HANDBOOK OF NEURO-ONCOLOGY NEUROIMAGING

SECOND EDITION

Edited by

HERBERT B. NEWTON
Director, Medical Neuro-Oncology Program,
Kettering Medical Center & Kettering Cancer Center, Kettering, OH, USA

Professor of Neurology & Neurosurgery (Retired),
Wexner Medical Center at the Ohio State University & James Cancer Hospital, Columbus, OH, USA



ELSEVIER

AMSTERDAM • BOSTON • HEIDELBERG • LONDON
NEW YORK • OXFORD • PARIS • SAN DIEGO
SAN FRANCISCO • SINGAPORE • SYDNEY • TOKYO
Academic Press is an imprint of Elsevier



Academic Press is an imprint of Elsevier
125 London Wall, London EC2Y 5AS, UK
525 B Street, Suite 1800, San Diego, CA 92101-4495, USA
50 Hampshire Street, 5th Floor, Cambridge, MA 02139, USA
The Boulevard, Langford Lane, Kidlington, Oxford OX5 1GB, UK

Copyright © 2016, 2008 Elsevier Ltd. All rights reserved.

No part of this publication may be reproduced or transmitted in any form or by any means, electronic or mechanical, including photocopying, recording, or any information storage and retrieval system, without permission in writing from the publisher. Details on how to seek permission, further information about the Publisher's permissions policies and our arrangements with organizations such as the Copyright Clearance Center and the Copyright Licensing Agency, can be found at our website: www.elsevier.com/permissions.

This book and the individual contributions contained in it are protected under copyright by the Publisher (other than as may be noted herein).

Notices
Knowledge and best practice in this field are constantly changing. As new research and experience broaden our understanding, changes in research methods, professional practices, or medical treatment may become necessary.

Practitioners and researchers must always rely on their own experience and knowledge in evaluating and using any information, methods, compounds, or experiments described herein. In using such information or methods they should be mindful of their own safety and the safety of others, including parties for whom they have a professional responsibility.

To the fullest extent of the law, neither the Publisher nor the authors, contributors, or editors, assume any liability for any injury and/or damage to persons or property as a matter of products liability, negligence or otherwise, or from any use or operation of any methods, products, instructions, or ideas contained in the material herein.

British Library Cataloguing-in-Publication Data
A catalogue record for this book is available from the British Library

Library of Congress Cataloging-in-Publication Data
A catalog record for this book is available from the Library of Congress

ISBN: 978-0-12-800945-1

For information on all Academic Press publications visit our website at https://www.elsevier.com/



Typeset by TNQ Books and Journals
www.tnq.co.in

Dedication

I would like to thank my wife, Cindy, and all of the children in my wonderful mixed family—Alex and Ashley Newton and Sammi, Skylar, and Cameron Burrell—for their love, patience, and support while I worked on this book project.

I would also like to thank my Neuro-Oncology patients and their families for their amazing courage and strength in the face of adversity, which was a constant inspiration.

Herbert B. Newton

Dedication

Ferenc A. Jolesz, M. D., B. Leonard Holman Professor of Radiology

The second edition of this book is dedicated to Dr Ferenc Jolesz, who was a wonderful editing partner while we worked together on the first edition of the *Handbook of Neuro-oncology Neuroimaging*. Unfortunately, Dr Jolesz was lost to all of us when he died suddenly and unexpectedly—from complications related to a pulmonary embolism—in late December 2014 while on vacation in Florida.

Dr Jolesz was born in Budapest, Hungary, on May 21, 1946. He earned his MD from the Semmelweis Medical School in 1971, followed by a research fellowship in biomedical engineering at the Kalman Kando College of Electrical Engineering and a residency in neurosurgery at the Institute for Neurosurgery in Budapest. He was then invited to the United States in 1979 to start a fellowship in neurology at the Massachusetts General Hospital and Boston Biomedical Research Institute. Afterward, he completed a research fellowship in physiology at Harvard Medical School (HMS). He was then asked to join the Brigham & Women's Hospital (BWH) Department of Radiology in 1982, initially as a clinical fellow in neuroradiology and then as a resident in diagnostic radiology. He joined the faculty of BWH and HMS in 1985 and became the Director of the Division of Magnetic Resonance Imaging for BWH in 1988. In 1993, he established the Image-Guided Therapy Program at BWH, and in 2000 he was appointed Vice Chair for Research in the Department of Radiology at BWH. In 1998, he was awarded the B. Leonard Holman Chair in Radiology at HMS.

In a career that spanned over 30 years, Dr Jolesz attained worldwide recognition as a clinician and scientist in the fields of neurosurgery, radiology, advanced magnetic resonance imaging, and image-guided therapy. In fact, he is considered by many to be the "father of modern-day image-guided therapy." He was a member of the Hungarian National Academy of Sciences and the Institute of Medicine of the National Academy of Sciences and had received the Outstanding Researcher Award from the Radiological Society of North America, as well as the Gold Medal of the International Society for Magnetic Resonance in Medicine.

In addition to his scientific accomplishments, Dr Jolesz was considered an excellent teacher, leader, and mentor, who always displayed compassion, generosity, and a gentle sense of humor to those around him. He is survived by his wife, Dr Anna Jolesz, and his two daughters—Dr Marta Jolesz and Ms Klara Jolesz.

List of Contributors

William Ankenbrandt Department of Radiology, North Shore University Health System, The University of Chicago Pritzker School of Medicine, Chicago, IL, USA

Isabel Arrillaga-Romany Department of Neurology, Massachusetts General Hospital and Harvard Medical School, Boston, MA, USA

K.K. Atsina Department of Neurosurgery, Yale School of Medicine, New Haven, CT, USA

Chaitra A. Badve Department of Diagnostic Radiology, University Hospitals Case Medical Center, Cleveland, OH, USA

J.M. Baehring Department of Neurosurgery, Yale School of Medicine, New Haven, CT, USA; Departments of Neurology and Medicine, Yale School of Medicine, New Haven, CT, USA

Randall Lawrence Baldassarre Department of Radiology, UCSD Medical Center, San Diego, CA, USA

Wenya Linda Bi Department of Neurosurgery, Brigham and Women's Hospital, Harvard Medical School, Boston, MA, USA

Peter M. Black Department of Radiology, Brigham and Women's Hospital, Harvard Medical School, Boston, MA, USA

Ingrid B. Boehm Department of Diagnostic, Interventional and Pediatric Radiology, College of Medicine, Bern University, Bern, Switzerland

Genevieve Bolles Department of Radiology, Division of Neuroradiology, Medical University of South Carolina, Charleston, SC, USA

Eric C. Bourekas Dardinger Neuro-Oncology Center, Departments of Radiology, Wexner Medical Center at The Ohio State University and James Cancer Hospital and Solove Research Institute, Columbus, OH, USA; Division of Neuro-Oncology, Departments of Neurology and Neurosurgery, Dardinger Neuro-Oncology Center, Wexner Medical Center at The Ohio State University and James Cancer Hospital and Solove Research Institute, Columbus, OH, USA

Nicole Petrovich Brennan Department of Radiology, Memorial Sloan-Kettering Cancer Center, New York, NY, USA

Marc Bussiere Department of Radiation Oncology, Massachusetts General Hospital and Harvard Medical School, Boston, MA, USA

Soonmee Cha Department of Radiology and Biomedical Imaging, University of California, San Francisco, CA, USA; Department of Neurological Surgery, University of California, San Francisco, CA, USA

Arnab Chakravarti Wexner Medical Center, Department of Radiation Oncology, Ohio State University, Columbus, OH, USA

Marc C. Chamberlain Department of Neurology and Neurological Sciences, Fred Hutchinson Cancer Research Center, University of Washington, Seattle, Washington, USA

Susan M. Chang Department of Neurological Surgery, University of California, San Francisco, CA, USA

Paul H. Chapman Department of Neurosurgery, Massachusetts General Hospital and Harvard Medical School, Boston, MA, USA

Clark C. Chen Center for Theoretical and Applied Neuro-Oncology, Division of Neurosurgery, Moores Cancer Center, University of California, San Diego, CA, USA

Susan N. Chi Dana-Farber/Boston Children's Cancer and Blood Disorder Center, Dana-Farber Cancer Institute and Boston Children's Hospital, Boston, MA, USA

D. Chourmouzi Department of Radiology, Interbalkan Medical Center, Thessaloniki, Greece

Gregory A. Christoforidis Department of Radiology, University of Chicago, Chicago, IL, USA

Ugonma Chukwueke Department of Neurology & Neurotherapeutics, University of Texas Southwestern Medical Center, Dallas, TX, USA

Jennifer L. Clarke Department of Neurology, University of California, San Francisco, CA, USA; Department of Neurological Surgery, University of California, San Francisco, CA, USA

John M. Collins Department of Radiology, University of Chicago, Chicago, IL, USA

L. Celso Hygino da Cruz Jr. CDPI – Clínica de Diagnóstico por Imagem, IRM Ressonância Magnética, Centro Médico Barrashopping Rio de Janeiro, RJ, Brazil

Parviz Dolati Department of Radiology, Brigham and Women's Hospital, Harvard Medical School, Boston, MA, USA

A. Drevelegas Department of Radiology, Interbalkan Medical Center, Thessaloniki, Greece

K. Drevelegas Department of Radiology, Interbalkan Medical Center, Thessaloniki, Greece; Karolinska Institute, Solna, Sweden

Sylvia Eisele Department of Neurology, University Hospitals Case Medical Center, Cleveland, OH, USA

Shehanaz Ellika Department of Radiology, Henry Ford Hospital, Detroit, MI, USA

Mark A. Ferrante Department of Neurology, University of Tennessee Health Science Center, Memphis, TN, USA

Nicholas C. Ferraro Department of Neurosurgery, University of Miami–Miller School of Medicine, Miami, FL, USA

Ryan Fisicaro Department of Radiology, Memorial Sloan-Kettering Cancer Center, New York, NY, USA

Alexandra J. Golby Department of Neurosurgery, Brigham and Women's Hospital, Harvard Medical School, Boston, MA, USA

Carlos R. Goulart Department of Neurological Surgery, The Ohio State University – Wexner Medical Center, The James Cancer Hospital, Columbus, OH, USA

Michael Guiou Wexner Medical Center, Department of Radiation Oncology, Ohio State University, Columbus, OH, USA

Nilendu Gupta Wexner Medical Center, Department of Radiation Oncology, Ohio State University, Columbus, OH, USA

Nobuhiko Hata Department of Radiology, Brigham and Women's Hospital, Harvard Medical School, Boston, MA, USA

David Hearshen Department of Radiology, Henry Ford Health System, Detroit, MI, USA

John W. Henson Piedmont Brain Tumor Center, Atlanta, GA, USA

Johannes T. Heverhagen Department of Diagnostic, Interventional, and Pediatric Radiology, College of Medicine, Bern University, Bern, Switzerland; Department of Radiology, College of Medicine, The Ohio State University, Columbus, OH, USA

Andrei Holodny Department of Radiology, Memorial Sloan-Kettering Cancer Center, New York, NY, USA

Tudor Hesketh Hughes Department of Radiology, UCSD Medical Center, San Diego, CA, USA

Masanori Ichise Molecular Neuroimaging Program, Molecular Imaging Center, National Institute of Radiological Sciences, Chiba, Japan

Michael E. Ivan Department of Neurosurgery, University of Miami–Miller School of Medicine, Miami, FL, USA

Rajan Jain Department of Radiology, New York University School of Medicine, New York, NY, USA

Ferenc A. Jolesz Department of Radiology, Brigham and Women's Hospital, Harvard Medical School, Boston, MA, USA

Justin T. Jordan Massachusetts General Hospital, Department of Neurology, Division of Neuro-Oncology, Boston, MA, USA

Daniel Kacher Department of Radiology, Brigham and Women's Hospital, Harvard Medical School, Boston, MA, USA

Alayar Kangarlu MRI Physics Psychiatry, Columbia University, New York, NY, USA

Arash Kardan Departments of Nuclear Medicine, /PET, Kettering Memorial Hospital, Kettering, OH, USA

Marie Foley Kijewski Department of Radiology, Brigham and Women's Hospital, Harvard Medical School, Boston, MA, USA

Margareth Kimura CDPI – Clínica de Diagnóstico por Imagem, Centro Médico Barrashopping, Rio de Janeiro, RJ, Brazil

John T. Kissel Division of Neuromuscular Diseases, Department of Neurology, VA Medical Center, Memphis, TN, USA

Ricardo J. Komotar Department of Neurosurgery, University of Miami–Miller School of Medicine, Miami, FL, USA

George Krol Division of Neuroradiology, Memorial Sloan Kettering Cancer Center, New York, NY, USA

Priya Kumthekar Department of Neurology, Northwestern University, Feinberg School of Medicine, Chicago, IL, USA

Joshua Lantos Department of Radiology, Memorial Sloan Kettering Cancer Center, New York, USA

Emilie Le Rhun Breast Unit, Department of Medical Oncology, Oscar Lambret Center, Lille Cedex, France; Department of Neuro-oncology, Neurosurgery, Roger Salengro Hospital, University Hospital, Lille Cedex, France

Michael H. Lev Neurovascular Laboratory, Massachusetts General Hospital, Boston, MA, USA and Harvard Medical School, Boston, MA, USA

Jay S. Loeffler Department of Radiation Oncology, Massachusetts General Hospital and Harvard Medical School, Boston, MA, USA

Stephan E. Maier Department of Radiology, Brigham and Women's Hospital, Harvard Medical School, Boston, MA, USA; Department of Radiology, Sahlgrenska University Hospital, Sahlgrenska Academy, Gothenburg University, Gothenburg, Sweden

Lonika Majithia Wexner Medical Center, Department of Radiation Oncology, Ohio State University, Columbus, OH, USA

Tobias A. Mattei Department of Neurosurgery, Brain & Spine Center – InvisionHealth, Buffalo, NY, USA

Brendan J. McCullough Radia Inc., Lynwood, WA, USA; Swedish Neuroscience Institute, Seattle, WA, USA; Department of Health Services, University of Washington, Seattle, WA, USA

Ehud Mendel Department of Neurological Surgery, The Ohio State University – Wexner Medical Center, The James Cancer Hospital, Columbus, OH, USA

Tom Mikkelsen Department of Neurosurgery, Henry Ford Health System, Detroit, MI, USA

Vesselin Z. Miloushev Neuroradiology, Department of Radiology, Columbia University Medical Center, New York, NY, USA

Pedro C. Miranda Institute of Biophysics and Biomedical Engineering, Faculty of Science, University of Lisbon, Lisbon, Portugal

Michelle Monje Department of Neurology, Stanford School of Medicine, Stanford, CA, USA

Prashant Nagpal Department of Radiology, University of Iowa Hospitals and Clinics, Iowa City, IA, USA

Ken Alexander Nakanote School of Medicine, University of California, San Diego, CA, USA

Herbert B. Newton Division of Neuro-Oncology, Departments of Neurology and Neurosurgery, Dardinger Neuro-Oncology Center, Wexner Medical Center at The Ohio State University and James Cancer Hospital and Solove Research Institute, Columbus, OH, USA

Erik B. Nine Department of Radiology, North Shore Medical Center, Salem, MA, USA

Nancy Ann Oberheim Bush Department of Neurology, University of California, San Francisco, CA, USA; Department of Neurological Surgery, University of California, San Francisco, CA, USA

Olutayo Olubiyi Department of Neurosurgery, Brigham and Women's Hospital, Harvard Medical School, Boston, MA, USA

S.B. Omay Department of Neurosurgery, Yale School of Medicine, New Haven, CT, USA

Nina Paleologos Rush Medical College, Rush University, Chicago, IL, USA

N. Papanicolaou Karolinska Institute, Solna, Sweden

Kunal S. Patel Center for Theoretical and Applied Neuro-Oncology, Division of Neurosurgery, Moores Cancer Center, University of California, San Diego, CA, USA

Tina Young Poussaint Department of Radiology, Division of Neuroradiology, Boston Children's Hospital, Harvard Medical School, Boston, MA, USA

Sanjay P. Prabhu Department of Radiology, Division of Neuroradiology, Boston Children's Hospital, Harvard Medical School, Boston, MA, USA

Jinrong Qu Department of Radiology, Henan Cancer Hospital, Zhengzhou, Henan, China

Jeffrey J. Raizer Department of Neurology, Northwestern University, Feinberg School of Medicine, Chicago, IL, USA

Haricharan Reddy Diversified Radiology, Denver, CO, USA

Tanvir Rizvi Radiology and Medical Imaging, University of Virginia Health System, Charlottesville, VA, USA

Lisa R. Rogers Department of Neurology, University Hospitals Case Medical Center, Seidman Cancer Center, Cleveland, OH, USA

Martin Satter Departments of Nuclear Medicine, /PET, Kettering Memorial Hospital, Kettering, OH, USA

Mithun G. Sattur Rose Ella Burkhardt Brain Tumor and NeuroOncology Center, Cleveland Clinic, Cleveland, OH, USA

David Schiff Department of Neurology, University of Virginia Health System, Charlottesville, VA, USA; Neuro-Oncology Center, University of Virginia Health System, Charlottesville, VA, USA

Kathleen Schmainda Department of Radiology, Medical College of Wisconsin, Milwaukee, WI, USA

Andrew D. Schweitzer Department of Radiology, Division of Neuroradiology, Weill Cornell Medicine New York, NY, USA

Victoria Michelle Silvera Department of Radiology, Boston Children's Hospital, Boston, MA, USA

H. Wayne Slone Dardinger Neuro-Oncology Center, Departments of Radiology, Wexner Medical Center at The Ohio State University and James Cancer Hospital and Solove Research Institute, Columbus, OH, USA

James Snyder Department of Neurosurgery, Henry Ford Health System, Detroit, MI, USA

Aaron D. Sodickson Department of Radiology, Brigham and Women's Hospital, Harvard Medical School, Boston, MA, USA

Daniel K. Sodickson Center for Advanced Imaging Innovation and Research (CAI^2R), Department of Radiology, New York University School of Medicine, New York, NY, USA

Lilja Bjork Solnes Division of Nuclear Medicine, Johns Hopkins, Baltimore, MD, USA

Maria Vittoria Spampinato Department of Radiology, Division of Neuroradiology, Medical University of South Carolina, Charleston, SC, USA

Yanping Sun Brigham and Women's Hospital, Harvard Medical School, Boston, MA, USA

Sophie Taillibert Department of Neurology Mazarin and Department of Radiation Oncology, Pitié-Salpétrière Hospital, University Pierre et Marie Curie, Paris VI, Paris, France

Ion-Florin Talos Department of Radiology, Brigham and Women's Hospital, Harvard Medical School, Boston, MA, USA

Suzanne Tharin Department of Neurosurgery, Stanford University, Palo Alto, CA, USA

Achala Vagal Neuroradiology Division, Department of Radiology, University of Cincinnati Medical Center, Cincinnati, OH, USA

Steven Vernino Department of Neurology & Neurotherapeutics, University of Texas Southwestern Medical Center, Dallas, TX, USA

Michael A. Vogelbaum Rose Ella Burkhardt Brain Tumor and NeuroOncology Center, Cleveland Clinic, Cleveland, OH, USA; Department of Surgery (Neurosurgery), Cleveland Clinic Lerner College of Medicine of Case Western Reserve University, Cleveland, OH, USA

Arastoo Vossough Children's Hospital of Philadelphia, Philadelphia, PA, USA and Hospital of the University of Pennsylvania, Philadelphia, PA, USA

Steve Walston Wexner Medical Center, Department of Radiation Oncology, Ohio State University, Columbus, OH, USA

Simon K. Warfield Department of Radiology, Brigham and Women's Hospital, Harvard Medical School, Boston, MA, USA

Michael A. Weicker Department of Neurological Surgery, The Ohio State University – Wexner Medical Center, The James Cancer Hospital, Columbus, OH, USA

D. Bradley Welling Department of Otology and Laryngology, Harvard Medical School, Massachusetts Eye and Ear and Massachusetts General Hospital, Boston, MA, USA

Cornelia Wenger Institute of Biophysics and Biomedical Engineering, Faculty of Science, University of Lisbon, Lisbon, Portugal

Patrick Y. Wen Center for Neuro-Oncology, Dana-Farber/ Brigham and Women's Cancer Center and Harvard Medical School, Boston, MA, USA

Max Wintermark Neuroradiology Division, Department of Radiology, Stanford University, Stanford, CA, USA

Eric T. Wong Brain Tumor Center & Neuro-Oncology Unit, Beth Israel Deaconess Medical Center & Harvard Medical School, Boston, MA, USA; Department of Physics, University of Massachusetts at Lowell, Lowell, MA, USA

E. Xinou Department of Radiology, Theagenio Cancer Hospital, Thessaloniki, Greece

Edward Yang Department of Radiology, Boston Children's Hospital, Boston, MA, USA

Randy Yeh Nuclear Medicine and Molecular Imaging, Department of Radiology, Columbia University Medical Center, New York, NY, USA

Geoffrey S. Young Department of Radiology, Brigham and Women's Hospital, Boston, MA, USA; Department of Radiology, Dana Farber Cancer Institute, Boston, MA, USA; Department of Radiology, Harvard Medical School, Boston, MA, USA

Robert J. Young Department of Radiology, Memorial Sloan Kettering Cancer Center, New York, USA; Brain Tumor Center, Memorial Sloan Kettering Cancer Center, New York, USA

Alicia M. Zukas Department of Neurology, University of Virginia Health System, Charlottesville, VA, USA; Neuro-Oncology Center, University of Virginia Health System, Charlottesville, VA, USA

Preface

Steady progress has taken place since 2010 in the various disciplines that comprise neuro-oncology neuroimaging, with even more widespread utilization of advanced imaging technologies in clinical practice. Advanced techniques in computed tomography, magnetic resonance imaging (MRI), and positron-emission tomography have further improved the visualization and localization of tumors and provided target definition for various therapeutic modalities. Additional refinements of newer imaging methods, such as MR spectroscopy, functional MRI, diffusion MRI, and diffusion tensor imaging. have allowed brain tumor patients to be diagnosed much earlier in the course of their illness and to be followed more carefully during surgery and subsequent treatment. In addition, newer imaging and treatment modalities have come into the clinic, such as the RANO criteria, tumor treating fields (i.e., the Optune electrical array), and the concept of pseudo-progression, which needed to be reviewed in detail. Overall, it seemed like the field had reached a "critical mass" of new and updated information and that it was the right time to update this book with a second edition of the *Handbook of Neuro-Oncology Neuroimaging*.

The second edition of this book should have broad appeal to anyone interested in the fields of neuro-oncology and neuroimaging, and especially to those who are involved in the care of patients with brain tumors. It will satisfy clinicians, who require in-depth overviews of various neuro-oncology topics along with "cutting edge" information regarding how to apply neuroimaging techniques to those areas of interest. In addition, the book can serve as a resource of background information to neuroimaging researchers and basic scientists with an interest in brain tumors and neuro-oncology. I sincerely hope that the world-class group of authors assembled herein can assist you in providing the best oncologic care for your patients.

I am very thankful to the publisher for providing the opportunity to update this extensive body of clinically relevant information to a larger professional audience. I would also like to thank all of our colleagues who contributed to this book and provided insight into the use of imaging methods in neuro-oncology.

Herbert B. Newton, M.D., FAAN
Columbus, Ohio, 2016

CHAPTER

1

Overview of Brain Tumor Epidemiology

Herbert B. Newton

Division of Neuro-Oncology, Departments of Neurology and Neurosurgery, Dardinger Neuro-Oncology Center, Wexner Medical Center at The Ohio State University and James Cancer Hospital and Solove Research Institute, Columbus, OH, USA

Brain tumors remain a significant health problem in the United States and worldwide. Overall, they comprise some of the most malignant tumors known to affect human beings and are generally refractory to all modalities of treatment. It is estimated that between 30,000 and 35,000 new cases of primary brain tumors (PBTs) will be diagnosed each year in the United States (1–2% of newly diagnosed cancers overall).[1–6] Metastatic brain tumors (MBTs) are even more common and affect between 150,000 and 170,000 new patients each year in this country.[7–11] Although significant advances have been made in our understanding of the molecular biology of brain tumors, further research is needed to improve our knowledge of the etiology and natural history of this disease.

EPIDEMIOLOGY OF PBTs

Most studies suggest that approximately 14 per 100,000 people in the United States will be diagnosed with a PBT each year.[2–6] Among this cohort with newly diagnosed tumors, 6–8 per 100,000 will have a high-grade neoplasm. Contemporary epidemiological studies suggest an increasing incidence rate for the development of PBT in children less than 14 years of age and in patients 70 years or older.[12] For people in the 15- to 44-year-old age group the overall incidence rates have remained fairly stable. The cause of the increased incidence of PBT in some age groups remains unclear, but may be due to improvements in diagnostic neuroimaging such as magnetic resonance imaging, greater availability of specially qualified neurosurgeons and neuropathologists, improved access to medical care for children and elderly patients, and more aggressive approaches to health care for elderly patients.[5,12] In other words, the increase in PBT incidence may be more apparent than real owing to ascertainment bias.

The prognosis and survival of patients with PBT remain poor.[1–6] Although uncommon neoplasms, they rank among the top 10 causes of cancer-related deaths in the United States and account for a disproportionate 2.4% of all yearly cancer-related deaths.[13] The median survival for a patient with glioblastoma multiforme (GBM) is approximately 14–18 months, a figure that has not improved substantially since the 1980s. For patients with a low-grade astrocytoma or oligodendroglioma, the median survival is still significantly curtailed and is about 6–10 years. For PBT patients in the United States as a whole, across all age groups and tumor types, the 5-year survival rate is 20%.[3] If a patient with a PBT survives for an initial 2 years, the probability of surviving another 3 years is 76.2%. In general, for any given tumor type, survival is better for younger patients than for older patients. The only exception to this generalization is for children with medulloblastoma and embryonal tumors, of which patients under 3 years of age have poorer survival rates than children between 3 and 14 years of age.[14] The 5-year survival rate for all children less than 14 years of age with a malignant PBT is 72%.

The median age at diagnosis for PBT is between 54 and 58 years.[1–6] Among the histological varieties of PBT, there is significant variability in the age of onset. A small secondary peak is also present in the pediatric age group, in children between the ages of 4 and 9. Overall, PBTs are more common in males than females, with the exception of meningiomas, which are almost twice as common in females. Tumors of the sellar region, and of the cranial and spinal nerves, are almost equally represented among males and females. In the United States, gliomas are more commonly diagnosed in whites than

Handbook of Neuro-Oncology Neuroimaging, Second Edition
http://dx.doi.org/10.1016/B978-0-12-800945-1.00001-X

© 2016 Elsevier Ltd. All rights reserved.

TABLE 1 Risk Factors that Have Been Investigated in Epidemiological Studies of Primary Brain Tumors

Hereditary syndromes (proven): tuberous sclerosis, neurofibromatosis types 1 and 2, nevoid basal cell carcinoma syndrome, Turcot syndrome, and Li-Fraumeni syndrome
Family history of brain tumors
Constitutive polymorphisms: glutathione transferases, cytochromes P-450 2D6 and 1A1, *N*-acetyltransferase, and other carcinogen metabolizing, DNA repair, and immune function genes
History of prior cancer
Exposure to infectious agents
Allergies (possible reduced risk)
Head trauma
Drugs and medications
Dietary history: *N*-nitroso compounds, oxidants, antioxidants
Tobacco usage
Alcohol consumption
Ionizing radiation exposure (proven)
Occupational and industrial chemical exposures: pesticides, vinyl chloride, synthetic rubber manufacturing, petroleum refining and production, agricultural workers, lubricating oils, organic solvents, formaldehyde, acrylonitrile, phenols, polycyclic aromatic hydrocarbons
Cellular telephones
Power frequency electromagnetic field exposure

Data adapted from references 2–6, 14–26.

blacks, whereas the incidence of meningiomas is relatively equal between the two groups.

Numerous epidemiological studies have been performed in an attempt to define risk factors involved in the development of brain tumors (see Table 1).[2–6] The vast majority of these potential risk factors have not been associated with any significant predisposition to brain tumors. One risk factor that has proven to be important is the presence of a hereditary syndrome with a genetic predisposition for developing tumors, some of which can affect the nervous system.[4,5,15] Several hereditary syndromes are associated with PBTs, including tuberous sclerosis, neurofibromatosis types 1 and 2, nevoid basal cell carcinoma syndrome, Li-Fraumeni syndrome, and Turcot syndrome. However, it is estimated that hereditary genetic predisposition may be involved in only 2–8% of all cases of PBT. Familial aggregation of brain tumors has also been studied, with conflicting results.[5,15] The relative risk for developing a tumor among family members of a patient with a PBT is quite variable, ranging from 1 to 10. One study that performed a segregation analysis of families of more than 600 adult glioma patients showed that a polygenic model most accurately explained the inheritance pattern.[16] A similar analysis of 2141 first-degree relatives of 297 glioma families did not reject a multifactorial model, but concluded that an autosomal recessive model fit the inheritance pattern more accurately.[17] Critics of these studies suggest that the common exposure of a family to a similar pattern of environmental agents could lead to a similar clustering of tumors. Other investigators have focused on genetic polymorphisms that might influence genetic and environmental factors to increase the risk for a brain tumor.[4,5] Alterations in genes involved in oxidative metabolism, detoxification of carcinogens, DNA stability and repair, and immune responses might confer a genetic predisposition to tumors. For example, Elexpuru-Camiruaga and colleagues demonstrated that cytochrome P-450 2D6 and glutathione transferase Theta were associated with an increased risk for brain tumors.[18] Other studies have not supported these results, but have found an increased risk for rapid *N*-acetyltransferase acetylation and intermediate acetylation.[19] In general, further studies with larger cohorts of patients will be necessary to determine if genetic polymorphisms of key metabolic enzyme systems play a significant role in the risk for developing a brain tumor.

Cranial exposure to therapeutic ionizing radiation is a potent risk factor for subsequent development of a brain tumor and is known to occur after a wide range of exposures.[1–6] Application of low doses of irradiation (1000–2000 cGy), such as were prescribed in the past for children with tinea capitis or skin hemangiomas, have been associated with relative risks of 18 for nerve sheath tumors, 10 for meningiomas, and 3 for gliomas.[5,20] Gliomas and other PBTs are also known to occur after radiotherapy for diseases such as leukemia, lymphoma, and head and neck cancers.[5,21,22] In addition, alternative methods of radiation exposure, such as nuclear bomb blasts and employment at nuclear production facilities, have also been implicated as significant risk factors for the development of brain tumors.[23,24]

Many other risk factors have been evaluated for their potential role in the genesis of brain tumors.[1–6] The majority of these factors have been proven to have little, if any, relationship to brain tumor development or to have an indeterminate association due to a mixture of positive and negative studies. Factors in this category include the history of a prior primary systemic malignancy, head injury, prenatal or premorbid ingestion of various types of medications, exposure to viruses and other types of infection (except for the human immunodeficiency virus, which is known to be associated with brain lymphoma), dietary history (i.e., ingestion of *N*-nitroso compounds, oxidants, and antioxidants), alcohol ingestion, smoking tobacco, residential chemical exposures, and proximity to electromagnetic fields. The relationship between industrial and occupational

chemical exposures and brain tumors is very complex and remains unclear.[2,4,5] Workers are exposed to chemicals that are potentially carcinogenic or neurotoxic, or both, including lubricating oils, organic solvents, formaldehyde, acrylonitrile, phenols and phenolic-based compounds, vinyl chloride, and polycyclic aromatic hydrocarbons. Preclinical studies have proven the ability of vinyl chloride to induce brain tumors in rat models, and some studies suggest an increased risk for chemical workers who handle this compound.[25] However, more recent and extensive analyses suggest that the relationship between vinyl chloride exposure and brain tumors remains inconclusive.[26] Similar inconclusive results for other chemicals are common in the epidemiology literature and demonstrate the difficulty of proving an association between workplace exposures and an uncommon form of cancer. At this time, no definitive associations have been proven between brain tumors and any specific chemicals found in the occupational or industrial setting, including those that are known to be definite or putative carcinogens.

Several large studies have evaluated the possibility of a link between the use of handheld cellular telephones and brain cancer, as well as other tumors of the head and neck region. Researchers from Denmark performed a nationwide review of 420,095 cell phone users and determined that the overall incidence of cancer was not elevated (OR = 0.89) in comparison to controls, including brain tumors, salivary gland tumors, and leukemias.[27] Other studies focusing on the incidence of high-grade gliomas in cellular telephone users have not been able to substantiate an increased incidence.[28–30] Several reports have focused on the use of cellular telephones and the incidence of acoustic schwannomas.[31,32] Neither study was able to discern a relationship between the duration of use, lifetime cumulative hours of use, or frequency of use of a cellular telephone and the risk of developing an acoustic schwannoma. The only positive report to date was a population-based, case–control study from Germany that evaluated 366 glioma, 381 meningioma, and 1494 control patients.[33] In this study, the overall risk for a brain tumor was not associated with the use of a cellular telephone. However, there was a small increased risk of glioma (OR = 2.20), but not meningioma (OR = 1.09), in patients that had used a cellular telephone for 10 years or more.

More recent molecular epidemiological studies in adult patients with high-grade glioma are beginning to show promise for further research efforts.[34] In a study of the association between human leukocyte antigens (HLAs) and related polymorphisms (HLA-A, -B, -C, -DRB1) and the onset and prognosis of GBM, 155 GBM patients and 157 controls were studied in the San Francisco area.[35] During multivariate logistical regression analysis, the HLA-B*13 and the HLA-B*07-Cw*07 haplotypes were positively associated with the occurrence of GBM ($p = 0.01$, $p < 0.001$, respectively). The Cw*01 variant had a negative association with the occurrence of GBM ($p = 0.05$). In addition, progression to death among GBM patients was slower in patients with HLA-A*32 (HR = 0.45, $p < 0.01$) and faster in those with HLA-B*55 (HR = 2.27, $p < 0.01$). In a study of polymorphisms of ERCC1 and ERCC2, genes that are important for DNA nucleotide excision repair, 450 adult glioma patients and 500 controls were analyzed.[36] Overall, the presence of ERCC1 and ERCC2 was not associated with an increased risk for GBM. However, among whites, glioma patients were significantly more likely than controls to be homozygous for variants in ERCC1 C8092A and ERCC2 K751Q (OR = 3.2). In a similar study, 556 astrocytic tumors were analyzed for the expression of p53, epidermal growth factor receptor (EGFR), murine double minute-2 (MDM2), and O^6-methylguanine-DNA-methyltransferase (MGMT) and then correlated with clinical parameters and risk factors.[37] The data confirmed the previously noted inverse relationship between p53 mutation and MDM2 ($p = 0.04$) or EGFR ($p = 0.004$) amplification. In addition, the presence of p53 mutations were more likely to occur in younger patients ($p < 0.001$). EGFR gene amplification was more likely to occur in older patients (mean 63 years of age amplified vs mean 48 years of age nonamplified; $p = 0.005$). The p53 mutations were more likely to occur in GBM among nonwhite patients than among white patients ($p = 0.004$). Patient carriers of the MGMT variant 84Phe allele were significantly less likely to have tumors with p53 overexpression (OR = 0.30) and somewhat less likely to have tumors with p53 mutations (OR = 0.47). The authors concluded that these molecular data demonstrated ethnic variation in the pathogenesis of glioma.

A 2014 study of occupational exposure to extremely low frequency magnetic fields (ELFs) and primary brain tumor risk suggests a causal association.[38] As part of the INTEROCC Study, 3761 adult brain tumor patients with glioma or meningioma were studied from seven different countries, from 2000 through 2004. Estimates of cumulative exposure to ELFs, average exposure, maximum exposure, and exposure duration were calculated for the lifetime, and for 1–4, 5–9, and 10+ years prior to the diagnosis of the brain tumor. There was no correlation between lifetime cumulative ELF exposure and glioma or meningioma risk. However, there was a positive association between cumulative ELF exposure 1–4 years prior to the diagnosis for glioma patients (OR = 1.67; $p < 0.0001$), as well as a weaker but still significant association with meningioma (OR = 1.23; $p = 0.02$). The authors suggested that ELF exposure in the recent past might influence the late stages of tumorigenesis (e.g., promotion and progression).

Of all the potential risk factors studied, the only one that might be associated with a protective effect for developing a brain tumor is the presence of an allergy.[39] The presence of any form of allergy was inversely associated with the development of a glioma (OR = 0.7), but not with meningiomas or acoustic neuromas. Similar inverse associations were noted for the presence of autoimmune diseases and the presence of both gliomas and meningiomas. The authors suggested that allergy-related immunological factors might play a protective role in the genesis of certain brain tumors. As a follow-up to this initial study, Schwartzbaum and colleagues performed a population-based case–control evaluation of 111 GBM patients and 422 controls, using germ-line polymorphisms associated with asthma and inflammation as biomarkers.[40] Self-reported asthma and eczema were inversely related to the incidence of GBM (OR = 0.64). In addition, interleukin (IL)-4RA Ser478Pro TC, CC and IL-4RA Gln551Arg AG, AA were positively associated with GBM (OR = 1.64), whereas IL-13 −1,112 CT, TT was negatively associated with GBM (OR = 0.56). The authors suggested that associations existed between IL-4RA, IL-13, and GBM that were independent of their role in allergic conditions.

EPIDEMIOLOGY OF MBTs

Brain metastases (MBTs) are the most common complication of systemic cancer, with estimated incidence rates of 8.3–11 cases per 100,000 population.[7–11,41] Hospital and autopsy-based studies estimate that these tumors develop in 20–40% of all adult cancer patients, which corresponds to approximately 150,000–170,000 new cases per year in the United States. More recent data using population-based estimates would suggest a lower incidence of MBTs, in the range of 10%.[42] The presence of an MBT does not always correlate with clinical sequelae; it is estimated that only 60–75% of patients with an MBT will become symptomatic. The frequency of MBT appears to be rising owing to more successful systemic treatment and longer patient survival, earlier detection and implementation of therapy, and improved imaging techniques. MBTs most often arise from primary tumors of the lung (50–60%), breast (15–20%), melanoma (5–10%), and gastrointestinal tract (4–6%).[7–11] Empirical screens of patients with newly diagnosed non-small-cell lung cancer (NSCLC) identify MBTs in 3–10% of cases.[41] However, MBTs can develop from virtually any systemic malignancy, including primary tumors of the prostate, ovary and female reproductive system, kidney, esophagus, soft tissue sarcoma, bladder, and thyroid.[43–52] In addition, between 10% and 15% of patients will develop MBT from an unknown primary.[8,53] Autopsy studies in adults would suggest that melanoma (20–45% of patients) has the most neurotropism of all primary tumors; however, small-cell lung, renal, breast, and testicular carcinomas also have a strong propensity for spread to the brain.[8] Tumors with a low degree of neurotropism include prostate, gastrointestinal tract, ovarian, and thyroid malignancies. In children and young adults, MBTs arise most often from sarcomas (e.g., osteogenic, Ewing), germ cell tumors, and neuroblastomas.[7–11,54] In 65–75% of patients, two or more metastatic tumors will develop simultaneously and be present at the time of cancer diagnosis. Single brain metastases are less common and are most often noted in patients with breast, colon, and renal cell carcinomas. Patients with malignant melanoma and lung carcinoma are more likely to have multiple metastatic lesions.

The prognosis for patients with MBT is quite poor and is dependent on the histological tumor type, number and size of the metastatic lesions, neurological status, and degree of systemic involvement. Overall, the presence of an MBT is associated with high morbidity and mortality, with approximately one-third of all patients dying from the brain tumor.[10] The natural history is such that, left untreated, patients with MBT will usually die of neurological deterioration within 4 weeks. The addition of steroids will typically extend survival to 8 weeks. External beam radiotherapy, the most common modality of treatment, can further extend survival to 12–20 weeks in many patients.[7–11] However, survival is also dependent on the type of primary malignancy, as shown in a report by Hall and colleagues.[55] In their study, the overall 2-year survival rate for patients with MBT was 8.1%, with a range from 1.7% in patients with small-cell-lung carcinoma up to 23.9% for those with ovarian cancer. Several studies have assessed how various prognostic factors relate to MBT patients at the time of diagnosis. A recursive partitioning analysis of three radiation therapy oncology group trials evaluated a wide range of prognostic factors and their impact on patient survival.[56] The most important favorable factors were younger age (younger vs older than 65 years; $p < 0.0001$), higher Karnofsky Performance Status (KPS) score (greater or less than 70; $p < 0.0001$), and limited extent of systemic disease (controlled vs widespread disease; $p < 0.0001$). Using these criteria, patients could be grouped into three distinct classes. Class 1 included patients who were less than 65 years of age, had KPS scores greater than 70, and had well-controlled systemic disease; class 3 consisted of all patients with KPS scores less than 70; and class 2 included all other patients who did not fit into class 1 or class 3. The median overall survival varied significantly between groups: 28.4 weeks for patients in class 1, 16.8 weeks for those in class 2, and 9.2 weeks for class 3 patients.

In addition, by univariate analysis, patients with multiple MBTs had a significantly reduced survival compared to those with solitary lesions ($p = 0.021$).

In a similar study by Nussbaum and colleagues, the number of metastatic lesions present at diagnosis was found to correlate with overall survival.[57] They noted a significant difference ($p = 0.0001$) in median survival between patients with solitary brain metastases and those with multifocal disease: 5 months versus 3 months, respectively.

The molecular events that lead to the metastatic phenotype in a given primary tumor, with subsequent metastases to systemic organs and to the brain, remain unclear. Over the past few decades, the predominant theory postulated that somatic mutations in rare cells of the primary tumor (i.e., less than 1 in 10 million) would lead to an acquired increase in metastatic capacity, with the ability to migrate through tissues, survive in blood and lymphatic fluid, invade distant organs, and establish metastatic nodules.[58] Although this theory was supported somewhat by animal models, there were no data to verify this process in human tumors. More recent evidence, based on expression microarray analyses of primary and metastatic tumors, supports the concept that metastatic potential is related to the intrinsic molecular biological state of the primary tumor as a whole, rather than to the emergence of a few rare cells.[59,60] The metastatic gene-expression signature consisted of a subset of eight genes that were upregulated (e.g., SNRPF, EIF4EL3, PTTG1) and a subset of nine genes that were downregulated (e.g., major histocompatibility complex class II DP-β1, RUNX1) in the primary cancer.[59] None of the genes were individual markers of the metastatic phenotype; they were predictive only when analyzed as a whole group. Patients with primary cancers that expressed the metastatic phenotypic signature had significantly shorter survival times in comparison to patients whose tumors did not express it ($p = 0.009$).

In a related study, Milas and colleagues attempted to identify biological markers that could predict brain MBT and treatment outcome in patients with NSCLC.[61] Twenty-nine patients with MBT, and matched controls without MBT, were analyzed using immunohistochemical techniques. Primary cancer and brain tumor tissue samples were analyzed for the expression of EGFR, cyclooxygenase-2 (COX-2), and BAX. Expression of COX-2 in brain lesions correlated with expression in primary cancers ($p = 0.023$), whereas the expression of BAX was lower in the MBTs in comparison to the primary cancer ($p = 0.045$). However, the overall expression of EGFR, COX-2, and BAX in primary NSCLC tumors did not differ between patients with MBT and those without MBT. Therefore, this set of molecular markers cannot be used to predict the likelihood of MBT in patients with NSCLC.

Acknowledgments

The authors thank Shawna Huckell and Nicole Ghaffari for research assistance. Dr. Newton was supported in part by National Cancer Institute Grant CA 16058 and the Dardinger Neuro-Oncology Center Endowment Fund.

References

1. Newton HB. Primary brain tumors: review of etiology, diagnosis, and treatment. *Am Fam Phys*. 1994;49:787–797.
2. Wrensch M, Minn Y, Chew T, Bondy M, Berger MS. Epidemiology of primary brain tumors: current concepts and review of the literature. *Neuro-Oncol*. 2002;4:278–299.
3. Davis FG, McCarthy BJ. Current epidemiological trends and surveillance issues in brain tumors. *Expert Rev Anticancer Ther*. 2001; 1:395–401.
4. Osborne RH, Houben MPWA, Tijssen CC, Coebergh JWW, van Duijn CM. The genetic epidemiology of glioma. *Neurol*. 2001;57: 1751–1755.
5. Ostrom QT, Bauchet L, Davis FG, et al. The epidemiology of glioma in adults: a "state of the science" review. *Neuro-Oncol*. 2014;16:896–913. pii:nou087.
6. Hess KR, Broglio DR, Bondy ML. Adult glioma incidence trends in the United States, 1977–2000. *Cancer*. 2004;101:2293–2299.
7. Newton HB. Neurological complications of systemic cancer. *Am Fam Phys*. 1999;59:878–886.
8. Soffietti R, Ruda R, Mutani R. Management of brain metastases. *J Neurol*. 2002;249:1357–1369.
9. Langer CJ, Mehta MP. Current management of brain metastases, with a focus on systemic options. *J Clin Oncol*. 2005;23:6207–6219.
10. Bajaj GK, Kleinberg L, Terezakis S. Current concepts and controversies in the treatment of parenchymal brain metastases: improved outcomes with aggressive management. *Cancer Investig*. 2005;23:363–376.
11. Lassman AB, DeAngelis LM. Brain metastases. *Neurol Clin N Am*. 2003;21:1–23.
12. Legler JM, Ries LA, Smith MA, et al. Cancer surveillance series [corrected]: brain and other central nervous system cancers: recent trends in incidence and mortality. *J Natl Cancer Inst*. 1999;91:1382–1390.
13. ACS (American Cancer Society). *Cancer Facts and Figures 2002*. Atlanta: American Cancer Society; 2002.
14. Grovas A, Fremgen A, Rauck A, et al. The National Cancer Data Base report on patterns of childhood cancers in the United States. *Cancer*. 1997;80:2321–2332.
15. Bondy M, Wiencke J, Wrensch M, Kryitsis AP. Genetics of primary brain tumors: a review. *J Neuro-Oncol*. 1994;18:69–81.
16. de Andrade M, Barnholtz JS, Amos CI, Adatto P, Spencer C, Bondy ML. Segregation analysis of cancer in families of glioma patients. *Genet Epidemiol*. 2001;20:258–270.
17. Malmer B, Gronberg H, Bergenheim AT, Lenner P, Henriksson R. Familial aggregation of astrocytoma in northern Sweden: an epidemiological cohort study. *J Cancer*. 1999;81:366–370.
18. Elexpuru-Camiruaga J, Buxton N, Kandula V, et al. Susceptibility to astrocytoma and meningioma: Influence of allelism at glutathione S-transferase (GSTT1 and GSTM1) and cytochrome P-450 (CYP2D6) loci. *Cancer Res*. 1995;55:4237–4239.
19. Trizna Z, de Andrade M, Kyritsis AP, et al. Genetic polymorphisms in glutathione S-transferase mu and theta, N-acetyltransferase, and CYP1A1 and risk of gliomas. *Cancer Epidemiol Biomarkers Prev*. 1998;7:553–555.
20. Karlsson P, Holmberg E, Lundell M, Mattsson A, Holm LE, Wallgren A. Intracranial tumors after exposure to ionizing radiation during infancy: a pooled analysis of two Swedish cohorts of 28,008 infants with skin hemangioma. *Radiat Res*. 1998;150: 357–364.

21. Salvatai M, Aratico M, Caruso R, Rocchi G, Orlando EER, Nucci F. A report on radiation-induced gliomas. *Cancer*. 1991;67: 392–397.
22. Yeh H, Matanoski GM, Wang N, Sandler DP, Comstock GW. Cancer incidence after childhood nasopharyngeal radium irradiation: a follow-up study in Washington County, Maryland. *Am J Epidemiol*. 2001;153:749–756.
23. Shintani T, Hayakawa N, Hoshi M, et al. High incidence of meningioma among Hiroshima atomic bomb survivors. *J Radiat Res*. 1999;40:49–57.
24. Loomis DP, Wolf SH. Mortality of workers at a nuclear materials production plant at Oak Ridge, Tennessee, 1947–1990. *Am J Ind Med*. 1996;29:131–141.
25. Wong O, Whorton MD, Follart DE, Ragland D. An industry-wide epidemiologic study of vinyl chloride workers, 1942–1982. *Am J Ind Med*. 1991;20:317–334.
26. McLaughlin JK, Lipworth L. A critical review of the epidemiologic literature on health effects of occupational exposure to vinyl chloride. *J Epidemiol Biostat*. 1999;4:253–275.
27. Johansen C, Boice JD, McLaughlin JK, Olsen JH. Cellular telephones and cancer – a nationwide cohort study in Denmark. *J Natl Cancer Inst*. 2001;93:203–207.
28. Muscat JE, Malkin MG, Thompson S, et al. Handheld cellular telephone use and risk of brain cancer. *JAMA*. 2000;284:3001–3007.
29. Inskip PD, Tarone RE, Hatch EE, et al. Cellular-telephone use and brain tumors. *N Engl J Med*. 2001;344:79–86.
30. Christensen HC, Schüz J, Kosteljanetz M. Cellular telephones and risk for brain tumors. A population-based, incident case-control study. *Neurol*. 2005;64:1189–1195.
31. Muscat JE, Malkin MG, Shore RE, et al. Handheld cellular telephones and risk of acoustic neuroma. *Neurol*. 2002;58:1304–1306.
32. Schoemaker MJ, Swerdlow AJ, Ahlbom A, et al. Mobile phone use and risk of acoustic neuroma: results of the Interphone case-control study in five north European countries. *Br J Cancer*. 2005;93: 842–848.
33. Schuz J, Bohler E, Berg G, et al. Cellular phones, cordless phones, and the risks of glioma and meningioma (Interphone Study Group, Germany). *Am J Epidemiol*. 2006;163:512–520.
34. Wrensch M, Fisher JL, Schwartzbaum JA, Bondy M, Berger M, Aldape KD. The molecular epidemiology of gliomas in adults. *Neurosurg Focus*. 2005;19:E5.
35. Tang J, Shao W, Dorak MT, et al. Positive and negative associations of human leukocyte antigen variants with the onset and prognosis of adult glioblastoma multiforme. *Cancer Epidemiol Biomarkers Prev*. 2005;14:2040–2044.
36. Wrensch M, Kelsey KT, Liu M, et al. ERCC1 and ERCC2 polymorphisms and adult gliomas. *Neuro-Oncol*. 2005;7:495–507.
37. Wiencke JK, Aldape K, McMillan A, et al. Molecular features of adult glioma associated with patient race/ethnicity, age, and a polymorphism in O^6-methylguanine-DNA-methyltransferase. *Cancer Epidemiol Biomarkers Prev*. 2005;14:1774–1783.
38. Turner MC, Benke G, Bowman JD, et al. Occupational exposure to extremely low frequency magnetic fields and brain tumour risk in the INTEROCC study. *Cancer Epidemiol Biomarkers Prev*. 2014;23:1863–1872. pii:cebp.0102.2014.
39. Brenner AV, Linet MS, Fine HA, et al. History of allergies and autoimmune diseases and risk of brain tumors in adults. *Int J Cancer*. 2002;99:252–256.
40. Schwartzbaum J, Ahlbom A, Malmer B, et al. Polymorphisms associated with asthma are inversely related to glioblastoma multiforme. *Cancer Res*. 2006;65:6459–6465.
41. Gavrilovic IT, Posner JB. Brain metastases: epidemiology and pathophysiology. *J Neuro-Oncol*. 2005;75:5–14.
42. Barnhholtz-Sloan JS, Sloan AE, Davis FG, Vigneau FD, Lai P, Sawaya RE. Incidence proportions of brain metastases in patients diagnosed (1973 to 2001) in the metropolitan Detroit Cancer Surveillance System. *J Clin Oncol*. 2004;22:2865–2872.
43. Leroux PD, Berger MS, Elliott JP, Tamimi HK. Cerebral metastases from ovarian carcinoma. *Cancer*. 1991;67:2194–2199.
44. Martinez-Manas RM, Brell M, Rumia J, Ferrer E. Case report. Brain metastases in endometrial carcinoma. *Gyn Oncol*. 1998;70: 282–284.
45. Mccutcheon IE, Eng DY, Logothetis CJ. Brain metastasis from prostate carcinoma. Antemortem recognition and outcome after treatment. *Cancer*. 1999;86:2301–2311.
46. Lowis SP, Foot A, Gerrard MP, et al. Central nervous system metastasis in Wilms' tumor. A review of three consecutive United Kingdom trials. *Cancer*. 1998;83:2023–2029.
47. Culine S, Bekradda M, Kramar A, et al. Prognostic factors for survival in patients with brain metastases from renal cell carcinoma. *Cancer*. 1998;83:2548–2553.
48. Qasho R, Tommaso V, Rocchi G, et al. Choroid plexus metastasis from carcinoma of the bladder: case report and review of the literature. *J Neuro-Oncol*. 1999;45:237–240.
49. Salvati M, Frati A, Rocchi G, et al. Single brain metastasis from thyroid cancer: report of twelve cases and review of the literature. *J Neuro-Oncol*. 2001;51:33–40.
50. Ogawa K, Toita T, Sueyama H, et al. Brain metastases from esophageal carcinoma. Natural history, prognostic factors, and outcome. *Cancer*. 2002;94:759–764.
51. Espat NJ, Bilsky M, Lewis JJ, et al. Soft tissue sarcoma brain metastases. Prevalence in a cohort of 33829 patients. *Cancer*. 2002;94: 2706–2711.
52. Schouten LJ, Rutten J, Huveneers HAM, Twijnstra A. Incidence of brain metastases in a cohort of patients with carcinoma of the breast, colon, kidney, and lung and melanoma. *Cancer*. 2002;94: 2698–2705.
53. Ruda R, Borgognone M, Benech F, Vasario E, Soffietti R. Brain metastases from unknown primary tumour. A prospective study. *J Neurol*. 2001;248:394–398.
54. Kebudi R, Ayan I, Görgün O, Agaoglu FY, Vural S, Darendeliler E. Brain metastasis in pediatric extracranial solid tumors: survey and literature review. *J Neuro-Oncol*. 2005;71:43–48.
55. Hall WA, Djalilian HR, Nussbaum ES, et al. Long-term survival with metastatic cancer to the brain. *Med Oncol*. 2000;17:279–286.
56. Gaspar L, Scott C, Rotman M, et al. Recursive partitioning analysis (RPA) of prognostic factors in three radiation therapy oncology group (RTOG) brain metastases trials. *Int J Rad Oncol Biol Phys*. 1997;37:745–751.
57. Nussbaum ES, Djalilian HR, Cho KH, Hall WA. Brain metastases: histology, multiplicity, surgery, and survival. *Cancer*. 1996;78: 1781–1788.
58. Poste G, Fidler IJ. The pathogenesis of cancer metastasis. *Nature*. 1980;283:139–146.
59. Bernards R, Weinberg RA. Metastasis genes: a progression puzzle. *Nature*. 2002;418:823.
60. Ramaswamy S, Ross KN, Lander ES, Golub TR. A molecular signature of metastasis in primary solid tumors. *Nat Genet*. 2003;33:49–54.
61. Milas I, Komaki R, Hachiya T, et al. Epidermal growth factor receptor, cyclooxygenase-2, and BAX expression in the primary non-small cell lung cancer and brain metastases. *Clin Cancer Res*. 2003;9:1070–1076.

CHAPTER

2

Overview of Pathology and Treatment of Primary Brain Tumors

Herbert B. Newton

Division of Neuro-Oncology, Departments of Neurology and Neurosurgery, Dardinger Neuro-Oncology Center, Wexner Medical Center at The Ohio State University and James Cancer Hospital and Solove Research Institute, Columbus, OH, USA

The epidemiology of primary brain tumors (PBTs) was reviewed in detail in Chapter 1. In this chapter, we provide an overview of the classification, pathology, and treatment of the common PBT. PBTs will be diagnosed in approximately 30,000–35,000 patients in the United States this year and are associated with significant morbidity and mortality.[1–6] Of the estimated 14 patients per 100,000 population that will develop a PBT this year, 6–8 per 100,000 will have a high-grade neoplasm, usually some form of glioma such as glioblastoma multiforme (GBM) or anaplastic astrocytoma (AA).

PATHOLOGY OF SELECTED PBTs

The application of appropriate therapeutic strategies is dependent on knowing the type of tumor affecting a given patient. In addition to assisting with treatment decisions, the tumor classification and grade provide important information regarding prognosis. This chapter follows the World Health Organization (WHO) classification that separates nervous system tumors into different nosological entities and assigns a grade of I–IV to each lesion (see Table 1), with grade I being biologically indolent and grade IV being biologically most malignant and having the worst prognosis.[7,8] Within the WHO classification, tumors of neuroepithelial and meningeal origin contain the two largest and most clinically relevant groups of neoplasms.

Tumors of neuroepithelial origin comprise a large and diverse group of neoplasms, with a mixture of slowly growing and malignant tumor types (see Table 2).[7–9] Gliomas (e.g., GBM, AA, oligodendrogliomas, medulloblastoma) are the largest subgroup within the neuroepithelial class of neoplasms and are also the most common type of PBT. Tumors of neuroepithelial origin, and gliomas in particular, can grow diffusely within the brain or be more circumscribed. Diffusely growing tumors are most common and include the astrocytomas, oligodendrogliomas, and mixed oligoastrocytomas. Any of these subtypes can undergo malignant transformation and degenerate into the most aggressive form of glioma, the GBM.

Diffuse Astrocytomas. The current WHO classification divides astrocytomas into diffuse and localized varieties (see Table 3).[7–9] The diffuse astrocytomas are intrinsically invasive and often travel along white matter tracts deep into normal brain. There are three groups of diffuse astrocytic neoplasms: astrocytoma (WHO grade II; peak age of 30–39 years), AA (WHO grade III; peak age of 40–49 years), and GBM (WHO grade IV; peak age of 50–69 years). Diffuse astrocytic tumors can be divided into fibrillary, protoplasmic, and gemistocytic forms, with the fibrillary form being most common. The presence of gemistocytic and protoplasmic cellular variations are most often seen in WHO grade II tumors. WHO grade II astrocytomas are considered low-grade tumors and usually occur in the cerebral white matter. These tumors are characterized by a relatively uniform population of proliferating neoplastic astrocytes in a fibrillary matrix, with minimal cellular and nuclear pleomorphism or atypia (see Figure 1). Tumor margins are poorly delineated and suggest significant infiltration into surrounding brain. Mitotic figures are absent and there is no evidence for vascular hyperplasia. Microcystic change is commonly noted in all variants of grade II astrocytoma. The Ki-67

Handbook of Neuro-Oncology Neuroimaging, Second Edition
http://dx.doi.org/10.1016/B978-0-12-800945-1.00002-1

© 2016 Elsevier Ltd. All rights reserved.

TABLE 1 WHO Classification: Tumors of the Central Nervous System

Tumors of neuroepithelial tissue
Tumors of cranial nerves and spinal nerves
Tumors of the meninges
Lymphomas and hemopoietic neoplasms
Germ-cell tumors
Tumors of the sellar region
Cysts and tumor-like lesions
Metastatic tumors

TABLE 2 WHO Classification: Tumors of Neuroepithelial Tissue

Astrocytic tumors
Oligodendroglial tumors
Ependymal tumors
Mixed gliomas
Choroid plexus tumors
Neuronal and mixed neuronal–glial tumors
Pineal parenchymal tumors
Neuroepithelial tumors of uncertain origin
Embryonal tumors

TABLE 3 WHO Classification: Astrocytic Tumors

DIFFUSE ASTROCYTOMAS
Astrocytoma (WHO grade II)
Fibrillary
Protoplasmic
Gemistocytic
Anaplastic astrocytoma (WHO grade III)
Glioblastoma multiforme (WHO grade IV)
Giant cell glioblastoma
Gliosarcoma
LOCALIZED ASTROCYTOMAS (WHO GRADE I)
Pilocytic astrocytoma
Pleomorphic xanthoastrocytoma
Subependymal giant cell astrocytoma

labeling index of WHO grade II astrocytomas is typically less than 4%, with a mean of approximately 2.0–2.5%.

Higher-grade diffuse astrocytomas include AA (WHO grade III) and GBM (WHO grade IV), as well as the GBM variants giant cell glioblastoma and gliosarcoma (WHO grade IV) (see Table 3).[7–10] Anaplastic astrocytomas are similar to grade II tumors, except for the presence of more prominent cellular and nuclear pleomorphism and atypia and mitotic activity (see Figure 2). In addition, grade III and IV tumors usually do not stain as intensely or as homogeneously with glial fibrillary acidic protein (GFAP). According to WHO criteria, the critical feature that upgrades a grade II tumor to an AA is the presence of mitotic activity, with anaplastic tumors having Ki-67 indices in the range of 5–10% in most cases. Other features of anaplasia can be present, such as multinucleated tumor cells, abnormal mitotic figures, and regions of vascular proliferation. Necrosis is absent in grade III astrocytomas.

Glioblastoma multiforme is classified as a WHO grade IV tumor and has histological features similar to those of AA, but with more pronounced anaplasia (see Figure 3(A)).[7–10] The presence of microvascular proliferation and/or necrosis in an otherwise malignant astrocytoma

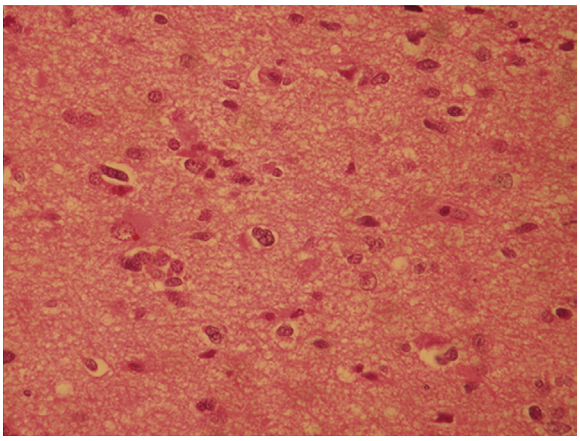


FIGURE 1 WHO grade II fibrillary astrocytoma. Note the neoplastic astrocytes in a fibrillary matrix, with mildly increased cellularity and pleomorphism. No mitoses or hypervascularity are present. Hematoxylin and eosin staining (H&E); original magnification 200×.

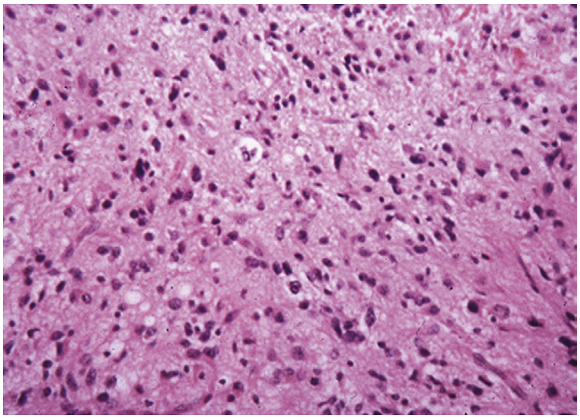


FIGURE 2 WHO grade III fibrillary astrocytoma (AA). The tumor is more densely cellular than grade II, with significant cellular and nuclear pleomorphism and atypia. Mitotic figures are evident. H original magnification 200×.

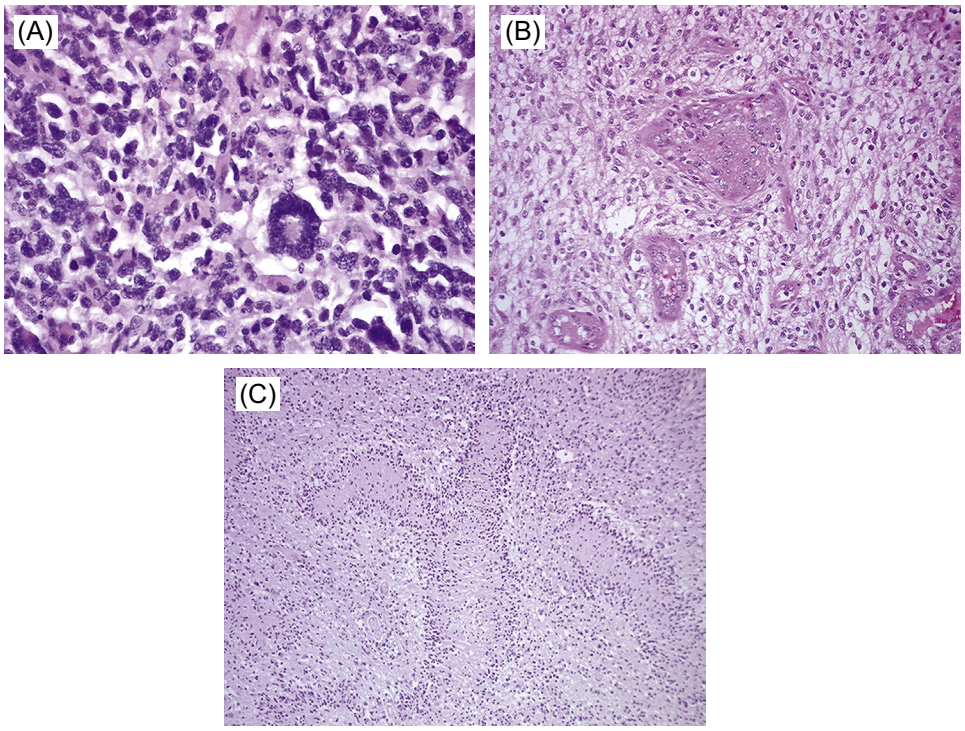


FIGURE 3 WHO grade IV fibrillary astrocytoma (GBM). (A) A highly cellular tumor with marked cellular and nuclear pleomorphism, numerous mitoses, giant cells (H original magnification 400×); (B) dense vascular proliferation (H original magnification 200×); and (C) regions of necrosis with pseudopalisading tumor nuclei (H original magnification 100×).

upgrades the tumor to a GBM. Vascular proliferation is defined as blood vessels with "piling up" of endothelial cells, including the formation of glomeruloid vessels (see Figure 3(B)). The glomeruloid vessels can form undulating garlands that surround necrotic zones in some cases. Necrosis can be noted in large amorphous areas, which appear ischemic in nature, or can appear as more serpiginous regions with surrounding palisading tumor cells (i.e., perinecrotic pseudopalisading; see Figure 3(C)). Necrosis with nuclear pseudopalisading is essentially pathognomonic for GBM. Other features of GBM that are typically prominent include marked cellular and nuclear pleomorphism and atypia, mitotic figures and multinucleated giant cells, and pronounced infiltrative capacity into the surrounding brain. Labeling indices with Ki-67 are usually in the range of 15–20%, but can be much higher in some tumors.

Localized Astrocytomas. In the WHO classification, the localized astrocytomas include the pilocytic astrocytoma (WHO grade I), pleomorphic xanthoastrocytoma (PXA; WHO grade II), and the subependymal giant cell astrocytoma (WHO grade I).[7–10] Pilocytic astrocytomas are slow-growing, relatively circumscribed tumors that usually occur in children (peak age 10–12 years) and young adults. These tumors have a predilection for the cerebellum, optic nerves and optic pathways, and hypothalamus. The distinctive histological feature is the presence of cells with slender, elongated nuclei and thin, hair-like (i.e., piloid), GFAP-positive, bipolar processes. These cells are found in a biphasic background, which consists of dense fibrillary regions alternating with loose, microcystic areas. Labeling index studies with Ki-67 report values of 0.5–1.5% in most tumors. The PXA is a supratentorial tumor with a predilection for the superficial temporal lobes that usually occurs in younger patients (mean age 15–18 years) with a long-standing history of seizure activity.[7–10] On histological examination, PXA demonstrates significant pleomorphism, with numerous atypical giant cells and astrocytes with prominent nucleoli.[11] Also present are large foamy (xanthomatous) cells with lipidized cytoplasm that express GFAP. Subependymal giant cell astrocytoma is an indolent, slowly growing tumor that typically arises in the walls of the lateral ventricles and is almost invariably associated with tuberous sclerosis.[7–10]

Oligodendrogliomas and Oligoastrocytomas. Oligodendrogliomas are a form of diffuse glioma that can be of pure or mixed histology and are classified as WHO grade II or III.[7–10] They typically occur in young to middle-aged adults (peak age 35–45 years) with a history of seizures, within the white matter of the frontal and temporal lobes. Pure low-grade oligodendroglial tumors (WHO grade II) are characterized histologically by a moderately cellular, monotonous pattern of cells with round nuclei and perinuclear halos (the classic "fried-egg" appearance; see Figure 4).[12] The perinuclear halos are an artifact of the formalin fixation process of the tumor tissue. Foci of

calcification are frequent and can be quite dense in some cases. Delicately branching blood vessels are prominent (i.e., "chicken-wire" vasculature), but do not display endothelial proliferation. Oligodendrogliomas have a pronounced invasive capacity and are known to invade the gray and white matter diffusely, with a strong tendency to form secondary structures of Scherer, in particular perineuronal satellitosis. Mitoses are absent or rare and necrosis is not present. Labeling studies with Ki-67 usually demonstrate indices less than 5%, with a mean of approximately 2%. The diagnosis of an anaplastic oligodendroglioma (WHO grade III) requires the presence of additional histologic features, including a higher degree of cellularity and mitotic activity, vascular endothelial hyperplasia, nuclear pleomorphism, and regions of necrosis (see Figure 5(A) and (B)). These tumors behave in a more aggressive fashion, with a higher proliferative rate (Ki-67 labeling index >5%) and capacity for invasion of surrounding brain. Mixed oligoastrocytomas can be classified as WHO grade II or III tumors.[7–10] Distinct populations of neoplastic oligodendroglial cells and astrocytes can be identified within the mass that have features similar to pure versions of the tumor. The percentage of each cell population can be quite variable, with an even mixture of cell types or with one cell type predominating.

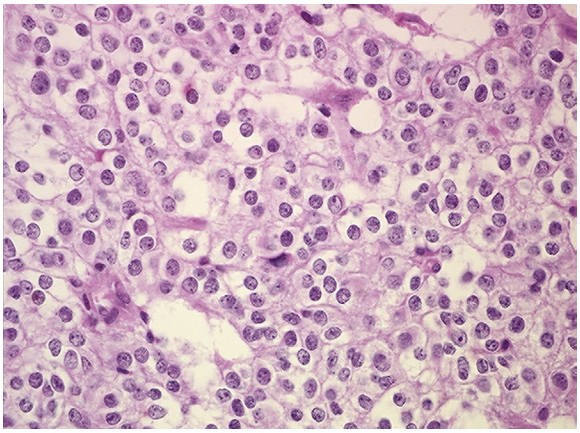


FIGURE 4 WHO grade II oligodendroglioma. This image demonstrates the classic features of typical oligodendroglioma, with moderate cellularity and numerous round cells with the "fried-egg" pattern of perinuclear halos and delicate "chicken-wire" vasculature. H original magnification 400×.

Advances in molecular neuropathology have begun to clarify the biological underpinnings of variability in response to treatment of oligodendrogliomas.[12–14] The majority of tumors demonstrate genetic losses on chromosome 1p (40–92%) and/or 19q (50–80%). There is a strong predilection for deletions of 1p and 19q to occur together, but in some tumors they can be singular events. Patients with oligodendrogliomas that contain deletions of 1p and 19q are consistently more responsive to irradiation and chemotherapy and have an overall median survival of 8–10 years. In contrast, patients with tumors that do not have deletion of 1p and 19q are more resistant to all forms of therapy and have an overall median survival of only 3–4 years.

Medulloblastoma and Other Embryonal Tumors. Embryonal tumors are a group of aggressive, malignant neoplasms that usually affect children. They are classified by the WHO as grade IV in all cases (see Table 4).[7–10] All embryonal tumors share the common features of high cellularity, frequent mitoses, regions of necrosis, and a propensity for metastases along cerebrospinal fluid (CSF) pathways. Medulloblastoma is the most common of the embryonal tumors and is considered a primitive neuroectodermal tumor (PNET) of the cerebellum. It usually arises in the midline in children, within the cerebellar vermis, whereas in adults it is more likely to have an off-center location within the cerebellar

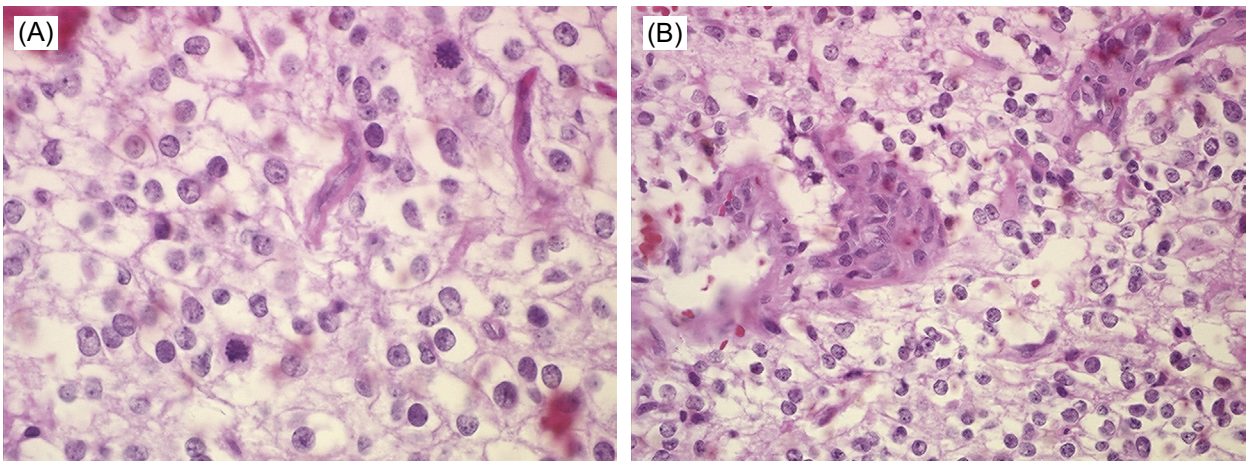


FIGURE 5 WHO grade III oligodendroglioma. A more densely cellular tumor with prominent cellular and nuclear pleomorphism, mitotic activity (A), and increased vascularity (B). H original magnification 400×.

hemispheres. The typical medulloblastoma is densely cellular and composed of undifferentiated cells with hyperchromatic, oval to carrot-shaped nuclei with scant cytoplasm (see Figure 6).[9,15] The nuclei have a tendency to mold against one another. Mitoses and single cell necrosis are frequently present. Evidence of anaplasia is variable and may include increased nuclear size, abundant mitoses, and the presence of large cells or similar aggressive cellular morphology. Some tumors may display immunohistochemical and morphological evidence for differentiation along neuronal, glial, or mesenchymal lines. Medulloblastomas are highly proliferative tumors, with Ki-67 labeling indices ranging from 15% to 50%.

Meningioma and Other Tumors of the Meninges. Tumors of the meninges comprise a large and diverse group of neoplasms that mostly have meningothelial or mesenchymal, nonmeningothelial origins (see Table 5).[8,9] The most common primary tumor of this group is the meningioma

TABLE 4 WHO Classification: Embryonal Tumors

Medulloepithelioma
Ependymoblastoma
Medulloblastoma
Desmoplastic medulloblastoma
Large-cell medulloblastoma
Medullomyoblastoma
Melanotic medulloblastoma
Supratentorial PNET
Neuroblastoma
Ganglioneuroblastoma
Atypical teratoid/rhabdoid tumor

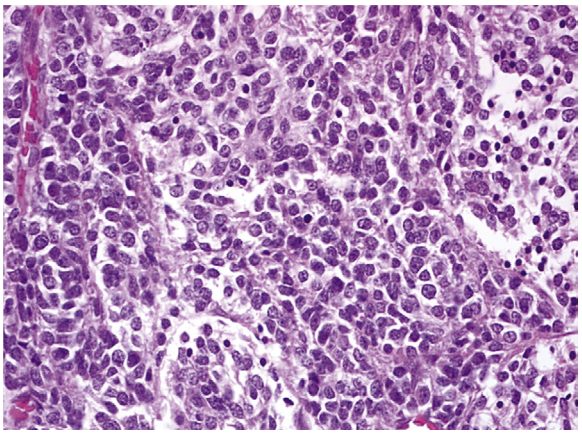


FIGURE 6 WHO grade IV medulloblastoma. Note the dense cellularity and presence of undifferentiated cells with hyperchromatic, oval to carrot-shaped nuclei with scant cytoplasm. The nuclei have a tendency to mold against one another. H original magnification 200×.

TABLE 5 WHO Classification: Tumors of the Meninges

TUMORS OF MENINGOTHELIAL CELLS (MENINGIOMAS)
Meningothelial
Fibrous (fibroblastic)
Transitional (mixed)
Psammomatous
Angiomatous
Microcystic
Secretory
Lymphoplasmacyte rich
Metaplastic
Clear cell
Chordoid
Atypical
Papillary
Rhabdoid
Anaplastic
MESENCHYMAL, NONMENINGOTHELIAL TUMORS
Lipoma
Angiolipoma
Hibernoma
Liposarcoma (intracranial)
Solitary fibrous tumor
Fibrosarcoma
Malignant fibrous histiocytoma
Leiomyoma
Leiomyosarcoma
Rhabdomyoma
Rhabdomyosarcoma
Chondroma
Chondrosarcoma
Osteoma
Osteosarcoma
Osteochondroma
Hemangioma
Epithelioid hemangioendothelioma
Hemangiopericytoma
Angiosarcoma
Kaposi sarcoma

Continued

TABLE 5 WHO Classification: Tumors of the Meninges—cont'd

PRIMARY MELANOCYTIC LESIONS
Diffuse melanocytosis
Melanocytoma
Malignant melanoma
Meningeal melanomatosis

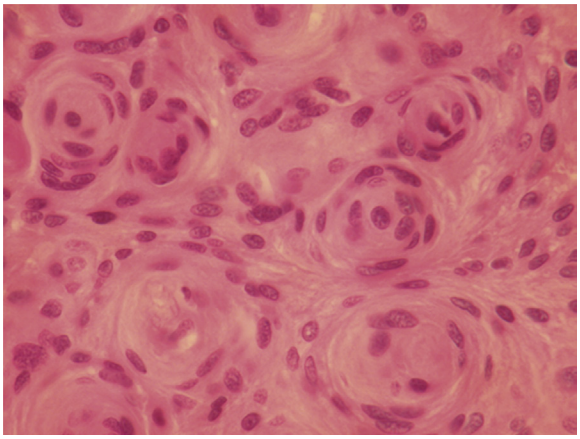


FIGURE 7 WHO grade II meningioma. The tumor demonstrates a moderately dense, uniform pattern of cells with oval-shaped nuclei and the presence of many cellular whorl patterns. H original magnification 200×.

(18–20% of intracranial tumors), which has meningothelial cell origins and is composed of neoplastic arachnoidal cap cells of the arachnoidal villi and granulations. Meningiomas can occur anywhere within the intracranial cavity, but favor the sagittal area along the superior longitudinal sinus, over the lateral cerebral convexities, at the tuberculum sellae and parasellar region, the sphenoidal ridge, and along the olfactory grooves. Numerous histologic variants of meningioma are described and recognized by the WHO (see Table 5). However, the histopathological description of most of these variants has no bearing on the clinical behavior of the tumor. Meningioma subtypes that have a more indolent nature and low risk for aggressive growth or recurrence are classified as WHO grade I and include the meningothelial, fibrous/fibroblastic, transitional (mixed), secretory, psammomatous, angiomatous, microcystic, lymphoplasmocyte-rich, and metaplastic variants.[16,17] Of this group, the meningothelial, fibrous, and transitional variants are most frequently diagnosed. The histological features common to most low-grade meningiomas are the presence of whorls (tightly wound, rounded collections of cells), psammoma bodies (concentrically laminated mineral deposits that often begin in the center of whorls), intranuclear pseudoinclusions (areas in which pink cytoplasm protrudes into a nucleus to produce a hollowed-out appearance), and occasional pleomorphic nuclei and mitoses (see Figure 7).[16,17]

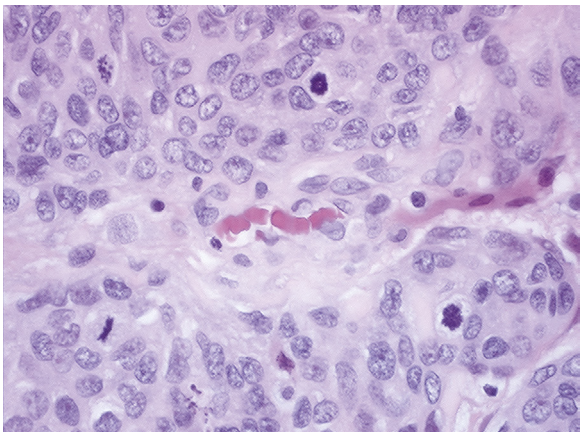


FIGURE 8 WHO grade III anaplastic meningioma. This higher power view demonstrates increased nuclear pleomorphism and frequent mitoses. H original magnification 400×.

Meningothelial meningiomas are composed of lobules of typical meningioma cells, with minimal whorl formation. The tumor cells are uniform in shape, with oval nuclei that may show central clearing. Fibrous variants have spindle-shaped cells resembling fibroblasts that form parallel and interlacing bundles within a matrix of collagen and reticulin.

Meningioma subtypes that are more likely to display aggressive clinical behavior and to recur are classified by the WHO as grade II (atypical, clear cell, chordoid) and grade III (rhabdoid, papillary, anaplastic).[8,9,16,17] On histological examination, all of the grade II tumors are likely to demonstrate increased cellularity, more frequent mitoses, diffuse or sheetlike growth, nuclear pleomorphism and atypia, and evidence for micronecrosis. Grade III tumors such as anaplastic meningioma show features consistent with frank malignancy, including a high mitotic rate, advanced cytological atypia, nuclear pleomorphism, and necrosis (see Figure 8). Invasion of underlying brain is frequently noted in grade III meningiomas, but can also occur in lower grade variants. Proliferation studies using Ki-67 demonstrate labeling indices ranging from 8% to 15%.

Primary Central Nervous System Lymphoma. Primary central nervous system lymphomas (PCNSLs) are malignant tumors classified as WHO grade IV that affect adults in the sixth or seventh decade of life.[8,9] They are often multifocal and usually arise in the deep supratentorial white matter, with a predilection for the periventricular region and basal ganglia. PCNSLs are composed of a clonal expansion of neoplastic lymphocytes, typically of the diffuse, large-cell, or immunoblastic variety. In 95% of the tumors, the cells have a B cell lineage, often with monoclonal IgMκ production. On histological examination, PCNSLs display a perivascular cellular orientation, with expansion of vessel walls and reticulin deposition (see Figure 9).[18] Regions

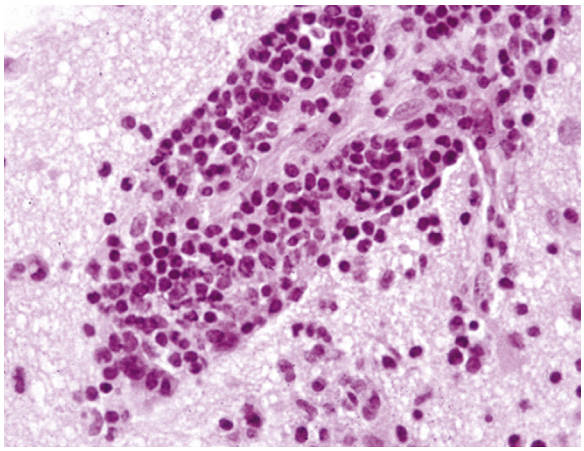


FIGURE 9 WHO grade IV primary CNS lymphoma. Note the presence of neoplastic lymphocytes in an angiocentric growth pattern, with nuclear pleomorphism and mitoses. H original magnification 100×.

of necrosis are common, especially if steroids have been administered prior to the biopsy. The lymphomatous cells are noncohesive and usually have large, irregular nuclei, prominent nucleoli, and scant cytoplasm. From the perivascular region, tumor cells are noted to invade the surrounding brain parenchyma, either in compact cellular aggregates or as singly infiltrating tumor cells. PCNSLs are highly proliferative tumors, with Ki-67 labeling indices ranging from 20% to 50% in most studies. The diagnosis can be confirmed by immunohistochemical positivity for leukocyte common antigen (CD45) and specific B cell markers (CD19, CD20, and CD79a).

SURGICAL THERAPY OF PBTs

Surgical intervention is the most common form of treatment for PBTs and is an important aspect of initial therapy in most patients. Indications for surgery include reduction of tumor burden, alleviation of mass effect, control of seizures and reversal of neurological deficit, confirmation of the histological diagnosis, diversion of CSF by shunting procedures in selected cases, and the introduction of local antineoplastic agents.[1,19,20] Advances in neurosurgical technology offer new approaches to tumor removal, such as frame-based and frameless stereotactic biopsy, preoperative functional magnetic resonance imaging (MRI) and intraoperative cortical mapping, neuronavigation and tumor resection in the awake patient, and the use of intraoperative MRI.[21–23] These techniques allow the surgeon to more carefully delineate tumor margins and to preserve surrounding regions of eloquent brain (e.g., Broca's area, primary motor cortex) and delicate vascular structures, while performing a more aggressive and thorough tumor resection. Complete removal of benign tumors such as meningioma, pilocytic astrocytoma, and schwannomas can be curative. For malignant tumors (i.e., GBM, AA), although the lack of a prospective, controlled randomized clinical trial still fosters debate in the literature, most neurosurgeons recommend a near-total or gross-total resection, whenever possible, of all enhancing tumor volume and regionally infiltrated brain as defined on T2-weighted or FLAIR MRI sequences. Gross-total tumor resection is not curative for these tumor types, but has been associated with longer overall and progression-free survival (PFS) in several studies, as well as improved neurological quality of life.[24,25] For tumors that are diffusely infiltrative or multifocal, a stereotactic biopsy is more likely to preserve neurological function than an attempt at resection and, in most cases, will be able to provide a histological diagnosis to guide further treatment. The accuracy of stereotactic biopsy is further improved when the region of interest is defined by contrast enhancement on MRI or abnormal signal on MRI spectroscopy or positron emission tomography.

RADIATION THERAPY OF PBTs

External beam fractionated radiation therapy is an appropriate form of treatment for virtually all patients with high-grade gliomas (i.e., GBM, AA, anaplastic oligodendroglioma (AO), medulloblastoma), as well as for selected low-grade PBTs that are surgically inaccessible or have progressed after initial resection.[1,26–29] Numerous randomized controlled trials have demonstrated a survival benefit for high-grade glioma patients receiving surgical resection and irradiation in comparison to resection alone (approximately 34–38 weeks vs 14–18 weeks, respectively). The mechanism of cell death appears to be the production of DNA strand damage by ionizing radiation and the generation of highly reactive oxygen radicals that induce further DNA damage and disrupt cellular processes. Sublethal or mortal damage to endothelial cells in tumor vessels may also be of importance. The standard approach is administered in the early postoperative phase and initially uses conformal radiation ports that encompass the T2-weighted target with a margin of 1–3 cm, using a dose of approximately 4500–4700 cGy in 180- to 200-cGy daily fractions. After this portion has been completed, a "cone down" is performed, targeting the T1-weighted contrast-enhancing volume of the tumor with a 1- to 3-cm margin, bringing the total dose to approximately 6000 cGy. Irradiation is performed over the course of 6–7 weeks, with the patient receiving treatment 5 days per week. Radiation therapy schedules can sometimes be modified with hypofractionation and/or an abbreviated treatment course for elderly patients or for those with a low performance

status, while maintaining a similar level of toxicity and overall survival.[30,31] More aggressive approaches to irradiation using hyperfractionation schemes have not been shown to improve tumor control and, in some reports, have been associated with worse outcomes.[28] Other techniques to increase localized radiation doses to the tumor resection cavity, such as brachytherapy with permanent or temporary radioactive seeds, have also had disappointing results in controlled trials.[32] In addition to the cranial dosage, spinal-axis radiation therapy is necessary for tumors that often seed the meninges, such as medulloblastoma, pineoblastoma, and anaplastic ependymoma.

Stereotactic radiosurgery, using a linear accelerator-based system (e.g., Cyberknife®) or a Co^{60}-based system (e.g., Gamma Knife®) to deliver a single (or a few) high-dose radiation fraction(s) to a defined volume using stereotactic localization, is another method to boost radiation doses in the tumor bed of a newly diagnosed or recurrent glioma, while sparing normal surrounding tissues.[33–35] Because of the diffuse, infiltrative nature of the growth pattern of these tumors, the application of focal treatment modalities such as radiosurgery remains controversial. Retrospective and single-armed, uncontrolled prospective trials suggest an improvement in local tumor control rates and survival when using either radiosurgical system. However, these results were not been confirmed in the randomized, controlled trial of radiosurgery for GBM reported by the Radiation Therapy Oncology Group (RTOG 93-05).[35,36] In this study, 203 GBM patients were randomized to receive radiosurgery followed by conventional irradiation (60 Gy) and intravenous carmustine chemotherapy (80 mg/m^2/day × 3 days every 8 weeks) or irradiation plus chemotherapy alone. The median survival for the radiosurgical and conventional treatment groups were 13.5 and 13.6 months, respectively ($p = 0.5711$). In addition, the 2- and 3-year survival rates and patterns of failure were similar between groups. There was no difference in general quality of life or retention of cognitive function between groups.

CHEMOTHERAPY OF PBTs

Chemotherapy is used as an adjunctive treatment for malignant PBTs (i.e., mostly high-grade gliomas—GBM, AA) and for selected low-grade gliomas that progress through initial surgical resection and irradiation.[1,37–40] The addition of chemotherapy has resulted in modest improvements in the survival of patients with malignant glioma, as demonstrated by two detailed meta-analyses.[41,42] Over the past two decades and until recently, nitrosourea alkylating drugs such as carmustine and lomustine (CCNU) were considered the most effective chemotherapeutic agents for these tumors.[37,38] Other agents with mild activity included procarbazine (administered alone or in combination with CCNU and vincristine), cisplatin, etoposide, carboplatin, and cyclophosphamide. For the treatment of PCNSL, methotrexate has been shown to be the most active agent, either alone or in combination with other drugs (e.g., cytarabine, rituximab).[43]

Since 2005, the focus has been on the second-generation alkylating agent temozolomide (TZM), which has an activity profile superior to those of the nitrosoureas and other agents. Temozolomide is an imidazotetrazine derivative of the alkylating agent dacarbazine, with activity against systemic and CNS malignancies.[37,38,44–47] The drug undergoes chemical conversion at physiological pH to the active species 5-(3-methyl-1-triazeno)imidazole-4-carboxamide. Temozolomide exhibits schedule-dependent antineoplastic activity by interfering with DNA replication through the process of methylation. The methylation of DNA is dependent on the formation of a reactive methyldiazonium cation, which interacts with DNA at the following sites: N^7-guanine (70%), N^3-adenine (9.2%), and O^6-guanine (5%). Because TZM is stable at acid pH, it can be taken orally in capsules. Oral bioavailability is approximately 100%, with rapid absorption of the drug. In addition, TZM has excellent penetration of the blood–brain barrier and brain tumor tissue.

Initial studies of TZM were in patients with recurrent AA and GBM and suggested significant activity.[37,38,44–47] Subsequent larger studies demonstrated unequivocal efficacy in the recurrent setting. The first study evaluated the use of TZM (150–200 mg/m^2/day × 5 days every 28 days) in a series of 162 patients with recurrent malignant gliomas, including 97 patients with AA.[48] In the AA cohort, there were 6 patients with complete response (CR), 27 with partial response (PR), and another 31 with stable disease (SD) (CR + PR + SD = 66%). The response rate was similar in patients that had failed prior chemotherapy or were chemotherapy-naïve. Median overall PFS was 5.4 months, with 6- and 12-months PFS rates of 46% and 24%, respectively. The median overall survival was 13.6 months, with 6- and 12-months survival rates of 75% and 56%, respectively. A similar comparative phase II trial evaluated the activity of TZM versus procarbazine (125–150 mg/m^2/day × 28 days every 8 weeks) in a cohort of 225 patients with GBM at first relapse.[49] Overall response rates (PR + SD) were significantly higher for patients in the TZM cohort (45.6% vs 32.7%; $p = 0.049$). Treatment with TZM resulted in a significant improvement in median PFS (12.4 weeks vs 8.32 weeks; $p = 0.0063$) and 6-month PFS (21% vs 8%; $p = 0.008$) in comparison to procarbazine. In addition, the 6-month overall survival rate was significantly higher for patients in the TZM arm of the study (60% vs 44%; $p = 0.019$).

Temozolomide has also been applied to GBM patients in the "up-front" setting by Stupp and colleagues in a set of phase II and III studies, in combination with standard external beam irradiation and monthly adjuvant chemotherapy.[37,38,50,51] For the phase III study, a total of 573 patients were randomly assigned to receive radiation alone (6000 cGy; 200 cGy/day × 5 days/week for 6 weeks) or radiotherapy in combination with daily TZM (75 mg/m^2/day × 7 days/week for 6 weeks).[51] After the completion of irradiation, each patient in the chemotherapy arm went on to receive six cycles of adjuvant single-agent TZM (150–200 mg/m^2/day × 5 days, every 28 days). The overall median survival was 14.6 months for the radiotherapy plus TZM cohort and 12.1 months for the cohort that received irradiation alone, for an overall median survival benefit of 2.5 months. The unadjusted hazard ratio (HR) for death due to the GBM for the radiotherapy plus TZM cohort was 0.63 ($p < 0.001$, log-rank test). The 2-year survival rate was 26.5% for the chemoradiation cohort and 10.4% for the cohort receiving radiotherapy alone. Responsiveness to chemoradiation and overall survival were found to correlate strongly with the presence of promoter methylation of the methylguanine-methyltransferase (MGMT) gene, which is important for tumor cell resistance to radiotherapy and chemotherapy. Since the publication of this report, chemoradiation using low-dose TZM, followed by adjuvant monthly TZM, has become FDA approved and is now the "standard of care" for newly diagnosed GBM patients in the United States and around the world. In a 5-year follow-up of this cohort of patients, Stupp and colleagues report a persistent and significant difference in survival between the group of patients that received radiotherapy and TZM versus the group that received radiotherapy alone.[52] For the chemoradiation group, overall survival at 4 and 5 years was 12.1% and 9.8%, respectively. In contrast, the radiotherapy-alone group had 4- and 5-year overall survivals of 3.0% and 1.9%, respectively. The differences in overall survival were highly significant, with a HR of 0.60 ($p < 0.0001$). Methylation of the MGMT promoter region was still a very strong predictor of response to TZM chemotherapy.

Dose-intensive or dose-dense schedules of TZM (e.g., 7 days on/7 days off, 3 weeks on/1 week off) have also been under investigation, because laboratory studies suggest that the higher cumulative dose may result in improved efficacy through augmented depletion of MGMT in tumor cells.[53] This premise was tested by the RTOG, in the RTOG-0525 phase III trial, in a cohort of 833 patients with newly diagnosed GBM.[54] Patients were treated with standard surgical resection and chemoradiation, and then randomized to receive either conventional TZM (5 days per month; 150–200 mg/m^2/day) or dose-dense TZM (21 days on/7 days off; 75–100 mg/m^2/day), for a total of 6–12 cycles. The two treatment groups were not statistically different at final analysis in terms of median overall survival (16.6 vs 14.9 months; HR = 1.03) or median PFS (5.5 vs 6.7 months; HR = 0.87). MGMT promoter methylation was associated with improved overall survival (21.2 vs 14 months; HR = 1.74), PFS (8.7 vs 5.7 months; HR = 1.63), and response rate.

Angiogenesis is a tightly controlled process that involves growth and maintenance of blood vessels within tissues and organs.[55–58] A delicate equilibrium exists between positive angiogenic factors (e.g., vascular endothelial growth factor (VEGF), transforming growth factor-β (TGF-β)) and inhibitory factors (e.g., thrombospondin-1, angiostatin, endostatin).[55–58] These factors interact with specific receptors on endothelial cells and the extracellular matrix, such as VEGF receptor-1 (VEGFR-1), VEGFR-2, VEGFR-3, TIE1, and TIE2.[57] There are several important stimuli for conversion to the angiogenic phenotype in GBM. The presence of hypoxia induces upregulation of secretion of VEGF and expression of VEGFRs in tumor endothelial cells and surrounding regional vasculature.[57] Another critical element for the switch to the angiogenic phenotype is overactivity of the major growth factor signaling pathways and loss of certain tumor suppressor genes.[59] Overexpression and excessive activity of platelet-derived growth factor (PDGF), epidermal growth factor (EGF), fibroblast growth factor, Ras, TGF-α, and TGF-β are critical to the development of the angiogenic phenotype.[60–62] In addition to growth factor activity, internal signal transduction mediators also appear to play a role in the angiogenic phenotype. The PI3K/Akt/PTEN signaling pathway is involved in the regulation of angiogenesis through the control of expression of VEGF, hypoxia-inducible factor-1, and thrombospondin-1.[63–65]

Numerous investigators have begun to focus on treatment approaches that capitalize on the prominence of VEGF signaling in solid tumor angiogenesis.[95] The most promising approaches include monoclonal antibodies against VEGF (e.g., bevacizumab) and VEGFR (e.g., IMC-1C11, DC101).[59,66–68] Bevacizumab (Avastin™) has advanced the farthest in terms of preclinical evaluation and clinical trials.[69,70] Bevacizumab is a humanized IgG1 monoclonal antibody that is specific for all isoforms of VEGF, preventing their binding to VEGFR. It has demonstrated significant activity in preclinical studies against a wide variety of solid tumors, including gliomas, as a single agent and in combination with conventional chemotherapy.[71–73]

The first report of the use of bevacizumab for brain tumor patients was by Stark-Vance in 2005, who treated 21 patients with malignant gliomas with bevacizumab in combination with irinotecan.[74] The response rate was

an impressive 43%, although there were two treatment-related deaths (intracranial hemorrhage, intestinal perforation). Based on this promising preliminary work, Vredenburgh and colleagues organized a prospective phase II trial of bevacizumab and irinotecan for patients with recurrent malignant gliomas.[75] Thirty-two patients were enrolled (GBM 23; anaplastic tumors 9) and received intravenous bevacizumab (10 mg/kg) and irinotecan (340 mg/m^2 on enzyme-inducing antiepileptic drugs (EIAED), 125 mg/m^2 not on EIAED) every 2 weeks. Radiographic responses were noted in 20 of 32 patients (63%; CR 1, PR 19), including 14 of 23 in the GBM cohort and 6 of 9 in the anaplastic glioma subgroup. The median overall PFS was 23 weeks: 20 weeks in GBM patients and 30 weeks in patients with anaplastic tumors. The 6-month PFS and overall survival rates were 38% and 72%, respectively. In updated reports from 68 patients (GBM 35; anaplastic tumors 33) the MRI response rate was similar (59%).[76,77] For the GBM cohort the 6-month PFS was 46%, with a 6-month overall survival of 77%. For the anaplastic glioma subgroup, the 6-month PFS rate was 61%, with a median PFS of 42 weeks. Eight patients were taken off the study for thrombotic complications, including pulmonary emboli (4), deep venous thrombosis (2), thrombotic thrombocytopenic purpura (1), and thrombotic stroke (1). The preliminary use of bevacizumab and irinotecan at other institutions resulted in similar results, in terms of MRI response rates, time to progression, and overall survival.[73,78–82] The Duke group has also performed a phase II study of bevacizumab and irinotecan that was restricted to only patients with recurrent grade III gliomas (25 AA, 8 AO).[83] There were two cohorts of patients: the first group of 9 patients received the standard combination regimen every 2 weeks, whereas the second group received bevacizumab (15 mg/kg every 3 weeks) and irinotecan (days 1, 8, 22, 29 of each cycle; 340 mg/m^2 on EIAED, 125 mg/m^2 on NEIAED) on a 6-week cycle. Objective responses were noted in 29 patients (61% with at least a PR). The 6-month PFS and overall survival rates were 55% and 79%, respectively. There was no difference in PFS or survival rates between the two treatment cohorts. Although bevacizumab has been well tolerated by the majority of patients, severe toxicity can occur, including hypertension, proteinuria, arterial and venous thromboembolic events, hemorrhage, gastrointestinal perforation, and impaired wound healing.[84]

The results of the BRAIN trial were reported by Friedman and colleagues in 2009.[73,85] This study was a phase II, multicenter, open-label, noncomparative trial evaluating the efficacy of bevacizumab, alone or in combination with irinotecan, in a group of 167 patients with GBM in first or second relapse. Patients were randomly assigned to receive bevacizumab (10 mg/kg) as a single agent or in combination with irinotecan (340 or 125 mg/m^2, depending on EIAED or NEIAED), on an every 2-weeks schedule. The primary endpoints for the study were 6-month PFS and objective response rate on follow-up MRI, with secondary endpoints of safety and overall survival. The 6-month PFS rates in the bevacizumab alone and bevacizumab plus irinotecan groups were 42.6% and 50.3%, respectively. Objective response rates on follow-up MRI were 28.2% for the bevacizumab alone cohort and 37.8% for the bevacizumab plus irinotecan group. Median PFS times for the bevacizumab alone and bevacizumab plus irinotecan cohorts were 4.2 and 5.6 months, respectively. The overall survival times were also similar between the single-agent bevacizumab and the bevacizumab plus irinotecan groups (9.2 months vs 8.7 months). There was a trend for patients on corticosteroids at the beginning of the trial to remain on stable or decreasing doses over time.[86] Grade 3 or 4 toxicity was more frequent in the bevacizumab plus irinotecan group (65.8%) in comparison to those receiving bevacizumab alone (46.4%). The most common adverse events were hypertension, fatigue, neutropenia, and seizures. Intracranial hemorrhage was uncommon in both groups (2.4% bevacizumab alone, 3.8% bevacizumab plus irinotecan; 5 total patients, only 1 was grade 4). The authors concluded that bevacizumab, alone or in combination with irinotecan, was active against recurrent GBM, with 6-month PFS rates that were far superior to the expected 15% rate for salvage chemotherapy and irinotecan alone.

Clinicians have begun to evaluate the safety and feasibility of using bevacizumab in combination with temozolomide during chemoradiation in newly diagnosed patients with high-grade gliomas.[73,87,88] An early pilot study of bevacizumab (10 mg/kg every 2 weeks) in combination with temozolomide (75 mg/m^2 during irradiation, followed by 150–200 mg/m^2 × 5 days every 4 weeks) was performed by Lai and colleagues in 10 patients with newly diagnosed GBM.[87] The toxicity was considered to be acceptable and consisted of fatigue, myelotoxicity, wound breakdown, DVT/PE, and one case of radiation-induced optic neuropathy. Preliminary efficacy analysis suggested an encouraging mean PFS (range 15–45 weeks). A similar feasibility study from Narayana et al. evaluated 15 patients with high-grade glioma, with the adjuvant therapy phase planned over 1 year (temozolomide 150 mg/m^2/day).[88] Thirteen patients (86.6%) completed the entire year of adjuvant treatment; radiographic responses were noted in 13 of 14 assessable patients (92.8%). The 1-year PFS and overall survival rates were 59.3% and 86.7%, respectively. Using a more aggressive approach, Vredenburgh et al. treated 75 patients with newly diagnosed GBM with standard chemoradiation plus bevacizumab (10 mg/kg every 2 weeks), followed by adjuvant temozolomide (200 mg/m^2 × 5 days every month) in combination with bevacizumab

and irinotecan (340 mg/m^2 on EIAED, 125 mg/m^2 on NEIAED) every 2 weeks.[89] The median PFS for the entire cohort was 14.2 months, with a median overall survival of 21.2 months. At 16-month follow-up, the overall survival rate was 65%. Another update by the Duke group reports the results from 125 newly diagnosed GBM patients who were treated with standard chemoradiation and temozolomide, in addition to bevacizumab (10 mg/kg intravenously every 2 weeks).[90] Overall, the combination of temozolomide and bevacizumab was tolerated well in the majority of patients, with 96% completing the full course of chemoradiation and 90% able to continue on with treatment into the adjuvant chemotherapy phase. Toxicities associated with treatment discontinuation included pulmonary emboli, CNS hemorrhage, pancytopenia, wound dehiscence, and colonic perforation.

Based on these intriguing preliminary studies, two large phase III clinical trials were performed to determine the impact of adding bevacizumab to standard chemoradiation with temozolomide in newly diagnosed GBM patients. The first study was the Avastin in Glioblastoma Trial (AVAglio), an international effort based mainly in Europe, which enrolled 921 patients and randomly assigned them to receive either bevacizumab (10 mg/kg every 2 weeks) or placebo, plus standard radiotherapy and concomitant temozolomide.[91] The coprimary endpoints of the study were PFS and overall survival. After chemoradiation was completed, patients received either bevacizumab or placebo every 2 weeks, along with adjuvant temozolomide (150–200 mg/m^2/day) for up to six cycles. After the completion of adjuvant temozolomide, patients would continue with single-agent bevacizumab (15 mg/kg every 3 weeks) or placebo until disease progression or unacceptable toxicity. The median PFS was longer in the bevacizumab group than in the placebo group (median 10.6 months vs 6.2 months; HR = 064; $p < 0.001$). Overall survival was not significantly different between the groups (median 16.8 months vs 16.7 months; HR = 0.88; $p = 0.10$). The overall survival rates of the bevacizumab and placebo groups were 72.4% and 66.3% at 1 year ($p = 0.049$) and 33.9% and 30.1% at 2 years ($p = 0.24$), respectively. Health-related quality of life and performance status were maintained longer in the bevacizumab group; in addition, they required a lower dose of corticosteroids. The other phase III trial was the RTOG 0825 study, which enrolled and randomized 637 patients with newly diagnosed GBM and had design and treatment groups similar to those of the AVAglio study, except that during the adjuvant treatment phase, patients could continue temozolomide for up to 12 cycles.[92] There was no difference between the bevacizumab and the placebo groups in terms of overall survival (median 15.7 months vs 16.1 months; HR = 1.13). The PFS was longer for the bevacizumab cohort (median 10.7 months vs 7.3 months; HR = 0.79), but was not considered significant because it did not reach the prespecified improvement target. During the course of the study, the bevacizumab group showed an increased symptom burden, worse quality of life, and a decline in neurocognitive function in comparison to the placebo group.

MOLECULAR OR "TARGETED" TREATMENT

As noted above, conventional chemotherapeutic approaches to treatment for malignant glioma are not predicated on the biology of the malignant phenotype. It has become apparent that the transformed phenotype of brain tumor cells is highly complex and results from the dysfunction of a variety of interrelated regulatory pathways.[93–95] The transformation process involves amplification or overexpression of oncogenes in combination with loss or lack of expression of tumor suppressor genes. Oncogenes and signal transduction molecules that have been demonstrated to be important for gliomagenesis include PDGF and its receptor (PDGFR), EGF and EGFR, CDK4, mdm-2, Ras, phosphoinositol-3 kinase (PI3K), Akt, and mTOR (mammalian target of rapamycin). Tumor suppressor genes of importance in glial transformation include p53, retinoblastoma, p16 and p15 (i.e., INK4a, INK4b), DMBT1, and PTEN. Most of these tumor suppressor genes function as negative regulators of the cell cycle, whereas others are inhibitors of important internal signal transduction pathways. The net effect of these acquired abnormalities is dysregulation of, and an imbalance between, the activity of the cell cycle and apoptotic pathways.

Because the survival of patients with high-grade gliomas has remained so poor using conventional chemotherapeutic approaches, new treatment modalities are being investigated that have a more molecular, "targeted" mechanism of action, with the ability to overcome the transformed phenotype.[59,60,96–98] Advances in growth factor and signal transduction biology are now providing the background for the development of "molecular therapeutics," a new class of drugs that manipulate and exploit these pathways. Molecular drugs targeting critical signal transduction pathway effectors, such as PDGFR, EGFR, Ras, PI3K, and mTOR, have entered clinical trials in brain tumor patients.[59,60,96–98] To date, numerous drugs have been tested in phase I, II, and III trials, designed to target various key receptors, signal transduction proteins, and cell membrane-related proteins such as EGFR (gefitinib, erlotinib, cetuximab), PDGFR (imatinib), Ras (tipifarnib, lonafarnib), mTOR (temsirolimus), integrins (cilengitide), and protein kinase C (enzastaurin), as well as multikinase drugs (e.g., lapatinib) that can target combinations of the above. Preliminary

results suggest only modest activity against recurrent high-grade gliomas when used as single agents. Current and subsequent clinical trials will investigate using molecular drugs in combination with conventional chemotherapeutic agents (e.g., TZM, hydroxyurea), with other molecular drugs that target different signal transduction pathways, and with irradiation.

Acknowledgments

The authors thank Shawna Huckell and Nicole Ghaffari for research assistance. Dr. Newton was supported in part by National Cancer Institute Grant CA 16058 and the Dardinger Neuro-Oncology Center Endowment Fund.

References

1. Newton HB. Primary brain tumors: review of etiology, diagnosis, and treatment. *Am Fam Phys*. 1994;49:787–797.
2. Preston-Martin S. Epidemiology of primary CNS neoplasms. *Neurol Clin*. 1996;14:273–290.
3. Davis FG, McCarthy BJ. Current epidemiological trends and surveillance issues in brain tumors. *Expert Rev Anticancer Ther*. 2001;1:395–401.
4. Osborne RH, Houben MPWA, Tijssen CC, Coebergh JWW, van Duijn CM. The genetic epidemiology of glioma. *Neurol*. 2001;57:1751–1755.
5. Wrensch M, Minn Y, Chew T, Bondy M, Berger MS. Epidemiology of primary brain tumors: current concepts and review of the literature. *Neuro-Oncol*. 2002;4:278–299.
6. Hess KR, Broglio DR, Bondy ML. Adult glioma incidence trends in the United States, 1977–2000. *Cancer*. 2004;101:2293–2299.
7. Rodriguez FJ, Giannini C. Diagnostic neuropathology of tumors of the central nervous system. *Handbk Clin Neurol*. 2012;104:77–107.
8. Kleihues P, Louis DN, Scheithauer BW, et al. The WHO classification of tumors of the nervous system. *J Neuropathol Exp Neurol*. 2002;61:215–225.
9. McLendon RE, Enterline DS, Tien RD, Thorstad WL, Bruner JM. Tumors of central neuroepithelial origin. In: Bigner DD, McLendon RE, Bruner JM, eds. *Russell & Rubinstein's Pathology of Tumors of the Nervous System*. *Sixth Edition*. *Volume 1*. London: Arnold; 1998;9: 307–571.
10. Li J, Sulman E, Aldape K. Molecular biology of brain tumors. *Handbk Clin Neurol*. 2012;104:23–34.
11. Sharma A, Nand Sharma D, Kumar JP, Kishor RG. Pleomorphic xanthoastrocytoma – a clinico-pathological review. *Neurol Neurochir Pol*. 2011;45:379–386.
12. Matthews S, Succar P, Jelinek H, et al. Diagnosis of oligodendroglioma: molecular and classical histological assessment in the twenty-first century. *Asia Pac J Clin Oncol*. 2012;8:213–216.
13. Jenkinson MD, Walker C, Brodbelt AR, et al. Molecular genetics, imaging and treatment of oligodendroglial tumours. *Acta Neurochir (Wien)*. 2010;152:1815–1825.
14. Bromberg JE, van den Bent MJ. Oligodendrogliomas: molecular biology and treatment. *Oncologist*. 2009;14:155–163.
15. Eberhart CG, Burger PC. Anaplasia and grading in medulloblastomas. *Brain Pathol*. 2003;13:376–385.
16. Lamszus K. Meningioma pathology, genetics, and biology. *J Neuropathol Exp Neurol*. 2004;63:275–286.
17. Perry A, Gutmann DH, Reifenberger G. Molecular pathogenesis of meningiomas. *J Neuro-Oncol*. 2004;70:183–202.
18. Deckert M, Engert A, Bruck W, et al. Modern concepts in the biology, diagnosis, differential diagnosis, and treatment of primary central nervous system lymphoma. *Leukemia*. 2011;25:1797–1807.
19. Parney IF, Berger MS. Principles of brain tumor surgery. *Handbk Clin Neurol*. 2012;104:187–213.
20. Dunn IF, Black PM. The neurosurgeon as local oncologist: cellular and molecular neurosurgery in malignant glioma therapy. *Neurosurg*. 2003;52:1411–1424.
21. Choi BD, Mehta AI, Batich KA, et al. The use of motor mapping to aid resection of eloquent gliomas. *Neurosurg Clin N Am*. 2012;23:215–225.
22. Orringer DA, Golby A, Jolesz F. Neuronavigation in the surgical management of brain tumors: current and future trends. *Expert Rev Med Devices*. 2012;9:491–500.
23. Liang D, Schulder M. The role of intraoperative magnetic resonance imaging in glioma surgery. *Surg Neurol Int*. 2012;3: S320–S327.
24. Lacroix M, Abi-Said D, Fourney DR, et al. A multivariate analysis of 416 patients with glioblastoma multiforme: prognosis, extent of resection, and survival. *J Neurosurg*. 2001;95:190–198.
25. Bloch O, Han SJ, Cha S, et al. Impact of extent of resection for recurrent glioblastoma on overall survival: clinical article. *J Neurosurg*. 2012;117:1032–1038.
26. Caruso C, Carcaterra M, Donato V. Role of radiotherapy for high grade glioma management. *J Neurosurg Sci*. 2013;57:163–169.
27. Wind JJ, Young R, Saini A, Sherman JH. The role of adjuvant radiation therapy in the management of high-grade gliomas. *Neurosurg Clin N Am*. 2012;23:247–258.
28. Minniti G, Goldsmith C, Brada M. Radiotherapy. *Handbk Clin Neurol*. 2012;104:215–228.
29. Kortmann RD, Jeremic B, Bamberg M. Radiotherapy in the management of low-grade gliomas. In: Petrovich Z, Brady LW, Apuzzo ML, Bamberg M, eds. *Combined Modality Therapy of Central Nervous System Tumors*. Vol. 16. Berlin: Springer; 2001:317–326.
30. Chang EL, Yi W, Allen PK, Levin VA, Sawaya RE, Maor MH. Hypofractionated radiotherapy for elderly or younger low-performance status glioblastoma patients: outcome and prognostic factors. *Int J Rad Oncol Biol Phys*. 2003;56:519–528.
31. Roa W, Brasher PMA, Bauman G, et al. Abbreviated course of radiation therapy in older patients with glioblastoma multiforme: a prospective randomized clinical trial. *J Clin Oncol*. 2004;22: 1583–1588.
32. Selker RG, Shapiro WR, Burger P, et al. The Brain Tumor Cooperative Group NIH trial 87-01: a randomized comparison of surgery, external radiotherapy, and carmustine versus surgery, interstitial radiotherapy boost, external radiation therapy, and carmustine. *Neurosurg*. 2002;51:343–357.
33. Elaimy AL, Mackay AR, Lamoreaux WT, et al. Clinical outcomes of gamma knife radiosurgery in the salvage treatment of patients with recurrent high-grade glioma. *World Neurosurg*. 2013;80:872–878.
34. Koga T, Saito N. Efficacy and limitations of stereotactic radiosurgery in the treatment of glioblastoma. *Neurol Clin Chir (Tokyo)*. 2012;52:548–552.
35. Tsao MN, Mehta MP, Whelan TJ, et al. The American Society for Therapeutic Radiology and Oncology (ASTRO) evidence-based review of the role of radiosurgery for malignant glioma. *Int J Rad Oncol Biol Phys*. 2005;63:47–55.
36. Souhami L, Seiferheld W, Brachman D, et al. Randomized comparison of stereotactic radiosurgery followed by conventional radiotherapy with carmustine to conventional radiotherapy with carmustine for patients with glioblastoma multiforme: report of Radiation Therapy Oncology Group 93-05 protocol. *Int J Rad Oncol Biol Phys*. 2004;60:853–860.
37. Newton HB. Chemotherapy of high-grade astrocytomas. In: Newton HB, ed. *Handbook of Brain Tumor Chemotherapy*. Vol. 24. London: Elsevier Medical Publishers-Academic Press; 2006:347–363.
38. Blakeley J, Grossman SA. Chemotherapy with cytotoxic and cytostatic agents in brain cancer. *Handbk Clin Neurol*. 2012;104:229–265.

39. Viaccoz A, Lekoubou A, Ducray F. Chemotherapy in low-grade gliomas. *Curr Opin Oncol*. 2012;24:694–701.
40. Malkin MG. Chemotherapy of low-grade astrocytomas. In: Newton HB, ed. *Handbook of Brain Tumor Chemotherapy*. Vol. 25. London: Elsevier Medical Publishers-Academic Press; 2006:364–370.
41. Fine HA, Dear KBG, Loeffler JS, Black PM, Canellos GP. Meta-analysis of radiation therapy with and without adjuvant chemotherapy for malignant gliomas in adults. *Cancer*. 1993;71:2585–2597.
42. Steward LA, Burdett S, Souhami RL, Stenning S. Chemotherapy in adult high-grade glioma: a systematic review and meta-analysis of individual patient data from 12 randomised trials. *Lancet*. 2002;359:1011–1018.
43. El Kamar FG, Abrey LE. Chemotherapy for primary central nervous system lymphoma. In: Newton HB, ed. *Handbook of Brain Tumor Chemotherapy*. Vol. 28. London: Elsevier Medical Publishers-Academic Press; 2006:395–406.
44. Stevens MFG, Newlands ES. From triazines and triazenes to temozolomide. *Eur J Cancer*. 1993;20A:1045–1047.
45. Newlands ES, O'Reilly SM, Glaser MG, et al. The Charing Cross Hospital experience with temozolomide in patients with gliomas. *Eur J Cancer*. 1996;2A:2236–2241.
46. Newlands ES, Stevens MFG, Wedge SR, Wheelhouse RT, Brock C. Temozolomide: a review of its discovery, chemical properties, pre-clinical development and clinical trials. *Cancer Treat Rev*. 1997;23:35–61.
47. Hvizdos KM, Goa KL. Temozolomide. *CNS Drugs*. 1999;12:237–243.
48. Yung WKA, Prados MD, Yaya-Tur R, et al. Multicenter phase II trial of temozolomide in patients with anaplastic astrocytoma or anaplastic oligoastrocytoma at first relapse. *J Clin Oncol*. 1999;17:2762–2771.
49. Yung WKA, Albright RE, Olson J, et al. A phase II study of temozolomide vs. procarbazine in patients with glioblastoma multiforme at first relapse. *Br J Cancer*. 2000;83:588–593.
50. Stupp R, Dietrich PY, Kraljevic SO, et al. Promising survival for patients with newly diagnosed glioblastoma treated with concomitant radiation plus temozolomide followed by adjuvant temozolomide. *J Clin Oncol*. 2002;20:1375–1382.
51. Stupp R, Mason WP, van den Bent MJ, et al. Radiotherapy plus concomitant and adjuvant temozolomide for glioblastoma. *New Engl J Med*. 2005;352:987–996.
52. Stupp R, Hegi ME, Mason WP, et al. Effects of radiotherapy with concomitant and adjuvant temozolomide versus radiotherapy alone on survival in glioblastoma in a randomized phase III study: 5-year analysis of the EORTC-NCIC trial. *Lancet Oncol*. 2009;10:459–466.
53. Strik HM, Marosi C, Kaina B, Neyns B. Temozolomide dosing regimens for glioma patients. *Curr Neurol Neurosci Rep*. 2012;12:286–293.
54. Gilbert MR, Wang M, Aldape KD, et al. Dose-dense temozolomide for newly diagnosed glioblastoma: a randomized phase III clinical trial. *J Clin Oncol*. 2013;31:4085–4091.
55. Cavallaro U, Christofori G. Molecular mechanisms of tumor angiogenesis and tumor progression. *J Neuro-Oncol*. 2000;50:63–70.
56. Webb CP, Vande Woude GF. Genes that regulate metastasis and angiogenesis. *J Neuro-Oncol*. 2000;50:71–87.
57. Plate KH. Mechanisms of angiogenesis in the brain. *J Neuropath Exp Neurol*. 1999;58:313–320.
58. Hardee ME, Zagzag D. Mechanisms of glioma-associated neovascularization. *Am J Pathol*. 2012;181:1126–1141.
59. Newton HB. Molecular neuro-oncology and the development of "targeted" therapeutic strategies for brain tumors. Part 2 – PI3K/Akt/PTEN, mTOR, SHH/PTCH, and angiogenesis. *Expert Rev Anticancer Ther*. 2004;4:105–128.
60. Newton HB. Molecular neuro-oncology and the development of "targeted" therapeutic strategies for brain tumors. Part 1 – growth factor and ras signaling pathways. *Expert Rev Anticancer Ther*. 2003;3:595–614.
61. Jensen RL. Growth factor-mediated angiogenesis in the malignant progression of glial tumors: a review. *Surg Neurol*. 1998;49:189–196.
62. Dunn IF, Heese O, Black PM. Growth factors in glioma angiogenesis: FGFs, PDGF, EGF, and TGFs. *J Neuro-Oncol*. 2000;50:121–137.
63. Zagzag D, Zhong H, Scalzitti JM, et al. Expression of hypoxia-inducible factor 1α in brain tumors. Association with angiogenesis, invasion, and progression. *Cancer*. 2000;88:2606–2618.
64. Jiang BH, Jiang G, Zheng JZ, et al. Phosphatidylinositol 3-kinase signaling controls levels of hypoxia-inducible factor 1. *Cell Growth Differ*. 2001;12:363–369.
65. Wen S, Stolarov J, Myers MP, et al. PTEN controls tumor-induced angiogenesis. *Proc Natl Acad Sci USA*. 2001;98:4622–4627.
66. Hicklin DJ, Ellis LM. Role of the vascular endothelial growth factor pathway in tumor growth and angiogenesis. *J Clin Oncol*. 2005;23:1011–1027.
67. Levine AM, Tulpule A, Quinn DI, et al. Phase I study of antisense oligonucleotide against vascular endothelial growth factor: decrease in plasma vascular endothelial growth factor with potential clinical efficacy. *J Clin Oncol*. 2006;24:1712–1719.
68. Wachsberger PR, Burd R, Cardi C, et al. VEGF trap in combination with radiotherapy improves tumor control in U87 glioblastoma. *Int J Rad Oncol Biol Phys*. 2007;67:1526–1537.
69. Ranieri G, Patruno R, Ruggieri E, Montemurro S, Valerio P, Ribatti D. Vascular endothelial growth factor (VEGF) as a target of bevacizumab in cancer: from the biology to the clinic. *Curr Med Chem*. 2006;13:1845–1857.
70. Shih T, Lindley C. Bevacizumab: an angiogenesis inhibitor for the treatment of solid malignancies. *Clin Ther*. 2006;28:1779–1802.
71. Kunkel P, Ulbricht U, Bohlen P, et al. Inhibition of intracranial glioma angiogenesis and growth in vivo by systemic treatment with a monoclonal antibody against vascular endothelial growth factor receptor-2. *Cancer Res*. 2001;61:6624–6628.
72. Stefanik DF, Fellows WK, Rizkalla LR, et al. Monoclonal antibodies to vascular endothelial growth factor (VEGF) and the VEGF receptor, FLT-1, inhibit the growth of C6 glioma in a mouse xenograft. *J Neuro-Oncol*. 2001;55:91–100.
73. Newton HB. Overview of angiogenesis and the use of bevacizumab in patients with malignant gliomas. *Curr Signal Transduct Ther*. 2013;8:25–35.
74. Stark-Vance V. Bevacizumab and CPT-11 in the treatment of relapsed malignant glioma. In: *World Federation of Neuro-Oncology Meeting*. 2005:91.
75. Vredenburgh JJ, Desjardins A, Herndon JE, et al. Phase II trial of bevacizumab and irinotecan in recurrent malignant glioma. *Clin Cancer Res*. 2007;13:1253–1259.
76. Goli KJ, Desjardins A, Herndon JE, et al. Phase II trial of bevacizumab and irinotecan in the treatment of malignant gliomas (abstract). *J Clin Oncol (Suppl)*. 2007;18S:75s.
77. Vredenburgh JJ, Desjardins A, Herndon JE, et al. Bevacizumab plus irinotecan in recurrent glioblastoma multiforme. *J Clin Oncol*. 2007;25:4722–4729.
78. Kang T, Jin T, Elinzano H, Peereboom D. Irinotecan and bevacizumab in progressive primary brain tumors, an evaluation of efficacy and safety. *J Neuro-Oncol*. 2008;89:113–118.
79. Gilbert MR, Wang M, Aldape K, Lassman A, Sorensen AG, Mikkelson T, et al. RTOG 0625: a phase II study of bevacizumab and irinotecan in recurrent glioblastoma (GBM) (abstract). *J Clin Oncol (Suppl)*. 2009;27:89s.
80. Ali SA, McHayleh WM, Ahmad A, Sehgal R, Braffet M, Rahman M, et al. Bevacizumab and irinotecan in glioblastoma multiforme: a series of 13 cases. *J Neurosurg*. 2008;109:268–272.
81. Bokstein F, Shpigel S, Blumenthal DT. Treatment with bevacizumab and irinotecan for recurrent high-grade glial tumors. *Cancer*. 2008;112:2267–2273.

82. Poulsen HS, Grunnet K, Sorensen M, et al. Bevacizumab plus irinotecan in the treatment of patients with progressive recurrent malignant brain tumours. *Acta Oncol*. 2009;48:52–58.
83. Desjardins A, Reardon DA, Herndon JE, et al. Bevacizumab plus irinotecan in recurrent WHO grade 3 malignant gliomas. *Clin Cancer Res*. 2008;14:7068–7073.
84. Gordon MS, Cunningham D. Managing patients treated with bevacizumab combination therapy. *Oncology*. 2005;69:25–33.
85. Friedman HS, Prados MD, Wen PY, et al. Bevacizumab alone and in combination with irinotecan in recurrent glioblastoma. *J Clin Oncol*. 2009;27:4733–4740.
86. Vredenburgh JJ, Cloughesy T, Samant M, et al. Corticosteroid use in patients with glioblastoma at first or second relapse treated with bevacizumab in the BRAIN study. *Oncology*. 2010;15:1329–1334.
87. Lai A, Filka E, McGibbon B, Nghiemphu PL, et al. Phase II pilot study of bevacizumab in combination with temozolomide and regional radiation therapy for up-front treatment of patients with newly diagnosed glioblastoma mutiforme: Interim analysis of safety and tolerability. *Int J Rad Oncol Biol Phys*. 2008;71:1372–1380.
88. Narayana A, Golfinos JG, Fischer I, et al. Feasibility of using bevacizumab with radiation therapy and temozolomide in newly diagnosed high-grade glioma. *Int J Rad Oncol Biol Phys*. 2008;72:383–389.
89. Vredenburgh JJ, Desjardins A, Reardon DA, et al. The addition of bevacizumab to standard radiation therapy and temozolomide followed by bevacizumab, temozolomide, and irinotecan for newly diagnosed glioblastoma. *Clin Cancer Res*. 2011;17:4119–4124.
90. Vredenburgh JJ, Adejardins A, Kirkpatrick JP, et al. Addition of bevacizumab to standard radiation therapy and daily temozolomide is associated with minimal toxicity in newly diagnosed glioblastoma multiforme. *Int J Rad Oncol Biol Phys*. 2012;82:58–66.
91. Chinot OL, Wick W, Mason W, et al. Bevacizumab plus radiotherapy-temozolomide for newly diagnosed glioblastoma. *New Engl J Med*. 2014;370:709–722.
92. Gilbert MR, Dignam JJ, Armstrong TS, et al. A randomized trial of bevacizumab for newly diagnosed glioblastoma. *New Engl J Med*. 2014;370:699–708.
93. Marumoto T, Saya H. Molecular biology of glioma. *Adv Exp Med Biol*. 2012;746:2–11.
94. Li J, Sulman E, Aldape K. Molecular biology of brain tumors. *Handbk Clin Neurol*. 2012;104:23–34.
95. Westphal M, Lamszus K. The neurobiology of gliomas: from cell biology to the development of therapeutic approaches. *Nat Rev Neurosci*. 2011;12:495–508.
96. Newton HB. Molecular neuro-oncology and the development of "targeted" therapeutic strategies for brain tumors. Part 5 – apoptosis and cell cycle. *Expert Rev Anticancer Ther*. 2005;5:355–378.
97. Sathornsumetee S, Rich JN. Molecularly targeted therapy in neuro-oncology. *Handbk Clin Neurol*. 2012;104:255–278.
98. Hamza MA, Gilbert M. Targeted therapy in gliomas. *Curr Oncol Rep*. 2014;16(4):379.

CHAPTER

3

Overview of Pathology and Treatment of Metastatic Brain Tumors

Herbert B. Newton

Division of Neuro-Oncology, Departments of Neurology and Neurosurgery, Dardinger Neuro-Oncology Center, Wexner Medical Center at The Ohio State University and James Cancer Hospital and Solove Research Institute, Columbus, OH, USA

The epidemiology of metastatic brain tumors (MBTs) was reviewed in detail in Chapter 1. In this chapter, we will provide an overview of the classification, pathology, and treatment of the common MBT. MBT arise in 20–40% of all adult cancer patients and are the most common complication of systemic neoplastic disease.[1–5] They are expected to be diagnosed in approximately 150,000–170,000 patients in 2015 in the USA and are associated with significant morbidity and mortality. Of the estimated 8.3–11 patients per 100,000 population that will develop an MBT this year, more than 75% will have underlying primary tumors of the lung, breast, and skin (i.e., melanoma) (see Table 1). However, virtually any primary tumor has the potential to metastasize to the brain.

PATHOLOGY OF MBTs

Systemic tumor cells usually travel to the brain by hematogenous spread through the arterial circulation, often after genetic alterations that produce a more motile and aggressive phenotype.[6–11] The metastasis most often originates from the lung, either from a primary lung tumor or from a pulmonary metastasis. Occasionally, cells reach the brain through the Batson's paravertebral venous plexus or by direct extension from adjacent structures (e.g., sinuses, skull). The distribution of brain metastases follows the relative volume of blood flow to each area, so that 80% of tumors arise in the cerebral hemispheres, 15% in the cerebellum, and 5% in the brain stem. Tumor cells typically lodge in small vessels at the gray–white junction and then spread into the brain parenchyma, where they proliferate and induce their own blood supply by neoplastic angiogenesis.[9] Expansion of the MBT disrupts the function of adjacent neural tissue through several mechanisms, including direct displacement of brain structures, perilesional edema, irritation of overlying gray matter, and compression of arterial and venous vasculature.

The metastatic phenotype is the result of a complex alteration of gene expression that affects tumor cell adhesion, motility, protease activity, and internal signaling pathways.[8–10] Initial changes involve downregulation of surface adhesion molecules, such as integrins and cadherins, which reduces cell-to-cell interactions and allows easier mobility through the surrounding extracellular matrix (ECM). Cell motility is also accelerated in response to specific ligands, such as scatter factor and autocrine motility factor.[7–10] Several oncogenes and signal transduction pathways are also commonly activated in these aggressive cells, including members of the Ras family, Src, Met, and downstream molecules such as Raf, MAPK 1/2, Rac/Rho, PI3-kinase, and focal adhesion kinase. Cellular invasive capacity is augmented in the metastatic phenotype by increased tumor cell secretion of matrix metalloproteinases (e.g., collagenases, gelatinases) and other enzymes that degrade the ECM.[9,10] In addition, metastatic cells often have downregulated secretion of tissue inhibitors of metalloproteinases (i.e., TIMP-1, TIMP-2), which further enhances their invasive potential and access to the vasculature. Loss of certain metastasis-suppressor genes has also been implicated in the metastatic phenotype, including nm23, KA11, KiSS1, PTEN, Maspin, and others.[9–11] Reduced expression of these genes removes inhibitory

Handbook of Neuro-Oncology Neuroimaging, Second Edition
http://dx.doi.org/10.1016/B978-0-12-800945-1.00003-3

© 2016 Elsevier Ltd. All rights reserved.

TABLE 1 Primary Sites of Metastatic Brain Tumors

Primary Tumor	Percentage (%)
Lung	50–60
Squamous cell	25–30
Adenocarcinoma	12–15
Small cell	10–13
Large cell	2
Breast	15–20
Melanoma	5–10
Gastrointestinal	4–6
Genitourinary	3–5
Unknown	4–8
Other	3–5

Data compiled from references 1–5.

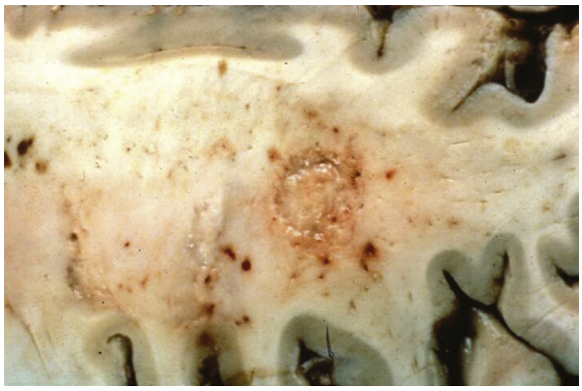


FIGURE 1 Gross specimen of brain demonstrating a metastatic brain tumor from a primary lung carcinoma, located at the gray–white junction. Note the well circumscribed nature of the lesion, with little infiltration into the surrounding brain.

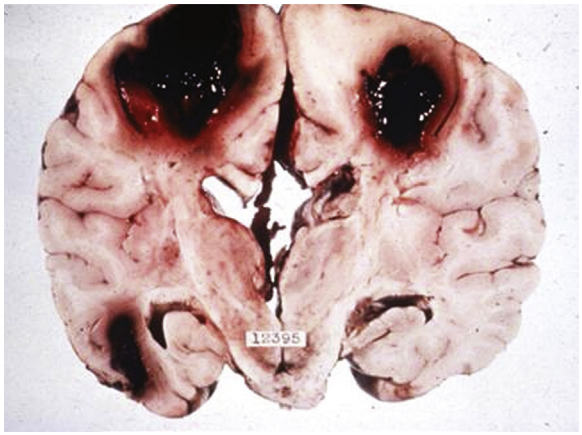


FIGURE 2 Gross specimen of brain demonstrating several metastatic brain tumors from malignant melanoma. Note the hemorrhagic nature of the lesions, along with significant surrounding edema and mass effect.

control over the formation of macroscopic metastases. A case control study of nonsmall cell lung cancer (NSCLCA) patients, with and without MBT, attempted to correlate the expression of epidermal growth factor receptor (EGFR), cyclooxygenase-2, and Bax with the risk of developing brain metastases.[12] It was found that expression of these biomarkers was similar for patients with and without MBT, and could not be used to predict the potential for developing an MBT. In addition, expression levels of EGFR, cyclooxygenase-2, and Bax did not correlate with patient survival in multivariate analysis.

Once the metastatic bolus of cells has traveled to the nervous system and has lodged within the brain, neoplastic angiogenesis is required for the tumor to grow to a clinically relevant size.[9,10,13,14] The angiogenic phenotype requires upregulation of angiogenic promoters such as vascular endothelial growth factor (VEGF), fibroblast growth factors (basic FGF, acidic FGF), angiopoietins (Ang-1, Ang-2), platelet-derived growth factor (PDGF), epidermal growth factor (EGF), transforming growth factors (TGFα and TGFβ), interleukins (IL-6, IL-8), and the various growth factor receptors (e.g., VEGFR, PDGFR, EGFR).[13,14] During the "angiogenic switch" to the metastatic phenotype, tumor cells also reduce secretion of angiogenesis inhibitors, such as thrombospondin-1, platelet factor-4, and interferons α and β.[13] This reduced concentration of inhibitory factors further "tips the balance" in the local environment to permit angiogenic activity within and around the tumor mass.

On macroscopic evaluation, MBT usually form rounded, discrete deposits in the brain parenchyma that are well circumscribed and demarcated from surrounding neural tissues (see Figures 1 and 2).[15,16] The most common locations for metastases are the frontal and temporal lobes, other lobes of the cerebrum, the cerebellum, and diencephalic region. The lesions can be single (25–35% of cases) or multiple (65–75% of cases), and may even present as a miliary pattern of numerous tiny masses. Primary tumors most likely to cause multifocal MBT include small cell and adenocarcinoma of the lung, melanoma, and choriocarcinoma. Single metastatic deposits are more likely to arise from renal cell, gastrointestinal, breast, prostatic, and uterine carcinomas. The tumor deposits may have areas of hemorrhage or necrosis, particularly in the center of large lesions. Primary tumors most likely to cause hemorrhagic brain metastases include melanoma, choriocarcinoma, lung carcinoma, and renal cell carcinoma. With or without hemorrhage, the tumor is usually surrounded by an extensive amount of vasogenic edema, which often seems out of proportion to the size of the mass, and contributes to regional mass effect.

On microscopic examination, the histological features of the MBT are usually similar, if not identical, to those of the primary neoplasm (see Figures 3 and 4).[15,16] In some

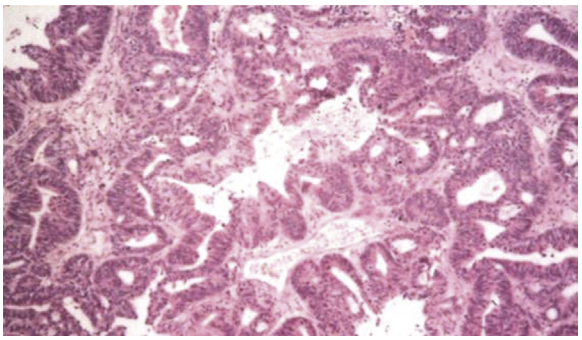


FIGURE 3 Microscopic preparation of tissue from a metastatic adenocarcinoma of the lung. Note that the metastatic tissue in the brain maintains the ability to form complete glandular structures. Hematoxylin and eosin staining (×200 magnification).

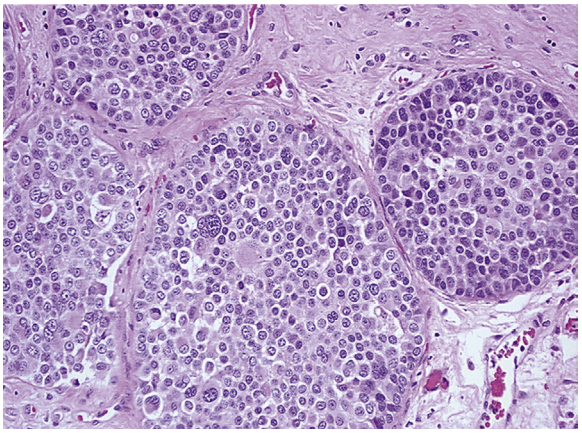


FIGURE 4 Microscopic preparation of tissue from a metastatic ductal carcinoma of the breast. Note tumor nodules are sharply demarcated from surrounding brain parenchyma, with no infiltration. Hematoxylin and eosin staining (×400 magnification).

cases, there may be a vigorous angiogenic response, with more prominent vascular proliferation and the formation of glomeruloid structures. In other tumors, there may be extensive necrosis, with only small regions of recognizable neoplastic tissue at the periphery of the lesion or adjacent to blood vessels. However, unlike glioblastoma multiforme, pseudopalisading of tumor nuclei around necrotic foci is very uncommon. The tumor mass will usually have well-defined borders, tending to displace adjacent brain parenchyma without significant infiltration. Areas of hemorrhage and gliosis are often noted. Initial review of the tissue morphology can often identify a major tumor category, such as metastatic carcinoma, melanoma, or lymphoma. For a more detailed determination of cellular differentiation and assignment to a specific histological category, immunocytochemical analysis is required.[15–17] The tissue is usually screened with a detailed antibody panel, which includes numerous cell- and tumor-specific markers (see Table 2). In some cases, further investigation with electron microscopy or molecular genetic techniques may be necessary to finalize the diagnosis.

TABLE 2 Immunocytochemical Staining Techniques Used in the Diagnosis of Metastatic Brain Tumors

INITIAL SCREENING PANEL
Epithelial membrane antigen
Cytokeratins
Glial fibrillary acidic protein
CELL-SPECIFIC MARKERS
Lung cancer: cytokeratin 7, surfactant
Breast cancer: cytokeratin 7, estrogen, and progesterone receptors
Gastrointestinal cancer: cytokeratin 20
Ovarian cancer: CA 125
Neuroendocrine: chromogranins, peptides
Thyroid cancer: thyroglobulin
Prostate cancer: prostate specific antigen, prostatic acid phosphatase
GERM CELL TUMORS
Placental alkaline phosphatase
SARCOMAS
Desmin
Smooth muscle actin
S-100
MALIGNANT MELANOMA
S-100
HMB45
MART-1
LYMPHOMA
CD45
CD3
CD20

Data derived from references 15–17.

SURGICAL THERAPY OF MBTs

In the modern era of neurosurgery, there is now an important role for surgical resection of MBT, in carefully selected patients.[18–21] Surgical removal should be considered in all patients with a magnetic resonance imaging (MRI)-documented solitary metastasis. Unfortunately, this constitutes only 25–35% of all patients. Among those patients with solitary lesions, only half will be appropriate for surgery because of factors such as inaccessibility of the tumor (e.g., brainstem, eloquent cortex), extensive systemic tumor burden, or other medical problems (e.g., cardiac ischemia, pulmonary insufficiency). Using second generation

image-guided, neuronavigation systems with frameless stereotaxy, patients with MBT can undergo aggressive surgical resection with significantly less risk of neurological injury.[22] In a review of 49 patients by Tan and Black, the use of image-guided craniotomy allowed for a gross total resection of the tumor and complete resolution of symptoms in 96% and 70% of the cohort, respectively. Neurological deterioration was only noted in two patients (3.6%), in whom significant deficits were present prior to surgery. The median survival for the entire group was 16.2 months, with a local recurrence rate of 16%. When neuronavigation and image-guidance is integrated with intraoperative MRI, the extent of surgical resection can be monitored and maximized in the operating room.[23,24] This often allows for a more complete resection of tumor and the potential for improved local control.

Class I evidence from two phase III trials is available to support the use of surgical resection in MBT patients.[18–21,25,26] In the seminal study by Patchell and colleagues, 48 patients with solitary MBT were randomly assigned to receive surgical resection plus irradiation or irradiation alone.[25] Local recurrence at the site of the original metastasis was significantly less frequent in the surgical cohort compared with the irradiation alone cohort (20% vs 52%; $p < 0.02$). Overall survival was significantly longer in the surgical group (median 40 weeks vs 15 weeks; $p < 0.01$). In addition, functional independence was maintained longer in the surgical cohort (median 38 weeks vs 8 weeks; $p < 0.005$). In a similar European phase III trial, 63 evaluable patients with solitary MBT were randomized to receive hyperfractionated irradiation (200 cGy × 2 per day; total of 4,000 cGy) with or without surgical resection.[26] The overall survival was significantly longer in the surgical cohort (median 10 months vs 6 months; $p = 0.04$). A survival advantage was also noted for the surgical group in the 12-month (41% vs 23%) and 24-month (19% vs 10%) overall survival rates. The effect of the surgical procedure on survival was most pronounced in the patient cohort with stable systemic disease, with significant differences in overall survival (median 12 months vs 7 months; $p = 0.02$), 12-month survival rate (50% vs 24%), and 24-month survival rate (27% vs 10%). For patients with active systemic disease, the surgical resection and irradiation alone cohorts had the same median overall survival (5 months). One negative phase III trial was reported by Mintz and coworkers in their review of 84 patients randomized to receive irradiation with or without surgical resection.[27] Overall survival was similar between the surgical and irradiation alone groups (median 5.6 months vs 6.3 months; $p = 0.24$). There was also no difference between treatment cohorts in the ability of patients to maintain Karnofsky Performance Status ≥70%. However, it should be mentioned that this study had several methodological shortcomings, including the fact that 73% of all patients had poorly controlled systemic disease, there was an unequal distribution of primary pathologies between treatment cohorts (i.e., more radioresistant colorectal cancer in the surgical group and more radiosensitive breast cancer in the irradiation alone group), and nonuniform calculation of survival times.[21]

There is also class II and III evidence to support the use of surgical resection for selected patients with a solitary MBT, mainly reflecting individual institutional experience.[18–22,28–32] This has been demonstrated in patients with solitary MBT from various types of primary tumors, including those from lung, breast, colon and rectum, melanoma, renal cell, and others. In general, these studies also demonstrate improved local control rates and longer survival in patients with solitary, accessible MBT that receive surgical resection followed by external beam irradiation.

For patients with multiple MBT, the use of surgical treatment is more controversial and remains unclear.[18–21] Some authors advocate the removal of all metastatic tumors, if the lesions are accessible and not located in eloquent regions of brain.[33] Using this approach with carefully selected patients, survival can be similar to that of patients undergoing surgery for solitary metastases. Other authors suggest limiting the use of surgical resection for the "dominant or symptomatic" lesion, if it is accessible.[20,32] The smaller and less symptomatic tumors can then be controlled by postoperative irradiation.

RADIATION THERAPY OF MBTs

Whole brain external beam irradiation (WBRT) remains the primary form of therapy for the majority of patients with brain metastases.[1–5,34–36] It is still the treatment of choice for tumors that are located in eloquent cortex or are too large or too numerous for surgical resection or radiosurgical approaches. Early randomized trials in the 1970s and 1980s by the Radiation Therapy Oncology Group (RTOG) and others evaluated variable dosing (10–54.4 Gy) and fractionation (1–34 fractions) schemes, in an attempt to determine the optimal therapeutic regimen.[35,36] The median survival across all studies ranged from 2.4 to 4.8 months, thereby proving that differences in dosing, timing, and fractionation schedules did not significantly influence the results in MBT patients. Objective tumor responses (i.e., complete response (CR), partial response (PR), minor response) were noted in approximately 60% of patients in the randomized RTOG trials. The most widely used WBRT regimen delivers a total of 30 Gy in 10 × 3 Gy fractions over 2 weeks. Although this dose has limited potential for

longterm tumor control, it is well tolerated and designed to minimize the neurotoxicity associated with WBRT. An analysis of RTOG clinical trial data suggests that this regimen can provide control of disease in roughly 50% of patients at 6 months. After receiving WBRT, most MBT patients note an improvement or stabilization of neurologic symptoms, including headache, seizures, impaired mentation, cerebellar dysfunction, and motor deficits.[35]

A randomized trial has also evaluated the utility of WBRT in the context of patients with a solitary MBT that have undergone surgical resection.[37] In this study, 95 patients with solitary MBT were treated with complete surgical resection and then randomized into a postoperative radiotherapy group or an observation group. The overall recurrence rate of MBT anywhere in the brain was significantly reduced in the radiotherapy group (18% vs 70%; $p < 0.001$). Postoperative WBRT was able to reduce the rate of MBT recurrence at the site of the original metastasis (10% vs 46%; $p < 0.001$) and at distant sites in the brain (14% vs 37%; $p < 0.01$). In addition, patients in the radiotherapy cohort were less likely to die of neurological causes than patients in the observation group (14% vs 44%; $p = 0.003$). However, there was no significant difference between groups in terms of the overall length of survival or the length of time that patients were able to maintain functional independence. This is not surprising as one would not expect WBRT to have any effect on the course of the systemic cancer.

Prophylactic cranial irradiation (PCI) is an "upfront" application of WBRT that is only appropriate for consideration in selected patients with lung cancer. The efficacy of PCI was first demonstrated in patients with small cell lung cancer (SCLCA), especially those with well-controlled systemic disease.[38,39] Initial reports demonstrated a survival benefit of 5.4% at 3 years, with a 25.3% reduction in the cumulative incidence of MBT in the cohort of patients achieving a complete systemic remission with chemotherapy.[38] A subsequent analysis of 505 patients that had participated in randomized trials further characterized the benefit of PCI in SCLCA patients.[39] The 5-year cumulative incidence of MBT as an isolated first site of relapse was 20% in the PCI cohort and 37% in control patients ($p < 0.001$). The overall 5-year incidence of MBT for the PCI and control groups was 43% and 59%, respectively (relative risk [RR] 0.50; $p < 0.001$). However, the effect on overall survival was modest, with 5-year rates for the PCI and control groups of 18% and 15%, respectively (RR 0.84; $p = 0.06$). Presumably, this is because the majority of SCLCA patients ultimately die of systemic metastases, an issue not addressed by PCI. PCI has also been investigated in patients with NSCLCA, but with less compelling evidence of benefits.[40,41] Although there does appear to be a reduction in the incidence of MBT in the PCI cohorts, no survival benefit has been observed. This view is consistent with a Cochrane Review of the use of PCI in NSCLCA patients.[42] The authors concluded that there was insufficient evidence at the time to recommend the use of PCI in clinical practice, and that it should only be offered in the context of a clinical trial.

Stereotactic radiosurgery (SRS) is a method of delivering focused irradiation to the boundaries of a tumor (i.e., conformal dosing), in a single or few fractions, using great precision.[34–36,43–47] SRS has become an important therapeutic option for brain metastases for several reasons, including the fact that most MBT are spherical and small at the time of diagnosis, the degree of infiltration into surrounding brain is usually limited, the gray–white matter junction is considered a relatively "noneloquent" area of the brain, and improved local control in the brain may extend patient survival. The treatment is most often administered using a Gamma Knife® (i.e., ^{60}Co sources); however, linear accelerator (e.g., Cyberknife®) and proton beam units are also used and demonstrate comparable local control and complication rates. SRS is most effective for tumors ≤3 cm in diameter. However, some authors recommend treatment of tumors up to 4 cm in diameter. Typical doses are in the range of 15–20 Gy to the margins of the tumor, with higher doses administered at the center of the mass. Optimal dosing will depend on the size of the tumor, previous exposure to irradiation, and proximity to delicate neural structures (e.g., optic chiasm).

There are two reports that provide class I evidence for the efficacy of SRS in the context of a boost to WBRT.[48,49] In the first study from the University of Pittsburgh, 27 patients with two to four MBT were randomized to receive WBRT (30 Gy over 12 fractions) plus SRS (tumor margin dose of 16 Gy) or WBRT alone.[48] Local control was improved by the use of the SRS boost, with local failure rates at 1 year of 8% for the combined treatment group and 100% for the WBRT alone group. The median time to local failure was 36 months for the WBRT plus SRS cohort and 6 months for the WBRT alone group ($p = 0.0005$). In addition, median time to overall brain failure (local or distant) was longer for the combined treatment cohort compared with the WBRT alone group (34 months vs 5 months; $p = 0.002$). However, the addition of the SRS boost did not significantly influence overall survival between the two groups (11 months vs 7.5 months, respectively; $p = 0.22$). Again, this lack of effect on overall survival could simply reflect the effects of systemic metastases in these patients. In a similar study by the RTOG (RTOG 9508), 333 patients with one to three MBT were randomized to receive either WBRT (37.5 Gy over 15 fractions) or WBRT plus an SRS boost of 15–24 Gy, depending on tumor size.[49] Local control at 1 year was significantly better for the SRS group compared with the WBRT alone group (82% vs 71%; $p = 0.01$). In addition, time to local progression was extended in the combined treatment cohort ($p = 0.0132$). Overall median survival was similar between groups;

however, for patients with a single MBT, median survival was longer in the WBRT plus SRS cohort (6.5 months vs 4.9 months; $p = 0.0393$). The Karnofsky Performance Status was more likely to be stable or improved at 6 months follow-up in the WBRT plus SRS group (43% vs 27%; $p = 0.03$). This is consistent with the multivariate analysis, which demonstrated improved survival in patients with RPA class I disease ($p < 0.0001$).

There are numerous reports in the literature describing class II and III evidence supporting the use of SRS for treatment of MBT.[34–36,43–47] A review of the larger trials (i.e., 100 or more patients) would suggest that SRS is as effective as, if not more effective than, WBRT.[50–61] In most of the studies, the median survival ranged between 5.5 and 13.5 months, with overall local control rates of 85–95%. The increase in local control rates did not translate into improved survival, with most patients dying of systemic disease progression. Several factors have been found to influence the degree of local control, including primary tumor histology (e.g., melanoma vs lung carcinoma), tumor volume, tumor location, presentation (e.g., new vs recurrent), and pattern of MRI enhancement (e.g., homogeneous vs heterogeneous vs ring). Some authors recommend the use of SRS as the primary, upfront mode of irradiation in high-performance patients with well-controlled systemic disease, instead of WBRT.[50–61] However, this view is not supported by the conclusions of an American Society for Radiation Oncology (ASTRO) meta-analysis of SRS treatment of MBT.[62] The ASTRO recommendations are to advise an SRS boost to WBRT in selected patients with one to four newly diagnosed MBT. The omission of WBRT results in significantly lower rates of local and distant brain control.

CHEMOTHERAPY OF MBTs

Chemotherapy has become a more viable option for the treatment of MBT, especially for recurrent disease.[63–69] The prior reluctance to use chemotherapy stemmed from concerns about the ability of chemotherapy drugs to cross the blood–brain barrier (BBB) and penetrate tumor cells, the intrinsic chemoresistance of metastatic disease, and the high probability of early death from systemic progression. However, animal data suggests that metastatic tumors that strongly enhance computed tomography (CT) or MRI have an impaired BBB and will allow entry of chemotherapeutic drugs.[63,65] In addition, systemic resistance to a given drug does not always preclude sensitivity of the metastasis within the brain.[63] Several types of MBTs are relatively chemosensitive and may respond, including breast cancer, small cell lung cancer, NSCLCA, germ cell tumors, and ovarian carcinoma.

The most common approach to chemotherapy for brain metastases is to administer it upfront, before or during conventional WBRT or SRS.[70–79] Several authors have demonstrated that combination regimens given intravenously can be active in this context. The most frequently used agents included cisplatin (CDDP), etoposide (VP16), and cyclophosphamide (CTX). In a series of 19 patients with small cell lung cancer and brain metastases, Twelves and coworkers used intravenous (IV) CTX, vincristine, and VP16 every 3 weeks before any form of irradiation.[70] Ten of the 19 patients (53%) had a radiological or clinical response. In nine patients, there was CT evidence of tumor shrinkage; while in one patient there was neurological improvement, without neuroimaging follow-up. The mean time to progression (TTP) was 22 weeks, with a median overall survival of 28 weeks. Cocconi and colleagues used upfront IV cisplatin and etoposide every 3 weeks for 22 evaluable patients with MBT from breast carcinoma.[71]

There were 12 objective responses, for an overall objective response rate of 55%. The median TTP was 25 weeks overall and 40 weeks in the objective response cohort. The overall median survival was 58 weeks. The same authors have expanded their series to include 89 patients with MBT from breast, nonsmall lung carcinoma, and malignant melanoma.[72] Objective responses were noted in the breast and lung cohorts. None of the patients with melanoma had objective responses. The overall objective response rate was 30% (34/89). The median TTP was 15 weeks, with a median survival for the cohort of 27 weeks. Similar responses have been noted in series of patients with MBT from lung and breast carcinoma.[73–79] However, although objective responses were noted in many of these studies, they did not translate into improvements in patient survival.

Topotecan is a semisynthetic camptothecan derivative that selectively inhibits topoisomerase I in the S phase of the cell cycle.[80] It demonstrates excellent penetration of the BBB in primate animal models and humans. Summating the data of more than 60 patients in several European studies of single agent topotecan, the objective response rates have been encouraging, with 30–60% of patients demonstrating CR or PR.[81–84] Topotecan is also being investigated in combination with radiotherapy and other cytotoxic chemotherapy agents, such as temozolomide. A phase I trial evaluated the tolerability of temozolomide (50–200 mg/m^2) and topotecan (1–1.5 mg/m^2), given daily for 5 days every 28 days.[85] Twenty-five patients with systemic solid tumors were treated. Toxicity was mainly hematological, with frequent neutropenia and thrombocytopenia. Three patients were noted to have a PR.

Temozolomide is an imidazotetrazine derivative of the alkylating agent dacarbazine with activity against systemic and central nervous system (CNS) malignancies.[65,86–88] The drug undergoes chemical conversion

at physiological pH to the active species 5-(3-methyl-1-triazeno)imidazole-4-carboxamide. Temozolomide exhibits schedule-dependent antineoplastic activity by interfering with DNA replication through the methylation of DNA at the following sites: N^7-guanine (70%), N^3-adenine (9.2%), and O^6-guanine (5%). Several reports have suggested activity of single agent temozolomide against MBT, with occasional objective responses.[89,90] Temozolomide is also under investigation as a radiation sensitizer, including a randomized phase II trial by Antonadou and associates.[91] In this study, 52 newly diagnosed MBT patients (lung and breast) were treated with either WBRT alone (40 Gy) or WBRT plus conventional temozolomide. The addition of temozolomide improved the objective response rate compared with WBRT alone (CR 38%, PR 58% vs CR 33%, PR 33%). In addition, neurologic improvement during treatment was more pronounced in the cohort of patients receiving chemotherapy. A similar randomized phase II trial by Verger and colleagues treated 82 patients with MBT (mostly lung and breast) using either combined WBRT (30 Gy) and temozolomide (75 mg/m^2/day during irradiation, plus two cycles of conventional adjuvant dosing) or WBRT alone.[92] The objective response rate and overall survival were similar between treatment groups. However, there was a significantly higher rate of progression-free survival at 90 days in the combined treatment cohort (72% vs 54%, $p = 0.03$). In addition, the percentage of patients dying from the MBT was lower in the chemotherapy arm (41% vs 69%; $p = 0.03$). Temozolomide has also been shown to have activity, as a single agent and in combination with other drugs (e.g., cisplatin, doxetaxel, thalidomide), against MBT from malignant melanoma.[93–96] A review of 21 published clinical trials using temozolomide for the treatment of progressive brain metastases from solid tumors concluded that the drug had modest activity as a single agent, as well as in combination with RT and other anticancer drugs.[97]

Interstitial or localized delivery of chemotherapy drugs (i.e., BCNU) into the resection cavity of resected tumors has been well established for high-grade gliomas, and is also under investigation for brain metastases.[98–100] Animal studies by Ewend and coworkers suggested that BCNU was more effective in this setting than carboplatin or camptothecin, and that local control of tumors and prolonged survival was better in the setting of radiation therapy (RT) + BCNU wafer implantation, compared with RT alone or BCNU wafers alone.[99] Early phase I and II trials using BCNU wafers in metastatic brain tumor patients were promising, with 100% local control of newly diagnosed and resected tumors, with or without adjuvant RT.[99] Brem and colleagues reported the use of BCNU wafer placement in a series of 59 patients with up to three brain metastases, with detailed neurocognitive follow-up.[101] All of the patients underwent resection of a solitary or "dominant" lesion (oligometastatic, two to three lesions), followed by wafer placement in the resection cavities, with radiosurgical treatment of any small nonresected tumors. In all but one patient, neurocognitive function improved in the domains of memory, executive function, and fine motor skills. The wafers were well tolerated, without any irreversible serious adverse reactions. The local recurrence rate was 28% at 1-year follow-up.

In an effort to improve dose intensity to MBT, some authors have given some or all of the chemotherapy drugs by the intraarterial (IA) route.[63,102–107] There are several advantages to IA administration of chemotherapy instead of the conventional IV route, including augmentation of the peak concentration of drug in the region of the tumor and an increase in the local area under the concentration–time curve.[102] Pathologically, MBTs are excellent candidates for IA approaches, because they tend to be well circumscribed and noninfiltrative.[16] In addition, MBT almost always enhance on MRI imaging, indicating excellent arterial vascularization and impairment of the BBB. Pharmacologic studies using animal models of IA and IV drug infusion have shown that the IA route can increase the intratumoral concentration of a given agent at least threefold to fivefold.[108,109] For chemosensitive tumors, improving the intratumoral concentrations of drug should augment tumor cell killing and the ability to achieve objective responses.[102] Initial applications of IA chemotherapy to MBT involved the use of BCNU and cisplatin.[103–107] Although objective responses were noted in patients with lung and breast tumors, significant neurotoxicity occurred (e.g., seizures, confusion). Other reports have used carboplatin as the primary IA agent, and have resulted in similar objective response rates, with significantly less neurotoxicity.[110–112]

The expansion of knowledge regarding the molecular biology of neoplasia and the metastatic phenotype has led to intense development of therapeutic strategies designed to exploit this new information.[113] Several targets of therapeutic intervention have been developed, including growth factor receptors and their tyrosine kinase activity, disruption of aberrant internal signal transduction pathways, inhibition of excessive matrix metalloproteinase activity, downregulation of cell cycle pathways, and manipulation of the apoptosis pathways. The most promising approach thus far has been the development of small molecule drugs or monoclonal antibodies to the major growth factor receptors (e.g., PDGFR, EGFR, Her2, CD20).[114–118] Monoclonal antibody agents such as rituximab (i.e., Rituxan®) and trastuzumab (i.e., Herceptin®) have proven to be clinically active against nonHodgkin lymphoma and breast cancer, respectively. Several small molecule inhibitors of the tyrosine kinase activity of the EGFR (e.g., geftinib, erlotinib) are under clinical evaluation in phase I trials of patients with solid

tumors.[115–117] Similar efforts are underway to develop agents that can target the tyrosine kinase activity of the PDGFR and the ras signaling pathway.[117,118] Other agents under development will be designed to target downstream effectors, such as Raf, MAPK, Rac/Rho, and angiogenesis. Targeted approaches to treatment of brain metastases have shown some evidence of activity.[119,120] An early report using imatinib, a tyrosine kinase inhibitor with activity against C-KIT and PDGFR, describes a 75-year-old male with a C-KIT positive gastrointestinal stromal tumor that developed neurological deterioration and gait difficulty.[121] An MRI scan demonstrated leptomeningeal disease with brain infiltration and edema. After treatment with imatinib mesylate (400 mg bid) for 2 months, his neurological function and gait improved. A follow-up MRI scan revealed complete resolution of the meningeal and intraparenchymal abnormalities. Several authors have described case reports of the use of gefitinib, an oral tyrosine kinase inhibitor of EGFR, in patients with MBT from NSCLCA.[122–126] A few of these initial patients had objective responses, including CR, that were durable. These early reports lead Ceresoli and colleagues to perform a prospective phase II trial of gefitinib in patients with MBT from NSCLCA.[127] Forty-one consecutive patients were treated with gefitinib (250 mg/day); 37 had received prior chemotherapy and 18 had undergone WBRT. There were four patients with a PR and seven with stable disease. The overall progression-free survival was only 3 months. However, the median duration of responses in the patients with a PR was an encouraging 13.5 months.

Bevacizumab (BEV), a humanized monoclonal antibody against VEGF, has been shown to have a potent antiangiogenesis effect in many systemic solid tumors, as well as in GBM.[119,120] There has been concern about using BEV in patients with MBT, due to the overall increased risk of hemorrhagic events. However, reports suggest that the risk of intratumoral hemorrhage is similar for MBT that have received BEV compared with those that have not received BEV.[128] In addition, a report by Zustuvich and coworkers shows that BEV has efficacy as a primary treatment modality against MBT.[129] In a series of 18 patients with mostly lung and renal adenocarcinoma and MBT, BEV was used as part of the primary chemotherapy regimen. There was a 60% partial response rate of the MBT, with another 40% with tumor stabilization. The progression-free survival of the cohort was 14 months, with an overall survival of 15 months. Clinical trials are underway to investigate the efficacy and safety of using BEV for patients with MBT from non-small lung cancer, breast cancer, and melanoma.

Patients with HER2-positive breast cancer and MBT are also being evaluated for molecular therapeutic approaches.[119,120] Several agents have been under investigation due to their potent antiHER2 activity, including trastuzumab and lapatinib. Thus far, lapatinib seems to be the most promising approach, especially in combination with capecitabine.[130,131] However, even when used as a single agent, lapatinib can lead to objective tumor shrinkage, as shown in a Japanese report.[132]

Molecular therapeutic approaches have also been applied to patients with MBT from malignant melanoma, with some success.[119,120,133,134] BRAF inhibitors have proven active against melanoma tumors harboring the V600 mutation, including vemurafenib, which is now approved by the Food and Drug Administration (FDA).[133–135] In a pilot study using vemurafenib in patients with symptomatic MBT, there was a 42% overall partial response rate for systemic and CNS disease, with another 38% with stable disease. Of 19 patients with measurable MBT, 3 (16%) achieved a partial response, while 7 (37%) showed a >30% reduction in tumor size.[135] A similar study evaluated the efficacy of dabrafenib, another BRAF inhibitor, in a series of 172 patients with melanoma and MBT, harboring either Val600Glu or Val600Lys BRAF mutations.[136] In patients with MBT that were newly diagnosed or had received prior therapy, dabrafenib was able to achieve objective responses of intracranial disease in 31–39% of the cases. Another approach has been to target the interaction between cytotoxic T lymphocyte-associated antigen (CTLA-4) and its ligands B7.1 and B7.2, thereby enhancing antitumor cellular immunity and reducing tolerance to tumor-associated antigens.[133,134] The FDA approved the monoclonal antibody, ipilimumab, target CTLA-4 and has been shown to be clinically active against primary and metastatic melanoma.[133,134,137] In addition, ipilimumab has been able to induce durable responses in melanoma metastatic to the brain.

Acknowledgments

The authors would like to thank Nicole Ghaffari and Shawna Huckell for research assistance. Dr. Newton was supported in part by National Cancer Institute grant, CA 16058 and the Dardinger Neuro-Oncology Center Endowment Fund.

References

1. Alexandru D, Bola DA, Linskey ME. Epidemiology of central nervous system metastases. *Prog Neurol Surg*. 2012;25:13–29.
2. Owonikoko TK, Arbiser J, Zelnak A, et al. Current approaches to the treatment of metastatic brain tumours. *Nat Rev Clin Oncol*. 2014;11:203–222. http://dx.doi.org/10.1038/nrclinonc.2014.25.
3. Langer CJ, Mehta MP. Current management of brain metastases, with a focus on systemic options. *J Clin Oncol*. 2005;23:6207–6219.
4. Bajaj GK, Kleinberg L, Terezakis S. Current concepts and controversies in the treatment of parenchymal brain metastases: improved outcomes with aggressive management. *Cancer Investig*. 2005;23:363–376.
5. Lassman AB, DeAngelis LM. Brain metastases. *Neurol Clin N Am*. 2003;21:1–23.

6. Wilhem I, Molnar J, Fazakas C, et al. Role of the blood–brain barrier in the formation of brain metastases. *Int J Mol Sci*. 2013;14:1383–1411.
7. Langley RR, Fidler IJ. The biology of brain metastasis. *Clin Chem*. 2013;59:180–189.
8. Yan J, Yang Q, Huang Q. Metastasis suppressor genes. *Histol Histopathol*. 2013;28:285–292.
9. Webb CP, Vande Woude GF. Genes that regulate metastasis and angiogenesis. *J Neuro-Oncol*. 2000;50:71–87.
10. Nathoo N, Chalhavi A, Barnett GH, Toms SA. Pathobiology of brain metastases. *J Clin Pathol*. 2005;58:237–242.
11. Yoshida BA, Sokoloff MM, Welch DR, Rinker-Schaeffer CW. Metastasis-suppressor genes: a review and perspective on an emerging field. *J Natl Cancer Inst*. 2000;92:1717–1730.
12. Milas I, Komaki R, Hachiya T, et al. Epidermal growth factor receptor, cyclooxygenase-2, and BAX expression in the primary non-small cell lung cancer and brain metastases. *Clin Cancer Res*. 2003;9:1070–1076.
13. Hanahan D, Folkman J. Patterns of emerging mechanisms of the angiogenic switch during tumorigenesis. *Cell*. 1996;86:353–364.
14. Beckner ME. Factors promoting tumor angiogenesis. *Cancer Investig*. 1999;17:594–623.
15. Metastatic tumours. In: Ironside JW, Moss TH, Louis DN, Lowe JS, Weller RO, eds. *Diagnostic Pathology of Nervous System Tumours*. Vol. 12. London: Churchill Livingstone; 2002:319–341.
16. Pekmezci M, Perry A. Neuropathology of brain metastases. *Surg Neurol Int*. 2013;4(suppl 4):S245–S255.
17. Perry A, Parisi JE, Kurtin PJ. Metastatic adenocarcinoma to the brain: an immunohistochemical approach. *Hum Pathol*. 1997; 28:938–943.
18. Brem S, Panattil JG. An era of rapid advancement: diagnosis and treatment of metastatic brain cancer. *Neurosurg*. 2005;57: S4-S5–S4-S9.
19. Vogelbaum MA, Suh JH. Resectable brain metastases. *J Clin Oncol*. 2006;24:1289–1294.
20. Hatiboglu MA, Wildrick DM, Sawaya R. The role of surgical resection in patients with brain metastases. *Ecancermedicalscience*. April 2013;18(7):308. http://dx.doi.org/10.3332/ecancer.2013.308.
21. Schodel P, Schebesch KM, Brawanski A, Proescholdt MA. Surgical resection of brain metastases – impact on neurological outcome. *Int J Mol Sci*. 2013;14:8708–8718.
22. Tan TC, Black PM. Image-guided craniotomy for cerebral metastases: techniques and outcomes. *Neurosurgery*. 2003;53:82–90.
23. Albayrak B, Samdani AF, Black PM. Intra-operative magnetic resonance imaging in neurosurgery. *Acta Neurochir (Wien)*. 2004; 146:543–556.
24. Nimsky C, Ganslandt O, von Keller B, Romstöck J, Fahlbusch R. Intraoperative high-field-strength MR imaging: implementation and experience in 200 patients. *Radiology*. 2004;233:67–78.
25. Patchell RA, Tibbs PA, Walsh JW, et al. A randomized trial of surgery in the treatment of single metastases to the brain. *New Engl J Med*. 1990;322:494–500.
26. Vecht CJ, Haaxma-Reiche H, Noordijk EM, et al. Treatment of single brain metastasis: radiotherapy alone or combined with neurosurgery? *Ann Neurol*. 1993;33:583–590.
27. Mintz AH, Kestle J, Rathbone MP, et al. A randomized trial to assess the efficacy of surgery in addition to radiotherapy in patients with a single cerebral metastasis. *Cancer*. 1996;78:1470–1476.
28. Arbit E, Wronski M, Burt M, Galicich JH. The treatment of patients with recurrent brain metastases. A retrospective analysis of 109 patients with nonsmall cell lung cancer. *Cancer*. 1995;76:765–773.
29. Wronski M, Arbit E, McCormick B. Surgical treatment of 70 patients with brain metastases from breast cancer. *Cancer*. 1997; 80:1746–1754.
30. Wronski M, Arbit E. Resection of brain metastases from colorectal carcinoma in 73 patients. *Cancer*. 1999;85:1677–1685.
31. O'Neill BP, Iturria NJ, Link MJ, Pollock BE, Ballman KV, O'Fallon JR. A comparison of surgical resection and stereotactic radiosurgery in the treatment of solitary brain metastases. *Int J Rad Oncol Biol Phys*. 2003;55:1169–1176.
32. Paek SH, Audu PB, Sperling MR, Cho J, Andrews DW. Reevaluation of surgery for the treatment of brain metastases: review of 208 patients with single or multiple brain metastases treated at one institution with modern neurosurgical techniques. *Neurosurgery*. 2005;56:1021–1034.
33. Bindal RK, Sawaya R, Leavens ME, Lee JJ. Surgical treatment of multiple brain metastases. *J Neurosurg*. 1993;79:210–216.
34. Berk L. An overview of radiotherapy trials for the treatment of brain metastases. *Oncology*. 1995;9:1205–1212.
35. McTyre E, Scott J, Chinnalyan P. Whole brain radiotherapy for brain metastasis. *Surg Neurol Int*. 2013;4(suppl 4):S236–S244.
36. Khuntia D, Brown P, Li J, Mehta MP. Whole-brain radiotherapy in the management of brain metastasis. *J Clin Oncol*. 2006;24:1295–1304.
37. Patchell RA, Tibbs PA, Regine WF, et al. Postoperative radiotherapy in the treatment of single metastases to the brain: a randomized trial. *JAMA*. 1998;280:1485–1489.
38. Aupérin A, Arriagada R, Pignon JP, et al. Prophylactic cranial irradiation for patients with small-cell lung cancer in complete remission. Prophylactic Cranial Irradiation Overview Collaborative Group. *New Engl J Med*. 1999;341:476–484.
39. Arriagada R, Le Chevalier T, Rivière A, et al. Patterns of failure after prophylactic cranial irradiation in small-cell lung cancer: analysis of 505 randomized patients. *Ann Oncol*. 2002;13:748–754.
40. Laskin JJ, Sandler AB. The role of prophylactic cranial radiation in the treatment of non-small-cell lung cancer. *Clin Adv Hem Oncol*. 2003;1:731–740.
41. Gore EM. Prophylactic cranial irradiation for patients with locally advanced non-small-cell lung cancer. *Oncology*. 2003;17:775–779.
42. Lester JF, MacBeth FR, Coles B. Prophylactic cranial irradiation for preventing brain metastases in patients undergoing radical treatment for non-small-cell lung cancer: a Cochrane Review. *Int J Rad Oncol Biol Phys*. 2005;63:690–694.
43. Halasz LM, Rockhill JK. Stereotactic radiosurgery and stereotactic radiotherapy for brain metastases. *Surg Neurol Int*. 2013;4(suppl 4): S185–S191.
44. Serizawa T, Higuchi Y, Nagano O. Stereotactic radiosurgery for brain metastases. *Neurosurg Clin N Am*. 2013;24:597–603.
45. Sheehan J, Niranjan A, Flickinger JC, Kondziolka D, Lunsford LD. The expanding role of neurosurgeons in the management of brain metastases. *Surg Neurol*. 2004;62:32–41.
46. McDermott MW, Sneed PK. Radiosurgery in metastatic brain cancer. *Neurosurgery*. 2005;57: S4-S45–S4-S53.
47. Bhatnagar AK, Flickinger JC, Kondziolka D, Lunsford LD. Stereotactic radiosurgery for four or more intracranial metastases. *Int J Rad Oncol Biol Phys*. 2006;64:898–903.
48. Kondziolka D, Patel A, Lunsford LD, Kassam A, Flickinger JC. Stereotactic radiosurgery plus whole brain radiotherapy versus radiotherapy alone for patients with multiple brain metastases. *Int J Rad Oncol Biol Phys*. 1999;45:427–434.
49. Andrews DW, Scott CB, Sperduto PW, et al. Whole brain radiation therapy with or without stereotactic radiosurgery boost for patients with one to three brain metastases: phase III results of the RTOG 9508 randomised trial. *Lancet*. 2004;363:1665–1672.
50. Flickinger JC, Kondziolka D, Lunsford LD, et al. A multi-institutional experience with stereotactic radiosurgery for solitary brain metastases. *Int J Rad Oncol Biol Phys*. 1994;28:797–802.
51. Alexander E, Moriarty TM, Davis RB, et al. Stereotactic radiosurgery for the definitive, noninvasive treatment of brain metastases. *J Natl Cancer Inst*. 1995;87:34–40.
52. Gerosa M, Nicolato A, Severi F, et al. Gamma knife radiosurgery for intracranial metastases: from local control to increased survival. *Stereotact Funct Neurosurg*. 1996;66:184–192.

53. Joseph J, Adler JR, Cox RS, Hancock SL. Linear accelerator-based stereotactic radiosurgery for brain metastases: the influence of number of lesions on survival. *J Clin Oncol*. 1996;14:1085–1092.
54. Pirzkall A, Debus J, Lohr F, et al. Radiosurgery alone or in combination with whole-brain radiotherapy for brain metastases. *J Clin Oncol*. 1998;16:3563–3569.
55. Chen JC, Petrovich Z, O'Day S, et al. Stereotactic radiosurgery in the treatment of metastatic disease to the brain. *Neurosurgery*. 2000;47:268–279.
56. Hoffman R, Sneed PK, McDermott MW, et al. Radiosurgery for brain metastases from primary lung carcinoma. *Cancer J*. 2001;7:121–131.
57. Gerosa M, Nicolato A, Foroni R, et al. Gamma knife radiosurgery for brain metastases: a primary therapeutic option. *J Neurosurg*. 2002;97:515–524.
58. Petrovich Z, Yu C, Giannotta SL, O'Day S, Apuzzo MLJ. Survival and pattern of failure in brain metastases treated with stereotactic gamma knife radiosurgery. *J Neurosurg*. 2002;97:499–506.
59. Hasegawa T, Kondziolka D, Flickinger JC, Germanwala A, Lunsford LD. Brain metastases treated with radiosurgery alone: an alternative to whole brain radiotherapy? *Neurosurgery*. 2003; 52:1318–1326.
60. Lutterbach J, Cyron D, Henne K, Ostertag CB. Radiosurgery followed by planned observation in patients with one to three brain metastases. *Neurosurgery*. 2003;52:1066–1073.
61. Muacevic A, Kreth FW, Tonn JC, Wowra B. Stereotactic radiosurgery for multiple brain metastases from breast carcinoma. *Cancer*. 2004;100:1705–1711.
62. Mehta MP, Tsao MN, Whelan TJ, et al. The American Society for Therapeutic Radiology and Oncology (ASTRO) evidence-based review of the role of radiosurgery for brain metastases. *Int J Rad Oncol Biol Phys*. 2005;63:37–46.
63. Newton HB. Chemotherapy of brain metastases. In: Newton HB, ed. *Handbook of Brain Tumor Chemotherapy*. Vol. 35. London: Elsevier Medical Publishers/Academic Press; 2006:475–489.
64. Newton HB. Chemotherapy for the treatment of metastatic brain tumors. *Expert Rev Anticancer Ther*. 2002;2:495–506.
65. Lee SH. Role of chemotherapy on brain metastasis. *Prog Neurol Surg*. 2012;25:110–114.
66. Tosoni A, Lumachi F, Brandes AA. Treatment of brain metastases in uncommon tumors. *Expert Rev Anticancer Ther*. 2004;4:783–793.
67. van den Bent MJ. The role of chemotherapy in brain metastases. *Eur J Cancer*. 2003;39:2114–2120.
68. Schuette W. Treatment of brain metastases from lung cancer: chemotherapy. *Lung Cancer*. 2004;45(suppl 2):S253–S257.
69. Bafaloukos D, Gogas H. The treatment of brain metastases in melanoma patients. *Cancer Treat Rev*. 2004;30:515–520.
70. Twelves CJ, Souhami RL, Harper PG, et al. The response of cerebral metastases in small cell lung cancer to systemic chemotherapy. *Br J Cancer*. 1990;61:147–150.
71. Cocconi G, Lottici R, Bisagni G, et al. Combination therapy with platinum and etoposide of brain metastases from breast carcinoma. *Cancer Investig*. 1990;8:327–334.
72. Franciosi V, Cocconi G, Michiarava M, et al. Front-line chemotherapy with cisplatin and etoposide for patients with brain metastases from breast carcinoma, nonsmall lung carcinoma, or malignant melanoma. A prospective study. *Cancer*. 1999;85:1599–1605.
73. Bernardo G, Cuzzoni Q, Strada MR, et al. First-line chemotherapy with vinorelbine, gemcitabine, and carboplatin in the treatment of brain metastases from non-small-cell lung cancer: a phase II study. *Cancer Investig*. 2002;20:293–302.
74. Rosner D, Nemoto T, Lane WW. Chemotherapy induces regression of brain metastases in breast carcinoma. *Cancer*. 1986;58:832–839.
75. Boogerd W, Dalesio O, Bais EM, Van Der Sande JJ. Response of brain metastases from breast cancer to systemic chemotherapy. *Cancer*. 1992;69:972–980.
76. Robinet G, Thomas P, Breton JL, et al. Results of a phase III study of early versus delayed whole brain radiotherapy with concurrent cisplatin and vinorelbine combination in inoperable brain metastasis of non-small-cell lung cancer: Groupe Français de Pneumo-Cancérologie (GFPC) protocol 95-1. *Ann Oncol*. 2001;12:59–67.
77. Postmus PE, Haaxma-Reiche H, Smit EF, et al. Treatment of brain metastases of small-cell lung cancer: comparing teniposide and teniposide with whole-brain radiotherapy – a phase III study of the European Organization for the Research and Treatment of Cancer Lung Cancer Cooperative Group. *J Clin Oncol*. 2000;18:3400–3408.
78. Ushio Y, Arita N, Hayakawa T, et al. Chemotherapy of brain metastases from lung carcinoma: a controlled randomized study. *Neurosurgery*. 1991;28:201–205.
79. Guerrieri M, Wong K, Ryan G, Millward M, Quong G, Ball DL. A randomized phase III study of palliative radiation with concomitant carboplatin for brain metastases from non-small cell carcinoma of the lung. *Lung Cancer*. 2004;46:107–111.
80. Slichenmyer WJ, Rowinsky EK, Donehower RC, Kaufmann SH. The current status of camptothecin analogues as antitumor agents. *J Natl Cancer Inst*. 1993;85:271–291.
81. Ardizzoni A, Hansen H, Dombernowsy P, et al. Topotecan, a new active drug in the second-line treatment of small-cell lung cancer: a phase II study in patients with refractory and sensitive disease. *J Clin Oncol*. 1997;15:2090–2096.
82. Korfel A, Oehm C, von Pawel J, et al. Response to topotecan of symptomatic brain metastases of small-cell lung cancer also after whole-brain irradiation: a multicentre phase II study. *Eur J Cancer*. 2002;38:1724–1729.
83. Oberhoff C, Kieback DG, Würstlein R, et al. Topotecan chemotherapy in patients with breast and brain metastases: results of a pilot study. *Onkologie*. 2001;24:256–260.
84. Wong ET, Berkenblit A. The role of topotecan in the treatment of brain metastases. *Oncology*. 2004;9:68–79.
85. Eckardt JR, Martin KA, Schmidt AM, White LA, Greco AO, Needles BM. A phase I trial of IV topotecan in combination with temozolomide daily time 5 every 28 days. *Proc ASCO*. 2002;21:83b.
86. Newlands ES, Stevens MFG, Wedge SR, et al. Temozolomide: a review of its discovery, chemical properties, pre-clinical development and clinical trials. *Cancer Treat Rev*. 1997;23:35–61.
87. Hvisdos KM, Goa KL. Temozolomide. *CNS Drugs*. 1999;12:237–243.
88. Stupp RK, Gander M, Leyvraz S, Newlands E. Current and future developments in the use of temozolomide for the treatment of brain tumors. *Lancet Oncol*. 2001;2:552–560.
89. Abrey LE, Olson JD, Raizer JJ, et al. A phase II trial of temozolomide for patients with recurrent or progressive brain metastases. *J Neuro-Oncol*. 2001;53:259–265.
90. Christodoulou C, Bafaloukos D, Kosmidos P, et al. Phase II study of temozolomide in heavily pretreated cancer patients with brain metastases. *Ann Oncol*. 2001;12:249–254.
91. Antonadou D, Paraskaveidis M, Sarris N, et al. Phase II randomized trial of temozolomide and concurrent radiotherapy in patients with brain metastases. *J Clin Oncol*. 2002;20:3644–3650.
92. Verger E, Gil M, Yaya R, et al. Temozolomide and concomitant whole brain radiotherapy in patients with brain metastases: a phase II randomized trial. *Int J Rad Oncol Biol Phys*. 2005;61:185–191.
93. Biasco G, Pantaleo MA, Casadei S. Treatment of brain metastases of malignant melanoma with temozolomide. *New Engl J Med*. 2001;345:621–622.
94. Agarwala SS, Kirdwood JM, Gore M, et al. Temozolomide for the treatment of brain metastases associated with metastatic melanoma: a phase II study. *J Clin Oncol*. 2004;22:2101–2107.
95. Bafaloukos D, Tsoutsos D, Fountzilas G, et al. The effect of temozolomide-based chemotherapy in patients with cerebral metastases from melanoma. *Melanoma Res*. 2004;14:289–294.

96. Hwu WJ, Raizer JJ, Panageas KS, Lis E. Treatment of metastatic melanoma in the brain with temozolomide and thalidomide. *Lancet Oncol*. 2001;2:634–635.
97. Zhu W, Zhou L, Qian JQ, et al. Temozolomide for treatment of brain metastases: a review of 21 clinical trials. *World J Clin Oncol*. 2014;5:19–27.
98. Haque RM, Amundson E, Dorsi M, Brem H. Interstitial chemotherapy and polymer-drug delivery. In: Newton HB, ed. *Handbook of Brain Tumor Chemotherapy*. Vol. 19. London: Elsevier Medical Publishers/Academic Press; 2006:274–294.
99. Attenollo F, Raza SM, Dimeco F, Olivi A. Chemotherapy for brain tumors with polymer drug delivery. *Handbk Clin Neurol*. 2012;104:339–353.
100. Abel TJ, Ryken T, Lesniak MS, Gabikian P. Gliadel for brain metastasis. *Surg Neurol Int*. 2013;4(suppl 4):S289–S293.
101. Brem S, Meyers CA, Palmer G, et al. Preservation of neurocognitive function and local control of 1 to 3 brain metastases treated with surgery and carmustine wafers. *Cancer*. 2013;119:3830–3838.
102. Stewart DJ. Pros and cons of intra-arterial chemotherapy. *Oncology*. 1989;3:20–26.
103. Yamada K, Bremer AM, West CR, et al. Intra-arterial BCNU therapy in the treatment of metastatic brain tumor from lung carcinoma. A preliminary report. *Cancer*. 1979;44:2000–2007.
104. Madajewicz S, West CR, Park HC, et al. Phase II study – intra-arterial BCNU therapy for metastatic brain tumors. *Cancer*. 1981;47: 653–657.
105. Cascino TL, Byrne TN, Deck MDF, Posner JB. Intra-arterial BCNU in the treatment of metastatic tumors. *J Neuro-Oncol*. 1983;1:211–218.
106. Madajewicz S, Chowhan N, Iliya A, et al. Intracarotid chemotherapy with etoposide and cisplatin for malignant brain tumors. *Cancer*. 1991;67:2844–2849.
107. Newton HB. Intra-arterial chemotherapy. In: Newton HB, ed. *Handbook of Brain Tumor Chemotherapy*. Vol. 17. London: Elsevier Medical Publishers/Academic Press; 2006:247–261.
108. Barth RF, Yang W, Rotaru JH, et al. Boron neutron capture therapy of brain tumors: enhanced survival following intracarotid injection of either sodium borocaptate or boronophenylalanine with or without blood–brain barrier disruption. *Cancer Res*. 1997;57:1129–1136.
109. Kroll RA, Neuwelt EA. Outwitting the blood–brain barrier for therapeutic purposes: osmotic opening and other means. *Neurosurgery*. 1998;42:1083–1100.
110. Gelman M, Chakares D, Newton HB. Brain tumors: complications of cerebral angiography accompanied by intra-arterial chemotherapy. *Radiology*. 1999;213:135–140.
111. Newton HB, Stevens C, Santi M. Brain metastases from fallopian tube carcinoma responsive to intra-arterial carboplatin and intravenous etoposide: a case report. *J Neuro-Oncol*. 2001;55:179–184.
112. Newton HB, Snyder MA, Stevens C, et al. Intra-arterial carboplatin and intravenous etoposide for the treatment of brain metastases. *J Neuro-Oncol*. 2003;61:35–44.
113. Garrett MD, Workman P. Discovering novel chemotherapeutic drugs for the third millennium. *Eur J Cancer*. 1999;35:2010–2030.
114. Livitzki A, Gazit A. Tyrosine kinase inhibition: an approach to drug development. *Science*. 1995;267:1782–1788.
115. Gibbs JB. Anticancer drug targets: growth factors and growth factor signaling. *J Clin Investig*. 2000;105:9–13.
116. Dillman RO. Monoclonal antibodies in the treatment of malignancy: basic concepts and recent developments. *Cancer Investig*. 2001;19:833–841.
117. Hao D, Rowinsky EK. Inhibiting signal transduction: recent advances in the development of receptor tyrosine kinase and ras inhibitors. *Cancer Investig*. 2002;20:387–404.
118. Newton HB. Molecular neuro-oncology and the development of "targeted" therapeutic strategies for brain tumors. Part 1 – growth factor and ras signaling pathways. *Expert Rev Anticancer Ther*. 2003;3:595–614.
119. Davies MA. Targeted therapy for brain metastases. *Adv Pharmacol*. 2012;65:109–142.
120. Soffietti R, Trevisan E, Ruda R. Targeted therapy in brain metastasis. *Curr Opin Oncol*. 2012;24:679–686.
121. Brooks BJ, Bani JC, Fletcher CDM, Demeteri GD. Response of metastatic gastrointestinal stromal tumor including CNS involvement to imatinib mesylate (STI-571). *J Clin Oncol*. 2002;20:870–872.
122. Cappuzzo F, Ardizzoni A, Soto-Parra H, et al. Epidermal growth factor receptor targeted therapy by ZD 1839 (Iressa) in patients with brain metastases from non-small cell lung cancer (NSCLC). *Lung Cancer*. 2003;41:227–231.
123. Cappuzzo F, Calandri C, Bartolini S, Crinò LZD. 1839 in patients with brain metastases from non-small cell lung cancer (NSCLC): report of four cases. *Br J Cancer*. 2003;89:246–247.
124. Poon ANY, Ho SSM, Yeo W, Mok TSK. Brain metastases responding to gefitinib alone. *Oncology*. 2004;67:174–178.
125. Ishida A, Kanoh K, Nishisaka T, et al. Gefitinib as a first line of therapy in non-small cell lung cancer with brain metastases. *Intern Med*. 2004;43:718–720.
126. Katz A, Zalewski P. Quality-of-life benefits and evidence of antitumor activity for patients with brain metastases treated with gefitinib. *Br J Cancer*. 2003;89:S15–S18.
127. Ceresoli GL, Cappuzzo F, Gregorc V, Bartolini S, Crinò L, Villa E. Gefitinib in patients with brain metastases from non-small cell lung cancer: a prospective trial. *Ann Oncol*. 2004;15:1042–1047.
128. Besse B, Lasserre SF, Compton P, et al. Bevacizumab safety in patients with central nervous system metastases. *Clin Cancer Res*. 2010;16:169–278.
129. Zustovich F, Ferro A, Lombardi G, et al. Bevacizumab as frontline treatment of brain metastases from solid tumors: a case series. *Anticancer Res*. 2013;33:4061–4065.
130. Azim HA, Azim Jr HA. Systemic treatment of brain metastases in HER2-positive breast cancer: current status and future directions. *Future Oncol*. 2012;8:135–144.
131. Larsen PB, Kumler I, Nielsen DL. A systematic review of trastuzumab and lapatinib in the treatment of women with brain metastases from HER2-positive breast cancer. *Cancer Treat Rev*. 2013;39:720–727.
132. Iwata H, Narabayashi M, Ito Y, et al. A phase II study of lapatinib for brain metastases in patients with HER2-overexpressing breast cancer following trastuzumab based systemic therapy and cranial radiotherapy: subset analysis of Japanese patients. *Int J Clin Oncol*. 2013;18:621–628.
133. Fonkem E, Uhlmann EJ, Floyd SR, et al. Melanoma brain metastasis: overview of current management and emerging targeted therapies. *Expert Rev Neurother*. 2012;12:1207–1215.
134. Lyle M, Long GV. The role of systemic therapies in the management of melanoma brain metastases. *Curr Opin Oncol*. 2014; 26:222–229.
135. Dummer R, Goldinger SM, Turtschi CP, et al. Vemurafenib in patients with BRAF(V600) mutation-positive melanoma with symptomatic brain metastases: final results of an open-label pilot study. *Eur J Cancer*. 2014;50:611–621.
136. Long GV, Trefzer U, Davies MA, et al. Dabrafenib in patients with Val600Glu or Val600Lys BRAF-mutant melanoma metastatic to the brain (BREAK-MB): a multicentre, open-label, phase 2 trial. *Lancet Oncol*. 2012;13:1087–1095.
137. Margolin KA, Di Giacomo AM, Maio M. Brain metastasis in melanoma: clinical activity of CTLA-4 antibody therapy. *Semin Oncol*. 2010;37:468–472.

CHAPTER

4

Overview of Spinal Cord Tumor Epidemiology

Herbert B. Newton

Division of Neuro-Oncology, Departments of Neurology and Neurosurgery, Dardinger Neuro-Oncology Center, Wexner Medical Center at The Ohio State University and James Cancer Hospital and Solove Research Institute, Columbus, OH, USA

Primary spinal cord tumors (SCT) are a group of neoplasms that arise from the parenchyma of the spinal cord or from tissues that comprise or are contained within the surrounding spinal canal, including meninges, nerves, fat, bone, and blood vessels.[1–4] Secondary SCT arise as metastatic deposits, within the spinal cord parenchyma or surrounding tissues, from a primary lesion outside of the central nervous system (CNS; see Chapters 6 and 7). Because of their location near delicate spinal cord structures that mediate motor control and sensation, even slowly growing benign SCT may cause severe neurologic sequelae. This chapter will provide an overview of the epidemiology of primary and metastatic tumors of the spinal cord, with a review of pathology and treatment to follow in the next two chapters.

EPIDEMIOLOGY OF PRIMARY SCT

Primary SCT are classified according to their cell of origin and the location of the mass in relation to the spinal cord parenchyma: either intramedullary or extramedullary (i.e., developing from cells that are intrinsic or extrinsic, respectively, to the spinal cord). Extramedullary SCT are further subdivided into intradural and extradural (i.e., developing inside or outside, respectively, the fibrous dural covering of the spinal cord; while remaining extrinsic to the spinal cord itself). In adults, more than 85% of SCT are extramedullary (see Table 1). Of this group, the intradural tumors are most frequent, with meningiomas and schwannomas comprising 55–60% of the total (see Table 2).[1–4] Less common extramedullary tumors are sarcomas, exophytic ependymomas and astrocytomas, epidermoids, and dermoids. Intramedullary tumors are much less common, accounting for roughly 10–12% of all SCT in adults (see Table 1).[1–4] Ependymomas and astrocytomas are responsible for more than 80% of these cases (see Table 2). In children, the distribution of SCT is different from that in adults, with a greater percentage of intramedullary tumors, especially astrocytomas and ependymomas (see Table 3).[5–7] Of the extramedullary tumors that do develop in children, neuroblastomas are common; meningiomas and neurofibromas are much less frequently diagnosed.

SCT are relatively rare, comprising 0.5% of all newly diagnosed tumors and 5–12% of all primary CNS neoplasms, with an annual incidence of approximately 1 case per 100,000 population per year.[1–4,8–13] The majority of SCT occur between the ages of 20 and 50 years, but can arise at any age. When all cases are taken into account (i.e., antemortem and postmortem), the incidence of SCT appears to increase with age, such that the age groups of 0–24, 25–44, 45–64, and 65 years and older have rates of 0.7, 1.0, 2.8, and 3.6 per 100,000 person-years, respectively.[8] If only antemortem cases are included, the incidence drops off dramatically for patients over 60 years of age. The prevalence of SCT is much lower than that of primary brain tumors, with a ratio of 1:4 to 1:8. Men and women develop SCT with equal overall incidence, although specific tumor types are known to be more common in women (i.e., meningiomas) and men (i.e., ependymomas). The incidence of SCT does not appear to be related to social class, occupation, or marital status.[11] However, among nonHispanic white patients, an increased incidence has been observed in Jewish females and those of either gender born in Eastern Europe.[11] The anatomical distribution of primary SCT is uneven, with 50–55% of tumors arising in the thoracic spinal canal, 25–30% involving the lumbosacral region, and the remaining 15–25% affecting the cervical spinal canal and foramen magnum.

http://dx.doi.org/10.1016/B978-0-12-800945-1.00004-5

© 2016 Elsevier Ltd. All rights reserved.

TABLE 1 Anatomic Distribution of Primary Spinal Cord Tumors in Adults

Location	%
Intramedullary	10–12
Extramedullary	88–90
Extradural	25
Intradural	60
Cauda equina	5

Adapted from Refs 1–4.

TABLE 2 Clinically Important Primary Spinal Cord Tumors in Adults

Extramedullary	(%)	Intramedullary	(%)
Schwannoma	29	Ependymoma	55
Meningioma	25	Astrocytoma	30
Exophytic ependymoma	13	Hemangioblastoma	5
Sarcoma	12	Other	5–10
		Mixed glioma	
Exophytic astrocytoma	6	Oligodendroglioma	
		Dermoid	
Other	10–15	Epidermoid	
Epidermoid		Teratoma	
Dermoid		**Total**	**100**
Teratoma			
Lipoma			
Vascular tumors			
Chordoma			
Total	**100**		

Adapted from Refs 1–4.

TABLE 3 Clinically Important Primary Spinal Cord Tumors in Children

Extramedullary	%	Intramedullary	%
Extradural		Astrocytoma	15
Neuroblastoma	16	Ependymoma	13
Ganglioneuroma	3	Hemangioma	3
Osseous	2	Ganglioglioma	1
Other	5	Other	5
Intradural		Lipoma	
Dermoid	9	Oligodendroglioma	
Teratoma	8	Epidermoid	
Neurofibroma	7	Dermoid	
Lipoma	4		
Meningioma	3		
Schwannoma	2		

Adapted from Refs 5–7.

The most common extramedullary tumors are peripheral nerve sheath tumors, which include schwannomas, neurofibromas, and meningiomas.[1–4,8–11] In patients with sporadic disease (i.e., do not have neurofibromatosis [NF1, NF2]), schwannomas are the most frequently diagnosed peripheral nerve sheath tumors of the spine.[14–16] They present as a solitary lesion attached to dorsal sensory branches. When schwannomas occur as a component of NF2, they are more likely to be multifocal and spread throughout the neuraxis. Schwannomas have an incidence rate similar to or slightly higher than meningiomas; however, some reports suggest they are significantly more common than meningiomas.[15] Schwannomas account for approximately one-quarter of all SCT and 25–35% of all intradural, extramedullary tumors. Specific incidence estimates range between 0.3 and 0.5 cases per 100,000 population per year. In most studies, the incidence is similar for males and females, although a few scattered reports suggest these tumors are more common in males (61% vs 39%).[14]

Meningiomas of the spine account for 12–15% of all meningiomas and for 20–25% of all primary SCT, making them the second most common spinal neoplasm.[1,2,8–11,17–19] They are usually noted in the thoracic region (80%), but may occur in the cervical (17%) and lumbosacral (3%) spine as well. The tumor is intradural and often noted near the nerve root exit sites, but does not directly involve the nerve root. In up to 15% of cases, there can be an extradural component of the mass. The mass generally presents as a solitary lesion; multiple tumors are only noted in 1–2% of patients, sometimes in association with neurofibromatosis. Spinal meningiomas have a strong predilection for female patients, with a female to male ratio of up to 5:1 in some series. However, the age of onset and age distribution is equivalent between males and females. The median age at diagnosis is in the mid-50s, with the majority of cases occurring between 40 and 70 years of age. Although spinal meningiomas are rare in children, younger patients can develop these tumors and often have a more aggressive course.[20] In this younger cohort, the tumors have a stronger predilection for the cervical spine and are more often associated with predisposing factors (e.g., NF2, radiation exposure). Spinal trauma and exposure to ionizing radiation are both considered to be risk factors for developing a spinal meningioma.[18] However, the risk has been more firmly established in patients with intracranial meningiomas.

Spinal ependymomas most often arise as an intraparenchymal mass or as an intradural, extramedullary lesion in the lumbosacral spine.[1,2,8–11] They comprise approximately 35% of all CNS ependymomas and 13–15% of all spinal tumors. Ependymomas are the most common intramedullary SCT in adults and account for 55–60% of all cases.[21–23] The tumor can develop at any age, but has a typical onset in the middle adult years. Although some studies show an equal distribution between male and female patients, the majority of reports suggest a male predominance. Intramedullary ependymomas have a predilection for the cervical spinal cord, such that 60–70% of tumors arise from or extend into this region. Syringomyelia is associated with ependymomas of the spinal parenchyma in two-thirds of cases, especially those arising in the cervical cord. In 40–45% of patients, intradural ependymomas originate from the conus medullaris (30%) or filum terminale (65%) within the lumbosacral thecal sac, and are considered to be extramedullary tumors.[2,21,24] The vast majority of these lesions are of the myxopapillary histological subtype. Myxopapillary ependymomas account for approximately 15–18% of all spinal ependymomas and tend to affect young adults, with a mean age of onset of 36 years. Similar to their intramedullary counterparts, ependymomas of the cauda equina region tend to have a male predominance, with a male to female ratio of 1.7:1 to 2:1.[24]

Spinal astrocytomas are relatively uncommon and only account for 3–4% of all CNS astrocytomas, with an incidence of 0.8–2.5 cases per 100,000 population per year.[1,2,12,13,25] In adults, they comprise 7–10% of all primary SCT and 30–35% of all intramedullary SCT. In children, they tend to be more common and are the most frequently diagnosed intramedullary tumor, comprising at least 90% of primary SCT in patients less than 10 years of age and up to 60% of primary SCT in adolescents.[5,7] Although spinal astrocytomas can occur at any age, they usually affect young adults, with an onset of symptoms between 30 and 35 years of age. Gender distribution between male and female patients is fairly even in some series, while others would suggest a slight male predominance.[25] The tumor arises in the cervical spinal cord or cervicothoracic region in approximately 60% of patients. Lesions of the lower thoracic and lumbosacral cord, conus medullaris, and filum terminale are less common. Tumors spanning the entire spinal cord (i.e., holocord tumors) can occur, but are very rare. In up to 40% of cervical and upper thoracic cases, there may be an associated syringomyelia.

Hemangioblastomas are slowly growing, highly vascular tumors of the spinal cord that can occur sporadically (75–80%) or in association with von-Hippel-Lindau Syndrome (VHL; 20–25%).[2,13,26,27] The tumor is usually a solitary mass in sporadic cases but can be multifocal in patients with VHL. Hemangioblastomas account for 2–8% of all intramedullary SCT and are the third most common intramedullary tumor. They can arise anywhere within the spinal cord, but have a predilection for the cervical and thoracic regions. This predilection for the cervical cord is more pronounced in patients with VHL. The mass is entirely intramedullary in 30% of cases, but more often will have intramedullary and extramedullary components (50–55%). In 15–20% of cases the lesion is located completely within the extramedullary compartment. The tumor usually affects young adults, with an age of onset between 35 and 40 years; it is relatively uncommon in pediatric patients. In patients with VHL, the age of onset tends to be 5–10 years earlier. Males are affected more often than females, with a male-to-female ratio of 1.7:1.

Spinal cord oligodendrogliomas are uncommon intramedullary tumors that represent 1–2% of all primary SCT and 1.5–2% of all CNS oligodendrogliomas.[1–7,28–30] They usually arise in the thoracic (30%) and cervical (25%) portions of the cord, but can involve multiple regions (e.g., thoraco-lumbar, 15%; holocord, 7.5%) and the lumbar spine (5%). The tumor is most often diagnosed in young adults; however, children and adolescents can be affected. There appears to be an even distribution between male and female patients.

Other less common neoplasms that may involve the spine include lipomas, maldevelopmental tumors (e.g., teratoma, dermoids, epidermoids), paragangliomas, chordomas, chondrosarcomas, sarcomas, and lymphomas.[1–7,11,31,32] Lipomas account for 1% of all intramedullary tumors and are the most common dysembryogenic lesion of the spine.[33] They are not true neoplasms and most likely arise from an inclusion of mesenchymal tissue within the spine. Dermoids, epidermoids, and teratomas can be intramedullary or extramedullary, but tend to involve the thoracolumbar and lumbar spine. Epidermoid tumors are more common in male patients. Paragangliomas are tumors of neural crest origin that usually arise from the filum terminale or cauda equina. Chordomas of the spine account for 4% of all spinal tumors and 11–15% of all CNS chordomas.[34] They are most often diagnosed in the fourth decade of life and have a predilection for males, with a male-to-female ratio of 2:1. Chondrosarcomas of the spine account for 4–8% of all chondrosarcomas and have a male-to-female ratio of 1.5:1.[35] They involve the true vertebrae in 30–35% of patients (usually thoracic), and affect the sacrum in another third. The age at presentation ranges between 45 and 50 years in most series. Primary sarcomas of the spine are very rare and account for 0.7% of all CNS tumors and 5.6% of all SCT.[36] Lymphomas of the spine are usually of B cell origin and can arise within the spinal cord parenchyma or extradurally; 13% will have bony involvement.[32] The onset of symptoms is typically in the fifth to seventh decade.

EPIDEMIOLOGY OF INTRAMEDULLARY SPINAL CORD METASTASES

Intramedullary spinal cord metastases (ISCM) are an uncommon neurological complication of systemic cancer.[37] Compared with neoplastic epidural spinal cord compression (see Chapter 7), ISCM are diagnosed much less frequently, with an incidence approximately one-sixteenth as high.[37–39] ISCM are estimated to affect between 0.5% and 2.0% of all patients with cancer, representing only 8.5% of all CNS metastases, and comprising 1–3% of all intramedullary SCT.[38–41] However, the true incidence may be somewhat higher, since ISCM are noted in 2–4% of all cancer patients studied at autopsy, suggesting that many patients with this complication never become symptomatic.

ISCM can arise from any primary systemic neoplasm, but are due to lung cancer in 50–60% of cases (see Table 4).[38–41] Small cell lung carcinoma (SCLC) accounts for approximately half of these cases, but any of the other histological subtypes can be involved. Overall, ISCM are estimated to occur in up to 5% of patients with SCLC, but in only around 1% of patients with nonSCLC.[40,42,43] Other primary malignancies with a tendency to metastasize to the spinal cord include breast cancer (10–13% of all ISCM), melanoma (9%), renal cell carcinoma (5–9%), lymphoma (5%), colorectal cancer (3%) and other gastrointestinal malignancies, thyroid carcinoma (2%), and ovarian cancer (1–2%).[44–47] The presence of ISCM suggests an advanced form of cancer and a biologically aggressive disease. For example, at the time of diagnosis of ISCM, 55–60% of patients will already have been diagnosed with brain metastases and another 25% will have leptomeningeal metastases.[38]

TABLE 4 Percentage of Intramedullary Spinal Cord Metastases by Primary Tumor Site

Primary Type	Percentage
Lung	50–60
SCLC	50–55
NonSCLC	45–50
Breast	10–13
Melanoma	9
Renal cell	5–9
Lymphoma	5
Colorectal and GI	3
Thyroid	2
Ovarian	1–2

Abbreviations: SCLC, small cell lung carcinoma; GI, gastrointestinal.
Adapted from Refs 38–47.

The mean age at presentation of ISCM in the literature is 58 years, with a range of 38–78 years.[38–41] Males are affected more often than females (64% vs 46%), but there does not appear to be any predilection for specific ethnic or racial groups. ISCM are distributed fairly evenly along the spinal cord parenchyma in most studies, affecting the cervical, thoracic, and lumbar regions in 24%, 22%, and 28% of cases, respectively. However, some reports would suggest a mild preponderance of involvement in the conus medullaris as, for example, the study by Schiff and O'Neill, in which the conus accounted for over half the cases.[38] The metastatic deposits are solitary in the majority of patients, with multifocal disease noted in approximately 15%.[40] ISCM usually occurs in the context of a well-established diagnosis of cancer. However, in some patients, ISCM can be the initial presentation of systemic cancer. This has been noted in up to 22.5% of ISCM patients in some reports.[38]

Acknowledgments

The authors would like to thank Nicole Ghaffari and Shawna Huckell for research assistance. Dr. Newton was supported in part by National Cancer Institute grant, CA 16058 and the Dardinger Neuro-Oncology Center Endowment Fund.

References

1. Engelhart HH, Villano JL, Porter KR, et al. Clinical presentation, histology, and treatment in 430 patients with primary tumors of the spinal cord, spinal meninges, or caude equina. *J Neurosurg Spine*. 2010;13:67–77.
2. Chamberlain MC, Tredway TL. Adult primary intradural spinal cord tumors: a review. *Curr Neurol Neurosci Rep*. 2011;11:320–328.
3. Mechtler LL, Nandigam K. Spinal cord tumors: new views and future directions. *Neurol Clin*. 2013;31:241–268.
4. Waters JD, Peran EM, Ciacci J. Malignancies of the spinal cord. *Adv Exp Med Biol*. 2012;760:101–113.
5. Hsu W, Jallo GI. Pediatric spinal tumors. *Handb Clin Neurol*. 2013; 112:959–965.
6. Baysefer A, Akay KM, Izci Y, Kayali H, Timurkaynak E. The clinical and surgical aspects of spinal tumors in children. *Pediatr Neurol*. 2004;31:261–266.
7. Auguste KI, Gupta N. Pediatric intramedullary spinal cord tumors. *Neurosurg Clin N Am*. 2006;17:51–61.
8. Sasanelli F, Beghi E, Kurland KT. Primary intraspinal neoplasms in Rochester, Minnesota 1935–1981. *Neuroepidemiol*. 1983;2:156–163.
9. Fogelholm R, Uutela T, Murros K. Epidemiology of central nervous system neoplasms. A regional survey in central Finland. *Acta Neurol Scand*. 1984;69:129–136.
10. Helseth A, Mork SJ. Primary intraspinal neoplasms in Norway, 1955 to 1986. A population-based survey of 467 patients. *J Neurosurg*. 1989;71:842–845.
11. Preston-Martin S. Descriptive epidemiology of primary tumors of the spinal cord and spinal meninges in Los Angeles County 1972–1985. *Neuroepidemiol*. 1990;9:106–111.
12. Preston-Martin S. Epidemiology of primary CNS neoplasms. *Neurol Clin*. 1996;14:273–290.
13. Tihan T, Chi JH, McCormick PC, Ames CP, Parsa AT. Pathologic and epidemiologic findings of intramedullary spinal cord tumors. *Neurosurg Clin N Am*. 2006;17:7–11.

14. Conti P, Pansini G, Mouchaty H, Capuano C, Conti R. Spinal neurinomas: retrospective analysis and long-term outcome of 179 consecutively operated cases and review of the literature. *Surg Neurol*. 2004;61:35–44.
15. Jinnai T, Hoshimaru M, Koyama T. Clinical characteristics of spinal nerve sheath tumors: analysis of 149 cases. *Neurosurgery*. 2005;6: 510–515.
16. Waldron J, Weinstein RP. Nerve sheath tumors of the spine. In: Berger MS, Prados MD, eds. *Textbook of Neuro-Oncology*. Vol. 63. Philadelphia: Elsevier Saunders; 2005:485–488.
17. Sandalcioglu IE, Hunold A, Muller O, et al. Spinal meningiomas: critical review of 131 surgically treated patients. *Eur Spine J*. 2008;17:1035–1041.
18. Cohen-Gadol AA, Krauss WE. Spinal meningiomas. In: Berger MS, Prados MD, eds. *Textbook of Neuro-Oncology*. Vol. 64. Philadelphia: Elsevier Saunders; 2005:489–492.
19. Peker S, Cerci A, Ozgen S, Isik N, Kalelioglu M, Pamir MN. Spinal meningiomas: evaluation of 41 patients. *J Neurosurg Sci*. 2005;49:7–11.
20. Cohen-Gadol AA, Zikel OM, Koch CA, Scheithauer BW, Krauss WE. Spinal meningiomas in patients younger than 50 years of age: a 21-year experience. *J Neurosurg*. 2003;98:258–263.
21. Schwartz TH, McCormick PC. Intramedullary ependymomas: clinical presentation, surgical treatment strategies and prognosis. *J Neuro-Oncol*. 2000;47:211–218.
22. Chang UK, Choe WJ, Chung SK, Chung CK, Kim HJ. Surgical outcome and prognostic factors of spinal intramedullary ependymomas in adults. *J Neuro-Oncol*. 2002;57:133–139.
23. Schwartz TH, Parsa AT, McCormick PC. Intramedullary ependymomas. In: Berger MS, Prados MD, eds. *Textbook of Neuro-Oncology*. Vol. 66. Philadelphia: Elsevier Saunders; 2005:497–500.
24. Parney IF, Parsa AT. Myxopapillary ependymomas. In: Berger MS, Prados MD, eds. *Textbook of Neuro-Oncology*. Vol. 65. Philadelphia: Elsevier Saunders; 2005:493–496.
25. Babu R, Karikari IO, Owens TR, Bagley CA. Spinal cord astrocytomas: a modern 20-year experience at a single institution. *Spine*. 2014;39:533–540.
26. Lonser RR, Oldfield EH. Spinal cord hemangioblastomas. *Neurosurg Clin N Am*. 2006;17:37–44.
27. Wanebo JE, Lonser RR, Glenn GM, Oldfield EH. The natural history of hemangioblastomas of the central nervous system in patients with von Hippel-Lindau disease. *J Neurosurg*. 2003;98:82–94.
28. Fortuna A, Celli P, Palma L. Oligodendrogliomas of the spinal cord. *Acta Neurochir*. 1980;52:305–329.
29. Pagni CA, Canavero S, Gaidolfi E. Intramedullary "holocord" oligodendroglioma: case report. *Acta Neurochir*. 1991;113:96–99.
30. Fountas KN, Karampelas I, Nikolakakos LG, Troup EC, Robinson JS. Primary spinal cord oligodendroglioma: case report and review of the literature. *Childs Nerv Syst*. 2005;21:171–175.
31. Waldron J, Ames C. Benign tumors of the spine. In: Berger MS, Prados MD, eds. *Textbook of Neuro-Oncology*. Vol. 65. Philadelphia: Elsevier Saunders; 2005:511–516.
32. Chou D, Gökaslan Z. Malignant primary tumors of the vertebral column. In: Berger MS, Prados MD, eds. *Textbook of Neuro-Oncology*. Vol. 70. Philadelphia: Elsevier Saunders; 2005:517–520.
33. Lee M, Rezai AR, Abbott R, et al. Intramedullary spinal cord lipomas. *J Neurosurg*. 1995;82:394–400.
34. Bjornsson J, Wold LE, Ebersold MJ, Laws ER. Chordoma of the mobile spine. A clinicopathologic analysis of 40 patients. *Cancer*. 1993;71:735–740.
35. York JE, Berk RH, Fuller GN, et al. Chondrosarcoma of the spine: 1954 to 1997. *J Neurosurg*. 1997;90:73–78.
36. Merimsky O, Lepechoux C, Terrier P, et al. Primary sarcomas of the central nervous system. *Oncology*. 2000;58:210–214.
37. Newton HB. Neurological complications of systemic cancer. *Am Fam Phys*. 1999;59:878–886.
38. Sung WS, Sung MJ, Chan JH, et al. Intramedullary spinal cord metastases: a 20-year institutional experience with a comprehensive literature review. *World Neurosurg*. 2013;79:576–584.
39. Rykken JB, Diehn FE, Hunt CH, et al. Intramedullary spinal cord metastases: MRI and relevant clinical features from a 13-year institutional case series. *Am J Neuroradiol*. 2013;34:2043–2049.
40. Chi JH, Parsa AT. Intramedullary spinal cord metastasis: clinical management and surgical considerations. *Neurosurg Clin N Am*. 2006;17:45–50.
41. Kalayci M, Cagavi F, Gul S, et al. Intramedullary spinal cord metastases: diagnosis and treatment – an illustrated review. *Acta Neurochir (Wien)*. 2004;146:1347–1354.
42. Nikolaou M, Koumpou M, Mylonakis N, Karabelis A, Pectasides D, Kosmas C. Intramedullary spinal cord metastases from atypical small cell lung cancer: a case report and literature review. *Cancer Investig*. 2006;24:46–49.
43. Potti A, Abdel-Raheem M, Levitt R, et al. Intramedullary spinal cord metastases (ISCM) and non-small cell lung carcinoma (NSCLC): clinical patterns, diagnosis and therapeutic considerations. *Lung Cancer*. 2001;31:319–323.
44. Villegas AE, Guthrie TH. Intramedullary spinal cord metastasis in breast cancer: clinical features, diagnosis, and therapeutic consideration. *Breast J*. 2004;10:532–535.
45. Conill C, Sanchez M, Puig S, et al. Intramedullary spinal cord metastases of melanoma. *Melanoma Res*. 2004;14:431–433.
46. Taniura S, Tatebayashi K, Watanabe K, Watanabe T. Intramedullary spinal cord metastasis from gastric cancer. Case report. *J Neurosurg (Spine 1)*. 2000;93:145–147.
47. Fakih M, Schiff D, Erlich R, Logan TF. Intramedullary spinal cord metastasis (ISCM) in renal cell carcinoma: a series of six cases. *Ann Oncol*. 2001;12:1173–1177.

CHAPTER

5

Overview of Pathology and Treatment of Primary Spinal Cord Tumors

Herbert B. Newton

Division of Neuro-Oncology, Departments of Neurology and Neurosurgery, Dardinger Neuro-Oncology Center, Wexner Medical Center at The Ohio State University and James Cancer Hospital and Solove Research Institute, Columbus, OH, USA

The epidemiology of primary spinal cord tumors (SCT) was reviewed in detail in Chapter 4. In this chapter, we will provide an overview of the classification, pathology, and treatment of common primary SCT. Primary SCT will be diagnosed in approximately 1500–2000 new patients in 2015 and are associated with significant morbidity and mortality.[1–6] Of the estimated one patient per 100,000 population that will develop a primary SCT in 2015 in the USA, the majority will have an intradural, extramedullary, low-grade neoplasm such as a schwannoma, meningioma, or neurofibroma. Less often, the tumor will be intramedullary and arise from the spinal cord parenchyma, such as an ependymoma or astrocytoma. Although high-grade SCT derived from parenchymal cells or surrounding tissues are occasionally noted, they are infrequent compared with their counterparts in the brain.

PATHOLOGY OF SELECTED PRIMARY SCT

Similar to the situation discussed in Chapter 2 for primary brain tumors, specific knowledge of SCT pathology is necessary before therapeutic strategies can be finalized. In addition to assisting with treatment decisions, tumor classification and grade can provide important prognostic information for patients and families. This chapter will follow the World Health Organization (WHO) classification that separates nervous system tumors into different nosological entities and assigns a grade of I–IV to each lesion (see Table 1), with grade I being biologically benign and grade IV being biologically the most malignant and having the worst prognosis.[7,8] Within the WHO classification, tumors of neuroepithelial and meningeal origin, as well as tumors of the cranial and spinal nerves, are the most clinically relevant groups when considering primary SCT pathology.

In general, the histologic features of primary SCT are similar to the same type of tumor when it occurs in the brain or intracranial cavity.[7,8] However, the distribution of histological variants and grade may be different for a given tumor type when it develops in the spine as opposed to the brain. Tumors arising in the extramedullary compartment are most common and represent 88–90% of all primary SCT. Of this large and diverse group, schwannomas, meningiomas, neurofibromas, myxopapillary ependymomas, chordomas, and hemangioblastomas are most frequently diagnosed.

Schwannomas. On gross pathological inspection, spinal schwannomas appear as discrete, rounded, firm, encapsulated masses arising from a nerve fascicle. The tumors may have variable amounts of cyst formation, yellowish areas of xanthomatous changes, and hemorrhage. During the early "intraneural" phase of growth, the tumor is fusiform in shape, similar to neurofibromas.[3,7–10] As the tumor enlarges, the adjacent nerve fascicles are compressed and displaced eccentrically. The nerve fascicles are usually not infiltrated by, or encased within the mass, although they may be incorporated superficially into the tumor capsule. On microscopic examination, "classic" schwannomas are composed of a heterogeneous, biphasic architecture that contains two distinct regions: Antoni A and Antoni B (see Figure 1).[9] In most tumors, the Antoni A regions predominate, and are organized into dense, compact rows or arrays of elongated, spindle-shaped cells that have hyperchromatic, rod-shaped nuclei and eosinophilic cytoplasm. The nuclei are often aligned into

Handbook of Neuro-Oncology Neuroimaging, Second Edition
http://dx.doi.org/10.1016/B978-0-12-800945-1.00005-7

© 2016 Elsevier Ltd. All rights reserved.

TABLE 1 WHO Classification: Tumors of the Central Nervous System

Tumors of neuroepithelial tissue
Tumors of cranial nerves and spinal nerves
Tumors of the meninges
Lymphomas and hemopoietic neoplasms
Germ cell tumors
Tumors of the sellar region
Cysts and tumor-like lesions
Metastatic tumors

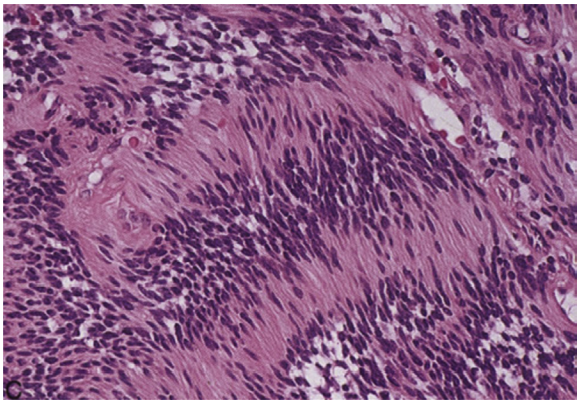


FIGURE 1 Spinal schwannoma. Classic schwannoma demonstrating biphasic architecture composed of Antoni A and Antoni B regions. Antoni A regions are characterized by dense, compact rows of elongated, spindle-shaped cells with rod-shaped nuclei and eosinophilic cytoplasm. Antoni B regions are loosely organized and contain large, vacuolated, stellate cells with areas of microcystic change and lipid accumulation. Hematoxylin and eosin staining (×400 magnification).

palisades that alternate with dense, anuclear zones of fibrillar eosinophilic material; these structures are called Verocay bodies. In some tumors, the cell bundles form whorls of various sizes. The Antoni B regions are loosely organized and composed of large, vacuolated, pleomorphic stellate cells with pyknotic or irregular nuclei. Areas of microcystic change, hyalinization of blood vessels, hemorrhage with perivascular hemosiderin deposition, lipid accumulation, and nuclear degenerative atypia are common. Mitoses and nuclear pleomorphism can be seen on occasion, but do not imply malignant potential. In addition to the classic microscopic appearance of these tumors, several less common forms exist, including the cellular, ancient, plexiform, melanotic, and malignant schwannoma variants.[9]

Meningiomas. Spinal meningiomas have meningothelial cell origins and are derived from neoplastic arachnoidal cap cells embedded within the dura of the spinal canal.[7,8,11] The tumors usually present as rounded or globoid masses, with a variable consistency (i.e., soft to

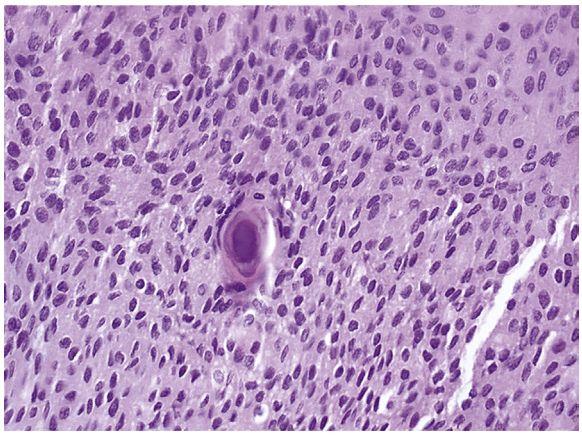


FIGURE 2 WHO grade I spinal meningioma. High-power view of classic spinal meningioma, demonstrating numerous oval to elongated meningothelial cells in a syncytial pattern. A solitary psammoma body is present in the center of the field. Hematoxylin and eosin staining (×400 magnification).

firm), that are attached to the dura and arise near the nerve root sleeve. Less often, the mass will have a carpet-like or "en plaque" configuration, extending along the dura. Cervical meningiomas are most likely to have an anterior location, while thoracic cases tend to occur more laterally. The microscopic features of spinal meningiomas are similar to meningiomas of the intracranial cavity (see Chapter 2), with the same spectrum of histological variants as recognized by the WHO. Meningioma subtypes that have a more indolent nature and low risk for aggressive growth or recurrence are classified as WHO grade I, and include the meningothelial, fibrous/fibroblastic, transitional (mixed), secretory, psammomatous, angiomatous, microcystic, lymphoplasmocyte-rich, and metaplastic variants.[12,13] Highly calcified, psammomatous lesions are the most frequent subtype noted in the spine. The histological features common to most low-grade meningiomas are the presence of whorls (tightly wound, rounded collections of cells), psammoma bodies (concentrically laminated mineral deposits that often begin in the center of whorls), intranuclear pseudoinclusions (areas in which pink cytoplasm protrudes into a nucleus to produce a hollowed-out appearance), and rare pleomorphic nuclei and mitoses (see Figure 2). In general, high-grade meningiomas, especially atypical and anaplastic varieties (WHO grades II and III, respectively), are rare in the spinal meninges. However, the clear cell variant (WHO grade II) is often noted in the lumbar region, an unusual location for other subtypes.

Neurofibromas. On gross pathological examination, spinal neurofibromas are soft, well-circumscribed, pedunculated, and unencapsulated gelatinous masses of a whitish or opalescent color.[3,7,8,10] Regions of cyst formation, xanthomatous changes, and hemorrhage are not seen as commonly as they are with schwannomas. During

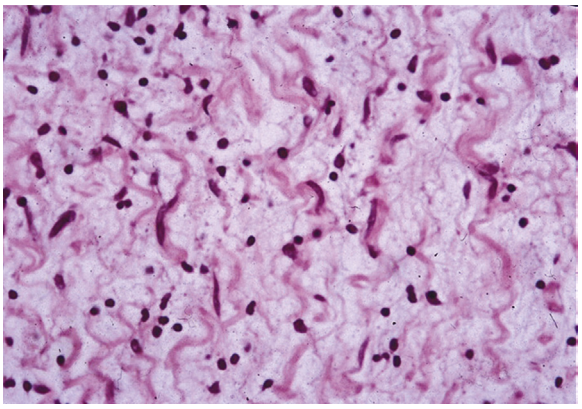


FIGURE 3 Spinal neurofibroma. Typical neurofibroma demonstrating interlacing bundles of fusiform Schwann cells with wavy nuclei. Hematoxylin and eosin staining (×200 magnification).

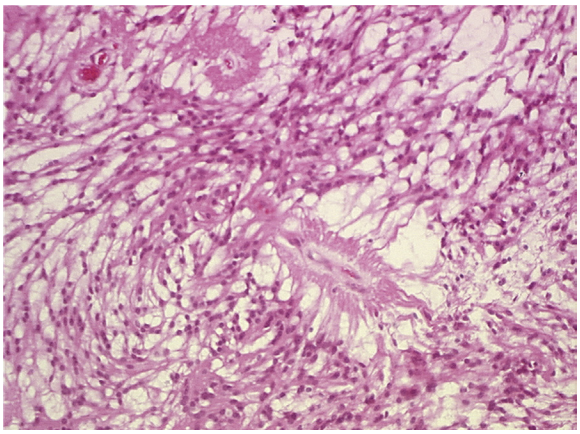


FIGURE 4 WHO grade I myxopapillary ependymoma. Medium-power view of classic myxopapillary ependymoma demonstrating the tumor cells forming perivascular radial arrangements (i.e., rosettes; at the center), within a background mucoid matrix. Note that some of the blood vessel walls (center and top left) display mucoid degeneration. Hematoxylin and eosin staining (×200 magnification).

initial phases of growth, the tumor infiltrates the parent nerve, causing a localized, fusiform swelling. As the tumor enlarges, the parent nerve and those nerves around it may develop gross alterations of shape (e.g., "bag of worms"), and can become encased within the mass. On microscopic histological examination, the typical spinal neurofibroma has interlacing bundles of fusiform Schwann cells with wavy nuclei within a matrix of collagen-rich and mucopolysaccharide-rich material (see Figure 3). Because of the infiltrative growth pattern of neurofibromas, axons of nerve fibers are easily demonstrated after silver impregnation of tumor tissue. Features common to schwannomas such as palisading, Verocay bodies, and whorling are noted infrequently. The architecture and cellular appearance can vary, producing several subtypes: storiform perineural fibroma, pacinian neurofibroma, epithelioid neurofibroma, and pigmented neurofibroma.[7,8]

Myxopapillary Ependymomas. Myxopapillary ependymomas arise predominantly in the region of the filum terminale and cauda equina, and present as elongated, sausage-shaped masses with a smooth, lobulated surface.[7,8,14,15] The tumor is usually well-defined and almost appears encapsulated, displacing or compressing the nerve roots of the cauda equina, with only a mild tendency to infiltrate or envelope neural structures. Some tumors can be large at presentation (e.g., 10 cm or greater in length), and are known to cause erosion and scalloping of the surrounding vertebral bodies and sacrum. On microscopic histological examination, myxopapillary ependymomas are classified as WHO grade I. Characteristic features include numerous small papillary structures, that are each surrounded by well-defined cuboidal or columnar cells, usually in a single layer (see Figure 4).[14,15] These cells have rounded, ependymal type nuclei with distinct margins and a delicate chromatin meshwork, without obvious cytoplasmic processes. The cores of the papillae have a myxoid appearance and consist of a central blood vessel surrounded by a mucinous matrix or are entirely filled by the mucinous material. In papillae with central blood vessels, extensive thickening and hyalinization of the vessel wall may be seen. Other regions of the tumor show a looser structure, with tumor cell nuclei embedded in a meshwork of fine cytoplasmic processes. The processes are often arranged in a radial fashion around the basement membranes of blood vessels and enclose numerous microcystic spaces. On occasion, more compact gliofibrillar areas resembling typical ependymomas can be noted, with the presence of perivascular pseudorosettes or even true ependymal rosettes. Degenerative features, such as microvascular hyalinization, thrombosis, hemorrhage, and hemosiderin, are often present. At the edge of the tumor, there is usually a sharp margin between neoplastic cells and normal tissue, although in some cases nerve roots can be enclosed. Mitotic figures and other features of anaplasia are not usually seen.

Chordomas. Chordomas of the spine present as slow-growing, unencapsulated neoplasms that are locally invasive within bone and, in some cases, regional soft tissues.[7,8,16–18] A pseudocapsule may be noted around tumors that grow into soft tissues or the dura mater. As the tumors enlarge, they often stretch spinal nerves and displace blood vessels. Grossly, the tumors are usually reddish or purple in color, with a nodular appearance to the surface. Internally, the mass is frequently gelatinous and soft; regions that contain cartilage or calcium are more firm. Foci of hemorrhage may be present and can be small or extensive. The size of the lesion can be variable, with lumbosacral tumors often becoming very large. On microscopic examination, chordomas can be grouped into several different histological categories, including a typical pattern, a chondroid pattern, and

tumors with features of malignant degeneration.[16–18] The typical or classic pattern of chordoma (65–80% of all cases) is distinguished by a lobular arrangement, with the neoplastic cells disposed in solid sheets or irregular intersecting cords (see Figure 5). The sheets and cords of cells are set in a stroma that contains an abundant mucinous matrix. The individual cells are large, often with vacuolated eosinophilic cytoplasm, and contain variable amounts of mucin. The cell type considered diagnostic for chordomas is called physaliphorous (i.e., bubble-bearing). These cells are distinctively large and vacuolated, with eccentric nuclei (see Figure 5). Nuclei tend to be hyperchromatic, with prominent nucleoli, and rarely demonstrate atypia. Potentially aggressive features such as mitoses, necrosis, hypervascularity, and spindle cells (i.e., sarcomatous degeneration) are typically absent or rare. Some authors contend that the chondroid pattern (15–30% of all cases) is a separate histological variant of chordoma, although this is controversial.[16–19] On histological examination, chondroid chordomas contain regions of typical chordoma with physaliphorous cells, against a background of areas characterized by cartilaginous matrix that have stellate tumor cells occupying lacunar spaces (resembling chondrocytes).[19] As in typical chordoma, anaplastic or aggressive features such as mitoses, necrosis, hypervascularity, and spindle cells are typically absent or rare.

Hemangioblastomas. Hemangioblastomas are red–brown tumors that are well circumscribed and can arise entirely within the spinal cord parenchyma, or be partly or entirely extramedullary.[1–3,7,8,20,21] Intraparenchymal tumors often have a superficial margin at the pial surface, which is usually covered by ectatic and tortuous blood vessels. Extra-axial tumors are usually well-defined masses growing out over the posterior surface of the cord, sometimes with a projection of neoplastic tissue into the cord parenchyma. In some cases, the tumor may appear as discrete nodules attached to the posterior nerve roots. Between 60% and 70% of hemangioblastomas are associated with a large cystic cavity, with the solid portion of the tumor embedded in the cyst wall as a mural nodule. In the spinal cord, the cysts are elongated syrinx cavities, which can extend over several levels above and below the solid portion of the tumor. The cyst usually contains yellow or rusty brown proteinaceous fluid and has a lining that is smooth and opaque. Cystic or syrinx cavities are not formed from tumor tissue; the lining is composed of a dense layer of gliotic cells that often incorporates Rosenthal fibers and hemosiderin pigment. On microscopic examination, the predominant features of hemangioblastomas are an extensive meshwork of delicate blood vessels and larger, sinusoidal, vascular spaces (see Figure 6).[7,8,20,21] All of these vessels have a capillary structure, with thin walls formed by plump endothelial cells. In between the vascular channels are variable numbers of intervascular or stromal cells arranged in strands and sheets. The cells are large and rounded or polygonal in shape, with abundant cytoplasm and small, rounded, central or eccentrically placed nuclei. The nuclei may occasionally have a vacuolated appearance. In most cells, the cytoplasm is foamy in appearance and swollen by neutral lipid. Although pleomorphic, multinucleated or giant stromal cells may be noted in some cases, mitotic figures are extremely rare. Overall, these tumors are considered to be low-grade neoplasms (i.e., WHO grade I) and do not display intrinsic tumor necrosis of cytological evidence of malignancy.

Tumors arising in the intramedullary compartment are less common, and represent 10–12% of all primary SCT in adults.[1–3] They are histologically similar to their counterparts in the brain, but are often of lower

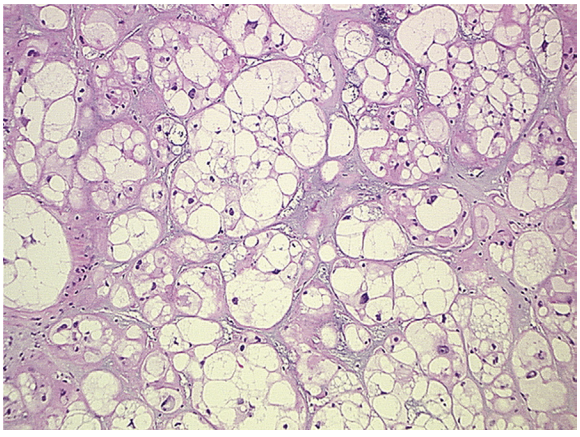


FIGURE 5 Spinal chordoma. Medium-power view of classic or typical chordoma, demonstrating physaliphorous (bubble-bearing) cells. Note the large size, vacuolization, and eccentric nuclei. Mitoses, spindle cells, and regions of necrosis are absent. Hematoxylin and eosin staining (×100 magnification).

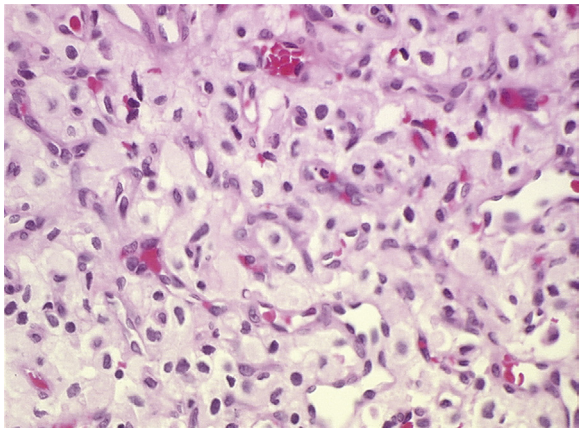


FIGURE 6 Spinal hemangioblastoma. High-power view of typical spinal hemangioblastoma, demonstrating the rich capillary network and large, vacuolated (i.e., lipid laden) stromal cells. Hematoxylin and eosin staining (×400 magnification).

grade.[7,8,22] Of this group, ependymomas, astrocytomas, hemangioblastomas, maldevelopmental tumors (e.g., epidermoid), and other glial tumors (e.g., oligodendroglioma) are most often diagnosed.

Ependymomas. Intramedullary ependymomas are derived from the ependymal lining cells of the central canal and arise as well circumscribed masses within the spinal cord parenchyma (usually in the cervical cord or at the cervicothoracic junction), with very little tendency to infiltrate adjacent neural tissue.[7,8,22–24] Spinal cord ependymomas are commonly divided into typical (WHO grade II) or anaplastic (WHO grade III) varieties. In addition, the WHO recognizes four histological variants of the typical ependymoma (all WHO grade II), including the cellular, papillary, clear cell, and tanycytic subtypes, as well as two low-grade (grade I) forms, myxopapillary ependymoma and subependymoma. On histological examination, WHO grade II ependymomas are densely cellular and composed of oval to carrot-shaped cells, with a dense speckled nucleus and tapering eosinophilic cytoplasm (see Figure 7).[22–25] Some tumors have cells with a more glial appearance and more background fibrillarity or more epithelioid cells and architecture. Perivascular pseudorosettes, which are commonly observed, are circular arrangements of tumor cells that send processes towards vessel walls, creating a perivascular "nuclear-free zone" that can be noted at low power. Less commonly, true ependymal rosettes, surrounding a true lumen, can be observed. Ependymomas are usually glial fibrillary acidic protein (GFAP) positive. Anaplastic ependymomas (WHO grade III) are less common in the spinal cord and have additional features such as increased cellularity, mitotic activity, pleomorphic nuclei, vascular hyperplasia, nuclear atypia, and necrosis.

Astrocytomas. Astrocytomas of the spinal cord tend to be of lower grade than their counterparts in the brain.[1–6] However, they remain infiltrative lesions that often span four to six spinal cord segments at the time of diagnosis. Approximately 50% of spinal astrocytomas are WHO grade I, 22% WHO grade II, 20% WHO grade III, and 8% WHO grade IV.[1,4,26,27] Grade I tumors (i.e., pilocytic astrocytomas) are more common in children, but can occur in young adults. They typically present as a homogeneous, well-demarcated mass, with a gliotic surrounding margin, or as an enhancing mural nodule associated with a large cyst.[7,8,26,27] The distinctive histological feature is the presence of cells with slender, elongated nuclei and thin, hair-like (i.e., piloid), GFAP positive, bipolar processes (see Figure 8). These cells are found in a biphasic background, which consists of dense fibrillary regions alternating with loose, microcystic areas. Also frequently noted are Rosenthal fibers, which are eosinophilic, refractile, corkscrew-shaped deposits. Spinal astrocytomas of higher grade (WHO grade II–IV) are considered diffuse tumors and are more infiltrative.[7,8,26,27] WHO grade II spinal astrocytomas are characterized by a relatively uniform population of proliferating neoplastic astrocytes in a fibrillary matrix, with minimal cellular and nuclear pleomorphism or atypia (see Figure 9). Grade II tumors may display diffuse and intense staining with GFAP. Mitotic figures are absent and there is no evidence for vascular hyperplasia. Spinal anaplastic astrocytomas (AA; WHO grade III) are similar to grade II tumors, but have more prominent cellular and nuclear pleomorphism and atypia, and mitotic activity (see Figure 10). According to WHO criteria, the critical feature that upgrades a grade II tumor to an AA is the presence of mitotic activity, with anaplastic tumors having Ki-67 indices in the range of 5–10% in most cases.

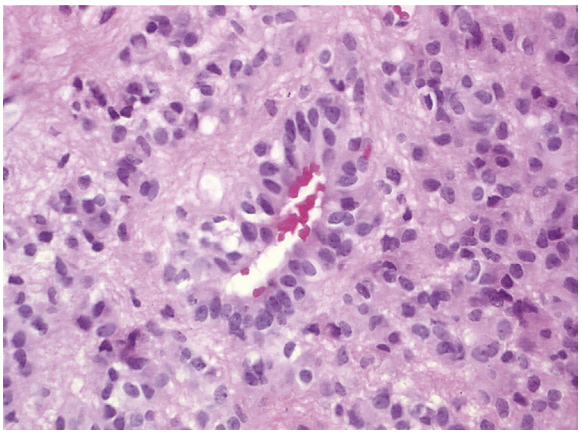


FIGURE 7 WHO grade II intramedullary ependymoma. High-power view of typical intramedullary ependymoma, demonstrating a perivascular pseudorosette, surrounded by groups of cells with oval nuclei and scant cytoplasm. Hematoxylin and eosin staining (×400 magnification).

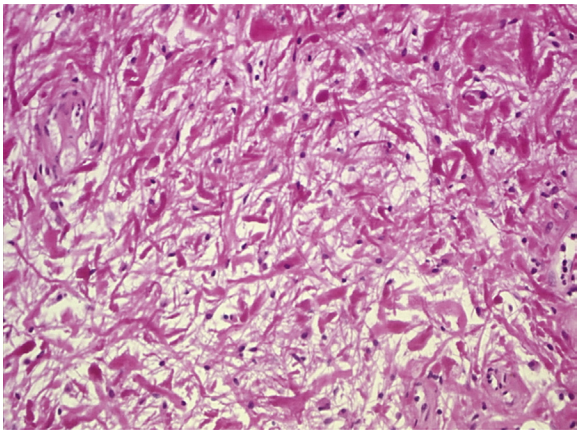


FIGURE 8 WHO grade I spinal pilocytic astrocytoma. Medium-power view of a classic spinal pilocytic astrocytoma, demonstrating numerous eosinophilic Rosenthal fibers and astrocytic cells with thin bipolar processes which crisscross within the background. Hematoxylin and eosin staining (×200 magnification).

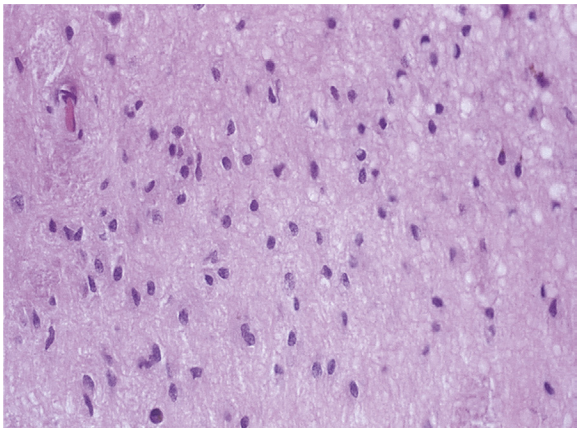


FIGURE 9 WHO grade II spinal astrocytoma. High-power view of a typical grade II spinal astrocytoma, demonstrating oval to elongated, mildly pleomorphic and hyperchromatic astrocytic nuclei infiltrating into the neuropil. Hematoxylin and eosin staining (×400 magnification).

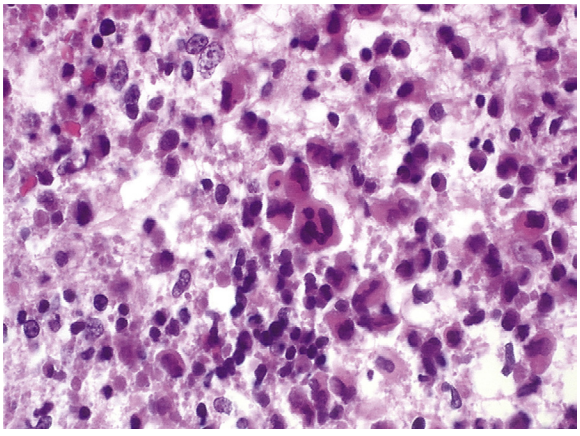


FIGURE 10 WHO grade III spinal anaplastic astrocytoma. High-power view of a grade III spinal astrocytoma, demonstrating increased cellularity, nuclear pleomorphism, multinucleated cells, and mitotic figures. No necrosis or vascular proliferation was present. Hematoxylin and eosin staining (×600 magnification).

Other features of anaplasia can be present, such as multinucleated tumor cells and abnormal mitotic figures. Spinal glioblastoma multiforme (GBM) is classified as a WHO grade IV tumor and has similar histological features to AA, but with more pronounced anaplasia (see Figure 11).[7,8] Microvascular proliferation and/or necrosis in an otherwise malignant astrocytoma upgrades the tumor to a GBM. Vascular proliferation is defined as blood vessels with "piling up" of endothelial cells, including the formation of glomeruloid vessels. Necrosis can be noted in large amorphous areas, which appear ischemic in nature, or can appear as more serpiginous regions with surrounding palisading tumor cells (i.e., perinecrotic pseudopalisading). Necrosis with nuclear pseudopalisading is essentially pathognomonic for GBM. Other features of GBM that are typically prominent include marked cellular and nuclear pleomorphism and atypia, mitotic figures and multinucleated giant cells, and pronounced infiltrative capacity into surrounding spinal cord.

SURGICAL THERAPY OF PRIMARY SCT

Once it is established that a patient has a lesion that is likely to be a primary SCT, surgical intervention is usually required to provide a definitive diagnosis and, if possible, to totally remove the mass.[1–6] Advances in technology have improved the results of operative therapy for SCT. These include the use of the operating microscope and microneurosurgical instrumentation, bipolar coagulation, surgical lasers, ultrasonic aspirators, intraoperative ultrasound localization, and the use of intraoperative spinal cord evoked potential monitoring. Intraoperative monitoring of sensory and motor evoked potentials should be considered for all patients undergoing surgery for an intramedullary spinal cord tumor.[2,28] A 50% decline in

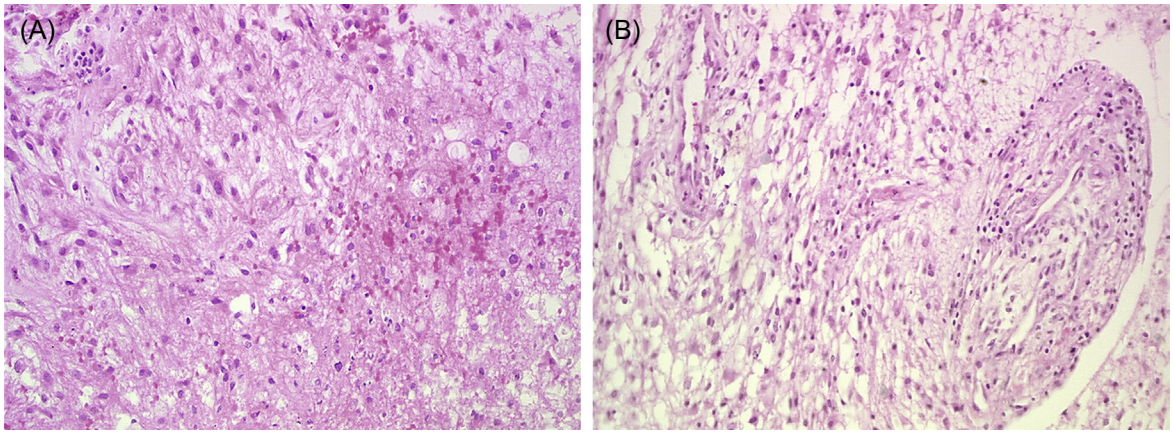


FIGURE 11 WHO grade IV spinal GBM. Medium-power views of a grade IV spinal astrocytoma, demonstrating increased cellularity, cellular and nuclear pleomorphism, areas of necrosis (A), and microvascular proliferation (B). Hematoxylin and eosin staining (×200 magnification).

evoked potential amplitude during the procedure may be an indication of a new, possibly permanent, postoperative motor deficit.

The majority of intradural extramedullary tumors are well circumscribed, noninfiltrative, benign lesions that are amenable to complete surgical resection.[1–3] They typically have clear cleavage planes that allow separation from surrounding structures. The typical surgical approach for spinal schwannomas and neurofibromas is to attempt complete resection, which can be curative in most cases. The operative approach is usually a midline partial or total laminectomy.[29–31] The tumors are always attached to at least one nerve root. Schwannomas can be completely resected in 85–90% of cases without sacrifice of the parent nerve root.[30,31] Radical resection is also possible for large, invasive tumors that extend into surrounding bones and soft tissues.[32] Neurofibromas can be completely resected in 90% of cases.[29] However, in 80–90% of these patients the parent nerve root must be sacrificed during tumor removal. Recurrences are rare for schwannomas and neurofibromas after complete resection. In patients with neurofibromatosis and multiple neurofibromas, surgical resection is restricted to the neurologically symptomatic tumors.[1,3,33] For most meningiomas, a posterior approach with laminectomy is adequate to visualize and access the tumor for resection.[1–3,11,34–36] Tumors placed more ventrally may require a posterolateral approach or pediculectomy to allow safe tumor removal without cord retraction. Regions of the dura infiltrated with tumor should be resected when technically feasible. If complete removal of the dura cannot be achieved, extensive electrocautery of the remaining dura should be performed. Cauterization of the dura instead of resection, in selected cases, has not been associated with significantly higher recurrence rates.[11] Patients with schwannomas, meningiomas, and neurofibromas that compress the spinal cord and cause myelopathy do well after surgical resection, often with various degrees of improvement in neurological status (50–80% in large series).[1–6,11] It is theorized that because the tumors grow so slowly, the damage to the spinal cord is mainly compressive and somewhat reversible, which would not be the case were the damage due to severe demyelination, loss of axons, or ischemia. Intradural extramedullary epidermoids, dermoids, lipomas, and teratomas can usually be removed completely.

The common intramedullary tumors, especially astrocytomas and ependymomas, are not as easily resected as the extramedullary tumors, although some authors advocate an aggressive approach.[1–6,37–39] Because these tumors usually lack a capsule and are more infiltrative, it is more difficult to discern a clear cleavage plane to separate tumor from surrounding normal tissues. Ependymomas of the cauda equina and conus medullaris are often adherent to surrounding neural structures and may erode into bone, making complete removal difficult without severe neurologic sequelae.[1–3,14,15,40] Gross total resection is recommended whenever feasible, but is only achieved in 22–42% of cases. In most patients, subtotal or incomplete piecemeal removal is performed and results in frequent recurrences and a compromise in survival. Spinal stabilization surgery (i.e., instrumentation and fusion) may also be of benefit for selected patients in whom tumor involvement with spinal elements has resulted in spinal instability. Intrinsic ependymomas can be completely resected in a greater percentage of patients because they tend to be more circumscribed than ependymomas of the filum terminale and cauda equina.[1–3,23,24,40–43] The majority of intramedullary ependymomas are low-grade, with very clear cleavage planes between tumor and surrounding normal cord tissue. For adequate visualization of the degree of infiltration of the mass and the clarity of the cleavage plane, an adequate myelotomy must be performed, that extends over the entire rostral–caudal extent of the tumor. If a clear cleavage plane is identified, the goal should be gross total removal of all tumor tissue within the cord. Large tumors may require internal decompression with an ultrasonic aspirator or laser during the procedure. If the tumor is more infiltrative, and a cleavage plane cannot be identified, then a biopsy should be obtained to establish a histologic diagnosis. Astrocytomas of the spinal cord vary in their degree of histologic malignancy and infiltrative capacity. In general, they tend to be of lower grade than similar tumors in the brain. Low-grade tumors that do not demonstrate severe infiltration into surrounding spinal segments can be aggressively resected, with good preservation of function and length of survival.[1–6,26,27,37,38,44–46] The surgical approach would require a laminectomy in adult patients and an osteoplastic laminotomy in children, including verification of the location of the tumor and any associated cysts using ultrasound guidance, followed by a midline myelotomy. The tumor is resected using a combination of suction aspiration and the ultrasonic aspirator, working from the inside outward. Low-grade astrocytomas with significant infiltration and all high-grade tumors cannot be completely resected without risk of significant injury to the patient. In these tumors, a biopsy or partial resection that does not further compromise neurologic function is appropriate.[47–49] Microsurgical resection is the primary treatment for hemangioblastomas of the spinal cord, but the approach will vary depending on whether the tumor is sporadic or associated with von Hippel-Lindau Syndrome (VHLS).[1–3,20,21,50–52] For patients with sporadic tumors, resection of the mass is often required to confirm the diagnosis and is appropriate before the onset of significant symptoms. In patients with VHLS, the indications for surgery are based on significant signs and symptoms attributable to the hemangioblastoma and its

associated syrinx. Asymptomatic tumors should be followed clinically and considered for resection only when the patient develops significant signs and symptoms. For most patients, a direct posterior approach to the tumor will be adequate, including laminectomies that provide exposure 1–2 cm above and below the rostral and caudal margins of the tumor.[20,52] Ultrasound guidance is usually necessary to locate the mass and allow proper placement of the midline dural incision. The tumor is then resected in a circumferential manner, separating the tumor capsule from surrounding spinal cord, and coagulating all of the individual small blood vessels associated with the capsule. The majority of dermoids, epidermoids, and teratomas can be partially or completely resected using standard microneurosurgical techniques.[1–3]

The surgical approach to extradural SCT, such as neuroblastoma, spinal chordoma, and osteosarcoma, is to completely resect the tumor, if possible, or at least debulk the mass and relieve pressure on the thecal sac and spinal cord.[1–3]

In general, the surgical approach to primary SCT in pediatric patients is similar to that of adults with the same type of tumor.[4–6,45] A complete surgical resection should be attempted in the majority of intradural, extramedullary SCT and virtually all extradural tumors. For intramedullary tumors, the preferred technique is osteoplastic laminotomy, with removal of the laminar roof in one piece, and replacement of the entire block of tissue after resection of the mass. This technique allows for preservation of the posterior tension band, restores normal spinal anatomy, and may result in bony fusion of the reapproximated lamina. In addition, there appears to be a reduced incidence of postoperative spinal deformity.

RADIATION THERAPY OF PRIMARY SCT

The majority of patients with primary SCT will not require external beam radiation therapy (RT) after surgical resection. Patients with completely resected extramedullary or extradural tumors (e.g., schwannoma, meningioma) should not receive RT, as it has not been shown to improve local tumor control or survival in this context.[1–6,10,11,14,20,24,27,37,38,53,54] These patients should be followed closely with regular neurologic examinations and magnetic resonance imaging (MRI) scans for evidence of SCT recurrence. At the time of recurrence, RT should be considered for those tumors not amenable to further surgical intervention.[1–3,54] Typical doses applied to the gross tumor volume are in the range of 45–55 Gy, with higher doses reserved for more histologically aggressive tumors. Other indications for RT are benign or low-grade SCT that cannot be completely resected, and all anaplastic or malignant tumors.[1–3,53,54] RT is applied most often to incompletely resected or recurrent spinal ependymomas.[1–3,14,24,55,56] Although there have been no controlled clinical trials, most authors agree that RT (50–55 Gy administered in 1.8 Gy daily fractions) improves local control and survival in properly selected spinal ependymoma patients. Patients with high-grade tumors and those who have undergone incomplete resection tend to have shorter disease-free intervals and survival.[54–56] An initial study of RT for spinal ependymoma reviewed 58 patients treated between 1950 and 1987, 43 of whom had received irradiation.[55] The 5- and 10-year cause-specific survival rates were 74% and 68%, respectively. Histological grade of the tumor was the only independent prognostic factor on multivariate analysis. However, RT was considered to be of benefit in the group of patients with incompletely resected tumors. In this cohort, the 5- and 10-year progression-free survival (PFS) rates were both 59%, and the cause-specific survival rates at 5 and 10 years were 69% and 62%, respectively. In a large multiinstitutional review of spinal cord gliomas, 126 patients with ependymoma were treated, 59 of whom received postoperative RT.[56] Overall, the use of RT compared with surgery alone did not improve PFS ($p = 0.11$). In addition, on univariate and multivariate analyses, the use of RT did not improve overall survival compared with surgery alone (adjusted hazard ratio 1.12, $p = 0.89$). These results are similar to those reported by other authors, such as Sgouros and colleagues, who also noted that RT did not confer a survival advantage.[57] However, it must be pointed out that the apparent lack of efficacy of RT may be at least partially due to a selection bias in the data. The patients that received RT were less likely to undergo complete resections (20% vs 82%; $p < 0.01$) and had a significantly higher percentage of high-grade ependymomas (0% vs 21%; $p < 0.01$). Following the use of RT, spinal ependymomas generally tend to fail within the radiation port. Craniospinal RT (36–39.6 Gy) is only recommended for malignant ependymomas or tumors with documented leptomeningeal spread (i.e., cerebrospinal fluid evaluation with positive cytology or MRI with unequivocal nonbulky spinal meningeal enhancement). Higher doses of craniospinal RT are recommended (54 Gy) for patients that have MRI evidence for bulky leptomeningeal disease.[2,3]

Spinal astrocytomas typically require postoperative RT because they are more infiltrative and cannot be completely resected as readily as ependymomas and other SCT.[1–4,26,27,44–49] For infiltrative low-grade tumors, the recommended RT dose is 50–54 Gy, administered in 1.8 Gy daily fractions. Anaplastic or malignant tumors require a higher dose, usually in the range of 55.8–59.4 Gy. The survival rates following RT are significantly affected by tumor grade. For example, in one older study, patients with low-grade astrocytomas had

a 5-year actuarial survival rate of 89%, while patients with malignant tumors did not survive beyond 3 years.[58] Another study noted that median survival was significantly shorter for high-grade spinal astrocytomas compared with lower grade tumors, but did not differ between AA and GBM.[49] In this study, the median survival was 33 months for low-grade astrocytomas and 10 months for both AA and GBM. Similar results were noted in the large retrospective study cited above, in their cohort of 57 spinal astrocytoma patients.[56] The risk of disease progression in patients with high-grade tumors was more than twice that of patients with low- or moderate-grade tumors (hazard ratio 2.67; $p = 0.02$). In this same study, multivariate analysis demonstrated a significant risk reduction for patients with low or moderate grade tumors that received postoperative RT (adjusted hazard ratio 0.24; $p = 0.02$). However, postoperative RT did not appear to be beneficial in patients with high-grade astrocytomas ($p = 0.67$). Postoperative RT did not improve overall survival on univariate or multivariate analyses. Similar to the data for ependymomas cited above, a selection bias was noted in the RT group in terms of a lower percentage of patients receiving complete resections (13% vs 53%; $p < 0.01$). Relapse of spinal astrocytomas is almost always local, often with dissemination to the leptomeninges. Nonetheless, RT is recommended for the majority of spinal astrocytoma patients following resection, despite the poor results in high-grade tumors.

RT is an important therapeutic consideration for many patients with locally invasive spinal chordomas that cannot be completely resected.[59] Unfortunately, chordomas have proved to be relatively radioresistant tumors. The clinical results in most RT trials have demonstrated only modest improvements in local control, recurrence-free survival, and overall survival.[59–62] In general, the best results have been in patients that have undergone irradiation and an aggressive partial resection. For example, York and colleagues studied 27 patients with sacral chordomas and noted a significant difference in the disease-free interval (24 months vs 8 months; $p < 0.02$) for patients receiving irradiation after subtotal resection.[63] In a study of 21 patients with chordomas of various sites, Keisch and colleagues concluded that irradiation prolonged the time to first relapse for tumors of the lower spine and sacrum but not for tumors of the skull base.[61] The overall 5- and 10-year actuarial survival rates were 74% and 46%, respectively. Irradiation of chordomas with charged particles (i.e., protons, helium, neon, carbon) has shown promise as a more efficacious therapeutic option.[59,64,65] The high linear energy transfer of charged particles allows for a more defined and superior dose distribution (i.e., steeper dose fall-off). Higher doses can be prescribed to the tumor volume with minimal risk of augmented toxicity to surrounding delicate structures (i.e., spinal cord). In a study using helium and neon particles, Berson and colleagues treated 25 patients with chordomas of the skull base and cervical spine and reported a 5-year local control rate of 55%.[60] For patients with unresectable sacral chordomas, carbon ion radiotherapy has also been effective.[65] The overall 5-year local control rate was 96%, with a 5-year overall survival rate of 52%.

Another technique being applied to selected primary SCT is the CyberKnife®, an image-guided frameless stereotactic radiosurgery system.[66] In a series of 125 spinal tumors, including 17 extramedullary lesions (e.g., neurofibroma, meningioma), the mean dose was 14 Gy at the 80% isodose line (range 12–20 Gy). Treatment was well tolerated by patients, and follow-up evaluation that ranged from 6 to 27 months showed that all of the primary tumors remained stable.

The spinal cord is sensitive to the effects of radiation.[2,3,54] Overdosage must be avoided to reduce the risk of radiation-induced myelopathy, which is irreversible. The accepted spinal cord tolerance level is 5000–5500 cGy, administered over 5–6 weeks using 180–200 cGy daily fractions. This is the appropriate dose for most spinal ependymomas and astrocytomas. Above this dose the therapeutic index falls sharply, so that the probability of myelopathy is 50% at 6500 cGy. The thoracic spinal cord segments are most radiation sensitive, while the cauda equina is the least sensitive.

CHEMOTHERAPY OF PRIMARY SCT

There is a paucity of data to evaluate the efficacy of chemotherapy for the treatment of primary SCT. Because most of these tumors are histologically benign and respond well to surgical and/or RT, chemotherapy is rarely indicated. For gliomatous SCT that progress after surgery and RT, chemotherapy similar to that used for intracranial gliomas can be attempted.[1–3,67–69] However, because of the rarity of SCT requiring chemotherapy, no phase III or large phase II trials have been reported. All of the available data have been from case reports or small institutional series that contain a handful of patients. Chemotherapy agents with potential activity include nitrosoureas (carmusine (BCNU), lomustine (CCNU)), procarbazine, vincristine, etoposide, cyclophosphamide, temozolomide, and carboplatin.

Patients with spinal cord astrocytomas have been treated with several forms of chemotherapy by a variety of authors.[67–75] Initial reports were in pediatric patients, including a 13-year-old girl with a thoracic AA that was treated with partial resection, multidrug chemotherapy,

and irradiation.[70] The chemotherapy regimen consisted of ifosphamide and etoposide alternating with cisplatin and cytarabine. Follow-up after RT demonstrated a complete response (CR) that was maintained for 16 months. Bouffet and coworkers, in their review of prognostic factors in spinal astrocytomas, reported a series of nine children that had received chemotherapy.[72] In three of these patients, chemotherapy was the sole mode of treatment, while in the other six patients it was used in combination with RT. Partial responses (PR) were noted in two of the patients that had only received chemotherapy. The same authors also reported a 30-year-old patient with a grade II astrocytoma that was treated with neoadjuvant chemotherapy (carboplatin and vincristine).[71] Treatment with the regimen over 11 cycles resulted in a CR, with improved neurological function, that was maintained during 14 months of follow-up. Allen and colleagues enrolled 13 pediatric patients with spinal astrocytomas (eight AA and four GBM) into the Children's Cancer Group 945 protocol, which used two cycles of "8-drugs-in-1-day" chemotherapy before RT and up to eight cycles afterwards.[73] The regimen included vincristine, carmustine, procarbazine, hydroxyurea, cisplatin, cytarabine, prednisone, and cyclophosphamide. PreRT chemotherapy resulted in three objective responses (one CR and two PR) in evaluable patients. However, the 5-year PFS and overall survival were only 46% and 54%, respectively. The authors concluded that 8-drugs-in-1-day chemotherapy did not offer a therapeutic advantage over the more traditional approach using CCNU and vincristine. Lowis and coworkers described two pediatric patients with spinal cord astrocytomas that had excellent responses to multiagent chemotherapy.[74] The first was a 19-month-old child with a spinal AA that progressed after partial resection. Chemotherapy was used instead of RT because of the young age, and consisted of carboplatin, vincristine, cyclophosphamide, methotrexate, and cisplatin. The patient improved neurologically and developed a CR that remained durable at 29 months follow-up. An excellent response was also noted in the other patient, a 4-year-old with a grade II astrocytoma, treated neoadjuvantly with carboplatin and vincristine. Similar responses have been noted in a report of three very young patients (26–41 months old) with low-grade gliomas of the spinal cord (two pilocytic astrocytoma, one ganglioglioma), treated monthly with a single agent carboplatin (560 mg/m^2).[69] Two of the patients developed PR, while the other had stable disease, all of which remained durable during 5–17 months follow-up. In another series of spinal cord gliomas in young children (age range 3 months–9.5 years), Doireau and colleagues used an aggressive brain regimen consisting of carboplatin, procarbazine, vincristine, cisplatin, etoposide, and cyclophosphamide.[68] After a 16 month course of chemotherapy, there were four patients with a CR, three with a PR, and one with stable disease. The overall survival rate was 87.5%, with an event-free survival rate at 2 and 4 years of 50%. Henson and coworkers described an adult patient with a low-grade astrocytoma of the conus medullaris, that initially responded well to RT.[75] Two years later the patient had clinical and MRI progression and was placed on cisplatin and etoposide. However, after further progression he was placed on PCV (procarbazine, CCNU, vincristine), which induced tumor shrinkage on MRI and improvement in neurological function. The response was durable for 23 months (11 cycles) before disease progression.

Temozolomide (TEM) has been shown to be active in low-grade gliomas of the brain, and is now being applied to spinal gliomas.[76–79] An early report by Chamoun and coworkers described the use of TEM (200 mg/m^2/day for 5 days, every 4 weeks) in two teenage patients with low-grade spinal astrocytomas.[76] Each patient was treated for a total of 10 cycles and had stabilization of disease clinically and by MRI scan. Several other authors have also had patients with high-grade spinal cord gliomas respond to TEM.[77–79] Kim et al. describe a series of six patients with newly diagnosed or recurrent high-grade astrocytoma and ependymoma who were treated with concomitant RT and TEM followed by adjuvant TEM, or adjuvant TEM alone.[77] Several of the patients responded with long-term stable disease. In a similar study of eight patients with high-grade spinal cord gliomas, TEM was able to achieve a median time-to-progression of 6.6 months (range 1–40 months) in the recurrent group, with a median overall survival of 16.6 months (range 1.2–64.5 months).[78] A case report described the use of TEM in an 18-year-old female with a primary spinal cord anaplastic oligodendroglioma (1p deleted).[79] After initial surgical resection and RT, the tumor recurred, requiring a re-resection, followed by adjuvant chemotherapy with TEM. After 6 months of treatment, there was a significant reduction if residual tumor, along with clinical improvement in lower extremity function.

Bevacizumab (BEV), a monoclonal antibody that targets vascular endothelial growth factor (VEGF) and has been shown to be active in adult GBM of the brain, has also been applied to spinal cord high-grade gliomas.[78,80] A series of six patients with progressive high-grade spinal cord gliomas was treated with BEV.[78] On follow-up MRI, there were five PR that correlated with clinical improvement. The median time-to-progression was 20.7 months (range 3.3–29.9 months), with a median overall survival of 22.8 months (range 3.3–31.8 months).

There are very few published reports of patients with spinal ependymomas receiving chemotherapy.[67] The largest experience is from Chamberlain, who describes the use of oral etoposide (50 mg/m^2/day for 21 days, every 5 weeks) in a series of 10 adult patients with

recurrent spinal cord ependymoma.[81,82] There were two patients with a PR and five patients with stable disease. The overall median response duration and median survival were 15 months and 17.5 months, respectively. A case report has also been described of a teenager with a progressive spinal myxopapillary ependymoma that was treated with the combination of tamoxifen (60 mg/m^2/day) and etoposide (50 mg/m^2/day), for 3 weeks each month.[83] The patient had a PR that was durable at 19 months follow-up.

MOLECULAR OR "TARGETED" TREATMENT

There are very few published reports specifically examining the molecular biology of primary SCT.[84–86] However, it is likely that many, if not all, of the genetic alterations noted in intracranial gliomas are involved in the transformation and malignant phenotype of SCT (see Chapter 2). It has become apparent that the transformed phenotype of neoplastic glial tumor cells is highly complex and results from the dysfunction of a variety of interrelated regulatory pathways.[87–89] The transformation process involves amplification or overexpression of oncogenes in combination with loss or lack of expression of tumor suppressor genes. Oncogenes and signal transduction molecules that have been demonstrated to be important for gliomagenesis include platelet-derived growth factor and its receptor (PDGF, PDGFR), epidermal growth factor and its receptor (EGF, EGFR), CDK4, mdm-2, Ras, phosphoinositol-3 kinase (PI3K), Akt, and mammalian target of rapamycin (mTOR). Tumor suppressor genes of importance in glial transformation include p53, retinoblastoma (Rb), p16 and p15 (i.e., INK4a, INK4b), DMBT1, NF2, and PTEN. Most of these tumor suppressor genes function as negative regulators of the cell cycle, while others are inhibitors of important internal signal transduction pathways. The net effect of these acquired abnormalities is dysregulation of, and an imbalance between, the activity of the cell cycle and apoptotic pathways.

Several reports have investigated the molecular genetics of spinal ependymomas.[90–93] In one study, five out of seven patients were noted to have mutations of the NF2 gene, which resulted in the production of a truncated protein product.[90] Other investigators have also found mutations in NF2, as well as loss of DNA sequences from chromosomes 22q and 17p, in sporadic intramedullary spinal ependymomas.[91] Another study reviewed the molecular aspects of a large series of 62 ependymal tumors, including cases from the brain and spine.[92] Allelic loss was noted of chromosomes 10q (five of 56 cases) and 22q (12 of 54 cases). In addition, somatic mutations of NF2 were present in six tumors, all of which were grade II intramedullary spinal ependymomas. A report on the methylation status of HIC-1, a putative tumor suppressor gene on chromosome 17p13.3, reviewed the findings in a series of 52 intracranial and spinal ependymomas.[93] There was a significant correlation between hypermethylation of HIC-1 and nonspinal localization of the tumor ($p = 0.019$).

Advances in growth factor and signal transduction biology are now providing the background for the development of "molecular therapeutics," a new class of drugs that manipulate and exploit these pathways.[94] Molecular drugs targeting critical signal transduction pathway effectors, such as PDGFR, EGFR, Ras, PI3K, and mTOR, have entered early clinical trials in brain tumor patients.[95–98] In the near future, clinicians will have the opportunity to apply this new class of drugs to recurrent or progressive SCT.

Acknowledgments

The authors would like to thank Julia Shekunov for research assistance. Dr. Newton was supported in part by National Cancer Institute grant, CA 16058 and the Dardinger Neuro-Oncology Center Endowment Fund.

References

1. Engelhart HH, Villano JL, Porter KR, et al. Clinical presentation, histology, and treatment in 430 patients with primary tumors of the spinal cord, spinal meninges, or caude equina. *J Neurosurg Spine*. 2010;13:67–77.
2. Mechtler LL, Nandigam K. Spinal cord tumors: new views and future directions. *Neurol Clin*. 2013;31:241–268.
3. Waters JD, Peran EM, Ciacci J. Malignancies of the spinal cord. *Adv Exp Med Biol*. 2012;760:101–113.
4. Hsu W, Jallo GI. Pediatric spinal tumors. *Handb Clin Neurol*. 2013;112:959–965.
5. Baysefer A, Akay KM, Izci Y, Kayali H, Timurkaynak E. The clinical and surgical aspects of spinal tumors in children. *Pediatr Neurol*. 2004;31:261–266.
6. Auguste KI, Gupta N. Pediatric intramedullary spinal cord tumors. *Neurosurg Clin N Am*. 2006;17:51–61.
7. Kleihues P, Louis DN, Scheithauer BW, et al. The WHO classification of tumors of the nervous system. *J Neuropathol Exp Neurol*. 2002;61:215–225.
8. Rodriguez FJ, Giannini C. Diagnostic pathology of tumors of the central nervous system. *Handb Clin Neurol*. 2012;104:77–107.
9. Kurtkaya-Yapicier O, Scheithauer B, Woodruff JM. The pathobiologic spectrum of schwannomas. *Histol Histopathol*. 2003;18:925–934.
10. Waldron J, Weinstein RP. Nerve sheath tumors of the spine. In: Berger MS, Prados MD, eds. *Textbook of Neuro-Oncology*. Vol. 63. Philadelphia: Elsevier Saunders; 2005:485–488.
11. Cohen-Gadol AA, Krauss WE. Spinal meningiomas. In: Berger MS, Prados MD, eds. *Textbook of Neuro-Oncology*. Vol. 64. Philadelphia: Elsevier Saunders; 2005:489–492.
12. Alahmadi H, Croul SE. Pathology and genetics of meningiomas. *Semin Diagn Pathol*. 2011;28:314–324.
13. Perry A, Gutmann DH, Reifenberger G. Molecular pathogenesis of meningiomas. *J Neuro-Oncol*. 2004;70:183–202.

14. Parney IF, Parsa AT. Myxopapillary ependymomas. In: Berger MS, Prados MD, eds. *Textbook of Neuro-Oncology*. Vol. 65. Philadelphia: Elsevier Saunders; 2005:493–496.
15. Takei H, Kosarac O, Powell SZ. Cytomorphologic features of myxopapillary ependymoma: a review of 13 cases. *Acta Cytol*. 2009;53:29–302.
16. Rich TA, Schiller A, Suit HD, Mankin HJ. Clinical and pathologic review of 48 cases of chordoma. *Cancer*. 1985;56:182–187.
17. Schoedel KE, Martinez AJ, Mahoney TM, Contis L, Becich MJ. Chordomas: pathological features; ploidy and silver nucleolar organizing region analysis. A study of 36 cases. *Acta Neuropathol*. 1995;89:139–143.
18. Crapanzano JP, Ali SZ, Ginsberg MS, Zakowski MF. Chordoma. A cytologic study with histologic and radiologic correlation. *Cancer*. 2001;93:40–51.
19. Ishida T, Dorfman HD. Chondroid chordoma versus low-grade chondrosarcoma of the base of the skull: can immunohistochemistry resolve the controversy? *J Neuro-Oncol*. 1994;18:199–206.
20. Lonser RR, Oldfield EH. Spinal cord hemangioblastomas. *Neurosurg Clin N Am*. 2006;17:37–44.
21. Lonser RR, Oldfield EH. Spinal cord hemangioblastomas. In: Berger MS, Prados MD, eds. *Textbook of Neuro-Oncology*. Vol. 68. Philadelphia: Elsevier Saunders; 2005:506–510.
22. McLendon RE, Enterline DS, Tien RD, Thorstad WL, Bruner JM. Tumors of central neuroepithelial origin. In: Bigner DD, McLendon RE, Bruner JM, eds. *Russell & Rubinstein's Pathology of Tumors of the Nervous System. Sixth Edition. Volume 1*. London: Arnold; 1998;9:307–571.
23. Schwartz TH, McCormick PC. Intramedullary ependymomas: clinical presentation, surgical treatment strategies and prognosis. *J Neuro-Oncol*. 2000;47:211–218.
24. Schwartz TH, Parsa AT, McCormick PC. Intramedullary ependymomas. In: Berger MS, Prados MD, eds. *Textbook of Neuro-Oncology*. Vol. 66. Philadelphia: Elsevier Saunders; 2005:497–500.
25. Rosenblum MK. Ependymal tumors: a review of their diagnostic surgical pathology. *Pediatr Neurosurg*. 1998;28:160–165.
26. Houten JK, Cooper PR. Spinal cord astrocytomas: presentation, management and outcome. *J Neuro-Oncol*. 2000;47:219–224.
27. Roonprapunt C, Houten JK. Spinal cord astrocytomas: presentation, management, and outcome. *Neurosurg Clin N Am*. 2006;17:29–38.
28. Morota N, Deletis V, Constantini S, Kofler M, Cohen H, Epstein FJ. The role of motor evoked potentials during surgery for intramedullary spinal cord tumors. *Neurosurgery*. 1997;41:1327–1336.
29. Seppala MT, Haltia MJ, Sankila RJ, Jaaskelainen JE, Heiskanen O. Long-term outcome after removal of spinal neurofibroma. *J Neurosurg*. 1995;82:572–577.
30. Seppala MT, Haltia MJ, Sankila RJ, Jaaskelainen JE, Heiskanen O. Long-term outcome after removal of spinal schwannoma: a clinicopathological study of 187 cases. *J Neurosurg*. 1995;83:621–626.
31. Conti P, Pansini G, Mouchaty H, Capuano C, Conti R. Spinal neurinomas: retrospective analysis and long-term outcome of 179 consecutively operated cases and review of the literature. *Surg Neurol*. 2004;61:35–44.
32. Sridhar K, Ramamurthi R, Vasudevan MC, Ramamurthi B. Giant invasive spinal schwannomas: definition and surgical management. *J Neurosurg (Spine 2)*. 2001;94:210–215.
33. Riccardi VM. The neurofibromatoses. *Hematol Oncol Ann*. 1994;2:119–128.
34. Gezen F, Kahraman S, Çanakci Z, Bedük A. Review of 36 cases of spinal cord meningioma. *Spine*. 2000;25:727–731.
35. Cohen-Gadol AA, Zikel OM, Koch CA, Scheithauer BW, Krauss WE. Spinal meningiomas in patients younger than 50 years of age: a 21-year experience. *J Neurosurg (Spine 3)*. 2003;98:258–263.
36. Peker S, Cerci A, Ozgen S, et al. Spinal meningiomas: evaluation of 41 patients. *J Neurosurg Sci*. 2005;49:7–11.
37. Cooper PR, Epstein F. Radical resection of intramedullary spinal cord tumors in adults. Recent experience in 29 patients. *J Neurosurg*. 1985;63:492–499.
38. Cooper PR. Outcome after operative treatment of intramedullary spinal cord tumors in adults: intermediate and long-term results in 51 patients. *Neurosurgery*. 1989;25:855–859.
39. Constantini S, Miller DC, Allen JC, Rorke LB, Freed D, Epstein FJ. Radical excision of intramedullary spinal cord tumors: surgical morbidity and long-term follow-up evaluation in 164 children and young adults. *J Neurosurg*. 2000;93:183–193.
40. Asazuma T, Toyama Y, Suzuki N, Fujimura Y, Hirabayshi K. Ependymomas of the spinal cord and cauda equina: an analysis of 26 cases and a review of the literature. *Spinal Cord*. 1999;37:753–759.
41. McCormick PC, Torres R, Post KD, Stein BM. Intramedullary ependymoma of the spinal cord. *J Neurosurg*. 1990;72:523–532.
42. Chang UK, Choe WJ, Chung SK, Chung CK, Kim HJ. Surgical outcome and prognostic factors of spinal intramedullary ependymomas in adults. *J Neuro-Oncol*. 2002;57:133–139.
43. Hanbali F, Fourney DR, Marmor E, et al. Spinal cord ependymoma: radical surgical resection and outcome. *Neurosurgery*. 2002;51:1162–1174.
44. Epstein FJ, Farmer J, Freed D. Adult intramedullary astrocytomas of the spinal cord. *J Neurosurg*. 1992;77:355–359.
45. Rossitch E, Zeidman SM, Burger PC, Curnes JT, et al. Clinical and pathological analysis of spinal cord astrocytomas in children. *Neurosurgery*. 1990;27:193–196.
46. Robinson CG, Prayson RA, Hahn JF, et al. Long-term survival and functional status of patients with low-grade astrocytoma of spinal cord. *Int J Rad Oncol Biol Phys*. 2005;63:91–100.
47. Cohen AR, Wisoff JH, Allen JC, Epstein F. Malignant astrocytomas of the spinal cord. *J Neurosurg*. 1989;70:50–54.
48. Ciappetta P, Salvati M, Capoccia G, Artico M, et al. Spinal glioblastomas: report of seven cases and review of the literature. *Neurosurgery*. 1991;28:302–306.
49. Santi M, Mena H, Wong K, Koeller K, Olsen C, Rushing EJ. Spinal cord malignant astrocytomas. Clinicopathologic features in 36 cases. *Cancer*. 2003;98:554–561.
50. Lonser RR, Weil RJ, Wanebo JE, DeVroom HL, Oldfield EH. Surgical management of spinal cord hemangioblastomas in patients with von Hippel-Lindau disease. *J Neurosurg*. 2003;98:106–116.
51. Huang JS, Chang CJ, Jeng CM. Surgical management of hemangioblastomas of the spinal cord. *J Formos Med Assoc*. 2003;102:868–875.
52. Lonser RR, Oldfield EH. Microsurgical resection of spinal cord hemangioblastomas. *Neurosurg (ONS Suppl 3)*. 2005;57:ONS-372–ONS-376.
53. Linstadt DE, Wara WM, Leibel SA, Gutin PH, et al. Postoperative radiotherapy of primary spinal cord tumors. *Int J Rad Oncol Biol Phys*. 1989;16:1397–1403.
54. Petrovich Z, Liker M, Jozsef G. Radiotherapy for tumors of the spine. In: Petrovich Z, Brady LW, Apuzzo ML, Bamberg M, eds. *Combined Modality Therapy of Central Nervous System Tumors*. Vol. 31. Berlin: Springer; 2001:547–561.
55. Whitaker SJ, Bessell EM, Ashley SE, Bloom HJG, et al. Postoperative radiotherapy in the management of spinal cord ependymoma. *J Neurosurg*. 1991;74:720–728.
56. Abdel-Wahab M, Etuk B, Palermo J, et al. Spinal cord gliomas: a multi-institutional retrospective analysis. *Int J Rad Oncol Biol Phys*. 2006;64:1060–1071.
57. Sgouros S, Malluci CL, Jackowski A. Spinal ependymomas – the value of postoperative radiotherapy for residual disease control. *Br J Neurosurg*. 1996;10:559–566.
58. Kopelson G, Linggood RM. Intramedullary spinal cord astrocytoma versus glioblastoma. The prognostic importance of histologic grade. *Cancer*. 1982;50:732–735.

59. Newton HB. Chordoma. In: 4th ed. Raghavan D, Brecher M, Johnson DH, Meropol NJ, Moots PL, Rose P, et al., eds. *Textbook of Uncommon Cancers*. Vol. 54. Chichester: Wiley; 2012:721–732.
60. Berson AM, Castro JR, Petti P, et al. Charged particle irradiation of chordoma and chondrosarcoma of the base of skull and cervical spine: the Lawrence Berkeley laboratory experience. *Int J Radiat Oncol Biol Phys*. 1998;15:559–565.
61. Keisch ME, Garcia DM, Shibuya RB. Retrospective long-term follow-up analysis in 21 patients with chordomas of various sites treated at a single institution. *J Neurosurg*. 1991;75:374–377.
62. Thieblemont C, Biron P, Rocher F, et al. Prognostic factors in chordoma: role of postoperative radiotherapy. *Eur J Cancer*. 1996;31: 2255–2259.
63. York JE, Kaczaraj A, Abi-Said D, et al. Sacral chordoma: 40-year experience at a major cancer center. *Neurosurgery*. 1999;44:74–80.
64. Noel G, Feuvret L, Calugaru V, et al. Chordomas of the base of the skull and upper cervical spine. One hundred patients irradiated by a 3D conformal technique combining photon and proton beams. *Acta Oncol*. 2005;44:700–708.
65. Imai R, Kamada T, Tsuji H, et al. Carbon ion radiotherapy for unresectable sacral chordomas. *Clin Cancer Res*. 2004;10:5741–5746.
66. Gerszten PC, Ozhasoglu C, Burton SA, et al. CyberKnife frameless stereotactic radiosurgery for spinal lesions: clinical experience in 125 cases. *Neurosurgery*. 2004;55:89–99.
67. Balmaceda C. Chemotherapy for intramedullary spinal cord tumors. *J Neuro-Oncol*. 2000;47:293–307.
68. Doireau V, Grill J, Zerah M, et al. Chemotherapy for unresectable and recurrent intramedullary glial tumours in children. *Br J Cancer*. 1999;81:835–840.
69. Hassall TEG, Mitchell AE, Ashley DM. Carboplatin chemotherapy for progressive intramedullary spinal cord low-grade gliomas in children: three case studies and a review of the literature. *Neuro-Oncology*. 2001;3:251–257.
70. Weiss E, Klingbiel T, Kortmann RD, Hess CF, Bamberg M. Intraspinal high-grade astrocytoma in a child – rationale for chemotherapy and more intensive radiotherapy? *Child's Nerv Syst*. 1997;13:108–112.
71. Bouffet E, Amat D, Devaux Y, Desuzinges C. Chemotherapy for spinal cord astrocytoma. *Med Pediatr Oncol*. 1997;29:560–562.
72. Bouffet E, Pierre-Kahn A, Marchal JC, et al. Prognostic factors in pediatric spinal cord astrocytoma. *Cancer*. 1998;83:2391–2399.
73. Allen JC, Aviner S, Yates AJ, et al. Treatment of high-grade spinal cord astrocytoma of childhood with "8-in-1" chemotherapy and radiotherapy: a pilot study of CCG-945. *J Neurosurg*. 1998;88:215–220.
74. Lowis SP, Pizer BL, Coakham H, Nelson RJ, Bouffet E. Chemotherapy for spinal cord astrocytoma: can natural history be modified? *Child's Nerv Syst*. 1998;14:317–321.
75. Henson JW, Thornton AF, Louis DN. Spinal cord astrocytoma: response to PCV chemotherapy. *Neurology*. 2000;54:518–520.
76. Chamoun RB, Alaraj AM, Al Kutoubi AO, Abboud MR, Haddad GF. Role of temozolomide in spinal cord low grade astrocytomas: results in two pediatric patients. *Acta Neurochir (Wien)*. 2006;148:175–180.
77. Kim WH, Yoon SH, Kim CY, et al. Temozolomide for malignant primary spinal cord glioma: an experience of six cases and a literature review. *J Neuro-Oncol*. 2011;101:247–254.
78. Kaley TJ, Mondesire-Crump I, Gavrilovic IT. Temozolomide or bevacizumab for spinal cord high-grade gliomas. *J Neuro-Oncol*. 2012;109:385–389.
79. Wang F, Qiao G, Lou X. Spinal cord anaplastic oligodendroglioma with 1p deletion: report of a relapsing case treated with temozolomide. *J Neuro-Oncol*. 2011;104:387–394.
80. Newton HB. Overview of angiogenesis and the use of bevacizumab in patients with malignant gliomas. *Curr Signal Transduct Ther*. 2013;8:25–35.
81. Chamberlain MC. Etoposide for recurrent spinal cord ependymoma. *Neurology*. 2002;58:1310–1311.
82. Chamberlain MC. Salvage chemotherapy for recurrent spinal cord ependymoma. *Cancer*. 2002;95:997–1002.
83. Madden JR, Fenton LZ, Weil M, Winston KR, Partington M, Foreman NK. Experience with tamoxifen/etoposide in the treatment of a child with myxopapillary ependymoma. *Med Pediatr Oncol*. 2001;37:67–69.
84. Parsa AT, Fiore AJ, McCormick PC, Bruce JN. Genetic basis of intramedullary spinal cord tumors and therapeutic implications. *J Neuro-Oncol*. 2000;47:239–251.
85. Parsa AT, Chi JH, Acosta FL, Ames CP, McCormick PC. Intramedullary spinal cord tumors: molecular insights and surgical innovation. *Clin Neurosurg*. 2005;52:1–9.
86. Chi JH, Cachola K, Parsa AT. Genetics and molecular biology of intramedullary spinal cord tumors. *Neurosurg Clin N Am*. 2006;17: 1–5.
87. Li J, Sulman E, Aldape K. Molecular biology of brain tumors. *Handb Clin Neurol*. 2012;104:23–34.
88. Cloughesy TF, Cavanee WK, Mischel PS. Glioblastoma: from molecular pathology to targeted treatment. *Annu Rev Pathol*. 2014;9:1–25.
89. Maher EA, Furnari FB, Bachoo RM, et al. Malignant glioma: genetics and biology of a grave matter. *Genes Dev*. 2001;15:1311–1333.
90. Birch BD, Johnson JP, Parsa AT, et al. Frequent type 2, neurofibromatosis gene transcript mutations in sporadic intramedullary spinal cord ependymomas. *Neurosurgery*. 1996;39:135–140.
91. von Haken MS, White EC, Daneshvar-Shyesther L, et al. Molecular genetic analysis of chromosome arm 17p and chromosome arm 22q DNA sequences in sporadic pediatric ependymomas. *Genes Chromosom Cancer*. 1996;17:37–44.
92. Ebert C, von Haken MS, Meyer-Puttlitz B, et al. Molecular genetic analysis of ependymal tumors: NF2 mutations and chromosome 22q loss occur preferentially in intramedullary spinal ependymomas. *Am J Pathol*. 1999;155:627–632.
93. Waha A, Koch A, Hartmann W, et al. Analysis of HIC-1 methylation and transcription in human ependymomas. *J Cancer*. 2004;110:542–549.
94. Adjei AA, Hidalgo M. Intracellular signal transduction pathway proteins as targets for cancer therapy. *J Clin Oncol*. 2005;23:5386–5403.
95. Newton HB. Molecular neuro-oncology and the development of "targeted" therapeutic strategies for brain tumors. Part 1 – growth factor and ras signaling pathways. *Expert Rev Anticancer Ther*. 2003;3:595–614.
96. Newton HB. Molecular neuro-oncology and the development of "targeted" therapeutic strategies for brain tumors. Part 2 – PI3K/Akt/PTEN, mTOR, SHH/PTCH, and angiogenesis. *Expert Rev Anticancer Ther*. 2004;4:105–128.
97. Newton HB. Molecular neuro-oncology and the development of "targeted" therapeutic strategies for brain tumors. Part 5 – apoptosis and cell cycle. *Expert Rev Anticancer Ther*. 2005;5:355–378.
98. Rich JN, Bigner DD. Development of novel targeted therapies in the treatment of malignant glioma. *Nat Rev Drug Discov*. 2004;3:430–446.

CHAPTER

6

Overview of Pathology and Treatment of Intramedullary Spinal Cord Metastases

Herbert B. Newton

Division of Neuro-Oncology, Departments of Neurology and Neurosurgery, Dardinger Neuro-Oncology Center, Wexner Medical Center at The Ohio State University and James Cancer Hospital and Solove Research Institute, Columbus, OH, USA

The epidemiology of intramedullary spinal cord metastases (ISCM) was reviewed in detail in Chapter 4. In this chapter, we will provide an overview of the classification, pathology, and treatment of ISCM. Metastases to the spinal cord parenchyma are very uncommon compared with primary spinal cord tumors (SCT) and neoplastic epidural spinal cord compression (see Chapter 7), affecting only 0.5–2.0% of all cancer patients.[1–5] However, they are often associated with significant morbidity and mortality, and often herald the onset of a more biologically aggressive and advanced form of the primary malignancy.[6,7] ISCM represent 8.5% of all central nervous system metastases and only 1–3% of all intramedullary SCT. Although ISCM can arise from virtually any primary systemic neoplasm, the vast majority are due to tumors of the lung and breast, malignant melanoma, and renal cell carcinoma (see Table 1).

PATHOLOGY OF ISCM

ISCM are distributed fairly evenly along the entire length of the spinal cord, with a possible subtle predilection for the conus medullaris.[2–5,8,9] The mechanism of metastatic spread of tumor cells from the primary neoplasm to the spinal cord parenchyma remains unclear. In the majority of cases, hematogenous dissemination is thought to be involved, usually via an arterial route.[4,8] This is corroborated by the common coexistence of pulmonary and brain metastasis in patients with ISCM. In addition, an arterial mechanism is consistent with spinal necropsy data demonstrating that ISCM typically involve the posterior horns, which contain spinal gray matter and have dense capillary beds, with five times the arterial perfusion compared with the surrounding spinal white matter.[4,10] Hematogenous spread through the vertebral venous plexus (i.e., Batson's venous plexus) has also been suggested as another mechanism in some patients with ISCM. In these cases, tumor cells gain access to the spinal cord parenchyma via retrograde movement through the plexus. Tumor cells may also gain access to the spinal cord directly from cerebrospinal fluid in patients with preexisting leptomeningeal metastases.[8,9] In this situation, tumor cells infiltrate the Virchow-Robin spaces of blood vessels entering the cord, and then penetrate the pial layer to gain access to spinal cord parenchyma. The last possible mechanism involves direct extension of tumor cells into the spinal cord from an adjacent primary neoplasm. The tumor cells are able to enter the cord parenchyma by extending directly through the dura or by perineural spread along nerve roots.

Once the metastatic bolus of cells has gained access to the spinal cord and has lodged within the cord parenchyma, neoplastic angiogenesis is required for the tumor to grow to a clinically relevant size.[11–13] The angiogenic phenotype requires upregulation of angiogenic promoters such as vascular endothelial growth factor (VEGF), fibroblast growth factors (basic FGF, acidic FGF), angiopoietins (Ang-1, Ang-2), platelet-derived growth factor (PDGF), epidermal growth factor (EGF), transforming growth factors (TGFα and TGFβ), interleukins (IL-6, IL-8), and the various growth factor receptors (e.g., VEGFR, PDGFR, EGFR).[12,13] Secretion of angiogenesis inhibitors, such as thrombospondin-1, platelet factor-4, and interferons α and β, is typically reduced in the ISCM, further "tipping the balance" in the local environment to permit angiogenic activity within and around the tumor mass.

http://dx.doi.org/10.1016/B978-0-12-800945-1.00006-9

© 2016 Elsevier Ltd. All rights reserved.

TABLE 1 Percentage of Intramedullary Spinal Cord Metastases by Primary Tumor Site

Primary Type	Percentage (%)
Lung	50–60
SCLC	50–55
NonSCLC	45–50
Breast	10–13
Melanoma	9
Renal cell	5–9
Lymphoma	5
Colorectal and GI	3
Thyroid	2
Ovarian	1–2

SCLC, small cell lung carcinoma; GI, gastrointestinal.
Adapted from Refs 2–5.

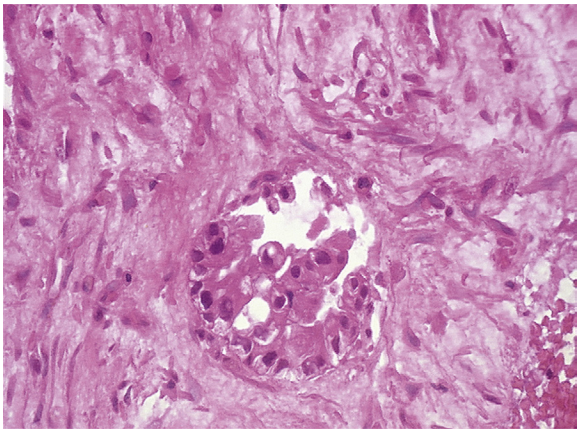


FIGURE 1 Low-power view of a bronchogenic carcinoma metastatic to the cervical spinal cord, demonstrating gliotic tissue surrounding the focus of tumor. Hematoxylin and eosin staining (x200 magnification).

On macroscopic evaluation, ISCM usually form rounded, discrete deposits in the spinal cord parenchyma that are well circumscribed and demarcated from surrounding neural tissues (see Figure 1).[2–4,8,9] Foci of hemorrhage may be noted within the tumor and involvement of the posterior nerve roots is often present. On microscopic examination, the histological features of the ISCM are usually similar, if not identical, to those of the primary neoplasm (see Figure 2).[14,15] The tumor mass will usually have well-defined borders, tending to displace adjacent spinal cord parenchyma without significant infiltration. Areas of hemorrhage and gliosis are frequently noted. Initial review of the tissue morphology can often identify a major tumor category, such as metastatic carcinoma or melanoma. However, in roughly 3% of ISCM cases, no known histopathological tissue pattern

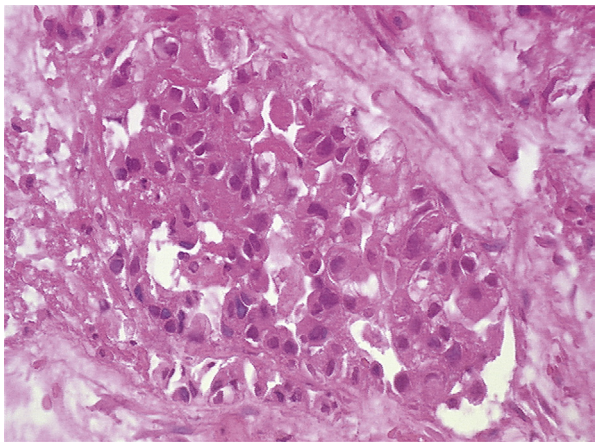


FIGURE 2 High-power view of the same intramedullary metastasis, revealing features of an adenocarcinoma, with the formation of complex glandular structures, as well as pleomorphic and hyperchromatic nuclei. Hematoxylin and eosin staining (x400 magnification).

can be discerned.[16] For a more detailed determination of cellular differentiation and assignment to a specific histological category, immunocytochemical analysis may be required.[14,15]

SURGICAL THERAPY OF ISCM

In the past, surgical approaches to treatment of ISCM were not attempted due to the frequent occurrence of neurological injury. Technical advances in neurosurgical techniques have improved the results of operative therapy for ISCM in carefully selected patients.[3–5,17,18] These advances include the use of the operating microscope and microneurosurgical instrumentation, bipolar coagulation, surgical lasers, ultrasonic aspirators, intraoperative ultrasound localization, and the use of intraoperative spinal cord evoked potential monitoring. Intraoperative monitoring of sensory and motor evoked potentials should be considered for all patients undergoing surgery for an ISCM.[18,19] A 50% decline in evoked potential amplitude during the procedure may be an indication of a new, possibly permanent, postoperative motor deficit.

Several reports suggest that carefully selected patients with ISCM can benefit from surgical resection.[3–5,16–18] Patients with a suspected ISCM that have an unknown primary tumor should be considered for a biopsy, to allow for a definitive pathological diagnosis. A more aggressive approach may not be possible for patients with poor general medical condition, widespread systemic disease, or concomitant brain metastases and/or leptomeningeal disease. For the cohort of patients with higher functional status and well-controlled systemic and neurological disease, an open spinal procedure should be attempted, using a similar technique to what has been described

for primary intramedullary SCT (see Chapter 5).[3,4,18] If there is a clear cleavage plane between the tumor margin and the surrounding normal spinal cord parenchyma, an aggressive gross total resection should be performed. If a clear cleavage plane cannot be discerned, a biopsy and decompressive laminectomy will be sufficient to allow for the development of an appropriate treatment plan. Using this treatment paradigm, Gasser and colleagues reviewed their experience with surgical therapy in a series of 13 patients with ISCM.[18] They were able to accomplish complete surgical removal of the tumor in six patients and an incomplete resection in the remaining seven patients. Eleven of the 13 patients were clinically stable in the postoperative period. The histology of the primary tumor appeared to affect the extent of resection and surgical outcome. A complete resection was possible for all ISCM from adenocarcinomas. However, tumors derived from sarcomas and poorly differentiated carcinomas could only be incompletely resected due to poor cleavage planes.

RADIATION THERAPY OF ISCM

The most common method of treatment for patients with ISCM has been a combination of dexamethasone and external beam irradiation of the spine.[2–7,16,17] Dexamethasone is able to acutely reduce peritumoral edema and can improve pain and neurological function in up to 85% of patients.[17] The use of dexamethasone provides neurological stabilization in the majority of patients while they are being prepared for more definitive therapy. Fractionated external beam radiotherapy (RT) is the treatment modality of choice for the vast majority of patients with ISCM, even if they have undergone an aggressive surgical resection.[2–5,16,17,20] Initial reports suggested that ISCM were often multiple and that RT of the entire spinal cord was necessary.[7–9] However, this approach often led to severe bone marrow toxicity and hematologic compromise. In the era of magnetic resonance imaging of the spine, it is now known that ISCM are usually solitary lesions and that multifocal disease only occurs in approximately 12–15% of patients.[2–4,21] Therefore, focal RT to the site of the lesion, with a 1–2 cm margin above and below the mass, will be appropriate for most patients. Various RT treatment schedules have been used, but most authors suggest a total dose between 30 and 40 Gy, administered in daily fractions of 200–300 cGy, over 2-3 weeks.[2–5,16,17]

The clinical response to RT is variable depending on several key factors, including the histology and radiosensitivity of the ISCM, the duration of the symptoms, and the extent of the neurological deficit at the time of treatment initiation. Irradiation is very effective in radiosensitive tumor types, such as small cell lung carcinoma (SCLC), lymphoma, and germ cell tumors.[2–5,16,17,22] Clinical stabilization or improvement can also be noted in patients with less sensitive tumors, including those from breast, prostate, ovary, and non-SCLC.[2–5,16,17,23,24] However, it must be noted that even some tumors that are traditionally considered to be insensitive to RT, such as renal cell carcinoma, can be stabilized if the treatment is initiated early in the course of ISCM.[25] Overall, it appears that early diagnosis and treatment of ISCM is even more important than sensitive histology.[2–4,7,16,17] The majority of patients, regardless of ISCM histology, will have the potential for clinical and neurological stabilization if RT (with or without surgical resection) and dexamethasone are utilized before the onset of significant spinal cord damage and weakness (i.e., myelopathy with paraparesis or tetraparesis). If RT and dexamethasone are initiated while the patient is still ambulatory, the prognosis for stabilization of function is very good. Regardless of the histologic subtype, if treatment of ISCM is started after the onset of severe myelopathy and limb weakness, the likelihood of any significant recovery is poor.

A new RT technique under evaluation for ISCM is image-guided, frameless stereotactic radiosurgery.[26–28] Several reports by Ryu and coworkers suggest that single dose radiosurgery, given as a boost after RT (6–8 Gy) or as "stand alone" treatment (10–60 Gy), can be safely delivered to the spine, is well tolerated, and often results in rapid pain control.[26,27] In their series, the incidence of tumor recurrence or progression into adjacent spinal regions was only 5%. Using the CyberKnife® radiosurgery system, Gerszten and colleagues have described their experience in a series of 125 patients with spinal tumors, including 108 with metastatic lesions.[28] For the entire cohort, the mean dose was 14 Gy at the 80% isodose line (range 12–20 Gy). The treatment was well tolerated by patients. During follow-up evaluation that ranged from 6 to 27 months, most of the metastatic tumors remained stable. In a series of nine patients with ISCM, Veeravagu et al. also used the CyberKnife radiosurgery platform, delivering 14–27 Gy (median 21 Gy) in 1–5 fractions (median 3).[29] Although overall survival was poor, due to advanced systemic disease (median survival 4.0 months), radiosurgical treatment resulted in excellent local control of disease in the majority of patients.

CHEMOTHERAPY OF ISCM

Chemotherapy has occasionally been applied to ISCM as indicated by tumor staging and prior responses.[2–5,9,16,25,30] However, there are no chemotherapy protocols or drug strategies specific for ISCM. Several authors suggest adding chemotherapy to RT in cases with

chemosensitive tumors (e.g., SCLC, lymphoma, germ cell tumors, breast carcinoma).[5,16,25] In addition, intrathecal chemotherapy can be used for patients with concomitant ISCM and leptomeningeal disease.[2–4] In a review of survival and prognosis by Connolly and colleagues, the addition of chemotherapy to RT imparted a significant extension of survival compared with RT alone ($p < 0.05$).[16] In their series, patients with melanoma had the best survival (43 weeks), while patients with lung and breast tumors only survived 19.7 and 13.0 weeks, respectively. Another report reviewed the results of chemotherapy as the sole treatment for two patients with ISCM from SCLC.[31] The first patient was treated with etoposide and nitrosoureas and had a partial response that lasted for 6 months. The second patient received cyclophosphamide, adriamycin, etoposide, and cisplatin and had a complete response before the addition of focal RT. Several other patients with lung carcinoma were also reported to respond to similar chemotherapy regimens, usually in combination with RT.[6,16,31]

Acknowledgments

The authors would like to thank Shawna Huckell and Nicole Ghaffari for research assistance. Dr. Newton was supported in part by National Cancer Institute grant, CA 16058 and the Dardinger Neuro-Oncology Center Endowment Fund.

References

1. Engelhard HH, Villano JL, Porter KR, et al. Clinical presentation, histology, and treatment of 430 patients with primary tumors of the spinal cord, spinal meninges, or cauda equina. *J Neurosurg Spine*. 2010;13:67–77.
2. Sung WS, Sung MJ, Chan JH, et al. Intramedullary spinal cord metastases: a 20-year institutional experience with a comprehensive literature review. *World Neurosurg*. 2013;79:576–584.
3. Rykken JB, Diehn FE, Hunt CH, et al. Intramedullary spinal cord metastases: MRI and relevant clinical features from a 13-year institutional case series. *AJNR Am J Neuroradiol*. 2013;34:2043–2049.
4. Chi JH, Parsa AT. Intramedullary spinal cord metastasis: clinical management and surgical considerations. *Neurosurg Clin N Am*. 2006;17:45–50.
5. Kalayci M, Cagavi F, Gul S, et al. Intramedullary spinal cord metastases: diagnosis and treatment – an illustrated review. *Acta Neurochir (Wien)*. 2004;146:1347–1354.
6. Grem JL, Burgess J, Trump DL. Clinical features and natural history of intramedullary spinal cord metastasis. *Cancer*. 1985;56:2305–2314.
7. Winkelman MD, Adelstein DJ, Karlins NL. Intramedullary spinal cord metastasis. Diagnostic and therapeutic considerations. *Arch Neurol*. 1987;44:526–531.
8. Costigan DA, Winkelman MD. Intramedullary spinal cord metastasis. A clinicopathological study of 13 cases. *J Neurosurg*. 1985;62:227–233.
9. Dunne JW, Harper CG, Pamphlett R. Intramedullary spinal cord metastases: a clinical and pathological study of nine cases. *Q J Med*. 1986;61:1003–1020.
10. Qui MG, Zhu XH. Aging changes of the angioarchitecture and arterial morphology of the spinal cord in rats. *Gerontology*. 2004;50:360–365.
11. Beckner ME. Factors promoting tumor angiogenesis. *Cancer Investig*. 1999;17:594–623.
12. Webb CP, Vande Woude GF. Genes that regulate metastasis and angiogenesis. *J Neuro-Oncol*. 2000;50:71–87.
13. Yoshida BA, Sokoloff MM, Welch DR, Rinker-Schaeffer CW. Metastasis-suppressor genes: a review and perspective on an emerging field. *J Natl Cancer Inst*. 2000;92:1717–1730.
14. Bruner JM, Tien RD. Secondary tumors. In: Bigner DD, McLendon RE, Bruner JM, eds. *Russell & Rubinstein's Pathology of Tumors of the Nervous System. Sixth Edition. Volume 2.* London: Arnold; 1998;17:419–450.
15. Metastatic tumours. In: Ironside JW, Moss TH, Louis DN, Lowe JS, Weller RO, eds. *Diagnostic Pathology of Nervous System Tumours*. Vol. 12. London: Churchill Livingstone; 2002:319–341.
16. Connolly ES, Winfree CJ, McCormick PC, Cruz M, Stein BM. Intramedullary spinal cord metastasis: report of three cases and review of the literature. *Surg Neurol*. 1996;46:329–337.
17. Gasser TG, Pospiech J, Stolke D, Schwechheimer K. Spinal intramedullary metastases. Report of two cases and review of the literature. *Neurosurg Rev*. 2001;24:88–92.
18. Gasser T, Sandalcioglu IE, El Hamawi B, van de Nes JAP, Stolke D, Wiedemayer H. Surgical treatment of intramedullary spinal cord metastases of systemic cancer: functional outcome and prognosis. *J Neuro-Oncol*. 2005;73:163–168.
19. Morota N, Deletis V, Constantini S, Kofler M, Cohen H, Epstein FJ. The role of motor evoked potentials during surgery for intramedullary spinal cord tumors. *Neurosurgery*. 1997;41:1327–1336.
20. Petrovich Z, Liker M, Jozsef G. Radiotherapy for tumors of the spine. In: Petrovich Z, Brady LW, Apuzzo ML, Bamberg M, eds. *Combined Modality Therapy of Central Nervous System Tumors*. Vol. 31. Berlin: Springer; 2001:547–561.
21. Li MH, Holtas S. MR imaging of spinal intramedullary tumors. *Acta Radiol*. 1991;32:505–513.
22. Nikolaou M, Kumpou M, Mylonakis N, et al. Intramedullary spinal cord metastases from atypical small cell lung cancer: a case report and literature review. *Cancer Investig*. 2006;24:46–49.
23. Potti A, Abdel-Raheem M, Levitt R, Schell DA, Mehdi SA. Intramedullary spinal cord metastases (ISCM) and non-small cell lung carcinoma (NSCLC): clinical patterns, diagnosis, and therapeutic considerations. *Lung Cancer*. 2001;31:319–323.
24. Vellegas AE, Guthrie TH. Intramedullary spinal cord metastasis in breast cancer: clinical features, diagnosis, and therapeutic consideration. *Breast J*. 2004;10:532–535.
25. Fakih M, Schiff D, Erlich R, Logan TF. Intramedullary spinal cord metastasis (ISCM) in renal cell carcinoma: a series of six cases. *Ann Oncol*. 2001;12:1173–1177.
26. Ryu S, Fang YF, Rock J, et al. Image-guided and intensity-modulated radiosurgery for patients with spinal metastasis. *Cancer*. 2003;97:2013–2018.
27. Ryu S, Rock J, Rosenblum M, Kim JH. Patterns of failure after single-dose radiosurgery for spinal metastasis. *J Neurosurg*. 2004;101:402–405.
28. Gerszten PC, Ozhasoglu C, Burton SA, et al. CyberKnife frameless stereotactic radiosurgery for spinal lesions: clinical experience in 125 cases. *Neurosurgery*. 2004;55:89–99.
29. Veeravagu A, Lieberson RE, Miener A, et al. CyberKnife stereotactic radiosurgery for the treatment of intramedullary spinal cord metastases. *J Clin Neurosci*. 2012;19:1273–1277.
30. Balmaceda C. Chemotherapy for intramedullary spinal cord tumors. *J Neuro-Oncol*. 2000;47:293–307.
31. Ferrior JP, Cadranel J, Khalil A, Lebreton C, Contant S, Milleron B. Intramedullary metastases of bronchogenic carcinoma. Two cases. *Rev Neurol (Paris)*. 1998;154:166–169.

CHAPTER

7

Epidural Spinal Cord Compression in Adult Neoplasms

Alicia M. Zukas, David Schiff

Department of Neurology, University of Virginia Health System, Charlottesville, VA, USA; Neuro-Oncology Center, University of Virginia Health System, Charlottesville, VA, USA

INTRODUCTION

Malignant spinal cord compression types can be thought of as affecting the intradural or extradural spaces. The intradural space comprises the subarachnoid space, where leptomeningeal metastases occur, and the intramedullary space comprises the spinal cord. These intradural spaces are less commonly invaded by metastases. The extradural space of the spinal cord is also known as the epidural space; it contains fat, lymphatics, vasculature, and nerve roots. For as many as 20% of patients with metastatic lesions, the first identified metastasis is within this epidural space.[1,2] This is because there is often significant morbidity with epidural metastases, with symptoms arising from painful bony involvement with periosteum sensitivity, vascular congestion, and compression.[3]

About 60% of epidural spinal cord compression (ESCC) occurs in the thoracic spine, with about 30% in the lumbosacral spine and 10% in the cervical spine.[4] The predilection for the thoracic region may be because of the larger number of vertebrae, its natural kyphosis, and the smaller diameter for symptomatic compression to occur in comparison to other areas of the spine. The thoracic spine is also more sensitive to radiation because of its poor vascular supply.

Tumor cells typically disseminate in the body via seeding of organs or body cavities, lymphatic spread, or hematogenous spread. It had been thought that metastases travel to the epidural space via the Batson plexus with posterior extension leading to dural compression. It was Batson himself who hypothesized that intrathoracic or intra-abdominal changes in pressure allowed for their embolization and venous reflux into the epidural space.[5] However, postmortem studies have reported that metastatic epidural tumors arise from the vertebral bodies.[6,7] The arterial system is suspected as the avenue for spread to these vertebral bodies' rich hematopoietic bone marrow. Less commonly metastases arise at the marrow-destitute posterior vertebral arch or via intraspinal spread derived from a vertebral neural foramen. Lymphomas or neuroblastomas may invade by way of the vertebral neuroforamina in about 15% of ESCCs.[8]

The damage done by epidural metastatic lesions is namely due to the vascular congestion and vascular edema through blockage of the epidural venous plexus. This congestion is prostaglandin driven and probably even vascular endothelial growth factor mediated based on intracranial studies. Vasogenic edema can result in spinal cord demyelination, infarction, and therefore irreversible neurological loss. Less commonly do the lesions cause direct compression of the cord, although they may also indirectly damage the spinal cord by destabilization of the spinal column through pathological fractures.[9]

ETIOLOGY

While some tumor types may be better able to survive migration after undergoing a metastatic cascade to take up new residence, it seems any cancer type has the propensity for epidural invasion. Metastases from the breast, lung, or prostate account for roughly 50% of all epidural metastatic lesions. About 70% of patients with advanced breast or prostate cancer have bone metastases on postmortem examination.[10,11] Coleman et al. even found bone metastases in 42% of patients with thyroid cancer and 35% with kidney cancers on postmortem examination.

Handbook of Neuro-Oncology Neuroimaging, Second Edition
http://dx.doi.org/10.1016/B978-0-12-800945-1.00007-0

© 2016 Elsevier Ltd. All rights reserved.

In prostate cancer patients, the additional risk of spinal cord compression is 24%; if the Gleason score is greater than or equal to 7, they are at 2.37 times higher risk.[12] While breast, lung, and prostate are statistically the most common cancers in adults, epidural metastases are also commonly seen in non-Hodgkin lymphoma, renal cell carcinoma, and multiple myeloma.[13]

In children, the most common culprits are sarcomas, neuroblastomas, germ cell tumors, and Hodgkin lymphoma.[14] In a large Danish population-based study of 1841 children with cancer, 1.6% developed bone metastases over 10 years and only 10% of these patients had spinal cord compression.[15] The majority (93%) of these children had solid tumors and survival was significantly poorer for these patients with bone metastases.

CLINICAL FEATURES

The symptoms associated with malignant spinal cord compression are directly related to the size and the location of the lesion. Typically, the cardinal clinical feature is back pain. Table 1 identifies pain as being present in 83–96% of patients at the time of presentation. With a metastasis starting in the vertebral body, its outward growth may stretch the sensitive periosteum, and this is perceived as localized pain. Over time, the pain usually intensifies and changes from a focal pain to a radicular pain as it invades the epidural space. Pain is often magnified with stressors to the vertebrae or stretching of the venous plexus as with position changes, recumbency, and straining.[4] Objective findings of weakness are seen in 61–85% of patients at the time of presentation. About two-thirds of all spinal cord compression patients are nonambulatory at the time of diagnosis[16] from either the myelopathy affecting the antigravity muscles of the lower extremities or pain. Sensory deficit complaints are less common than complaints of weakness but can often be discovered on close examination.[8] Lhermitte phenomena may be elicited if there is dorsal compression at the level of the cervical or thoracic spine.

TABLE 1 Clinical Presentation of Malignant Spinal Cord Compression

Patients	Pain (%)	Weakness (%)	Sensory Deficits (%)	Autonomic Dysfunction (%)
398	83	67	90	48
153	88	61	78	40
130	96	76	51	57
79	70	91	46	44
77	94	85	57	52

Prasad D, Schiff D. Malignant spinal-cord compression. Lancet Oncol. *2005;6:15-24.*

Cauda equina involvement should be suspected if there are saddle sensory complaints or consistent bowel or bladder symptoms. Compression on the lateral spinal cord may manifest as isolated ataxia by affecting descending spinocerebellar tracts.

DIAGNOSIS

Certainly history and clinical examination are indispensable in terms of identifying a lesion. Magnetic resonance imaging (MRI) is the principal modality for confirming clinical suspicion, by establishing a precise localization and determining the degree of destruction to surrounding tissues. If MRI is not available or contraindicated, computerized tomography or invasive cisternal and lumbar myelography are second-line imaging modalities. The standard MRI protocol for ESCC detection involves sagittal T1-weighted, short TI inversion recovery sequences, and fat-suppressed T2 fast-spin-echo-weighted sequences with T1- and/or T2-weighted axial planes. The entire spine should be imaged, as 30% of patients presenting with an ESCC have additional lesions.[17] The vertebral metastasis is hypointense on T1 and easily seen against normal high-signal fatty tissue of the vertebral bodies. Consequently, the lesion is hyperintense on T2 sequences and edematous spinal cord will have increased T2 signal, indicative of vascular congestion. The lesion may show contrast enhancement, helping differentiate its extra- versus intradural location and can evaluate for extraosseous extension.

CORTICOSTEROIDS

Systemic corticosteroids have been shown to be effective for symptom management as well as in delaying irreversible neurological deficits. They work by decreasing capillary permeability and by providing analgesia through inhibiting prostaglandin synthesis. Steroids are recommended for anyone undergoing radiotherapy unless otherwise contraindicated. Recommended doses may range from 16 to 100 mg of dexamethasone per day. A standard initial dose may be 10 mg followed by 16 mg total daily dose, usually in divided dosing. For patients with dense neurological disability, a 100-mg bolus may even be used with high maintenance doses.[18] One randomized controlled trial by Graham et al. was not able to derive an optimal dose for systemic corticosteroids.[19] Steroids can be generally weaned after 2 weeks of treatment initiation.[13] In general, anti-inflammatory drugs should be given at the lowest effective dose and in monotherapy, to reduce the risk of gastric ulceration. With steroids alone, there is a 1.8 times risk of gastric ulceration, but in combination with nonsteroidal

anti-inflammatory drugs, this poses 12 times the risk for perforation, thus driving the recommendation for gastrointestinal prophylaxis.[20,21]

TREATMENT

The treatment for ESCC is interdisciplinary, and typically comprises some combination of corticosteroids, surgery, and radiation. Chemotherapy is considered if the cancer is chemosensitive and may be able to capture other disseminated tumor cells. Indications for surgery of ESCC include pathological fracture resulting in bone fragments impinging on the spinal cord, radioresistant tumor, or a need for tissue for diagnosis. Bisphosphonates can also be offered for risk of pathological vertebral collapse. The success of surgical decompression is dependent in large part on the severity and location of the compression and whether the expected survival is greater than 3 months.[12] Initial surgical decompressions are generally done with laminectomies and vertebral corpectomies; however, these are followed by radiotherapy or radiosurgery for residual tumor.

In 2005, a landmark study identified that surgery plus radiation is superior to radiation alone. Patchell et al. performed a randomized controlled trial of 101 patients with metastatic extradural spinal cord compression.[13] Patients were randomized to receive either decompressive surgery with radiotherapy 14 days later or radiotherapy alone, with both arms receiving 30 Gy in 10 fractions and high-dose dexamethasone. The authors found that the patients treated with the combined modalities had improved ambulation outcomes, improved urinary continence, and even improved overall survival (median 126 days vs 100 days; $p = 0.033$). Several groups then looked at patients with radioresistant tumor types and found that those with renal cell cancer have similar ambulatory outcomes after surgery and radiotherapy compared to those with classically radiosensitive epidural metastases.

As higher doses of radiation may lead to late radiation injury to the spinal cord, the optimal fractionation dose for patients with a shorter life expectancy was investigated by Maranzano et al. They found that there was no significant difference in time to ambulation, bladder function, or pain relief between patients receiving a split course (5 Gy × 3 days + 3 Gy × 5 days) and those receiving a short course (8 Gy × 2 days) of radiotherapy.[22] In 2009, Maranzano et al. then found no significant difference among 303 patients with variable prognoses: 16 Gy in two fractions versus 8 Gy in one fraction.[23] Ultimately, a nonrandomized study comparing a short course versus a long course of radiotherapy in 265 patients found that the long-course radiotherapy improved 12-month progression-free survival by 72% versus 55%, $p = 0.034$, as well as local control rates—81% vs 61%, $p = 0.005$.[24] Intrinsic radiosensitivity of the tumor, acuteness of the onset of neurological deficits, the extent of pretreatment deficits, and the extent of anatomic compression of the spinal cord are all factors in clinical outcomes following radiotherapy.[25]

Spinal radiosurgery is a noninvasive delivery of a large radiation dose to a localized site while driving the radiation beam with radiographic tracking. This is a good alternative for a lesion with little mass effect upon the cord but necessitating open surgery, if the patient has additional surgical comorbidities, or if the lesion is in a surgically inaccessible location.[26] This targeted dose also spares surrounding healthy tissue in a radiation field. This is typically reserved for patients with limited disease and greater than 3 months of expected survival. After one to five sessions of radiosurgery, Sheehan et al. reported that 40% of patients had improvement in their neurological function and 85% of patients had rapid improvement in pain level. Chang et al. also found that there was radiological control of spinal metastases after radiosurgery in 80% of treated patients after 12 months.[27]

PROGNOSIS

Even without epidural disease, the burden of metastatic disease and presence of bony metastatic lesions are poor prognostic indicators. With metastatic disease to the spinal cord, the pretreatment performance status best predicts for posttreatment neurological status. Preservation of ambulation appears to be an independent factor in life expectancy. Combining surgery with radiation has provided the best outcome for improved ambulation, urinary continence, and overall survival. Radiation therapy has proven utility both in reducing pain and in preserving neurological function in patients with ESCC. One possible latent detrimental consequence of radiotherapy is radiation myelopathy. While rare, it may begin as early as 9 months after treatment, with the risk reduced with careful planning and dose selection. With median survival between 3 and 7 months, and 36% probability of survival to 12 months,[12] the concern for this latent adverse event must be weighed against the need for acute management performed with the intention of prolonging survival and quality of life. If there is lesion recurrence, treatment options may again be revisited, including reirradiation, chemotherapy, and surgery.

References

1. Loblaw DA, Laperriere NJ, Mackillop WJ. A population-based study of malignant spinal cord compression in Ontario. *Clin Oncol*. 2003;15:211–217.
2. Schiff D, O'Neill BP, Suman VJ. Spinal epidural metastasis as the initial manifestation of malignancy: clinical features and diagnostic approach. *Neurology*. 1997;49:452–456.

3. Bach F, Larsen BH, Rohde, et al. Metastatic spinal cord compression. Occurrence, symptoms, clinical presentations and prognosis in 398 patients with spinal cord compression. *Acta Neurochir*. 1990;107(1–2):37–43.
4. Schiff D. Spinal cord compression. *Neurol Clin N Am*. 2003;21: 67–86.
5. Coman DR, DeLong RP. The role of the vertebral venous system in the metastasis of cancer to the spinal column: experiments with tumor-cell suspensions in rats and rabbits. *Cancer*. 1951;4:610–618.
6. Wong DA, Fornasier VL, MacNab I. Spinal metastases: the obvious, the occult, and the imposters. *Spine*. 1990;15:1–4.
7. Arguello F, Baggs RB, Duerst RE, Johnstone L, McQueen K, Frantz CN. Pathogenesis of vertebral metastases and epidural spinal cord compression. *Cancer*. 1990;65:98–106.
8. Gilbert RW, Kim JH, Posner JB. Epidural spinal cord compression from metastatic tumor diagnosis and treatment. *Ann Neurol*. 1978;3:40–51.
9. Ushio Y, Posner R, Posner JB, et al. Experimental spinal cord compression by epidural neoplasm. *Neurology*. 1977;27:422–429.
10. Roodman GD. Mechanisms of bone metastasis. *N Engl J Med*. 2004;350:1655–1664.
11. Coleman RE. Clinical features of metastatic bone disease and risk of skeletal morbidity. *Clin Cancer Res*. 2006;12:6243s–6249s.
12. Sutcliffe P, Connock M, Shyangdan D, Court R, Kandala NB, Clarke A. A systematic review of evidence on malignant spinal metastases: natural history and technologies for identifying patients at high risk of vertebral fracture and spinal cord compression. *Health Technol Assess*. September 2013;17(42).
13. Patchell RA, Tibbs PA, Reine WF, et al. Direct decompressive surgical resection in the treatment of spinal cord compression caused by metastatic cancer: a randomized trial. *Lancet*. 2005;366: 643–648.
14. Klein SL, Sanford RA, Muhlbauer MS. Pediatric spinal epidural metastases. *J Neurosurg*. 1991;74:70–75.
15. Hernandez R, Maegbaek ML, Liede A, Sorense HT, Ehrenstein VA. *J Pediatr Hematol Oncol*. October 2014;36(7):528–533.
16. Husband DJ. Malignant spinal cord compression: prospective study of delays in referral and treatment. *BMJ*. 1998;317:18–21.
17. Schiff D, O'Neill BP, Wang CH, O'Fallon JR. Neuroimaging and treatment implications of patients with multiple epidural spinal metastases. *Cancer*. 1998;83:1593–1601.
18. Sorensen S, Helweg-Larsen S, Mouridsen H, et al. Effect of high-dose dexamethasone in carcinomatous metastatic spinal cord compression treated with radiotherapy: a randomised trial. *Eur J Cancer*. 1994;1:22–27.
19. Graham PH, Capp A, Delaney G, et al. A pilot randomised comparison of dexamethasone 96 mg vs 16 mg per day for malignant spinal cord compression treated by radiotherapy: TROG 01.05 Superdex study. *Clin Oncol R Coll Radiol*. 2006;18:70–76.
20. Heimdal K, Hirschberg H, Slettebo H, et al. High incidence of serious side effects of high-dose dexamethasone treatment in patients with epidural spinal cord compression. *J Neurooncol*. 1992;12:141–144.
21. Hernández-Díaz S, Rodríguez L. Steroids and risk of upper gastrointestinal complications. *Am J Epidemiol*. 2001;153:1089–1093.
22. Maranzano E, Bellavita R, Rossi R, et al. Short course radiotherapy in metastatic spinal cord compression: results of a phase III, randomized, multicenter trial. *J Clin Oncol*. 2005;23:3358–3365.
23. Maranzano E, Trippa F, Casale M, et al. 8 Gy single-dose radiotherapy is effective in metastatic spinal cord compression: results of a phase III randomizedmulticentre Italian trial. *Radiother Oncol*. 2009;93:174–179.
24. Rades D, Lange M, Veninga T, et al. Final results of a prospective study comparing the local control of short-course and long-course radiotherapy for metastatic spinal cord compression. *Int J Radiat Oncol Biol Phys*. 2011;79:524–530.
25. Schiff D. Metastatic spinal cord disease. *Continuum*. 2005;11(5): 30–46.
26. Sheehan JP, Shaffrey CI, Shlesinger D, Williams BJ, Arlet V, Larner J. Radiosurgery in the treatment of spinal metastases: tumor control, survival, and quality of life after helical tomotherapy. *Neurosurgery*. 2009;65:1052–1062.
27. Chang UK, Cho WI, Kim MS, Cho CK, Lee DH, Rhee CH. Local tumor control after retreatment of spinal metastasis using stereotactic body radiotherapy;comparison with initial treatment group. *Acta Oncol*. 2012;51(5):589–595.

CHAPTER

8

Neoplastic Meningitis

Sophie Taillibert[1], *Emilie Le Rhun*[2,3], *Marc C. Chamberlain*[4]

[1]Department of Neurology Mazarin and Department of Radiation Oncology, Pitié-Salpétrière Hospital, University Pierre et Marie Curie, Paris VI, Paris, France; [2]Breast Unit, Department of Medical Oncology, Oscar Lambret Center, Lille Cedex, France; [3]Department of Neuro-oncology, Neurosurgery, Roger Salengro Hospital, University Hospital, Lille Cedex, France; [4]Department of Neurology and Neurological Sciences, Fred Hutchinson Cancer Research Center, University of Washington, Seattle, Washington, USA

EPIDEMIOLOGY

Neoplastic meningitis (NM) is diagnosed in 3–5% of patients with solid tumors (termed carcinomatous meningitis), 5–15% of patients with leukemia and lymphoma (termed leukemic or lymphomatous meningitis, respectively), and 1–2 % of patients with primary brain tumors.[1–5] Autopsy studies show that 19% of patients with cancer and neurologic signs and symptoms have evidence of meningeal involvement.[6] Adenocarcinoma is the most frequent histology and breast, lung, and melanoma are the most common primary sites to metastasize to the leptomeninges (Table 1).[3,7,8] Although small cell lung cancer (SCLC) and melanoma have the highest rates of spread to the leptomeninges (11% and 20%, respectively), [9,10] because of the higher incidence of breast cancer (with a 5% rate of spread), [11] the latter accounts for most cases in large series of the disorder.[1,7] In breast cancer, risk factors for the development of NM are an infiltrating lobular carcinoma type, and estrogen receptor and progesterone receptor negative status.[12–17] Triple negative status of breast cancer has also previously been reported to be a risk factor for development of NM.[18] NM is still a relatively rare manifestation of HER2 positive breast cancers (3–5%), notwithstanding the increased incidence of parenchymal brain metastasis (Table 2).[19]

Treatment of systemic cancer metastatic to the central nervous system (CNS) appears to influence the incidence of NM accounting in part for the apparent increase incidence of NM. Among these factors, surgical resection of parenchymal cerebellar metastases increases the risk of subsequent development of NM.[20–22] Resection of supratentorial brain metastasis that results in entry into the ventricular system also appears to increase the risks of developing NM.[20, 23–25] The presumed mechanism in both instances suggests spillage of cancer cells directly into the cerebrospinal fluid (CSF) and subsequent dissemination. Another, and likely most important, factor contributing to the increased incidence of NM and other CNS metastases includes the use of more effective systemic therapy, both adjuvant and salvage. This can lead to improved and prolonged survival that penetrates the CNS poorly, resulting in a pharmacologic sanctuary within the CNS. An example is the use of newer targeted therapies with poor CNS penetration such as trastuzumab (HER2 positive breast cancer) and rituximab (lymphoma).[26–28] The meninges and CSF compartments are a pharmacological sanctuary for most cytotoxic agents, a reflection of the poor penetration by these agents in crossing an intact blood–CSF barrier.[29]

NM usually presents in patients with widely disseminated and progressive systemic cancer (>70%) but may present after a disease-free interval (20%) and may even be the first manifestation of cancer (5–10%), occasionally in the absence of other evidence of systemic disease.[7,30–32]

PATHOGENESIS

Cancer cells reach the meninges by various routes including (1) hematogenous spread, either by arterial dissemination in most cancers, or through the Batson's venous plexus in pelvic cancers; (2) direct extension from contiguous tumor deposits such as brain intraparenchymal metastases or primary brain tumors; and

Handbook of Neuro-Oncology Neuroimaging, Second Edition
http://dx.doi.org/10.1016/B978-0-12-800945-1.00008-2

© 2016 Elsevier Ltd. All rights reserved.

TABLE 1 Most Frequent Primary Tumors[3,7,8]

Primary Site of Cancer	Percent
Breast cancer	27–50%
Lung cancer	22–36%
adenocarcinoma	50–56%
squamous cell carcinoma	26–36%
small cell carcinoma	13–14%
Malignant melanoma	12%
Genitourinary	5%
Head and neck	2%
Adenocarcinoma of unknown primary	2%

TABLE 2 Prognosis by Tumor Histology[20,52,62,80]

Tumor Histology	Median Survival (Months)	Range (Months)
Breast (N = 32)[37]	7.5	1.5–16
Nonsmall cell lung cancer (N = 32)[112]	5	1–12
Melanoma (N = 16)[89]	4	2–8
High-grade glioma (N = 20)[167]	3.5	1–6

(3) through centripetal migration from systemic tumors along perineural or perivascular spaces in vertebral and paravertebral metastases (particularly from breast and lung cancers), and in head and neck cancers.[33–35]

Once cancer cells have entered the subarachnoid space, cells are transported by CSF flow resulting in disseminated and multifocal neuraxis seeding of the leptomeninges. Tumor infiltration is most prominent in the base of the brain (specifically the basilar cisterns) and the dorsal surface of the spinal cord (in particular the cauda equina).[5,36] Hydrocephalus or impairment of CSF flow may occur as a result of ependymal nodules or tumor deposits obstructing CSF outflow, particularly at the level of the fourth ventricle, basal cisterns, cerebral convexity, or spinal subarachnoid space.

CLINICAL FEATURES

NM classically presents with pleomorphic clinical manifestations encompassing symptoms and signs in three domains of neurological function: (1) the cerebral hemispheres; (2) the cranial nerves; and (3) the spinal cord and associated roots. Signs on examination generally exceed patient-reported symptoms.

The most common manifestations of cerebral hemisphere dysfunction are headaches and mental status changes. Other signs include confusion, dementia, seizures, and hemiparesis. Diplopia is the most common symptom of cranial nerve dysfunction with cranial nerve VI being the most frequently affected, followed by cranial nerves III and IV. Trigeminal sensory or motor loss, cochlear dysfunction, and optic neuropathy are also common findings. Spinal signs and symptoms include weakness (lower extremities more often than upper), dermatomal or segmental sensory loss, and pain in the neck and/or back, or following radicular patterns. Nuchal rigidity is only present in 15% of cases.[3,7,8,31] Gait instability, headache, nausea, and vomiting due to elevated intracranial pressure resulting from impaired CSF resorption may also manifest during the course of the disease. Seizures in general are comparatively rare in NM (<10% incidence).

Caution should be exercised when make a diagnosis of NM. The finding of multifocal neuraxis disease in a patient with known malignancy is strongly suggestive of NM, but it is also common for patients with NM to present with isolated syndromes such as symptoms of raised intracranial pressure, cauda equina syndrome, or cranial neuropathy.

New neurological signs and symptoms may represent progression of NM but must be distinguished from the manifestations of parenchymal disease (30–40% of patients with NM will have coexistent parenchymal brain metastases), and from side effects of chemotherapy or radiation used for treatment, and are rarely from paraneoplastic syndromes. At presentation, NM must also be differentiated from chronic meningitis due to tuberculosis, fungal infection, or sarcoidosis, as well as from metabolic and toxic encephalopathies in the appropriate clinical setting.[7,37]

DIAGNOSIS

CSF Analysis

The most useful laboratory test in the diagnosis of NM is CSF analysis. Abnormalities include increased opening pressure (>200 mm of H_2O), increased leukocytes (>4/mm^3), elevated protein (>50 mg/dl), or decreased glucose (<60 mg/dl), which are suggestive of NM but not diagnostic. The presence of malignant cells in the CSF is diagnostic of NM but, in general, as is true for most cytological analyses, assignment to a particular tumor is not possible.[38]

In patients with positive CSF cytology (see below), up to 45% will be cytologically negative on initial examination.[6] The yield is increased to 80% with a second CSF analysis but little benefit is obtained from repeat lumbar punctures after two lumbar punctures.[7] Of note, a series including lymphomatous and leukemic meningitis by Kaplan et al.[3] observed the frequent dissociation between CSF cell count and malignant

cytology (29% of cytologically positive CSF had concurrent CSF counts of less than 4/mm^3). Murray et al.[39] showed that CSF levels of protein, glucose, and malignant cells[40] vary at different levels of the neuraxis even if there is no obstruction of the CSF flow. This finding reflects the multifocal nature of NM and explains why CSF obtained from a site distant to that of the pathologically involved meninges may yield a negative cytology.

Of the 90 patients reported by Wasserstrom et al.[7], 5% had positive CSF cytology only from either the ventricles or the cisterna magna. In a series of 60 patients with NM, positive lumbar CSF cytology at diagnosis and no evidence of CSF flow obstruction, ventricular and lumbar cytologies obtained simultaneously were discordant in 30% of cases.[41] The authors observed that in the presence of spinal signs or symptoms, the lumbar CSF was more likely to be positive and, conversely, in the presence of cranial signs or symptoms, the ventricular CSF was more likely to be positive. Not obtaining CSF from a site of symptomatic or radiographically demonstrated disease was found to correlate with false negative cytology results in a prospective evaluation of 39 patients, as did withdrawing small CSF volumes (<10.5 ml), delayed processing of specimens, and obtaining fewer than two samples.[42] Even after correcting for these factors there remains a substantial group of patients with NM and persistently negative CSF cytology. Glass et al. reviewed postmortem evaluation, evaluating the value of premortem CSF cytology, and demonstrated that up to 40% of patients with clinically suspected NM proven at the time of autopsy were cytologically negative.[6] This figure increased to greater than 50% in patients with focal NM.

The low sensitivity of CSF cytology makes it difficult not only to diagnose NM but also to assess the response to treatment. Biochemical markers, immunohistochemistry, and molecular biology techniques applied to CSF have been explored in an attempt to find a reliable biological marker of disease.

Numerous biochemical markers have been evaluated, but in general their use has been limited by poor sensitivity and specificity. Tumor markers such as carcinoembryogenic antigen (CEA) from adenocarcinomas, and α-fetoprotein and β-human chorionic gonadotropin from testicular cancers and primary extragonadal CNS tumors can be relatively specific for NM when elevated in CSF and in the absence of markedly elevated serum levels.[34,43] Candidate biomarkers for NM such as vascular endothelial growth factor (VEGF), urokinase-type plasminogen activator, and tissue plasminogen activator (small molecules involved in angiogenesis), have also been evaluated. In the majority of studies, VEGF levels were increased in patients with NM, but sensitivities and specificities have varied widely, from 51.4 to 100% and from 71 to 100%, respectively.[44–49] Combinations of different CSF biomarkers have been suggested as a method to increase the sensitivity of these markers.[48] Profiling proteins involved in the metastatic process using CSF proteomics may have a potential diagnostic and prognostic value. This method has been evaluated by mass spectrometry and multiplex immunoassay.[49–53]

The use of monoclonal antibodies for immunohistochemical analysis of CSF in NM does not significantly increase the sensitivity of cytology alone.[54–56] However, in the case of leukemia and lymphoma, antibodies against surface markers can be used to distinguish between reactive and neoplastic lymphocytes in the CSF.[57]

Cytogenetic studies have also been evaluated in an attempt to improve the diagnostic accuracy of NM. Flow cytometry and DNA single cell cytometry, techniques that measure the chromosomal content of cells, and fluorescent *in* situ hybridization, a method that detects numerical and structural genetic aberrations as a sign of malignancy, can give additional diagnostic information, but still have a low sensitivity.[58–60] Polymerase chain reaction can establish a correct diagnosis when cytology is inconclusive, but the genetic alteration of the cancer must be known for it to be amplified with this technique, and this is generally not the case, particularly in solid tumors.[61] Another new promising method using the CellSearch® technology may allow identification and precise quantification of malignant cells in the CSF in NM.[62–65] Cellsave Preservative tubes, used for this evaluation, introduce a 3-day delay in processing. Several adaptations have been used for the identification of malignant cells in the CSF. Further evaluations of this technology with a simplified method are now ongoing.

CSF flow cytometry is a quantitative analysis of tumor cells in CSF and a method that has been increasingly used in hematological cancers either in addition to CSF cytology or as the sole assessment method.[66–71] The advantages of CSF flow cytometry are that it requires small volumes of CSF (<2 ml), is rapidly available, and quantitates tumor volume in CSF.[72] Disadvantages are that the meaning of very low tumor cell counts in CSF is unclear, and currently that it is unable to be used for solid cancers primarily because of a lack of tumor-specific probes.[73,74] Another limitation of CSF flow cytometry is that the cancer cells deteriorate rapidly; however, a fixative added following acquisition of CSF (e.g., TransFix® or use of Cellsave Preservative Tubes) may obviate this methodological problem.[75,76] This technique has been standardized in many centers in the USA as well as in Spain.[42,75–77]

In cases where there is no evidence of systemic cancer and CSF analysis remains inconclusive, a meningeal biopsy may be diagnostic. The yield of this test increases if the biopsy is taken from an enhancing region identified by magnetic resonance imaging (MRI).[78]

Neuroradiographic Studies

MRI with gadolinium enhancement (MR-Gd) is the technique of choice to evaluate patients with suspected leptomeningeal metastasis.[79] Because NM involves the entire neuraxis, imaging of the entire CNS is required in patients considered for further treatment. T1-weighted sequences, with and without contrast, combined with fat suppression T2-weighted sequences constitute the standard examination.[80] MRI has been shown to have a higher sensitivity than cranial contrast-enhanced computed tomography (CT) in several series[79–81], and is similar to CT myelography for the evaluation of the spine, but significantly better tolerated.[82,83]

Any irritation of the leptomeninges (i.e., blood, infection, and cancer) will result in their enhancement on MRI, which is seen as a fine signal-intense layer that follows the gyri and superficial sulci. Subependymal involvement of the ventricles often results in ventricular enhancement. Some changes such as cranial nerve enhancement on cranial imaging and intradural extramedullary enhancing nodules on spinal MR (most frequently seen in the cauda equina) can be considered diagnostic of NM in patients with cancer.[84] Lumbar puncture itself can, in rare cases, cause a meningeal reaction leading to dural-arachnoidal enhancement so imaging should be obtained preferably prior to the procedure.[85] MR-Gd has a 30% incidence of false negative results so that a normal study does not exclude a diagnosis of NM. On the other hand, in cases with a typical clinical presentation, abnormal MR-Gd alone is adequate to establish the diagnosis of NM.[84,86]

Radionuclide studies using either ^{111}Indium-diethylenetriamine pentaacetic acid or ^{99}Tc macroaggregated albumin are the techniques of choice to evaluate CSF flow dynamics.[35,87] Abnormal CSF circulation has been demonstrated in 30–70% of patients with NM, with blocks commonly occurring at the skull base, the spinal canal, and over the cerebral convexities.[83,87,88] Patients with interruption of CSF flow demonstrated by radionuclide ventriculography have been shown in three clinical series to have decreased survival compared with those with normal CSF flow.[87,89,90] Involved field radiotherapy to the site of CSF flow obstruction, restores flow in 30% of patients with spinal disease and 50% of patients with intracranial disease.[91] Reestablishment of CSF flow with involved-field radiotherapy followed by intraCSF chemotherapy led to longer survival, lower rates of treatment -related morbidity, and lower rate of death from progressive NM, compared with the group that had persistent CSF blocks.[87,89] These findings may reflect how CSF flow abnormalities prevent homogeneous distribution of intraCSF chemotherapy, resulting in: (1) protected sites where tumor can progress; and (2) an accumulation of drug at other sites leading to neurotoxicity and systemic toxicity. Based on this, many authors recommend that intraCSF chemotherapy is preceded by a radionuclide flow study and, if a block is found, that radiotherapy (RT) is administered in an attempt to reestablish normal flow.[34,92]

STAGING

In summary, patients with suspected NM should undergo one or two lumbar punctures, cranial MR-Gd, complete spinal MR-Gd, and a radioisotope CSF flow study to rule out sites of CSF block. If cytology remains negative and radiological studies are not definitive, consideration may be given to ventricular or lateral cervical CSF analysis based on suspected site of predominant disease. If the clinical scenario or radiological studies are highly suggestive of NM, treatment is warranted despite persistently negative CSF cytology.

PROGNOSIS

The median survival of untreated patients with NM is 4–6 weeks and death generally occurs as a result of progressive neurological dysfunction.[7] Treatment is intended to improve or stabilize the neurological status and to prolong survival. Fixed neurological defects are rarely improved with treatment but progression of neurological deterioration may be halted in some patients and median survival increased to 4–6 months[34]. The type of primary cancer is known to be a major prognostic factor.[93,94] Multivariate analysis confirmed the association between survival and primary tumor type. For example, survival is better in breast cancer compared with lung cancer or melanoma-related NM.[45,95,96] Breast cancer NM has a comparatively good prognosis with a median survival estimated at 3.3–5 months.[13,37,43,97–101] Improvements have been observed in lung cancer-related NM, particularly with the use of targeted agents such as epidermal growth factor receptor (EGFR) and anaplastic lymphoma kinase inhibitors, reporting median survival of 3–4.3 months.[102,103] Melanoma complicated by NM continues to demonstrate the worst prognosis with a median survival estimated at less than 2.5 months prior to the era of the immunotherapy.[104]

Numerous prognostic factors for survival and response have been evaluated (e.g., age, gender, duration of signs of NM, increased protein or low glucose in CSF, and ratio of lumbar/ventricular CEA), but many remain controversial.[104] It is commonly accepted, however, that patients will do poorly with intensive treatment of NM if they have a poor performance status, multiple fixed neurologic deficits, bulky CNS disease, coexistent carcinomatous encephalopathy, and CSF flow abnormalities demonstrated by radionuclide ventriculography.

In general, patients with widely metastatic aggressive cancers that do not respond well to systemic chemotherapies are also less likely to benefit from intensive therapy.[34,105,106] What appears clear is that, optimally, NM should be diagnosed in the early stages of disease to prevent the progression of disabling neurological deficits, analogous to the clinical situation of epidural spinal cord compression.

EVALUATION AND RESPONSE TO TREATMENT

No standardized criteria to evaluate the response to treatment of NM have been clearly defined or universally agreed upon. New clinical signs and symptoms must be distinguished from manifestations of parenchymal disease, side effects of intraCSF treatment, systemic treatment or radiation, comedication, neurological or extra-neurological intercurrent disease, and, in rare cases, paraneoplastic syndromes[107]. Transient neurological deficits or symptoms should not be misconstrued as NM-related neurological progression. Despite these complexities, the neurological examination best reflects response to treatment of NM. The one-dimensional Response Evaluation Criteria in Solid Tumors criteria are not appropriate for the evaluation of NM as the imaging features of (subarachnoid, ventricular or parenchymal enhancing nodules, focal or diffuse pial enhancement, ependymal, sulcal, folia, or cranial nerve enhancements) in general are not measurable. CSF cytology (solid cancers) or flow cytometry (hematological cancers) remain the gold standard for the identification of malignant cells in the CSF. Nevertheless, the sensitivity of a first CSF cytology examination varies from 45 to 55%. Two successive CSF cytology samples separated in time are required to evaluate cytological response. In conclusion, new consensual criteria regarding evaluation and response to treatment in NM are needed to better adjudicate outcome and to permit more uniform conduct of clinical trials with novel agents. A Response Assessment in Neuro-Oncology working group was created in 2012 in order to consolidate current literature and suggest new criteria for evaluating patients with NM.

TREATMENT

The evaluation of treatment of NM is complicated by the lack of standard treatments, the difficulties of determining response to treatment given the suboptimal sensitivity of the diagnostic procedures, the fact that most patients will die of systemic disease, and because most studies are small, nonrandomized, and retrospective.[101] However, it is clear that treatment of NM can provide effective palliation and, in some cases, result in prolonged survival. In most cases, treatment requires the combination of surgery, irradiation, and chemotherapy. Figure 1 outlines a treatment algorithm for NM.

Surgery

Surgery is used in the treatment of NM for the placement of (1) intraventricular catheters and subgaleal reservoirs for administration of cytotoxic drugs and (2) ventriculoperitoneal shunts in patients with symptomatic hydrocephalus.

Drugs can be instilled into the subarachnoid space by lumbar puncture or via an intraventricular reservoir system. The latter is the preferred approach because it is simpler, more comfortable for the patient, and safer than repeated lumbar punctures. It also results in a more uniform distribution of the drug in the CSF space and produces the most consistent CSF levels. In up to 10% of lumbar punctures the drug is delivered to the epidural space, even if there is CSF return after placement of the needle, and drug distribution has been shown to be better after drug delivery through a reservoir.[108]

There are two basic types of reservoirs: the Rickham style reservoir, a flat rigid reservoir placed over a burr hole; and the Ommaya reservoir, a dome-shaped reservoir that can be palpated easily. They are generally placed over the right (nondominant) frontal region using a small C-shaped incision. The catheter is placed in the frontal horn of the lateral ventricle or close to the foramen of Monroe through a standard ventricular puncture. In most cases anatomical landmarks suffice but ultrasonographic or CT guidance can be helpful in some situations.[109] It is very important to be sure that the tip and the side perforations of the catheter be inserted completely into the ventricle to avoid drug instillation into the brain parenchyma. Correct placement of the catheter should be checked by noncontrast CT prior to its use for drug administration and it will frequently show a small amount of air in both frontal horns.[110]

NM often causes communicating hydrocephalus leading to symptoms of raised intracranial pressure. Relief of sites of CSF flow obstruction with involved-field radiation should be attempted to avoid the need for CSF shunting. If hydrocephalus persists, a ventriculoperitoneal shunt should be placed to relieve the pressure as relief of pressure often results in clinical improvement. If possible an in-line on/off valve and a reservoir should be used to permit the administration of intraCSF chemotherapy, although some patients cannot tolerate having the shunt turned off to allow the circulation of the drug.[35]

Furthermore, in patients with a persistent blockage of ventricular CSF, a lumbar catheter and reservoir can be used in addition to a ventricular catheter to allow treatment of the spine with intrathecal chemotherapy,

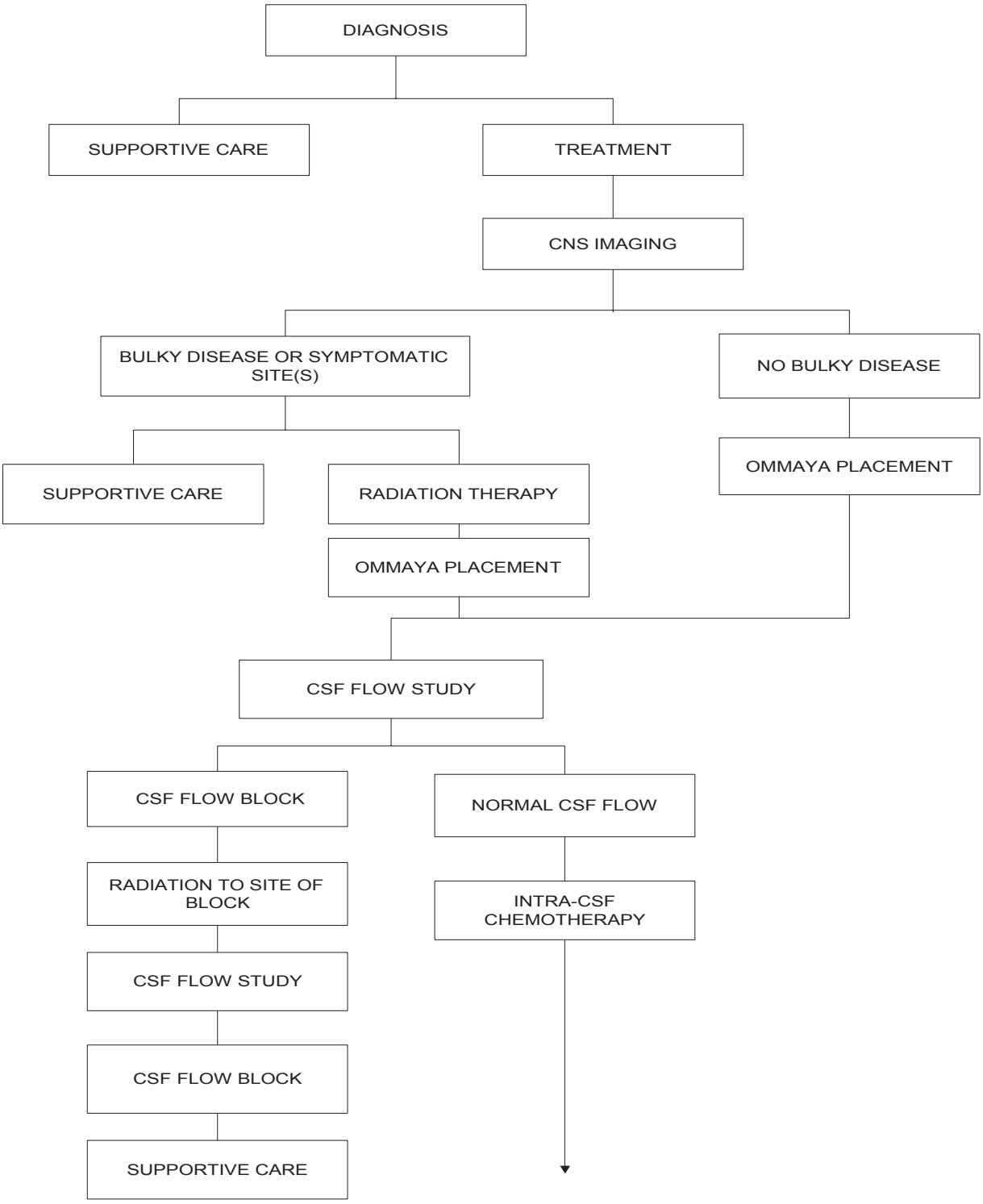


FIGURE 1 Treatment algorithm of neoplastic meningitis.

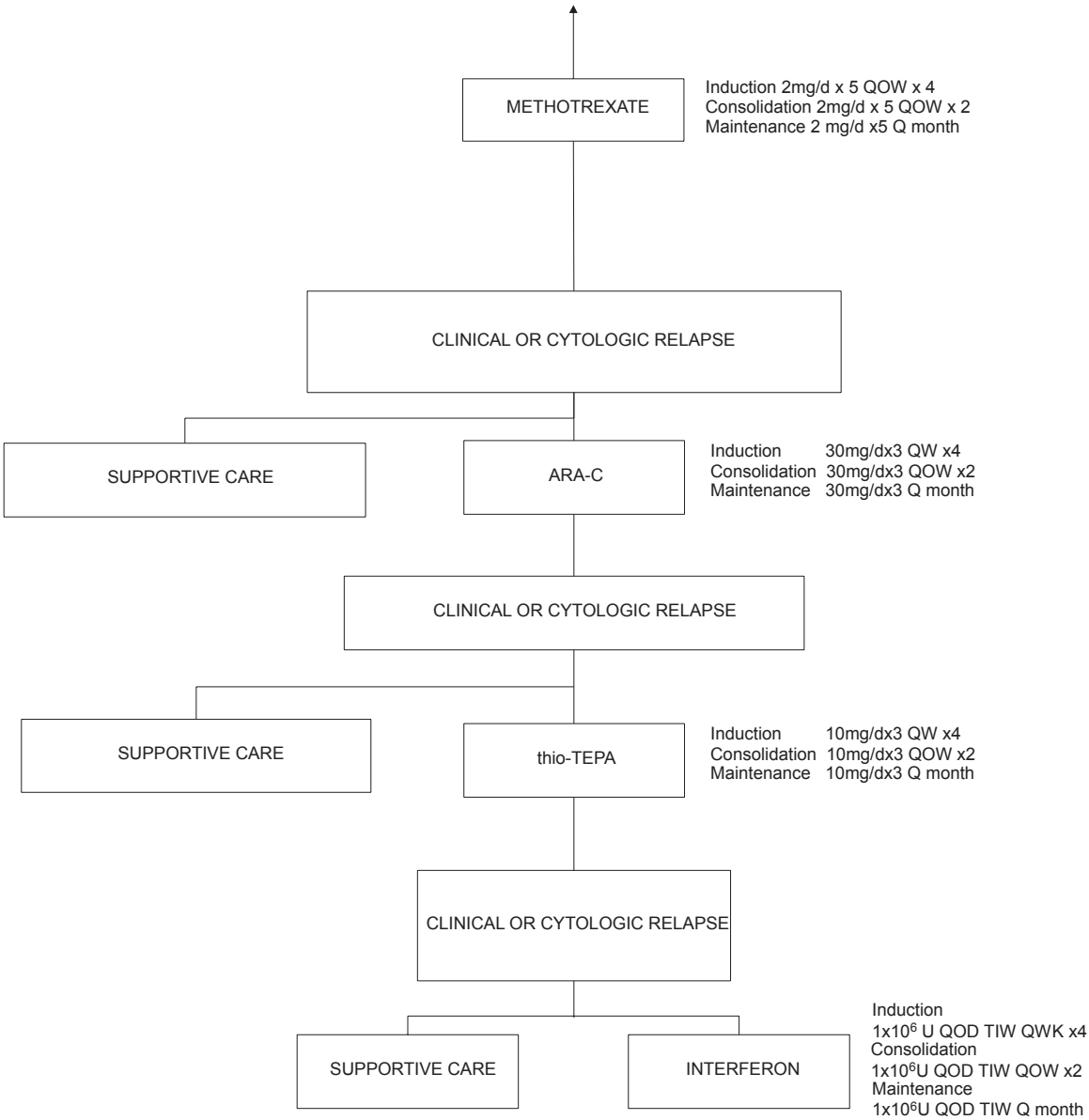


FIGURE 1 CONT'D

although as discussed earlier, patients with persistent CSF flow blocks after radiation are probably best managed by supportive care alone.

Finally, occasionally patients may undergo a meningeal biopsy, to pathologically confirm NM. However, given that most patients demonstrate MR leptomeningeal abnormalities, an abnormal CSF profile, or a clinical examination consistent with NM, meningeal biopsies are rarely performed.

Radiotherapy

RT is used in the treatment of NM— (1) for palliation of symptoms, such as a cauda equina syndrome; (2) to decrease bulky disease such as coexistent parenchymal brain metastases; and (3) to correct CSF flow abnormalities demonstrated by radionuclide ventriculography. Patients may have significant symptoms without radiographic evidence of bulky disease and still benefit from radiation. For example, patients with low back pain and leg weakness should be considered for radiation to the cauda equina, and those with cranial neuropathies should be offered whole-brain RT (WBRT) or base of skull RT.[43]

RT of bulky disease is indicated as intraCSF chemotherapy is limited by diffusion to 2–3 mm penetration into tumor nodules. In addition, involved-field radiation can correct CSF flow abnormalities and this has been

shown to improve patient outcome as discussed above. Unlike brain metastases, the impact of WBRT on overall survival is unclear in NM as reported results have been contradictory.[102,103] Whole neuraxis radiation is rarely indicated in the treatment of NM from solid tumors because it is associated with significant systemic toxicity (severe myelosuppression and mucositis among other complications) and is not curative.

Chemotherapy

Chemotherapy is the only treatment modality that can treat the entire neuraxis. Chemotherapy may be administered systemically or intrathecally.

IntraCSF THERAPY

IntraCSF chemotherapy is the mainstay of treatment for NM, although its superiority compared with systemic treatment, or when added to systemic treatment and compared with this one alone, has not been established in randomized trials; and the efficacy of intraCSF treatment consequently is uncertain. Retrospective analysis or comparison with historical series suggests that the administration of chemotherapy to the CSF improves the outcome of patients with NM.[1,37,84,111,112] However, it is noted that most series will exclude patients that are too sick to receive any treatment, which may be up to one-third of patients with NM.[113] This is particularly evident in series of patients with NSCLC-related NM.[102,103]

Three agents are routinely used: methotrexate, cytarabine (including liposomal cytarabine or DepoCyt®), and thioTEPA. No difference in response has been seen when comparing single agent methotrexate with thioTEPA[34] or when using multiple agent (methotrexate, thioTEPA and cytarabine or methotrexate and cytarabine) compared with single agent methotrexate in adult randomized studies of NM.[114–116] Table 3 outlines the common treatment regimens for these drugs. A sustained-release liposomal form of cytarabine (DepoCyt®) results in cytotoxic cytarabine levels in the CSF for at least 10 days and when given bimonthly and compared with biweekly methotrexate, resulted in longer time to neurological progression in patients with NM due to solid tumors.[117] Furthermore, quality of life and cause of death favored DepoCyt® over methotrexate. These findings were confirmed in a study of lymphomatous meningitis and in an open label study suggesting that DepoCyt® should be considered the drug of first choice in the treatment of NM when experimental therapies are unavailable.[118,119]

Complications of intraCSF chemotherapy include those related to the ventricular reservoir and those related to the chemotherapy administered. The most frequent complications of ventricular reservoir placement are malposition (rates reported between 3 and 12%), obstruction, and infection (usually skin flora). CSF infection occurs in 2–13% of patients receiving intraCSF chemotherapy. It commonly presents with headache, changes in neurologic status, fever, and malfunction of the reservoir. CSF pleocytosis is commonly encountered. The most frequently isolated organism is *Staphylococcus epidermidis*. Treatment requires intravenous antibiotics, with or without oral and intraventricular antibiotics. Some authors advocate the routine removal of the ventricular reservoir, while others reserve device removal for those that do not clear with antibiotic therapy. Routine culture of CSF is not recommended because of the high rate of contamination with skin flora in the absence of infection.[1,5,71,110,120] Myelosuppression can occur after administration of intrathecal chemotherapies and it is recommended that folinic acid rescue (10 mg every 6 h for 24 h) is given orally after the administration of methotrexate to mitigate this complication. Chemical aseptic meningitis occurs in nearly half of all patients treated by intraventricular administration and is characterized by fever, headache, nausea, vomiting, meningismus, and photophobia. In the majority of patients this inflammatory reaction can be treated in the outpatient setting with oral antipyretics, antiemetics, and corticosteroids. Rarely, treatment-related neurotoxicity occurs and may result in a symptomatic subacute leukoencephalopathy or myelopathy. However, in patients with NM and prolonged survival, the combination of RT and chemotherapy frequently results in a late leukoencephalopathy evident on neuroradiographic studies, and is occasionally symptomatic.[1,5,121]

SYSTEMIC THERAPY

The rationale to give intraCSF chemotherapy is based on the presumption that most chemotherapeutic agents when given systemically have poor CSF penetration and do not reach therapeutic levels (as mentioned above). Exceptions to this would be systemic high-dose methotrexate, cytarabine, and thioTEPA, all of which result in cytotoxic CSF levels. Their systemic administration, however, is limited by systemic toxicity and the difficulty to integrate these regimens into other chemotherapeutic programs being used to manage systemic disease. Some authors argue that intraCSF chemotherapy does not add to improved outcome in the treatment of NM, since systemic therapy can obtain access to the subarachnoid deposits through their own vascular supply.[113] In a retrospective comparison of patients treated with systemic chemotherapy and radiation to involved areas, plus or minus intrathecal chemotherapy, Bokstein et al. did not find significant differences in response rates, median survival, or proportion of long-term survivors

TABLE 3 Regional Chemotherapy for NM

	Induction Regimens		Consolidation Regimen		Maintenance Regimen	
Drugs	**Bolus Regimen**	**CxT Regimen**	**Bolus Regimen**	**CxT Regimen**	**Bolus Regimen**	**CxT Regimen**
Methotrexate	10–15 mg twice weekly (total 4 weeks)	2 mg/day for 5 days every other week (total 8 weeks)	10–15 mg once weekly (total 4 weeks)	2 mg/day for 5 days every other week (total 4 weeks)	10–15 mg once a month	2 mg/day for 5 days once a month
Cytarabine	25–100 mg 2 or 3 times weekly (total 4 weeks)	25 mg/day for 3 days weekly (total 4 weeks)	25–100 mg once weekly (total 4 weeks)	25 mg/day for 3 days every other week (total 4 weeks)	25–100 mg once a month	25 mg/day for 3 days once a month
DepoCyt®	50 mg every 2 weeks (total 8 weeks)		50 mg every 4 weeks (total 24 weeks)			
ThioTEPA	10 mg 2 or 3 times weekly (total 4 weeks)	10 mg/day for 3 days weekly (total 4 weeks)	10 mg once weekly (total 4 weeks)	10 mg/day for 3 days every other week (total 4 weeks)	10 mg once a month	10 mg/day for 3 days once a month
α-Interferon	1×10^6 u 3 times weekly (total 4 weeks)		1×10^6 u 3 times weekly every other week (total 4 weeks)		1×10^6 u 3 times weekly (1 week per month)	
Trastuzumab Phase I	25 to 125 mg per week (total 8 weeks)					
Rituximab	10 or 25 or 50 mg twice a week (total 9 doses)					
Topotecan	0.4 mg twice weekly (total 6 weeks)					
Etoposide		0.5 mg/d 5 days per week every other week (total 8 weeks)				

among the two groups but, of course, the group that did not receive the intrathecal treatment was spared the complications of this modality.[122] Glantz et al. treated 16 patients with high-dose intravenous methotrexate and compared their outcome with a reference group of 15 patients treated with intraCSF methotrexate.[123] They found response rates and survival were significantly better in the group treated with intravenous therapy.

In breast cancer, capecitabine, an oral prodrug of 5-fluorouracil, has induced encouraging long-lasting responses and stabilization in a limited number of patients with NM from breast cancer.[124–128] Similar to capecitabine, hormonal agents such as tamoxifen, letrozole, anastrozole, and megestrol have occasionally been useful in breast cancer NM, but like capecitabine these reports usually comprise a single patient and it is difficult to draw any conclusions as to effectiveness of either hormonal agents or capecitabine in breast cancer-related NM.[129–131]

Park and colleagues reported that administration of systemic chemotherapy after diagnosis of NM in NSCLC patients was a significant factor in improving survival compared with patients not receiving systemic therapy.[103] In this retrospective series, 22 patients (44%) received systemic chemotherapy (cytotoxic chemotherapy or EGFR inhibitor) after being diagnosed with NM. Patients treated with combined therapy had a prolonged survival (11.5 vs 1.4 months, $p < 0.001$) and the authors concluded that a proportion of NSCLC patients with NM may benefit from further systemic chemotherapy. In terms of patients who could be good candidates for aggressive NM-directed treatment, patients with a good performance status and patients with NM at the time of initial NSCLC diagnosis appear to represent the most favorable subpopulation.

The EGFR tyrosine kinase inhibitors (TKIs) erlotinib and gefitinib show activity in NSCLC, especially in

women, nonsmokers, patients of Asian ethnicity, those with adenocarcinoma, and those with specific activating mutations of the EGFR. Several studies have suggested that a subset of patients with NM from NSCLC may benefit with long-lasting remission (11–12 months) from erlotinib and gefitinib at normal or higher dose if an EGFR mutation is present.[102,132–138] Studies, including a large retrospective series, have demonstrated particularly encouraging results with the use of these agents. In a US series, the median survival of the nine patients with known EGFR mutations, NSCLC, and NM (all of whom received TKI at some point) was 14 months (range 1–28 months).[102] In a Korean series, 14 patients (28%) with NM who were treated with an EGFR TKI had a median survival of 19.2 months.[103] Thirteen of the 14 patients were never-smokers with adenocarcinoma. EGFR mutation data was available in 16 patients in the Korean series, and of the 11 EGFR-mutant patients, the median survival of 6 patients who received EGFR TKI after being diagnosed with NM has not been reached, compared with 1.7 months in 5 patients who did not receive EGFR TKI. In conclusion, EGFR TKI, a new generation chemotherapeutic agent, may be a valuable option in patients with NM and NSCLC, particularly in patients with activating EGFR mutations.

Median CSF levels and CSF/serum indexes of VEGF have been measured in several studies and were significantly higher in patients with NM, supporting the hypothesis that angiogenesis contributes to NM. VEGF was also negatively correlated with survival in these patients.[46,139–141] Bevacizumab is a monoclonal antibody that targets the VEGF ligand. This agent is widely prescribed in metastatic colorectal cancer and in metastatic NSCLC. Retrospective data suggested that bevacizumab is safe in CNS metastases especially when lesions are asymptomatic and are of comparatively small volume.[142] Intratumoral (intrametastatic) hemorrhages appear not to increase with bevacizumab treatment. Prospective studies in NM are ongoing to confirm benefits in the use of antiVEGF directed therapy.

Patients with NM and melanoma have a poor prognosis, with a median survival less than 2 months. IntraCSF chemotherapy may delay the progression of neurologic signs and symptoms, but benefits are limited and systemic chemotherapy (temozolomide, DTIC, and fotemustine) have generally had only limited efficacy. Currently there is limited data on the utility of BRAF or immune checkpoint inhibitors in the treatment of NM and melanoma, notwithstanding increasing use of these agents in the treatment of melanoma. Clinical results from the development of immunotherapy agents such as the antiCTLA4 monoclonal antibody ipilimumab and targeted therapies targeting mutated BRAF, such as vemurafenib and dabrafenib, suggest these agents may play a role in the multidisciplinary management of melanoma patients with brain metastases.[143–147] Leptomeningeal involvement may also be responding to these new therapies as illustrated with ipilimumab or dabrafenib in a case report.[148–149]

EXPERIMENTAL AGENTS

IntraCSF Experimental Agents

Intralumbar or intraventricular (intraCSF) chemotherapy remains the preferred treatment route for NM. Several new drugs have been evaluated in patients with NM in an exploration to find improved therapies for this disease.

IntraCSF etoposide has been evaluated in two feasibility studies and one phase II study.[150–152] In the phase II trial, 27 patients were enrolled, of whom 26% had a cytological response and either stable or improved neurologic status at the end of induction. In responding patients, time to neurologic progression ranged from 8–40 weeks (median 20 weeks). The 6-month neurologic disease progression-free survival was 11%. The modest efficacy in a variety of tumors with varying prognosis makes these studies difficult to interpret.

Topotecan is a topoisomerase I inhibitor that has been evaluated in a phase II nonrandomized study in 62 patients.[153] Sixty-five percent of patients completed the 6-week induction period of whom 21% had CSF clearance of malignant cells, and the overall median survival was 15 weeks. Chemical meningitis was the most common side effect (32% of patients, 5% grade III). IntraCSF topotecan was well-tolerated, but it is unclear if this agent provides any added benefit over other intraCSF methotrexate or cytarabine. As noted above several different types of primary tumors were treated with intraCSF topotecan (breast, NSCLC, CNS, other), thus making the interpretation of results difficult due to the differing prognosis in this heterogeneous population.

NM remains relatively rare (3–5%) in HER2 positive breast cancer patients compared with brain metastases (around 30%).[154–156] In NM, a high level of consistency in the tumor HER2 status has been reported between primary tumors and malignant cells in the CSF, unlike the situation in parenchymal brain metastasis.[155,157] IntraCSF trastuzumab has been administered at varying doses (5–100 mg) with clinical and cytological success reported in case studies of patients with NM and HER2 breast cancer.[158–165] Occasional prolonged survival has also been reported (>72 months). A complete response (necropsy) has been achieved in a single patient who survived 27 months after NM diagnosis and received 67 cycles of weekly 25 mg intralumbar trastuzumab with marked clinical improvement.[161] These results are encouraging, but the intraCSF use of trastuzuzmab

remains investigational, as more data and experience are necessary before this regimen can be considered standard. Attempts to develop intraCSF use of trastuzumab in the context of prospective phase I or II trials are ongoing in France and in the USA.

Supportive Care

Not all patients with NM are candidates for the aggressive treatment outlined above. Most authors agree that combined modality therapy should be offered to patients with life expectancy greater than 3 months and a Karnofsky performance status of greater than 60%.

Supportive care that should be offered to every patient, regardless of whether they receive NM-directed therapy, include anticonvulsants for seizure control (seen in 10–15% of patients with NM), adequate analgesia with opioid drugs, as well as antidepressants and anxiolytics, if necessary. Corticosteroids have a limited use in NM-related neurological symptoms, but can be useful to treat vasogenic edema associated with intraparenchymal or epidural metastases, or for the symptomatic treatment of nausea and vomiting together with routine antiemetic drugs. In case of hydrocephalus secondary to CSF blockade, a course of steroids during whole brain or skull base radiotherapy is sometimes appropriate but shunting is often required in this situation.[43,166] Decreased attention and somnolence secondary to whole brain radiation can be treated with psychostimulants.[5]

CONCLUSIONS

NM is a complicated disease for a variety of reasons. First, most reports concerning NM treat all subtypes as equivalent with respect to CNS staging, treatment, and outcome. However, clinical trials in oncology are based on specific tumor histology. Comparing responses in patients with carcinomatous meningitis resulting from breast cancer to patients with NSCLC outside of investigational new drug trials may be misleading. A general consensus is that breast cancer is inherently more chemosensitive than NSCLC or melanoma and therefore survival following chemotherapy is likely to be different. This observation has been substantiated in patients with systemic metastases though comparable data regarding CNS metastases, in particular NM, is meager.

Second feature of NM, which complicates therapy, is deciding whom to treat. Not all patients necessarily warrant aggressive CNS-directed therapy. However, few guidelines exist permitting appropriate choice of therapy. Based on the prognostic variables determined clinically and by evaluation of extent of disease, a sizable minority of patients will not be candidates for aggressive NM-directed therapy. Therefore, supportive comfort care (RT to symptomatic disease, antiemetic drugs, and narcotics) is offered to patients with NM considered poor candidates for aggressive therapy as seen in Figure 1.

Third, optimal treatment of NM remains poorly defined. Given these constraints, the treatment of NM today is palliative and rarely curative with a median patient survival of 2–3 months based on data of the 4 prospective randomized trials in this disease. However, palliative therapy of NM often affords the patient protection from further neurological deterioration and consequently an improved neurologic quality of life. No studies to date have attempted an economic assessment of the treatment of NM and therefore no information is available regarding a cost-benefit analysis as has been performed for other cancer-directed therapies.

Finally, in patients with NM, the response to treatment is primarily a function of CSF cytology and secondarily of clinical improvement of neurologic signs and symptoms. Other than CSF cytology and possible biochemical markers, no other CSF parameters predict response. Furthermore, because CSF cytology may manifest a rostra-caudal disassociation, consecutive negative cytology samples (defined as a complete response to treatment) requires confirmation by both ventricular and lumbar CSF cytologies. In general, only pain-related neurologic symptoms improve with treatment. Neurologic signs such as confusion, cranial nerve deficit(s), ataxia, and segmental weakness minimally improve or stabilize with successful treatment.

References

1. Shapiro WR, Posner JB, Ushio Y, et al. Treatment of meningeal neoplasms. *Cancer Treat Rep*. 1977;61(4):733–743.
2. Nugent JL, Bunn Jr PA, Matthews MJ, et al. CNS metastases in small cell bronchogenic carcinoma: increasing frequency and changing pattern with lengthening survival. *Cancer*. 1979;44(5):1885–1893.
3. Kaplan JG, DeSouza TG, Farkash A, et al. Leptomeningeal metastases: comparison of clinical features and laboratory data of solid tumors, lymphomas and leukemia's. *J Neuro-Oncol*. 1990;9(3):225–229.
4. Siegal T, Lossos A, Pfeffer MR. Leptomeningeal metastases: analysis of 31 patients with sustained off- therapy response following combined-modality therapy. *Neurology*. 1994;44(8):1463–1469.
5. Chamberlain MC. Carcinomatous meningitis. *Arch Neurol*. 1997;54(1):16–17.
6. Glass JP, Melamed M, Chernik NL, et al. Malignant cells in cerebrospinal fluid (CSF): the meaning of a positive CSF cytology. *Neurology*. 1979;29(10):1369–1375.
7. Wasserstrom WR, Glass JP, Posner JB. Diagnosis and treatment of leptomeningeal metastases from solid tumors: experience with 90 patients. *Cancer*. 1982;49(4):759–772.
8. Little JR, Dale AJ, Okazaki H. Meningeal carcinomatosis. Clinical manifestations. *Arch Neurol*. 1974;30(2):138–143.
9. Rosen ST, Aisner J, Makuch RW, et al. Carcinomatous leptomeningitis in small cell lung cancer: a clinicopathologic review of the National Cancer Institute experience. *Medicine (Baltimore)*. 1982;61(1):45–53.

10. Amer MH, Al Sarraf M, Baker LH, et al. Malignant melanoma and central nervous system metastases: incidence, diagnosis, treatment and survival. *Cancer*. 1978;42(2):660–668.
11. Yap HY, Yap BS, Tashima CK, et al. Meningeal carcinomatosis in breast cancer. *Cancer*. 1978;42(1):283–286.
12. Altundag K, Bondy ML, Mirza NQ, et al. Clinicopathologic characteristics and prognostic factors in 420 metastatic breast cancer patients with central nervous system metastasis. *Cancer*. 2007;110:2640.
13. Gauthier H, Guilhaume MN, Bidard FC, et al. Survival of breast cancer patients with meningeal carcinomatosis. *Ann Oncol*. 2010;21(11):2183–2187.
14. Lamovec J, Zidar A. Association of leptomeningeal carcinomatosis in carcinoma of the breast with infiltrating lobular carcinoma. An autopsy study. *Arch Pathol Lab Med*. 1991;115:507.
15. Lamovec J, Bracko M. Metastatic pattern of infiltrating lobular carcinoma of the breast: an autopsy study. *J Surg Oncol*. 1991;48:28.
16. Lin NU, Claus E, Sohl J, Razzak AR, Arnaout A, Winer EP. Sites of distant recurrence and clinical outcomes in patients with metastatic triple-negative breast cancer: high incidence of central nervous system metastases. *Cancer*. November 15, 2008;113(10):2638–2645.
17. Le Rhun E, Taillibert S, Zairi F, et al. Clinicopathological features of breast cancers predict the development of leptomeningeal metastases: a case-control study. *J Neuro Oncol*. November 2011;105(2):309–315.
18. Lin M, Chen ZQ, Bao Y, et al. Relationship between breast cancer molecular subtypes with clinicopathological characteristics and prognosis. *Zhonghua Bing Li Xue Za Zhi*. June 2010;39(6):372–376. Chinese.
19. Rakha EA, El-Sayed ME, Green AR, Lee AH, Robertson JF, Ellis IO. Prognostic markers in triple-negative breast cancer. *Cancer*. 2007;109:25–32.
20. DeAngelis NM, Mandell LR, Thaler HT, et al. The role of postoperative radiotherapy after resection of single brain metastases. *Neurosurgery*. 1989;24:798.
21. Norris LK, Grossman SA, Olivi A. Neoplastic meningitis following surgical resection of isolated cerebellar metastasis: a potentially preventable complication. *J Neuro Oncol*. 1997;32:215.
22. Sawaya R, Hammoud M, Schoppa D, et al. Neurosurgical outcomes in a modern series of craniotomies for treatment of parenchymal tumors. *Neurosurgery*. 1998;42:1044–1056.
23. Ahn JH, Lee SH, Kim S, et al. Risk for leptomeningeal seeding after resection for brain metastases: Implication of tumor location with mode of resection. *J Neurosurg*. 2012;116:984–993.
24. Elliott JP, Keles GE, Waite M, et al. Ventricular entry during resection of malignant gliomas: effect on intracranial cerebrospinal fluid tumor dissemination. *J Neurosurg*. 1994;80:834.
25. van der Ree TC, Dippel DW, Avezaat CJ. Sillevis Smitt PA, Vecht CJ, van den Bent MJ: Leptomeningeal metastasis after surgical resection of brain metastases. *J Neurol Neurosurg Psychiatry*. 1999;66:225–227.
26. Bendell JC, Domchek SM, Burstein HJ, et al. Central nervous system metastases in women who receive trastuzumab-based therapy for metastatic breast carcinoma. *Cancer*. 2003;97:2972.
27. Omuro AM, Kris MG, Miller VA, et al. High incidence of disease recurrence in the brain and leptomeninges in patients with nonsmall cell lung carcinoma after response to gefitinib. *Cancer*. 2005;103:2344.
28. Lai R, Dang CT, Malkin MG, Abrey LE. The risk of central nervous system metastases after trastuzumab therapy in patients with breast carcinoma. *Cancer*. 2004;101:810.
29. Laterra J, Keep R, Betz LA, Goldstein GW. Blood—cerebrospinal fluid barrier. In: Siegel GJ, Agranoff BW, Albers RW, et al., eds. *Basic Neurochemistry: Molecular, Cellular and Medical Aspects*. 6th ed. Philadelphia: Lippincott-Raven; 1999.
30. van Oostenbrugge RJ, Twijnstra A. Presenting features and value of diagnostic procedures in leptomeningeal metastases. *Neurology*. 1999;53(2):382–385.
31. Balm M, Hammack J. Leptomeningeal carcinomatosis. Presenting features and prognostic factors. *Arch Neurol*. 1996;53(7): 626–632.
32. Sorensen SC, Eagan RT, Scott M. Meningeal carcinomatosis in patients with primary breast or lung cancer. *Mayo Clin Proc*. 1984;59(2):91–94.
33. Gonzalez-Vitale JC, Garcia-Bunuel R. Meningeal carcinomatosis. *Cancer*. 1976;37(6):2906–2911.
34. Grossman SA, Krabak MJ. Leptomeningeal carcinomatosis. *Cancer Treat Rev*. 1999;25(2):103–119.
35. Chamberlain MC. Radioisotope CSF flow studies in leptomeningeal metastases. *J Neuro-Oncol*. 1998;38(2–3):135–140.
36. Boyle R, Thomas M, Adams JH. Diffuse involvement of the leptomeninges by tumour–a clinical and pathological study of 63 cases. *Postgrad Med J*. 1980;56(653):149–158.
37. Chamberlain MC, Kormanik PR. Carcinomatous meningitis secondary to breast cancer: predictors of response to combined modality therapy. *J Neuro-Oncol*. 1997;35(1):55–64.
38. Kolmel HW. Cytology of neoplastic meningosis. *J Neuro-Oncol*. 1998;38(2–3):121–125.
39. Murray JJ, Greco FA, Wolff SN, et al. Neoplastic meningitis. Marked variations of cerebrospinal fluid composition in the absence of extradural block. *Am J Med*. 1983;75(2):289–294.
40. Rogers LR, Duchesneau PM, Nunez C, et al. Comparison of cisternal and lumbar CSF examination in leptomeningeal metastasis. *Neurology*. 1992;42(6):1239–1241.
41. Chamberlain MC, Kormanik PA, Glantz MJ. A comparison between ventricular and lumbar cerebrospinal fluid cytology in adult patients with leptomeningeal metastases. *Neuro-Oncol*. 2001;3(1):42–45.
42. Glantz MJ, Cole BF, Glantz LK, et al. Cerebrospinal fluid cytology in patients with cancer: minimizing false- negative results. *Cancer*. 1998;82(4):733–739.
43. DeAngelis NM. Current diagnosis and treatment of leptomeningeal metastasis. *J Neuro-Oncol*. 1998;38(2–3):245–252.
44. Stockhammer G, Poewe W, Burgstaller S, et al. Vascular endothelial growth factor in CSF: a biological marker for carcinomatous meningitis. *Neurology*. 2000;54:1670–1676.
45. Herrlinger U, Fösrschier H, Küker W, Meyermann R, et al. Leptomeningeal metastasis; survival and prognosis in 155 patients. *J Neurol Sci*. 2004;223(2):167–178.
46. van de Lagerijt B, Gijtenbeek JM, de Reus HP, et al. CSF levels of growth factors and plasminogen activators in leptomeningeal metastases. 2006; 67(1): 114–119.
47. Corsini E, Bernardi G, Gaviani P, et al. Intrathecal synthesis of tumor markers is a highly sensitive test in the diagnosis of leptomeningeal metastasis from solid cancers. *Clin Chem Lab Med*. 2009;47(7):874–879.
48. Groves MD, Hess KR, Puduvalli VK, et al. Biomarkers of disease: cerebrospinal fluid vascular endothelial growth factor (VEGF) and stromal cell derived factor (SDF)-1 levels in patients with neoplastic meningitis (NM) due to breast cancer, lung cancer and melanoma. *J Neuro-Oncol*. 2009;94:229–234.
49. Grewal J, Saria MG, Kesari S. Novel approaches to treating leptomeningeal metastases. *J Neuro-Oncol*. 2012;106(2):225–234.
50. Brandsma D, Voest EE, de Jager W, et al. CSF protein profiling using Multiplex Immuno-assay: A potenteoal new diagnostic tool for leptomeningeal metastases. *J Neurol*. 2006; 253(9):1177–1184.
51. Dekker LJ, Boogerd W, Stockhammer G, et al. MALDI-TOF mass spectrometry analysis of cerebrospinal fluid tryptic peptide profiles to diagnose leptomeningeal metastases in patients with breast cancer. *Mol Cell Proteomics*. 2005;4(9):1341–1349.

52. Römpp A, Dekker L, Taban I, et al. Identification of leptomeningeal metastasis-related proteins in cerebrospinal fluid of patients with breast cancer by a combination of MALDI-TOF, MALDI-FTICR and nano LC-FTICR MS. *Proteomics*. 2007;7(3):474–481.
53. Weston CL, Glantz MJ, Connor JR. Detection of cancer cells in the cerebrospinal fluid: current methods and future directions. *Fluids Barriers CNS*. 2011;8:14.
54. Garson JA, Coakham HB, Kemshead JT, et al. The role of monoclonal antibodies in brain tumour diagnosis and cerebrospinal fluid (CSF) cytology. *J Neuro-Oncol*. 1985;3(2):165–171.
55. Hovestadt A, Henzen-Logmans SC, Vecht CJ. Immunohistochemical analysis of the cerebrospinal fluid for carcinomatous and lymphomatous leptomeningitis. *Br J Cancer*. 1990;62(4):653–654.
56. Boogerd W, Vroom TM, van Heerde P, et al. CSF cytology versus immunocytochemistry in meningeal carcinomatosis. *J Neurol Neurosurg Psychiatry*. 1988;51(1):142–145.
57. van Oostenbrugge RJ, Hopman AH, Ramaekers FC, et al. In situ hybridization: a possible diagnostic aid in leptomeningeal metastasis. *J Neuro-Oncol*. 1998;38(2–3):127–133.
58. Cibas ES, Malkin MG, Posner JB, et al. Detection of DNA abnormalities by flow cytometry in cells from cerebrospinal fluid. *Am J Clin Pathol*. 1987;88(5):570–577.
59. Biesterfeld S, Bernhard B, Bamborschke S, et al. DNA single cell cytometry in lymphocytic pleocytosis of the cerebrospinal fluid. *Acta Neuropathol (Berl)*. 1993;86(5):428–432.
60. van Oostenbrugge RJ, Hopman AH, Arends JW, et al. The value of interphase cytogenetics in cytology for the diagnosis of leptomeningeal metastases. *Neurology*. 1998;51(3):906–908.
61. Rhodes CH, Glantz MJ, Glantz L, et al. A comparison of polymerase chain reaction examination of cerebrospinal fluid and conventional cytology in the diagnosis of lymphomatous meningitis. *Cancer*. 1996;77(3):543–548.
62. Nayak L, Fleisher M, Gonzalez-Espinosa R, et al. Rare cell capture technology for the diagnosis of leptomeningeal metastaseis in slide tumors. *Neurology*. 2013;80:1598–1605.
63. Patel AS, Allen JE, Dicker DT, et al. Identification and enumeration of circulating tumor cells in the cerebrospinal fluid of breast cancer patients with central nervous system metastases. *Oncotarget*. 2011;2(10):752–760.
64. Le Rhun E, Tu Q, de Carvalho Bittencourt M, et al. Detection and quantification of CSF malignant cells by the CellSearch(®) technology in patients with melanoma leptomeningeal metastasis. *Med Oncol*. 2013;30(2):538.
65. Le Rhun E, Massin F, Tu Q, Bonneterre J, de Carvalho Bittencourt M, Faure GC. Development of a new method for identification and quantification in cerebrospinal fluid of malignant cells from breast carcinoma leptomeningeal metastasis. *BMC Clin Pathol*. 2012;12:21.
66. Nuckel H, Novotny J, Noppeney R, et al. Detection of malignant haematopoietic cells in the cerebrospinal fluid by conventional cytology and flow cytometry. *Clin Lab Haem*. 2006;28:22–29.
67. Chamberlain MC, Glantz M, Groves MD, Wilson WH. Diagnostic tools for neoplastic meningitis: detecting disease, identifying patient risk, and determining benefit of treatment. *Semin Oncol*. 2009;36(Suppl 2):S35–S45.
68. Hegde U, Filie A, Little RF, et al. High incidence of occult leptomeningeal disease detected by flow cytometry in newly diagnosed aggressive B-cell lymphomas at risk for central nervous system involvement: the role of flow cytometry versus cytology. *Blood*. 2005;105:496–502.
69. French CA, Dorfman DM, Shaheen G, Cibas ES. Diagnosing lymphoproliferative disorders involving the cerebro- spinal fluid: increased sensitivity using flow cytometric analysis. *Diagn Cytopathol*. 2000;23:369–374.
70. Bromberg JEC, Breems DA, Kraan J, et al. CSF flow cytometry greatly improves diagnostic accuracy in CNS hematologic malignancies. *Neurology*. 2008;68:1674–1679.
71. Brem SS, Bierman PJ, Black P, et al. NCCN clinical practice guidelines in oncology. *Cent Nerv Syst Cancers*. 2008;1. Available at http://www.nccn.org/professionals/physician_gls/PDF/cns.pdf. Accessed 23.01.09.
72. Aune MW, Becker JL, Brugnara C, et al. Automated flow cytometric analysis of blood cells in cerebrospinal fluid: analytic performance. *Am J Clin Pathol*. 2004;121:690–700.
73. Sancho JM, Orfao A, Quijano S, et al. Clinical significance of occult cerebrospinal fluid involvement assessed by flow cytometry in non-Hodgkin's lymphoma patients at high risk of central nervous system disease in the rituximab era. *Eur J Haematol*. 2010;85:321–328.
74. Strik H, Luthe H, Nagel I, Ehrlich B, Bahr M. Automated cerebrospinal fluid cytology: limitations and reasonable applications. *Anal Quant Cytol Histol*. 2005;27:167–173.
75. Dux R, Kindler-Röhrborn A, Annas M, Faustmann P, Lennartz K, Zimmermann CW. A standardized protocol for flow cytometric analysis of cells isolated from cerebrospinal fluid. *J Neurol Sci.* 1994;121:74–78.
76. de Jongste AH, Kraan J, Broek PD, et al. Use of TransFix™ cerebrospinal fluid storage tubes prevents cellular loss and enhances flow cytometric detection of malignant hematological cells after 18 hours of storage. *Cytometry B Clin Cytom*. 2013:14. http://dx.doi.org/10.1002/cyto.b.21097. [Epub ahead of print].
77. Subirá D, Castañón S, Aceituno E, et al. Flow cytometric analysis of cerebrospinal fluid samples and its usefulness in routine clinical practice. *Am J Clin Pathol*. June 2002;117(6):952–958.
78. Cheng TM, O'Neill BP, Scheithauer BW, et al. Chronic meningitis: the role of meningeal or cortical biopsy. *Neurosurgery*. 1994;34(4):590–595.
79. Chamberlain MC, Sandy AD, Press GA. Leptomeningeal metastasis: a comparison of gadolinium-enhanced MR and contrast-enhanced CT of the brain. *Neurology*. 1990;40(3 Pt 1):435–438.
80. Schumacher M, Orszagh M. Imaging techniques in neoplastic meningiosis. *J Neuro-Oncol*. 1998;38(2–3):111–120.
81. Sze G, Soletsky S, Bronen R, et al. MR imaging of the cranial meninges with emphasis on contrast enhancement and meningeal carcinomatosis. *AJR Am J Roentgenol*. 1989;153(5):1039–1049.
82. Schuknecht B, Huber P, Buller B, et al. Spinal leptomeningeal neoplastic disease. Evaluation by MR, myelography and CT myelography. *Eur Neurol*. 1992;32(1):11–16.
83. Chamberlain MC. Comparative spine imaging in leptomeningeal metastases. *J Neuro-Oncol*. 1995;23(3):233–238.
84. Freilich RJ, Krol G, DeAngelis NM. Neuroimaging and cerebrospinal fluid cytology in the diagnosis of leptomeningeal metastasis. *Ann Neurol*. 1995;38(1):51–57.
85. Mittl Jr RL, Yousem DM. Frequency of unexplained meningeal enhancement in the brain after lumbar puncture. *AJNR Am J Neuroradiol*. 1994;15(4):633–638.
86. Chamberlain MC. Cytologically negative carcinomatous meningitis: usefulness of CSF biochemical markers. *Neurology*. 1998;50(4):1173–1175.
87. Glantz MJ, Hall WA, Cole BF, et al. Diagnosis, management, and survival of patients with leptomeningeal cancer based on cerebrospinal fluid-flow status. *Cancer*. 1995;75(12):2919–2931.
88. Trump DL, Grossman SA, Thompson G, et al. CSF infections complicating the management of neoplastic meningitis. Clinical features and results of therapy. *Arch Intern Med*. 1982;142(3):583–586.
89. Chamberlain MC, Kormanik PA. Prognostic significance of 111indium-DTPA CSF flow studies in leptomeningeal metastases. *Neurology*. 1996;46(6):1674–1677.
90. Mason WP, Yeh SD, DeAngelis NM. 111Indium-diethylenetriamine pentaacetic acid cerebrospinal fluid flow studies predict distribution of intrathecally administered chemotherapy and outcome in patients with leptomeningeal metastases. *Neurology*. 1998;50(2):438–444.

91. Chamberlain MC, Corey-Bloom J. Leptomeningeal metastases: 111indium-DTPA CSF flow studies. *Neurology*. 1991;41(11):1765–1769.
92. Chamberlain MC, Kormanik P, Jaeckle KA, et al. 111Indium-diethylenetriamine pentaacetic acid CSF flow studies predict distribution of intrathecally administered chemotherapy and outcome in patients with leptomeningeal metastases. *Neurology*. 1999;52(1):216–217.
93. Chamberlain MC, Glantz M, Groves MD, et al. Diagnostic tools for neoplastic meningitis: detecting disease, identifying patient risk, and determining benefit of treatment. *Semin Oncol*. 2009;36(4 Suppl 2):S35–S45.
94. Taillibert S, Laigle-Donadey F, Chodkiewicz C, Sanson M, Hoang-Xuan K, Delattre JY. Leptomeningeal metastases from solid malignancy: a review. *J Neuro-Oncology*. 2005;75(1):85–99.
95. Clarke JL, Perez HR, Jacks NM, et al. Leptomeningeal metastases in the MRI era. *Neurology*. 2010;74:1449.
96. Oechsle K, Lange-Brock V, Kruell A, Bokemeyer C, de Wit M. Prognostic factors and treatment options in patients with leptomeningeal metastases of different primary tumors: a retrospective analysis. *J Cancer Res Clin Oncol*. 2010;136(11):1729–1735.
97. Clatot F, Philippin-Lauridant G, Ouvrier MJ, et al. Clinical improvement and survival in breast cancer leptomeningeal metastasis correlate with the cytologic response to intrathecal chemotherapy. *J Neuro-Oncology*. 2009;95(3):421–426.
98. Rudnicka H, Niwinska A, Murawska M. Breast cancer leptomeningeal metastasis—the role of multimodality treatment. *J Neuro-Oncology*. 2007;84:57–62.
99. Lee S, Ahn HK, Park YH, et al. Leptomeningeal metastases from breast cancer: intrinsic subtypes may affect unique clinical manifestations. *Breast Cancer ResTreat*. 2011;129(3):809–817.
100. de Azevedo CR, Cruz MR, Chinen LT, et al. Meningeal carcinomatosis in breast cancer: prognostic factors and outcome. *J Neuro-Oncology*. 2011;104(2):565–572.
101. Hildebrand J. Prophylaxis and treatment of leptomeningeal carcinomatosis in solid tumors of adulthood. *J Neuro-Oncol*. 1998;38(2–3):193–198.
102. Morris PG, Reiner AS, Szenberg OR, et al. Leptomeningeal Metastasis from Non-small Cell Lung Cancer : Survival and the Impact of Whole Brain Radiotherapy. *J Thorac Oncol*. 2012;7(2):382–385.
103. Park JH, Kim YJ, Lee JO, et al. Clinical outcomes of leptomeningeal metastasis in patients with non-small cell lung cancer in the modern chemotherapy era. *Lung Cancer*. 2012;76(3):387–392.
104. Harstad L, Hess KR, Groves MD. Prognostic factors and outcomes in patients with leptomeningeal melanomatosis. *J Neuro-Oncol*. 2008;10:1010–1018.
105. Chamberlain MC, Kormanik PA. Prognostic significance of coexistent bulky metastatic central nervous system disease in patients with leptomeningeal metastases. *Arch Neurol*. 1997;54(11):1364–1368.
106. Chamberlain MC. Neoplastic meningitis–related encephalopathy: prognostic significance. *Neurology*. 2003;60(5):A17–A18.
107. Chamberlain MC. Neoplastic meningitis. *Oncologist*. 2008;13:967–977.
108. Shapiro WR, Young DF, Mehta BM. Methotrexate: distribution in cerebrospinal fluid after intravenous, ventricular and lumbar injections. *N Engl J Med*. 1975;293(4):161–166.
109. Berweiler U, Krone A, Tonn JC. Reservoir systems for intraventricular chemotherapy. *J Neuro-Oncol*. 1998;38(2–3):141–143.
110. Sandberg DI, Bilsky MH, Souweidane MM, et al. Ommaya reservoirs for the treatment of leptomeningeal metastases. *Neurosurgery*. 2000;47(1):49–54.
111. Sause WT, Crowley J, Eyre HJ, et al. Whole brain irradiation and intrathecal methotrexate in the treatment of solid tumor leptomeningeal metastases–a Southwest Oncology Group study. *J Neuro-Oncol*. 1988;6(2):107–112.
112. Chamberlain MC, Kormanik P. Carcinoma meningitis secondary to non-small cell lung cancer: combined modality therapy. *Arch Neurol*. 1998;55(4):506–512.
113. Siegal T. Leptomeningeal metastases: rationale for systemic chemotherapy or what is the role of intra-CSF-chemotherapy? *J Neuro-Oncol*. 1998;38(2–3):151–157.
114. Giannone L, Greco FA, Hainsworth JD. Combination intraventricular chemotherapy for meningeal neoplasia. *J Clin Oncol*. 1986;4(1):68–73.
115. Hitchins RN, Bell DR, Woods RL, et al. A prospective randomized trial of single-agent versus combination chemotherapy in meningeal carcinomatosis. *J Clin Oncol*. 1987;5(10):1655–1662.
116. Bleyer WA, Drake JC, Chabner BA. Neurotoxicity and elevated cerebrospinal-fluid methotrexate concentration in meningeal leukemia. *N Engl J Med*. 1973;289(15):770–773.
117. Glantz MJ, Jaeckle KA, Chamberlain MC, et al. A randomized controlled trial comparing intrathecal sustained-release cytarabine (DepoCyt) to intrathecal methotrexate in patients with neoplastic meningitis from solid tumors. *Clin Cancer Res*. 1999;5(11):3394–3402.
118. Glantz MJ, LaFollette S, Jaeckle KA, et al. Randomized trial of a slow release versus a standard formulation of cytarabine for the intrathecal treatment of lymphomatous meningitis. *J Clin Oncol*. 1999;17:3110–3116.
119. Chamberlain MC, Kormanik PA, Barba D. Complications associated with intraventricular chemotherapy in patients with leptomeningeal metastases. *J Neurosurg*. 1997;87:694–699.
120. Siegal T, Pfeffer MR, Steiner I. Antibiotic therapy for infected Ommaya reservoir systems. *Neurosurgery*. 1988;22(1 Pt 1):97–100.
121. Kerr JZ, Berg S, Blaney SM. Intrathecal chemotherapy. *Crypt Rev Oncol Hematol*. 2001;37(3):227–236.
122. Bokstein F, Lossos A, Siegal T. Leptomeningeal metastases from solid tumors: a comparison of two prospective series treated with and without intra-cerebrospinal fluid chemotherapy. *Cancer*. 1998;82(9):1756–1763.
123. Glantz MJ, Cole BF, Recht L, et al. High-dose intravenous methotrexate for patients with nonelukemic leptomeningeal cancer: is intrathecal chemotherapy necessary? *J Clin Oncol*. 1998;16(4):1561–1567.
124. Giglio P, Tremont-Lukats IW, Groves MD. Response of neoplastic meningitis from solid tumors to oral capecitabine. *J Neuro-Oncol*. 2003;65:167.
125. Rogers LR, Remer SE, Tejwani S. Durable response of breast cancer leptomeningeal metastasis to capecitabine monotherapy. *Neuro Oncol*. 2004;6:63.
126. Shigekawa T, Takeuchi H, Misumi M, et al. Successful treatment of leptomeningeal metastases from breast cancer using the combination of trastuzumab and capecitabine: a case report. *Breast Cancer*. 2009;16:88.
127. Ekenel M, Hormigo AM, Peak S, et al. Capecitabine therapy of central nervous system metastases from breast cancer. *J Neuro-Oncol*. 2007;85:223.
128. Tham YL, Hinckley L, Teh BS, Elledge R. Long-term clinical response in leptomeningeal metastases from breast cancer treated with capecitabine monotherapy: a case report. *Clin Breast Cancer*. 2006;7:164.
129. Boogerd W, Dorresteijn LD, van Der Sande JJ, de Gast GC, Bruning PF. Response of leptomeningeal metastases from breast cancer to hormonal therapy. *Neurology*. 2000;55:117–119.
130. Chamberlain MC. Response of leptomeningeal metastases from breast cancer to hormonal therapy. *Neurology*. 2001;56(3):425–426.
131. Ozdogan M, Samur M, Bozcuk HS, et al. Durable remission of leptomeningeal metastasis of breast cancer with letrozole: a case report and implications of biomarkers on treatment selection. *Jpn J Clin Oncol*. 2003;33:229–231.

132. Tetsumoto S, Osa A, Kijima T, et al. Two cases of leptomeningeal metastases from lung adenocarcinoma which progressed during gefitinib therapy but responded to erlotinib. *Int J Clin Oncol*. April 2012;17(2):155–159.
133. Clarke JL, Pao W, Wu N, et al. High dose weekly erlotinib achieves therapeutic concentrations in CSF and is effective in leptomeningeal metastases from epidermal growth factor receptor mutant lung cancer. *J Neuro-Oncol*. 2010;99:283.
134. Kanaji N, Bandoh S, Nagamura N, et al. Significance of an epidermal growth factor receptor mutation in cerebrospinal fluid for carcinomatous meningitis. *Intern Med*. 2007;46:1651.
135. Sakai M, Ishikawa S, Ito H, et al. Carcinomatous meningitis from non-small-cell lung cancer responding to gefitinib. *Int J Clin Oncol*. 2006;11:243.
136. Hashimoto N, Imaizumi K, Honda T, et al. Successful re-treatment with gefitinib for carcinomatous meningitis as disease recurrence of non-small-cell lung cancer. *Lung Cancer*. 2006;53:387.
137. Yi HG, Kim HJ, Kim YJ, et al. Epidermal growth factor receptor (EGFR) tyrosine kinase inhibitors (TKIs) are effective for leptomeningeal metastasis from non-small cell lung cancer patients with sensitive EGFR mutation or other predictive factors of good response for EGFR TKI. *Lung Cancer*. 2009;65:80–84.
138. Jackman DM, Holmes AJ, Lindeman N, et al. Response and resistance in a non-small cell lung cancer patient with an epider- mal growth factor receptor mutation and leptomeningeal metastases treated with high-dose gefitinib. *J Clin Oncol*. 2006;24: 4517–4520.
139. Reijneveld JC, Taphoorn MJ, Kerckhaert OA, Drixler TA, Boogerd W, Voest EE. Angiostatin prolongs the survival of mice with leptomeningeal metastases. *Eur J Clin Invest*. 2003;33:76–81.
140. Reijneveld JC, Brandsma D, Boogerd W, et al. CSF levels of angiogenesis-related proteins in patients with leptomeningeal metastases. *Neurology*. 2005;65(7):1120–1122.
141. Groves MD. CSF levels of angiogenesis-related proteins in patients with leptomeningeal metastases. *Neurology*. May 23, 2006;66(10):1609–1610.
142. Besse B, Lasserre SF, Compton P, et al. Bevacizumab safety in patients with central nervous system metastases. *Clin Cancer Res*. 2010;16(1):269–278.
143. Margolin K, Ernstoff MS, Hamid O, et al. Ipilimumab in patients with melanoma and brain metastases. An open-label phase 2 trial. *Lancet Oncol é*. 2012;13:459–465.
144. Weber JS, Amin A, Minor D, Siegel J, Berman D, O'Day SJ. Safety and clinical activity of ipilimumab in melanoma patients with brain metastases: retrospective analysis of data from a phase 2 trial. *Melanoma Res*. 2011;21:530–534.
145. Rochet NM, Kottschade LA, Markovic SN. Vemurafenib for melanoma metastases to the brain. *N Engl J Med*. December 2011;365(25):2439–2441.
146. Dummer R, et al. An open-label pilot study of vemurafenib in previously treated metastatic melanoma patients with brain metastases. *J Clin Oncol*. 2011;29:537s.
147. Falchook GS, Long GV, Kurzrock R, et al. Dabrafenib in patients with melanoma, untreated brain metastases, and other solid tumours: a phase 1 dose-escalation trial. *The Lancet*. 2012;379(9829):1893–1901.
148. Simeone E, De Maio E, Sandomenico F, et al. Neoplastic leptomeningitis presenting in a melanoma patient treated with dabrafenib (a V600EBRAF inhibito): a case report. *J Med Case Rep*. 2012;6(1):131.
149. Bot I, Blank CD, Brandsma D. Clinical and radiological response of leptomeningeal melanoma after whole brain radiotherapy and ipilimumab. *J Neurol*. March 2012. [Epub online].
150. Slavc I, Schuller E, Falger J, et al. Feasibility of long-term intraventricular therapy with mafosfamide (n = 26) and etoposide (n = 11): experience in 26 children with disseminated malignant brain tumors. *J Neurooncol*. 2003;64:239.
151. Fleischhack G, Reif S, Hasan C, et al. Feasibility of intraventricular administration of etoposide in patients with metastatic brain tumours. *Br J Cancer*. 2001;84:1453.
152. Chamberlain MC, Tsao-Wei DD, Groshen S. Phase II trial of intracerebrospinal fluid etoposide in the treatment of neoplastic meningitis. *Cancer*. 2006;106:2012.
153. Groves MD, Glantz MJ, Chamberlain MC. A multicenter phase II trial of intrathecal topotecan in patients with meningeal malignancies. *Neuro oncology*. 2008;10(6):1010–1018.
154. Nam BH, Kim SY, Han HS, et al. Breast cancer subtypes and survival in patients with brain metastases. *Breast Cancer Res*. 2008;10(1):R20. [Epub 28.02.08].
155. Lin NU. Concordance of HER2 in primary tumor and leptomeningeal metastases: now what? *Breast Cancer Res Treat*. 2010.
156. Bendell JC, Domchek SM, Burstein HJ, et al. Central nervous system metastases in women who receive trastuzumab-based therapy for metastatic breast carcinoma. *Cancer*. June 15, 2003;97(12):2972–2977.
157. Park IH, Kwon Y, Ro JY, Lee KS, Ro J. Concordant HER2 status between metastatic breast cancer cells in CSF and primary breast cancer tissue. *Breast Cancer Res Treat*. August 2010;123(1):125–128.
158. Stemmler HJ, Schmitt M, Harbeck N, et al. Application of intrathecal trastuzumab (Herceptin) for treatment of meningeal carcinomatosis in HER2- overexpressing metastatic breast cancer. *Oncol Rep*. 2006;15:1373–1377.
159. Stemmler HJ, Schmitt M, Willems A, et al. Ratio of trastuzumab levels in serum and cerebrospinal fluid is altered in HER2-positive breast cancer patients with brain metastases and impairment of blood–brain barrier. *Anticancer Drugs*. 2007;18:23–28.
160. Stemmler HJ, Mengele K, Schmitt M, et al. Intrathecal trastuzumab (Herceptin) and methotrexate for meningeal carcinomatosis in HER-2 overexpressing metastatic breast cancer: a case report. *Anticancer Drugs*. 2008;19:832–836.
161. Oliveira M, Braga S, Passos-Coelho JL, Fonseca R, Oliveira J. Complete response in HER2+ leptomeningeal carcinomatosis from breast cancer with intrathecal trastuzumab. *Breast Cancer Res Treat*. June 2011;127(3):841–844. [Epub 3.03.11].
162. Hofer S, Mengele K, Stemmler HJ, Schmitt M, Pestalozzi B. Intrathecal trastuzumab: dose matters. *Acta Oncol*. April 23, 2012. [Epub ahead of print].
163. Laufman LR, Forsthoefel KF. Use of intrathecal trastuzumab in a patient with carcinomatous meningitis. *Clin Breast Cancer*. 2001;2:235.
164. Mir O, Ropert S, Alexandre J, Lemare F, Goldwasser F. High-dose intrathecal trastuzumab for leptomeningeal metastases secondary to HER-2 overexpressing breast cancer. *Ann Oncol*. 2008;19(11):1978–1980.
165. Platini C, Long J, Walter S. Meningeal carcinomatosis from breast cancer treated with intrathecal trastuzumab. *Lancet Oncol*. 2006;7:778–780.
166. Glantz MJ, Hall WA, Cole BF, et al. Diagnosis, management, and survival of patients with leptomeningeal cancer based on cerebrospinal fluid-flow status. *Cancer*. 1995;75:2919–2931.
167. Chamberlain MC. Combined modality treatment of leptomeningeal gliomatosis. *Neurosurgery*. 2003;52:324–330.

CHAPTER

9

Vascular Disorders: Epidemiology

Sylvia Eisele[1], *Lisa R. Rogers*[2]

[1]Department of Neurology, University Hospitals Case Medical Center, Cleveland, OH, USA; [2]Department of Neurology, University Hospitals Case Medical Center, Seidman Cancer Center, Cleveland, OH, USA

INTRODUCTION

Central nervous system vascular disease is a well-recognized complication of cancer. It may result from the direct or indirect effects of cancer and cancer treatment on blood vessels, from coagulopathies associated with cancer or cancer treatment, and from infection.[1,2] Until recent years, most clinical and pathology data relevant to these conditions were available only from retrospective reviews or case reports. Prospective studies have better identified the risk for cerebrovascular disease in cancer patients and have elucidated the role of treatment-related vascular injury and provided new information regarding the risk factors and incidence of these syndromes. The largest prospective study to date is that of Zoller et al., who followed 820,491 Swedish cancer patients from first hospitalization for hemorrhagic or ischemic stroke and compared the stroke risk with that of controls.[3] The risk of hemorrhagic and ischemic stroke was highest during the first 6 months of cancer diagnosis (2.2 and 1.6, respectively).[4] In children with cancer, Noje et al. found that the prevalence of stroke is approximately 1%, with equal distribution of ischemic versus hemorrhagic stroke.[4] The strongest association was found for children with leukemia and primary brain tumors.

COAGULOPATHY

Cancer can be complicated by alterations in the coagulation system that result in thrombosis, hemorrhage, or a combination of these. The thrombotic coagulopathy results from a complex interplay of tumor-related changes in the coagulation cascade and fibrinolytic system and the production of procoagulants by the tumor.[5] The predominant result of these abnormalities is activation of the extrinsic coagulation pathway through overexpression of tissue factor, a cell surface glycoprotein, generating thrombin, which converts fibrinogen into fibrin.[6] Tissue factor also activates platelets. It is speculated that an imbalance between tissue factor and its main inhibitor, tissue factor pathway inhibitor, contributes to a clinically apparent thrombotic coagulopathy in cancer patients. Another procoagulant that is expressed by tumor cells, termed cancer procoagulant, is a cysteine protease that is capable of initiating the coagulation process via alteration of the fibrinolytic process.[7] In addition, cancer cells can also alter coagulation by promoting platelet activation and aggregation through release of adenosine triphosphate, thrombin, and other proteases.[5] Release of proinflammatory and proangiogenic cytokines from the tumor may also contribute to thrombosis.

Disseminated intravascular coagulation, thrombocytopenia, and nutritional deficiency (especially vitamin K) may lead to systemic and central nervous system hemorrhages. Brain hemorrhage is most common in acute myelogenous leukemias, especially acute promyelocytic leukemia, early in its treatment. In this setting, disseminated intravascular coagulation is due to the release of procoagulant substances associated with tumor lysis. In addition, annexin II is highly expressed by leukemic cells and in cerebral microvascular endothelial cells.[8] This protein has high affinity to plasminogen and tissue plasminogen activator and also acts as a cofactor of plasminogen activation, hence enhancing plasmin activity. Thrombocytopenia is most commonly caused by bone marrow deficiency due to tumor infiltration, treatment toxicity, or immune-mediated platelet destruction. There is a high incidence of brain hemorrhage associated with bone marrow transplant to treat leukemia; in one study, intracranial hemorrhage was observed in 32% of 180 such patients.[9] In addition to disseminated intravascular coagulation, liver dysfunction, thrombocytopenia, and lumbar puncture can be precipitating factors in patients treated for leukemia or brain tumors.[10–12]

Handbook of Neuro-Oncology Neuroimaging, Second Edition
http://dx.doi.org/10.1016/B978-0-12-800945-1.00009-4

© 2016 Elsevier Ltd. All rights reserved.

ISCHEMIC CEREBROVASCULAR EVENTS

Investigations have revealed that the annual rate of age-adjusted cancer incidence is higher among ischemic stroke patients compared with the general population.[13] In addition, Navi et al. identified that the 3-month cumulative incidence of ischemic stroke is higher in patients with cancer, especially those with lung, pancreatic, and colorectal cancers, compared with matched controls.[14]

Cerebral ischemia in cancer patients is most commonly due to a thrombotic coagulopathy associated with the tumor or its treatment. A retrospective review of cerebral ischemic events in 96 cancer patients identified coagulation disorders in association with cerebral embolism as the most common etiologic factor.[2] Inflammatory and immune processes may play a role also.[15] Nonbacterial thrombotic endocarditis (NBTE) is a common cause of thrombotic and embolic ischemic stroke related to systemic thrombotic coagulopathy and sterile cardiac valve vegetations. It typically develops in patients with widely disseminated cancer, but stroke from NBTE can also be the presenting sign of cancer.[16,17]

The second most common cause of cerebral ischemia is the direct effect of a tumor on cerebral blood vessels. This includes tumor embolism in patients with primary or metastatic cardiac or lung tumors and cerebral intravascular obstruction by neoplastic cells in hematological malignancies with hyperleukocytosis, such as acute myelogenous leukemia and chronic lymphocytic leukemia, and with polycythemia vera. Leptomeningeal metastasis infiltrating vessel walls and extra- or intracranial tumors causing external vascular obstruction are also causes of cerebral infarction.

Intravascular lymphomatosis is a rare variant of extranodal B-cell non-Hodgkin lymphoma. Malignant cells proliferate within the vessels of systemic organs and the brain, causing diffuse thrombosis. The clinical manifestations are varied and the diagnosis is often not made until autopsy when the nervous system is preferentially involved, but antemortem diagnosis is important because therapy can be effective.[18] Thrombosis from tumor cell proliferation can also occur in leukemia when the leukemic cell count is very high (hyperleukocytosis). This type of vascular thrombosis can result in cerebral infarction or hemorrhage.

When a systemic solid tumor metastasizes to the brain via the arterial circulation, the tumor embolus may be large enough to cause obstruction of a large- or medium-size vessel and result in transient or permanent cerebral ischemia.[19] The underlying tumor almost always originates in the heart or lung. Sarcoma is the most common cardiac tumor to cause symptomatic cerebral embolization. Lung tumors may be primary or metastatic. There are rare reports of brain embolism occurring from manipulation of the lung at the time of surgical removal of a lung tumor.

Cerebral venous thrombosis, typically involving the superior sagittal sinus, can result from a thrombotic coagulopathy associated with cancer.[20] Most often it occurs secondary to cancer treatment, especially L-asparaginase administered for childhood leukemia and lymphoma. Steroids also contribute to the risk in children and lumbar puncture for intrathecal chemotherapy in adults.[21,22] There is a high rate of recurrence of venous thrombosis in patients with myeloproliferative neoplasms.[23]

INTRACRANIAL TUMOR

Tumor in the skull or dura can result in epidural, subdural, or subarachnoid hemorrhage. The most common syndrome is subdural hemorrhage resulting from dural metastasis of carcinomas, typically originating in the breast, lung, or prostate, or of lymphoma. Subdural hemorrhages also occur in patients with leukemia.[24] The mechanism of hemorrhage is speculated to be congestion or stretching of vessels in the dura. Primary dural tumors, typically meningiomas, also bleed, but this is uncommon.[25]

Intracranial hemorrhage in the setting of cancer is most commonly due to bleeding into brain metastases. The most common underlying tumor is lung adenocarcinoma; other tumors that are prone to bleeding include melanoma and thyroid, renal cell, and hepatocellular cancer. Bleeding in this setting is caused predominantly by the altered structure of neoplastic blood vessels, which lack normal endothelial cell tight junctions or a fully matured blood–brain barrier and therefore are prone to rupture.[26] Additional mechanisms are rapid tumor growth with rupture of neoplastic vessels or invasion of adjacent cerebral vessels. Higher vascular endothelial growth factor expression and neovascularity in hemorrhagic, rather than nonhemorrhagic, brain metastases have been demonstrated.[27] The most common primary brain tumors to be associated with hemorrhage are pituitary adenomas, meningiomas, and gliomas. Rarely, arterial tumor emboli from systemic cancer result in damage to cerebral vessels, resulting in neoplastic aneurysms with subsequent rupture and parenchymal or subarachnoid hemorrhages.

Tumors can also encase, compress, or invade cerebral venous structures. Such tumors can be primary or metastatic and are typically located in the skull or dura. The occurrence is rare: Komotar et al. retrospectively reviewed the records of 1617 patients with meningiomas and identified only three patients with neurological symptoms attributed to internal carotid artery compression.[28] Rarely, primary or metastatic tumor in the leptomeninges surrounds and/or compresses vessels in the Virchow–Robin space, resulting in infarction.[29,30] Invasion of the arterial wall and subsequent

vascular occlusion by parenchymal brain tumors is rare, but is reported in glioblastoma.[31,32]

Treatment Effects

Chemotherapy can increase the risk of systemic and cerebral thrombosis or hemorrhage. Some chemotherapies exaggerate the hypercoagulable state, whereas others may injure the endothelium or cause vasospasm. In other instances, thromboses are due to the release of tumor-derived coagulation factors into the bloodstream. L-Asparaginase is an enzymatic inhibitor of protein synthesis, which is often used in the induction therapy of acute leukemia. It depletes plasma proteins involved in coagulation and fibrinolysis. It is most commonly associated with cerebral venous sinus thrombosis but, in a small percentage of patients, is associated with intraparenchymal thrombosis or hemorrhage.[33] Inherited or acquired coagulation defects may render patients more susceptible to the thrombotic complications of L-asparaginase. In a retrospective review of 19 pediatric patients with leukemia or lymphoma administered L-asparaginase-containing regimens, low levels of coagulation factors in association with increased plasma D-dimer levels during or after L-asparaginase administration, combined with fresh-frozen plasma infusion, were associated with thrombosis.[34] Subdural hemorrhages occur in some patients with leukemia who are treated with bone marrow transplant.[11] The hemolytic uremic syndrome is a rare complication of chemotherapy, typically occurring in patients with carcinoma, that can result in brain hemorrhage.

Tamoxifen, used most commonly in the treatment of breast cancer, is well known to be associated with an increased risk of systemic venous thrombosis. However, the risk of cerebral ischemia is disputed.

The posterior reversible encephalopathy syndrome, presenting clinically with signs of elevated intracranial pressure, seizures, and confusion, has been associated with an increasing number of systemic antineoplastic agents, commonly cisplatin, 5-fluorouracil, doxorubicin, bevacizumab, and rituximab. Postulated mechanisms are treatment-related blood pressure elevation and toxic endothelial alterations, which lead to disruption of the blood–brain barrier and cerebral edema.[35–38]

Radiotherapy can produce or accelerate atherosclerosis and it is a causative factor in transient or permanent cerebral ischemia in some patients radiated for head and neck cancer. Because of the location of treatment portals, extensive areas of the common carotid artery and its branches in the neck are radiated. In a retrospective study, Dorth et al. found that 14% of patients had evidence of carotid stenosis at 4 years after radiotherapy compared to 4.2% in the general population.[39] In a report of stroke in patients younger than 60 years of age who received therapeutic neck radiation for head and neck tumors, Dorresteijn et al. reported a 12% 15-year cumulative risk of stroke.[40] Other factors may also contribute to the development of carotid stenosis. In one study of duplex ultrasonography in patients treated for head and neck cancers, independent risk factors for severe postradiation carotid stenosis included smoking history, interval from radiation of more than 5 years, no prior oncological surgery, and cerebrovascular symptoms.[41] Survivors of childhood Hodgkin lymphoma are also at risk for stroke if they received mantle radiation exposure. In these patients cerebral ischemia may be related to carotid artery disease or to cardiac valve disease with embolism.[42] In a separate study, De Bruin et al. reported that 5-year survivors of Hodgkin lymphoma who were treated before age 51 years have a significantly increased risk of stroke and transient ischemic attack compared with the general population. The risk of vascular events remained elevated after prolonged follow-up.[43] In addition, Bowers et al. documented the incidence of and risk factors for strokes occurring in long-term survivors of childhood leukemia and brain tumors.[44] These patient groups were compared with a random sampling of siblings of cancer survivors. The relative risk of stroke for leukemia survivors compared with the siblings was 64 (95% CI, 3.0–13.8; p, 0.0001) and for brain tumor survivors was 29 (95% CI, 13.8–60.6; p, 0.0001). An increased risk of stroke was found with a mean cranial radiation therapy dose of 30 Gy.

There is no significant increase in the 10-year risk for stroke in breast cancer patients treated with supraclavicular radiation.[45] The lack of strokes in these patients might be explained by the lower radiation dose administered and the smaller volume of irradiated vessel, compared to radiation for head and neck cancer.

Radiation-induced cerebral vasculopathy, resulting in multifocal vessel occlusions and sometimes resulting in infarction or hemorrhage, is a less common toxicity and is reported primarily in children.[46] A variety of miscellaneous and rare vascular disorders attributed to radiation of brain tumors are reported, including pseudoaneurysms and cavernous malformations.[47] Stroke-like migraine attacks after radiation therapy (SMART) syndrome represents the occurrence of reversible cerebral symptoms and signs associated with migraine headaches and cortical enhancement on magnetic resonance imaging. This is a rare syndrome occurring within years of brain radiation and in general has a good prognosis. The mechanism is not known, but is speculated to be a delayed manifestation of vascular injury.[48,49]

INFECTION

Immunosuppression in cancer patients renders them susceptible to opportunistic infections, especially fungal sepsis. Cerebral septic emboli are typically due to

Aspergillus, *Candida*, or mucormycosis species and occur most often in patients with leukemia or lymphoma or after bone marrow transplant. In the immunocompromised state, varicella zoster reactivation is common and may lead to cerebral vasculopathy presenting as ischemic stroke, hemorrhage, or central nervous system vasculitis.[50]

OTHER

Rarely, central nervous system angiitis is the presenting sign of non-Hodgkin lymphoma, Hodgkin disease, or other hematologic malignancies.[51,52] The mechanism for this association is not known. Idiopathic thrombocytopenic purpura, predisposing to intracranial hemorrhage, can complicate chronic leukemia or lymphoma.

References

1. Graus F, Rogers LR, Posner JB. Cerebrovascular complications in patients with cancer. *Medicine*. 1985;64:16–35.
2. Cestari DM, Weine DM, Panageas KS, Segal AZ, DeAngelis LM. Stroke in patients with cancer incidence and etiology. *Neurology*. 2004;62:2025–2030.
3. Zoller B, Sundquist JJ, Sundquist K. Risk of haemorrhagic and ischaemic stroke in patients with cancer: a nationwide follow-up study from Sweden. *Eur J Cancer*. 2012;48:1875–1883.
4. Noje C, Cohen K, Jordan LC. Hemorrhagic and ischemic stroke in children with cancer. *Pediatr Neurol*. 2013;49:237–242.
5. Noble S, Pasi J. Epidemiology and pathophysiology of cancer-associated thrombosis. *Br J Cancer*. 2010;102:S2–S9.
6. Rickles FR, Brenner B. Tissue factor and cancer. *Semin Thromb Hemost*. 2008;34:143–145.
7. Prandoni P, Falanga A, Piccioli A. Cancer and venous thromboembolism. *Lancet Oncol*. 2005;6:401–410.
8. Menell JS, Cesarman GM, Jacovina AT, McLaughlin MA, Lev EA, Hajjar KA. Annexin II and bleeding in acute promyelocytic leukemia. *N Engl J Med*. 1999;340:994–1004.
9. Blegi-Torres LF, Werner B, Gasparetto EL, de Medeiros BC, Pasquini R, de Medeiros CR. Post-transplant complications. Intracranial hemorrhage following bone marrow transplantation: an autopsy study of 58 patients. *Bone Marrow Transplant*. 2002;29:29–32.
10. Coplin WM, Cochran MS, Levine SR, Crawford SW. Stroke after bone marrow transplantation – frequency, aetiology and outcome. *Brain*. 2001;124:1043–1051.
11. Graus F, Saiz A, Sierra J, et al. Neurologic complications of autologous and allogeneic bone marrow transplantation in patients with leukemia: a comparative study. *Neurology*. 1996;46:1004–1009.
12. Kyrnetskiy EE, Kun LE, Boop FA, Sanford RA, Khan RB. Types, causes, and outcome of intracranial hemorrhage in children with cancer. *J Neurosurg*. 2005;102(1 Suppl.):31–35.
13. Qureshi AI, Malik AA, Saeed O, et al. Incident cancer in a cohort of 3247 cancer diagnosis free ischemic stroke patients. *Cerebrovasc Dis*. 2015;39:262–268.
14. Navi BB, Reiner AS, Kamel H, et al. Association between incident cancer and subsequent stroke. *Ann Neurol*. 2015;77:291–300.
15. Karlinska AG, Gromadzka G, Karlinski MA, Czlonkowska A. The activity of malignancy may determine stroke pattern in cancer patients. *J Stroke Cerebrovasc Dis*. 2010;24:778–783.
16. Rogers LR, Cho E-S, Kempin S, Posner JB. Cerebral infarction from nonbacterial thrombotic endocarditis: clinical and pathological study including the effects of anticoagulation. *Am J Med*. 1987;83:746–756.
17. Wong SF, Seow J, Profitis K, Johns J, Barnett S, John T. *Intern Med J*. 2013;43:211–214.
18. Fonkem E, Lok E, Robison D, Gautam S, Wong ET. The natural history of intravascular lymphomatosis. *Cancer Med*. 2014;3:1010–1024.
19. O'Neill BP, Dinapoli RP, Okazaki H. Cerebral infarction as a result of tumor emboli. *Cancer*. 1987;60:90–95.
20. Raizer JJ, DeAngelis LM. Cerebral sinus thrombosis diagnosed by MRI and MR venography in cancer patients. *Neurology*. 2000;54:1222–1226.
21. Ranta S, Tuckuviene R, Makipernaa A, et al. Cerebral sinus venous thromboses in children with acute lymphoblastic leukemia-a multicentre study from the Nordic Society of Paediatric Haematology and Oncology. *Br J Haematol*. 2015;168:547–552.
22. Zurrbier SM, Lauw MN, Coutinho JM, et al. Clinical course of cerebral venous thrombosis in adult acute lymphoblastic leukemia. *J Stroke Cerebrovasc Dis*. 2015;24:1679–1684.
23. Martinelli I, De Stefano V, Carobbio A, et al. Cerebral vein thrombosis in patients with Philadelphia-negative myeloproliferative neoplasms. An European Leukemia Net study. *Am J Hematol*. 2014;89:E200–E205.
24. Reichman J, Singer S, Navi B, et al. Subdural hematoma in patients with cancer. *Neurosurgery*. 2012;71:74–79.
25. Bosnjak R, Derham C, Popovic M, Ravnik J. Spontaneous intracranial meningioma bleeding: clinicopathological features and outcome. *J Neurosurg*. 2005;103:473–484.
26. Katz JM, Segal AZ. Incidence and etiology of cerebrovascular disease in patients with malignancy. *Curr Atheroscler Rep*. 2005;7:280–288.
27. Jung S, Moon K-S, Jung T-Y, et al. Possible pathophysiological role of vascular endothelial growth factor (VEGF) and matrix metalloproteinases (MMPs) in metastatic brain tumor-associated intracerebral hemorrhage. *J Neurooncol*. 2006;76:257–263.
28. Komotar RJ, Keswani SC, Wityk RJ. Meningioma presenting as stroke: report of two cases and estimation of incidence. *J Neurol Neurosurg Psychiatry*. 2003;74:136–137.
29. Herman C, Kupsky WJ, Rogers L, Duman R, Moore P. Leptomeningeal dissemination of malignant glioma simulating cerebral vasculitis: case report with angiographic and pathological studies. *Stroke*. 1995;26:2366–2370.
30. Klein P, Haley EC, Wooten GF, et al. Focal cerebral infarctions associated with perivascular tumor infiltrates in carcinomatous leptomeningeal metastases. *Arch Neurol*. 1989;46:1149–1152.
31. Rojas-Marcos I, Martin-Duverneuil N, Laigle-Donadey F, Taillibert S, Delattre JY. Ischemic stroke in patients with glioblastoma multiforme. *J Neurol*. 2005;252:488–489.
32. Pina S, Camero A, Rodrigues T, et al. Acute ischemic stroke secondary to glioblastoma. A case report. *Neuroradiol J*. 2014;27:85–90.
33. Wani NA, Kosar T, Pala NA, Quereshi UA. Sagittal sinus thrombosis due to L-asparaginase. *J Pediatr Neurosci*. 2010;5:32–35.
34. Kiyosawa N, Kano G, Yoshioka H, Sugimoto T, Imashuku S. Cerebral thrombotic complications in adolescent leukemia/lymphoma patients treated with L-asparaginase-containing chemotherapy. *Leuk Lymphoma*. 2005;46:729–735.
35. Arrillaga-Romany IC, Dietrich J. Imaging findings in cancer therapy-associated neurotoxicity. *Semin Neurol*. 2012;32:476–486.
36. Marinella MA, Markert RJ. Reversible posterior leucoencephalopathy syndrome associated with anticancer drugs. *Intern Med J*. 2009;39:826–834.
37. Ryan SA, Maceneaney P, O'Reilly SP, Moylan EJ, Power DG. Reversible posterior leukoencephalopathy induced by carboplatin and etoposide. *Med Oncol*. 2012;29:1287–1291.
38. Bartynski WS. Posterior reversible encephalopathy syndrome, part 2. *Am J Neurolradiol*. 2008;29:1042–1043.
39. Dorth JA, Patel PR, Broadwater G, Brizel DM. Incidence and risk factors of significant carotid artery stenosis in asymptomatic survivors of head and neck cancer after radiotherapy. *Head Neck*. 2014;36:215–219.

40. Dorresteijn LD, Kappelle AC, Boogerd W, et al. Increased risk of ischemic stroke after radiotherapy on the neck in patients younger than 60 years. *J Clin Oncol*. 2002;20:282–288.
41. Cheng SW, Ting AC, Lam LK, Wei WI. Carotid stenosis after radiotherapy for nasopharyngeal carcinoma. *Arch Otolaryngol Head Neck Surg*. 2000;126:517–521.
42. Bowers DC, McNeil DE, Liu Y, et al. Stroke as a late treatment effect of Hodgkin's disease: a report from the Childhood Cancer Survivor Study. *J Clin Oncol*. 2005;23:6508–6515.
43. De Bruin ML, Dorresteijn LD, van't Veer MB, et al. Increased risk of stroke and transient ischemic attack in 5-year survivors of Hodgkin lymphoma. *J Natl Cancer Inst*. 2009;101:928–937.
44. Bowers DC, Liu Y, Leisenring W, et al. Late-occurring stroke among long-term survivors of childhood leukemia and brain tumors: a report from the Childhood Cancer Survivor Study. *J Clin Oncol*. 2006;24:5277–5282.
45. Woodward WA, Giordano SH, Duan Z, Hortobagyi GN, Buchholz TA. Supraclavicular radiation for breast cancer does not increase the 10-year risk of stroke. *Cancer*. 2006;106:2556–2562.
46. Wang C, Roberts KB, Bindra RS, Chiang VL, Yu JB. Delayed cerebral vasculopathy following cranial radiation therapy for pediatric tumors. *Pediatr Neurol*. 2014;50:549–556.
47. Lau WY, Chow CK. Radiation-induced petrous internal carotid artery aneurysm. *Ann Otol Rhinol Laryngol*. 2005;114:939–940.
48. Pruitt A, Dalmau J, Detre J, Alavi A, Rosenfeld MR. Episodic neurologic dysfunction with migraine and reversible imaging findings after radiation RRH. *Neurology*. 2006;67:676–678.
49. Black DF, Bartleson JD, Bell ML, Lachance DH. SMART: stroke-like migraine attacks after radiation therapy. *Cephalalgia*. 2006;26: 1137–1142.
50. Nagel MA, Gilden D. Neurological complications of varicella zoster virus reactivation. *Curr Opin Neurol*. 2012;27:356–360.
51. Le Guennec L, Roos-Weil D, Mokhtari K, et al. Granulomatous angiitis of the CNS revealing a Hodgkin lymphoma. *Neurology*. 2013;80:323–324.
52. Morotti A, Malagola M, Cancelli V, et al. Central nervous system angiitis in Hodgkin's disease. *J Neurol*. 2013;260:2897–2899.

CHAPTER

10

Intracranial Hemorrhage in Cancer Patients

Chaitra A. Badve[1], *Lisa R. Rogers*[2]

[1]Department of Diagnostic Radiology, University Hospitals Case Medical Center, Cleveland, OH, USA; [2]Department of Neurology, University Hospitals Case Medical Center, Seidman Cancer Center, Cleveland, OH, USA

INTRODUCTION

The most common location of intracranial hemorrhage (ICH) in cancer patients is the brain parenchyma, followed by the subdural, subarachnoid, and epidural spaces.[4] The etiology, clinical presentation, diagnostic evaluation, and management of ICH in the cancer setting are different from those in the general population and are closely related to the type of malignancy and antineoplastic therapy.[11,19] The most common tumors associated with ICH are lung, melanoma, breast, and glioblastoma, among patients with solid tumors, and leukemia among patients with hematological malignancies.[19]

ETIOLOGY

The most common causes of ICH in cancer are systemic coagulopathy, presence of intracranial tumor, and complications of cancer treatment.

Coagulopathy

Coagulopathy leading to ICH in cancer patients may be associated with disseminated intravascular coagulation (DIC), thrombocytopenia due to bone marrow suppression or infiltration by tumor, liver failure, or vitamin K deficiency. Chen et al. reported ICH in 2.8% (72 patients) of 2574 patients with hematologic malignancies.[3] The most common causes were thrombocytopenia, sepsis, and prolonged prothrombin time. Hemorrhage associated with DIC is most common in acute myelogenous leukemias, especially early in the treatment of acute promyelocytic leukemia (APML). In a review of 90 cancer patients with subdural hematomas diagnosed at Sloan Kettering Cancer Center, gliomas, leukemia, and prostate cancer were the most common malignancies. Coagulopathy and head trauma were the most common causes.[15] Idiopathic thrombocytopenic purpura, complicating chronic leukemia, or lymphoma is a rare cause of ICH.

Tumor-Related Hemorrhages

The most common tumors associated with parenchymal hemorrhage are brain metastases, particularly from melanoma and thyroid, renal cell, hepatocellular, or lung cancer origin.[16,17] Lymphoma is the most common hematologic malignancy to underlie parenchymal hemorrhage.[3] A variety of primary brain tumors are also associated with hemorrhage, including glioblastoma multiforme, pituitary macroadenomas, and meningiomas. The mechanism of intratumoral hemorrhage is speculated to be rapid tumor growth, which results in the rupture of neoplastic vessels or of adjacent cerebral vessels. Vascular endothelial growth factor (VEGF) may play a role in hemorrhage into brain metastases: Jung et al. demonstrated higher VEGF expression and neovascularity in hemorrhagic, rather than nonhemorrhagic, brain metastases.[7]

The most common skull or dural tumors associated with subdural hemorrhage are breast, lung, prostate, or lymphoma metastasis.[19] Primary dural tumors, typically meningiomas and hemangiopericytomas, also hemorrhage, but this is less common.[2] Tumor-related congestion or stretching of vessels in the dura is speculated to be the reason for subdural hemorrhage. Epidural hemorrhage is a rare complication of skull or dural tumor.[8]

Hyperleukocytosis (peripheral blast count >100,000/mm^3) in acute myelogenous leukemia can result in brain hemorrhage because of leukostasis (plugging of small cerebral vessels) or because of the growth of leukemic nodules, which damages blood vessels. Rarely, arterial tumor emboli from systemic cancer form neoplastic aneurysms, which rupture and cause bleeding into the brain or subarachnoid space.[13]

Handbook of Neuro-Oncology Neuroimaging, Second Edition
http://dx.doi.org/10.1016/B978-0-12-800945-1.00010-0

© 2016 Elsevier Ltd. All rights reserved.

Treatment Effects

Systemic agents administered for cancer increase the risk of systemic and cerebral hemorrhage. In APML patients undergoing chemotherapy, acute DIC is caused by procoagulant substances in the leukemic cells released during tumor lysis.[9,12,19] L-Asparaginase, which is typically associated with cerebral venous thrombosis, can also rarely result in brain hemorrhage. There is anecdotal evidence that imatinib may contribute to subdural hemorrhage when used to treat chronic myelogenous leukemia and, when administered with systemic and intrathecal chemotherapy, is associated with a small risk of subdural hemorrhage in Philadelphia chromosome-positive, but not Philadelphia chromosome-negative, acute lymphoblastic leukemia.[14,18]

A common clinical setting for ICH is following bone marrow transplant to treat leukemia. In a study by Blegi-Torres and colleagues, ICH hemorrhage was identified in 32% of 180 patients.[1] The site of bleeding is often subdural.[5]

The hemolytic uremic syndrome is a rare complication of chemotherapy, typically occurring in patients with carcinoma, which can result in brain hemorrhage. In addition, a variety of miscellaneous and rare vascular disorders attributed to radiation of brain tumors are reported, including pseudoaneurysms and cavernous malformations, which may cause subarachnoid or intraparenchymal hemorrhage.[10]

CLINICAL PRESENTATION

As in patients without cancer who develop parenchymal or subdural hemorrhage, signs may be acute or subacute and include headache, encephalopathy, focal neurological deficits, or a seizure. In systemic coagulopathy and acute DIC there will usually be signs of systemic thrombosis or hemorrhage. The onset of neurological signs in intratumoral hemorrhage is usually acute. In some instances, however, the onset of signs is chronic and indistinguishable from those of preexisting tumor. Depending on the location of the bleed, focal neurologic signs may be present.

DIAGNOSIS

A detailed clinical history and clinical examination are essential for directing focused diagnostic tests and reaching a rapid and accurate diagnosis. Systemic coagulopathy, especially DIC, will be associated with abnormalities of platelet count, coagulation function, D-dimer, and fibrinogen levels. Clinical and laboratory signs will be abnormal in the presence of sepsis and liver failure. Cross-sectional imaging with noncontrast computed tomography (CT) is the test of choice for rapid screening for ICH in acutely ill patients. Acute intraparenchymal, subarachnoid, subdural, and epidural hemorrhages can be easily detected by the characteristic appearance and location of hematoma. Acute ICH is often hyperdense on CT; however, caution is indicated in the setting of coagulopathy and hyperacute bleeding in which the hematoma may appear isodense to the brain parenchyma. Magnetic resonance imaging (MRI) is the investigation of choice in evaluating intratumoral hemorrhages, hemorrhagic transformations of stroke, and subdural hemorrhages due to tumoral infiltrations or coagulopathy. The early presence of edema and enhancement associated with intraparenchymal hemorrhage suggest associated brain metastasis. Figure 1 shows early edema associated with intratumor hemorrhage in a patient with brain metastasis. In addition, atypical locations of hemorrhage at the gray–white junction, persistent edema, and delayed evolution of blood products on follow-up imaging are suspicious for intratumoral hemorrhage.

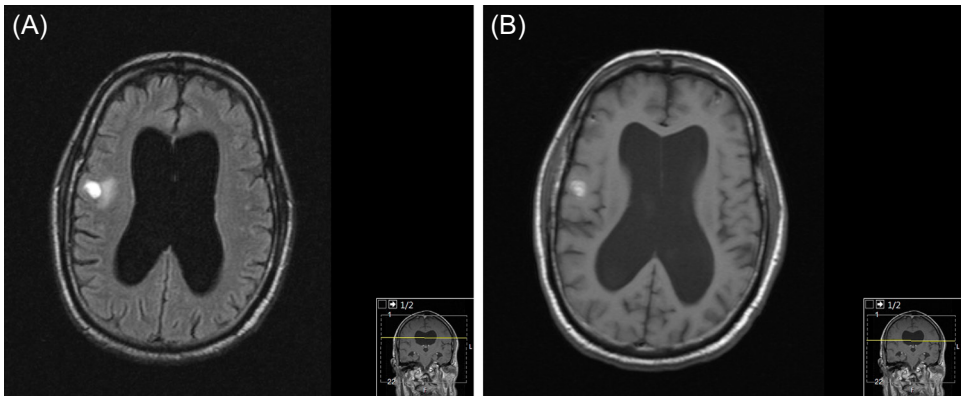


FIGURE 1 (A) T1-weighted unenhanced MRI shows hyperintense signal attributed to a new hemorrhage into brain metastasis. (B) Fluid-attenuated inversion recovery image shows early edema surrounding the bleed.

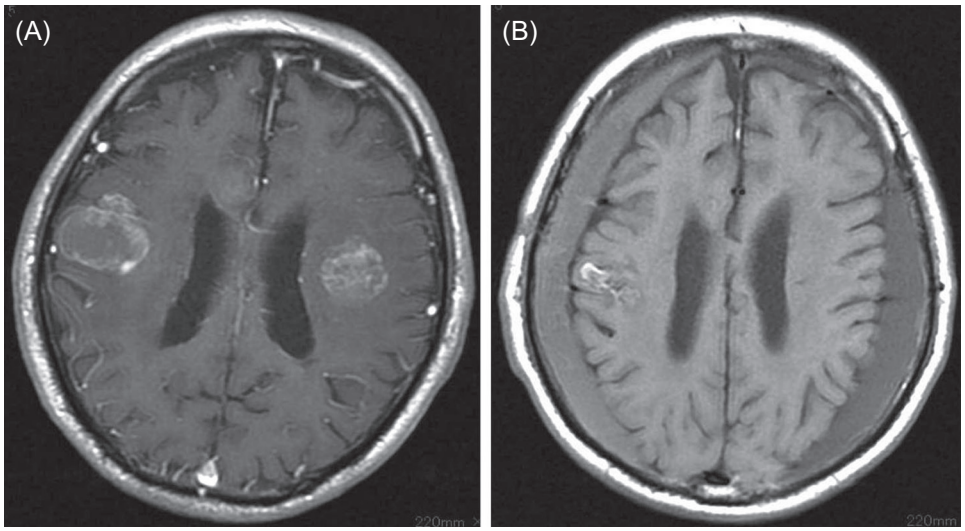


FIGURE 2 (A) Brain MR image taken on admission shows bilateral masses in the brain. (B) Brain MR image taken on deterioration of symptoms shows bilateral crescent-shaped isointensity lesions and a shrunken brain mass. *Reproduced with permission from Ref. 6*

Subdural hemorrhages associated with primary or metastatic tumors to the skull or dura can be recognized by hematomas with coexistent skull expansion, destruction, dural thickening, and enhancement. In some instances, the tumor is microscopic.[6] Figure 2 shows the sudden development of bilateral subdural hematomas in a patient with brain metastasis from lung cancer in whom there was no imaging evidence of dural or skull metastasis. Diagnosis was made only at examination of the subdural fluid (Figure 3). CT or MRI scan can identify epidural hemorrhage associated with skull metastasis.

MR angiography and venography can evaluate arterial and venous structures in the setting of suspected venous thrombosis or subarachnoid bleed. Digital subtraction angiography is the gold standard for diagnosis of tumor- or therapy-related intracranial aneurysms, pseudoaneurysms, and vascular malformations.

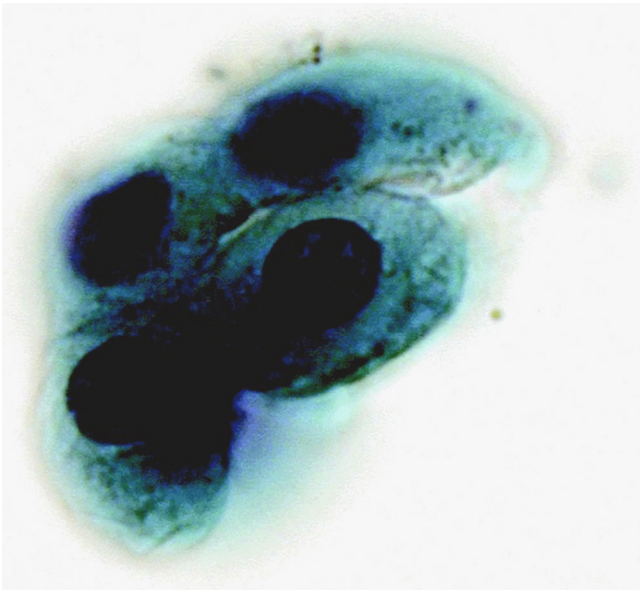


FIGURE 3 Adenocarcinoma cells detected in hematoma fluid. *Reproduced with permission from Ref. 6*

MANAGEMENT

Steroids play an important role in decreasing mass effect associated with ICH. Treatment of systemic coagulopathy is aimed at correcting the underlying cause and may include platelets, fresh-frozen plasma, coagulation factors, vitamin K, or treatment of sepsis. Treatment of DIC remains controversial, as there is a need to control the underlying thrombotic disorder and also to replace clotting factors. Treatment of subdural hematomas is dictated by the clinical status and presence of coagulopathy and may include resection, treatment of coagulopathy, or both.[5]

Resection of a tumor-related hemorrhage is indicated when the hemorrhage is life threatening but, in many instances, surgery is not required and standard therapy should be directed to the tumor, typically radiation. A neoplastic subdural or epidural hemorrhage may be large enough to require drainage to relieve mass effect. Definitive therapy for skull or dural metastasis is radiation or chemotherapy, depending on the tumor type. Therapy for the rare occurrence of bleeding from a neoplastic aneurysm should be radiation, with or without chemotherapy.

References

1. Blegi-Torres LF, Werner B, Gasparetto EL, de Medeiros BC, Pasquini R, de Medeiros CR. Post-transplant complications. Intracranial hemorrhage following bone marrow transplantation: an autopsy study of 58 patients. *Bone Marrow Transplant*. 2002;29:29–32.
2. Bosnjak R, Derham C, Popovic M, Ravnik J. Spontaneous intracranial meningioma bleeding: clinicopathological features and outcome. *J Neurosurg*. 2005;103:473–484.
3. Chen C-Y, Tai C-H, Cheng A, et al. Intracranial hemorrhages in adult patients with hematological malignancies. *BMC Med*. 2012;10:97.
4. Graus F, Rogers LR, Posner JB. Cerebrovascular complications in patients with cancer. *Medicine*. 1985;64:16–35.
5. Graus F, Saiz A, Sierra J, et al. Neurologic complications of autologous and allogeneic bone marrow transplantation in patients with leukemia: a comparative study. *Neurology*. 1996;46:1004–1009.
6. Hata A, Fujita S, Katakami N, Sakai C, Imai Y. Bilateral subdural hematoma associated with central nervous system metastases from lung cancer. *J Thorac Oncol*. 2011;6:207–208.
7. Jung S, Moon K-S, Jung T-Y, et al. Possible pathophysiological role of vascular endothelial growth factor (VEGF) and matrix metalloproteinases (MMPs) in metastatic brain tumor-associated intracerebral hemorrhage. *J Neurooncol*. 2006;76:257–263.
8. Kim B, Yoon S, Bae H, Yun I. Spontaneous intracranial epidural hematoma originating from dural metastasis of hepatocellular carcinoma. *J Korean Neurosurg Soc*. 2010;48:166–169.
9. Kyrnetskiy EE, Kun LE, Boop FA, Sanford RA, Khan RB. Types, causes, and outcome of intracranial hemorrhage in children with cancer. *J Neurosurg*. 2005;102(1 Suppl.):31–35.
10. Lau WY, Chow CK. Radiation-induced petrous internal carotid artery aneurysm. *Ann Otol Rhinol Laryngol*. 2005;114:939–940.
11. Morgenstern LB, Hemphill JC, Anderson C, et al. Guidelines for the management of spontaneous intracerebral hemorrhage: a guideline for healthcare professionals from the American Heart Association/American Stroke Association. *Stroke*. 2010;41:2108–2129.
12. Navi BB, Reichman JS, Berlin D, et al. Intracerebral and subarachnoid hemorrhage in patients with cancer. *Neurology*. 2010;74:494–501.
13. Nomura R, Yoshida D, Kim K, Kobayashi S, Teramoto A. Intracerebral hemorrhage caused by a neoplastic aneurysm from pleomorphic lung carcinoma: case report. *Neurol Med Chir (Tokyo)*. 2009;49:33–36.
14. Patel SB, Gojo I, Tidwell ML, Sausville EA, Baer MR. Subdural hematomas in patients with Philadelphia chromosome-positive acute lymphoblastic leukemia receiving imatinib mesylate in conjunction with sytemic and intrathecal chemotherapy. *Leuk Lymphoma*. 2011;52:1211–1214.
15. Reichman J, Singer S, Navi B, et al. Subdural hematoma in patients with cancer. *Neurosurgery*. 2012;71:74–79.
16. Schouten LJ, Rutten J, Huveneers HA, Twijnstra A. Incidence of brain metastases in a cohort of patients with carcinoma of the breast, colon, kidney, and lung and melanoma. *Cancer*. 2002;94:2698–2705.
17. Seidel C, et al. A comprehensive analysis of vascular complications in 3889 glioma patients from the German Glioma Network. *J Neurol*. 2013;260(3):847–855.
18. Song KW, Rifkind J, Al-Beirouti B, Yee K, et al. Subdural hematomas during CML therapy with imatinib mesylate. *Leuk Lymphoma*. 2004;8:1633–1636.
19. Velander AJ, DeAngelis LM, Navi BB. Intracranial hemorrhage in patients with cancer. *Curr Atheroscler Rep*. 2012;14:373–381.

CHAPTER

11

Central Nervous System Infarction

Achala Vagal[1], *Arastoo Vossough*[2], *Michael H. Lev*[3], *Max Wintermark*[4]

[1]Neuroradiology Division, Department of Radiology, University of Cincinnati Medical Center, Cincinnati, OH, USA; [2]Children's Hospital of Philadelphia, Philadelphia, PA, USA and Hospital of the University of Pennsylvania, Philadelphia, PA, USA; [3]Neurovascular Laboratory, Massachusetts General Hospital, Boston, MA, USA and Harvard Medical School, Boston, MA, USA; [4]Neuroradiology Division, Department of Radiology, Stanford University, Stanford, CA, USA

INTRODUCTION

Symptomatic cerebral infarction or stroke affects more than 795,000 Americans each year, killing almost 130,000 yearly.[1,2] On average, one American dies from stroke every 4 min. [1,2] Stroke is a leading cause of long-term disability with a profound socioeconomic impact. The estimated direct and indirect cost of stroke is $36.5 billion each year.[3] Approximately 85% of strokes are nonhemorrhagic and 15% are hemorrhagic. In western populations, the major causes of central nervous system (CNS) infarcts include emboli from large vessels (e.g., atherosclerotic carotid disease), emboli from the heart, small vessel (i.e., lacunar) disease, and other causes, including hypercoagulable states, intracranial atherosclerosis, extracranial and intracranial arterial dissection, vasculitis, other vasculopathies, and various causes of venous infarction.

IMAGING EVALUATION OF CNS INFARCTION

Neuroimaging of acute stroke should answer a few key issues[4,5]: (1) whether hemorrhage is present; (2) the extent of ischemia; (3) whether there is an intravascular clot that can be targeted for thrombolysis; (4) whether a penumbra of ischemic, but potentially salvageable tissue is present; (5) exclusion of stroke mimics; (6) the etiology of the stroke; and (7) whether there is a risk of recurrence. To answer these and related questions, a variety of imaging techniques are used in the evaluation of CNS infarcts. Currently, the standard of care is a noncontrast head computed tomography (CT) scan. Multimodal imaging techniques are increasingly being used to identify treatment-related imaging targets and potentially powerful means of patient triage in the setting of acute stroke; this is an area of active research.[5,6]

Computed Tomography

Noncontrast Computed Tomography (NCCT)

CT is used to exclude hemorrhage in acute stroke, but can also show early ischemic changes. The classic signs of early ischemic change on NCCT include:[7–9]

1. Hypodensity. Early parenchymal hypoattenuation and loss of gray–white differentiation are the earliest parenchymal signs of acute infarct. They may manifest as hypodensity in the basal ganglia, loss of the normal insular ribbon, or loss of cortex–white matter differentiation in the cerebral hemispheres (Figure 1(A)). The mechanism of hypodensity on CT is thought to represent cytotoxic edema or decreased blood volume.[7] The low-density region seen on NCCT represents infarcted tissue. Reported sensitivity of CT in hyperacute stroke in the first 6 hours is in the range of 38–45%.[10,11] It has been shown that use of narrow window settings can improve the conspicuity of subtle ischemic hypodensity by accentuating the gray–white matter differentiation (Figure 1(B)).[12] Frank hypodensity in greater than one-third of the middle cerebral artery (MCA) territory has been reported as a risk factor for hemorrhagic transformation.[7]

Handbook of Neuro-Oncology Neuroimaging, Second Edition
http://dx.doi.org/10.1016/B978-0-12-800945-1.00011-2

© 2016 Elsevier Ltd. All rights reserved.

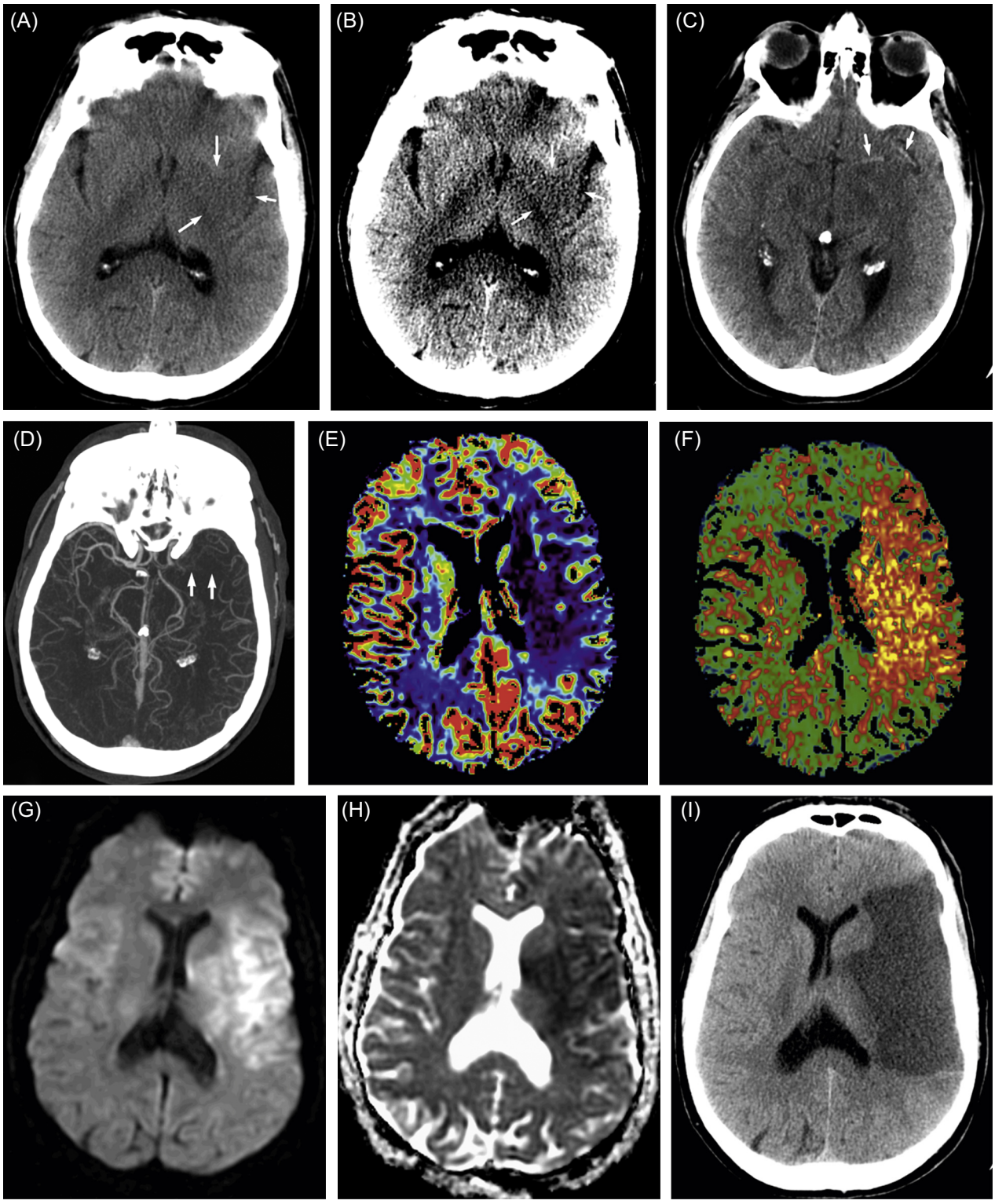


FIGURE 1 Acute left MCA territory infarct. (A) CT scan shown in standard brain windows shows subtle left basal ganglia hypodensity and loss of insular ribbon (arrows). (B) Same CT slice as in Figure 1(A), but with narrow window settings shows a much more conspicuous appearance of the left basal ganglia hypodensity and insular ribbon loss (arrows). (C) NCCT shows dense MCA secondary to thrombus in the left MCA (arrows). (D) Maximum intensity projection of CTA shows no flow and occlusion in the proximal left MCA (arrows). (E) CT perfusion color-coded CBF map demonstrating an area of decreased flow in the left MCA territory. (F) CT perfusion color-coded MTT map in the same slice as in Figure 1(E), demonstrating a much larger area of increased MTT compared to the area of decreased flow (perfusion mismatch). (G) Diffusion-weighted MRI image performed 2 hours later shows high DWI signal in the left MCA territory. (H) ADC map corresponding to DWI slice in Figure 1(G), showing decreased signal and confirming restricted diffusion in the left MCA territory. (I) Follow-up CT scan 7 days later demonstrates the final area of infarct in the left MCA territory, which in this patient corresponds more closely with the area of decreased CBF. This patient was not a thrombolysis candidate at the time of presentation.

2. Subtle effacement of cortical sulci and basilar cisterns with narrowing of the sylvian fissure may also be seen. Gaze deviation toward the side of the stroke may be an additional helpful hint for early diagnosis of acute infarct on NCCT.
3. Vessel hyperdensity. This finding is due to the presence of a fibrin-rich occlusive thrombus in a vessel, most commonly in the M1 segment of the MCA known as the hyperdense MCA sign (Figure 1(C)).[13] This finding is associated with a poorer prognosis.[14] A dense thrombus may also be seen in cases of basilar artery or posterior cerebral artery occlusive disease. Arterial microcalcifications and high hematocrit levels can cause false positives.

CT Angiography (CTA)

CTA in the setting of ischemic stroke is used to evaluate the presence of arterial thrombosis, arterial stenosis, and potentially evaluate the collateral pathways (Figure 1(D)). CTA is performed by dynamic intravenous injection of contrast, with optimized timing to image the arterial vessels at their peak enhancement. For acute stroke, imaging of both the intracranial vasculature and the cervical vessels from the aortic arch should be performed. Protocols vary within institutions, but in all cases, the CTA protocols should be optimized to find a balance between image quality and noise, slice thickness, pitch, table speed, gantry rotation rate, contrast dose, contrast flow rate, and radiation dose. The newer multidetector scanners can help reduce contrast dose, scanning time, and potentially reduce radiation dose by automated tube modulation. The use of a saline chaser can help reduce contrast dose and decrease streak artifact from dense venous contrast in the thoracic inlet. The use of multiphasic injection rates can also help optimize contrast enhancement in the vessels and decrease contrast use. The use of bolus tracking or a test bolus prior to the actual scan can help optimize timing of the contrast bolus.

Once the CTA scan is performed, the source images can be viewed on the scanner to look for obvious areas of vessel occlusion or stenosis. Various two-dimensional and three-dimensional reconstruction methods can be utilized to visualize the vessels. These include maximum intensity projections (MIP), multiplanar reformats, curved reformats in which the vessels are straightened via a computer algorithm, shaded surface display, and finally volume rendering. Some of these methods are time-consuming and may require work on a dedicated workstation. In urgent situations, the CT technologists can produce triplanar thick slab MIP images (e.g., 30 mm thick slabs at 5 mm overlapping intervals) on the scanner console rapidly for quick interpretation before the detailed three-dimensional images are reconstructed (Figure 1(D)).

The main advantages of CTA include widespread availability, speed of acquisition, the fact that they can be obtained at the same time as NCCT, higher accuracy compared with magnetic resonance angiography (MRA), and lower risk compared with catheter angiography. The relative disadvantages of CTA include iodinated contrast risk, radiation, limited field of view on older scanners, beam-hardening artifact from dental fillings and implants, and lack of physiological data such as flow velocity and directionality that could be obtained by magnetic resonance imaging (MRI). Another limitation of CTA is that in areas of dense or circumferential calcification, there is substantial beam-hardening artifact, which limits accurate measurement of vessel lumen diameter.

CTA has been shown to be 98% sensitive and specific for proximal intracranial thrombus detection.[15] CTA has been shown to be accurate and superior to ultrasonography in assessing degree of stenosis, the presence of hairline vessel lumen, and atherosclerotic plaque ulceration.[16] CTA is the most common first-line noninvasive vascular test in the acute setting for neurovascular disease. CTA source images (CTA-SI) provide relevant data concerning tissue-level perfusion and it has been suggested that CTA-SI are blood volume weighted by theoretical modeling,[17] and hence can be used to define infarct core. CTA can also give valuable information regarding the baseline leptomeningeal collateral status, which is an independent determinant of clinical outcome among patients with acute ischemic stroke.

CT Perfusion (CTP)

Within minutes of a vessel occlusion, an area of brain parenchyma develops irreversible damage or infarction, defined as the "core". A severely hypoperfused tissue which is not irreversibly damaged and potentially salvageable surrounds this core; defined as the "ischemic penumbra". Perfusion imaging is utilized to delineate this ischemic penumbra in acute stroke. An imaging test which can thus physiologically define the core and penumbra can potentially extend the thrombolysis treatment window and a "tissue clock" instead of the "time clock" for triaging stroke patients.[18] CTP measures tissue-level capillary blood flow in the brain.[19] Cerebral perfusion can be described by three parameters. Cerebral blood volume (CBV) is the total volume of blood in a given unit volume of brain tissue. Cerebral blood flow (CBF) is the volume of blood moving through a given unit volume of brain per unit time. Mean transit time (MTT) is the average of the transit time of blood through a region of brain parenchyma. These parameters are related to each other by the "central volume" formula MTT = CBV/CBF. Another important parameter is Tmax, the time to maximum of the residue function obtained by deconvolution.

Quantitative CTP is often performed by continuous cine-CT acquisition of a fixed brain region during dynamic intravenous contrast administration at a rate of 4–7 ml/s.[20] Previously, only a limited number of slices could be covered, but with the advent of higher detector scanners, larger volumes of the brain—including the entire brain parenchyma—can be imaged using CTP techniques. Once the data is acquired, various postprocessing methods are utilized to produce perfusion parameter (CBV, CBF, and MTT) maps using a variety of deconvolution and nondeconvolution methods (Figure 1).

The advantages of CTP include widespread availability of CT, lower costs, relative ease and higher speed of scanning, especially in very ill patients, and use in patients with contraindications to MRI. CTP can provide quantitative perfusion information compared to MR perfusion, and is not limited by susceptibility effects from adjacent structures or large vessel contamination.[20] The disadvantages of CTP include use of ionizing radiation, the risks associated with iodinated contrast use, limited brain coverage with current scanner technology, and more complex image postprocessing requirements. One of the biggest disadvantages of both CT and MR perfusion is lack of standardization and validation of acquisition techniques, postprocessing algorithms, and thresholds to define penumbra and core.

The earlier operational ischemic penumbra in CTP was defined as the area of CBV–CBF mismatch (Figure 1(E) and (F)); the region of decreased CBV being the core and area of CBV–CBF/MTT mismatch as the penumbra.[21] Recent literature supports the use of CBF to define core.[22,23] The time maps including MTT and Tmax are used to estimate the penumbra. It is hypothesized that patients with no mismatch or with early complete recanalization will show no or little lesion progression.[20] Untreated or unsuccessfully treated patients with large mismatch may show substantial growth of the infarcted tissue on follow-up imaging (Figure 1(I)). However, the utility of mismatch as a physiological triage tool for thrombolysis candidate selection is a highly debated topic. There is considerable ongoing research in better defining perfusion thresholds to more accurately define and characterize the infarct core and ischemic penumbra, and their relationship to clinical outcome and hemorrhagic risk.

Magnetic Resonance

Conventional MRI

Diffusion-Weighted Imaging (DWI)

Diffusion imaging techniques are discussed in more detail in Chapters 27 and 28. DWI is highly sensitive and specific in detection of hyperacute and acute stroke, ranging from 86 to 100%[24] and with the highest level of evidence for accurate diagnosis of ischemic stroke. On diffusion imaging, acute infarcts present as bright areas on DWI images and dark on apparent diffusion coefficient (ADC) maps (Figure 1(G) and (H)). Diffusion restriction can be also be seen in patients with cerebral abscesses, highly cellular tumors including high-grade glioma, venous infarcts, acute demyelinating lesions, infections such as herpes encephalitis, Creutzfeldt-Jacob disease, status epilepticus, hemiplegic migraine, transient global amnesia, reversible posterior encephalopathy, and diffuse axonal injury. However, infarcts can usually be differentiated from the above disease processes based on additional MR features. False negative infarcts on DWI are seen in brainstem infarcts, or small lacunar infarctions. In these cases, persistence of the specific neurological deficit on examination may prompt early follow-up imaging which often shows the abnormality not seen on the initial scan.

DWI is also helpful in the aging of infarcts, particularly detection of acute infarcts in the setting of subacute infarcts; this differentiation is difficult on NCCT. In the absence of thrombolysis, reversibility of DWI lesions is relatively rare and often in cases of transient ischemic attack, transient global amnesia, status epilepticus, and venous sinus thrombosis.[25] With thrombolysis a portion of the DWI abnormality may be reversible, especially in the white matter, although still uncommon. Lower ADC values in areas of infarct are associated with higher risk of hemorrhagic transformation and larger volumes of diffusion abnormality are associated with worse clinical outcome.[24]

In the hyperacute stage of stroke (0–6 hours), there may be loss of the normal vessel flow voids on T2-weighted images. On fluid attenuation inversion recovery (FLAIR) sequences, there may be high intravascular signal within the vessels, a finding that can be seen in up to 65% of cases.[26] The sensitivity of parenchymal signal changes on T2-weighted or FLAIR images in the first 6 hours of stroke are only 18–29%.[11,27,28] Acute infarcts are seen as hyperintense, swollen cortical gyri on FLAIR images, representing cytotoxic edema. Gradient echo T2*-weighted susceptibility images may also show the intravascular thrombus as a linear region of low signal susceptibility, due to the presence of deoxyhemoglobin within the clot. In one study, this finding had 83% sensitivity compared with 52% sensitivity of the dense vessel sign on noncontrast CT.[29] Contrast-enhanced T1-weighted images may show arterial enhancement without parenchymal enhancement in 50% of hyperacute strokes, believed to represent collateral flow, slow flow, or hyperperfusion after early recanalization.[30,31]

In the acute stage of stroke (6–24 hours), there is increase in water content and the infarct is seen as hyperintensity on T2-weighted and FLAIR images with a sensitivity approaching 90% at 24 hours.[31]

Diffusion restriction (bright DWI and dark ADC signal) can be seen in acute infarcts up to 10–14 days, after which the ADC maps start to normalize.

In the subacute stage of stroke (24 hours–2 weeks), T2 and FLAIR hyperintensity persist, and T1 hypointensity starts to develop. The DWI signal is usually bright, although there is no corroborating ADC darkness (T2 shine through). Brain swelling increases and peaks at day three, manifesting as effacement of sulci, cisterns, and ventricles, gyral thickening, midline shift, and various forms of herniation. Arterial enhancement and meningeal enhancement are seen, which often resolve by 1 week. Gyriform parenchymal enhancement occurs at this stage and may persist up to 8 weeks.[30]

In the chronic stage of stroke, the edema resolves and gliosis and tissue loss develops, characterized by T2 hyperintensity, T1 hypointensity, focal volume loss, and possibly cystic encephalomalacia. After 8 weeks, no parenchymal, vascular or meningeal enhancement is seen. With larger infarcts, Wallerian degeneration develops, manifested by volume loss and T2 hyperintensity in the corticospinal tract pathway.

Hemorrhagic transformation of brain infarction can range from small petechial bleeds to large parenchymal hematomas. It has a cumulative incidence of up to 43% in the first month and overall risk factors include embolic stroke etiology, hypertension, high glucose levels, higher National Institute of Health Stroke Scale score, reperfusion, good collateral circulation, longer time to recanalization after thrombolysis, anticoagulant therapy, and thrombolytic therapy.[32–35] A common grading scheme uses the hemorrhagic infarcts (HI1 and HI2) and parenchymal hematoma (PH1 and PH2) classification.[36] Gradient echoT2*-weighted sequences are best utilized in detecting these areas of intraparenchymal hemorrhage and it has been shown to have equivalent sensitivity compared with CT.[37,38] As time passes and blood products pass through the methemoglobin stage, they may manifest as areas of hyperintensity on T1-weighted images.

Conventional MRI is an adjunct to CTA or MRA in the diagnosis of cervicocranial vessel dissection. Fat-saturated T1-weighted images may show a bright methemoglobin signal in the vessel wall hematoma caused by dissection. The caveat in the use of this technique is that the hematoma may not be seen in very early cases and also in chronic dissections.

MR Angiography (MRA)

MRA is used to evaluate the intracranial and cervical vascular supply to the brain. Both noncontrast (time-of-flight and phase-contrast) and contrast-enhanced (CE) MRA techniques are available. Images obtained from these various techniques are often postprocessed via MIP to better depict the vascular anatomy.

Time-of-Flight (TOF) MRA

TOF MRA is a gradient echo sequence that is performed by repeatedly applying a radiofrequency (RF) pulse, followed by dephasing and rephasing gradients. Stationary tissues become saturated and lose signal by the repeated RF pulse, whereas flowing blood is bright as it brings unsaturated spins into the imaging volume.[32] This is known as "flow-related enhancement." Saturation bands are applied to suppress signal from incoming veins in the other direction. TOF MRA can be performed in a two-dimensional or three-dimensional acquisition. It is generally used as an initial screening tool or in instances where contrast enhanced MRA of the neck cannot be performed or has failed, or when information of flow directionality is important. Three-dimensional TOF MRA is typically used to evaluate the intracranial circulation. Two-dimensional TOF is often the technique used in magnetic resonance venography (MRV) of the dural venous sinuses.

Phase Contrast (PC) MRA

This is a gradient echo sequence, which applies a pair of equal, but opposing direction dephasing and rephasing RF pulses to the imaging volume. Stationary tissues have no net change in phase because they encounter equal but opposite direction dephasing and rephasing pulses, but moving blood acquires a phase shift. The amount of phase shift is proportional to the velocity of moving blood. PC MRA can also be performed in a two-dimensional or three-dimensional fashion. PC MRA is usually only reserved for instances where there is a concern that a venous or arterial subacute clot (intrinsically bright T1 signal) is mimicking flow-related enhancement.

Contrast Enhanced MRA

CE MRA uses a three-dimensional fast gradient-echo sequence in conjunction with a dynamic bolus injection of gadolinium. The acquisition is carefully timed during passage of the bolus of gadolinium through the arteries of interest. A preliminary test injection of gadolinium can be done to time the arrival of contrast into the arteries. With recent scanners, a fluoro technique can be used to monitor the region of interest in real time and start the acquisition when contrast is first seen or even use automated bolus detection. Due to a very low echo time, there is good background fat suppression. Acquisition time can generally be less than 30 s. Similar techniques can be used for CE MRV of the venous sinuses.[39]

Clinical Utility of MRA

CE MRA of the neck is reported to have a sensitivity of 94–97%, and a specificity of 81–95%, compared with angiography (the gold standard) for stratifying surgical from nonsurgical cases of carotid stenosis and correlation of $r = 0.94$ to 0.96.[40–42] Three-dimensional TOF MRA

of the intracranial circulation is reported to have a sensitivity of 88–100% and a specificity of 95–97% compared with digital subtraction angiography in diagnosis of intracranial occlusion and MCA disease, respectively.[43,44]

MR Perfusion Imaging

MR perfusion-weighted imaging (PWI) techniques are discussed in more detail in Chapter 31. Like CT perfusion, MR perfusion provides CBV–CBF–MTT–Tmax maps. One of the biggest advantages of utilizing MRI as a perfusion test is that the core can be delineated accurately using the region of diffusion restriction on the DWI sequence, rather than being inferred from perfusion data. The volume difference between DWI core and Tmax (greater than 6 s) images constitute the operational DWI-PWI mismatch or a stroke MRI correlate of the ischemic penumbra (Diffusion and Perfusion Imaging Evaluation for Understanding Stroke Evolution Study 2). Although the mismatch model has been proposed to identify acute stroke patients who benefit from reperfusion therapy, the optimal definition and threshold of a mismatch is uncertain. This model also does not take into account that the PWI lesion also assesses areas of oligemia, which are not in danger of irreversible injury.

Additional advantages of MR perfusion imaging in stroke include whole brain coverage and simpler postprocessing methodology. The disadvantages of dynamic contrast MR PWI include susceptibility artifact due to metallic objects and near bone and air interfaces, the need for high flow rate injections, sensitivity to patient motion, unreliability in calculating absolute values of perfusion parameters, and the possibility that the patient has a contraindication to MRI. The biggest disadvantage of MRI in acute stroke is that it is not easily available in the acute setting and has longer scan times.

Catheter Angiography

Catheter angiography no longer has a significant diagnostic role in evaluation of ischemic CNS infarction given the increased diagnostic utility of less invasive imaging techniques. The exception is in the evaluation of vasculopathies, including vasculitis, vasospasm, and rarely for confirmation of arterial dissection. Its diagnostic role in evaluation of aneurysms and arteriovenous malformations has also relatively decreased, but it remains an important modality in cases in which less invasive techniques do not provide adequate information. Nevertheless, endovascular techniques play a crucial role in the management of stroke patients for intraarterial thrombolysis, mechanical thrombolysis, and vasospasm treatment. Endovascular techniques are also employed in carotid, vertebral, and intracranial vessel angioplasty/stenting for the prevention and treatment of stroke.

CT and MR imaging techniques can be considered as equivalent tools and the selection of the modality depends mainly primarily on the institutional workflow. It is important to remember that the ultimate goal in acute stroke is to image rapidly and improve the efficiency of thrombolytic therapy.

CNS INFARCTION IN NEUROONCOLOGY

Neurooncologic patients are at increased risk for CNS infarcts, whether due to the direct effects of CNS tumors on the brain and spinal cord or as a result of treatment for these neoplasms. CNS infarcts also occur in higher frequency in patients with systemic neoplasia (detailed further in Chapter 62).

CNS Infarction Caused by Brain Tumors

Mass effect from brain tumors can cause displacement, kinking, and resultant narrowing or occlusion of cerebral vessels, leading to infarction. Examples include cases of subfalcine herniation causing compression of the anterior cerebral arteries against the falx (Figure 2(A–D)). Also mass effect or acute hydrocephalus causing transtentorial herniation may lead to compression of the posterior cerebral arteries against the tentorium and resultant occipital lobe infarction (Figure 2(E)) or compression of the superior cerebellar arteries.[45]

Primary or metastatic tumors of the brain, meninges, or skull can infiltrate and compress the arterial supply or venous drainage systems and cause arterial or venous infarcts.[46] Examples include convexity meningiomas compressing or infiltrating the venous sinuses and also sellar/parasellar tumors infiltrating and occluding the carotid arteries in the cavernous sinus. However, these vascular occlusions may not necessarily lead to infarcts since the associated neoplasms frequently grow at a slow rate, often providing adequate time for the development of collateral pathways in the vascular supply or drainage systems.

Tumor infiltration in the Virchow-Robin perivascular spaces can cause vessel compression, spasm, or thrombosis leading to infarction, for example, in diffuse leptomeningeal gliomatosis.[47] Intravascular lymphomatosis is a rare entity that often involves the CNS and can cause infarcts, which could be related to proliferation of lymphoma cells in the vessel lumen (Figure 3).

CNS Infarction as a Result of Treatment of Brain Tumors

After surgical resection of gliomas, focal areas of restricted diffusion adjacent to the resection cavity have been reported in 64–70% of cases.[48,49] These areas of

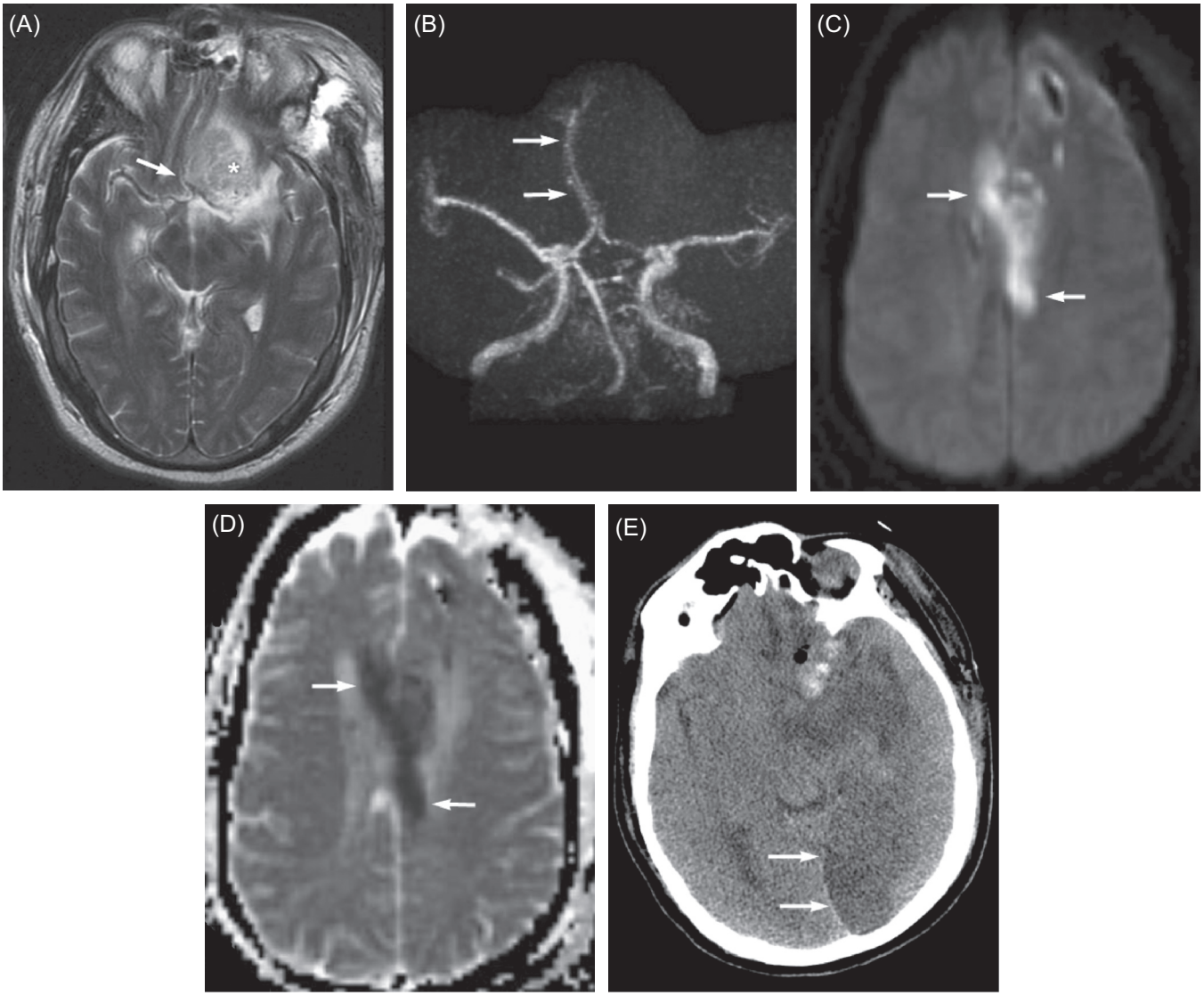


FIGURE 2 Infarcts caused by mass effect from brain tumor and displacement and compression of cerebral blood vessels. (A) Left frontal glioblastoma multiforme (asterisk) causing leftward subfalcine herniation and displacement of the anterior cerebral arteries (arrows). (B) Rightward displacement of ACAs. (C) DWI image showing bilateral ACA territory infarcts (arrows). (D) ADC map confirming bilateral ACA territory infarcts (arrows). (E) CT scan from a few days later in same patient showing left occipital lobe infarct (arrows) caused by transtentorial herniation and compression of the posterior cerebral artery against the tentorium.

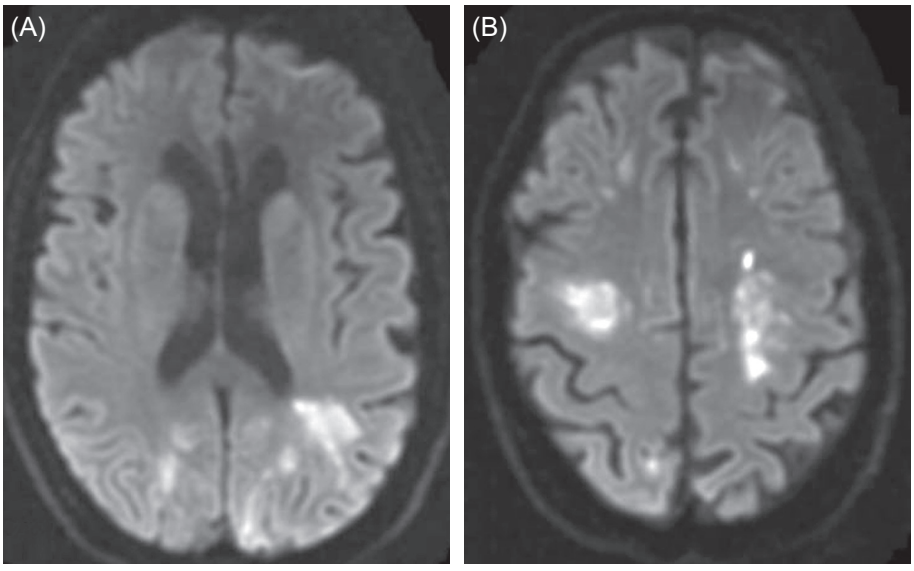


FIGURE 3 Cerebral infarcts in a patient with proven intravascular lymphomatosis. (A) and (B) Diffusion-weighted images show multiple scattered bilateral areas of high DWI signal, consistent with acute infarcts. None of these areas demonstrated contrast enhancement at this time (not shown).

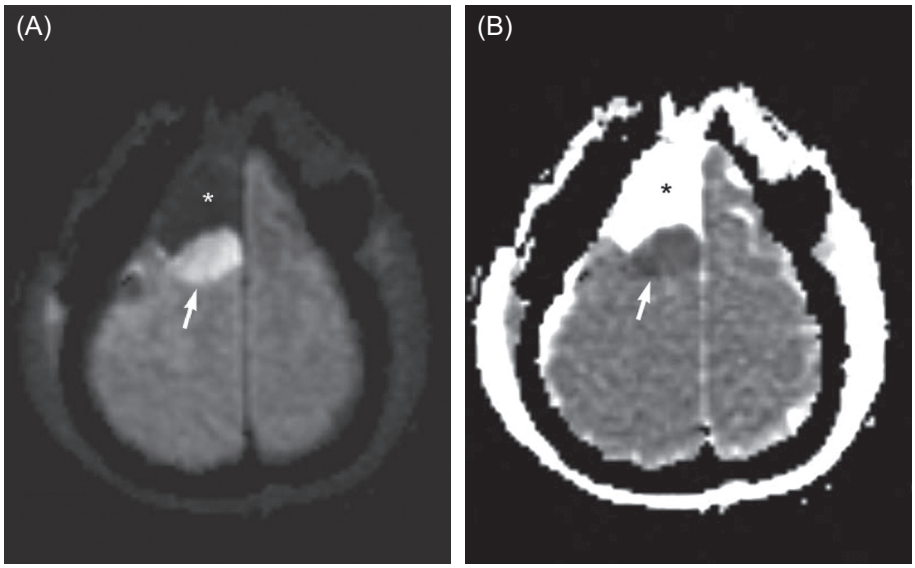


FIGURE 4 Area of diffusion restriction in right frontal lobe adjacent to surgical resection cavity (asterisks), status post resection of right frontal oligodendroglioma. (A) DWI image showing high-signal area (arrow) posterior to resection cavity. (B) ADC map showing low diffusion coefficient (arrow) in same area. These areas of diffusion restriction in the surgical bed are usually transient and reflect ischemia and postoperative injury.

diffusion restriction are usually transient, may or may not be associated with neurological deficits, can demonstrate enhancement in the subacute phase, and are usually a combination of ischemia and postoperative injury, including retraction injury (Figure 4).

Injury to the internal carotid arteries can occur during transsphenoidal surgery for pituitary/sellar tumors. Even in the absence of direct carotid injury, postexcision packing of the tumor cavity, intrasellar postoperative hemorrhage, and massive postoperative tumor swelling after partial resection have all been reported to cause infarcts presumably due to compression of the internal carotid arteries.[50] Cortical venous infarcts can occur after surgery in cases of firmly adherent extraaxial tumors to the cortex.[51]

Radiation therapy for treatment of head and neck cancer can lead to accelerated atherosclerosis of the cervical arterial supply to the brain and cause premature infarcts.[46] Radiation therapy for brain tumors can also cause a similar phenomenon in intracranial vessels.

Spinal Cord Infarction in Neurooncology

Spinal cord infarcts are rare and are often caused by interruption of the spinal cord blood supply secondary to thromboemboli or iatrogenic interruption of the supply after aortic or retroperitoneal surgery, or endovascular procedures. Neurooncologic patients may be at higher risk for spinal cord infarcts. Spinal cord infarction has been reported in acute hydrocephalus due to a colloid cyst of the third ventricle and downward brain herniation, presumably by pressure on the spinal artery.[52] Intravascular lymphomatosis can also cause spinal cord infarcts.[53] Spinal cord infarcts have also been reported as rare complications of posterior fossa and pineal surgery in the sitting position.[54]

Application of diffusion MRI to imaging of the spinal cord is challenging secondary to susceptibility artifact from surrounding structures, motion from CSF pulsation, respiratory motion, carotid–vertebral pulsations, and the small size of the spinal cord. Many different methods for early detection of spinal cord infarcts have been proposed.[55] These include older techniques such as line scan diffusion, with minimal susceptibility artifact, without the need for cardiac or respiratory gating, or flow compensation, all in a reasonable clinical timeframe.[56] Newer methods include nonechoplanar fast spin-echo techniques with multiple overlapping blades of k-space acquisition and also readout segmented multishot echoplanar techniques. These sequences may take longer to acquire but are superior in reducing susceptibility effects and geometric distortion in spinal diffusion imaging.

CONCLUSION

Neurooncologic patients are at increased risk for CNS infarcts. A variety of imaging modalities are available for rapid evaluation and diagnosis of CNS infarcts in order to optimize the triage and management of these patients.

References

1. Kochanek KD, Kirmeyer SE, Martin JA, Strobino DM, Guyer B. Annual summary of vital statistics: 2009. *Pediatrics*. 2012:2011–3435.
2. Go AS, Mozaffarian D, Roger VL, et al. Heart disease and stroke statistics–2014 update: a report from the American Heart Association. *Circulation*. 2014;129(3):e28.

3. Thom T. *Heart Disease and Stroke Statistics – 2006 Update*. Dallas: American Heart Association; 2006.
4. Shetty SK, Lev MH. CT perfusion in acute stroke. *Semin Ultrasound CT MR*. December 2005;26(6):404–421.
5. Wintermark M, Albers GW, Broderick JP, et al. Acute stroke imaging research roadmap II. *Stroke*. 2013;44(9):2628–2639.
6. Gonzalez RG. Imaging-guided acute ischemic stroke therapy: from "time is brain" to "physiology is brain". *Am J Neuroradiol*. April 2006;27(4):728–735.
7. Vu D, Lev MH. Noncontrast CT in acute stroke. *Semin Ultrasound CT MR*. December 2005;26(6):380–386.
8. Kucinski T. Unenhanced CT and acute stroke physiology. *Neuroimaging Clin N Am*. May 2005;15(2):397–407, xi–xii.
9. Camargo EC, Gonzalez G, Gonzalez RG, Lev MH. Unenhanced Computed Tomography. In: Gonzalez RG, Hirsch JA, Koroshetz WJ, Lev MH, Schaefer PW, eds. *Acute Ischemic Stroke: Imaging and Intervention*. Berlin: Springer-Verlag; 2006:41–56.
10. Mohr JP, Biller J, Hilal SK, et al. Magnetic resonance versus computed tomographic imaging in acute stroke. *Stroke*. May 1995;26(5):807–812.
11. Gonzalez RG, Schaefer PW, Buonanno FS, et al. Diffusion-weighted MR imaging: diagnostic accuracy in patients imaged within 6 hours of stroke symptom onset. *Radiology*. January 1999;210(1):155–162.
12. Lev MH, Farkas J, Gemmete JJ, et al. Acute stroke: improved nonenhanced CT detection–benefits of soft-copy interpretation by using variable window width and center level settings. *Radiology*. October 1999;213(1):150–155.
13. Pressman BD, Tourje EJ, Thompson JR. An early CT sign of ischemic infarction: increased density in a cerebral artery. *Am J Roentgenol*. September 1987;149(3):583–586.
14. Tomsick T, Brott T, Barsan W, et al. Prognostic value of the hyperdense middle cerebral artery sign and stroke scale score before ultraearly thrombolytic therapy. *Am J Neuroradiol*. January 1996;17(1):79–85.
15. Lev MH, Farkas J, Rodriguez VR, et al. CT angiography in the rapid triage of patients with hyperacute stroke to intraarterial thrombolysis: accuracy in the detection of large vessel thrombus. *J Comput Assist Tomogr*. July–August 2001;25(4):520–528.
16. Sheikh SF, Gonzalez RG, Lev MH. Stroke CT angiography. In: Gonzalez RG, Hirsch JA, Koroshetz WJ, Lev MH, Schaefer PW, eds. *Acute Ischemic Stroke: Imaging and Intervention*. Berlin: Springer-Verlag; 2006:57–86.
17. Hunter GJ, Hamberg LM, Ponzo JA, et al. Assessment of cerebral perfusion and arterial anatomy in hyperacute stroke with three-dimensional functional CT: early clinical results. *Am J Neuroradiol*. January 1998;19(1):29–37.
18. Rother J. Imaging-guided extension of the time window: ready for application in experienced stroke centers? *Stroke*. February 2003;34(2):575–583.
19. Villringer A, Rosen BR, Belliveau JW, et al. Dynamic imaging with lanthanide chelates in normal brain: contrast due to magnetic susceptibility effects. *Magn Reson Med*. February 1988;6(2):164–174.
20. Shetty SK, Lev MH. CT perfusion in acute stroke. *Neuroimaging Clin N Am*. August 2005;15(3):481–501, ix.
21. Wintermark M, Flanders AE, Velthuis B, et al. Perfusion-CT assessment of infarct core and penumbra receiver operating characteristic curve analysis in 130 patients suspected of acute hemispheric stroke. *Stroke*. 2006;37(4):979–985.
22. Campbell BC, Christensen S, Levi CR, et al. Cerebral blood flow is the optimal CT perfusion parameter for assessing infarct core. *Stroke*. 2011;42(12):3435–3440.
23. Kamalian S, Kamalian S, Maas MB, et al. CT cerebral blood flow maps optimally correlate with admission diffusion-weighted imaging in acute stroke but thresholds vary by postprocessing platform. *Stroke*. 2011;42(7):1923–1928.
24. Schaefer PW, Kiruluta A, Gonzalez RG, Lev MH. Diffusion MRI of acute stroke. In: Gonzalez RG, Hirsch JA, Koroshetz WJ, Lev MH, Schaefer PW, eds. *Acute Ischemic Stroke: Imaging and Intervention*. Berlin: Springer-Verlag; 2006:139–171.
25. Grant PE, He J, Halpern EF, et al. Frequency and clinical context of decreased apparent diffusion coefficient reversal in the human brain. *Radiology*. October 2001;221(1):43–50.
26. Maeda M, Koshimoto Y, Uematsu H, et al. Time course of arterial hyperintensity with fast fluid-attenuated inversion-recovery imaging in acute and subacute middle cerebral arterial infarction. *J Magn Reson Imaging*. June 2001;13(6):987–990.
27. Perkins CJ, Kahya E, Roque CT, Roche PE, Newman GC. Fluid-attenuated inversion recovery and diffusion- and perfusion-weighted MRI abnormalities in 117 consecutive patients with stroke symptoms. *Stroke*. December 1, 2001;32(12):2774–2781.
28. Shimosegawa E, Inugami A, Okudera T, et al. Embolic cerebral infarction: MR findings in the first 3 hours after onset. *Am J Roentgenol*. May 1993;160(5):1077–1082.
29. Flacke S, Urbach H, Keller E, et al. Middle cerebral artery (MCA) susceptibility sign at susceptibility-based perfusion MR imaging: clinical importance and comparison with hyperdense MCA sign at CT. *Radiology*. May 2000;215(2):476–482.
30. Crain MR, Yuh WT, Greene GM, et al. Cerebral ischemia: evaluation with contrast-enhanced MR imaging. *Am J Neuroradiol*. July–August 1991;12(4):631–639.
31. Yuh WT, Crain MR, Loes DJ, Greene GM, Ryals TJ, Sato Y. MR imaging of cerebral ischemia: findings in the first 24 hours. *Am J Neuroradiol*. July–August 1991;12(4):621–629.
32. Vu D, Gonzalez RG, Schaefer PW. Conventional MRI and MR angiography of stroke. In: Gonzalez RG, Hirsch JA, Koroshetz WJ, Lev MH, Schaefer PW, eds. *Acute Ischemic Stroke: Imaging and Intervention*. Berlin: Springer-Verlag; 2006:115–137.
33. Kidwell CS, Saver JL, Carneado J, et al. Predictors of hemorrhagic transformation in patients receiving intra-arterial thrombolysis. *Stroke*. March 2002;33(3):717–724.
34. Hornig CR, Dorndorf W, Agnoli AL. Hemorrhagic cerebral infarction–a prospective study. *Stroke*. March–April 1986;17(2):179–185.
35. Hakim AM, Ryder-Cooke A, Melanson D. Sequential computerized tomographic appearance of strokes. *Stroke*. November–December 1983;14(6):893–897.
36. Fiorelli M, Bastianello S, von Kummer R, et al. Hemorrhagic transformation within 36 hours of a cerebral infarct: relationships with early clinical deterioration and 3-month outcome in the European Cooperative Acute Stroke Study I (ECASS I) cohort. *Stroke*. November 1999;30(11):2280–2284.
37. Hermier M, Nighoghossian N, Derex L, et al. MRI of acute post-ischemic cerebral hemorrhage in stroke patients: diagnosis with T2*-weighted gradient-echo sequences. *Neuroradiology*. October 2001;43(10):809–815.
38. Kidwell CS, Chalela JA, Saver JL, et al. Comparison of MRI and CT for detection of acute intracerebral hemorrhage. *JAMA*. October 20, 2004;292(15):1823–1830.
39. Farb RI, Scott JN, Willinsky RA, Montanera WJ, Wright GA, terBrugge KG. Intracranial venous system: gadolinium-enhanced three-dimensional MR venography with auto-triggered elliptic centric-ordered sequence–initial experience. *Radiology*. January 2003;226(1):203–209.
40. Nederkoorn PJ, Elgersma OE, van der Graaf Y, Eikelboom BC, Kappelle LJ, Mali WP. Carotid artery stenosis: accuracy of contrast-enhanced MR angiography for diagnosis. *Radiology*. September 2003;228(3):677–682.
41. UK-I JM, Hollingworth W, Trivedi RA, et al. Contrast-enhanced MR angiography vs intra-arterial digital subtraction angiography for carotid imaging: activity-based cost analysis. *Eur Radiol*. April 2004;14(4):730–735.

42. Alvarez-Linera J, Benito-Leon J, Escribano J, Campollo J, Gesto R. Prospective evaluation of carotid artery stenosis: elliptic centric contrast-enhanced MR angiography and spiral CT angiography compared with digital subtraction angiography. *Am J Neuroradiol*. May 2003;24(5):1012–1019.
43. Korogi Y, Takahashi M, Mabuchi N, et al. Intracranial vascular stenosis and occlusion: diagnostic accuracy of three-dimensional, Fourier transform, time-of-flight MR angiography. *Radiology*. October 1994;193(1):187–193.
44. Stock KW, Radue EW, Jacob AL, Bao XS, Steinbrich W. Intracranial arteries: prospective blinded comparative study of MR angiography and DSA in 50 patients. *Radiology*. May 1995;195(2):451–456.
45. Wang KC, Hong SK, Kim IO, Cho BK, Han DH. Infarction of the territory supplied by the contralateral superior cerebellar artery in a case of descending transtentorial herniation. *Childs Nerv Syst*. July 1995;11(7):432–435.
46. Rogers LR. Cerebrovascular complications in patients with cancer. *Semin Neurol*. December 2004;24(4):453–460.
47. Singh M, Corboy JR, Stears JC, Kleinschmidt-DeMasters BK. Diffuse leptomeningeal gliomatosis associated with multifocal CNS infarcts. *Surg Neurol*. October 1998;50(4):356–362; discussion 362.
48. Smith JS, Cha S, Mayo MC, et al. Serial diffusion-weighted magnetic resonance imaging in cases of glioma: distinguishing tumor recurrence from postresection injury. *J Neurosurg*. September 2005;103(3):428–438.
49. Ulmer S, Thiago AB, Barker GJ, Lev MH, Gonzalez RG, Henson JW. Clinical and radiographic features of peritumoral infarction following resection of gioblastoma. *Neurology*. 2006;67(9):1668–1670.
50. Kurschel S, Leber KA, Scarpatetti M, Roll P. Rare fatal vascular complication of transsphenoidal surgery. *Acta Neurochir (Wien)*. March 2005;147(3):321–325; discussion 325.
51. Kiya K, Satoh H, Mizoue T, Kinoshita Y. Postoperative cortical venous infarction in tumours firmly adherent to the cortex. *J Clin Neurosci*. May 2001;8(suppl 1):109–113.
52. Siu TL, Bannan P, Stokes BA. Spinal cord infarction complicating acute hydrocephalus secondary to a colloid cyst of the third ventricle. Case report. *J Neurosurg Spine*. July 2005;3(1):64–67.
53. Kinoshita T, Sugihara S, Matusue E, et al. Intravascular malignant lymphomatosis: diffusion-weighted magnetic resonance imaging characteristics. *Acta Radiol*. May 2005;46(3):246–249.
54. Morandi X, Riffaud L, Amlashi SF, Brassier G. Extensive spinal cord infarction after posterior fossa surgery in the sitting position: case report. *Neurosurgery*. June 2004;54(6):1512–1515; discussion 1515–1516.
55. Schwartz ED, Chin CL, Takahashi M, Hwang SN, Hackney DB. Diffusion-weighted imaging of the spinal cord. *Neuroimaging Clin N Am*. February 2002;12(1):125–146.
56. Maier SE, Gudbjartsson H, Patz S, et al. Line scan diffusion imaging: characterization in healthy subjects and stroke patients. *Am J Roentgenol*. July 1998;171(1):85–93.

CHAPTER

12

Intracranial Veno-occlusive Disease

Chaitra A. Badve[1], *Lisa R. Rogers*[2]

[1]Department of Diagnostic Radiology, University Hospitals Case Medical Center, Cleveland, OH, USA; [2]Department of Neurology, University Hospitals Case Medical Center, Seidman Cancer Center, Cleveland, OH, USA

INTRODUCTION

Cerebral venous thrombosis (CVT) in the setting of cancer is most commonly caused by a hypercoagulable state induced by the cancer or cancer treatments or by a tumor that is adjacent to the venous system that compresses or invades the vessel.[1] Neurosurgical procedures, lumbar puncture, jugular catheter occlusion, and steroid therapy are independent risk factors for CVT that may coexist in the cancer patient. The most common location of CVT in the cancer patient is the superior sagittal sinus.[2]

ETIOLOGY

Nonmetastatic Cerebral Venous Thrombosis

The most common cause of spontaneous CVT is a systemic coagulopathy that is associated with cancer or follows the administration of chemotherapy.[2–4] The most common chemotherapy to be associated with CVT is L-asparaginase administered for acute leukemia or lymphoma. Steroids may cause or contribute to CVT in this setting.[5]

L-Asparaginase is an enzymatic inhibitor of protein synthesis and depletes plasma proteins involved in coagulation and fibrinolysis. In a retrospective review of 19 pediatric patients with leukemia or lymphoma who were administered L-asparaginase-containing regimens, low levels of coagulation factors in association with increased plasma D-dimer levels during or after L-asparaginase administration, combined with fresh-frozen plasma infusion, were associated with vascular thrombosis.[6] Acquired or inherited coagulation defects may render patients more susceptible to the thrombotic complications of L-asparaginase.[7]

CVT can result in venous infarction, which is often hemorrhagic. It is the most common cause of cerebral infarction in children with acute lymphocytic leukemia (ALL). A large multicenter retrospective analysis of stroke among 2318 children treated for ALL identified a prevalence of 0.47%, all of which were due to CVT.[3]

Metastatic Cerebral Venous Thrombosis

Tumors arising in the skull or dura may compress or invade adjacent venous sinuses resulting in altered venous flow, which leads to stasis and thrombosis. The most common primary tumor to be associated with CVT is meningioma. A variety of systemic tumors can metastasize to the skull or dura, resulting in CVT. Rarely, CVT is associated with metastasis to the leptomeninges.[8] The superior sagittal sinus is the most common venous structure affected by compression or infiltration by tumor, but other sites of compression can occur, depending upon the location of the tumor.

CLINICAL FEATURES

The clinical signs of spontaneous CVT, similar to patients without cancer who develop CVT, include headache, vomiting, papilledema, and seizures, occurring alone or in combination. Additionally, focal neurological signs or encephalopathy may manifest if there is associated cerebral infarction or hemorrhage. The neurological symptoms usually develop acutely but in rare instances CVT can present with chronic headache, and papilledema can be identified on the physical examination.

Nonmetastatic CVT in adults or children is predominantly associated with hematologic malignancies, especially acute leukemia.[2,9,10] The most common venous structure to be affected is the superior sagittal sinus. When associated with L-asparaginase therapy, it typically occurs during or shortly after the induction therapy, but there are instances of delayed thrombosis.[11] In contrast to nonneoplastic CVT, thrombosis produced by skull or

Handbook of Neuro-Oncology Neuroimaging, Second Edition
http://dx.doi.org/10.1016/B978-0-12-800945-1.00012-4

© 2016 Elsevier Ltd. All rights reserved.

dural metastasis more often presents in a subacute fashion, with symptoms and signs of increased intracranial pressure such as headache, vomiting, and papilledema. There may also be focal neurologic signs or encephalopathy if CVT results in venous infarction or hemorrhage.

DIAGNOSIS

A detailed clinical history and clinical examination are essential for directing focused diagnostic tests and reaching a rapid and accurate diagnosis. Magnetic resonance imaging (MRI) is the procedure of choice to identify CVT. Unenhanced MRI allows for visualization of the thrombus and also parenchymal abnormalities that may be present owing to infarction or hemorrhage. CVT was complicated by brain hemorrhage in a pediatric patient treated for ALL (Figure 1). Contrast-enhanced computed tomography (CT) or MRI will sometimes demonstrate the "empty delta" sign within the venous sinus owing to lack of contrast filling in the area of thrombosis (Figure 2). The signal within the sinus may be difficult to interpret on unenhanced MRI if venous flow is slow, rather than obstructed, or if the occlusion is acute. In these instances, or if a CVT is suspected but is not visible on brain MRI or CT, contrast-enhanced magnetic resonance venography (MRV) or CT venography can be diagnostic. Multiple areas of CVT were identified on MRV (Figure 3). Imaging, particularly with MRI, is also useful to identify CVT associated with skull or dural

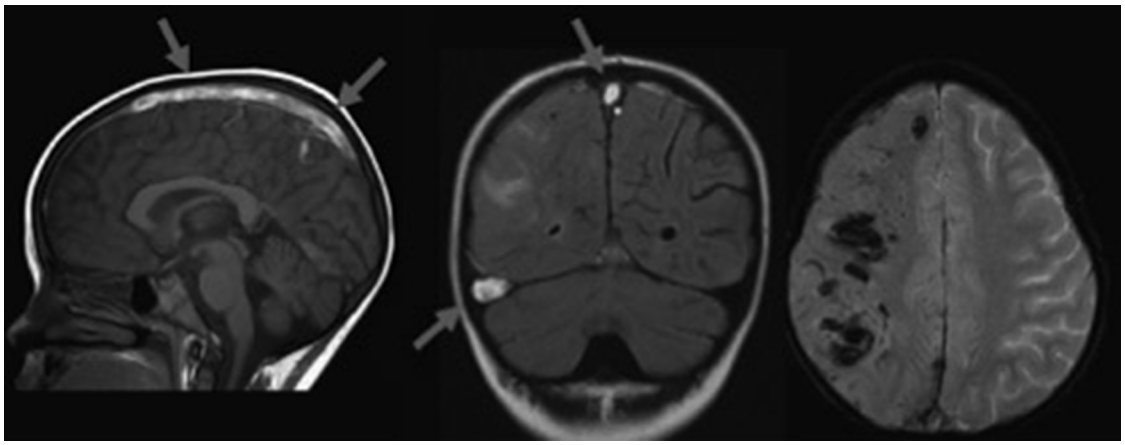


FIGURE 1 MR images (sagittal T1, coronal T2 fluid attenuated inversion recovery, and axial T2*) demonstrate signs of thrombus in the superior sagittal sinus and right transverse sinus (arrows) and extensive right frontoparietal hemorrhage and edema. *Reproduced with permission from Bhatia R, Rowley HD, Mosher JC, et al. Extensive sinovenous thrombosis and hemorrhagic infarction during therapy for T-cell acute lymphoblastic leukemia.* Pediatr Emerg Care. *2013;29(1):93–97. Wolters Kluwer Health, Inc.*

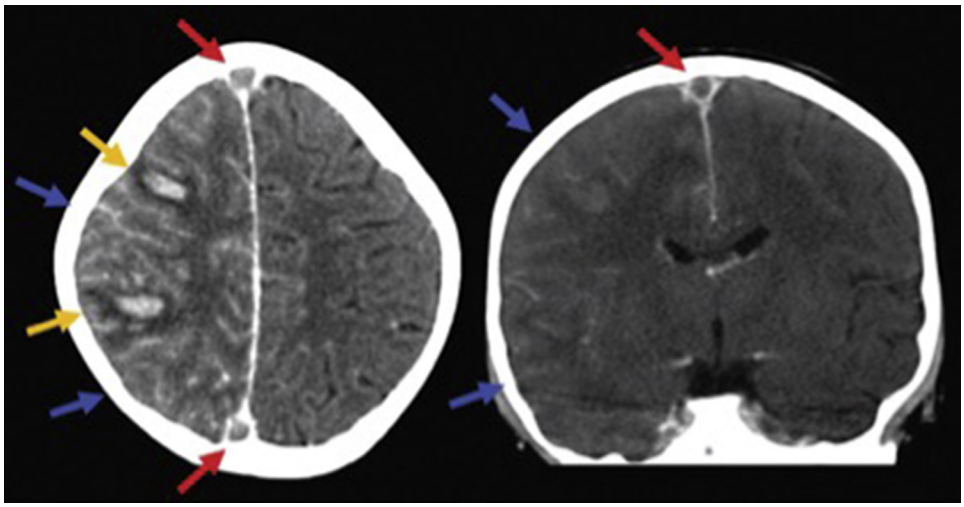


FIGURE 2 Axial and coronal reconstructions of a contrast-enhanced head CT exhibit the "empty delta" sign (red arrows), which denotes a filling defect (clot) within the superior sagittal sinus. Multifocal hyperdense right frontoparietal hemorrhage is noted (yellow arrows), a finding consistent with hemorrhagic venous infarction from dural venous sinus occlusion. There is also right holohemispheric cortical venous engorgement (blue arrows). *Reproduced with permission from Bhatia R, Rowley HD, Mosher JC, et al. Extensive sinovenous thrombosis and hemorrhagic infarction during therapy for T-cell acute lymphoblastic leukemia.* Pediatr Emerg Care. *2013;29(1):93–97. Wolters Kluwer Health, Inc.*

tumor.[12] Thrombosis of the superior sagittal sinus due to compression by a skull metastasis is visible on MRI and MRV (Figure 4). As in nonmetastatic CVT, contrast-enhanced venography by MRI or CT can be diagnostic of CVT if standard brain imaging is unclear (Figure 5).

TREATMENT

Spontaneous resolution or recanalization of nonmetastatic CVT can occur, especially when it occurs early in the course of cancer and when the tumor is responding

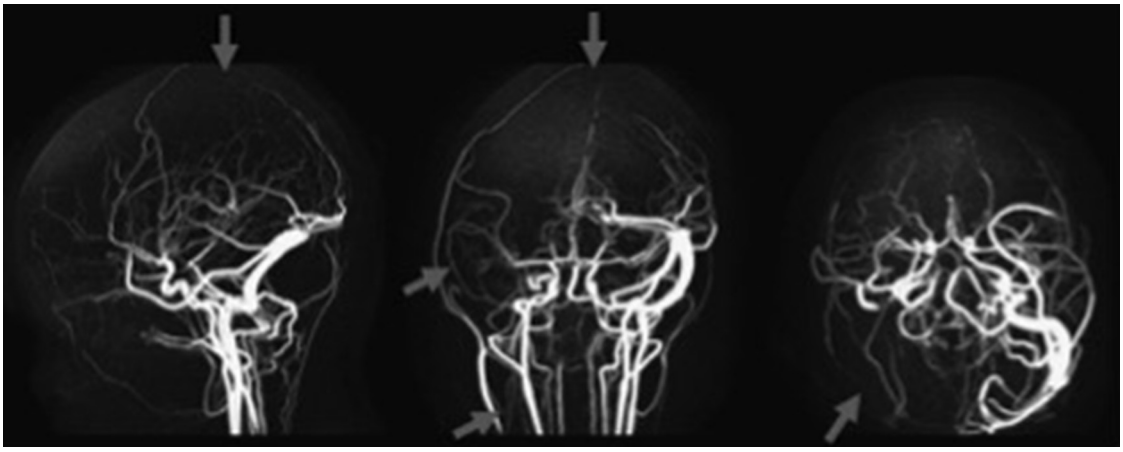


FIGURE 3 Three-dimensional phase-contrast MR venogram (sagittal, coronal, and axial maximum intensity projections) demonstrates complete occlusion of the superior sagittal sinus, right transverse sinus, right sigmoid sinus, and right internal jugular vein (arrows). There is also poor flow in the deep system including the straight sinus. *Reproduced with permission from Bhatia R, Rowley HD, Mosher JC, et al. Extensive sinovenous thrombosis and hemorrhagic infarction during therapy for T-cell acute lymphoblastic leukemia.* Pediatr Emerg Care. *2013;29(1):93–97. Wolters Kluwer Health, Inc.*

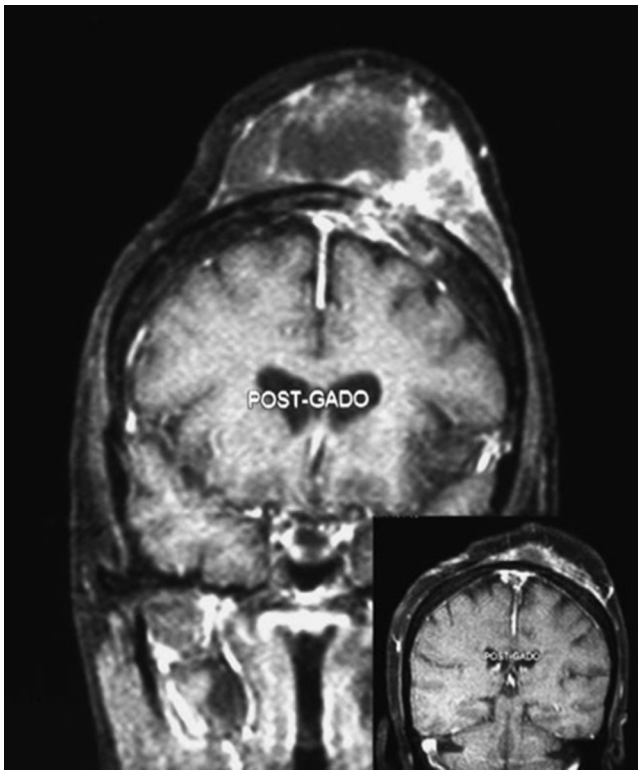


FIGURE 4 T1-weighted postgadolinium magnetic resonance coronal image showing midline scalp swelling with direct invasion to both tables of skull and thickening of adjacent dura matter. The inset shows thrombosis of the superior sagittal sinus. *Reproduced with permission from Abhishek A, Ouseph MM, Sharma P, Kamal V, Sharma M. Bulky scalp metastasis and superior sagittal sinus thrombosis from a cervical adenocarcinoma: an unusual case.* J Med Imaging Radiat Oncol. *2008;52:91–94. John Wiley & Sons Ltd.*

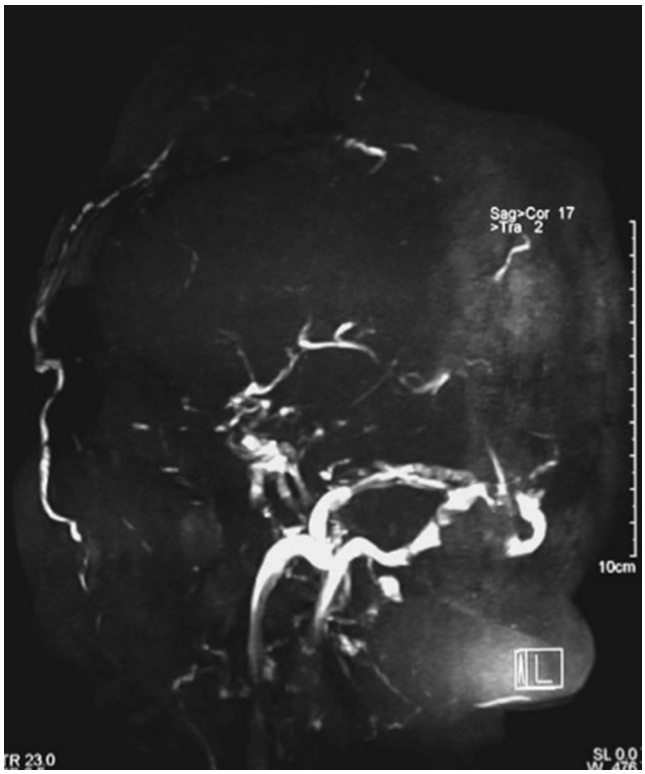


FIGURE 5 MR venogram image showing nonvisualization of superior sagittal sinus, suggestive of complete thrombosis of superior sagittal sinus. *Reproduced with permission from Abhishek A, Ouseph MM, Sharma P, Kamal V, Sharma M. Bulky scalp metastasis and superior sagittal sinus thrombosis from a cervical adenocarcinoma: an unusual case.* J Med Imaging Radiat Oncol. *2008;52:91–94. John Wiley & Sons Ltd.*

to treatment. No therapy is indicated in these instances. Treatment directed to the thrombosis should be considered for persistent and symptomatic cases. Anticoagulation, urokinase, and endovascular thrombolysis are useful treatments when sinus occlusion occurs in patients without cancer, but have not been extensively studied in cancer patients, although anecdotal reports indicate it is safe.[13,14] The safety of anticoagulation in ALL patients has been reported in small numbers of patients.[3,5] The prognosis for recovery in some patients with CVT is poor, despite therapy, when there is involvement of the deep venous sinuses.[15] The prognosis for recovery is also poor in patients with prothrombotic risk factors.[7]

In contrast to nonmetastatic CVT, the thrombosis in metastatic CVT is less likely to spontaneously remit or recanalize. The clinical course is generally progressive in these patients if the tumor is not treated.[16] Depending on the type and location of tumor, radiation therapy or surgical intervention should be considered. There are no data to support the use of anticoagulation in this condition.

References

1. Saposnik G, Barinagarrementeria F, Brown RD, et al. Diagnosis and management of cerebral venous thrombosis a statement for healthcare professionals from the American Heart Association/American Stroke Association. *Stroke*. 2011;42:1158–1192.
2. Raizer JJ, DeAngelis LM. Cerebral sinus thrombosis diagnosed by MRI and MR venography in cancer patients. *Neurology*. 2000;54:1222–1226.
3. Santoro N, Giordano P, Del Vecchio GC, et al. Ischemic stroke in children treated for acute lymphoblastic leukemia. A retrospective study. *J Pediatr Hematol Oncol*. 2005;27:153–157.
4. Masjuan J, Pardo J, Callejo JM, et al. Tamoxifen: a new risk factor for cerebral sinus thrombosis. *Neurology*. 2004;62:334–335.
5. Ranta S, Tuckuviene R, Makipernaa A, et al. Cerebral sinus venous thromboses in children with acute lymphoblastic leukaemia—a multicentre study from the Nordic Society of Paediatric Haematology and Oncology. *Br J Haematol*. 2015;4:547–552.
6. Kiyosawa N, Kano G, Yoshioka H, Sugimoto T, Imashuku S. Cerebral thrombotic complications in adolescent leukemia/lymphoma patients treated with L-asparaginase-containing chemotherapy. *Leuk Lymphoma*. 2005;46:729–735.
7. Wermes C, Fleischhack G, Junker R, et al. Cerebral venous sinus thrombosis in children with acute lymphoblastic leukemia carrying the MTHFR TT677 genotype and further prothrombotic risk factors. *Klin Padiatr*. 1999;211:211–214.
8. Oda N, Sakugawa M, Bessho A, et al. Cerebral venous sinus thrombosis concomitant with leptomeningeal carcinomatosis in a patient with epidermal growth factor receptor-mutated lung cancer. *Oncol Lett*. 2014;8:2489–2492.
9. Reddingius RE, Patte C, Couanet D, Kalifa C, Lemerle J. Dural sinus thrombosis in children with cancer. *Med Pediatr Oncol*. 1997;29:296–302.
10. Bhatia R, Rowley HD, Mosher JC, et al. Extensive sinovenous thrombosis and hemorrhagic infarction during therapy for T-cell acute lymphoblastic leukemia. *Pediatr Emerg Care*. January 2013;29(1):93–97.
11. Corso A, Castagnola C, Bernasconi C. Thrombotic events are not exclusive to the remission induction period in patients with acute lymphoblastic leukemia: a report of two cases of cerebral sinus thrombosis. *Ann Hematol*. 1997;75:117–119.
12. Abhishek A, Ouseph MM, Sharma P, Kamal V, Sharma M. Bulky scalp metastasis and superior sagittal sinus thrombosis from a cervical adenocarcinoma: an unusual case. *J Med Imaging Radiat Oncol*. 2008;52:91–94.
13. de Bruijn SF, Stam J. Randomized, placebo-controlled trial of anticoagulant treatment with low-molecular-weight heparin for cerebral sinus thrombosis. *Stroke*. 1999;30:484–488.
14. Soleau SW, Schmidt R, Stevens S, Osborn A, MacDonald JD. Extensive experience with dural sinus thrombosis. *Neurosurgery*. 2003;52:534–544.
15. Ferro JM, Canhão P, Stam J, et al. Prognosis of cerebral vein and dural sinus thrombosis results of the International Study on Cerebral Vein and Dural Sinus Thrombosis (ISCVT). *Stroke*. 2004;35:664–670.
16. López-Peláez MF, Millán JM, de Vergas J. Fatal cerebral venous sinus thrombosis as major complication of metastatic cervical mass: computed tomography and magnetic resonance findings. *J Laryngol Otol*. 2000;114:798–801.

CHAPTER

13

Paraneoplastic Syndromes

Ugonma Chukwueke, Steven Vernino

Department of Neurology & Neurotherapeutics, University of Texas Southwestern Medical Center, Dallas, TX, USA

INTRODUCTION

Patients with cancer may develop neurological problems as a direct result of tumor invasion into the nervous system or through other, indirect mechanisms including, but not limited to, coagulopathy and metabolic or nutritional disturbances. Paraneoplastic syndromes are complications of cancer that cannot be attributed to direct effects of the neoplasm or its metastases. Some of these disorders result from tissue-specific autoimmunity initiated by the immune response against cancer. The most dramatic examples of cancer-related autoimmunity are the paraneoplastic neurological disorders (PNDs). Certain cancers that express onconeural proteins (proteins that are usually restricted to the nervous system) are particularly prone to inducing neurological autoimmunity. The pathogenesis of many PNDs is thought to involve cytotoxic T-lymphocytes, which presumably recognize autoantigens in the context of major histocompatibility complex class I on both tumor cells and neurons.[1] Antibodies against neuronal antigens may be produced as well. These paraneoplastic autoantibodies are useful diagnostic markers even in syndromes in which they are not directly pathogenic.

The PNDs can involve any part of the nervous system and may affect multiple areas simultaneously (Table 1). Some PNDs have unique clinical characteristics and should be easily recognized (e.g., paraneoplastic cerebellar degeneration, sensory neuronopathy, and limbic encephalitis). Others may be indistinguishable from more common neurological disorders (e.g., peripheral neuropathy, myasthenia gravis, motor neuron disease, and myelitis). In these cases, the association with cancer may be underrecognized because of the absence of clinical suspicion.

Although the neurological symptoms vary between disorders, most PNDs share some common clinical features. The neurological syndromes typically have a subacute onset and progressive course. Symptoms typically develop over weeks or months, but can progress more rapidly (over a few days) in some cases. The neurological illness precedes the diagnosis of cancer in the majority of cases; and the cancer may be in the early stages, proving difficult to detect at the time of neurological presentation. It has been suggested that patients in whom a PND is suspected (classic syndrome or positive serological markers), but no cancer has been identified, should have regular cancer screenings for a period of 5 years.[2,3] Misdiagnosis or delay in diagnosis of PND is common. In those patients with a recent cancer diagnosis, the presence of new neurologic symptoms, specifically in the absence of other etiologies or cancer treatment, should raise suspicion of a paraneoplastic process. In patients with a previous history of cancer, the onset of neurological symptoms may herald cancer recurrence.

Even when the diagnosis of PND is suspected, the initial search for malignancy may be unrevealing. Tumors, when found, tend to be limited in stage.[4] Several reports suggest that patients with PND have a favorable cancer outcome (better survival and treatment response) compared to those with identical tumors without PND.[5–8] This observation may reflect earlier diagnosis of small tumors with limited metastasis or may be a consequence of a vigorous immune response directed against the malignant cells.

The neurological disorder, on the other hand, may progress relentlessly despite treatment, and patients are often left with significant neurological disability.[5,9,10] Those PNDs affecting the peripheral nervous system (PNS) are most likely to improve with treatment.[31] Those primarily affecting the central nervous system (CNS) tend to be refractory to treatment, probably owing to permanent neuronal cell loss, which occurs early on in the disease process.[31]

The median age of onset of PND is 65 years. In American studies, female patients predominate at a ratio of 2/1, even when cases of gender-specific tumors (breast, ovary, and testes) are not considered.[2,3] In general, PNDs

Handbook of Neuro-Oncology Neuroimaging, Second Edition
http://dx.doi.org/10.1016/B978-0-12-800945-1.00013-6

© 2016 Elsevier Ltd. All rights reserved.

TABLE 1 Paraneoplastic Neurological Syndromes

BRAIN AND EYE
Cerebellar degeneration
Limbic encephalitis[15]
Brain-stem encephalitis[18]
Opsoclonus–myoclonus
Chorea[19]
Optic neuropathy
Retinal degeneration
SPINAL CORD
Myelopathy
Myelitis with rigidity and spasms ("stiff-person" and "stiff-limb" syndromes)
Motor neuronopathy
NERVE
Sensory neuronopathy (pure sensory neuropathy)
Sensorimotor peripheral neuropathy (subacute or chronic)[20]
Autonomic neuropathy, gastrointestinal dysmotility[2]
NEUROMUSCULAR JUNCTION/MUSCLE
Lambert–Eaton myasthenic syndrome
Myasthenia gravis
Dermatomyositis
Neuromyotonia
MULTIFOCAL DISORDERS (ENCEPHALOMYELONEUROPATHIES)
Combination of those above and others

are quite rare, estimated at 0.01% of cancer patients.[11] Certain malignancies are more likely to be associated with PND. About 30% of patients with thymoma have some form of neurological autoimmunity, mostly myasthenia gravis.[12] Small-cell carcinoma, most commonly arising in the lung, is associated with one or more PNDs in up to 3% of cases.[13,14] Other malignancies with definite PND associations include gynecological malignancies arising from the breast, ovary, fallopian tube, and peritoneum; Hodgkin and non-Hodgkin lymphoma; testicular cancer; and neuroblastoma. PNDs occur at a much lower frequency in patients with non-small-cell lung, renal, uterine, and melanotic skin cancers.

All PNDs are rare, but several classical syndromes are distinctive and common enough to warrant specific attention. Additionally, the demographics of the patient and the presence of cancer risk factors or constitutional symptoms should increase suspicion of a paraneoplastic etiology. Diagnostic criteria have been established to assist with early identification and treatment of PNDs. These criteria may now serve as a guide for determining the appropriateness of malignancy screening (Tables 2 and 3). Certain features, independent of established diagnostic criteria, should raise concern for PND: (1) subacute and progressive course, (2) multifocal pattern of neurological deficits, and (3) constitutional symptoms or cancer risk factors.[27] Neuroimaging is important in the evaluation of PND of the CNS, mainly to evaluate for other etiologies, such as metastatic disease, vascular disorders, or inflammation. For PND restricted to the PNS, neuroimaging generally does not contribute much to the diagnosis. Body imaging studies, including metabolic imaging, are very important in determining the presence and location of an underlying malignancy.

PARANEOPLASTIC CEREBELLAR DEGENERATION

Paraneoplastic cerebellar degeneration (PCD) presents as nonspecific gait unsteadiness, which progresses to severe cerebellar ataxia over a few weeks or months. Occasionally, an acute onset may suggest brain-stem or cerebellar stroke. More insidious onset may be confused with the inherited or degenerative ataxias. The typical clinical features are disabling incoordination of gait, trunk, and limbs and an ataxic dysarthria. Often, severe vertigo with nausea, diplopia, nystagmus, and oscillopsia are early complaints. Within a few months, most patients will lose the ability to walk or even sit independently, lose the ability to write or feed themselves, and lose the ability to communicate effectively.[8,9] Dramatic tremors of the limbs and head (titubation) may occur. Symptoms often stabilize spontaneously, but usually leave the patient with severe ataxia and loss of independence. PCD has been most commonly associated with solid tumor malignancies, specifically of the ovaries, breast, and lung, and usually precedes the diagnosis of cancer. Autoantibodies reactive against the cytoplasm of cerebellar Purkinje cells (Purkinje cell antibody type 1; PCA-1 or "anti-Yo") may be found in the serum or cerebrospinal fluid (CSF) as markers of the gynecological tumors. Several different antibody markers have been associated with PCD in the context of small-cell lung cancer including antineuronal nuclear antibody (ANNA-1 or anti-Hu) or P/Q-type calcium channel antibodies. PCD may also be associated with hematologic cancers including Hodgkin and non-Hodgkin lymphoma with different antibody markers (Table 2).

LIMBIC ENCEPHALITIS

Over the past several years, significant progress has been made in characterizing the features of limbic encephalitis, specifically in distinguishing paraneoplastic from

TABLE 2 Neuronal Paraneoplastic Autoantibodies

Antibody	Usual Tumor	Commonly Associated Syndromes
NEURONAL ANTIBODIES AGAINST NUCLEAR OR CYTOPLASMIC ANTIGENS		
ANNA-1 (anti-Hu)[2]	SCLC	Limbic encephalitis, ataxia, sensory neuronopathy, autonomic and sensorimotor neuropathies
CRMP-5 (anti-CV2)[22]	SCLC or thymoma	Encephalomyelitis, chorea, neuropathy, optic neuritis
PCA-1 (anti-Yo)	Ovarian or breast	Paraneoplastic cerebellar degeneration
Anti-Ma[18]	Lung, breast, or testicular	Limbic and brain-stem encephalitis
Amphiphysin	Lung or breast cancer	Encephalomyelitis, neuropathy, "stiff-person syndrome"
PCA-2	SCLC	Encephalomyelitis
ANNA-2 (anti-Ri)	Lung or breast cancer	Ataxia, opsoclonus–myoclonus, neuropathy
PCA-Tr (anti-Tr)	Hodgkin lymphoma	Paraneoplastic cerebellar degeneration
ANNA-3	SCLC	Encephalomyelitis
Anti-Zic4	SCLC	Ataxia
Recoverin	SCLC	Cancer-associated retinopathy
Retinal bipolar cell	Melanoma, colon adenocarcinoma	Cancer-associated retinopathy
CASPR2	Thymoma, lung cancer	Neuromyotonia, encephalitis
LGI1	Thymoma	Limbic encephalitis
ION CHANNEL AUTOANTIBODIES		
P/Q-type VGCC	SCLC (60%)	Lambert–Eaton syndrome Cerebellar degeneration
N-type VGCC	Lung or breast cancer	Encephalomyelitis, neuropathy
Muscle AChR	Thymoma (15%)	Myasthenia gravis
VGKC complex	Thymoma or SCLC	Neuromyotonia, limbic encephalitis
mGluR1	Hodgkin lymphoma	Paraneoplastic cerebellar degeneration
GABA-B receptor	SCLC	Limbic encephalitis
AMPA receptor	SCLC, thymoma, breast cancers	Limbic encephalitis
NMDA receptor	Teratoma	Anti-NMDA receptor encephalitis
Neuronal AChR	SCLC	Autonomic neuropathy
Glycine receptor	SCLC	Progressive encephalomyelitis with rigidity and myoclonus

Alternate nomenclature is indicated in parentheses.

nonparaneoplastic or autoimmune etiologies. A better description of clinical syndromes and serological markers has improved the accuracy of the diagnostic evaluation.

Paraneoplastic limbic encephalitis (PLE) is characterized by the triad of short-term memory impairment, temporal lobe seizures, and psychiatric symptoms (commonly depression, psychosis, or change in personality). The differential diagnosis of this presentation includes nonparaneoplastic or autoimmune limbic encephalitis, viral encephalitis, rapidly progressing dementia such as Creutzfeld–Jakob disease, vasculitis, other steroid-responsive encephalopathy, or a primary psychiatric illness.[16]

Two-thirds of patients have overt seizures (usually complex partial temporal lobe seizures), which may be difficult to control.[15] PLE tends to have a monophasic course; however, patients may stabilize or partially improve following treatment of the cancer or treatment with immunomodulatory therapies.[25] Most are left with residual memory impairment and seizures.

The most common tumors associated with PLE are small-cell lung carcinoma (SCLC), testicular cancer, breast cancer, and thymoma. The neurological syndrome antedates the diagnosis of cancer in most cases. Several autoantibody markers have been associated with PLE, including anti-Hu (ANNA-1) and anti-Ma (Table 2).

TABLE 3 Paraneoplastic Neurological Disorders

ABSOLUTE PNS CRITERIA
1. Detection of a classical neurologic syndrome (encephalomyelitis, limbic encephalitis, subacute cerebellar degeneration, sensory neuropathy, opsoclonus–myoclonus, Lambert–Eaton myasthenic syndrome, and dermatomyositis)
2. Significant recovery in a nonclassical syndrome following the cancer treatment
3. Detection of antineuronal antibody together with the nonclassical syndrome and cancer
4. Detection of a well-characterized antineuronal antibody (anti-Ri, anti-Hu, anti-Yo, anti-Ma2, anti-CV2, and antiamphiphysin) together with the neurologic syndrome in the absence of accompanied cancer
POSSIBLE PNS CRITERIA
1. Undetectable underlying cancer and antibody but high risk of underlying tumor in a patient with classical neurologic syndrome
2. Detection of antineuronal antibody despite absence of neurologic syndrome or cancer
3. Presence of classical neurologic syndrome and cancer (within 2 years of diagnosis of syndrome) in a patient without antineuronal antibodies

More recent work has demonstrated that, in patients with SCLC and LE, previously considered "seronegative," the antibody against the GABA receptor, type B, was the most commonly identified antibody.[24] The autoantibody findings are very useful in directing the search for occult malignancy, but up to 30% of patients with PLE and cancer have negative antibody studies.[15] In those cases, a search for malignancy must be conducted according to the patient's individual cancer risk factors.

It is also important to note that some cases of noninfectious limbic encephalitis are not associated with cancers. These are collectively referred to as nonparaneoplastic or autoimmune encephalitis (AE). Clinically, the disease is very similar to PLE, with primarily neuropsychiatric symptoms, short-term memory loss, cognitive impairment, confusion, and affective changes progressing over weeks to months.[30] Different sets of autoantibodies have been associated with AE, including those specific for *N*-methyl-D-aspartate receptors (NMDARs), LGI1 (and other voltage-gated potassium channel-associated proteins), AMPA receptors, and GABA-B and GABA-A receptors.

Anti-NMDAR encephalitis was first recognized less than 10 years ago but has quickly become the most recognized and best characterized of the AEs. Antibodies in these patients are directed against the NR1 subunit of the NMDA-type glutamate receptor.[23,32] There is a female predominance with 80% of cases being in women.[23] Prior to onset of neuropsychiatric manifestations, there may be a viral prodrome, which is then followed by a neurologic syndrome similar to PLE, with additional clinical features including catatonia, orolingual–facial dyskinesias, choreoathetosis, central hypoventilation, and autonomic instability (due to hypothalamic dysfunction), as well as seizures and status epilepticus.[23] Patients older than 45 may present primarily with memory difficulties, lending consideration to other etiologies of rapidly progressing dementias. An electroencephalogram pattern described as a "delta brush" has been identified in patients with anti-NMDAR encephalitis. This condition can affect children, in whom initial presentation is characterized by irritability and intractable seizures or status epilepticus; 40% of patients with anti-NMDAR encephalitis are younger than 18. In this population, diagnosis is often difficult, as presenting symptoms of irritability, hyperactivity, and temper changes are common in young children.

In children younger than 12, the likelihood of tumor is low (<9%); however, in 50% of young adult women with anti-NMDAR encephalitis, an underlying ovarian teratoma is identified (either uni- or bilateral).[25] Removal of the teratoma has been associated with hastened recovery and decreased frequency of relapses.[24] Hence, identification of the NMDAR antibodies should prompt search for ovarian teratoma. The search for malignancy should take into consideration the age and sex of the patient. However, if the initial search for malignancy is unrevealing, the majority of other cases of anti-NMDAR encephalitis are not paraneoplastic.

BRAIN-STEM ENCEPHALITIS

Paraneoplastic brain-stem encephalitis is characterized by prominent eye-movement abnormalities (vertical gaze palsy, ophthalmoplegia, double vision, complex nystagmus, or other involuntary eye movements) often associated with disorders of sleep and wakefulness (including excessive somnolence or central sleep apnea). Other cranial nerve findings include ptosis, facial weakness, flaccid dysarthria, dysphagia, subacute hearing loss, and jaw or eyelid dystonia.[17,18] Patients with anti-Hu antibodies present with primarily medullary involvement, often manifesting with central hypoventilation.[26] In those with antineuronal nuclear antibody, type 2 (anti-Ri), clinical features include opsoclonus, extrapyramidal rigidity, ataxia, and postural instability. Additionally, jaw dystonia and laryngospasm have been noted. Symptoms of brain-stem encephalitis may occur in combination with those of PLE, PCD, or opsoclonus–myoclonus. Several different cancers have been associated, including SCLC and testicular and breast cancer.

OPSOCLONUS–MYOCLONUS

Opsoclonus refers to involuntary, chaotic, high-amplitude conjugate eye movements often associated with diffuse or focal myoclonus (involuntary brief muscle jerks of the trunk or limbs). The opsoclonus–myoclonus syndrome (OMS) has been well described in children, often accompanying neuroblastoma. In children, OMS may improve with treatment of the neuroblastoma along with adrenocorticotropic hormone or prednisone, although many children are left with some degree of neurological and behavioral sequelae. In adults, less than half of patients with opsoclonus–myoclonus have cancer. If a malignancy is present, breast adenocarcinoma and small-cell carcinoma are known associations. Adults with a presumed idiopathic diagnosis have been assumed to have parainfectious causes of OMS, with human immunodeficiency virus being a leading cause.[29] Patients without cancer may respond to immunomodulatory treatment and make a good recovery. Adults with paraneoplastic OMS may also have features of PCD, PLE, or brain-stem encephalitis.

PARANEOPLASTIC CHOREA

Tremor and other movement disorders may occur in cancer patients but are usually not manifestations of paraneoplastic autoimmunity.[19] However, the subacute onset of generalized or focal chorea in an adult may represent a PND. Chorea refers to involuntary, random, and coordinated but purposeless movements of one or more parts of the body. Chorea is a slow movement, often described as writhing or "snake-like." Chorea of the face (orofacial dyskinesia) consists of excessive pursing of the lips, grimacing, or blinking, and may be associated with a strained voice. Patients are often unconcerned by or even unaware of these movements. Observers may attribute the movements to restlessness or fidgeting. Chorea in adults can have diverse causes, but subacute onset in a patient over 60 years of age and association with other neurological symptoms should strongly raise the possibility of a paraneoplastic disorder.[19] Paraneoplastic chorea may also present with significant side-to-side asymmetry. Based on pathological and radiological findings, paraneoplastic chorea appears to be the result of inflammation affecting extrapyramidal circuits including the caudate (striatal encephalitis). Many patients have autoantibodies against the CRMP-5 protein (also known as "anti-CV2" antibodies) in serum and CSF, and the most commonly associated malignancy is SCLC.

PERIPHERAL NERVOUS SYSTEM DISORDERS

Signs and symptoms of a peripheral sensorimotor neuropathy (numbness in the feet and fingers or distal weakness) are very common in cancer patients. Neuropathy may present well in advance of the cancer diagnosis and is arguably the most common PND. One study estimated that 4.5% of patients with unexplained adult-onset axonal sensorimotor neuropathy have a malignancy.[20] The exact incidence of neuropathy as a PND, however, remains uncertain. In many cases, the characteristics of a paraneoplastic peripheral neuropathy are those of a mixed sensory and motor length-dependent axonal neuropathy indistinguishable from the nonparaneoplastic neuropathies commonly encountered in the neurology clinic. A few clinical features should increase the suspicion of PND. The onset of paraneoplastic neuropathy tends to be more rapid, with progression of symptoms, signs, and electrophysiological changes over weeks or months. Onset in the upper extremity and pain are typical. Analysis of CSF may show mild abnormalities. Peripheral neuropathy has been associated with a number of cancers (SCLC and non-SCLC, breast cancer, and thymoma) and with several autoantibody markers (Table 2). However, antibody studies are negative in many patients with paraneoplastic peripheral sensorimotor neuropathy.[20]

Progressive neuropathy that exclusively affects the sensory nerves has been termed pure sensory neuropathy, sensory ganglionopathy, or sensory neuronopathy. This disorder is more easily recognized as a PND. About 20% of cases of sensory neuronopathy are paraneoplastic; the remainder are either idiopathic or associated with systemic autoimmune disease (notably Sjögren syndrome) or toxin exposure (including chemotherapy agents). Initial symptoms may commence in the upper or lower extremity and consist of distal pain, numbness, and paresthesias, which can be asymmetric. Because of marked loss of proprioception, clumsiness and gait unsteadiness develop (sensory ataxia). With eyes closed, the loss of balance and coordination becomes much worse (positive Romberg sign), and slow wandering movements of the digits or limbs (pseudoathetosis) may be seen. Muscle stretch reflexes are usually absent. Often, the disorder progresses relentlessly over weeks or months and leads to significant disability. Because of profound sensory loss, the patient may be unaware of serious injuries to the extremities. Any of several paraneoplastic antibodies may be found, but the typical correlation is with the anti-Hu (ANNA-1) antibody. SCLC is the most commonly associated tumor. Typically, the neurological syndrome precedes the diagnosis of cancer, and the detection of cancer may be delayed by over a year despite frequent surveillance.

MYASTHENIA GRAVIS AND LAMBERT–EATON SYNDROME

Myasthenia gravis (MG) and Lambert–Eaton myasthenic syndrome differ from the disorders described earlier in two important respects. First, the antibodies in these disorders are directed against ion channels at the neuromuscular junction and not only are a specific diagnostic marker but also directly cause the disease. Second, patients often respond well to treatment. MG is the prototypical autoimmune neurological disorder. Patients present with fatigable weakness, which usually affects the eyes (causing ptosis and diplopia). Antibodies against acetylcholine receptors (AChR) at the neuromuscular junction (muscle AChR) cause the disease and can be detected in the serum in about 90% of patients with generalized symptoms.[27] About 15% of patients with MG have a paraneoplastic disorder usually associated with thymoma. Patients with paraneoplastic MG are essentially always seropositive for AChR antibodies and typically have clinical manifestation of generalized weakness. Patients with predominantly ocular MG and those who do not have AChR antibodies are unlikely to harbor an underlying malignancy.[27]

In Lambert–Eaton syndrome (LES), antibodies against P/Q-type voltage-gated calcium channels on the motor nerve terminal lead to inefficiency of neuromuscular transmission. LES is a paraneoplastic disorder associated with SCLC in about 60% of adult patients, although other cancers such as leukemia and prostate cancer have been reported. Patients with paraneoplastic LES usually present after age 40 with complaints of generalized weakness and fatigue, typically rapid in progression. Characteristically, recognition of the neurologic syndrome precedes the diagnosis of cancer, and cancer diagnosis may be delayed by as much as 5–6 years after neurological symptoms.[28] When LES is associated with SCLC, features of other neurological syndromes may coexist, and other paraneoplastic antibodies may be detected in addition to calcium channel antibodies.[27]

LABORATORY FINDINGS

As PND usually predates the diagnosis of cancer and routine laboratory tests in patients with these disorders are usually normal, diagnosis of PND requires an initial clinical suspicion. Analysis of the CSF may be normal or show only mild lymphocytic pleocytosis and elevated protein. Oligoclonal bands and increased CSF IgG synthesis rate are seen in a minority of cases. The advent and expansion of testing for paraneoplastic neurological autoantibodies have been a great help in diagnosing PND.

Paraneoplastic antibodies are important as surrogate markers of a specific immune response to cancer. Neuronal nuclear and cytoplasmic antibodies are highly specific for the presence of cancer and also predictive of the cancer type. Nearly 90% of patients with ANNA-1 antibodies have SCLC, and over 90% of patients with PCA-1 have cancer (76% ovarian or related peritoneal tumors and 13% breast cancer).[2,21] Thus, finding a neuronal nuclear or cytoplasmic antibody in a patient with a neurological syndrome should mandate a thorough evaluation for occult malignancy and close oncological follow-up if cancer is not detected on the initial search. The antibody specificity helps direct the search for cancer by predicting the most likely cancer. Unfortunately, even comprehensive testing for all known paraneoplastic antibodies lacks the sensitivity to completely exclude a PND.

EVALUATION AND TREATMENT

The evaluation of a PND requires an initial clinical suspicion. These disorders usually precede a diagnosis of cancer, and the tumors are typically limited in stage. Some clinical syndromes (including those described above) should immediately raise the possibility of PND and lead to a cancer evaluation regardless of serological results. Many other patients with PND have atypical, unusual, or multifocal neurological complaints that are hard to characterize or localize neuroanatomically. Testing for paraneoplastic antibodies can help confirm the diagnosis of PND and direct the search for occult malignancy. Neurological imaging studies are an important part of the evaluation, especially to help exclude alternative diagnoses, such as metastases, infection, demyelinating disease, and cerebrovascular disorders.

Cancer evaluation starts with a complete medical history and examination. The search for malignancy then relies heavily on body imaging studies. Suspicious lesions on these imaging studies should be subjected to biopsy to confirm the cancer diagnosis and guide treatment.

Management of PND is twofold, involving treatment of both the neurologic syndrome and the underlying malignancy. Antibody removal often results in neurologic recovery in those PND cases in which the antibody has a direct effect on neuromuscular junction function (MG, Lambert–Eaton myasthenic syndrome). Plasma exchange and intravenous immunoglobulins are treatment options in these instances. For antibody-mediated disorders of the CNS (anti-NMDAR encephalitis), immunotherapies such as corticosteroids, plasma exchange, cyclophosphamide, or rituximab may be employed.[23]

Tumor removal has been associated with stabilization and improvement of PND. Hence, early tumor diagnosis and prompt institution of therapy are critical. In addition to eliminating the tumor as the stimulus for

the autoimmune syndrome, many chemotherapy regimens also provide direct immunosuppressive effects. Once a tumor remission is achieved, the serum titers of paraneoplastic antibodies tend to decline slowly over time but may never normalize. A relapse of neurological symptoms or onset of a new unexplained neurological syndrome may herald tumor recurrence. A rise in the paraneoplastic antibody titer can also signal the return of cancer, but monitoring of paraneoplastic serology over time is not efficient or reliable for this purpose. In cases of PND in which cancer cannot be identified despite an exhaustive search or where the neurological symptoms progress despite cancer remission, immunomodulatory therapies can be considered.[5]

References

1. Albert ML, Darnell JC, Bender A, et al. Tumor-specific killer cells in paraneoplastic cerebellar degeneration. *Nat Med*. 1998;4(11):1321–1324.
2. Lucchinetti CF, Kimmel DW, Lennon VA. Paraneoplastic and oncologic profiles of patients seropositive for type 1 antineuronal nuclear autoantibodies. *Neurology*. 1998;50(3):652–657.
3. Candler PM, Hart PE, Barnett M, et al. A follow up study of patients with paraneoplastic neurological disease in the United Kingdom. *J Neurol Neurosurg Psychiatry*. 2004;75(10):1411–1415.
4. Graus F, Dalmou J, Rene R, et al. Anti-Hu antibodies in patients with small-cell lung cancer: association with complete response to therapy and improved survival. *J Clin Oncol*. 1997;15(8):2866–2872.
5. Vernino S, O'Neill BP, Marks RS, et al. Immunomodulatory treatment trial for paraneoplastic neurological disorders. *Neuro Oncol*. 2004;6:55–62.
6. Maddison P, Newsom-Davis J, Mills KR, Souhami RL. Favourable prognosis in Lambert–Eaton myasthenic syndrome and small-cell lung carcinoma. *Lancet*. 1999;353(9147):117–118.
7. Altman AJ, Baehner RL. Favorable prognosis for survival in children with coincident opso-myoclonus and neuroblastoma. *Cancer*. 1976;37(2):846–852.
8. Hammack JE, Kimmel DW, O'Neill BP, Lennon VA. Paraneoplastic cerebellar degeneration: a clinical comparison of patients with and without Purkinje cell cytoplasmic antibodies. *Mayo Clin Proc*. 1990;65(11):1423–1431.
9. Rojas I, Graus F, Keime-Guibert F, et al. Long-term clinical outcome of paraneoplastic cerebellar degeneration and anti-Yo antibodies. *Neurology*. 2000;55(5):713–715.
10. Dalmau J, Graus F, Rosenblum M, Posner J. Anti-Hu associated paraneoplastic encephalomyelitis/sensory neuronopathy. A clinical study of 71 patients. *Med Baltim*. 1992;71:59–72.
11. Darnell RB, Posner JB. Paraneoplastic syndromes involving the nervous system. *N Engl J Med*. 2003;349(16):1543–1554.
12. Vernino S, Lennon VA. Autoantibody profiles and neurological correlations of thymoma. *Clin Cancer Res*. 2004;10:7270–7275.
13. Elrington GM, Murray NM, Spiro SG, Newsom-Davis J. Neurological paraneoplastic syndromes in patients with small cell lung cancer. A prospective survey of 150 patients. *J Neurol Neurosurg Psychiatry*. 1991;54(9):764–767.
14. Sculier JP, Feld R, Evans WK, et al. Neurologic disorders in patients with small cell lung cancer. *Cancer*. 1987;60(9):2275–2283.
15. Lawn ND, Westmoreland BF, Kiely MJ, et al. Clinical, magnetic resonance imaging, and electroencephalographic findings in paraneoplastic limbic encephalitis. *Mayo Clin Proc*. 2003;78(11):1363–1368.
16. Thieben MJ, Lennon VA, Boeve BF, et al. Potentially reversible autoimmune limbic encephalitis with neuronal potassium channel antibody. *Neurology*. 2004;62(7):1177–1182.
17. Pittock SJ, Lucchinetti CF, Lennon VA. Anti-neuronal nuclear autoantibody type 2: paraneoplastic accompaniments. *Ann Neurol*. 2003;53(5):580–587.
18. Voltz R, Gultekin SH, Rosenfeld MR, et al. A serologic marker of paraneoplastic limbic and brain-stem encephalitis in patients with testicular cancer. *N Engl J Med*. 1999;340(23):1788–1795.
19. Vernino S, Tuite P, Adler CH, et al. Paraneoplastic chorea associated with CRMP-5 neuronal antibody and lung carcinoma. *Ann Neurol*. 2002;51(5):625–630.
20. Antoine JC, Mosnier JF, Absi L, et al. Carcinoma associated paraneoplastic peripheral neuropathies in patients with and without anti-onconeural antibodies. (see comment). *J Neurol Neurosurg Psychiatry*. 1999;67(1):7–14.
21. Pittock SJ, Kryzer TJ, Lennon VA. Paraneoplastic antibodies coexist and predict cancer, not neurological syndrome. *Ann Neurol*. 2004;56(5):715–719.
22. Yu Z, Kryzer TJ, Griesmann GE, et al. CRMP-5 neuronal autoantibody: marker of lung cancer and thymoma-related autoimmunity. *Ann Neurol*. 2001;49(2):146–154.
23. Rosenfeld MR, Dalmau J. Diagnosis and management of paraneoplastic neurologic disorders. *Curr Treat Options Oncol*. 2013;14(4):528–538.
24. Titulaer MJ, McCracken L, Gabilondo I, et al. Treatment and prognostic factors for long-term outcome in patients with anti-NMDA receptor encephalitis: an observational cohort study. *Lancet Neurol*. 2013;12(2):157–165.
25. Dalmau J, Rosenfeld MR. Autoimmune encephalitis update. *Neuro Oncology*. 2014;16(6):771–778.
26. Graus F, Dalmau J. Paraneoplastic neurological syndromes. *Curr Opin Neurol*. 2012;25(6):795–801.
27. Sharp L, Vernino S. Paraneoplastic neuromuscular disorders. *Muscle Nerve*. 2012;46(6):841–850.
28. Wirtz PW, Smallegange TM, Wintzen AR, et al. Differences in clinical features between the Lambert–Eaton myasthenic syndrome with and without cancer: an analysis of 227 published cases. *Clin Neurol Neurosurg*. 2002;104(4):359–363.
29. Klaas JP, Ahlskog JE, Pittock SJ, et al. Adult-onset opsoclonus–myoclonus syndrome. *Arch Neurol*. 2012;69(12):1598–1607.
30. Radja GK, Cavanna AE. Treatment of VGKC complex antibody-associated limbic encephalitis: a systematic review. *J Neuropsych Clin Neurosci*. 2013;25(4):264–271.
31. Rosenfeld MR, Dalmau J. Update on paraneoplastic and autoimmune disorders of the central nervous system. *Semin Neurol*. 2010;30(3):320–331.
32. Lancaster E, Martinez-Hernandez E, Titulaer MJ, et al. Antibodies to metabtropic glutamate receptor 5 in the Ophelia syndrome. *Neurology*. 2011;77(18):1698–1701.

CHAPTER

14

Neoplastic Plexopathies

Mark A. Ferrante[1], *John T. Kissel*[2]

[1]Department of Neurology, University of Tennessee Health Science Center, Memphis, TN, USA; [2]Division of Neuromuscular Diseases, Department of Neurology, VA Medical Center, Memphis, TN, USA

INTRODUCTION

The cervical, brachial, lumbar, and sacral plexuses constitute the primary plexuses of the peripheral nervous system (PNS), with the lumbar and sacral plexuses typically discussed together as the lumbosacral (LS) plexus. Neoplastic processes may involve any of these plexuses and, typically, have significant adverse effects on patient quality of life. When misattributed to other orthopedic or neuromuscular conditions, therapeutic delays further adversely affect outcome. In general, patients with metastatic involvement have advanced neoplastic spread and die from vital organ complications. To improve survival and quality of life, clinicians must possess an understanding of plexus anatomy, the clinical features associated with plexopathies and the diagnostic and therapeutic options available.

CLASSIFICATION

In 2000, the World Health Organization classified peripheral nerve tumors into four categories: neurofibromas, schwannomas, perineuriomas (intraneural and extraneural), and malignant neural sheath tumors (NSTs). The latter, which are also called neurogenic sarcomas, include malignancies of peripheral nerve origin or with nerve sheath differentiation, excluding tumors of epineurial or vascular origin.[1] A more practical approach uses two features, malignant status and cell of origin, to classify these tumors into four categories:

1. Benign NSTs
2. Benign nonNSTs
3. Malignant NSTs
4. Malignant non-NSTs (This category includes all malignant tumors of extraplexal origin that invade the plexus by direct extension or metastasis.)

PLEXUS ANATOMY

Cervical Plexus

Upon exiting the intervertebral foramen, each spinal nerve gives off a posteriorly directed posterior primary ramus and then continues as the anterior primary ramus (APR). The cervical plexus is derived from the C1–C4 APR and is located superficial to the scalenus medius and levator scapulae and deep to the sternocleidomastoid (Figure 1). The sensory nerves from this plexus (lesser occipital, greater auricular, transverse cutaneous, and supraclavicular nerves) supply sensation to the back of the head, neck, and cape area. Its motor branches supply the diaphragm, infrahyoid, scalenus medius, trapezius, levator scapulae, and C1–C4 paravertebral muscles. Postganglionic sympathetic fibers, derived from the superior cervical ganglion, also traverse this plexus.[2,3]

Brachial Plexus

The brachial plexus (BP) is composed of five roots (C5–T1), three trunks (upper, middle, and lower), six divisions (three anterior and three posterior), three cords (lateral, posterior, and medical), and several terminal nerves (musculocutaneous, axillary, radial, median, and ulnar; Figure 2). Other nerves containing BP-derived axons include the phrenic (C5 APR), dorsal scapular (C5 APR), long the rack (C5–C7 APR),suprascapular (upper trunk), and the lateral pectoral (lateral cord), as well as those derived from the

http://dx.doi.org/10.1016/B978-0-12-800945-1.00014-8
© 2016 Elsevier Ltd. All rights reserved.

posterior cord (subscapular, thoracodorsal, axillary, and radial nerves) and from the medial cord (medial pectoral, medial brachial cutaneous, medial antebrachial cutaneous, and ulnar nerves).[2] The supraclavicular plexus is divided into three parts: upper plexus (upper trunk; C5 and C6 roots), middle plexus (middle trunk; C7 root), and lower plexus (lower trunk; C8 and T1 roots). Many tumors associated with metastatic BP lesions drain to the lateral axillary lymph nodes near the lower trunk (and its divisions), producing lower plexopathies. Because the upper trunk and its divisions are relatively free of lymph nodes, the upper plexus is less commonly the onset site for metastatic disease arising from the lymphatic system.[4]

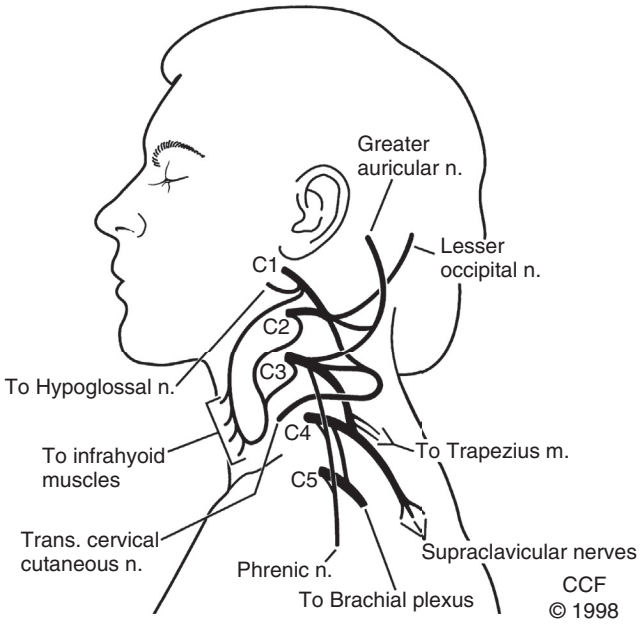


FIGURE 1 The cervical plexus.

Lumbosacral Plexus

The LS plexus, which lies in the retroperitoneal space (Figure 3), receives nerve fibers from the L1–L4 APR and, often, the T12 APR. Fibers from the L4 and L5 APR join to form the LS trunk which, in turn, joins the S1–S4 APR to form the sacral plexus. The LS plexus gives off the iliohypogastric, ilioinguinal, genitofemoral, obturator, femoral, lateral femoral cutaneous, sciatic common peroneal, tibial, superior and inferior gluteal, pudendal, and posterior femoral cutaneous nerves, as well as motor branches to the psoas and iliacus muscles. A portion of the S4 APR contributes to the coccygeal plexus. The lumbar plexus is situated within the upper two-thirds of the psoas major. The iliohypogastric, ilioinguinal, and genitofemoral nerves descend posterior to the iliac fascia and paraaortic and iliac lymph nodes. The sacral plexus lies within the pelvis adjacent to the rectum, colon, and ureter. The lumbar and sacral plexuses receive their blood supply from lumbar arteries derived from the abdominal aorta and internal iliac artery, respectively.[2]

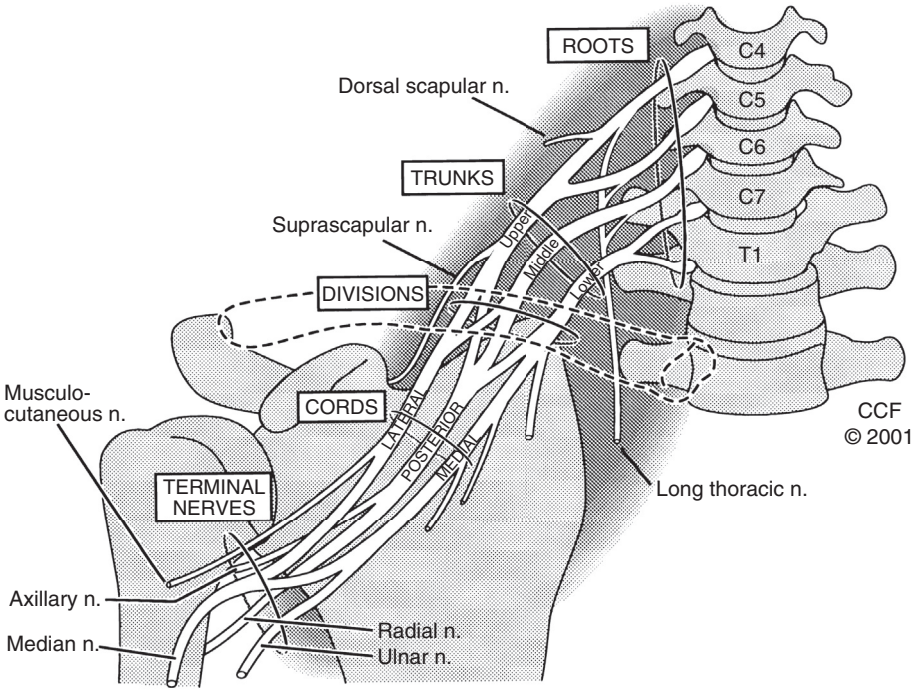


FIGURE 2 The brachial plexus.

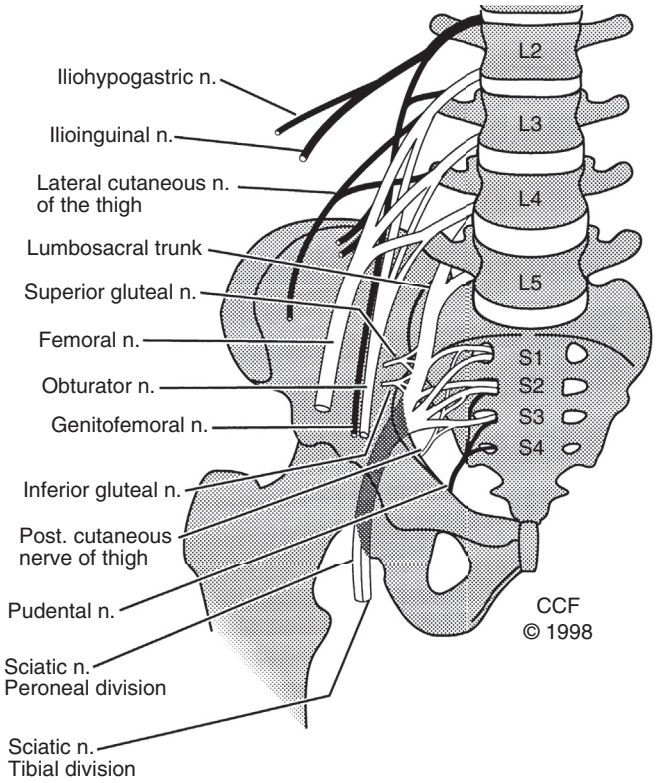


FIGURE 3 The lumbosacral plexus.

EPIDEMIOLOGY AND RISK FACTORS

Although only 1% of cancer patients have plexus involvement, approximately 15% of all BP lesions are due to plexus tumors, most commonly neurofibromas and schwannomas.[5–7] Neurofibromas are more common in patients with neurofibromatosis 1 (NF1),[8,9] but only 10% of patients with solitary neurofibromas have NF1.[10] In general, neurofibromas associated with NF1 are larger, manifest at an earlier age, and are more frequently multiple or plexiform.[7,11] Sporadic neurofibromas are more frequently right-sided and are more common in women.[11] The risk of malignant degeneration in solitary neurofibromas is low, but occurs in 5–10% of NF1 patients.[12,13] Schwannomas are more common in the head and neck and along major nerve trunks.[14] Their incidence peaks in the fourth and fifth decades and is higher in women.[7,11,15,16]

The incidence of non-NSTs is lower than that of NSTs. Although the incidence of malignant NSTs, which account for 10% of sarcomas, is very low (0.001%), this value is much higher in NF1 patients (4.6%).[17,18] In fact, 50% of malignant NSTs occur in NF1 patients, generating a lifetime risk of 2–10% and an expected life reduction of 10–15 years.[19–21] Overall, NF1 patients with malignant NSTs present one to two decades earlier.[22]

The incidence of metastatic plexopathies is less clear because plexus evaluations may not be undertaken when study results would not affect management or when patients are too ill or refuse such evaluations. Overall, the most common metastatic lesion to involve the peripheral nerves, usually the BP, is breast carcinoma,[8,15] which most frequently involves middle-aged to elderly females.

The incidence of primary neoplastic plexopathies varies among the plexuses; most involve the BP.[23] In adults with solitary neurofibromas, the supraclavicular plexus is most commonly involved, especially the upper and middle plexuses[6,7,11,15,24,25]; the distribution is more uniform among NF1 patients.[6,7] Schwannomas, which also more commonly involve the upper plexus, are rarely observed in NF1 patients.[6,7,15]

Although fewer than 1% of patients with neoplasms have LS plexus involvement,[26,27] malignancy constitutes the most common diagnosis in patients presenting with LS plexopathies.[28,29] Risk factors for the primary neoplastic plexopathies include NF1, NF2, and prior radiation to the area. About 11% of malignant NSTs follow radiation, with a latency period ranging from 4 to 41 years (average, 15 years).[30,31]

PATHOGENESIS AND PATHOPHYSIOLOGY

The pathological features of primary neoplastic plexopathies vary with the type of neoplasm. Schwannomas typically are solitary, paraneural, benign, slow-growing tumors arising anywhere along the neural sheath, especially on spinal roots at the myelination transition zone (where Schwann cells and oligodendrocytes abut). Larger lesions may compress adjacent nerves. Rarely, schwannomas are multiple or undergo malignant transformation.[32] Solitary neurofibromas, which probably arise from perineural fibroblasts, involve the entire cross-section of the nerve.[7,8,15,33] Because plexiform neurofibromas do not have a capsule, they are infiltrative and typically many inches long at presentation.[23] Malignant NSTs commonly arise de novo or via the malignant transformation of a plexiform neurofibroma; they arise less commonly from a solitary neurofibroma or ganglioneuroma and rarely from a schwannoma.[21,34] Malignant NSTs spread via direct extension or blood-borne metastasis.

Secondary neoplastic plexopathies reflect direct invasion from adjacent primary tumor or indirect invasion via metastatic spread to adjacent tissue (soft tissue; bone) or lymph node metastases. Metastases to intraneural plexus elements rarely occur. Infiltration may occur through the blood in hematological malignancies and via the spinal fluid in both hematologic and certain solid malignancies (especially breast and lung cancer and melanoma).[35] Neurolymphomatosis is the term

used to describe nerve infiltration by neoplastic cells in non-Hodgkin's lymphoma and acute leukemia. Compression may also disrupt plexus fiber integrity (e.g., metastatic axillary lymphadenopathy).[36–38] Indirect BP involvement may follow thoracic outlet infection related to chemotherapy-induced immunosuppression.[39–41] Leukemic infiltrates may produce vascular occlusion and plexus infarction.

Although nerve fibers can be damaged by neoplastic processes in a variety of ways, their pathologic responses are limited to axon disruption (the most common pathology associated with neoplastic nerve fiber involvement) and myelin disruption (focal demyelination). Although axon disruption induces Wallerian degeneration distally, myelin disruption remains focal. Depending on the fiber type affected, axon disruption results in conduction failure, which, in turn, produces weakness, sensory loss, and dysautonomia. Depending on its severity, demyelination produces either conduction block, when nerve impulses cannot traverse the lesion site (results in weakness and sensory loss), or conduction slowing, when the impulses traverse the lesion site, but at a slower rate (typically asymptomatic or associated with paresthesias).

CLINICAL FEATURES

The main clinical features associated with neoplastic plexopathies are pain and sensorimotor dysfunction, depending on the plexus region and fiber types involved and the underlying neoplasm. Benign NSTs usually present as painless, palpable masses over the course of a nerve, often with Tinel's sign and lateral, but not longitudinal, mobility.[23,42] Due to their slow growth rate, pain, and neurologic deficits are infrequent (more common with neurofibromas).[8,15,34,42–44] Although malignant NSTs can occur sporadically, they more commonly develop from preexisting plexiform neurofibromas. They present as painful, rapidly expanding masses with progressive neurologic dysfunction.[11,13] Patients with metastatic plexopathies typically present with severe pain. Most of these patients are already known to harbor a malignancy, have already been treated, and have widely metastatic disease.

With metastatic cervical plexopathies, pain radiating to the neck, shoulder, or throat that worsens with swallowing or neck movement is the primary symptom.[27] Sensory disturbances are frequent. Motor involvement may go unrecognized when the affected muscle is multiply innervated, not easily assessed, or does not impede activities of daily living.[3,27,45,46] With intraspinal canal extension, respiratory paralysis (epidural spinal cord compression), and Horner's syndrome (sympathetic trunk involvement) may occur. Mass lesions or lymphadenopathy may be noted on general examination.

Most metastatic brachial plexopathies present with pain involving the shoulder or axilla that radiates along the medial aspects of the arm, forearm, and hand.[4] As the malignancy spreads, progressive neurologic dysfunction occurs. With upper plexopathies weakness (involves C5 and C6 muscles) may cause the arm to assume the "waiter's tip" position (i.e., adduction and internal rotation of the shoulder, extension and pronation of the arm and forearm, and posterolateral rotation of the palm). Sensory disturbances occur along the lateral aspects of the arm, forearm, and hand, and the biceps and brachioradialis reflexes may be lost. With middle plexopathies, weakness is confined to C7 muscles; sensory abnormalities occur along the posterolateral arm, dorsal forearm, and lateral hand; and the triceps reflex may be affected. With lower plexus involvement, weakness involves C8 and T1 muscles and sensory disturbances occur along the medial arm, forearm, and hand. An ipsilateral Horner's sign occurs in 25% of cases[5] and the finger flexor reflex may be affected. The distribution of the hand symptoms reflects the cell bodies of origin from which the affected sensory and motor nerve fibers originate.[47] Lateral cord lesions may produce weakness of the biceps, brachialis, pronator teres, and flexor carpi radialis and sensory disturbances in the lateral forearm or hand. Posterior cord lesions may cause weakness in muscles innervated by the subscapular, thoracodorsal, axillary, and radial nerves and sensory disturbances in the upper and lower lateral brachial cutaneous, posterior brachial and antebrachial cutaneous, and superficial radial nerves. Medial cord lesions may generate weakness in C8/T1–ulnar, C8/T1–median, or C8–radial nerve innervated muscles, as well as sensory disturbances in the medial brachial cutaneous, medial antebrachial cutaneous, and ulnar nerve distributions. Terminal nerve involvement produces sensorimotor abnormalities restricted to the domains of the affected nerve.

Approximately 15% of patients with neoplastic LS plexopathies present without a known malignancy.[26] Pain is the most common and, often, the most disabling feature, typically preceding any other symptom by weeks to months.[26,27,48,49] With lumbar plexopathies, pain occurs in the lower torso, buttock, hip, anterolateral thigh, and medial leg regions, whereas with sacral plexus involvement, it more commonly occurs in the posterolateral thigh, the remainder of the leg and the foot.[26,50] The pain may be elicited or exacerbated by reverse straight leg testing (lumbar plexus) or by straight leg testing (sacral plexus). Upper lumbar plexopathies are associated with sensory disturbances in the cutaneous distributions of the iliohypogastric, ilioinguinal, and genitofemoral nerves. More inferior lesions affect

fibers destined for the femoral (anteromedial thigh and medial leg sensation; hip flexor and knee extensor strength; and quadriceps reflex), obturator (superomedial thigh sensation, thigh adductor strength, and adductor reflex), or lateral femoral cutaneous nerve. When LS trunk or upper sacral plexus involvement affects fibers destined for the deep peroneal nerve, foot drop may result. Lower sacral plexopathies produce weakness in the thigh extensors and abductors, leg flexors, and foot muscles. Sensory disturbances in the posterior thigh, leg (sparing the medial aspect) and foot occur and, when S1-derived nerve fibers are involved, ankle reflex changes result. Patients with deep pelvic tumors often present with sensory disturbances in the perineum and perianal area prior to leg pain or weakness. Other features associated with pelvic malignancy include sciatic notch tenderness, anal sphincter tone abnormalities, urinary incontinence, leg or penile edema, thrombophlebitis, ascites, hepatosplenomegaly, and generalized lymphadenopathy.[27,48–51] When retroperitoneal lymph node metastases involve the LS plexus, findings include vertebral body destruction, leg edema, and features of ureteral obstruction.[52,53]

ASSOCIATED NEOPLASTIC DISORDERS

Most neoplastic cervical plexopathies are due to the direct invasion of tumor from adjacent tissues; invasion via adjacent metastases is less frequent.[27] Breast and lung cancers account for 70% of the primary tumors involving the BP.[4] Apical lung cancers are the most common nonmetastatic malignancy to involve the BP.[54] Other sources include lymphoma, sarcoma, melanoma, thyroid, testicular, bladder, gastrointestinal, and head and neck cancer.[5,15,43] Intraneural metastasis is rare, but has been reported with carcinoid and hematologic malignancies.[55–61] Colorectal carcinoma, sarcoma, breast cancer, lymphoma, and carcinoma of the cervix usually affect the LS plexus.[5,15]

Primary neoplastic plexopathies are infrequent and usually occur in the BP.[8] Of these, schwannomas and neurofibromas predominate, most of which are benign.[6,7] Benign non-NSTs include desmoid, lipoma, hamartoma, ganglioneuroma, myoblastoma, lymphangioma, myositis ossificans, osteochondroma, and vascular tumors (e.g., venous angioma, hemangiopericytoma, glomus tumor, and hemangioblastoma).[6,7,62,63] Malignant non-NSTs can directly extend or metastasize to nerve. Breast and lung cancer and melanoma account for most malignant non-NSTs involving the BP.

While most secondary malignancies of the BP do not involve particular plexus regions,[4] breast, head and neck, and apical lung cancers are exceptions. Breast cancer favors the infraclavicular plexus when it metastasizes to the lateral axillary lymph nodes, head and neck cancer favors the upper plexus when it infiltrates from above, and apical lung cancers favor the lower plexus with infiltration from below. Other common BP malignancies include lymphoma, melanoma, and esophageal and bladder cancer.[64]

A variety of malignant carcinomas and lymphoreticular tumors involve the LS plexus. These may be restricted to the lumbar (31%), sacral (51%), or LS (18%) plexus.[26] Most secondary lesions reflect direct invasion from primary pelvic malignancies; less commonly, metastatic growth from regional lymph nodes or bone occurs.[5] Direct extension from an intraabdominal source more commonly affects the lumbar plexus, whereas metastatic involvement more commonly involves the sacral plexus.[26] The most common neoplastic LS plexopathy is invasive colorectal carcinoma,[65] while breast cancer is the most common cause of metastatic plexopathy.[26] Other common sources include uterine and cervical malignancies, retroperitoneal sarcoma, lymphoma, melanoma, and myeloma, as well as lung, testicular, thyroid, renal, and bladder carcinoma.[5,26,27,29,65] Malignant psoas syndrome is observed in patients with advanced solid tumors of the genitourinary tract, prostate, and colorectum, a reflection of their patterns of spread.

Benign neoplasms, most commonly neurofibromas and schwannomas, infrequently affect the LS plexus[11,65–67] and are often incidentally discovered when individuals with sensorimotor disturbances are referred for electrodiagnostic (EDX) testing, which localizes the lesion and directs imaging. Compression from benign tumors (dermoid cyst and uterine leiomyoma) may affect the LS plexus.[65]

Pancoast Syndrome

Apical lung cancers comprise approximately 3% of all bronchogenic carcinomas. Unlike most lung cancers, they are predominantly extrapulmonary, slow growing, locally aggressive, infrequently metastatic, and radiosensitive.[68–70] Through tissue contiguity, they spread into the thoracic inlet and apical chest wall structures, including the lower plexus. Most patients are elderly males with smoking histories who present with severe, unrelenting shoulder pain from pleural involvement. The pain usually extends into the axilla and medial arm (via C8–T2 axon involvement), is worse at night and interferes with sleep. Medial scapular pain follows tumor extension into the superior mediastinum or the posterior primary rami.[71] Invasion of the lower plexus, paravertebral sympathetic chain, or the inferior cervical (stellate) ganglion produce Horner syndrome. Hand weakness and atrophy, along with sensory loss involving the medial aspects of the hand, forearm, and arm, as well as the axilla, are

typical. Other features include supraclavicular fullness, venous distension, and upper extremity edema (subclavian vein obstruction). Bone destruction of the upper thoracic ribs and, less often, the adjacent vertebrae occurs.[72,73] Although bronchogenic carcinoma is the most common cause of this disorder, Pancoast syndrome may follow any thoracic inlet disorder, including other tumors, inflammatory processes, and infections.[39–41,73–77]

DIFFERENTIAL DIAGNOSIS

A palpable mass with pain or paresthesias in a plexus distribution is suggestive of a primary neoplastic plexopathy. Other considerations include benign cysts, nerve hamartomas, and traumatic neuromas. Neoplastic cervical plexopathies may be mimicked by neoplastic meningitis or epidural tumor spread involving cervical roots. When patients develop cervical plexus dysfunction following radical neck dissections, the relationship between symptoms and surgery helps differentiate an iatrogenic process from tumor recurrence. Cervical plexopathies may also follow radiation therapy.[78]

The differential diagnosis of BP lesions among cancer patients is much more extensive. The two most common causes are metastatic plexopathy and postradiation plexopathy (in those who received radiation). Other considerations include neoplastic advancement (e.g., epidural extension and neoplastic meningitis), treatment-related (e.g., subclavian artery occlusion; effects of chemotherapy), iatrogenic (e.g., surgical intervention; anesthetic administration), orthopedic conditions (e.g., rotator cuff tear), and other nontraumatic entities.[4,24,64,79–81]

LS plexopathies must be differentiated from more proximal and more distal lesions. When patients with known malignancies develop LS plexopathies, metastatic spread to the plexus or cauda equina and neoplastic meningitis are considerations. When severe, unilateral, local or radicular pain is present, disc herniation is a possibility. If the patient has received pelvic irradiation, postradiation plexopathy is a concern. Treatment with chemotherapy via internal iliac artery injection may affect the LS plexus through ischemic or neurotoxic mechanisms. Intragluteal injections of analgesics can also damage the LS plexus, presumably due to vasospasm and thrombosis of the sacral plexus blood supply.[29,82] Patients with retroperitoneal hemorrhage (e.g., leukemia) may develop abnormalities in the distribution of the particular plexus fibers affected. When the bleeding is limited to the iliacus muscle, an isolated femoral neuropathy may develop. With more extensive bleeding into the psoas muscle, the lumbar plexus or, less commonly, both lumbar and sacral plexus may be involved.[65,83,84] Several features of diabetic amyotrophy and peripheral nerve vasculitis suggest malignancy (e.g., older age, progressive weight loss, and persistent lower extremity pain). Normal imaging studies help exclude malignancy.

Postradiation Plexopathy

Although peripheral nerve fibers are relatively radioresistant,[85] radiation therapy (XRT) may have toxic effects on nerve fibers and vasa nervorum, with resultant demyelination, impaired circulation, and fibrosis (postradiation plexopathy).[50,86–90] The interval between the last dose of XRT and the onset of symptoms may vary from a few weeks to more than 30 years, although symptoms usually occur within 12–20 months.[38,64,91] The initial clinical features reflect demyelination, with resultant paresthesias, often in a lateral cord distribution. A presumed diagnosis of radiculopathy or carpal tunnel syndrome may result in unnecessary surgical procedures. Pain at onset is a major symptom in only a third of cases. Weakness and sensory loss follow, sometimes with limb edema. As the disorder progresses, the demyelination converts to axon disruption and the arm becomes atrophic, flail, insensate, edematous, and painful.[29,50] Risk factors for this disorder include higher XRT doses, higher fraction sizes, the three-field technique, and concomitant chemotherapy. Over the past few decades, risk factor modification has significantly reduced the incidence of this disorder.[92–94] Subclavian artery thrombosis with resultant plexus fiber ischemia and permanent, painless weakness, and sensory loss infrequently follow XRT. A lower motor neuron syndrome can occur 3–5 years after XRT to the cauda equina.[64,65]

Differentiating postradiation plexopathy from neoplastic plexopathy can be challenging. Features predicting tumor recurrence include early and severe pain, rapid progression, lower plexus involvement (regarding the BP), lower and usually unilateral (regarding the LS plexus), positron emission tomography (PET) scan positivity, and the presence of metastatic disease in other body regions, whereas findings suggesting postradiation plexopathy include painless paresthesias at onset, lateral cord distribution (regarding the BP), bilateral (regarding the LS plexus), slow progression, PET scan negativity, and certain EDX features (i.e., demyelinating conduction block, fasciculations, grouped repetitive discharges, and myokymic discharges).[4,38,91,95–98] Features of postradiation plexopathy never exclude tumor recurrence, as the two may occur concomitantly. Surgical confirmation may be necessary, although a negative biopsy does not exclude tumor recurrence.[4]

EVALUATION

The diagnosis of neoplastic plexopathies requires the coupling of historical and examination data with laboratory findings and imaging and EDX studies. Pertinent historical data include the growth rate of the lesion, the presence and progression of pain or neurologic deficits, the presence of other masses, a personal or family history of NF or cancer, previous cancer treatments, and the presence of constitutional symptoms (e.g., fever, weight loss). On examination, the size and location of the lesion and the presence of tenderness, Tinel's sign, neurologic deficit, other tumors, and NF1 stigmata are sought. Plain X-rays and computed tomography (CT) scans may identify bony neoplastic destruction or radiation exposure and spinal column instability, while radionuclide bone scans identify extraplexal metastases. Magnetic resonance imaging (MRI) is the procedure of choice for defining the location and margins of the tumor, its relationship to adjacent structures, and lymphadenopathy.[21,99,100] On MRI, NSTs appear as fusiform or spherical enlargements; often, the capsule and the nerve from which it arises are visualized.[99,101] Multiple or plexiform lesions suggest NF1.[23] When malignant cells track along the connective tissue of a plexus, visualization by MRI may be impossible. Radiographic studies do not distinguish neurofibromas from schwannomas or benign lesions from malignant ones.[102] Heterogeneous signal and bone erosion are seen with benign NSTs and, in addition, benign plexiform neurofibromas may have irregular infiltrative borders.[103–105] PET scanning may be useful for identifying neoplastic changes within a plexus and for differentiating benign and malignant plexiform neurofibromas; magnetic resonance neurography differentiates intraneural and perineural masses.[5,106,107] Angiography defines tumor vascularity and the relationship between the tumor and any neighboring vessels.[21] Cerebrospinal fluid (CSF) examination is performed when neoplastic meningitis is a consideration. EDX studies localize and characterize the plexopathy, identify subclinical lesions, identify features of postradiation plexopathy, direct imaging studies, and assess progression, and treatment response. EDX studies are often normal until persistent sensorimotor deficits are present.[23]

Accurate diagnosis requires histologic studies of tumor tissue or enlarged lymph nodes. Unfortunately, when benign plexus tumors are mistaken for nonneural lesions and improperly biopsied or excised, severe, permanent and unnecessary neurologic deficits, and pain may result.[7,15,43] Consequently, whenever a mass lesion is associated with neurologic dysfunction or Tinel's sign, referral to an experienced neurosurgeon is indicated. When a malignant NST is suspected, a metastatic evaluation, including chest films, bone scan, chest and abdominal CT, and MRI of the surrounding structures is performed. Definitive diagnosis is made by biopsy.[8] When a malignant plexopathy is suspected and the MRI is normal, surgical exploration and studies to search for extraplexal lesions may be required. When the results are negative, reimaging and reexploration should be carried out 3–6 months later.[4]

Other aspects of the evaluation reflect the plexus under consideration. When malignancy involves the cervical plexus, a thorough head and neck examination is mandatory, preferably by an otolaryngologist. Plain films and CT scans of the neck identify bone erosion and neck instability and chest films may identify benign NSTs or hemidiaphragmatic paralysis. With the latter, determination of whether the lesion reflects phrenic nerve (more common) or cervical plexus involvement is needed.[23,29,108] When tumor infiltration of the cervical plexus does not produce a recognizable mass, a repeat scan or surgical exploration may be warranted.[27]

With suspected neoplastic brachial plexopathies, the neck, supraclavicular fossa, shoulder region, and axilla are palpated for masses. Horner's syndrome is sought because it is associated with epidural spinal cord compression among patients with metastatic lesions.[38] Plain films of the chest, cervical spine, clavicle, scapula, shoulder, and humerus help identify lung lesions (e.g., superior sulcus masses) and bone abnormalities related to malignant erosion or radiation necrosis. Axial MRI images best assess the APR and trunk elements (due to their horizontal orientation), while coronal images better assess the divisions and cords. In the setting of Pancoast syndrome, MRI is utilized to define the extent of tumor invasion. A fairly new MRI technique, magnetic resonance myelography, images proximal BP elements traversing the CSF.[109,110] Following three-dimensional reconstruction, it produces T2-weighted myelogram-like images of the CSF.

With suspected neoplastic LS plexopathies, pelvic CT scanning can visualize nerve sheath tumors and is abnormal at presentation in up to 96% of patients with metastatic disease.[26]

Other studies may also be helpful. Apical lordotic chest films identify apical lung cancers, typically with extension through the visceral pleura into the parietal pleura and chest wall. CT scanning and MRI of the neck, chest, and upper abdomen help with tumor staging (extent, epidural spread) and dictate appropriate surgical intervention.[76,102] Percutaneous transthoracic needle biopsy has a diagnostic yield of 95%.[102] Bone, liver, and brain imaging assess for metastatic lesions.[76] Open biopsy to delineate the tumor cell type usually is unnecessary prior to treatment.[76] With neoplastic LS plexopathies, plain films of the spine and pelvis may reveal bony erosion or loss of the psoas shadow, suggesting a retroperitoneal mass. Lower abdominal and pelvic CT scanning can identify solid tumors, calcifications, bony erosion, spinal column

instability, bleeding, and radiation osteitis.[29,50] Modern scanners permit visualization of plexus elements when oral, intravenous, and urographic contrast agents are administered. Although 96% of patients presenting with neoplastic LS plexopathies have abnormal CT scans, CT cannot categorize lesions and does not recognize nonstructural plexus lesions, such as vasculitis. CT–myelography may identify intraspinal neoplastic involvement of the cauda equina or epidural space.[26]

MRI shows the greatest anatomic detail and is the most sensitive radiologic modality for identifying neoplastic plexopathies.[111] Neoplastic invasion, NSTs, and some metastatic lesions require gadolinium for visualization. When the scan does not show a mass lesion, repeat scanning in 4–6 weeks often discloses tumor that was not apparent on the initial imaging study.[98] Magnetic resonance myelography can delineate structures proximal to the termination site of the nerve root sleeve, such as thecal margins, nerve roots and their sheaths, and the cauda equina and conus medullaris. In the setting of stronger magnetic resonance imagers, improved coils, and advanced imaging techniques, the spatial resolution, and soft tissue contrast provided by magnetic resonance neurography can be used to generate detailed images of the LS plexus and its branches.[112] Diffusion tensor imaging with tractography may be used to demonstrate fiber tract displacement, infiltration, and disruption related to neoplastic plexus involvement.[113] Other useful radiographic modalities include isotope bone scans (bony metastases), ultrasonography (lower abdominal and pelvic masses), and intravenous pyelography and barium enemas (distortion of bladder, ureter, or bowel).

EDX testing is useful for plexus assessment, including lesion localization, lesion characterization, and assessment of severity and prognostication. Because of the high innervation ratio of lower extremity muscles, EDX testing can identify even minimal motor axon loss. Also, with neoplastic LS plexopathies, it frequently identifies abnormalities outside of the region of the imaged mass, including contralateral LS plexus involvement. For this reason, a normal EDX examination argues against a neoplastic plexopathy. Because of the limited number of reliable sensory nerve conduction studies available to assess the LS plexus, normal sensory responses cannot be used to exclude a plexopathy and abnormal ones may be related to multiple nerve involvement rather than a plexopathy. EDX features of postradiation plexopathy may also be noted.[114,115]

Surgical biopsy typically is required when a mass lesion of unknown primary is identified. Serological testing may be helpful, including serum sedimentation rate, testing for diabetes, and specific antigen testing (e.g., prostate-specific antigen, carcinoembryonic antigen, and CA-125). When patients with known primaries develop widely metastatic disease and present with LS plexus involvement, diagnostic testing may not be pursued, especially when the primary was known to neighbor the LS plexus.

MANAGEMENT

The diversity of neoplastic plexopathies requires individualized treatment plans that reflect tumor characteristics, sensitivity to radiation and chemotherapy, the degree of spread, and the general health and wishes of the patient. Surgical resection is the treatment of choice for most nonmetastatic plexus tumors, the goals of which include cure, restoration of function, symptom relief, palliation, and cosmetic improvement. Excision types include intralesional (excision leaves visible tumor), marginal (excision includes surrounding capsule or reactive zone), wide (excision includes a cuff of normal surrounding tissue), or radical (includes the entire anatomical compartment).[21] Intralesional and marginal resections usually are indicated for benign tumors, whereas wide and radical resections are reserved for malignant lesions. Chemotherapy and XRT typically are adjunctive treatments.

With benign tumors, surgical indications include pain, neurologic dysfunction, suspicion of malignant transformation (e.g., rapid growth), and disfigurement.[15,23] Schwannomas are encapsulated and, when symptomatic, often can be excised without deficit or recurrence. Because neurofibromas arise within the fascicle, their surgical excision requires sacrifice of nonfunctioning parent and adjacent fascicles. Intraoperative EDX studies permit total tumor resection without added deficit from sacrifice of functioning fascicles.[15,23] The poor delineation, increased vascularity, and infiltrative nature of plexiform neurofibromas increase the chance of postoperative neurologic dysfunction to roughly one-half and reduce the likelihood of complete resection.[8,23,116,117] Postoperative neurologic deficits are more common among NF1 patients, occurring in approximately one-third with solitary tumors.[118] A phase I trial of pegylated interferon alpha-2b in patients with unresectable, progressive, symptomatic, or life-threatening plexiform neurofibromas provided class III evidence that this agent could result in growth cessation and improvement.[119] When nerve function cannot be preserved, nerve grafting may be performed. Benign non-NSTs that grow extrinsic to their parent fascicles and intraneural lipomas can often be excised without neurologic deficit.[118]

Malignant NSTs have a high risk of local and distant spread and marked resistance of chemotherapy and radiotherapy. Survival requires surgical excision coupled with adjuvant high-dose XRT.[120,121] Although postoperative XRT provides local control and delays recurrence, especially when resection is incomplete, better long-term

survival has not been proven with this regimen and there is a risk of generating malignant NSTs among unaffected fibers.[116,122] The roles of brachytherapy and intraoperative electron beam irradiation are unresolved.[116] The role of chemotherapy is unclear. A meta-analysis showed no difference in survival despite improved progression-free survival and reduced 10-year relapse rates with chemotherapy.[123] Although chemotherapy has no role in the initial treatment of patients without metastatic disease when gross total tumor resection is accomplished, it may be considered when complete resection is impossible, when extremity amputation is to be avoided, with widely metastatic disease, as an alternative to radiotherapy or with treatment failures.[22,116,121] The surgical goal is complete resection with wide tumor margins.[120] Extremity amputation well above the lesion may be required,[8,15] although even this may not prevent metastases or improve survival.[9] In selected patients, limb-sparing procedures, which include wide local resection, radiation, and chemotherapy, have been performed with good to excellent survival rates.[8] Neural sacrifice usually is unavoidable. Unfortunately, the large area resected and the adverse effects of postoperative XRT on graft tissue preclude nerve grafting.[22] Survivin, a member of the inhibitor of apoptosis family that is highly expressed during embryogenesis and largely undetectable in normal adult tissue, is overexpressed in transformed cells, including human malignant NSTs, prompting clinical trials using antisurvivin strategies.[124] In addition, tamoxifen has been shown to inhibit malignant NST growth in an estrogen receptor-independent manner, thereby providing a rationale for clinical trials with this agent in patients with malignant NSTs.[125]

Metastatic plexopathies typically occur late in the course of the malignancy, are relatively resistant to chemotherapy and radiotherapy, and are incurable. Treatment is palliative and responses modest and short-lived.[5,8,27] With metastatic breast carcinoma, however, the malignancy often does not invade beyond the epineurial level; thus, external neurolysis and tumor removal is an option. Likewise, with melanoma and lymphoma, tumor removal from epineurial attachments, followed by local radiation, may be beneficial.[8]

The pain associated with neoplastic plexopathies is usually severe in degree, unrelenting in nature, and difficult to control. Opioid monotherapy, the mainstay of analgesic treatment, is associated with multiple side effects and may be inefficacious. Dose-limiting side effects may respond to continuous delivery (transdermal and subcutaneous). Nonopioid analgesics (e.g., antiepileptic drugs, tricyclic antidepressants, and dexamethasone) are also helpful. When these agents are started early and at dosages adequate to achieve pain control, pain severity, and adverse effects may be significantly diminished. In one study of seven patients with neoplastic plexopathies and severe pain unresponsive to opioids and adjunctive therapies, the addition of levetiracetam led to pain control within 2 weeks in all patients and, in addition, to decreased opioid use.[126] Other approaches include transcutaneous electric nerve stimulation (TENS), local anesthesia (e.g., paravertebral nerve blocks), and implantable intrathecal pumps. Surgical procedures (e.g., dorsal root entry zone procedure, contralateral percutaneous cordotomies at C1–C2, and selective rhizotomies) may be required for severe intractable pain. In one study, selective dorsal root rhizotomy in six patients with refractory pain related to neoplastic LS plexopathies related to terminal pelvic cancer experienced significant reduction in pain ratings and daily narcotic usage.[127] More destructive procedures (e.g., limb amputations) are ineffective.[4,27,29,38] Ultrasound-guided pulsed radiofrequency treatment of intractable pain related to neoplastic brachial plexopathies was reported to provide moderate control in three patients.[128]

Occupational therapy consultation for assistive devices to maximize remaining neurologic function and to prevent neuromuscular complications (e.g., painful contractures, deep venous thromboses, ulcerations, and compression neuropathies) should also be employed to optimize quality of life. Compressive devices and extremity elevation may benefit lymphedema.

The current treatment of Pancoast syndrome is surgical resection, with many patients—even some with extensive BP or spinal column involvement—achieving curative resections.[111,129] Surgical contraindications include extensive invasion, mediastinal lymphadenopathy, and peripheral metastases, although palliative surgery may be employed for epidural compression, mechanical instability, or pain unresponsive to radiation.[76,129] Induction chemoradiotherapy increases the chance of performing a complete resection and is the standard of care for any potentially resectable Pancoast tumor.[130,131] The prognosis primarily reflects tumor stage, response to preoperative chemoradiation, and resection completeness.[131] Most studies have failed to demonstrate a survival advantage using either postoperative XRT or intraoperative brachytherapy.[130] Recurrence is common and may be local or, more commonly, through distant metastases, especially to the brain.[131] Selected patients with a solitary brain metastasis seem to benefit from resection or stereotactic radiosurgery.[132] The pain associated with Pancoast syndrome can be unbearable and the relief following induction chemoradiotherapy typically is short-lived. Combinations of opioid and nonopioid analgesics, steroids, tricyclics, antiepileptics, ketamine, and TENS may be ineffective. Continuous administration of local anesthetics into the BP region was successful in six patients.[133] Adequate pain relief may follow percutaneous cervical cordotomy; however, the success rate of other invasive techniques (e.g., scalenotomy,

spinothalamic tractotomy, myelotomy, cingulotomy, dorsal column stimulators, and subarachnoid phenol or alcohol) is unclear.[133]

There is no effective treatment for postradiation plexopathy and treatment is symptomatic.[5,11,29,64] Physical therapy can prevent atrophy, capsulitis, contractures and lymphedema, and orthotics help maintain function. Medications, TENS, and dorsal column stimulators may reduce pain.[38] External neurolysis can break up perineural adhesions and scar tissue. Although this may lessen pain, progression usually continues.[5,15] Because of its ability to maintain blood flow in vessels with radiation-induced endothelial damage, anticoagulation has been suggested as a potential treatment for postradiation plexopathy, but remains of unproven value.[134,135]

PROGNOSIS AND FUTURE PERSPECTIVES

The prognosis for neurologic recovery primarily reflects the underlying malignancy. The prognosis is excellent for most benign NSTs and non-NSTs. Following tumor resection, worsening of pain, or motor dysfunction is infrequent and the recurrence rate is less than 5%,[23,62,116,136] although desmoid tumors tend to recur despite thorough excision.[15] The total removal of plexiform tumors causes loss of function and subtotal removal permits progression of tumor growth. Thus, these tumors are associated with functional loss of the involved nerve.[23] Malignant NSTs have a high recurrence rate; about one-fourth of non-NF1 patients experience local recurrence within 2 years with an even higher rate among NF1 patients.[13,135] The 5-year survival rate for non-NF1 patients is about two-thirds and for NF1 patients about 25%.[9,21,32,116] Poor prognostic factors include tumor size above 5 cm in diameter, high histological grade, positive surgical margins, and the presence of NF1. Patients with involvement of proximal PNS structures do worse because of incomplete resection and spread into the CNS.[13]

The prognosis for patients with metastatic plexopathies is poor. Typically, the lesion expands, pain is difficult to control and widespread metastatic disease ensues.[26,27,29] Most patients die from neoplastic involvement of vital organs within 2 years with pain and motor dysfunction adversely affecting quality of life.[26,27] Patients with lymphoma, breast cancer, and certain head and neck malignancies may achieve better pain control and functional improvement.

With Pancoast syndrome, the degree of local invasion at presentation determines the resectability of the tumor and survival.[129] Favorable features include absence of metastatic disease, lack of lymph node involvement, and resolution of pain following preoperative XRT.[69,70,137] Conversely, extensive invasion of the BP, spinal column invasion, and cord compression portend a poor prognosis.[137] Tumor cell type does not seem to influence survival.[70] Future studies are needed to determine the best combination of chemotherapy and biological agents and whether prophylactic cranial irradiation would reduce the occurrence of brain metastases following treatment.[130]

The prognosis for patients with postradiation plexopathy is poor because the disorder often is inexorably progressive, spreading through the plexus and pathologically converting from chronic demyelination to severe axon loss.[27,47,50,64,84] Many patients with arm involvement develop a useless, swollen, painful limb.[64,91] Even when the lesion is incomplete, sensory ataxia often severely limits useful function.[29]

Radiologic innovations continue to improve the ability to diagnose plexus tumors and surgical advancements continuously improve functional outcome and reduce surgical morbidity. Advances in genetics and oncology should provide new therapeutic options that will extend and improve the quality of life of those affected. An excellent example of these advances relates to NF1, where tumorigenesis may reflect loss of neurofibromin function and resultant overactivity of the p21-ras signaling pathway.[116] Clinical trials of antiras drugs and, for plexiform neurofibromas, interferon-alpha2b (an antiangiogenic agent thought to impede or prevent tumor growth have been performed).[120,138]

References

1. Kleihues P, Cavenee WK. *World Health Organization Classification of Tumours: Pathology and Genetics of Tumours of the Nervous System*. Lyon: AZRC Press; 2000.
2. Clemente CD. *Gray's Anatomy*. 30th ed. (American) Baltimore: Williams & Wilkins; 1985.
3. Brazis PW, Masdeu JC, Biller J. *Localization in Clinical Neurology*. 2nd ed. Boston: Little Brown; 1990.
4. Kori SH, Foley KM, Posner JB. Brachial plexus lesions in patients with cancer: 100 cases. *Neurology*. 1981;31:45–50.
5. Jaeckle KA. Neurological manifestations of neoplastic and radiation-induced plexopathies. *Semin Neurol*. 2004;24:385–393.
6. Kim DH, Cho YJ, Tiel RL, Kline DG. Outcomes of surgery in 1019 brachial plexus lesions treated at Louisiana State University Health Sciences Center. *J Neurosurg*. 2003;98:1005–1016.
7. Ganju A, Roosen N, Kline DG, Tiel RL. Outcomes in a consecutive series of 111 surgically treated plexal tumors: a review of the experience at the Louisiana State University Health Sciences Center. *J Neurosurg*. 2001;95:51–60.
8. Chang SD, Kim DH, Hudson AR, Kline DG. Peripheral nerve tumors. In: Katirji B, Kaminski HJ, Preston DC, Ruff RL, Shapiro BE, eds. *Neuromuscular Disorders in Clinical Practice*. Boston: Butterworth Heinemann; 2002:828–837.
9. Park JK. Peripheral nerve tumors. In: Samuels MA, Feske SK, eds. *Office Practice of Neurology*. 2nd ed. Philadelphia: Churchill Livingstone; 2003:1118–1121.
10. Geschickter CF. Tumors of peripheral nerve. *Am J Cancer*. 1935;25:377–410.
11. Kline DG, Hudson AR. *Nerve Injuries*. Philadelphia: Saunders; 1995.

12. Ferner RE, O'Doherty MJ. Neurofibroma and schwannoma. *Curr Opin Neurol*. 2002;15:679–684.
13. Baehring JM, Betensky RA, Batchelor TT. Malignant peripheral nerve sheath tumor: the clinical spectrum and outcome of treatment. *Neurology*. 2003;61:696–698.
14. Moukarbel RV, Sabri AN. Current management of head and neck schwannomas. *Curr Opin Otolaryngol Head Neck Surg*. 2005;13:117–122.
15. Lusk MD, Kline DG, Garcia CA. Tumors of the brachial plexus. *Neurosurgery*. 1987;21:439–453.
16. Pilavaki M, Chourmouzi D, Kiziridou A, Skordalaki A, Zarampoukas T, Drevelengas A. Imaging of peripheral nerve sheath tumors with pathologic correlation: pictorial review. *Eur J Radiol*. 2004;52:229–239.
17. Ducatman BS, Scheithauer BW, Piepgras DG, Reiman HM, Ilstrup DM. Malignant peripheral nerve sheath tumors. A clinicopathologic study of 120 cases. *Cancer*. 1986;57:2006–2021.
18. Collin C, Godbold J, Hajdu S, Brennan M. Localized extremity soft tissue sarcoma: an analysis of factors affecting survival. *J Clin Oncol*. 1987;5:601–612.
19. Zoller M, Rembeck B, Akesson H, Angervall L. Life expectancy, mortality and prognostic factors in neurofibromatosis type 1. A twelve-year follow-up of an epidemiological study in Goteborg, Sweden. *Acta Derm Venereol*. 1995;75:136–140.
20. Korf BR. The neurofibromatoses. In: Samuels MA, Feske SK, eds. *Office Practice of Neurology*. 2nd ed. Philadelphia: Churchill Livingstone; 2003:1076–1082.
21. Lee DH, Dick HM. Management of peripheral nerve tumors. In: Omer Jr GE, Spinner M, Van Beek AL, eds. *Management of Peripheral Nerve Problems*. 2nd ed. Philadelphia: Saunders; 1998.
22. Perrin RG, Guha A. Malignant peripheral nerve sheath tumors. *Neurosurg Clin N Am*. 2004;15:203–216.
23. Donner TR, Voorhies RM, Kline DG. Neural sheath tumors of major nerves. *J Neurosurg*. 1994;81:362–373.
24. Wilbourn AJ. Brachial plexopathies. In: Katirji B, Kaminski HJ, Preston DC, Ruff RL, Shapiro BE, eds. *Neuromuscular Disorders in Clinical Practice*. Boston: Butterworth Heinemann; 2002:884–906.
25. Wilbourn AJ, Ferrante MA. Clinical electromyography. In: Joynt RJ, Griggs RC, eds. *Baker's Clinical Neurology on CD-ROM*. Philadelphia: Lippincott; 2003.
26. Jaeckle KA, Young DF, Foley KM. The natural history of lumbosacral plexopathy in cancer. *Neurology*. 1985;35:8–15.
27. Jaeckle KA. Nerve plexus metastases. *Neurol Clin*. 1991;9:857–866.
28. Mumenthaler M, Schliack H. *Peripheral Nerve Lesions: Diagnosis and Therapy*. New York: Thieme; 1991.
29. Wilbourn AJ, Ferrante MA. Plexopathies. In: Pourmand R, ed. *Neuromuscular Diseases: Expert Clinicians' Views*. Boston: Butterworth Heinemann; 2001:493–527.
30. Foley KM, Woodruff JM, Ellis FT, Posner JB. Radiation-induced malignant and atypical peripheral nerve sheath tumors. *Ann Neurol*. 1980;7:288–296.
31. Ducatman BS, Scheithauer BW. Postirradiation neurofibrosarcoma. *Cancer*. 1983;51:1028–1033.
32. Ghosh BC, Ghosh L, Huvos AG, Fortner JG. Malignant schwannoma: a clinicopathologic study. *Cancer*. 1973;31:184–190.
33. Enzinger FM, Weiss SW. *Soft Tissue Tumors*. 2nd ed. St Louis: CV Mosby; 1988.
34. Harkin JC, Reed RJ. Tumors of the peripheral nervous system. In: *Atlas of Tumor Pathology, 2nd Series, Fascicle 3*. Washington DC: Armed Forces Institute of Pathology; 1969.
35. Mackinnon SE, Dellon AL. Tumors of the peripheral nerve. In: *Surgery of the Peripheral Nerve*. Stuttgart: Thieme; 1988:535–548.
36. Van Echo DA, Sickles EA, Wiernik PH. Thoracic outlet syndrome, supraclavicular adenopathy, Hodgkin's disease. *Ann Int Med*. 1973;78:608–609.
37. Felice KJ, Donaldson JO. Lumbosacral plexopathy due to benign uterine leiomyoma. *Neurology*. 1995;45:1943–1944.
38. Kori SH. Diagnosis and management of brachial plexus lesions in cancer patients. *Oncology*. 1995;9:756–765.
39. Winston DJ, Jordan MC, Rhodes J. *Allescheria boydii* infections in the immunosuppressed host. *Am J Med*. 1977;63:830–835.
40. Simpson FG, Morgan M, Cooke NJ. Pancoast's syndrome associated with invasive aspergillosis. *Thorax*. 1986;41:156–157.
41. Shamji FM, Leduc JR, Bormanis J, Sachs HJ. Acute Pancoast's syndrome caused by fungal infection. *Can J Surg*. 1988;31:441–443.
42. Dodge Jr HW, Craig WM. Benign tumors of peripheral nerves and their masquerade. *Minn Med*. 1957;40:294–301.
43. Dart Jr LH, MacCarty CS, Love JG, Dockerty MB. Neoplasms of the brachial plexus. *Minn Med*. 1970;53:959–964.
44. Fisher RG, Tate HB. Isolated neurilemmomas of the brachial plexus. *J Neurosurg*. 1970;32:463–467.
45. Haymaker W, Woodhall B. *Peripheral Nerve Injuries: Principles of Diagnosis*. Philadelphia: Saunders; 1953.
46. Schaafsma SJ. Plexus injuries. In: Vinken PJ, Bruyn GW, eds. *Handbook of Clinical Neurology*. Diseases of Nerves, Part 1; Vol. 7. Amsterdam: Elsevier; 1987:402–429.
47. Ferrante MA, Wilbourn AJ. The utility of various sensory nerve conduction responses in assessing brachial plexopathies. *Muscle Nerve*. 1995;18:879–889.
48. Pettigrew LC, Glass JP, Moar M, Zornoza J. Diagnosis and treatment of lumbosacral plexopathies in patients with cancer. *Arch Neurol*. 1984;41:1282–1285.
49. Chad DA, Bradley WG. Lumbosacral plexopathy. *Semin Neurol*. 1987;7:97–107.
50. Thomas JE, Cascino TL, Earle JD. Differential diagnosis between radiation and tumor plexopathy of the pelvis. *Neurology*. 1985;35:1–7.
51. McKinney AS. Neurologic findings in retroperitoneal mass lesions. *South Med J*. 1973;66:862–864.
52. Van Nagell JR, Sprague AD, Roddick JW. The effect of intravenous pyelography and cystoscopy on the staging of cervical cancer. *Gynecol Oncol*. 1975;3:87–91.
53. Saphner T, Gallion HH, Van Nagell JR, Kryscio R, Patchell RA. Neurologic complications of cervical cancer. *Cancer*. 1989; 64:1147–1151.
54. Vargo MM, Flood KM. Pancoast tumor presenting as cervical radiculopathy. *Arch Phys Med Rehabil*. 1990;71:606–609.
55. Liang R, Kay R, Maisey MN. Brachial plexus infiltration by non-Hodgkin's lymphoma. *Brit J Radiol*. 1985;58:1125–1127.
56. Grisold W, Jellinger K, Lutz D. Human neurolymphomatosis in a patient with chronic lymphatic leukemia. *Clin Neuropathol*. 1990;9:224–230.
57. Diaz-Arrastia R, Younger DS, Hair L, et al. Neurolymphomatosis: a clinicopathological syndrome reemerges. *Neurology*. 1992;42:1136–1141.
58. Glass J, Hochberg FH, Miller DC. Intravascular lymphomatosis: a systemic disease with neurologic manifestations. *Cancer*. 1993;71:3156–3164.
59. Levin KH, Lutz G. Angiotrophic large cell lymphoma with peripheral nerve and skeletal muscle involvement: early diagnosis and treatment. *Neurology*. 1996;47:1009–1011.
60. van den Bent MJ, de Bruin HG, Bos GM, Brutel de la Rivere G, Sillevis Smitt PA. Negative sural nerve biopsy in neuro-lymphomatosis. *J Neurol*. 1999;246:1159–1163.
61. Grisold W, Piza-Katzer H, Jahn R, Herczeg E. Intraneural nerve metastasis with multiple mononeuropathies. *JPNS*. 2000;5:163–167.
62. Huang JH, Zaghloul K, Zager EL. Surgical management of brachial plexus region tumors. *Surg Neurol*. 2004;61:372–378.
63. Todd M, Shah GV, Mukherji SK. MR imaging of brachial plexus. *Top Magn Reson Imaging*. 2004;15:113–125.
64. Wilbourn AJ. Brachial plexus lesions. In: Dyck PJ, Thomas PK, eds. *Peripheral Neuropathy*. 4th ed. Philadelphia: Elsevier Saunders; 2005:1339–1373.

65. Donaghy M. Lumbosacral plexus lesions. In: Dyck PJ, Thomas PK, eds. *Peripheral Neuropathy*. 4th ed. Philadelphia: Elsevier Saunders; 2005:1375–1390.
66. Benzel EC, Morris DM, Fowler MR. Nerve sheath tumors of the sciatic nerve and sacral plexus. *J Surg Oncol*. 1988;39:8–16.
67. Hunter VP, Burke TW, Crooks LA. Retroperitoneal nerve sheath tumors: an unusual cause of pelvic mass. *Obstet Gynecol*. 1988;71:1050–1052.
68. Komaki R, Roh J, Cox JD, et al. Superior sulcus tumors: results of irradiation in 36 patients. *Cancer*. 1981;48:1563–1568.
69. Kanner RM, Martini N, Foley KM. Incidence of pain and other clinical manifestations of superior pulmonary sulcus (Pancoast) tumors. In: Bonica JJ, Ventafridda V, Pagni CA, eds. *Advances in Pain Research and Therapy*. Vol. 4. New York: Raven Press; 1982:27–39.
70. Ricci C, Rendina EA, Venuta F, et al. Superior pulmonary sulcus tumors: radical resection and palliative treatment. *Int Surg*. 1989;74:175–179.
71. Hepper NGG, Herskovic T, Witten DM, Mulder DW, Woolner LB. Thoracic inlet tumors. *Ann Int Med*. 1966;64:979–989.
72. Pancoast HK. Superior pulmonary sulcus tumor. *J Am Med Assoc*. 1932;99:1391–1396.
73. Attar S, Miller JE, Satterfield J, et al. Pancoast's tumor: irradiation or surgery? *Ann Thor Surg*. 1979;28:578–586.
74. Stathatos C, Kontaxis AN, Zafiracopoulos P. Pancoast's syndrome due to hydatid cysts of the thoracic outlet. *J Thorac Cardiovasc Surg*. 1969;58:764–768.
75. Omenn GS. Pancoast syndrome due to metastatic carcinoma from the uterine cervix. *Chest*. 1971;60:268–270.
76. Urschel Jr HC. Superior pulmonary sulcus carcinoma. *Surg Clin*. 1988;68:497–509.
77. Silverman MS, MacLeod JP. Pancoast's syndrome due to staphylococcal pneumonia. *Can Med Assoc J*. 1990;142:343–345.
78. Westling P, Svensson H, Hele P. Cervical plexus lesions following post-operative radiation therapy of mammary carcinoma. *Acta Radiol Ther Phys Biol*. 1972;11:209–216.
79. Jackson L, Keats AS. Mechanisms of brachial plexus palsy following anesthesia. *Anesthesiology*. 1965;26:190–194.
80. Pezzimenti JF, Bruckner HW, DeConti RC. Paralytic brachial neuritis in Hodgkin's disease. *Cancer*. 1973;31:626–629.
81. Thyagarajan D, Cascino T, Harms G. Magnetic resonance imaging in brachial plexopathy of cancer. *Neurology*. 1995;45:421–427.
82. Stoehr M, Dichgans J, Dorstelmann D. Ischaemic neuropathy of the lumbosacral plexus following intragluteal injection. *J Neurol Neurosurg Psychiatr*. 1980;43:489–494.
83. Emery S, Ochoa J. Lumbar plexus neuropathy resulting from retroperitoneal hemorrhage. *Muscle Nerve*. 1978;1:330–334.
84. Stewart JD. *Focal Peripheral Neuropathies*. 3rd ed. Philadelphia: Lippincott Williams & Wilkins; 2000.
85. Fajardo LF. Vascular lesions following radiation. *Pathol Annu*. 1988;23:297–330.
86. Greenfield MM, Stark FM. Post-irradiation neuropathy. *Am J Radiol*. 1948;60:617–622.
87. Stoll BA, Andrews JT. Radiation-induced peripheral neuropathy. *Br Med J*. 1966;1:834–837.
88. Haymaker N, Lindgren M. Nerve disturbances following exposure to ionizing radiation. In: Vinken PJ, Bruyn GW, eds. *Handbook of Clinical Neurology*. Amsterdam: North Holland; 1970.
89. Burns RJ. Delayed radiation-induced damage to the brachial plexus. *Clin Exp Neurol*. 1978;15:221–227.
90. Johannson S, Svensson H, Larson LG, Denekamp J. Brachial plexopathy after postoperative radiotherapy of breast cancer patients. *Acta Oncol*. 2000;39:373–382.
91. Wilbourn AJ, Levin KH, Lederman RJ. Radiation-induced brachial plexopathy: electrodiagnostic changes over 13 years (abstract). *Muscle Nerve*. 1994;17:1108.
92. Pierce SM, Recht A, Lingos TI, et al. Long-term radiation complications following conservative surgery (CS) and radiation therapy (RT) in patients with early stage breast cancer. *Int J Radiat Oncol Biol Phys*. 1992;23:915–923.
93. Olsen NK, Pfeiffer P, Johanssen L, Schroder H, Rose C. Radiation-induced brachial plexopathy: neurological follow-up in 161 recurrence-free breast cancer patients. *Int J Radiat Oncol Biol Phys*. 1993;26:43–49.
94. Schierle C, Winograd JM. Radiation-induced brachial plexopathy: review. Complication without a cure. *J Reconstr Microsurg*. 2004;20:149–152.
95. Allen AA, Albers JW, Bastron JA, Daube JR. Myokymic discharges following radiotherapy for malignancy (abstract). *Electroenceph Clin Neurophysiol*. 1977;43:148.
96. Lederman RJ, Wilbourn AJ. Brachial plexopathy: recurrent cancer or radiation? *Neurology*. 1984;34:1331–1335.
97. Harper CM, Thomas JE, Cascino TL, Litchy WJ. Distinction between neoplastic and radiation-induced brachial plexopathy, with emphasis on the role of EMG. *Neurology*. 1989;39:502–506.
98. Jaeckle KA. Nerologic manifestations of neoplastic and radiation-induced plexopathies. *Semin Neurol*. 2010;30:254–262.
99. Cerofolini E, Landi A, DeSantis G, Maiorana A, Canossi G, Romagnoli R. MR of benign peripheral nerve sheath tumors. *J Comput Assist Tomogr*. 1991;15:593–597.
100. Rapoport S, Blair DN, McCarty SM, Desser TS, Hammers LW, Sostman HD. Brachial plexus: correlation of MR imaging with CT and pathologic findings. *Radiology*. 1988;167:161–165.
101. Smith W, Amis JA. Neurilemmoma of the tibial nerve: a case report. *J Bone Jt Surg Am*. 1992;74:443–444.
102. Mukherji SK, Castillo M, Wagle AG. The BP. *Sem US CT MRI*. 1996;17:519–538.
103. Petasnick JP, Turner DA, Charters JR, Gritelis S, Zacharias CE. Soft tissue masses of the locomotor system: comparison of MRI with CT. *Radiology*. 1986;160:125–133.
104. Levine E, Huntrakoon M, Wetzel LH. Malignant nerve sheath neoplasms in neurofibromatosis: distinction from benign tumors by using imaging techniques. *Am J Radiol*. 1987;149:1059–1064.
105. Kransdorf MJ, Jelinek JS, Moser RP, et al. Soft tissue masses: diagnosis using MR imaging. *Am J Radiol*. 1989;153:541–547.
106. Howe FA, Filler AG, Bell BA, Griffiths JR. Magnetic resonance neurography. *Magn Reson Med*. 1992;28:328–338.
107. Ferner RE, Lucas JD, O'Doherty MJ, et al. Evaluation of (18) fluorodeoxyglucose positron emission tomography ((18)FDG PET) in the detection of malignant peripheral nerve sheath tumours arising from within plexiform neurofibromas in neurofibromatosis 1. *J Neurol Neurosurg Psychiatr*. 2000;68:353–357.
108. Gyhra A, Israel J, Santander C, Acuna D. Schwannoma of the brachial plexus with intrathoracic extension. *Thorax*. 1980;35:703–704.
109. Krudy AG. MR myelography using heavily T2-weighted fast spin-echo pulse sequences with fat presaturation. *Am J Radiol*. 1992;159:1315–1320.
110. Toshiyasu N, Yabe Y, Horiuchi Y, Takayama S. Magnetic resonance myelography in brachial plexus injury. *J Bone Jt Surg Br*. 1997;79B:764–769.
111. Taylor BV, Kimmel DW, Krecke KN, Cascino TL. Magnetic resonance imaging in cancer-related lumbosacral plexus. *Mayo Clin Proc*. 1997;72:823–829.
112. Soldatos T, Andreisek G, Thawait GK, et al. High-resolution 3-T MR neurography of the lumbosacral plexus. *Radiographics*. 2013;33:967–987.
113. Vargas MI, Viallon M, Nguyen D, Delavelle J, Becker M. Diffusion tensor imaging (DTI) and tractography of the brachial plexus: feasibility and initial experience in neoplastic conditions. *Neuroradiology*. 2010;52:237–245.
114. Aho K, Sainio K. Late irradiation-induced lesions of the lumbosacral plexus. *Neurology*. 1983;33:953–955.

115. Albers JW, Allen Jr AA, Bastron JA, Daube JR. Limb myokymia. *Muscle Nerve*. 1981;4:494–504.
116. Huang JH, Johnson VE, Zager EL. Tumors of the peripheral nerves and plexuses. *Curr Treat Options Neurol*. 2006;8:299–308.
117. Tiel R, Kline D. Peripheral nerve tumors: surgical principles, approaches, and techniques. *Neurosurg Clin N Am*. 2004;15:167–175.
118. Louis DS. Peripheral nerve tumors in the upper extremity. *Hand Clin*. 1987;3:311–318.
119. Jakacki RI, Dombi E, Potter DM, et al. Phase I trial of pegylated interferon-alpha-2b in young pts with plexiform neurofibromas. *Neurology*. 2011;76:265–272.
120. Ferner RE, Gutmann DH. International consensus statement on malignant peripheral nerve sheath tumors in neurofibromatosis. *Cancer Res*. 2002;62:1573–1577.
121. Rawal A, Yin Q, Roebuck M, et al. Atypical and malignant peripheral nerve-sheath tumors of the brachial plexus: report of three cases and review of the literature. *Microsurgery*. 2006;26:80–86.
122. Khanfir K, Alzieu L, Terrier P, et al. Does adjuvant radiation therapy increase loco-regional control after optimal resection of soft-tissue sarcoma of the extremities? *Eur J Cancer*. 2003;39:1872–1880.
123. Tierney JF, Stewart LA, Parmar MKB, et al. Adjuvant chemotherapy for localised resectable soft tissue sarcoma of adults: meta-analysis of individual data. Sarcoma meta-analysis collaboration. *Lancet*. 1997;350:1647–1654.
124. Ghadimi MP, Young ED, Belousov R, et al. Survivin is a viable target for the treatment of malignant peripheral nerve sheath tumors. *Clin Cancer Res*. 2012;18:2545–2557.
125. Byer SJ, Eckert JM, Brossier NM, et al. Tamoxifen inhibits malignant peripheral nerve sheath tumor growth in an estrogen receptor-independent manner. *Neuro-Oncology*. 2011;13:28–41.
126. Dunteman ED. Levetiracetam an an adjunctive analgesic in neoplastic plexopathies: case series and commentary. *J Pain Palliat Care Pharmacother*. 2005;19:35–43.
127. Son BC, Yoon JH, Kim DR, Lee SW. Dorsal rhizotomy for pain from neoplastic lumbosacral plexopathy inn advanced pelvic cancer. *Stereotact Funct Neurosurg*. 2014;92:109–116.
128. Arai YC, Nishihara M, Aono S, et al. Pulsed radiofrequency treatment within brachial plexus for the management of intractable neoplastic plexopathic pain. *J Anesth*. 2013;27:298–301.
129. Bilsky MH, Vitaz TW, Boland PJ, Bains MS, Rajaraman V, Rusch VW. Surgical treatment of superior sulcus tumors with spinal and brachial plexus involvement. *J Neurosurg (Spine 3)*. 2002;97:301–309.
130. Pitz CC, de la Riviere AB, van Swieten HA, Duurkens VA, Lammers JW, van den Bosch JM. Surgical treatment of pancoast tumours. *Eur J Cardiothorac Surg*. 2004;26:202–208.
131. Foroulis CN, Zarogoulidis P, Darwiche K, et al. Superior sulcus (pancoast) tumors: current evidence on diagnosis and radical treatment. *J Thorac Dis*. 2013;5(S4):S342–S358.
132. Kozower BD, Larner JM, Detterbeck FC, Jones DR. Special treatment issues in non-small cell lung cancer: diagnosis and management of lung cancer, 3rd ed.: American College of Chest Physicians evidence-based clinical practice guidelines. *Chest*. 2013;143(5 Suppl.):e368S–e399S.
133. Vranken JH, Zuurmond WW, de Lange JJ. Continuous brachial plexus block as treatment for the pancoast syndrome. *Clin J Pain*. 2000;16:327–333.
134. Glantz MJ, Burger PC, Friedman AH, Radtke RA, Massey EW, Schold Jr SC. Treatment of radiation-induced nervous tissue injury with heparin and warfarin. *Neurology*. 1994;44:2020–2027.
135. Soto O. Radiation-induced conduction block: resolution following anticoagulant therapy. *Muscle Nerve*. 2005;31:642–645.
136. Artico M, Cervoni L, Wierzbicki V, D'Andrea V, Nucci F. Benign neural sheath tumours of major nerves: characteristics in 119 surgical cases. *Acta Neurochir*. 1997;139:1108–1116.
137. Sundaresan N, Hilaris BS, Martini N. The combined neurosurgical-thoracic management of superior sulcus tumors. *J Clin Oncol*. 1987;5:1739–1745.
138. NIH Clinical Research Studies (protocol number: 05-C-0232). A phase 1 trial of peginterferon Alfa-2b (Peg-Intron) for plexiform neurofibromas. http://clinicalstudies.info.nih.gov/detail/a_2005-c-0232.html.

CHAPTER

15

Neurologic Complications of Oncologic Therapy

Isabel Arrillaga-Romany[1], *Michelle Monje*[2], *Patrick Y. Wen*[3]

[1]Department of Neurology, Massachusetts General Hospital and Harvard Medical School, Boston, MA, USA; [2]Department of Neurology, Stanford School of Medicine, Stanford, CA, USA; [3]Center for Neuro-Oncology, Dana-Farber/Brigham and Women's Cancer Center and Harvard Medical School, Boston, MA, USA

COMPLICATIONS OF RADIOTHERAPY

Radiation therapy is one of the most important causes of neurotoxicity in patients with cancer. It may affect the nervous system by: (1) direct injury to neural structures included in the radiation portal; or (2) indirectly by damaging blood vessels or endocrine organs necessary for functioning of the nervous system or by producing tumors. Radiation injury may occur acutely, but more commonly occurs after a delay of months or years. Many factors determine whether radiation injury will occur. These include the radiation dose, fraction size, duration of treatment, location and volume treated, the length of survival following radiation therapy, and the presence of other therapies and systemic diseases.[1,2]

The complications of radiotherapy are classically categorized in terms of acute, early–delayed, and late–delayed forms (Table 1).[3] Radiation toxicity occurs in all parts of the nervous system: the brain, spinal cord, and peripheral nerves.

Brain

Acute (0–14 Days)

Acute Encephalopathy

Following cranial radiotherapy, acute encephalopathy may occur. Symptoms include nausea/vomiting, drowsiness, headache, and/or possibly worsening of preexisting neurological deficits. This syndrome may be associated with fever. The risk of acute encephalopathy increases with radiation fraction size exceeding 2 Gy. The etiology appears to be disruption of the blood–brain barrier, with resultant vasogenic edema and subsequently increased intracranial pressure (ICP).[4] A transient increase in white matter edema may be seen on neuroimaging. The prognosis is generally excellent, however, herniation and death are possible if the ICP is already increased, especially in cases with posterior fossa or intraventricular tumors. Acute radiation-induced encephalopathy usually responds to corticosteroid therapy. Patients with large tumors and mass effect should receive corticosteroids and undergo surgery prior to beginning radiotherapy to prevent acute encephalopathy.

Fatigue

A significant number of patients undergoing cranial irradiation experience severe and progressive fatigue. This occurs partway through the course of radiotherapy, typically between weeks three and six of radiotherapy for primary brain tumors and near the end of radiotherapy to several weeks after the completion of radiotherapy for metastatic disease.[3] In one study of 104 patients with metastatic disease to brain, the incidence of excessive fatigue was reported to be 85% in patients who underwent whole brain radiotherapy plus radiosurgery, compared with 28% in patients undergoing radiosurgery alone.[5] Though used by some to help reduce severity of fatigue, there is no evidence to date that supports the clinical utility of methylphenidate, modafinil, and armodafinil for this purpose.[6–8]

Early Delayed (4 Weeks to Months)

Several neurological syndromes occur between 4 weeks to several months after radiation therapy. The precise etiology is unclear but may be related to transient

Handbook of Neuro-Oncology Neuroimaging, Second Edition
http://dx.doi.org/10.1016/B978-0-12-800945-1.00015-X

© 2016 Elsevier Ltd. All rights reserved.

TABLE 1 Summary of Radiation-Induced Neurologic Complications

Neurologic Complications of Radiation Therapy to the Brain
DIRECT EFFECTS OF RADIATION THERAPY
• Acute reactions (hours or days) Cerebral edema: headaches, nausea, vomiting, lethargy • Early delayed reactions (2 weeks to 4 months) Drowsiness, increased cognitive dysfunction, exacerbation of neurologic deficits • Late delayed reactions (4 months to several years) Mild to moderate cognitive decline Dementia Cerebral necrosis Leukoencephalopathy Normal pressure hydrocephalus
INDIRECT EFFECTS OF RADIATION THERAPY
Cerebrovascular disorders Large and small vessel disease, moyamoya, telangiectasias, cavernomas, angiomatous malformations, aneurysms Radiation-induced neoplasms Meningiomas, sarcomas, gliomas, schwannomas Endocrine dysfunction Hypothyroidism, hypogonadism, growth hormone deficiency, hypoadrenalism
NEUROLOGIC COMPLICATIONS OF RADIATION THERAPY TO THE SPINAL CORD
Early delayed radiation myelopathy Late delayed radiation myelopathy Delayed radiation myelopathy (DRM) Radiogenic lower motor neuron disease Spinal vasculopathy and hemorrhage
NEUROLOGIC COMPLICATIONS OF RADIATION THERAPY TO THE BRACHIAL PLEXUS
Early delayed brachial plexopathy Late delayed brachial plexopathy Neurologic complications of radiation therapy to peripheral nerves Cranial neuropathies Peripheral neuropathy Nerve sheath tumor

demyelination and remyelination. These syndromes usually resolve spontaneously.

Somnolence Syndrome

The somnolence syndrome consists of drowsiness, lethargy, excessive sleep, headache, nausea, and anorexia, and is more common in children. It occurs several weeks after cranial irradiation and the course is usually monophasic, resolving within a few weeks.[9–11] The reported incidence varies greatly, depending on factors such as radiation dose, fractionation, tumor type/location, and diagnostic criteria. The somnolence syndrome was suggested to be a predictor of long-term cognitive outcome in one series, but this finding was not reproduced in subsequent studies.[12–14] Informing patients of the probability of somnolence for a period after radiotherapy greatly reduces anxiety.

Pseudoprogression

Roughly 10–30% of patients treated with combined chemoradiation for malignant glioma may exhibit magnetic resonance imaging (MRI) findings indistinguishable from tumor progression that represent a specific form of radiation-induced tissue injury termed pseudoprogression.[15] These imaging findings typically present within 3 months of completion of combined chemoradiation.[16] In the minority of patients associated neurological symptoms may occur. They are typically self-limited but can be treated with corticosteroids as needed. Promoter methylation of the repair enzyme O^6-methyl guanine DNA methyltransferase of glioblastoma has been reported to be associated with a higher incidence of pseudoprogression in some studies,[17,18] but not in others.[19] No imaging study can reliably differentiate pseudoprogression from tumor progression but dynamic susceptibility contrast MRI (dynamic susceptibility contrast (DSC) or perfusion MRI) shows the most promise. DSC-MRI measures the signal intensity change related to T2/T2* relaxation during first-pass bolus of paramagnetic contrast agents and can be used to derive relative cerebral blood volumes which are increased in recurrent tumors but not pseudoprogression[20–22]. Fludeoxyglucose positron emission tomography (FDG-PET) can be useful in the differentiation of radiation necrosis from residual or progressive tumor but has a variable degree of sensitivity (60–90%) and specificity (40–100%).[23] Amino acid PET, including [^{11}C-methyl]-methionine, L-1-[^{11}C]-tyrosine, O-(2-[^{18}F]-fluoroethyl)-L-tyrosine, and 3,4-dihydroxy-6-[^{18}F]-fluoro-L-phenylalanine may be more useful than FDG-PET but are currently not widely available.[24–26] Acquisition of tissue via biopsy or resection is sometimes required for definitive diagnosis.

Transient Cognitive Impairment

A transient decline in cognition, distinct from the late onset progressive cognitive decline described below, may occur. This type of cognitive dysfunction, predominantly verbal memory dysfunction, carries a good prognosis and does not appear to predict development of the late-delayed cognitive syndrome.[27,28]

Subacute Rhombencephalitis

A subacute rhombencephalitis may occur 1-3 months after treatment when radiation portals involve the brainstem, such as with ocular, pituitary or head and neck tumors. This syndrome is distinct from the brainstem radionecrosis that can occur later. Clinically, patients present with diplopia, nystagmus, ataxia, dysarthria and other brainstem symptoms and signs. CSF evaluation may show signs of inflammation. Neuroimaging reveals brainstem white matter abnormalities, with lesions that are T1 hypointense and T2 hyperintense; the lesions may enhance with

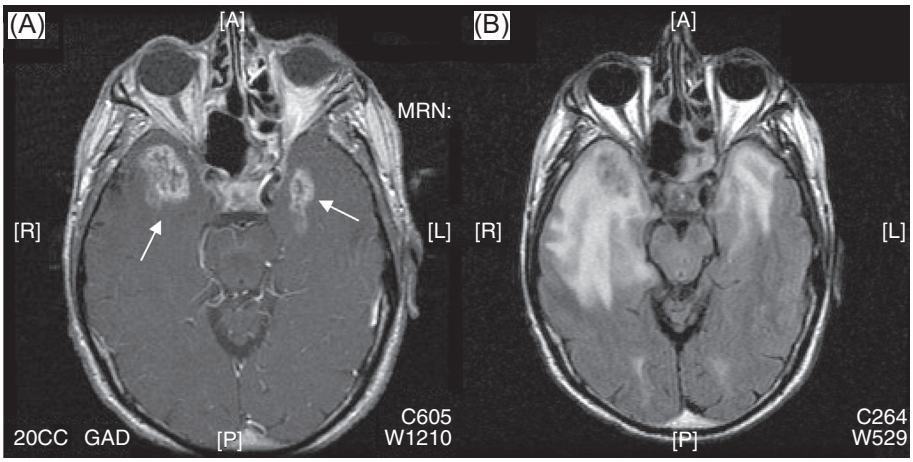


FIGURE 1 A 49-year-old man with T4 squamous cell carcinoma of the paranasal sinuses treated with radiotherapy 6 years previously presenting with confusion and memory loss. (A) T1-weighted axial MRI with gadolinium showing enhancing necrotic areas in both temporal lobes (white arrows); (B) axial FLAIR MRI showing edema around necrotic areas. FDG-PET scan showed no uptake, suggesting that the areas of enhancement were necrosis.

gadolinium.[29] Prognosis is generally good, with progressive improvement over weeks to months, but death has been reported.[30]

Late Delayed (Months to Years)

Radionecrosis

Radiation necrosis has been reported following treatment of both intracranial and extracranial tumors, such as nasopharyngeal carcinoma (Figure 1). Radiation necrosis typically occurs 1–2 years after radiation, but latency as short as 3 months and as long as 30 years have been reported.[31] Recognition of the risk factors for radiation necrosis has resulted in a decrease in incidence. Radiation total dose and fraction size are important risk factors and a total external beam dose of 55–60 Gy delivered in 1.8–2.0 Gy fractions constitutes the upper limits of "safe" dose. Other risk factors include lesion volume and location, old age, associated chemotherapy, and vascular risk factors such as diabetes. Therapies that attempt to increase the dose of radiation delivered to the tumor volume, such as interstitial brachytherapy and stereotactic radiosurgery, also result in an increased incidence of radiation necrosis.[32,33]

Radiation necrosis can result in devastating clinical consequences. Patients present with focal neurological symptoms, often recapitulating the presenting symptoms of the patient's initial disease in the case of primary brain tumors, severe cognitive deficits, signs and symptoms of ICP, and/or seizures.

Imaging characteristics of radiation necrosis are very similar to recurrent tumor. Computed tomography (CT) reveals hypodensity and variable contrast enhancement. MRI shows T1 hypointensity and T2 hyperintensity, predominantly involving white matter. Lesions frequently enhance with gadolinium.[34,35] Mass effect may be present. PET or single photon emission computerized tomography (SPECT) imaging, MR spectroscopy, or diffusion tensor imaging may be employed to help differentiate radiation necrosis from malignancy.[36,37]

In one series, a (201)T1-SPECT technique yielded diagnostic sensitivity of 0.88 and a specificity of 0.83, compared with routine neuroanatomical imaging (CT and MRI), which was found to have a sensitivity of 0.63 and a specificity of 0.59.[37] A separate study of 20 patients with recurrent glioma and 15 with radiation necrosis highlighted the potential utility of diffusion tensor imaging in differentiating between these two processes. An apparent diffusion coefficient ratio <1.65 and/or a fractional anisotropy ratio >0.36 within the area of contrast enhancement predicted tumor recurrence over treatment effect.[38] Perfusion MRI may be useful. However, biopsy remains the only definitive means of diagnosis.[39]

Histopathologically, the lesions of radiation necrosis predominantly affect white matter. Vascular changes include vessel wall hyalinization, thickening and fibrinoid necrosis, fibrinous exudates, vascular hemorrhage, and thrombosis. These changes affect the small arteries and arterioles. Demyelination is also evident.[40] The etiology of radiation necrosis is not yet clear. Histopathology reveals vascular damage and demyelination, implicating the vascular cells and/or oligodendrocytes as the targets of radiation injury.[16]

Classically, radiation injury has been attributed to either the vascular hypothesis or the glial hypothesis. The vascular hypothesis states that radiation-induced vasculopathy and the resultant ischemic necrosis account for radiation injury. The glial hypothesis proposes that radiation-induced damage to oligodendrocytes and their precursors, or neur is the underlying cause of radiation injury. However, the lesions of radiation necrosis are not typical of either pure vascular or demyelinating disease, so neither

hypothesis is sufficient to account for all of the facets of radiation necrosis. Impaired neurogenesis is also a factor.[41]

Treatment of radiation necrosis has historically involved surgical excision and steroid therapy. Additional therapies have been proposed, including anticoagulants, hyperbaric oxygen, and α-tocopherol, but their clinical utility has yet to be proven.[22–24,39] Bevacizumab, a humanized monoclonal anti-vascular endothelial growth factor (VEGF) antibody, has surfaced as a promising treatment option in certain cases of radiation-induced necrosis.[42–45] In a small double-blinded randomized trial of 14 patients with radiation necrosis, patients receiving bevacizumab had significant radiographic and clinical improvement compared with patients receiving placebo.[44] No significant adverse events were reported,[44] but additional trials should be considered both to determine the safety profile of this agent in this indication, and to determine the optimum dose and duration of treatment. Several case series have raised concerns regarding cessation of treatment, with evidence of relapse shortly after discontinuation in a substantial portion of patients.

Leukoencephalopathy

Diffuse white matter changes may occur as a late delayed effect of radiation alone, a combination of radiotherapy and chemotherapy, or, more rarely, after chemotherapy alone. In addition to concomitant chemotherapy such as methotrexate, risk factors for radiation-induced leukoencephalopathy include higher radiation dose and age greater than 60 years.[4,46] This diffuse white matter injury is an entity distinct from radiation necrosis. Histopathology reveals rarefication of white matter, reactive astrogliosis and foci of necrosis.[46,47] In the most severe form, disseminated necrotizing leukoencephalopathy, necrotic foci become confluent and a prominent axonopathy is noted ultrastructurally.[28] Neuroimaging (Figure 2) reveals diffuse increased periventricular T2/fluid-attenuated inversion recovery (FLAIR) signal in the white matter.[48] Enhancement can occur in severe cases, but is not the norm. Diffuse atrophy is often seen. MR spectroscopy reveals loss of *N*-acetyl aspartate, choline, and creatine, implying axonal and membrane damage in the abnormal-appearing white matter.

Dementia

A large metaanalysis of the literature found an incidence of postradiation dementia to be 12%.[49] The dementia is typically characterized by deficits in memory, attention, and intellectual function. Cortical functions such as apraxia and language are relatively spared. Typical onset is within 2 years of radiation exposure and the course is usually progressive. Risk factors are the same as for leukencephalopathy, including radiation dose, fraction size, volume of brain irradiated, older age, and concomitant chemotherapy. As the survival of brain tumor patients improves, an increasing number develop impairment of normal cerebrospinal fluid reabsorption through the arachnoid granulations. This leads to a communicating hydrocephalus with cognitive impairment, gait unsteadiness, and urinary symptoms. Some of these patients may benefit from placement of a ventriculoperitoneal shunt.[50]

Mild to Moderate Cognitive Impairment

Cognitive dysfunction, characterized by prominent dysfunction of short-term memory, is perhaps the most common sequela of radiotherapy.[49,51–53] Months to years after cranial radiation exposure, patients exhibit progressive deficits in short-term memory, spatial relations, visual motor processing, quantitative abilities, and attention.[54] Hippocampal dysfunction is a prominent feature of these neuropsychological sequelae.[55] In fact, the severity of the cognitive deterioration appears to depend upon the radiation dosage delivered to the medial temporal lobes[56]

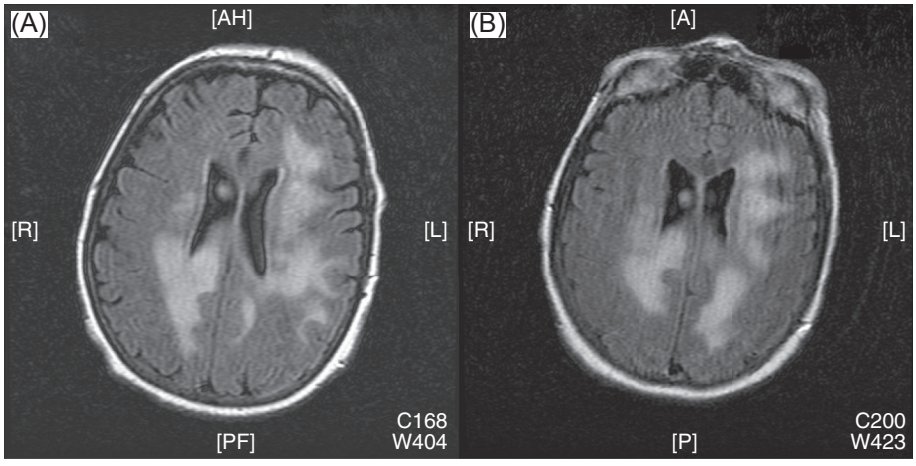


FIGURE 2 A 70-year-old woman with central nervous system lymphoma treated with methotrexate and radiation therapy. Axial FLAIR MRI of the brain showing increased periventricular leucoencephalopathy on 2 axial images (A and B).

The incidence of treatment-induced impairment in cognition has been very well described in children. It is estimated that, when irradiated at age less than 7 years, nearly 100% of children require special education; after 7 years of age approximately 50% of children require special education.[57] Some degree of memory dysfunction is thought to occur in the majority of children. The incidence of memory dysfunction in adult patients has been difficult to quantify, largely due to a lack of uniformity in neuropsychometric testing in the literature. Nonetheless, a review of the available adult literature suggests that whole brain radiotherapy has deleterious effects on neurocognitive function.[58] Mild to moderate cognitive dysfunction is inconsistently associated with radiological findings and frequently occurs in patients with normal-appearing neuroimaging.[59] Clinically significant memory deficits in the absence of radiological findings implicates damage to a subtle process with robust physiological consequences.

One such process is hippocampal neurogenesis. Studies in animal models have demonstrated that therapeutic doses of cranial irradiation virtually ablate neurogenesis and that this inhibition of neurogenesis correlates with impaired performance on hippocampal-dependent memory tests.[57,60,61] Surprisingly, irradiation does not simply deplete the stem cell population, but rather disrupts the microenvironment that normally supports hippocampal neurogenesis.[60,62] This microenvironmental perturbation is due largely to irradiation-induced microglial inflammation, and therapy with the nonsteroidal antiinflammatory agent indomethacin partially restores hippocampal neurogenesis and function in rodents.[62] Additional possible mechanisms underlying radiation-induced cognitive dysfunction include white matter dysfunction, altered regional blood flow due to microvascular disease, and acute and chronic oxidative stress and inflammatory responses.[2,63,64]

To date, treatment with mementine is the only evidence-based strategy to help prevent cognitive decline in those treated with whole brain irradiation. Mementine is an *N*-methyl-D-aspartate antagonist approved by the Food and Drug Administration for use in the treatment of moderate to severe Alzheimer's disease. A randomized placebo controlled trial demonstrated that treatment with memantine for 24 weeks during and after radiation delayed time to cognitive decline and reduced the rate of decline in memory, executive function, and processing speed.[65]

Under active research, hippocampal sparing is another strategy aimed at protecting against whole brain radiation-induced cognitive impairment.[66,67] The motivation for this strategy stems from observations that radiation affects hippocampal dependent learning, memory, and spatial processing likely through effects on adult hippocampal neurogenesis,[68] and knowledge that metastases rarely affect this critical brain structure.[68] A phase II Radiation Therapy Oncology Group trial evaluating the clinical benefit of hippocampal sparing in patients undergoing whole brain radiation therapy for brain metastasis is ongoing.

Radiotherapy-Induced Tumors

Criteria for definition as a radiation-induced tumor include a long latency (years to decades) to occurrence of the second tumor and location of the tumor within the radiation portal. Although uncommon, secondary tumors do occur following cranial irradiation, particularly meningiomas, gliomas (Figure 3), and sarcomas. The relative proportion of secondary cranial tumors is roughly 70%, 20%, and 10%, respectively. Overall,

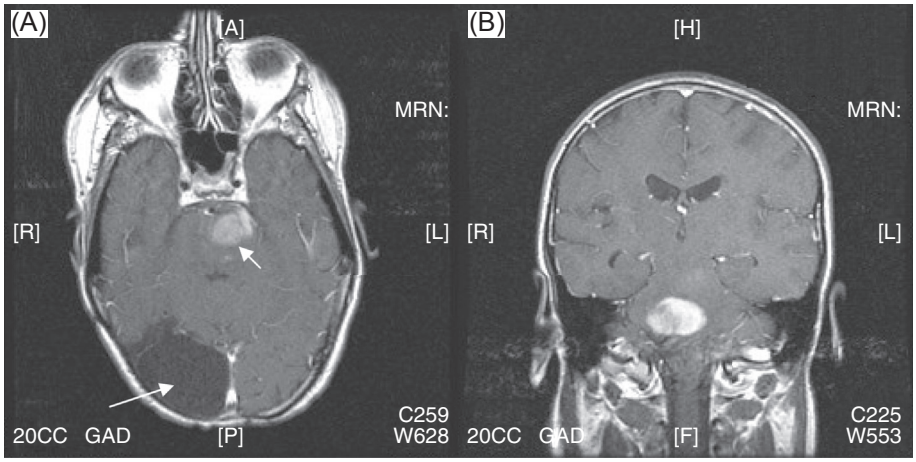


FIGURE 3 A 25-year-old with a history of right parietal cerebral neuroblastoma at age 3 treated with surgical resection and radiotherapy who presented with a 2 month history of ataxia, headaches, and drowsiness. (A) Axial and (B) coronal T1-weighted MRI with gadolinium shows enhancing brainstem lesion. The right parietal surgical cavity from his prior surgery for neuroblastoma is visible (longer arrow). Biopsy showed anaplastic astrocytoma, presumably induced by prior radiotherapy.

radiation-induced malignancies have been estimated at roughly 1–2% per decade following treatment.[69] In an Israeli study of 10,834 patients exposed in childhood to an average dose of only 1.5 Gy for *Tinea capitis*, the relative risk of developing a neural tumor was found to be 6.9. In patients receiving 2.5 Gy, the relative risk was close to 20.[70] After cranial irradiation for childhood leukemia, one series found a relative risk for secondary tumor of 22.[71]

Meningiomas are the most common brain neoplasm to be induced by ionizing radiation.[72,73] More than 300 cases of radiation-induced meningiomas have been reported.[71] Authors frequently differentiate between low-dose (10 Gy) irradiation and high-dose (20 Gy) irradiation-induced meningiomas. The latency from time of treatment to meningioma development ranges from one to three decades.[71,74,75] There is an increased incidence of cellular atypia and aggressive subtypes following irradiation.[76] Cytogenetic studies of radiation induced meningiomas revealed abnormalities involving chromosome 1p.[77,78]

More than 100 cases of secondary gliomas have been reported (see Figure 3); of these, approximately 40% are glioblastoma. Gliomas arise after a mean latency of 9.6 years.[79] Prognosis is often slightly worse or comparable to that of patients with spontaneous gliomas relative to spontaneous forms,[80] due either to a more aggressive behavior or because treatment options are limited by previous exposures.

Rarely, sarcomas involving the skull base, calvaria, or dura may occur. Osteosarcoma, fibrosarcoma, and chondrosarcoma have also been reported.

VASCULOPATHY

Large Vessel Atherosclerosis

Radiation of head and neck cancers or lymphoma can cause accelerated atherosclerosis of the carotid arteries.[81,82] Intracranial accelerated atherosclerosis also occurs,[83] as can secondary moyamoya disease,[84,85] a stenosis or occlusion of large and intermediate cerebral arteries, abnormal net-like vessels, and transdural anastomoses. Treatment involves aggressive control of vascular risk factors such as hyperlipidemia and hypertension. Carotid endarterectomy may be pursued when indicated, but may be more complicated due to vascular fibrosis and postradiation skin changes that may impair healing and increase risk of infection.

Vascular Malformations

Radiation-induced vascular malformations occur more frequently in children than in adults and carry a significant risk of hemorrhage. In one series, 20% of children who had undergone cranial irradiation exhibited radiological evidence of at least one new telangiectasia, defined as small low-signal intensity foci on T2 MR images.[86] In another series, 5 out of 20 patients with postirradiation telangiectasias developed hematoma formation at the site of previously identified T2 shortening.[77] Postmortem histopathology revealed thin-walled vessels surrounded by hemosiderin and gliosis.[87] Radiation-induced retinal telangiectasias and microaneurysms have also been reported.[88] Cavernous angiomas also develop after cranial irradiation, particularly when radiation exposure occurs during childhood.[86] The reported latency between irradiation and diagnosis ranges from 3 to 41 years.[86,89] These lesions are of great concern given their hemorrhagic potential, which appears to be greater for radiation-induced cases than for spontaneous cavernomas[87,89]

Small Vessel Disease

Radiation injury to the microvasculature has been extensively described. Mineralizing microangiopathy occurs more frequently in children than in adults, resulting in calcifications in the basal ganglia, subcortical white matter, or dentate nuclei.[90] The etiology is radiation-induced intimal injury to small vessels, subsequent tissue ischemia, and dystrophic calcification. Lacunar infarctions have also been reported to be a consequence of cranial irradiation.[91] In one series of 421 children treated with cranial radiotherapy, 25 (6%) developed asymptomatic lacunes at a median latency of 2 years. The burden of lacunar disease increased with time from irradiation. The most significant risk factor for development of lacunar disease in this series was age less than 5 years at the time of irradiation.[92]

Neuroendocrine Dysfunction

The hypothalamic–pituitary axis is exquisitely sensitive to irradiation.[93] Endocrine disorders can be the consequence of direct irradiation of an endocrine gland (e.g., 50% of patients developing hypothyroidism within 20 years following radiotherapy for Hodgkin's disease as a result of irradiation of the thyroid gland) or as a result of hypothalamic–pituitary dysfunction secondary to cranial irradiation.[93,94] In children, the most common endocrinopathy is growth hormone deficiency. Gonadotrophin deficiency and secondary and tertiary hypothyroidism occur less frequently. In adults, although growth hormone deficiency is common, it is rarely symptomatic. Approximately 67% of adult males experience sexual difficulties, usually decreased libido and impotence, within 2 years of radiotherapy. These problems are thought to result

from gonadotrophin deficiency from hypothalamic damage. Hypothyroidism and hypoadrenalism occur less commonly and may require hormone replacement. Hyperprolactinemia may also occur.[95]

SPINAL CORD

The spinal cord may be affected by radiotherapy for primary spinal tumors, epidural metastases, tumors of the head and neck, or tumors near the spinal cord, such as Hodgkin's lymphoma.

Acute

Acute complications of the spinal cord are exceedingly rare and acute neurological worsening should lead to an evaluation for intratumoral hemorrhage or tumor progression.[4]

Early–Delayed Radiation Myelopathy

This complication occurs 6 weeks to 6 months after radiotherapy and generally presents as Lhermitte's sign, an unpleasant sensation of tingling, numbness, and/or electrical-like feeling that travels down the spine and to the extremities following neck flexion. Symptoms typically self-resolve within 2–9 months after symptom onset.[96,97] There are no radiological findings. The etiology is thought to be a transient demyelination due to radiation-induced oligodendrocyte apoptosis; rebound of the oligodendrocyte precursor population several weeks after radiation exposure likely accounts for recovery.[98,99]

Late–Delayed Radiation Myelopathy

Late–delayed myelopathy takes two main forms—a progressive radiation myelopathy and a rare radiogenic lower motor neuron disease. Compared with the early delayed myelopathy, the late forms of myelopathy carry a poor prognosis.

Delayed Radiation Myelopathy (DRM)

This complication typically occurs 6 months to 10 years after radiation exposure. Risk factors include higher doses, larger fraction sizes, previous radiation exposure (therapeutic or incidental), old age, concurrent radiosensitizing chemotherapies, and radiation sites in the lower thoracic and lumbar spine.[96,100] Doses of 50, 60, and 69 Gy encompassing the complete cross-section of the spine and using a conventional fractionated schedule of 2 Gy per day was associated with 0.2, 6, and 50% risk of chronic myelopathy, respectively.[100] Clinical presentation may be acute or insidious in onset, progressing to paraparesis or quadriparesis with variable sensory disturbances, bowel and bladder dysfunction, or diaphragmatic weakness in the case of high cervical lesions. Patients may present with a Brown-Sequard hemicord syndrome or a transverse myelitis. Pathology reveals findings similar to cerebral radionecrosis, with areas of focal necrosis, hyalinization, and fibrinoid necrosis of the vasculature, demyelination, and telangeictasias with focal hemorrhage.[101] As in cerebral radiation injury, the etiology is thought to be either radiation-induced vascular and/or glial injury, but the pathogenesis is incompletely understood. MRI can initially be normal with subsequent cord edema and enhancement early in the course and atrophy late in the course.[48,102] PET/CT scans may be helpful in differentiating from primary or secondary spinal cord malignancies.[103] Prognosis is poor but there have been reports of partial recovery.[104,105] There is no effective treatment, although hyperbaric oxygen, anticoagulation, and steroid therapies have been suggested. Bevacizumab may also be clinically beneficial.[106] To minimize risk of this terrible complication, radiation to the spinal cord is generally limited to 4500 cGy in 22–25 fractions.

Radiogenic Lower Motor Neuron Disease

A lower motor neuron syndrome is a rare complication of radiotherapy to the lower spinal cord, cauda equina, or paraspinal tumors.[107–110] This complication predominately affects the lower extremities; in one series of 47 patients, only one had upper extremity weakness.[108] Reported latency from irradiation to presentation ranges from 4 to 312 months.[108] There is no apparent dose dependence and authors have suggested that the etiology of radiogenic lower motor neuron disease may be multifactorial.[108] There is evidence to suggest the anterior horn cells are involved, or alternatively motor nerve roots.[111]

Vascular Changes

Rarely, spinal cord hemorrhage may occur. This is likely to be related to formation of spinal telangiectesias or cavernous malformations.[112]

PLEXUSES AND PERIPHERAL NERVE

Plexopathies

Irradiation of supraclavicular, infraclavicular, or axillary lymph nodes can cause a brachial plexopathy, while irradiation of the pelvic and retroperitoneal lymph nodes can rarely result in a lumbosacral plexopathy. An early–delayed variant of brachial plexopathy presents several months after irradiation, occurring in 1–2% of patients irradiated for breast cancer.[113] Early–delayed brachial

plexopathy is generally reversible. Late–delayed brachial plexopathy occurs years after irradiation, with a progressive course.[114] Pathology of late–delayed plexopathy reveals perineural fibrosis and endoneural thickening, demyelination, axon loss, and small vessel changes. It is sometimes difficult to distinguish a radiation-induced plexopathy from recurrent tumor. The presence of myokymia on electromyography is suggestive of radiation plexopathy.[115] Neuroimaging studies such as MRI or PET may also be helpful in differentiating tumor infiltration from radiation plexopathy.

Peripheral Nerve

Peripheral Neuropathy

The peripheral nerves are relatively radioresistant and radiation-induced injury is rare.

Nerve Sheath Tumors

Rarely, malignant nerve sheath tumors can develop.[116–118]

Cranial Neuropathies

The optic nerve (strictly speaking, part of the central nervous system) is the most frequently affected cranial nerve. Other cranial nerves affected by radiotherapy include the olfactory nerve (also part of the central nervous system), hypoglossal nerve, and the spinal accessory nerve.[119] Multiple cranial neuropathies are also possible. Symptoms are usually observed 6 months to 16 years following treatment.[120] Myokimic discharges are typical electromyographic features.[121] Involvement of the oculomotor, trochlear, and abducens nerves are rare.

COMPLICATIONS OF CHEMOTHERAPY

CHEMOTHERAPY-INDUCED COGNITIVE IMPAIRMENT

A growing body of evidence suggests that chemotherapy can negatively impact cognitive functioning both in the acute and delayed setting.[122–130] The incidence of posttreatment cognitive impairment can range from 15 to 61%[131] and may be among the most frequently reported posttreatment symptoms of cancer survivors.[132] Effects can be worse immediately after treatment with some improvement over time[131] or with little recovery, leading to long lasting impairment.[124,130,133,134] Alternatively, patients may develop symptoms months to years following treatment.[128] Deficits in memory, executive function, processing speed, and attention appear most frequently.[135] Age[136,137] and baseline cognitive reserve[136] have been identified as risk factors to neurotoxic effects of chemotherapy.

The mechanisms underlying effects of chemotherapy on the brain remain elusive, but may involve direct neurotoxic injury of hippocampal progenitor cells.[138–140] Such effects on hippocampal neurogenesis may help explain the delayed impact of treatment on cognition. Chemotherapy-induced increases in oxidative stress,[141] white matter damage,[139,142] and reduced brain vascularization[131] may also be involved. Imaging studies have provided additional information about the structural and functional pathology associated with chemotherapy exposure. Reductions in hippocampal and frontal white and gray matter, have been documented in cancer patients treated with chemotherapy.[143,144] Advanced imaging studies using functional MRI, PET, and diffusion tensor MRI have provided additional, albeit limited, understanding of the pathophysiology of cognitive changes associated with chemotherapy.[131]

Additional complications of chemotherapy include acute encephalopathy, seizures, headaches, aseptic meningitis, acute cerebellar syndrome, vasculopathy and stroke, neuropathy, visual loss, myelopathy, posterior reversible encephalopathy syndrome (PRES), and dementia (Table 2). Complications can result from direct toxic effects, secondary metabolic derangements, cerebrovascular insult, or inflammation. The following section will focus on the drugs that frequently cause neurotoxicity.

Antimetabolites

Methotrexate

Methotrexate is a dihydrofolate reductase inhibitor used in the treatment of leukemia, lymphomas (including central nervous system lymphoma), choriocarcinoma, breast cancer, osteosarcoma, and leptomeningeal metastases. The manifestations of methotrexate toxicity depend of the route of administration, dose, and the use of other treatment modalities such as irradiation.

Intrathecal methotrexate produces aseptic meningitis in about 10% of patients. Symptoms of headache, nuchal rigidity, back pain, nausea, vomiting, fever, and lethargy begin 2–4 h after the drug is administered into the intrathecal space and persist for 12–72 h.[145] Transverse myelopathy is also possible, presenting as back or leg pain, followed by paraplegia, sensory loss, and sphincter dysfunction. This can occur 30 min to up to 2 weeks later, but typically happens within 2 days; variable recovery ensues.[146] Rarely, intrathecal methotrexate can results in acute encephalopathy, subacute focal neurological deficits, neurogenic pulmonary edema, and death.[147,148]

Low-dose systemic methotrexate toxicity is associated with dizziness, headache, and mild cognitive impairment. Symptoms resolve after discontinuation

TABLE 2 Neurological Complications of Chemotherapy, Biological Response Modifiers, and Targeted Molecular Agents

Acute Encephalopathy
- Asparaginase
- 5-Azacytidine
- BCNU (IA or HD)
- Chlorambucil
- Cisplatin
- Corticosteroids
- Cytosine arabinoside (HD)
- Dacarbazine
- Doxorubicin
- Etoposide (HD)
- Fludarabine
- 5-Fluorouracil (5-FU)
- Hexamethylmelamine
- Hydroxyurea
- Ibritumomab
- Ifosfamide
- Imatinib
- Interferons
- Interleukins 1 and 2
- Mechloramine
- Methotrexate
- Misonidazole
- Mitomycin C
- Nelarabine
- Paclitaxel
- Pentostatin
- Procarbazine
- Tamoxifen
- Thalidomide
- ThioTepa (HD)
- Tumor necrosis factor
- Vinca alkaloids
- Zarnestra

Dementia
- BCNU (IA and HD)
- Corticosteroids
- Cytosine arabinoside
- Dacarbazine
- 5-FU _ Levamisole
- Fludarabine
- Interferon-alpha
- Methotrexate

Cranial neuropathy
- BCNU (IA) (ototoxicity)
- Cisplatin (ototoxicity)
- Cytosine arabinoside
- Ifosfamide
- Methotrexate
- Nelarabine
- Vincristine (extraocular palsies)

Acute Cerebellar Syndrome
- Cytosine arabinoside
- 5-FU
- Hexamethylmelamine
- Ifosfamide
- Interleukin-2
- Procarbazine
- Tamoxifen
- Thalidomide
- Vinca alkaloids
- Zarnestra

Leukoencephalopathy
- Capecitabine
- Cisplatin
- Cytarabine (IT)
- 5-FU with levamisole
- Cyclosporin-A
- Methotrexate (IT)
- Nelarabine
- Sunitinib malate

Headache
- Asparaginase
- Capecitabine
- Cetuximab
- Cisplatin
- Corticosteroids
- Cytosine arabinoside
- Danazol
- Estramustine
- Etoposide
- Fludarabine
- Gefitinib (ZD1839)
- Hexamethylmelamine
- Interferons
- Interleukins 1, 2, 4
- Ibritumomab
- Levamisole
- Mechlorethamine
- Methotrexate (IT)
- Nelarabine
- Octreotide
- Oprelvekin
- Plicamycin
- Rituximab
- Retinoic acid
- SU5416
- Tamoxifen
- Temozolomide
- ThioTepa (IT)
- Topotecan
- Tositumomab
- Trastuzumab

Seizures
- Amifostine
- Asparaginase
- BCNU
- Busulphan (HD)
- Chorambucil
- Cisplatin
- Corticosteroids
- Cytosine arabinoside
- Dacarbazine
- Etanercept
- Etoposide
- 5-FU
- Ifosfamide
- Interferon
- Interleukin-2
- Letrozole
- Levamisole
- Mechloramine
- Methotrexate
- Octreotide
- Paclitaxel
- Pentostatin
- Suramin
- Teniposide
- Thalidomide
- Vinca alkaloids

Vasculopathy and stroke
- Asparaginase
- Bevacizumab
- BCNU (IA)
- Bleomycin
- Carboplatin (IA)
- Cisplatin (IA)
- Doxorubicin
- Erlotinib
- Estramustine
- 5-FU
- Imatinib mesylate
- Methotrexate
- Nelarabine
- Tamoxifen

Aseptic meningitis
- Cytosine arabinoside (IT)
- Levamisole
- Methotrexate (IT)
- ThioTepa (IT)

Syncope
- Bevacizumab
- Erlotinib
- Nelarabine

Neuropathy
- 5-Azacytidine
- Bortezomib
- Capecitabine
- Carboplatin
- Cisplatin
- Cytosine arabinoside
- Docetaxel
- Eribulin
- Etoposide
- 5-FU
- Gemcitabine
- Hexamethylmelamine
- Ifosphamide
- Interferon-α
- Misonidazole
- Nelarabine
- Oprelvekin
- Oxaliplatin
- Paclitaxel
- Pemetrexed
- Procarbazine
- Purine analogs (fludarabine, cladribine, pentostatin)
- Sorafenib
- Sunitinib malate
- Suramin
- Teniposide (VM-26)
- Thalidomide
- Tumor necrosis factor
- Vinca alkaloids
- Zarnestra

Myelopathy
- Cisplatin
- Cladribine
- Corticosteroids
- Cytosine arabinoside
- Doxorubicin
- Fludarabine
- Interferon alpha
- Methotrexate (IT)
- Mitoxantrone (IT)
- Docetaxel
- ThioTepa (IT)
- Vincristine (IT)

Visual loss
- BCNU (IA)
- Bevacizumab
- Cisplatin
- Etanercept
- Fludarabine
- Methotrexate (HD)
- Tamoxifen

Abbreviations: HD, high dose; IA, intraaterial; IT, intrathecal.

of methotrexate. High-dose systemic methotrexate can result in an acute encephalopathy syndrome presenting within 24 h of treatment with seizures, confusion, and somnolence.[149] Subacutely, high-dose methotrexate can cause a stroke-like syndrome, characterized by transient focal neurological deficits, confusion, and sometimes seizures. This appears within 6 days of exposure to methotrexate and resolves completely within 72 h. Chronically, methotrexate can cause leukoencephalopathy, either alone or in combination with

radiotherapy[150,151](see Figure 2). Polymorphisms of genes related to neurogenesis may help predict vulnerability.[152] There are no effective treatments. The manifestations and consequences of leukoencephalopathy were discussed above.

5-Fluorouracil

5-Fluorouracil (5-FU) is a fluorinated pyrimidine that disrupts DNA synthesis and is used in treatment of many cancers, including colon and breast cancers. 5-FU crosses the blood–brain barrier and the highest concentration is found in the cerebellum, where it is toxic to Purkinje and granule cells.[153] An acute cerebellar syndrome can occur and is characterized by acute onset of ataxia, dysmetria, dysarthria, and nystagmus.[154] Onset begins weeks to months after initiation of treatment[154] and the drug should be discontinued when symptoms emerge. Complete recovery is the rule. Patients with decreased dihydropyrimidine dehydrogenase activity are at an increased risk for developing severe neurologic toxicity following 5-FU chemotherapy.[155,156] Other toxicities of 5-FU include encephalopathy,[157,158] optic neuropathy,[159] focal dystonia,[160] Parkinsonian syndromes, eye movement abnormalities, and cerebrovascular disorders.[161] Peripheral neuropathy has also been reported.[162] The mechanism of toxicity might involve damage to myelinated tracts and altered translational regulation of oligodendrocytes.[163] The combination of 5-fluorouracil and levamisole used to treat colon cancer has been rarely associated with the development of a multifocal leukoencephalopathy.[164] Capecitabine, a prodrug that is metabolized to 5-FU by the enzyme thymidine phosphorylase, is used to treat breast and gastrointestinal malignancies. Neurologic complications are uncommon, but some patients experience paresthesias, headaches, and cerebellar symptoms. Several cases of neuropathies[165,166] and multifocal leukoencephalopathy have also been described.[167]

Cytosine Arabinoside (Cytarabine, Ara-C)

Ara-C is a pyrimidine analogue that disrupts DNA synthesis and is used in the treatment of leukemias, lymphomas, and leptomeningeal metastases. Standard doses are associated with few neurological complications. At higher doses, however, an acute cerebellar syndrome may develop in 10–25% of patients,[168] particularly those with renal impairment.[169,170] Somnolence is another frequent symptom. Initially, imaging is typically unremarkable. Several months later there is subsequent development of cerebellar atrophy on MRI correlating with widespread loss of Purkinje cells.[48] The syndrome is typically reversible, though rarely can produce permanent symptoms.[171] Occasionally, high-dose Ara-C produces encephalopathy, seizures, reversible ocular toxicity, lateral rectus syndrome, bulbar and psuedobulbar palsy, Horner's syndrome, aseptic meningitis, anosmia, and/or an extrapyramidal syndrome.[168,172,173] When administered intrathecally, Ara-C can also result in a transverse myelitis.[174]

Alkylating Agents

Ifosfamide

Ifosfamide is an alkylating agent that causes cross-linking of DNA and is used in the treatment of many cancers, including a number of sarcomas and gynecological cancers. It produces an acute encephalopathy in 10–30% of patients that presents hours to days after exposure.[175–179] Clinical manifestations include confusion, hallucinations, cerebellar dysfunction, seizures, cranial neuropathies, and occasionally coma.[180–182] The etiology appears to be accumulation of chloracetaldehyde, a breakdown product of ifosfamide. Patients with a history of prior cisplatin use, kidney dysfunction, low serum albumin or who are concurrent taking aprepitant, may be at increased risk for this complication.[176,181,183–186] The encephalopathy typically resolves without intervention in 28–72 h from discontinuation of the ifosfamide.[187] Methylene blue and benzodiazepines have been used to accelerate recovery. Thiamine and dexmedetomidine may also have clinical utility.[182,188–193] Other more rare but notable neurologic complications of this agent include asterixis, myoclonus, postural tremor,[179] neuropathies,[194] and extrapyramidal symptoms.[195,196]

Busulfan

Another alkylating agent, busulfan, is used in conditioning regimens for hematopoietic stem cell transplant. At high doses busulfan can induce generalized seizures, usually after the third or fourth day of administration.[197] Seizure prophylaxis is often warranted and phenytoin, benzodiazepines, and levicitacetram have all been used to this effect.[198,199]

Platinum-Based Agents

Cisplatin

Cisplatin is a platinum-based agent that produces DNA cross-linking and is used to treat medulloblastoma, head and neck, ovarian, germ cell, cervical, lung, and bladder cancers. Cisplatin produces a neuropathy that affects predominantly large myelinated sensory fibers at the level of the dorsal root ganglion,[200,201] causing proprioceptive loss, numbness, and paresthesias.[201,202] Sural nerve biopsy shows demyelination and axonal loss. The neuropathy is related to a total cumulative dose, with symptom presentation typically at a dose of 300 mg/m^2 or greater, and usually improves with time after cessation of treatment. Coasting is a unique feature

of cisplatin-induced peripheral neuropathy and is term used to describe the typical delay in recovery following discontinuation of the drug.[203] Onset of the neuropathy following completion of cisplatin therapy can also be seen. The mechanism of neurotoxicity is believed to involve direct toxicity to dorsal root ganglion cells, or indirect toxicity via oxidative stress or mitochondrial dysfunction. Patients with polymorphisms in glutathione S-transferase, an enzyme responsible for metabolism of cisplatin, may be most susceptible to this neuropathy.[204,205] There are no effective preventive strategies or treatments for chemotherapy-induced peripheral neuropathy.[206] Duloxetine, other antidepressants and/or anticonvulsants can be tired to help ameliorate symptoms. The mechanism likely involves oxidative stress and mitochondrial dysfunction,[207,208] or an alteration in cell cycle kinetics leading postmitotic dorsal root ganglion cells to reenter the cell cycle.[209] Both of these mechanistic pathways are purported to triggering an increase in neuronal apoptosis.

Cisplatin also commonly causes ototoxicity with high-frequency sensorineural hearing loss and tinnitus due to dose-related damage to the hair cells in the organ of Corti.[210,211] Audiometric hearing loss is present in 74–88% of patients, with symptomatic hearing loss in 16–20% of patients. Irradiation increases the risk of hearing loss.[212,213] There remains insufficient data to recommend a particular agent for the prevention of cisplatin-induced ototoxicity, but intratympanic dexamethasone,[214] amifostine,[211,215,216] and sodium thiosulfate[217] are sometimes used. Lhermitte's sign occurs in 20–40% of patients receiving cisplatin. Rarely, cisplatin may cause encephalopathy, reversible posterior leukoencephalopathy, late vascular toxicity, taste disturbance, and a myasthenic syndrome.

Oxaliplatin

Oxaliplatin is another platinum-based chemotherapy most often used for the treatment of metastatic colorectal cancer. Like cisplatin, this agent can produce a cumulative and dose-limiting distal sensory neuropathy. In addition, oxaliplatin can cause a unique type of acute neuropathy-like syndrome in over 80% of treated patients.[218] Symptoms occur within hours to days of drug administration, are not cumulative and for the most part resolve within a few week.[219] Patients with severe symptoms can be vulnerable to longer-term peripheral neuropathies.[220] Symptoms include sensitivity to cold, throat discomfort, dyspnea, muscle pain, and paresthesias of the hands, feet, and perioral region.[218] No clear evidence-based preventive strategies exist to date.[206] In the appropriate clinical setting, dose reduction or interruption of therapy can be employed to help ameliorate symptoms. Duloxetine, other antidepressants and/or anticonvulsants can be tired to help ameliorate symptoms.

Carboplatin

Cisplatin is a third platinum-based agent used to treat nonsmall cell lung cancer and ovarian cancer, among other indications. At standard doses, carboplatin rarely produces neuropathy. However, a neuropathy can be seen at higher doses such as those employed in hematopoietic stem cell transplant.[221]

Taxanes (Paclitaxel and Docetaxel)

Taxanes inhibit microtubule function and are used in the treatment of many cancers including nonsmall cell lung, ovary, and breast cancers. Paclitaxel and docetaxel both produces a dose-limiting peripheral neuropathy in 60% and 15% of patients receiving treatment, respectively.[222,223] Severity of symptoms are usually greater with paclitaxel, though its neurotoxic threshold is 1000 mg/m^2, significantly higher than that of docetaxel at 400 mg/m^2.[224] The neuropathy is predominantly sensory, affecting both small and large fibers and manifesting clinically as burning paresthesias of the hands and feet and loss of reflexes. It does not commonly progress. Motor and autonomic neuropathies have also been reported with both agents.

Rarely, paclitaxel causes seizures and encephalopathy. Docetaxel can occasionally result in Lhermittes's sign.[126]

Vincristine

Vincristine is a vinca alkaloid that disrupts microtubules and is used to treat many cancers including leukemia, lymphoma, sarcomas, and brain tumors. It causes an axonal neuropathy affecting both sensory and motor fibers in almost all patients.[225] Small sensory fibers are particularly affected. Clinical manifestations include fingertip and foot paresthesias, muscle cramps, foot and wrist drop, and sensory loss of varying degrees. Focal neuropathies and cranial neuropathies are also possible. Patient with hereditary neuropathies (such as Charcot-Marie-Tooth),[226,227] or on concurrent inhibitors of CYP3A4 (such as antifungals),[228,229] or hematopoietic colony stimulating factors[230] are particularly vulnerable this neuropathy.

In addition to the sensory and motor neuropathy, vincristine commonly causes an autonomic neuropathy, characterized by gastrointestinal, urinary, and/or sexual dysfunction.[231] Focal cranial nerve neuropathies, most commonly involving the oculomotor nerve, can also occur.[232] Rarely, vincristine causes the syndrome of inappropriate antidiuretic hormone, resulting in hyponatremia leading to metabolic encephalopathy and seizures.[233] Vincristine should never be administered intrathecally and accidental administration of vincristine

into the cerebrospinal fluid produces a rapidly ascending myelopathy, coma, and death.[234] Other vinca alkaloids such as vinblastine and vinorlbine are associated with a lower incidence of neuropathies.

L-Asparaginase

L-asparaginase is used in the treatment of acute lymphocytic leukemia and functions by catalyzing asparagine into aspartate and ammonia, thereby inhibiting protein synthesis. A hyperammoniemic encephalopathy can occur. The severity of the encephalopathy correlates with the amount of slow wave activity on the electroencephalogram, but not with the degree of hyperammoniemia.[235] L-asparaginase can cause a deficiency in antithrombin III, plasminogen, and fibrinogen. This predisposes patients to thrombotic and hemorrhagic cerebrovascular disease,[236] especially venous sinus thrombosis.[237] Patients receiving L-asparaginase who present with confusion, obtundation, seizure, or new focal neurological deficit should be evaluated for venous sinus thrombosis.[238]

Anthracycline Antibiotics (Daunorubicin, Doxorubicin, Mitoxantrone)

The anthracycline antibiotics exert their antineoplastic action by intercalating between DNA bases, causing uncoiling of the double helix structure of DNA. Side effects of the anthracylines on the nervous system are indirect. The anthracyclines can cause a cardiomyopathy and, subsequently, reduced ventricular contractility can promote intraventricular thrombus formation. These thrombi can cause cardioembolic strokes or transient ischemic attacks.[238]

Monoclonal Antibodies

Bevacizumab (Avastin)

Bevacizumab is a monoclonal antibody against VEGF used for various malignancies including glioblastoma. Along with other inhibitors of VEGF and the VEGF receptor (VEGFR), bevacizumab has been associated with PRES in 0.1% of treated patients. PRES is a leukoencephalopathy syndrome characterized by seizures, headaches, vision loss, and confusion. Hypertension may be present and in the absence of causative agents, is usually a precipitating factor. Imaging reveals nonenhancing subcortical leukoencephalopathy in a distal vascular distribution. Discontinuing the causative agent usually results in complete resolution of symptoms and signs.

Bevacizumb also increases the risk of arterial-thrombotic events 1.6-fold[239] thereby increasing the risk of transient ischemic attacks and strokes. There is an additional but small increased risk of hemorrhage in brain, possibly slightly higher in patients with primary brain tumors or metastasis.[240,241] Regardless, anticoagulation appears generally well tolerated by patients on anti-VEGF therapy.[242]

Ipilumimab

Ipilumimab is a monoclonal antibody against the CTLA-4 on the cell surface of T cells that works to activate the immune system and is currently approved for the treatment of melanoma. Observed neurological complications are immune-mediated and include lymphocytic hypophysitis,[243] Guillain–Barre,[244] myasthenia gravis, sensory and motor neuropathies, transverse myelitis,[245] PRES,[246] and hypopituitarism.[245,247,248] High-dose steroids or plasmapheresis can be considered for treatment.

Others

Rituximab is a monoclonal antibody against CD20 typically used to treat lymphomas with rare neurological complications, but can be associated with nonspecific symptoms including headaches and dizziness. An extremely serious but rare complication of rituximab and alemtuzumab, another humanized monoclonal antibody that targets CD25 and is used to treat chronic lymphocytic leukemia, is the development of progressive multifocal leukoencephalopathy.[249,250] Trastuzumab is a humanized anti-HER2 monoclonal antibody used in the treatment of breast cancer. Neurologic side effects are rare but patients may experience headaches, paresthesias, and dizziness after infusions.[251] Cetuximab is a chimeric mouse–human monocloncal antibody targeting epidermal growth factor used for colorectal and head and neck cancers. Headaches are common after treatment and patients may develop fatigue and cramps, possibly related to hypomagnesaemia.[252]

SUMMARY

Neurologic complications of oncologic therapies are occurring with increasing frequency in cancer patients. This is a result of the availability of a growing number of treatments associated with neurotoxicities and prolonged patient survival. Increased understanding of the underlying mechanisms for these neurologic complications and methods to prevent them will be an important challenge for the future and will hopefully lead to reduced neurologic morbidity in cancer patients.

References

1. Rinne ML, Lee EQ, Wen PY. Central nervous system complications of cancer therapy. *J Support Oncol*. 2012;10(4):133–141.
2. Soussain C, Ricard D, Fike JR, et al. CNS complications of radiotherapy and chemotherapy. *Lancet*. 2009;374:1639–1651.
3. Sheline GE, Wara WM, Smith V. Therapeutic irradiation and brain injury. *Int J Radiat Oncol Biol Phys*. 1980;6:1215–1228.
4. Behin A, Delattre JY. Complications of radiation therapy on the brain and spinal cord. *Semin Neurol*. 2004;24:405–417.
5. Kondziolka D, Niranjan A, Flickinger JC, Lunsford LD. Radiosurgery with or without whole-brain radiotherapy for brain metastases: the patients' perspective regarding complications. *Am J Clin Oncol*. 2005;28:173–179.
6. Gehring K, Patwardhan SY, Collins R, et al. A randomized trial on the efficacy of methylphenidate and modafinil for improving cognitive functioning and symptoms in patients with a primary brain tumor. *J Neuro-Oncol*. 2012;107:165–174.
7. Lee EQ, Muzikansky A, Kesari S, et al. A randomized, placebo-controlled pilot trial of armodafinil for fatigue in patients with gliomas undergoing radiotherapy. *J Clin Oncol*. 2014;32:5s.
8. Butler Jr JM, Case LD, Atkins J, et al. A phase III, double-blind, placebo-controlled prospective randomized clinical trial of d-threo-methylphenidate HCl in brain tumor patients receiving radiation therapy. *Int J Radiat Oncol Biol Phys*. 2007;69:1496–1501.
9. Garwicz S, Aronson S, Elmqvist D, Landberg T. Postirradiation syndrome and eeg findings in children with acute lymphoblastic leukaemia. *Acta Paediatr Scand*. 1975;64:399–403.
10. Ryan J. Radiation somnolence syndrome. *J Pediatr Oncol Nurs*. 2000;17:50–53.
11. Powell C, Guerrero D, Sardell S, et al. Somnolence syndrome in patients receiving radical radiotherapy for primary brain tumours: a prospective study. *Radiother Oncol*. 2011;100:131–136.
12. Berg RA, Ch'ien LT, Lancaster W, et al. Neuropsychological sequelae of postradiation somnolence syndrome. *J Dev Behav Pediatr*. 1983;4:103–107.
13. Ch'ien LT, Aur RJ, Stagner S, et al. Long-term neurological implications of somnolence syndrome in children with acute lymphocytic leukemia. *Ann Neurol*. 1980;8:273–277.
14. Trautman PD, Erickson C, Shaffer D, et al. Prediction of intellectual deficits in children with acute lymphoblastic leukemia. *J Dev Behav Pediatr*. 1988;9:122–128.
15. Brandsma D, Stalpers L, Taal W, et al. Clinical features, mechanisms, and management of pseudoprogression in malignant gliomas. *Lancet Oncol*. 2008;9:453–461.
16. Fink J, Born D, Chamberlain MC. Radiation necrosis: relevance with respect to treatment of primary and secondary brain tumors. *Curr Neurol Neurosci Rep*. 2012;12:276–285.
17. Schiff D, Wen PY, van den Bent MJ. Neurological adverse effects caused by cytotoxic and targeted therapies. 2009; 6: 596–603.
18. Brandes AA, Franceschi E, Tosoni A, et al. MGMT promoter methylation status can predict the incidence and outcome of pseudoprogression after concomitant radiochemotherapy in newly diagnosed glioblastoma patients. *J Clin Oncol*. 2008;26:2192–2197.
19. Wick W, Chinot OL, Mason WP, et al. Patterns of tumor progression in a phase 3 study of bevacizumab (Bv) plus radiotherapy (RT) plus temozolomide (T) for newly diagnosed glioblastoma (GB). *J Clin Oncol*. 2014;32(5s):32.
20. Rosen BR, Belliveau JW, Vevea JM, Brady TJ. Perfusion imaging with NMR contrast agents. *Magn Reson Med*. 1990;14:249–265.
21. Hu LS, Eschbacher JM, Heiserman JE, et al. Reevaluating the imaging definition of tumor progression: perfusion MRI quantifies recurrent glioblastoma tumor fraction, pseudoprogression, and radiation necrosis to predict survival. *Neuro Oncol*. 2012; 14:919–930.
22. Tsien C, Galban CJ, Chenevert TL, et al. Parametric response map as an imaging biomarker to distinguish progression from pseudoprogression in high-grade glioma. *J Clin Oncol*. 2010;28:2293–2299.
23. Hustinx R, Pourdehnad M, Kaschten B, Alavi A. PET imaging for differentiating recurrent brain tumor from radiation necrosis. *Radiol Clin North Am*. 2005;43:35–47.
24. Pauleit D, Floeth F, Hamacher K, et al. O-(2-[^{18}F]fluoroethyl)-L-tyrosine PET combined with MRI improves the diagnostic assessment of cerebral gliomas. *Brain*. 2005;128:678–687.
25. Dunet V, Rossier C, Buck A, et al. Performance of 18F-fluoroethyl-tyrosine (18F-FET) PET for the differential diagnosis of primary brain tumor: a systematic review and Metaanalysis. *J Nucl Med*. 2012;53:207–214.
26. Singhal T, Narayanan TK, Jacobs MP, et al. 11C-methionine PET for grading and prognostication in gliomas: a comparison study with 18F-FDG PET and contrast enhancement on MRI. *J Nucl Med*. 2012;53:1709–1715.
27. Armstrong CL, Corn BW, Ruffer JE, et al. Radiotherapeutic effects on brain function: double dissociation of memory systems. *Neuropsychiatry Neuropsychol Behav Neurol*. 2000;13:101–111.
28. Vigliani MC, Sichez N, Poisson M, Delattre JY. A prospective study of cognitive functions following conventional radiotherapy for supratentorial gliomas in young adults: 4-year results. *Int J Radiat Oncol Biol Phys*. 1996;35:527–533.
29. Creange A, Felten D, Kiesel I, et al. Subacute leukoencephalopathy of the rhombencephalon after pituitary radiotherapy. *Rev Neurol Paris*. 1994;150:704–708.
30. Lampert P, Tom MI, Rider WD. Disseminated demyelination of the brain following Co60 (gamma) radiation. *Arch Pathol*. 1959;68:322–330.
31. Oppenheimer JH, Levy ML, Sinha U, et al. Radionecrosis secondary to interstitial brachytherapy: correlation of magnetic resonance imaging and histopathology. *Neurosurgery*. 1992;31:336–343.
32. Minniti G, Clarke E, Lanzetta G, et al. Stereotactic radiosurgery for brain metastases: analysis of outcome and risk of brain radionecrosis. *Radiat Oncol*. 2011;6:48.
33. Gabayan AJ, Green SB, Sanan A, et al. GliaSite brachytherapy for treatment of recurrent malignant gliomas: a retrospective multiinstitutional analysis. *Neurosurgery*. 2006;58:701–709; discussion 701–709.
34. Shah R, Vattoth S, Jacob R, et al. Radiation necrosis in the brain: imaging features and differentiation from tumor recurrence. *Radiographics*. 2012;32:1343–1359.
35. Kumar AJ, Leeds NE, Fuller GN, et al. Malignant gliomas: MR imaging spectrum of radiation therapy- and chemotherapy-induced necrosis of the brain after treatment. *Radiology*. 2000;217:377–384.
36. Rock JP, Scarpace L, Hearshen D, et al. Associations among magnetic resonance spectroscopy, apparent diffusion coefficients, and image-guided histopathology with special attention to radiation necrosis. *Neurosurgery*. 2004;54:1111–1117; discussion 1117–1119.
37. Gomez-Rio M, Martinez Del Valle Torres D, Rodriguez-Fernandez A, et al. (201)Tl-SPECT in low-grade gliomas: diagnostic accuracy in differential diagnosis between tumour recurrence and radionecrosis. *Eur J Nucl Med Mol Imaging*. 2004;31:1237–1243.
38. Xu JL, Li YL, Lian JM, et al. Distinction between postoperative recurrent glioma and radiation injury using MR diffusion tensor imaging. *Neuroradiology*. 2010;52:1193–1199.
39. Chao ST, Ahluwalia MS, Barnett GH, et al. Challenges with the diagnosis and treatment of cerebral radiation necrosis. *Int J Radiat Oncol Biol Phys*. 2013;87:449–457.
40. Yoshihiko YY. Pathological review of late cerebral radionecrosis. *Brain Tumor Pathol*. 2008;25:51–58.
41. Monje ML, Palmer T. Radiation injury and neurogenesis. *Curr Opin Neurol*. 2003;16:129–134.

42. Gonzalez J, Kumar AJ, Conrad CA, Levin VA. Effect of bevacizumab on radiation necrosis of the brain. *Int J Radiat Oncol Biol Phys*. 2007;67:323–326.
43. Torcuator R, Zuniga R, Mohan YS, et al. Initial experience with bevacizumab treatment for biopsy confirmed cerebral radiation necrosis. *J Neuro-Oncol*. 2009;94:63–68.
44. Levin VA, Bidaut L, Hou P, et al. Randomized double-blind placebo-controlled trial of bevacizumab therapy for radiation necrosis of the central nervous system. *Int J Radiat Oncol Biol Phys*. 2011;79:1487–1495.
45. Deibert CP, Ahluwalia MS, Sheehan JP, et al. Bevacizumab for refractory adverse radiation effects after stereotactic radiosurgery. *J Neuro-Oncol*. 2013;115:217–223.
46. Wassenberg MW, Bromberg JE, Witkamp TD, et al. White matter lesions and encephalopathy in patients treated for primary central nervous system lymphoma. *J Neuro-Oncol*. 2001;52:73–80.
47. Wang AM, Skias DD, Rumbaugh CL, et al. Central nervous system changes after radiation therapy and/or chemotherapy: correlation of CT and autopsy findings. *AJNR Am J Neuroradiol*. 1983;4:466–471.
48. Arrillaga-Romany IC, Dietrich J. Imaging findings in cancer therapy-associated neurotoxicity. *Semin Neurol*. 2012;32:476–486.
49. Crossen JR, Garwood D, Glatstein E, Neuwelt EA. Neurobehavioral sequelae of cranial irradiation in adults: a review of radiation-induced encephalopathy. *J Clin Oncol*. 1994;12:627–642.
50. Thiessen B, DeAngelis LM. Hydrocephalus in radiation leukoencephalopathy: results of ventriculoperitoneal shunting. *Arch Neurol*. 1998;55:705–710.
51. Roman DD, Sperduto PW. Neuropsychological effects of cranial radiation: current knowledge and future directions. *Int J Radiat Oncol Biol Phys*. 1995;31:983–998.
52. Anderson VA, Godber T, Smibert E, et al. Cognitive and academic outcome following cranial irradiation and chemotherapy in children: a longitudinal study. *Br J Cancer*. 2000;82:255–262.
53. Surma-aho O, Niemela M, Vilkki J, et al. Adverse long-term effects of brain radiotherapy in adult low-grade glioma patients. *Neurology*. 2001;56:1285–1290.
54. Armstrong GT, Reddick WE, Petersen RC, et al. Evaluation of memory impairment in aging adult survivors of childhood acute lymphoblastic leukemia treated with cranial radiotherapy. *J Natl Cancer Inst*. 2013;105:899–907.
55. Monje M, Dietrich J. Cognitive side effects of cancer therapy demonstrate a functional role for adult neurogenesis. *Behav Brain Res*. 2012;227:376–379.
56. Abayomi OK. Pathogenesis of cognitive decline following therapeutic irradiation for head and neck tumors. *Acta Oncol*. 2002;41:346–351.
57. Monje M. Cranial radiation therapy and damage to hippocampal neurogenesis. *Dev Disabil Res Rev*. 2008;14:238–242.
58. McDuff SG, Taich ZJ, Lawson JD, et al. Neurocognitive assessment following whole brain radiation therapy and radiosurgery for patients with cerebral metastases. *J Neurol Neurosurg Psychiatry*. 2013;84:1384–1391.
59. Dropcho EJE. Central nervous system injury by therapeutic irradiation. *Neurol Clin*. 1991;9:969–988.
60. Monje ML, Mizumatsu S, Fike JR, Palmer TD. Irradiation induces neural precursor-cell dysfunction. *Nat Med*. 2002;8:955–962.
61. Raber J, Rola R, LeFevour A, et al. Radiation-induced cognitive impairments are associated with changes in indicators of hippocampal neurogenesis. *Radiat Res*. 2004;162:39–47.
62. Monje ML, Toda H, Palmer TD. Inflammatory blockade restores adult hippocampal neurogenesis. *Science*. 2003;302:1760–1765.
63. Zhao W, Diz DI, Robbins ME. Oxidative damage pathways in relation to normal tissue injury. *Br J Radiol*. 2007;80(1):S23–S31.
64. Lee WH, Sonntag WE, Mitschelen M, et al. Irradiation induces regionally specific alterations in pro-inflammatory environments in rat brain. *Int J Radiat Biol*. 2010;86:132–144.
65. Brown PD, Pugh S, Laack NN, et al. Memantine for the prevention of cognitive dysfunction in patients receiving whole-brain radiotherapy: a randomized, double-blind, placebo-controlled trial. *Neuro Oncol*. 2013;15:1429–1437.
66. Shaw MG, Ball DL. Treatment of brain metastases in lung cancer: strategies to avoid/reduce late complications of whole brain radiation therapy. *Curr Treat Options Oncol*. 2013;14:553–567.
67. Gondi V, Pugh SL, Tome WA, et al. Preservation of memory with conformal avoidance of the hippocampal neural stem-cell compartment during whole-brain radiotherapy for brain metastases (RTOG 0933): a phase II multi-institutional trial. *J Clin Oncol*. 2014;32(34):3810–3816.
68. Gondi V, Tome WA, Marsh J, et al. Estimated risk of perihippocampal disease progression after hippocampal avoidance during whole-brain radiotherapy: safety profile for RTOG 0933. *Radiother Oncol*. 2010;95:327–331.
69. Prasad G, Haas-Kogan DA. Radiation-induced gliomas. *Expert Rev Neurother*. 2009;9:1511–1517.
70. Ron E, Modan B, Boice Jr JD, et al. Tumors of the brain and nervous system after radiotherapy in childhood. *N Engl J Med*. 1988;319:1033–1039.
71. Amirjamshidi A, Abbassioun K. Radiation-induced tumors of the central nervous system occurring in childhood and adolescence. Four unusual lesions in three patients and a review of the literature. *Childs Nerv Syst*. 2000;16:390–397.
72. al-Mefty O, Kersh JE, Routh A, Smith RR. The long-term side effects of radiation therapy for benign brain tumors in adults. *J Neurosurg*. 1990;73:502–512.
73. Umansky F, Shoshan Y, Rosenthal G, et al. Radiation-induced meningioma. *Neurosurg Focus*. 2008;24:E7.
74. Godlewski B, Drummond KJ, Kaye AH. Radiation-induced meningiomas after high-dose cranial irradiation. *J Clin Neurosci*. 2012;19:1627–1635.
75. Banerjee J, Paakko E, Harila M, et al. Radiation-induced meningiomas: a shadow in the success story of childhood leukemia. *Neuro Oncol*. 2009;11:543–549.
76. Strojan P, Popovic M, Jereb B. Secondary intracranial meningiomas after high-dose cranial irradiation: report of five cases and review of the literature. *Int J Radiat Oncol Biol Phys*. 2000;48:65–73.
77. Zattara-Cannoni H, Roll P, Figarella-Branger D, et al. Cytogenetic study of six cases of radiation-induced meningiomas. *Cancer Genet Cytogenet*. 2001;126:81–84.
78. Lillehei KO, Donson AM, Kleinschmidt-DeMasters BK. Radiation-induced meningiomas: clinical, cytogenetic, and microarray features. *Acta Neuropathol*. 2008;116:289–301.
79. Salvati M, Frati A, Russo N, et al. Radiation-induced gliomas: report of 10 cases and review of the literature. *Surg Neurol*. 2003;60:60–67; discussion 67.
80. Paulino AC, Mai WY, Chintagumpala M, et al. Radiation-induced malignant gliomas: is there a role for reirradiation? *Int J Radiat Oncol Biol Phys*. 2008;71:1381–1387.
81. Murros KE, Toole JF. The effect of radiation on carotid arteries. A review article. *Arch Neurol*. 1989;46:449–455.
82. Santoro A, Bristot R, Paolini S, et al. Radiation injury involving the internal carotid artery. Report of two cases. *J Neurosurg Sci*. 2000;44:159–164.
83. Laplane D, Carydakis C, Baulac M, et al. Intracranial artery stenoses 44 years after craniofacial radiotherapy. *Rev Neurol Paris*. 1986;142:65–67.
84. Kondoh T, Morishita A, Kamei M, et al. Moyamoya syndrome after prophylactic cranial irradiation for acute lymphocytic leukemia. *Pediatr Neurosurg*. 2003;39:264–269.

85. Bitzer M, Topka H. Progressive cerebral occlusive disease after radiation therapy. *Stroke*. 1995;26:131–136.
86. Jain R, Robertson PL, Gandhi D, et al. Radiation-induced cavernomas of the brain. *AJNR Am J Neuroradiol*. 2005;26:1158–1162.
87. Singla A, Brace O'Neill JE, Smith E, Scott RM. Cavernous malformations of the brain after treatment for acute lymphocytic leukemia: presentation and long-term follow-up. *J Neurosurg Pediatr*. 2013;11:127–132.
88. Bagan SM, Hollenhorst RW. Radiation retinopathy after irradiation of intracranial lesions. *Am J Ophthalmol*. 1979;88:694–697.
89. Keezer MR, Del Maestro R. Radiation-induced cavernous hemangiomas: case report and literature review. *Can J Neurol Sci*. 2009;36:303–310.
90. Shanley DJ. Mineralizing microangiopathy: CT and MRI. *Neuroradiology*. 1995;37:331–333.
91. Shobha N, Smith EE, Demchuk AM, Weir NU. Small vessel infarcts and microbleeds associated with radiation exposure. *Can J Neurol Sci*. 2009;36:376–378.
92. Fouladi M, Langston J, Mulhern R, et al. Silent lacunar lesions detected by magnetic resonance imaging of children with brain tumors: a late sequela of therapy. *J Clin Oncol*. 2000;18:824–831.
93. Constine LS, Woolf PD, Cann D, et al. Hypothalamic-pituitary dysfunction after radiation for brain tumors. *N Engl J Med*. 1993;328:87–94.
94. Samaan NA, Schultz PN, Yang KP, et al. Endocrine complications after radiotherapy for tumors of the head and neck. *J Lab Clin Med*. 1987;109:364–372.
95. Toogood AA. Endocrine consequences of brain irradiation. *Growth Horm IGF Res*. 2004;14(suppl A):S118–S124.
96. Rampling R, Symonds P. Radiation myelopathy. *Curr Opin Neurol*. 1998;11:627–632.
97. Lewanski CR, Sinclair JA, Stewart JS. Lhermitte's sign following head and neck radiotherapy. *Clin Oncol R Coll Radiol*. 2000;12:98–103.
98. Li YQ, Guo YP, Jay V, et al. Time course of radiation-induced apoptosis in the adult rat spinal cord. *Radiother Oncol*. 1996;39:35–42.
99. Atkinson SL, Li YQ, Wong CS. Apoptosis and proliferation of oligodendrocyte progenitor cells in the irradiated rodent spinal cord. *Int J Radiat Oncol Biol Phys*. 2005;62:535–544.
100. Kirkpatrick JP, van der Kogel AJ, Schultheiss TE. Radiation dose-volume effects in the spinal cord. *Int J Radiat Oncol Biol Phys*. 2010;76:S42–S49.
101. Okada S, Okeda R. Pathology of radiation myelopathy. *Neuropathology*. 2001;21:247–265.
102. Wang PY, Shen WC, Jan JS. MR imaging in radiation myelopathy. *AJNR Am J Neuroradiol*. 1992;13:1049–1055; discussion 1056–1048.
103. Kadir T, Sarica FB, Ozgur K, et al. Delayed radiation myelopathy: differential diagnosis with positron emission tomography/computed tomography examination. *Asian J Neurosurg*. 2012;7:206–209.
104. Esik O, Emri M, Csornai M, et al. Radiation myelopathy with partial functional recovery: PET evidence of long-term increased metabolic activity of the spinal cord. *J Neurol Sci*. 1999;163:39–43.
105. Lengyel Z, Reko G, Majtenyi K, et al. Autopsy verifies demyelination and lack of vascular damage in partially reversible radiation myelopathy. *Spinal Cord*. 2003;41:577–585.
106. Chamberlain MC, Eaton KD, Fink J. Radiation-induced myelopathy: treatment with bevacizumab. *Arch Neurol*. 2011;68:1608–1609.
107. Feistner H, Weissenborn K, Munte TF, et al. Post-irradiation lesions of the caudal roots. *Acta Neurol Scand*. 1989;80:277–281.
108. Esik O, Vonoczky K, Lengyel Z, et al. Characteristics of radiogenic lower motor neurone disease, a possible link with a preceding viral infection. *Spinal Cord*. 2004;42:99–105.
109. Tallaksen CM, Jetne V, Fossa S. Postradiation lower motor neuron syndrome–a case report and brief literature review. *Acta Oncol*. 1997;36:345–347.
110. De Carolis P, Montagna P, Cipulli M, et al. Isolated lower motoneuron involvement following radiotherapy. *J Neurol Neurosurg Psychiatry*. 1986;49:718–719.
111. Bowen J, Gregory R, Squier M, Donaghy M. The post-irradiation lower motor neuron syndrome neuronopathy or radiculopathy? *Brain*. 1996;119(Pt 5):1429–1439.
112. Yoshino M, Morita A, Shibahara J, Kirino T. Radiation-induced spinal cord cavernous malformation. Case report. *J Neurosurg*. 2005;102(1 Suppl):101–104.
113. Salner AL, Botnick LE, Herzog AG, et al. Reversible brachial plexopathy following primary radiation therapy for breast cancer. *Cancer Treat Rep*. 1981;65:797–802.
114. Gillette EL, Mahler PA, Powers BE, et al. Late radiation injury to muscle and peripheral nerves. *Int J Radiat Oncol Biol Phys*. 1995;31:1309–1318.
115. Cross NE, Glantz MJ. Neurologic complications of radiation therapy. *Neurol Clin*. 2003;21:249–277.
116. Paolini S, Raco A, Di Stefano D, et al. Post-radiation intramedullary malignant peripheral nerve sheath tumor. *J Neurosurg Sci*. 2006;50:49–53.
117. Foley KM, Woodruff JM, Ellis FT, Posner JB. Radiation-induced malignant and atypical peripheral nerve sheath tumors. *Ann Neurol*. 1980;7:311–318.
118. Adamson DC, Cummings TJ, Friedman AH. Malignant peripheral nerve sheath tumor of the spine after radiation therapy for Hodgkin's lymphoma. *Clin Neuropathol*. 2004;23:245–255.
119. Chew NK, Sim BF, Tan CT, et al. Delayed post-irradiation bulbar palsy in nasopharyngeal carcinoma. *Neurology*. 2001;57:529–531.
120. Rong X, Tang Y, Chen M, et al. Radiation-induced cranial neuropathy in patients with nasopharyngeal carcinoma. A follow-up study. *Strahlenther Onkol*. 2012;188:282–286.
121. Shin HY, Park HJ, Choi YC, Kim SM. Clinical and electromyographic features of radiation-induced lower cranial neuropathy. *Clin Neurophysiol*. 2013;124:598–602.
122. van Dam FS, Schagen SB, Muller MJ, et al. Impairment of cognitive function in women receiving adjuvant treatment for high-risk breast cancer: high-dose versus standard-dose chemotherapy. *J Natl Cancer Inst*. 1998;90:210–218.
123. Schagen SB, van Dam FS, Muller MJ, et al. Cognitive deficits after postoperative adjuvant chemotherapy for breast carcinoma. *Cancer*. 1999;85:640–650.
124. Brezden CB, Phillips KA, Abdolell M, et al. Cognitive function in breast cancer patients receiving adjuvant chemotherapy. *J Clin Oncol: Official J Am Soc Clin Oncol*. 2000;18:2695–2701.
125. Hurria A, Rosen C, Hudis C, et al. Cognitive function of older patients receiving adjuvant chemotherapy for breast cancer: a pilot prospective longitudinal study. *J Am Geriatrics Soc*. 2006;54:925–931.
126. Ahles TA, Saykin A. Cognitive effects of standard-dose chemotherapy in patients with cancer. *Cancer Invest*. 2001;19:812–820.
127. Schagen SB, Muller MJ, Boogerd W, et al. Late effects of adjuvant chemotherapy on cognitive function: a follow-up study in breast cancer patients. *Ann Oncol : Official J Eur Soc Med Oncol/ESMO*. 2002;13:1387–1397.
128. Wefel JS, Lenzi R, Theriault RL, et al. The cognitive sequelae of standard-dose adjuvant chemotherapy in women with breast carcinoma: results of a prospective, randomized, longitudinal trial. *Cancer*. 2004;100:2292–2299.
129. Schagen SB, Muller MJ, Boogerd W, et al. Change in cognitive function after chemotherapy: a prospective longitudinal study in breast cancer patients. *J Natl Cancer Inst*. 2006;98:1742–1745.
130. Weis J, Poppelreuter M, Bartsch HH. Cognitive deficits as long-term side-effects of adjuvant therapy in breast cancer patients: 'subjective' complaints and 'objective' neuropsychological test results. *Psycho-Oncology*. 2009;18:775–782.

131. Ahles TA, Root JC, Ryan EL. Cancer- and cancer treatment-associated cognitive change: an update on the state of the science. *J Clin Oncol: Official J Am Soc Clin Oncol*. 2012;30:3675–3686.
132. Boykoff N, Moieni M, Subramanian SK. Confronting chemobrain: an in-depth look at survivors' reports of impact on work, social networks, and health care response. *J Cancer Surviv*. 2009; 3:223–232.
133. Ahles TA, Saykin AJ, Furstenberg CT, et al. Neuropsychologic impact of standard-dose systemic chemotherapy in long-term survivors of breast cancer and lymphoma. *J Clin Oncol*. 2002; 20:485–493.
134. Schagen SB, Hamburger HL, Muller MJ, et al. Neurophysiological evaluation of late effects of adjuvant high-dose chemotherapy on cognitive function. *J Neuro-Oncol*. 2001;51:159–165.
135. Janelsins MC, Kohli S, Mohile SG, et al. An update on cancer- and chemotherapy-related cognitive dysfunction: current status. *Seminars Oncol*. 2011;38:431–438.
136. Ahles TA, Saykin AJ, McDonald BC, et al. Longitudinal assessment of cognitive changes associated with adjuvant treatment for breast cancer: impact of age and cognitive reserve. *J Clin Oncol*. 2010;28:4434–4440.
137. Kesler SR, Kent JS, O'Hara R. Prefrontal cortex and executive function impairments in primary breast cancer. *Arch Neurol*. 2011;68:1447–1453.
138. Dietrich J, Han R, Yang Y, et al. CNS progenitor cells and oligodendrocytes are targets of chemotherapeutic agents in vitro and in vivo. *J Biol*. 2006;5:22.
139. Han R, Yang YM, Dietrich J, et al. Systemic 5-fluorouracil treatment causes a syndrome of delayed myelin destruction in the central nervous system. *J Biol*. 2008;7:12.
140. Hyrien O, Dietrich J, Noble M. Mathematical and experimental approaches to identify and predict the effects of chemotherapy on neuroglial precursors. *Cancer Res*. 2010;70:10051–10059.
141. Konat GW, Kraszpulski M, James I, et al. Cognitive dysfunction induced by chronic administration of common cancer chemotherapeutics in rats. *Metab Brain Dis*. 2008;23:325–333.
142. Ahles TA, Saykin AJ. Candidate mechanisms for chemotherapy-induced cognitive changes. Nature reviews. *Cancer*. 2007;7: 192–201.
143. McDonald BC, Conroy SK, Ahles TA, et al. Gray matter reduction associated with systemic chemotherapy for breast cancer: a prospective MRI study. *Breast Cancer Res Treat*. 2010;123: 819–828.
144. Deprez S, Amant F, Smeets A, et al. Longitudinal assessment of chemotherapy-induced structural changes in cerebral white matter and its correlation with impaired cognitive functioning. *J Clin Oncol*. 2012;30:274–281.
145. Geiser CF, Bishop Y, Jaffe N, et al. Adverse effects of intrathecal methotrexate in children with acute leukemia in remission. *Blood*. 1975;45:189–195.
146. Gagliano RG, Costanzi JJ. Paraplegia following intrathecal methotrexate: report of a case and review of the literature. *Cancer*. 1976;37:1663–1668.
147. Baehring JM, Fulbright RK. Delayed leukoencephalopathy with stroke-like presentation in chemotherapy recipients. *J Neurol Neurosurg Psychiatry*. 2008;79:535–539.
148. Bond J, Hough R, Moppett J, et al. 'Stroke-like syndrome' caused by intrathecal methotrexate in patients treated during the UKALL 2003 trial. *Leukemia*. 2013;27:954–956.
149. Rubnitz JE, Relling MV, Harrison PL, et al. Transient encephalopathy following high-dose methotrexate treatment in childhood acute lymphoblastic leukemia. *Leukemia*. 1998;12:1176–1181.
150. Rubinstein LJ, Herman MM, Long TF, Wilbur JR. Disseminated necrotizing leukoencephalopathy: a complication of treated central nervous system leukemia and lymphoma. *Cancer*. 1975;35: 291–305.
151. Pizzo PA, Poplack DG, Bleyer WA. Neurotoxicities of current leukemia therapy. *Am J Pediatr Hematol Oncol*. 1979;1:127–140.
152. Bhojwani D, Sabin ND, Pei D, et al. Methotrexate-induced neurotoxicity and leukoencephalopathy in childhood acute lymphoblastic leukemia. *J Clin Oncol*. 2014;32:949–959.
153. Riehl JL, Brown WJ. Acute cerebellar syndrome secondary to 5-fluorouracil therapy. *Neurology*. 1964;14:961–967.
154. Gottlieb JA, Luce JK. Cerebellar ataxia with weekly 5-fluorouracil administration. *Lancet*. 1971;1:138–139.
155. Takimoto CH, Lu ZH, Zhang R, et al. Severe neurotoxicity following 5-fluorouracil-based chemotherapy in a patient with dihydropyrimidine dehydrogenase deficiency. *Clin Cancer Res*. 1996;2:477–481.
156. Johnson MR, Hageboutros A, Wang K, et al. Life-threatening toxicity in a dihydropyrimidine dehydrogenase-deficient patient after treatment with topical 5-fluorouracil. *Clin Cancer Res*. 1999; 5:2006–2011.
157. Nott L, Price TJ, Pittman K, et al. Hyperammonemia encephalopathy: an important cause of neurological deterioration following chemotherapy. *Leuk Lymphoma*. 2007;48:1702–1711.
158. Liaw CC, Wang HM, Wang CH, et al. Risk of transient hyperammonemic encephalopathy in cancer patients who received continuous infusion of 5-fluorouracil with the complication of dehydration and infection. *Anticancer Drugs*. 1999;10:275–281.
159. Delval L, Klastersky J. Optic neuropathy in cancer patients. Report of a case possibly related to 5 fluorouracil toxicity and review of the literature. *J Neuro-Oncol*. 2002;60:165–169.
160. Brashear A, Siemers E. Focal dystonia after chemotherapy: a case series. *J Neuro-Oncol*. 1997;34:163–167.
161. El Amrani M, Heinzlef O, Debroucker T, et al. Brain infarction following 5-fluorouracil and cisplatin therapy. *Neurology*. 1998;51:899–901.
162. Werbrouck BF, Pauwels WJ, De Bleecker JL. A case of 5-fluorouracil-induced peripheral neuropathy. *Clin Toxicol (Phila)*. 2008;46: 264–266.
163. Han R, Yang YM, Dietrich J, et al. Systemic 5-fluorouracil treatment causes a syndrome of delayed myelin destruction in the central nervous system. *J Biol*. 2008;7:12.
164. Luppi G, Zoboli A, Barbieri F, et al. Multifocal leukoencephalopathy associated with 5-fluorouracil and levamisole adjuvant therapy for colon cancer. A report of two cases and review of the literature. The INTACC. Intergruppo Nazionale Terpia Adiuvante Colon Carcinoma. *Ann Oncol*. 1996;7:412–415.
165. Dasgupta S, Adilieje C, Bhattacharya A, et al. Capecitabine and sixth cranial nerve palsy. *J Cancer Res Ther*. 2010;6:80–81.
166. Saif MW, Wood TE, McGee PJ, Diasio RB. Peripheral neuropathy associated with capecitabine. *Anticancer Drugs*. 2004;15: 767–771.
167. Niemann B, Rochlitz C, Herrmann R, Pless M. Toxic encephalopathy induced by capecitabine. *Oncology*. 2004;66:331–335.
168. Hwang TL, Yung WK, Estey EH, Fields WS. Central nervous system toxicity with high-dose Ara-C. *Neurology*. 1985;35:1475–1479.
169. Winkelman MD, Hines JD. Cerebellar degeneration caused by high-dose cytosine arabinoside: a clinicopathological study. *Ann Neurol*. 1983;14:520–527.
170. Smith GA, Damon LE, Rugo HS, et al. High-dose cytarabine dose modification reduces the incidence of neurotoxicity in patients with renal insufficiency. *J Clin Oncol*. 1997;15:833–839.
171. Friedman JH, Shetty N. Permanent cerebellar toxicity of cytosine arabinoside (Ara C) in a young woman. *Mov Disord*. 2001;16:575–577.
172. Hoffman DL, Howard Jr JR, Sarma R, Riggs JE. Encephalopathy, myelopathy, optic neuropathy, and anosmia associated with intravenous cytosine arabinoside. *Clin Neuropharmacol*. 1993;16:258–262.
173. Luque FA, Selhorst JB, Petruska P. Parkinsonism induced by high-dose cytosine arabinoside. *Mov Disord*. 1987;2:219–222.

174. Dunton SF, Nitschke R, Spruce WE, et al. Progressive ascending paralysis following administration of intrathecal and intravenous cytosine arabinoside. A Pediatric Oncology Group study. *Cancer*. 1986;57:1083–1088.
175. Meanwell CA, Blake AE, Kelly KA, et al. Prediction of ifosfamide/mesna associated encephalopathy. *Eur J Cancer Clin Oncol*. 1986;22:815–819.
176. David KA, Picus J. Evaluating risk factors for the development of ifosfamide encephalopathy. *Am J Clin Oncol*. 2005;28:277–280.
177. Rieger C, Fiegl M, Tischer J, et al. Incidence and severity of ifosfamide-induced encephalopathy. *Anticancer Drugs*. 2004;15: 347–350.
178. Lorigan P, Verweij J, Papai Z, et al. Phase III trial of two investigational schedules of ifosfamide compared with standard-dose doxorubicin in advanced or metastatic soft tissue sarcoma: a European Organisation for Research and Treatment of Cancer Soft Tissue and Bone Sarcoma Group Study. *J Clin Oncol*. 2007;25:3144–3150.
179. Savica R, Rabinstein AA, Josephs KA. Ifosfamide associated myoclonus-encephalopathy syndrome. *J Neurol*. 2011;258:1729–1731.
180. Meanwell CA, Kelly KA, Blackledge G. Avoiding ifosfamide/mesna encephalopathy. *Lancet*. 1986;2:406.
181. Pratt CB, Goren MP, Meyer WH, et al. Ifosfamide neurotoxicity is related to previous cisplatin treatment for pediatric solid tumors. *J Clin Oncol*. 1990;8:1399–1401.
182. Watkin SW, Husband DJ, Green JA, Warenius HM. Ifosfamide encephalopathy: a reappraisal. *Eur J Cancer Clin Oncol*. 1989;25:1303–1310.
183. Durand JP, Gourmel B, Mir O, Goldwasser F. Antiemetic neurokinin-1 antagonist aprepitant and ifosfamide-induced encephalopathy. *Ann Oncol*. 2007;18:808–809.
184. Howell JE, Szabatura AH, Hatfield Seung A, Nesbit SA. Characterization of the occurrence of ifosfamide-induced neurotoxicity with concomitant aprepitant. *J Oncol Pharm Pract*. 2008;14:157–162.
185. Hansen H, Yuen C. Aprepitant-associated ifosfamide neurotoxicity. *J Oncol Pharm Pract*. 2010;16:137–138.
186. Jarkowski 3rd A. Possible contribution of aprepitant to ifosfamide-induced neurotoxicity. *Am J Health Syst Pharm*. 2008;65:2229–2231.
187. Ajithkumar T, Parkinson C, Shamshad F, Murray P. Ifosfamide encephalopathy. *Clin Oncol R Coll Radiol*. 2007;19:108–114.
188. Kupfer A, Aeschlimann C, Wermuth B, Cerny T. Prophylaxis and reversal of ifosfamide encephalopathy with methylene-blue. *Lancet*. 1994;343:763–764.
189. Pelgrims J, De Vos F, Van den Brande J, et al. Methylene blue in the treatment and prevention of ifosfamide-induced encephalopathy: report of 12 cases and a review of the literature. *Br J Cancer*. 2000;82:291–294.
190. Buesa JM, Garcia-Teijido P, Losa R, Fra J. Treatment of ifosfamide encephalopathy with intravenous thiamin. *Clin Cancer Res*. 2003; 9:4636–4637.
191. Bernard PA, McCabe T, Bayliff S, Hayes Jr D. Successful treatment of ifosfamide neurotoxicity with dexmedetomidine. *J Oncol Pharm Pract*. 2010;16:262–265.
192. Imtiaz S, Muzaffar N. Ifosfamide neurotoxicty in a young female with a remarkable response to thiamine. *J Pak Med Assoc*. 2010;60:867–869.
193. Hamadani M, Awan F. Role of thiamine in managing ifosfamide-induced encephalopathy. *J Oncol Pharm Pract*. 2006;12:237–239.
194. Patel SR, Forman AD, Benjamin RS. High-dose ifosfamide-induced exacerbation of peripheral neuropathy. *J Natl Cancer Inst*. 1994;86:305–306.
195. Pallotta MG, Velazco A, Sadler A. Ifosfamide extrapyramidal neurotoxicity. *Cancer*. 1992;70:2743–2745.
196. Ames B, Lewis LD, Chaffee S, et al. Ifosfamide-induced encephalopathy and movement disorder. *Pediatr Blood Cancer*. 2010;54:624–626.
197. Ciurea SO, Andersson BS. Busulfan in hematopoietic stem cell transplantation. *Biol Blood Marrow Transpl*. 2009;15:523–536.
198. Soni S, Skeens M, Termuhlen AM, et al. Levetiracetam for busulfan-induced seizure prophylaxis in children undergoing hematopoietic stem cell transplantation. *Pediatr Blood Cancer*. 2012;59:762–764.
199. Diaz-Carrasco MS, Olmos R, Blanquer M, et al. Clonazepam for seizure prophylaxis in adult patients treated with high dose busulfan. *Int J Clin Pharm*. 2013;35:339–343.
200. Winkelman MD, Hines JD. Cerebellar degeneration caused by high-dose cytosine arabinoside: a clinicopathological study. *Ann Neurol*. 1983;14:520–527.
201. Roelofs RI, Hrushesky W, Rogin J, Rosenberg L. Peripheral sensory neuropathy and cisplatin chemotherapy. *Neurology*. 1984;34:934–938.
202. Argyriou AA, Bruna J, Marmiroli P, Cavaletti G. Chemotherapy-induced peripheral neurotoxicity (CIPN): an update. *Crit Rev Oncol Hematol*. 2012;82:51–77.
203. von Schlippe M, Fowler CJ, Harland SJ. Cisplatin neurotoxicity in the treatment of metastatic germ cell tumour: time course and prognosis. *Br J Cancer*. 2001;85:823–826.
204. Khrunin AV, Moisseev A, Gorbunova V, Limborska S. Genetic polymorphisms and the efficacy and toxicity of cisplatin-based chemotherapy in ovarian cancer patients. *Pharmacogenomics J*. 2010;10:54–61.
205. Oldenburg J, Kraggerud SM, Brydoy M, et al. Association between long-term neuro-toxicities in testicular cancer survivors and polymorphisms in glutathione-s-transferase-P1 and -M1, a retrospective cross sectional study. *J Transl Med*. 2007;5:70.
206. Hershman DL, Lacchetti C, Dworkin RH, et al. Prevention and management of chemotherapy-induced peripheral neuropathy in survivors of adult cancers: American Society of Clinical Oncology clinical practice guideline. *J Clin Oncol*. 2014;32:1941–1967.
207. Zhang H, Mizumachi T, Carcel-Trullols J, et al. Targeting human 8-oxoguanine DNA glycosylase (hOGG1) to mitochondria enhances cisplatin cytotoxicity in hepatoma cells. *Carcinogenesis*. 2007;28:1629–1637.
208. Scuteri A, Galimberti A, Maggioni D, et al. Role of MAPKs in platinum-induced neuronal apoptosis. *Neurotoxicology*. 2009; 30:312–319.
209. Gill JS, Windebank AJ. Cisplatin-induced apoptosis in rat dorsal root ganglion neurons is associated with attempted entry into the cell cycle. *J Clin Invest*. 1998;101:2842–2850.
210. Rademaker-Lakhai JM, Crul M, Zuur L, et al. Relationship between cisplatin administration and the development of ototoxicity. *J Clin Oncol*. 2006;24:918–924.
211. Brock PR, Knight KR, Freyer DR, et al. Platinum-induced ototoxicity in children: a consensus review on mechanisms, predisposition, and protection, including a new International Society of Pediatric Oncology Boston ototoxicity scale. *J Clin Oncol*. 2012;30:2408–2417.
212. Moroso MJ, Blair RL. A review of cis-platinum ototoxicity. *J Otolaryngol*. 1983;12:365–369.
213. Schell MJ, McHaney VA, Green AA, et al. Hearing loss in children and young adults receiving cisplatin with or without prior cranial irradiation. *J Clin Oncol*. 1989;7:754–760.
214. Marshak T, Steiner M, Kaminer M, et al. Prevention of cisplatin-induced hearing loss by intratympanic dexamethasone: a randomized controlled study. *Otolaryngol Head Neck Surg*. 2014;150:983–990.
215. Gurney JG, Bass JK, Onar-Thomas A, et al. Evaluation of amifostine for protection against cisplatin-induced serious hearing loss in children treated for average-risk or high-risk medulloblastoma. *Neuro Oncol*. 2014;16:848–855.
216. Fouladi M, Chintagumpala M, Ashley D, et al. Amifostine protects against cisplatin-induced ototoxicity in children with average-risk medulloblastoma. *J Clin Oncol*. 2008;26:3749–3755.

217. Freyer D. The effects of sodium thiosulfate (STS) on cisplatin-induced hearing loss: a report from the Children's Oncology Group (abstract). *J Clin Oncol*. 2014;32.
218. Argyriou AA, Cavaletti G, Briani C, et al. Clinical pattern and associations of oxaliplatin acute neurotoxicity: a prospective study in 170 patients with colorectal cancer. *Cancer*. 2013;119:438–444.
219. Pachman DR, Qin R, Seisler DK, et al. Clinical course of patients with oxaliplatin-associated neuropathy. *J Clin Oncol*. 2014;32.
220. Velasco R, Bruna J, Briani C, et al. Early predictors of oxaliplatin-induced cumulative neuropathy in colorectal cancer patients. *J Neurol Neurosurg Psychiatry*. 2014;85:392–398.
221. Heinzlef O, Lotz JP, Roullet E. Severe neuropathy after high dose carboplatin in three patients receiving multidrug chemotherapy. *J Neurol Neurosurg Psychiatry*. 1998;64:667–669.
222. Freilich RJ, Balmaceda C, Seidman AD, et al. Motor neuropathy due to docetaxel and paclitaxel. *Neurology*. 1996;47:115–118.
223. Lee JJ, Swain SM. Peripheral neuropathy induced by microtubule-stabilizing agents. *J Clin Oncol*. 2006;24:1633–1642.
224. Grisold W, Cavaletti G, Windebank AJ. Peripheral neuropathies from chemotherapeutics and targeted agents: diagnosis, treatment, and prevention. *Neuro Oncol*. 2012;14(suppl 4):iv45–iv54.
225. Casey EB, Jellife AM, Le Quesne PM, Millett YL. Vincristine neuropathy. Clinical and electrophysiological observations. *Brain*. 1973;96:69–86.
226. Naumann R, Mohm J, Reuner U, et al. Early recognition of hereditary motor and sensory neuropathy type 1 can avoid life-threatening vincristine neurotoxicity. *Br J Haematol*. 2001;115:323–325.
227. Hogan-Dann CM, Fellmeth WG, McGuire SA, Kiley VA. Polyneuropathy following vincristine therapy in two patients with Charcot-Marie-Tooth syndrome. *JAMA*. 1984;252:2862–2863.
228. Teusink AC, Ragucci D, Shatat IF, Kalpatthi R. Potentiation of vincristine toxicity with concomitant fluconazole prophylaxis in children with acute lymphoblastic leukemia. *Pediatr Hematol Oncol*. 2012;29:62–67.
229. Harnicar S, Adel N, Jurcic J. Modification of vincristine dosing during concomitant azole therapy in adult acute lymphoblastic leukemia patients. *J Oncol Pharm Pract*. 2009;15:175–182.
230. Weintraub M, Adde MA, Venzon DJ, et al. Severe atypical neuropathy associated with administration of hematopoietic colony-stimulating factors and vincristine. *J Clin Oncol*. 1996;14:935–940.
231. Legha SS. Vincristine neurotoxicity. Pathophysiology and management. *Med Toxicol*. 1986;1:421–427.
232. Pal PK. Clinical and electrophysiological studies in vincristine induced neuropathy. *Electromyogr Clin Neurophysiol*. 1999;39:323–330.
233. Robertson GL, Bhoopalam N, Zelkowitz LJ. Vincristine neurotoxicity and abnormal secretion of antidiuretic hormone. *Arch Intern Med*. 1973;132:717–720.
234. Gaidys WG, Dickerman JD, Walters CL, Young PC. Intrathecal vincristine. Report of a fatal case despite CNS washout. *Cancer*. 1983;52:799–801.
235. Leonard JV, Kay JD. Acute encephalopathy and hyperammonaemia complicating treatment of acute lymphoblastic leukaemia with asparaginase. *Lancet*. 1986;1:162–163.
236. Feinberg WM, Swenson MR. Cerebrovascular complications of L-asparaginase therapy. *Neurology*. 1988;38:127–133.
237. Kieslich M, Porto L, Lanfermann H, et al. Cerebrovascular complications of L-asparaginase in the therapy of acute lymphoblastic leukemia. *J Pediatr Hematol Oncol*. 2003;25:484–487.
238. Plotkin SR, Wen PY. Neurologic complications of cancer therapy. *Neurol Clin*. 2003;21:279–318.
239. Schutz FA, Je Y, Azzi GR, et al. Bevacizumab increases the risk of arterial ischemia: a large study in cancer patients with a focus on different subgroup outcomes. *Ann Oncol*. 2011;22:1404–1412.
240. Yang JC, Haworth L, Sherry RM, et al. A randomized trial of bevacizumab, an anti-vascular endothelial growth factor antibody, for metastatic renal cancer. *N Engl J Med*. 2003;349:427–434.
241. Gordon MS, Margolin K, Talpaz M, et al. Phase I safety and pharmacokinetic study of recombinant human anti-vascular endothelial growth factor in patients with advanced cancer. *J Clin Oncol*. 2001;19:843–850.
242. Johnson DH, Fehrenbacher L, Novotny WF, et al. Randomized phase II trial comparing bevacizumab plus carboplatin and paclitaxel with carboplatin and paclitaxel alone in previously untreated locally advanced or metastatic non-small-cell lung cancer. *J Clin Oncol*. 2004;22:2184–2191.
243. Hodi FS, O'Day SJ, McDermott DF, et al. Improved survival with ipilimumab in patients with metastatic melanoma. *N Engl J Med*. 2010;363:711–723.
244. Wilgenhof S, Neyns B. Anti-CTLA-4 antibody-induced Guillain-Barre syndrome in a melanoma patient. *Ann Oncol*. 2011;22:991–993.
245. Liao B, Shroff S, Kamiya-Matsuoka C, Tummala S. Atypical neurological complications of ipilimumab therapy in patients with metastatic melanoma. *Neuro Oncol*. 2014;16:589–593.
246. Maur M, Tomasello C, Frassoldati A, et al. Posterior reversible encephalopathy syndrome during ipilimumab therapy for malignant melanoma. *J Clin Oncol*. 2012;30:e76–78.
247. Chodakiewitz Y, Brown S, Boxerman JL, et al. Ipilimumab treatment associated pituitary hypophysitis: clinical presentation and imaging diagnosis. *Clin Neurol Neurosurg*. 2014;125C:125–130.
248. Juszczak A, Gupta A, Karavitaki N, et al. Ipilimumab: a novel immunomodulating therapy causing autoimmune hypophysitis: a case report and review. *Eur J Endocrinol*. 2012;167:1–5.
249. Piccinni C, Sacripanti C, Poluzzi E, et al. Stronger association of drug-induced progressive multifocal leukoencephalopathy (PML) with biological immunomodulating agents. *Eur J Clin Pharmacol*. 2010;66:199–206.
250. Carson KR, Evens AM, Richey EA, et al. Progressive multifocal leukoencephalopathy after rituximab therapy in HIV-negative patients: a report of 57 cases from the Research on Adverse Drug Events and Reports project. *Blood*. 2009;113:4834–4840.
251. Cobleigh MA, Vogel CL, Tripathy D, et al. Multinational study of the efficacy and safety of humanized anti-HER2 monoclonal antibody in women who have HER2-overexpressing metastatic breast cancer that has progressed after chemotherapy for metastatic disease. *J Clin Oncol*. 1999;17:2639–2648.
252. Pfeiffer P, Nielsen D, Yilmaz M, et al. Cetuximab and irinotecan as third line therapy in patients with advanced colorectal cancer after failure of irinotecan, oxaliplatin and 5-fluorouracil. *Acta Oncol*. 2007;46:697–701.

CHAPTER

16

Physics of Computed Tomography Scanning

Johannes T. Heverhagen

Department of Diagnostic, Interventional, and Pediatric Radiology, College of Medicine, Bern University, Bern, Switzerland; Department of Radiology, College of Medicine, The Ohio State University, Columbus, OH, USA

Conventional radiography projects a three-dimensional object onto a two dimensional image. The major limitation is that different overlaying tissues are superimposed on the image.

Computed tomography (CT) avoids this problem by scanning thin slices with a rotating narrow X-ray beam. The basic data simply consist of measurements of the X-ray attenuation coefficients along the beam path. From this information, a reconstruction algorithm must produce a cross-section image of tissue attenuation characteristics. In general, tissues have different attenuation properties, depending on their physical density and anatomic dimensions.

HISTORICAL DEVELOPMENT

Translate/Rotate Geometry: The first head CT scanner was introduced in 1972 by Sir Godfrey Hounsfield and was called the EMI Mark 1. The principle mathematical basis behind this technology had already been published in 1917 by J. Radon. The first CT scanner produced images with an 80-by-80 matrix of 3 mm pixel resolution and required approximately 5 min of scan time per pair of slices.[1] In this type of system a pencil beam with only two X-ray detectors is used. The X-ray tube and the detector translates linearly across the patient at a particular angle. The system then rotates at an angle of one degree and translates back across the patient. During a total examination time of 5 min the row data of one image pair is acquired with a total gantry rotation of 180°. This system was the sole CT scanner that used parallel beam geometry.[2] The pencil beam geometry provided very efficient scatter reduction, but was an inefficient utilization of X-ray source. In the second generation of CT scanners, the pencil beam expanded to a small, fan-shaped beam and the detector increased to a linear array of 30 detectors. The translate/rotate configuration was still used but this new development reduced the acquisition time of 18 s per slice and made more efficient use of the X-ray beam.

Rotate/Rotate Geometry: The third generation scanners opened up the X-ray fan beam to include the entire patient in the fan. This geometry involves an expanded detector array with more than 800 detector elements. This type of scanner eliminated the time-consuming translation movement and allows a fast image acquisition, approximately 2 s per slice. The geometry of third generation scanners is especially sensitive to detector miscalibration because the detectors are permanently irradiated. Because they are constantly moving and vibrating, their calibration could drift significantly.

Rotate/Stationary Geometry: In the next type of CT generation, only the X-ray source rotated around the patient and the X-rays were detected using a stationary 360° ring of detectors. This allowed for very fast image acquisition, as short as half a second. These fourth generation CT scanners required many detectors. Modern scanners use about 4800 detector elements for the whole ring. The fixed detectors avoided calibration problems, found in the third generation, because the beam always irradiated a newly calibrated detector.

Stationary/Stationary Geometry: In the next step, a so-called cine-CT scanner or electron beam scanner dedicated for cardiac tomography was developed. It seemed like a huge X-ray tube, which the patient entered. A large anode arc of tungsten encircled the patient semicircularly. A moving electron beam swept across the anode and generated the X-rays. By using multiple target layers in anode material, it was possible to produce up to eight fan beams simultaneously. Consequently, electron beam CT scanners were able to acquire eight slices within a very short time of 50 ms. The production of such a CT scanner was double the cost of a conventional CT scanner. Today, only 120 of these scanners exist worldwide.

http://dx.doi.org/10.1016/B978-0-12-800945-1.00016-1

© 2016 Elsevier Ltd. All rights reserved.

Helical CT: In the early 1990s, the newly developed slip-ring technology for X-ray tube and detector connections replaced the old CT scanner equipment, which worked with spooled cable technology. Now, the gantry was able to rotate continuously around the patient during the entire examination. Implementation of the helical CT, or commonly called spiral CT, revolutionized CT development as well as clinical practice.[3] During scanning, data acquisition is combined with continuous movement of the patient through the gantry. The path of the X-ray beam around the patient can be described as a spiral. Whereas, conventional CT required a step-and-shoot acquisition procedure, helical CT uses much faster and nonstop technology to acquire multiple transverse slices.[4] These advances have revolutionized CT scanning in clinical routine. Entire organs such as liver or lung can be scanned in a single breath-hold.[5] This approach enables to image continuous sections without gaps as a result of changes in respiration levels between acquisitions of individual slices. Such gaps could lead to masking of lesions hidden in those gaps. Due to the better resolution, it is also possible to detect smaller lesions. Furthermore, application of intravenous contrast agents can be better tailored to the acquisition protocol and thinner slices can be obtained. New applications and expansion of existing techniques have improved clinical diagnosis. The data obtained from spiral CT are truly three dimensional and allow multiplanar image reconstruction as a consequence of the lack of motion misregistration and the increased through-plane resolution.[6] The ability to acquire volume data also paved the way for the development of three-dimensional image processing techniques.

The helical trajectory of the spiral data acquisition does not allow for the direct reconstruction of a cross-section of the patient. Before reconstruction, the raw data from helical data set must be interpolated to the reconstruction plane of interest.[7,8] Helical scan protocols have introduced a new parameter, called pitch. The pitch is determined by table speed (in mm/sec) divided by beam collimation (in mm) multiplied by the gantry rotation period.

$$Pitch = \frac{table\ movement\ per\ 360\text{-}degree\ gantry\ rotation}{collimator\ width}$$

In other words, the pitch factor is a ratio without units which provides information about table movement relative to beam collimation. A pitch of less than one means that the data is oversampled which may result in better image quality but higher radiation dose for the patient. Therefore, pitch factors greater than 1 and up to 1.5 are commonly used in clinical routine. However, the key limitation is that slice thickness is still determined by the collimation of the X-ray beam. Opening up the collimator increases the slice thickness which improves X-ray beam utilization but reduces the through plane resolution.

Multiple Detector Array CT: Multislice CT represents another major shift in CT technology. By using multiple detector arrays, the collimator spacing of the X-ray beam is wider and therefore more X-rays are used in producing image data. With the introduction of this approach, the slice thickness is determined by the detector size and not by the collimator.[9] This allows the acquisition of several images simultaneously.[10] Modern scanners are available with up to 382 detector rows. The main benefit is an improved scan speed and the availability of isotropic images. In multislice CT, the beam is split into several slices and therefore the definition of the pitch factor is different than in single detector spiral CT scanners.[11] For example, a four-detector array multislice scanner is acquiring 2.5 mm-thick slices at a tabletop speed of 15 mm per 1-s gantry rotation. This results in a pitch of 6 (15 mm/2.5 mm). That corresponds to a single collimator pitch of 1.5.

$$Pitch = \frac{table\ movement\ per\ 360\text{-}degree\ gantry\ rotation}{collimator\ width \times number\ of\ detectors}$$

Dual Source CT: The dual source CT scanner is the newest step of development in CT technology. This type of system uses two X-ray sources with two corresponding detector arrays which are mounted onto a rotating gantry with an offset of 90°. The X-ray tubes can operate with two different energies simultaneously.[12] Alternatively, it is possible to acquire image data in half the time unlike conventional technology. For example, a dual-source multi detector row scanner can acquire an entire cardiac study within a heart beat.

IMAGE RECONSTRUCTION

Each registered beam is just a projection of attenuation characteristics of the irradiated tissue. The aim of the reconstruction algorithm is to estimate how the tissue absorptions are distributed along the X-ray path. This goal is not achievable using a single projection profile. Instead it needs a large number of projections for many different angles. The acquired projection profile can be displayed as a sinogram (Figure 1). Sinograms are not used for clinical routine, but they are relevant for understanding tomographic principles. The horizontal axis of the sinogram represents the different projection profiles. The vertical axis in the sinograms corresponds to each angle of projections. Objects closer to the center of the field of view produce small sinusoid amplitudes in the sinogram, and objects closer to the edge produce heightened sinusoidal amplitudes.

Reconstructing an image from the projection profiles is a classical inverse problem. Early attempts at CT reconstruction used an iterative approach called algebraic reconstruction algorithm.[13] This algorithm starts with an assumed image, computes projections from the image, compares the original projection data, and updates the

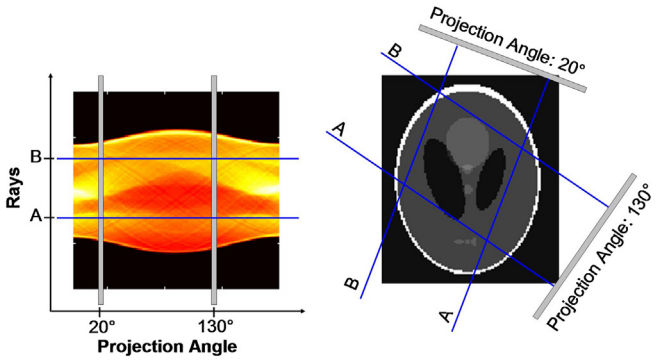


FIGURE 1 The sinogram contains the raw data of a CT acquisition. The horizontal axis corresponds to each angle of acquired projection profiles. The vertical axis corresponds to the rays in each projection. Here, there are two rays (A and B) and two different projection profiles (20° and 130°) illustrated.

image based on errors between projections that would be obtained from the current pixels, values, and actual projection. This method was very time-consuming and computationally intensive. A faster CT reconstruction approach has been developed called filtered back-projection.[14] It became widely accepted because reconstruction of the images is completed as soon as the CT examination is finished.

Figure 2 shows a simplified 3-by-3 matrix array containing nine pixels, with each pixel having specific values of absorption coefficients. In such a way a high attenuation pixel is in the center, and lighter attenuation pixels are in the periphery. Three projection profiles pass through the array vertically, horizontally, and diagonally. By using the direct back-projection procedure alone, the record measurement reading for each detector element is distributed evenly along the path of the X-ray. Subsequently, each pixel is set to the average of all angularity of beams that traverse that pixel. Now the measurement reading is back-projected and averaged into each pixel. The reconstructed image resembles the original, but is modified by a blurring map.

By virtue of the extensive blurring, the direct back-projection yielded no suitable outcomes. In practice, before back-transformation is carried out, each projection profile is filtered. The mathematical filtering step involves convolving the projection data with a convolution kernel. The filtered back-projection is easiest to implement in the frequency domain using a special Fourier transformation called the Fourier slice theorem. The Fourier slice theorem states that the one-dimensional Fourier transform of the projection profile is equal to the two-dimensional Fourier transform of the image evaluated on the radial line that the projection was taken on.[15] Once the two-dimensional Fourier transform space is filled from the individual one-dimensional Fourier transforms of the projection profiles, the image can be generated by applying an inverse two-dimensional Fourier transform to this space. Before the inverse transform is done, the user can apply different convolution kernels as filter procedures to create an appropriate character

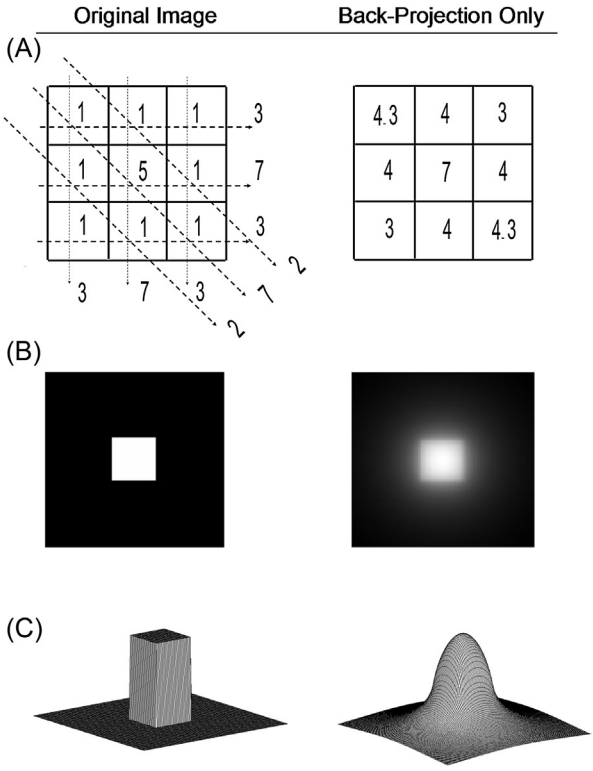


FIGURE 2 Image reconstruction using a simple back-projection. Back-projection alone produces a blurred image. (A) The left 3-by-3 pixel array represents the original grid with a pixel of high attenuation in the center and pixels of weaker attenuation in the periphery. The right array shows the reconstructed grid by a simple back-projection. (B) Represents the corresponding images and (C) illustrates the same smearing effect by a relief figure.

of the diagnostic image. The most common kernels are derived by a Ram-Lak filter multiplied with a low-pass filter.[16] In filter procedures, the shape of the kernel would be impressed to each projection profile and avoiding the blurring effects in reconstructed images (Figure 3).

Today, faster computer processors are allowing for the use of iterative reconstruction algorithms again.[17] These algorithms begin to replace filtered back-projection algorithms because they permit reduced image noise with low milliampere/peak kilovolt settings. As described above, such algorithms use approximations of voxel attenuation to calculate projection data; these approximations of voxel attenuation are iteratively adjusted to decrease the difference between the measured data and the estimated data. The signal-to-noise ratios obtained by iterative reconstruction techniques are better compared with filtered back-projection while simultaneously conserving spatial resolution.[18] Studies have demonstrated dose reductions of 32–65% compared with filtered back-projection techniques without a noticeable decrease in signal-to-noise ratio.[19,20] Clinical studies confirm these findings in vivo determining that iterative reconstruction techniques can provide a similar diagnostic image quality with reduced radiation exposure.[21,22]

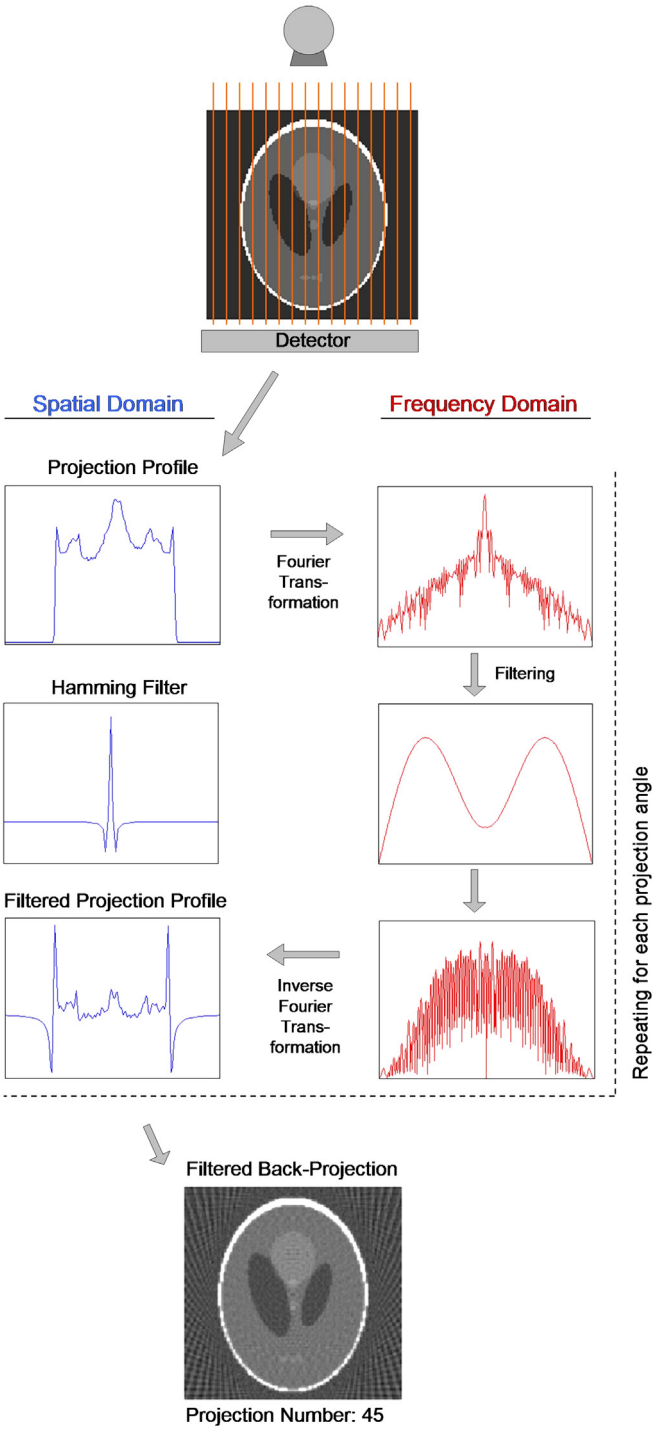


FIGURE 3 Schematic illustration of the steps in filtered back-projection. Each single acquired projection profile will be converted to the frequency domain using Fourier transformation. In the frequency domain, the mathematical filter operation (convolution) is easy to apply using multiplication with a frequency domain filter kernel. The resulting product will be reconverted to the spatial domain by applying the inverse Fourier transform and is ready to be back-projected. These steps would be repeated for each angle. The illustration shows a reconstruction result of an original object using 45 projections.

After CT reconstruction but before storing and displaying, CT images are normalized and truncated to integer values. These values are called Hounsfield units (HU), or CT numbers, and represent quantitative data with specific values for each tissue quality.[17] In general, they are related to the attenuation coefficient of water, because most tissues have linear attenuation coefficients very similar to that of water over a large photon–energy interval. This is the reason for introducing the dimensionless unit, Hounsfield:

$$HU = \frac{\mu_{tissue} - \mu_{water}}{\mu_{water}} \cdot 1000$$

Where μ is the linear attenuation coefficient of the material in the irradiated pixel and μ_{water} represents the attenuation coefficient of water. Each HU is equivalent to 0.1% of the attenuation of water.[18] These normalized results typically range from −1000 to +3000 HU, where −1000 HU corresponds to air, soft tissue range from −100 to +100 HU, water is 0 HU, and dense bone and areas filled with contrast agent range up to +3000 HU. HUs are quantitative and provide important information leading to a more accurate diagnosis in many clinical settings. For example, the identification of calcified or noncalcified pulmonary nodules can be determined from CT images based on mean HU of the nodule. CT scanners can measure bone density with good accuracy. Furthermore, the quantitative image pixels are used for radiotherapy dose planning. The accuracy of dose calibrations based on such CT data is partly determined by the precision of the calibration of CT HUs to relative electron density.

CT images typically possess 12 bits of gray scale, for a total of 4096 shades of gray. This corresponds to the range of −1000 to 3095 HU. However, human eyes cannot resolve that many shades of gray in medical images. If the full value range (−1000 to +3095) was displayed, the particular tissues of interest would be limited to a relatively small range of HUs. Consequently, the visualization and medical diagnoses would be limited. The most common way to adjust the intensity values of the anatomic tissues of interest to the dynamic range of human eyes is applying a look-up table. A look-up table lists the relationship between stored HUs and their corresponding gray scale values of the output image. Contrast can be enhanced by assigning a narrow interval of HUs to the entire gray scale on the display monitor. This post-processing procedure is called windowing and leveling. The window width determines the contrast of the image. A narrower window results in greater contrasts (Figure 4). The level is the HU at the center of the window and selects the structures in the image displayed on the gray scale, that is, from black to white. For example, a head CT image viewed at a center of +50 and a window

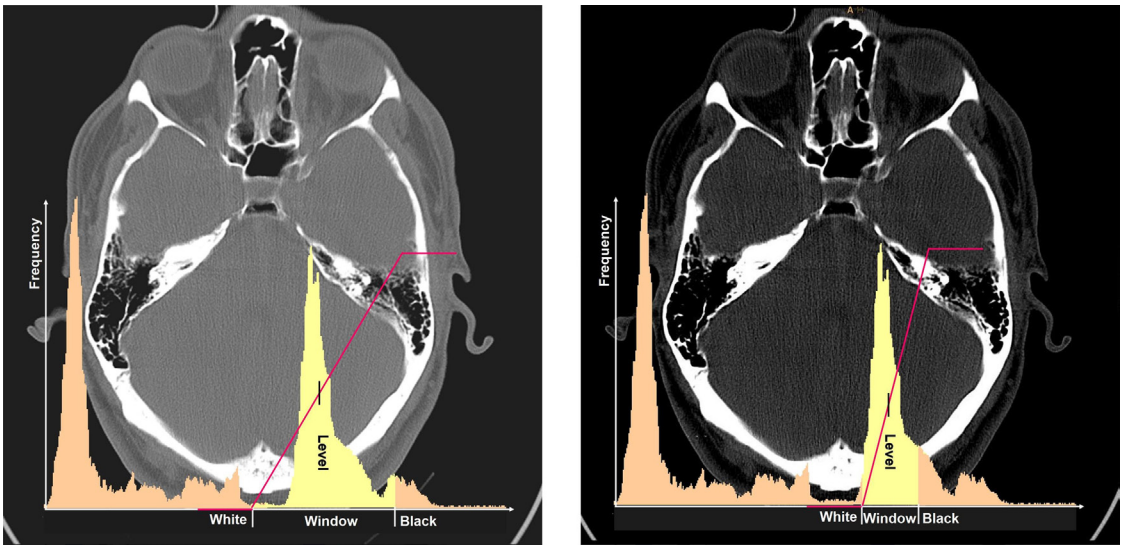


FIGURE 4 The images show the effect of changes in window width. The level is the Hounsfield unit (HU), which corresponds to the center of the window. Only the HUs inside the window are displayed in the image. Structures outside the window width are displayed either completely black or white. The left image shows a window of 1400 HU by a level of 250 HU. The right image shows the same level but with a narrower window of 700 HU. This narrow window generates a very high contrast image.

of 200 HU is optimized for gray and white matter contrast. The center of +50 HU corresponds to the approximate HU of gray and white matter, and it is these tissues that will be displayed with the mid-gray illumination. A window of 200 HU implies a range from −50 to +150 HU. Consequently, all tissues having 150 HU or above will be displayed as white, while all tissues of at −50 HU and below will be displayed as black. It is routine to display CT images using several different window and level settings for each image in order to enhance the depiction of various tissues, such as lung, soft tissues, and bones.

References

1. Beckmann EC. CT scanning the early days. *Br J Radiol*. 2006;79:5–8.
2. Robb RA. X-ray computed tomography: from basic principles to applications. *Annu Rev Biophys Bioeng*. 1982;11:177–201.
3. Kalender WA, Polacin A. Physical performance characteristics of spiral CT scanning. *Med Phys*. 1991;18:910–915.
4. Kalender WA. Thin-section three-dimensional spiral CT: is isotropic imaging possible? *Radiology*. 1995;197:578–580.
5. Kalender WA, Seissler W, Klotz E, Vock P. Spiral volumetric CT with single-breath-hold technique, continuous transport, and continuous scanner rotation. *Radiology*. 1990;176:181–183.
6. Hu H. Multi-slice helical CT: scan and reconstruction. *Med Phys*. 1999;26:5–18.
7. Flohr TG, Schaller S, Stierstorfer K, Bruder H, Ohnesorge BM, Schoepf UJ. Multi-detector row CT systems and image-reconstruction techniques. *Radiology*. 2005;235:756–773.
8. Taguchi K, Aradate H. Algorithm for image reconstruction in multi-slice helical CT. *Med Phys*. 1998;25:550–561.
9. Kohl G. The evolution and state-of-the-art principles of multislice computed tomography. *Proc Am Thorac Soc*. 2005;2:470–500.
10. Flohr T, Stierstorfer K, Bruder H, Simon J, Schaller S. New technical developments in multislice CT–Part 1: approaching isotropic resolution with sub-millimeter 16-slice scanning. *Rofo*. 2002;174:839–845.
11. Lewis MA. Multislice CT: opportunities and challenges. *Br J Radiol*. 2001;74:779–781.
12. Flohr TG, McCollough CH, Bruder H, et al. First performance evaluation of a dual-source CT (DSCT) system. *Eur Radiol*. 2006;16:256–268.
13. Brooks RA, Di CG. Theory of image reconstruction in computed tomography. *Radiology*. 1975;117:561–572.
14. Stark H, Woods J, Paul I, Hingorani R. Direct Fourier reconstruction in computer tomography. *Acoust Speech, Signal Process IEEE*. 1981;29:237–245.
15. Edelheit LS, Herman GT, Lakshminarayanan AV. Reconstruction of objects from diverging x rays. *Med Phys*. 1977;4:226–231.
16. Ramachandran GN, Lakshminarayanan AV. Three-dimensional reconstruction from radiographs and electron micrographs: application of convolutions instead of Fourier transforms. *Proc Natl Acad Sci U. S. A*. 1971;68:2236–2240.
17. Wang G, Yu H, De Man B. An outlook on x-ray CT research and development. *Med Phys*. 2008;35(3):1051–1064.
18. Thibault JB, Sauer KD, Bouman CA, Hsieh J. A three-dimensional statistical approach to improved image quality for multislice helical CT. *Med Phys*. 2007;34(11):4526–4544.
19. Hara AK, Paden RG, Silva AC, Kujak JL, Lawder HJ, Pavlicek W. Iterative reconstruction technique for reducing body radiation dose at CT: feasibility study. *AJR Am J Roentgenol*. 2009;193(3):764–771.
20. Christe A, Heverhagen J, Ozdoba C, Weisstanner C, Ulzheimer S, Ebner L. CT dose and image quality in the last three scanner generations. *World J Radiol*. 2013;5(11):421–429.
21. Ebner L, Knobloch F, Huber A, Landau J, Ott D, Heverhagen JT, et al. Feasible dose reduction in routine chest computed tomography maintaining constant image quality using the last three scanner generations: from filtered back projection to sinogram-affirmed iterative reconstruction and impact of the novel fully integrated detector design minimizing electronic noise. *J Clin Imaging Sci*. 2014;4:38.
22. Klink T, Obmann V, Heverhagen J, Stork A, Adam G, Begemann P. Reducing CT radiation dose with iterative reconstruction algorithms: the influence of scan and reconstruction parameters on image quality and CTDIvol. *Eur J Radiol*. 2014;83(9):1645–1654.

CHAPTER

17

Physics of Computed Tomography: Contrast Agents

Ingrid B. Boehm[1], *Johannes T. Heverhagen*[1,2]

[1]Department of Diagnostic, Interventional and Pediatric Radiology, College of Medicine, Bern University, Bern, Switzerland; [2]Department of Radiology, College of Medicine, The Ohio State University, Columbus, OH, USA

This chapter focuses on water-soluble intravenously administered iodinated positive-contrast agents only. Negative (gases, e.g., air or CO_2), barium-based (gastrointestinal), and water-insoluble or oily contrast agents have major applications too, but are not discussed because they do not have any significant application in the brain. For further information about these contrast agents, the interested reader is referred to Speck[1].

HISTORY

Whereas the discovery of X-rays revolutionized modern medicine, many soft-tissue structures in the human body remained invisible on classic X-ray images and, later on, computed tomography (CT) images. Shortly after the discovery of X-rays in 1895, the need for substances that improve the contrast of soft tissues and organs became evident. Unfortunately, the first agents used as contrast materials (CMs), such as bismuth or lead salts, were too toxic. As early as in the 1920s, the first iodine-containing agents were used for angiographic and pyelographic examinations.[2] In 1953, the basic molecule—namely tri-iodobenzoic acid (Figure 1)—for all currently approved iodinated contrast media, was introduced.[2] Initially, tri-iodobenzoic acid derivatives were ionic molecules of high osmolarity, and in the late 1960s nonionic compounds of low osmolarity were produced.[3]

The development of X-ray contrast agents has made significant progress over the past century to accommodate diagnostic requirements and in the design of safely applicable products. Even though new generations of CT technology as well as modalities with better soft-tissue contrast, for example, magnetic resonance imaging (MRI) and ultrasound (US), have improved the capabilities of native scans, contrast agents are employed routinely in CT. Their functions are to depict morphology by creating or increasing the contrast between anatomic structures and to visualize function, for example, perfusion, integrity of the blood–brain barrier, or capacity of elimination processes via the kidneys or the liver.

GENERAL PRINCIPLE OF X-RAY CONTRAST AGENTS

Contrast in X-ray images is determined by the absorption of X-rays depending on atomic number, concentration, and volume of the absorbing material. In some regions of the body, different tissues provide enough inherent contrast, for example, in the chest, but in other regions where the properties of the organs present are similar, for example, the abdomen, virtually no intrinsic contrast is present. Therefore, the introduction of materials that reduce (gases, negative-contrast agents) or increase (iodine, barium, positive-contrast agents) absorption, and as a result enhance contrast, is necessary.

The contrast induced by iodinated contrast agents is based on the physicochemical properties of iodine (high density, firm binding to benzene, and low toxicity) and the availability of positions 1, 3, and 5 for the introduction of side chains to modify the biological and chemical properties of the complex (Figure 1).[4,5]

Soon, it became obvious that the side effects of these contrast agents were attributable to the high osmolality of the agents, and substances with lower osmolality (nonionic contrast agents) were formulated.[3] In addition

Handbook of Neuro-Oncology Neuroimaging, Second Edition
http://dx.doi.org/10.1016/B978-0-12-800945-1.00017-3

© 2016 Elsevier Ltd. All rights reserved.

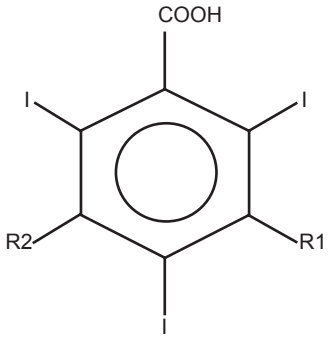


FIGURE 1 Tri-iodinated contrast agent. Aromate, parent substance; I, iodine, contrast enhancement; COOH, water solubility; R1, R2, reduction of toxicity.

to the lower osmolality, the nonionic contrast agents have two distinct advantages over ionic ones:

1. The incidence of general reactions and of allergic reactions that can be life-threatening is markedly reduced.[6–8] The improved tolerance of nonionic versus ionic substances is rooted in several physicochemical properties, such as the absence of any electrical charges or cations and significantly better shielding by hydrophilic side chains.
2. Neural tolerance is improved owing to the blood-isotonic character of the substances.

Therefore, nonionic contrast agents have replaced ionic ones virtually completely.

CURRENT APPLICATIONS OF CONTRAST AGENTS IN COMPUTED TOMOGRAPHY

Initially, it was thought that the high soft-tissue contrast of CT would make the administration of contrast agents unnecessary. However, nowadays the use of contrast agents in CT is routine and used in a wide variety of applications. These applications range from mechanical filling of cavity structures in CT myelography (intrathecal administration) over the purely anatomical depiction of perfusion defects in stroke, the differentiation between necrotic brain areas and the so-called penumbra in stroke patients, to the functional assessment of the blood–brain barrier in the diagnosis of brain tumors (intravenous application).

If injected intrathecally the contrast agent mixes with the cerebral spinal fluid and fills and opacifies the luminal area of the spinal canal. Thereby, it unmasks luminal changes, such as stenoses or cavities.[9] Intravenous application can reveal perfusion defects caused by occlusion of a vessel and can depict vascular anatomy. The CT scan then shows not only the occluded vessel but also the affected area of the brain by a lack of contrast enhancement in that area. Intravenous application also demonstrates bleeding due to rupture of a vessel or an aneurysm. Here, the contrast agent leaks out of the ruptured vessel into the surrounding tissue and reveals the extent of hemorrhage in the brain. It also indicates intraluminal filling defects in sinus thrombosis and can enhance the entire vasculature in CT angiography. Leaking of the contrast through the blood–brain barrier into the parenchyma of the brain represents functional disruption of the blood–brain barrier by a tumor with immature, leaky vasculature.[10]

Modern multislice spiral CT scanners allow the acquisition of serial, time-resolved images of the same slice, even of the same volume, after injection of the contrast agent (dynamic CT). These time series represent the first pass of contrast agent through the tissue, allowing one to follow the density patterns in the observed volume over time. The individual time–density curve (arrival and washout of the contrast agent) permits conclusions about the functional status and distribution of the contrast agent. In addition, pharmacologically induced functional changes can be observed.[11]

SIDE EFFECTS AND TOXICITY

X-ray contrast agents are usually injected in high volumes and at high rates. Therefore, important prerequisites of contrast agents are low toxicity and safe application. Moreover, for diagnostic substances a higher safety profile is expected than for therapeutics.

A major improvement in patient safety has been the step from ionic to nonionic contrast agents. For ionic agents, the incidence of side effects is high depending on the patient's condition, the type of examination, the contrast agent, its dose, and the circumstances of the examination: elective versus emergency conditions. Of special interest are severe or fatal adverse events. The numbers for these incidents vary greatly between 1 of every 116,000 patients and 1 of every 10,000 patients. Nonionic contrast agents are generally better tolerated (Table 1). It has been shown that the incidence of systemic reactions has been reduced using nonionic contrast agents.[6,12] The frequency of severe reactions has also been reduced. However, as of this writing no conclusion can be drawn about the frequency of fatal incidents. But because life-threatening events are reduced by using nonionic contrast agents, it is very likely that they also reduce the number of fatalities.

Nevertheless, it has to be stressed that only the frequency of side effects is reduced by nonionic contrast agents and that the same kind of side effects do occur. Therefore, if administering contrast agents, even nonionic ones, one has to be prepared to treat reactions.

With the introduction of nonionic contrast agents, delayed reactions (arising more than 1 h up to 1 week

TABLE 1 Tolerance of Ionic and Nonionic Contrast Agents in Comparison

Reactions, Side Effects	Ionic Contrast Agents	Nonionic Contrast Agents
General reactions	–	+
Osmolality-dependent effects	–	+
General renal tolerance (intravenous application)	O	O
Renal angiography (intra-arterial application)	–	+
Cardiodepression (due to calcium binding)	–	+
Neural tolerance	–	+

–: worse than; +: better than; O: no difference.

after contrast medium application) have been described that are more common after dimeric than after monomeric contrast agents.[13] These reactions include skin manifestations (the most common reaction is maculopapular exanthema[14]), parotitis, and possibly other reactions, such as headache and nausea. No differences between ionic and nonionic contrast agents could be demonstrated for delayed reactions.[12] However, for nonionic contrast agents it has been demonstrated that delayed reactions were twice as common as early reactions occurring within the first 30 min after administration.[15] This should lead the attending physician to draw the patient's attention to possible delayed reactions, even though these reactions are usually mild in intensity.

Adverse events after contrast medium application can be classified into two main reaction types:

- Dose-dependent side effects or so-called type A reactions[16]: These effects can be explained by direct pharmacological mechanisms including the osmolality of the contrast agent. Typical manifestations are pain at the injection site, a sensation of heat, erythema (skin redness), headache, cardiovascular effects (e.g., increase in blood pressure), renal damage (contrast-induced acute kidney injury (AKI), formerly called contrast-induced nephropathy), taste alteration, vertigo, and thyrotoxic effects. Nonionic contrast agents have distinct advantages over ionic ones owing to fewer incidences of these kinds of reactions (except thyrotoxic events). Consequently, they are superior in pain-intensive applications and angiography.
- Dose-independent and unpredictable side effects or so-called type B reactions (i.e., hypersensitivity including anaphylactic reactions)[16]: These effects do not depend on the osmolality or other pharmacological characteristics of the injected contrast agent.

Although the exact underlying mechanisms are currently far from clear there is a body of evidence that these reactions can be further subdivided into allergic and nonallergic (pseudo-allergic or allergy-like) reactions. The reactions range from mild (localized urticaria and dizziness) to severe (cardiac arrest and anaphylactic shock). The mortality with ionic contrast agents is reported to range from 1 in every 10,000 to 1 in 100,000 patients.
Although these reactions can occur with ionic and nonionic agents, they occur less frequently with nonionic agents. Often, in patients who had repeated reactions to ionic contrast agents, nonionic ones are tolerated without any symptoms.[6–8, 17] In patients at risk, with a prior history of anaphylactic/allergic reactions to CMs or with an acute severe allergic reaction,[18] an allergy workup is useful to identify tolerated and not tolerated contrast agents[19] and possibly other substances (e.g., latex and heparin) that are responsible for a hypersensitivity.[20] If such a diagnostic is not possible the use of another iodinated CM (not the culprit) and a prophylactic medication reduces the frequency and severity of anaphylaxis. However, it does not rule out anaphylactic reactions, and moreover it does not alleviate other reactions or side effects. Possible premedications include antihistaminics (H_1 blockers) alone or in combination with corticosteroids. The premedication can be given intravenously 30–60 min before the administration of the contrast agent or orally in doses of 32 mg methylprednisolone twice (e.g., 6 and 2 h) before the injection. One should be aware that as of this writing no standardized prophylactic drug regimen exists.[21] Patients without any risk factors do not benefit from prophylaxis.[22]

Certain conditions demand special attention and special measures before an iodinated contrast agent is applied. An overview of the spectrum of adverse reactions is presented elsewhere.[23] An effective prophylaxis of patients with a history of previous adverse CM-induced reactions depends on their exact clinical characterization and documentation. In addition, certain precautions have to be taken and arrangements have to be made in case a reaction occurs. In the following paragraphs, some critical scenarios are described:

Pregnant and breast-feeding patients: X-ray contrast agents have not been proven to be safe in pregnant patients. However, because exposure to X-rays should be avoided during pregnancy (and alternative investigations, such as MRI or US, are preferred), the application of X-ray contrast agents during pregnancy does not pose a real imminent problem. Contrast agents do not (or only minimally) enter the breast milk and therefore do not pose a threat to the infant.

Iodine-induced hyperthyroidism: In patients with struma or hyperthyroidism the injection of iodine (diagnostic or therapeutic) can induce serious metabolic side effects as severe as thyrotoxic crisis. Therefore, hyperthyroidism has to be excluded prior to iodinated contrast agent injection. The risk of hyperthyroidism is exclusively determined by the injection of iodine. As a result, the risk of hyperthyroidism is not alleviated by the use of nonionic contrast agents. It is the same for ionic and nonionic ones. Iodine-induced hyperthyroidism does occur weeks or months after the iodine administration, and patients have to be alerted to watch for symptoms. In patients with hyperthyroidism and a mandatory application of iodinated contrast agent, a double prophylactic medication should be administered. It consists of perchlorate (3 × 300 mg daily) for 2 days prior to and 1 week after and of thiamazole (2 × 20 mg daily) for 2 days prior to and 3 weeks after contrast agent application.

Contrast-induced AKI: Intravenously administered contrast agents in CT are renally eliminated. In patients without risk factors, the possibility of impairment of the renal function is not imminent.[24, 25] Contrast-induced AKI is defined as an increase in serum creatinine of ≥25% or ≥0.5 mg/dl 48 h after CM administration. In patients with risk factors such as renal insufficiency, insulin-dependent diabetes mellitus, dehydration, cardiac insufficiency, and/or medication with nephrotoxic drugs, contrast-induced AKI may occur. Therefore, alternative procedures such as MRI and US should be chosen. If the application of iodinated contrast agents cannot be avoided, various prophylactic measures are recommended. They include appropriate hydration up to 24 h after contrast medium injection, discontinuation of nephrotoxic drugs, and avoiding multiple examinations with contrast agent application within a short time frame. Now the administration of special drugs such as acetylcysteine is debated.

Metformin-induced lactic acidosis: Care should be taken in the choice of the medication given to the patient. The administration of iodinated contrast medium in diabetes patients receiving the oral antidiabetic drug metformin has a risk of lactic acidosis especially if the renal function is reduced. Although a rare condition, it is a very severe one, with a mortality of up to 50%.[26] The incidence is reported to be 9 per 100,000 patients and year of metformin intake, much of which can be attributed to contraindications such as congestive heart failure, renal failure, advanced age, and states with tissue hypoxemia. Because metformin clearance is reduced by 74–78% in moderate or severe renal impairment,[27] the risk for metformin retention followed by lactic acidosis is higher in patients with stage 3 chronic kidney disease.[28] Therefore, in cases with renal dysfunction metformin should be withdrawn 48 h before and restarted 48 h after contrast medium application.[29] When the patient has a normal renal function, metformin medication should be stopped at the time of CM administration and should be restarted, at the earliest, 48 h later, if a normal renal function is diagnosed by serum creatinine determination. These guidelines have been updated by the European Society of Urogenital Radiology and published online.[30]

For guidelines for therapy and prophylaxis of adverse reactions to contrast agents, please also refer to Bush and Swanson.[31] Even though such reactions are rare, the administering physician always has to be prepared to react to an emergency and treat possible side effects.

References

1. Speck U. *Contrast Media – Overview, Use and Pharmaceutical Aspects*. 4th Edition Springer; 1999(Speck U ed.).
2. Quader MA, Sawmiller CJ, Sumpio BE. Radio contrast agents: history and evolution. In: Chang JB, ed. *Textbook of Angiology*. Springer; 2000:775–783.
3. Almen T. Contrast agent design. Some aspects on the synthesis of water soluble contrast agents of low osmolality. *J Theor Biol*. 1969;24:216–226.
4. Yamamoto Y, Satoh T, Sakurai M, Asari S, Sadamoto K. Minimum dose contrast bolus in computed angiotomography of the brain. *J Comput Assist Tomogr*. 1982;6:575–585.
5. Huang HK, Chamberlin K, Schellinger D, Raptopoulos V, Garnic JD. A subtraction technique comparing pre- and post-contrast medium enhancement CT scans. *Comput Tomogr*. 1977;1:267–271.
6. Katayama H, Yamaguchi K, Kozuka T, et al. Adverse reactions to ionic and nonionic contrast media. A report from the Japanese Committee on the Safety of Contrast Media. *Radiology*. 1990;175:621–628.
7. Rapoport S, Bookstein JJ, Higgins CB, et al. Experience with metrizamide in patients with previous severe anaphylactoid reactions to ionic contrast agents. *Radiology*. 1982;143:321–325.
8. Wolf GL, Arenson RL, Cross AP. A prospective trial of ionic vs nonionic contrast agents in routine clinical practice: comparison of adverse effects. *AJR*. 1989;152:939–944.
9. Saifuddin A. The imaging of lumbar spinal stenosis. *Clin Radiol*. 2000;55:581–594.
10. Haider MA, Milosevic M, Fyles A, et al. Assessment of the tumor microenvironment in cervix cancer using dynamic contrast enhanced CT, interstitial fluid pressure and oxygen measurements. *Int J Radiat Oncol Biol Phys*. 2005;62:1100–1107.
11. Rydberg J, Buckwalter KA, Caldemeyer KS, et al. Multisection CT: scanning techniques and clinical applications. *Radiographics*. 2000;20:1787–1806.
12. McCullough M, Davies P, Richardson R. A large trial of intravenous Conray 325 and Niopam 300 to assess immediate and delayed reactions. *Br J Radiol*. 1989;62:260–265.
13. Schild HH, Kuhl CK, Hübner-Steiner U, Böhm I, Speck U. Adverse events after unenhanced and monomeric and dimeric contrast-enhanced CT: a prospective randomized controlled trial. *Radiology*. July 2006;240(1):56–64.
14. Böhm I, Schild HH. A practical guide to diagnose lesser-known immediate and delayed contrast media-induced adverse cutaneous reactions. *Eur Radiol*. 2006;16(7):1570–1579.
15. Christiansen C. X-ray contrast media – an overview. *Toxicology*. 2005;209:185–187.
16. Rawlins MD, Thompson JW. Mechanisms of adverse drug reactions. In: Davies DM, ed. *Textbook of adverse drug reaction*. New York: Oxford University Press; 1991:18–45.
17. Holtas S. Iohexol in patients with previous adverse reactions to contrast media. *Invest Radiol*. 1984;19:563–565.

18. Boehm I. Contrast medium and patients at risk: asthma. *Acta Radiol*. 2009;50(3):348.
19. Böhm I, Pfützner W, Klose KJ. Individual management permits contrast media enhanced CT examination without premedication. *Röfo*. December 2012;184(12):1161–1162.
20. Böhm I, Alfke H, Klose KJ. Hypersensitivity reactions and contrast medium injection: are they always related? *Eur J Radiol*. November 2011;80(2):368–372.
21. Tramèr MR, von Elm E, Loubeyre P, Hauser C. Pharmacological prevention of serious anaphylactic reactions due to iodinated contrast media: systematic review. *BMJ*. September 30, 2006;333(7570):675.
22. Reimann HJ, Tauber R, Kramann B, et al. Premedication with H1- and H2-receptor antagonists for intravenous urography using contrast media. *Röfo*. 1986;144:169–173.
23. Böhm I, Heverhagen JT, Klose KJ. Classification of acute and delayed contrast media-induced reactions: proposal of a three-step system. *Contrast Media Mol Imaging*. November–December 2012;7(6):537–541.
24. Cramer BC, Parfrey PS, Hutchinson TA, et al. Renal function following infusion of radiologic contrast material. A prospective controlled study. *Arch Intern Med*. 1985;145:87–89.
25. Heller CA, Knapp J, Halliday J, O'Connell D, Heller RF. Failure to demonstrate contrast nephrotoxicity. *Med J Aust*. 1991;155:329–332.
26. Stang M, Wysowski DK, Butler-Jones D. Incidence of lactic acidosis in metformin users. *Diabetes Care*. 1999;22:925–927.
27. Sambol NC, Chiang J, Lin ET, et al. Kidney function and age are both predictors of pharmacokinetics of metformin. *J Clin Pharmacol*. 1995;35:1094–1102.
28. Thomsen HSMS, Almén T, Aspelin P, et al. Metformin and contrast media. *Radiology*. 2010;256:672–673.
29. Thomsen HS, Morcos SK. ESUR guidelines on contrast media. *Abdom Imaging*. 2006;31:131–140.
30. *ESUR Guidelines on Contrast Media*. European Society of Urogenital Radiology Web site. http://www.esur.org/esur-guidelines/.
31. Bush WH, Swanson DP. Acute reactions to intravascular contrast media: types, risk factors, recognition, and specific treatment. *AJR*. 1991;157:1153–1161.

CHAPTER

18

Introductory Magnetic Resonance Imaging Physics

Aaron D. Sodickson[1], *Daniel K. Sodickson*[2]

[1]Department of Radiology, Brigham and Women's Hospital, Harvard Medical School, Boston, MA, USA; [2]Center for Advanced Imaging Innovation and Research (CAI[2]R), Department of Radiology, New York University School of Medicine, New York, NY, USA

EXTERNAL MAGNETIC FIELD, PROTONS, AND EQUILIBRIUM MAGNETIZATION

Much of the bulk of the magnetic resonance imaging (MRI) scanner apparatus is dedicated to producing an extremely strong magnetic field, denoted as B_0. Common present day whole-body clinical systems operate at field strengths of 1.5 Tesla (T) (30,000 times the strength of the Earth's magnetic field), or 3 T. Higher field systems at 7 T and above are commercially available, though as of yet mostly limited to research use.

The great majority of clinical MRI applications image protons, present in vast numbers throughout the body in all molecules containing hydrogen nuclei. These protons have a physical characteristic, the nuclear spin, which imparts magnetic properties to the nucleus that are vital to MR image formation.

When placed into the strong B_0 magnetic field, a small excess of the nuclear spins align along rather than opposed to the field direction and their microscopic magnetizations sum into a net equilibrium magnetization vector, denoted M_0 (Figure 1). The strength of M_0 (and consequently the maximum available signal strength) scales with the size of B_0, providing the primary motivation for the development and use of higher B_0 field strength systems.

LARMOR PRECESSION AND MRI SIGNAL

Once M_0 is perturbed away from its equilibrium z-axis, it behaves like a classical bar magnet that is fixed in location but free to rotate. It precesses about B_0 at a characteristic frequency, the Larmor frequency $\omega_0 = \gamma B_0$. This precession frequency scales with the strength of the external magnetic field B_0, with a proportionality constant, the gyromagnetic ratio γ, that is an intrinsic property of the nucleus being interrogated and is the same for all protons throughout the body. At typical clinical MRI field strengths, the proton Larmor frequency is in the megahertz or radiofrequency (RF) range.

When surrounded by a loop of wire, "the coil," the time varying magnetic field created by the precessing magnetization vector induces a current, "the signal," which forms the basis for image formation in MRI (Figure 2).

RADIOFREQUENCY ENERGY AND RESONANCE

In order to precess and induce a signal, M_0 must first be tilted away from its equilibrium "longitudinal" z-axis orientation and into the "transverse" x–y plane. In fact, the magnetization vector may best be thought of in terms of its longitudinal component M_L, which remains fixed along the z-axis, and its transverse component M_T, which precesses about B_0 in the x–y plane (see Figure 2). MRI relies on the use of RF magnetic fields, denoted B_1, to convert longitudinal magnetization into transverse magnetization, or equivalently, to tilt the magnetization vector into the transverse plane.

The weak B_1 magnetic fields are aligned in the transverse plane, perpendicular to the z-axis. By its nature, M_0 will precess about any externally applied magnetic field, so this B_1 field will tilt the magnetization away

Handbook of Neuro-Oncology Neuroimaging, Second Edition
http://dx.doi.org/10.1016/B978-0-12-800945-1.00018-5

© 2016 Elsevier Ltd. All rights reserved.

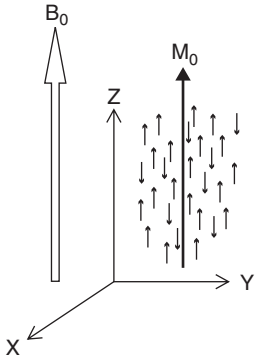


FIGURE 1 The direction of the external static magnetic field B_0 defines the z-axis, or longitudinal axis, of the MRI apparatus. The perpendicular x–y plane is often denoted the transverse plane. A vector sum of the microscopic nuclear spin magnetizations yields the net equilibrium magnetization vector M_0 oriented along the z-axis.

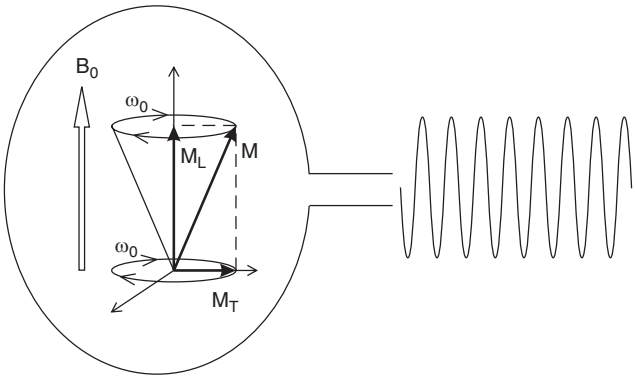


FIGURE 2 Precessing magnetization vector M, separated into its longitudinal component M_L, which remains fixed along the z-axis, and its transverse component M_T, which precesses about the z-axis in the x–y plane. The time varying magnetic field produced by the precessing magnetization induces an oscillating current in the coil surrounding the magnetization vector.

from its equilibrium z-axis. However, the strength of the applied B_1 field is so tiny compared with B_0 that if its direction remained fixed, it would have a negligible net effect due to the rapid precession of the magnetization vector about the z-axis. MRI works in this setting by rotating the axis of the B_1 field about the z-axis exactly in concert with the precessing magnetization vector. When the direction of the applied B_1 field is altered in step with the Larmor precession of M_0, the effect of the weak B_1 field can accumulate over time and cause a net tilting of M_0 toward the transverse plane (Figure 3). This precise matching of the two frequencies is the "resonance" criterion from which MRI borrows its name and it sets the B_1 frequency in the megaHertz RF range.

Resonant RF energy is typically applied as RF pulses, whose combination of amplitude and duration produces a predictable net tilting of the magnetization vector away from the z-axis by a prescribed angle. A 90° pulse takes M_0 from the z-axis fully into the transverse plane, while a 180° pulse produces an excursion from +z to the −z-axis (Figure 3).

RELAXATION

T1 and T2 Relaxation

After the net magnetization vector has been perturbed away from equilibrium, it will eventually return to its equilibrium state, with restoration of M_0 along the +z-axis. This occurs through simultaneous recovery of the longitudinal magnetization component M_L along the z-axis via T1 relaxation, and disappearance of the transverse magnetization component M_T via T2 relaxation. The two relaxation rates, denoted T1 and T2, are intrinsic features of the underlying tissue (related to tissue structure and microscopic proton motion) and vary with tissue type.

Figure 4 demonstrates the relaxation curves of the longitudinal and transverse magnetization components following a 90° RF pulse. The 90° pulse converts all of the longitudinal magnetization into transverse magnetization, leaving no residual M_L, and a maximal value of M_T. M_L then regrows from zero to its equilibrium value M_0 along +z, recovering most rapidly for fat and most slowly for cerebral spinal fluid (CSF). M_T decays away to zero at the T2 relaxation rate, with loss of M_T (and thus signal strength) occurring most rapidly for fat and most slowly for CSF.

T2* Relaxation

Signal strength actually decays at the T2 relaxation rate only in an ideal situation, in which all spins experience exactly the same external magnetic field. In reality, any source of inhomogeneity in this field causes nearby spins to precess at different frequencies and to dephase more rapidly, resulting in more rapid signal loss with a shortened relaxation time, T2*. Common sources of these inhomogeneities include the inability to engineer an absolutely uniform magnetic field and "susceptibility effects" in which differences in the magnetic properties of nearby materials (air, metal, and blood products) distort the magnetic field.

IMAGE CONTRAST MECHANISMS

Basic Pulse Sequence and Imaging Parameters Repetition Time and Echo Time

Figure 5 outlines a simplified pulse sequence diagram and defines two key variables, echo time (TE) and repetition time (TR), that may be adjusted to alter the image contrast. The TE may be thought of as the delay after the RF pulse until the signal is gathered. The TR denotes the time interval between subsequent excitations by RF

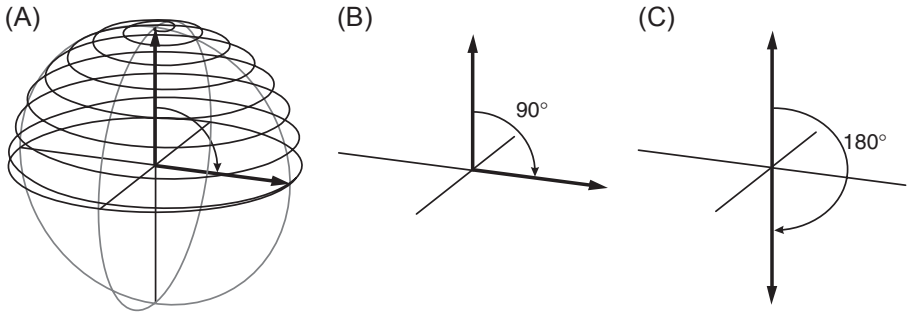


FIGURE 3 (A) In the presence of the RF field, the magnetization vector spirals down from the z-axis into the transverse plane. (B) Net effect of a 90° RF-pulse. (C) Net effect of a 180° RF-pulse.

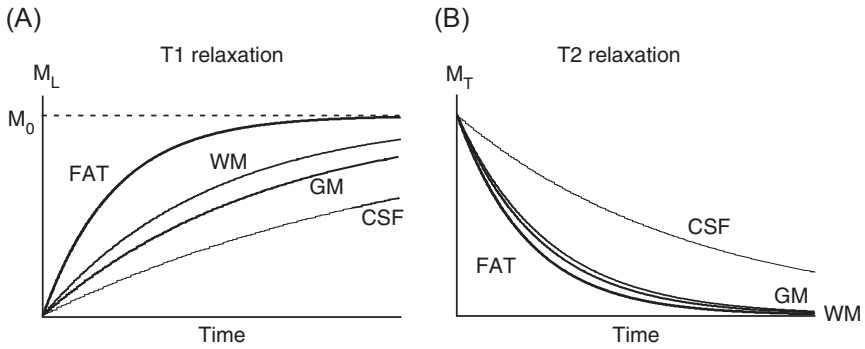


FIGURE 4 (A) T1 relaxation curves describing recovery of longitudinal magnetization toward equilibrium following a 90° RF pulse. (B) T2 relaxation curves describing the decay of transverse magnetization toward zero following a 90° RF pulse. In sequence from shortest to longest relaxation times (fastest to slowest relaxation rates): fat, white matter (WM), gray matter (GM), and cerebrospinal fluid (CSF). As T1 relaxation represents recovery of longitudinal magnetization toward M_0, while T2 relaxation represents decay of transverse magnetization toward zero, the directions of the curves are reversed from (A) to (B).

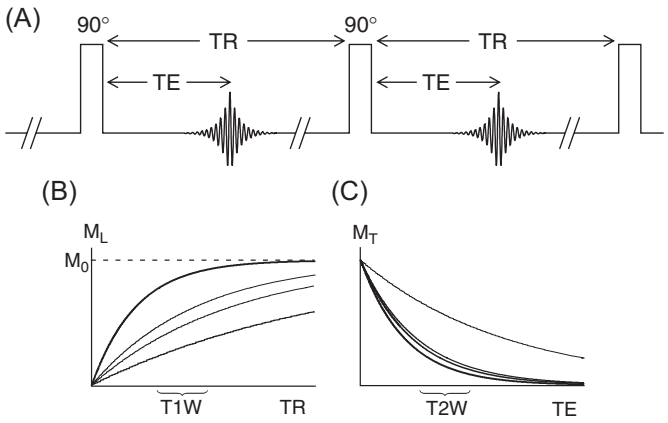


FIGURE 5 (A) Schematic pulse sequence diagram. (B) T1 relaxation occurs during each repetition time (TR) between subsequent 90° RF pulses. Choice of TR thus determines the extent of T1 weighting in the image. (C) T2 relaxation occurs during each echo time (TE), which defines the timing of signal collection after each RF pulse. Choice of TE thus determines the amount of T2 weighting in the image. TR and TE ranges to produce T1-weighted and T2-weighted images are bracketed in (B) and (C).

pulses. The process of creating an image requires numerous repetitions of this basic building block (see below).

During each TR, longitudinal magnetization is allowed to grow back along +z, to a degree depending on the tissue's T1 relaxation rate. Adjusting TR in this pulse sequence thus controls the extent of T1-weighted contrast introduced into the image (see below).

Immediately following the subsequent RF pulse, each tissue has its maximal amount of transverse magnetization. This transverse magnetization then decays toward zero during TE, to a degree depending on the tissue's T2 relaxation rate. Adjusting the length of the TE delay before collecting the induced signal thus controls the extent of T2-weighted contrast introduced into the image (see below).

Proton Density, T1-Weighted, and T2-Weighted Images

The proton density refers to the number of hydrogen nuclei per unit volume. A region with a greater number of spins will contribute more magnetization and

TABLE 1 Appropriate Choices of TR and TE to Create T1-Weighted, T2-Weighted, and Proton Density Images

	Proton density	*T1-weighted*	*T2-weighted*
TR	As long as possible	**Relatively short**	As long as possible
TE	As short as possible	As short as possible	**Relatively long**

thus more signal than an equivalent region containing fewer spins. Proton density images are designed to show purely this underlying density variation. T1- and T2-weighted images then superimpose additional image contrast based on the differing relaxation times of the tissues, to degrees depending on the TR and TE values chosen for the scan. It must be emphasized that T1 and T2 are fixed parameters reflecting physical characteristics of the tissue, while TR and TE are imaging variables that are adjusted at the MR scanner to accentuate image contrast between tissues.

The magnitude of the signal collected for a given tissue type is determined by multiplying the underlying proton density distribution by the values of the T1 and T2 relaxation curves of Figure 5 for each particular tissue at the chosen TR and TE times.

$$Signal = PD \times \left(1 - e^{-TR/T1}\right) \times e^{-TE/T2}$$

The appropriate choices of TR and TE values are shown in Table 1 and discussed below.

Proton Density Images

Proton density images rely on a very long TR value to eliminate T1-weighted contrast and a very short TE value to eliminate T2-weighted contrast. The long TR allows recovery of full equilibrium magnetization for all tissues. The next RF pulse transfers this magnetization to the transverse plane, where it precesses and induces the signal that is recorded immediately (at a very short TE) before significant T2 relaxation can take place. The resulting image then reflects the spatial distribution of proton density across the patient, without additional T1- or T2-weighted contrast.

T1-Weighted Images

T1-weighted images rely on relatively short values of TR to introduce T1-weighted contrast and very short TE values to eliminate T2-weighting. The short value of TR establishes differences in longitudinal magnetization values for different tissue types (see Figure 5(B)). Following the subsequent RF pulse to transfer this magnetization to the transverse plane, the induced signal is collected rapidly (at a short TE) to minimize T2-weighting. This combination produces a T1-weighted image while eliminating the confounding effects of T2-weighting.

T2-Weighted Images

T2-weighted images rely on a very long TR value to eliminate T1-weighting and a relatively long TE value to introduce T2-weighted contrast by creating differences in transverse magnetization between different tissue types. The long TR allows recovery of full equilibrium magnetization for all tissues. Following the subsequent RF pulse to transfer this magnetization to the transverse plane, signal is not collected until a long enough TE has passed to highlight differences in transverse magnetization based on T2-relaxation differences (see Figure 5(C)). This combination produces a T2-weighted image while eliminating the confounding effects of T1-weighting.

Figure 6 shows examples of the different image types, achieved by appropriate adjustment of TR and TE.

Inversion Recovery

Inversion recovery sequences add an additional 180° RF pulse to the basic pulse sequence building block of Figure 5. Following this pulse, there is a delay time (τ) before the subsequent 90° pulse and signal collection at TE (Figure 7). TE and TR are chosen to produce T2-weighted images, but the additional imaging variable τ provides a mechanism to use T1 relaxation differences to uniformly suppress signal from a tissue of interest (water in fluid attenuated inversion recovery (FLAIR) images and fat in short tau inversion recovery (STIR) images).

FLUID ATTENUATED INVERSION RECOVERY

In FLAIR images, τ is chosen to correspond to the zero-crossing point in the T1 relaxation curve of water. The 90° RF pulse is applied at just the moment that the longitudinal magnetization of cerebrospinal fluid crosses through zero, so that there is no formation of transverse magnetization to produce signal from the CSF. Other tissue types with faster T1 relaxation have recovered significant portions of their equilibrium magnetization, so the 90° pulse does produce transverse magnetization and MR signal for these tissues. Figure 6(C) provides a sample image.

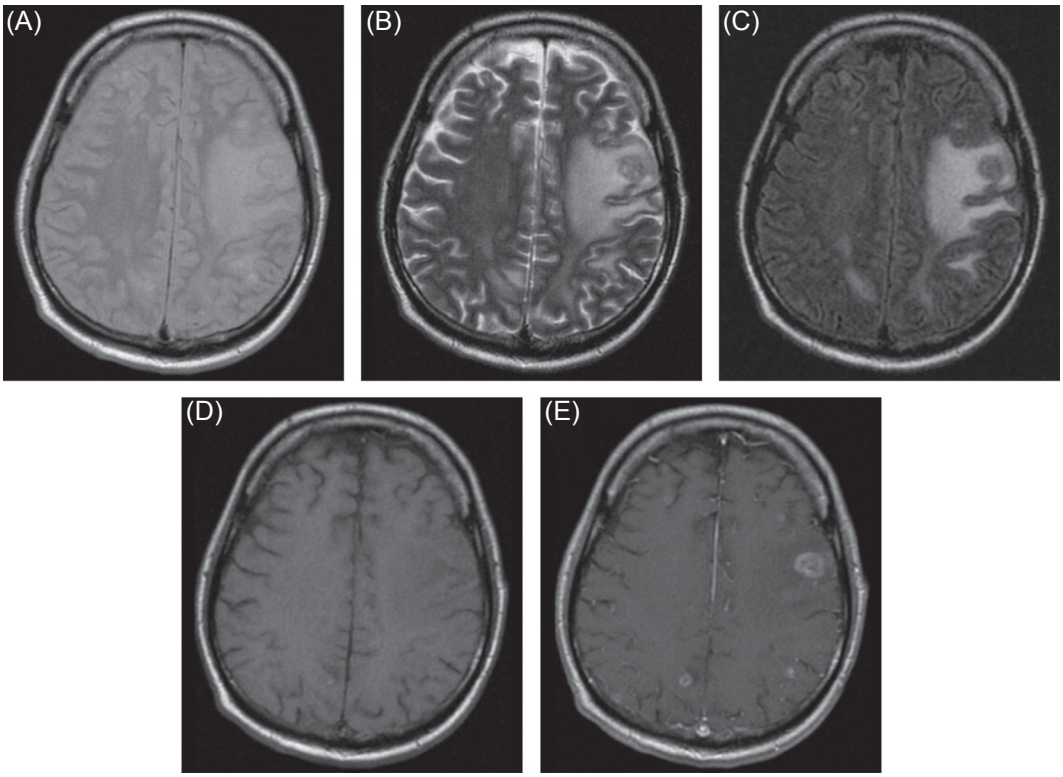


FIGURE 6 Different types of image contrast in a patient with melanoma metastases. (A) Proton density, (B) T2-weighted, (C) FLAIR, (D) T1-weighted, and (E) T1-weighted following intravenous gadolinium administration. Note the slightly lower signal intensity of white matter relative to gray matter on the T2-weighted and FLAIR images (because the more rapid T2 relaxation of white matter causes its transverse magnetization to disappear more rapidly during TE), as opposed to its slightly higher relative intensity on the T1-weighted image (because the more rapid T1 relaxation of white matter produces greater longitudinal magnetization during TR). In (E), the metastases enhance due to the T1-shortening effect of gadolinium in regions where it enters tissues across a disrupted blood–brain barrier. The shorter T1 time leads to greater recovery of longitudinal magnetization during each TR and produces greater signal after the subsequent RF pulse. In (C) the FLAIR image eliminates the signal from CSF, while continuing to demonstrate the vasogenic edema surrounding the metastases.

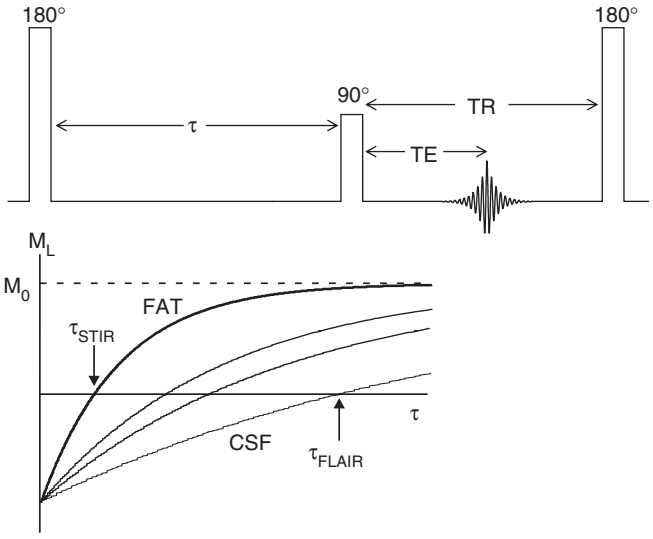


FIGURE 7 Immediately following the 180° inversion pulse, all of the equilibrium magnetization has been flipped to the −z-axis. The longitudinal magnetization recovers from −z to +z at the characteristic T1 relaxation rates of the different tissues. Appropriate selection of τ eliminates subsequent signal production from water in FLAIR images and from fat in STIR images. At the FLAIR timing shown in the image, the 90° pulse occurs at the T1 relaxation null of water, which thus produces no transverse magnetization or signal, while other tissues do generate a signal.

SHORT TAU INVERSION RECOVERY

In STIR images, τ is chosen to match the zero-crossing point in the T1 relaxation curve of fat. As a result, STIR provides a robust method of uniform fat suppression and is particularly helpful in accentuating soft tissue edema within fat-containing tissues such as bone marrow.

MAKING AN IMAGE

Spatial Localization by Magnetic Field Gradients

Spatial localization in MR images is primarily achieved through magnetic field gradients. These gradients (G) are spatially varying magnetic fields whose strength increases linearly with position along a given direction and are applied in addition to the uniform B_0 field that is present at baseline. For example, when an x-axis gradient is applied, the total magnetic field strength is slightly weaker on one side of the imaging volume (−x locations) and stronger on the other (+x locations) (Figure 8). Because the Larmor precession

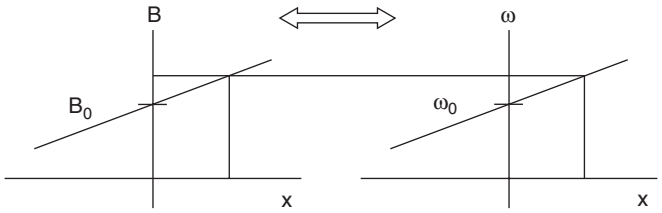


FIGURE 8 In the presence of the magnetic field gradient, magnetic field strength B varies linearly with position. As a result, corresponding precession frequencies vary linearly with position.

frequency is directly proportional to magnetic field strength, the result is that signal from one side of the patient oscillates at slightly slower frequencies than signal from the other side of the patient.

All of these signal components are simultaneously detected in the surrounding coil, but may be separated into the individual frequency components through use of the Fourier transform. The amount of signal oscillating at a given frequency corresponds to the amount of magnetization precessing at the corresponding magnetic field strength, which determines the spatial location of that magnetization along the gradient direction. In this way, magnetic field gradients create a mapping of frequency to position, a property which is crucial to MR image formation.

k-space

The concept of frequency-to-position mapping produced by magnetic field gradients is most intuitive in a single dimension, but is more challenging to conceptualize in multidimensional images. The k-space formalism is a convenient way to describe gradient encoding along one or more dimensions.

Magnetic Field Gradients, Spatial Frequencies, and k-space

As magnetic field gradients establish different precession frequencies across the imaging volume, evolution in a gradient over a specified time creates a spatial distribution of magnetization that varies along the gradient direction. Greater amounts of evolution in the gradient produce progressively tighter spatial oscillations across the patient, or oscillations of progressively higher spatial frequency (Figure 9(A)).

The basic tenet of Fourier transform mathematics is that any given shape may be defined as an appropriate combination of spatially oscillating distributions. k-space tabulates the contributions of these spatial frequency components. It is the mathematical domain in which MRI signal is collected and is in fact related to the actual image by means of Fourier transformation.

Each data point of collected signal occupies a particular location in k-space and contains information about the corresponding spatial frequency of magnetization distributed across the imaging volume. The $k=0$ data point represents magnetization uniformly distributed across the imaging volume. The $k=\pm1$ data points describe distributions of magnetization with a single cycle of oscillation from one end of the imaging volume to the other, $k=\pm2$ with two cycles of oscillation, and so on (Figure 9(B)). A complete set of these data points specifies the amount of each spatial frequency component and uniquely determines the true spatial map of magnetization. This k-space "map" of spatial frequencies is converted via the Fourier transform to the "spatial domain" to produce the image.

Each spatial frequency component is interrogated by creating the appropriate spatial oscillation via increasing intervals or "steps" of gradient evolution. In practice, this may be done by allowing evolution for longer time intervals under a gradient of fixed strength—the frequency encoding approach (Figure 9(C)), or by producing evolution for a fixed time interval under gradients of increasing strength—the phase encoding approach (Figure 9(D)). The signal produced by each gradient evolution step reflects the size of the corresponding spatial frequency component and "fills" the corresponding k-space position.

Frequency Encoding

During the signal collection phase of the pulse sequence, a frequency encoding gradient or "readout" gradient is applied. This gradient maps precession frequency to spatial position. Fourier transformation decomposes the collected signal into its component frequencies, whose magnitudes correspond to the amount of magnetization at each position, and yield a one-dimensional image.

In the k-space description, gradient evolution steps are defined by successive time intervals under a readout gradient of fixed strength. Each associated signal data point fills the corresponding k-space position (Figure 10). All of the data points needed to fill the complete line of k-space may be acquired after a single RF pulse and Fourier transformation yields a one-dimensional projection image.

Phase Encoding

Phase encoding is used to encode spatial information in the second dimension and typically uses a gradient along an axis perpendicular to the frequency encoding direction. Unlike frequency encoding, phase encoding steps are generally achieved via stepwise changes in the strength of the phase encoding gradient, with the evolution interval remaining fixed (see Figure 10).

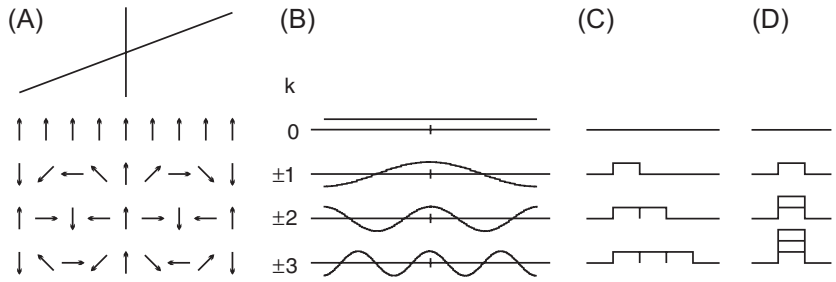


FIGURE 9 Creation of spatial distributions via gradient evolution. (A) Relative to the center position, rightward magnetizations precess at increasing clockwise rates, and leftward magnetization at increasing counterclockwise rates. The top row is a uniform distribution of magnetization prior to gradient evolution, lower rows show the spatial distribution after progressive steps of gradient evolution. (B) Corresponding spatial distributions and k-space values (C) and (D). Equivalent gradient evolution steps: (C) frequency encoding approach, with fixed gradient strength and increasing evolution time intervals; (D) phase encoding approach, with fixed evolution times, but increasing gradient strengths.

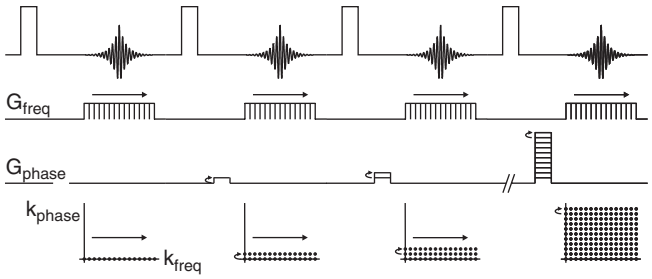


FIGURE 10 Spatial encoding technique combining frequency and phase encoding. Signal collected during each frequency encoding gradient fills a horizontal line in k-space (straight arrows). Each phase encoding gradient step toggles to the next vertical k-space position (curved arrows). After a complete set of phase encode steps, a full plane of k-space data is filled, allowing two-dimensional image reconstruction by Fourier transformation.

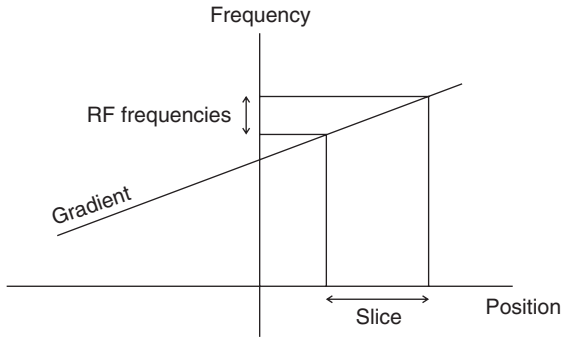


FIGURE 11 Slice selection. The position of the slice is determined by the center frequency of the RF pulse and the slope of the magnetic field gradient, while the slice thickness is determined by the range of frequencies contained in the RF pulse and by the slope of the gradient.

Phase encoding is otherwise entirely analogous to frequency encoding, as each encoding step provides information about a different spatial frequency component and fills the corresponding position in k-space.

Each phase encoding evolution step must be performed after a new RF pulse, which requires numerous repetitions of the pulse sequence building block in order to collect all of the required signal data. Data collected after a full set of frequency and phase encoding steps then fills a full plane of k-space, which may be Fourier transformed into a two-dimensional image.

Slice Selection

In order to spatially encode the third dimension, a slice selection step is often employed, in which the RF pulses are applied in the presence of a slice selection magnetic field gradient. The RF pulses contain an adjustable range of frequencies. As discussed in the section on RF energy and resonance, the RF excitation frequency must match the spin precession frequency in order to tilt magnetization into the transverse plane. As a result, each RF pulse only excites spins with a matching range of precession frequencies, which corresponds to a predictable range of locations along the gradient direction (Figure 11).

Expanded Pulse Sequence Diagram and Two-Dimensional versus Three-Dimensional Imaging Techniques

Figure 12 contains a simplified schematic pulse sequence diagram for two-dimensional imaging, in which slice selection, phase encoding, and frequency encoding extract spatial information along each of the three perpendicular axes. For each slice selection step, in-plane spatial encoding is performed with a combination of phase and frequency encoding. Each slice requires a full set of phase encoding steps, each of which in turn requires its own TR.

It is primarily this need to repeat numerous excitations with different slice selection and phase encoding steps that accounts for the lengthy scan times of MRI (although in reality data acquisition from different slices may be interleaved to save some time).

Rather than performing slice selection as above, three-dimensional imaging techniques instead add an additional nested phase encoding cycle to spatially encode

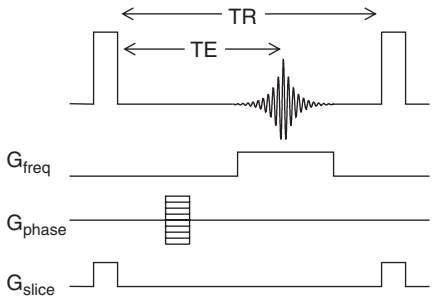


FIGURE 12 Schematic two-dimensional imaging pulse sequence diagram (several practical details omitted). The slice selection gradient is applied during the RF pulses. The phase encoding gradients step in amplitude during successive TR repetitions. The frequency encoding gradients are applied during signal readout.

the third dimension, again requiring repetition through multiple excitations.

Echoes

In actual practice, it is generally necessary to acquire signal data from both positive and negative sides of k-space. In order to do this, data are collected during symmetric echoes, with the center point of the echo corresponding to k = 0. There are two general techniques to do this, called, respectively, spin echo and gradient echo.

Spin Echoes

Spin echoes are formed by placing a 180° pulse in the center of the TE time (left out of the pulse sequence diagrams for simplicity). This additional 180° pulse has the effect of refocusing any dephasing of transverse magnetization caused by persistent magnetic field inhomogeneities as discussed above. The result is an echo height determined by T2 rather than T2*, which not only produces greater signal strength but also better reflects intrinsic tissue properties. A commonly used analogy is to visualize runners on a track, who run at different speeds in one direction and spread out along the track for TE/2 before the sound of a whistle (the 180° pulse) causes them all to reverse directions but to maintain their individual speeds. After the second TE/2, they all rejoin one another in an "echo" at the starting line before again beginning to "dephase" around the track in the other direction.

Gradient Echoes

Gradient echoes do not use any additional RF pulses during TE. Instead, the strength of the frequency encoding readout gradient is reversed to form an echo. The track runner analogy to a gradient echo is that after running for a length of time, the whistle (the gradient reversal) causes the fastest and slowest runners each to adopt the other's previous running speed. After an equivalent time interval, the two again meet, coming momentarily back "in phase" with one another.

Because fixed magnetic field inhomogeneities are not corrected by gradient echo sequences, such sequences are more prone to susceptibility effects, which create local magnetic field inhomogeneities. These may be intended, as with use of gradient echo sequences to improve detectability of subtle foci of hemorrhage, or undesired, in the form of susceptibility artifacts arising from dental or surgical metal, or from air–tissue interfaces in diffusion-weighted images.

ADDITIONAL TOPICS RELEVANT TO NEUROIMAGING

There are numerous other techniques available to create image contrast that highlights specific tissue characteristics, and/or to improve image quality and imaging efficiency. We will briefly touch on some of these techniques, many of which are discussed in greater detail elsewhere in this book.

Chemical Shift Fat Saturation

Chemical shift refers to the slight difference in Larmor precession frequency of different tissues based on the different chemical environments of their protons or other MR-active nuclei. These different precession frequencies may be used to advantage in spectroscopy applications (described elsewhere in this book). Just as slice selection pulses can be used to selectively excite spins precessing at a specific frequency within an applied magnetic field gradient, frequency-selective RF pulses can be used that contain just the right frequencies to selectively excite fat protons. The associated transverse magnetization may then be destroyed by dephasing in a magnetic field gradient (or else a fat-selective inversion recovery process may be employed), so that subsequent RF excitations can then be used in standard fashion to create images that lack signal contributions from fat.

Since these methods depend on matching the RF frequencies with the resonant frequency of fat, they are prone to inhomogeneous fat suppression whenever the underlying B_0 magnetic field is not perfectly homogeneous. As a result, chemical shift fat saturation is generally less robust for uniform fat saturation than STIR, but can, for example, be used effectively in the neck to remove fat signal around the vessels in order to highlight bright methemoglobin from vascular dissection on T1-weighted images. More advanced approaches for robust separation of fat signal from water signal, such as so-called Dixon techniques, are also available, but are less common in routine clinical use.

Diffusion-Weighted Imaging (DWI)

DWI techniques (discussed in greater detail elsewhere in this book) create image contrast based on differences in local proton diffusivity. The basic technique involves use of a strong magnetic field gradient to create a tightly oscillating spatial distribution of transverse spin magnetization (as in Figure 9(B)). In the absence of proton diffusion, application of the reverse gradient results in a realignment of these spins, with restoration of the initial uniform transverse magnetization and a corresponding high signal magnitude, producing a gradient echo. However, diffusion of protons during the interval between the winding and unwinding gradients results in redistribution of protons between the peaks and troughs of the spatial modulation, which produces an essentially uniform reduction in the amplitude of the modulation, and a corresponding loss of signal after the refocusing gradient.

The degree of signal loss depends on how freely the protons can diffuse, and on the strength of and time interval between the magnetic field gradients. More freely diffusing protons undergo greater loss of signal than those with restricted diffusion. Since proton diffusion distances during typical MR timescales are on the order of tens of micrometers, the relevant restrictions are predominantly microscopic, and diffusion-weighted images therefore carry valuable information regarding the tissue microenvironment.

In order to separate signal loss due to diffusion from losses due to relaxation or other mechanisms, data are acquired using at least two distinct gradient strengths characterized by a so-called b-value, typically including a high value (such as $b = 1000$) and a zero gradient strength ($b = 0$). From these two acquisitions, an apparent diffusion coefficient map can be calculated to isolate the differences based solely on diffusivity. Areas with restricted diffusion appear darker on these images as they have a lower apparent diffusion coefficient than is found in areas of unrestricted diffusion.

Diffusion tensor imaging (DTI) is an extension of DWI methods, in which diffusion encoding gradients are applied along multiple successive directions, enabling the determination of preferential directions for diffusivity within each voxel. DTI is used in applications such as fiber tractography, which creates maps of the three-dimensional course of white matter tracts based on the greater diffusivity of water parallel rather than perpendicular to axons and fiber tracts.

Susceptibility-Weighted Imaging (SWI)

As described above, gradient echo sequences are sensitive to variations in magnetic susceptibility that lead to local variations in magnetic field strength and associated signal dephasing, leading to signal dropout or "blooming" artifacts in addition to anomalous signal phase accumulations. SWI uses these artifacts to its advantage, incorporating information about the phase of the signal in the transverse plane in order to highlight foci containing increased concentrations of paramagnetic (e.g., iron) or diamagnetic (e.g., calcium) materials whose magnetic susceptibility properties differ from those of surrounding tissues.[1] SWI may be used, for example, to assess iron content in microhemorrhages or small vessels.

Motion Compensation

Patient motion is a common challenge in brain imaging. In traditional pulse sequences, multiple repetitions are needed to accomplish the required phase encoding. Patient motion creates misregistration of the relevant k-space data, which manifests as motion artifact along the phase encoding direction in the reconstructed images.

Numerous strategies for compensation of motion-related artifacts have been devised over time. One strategy which has seen increasing use in neuroimaging applications is the PROPELLER technique, in which the direction of encoding gradients is shifted to fill in bands of k-space data at progressively advancing angles, like the blades of a propeller.[2] These bands, or blades, are designed to overlap and produce redundant data in the center of k-space, which encodes overall image intensity and broad spatial variations. Differences in the central k-space data between the blades can be used to detect and correct for motion-related offsets. At the same time, the blades are spaced in such a way that there is sufficient sampling of the periphery of k-space to capture high frequency edge details in the images.

Parallel Imaging

Another means of reducing motion artifacts or other time-dependent image distortions is to increase imaging speed. The history of MRI has been marked by progressive increases in speed, enabled by advances both in hardware (gradient strength and switching rate, B_0 field strength, etc.) and in software (e.g., efficient pulse sequences).

One class of rapid imaging approaches now in routine use across many scanners and pulse sequence types is parallel imaging, which uses arrays of RF detectors to encode image information in parallel, rather than in a traditional sequential order.[3–5] Rather than relying entirely on successive applications of encoding gradients, as has been described earlier in this chapter, parallel imaging methods use a reduced number of gradient steps and fill in the missing data via combinations of signals acquired simultaneously in multiple coil array elements, thereby circumventing traditional limits on sequential acquisition

speed. Each coil in a suitably configured array provides a distinct view of the body, and prior knowledge of the spatial sensitivity patterns underlying these views may be used in parallel image reconstruction algorithms to fill in holes in k-space or otherwise to resolve ambiguities in the undersampled datasets.

The advent of parallel imaging has led to a notable expansion in the number of receiver channels on commercially available MR scanners, and to a profusion of many-element coil arrays, which have the added benefit of providing increased baseline signal-to-noise ratio for neuroimaging and other applications. Parallel imaging has been used not only to reduce motion artifacts but also to decrease susceptibility-related distortions, and of course to reduce overall scan time or else to enable the acquisition of more anatomical or functional information per unit time. Meanwhile, development of new methods to increase acquisition speed and efficiency still further continues, with methods such as compressed sensing[6] promising to provide access to heretofore inaccessible spatial and temporal scales.

CONCLUSION

This chapter has introduced many of the key conceptual underpinnings of MRI physics. Several good references contain extensive sections that expand further upon these crucial concepts and typical imaging methods.[7–11] A basic understanding of these principles is vital to a firm grasp of clinical MR image content and forms the foundation for understanding more advanced MR imaging techniques.

References

1. Haacke EM, Mittal S, Wu Z, Neelavalli J, Cheng YC. Susceptibility-weighted imaging: technical aspects and clinical applications, part 1. *Am J Neuroradiol*. 2009;30(1):19–30.
2. Pipe JG. Motion correction with PROPELLER MRI: application to head motion and free-breathing cardiac imaging. *Magn Reson Med*. 1999;42(5):963–969.
3. Sodickson DK, Manning WJ. Simultaneous acquisition of spatial harmonics (SMASH): fast imaging with radiofrequency coil arrays. *Magn Reson Med*. 1997;38(4):591–603.
4. Pruessmann KP, Weiger M, Scheidegger MB, Boesiger P. SENSE: sensitivity encoding for fast MRI. *Magn Reson Med*. 1999;42(5): 952–962.
5. Griswold MA, Jakob PM, Heidemann RM, Nittka M, Jellus V, Wang J, et al. Generalized autocalibrating partially parallel acquisitions (GRAPPA). *Magn Reson Med*. 2002;47(6):1202–1210.
6. Lustig M, Donoho D, Pauly JM. Sparse MRI: the application of compressed sensing for rapid MR imaging. *Magn Reson Med*. 2007;58(6):1182–1195.
7. Stark DD, Bradley WG. *Magnetic Resonance Imaging*. 3rd ed. St Louis: Mosby; 1999.
8. Edelman RR, Hesselink JR, Zlatkin M. *Clinical Magnetic Resonance Imaging*. 3rd ed. Philadelphia: Saunders; 2005.
9. Hornak JP. The Basics of MRI. http://www.cis.rit.edu/htbooks/mri/.
10. Higgins CB, Hricak H, Helms CA. *Magnetic Resonance Imaging of the Body*. 3rd ed. Philadelphia: Lippincott-Raven; 1996.
11. Brown RW, Cheng TN, Haacke EM, Thompson MR, Venkatesan R. *Magnetic Resonance Imaging: Physical Principles and Sequence Design*. 2nd ed. John Wiley & Sons; 2014.

CHAPTER

19

Advanced Magnetic Resonance Imaging of Brain Tumors

Geoffrey S. Young[1,2,3], *Jinrong Qu*[4]

[1]Department of Radiology, Brigham and Women's Hospital, Boston, MA, USA; [2]Department of Radiology, Dana Farber Cancer Institute, Boston, MA, USA; [3]Department of Radiology, Harvard Medical School, Boston, MA, USA; [4]Department of Radiology, Henan Cancer Hospital, Zhengzhou, Henan, China

This chapter outlines the basic underlying physics, physiology, acquisition technique, and clinical application of the advanced brain tumor magnetic resonance imaging (MRI) techniques most widely used in clinical diagnosis, prognosis, therapeutic planning, and follow-up: diffusion-weighted imaging, diffusion tensor imaging, MR spectroscopy, dynamic susceptibility contrast perfusion imaging, and dynamic contrast-enhanced permeability imaging.

DIFFUSION-WEIGHTED IMAGING

Diffusion-weighted imaging (DWI) contrast reflects the mean distances traveled during the pulse sequence by free water protons in tissue owing to Brownian motion—distances on the order of 10 μm. Diffusivity is characterized by the "apparent diffusion coefficient" (ADC), a scalar parameter with units of mm^2/s.[1] Intracellular organelles and membranes result in an intracellular water diffusion path length that is an order of magnitude shorter than the diffusion path length of extracellular water. For this reason, the fraction of each voxel comprising extracellular space, known as the extracellular volume fraction, is the primary determinant of ADC in that voxel.

Because routine DWI is produced from a T2*-weighted spin-echo echoplanar (SE-EPI) sequence with diffusion sensitization gradients added before and after the 180° pulse, the contrast reflects susceptibility weighting and T2 weighting as well as diffusion weighting. The magnitude and timing of each of the three roughly orthogonal diffusion sensitization gradients determine the degree of diffusion weighting, expressed in terms of a b-value with units of s^2/mm. In current practice, b-values of $1000\,s^2/mm$ are most common. To separate the contributions of diffusion weighting and of T2 weighting to the observed signal intensity (SI) on DWI images, ADC maps are calculated from the DWI and from an image set acquired with the diffusion gradient magnitude set to zero (B0). Although b-values of 1500–2500 may allow more accurate estimates of cellularity, the lower signal-to-noise ratio (SNR), increased sensitivity to artifact, and longer scan time associated with these stronger gradient settings have kept them from widespread clinical use.[2]

The measured ADC represents the relative contributions from the fraction of tissue water in the extracellular space and the fraction of water within the cell body or associated with the cell membrane. Flow within the intravascular compartment also affects the measured ADC. The ADC estimate of the "true" net diffusivity (D) can be improved by excluding the pseudo-diffusion effects due to blood flow, using an analytic technique referred to as intravoxel incoherent motion (IVIM) analysis performed on a multiple b-value DWI dataset,[3] but several studies have reported no significant difference between this improved estimate D and the simpler ADC measurement.[4,5]

Differential Diagnosis, Grading, Monitoring of Progression, and Response

Very low ADC in the viscous contents of epidermoid cysts and abscesses can be used to distinguish these lesions from arachnoid cyst, tumefactive demyelination, and necrotic tumor with accuracy greater than 90%.[6–9] Vasogenic edema and necrosis decrease net cellularity

Handbook of Neuro-Oncology Neuroimaging, Second Edition
http://dx.doi.org/10.1016/B978-0-12-800945-1.00019-7

© 2016 Elsevier Ltd. All rights reserved.

and thus increase ADC, whereas highly cellular tumors (primitive neuroectodermal tumor, glioblastoma multiforme (GBM), meningioma, lymphoma, metastases) increase cellularity, thus lowering ADC. Low ADC in an intra-axial lesion should suggest lymphoma or metastasis and, in a peripheral lesion, meningioma or dural metastasis likelier than glioma but, because low ADC is seen in a small number of glioblastomas, correlation with other advanced and conventional neuroimaging data is required for reliable clinical interpretation.[10–14]

Minimum ADC (ADCmin) correlates well with histologic measures of tumor cellularity in high- and low-grade glioma, lymphoma, medulloblastoma, meningioma, and metastases, among other tumors.[10,15–19] ADCmin below a threshold of 1.7–2.5 can contribute to the distinction of high-grade from low-grade glioma,[20,21] but overlap between tumor grades makes correlation with other MRI data mandatory.[13,20,22,23] Wide variations in ADCmin and cellularity among GBM are not only likely in part to be due to variable necrosis, hemorrhage, and calcification, but also may also reflect genotypic heterogeneity since these measures correlate well with radiation responsiveness.[24,25] Conversely, ADC cannot be used to distinguish accurately typical from atypical meningioma since variation in cellularity between individual tumors is greater than the difference between the groups.[18] In the postoperative patient, low ADC at the resection margin or in the cavity can alter management by suggesting ischemia or abscess, respectively, when conventional MR sequences exclude artifact from hematoma and are consistent with these diagnoses.[26,27] Because increases or decreases in ADC from baseline are sensitive markers of cytoreductive response to radiation therapy/chemotherapy or recurrence, respectively, functional diffusion mapping and other means of presenting longitudinal DWI data are under development (Figures 1 and 2).[16,17,28–34] In addition, deconvolution of the intravascular water motion from the tissue water diffusion has been demonstrated using multiple b-value DWI data. This analysis, referred to as IVIM analysis, yields an improved estimate of extravascular water tissue diffusion coefficient (*D* or *D*slow) and an estimate of the intracapillary water diffusion coefficient (*D** or *D*fast) as well as an estimate of the intravascular water fraction in each voxel (*f*). While this allows an intriguing noncontrast estimate of *D** and *f* correlated to blood volume and thus tumor grade, it remains to be demonstrated that IVIM estimates of *D* will allows improved correlation with tumor grade or that IVIM will add independent information to tumor imaging with perfusion-weighted imaging (PWI).[35]

DWI sequences have been adapted to perform diffusion tensor imaging (DTI) by acquiring data in six or more directions. This yields sufficient data to define fully a three-dimensional (3-D) tensor (vector) matrix describing the direction and magnitude of water diffusion in each voxel. Increasing the number of diffusion-gradient directions allows more precise estimation of the preferred direction of water diffusion. The degree to which water diffuses faster in one direction than another within a given voxel is referred to as the degree of anisotropy and can be characterized by a large number of derived scalar measures, the most commonly used of which is called fractional anisotropy (FA).[36,37] FA and other anisotropy measures reflect the existence of tissue microstructures—such as myelinated axonal bundles—and physiological processes—such as axonal transport—that facilitate the diffusion of water in one or more directions and hinder it in other directions. DTI data can be used to generate a voxel-by-voxel map of anisotropy and of other scalar measures and to produce a map depicting the principal diffusion direction in each voxel as a vector superimposed on the anatomic image.

Diffusion Tensor Imaging for Preoperative Assessment, Surgical Guidance, and Follow-up

Numerous mathematical "tractography" algorithms have been published that connect the principal direction or directions of preferred water diffusion in each voxel to those of neighboring voxels to trace out 3-D curves depicting the major white matter (WM) tracts in the brain. In normal WM the high anisotropy produced by the tightly bundled myelin sheaths of the major tracts allows reliable tractography. Although more technically challenging, the depiction of eloquent WM tracts infiltrated and displaced by a tumor has been shown to be useful in surgical planning and in prediction of postoperative dysfunction related to WM tract injury.[38–44] However, the use of DTI in surgical planning remains investigational because no controlled studies have demonstrated improvement in clinical outcome due to the use of DTI in surgical guidance to date, and different techniques in current use may produce significantly different depictions of the location of eloquent WM tracts.[45,46]

Initial experience suggests that DTI can contribute to the assessment of WM microinvasion by infiltrating glioma and thus assist in differentiating tumor recurrence from radiation necrosis, edema, and gliosis.[38,47–50] The multiple DTI-based parameters from the voxel-based diffusion tensor-based clustered images (DTcls) can help differentiate between low- and high-grade gliomas by obtaining novel clustering images called DTcls, and the new approach could lead to more accurate noninvasive grading and more appropriate treatment.[51] Although published attempts to use FA and related anisotropy measures clinically to define the margin of glioma WM infiltration and to distinguish vasogenic edema around metastases from tumor infiltration around glioma have not been uniformly successful,[25,48,52–57] work continues on more sophisticated model-based analyses of WM microstructure.

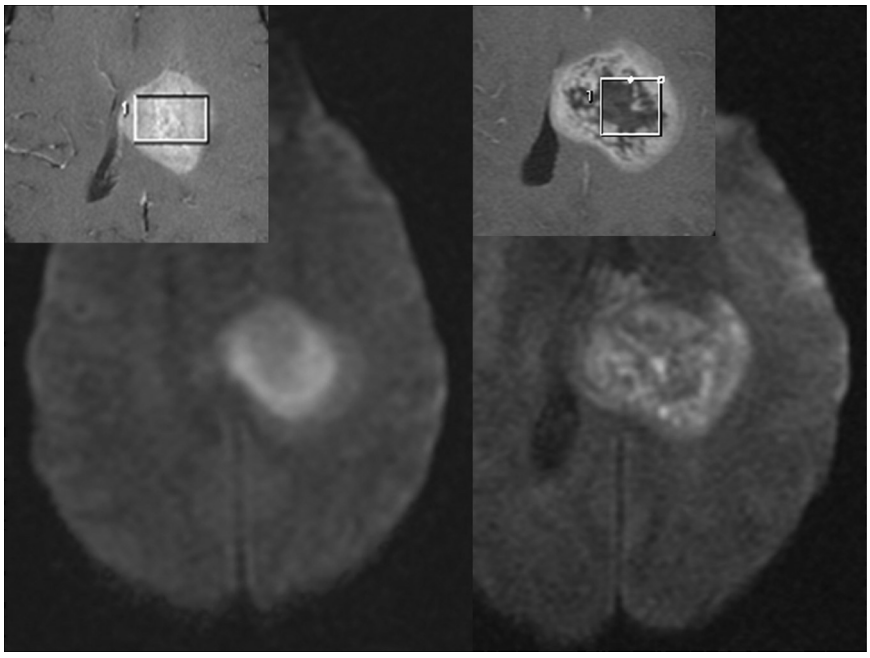


FIGURE 1 Increasing ADC suggestive of decreasing cellularity in a patient whose spectroscopy is presented in Figure 5 supports the impression that the enlargement of the Gd-enhancing lesion is due to radiation necrosis rather than tumor recurrence.

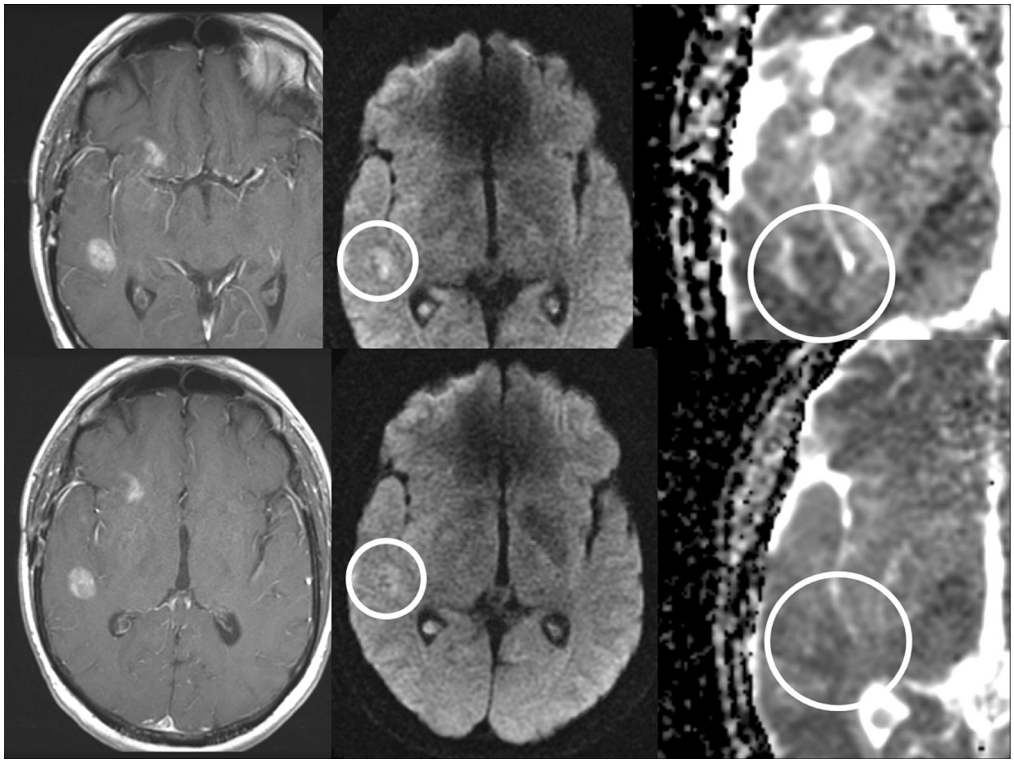


FIGURE 2 Post-Gd T1WI (left), DWI (center), and ADC (right) at baseline (top row) and after 1 month of chemoradiation (bottom row) demonstrate marked decrease in cellularity, which, despite unchanged enhancement, suggests good therapeutic response.

MAGNETIC RESONANCE SPECTROSCOPY

$^1H_0$ MR spectroscopy (MRS) is essentially proton nuclear magnetic resonance (NMR) spectroscopy modified by use of point-resolved spin echo (PRESS)- or stimulated echo-based anatomic localization schemes performed on standard MRI systems. PRESS produces higher SNR and fewer artifacts but cannot be performed at very short echo time (TE), so both sequences are in

widespread use. Simultaneous localization of MRS from multiple voxels to increase spatial resolution is called magnetic resonance spectroscopic imaging (MRSI) or chemical shift imaging. At clinical scanner field strengths (1–2 orders of magnitude lower than analytic NMR spectrometers), employing standard chemical shift-selective suppression of more than 99.99% of the free water proton signal (needed because the metabolites of interest are present in concentrations 4–5 orders of magnitude lower than water), with localization of MRSI data to 1-cm^3 voxels, the available SNR is so low that current MRSI techniques require long acquisition times (more than 10 min in some cases) and are thus very sensitive to patient motion and other artifacts. Single-voxel spectroscopy of large regions of interest (ROIs) is less time-consuming but yields far fewer useful data, since the large voxels may contain a mixture of necrotic tumor, high-grade tumor, low-grade tumor, and surrounding brain tissue, so technical development of faster 3-D MRSI techniques with greater anatomic coverage and smaller voxel sizes continues.[58–64]

$^1H_0$ MRS and NMR separate signals from chemically distinct hydrogen protons based on the slightly different "chemical shift" of each $^1H_0$ resonant frequency due to differences in the charge density of the surrounding covalent electron-bond cloud. The resulting $^1H_0$ MR spectrum is graphed with the SI of each distinct species on the *y*-axis expressed in arbitrary units and the chemical shift of each species on the *x*-axis expressed in parts per million (ppm) of the resonant-frequency tetramethylsilane protons. The use of ppm rather than Hz produces spectra that are similar regardless of scanner field strength. Because the SI detected from each $^1H_0$ species depends on a host of technical factors that vary from scan to scan, peak areas vary by 20% between serial scans even under ideal conditions.[65] Absolute quantitation of metabolite concentrations is generally reserved for the laboratory[66] and, instead, clinical spectra are presented scaled to the highest peak in the spectrum.

Because peak height is subject to less measurement error than peak area, clinical interpretation focuses on ratios of peak heights in the area of interest relative to one another and to normal-appearing voxels in the contralateral brain. The main peaks of interest in brain tumor MRS are branched-chain amino acids (AA; 0.9–1.0 ppm), lipids (Lip; 0.9–1.5 ppm), lactate (Lac; 1.3 ppm), alanine (Ala; 1.5 ppm), *N*-acetylaspartate (NAA; 2.0 ppm), choline (Cho; 3.2 ppm), creatine (Cr; 3.0 and 3.9 ppm), and myoinositol (mI; 3.6 ppm). The two Cr peaks and the broad Lip and AA peaks reflect the presence of multiple nonequivalent proton species in these molecules. Occasionally, when definite resolution of the overlapping AA, Lac, and Lip peaks is clinically important, combinations of short (<45 ms), intermediate (130–140 ms), and/or long (270–280 ms) echo times are used to differentiate them based on the phase difference of AA, Lac, and Ala with respect to Lip, NAA, Cr, and Cho.

NAA, found only in neurons, is involved in lipid metabolism, nitrogen balance, neuronal–glial signaling, and energy metabolism, among other processes. NAA varies in concentration with anatomic region and patient age and is decreased by all processes that impair neuronal function or kill neurons, including tumor, necrosis, demyelination, ischemia, neurodegeneration, etc.[67–69] Cr, an important high-energy phosphate buffer substrate for Cr kinase, has an important role in maintaining vital cellular levels of ATP.[70] Because Cr varies in concentration with anatomic region, diet, and pathophysiology, great care is needed when using it as an internal reference for evaluating other peak heights.[71] Cho-containing compounds play a key role in biosynthesis of phosphatidylcholine, other membrane lipids, and acetylcholine. Brain Cho concentration varies with anatomic region and dietary Cho intake and is very useful as a marker of cell membrane synthesis and degradation in glial growth, injury, and repair.[72,73] In contrast to Cr, NAA, and Cho peaks present in normal brain spectra, Lip is observed only in disease states producing frank necrosis or partial volume averaging of fat in scalp, marrow, lipoma, or teratoma. Lac, observed as a doublet in MRSI because of J-coupling between its protons, is present only in disease states producing anaerobic glycolysis. Because the Lip and Lac peaks are often observed together in pathologic processes producing anaerobic metabolism together with frank necrosis, distinction of the two is often diagnostically unimportant, in which case the term "Lip-Lac" is used to refer to both overlapping peaks.

Because of the distinct T2s of Cr (150–160 ms), Cho (240–250 ms), and NAA (250–300 ms), different fractions of the total signal from each metabolite will have decayed at a given echo time and so both relative and absolute peak heights will vary considerably with TE. In addition, the T2 of these metabolites varies with their anatomic location,[69,74] so careful reference to normal spectra acquired in the same anatomic location at the same TE is required to interpret spectroscopy correctly. The T2 of mI, among other metabolites including glutamate and glucose, is so short that short TE spectroscopy (by convention, less than 35 ms) is required to detect it.

Magnetic Resonance Spectroscopy in Differential Diagnosis, Grading, Surgical Planning, and Follow-up

Because Cho concentrations are increased by glial membrane injury in ischemia and demyelination, and by glial division in gliosis and glial neoplasia, high Cho may be seen in the spectra of a wide variety of pathologic lesions. Similarly, demyelination, ischemia, and glioma all injure neurons and decrease NAA. Finally,

ischemia and neoplasia both may produce Lac and Lip since anaerobic glycolysis and cellular necrosis occur in both pathophysiologies. Predictably, numerous studies have demonstrated that MRS is of no significant benefit in differential diagnosis of brain tumor from nonneoplastic brain lesions.[75-78] The only major exception to this rule is the use of MRS in rim-enhancing lesions to distinguish bacterial abscess and parasitic cyst from necrotic tumor by demonstrating the presence of AA in the cystic contents. Because AA represent lysosomal breakdown products their detection implies the presence of activated polymorphonuclear leukocytes—a finding nearly pathognomonic of infection.[7,79]

MRS has a similarly limited value for differentiating glial from nonglial neoplasms since both meningioma, which contains no neurons, and necrotic GBM, in which the neurons have died, produce very high Cho and little or no NAA. Although some meningiomas have very high concentrations of Ala, up to 80% of them contain only low levels, similar to the concentrations detected in metastases and schwannomas. Finally, MRS has no role in the differentiation of metastasis from GBM, since both may have high Cho and low or no NAA and may have prominent Lac and Lip.[80]

Although not useful in differential diagnosis, MRS estimation of the Cho/NAA ratio (CNR) is valuable for preoperative estimation of the grade of known or suspected glioma, since Cho increases and NAA decreases in proportion to increasing tumor grade from grade I to grade III. Although frequent necrosis in grade IV glioma makes GBM CNR somewhat variable, either a CNR greater than 1.5 or the presence of Lac-Lip should suggest a grade IV lesion.[21,81–85] Because the high blood volume observed in all grades of oligodendroglioma makes prediction of oligodendroglioma grade by perfusion unreliable, MRS remains especially useful in grading this glioma subtype.[86–89] MRS may also be more useful than perfusion in areas where radiation necrosis mixed with recurrent tumor lowers the apparent blood volume, but this remains to be proven.[90,91] Similarly, whole-brain NAA and CH2/CH3 ratios in normal-appearing brain have been proposed as alternative ways to measure glioma WM infiltration, but these measures have not yet been clinically validated (Figures 3 and 4).[92,93]

MRS targeting of foci with high CNR improves the accuracy of biopsy by reducing false negatives and undergrading and it has been used to guide radiosurgery and resection.[94–99]

Magnetic Resonance Spectroscopy in Assessment of Treatment Response

Because both recurrent GBM and radiation necrosis may produce Lac-Lip, high Cho, and low NAA, MRS performed at a single time point is not useful in glioma follow-up, except in foci where florid necrosis produces a complete absence of all metabolites.[100] Longitudinal CNR decrease (suggesting necrosis) or increase

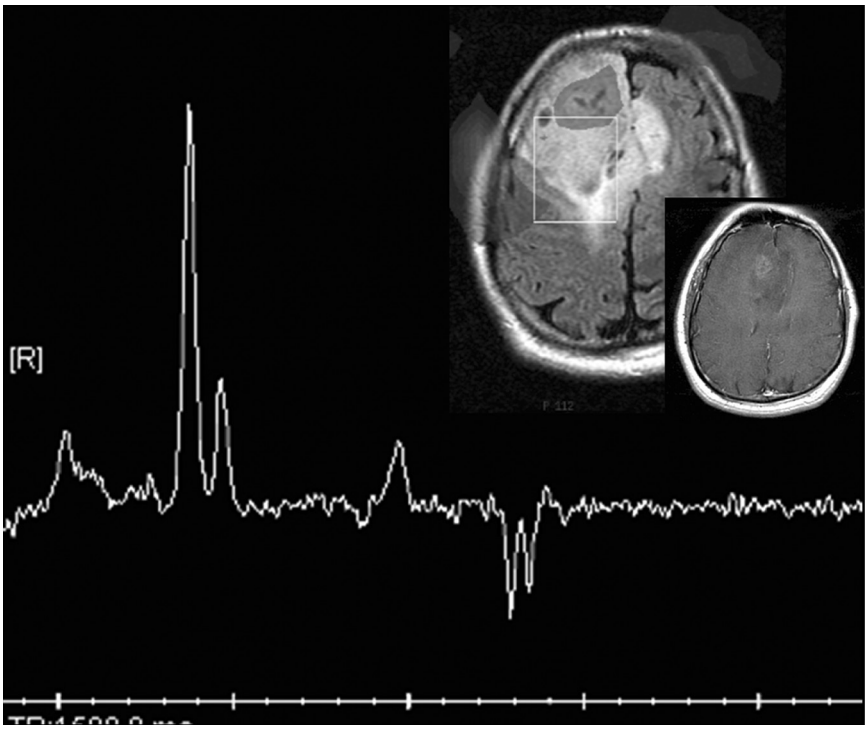


FIGURE 3 Intermediate TE (144 ms) single-voxel MRS of anaplastic oligoastrocytoma reveals CNR 0.4 and prominent lactate peak consistent with high-grade glioma.

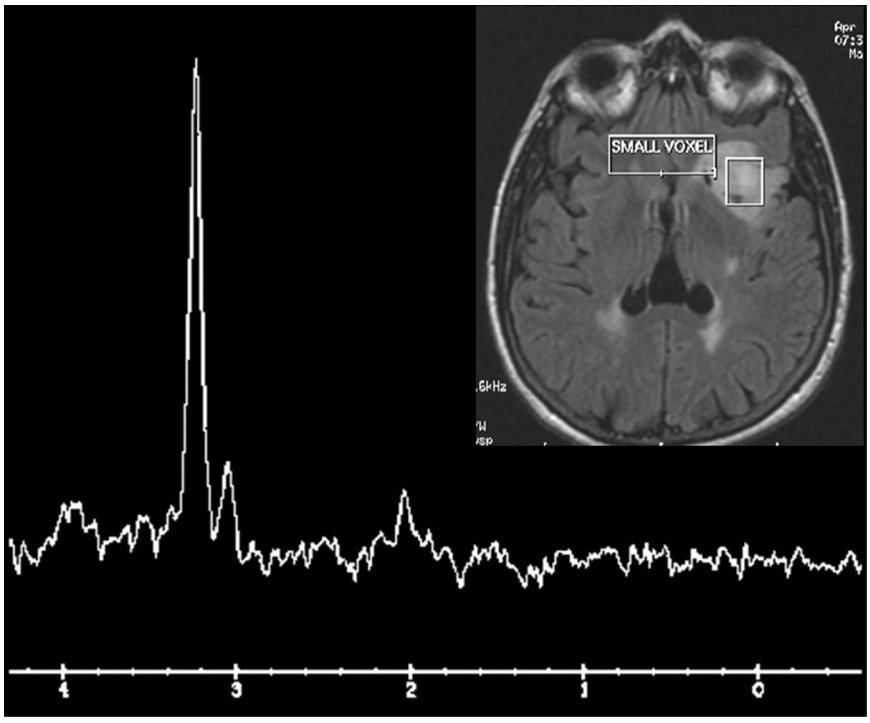


FIGURE 4 Extremely high Cho peak and CNR in oligodendroglioma suggest high WHO grade. MRS is preferred for grading of oligodendroglioma because the elevated relative capillary blood volume (rCBV) seen in all grades makes perfusion MR grading less reliable.

(suggesting recurrence) over time has been demonstrated to be much more useful when performed by groups with the resources to apply consistently meticulous technical acquisition and postprocessing standards to produce reliable data integrated with diffusion, perfusion, and anatomic imaging.[95,97,101–103] However, outside of a handful of major laboratories, the experience in routine clinical practice using currently available hardware and software is quite disappointing, because the temporal variation in metabolite concentrations on sequential scans is often far smaller than the variations in spectra due to changes in voxel location, differences in acquisition parameters, scalp lipid averaging, susceptibility artifacts, and other technical factors. In essence, reliable MRSI glioma follow-up can be achieved only when staffing and scan time are sufficient to allow a trained technical spectroscopy specialist to monitor each individual MRS scan under the direct supervision of the interpreting radiologist. This is impossible to achieve at most centers because MRS is currently not reimbursed and so the associated personnel and scanner-time costs of performing it are prohibitive (Figure 5).

Isocitrate dehydrogenase (IDH) enzyme mutations result in accumulation of the metabolite 2-hydroxyglutarate (2-HG) in up to 86% of gliomas, but are much more common in low-grade glioma (LGG) than in high-grade glioma (HGG). IDH-1 mutation has emerged as a useful clinical diagnostic marker to help distinguish LGG from other pathologies and a prognostic marker that identifies a subgroup of GBM with a better 5-year survival rate than IDH-1 wild-type GBM patients. The prevailing hypothesis is that the IDH-1 mutant group represents GBM resulting from high-grade transformation of LGG. As such, reports of noninvasive detection of 2-HG by MRS in vivo validated by correlation with ex vivo measurements in the corresponding tumor samples promise a very exciting advance and the first direct MRI detection of metabolic abnormality related to cancer mutation.[104–106]

MICROVASCULAR IMAGING IN BRAIN TUMORS: PERFUSION-WEIGHTED IMAGING AND T1-WEIGHTED PERMEABILITY IMAGING

Imaging of tumor neovasculature directly assesses several of the cardinal features of HGG of great importance in assessment and monitoring of patients taking angiogenesis inhibitors. While much active investigation focuses on more advanced techniques such as first-pass permeability estimation, arterial spin labeling, and vascular morphologic imaging, these techniques have not been validated sufficiently for routine clinical use. Thus this discussion will focus on the widely accepted use of susceptibility-weighted first-pass techniques (PWI) to estimate blood volume and T1-weighted techniques (T1-weighted permeability imaging, or T1P) to estimate

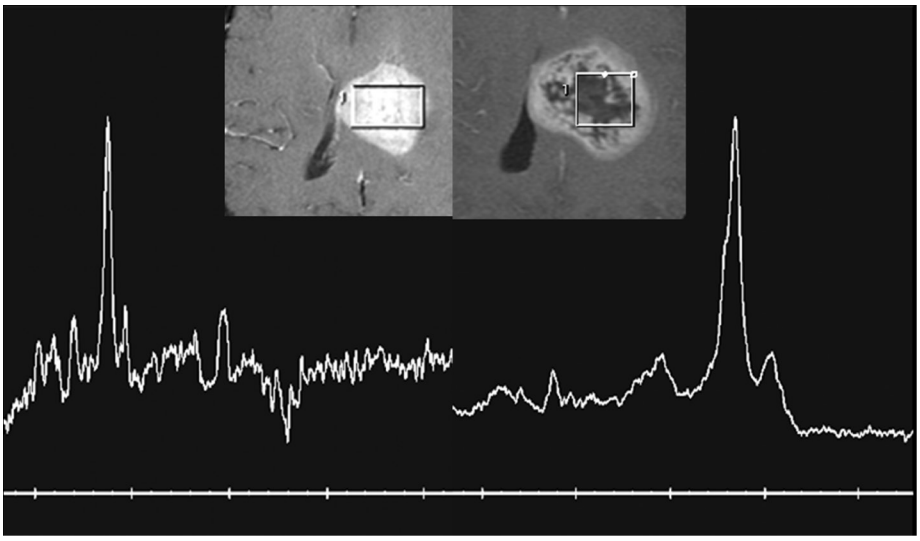


FIGURE 5 Despite the enlargement of the area of abnormal enhancement following chemoradiation, serial TE 5 144-ms small-voxel MRS showing disappearance of Cho and dramatic increase in Lip suggests radiation necrosis. Note that the presence of Lac, seen as a small inverted doublet on the earlier (left) spectrum, can no longer be assessed on the later spectrum (right) because of the dominant overlapping Lip peak.

capillary permeability.[107] Advanced IVIM-model-based analysis of noncontrast multiple b-value DWI data can be used to characterize the diffusivity (*D*fast) and perfusion volume (*f*) of a fast-diffusing tissue component felt to represent the intracapillary water, which differs significantly between low- and high-grade tumors and shows some correlation with capillary blood volume (CBV) from PWI.[5] Whether this will prove to be translatable to clinical use and what advantage it might have over contrast-based methods remains to be seen.

Perfusion-Weighted Imaging

Because the signal change exploited by PWI results from the susceptibility effect of a concentrated intravascular bolus of paramagnetic Gd contrast agent, production of reliable PWI maps requires high-pressure power injection through an 18- to 20-gauge antecubital intravenous catheter of a high-contrast dose (typically 0.2 mmol/kg or twice the standard dose) at a high rate (typically 4 ml/s or higher). The data acquisition typically consists of a single-shot echoplanar (EPI) sequence covering the whole brain every 1–2 s, which is repeated continuously for 40–60 s starting about 10 s before the arrival of the bolus in the brain and ending 10–20 s after recirculation of the first pass of contrast agent. Among EPI sequences, SE-EPI remains the gold standard, despite the slightly higher contrast requirements of this sequence, because of its contrast sensitivity to 1- to 2-μm neovessels and its lower sensitivity to the susceptibility artifacts that remain a significant limitation of PWI.[91,108] Postprocessing of the time-series data yields a time-signal intensity curve (TIC) for each voxel from which the relative CBV (rCBV) in the voxel can be derived by integrating the area under the TIC during the passage of the contrast bolus. rCBV is displayed as a rainbow-colored map, windowed by convention to display high gray matter (GM) rCBV in red and lower WM rCBV in blue. These data are supplemented by inspection of the TIC in the ROI within the lesion and a corresponding equally sized ROI within normal-appearing (ideally, contralateral) brain and, when needed, calculation of normalized CBV (nCBV) ratios between the two ROIs.[109] Overlaying these maps on higher resolution anatomic images is critical for interpretation because, despite ongoing work to develop faster and higher resolution methods,[108,110] the limit of resolution of clinical PWI using commercial hardware and software remains 2- to 4-mm in-plane voxel dimensions, 5- to 10-mm sections, and 1- to 2-s temporal resolution.

Perfusion-Weighted Imaging in Diagnosis, Grading, Operative Planning, and Follow-up

Visual inspection of TIC and source images is essential for interpretation because the effects of patient motion, susceptibility, SNR, bolus rate, and timing, as well as partial-volume averaging artifacts, cannot be assessed from color maps alone. Because the arterial input function is difficult to estimate accurately from signal loss techniques such as Gd bolus imaging, clinically available rCBV maps remain qualitative, rather than quantitative. Nevertheless, knowledge that the normal CBV of GM is approximately two to three times that of WM[111,112] allows effective clinical interpretation of tumor rCBV maps, since a maximum tumor rCBV two to three times that of normal-appearing WM (NAWM) has been demonstrated to be a strong predictor of the presence of HGG.[99,113] Thus, correctly thresholded and windowed

rCBV maps, corroborated by inspection of ROI, TIC, and nCBV ratios, that show tumor blood volume similar to or higher than normal-appearing GM are strongly predictive of hypervascularity and thus HGG. Low-grade tumor rCBV, on the other hand, tends to be less than or equal to that of NAWM. Focal areas of rCBV intermediate between NAWM and GM deserve careful attention to TIC and nCBV ratios, prior comparison with PWI, and close-interval follow-up. In all cases, comparison of rCBV maps to prior maps to detect longitudinal change and correlation of rCBV with independent advanced data and anatomic MR images are critical (Figure 6).

Inspection of TIC, as required for reliable interpretation, also allows detection of significant first-pass contrast leakage that violates the central volume theorem assumption of a nondiffusible tracer[114] and complicates calculation of CBV.[115] Although multiple curve-fitting algorithms[116–121] have been reported to address this, standard commercial curve integration software still relies on simple interpolated and constant baseline methods. Since the former will systematically underestimate and the latter systematically overestimate CBV in high-permeability lesions, inspection of both may be necessary in highly permeable lesions. While the GBM neovessel blood–brain barrier (BBB) is often impaired and may produce a TIC that returns as little as halfway to baseline, detection of very high first-pass leak with minimal or no return to baseline on lesion TIC should suggest a nonglial tumor such as meningioma, choroid plexus papilloma, metastases, or lymphoma, since capillaries within these lesions have essentially no BBB.[120,122,123] When interpreted in the context of DWI and conventional imaging, this visual TIC analysis can be quite useful in helping to distinguish such lesions from GBM and oligodendroglioma. In a rim-enhancing lesion, peripheral rCBV less than or equal to that of the surrounding WM should suggest the possibility of abscess and indicates a need for careful correlation with DWI, MRS, and anatomic images.[8] The usefulness of rCBV to distinguish glioma from metastases remains undefined. Published data show that the rCBV of metastases varies with the vascularity of the primary tumor in a range overlapping that of GBM, but it is unclear how this applies to standard SE-EPI technique.[13,124–126] Thus, although DWI and MRS remain the primary advanced techniques for differentiating abscess from cystic metastasis, SE-EPI PWI demonstration of peripheral high rCBV argues against abscess. In a solid enhancing intra-axial lesion, SE-EPI demonstration of low rCBV should suggest consideration of lymphoma or metastasis.[13,122] In a cortical or subcortical lesion with conventional imaging features suggestive of focal circumscribed LGG, demonstration of rCBV greater than or equal to GM strongly suggests oligodendroglioma (Figures 7 and 8).

Because "chicken-wire" capillaries produce high rCBV in all grades of oligodendroglioma, MRS should be

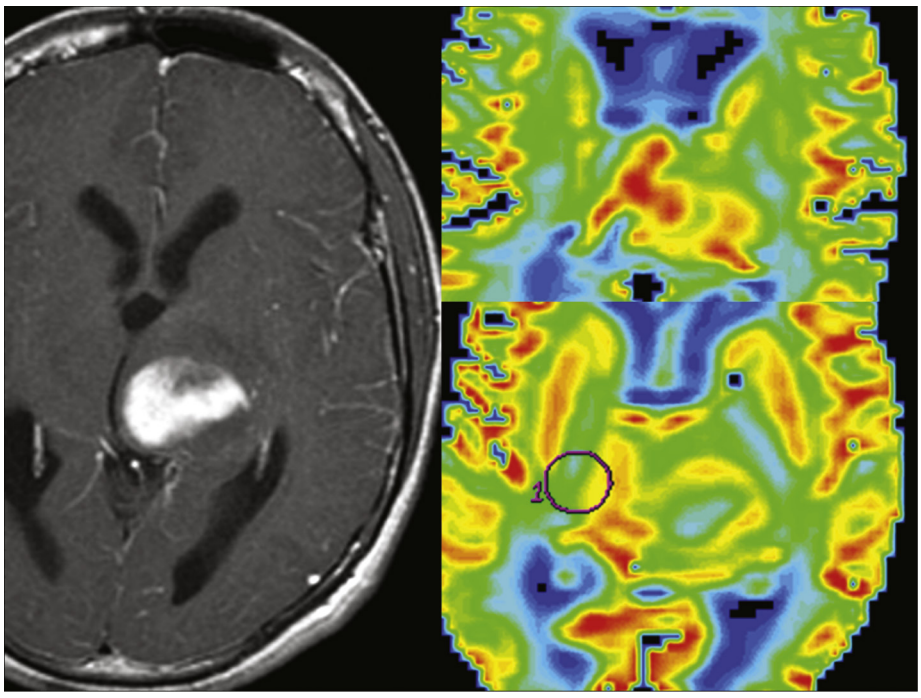


FIGURE 6 Perfusion MR of this astrocytoma reveals rCBV higher than cortical GM at the periphery and just outside of the area of abnormal enhancement (upper right), but lower blood volume in the center and inferior portion of the lesion (lower right). This information about the heterogeneous spatial distribution of high-grade tumor can be useful in preventing false negative or undergraded biopsy results and in directing focal resection or ablation to areas of unsuspected hypervascular glioma.

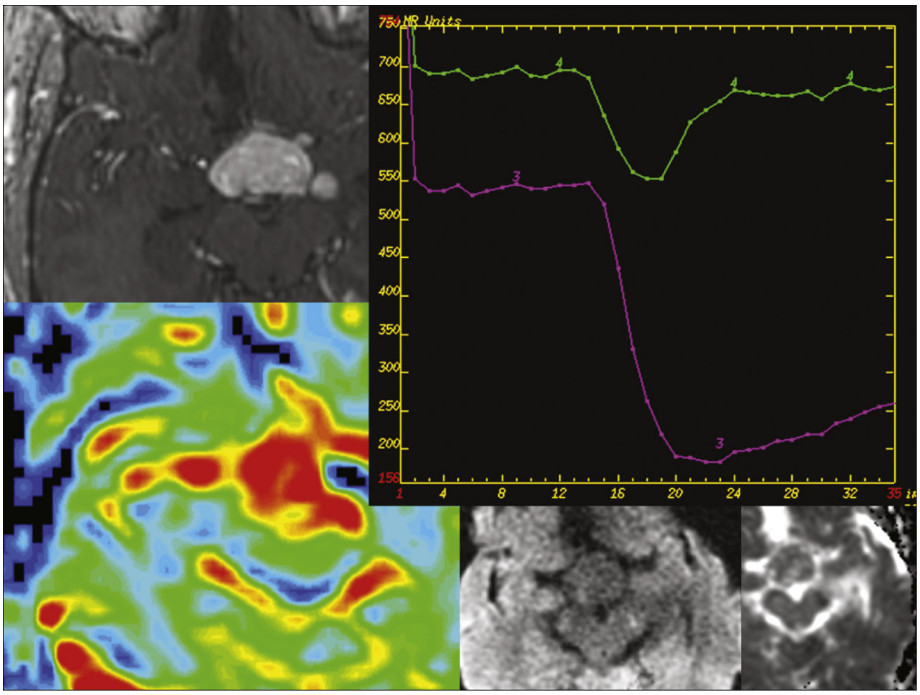


FIGURE 7 Although the intermediate ADC of this enhancing lesion does not indicate sufficiently high cellularity to be definitive, the SE-EPI perfusion imaging findings are characteristic of meningioma. The TIC within the lesion (purple curve) demonstrates near-complete leak of contrast during first pass consistent with a lesion of nonglial origin, and both the TIC and the rCBV color map (left) demonstrate very high blood volume compared to a reference ROI (green curve).

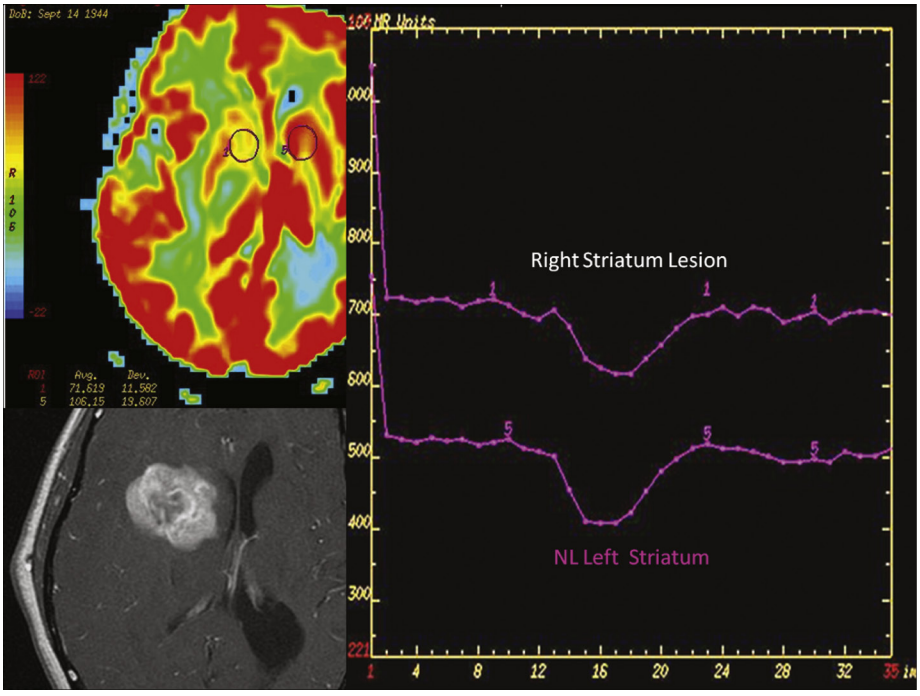


FIGURE 8 rCBV color map (upper left) demonstrates lower blood volume in the right basal ganglia lesion ROI than in the contralateral anatomically appropriate left basal ganglia ROI. In this prominently enhancing solitary right basal ganglia periventricular lesion (lower left) the PWI is suggestive of central nervous system lymphoma. The relatively little first-pass leak seen in the TIC (right) in this lesion may be due to prior high-dose steroid therapy.

performed in grading of such lesions.[86–89] In astrocytoma, on the other hand, rCBVmax is a strong predictor of grade and rCBV greater than that of normal GM should raise concern for GBM, in which mean rCBVmax values are often four to six times those of WM.[99,127–132] This strong correlation also forms the basis for the demonstrated efficacy of rCBV maps in targeting the high-grade areas of heterogeneous glioma for biopsy, ablation, or resection.[115,132,133]

Pronounced variation of rCBV within and between patients makes it essential to obtain baseline PWI data using an equivalent technique if PWI is to be used in assessing treatment response.[115] After chemoradiation of glioma, increasing rCBV within an area of abnormal enhancement or T2 prolongation suggests recurrence, whereas low rCBV, especially when correlated with increasing ADC, suggests radiation necrosis.[30,134–136] Good correlation between rCBV and expression of proangiogenic cytokines suggests that this will remain an important method of follow-up in the era of angiogenesis inhibition.[129] The pronounced effect of steroids on vascular permeability in glioma and the difficulty of completely deconvolving permeability from blood volume with current techniques may explain the mixed conclusions reached by studies examining the effects of steroid dose on CBV and certainly suggest attention to steroid dosing during follow-up at present.[137–139]

T1-Weighted Permeability Imaging

Because increasing secretion of proangiogenic factors correlates with tumor grade, both permeability of coopted native capillaries and formation of fenestrated neocapillaries increase with tumor grade.[140] These different degrees of abnormal permeability are difficult to differentiate on delayed post-Gd T1-weighted imaging (Gd-T1WI), probably accounting for its imperfect performance in distinguishing LGG and HGG.[141]

Dynamic Gd-enhanced T1P, a semiquantitative dynamic adaptation of Gd-T1WI, allows a much more sensitive assessment of microvessel permeability by acquiring data continuously throughout the first few passes of Gd recirculation. Serial fast Gd-T1WI, usually acquired with the radiofrequency spoiled-gradient echo technique, is performed continuously throughout the first 2–5 min after bolus Gd injection. TIC calculated in T1P demonstrates an increase in available signal—due to Gd augmentation of the T1 relaxation rate of adjacent water protons—that is far more easily quantifiable than the signal loss seen in DSC PWI. Because the TIC reflects several passes through the brain at a somewhat lower temporal resolution than PWI, curve fitting, deconvolution of the initial first-pass effect, and one- or two-compartment pharmacokinetic modeling must be applied to calculate parameters that reliably reflect the degree of BBB impairment. The most widely used parameters are derived from the slope of the delayed plateau phase of the TIC. When appropriately corrected for first-pass effects, T2* effects, and large vessel concentrations, this slope should provide a good estimate of the net forward volume transfer constant (*K*trans), reflecting the net rate of passage of Gd from the intravascular space to the extravascular extracellular space. The validity of the assumptions underlying the mathematics of *K*trans calculation depend heavily on the repetition time (TR) and TE of the sequence, since Gd has T2 and T2* shortening as well as T1 shortening effects. T1 mapping can be performed prior to T1P to allow better quantitation, if required by the pulse sequence parameters and analysis employed. Even so, the rate of Gd diffusion across the BBB depends on variable cerebral blood flow (CBF), variable intravascular Gd concentration, capillary surface area (which is abnormal in neocapillaries), and pressure gradients across the BBB that result from a combination of tumor interstitial oncotic pressure and intravascular and tissue hydrostatic pressure, as well as BBB permeability. Thus, although in general the T1 method described here is far less controversial than the more recently reported T2*-based first-pass methods, the calculation of a true *K*trans is not trivial. Because controversy persists over the degree to which parameters calculated from T1P reflect pure *K*trans or an admixture of *K*trans with CBF, surface area, and other factors, and over the relative advantages of *K*trans versus other compound metrics such as permeability surface area (*K*ps), the term "measures of permeability" is used below to recognize that most of the large variety of published delayed phase measures depend heavily, but not exclusively, on *K*trans. In addition, a number of measures reflecting aspects of permeability dynamics other than the slope of the delayed phase, have been devised in the quest for a practical, reproducible, and informative metric, including the maximum rate of enhancement during the first pass (max *dI/dt*, rR, etc.).[142–145] It seems likely that these two types of metrics each reflect different aspects of the underlying endothelial abnormality.

T1-Weighted Permeability Imaging in Diagnosis, Grading, and Follow-up

Assuming reliable T1P technique, increasing permeability correlates well with increasing tumor grade.[142,144–147] Although some reports suggest that rCBV may be slightly more predictive, the two measures are independent but strongly correlated in HGG, suggesting that some combination of both may prove ideal.[107,113,148] Like rCBV, T1P can be used to aid the differentiation of recurrent glioma from radiation necrosis,[143,146] but it is much less widely used owing to a combination of imaging time, profusion of reported permeability measures, and lack of robust and user-friendly postprocessing software. As these technical needs are answered over the

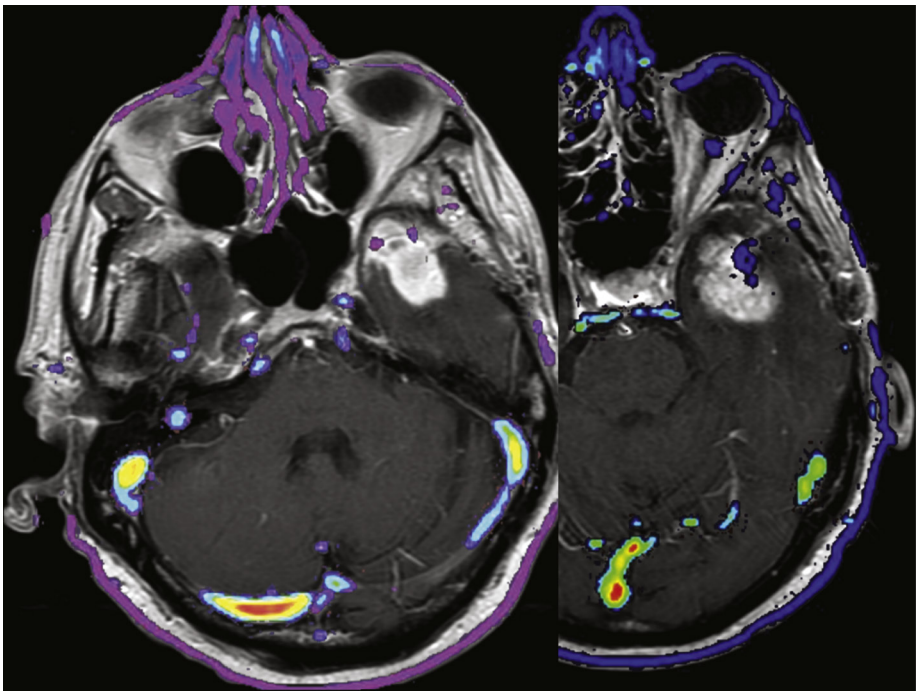


FIGURE 9 Despite differences in windowing and slice registration, a 4-week follow-up permeability *K*ps map (right) superimposed on post-Gd T1WI demonstrates increasing permeability (similar to systemic scalp capillaries) in the rapidly expanding lateral aspect of the left temporal recurrent HGG. This type of data holds promise for distinguishing recurrent tumor from necrosis, but clinical validation and routine application await improvements in postprocessing and display technique to achieve practical longitudinally comparable maps. *Postprocessing software courtesy of Timothy Roberts, Ph.D., Children's Hospital of Philadelphia.*

next few years, T1P will probably become a significant clinical tool (Figures 9 and 10).

CONCLUSION

The techniques discussed here can produce data on brain tumor cellularity, tissue invasion, metabolism, and microvasculature that, when appropriately integrated with anatomic MRI in a multidimensional brain tumor imaging protocol, can contribute significantly to differential diagnosis, estimation of tumor grade, planning of biopsy and focal resection/ablation, and therapeutic monitoring. Meticulous attention to acquisition and postprocessing technique, reference to source images and graphical data, and comparison with identically acquired preoperative baseline and serial follow-up data are essential for the safe and effective clinical use of all of these techniques. Although space limitations have prevented more than a cursory allusion to the potential pitfalls of advanced imaging, the importance of integrating all available advanced MRI data and interpreting them in the context of the anatomic imaging should be clear. Similarly, now that such a wealth of tumor-specific information is available, the importance of correlation with accurate history regarding tumor histology, radiation therapy, steroid administration, and cytotoxic and antiangiogenic chemotherapy cannot be overstated.

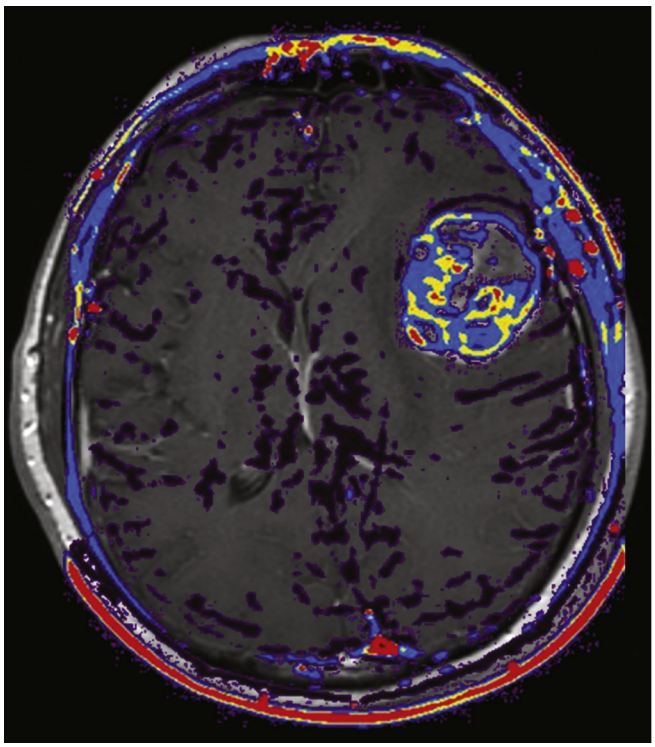


FIGURE 10 Permeability *K*ps color map superimposed on post-Gd T1WI depicts heterogeneous permeability within a lung cancer metastasis. Permeability similar to systemic capillaries in scalp is seen in a portion of the lesion. *Postprocessing software courtesy of Timothy Roberts, Ph.D., Children's Hospital of Philadelphia.*

References

1. Provenzale JM, Mukundan S, Barboriak DP. Diffusion-weighted and perfusion MR imaging for brain tumor characterization and assessment of treatment response. *Radiology*. 2006;239(3):632–649.
2. Mardor Y, Pfeffer R, Spiegelmann R, et al. Early detection of response to radiation therapy in patients with brain malignancies using conventional and high b-value diffusion-weighted magnetic resonance imaging. *J Clin Oncol*. 2003;21(6):1094–1100.
3. Le Bihan D. Diffusion, confusion and functional MRI. *Neuroimage*. 2012;62(2):1131–1136.
4. Iima M, Reynaud O, Tsurugizawa T, et al. Characterization of glioma microcirculation and tissue features using intravoxel incoherent motion magnetic resonance imaging in a rat brain model. *Invest Radiol*. 2014;49(7):485–490.
5. Suh CH, Kim HS, Lee SS, et al. Atypical imaging features of primary central nervous system lymphoma that mimics glioblastoma: utility of intravoxel incoherent motion MR imaging. *Radiology*. 2014;272(2):504–513.
6. Reddy JS, Mishra AM, Behari S, et al. The role of diffusion-weighted imaging in the differential diagnosis of intracranial cystic mass lesions: a report of 147 lesions. *Surg Neurol*. 2006;66(3):246–250. discussion 250–251.
7. Mishra AM, Gupta RK, Jaggi RS, et al. Role of diffusion-weighted imaging and in vivo proton magnetic resonance spectroscopy in the differential diagnosis of ring-enhancing intracranial cystic mass lesions. *J Comput Assist Tomogr*. 2004;28(4):540–547.
8. Erdogan C, Hakyemez B, Yildirim N, Parlak M. Brain abscess and cystic brain tumor: discrimination with dynamic susceptibility contrast perfusion-weighted MRI. *J Comput Assist Tomogr*. 2005;29(5):663–667.
9. Tsui EY, Leung WH, Chan JH, et al. Tumefactive demyelinating lesions by combined perfusion-weighted and diffusion weighted imaging. *Comput Med Imaging Graph*. 2002;26(5):343–346.
10. Guo AC, Cummings TJ, Dash RC, Provenzale JM. Lymphomas and high-grade astrocytomas: comparison of water diffusibility and histologic characteristics. *Radiology*. 2002;224(1):177–183.
11. Okamoto K, Ito J, Ishikawa K, et al. Diffusion-weighted echo-planar MR imaging in differential diagnosis of brain tumors and tumor-like conditions. *Eur Radiol*. 2000;10(8):1342–1350.
12. Toh CH, Chen YL, Hsieh TC, et al. Glioblastoma multiforme with diffusion-weighted magnetic resonance imaging characteristics mimicking primary brain lymphoma. Case report. *J Neurosurg*. 2006;105(1):132–135.
13. Calli C, Kitis O, Yunten N, et al. Perfusion and diffusion MR imaging in enhancing malignant cerebral tumors. *Eur J Radiol*. 2006;58(3):394–403.
14. Krabbe K, Gideon P, Wagn P, et al. MR diffusion imaging of human intracranial tumours. *Neuroradiology*. 1997;39(7):483–489.
15. Kotsenas AL, Roth TC, Manness WK, Faerber EN. Abnormal diffusion-weighted MRI in medulloblastoma: does it reflect small cell histology? *Pediatr Radiol*. 1999;29(7):524–526.
16. Chenevert TL, Stegman LD, Taylor JM, et al. Diffusion magnetic resonance imaging: an early surrogate marker of therapeutic efficacy in brain tumors. *J Natl Cancer Inst*. 2000;92(24):2029–2036.
17. Chenevert TL, McKeever PE, Ross BD. Monitoring early response of experimental brain tumors to therapy using diffusion magnetic resonance imaging. *Clin Cancer Res*. 1997;3(9):1457–1466.
18. Filippi CG, Edgar MA, Ulug AM, et al. Appearance of meningiomas on diffusion-weighted images: correlating diffusion constants with histopathologic findings. *AJNR Am J Neuroradiol*. 2001;22(1):65–72.
19. Hayashida Y, Hirai T, Morishita S, et al. Diffusion-weighted imaging of metastatic brain tumors: comparison with histologic type and tumor cellularity. *AJNR Am J Neuroradiol*. 2006;27(7):1419–1425.
20. Sugahara T, Korogi Y, Kochi M, et al. Usefulness of diffusion-weighted MRI with echo-planar technique in the evaluation of cellularity in gliomas. *J Magn Reson Imaging*. 1999;9(1):53–60.
21. Catalaa I, Henry R, Dillon WP, et al. Perfusion, diffusion and spectroscopy values in newly diagnosed cerebral gliomas. *NMR Biomed*. 2006;19(4):463–475.
22. Yang D, Korogi Y, Sugahara T, et al. Cerebral gliomas: prospective comparison of multivoxel 2D chemical-shift imaging proton MR spectroscopy, echoplanar perfusion and diffusion-weighted MRI. *Neuroradiology*. 2002;44(8):656–666.
23. Bulakbasi N, Kocaoglu M, Ors F, et al. Combination of single-voxel proton MR spectroscopy and apparent diffusion coefficient calculation in the evaluation of common brain tumors. *AJNR Am J Neuroradiol*. 2003;24(2):225–233.
24. Mardor Y, Roth Y, Ochershvilli A, et al. Pretreatment prediction of brain tumors' response to radiation therapy using high b-value diffusion-weighted MRI. *Neoplasia*. 2004;6(2):136–142.
25. Castillo M, Smith JK, Kwock L, Wilber K. Apparent diffusion coefficients in the evaluation of high-grade cerebral gliomas. *AJNR Am J Neuroradiol*. 2001;22(1):60–64.
26. Khan RB, Gutin PH, Rai SN, et al. Use of diffusion weighted magnetic resonance imaging in predicting early postoperative outcome of new neurological deficits after brain tumor resection. *Neurosurgery*. 2006;59(1):60–66.
27. Schaefer PW, Grant PE, Gonzalez RG. Diffusion-weighted MR imaging of the brain. *Radiology*. 2000;217(2):331–345.
28. Hein PA, Eskey CJ, Dunn JF, Hug EB. Diffusion-weighted imaging in the follow-up of treated high-grade gliomas: tumor recurrence versus radiation injury. *AJNR Am J Neuroradiol*. 2004;25(2):201–209.
29. Chan YL, Yeung DK, Leung SF, Chan PN. Diffusion-weighted magnetic resonance imaging in radiation-induced cerebral necrosis. Apparent diffusion coefficient in lesion components. *J Comput Assist Tomogr*. 2003;27(5):674–680.
30. Tsui EY, Chan JH, Ramsey RG, et al. Late temporal lobe necrosis in patients with nasopharyngeal carcinoma: evaluation with combined multi-section diffusion weighted and perfusion weighted MR imaging. *Eur J Radiol*. 2001;39(3):133–138.
31. Moffat BA, Chenevert TL, Lawrence TS, et al. Functional diffusion map: a noninvasive MRI biomarker for early stratification of clinical brain tumor response. *Proc Natl Acad Sci USA*. 2005;102(15):5524–5529.
32. Hamstra DA, Chenevert TL, Moffat BA, et al. Evaluation of the functional diffusion map as an early biomarker of time-to-progression and overall survival in high-grade glioma. *Proc Natl Acad Sci USA*. 2005;102(46):16759–16764.
33. Ellingson BM, Cloughesy TF, Lai A, et al. Quantitative probabilistic functional diffusion mapping in newly diagnosed glioblastoma treated with radiochemotherapy. *Neuro Oncol*. 2013;15(3):382–390.
34. Ellingson BM, Cloughesy TF, Zaw T, et al. Functional diffusion maps (fDMs) evaluated before and after radiochemotherapy predict progression-free and overall survival in newly diagnosed glioblastoma. *Neuro Oncol*. 2012;14(3):333–343.
35. Bisdas S, Koh TS, Roder C, et al. Intravoxel incoherent motion diffusion-weighted MR imaging of gliomas: feasibility of the method and initial results. *Neuroradiology*. 2013;55(10):1189–1196.
36. Inoue T, Ogasawara K, Beppu T, et al. Diffusion tensor imaging for preoperative evaluation of tumor grade in gliomas. *Clin Neurol Neurosurg*. 2005;107(3):174–180.
37. Field AS, Wu YC, Alexander AL. Principal diffusion direction in peritumoral fiber tracts: color map patterns and directional statistics. *Ann NY Acad Sci*. 2005;1064:193–201.
38. Goebell E, Fiehler J, Ding XQ, et al. Disarrangement of fiber tracts and decline of neuronal density correlate in glioma patients–a combined diffusion tensor imaging and 1H-MR spectroscopy study. *AJNR Am J Neuroradiol*. 2006;27(7):1426–1431.

39. Yu CS, Li KC, Xuan Y, et al. Diffusion tensor tractography in patients with cerebral tumors: a helpful technique for neurosurgical planning and postoperative assessment. *Eur J Radiol*. 2005;56(2):197–204.
40. Nimsky C, Grummich P, Sorensen AG, et al. Visualization of the pyramidal tract in glioma surgery by integrating diffusion tensor imaging in functional neuronavigation. *Zentralbl Neurochir*. 2005;66(3):133–141.
41. Lazar M, Alexander AL, Thottakara PJ, et al. White matter reorganization after surgical resection of brain tumors and vascular malformations. *AJNR Am J Neuroradiol*. 2006;27(6):1258–1271.
42. Schonberg T, Pianka P, Hendler T, et al. Characterization of displaced white matter by brain tumors using combined DTI and fMRI. *Neuroimage*. 2006;30(4):1100–1111.
43. Bondiau PY, Konukoglu E, Clatz O, et al. Biocomputing: numerical simulation of glioblastoma growth and comparison with conventional irradiation margins. *Phys Med*. 2011;27(2):103–108.
44. Kovanlikaya I, Firat Z, Kovanlikaya A, et al. Assessment of the corticospinal tract alterations before and after resection of brainstem lesions using Diffusion Tensor Imaging (DTI) and tractography at 3T. *Eur J Radiol*. 2011;77(3):383–391.
45. Potgieser AR, Wagemakers M, van Hulzen AL, et al. The role of diffusion tensor imaging in brain tumor surgery: a review of the literature. *Clin Neurol Neurosurg*. 2014;124C:51–58.
46. Fu C, Feng X, Bian D, et al. Simultaneous changes of magnetic resonance diffusion-weighted imaging and pathological microstructure in locally advanced cervical cancer caused by neoadjuvant chemotherapy. *J Magn Reson Imaging*. August 2015;42(2):427–435.
47. Stieltjes B, Schluter M, Didinger B, et al. Diffusion tensor imaging in primary brain tumors: reproducible quantitative analysis of corpus callosum infiltration and contralateral involvement using a probabilistic mixture model. *Neuroimage*. 2006;31(2):531–542.
48. Lu S, Ahn D, Johnson G, et al. Diffusion-tensor MR imaging of intracranial neoplasia and associated peritumoral edema: introduction of the tumor infiltration index. *Radiology*. 2004;232(1):221–228.
49. van Westen D, Latt J, Englund E, et al. Tumor extension in high-grade gliomas assessed with diffusion magnetic resonance imaging: values and lesion-to-brain ratios of apparent diffusion coefficient and fractional anisotropy. *Acta Radiol*. 2006;47(3):311–319.
50. Sundgren PC, Fan X, Weybright P, et al. Differentiation of recurrent brain tumor versus radiation injury using diffusion tensor imaging in patients with new contrast-enhancing lesions. *Magn Reson Imaging*. 2006;24(9):1131–1142.
51. Lee EY, Yu X, Chu MM, et al. Perfusion and diffusion characteristics of cervical cancer based on intraxovel incoherent motion MR imaging-a pilot study. *Eur Radiol*. 2014;24(7):1506–1513.
52. Provenzale JM, McGraw P, Mhatre P, et al. Peritumoral brain regions in gliomas and meningiomas: investigation with isotropic diffusion-weighted MR imaging and diffusion-tensor MR imaging. *Radiology*. 2004;232(2):451–460.
53. Price SJ, Burnet NG, Donovan T, et al. Diffusion tensor imaging of brain tumours at 3T: a potential tool for assessing white matter tract invasion? *Clin Radiol*. 2003;58(6):455–462.
54. Lu S, Ahn D, Johnson G, Cha S. Peritumoral diffusion tensor imaging of high-grade gliomas and metastatic brain tumors. *AJNR Am J Neuroradiol*. 2003;24(5):937–941.
55. Chiang IC, Kuo YT, Lu CY, et al. Distinction between high-grade gliomas and solitary metastases using peritumoral 3-T magnetic resonance spectroscopy, diffusion, and perfusion imagings. *Neuroradiology*. 2004;46(8):619–627.
56. Kono K, Inoue Y, Nakayama K, et al. The role of diffusion-weighted imaging in patients with brain tumors. *AJNR Am J Neuroradiol*. 2001;22(6):1081–1088.
57. Stadnik TW, Chaskis C, Michotte A, et al. Diffusion-weighted MR imaging of intracerebral masses: comparison with conventional MR imaging and histologic findings. *AJNR Am J Neuroradiol*. 2001;22(5):969–976.
58. Star-Lack J, Vigneron DB, Pauly J, et al. Improved solvent suppression and increased spatial excitation bandwidths for three-dimensional PRESS CSI using phase-compensating spectral/spatial spin-echo pulses. *J Magn Reson Imaging*. 1997;7(4):745–757.
59. Tran TK, Vigneron DB, Sailasuta N, et al. Very selective suppression pulses for clinical MRSI studies of brain and prostate cancer. *Magn Reson Med*. 2000;43(1):23–33.
60. Duyn JH, Gillen J, Sobering G, et al. Multisection proton MR spectroscopic imaging of the brain. *Radiology*. 1993;188(1):277–282.
61. Duyn JH, Moonen CT. Fast proton spectroscopic imaging of human brain using multiple spin-echoes. *Magn Reson Med*. 1993;30(4):409–414.
62. Adalsteinsson E, Irarrazabal P, Spielman DM, Macovski A. Three-dimensional spectroscopic imaging with time-varying gradients. *Magn Reson Med*. 1995;33(4):461–466.
63. Posse S, Tedeschi G, Risinger R, et al. High speed 1H spectroscopic imaging in human brain by echo planar spatial-spectral encoding. *Magn Reson Med*. 1995;33(1):34–40.
64. Zhang Y, Gabr RE, Zhou J, et al. Highly-accelerated quantitative 2D and 3D localized spectroscopy with linear algebraic modeling (SLAM) and sensitivity encoding. *J Magn Reson*. 2013;237:125–138.
65. Marshall I, Wardlaw J, Cannon J, et al. Reproducibility of metabolite peak areas in 1H MRS of brain. *Magn Reson Imaging*. 1996;14(3):281–292.
66. Calvar JA. Accurate 1H tumor spectra quantification from acquisitions without water suppression. *Magn Reson Imaging*. 2006;24(9):1271–1279.
67. Birken DL, Oldendorf WH. N-acetyl-L-aspartic acid: a literature review of a compound prominent in 1H-NMR spectroscopic studies of brain. *Neurosci Biobehav Rev*. 1989;13(1):23–31.
68. Moffett JR, Ross B, Arun P, et al. N-Acetylaspartate in the CNS: from neurodiagnostics to neurobiology. *Prog Neurobiol*. 2007;81(2):89–131.
69. Christiansen P, Toft P, Larsson HB, et al. The concentration of N-acetyl aspartate, creatine + phosphocreatine, and choline in different parts of the brain in adulthood and senium. *Magn Reson Imaging*. 1993;11(6):799–806.
70. Wyss M, Kaddurah-Daouk R. Creatine and creatinine metabolism. *Physiol Rev*. 2000;80(3):1107–1213.
71. Degaonkar MN, Pomper MG, Barker PB. Quantitative proton magnetic resonance spectroscopic imaging: regional variations in the corpus callosum and cortical gray matter. *J Magn Reson Imaging*. 2005;22(2):175–179.
72. Kent C. Regulatory enzymes of phosphatidylcholine biosynthesis: a personal perspective. *Biochim Biophys Acta*. 2005;1733(1):53–66.
73. Babb SM, Ke Y, Lange N, et al. Oral choline increases choline metabolites in human brain. *Psychiatry Res*. 2004;130(1):1–9.
74. Brief EE, Whittall KP, Li DK, MacKay A. Proton T1 relaxation times of cerebral metabolites differ within and between regions of normal human brain. *NMR Biomed*. 2003;16(8):503–509.
75. Gajewicz W, Papierz W, Szymczak W, Goraj B. The use of proton MRS in the differential diagnosis of brain tumors and tumor-like processes. *Med Sci Monit*. 2003;9(9):MT97–105.
76. Preul MC, Caramanos Z, Collins DL, et al. Accurate, noninvasive diagnosis of human brain tumors by using proton magnetic resonance spectroscopy. *Nat Med*. 1996;2(3):323–325.
77. Del Sole A, Falini A, Ravasi L, et al. Anatomical and biochemical investigation of primary brain tumours. *Eur J Nucl Med*. 2001;28(12):1851–1872.
78. Delorme S, Weber MA. Applications of MRS in the evaluation of focal malignant brain lesions. *Cancer Imaging*. 2006;6:95–99.
79. Lai PH, Ho JT, Chen WL, et al. Brain abscess and necrotic brain tumor: discrimination with proton MR spectroscopy and diffusion-weighted imaging. *AJNR Am J Neuroradiol*. 2002;23(8):1369–1377.

80. Cho YD, Choi GH, Lee SP, Kim JK. (1)H-MRS metabolic patterns for distinguishing between meningiomas and other brain tumors. *Magn Reson Imaging*. 2003;21(6):663–672.
81. Devos A, Lukas L, Suykens JA, et al. Classification of brain tumours using short echo time 1H MR spectra. *J Magn Reson*. 2004;170(1):164–175.
82. Li X, Vigneron DB, Cha S, et al. Relationship of MR-derived lactate, mobile lipids, and relative blood volume for gliomas in vivo. *AJNR Am J Neuroradiol*. 2005;26(4):760–769.
83. Law M, Yang S, Wang H, et al. Glioma grading: sensitivity, specificity, and predictive values of perfusion MR imaging and proton MR spectroscopic imaging compared with conventional MR imaging. *AJNR Am J Neuroradiol*. 2003;24(10):1989–1998.
84. Fayed N, Morales H, Modrego PJ, Pina MA. Contrast/Noise ratio on conventional MRI and choline/creatine ratio on proton MRI spectroscopy accurately discriminate low-grade from high-grade cerebral gliomas. *Acad Radiol*. 2006;13(6):728–737.
85. Chen J, Huang SL, Li T, Chen XL. In vivo research in astrocytoma cell proliferation with 1H-magnetic resonance spectroscopy: correlation with histopathology and immunohistochemistry. *Neuroradiology*. 2006;48(5):312–318.
86. Jenkinson MD, Smith TS, Joyce K, et al. MRS of oligodendroglial tumors: correlation with histopathology and genetic subtypes. *Neurology*. 2005;64(12):2085–2089.
87. White ML, Zhang Y, Kirby P, Ryken TC. Can tumor contrast enhancement be used as a criterion for differentiating tumor grades of oligodendrogliomas? *AJNR Am J Neuroradiol*. 2005; 26(4):784–790.
88. Lev MH, Ozsunar Y, Henson JW, et al. Glial tumor grading and outcome prediction using dynamic spin-echo MR susceptibility mapping compared with conventional contrast-enhanced MR: confounding effect of elevated rCBV of oligodendrogliomas [corrected]. *AJNR Am J Neuroradiol*. 2004;25(2):214–221.
89. Xu M, See SJ, Ng WH, et al. Comparison of magnetic resonance spectroscopy and perfusion-weighted imaging in presurgical grading of oligodendroglial tumors. *Neurosurgery*. 2005;56(5):919–926.
90. Chernov M, Hayashi M, Izawa M, et al. Differentiation of the radiation-induced necrosis and tumor recurrence after gamma knife radiosurgery for brain metastases: importance of multi-voxel proton MRS. *Minim Invasive Neurosurg*. 2005;48(4):228–234.
91. Sugahara T, Korogi Y, Kochi M, et al. Perfusion-sensitive MR imaging of gliomas: comparison between gradient-echo and spin-echo echo-planar imaging techniques. *AJNR Am J Neuroradiol*. 2001;22(7):1306–1315.
92. Matulewicz L, Sokol M, Wydmanski J, Hawrylewicz L. Could lipid CH2/CH3 analysis by in vivo 1H MRS help in differentiation of tumor recurrence and post-radiation effects? *Folia Neuropathol*. 2006;44(2):116–124.
93. Cohen BA, Knopp EA, Rusinek H, et al. Assessing global invasion of newly diagnosed glial tumors with whole-brain proton MR spectroscopy. *AJNR Am J Neuroradiol*. 2005;26(9):2170–2177.
94. Gajewicz W, Grzelak P, Gorska-Chrzastek M, et al. The usefulness of fused MRI and SPECT images for the voxel positioning in proton magnetic resonance spectroscopy and planning the biopsy of brain tumors: presentation of the method. *Neurol Neurochir Pol*. 2006;40(4):284–290.
95. Hall WA, Martin A, Liu H, Truwit CL. Improving diagnostic yield in brain biopsy: coupling spectroscopic targeting with real-time needle placement. *J Magn Reson Imaging*. 2001;13(1):12–15.
96. Payne GS, Leach MO. Applications of magnetic resonance spectroscopy in radiotherapy treatment planning. *Br J Radiol*. 2006;79:S16–S26. Spec No 1.
97. Graves EE, Nelson SJ, Vigneron DB, et al. A preliminary study of the prognostic value of proton magnetic resonance spectroscopic imaging in gamma knife radiosurgery of recurrent malignant gliomas. *Neurosurgery*. 2000;46(2):319–326. discussion 326–328.
98. Graves EE, Pirzkall A, Nelson SJ, et al. Registration of magnetic resonance spectroscopic imaging to computed tomography for radiotherapy treatment planning. *Med Phys*. 2001;28(12):2489–2496.
99. Hakyemez B, Erdogan C, Ercan I, et al. High-grade and low-grade gliomas: differentiation by using perfusion MR imaging. *Clin Radiol*. 2005;60(4):493–502.
100. Chan YL, Yeung DK, Leung SF, Cao G. Proton magnetic resonance spectroscopy of late delayed radiation-induced injury of the brain. *J Magn Reson Imaging*. 1999;10(2):130–137.
101. Graves EE, Nelson SJ, Vigneron DB, et al. Serial proton MR spectroscopic imaging of recurrent malignant gliomas after gamma knife radiosurgery. *AJNR Am J Neuroradiol*. 2001;22(4):613–624.
102. Plotkin M, Eisenacher J, Bruhn H, et al. 123I-IMT SPECT and 1H MR-spectroscopy at 3.0 T in the differential diagnosis of recurrent or residual gliomas: a comparative study. *J Neurooncol*. 2004;70(1):49–58.
103. Hollingworth W, Medina LS, Lenkinski RE, et al. A systematic literature review of magnetic resonance spectroscopy for the characterization of brain tumors. *AJNR Am J Neuroradiol*. 2006;27(7):1404–1411.
104. Schreuder SM, Lensing R, Stoker J, Bipat S. Monitoring treatment response in patients undergoing chemoradiotherapy for locally advanced uterine cervical cancer by additional diffusion-weighted imaging: a systematic review. *J Magn Reson Imaging*. September 2015;42(3):572–594.
105. Farquharson S, Tournier JD, Calamante F, et al. White matter fiber tractography: why we need to move beyond DTI. *J Neurosurg*. 2013;118(6):1367–1377.
106. Inano R, Oishi N, Kunieda T, et al. Voxel-based clustered imaging by multiparameter diffusion tensor images for glioma grading. *Neuroimage Clin*. 2014;5:396–407.
107. Provenzale JM, York G, Moya MG, et al. Correlation of relative permeability and relative cerebral blood volume in high-grade cerebral neoplasms. *AJR Am J Roentgenol*. 2006;187(4):1036–1042.
108. Cha S. Dynamic susceptibility-weighted contrast-enhanced perfusion MR imaging in pediatric patients. *Neuroimaging Clin N Am*. 2006;16(1):137–147. [ix].
109. Cha S, Knopp EA, Johnson G, et al. Intracranial mass lesions: dynamic contrast-enhanced susceptibility-weighted echo-planar perfusion MR imaging. *Radiology*. 2002;223(1):11–29.
110. Lupo JM, Lee MC, Han ET, et al. Feasibility of dynamic susceptibility contrast perfusion MR imaging at 3T using a standard quadrature head coil and eight-channel phased-array coil with and without SENSE reconstruction. *J Magn Reson Imaging*. 2006;24(3):520–529.
111. Nakagawa T, Tanaka R, Takeuchi S, Takeda N. Haemodynamic evaluation of cerebral gliomas using XeCT. *Acta Neurochir (Wien)*. 1998;140(3):223–233. discussion 233–234.
112. Muizelaar JP, Fatouros PP, Schroder ML. A new method for quantitative regional cerebral blood volume measurements using computed tomography. *Stroke*. 1997;28(10):1998–2005.
113. Law M, Young R, Babb J, et al. Comparing perfusion metrics obtained from a single compartment versus pharmacokinetic modeling methods using dynamic susceptibility contrast-enhanced perfusion MR imaging with glioma grade. *AJNR Am J Neuroradiol*. 2006;27(9):1975–1982.
114. Stewart GN. Researches on the Circulation Time in Organs and on the Influences which affect it: Parts I.-III. *J Physiol*. 1893;15(1–2):1–89.
115. Lupo JM, Cha S, Chang SM, Nelson SJ. Dynamic susceptibility-weighted perfusion imaging of high-grade gliomas: characterization of spatial heterogeneity. *AJNR Am J Neuroradiol*. 2005;26(6):1446–1454.
116. Uematsu H, Maeda M. Double-echo perfusion-weighted MR imaging: basic concepts and application in brain tumors for the assessment of tumor blood volume and vascular permeability. *Eur Radiol*. 2006;16(1):180–186.

117. Vonken EJ, van Osch MJ, Bakker CJ, Viergever MA. Measurement of cerebral perfusion with dual-echo multi-slice quantitative dynamic susceptibility contrast MRI. *J Magn Reson Imaging*. 1999;10(2):109–117.
118. Vonken EP, van Osch MJ, Bakker CJ, Viergever MA. Simultaneous quantitative cerebral perfusion and Gd-DTPA extravasation measurement with dual-echo dynamic susceptibility contrast MRI. *Magn Reson Med*. 2000;43(6):820–827.
119. Daldrup-Link HE, Brasch RC. Macromolecular contrast agents for MR mammography: current status. *Eur Radiol*. 2003;13(2):354–365.
120. Yang S, Law M, Zagzag D, et al. Dynamic contrast-enhanced perfusion MR imaging measurements of endothelial permeability: differentiation between atypical and typical meningiomas. *AJNR Am J Neuroradiol*. 2003;24(8):1554–1559.
121. Boxerman JL, Schmainda KM, Weisskoff RM. Relative cerebral blood volume maps corrected for contrast agent extravasation significantly correlate with glioma tumor grade, whereas uncorrected maps do not. *AJNR Am J Neuroradiol*. 2006;27(4):859–867.
122. Hartmann M, Heiland S, Harting I, et al. Distinguishing of primary cerebral lymphoma from high-grade glioma with perfusion-weighted magnetic resonance imaging. *Neurosci Lett*. 2003;338(2):119–122.
123. Rollin N, Guyotat J, Streichenberger N, et al. Clinical relevance of diffusion and perfusion magnetic resonance imaging in assessing intra-axial brain tumors. *Neuroradiology*. 2006;48(3):150–159.
124. Essig M, Waschkies M, Wenz F, et al. Assessment of brain metastases with dynamic susceptibility-weighted contrast-enhanced MR imaging: initial results. *Radiology*. 2003;228(1):193–199.
125. Kremer S, Grand S, Berger F, et al. Dynamic contrast-enhanced MRI: differentiating melanoma and renal carcinoma metastases from high-grade astrocytomas and other metastases. *Neuroradiology*. 2003;45(1):44–49.
126. Kremer S, Grand S, Remy C, et al. Contribution of dynamic contrast MR imaging to the differentiation between dural metastasis and meningioma. *Neuroradiology*. 2004;46(8):642–648.
127. Knopp EA, Cha S, Johnson G, et al. Glial neoplasms: dynamic contrast-enhanced T2*-weighted MR imaging. *Radiology*. 1999;211(3):791–798.
128. Sugahara T, Korogi Y, Kochi M, et al. Correlation of MR imaging-determined cerebral blood volume maps with histologic and angiographic determination of vascularity of gliomas. *AJR Am J Roentgenol*. 1998;171(6):1479–1486.
129. Maia Jr AC, Malheiros SM, da Rocha AJ, et al. MR cerebral blood volume maps correlated with vascular endothelial growth factor expression and tumor grade in nonenhancing gliomas. *AJNR Am J Neuroradiol*. 2005;26(4):777–783.
130. Shin JH, Lee HK, Kwun BD, et al. Using relative cerebral blood flow and volume to evaluate the histopathologic grade of cerebral gliomas: preliminary results. *AJR Am J Roentgenol*. 2002;179(3):783–789.
131. Aronen HJ, Gazit IE, Louis DN, et al. Cerebral blood volume maps of gliomas: comparison with tumor grade and histologic findings. *Radiology*. 1994;191(1):41–51.
132. Chaskis C, Stadnik T, Michotte A, et al. Prognostic value of perfusion-weighted imaging in brain glioma: a prospective study. *Acta Neurochir (Wien)*. 2006;148(3):277–285. discussion 285.
133. Maia Jr AC, Malheiros SM, da Rocha AJ, et al. Stereotactic biopsy guidance in adults with supratentorial nonenhancing gliomas: role of perfusion-weighted magnetic resonance imaging. *J Neurosurg*. 2004;101(6):970–976.
134. Tsui EY, Chan JH, Leung TW, et al. Radionecrosis of the temporal lobe: dynamic susceptibility contrast MRI. *Neuroradiology*. 2000;42(2):149–152.
135. Siegal T, Rubinstein R, Tzuk-Shina T, Gomori JM. Utility of relative cerebral blood volume mapping derived from perfusion magnetic resonance imaging in the routine follow up of brain tumors. *J Neurosurg*. 1997;86(1):22–27.
136. Sugahara T, Korogi Y, Tomiguchi S, et al. Posttherapeutic intraaxial brain tumor: the value of perfusion-sensitive contrast-enhanced MR imaging for differentiating tumor recurrence from nonneoplastic contrast-enhancing tissue. *AJNR Am J Neuroradiol*. 2000;21(5):901–909.
137. Ostergaard L, Hochberg FH, Rabinov JD, et al. Early changes measured by magnetic resonance imaging in cerebral blood flow, blood volume, and blood–brain barrier permeability following dexamethasone treatment in patients with brain tumors. *J Neurosurg*. 1999;90(2):300–305.
138. Bastin ME, Carpenter TK, Armitage PA, et al. Effects of dexamethasone on cerebral perfusion and water diffusion in patients with high-grade glioma. *AJNR Am J Neuroradiol*. 2006;27(2):402–408.
139. Wilkinson ID, Jellineck DA, Levy D, et al. Dexamethasone and enhancing solitary cerebral mass lesions: alterations in perfusion and blood-tumor barrier kinetics shown by magnetic resonance imaging. *Neurosurgery*. 2006;58(4):640–646.
140. Liebner S, Fischmann A, Rascher G, et al. Claudin-1 and claudin-5 expression and tight junction morphology are altered in blood vessels of human glioblastoma multiforme. *Acta Neuropathol*. 2000;100(3):323–331.
141. Ginsberg LE, Fuller GN, Hashmi M, et al. The significance of lack of MR contrast enhancement of supratentorial brain tumors in adults: histopathological evaluation of a series. *Surg Neurol*. 1998;49(4):436–440.
142. Roberts HC, Roberts TP, Ley S, et al. Quantitative estimation of microvascular permeability in human brain tumors: correlation of dynamic Gd-DTPA-enhanced MR imaging with histopathologic grading. *Acad Radiol*. 2002;9(suppl 1):S151–S155.
143. Hazle JD, Jackson EF, Schomer DF, Leeds NE. Dynamic imaging of intracranial lesions using fast spin-echo imaging: differentiation of brain tumors and treatment effects. *J Magn Reson Imaging*. 1997;7(6):1084–1093.
144. Uematsu H, Maeda M, Sadato N, et al. Vascular permeability: quantitative measurement with double-echo dynamic MR imaging–theory and clinical application. *Radiology*. 2000;214(3):912–917.
145. Roberts HC, Roberts TP, Brasch RC, Dillon WP. Quantitative measurement of microvascular permeability in human brain tumors achieved using dynamic contrast-enhanced MR imaging: correlation with histologic grade. *AJNR Am J Neuroradiol*. 2000;21(5):891–899.
146. Provenzale JM, Wang GR, Brenner T, et al. Comparison of permeability in high-grade and low-grade brain tumors using dynamic susceptibility contrast MR imaging. *AJR Am J Roentgenol*. 2002;178(3):711–716.
147. Law M, Yang S, Babb JS, et al. Comparison of cerebral blood volume and vascular permeability from dynamic susceptibility contrast-enhanced perfusion MR imaging with glioma grade. *AJNR Am J Neuroradiol*. 2004;25(5):746–755.
148. Jackson A, Kassner A, Annesley-Williams D, et al. Abnormalities in the recirculation phase of contrast agent bolus passage in cerebral gliomas: comparison with relative blood volume and tumor grade. *AJNR Am J Neuroradiol*. 2002;23(1):7–14.

CHAPTER

20

Magnetic Resonance Contrast Agents for Neuroradiology: Current Status

Genevieve Bolles, Maria Vittoria Spampinato

Department of Radiology, Division of Neuroradiology, Medical University of South Carolina, Charleston, SC, USA

INTRODUCTION

Since U.S. Food and Drug Administration (FDA) approval in 1988, magnetic resonance imaging (MRI) using gadolinium-based contrast agents (GBCAs) has been routinely used in the diagnosis and follow-up of many pathologies involving the central nervous system (CNS), including but not limited to neoplasms and inflammatory, infectious, degenerative, and vascular pathologies. The chemical and physical aspects of the common GBCA safety, biodistribution, and relaxation effects have been well documented,[1–5] and there is an enormous body of literature regarding their application in neuroradiological MR examinations. See Table 1 for a current list of FDA-approved GBCAs in the United States at the time of publication.[6–10] Although there are some clinical differences, all these agents have similar efficacies, biodistributions, and half-lives and low rates of similar adverse drug reactions. In neuroradiological MRI examinations, venous injection of approximately 20 ml of the agent, typically resulting in concentrations of approximately 0.1 mM/kg, is routine. Power injectors for controlled bolus injections at rates from 1 to 10 ml/s are in common use and are recommended when using the agent for "first-pass perfusion" studies in the brain (see below).

CONTRAST MEDIA IN NEUROIMAGING

Contrast enhancement is observed in many CNS tumors, "active" multiple sclerosis lesions, inflammation, and radiation necrosis. To varying degrees, the use of gadolinium agents helps demarcate the extent and pattern of such pathologies and can make small lesions, like acoustic neuromas, more conspicuous. In general, however, the enhancement must be considered more sensitive than specific. Following intravenous injection, the GBCAs distribute themselves through the vasculature and then, with the exception of neural tissue with an intact blood–brain barrier (BBB), throughout the extracellular space. Only vascular structures and areas of the brain without a BBB, such as nasal/sinus mucosa, choroid plexus, portions of the cranial nerves, pineal gland, infundibulum, and pituitary gland, will show varying degrees of physiologic enhancement after injection. Pathologic enhancement in neuroimaging may occur for several reasons or a combination thereof, including neoangiogenesis and increased permeability of blood vessels, enhancement of structures that are extra-axial and do not have a BBB, and/or breakdown of the BBB with leakage of contrast.[11]

In clinical practice, contrast-enhanced MRI is most often performed using T1-weighted sequences, with either spin-echo (SE) or gradient-echo (GRE) acquisitions. SE images provide better contrast enhancement of the brain lesions and have been preferred, although GRE images demonstrate improved spatial resolution with shorter imaging time and decreased artifact from motion.[12–16] The use of GBCAs increases the sensitivity and specificity of MRI in the detection of CNS pathology. T1-weighted sequences rely on the T1-shortening property of the gadolinium ion, which is how GBCAs were used the first 20 years after FDA approval. GBCAs concentrate in the extracellular space. The GBCA T1-shortening property causes faster longitudinal magnetization recovery and therefore greater MR signal intensity (enhancement) in the tissue compared to noncontrasted images. The greater the gadolinium contrast concentration is, the greater the T1-shortening effect, and therefore, signal enhancement is observed. The wash-in to the extracellular space is followed by a washout phase as

Handbook of Neuro-Oncology Neuroimaging, Second Edition
http://dx.doi.org/10.1016/B978-0-12-800945-1.00020-3

© 2016 Elsevier Ltd. All rights reserved.

TABLE 1 FDA-Approved Gadolinium-Based Contrast Agents for Use in the United States

Generic Name	Trade Name	Manufacturer	Formulation	Concentration (mol/l)	Group (NSF)[a]
Gadodiamide	Omniscan	GE Healthcare	Nonionic linear	0.5	1
Gadopentetate dimeglumine	Magnevist	Bayer Healthcare	Ionic linear	0.5	1
Gadoversetamide	OptiMARK	Covidien	Nonionic linear	0.5	1
Gadobenate dimeglumine	MultiHance	Bracco Diagnostics	Ionic linear	0.5	2
Gadoteridol	ProHance	Bracco Diagnostics	Macrocyclic	0.5	2
Gadoteric acid	Dotarem	Guerbet	Macrocyclic	0.5	2
Gadobutrol	Gadavist	Bayer Healthcare	Macrocyclic	1	2
Gadofosveset	Ablavar	Lantheus Medical	Macrocyclic	0.25	3
Gadoxetic acid	Eovist	Bayer Healthcare	Ionic linear	0.25	3

[a]***Group 1,*** *agents associated with greatest number of NSF cases;* ***group 2,*** *agents associated with few, if any, unconfounded cases of NSF;* ***group 3,*** *agents that have only recently appeared on the market.*

the gadolinium agents are cleared from the blood by the kidneys and, by extension, from the extracellular spaces back to the blood for renal excretion. Neural tissue is special in regard to these gadolinium agents in that an intact BBB minimizes the effect of the agent in typical T1-weighted scans.[17] The magnitude of T1 shortening is called relaxivity.[18]

In addition to T1-weighted sequences, contrast enhancement can also be seen on fluid-attenuated inversion recovery (FLAIR) images of the brain owing to a mild T1 effect of the long inversion time used to cancel out the signal intensity of water. However, vasculature does not enhance, making contrast-enhanced FLAIR images useful in visualizing superficial abnormalities, such as carcinomatosis or leptomeningeal inflammation (Figure 1).[10,19,20] Susceptibility-weighted imaging (SWI) is useful for detecting and differentiating intra-axial bleeds and calcifications. SWI sequences can be obtained after the administration of GBCAs without affecting the image quality.[10,21,22] Contrast-enhanced SWI can be used to evaluate arteriovenous shunts and/or the architecture of brain neoplasms.[10,23,24]

The goals of imaging for neoplastic disease processes are numerous, and contrast-enhanced MR imaging is essential throughout the course of the disease process.[25] Upon presentation, the roles of contrast-enhanced MRI include attempting to differentiate nonneoplastic from neoplastic conditions, making a diagnosis or differential diagnosis, evaluating the location and extent of the lesion, and establishing the grade of the tumor and possible complications.[26–29] During treatment, contrast-enhanced MR imaging is important for guiding surgical and/or radiation therapy.[30–33] During follow-up, imaging helps to monitor progression and response as well as to evaluate for posttreatment complications. Conventional contrast-enhanced MR imaging is limited, though, in the differential diagnosis of recurrent tumor, pseudo-progression, and radiation necrosis.[34]

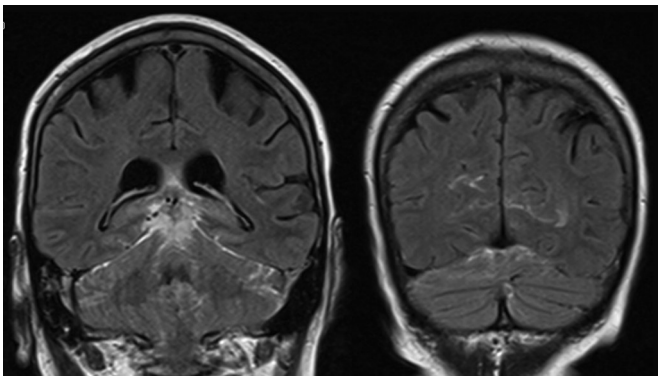


FIGURE 1 Leptomeningeal carcinomatosis. Coronal postcontrast FLAIR images in a patient with breast cancer reveal occipital and cerebellar leptomeningeal enhancement.

SAFETY

Adverse Reactions

Gadolinium chelates, approved for intravenous use since the late 1980s, are well tolerated with very low rates of acute adverse reactions. These rates are lower than is seen with iodinated contrast administration. The frequency of all acute adverse events after a standard dose of GBCA ranges from 0.07% to 2.4%; however, most of these reactions are mild (e.g., coldness or warmth at injection site, nausea, headache, pruritus, etc.). Even rarer are allergic-like reactions, ranging in frequency from 0.004% to 0.7%, with urticaria or hives being the most common reaction. True life-threatening reactions are extremely rare, with frequency ranging from 0.001%

to 0.01%. If the patient reports a history of prior adverse reaction to GBCA, there is increased risk (approximately eight times higher) of a future acute adverse reaction, which can be more severe. Patients with asthma and other allergies have an increased risk of adverse reactions, including previous allergic-like reactions to iodinated contrast administration, although there is no cross-reactivity.[35]

If the patient reports a previous reaction to GBCA, certain precautions should be taken. There should be a conversation between the ordering physician, the patient, and the radiologist about whether the examination requiring GBCA administration is necessary or could be replaced by a different examination, whether a different brand of GBCA could be used, and if the patient could be premedicated with corticosteroids and antihistamines, especially in patients with prior moderate to severe reaction. Treatment of acute adverse reactions is similar to adverse reactions from iodinated contrast. It is important that the personnel at the imaging site are trained in recognizing, handling, and treating adverse reactions. The patient should be taken out of the imaging room and away from the magnet to prevent hazards occurring from the resuscitation equipment. Generally, the patient should be immediately examined and the radiologist or person responding to the reaction should assess the general appearance of the patient, the ability to communicate, followed by an evaluation of the patient's breathing supplemented with lung auscultation; a set of vital signs should be immediately obtained. This information will allow evaluation of the severity of the reaction. Please see the most current edition of the American College of Radiology (ACR) *Manual on Contrast Media* for the most up-to-date treatments of acute contrast reactions. Extravasation of contrast is a potential complication of GBCA administration; however, studies have shown that GBCAs are less toxic to the skin when comparing equal volumes of iodinated contrast material. Also, the volume of GBCA injected is usually less for MR imaging, making the chances of compartment syndrome much smaller.[9] At approved dosages for MR imaging, there appear to be no nephrotoxic effects of GBCAs.

Nephrogenic Systemic Fibrosis

Nephrogenic systemic fibrosis (NSF), first described in 2000, is a potentially lethal fibrosing disease that primarily involves the skin but can also involve other tissues such as the lungs, skeletal muscles, esophagus, and heart.[36] Initial symptoms can include skin thickening and/or pruritus, which can progress to immobility and contractures of the joints. These signs and symptoms may develop and progress rapidly, making this condition potentially fatal.

When first described in 2000, it was noted to occur mostly in patients with end-stage chronic kidney disease (CKD), especially in patients requiring dialysis. Because no cases were reported prior to 1997, it was thought that a recently introduced agent might play a factor. In 2006, several groups noted a strong association between cases of NSF and the administration of GBCAs to patients with renal disease.[37,38] It is now widely accepted that GBCA administration is necessary in the development of NSF. The exact mechanism between GBCA administration and development of NSF is not definitively understood. The prevailing hypothesis includes that the development of NSF is related to the release of gadolinium from the chelates that constitute different GBCAs. This may partly explain why there are differences in the number of cases for different GBCAs. Most cases have been reported after administration of gadodiamide (Omniscan, GE Healthcare), gadopentetate dimeglumine (Magnevist, Bayer HealthCare Pharmaceuticals), or gadoversetamide (OptiMARK, Covidien), which are now considered group 1 agents, although other factors such as reporting bias and number of years in use may contribute to differences in reported cases (Table 1). Group 2 agents include gadobenate dimeglumine (MultiHance, Bracco Diagnostics), gadoteridol (ProHance, Bracco Diagnostics), gadoteric acid (Dotarem, Guerbet), and gadobutrol (Gadavist, Bayer HealthCare Pharmaceuticals). Group 3 agents include gadofosveset (Ablavar, Lantheus) and gadoxetic acid (Eovist, Bayer HealthCare Pharmaceuticals).

The onset of most cases of NSF occur within days to months following GBCA exposure; however, there have been rare reports of symptom development years after the last reported GBCA administration.[39] Whereas the precise mechanism is unclear, the postulated mechanism involves the gadolinium ions dissociating from chelates in GBCAs in patients with significant chronic or acute renal disease, probably due to prolonged clearance times as well as other metabolic factors intrinsic to renal disease. Then, the free gadolinium ion binds with an anion and gets deposited in various tissues as an insoluble complex, with resultant fibrosis occurring.[40–42] This is supported by the existence of gadolinium in affected tissues of NSF patients[43,44]; however, detection of such is not a requirement for NSF. It is believed that higher doses, either as a single administration or as the accumulation of multiple administrations over time, have a stronger association with development of NSF.[45,46] It should be noted that there are case reports of NSF in patients following administration of a single, standard dose of GBCA.[39,47]

It is estimated that patients with end-stage (CKD stage 5, eGFR <15 ml/min/1.73 m^2) and severe (CKD stage 4, eGFR 15–29 ml/min/1.73 m^2) CKD have a 1–7% chance of developing NSF after GBCA administration (Box 1).[37–40,45,48,49] However, most cases of NSF

BOX 1

PATIENTS AT RISK FOR NSF (ACR COMMITTEE ON DRUGS AND CONTRAST MEDIA)

- On any form of dialysis
- End-stage CKD (CKD 4 or 5, eGFR < 30 ml/min/1.73 m^2) without dialysis
- eGFR 30–40 ml/min/1.73 m^2 without dialysis because eGFR may fluctuate
- Acute kidney injury

have occurred in patients with end-stage CKD and on dialysis. In NSF patients with severe CKD, the eGFR was usually closer to 15 ml/min/1.73 m^2. However, it is important to remember that this is a rare disease and most patients with severe CKD who received GBCAs have not developed NSF. It is thought that 12–20% of cases of NSF have occurred in patients with acute kidney injury (AKI), either alone or superimposed on CKD; therefore AKI is also a risk factor for development of NSF.[50,51]

Screening for acute or chronic renal disease is important before administering GBCAs:

1. Outpatients: Asking the patient and/or caregiver if the patient has a problem with his or her kidneys is not an effective screening tool and may fail to detect AKI and CKD.[52] Suggested risk factors that should be screened based on published data and expert opinion include the following: age >60, history of dialysis, kidney transplant, single kidney, kidney surgery, cancer involving the kidneys, medically treated hypertension, and history of diabetes mellitus.[53,54] If the patient is on dialysis, no further testing is necessary. If the patient is deemed at risk for impaired renal function based on the screening form, eGFR should be calculated via existing or new laboratory testing. The Modification of Diet in Renal Disease equation should be used to calculate eGFR for adults,[55] and the Schwartz equation should be used for children.[56] Suggested timelines exist for the timing of laboratory studies/calculated eGFR and administration of GBCA, although no high-powered evidence exists to guide this (see the most up to date ACR *Manual on Contrast Media*, http://www.acr.org/quality-safety/resources/contrast-manual).
2. Inpatients: eGFR should be calculated within 2 days of administering GBCAs for all inpatients. Also, inpatients should be evaluated for AKI, as eGFR does not detect all cases of AKI.

Recommendations for imaging patients deemed at risk for NSF: Generally, once a patient is deemed at risk for NSF, there should be a conversation between the ordering physician, the radiologist, and the patient that involves potentially performing a different study that does not involve GBCA administration, avoiding group 1 agents (gadodiamide, gadopentetate dimeglumine, and gadoversetamide), and using the lowest contrast dose possible without hindering diagnostic information. Documentation about the decision-making process is key. Risks of developing NSF must be balanced against the potential risks of not performing the gadolinium-enhanced MRI.

Few cases of pediatric NSF have been reported (none under 6 years of age); however, the same guidelines used for adults should be followed for GBCA administration, as there is not enough information to demonstrate that NSF is less likely to occur in children.

Increasing awareness and subsequent precautions have already resulted in a decrease in new NSF cases.[57] Of note, research on NSF is still evolving. Please see the most up to date ACR *Manual on Contrast Media* as well as any publications after the time of print of this textbook chapter.[9]

ADVANCED TECHNIQUES USING CONTRAST MEDIA

Although intravenous contrast administration is important to characterize abnormalities in the CNS as previously mentioned in this chapter, it is a nonspecific reflection of breakdown of the BBB and/or increased vascularity. Advanced MRI techniques involving injection of GBCAs now exist that provide physiological information such as tissue perfusion and capillary permeability quantification.[25,58]

There are two main categories of dynamic contrast-enhanced perfusion MR imaging: dynamic susceptibility contrast-weighted imaging using T2- or T2*-weighted imaging (DSC-MRI) and dynamic contrast-enhanced MRI using T1-weighted imaging (DCE-MRI). In DSC-MRI the first pass of an administered GBCA contrast bolus (0.1 mmol/kg) through brain tissue is monitored using a

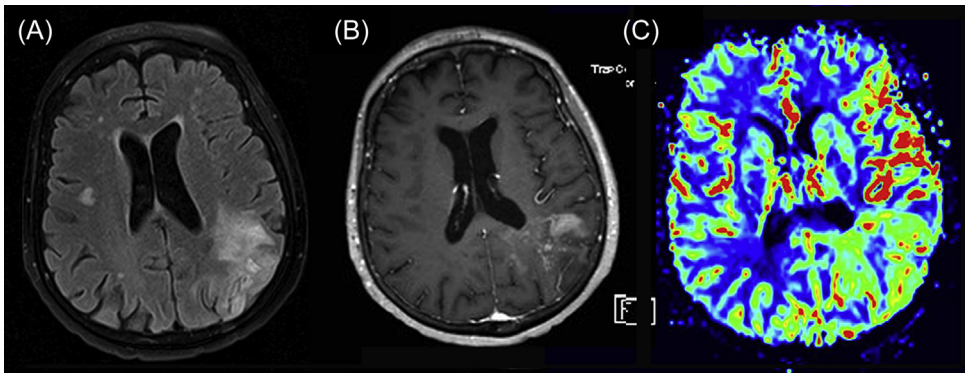


FIGURE 2 Glioblastoma multiforme. (A) Axial FLAIR image demonstrates T2 hyperintensity consistent with infiltrative tumor in the left parietal and occipital lobe. (B) Axial post-gadolinium T1 and (C) rCBV map demonstrate contrast enhancement and increased cerebral blood volume, indicating disruption of the blood–brain barrier and high tumor vascularity consistent with high-grade glioma.

dynamic series of T2- or T2*-weighted images. T2- or T2*-weighted images can be obtained using a multislice SE or GRE technique, respectively. Whereas both sequences have advantages and disadvantages, it is believed that the GRE echo-planar imaging is superior to SE echo-planar imaging to predict glioma grade and is the most widely used technique in clinical practice.[59,60] The susceptibility effect of a paramagnetic contrast agent results in signal loss in the signal intensity–time curve. This information is used to calculate hemodynamic parameters such as cerebral blood flow, cerebral blood volume (CBV), mean transit time, and time to peak contrast concentration.[61,62] Generally, postprocessing methods provide qualitative CBV maps that can be interpreted visually (Figure 2). Accurate quantification of relative CBV (rCBV) by using standard processing models applied to first-pass data requires exclusive intravascular localization of the GBCA. However, malignant brain tumors often have a leaky BBB, especially after chemoradiation. This may result in an underestimation of rCBV. Several correction methods have been developed to discard the effects of contrast leakage. Preload dosing of GBCAs (0.025–0.1 mmol/kg administered 5–10 min before the DSC-MRI acquisition) before DSC-MRI saturates the interstitial space T1-weighted signal intensity, thereby minimizing the T1-weighted leakage effects and subsequent T1-induced signal intensity increases during DSC administration. In addition to contrast preload, postprocessing leakage correction is recommended. Studies have shown that preload with postprocessing leakage correction and implicit correction of T1 leakage effects with a dual-echo acquisition technique are the best methods to differentiate tumor from normal brain on rCBV maps.[63] In clinical practice, semiquantitative calculations can be interpreted by comparing rCBV in tumor regions of interest (ROI) to rCBV in the contralateral normal-appearing brain. The most widely used metric is the rCBV ratio (tumoral rCBV/normal contralateral rCBV). The maximal rCBV ratio should be determined by placing multiple ROI in several tumoral hot spots.[64]

DSC-MRI measurements of tumor rCBV have been widely used in neuro-oncology for glioma grading,[65–67] prognosis prediction,[66,68–70] and differentiating recurrent tumor from radiation necrosis.[71–73] Although the WHO classification remains the gold standard for prognosis and treatment in brain tumors, DSC-MRI can help predict glioma grade and therefore better direct therapy.[65] rCBV ratios also have greater accuracy in glioma grading than conventional contrast-enhanced MRI.[65,74,75] rCBV is a strong predictor of prognosis, perhaps independent of or even better than histopathological grading, especially in cases that undergo partial resection or stereotactic biopsy, probably owing to tumor sampling errors or other variability sources in histopathology grading. DSC-MRI can also help locally guide biopsy and treatment based on the portion of the tumor that appears the most aggressive, which is not necessarily the part of the tumor that most avidly enhances.[76] Studies have shown that an area of increased rCBV (rCBV ratio > 1.75) in a low-grade glioma is associated with malignant transformation and poor prognosis.[69] Furthermore, this finding may be seen months earlier than contrast enhancement of the same site.[77] As a result, a threshold rCBV ratio of 1.75 was found to be predictive of time to progression and survival in gliomas.[69] rCBV measurements can also help differentiate between nonneoplastic processes such as abscess versus cystic brain tumor (lower rCBV ratio in abscess wall), between tumefactive demyelinating lesion (TDL) and glioma (lower rCBV ratio in TDL), and between lymphoma and glioma (lower rCBV ratio in lymphoma).[78–81] DSC-MRI has several limitations, such as lack of technique standardization across institutions and frequent inadequate reporting of technical parameters (e.g., GRE vs SE, contrast bolus description, flow rate, preload, and postprocessing method). Furthermore, susceptibility artifacts should be recognized and reported (i.e., surgical hardware, hemorrhagic foci, tumor near bone–air at skull base).[76,82]

DCE-MRI estimates the permeability of the BBB and therefore can characterize its integrity. It is commonly referred to as "permeability MRI" or "T1 perfusion MRI." It is typically performed before DSC-MRI, so that the first contrast bolus acts as the preload dose for DSC-MRI. Using T1-weighted DCE-MRI, the GBCA accumulation results in T1 shortening and therefore positive enhancement.[83] These images are usually obtained using a T1-weighted GRE sequence. The most commonly used DCE-MRI parameter is K^{Trans} (the volume transfer constant, aka vascular permeability). Other parameters that can be obtained from DCE-MRI include total plasma space volume (V_p), total extravascular–extracellular space volume (V_e), and the rate constant between extracellular space (EES) and blood plasma. DCE-MRI analysis is generally more complex and challenging than DSC-MRI, but this technique has been increasingly used at academic medical centers.

Both perfusion techniques can help in the evaluation of previously treated gliomas. In fact, contrast enhancement of previously treated gliomas can be a nonspecific finding, and additional information is needed to differentiate post-treatment changes from residual disease/recurrence.[25]

1. Glioma versus radiation necrosis or pseudo-progression: It is known that rCBV is elevated in recurrent high-grade glioma but not in radiation necrosis.[71,73,84] Delayed radiation necrosis should be differentiated from pseudo-progression. Delayed radiation necrosis occurs months to years after radiation treatment completion. Pseudo-progression occurs in high-grade gliomas when treated with chemoradiotherapy with temozolomide during the first 3–6 months of therapy. On conventional imaging both entities present with an increase in size and/or enhancement of previously treated tumor.[85,86] However, pseudo-progression usually represents a combination of viable neoplasm and chemoradiation-induced changes. As a result, recurrent tumor and pseudo-progression may demonstrate overlapping rCBV values, making the differentiation between these two entities a diagnostic challenge. There is more definitive evidence in the literature for the use of rCBV in the differentiation of recurrent high-grade glioma from delayed radiation necrosis (typically months to years after radiation treatment completion) than in the differentiation of recurrent high-grade glioma from pseudo-progression (typically 3–6 months after chemoradiotherapy with temozolomide).[87–90]
2. Pseudo-response: Antiangiogenic agents, such as bevacizumab or cediranib, may cause rapid decrease in general enhancement in patients with glioblastoma multiforme because of decreased vessel permeability instead of actual disease regression (Figure 3).[86,91,92] An initial imaging response lasting days or weeks, or pseudo-response, can occur in this patient population. As a result, it is important to carefully evaluate not only the enhancement pattern on contrast-enhanced T1-weighted images but also the extent of tumor infiltration on FLAIR images in patients treated with antiangiogenic agents. Again, DSC imaging may be able to predict time to progression in patients with glioblastoma.[76,93]

MAGNETIC RESONANCE ANGIOGRAPHY

The two primary imaging methods used in MRI to highlight blood vessels, also known as magnetic resonance angiography (MRA), are the time-of-flight (TOF) technique and the phase-contrast (PC) technique. To some degree, judicious use of gadolinium contrast can

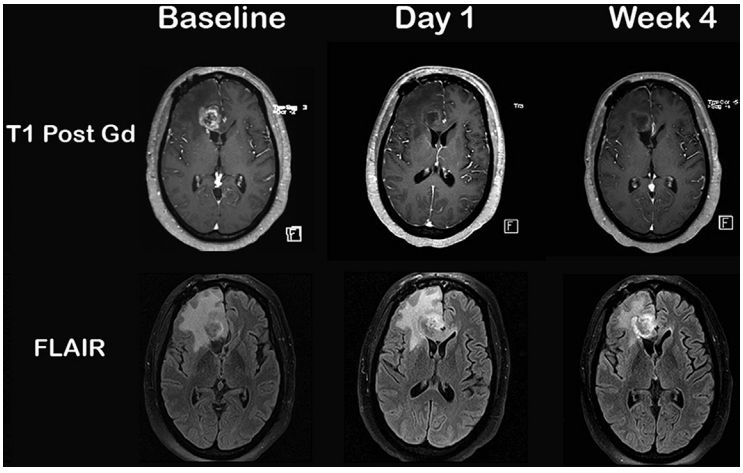


FIGURE 3 Glioblastoma multiforme treated with antiangiogenic agents. Compared to the baseline scan, decreased contrast enhancement of a right frontal lesion is observed 1 day after initiation of bevacizumab treatment. After 4 weeks there is further reduction of T2 signal abnormality on FLAIR images.

enhance the value of either MRA method by essentially allowing better visualization of the smaller distal branches owing to the (transient) shortened T1 of blood.[94–98] With TOF, for example, rapid radio-frequency (RF) pulsing of selected tissue sections serves to T1 saturate static spins within the section while spins flowing into the section have seen none, or only a few, of the RF pulses. These spins are thus largely T1 unsaturated and so appear bright, allowing the separation of flowing blood within vessels from the surrounding tissue. The bright vessels are most often displayed using maximum intensity projection algorithms to generate MR angiograms. TOF methods inherently utilize T1 saturation effects so that lowering blood T1 values with gadolinium contrast helps the blood remain unsaturated even for slow-flowing blood in small vessels, which may experience many RF pulses. Similarly, PC techniques (where the term "contrast" here refers to the contrast generated by the phase as opposed to magnitude of the MR signal and not to the "contrast" associated with the gadolinium agent contrast material) primarily utilize rapid GRE sequences whose signals will generally benefit from shortened blood T1 values. Thus, at appropriate doses, gadolinium contrast can enhance the value of TOF and PC MRA, though at a cost, including enhancement of some surrounding tissues and additional enhancement of the venous system, that can confound the interpretation of arterial signals that may be of greater interest. As both two- and three-dimensional TOF acquisitions have become faster, the timing of bolus injections of gadolinium contrast is more and more often coordinated with the actual acquisitions so that the various phases of arterial and venous enhancement can be separately visualized. The use of gadolinium contrast agents in MRA is not necessary and can add to the cost and complexity of the exam but, when used properly, can also enhance the utility of a given MRA study.

FUTURE APPLICATIONS

New contrast agents and new ideas for their use in magnetic resonance neuroimaging continue to be explored. In recent times, there has been much research involving paramagnetic liposomal MRI contrast agents. An extensive library of gadolinium-containing liposomal MRI contrast agents is available for imaging of CNS disease-specific markers and for image-guided drug delivery.[99] The properties and composition of liposomal MRI contrast agents influence their pharmacodynamic behavior. These compounds can be used for passive accumulation in neoplastic tissue. In fact, angiogenic neoplastic microvasculature is disorganized and presents large endothelial gaps.[100] As a result, nontargeted liposome nanoparticles with size ranging from 10 to 100 nm can extravasate into the tumor interstitium.[101] In addition, ligand-conjugated (targeted) paramagnetic liposomes can be used to target specific pathologic processes such as angiogenesis or inflammation or can be loaded with drugs for therapeutic intervention.[102] Another class of contrast agents known as ultrasmall superparamagnetic iron oxide particles (USPIOs) has been used to investigate BBB breakdown, for example, in inflammatory and neoplastic CNS disease; to assess tumor perfusion;[103] and as vehicles for MR-monitored glioma-targeted drug delivery.[104] Because enhancement peaks 24 h after intravenous infusion of these compounds and persists after 48 h, USPIO contrast-enhanced MRI has been used to evaluate for residual tumor in intraoperative MRI and postoperative MRI without the need for further administration of contrast material.[105] USPIOs have also been used as blood pool contrast agents in the evaluation of tumor perfusion using a time-series T2*-weighted technique (DSC).[106] Gahramanov et al. have found that perfusion MRI with ferumoxytol, an FDA-approved USPIO compound, can be used to diagnose pseudo-progression in glioblastomas treated with chemoradiotherapy.[107] Molecular imaging applications of USPIOs are also under investigation.[103] Animal studies have shown that activated microglia present within and surrounding malignant brain tumors can be labeled using USPIOs, and activated labeled microglia provide a fairly accurate tumor map on USPIO-enhanced MRI.[108] Limitations of USPIOs compared to GBCAs include the fact that they must be administered over approximately 30 min to limit adverse reactions, and MRI is typically performed 24 h after the infusion, although this limitation does not apply to the use as blood pool agents. Conversely, USPIOs have the advantage of being potential replacements for GBCAs in patients with chronic renal disease at risk for NSF[109] and of providing more accurate measurements of CBV and blood flow than GBCAs.[103]

In conclusion, although GBCAs remain a clearly better screening tool in clinical practice and are currently irreplaceable, novel compounds such as USPIOs and paramagnetic liposomal contrast agents are exciting tools with promising applications in many CNS pathologies and may become routinely utilized in clinical practice for diagnostic and treatment purposes in the near future.

References

1. Caravan P, Ellison JJ, McMurry TJ, Lauffer RB. Gadolinium(III) chelates as MRI contrast agents: structure, dynamics, and applications. *Chem Rev*. September 8, 1999;99(9):2293–2352.
2. Shellock FG, Kanal E. Safety of magnetic resonance imaging contrast agents. *J Magn Reson Imaging*. September 1999;10(3):477–484.
3. Yoshikawa K, Davies A. Safety of ProHance in special populations. *Eur Radiol*. 1997;7(Suppl 5):246–250.

4. Filippi M, Rovaris M, Capra R, et al. A multi-centre longitudinal study comparing the sensitivity of monthly MRI after standard and triple dose gadolinium-DTPA for monitoring disease activity in multiple sclerosis. Implications for phase II clinical trials. *Brain*. October 1998;121(Pt 10):2011–2020.
5. Oksendal AN, Hals PA. Biodistribution and toxicity of MR imaging contrast media. *J Magn Reson Imaging*. January–February 1993;3(1):157–165.
6. Sherry AD, Caravan P, Lenkinski RE. Primer on gadolinium chemistry. *J Magn Reson Imaging*. December 2009;30(6): 1240–1248.
7. de Haen C, Cabrini M, Akhnana L, Ratti D, Calabi L, Gozzini L. Gadobenate dimeglumine 0.5 M solution for injection (MultiHance) pharmaceutical formulation and physicochemical properties of a new magnetic resonance imaging contrast medium. *J Comput Assist Tomogr*. November 1999;23(Suppl 1): S161–S168.
8. Tombach B, Benner T, Reimer P, et al. Do highly concentrated gadolinium chelates improve MR brain perfusion imaging? Intraindividually controlled randomized crossover concentration comparison study of 0.5 versus 1.0 mol/L gadobutrol. *Radiology*. March 2003;226(3):880–888.
9. Drugs ACo, Media aC. *ACR Manual on Contrast Media*; 2013;9.
10. Kim BS, Gutierrez JE. Contrast-enhanced MR imaging in neuroimaging. *Magn Reson Imaging Clin N Am*. November 2012; 20(4):649–685.
11. Essig M, Dinkel J, Gutierrez JE. Use of contrast media in neuroimaging. *Magn Reson Imaging Clin N Am*. November 2012;20(4):633–648.
12. Cherryman G, Golfieri R. Comparison of spin echo T1-weighted and FLASH 90 degrees gadolinium-enhanced magnetic resonance imaging in the detection of cerebral metastases. *Br J Radiol*. September 1990;63(753):712–715.
13. Mirowitz SA. Intracranial lesion enhancement with gadolinium: T1-weighted spin-echo versus three-dimensional Fourier transform gradient-echo MR imaging. *Radiology*. November 1992;185(2):529–534.
14. Mugler 3rd JP, Brookeman JR. Theoretical analysis of gadopentetate dimeglumine enhancement in T1-weighted imaging of the brain: comparison of two-dimensional spin-echo and three-dimensional gradient-echo sequences. *J Magn Reson Imaging*. September–October 1993;3(5):761–769.
15. Pui MH, Fok EC. MR imaging of the brain: comparison of gradient-echo and spin-echo pulse sequences. *AJR Am J Roentgenol*. October 1995;165(4):959–962.
16. Li D, Haacke EM, Tarr RW, Venkatesan R, Lin W, Wielopolski P. Magnetic resonance imaging of the brain with gadopentetate dimeglumine-DTPA: comparison of T1-weighted spin-echo and 3D gradient-echo sequences. *J Magn Reson Imaging*. May–June 1996;6(3):415–424.
17. Steen RG, Reddick WE, Ogg RJ, Langston JW. Effect of a gadodiamide contrast agent on the reliability of brain tissue T1 measurements. *Magn Reson Imaging*. February 1999;17(2):229–235.
18. Kanal E. Gadolinium-based magnetic resonance contrast agents for neuroradiology: an overview. *Magn Reson Imaging Clin N Am*. November 2012;20(4):625–631.
19. Fukuoka H, Hirai T, Okuda T, et al. Comparison of the added value of contrast-enhanced 3D fluid-attenuated inversion recovery and magnetization-prepared rapid acquisition of gradient echo sequences in relation to conventional postcontrast T1-weighted images for the evaluation of leptomeningeal diseases at 3T. *AJNR Am J Neuroradiol*. May 2010;31(5):868–873.
20. Galassi W, Phuttharak W, Hesselink JR, Healy JF, Dietrich RB, Imbesi SG. Intracranial meningeal disease: comparison of contrast-enhanced MR imaging with fluid-attenuated inversion recovery and fat-suppressed T1-weighted sequences. *AJNR Am J Neuroradiol*. March 2005;26(3):553–559.
21. El-Koussy M, Schroth G, Gralla J, et al. Susceptibility-weighted MR imaging for diagnosis of capillary telangiectasia of the brain. *AJNR Am J Neuroradiol*. April 2012;33(4):715–720.
22. Noebauer-Huhmann IM, Pinker K, Barth M, et al. Contrast-enhanced, high-resolution, susceptibility-weighted magnetic resonance imaging of the brain: dose-dependent optimization at 3 tesla and 1.5 tesla in healthy volunteers. *Invest Radiol*. March 2006;41(3):249–255.
23. Jagadeesan BD, Delgado Almandoz JE, Benzinger TL, Moran CJ. Postcontrast susceptibility-weighted imaging: a novel technique for the detection of arteriovenous shunting in vascular malformations of the brain. *Stroke*. November 2011;42(11):3127–3131.
24. Hori M, Ishigame K, Kabasawa H, et al. Precontrast and postcontrast susceptibility-weighted imaging in the assessment of intracranial brain neoplasms at 1.5 T. *Jpn J Radiol*. May 2010;28(4):299–304.
25. Essig M, Anzalone N, Combs SE, et al. MR imaging of neoplastic central nervous system lesions: review and recommendations for current practice. *AJNR Am J Neuroradiol*. May 2012;33(5): 803–817.
26. Asari S, Makabe T, Katayama S, et al. Evaluation of MRI score in the differentiation between glioblastoma multiforme and metastatic adenocarcinoma of the brain. *Acta Neurochir (Wien)*. 1993;122(1–2):54–59.
27. Vaghi MA, Strada L, Visciani A, Passerini A, Longone V, Broggi G. Magnetic resonance imaging in intracranial gliomas. Comparison with computed tomography and serial stereotactic biopsy. *Acta Radiol Suppl*. 1986;369:151–153.
28. Mut M, Turba UC, Botella AC, Baskurt E, Lopes MB, Shaffrey ME. Neuroimaging characteristics in subgroup of GBMs with p53 overexpression. *J Neuroimaging*. April 2007;17(2):168–174.
29. Schumacher DJ, Tien RD, Friedman H. Gadolinium enhancement of the leptomeninges caused by hydrocephalus: a potential mimic of leptomeningeal metastasis. *AJNR Am J Neuroradiol*. April 1994;15(4):639–641.
30. Schad LR, Boesecke R, Schlegel W, et al. Three dimensional image correlation of CT, MR, and PET studies in radiotherapy treatment planning of brain tumors. *J Comput Assist Tomogr*. November–December 1987;11(6):948–954.
31. Shuman WP, Griffin BR, Haynor DR, et al. The utility of MR in planning the radiation therapy of oligodendroglioma. *AJR Am J Roentgenol*. March 1987;148(3):595–600.
32. Krol G, Galicich J, Arbit E, Sze G, Amster J. Preoperative localization of intracranial lesions on MR. *AJNR Am J Neuroradiol*. May–June 1988;9(3):513–516.
33. Zamorano L, Dujovny M, Chavantes C, Malik G, Ausman J. Image-guided stereotactic centered craniotomy and laser resection of solid intracranial lesions. *Stereotact Funct Neurosurg*. 1990;54–55:398–403.
34. Dequesada IM, Quisling RG, Yachnis A, Friedman WA. Can standard magnetic resonance imaging reliably distinguish recurrent tumor from radiation necrosis after radiosurgery for brain metastases? A radiographic-pathological study. *Neurosurgery*. November 2008;63(5):898–903. Discussion 904.
35. Hunt CH, Hartman RP, Hesley GK. Frequency and severity of adverse effects of iodinated and gadolinium contrast materials: retrospective review of 456,930 doses. *AJR Am J Roentgenol*. October 2009;193(4):1124–1127.
36. Kuo PH, Kanal E, Abu-Alfa AK, Cowper SE. Gadolinium-based MR contrast agents and nephrogenic systemic fibrosis. *Radiology*. March 2007;242(3):647–649.
37. Grobner T. Gadolinium–a specific trigger for the development of nephrogenic fibrosing dermopathy and nephrogenic systemic fibrosis? *Nephrol Dial Transpl: Official Publ Eur Dial Transpl Assoc–Eur Ren Assoc*. April 2006;21(4):1104–1108.
38. Marckmann P, Skov L, Rossen K, et al. Nephrogenic systemic fibrosis: suspected causative role of gadodiamide used for contrast-enhanced magnetic resonance imaging. *J Am Soc Nephrol: JASN*. September 2006;17(9):2359–2362.

39. Shabana WM, Cohan RH, Ellis JH, et al. Nephrogenic systemic fibrosis: a report of 29 cases. *AJR Am J Roentgenol*. March 2008;190(3):736–741.
40. Collidge TA, Thomson PC, Mark PB, et al. Gadolinium-enhanced MR imaging and nephrogenic systemic fibrosis: retrospective study of a renal replacement therapy cohort. *Radiology*. October 2007;245(1):168–175.
41. Abraham JL, Thakral C, Skov L, Rossen K, Marckmann P. Dermal inorganic gadolinium concentrations: evidence for in vivo transmetallation and long-term persistence in nephrogenic systemic fibrosis. *Br J Dermatol*. February 2008;158(2):273–280.
42. Rosenkranz AR, Grobner T, Mayer GJ. Conventional or gadolinium containing contrast media: the choice between acute renal failure or nephrogenic systemic fibrosis? *Wien Klin Wochenschr*. 2007;119(9–10):271–275.
43. Christensen KN, Lee CU, Hanley MM, Leung N, Moyer TP, Pittelkow MR. Quantification of gadolinium in fresh skin and serum samples from patients with nephrogenic systemic fibrosis. *J Am Acad Dermatol*. January 2011;64(1):91–96.
44. High WA, Ayers RA, Chandler J, Zito G, Cowper SE. Gadolinium is detectable within the tissue of patients with nephrogenic systemic fibrosis. *J Am Acad Dermatol*. January 2007;56(1): 21–26.
45. Wertman R, Altun E, Martin DR, et al. Risk of nephrogenic systemic fibrosis: evaluation of gadolinium chelate contrast agents at four American universities. *Radiology*. September 2008;248(3):799–806.
46. Kallen AJ, Jhung MA, Cheng S, et al. Gadolinium-containing magnetic resonance imaging contrast and nephrogenic systemic fibrosis: a case-control study. *Am J Kidney Dis*. June 2008; 51(6):966–975.
47. Pryor JG, Scott GA. Nephrogenic systemic fibrosis: a clinicopathologic study of 6 cases. *J Am Acad Dermatol*. November 2007;57(5):902–903.
48. Broome DR, Girguis MS, Baron PW, Cottrell AC, Kjellin I, Kirk GA. Gadodiamide-associated nephrogenic systemic fibrosis: why radiologists should be concerned. *AJR Am J Roentgenol*. February 2007;188(2):586–592.
49. Sadowski EA, Bennett LK, Chan MR, et al. Nephrogenic systemic fibrosis: risk factors and incidence estimation. *Radiology*. April 2007;243(1):148–157.
50. Abu-Alfa AK. Nephrogenic systemic fibrosis and gadolinium-based contrast agents. *Adv Chronic Kidney Dis*. May 2011;18(3):188–198.
51. Prince MR, Zhang H, Morris M, et al. Incidence of nephrogenic systemic fibrosis at two large medical centers. *Radiology*. September 2008;248(3):807–816.
52. Coresh J, Byrd-Holt D, Astor BC, et al. Chronic kidney disease awareness, prevalence, and trends among U.S. adults, 1999 to 2000. *J Am Soc Nephrol: JASN*. January 2005;16(1):180–188.
53. Choyke PL, Cady J, DePollar SL, Austin H. Determination of serum creatinine prior to iodinated contrast media: is it necessary in all patients? *Tech Urol*. June 1998;4(2):65–69.
54. Tippins RB, Torres WE, Baumgartner BR, Baumgarten DA. Are screening serum creatinine levels necessary prior to outpatient CT examinations? *Radiology*. August 2000;216(2):481–484.
55. Levey AS, Coresh J, Greene T, et al. Expressing the Modification of Diet in Renal Disease Study equation for estimating glomerular filtration rate with standardized serum creatinine values. *Clin Chem*. April 2007;53(4):766–772.
56. Schwartz GJ, Munoz A, Schneider MF, et al. New equations to estimate GFR in children with CKD. *J Am Soc Nephrol: JASN*. March 2009;20(3):629–637.
57. Altun E, Martin DR, Wertman R, Lugo-Somolinos A, Fuller 3rd ER, Semelka RC. Nephrogenic systemic fibrosis: change in incidence following a switch in gadolinium agents and adoption of a gadolinium policy–report from two U.S. universities. *Radiology*. December 2009;253(3):689–696.
58. Ferre JC, Shiroishi MS, Law M. Advanced techniques using contrast media in neuroimaging. *Magn Reson Imaging Clin N Am*. November 2012;20(4):699–713.
59. Donahue KM, Krouwer HG, Rand SD, et al. Utility of simultaneously acquired gradient-echo and spin-echo cerebral blood volume and morphology maps in brain tumor patients. *Magn Reson Med*. June 2000;43(6):845–853.
60. Sugahara T, Korogi Y, Kochi M, Ushio Y, Takahashi M. Perfusion-sensitive MR imaging of gliomas: comparison between gradient-echo and spin-echo echo-planar imaging techniques. *AJNR Am J Neuroradiol*. August 2001;22(7):1306–1315.
61. Calamante F, Thomas DL, Pell GS, Wiersma J, Turner R. Measuring cerebral blood flow using magnetic resonance imaging techniques. *J Cereb Blood Flow Metab: Official J Int Soc Cereb Blood Flow Metab*. July 1999;19(7):701–735.
62. Zaharchuk G. Theoretical basis of hemodynamic MR imaging techniques to measure cerebral blood volume, cerebral blood flow, and permeability. *AJNR Am J Neuroradiol*. November–December 2007;28(10):1850–1858.
63. Paulson ES, Schmainda KM. Comparison of dynamic susceptibility-weighted contrast-enhanced MR methods: recommendations for measuring relative cerebral blood volume in brain tumors. *Radiology*. November 2008;249(2):601–613.
64. Wetzel SG, Cha S, Johnson G, et al. Relative cerebral blood volume measurements in intracranial mass lesions: interobserver and intraobserver reproducibility study. *Radiology*. September 2002;224(3):797–803.
65. Law M, Yang S, Wang H, et al. Glioma grading: sensitivity, specificity, and predictive values of perfusion MR imaging and proton MR spectroscopic imaging compared with conventional MR imaging. *AJNR Am J Neuroradiol*. November-December 2003;24(10):1989–1998.
66. Lev MH, Ozsunar Y, Henson JW, et al. Glial tumor grading and outcome prediction using dynamic spin-echo MR susceptibility mapping compared with conventional contrast-enhanced MR: confounding effect of elevated rCBV of oligodendrogliomas [corrected]. *AJNR Am J Neuroradiol*. February 2004;25(2):214–221.
67. Spampinato MV, Smith JK, Kwock L, et al. Cerebral blood volume measurements and proton MR spectroscopy in grading of oligodendroglial tumors. *AJR Am J Roentgenol*. January 2007;188(1):204–212.
68. Bisdas S, Kirkpatrick M, Giglio P, Welsh C, Spampinato MV, Rumboldt Z. Cerebral blood volume measurements by perfusion-weighted MR imaging in gliomas: ready for prime time in predicting short-term outcome and recurrent disease? *AJNR Am J Neuroradiol*. April 2009;30(4):681–688.
69. Law M, Young RJ, Babb JS, et al. Gliomas: predicting time to progression or survival with cerebral blood volume measurements at dynamic susceptibility-weighted contrast-enhanced perfusion MR imaging. *Radiology*. May 2008;247(2):490–498.
70. Spampinato MV, Schiarelli C, Cianfoni A, et al. Correlation between cerebral blood volume measurements by perfusion-weighted magnetic resonance imaging and two-year progression-free survival in gliomas. *Neuroradiol J*. August 2013;26(4):385–395.
71. Barajas Jr RF, Chang JS, Segal MR, et al. Differentiation of recurrent glioblastoma multiforme from radiation necrosis after external beam radiation therapy with dynamic susceptibility-weighted contrast-enhanced perfusion MR imaging. *Radiology*. November 2009;253(2):486–496.
72. Hoefnagels FW, Lagerwaard FJ, Sanchez E, et al. Radiological progression of cerebral metastases after radiosurgery: assessment of perfusion MRI for differentiating between necrosis and recurrence. *J Neurol*. June 2009;256(6):878–887.
73. Hu LS, Baxter LC, Smith KA, et al. Relative cerebral blood volume values to differentiate high-grade glioma recurrence from post-treatment radiation effect: direct correlation between image-guided tissue histopathology and localized dynamic susceptibility-weighted contrast-enhanced perfusion MR imaging measurements. *AJNR Am J Neuroradiol*. March 2009;30(3):552–558.

74. Aronen HJ, Perkio J. Dynamic susceptibility contrast MRI of gliomas. *Neuroimaging Clin N Am*. November 2002;12(4):501–523.
75. Shin JH, Lee HK, Kwun BD, et al. Using relative cerebral blood flow and volume to evaluate the histopathologic grade of cerebral gliomas: preliminary results. *AJR Am J Roentgenol*. September 2002;179(3):783–789.
76. Lacerda S, Law M. Magnetic resonance perfusion and permeability imaging in brain tumors. *Neuroimaging Clin N Am*. November 2009;19(4):527–557.
77. Danchaivijitr N, Waldman AD, Tozer DJ, et al. Low-grade gliomas: do changes in rCBV measurements at longitudinal perfusion-weighted MR imaging predict malignant transformation? *Radiology*. April 2008;247(1):170–178.
78. Cha S, Pierce S, Knopp EA, et al. Dynamic contrast-enhanced T2*-weighted MR imaging of tumefactive demyelinating lesions. *AJNR Am J Neuroradiol*. June–July 2001;22(6):1109–1116.
79. Chiang IC, Hsieh TJ, Chiu ML, Liu GC, Kuo YT, Lin WC. Distinction between pyogenic brain abscess and necrotic brain tumour using 3-tesla MR spectroscopy, diffusion and perfusion imaging. *Br J Radiol*. October 2009;82(982):813–820.
80. Holmes TM, Petrella JR, Provenzale JM. Distinction between cerebral abscesses and high-grade neoplasms by dynamic susceptibility contrast perfusion MRI. *AJR Am J Roentgenol*. November 2004;183(5):1247–1252.
81. Weber MA, Zoubaa S, Schlieter M, et al. Diagnostic performance of spectroscopic and perfusion MRI for distinction of brain tumors. *Neurology*. June 27, 2006;66(12):1899–1906.
82. Cha S, Knopp EA, Johnson G, Wetzel SG, Litt AW, Zagzag D. Intracranial mass lesions: dynamic contrast-enhanced susceptibility-weighted echo-planar perfusion MR imaging. *Radiology*. April 2002;223(1):11–29.
83. Tofts PS, Brix G, Buckley DL, et al. Estimating kinetic parameters from dynamic contrast-enhanced T(1)-weighted MRI of a diffusable tracer: standardized quantities and symbols. *J Magn Reson Imaging*. September 1999;10(3):223–232.
84. Gasparetto EL, Pawlak MA, Patel SH, et al. Posttreatment recurrence of malignant brain neoplasm: accuracy of relative cerebral blood volume fraction in discriminating low from high malignant histologic volume fraction. *Radiology*. March 2009;250(3):887–896.
85. Clarke JL, Chang S. Pseudoprogression and pseudoresponse: challenges in brain tumor imaging. *Curr Neurol Neurosci Rep*. May 2009;9(3):241–246.
86. Hygino da Cruz Jr LC, Rodriguez I, Domingues RC, Gasparetto EL, Sorensen AG. Pseudoprogression and pseudoresponse: imaging challenges in the assessment of posttreatment glioma. *AJNR Am J Neuroradiol*. December 2011;32(11):1978–1985.
87. Hu LS, Eschbacher JM, Heiserman JE, et al. Reevaluating the imaging definition of tumor progression: perfusion MRI quantifies recurrent glioblastoma tumor fraction, pseudoprogression, and radiation necrosis to predict survival. *Neuro-Oncology*. July 2012;14(7):919–930.
88. Kong DS, Kim ST, Kim EH, et al. Diagnostic dilemma of pseudoprogression in the treatment of newly diagnosed glioblastomas: the role of assessing relative cerebral blood flow volume and oxygen-6-methylguanine-DNA methyltransferase promoter methylation status. *AJNR Am J Neuroradiol*. February 2011;32(2):382–387.
89. Tsien C, Galban CJ, Chenevert TL, et al. Parametric response map as an imaging biomarker to distinguish progression from pseudoprogression in high-grade glioma. *J Clin Oncol: Official J Am Soc Clin Oncol*. May 1, 2010;28(13):2293–2299.
90. Young RJ, Gupta A, Shah AD, et al. MRI perfusion in determining pseudoprogression in patients with glioblastoma. *Clin Imaging*. January–February 2013;37(1):41–49.
91. Norden AD, Drappatz J, Muzikansky A, et al. An exploratory survival analysis of anti-angiogenic therapy for recurrent malignant glioma. *J Neuro-Oncol*. April 2009;92(2):149–155.
92. Batchelor TT, Sorensen AG, di Tomaso E, et al. AZD2171, a pan-VEGF receptor tyrosine kinase inhibitor, normalizes tumor vasculature and alleviates edema in glioblastoma patients. *Cancer Cell*. January 2007;11(1):83–95.
93. Sawlani RN, Raizer J, Horowitz SW, et al. Glioblastoma: a method for predicting response to antiangiogenic chemotherapy by using MR perfusion imaging–pilot study. *Radiology*. May 2010;255(2):622–628.
94. Ozsarlak O, Van Goethem JW, Maes M, Parizel PM. MR angiography of the intracranial vessels: technical aspects and clinical applications. *Neuroradiology*. December 2004;46(12):955–972.
95. Mathews VP, Elster AD, King JC, Ulmer JL, Hamilton CA, Strottmann JM. Combined effects of magnetization transfer and gadolinium in cranial MR imaging and MR angiography. *AJR Am J Roentgenol*. January 1995;164(1):169–172.
96. Marchal G, Michiels J, Bosmans H, Van Hecke P. Contrast-enhanced MRA of the brain. *J Comput Assist Tomogr*. January–February 1992;16(1):25–29.
97. Jager HR, Ellamushi H, Moore EA, Grieve JP, Kitchen ND, Taylor WJ. Contrast-enhanced MR angiography of intracranial giant aneurysms. *AJNR Am J Neuroradiol*. November–December 2000;21(10):1900–1907.
98. Jung HW, Chang KH, Choi DS, Han MH, Han MC. Contrast-enhanced MR angiography for the diagnosis of intracranial vascular disease: optimal dose of gadopentetate dimeglumine. *AJR Am J Roentgenol*. November 1995;165(5):1251–1255.
99. Langereis S, Geelen T, Grull H, Strijkers GJ, Nicolay K. Paramagnetic liposomes for molecular MRI and MRI-guided drug delivery. *NMR Biomed*. July 2013;26(7):728–744.
100. Maeda H. Tumor-selective delivery of macromolecular drugs via the EPR effect: background and future prospects. *Bioconjugate Chem*. May 19, 2010;21(5):797–802.
101. Danhier F, Feron O, Preat V. To exploit the tumor microenvironment: passive and active tumor targeting of nanocarriers for anticancer drug delivery. *J Control Release: Official J Control Release Soc*. December 1, 2010;148(2):135–146.
102. Kelkar SS, Reineke TM. Theranostics: combining imaging and therapy. *Bioconjugate Chem*. October 19, 2011;22(10):1879–1903.
103. Weinstein JS, Varallyay CG, Dosa E, et al. Superparamagnetic iron oxide nanoparticles: diagnostic magnetic resonance imaging and potential therapeutic applications in neurooncology and central nervous system inflammatory pathologies, a review. *J Cereb Blood Flow Metab: Official J Int Soc Cereb Blood Flow Metab*. January 2010;30(1):15–35.
104. Chertok B, Moffat BA, David AE, et al. Iron oxide nanoparticles as a drug delivery vehicle for MRI monitored magnetic targeting of brain tumors. *Biomaterials*. February 2008;29(4):487–496.
105. Hunt MA, Bago AG, Neuwelt EA. Single-dose contrast agent for intraoperative MR imaging of intrinsic brain tumors by using ferumoxtran-10. *AJNR Am J Neuroradiol*. May 2005;26(5):1084–1088.
106. Neuwelt EA, Varallyay CG, Manninger S, et al. The potential of ferumoxytol nanoparticle magnetic resonance imaging, perfusion, and angiography in central nervous system malignancy: a pilot study. *Neurosurgery*. April 2007;60(4):601–611. Discussion 611–602.
107. Gahramanov S, Muldoon LL, Varallyay CG, et al. Pseudoprogression of glioblastoma after chemo- and radiation therapy: diagnosis by using dynamic susceptibility-weighted contrast-enhanced perfusion MR imaging with ferumoxytol versus gadoteridol and correlation with survival. *Radiology*. March 2013;266(3):842–852.
108. Fleige G, Nolte C, Synowitz M, Seeberger F, Kettenmann H, Zimmer C. Magnetic labeling of activated microglia in experimental gliomas. *Neoplasia*. November–December 2001;3(6):489–499.
109. Neuwelt EA, Hamilton BE, Varallyay CG, et al. Ultrasmall superparamagnetic iron oxides (USPIOs): a future alternative magnetic resonance (MR) contrast agent for patients at risk for nephrogenic systemic fibrosis (NSF)? *Kidney Int*. March 2009;75(5):465–474.

CHAPTER

21

Physics of High-Field Magnetic Resonance Imaging and Applications to Brain Tumor Imaging

Alayar Kangarlu

MRI Physics Psychiatry, Columbia University, New York, NY, USA

INTRODUCTION

Magnetic resonance is a powerful phenomenon that has offered the medical field an imaging technique (magnetic resonance imaging—MRI) that has revolutionized medicine for the past 3 decades. The magnetic field of MRI scanners plays a central role in the quality of images and as such there has been a relentless drive toward higher magnetic fields.[1–5] The higher fields, however, present formidable challenges such as high magnetic susceptibility, radio frequency (RF) inhomogeneities, and patient safety.[6,7] Almost all modern whole-body scanners use superconducting wires wound around cylinders with diameters of about 1 m and a length of about 2 m. The magnetic field strength of the majority of clinical scanners as of this writing is 1.5 T. In the early 1990s, a few 4-T research whole-body scanners were introduced by the major manufacturers and these units established the basis for a gradual introduction of higher fields into clinical settings.[1–4] Today, 3-T whole-body scanners are appearing in clinics and hospitals at a rapid rate. In 1997, an 8-T whole-body scanner was debuted by Ohio State University,[5] whose proof of safe exposure of human subjects[6,7] prepared the stage for manufacturers to follow suit and consider the feasibility of high-field (HF) MRI for medical imaging. Today, more than 50 academic institutions and research laboratories around the world operate 7-T whole-body scanners. This has changed the classification of MRI scanners as low field, HF, or ultrahigh field (UHF), as they have been transformed every decade. While as late as 2005 a 3-T scanner was considered to be a UHF magnet for research, today this field strength is viewed simply as HF for clinical applications and low-field or medium-field strength for research applications. And 7-T and higher field scanners, which were considered UHF at their debut, are now simply considered to be HF scanners. Such rapid change in taxonomy and proliferation of HF technology was achieved owing to the feasibility and stringent safety work that was demonstrated by the 8-T scanner. Another by-product of this rapid increase in the number of HF scanners is the interest of many scientists and engineers in its potential leading to developments such as parallel imaging in hardware,[8,9] diffusion tensor imaging (DTI) in pulse sequences, and molecular imaging in the area of contrast agents.

In this review, we present a summary of the physics of MRI, in which the advantages of HF MRI are identified. In addition, the inevitable disadvantages are described, and opportunities for engineering innovations for their minimization or elimination are surveyed. Considering that HF scanners are approaching the limits of existing superconducting materials' tolerance for magnetic flux, ways of understanding these limits and working with or around them are also illustrated.

MAGNETIC RESONANCE IMAGING PHYSICS

To better understand the role of the latest developments in enhancing sensitivity and specificity of MRI in augmenting its diagnostic capabilities, a brief review of the process of signal generation by magnetic resonance is necessary. The underlying process in this technique is nuclear magnetization, which all elements in nature exhibit. Hydrogen (^{1}H) is the most abundant element in

Handbook of Neuro-Oncology Neuroimaging, Second Edition
http://dx.doi.org/10.1016/B978-0-12-800945-1.00021-5

© 2016 Elsevier Ltd. All rights reserved.

biological tissues that has a large gyromagnetic ratio (γ). γ represents the nuclear magnetic dipole (μ) and its rotational dynamic that governs the ways in which individual μ's from spin and orbital motion of different protons and neutrons add to constitute the nuclear magnetic moment, ultimately causing a detectable signal from outside the body.[10] All elements with odd numbers of protons or neutrons in their nucleus have a nonzero angular momentum and magnetic moment. In this regard, ^{1}H is a unique element with the smallest odd number of protons. By the same token, other nuclei with odd numbers of nucleons (protons and neutrons) exhibit intrinsic magnetic moment, which is the result of individual magnetic moments. In the same manner in which tiny magnetic moments (fields) of the nucleons of an individual nucleus add to make up the elemental μ such as μ (^{1}H), the magnetic fields generated by each atom of a nucleus within an imaging voxel add to make up the magnetization vector associated with that voxel.

Upon exposure of an object to a strong static magnetic field (B_0), it interacts with the spin motion splitting its randomly distributed population into two groups of parallel (N^+) and antiparallel (N^-) protons with respect to the direction of B_0. The population difference between the two groups is governed by the Boltzmann distribution function,

$$\frac{N^+}{N^-} = e^{\frac{\Delta E}{kT}},$$

where $\Delta E = \gamma(h/2\pi)\, B_0$, T is the room temperature, and k is the Boltzmann constant (1.38×10^{-23} J/K).

For ^{1}H with a $\gamma = 42.575$ MHz/T a field strength of $B_0 = 1$ T will split the ^{1}H population with two groups whose energies are $\Delta E = 2.82 \times 10^{-26}$ J apart. Considering that human MRI is performed at room temperature, $kT = 4.01 \times 10^{-21}$ J or about 25 meV, the ratio of $\Delta E/kT$ becomes an infinitesimally small number, on the order of $<10^{-6}$. For such a small number, exponential terms on the right side of the equation could be approximated by $\sim 1 + \Delta E/kT$ or expressed in terms of the excess proton or population difference of $\Delta N = N^+ - N^-$, which, for such fields and temperatures, amounts to a ΔN/N of 3 ppm. This simple analysis implies that a magnetic field of 1 T will divide every group of 1 million water molecules, with 2 million hydrogen atoms, into two almost equal groups of about 1,000,000 hydrogen atoms. In other words, the population difference caused by a 1-T magnetic field amounts to only three more parallel protons (N^+) than antiparallel ones (N^-). This tiny population difference for such a relatively large external field is the reason for MRI's insensitivity. Were it possible to probe every hydrogen atom of the water molecules within the body, the signal-to-noise ratio (SNR) of MRI would have been more than 100,000 times stronger. Such increase in the SNR would have easily placed cellular and even molecular imaging within the reach of clinical magnets operating at 1.5 T. But this is not the case, and we had to work around this inherent insensitivity of MRI. So, once again, resorting to HF remains the only way to increase SNR.

On the other hand, given the high concentration of water in the body, each 1 μl or 1 mm^3 of biological tissues contains about 10^{15} excess protons, ΔN. Such a population of uncompensated protons will generate an SNR of <10 compared to the background noise. This is the reason why, despite the nuclear magnetic resonance insensitivity, we can still generate images representing voxels of ~μl. But, not much smaller! This warrants a discussion on how HF MRI can be further sensitized to become a cancer-specific diagnostic imaging tool. In the following, we discuss the principles of operation of critical technologies in HF MRI and those areas of highest potential for increasing MRI sensitivity toward the limits needed to visualize preangiogenic tumor pathology.[11]

MAGNETIC RESONANCE IMAGING OF BRAIN TUMORS—STATE OF THE ART

Despite the availability of whole-body HF scanners for a decade, few applications in cancer have surfaced as of this writing.[12,13] Aside from HF, the state of the art in brain tumor imaging is the incorporation of fast techniques and new contrast agents in visualizing the tumor. Yet, for most tumors and their metastases, the current state of the art in clinical MRI is unable to detect the tumor until after it has developed neovasculature.[14] While the ability to visualize microstructures by clinical scanners based on the indigenous contrast of deoxyhemoglobin is low, administration of contrast agents in animals has shown some promising results. Reliable vascular density quantification by contrast agents will help make routine MRI a better indicator of tumor activity. Correlations between microvascular density and cell proliferation in human gliomas found by immunohistochemical methods highlight the significance of such imaging capability for human cerebral gliomas.[14] They also emphasize the significance of HF in vivo detection of microvessels of about 100 μm diameter, which cannot be easily detected by 1.5-T scanners.

INDIRECT MEASURE OF PATHOLOGY

The primary collateral damages caused by cancer to brain tissues detectable by routine MRI are edema and hemorrhage. Also, owing to the ability of diffusion imaging at 1.5 T to distinguish fiber structures, such techniques can be used to detect any damage to myelinated axons. But, other than these indirect measures of tumor etiology, clinical MRI lacks specificity for prediction of

underlying pathology or histologic grade of tumors. So, one mission for MRI could be the enhancement of such specificity. In therapeutics, MRI could develop into a tool to make a distinction between tumor recurrence and consequences of radiation therapy, such as tumor necrosis. As of this writing, all means of assessment of tumor activity offered by MRI, such as vascular, metabolic, and physiological, are indirect. Metabolic quantification offered by magnetic resonance spectroscopy (MRS) enables measurement of choline, which is a good marker of membrane turnover that could precede the formation of necrotic lesions. High-resolution ^{1}H MRS will provide a measure of this activity. MRI studies to date have visualized brain tumors in contrast with normal tissues. The mechanism of signal generation in MRI has not been proven to correlate with the underlying pathology of cancer, although the consequences of cancer, such as breakdown of the blood–brain barrier (BBB), necrosis, hemorrhage, edema, and inflammation, have MRI implications that have been used in the past for visualization of tumors. However, a correlation between these measures and clinical manifestations of the disease has not yet been established.

A DIRECT MEASURE OF PATHOLOGY

The ideal feature in MRI for cancer studies would be an ability to monitor directly the pathologic processes associated with cancer. Imaging techniques could be sensitized for particular structural or physiological characteristics that best represent a particular pathology. In cancer, angiogenesis lends itself well to MRI optimizations for cancer imaging. For example, routine MRI operating at 1.5 T has come a long way since its early days in imaging brain tumors. Today's 1.5-T images have higher SNR, higher contrast-to-noise ratio (CNR), and fewer artifacts than their earlier counterparts. This level of progress has enabled clinicians to use spectroscopy, perfusion, DTI, and, soon, functional MRI (fMRI), at 1.5 T, as approved tools of medical diagnosis. But, despite these many innovations to improve the quality of images and speed up acquisition, the underlying insensitivity of MRI has prevented this modality from being able to detect tumors directly at their inception, based on their etiology and not collateral consequences. Beyond the HF increase in SNR, affiliated technologies such as RF coils, pulse sequences, and gradient technology have reached the level of maturity that engineering and safety limits allow. Further enhancement in MRI ability of tumor detection requires extension of its reach into microscopic aspects of tissue architecture. One active area for sensitization of MRI to cancer pathology is the application of contrast agents. A new class of contrast-enhancing agents with the ability to target directly pathological sites has raised hopes for achieving molecular-level detection of cancer with whole-body MRI scanners. When this happens, it will amount to a second revolution in diagnostic imaging, the first being the appearance of MRI as a routine radiological device.

HOW MAGNETIC RESONANCE IMAGING COMPARES WITH OTHER IMAGING TECHNIQUES

One of the major disadvantages of MRI is its long acquisition time compared to optical imaging, computer-assisted tomography (CT), and positron emission tomography (PET). But all of these other techniques are beset by difficulties of their own. CT scanning involves the use of ionizing radiation. Optical imaging suffers from very small penetration depth within the human body. PET images can be produced only at low resolution (5 mm) and are invasive. MR images produce a high soft-tissue contrast at a high resolution. But the primary contrast mechanisms are the magnetization relaxation times, T1 and T2. Considering that T1s are on the order of 1 s and T2s 0.1 s, and spatial encoding of the resonant spins requires phase encoding in at least one dimension of a two-dimensional image, the acquisition times become long, on the order of 5 min per pulse sequence. Since its inception, MRI has constantly witnessed faster imaging sequences to deal with this drawback. Imaging in steady-state, single-shot excitation techniques such as echoplanar imaging (EPI) and multiple-refocusing techniques such as fast spin echo (FSE), etc., has considerably reduced imaging time, but not down to real time yet.

HIGH-FIELD IMAGING: PROS AND CONS

In assessing the role of HF MRI in cancer, the underlying pathology should be kept in perspective. Existing imaging techniques have been proven to be insensitive for the detection of most tumors or their metastases at their early stages. Subsequent to tumor neovascularization, MRI can use the contrast generated by the presence of extra paramagnetic enhancement to visualize neovasculature or other concurring or ensuing events such as edema. The dependence of 1.5-T MRI on collateral events such as edema for visualization of tumors has set a ceiling for the utility of this tool for noninvasive monitoring of the progression of the disease and therapeutic efficacy. This is why the search for techniques capable of accessing the microstructure of the brain tissues is at full throttle. Few alternatives are available to sensitize MRI to cancer pathology at a microscopic level. High magnetic field (B_0) is one such option, representing the ultimate limit of the SNR of images. The SNR is directly proportional to B_0 and

is the primary determinant of the image resolution.[15,16] HF MRI is also critically dependent on RF coil technology and gradient design. Particularly, RF plays an important role in the quality of HF images. This issue and ways of improving it are analyzed in this chapter. Improvement of the image quality to the extent of microscopic resolution in MRI is a significant goal for cancer and must be rigorously pursued. In this regard, while the advantages of HF MRI in its application to cancer are well known,[17] the disadvantages and challenges in materializing its goals must also be fully scrutinized. Understanding of these challenges will translate them into engineering topics for research that will ultimately help improve the technology and sharpen its usefulness.[18]

HIGH-RESOLUTION IMAGING

In further enhancing the visibility of cancer pathology to HF MRI, the visualization of the normal tissues and the etiology of the cancer must be considered. The most striking aspect of images published by HF whole-body MRI scanners provides evidence that acquisition of microscopic resolution from the human body within clinically acceptable time is possible, as shown in Figure 1.

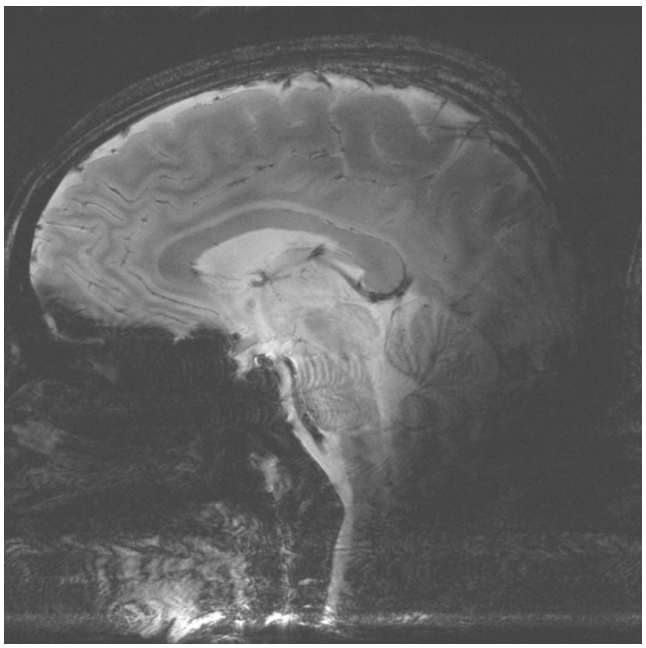


FIGURE 1 A sagittal GRE image of a human brain at 8 T. A number of artifacts appear on this image including (A) strong signal void due to the tissue–air interface in the prefrontal cortex around the sinuses and orbitals, (B) loss of all tissues in the oral cavity, and (C) RF ripple artifact originating from multiple flip angle, the off-center placement of the head in the coil causing signal loss in the posterior region, and inadequate insertion of the head into the coil, subjecting the lower portion of the image to inhomogeneous B_1 causing strong distortion in tissue representation.

Such resolution is achieved[17] while staying within regulatory guidelines concerning RF power deposition and gradient switching. In addition, each pulse sequence has an RF energy associated with it, which is a function of sequence parameters. These sequence parameters could be adjusted to prevent most sequences from posing a safety hazard at HF strengths.[7] For example, gradient echo (GRE) contains less RF energy than does spin echo (SE). This makes it ideal for HF applications. This is particularly true, since GRE has a high sensitivity for the detection of microvasculature, such as capillaries and venules.[17] The high paramagnetic effect produced by deoxyhemoglobin will generate an inhomogeneous magnetic field in the near vicinity of these vessels, causing rapid dephasing in precessional coherence, i.e., drastically reducing T2*. Such a dephasing effect is a function of the magnetic field, giving rise to a more striking signature for these vessels at higher fields as is shown in Figures 1 and 2. At HF, GRE gains additional sensitivity that is particularly useful for visualization of neovasculature around and within the tumor. While 100-μm-resolution images of the whole head from an awake subject are possible, in the absence of ultrafast techniques, acquisition of these images is long. However, given the prevalence of 200- to 300-μm vessels in most brain tumors, GRE could be further routinely sensitized to detect neovasculature in vivo. This aspect of HF MRI lends itself to the development of new noninvasive tools

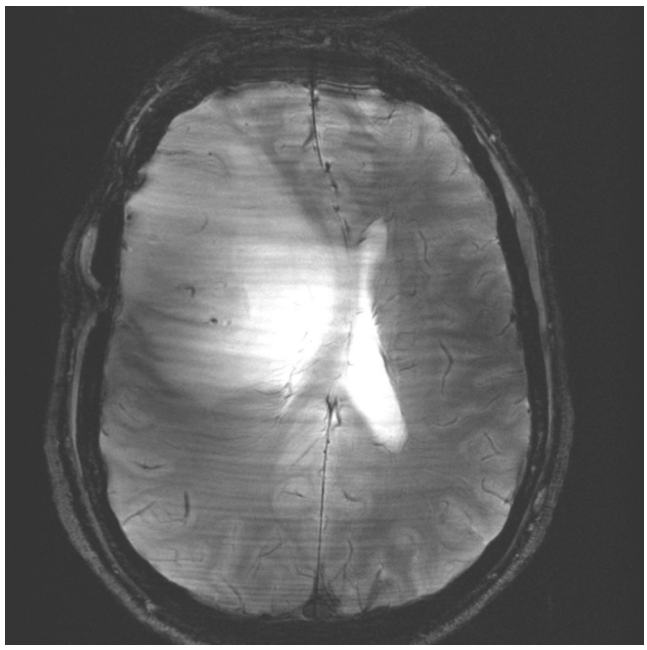


FIGURE 2 An axial GRE image of a brain tumor at 8 T. Distinct features are (A) high SNR as translated into 200-μm in-plane resolution, (B) bright center or dielectric resonances, (C) no signal from the skull because of its short T2* and high susceptibility, and (D) horizontal striped artifacts due to a repetitive motion caused by pulsatile motions in the disproportionate amount of cerebrospinal fluid within the slice plane.

for monitoring tumor progression and identifying and validating biological endpoints whereby novel antiangiogenesis agents can be more rapidly evaluated regarding their angiostatic efficacy and clinical relevance. Other sequences have the potential for cancer-specific enhancement. These include diffusion-based images and spectroscopic techniques. While diffusion as a thermally induced process is not field dependent, the high SNR of HF will generate a high CNR that enhances conspicuity of the diffusion-modifying pathology. Edema, in particular, has a strong diffusion signature. Even with diffusion-weighted imaging (DWI) and a spatial resolution of $250 \times 250 \times 1000$ μm, images of regional morphological and functional heterogeneity in the tumor could be obtained at HF. This resolution, however, is not sufficient to resolve the microvasculature. Reports of sequences visualizing cortical microanatomy in brain samples have shown a contrast superior to any clinical imaging techniques that rival histology.[18] Others have been able to optimize the resolution of 3-T scanners to observe cortical layers in human brain.[19] Observation of multilaminar structures in the cortical gray matter is a milestone in in vivo detection of brain microstructures and they can be clearly seen in images from today's HF scanners. While high SNR in HF MRI has already found many applications, its help in cancer diagnosis and therapy has not been immediate. But it holds promise that should be further explored, while considering other means of image enhancement, such as data acquisition, RF coils, relaxation effects, susceptibility contrast, and contrast agents. Innovations in these areas, just within the short time since the 8 T debut, have made great strides in making HF scanners a viable investment in radiology. Scientists are actually designing experiments with their 7-T whole-body scanners that were inconceivable with clinical imaging at 1.5 T. Development of MR microscopy (MRM) for in vivo application neuroimaging has the potential to produce results that would correlate the clinical deficit with the presence or absence of various types of tumors. Development of in vivo human MRM with a 50- to 100-μm resolution is not far from reach and will further inform tumor studies. Our ability to routinely acquire images with a 200-μm resolution has set the stage for further innovations in lesion microscopy.[17] In vivo human MRM will be the precursor to in vivo human cellular imaging. The technical issues on the path to full realization of in vivo MRM are currently the subject of many engineering studies in MRI.

MAGNETIC SUSCEPTIBILITY

The inhomogeneity of living tissues combined with compartmentalized organs and cavities introduces a challenge in MRI. This is due to the necessity in MRI for a highly homogeneous magnetic field at the imaged site. This stringent homogeneity requirement, i.e., about 0.1 ppm/cm, is the primary reason for the size and price of the MRI magnets. Tissue heterogeneity modifies B_0 homogeneity and must be compensated for by shimming schemes, pulse sequence design, or postprocessing. In humans, tissue contents vary from solid to gaseous and various consistencies of liquid in between. This drastic variation in consistency has profound contrast implications, particularly on HF MR images owing to magnetic susceptibility (χ) effects on magnetization (M) of the tissue within each voxel. As $\boldsymbol{B}_0 = \mu_0(1 + \chi)\mathbf{H}$, where $\mathbf{M} = \chi\mathbf{H}$, μ_0 is the permeability of air, and $\mathbf{H}$ is the magnetic flux, variation of χ causes changes in B_0, which deteriorates B_0 homogeneity over the sample. Despite the fact that susceptibility causes a loss of signal, an accurate account of its magnitude could enable countermeasures to minimize its adverse effects and enable one to use its T2* contrast potentials to their advantage.[20] At HF, susceptibility-induced T2* effects could be used as a source of contrast to achieve very high resolution to enhance MR images to the limit of microscopy. While magnetic susceptibility causes artifacts leading to signal loss in brain near air-filled sinuses, the T2*-based gradient recalled echo (GRE) sequence has shown much potential on high-resolution images at 7 T and higher. GRE uses a gradient reversal to rephrase the transverse magnetization (**M**), in contrast to SE sequence that use a 180° RF pulse.[21,22] As gradients are unable to rephrase the dephasing caused by local susceptibility-induced inhomogeneities, the heterogeneous nature of the tissues drastically reduces the T2* at HF, making it suitable for microstructure depiction. The 8-T GRE images[14,17] made the case for the utility of GRE in neurology applications, such as brain tumor studies, by highlighting its unique capability in showing microvasculature. However, GRE images bear testimony to artifacts that go beyond the voxel point spread function, as seen in Figures 1 and 3. Any large source of magnetic susceptibility will cast a large dark shadow on the images. Susceptibility-induced artifacts due to sinuses, vestibular tube, or dental fillings are particularly pronounced at HF and could wipe out signal in a large portion of the image. GRE artifacts can also lower the efficiency of fat suppression as the fat and water resonances are only 3.5 ppm apart. Susceptibility could also have a detrimental effect on diffusion-based contrasts such as DWI, apparent diffusion constant, and DTI. The effect of magnetic susceptibility on diffusion is due to a diffusion theory assumption that signal loss from various molecules is a function of their state of motion alone. Magnetic susceptibility and its variation across the sample add complications to this picture that should be taken into account for diffusion image interpretation. The initial studies at 8 T highlighted the contrast between strong T2* of GRE and T2 of SE by

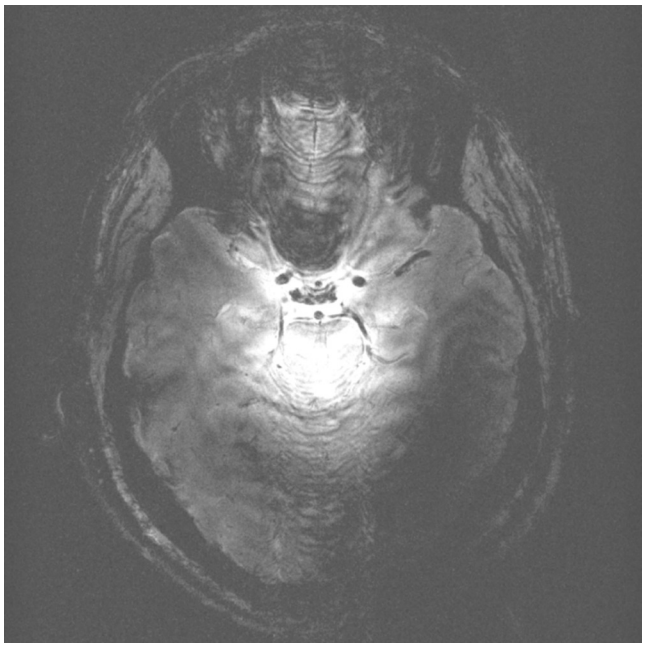


FIGURE 3 An axial GRE view of a human head image acquired at 8 T. This image has a strong dielectric resonance at the central regions and a strong susceptibility source inferior to the slice location. The susceptibility inhomogeneity caused in the inferior regions of this slice extends over a large region including the superior occipital gyrus, calcarine sulcus, and fusiform gyrus.

investigating the feasibility of FSE sequences, such as rapid acquisition by relaxation enhancement (RARE).[23] The use of FSE sequences was viewed with caution for HF applications because of their high RF power content caused by RF refocusing. But the ability of FSE for suppression of the T2* mechanism, thereby increasing SNR and enabling the use of the T2 mechanism for brain studies, provided motivation for investigation into the health and feasibility consequences of their use at HF.[6,7,23,24]

As mentioned above, the T2* could also be used as a source of contrast. Such is the case in blood oxygen level-dependent (BOLD) mechanisms that generate a T2*-based change in SNR, also called activation SNR, in fMRI studies. BOLD SNR increases proportional to T2* generating functional contrast in brain tissues based on the difference in susceptibility $\Delta\chi$ of oxyhemoglobin and deoxyhemoglobin. Such $\Delta\chi$ in tissue translates into ΔR^*, or a difference in relaxivity, which is a measure of the hemodynamic response function (HRF) to an external neurological stimulation (NS). The establishment of a mathematical relationship between HRF and NS will advance our knowledge of the inner workings of the brain. Such relationships could in turn be used as a measure of functional performance of the brain, which could be useful in the evaluation of the damage to brain tissue outside the visible tumor boundaries. fMRI maps have shown great potential for presurgery planning, and refinement of their results will strengthen the neurosurgeon's hand in the process of tumor resection.

In other applications, susceptibility-induced signal dephasing is used to advantage. The so-called iron oxide-based contrast agents, such as ultrasmall superparamagnetic iron oxide particles (USPIOs), with their ability to kill MRI signal in their near vicinity, are a promising candidate for negative contrast. In addition, gadolinium-based molecules, such as Gd-DTPA, through their ability for T1 relaxivity enhancement, are used as positive contrast agents. This means that negative agents or T2 agents cause darkening of images on their sites, and positive agents or T1 agents brighten the images in the regions where they reside. The role of molecular dynamics in the determination of lanthanide-based contrast agents has given rise to simulation research to improve our understanding of the bonding dynamics and dipole–dipole interactions that will enable the design of cancer-specific contrast agents with higher detectability. While both of these classes of contrast agents, i.e., T2-reducing and T1-reducing contrast agents, are used as passive agents for detection of abnormalities of the BBB, their potential for active uses has generated considerable interest.[25] Both USPIOs and Gd-contrast agents could also be used as targeted agents through conjugation with ligand-mediated pathology-specific molecules such as vascular endothelial growth factor. The application of targeted molecular imaging at HFs has great potential that could be explored with HF and UHF animal magnets on animal models of cancer. Strong susceptibility artifacts and dipole–dipole interactions and the freedom to use higher doses than are known to be safe for humans have made UHF animal magnets a rapidly proliferating research tool in cancer research.

STATIC MAGNETIC FIELD: SIGNAL-TO-NOISE RATIO

The most fundamental parameter in enhancing the sensitivity of MRI to cancer pathology is SNR. As 8-T MRI has demonstrated, through producing high SNR, depiction of the microvasculature in human subjects in vivo is feasible (see Figures 1 and 2). Regarding its benefits to cancer research, high SNR could be used in three major areas:

1. visualization of neovasculature,
2. tumor properties-based contrast, and
3. localization and demarcation of tumors.

The first application is one of the most important potential uses of high SNR that have not yet been fully realized.[13,14] Enhancing the visibility of blood vessels enables a clearer depiction of high tortuosity, irregular vascular patterns, and longer vessels within and around

the tumor. The ability to visualize and map out these features of the mass, in comparison with normal blood vessels and other landmarks, could provide an independent measure of in vivo staging of brain tumors. High SNR's capability for microstructure depiction can be used for imaging-based distinction of neovasculature from mature blood vessels. This is an important diagnostic capability that radiology currently lacks. Its availability will offer a significant capability for antiangiogenic therapy. Results of microvascular density could also be used, along with dynamic contrast-enhanced MRI to obtain an account of vascular leakiness. High SNR and high susceptibility have the potential in HF MRI to enable detection of neovasculature in a longitudinal study that keeps track of vascular density, making them distinct from mature blood vessels. Eight-tesla images have shown that susceptibility enhances the contrast between microvasculature and brain parenchyma to the point of visualization of subvoxel structures. Histopathologic findings have highlighted the importance of in vivo distinction between neovasculature and mature blood vessels in the early stages of the disease.[11] More work is needed to show how high SNR can help to achieve such a distinction.

To enhance the role of SNR in brain tumor imaging beyond vasculature depiction, other tumor properties such as microstructure and physiology could be used. The ability to stage tumors, as is done by histologic methods, could be a useful role for HF MRI. High SNR will help in the use of other tumor properties such as hypoxia and acidity to enable MRI to determine histologic type and grade in brain tumors noninvasively. Hypoxic mapping by BOLD contrast in HF MRI using EPI could provide an estimation of the pathophysiology of a tumor and a measure of therapeutic efficacy. Acidity could be obtained from MRS detection of lactic peaks. At HF, higher SNR is combined with larger chemical shift dispersion, enabling spectroscopy (MRS) peaks to become both stronger and farther from each other. Both of these HF effects contribute to a better resolution of the metabolite peaks. Chemical-shift imaging maps offer measures of *N*-acetylaspartate (NAA), choline, creatine, and lactate in the brain. High SNR will make more peaks accessible, and measures such as acidity and choline content could help with the determination of malignancy. The SNR at 1.5 T is sufficient for relative quantification of metabolites like creatine/NAA, while high SNR could allow absolute quantification of maps of all these metabolites at HF. Such capabilities will elevate MRI to a true noninvasive neuropathologic method.

The relationship between high SNR and the ability to detect tumor boundaries more reliably is not clear. In general, enhanced sensitivity will enhance the capability for signal modulation as a function of tissue microstructure and physiology. Independence of relaxation mechanisms in creating contrast for tumor detection from SNR, and its ability to detect signals from smaller voxels, increases the possibility of a better demarcation of the tumor boundaries owing to a less severe partial volume effect at the tumor boundaries. Furthermore, events such as increased cellularity and diffuse calcification have the potential for additional contrast generation. Both processes will become visible earlier as their contribution to the determination of voxel SNR becomes more dependent on the fraction of voxel occupied by calcified particles and higher cellular density.

As mentioned in the susceptibility section, small animal models could be used in UHF MRI scanners to allow the testing of hypothesis-driven experiments to determine the viability of the model to enhance tumor visibility and to evaluate the therapeutic efficacy of new drugs. The high SNR of UHF animal scanners provides a powerful tool to push the boundaries of resolution toward microscopy and contrast-free molecular imaging. Since the results of animal studies, as well as new MRI techniques, are directly applicable to human scanners, they reduce the bench-to-bed development time and offer a realistic alternative to research involving human subjects.

RADIO FREQUENCY PENETRATION

The Larmor equation is given by $\omega_0 = \gamma B_0$ and determines the precessional frequency of a proton within a magnetic field B_0. As B_0 increases, so does the rotational frequency of protons, ω_0. The resonance effect in MRI requires irradiation of the subject with an electromagnetic wave of the same frequency as ω_0 to deflect proton magnetic moments away from B_0, i.e., excitation. Considering the $^1H\gamma$ and the range of B_0 used in clinical MRI, the frequency of electromagnetic fields needed in MRI falls in the 63.5 (at 1.5 T) to 128 MHz (at 3 T) range, which falls in the RF category. For whole-body research magnets, RF goes up to 400 MHz at 9.4 T. This range (>300 MHz) corresponds to the UHF band used for television broadcasting. With the increase in RF, the electrodynamic properties of tissues will vary proportional to ω_0. Tissue conductivity is a function of frequency that increases at HFs and, as a result, increases the RF absorption by the tissue. This extra RF absorption requires higher power to achieve the same deflection angle at HF compared to lower fields. So, RF power content of pulse sequences increases at HF. The electric field (E or E_1) associated with the RF magnetic field (B_1) that is used to excite the spins causes tissue heating.[27] Delivery of RF to a voxel occupied by a tissue of conductivity σ (ohm^{-1}) and density ρ (kg/m^3) requires an electric field E_1 (V/m) that will cause RF absorption

or specific absorption rate (SAR [W/kg]) given by the equation $SAR = \sigma E^2/2\rho$. SAR is a standard measure of tissue heating, and regulatory bodies such as the US Food and Drug Administration (FDA) provide guidelines for RF limits used in human applications.[7] As of this writing, values for SAR suggested by the FDA since July 14, 2003, stand at SAR = 3 W/kg averaged overhead for 10 min. While SAR implies absorption of RF by the tissue in a uniform manner, RF distribution across the body parts, e.g., the human head, is by no means uniform. The heterogeneous nature of the biological tissues causes this nonuniformity that leads to a nonuniform local SAR across the head.[28] Other factors, such as head size and coil size, also affect the extent of nonuniform distribution of RF within the brain.[27,28] While higher absorption at HF attenuates the RF penetration into the tissue, other properties of the human body, i.e., high dielectric constant, cause opposite effects as is discussed in the following section.[26,29] In fact, the dielectric effects are so strong that they dominate the B_1 distribution generating the bright center, a hallmark of HF images as seen on the 8- and 7-T images of the human head shown in Figures 2–4. Aside from the safety considerations of inhomogeneous RF distribution, penetration effects must be addressed as an image quality issue as well. Such RF distribution has been addressed by offering solutions that use innovative coil design and excitation schemes.[27]

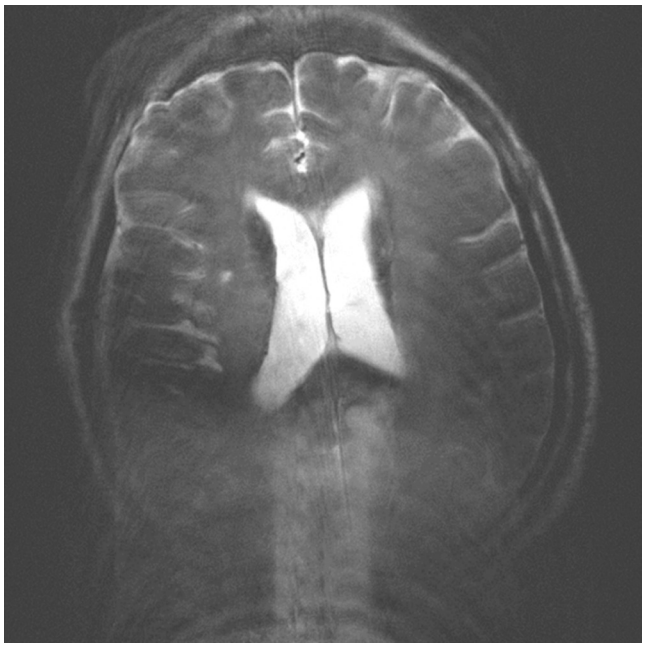


FIGURE 4 A RARE image obtained with a 512 × 512 matrix size. This image is heavily T2 weighted with a cerebrospinal fluid flow artifact extended along the phase-encoding direction. Also seen here are motion artifacts and strong loss of signal in the posterior aspect of the slice.

OTHER RADIO FREQUENCY ISSUES

Biological tissues have a high dielectric constant, ε, of about 50. This is due to the high water content, and ε (water) is around 80. The unique molecular structure of water is the primary determinant of its high dielectric properties. Within the human body, as in water, electromagnetic waves experience pronounced changes in their wave properties, such as wavelength, that influence their propagation and distribution. The dimensions of imaged objects also play as a factor in the formation of dielectric effects. The typical dimension, d, of a human head is about 10 cm, while the same d for the human torso is about 25 cm. At the same time, after RF enters the body its wavelength within the tissue changes and is given by $\lambda_t = \lambda_0/\sqrt{\varepsilon_r}$, where λ_t is the RF wavelength inside the tissue, λ_0 is the RF wavelength in air, and ε_r is the relative permittivity of the tissue. Evidence for dielectric effects begin to appear as λ_t approaches d from above, which is caused by B_0 increase, and becomes more severe as λ_t becomes smaller than d.

Dielectric resonance, or center brightness effects, begin to appear on MR images at around 2 T, when the patterns of inhomogeneity across MR images grow in severity and complexity.[29] At 8 T, as seen in Figures 2 and 3, the dielectric patterns clearly cause a significantly stronger B_1 at the central regions, making these regions of the image considerably brighter than the peripheral regions. While undesirable in general, this feature of HF MRI lends itself to studies involving the center of the brain, as it enables signal to be focused selectively in those regions. For all other applications requiring a homogeneous distribution of image intensity, new techniques in coil design and pulse sequences have shown to be able largely to suppress this effect.[8,9]

For magnetic fields above 7 T, a unique coil design called a transverse electromagnetic, or TEM, resonator is used.[30,31] HF MRI at 4 T and above has benefited from the electromagnetic characteristics of TEM coil design.[32] TEM coils incorporate a distributed capacitor concept in their construction, unlike the low-field RF coil's birdcage-like designs, which use a lumped-element concept for capacitor/inductor use. While unable to suppress the artifacts such as center brightness at HF, as seen in Figures 2 and 3, the TEM resonator has been able to address some fundamental issues, such as high electric field concentration around capacitors of lumped-element coils and radiation damping that becomes severe in the birdcage design at HF. The issue of radiation damping in birdcage RF coils[28,32] refers to the leaking of RF power as radiation in an outwardly direction that takes energy away from the internal regions of the coil where that energy is needed for spin excitation. This effect in birdcage coils degrades image homogeneity at proton frequencies owing to a need for more RF power

that introduces more electric noise into the body, reducing SNR and flip angle uniformity across the sample.

One remedy for dielectric effects is the choice of phase array volume coils and multichannel coils in a scheme called parallel imaging.[8,9,28] Phase array coils and multichannel coils are made up of a set of surface coils in tandem wrapped around the imaged body. Multichannel coils and phase array coils take advantage of their surface elements that generate stronger signal in the near proximity of the coil. This characteristic of multichannel coils offers higher SNR in peripheral regions compared to deep tissues. This effect acts opposite to dielectric effects and compensates for the center brightness, thereby restoring the intensity homogeneity to HF MR images. Multichannel coils could comprise traditional surface coil elements, or structures such as TEM coils could be used in such a way that their individual elements receive signals independently within a parallel receive (pRX) mode. Multichannel coils have been used in pRX mode in different partial parallel imaging schemes such as sensitivity encoding (SENSE)[8] and simultaneous acquisition of spatial harmonics (SMASH),[9] which are two variants of RF coil array reception techniques. Both SENSE and SMASH have the dual advantage of homogeneity and fast acquisition. The fast imaging is achieved by shortening the readout duration as it is for individual surface coils' ability to skip *k*-space lines. At lower fields, parallel imaging is used to reduce scan time for dynamic imaging studies and others in need of higher temporal resolution. As far as the use of parallel imaging for restoration of the homogeneity of RF (B_1) distribution is concerned, there are two opportunities for reinstating image homogeneity, one during transmit and the other during receive, which leads into a multitude of configurations for parallel imaging. These configurations include the use of (a) single-channel transceiver (Tx/Rx) volume coil, (b) single-channel transmit/parallel receive (Tx/pRx), and (c) parallel transmit/parallel receive (pTx/pRx), also called transmit SENSE/receive SENSE. These configurations have different advantages and disadvantages in terms of RF power, SAR, image uniformity, and SNR.

Parallel imaging has another benefit related to the economics of RF power generation and delivery technology. As RF power per unit flip angle excitation increases at HF, it becomes increasingly more expensive and difficult to incorporate RF amplifiers with the capability for high-fidelity pulse generation needed for spin excitation in HF scanners. A typical RF power amplifier for a 7-T scanner should have 10–30 kW of power for delivery for various applications. This makes pTx/pRx even more attractive. It is more economical to use multiple smaller transmitters feeding individual coil elements than to deliver massive amounts of RF power to an individual volume coil. This means that at HF one could use the smallest possible Tx coils to their advantage, since they can produce larger B_1 with the same amount of RF power compared to volume coils. On the other hand, for each unit of RF power, smaller elements of pRx coils can produce a more intense and shorter pulse that has a high bandwidth (BW). Such high-BW pulses allow more versatile sequence designs with better image contrast. Shorter echo times and higher sensitivity are achieved by pRx, in addition to high SNR advantages of the pRx mode, making this technology more favored for HF MRI studies.

Small HF and UHF animal scanners have already made a foothold for imaging of central nervous system tumor models. These scanners operating at fields of 7–14 T have demonstrated the gain in most of the fundamental MRI parameters like SNR, CNR, resolution, etc. The ability to generate a three-dimensional image of a tumor at 0.1 m^3 will open the path for conducting the most basic evaluation of therapeutic efficacy in humans, as is now done in animal models of brain tumors. Examples of in vivo anatomical imaging obtained at 8 T (see Figures 1–3) have voxels about 10 times bigger than 0.1 mm^3. Other chapters in this book also illustrate 8-T images with excellent SNR characteristics, raising hope that HF is truly advancing and will eventually bring anatomical, functional, and molecular imaging with MRI possible at submillimeter resolution. Another quantum leap in this technology will be made upon optimization of parallel imaging in the next generation of MRI scanners. In addition, targeted contrast agents should make it possible to achieve resolutions of about 0.1 mm^3 throughout the human brain in reasonable scan times. This will lead to a reassertion of MRI as the most effective tool in the diagnostic and therapeutic aspects of cancer care.

CONCLUSION

The drive toward higher magnetic fields has significantly improved the quality of MR images since 1995. Since the debut of 8-T MRI in 1998,[5] HF has shown even more potential for empowering diagnostic imaging. HF has shown that it has much to offer to cancer diagnosis and monitoring of therapy. As field strength increases, so does the sensitivity, magnetic susceptibility, T1 relaxation, and chemical shift. Gain in SNR has the most profound effect on new capabilities that open new applications to MRI. HF MRI has already shown that it is capable of acquisition of images with submillimeter resolution, microvascular visualization, reliable brain metabolite mapping, and high temporal resolution dynamic imaging. fMRI is another feature that MRI has offered to cancer research with a great deal of potential at HF in the arena of neurosurgery planning. Other developments such as tumor-specific contrast agents, parallel imaging, DTI, and complex new pulse sequences are further empowering HF MRI, helping its

march toward a true quantitative imaging technique with potential to develop specificity for imaging-based tumor staging. Within less than a decade since its appearance, parallel imaging has increased the number of channels for simultaneous acquisition to 128, which makes single-shot *k*-space readout acquisition possible. Such rapid developments will substantially facilitate HF MRI's ascension to a noninvasive neuropathological tool, with the potential for real-time therapeutic monitoring as well.[33–36]

Acknowledgments

I wish to thank Gregory Christoforidis of Ohio State University, Department of Radiology (currently at the University of Chicago Medical Center, Department of Radiology), for providing images for this chapter.

References

1. Vetter J, Ries G, Reichert T. A 4-tesla superconducting whole-body magnet for MR imaging and spectroscopy. *IEEE Trans Magn*. 1988;24:1285–1287.
2. Barfuss H, Fischer H, Hentschel D, Ladebeck R, Vetter J. Whole-body MR imaging and spectroscopy with a 4-T system. *Radiology*. 1988;169:811–816.
3. Barfuss H, Fischer H, Hentschel D, et al. In vivo magnetic resonance of humans with a 4T whole-body magnet. *NMR Biomed*. 1990;1:31–45.
4. Bomsdorf H, Helzel T, Kunz D, Roschmann P, Tschendel O. Spectroscopy and imaging with a 4 tesla whole-body MR system. *NMR Biomed*. 1988;1:151–156.
5. Robitaille PML, Abduljalil AM, Kangarlu A, et al. Human magnetic resonance imaging at 8T. *NMR Biomed*. 1998;11:263–265.
6. Kangarlu A, Zhu H, Burgess RE, Hamlin RL, Robitaille PML. Cognitive, cardiac, and physiological safety studies in ultra high field magnetic resonance imaging. *Magn Reson Imaging*. 1999;17:1407–1416.
7. Kangarlu A, Robitaille P. Biological effects and health implications in magnetic resonance imaging. *Concepts Magn Reson*. 2000;12:321–359.
8. Prussemann KP, Weiger M, Scheidegger MB, Boesiger P. SENSE: sensitivity encoding for fast MRI. *Magn Reson Med*. 1999;42:952–962.
9. Sodickson DK, Manning WJ. Simultaneous acquisition of spatial harmonics (SMASH): fast imaging with radiofrequency coil arrays. *Magn Reson Med*. 1997;38:591–603.
10. Abragam A. *Principles of Nuclear Magnetism*. Oxford: Oxford Science Publication; 1994.
11. McDonald DM, Choyke PL. Imaging of angiogenesis: from microscope to clinic. *Nat Med*. 2003;9:713–725.
12. Christoforidis GA, Kangarlu A, Abduljalil AM, et al. Susceptibility-based imaging of glioblastoma microvascularity at 8T: correlation of MR imaging and postmortem pathology. *Am J Neuroradiol*. 2004;25:756–760.
13. Christoforidis GA, Kangarlu A, Abduljalil AM, et al. Visualization of microvascularity in glioblastoma multiforme with 8-T high-spatial-resolution MR imaging. *Am J Neuroradiol*. 2002;23:1553–1556.
14. Tynninen O, Aronen HJ, Ruhala M, et al. MRI enhancement and microvascular density in gliomas: correlation with tumor cell proliferation. *Invest Radiol*. 1999;34:427–434.
15. Chen CN, Sank VJ, Cohen SM, Hoult DI. The field dependence of NMR imaging: I. Laboratory assessment of signal-to-noise ratio and power deposition. *Magn Reson Med*. 1986;3:722–729.
16. Hoult DI, Chen CN, Sank VJ. The field dependence of NMR imaging: II. Arguments concerning an optimal field strength. *Magn Reson Med*. 1986;3:730–746.
17. Robitaille PML, Abduljalil AM, Kangarlu A. Ultra high resolution imaging of the human head at 8T: 2K × 2K for Y2K. *J Comput Assist Tomogr*. 2000;24:2–8.
18. Kangarlu A, Bourekas BC, Ray-Chaudhry A, Rammohan KW. Cerebral cortical lesions in multiple sclerosis detected by magnetic resonance imaging at 8T. *Am J Neuroradiol*. 2007;28(2):262–266.
19. Koretsky AP. New developments in magnetic resonance imaging of the brain. *NeuroRx*. 2004;1:155–164.
20. Schenck JF. The role of magnetic susceptibility in magnetic resonance imaging: MRI, magnetic compatibility of the first and second kinds. *Med Phys*. 1996;23:815–850.
21. Abduljalil AM, Robitaille PML. Macroscopic susceptibility in ultra high field MRI. *J Comput Assist Tomogr*. 1999;23:823–841.
22. Abduljalil AM, Kangarlu A, Robitaille PML. Macroscopic susceptibility in ultra high field MRI-II: acquisition of spin echo images from the human head. *J Comput Assist Tomogr*. 1999;23:842–844.
23. Kangarlu A, Abduljalil A, Norris DG, Schwartzbauer C, Robitaille P. Human RARE imaging at 8T: RF intense imaging without SAR violation. *Magn Reson Mater Phys Biol Med*. 1999;9:81–84.
24. Norris DG, Kangarlu A, Abduljalil A, Schwartzbauer C, Robitaille P. Human MDEFT imaging at 8T. *Magn Reson Mater Phys Biol Med*. 1999;9:92–96.
25. Lubbe AS, Bergemann C, Brook J, McClure DG. Physiological aspects in magnetic drug targeting. *J Magn Magn Mater*. 1999;194:149–156.
26. Robitaille P, Kangarlu A, Abduljalil A. RF penetration in ultra high field magnetic resonance imaging (UHF MRI): challenges in visualizing details within the center of the human brain. *J Comput Assist Tomogr*. 1999;23:845–849.
27. Kangarlu A, Ibrahim TS, Shellock F. Effects of RF coil design and field polarization on RF heating inside of a head phantom. *Magn Reson Imaging*. 2005;23:53–60.
28. Ibrahim TS, Lee R, Baertlein BA, Kangarlu A, Robitaille P. Application of finite difference time domain method in RF coil design using multi-port excitation. *Magn Reson Imaging*. 2000;18:733–742.
29. Kangarlu A, Baertlein BA, Lee R, Ibrahim T, Abduljalil AM, Robitaille PML. Dielectric resonance phenomena in ultra high field magnetic resonance imaging. *J Comput Assist Tomogr*. 1999;23:820–831.
30. Roschmann P. Radiofrequency penetration and absorption in the human body: limitations to high-field whole-body nuclear magnetic resonance imaging. *Med Phys*. 1987;14:922–931.
31. Vaughn JT, Hetherington HP, Otu JO, Pan JW, Pohost GM. High frequency volume coils for clinical NMR imaging and spectroscopy. *Magn Reson Med*. 1994;32:206–218.
32. Baertlein BA, Ozbay O, Ibrahim T, et al. Theoretical model for a MRI radio frequency resonator. *IEEE Trans Biomed Eng*. 2000;47:535–546.
33. van der Kolk AG, Hendrikse J, Zwanenburg JM, Visser F, Luiten PR. Clinical applications of 7T MRI in the brain. *Eur J Radiol*. 2013;82(5):708–718.
34. Pinker K, Bogner W, Baltzer P, et al. Clinical application of bilateral high temporal and spatial resolution dynamic contrast-enhanced magnetic resonance imaging of the breast at 7T. *Eur Radiol*. 2013;24(4):913. http://dx.doi.org/10.1007/s00330-013-3075-8.
35. Beeman SC, Shui YB, Perez-Torres CJ, Engelbach JA, Ackerman JJ, Garbow JR. O_2-sensitive MRI distinguishes brain tumor versus radiation necrosis in murine models. *Magn Reson Med*. 2015. http://dx.doi.org/10.1002/mrm.25821. 26175346.
36. Zhang Q, Rajan SS, Tyner KM, et al. Effects of iron oxide nanoparticles on biological responses and MR imaging properties in human mammary healthy and breast cancer epithelial cells. *J Biomed Mater Res B Appl Biomater*. 2015. http://dx.doi.org/10.1002/jbm.b.33450. 26013845.

CHAPTER

22

Magnetic Resonance Image-Guided Neurosurgery*

Ferenc A. Jolesz†, *Parviz Dolati*, *Ion-Florin Talos*, *Simon K. Warfield*, *Daniel Kacher*, *Nobuhiko Hata*, *Peter M. Black*

Department of Radiology, Brigham and Women's Hospital, Harvard Medical School, Boston, MA, USA

Magnetic resonance imaging (MRI) has evolved into the premier neuroimaging modality since its introduction as a diagnostic tool in the mid-1980s. With the introduction of higher field magnets, we are now able to achieve spatial resolutions of such superb quality that even the most exquisite details of brain anatomy can be visualized. Owing to these advantages, MRI has had a great impact on the diagnosis of neurosurgical conditions and, with the implementation of intraoperative MRI, on surgical therapy as well. With intraoperative image updates, brain deformations throughout the course of surgery are detected in near-real time and the resection progress is readily monitored; this enables accurate neuronavigation. Intraoperative MRI (iMRI) is approaching the point at which it will be used not only to localize, target, and guide resection of brain tumors and other intracranial lesions, but also to provide a comprehensive picture of the surrounding functional anatomy. In addition to new imaging methods such as diffusion tensor imaging, multivoxel spectroscopy, and functional MRI (fMRI), novel therapeutic approaches have been added to the arsenal of MR-guided therapy. Among these, the promising results in MRI-guided focused ultrasound surgery, in which the noninvasive thermal ablation of tumors is monitored and controlled by MRI, are especially encouraging. With the clinical introduction of these advances, iMRI is changing the face of neurosurgery today.

Modern neurosurgery requires ever more comprehensive integration of sophisticated morphologic and functional imaging techniques into the surgical flow. This integration process includes the incorporation of interactive dynamic imaging, high-performance computing, and real-time image processing in the operating room.

The evolution of novel intraoperative imaging techniques has driven the development of several revolutionary image-guided therapy methods currently in process of implementation into neurosurgical practice.

In the following sections, we will present the various intraoperative systems in use as of this writing. We will then review the state of image-guided brain tumor surgery, including the role of multimodal imaging for guiding tumor resection and methods employed for image fusion and visualization. We will conclude with a brief presentation of novel, minimally invasive therapeutic approaches, including high-intensity focused ultrasound.

IMAGE-GUIDED THERAPY SYSTEMS

Owing to the ever-growing need for fast, high-resolution morphologic and functional imaging, competitors in the MRI market have begun to pursue higher field MR scanner solutions. Closed (cylindrical)-bore MR systems are marketed at a field strength of 3T, while open systems are now being introduced at 1.0T. The migration to higher field solutions is expected to continue, since the dominant competitors are currently pursuing even higher field solutions for the research community, that range from 4 to 9.4T. The US Food and Drug Administration has designated 7T as nonsignificant risk.

One of the implications of this migration is the recalibration of field strength definitions.[1] Demand for the 3-T systems has been so great that a subsegment has developed to describe more accurately the change that is taking place. For the purposes of this review, the 3-T market will be designated as the very high field. The

† Deceased

* Reproduced from the first edition, *Handbook of Neuro-Oncology Neuroimaging*, ed. F. Jolesz and H. Newton, Academic Press, 2007.

http://dx.doi.org/10.1016/B978-0-12-800945-1.00022-7
Copyright © 2008 Elsevier Ltd. All rights reserved.

high-field segment will include only those scanners with a field strength of 1.5 T. Midfield scanners will now include field strengths from 0.5 to 1 T, while low-field scanners are less than 0.5 T. A second trend in MRI scanner design includes decreasing bore length and increasing bore diameter, which greatly benefit access during interventional procedures and provide greater flexibility in patient positioning.

Choice of Magnetic Resonance Imaging Scanner and Procedural Flow

At the time of this publication, scanners ranging from 0.12 to 3 T are in use for MRI-guided neurosurgery with a range of configurations (Figure 1). The choice of scanner may strongly influence operating room architecture and the need to move the patient in between imaging cycles (Figure 1(A) and (B)). Figure 1 shows the use of a dedicated portable scanner (Figure 1(D)); horizontally open scanners (Figure 1(C)) or conventional closed-bore scanners (Figure 1(E) and (F)), which require that the patient be moved for intraoperative image updates by translating or pivoting a table up to 180° (with this configuration, the surgery takes place outside the 5-G line); and mobile closed-bore scanners, which move to the patient (Figure 1(G) and (H)). Different procedures are enabled by certain scanner capabilities. Greater signal-to-noise ratio and faster scan times, characteristic of the higher field, closed-bore scanners, enable intraoperative fMRI, diffusion tensor MRI (DT-MRI), and MR spectroscopy acquisitions, which may facilitate tumor resections. The high-field scanners, moreover, have greater sensitivity to temperature changes during thermal ablations, which is ideal for minimally invasive procedures, such as laser ablation and focused ultrasound ablation.[2,3] Lower-field open scanners offer greater patient access for biopsy and therapeutic probe placement. The tradeoffs of these scanners are listed in Table 1.

Safety

The complexity of controlling access increases in situations in which a single iMRI room services multiple operating rooms. Depending on layout, more entrances into the iMRI room may be necessary. Moreover, moving an intubated patient between the surgical station and the scanner poses a clinical safety concern. When the surgery occurs within the 5-G line, the use of custom-made, nonferrous instruments is mandatory (see Figure 1(A) and (F)). Solutions in which surgery occurs outside the 5-G line enable the use of conventional, more readily available instruments. However, great pains must be taken to prevent instruments from coming too close to the scanner, where they may become projectiles. This point is critical to the safety of the patient and staff.

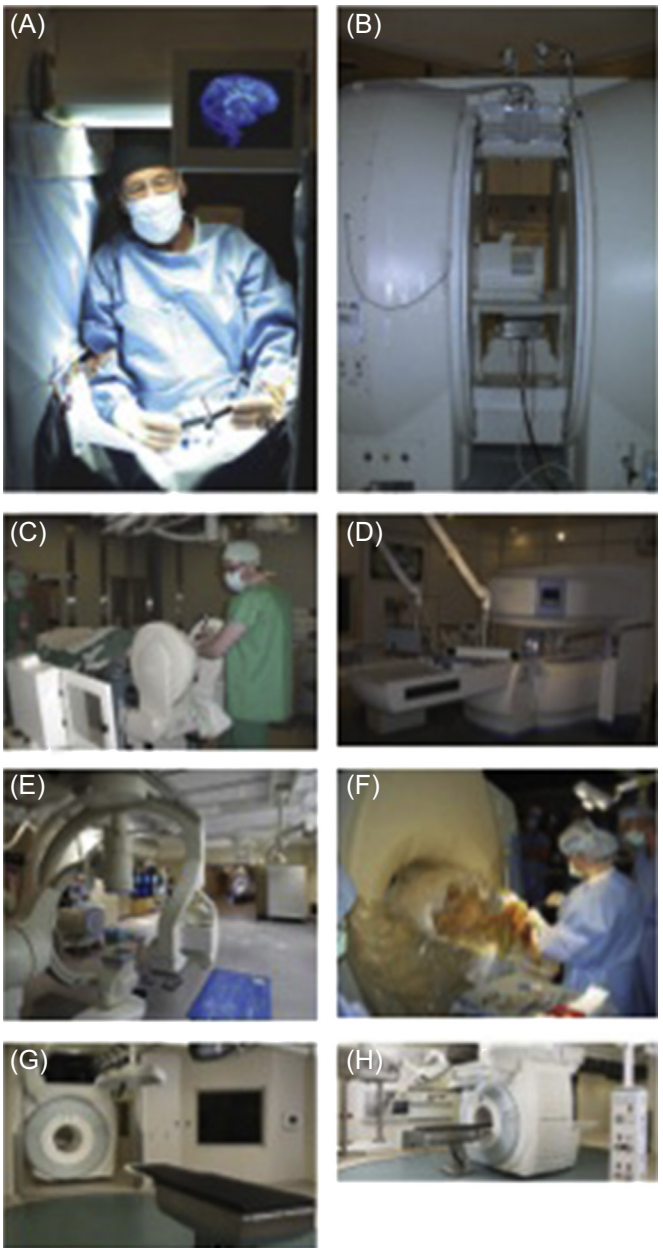


FIGURE 1 Solutions for MRI-guided neurosurgery. (A) Vertical open superconducting 0.5-T interventional scanner with integrated optical tracking system for neuronavigation. (B) Same system shown with integrated fluoro-X-ray system. *(Courtesy Rebecca Farhig.)* (C) Portable dedicated low-field system. *(Courtesy Medtronic.)* (D) Horizontal open permanent-magnet low-field system. *(Courtesy Roberto Blanco.)* (E) Two-room suite with closed-bore 3-T scanner and biplane fluoro-X-ray system. *(Courtesy Walter Kucharczyk.)* (F) One-room solution with 3-T scanner; surgery occurs at the back of the scanner to minimize excursion between surgical location and imaging location. (G, H) Mobile 1.5-T scanner; subsequent to image acquisition, scanner is moved to garage.

Patient Positioning

Many iMRI procedures require general anesthesia. It is essential the patient is positioned properly and all pressure points must be appropriately padded

TABLE 1 Possible MRI Configurations for Intraoperative and Interventional Imaging

Configuration	Field	Direct Access	Advantages
Long bore (closed)	1–3 T	No	Highest image quality
Short/wide bore (closed)	1.5 T	Limited	Moderate homogeneity and gradient speed
Horizontal open gap	0.02–1.0 T	Limited	Safety and instrument compatibility
Vertical open gap	0.5 T	Full	Intraoperative imaging; flexible positioning

to maintain good circulation. When the head has to be pinned in a head holder, as is the case with most neurosurgical procedures, centering the head in the sweet spot of the imaging volume may interfere with achieving the ideal surgical position. These requirements may sometimes preclude fitting of a large patient into the bore of the scanner.

BRAIN TUMOR RESECTION UNDER INTRAOPERATIVE MAGNETIC RESONANCE IMAGING GUIDANCE

Rationale

As of this writing, there is no generally accepted management standard for primary brain tumors. With the exception of patients with intractable epilepsy and symptomatic mass effect, the role of surgery remains controversial. However, an increasing number of studies suggest a beneficial effect of gross total tumor resection on overall and recurrence-free survival in patients with low- and high-grade gliomas.[4–7]

The fundamental goal of neurosurgery is to target, access, and remove intracranial lesions without causing damage to normal brain tissue or vascular structures. The overall concern is the preservation of neurological function, which requires precise delineation of functional anatomy and correct definition of the resection target volume. Intraoperative MRI has become the method of choice for achieving the safest and most accurate resection of glial neoplasms. Visual inspection is often unreliable in distinguishing tumor from normal brain tissue. Compared with visual inspection and other imaging modalities (computed tomography, ultrasound), MRI has a much higher sensitivity in detecting these lesions. However, the usefulness of preoperatively acquired MR images for surgical guidance is limited by changes in brain configuration, which inevitably occur during surgery. At the outset of any given procedure, surgical manipulations and anesthesia result in a change in the anatomic position of brain structures and intracerebral tumors. For example, the initial loss of cerebrospinal fluid following a craniotomy, retraction and resection of tissue, tissue hydration state, and partial arterial CO_2 pressure all play a role in the intraoperative brain shift.[8,9] Hence, localization and targeting of brain tumors based on preoperatively acquired images are unreliable. In fact, literature data show that, in the absence of intraoperative image updates, visual inspection of the surgical field alone fails to detect residual tumor otherwise accessible for resection.[7,10–12] Another major challenge when attempting gross total tumor resection is determining the relationship between lesion and functionally critical cortical areas and white matter tracts. A 2006 analysis of a large patient series harboring supratentorial gliomas, operated on with intraoperative anatomic MRI guidance, has shown that the main predictors for incomplete tumor resection are, in addition to large tumor volume and oligodendroglioma histopathology, tumor involvement of eloquent cortex and large fiber tracts, such as the corticospinal tract.[13] These findings highlight the importance of multimodal imaging, such as fMRI and DT-MRI, for surgical guidance.

Multimodality Imaging for Guiding Brain Tumor Resection

Functional MRI provides information about cortical function by noninvasive means. Such functional information is of paramount value for surgical planning in lesions located in or around eloquent cortex.

Basically, neural activation is accompanied by a hemodynamic response, i.e., increased supply of arterial (oxygenated) blood to the activated cortical regions. This results in a local increase of the oxyhemoglobin-to-deoxyhemoglobin ratio. Given the fact that oxyhemoglobin is diamagnetic and deoxyhemoglobin is paramagnetic, the hemodynamic response during activation leads to an alteration in local magnetic susceptibility, which can be readily detected with appropriate MRI sequences, such as echoplanar gradient-echo imaging.[14]

The interpretation of fMRI data is based on statistical analysis of the temporal variations in voxel intensity distribution during rest and activation. The functional maps are obtained by displaying the distribution of the voxels activated by various physiological tasks (i.e., motor, sensory, visual). Although fMRI data do not alter the diagnosis, they can contribute substantially to surgical planning by providing critical information about optimal positioning of craniotomy and corticotomy sites, surgical excision margins, and access routes to the lesions. Functional MRI-based surgical planning also yields various potential strategies that enable the surgeon to avoid targeting the lesion too close to eloquent cortex or to other essential structures.

The relationship between intra-axial infiltrative brain tumors, such as low- and high-grade glial neoplasm, and

the functionally active neural tissue has not been entirely elucidated. Large-population magnetoencephalography studies[15,16] demonstrated the presence of functionally active tissue within the tumor as defined by MRI in 18% of grade II, 17% of grade III, and 8% of grade IV tumors. Thus, obtaining functional information well in advance of the surgical procedure is critical in defining the safest surgical strategy. Moreover, the incorporation of preoperative fMRI information into frameless, stereotactic systems is becoming routine at some institutions.[17]

In our experience, preoperative fMRI data have proven very useful in guiding electrophysiological, cortical mapping. Furthermore, such information may be crucial to stereotactic biopsies, in which, owing to the small skull opening, cortical stimulation is not practicable. However, the intraoperative use of fMRI data is limited by the changes in the brain's shape, which inevitably occur during any neurosurgical procedure. Intraoperative fMRI acquisitions are not practical in low- and midfield iMRI systems. The high-field systems, however, do not suffer from this limitation.[18]

DT-MRI can add important information about the proximity of tumors to critical white matter fiber tracts.[19,20] Precise knowledge of white matter fiber tract locations as well as their topographic relationship with the lesion is essential not only to accurate surgical planning, but also to understanding and predicting neurological function both before and after surgery. White matter fiber tracts can be depicted by displaying the eigenvectors of the diffusion tensor or by color-coding the directional information. With such information overlaid on anatomical images, fiber tract alterations such as displacement, infiltration, or disruption can be readily observed. However, it is important to note the difficulty of identifying a tract in a two-dimensional plane.

Since 2000, several algorithms for three-dimensional tracking of water diffusion have been developed (3D tractography).[21–23] Unlike the task of detecting white matter fiber tracts within a two-dimensional plane, the 3D approach enables more precise tract identification and produces more reliable anatomic information. By registering multiple image data, such as fMRI, diffusion-weighted tensor images, and structural images including gadolinium contrast-enhanced images in three dimensions, and by rendering all information onto a 3D brain model, the surgeon can interpret the overall view of the tumor and white matter fiber relationship with relative ease.

Rigid and Nonrigid Image Registration for Surgical Guidance

New sophisticated image registration techniques have enabled the use of preoperatively acquired multimodal images for surgical navigation.

Registration has been extensively studied and excellent techniques are now available to achieve alignment of several different types of images. Different registration algorithms are distinguished by the alignment metric used to assess alignment quality and the nature of the transform that may be estimated. Different choices for these parameters lead to different performance characteristics, different levels of robustness to signal variation, to the type of geometrical change that may be identified automatically, and to changes in the capture range and speed of execution. Excellent reviews of work in image registration algorithms and strategies for registration validation are available.[24–26]

In our work we have focused on robust methods, able to be executed within the time constraints of surgery,[27] and fast implementations of methods suitable for multimodality data.[28] Alignment of preoperative data can utilize transformation models suitable for the capture of rigid body motion alone. Figure 2 illustrates the fusion of fMRI, DT-MRI, and structural MRI for the purpose of enhancing preoperative surgical planning. We applied a previously described segmentation strategy[29,30] to high-resolution MRI (spoiled gradient-echo (SPGR) at $0.9375 \times 0.9375 \times 1.3\,mm^3$ acquired on a GE 3-T scanner) and a T2W ($0.46{,}875 \times 0.46{,}875 \times 5.0\,mm^3$). We aligned the T2W fast spine echo scan, and also preoperative DT-MRI and fMRI to the SPGR scan, as shown in Figure 2. The distance between regions of activation in a language fMRI paradigm, the critical white matter fiber tracts, and the projected area of resection was carefully considered.

Rigid registration is able to compensate for translational and rotational differences, but nonrigid registration transformations are necessary to compensate for brain shift. A 2005 review[31] describes the motivation and methods for successfully capturing such intraoperative deformations, and a robust, rapid, and effective registering method for whole-brain preoperative MRI to iMRI has been described.[32]

One predictor of neurological deficit following neurosurgery is the distance between the resected tissue and the activation observed with fMRI.[33] We have recently experimented with the alignment of preoperative fMRI to iMRI during neurosurgical cases. We repeatedly updated the alignment as new iMRI was acquired over the course of the surgery and utilized rigid followed by nonrigid registration[32] to project the fMRI and DT-MRI into alignment with the patient's brain as the surgery proceeded. Reorientation of the DT-MRI was carried out using the method of Ruiz-Alzola.[34] The surgeon was able to visualize the spatial relationship between preoperative fMRI, DT-MRI, the location of the tumor, and the region of the tumor resection. This is illustrated in Figure 3.

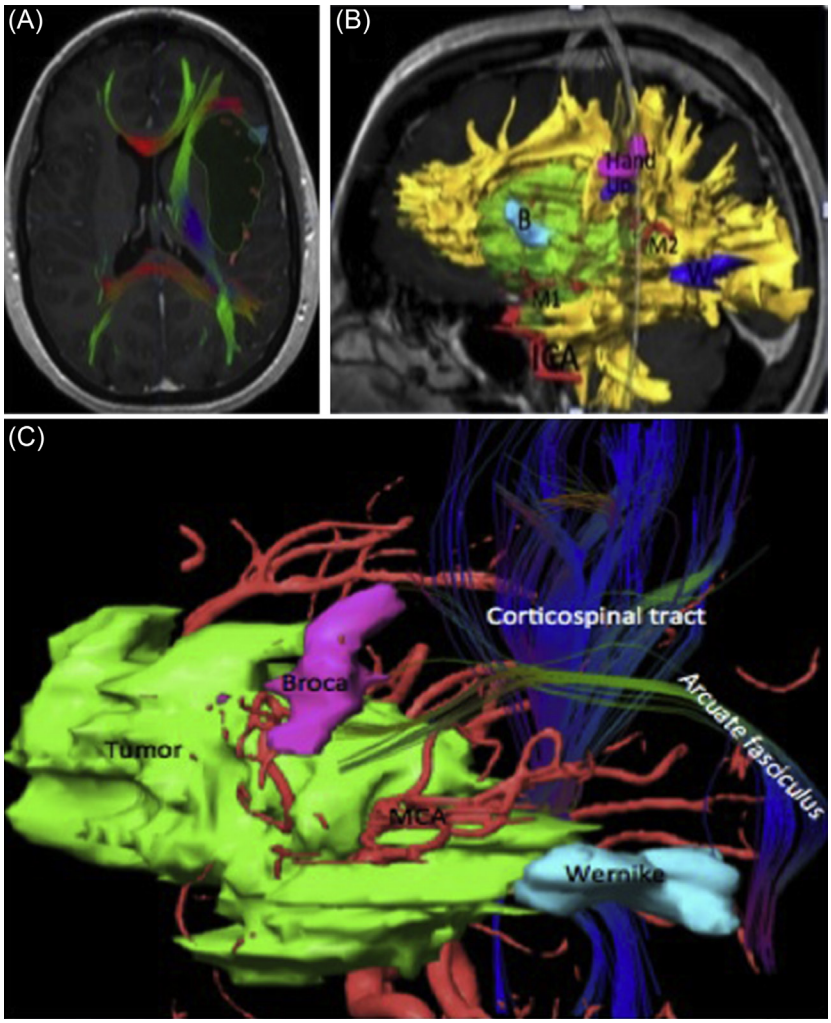


FIGURE 2 A 50-year-old male with a low-grade glioma involving the left frontotemporal lobes. (A) Axial and (B) sagittal view after 3D reconstruction and object creation. Segmentation and fusion of the preoperative structural MRI, fMRI, and DT-MRI have been performed. This type of visualization enables ready appreciation of the 3D relationship between anatomical structures, the tumor, and the critical fiber pathways. Green: brain tumor; yellow: fiber tracts; B: Broca area; W: Wernicke area; M1 and M2: middle cerebral artery branches. (C) Shows 3D object creation from the tumor, Broca and Wernicke areas, corticospinal tract, and arcuate fasciculus.

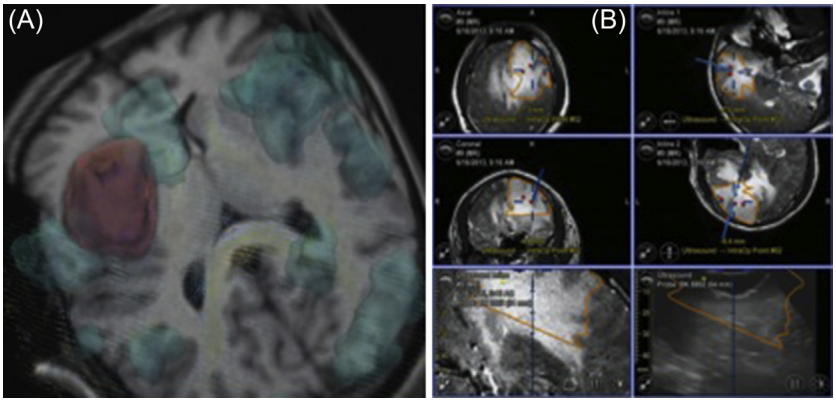


FIGURE 3 (A) Visualization of fusion of preoperative and intraoperative MRI. Functional MRI activation is represented in blue and DT-MRI is represented by line glyphs indicating the orientation of local white matter fibers. The preoperative appearance of the tumor is indicated by surface rendering in red, and cross-sectional slices through intraoperative volumetric MRI are shown. (B) The orange line highlights the limit of tumor in preoperative MRI (preoperative segmentation), which has been fused and overlaid on the intraoperative T2 MRI after first resection. The right bottom picture also shows coregistration of iMRI with ultrasound (US), confirming the tumor hyper echo signal within that orange outline. US will help the surgeon to overcome the brain shift regardless of the presence of iMRI.

Intraoperative Dynamic Contrast Imaging

One characteristic of high-grade glial neoplasms is their capacity to induce formation of new, abnormal vessels (tumor angiogenesis). These abnormal vessels lack a blood–brain barrier and are inherently highly permeable. Dynamic contrast enhancement studies performed during image-guided resection procedures have demonstrated a higher rate and degree of enhancement at sites of tumor recurrence, compared with areas associated with radiation necrosis, which results from damage of existing vessels.[35]

In this technique an SPGR scan is performed sequentially while gadolinium is injected intravenously (2D FSPGR, with echo time (TE) minimum; 45° flip angle; 1 NEX; sequential, multiphase, interleaved, variable bandwidth; and extended dynamic range; 10 phases/location; 22-cm field of view; 256 × 128; 1.87 s/image). This technique produces a series of images depicting regional rates of enhancement through the tumor volume.

A series of 24 patients who underwent dynamic MRI while in the intraoperative magnet was reported by Schwartz et al.[35] In patients with tumor recurrence, the signal intensity at first pass through active tumor had increased approximately 50% over baseline, while the maximal signal intensity change at first pass in patients without evidence of recurrent tumor was only approximately 15% over baseline. These data suggest that dynamic MRI can at once establish whether active tumor is likely to be present within a treated tumor bed and direct the surgeon to these sites; we now routinely use it for these purposes.

Schwartz et al. demonstrated an accuracy of 90% for this method in distinguishing patients with recurrent tumor from those with radiation necrosis.

Intraoperative Detection of Complications

One of the great advantages of performing surgery within the iMRI system is the ability of the operator to evaluate for intraoperative or perioperative hemorrhage. To this end, we routinely use a "heme-susceptibility sequence" that consists of a series of gradient-echo images with a time to recovery (TR) of 600 ms, a 30° flip angle, 1 NEX, and TEs of 9, 20, 40, and 60 ms. These images are acquired as two sets of double echoes: one with TEs of 9 and 40 ms and the other with TEs of 20 and 60 ms.

We have found that gradient-echo sequences with long TEs (i.e., 40–60 ms) show dark signal ("blooming") due to hyperacute blood collections, which is not evident on conventional imaging sequences or on shorter gradient-echo (GRE) sequences. This most likely reflects the greater sensitivity of the long-TE GRE sequence to the presence of small amounts of deoxyhemoglobin that develop in the periphery of a hyperacute blood collection. Atlas and Thulborn[36] have suggested that the low partial pressure of dissolved oxygen in the brain when compressed by the hematoma leads to deoxygenation of blood at the hematoma–brain interface. Hence, deoxyhemoglobin can be visualized only on long-TE GRE images and the attendant conspicuity of blood is directly correlated with increasing TE. It is important, however, to compare these images with conventional sequences to differentiate acute blood from postoperative air collections, which are visible as signal voids on all imaging sequences.

By understanding the changing appearance of the operative site on GRE images as a function of increasing TE, we can measure intraoperatively the amount of acute blood in a way that positively influences the outcome of intracranial surgery performed in the iMRI system. In 15 of the 18 cases studied, a small amount of hemorrhage was noted on the periphery of the operative cavity, but was considered too small to warrant any further action by either the radiologist or the surgeon. In three cases, however, the collections produced significant mass effect on surrounding brain structures or were enlarging and were subsequently drained using MR guidance. In the most extreme case, in which acute blood was exerting mass effect on surrounding brain and rapidly increasing in size, the collection was removed under MR guidance. Since diffusion-weighted MRI can detect ischemic injury, this method shows great potential for detecting white matter tracts as well as avoiding surgical complications related to vascular spasm and occlusion. As a proof of concept, intraoperative line scan diffusion imaging on a 0.5-T interventional MRI was performed during neurosurgery in three patients. Diffusion trace images were obtained in acute ischemic cases. Diagnosis of acutely developed vascular occlusion was confirmed with follow-up scans.[37]

Instrument Tracking and Neuronavigation

Early work with brain stereotaxis has established the importance and value of image guidance through better determination of tumor margins, better localization of lesions, and optimization of the targeting. Frame-based and frameless stereotaxis using 2D and 3D images have shown that neurosurgery can be performed through less invasive approaches, with greater accuracy. Today, the field of computer-assisted, image-guided surgery has replaced stereotactic neurosurgery.

With the introduction of iMRI, the need for frame of reference transformation and registration has been eliminated. The lesion localization in the 3D space is accomplished using image coordinates. Furthermore, with intraoperative image updates, the localization can be updated in a dynamic fashion. These features have dramatically enhanced the ability to obtain accurate biopsies and correct resection margins. Interactive use of MRI allows the selection of the optimal trajectories for

various neurosurgical approaches. Brain surgeries can be carefully planned and then executed under MRI guidance, which allows the surgical exposure and the related damage to the normal brain to be minimized.

Interactive instrument tracking is the process by which interactive localization is possible at any time during the surgery. Various tracking methods include articulated arms, optical tracking, passive systems, sonic digitizers, and electromagnetic sensors. Active optical trackers use multiple video cameras to triangulate the 3D location of flashing light-emitting diodes (LEDs) that may be mounted on any surgical instrument. Passive tracking systems use single or multiple video cameras to localize markers that have been placed on surgical instruments. Such passive systems do not require a power cable to be attached to the handheld localizer. Unfortunately, both LED and passive vision localization systems require line of sight between (at least some of) the landmarks or emitters and the imaging sensor at all times when an object is to be tracked. Electromagnetic digitizers operate without such a restriction and offer the ability to track objects out of view or instruments placed inside the body.

Interventional imaging and display provide the neurosurgeon with an enhanced and dynamic view of the anatomy. Coupled with a stereotactic system, such as the optical tracking system described earlier, this allows the surgeon to navigate the surgical instruments within the surgical field, based on preoperative and/or intraoperative imaging information.

Efforts to refine the integration of neuronavigation tools into iMRI systems further are rather critical for closed-bore and horizontal-gap MRI scanner configurations, in which images and anatomy have to be correlated outside the scanner after the imaging is completed and the patient is taken out of the scanner. The neuronavigation system is then used to register the image updates to the patient's frame of reference. After accomplishing this critical step, the neuronavigation system is used for guiding tumor resection.

Modern neuronavigation systems are not limited to tracking handheld surgical instruments. Nimsky et al. have reported 22 cases in which a surgical microscope was integrated with the tracking system and used for guiding the tumor resection. The authors found that the combination of intraoperative imaging with functional neuronavigation offers the opportunity for more radical resections and may help decrease surgical morbidity.[38] Iseki et al. reported their setup of an MRI-guided surgery suite with a horizontal gap scanner and in-house neuronavigation software.[39] Similar efforts to combine neuronavigation and open-MRI scanners can be also found in Mursch et al. and Samset et al.[40,41] A unique approach of combining a neuronavigation system with a compact mobile MRI scanner designed for use in a conventional operating room has been described by Schulder et al.[42]

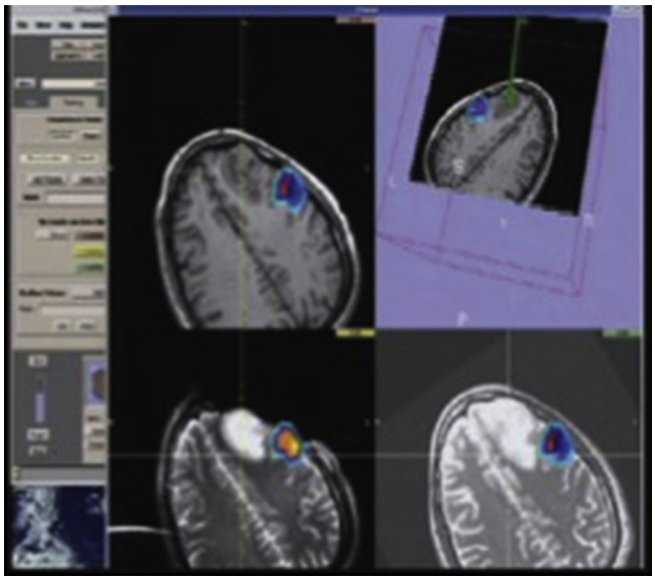


FIGURE 4 Neuronavigation using the 3D-Slicer. Preoperative fMRI registered and displayed on top of a preoperative T1 (top left), intraoperative T2 (bottom left), and preoperative T2 (bottom left) image. Note the virtual surgical probe (green bar) in the 3D view window (top right), which indicates the position of the surgical instrument used by the physician to navigate the multimodal image volume.

The development of neuronavigation systems for use within the iMRI environment has been a constant research focus at our institution. As a result of these efforts, we have developed the 3D-Slicer software package. This is a modular image-processing software package that features capabilities such as segmentation, registration, 3D-model generation, DT-tractography, multilayered display, and multiplanar image reformatting, along with instrument tracking capabilities (Figure 4). The 3D-Slicer has become an integral part of our iMRI system and has been successfully used for guiding brain biopsies and brain tumor resections for the past 7 years on a routine basis. Rigid and nonrigid fusion of preoperative, multimodal images with intraoperative image updates can be accomplished within the time constraints imposed by the ongoing surgery in this environment. The resulting updated multimodal datasets are employed for surgical guidance.[43]

After the multimodal preoperative images are registered with the intraoperative scans, the composite volume can be immediately used for surgical navigation ("virtual intraoperative scan") (Figure 5).

COREGISTRATION OF ULTRASOUND WITH PREOPERATIVE MRI AND iMRI

To validate the accuracy of preoperative MRI and iMRI, we have coregistered these navigation modalities

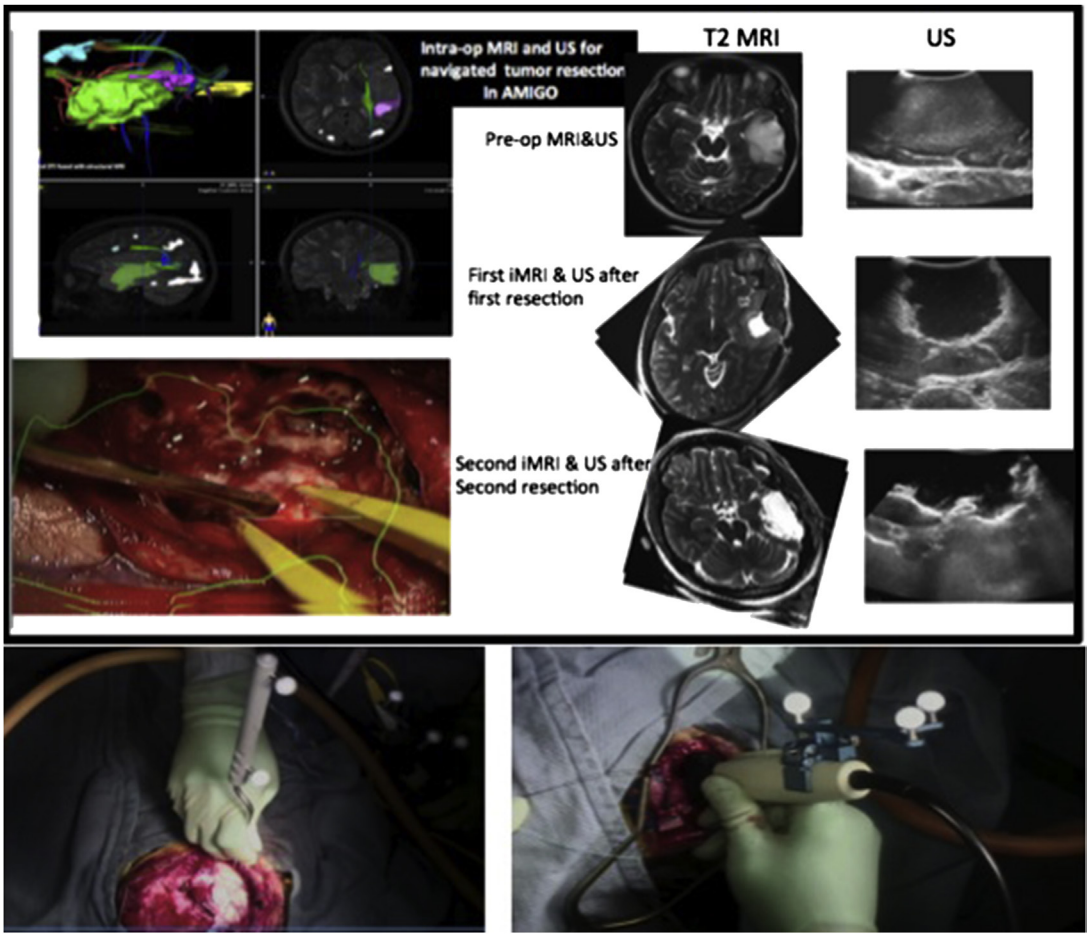


FIGURE 5 Coregistration of the preoperative and intraoperative MRI with ultrasound (US). Intraoperative real-time US helps us to determine the degree of brain shift and residual tumor when preoperative MRI is not able to show these changes. The top picture shows how iMRI and US are correlating with each other as we resect more tumors. The left bottom image shows the BrainLab navigation probe and bottom right shows the BrainLab cranial ultrasound module, coregistered to the iMRI via the BrainLab navigation system.

with real-time-tracked ultrasound (iUS) imaging, as a conavigation tool for the resection of brain tumors. Real-time US navigation will certainly help in cases of brain shift and we can be aware of misregistration from structural or functional MRI. To do this, the patient's head position is registered to the BrainLab neuronavigation system. Neuronavigation is performed by fusion of pre- and intraoperatively acquired MRI data. For all patients a 2D iUS with an 8-MHz probe is done after craniotomy, after dural opening, and at each stage of tumor resection to examine residual tumor. The iUS is calibrated and tracked using the BrainLab cranial US module, yielding registered and resliced views of the MRI in the same plane as the US. Our results from AMIGO (advanced multimodality image-guided operating room) at Brigham and Women's Hospital showed that in all cases, image quality and character of both iUS and iMRI, in detecting and navigating the lesion, were the same. We found 10% rates for brain shift and mismatch between preoperative MRI and real-time US as a navigational tools (Figure 5).[44]

Magnetic Resonance Imaging-Guided Thermal Ablations and Focused Ultrasound Surgery

With the introduction of MRI as a monitoring method for thermal therapies, a novel mechanism for controlling energy deposition became available. It was recognized that many MRI parameters are sensitive to temperature changes, which makes MRI suitable for monitoring thermal ablations by noninvasive means. Furthermore, one can take advantage of diffusion MRI, which detects changes in water mobility and compartmentalization, to identify reversible as well as irreversible thermally induced tissue changes.[44,45] It became obvious, however, that MRI monitoring of thermal ablation is feasible only if the imaging and therapy-delivery systems are integrated.

The role of MRI during thermal ablations is to monitor temperature levels and to ensure that the thermal coagulation is restricted to the targeted tissue volume. MRI can also detect irreversible tissue necrosis and demonstrate permanent changes within the treated tissue

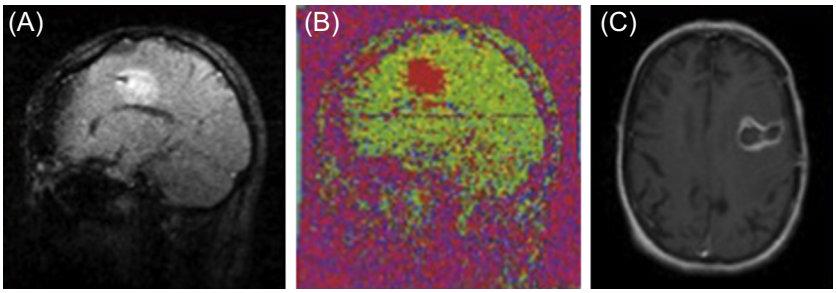


FIGURE 6 (A) Intraoperative image guiding the insertion of the laser fiber into the tumor. (B) MR thermal mapping during laser deposition. (C) Postoperative Gd-enhanced image.

volume. Physiologic effects such as perfusion or metabolic response to elevated temperature can also be used for monitoring the ablation. Both flow and tissue perfusion can affect the rate and extent of energy delivery and the size of the treated tissue volumes.[46]

Since the original description of MRI monitoring and control of laser–tissue interactions, MRI-guided tissue ablation (ILT) has become a clinically tested and accepted minimally invasive treatment option. It is a relatively simple straightforward method, which can be well adapted to the interventional MRI environment.

Overall, early results suggest that ILT is a safe therapy method. Although no definitive conclusion can be drawn based on the currently available data, it appears that ILT can be of benefit in patients with low-grade gliomas (Figure 6).[47,48] In malignant gliomas, thermal therapy has been essentially unsuccessful—a predictable outcome, since such tumors extend far beyond the area of MRI contrast enhancement.

Among currently developed thermal therapy methods, focused ultrasound (FUS) appears to be the most promising, since its use does not require any invasive intervention. The potential therapeutic use of US energy for intracranial pathology has long been acknowledged.[49] There is no more convincing example of the FUS benefits than in the brain, where deep lesions can be induced without any associated damage along the path of the acoustic beam.[49,50] In the brain, where most injuries have detectable functional consequences, it is extremely important to limit tissue damage to the targeted area. This necessitates the use of an imaging technique for localization, targeting, and real-time intraoperative monitoring and to control the spatial extent of heat deposition.[51] By combining FUS with MRI-based guidance and control, it may be possible to achieve complete tumor ablation without any associated structural injury or functional deficit.

Since the skull bone scatters and attenuates the propagation of the US beam, most clinical trials have been performed following craniotomy in order to provide an US window. However, the transcranial application of FUS, although challenging, is not impossible.[49] Although bone scatters and absorbs most of the acoustic energy, a small fraction can penetrate through the skull. Simulation and experimental studies have demonstrated the feasibility of accurately focusing US through the intact skull by using an array of multiple US transducers arranged over a large surface area.[50] To correct for beam distortion, the driving signal for the transducer elements of the array is individually adjustable, either based on measurements obtained with an invasive hydrophone probe or, better, based on detailed MRI.

Because of the large surface area, the US energy is distributed in such a manner as to avoid heating and consequent damage of skin, bone, meninges, or surrounding normal brain parenchyma, while being able to coagulate the tissue at the focus. The experimental data are extremely promising and a clinical trial is in progress at Harvard Medical School. From the preliminary results we conclude that it appears possible to coagulate brain tumors thermally through the intact skull under MRI thermometry control using MR-compatible arrays.

By applying multiple, smaller transducers around the skull in a helmet-like phased-array system, sufficient amounts of energy can be deposited in the target tissue. Unfortunately, the skull thickness is uneven, causing variable delays of the acoustic waves originating from individual phased-array elements. Phase incoherence can be corrected, however, if the skull thickness is known from preoperative X-ray computed tomography scans. In an experimental setup, successful focusing through the skull was achieved and verified by MRI, thus providing the foundation for developing the first human MRI-guided FUS system for brain tumor treatment.

Beyond thermal coagulation of tissue, FUS has various other effects that can be therapeutically exploited and thus open the way for potentially innovative vascular and functional neurosurgery applications and for targeted drug delivery to the central nervous system. Among the most important, the capability of occluding vessels could make FUS a therapeutic tool for the treatment of vascular malformations.[52]

FUS can be used selectively to open the blood–brain barrier, without damaging the surrounding brain

parenchyma.[53,54] For this effect to be achieved, preformed gas bubbles must be introduced into the vasculature, as is routinely done with US contrast agents. The gas bubbles implode and release cavitation-related energy, which transiently inactivates the tight junctions. As a consequence, large molecules can pass through the artificially created "window" in the blood–brain barrier.[55] These large molecules can be chemotherapeutic or neuropharmacological agents. FUS-based targeted selective drug delivery to the brain could result in novel therapeutic interventions for movement and psychiatric disorders.

Such MRI-guided focal opening of the blood–brain barrier, combined with US technology that permits sonication through the intact skull, will open the way for new, noninvasive, targeted therapies. Specifically, it would provide targeted access for chemotherapeutic and gene therapy agents,[56] as well as monoclonal antibodies, and could even provide a vascular route for performing neurotransplantations.

CONCLUSION

The role of imaging for both diagnosis and therapy has become well established. The increasing favorable reception and dissemination of minimally invasive procedures has resulted in the recognition of the feasibility of image-guided approaches. Although radiology has combined imaging with various novel therapeutic methods, the full utilization of advanced imaging technology has not yet been accomplished. Current research focuses on the development of therapy delivery systems in which advanced imaging modalities are closely linked with high-performance computing. Obviously, the operating room of the future will accommodate various instruments, tools, and devices that are attached to the imaging systems and controlled by image-based feedback.

References

1. US MRI scanners and Coils markets A435–50. 2003:2–7 [Frost and Sullivan Marketing Report].
2. Jolesz FA. Future perspectives for intraoperative MRI. *Neurosurg Clin N Am*. 2005;16(1):201–213.
3. Jolesz FA, Hynynen K, McDannold N, Tempany C. MR imaging-controlled focused ultrasound ablation: a noninvasive image-guided surgery. *Magn Reson Imag Clin N Am*. 2005;13(3):545–560.
4. Keles GE, Lamborn KR, Berger MS. Low-grade hemispheric gliomas in adults: a critical review of extent of resection as a factor influencing outcome. *J Neurosurg*. 2001;95(5):735–745.
5. Lacroix M, Abi-Said D, Fourney DR, et al. A multivariate analysis of 416 patients with glioblastoma multiforme: prognosis, extent of resection, and survival. *J Neurosurg*. 2001;95(2):190–198.
6. Claus EB, Horlacher A, Hsu L, et al. Survival rates in patients with low-grade glioma after intraoperative magnetic resonance image guidance. *Cancer*. 2005;103(6):1227–1233.
7. Schneider JP, Trantakis C, Rubach M, et al. Intraoperative MRI to guide the resection of primary supratentorial glioblastoma multiforme – a quantitative radiological analysis. *Neuroradiology*. 2005;47(7):489–500.
8. Nabavi A, Black PM, Gering DT, et al. Serial intraoperative magnetic resonance imaging of brain shift. *Neurosurgery*. 2001;48(4):787–797. [discussion 797–798].
9. Nimsky C, Ganslandt O, Cerny S, et al. Quantification of, visualization of, and compensation for brain shift using intraoperative magnetic resonance imaging. *Neurosurgery*. 2000;47(5):1070–1079. [discussion 1079–1080].
10. Schneider JP, Schulz T, Schmidt F, et al. Gross-total surgery of supratentorial low-grade gliomas under intraoperative MR guidance. *Am J Neuroradiol*. 2001;22(1):89–98.
11. Black PM, Alexander 3rd E, Martin C, et al. Craniotomy for tumor treatment in an intraoperative magnetic resonance imaging unit. *Neurosurgery*. 1999;45(3):423–431. [discussion 431–433].
12. Hadani M, Spiegelman R, Feldman Z, et al. Novel, compact, intraoperative magnetic resonance imaging-guided system for conventional neurosurgical operating rooms. *Neurosurgery*. 2001;48(4):799–807. [discussion 807–809].
13. Talos IF, Zou KH, Ohno-Machado L, et al. Supratentorial low-grade glioma resectability: statistical predictive analysis based on anatomic MR features and tumor characteristics. *Radiology*. 2006;239(2):506–513.
14. Logothetis NK, Pfeuffer J. On the nature of the BOLD fMRI contrast mechanism. *Magn Reson Imaging*. 2004;22(10):1517–1531.
15. Schiffbauer H, Berger MS, Ferrari P, et al. Preoperative magnetic source imaging for brain tumor surgery: a quantitative comparison with intraoperative sensory and motor mapping. *J Neurosurg*. 2002;97(6):1333–1342.
16. Schiffbauer H, Berger MS, Ferrari P, et al. Preoperative magnetic source imaging for brain tumor surgery: a quantitative comparison with intraoperative sensory and motor mapping. *Neurosurg Focus*. 2003;15(1):E7.
17. Rohlfing T, West JB, Beier J, et al. Registration of functional and anatomical MRI: accuracy assessment and application in navigated neurosurgery. *Comput Aided Surg*. 2000;5(6):414–425.
18. Nimsky C, Ganslandt O, Kober H, et al. Integration of functional magnetic resonance imaging supported by magnetoencephalography in functional neuronavigation. *Neurosurgery*. 1999;44(6):1249–1255. [discussion 1255–1256].
19. Witwer BP, Moftakhar R, Hasan KM, et al. Diffusion tensor imaging of white matter tracts in patients with cerebral neoplasm. *J Neurosurg*. 2002;97(3):568–575.
20. Talos IF, O'Donnell L, Westin CF, et al. Diffusion tensor and functional MRI fusion with anatomical MRI for image-guided neurosurgery. *Lect Notes Comp Sci*. 2003;2878:407–415.
21. Basser PJ, Pajevic S, Pierpaoli C, et al. In vivo fiber tractography using DT-MRI data. *Magn Reson Med*. 2000;44(4):625–632.
22. Mori S, van Zijl PC. Fiber tracking: principles and strategies a technical review. *NMR Biomed*. 2002;15(7–8):468–480.
23. Westin CF, Maier SE, Mamata H, et al. Processing and visualization for diffusion tensor MRI. *Med Image Anal*. 2002;6(2):93–108.
24. Pluim JP, Maintz JB, Viergever MA. Mutual-information based registration of medical images: a survey. *IEEE Trans Med Imaging*. 2003;22(8):986–1004.
25. West J, Fitzpatrick JM, Wang MY, et al. Comparison and evaluation of retrospective intermodality brain image registration techniques. *J Comput Assist Tomogr*. 1997;21(4):554–566.
26. Maintz JB, Viergever MA. A survey of medical image registration. *Med Image Anal*. 1998;2(1):1–36.
27. Warfield SK, Jolesz FA, Kikinis R. A high performance computing approach to the registration of medical imaging data. *Parallel Comput*. 1998;24(9–10):1345–1368.

28. Wells 3rd WM, Viola P, Atsumi H, et al. Multi-modal volume registration by maximization of mutual information. *Med Image Anal*. 1996;1(1):35–51.
29. Warfield SK. *Medical Image Analysis for Image Guided Therapy*. DICTA; 2005.
30. Grau V, Mewes AU, Alcaniz M, et al. Improved watershed transform for medical image segmentation using prior information. *IEEE Trans Med Imaging*. 2004;23(4):447–458.
31. Warfield SK, Haker SJ, Talos IF, et al. Capturing intraoperative deformations: research experience at Brigham and Women's Hospital. *Med Image Anal*. 2005;9(2):145–162.
32. Clatz O, Delingette H, Talos IF, et al. Robust nonrigid registration to capture brain shift from intraoperative MRI. *IEEE Trans Med Imaging*. 2005;24(11):1417–1427.
33. Krishnan R, Raabe A, Hattingen E, et al. Functional magnetic resonance imaging-integrated neuronavigation: correlation between lesion-to-motor cortex distance and outcome. *Neurosurgery*. 2004;55(4):904–914. [discusssion 914–915].
34. Ruiz-Alzola J, Westin CF, Warfield SK, et al. Nonrigid registration of 3D tensor medical data. *Med Image Anal*. 2002;6(2):143–161.
35. Schwartz RB, Hsu L, Kacher DF, et al. Intraoperative dynamic MRI: localization of sites of brain tumor recurrence after high-dose radiotherapy. *J Magn Reson Imaging*. 1998;8(5):1085–1089.
36. Atlas SW, Thulborn KR. MR detection of hyperacute parenchymal hemorrhage of the brain. *Am J Neuroradiol*. 1998;19(8):1471–1477.
37. Mamata Y, Mamata H, Nabavi A, et al. Intraoperative diffusion imaging on a 0.5 Tesla interventional scanner. *J Magn Reson Imaging*. 2001;13(1):115–119.
38. Nimsky C, Ganslandt O, Kober H, et al. Intraoperative magnetic resonance imaging combined with neuronavigation: a new concept. *Neurosurgery*. 2001;48(5):1082–1089. [discussion 1089–1091].
39. Iseki H, Muragaki Y, Nakamura R, et al. Intelligent operating theater using intraoperative open-MRI. *Magn Reson Med Sci*. 2005;4(3):129–136.
40. Mursch K, Gotthardt T, Kroger R, et al. Minimally invasive neurosurgery within a 0.5 Tesla intraoperative magnetic resonance scanner using an off-line neuro-navigation system. *Minim Invasive Neurosurg*. 2005;48(4):213–217.
41. Samset E, Hogetveit JO, Cate GT, Hirschberg H. Integrated neuronavigation system with intraoperative image updating. *Minim Invasive Neurosurg*. 2005;48(2):73–76.
42. Schulder M, Sernas TJ, Carmel PW. Cranial surgery and navigation with a compact intraoperative MRI system. *Acta Neurochir Suppl*. 2003;85:79–86.
43. Nabavi A, Gering DT, Kacher DF, et al. Surgical navigation in the open MRI. *Acta Neurochir Suppl*. 2003;85:121–125.
44. Dolati P, Olubios O, Norton I, Golby A. Ultrasound imaging for navigated brain tumor resection: a prospective validation study. In: *Electronic Poster at the 82nd AANS Annual Scientific Meeting, SF. CA, USA.* ; April 2014.
45. Bleier AR, Jolesz FA, Cohen MS, et al. Real-time magnetic resonance imaging of laser heat deposition in tissue. *Magn Reson Med*. 1991;21(1):132–137.
46. MacFall J, Prescott DM, Fullar E, Samulski TV. Temperature dependence of canine brain tissue diffusion coefficient measured in vivo with magnetic resonance echoplanar imaging. *Int J Hyperth*. 1995;11(1):73–86.
47. McDannold NJ, Jolesz FA. Magnetic resonance image-guided thermal ablations. *Top Magn Reson Imaging*. 2000;11(3):191–202.
48. Kahn T, Bettag M, Ulrich F, et al. MRI-guided laser-induced interstitial thermotherapy of cerebral neoplasms. *J Comput Assist Tomogr*. 1994;18(4):519–532.
49. Bettag M, Ulrich F, Schober R, et al. Stereotactic laser therapy in cerebral gliomas. *Acta Neurochir Suppl (Wien)*. 1991;52:81–83.
50. Hynynen K, Jolesz FA. Demonstration of potential noninvasive ultrasound brain therapy through an intact skull. *Ultrasound Med Biol*. 1998;24(2):275–283.
51. Clement GT, White J, Hynynen K. Investigation of a large-area phased array for focused ultrasound surgery through the skull. *Phys Med Biol*. 2000;45(4):1071–1083.
52. McDannold K, Hynynen D, Wolf G, et al. MRI evaluation of thermal ablation of tumors with focused ultrasound. *J Magn Reson Imaging*. 1998;8(1):91–100.
53. Hynynen K, Colucci V, Chung A, Jolesz F. Noninvasive arterial occlusion using MRI-guided focused ultrasound. *Ultrasound Med Biol*. 1996;22(8):1071–1077.
54. Hynynen K, McDannold N, Sheikov NA, et al. Local and reversible blood–brain barrier disruption by noninvasive focused ultrasound at frequencies suitable for trans-skull sonications. *Neuroimage*. 2005;24(1):12–20.
55. McDannold N, Vykhodtseva N, Hynynen K. Targeted disruption of the blood–brain barrier with focused ultrasound: association with cavitation activity. *Phys Med Biol*. 2006;51(4):793–807.
56. Kinoshita M, McDannold N, Jolesz FA, Hynynen K. Targeted delivery of antibodies through the blood–brain barrier by MRI-guided focused ultrasound. *Biochem Biophys Res Commun*. 2006;340(4):1085–1090.

CHAPTER

23

Neurosurgical Treatment Planning

Wenya Linda Bi[1], *Olutayo Olubiyi*[1], *Suzanne Tharin*[2], *Alexandra J. Golby*[1]

[1]Department of Neurosurgery, Brigham and Women's Hospital, Harvard Medical School, Boston, MA, USA;
[2]Department of Neurosurgery, Stanford University, Palo Alto, CA, USA

INTRODUCTION

Safe neurosurgery, for any indication, is predicated on intimate knowledge of anatomic corridors and physiological response. In the case of brain tumors, maximal excision with minimal incurrence of neurologic deficit is a goal for most disease subtypes. A technically flawless surgery imparts limited value to the patient in the face of impaired function, which may result from injury to cortical areas abutting a lesion or to white matter tracts encountered along the surgical approach. The amalgamation of conventional imaging for anatomic structures and functional mapping techniques has revolutionized the surgical approach to and clinical outcomes of brain tumors. While neurosurgeons have long used invasive brain mapping techniques, technological advances have led to less invasive methods for mapping brain function. These methods differ in their methodology, physiologic basis, spatial and temporal resolution, and cost. This chapter briefly presents the indications and limitations of perioperative imaging strategies for brain tumors, with a focus on functional imaging studies.

GENERAL CONSIDERATIONS IN BRAIN TUMOR SURGERY

Primary goals of neurosurgical intervention include obtaining tissue diagnosis and reduction of mass effect. Surgical resection may achieve a curative goal for some benign extrinsic lesions, such as meningiomas or pituitary tumors. This is not always true for higher-grade lesions or those that have infiltrated neurovascular structures by the time of presentation. Furthermore, intrinsic brain tumors are typically associated with insidious invasion and multifocal seeding, beyond the spectrum of visual detection at the time of surgery. Owing to their infiltrative nature, gliomas may have functional tissue within the tumor.[1,2] Infiltrative tumors may also contain white matter tracts within their boundaries, challenging the feasibility of complete resection.

Multiple studies have demonstrated that increased extent of resection improves survival for glioblastomas, both on initial diagnosis and at recurrence.[3,4] However, median survival remains around 14 months, despite adjuvant chemoradiation therapies.[5] This poor prognosis highlights the importance of expeditious postoperative recovery and minimization of even transient deficits. Similarly, patients with brain metastases usually have limited life expectancy, so palliative surgery must be balanced with preservation of quality of life. In the case of low-grade gliomas, the impact of extent of resection on survival is qualified by the genomic features of the tumor, such as *IDH1/2* mutation status.[6] As such, imaging of molecular signatures may play an increasingly important role in future decision-making.[7]

Neurosurgical treatment planning for tumors can be stratified into preoperative, intraoperative, and postoperative stages. Preoperative imaging dictates the decision to operate or not, the surgical approach, and anticipated extent of resection. Intraoperative imaging modalities navigate the surgical corridor, monitor neurologic function, and provide real-time feedback on operative margins. Postoperative imaging augurs risk and tempo for recurrence, reveals the presence of unanticipated complications, and sets a baseline for disease follow-up. In each stage, surgeons can choose among numerous strategies based on the desired data output, institutional experience, and availability.

PREOPERATIVE IMAGING STRATEGIES

Conventional magnetic resonance imaging (MRI) remains the mainstay of preoperative imaging for tumor surgical planning. Vascular anatomy is also frequently

http://dx.doi.org/10.1016/B978-0-12-800945-1.00023-9
© 2016 Elsevier Ltd. All rights reserved.

helpful in planning of surgical approaches for both intrinsic and extrinsic tumors. This can be elucidated by MR angiography/venography (MRA/V), computed tomographic (CT) angiography/venography (CTA/V), dynamic CTA/V, or digital subtraction angiography, with varying sensitivity, specificity, and associated risks. Further advanced imaging modalities provide insight into white matter tracts and localization of neurologic function, as described below. Appropriate selection of the optimal methodology is influenced by the goals of surgery.

Diffusion Tensor Imaging

Surgeons increasingly appreciate that perturbation of white matter tracts can result in significant permanent neurologic deficits and incorporate tractography in routine operative planning. The most common method by which white matter tracts are demonstrated is diffusion tensor imaging (DTI), which measure the direction of diffusion of water molecules as a marker for the axis of these tracts. DTI takes the assumption that axonal membranes and myelin directionally restrict the diffusion of water. Water diffuses most in the direction parallel to fiber tracts and least perpendicular to tracts, resulting in anisotropic diffusion in regions of tightly packed white matter tracts.[8] In contrast, in cerebrospinal fluid (CSF) or the gray matter, water diffusion is equal in all directions, or isotropic. In DTI, magnetic field gradients are applied in multiple orientations and a mathematical model, the diffusion tensor, is used to estimate the direction of maximum diffusivity of water molecules for every voxel, which corresponds to the dominant axis of white matter tracts in that voxel.[9] DTI can successfully demonstrate major white matter tracts, including the corticospinal, corticobulbar, and corticopontine tracts; arcuate fasciculus, uncinate fasciculus, superior and inferior occipitofrontal fasciculi, and occipitotemporal fasciculus; optic radiations; corpus callosum; cingulum; and anterior commissure.[9]

These tracts have been observed to be altered by neoplasms following four patterns: normal signal with altered position or direction, corresponding to tract displacement; decreased but present signal with normal direction and location, thought to correspond to vasogenic edema; decreased signal with disrupted direction maps, thought to correspond to infiltration; and loss of anisotropic signal, corresponding to fiber tract obliteration or destruction (Figure 1).[9] Superresolution track density imaging reconstruction of tractography data has shown histopathologic correlation between track density values and architectural disruption or cellularity of tissue.[10] Other advanced computational algorithms have also shown promise in building more robust tract outputs in the setting of peritumoral edema.[11] Further studies are merited to validate the pathologic correlates of these computational products. One team-based effort to tackle current limitations of DTI in neurosurgical treatment planning is the annual Medical Image Computing and Computer Assisted Intervention DTI challenge, which brings together international teams to resolve tractography solutions on a standardized set of challenging brain tumor cases.[12] Such efforts to promote discourse and foster innovation in tractography hold promise for its continued evolution.

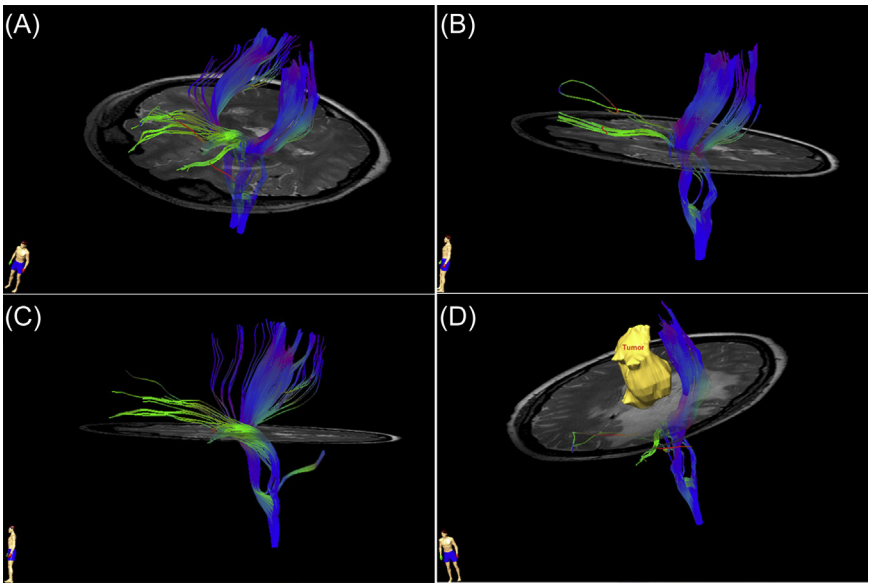


FIGURE 1 Corticospinal tracts as constructed through DTI in the setting of a left frontal tumor. Reconstruction showing disruption of normal tract anatomy by an intrinsic tumor. (A) Bilateral corticospinal tracts from a left anterior oblique view. (B) Intact corticospinal tracts on the right side, as appreciated from a left lateral view. (C) Disrupted corticospinal tracts on the left side (note the deficient fibers in the anterior half of the fiber bundle), with (D) closely juxtaposed glioma. *Images from the Golby Lab, Brigham and Women's Hospital, Harvard Medical School, Boston, MA.*

DTI faces several limitations. It remains susceptible to artifacts from air spaces and becomes less reliable in instances of crossing fiber tracts, although newer tractography methods have begun to solve these challenges.[13,14] Furthermore, the demonstration of anatomic location does not necessarily offer information on the functional status of these tracts, for which other modalities provide complementary data. DTI has also capitalized upon peritumoral edema to distinguish between primary and metastatic brain tumors. In the area of edema surrounding a metastasis, there is an increase in the diffusion of water along white matter tracts, whereas a decrease in diffusion is generally noted in primary brain tumors, presumably owing to their infiltrative nature.[15,16] DTI may also be used to image the effect of tumor on fiber tracts.[17] Taken together, increased appreciation for anatomic distortions of white matter tracts may allow greater confidence in operating on an area of expected white matter tract that has been destroyed or deflected, as well as avoiding injury to displaced tracts.

Functional Magnetic Resonance Imaging

Functional MRI (fMRI) is one of the most frequently used modalities to localize and assess cortical function. fMRI measures changes in cerebral blood flow as a surrogate for neuronal activity, most commonly with blood oxygen level-dependent (BOLD) changes in the MR signal. Neuronal activity results in increased blood flow through local capillaries. The increased perfusion outstrips the increased demand, resulting in an increase in the ratio of oxyhemoglobin (oxy-Hb) to deoxyhemoglobin (deoxy-Hb).[18] The iron in deoxy-Hb is paramagnetic and reduces the T2 signal. In other words, neuronal activity results in a relative increase in oxy-Hb concentration and consequent increase in T2 or BOLD signal.[19] For each voxel, the BOLD signal during performance of a task is compared to that during the resting, or low-level, control state. BOLD signal change represents a ratio rather than an absolute physiologic measure. The change in signal is small, on the order of 0.5–5%.[20] To obtain an acceptable signal-to-noise ratio, the BOLD signal is averaged over multiple repeated trials and then superimposed on a structural MRI. Not surprisingly, accurate fMRI maps may be difficult to achieve in patients with neurologic deficits, as adequate task performance is a prerequisite for accurate functional maps. More recently, the discovery of resting-state fMRI has led to investigation of task-free paradigms, which may provide a viable alternative in brain tumor operative planning, particularly in patients with neurologic deficits (Figure 2).[21,22]

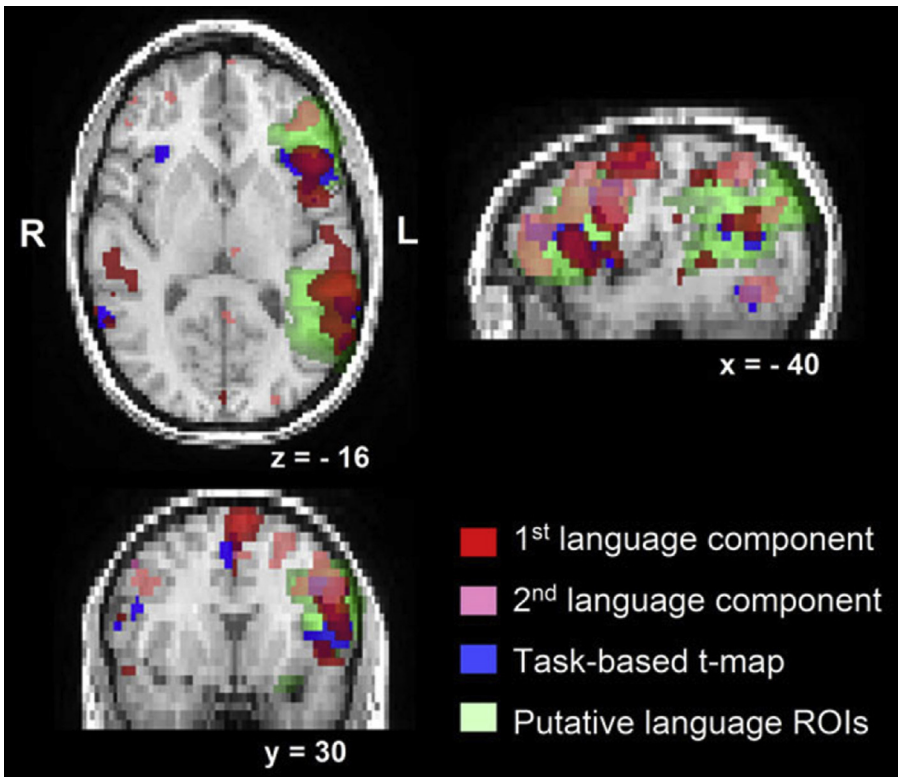


FIGURE 2 **Resting-state fMRI for language.** Superimposed cerebral activation maps from resting-state fMRI and task-based fMRI, overlaid on T1-weighted structural images. This subject had two consensus language components (first and second language components shown in red and pink, respectively). *Adapted from Tie et al.*[22]

fMRI has been compared against positron emission tomography (PET), transcranial magnetic stimulation (TMS), and electrocortical stimulation (ECS) testing for localization of the motor cortex in patients with lesions involving the central sulcus, demonstrating overlapping maps in the majority of cases. The typical spatial resolution of fMRI is 2–5 mm. Advanced MRI techniques, including higher field strengths and parallel imaging, can provide increased signal-to-noise ratio, increased spatial resolution, and shortened acquisition times.[23,24] The latency of the observed signal change in BOLD imaging is several seconds, making the temporal resolution of fMRI poor compared with techniques such as ECS or electroencephalography (EEG), though this is probably of little relevance for surgical planning.

fMRI is sensitive to motion-related artifacts, including those arising from heartbeat, breathing, and head motion. Disruption of the signal from face movement associated with vocalization has generally precluded the use of tasks involving overt spoken speech for language mapping. High-grade central nervous system tumors are also associated with hemodynamic–neural uncoupling and have altered regional blood flow, which may influence the BOLD signal. fMRI data must be interpreted with this in mind.

Benefits of fMRI include its noninvasive nature, the ability to interrogate function in the sulcal depths, and the ability to be integrated with multiple other imaging modalities for preoperative planning. The ability to repeat fMRI modules allows for multiple runs in a single session and serial sessions to follow patients over time. fMRI also localizes, in addition to lateralizes, critical functions such as language and memory, compared to Wada testing. In addition, fMRI can demonstrate functional activation in the depths of cortical sulci, an advantage over even the gold standard ECS, which restricts to the cortical surface.

Magnetoencephalography

Another noninvasive method of measuring brain activity is magnetoencephalography (MEG), which measures the magnetic fields that accompany neuronal activity (Figure 3). MEG is similar to EEG but is based on magnetic field changes rather than voltage changes. The summation of postsynaptic potentials generated by synchronous neuronal firing can be detected at the scalp surface using a biomagnetometer, made up of wire induction coils arranged in an array covering the head. The magnetic fields are then reconstructed to create an image of the distribution of evoked neural electrical activity in real time of brain function. Superconducting quantum interference devices are used to record the conductance change caused by the small magnetic fields associated with neuronal activity. During MEG functional mapping, a time-locked stimulus task is presented multiple times. The resulting evoked neuromagnetic signals are then averaged over several trials to separate the signal produced by a focal population of active neurons from background activity.

While MEG has most commonly been used to localize epileptogenic foci for resection,[25] it is increasingly applied to guide surgery of lesions adjacent to eloquent cortex.[26] Magnetic source imaging is the coregistration of MEG data to a structural image to facilitate the anatomic–functional correlations and to incorporate this information into stereotactic neuronavigation systems. Several studies report good correlation between preoperative MEG functional data and intraoperative maps of

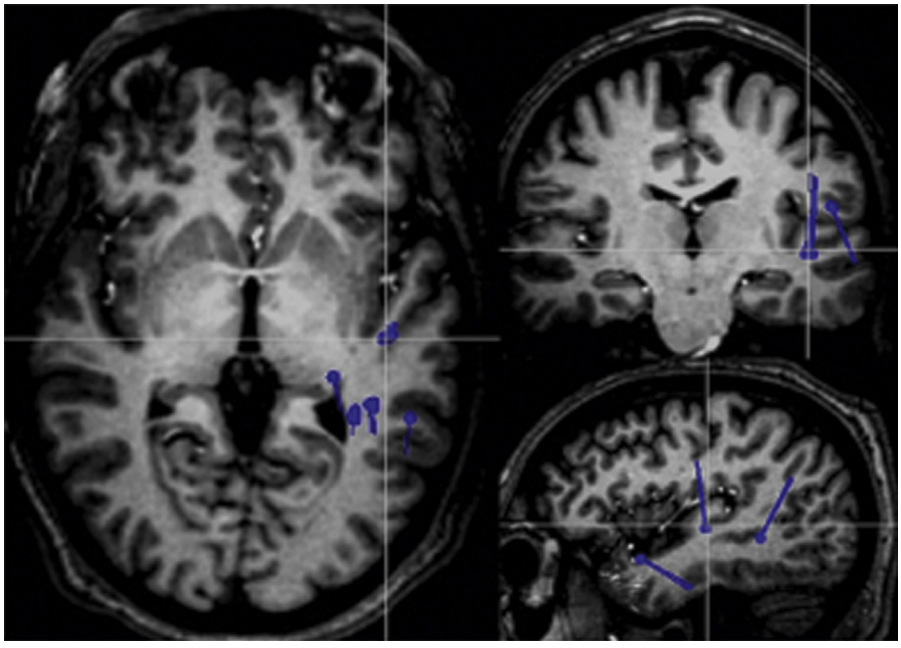


FIGURE 3 **MEG maps obtained during a language task.** Note dipoles primarily localize to the left temporal region.

sensory- and motor-evoked potentials and electrocortical mapping.[27–30] MEG offers excellent temporal resolution, while being more constrained to create spatially detailed functional activation maps. MEG detection of the current source often projects a distributed region over the cortical surface and is less reliable for focal anatomic localization. Therefore, many groups have merged MEG data with anatomic data or fMRI to locate key functional cortices near and within intrinsic neoplasms for preoperative and intraoperative planning.[31,32]

Transcranial Magnetic Stimulation

In contrast to the passive detection of magnetic currents, TMS actively delivers a magnetic field at the scalp to stimulate or inhibit neuronal electrical activity.[33] A current is discharged into an electromagnetic coil held over the skull, which induces a perpendicular electric field through the skin and skull, resulting in an electric current in the cortex, without causing pain to the patient.[34] TMS is relatively noninvasive, though repetitive stimulation carries a risk of causing seizures. Disadvantages include poor spatial resolution and limited availability.[34] More recent experience integrating TMS with stereotactic navigation, or navigated TMS (nTMS), allows coregistration of structural scans to localize delivery of TMS pulses.[35] TMS has been compared with ECS in patients with tumors near the central sulcus.[36] Furthermore, continued refinements in nTMS have demonstrated improving correlation with MEG and direct cortical stimulation in language mapping.[37,38]

Electrocorticography and Electrical Cortical Stimulation

Electrocorticography is the direct recording of electrical potentials associated with brain activity from the cerebral cortex. Since the 1930s, direct ECS testing has been the gold standard method for mapping brain function in preparation for surgical resection (Figure 4).[39,40] Invasive stimulation and recording from the human brain can provide unique opportunities to study fundamental processes at fine temporal and spatial resolution.[41] A widely used application of electrocorticography is the localization of the central sulcus by means of phase reversal of somatosensory-evoked potentials.[42] Intraoperatively, the motor cortex may be localized by stimulating the precentral and postcentral gyri, eliciting motor or somatosensory responses, respectively. ECS for motor mapping may be performed under general anesthesia as long as muscle relaxants are not used. Low- or high-frequency stimulation delivered to the motor cortex causes contralateral muscular contractions. Alterations in motor-evoked potentials (MEPs) after high-frequency repetitive ECS are concerning for potential postoperative impairment, although the amplitude and duration of MEP changes that are considered significant vary by pathology and surgical procedure.[43–45]

Cortical stimulation testing is limited by its invasive nature requiring craniotomy and generally specialized surgical and anesthesia teams. ECS is limited in its ability to examine the functional cortex within the sulcal

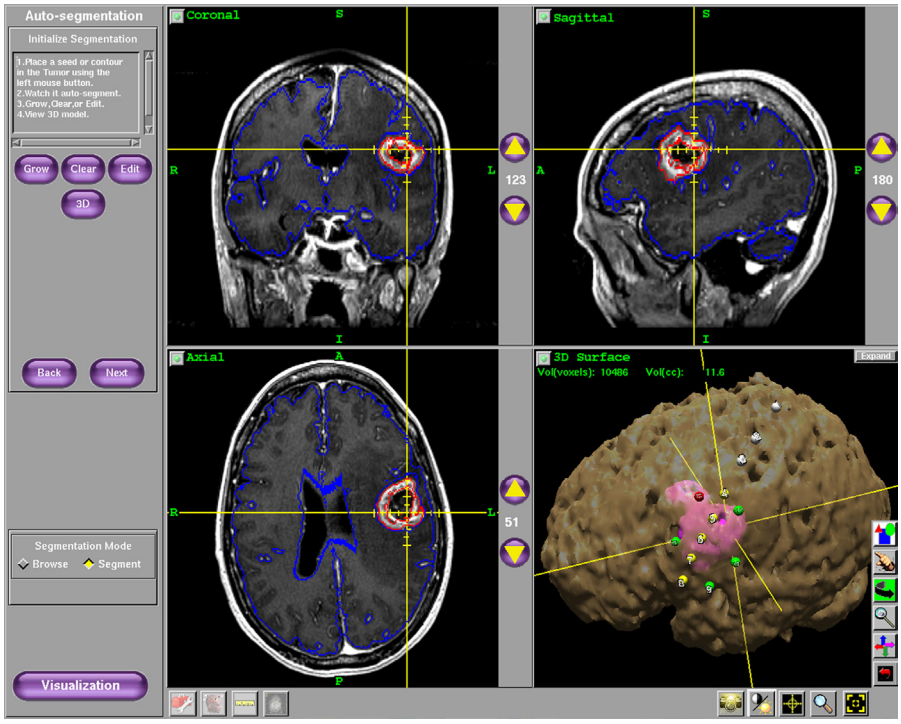


FIGURE 4 Intraoperative view of integrated images including segmented tumor in the left frontal lobe (outlined in red) and intraoperative recording sites (yellow spheres). Negative intraoperative stimulation sites are represented by green spheres, while positive sites are shown in red.

depths that comprise as much as two-thirds of the cortical surface, the deep structures of the mesial temporal lobe, or the underlying white matter. For example, it is not uncommon for patients who have undergone cortical mapping and resection respecting the boundaries of the eloquent cortex, nevertheless, to be left with neurological deficits secondary to damage to associated white matter tracts. To minimize such occurrences, some have applied intraoperative stimulation of white matter to define critical tracts.[46] Emerging experience with subcortical stimulation provides promising localization of motor, language, and visual tracts.[46–48] However, the precise distance from a functional tract at which responses are elicited is unclear and merits further study on the whole. Comparison of surgical series from recent decades reveals that intraoperative stimulation mapping may result in fewer late severe neurologic deficits and a greater extent of resection, especially in eloquent regions, for gliomas.[49]

Wada Testing

The intracarotid amytal, or Wada, test is a method in which sodium amytal is injected into the internal carotid artery (ICA), temporarily anesthetizing the brain in the territory of that ICA. Following confirmation of clinical effect by the onset of contralateral hemiparesis and EEG changes, a battery of behavioral tests is administered. Wada testing was initially developed to lateralize language dominance in patients undergoing electroconvulsive therapy, but has long been used for language lateralization in preoperative patients.[50] The Wada test was subsequently modified to test lateralization of memory and to assess the risk of postoperative amnesia in patients undergoing temporal lobectomy for medial temporal lobe epilepsy.[51] The spatial resolution of the Wada test is usually hemispheric. However, Wada testing has been employed in a more highly localized manner with selective catheterization, for instance, to investigate function of the mesial temporal structures in epilepsy patients.[52]

Wada testing is limited in that the examiner has only a few minutes to test each hemisphere. The test is invasive, carrying a 0.6–1% risk of stroke.[53] Agitation or obtundation can preclude cognitive testing in some individuals. Because of its invasive nature, Wada testing is not readily repeatable. Technically, the test may potentially be confounded by cross flow between hemispheres, resulting in anesthesia of both hemispheres from a unilateral injection. Furthermore, despite the Wada test being the gold standard historically, noninvasive functional imaging may provide better predictive efficacy in the contemporary era.[54,55] Increasingly, fMRI is substituted for Wada testing for the preoperative determination of language and memory lateralization.[56–60] MEG also shows promise in high correlation with Wada testing for language lateralization and presents a viable alternative in some centers.[61]

FUNCTIONAL APPLICATIONS

Localization and preservation of critical neurologic functions, including movement and language, garner special attention in operative planning. Functional imaging and tractography have also been applied for preservation of other modalities, such as vision, but will not be explored in depth here.[62]

Motor Mapping

Voluntary movement is associated with activation of primary motor cortex, premotor area, supplementary motor area, and superior parietal lobule. fMRI is the most common preoperative modality to delineate brain regions activated by motor tasks. fMRI has been validated against ECS in localizing motor areas.[63–67] More recently, preoperative nTMS and MEG data have shown reasonable concordance with direct cortical stimulation.[68] Subcortical motor pathways, as demonstrated through DTI, have also been combined with fMRI and ECS to evaluate the motor cortex and its descending (pyramidal) tracts in patients with tumors near the motor cortex.[17,69,70] However, the reconstructed motor fiber tracks can be significantly influenced by the choice of computational model and face significant limitations in accurate portrayal of lateral motor tracts.[71] Tumors and peritumoral edema near motor areas can also distort motor maps. The motor cortex, as well as descending tracts, is frequently shifted by mass lesions.[63,72] Nevertheless, integration of fMRI and DTI data into neuronavigation systems is becoming increasingly standard and valuable for operative guidance (Figure 5).[73]

Language Localization

Language networks are classically defined as an area controlling expressive aspects of language, or Broca's area, connected to an area controlling receptive aspects of language, or Wernicke's area (Figure 6).[74–78] Contemporary functional imaging and stimulation mapping have elucidated a more nuanced model of phonological and semantic language processing, with implications for tumor resection.[79] Furthermore, pathologic lesions, especially slow-growing low-grade gliomas, are recognized to induce cortical reorganization and plasticity with redistribution of eloquent language areas.[79,80]

Initial diagnostic studies focused on language lateralization, using fMRI and Wada. fMRI has demonstrated up to 97% concordance with Wada results in typical language lateralization and approximately 50% concordance in atypical language lateralization.[81,82] More recently, noninvasive functional imaging has also been suggested to have potentially better predictive efficacy of postoperative language and memory deficits than Wada testing.[55] The language task performed may influence

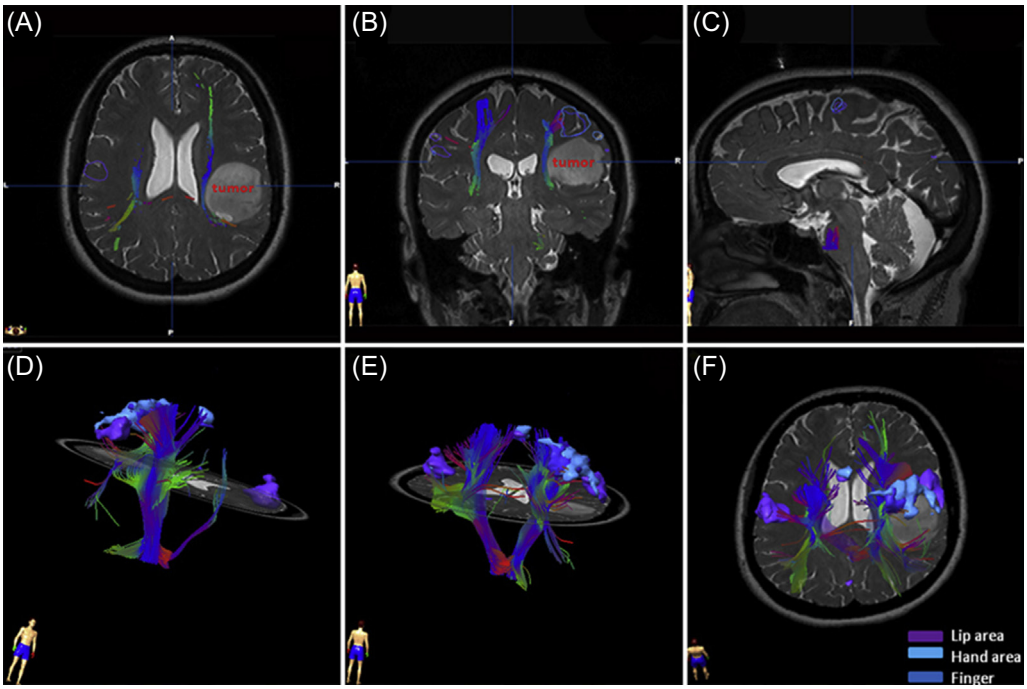


FIGURE 5 **fMRI for motor tasks with superimposed DTI-derived corticospinal tracts.** T2-weighted MRI with fMRI-mapped cortical motor areas, bilateral corticospinal tracts (CST), and a right frontoparietal glioma (tumor) in (A) sagittal, (B) coronal, and (C) axial views. (D) Three-dimensional reconstruction of right-side motor areas with associated right CST, in right anterior oblique view. (E) Three-dimensional reconstruction of right-side motor hand and bilateral lip areas with associated bilateral CST, in left posterior oblique view. (F) Three-dimensional reconstruction of right-side motor hand and bilateral lip areas with associated bilateral CST and T2-weighted axial slice. *Images from the Golby Lab, Brigham and Women's Hospital, Harvard Medical School, Boston, MA.*

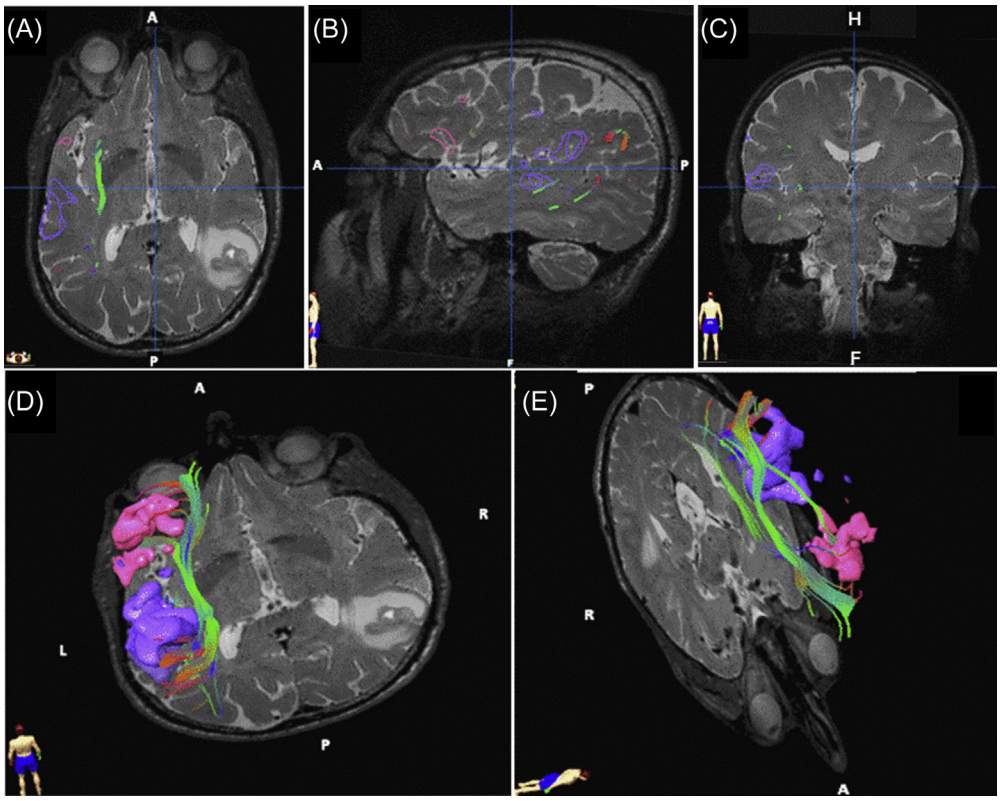


FIGURE 6 **fMRI for language activation with superimposed tract reconstruction of the arcuate fasciculus.** Two-dimensional images of fMRI mapped language areas with super-imposed DTI fiber tracking of arcuate fasciculus (green fibers) in (A) axial, (B) sagittal, and (C) coronal sections. Three-dimensional reconstruction of fMRI mapped language areas (magenta: frontal lobe language area; purple: temporal lobe language area) with super-imposed arcuate fasciculus in (D) posterior oblique and (E) right anterior oblique views. *Images from the Golby Lab, Brigham and Women's Hospital, Harvard Medical School, Boston, MA.*

the correlation of fMRI language maps and Wada results and should be considered during interpretation of data.[83]

Preoperative fMRI demonstrates atypical (bilateral or right-dominant) language dominance in 22–24% of non-right-handed subjects,[84,85] which agrees with earlier findings from Wada testing of left-handed epileptic patients.[86] A linear relationship is observed between the intensity of right-hemispheric activation on fMRI and the severity of language deficits observed on Wada testing of right-dominant individuals,[57] suggesting a role for fMRI in predicting the severity of language deficits in right-hemisphere surgery in this population and a possible advantage of fMRI, with its graded output, over the Wada test, with binary output. In comparison, fMRI also carries fewer risks, is less time-consuming, and is more cost-effective than Wada testing.[87]

Other functional modalities, including TMS and MEG, are increasingly applied to determine language localization. Repetitive TMS is used to disrupt language processing[88–90] and shows promising fidelity in multimodality comparisons against direct cortical stimulation.[91] MEG imaging has been found to have higher specificity and sensitivity in determining hemispheric language dominance compared to the Wada test.[61] Multimodality approaches with MEG, navigated repetitive TMS, and intraoperative cortical stimulation also show promise for further development.[38] Furthermore, MEG may demonstrate temporal language areas most robustly, while fMRI preferentially highlights frontal language areas, indicating an opportunity for complementary techniques.[92]

Owing to the vagaries of noninvasive preoperative language localization, cortical stimulation is considered the gold standard by some surgeons for accurate language mapping. ECS language mapping requires that the patient be able to cooperate in performing language tasks during an awake craniotomy, which is typically performed using a combination of local anesthetic field block and short-acting general agents. Once the scalp, skull, and dura are opened, the sedation is allowed to wear off so that the patient may cooperate with behavioral testing. During testing, the patient is awake and asked to perform language tests such as counting or naming while the surgeon stimulates the cortical surface. Naming, repetition, counting, and reading are all common tasks solicited from the patient during language mapping. Cortical stimulation of an area considered essential for language function can induce several forms of alterations, from speech arrest to aphasias, and is employed as an inhibition technique causing disruption in normal neuronal firing.

Speech arrest is induced with stimulation of the pars opercularis of the precentral gyrus in the dominant hemisphere, but has also been noted after stimulation of the nondominant pars opercularis.[93] Aphasic errors are noted on stimulation of the posterior inferior frontal gyrus, posterior temporal, and inferior parietal regions of the dominant hemisphere.[40,94] Although generalized maps for language localization are well accepted, marked variations, especially in the setting of a tumor that induces neuronal plasticity, call for language mapping in individual settings. Essential language sites are usually localized to spatially discrete areas in cortical stimulation mapping, compared to the broader distribution observed on fMRI. While ECS can produce speech disruptions with stimulation of both frontal and temporal cortex, different noninvasive functional mapping paradigms will preferentially demonstrate some language areas over others. A critical benefit of ECS during an awake craniotomy for tumor resection is that it distinguishes essential from nonessential but participating, language areas, as might be revealed on fMRI. In other words, fMRI language maps yield less insight into functional dependence than ECS. Cortical mapping during glioma surgery resulted in less than 2% persistent language deficit 6 months after glioma resection, in a series of 250 patients.[94]

Language mapping through cortical stimulation also faces several challenges. Even cooperative patients may have trouble maintaining task performance over the course of the operation, imposing limits on the available testing window. Risk of seizure and adequate airway control are additional concerns. Awake craniotomy generally requires dedicated neuroanesthesia support and a sufficient caseload to provide training and expertise and, hence, may not be available in some centers. These limitations call for continued investigations into noninvasive language localization techniques, using ECS as a standard for comparison.

INTRAOPERATIVE IMAGE-GUIDED SURGERY

Maximal tumor resection, as permitted by preservation of postoperative neurologic function, is a general goal of tumor surgery. Increased tumor resection has been associated with increased survival in both extra-axial and intra-axial tumors.[3,4,95] However, surgeons often overestimate the perceived extent of tumor resection, especially for intrinsic tumors.[96] As such, adjunctive modalities, including intraoperative imaging and improved real-time detection of tumor margins, are increasingly integrated with traditional surgical strategies.

Since the initial introduction of the low-field (0.5 T) intraoperative MRI in 1997,[97] modern intraoperative navigation suites have evolved to integrate high-field MRI, three-dimensional ultrasound, PET-CT, fluoroscopy, and intraoperative molecular diagnostic capabilities (Figure 7). MR instruments with increasingly higher field strengths offer unique opportunities for detailed anatomic resolution, tractography, and research investigations. However, intraoperative navigation also faces a number of biological and technical impediments.

One major challenge to the intraoperative use of preoperative mapping data is the brain shift that ensues after



FIGURE 7 The advanced multimodality image guided operating (AMIGO) suite at Brigham and Women's Hospital, Harvard Medical School, Boston, MA, USA. Integrated MRI, PET-CT, and angiographic capabilities are integrated with a state-of-the-art operating suite.

dural opening and debulking of a lesion. Causes of brain shift include patient positioning and effects of gravity, edema, administration of osmotic diuretics, drainage of CSF, retraction, and resection.[98,99] Investigations of brain shift have also revealed that displacement of the cortical surface and that of deeper structures are uncorrelated.[100] To overcome these dynamic alterations in structural landmarks, intraoperative MRI (ioMRI) provides critical real-time feedback, which may be further aided by algorithms to compensate for brain shifts.[97,101,102]

Intraoperative acquisition of functional data, such as intraoperative DTI and fMRI, provides additional insight into connectivity maps during tumor resection.[103–106] Comparison of preoperatively and intraoperatively acquired DTI data reveals variable shifting of white matter tracts, from 8 mm inward to 15 mm outward, during resection of adjacent mass lesions.[103] Resection of contrast-enhancing lesions produces a significantly larger shift in the tumor-to-corticospinal tract distance than debulking of non-contrast-enhancing lesions.[107] Intraoperative fMRI has also been utilized by several groups, in both low-field and higher-field settings, but remains limited by time constraints and sensitivity.[105,106,108]

As the application and availability of intraoperative navigation modalities continue to mature, several limitations need to be addressed. Intraoperative MRI imposes additional restrictions on compatible instruments, intraoperative neurophysiologic monitoring, and safety precautions. Access, ioMRI operative room time allotment and staffing, and dedicated equipment call for judicious resource utilization for cases that might be best served by immediate visual feedback of surgical results, including intra-axial neoplasms, suprasellar and parasellar lesions, and resection of seizure focus.

LIMITATIONS AND FUTURE DIRECTIONS

Current functional brain mapping techniques suffer from limitations in either temporal or spatial resolution or are highly invasive. It follows that resolution and quality of data can be improved by integrating, or coregistering, data from multiple complementary sources,[109] including conventional imaging data and neuronavigation systems (Figure 8).[110,111] While pre- and intraoperative coregistration

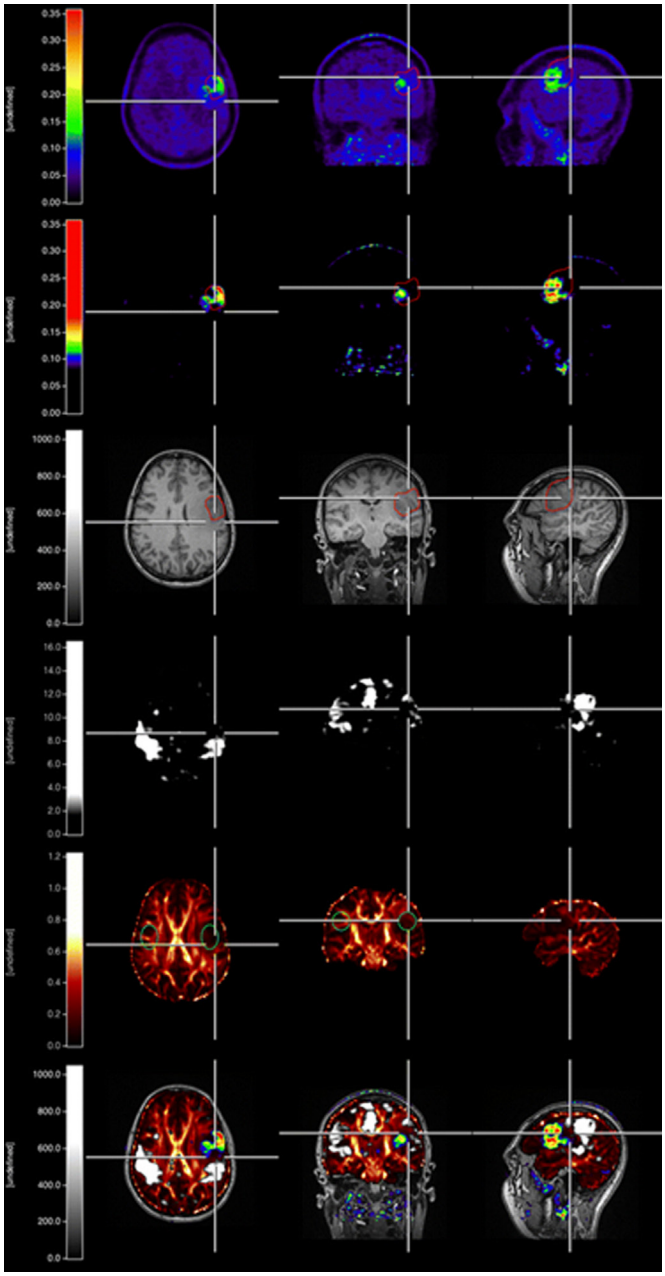


FIGURE 8 Integrated structural MRI, fMRI, PET, and DTI in tumor operative planning. PET data (rows 1 and 2), anatomic MRI (row 3), resting state fMRI (row 4), and DTI (row 5) demonstrate metabolic uptake by a left frontal tumor, which disturbs the attention–resting state network and impedes the surrounding white matter tracts. An overlay of PET, fMRI, and DTI data is demonstrated in the bottom row. *Adapted from Neuner et al.*[113]

of data from multiple functional mapping techniques has yet to find its way into mainstream use, an increasing number of studies suggest its future utility. For example, neuronavigation-integrated fMRI has been combined with intraoperative ECS to predict and minimize the risk of new postoperative neurologic deficit in resection of tumors near the motor cortex.[112] There will probably be an increased role for functional imaging in guidance of minimally invasive techniques such as focused ultrasound, laser thermal ablation, stereotactic radiosurgery, and other emerging techniques in patients with brain tumors for which traditional functional mapping may not be possible.

CONCLUSION

The combination of functional imaging with conventional imaging, image-guidance, and intraoperative imaging systems will improve our ability to perform more complete and precise resections of lesions while preserving neurological functions. Functional brain mapping stands to change the way intracranial processes are treated by creating a road map of neural function that not only defines eloquent "no-go" areas, but also illuminates potential functional targets. Such noninvasively derived road maps will be critical to the development of minimally invasive therapies.

References

1. Skirboll SS, Ojemann GA, Berger MS, Lettich E, Winn HR. Functional cortex and subcortical white matter located within gliomas. *Neurosurgery*. April 1996;38(4):678–684.
2. Ojemann JG, Miller JW, Silbergeld DL. Preserved function in brain invaded by tumor. *Neurosurgery*. August 1996;39(2):253–259.
3. Sanai N, Polley MY, McDermott MW, Parsa AT, Berger MS. An extent of resection threshold for newly diagnosed glioblastomas. *J Neurosurg*. July 2011;115(1):3–8.
4. Bloch O, Han SJ, Cha S, et al. Impact of extent of resection for recurrent glioblastoma on overall survival: clinical article. *J Neurosurg*. December 2012;117(6):1032–1038.
5. Stupp R, Mason WP, van den Bent MJ, et al. Radiotherapy plus concomitant and adjuvant temozolomide for glioblastoma. *N Engl J Med*. March 2005;352(10):987–996.
6. Beiko J, Suki D, Hess KR, et al. IDH1 mutant malignant astrocytomas are more amenable to surgical resection and have a survival benefit associated with maximal surgical resection. *Neuro Oncol*. January 2014;16(1):81–91.
7. Andronesi OC, Rapalino O, Gerstner E, et al. Detection of oncogenic IDH1 mutations using magnetic resonance spectroscopy of 2-hydroxyglutarate. *J Clin Invest*. September 2013;123(9):3659–3663.
8. Moseley ME, Cohen Y, Kucharczyk J, et al. Diffusion-weighted MR imaging of anisotropic water diffusion in cat central nervous system. *Radiology*. August 1990;176(2):439–445.
9. Jellison BJ, Field AS, Medow J, Lazar M, Salamat MS, Alexander AL. Diffusion tensor imaging of cerebral white matter: a pictorial review of physics, fiber tract anatomy, and tumor imaging patterns. *AJNR Am J Neuroradiol*. March 2004;25(3):356–369.
10. Barajas Jr RF, Hess CP, Phillips JJ, et al. Super-resolution track density imaging of glioblastoma: histopathologic correlation. *AJNR Am J Neuroradiol*. July 2013;34(7):1319–1325.
11. Chen ZT Y, Olubiyi O, Rigolo L, Mehrtash A, Norton I, Pasternak O, et al. Reconstruction of the arcuate fasciculus for surgical planning in the setting of peritumoral edema using two-tensor unscented Kalman filter tractography. *Neuroimage Clin*. March 2015;7:815–822.
12. Pujol S, Golby A, Wells W, et al. The DTI Challenge initiative on the standardized evaluation of DTI tractography for neurosurgical planning. In: *Proceedings of the 100th Annual Meeting of the Radiological Society of North America*; 2014. Chicago, IL.
13. Fernandez-Miranda JC, Pathak S, Engh J, et al. High-definition fiber tractography of the human brain: neuroanatomical validation and neurosurgical applications. *Neurosurgery*. August 2012;71(2):430–453.
14. Kuhnt D, Bauer MH, Egger J, et al. Fiber tractography based on diffusion tensor imaging compared with high-angular-resolution diffusion imaging with compressed sensing: initial experience. *Neurosurgery*. January 2013;72(suppl 1):165–175.
15. Lu S, Ahn D, Johnson G, Law M, Zagzag D, Grossman RI. Diffusion-tensor MR imaging of intracranial neoplasia and associated peritumoral edema: introduction of the tumor infiltration index. *Radiology*. July 2004;232(1):221–228.
16. Provenzale JM, McGraw P, Mhatre P, Guo AC, Delong D. Peritumoral brain regions in gliomas and meningiomas: investigation with isotropic diffusion-weighted MR imaging and diffusion-tensor MR imaging. *Radiology*. August 2004;232(2):451–460.
17. Witwer BP, Moftakhar R, Hasan KM, et al. Diffusion-tensor imaging of white matter tracts in patients with cerebral neoplasm. *J Neurosurg*. September 2002;97(3):568–575.
18. Fox PT, Raichle ME. Focal physiological uncoupling of cerebral blood flow and oxidative metabolism during somatosensory stimulation in human subjects. *Proc Natl Acad Sci USA*. February 1986;83(4):1140–1144.
19. Ogawa S, Lee TM, Kay AR, Tank DW. Brain magnetic resonance imaging with contrast dependent on blood oxygenation. *Proc Natl Acad Sci USA*. December 1990;87(24):9868–9872.
20. Bandettini PA, Wong EC, Hinks RS, Tikofsky RS, Hyde JS. Time course EPI of human brain function during task activation. *Magnetic Reson Med*. June 1992;25(2):390–397.
21. Fox MD, Snyder AZ, Vincent JL, Raichle ME. Intrinsic fluctuations within cortical systems account for intertrial variability in human behavior. *Neuron*. October 2007;56(1):171–184.
22. Tie Y, Rigolo L, Norton IH, et al. Defining language networks from resting-state fMRI for surgical planning–a feasibility study. *Hum Brain Mapp*. March 2014;35(3):1018–1030.
23. Pfeuffer J, Adriany G, Shmuel A, et al. Perfusion-based high-resolution functional imaging in the human brain at 7 Tesla. *Magnetic Reson Med*. May 2002;47(5):903–911.
24. Lin FH, Huang TY, Chen NK, et al. Functional MRI using regularized parallel imaging acquisition. *Magnetic Reson Med*. August 2005;54(2):343–353.
25. Lau M, Yam D, Burneo JG. A systematic review on MEG and its use in the presurgical evaluation of localization-related epilepsy. *Epilepsy Res*. May 2008;79(2–3):97–104.
26. Stufflebeam SM. Clinical magnetoencephalography for neurosurgery. *Neurosurg Clin N Am*. April 2011;22(2):153–167.
27. Gallen CC, Schwartz BJ, Bucholz RD, et al. Presurgical localization of functional cortex using magnetic source imaging. *J Neurosurg*. June 1995;82(6):988–994.
28. Kamada K, Takeuchi F, Kuriki S, Oshiro O, Houkin K, Abe H. Functional neurosurgical simulation with brain surface magnetic resonance images and magnetoencephalography. *Neurosurgery*. August 1993;33(2):269–272.

29. Rezai AR, Hund M, Kronberg E, et al. Introduction of magnetoencephalography to stereotactic techniques. *Stereotact Funct Neurosurg*. 1995;65(1–4):37–41.
30. Sutherling WW, Crandall PH, Darcey TM, Becker DP, Levesque MF, Barth DS. The magnetic and electric fields agree with intracranial localizations of somatosensory cortex. *Neurology*. November 1988;38(11):1705–1714.
31. Rezai AR, Hund M, Kronberg E, et al. The interactive use of magnetoencephalography in stereotactic image-guided neurosurgery. *Neurosurgery*. July 1996;39(1):92–102.
32. McDonald JD, Chong BW, Lewine JD, et al. Integration of preoperative and intraoperative functional brain mapping in a frameless stereotactic environment for lesions near eloquent cortex. Technical note. *J Neurosurg*. March 1999;90(3):591–598.
33. Barker AT, Jalinous R, Freeston IL. Non-invasive magnetic stimulation of human motor cortex. *Lancet*. May 1985;1(8437):1106–1107.
34. Sack AT, Linden DE. Combining transcranial magnetic stimulation and functional imaging in cognitive brain research: possibilities and limitations. *Brain Res Brain Res Rev*. September 2003;43(1):41–56.
35. Neggers SF, Langerak TR, Schutter DJ, et al. A stereotactic method for image-guided transcranial magnetic stimulation validated with fMRI and motor-evoked potentials. *NeuroImage*. April 2004;21(4):1805–1817.
36. Krings T, Buchbinder BR, Butler WE, et al. Stereotactic transcranial magnetic stimulation: correlation with direct electrical cortical stimulation. *Neurosurgery*. December 1997;41(6): 1319–1325.
37. Krieg SM, Shiban E, Buchmann N, et al. Utility of presurgical navigated transcranial magnetic brain stimulation for the resection of tumors in eloquent motor areas. *J Neurosurg*. May 2012;116(5):994–1001.
38. Tarapore PE, Findlay AM, Honma SM, et al. Language mapping with navigated repetitive TMS: proof of technique and validation. *NeuroImage*. November 2013;82:260–272.
39. Penfield W. The cerebral cortex and consciousness. *Harvey Lect*. 1937.
40. Ojemann G, Ojemann J, Lettich E, Berger M. Cortical language localization in left, dominant hemisphere. An electrical stimulation mapping investigation in 117 patients. *J Neurosurg*. September 1989;71(3):316–326.
41. Engel AK, Moll CK, Fried I, Ojemann GA. Invasive recordings from the human brain: clinical insights and beyond. *Nat Rev Neurosci*. January 2005;6(1):35–47.
42. Wood CC, Spencer DD, Allison T, McCarthy G, Williamson PD, Goff WR. Localization of human sensorimotor cortex during surgery by cortical surface recording of somatosensory evoked potentials. *J Neurosurg*. January 1988;68(1):99–111.
43. Neuloh G, Pechstein U, Cedzich C, Schramm J. Motor evoked potential monitoring with supratentorial surgery. *Neurosurgery*. July 2007;61(1 suppl):337–346.
44. Krieg SM, Schaffner M, Shiban E, et al. Reliability of intraoperative neurophysiological monitoring using motor evoked potentials during resection of metastases in motor-eloquent brain regions: clinical article. *J Neurosurg*. June 2013;118(6):1269–1278.
45. Macdonald DB, Skinner S, Shils J, Yingling C. American Society of Neurophysiological Monitoring. Intraoperative motor evoked potential monitoring – a position statement by the American Society of Neurophysiological Monitoring. *Clin Neurophysiol*. December 2013;124(12):2291–2316.
46. Keles GE, Lundin DA, Lamborn KR, Chang EF, Ojemann G, Berger MS. Intraoperative subcortical stimulation mapping for hemispherical perirolandic gliomas located within or adjacent to the descending motor pathways: evaluation of morbidity and assessment of functional outcome in 294 patients. *J Neurosurg*. March 2004;100(3):369–375.
47. Leclercq D, Duffau H, Delmaire C, et al. Comparison of diffusion tensor imaging tractography of language tracts and intraoperative subcortical stimulations. *J Neurosurg*. March 2010;112(3):503–511.
48. Gras-Combe G, Moritz-Gasser S, Herbet G, Duffau H. Intraoperative subcortical electrical mapping of optic radiations in awake surgery for glioma involving visual pathways. *J Neurosurg*. September 2012;117(3):466–473.
49. De Witt Hamer PC, Robles SG, Zwinderman AH, Duffau H, Berger MS. Impact of intraoperative stimulation brain mapping on glioma surgery outcome: a meta-analysis. *J Clin Oncol*. July 2012;30(20):2559–2565.
50. Wada J, Rasmussen T. Intracarotid injection of sodium amytal for the lateralization of cerebral speech dominance. 1960. *J Neurosurg*. June 2007;106(6):1117–1133.
51. Milner B, Branch C, Rasmussen T. Study of short-term memory after intracarotid injection of sodium amytal. *Trans Am Neurol Assoc*. 1962;87:224–226.
52. Brassel F, Weissenborn K, Ruckert N, Hussein S, Becker H. Superselective intra-arterial amytal (Wada test) in temporal lobe epilepsy: basics for neuroradiological investigations. *Neuroradiology*. July 1996;38(5):417–421.
53. Hankey GJ, Warlow CP, Sellar RJ. Cerebral angiographic risk in mild cerebrovascular disease. *Stroke*. February 1990;21(2):209–222.
54. Papanicolaou AC, Rezaie R, Narayana S, et al. Is it time to replace the Wada test and put awake craniotomy to sleep? *Epilepsia*. May 2014;55(5):629–632.
55. Binder JR, Sabsevitz DS, Swanson SJ, Hammeke TA, Raghavan M, Mueller WM. Use of preoperative functional MRI to predict verbal memory decline after temporal lobe epilepsy surgery. *Epilepsia*. August 2008;49(8):1377–1394.
56. Detre JA, Maccotta L, King D, et al. Functional MRI lateralization of memory in temporal lobe epilepsy. *Neurology*. April 1998;50(4):926–932.
57. Binder JR, Swanson SJ, Hammeke TA, et al. Determination of language dominance using functional MRI: a comparison with the Wada test. *Neurology*. April 1996;46(4):978–984.
58. Abou-Khalil B. An update on determination of language dominance in screening for epilepsy surgery: the Wada test and newer noninvasive alternatives. *Epilepsia*. March 2007;48(3):442–455.
59. Binder JR. Functional MRI is a valid noninvasive alternative to Wada testing. *Epilepsy Behav*. February 2011;20(2):214–222.
60. Golby AJ, Poldrack RA, Illes J, Chen D, Desmond JE, Gabrieli JD. Memory lateralization in medial temporal lobe epilepsy assessed by functional MRI. *Epilepsia*. August 2002;43(8):855–863.
61. Findlay AM, Ambrose JB, Cahn-Weiner DA, et al. Dynamics of hemispheric dominance for language assessed by magnetoencephalographic imaging. *Ann Neurol*. May 2012;71(5):668–686.
62. Tummala RP, Chu RM, Liu H, Truwit CL, Hall WA. Application of diffusion tensor imaging to magnetic-resonance-guided brain tumor resection. *Pediatr Neurosurg*. July 2003;39(1):39–43.
63. Yousry TA, Schmid UD, Jassoy AG, et al. Topography of the cortical motor hand area: prospective study with functional MR imaging and direct motor mapping at surgery. *Radiology*. April 1995;195(1):23–29.
64. Roux FE, Boulanouar K, Ranjeva JP, et al. Usefulness of motor functional MRI correlated to cortical mapping in Rolandic low-grade astrocytomas. *Acta Neurochir*. 1999;141(1):71–79.
65. Roux FE, Boulanouar K, Ibarrola D, Tremoulet M, Chollet F, Berry I. Functional MRI and intraoperative brain mapping to evaluate brain plasticity in patients with brain tumours and hemiparesis. *J Neurol Neurosurg Psychiatry*. October 2000;69(4):453–463.
66. Roessler K, Donat M, Lanzenberger R, et al. Evaluation of preoperative high magnetic field motor functional MRI (3 Tesla) in glioma patients by navigated electrocortical stimulation and postoperative outcome. *J Neurol Neurosurg Psychiatry*. August 2005;76(8):1152–1157.

67. Majos A, Tybor K, Stefanczyk L, Goraj B. Cortical mapping by functional magnetic resonance imaging in patients with brain tumors. *Eur Radiol*. June 2005;15(6):1148–1158.
68. Tarapore PE, Tate MC, Findlay AM, et al. Preoperative multimodal motor mapping: a comparison of magnetoencephalography imaging, navigated transcranial magnetic stimulation, and direct cortical stimulation. *J Neurosurg*. August 2012;117(2):354–362.
69. Parmar H, Sitoh YY, Yeo TT. Combined magnetic resonance tractography and functional magnetic resonance imaging in evaluation of brain tumors involving the motor system. *J Comput Assisted Tomogr*. July–August 2004;28(4):551–556.
70. Berman JI, Berger MS, Mukherjee P, Henry RG. Diffusion-tensor imaging-guided tracking of fibers of the pyramidal tract combined with intraoperative cortical stimulation mapping in patients with gliomas. *J Neurosurg*. July 2004;101(1):66–72.
71. Mandelli ML, Berger MS, Bucci M, Berman JI, Amirbekian B, Henry RG. Quantifying accuracy and precision of diffusion MR tractography of the corticospinal tract in brain tumors. *J Neurosurg*. August 2014;121(2):349–358.
72. Krings T, Topper R, Willmes K, Reinges MH, Gilsbach JM, Thron A. Activation in primary and secondary motor areas in patients with CNS neoplasms and weakness. *Neurology*. February 2002;58(3):381–390.
73. Nimsky C, Ganslandt O, Fahlbusch R. Implementation of fiber tract navigation. *Neurosurgery*. April 2006;58(4 suppl 2). ONS-292-303.
74. Berker EA, Berker AH, Smith A. Translation of Broca's 1865 report. Localization of speech in the third left frontal convolution. *Arch Neurol*. October 1986;43(10):1065–1072.
75. Geschwind N. Disconnexion syndromes in animals and man. I. *Brain*. June 1965;88(2):237–294.
76. Geschwind N. Disconnexion syndromes in animals and man. II. *Brain*. September 1965;88(3):585–644.
77. Wernicke C. Der aphasische symptomencomplex: eine psychologische studie auf anatomischer basis. In: Eggert GH, ed. *Wernicke's Works on Aphasia: a Sourcebook and Review*. Hague: Mouton; 1977:91–145.
78. Mohr JP, Pessin MS, Finkelstein S, Funkenstein HH, Duncan GW, Davis KR. Broca aphasia: pathologic and clinical. *Neurology*. April 1978;28(4):311–324.
79. Chang EF, Raygor KP, Berger MS. Contemporary model of language organization: an overview for neurosurgeons. *J Neurosurg*. February 2015;122(2):250–261.
80. Benzagmout M, Gatignol P, Duffau H. Resection of World Health Organization Grade II gliomas involving Broca's area: methodological and functional considerations. *Neurosurgery*. October 2007;61(4):741–752.
81. Woermann FG, Jokeit H, Luerding R, et al. Language lateralization by Wada test and fMRI in 100 patients with epilepsy. *Neurology*. September 9, 2003;61(5):699–701.
82. Bauer PR, Reitsma JB, Houweling BM, Ferrier CH, Ramsey NF. Can fMRI safely replace the Wada test for preoperative assessment of language lateralisation? A meta-analysis and systematic review. *J Neurol Neurosurg Psychiatry*. May 2014;85(5):581–588.
83. Lehericy S, Cohen L, Bazin B, et al. Functional MR evaluation of temporal and frontal language dominance compared with the Wada test. *Neurology*. April 2000;54(8):1625–1633.
84. Pujol J, Deus J, Losilla JM, Capdevila A. Cerebral lateralization of language in normal left-handed people studied by functional MRI. *Neurology*. March 1999;52(5):1038–1043.
85. Szaflarski JP, Binder JR, Possing ET, McKiernan KA, Ward BD, Hammeke TA. Language lateralization in left-handed and ambidextrous people: fMRI data. *Neurology*. July 2002;59(2):238–244.
86. Rasmussen T, Milner B. The role of early left-brain injury in determining lateralization of cerebral speech functions. *Ann NY Acad Sci*. September 1977;299:355–369.
87. Medina LS, Aguirre E, Bernal B, Altman NR. Functional MR imaging versus Wada test for evaluation of language lateralization: cost analysis. *Radiology*. January 2004;230(1):49–54.
88. Pascual-Leone A, Gates JR, Dhuna A. Induction of speech arrest and counting errors with rapid-rate transcranial magnetic stimulation. *Neurology*. May 1991;41(5):697–702.
89. Jennum P, Friberg L, Fuglsang-Frederiksen A, Dam M. Speech localization using repetitive transcranial magnetic stimulation. *Neurology*. February 1994;44(2):269–273.
90. Knecht S, Floel A, Drager B, et al. Degree of language lateralization determines susceptibility to unilateral brain lesions. *Nat Neurosci*. July 2002;5(7):695–699.
91. Picht T, Krieg SM, Sollmann N, et al. A comparison of language mapping by preoperative navigated transcranial magnetic stimulation and direct cortical stimulation during awake surgery. *Neurosurgery*. May 2013;72(5):808–819.
92. Kamada K, Takeuchi F, Kuriki S, Todo T, Morita A, Sawamura Y. Dissociated expressive and receptive language functions on magnetoencephalography, functional magnetic resonance imaging, and amobarbital studies. Case report and review of the literature. *J Neurosurg*. April 2006;104(4):598–607.
93. Penfield W, Roberts L. *Speech and Brain Mechanisms*. Princeton, NJ: Princeton University Press; 1959.
94. Sanai N, Mirzadeh Z, Berger MS. Functional outcome after language mapping for glioma resection. *N Engl J Med*. January 2008;358(1):18–27.
95. Simpson D. The recurrence of intracranial meningiomas after surgical treatment. *J Neurol Neurosurg Psychiatry*. February 1957;20(1):22–39.
96. Orringer D, Lau D, Khatri S, et al. Extent of resection in patients with glioblastoma: limiting factors, perception of resectability, and effect on survival. *J Neurosurg*. November 2012;117(5):851–859.
97. Black PM, Moriarty T, Alexander 3rd E, et al. Development and implementation of intraoperative magnetic resonance imaging and its neurosurgical applications. *Neurosurgery*. October 1997;41(4):831–842.
98. Nimsky C, Ganslandt O, Cerny S, Hastreiter P, Greiner G, Fahlbusch R. Quantification of, visualization of, and compensation for brain shift using intraoperative magnetic resonance imaging. *Neurosurgery*. November 2000;47(5):1070–1080.
99. Hartkens T, Hill DL, Castellano-Smith AD, et al. Measurement and analysis of brain deformation during neurosurgery. *IEEE Trans Med Imaging*. January 2003;22(1):82–92.
100. Reinges MH, Nguyen HH, Krings T, Hutter BO, Rohde V, Gilsbach JM. Course of brain shift during microsurgical resection of supratentorial cerebral lesions: limits of conventional neuronavigation. *Acta Neurochir*. April 2004;146(4):369–377.
101. Hall WA, Liu H, Martin AJ, Pozza CH, Maxwell RE, Truwit CL. Safety, efficacy, and functionality of high-field strength interventional magnetic resonance imaging for neurosurgery. *Neurosurgery*. March 2000;46(3):632–641.
102. Clatz O, Delingette H, Talos IF, et al. Robust nonrigid registration to capture brain shift from intraoperative MRI. *IEEE Trans Med Imaging*. November 2005;24(11):1417–1427.
103. Nimsky C, Ganslandt O, Hastreiter P, et al. Preoperative and intraoperative diffusion tensor imaging-based fiber tracking in glioma surgery. *Neurosurgery*. 2005;56(1):130–138.
104. Nimsky C, Ganslandt O, Merhof D, Sorensen AG, Fahlbusch R. Intraoperative visualization of the pyramidal tract by diffusion-tensor-imaging-based fiber tracking. *NeuroImage*. May 2006;30(4):1219–1229.
105. Azmi H, Biswal B, Salas S, Schulder M. Functional imaging in a low-field, mobile intraoperative magnetic resonance scanner: expanded paradigms. *Neurosurgery*. January 2007;60(1):143–149.
106. Gasser T, Szelenyi A, Senft C, et al. Intraoperative MRI and functional mapping. *Acta Neurochir Suppl*. 2011;109:61–65.

107. Shahar T, Rozovski U, Marko NF, et al. Preoperative imaging to predict intraoperative changes in tumor-to-corticospinal tract distance: an analysis of 45 cases using high-field intraoperative magnetic resonance imaging. *Neurosurgery*. July 2014;75(1):23–30.
108. Gasser T, Ganslandt O, Sandalcioglu E, Stolke D, Fahlbusch R, Nimsky C. Intraoperative functional MRI: implementation and preliminary experience. *NeuroImage*. July 2005;26(3):685–693.
109. Dale AM, Halgren E. Spatiotemporal mapping of brain activity by integration of multiple imaging modalities. *Curr Opin Neurobiol*. April 2001;11(2):202–208.
110. Roux FE, Ibarrola D, Tremoulet M, et al. Methodological and technical issues for integrating functional magnetic resonance imaging data in a neuronavigational system. *Neurosurgery*. November 2001;49(5):1145–1156.
111. O'Shea JP, Whalen S, Branco DM, Petrovich NM, Knierim KE, Golby AJ. Integrated image- and function-guided surgery in eloquent cortex: a technique report. *Int J Med Robot*. March 2006;2(1):75–83.
112. Krishnan R, Raabe A, Hattingen E, et al. Functional magnetic resonance imaging-integrated neuronavigation: correlation between lesion-to-motor cortex distance and outcome. *Neurosurgery*. October 2004;55(4):904–914.
113. Neuner I, Kaffanke JB, Langen KJ, et al. Multimodal imaging utilising integrated MR-PET for human brain tumour assessment. *Eur Radiol*. December 2012;22(12):2568–2580.

CHAPTER

24

Use of Neuroimaging for Radiation Therapy Planning

Lonika Majithia, Steve Walston, Michael Guiou, Nilendu Gupta, Arnab Chakravarti

Wexner Medical Center, Department of Radiation Oncology, Ohio State University, Columbus, OH, USA

INTRODUCTION

Intracranial tumors are a diverse group of malignancies that can generally be classified as primary (originating from the brain) or secondary (metastases from other organs). The overall incidence of all primary intracranial malignancies was 21.03 cases per 100,000 individuals in the United States from 2006 to 2010, which reflects international trends.[1] The largest histological category of primary brain tumors are the gliomas, which have an incidence of 6.02 cases per 100,000 individuals in the United States. The preferred treatment modality for benign tumors in general is surgical resection, with less frequent use of radiotherapy or chemotherapy. For malignant intracranial tumors, multimodality treatment is frequently used, which includes systemic therapy and radiotherapy. The goal of radiotherapy for intracranial tumors is to eradicate gross and microscopic disease while limiting normal tissue toxicities. Various radiation modalities are used, including fractionated external beam radiation therapy, stereotactic radiosurgery (SRS), and proton beam irradiation. We will review the imaging modalities used for intracranial tumor delineation and their role in radiation planning.

NEUROIMAGING

The field of neuroradiology has advanced immensely in the past decades. Historic invasive imaging, including cerebral angiography and pneumoencephalography, has been replaced by modern noninvasive modalities with improved image resolution. The most common imaging modality used today to define primary and metastatic brain tumors is magnetic resonance imaging (MRI) with gadolinium contrast, or computed tomography (CT) when MRI is contraindicated. MRI uses magnetic and radio waves to form a three-dimensional (3D) image of the anatomy with improved soft-tissue contrast compared to CT. T1-weighted MRI sequences are useful in distinguishing tumor from normal anatomy. In general, tumors are hypointense or isointense on T1-weighted MRI. High-grade and metastatic tumors may have areas of central tumor necrosis. Low-grade tumors generally have minimal to no contrast enhancement compared to high-grade and metastatic tumors. T2-weighted MRI or fluid-attenuated inversion recovery (FLAIR) sequences evaluate for infiltrative tumor and vasogenic edema, when the blood–brain barrier has been injured, commonly seen in high-grade and metastatic tumors (Figures 1 and 2).

Other imaging modalities less often used include MR spectroscopy (MRS), MR perfusion, and positron emission tomography (PET), which are used to distinguish disease progression from tumor necrosis or pseudoprogression (PsP).

RADIATION PLANNING AND DELIVERY

Radiotherapy plays an important role in the management of primary central nervous system (CNS) tumors and brain metastases. Historically, with X-ray-based radiation planning, whole-brain irradiation was the standard of care. With the introduction of CT, radiation treatment planning systems and algorithms were developed to estimate radiation dose deposition from electron-density mappings. Current practices in radiation oncology utilize CT-based radiotherapy planning for intracranial tumors. For the majority of CNS tumors, the radiation

Handbook of Neuro-Oncology Neuroimaging, Second Edition
http://dx.doi.org/10.1016/B978-0-12-800945-1.00024-0

© 2016 Elsevier Ltd. All rights reserved.

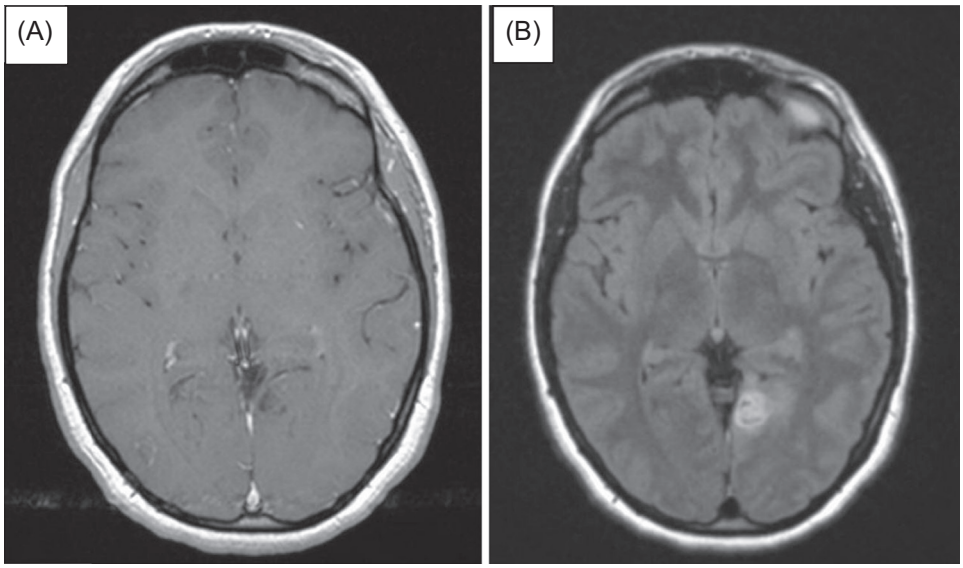


FIGURE 1 Grade II glioma at medial left occipital lobe. (A) Gadolinium-enhanced T1 MRI shows no enhancement or mass effect from lesion. (B) T2 FLAIR MRI shows well-defined signal abnormality in left occipital lobe with minimal vasogenic edema.

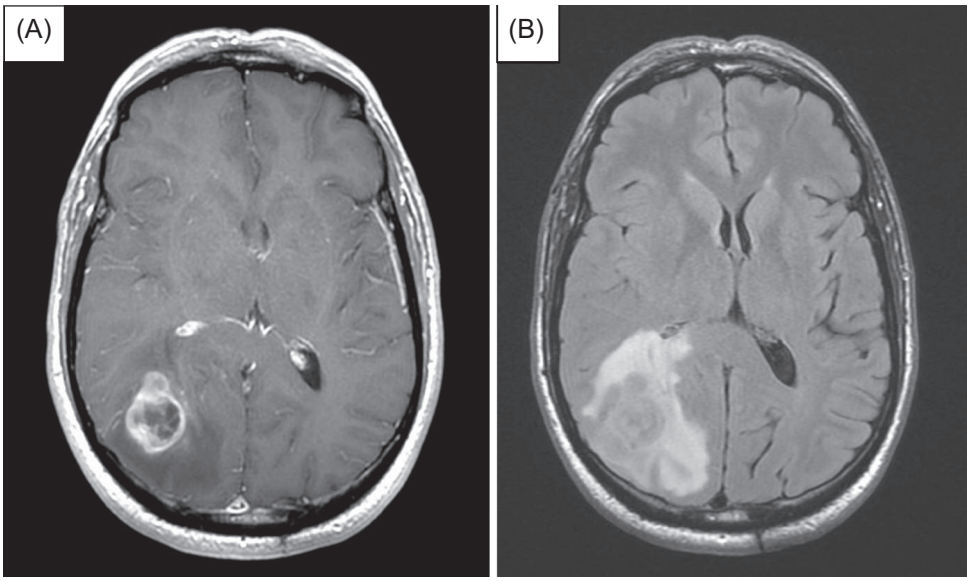


FIGURE 2 Glioblastoma multiforme at right parietal lobe. (A) Gadolinium-enhanced T1 MRI enhancement of tumor with central necrosis and mass effect. (B) T2 FLAIR MRI with signal abnormality in the right parietal lobe with significant vasogenic edema.

planning CT is done in the supine position with a head mask for immobilization and treatment reproducibility. Pre- and/or postoperative MR images are then registered with the planning CT, allowing for more accurate delineation of tumor and normal anatomy. The gross tumor volume (GTV)[2] is most often contoured using MRI given the resolution of this technique. Two expansions are then applied to the GTV. The first expansion is the clinical target volume (CTV),[2] which accounts for microscopic spread of disease. The second expansion is the planned target volume (PTV),[2] which accounts for patient motion and daily setup errors. The radiation dose is prescribed to the PTV to ensure all areas at risk for tumor involvement are treated while accounting for all uncertainties. Isodose lines, a topographic mapping of tumor dose deposition, as well as dose deposition statistics for treatment targets and critical structures called dose–volume histograms (DVHs)[3] are constructed and evaluated for conformity to target volumes as well as avoidance of critical normal structures.

Using a linear accelerator (LINAC), the whole or partial brain can be treated in a series of treatments or fractions. Smaller tumors (either single or multiple) can be treated with ablative doses in a single fraction with advanced immobilization and localization using a technique called SRS. For whole-brain irradiation, two opposed lateral fields are used to deliver high-energy

photon beams to the cranial vault. Small, moveable leaves (called multileaf collimators) can be used to block a portion of the treatment field to shape the dose and block normal structures such as the lenses, face, oral cavity, and throat. Common dosing schedules for whole-brain irradiation include 37.5 Gy in 15 fractions, 30 Gy in 10 fractions, and 20 Gy in 5 fractions. Whole-brain radiotherapy still remains a reasonable treatment option for brain metastases, for gliomatosis cerebri, and as a component of craniospinal irradiation. With the introduction of CT- and MRI-based tumor delineation, partial brain irradiation became the standard of care for well-localized tumors to reduce late neurocognitive deficits associated with whole-brain irradiation. Three-dimensional conformal, intensity-modulated radiation therapy (IMRT) and volumetric-modulated arc therapy (VMAT) planning methods are used for partial brain irradiation to maximize tumor coverage and minimize dose to critical normal structures such as the spinal cord, brainstem, optic chiasm, optic nerves, cochlea, and hippocampus. A DVH of the target structures and organs at risk (OARs) is created to judge the quality of a radiation plan. Priority in treatment planning is given to very critical OARs, such as the brainstem, followed by prioritizing coverage of the target volume.

QUALITY ASSURANCE OF IMAGING AND DOSE DELIVERY

The treatment planning process for intracranial targets invariably requires registration of MRI and other images with a treatment planning CT. This necessitates attention to the performance of quality assurance (QA) checks to characterize the geometric accuracy and the spatial distortions, especially for MR images. The QA needs are more acute for use of MR images coregistered for radiosurgery treatment planning. Several commercial 3D-distortion QA phantoms are available to perform such checks periodically to ensure image distortions are within acceptable limits.[4] Overall accuracy and precision checks through the full treatment planning chain of multimodality imaging, image registration, target localization, and treatment delivery also need to be performed, especially for radiosurgery treatment delivery. End-to-end QA phantoms are available to perform such tests.[5]

STEREOTACTIC RADIOSURGERY

SRS is a highly conformal radiation technique that uses a single high-dose radiation fraction to ablate an intracranial tumor. It was initially developed by the Swedish neurosurgeon Lars Leksell in 1951. This has now developed into the Elekta Gamma Knife system, which is a fixed-beam multisource delivery system that uses a cobalt-60 radiation source. A rigid head frame is placed by the neurosurgeon to reduce setup error and to establish a 3D coordinate system. This 3D coordinate system is matched to the diagnostic MRI scans, allowing proper localization of the tumor in reference to the frame. Only high-resolution MRI sequences with square voxels can be used for Gamma Knife radiosurgery planning. The tumor is delineated on the diagnostic MRI and the position is confirmed using the 3D coordinate system. Radiation dose varies depending on the volume of disease and proximity to critical structures. In 2000, Shaw et al. published the results of Radiation Therapy Oncology Group (RTOG) 90-05, which determined the maximum tolerated SRS dose in patients with recurrent primary brain tumors (previously irradiated) and brain metastases.[2] The maximum tolerated dose in a single-fraction SRS treatment was size dependent: 24 Gy for lesions ≤20 mm, 18 Gy for lesions 21–30 mm, and 15 Gy for 31–40 mm.[6] The radiation dose is typically prescribed to the 50% isodose line for Gamma Knife SRS, but varies more for other techniques of SRS delivery, including LINAC-based therapy. LINAC-based SRS is feasible, well tolerated, and less invasive. A face mask is created for immobilization in the supine position. Treatment planning systems create a highly conformal dose distribution using a VMAT technique. With LINAC-based treatment, larger volumes can also be treated over two to five fractions, called fractionated stereotactic radiotherapy (Figure 3).

PRACTICAL APPLICATION OF RADIOTHERAPY IN HIGH-GRADE GLIOMA

Historically, the treatment of malignant gliomas has been maximal surgical resection. However, surgery alone results in high rates of local recurrence. The suboptimal response was not understood until the infiltrative nature of the disease was described by Harvey Cushing in the early 1900s.[7] Owing to the inability to fully clear disease with surgery alone without significant morbidity, radiotherapy and chemotherapy were introduced into the treatment paradigm and overall survival improved.[8,9] Several trials aimed to improve this paradigm have been attempted, but the standard of care remains optimal surgical resection followed by sequential or concurrent chemoradiation.

Historically, radiotherapy for malignant gliomas consisted of whole-brain irradiation using opposed lateral fields. The Brain Tumor Cooperative Group 80-01 trial compared multiple adjuvant glioma therapy options.[10] One aspect of this study was to compare adjuvant whole-brain irradiation (6020 rad) with a mixed course of whole-brain irradiation (4300 rad) followed by a cone-down boost (1720 rad). No survival difference was noted

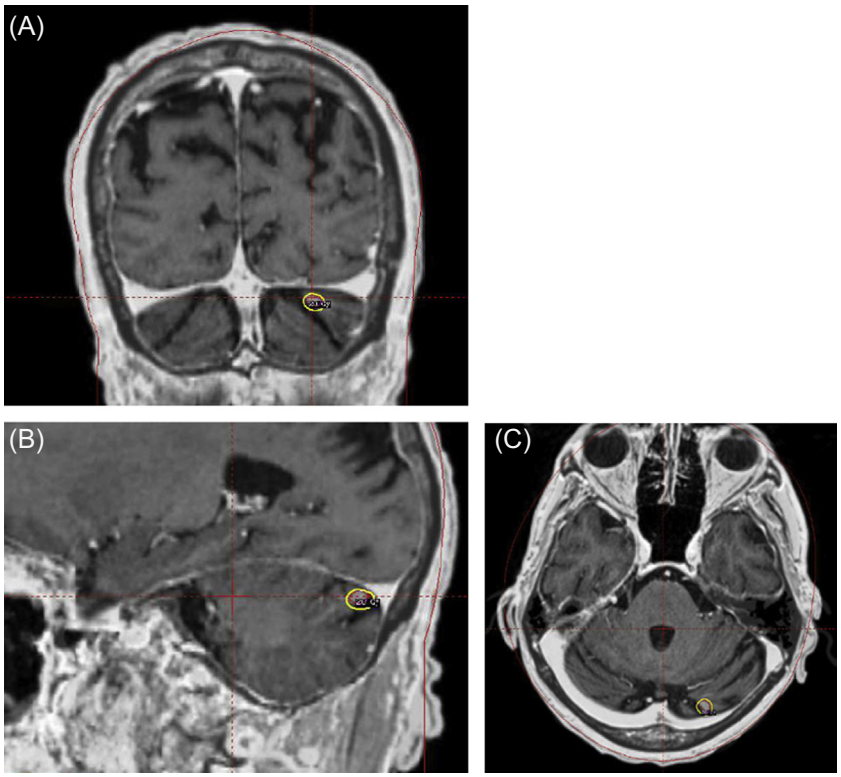


FIGURE 3 Patient with lung cancer metastasis to the left cerebellum that was treated with Gamma Knife SRS, 20 Gy to the 50% isodose line. (A) Coronal view of treatment plan on T1 spoiled gradient recalled acquisition (SPGR) MRI. (B) Sagittal view of treatment plan. (C) Axial view of treatment plan.

between these arms and thus the treatment paradigm shifted toward partial brain irradiation. An understanding of disease progression and recurrence patterns was needed to determine the parameters for partial brain irradiation. A historic paper published by Hochberg showed that, based on CT planning, 90% of disease recurrence occurred within 2 cm of the initial tumor volume.[11] This has been demonstrated in numerous studies thereafter and is valid under various dose schedules.

Current practices in radiation oncology utilize CT-based radiotherapy planning for adjuvant malignant glioma treatment. Following optimal resection of grade III and grade IV gliomas, patients undergo a postoperative gadolinium-contrast MRI of the brain within 24–48 h of surgery to determine the extent of tumor resection. The pre- and postoperative MR images are registered with the planning CT, allowing a composite treatment volume to be created. For both grade III and grade IV malignant gliomas, tumor volumes are defined using both the T1-weighted and the T2/FLAIR MR images. The primary tumor or resection cavity is defined on the T1-weighted contrast-enhanced MR image. The MRI T2 or FLAIR images allow determination of potential microscopic tumor extension along white matter pathways. Treatment volumes should incorporate potential tracks of tumor spread such as the corpus callosum, as demonstrated in Figure 4.

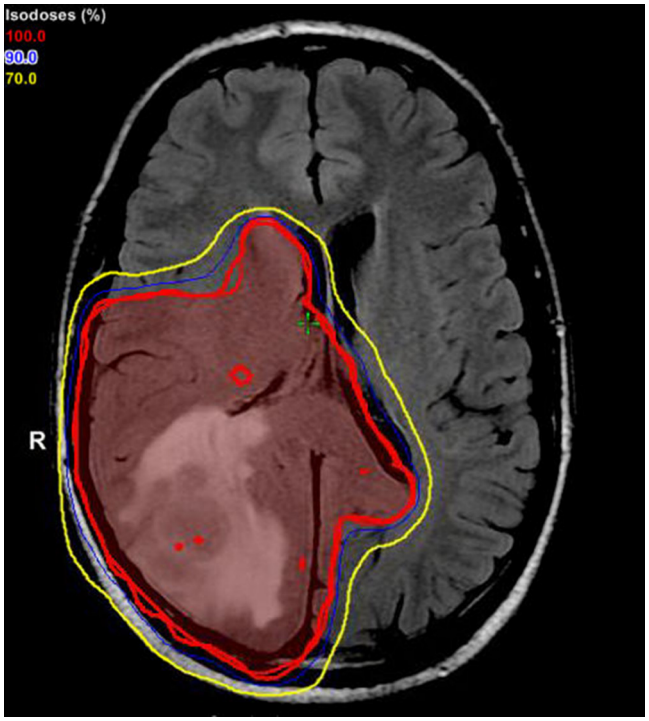


FIGURE 4 Axial T2 FLAIR MR imaging of the brain. A tumor in the right parietal lobe with vasogenic edema is shown. PTV is shaded in red. Three isodose lines are demonstrated: 100% (red), 95% (blue), and 70% (yellow). Note the extension of the PTV into the contralateral cerebrum owing to tumor tracking along the splenium of the corpus callosum.

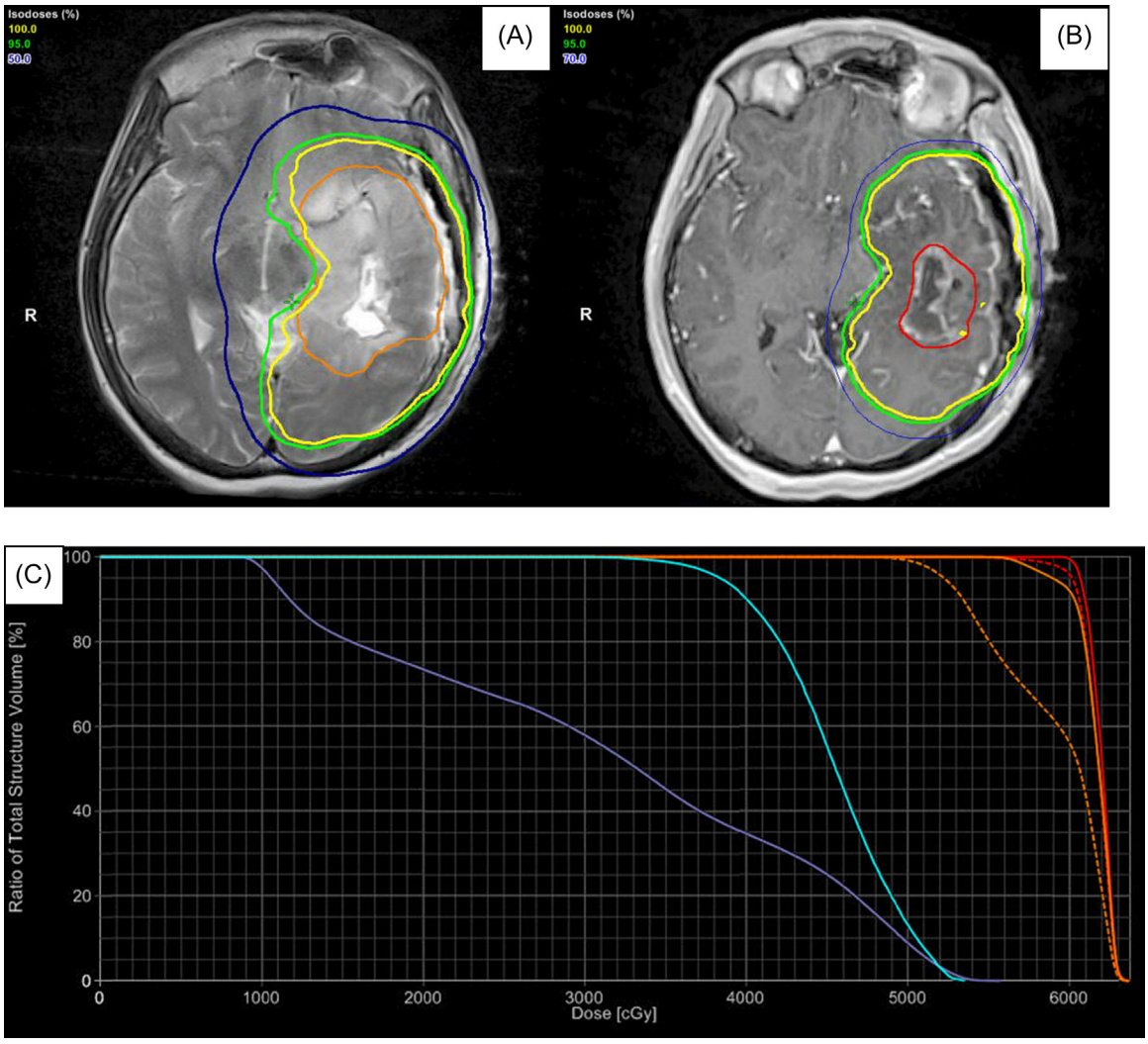


FIGURE 5 Radiation treatment plan for a patient with grade III glioma status post-gross tumor resection. (A) T2-weighted MRI with tumor and peritumoral edema CTV contoured in orange treated to 45 Gy. (B) Gadolinium-enhanced T1 MRI with tumor CTV contoured in red treated to 59.4 Gy. Three isodose lines are demonstrated: 100% (yellow), 95% (green), and 70% (blue). (C) Dose–volume histogram of the combined plan. The red and orange dotted lines depict the PTV volumes, the solid red and orange lines depict the GTV. The optic chiasm is the cyan structure and the brainstem is the purple structure.

For grade III gliomas, a guideline for treatment is derived from the results of RTOG 9402, a phase III trial evaluating chemoradiation for anaplastic oligodendroglioma patients.[12] Adjuvant radiotherapy was delivered in two phases. Initially the T2-weighted abnormality (tumor or resection cavity with edema) with a 2-cm margin was treated to 50.4 Gy in 28 fractions delivered once daily. This was sequentially followed by treating the T1-weighted abnormality (tumor or resection cavity) with a 1-cm margin to 9 Gy in five fractions.

For grade IV gliomas, the guideline for treatment is derived from RTOG 0825. Initially the T2-weighted abnormality is treated to 46 Gy in 23 fractions to a 2- to 3-cm margin, given once daily followed by a 14-Gy boost to the T1-weighted enhancing abnormality with a 1-cm margin. Various planning techniques, including IMRT and VMAT, are used to maximize tumor coverage and minimize dose to critical normal structures (Figure 5). The quality of a plan is assessed using both two-dimensional (2D) and 3D depictions of the CT along with assessment of the DVH. The DVH (Figure 5(C)) converts a 3D dose distribution into a 2D histogram of radiation dose versus structure volume. Both target volumes and OAR volumes can be evaluated. Target volumes receive the highest dose and thus are farthest to the right on the DVH. An optimal DVH for the target volume would have a steep slope that indicates full dose to the PTV with a sharp dose gradient. The maximum and mean doses to OARs are also evaluated by this method. A radiation plan is then approved based on the balance of tumor coverage and OAR dose (Figure 6).

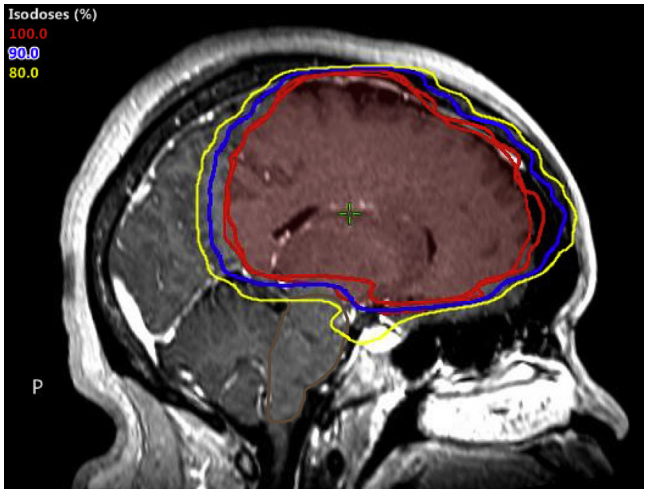


FIGURE 6 Sagittal view of CT-based radiation treatment plan for patient with glioblastoma multiforme. The PTV is shaded in red and brainstem volume in brown. Note how the 100% isodose line (red) is pulled away from the brainstem (brown) to reduce toxicity.

TREATMENT TOXICITY

The follow-up of patients with brain tumors after receiving surgery, radiation, and/or chemotherapy is aimed at closely evaluating disease recurrence as well as treatment-related toxicity. The preferred imaging method is T1 contrast-enhanced and T2/FLAIR sequences at 4 weeks following the completion of radiation therapy and then scans every 2–4 months for 2–3 years. After this time, the scanning interval can be adjusted at the physician's discretion. Radiation-induced brain injury is a complex and incompletely understood process. Total radiation dose, fraction size, treatment volume, and cell population treated can affect the level of brain injury. The mechanisms for this injury include vascular leakage resulting in edema, endothelial damage and loss resulting in hypoxia, reactive gliosis, activation of microglia by inflammatory factors, and other potential host factors.[13] Furthermore, it is often difficult to clearly distinguish treatment-related toxicity from tumor recurrence.

The toxicity of brain radiation is generally categorized as acute (less than 6 weeks following completion of radiation therapy), subacute (between 6 weeks and 6 months), and late (following 6 months) phase. Symptoms in the acute phase, such as fatigue, headache, and drowsiness, are generally thought to result from vascular leakage and peritumoral edema. This can lead to increased intracranial pressure resulting in nausea and vomiting. Toxicity related to increased peritumoral edema can be effectively managed with corticosteroids, although prolonged steroid-resistant swelling may require more intensive treatment with agents such as bevacizumab. Toxicity in the subacute phase is theorized to be related to enhanced capillary permeability and transient demyelination of oligodendroglial cells. The most common symptoms during this phase are fatigue, somnolence, headache, and worsening of previous neurologic deficits. Like with acute toxicity, corticosteroids are effective at mitigating these side effects and are therefore frequently employed. However, PsP and true disease progression can commonly occur between 6 weeks and 6 months and, as discussed below, these entities can be very difficult to distinguish. Unlike the previous phases, late toxicities are typically irreversible and progressive with the most profound effect on quality of life. Evidence suggests these effects are caused by white matter damage resulting from vascular injury, demyelination, and necrosis. The most serious late toxicity is radiation necrosis (RN), which is further discussed below. Another feared long-term complication is neuropsychological and neurocognitive decline, which have been reported to occur in 50–90% of patients who receive either whole-brain or partial brain radiation therapy.[14] Although the impact of radiotherapy on neurocognitive function is well known, there is evidence to suggest surgery and chemotherapy can play integral roles in the development of these impairments as well.[14] In the posttreatment setting, patients can experience difficulties with memory, attention, and executive function.[15] Often the detriment to quality of life is very significant and this has become an important endpoint in brain tumor studies.[16] Radiation-induced cognitive impairment is currently hypothesized to occur because of dynamic interactions between the multiple brain cell types, including astrocytes, endothelial cells, microglia, neurons, and oligodendrocytes.[15] Additionally, more recent studies have shown that radiation can inhibit hippocampal neurogenesis.[15] Promising new treatment and prevention strategies are being studied and have shown some impressive results, including using methylphenidate, memantine, and hippocampal avoidance.[17,18] Further studies will be needed to more completely understand the pathophysiology of radiation-induced brain damage and how to optimize prevention and management. Other less common toxicities that arise in the late phase include hearing loss, vestibular damage, retinopathy, cataract formation, and hypothalamic–pituitary axis deficiency.

DELINEATING PSEUDO-PROGRESSION, TRUE DISEASE PROGRESSION, AND RADIATION NECROSIS

PsP is a clinical entity that develops in a large proportion of patients following glioma treatment, whereby the treated region displays increased contrast enhancement with or without the development of neurological decline, which then improves without alteration in therapy.[19] It has been theorized that these imaging changes could be related to treatment effects resulting in disruption of the

blood–brain barrier or to RN.[19] RN is a late-delayed toxicity, generally occurring between 6 months and 3 years after receiving radiation therapy, with incidences documented as early as 1–2 months and as late as 13 years.[20–22] RN is described as a space-occupying necrosis producing mass effect and associated progressive neurological dysfunction, which is generally associated with considerable morbidity and mortality despite therapy.[20,21] Traditionally, RN has been a pathologic diagnosis requiring surgical resection and therefore it is unknown how many patients diagnosed with PsP, who then spontaneously improve, also harbor some amount of RN.[19] A logical explanation could be that PsP is induced by pronounced tissue inflammation, edema, and abnormal vascular permeability as an early (1–2 months) reaction and in more severe cases may result in RN (3 months–3 years).[22] Neither of these entities is discernible from early disease progression (EP) without surgical resection and tissue analysis. This uncertainty creates a clinical dilemma, as trials reporting radiographic response and progression-free survival have focused on imaging analysis for these endpoints and clearly this is unable to accurately delineate true progression from treatment-related effect, which may have resulted in incorrect reporting.[23] Also, this continues to present challenges in patient management, as the treatment strategy for true progression should include a change in treatment, while the management of PsP includes continuing the treatment course.

With the use of modern treatment paradigms including temozolomide (TMZ) and radiation therapy, the incidence of PsP appears to be approximately 20%.[24–30] However, imaging findings concerning for progression between 1 and 6 months following chemoradiation therapy occur in about 50% of patients and therefore 40% of those patients having improvement or stabilization without changes in intervention.[24–30] Whether TMZ has increased the rates of PsP is incompletely understood as studies prior to the implementation of TMZ less frequently used posttherapy MRI and therefore were less sensitive in detecting PsP.[31] One study that did have posttreatment MRI scans available determined that the rate of PsP in patients treated with radiotherapy alone was 23% and in those with radiotherapy plus TMZ was 29% (HR 1.3, $p = 0.55$).[31]

The incidence of RN with standard fractionation is estimated at between 3% and 6% but rates as high as 24% have been reported in aggressive regimens for intracranial lesions.[21,22,32] Development of RN displays a direct relationship with total dose of radiation and radiated volume.[22] For standard fractionation (2 Gy/fraction), a 5% and 10% risk of symptomatic RN is predicted to occur at a biologically effective dose of 120 and 150 Gy3 (α/β ratio equals 3), respectively.[33] Furthermore, there is a steep increase in RN when doses exceed 65 Gy (BED = 108 Gy3) with standard fractionation.[22] Additional risk factors, including dose per fraction (>2.5 Gy/fraction), hyperfractionation, location (brainstem, corpus callosum), and subsequent or concurrent chemotherapy administration, have been reported with retrospective and anecdotal evidence.[20–22,32,33] The best treatment for RN is symptomatic control with corticosteroids, followed by surgical debulking, if necessary. Other methods for management include bevacizumab or hyperbaric oxygen, but no randomized trials have confirmed their utility.

The appearance of PsP portends an improved overall survival compared with progressive disease in several studies, with an average improvement in median survival of 17 months.[28–30,34,35] This improvement was still an independent predictor of improved outcome when methylguanine–methyltransferase status was considered with multivariate analysis.[36] However, when examining differences between PsP and those with stable or improved initial imaging, there are mixed results, with no studies supporting a statistical difference in survival.[28–30,34,35] All efforts to delineate the underlying origin of posttherapy imaging changes with clinical evaluation, biomarkers, and imaging techniques have resulted in suboptimal accuracy in predicting disease progression or PsP. Several studies indicate that patients with early progressive disease have neurologic deterioration versus those with PsP.[24,28,36] These studies noted that patients proven to have PsP had a rate of neurologic deterioration 1 month following treatment of 21%, 33%, and 34%, while those who were determined to have disease progression had worsening symptoms 52%, 56%, and 67% of the time.[24,28,36] However, these differences did not have sufficient power to reach statistical significance and the presence of symptoms at 1 month cannot accurately predict PsP.

Owing to the presumed mechanistic difference between PsP and true disease progression, it appears feasible that an imaging technique could delineate the two in a timely fashion without an invasive procedure. Both conventional imaging with MRI and PET scan and more advanced techniques, including MRS, diffusion-weighted imaging (DWI), MR perfusion imaging, diffusion-tensor imaging, and novel PET tracers, have been evaluated with various results.[19]

Tissue signal intensity on T2-weighted and T1 contrast-enhanced weighted images does not reliably differentiate progressive disease (PD) from PsP as both conditions have enlargement with mass effect and increased gadolinium enhancement in the periphery of the resection cavity. Studies assessing conventional MRI have shown that subependymal enhancement on the first MRI following treatment significantly correlated with the diagnosis of EP, but the negative predictive value was only 41%, decreasing the clinical utility of this finding.[37] Conventional MRI may be adequate in situations in which

new enhancement develops outside of the treatment region, but in all other scenarios, it does not provide enough sensitivity or negative predictive value to be reliable. DWI has been considered a means to characterize and differentiate morphologic features, including edema, necrosis, and tumor tissue, by measuring differences in apparent diffusion coefficient (ADC) caused by water proton mobility alterations.[38] Areas with high cellularity, such as tumors, result in a low ADC, but gliosis, necrosis, and scar formation can also have an impact on ADC.[38] Two small studies have corroborated the finding that EP has a significantly reduced ADC ratio and mean ADC value compared with PsP.[38,39] However, there were cases of RN proven to have reduced ADC values and the overall utility of this method requires validation in a large prospective fashion. Furthermore, there are numerous limitations with DWI, including spatial and temporal sampling errors. Because the biology is dynamic through time and also measurements are dependent on what spatial areas are included, it is impossible to obtain a characteristic ADC measurement at a single time point.

Dynamic susceptibility-weighted contrast material-enhanced perfusion MRI is a technique that can provide physiologic information about vascular endothelial proliferation, vascular density, and angiogenesis.[40] These techniques can ascertain levels of absolute cerebral blood flow, cerebral blood volume (CBV), and relative CBV (rCBV), and as tumor progression occurs there is presumed to be increased blood volume and flow.[19] Several investigations concluded that areas of posttreatment enhancement have significantly lower rCBV values than those for recurrent tumor.[35,41,42] However, universal application is currently problematic as all of these studies used different cutoff values for rCBV ranging from 0.71 to 1.75.[35,41,42] Furthermore, with a breakdown of the blood–brain barrier, which can occur with chemoradiation therapy, gadolinium-based contrast can leak out and result in an underestimation of the true rCBV.[43] Feromoxytol (iron oxide nanoparticle)-based contrast appears to alleviate this inaccuracy as it does not leak out through a disrupted blood–brain barrier and experience using this technique showed that those with an rCBV value ≤1.75 had a median survival of 591 days versus those with a value >1.75, who had a median survival of 163 days ($p<0.001$).[44] Although this was not analyzed directly, it is suspected that these survival differences represent true progression for those with the low rCBV, and PsP in the others[44] (Figure 7).

MRS is a method of detecting metabolites in tissues, and within the brain specifically there is interest in choline (Cho), *N*-acetylaspartate (NAA), creatinine (Cr), lipid, and lactate. The distribution of these molecules in brain tissue is useful as tumors usually have elevated levels of Cho as a result of increased membrane phospholipids and decreased NAA compared with normal white matter, while necrotic tissues demonstrate elevated levels of lipid and lactate. By using Cho/NAA and Cho/Cr ratios (using a cutoff ratio of 1.71) in 28 patients with early imaging changes, the sensitivity, specificity, and diagnostic accuracy of 3D-MRS was found to be 94.1%, 100%, and 96%, respectively.[45] In a dosimetric study of 34 patients, it was noted the tumor volume defined by multivoxel MRS was significantly larger than the volume defined on T1-weighted contrast-enhanced MRI. Although the MRS and T2-weighted tumor volumes were similar, 88% of patients had extension of the MRS-defined volume past the T2-defined volume up to 2.8 cm.[46] When combining MRS data with DWI in 55 patients, the MRS data were able to correctly classify 85.5% of the patients, with the diagnostic yield being enhanced with the addition of DWI to 96.4%.[47] Such combinatorial techniques appear feasible and useful, but would need to be validated prospectively.

Owing to high glucose activity within the brain, the utility of[18] F-labeled fluorodeoxyglucose PET scans has been minimally effective in differentiating PsP and EP, with sensitivities of about 70% and high false-negative and -positive results. Several novel PET tracers have been attempted to selectively target tumor recurrence

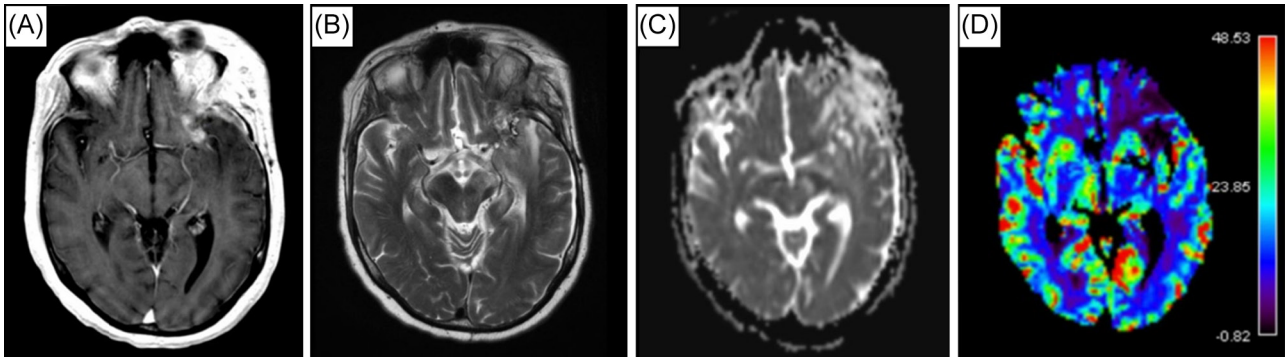


FIGURE 7 Patient with resected left frontal lobe glioblastoma multiforme and postoperative radiotherapy. He was noted to have enhancement at the resection border on T1 contrast MRI (A), which was associated with no FLAIR changes (B), high ADC difference (C) on DWI, and reduced rCBV with perfusion MRI (D). Findings are consistent with gliosis and radiation fibrosis.

by being actively incorporated into tumors. [^{11}C]Methionine (C-Met) is an amino acid tracer that is taken up by tumors via neural L-amino acid transporters.[48] This tracer showed promise in a small study consisting of only 11 patients, with a sensitivity of 100%, specificity of 60%, and diagnostic accuracy of 82% for detecting tumor recurrence.[49] However, subsequent studies were not able to reproduce these results and C-Met PET was worse in differentiating recurrence from PsP than DWI.[50,51] F-FDOPA is an F-labeled dopamine precursor believed to require active transport and will not passively diffuse through a disruption in the blood–brain barrier and therefore may be uniquely able to delineate tumor recurrence from PsP.[18] This method was shown to have a 97% sensitivity and an 86% specificity for detecting tumor recurrence in a group of 51 patients who had early imaging changes postchemoradiation.

Assuming that PsP and RN exist on the same continuum of treatment-related effects, it is reasonable to postulate that PsP tends to occur earlier and has milder symptoms than RN in the majority of cases. Therefore early and less symptomatic imaging changes can be managed with continued adjuvant treatment. If, however, the imaging changes are associated with neurologic decline, then tissue sampling is the best strategy to direct therapy. If there is evidence of necrosis without mitotically active malignant cells, then RN is assumed and can be treated with steroids, surgical excision, or bevacizumab.[22,52] When tumor recurrence is evident on pathology, surgical resection, alteration in systemic therapy, or consideration of reirradiation are valid treatment strategies. Although there have been many attempts at developing imaging to clearly delineate PsP from EP, none have been proven effective enough to guide treatment. Perhaps combining MRI and PET imaging modalities will provide enough diagnostic accuracy to guide treatment while avoiding surgical intervention, but these strategies need to be validated with large prospective trials.

FUTURE DIRECTIONS

Radiotherapy planning and neuroimaging technologies have made dramatic advances since 1995. Researchers improving tumor delineation for intracranial disease are working to understand the true extension of tumors based on functional and metabolic imaging studies. Radiotherapy planning itself is moving forward on several fronts. Radiation dose calculation algorithms have become more rigorous and accurate over time. Second, newer imaging modalities are being tested for treatment planning purposes. Since 2005–2006, there has been renewed interest in using MRI simulation for treatment planning rather than CT-based planning. The major hurdle thus far had been the lack of electron-density measurement with MRI. Thus electron-density numbers (in Hounsfield units) are derived and matched to the MRI voxels. Several studies have validated the synthetic CT model allowing MRI-based dose calculations with good results.[53,54] Newer treatment models are being developed that are trying to incorporate MRI into LINACs, allowing improved tumor visualization at the time of radiation delivery compared to CT. As imaging and molecular diagnostics become more integrated, the use of biomarkers may yield improved diagnostic tests for patients. Ongoing studies in genomic and molecular oncology have unraveled a complex cascade of biomarkers of tumorigenesis that are bringing in a new array of targeted antineoplastic agents. The roles of other therapies, including protons, carbon ions, and alternating magnetic fields, remain under evaluation. We continue to make significant advances in the therapy for intracranial tumors, with exciting new prospects on the horizon.

CONCLUSION

Intracranial tumors are a complex group of diseases that have incorporated, in varying degrees, surgery, chemotherapy, and radiotherapy. Significant progress has been made since 2005 in improving the resolution and utility of neuroimaging for tumor delineation and in producing more conformal radiotherapy delivery. These two factors allow improved tumor targeting and reduced treatment toxicities. Future advances in imaging and radiation planning will probably further fuse the worlds of neuroradiology and radiation oncology together.

References

1. Ostrom QT, Gittleman H, Farah P, et al. CBTRUS statistical report: primary brain and central nervous system tumors diagnosed in the United States in 2006–10. *Neuro Oncol*. 2013;15(Suppl 2):ii1–56.
2. Wambersie A, Landberg T, Gahbauer R. Prescribing, recording and reporting photon beam therapy: the problem of margins (the recent ICRU recommendations, Report #62, 1999). *Patras Med Phys*. 1999;99:25–31.
3. Drzymala RE, Mohan R, Brewster L, et al. Dose-volume histograms. *Int J Radiat Oncol Biol Phys*. 1991;21(1):71–78.
4. Walker A, Liney G, Metcalfe P, Holloway L. MRI distortion: considerations for MRI based radiotherapy treatment planning. *Australas Phys Eng Sci Med*. 2014;37(1):103–113.
5. Ramaseshan R, Heydarian M. Comprehensive quality assurance for stereotactic radiosurgery treatments. *Phys Med Biol*. 2003;48(14):N199–N205.
6. Shaw E, Scott C, Souhami L, et al. Single dose radiosurgical treatment of recurrent previously irradiated primary brain tumors and brain metastases: final report of RTOG protocol 90-05. *Int J Radiat Oncol Biol Phys*. 2000;47(2):291–298.
7. Maher EA, Furnari FB, Bachoo RM, et al. Malignant glioma: genetics and biology of a grave matter. *Genes Dev*. 2001;15(11):1311–1333.

8. Walker MD, Strike TA, Sheline GE. An analysis of dose-effect relationship in the radiotherapy of malignant gliomas. *Int J Radiat Oncol Biol Phys*. 1979;5(10):1725–1731.
9. Walker MD, Alexander Jr E, Hunt WE, et al. Evaluation of BCNU and/or radiotherapy in the treatment of anaplastic gliomas. A cooperative clinical trial. *J Neurosurg*. 1978;49(3):333–343.
10. Shapiro WR, Green SB, Burger PC, et al. Randomized trial of three chemotherapy regimens and two radiotherapy regimens and two radiotherapy regimens in postoperative treatment of malignant glioma. Brain Tumor Cooperative Group Trial 8001. *J Neurosurg*. 1989;71(1):1–9.
11. Hochberg FH, Pruitt A. Assumptions in the radiotherapy of glioblastoma. *Neurology*. 1980;30(9):907–911.
12. Cairncross G, Wang M, Shaw E, et al. Phase III trial of chemoradiotherapy for anaplastic oligodendroglioma: long-term results of RTOG 9402. *J Clin Oncol*. 2013;31(3):337–343.
13. Xu Y, Hu W, Liu Y, et al. P2Y6 Receptor-Mediated Microglial Phagocytosis in radiation-induced brain injury. *Mol Neurobiol*. 2015:1–13.
14. Crossen JR, Garwood D, Glatstein E, Neuwelt EA. Neurobehavioral sequelae of cranial irradiation in adults: a review of radiation-induced encephalopathy. *J Clin Oncol*. 1994;12(3):627–642.
15. Greene-Schloesser D, Robbins ME. Radiation-induced cognitive impairment–from bench to bedside. *Neuro Oncol*. 2012;14(Suppl 4):iv37–44.
16. Liu R, Page M, Solheim K, et al. Quality of life in adults with brain tumors: current knowledge and future directions. *Neuro Oncol*. 2009;11(3):330–339.
17. Gondi V, Pugh SL, Tome WA, et al. Preservation of memory with conformal avoidance of the hippocampal neural stem-cell compartment during whole-brain radiotherapy for brain metastases (RTOG 0933): a phase II multi-institutional trial. *J Clin Oncol*. 2014;32(34):3810–3816.
18. Brown PD, Pugh S, Laack NN, et al. Memantine for the prevention of cognitive dysfunction in patients receiving whole-brain radiotherapy: a randomized, double-blind, placebo-controlled trial. *Neuro Oncol*. 2013;15(10):1429–1437.
19. Kruser TJ, Mehta MP, Robins HI. Pseudoprogression after glioma therapy: a comprehensive review. *Expert Rev Neurother*. 2013;13(4):389–403.
20. Fink J, Born D, Chamberlain MC. Radiation necrosis: relevance with respect to treatment of primary and secondary brain tumors. *Curr Neurol Neurosci Rep*. 2012;12(3):276–285.
21. Ruben JD, Dally M, Bailey M, Smith R, McLean CA, Fedele P. Cerebral radiation necrosis: incidence, outcomes, and risk factors with emphasis on radiation parameters and chemotherapy. *Int J Radiat Oncol Biol Phys*. 2006;65(2):499–508.
22. Brandsma D, Stalpers L, Tall W, Sminia P, van den Bent MJ. Clinical features, mechanisms, and management of pseudoprogression in malignant gliomas. *Lancet Oncol*. 2008;9(5):453–461.
23. Macdonald DR, Cascino TL, Schold Jr SC, Cairncross JG. Response criteria for phase II studies of supratentorial malignant glioma. *J Clin Oncol*. 1990;8(7):1277–1280.
24. Taal W, Brandsma D, de Bruin HG, et al. Incidence of early pseudoprogression in a cohort of malignant glioma patients treated with chemoirradiation with temozolomide. *Cancer*. 2008;113(2):405–410.
25. Brandes AA, Tosoni A, Spagnolli F, et al. Disease progression or pseudoprogression after concomitant radiochemotherapy treatment: pitfalls in neurooncology. *Neuro Oncol*. 2008;10(3):361–367.
26. Chaskis C, Neyns B, Michotte A, De Ridder M, Everaert H. Pseudoprogression after radiotherapy with concurrent temozolomide for high-grade glioma: clinical observations and working recommendations. *Surg Neurol*. 2009;72(4):423–428.
27. Clarke JL, Iwamoto FM, Sul J, et al. Randomized phase II trial of chemoradiotherapy followed by either dose-dense or metronomic temozolomide for newly diagnosed glioblastoma. *J Clin Oncol*. 2009;27(23):3861–3867.
28. Gunjur A, Lau E, Taouk Y, Ryan G. Early post-treatment pseudoprogression amongst glioblastoma multiforme patients treated with radiotherapy and temozolomide: a retrospective analysis. *J Med Imaging Radiat Oncol*. 2011;55(6):603–610.
29. Roldan GB, Scott JN, McIntyre JB, et al. Population-based study of pseudoprogression after chemoradiotherapy in GBM. *Can J Neurol Sci*. 2009;36(5):617–622.
30. Sanghera P, Perry J, Sahgal A, et al. Pseudoprogression following chemoradiotherapy for glioblastoma multiforme. *Can J Neurol Sci*. 2010;37(1):36–42.
31. Gerstner ER, McNamara MB, Norden AD, Lafrankie D, Wen PY. Effect of adding temozolomide to radiation therapy on the incidence of pseudo-progression. *J Neurooncol*. 2009;94(1):97–101.
32. Siu A, Wind JJ, Iorgulescu JB, Chan TA, Yamada Y, Sherman JH. Radiation necrosis following treatment of high grade glioma-a review of the literature and current understanding. *Acta Neurochir*. 2012;154(2):191–201.
33. Lawrence YR, Li XA, el Naqa I, et al. Radiation dose-volume effects in the brain. *Int J Radiat Oncol Biol Phys*. 2010;76(Suppl 3):S20–S27.
34. Kang HC, Kim CY, Han JH, et al. Pseudoprogression in patients with malignant gliomas treated with concurrent temozolomide and radiotherapy: potential role of p53. *J Neurooncol*. 2011;102(1):157–162.
35. Kong DS, Kim ST, Kim EH, et al. Diagnostic dilemma of pseudoprogression in the treatment of newly diagnosed glioblastomas: the role of assessing relative cerebral blood flow volume and oxygen-6-methylguanine-DNA methyltransferase promoter methylation status. *AJNR Am J Neuroradiol*. 2011;32(2):382–387.
36. Brandes AA, Franceschi E, Tosoni A, et al. MGMT promoter methylation status can predict the incidence and outcome of pseudoprogression after concomitant radiochemotherapy in newly diagnosed glioblastoma patients. *J Clin Oncol*. 2008;26(13):2192–2197.
37. Young RJ, Gupta A, Shah AD, et al. Potential utility of conventional MRI signs in diagnosing pseudoprogression in glioblastoma. *Neurology*. 2011;76(22):1918–1924.
38. Hein PA, Eskey CJ, Dunn JF, Hug EB. Diffusion-weighted imaging in the follow-up of treated high-grade gliomas: tumor recurrence versus radiation injury. *AJNR Am J Neuroradiol*. 2004;25(2):201–209.
39. Asao C, Korogi Y, Kitajima M, et al. Diffusion-weighted imaging of radiation-induced brain injury for differentiation from tumor recurrence. *AJNR Am J Neuroradiol*. 2005;26(6):1455–1460.
40. Law M, Young RJ, Babb JS, et al. Gliomas: predicting time to progression or survival with cerebral blood volume measurements at dynamic susceptibility-weighted contrast-enhanced perfusion MR imaging. *Radiology*. 2008;247(2):490–498.
41. Hu LS, Baxter LC, Smith KA, et al. Relative cerebral blood volume values to differentiate high-grade glioma recurrence from posttreatment radiation effect: direct correlation between image-guided tissue histopathology and localized dynamic susceptibility-weighted contrast-enhanced perfusion MR imaging measurements. *AJNR Am J Neuroradiol*. 2009;30(3):552–558.
42. Gahramanov S, Raslan AM, Muldoon LL, et al. Potential for differentiation of pseudoprogression from true tumor progression with dynamic susceptibility-weighted contrast-enhanced magnetic resonance imaging using ferumoxytol vs. gadoteridol: a pilot study. *Int J Radiat Oncol Biol Phys*. 2011;79(2):514–523.
43. Gahramanov S, Muldoon LL, Li X, Neuwelt EA. Improved perfusion MR imaging assessment of intracerebral tumor blood volume and antiangiogenic therapy efficacy in a rat model with ferumoxytol. *Radiology*. 2011;261(3):796–804.
44. Gahramanov S, Muldoon LL, Varallyay CG, et al. Pseudoprogression of glioblastoma after chemo- and radiation therapy: diagnosis by using dynamic susceptibility-weighted contrast-enhanced perfusion MR imaging with ferumoxytol versus gadoteridol and correlation with survival. *Radiology*. 2013;266(3):842–852.

45. Zeng QS, Li CF, Zhang K, Liu H, Kang XS, Zhen JH. Multivoxel 3D proton MR spectroscopy in the distinction of recurrent glioma from radiation injury. *J Neurooncol*. 2007;84(1):63–69.
46. Pirzkall A, McKnight TR, Graves EE, et al. MR-spectroscopy guided target delineation for high-grade gliomas. *Int J Radiat Oncol Biol Phys*. 2001;50(4):915–928.
47. Zeng QS, Li CF, Liu H, Zhen JH, Feng DC. Distinction between recurrent glioma and radiation injury using magnetic resonance spectroscopy in combination with diffusion-weighted imaging. *Int J Radiat Oncol Biol Phys*. 2007;68(1):151–158.
48. Schober O, Duden C, Meyer GJ, Müller JA, Hundeshagen H. Non selective transport of [11C-methyl]-L-and D-methionine into a malignant glioma. *Eur J Nucl Med*. 1987;13(2):103–105.
49. Tsuyuguchi N, Takami T, Sunada I, et al. Methionine positron emission tomography for differentiation of recurrent brain tumor and radiation necrosis after stereotactic radiosurgery–in malignant glioma. *Ann Nucl Med*. 2004;18(4):291–296.
50. Terakawa Y, Tsuyuguchi N, Iwai Y, et al. Diagnostic accuracy of 11C-methionine PET for differentiation of recurrent brain tumors from radiation necrosis after radiotherapy. *J Nucl Med*. 2008;49(5):694–699.
51. Kim YH, Oh SW, Lim YJ, et al. Differentiating radiation necrosis from tumor recurrence in high-grade gliomas: assessing the efficacy of 18F-FDG PET, 11C-methionine PET and perfusion MRI. *Clin Neurol Neurosurg*. 2010;112(9):758–765.
52. Matuschek C, Bölke E, Nawatny J, et al. Bevacizumab as a treatment option for radiation-induced cerebral necrosis. *Strahlenther Onkol*. 2011;187(2):135–139.
53. Gudur MS, Hara W, Le QT, Wang L, Xing L, Li R. A unifying probabilistic Bayesian approach to derive electron density from MRI for radiation therapy treatment planning. *Phys Med Biol*. 2014;59(21):6595–6606.
54. Paulson ES, Erickson B, Schultz C, Allen Li X. Comprehensive MRI simulation methodology using a dedicated MRI scanner in radiation oncology for external beam radiation treatment planning. *Med Phys*. 2015;42(1):28–39.

CHAPTER

25

TTFields Therapy: Preclinical and Clinical Data

Joshua Lantos[1], *Robert J. Young*[1,2], *Pedro C. Miranda*[3], *Cornelia Wenger*[3], *Eric T. Wong*[4,5]

[1]Department of Radiology, Memorial Sloan Kettering Cancer Center, New York, USA; [2]Brain Tumor Center, Memorial Sloan Kettering Cancer Center, New York, USA; [3]Institute of Biophysics and Biomedical Engineering, Faculty of Science, University of Lisbon, Lisbon, Portugal; [4]Brain Tumor Center & Neuro-Oncology Unit, Beth Israel Deaconess Medical Center & Harvard Medical School, Boston, MA, USA; [5]Department of Physics, University of Massachusetts at Lowell, Lowell, MA, USA

INTRODUCTION AND OUTLINE

Tumor Treating Fields (TTFields) is a novel antimitotic cancer treatment modality that works with specialized low-intensity (1–3 V/cm) and intermediate frequency (~200 kHz) electric fields. TTFields for glioblastoma multiforme (GBM) patients are delivered noninvasively through two orthogonal pairs of transducer arrays placed on the shaved scalp. Tumor cells are disrupted during mitosis, with the specific frequency tuned for distinct cancer cell lines, while quiescent cells are not affected.

This chapter covers a short introduction to the basics of electric fields including a description of the mechanisms of action of TTFields. Preclinical findings are outlined and the clinical application of TTFields discussed. The induced electric field distribution within the cranium is explained and illustrated with computational modeling. The last part of the chapter will comment on neuroimaging in patients treated with TTFields including a discussion of response criteria, pseudoprogression, and other treatment-related changes in patients.

BASIC PRINCIPLES OF TTFIELDS AND PRECLINICAL FINDINGS

Introduction to the Physics of Electric Fields

It is important to have an understanding of the physical effects of the electric fields exerted on intracellular macromolecules and proteins. These effects arise from the fact that most of these molecules have a net electric charge (charged molecules) and/or an electric dipole moment (polar molecules). These physical properties subserve important cellular and biological functions mediated by electrical interactions between such molecules. The charged or polar molecules are also responsive to an applied electric field.

An electric field can be defined as the electric force per unit positive charge. Thus the direction of the electric field is radially outward from a positive charge (Figure 1(A)). In this field, a positive charge will move radially outwards, whereas a negative charge will move radially inwards. Molecules with net charges of opposite signs attract each other whereas molecules with net charges of the same sign repel each other. The electric field can be visualized by drawing directed curved lines (electric field lines) to indicate both the magnitude and the direction of the field. A uniform field is represented by parallel field lines (Figure 1(B)) whereas a nonuniform field is characterized by converging or diverging field lines (Figure 1(A) and (D)).[1] In an electrostatic field, where the source charges remain the same over time, a test charge will move toward the oppositely charged source (Figure 1(B)). In a field with time-varying or alternating source charges this charge will migrate back and forth (Figure 1(C), right). In polar molecules, the spatial separation of the positively and negatively charged poles gives rise to an electric dipole. In a uniform field, no net force is exerted on a dipole; specifically the forces acting at the ends with opposite polarity balance out and there is no movement in either direction.[2] Nonetheless the electric field induces a torque that rotates the dipole so it aligns with the direction of the field

Handbook of Neuro-Oncology Neuroimaging, Second Edition
http://dx.doi.org/10.1016/B978-0-12-800945-1.00025-2

© 2016 Elsevier Ltd. All rights reserved.

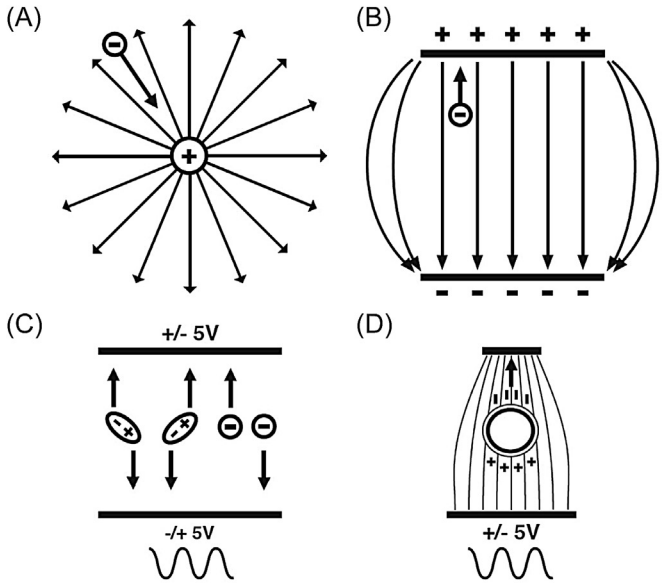


FIGURE 1 Electric field theory. (A) Opposite charges attract. (B) A constant, uniform, electric field. (C) Charges and dipoles in a time-varying, uniform electric field. (D) A dipole in a time-varying, nonuniform electric field (dielectrophoresis). *From Gutin PH and Wong ET (2012) with permission.*

(Figure 1(C), left). In a nonuniform field, the forces exerted on the positive and negative poles that make up the dipole are unequal, resulting in a net force and translational motion toward higher field intensity regions (Figure 1(D)). This phenomenon is termed dielectrophoresis, a function of frequency that is thoroughly described by Pohl.[2,3] Dielectrophoretic forces are actionable on neutral particles that are polarizable, proportional to the size of the particle, the degree of nonuniformity of the field, and the difference between dielectric properties of the particle and the suspending medium.

Mechanisms of Action of TTFields

The effects of the application of electric fields on biological cells are an often-discussed topic within the last few decades. Analytical descriptions and theoretical investigations have led to numerous techniques for cellular characterization and manipulation, which were translated into clinical applications. Low-frequency alternating fields are employed for nerve and muscle stimulation, while high-frequency fields find medical relevance in techniques such as tissue heating or tumor ablation. The biological effects of intermediate frequency fields in the kHz region have not been extensively studied, but investigations have uncovered a number of subtle biological effects on dividing cells.

Many of the subcellular particles that are responsible for mitosis and cytokinesis are highly polar structures. Thus, particles like tubulin, actin, and DNA are very susceptible to an applied electric field. TTFields are alternating electric fields of intermediate frequency (100–300 kHz) and low intensity (1–3 V/cm). The application of these fields is hypothesized to have distinct effects. For example, TTFields is believed to act by disrupting the formation of a properly functioning mitotic spindle during metaphase and by further disrupting normal cytokinesis during telophase, which leads to apoptosis. The first mechanism of action is explained by the fact that tubulin subunits align in the direction of the applied electric field, which prevents or prolongs the normal polymerization of the mitotic spindle (Figure 2(A)). The penetration of TTFields into the cell's interior was tested with computational modeling. The induced electric field distribution in and around a spherical cell exposed to TTFields during metaphase was computed using Comsol Multiphysics. The kHz frequency range marks a transition region where the intracellular field changes rapidly. For low frequencies, <10 kHz, the intracellular field is almost zero, whereas for high frequencies the impedance of the cell membrane is low and thus the cell becomes "electrically invisible" (Figure 2(B)).

The second mechanism of action results from the specific shape of the cell during anaphase and telophase. Within a dividing cell, the induced electric field is highly nonuniform with increased field intensity at the narrow furrow region. This nonuniform electric field within the cell generates dielectrophoretic forces that act on polar and charged elements in the cell, pushing them toward the cytokinetic furrow and leading to violent blebbing of the plasma membrane (Figure 2(C)).[1] The induced nonuniform field within the cell during different stages of cytokinesis, including the high field intensity region at the furrow, was examined by computational modeling (Figure 2(D), left). The dielectrophoretic force that is proportional to the gradient of the electric field squared was also calculated with this model. The normalized dielectrophoretic force induced in the cell during a late stage of cytokinesis was displayed as a function of frequency (Figure 2(D), right). The shape of the function predicts a very well-defined peak frequency at 150 kHz.

Cell Biology Effects of TTFields, Preclinical Findings, and Pilot Trials

In order to test these believed mechanisms of actions, in vitro experiments were conducted with different cancer cell lines exposed to TTFields. First, field-induced disruptions included violent blebbing, aberrant mitotic exit, and cellular derangement consisting of incompletely or poorly divided cells that have tetraploidy, asymmetric chromosome segregation leading to aneuploidy, or slippage into a G_0 state (Figure 3).[4,5] Second, once these cells re-enter into the next cycle of mitosis, they may trigger subsequent G_1 or G_2/M checkpoint leading to apoptosis. Apoptotic cells were readily seen in cell cultures treated

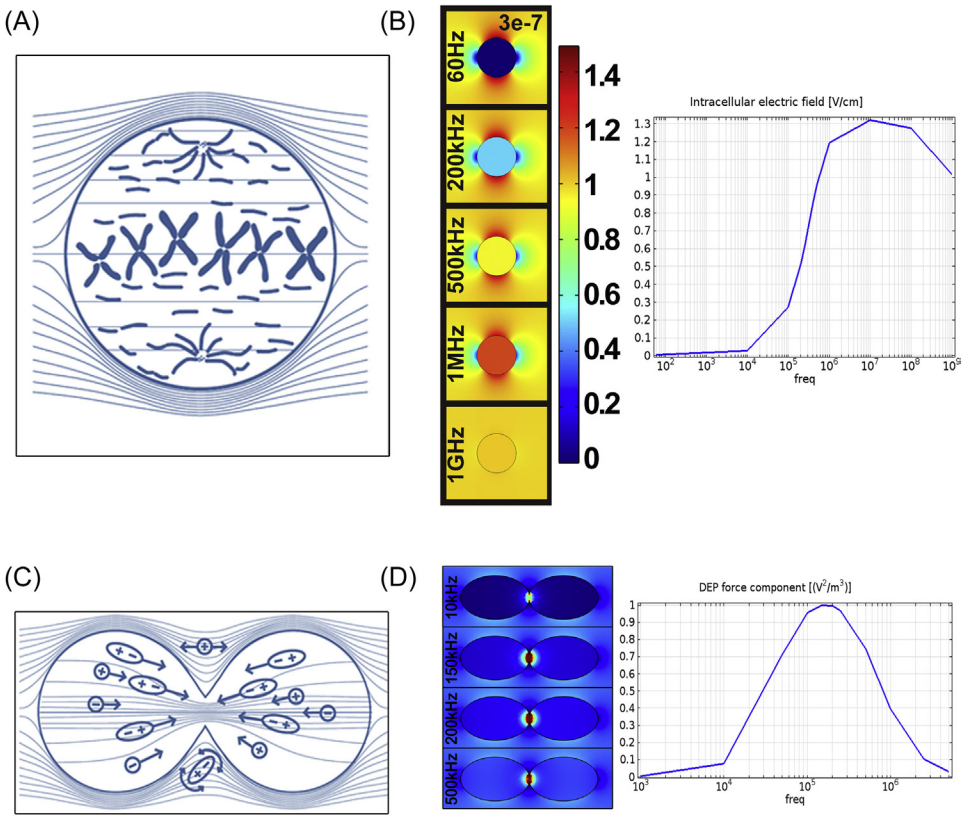


FIGURE 2 (A) Schematic drawing of the metaphase cell interior during TTFields treatment. Polar particles line up with the impressed field disrupting the proper formation of a functioning mitotic spindle. (B) Corresponding simulation results for the electric field distribution in and around a spherical cell exposed to TTFields of 1 V/cm. The intracellular field intensity is function of frequency. A rapid transition occurs in the kHz range, from a zero field at low frequencies to complete penetration at very high frequencies. (C) Schematic drawing of the telophase cell during TTFields treatment. The hourglass shape of the dividing cell induces a nonuniform field with high field intensities at the furrow region which induces dielectrophoretic force that pulls polarized particles toward it. (D) Corresponding simulation results for the electric field distribution in and around a dividing cell exposed to TTFields of 1 V/cm. The induced intracellular field is highly nonuniform with increased field strength at the furrow region. On the right, the normalized dielectrophoretic force induced in the cell when cytokinesis is almost complete is displayed as a function of frequency. The shape of the function predicts a very well defined peak frequency at 150 kHz. *From Novocure Inc. with permission.*

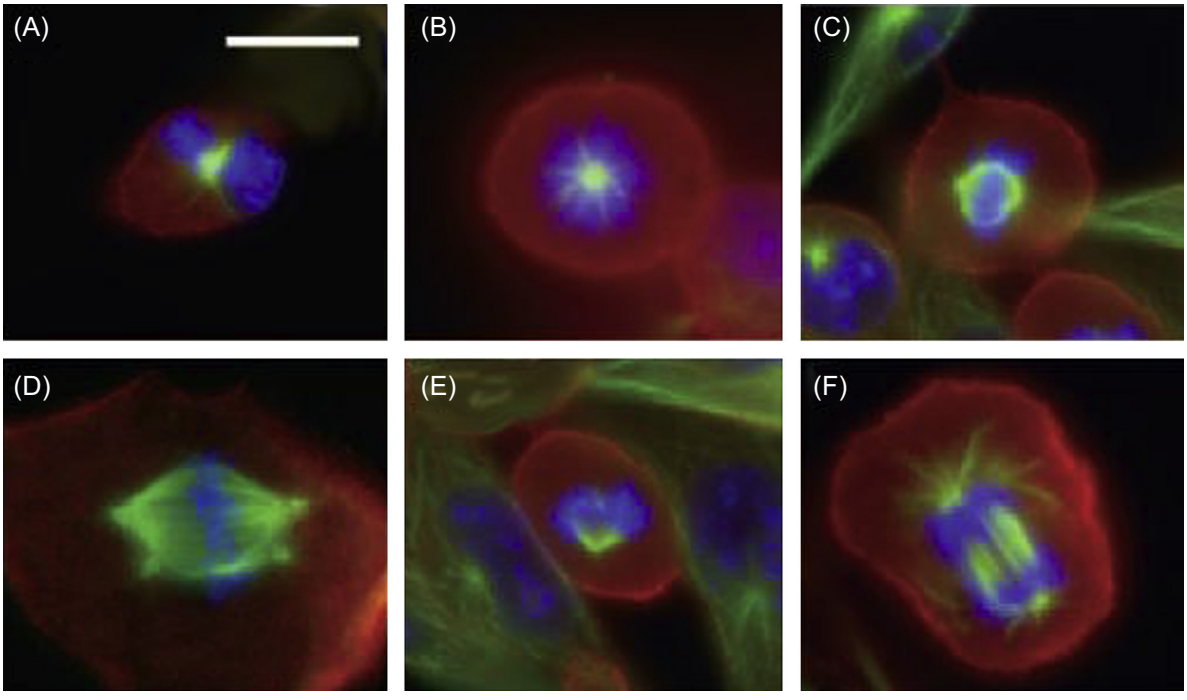


FIGURE 3 Immunohistochemical staining of abnormal mitotic figures in TTFields-treated cultures. Malignant melanoma cultures (n = 4) were treated for 24 h at 100 kHz and then stained with monoclonal antibodies for microtubules (green), actin (red), and DNA (blue). The photomicrographs show exemplary abnormal mitoses including: polyploid prophase (A); rosette (B); ill-separated metaphase (C); multispindled metaphase (D); single-spindled metaphase (E); and asymmetric anaphase (F). *From Kirson ED, Gurvich Z, Schneiderman R, et al (2004) with permission.*

with TTFields. Lastly, the violent membrane blebbing created cytoplasmic stress resulting in the expression of calreticulin on the plasma membrane and secretion of high-mobility group protein B1 into the extracellular space which, in concert, marks the cells for immune destruction.[6] This type of immunogenic cell death that occurs after induction of cellular stress has also been observed after treatment with specific immunostimulating chemotherapies, like oxaliplatin and cyclophosphamide.[7] This is also similar to the abscopal effect from radiation, which relies on the release of intracellular tumor antigen for sensitization of the host's immune system for destruction.[8]

In vitro experiments and experiments in animal tumor models have shown that the efficacy of TTFields depends on the intensity, frequency, and direction of the applied electric fields.[4,9] The cell biology effects of alternating electric fields were tested in various tumor cell lines, including the F98 glioma cell line from the rat. The inhibitory effects of TTFields on proliferation increase with intensity. For rat glioma complete proliferation arrest was observed after a 24 h exposure of a TTField intensity of 2.25 V/cm.[4] The optimal frequency varies among cell lines; glioma cells in tissue culture showed the strongest inhibition of cell division at a frequency of 200 kHz.[9] In mouse melanoma cultures, cellular damage was greatest when the applied electric field and the axis of cell division were parallel, in which case there were five times more damaged cells than live cells. This ratio was much closer to one when the angle between the electric field and the axis of cell division was close to 45° and to 90°.[4] Cells that were not actively dividing remained morphologically and functionally intact.[4] The antitumor effects of TTFields were confirmed in an intradermal mouse model for melanoma and an intracranial rat model for glioma.[9] In rats inoculated intracranially with glioma cells, treatment for 6 days using external electrodes to produce an electric field amplitude of 2 V/cm at 200 kHz caused a tumor volume reduction of 42.6% and 53.4% for two and three field directions, respectively, when compared with untreated tumors.[9]

Later, a small pilot trial of TTFields in 10 patients with recurrent glioblastoma demonstrated a median time to tumor progression of 26.1 (range 3.0–124.0) weeks, an overall survival (OS) of 62.2 (range 20.3–124.0) weeks, and a 1-year survival rate of 67.5%.[9] This promising outcome led to a pivotal trial which in turn resulted in the United States Food and Drug Administration (FDA) approval of TTFields as a therapy for recurrent GBM patients, as will be discussed in the next section.

The combined efficacy of TTFields and chemotherapies has been investigated. Using the IC_{50} as a measure, there was a 1000-fold drop in the IC_{50} of MDA-MB-231 cells when exposed to TTFields and paclitaxel in combination, as compared to paclitaxel alone.[10] Similar albeit smaller drops in the IC_{50}, 20-fold and 150-fold, were observed in the same cell line when exposed to TTFields and doxorubicin as well as TTFields and cyclophosphamide, respectively.

CLINICAL APPLICATION OF TTFields

Efficacy of Alternating Electric Fields Therapy for Glioblastoma

The NovoTTF-100A device was approved by the FDA in April 2011 for treating recurrent glioblastoma. The alternating electric fields are delivered by two pairs of transducer arrays positioned orthogonally onto the shaved scalp (Figure 4).[11] The arrays are connected to an electric field generator and a battery pack.[11] The recommended usage is ≥75% compliance or ≥18 h daily.

In the pivotal phase III EF-11 clinical trial, the NovoTTF-100A device was demonstrated to have equivalent efficacy when compared to Best Physician's Choice chemotherapy while sparing patients the toxicities associated with systemic chemotherapies.[11,12] As shown in Figure 5, the respective median OS was 6.6 months for NovoTTF-100A (n = 120) and 6.0 months for chemotherapy (n = 117), with a hazard ratio (HR) of 0.86 (95% confidence interval (CI) 0.66–1.12; P = 0.27). The respective median progression-free survival (PFS) was 2.2



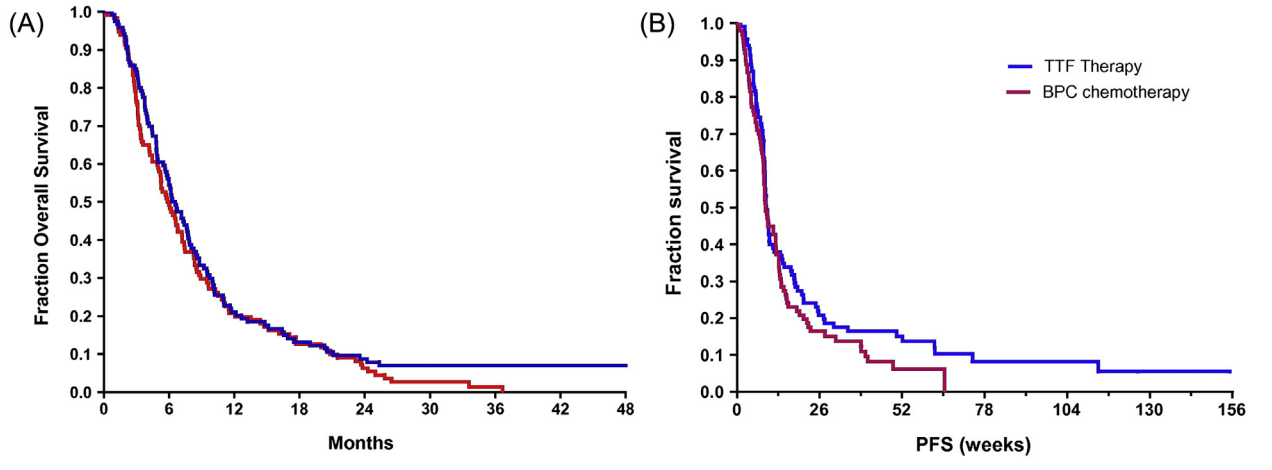
FIGURE 4 The NovoTTF-100A device. Two opposing pairs of transducer arrays are applied to the scalp and the cables are linked to the electric fields generator and a battery pack. *From Novocure Inc. with permission.*

and 2.1 months, with an HR of 0.81 (95% CI 0.60–1.09; P = 0.16). The PFS rate at 6 months was 21.4% (95% CI 13.5–29.3) and 15.1% (95% CI 7.8–22.3) (P = 0.13). The 1-year survival rate was 20% in the NovoTTF-100A cohort and 20% in the chemotherapy cohort. The most common toxicity associated with the NovoTTF-100A device was dermatological irritation, which occurred in 14% of patients with grade I or II severity; none of them had severe grade III or IV toxicity. Notably, the NovoTTF-100A cohort had fewer grade two or greater hematological toxicities compared with the chemotherapy cohort, 3% versus 17%, respectively, and fewer adverse gastrointestinal events, 4% versus 17%. Quality of life analysis (Figure 6) showed that patients treated with NovoTTF-100A had better cognitive and emotional function than those treated with chemotherapy. In contrast, appetite loss, constipation, diarrhea, fatigue, nausea, vomiting, and pain occurred more often in patients treated with chemotherapy than with NovoTTF-100A. Taken together, NovoTTF-100A had equivalent efficacy when compared to chemotherapy in patients with recurrent glioblastoma, while the toxicities associated with the device were mild and compared favorably to chemotherapy.

A post hoc analysis of responders and nonresponders in the EF-11 trial found that secondary glioblastomas were found in a higher frequency in responders than nonresponders in the NovoTTF-100A arm.[13] Additionally, all responders in the NovoTTF-100A arm had a significantly lower dexamethasone burden that statistically varied from the population as a whole, while dexamethasone had a lesser effect in the chemotherapy cohort (Figure 7).[13] Because dexamethasone can induce global immunosuppression, this finding further suggests that dexamethasone not only predisposes glioblastoma patients to infections, but also likely disables their anticancer immunity.[14]

Mrugala et al.[15] published data from the Patient Registry Dataset (PRiDe) for the 457 recurrent glioblastoma patients treated with NovoTTF-100A across 91 US medical centers. Compared with the EF-11 trial, more patients in the PRiDe received NovoTTF Therapy for first recurrence (33% vs 9%) but had also received previous bevacizumab regimens (55% vs 19%). First or second recurrence (vs third or later recurrence) and no prior bevacizumab use were positive prognostic factors. They found longer median OS with NovoTTF therapy in clinical practice (9.6 months) than in the EF-11 trial (6.6 months), and greater than double the 1-year OS rate (44% vs 20%). These results suggest that NovoTTF can offer favorable clinical benefit to patients with recurrent glioblastoma, while maintaining patient tolerability and safety.

The efficacy of NovoTTF therapy for newly diagnosed glioblastoma is currently being prospectively investigated in EF-14, a randomized multicenter trial of NovoTTF therapy plus adjuvant temozolomide compared with adjuvant temozolomide alone that are administered after completion of initial involved-field cranial irradiation and concomitant daily temozolomide.[16] The primary endpoint is PFS and secondary endpoints include OS, PFS at 6 months, survival at 1 and 2 years, as well as quality of life assessment. All 700 subjects have been accrued and randomized in a 2:1 fashion to NovoTTF therapy plus adjuvant temozolomide:adjuvant temozolomide. The sample size has the power to



At risk	0 m	6 m	12 m	18 m	24 m	30 m	36 m	42 m	48 m
TTF	120	63	24	15	9	7	4	2	1
BPC	117	56	22	14	6	2	1	0	0

0 m	13 w	26w	39w	52w	65 w	78 w	91 w
120	38	19	14	11	6	4	3
117	34	14	10	3	1	0	0

FIGURE 5 Overall survival (A) and progression-free survival (B) Kaplan–Meier curves. *From Stupp R, Wong ET, Kanner AA, et al (2012) with permission.*

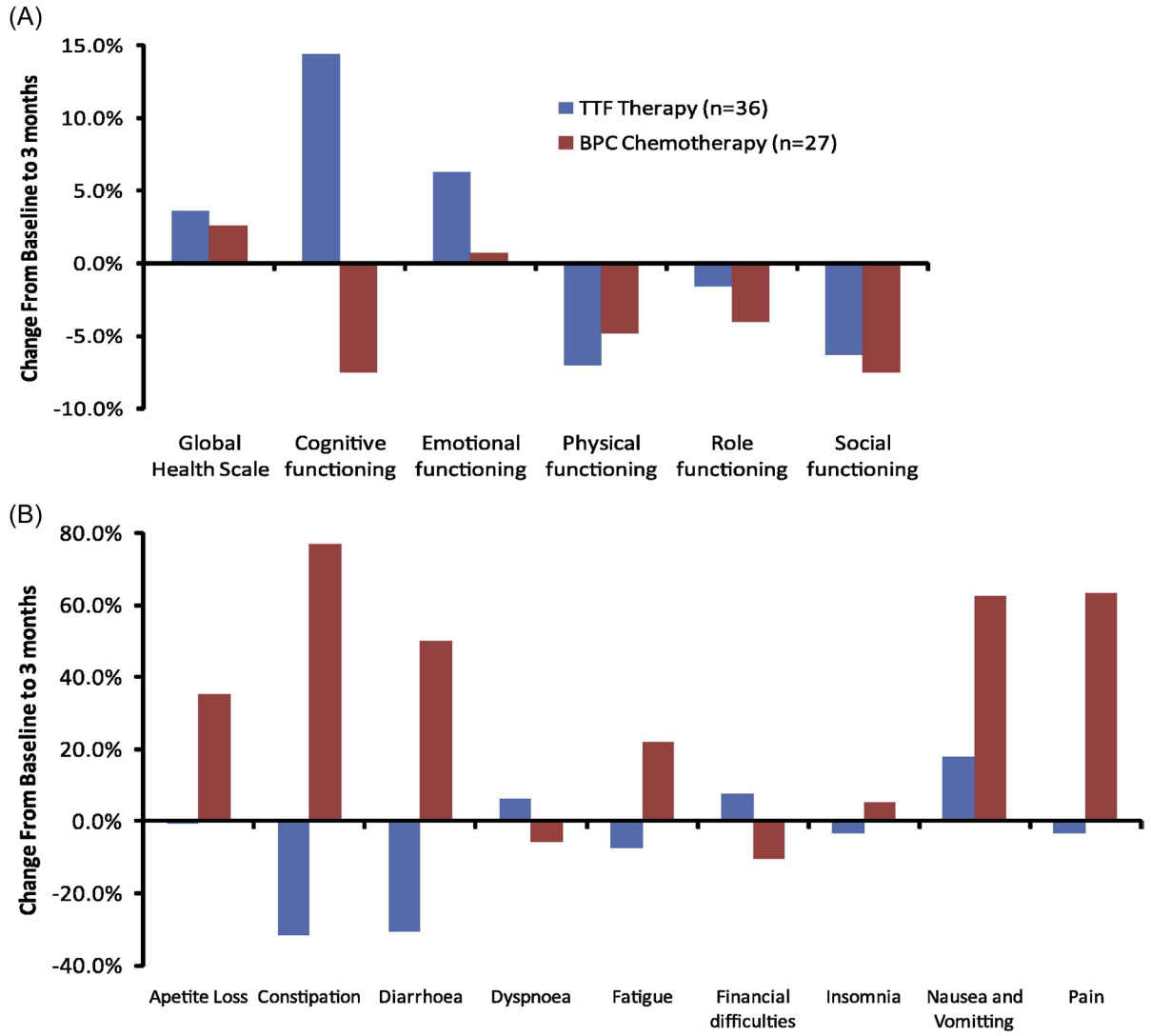


FIGURE 6 European Organization for Research and Treatment of Cancer quality of life questionnaire (QLQ) C30 longitudinal change from baseline to 3 months. (A) General functional scales (an increase in percentage corresponds to an increase in quality of life). (B) Symptom scales (an increase in percentage corresponds to a decrease in quality of life).

detect an HR of <0.78 for PFS and <0.76 for OS. The data were presented after a prespecified interim analysis of the first 315 subjects after a minimum follow up of 18 months.[17] In the intent-to-treat (ITT) population, there were 210 subjects randomized to the NovoTTF therapy plus adjuvant temozolomide arm and received a median of six cycles of treatment, while 105 subjects were randomized to the adjuvant temozolomide alone arm and received a median of four cycles of treatment. The per protocol (PP) population consisted of subjects that started their second cycle of treatment, or 196 in the former and 84 in the latter. Patient characteristics were balanced with respect to age, Karnofsky performance score, extent of resection, promoter methylation status of O^6-methylguanine-DNA methyltransferase, and time from diagnosis to randomization. The primary endpoint analysis showed that treatment with NovoTTF therapy plus adjuvant temozolomide was superior to adjuvant temozolomide alone, with a respective median PFS of 7.1 (95% CI 5.9–8.2) months versus 4.0 (95% CI 3.0–4.3) months (HR = 0.6, log rank P = 0.0014). The median OS in the former cohort, compared with the latter cohort, was also superior in both the ITT population, 19.6 (95% CI 16.5–24.1) months versus 16.6 (95% CI 13.5–19.1) months, respectively (HR = 0.75, log rank P = 0.034), and in the PP population, 20.5 (95% CI 16.5–24.1) months versus 15.5 (95% CI 13.5–19.1) months, respectively (HR = 0.67, log rank P = 0.0072). There were no unexpected adverse events. Expected grade III and IV hematological side effects (12% vs 9%), gastrointestinal disorders (5% vs 2%), and convulsions (7% vs 7%) were similar between the two cohorts. Scalp reaction was more common in the NovoTTF therapy-treated than the temozolomide-only group, 49% vs 5%, respectively, for

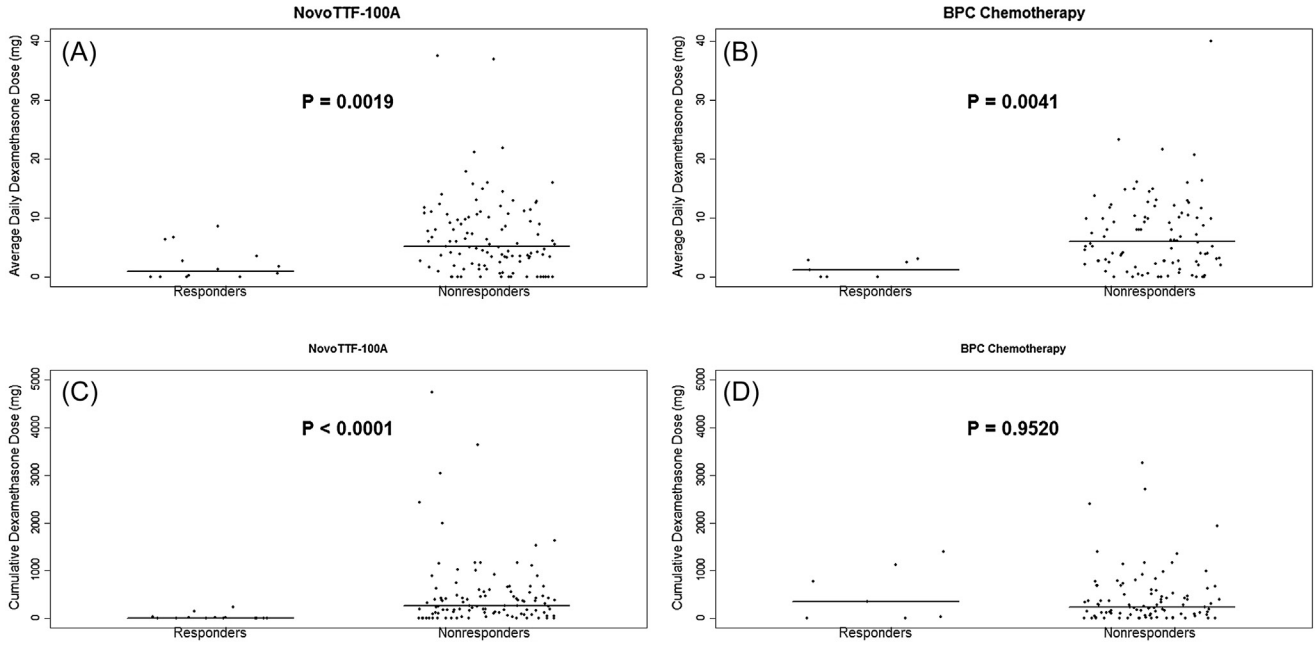


FIGURE 7 Scatter plot of mean daily dexamethasone and cumulative dexamethasone dose in responders and nonresponders. (A) In the NovoTTF-100A cohort, the respective median and mean daily dexamethasone dose was 1.0 and 2.3 (95% CI 0.8–3.8) mg for responders versus 5.2 and 6.8 (95% CI 5.6–8.1) mg for nonresponders (P = 0.0019). (B) In the BPC cohort, the respective median and mean daily dexamethasone dose was 1.2 and 1.4 (95% CI 0.3–2.4) mg for responders versus 6.0 and 7.2 (95% CI 6.0–8.4) mg for nonresponders (P = 0.0041). (C) In the NovoTTF-100A cohort, the respective median and mean cumulative dexamethasone dose was 7.1 and 35.9 (95% CI N/A–72.5) mg for responders versus 261.7 and 485.6 (95% CI 347.9–623.4) mg for nonresponders (P < 0.0001). (D) In the BPC cohort, the respective median and mean cumulative dexamethasone dose was 348.5 and 525.6 (95% CI 96.5–954.7) mg for responders versus 242.3 and 431.0 (95% CI 328.1–533.8) mg for nonresponders (P = 0.9520). BPC, Best Physician's Choice; CI, confidence interval; N/A, not available.

grade I and II toxicities as well as 7% vs 5%, respectively for grade III and IV toxicities.

ELECTRIC FIELD DISTRIBUTION WITHIN CRANIUM AND BRAIN

Experimental Evidence

The dependence of the efficacy of TTFields on the electric field strength has been described earlier. Measurement of the applied electric field in cell cultures and in animals is straightforward. Verification of the field strength inside the human head during TTFields treatment would be desirable, but is fraught with difficulties. A single intracranial measurement has been reported in the literature, showing that an electric field intensity of 1–2 V/cm could be produced in the center of the brain by applying a potential difference of approximately 50 V between the transducer arrays.[9]

Computational Model

Computational modeling provides a practical means to estimate the intensity of the electric field in the brain and, more generally, to examine the effect of the shape and physical properties of the different tissues of the head on the electric field distribution. This can be achieved by combining a realistic three-dimensional representation of the head with a numerical method to calculate the electric field. The three-dimensional model is defined in terms of surfaces that correspond to the boundaries between adjacent tissues. These surfaces are represented by small triangles that make up the surface meshes (see top row of Figure 8). The bulk of the tissue is represented by small volume elements with four triangular surfaces (tetrahedra) that make up the volume meshes. The volume meshes and the surface meshes match at the boundaries. The finite element method is used to solve Maxwell's equations, based on the spatial discretization provided by the volume mesh. The numerical solution of these equations yields an estimate of the electric potential and the electric field within the head (for more details see Miranda et al.[18]).

The head model shown in the top row of Figure 8 was created by segmenting T1- and T2-weighted MR images of a single healthy subject.[18] It consists of five different tissue types: scalp, skull, cerebrospinal fluid (CSF), gray matter (GM), and white matter (WM). The ventricles were assumed to have the same properties as the CSF. Two concentric spheres were introduced

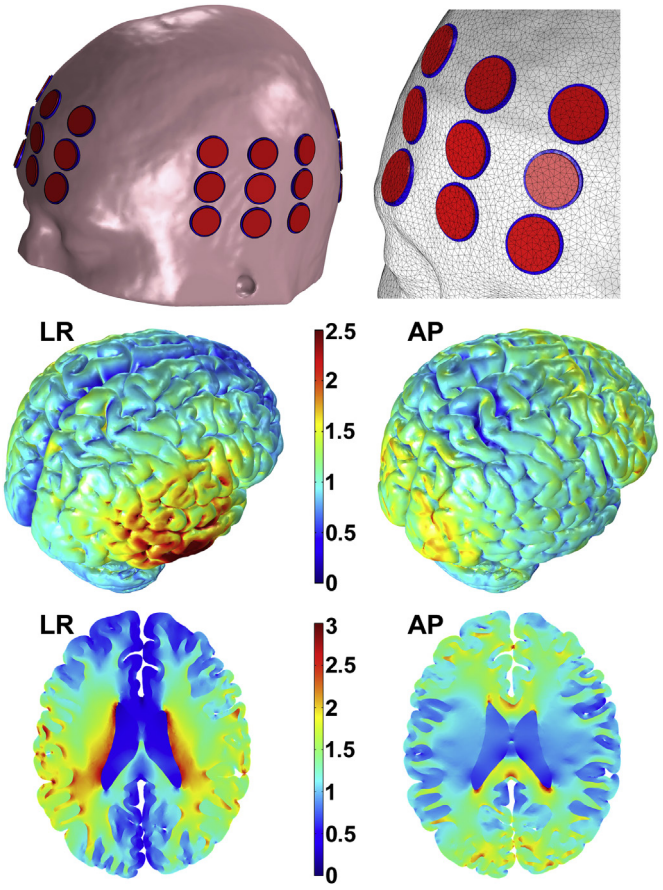


FIGURE 8 Top row: The scalp surface with transducer arrays in red and gel layers in blue. On the right, a close-up of the anterior array also shows the triangular surface mesh elements. Middle row: The magnitude of the electric field on the cortical surface. Bottom row: The magnitude of the electric field in an axial slice at the level of the ventricles. The electric field is expressed in V/cm.

in the model to mimic the presence of a tumor with a necrotic core placed in the WM near a lateral ventricle. The necrotic core has a diameter of 1.4 cm and is surrounded by a 3 mm active shell. Four transducer arrays that faithfully reproduce those used with the NovoTTF-100A device were placed on the scalp. Each array consists of nine interconnected transducers, capacitively coupled to the scalp. The frequency of the impressed current was set to 200 kHz, and the amplitude of the current through each transducer in an active array was set to 100 mA. Transducer arrays were activated in pairs: the left–right (LR) pair and the anterior–posterior (AP) pair. In addition to the influence of the complex shape of the tissue interfaces, the intensity of the electric field also depends on the electrical properties of the tissues. The values for the electrical conductivity and permittivity used in this model were obtained from the literature (see Table 1). The electric fields were calculated using the finite element method, as described previously.[19] The amplitude of the potential difference

TABLE 1 Electrical Properties of Tissues and Other Materials Used in this Study[19]

	Conductivity (S/m)	Relative Permittivity
Scalp	0.25	10,000
Skull	0.013	200
CSF	1.79	110
GM	0.25	3000
WM	0.12	2000
Tumor shell	0.24	2000
Tumor core	1.0	110
Gel	0.1	100
Transducer	0	10,000

applied between transducer arrays was 106 V for the AP pair and 75 V for the LR pair.

Modeling Results

The plots in the bottom rows of Figure 8 show the magnitude of the electric field on the cortical surface and in the brain. The distribution is noticeably nonuniform, with local high electric field regions (hotspots) arising far away from the transducers. Nonetheless, in general, the electric field is highest in the regions close to the active arrays and decreases slowly as a function of distance from these arrays. The electric field exceeds 1 V/cm over large areas of the slices shown and also over a large part of the brain in the inferior–superior direction, due to the large dimensions of the arrays (about 6.2 cm by 8.4 cm). In both configurations, the magnitude of the electric field exceeded 1 V/cm in more than 60% of the total brain volume (WM + GM), and it exceeded 2 V/cm in less than 5% of the total brain volume.

The observed nonuniform field distribution is due to tissue heterogeneity. At a boundary, the component of the electric field that is perpendicular to that boundary is enhanced in the low conductivity tissue and reduced in the high conductivity tissue, giving rise to a discontinuity in the electric field intensity. This effect is particularly visible near the ventricles in the LR configuration, where part of the WM–CSF boundary is perpendicular to the applied electric field (see bottom row in Figure 8). It is also visible near WM–GM interfaces under the transducers, but the effect is less marked because the difference between the conductivities of these two tissues is not as great as at the WM–CSF interface (see AP and LR fields). Note that the electric field in the ventricles is extremely low due to the high conductivity of CSF.

The electric field in and around the tumor is also affected by tissue heterogeneity.[20] In this model, the presence of a high conductivity necrotic core boosts

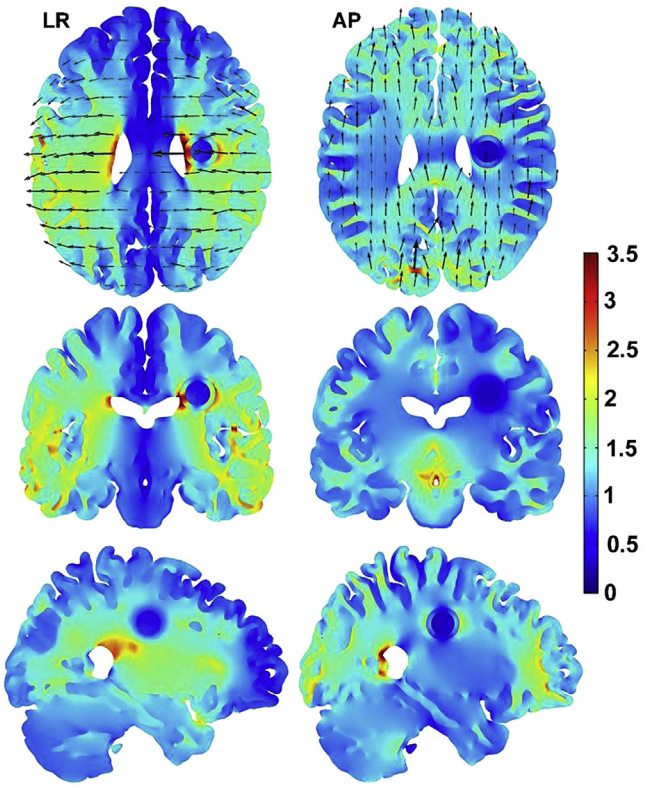


FIGURE 9 The magnitude of the electric field in axial (top row), coronal (middle row), and sagittal (bottom row) slices through the virtual lesion. The arrows in the axial slice indicate the direction of the alternating field. The electric field is expressed in V/cm.

the electric field in the surrounding tumor and WM (Figure 9). Again, the hotspots occur where the interfaces are perpendicular to the applied electric field. This implies that in the high electric field regions in the tumor, the field direction is always approximately perpendicular to the tissue boundaries. Also, the existence of these directional effects points to another advantage of applying the electric field in two or more directions: different directions may increase the field in different parts of the tumor. The plots in this figure also show that the electric field intensity at the tumor site is strongly influenced by the proximity to the ventricles. It is also influenced by the distance between the tumor and the active arrays, which suggests that a simple rule to place the arrays on the scalp is to minimize their distance to the tumor.

Future Modeling Developments

The computational model used to calculate the electric field inside the head is based on classical physics and well-known numerical methods, and therefore the results are thought to be reliable. Nevertheless, there is an uncertainty in the predicted values that is due mainly to the uncertainty in the dielectric properties of the tissues. Given the range of values reported in the literature, the uncertainty in the electric field could amount to about 50%. In the future, we plan to reduce this uncertainty in new head models by incorporating electrical conductivity data derived from diffusion tensor imaging (DTI). This is particularly important for calculating the electric fields within the tumor since the data available in the literature are scarce and so DTI data may provide better estimates of the conductivity in the necrotic core, the cancerous shell, and the edema that surrounds it. DTI does not provide information about the permittivity of the tissues, but this property has a small impact on the electric field in the frequency range of TTFields. Also, DTI data may be useful for image segmentation as it may provide a better distinction of the tumor borders and a better definition of the edema region.

IMAGING IN PATIENTS TREATED WITH TTFields THERAPY

TTFields represents a unique treatment for glioblastoma that does not fall into the traditional categories of surgery, radiation, or chemotherapy. Compared with conventional cytotoxic therapies intended to kill tumor cells, TTFields represent a novel anticancer treatment that inhibits cell division by interfering with the formation of the mitotic spindle and by affecting polar molecules from metaphase to telophase.[4,9] Interpretation of imaging changes caused by treatment with TTFields therefore relies on understanding the mechanism of action and familiarity with potentially variable patterns of treatment response as well as failure. This section will discuss standard response criteria, typical imaging changes seen with conventional and investigational therapies, and early experience with TTFields.

Response Criteria

Most clinical treatment decisions rely on changes in the size of the enhancing tumor(s): increasing size and/or number represents tumor progression and requires a change in treatment, while decreasing size and/or number represent tumor response. In 1990, in order to facilitate comparisons of treatments being tested in different clinical trials Macdonald et al.[21] proposed standardized response criteria that defined progressive disease (PD) as ≥25% increase in the size of enhancing tumor(s) (measured bidimensionally by taking the sum of the product of perpendicular diameters) or the presence of new enhancing tumor(s). Recognizing that newer treatments could induce transient increases in enhancing lesion(s) representing treatment related changes rather than tumor, the Macdonald criteria were updated in 2010 by

the Response Assessment in Neuro-Oncology (RANO) working group with several important additions.[22] First, an allowance was made for early treatment-related changes termed pseudoprogression. Any increase in size of enhancing lesion(s) ≤3 months after completion of radiation therapy located within the high-dose radiation field (80% isodose line) were no longer considered to represent PD, unless there was histopathologic evidence of tumor. New enhancing lesion(s) located outside the high-dose radiation field were still considered PD. After the first 3 months, RANO also defined recurrence as ≥25% increase of the enhancing lesions. Second, in recognition of progression of nonenhancing tumor in the setting of antiangiogenic therapy (e.g., bevacizumab), "significant" increases in T2/fluid attenuated inversion recovery (FLAIR) hyperintense signal became a new criterion for PD. This pseudoresponse, where rapid decrease in enhancing disease is not correlated with tumor response, is a well-described phenomenon with antiangiogenic therapies but unlikely to occur with treatments that do not directly affect the blood–brain barrier.

Pseudoprogression and Other Treatment-Related Changes

Pseudoprogression is a subacute treatment induced phenomenon that presents with new and/or increasing enhancing lesion(s) that spontaneously stabilize or resolve without further therapy. Thought to represent an inflammatory response to treatment,[23,24] pseudoprogression is most familiar in high-grade gliomas after treatment with radiation therapy and concomitant daily temozolomide as per Stupp et al.[25] Similar treatment-related changes with transient imaging worsening have been described with other older therapies,[26–28] as well as newer therapies—notably immune modulating agents.[29] Wolchok et al.[29] described treatment response and improved survival in patients with systemic metastatic melanoma treated with ipilimumab, despite an increased burden of enhancing lesions and the presence of new enhancing lesions. They therefore proposed new immune-related response criteria to better characterize these treatment-related changes and avoid overestimations of PD, and may also be applicable after treatment with TTFields, despite the more common use of RANO criteria.

Diagnosis of treatment-related changes often requires clinical and imaging follow-up to determine stability or resolution on subsequent scans, or repeat surgery with histopathologic confirmation of necrosis without tumor. Accurate determination of treatment-related changes versus tumor is necessary, because the two involve antithetical management. Treatment-related changes may require steroids or other therapy for relief of symptomatic edema and/or mass effect, or in unrelenting cases of radiation necrosis may also necessitate surgery or antiangiogenic therapy.[30–32] Patients should in many cases continue their current, probably effective therapy. In contrast, recurrent tumor requires discontinuation of current ineffective therapy and consideration of new therapy.

Advanced Imaging Techniques

The changes in size used by most response criteria to determine treatment response may occasionally lag behind alterations in tumor biology, where effective therapy may decrease metabolically active tumor that remains stable in size. In other situations, changes in size may be misleading when accelerated cell killing, treatment-related inflammatory changes, and blood–brain barrier disruption—as occurs with pseudoprogression—may induce an increase in enhancing lesions and edema to mimic worsening tumor. To complement traditional magnetic resonance imaging (MRI) sequences, advanced imaging techniques enable measurement of biological changes that do not depend upon changes in size. These technologies interrogate different aspects of tumor pathophysiology and may provide independent predictors of patient outcome, confirmation of suspected progression or treatment effects in clinical trials, as well as measurement of biological effects of investigational drugs. Popular techniques that are briefly discussed below include MR perfusion, MR spectroscopy, and positron emission tomography (PET).

Dynamic contrast enhanced (DCE) T1, dynamic susceptibility contrast T2*, and arterial spin labeling perfusion MR techniques provide information about tumor microvascularity, neoangiogenesis, and blood–brain barrier disruption. Multiple studies have shown utility in differentiating between recurrent tumor and radiation injury, including pseudoprogression. For example, while both recurrent tumor and radiation injury can show increases in size of enhancing and T2/FLAIR lesions, an increase in the relative cerebral blood volume, as measured by MR perfusion, is seen with recurrent tumors but not in radiation necrosis.[24,33–35] Increases in perfusion in the setting of tumor progression are related to increased microscopic vessel density from tumor neoangiogenesis. The enhancing lesions of radiation injury instead reflect increased leakiness with inflammatory mediators and blood–brain barrier disruption.

MR spectroscopy provides the semiquantification of metabolites that can characterize the composition of a lesion in the brain. This can aid in the diagnosis of radiation injury, which typically demonstrates low choline (a cell membrane marker) and possibly high lipid/lactate peaks (indicating necrosis). In contrast, tumors typically demonstrate high choline and low *N*-acetylaspartate (NAA), which may also be expressed as a choline/NAA ratio.[36,37]

PET uses metabolic tracers (most commonly, the glucose analogue 2-deoxy-2-(^{18}F)fluoro-D-glucose (FDG)) to study brain lesion metabolism. FDG is preferentially taken up by hypermetabolic tumor cells, and not by radiation injury. Although studies have suggested accuracy for distinguishing tumor recurrence from radiation changes, the high basal uptake of FDG in the brain that results in high background signal continues to represent a technical challenge.[38–40] Other nonFDG PET agents may prove to be more sensitive and specific to treatment changes, but these are still being investigated in clinical trials and not widely available.

Imaging in Patients Treated with NovoTTF Therapy: Early Experience

The unique mechanisms of action of TTFields and its effects on tumor biology present additional challenges to traditional response criteria based on changes in the size of the enhancing tumor. The electric fields interfere with the organized coalescence of the mitotic spindle and affects polar molecules from metaphase to telophase to prevent cell division at the G_1 or G_2/M checkpoints. As cells are required to be in active mitosis, any immune-mediated apoptosis induced by treatment may therefore be expected to require some time to occur.

Some patients may have a delay in radiographic response after treatment with TTFields. In a post hoc analysis of pilot and phase III trial data, Vymazal and Wong[41] reported that the median time to response was delayed by 5.2 months. This delay suggests that the relatively slow TTFields induced tumor cell death may be insufficient in symptomatic patients with rapidly progressive tumors. This is despite the fact that tumor cells with active mitoses are most susceptible to the electrical fields. While delayed, the response may be durable with a median response duration of 12.9 months.[41]

Some patients may also demonstrate transient increases in enhancing lesion size that do not represent tumor growth (Figure 10). This is similar to the pseudoprogression that is most familiar after standard radiation therapy and temozolomide chemotherapy. In these delayed responders with initial tumor growth, the median time to reversal of tumor growth was 4 months (95% CI, 2.3–7.4).[41] Villano et al.[42] described a patient who survived greater than 6 years using TTFields as monotherapy, where initial growth of the enhancing recurrent glioblastoma was followed by slow decrease. These observations are consistent with kinetic model stimulations in which tumor growth is maximum at 1 month followed by a reduction of tumor volume to 35% near 6.8 months, which is equivalent to a 50% decrease or partial response in bidimensional tumor measurement according to Macdonald or RANO criteria.[41]

Given the possibility for delayed treatment response, caution should be applied when interpreting worsening imaging results in patients treated with TTFields. New enhancing lesions within the treatment field should be considered possible tumor progression or treatment-related change (e.g., pseudoprogression), and investigated using additional or advanced imaging to confirm the diagnosis. Confirmation should be sought using advanced imaging, with the choice of MR perfusion, spectroscopy, PET/computed tomography (CT) or other techniques depending on the local expertise and available technology. New enhancing lesions outside the treatment field, however, should be considered tumor progression as per the RANO criteria.

Another consideration in evaluating response in patients treated with TTFields pertains to the treatment fields themselves. Treatment fields are nonuniform and different parts of the brain may receive different "doses" based on field strength and positioning.[19] Tumor progression may occur more frequently at the edges of the treatment fields due to lowered field strengths at the periphery.[20] It is important to recognize that treatment design, field strength, and cell size may all play a role in out-of-field recurrences. If recurrence occurs, new enhancing tumors outside of the tumor treatment field may be treated by adjusting the treatment field maps using the NovoTAL software.

CONCLUSIONS

Alternating electric fields represent a novel treatment strategy for patients with recurrent glioblastoma, and a viable alternative to conventional chemotherapies. This is because these fields interfere with tumor cell division at a different part of the cell cycle, rendering it unique to other oncolytic agents. In vitro, TTFields can be combined with specific chemotherapies to achieve at least an additive anticancer effect. The modeling study clearly demonstrates the need for patient-specific head models in order to predict the electric field as accurately as possible. Such models could be used in a retrospective study to establish the link between the electric field distribution and treatment outcome, both positive and negative. They could also be used prospectively for treatment planning. In this case, the positions of the transducer arrays and the current delivered through each pair could be used a priori to optimize the electric fields delivered to the tumor could be determined a priori. Typical optimization criteria would include high intensity and uniformity of the electric field in the area containing tumor and edema, as well as low field intensity in the surrounding brain tissues.[43,44]

Early clinical experience has demonstrated that the NovoTTF therapy-induced cell death may in some

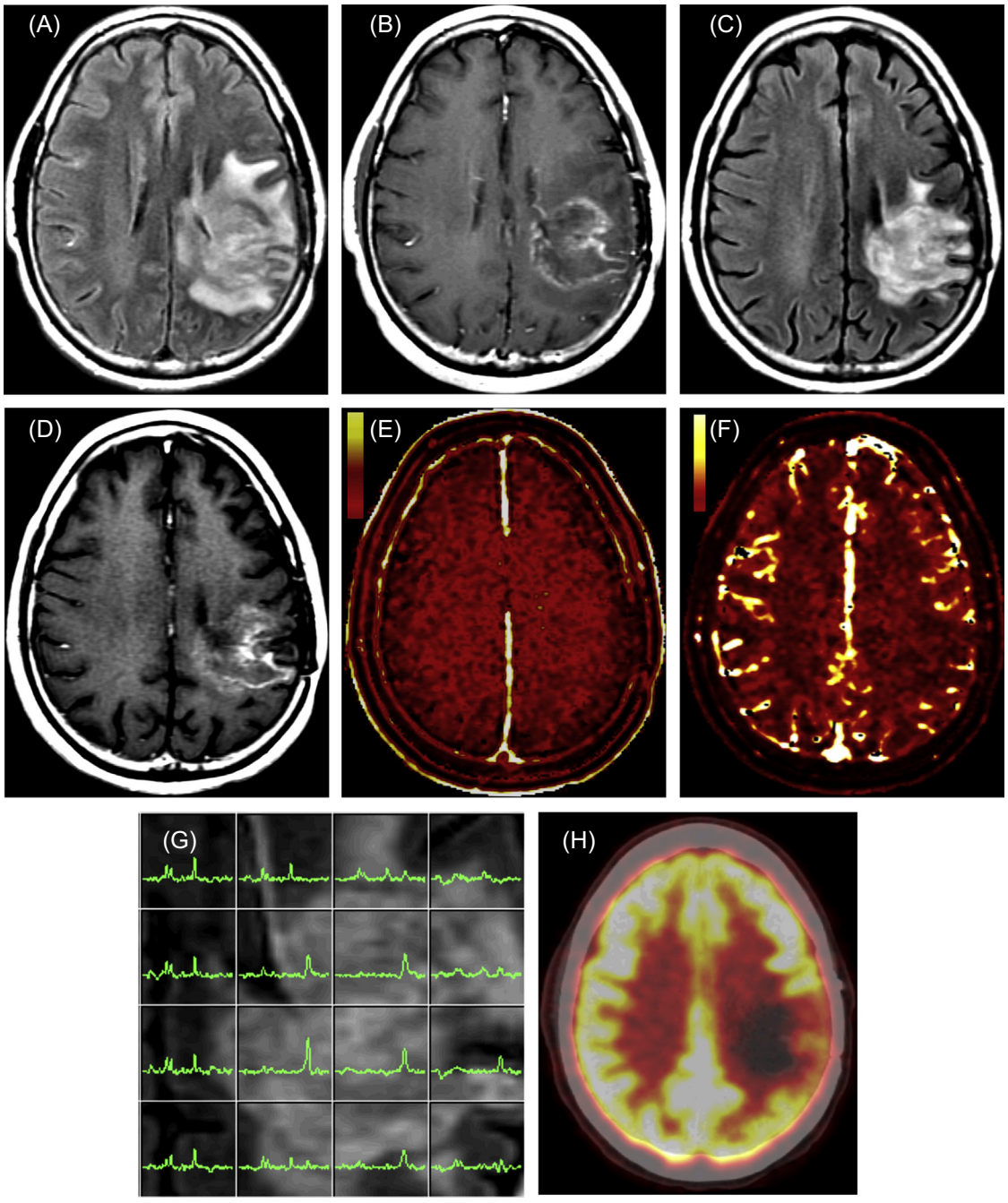


FIGURE 10 Patient with glioblastoma 18 months after completion of radiation therapy and temozolomide followed by adjuvant temozolomide, with bevacizumab added 5 months earlier for recurrent tumor. Axial FLAIR (A) and contrast T1-weighted (B) images demonstrate nonenhancing hyperintense and enhancing disease, respectively, indicating failure of treatment. The bevacizumab was discontinued and the patient began CPT-11 and NovoTTF-100A. Two months later, there is decreased nonenhancing (C) and enhancing (D) disease. DCE MRI perfusion shows no leakiness on the Ktrans map (E) or hyperperfusion on the plasma volume map (F) multivoxel MRI spectroscopy (G) demonstrates a lipid/lactate peak with decreased remaining metabolites, and FDG PET/CT (H) confirms absence of hypermetabolic activity. These are all consistent with absence of active high-grade tumor. CPT-11 was discontinued 17 months later due to fatigue and excessive number of cycles, while NovoTTF-100A was continued as monotherapy for another 5 months before another progression (not shown). BCNU (bis-chloroethylnitrosourea) was added to the treatment regimen for the patient who survived another 2 years.

patients result in a delayed treatment response or transient worsening before response. Since it may be unclear whether this worsening detected by conventional MRI is due to tumor progression or evolving treatment-related changes, advanced imaging techniques, and follow up should be performed to confirm the diagnosis whenever possible. Future experience will help determine the rate and time frame of these

treatment-related changes, and the optimal imaging strategy to diagnose treatment response or tumor progression.

References

1. Gutin PH, Wong ET. Noninvasive application of alternating electric fields in glioblastoma: a fourth cancer treatment modality. *ASCO 2012 Education Book*. 2012:126–131.
2. Zimmermann U, Vienken J. Electric field-induced cell-to-cell fusion. *J Membr Biol*. 1982;67(3):165–182.
3. Pohl HA. *Dielectrophoresis*. Cambridge University Press; 1978.
4. Kirson ED, Gurvich Z, Schneiderman R, et al. Disruption of cancer cell replication by alternating electric fields. *Cancer Res*. 2004;64(9):3288–3295.
5. Lee SX, Tunkyi A, Wong ET, Swanson KD. Mitosis interference of cancer cells by NovoTTF-100A causes decreased cellular viability. *Neuro Oncol*. 2012;14(suppl 6):vi9.
6. Lee SX, Wong ET, Swanson KD. Disruption of cell division within anaphase by tumor treating fields (TTFields) leads to immunogenic cell death. *Neuro Oncol*. 2013;15(suppl 3):iii66–iii67.
7. Zitvogel L, Apetoh L, Ghiringhelli F, Kroemer G. Immunological aspects of cancer chemotherapy. *Nat Rev Immunol*. 2008;8(1):59–73.
8. Postow MA, Callahan MK, Barker CA, et al. Immunologic correlates of the abscopal effect in a patient with melanoma. *N Engl J Med*. 2012;366(10):925–931.
9. Kirson ED, Dbaly V, Tovarys F, et al. Alternating electric fields arrest cell proliferation in animal tumor models and human brain tumors. *Proc Natl Acad Sci USA*. 2007;104(24):10152–10157.
10. Kirson ED, Schneiderman RS, Dbaly V, et al. Chemotherapeutic treatment efficacy and sensitivity are increased by adjuvant alternating electric fields (TTFields). *BMC Med Phys*. 2009;9:1.
11. Fonkem E, Wong ET. NovoTTF-100A: a new treatment modality for recurrent glioblastoma. *Expert Rev Neurother*. 2012;12(8):895–899.
12. Stupp R, Wong ET, Kanner AA, et al. NovoTTF-100A versus physician's choice chemotherapy in recurrent glioblastoma: a randomised phase III trial of a novel treatment modality. *Eur J Cancer*. 2012;48(14):2192–2202.
13. Wong ET, Lok E, Swanson KD, et al. Response assessment of NovoTTF-100A versus best physician's choice chemotherapy in recurrent glioblastoma. *Cancer Med*. 2014;3(3):592–602.
14. Hughes MA, Parisi M, Grossman S, Kleinberg L. Primary brain tumors treated with steroids and radiotherapy: low CD4 counts and risk of infection. *Int J Radiat Oncol Biol Phys*. 2005;62(5):1423–1426.
15. Mrugala MM, Engelhard HH, Dinh Tran D, et al. Clinical practice experience with NovoTTF-100A system for glioblastoma: the patient registry dataset (PRiDe). *Semin Oncol*. 2014 October;41(suppl 6):S4–S13. http://dx.doi.org/10.1053/j.seminoncol.2014.09.010. Epub 2014 Sep 16.
16. www.clinicaltrials.gov/ct2/show/NCT00916409.
17. Stupp R, Wong E, Scott C, et al. Interim analysis of the EF-14 trial: a prospective, multi-center trial of NovoTTF-100A together with temozolomide compared to temozolomide alone in patients with newly diagnosed GBM. *Neuro Oncol*. 2014;16(suppl 5):167.
18. Miranda PC, Mekonnen A, Salvador R, Ruffini G. The electric field in the cortex during transcranial current stimulation. *Neuroimage*. 2013;70:48–58.
19. Miranda PC, Mekonnen A, Salvador R, Basser PJ. Predicting the electric field distribution in the brain for the treatment of glioblastoma. *Phys Med Biol*. 2014;59(15):4137–4147.
20. Turner SG, Gergel T, Wu H, Lacroix M, Toms SA. The effect of field strength on glioblastoma multiforme response in patients treated with the NovoTTF-100A system. *World J Surg Oncol*. 2014;12:162.
21. Macdonald DR, Cascino TL, Schold Jr SC, Cairncross JG. Response criteria for phase II studies of supratentorial malignant glioma. *J Clin Oncol*. 1990;8(7):1277–1280.
22. Wen PY, Macdonald DR, Reardon DA, et al. Updated response assessment criteria for high-grade gliomas: response assessment in neuro-oncology working group. *J Clin Oncol*. 2010;28(11):1963–1972.
23. Linhares P, Carvalho B, Figueiredo R, Reis RM, Vaz R. Early pseudoprogression following chemoradiotherapy in glioblastoma patients: the value of RANO evaluation. *J Oncol*. 2013;2013:690585.
24. Hygino da Cruz Jr LC, Rodriguez I, Domingues RC, Gasparetto EL, Sorensen AG. Pseudoprogression and pseudoresponse: imaging challenges in the assessment of posttreatment glioma. *AJNR Am J Neuroradiol*. 2011;32(11):1978–1985.
25. Stupp R, Mason WP, van den Bent MJ, et al. Radiotherapy plus concomitant and adjuvant temozolomide for glioblastoma. *N Engl J Med*. 2005;352(10):987–996.
26. Watne K, Hager B, Heier M, Hirschberg H. Reversible oedema and necrosis after irradiation of the brain. Diagnostic procedures and clinical manifestations. *Acta Oncol*. 1990;29(7):891–895.
27. Graeb DA, Steinbok P, Robertson WD. Transient early computed tomographic changes mimicking tumor progression after brain tumor irradiation. *Radiology*. 1982;144(4):813–817.
28. de Wit MC, de Bruin HG, Eijkenboom W, Sillevis Smitt PA, van den Bent MJ. Immediate post-radiotherapy changes in malignant glioma can mimic tumor progression. *Neurology*. 2004;63(3):535–537.
29. Wolchok JD, Hoos A, O'Day S, et al. Guidelines for the evaluation of immune therapy activity in solid tumors: immune-related response criteria. *Clin Cancer Res*. 2009;15(23):7412–7420.
30. Boothe D, Young R, Yamada Y, Prager A, Chan T, Beal K. Bevacizumab as a treatment for radiation necrosis of brain metastases post stereotactic radiosurgery. *Neuro Oncol*. 2013;15(9):1257–1263.
31. Gonzalez J, Kumar AJ, Conrad CA, Levin VA. Effect of bevacizumab on radiation necrosis of the brain. *Int J Radiat Oncol Biol Phys*. 2007;67(2):323–326.
32. Wong ET, Huberman M, Lu XQ, Mahadevan A. Bevacizumab reverses cerebral radiation necrosis. *J Clin Oncol*. 2008;26(34):5649–5650.
33. Young RJ, Gupta A, Shah AD, et al. MRI perfusion in determining pseudoprogression in patients with glioblastoma. *Clin Imaging*. 2013;37(1):41–49.
34. Barajas RF, Chang JS, Sneed PK, Segal MR, McDermott MW, Cha S. Distinguishing recurrent intra-axial metastatic tumor from radiation necrosis following gamma knife radiosurgery using dynamic susceptibility-weighted contrast-enhanced perfusion MR imaging. *AJNR Am J Neuroradiol*. 2009;30(2):367–372.
35. Mangla R, Singh G, Ziegelitz D, et al. Changes in relative cerebral blood volume 1 month after radiation-temozolomide therapy can help predict overall survival in patients with glioblastoma. *Radiology*. 2010;256(2):575–584.
36. Schlemmer HP, Bachert P, Herfarth KK, Zuna I, Debus J, van Kaick G. Proton MR spectroscopic evaluation of suspicious brain lesions after stereotactic radiotherapy. *AJNR Am J Neuroradiol*. 2001;22(7):1316–1324.
37. Al-Okaili RN, Krejza J, Wang S, Woo JH, Melhem ER. Advanced MR imaging techniques in the diagnosis of intraaxial brain tumors in adults. *Radiographics*. 2006;26(suppl 1):S173–S189.
38. Hatzoglou V, Ulaner GA, Zhang Z, Beal K, Holodny AI, Young RJ. Comparison of the effectiveness of MRI perfusion and fluorine-18 FDG PET-CT for differentiating radiation injury from viable brain tumor: a preliminary retrospective analysis with pathologic correlation in all patients. *Clin Imaging*. 2013;37(3):451–457.

39. Ericson K, Kihlstrom L, Mogard J, et al. Positron emission tomography using 18F-fluorodeoxyglucose in patients with stereotactically irradiated brain metastases. *Stereotact Funct Neurosurg*. 1996;66(suppl 1):214–224.
40. Chao ST, Suh JH, Raja S, Lee SY, Barnett G. The sensitivity and specificity of FDG PET in distinguishing recurrent brain tumor from radionecrosis in patients treated with stereotactic radiosurgery. *Int J Cancer*. 2001;96(3):191–197.
41. Vymazal J, Wong ET. Response patterns of recurrent glioblastomas treated with tumor treating fields (TTFields). *Semin Oncol*. 2014 October;41(suppl 6):S14–S24. http://dx.doi.org/10.1053/j.seminoncol.2014.09.009. Epub 2014 Sep 16.
42. Villano JL, Williams LE, Watson KS, et al. Delayed response and survival from NovoTTF-100A in recurrent GBM. *Med Oncol*. 2013;30(1):338.
43. Dmochowski JP, Datta A, Bikson M, Su Y, Parra LC. Optimized multi-electrode stimulation increases focality and intensity at target. *J Neural Eng*. 2011;8(4):046011.
44. Ruffini G, Fox MD, Ripolles O, Miranda PC, Pascual-Leone A. Optimization of multifocal transcranial current stimulation for weighted cortical pattern targeting from realistic modeling of electric fields. *Neuroimage*. 2014;89:216–225.

CHAPTER

26

Applications of Stereotactic Radiosurgery in Neuro-Oncology

Kunal S. Patel[1], *Paul H. Chapman*[2], *Marc Bussiere*[3], *Jay S. Loeffler*[3], *Clark C. Chen*[1]

[1]Center for Theoretical and Applied Neuro-Oncology, Division of Neurosurgery, Moores Cancer Center, University of California, San Diego, CA, USA; [2]Department of Neurosurgery, Massachusetts General Hospital and Harvard Medical School, Boston, MA, USA; [3]Department of Radiation Oncology, Massachusetts General Hospital and Harvard Medical School, Boston, MA, USA

INTRODUCTION

The AANS/CNS/ASTRO definition of stereotactic radiosurgery is a technique that generates ionizing radiation (IR) in certain cases to inactivate or eradicate a defined target in the head or spine.[1] Conformal delivery is accomplished by converging multiple IR beams on the tumor and minimizing the radiation delivered by each unique beam (see Figure 1).[2] Because there is a significant fall-off in dose outside of the treatment target, the target receives maximal effect while the radiation to surrounding nontarget tissue is limited. Although most often performed in a single session, radiosurgery can involve up to five sessions,[1] with marginal doses ranging between 11 and 70 Gy.[3,4] In contrast, multistage radiosurgery is a scheme in which a different region of the target is irradiated in each session, separated by 3–12 months.[5]

FOUNDATIONS OF RADIOSURGERY

Target Size

As the size of the target increases, incidental radiation to the surrounding nontarget tissues also increases. Therefore, the maximal tolerable dose in radiosurgery is a function of tumor size.[6] To limit radiation-associated morbidity to <20%, the RTOG 90-05 study recommends doses of 24, 18, and 15 Gy for lesions less than or equal to 2, 3, and 4 cm, respectively.[7] Because of this trade-off, radiosurgery of lesions >4 cm cannot use an effective dose without an unacceptable level of radiation toxicity.

Target Location

The risk of radiosurgical morbidity varies with the region irradiated.[8] For instance, 12 Gy irradiation of the basal ganglia/thalamus region is associated with a 20% morbidity, whereas the same dose to the cerebral cortex is associated with a <1% morbidity. Therefore, it is important to identify regions at high risk in radiosurgery, which can be safely irradiated by radiotherapy.

Radiosurgery of lesions near the ventricular system is associated with an increased rate of hydrocephalus. For example, 10% of patients with vestibular schwannomas develop communicating hydrocephalus after radiosurgery.[9] Although this is likely to be due to tumor necrosis leading to cerebrospinal fluid (CSF) malabsorption, the true etiology of this hydrocephalus is unclear.

Radiation to the internal carotid artery (ICA), as in radiosurgery to cavernous sinus lesions, involves a risk of ICA stenosis. In the thousands of pituitary/cavernous sinus lesions treated with radiosurgery, only a few cases of ICA stenosis have been described.[10–13] Radiation exposure to the ICA should be limited, especially in cases in which ICA patency is already compromised by tumor compression. Although there is no consensus on how best to avoid this, recommendations have included doses of <50% of the ICA vessel diameter[12] or <30 Gy.[14] In contrast, no instances of venous complications (scarring or thrombosis) after radiation have been reported.

Handbook of Neuro-Oncology Neuroimaging, Second Edition
http://dx.doi.org/10.1016/B978-0-12-800945-1.00026-4

© 2016 Elsevier Ltd. All rights reserved.

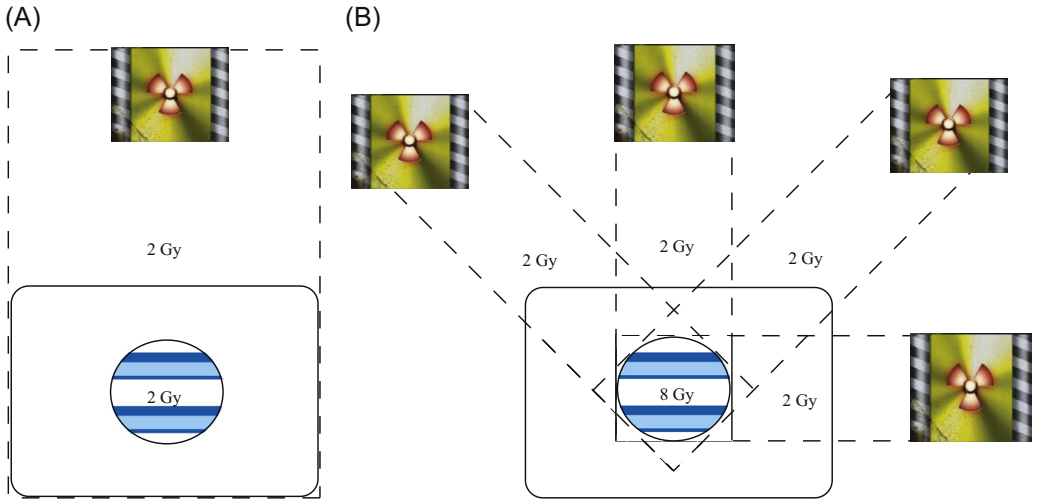


FIGURE 1 **Radiotherapy and radiosurgery.** (A) In radiotherapy, radiation is delivered to both normal and cancer tissues. The therapeutic efficacy is derived from the increased DNA repair capacity of normal cells relative to tumor cells when repeatedly exposed to small doses of radiation. In the illustration, the dashed line represents the radiation field. The solid square represents the intracranial space. The striped circle represents the tumor volume. In this theoretic illustration, both the tumor and the normal tissue receive 2 Gy of ionization radiation. (B) In radiosurgery, multiple, nonparallel radiation beams are converged on the tumor volume. The radiation received by the normal tissue in each beam path is minimal relative to the point of beam convergence. In this illustration, the dashed line represents the radiation field. The solid square represents the intracranial space. The striped circle represents the tumor volume. The tumor volume receives 8 Gy of radiation from four radiation sources, whereas the surrounding tissues receive significantly lower doses of radiation.

Target Proximity to Cranial Nerves

Proximity of the target tissue to radiosensitive cranial nerves increases the risk of cranial neuropathy. Cranial nerves II and VIII are especially radiosensitive. Therefore, radiosurgery may not be the optimal choice in cases in which the target is near these radiosensitive nerves.[3,15–17]

The optic apparatus is also sensitive to radiation. This is affected by previous damage to the nerve, the total volume affected, and the dose level administered.[18,19] Optic neuropathy has been reported at rates of 0–3% with doses of 8 Gy to the optic apparatus[12,20] and in select cases in which even higher doses were given.[17] These data suggest that radiation to any part of the optic apparatus exceeding 10 Gy should be avoided.

It is difficult to determine the radiosensitivity of cranial nerve VIII because it is almost always irradiated in the context of an acoustic neuroma. It is impossible to differentiate between damage from the tumor and damage from radiation. Studies with quantitative audiologic testing have reported hearing loss of >20 dB after radiosurgery (12–17 Gy),[15,16,21] generally consistent with studies using more qualitative audiologic assessments.[22–24] These data suggest that the risk of hearing loss via cranial VIII injury after radiosurgery for acoustic neuroma, with a marginal dose of 12 Gy, is approximately 60%.

Other cranial nerves are less radiosensitive. Whereas doses of 15–40 Gy to the cavernous sinus lead to a 10–15% risk of cranial nerve III–VI neuropathy, this is prevented with doses of <15 Gy.[20] In addition, there is only a <1% incidence of cranial nerve VII neuropathy with doses of 11–15 Gy in radiosurgery for acoustic neuroma.[25] Last, cranial nerve IX–XI neuropathy rates of 0–2% have been reported after radiosurgery with doses of 8–12 Gy.[26–29] These data show that higher radiation doses can be applied to lesions close to the less radiosensitive cranial nerves.

DELIVERY OF RADIOSURGERY

Photon and Proton Radiosurgery

Both photons and protons can be used to transfer energy in radiosurgery. Photons are discrete aliquots of energy produced in gamma- or X-irradiation. Whereas both gamma- and X-rays consist of photons, their photons are produced in different ways. Gamma-rays, used in Gamma Knife radiosurgery, use photons created by radioactive decay, whereas X-rays, used in linear accelerator (LINAC) radiosurgery, use photons created by LINACs. Because both Gamma Knife and LINAC radiosurgery use photon-based IR, their clinical outcomes are similar.[30]

Protons are created by removing an electron from an atom and accelerating the remaining proton in the magnetic field of a cyclotron or a synchrocyclotron.[31] Relative to photon radiosurgery, proton radiosurgery is new. Access to proton radiosurgery remains limited, although the number of centers is rapidly growing. As of this writing, there are 49 operating proton radiotherapy centers worldwide with 30 more planned. As for the older, photon-based radiosurgery platforms, there are hundreds of Gamma Knife and LINAC radiosurgery centers.[32]

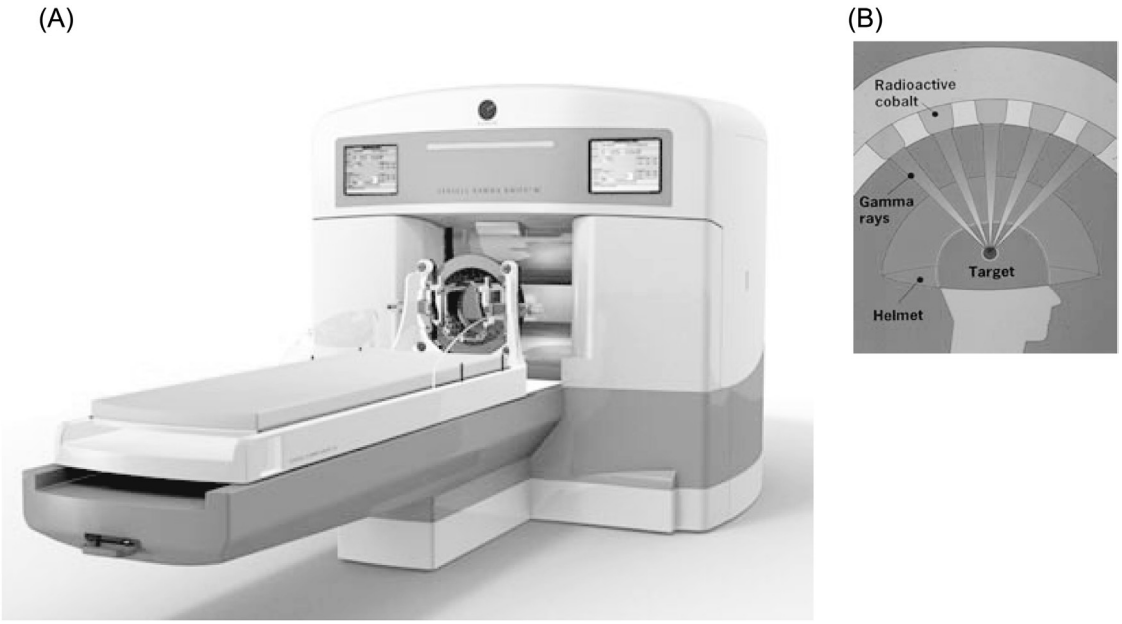


FIGURE 2 **Gamma Knife radiosurgery.** (A) The Gamma Knife device consists of an 18,000-kg shield surrounding a hemispheric array of 201 cobalt-60 sources. (B) The sources are oriented such that all 201 beams converge at a single point (also known as the isocenter of the Gamma Knife).

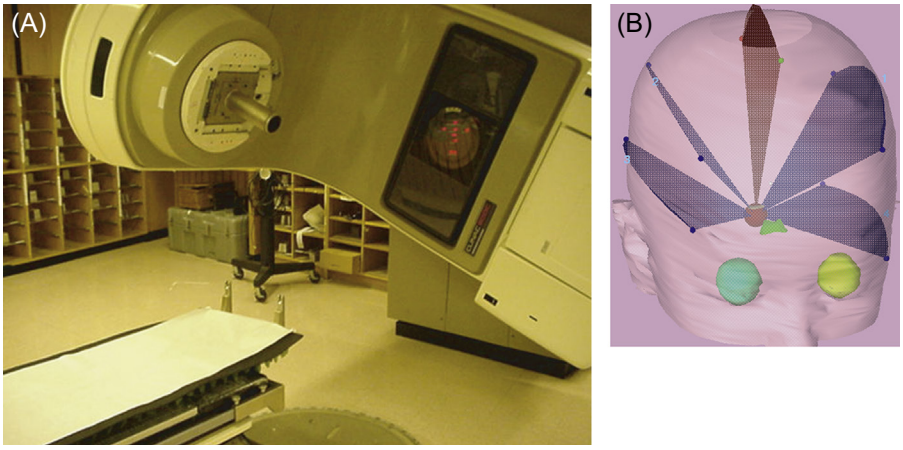


FIGURE 3 **LINAC radiosurgery.** (A) A LINAC apparatus. The source of radiation can be rotated relative to the treatment couch. (B) Schematic depiction of multiple non-coplanar arcs of radiation that intersect at the target volume.

Gamma Knife Radiosurgery

The Gamma Knife system is used to administer photon-based radiosurgery. First, a stereotactic head frame is placed. An 18,000-kg shield surrounding an array of 201 cobalt-60 sources (see Figure 2) produces beams that converge at the isocenter of the Gamma Knife, producing an accuracy of 0.1–1 mm.[33]

LINAC Radiosurgery

LINAC also delivers photon-based radiosurgery. Like in Gamma Knife, a stereotactic head frame is placed. Instead of using an array of fixed cobalt sources, LINAC radiosurgery utilizes multiple non-coplanar arcs of radiation that intersect at the target volume (see Figure 3). However, this radiation involves X-rays instead of the gamma-rays used in Gamma Knife. LINAC-based devices also achieve an accuracy of 0.1–1 mm.[33]

CyberKnife Radiosurgery

The CyberKnife platform combines a mobile LINAC with an image-guided robotic system to deliver photon-based radiosurgery (see Figure 4). Unlike LINAC or Gamma Knife, the placement of a stereotactic head frame is not required with CyberKnife. Prior to treatment, computed tomography (CT) images are taken to analyze the relationship between the patient's bony anatomy and the target volume. During treatment, the patient



FIGURE 4 **CyberKnife radiosurgery.** The CyberKnife device combines a mobile linear accelerator with an image-guided robotic system. During the treatment, patient movement is monitored with minimal time lag by the system's low-dose X-ray cameras. These planar images are compared to digitally reconstructed radiographs derived from the pretreatment CT scan. Based on calculations derived from these comparisons, the computer-controlled robotic arm maneuvers the mobile linear accelerator in response to any changes in patient position during treatment. 1: Diagnostic X-ray tubes; 2: Mobile LINAC; 3: Camera; 4: Couch; 5: Robotic arm.

is monitored by X-ray cameras. Comparing this image to that of the pretreatment scan, the mobile LINAC is automatically moved in response to patient movement, leading to an accuracy of <1 mm.[34]

Proton Beam Radiosurgery

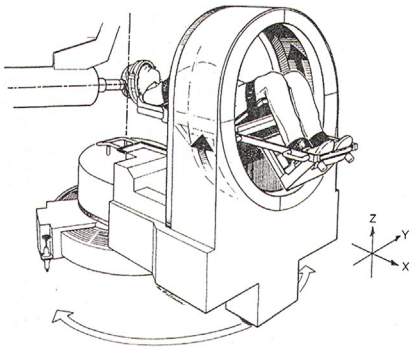
There are several devices designed specifically for proton radiosurgery. With the STAR device (stereotactic alignment for radiosurgery apparatus; see Figure 5), a head frame attached to a couch apparatus is placed and can be rotated relative to a fixed beam portal. Alternatively, the beam source can be mobilized on a rotating gantry (see Figure 6). Using both methods, accuracy is approximately 0.1 mm.

Only select patients should be referred for proton beam radiosurgery, as the number of facilities is limited. Proton radiosurgery is not indicated for small (<10 cc in volume), spherically shaped lesions that are: (1) not in proximity to critical anatomic structures, (2) in eloquent regions, (3) in deep subcortical areas, or (4) in previously radiated volumes. For these cases, equal results can be obtained with photon-based radiosurgery.

NEUROIMAGING AND RADIOSURGERY

Computerized Tomography

CT imaging facilitates accurate radiosurgical planning in two ways: (1) by providing anatomic visualization of the target plus surrounding areas and (2) by conversion to electron-density maps. The latter is possible because the intensity of each voxel on the CT image is proportional to the electron density of the tissues



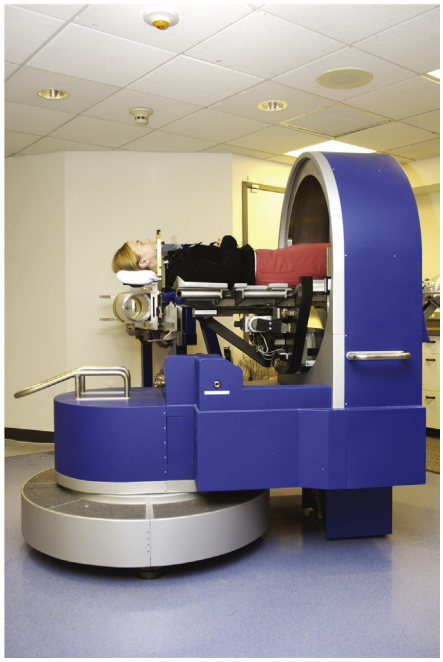


FIGURE 5 **The STAR (stereotactic alignment radiosurgery) system at the MGH Northeast Proton Therapy Center.** An isocentric patient-positioning device is designed to rotate the patient around a fixed proton-beam line. The unit has five degrees of freedom, three linear and two rotational. Using these axes of movement, the patient is positioned such that the target lesion is at the center of the beam isocenter.

imaged. Use of electron-density maps allows for definition of isodose lines. Without this, the actual dose delivered can differ from the desired dose by up to 20%.[35]

Magnetic Resonance Imaging

Magnetic resonance (MR) imaging is superior in the delineation of soft tissue structures, especially for targets in the cranial base, and therefore provides considerable information beyond CT imaging in regard to target delineation. However, MR imaging is subject to several sources of error that contribute to image distortion. Examples include gradient field nonlinearity (<1 mm distortion after computation correction)[36] and resonance offset (up to 2 mm distortion).[37–39] In addition, motion artifact from patient movement during the prolonged image acquisition period can compromise accuracy of the image. Owing to these effects, the localization error of MR as stand-alone imaging is approximately 2–3 mm[40–43], although errors as high as 8 mm have been reported.[44] This uncertainty fails to meet the radiosurgical standard of <1 mm established by the American Society of Therapeutic Radiology and Oncology.[45–47] Another disadvantage of MR imaging relative to CT is the lack of electron density information, which leads to suboptimal radiosurgical planning.[48] Despite the superior anatomic visualization of MR imaging, various distortion effects, lack of electron-density information, and motion artifact makes its stand-alone use in radiosurgery prohibitive.

CT–MR Image Integration

The combination of information from MR and CT imaging produces radiosurgery plans superior to those derived from each modality alone.[49–52] Algorithms have been designed to add the geometric accuracy of CT imaging (due to the lack of spatial distortion effects) to the diagnostic accuracy of MR imaging (due to enhanced soft-tissue resolution). The first method is termed prospective image coregistration.[46] In this method, the patient is placed in a stereotactic head frame to minimize motion artifacts. Fiduciary markers are placed to provide a spatial relationship between the patient's anatomy and the head frame as well as to serve as coregistration points between the two imaging modalities. This leads to an accuracy to 1–2 mm.[46] Another method is retrospective coregistration. Instead of acquiring the images in a predetermined manner, the two imaging modalities are integrated by aligning anatomic landmarks.[53] Various computation techniques have been used to carry out this alignment and result in an uncertainty of 2–3 mm.[46,54,55]

Functional Imaging

Definition of target tumor volumes is based on contrast-enhancing volumes. Therefore, non-contrast-enhancing tumors are incompletely treated. Various functional imaging techniques have been evaluated alongside traditional imaging to better identify non-contrast-enhancing tumor targets for radiosurgery.

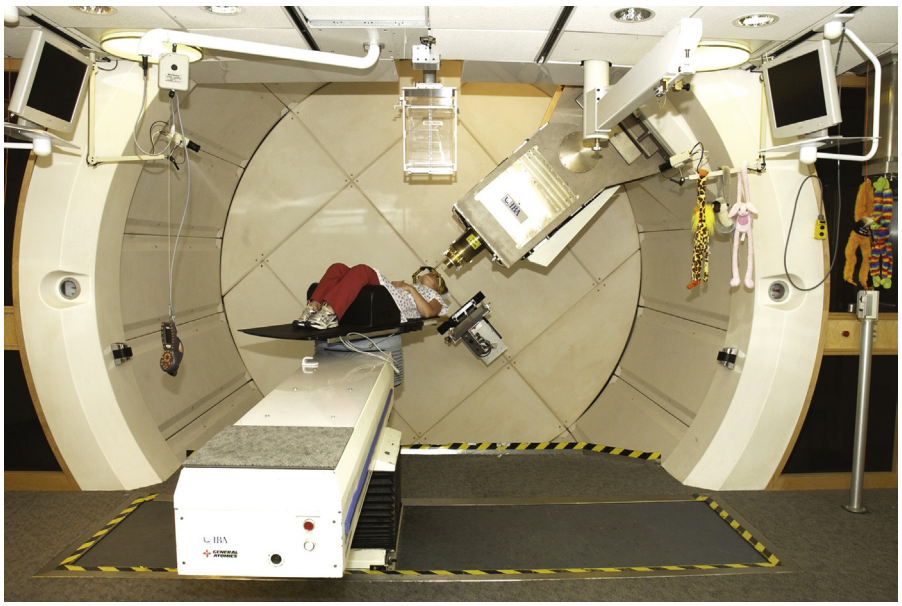


FIGURE 6 **The proton gantry system at the MGH Northeast Proton Therapy Center.** An isocentric gantry with a mobile proton-beam source is used in conjunction with a robotic patient-positioning treatment couch. The robotic unit has six degrees of freedom, three linear and three rotational. The patient is positioned to place the target lesion at the center of the beam isocenter.

MR spectroscopy takes advantage of differences in metabolites between tumor and nontumor tissue to identify neoplastic tissue.[56] MR spectroscopy has been reported to identify abnormalities outside the volume delineated by contrast enhancement on MR imaging in 88% of patients with malignant glioma.[57] Furthermore, untreated MR spectroscopy abnormalities are associated with decreased median survival.[58–63] These data suggest that MR spectroscopy abnormalities outside the contrast-enhancing region should be considered in the treatment of gliomas.

MR diffusion-weighted imaging takes advantage of differences in water molecule diffusion to calculate measures such as the apparent diffusion coefficient (ADC). Because malignant gliomas distort the cerebral architecture, and therefore water molecule diffusion, abnormal ADC can predict the presence of tumor. ADC maps may be helpful in identification of non-contrast-enhancing tumor volume.

CLINICAL APPLICATIONS OF RADIOSURGERY

Radiotherapy and radiosurgery are treatment options for patients with brain tumors who are poor surgical candidates. The applications of radiosurgery in neuro-oncology include the treatment of cerebral metastases, meningiomas, acoustic neuromas, pituitary adenomas, and gliomas.

Cerebral Metastases

The current treatment for cerebral metastases is surgery, chemotherapy, and whole-brain radiation therapy (WBRT), and it lengthens median survival only by 2–4 months.[64]

The discovery that metastases resistant to WBRT are not resistant to radiosurgery[65,66] led to a variety of studies investigating the use of radiosurgery plus WBRT for treatment of cerebral metastases.[30,67–69] The local control rate at the 1-year follow-up was superior, with WBRT plus radiosurgery at 82–92% relative to WBRT alone at 0–71% ($p < 0.05$), suggesting that radiosurgery is an effective means of augmenting WBRT in preventing intracranial tumor growth. In addition, patients with WBRT plus radiosurgery had better neurologic outcomes as well as decreased steroid use at 6 months follow-up.[30] However, although local control is improved by the combination therapy, patient survival remains unaffected, as patients die from progression of the primary disease. No statistically significant difference in short-term toxicity was observed between WBRT with and without radiosurgery. In these patients, the cognitive impairment associated with WBRT >7 years after treatment is avoided, as they rarely achieve such survival levels.[70,71]

TABLE 1 Randomized Controlled Trials Evaluating Radiosurgery versus Radiosurgery Plus WBRT as Treatment for Intracranial Metastases

Study	Patients	Overall Survival (m)	Local Control	Freedom from New Metastasis
Chougule et al.[67]	37/31	No difference	87%/91% ($p > 0.05$)	Not reported
JROSG99-1[174]	67/65	7.5/8.0	72%/89% ($p = 0.002$)	64%/42% ($p = 0.003$)
Chang et al.[80a]	30/28	Not reported	27%/73% ($p < 0.001$)	Not reported
EORTC 22952-26001[79]	100/99	10.9/10.7	69%/81% ($p = 0.04$)	52% vs 67% ($p = 0.023$)

WBRT – whole-brain radiation therapy.
[a]*This trial was stopped early due to neurocognitive dysfunction in patients with combination therapy.*

The addition of temozolomide or erlotinib to WBRT plus radiosurgery in non-small-cell lung cancer did not improve survival (6.3 vs 13.4 months).[72] In fact, central nervous system progression, new metastases, and toxicity were less common with WBRT/radiosurgery alone, suggesting that the addition of chemotherapy potentially worsens outcomes.

Radiosurgery is also used without WBRT for treatment of cerebral metastases. Most studies suggest radiosurgery alone is as effective as radiosurgery plus WBRT (see Table 1).[67,69,73–79] The EORTC 22952-26001 trial found no change in median survival (10.9 vs 10.7 months) between radiosurgery and radiosurgery/WBRT. This lack of difference in overall survival was also seen in the Aoyama study, in which the median survival time was similar in both groups (7.5 vs 8.0 months). However, there is a discrepancy in the differences in local control rates. An earlier study reported comparable 1-year local control rates (87 vs 91%) between radiosurgery alone and WBRT plus radiosurgery.[67] Studies following this have yielded different data. The JROSG99-1 and the NCT00548756 trials both showed a significantly worse 1-year local control rate with radiosurgery alone (72% vs 89%, $p = 0.002$, and 27% vs 73%, $p < 0.001$, respectively). Similarly, in the EORTC 22952-26001 trial, the 2-year relapse rate at initial sites (31% vs 19%, $p = 0.04$) was lower in the WBRT/radiosurgery arm versus radiosurgery alone.[79] This study also found that death by intracranial progression was decreased with combination therapy (44% vs 28%). These data suggest that although local control may be worse than in combination therapy, there is no difference in overall survival. In addition, the discrepancy in local control rates suggests that differences in the administration or dosing regimens of radiosurgery may influence outcomes.

In patients with numerous metastases, WBRT may be more feasible than radiosurgery on each individual lesion.

However, the JLGK0901 study showed no significant difference in overall survival (10.8 months in 531 patients with 2–4 metastatic lesions vs 10.8 months in 208 patients with 5–10 metastatic lesions, p = 0.78) or radiosurgery-induced adverse events (9% vs 9%, p = 0.89), suggesting that stand-alone radiosurgery can be effective for patients with multiple metastases.[78]

Unlike WBRT, radiosurgery cannot treat micrometastases, and therefore the risk of new intracranial metastases is higher in patients with radiosurgery alone. The JROSG99-1 study found that freedom from new intracranial metastases was 82% with combined treatment versus 48% with radiosurgery alone.[73] Similarly, the EORTC 22952-26001 trial showed higher relapse rates at new sites (48% vs 33%, p = 0.02) with radiosurgery alone.[79] However, with salvage therapy (either in the form of WBRT or radiosurgery) patient survival is comparable to that achieved by up-front combined WBRT/radiosurgery.[76]

Whereas multiple studies have shown that survival is comparable with and without WBRT, the EORTC 22952-26001 trial also showed no difference in functional independence with WBRT/radiosurgery versus radiosurgery alone. This study reported no difference in time to WHO performance status of greater than 2 (9.5 vs 10.0 months, p = 0.71).[79] Furthermore, one randomized control trial comparing WBRT/radiosurgery versus radiosurgery alone, NCT00548756,[80] was stopped early as there was a 96% probability that patients with WBRT/radiosurgery were significantly more likely to decline in neurocognitive function. McDuff et al. analyzed the results of studies comparing radiosurgery alone versus combination therapy and concluded that WBRT may have deleterious effects on neurocognitive functioning.[81] Avoiding WBRT in favor of sequential radiosurgery may be useful in select patients, given the cognitive impairment associated with WBRT.[70]

Overall, several critical issues remain unsolved in the clinical application of radiosurgery for patients with intracranial metastases. The differences in data on local control raises questions as to factors contributing to the discrepancy. These factors should be studied to define guidelines for how radiosurgery is delivered. Equally important, the long-term efficacy of radiosurgery in patients with metastasis needs to be quantified. This issue will be increasingly important as the overall survival of cancer patients continues to increase.

Meningiomas

Given the slow growth rate of meningiomas (0.8–5 cc/year),[82] the treatment of choice for stable asymptomatic meningiomas is observation. In contrast, the treatment of choice for symptomatic or progressively enlarging meningiomas is resection.

Radiotherapy and radiosurgery are alternatives to surgery. In contrast to surgery, by which symptomatic relief is achieved by tumor debulking, the goal of radiation treatment is to slow tumor growth, although tumor shrinkage is possible.[26,27,83–87] Long-term results (see Table 2) suggest that radiotherapy and radiosurgery are comparably efficacious in controlling the growth of meningiomas, while also yielding comparable rates of posttreatment complications. Conventional radiotherapy achieves local control rates of 76–98% at 5 years and 77–96% at 10 years, with complication rates between 3.3 and 10%.[83–86] For radiosurgery, local control rates are 93–98% at 5 years and 79–98% at 10 years, with complications ranging between 1.3 and 10%.[26,27,87–90] These data suggest that the efficacy of radiosurgery in the initial treatment of meningiomas is comparable to radiotherapy or Simpson grade 1 resection.[91] Additionally, with low complication rates, radiosurgery is a feasible method for treating meningiomas. Therefore, for meningiomas located in regions where adequate resection cannot be safely achieved (skull-base meningiomas or those involving the cavernous sinus), primary radiosurgery or radiotherapy should be pursued.[92]

Radiosurgery can also be used for recurrent meningiomas as its efficacy is similar to that of radiosurgery for primary meningiomas.[90] However, for surgically accessible meningiomas in certain areas (convexity, falx, and parasagittal region), complete resection should be the treatment of choice, as radiotherapy and radiosurgery of these regions are associated with significant peritumoral edema and neurologic morbidity.[3]

TABLE 2 Studies Evaluating Radiosurgery as Treatment for Meningiomas

Study[a]	Patients	Marginal Dose (Median)	Follow-Up	Actuarial Control	Complication Rate
Kobayashi et al.[87]	54	14.5 Gy	5 years	89%	5.5%
Eustacchio et al.[26]	121	13 Gy	6 years	98%	3.3%
Kreil et al.[175]	200	12 Gy	8 years	98%	2.5%
Santacroce et al.[88]	4565	14 Gy	8 years	93%	6.6%
Starke et al.[89]	255	14 Gy	6.5 years	86%	10%
Kondziolka et al.[90]	290	15 Gy	9 years	91%	3.1%

[a]*Only studies with >5 year median follow-up are included.*

Acoustic Neuromas

Surgical resection has been the treatment of choice for acoustic neuromas, but in recent years, radiosurgery has emerged as an alternative for small acoustic neuromas (<3 cm).

TABLE 3 Studies Evaluating Radiosurgery as Treatment for Acoustic Neuroma

Study	Patients	Marginal Dose	Follow-Up	Actuarial Control	Loss of Hearing[a]	CN V Neuropathy	CN VII Neuropathy
Andrews et al.[30]	69	12 Gy	2 years	98% (5 years)	67%	5%	2%
Lundsford et al.[176]	829	13 Gy	n/a	97% (12 years)	23–50%	3.1%	1%
Hasegawa et al.[177]	73	15 Gy	11 years	87% (10 years)	63%	5%	5%
Chung et al.[178]	195	13 Gy	3 years	95% (7 years)	40%	1%	1%
Chung et al.[95]	21	12 Gy	4 years	91% (4 years)	100%	0%	0%
Milligan et al.[96]	22	12 Gy	6 years	82% (5 years)	53%	14%	8%
Carlson et al.[97]	44	12 Gy	9 years	n/a	82%	n/a	n/a

[a]*Percentage of patients who retained serviceable hearing after treatment.*

Ten-year follow-up has been reported for 827 patients, indicating a local control rate of 97%.[25] Other studies have reported local control rates of 82–98% at 5–10 year follow-up (see Table 3).[9,24,93–97] Complications of radiosurgery include facial neuropathy (1–8%), trigeminal neuropathy (1–14%), loss of serviceable hearing (40–100%), and hydrocephalus (10–15%). Other than the risk of hydrocephalus, which does not exist with surgical resection, outcomes of surgical resection and radiosurgery are comparable.[22,23]

However, hearing appears to be better preserved by stereotactic radiotherapy relative to radiosurgery. Serviceable hearing after treatment was lost in 67% of patients after radiosurgery but only 19–29% of patients after radiotherapy.[9,24,93] Similarly, hearing loss defined by a pure tone average elevation of >20 dB was found in 69% of patients after radiosurgery and 21% of patients after radiotherapy.[15,16]

Whereas surgery should continue to be the treatment for symptomatic, large acoustic neuromas, for smaller tumors (<3 cm), radiotherapy or radiosurgery should be considered and with this the increased preservation of hearing with stereotactic radiotherapy.

Pituitary Adenomas

Given the benign nature of the pituitary adenomas, therapeutic intervention is limited to lesions that are (1) symptomatic via hormonal secretion or mass effect or (2) increasing in size. The role of radiosurgery therefore differs by subtype of pituitary adenoma.

Prolactinomas

The primary treatment for prolactinomas is a dopamine agonist. Surgery, radiotherapy, and radiosurgery are reserved for patients who fail to tolerate or respond to medical therapy. Surgery is the treatment of choice after medical therapy because surgery provides the fastest relief of hormonal hypersecretion and therefore symptomatology.[98–100]

TABLE 4 Efficacy of Surgery, Radiation Therapy, and Radiosurgery in the Treatment of Pituitary Adenomas

Pathology	Surgery	Radiotherapy	Radiosurgery
Prolactinoma[a]	65%	30–50%	30–50%
GH secreting[a]	60%	60–80%[b]	42%
ACTH secreting[a]	80%	80%	50–80%
Nonfunctioning	90%	55%	78%

The numbers shown indicate the percentage of patients with >5 year progression-free survival.
[a]*Time to endocrine normalization considerably shorter after radiosurgery.*
[b]*Using GH < 10 ng/ml as endocrine normalization.*

Poor surgical candidates may be treated with radiotherapy or radiosurgery. Without surgery or medical therapy, prolactin normalization was achieved in 30–50% of the patients 7–11 years (mean 7.3 years) after radiotherapy (45–50 Gy).[101–103] Radiation-induced pituitary hormone deficits ranged between 20% and 30%.[103] Radiosurgery has efficacy comparable to that of radiotherapy. Short-term prolactin normalization has been shown in 20–60% of patients[104] and long-term (>5 years) normalization has been reported in 41% of patients (16–35 Gy) (see Table 4).[105] Surgery improves the efficacy of radiotherapy or radiosurgery, as higher tumor volume is a risk factor for remission after radiation treatment.[105] The risk of postradiosurgery pituitary deficits is comparable those of to surgery and radiotherapy. The rate of these hormonal deficits increases with time (20% at 2 years and 30% at 5 years); they are most commonly a single hormone deficiency and are more common in patients with suprasellar tumor extension.[105,106] Because pituitary deficits can occur years after treatment, long-term follow-up is necessary.[105]

Growth Hormone-Secreting Adenomas

The consensus definition for the posttreatment remission of acromegaly is a serum IGF-1 level in the age- and sex-adjusted normal range and a random growth hormone (GH) level of <1 ng/ml.[107] Medical therapy with

somatostatin analogues normalizes serum IGF-1 levels in up to 2/3 of patients with acromegaly. However, side effects associated with medical treatment, such as abdominal pain, diarrhea, or constipation, combined with its high cost, make long-term medical therapy tenuous.[108]

Because surgery has the fastest rate of endocrine correction, it remains the first-line treatment for GH-secreting adenomas. Transsphenoidal resection for GH-secreting adenomas achieves a remission rate of 60%.[109,110] Recurrence rates are <10%[110] and complications include CSF leak (1–5%), septal perforation (0–5%), and pituitary insufficiency (20–30%).

Radiotherapy is an alternative option for poor surgical candidates or patients with recurrence. Following radiotherapy, 60–80% of treated patients achieved GH <10 ng/ml after 10 years.[111–113] As in prolactinomas, the therapeutic effects of surgery and radiation are additive.[114]

Radiosurgery is another option for poor surgical candidates or patients with recurrence. Owing to the variability in remission definitions and radiosurgery planning, the literature on radiosurgery for GH-secreting adenomas shows extremely variable success rates.[104,115] However, using the consensus criteria, Castinetti et al. reported a remission rate of 42% in patients with long-term follow-up (>5 years) (see Table 4).[105] This study reported a mean time to remission of 4 years, which was longer than for other secretory pituitary adenomas (2 years).[105] Complications included pituitary deficits (21%), cranial nerve palsy (4%), and trigeminal neuralgia (1%). These results suggest comparable disease control by radiosurgery and radiotherapy, although the effect of radiosurgery is faster. Like with prolactinomas, rates of pituitary deficits are similar to radiotherapy and necessitate long-term follow-up as new pituitary deficits can occur years after treatment.

Adrenocorticotropic Hormone-Secreting Adenomas

As long-term medical therapy is associated with serious side effects, surgery remains the treatment for adrenocorticotropic hormone (ACTH)-secreting pituitary adenomas. Success with surgery of ACTH-secreting adenomas has been reported in 60% of macroadenomas along with recurrence rates of 30%[116] and mortality and morbidity rates of 0.5–2% and 3.3–9.3%, respectively.[117–120]

The role of radiotherapy or radiosurgery is reserved for poor surgical candidates or patients with recurrence. Endocrine normalization is comparable between radiotherapy and radiosurgery. Within 2 years after radiotherapy in patients with incomplete resection, 80% achieve endocrine normalization.[121,122] Radiosurgery is associated with a success rate of 50–80% (see Table 4).[104,105] However, the median time to endocrine normalization was 1–3 months shorter with radiosurgery than with radiotherapy.[3,104,123] Rates of pituitary deficits related to radiotherapy or radiosurgery appear comparable at around 30%.[106] Recurrence after remission can occur as late as 8 years postradiosurgery. Because both recurrence and pituitary deficits can develop years after treatment, long-term follow-up is necessary.

Nonfunctioning Adenomas

Surgery is also the primary intervention for nonfunctioning adenomas. Eighty-four to eighty-seven percent of patients with visual deficits experience restitution of normal visual function postoperatively.[99,124] Given the effectiveness of surgery, postoperative radiation of residual tumor is not necessary.[125]

Outcomes are similar for both radiotherapy and radiosurgery in the treatment of recurrent nonfunctioning adenomas. Progression-free survival has been reported to be 96–97% at 5 years, 78% at 10 years, and 76% at 20 years.[126,127] Tumor recurrence occurs around 5 years posttreatment, but can occur even 10 years after treatment.[128] Rates of pituitary deficits are similar to those of secreting pituitary adenomas (20–40%).[106,127,128] The risk increases over time, reported as 23–31% at 5 years and 47–51% at 10 years.[127] The chance of recurrence and pituitary deficits years posttreatment necessitates long-term follow-up.

Another indication for radiotherapy or radiosurgery is up-front therapy in asymptomatic but enlarging nonfunctional adenomas in poor surgical candidates. For these patients, the 10-year progression-free survival is approximately 55%.[129] In contrast, 75% of the patients who underwent both surgery and radiation therapy remain disease free at 10 years.[129] This additive effect of surgery to radiation therapy is similar to that seen with secretory pituitary adenomas.[105,106,127,130]

With the exception of prolactinomas, for which dopamine agonists remain the mainstay of therapy, surgery is the treatment of choice for pituitary adenomas. Radiation therapy and radiosurgery represent treatment options for residual/recurrent tumors or as primary treatment in poor surgical candidates. Radiotherapy and radiosurgery appear equally efficacious in inducing endocrine normalization of secretory adenomas. Regardless of secretory status, risk of recurrence and pituitary deficits require long-term follow-up.

Gliomas

Grade I gliomas

Because WHO grade I gliomas can be cured with complete excision, surgery remains the primary therapy. For example, complete removal of pilocytic astrocytomas produces a 100% progression-free survival at 10 years.[131] In cases of recurrent or unresectable tumor,

radiotherapy and radiosurgery are similarly efficacious, with an 85–95% progression-free survival at 5 years.[132–134] In addition, progression after the first radiation treatment can be controlled with a second treatment.[132] Single high-dose radiation of tumors located in select regions, such as the hypothalamic region, may be associated with significant toxicity.[8] Therefore, the choice of radiotherapy versus radiosurgery is based on tumor location.

Grade II gliomas

Surgical resection is the first-line therapy for WHO grade II gliomas. With complete resection alone, the 10-year survival rate is around 68%.[135] The 10-year survival falls to 30–50% with subtotal resections (<50% tumor mass resected), but with adjuvant radiotherapy, the 5-year survival rate increases to 43–75%.[136–139]

Two randomized controlled trials have shown that a radiation dose around 50 Gy is the optimal radiation dose for the treatment of low-grade gliomas. There was no difference in 5-year overall and progression-free survival between 45- versus 59.4-Gy[140] and 50.4- versus 64.8-Gy[141] dose groups. In addition, although there was no survival benefit in patients given immediate postoperative radiotherapy, these patients had an improved 5-year progression-free survival (44% vs 37%; $p < 0.05$). These results suggest that radiotherapy is effective as both an up-front and a salvage modality.

Whereas clinical experience for radiosurgery as up-front treatment for low-grade glioma has been reported as similar to that of radiotherapy (progression-free survival of 37–54% at 5 years, 37% at 10 years),[133,142] the diffusely infiltrating nature of the disease and the large volume irradiated renders radiosurgery suboptimal as up-front therapy in most cases.

Grade III and IV gliomas

Surgery remains the therapy of choice for the treatment of malignant gliomas. Radiotherapy with a cumulative dose of 60 Gy prolongs survival (median 12 months) in patients with malignant glioma.[143–145] Although survival is further improved with dose escalation to 90 Gy using proton irradiation (median 18.6 months), almost all patients develop radiation necrosis and neurologic deterioration.[146] Therefore, the current regimen of radiotherapy limits the cumulative dose to 60 Gy.

Recurrence in malignant gliomas often occurs within 2 cm of the enhancing margin of the primary tumor[147] and rarely recurs with metastatic disease.[148] Therefore, supplementing standard adjuvant radiotherapy plus chemotherapy with radiosurgery to the tumor margins could serve as a potential boost therapy. Although several retrospective[149–154] and prospective reports[155,156] suggested that this boost therapy increased patient survival, a randomized controlled trial found no advantage in median survival (13.6 vs 13.5 months; $p = 0.5711$).[157,158] This lack of improvement in survival is supported by multiple prospective studies.[159–161] Reanalysis of the initial retrospective series revealed that the benefit found was probably due to selection bias.[150,162,163] Similar to results on survival, there were no differences in quality of life (via the Spitzer index) or rate of cognitive decline (via Mini Mental Status Exam) with and without radiosurgery boost therapy.[158] Last, radiosurgery boost was associated with increased toxicity, including cerebral edema and radiation necrosis.[158] Overall, radiosurgery boost has not been shown to improve survival or quality of life, yet it involves an increased risk of toxicity.

Although there is no randomized controlled trial on the use of radiosurgery as salvage therapy for recurrent malignant gliomas, several prospective[164–166] and retrospective[167–169] studies have demonstrated a median survival of 6–12 months. Similarly, tumor control with salvage radiosurgery has not been compared to alternative strategies, but has been associated with an 80–85% local or marginal failure and median progression-free survival of 3.75–4 months[165,166,168] as well as radiosurgery-associated side effect rates of 22–35%.[164,168] Although there is potential use of radiosurgery as salvage therapy for recurrent malignant glioma, this awaits confirmation by randomized trial.

Radiation therapy is effective in the treatment of grade I, II, III, and IV gliomas. However, the specific role of radiosurgery in the treatment of gliomas remains poorly defined.

Radiation-Associated Tumor Formation

Radiation-associated tumor formation has been described after radiation treatment, whereby initial tumor formation can occur between 6 and 32 years after radiation.[170–172] The risk of tumor formation 30 years after radiotherapy is 0.8–1.9%.[170–172] Radiosurgery should have a lower risk of tumor formation because of the smaller irradiated area and lower dose administered to nontarget areas. To date, only nine cases of radiosurgery-associated tumor formation have been reported.[173] Although the incidence is very low, the possibility of radiosurgery-associated tumor formation warrants communication of this risk to patients before treatment as well as posttreatment surveillance.

CONCLUSION

Radiosurgery is an important treatment option in neuro-oncology. Radiosurgery is effective in the treatment of cerebral metastases, meningiomas, acoustic neuromas, pituitary adenomas, and gliomas. However, the exact role of radiosurgery in the therapeutic paradigm

of each disease is unclear. Understanding of the specific clinical contexts to which radiosurgery is better suited than radiotherapy may serve to optimize its role in neuro-oncology.

References

1. American Association of Neurological Surgeons CoNS and American Society for Therapeutic Radiation Oncology. *AANS/CNS/ASTRO Definition of Stereotactic Radiosurgery*; 2009.
2. Leksell L. The stereotaxic method and radiosurgery of the brain. *Acta Chir Scand*. 1951;102:316–319.
3. Chan A, Cardinale R, Loeffler J. Stereotactic irradiation. In: Perez C, Brady L, Halperin E, Schmidt-Ullrich R, eds. *Principles and Practice of Radiation Oncology*. Philadelphia: Lippincott Williams & Wilkins; 2004:410–428.
4. Duma C, Jacques D, Kopyov O. The treatment of movement disorders using Gamma Knife stereotactic radiosurgery. *Neurosurg Clin N Am*. 1999;10(2):379–389.
5. Pollock BE, Lunsford LD. A call to define stereotactic radiosurgery. *Neurosurgery*. 2004;55(6):1371–1373.
6. Shiau CY, Sneed PK, Shu HK, et al. Radiosurgery for brain metastases: relationship of dose and pattern of enhancement to local control. *Int J Radiat Oncol Biol Phys*. 1997;37(2):375–383.
7. Shaw E, Scott C, Souhami L, et al. Single dose radiosurgical treatment of recurrent previously irradiated primary brain tumors and brain metastases: final report of RTOG protocol 90-05. *Int J Radiat Oncol Biol Phys*. 2000;47(2):291–298.
8. Flickinger JC, Kondziolka D, Lunsford LD, et al. Development of a model to predict permanent symptomatic postradiosurgery injury for arteriovenous malformation patients. Arteriovenous Malformation Radiosurgery Study Group. *Int J Radiat Oncol Biol Phys*. 2000;46(5):1143–1148.
9. Sawamura Y, Shirato H, Sakamoto T, et al. Management of vestibular schwannoma by fractionated stereotactic radiotherapy and associated cerebrospinal fluid malabsorption. *J Neurosurg*. 2003;99(4):685–692.
10. Lim YL, Leem W, Kim TS, Rhee BA, Kim GK. Four years' experiences in the treatment of pituitary adenomas with gamma knife radiosurgery. *Stereotact Funct Neurosurg*. 1998;70(suppl 1):95–109.
11. Muramatsu J, Yoshida M, Shioura H, et al. Clinical results of LINAC-based stereotactic radiosurgery for pituitary adenoma. *Nippon Igaku Hoshasen Gakkai Zasshi*. 2003;63(5):225–230.
12. Pollock BE, Nippoldt TB, Stafford SL, Foote RL, Abboud CF. Results of stereotactic radiosurgery in patients with hormone-producing pituitary adenomas: factors associated with endocrine normalization. *J Neurosurg*. 2002;97(3):525–530.
13. Abeloos L, Levivier M, Devriendt D, Massager N. Internal carotid occlusion following gamma knife radiosurgery for cavernous sinus meningioma. *Stereotact Funct Neurosurg*. 2007;85(6):303–306.
14. Shin M, Kurita H, Sasaki T, et al. Stereotactic radiosurgery for pituitary adenoma invading the cavernous sinus. *J Neurosurg*. 2000;93(suppl 3):2–5.
15. Ito K, Kurita H, Sugasawa K, Mizuno M, Sasaki T. Analyses of neuro-otological complications after radiosurgery for acoustic neurinomas. *Int J Radiat Oncol Biol Phys*. 1997;39(5):983–988.
16. Sakamoto T, Shirato H, Sato N, et al. Audiological assessment before and after fractionated stereotactic irradiation for vestibular schwannoma. *Radiother Oncol*. 1998;49(2):185–190.
17. Stafford SL, Pollock BE, Leavitt JA, et al. A study on the radiation tolerance of the optic nerves and chiasm after stereotactic radiosurgery. *Int J Radiat Oncol Biol Phys*. 2003;55(5):1177–1181.
18. Leber KA, Bergloff J, Langmann G, Mokry M, Schrottner O, Pendl G. Radiation sensitivity of visual and oculomotor pathways. *Stereotact Funct Neurosurg*. 1995;64(suppl 1):233–238.
19. Leber KA, Bergloff J, Pendl G. Dose-response tolerance of the visual pathways and cranial nerves of the cavernous sinus to stereotactic radiosurgery. *J Neurosurg*. 1998;88(1):43–50.
20. Tishler RB, Loeffler JS, Lunsford LD, et al. Tolerance of cranial nerves of the cavernous sinus to radiosurgery. *Int J Radiat Oncol Biol Phys*. 1993;27(2):215–221.
21. Paek SH, Chung HT, Jeong SS, et al. Hearing preservation after gamma knife stereotactic radiosurgery of vestibular schwannoma. *Cancer*. 2005;104(3):580–590.
22. Karpinos M, Teh B, Zeck O, et al. Treatment of acoustic neuroma: stereotactic radiosurgery vs. microsurgery. *Int J Radiat Oncol Biol Phys*. 2002;54(5):1410–1421.
23. Pollock B, Lunsford L, Kondziolka D, et al. Outcome analysis of acoustic neuroma management: a comparison of microsurgery and stereotactic radiosurgery. *Neurosurgery*. 1995;36(1):215–224.
24. Andrews DW, Suarez O, Goldman HW, et al. Stereotactic radiosurgery and fractionated stereotactic radiotherapy for the treatment of acoustic schwannomas: comparative observations of 125 patients treated at one institution. *Int J Radiat Oncol Biol Phys*. 2001;50(5):1265–1278.
25. Lunsford LD, Niranjan A, Flickinger JC, Maitz A, Kondziolka D. Radiosurgery of vestibular schwannomas: summary of experience in 829 cases. *J Neurosurg*. 2005;102(suppl):195–199.
26. Eustacchio S, Trummer M, Fuchs I, Schrottner O, Sutter B, Pendl G. Preservation of cranial nerve function following Gamma Knife radiosurgery for benign skull base meningiomas: experience in 121 patients with follow-up of 5 to 9.8 years. *Acta Neurochir Suppl*. 2002;84:71–76.
27. Kreil W, Luggin J, Fuchs I, Weigl V, Eustacchio S, Papaefthymiou G. Long term experience of gamma knife radiosurgery for benign skull base meningiomas. *J Neurol Neurosurg Psychiatry*. 2005;76(10):1425–1430.
28. Muthukumar N, Kondziolka D, Lunsford LD, Flickinger JC. Stereotactic radiosurgery for jugular foramen schwannomas. *Surg Neurol*. 1999;52(2):172–179.
29. Zhang N, Pan L, Dai JZ, Wang BJ, Wang EM, Cai PW. Gamma knife radiosurgery for jugular foramen schwannomas. *J Neurosurg*. 2002;97(suppl 5):456–458.
30. Andrews DW, Scott CB, Sperduto PW, et al. Whole brain radiation therapy with or without stereotactic radiosurgery boost for patients with one to three brain metastases: phase III results of the RTOG 9508 randomised trial. *Lancet*. 2004;363(9422):1665–1672.
31. Lawrence E, Edlefsen N. On the production of high speed protons. *Science*. 1930;72:376.
32. Sisterson J. Particle Therapy Co-Operative Group (PTCOG). *Particles Newsletter*. 2005:35.
33. Schwartz M. Stereotactic radiosurgery: comparing different technologies. *CMAJ*. 1998;158(5):625–628.
34. Kuo JS, Yu C, Petrovich Z, Apuzzo ML. The CyberKnife stereotactic radiosurgery system: description, installation, and an initial evaluation of use and functionality. *Neurosurgery*. 2003;53(5):1235–1239; discussion 1239.
35. Battista J, Rider W, Van DJ. Computed tomography for radiotherapy planning. *Int J Radiat Oncol Biol Phys*. 1980;6(1):99–107.
36. Chang H, Fitzpatrick J. A technique for accurate magnetic resonance imaging in the presence of field inhomogeneities. *IEEE Trans Med Imaging*. 1992;11:319–329.
37. Sumanaweera TS, Adler Jr JR, Napel S, Glover GH. Characterization of spatial distortion in magnetic resonance imaging and its implications for stereotactic surgery. *Neurosurgery*. 1994;35(4):696–703; discussion 703–694.
38. Sumanaweera T, Glover G, Song S, Adler J, Napel S. Quantifying MRI geometric distortion in tissue. *Magn Reson Med*. 1994;31:40–47.
39. Sumanaweera T, Glover G, Binford T, Adler J. MR susceptibility misregistration correction. *IEEE Trans Med Imaging*. 1993;12:251–259.

40. Walton L, Hampshire A, Forster DM, Kemeny AA. A phantom study to assess the accuracy of stereotactic localization, using T1-weighted magnetic resonance imaging with the Leksell stereotactic system. *Neurosurgery*. 1996;38(1):170–176; discussion 176–178.
41. Orth RC, Sinha P, Madsen EL, et al. Development of a unique phantom to assess the geometric accuracy of magnetic resonance imaging for stereotactic localization. *Neurosurgery*. 1999;45(6):1423–1429; discussion 1429–1431.
42. Kondziolka D, Dempsey PK, Lunsford LD, et al. A comparison between magnetic resonance imaging and computed tomography for stereotactic coordinate determination. *Neurosurgery*. 1992;30(3):402–406; discussion 406–407.
43. Bednarz G, Downes MB, Corn BW, Curran WJ, Goldman HW. Evaluation of the spatial accuracy of magnetic resonance imaging-based stereotactic target localization for gamma knife radiosurgery of functional disorders. *Neurosurgery*. 1999;45(5):1156–1161; discussion 1161–1153.
44. Walton L, Hampshire A, Forster DM, Kemeny AA. Stereotactic localization with magnetic resonance imaging: a phantom study to compare the accuracy obtained using two-dimensional and three-dimensional data acquisitions. *Neurosurgery*. 1997;41(1):131–137; discussion 137–139.
45. Shaw E, Kline R, Gillin M, et al. Radiation Therapy Oncology Group: radiosurgery quality assurance guidelines. *Int J Radiat Oncol Biol Phys*. 1993;27(5):1231–1239.
46. Khoo VS, Dearnaley DP, Finnigan DJ, Padhani A, Tanner SF, Leach MO. Magnetic resonance imaging (MRI): considerations and applications in radiotherapy treatment planning. *Radiother Oncol*. 1997;42(1):1–15.
47. Consensus statement on stereotactic radiosurgery quality improvement. The American Society for Therapeutic Radiology and Oncology, Task Force on Stereotactic Radiosurgery and the American Association of Neurological Surgeons, Task Force on Stereotactic Radiosurgery. *Int J Radiat Oncol Biol Phys*. 1994;28(2):527–530.
48. Schad LR, Gademann G, Knopp M, Zabel HJ, Schlegel W, Lorenz WJ. Radiotherapy treatment planning of basal meningiomas: improved tumor localization by correlation of CT and MR imaging data. *Radiother Oncol*. 1992;25(1):56–62.
49. Ten Haken RK, Thornton Jr AF, Sandler HM, et al. A quantitative assessment of the addition of MRI to CT-based, 3-D treatment planning of brain tumors. *Radiother Oncol*. 1992;25(2):121–133.
50. Shuman WP, Griffin BR, Haynor DR, et al. The utility of MR in planning the radiation therapy of oligodendroglioma. *AJR Am J Roentgenol*. 1987;148(3):595–600.
51. Shuman WP, Griffin BR, Haynor DR, et al. MR imaging in radiation therapy planning. Work in progress. *Radiology*. 1985;156(1):143–147.
52. Just M, Rosler HP, Higer HP, Kutzner J, Thelen M. MRI-assisted radiation therapy planning of brain tumors–clinical experiences in 17 patients. *Magn Reson Imaging*. 1991;9(2):173–177.
53. Pelizzari CA, Chen GT, Spelbring DR, Weichselbaum RR, Chen CT. Accurate three-dimensional registration of CT, PET, and/or MR images of the brain. *J Comput Assist Tomogr*. 1989;13(1):20–26.
54. Judnick JW, Kessler ML, Fleming T, Petti P, Castro JR. Radiotherapy technique integrates MRI into CT. *Radiol Technol*. 1992;64(2):82–89.
55. Evans PM, Gildersleve JQ, Morton EJ, et al. Image comparison techniques for use with megavoltage imaging systems. *Br J Radiol*. 1992; 65(776):701–709.
56. Nelson SJ, Cha S. Imaging glioblastoma multiforme. *Cancer J*. 2003;9(2):134–145.
57. Pirzkall A, McKnight TR, Graves EE, et al. MR-spectroscopy guided target delineation for high-grade gliomas. *Int J Radiat Oncol Biol Phys*. 2001;50(4):915–928.
58. Chan A, Nelson S. Use of 1H magnetic resonance spectroscopic imaging in managing recurrent glioma patients undergoing radiosurgery. In: *ISMRM Workshop Proceedings on MR of Cancer*. 2002:227.
59. Nelson SJ, Graves E, Pirzkall A, et al. In vivo molecular imaging for planning radiation therapy of gliomas: an application of 1H MRSI. *J Magn Reson Imaging*. 2002;16(4):464–476.
60. McKnight TR, von dem Bussche MH, Vigneron DB, et al. Histopathological validation of a three-dimensional magnetic resonance spectroscopy index as a predictor of tumor presence. *J Neurosurg*. 2002;97(4):794–802.
61. Graves EE, Nelson SJ, Vigneron DB, et al. Serial proton MR spectroscopic imaging of recurrent malignant gliomas after gamma knife radiosurgery. *AJNR Am J Neuroradiol*. 2001;22(4):613–624.
62. Graves EE, Nelson SJ, Vigneron DB, et al. A preliminary study of the prognostic value of proton magnetic resonance spectroscopic imaging in gamma knife radiosurgery of recurrent malignant gliomas. *Neurosurgery*. 2000;46(2):319–326; discussion 326–318.
63. Chan AA, Lau A, Pirzkall A, et al. Proton magnetic resonance spectroscopy imaging in the evaluation of patients undergoing gamma knife surgery for Grade IV glioma. *J Neurosurg*. 2004;101(3):467–475.
64. Agboola O, Benoit B, Cross P, et al. Prognostic factors derived from recursive partition analysis (RPA) of Radiation Therapy Oncology Group (RTOG) brain metastases trials applied to surgically resected and irradiated brain metastatic cases. *Int J Radiat Oncol Biol Phys*. 1998;42(1):155–159.
65. Alexander 3rd E, Moriarty TM, Davis RB, et al. Stereotactic radiosurgery for the definitive, noninvasive treatment of brain metastases. *J Natl Cancer Inst*. 1995;87(1):34–40.
66. Brown PD, Brown CA, Pollock BE, Gorman DA, Foote RL. Stereotactic radiosurgery for patients with "radioresistant" brain metastases. *Neurosurgery*. 2002;51(3):656–665; discussion 665–657.
67. Chougule P, Burton-Williams M, Saris S. Randomized treatment of brain metastasis with gamma knife radiosurgery. *Int J Radit Oncol Biol Phys*. 2000;48:114.
68. Kondziolka D, Patel A, Lunsford LD, Kassam A, Flickinger JC. Stereotactic radiosurgery plus whole brain radiotherapy versus radiotherapy alone for patients with multiple brain metastases. *Int J Radiat Oncol Biol Phys*. 1999;45(2):427–434.
69. Mehta MP, Tsao MN, Whelan TJ, et al. The American Society for Therapeutic Radiology and Oncology (ASTRO) evidence-based review of the role of radiosurgery for brain metastases. *Int J Radiat Oncol Biol Phys*. 2005;63(1):37–46.
70. Surma-aho O, Niemela M, Vilkki J, et al. Adverse long-term effects of brain radiotherapy in adult low-grade glioma patients. *Neurology*. 2001;56(10):1285–1290.
71. Taphoorn MJ, Klein M. Cognitive deficits in adult patients with brain tumours. *Lancet Neurol*. 2004;3(3):159–168.
72. Sperduto PW, Wang M, Robins HI, et al. A phase 3 trial of whole brain radiation therapy and stereotactic radiosurgery alone versus WBRT and SRS with temozolomide or erlotinib for non-small cell lung cancer and 1 to 3 brain metastases: Radiation Therapy Oncology Group 0320. *Int J Radiat Oncol Biol Phys*. 2013;85(5):1312–1318.
73. Aoyama H, Shirato H, Nakagawa K. Interim report of the JROSG99-1 multi-institutional randomized trial, comparing radiosurgery alone vs. radiosurgery plus whole brain irradiation for 1-4 brain metastases [abstract]. In: *Proceedings from the 40th Annual Meeting of the American Society of Clinical Oncology*. 2004:108S.
74. Lutterbach J, Cyron D, Henne K, Ostertag CB. Radiosurgery followed by planned observation in patients with one to three brain metastases. *Neurosurgery*. 2003;52(5):1066–1073; discussion 1073–1064.
75. McDermott M, Sneed P. Radiosurgery in metastaic brain cancer. *Neurosurgery*. 2005;57(5):45–53.
76. Sneed PK, Lamborn KR, Forstner JM, et al. Radiosurgery for brain metastases: is whole brain radiotherapy necessary? *Int J Radiat Oncol Biol Phys*. 1999;43(3):549–558.

77. Yamamoto M, Serizawa T, Shuto T, et al. Stereotactic radiosurgery for patients with multiple brain metastases (JLGK0901): a multi-institutional prospective observational study. *Lancet Oncol*. 2014;15(4):387–395.
78. Aoyama H, Shirato H, Tago M, et al. Stereotactic radiosurgery plus whole-brain radiation therapy vs stereotactic radiosurgery alone for treatment of brain metastases: a randomized controlled trial. *JAMA*. 2006;295(21):2483–2491.
79. Kocher M, Soffietti R, Abacioglu U, et al. Adjuvant whole-brain radiotherapy versus observation after radiosurgery or surgical resection of one to three cerebral metastases: results of the EORTC 22952-26001 study. *J Clin Oncol*. 2011;29(2):134–141.
80. Chang EL, Wefel JS, Hess KR, et al. Neurocognition in patients with brain metastases treated with radiosurgery or radiosurgery plus whole-brain irradiation: a randomised controlled trial. *Lancet Oncol*. 2009;10(11):1037–1044.
81. McDuff SG, Taich ZJ, Lawson JD, et al. Neurocognitive assessment following whole brain radiation therapy and radiosurgery for patients with cerebral metastases. *J Neurol Neurosurg Psychiatry*. 2013;84(12):1384–1391.
82. Nakamura M, Roser F, Michel J, Jacobs C, Samii M. The natural history of incidental meningiomas. *Neurosurgery*. 2003;53(1):62–70; discussion 70–61.
83. Condra KS, Buatti JM, Mendenhall WM, Friedman WA, Marcus Jr RB, Rhoton AL. Benign meningiomas: primary treatment selection affects survival. *Int J Radiat Oncol Biol Phys*. 1997;39(2):427–436.
84. Glaholm J, Bloom H, Crow J. The role of radiotherapy in the management of intracranial meningiomas: The Royal Marsden Hospital experience with 186 patients. *Int J Rad Biol Phys*. 1990;18:755–761.
85. Goldsmith B, Wara W, Wilson C, Larson D. Postoperative irradiation for subtotally resected meningiomas. *J Neurosurg*. 1994;1994(80):195–201.
86. Nutting C, Brada M, Brazil L, et al. Radiotherapy in the treatment of benign meningioma of the skull base. *J Neurosurg*. 1999;90(5):823–827.
87. Kobayashi T, Kida Y, Mori Y. Long-term results of stereotactic gamma radiosurgery of meningiomas. *Surg Neurol*. 2001;55(6):325–331.
88. Santacroce A, Walier M, Régis J, et al. Long-term tumor control of benign intracranial meningiomas after radiosurgery in a series of 4565 patients. *Neurosurgery*. 2012;70(1):32–39; discussion 39.
89. Starke RM, Williams BJ, Hiles C, Nguyen JH, Elsharkawy MY, Sheehan JP. Gamma knife surgery for skull base meningiomas. *J Neurosurg*. 2012;116(3):588–597.
90. Kondziolka D, Patel AD, Kano H, Flickinger JC, Lunsford LD. Long-term outcomes after gamma knife radiosurgery for meningiomas. *Am J Clin Oncol*. 2014.
91. Pollock BE, Stafford SL, Utter A, Giannini C, Schreiner SA. Stereotactic radiosurgery provides equivalent tumor control to Simpson Grade 1 resection for patients with small- to medium-size meningiomas. *Int J Radiat Oncol Biol Phys*. 2003;55(4):1000–1005.
92. Pollock BE, Stafford SL, Utter A, Giannini C, Schreiner SA. Stereotactic radiosurgery provides equivalent tumor control to Simpson Grade 1 resection for patients with small- to medium-size meningiomas. *Int J Radiat Oncol Biol Phys*. 2003;55(4):1000–1005.
93. Chan AW, Black P, Ojemann RG, et al. Stereotactic radiotherapy for vestibular schwannomas: favorable outcome with minimal toxicity. *Neurosurgery*. 2005;57(1):60–70; discussion 60–70.
94. Combs SE, Volk S, Schulz-Ertner D, Huber PE, Thilmann C, Debus J. Management of acoustic neuromas with fractionated stereotactic radiotherapy (FSRT): long-term results in 106 patients treated in a single institution. *Int J Radiat Oncol Biol Phys*. 2005;63(1):75–81.
95. Chung WY, Pan DH, Lee CC, et al. Large vestibular schwannomas treated by Gamma Knife surgery: long-term outcomes. *J Neurosurg*. 2010;113(suppl):112–121.
96. Milligan BD, Pollock BE, Foote RL, Link MJ. Long-term tumor control and cranial nerve outcomes following γ knife surgery for larger-volume vestibular schwannomas. *J Neurosurg*. 2012;116(3):598–604.
97. Carlson ML, Jacob JT, Pollock BE, et al. Long-term hearing out comes following stereotactic radiosurgery for vestibular schwannoma: patterns of hearing loss and variables influencing audiometric decline. *J Neurosurg*. 2013;118(3):579–587.
98. Hamilton DK, Vance ML, Boulos PT, Laws ER. Surgical outcomes in hyporesponsive prolactinomas: analysis of patients with resistance or intolerance to dopamine agonists. *Pituitary*. 2005;8(1):53–60.
99. Jane Jr JA, Laws Jr ER. The surgical management of pituitary adenomas in a series of 3,093 patients. *J Am Coll Surg*. 2001;193(6):651–659.
100. Webb SM, Rigla M, Wagner A, Oliver B, Bartumeus F. Recovery of hypopituitarism after neurosurgical treatment of pituitary adenomas. *J Clin Endocrinol Metab*. 1999;84(10):3696–3700.
101. Grossman A, Cohen BL, Charlesworth M, et al. Treatment of prolactinomas with megavoltage radiotherapy. *Br Med J (Clin Res Ed)*. 1984;288(6424):1105–1109.
102. Tsagarakis S, Grossman A, Plowman PN, et al. Megavoltage pituitary irradiation in the management of prolactinomas: long-term follow-up. *Clin Endocrinol (Oxf)*. 1991;34(5):399–406.
103. Tsang RW, Brierley JD, Panzarella T, Gospodarowicz MK, Sutcliffe SB, Simpson WJ. Role of radiation therapy in clinical hormonally-active pituitary adenomas. *Radiother Oncol*. 1996;41(1):45–53.
104. Sheehan JP, Niranjan A, Sheehan JM, et al. Stereotactic radiosurgery for pituitary adenomas: an intermediate review of its safety, efficacy, and role in the neurosurgical treatment armamentarium. *J Neurosurg*. 2005;102(4):678–691.
105. Castinetti F, Nagai M, Morange I, et al. Long-term results of stereotactic radiosurgery in secretory pituitary adenomas. *J Clin Endocrinol Metab*. 2009;94(9):3400–3407.
106. Xu Z, Lee Vance M, Schlesinger D, Sheehan JP. Hypopituitarism after stereotactic radiosurgery for pituitary adenomas. *Neurosurgery*. 2013;72(4):630–637; 636–637.
107. Giustina A, Chanson P, Bronstein MD, et al. A consensus on criteria for cure of acromegaly. *J Clin Endocrinol Metab*. 2010;95(7):3141–3148.
108. McKeage K, Cheer S, Wagstaff AJ. Octreotide long-acting release (LAR): a review of its use in the management of acromegaly. *Drugs*. 2003;63(22):2473–2499.
109. Hardy J, Somma M, Vezina J. *Treatment of acromegaly: radiation or surgery?* Philadelphia: WB Saunders; 1976.
110. Kreutzer J, Vance ML, Lopes MB, Laws Jr ER. Surgical management of GH-secreting pituitary adenomas: an outcome study using modern remission criteria. *J Clin Endocrinol Metab*. 2001;86(9):4072–4077.
111. Dowsett RJ, Fowble B, Sergott RC, et al. Results of radiotherapy in the treatment of acromegaly: lack of ophthalmologic complications. *Int J Radiat Oncol Biol Phys*. 1990;19(2):453–459.
112. Lamberg BA, Kivikangas V, Vartianen J, Raitta C, Pelkonen R. Conventional pituitary irradiation in acromegaly. Effect on growth hormone and TSH secretion. *Acta Endocrinol (Copenh)*. 1976;82(2):267–281.
113. Sheline G, Wara W. Radiation therapy of acromegaly and nonsecretory chromophobe adenomas of the pituitary. In: Seydel H, ed. *Tumors of the Central Nervous System*. New York: Wiley; 1975:119–131.
114. Volker S, Stolke D, Hubertus M, Hoffmann B. Clinical and radiological evaluation of long-term results of stereotactic proton beam radiosurgery in patients with cerebral arteriovenous malformation. *J Neurosurg*. 1994;81:683–689.
115. Marko NF, LaSota E, Hamrahian AH, Weil RJ. Comparative effectiveness review of treatment options for pituitary microadenomas in acromegaly. *J Neurosurg*. 2012;117(3):522–538.

116. Benveniste RJ, King WA, Walsh J, Lee JS, Delman BN, Post KD. Repeated transsphenoidal surgery to treat recurrent or residual pituitary adenoma. *J Neurosurg*. 2005;102(6):1004–1012.
117. De Tommasi C, Vance ML, Okonkwo DO, Diallo A, Laws Jr ER. Surgical management of adrenocorticotropic hormone-secreting macroadenomas: outcome and challenges in patients with Cushing's disease or Nelson's syndrome. *J Neurosurg*. 2005;103(5):825–830.
118. Robert F, Hardy J. Cushing's disease: a correlation of radiological, surgical and pathological findings with therapeutic results. *Pathol Res Pract*. 1991;187(5):617–621.
119. Semple PL, Laws Jr ER. Complications in a contemporary series of patients who underwent transsphenoidal surgery for Cushing's disease. *J Neurosurg*. 1999;91(2):175–179.
120. Thapar K, Laws E. In: Kaye A, Laws E, eds. *Brain Tumors: An Encyclopedia Approach*. London: Churchill Livingstone; 2001:803–853.
121. Estrada J, Boronat M, Mielgo M, et al. The long-term outcome of pituitary irradiation after unsuccessful transsphenoidal surgery in Cushing's disease. *N Engl J Med*. 1997;336(3):172–177.
122. Jennings AS, Liddle GW, Orth DN. Results of treating childhood Cushing's disease with pituitary irradiation. *N Engl J Med*. 1977;297(18):957–962.
123. Sheehan JM, Vance ML, Sheehan JP, Ellegala DB, Laws Jr ER. Radiosurgery for Cushing's disease after failed transsphenoidal surgery. *J Neurosurg*. 2000;93(5):738–742.
124. Jane Jr JA, Laws Jr ER. Surgical management of pituitary adenomas. *Singapore Med J*. 2002;43(6):318–323.
125. Dekkers OM, Pereira AM, Roelfsema F, et al. Observation alone after transsphenoidal surgery for non-functioning pituitary macroadenoma. *J Clin Endocrinol Metab*. 2006;28:28.
126. Flickinger JC, Nelson PB, Martinez AJ, Deutsch M, Taylor F. Radiotherapy of nonfunctional adenomas of the pituitary gland. Results with long-term follow-up. *Cancer*. 1989;63(12):2409–2414.
127. Park KJ, Kano H, Parry PV, et al. Long-term outcomes after gamma knife stereotactic radiosurgery for nonfunctional pituitary adenomas. *Neurosurgery*. 2011;69(6):1188–1199.
128. Gopalan R, Schlesinger D, Vance ML, Laws E, Sheehan J. Long-term outcomes after Gamma Knife radiosurgery for patients with a nonfunctioning pituitary adenoma. *Neurosurgery*. 2011;69(2):284–293.
129. Urdaneta N, Chessin H, Fischer JJ. Pituitary adenomas and craniopharyngiomas: analysis of 99 cases treated with radiation therapy. *Int J Radiat Oncol Biol Phys*. 1976;1(9–10):895–902.
130. Bunting SF, Callén E, Wong N, et al. 53BP1 inhibits homologous recombination in Brca1-deficient cells by blocking resection of DNA breaks. *Cell*. 2010;141(2):243–254.
131. Forsyth PA, Shaw EG, Scheithauer BW, O'Fallon JR, Layton Jr DD, Katzmann JA. Supratentorial pilocytic astrocytomas. A clinicopathologic, prognostic, and flow cytometric study of 51 patients. *Cancer*. 1993;72(4):1335–1342.
132. Boethius J, Ulfarsson E, Rahn T, Lippittz B. Gamma knife radiosurgery for pilocytic astrocytomas. *J Neurosurg*. 2002;97(suppl 5):677–680.
133. Heppner PA, Sheehan JP, Steiner LE. Gamma knife surgery for low-grade gliomas. *Neurosurgery*. 2005;57(6):1132–1139; discussion.
134. Kidd EA, Mansur DB, Leonard JR, Michalski JM, Simpson JR, Perry A. The efficacy of radiation therapy in the management of grade I astrocytomas. *J Neurooncol*. 2006;76(1):55–58. Epub 2005 August 2011.
135. Janny P, Cure H, Mohr M, et al. Low grade supratentorial astrocytomas. Management and prognostic factors. *Cancer*. 1994;73(7):1937–1945.
136. Fazekas J. Treatment of grades I and II brain astrocytomas: the role of radiotherapy. *Int J Rad Biol Phys*. 1977;2:661–666.
137. Garcia D, Fulling K, Marks J. The value of radiation therapy in addition to surgery for astrocytomas of the adult cranium. *Cancer*. 1985;55:919–927.
138. Medbery C, Straus K, Steinberg S, Cotelingam J, Fisher W. Low-grade astrocytomas: treatment results and prognostic variables. *Int J Rad Biol Phys*. 1988;15:837–841.
139. Shaw E, Dumas-Duport C, Scheithauer B, et al. Radiation therapy in the management of low-grade supratentorial astrocytomas. *J Neurosurg*. 1989;70:853–861.
140. Karim AB, Maat B, Hatlevoll R, et al. A randomized trial on dose-response in radiation therapy of low-grade cerebral glioma: European Organization for Research and Treatment of Cancer (EORTC) Study 22844. *Int J Radiat Oncol Biol Phys*. 1996;36(3):549–556.
141. Shaw E, Arusell R, Scheithauer B, et al. Prospective randomized trial of low- versus high-dose radiation therapy in adults with supratentorial low-grade glioma: initial report of a North Central Cancer Treatment Group/Radiation Therapy Oncology Group/Eastern Cooperative Oncology Group study. *J Clin Oncol*. 2002;20(9):2267–2276.
142. Park KJ, Kano H, Kondziolka D, Niranjan A, Flickinger JC, Lunsford LD. Early or delayed radiosurgery for WHO grade II astrocytomas. *J Neurooncol*. 2011;103(3):523–532.
143. Bleehen NM, Wiltshire CR, Plowman PN, et al. A randomized study of misonidazole and radiotherapy for grade 3 and 4 cerebral astrocytoma. *Br J Cancer*. 1981;43(4):436–442.
144. Sheline GE. Radiotherapy for high grade gliomas. *Int J Radiat Oncol Biol Phys*. 1990;18(4):793–803.
145. Walker MD, Strike TA, Sheline GE. An analysis of dose-effect relationship in the radiotherapy of malignant gliomas. *Int J Radiat Oncol Biol Phys*. 1979;5(10):1725–1731.
146. Fitzek M, Thornton A, Rabinov J, et al. Accelerated fractionated proton/photon irradiation to 90 cobalt gray equivalent for glioblastoma multiforme: results of a phase II prospective trial. *J Neurosurg*. 1999;91:251–260.
147. Hochberg FH, Pruitt A. Assumptions in the radiotherapy of glioblastoma. *Neurology*. 1980;30(9):907–911.
148. Erlich SS, Davis RL. Spinal subarachnoid metastasis from primary intracranial glioblastoma multiforme. *Cancer*. 1978;42(6):2854–2864.
149. Buatti JM, Friedman WA, Bova FJ, Mendenhall WM. Linac radiosurgery for high-grade gliomas: the University of Florida experience. *Int J Radiat Oncol Biol Phys*. 1995;32(1):205–210.
150. Larson DA, Gutin PH, McDermott M, et al. Gamma knife for glioma: selection factors and survival. *Int J Radiat Oncol Biol Phys*. 1996;36(5):1045–1053.
151. Nwokedi EC, DiBiase SJ, Jabbour S, Herman J, Amin P, Chin LS. Gamma knife stereotactic radiosurgery for patients with glioblastoma multiforme. *Neurosurgery*. 2002;50(1):41–46; discussion 46–47.
152. Prisco FE, Weltman E, de Hanriot RM, Brandt RA. Radiosurgical boost for primary high-grade gliomas. *J Neurooncol*. 2002;57(2):151–160.
153. Sarkaria JN, Mehta MP, Loeffler JS, et al. Radiosurgery in the initial management of malignant gliomas: survival comparison with the RTOG recursive partitioning analysis. Radiation Therapy Oncology Group. *Int J Radiat Oncol Biol Phys*. 1995;32(4):931–941.
154. Shrieve DC, Alexander 3rd E, Black PM, et al. Treatment of patients with primary glioblastoma multiforme with standard postoperative radiotherapy and radiosurgical boost: prognostic factors and long-term outcome. *J Neurosurg*. 1999;90(1):72–77.
155. Loeffler JS, Alexander E, Shea WM, et al. Radiosurgery as part of the initial management of patients with malignant gliomas. *J Clin Oncol*. 1992;10(9):1379–1385.
156. Mehta MP, Masciopinto J, Rozental J, et al. Stereotactic radiosurgery for glioblastoma multiforme: report of a prospective study evaluating prognostic factors and analyzing long-term survival advantage. *Int J Radiat Oncol Biol Phys*. 1994;30(3):541–549.

157. Tsao MN, Mehta MP, Whelan TJ, et al. The American Society for Therapeutic Radiology and Oncology (ASTRO) evidence-based review of the role of radiosurgery for malignant glioma. *Int J Radiat Oncol Biol Phys*. 2005;63(1):47–55.
158. Souhami L, Seiferheld W, Brachman D, et al. Randomized comparison of stereotactic radiosurgery followed by conventional radiotherapy with carmustine to conventional radiotherapy with carmustine for patients with glioblastoma multiforme: report of Radiation Therapy Oncology Group 93-05 protocol. *Int J Radiat Oncol Biol Phys*. 2004;60(3):853–860.
159. Shenouda G, Souhami L, Podgorsak EB, et al. Radiosurgery and accelerated radiotherapy for patients with glioblastoma. *Can J Neurol Sci*. 1997;24(2):110–115.
160. Gannett D, Stea B, Lulu B, Adair T, Verdi C, Hamilton A. Stereotactic radiosurgery as an adjunct to surgery and external beam radiotherapy in the treatment of patients with malignant gliomas. *Int J Radiat Oncol Biol Phys*. 1995;33(2):461–468.
161. Stea B, Rossman K, Kittelson J, et al. A comparison of survival between radiosurgery and stereotactic implants for malignant astrocytomas. *Acta Neurochir Suppl*. 1994;62:47–54.
162. Ulm 3rd AJ, Friedman WA, Bradshaw P, Foote KD, Bova FJ. Radiosurgery in the treatment of malignant gliomas: the University of Florida experience. *Neurosurgery*. 2005;57(3):512–517; discussion 512–517.
163. Tsao MN, Mehta MP, Whelan TJ, et al. The American Society for Therapeutic Radiology and Oncology (ASTRO) evidence-based review of the role of radiosurgery for malignant glioma. *Int J Radiat Oncol Biol Phys*. 2005;63(1):47–55.
164. Chamberlain MC, Barba D, Kormanik P, Shea WM. Stereotactic radiosurgery for recurrent gliomas. *Cancer*. 1994;74(4):1342–1347.
165. Hall WA, Djalilian HR, Sperduto PW, et al. Stereotactic radio surgery for recurrent malignant gliomas. *J Clin Oncol*. 1995;13(7): 1642–1648.
166. Larson DA, Prados M, Lamborn KR, et al. Phase II study of high central dose Gamma Knife radiosurgery and marimastat in patients with recurrent malignant glioma. *Int J Radiat Oncol Biol Phys*. 2002;54(5):1397–1404.
167. Larson DA, Gutin PH, McDermott M, et al. Gamma knife for glioma: selection factors and survival. *Int J Radiat Oncol Biol Phys*. 1996;36(5):1045–1053.
168. Shrieve DC, Alexander E, Wen PY, et al. Comparison of stereotactic radiosurgery and brachytherapy in the treatment of recurrent glioblastoma multiforme. *Neurosurgery*. 1995;36(2):275–282; discussion 282–274.
169. Sarkar A, Pollock BE, Brown PD, Gorman DA. Evaluation of gamma knife radiosurgery in the treatment of oligodendrogliomas and mixed oligodendroastrocytomas. *J Neurosurg*. 2002;97(suppl 5):653–656.
170. Brada M, Ford D, Ashley S, et al. Risk of second brain tumour after conservative surgery and radiotherapy for pituitary adenoma. *BMJ*. 1992;304(6838):1343–1346.
171. Kimball Dalton VM, Gelber RD, Li F, Donnelly MJ, Tarbell NJ, Sallan SE. Second malignancies in patients treated for childhood acute lymphoblastic leukemia. *J Clin Oncol*. 1998;16(8):2848–2853.
172. Sadetzki S, Flint-Richter P, Ben-Tal T, Nass D. Radiation-induced meningioma: a descriptive study of 253 cases. *J Neurosurg*. 2002;97(5):1078–1082.
173. Niranjan A, Kondziolka D, Lunsford LD. Neoplastic transformation after radiosurgery or radiotherapy: risk and realities. *Otolaryngol Clin North Am*. 2009;42(4):717–729.
174. JROSG99-1. 2006.
175. Kreil et al. 2004.
176. Lundsford et al. 2005.
177. Hasegawa et al. 2005.
178. Chung et al. 2005.

CHAPTER

27

Diffusion Magnetic Resonance Imaging in Brain Tumors

L. Celso Hygino da Cruz Jr.[1], *Margareth Kimura*[2]

[1]CDPI – Clínica de Diagnóstico por Imagem, IRM Ressonância Magnética, Centro Médico Barrashopping Rio de Janeiro, RJ, Brazil; [2]CDPI – Clínica de Diagnóstico por Imagem, Centro Médico Barrashopping, Rio de Janeiro, RJ, Brazil

INTRODUCTION

The incidence of primary neoplasms of the central nervous system (CNS) is around 14,000 new cases annually in the United States, and it is estimated that brain tumors cause the deaths of 13,000 patients every year. Although this incidence represents only 1.4% annually of all new cases of cancer, brain tumors correspond to 2.4% of all deaths caused by cancer.[1] Brain metastases occur in approximately 30% of all patients with disseminated cancer.[2] When metastatic lesions are included, brain tumors are estimated to cause the death of 90,000 patients every year.[3–5] Gliomas are the leading cause of primary CNS tumor, accounting for 40–50% of cases and 2–3% of all cancers.[6,7] Despite new techniques of treatment, patient survival still remains very low, varying between 16 and 53 weeks.[8]

A variety of imaging techniques have been developed for assessing brain tumors. This task of assessment includes initial detection, diagnosis, grading and guiding intervention, monitoring after therapy, and overall prognosis. More recently, with the advances in genomic analysis of brain tumors, it has become possible to classify tumors according to their genetic and molecular characteristics. This classification based on gene expression of brain tumors has been suggested by many authors and may become a better predictor of key outcomes than the traditional histologic classification used for such neoplasms.[9–16] In line with these findings, it has been observed by researchers that magnetic resonance imaging (MRI) can predict genetic characteristics of brain tumors noninvasively. For more than 20 years, conventional MRI, typically T1- and T2-weighted imaging, has been used for this purpose.[17] Although in clinical practice nearly all detected lesions undergo some type of surgical intervention, such as biopsy or excision, and therefore histologic diagnosis is available, some cases will still require a determination of tumor grade. For example, surgical excision of the visible abnormality is often attempted, despite a consensus that conventional MRI tends to underestimate the extent of the tumor, which in turn many suspect leads to suboptimal treatment.[18] In part this is because most primary brain neoplasms infiltrate the brain parenchyma out beyond the enhancing portion of the lesion. High-grade gliomas have the ability to infiltrate the brain parenchyma. This infiltration appears to follow the main fiber bundles, possibly along the vessel channels, without disrupting the blood–brain barrier.[19]An ability to detect these bundles, therefore, might allow better determination of tumor growth directions and extent. Many other imaging techniques are under development to attempt to answer these and related questions.[20]

Physiology-based MRI methods, such as diffusion-weighted imaging (DWI), permeability, perfusion-weighted imaging, and MR spectroscopy (MRS), have been widely used to determine the grade, heterogeneity, and extent of these primary and secondary brain tumors. DWI first came into wide use because of its ability to detect hyperacute infarcts (Figure 1). Since 2005, diffusion has been studied extensively in the evaluation of other pathologies, including brain tumors. DWI has been thoroughly investigated as an imaging biomarker for cancer treatment response and as a prognostic marker for treatment outcomes by some tumors.[21–24] It has been demonstrated that diffusion tensor MR imaging (DTI) can assess tumor treatment response after chemotherapy, radiation, and antiangiogenic agents because it is sensitive to macromolecular and microstructural changes that usually occur at

http://dx.doi.org/10.1016/B978-0-12-800945-1.00027-6

© 2016 Elsevier Ltd. All rights reserved.

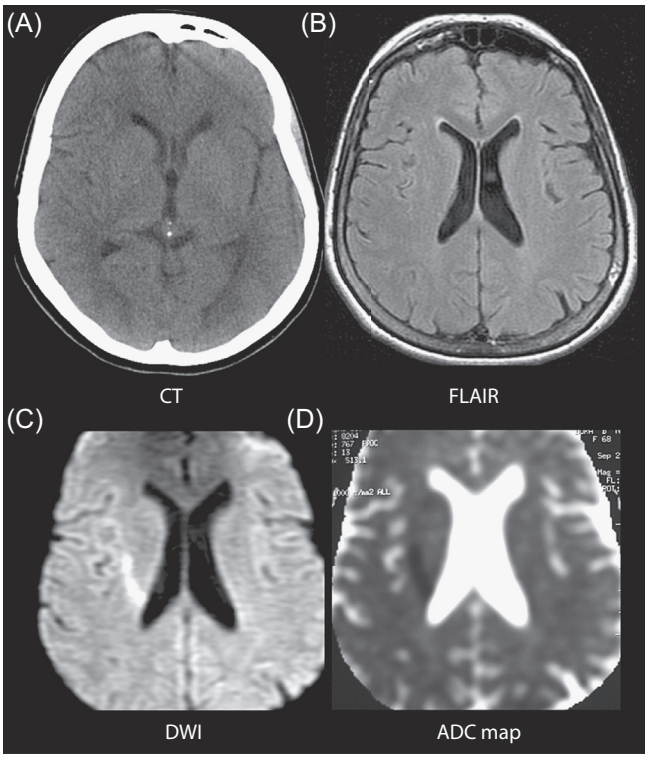


FIGURE 1 A 67-year-old woman presenting with new onset of left hemiparesis at 2 h. (A) Nonenhancing computed tomography and (B) T2-weighted image do not demonstrate any abnormality. (C) Diffusion-weighted image demonstrates a hyperintense area in the posterior limb of the right internal capsule and corona radiata. (D) An area of hyperacute infarct could be diagnosed, based on the findings of restricted diffusion, reflecting cytotoxic edema, confirmed by the apparent diffusion coefficient map—black area on the ADC map.

a molecular level earlier than anatomical changes during therapy.[25]

DTI is an MR method that may be able to delineate more accurately between the core of the tumor, infiltrating tumor, peritumoral edema, and normal brain parenchyma.[26] DTI has been widely used because of its apparent ability to illustrate the relationship of a tumor with the nearby main fiber tracts, though this remains difficult to validate. Because of these early findings, some have suggested that DTI might also be used to aid in surgical planning,[27] possibly in some services in radiotherapy planning,[28] and as a predictive biomarker of brain chemoradiotherapy adverse effects,[25] as well as to monitor for tumor recurrence or tumor response to treatment[29] or even to differentiate inflammatory from neoplastic lesions.[30]

Whereas these new applications have not yet been validated and standardized, or even widely studied in multicenter clinical trials, many individual practitioners are nevertheless actively using DTI. The reasoning behind such use typically begins with the logic that the aim of a surgical brain tumor treatment is as complete a resection of the lesion as possible without harming vital brain functions.[31,32] Therefore, a preoperative approach that maps, even imperfectly, the tumor and its relationship to nearby functional structures may facilitate the patient's outcome.[33] Since 2005, diffusion techniques that enable the assessment of diffusional non-Gaussian properties of water diffusion have been explored for their possible ability to evaluate the microstructural complexity of brain tissue and tumors. High-angular-resolution diffusion imaging (HARDI), diffusion spectrum imaging (DSI), and diffusional kurtosis imaging constitute some of these techniques. Diffusion kurtosis imaging (DKI) is the simpler and quicker choice to be performed in the clinical setting. DKI is an extension of DWI and DTI and requires the use of at least 2 nonzero b values and 15 diffusion gradient directions and jointly generates DTI and DKI metrics. DKI allows the quantification of additional non-Gaussian diffusion metrics. Such non-Gaussian diffusional kurtosis imaging metrics are believed to be sensitive to microstructural alterations within gliomas and may be helpful in tumor grading, possibly better than conventional DWI and DTI.[34–38]

Because of this logic and related rationales, considerable interest in DKI and radiogenomics involving diffusion-based techniques has arisen. In this chapter, therefore, we review the methodology and uses of DWI, DTI, and DKI as they have been studied in these anecdotal and early studies.

PHYSICAL BASIS

Diffusion-Weighted MR Imaging

DWI is able to detect water movement at a molecular level. It is based on the random or Brownian motion of water molecules, typically in relation to their thermal energy, although influenced by the surrounding environment. In the brain, the presence of some tissue structures restricts free water motion[39]; for example, the diffusion of water molecules is higher in the ventricles than in the parenchyma, as there are few barriers. This is because diffusion in tissue is affected by the presence of semipermeable membranes and oriented microstructures in the intracellular, extracellular, and vascular compartments, which results in preferential movement of water parallel to these obstacles. MRI makes it possible to estimate the diffusivity of water molecules.

Most diffusion measurements today are made using a variant of the diffusion-weighted sequence first described by Stejskal and Tanner. Their initial approach described a spin-echo (SE) sequence together with two equal and opposite extragradient pulses[40]; the amount of signal loss can be related to the magnitude of diffusion. For practical purposes, an echo-planar imaging SE T2-weighted sequence is utilized, because of its ability to reduce motion artifacts and its rapid acquisition time.[41] Stejskal and Tanner's approach uses two magnetic pulses or gradients to

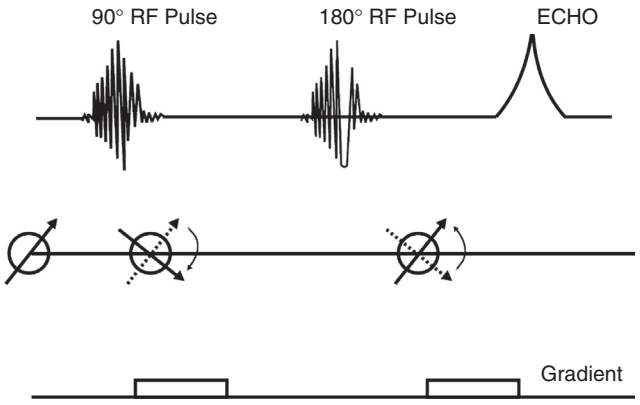


FIGURE 2 A schematic figure demonstrating the diffusion-weighted sequence described by Stejskal and Tanner.

label the spins: the application of the first diffusion gradient causes a dephasing of water protons; because they move randomly, not all water protons are in place for rephrasing from the application of the second diffusion gradient. Thus, there is a signal decrease that depends on how far the water molecules have moved (Figure 2).[42] The net signal on the final DWI is therefore influenced by both the T2 tissue effect and the tissue diffusion characteristics. By acquiring an image with little diffusion weighting and another image with substantial diffusion weighting, the apparent diffusion coefficient (ADC) can be calculated on a voxel-by-voxel basis, allowing the generation of a map that reflects solely the diffusion influence excluding the T2 effects, which prevents misinterpretation from the so-called "T2 shine-through" effect.[43,44]

Some pathologic processes appear to change the characteristics of the brain microenvironment, which in turn results in alteration of the ADC.[42] In clinical practice, diffusion imaging has been used to assess acute cerebral ischemia[44–46], as diffusion water motion decreases after the onset of ischemia. The biophysical mechanisms underlying the observed decrease in ADC in acute ischemia are still poorly understood. Failure of the Na^+/K^+ adenosine triphosphatase pump is believed to play an important role in this pathophysiological process, however, and this state of ischemia is often referred to as cytotoxic edema.[47,48] Other possible explanations for the decrease in ADC are intracellular and extracellular relative volume changes, extracellular space tortuosity increase. and reduction in the cytoplasmic circulation of the intracellular compartment[49]. Whereas ischemia was the first application of DWI, diffusion imaging has also been applied to the evaluation of many other neurological conditions. The appearance of lesions in diseases such as multiple sclerosis (Figure 3)[48,50,51], venous infarctions, hypoglycemia, diffuse axonal injury, transient global amnesia, metronidazole toxicity, osmotic myelinolysis, carbon monoxide poisoning[49], encephalitis[52], and Creutzfeldt–Jakob disease[53] (Figure 4) can be contrasted with the appearance of diffusion in neoplastic brain lesions (see later figures).

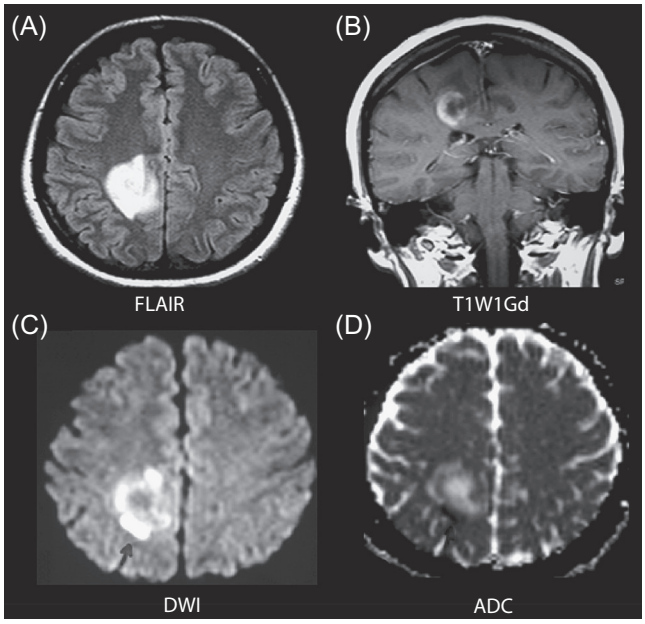


FIGURE 3 (A) Axial FLAIR image showing the presence of demyelinating plaques on the brain stem and in the cerebellum peduncles that are enhanced in the postcontrast T1-weighted image (B, C). These lesions may consist of acute demyelinating plaques. (D) Most acute multiple sclerosis plaques may have restricted diffusion, characterized by hyperintensity on DWI and low ADC values on an ADC map.

Diffusion Tensor MR Imaging

The mathematical description of the movement of water can be complex. Whereas water motion occurs in all three cardinal directions, the description of this movement may be highly variable depending on local restrictions. In an attempt to simplify the analysis of diffusion imaging, often water mobility is assumed to behave in a manner that can be described using a Gaussian approximation. As we will see below, this is a powerful approach and is widely popular; however, the limitations of this technique have begun to become apparent, as will also be discussed below. Nevertheless, the Gaussian approximation has definite utility, and therefore we will use this approximation as well for much of this chapter.

When water molecules diffuse equally in all directions, this is termed isotropic diffusion. This phenomenon is typical in the ventricles, and at the resolution of typical clinical MRI, such isotropic behavior seems to be the case in the gray matter. In the white matter, however, free water molecules diffuse anisotropically, that is, the water diffusion is not equal in all three orthogonal directions.[54,55] This is probably because tissue structures impede the water motion; these structures probably include the cell membranes, organelles, and distinct water compartments.[56] The myelin sheath is able to modulate the degree of anisotropy.[56] Put another way, isotropic diffusion can be graphically represented as a sphere, whereas anisotropic

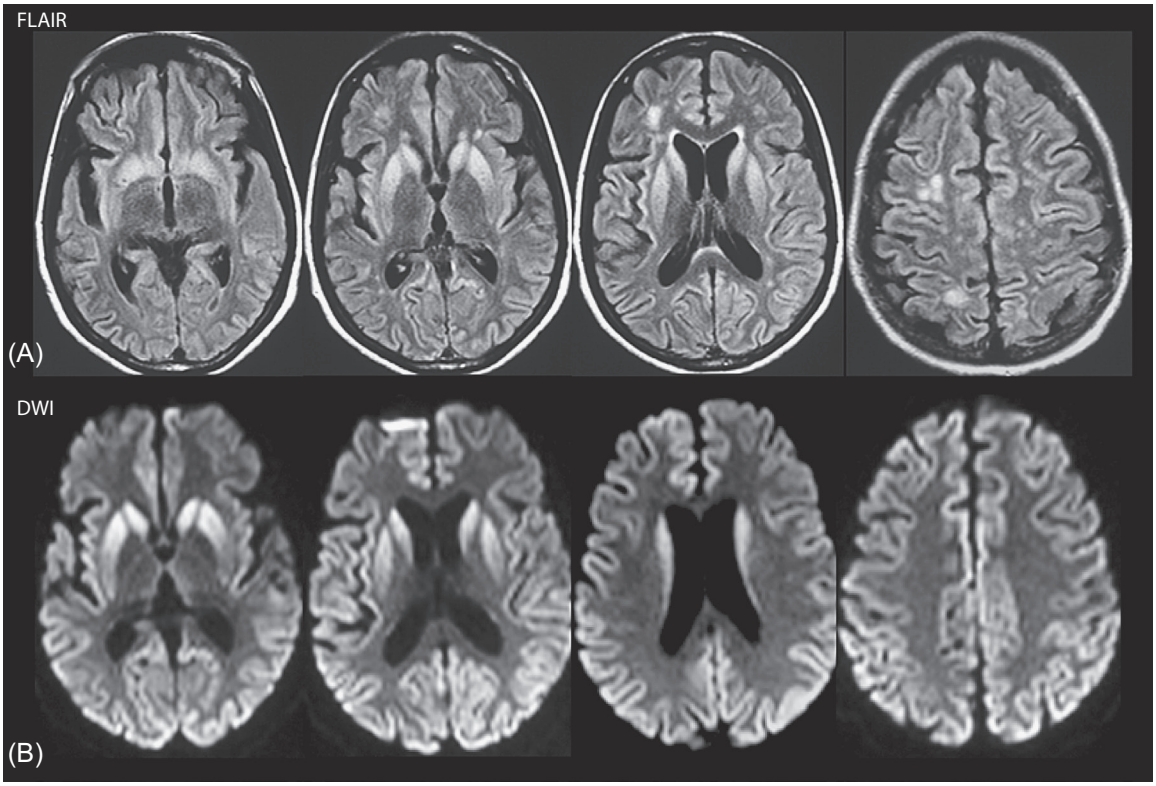


FIGURE 4 A 45-year-old woman complaining of mental disturbance with the diagnosis of Creutzfeldt–Jakob disease. (A) Axial FLAIR images and (B) diffusion-weighted images demonstrate gyriform increased signal intensity predominantly in the cortex of the occipitoparietal lobes and also in the basal ganglia, consistent with restricted diffusion.

diffusion can be graphically expressed as an ellipsoid,[57] with water molecules moving farther along the long axis of a fiber bundle and less perpendicularly (Figure 5).[58]

In a tensor model, water mobility is described by a 3×3 matrix. To estimate the nine-tensor matrix elements, the diffusion gradients must be applied to at least six noncollinear directions (it is six rather than nine because only some degree of symmetry is assumed, and so only six of the nine elements are unique under this assumption).[58] The eigenvalues represent the three principal diffusion coefficients measured along the three coordinate directions of the ellipsoid.[58] The eigenvectors represent the directions of the tensor.[59] Because interpreting a tensor representation can be nonintuitive, scalar metrics have been proposed to simplify DTI data.[57] For example, fractional anisotropy (FA) measures the fraction of the total magnitude of diffusion anisotropy. FA values vary from completely isotropic diffusion (graded as 0) up to completely anisotropic diffusion (graded as 1).[57,58]

In addition to assessment of the diffusion in a single voxel, DTI has been used to attempt to map the white matter fiber tracts. This is typically done by connecting each voxel eigenvector to its adjacent in accordance with the direction the fibers are pointing.[60,61] DTI can also determine a color-coded FA map of fiber orientation.[62] A different color has been attributed to represent a different fiber orientation along the three orthogonal spatial axes: in the standard convention, red stands for the left–right direction of x-oriented fibers, blue stands for the superior–inferior direction of y-oriented fibers, and green for the anterior–posterior direction of z-oriented fibers (Figure 6).[62–64]

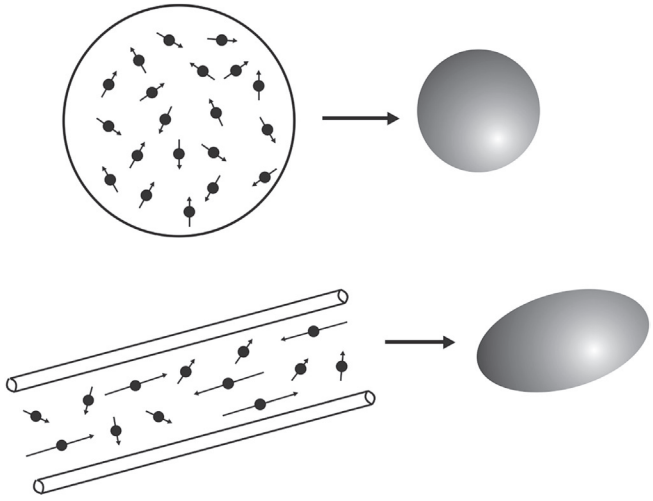


FIGURE 5 Free water molecules diffuse equally in all directions. This is termed isotropic diffusion and can be graphically represented as a sphere. When there is a preferred direction for the free water molecules to diffuse, the diffusion is termed anisotropic and can be graphically represented as an ellipsoid.

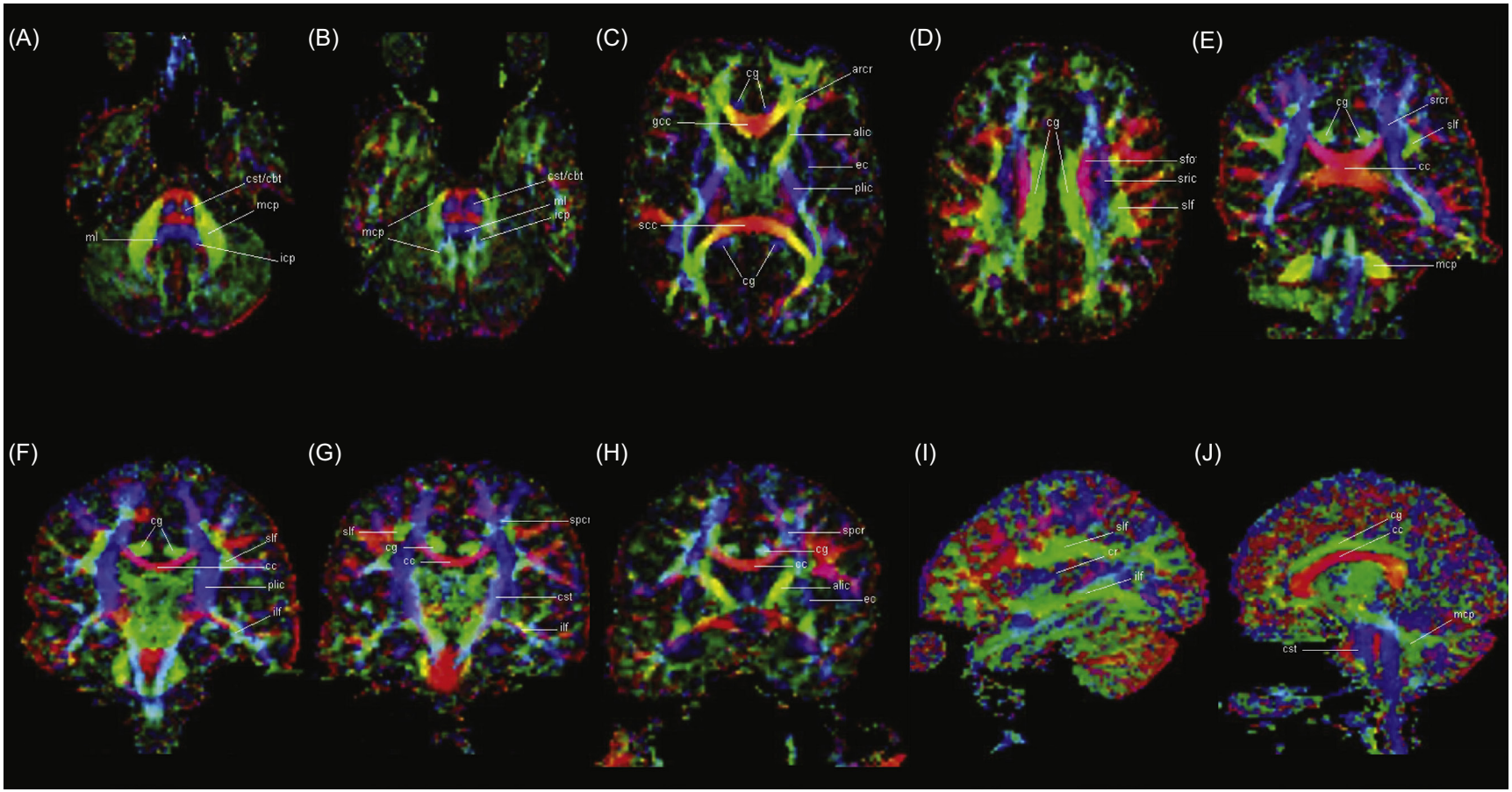


FIGURE 6 Diffusion tensor imaging color-coded map of a healthy volunteer. Locations of white matter tracts are assigned on color maps. The direction of the main fiber tracts is represented by red (right–left), green-yellow (anterior–posterior), and blue (superior–inferior). Several main fiber tracts visible on color maps are annotated on the basis of anatomic knowledge. (A–D) Axial fractional anisotropic (FA) color maps. (E–H) Coronal FA color maps. (I, J) Sagittal FA color maps. mcp, middle cerebral peduncle; cst, corticospinal tract; cbt, corticobulbar tract; ml, medial lemniscus; icp, inferior cerebellar peduncle; cg, cingulum; cc, corpus callosum; gcc, genu of corpus callosum; scc, splenium of corpus callosum; arcr, anterior region of corona radiata; alic, anterior limb of internal capsule; plic, posterior limb of internal capsule; ec, external capsule; sric, superior region of internal capsule; sfof, superior fronto-occiptal fasciculus; ifof, inferior fronto-occiptal fasciculus; slf, superior longitudinal fasciculus; ilf, inferior longitudinal fasciculus.

Diffusion Kurtosis MR Imaging

DKI is an extension of DWI and DTI and is clinically feasible, which enables the assessment of non-Gaussian properties of water diffusion.[34–36] Whereas in the DTI technique water mobility is based on the assumption that the displacement probability function of water diffusion follows a Gaussian distribution, DKI assumes a non-Gaussian probability of water diffusion. In probability theory, the normal (or Gaussian) distribution is a very commonly occurring continuous probability distribution. It is perhaps the most used distribution in all of science and sometimes it is informally called the bell curve. On the other side, kurtosis in probability distribution represents the extent to which the diffusion pattern of the water molecules deviates from a perfect Gaussian curve. Mathematically, kurtosis is a dimensionless statistical metric for quantifying the non-Gaussianity of an arbitrary probability of distribution.

In biological tissues, such as the brain, it is believed that the non-Gaussian behavior of water might occur as a consequence of a heterogeneous environment characterized by multiple compartments, organelles, and semipermeable membranes. In this context, DKI has been considered a technique that can provide other additional information than DTI about the microstructure in the brain.[34–36]

Typically for MRI, DKI is acquired using at least 3 distinct b values, including b 0, and at least 15 independent diffusion directions must be applied in tissues with anisotropic properties. Scan times of 10 min are noted for 1.5 and 3.0 T clinical MR imaging systems. Diffusion kurtosis sequence jointly generates DTI and DKI metrics; these last are named mean kurtosis, axial and radial diffusion kurtosis, and FA (Figure 7). Diffusion kurtosis can potentially be more sensitive to some tissue properties, such as heterogeneity of the regional brain environment, and it can study isotropic tissues such as gray matter.[35]

Furthermore, some promising preliminary results for the evaluation of several brain diseases have been described in the literature over the past few years, including the possibility of resolving fiber crossing with the use of DKI tractography.[65–73] A study on neuromyelitis optica patients, however, reported FA derived from DTI to be more sensitive at detecting microstructural alterations in white matter tracts with high anisotropy compared to the FA derived from DKI in neuromyelitis optica patients.[74] In contrast, two other studies conducted to characterize the non-Gaussian diffusion patterns of cerebral glioma microstructure reported

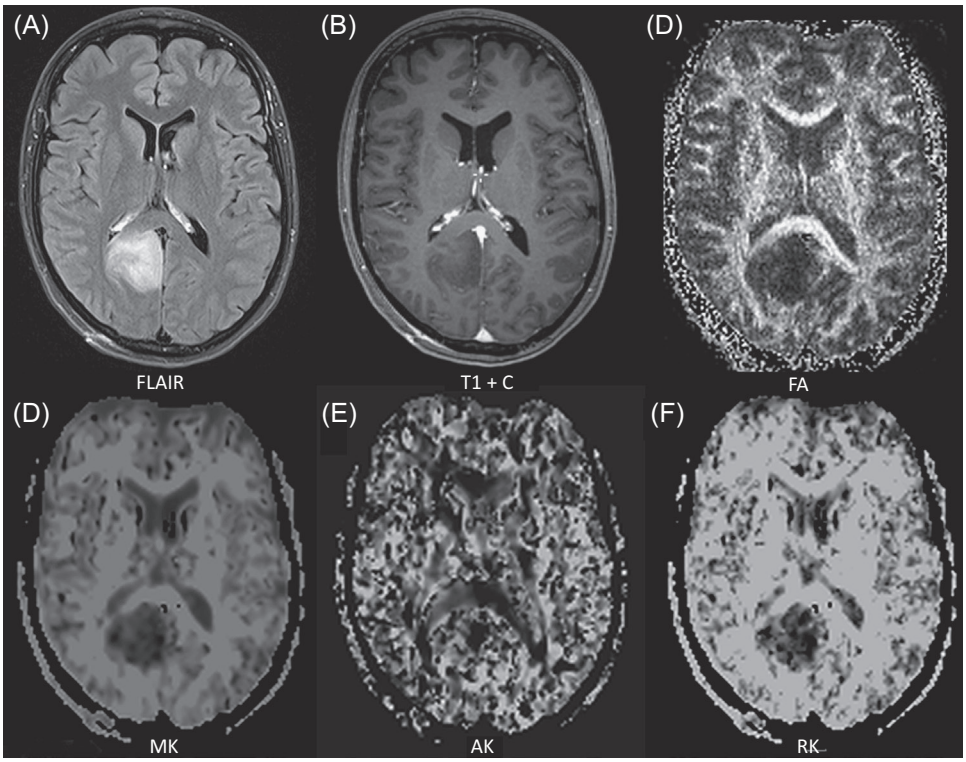


FIGURE 7 A 23-year-old-woman with a biopsy-proven diagnosis of low-grade astrocytoma. (A) Flair image and (B) axial contrast-enhanced T1-weighted image demonstrate an expansive lesion with no enhancement areas located on the right occipital lobe that infiltrates part of the splenium of the corpus callosum. (C–F) The maps of the metrics obtained with a diffusion kurtosis imaging sequence at a 3-Tesla MR scanner, named fractional anisotropy (FA), mean kurtosis (MK), axial kurtosis (AK), and radial kurtosis (RK), are shown.

that DKI was able to better differentiate glioma grades in cases of nonenhancing brain tumors.[7,38] The authors highlighted the fact that the principal metric derived from DKI, mean kurtosis, which is thought to be an index of microstructural complexity, enabled the imaging characterization of different glioma grades. Then, mean kurtosis can have an advantage over FA in some circumstances, because it does not rely on spatially oriented tissue structures. Overall, it is important to mention that DKI metrics are pure diffusion measures and they lack microstructural and pathological specificity, so they must be augmented with a tissue model to help interpret the physical meaning of any changes associated with disease processes.[36] Also, the exact nature of non-Gaussian behavior of water diffusion still needs to be elucidated.[36]

Taking all of this into consideration, one should consider that DWI and DTI are mature imaging techniques with several established brain applications, including ischemic stroke, brain tumors, and fiber tracking. DKI, although promising, still needs to be verified in its sensitivity and possible applications of its different metrics.

CLINICAL USE

As mentioned above, there are no multicenter clinical trials demonstrating the benefit of DTI (or DWI) in brain tumors. Therefore, formally speaking, there is no scientific evidence for the utility of DTI in tumor imaging. Nevertheless, in the following sections we summarize current opinion based on single-center studies and clinical anecdotes; clearly, more well-controlled studies are needed to definitively state the benefit of these techniques to patients.

ASSESSMENT OF EXTRA-AXIAL TUMORS

The diagnosis of epidermoid tumor can be challenging in clinical practice, as its signal intensity is frequently quite similar to that of cerebrospinal fluid (CSF) on conventional T1- and T2-weighted images. Under special conditions, arachnoid cysts may have an atypical appearance on conventional MRI, because of blood and high protein contents, complicating the differential diagnosis between these two extra-axial lesions.[42] DWI can also be used as an effective way of differentiating an arachnoid cyst from epidermoid tumors.[75] Both lesions present the same T1 and T2 signal intensity characteristic of CSF. On DWI, epidermoid tumors are hyperintense, because they are solidly composed, whereas arachnoid cysts are hypointense, demonstrating high diffusivity.[75] The ADC values of epidermoid tumors are similar to or slightly lower than those of the brain parenchyma, whereas the ADC values of arachnoid cysts are similar to those of CSF.[76] Water molecules in arachnoid cyst demonstrate a high diffusibility, as there is no structure impeding their motion (see Figure 8). On the other hand, the water molecules are impeded by tumor contents, such as keratinous debris (see Figure 9).[77] As a result, DWI can be used to better assess follow-up of surgically resected epidermoid tumors, proving efficacious in the detection of residual lesions (see Figure 10).[78] FLAIR sequence can also be used to make such differentiation, as epidermoid tumors present isointense to slightly hyperintense signal intensity.

Most meningiomas are not difficult to diagnosis on conventional MR imaging. The preoperative measurement of ADC values may predict the malignancy of meningiomas, which may be useful in deciding

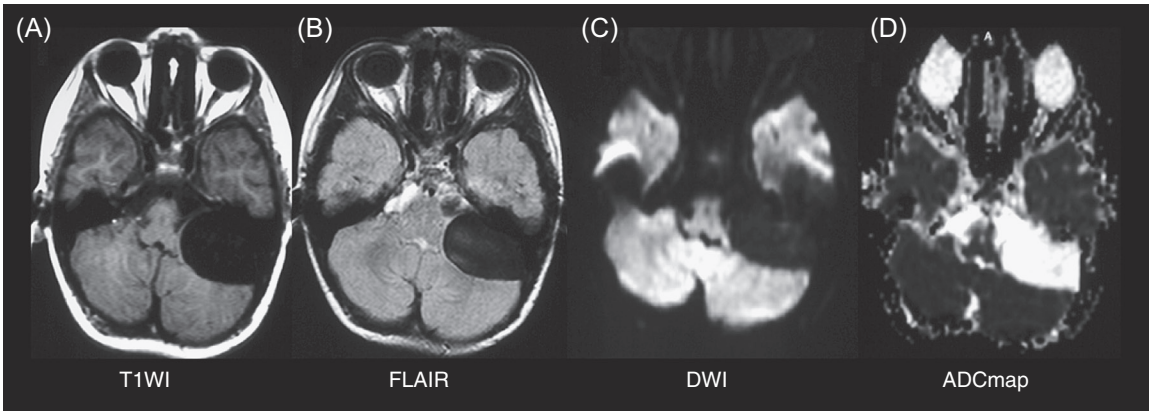


FIGURE 8 A 3-year-old girl with arachnoid cyst in the left cerebellopontine angle cistern. (A) Axial T1-weighted image and (B) FLAIR image show a hypointense round lesion on the left cerebellopontine angle cistern that causes compression to the left cerebellum hemisphere. (C) Diffusion-weighted image demonstrates a hypointense signal, with high diffusibility seen on the apparent diffusion coefficient map (D), which is isointense relative to cerebrospinal fluid.

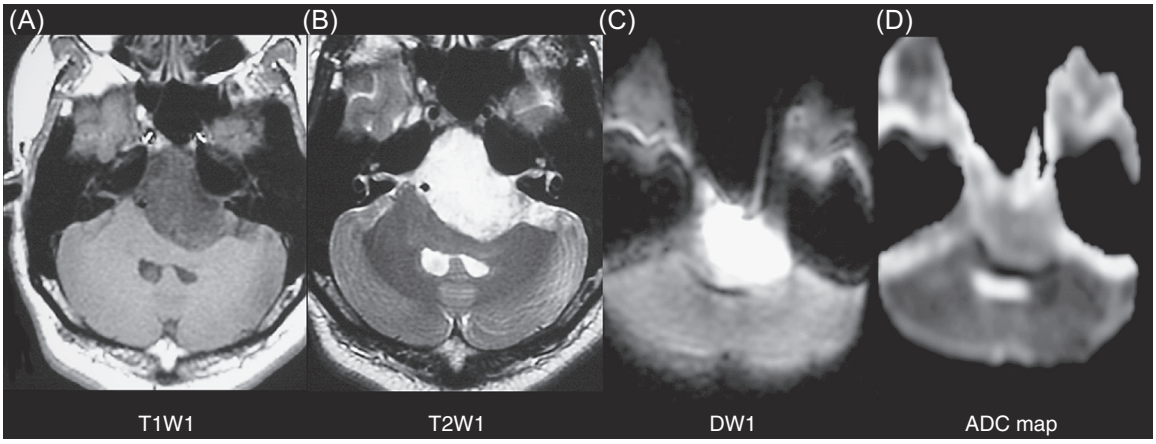


FIGURE 9 A 27-year-old man with epidermoid tumor in the left cerebellopontine angle cistern. An expansive rounded lesion in the left cerebellopontine angle cistern presenting as (A) hypointense on axial T1-weighted image and (B) hyperintense on axial T2-weighed image is shown. (C) Axial diffusion-weighted image shows a hyperintense lesion, which an apparent diffusion coefficient map (D) shows as nearly isointense relative to normal brain parenchyma.

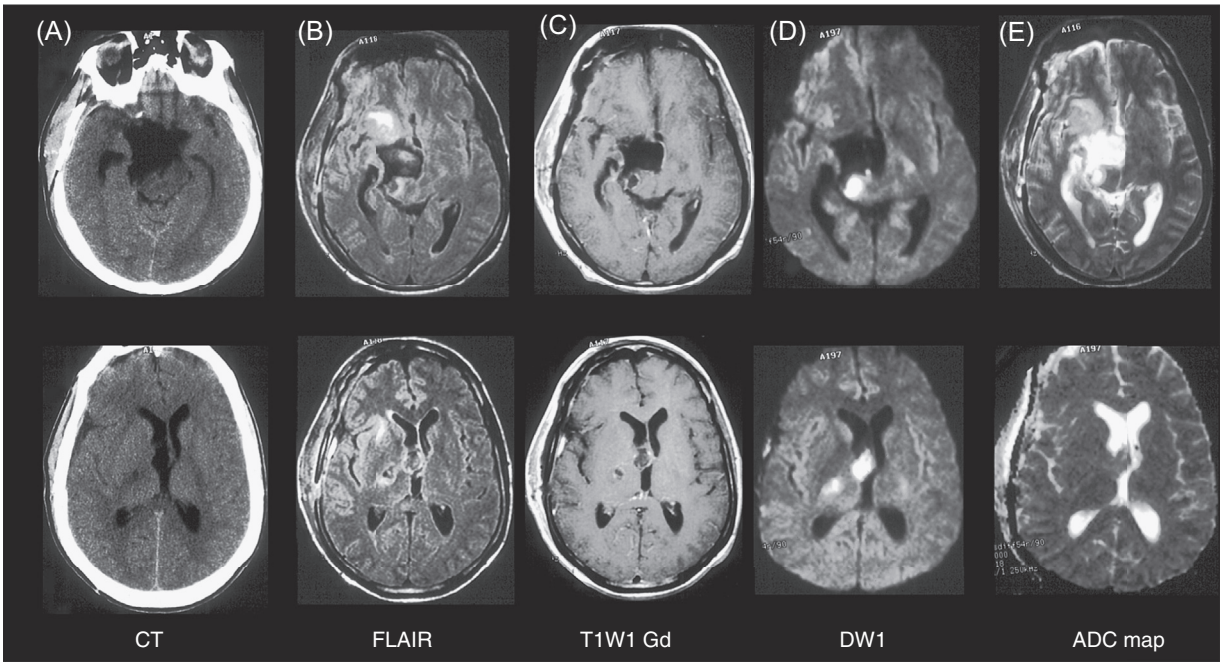


FIGURE 10 Follow-up MR exam performed 3 months after surgical resection of an epidermoid tumor in a 38-year-old man. (A) CT images show an abnormal hypodense area at the surgical site. (B) Axial FLAIR images and (C) axial contrast-enhanced T1-weighted images show postsurgical changes in the brain parenchyma, as well as an area of slight hyperintensity on FLAIR images and isointensity on T1-weighted images that may represent residual tumor. (D) Axial diffusion-weighted images can easily show a hyperintense lesion, which represents residual tumor, surrounded by a hypointense area, corresponding to postsurgical changes. (E) ADC maps obtained also demonstrate the difference between the residual tumor, with isointensity relative to normal brain tissue, and the hyperintense area corresponding to postsurgical changes, filled with cerebrospinal fluid.

on the surgical strategy or for prescribing potential adjunctive therapy. As a consequence, a more accurate prognosis may be obtained. Malignant and atypical samples demonstrated a restricted diffusion, displaying low ADC values, compared with typical meningiomas (see Figure 11).[79,80] Some aspects have been postulated to contribute to decreased ADC values in malignant and atypical meningiomas—hypercellularity, a high nuclear-to-cytoplasmic ratio, prominent nucleoli, and decreased extracellular water.[80]

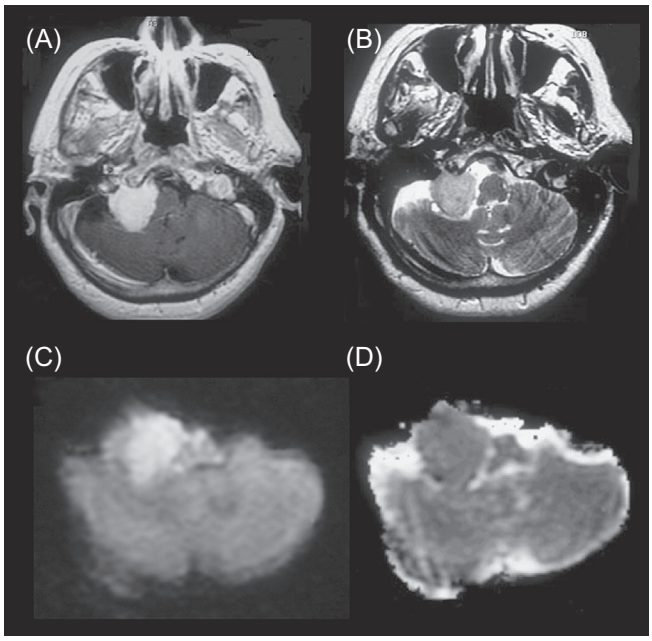


FIGURE 11 An 84-year-old woman with meningioma. (A) Axial post-contrast-enhanced T1-weighted image and (B) axial T2-weighted image show an extra-axial enhancing lesion in the right cerebellopontomedullary angle cistern. (C) Axial DWI demonstrates increased signal intensity owing to restricted diffusion, caused by increase in cellularity with low ADC values on ADC map (D).

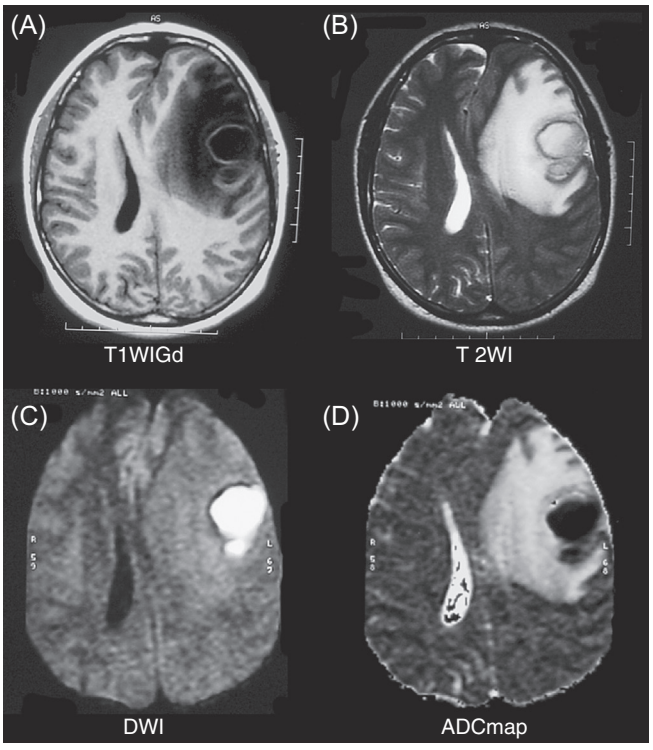


FIGURE 12 A 23-year-old man presenting with early onset of headache and speech difficulties. (A) Axial postcontrast T1-weighted image and (B) T2-weighted image show an expansive, necrotic rim-enhancing lesion, surrounded by vasogenic edema, causing mass effect to the adjacent brain parenchyma compressing the ipsilateral ventricle. The lesion has restricted diffusion, owing to its high viscosity content, presenting with high signal intensity on (C) DWI and (D) low ADC values.

CHARACTERIZATION OF INTRA-AXIAL CYSTIC MASSES

A number of groups have suggested that DWI can aid in the distinction between brain abscesses and necrotic and cystic neoplasms on MRI. This differentiation is still a challenge in both clinical and radiological settings. Early studies suggested that DWI can provide a sensitive and specific method for differentiating tumor from abscess in certain settings.[81–84] The abscesses have a high signal on DWI and a reduced ADC within the cavity (see Figure 12). This restricted diffusion is thought to be related to the characteristic of the pus in the cavity. Because pus is a viscous fluid that consists of inflammatory cells, debris, and macromolecules such as fibrinogen[85], this may, in turn, lead to reduced water mobility, lower ADC, and bright signal on DWI. On the other hand, necrotic and cystic tumors display a low signal on DWI (similar to the CSF in the ventricles), with an increased ADC as well as isointense or hypointense DWI signal intensity in the lesion margins (see Figure 13).[83] Although these findings can be helpful, they are of course not absolute: under certain conditions, restricted diffusion has been documented in hemorrhagic metastases, radiation necrosis, and cystic astrocytoma.[86] Moreover, the ADC values may vary greatly with the age of an abscess, the course of the therapy, the size of the lesion, and the immune status of the host. DTI can be helpful in assessing brain abscesses, adding new information to their differentiation from necrotic glioblastomas and cystic metastatic brain tumors. In an earlier paper, neoplastic lesions presented a hyperintense FA rim in the immediate zone of peritumoral edema, but not for the abscesses.[87] It has been described that FA values from the enhancing region of glioblastomas were significantly higher than those of brain metastases, and a classification model based on FA to differentiate glioblastomas from brain metastases was then reported.[88]

TUMOR GRADING

There is an attempt to determine standards for measurements, analysis, and display in order to establish the use of DWI in oncologic imaging.[89] Nevertheless, despite the numerous publications about its use in oncology, no accepted standards in measurement or analysis methods have been established. Tumor grading is very important in treatment decision and evaluation of prognosis.

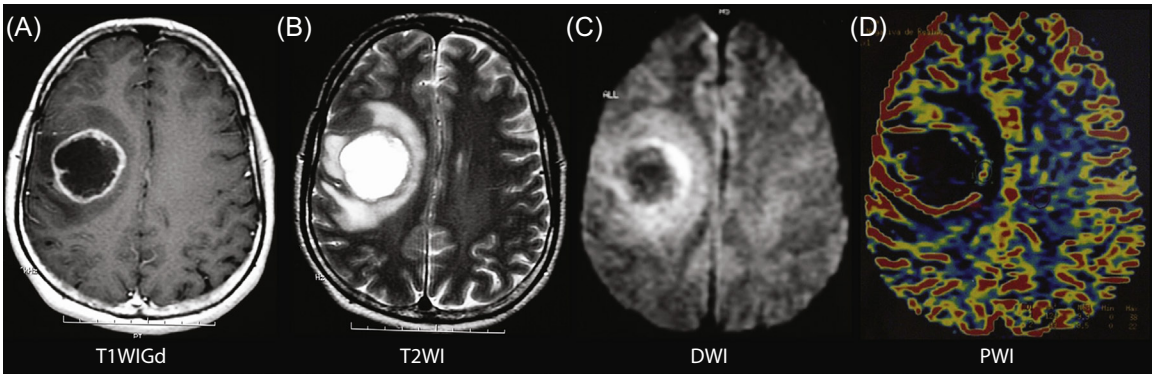


FIGURE 13 A 48-year-old man with glioblastoma multiforme. (A) Contrast-enhanced, axial T1-weighted image shows an enhancing necrotic mass, surrounded by abnormal hyperintense area on (B) the axial T2-weighted image. This abnormal hyperintense T2-weighted image area can represent peritumoral edema and/or infiltrating tumor. The tumor is iso–hypointense on the T2-weighted image, indicating high cellularity, which is also demonstrated as a restricted diffusion on (C) the DWI and high perfusion on (D) the Perfusion Weighted Imaging (PWI) map.

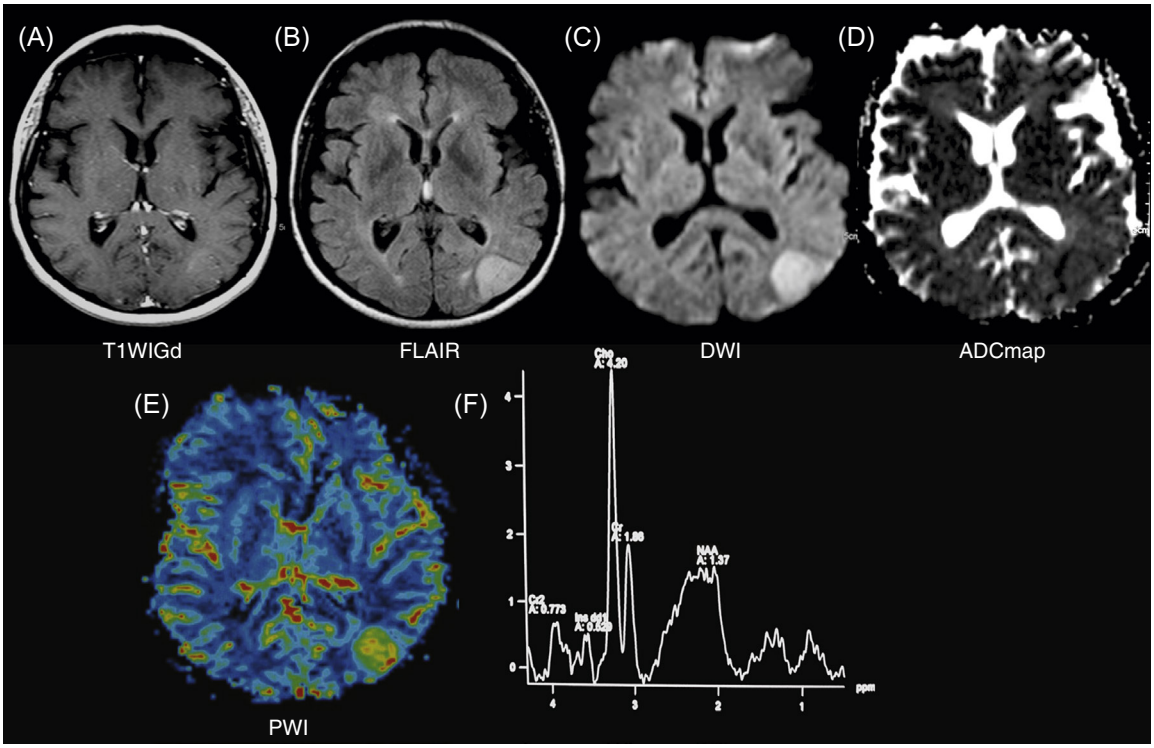


FIGURE 14 A 65-year-old man complaining of cognitive impairment with anaplastic astrocytoma. (A) Contrast-enhanced, axial, T1-weighted image shows a round cortical lesion with a slight contrast enhancing in the left occipitoparietal lobe, with hyperintensity on (B) FLAIR and (C) diffusion-weighted images and restricted diffusion on (D) ADC maps. (E) The lesion also has hyperperfusion representing neoangiogenesis. (F) Magnetic resonance spectroscopy shows markedly elevated choline peak and low *N*-acetylaspartate peak.

Whereas tissue samples are obtained as part of most therapeutic approaches, heterogeneity in tissue sampling, as well as monitoring malignant dedifferentiation and other needs, has led to a desire to use imaging to better ascertain tumor grade. In certain settings, diffusion imaging appears to increase both the sensitivity and the specificity of MR imaging in the evaluation of brain tumors by providing information about tumor cellularity, which may, in turn, improve the prediction of tumor grade.[26,90–98] The mechanism by which DWI may help in tumor grading is based on the restriction of free water molecules caused by high cellularity, high nuclear/cytoplasmic ratios, or reduction in extracellular space.[58,99] The reduction in extracellular space as well as the high nuclear/cytoplasmic ratios of some cancer cells causes a relative reduction in the ADC values (see Figure 14).[100] Some studies suggest a correlation between the ADC values and tumor cellularity,[79,99] with lower ADC values suggesting high-grade lesions (see Figure 15).[79,101] In some studies, however, ADC values found in high- and low-grade gliomas have

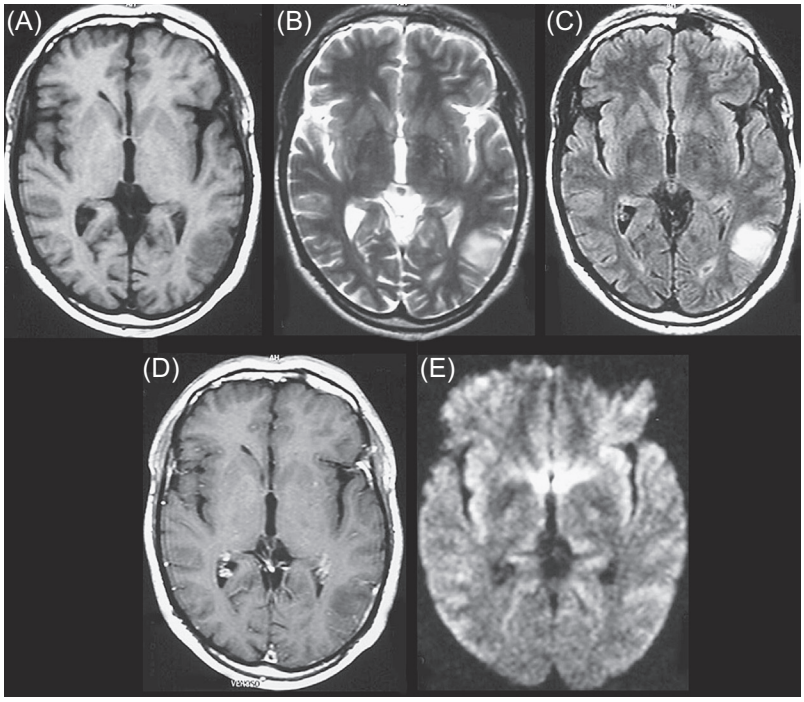


FIGURE 15 A biopsy-proven low-grade glioma in a 43-year-old man presenting with focal partial seizures in the right arm for 15 days. (A) An expansive lesion with hypointensity on T1-weighted image and (B) hyperintensity on T2-weighted image and (C) FLAIR image, which does not enhance in (D) the post-contrast-enhanced T1-weighted image. (E) Axial diffusion-weighted image does not show restricted diffusion.

overlapped somewhat.[79] This is caused by the heterogeneity of gliomas across different grades, or even within the same grade. Then, the range of ADC values within a given glioma can vary markedly. The DKI technique has also been reported by some authors as a sensitive technique to analyze tissue heterogeneity in gliomas, allowing for the differentiation between high- and low-grade gliomas.[37,38] The principal metric of DKI is mean kurtosis, which is a qualitative metric able to measure overall diffusional heterogeneity in brain tissue. This metric is independent of direction and has been reported to increase in high-grade gliomas.[37,38] High-grade gliomas are characterized by higher cellularity, more nuclear atypia, more prominent pleomorphism, and more vascular hyperplasia and necrosis, all of which restrict the diffusion of water. Consequently, microstructural complexity and heterogeneity are higher in high-grade gliomas than in low-grade gliomas. Because heterogeneity of the diffusion environment from compartmentalization also results in non-Gaussian probability distribution of water diffusion, DKI is able to quantify it.

Diffusion tensor imaging has also been used to attempt grading of brain neoplasms and seems to provide some utility by assessment of tumor cellularity. To date, the additional information provided by DTI has not yet been shown to correlate with tumor cellularity,[102] because a high degree of fiber tract disorganization in the tumor core is thought to be present.[103] Nevertheless, one report has argued that FA can distinguish high-grade gliomas from low-grade gliomas.[104] This study found a significant difference between the FA when only the solid portion of the lesion was analyzed, avoiding the necrotic and cystic portions. The FA values in high-grade gliomas were higher than those in the low-grade gliomas, which was taken to suggest higher symmetry of histologic organization. However, these results are somewhat contradictory to the usual understanding of the microstructure of high-grade gliomas. The histological characteristics of high-grade gliomas compared with those of low-grade gliomas typically reveal pleomorphologic structures and a regressive organization, rather than an increase in parallel histological organization.[104] A separate report found no differences between low- and high-grade gliomas with regard to FA values in the tumor center. This may be consistent with the disorganization of fiber tracts in the center of both entities, resulting in a loss of structural organization.[103]

The hope for mean diffusibility of brain tumors to be a parameter for tumor classification has yet to be fulfilled. Further complicating this situation is that mean diffusibility in brain tumors is probably influenced by tumor cellularity, intra- or extracellular edema, and tumor necrosis, at least at the typical b value of 1000 s/mm^2. This multifactorial influence probably makes mean diffusibility too nonspecific of a parameter for tumor grade or infiltration and does not give a specific perception of tumor classification.[103]

Owing to all of these issues, evaluation of tumor grade with diffusion imaging remains uncertain in clinical practice. But there is accumulating evidence about the biological meaning of DWI, DTI, and DKI in oncologic imaging.

STRATIFYING TUMOR HISTOLOGY

The use of DWI in the evaluation of neoplasms provides information on microstructural characteristics of a tumor. ADC is a remarkable quantitative biomarker of cellularity, and this has been described as a means to help stratify tumor histology.[105–107] With the wide clinical availability of DWI, measurements of ADC values are more frequently integrated into conventional imaging analysis and may help stratify some differential histologic diagnoses. In some studies, lymphoma, a highly cellular tumor, has been found to present hyperintense signal intensity on DWI and reduced ADC values,[108] and it may be in differentiating lymphoma from other CNS lesions that DWI has its greatest value (see Figure 16). In a previous study, the ratio of ADC values in the center of rim-enhancing intracranial lesions relative to normal-appearing white matter was significantly higher in patients with toxoplasmosis than in patients with lymphoma.[109]

DWI may also be helpful in distinguishing medulloblastoma, a primitive neuroectodermal tumor, from other pediatric brain tumors. Some investigators report that medulloblastoma displays restricted diffusion, again presumably because of the densely packed tumor cells and high nuclear-to-cytoplasmic ratio (see Figure 17).[110,111] In one report, the solid enhancing portion of cerebellar hemangioblastomas on postcontrast T1-weighted images was, together with other posterior fossa neoplasms, the only one to demonstrate hypointensity on DWI. The main explanation for the high ADC values in these tumors was suggested to be the rich vascular spaces present in hemangioblastomas.[112]

DWI can add important insights regarding the differentiation of pediatric posterior fossa tumors, such as pilocytic astrocytoma, medulloblastoma, and ependymoma.[105] ADC values may play a potentially important role in the presurgical management of children with posterior fossa tumors. It may be proposed that if high ADC values are present, a patient may go directly to surgery without additional imaging of the spine, given that pilocytic astrocytomas demonstrate high values of ADC compared to medulloblastomas and ependymomas, and they are unlikely to metastasize.[105]

As described, DWI is also important in the assessment of patients with pineal tumors, helping in the

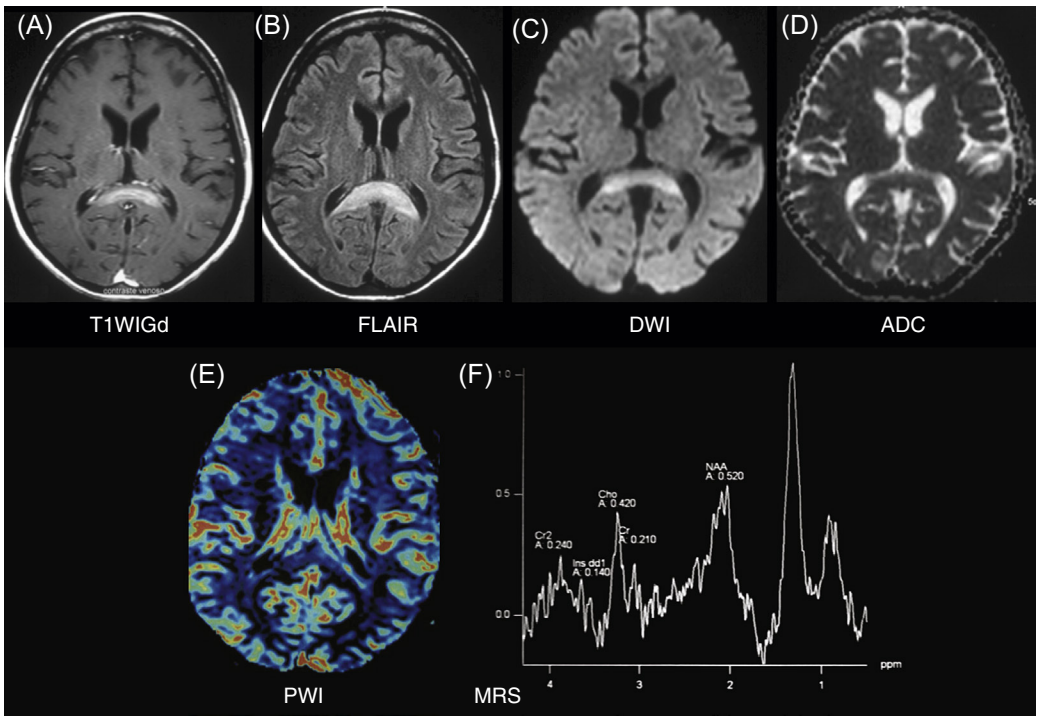


FIGURE 16 A 72-year-old female presenting with cognitive impairment and mental and language disturbance for 20 days, with a biopsy-proven diagnosis of lymphoma. (A) Axial T1-weighted image shows a lesion in the splenium of the corpus callosum, which enhances after intravenous injection of contrast and (B) has hyperintensity on the FLAIR image. (C) The lesion has restricted diffusion demonstrated by hyperintensity on diffusion-weighted image, confirmed by (D) low apparent diffusion coefficient values. (E) It does not have hyperperfusion on relative cerebral blood volume maps. (F) Magnetic resonance spectroscopy demonstrates markedly elevated lactate/lipids peaks and a low *N*-acetylaspartate peak. There is also noted a slight increase in the choline peak.

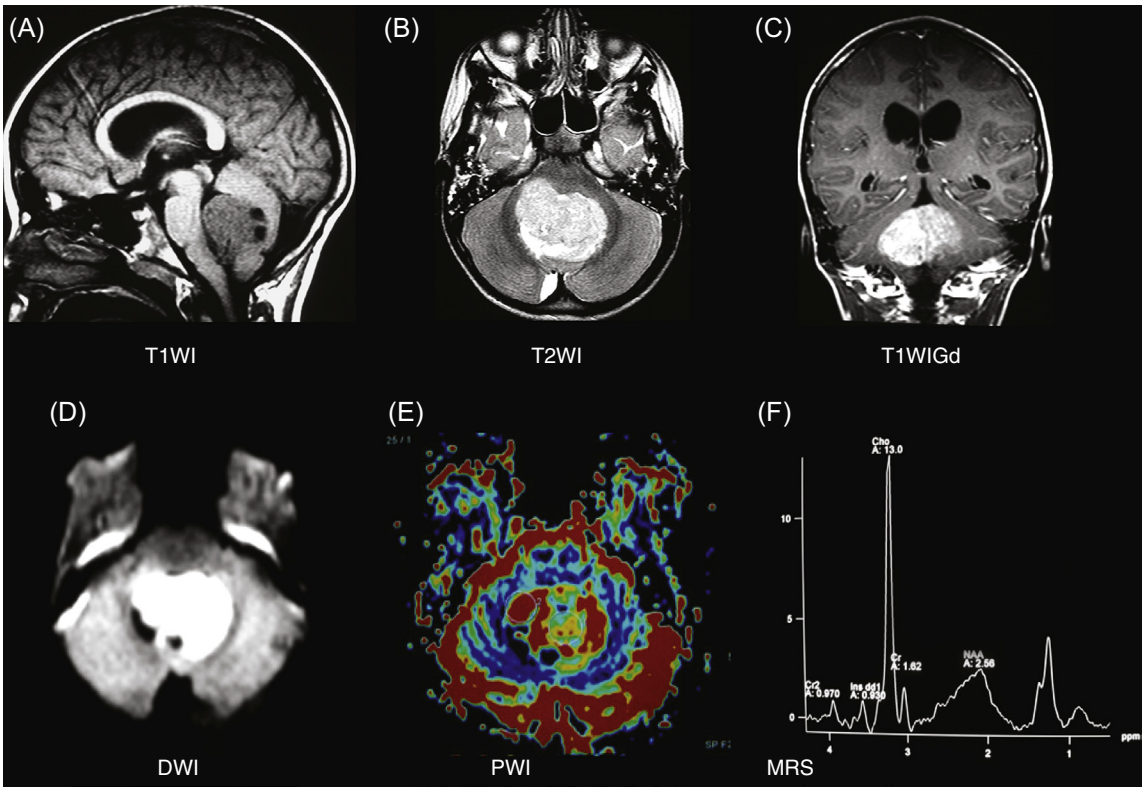


FIGURE 17 A 7-year-old boy with medulloblastoma, presenting with headache, vomiting, gait disturbance, and behavior impairment. (A) An expansive heterogeneous lesion, localized in the fourth ventricle, has isointense signal intensity on T1-weighted axial image, (B) is hyperintense on T2-weighted axial image, and (C) is enhanced after contrast intravenous injection. (D) The lesion has restricted diffusion on diffusion-weighted image, owing to the hypercellularity. (E) The lesion also presents hyperperfusion and (F) on MRS a high peak of choline, low peak of *N*-acetylaspartate, and elevation of lactate/lipids levels are also noted.

differentiation between germinomas and pineal cell origin tumors.[106] In addition, FA and ADC have been reported to allow the differentiation between primary cerebral lymphoma and glioblastoma. FA and ADC values were significantly lower for lymphoma.[107] In all these examples, the stratification was based on ADC qualitative and quantitative analysis with cutoff values. Thus, microstructural information added to conventional MRI information helps to stratify tumor histology. This kind of information may be valuable in pretreatment evaluation and surgical planning. In the case of tumors of pineal cell origin and those of germ cell origin, there is a difference between them in prognosis and treatment.[106]

To date, ADC is the noninvasive technique able to stratify tumor aggressiveness on an easy, quick, and clinically feasible basis.

PREOPERATIVE PLANNING AND PERITUMORAL MARGINS

The precise determination of the margins of the tumor is considered by many investigators to be of the utmost importance for the management of brain tumors. The goal of a surgical approach to the brain neoplasm is the complete resection of the tumor, coupled with minimum neurological deficit.[114] A variety of approaches have been used, and diffusion imaging has also been enlisted in the attempt to determine the margins of tumors in the brain. Some suggest that DWI can provide information about peritumoral neoplastic cell infiltration,[26,90–95] and perhaps even help discriminate the boundaries between tumor, infiltrating tumor, peritumoral edema, and normal brain parenchyma.[26,43,90,115] It is well-known that high-grade tumors tend to spread diffusely across the brain, moving along the fiber tracts.[116,117] However, not all studies have found DWI to be helpful in the evaluation of tumor infiltration,[79,98,118] most likely because of the difficulty in finding the borders of some tumors, even on histopathology. Given these conflicting findings, it remains unclear whether DWI or DTI is a useful tool to predict the true extent of a brain tumor. Owing to the challenges of obtaining a histological standard of reference ("gold standard"), it is reasonable to question DWI's ability to distinguish neoplastic cell infiltration beyond the enhancing portion of the lesion on the abnormal hyperintense T2-weighted image (T2WI),

which traditionally is thought to represent vasogenic edema with or without tumor invasion.

Some investigators believe that metastases with perilesional edema have higher ADC values than a primary brain tumor with peritumoral edema, and these investigators have suggested that higher ADC values may allow better differentiation between metastases and primary lesions.[92] In high-grade gliomas, the abnormal hyperintense T2 WI is thought to represent not only vasogenic edema, but also infiltrative neoplastic cells. The normal white matter extracellular space contains a complex matrix, which restricts the free motion of water molecules.[119] Increased permeability of the blood–brain barrier produces a vasogenic edema that surrounds the brain tumor.[120] Invasive neoplastic cells have been found to destroy the extracellular matrix.[121] Following this logic, cell infiltration alters the integrity of the extracellular matrix, reducing the obstruction for free water molecules to diffuse. However, this logic is somewhat speculative, and vasogenic edema with neoplastic cell infiltration may be found in high-grade gliomas, whereas in cases of meningiomas, metastases, and low-grade gliomas vasogenic edema without neoplasm infiltration is seen—both with similar ADC values.

Whereas the specific biophysics of perilesional edema remains unclear, and ADC alone may not differentiate peritumoral edema with infiltration from peritumoral edema without infiltration, a number of investigators have reported that DTI can detect variations in FA values around lesions. This has in turn led some to speculate that these variations may be due to the presence of infiltrative tumor. However, it is not clear if infiltrating tumor will destroy fibers, and therefore result in lower FA, or if the tumor infiltrating along the fibers actually increases FA by having more ultrastructural alignment with the fibers. One report did not find any significant difference between the FA values of the enhancing and the nonenhancing portion of the two neoplastic lesions,[122] but another report has verified that the periphery of low-grade gliomas, without abnormal hyperintense signal on the T2 WIs images, contains a considerable amount of preserved fiber tracts (high FA values), whereas most tracts are disarranged in high-grade gliomas (low FA values).[103] Diffusion tensor imaging seems to demonstrate that the periphery of low-grade gliomas contains preserved fiber tracts, whereas most tracts are disarranged in grade III gliomas. However, the presence of edema can obscure fiber tracts that are present.

The involvement of the white matter tracts can often be identified in brain tumor patients by using either anisotropy maps (FA maps are the most widely used) or tractography or both. Based on DTI findings resulting from studies of brain tumor patients, the white matter involvement by a tumor can be arranged into five different categories[96,97]:



FIGURE 18 Pattern of main fiber tract involvement: displaced. Maintained normal or slightly decreased anisotropy, situated in an abnormal location or presenting in an abnormal orientation. It confirmed an intact tract.

1. Displaced: maintained normal or slightly decreased anisotropy relative to the contralateral tract in the corresponding location but situated in an abnormal T2WI signal-intensity area or presented in an abnormal orientation (see Figure 18);
2. Invaded: reduced anisotropy; the main fiber tracts remain identifiable on oriented color-coded FA maps (see Figure 19);
3. Disrupted: marked reduced anisotropy; the main fiber tracts are unidentifiable on oriented color-coded FA maps (see Figure 20);
4. Infiltrated: slightly reduced anisotropy without displacement of white matter architecture; the fibers remaining identifiable on orientation maps (see Figure 21);
5. Edematous: marked reduced anisotropy with normal oriented on color-coded FA maps, but located in an abnormal T2WI signal-intensity area (see Figure 22).[102]

Displacement rather than destruction of white matter fibers (as suggested by FA) around low-grade gliomas has been described[28,113], and this is consistent with structural imaging approaches. Low-grade neoplasms (see Figure 5) are typically well-circumscribed lesions that do not cause invasion or destruction of fiber tracts.

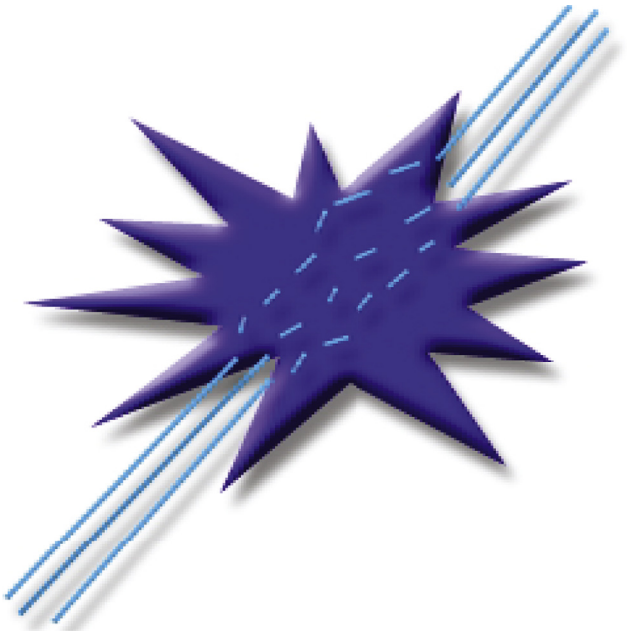


FIGURE 19 Pattern of main fiber tract involvement: disrupted. Marked reduced anisotropy and unidentifiable orientation color-coded fractional anisotropy maps.

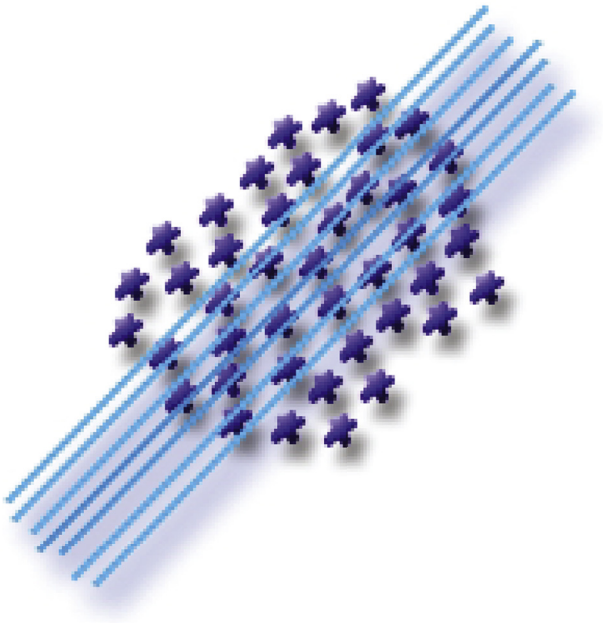


FIGURE 21 Pattern of main fiber tract involvement: infiltrated. Slightly decreased anisotropy without displacement of white matter architecture, remaining identifiable on orientation color-coded fractional anisotropy maps and tractography.

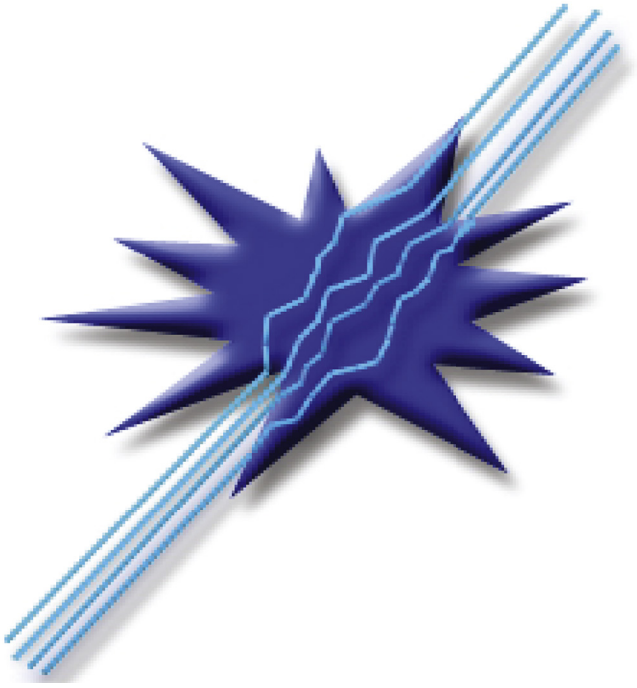


FIGURE 20 Pattern of main fiber tract involvement: invaded. Reduced anisotropy, but remaining identifiable on orientation color-coded fractional anisotropy maps.

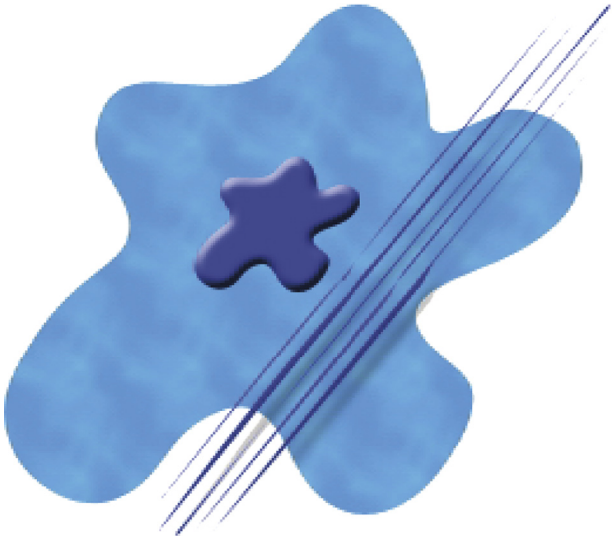


FIGURE 22 Pattern of main fiber tract involvement: edematous. Marked reduced anisotropy with normal orientation, but located in an abnormal T2-weighted signal-intensity area.

Such lesions tend to produce a displacement or deviation of surrounding white matter fibers (see Figure 23). This is not absolute: one study described a case in which the corticospinal tract had been infiltrated by an oligodendroglioma that, nevertheless, had spared the motor strip and the posterior limb of the internal capsule.[123] Furthermore, displacement rather than infiltration of the adjacent white matter tracts has also been described in cerebral metastases[28] and meningiomas.[124] Finally, in some cases of high-grade gliomas, the tumor could cause not only invasion and disruption of the main fiber tracts but also associated displacement

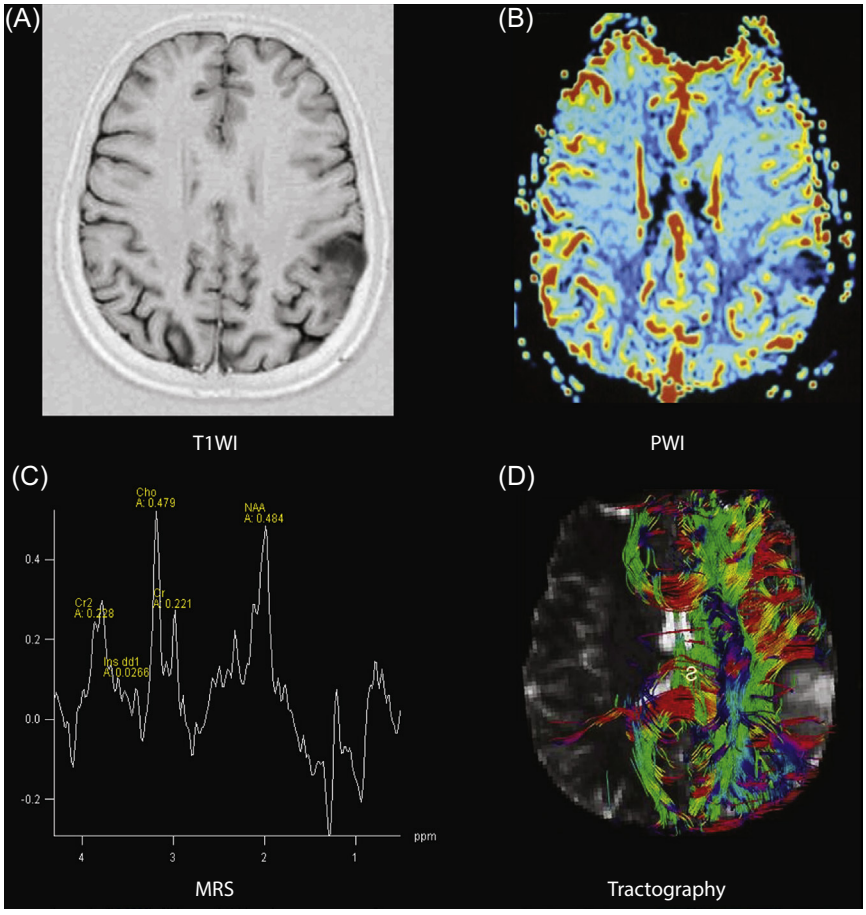


FIGURE 23 A 42-year-old man with a diagnosis of a low-grade astrocytoma presented with early onset of focal seizures. (A) The MRI examination demonstrates an expansive lesion in the peri-rolandic area, (B) which does not have hyperperfusion. (C) Magnetic resonance spectroscopy depicts increased peak of choline, reduced *N*-acetylaspartate and no lactate/lipids. (D) The mass lesion causes displacement of the main fiber tracts adjacent to the tumor, which is well demonstrated on tractography. There seems to be invasion or disruption of these tracts.

(see Figure 24). So although DTI can identify tracts and help determine the presence or absence of invasion versus displacement, the presence or absence of displacement does not appear to be highly diagnostic for high- or low-grade malignancy.

Both vasogenic edema and tumor tissue appear to be more isotropic than normal white matter. Thus, the anisotropy in the T2WI hyperintense area that surrounds the tumor is typically reduced, either because of invasion of neoplastic cells or because of edema. One report has noted that in patients with high-grade gliomas, but not with low-grade gliomas or cerebral metastases, the anisotropy is also low in the white matter areas adjacent to tumors that look normal on T2WI (compared with the contralateral hemisphere).[28] The same situation has been reported in lymphomas. Compared with the abnormal white matter adjacent to metastases, decreased anisotropy in the abnormal white matter that surrounds the gliomas was demonstrated.[123] FA values decrease in the abnormal area that surrounds high-grade tumors on T2-weighted imaging. Again, this presumably happens because of increased water content and also tumor invasion.[29] This is not uniform: a certain number of studies have not found any difference in the analyses of abnormal white matter adjacent to high-grade gliomas and metastases.[29]

One important finding, the presence of tract disruption, is mostly found in high-grade tumors and is thought to be caused by a combination of peritumoral edema, tumor mass effect, and tumor infiltration effect (see Figure 25).[28,124] Although anatomic disruption and functional disruption are not necessarily equivalent, the ability to visualize tracts has led to a number of investigations in this area. The main fiber tracts are infiltrated in cases of gliomatosis cerebri, which has a specific histopathologic behavior. In this lesion, the neoplastic cells form parallel rows among nerve fibers, preserving them. However, there is destruction of the myelin sheaths. Thus, the anisotropy is slightly reduced compared to normal subjects but increased compared to high-grade gliomas.[125] The main fiber tracts can remain

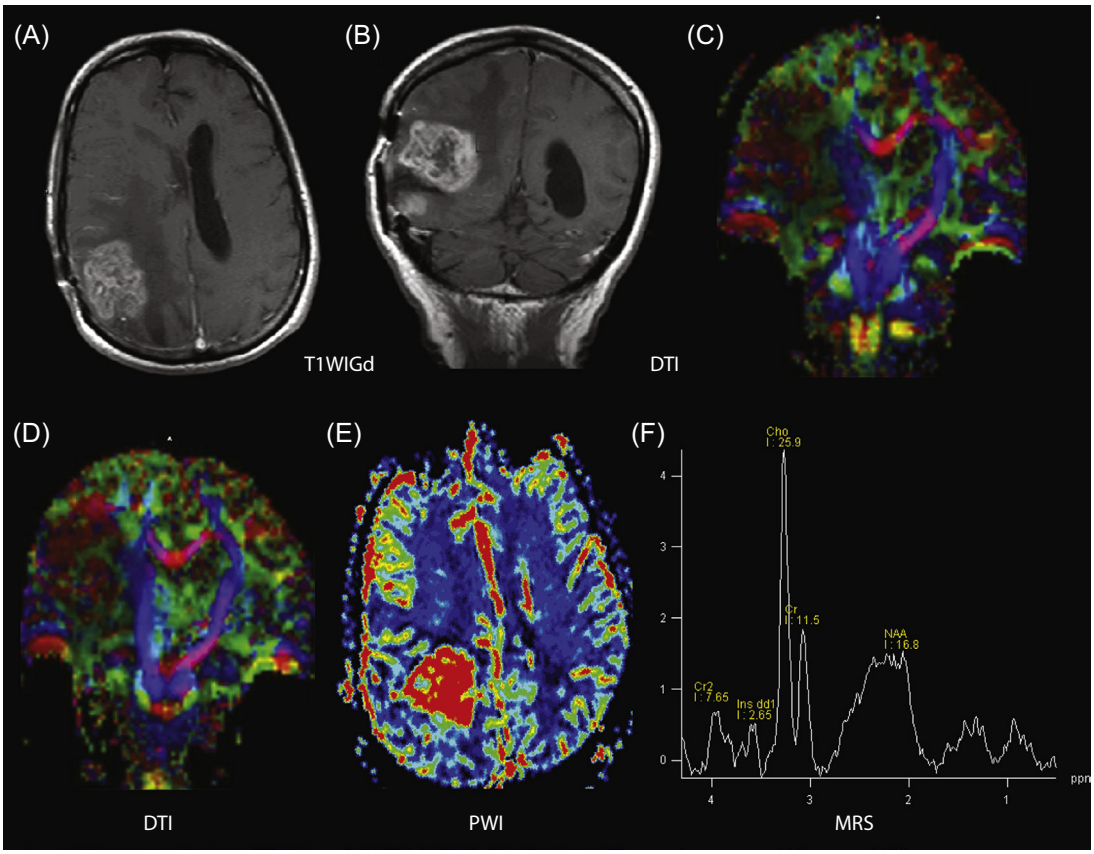


FIGURE 24 (A, B) An expansive and infiltrating lesion in a 73-year-old man with left hemiparesis and seizures, with the diagnosis of glioblastoma multiforme. (C) The lesion has hyperperfusion and (D) markedly elevated choline and lactate/lipids peaks and a low *N*-acetylaspartate peak. (E, F) Coronal diffusion tensor imaging–fractional anisotropy color-coded maps show that the lesion dislocates and infiltrates the corticospinal tract and the superior longitudinal fasciculus. There is also distortion of the corpus callosum.

identifiable on orientation maps and also on the tractography (see Figure 26).

Metastatic lesions are surrounded by abnormal T2WI that most likely consists of vasogenic edema. The edematous areas have reduced FA values. This fact is typically explained by an increase in water content rather than by destruction or invasion of nerve fibers to be consistent with neuropathologic findings (see Figure 27). DTI has not been reported to help in the differentiation of apparently normal white matter from edematous brain and enhancing peritumoral margins.[126] The drop in FA values of the area infiltrated by tumor cells is lower than that in the peritumoral edema.[3,27,102] DTI can distinguish edematous areas with intact fibers—mostly found in metastases—from disrupted fibers—mostly found in high-grade gliomas.[127] However, the drop in FA values can vary depending on the degree of neoplasm infiltration and the amount of peritumoral edema.

Intracranial neoplasms may involve both the functional cortex and the corresponding white matter tracts. The preoperative identification of eloquent areas through noninvasive methods, such as blood-oxygen-level-dependent (BOLD) functional MR imaging (fMRI) and DTI tractography, offers some advantages; not only can it reduce the time of surgery in some instances, but also it may minimize some intraoperative cortical stimulation methods, such as the identification of the language cortex.[127] Until recently, preoperative and perioperative methods to evaluate brain function of patients with brain tumors were restricted to cortical activation studies. Increasingly, however, investigators are beginning to combine fMRI with DTI. The attraction is that fMRI can be an accurate and noninvasive method used to map the functional cerebral cortex, identifying eloquent areas in the cortex, and displaying their relationship to the lesion,[128] whereas DTI may be able to accurately identify the main fiber tracts to be avoided during surgery so as to safely guide the tumor resection.[3] Consequently, the combination of DTI tractography and fMRI might allow us to precisely map an entire functional circuit (see Figure 28).[129] Even though fMRI locates eloquent cortical areas, determination of the course and integrity of the fiber tracts remains essential to the surgical planning.[127,130] This identification of the fiber tracts can facilitate reaching a decision regarding the likelihood of an operation.[3] As a result, neurosurgeons may have more

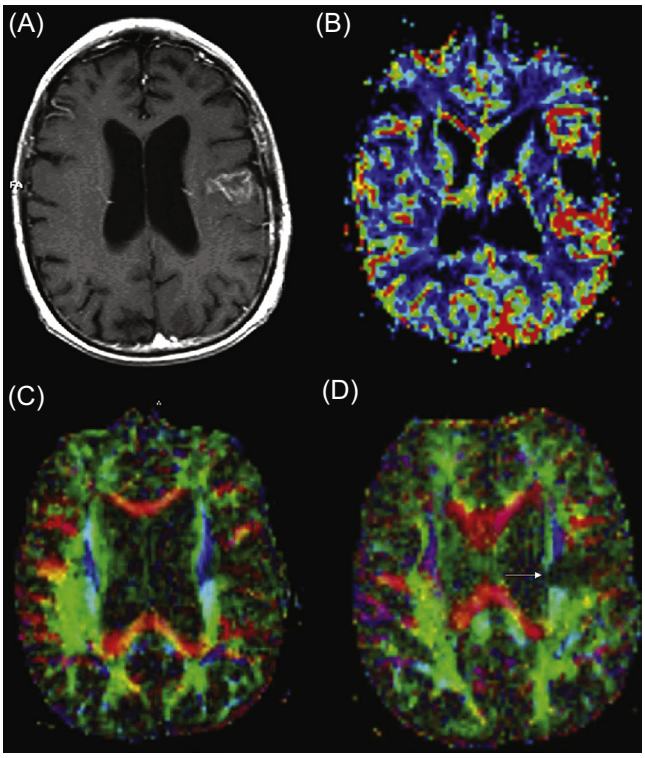


FIGURE 25 A 56-year-old man with an anaplastic astrocytoma, presented with right hemiparesis. (A) The contrast-enhanced T1-weighted image shows a left frontal lesion that has hyperperfusion on (B) the relative cerebral blood volume map—note the black signal caused by excessive enhancement with resulting T1 effect. (C, D) The axial diffusion tensor imaging–fractional anisotropy color-coded maps demonstrate disruption of the left corona radiata (arrow).

information to inform the choice of surgical approach to be taken. This better evaluation of risks by neurosurgeons is possible if they can know the spatial relation between the tumor and the major fiber tracts,[63] thereby avoiding postoperative neurological deficit.[4,130] However, this remains to be proven in randomized trials.

Many investigators hope that the combined use of fMRI and DTI tractography might define the structural basis of functional connectivity in normal and pathological brains[131] and allow for improved intraoperative guidance. Because fMRI is in many instances able to depict the exact location of the motor cortex, it should be possible to delineate the corticospinal tract by DTI tractography. Modern neurosurgical navigation systems typically provide a probe-guided intraoperative MR display of the brain.[132] Such systems are already widely used and in some cases able to combine the information of fMRI[127,132] with that of DTI tractography[129,133] or even of both together.[124,128]

INTRAOPERATIVE DIFFUSION IMAGING

The extent of resection of a brain tumor appears to be a prognostic factor for survival and time to recurrence.[134,135] Therefore, the ability to determine intraoperatively whether the resection is incomplete should be highly advantageous.[136] Intraoperative MR imaging (iMRI) has been used to guide brain tumor resection.[137] With the advent of DTI, iMRI can be used to assist in the preservation of the main fiber tracts; this is desirable to avoid postoperative neurological deficits.

The rationale for iMRI is straightforward: surgical manipulations and maneuvers alter the anatomic positions of brain structures and the tumor,[138] and morphological changes in the brain may also occur between the time of the preoperative MRI exams and the time of the surgery.[139] Therefore, the exact location of brain tumors based on preoperative exams may not be the same (i.e., brain shift).[140] Intraoperative MRI has been proposed as a possible way to enable neurosurgeons to optimize their surgical approaches by avoiding critical structures and the adjacent normal brain parenchyma.[138] Some reports suggest that in 65–92% of the cases in which neurosurgeons believed they had performed a complete and thorough tumor resection, the iMRI still demonstrates tissue to be resected,[137,141] because such lesions can be difficult to differentiate from the normal brain parenchyma visually.

In a similar manner, many investigators have suggested that DTI performed intraoperatively could add information regarding the integrity of main fiber tracts, which again may have shifted during the procedure. Findings from iMRI led to the modification of surgical procedure in almost 30% of patients in a 2004 report,[140] with investigators reporting that intraoperative DTI was able to depict changes in fiber orientation secondary to craniotomy or burr-hole procedures.[136]

Intraoperative MRI can have the full range of MRI capabilities, including functional sequences such as fMRI[137] and DWI (e.g., screening for intraoperative development of hyperacute cerebral ischemia).[133] DTI, together with a neuronavigation system, can give the neurosurgeon new insights regarding important information during the excision of a tumor. Registration of the relation between brain tumor lesion and main fiber tracts in the neuronavigator system facilitates the preservation of these fibers. For this purpose, to compensate the brain shift, updating the neuronavigating information with intraoperative data should be necessary.[136]

A study was performed to evaluate the practical value of 3.0-T intraoperative MRI with intraoperative DTI in surgery close to the corticospinal tract and to compare high-field DTI with intraoperative neurophysiological corticospinal tract mapping during glioma and metastasis resection in a routine setting. Intraoperative image distortion appeared in 36% of the cases and, even though the combination of the two methods in selected cases could help increase the safety of tumor resection close to the corticospinal tract,

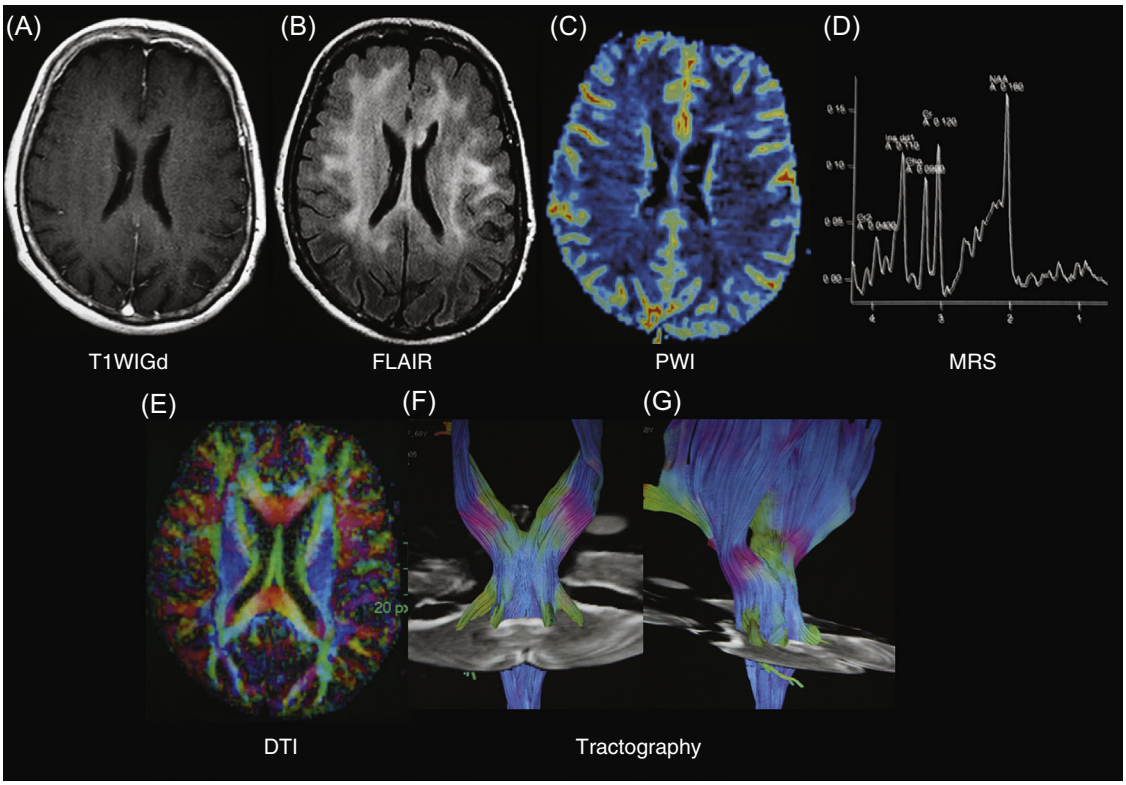


FIGURE 26 An invading white matter lesion that extends to both hemispheres, involving the frontoparietal lobes through the corpus callosum in a 68-year-old woman who presented with cognitive impairment. The diagnosis of gliomatosis cerebri was made after a biopsy. (A) The lesion does not enhance on the postcontrast T1-weighted image, (B) has hyperintense signal on the FLAIR image, and (C) does not have hyperperfusion on the relative cerebral blood volume map. (D) Magnetic resonance spectroscopy shows a high myoinositol peak, a moderately high choline peak, and a subtle reduction on the *N*-acetylaspartate peak. (E) The diffusion tensor images–fractional anisotropy color-coded map and (F, G) tractography demonstrate that the main fiber tracts are preserved. This is probably explained by the fact that gliomatosis cerebri is a diffusely invading lesion that preserves the normal underlying cytoarchitectural pattern because it does not destroy the nerve fibers.

the neurophysiological subcortical mapping remained superior to DTI.[142]

Although anecdotal, such reports suggest that intraoperative diffusion imaging may provide important clinical information, adding substantially to the intraoperative information available about the pathologic state of the brain parenchyma and the structure of white matter.

POSTTREATMENT EVALUATION

Assessment of treatment response typically relies on the assessment of contrast enhancement on subsequent imaging studies within 24–48 h after the surgical procedure[143] and then later by the evaluation of tumor size weeks to months after conclusion of therapy.[144] The appearance of a new enhancing area often results in management alterations, leading frequently to adjuvant therapy. A 2005 report observed the benefits of performing DWI in immediate postoperative MR examinations.[143] Areas of restricted diffusion were described adjacent to low- or high-grade glioma tumor resection cavity. Follow-up MR examinations revealed that these areas of restricted diffusion resolved, and that contrast enhancing appeared in the corresponding location. This enhancement subsequently regressed to form an area of encephalomalacia. Because conventional MR examination at the time of the enhancement period is easily misdiagnosed as tumor recurrence or tumor progression, such findings can lead to erroneous interpretation of treatment failed and the initiation of a new adjuvant therapy. Investigators have concluded that a corresponding area of restricted diffusion almost always precedes the delayed contrast enhancement described, which invariably evolves into encephalomalacia or a gliotic cavity on long-term follow-up studies. Although this needs to be reproduced in other studies, one can speculate that reduced diffusibility in and around the surgery bed may represent areas of infarct, ischemia, or even venous congestion, secondary to acute cellular damage, such as surgical trauma, retraction and vascularity damage, and tumor devascularization.[100]

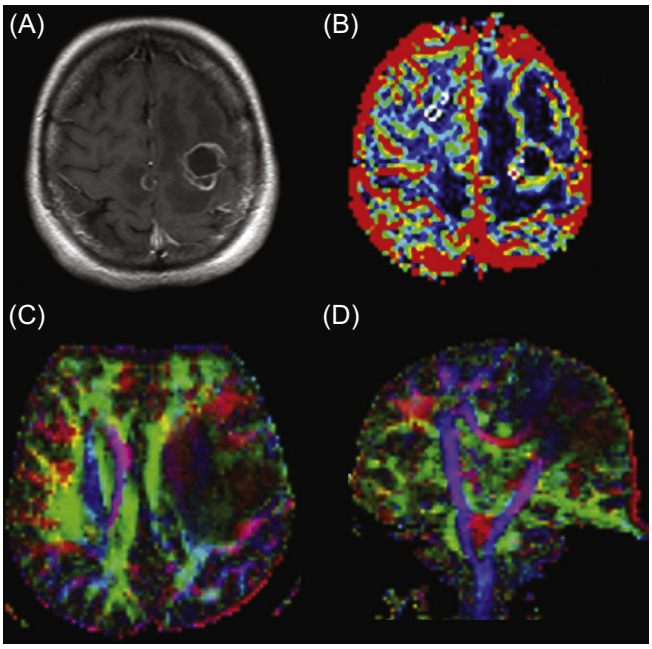


FIGURE 27 A 50-year-old woman with new onset of seizures and history of breast cancer. (A) A round rim-enhancing lesion with a necrotic center and (B) hyperperfusion is surrounded by peritumoral edema, consisting of breast cancer metastasis. (C) Axial and (D) coronal diffusion tensor images–fractional anisotropy maps show the edematous changes in the FA values. Thus, it is difficult to identify the main fiber tracts within the vasogenic edema. This does not necessarily mean that these fibers are infiltrated or disrupted, however.

Such findings are unlikely to represent early recurrence (see Figure 29).

DWI might also be a biomarker for the response to therapy because of changes in tumor water diffusibility, which may occur secondarily to changes in cell density, a method referred to as "functional diffusion imaging." In this methodology, ADC values are measured over time and compared on a coregistered voxel-by-voxel basis. In this setting, ADC appears to be a sensitive and early predictor of therapeutic efficacy.[145] Specifically, investigators prospectively compared tumor diffusion values at 3 weeks after initiation of therapy with pretreatment images so as to measure ADC changes induced by therapy.[146] If this methodology holds up in multicenter trials, it would allow a lack of change in ADC values in the tumor to indicate a failure in therapy. This would in turn provide an opportunity to switch to a more beneficial therapy, minimizing the morbidity associated with a prolonged and inefficient treatment. The logic behind this methodology is that successful treatment will result in extensive cell damage, leading to a reduction in cell density. The neoplastic cell loss results in an increase in extracellular space, thereby increasing free water molecule diffusibility. As increases in brain tumor ADC correspond to decreases in tumor volume in long-term follow-up studies, DWI may, therefore, be an important surrogate marker for quantification of treatment response (see Figure 30).

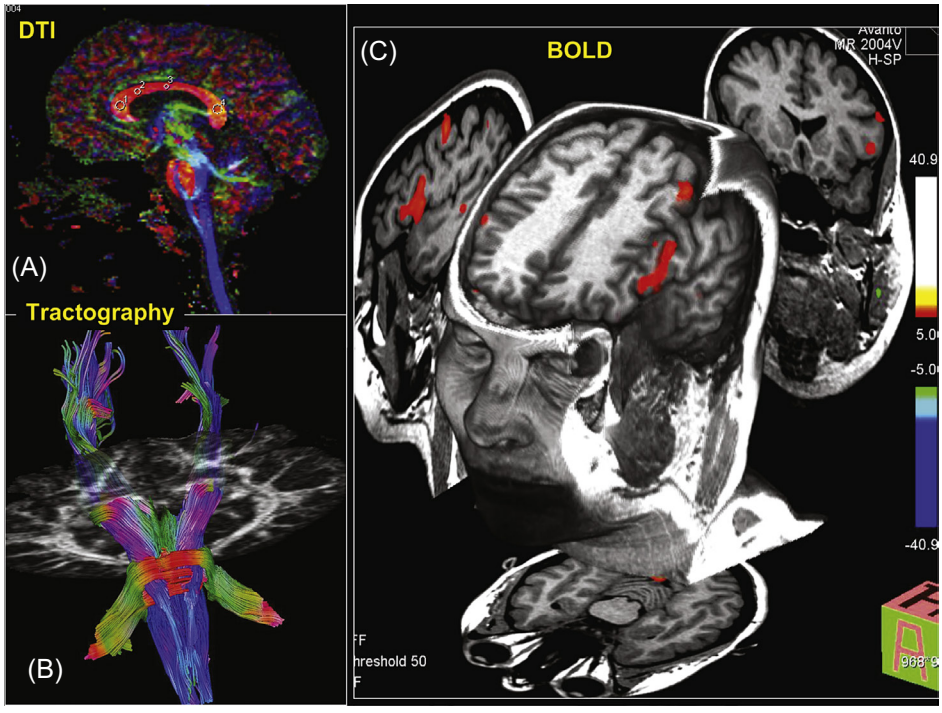


FIGURE 28 The whole brain functional circuit demonstrated with (A) the diffusion tensor MR image and (B) tractography together with (C) the BOLD sequence.

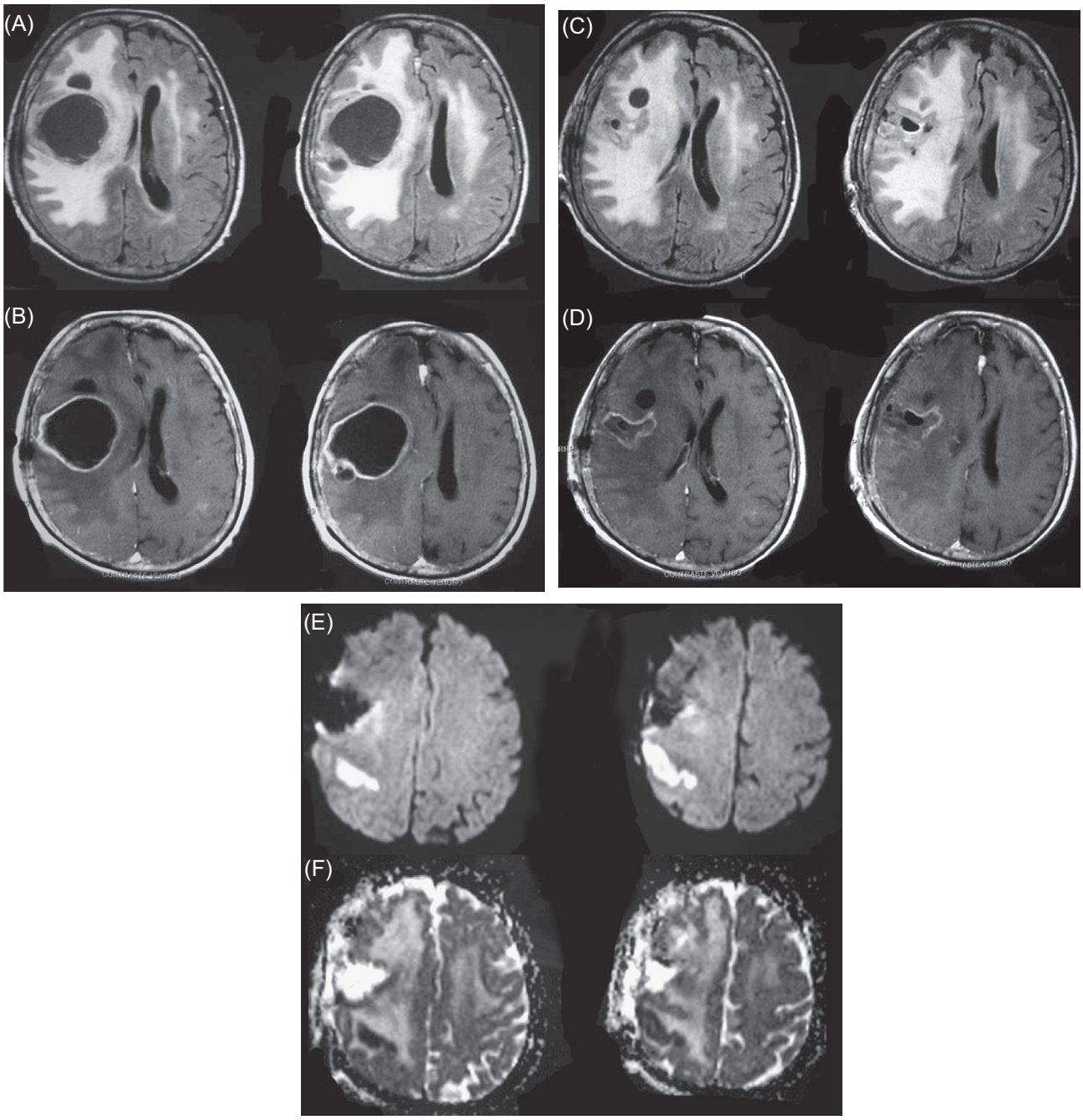


FIGURE 29 (A)A patient presenting with an expansive round rim-enhancing lesion on the postcontrast T1-weighted images, (B) with necrotic center and surrounded by hyperintense area on FLAIR images, that may consist of neoplastic infiltration and/or vasogenic edema. The diagnosis of glioblastoma multiforme was made after brain biopsy. (C, D) The follow-up exam, after surgery, shows a partial resection of the lesion. (E) The diffusion-weighted images and (F) the apparent diffusion coefficient maps show an area of restricted diffusion just adjacent to the surgery bed, consisting of acute infarct.

Last, in oncologic imaging, DWI has been linked to tumor response, and we will stress the reasons parameters derived from DWI are appealing as imaging biomarkers. First, the DWI acquisition is noninvasive, does not require any exogenous contrast agents, does not use ionizing radiation, yet is quantitative and can be obtained relatively rapidly.[89]

Since 2005, advances in molecular imaging have advanced the understanding of cancer development, growth, and spread. As a consequence, novel oncologic drugs designed to disrupt specific biological pathways of cancer growth were created. These drugs include antiangiogenic and antivascular agents. DWI can evaluate the anticancer therapy,[147] for example, the

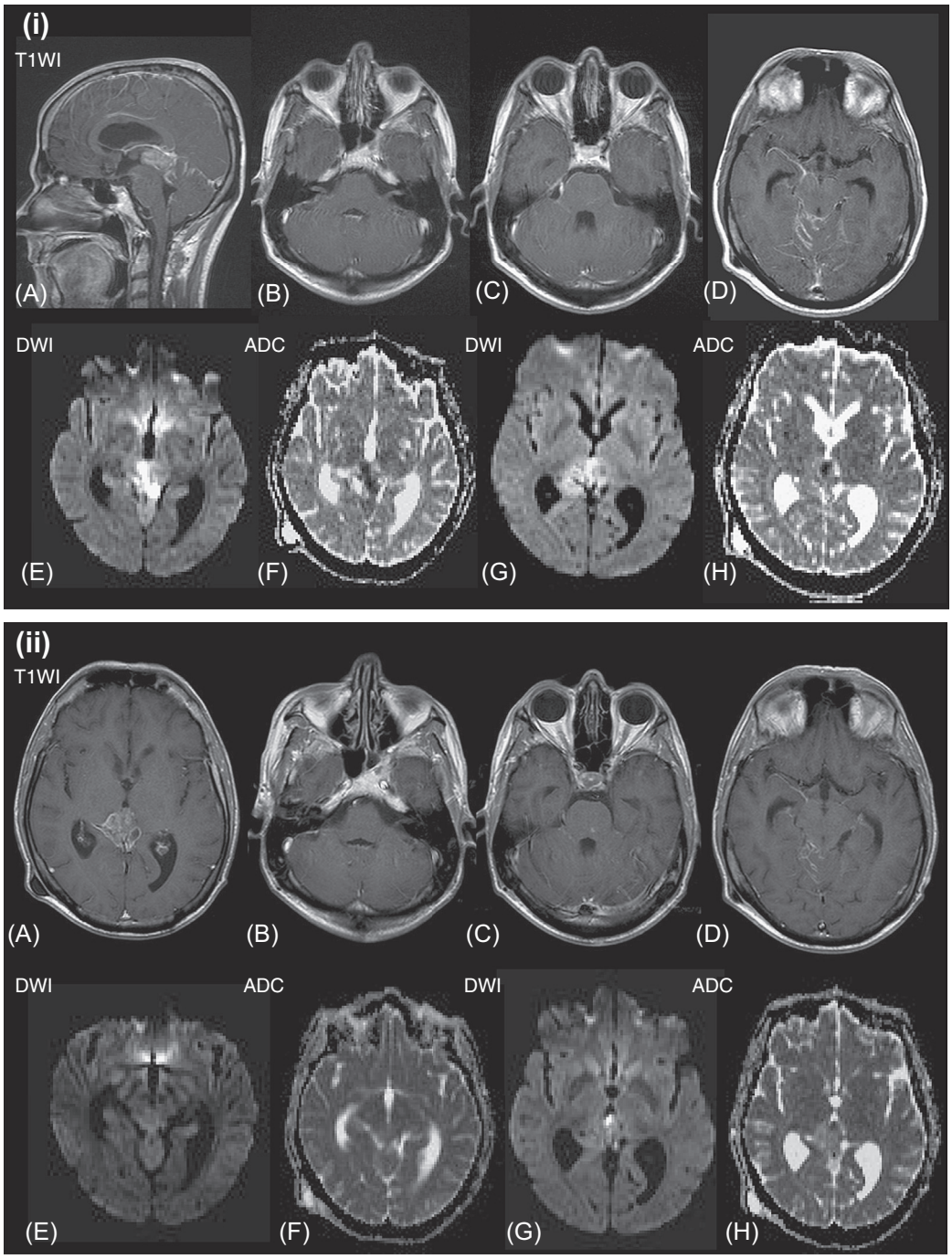


FIGURE 30 A 43-year-old man with a biopsy-proven diagnosis of pinealoblastoma. (i, A–D) The postcontrast T1-weighted images show an expansive enhancing round lesion in the pineal. There is also leptomeningeal dissemination to the cranial nerves and the cerebellum sulcus. (i, E–H) The lesion also has areas of restricted diffusion. (ii, A–D) The follow-up exam after chemotherapy and radiotherapy shows that the lesion decreased in size; there is no more leptomeningeal enhancement on the postcontrast T1-weighted images. (ii, E–H) In the axial diffusion-weighted images there are no more restricted diffusion areas within the lesion. The apparent diffusion coefficient values are higher; this might suggest a positive response to therapy.

evaluation of antiangiogenesis therapy in the treatment of high-grade gliomas by interfering with the vascular endothelial growth factor pathway. The monoclonal antibodies that block growth factors or receptors cause reductions in tumor ADC values that coincide with reductions in contrast enhancement. The principal explanation appears to be a reduction in the lesion extravascular–extracellular space secondary to vascular normalization and lowering of vascular permeability.[147] However, increases in ADC values can happen if

there is significant tumor necrosis caused by treatment. Similarly, vascular disrupting agents, which induce massive necrosis, can also cause an increase in ADC values[148,149] Thus, DWI detects apoptotic and angiolytic drug effects that alter the microenvironmental architecture.[147] In other words, any therapy that causes necrosis or cellular lysis will create increases in ADC.

Restricted diffusion can also be observed preceding the appearance of enhancing tumor in a patient under antiangiogenic therapy. Areas of low ADC values may correspond to tumor cell infiltration leading to tumor spread, whereas there is no abnormal contrast enhancement. This observation was described as a "pseudoresponse."[150] DWI has been also described to be an important tool to detect acute white matter neurotoxicity in patients using methotrexate.[151]

DTI may also play a role in the management of patients undergoing radiation therapy and chemotherapy. By adding information about the location of white matter tracts, DTI tractography might be successfully utilized alongside fMRI for radiosurgery planning. In theory, this should allow a reduction of the dose applied as well as of the volume of normal brain irradiated with a high dose, hopefully reducing necrosis.[28] DTI may also help in the early detection of white matter injuries caused by chemotherapy and radiation therapy. A report showed a correlation between reductions in FA values, young age at treatment, increased interval since the beginning of treatment, and poor intellectual outcome in patients with medulloblastoma.[152] The possibility of using FA or other DTI changes as a biomarker for neurotoxicity is enticing.

POTENTIAL FUTURE APPLICATIONS

Although DWI has been used to assess brain tumor diagnoses and treatments, to help in preoperative planning, and to guide surgery intraoperatively, there are still a number of new areas and possible future applications. These include therapy monitoring (such as the functional diffusion method described above); monitoring radiation or other treatments via quantitative assessment of white matter changes as a marker for toxicity, plasticity after surgery, radiation, or other treatment; and so on. However, many of these techniques will require improved image quality. Therapy monitoring is especially important for clinical therapeutic efficacy and personalized treatment and pharmaceutical perspectives because DWI can be used as a tool to help in the decision-making in the drug development process.[89] Specifically, DWI is an echo-planar sequence that suffers from a low signal-to-noise ratio (SNR) owing to the need for rapid acquisition approaches. The types of quantification of diffusibility or anisotropy that might allow these advanced applications are very sensitive to inadequate SNR. Mean diffusibility and FA values may vary with SNR. With the appropriate SNR, and if more powerful gradients could be used, a smaller voxel could be obtained in a clinically acceptable measurement time. The voxel size typically used in diffusion images is large enough to cause partial-volume effects and thus make it difficult to identify crossing fibers. A smaller voxel size may be helpful in solving the problem of crossing fibers and can be useful to delineate small white matter structures. Some have demonstrated a better SNR in a 3.0-T scanner. However, some challenges remain, including geometric distortions.[153] More importantly for the future, however, will be the move beyond the tensor representation of diffusion. This model fails to account for cases of intersection and dispersion of fibers in the same voxel.[154] Because insertion of fibers is the key event in linking white matter to gray matter, and because so much of the brain is composed of regions of intersecting fibers, it seems highly likely that whatever method can go beyond the tensor, to so-called "supertensor" representations, will become useful once the technology allows these techniques to be practical. One such approach is called DSI; other variants of this same approach go by other acronyms (e.g., HARDI), but the concept is the same: to move beyond the limitations of the tensor model. More recently, an analytical representation of the kurtosis equation gives the leading non-Gaussian corrections for the diffusion orientation distribution function that is a natural foundation for DKI-based fiber tractography. Potential advantages of DKI-based tractography over a DTI-based approach are greater accuracy in the estimation of fiber bundle directions and the ability to resolve intravoxel fiber crossings. It can improve fiber tractography in white matter regions, such as the centrum semiovale, where fiber crossings are common.[73] Considering the new perspective of DKI tractography and taking into consideration that a full brain DKI acquisition can be obtained in less than 10 min, whereas a full brain DSI acquisition typically requires about 30 min to 1 h, one can choose what is more feasible for its requirement. Another advanced approach for tractography is the Q-ball. It shows more dependence on the *b* value, with the accuracy improving as the *b* value increases.[73] The better understanding and assessment of both large and small fibers will almost certainly help in the evaluation of the relationship between brain neoplasm lesions and the underlying normal anatomy.

Limitations

Although initial reports suggest advantages of DWI, DTI, and DKI in the evaluation of patients with brain tumors, these reports are largely single-center, uncontrolled, preliminary findings. Therefore these results must be cautiously interpreted. Multicenter studies are

sorely needed. There are difficulties in designing prospective studies that assess certain methods, such as intraoperative MRI, for which blinding is difficult and bias inevitably is present.

As suggested above, there remain substantial technical hurdles, even though the rapid evolution of MRI systems is making ever more powerful approaches possible. Susceptibility artifacts can cause image distortion that prevents DTI data from being accurately analyzed,[27] and numerous other technical challenges remain.

SUMMARY

Diffusion imaging seems to offer the possibility of adding important information to presurgical planning and posttreatment evaluation. DTI seems to provide useful local information about the structures near the tumor, and this appears to be useful in planning, and DKI seems to be able to grade gliomas and help in fiber-crossing tractography. In the future, DTI may provide an improved way to monitor intraoperative surgical procedures as well as their complications. Furthermore, evaluation of the response to treatment with chemotherapy, antiangiogenic drugs, antivascular agents, and radiation therapy might also be possible. Although diffusion imaging has some limitations, it remains as an area of active investigation and implementation in clinical practice.

References

1. Ostrom QT, Gittleman H, Farah P, et al. CBTRUS Statistical Report: Primary Brain and Central Nervous System Tumors Diagnosed in the United States in 2006-2010. *Neuro Oncol*. 2013;15(2):1–56.
2. Knisely JPS, Rockwell S. Importance of hypoxia in the biology and treatment of brain tumors. *Neuroimag Clin N Am*. 2002;12:525–536.
3. Landis SH, Murray T, Bolden S. Cancer statistics, 1998. *CA Cancer J Clin*. 1998;48:6–29.
4. Berens ME, Rutka JT, Rosenblum ML. Brain tumor epidemiology, growth, and invasion. *Neurosurg Clin North Am*. 1990;1:1–18.
5. Jemal A, Thomas A, Murray T, et al. Cancer statistics 2002. *CA*. 2002;52(1):23–47.
6. Koeller KK, Henry JM. Superficial gliomas: radiologic-pathologic correlation. *Radiographics*. 2001;21:1533–1556.
7. Hunt D, Treasure P. *Year of life lost due to cancer in East Anglia 1990-1994*. Cambridge: East Anglian Cancer Intelligence Unit, Institute of Public Health; 1998.
8. Brain MRC, Tumor Working Party. Prognostic factor for high-grade malignant glioma: development of a prognostic index. A report of the Medical Research Council Brain Tumor Working Party. *J Neuro Oncol*. 1990;9:47–55.
9. Nutt CL, Mani DR, Betensky RA, et al. Gene expression-based classification of malignant gliomas correlates better with survival than histological classification. *Cancer Res*. 2003;63:1602–1607.
10. Hegi ME, Diserens AC, Gorlia T, et al. MGMT gene silencing and benefit from temozolomide in glioblastoma. *N Engl J Med*. 2005;352(10):997–1003.
11. Esteller M, Garcia-Foncillas J, Andion E, et al. Inactivation of the DNA-repair gene MGMT and the clinical response of gliomas to alkylating agents. *N Eng J Med*. 2000;343(19):1350–1354.
12. Yan H, Parsons DW, Jin G, et al. IDH1 and IDH2 mutations in gliomas. *N Engl J Med*. 2009;360(8):765–773.
13. Barajas RF, Hodgson JG, Chang JS, et al. Glioblastoma multiforme regional genetic and cellular expression patterns: influence on anatomic and physiologic MR imaging. *Radiology*. 2010;254(2):564–576.
14. Esmaeili M, Vettukattil R, Bathen TF. 2-Hydroxyglutarate as a magnetic resonance biomarker for glioma subtyping. *Transl Oncol*. 2013;6(2):92–98.
15. Juratli TA, Kirsch M, Robel K, et al. IDH mutations as an early and consistent marker in low-grade astrocytomas WHO grade II and their consecutive secondary high-grade gliomas. *Neuro Oncol*. 2012;108:403–410.
16. SongTao Q, Lei Y, Si G, et al. IDH mutations predict longer survival and response to temozolomide in secondary glioblastoma. *Cancer Sci*. 2012;103:269–273.
17. Felix R, Schorner W, Laniado M, et al. Brain tumors: MR imaging with gadolin-DPTA. *Radiology*. 1985;156:681–688.
18. Tovi M. MR imaging in cerebral gliomas analysis of tumor tissue components. *Acta Radiol Suppl*. 1993;384:1–24.
19. Knopp EA, Cha S, Johnson G, et al. Glial neoplams: dynamic contrast-enhanced T2*-weighted MR imaging. *Radiology*. 1999;211:791–798.
20. Sorensen AG. Magnetic resonance as a cancer imaging biomarker. *J Clin Oncol*. 2006;24:3274–3281.
21. Valles FE, Perez-Valles CL, Regalado S, Barajas RF, Rubenstein JL, Cha S. Combined diffusion and perfusion MR imaging as biomarkers of prognosis in immunocompetent patients with primary central nervous system lymphoma. *J Neuroradiol*. 2013;34:35–40.
22. Pope WB, Qiao XJ, Kim HJ, et al. Apparent diffusion coefficient histogram analysis stratifies progression-free and overall survival in patients with recurrent GBM treated with bevacizumab: a multi-center study. *J Neuro Oncol*. 2012;108:491–498.
23. Hwang EJ, Cha Y, Leum Lee A, et al. Early response evaluation for recurrent high grade gliomas treated with bevacizumab: a volumetric analysis using diffusion-weighted imaging. *J Neuro Oncol*. 2013;112:427–435.
24. Gerstner ER, Chen PJ, Wen PY, et al. Infiltrative patterns of glioblastoma spread detected via diffusion MRI after treatment with cediranib. *Neuro-Oncol*. 2010;12(5):466–472.
25. Chapman CH, Nazem-Zadeh M, Lee OE, Schipper MJ, Tsien CI, et al. Regional variation in brain white matter diffusion index changes following chemoradiotherapy: a prospective study using tract-based spatial statistics. *PLoS ONE*. 2013;8(3):e57768.
26. Brunberg JA, Chenevert TL, McKeever PE, Ross DA, Junck LR, Muraszko KM, et al. In vivo MR determination of water diffusion coefficients and diffusion anisotropy: correlation with structural alteration in gliomas of the cerebral hemispheres. *AJNR Am J Neuroradiol*. 1995;16:361–371.
27. Mori S, Frederiksen K, Van Zijl PCM, Stieltjes B, Kraut MA, Slaiyappan M, et al. Brain white matter anatomy of tumor patients evaluated with diffusion tensor imaging. *Ann Neurol*. 2002;51:377–380.
28. Price SJ, Burnet NG, Donovan T, Green HAL, Pena A, Antoun NM, et al. Diffusion tensor imaging of brain tumors at 3T: a potential tool for assessing white matter tract invasion. *Clin Radiol*. 2003;58:455–462.
29. Lu S, Ahn D, Johnson G, Cha S. Peritumoral Diffusion tensor imaging of high-grade gliomas and metastatic brain tumors. *AJNR Am J Neuroradiol*. 2003;24:937–941.
30. Toh CH, Wei K-C, Ng S-H, Wan Y-L, Lin C-P, Castillo M. Differentiation of brain abscesses from necrotic glioblastomas and cystic metastatic brain tumors with diffusion tensor imaging. *AJNR Am J Neuroradiol*. 2011;32:1646–1651.
31. Maldjian JA, Schulder M, Liu WC, Mun IK, Hirschorn D, Murthy R, et al. Intraoperative functional MRI using a real-time neurosurgical navigation system. *J Comput Assist Tomogr*. 1997;21:910–912.

32. Schulder M, Maldjian JA, Liu WC, Holodny AI, Kalnin AT, Mun IK, et al. Functional image-guided surgery of intracranial tumors located in or near the sensorimotor cortex. *J Neurosurg*. 1998;89:412–418.
33. Laundre BJ, Jellinson BJ, Badie B, et al. Diffusion tensor imaging of the corticospinal tract before and after mass resection as correlated with clinical motor findings: preliminary data. *AJNR Am J Neuroradiol*. 2005;26:791–796.
34. Jensen J, Helpern J, Ramani A, et al. Diffusional kurtosis imaging: the quantification of non-gaussian water diffusion by means of magnetic resonance imaging. *Magn Reson Med*. 2005;53:1432–1440.
35. Jensen JH, Helpern JA. MRI quantification of non-Gaussian water diffusion by kurtosis analysis. *NMR Biomed*. 2010;23:698–710.
36. Fieremans E, Jensen JH, Helpern JA. White matter characterization with diffusional kurtosis imaging. *NeuroImage*. 2011;58:177–188.
37. Raab P, Hattingen E, Franz K, et al. Cerebral gliomas: diffusional kurtosis imaging analysis of microstructural differences. *Radiology*. 2010;254:876–881.
38. Van Cauter S, Veraart J, Sijbers J, et al. Gliomas: diffusion kurtosis MR imaging in grading. *Radiology*. 2012;263:492–501.
39. Holodny AI, Ollenschlager M. Diffusion imaging in brain tumor. *Neuroimaging Clin N Am*. 2002;12:107–124.
40. Stejskal E, Tanner J. Spin diffusion measurements: spin echos in the presence of time-dependent field gradient. *J Chem Phys*. 1965;42:288–292.
41. Romero JM, Schaefer PW, Grant PE, Becerra L, Gonzáles RG. Diffusion MR imaging of acute ischemic stroke. *Neuroimaging Clin N Am*. 2002;12:35–53.
42. Barboriak DP. Imaging of brain tumors with diffusion-weighted and diffusion tensor MR imaging. *Magn Reson Imaging Clin N Am*. 2003;11:379–401.
43. Maier SE, Gudbjartsson H, Patz S, Hsu L, Lovblad KO, Edelman RR, et al. Line scan diffusion imaging: characterization in healthy subjects and stroke patients. *Am J Roentgenol*. 1998;171:85–93.
44. Warach S, Chien D, Li W, Ronthal M, Edelman RR. Fast magnetic resonance diffusion-weighted imaging of acute human stroke. *Neurology*. 1992;42:1717–1723.
45. Sunshine JL, Tarr RW, Lanzieri CF, Landis DM, Selman WR, Lewin JS. Hyperacute stroke: ultrafast MR imaging to triage patients prior to therapy. *Radiology*. 1999;212:325–332.
46. Beauchamp NJ, Uluğ AM, Passe TJ, van Zijl PC. MR diffusion imaging in stoke: review and controversies. *RadioGraphics*. 1998;18:1269–1283.
47. Schaefer PW. Applications of DWI in clinical neurology. *J Neurol Sci*. 2001;186(1):25–35.
48. Larsson HBW, Thomsen C, Frederiksen J, Stubgaard M, Henriksen O. In vivo magnetic resonance measurement in the brain of patients with multiple sclerosis. *Magn Reson Imaging*. 1993;10:712.
49. Fung SH, Roccatagliata L, Gonzales GR, Schaefer P. MR Diffusion imaging in ischemic stroke. *Neuroimag Clin N Am*. 2011;21:345–377.
50. Horsfield MA, Lai M, Webb SL, Barker GJ, Tofts PS, Turner R, et al. Apparent diffusion coefficients in benign and secondary progressive multiple sclerosis by nuclear magnetic resonance. *Magn Reson Med*. 1996;36:393–400.
51. Castriota-Scanderberg A, Tomaiuolo F, Sabatini U, Nocentini U, Grasso MG, Caltagirone C. Demyelinating plaques in relapsing-remitting and secondary proggressive multiple sclerosis: assessment with diffusion MR imaging. *AJNR Am J Neuroradiol*. 2000;21:862–868.
52. Tsuchiya K, Katase S, Yoshino A, Hachiya J. Diffusion-weighted MR imaging of encephalitis. *AJR Am J Roentegenol*. 1999;173: 1097–1099.
53. Na DL, Suh CK, Choi SH, Moon HS, Seo DW, Kim SE, et al. Diffusion-weighted magnetic resonance imaging in probable Creutzfeldt-Jakob disease. *Arch Neurol*. 1999;56:951–957.
54. Chenevert TL, Brunberg JA, Pipe JG. Anisotropic diffusion in human white matter: demonstration with MR techniques in vivo. *Radiology*. 1990;177:401–405.
55. Moseley ME, Cohen Y, Kucharczyk W, Mintorovitch J, Asgari HS, Wendland MF. Diffusion-weighted MR imaging of anisotropic water diffusion in cat central nervous system. *Radiology*. 1990;176:439–445.
56. Christian B. The basis of anisotropic water diffusion in the nervous system – a technical review. *NMR Biomed*. 2002;15:435–455.
57. Ito R, Mori S, Melhem ER. Diffusion tensor MR imaging and tractography. *Neuroimagin Clin N Am*. 2002;12(1):1–19.
58. Pierpaoli C, Jezzard P, Basser P, Barnett A, Di Chiro G. Diffusion tensor MR imaging of the human brain. *Radiology*. 1996;201: 637–648.
59. Basser PJ, Mattiello J, LeBihan D. Estimation of the effective self-diffusion tensor from the NMR spin echo. *J Mang Reson B*. 1994;103:247–254.
60. Melhem ER, Mori S, Mukundan G, Kraut MA, Pomper MG, Van Zijl PCM. Diffusion tensor MR imaging of the brain and white matter tractography. *AJR Am J Roentgenol*. 2002;178(1):3–16.
61. Basser PJ, Pajevic S, Pierpaoli C, Duda J, Aldroubi A. In vivo fiber tractography using DT-MRI data. *Magn Reson Med*. 2000;44: 625–632.
62. Mamata H, Mamata Y, Westin CF, Shenton ME, Kikinis R, Jolesz FA, et al. High-resolution line scan diffusion tensor MR imaging of white matter fiber tract anatomy. *AJNR Am J Neuroradiol*. 2002;23:67–75.
63. Douek P, Turner R, Pekar J, Patronas N, Le Bihan D. MR color mapping of myelin fiber orientation. *J Comput Assist Tomogr*. 1991;15(6):923–929.
64. Pajevic S, Pierpaoli C. Color schemes to represent the orientation of anisotropic tissues from diffusion tensor data: application to white matter fiber tract mapping in the human brain. *Magn Reson Med*. 1999;42:526–540.
65. Helpern JA, Adisetiyo V, Falangola MF, et al. Preliminary evidence of altered gray and white matter microstructural development in the frontal lobe of adolescents with attention-deficit hyperactivity disorder: a diffusional kurtosis imaging study. *J Magn Reson Imaging*. 2011;33:17–23.
66. Grossman EJ, Ge Y, Jensen JH, et al. Thalamus and cognitive impairment in mild traumatic brain injury: a diffusional kurtosis imaging study. *J Neurotrauma*. 2012;29:2318–2327.
67. Blockx I, Verhoye M, Audekerke JV, et al. Identification and characterization of Huntington related pathology: an in vivo DKI imaging study. *Neuroimage*. 2012;63:653–662.
68. Raz E, Bester M, Sigmund EE, et al. A better characterization of spinal cord damage in multiple sclerosis: a diffusional kurtosis imaging study. *AJNR Am J Neuroradiol*. 2013;34:1846–1852.
69. Fieremans E, Benitez A, Jensen MF, et al. Novel white matter tract integrity metrics sensitive to alzheimer disease progression. *AJNR Am J Neuroradiol*. 2013;34:2105–2112.
70. Jansen JFA, Stambukb HE, Koucher JA, et al. Non-Gaussian analysis of diffusion-weighted MR imaging in head and neck squamous cell carcinoma: a feasibility study. *AJNR Am J Neuroradiol*. 2010;31:741–748.
71. Hui ES, Du F, Huang S, et al. Spatiotemporal dynamics of diffusional kurtosis, mean diffusivity and perfusion changes in experimental stroke. *Brain Res*. 2012;1451:100–109.
72. Gong NJ, Wong CS, Chan CC, et al. Correlations between microstructural alterations and severity of cognitive deficiency in Alzheimer's disease and mild cognitive imparirment: a diffusional kurtosis imaging study. *Magn Reson Imaging*. 2013;31: 688–694.
73. Jensen JH, Helpern JA, Tabesh A, et al. Leading non-Gaussian corrections for diffusion orientation distribution function. *NMR Biomed*. 2014;27:202–211.

74. Kimura MCG, Doring TM, Rueda FC, Tukamoto G, Gasparetto EL. In vivo assessment of white matter damage in neuromyelitis optica: a diffusion tensor and diffusion kurtosis MR imaging study. *JNS J Neurol Sci*. 2014. http://dx.doi.org/10.1016/j.jns.2014.07.035.
75. Tsuruda JS, Chew WM, Moseley ME, Norman D. Diffusion-weighted MR imaging of the brain: value of differentiating between extra-axial cysts and epidermoid tumors. *Am J Neuroradiol*. 1990;155(5):1049–1065.
76. Chen S, Ikawa F, Kurisu K, Arita K, Takaba J, Kanou Y. Quantitative MR evaluation of intracranial epidermoid tumors by fast fluid-attenuated inversion recovery imaging and echo-planar diffusion-weighted imaging. *AJNR Am J Neuroradiol*. 2001;22(6):1089–1096.
77. Tsuruda JS, Chew WM, Moseley ME, et al. Diffusion-weighted MR imaging of extraaxial tumors. *Magn Reson Med*. 1999;9:352–361.
78. Laing AD, Mitchell PJ, Wallace D. Diffusion-weighted magnetic resonance imaging of intracranial epidermoid tumors. *Aust Radiol*. 1999;43:16–19.
79. Kono K, Inoue Y, Nakayama K, Shakudo M, Morino M, Ohata K, et al. The role of diffusion-weighted imaging in patients with brain tumors. *AJNR Am J Neuroradiol*. 2001;22:1081–1088.
80. Filippi CG, Edgar MA, Ulug AM, et al. Appearance of meningiomas on diffusion-weighted images: correlation diffusion constants with histopathologic findings. *AJNR Am J Neuroradiol*. 2001;22:65–72.
81. Guo AC, Provenzale JM, Cruz Jr LCH, Petrella JR. Cerebral abscesses: investigation using apparent diffusion coefficient maps. *Neuroradiology*. 2001;43:370–374.
82. Bergui M, Zhong J, Bradac GB, Sales S. Diffusion-weighted images of intracranial cyst-like lesions. *Neuroradiology*. 2001;439(10): 824–829.
83. Chang SC, Lai PH, Chen WL, Weng HH, Ho JT, Wang JS. Diffusion-weighted MRI features of brain abscess and cystic or necrotic brain tumors: comparison with conventional MRI. *Clin Imaging*. 2002;26(4):227–236.
84. Chan JH, Tsui EY, Chau LF, Chow KY, Chan MS, Yuen MK, et al. Discrimination of an infected brain tumor from a cerebral abscess by combined MR perfusion and diffusion imaging. *Comput Med Imaging Graph*. 2002;26(1):19–23.
85. Ebisu T, Tanaka C, Umeda M, Kitamura M, Naruse S, Higuichi T, et al. Discrimination of brain abscess from necrotic or cystic tumors by diffusion-weighted echo planar imaging. *Reson Imaging*. 1996;14(9):1113–1116.
86. Hartmann M, Jansen O, Heiland S, Sommer C, Munkel K, Sartor K. Restricted diffusion within ring enhancement is not pathognomonic for brain abscess. *AJNR Am J Neuroradiol*. 2001; 22(9):1738–1742.
87. Toh CH, Wei KC, NG SH, et al. Differentiation of brain abscesses from necrotic glioblastomas and cystic metastatic brain tumors with Diffusion Tensor Imaging. *AJNR Am J Neuroradiol*. 2011;32: 1646–1651.
88. Wang S, Kim SJ, Poptani H, et al. Diagnostic utility of diffusion tensor imaging in differentiating glioblastomas from brain metastases. *AJNR Am J Neuroradiol*. 2014;35:928–934.
89. Padhani AR, Liu G, Mu-Koh D, et al. Diffusion-weighted magnetic resonance imaging as a cancer biomarker: consensus and recommendations. *Neoplasia*. 2009;11:102–125.
90. Tien RD, Feldesberg GJ, Friedman H, Brown M, MacFall J. MR imaging of high-grade cerebral gliomas: value of diffusion-weighted echo-planar pulse sequence. *AJR Am J Roentgenol*. 1994; 162:671–677.
91. Eis M, Els T, Hoehn-Berlage M, Hossman KA. Quantitative diffusion MR imaging of cerebral tumor and edema. *Acta Neuro-chir Suppl (Wien)*. 1994;60:344–346.
92. Krabbe K, Gideon P, Wang P, Hansen U, Thomsen C, Madsen F. MR diffusion imaging of human intracranial tumours. *Neuroradiology*. 1997;39:483–489.
93. Le Bihan D, Douek P, Argyropoulou M, Turner R, Patronas N, Fulham M. Diffusion and perfusion magnetic resonance imaging in brain tumors. *Top Mang Reson Imaging*. 1993;5:25–31.
94. Tsuruda JS, Chew WM, Moseley ME, Norman D. Diffusion-weighted MR imaging of extraaxial tumors. *Magn Reson Med*. 1991;19:316–320.
95. Yanaka K, Shirai S, Kimura H, Kamezaki T, Matsumura A, Nose T. Clinical application of diffusion-weighted magnetic resonance imaging to intracranial disorders. *Neurol Med Chir*. 1995;16:361–371.
96. Cruz Jr LCH, Sorensen GS. Diffusion tensor magnetic resonance imaging of brain tumors. *Neurosurg Clin N Am*. 2005;16:115–134.
97. Cruz Jr LCH, Sorensen GS. Diffusion tensor magnetic resonance imaging of brain tumors. *Magn Reson Imaging Clin N Am*. 2006;14(2):183–202.
98. Stadnik TW, Chaskis C, Michotte A, Shabana WM, van Rompaey K, Luypaert R, et al. Diffusion-weighted MR imaging of intracerebral masses: comparison with conventional MR imaging and histologic findings. *AJNR Am J Neuroradiol*. 2001;22: 969–976.
99. Sugahara T, Korogi Y, Kochi M, Ikushima I, Shigematu Y, Hirai T, et al. Usefulness of diffusion-weighted MRI with echo-planar technique in the evaluation of cellularity in gliomas. *J Mag Reson Imaging*. 1999;9:53–60.
100. Cha S. Update on brain tumor imaging: from anatomy to physiology. *AJNR Am J Neuroradiol*. 2006;27:475–487.
101. Noguchi K, Watanabe N, Nagayoshi T, Kanazawa T, Toyoshima S, Shimizu M, et al. Role of diffusion-weighted echo-planar MRI in distinguishing between brain abscess and tumor: a preliminary report. *Neuroradiology*. 1999;41:171–174.
102. Witwer BP, Moftakhar R, Hasan KM, Deshmukh P, Haughton V, Field A, et al. Diffusion-tensor imaging of white matter tracts in patients with cerebral neoplasm. *J Neurosurg*. 2002;97:568–575.
103. Goebell E, Paustenbach S, Vaeterlein O, et al. Low-grade and anaplastic gliomas: differences in architecture evaluated with diffusion-tensor MR imaging. *Radiology*. 2006;239:217–222.
104. Inoue T, Ogasawara K, Beppu T, Ogawa A, Kabasawa H. Diffusion tensor imaging for preoperative evaluation of tumor grade in gliomas. *Clin Neurol Neurosurg*. 2005;107:174–180.
105. Rumboldt Z, Camacho DLA, Lake D, et al. Apparent diffusion coefficients for differentiation of cerebelar tumours in children. *AJNR Am J Neuroradiol*. 2006;27:1362–1369.
106. Dumrongpisutikul N, Intrapiromkul J, Yousem DM. Distinguishing between germinomas and pineal cell tumors on MR imaging. *AJNR Am J Neuroradiol*. 2012;33:550–555.
107. Toh CH, Castillo M, Wong AM-C, et al. Primary cerebral lymphoma and glioblastoma multiforme: differences in diffusion characteristics evaluated with diffusion tensor imaging. *AJNR Am J Neuroradiol*. 2008;29:471–475.
108. Guo AC, Cummings TJ, Dash RC, Provenzale JM. Lymphomas and high-grade astrocytomas: comparison of water diffusibility and histologic characteristics. *Radiology*. 2002;224(1): 177–183.
109. Camacho DLA, Smith JK, Castillo M. Differentiation of toxoplasmosis and lymphoma in AIDS patients by using apparent diffusion coefficients. *Am J Neuroradiol*. 2003;24(4):633–637.
110. Gauvain KM, McKinstry RC, Mukherjee P, et al. Evaluating pediatric brain tumor cellularity with diffusion-tensor imaging. *AJR Am J Roentgenol*. 2001;177:449–454.
111. Koetsenas AL, Roth TC, Manness WK, Faeber EN. Abnormal diffusion-weighted MRI in medulloblastoma: Does it reflect small cell histology? *Pediatric Radiol*. 1999;29:524–526.
112. Quadrery FA, Okamoto K. Diffusion-weighted MRI of haemangioblastomas and other cerebellar tumours. *Neuroradiology*. 2003;45(4):212–219.

113. Weishmann UC, Symms MR, Parker GJM, Clark CA, Lemieux L, Barker GJ, et al. Diffusion tensor imaging demonstrates deviation of fibers in normal appearing white matter adjacent to a brain tumour. *J Neurol Neurosurg Psychiatry*. 2000;68:501–503.
114. Jellinson BJ, Field AS, Medow J, et al. Diffusion tensor imaging of cerebral white matter: a pictorial review of physics, fiber tract anatomy, and tumor imaging patterns. *AJNR Am J Neuroradiol*. 2004;23:356–369.
115. Yoshiura T, Wu O, Zaheer A, Reese TG, Sorensen AG. Highly diffusion-sensitized MRI of brain: dissociation of gray and white matter. *Magn Reson Med*. 2001;45:734–740.
116. Burger PC, Heinz ER, Shibata T, Kleihues P. Topographic anatomy and CT correlations in the untreated glioblastoma multiforme. *J Neurosurg*. 1988;68:698–704.
117. Johnson PC, Hunt SJ, Drayer BP. Human cerebral gliomas: correlation of postmortem MR imaging and neuropathologic findings. *Radiology*. 1989;170:211–217.
118. Castillo M, Smith JK, Kwock L, Wilber K. Apparent diffusion coefficients in the evaluation of high-grade cerebral gliomas. *AJNR J Neuroradiol*. 2001;22(1):60–64.
119. Giese A, Westphal M. Glioma invasion in the central nervous system. *Neurosurgery*. 1996;39:235–252.
120. Papadopoulos MC, Saadoun S, Davies DC, Bell BA. Emerging molecular mechanisms of brain tumour oedema. *Br J Neurosurg*. 2001;15:101–108.
121. Yamamoto M, Ueno Y, Hayashi S, Fukushima T. The role of proteolysis in tumor invasiveness in glioblastoma multiforme and metastatic brain tumors. *Anticancer Res*. 2002;22:4265–4268.
122. Tsuchiya K, Fujikawa A, Nakajima M, Honya K. Differentiation between solitary metastasis and high-grade gliomas by diffusion tensor imaging. *Br J Radiol*. 2005;78:533–537.
123. Holodny AI, Schwartz TH, Ollenschleger M, Liu WC, Schulder M. Tumor involvement of the corticospinal tract: diffusion magnetic resonance tractography with intraoperative correlation. *J Neurosurg*. 2001;95(6):1082.
124. Holodny AI, Ollenschleger M, Liu WC, Schulder M, Kalnin AJ. Identification of the corticospinal tracts achieved using blood-oxygen-level-dependent and diffusion functional MR imaging in patients with brain tumors. *Am J Neuroradiol*. 2001;22:83–88.
125. Akai H, Mori H, Aoki S, et al. Diffusion tensor tractography of gliomatosis cerebri: fiber tracking through the tumor. *J Comput Assist Tomogr*. 2005;29(1):127–129.
126. Sha S, Bastin ME, Whittle IR, Wardlaw JM. Diffusion tensor MR imaging of high-grade cerebral gliomas. *AJNR Am J Neuroradiol*. 2002;23:520–527.
127. Tummala RP, Chu RM, Liu H, Truwit C, Hall WA. Application of diffusion-tensor imaging to magnetic-resonance-guided brain tumor resection. *Pediatr Neurosurg*. 2003;39:39–43.
128. Schulder M, Maldjian JA, Liu W-C, Holodny AI, Kalnin AT, Mun IK, et al. Functional image-guided survery of intracranial tumors located in or near the sensorimotor cortex. *J Neurosurg*. 1998;89:412–418.
129. Krings T, Reiges MH, Thiex R, Gilsbach JM, Thron A. Functional and diffusion-weighted magnetic resonance images of space-occupying lesions affecting the motor system: imaging the motor cortex and pyramidal tracts. *J Neurosurg*. 2001;95(5):816–824.
130. Mamata Y, Mamata H, Nabavi A, Kacher DF, Pegolizzi Jr RS, Schwartz RB, et al. Intraoperative diffusion imaging on a 0.5 Tesla interventional scanner. *J Magn Reson Imaging*. 2001;13:115–119.
131. Guye M, Parker GJM, Symms M, Boulby P, Wheeler-Kingshott CAM, Salek-Haddadi A, et al. Combined functional MRI and tractography to demonstrate the connectivity of the human primary motor cortex in vivo. *Neuroimage*. 2003;19:1349–1360.
132. Maldjian JA, Schulder M, Liu W-C, Mun I-K, Hirschorn D, Murthy R, et al. Intraoperative functional MRI using a real-time neurosurgical navigation system. *J Comput Assist Tomogr*. 1997;21(6):910–912.
133. Krings T, Coenen VA, Axer H, Reinges MHT, Holler M, von Keyserlingk DG, et al. In vivo 3D visualization of normal pyramidal tracts in human subjects using diffusion weighted magnetic resonance imaging and a neuronavigator system. *Neurosci Lett*. 2001;307:192–196.
134. Keles GE, Chang EF, Lamborn KR, et al. Volumetric extent of resection and residual contrast enhancement on initial surgery as predictors of outcome in adult patients with hemispheric anaplastic astrocytoma. *J Neurosurg*. 2006;105(1):34–40.
135. Keles GE, Anderson B, Berger MS. The effect of extent of resection on time to tumor progression and survival in patients with glioblastoma multiforme of the cerebral hemisphere. *Surg Neurol*. 1999;52(4):371–379.
136. Nimsky C, Ganslandt O, Hastreiter P, et al. Intraoperative diffusion-tensor MR imaging: shifting of white matter tracts during neurosurgical procedures – initial experience. *Radiology*. 2005;234:218–225.
137. Bradley WG. Achieving gross total resection of brain tumors: intraoperative MR imaging can make a big difference (editorial). *AJNR Am J Neuroradiol*. 2002;23:348–349.
138. Jolesz FA, Talos I-F, Schwartz RB, Mamat H, Kacher DF, Hynynen K, et al. Intraoperative magnetic resonance imaging and magnetic resonance imaging-guided therapy of brain tumors. *Neuroimag Clin N Am*. 2002;12:665–683.
139. Martin AJ, Hall WA, Liu H, Pozza CH, Michel E, Casey SO, et al. Brain tumor resection: intraoperative monitoring with high-filed-strength MR imaging-initial results. *Radiology*. 2000;215:221–228.
140. Nimsky C, Ganslandt O, Keller BV, Romstock J, Fahlbush R. Intraoperative high-field-strength MR imaging: implement and experience in 200 patients. *Radiology*. 2004;233:67–78.
141. Albert FK, Forsting M, Sartor K, Adams HP, Kunze S. Early postoperative magnetic resonance imaging after resection of malignant glioma: objective evaluation of residual tumor growth and its influence on regrowth and prognosis. *Neurosurg*. 1994;34:45–61.
142. Ostrý S, Belšan T, Otáhal J, et al. Is intraoperative diffusion tensor imaging at 3.0T comparable to subcortical corticospinal tract mapping? *Neurosurgery*. 2013;73(5):797–807.
143. Smith JS, Cha S, Catherine M, et al. Serial diffusion-weighted magnetic resonance imaging in case of glioma: distinguishing tumor recurrence from postresection injury. *J Neurosurg*. 2005;103:428–438.
144. James K, Eisenhauer E, Christian M, et al. *J Natl Cancer Inst*. 1999;91:523–528.
145. Ross BD, Chenevert TL, Kim B, Ben-Joseph O. Magnetic resonance imaging and spectroscopy: application to experimental neuro-oncology. *Q Magn Reson Biol Med*. 1994;1:89–106.
146. Moffat BA, Chenevert TL, Lawrence TS, et al. Functional diffusion map: a noninvasive MRI biomarker for early stratification of clinical brain tumor response. *Proc Natl Acad Sci USA*. 2005;102(15):5524–5529.
147. Figueiras RG, Padhani AR, Goh VJ, et al. Novel oncologic drugs: what they do and how they affect images. *RadioGraphics*. 2011;31:2059–2091.
148. Sorensen AG, Batchelor TT, Wen PY, Zhang WT, Jain RK. Response criteria for glioma. *Nat Clin Pract Oncol*. 2008;5(11):634–644.
149. Rieger J, Bähr O, Ronellenfitsch MW, Steinbach J, Hattingen E. Bevacizumab-induced diffusion restriction in patients with glioma: tumor progression or surrogate marker of hypoxia? *J Clin Oncol*. 2010;28(27):e477.
150. Hygino da Cruz Jr LC, Rodriguez I, Domingues RC, Gasparetto EL, Sorensen AG. Pseudoprogression and pseudoresponse: imaging challenges in the assessment of posttreatment glioma. *AJNR Am J Neuroradiol*. 2011;32(11):1978–1985.

151. Fisher MJ, Khademian ZP, Simon EM, Zimmerman RA, Bilaniuk LT. Diffusion-weighted MR imaging of early methotrexate-related neurotoxicity in children. *AJNR Am J Neuroradiol*. 2005;26:1686–1689.
152. Khong P-L, Kwong DL, Chan GCF, Sham JST, Cham F-L, Ooi G-C. Diffusion-tensor imaging for the detection and qualification of treatment-induced white matter injury in children with medulloblastoma: a pilot study. *AJNR Am J Neuroradiol*. 2003;24:734–740.
153. Hunsche S, Mosely ME, Stoeter P, Hedehus M. Diffusion-tensor MR imaging at 1.5T and 3.0T: initial observations. *Radiology*. 2001;221:550–556.
154. Wiegell MR, Larsson HBW, Wedeen VJ. Fiber crossing in human brain depicted with diffusion tensor MR imaging. *Radiology*. 2000;217:897–903.

CHAPTER

28

Diffusion Imaging of Brain Tumors

Stephan E. Maier

Department of Radiology, Brigham and Women's Hospital, Harvard Medical School, Boston, MA, USA; Department of Radiology, Sahlgrenska University Hospital, Sahlgrenska Academy, Gothenburg University, Gothenburg, Sweden

MAGNETIC RESONANCE DIFFUSION IMAGING

The capability of magnetic resonance (MR) to measure and image molecular diffusion has provided a new source of image contrast that gives information clearly different from that provided by T1- and T2-weighted images. Stejskal and Tanner[1] introduced a spin-echo sequence with strong magnetic field gradient pulses on both sides of the inverting 180° radio frequency pulse. In clinical scanners, each gradient is typically applied for a duration of several tens of milliseconds, during which time the average water molecule in brain tissues may migrate 10 or more micrometers in a random direction. In pure water, the irregularity of molecular motion causes an attenuation of the MR signal according to a monoexponential function $\exp(-Db)$, where D is the diffusion coefficient and b the diffusion weighting exerted by the gradients. In tissues, the diffusion coefficient of water is much lower than the diffusion coefficient of pure water, since molecular displacement of water is impeded by many intracellular and extracellular structures, such as macromolecules, organelles, and membranes. An obvious diagnostic application of this difference in diffusion is the differentiation between fluid-filled cysts and tissue. Diffusion differences among diverse tissues and their pathologic alterations are less striking, but may still aid in diagnostic image interpretation. To eliminate signal variations due to T2 decay and nonuniform proton density, usually at least two measurements, one with diffusion gradients and one without, are obtained and maps of the diffusion coefficients are then reconstructed. To avoid any ambiguities in the image interpretation, due to the orientationally dependent restricted diffusion in white matter tracts, image data are collected sequentially with diffusion weighting along three orthogonal or more directions, and the directionally independent "trace" or "mean" diffusion-weighted images and apparent diffusion constant (ADC) maps are calculated.

Measuring micrometer diffusion in the presence of involuntary head motion and physiologic brain deformation[2] poses a great challenge. Owing to the inherent motion robustness and possibility of rapid acquisition, single-shot echoplanar diffusion imaging[3] is the preferred acquisition method for clinical routine diffusion imaging. Unfortunately, single-shot echoplanar imaging is also very sensitive to magnetic field susceptibility variations, chemical shift, and eddy currents; particularly in conjunction with inadequate shimming, this can lead to image distortions and or complete signal loss. Such artifacts are typically present near large air-filled bone structures, such as the frontal and maxillary cavities, orbits, or skull base. The distortions increase proportionally with field strength, but can be reduced with parallel imaging technology,[4] albeit only to some extent. Alternatively, multishot acquisitions, which feature navigators to correct for shot-to-shot motion-related changes of the MR signal, can be used to obtain diffusion-weighted image data with high or even very high geometric fidelity.[5–9] With incomplete sampling and advanced reconstruction methods,[9] the manyfold increased scan time of such multishot diffusion imaging sequences can be diminished. But reconstruction methods like compressed sensing, which achieve acceleration by incomplete data sampling, can also be applied with conventional single-shot imaging to measure a large number of different diffusion weightings and encoding directions within clinically acceptable scan times.[10]

Most image data presented here were collected with the so-called line-scan diffusion imaging (LSDI) technique.[11] While this technique is inherently slower than the more commonly used single-shot echoplanar diffusion imaging technique,[3] image distortions due to susceptibility variations are greatly reduced.[12,13] Moreover, since chemical shift artifacts tend to be negligible with LSDI, fat signal suppression is not required.

http://dx.doi.org/10.1016/B978-0-12-800945-1.00028-8

© 2016 Elsevier Ltd. All rights reserved.

Unless otherwise noted, LSD images were obtained with a rectangular 128 × 96 imaging matrix interpolated to a 256 × 192 matrix, 220 × 165-mm field of view, and 4-mm slice thickness, 2592-ms repetition time (TR), and 69-ms echo time (TE).

CHARACTERIZATION OF BRAIN TUMORS WITH A SINGLE DIFFUSION COEFFICIENT DERIVED FROM CONVENTIONAL DIFFUSION-WEIGHTED IMAGES

In clinical diffusion imaging and many research studies, images are sampled for only two or at most a few b-factors from 0 up to 1000 s/mm^2, and results obtained in tissues are analyzed assuming a monoexponential signal decay as observed in pure water. There is a small perfusion-related deviation at b-factors up to 300 s/mm^2.[14–16] Owing to the small size of this component it can usually be ignored or largely avoided by using a lower b-factor limit of 100 s/mm^2. With a highest diffusion weighting of typically 1000 s/mm^2, the lowest tolerable signal-to-noise ratio limits spatial resolution down to about 2.5 mm isotropic, i.e., a resolution considerably inferior to the resolution achieved with conventional T1- and T2-weighted sequences. Higher in-plane resolution is associated with more severe distortions, unless multishot sequences are employed instead. Typically a minimum of three orthogonal diffusion encoding directions are collected, but often more directions are sampled to obtain directional information about the diffusion process and to improve signal-to-noise ratio in the images showing mean diffusion. Examples of trace diffusion-weighted images and trace diffusion maps with the corresponding T1-weighted and T2-weighted images from brain tumor patients are presented in Figures 1 and 2.

For diffusion measurements over a normal b-factor range, white and gray matter exhibit very similar mean diffusion constants, whereas diffusion constants of brain lesions differ by almost a magnitude. In general, diffusion constants of tumor tissue are higher than the diffusion constants of normal white and gray matter. The highest diffusion values are found in cystic and necrotic parts of lesions. One of the first reported diagnostic applications of diffusion imaging in brain tumors was the differentiation between epidermoid tumors and extra-axial cysts.[17,18] Although fluid-attenuated inversion recovery imaging is also capable of this differentiation, diffusion-weighted imaging provides the best lesion conspicuity.[19] The water molecules in the fluid of cystic lesions experience no hindrance by cell structures and the diffusion coefficient is therefore similar to diffusion in pure water at body temperature and can easily be distinguished from the diffusion coefficient of any other tissue, including tumor tissue (see Figure 3). Large areas of necrosis can readily be detected and delineated based on the elevated diffusion coefficient within the lesion. However, owing to the inferior spatial resolution of diffusion MR imaging, isolated areas of necrosis within viable tumor tissue can be difficult to detect, but impress by an overall elevated ADC. Diffusion coefficients are also helpful to achieve a higher confidence in differentiating cystic or necrotic tumor lesions from an abscess than with conventional MR imaging alone.[20–23] Abscesses are characterized by a diffusion coefficient that is slightly lower than the diffusion coefficient of white and gray matter. Thus, with the exception of the early stage of tumor necrosis[22,24] that may also appear hyperintense on diffusion-weighted images, a cerebral abscess should be suspected in all cases of cystic or necrotic masses with high signals on diffusion-weighted images and low values on the diffusion maps.

Different tumors exhibit a wide range of consistent and dissimilar diffusion values. Some pertinent literature values and their standard deviations are presented in Table 1. Figure 4 shows how some of the values listed in Table 1 stack up along the ADC scale. The most comprehensive list of brain tumor values can be found in a study by Yamasaki et al.[25] The values published by Yamasaki et al. agree well with values of several other studies that were smaller in scope[26–30] and also with values derived from the image data presented here. A consistent finding is that diffusion values of neuroepithelial tumors seem to be negatively correlated with their respective World Health Organization (WHO) grade. In agreement with the observed correlation it has been confirmed both qualitatively[31–33] and quantitatively[29,34–38] that the diffusion value in tumors is inversely correlated with cell density and/or nucleus-to-cytoplasm ratio. Ruy et al.[39] observed that measures of ADC texture within the tumor also permit differentiation between high- and low-grade gliomas. For xenografts of various human melanoma cell lines Lyng et al.[40] confirmed histologically a negative correlation between diffusion and cell density. Moreover, other lesions with very high cell density, such as malignant lymphoma[29] and abscess,[41] are characterized by water diffusion that is equally severely hindered as in gray and white matter. However, it is difficult to generalize such correlation findings, since they seem rather to apply only within respective tumor categories. For example, the diffusion coefficient of schwannomas is relatively high, while the high cell density of such tumors would indicate severely hindered diffusion. Finally, to some extent the elevated diffusion coefficients in tumors may also be explained by edema within the tumor.[42]

Unfortunately, there is a considerable overlap between the tumor-specific ranges of diffusion values. Therefore, the observed diffusion value by itself, despite

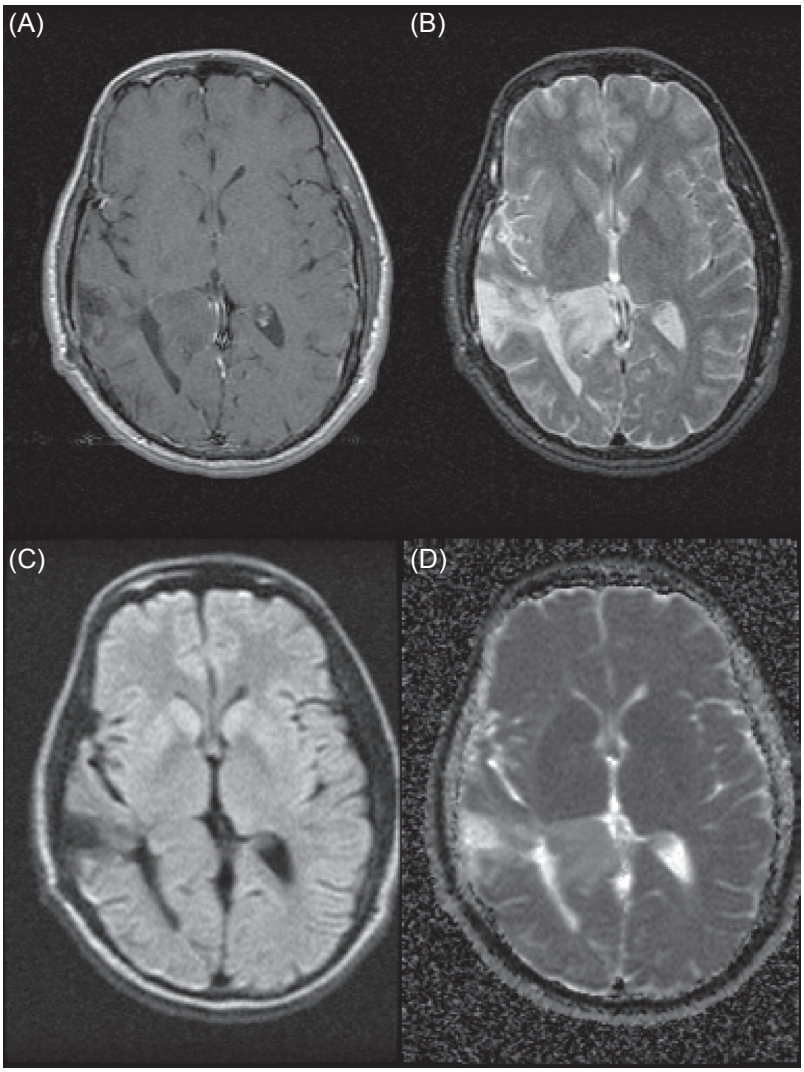


FIGURE 1 Axial brain images of a 43-year-old male patient with a recurrent low-grade astrocytoma. (A) T1-weighted postcontrast spin-echo image (TR 700 ms/TE 14 ms) shows a nonenhancing lesion. (B) T2-weighted spin-echo image (TR 3000 ms/TE 80 ms) shows the lesion and minor edema. (C) Trace diffusion-weighted image (b-factor 1000 s/mm^2) reveals a distorted geometry of the right ventricle and brain surface. (D) On the trace diffusion map, in accordance with a high diffusion, the cerebrospinal fluid space appears bright (D = 3.21 µm^2/ms). The diffusion within the tumor lesion is elevated (D = 1.36 µm^2/ms). Gray and white matter show no obvious difference and appear dark gray (D = 0.80 µm^2/ms).

the very intriguing correlation with cell architecture, generally does not permit the diagnosis of a particular brain tumor. Another confounding factor is that the range of diffusion values representative of peritumoral edema overlaps with the diffusion value range of most (malignant) tumors and, therefore, mean diffusion values are of limited value to demarcate tumor lesion boundaries (see also Figure 2). Morita et al.[43] found that the higher diffusion values of the peritumoral edema observed in high-grade gliomas (see Table 1) may reflect the destruction of the extracellular matrix ultrastructure by malignant cell infiltration. Lemercier et al.[44] observed for the peritumoral edema of glioblastoma a characteristic ADC gradient, whereas ADCs in the peritumoral edema of solitary metastatic lesions appeared homogeneous. Nevertheless, diffusion-weighted imaging does certainly aid in the diagnostic decision based on anatomic features and signal intensities manifest on the T1- and T2-weighted images. Yamasaki et al.[25] point out that once more confidence has been gained with the diffusion values of certain tumor types, diffusion-weighted imaging may play an important role to differentiate between meningiomas and schwannomas, as well as between craniopharyngiomas and pituitary adenomas or meningiomas (see Table 1).

Diffusion measurements are also useful to predict treatment outcome. Brynolfsson et al.[45] found that for high-grade gliomas, certain pretreatment ADC texture characteristics hold prognostic information. A unique ability of diffusion-weighted imaging is to follow

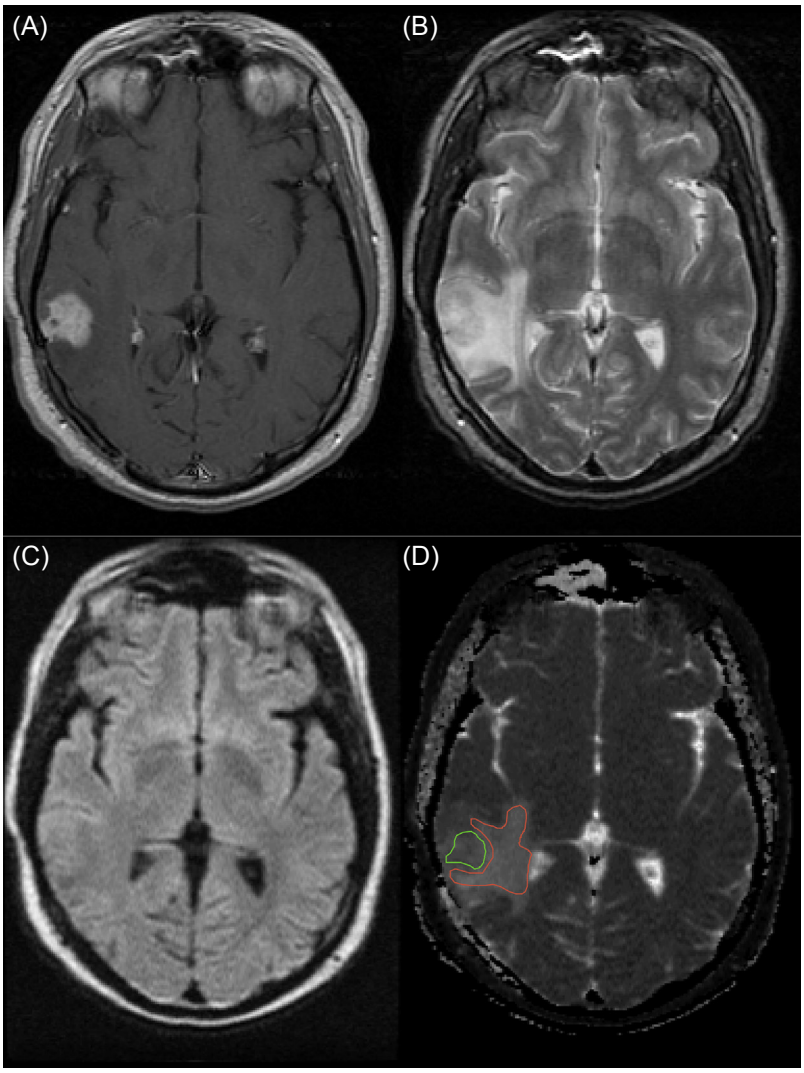


FIGURE 2 Axial brain images of a 40-year-old female patient with a glioblastoma. (A) T1-weighted postcontrast spin-echo image (TR 600 ms/TE 14 ms) shows an enhancing lesion. (B) T2-weighted spin-echo image (TR 3000 ms/TE 92 ms) shows the lesion and larger area with edema. (C) The same area on the LSDI mean diffusion-weighted image (b-factor 1000 s/mm^2) appears isointense with the surrounding normal tissue. There is evidence, however, of slight deformation of the ventricle and sulcus anatomy. (D) Mean diffusion coefficient map exhibits elevated diffusion within both the lesion and the edema. ADC measured within the green region of interest (ROI) outline for tumor (defined on the T1-weighted image) is 1.18 μm^2/ms and within the red ROI outline for edema 1.35 μm^2/ms. Gray and white matter show no obvious difference in diffusion and appear dark gray (ADC = 0.76 μm^2/ms). *From Ref. 98 with permission.*

therapy-induced changes in brain tumors. Different tissue reactions can be documented[46] (see Figure 5): Tumor areas resistant to therapy exhibit unaltered diffusion values. Areas of transient cell swelling or ischemia are characterized by decreased diffusion values. Meanwhile, areas experiencing cell lysis or apoptosis present increased diffusion values. Analysis of such diffusion changes during different stages of therapy, preferably with the image data coregistered to pretreatment scans, permits a quantitative documentation of the response to drug,[47] radiation,[46,48] or gene[49] therapy. It has also been demonstrated that changes observed during the early stages of therapy are an early indicator of the final treatment response[46,50,51] and the correct interpretation, should a tumor be unresponsive to therapy, may facilitate a timely decision for alternative therapy. Diffusion imaging at a later stage can be used to document radiation-induced cerebral injury.[52] Differentiation of posttherapeutic pseudoprogression from tumor progression and pseudoresponse from tumor regression with diffusion imaging and other methods remains a challenge.[53] Lee et al.[54] found that in high-grade gliomas diffusion-weighted images were useful to differentiate pseudoprogression from tumor progression, whereas Hu et al.[55] demonstrated that the combination of diffusion and perfusion parameters was a promising approach to differentiate radiation necrosis from recurrent tumor.

TABLE 1 Diffusion Values of Normal and Pathological Tissues in the Brain

Normal Brain Tissue	**ADC μm²/ms**
Normal white matter[12]	0.705 ± 0.014
Deep gray matter[99]	0.75 ± 0.03
Neuroepithelial Tumors	**ADC μm²/ms**
WHO grade I, dysembryoplastic neuroepithelial tumor[25]	2.546 ± 0.135
WHO grade I, pilocytic astrocytoma[25]	1.659 ± 0.260
WHO grade II, diffuse astrocytoma[25]	1.530 ± 0.148
WHO grade II, oligodendroglioma[25]	1.455
WHO grade II, ependymoma[25]	1.230 ± 0.119
WHO grade III, anaplastic astrocytoma[25]	1.245 ± 0.153
WHO grade III, anaplastic oligodendroglioma[25]	1.222 ± 0.093
WHO grade III, anaplastic ependymoma[25]	1.103 ± 0.101
WHO grade IV, glioblastoma[25]	1.079 ± 0.154
WHO grade IV, primitive neuroectodermal tumor (PNET)[25]	0.835 ± 0.122
WHO grade IV, medulloblastoma[26]	0.66 ± 0.15
Other Brain Tumors	**ADC μm²/ms**
Craniopharyngioma[25]	1.572 ± 0.210
Schwannoma[25]	1.384 ± 0.140
Epidermoid tumor[25]	1.263 ± 0.174
Germ-cell tumor[25]	1.189 ± 0.175
Metastatic tumor[25]	1.149 ± 0.192
Pituitary adenoma[25]	1.121 ± 0.202
Typical meningioma[100]	1.17 ± 0.21
Atypical/malignant meningioma[100]	0.75 ± 0.21
Malignant lymphoma[25]	0.725 ± 0.192
Secondary Changes and Other Pathologies	**ADC μm²/ms**
Vasogenic (peritumoral) edema[27]	1.30 ± 0.11
Peritumoral edema (high-grade glial tumor)[43]	1.825 ± 0.115
Cytotoxic (ischemic) edema[27]	1.04 ± 0.05
Cystic/necrotic tumor area[22]	2.70 ± 0.31
Abscess[22]	0.65 ± 0.16
Acute stroke[101]	0.401 ± 0.143

From Ref. 98 with permission.

CHARACTERIZATION OF BRAIN TUMORS WITH MULTIPLE DIFFUSION PARAMETERS DERIVED FROM HIGHLY DIFFUSION-WEIGHTED IMAGES

Diffusion-weighted brain images with very high b-factors of 5000 s/mm² or higher, which clearly depict tissue structures above the noise threshold, can readily be obtained on clinical scanners.[56,57] The signal loss resulting from the higher diffusion weighting can be compensated for by the use of a lower spatial resolution. Examples of high *b* diffusion data obtained in a brain tumor patient are presented in Figures 6 and 7. As can be appreciated with the signal versus b-factor plot shown in Figure 7, the diffusion-weighted signal decays slower than one might expect from a

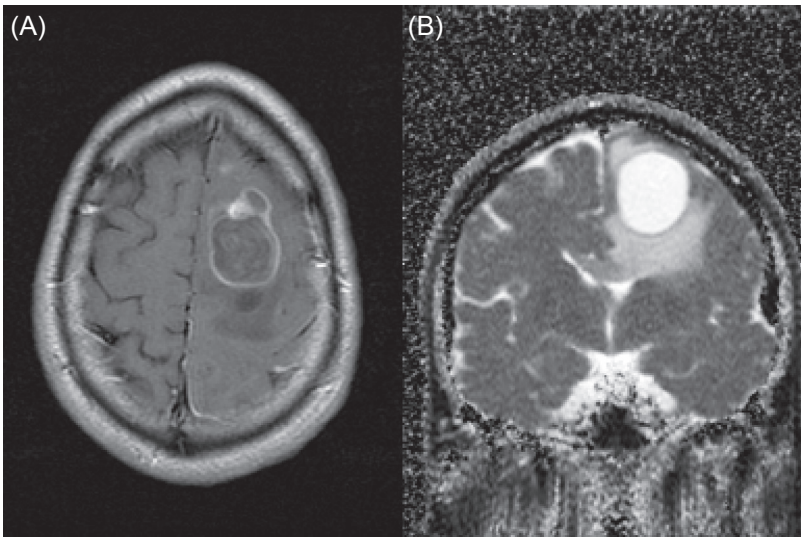


FIGURE 3 Brain images of a giant cell astrocytoma with cyst formation in a 51-year-old male patient. (A) Axial T1-weighted postcontrast spin-echo image (TR 600 ms/TE 19 ms) shows a round lesion with an enhancing rim. (B) The same lesion is shown in a coronal trace diffusion map. The nonenhancing central portion discerned on the T1-weighted image is distinguished by a high diffusion constant ($D = 2.82\,\mu m^2/ms$), which is comparable to the diffusion constant of water at body temperature. The diffusion within the enhancing rim is much lower, but partial volume effects do not permit an exact determination of the diffusion constant. The diffusion within the corpus callosum on the contralateral side is elevated owing to edema formation ($D = 1.18\,\mu m^2/ms$) (see also Figure 9).

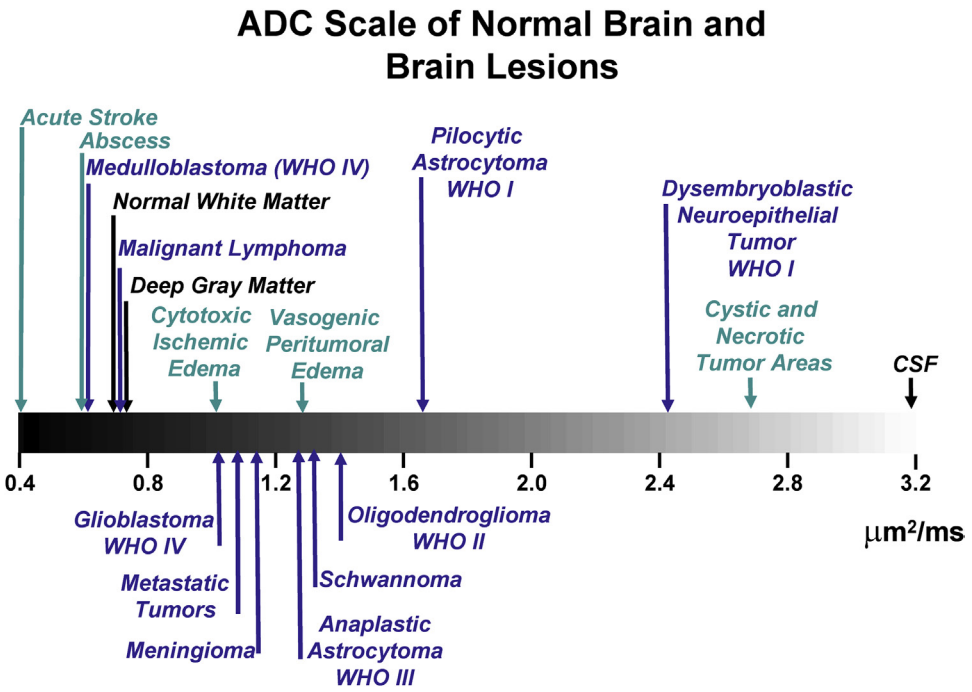


FIGURE 4 Selected values listed in Table 1 are shown in reference to an ADC scale.

monoexponential extrapolation of data measured between $b = 0$ and $1000\,s/mm^2$. Several analysis models have been proposed to describe the nonmonoexponential diffusion-related signal decay. The physically motivated biexponential or multiexponential model yields two or more diffusion constants and respective volume fractions. Empirical models include the "stretched exponential" model,[58] which yields a diffusion coefficient and an exponential stretch-parameter, α, and the "kurtosis" model,[59,60] which yields a diffusion coefficient and an excess kurtosis parameter, K. These models tend to fit real data less well than the physically

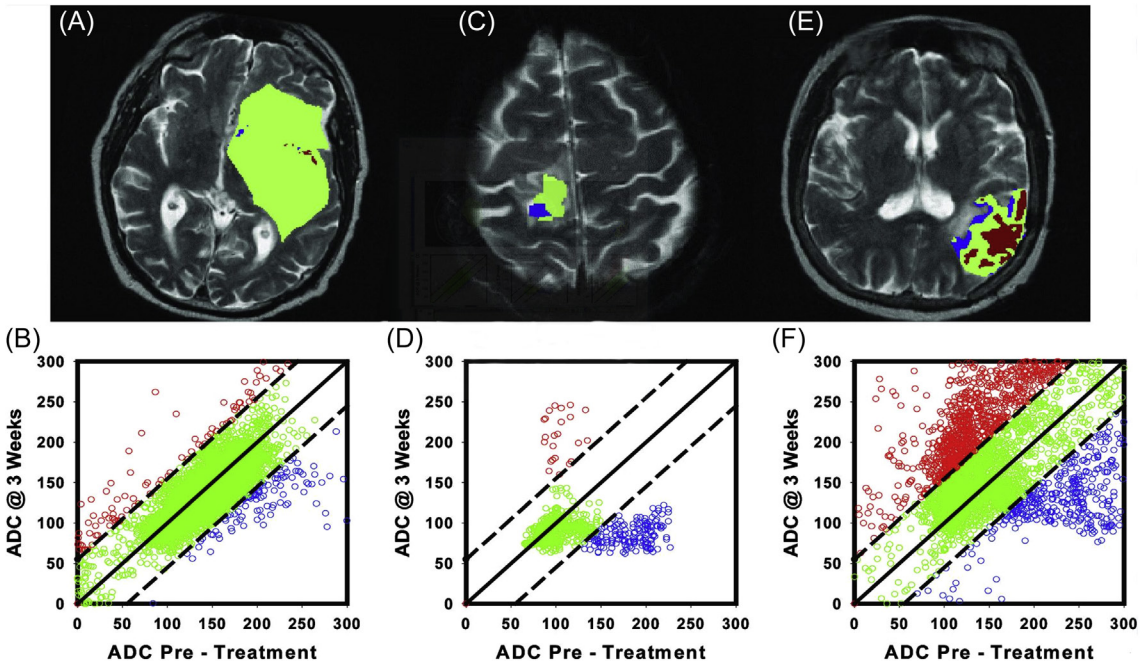


FIGURE 5 MR images of three patients with oligodendrogliomas. MR image datasets obtained from three different patients diagnosed with anaplastic oligodendrogliomas. Images shown are at 3 weeks into a 7-week fractionated ionizing radiation regimen. Regions of interest were drawn for each tumor image by using anatomical images. (A, C, and E) shown are the regional spatial distributions of ADC changes (functional diffusion maps) for a single slice through each tumor as color overlays for patients PD, SD, and PR, respectively. The red pixels indicate areas of increased diffusion, whereas the blue and green pixels indicate regions of decreased and unchanged ADC, respectively. The scatter plots (B, D, and F) show quantitatively the distribution of ADC changes for the entire three-dimensional tumor volume for each corresponding patient (A, C, and E). *From Ref. 46 with permission.*

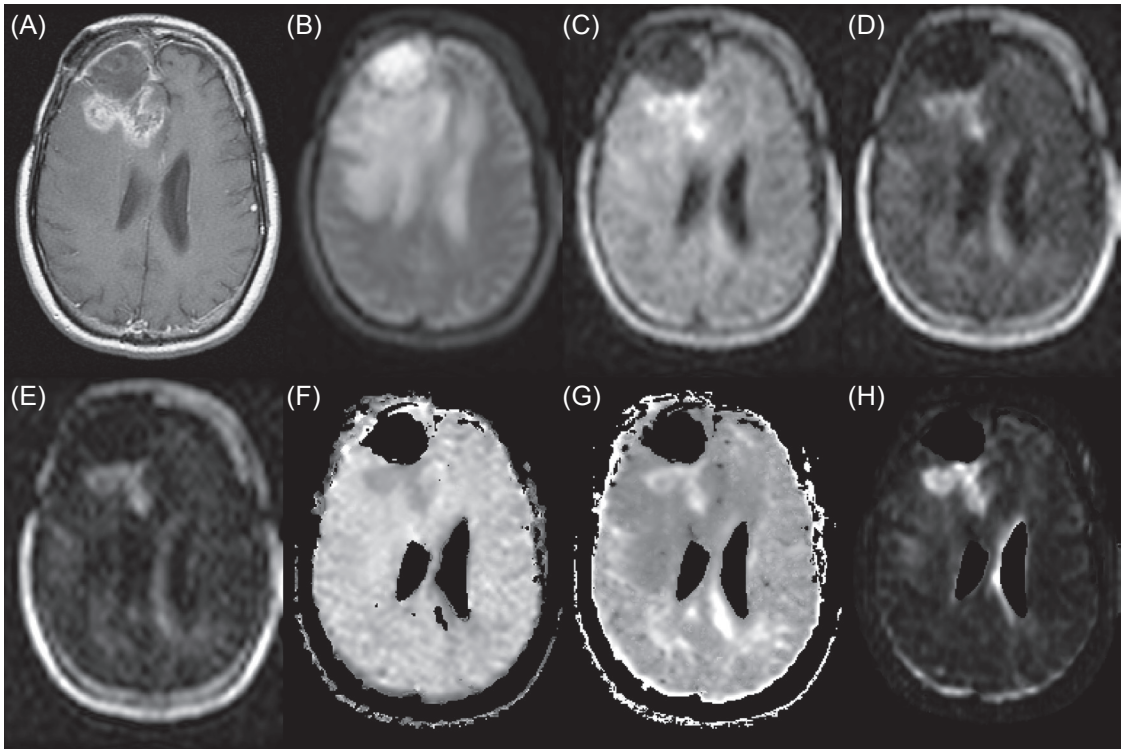


FIGURE 6 Axial brain images of a frontal glioblastoma with postoperative cyst formation in a 38-year-old male patient. (A) Axial T1-weighted postcontrast spin-echo image (TR 600 ms/TE 25 ms) predominantly shows the margins and not the solid part of the tumor. (B) LSD image (64×48 imaging matrix interpolated to a 256×192 matrix, 220×165-mm field of view, 7.3-mm slice thickness, 2040-ms TR, and 94-ms TE) with a b-factor of 5 s/mm^2 appears basically T2 weighted and visualizes the extent of edema. (C) LSD image with a b-factor of 1000 s/mm^2 demonstrates the appearance using conventional diffusion weighting. (D) Highly diffusion-weighted LSD image with a b-factor of 3000 s/mm^2. (E) Very high diffusion-weighted LSD image with a b-factor of 5000 s/mm^2 exhibits signal above the noise threshold for all tissues. Extraordinarily high residual signal, despite high diffusion weighting, is observed in the solid part of the tumor. LSD images were all obtained with a single diffusion encoding direction. (F) α map obtained with a stretched exponential fit.[58] Compared to normal brain tissue, tumor tissue appears hypointense and edematous tissue slightly hyperintense. (G) Map of excess kurtosis K.[59,60] Compared to normal brain tissue, tumor tissue appears hyperintense and edematous tissue hypointense. White matter tracts running orthogonal to the diffusion encoding direction also appear hyperintense. (H) Computed χ^2 error map of the monoexponential fit to the diffusion-related signal decay reveals hyperintensity of the solid part of the tumor and slightly higher intensity within the edematous tissue. Other areas of hyperintensity are due to partial volume effects in voxels with nonuniform tissues or fluid content.

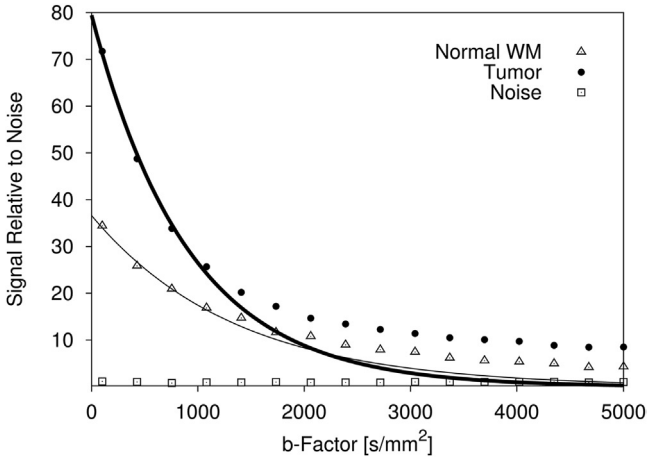


FIGURE 7 Plot of diffusion-attenuated signal versus b-factor for normal white matter (WM), tumor, and noise (measurement of the case shown in Figure 6. The solid lines show the signal decay predicted by a monoexponential fit through the first four signal values up to a b-factor of 1000 s/mm^2. Evidently the signal decays much more slowly than a monoexponential fit of the signal measured over the conventional b-factor range would predict. The diffusion values measured with conventional diffusion imaging ($b = 1000$ s/mm^2) were 1.10 μm^2/ms for tumor and 0.74 μm^2/ms for normal-appearing white matter.

motivated multiexponential models. However, since their mathematical functions are described with only three free parameters as opposed to the four free parameters needed for a biexponential model, fits are inherently more stable, requiring fewer data points (diffusion weightings) and producing parameter maps with less noise.

High diffusion weighting, unlike conventional diffusion weighting, permits a clear separation of normal gray and white matter.[61,62] An established interpretation for white and gray matter is that different diffusion-weighted signal decays occur in intra-axonal (restricted diffusion) and extra-axonal (hindered diffusion) water compartments, respectively, and that this gives rise to a biexponential decay.[63] For tumor characterization, the additional information gained by high b diffusion-weighted imaging without further postprocessing is fairly limited.[64,65] Maier et al.[66] also found that biexponential fit parameters derived from wide-range diffusion-weighted image scans are useful for tumor tissue characterization. They demonstrated that tumor tissue can be differentiated from both normal and edematous white matter: from normal white matter by the elevated diffusion constant of the fast-diffusing component and from edematous white matter by the elevated volume fraction of the slow-diffusing component. Similarly, Schwarcz et al.[67] found biexponential tissue water diffusion analysis useful to better characterize vasogenic edema.

Biexponential diffusion parameter maps seem to potentially provide valuable information, but the computed maps are plagued by low signal-to-noise ratio and limited spatial resolution. Moreover, the simultaneous interpretation of multiple computed parameter maps is cumbersome and if potential physical interpretation is not a priority, the display of the departure from a simple monoexponential decay in a single parameter map with high contrast-to-noise ratio may be more useful for diagnostic purposes. The studies by Raab[68] and Van Cauter[69] found that diffusion kurtosis maps computed from high b diffusion data permitted better grading of glioma lesions than conventional diffusion imaging. Kwee et al.[70] found that the stretched exponential parameter α in high-grade glioma was significantly different from α measured in normal brain structures. Maier et al.[71] reported that the χ^2 error parameter associated with monoexponential fits of the tissue water signals, measured typically at between 4 and 16 different b-factors, can be used to characterize the deviation from a simple monoexponential signal decay on a pixel-by-pixel basis (a comparison with the stretched exponential parameter α and excess kurtosis parameter K in a glioma case can be seen in Figure 6). It appears that for brain tumors such χ^2 maps permit good visualization of spatial details and that the resulting lesion contrast by far exceeds the contrast of biexponential parameter maps. In peritumoral edema, χ^2 values were on average 68% higher than in normal white matter. A remarkable departure from a simple monoexponential signal decay, with average χ^2 values almost 400% higher than in normal white matter, occurred in highly malignant primary brain tumors, such as glioblastomas (see Figure 6) or anaplastic astrocytomas. Unlike the enhancement of T1-weighted postcontrast images, such enhancement was consistently observed in the solid part of tumors. On the other hand, low-grade astrocytomas, one case of ganglioglioma (see Figure 8), and metastases demonstrated χ^2 values that were not profoundly different from the χ^2 value of white matter.

At the time of writing, clinical routine MR imaging characterizes the extent of brain tumors by the appearance of the margins on T1-weighted contrast-enhanced images. In brain tumors, the mechanism of T1-weighted contrast after paramagnetic contrast agent injection is known to be a local breakdown of the blood–brain barrier. However, tumor growth is not always associated with a leaking blood–brain barrier and the contrast agent enhancement is not specific. It could be due to tumor tissue itself, inflammation, increased permeability of blood vessels, or other abnormal changes. High b diffusion-weighted imaging together with appropriate analysis seems to provide tumor contrast clearly different from the contrast observed on T1-weighted images. It should be added

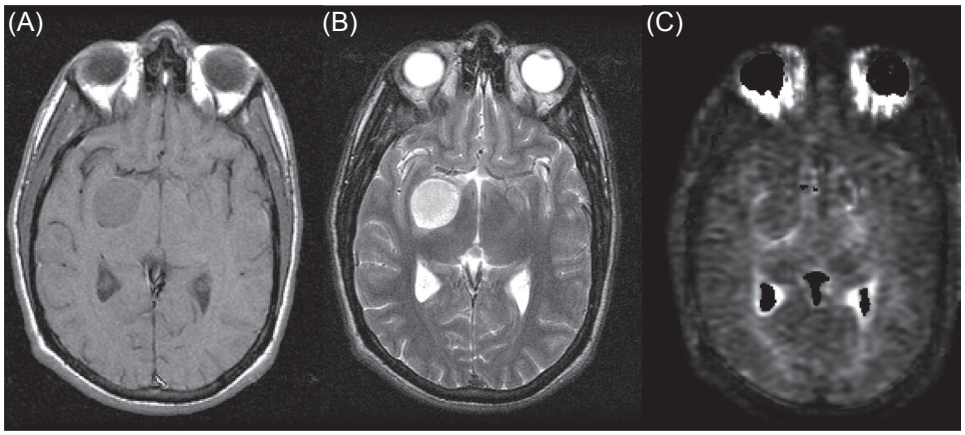


FIGURE 8 Axial brain images of a 24-year-old male patient with a ganglioglioma (WHO grade I). (A) The T1-weighted postcontrast spin-echo image (TR 500 ms/TE 14 ms) exhibits no enhancement at the location of the tumor. (B) The T2-weighted spin-echo image (TR 5600 ms/TE 96 ms) shows the tumor lesion. (C) The χ^2 error parameter map computed from trace LSDI data shows no enhancement, except along the rim of the tumor. The enhancement in the orbital cavity visible on the χ^2 map is artifactual and caused by eye motion. The tumor diffusion value measured with conventional diffusion imaging ($b = 1000\,s/mm^2$) was 1.37 $\mu m^2/ms$. LSD image parameters were 128 × 96 imaging matrix interpolated to a 256 × 192 matrix, 220 × 165-mm field of view, 6-mm slice thickness, 2682-ms TR, and 92-ms TE.

that diffusion-based tissue differentiation does not depend on the effect of contrast agents, since with the common imaging protocols the diffusion-weighted images are only minimally T1 weighted. A remarkable finding of the analysis of the nonmonoexponential diffusion-related signal decay in tumor patients is the observation of strong enhancement outside the tumor boundaries confirmed by T1 contrast-enhanced imaging. Although, in some instances, this can be attributed to partial volume effects, such enhancement seems to indicate malignant cell infiltration.[71] Indeed, average cell size (cell density), cell-size distribution (cell-size irregularity), and nucleus-to-cytoplasm size ratio are contrast agent-independent parameters that appear to have profound effects on diffusion and, in particular, the observed deviation from a monoexponential signal decay. The very same parameters permit definitive differentiation between pathologic and normal tissue, when histological analysis is applied.

ASSESSMENT OF NERVE FIBER TRACT INTEGRITY

A general model for hindered or restricted diffusion is well represented by the work of Basser and colleagues, who have incorporated the diffusion tensor formalism into diffusion data analyses.[72] With diffusion-tensor imaging (DTI) a minimum of six diffusion-weighted images with different diffusion encoding directions is acquired. Subsequent computation of the diffusion tensor yields for each voxel three diffusion coefficients (diffusion eigenvalues) along three orthogonal principal directions (diffusion eigenvectors). In white matter, the eigenvector direction associated with the largest eigenvalue coincides with the dominant fiber orientation,[73] i.e., the parallel arrangement of axons and myelin sheaths modulates water diffusion, such that water diffusion parallel to the white matter is less impeded than the water diffusion perpendicular to it. Most DTI studies use a diffusion weighting of $1000\,s/mm^2$. With higher diffusion weighting and a large number of encoding directions more complex diffusion models can be applied and crossing fibers can be detected.[74]

In many tissues, when averaged over the macroscopic scale of image voxels, the diffusion hindrance or restriction exerted by the intra- or extracellular structures is identical in every direction, i.e., the observed diffusion is isotropic. Gray matter exhibits such diffusion that is largely isotropic. The directional variability of water diffusion is usually quantified by the rotationally invariant fractional anisotropy (FA) index,[75] which ranges from 0 (isotropic diffusion) to 1.0 (totally restricted diffusion along two of the three eigenvector directions). The different white matter tracts are well characterized by their different anisotropy values[76,77] and range from 0.81 in the corpus callosum, over 0.62 in the internal capsule, to 0.09 in the cortical gray matter.[77]

Diffusion in tumors, except for areas where the tumor invades white matter, shows little anisotropy. Therefore, the primary value of imaging the preferred diffusion orientation and diffusion anisotropy in brain tumor patients lies rather in the evaluation of white matter fiber tract integrity than tumor tissue characterization.

Based on geometry, principal eigenvector direction, and the degree of anisotropy loss, there are four basic categories of white matter changes caused by tumor growth that can be differentiated:

1. White matter tract dislocation, caused by the mass effect of the tumor and edema: The white matter tracts on anisotropy maps exhibit loss of symmetry, distorted appearance, and abnormal location. The principal eigenvectors within the tract remain aligned with the course of the tract. In the absence of edema there is no change in anisotropy.
2. White matter tract swelling by edema: This is characterized by uniformly reduced white matter anisotropy, increased tract cross section, and absence of localized areas with anisotropy loss. The principal eigenvectors within the tract remain aligned with the course of the tract.
3. White matter tract tumor infiltration or invasion: This is characterized by nonuniformly reduced white matter anisotropy. The principal eigenvectors within the tract remain aligned with the course of the tract. The differentiation from edema may be difficult, but localization close to a highly malignant tumor or the absence of edema on corresponding T2-weighted images may be strong sign of infiltration or invasion rather than edema only.
4. White matter tract destruction: Replacement of the original white matter with tumor tissue produces a significant loss in diffusion anisotropy and lack of coherence of the principal eigenvector directions. These changes can be very localized, within an otherwise intact-appearing tract.

Often, more than one of these distinctive changes is present and a clear categorization may not be possible. Figure 9 shows a case in which DTI adds valuable information regarding fiber tract dislocation and swelling. A case in which DTI reveals partial destruction of a fiber tract by tumor infiltration can be seen in Figure 10. An example of complete fiber tract disruption visualized with diffusion anisotropy imaging is documented in Figure 11. Several studies have explored the potential of DTI to detect white matter tumor infiltration.[78–80] In high-grade gliomas and meningiomas both Tropine et al.[80] and Provenzale et al.[79] observed for the peritumoral region with increased T2 signal a trend toward greater FA reduction in high-grade gliomas. However, in high-grade gliomas compared to cerebral metastases, the FA reduction within the peritumoral edema is significantly larger for the metastatic lesions.[81] Within the normal-appearing peritumoral white matter, FA reduction in high-grade gliomas was significantly larger than the FA reduction in meningiomas[79] or metastases.[78] These findings suggest a potential role for diffusion imaging in the detection of tumoral infiltration, particularly in areas that appear normal on conventional

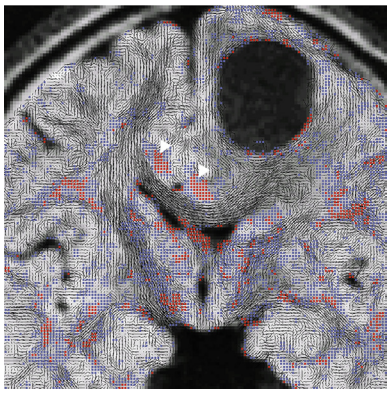


FIGURE 9 Coronal diffusion tensor map of giant cell astrocytoma with cyst (same patient as shown in Figure 3). In-plane component of the primary diffusion eigenvector is depicted with lines overlaid on the diffusion-weighted image. The out-of-plane component of the eigenvector is visualized with red (strong component) and blue (intermediate-size component) dots. The diffusion tensor map reveals a marked lateral shift of the corpus callosum and the cingulum tracts (arrows). Moreover, a widening of the left half of the corpus callosum can be discerned. In the immediate surrounding of the cyst, fiber structures appear to be intact, but severely distorted.

MR images. Saksena et al.[82] however, found that not all anisotropy changes in edema-free areas are caused by tumor cell infiltration. They investigated patients with unilateral glioblastoma multiforme or solitary brain metastases with no midline corpus callosum infiltration. Compared to healthy controls, anisotropy in the corpus callosum of both patient groups was significantly reduced and the authors attributed this change to Wallerian degeneration rather than tumor infiltration.

Only very few studies have explored diffusion anisotropy inside brain tumors and its potential value for tissue characterization. An early study[83] reported FA values for the nonenhancing core of high-grade glioma tumors (0.09), the enhancing tumor core (0.13), and the enhancing tumor margin (0.16). It was concluded that diffusion anisotropy added no benefit to tissue differentiation. In a later study,[84] it was found that FA values differ significantly between low-grade and high-grade gliomas in the tumor margin but not in the tumor center. This significant difference was believed to be the result of more extensive fiber-tract destruction in high-grade gliomas than in low-grade gliomas, whereas in the center of both low-grade and high-grade gliomas virtually no fibers remain intact. Inoue et al.[85] measured the lowest anisotropy in grade I gliomas (FA = 0.150) and the highest anisotropy in grade III and IV gliomas (FA = 0.230 and 0.229). The same group of investigators concluded that FA in glioblastomas is a good indicator of cell density and proliferation activity.[86] The authors also concluded the possibility of residual white matter as a factor contributing to the observed diffusion anisotropy in glioblastomas, but in addition suggested that typical regular tumor cell arrangement (similar to pseudopalisading) could also elevate FA values.

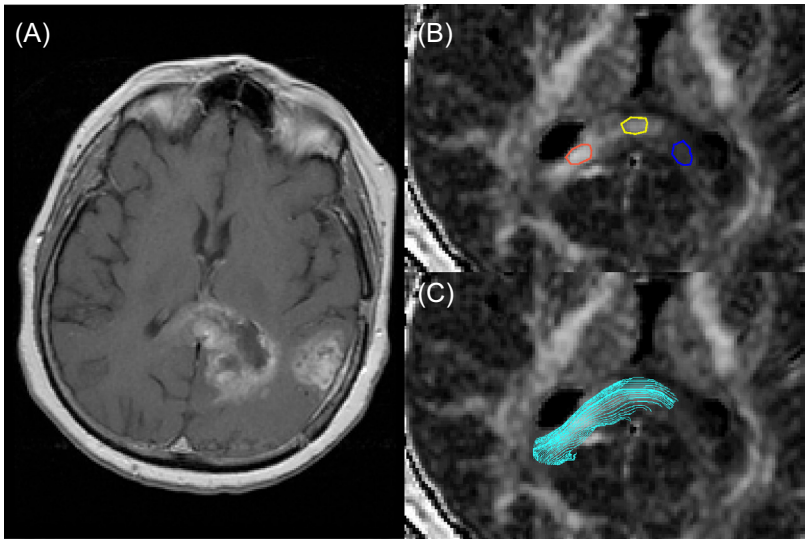


FIGURE 10 Axial brain images of a 57-year-old female patient with a multifocal glioblastoma. (A) The T1-weighted postcontrast spin-echo image (TR 750 ms/TE 14 ms) shows two lesions, one of them with invasion into the splenium of the corpus callosum. (B) Detail of diffusion anisotropy map with three regions of interest (ROI) drawn in the splenium of the corpus callosum (FA: red ROI 0.65, yellow ROI 0.46, blue ROI 0.20). (C) Same anisotropy map as shown in (B) with overlaid in-plane fiber-tracking path, documenting the presence of intact fibers in the tumor-invaded splenium.

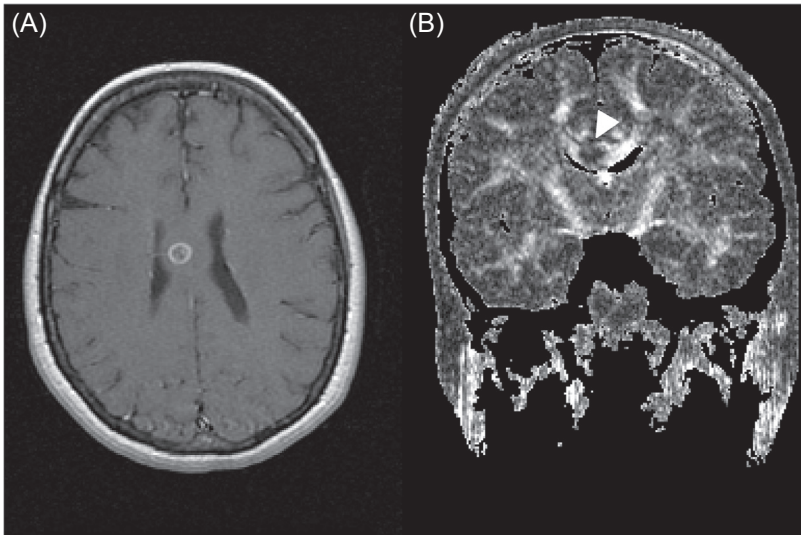


FIGURE 11 Brain images of a 52-year-old female patient with a melanoma metastasis. (A) The axial T1-weighted postcontrast spin-echo image (TR 750 ms/TE 14 ms) shows a small lesion with an enhancing rim within the body of the corpus callosum. (B) On coronal anisotropy map the same lesion is clearly discerned (arrow) as an area with low anisotropy (FA: 0.11; $D = 0.99\,\mu m^2/ms$) within the high-anisotropy region of the corpus callosum.

Indeed, in a rat tumor model, Zhang et al.[87] observed elevated FA values in the tumor rim area. Water-diffusion eigenvectors formed a circular pattern for 9L and F98 tumors and a radial pattern for human glioblastoma xenografts. Histologic validation confirmed a regular arrangement of tumor cells in agreement with the preferred orientation of diffusion. A modifying or cautionary detail to be considered when evaluating areas of low anisotropy is the difficulty in obtaining reliable anisotropy measures under unfavorable signal-to-noise ratio conditions.[75,77] Thus, the observed glioma grade dependency of the FA value may also be the effect of different signals within the lesion and consequently different signal-to-noise ratios rather than orientationally dependent diffusion restrictions. Moreover, low anisotropy can also be caused by orientation dispersion of microstructures with preferential diffusion orientations. Indeed, Szczepankiewicz et al.[88] demonstrated, using unique gradient pulses for diffusion encoding, that meningioma tumors and gray matter exhibit high anisotropy at the microstructure level, whereas glioblastoma tumors lack such microstructure anisotropy.

Anatomic mapping of tracts with DTI is of fundamental importance to avoid or minimize damage to displaced, but still functional, fiber tracts during neurosurgery or radiation therapy.[89,90] Although T2-weighted images permit white and gray matter differentiation, they do not contain information about the course of individual tracts and fail to discriminate white and gray matter in the presence of edema. Diffusion-tensor data can also be obtained during surgical procedures, when brain structures are likely to shift position.[91] Diffusion tensor tractography[92] has emerged as a diagnostically helpful application to visualize the course of tracts over longer distances. Diffusion tensor tractography uses the principal diffusion direction measured with DTI to compute the pathways of complete nerve fiber tracts. The tracing is performed by first defining positions of interest in a white matter tract. By following repetitively and in small steps along spatially interpolated directions of maximum diffusion, a contiguous path that passes through the initial seed positions is defined. Visualized with suitable software in two or three dimensions, these tracts depict the involved anatomy of white matter fibers (see Figure 10). Thus the departure from the basic assessment of the anisotropy of each diffusion tensor to the more elaborate analysis of neighbor relations among diffusion tensors opens the possibility for assessing in vivo axonal fiber connectivity and functional links between brain regions. Diffusion tensor tractography, especially fused together with conventional and functional image information, provides a powerful tool to avoid or minimize the injury of displaced but still intact fiber tracts during neurosurgery or radiation therapy.[89–91,93] It has also been suggested that tract anatomy derived from diffusion data can be used to estimate tumor progression along nerve fiber tracts and that this information may allow one to determine the optimal margin for resection in malignant brain tumors.[94,95] However, it should be remarked that tract course estimation over longer distances can be unreliable owing to noise, distortions, and small deviations between selected and actual diffusion encoding direction.[96]

CONCLUSION

Diffusion imaging clearly adds a new dimension to the diagnostic imaging of brain tumors. Of all the parameters that can be obtained with diffusion imaging, mean diffusion appears to be the most ubiquitously useful and most readily interpreted parameter. The value of this parameter lies not in the demarcation of tumor boundaries, but rather in the definitive tissue characterization in some cases in which T1- and T2-weighted images alone do not provide enough diagnostic information. The ability of diffusion imaging to document cellular response during drug or radiation therapy is also unique, but requires image registration for reliable detection of changes. The application of an extended b-factor range and analysis of the nonmonoexponential diffusion signal decay shows some interesting potential for diagnostic imaging in brain tumors. The diffusion anisotropy parameter, which can be obtained with DTI, seems to provide useful local information about white matter integrity. DTI is also valuable in the precise localization of white matter tracts. Tractography gives a quick and intuitive overview of the displaced course of white matter tracts in two- or three-dimensional space.

One major limitation of the MR diffusion images in comparison to the standard T1- and T2-weighted images is the inherent low signal-to-noise ratio and coarse spatial resolution. Partial volume effects prevent an equally good delineation of lesion boundaries and the images obtained with the commonly used single-shot echoplanar diffusion imaging method are plagued by geometric distortions. Such distortions may severely limit the use of such images for surgical planning or tractography.[97] Image postprocessing or multishot acquisition techniques can overcome these limitations. New advances in acquisition acceleration and image reconstruction may render protocols that acquire a large number of b-factors and diffusion encoding directions feasible in a clinical setting.

Acknowledgment

Some of the research data presented in this chapter were obtained with grant support from the National Institute of Neurological Disorders and Stroke (R01 NS39335) and the National Institute of Biomedical Imaging (R01 EB006867 and R01 EB010195).

References

1. Stejskal EO, Tanner JE. Spin diffusion measurements: spin echoes in the presence of a time-dependent field gradient. *J Chem Phys*. 1965;42:288–292.
2. Maier SE, Hardy CJ, Jolesz FA. Real-time quantification of brain and CSF motion with M-mode MR. *Radiology*. 1994;193:477–483.
3. Turner R, Le Bihan D, Maier J, Vavrek R, Hedges LK, Pekar J. Echo-planar imaging of intravoxel incoherent motions. *Radiology*. 1990;177:407–414.
4. Jaermann T, Crelier G, Pruessmann K, et al. SENSE-DTI at 3 T. *Magn Reson Med*. 2004;51(2):230–236.
5. Pipe JG, Farthing VG, Forbes KP. Multishot diffusion-weighted FSE using PROPELLER MRI. *Magn Reson Med*. 2002;47(1):42–52.
6. Holdsworth SJ, Skare S, Newbould RD, Bammer R. Robust GRAPPA-accelerated diffusion-weighted readout-segmented (RS)-EPI. *Magn Reson Med*. 2009;62(6):1629–1640.
7. Porter D, Heidemann RM. High resolution diffusion-weighted imaging using readout-segmented echo-planar imaging, parallel imaging and a two-dimensional navigator-based reacquisition. *Magn Reson Med*. 2009;62(2):468–475.
8. Chen N, Guidon A, Chang H, Song A. A robust multi-shot scan strategy for high-resolution diffusion weighted MRI enabled by multiplexed sensitivity-encoding (MUSE). *Neuroimage*. 2013;72:41–47.

9. Madore B, Chiou JY, Chu R, Chao TC, Maier SE. Accelerated multi shot diffusion imaging. *Magn Reson Med*. 2014;72(2):324–336.
10. Kuhnt D, Bauer MH, Egger J, et al. Fiber tractography based on diffusion tensor imaging compared with high-angular-resolution diffusion imaging with compressed sensing: initial experience. *Neurosurgery*. 2013;72(suppl 1):165–175.
11. Gudbjartsson H, Maier SE, Mulkern RV, oMrocz IA, Patz S, Jolesz FA. Line scan diffusion imaging. *Magn Reson Med*. 1996;36(4):509–519.
12. Maier SE, Gudbjartsson H, Patz S, et al. Line scan diffusion imaging: characterization in healthy subjects and stroke patients. *Am J Roentgenol*. 1998;17(1):85–93.
13. Maeda M, Maier SE, Sakuma H, Ishida M, Takeda K. Apparent diffusion coefficient in malignant lymphoma and carcinoma involving cavernous sinus evaluated by line scan diffusion-weighted imaging. *J Magn Reson Imaging*. 2006;24(3):543–548.
14. Chenevert TL, Pipe JG, Williams DM, Brunberg JA. Quantitative measurement of tissue perfusion and diffusion in vivo. *Magn Reson Med*. 1991;17:197–212.
15. van Rijswijk CS, Kunz P, Hogendoorn PC, Taminiau AH, Doornbos J, Bloem JL. Diffusion-weighted MRI in the characterization of soft-tissue tumors. *J Magn Reson Imaging*. 2002;15(3):302–307.
16. Bisdas S, Koh TS, Roder C, et al. Intravoxel incoherent motion diffusion-weighted MR imaging of gliomas: feasibility of the method and initial results. *Neuroradiology*. 2013;55(10):1189–1196.
17. Tsuruda JS, Chew WM, Moseley ME, Norman D. Diffusion-weighted MR imaging of the brain: value of differentiating between extraaxial cysts and epidermoid tumors. *Am J Neuroradiol*. 1990;11(5):925–931.
18. Maeda M, Kawamura Y, Tamagawa Y, et al. Intravoxel incoherent motion (IVIM) MRI in intracranial, extraaxial tumors and cysts. *J Comput Assist Tomogr*. 1992;16(4):514–518.
19. Chen S, Ikawa F, Kurisu K, Arita K, Takaba J, Kanou Y. Quantitative MR evaluation of intracranial epidermoid tumors by fast fluid-attenuated inversion recovery imaging and echo-planar diffusion-weighted imaging. *Am J Neuroradiol*. 2001;22(6):1089–1096.
20. Ebisu T, Tanaka C, Umeda M, et al. Discrimination of brain abscess from necrotic or cystic tumors by diffusion-weighted echo planar imaging. *Magn Reson Imaging*. 1996;14(9):1113–1116.
21. Noguchi K, Watanabe N, Nagayoshi T, et al. Role of diffusion-weighted echo-planar MRI in distinguishing between brain abscess and tumour: a preliminary report. *Neuroradiology*. 1999;41(3):171–174.
22. Chang SC, Lai PH, Chen WL, et al. Diffusion-weighted MRI features of brain abscess and cystic or necrotic brain tumors: comparison with conventional MRI. *Clin Imaging*. 2002;26(4):227–236.
23. Reddy JS, Mishra AM, Behari S, et al. The role of diffusion-weighted imaging in the differential diagnosis of intracranial cystic mass lesions: a report of 147 lesions. *Surg Neurol*. 2006;66(3):246–250.
24. Holtas S, Geijer B, Stromblad LG, Maly-Sundgren P, Burtscher IM. A ring-enhancing metastasis with central high signal on diffusion-weighted imaging and low apparent diffusion coefficients. *Neuroradiology*. 2000;42(11):824–827.
25. Yamasaki F, Kurisu K, Satoh K, et al. Apparent diffusion coefficient of human brain tumors at MR imaging. *Radiology*. 2005;235(3):985–991.
26. Rumboldt Z, Camacho DL, Lake D, Welsh CT, Castillo M. Apparent diffusion coefficients for differentiation of cerebellar tumors in children. *Am J Neuroradiol*. 2006;27(6):1362–1369.
27. Pronin IN, Kornienko VN, Fadeeva LM, Rodionov PV, Golanov AV. Diffusion-weighted image in the study of brain tumors and peritumoral edema (article in Russian). *Zh Vopr Neirokhir Im N N Burdenko*. July–September 2000;(3):14–16.
28. Dorenbeck U, Grunwald IQ, Schlaier J, Feuerbach S. Diffusion-weighted imaging with calculated apparent diffusion coefficient of enhancing extra-axial masses. *J Neuroimaging*. 2005;15(4):314–317.
29. Guo AC, Cummings TJ, Dash RC, Provenzale JM. Lymphomas and high-grade astrocytomas: comparison of water diffusibility and histologic characteristics. *Radiology*. 2002;224(1):177–183.
30. Kono K, Inoue Y, Nakayama K, et al. The role of diffusion-weighted imaging in patients with brain tumors. *Am J Neuroradiol*. 2001;22(6):1081–1088.
31. Uhl M, Altehoefer C, Kontny U, Il'yasov K, Buchert M, Langer M. MRI-diffusion imaging of neuroblastomas: first results and correlation to histology. *Eur Radiol*. 2002;12(9):2335–2338.
32. Rodallec M, Colombat M, Krainik A, Kalamarides M, Redondo A, Feydy A. Diffusion-weighted MR imaging and pathologic findings in adult cerebellar medulloblastoma. *J Neuroradiol*. 2004;31(3):234–237.
33. Herneth A, Guccione S, Bednarski M. Apparent diffusion coefficient: a quantitative parameter for in vivo tumor characterization. *Eur J Radiol*. 2003;45(3):208–213.
34. Sugahara T, Korogi Y, Kochi M, et al. Usefulness of diffusion-weighted MRI with echo-planar technique in the evaluation of cellularity in gliomas. *J Magn Reson Imaging*. 1999;9(1):53–60.
35. Gupta RK, Cloughesy TF, Sinha U, et al. Relationships between choline magnetic resonance spectroscopy, apparent diffusion coefficient and quantitative histopathology in human glioma. *J Neurooncol*. 2000;50(3):215–226.
36. Gauvain KM, McKinstry RC, Mukherjee P, et al. Evaluating pediatric brain tumor cellularity with diffusion-tensor imaging. *Am J Roentgenol*. 2001;177(2):449–454.
37. Hayashida Y, Hirai T, Morishita S, et al. Diffusion-weighted imaging of metastatic brain tumors: comparison with histologic type and tumor cellularity. *Am J Neuroradiol*. 2006;27(7):1419–1425.
38. Ellingson BM, Malkin MG, Rand SD, et al. Validation of functional diffusion maps (fDMs) as a biomarker for human glioma cellularity. *J Magn Reson Imaging*. 2010;31(3):538–548.
39. Ryu YJ, Choi SH, Park SJ, Yun TJ, Kim JH, Sohn CH. Glioma: application of whole-tumor texture analysis of diffusion-weighted imaging for the evaluation of tumor heterogeneity. *PLoS One*. 2014;9(9):1–9.
40. Lyng H, Haraldseth O, Rofstad E. Measurement of cell density and necrotic fraction in human melanoma xenografts by diffusion weighted magnetic resonance imaging. *Magn Reson Med*. 2000;43(6):828–836.
41. Mishra AM, Gupta RK, Saksena S, et al. Biological correlates of diffusivity in brain abscess. *Magn Reson Med*. 2005;54(4):663–667.
42. Steen RG. Edema and tumor perfusion: characterization by quantitative 1H MR imaging. *Am J Roentgenol*. 1992;158(2):259–264.
43. Morita K, Matsuzawa H, Fujii Y, Tanaka R, Kwee IL, Nakada T. Diffusion tensor analysis of peritumoral edema using lambda chart analysis indicative of the heterogeneity of the microstructure within edema. *J Neurosurg*. 2005;102(2):336–341.
44. Lemercier P, Paz Maya S, Patrie JT, Flors L, Leiva-Salinas C. Gradient of apparent diffusion coefficient values in peritumoral edema helps in differentiation of glioblastoma from solitary metastatic lesions. *Am J Roentgenol*. 2014;203(1):163–169.
45. Brynolfsson P, Nilsson D, Henriksson R, et al. ADC texture – an imaging biomarker for high-grade glioma? *Med Phys*. 2014;41(10):1–7.
46. Moffat BA, Chenevert TL, Lawrence TS, et al. Functional diffusion map: a noninvasive MRI biomarker for early stratification of clinical brain tumor response. *Proc Natl Acad Sci USA*. 2005;102(15):5524–5529.
47. Mardor Y, Roth Y, Lidar Z, et al. Monitoring response to convection-enhanced taxol delivery in brain tumor patients using diffusion-weighted magnetic resonance imaging. *Cancer Res*. 2001;61(13):4971–4973.
48. Mardor Y, Pfeffer R, Spiegelmann R, et al. Early detection of response to radiation therapy in patients with brain malignancies using conventional and high b-value diffusion weighted MRI. *J Clin Oncol*. 2003;21(6):1094–1100.

49. Valonen PK, Lehtimäki KK, Väisänen TH, et al. Water diffusion in a rat glioma during ganciclovir-thymidine kinase gene therapy-induced programmed cell death in vivo: correlation with cell density. *J Magn Reson Imaging*. 2004;19(4):389–396.
50. Mardor Y, Roth Y, Ochershvilli A, et al. Pre-treatment prediction of brain tumors response to radiation therapy using high b-value diffusion-weighted MRI. *Neoplasia*. 2004;6(2):136–142.
51. Moffat BA, Chenevert TL, Meyer CR, et al. The functional diffusion map: an imaging biomarker for the early prediction of cancer treatment outcome. *Neoplasia*. 2006;8(4):259–267.
52. Chan YL, Yeung DK, Leung SF, Chan PN. Diffusion-weighted magnetic resonance imaging in radiation-induced cerebral necrosis. apparent diffusion coefficient in lesion components. *J Comput Assist Tomogr*. 2003;27(5):674–680.
53. Huang RY, Neagu MR, Reardon DA, Wen YP. Pitfalls in the neuroimaging of glioblastoma in the era of antiangiogenic and immuno/targeted therapy – detecting illusive disease, defining response. *Front Neurol*. 2015;6(33):1–16.
54. Lee WJ, Choi SH, Park CK, et al. Diffusion-weighted MR imaging for the differentiation of true progression from pseudoprogression following concomitant radiotherapy with temozolomide in patients with newly diagnosed high-grade gliomas. *Acad Radiol*. 2012;19(11):1353–1361.
55. Hu X, Wong KK, Young GS, Guo L, Wong ST. Support vector machine multiparametric MRI identification of pseudoprogression from tumor recurrence in patients with resected glioblastoma. *J Magn Reson Imaging*. 2011;33(2):296–305.
56. Mulkern RV, Gudbjartsson H, Westin CF, et al. Multicomponent apparent diffusion coefficients in human brain. *NMR Biomed*. 1999;12:51–62.
57. Maier SE, Vajapeyam S, Mamata H, Westin CF, Jolesz FA, Mulkern RV. Biexponential diffusion tensor analysis of human brain diffusion data. *Magn Reson Med*. 2004;51(2):321–330.
58. Bennett KM, Schmainda K, Bennett R, Rowe D, Lu H, Hyde J. Characterization of continuously distributed cortical water diffusion rates with a stretched-exponential model. *Magn Reson Med*. 2003;50(4):727–734.
59. Kiselev VG, Il'yasov KA. Is the "biexponential diffusion" biexponential? *Magn Reson Med*. 2007;57(3):464–469.
60. Jensen JH, Helpern JA, Ramani A, Lu H, Kaczynski K. Diffusional kurtosis imaging: the quantification of non-gaussian water diffusion by means of magnetic resonance imaging. *Magn Reson Med*. 2005;53(6):1432–1440.
61. Yoshiura T, Wu O, Zaheer A, Reese TG, Sorensen AG. Highly diffusion-sensitized MRI of brain: dissociation of gray and white matter. *Magn Reson Med*. 2001;45(5):734–740.
62. Maier SE, Mulkern RV. Biexponential analysis of diffusion related signal decay in normal human cortical and deep gray matter. *Magn Reson Imaging*. 2008;26(7):897–904.
63. Assaf Y, Basser PJ. Composite hindered and restricted model of diffusion (CHARMED) MR imaging of the human brain. *Neuroimage*. 2005;27(1):48–58.
64. DeLano MC, Cooper TG, Siebert JE, Potchen MJ, Kuppusamy K. High-b-value diffusion-weighted MR imaging of adult brain: image contrast and apparent diffusion coefficient map features. *Am J Neuroradiol*. 2000;21(10):1830–1836.
65. Burdette JH, Durden DD, Elster AD, Yen YF. High b-value diffusion-weighted MRI of normal brain. *J Comput Assist Tomogr*. 2001;25(4):515–519.
66. Maier SE, Bogner P, Bajzik G, et al. Normal brain and brain tumor: multicomponent apparent diffusion coefficient line scan imaging. *Radiology*. 2001;219:842–849.
67. Schwarcz A, Ursprung Z, Berente Z, et al. In vivo brain edema classification: new insight offered by large b-value diffusion-weighted MR imaging. *J Magn Reson Imaging*. 2007;25(1):26–31.
68. Raab P, Hattingen E, Franz K, Zanella F, Lanfermann H. Cerebral gliomas: diffusional kurtosis imaging analysis of microstructural differences. *Radiology*. 2010;254(3):876–881.
69. Van Cauter S, Veraart J, Sijbers J, et al. Gliomas: diffusion kurtosis MR imaging in grading. *Radiology*. 2012;263(2):492–501.
70. Kwee TC, Galban CJ, Tsien C, et al. Comparison of apparent diffusion coefficients and distributed diffusion coefficients in high-grade gliomas. *J Magn Reson Imaging*. 2010;31(3):531–537.
71. Maier SE, Mamata H, Mulkern RV. Characterization of normal brain and brain tumor pathology by chisquares parameter maps of diffusion-weighted image data. *Eur J Radiol*. 2003;45(3):199–207.
72. Basser P, Mattiello J, Le Bihan D. MR diffusion tensor spectroscopy and imaging. *Biophys J*. 1994;66(1):259–267.
73. Lin CP, Tseng WY, Cheng HC, Chen JH. Validation of diffusion tensor magnetic resonance axonal fiber imaging with registered manganese-enhanced optic tracts. *Neuroimage*. 2001;14(5):1035–1047.
74. Tuch DS. Q-ball imaging. *Magn Reson Med*. 2004;52(6):1358–1372.
75. Papadakis NG, Xing D, Houston GC, et al. A study of rotationally invariant and symmetric indices of diffusion anisotropy. *Magn Reson Imaging*. 1999;17(6):881–892.
76. Pierpaoli C, Jezzard P, Basser P, Barnett A, Di Chiro G. Diffusion tensor MR imaging of the human brain. *Radiology*. 1996;201(3):637–648.
77. Mamata H, Jolesz FA, Maier SE. Characterization of central nervous system structures by magnetic resonance diffusion anisotropy. *Neurochem Int*. 2004;45(4):553–560.
78. Price S, Burnet N, Donovan T, et al. Diffusion tensor imaging of brain tumours at 3T: a potential tool for assessing white matter tract invasion? *Clin Radiol*. 2003;58(6):455–462.
79. Provenzale JM, McGraw P, Mhatre P, Guo AC, Delong D. Peritumoral brain regions in gliomas and meningiomas: investigation with isotropic diffusion-weighted MR imaging and diffusion-tensor MR imaging. *Radiology*. 2004;232(2):451–460.
80. Tropine A, Vucurevic G, Delani P, et al. Contribution of diffusion tensor imaging to delineation of gliomas and glioblastomas. *J Magn Reson Imaging*. 2004;20(6):905–912.
81. Byrnes TJ, Barrick TR, Bell BA, Clark CA. Diffusion tensor imaging discriminates between glioblastoma and cerebral metastases in vivo. *NMR Biomed*. 2011;24(1):54–60.
82. Saksena S, Jain R, Schultz L, et al. The corpus callosum Wallerian degeneration in the unilateral brain tumors: evaluation with diffusion tensor imaging (DTI). *J Clin Diagn Res*. 2013;7(2):320–325.
83. Sinha S, Bastin ME, Whittle IR, Wardlaw JM. Diffusion tensor MR imaging of high-grade cerebral gliomas. *Am J Neuroradiol*. 2002;23(4):520–527.
84. Goebell E, Paustenbach S, Vaeterlein O, et al. Low-grade and anaplastic gliomas: differences in architecture evaluated with diffusion-tensor MR imaging. *Radiology*. 2006;239(1):217–222.
85. Inoue T, Ogasawara K, Beppu T, Ogawa A, Kabasawa H. Diffusion tensor imaging for preoperative evaluation of tumor grade in gliomas. *Clin Neurol Neurosurg*. 2005;107(3):174–180.
86. Beppu T, Inoue T, Shibata Y, et al. Fractional anisotropy value by diffusion tensor magnetic resonance imaging as a predictor of cell density and proliferation activity of glioblastomas. *Surg Neurol*. 2005;63(1):56–61.
87. Zhang J, van Zijl PC, Laterra J, et al. Unique patterns of diffusion directionality in rat brain tumors revealed by high-resolution diffusion tensor MRI. *Magn Reson Med*. 2007;58(3):454–462.
88. Szczepankiewicz F, Lasic S, van Westen D, et al. Quantification of microscopic diffusion anisotropy disentangles effects of orientation dispersion from microstructure: applications in healthy volunteers and in brain tumors. *Neuroimage*. 2015;104:241–252.
89. Holodny AI, Schwartz TH, Ollenschleger M, Liu WC, Schulder M. Tumor involvement of the corticospinal tract: diffusion magnetic resonance tractography with intraoperative correlation. *J Neurosurg*. 2001;95(6):1082.

90. Yu CS, Li KC, Xuan Y, Ji XM, Qin W. Diffusion tensor tractography in patients with cerebral tumors: a helpful technique for neurosurgical planning and postoperative assessment. *Eur J Radiol*. 2005;56(2):197–204.
91. Nimsky C, Ganslandt O, Hastreiter P, et al. Preoperative and intraoperative diffusion tensor imaging-based fiber tracking in glioma surgery. *Neurosurgery*. 2005;56(1):130–137.
92. Basser PJ, Pajevic S, Pierpaoli C, Duda J, Aldroubi A. In vivo fiber tractography using DT-MRI data. *Magn Reson Med*. 2000;44(4):625–632.
93. Maesawa S, Fujii M, Nakahara N, et al. Clinical indications for high-field 1.5 T intraoperative magnetic resonance imaging and neuronavigation for neurosurgical procedures. review of initial 100 cases. *Neurol Med Chir (Tokyo)*. 2009;49(8):340–349.
94. Bondiau PY, Clatz O, Sermesant M, et al. Biocomputing: numerical simulation of glioblastoma growth using diffusion tensor imaging. *Phys Med Biol*. 2008;53(4):879–893.
95. Mosayebi P, Cobzas D, Murtha A, Jagersand M. Tumor invasion margin on the Riemannian space of brain fibers. *Med Image Anal*. 2012;16(2):361–373.
96. Mandelli ML, Berger MS, Bucci M, Berman JI, Amirbekian B, Henry RG. Quantifying accuracy and precision of diffusion MR tractography of the corticospinal tract in brain tumors. *Neurosurg*. 2014;121(2):349–358.
97. Hahn HK, Klein J, Nimsky C, Rexilius J, Peitgen HO. Uncertainty in diffusion tensor based fibre tracking. *Acta Neurochir Suppl*. 2006;98:33–41.
98. Maier SE, Sun Y, Mulkern RV. Diffusion imaging of brain tumors. *NMR Biomed*. 2010;23(7):849–864.
99. Helenius J, Soinne L, Perkio J, et al. Diffusion-weighted MR imaging in normal human brains in various age groups. *Am J Neuroradiol*. 2002;23(2):194–199.
100. Hakyemez B, Yildirim N, Gokalp G, Erdogan C, Parlak M. The contribution of diffusion-weighted MR imaging to distinguishing typical from atypical meningiomas. *Neuroradiology*. 2006;48(8):512–520.
101. Marks MP, de Crespigny A, Lentz D, Enzmann DR, Alberts GW, Moseley ME. Acute and chronic stroke: navigated spin-echo diffusion-weighted MR imaging. *Radiology*. 1996;199:403–408.

CHAPTER

29

Functional Magnetic Resonance Imaging

Ryan Fisicaro, Nicole Petrovich Brennan, Andrei Holodny

Department of Radiology, Memorial Sloan-Kettering Cancer Center, New York, NY, USA

INTRODUCTION

In brain tumor patients, treatment often entails resection of the brain tumor. Of utmost importance in the clinical management of brain tumor patients is quality of life. Thus, the goals of brain tumor surgery are twofold: (1) to maximize resection of the tumor and (2) not to resect important brain structures adjacent to the tumor. Maximizing resection aids in improving survival and quality of life, while not resecting important brain structures adjacent to the tumor avoids neurosurgical complications. To achieve these goals, knowing the location of eloquent brain regions in relation to the tumor is paramount. Awareness of eloquent brain regions helps to plan the surgical approach and techniques used in surgery.

Many techniques are used to localize brain function in the brain tumor patient, such as blood oxygen level-dependent functional magnetic resonance imaging (BOLD fMRI), positron emission tomography, near-infrared spectroscopy, direct cortical stimulation (DCS), magnetoencephalography, and transcranial magnetic spectroscopy. Each test has distinct advantages, but BOLD fMRI is the most frequently utilized clinical test for brain tumor patients. The reasons for the popularity of BOLD fMRI are that it is a noninvasive procedure with no known risks, has a sufficient signal-to-noise ratio on a standard clinical 1.5-T magnet, and has excellent spatial resolution.[1] BOLD fMRI, in addition to helping in mapping and planning preoperatively, also aids intraoperative mapping techniques such as DCS.

In this chapter, we discuss the use of BOLD fMRI in the management of brain tumor patients. We focus on the physics behind the BOLD fMRI signal, paradigm optimization, application to motor and language mapping, and artifacts and pitfalls in fMRI map interpretation. Last, we will cover the effects of fMRI on surgical outcomes and future developments of fMRI.

GENERAL fMRI CONSIDERATIONS

The basis of BOLD fMRI signals is the relative concentrations of the differing states of hemoglobin, namely diamagnetic oxyhemoglobin (HbO_2) and paramagnetic deoxyhemoglobin (dHb). Additionally, the signal relies on changes in the vasculature being tied to neuronal activity in a process called neurovascular coupling (NVC). Neuronal activity causes a secondary increase in cerebral blood flow (CBF), cerebral blood volume (CBV), and cerebral metabolic rate of oxygen ($CMRO_2$). It is the changes in these parameters that yield the BOLD effect.[2] When neuronal activity occurs, there is an increase in both CBF and $CMRO_2$. The delivery of oxygenated blood to the active area due to the increase in CBF is greater than the extraction of oxygen by $CMRO_2$. This overshoot of oxygenated blood causes an increase in HbO_2 relative to dHb and thus causes an increase in the BOLD fMRI signal.[3] This means that the fMRI signal will differ in the motor gyrus of a patient while at rest and during finger movements. As the generation of fMRI maps necessitates statistical comparisons, these periods of rest and activity are repeated multiple times to generate statistical power. Tasks designed to stimulate neuronal activity are called paradigms.

For fMRI mapping, there are two main types of stimulus presentation paradigms. Figure 1 illustrates the main difference between event-related and block design. A block paradigm consists of alternating cycles between the task, called the "on" state, and breaks, called the "off" state.[1] These alternating cycles are repeated 3–10 times during the scan and can be of equal or unequal duration. An example block paradigm includes a patient resting or fixating on a crosshair for 20 s and then naming pictures for 20 s. Event-related paradigms, while having similar off states, differ from block paradigms because patients perform a single event, such as toe movement, that has a much shorter duration than the on state of

Handbook of Neuro-Oncology Neuroimaging, Second Edition
http://dx.doi.org/10.1016/B978-0-12-800945-1.00029-X

© 2016 Elsevier Ltd. All rights reserved.

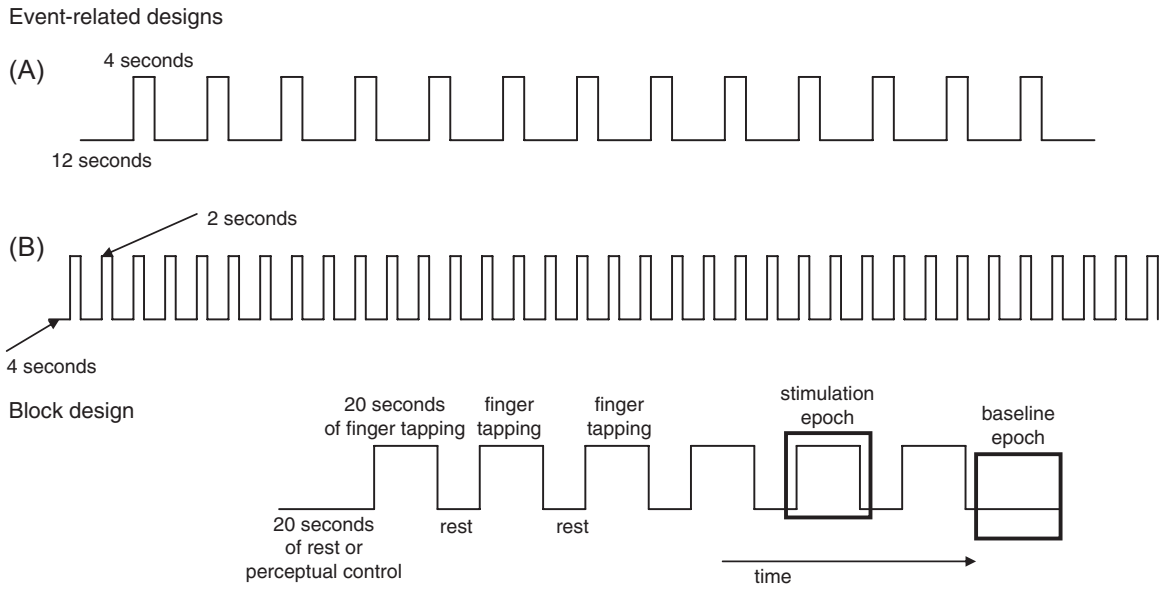


FIGURE 1 Two main types of stimulus delivery protocols. The block design groups stimuli of the same type with multiple repetitions per epoch. The example shown here is for finger tapping, but the stimulus is easily replaced with pictures or some other linguistic task for language assessment. Slow (A) and fast (B) event-related designs allow the estimation of the hemodynamic response to a single stimulus (or minimal number of stimuli). Block design alternates blocks of stimuli of the same type and is generally preferred for use with brain tumor patients when there is no need for temporal information and the goal is to assess basic function.

block paradigms. Event-related paradigms are better than block paradigms at estimating the hemodynamic response, while block paradigms have better statistical power due to acquiring more images per acquisition.[4]

In our experience, block designs are unequivocally better for brain tumor patients. This may be because their performance is variable and benefits from signal averaging. Regardless, using event-related designs with patients in our institution is driven only by necessity. These paradigms are helpful to researchers interested in the effects of a brain tumor on brain functioning, as the specific brain-based responses can be studied in detail. Additionally, event-related designs have proven useful with patients performing vocalized speech paradigms in which head motion is an issue and the contaminated images can be easily extracted when they are in isolation.

SENSORY/MOTOR fMRI

The sensory/motor system is one of the most straightforward to map using fMRI. The motor cortex, located in the precentral gyrus, has great responsibility in the actual performance of movements. The various motor functions map to specific locations in the motor cortex in a topographic manner called a homunculus.[5] Notable functional areas include the foot medially, the tongue laterally, and the hand in between. The hand is easy to localize with paradigms such as finger tapping and fist clenching and has a distinct anatomical landmark referred to as a "reverse omega" sign.[6] Moving more medially or laterally/inferiorly from the hand makes localizing the motor gyrus and eloquent centers relative to a lesion more difficult.[7] For a more lateral/inferior lesion, the inclusion of a tongue-movement paradigm might prove beneficial. Figure 2 shows how tongue and hand motor tasks can effectively map the different cortical representations of the motor homunculus. Localizing the foot at the most medial aspect of the motor strip can nicely define the location of the foot and leg relative to the supplementary motor area (SMA). A smaller matrix size will enable more specific, segregated maps of function (Figure 2). In some cases, the sacrifice in the signal-to-noise ratio that makes going from 64×64 to 128×128 may be advantageous. In our experience, the motor signal tends to be strong and resilient to head motion even in brain tumor patients, allowing use of the higher spatial resolution of 128×128.

The sensory cortex, located in the postcentral gyrus, has a homunculus pattern much like that of the motor cortex. A common paradigm used in sensory mapping is scrubbing a patient's hand with a textured object. While this paradigm is helpful in localizing the sensory cortex, another important consideration is the reciprocity of neural connectivity between the precentral and the postcentral gyri. This reciprocity allows for passive sensory movements to aid in mapping functional motor areas in patients who cannot perform a specific task because of a lesion or mass effect. When planning fMRI paradigms, one should consider how the neurosurgeon will use the map to plan or guide oncologic surgery. The map serves to confirm the surgeon's

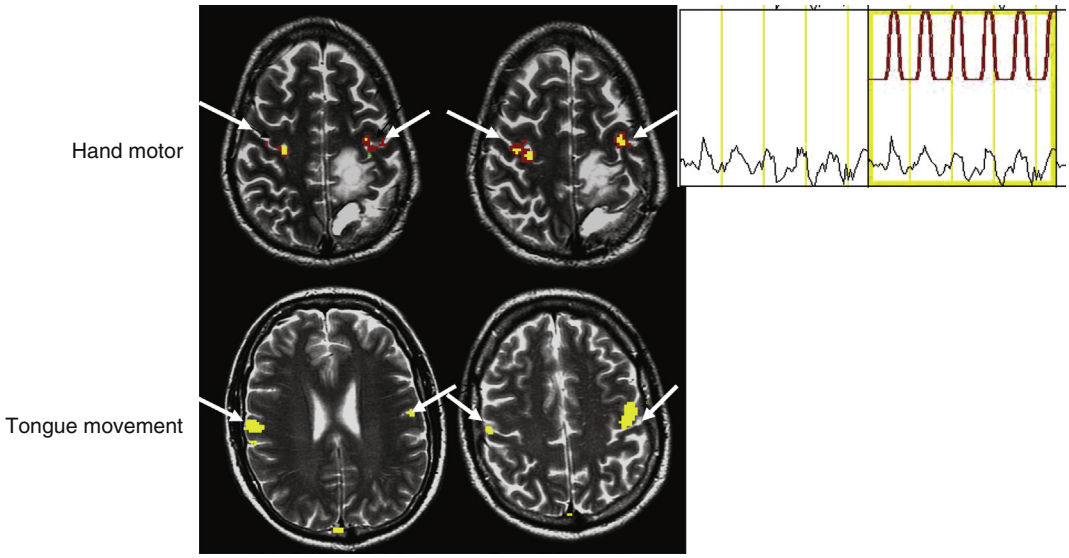


FIGURE 2 Hand motor fMRI and tongue movement fMRI in two brain tumor patients illustrating the ability of fMRI to distinguish between the more dorsal/superior and the lateral/inferior portions of the motor homunculus. Arrows indicate the locations of the central sulcus. The boxes represent the actual signal in two voxels in the motor cortex. The black is the measured signal and the red is the ideal or model for the stimulus presentation. In this case, the patient was instructed to move fingers six times, each separated by rest.

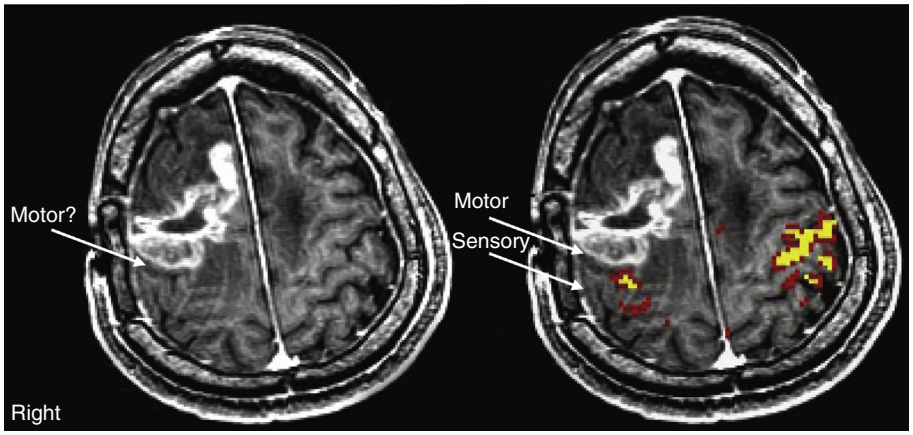


FIGURE 3 T_1-postcontrast image of a patient with a glioblastoma multiforme in the right hemisphere. This extensive lesion makes it difficult to determine whether the lesion is within the motor gyrus. fMRI of bilateral finger tapping makes this determination clearer. Note both the more anterior motor activity and the posterior sensory activity.

impression of the location of the lesion relative to the motor gyrus by noting whether the lesion is in the motor cortex itself or anterior or posterior to it. These judgments can be difficult based on a patient's clinical presentation alone and fMRI helps in clearing up ambiguities.

Additionally, a tumor may have mass effect that effaces sulci and renders them difficult to discern via traditional imaging. Figure 3 shows a T_1-postcontrast image of a patient with an extensive glioblastoma multiforme in the right hemisphere. Without fMRI, it was difficult to know whether this lesion extended into the motor gyrus itself. Following fMRI mapping, it was determined that the lesion was within the motor gyrus and the patient had an awake intraoperative procedure as a result.

Intraoperative DCS is considered the "gold standard" in neurosurgery to localize function. DCS mapping can be guided by fMRI as fMRI uses T_2*-weighted imaging that, while having lower spatial resolution, is highly sensitive to the susceptibility differences in the states of hemoglobin. The fMRI map can be fused to the intraoperative guidance system allowing the surgeon to begin stimulation based on not only anatomical landmarks, but also the fMRI localization. Figure 4 shows the integration of the hand and foot fMRI on the patient in Figure 3 into a neurosurgical navigation system. The surgeon was able to direct the intraoperative DCS before resection of this lesion. The hand fMRI was concordant with the DCS (foot/leg was not attempted).

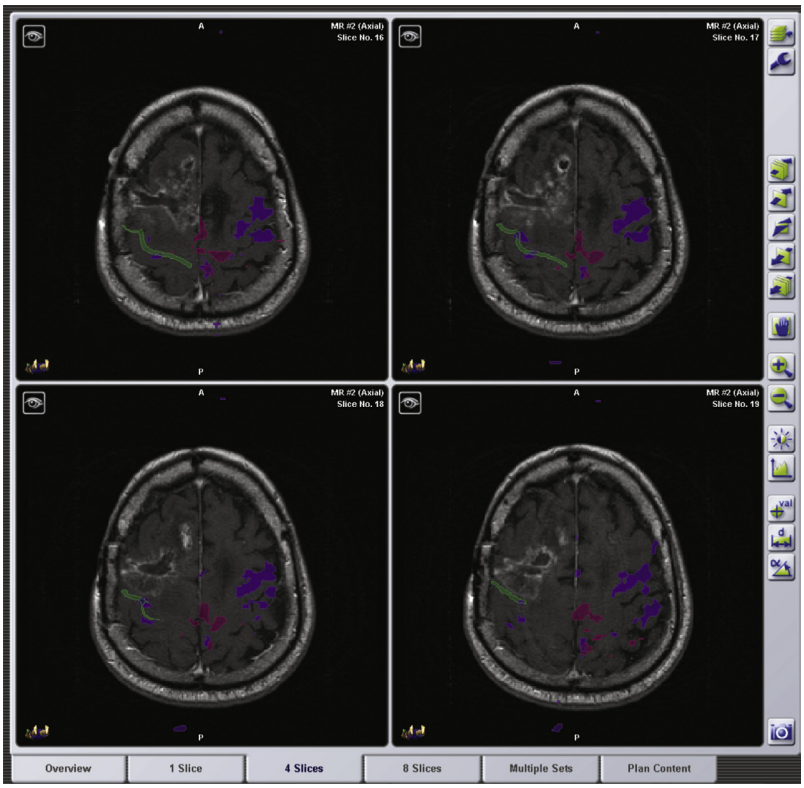


FIGURE 4 Integration of foot (pink) and hand (purple) fMRI on the patient from Figure 3 into a neurosurgical navigation system. The green line indicates the location of central sulcus.

LANGUAGE fMRI

Language lateralization and language localization are the two main types of language mapping for oncologic neurosurgery.

LATERALIZATION

The intracarotid sodium amobarbital procedure, better known as the WADA test, is currently the gold standard for determining language and memory dominance in patients.[8] It entails anesthetizing one hemisphere of the brain at a time while a clinician monitors the patient's performance on language and memory tasks. However, the WADA test is invasive and can cause stroke or other complications. Consequently, there is a significant effort to replace the WADA test. For the purpose of language lateralization, there are a number of studies confirming the concordance of fMRI with WADA and DCS.[7,9–11]

While there are a variety of language tasks, it is important to note that there is no consensus on standard paradigms. This is helpful clinically because it allows freedom in designing paradigms to best fit the capabilities of the patient and answer clinical questions. Language paradigms are categorized as productive or receptive speech tasks. Productive speech tasks require patients to generate words in response to a cue. An example task is verb generation, wherein a noun is given as a cue followed by the patient generating verbs. Receptive language paradigms include tasks such as listening to aurally presented words. Regardless of the chosen paradigm, activation is seen in both frontal and temporoparietal language areas. Because of this, designing multiple tasks covering both productive and receptive speech functions is important for better patient care.

Typically, the most useful way to measure essential language function for presurgical planning for brain tumor patients is to do a combined task analysis, as described by Ramsey et al.[11] The output of this analysis shows what is activated in common during different language tasks. This helps to decrease variability in the fMRI map by deemphasizing supportive language areas.

LOCALIZATION

The left hemisphere is dominant in language function for nearly all right-handed people and is usually dominant or codominant in left-handed people.[12] While Broca's area is located in the posterior inferior frontal

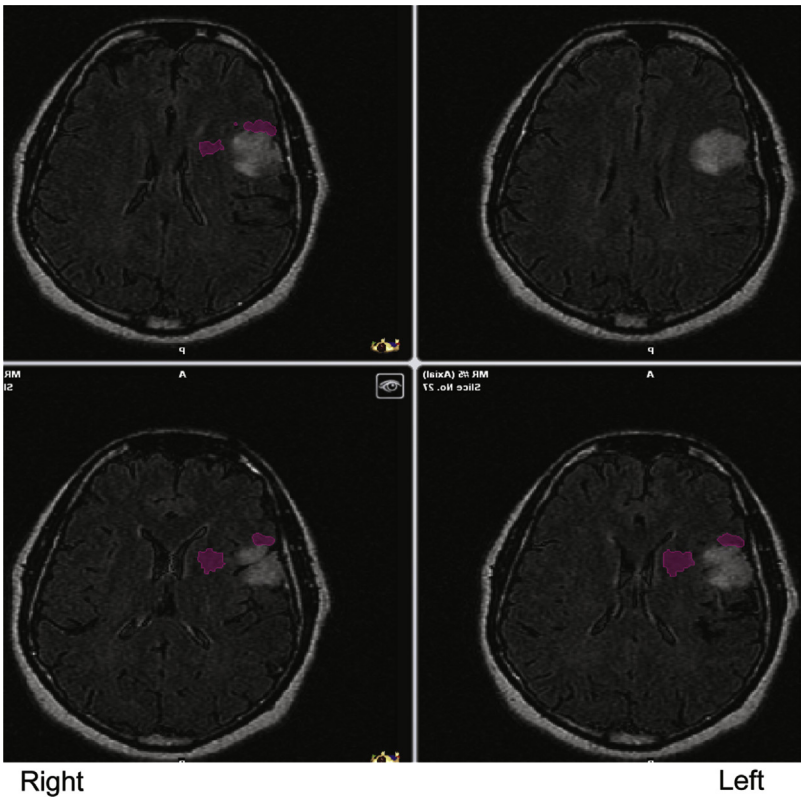


FIGURE 5 Fluid-attenuated inversion recovery image of a right-handed man with dysarthria and seizures. MRI revealed a low-grade minimally enhancing lesion in the expected location of Broca's area. fMRI revealed both insular and inferior frontal activity. The patient was operated on awake with direct cortical stimulation, and the location of Broca's area (speech arrest) was concordant with intraoperative cortical stimulation.

gyrus and Wernicke's area is located in the posterior superior temporal gyrus, mapping for neurosurgical planning is nuanced. Ideally, fMRI would localize essential language networks such that the surgeon could plan margins during oncologic surgery. But, fMRI activations are subject to variations in size depending on the type of statistical analysis and statistical thresholding. For example, decreasing the correlation coefficient on a language map increases the spatial extent of fMRI activity. This increase in spatial extent does not necessarily reflect the actual extent of neuronal activity, thus not allowing for surgical margins based on fMRI maps.

In addition to the spatial extent of fMRI activations, fMRI language maps reveal both essential and supportive function. In addition to Broca's and Wernicke's areas, many other areas participate in language function, such as the SMA, middle frontal gyrus, supramarginal gyrus, angular gyrus, and middle and inferior temporal gyri. As there are a great number of areas contributing to language function, there is no way as of this writing to discern between essential and supportive areas. This makes other mapping techniques, like DCS, necessary in many cases for surgical decision-making.

Figure 5 illustrates how language localization can guide the surgeon and aid in risk assessment and patient counseling. A 54-year-old man presented with seizures and slight dysarthria. MRI revealed a low-grade slightly enhancing lesion on T1. fMRI (during phenomic fluency) placed the lesion within Broca's area and lateral to insular language activity. The patient was counseled as to the risk of operating given the fMRI localization. The patient was operated on awake and DCS confirmed the location of Broca's area as measured by fMRI. In this case, only a biopsy was attempted because of the location of the tumor within Broca's area flanked by fMRI activity. The patient had no new deficits following surgery.

SPECIAL CONSIDERATIONS FOR fMRI MEASUREMENTS USING BRAIN TUMOR PATIENTS

When designing paradigms for patients, there are four main considerations. The first consideration is the questions and concerns the neurosurgeon has in developing the treatment plan. Second, patient status is important in regard to which tasks can be properly performed. Third, paradigm planning should be based on establishing the relative location of the lesion to

the expected functional neuroanatomy. Fourth, head motion is the most frequent cause of fMRI test failures, so paradigm design for each patient should keep head motion to a minimum.[13]

As the previously mentioned considerations help shape paradigm design, patient performance determines the quality of fMRI maps. To help increase patient performance, many steps can be taken. Early arrival by the patient allows for assessment of patient status and for thorough explanation and practice of paradigm tasks. This time can highlight any complications and allow for paradigm alterations. Motion and proper positioning also greatly affect fMRI maps. Addressing motion before the scan starts, by ensuring patient comfort and minimizing motion related to task performance, greatly improves results. For most motor paradigms, the scanning plane is parallel to the axial plane.[14] Misalignment of the scanning plane or patient positioning may cause the motor strip to fall off the back of images. To ensure patient performance, communication and monitoring systems are available to use during scans.

THE EFFECTS OF BRAIN TUMORS AND PRIOR SURGERY ON THE BOLD fMRI SIGNAL

As discussed previously, the basis for BOLD fMRI is NVC. However, in tumors, especially high-grade tumors, the vasculature is both morphologically and functionally abnormal and causes neurovascular uncoupling (NVU). In NVU, changes in vascular parameters are not tied to neuronal activity, thus not allowing for an increase in the BOLD fMRI signal. Morphologically, tumor vasculature is tortuous and disorganized and has increased angiogenesis.[15,16] Functionally, Holodny et al. demonstrated in patients with brain tumors in the motor strip that the hemisphere affected by the tumor had a significantly decreased fMRI signal volume during finger tapping compared to the unaffected hemisphere.[17] Additionally, Hou et al. characterized this difference further and showed an inverse relationship between perfusion (relative CBV) and the fMRI activation volume in grade IV gliomas.[18] That is, as perfusion measures increased, fMRI volume decreased.

Prior surgery is common when brain tumor patients come for treatment. This is an important consideration because those with prior surgery possibly have titanium plates, metallic staples, blood products, or residual surgical metal that can distort the magnetic field and alter T2*-weighted images.[1] Kim et al. showed a reduction in the volume of fMRI activity in the motor strip in the hemisphere with prior surgery when comparing fMRI volumes of activity during finger tapping in hemispheres unaffected and affected by prior surgery.[19]

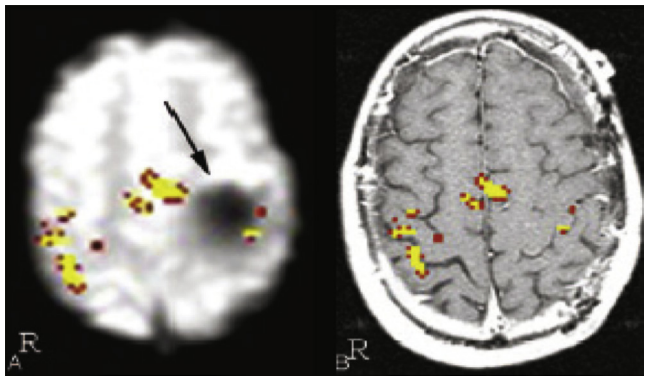


FIGURE 6 The signal dropout in the T_2* signal due to the effects of prior surgery. Also note that the volume of fMRI activity is decreased relative to the unaffected hemisphere. *From Ref. 19, ©American Society of Neuroradiology.*

Figure 6 demonstrates the type of signal void that can affect T2* scans. Of course, such a dropout will adversely affect the accuracy of the fMRI measurement. As a result, the authors suggest that the raw T2* images be inspected before data analysis to avoid misleading interpretations of the fMRI data.

Peck et al. did a similar study in patients with brain tumors, but asked whether the fMRI-determined laterality index (a measurement of the degree of language laterality) is affected in patients with prior surgery when using DCS as a ground truth.[20] There were no statistically significant differences in the hemispheric determination of language laterality between patients with or without prior surgery. However, there were discrepancies in the region of interest (Broca's area), laterality indices, and the results of intraoperative mapping. In conclusion, in cases in which the patient has an extensive malignant lesion and/or prior surgery, the fMRI should be interpreted with caution.

INTERPRETATION PITFALLS

The value of the fMRI map in clinical practice is directly related to the end-stage interpretation of the fMRI data. Consequently, it is worth outlining some of the more common mistakes in fMRI interpretation. In motor mapping, most postprocessing protocols include some degree of spatial smoothing. This is widely accepted and boosts the signal-to-noise ratio in addition to enhancing the appearance of fMRI activations. Depending on how much smoothing is applied, motor activations can be displaced. The posterior banks of the motor and sensory gyri are the portions of gray matter that typically activate in an fMRI scan. Using a 3-T scanner requires minimal smoothing and allows easy visualization of the spatial extent of the gray matter participating. Most institutions use 1.5-T scanners that allow one-fourth of

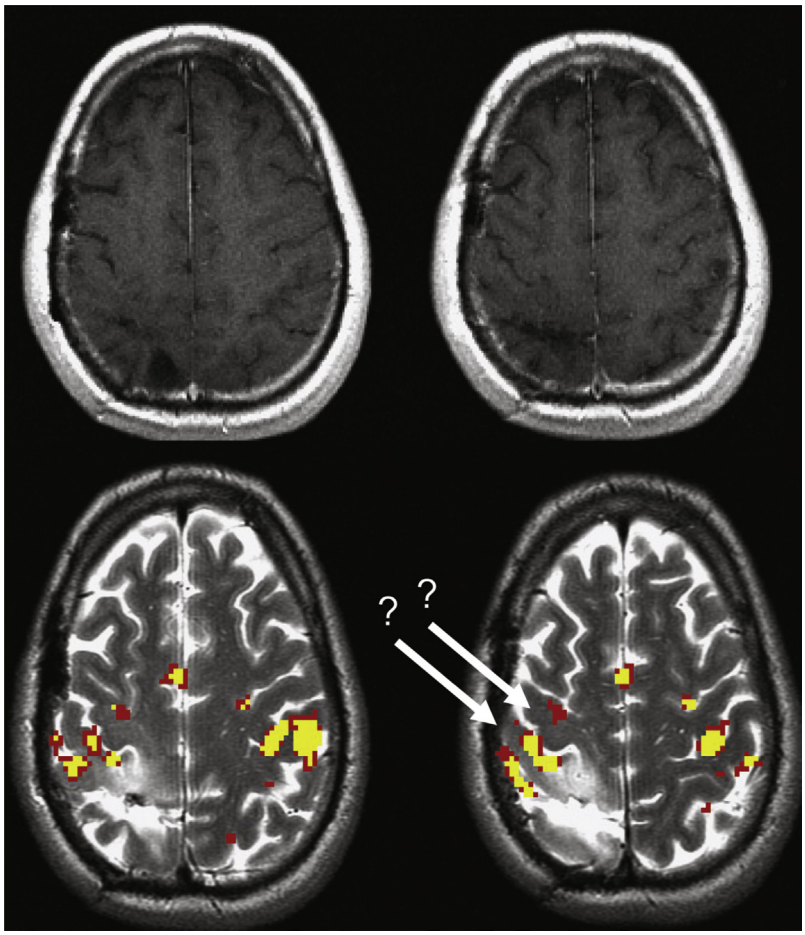


FIGURE 7 A common interpretation pitfall. While the distribution of fMRI activity on this 1.5-T finger-tapping fMRI (spatially smoothed at 4 mm) might lead one to believe that the posterior gyrus is the motor gyrus, the correct answer is the anterior gyrus, as it is the posterior bank of the motor and sensory gyri that activate during an fMRI task. This T2* scan was not misregistered with the anatomical scan and is a common spatial distribution.

the signal. When smoothing is applied, misleading activations can be seen without knowledge of both how smoothing extends activation volumes and the exact anatomy expected to activate. With information about physiology and spatial smoothing, the correct interpretation places the motor gyrus as the more anterior gyrus in Figure 7. It is also important to ensure no misregistration between anatomical and functional scans as a cause of misinterpretation.

In language mapping, while the left hemisphere is dominant for language function in nearly all right-handed individuals, there is often some right hemispheric activity during language tasks as well. Because the laterality index is a measure of ratios of activity between the hemispheres, right-hemispheric activity may decrease the laterality index but tends not to alter the determined dominant hemisphere. As the right-hemisphere Broca's hemisphere is commonly attributed to the prosodic component of speech, it is important to expect activity in both hemispheres during language activity. This is especially important in brain tumor patients in whom compensation may occur. In Figure 8, a patient with a low-grade glioma in the left superior frontal and frontal lobes responded silently to aurally presented questions and generated words silently to visually presented letters. In the responsive questions task, there is a significant amount of bilateral activity that is not expected. However, during word generation, the patient demonstrates the expected strong left dominance. The figure demonstrates the variability of the fMRI measurement and the need to scan patients on multiple language trials before final interpretation.

While brain-based compensation in brain tumor patients may not change a patient's management, there are instances of reorganization that are clinically relevant. A 100% right-handed 62-year-old man with a low-grade neoplasm in the superior temporal gyrus (the expected location of Wernicke's area) was seen at our institution.[21] He was completely intact on aphasia testing and fMRI suggested that while his Broca's function

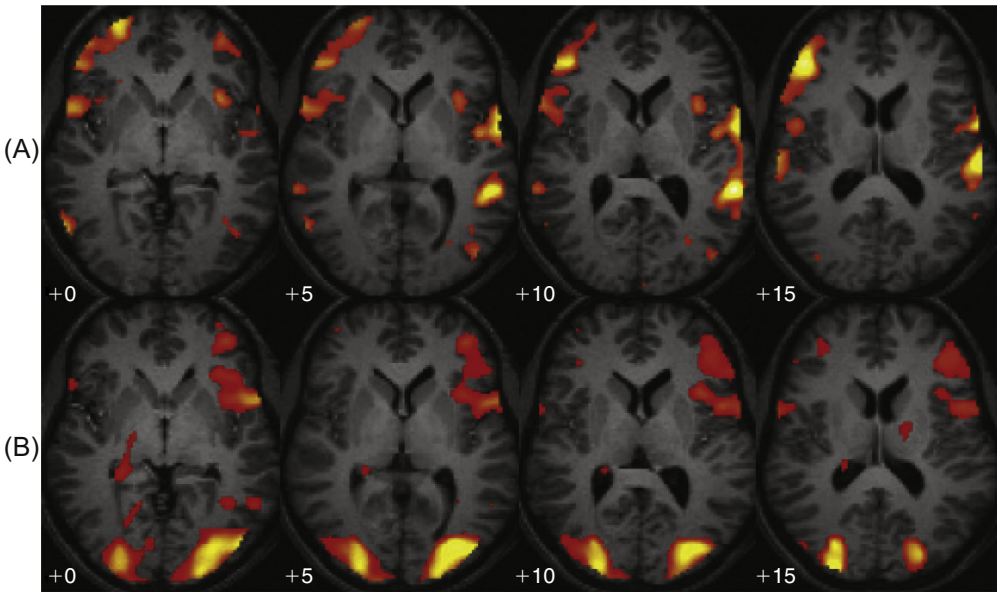


FIGURE 8 Further potential for an error in interpretation. An fMRI map of a right-handed patient with a left-hemispheric lesion in the SMA. (A) Patient silently responded to aural autobiographical questions. (B) Silent word generation to visually presented letters. The patient was left-hemisphere dominant on direct cortical stimulation. The examples illustrate the need to examine more than one task when determining dominance for language.

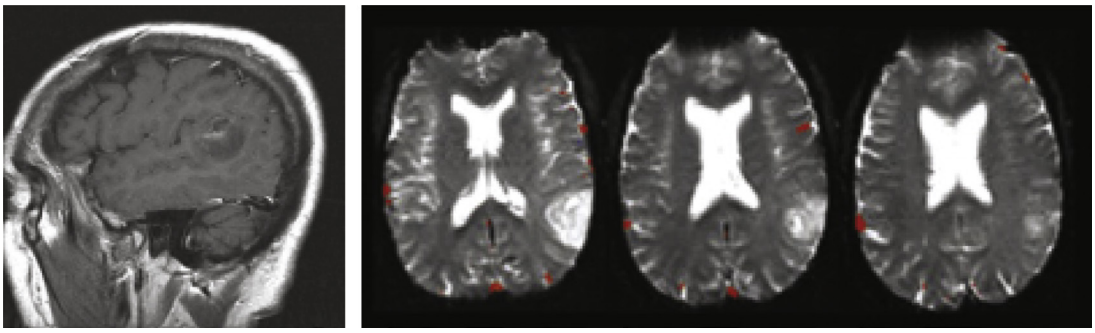


FIGURE 9 A 62-year-old man with a minimally enhancing low-grade glioma in the expected location of Wernicke's area (left-superior temporal gyrus). fMRI suggested translocation of the patient's Wernicke's function, which was confirmed with both direct cortical stimulation and gross total resection.

was nicely lateralized to the left hemisphere as expected, his Wernicke's area activated only in the right hemisphere. DCS confirmed the translocation and the patient was completely intact after a gross total resection of the lesion (Figure 9). This case nicely evidences the fact that while fMRI has its limitations in brain tumor patients, it can be a powerful first step to further testing when atypical patterns of activity are found.

SURGICAL OUTCOMES AND FUTURE DEVELOPMENTS

While it is helpful to know how fMRI can aid in preoperative planning and intraoperative mapping, knowing its effect on surgical outcomes helps to validate its use. Petrella et al. evaluated the effect of fMRI localization of language and motor areas in surgical decision-making and outcomes in brain tumor patients.[22] They found that fMRI allows for a more aggressive surgical approach and in certain patients allows for decreased surgical time, decreased craniotomy size, and increased extent of tumor resection. More recently, fMRI has been shown to help in presurgical prognosis and to lower the risk of postoperative neurological deficits.[23]

In fMRI, task-based paradigms drive the generation and understanding of fMRI maps and brain function. What these maps show is that brain functions do not localize to specific centers in the brain, but instead, tend to be organized in networks. A newer fMRI technique, called resting-state fMRI (RS-fMRI), identifies these networks in the absence of paradigms by detecting synchronous activations between separate, spatially distinct brain areas. RS-fMRI is sensitive to spontaneous

low-frequency fluctuations in the BOLD signal and is reliable across sessions and subjects, with some variability in loci between subjects.[24] In patients with tumors distorting the sensorimotor cortex, RS-fMRI is able to localize the motor cortex.[25] Additionally, Otten et al. demonstrated that motor network connectivity strength provides insight into motor weakness and motor performance using RS-fMRI.[26] Because RS-fMRI does not require task performance and can identify many networks simultaneously, RS-fMRI can save scanning time and be used in patients unable to properly perform paradigms. While in need of further investigation, RS-fMRI may provide more clinical applications of fMRI.

References

1. Bogomolny DL, Petrovich NM, Hou BL, et al. Functional MRI in the brain tumor patient. *Top Magn Reson Imaging*. 2004;15(5): 325–335.
2. Ogawa S, Lee T-M, Kay AR, et al. Brain magnetic resonance imaging with contrast dependent on blood oxygenation. *Proc Natl Acad Sci USA*. 1990;87:9868–9872.
3. Buxton RB, Uludag K, Dubowitz DJ, et al. Modeling the hemodynamic response to brain activation. *Neuroimage*. 2004;23(Suppl 1): S220–S233.
4. Birn RM, Cox RW, Bandettini PA. Detection versus estimation in event-related fMRI: choosing the optimal stimulus timing. *Neuroimage*. 2002;15(1):252–264.
5. Brennan NP. Preparing the patient for the fMRI study and optimization of paradigm selection and delivery. In: Holodny AI, ed. *Functional Neuroimaging: A Clinical Approach*. New York: Informa Healthcare USA, Inc.; 2008:13–21.
6. Yousry TA, Schmid UD, Alkhadhi H, et al. Localization of the motor hand area to a knob on the precentral gyrus: a new landmark. *Brain*. 1997;120:141–157.
7. Hirsch J, Ruge MI, Kim KH, et al. An integrated functional magnetic resonance imaging procedure for preoperative mapping of cortical areas associated with tactice, motor, language, and visual functions. *Neurosurgery*. 2000;47(3):711–721. [discussion 721–722].
8. Wada J. A new method for determination of the side of cerebral speech dominance: a preliminary report on the intracarotid injection of sodium amytal in man. *Iqakaa te Seibutzuquki*. 1949;14: 221–222.
9. Medina L, Aguierre E, Bernal B, Altman N. Functional MR imaging versus Wada test for evaluation of language lateralization: cost analysis. *Radiology*. 2004;230:49–54.
10. Gaillard W, Balsamo M, Xu B, et al. Language dominance in partial epilepsy patients identified with an fMRI reading task. *Neurology*. 2002;59:256–265.
11. Ramsey NF, Sommer IE, Rutten GJ, Kahn RS. Combined analysis of language tasks in fMRI improves assessment of hemispheric dominance for language functions in individual subjects. *Neuroimage*. 2001;13(4):719–733.
12. Isaacs KL, Barr WB, Nelson PK, et al. Degree of handedness and cerebral dominance. *Neurology*. 2006;66(12):1855–1858.
13. Krings T, Reinges MH, Erberich S, et al. Functional MRI for presurgical planning: problems, artefacts, and solution strategies. *J Neurol Neurosurg Psychiatry*. 2001;70(6):749–760.
14. Holodny AI, Shevzov-Zeburn N, Brennan N, Peck KK. Motor and sensory mapping. *Neurosurg Clin N Am*. 2011;22:207–218.
15. Plate KH, Mennel HD. Vascular morphology and angiogenesis in glial tumors. *Exp Toxicol Pathol*. 1995;47(2–3):89–94.
16. Jain RK, di Tomaso E, Duda DG, Loeffler JS, Sorensen AG, Batchelor TT. Angiogenesis in brain tumours. *Nat Rev Neurosci*. 2007;8:610–622.
17. Holodny AI, Schulder M, Liu WC, Wolko J, Maldijian JA, Kalnin AJ. The effect of brain tumors on BOLD functional MR imaging activation in the adjacent motor cortex: implications for image-guided neurosurgery. *AJNR Am J Neuroradiol*. 2002;21(8):1415–1422.
18. Hou BL, Bradbury M, Peck KK, Petrovich NM, Gutin PH, Holodny AI. Effect of brain tumor neovasculature defined by rCBV on BOLD fMRI activation volume in the primary motor cortex. *Neuroimage*. 2006;32(2):489–497.
19. Kim MJ, Holodny AI, Hou BL, et al. The effect of prior surgery on blood oxygen level-dependent functional MR imaging in the preoperative assessment of brain tumors. *AJNR Am J Neuroradiol*. 2005;26(8):1980–1985.
20. Peck K, Brennan N, Hou B, Gutin P, Tabar V, Holodny A. *The Reliability of preSurgical fMRI Language Lateralization in Patients with Primary Brain Tumors and Prior Surgery*. 14th ISMRM, Seattle, Washington, USA; May 2006:604.
21. Petrovich NM, Holodny AI, Brennan CW, Gutin PH. Isolated translocation of Wernicke's area to the right hemisphere in a 62-year-old man with a temporo-parietal glioma. *AJNR Am J Neuroradiol*. 2004;25(1):130–133.
22. Petrella JR, Shah LM, Harris KM, et al. Preoperative functional MR imaging localization of language and motor areas: effect on therapeutic decision making in patients with potentially resectable brain tumors. *Radiology*. 2006;240(3):793–802.
23. Tymowski M, Majchrzak K, Bobek-Billewicz B, Ladzinski P, Majchrzak H. The use of functional magnetic resonance imaging in reducing a risk of postoperative neurological defecits in the patients with brain tumour. *Neurochir Pol*. 2013;47(6):547–554.
24. Lee MH, Smyser CD, Shimony JS. Resting-state fMRI: a review of methods and clinical applications. *AJNR Am J Neuroradiol*. 2013;34(10):1866–1872.
25. Zhang D, Johnston JM, Fox D, et al. Preoperative sensorimotor mapping in brain tumor patients using spontaneous fluctuations in neuronal activity imaged with functional magnetic resonance imaging: initial experience. *Neurosurgery*. 2009;65:226–236.
26. Otten ML, Mikell CB, Youngerman BE, et al. Motor defecits correlate with resting state motor network connectivity in patients with brain tumours. *Brain*. 2012;135:1017–1026.

CHAPTER

30

Magnetic Resonance Spectroscopy

Tom Mikkelsen[1], *James Snyder*[1], *David Hearshen*[2]

[1]Department of Neurosurgery, Henry Ford Health System, Detroit, MI, USA; [2]Department of Radiology, Henry Ford Health System, Detroit, MI, USA

INTRODUCTION

Proton magnetic resonance spectroscopy (^{1}H MRS) has been used in a number of applications for the diagnosis and management of patients with glioma. The technique uses a method that suppresses the water proton signal and allows the resolution of spectral signals from other molecules biochemically related to the biology of the tumor. These are identifiable by their resonance frequencies and typically include choline (Cho), which is thought to reflect membrane turnover; creatine (Cr); and *N*-acetylaspartate (NAA), a neuronal marker; and a frequency range containing overlapping signals, which consists of resonances from lipid and lactate, associated with necrosis. Because these molecules are many times less abundant than water, larger voxels of acquisition are required. In addition, there are significant issues related to partial volume averaging from mixed tissues and those related to tissue/fluid boundaries, which may confound signal acquisition. Magnetic resonance spectroscopy imaging (MRSI) (also called chemical shift imaging) can be generated by integrating the signals beneath these metabolite peaks, but the large volumes of acquisition required limit image resolution. There are also technical issues with regard to normalization, and a number of different metabolite ratios are typically generated. Few validation studies have been carried out to verify the utility of these methods in glioma management, but several studies have correlated signal characteristics with tissue histology.[1–5]

CLINICAL APPLICATIONS

The application of so-called metabolic imaging in glioma continues to be a promising area of advancement with significant clinical benefit when placed into context with other physiologic imaging techniques, including diffusion-weighted imaging, diffusion tensor imaging, and dynamic susceptibility contrast-enhanced magnetic resonance imaging (MRI).

Neoplastic versus Nonneoplastic

Although MRSI has been used to distinguish neoplastic from nonneoplastic lesions, the detection of gliomas is typically not a major issue.[6,7] MRSI has shown benefits in distinguishing primary brain tumors from metastatic disease when an elevated Cho/Cr ratio is observed in surrounding fluid-attenuated inversion recovery (FLAIR) tissue.[8]

Grading and Differential Diagnosis

A major issue in the assessment of brain tumors is grading and differential diagnosis.[9] Several investigators have used statistical correlation with primary diagnosis and predictive modeling to suggest that MRSI is able to define lesion type and grade.[10] The number of independent variables available from the analysis of MRSI data is large and there are many analytic approaches, including qualitative, quantitative, and pattern recognition techniques. Most of these studies employ quantitative analysis, using measures combining multiple parameters to increase sensitivity and decrease the number of dimensions in the statistical analysis.[1,10–12] These measures usually involve ratios of metabolic indices with the numerator and denominator from the same volume (ipsilateral) or denominator from normal-appearing tissue, usually white matter (contralateral). Cho/NAA_{ips}, Cho/Cr_{ips}, Cho/Cr_{con}, and Cho/Cho_{con} are widely used. Measures involving lactate and lipid signals have also been used.[13] Lactate, reflecting anaerobic metabolism, is visible in various stages of both treatment-naïve and

© 2016 Elsevier Ltd. All rights reserved.

treated tumor metabolism and also in the response of normal tissue to treatment. Signal from lipid is not seen in MRSI of normal brain tissue, but is observed in both tumor and radiation necrosis. Measures involving lipid and lactate are subject to greater variability owing to overlap between lipid and lactate resonance frequencies and the range and overlap of resonance frequencies between various types of lipids that are present in necrotic tissue in variable amounts. Lactate-editing sequences have been used to separate lactate and lipid signals and may be useful in characterizing stages in treated tumor metabolism.[14] Infusion of labeled glucose with ^{13}C MRS is used to evaluate the kinetics of glucose metabolism within the tricarboxylic acid (TCA) cycle, which reveals a variety of enzymatic reactions in tumor populations,[15,16] thus providing information as to tumor kinetics, drug response, and vulnerable windows of treatment opportunity.[5,17]

An analogous but distinct issue is the definition of lesion boundaries. This, of course, is related directly to prognosis, the measurement of the extent of resection, the definition of radiation ports, and efficacy measurement. Gliomas, particularly anaplastic gliomas, infiltrate and spread great distances in the brain.[18] Regional infiltration during tumor progression has been most strikingly shown in the whole-mount studies of Scherer and Burger, in which glioblastomas have a central area of necrosis, a highly vascularized cellular rim of tumor, and a peripheral zone of infiltrating cells.[19,20] Studies have shown that tumor cells have migrated from the primary site of malignant gliomas, resulting in the almost inevitable local recurrence and tumor progression seen clinically.[20] Recurrence of human gliomas following surgery and radiation is most commonly seen in the margin adjacent to the initial tumor where leaking tumor neovasculature is permeable to imaging contrast agents, but may also be remote.[21]

Biopsy studies have shown that the conventional contrast-enhancing margin in MRI does not accurately reflect the lesion boundary. As a result, we have carried out a number of studies employing the techniques of multivoxel MRSI and directed surgical biopsies to validate alternative measures of the burden of disease.[1] Because conventional MRI does not adequately reflect the intratumoral heterogeneity of gliomas, we sought to determine a correlation between different ^{1}H MRSI metabolic ratios and the degree of tumor infiltration in diffusely infiltrating gliomas. Image-guided biopsies with semiquantitative and qualitative histopathological analyses from a series of 31 untreated patients with low- and high-grade gliomas were correlated with multivoxel ^{1}H MRSI referenced to the same spatial coordinates. With 247 tissue samples and 307 observations, choline-containing compounds using contralateral creatine and choline for normalization, or ipsilateral NAA, appeared to correlate best with the degree of tumor infiltration, regardless of tumor histologic grade. Our results show that MRSI is more accurate than conventional MRI in defining indistinct tumor boundaries and quantifying the degree of tumor infiltration. These data suggest that MRSI could play a role in the selection of stereotactic biopsy sites, especially in nonenhancing tumors. We would caution, though, that MRSI should not be used as a substitute for histopathological diagnosis. A corollary would be that it may be possible to assist in the planning of surgical resection using this technique. It follows also that the assessment of residual disease after surgery is another important potential application. This would be particularly true for low-grade glioma or nonenhancing tumor components in high-grade lesions. Data from high-grade glioma suggest improved prognosis in patients who have gross-total resections or imaging-complete resections employing contrast enhancement.[22,23] Measurement of the contrast-enhancing compartment may also not be the optimal parameter for tumor response assessment. This holds true especially in this era of cytostatic agents, which interfere with the proliferation, invasion, angiogenesis, and differentiation processes. Several correlative histopathological studies have shown that the contrast-enhancing margin is not representative of the lesion boundary.[24,25]

MRSI utilized with other modalities, such as perfusion and diffusion imaging, has demonstrated the most promise in the evaluation of tumor burden and in grading outside contrast-enhancing margins.[5,26–28] MRSI has shown benefits in distinguishing primary brain tumors from metastatic disease when an elevated Cho/Cr ratio is observed in surrounding FLAIR tissue.[8]

Prognosis and Survival

Several investigators have suggested that MRSI features, including maximal choline and lactate levels, correlate with survival at least as well as standard clinicopathological parameters.[29] Prospective validation studies, however, have not been done.[29–32] Use of d-2-hydroxyglutarate (2HG) as a direct marker of isocitrate dehydrogenase (IDH) mutation may provide a noninvasive method to assess IDH mutation status with improved prognostic implications.[33]

MRSI Guidance for Therapy

Surgical Planning

Determination of the extent of resection and biopsy site choice are two perisurgical applications for MRSI. There are problems, typically, in performing MRSI studies immediately postoperatively, as such studies are often confounded by postoperative features, including intracavitary air and tissue/fluid boundaries, each of which can introduce significant artifacts.[23]

Radiation Planning[34–36]

Another use for MRSI is in image-guided therapy, including definition of radiation ports. Enhancement on MRI of gliomas acquired after the administration of contrast agents containing gadolinium (Gd) has traditionally been used to delineate the tumor margin for surgical and radiation treatment planning. However, increased Cho and/or decreased NAA has been found well outside these margins,[35] implying that images of Cho, NAA, or Cho/NAA_{ips} (MRSI) may better reflect the distribution of infiltrating tumor. An example is shown in Figure 1.

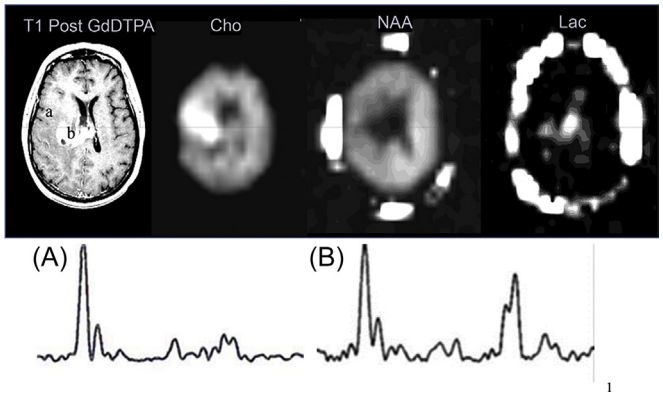


FIGURE 1 Images and spectra depicting spectroscopic abnormalities associated with a high-grade glioblastoma multiforme. Upper left shows Gd enhancement of a mass within the periventricular white matter with invasion of the lateral ventricles. Spectroscopic images show increased choline (Cho) (top middle left) and decreased *N*-acetylaspartate (NAA) (top middle right) over a much larger area, whereas the image of lactate (Lac) (top right) shows increased anaerobic metabolism in the medial aspect of the lesion. Decreased NAA and increased Cho indicate infiltrating disease at the lateral aspect of the abnormality (A) and (B) refer to spectra—the line drawings derived from the sites on the left-most panel directly above labeled T1 post-Gd MRI.

Though Gd enhancement is restricted to a small volume near the lateral ventricles, significantly increased Cho is found in a much larger volume, extending out to the cortical surface. This has prompted the development of strategies to combine MRI and MRSI in radiation treatment planning.[36] Because MRSI has inherently lower resolution, these images are fused with higher resolution MRI, acquired during the same examination. Many treatment plans are generated using computed tomography (CT) images. This requires an intermediate fusion of the CT and magnetic resonance coordinate systems.[37] An example of MRSI and MRI retrospectively fused with a treatment plan is shown in Figure 2. In this case, increased Cho suggestive of a tumor is found outside the 80% isodose line. Subsequent MRI and tumor resection 9 months later indicated a tumor in this region. In a retrospective review of radiation treatment plans for 10 patients, MRSI acquired prior to the treatment plan (but not used for planning) demonstrated increased Cho outside the 80% isodose line in 3 cases. Radiation treatment plans that rely on Gd enhancement may underestimate areas of infiltrative disease, whereas T2-weighted MRIs probably overestimate its extent. MRSI adds additional information that may help to refine the treatment plans; however, MRSI has invariably lower resolution than MRI and the margins delineated by features on either image should be interpreted with caution when superimposed on the other.

These preliminary data suggest that maximal efficacy from local field radiation treatment will not be achieved unless the spectroscopic abnormality is included within the treatment ports.[38] MRSI would theoretically be a more appropriate tool for target delineation for glioma radiation treatment planning; however, several series using modern

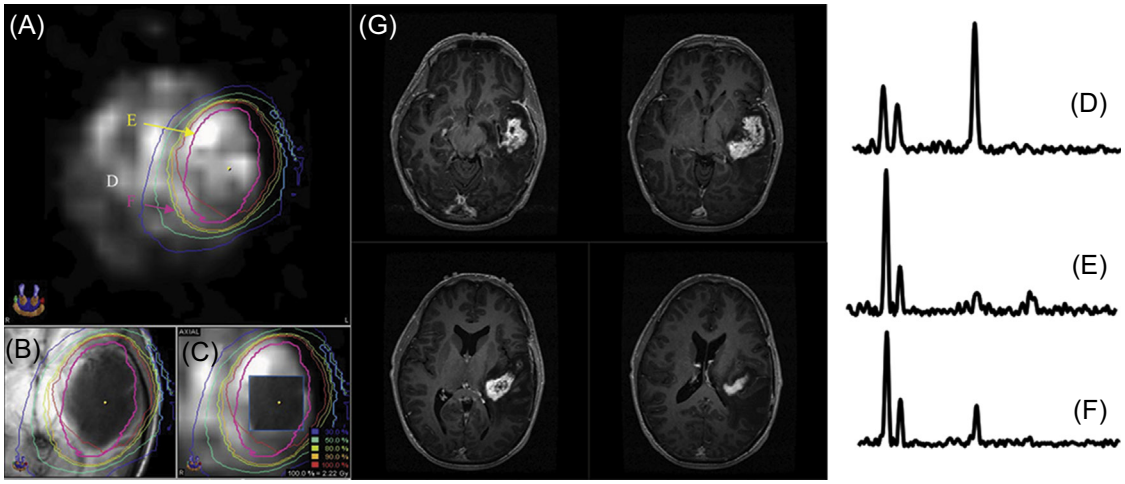


FIGURE 2 The presenting diagnosis for this patient was grade 2 astrocytoma with atypical features. Only subtle contrast enhancement is shown (B). The radiation treatment plan is shown fused to SI and Gd MRI in (A), (B), and (C). The isodose curve representing 80% of the 2.22 Gy delivered to the target is shown in green. Normal appearing contralateral white matter is shown in (D). The heterogeneous lesion has a solid component (very high choline (Cho) and very low *N*-acetylaspartate (NAA), spectrum (E)) within the 80% isodose curve and a component suggesting infiltrating disease (Cho not as high as (E) and NAA higher, spectrum (F)) outside the 80% isodose line. Follow-up MRI at 9 months after initial radiation treatment showed a new area of contrast enhancement (G) confirmed as a recurrent tumor.

radiation techniques with three-dimensional conformal planning, with or without dose escalation, have shown that the majority of recurrences still occur in-field and not remotely or at the margin.[21] In this setting, MRSI appears unlikely to improve local control or change the pattern of recurrence of fractionated radiation therapy unless it proves to be more specific than conventional MRI. This technique would be particularly useful if higher doses appeared to be better tolerated by minimizing inclusion of normal brain parenchyma.[39] Unfortunately, even with aggressive dose escalation for the treatment of glioblastoma, a high in-field failure rate is still observed.[40]

Assessment of Treatment Efficacy/Response

The role of MRSI in efficacy evaluation was the subject of a National Cancer Institute workshop report in 2005.[41]

Radiation

The effects of therapeutic radiation on the brain, including decreases in NAA and subacute increases in choline, have been described and can be difficult to discriminate from disease progression.[42–44]

Chemotherapy

Decreases in choline signal in response to chemotherapy have been seen and monitored using MRSI.[42,45–48] The technical issues of which volumes or features should be used in such monitoring, such as the peak heights, medians, or mean values, and which normalization corrections should be done remain to be determined. Identifying biomarkers of targeted chemotherapy as feedback for drug efficacy is a promising area of research in MRSI.[17]

Serial

Serial monitoring using MRSI appears to be a promising tool for tumor response assessment with novel noncytotoxic agents. It will need to be compared with conventional contrast enhancement measurements.[13,35] Validation studies, including prospective use of these imaging modalities, will be necessary before they can be used reliably as effective surrogates for therapy efficacy. In vivo ^{13}C MRS assessment of tumor metabolism, as measured by the conversion of glucose to metabolite, is a promising area of investigation that may provide insight into treatment response and tumor behavior.[15,16]

Differential Diagnosis

Recurrent Disease

Given the impact of specific treatment modalities on the MRSI parameters described above in newly diagnosed patients, it has been noted that the spectroscopic features of recurrent disease are rather different from those of treatment-naïve tumors. This obviously must lead to caution regarding the interpretation of MRSI in suspected recurrent disease using values derived from studies on newly diagnosed patients.[2,49,50]

Malignant Transformation of Low-Grade Tumors

Malignant degeneration in low-grade neoplasms of the brain has also been detected using MRSI.[51] Discordant conventional and spectroscopic findings may also be used to define a more aggressive clinical course with earlier disease progression.[28,52]

Differentiation of Radiation Necrosis and Recurrent Tumor

Early studies using single-voxel techniques could not adequately sample heterogeneous tissues found at various stages in the treatment of gliomas. Because recurrent tumor and radiation necrosis can both result in enhancement with Gd, studies utilizing MRSI have examined spectral patterns from tissues exhibiting different features on MRI, with and without administration of Gd, in an attempt to differentiate recurrent tumor from radiation necrosis. Multivoxel MRSI allows simultaneous sampling of necrotic core, lesion margin defined by enhancement with Gd, and abnormal tissue outside lesion margins defined by hyperintensity on T2-weighted MRI, which may include remote foci and/or infiltrative disease.

Figure 3 shows an MRSI study comparison of an image-guided-biopsy-proven recurrence at the inferior location (seen on the left, site b) and biopsy-proven radiation necrosis at the superior location (seen on the right, site c). It is of note that at the radiation necrosis biopsy

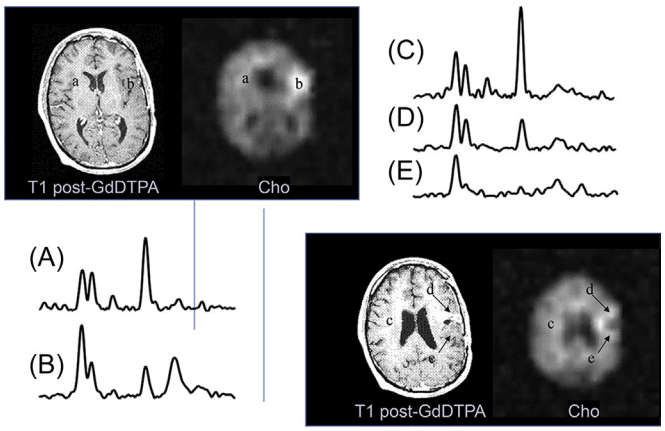


FIGURE 3 Images and spectra of a patient with initial glioblastoma multiforme who was evaluated for recurrent disease versus radiation necrosis. Image-guided stereotactic biopsy was performed within 24 h of the magnetic resonance examination. Biopsy confirmed both recurrent tumor (B) in the inferior location and radiation necrosis on the superior slice (D and E). Note that the Cho/NAA_{ips} on (D) and (E) is clearly abnormal, but the Cho/Cho_{con} is 1, whereas the Cho/Cho_{con} is 0.1 at the recurrent tumor location (B). (A) and (C) refer to spectra (line drawings derived at the specific locations designated A (normal in MR image in the panel above) and C (normal) in the image below.

site, the ipsilateral Cho/NAA ratio is clearly abnormal, which would suggest tumor recurrence, but the Cho/Cho_{con} ratio is less than 1. This situation might arise if treatment-naïve tumor and either treated tumor or radiation necrosis had either a different spectral pattern or different admixtures of tissue types within the MRSI voxel itself.

The spectral characteristics of radiation-induced changes in normal and tumor tissue depend on the time interval between the application of radiation and the acquisition of MRSI. Reports of early changes to normal tissue include an increase in Cho and a moderate decrease in NAA, whereas spectral features of delayed radiation-induced necrosis have been reported to include an overall decrease in Cho, Cr, and NAA, as well as the presence of lipid and/or lactate. An example of early-induced radiation change is shown in Figure 4. The MRSI was acquired approximately 1 month after treatment with 2.22 Gy targeted to the Gd-enhanced volume. Note that the increased Cho in white matter contralateral to the site of the original lesion coincides with the 30% isodose line, a relatively low radiation dose. This is in contrast to the MRSI from the superior location (see Figure 4(C)), in which the time interval between treatment and acquisition of MRSI was 9 months.

Our group has used the intraoperative biopsy correlation method to attempt to define diagnostic imaging parameters capable of discriminating recurrent tumor from radiation necrosis.[44] In that study, we looked at 27 patients who had been treated previously with surgery, radiotherapy, and chemotherapy and reoperated on for clinical and/or radiographic signs that caused suspicion for recurrent disease. Tissues were categorized into four groups: (1) spectroscopically normal; (2) pure tumor; (3) mixed tumor with necrosis; and (4) pure radiation necrosis.

Analysis was performed on 99 ^{1}H MRSI observations to determine whether the ^{1}H MRSI ratios varied according to tissue category. ^{1}H MRSI ratios were found to distinguish pure tumor from pure necrosis. No values suggested that mixed specimens could be distinguished in a statistically significant way from either pure tumor or pure necrosis. The data suggest that metabolite ratios derived on the basis of ^{1}H MRSI spectral patterns do allow reliable differential diagnostic statements to be made when the tissues are composed of either pure tumor or pure necrosis, but the spectral patterns are less definitive when tissues composed of varying degrees of mixed tumor and necrosis are examined.[2]

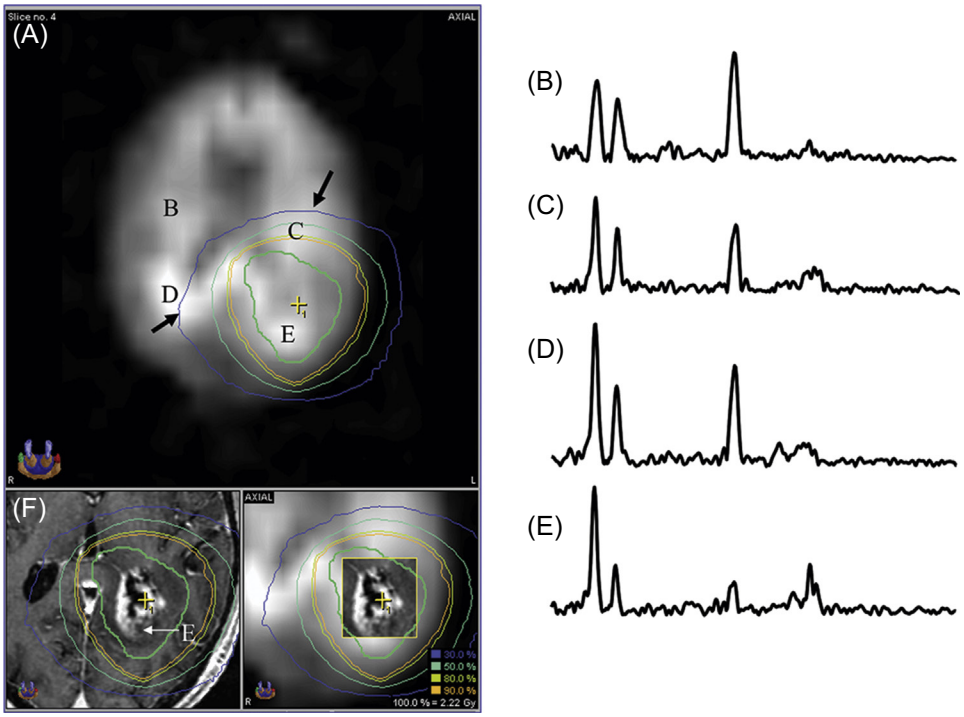


FIGURE 4 Radiation treatment plan fused to SI and MRI (A); Cho image, top, and Gd MRI, lower left). MRSI was collected 1 month after 2.22 Gy was delivered to the target (80% isodose curve depicted in light green). Site (B) was normal contralateral white matter. Site (C) showed increased Cho, decreased Cr and NAA, along with the presence of lactate/lipid indicating tumor (spectra acquired from rim of contrast enhancement). At site (D) Cho is increased through the white matter tracts of the corpus callosum, but normal amounts of Cr and NAA suggest early radiation injury or infiltrative disease. Site (E) shows increased Cho, decreased Cr and NAA, along with the presence of lactate/lipid indicating tumor (spectra acquired from center of lesion). At the right parietal area of increased Cho, NAA occurs at normal levels and lactate/lipid is not present. Both of these findings are consistent with early radiation effect.

An MRSI nominal voxel volume of 1 ml can still include admixtures of different tissue types in heterogeneous lesions as well as normal tissue, which potentially exist, even on high-resolution MRI used for reference. In a preliminary study comparing MRSI with image-guided stereotactic biopsies contained within the MRSI voxel and characterized as greater than 80% pure tumor, lesions prior to and following therapy had significantly different spectroscopic features, probably reflecting the presence of micronecrosis in the treated voxel.[53] This suggests that given the current resolution constraints in MRSI, it may not be possible to isolate the spectral characteristics of "pure" treated or recurrent tumor. It is also possible that MRSI voxels contain admixtures of tumor, radiation necrosis, and normal tissues.

There are several ways to apply MRSI in the management of patients with malignant gliomas. Although a number of proof-of-concept studies have been done as demonstrations, no prospective studies validating MRSI methods as a surrogate for treatment or differential diagnosis have been completed. However, promising data suggest that these methods may find a role in the assessment of therapeutic efficacy and differential diagnosis.

Future Directions

MRSI is a noninvasive modality of tissue characterization with potential for dynamic evaluation of tumor response to treatment, enzymatic processes, and chemical shift. Metabolic profiles obtained using high-resolution magic angle spinning (HR-MAS) are used to evaluate the histopathologic properties of tissue, with preservation of the specimen for further analysis. HR-MAS utilizes reduced molecular motion restriction resembling a semiliquid phase by rapidly spinning the sample at an optimal angle to the magnetic field.[54] Opportunities for HR-MAS, regarding the extent of resection and grading characteristics, may extend into the perioperative setting.[5,55] HR-MAS has been used ex vivo with translation to in vivo MRSI metabolomic glioma characterization.[56]

IDH mutational status defines a distinct clinical subset in glioma with prognostic as well as therapeutic implications. IDH1 mutation is thought to be an early oncogenetic alteration currently under investigation as a therapeutic target, most commonly found in secondary glioblastoma, with extended median patient survival.[57] MRSI of 2HG can be used clinically as a steady-state marker of IDH mutational status distinct from wild-type IDH status, in which 2HG is not routinely detectible.[58] Mutant IDH lacks the capacity of carboxylation leading to an accumulation of 2HG, which is readily detected with ^{1}H MRSI. 2HG used in concert with distinct MRSI metabolomic profiles as a function of specific genetic or epigenetic states can predict malignant transformation of low-grade gliomas and differentiate primary versus secondary subtypes.[56] Infusion of ^{13}C-labeled probes can be used to study the kinetics of glucose and the TCA cycle, providing an in vivo evaluation of tumor enzymatic reactions and targeted drug efficacy.[5,15–17] α-[1-^{13}C]ketoglutarate probes are used as real-time in vivo markers of IDH1 mutational status in glioma.[59] Clinical translation of dynamic mutated IDH mutational activity includes in vivo therapeutic target and efficacy assessment, biopsy selection, prognosis, and drug development.

References

1. Croteau D, Scarpace L, Hearshen D, et al. Correlation between magnetic resonance spectroscopy imaging and image-guided biopsies: semiquantitative and qualitative histopathological analyses of patients with untreated glioma. *Neurosurgery*. October 2001;49(4):823–829.
2. Rock JP, Scarpace L, Hearshen D, et al. Associations among magnetic resonance spectroscopy, apparent diffusion coefficients, and image-guided histopathology with special attention to radiation necrosis. *Neurosurgery*. May 2004;54(5):1111–1117.
3. Cheng LL, Chang IW, Louis DN, Gonzalez RG. Correlation of high-resolution magic angle spinning proton magnetic resonance spectroscopy with histopathology of intact human brain tumor specimens. *Cancer Res*. May 1, 1998;58(9):1825–1832.
4. Dowling C, Bollen AW, Noworolski SM, et al. Preoperative proton MR spectroscopic imaging of brain tumors: correlation with histopathologic analysis of resection specimens. *AJNR Am J Neuroradiol*. April 2001;22(4):604–612.
5. Kalpathy-Cramer J, Gerstner ER, Emblem KE, Andronesi OC, Rosen B. Advanced magnetic resonance imaging of the physical processes in human glioblastoma. *Cancer Res*. September 1, 2014;74(17):4622–4637.
6. Vuori K, Kankaanranta L, Hakkinen AM, et al. Low-grade gliomas and focal cortical developmental malformations: differentiation with proton MR spectroscopy. *Radiology*. March 2004;230(3):703–708.
7. Hourani R, Horska A, Albayram S, et al. Proton magnetic resonance spectroscopic imaging to differentiate between nonneoplastic lesions and brain tumors in children. *J Magn Reson Imag*. February 2006;23(2):99–107.
8. Bangiyev L, Rossi Espagnet MC, Young R, et al. Adult brain tumor imaging: state of the art. *Semin Roentgenol*. January 2014;49(1):39–52.
9. Gruber S, Stadlbauer A, Mlynarik V, Gatterbauer B, Roessler K, Moser E. Proton magnetic resonance spectroscopic imaging in brain tumor diagnosis. *Neurosurg Clin N Am*. January 2005;16(1):101–114, vi.
10. Preul MC, Caramanos Z, Collins DL, et al. Accurate, noninvasive diagnosis of human brain tumors by using proton magnetic resonance spectroscopy. *Nat Med*. March 1996;2(3):323–325.
11. Cohen BA, Knopp EA, Rusinek H, Babb JS, Zagzag D, Gonen O. Assessing global invasion of newly diagnosed glial tumors with whole-brain proton MR spectroscopy. *AJNR Am J Neuroradiol*. October 2005;26(9):2170–2177.
12. Stadlbauer A, Gruber S, Nimsky C, et al. Preoperative grading of gliomas by using metabolite quantification with high-spatial-resolution proton MR spectroscopic imaging. *Radiology*. March 2006;238(3):958–969.
13. Li X, Vigneron DB, Cha S, et al. Relationship of MR-derived lactate, mobile lipids, and relative blood volume for gliomas in vivo. *AJNR Am J Neuroradiol*. April 2005;26(4):760–769.

14. Star-Lack J, Spielman D, Adalsteinsson E, Kurhanewicz J, Terris DJ, Vigneron DB. In vivo lactate editing with simultaneous detection of choline, creatine, NAA, and lipid singlets at 1.5 T using PRESS excitation with applications to the study of brain and head and neck tumors. *J Magn Reson*. August 1998;133(2):243–254.
15. Park I, Larson PE, Zierhut ML, et al. Hyperpolarized ^{13}C magnetic resonance metabolic imaging: application to brain tumors. *Neuro-oncology*. February 2010;12(2):133–144.
16. Wijnen JP, Van der Graaf M, Scheenen TW, et al. In vivo ^{13}C magnetic resonance spectroscopy of a human brain tumor after application of ^{13}C-1-enriched glucose. *Magn Reson Imaging*. June 2010;28(5):690–697.
17. Ward CS, Venkatesh HS, Chaumeil MM, et al. Noninvasive detection of target modulation following phosphatidylinositol 3-kinase inhibition using hyperpolarized ^{13}C magnetic resonance spectroscopy. *Cancer Res*. February 15, 2010;70(4):1296–1305.
18. Mikkelsen T, Bjerkvig R, Laerum OD, Rosenblum ML, eds. *Brain tumor invasion: biological, clinical, and therapeutic considerations*. New York: Wiley-Liss; 1998.
19. Scherer HJ. The forms of growth in gliomas and their practical significance. *Brain*. March 1, 1940;63(1):1–35.
20. Burger PC, Kleihues P. Cytologic composition of the untreated glioblastoma with implications for evaluation of needle biopsies. *Cancer*. May 15, 1989;63(10):2014–2023.
21. Hochberg FH, Pruitt A. Assumptions in the radiotherapy of glioblastoma. *Neurology*. September 1980;30(9):907–911.
22. Keles GE, Lamborn KR, Berger MS. Low-grade hemispheric gliomas in adults: a critical review of extent of resection as a factor influencing outcome. *J Neurosurg*. November 2001;95(5):735–745.
23. Fountas KN, Kapsalaki EZ. Volumetric assessment of glioma removal by intraoperative high-field magnetic resonance imaging. *Neurosurgery*. May 2005;56(5):E1166.
24. Burger PC, Dubois PJ, Schold Jr SC, et al. Computerized tomographic and pathologic studies of the untreated, quiescent, and recurrent glioblastoma multiforme. *J Neurosurg*. February 1983;58(2):159–169.
25. Daumas-Duport C, Monsaigneon V, Blond S, et al. Serial stereotactic biopsies and CT scan in gliomas: correlative study in 100 astrocytomas, oligo-astrocytomas and oligodendrocytomas. *J Neurooncol*. 1987;4(4):317–328.
26. Chawla S, Wang S, Wolf RL, et al. Arterial spin-labeling and MR spectroscopy in the differentiation of gliomas. *AJNR Am J Neuroradiol*. October 2007;28(9):1683–1689.
27. Di Costanzo A, Scarabino T, Trojsi F, et al. Proton MR spectroscopy of cerebral gliomas at 3 T: spatial heterogeneity, and tumour grade and extent. *Eur Radiol*. August 2008;18(8):1727–1735.
28. Sahin N, Melhem ER, Wang S, et al. Advanced MR imaging techniques in the evaluation of nonenhancing gliomas: perfusion-weighted imaging compared with proton magnetic resonance spectroscopy and tumor grade. *Neuroradiol J*. October 2013;26(5):531–541.
29. Kuznetsov YE, Caramanos Z, Antel SB, et al. Proton magnetic resonance spectroscopic imaging can predict length of survival in patients with supratentorial gliomas. *Neurosurgery*. September 2003;53(3):565–574.
30. Oh J, Henry RG, Pirzkall A, et al. Survival analysis in patients with glioblastoma multiforme: predictive value of choline-to-N-acetylaspartate index, apparent diffusion coefficient, and relative cerebral blood volume. *J Magn Reson Imaging*. May 2004;19(5):546–554.
31. Li X, Jin H, Lu Y, Oh J, Chang S, Nelson SJ. Identification of MRI and ^{1}H MRSI parameters that may predict survival for patients with malignant gliomas. *NMR Biomed*. February 2004;17(1):10–20.
32. Fountas KN, Karampelas I. Proton magnetic resonance spectroscopic imaging can predict length of survival in patients with supratentorial gliomas. *Neurosurgery*. July 2004;55(1):257–258.
33. Choi C, Ganji SK, DeBerardinis RJ, et al. 2-hydroxyglutarate detection by magnetic resonance spectroscopy in IDH-mutated patients with gliomas. *Nat Med*. April 2012;18(4):624–629.
34. Pirzkall A, Li X, Oh J, et al. 3D MRSI for resected high-grade gliomas before RT: tumor extent according to metabolic activity in relation to MRI. *Int J Radiat Oncol Biol Phys*. May 1, 2004;59(1):126–137.
35. Nelson SJ, Vigneron DB, Dillon WP. Serial evaluation of patients with brain tumors using volume MRI and 3D ^{1}H MRSI. *NMR Biomed*. May 1999;12(3):123–138.
36. Nelson SJ, Graves E, Pirzkall A, et al. In vivo molecular imaging for planning radiation therapy of gliomas: an application of ^{1}H MRSI. *J Magn Reson Imaging*. October 2002;16(4):464–476.
37. Chang J, Thakur S, Perera G, et al. Image-fusion of MR spectroscopic images for treatment planning of gliomas. *Med Phys*. January 2006;33(1):32–40.
38. Chan AA, Lau A, Pirzkall A, et al. Proton magnetic resonance spectroscopy imaging in the evaluation of patients undergoing gamma knife surgery for Grade IV glioma. *J Neurosurg*. September 2004;101(3):467–475.
39. Ken S, Vieillevigne L, Franceries X, et al. Integration method of 3D MR spectroscopy into treatment planning system for glioblastoma IMRT dose painting with integrated simultaneous boost. *Radiat Oncol*. 2013;8:1.
40. Souhami L, Seiferheld W, Brachman D, et al. Randomized comparison of stereotactic radiosurgery followed by conventional radiotherapy with carmustine to conventional radiotherapy with carmustine for patients with glioblastoma multiforme: report of Radiation Therapy Oncology Group 93-05 protocol. *Int J Radiat Oncol Biol Phys*. November 1, 2004;60(3):853–860.
41. Evelhoch J, Garwood M, Vigneron D, et al. Expanding the use of magnetic resonance in the assessment of tumor response to therapy: workshop report. *Cancer Res*. August 15, 2005;65(16):7041–7044.
42. Lichy MP, Bachert P, Henze M, Lichy CM, Debus J, Schlemmer HP. Monitoring individual response to brain-tumour chemotherapy: proton MR spectroscopy in a patient with recurrent glioma after stereotactic radiotherapy. *Neuroradiology*. February 2004;46(2):126–129.
43. Kaminaga T, Shirai K. Radiation-induced brain metabolic changes in the acute and early delayed phase detected with quantitative proton magnetic resonance spectroscopy. *J Comput Assist Tomogr*. May–June 2005;29(3):293–297.
44. Rock JP, Hearshen D, Scarpace L, et al. Correlations between magnetic resonance spectroscopy and image-guided histopathology, with special attention to radiation necrosis. *Neurosurgery*. October 2002;51(4):912–919. discussion 919–920.
45. Balmaceda C, Critchell D, Mao X, et al. Multisection ^{1}H magnetic resonance spectroscopic imaging assessment of glioma response to chemotherapy. *J Neurooncol*. January 2006;76(2):185–191.
46. Murphy PS, Viviers L, Abson C, et al. Monitoring temozolomide treatment of low-grade glioma with proton magnetic resonance spectroscopy. *Br J Cancer*. February 23, 2004;90(4):781–786.
47. Preul MC, Caramanos Z, Villemure JG, et al. Using proton magnetic resonance spectroscopic imaging to predict in vivo the response of recurrent malignant gliomas to tamoxifen chemotherapy. *Neurosurgery*. February 2000;46(2):306–318.
48. Lodi R, Setola E, Tonon C, et al. Gliomatosis cerebri: clinical, neurochemical and neuroradiological response to temozolomide administration. *Magn Reson Imaging*. November 2003;21(9):1003–1007.
49. Lehnhardt FG, Bock C, Rohn G, Ernestus RI, Hoehn M. Metabolic differences between primary and recurrent human brain tumors: a ^{1}H NMR spectroscopic investigation. *NMR Biomed*. October 2005;18(6):371–382.
50. Preul MC, Leblanc R, Caramanos Z, Kasrai R, Narayanan S, Arnold DL. Magnetic resonance spectroscopy guided brain tumor resection: differentiation between recurrent glioma and radiation change in two diagnostically difficult cases. *Can J Neurol Sci*. February 1998;25(1):13–22.

51. Tedeschi G, Lundbom N, Raman R, et al. Increased choline signal coinciding with malignant degeneration of cerebral gliomas: a serial proton magnetic resonance spectroscopy imaging study. *J Neurosurg*. October 1997;87(4):516–524.
52. Wu WC, Chen CY, Chung HW, Juan CJ, Hsueh CJ, Gao HW. Discrepant MR spectroscopic and perfusion imaging results in a case of malignant transformation of cerebral glioma. *AJNR Am J Neuroradiol*. November–December 2002;23(10):1775–1778.
53. Hearshen D, Scarpace L, Rock J, et al. Comparison of MRSI and image guided histopathology in treatment naive and treated patients with malignant glioma. *Proc Intl Soc Mag Reson Med*. 2004;11:389.
54. Esmaeili M, Vettukattil R, Bathen TF. 2-hydroxyglutarate as a magnetic resonance biomarker for glioma subtyping. *Transl Oncol*. April 2013;6(2):92–98.
55. Croitor Sava A, Martinez-Bisbal MC, Van Huffel S, Cerda JM, Sima DM, Celda B. Ex vivo high resolution magic angle spinning metabolic profiles describe intratumoral histopathological tissue properties in adult human gliomas. *Magn Reson Med*. February 2011;65(2):320–328.
56. Elkhaled A, Jalbert L, Constantin A, et al. Characterization of metabolites in infiltrating gliomas using ex vivo ^{1}H high-resolution magic angle spinning spectroscopy. *NMR Biomed*. May 2014;27(5):578–593.
57. Yan H, Parsons DW, Jin G, et al. IDH1 and IDH2 mutations in gliomas. *New Engl J Med*. February 19, 2009;360(8):765–773.
58. Andronesi OC, Rapalino O, Gerstner E, et al. Detection of oncogenic IDH1 mutations using magnetic resonance spectroscopy of 2-hydroxyglutarate. *J Clin Invest*. September 3, 2013;123(9):3659–3663.
59. Chaumeil MM, Larson PE, Yoshihara HA, et al. Non-invasive in vivo assessment of IDH1 mutational status in glioma. *Nat Commun*. 2013;4:2429.

CHAPTER

31

Perfusion Imaging for Brain Tumor Characterization and Assessment of Treatment Response

Kathleen Schmainda

Department of Radiology, Medical College of Wisconsin, Milwaukee, WI, USA

INTRODUCTION

This chapter elucidates the more common types of magnetic resonance imaging (MRI) and computed tomography (CT) perfusion imaging methods to assess brain tumors. These methods require dynamic imaging such that images are acquired quickly to capture the fast physiologic (i.e., perfusion) information. Dynamic MRI methods for which an exogenous contrast agent is administered are referred to as dynamic contrast-enhanced (DCE) or dynamic susceptibility contrast (DSC) studies, depending on the primary sensitivity of the examination to either relaxivity (T1) or susceptibility (T2, T2*) contrast agent characteristics. While most perfusion techniques (both MRI and CT) rely on the administration of an exogenous contrast agent, newer dynamic MRI perfusion techniques, referred to as arterial spin-labeling (ASL) techniques, do not. Instead they are capable of noninvasively "labeling" blood water with a radio frequency (RF) pulse resulting in MRI signal changes proportional to tissue perfusion.

Because dynamic contrast agent-enhanced MRI perfusion methods represent the majority of perfusion studies performed in brain tumors, the primary focus of this chapter is on those methods. The general methodology for performing these studies is discussed along with a review of existing data and challenges to applying these methods for diagnosis and assessment of treatment response. That discussion will be followed by a more concise summary of dynamic CT and ASL MRI techniques for the study of brain tumors.

DYNAMIC CONTRAST AGENT MRI PERFUSION TECHNIQUES

The term perfusion, as employed in the MRI literature, is typically used as an all-encompassing term describing both morphologic and functional parameters that can be derived from dynamic contrast agent studies. This more generalized definition of perfusion differs from other non-MRI approaches that define perfusion specifically as the delivery of an agent to the tissue in milliliters per second per gram of tissue. Instead, while MRI perfusion studies can include measures of cerebral blood flow (CBF), which is measured in milliliters per second per milliliter of tissue, they also include measures of cerebral blood volume (CBV) and other derived parameters such as the tissue mean transit time (MTT), mean vessel diameter (mVD), plasma-tissue contrast agent transfer constant (K^{trans}) and compartmental volumes, such as v_e or EES, i.e., the extravascular–extracellular space. These derived parameters are of great interest as indicators of tumor angiogenesis, which is the new vessel formation required for tumor growth. As such, the parameters have potential applications in diagnosis, determining patient prognosis, predicting which patients will respond to a particular treatment, and evaluating treatment efficacy.

With MRI there exist two general approaches to the dynamic imaging of contrast agents for the purposes of measuring perfusion parameters. The first approach relies on collecting T1-weighted images, over many minutes, during the uptake and accumulation of a Gd (gadolinium)-chelated contrast agent, typically at a

Handbook of Neuro-Oncology Neuroimaging, Second Edition
http://dx.doi.org/10.1016/B978-0-12-800945-1.00031-8

© 2016 Elsevier Ltd. All rights reserved.

dose of 0.1 mmol Gd/kg. This dynamic T1-weighted approach is referred to as DCE imaging. The second approach, termed DSC imaging, relies on collecting T2- or T2*-weighted images over a period of seconds during which a concentrated bolus dose of Gd contrast agent passes through the tissue. Note that the overall dose used for DSC imaging is typically the same as is used for other postcontrast MRI or DCE studies, but since it is injected quickly—i.e., as a bolus, local concentration is "high" for a brief amount of time, which creates a difference in susceptibility between the blood and the tissue. Each approach measures a different subset of perfusion parameters and has a different set of challenges for the evaluation of tumors, as described below.

DYNAMIC CONTRAST-ENHANCED IMAGING

Basic Principles

DCE MRI is the acquisition of a time series of T1-weighted MR images acquired during the administration of a Gd-chelated contrast agent. In most studies the Gd chelate used is a low-molecular-weight agent because, for many years, only these agents have been approved by the US Food and Drug Administration (FDA) for clinical use. Outside of the brain these agents distribute as extracellular agents, meaning that they distribute throughout the tissue but are excluded from intact cells. However, in brain in which the blood–brain barrier (BBB) is intact, low-molecular-weight Gd chelates remain intravascularly distributed throughout the plasma space. These organ-dependent distributions dictate in part the utility of DCE methods for deriving tissue-specific information. For some animal DCE studies, high-molecular-weight Gd agents are also used. Because these agents are not cleared as readily from the vascular space, they offer some distinct advantages for more specifically measuring vascular permeability and volume, as described in more detail below. Here we will first describe DCE methods assuming an extracellular distribution, which reflects how the models were initially derived.

Unlike conventional contrast agent-enhanced MRI, which simply provides a snapshot of enhancement at one time point, DCE MRI provides a fuller description of the inflow ("wash-in") and outflow ("washout") contrast kinetics within tissue. Often the analysis of such data has taken the form of simple descriptors such as time to peak (i.e., enhancement slope) or peak enhancement. These parameters have been used in an attempt to differentiate tumor types and predict tumor grade, with mixed results.[1–6] In an effort to provide more quantitative data directly related to underlying tissue parameters, a variety of pharmacokinetic models have been applied to fit the data. Of the various models used to analyze DCE MRI data, the most commonly applied have been those that are variations of the Tofts and Kermode model first described in 1991.[7] This model is described by the following equation:

$$dC_t/dt = K^{trans}(C_p - C_t/v_e) \quad (1)$$

where C_p and C_t are the plasma and tissue contrast agent concentrations, K^{trans} is the volume transfer constant, and v_e is the fractional extravascular–extracellular volume. The parameter labels and definitions used in Eqn (1) are those recommended by an international group of scientists who reached a consensus regarding the DCE pharmacokinetic model and the underlying assumptions, definitions, and labeling of the fitted parameters.[8] Therefore, this model is often referred to as the consensus DCE model.

The transfer constant K^{trans}, which is equivalent to the product of extraction fraction (E) and flow (F), is a function of flow and the permeability–surface area product ($EF = F(1 - \exp^{(-PS/F)})$), which has been extensively described in the tracer kinetic literature earlier. The EF product has several physiologic interpretations, depending on the balance between capillary permeability and blood flow. This balance must be well understood for the proper interpretation of studies measuring this index. Under high permeability conditions where PS is much greater than blood flow (F), the flux of contrast agent across the capillary membrane is flow-limited, meaning that K^{trans} is primarily a measure of flow ($K^{trans} \approx F$). Conversely, when the permeability is low such that $PS << F$, K^{trans} is more accurately used as an index of vascular permeability ($K^{trans} \approx PS$). Therefore, whether K^{trans} is more appropriately interpreted as an indicator of flow or vascular permeability, or some combination thereof, depends on the relative condition of the capillary membrane, flow rates, and contrast agent size. So, especially for low-molecular-weight extracellular Gd contrast agents, K^{trans} is not a pure index and must not be interpreted as such.

Alternatively, distributed parameter models have been proposed that enable the measurement of both PS and F separately rather than indirectly through the measure of K^{trans}.[9,10] These approaches have shown some promise for the characterization of gliomas[11,12] and information about the tumor microenvironment that enables discrimination of tumor types such as gliomas, meningiomas, and brain metastases.[13] However, as with any multiparameter-fitting approach, such approaches can be very sensitive to initial conditions; estimating an increasing number of parameters leads to increasing instability of a model, especially when the signal-to-noise ratio (SNR) is low. Accordingly, a low contrast-to-noise ratio

can prevent a fit on a per-voxel basis. Furthermore, the contrast material dosage may not be increased in a sufficient manner both because of FDA limits on total dose of contrast agent that can be administered and because of the need to avoid saturating the arterial input function (AIF; C_p in Eqn (1)).[14]

Another approach to the measure of vascular permeability is to use high-molecular-weight agents. For these agents, $PS \ll F$, even under many pathological conditions, making it more likely that K^{trans} is a more direct measure of vascular PS. Several animal studies have demonstrated that high-molecular-weight contrast agents, such as albumin–Gd–diethylenetriaminepentaacetic acid (DTPA)[15,16] or Gadomer-17,[14] may be more effective in detecting small permeability differences than Gd-DTPA.[14,17] The disadvantage to this approach is that high-molecular-weight Gd contrast agents, which have been used in animal models, have not been approved for human use.

In the original consensus model (see Eqn (1)), the assumption is made that the effective vascular space is negligible. While this may be valid in some normal tissues such as brain and muscle, whose vascular fractions are only a few percent,[8] it most assuredly is not true in highly vascular tumors. The assumption has been charged with resulting in erroneously high K^{trans} values. For these reasons several investigators have modified the original consensus model to include the fractional vascular volume, so that Eqn (1) is recast to define the transfer and rate constants explicitly in terms of the plasma and EES tracer,

$$v_e dC_e/dt = K^{trans}\left(C_p - C_e\right) \tag{2}$$

where C_e is the contrast agent concentration in the EES, and the contribution of the intravascular tracer is then added to give the total tissue contrast agent concentration,

$$C_t = v_p C_p + v_e C_e \tag{3}$$

where v_p is the fractional volume of the intravascular (plasma) space. To determine the effect of this modification, Harrer et al.[12] compared the original model[7] (which also used an AIF previously determined from a sample of the normal population), with DCE imaging, for which v_p was not assumed negligible and the AIF was measured for each glioma patient. Their results suggest that more accurate values of K^{trans} were, in fact, obtained. Areas of high K^{trans}, as determined with the original model, were visible as areas of high v_p on the maps that included AIF measurements and v_p. The model that includes terms to represent the vascular volume is frequently referred to as the "Extended Tofts Model."[18]

Alternatively, the multiple-time-graphic method or Patlak plot[19] has been used to analyze the dynamic T1-weighted data, thereby also providing measures of the vascular transfer constants (K^{trans}) and plasma volume fraction (v_p).[20,21] The theory underlying this approach is the same as that described above. The difference is that the Patlak model assumes that the measurement is made during the period in which the plasma concentration is linear and no back-flux of contrast agent from the extravascular space occurs. Under these conditions the accumulation of tissue Gd is described by

$$C_t(t)/C_p(t) = K^{trans}\int C_p(t')dt' + v_p \tag{4}$$

Plotting the ratio of $C_t(t)/C_p(t)$ as a function of $\int C_p(t')\,dt'$ gives a plot in which the slope is equal to K^{trans} and the intercept equal to v_p. The transfer constants determined with this approach were found to agree with those determined with [^{14}C]sucrose measurements.[21]

Imaging Methodology

The general approach to collection of DCE imaging data is to use a fast gradient-echo T1-weighted sequence. Typically some variation of a three-dimensional spoiled gradient-echo (SPGR) image with short TR (TR < 7 ms), minimum TE (TE < 1.5 ms), and low flip angle (≈30°) is used[22] to acquire a time series of data before and after an injection of a Gd contrast agent. The images are acquired with a temporal resolution of tens of seconds to minutes. Precontrast T1 ($T1_0$) measurements are collected beforehand to convert the signal intensities from T1-weighted images into a change in the T1 relaxation rate as a function of time (i.e., $\Delta R1(t)$). The $\Delta R1(t)$ is directly proportional to the tissue contrast agent concentration time course (C(t)) (assuming fast water exchange between all compartments) to which the pharmacokinetic models are applied and from which the relevant physiologic parameters are extracted. A common method to measure T1 is variable flip-angle (VFA) imaging using an SPGR sequence.[23] This approach is widely used because it is time efficient and allows rapid three-dimensional volumetric T1 mapping with the same pulse sequence used to measure the contrast agent uptake. However, these VFA methods can suffer from B1 inhomogeneities, which cause variations in the flip angle spatially and in reference to the user-chosen value. Knowing the correct flip angle is essential for the accurate determination of T1 maps when using the VFA approach. A solution is to measure variations in the B1 (i.e., RF) field and take these into account when computing T1.[23–25]

For the contrast agent injection it is recommended that a power injector be used to minimize interstudy variation.[26] The total contrast dose should be administered over 15–30 s, followed immediately by a saline flush. When using pharmacokinetic models, a measure

of the AIF is required. To obtain the AIF the measurement protocol must have sufficient temporal resolution,[27] especially when the contrast agent is administered as a bolus. Often the AIF cannot be measured directly and a common AIF is used. However, determination of individualized AIFs has been shown to improve study reproducibility.[28] Since the standard approach to the collection of DCE imaging data has been to use fast gradient-echo methods the achievable temporal resolution is at best 6–15 s. Yet early theoretical estimates determined that the most accurate assessments of the various DCE-derived parameters would be obtained if the temporal resolution were closer to 1 s.[29] This was reiterated more recently with a report showing that the reliability of DCE-derived parameters worsens with decreased sampling rates.[30] Consequently, methods with both sufficient temporal and sufficient spatial resolution are needed for best DCE MRI results.

More recently, imaging methods based on echoplanar or spiral imaging have been developed with which DCE imaging data can be acquired simultaneous with DSC imaging data.[31–35] This is made possible with the collection of data at a very short TE and a longer TE. An added advantage to this approach is that the temporal resolution can be much higher, with times close to those previously theorized as optimum.[29,30] However, this is currently at the cost of worse spatial resolution. But with the eventual incorporation of parallel imaging[36] or multiband methods,[37] obtaining both high temporal and high spatial resolution should soon be possible.

Use of to Characterize Non-CNS Tumors

Some of the fundamental data validating DCE imaging techniques in the assessment of tumors have come from investigations of non-central nervous system (CNS) tumors.[22,38–40] Of the parameters determined, K^{trans}, i.e., the plasma–tissue contrast agent transfer constant, has thus far proven to be the most promising by showing changes in response to antiangiogenesis therapy[41] and a correlation with tumor vascular endothelial growth factor (VEGF) expression and microvascular density in breast tumors.[42,43] In another study, investigators attempted to increase the specificity for predicting breast tumor malignancy based on permeability measurements by employing a macromolecular contrast agent.[17] This study used dynamic data to yield estimates of the endothelial transfer coefficient, K^{PS} [$= K^{trans}$] and the fractional plasma volume of the tumors. The authors found a moderate yet statistically significant correlation for K^{PS} with presence of malignant histological features but did not find such a correlation for fractional plasma volume. Using a criterion that a K^{PS} value greater than 0 indicated a malignant lesion, the investigators found both a sensitivity and a specificity for detecting malignant tumor of 0.73 and a positive predictive value of 0.79.

Use of DCE to Characterize Gliomas and Predict Treatment Response

The results of using DCE MRI to study brain tumors, though fewer in number compared to non-CNS tumors, demonstrate promise for characterizing tumor biology and predicting response to treatment. While the results of using DCE MRI to distinguish primary brain tumor from metastases are mixed,[44,45] investigators have found a good correlation between several of the measures available from DCE-based studies and tumor grade. Good correlation between fractional vascular volume and brain tumor grade was observed[46] and the parameters K^{trans} and v_e demonstrated the ability to distinguish between low- and high-grade gliomas.[47,48] Potentially of greater importance, K^{trans} has been shown to be predictive of methylguanine-methyltransferase methylation status,[49] important for predicting response to the chemotherapeutic temozolomide, and to provide a distinction between tumor and treatment effect,[50,51] all of which are critically important for treatment management decisions. Example DCE results obtained from an 11-year-old patient with a brain tumor are shown in Figure 1.

Limitations of using DCE MRI in brain derive in part from its dependence on the permeability of the BBB. While this dependence is a strength in that the parameter K^{trans} can serve as an imaging biomarker of BBB permeability, it can also confound interpretation. Specifically, since patients with brain tumors are routinely treated with steroids, which act to decrease the BBB permeability, a low K^{trans} in such cases may falsely underestimate the tumor condition or overestimate treatment response. Furthermore, the contrast-to-noise ratio (CNR) of the measured signal may be low in areas of low BBB permeability owing to the combined effect of lack of contrast agent uptake into brain parenchyma and low vascular fraction in normal brain. This makes the assessment of DCE imaging parameters in brain more challenging, compared to non-CNS applications, in which there is significantly greater contrast agent extravasation. It is the reason some resort to a mean DCE signal derived from a region of interest (ROI), rather than a voxel-wise determination of the signal and derived parameters, thereby losing important spatial information. So although some may choose DCE methods, because of the higher quality of individual anatomic images provided, the ability to extract reliable voxel-wise information from the dynamic signal kinetics may diminish this advantage.

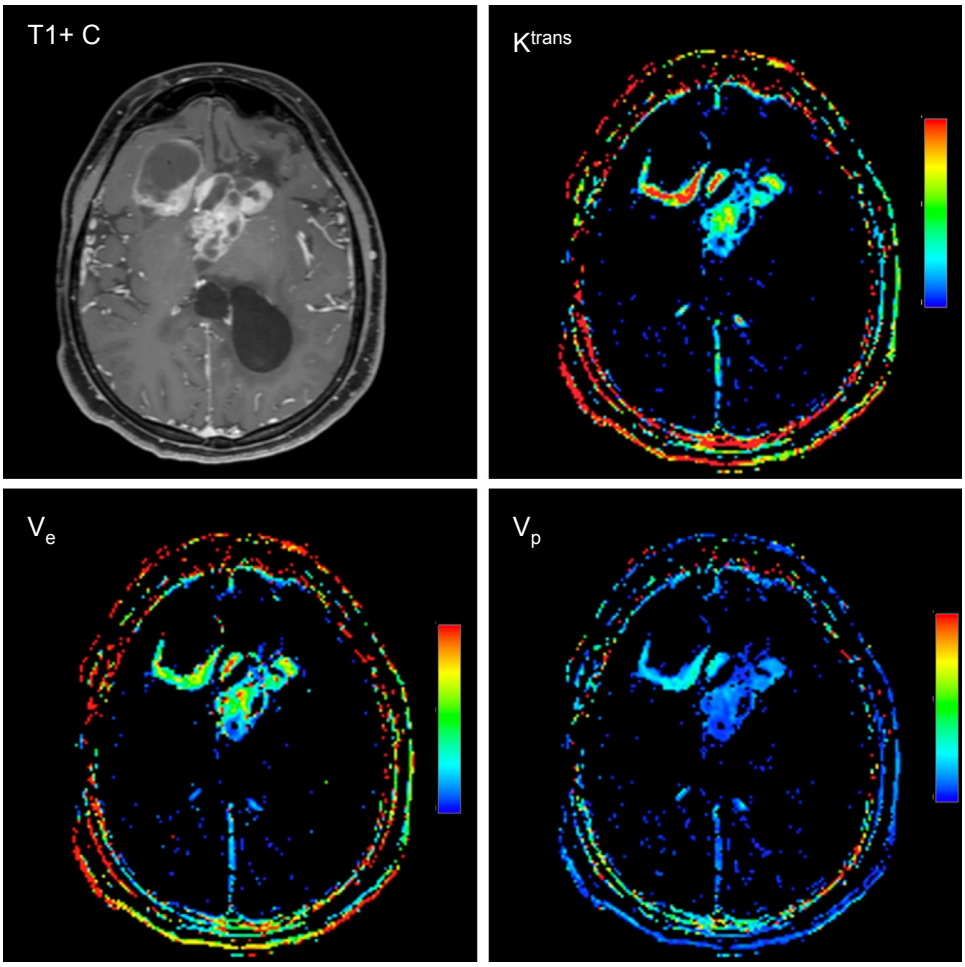


FIGURE 1 Postcontrast T1-weighted images (T1+C) and DCE parameter maps obtained from an 11-year-old child with a brain tumor. *Images courtesy of Dr. Harry Hu, Phoenix Children's Hospital, Arizona, with postprocessing software and analysis provided by Imaging Biometrics LLC.*

Toward Standardization of DCE Acquisition and Postprocessing Methods

A variety of factors in DCE MRI data acquisition and analysis can affect the accuracy and precision of the derived parameters and therefore the utility of this method to provide useful clinical information. Therefore many efforts are under way to understand discrepancies with a goal of working toward a consensus approach to acquisition and analysis. To emphasize the importance of these efforts a study was undertaken to compare the DCE-output parameters using 12 software tools applied to the same DCE MRI datasets.[52] Considerable parameter variations were reported. Yet nearly all algorithms provided good to excellent early prediction of therapy response. These results suggest that while parameter variations may be large, they do not affect the utility of DCE MRI for the evaluation of therapy. However, to enable interstudy comparisons and multicenter studies, consistency in the approach to acquisition and analysis must be improved.

DYNAMIC SUSCEPTIBILITY CONTRAST IMAGING

Basic Principles

In 1990, Rosen et al.[53] demonstrated that if imaging were performed during administration of a bolus of a Gd-chelated contrast agent, a transient decrease in signal intensity could be seen (see Figure 2). This approach is based on the principle of susceptibility contrast. Specifically, if a high concentration of a Gd contrast agent is confined to the vasculature, as is the case under bolus conditions, a difference in susceptibility or "magnetizability" between the contrast-containing vessel and the tissue occurs. The signal change can be converted into a relaxation rate change, which is proportional to the fraction of blood volume within each image voxel. Because the arterial contrast agent concentration is often not measured, the resulting CBV image maps show relative CBV values and are therefore termed rCBV maps.

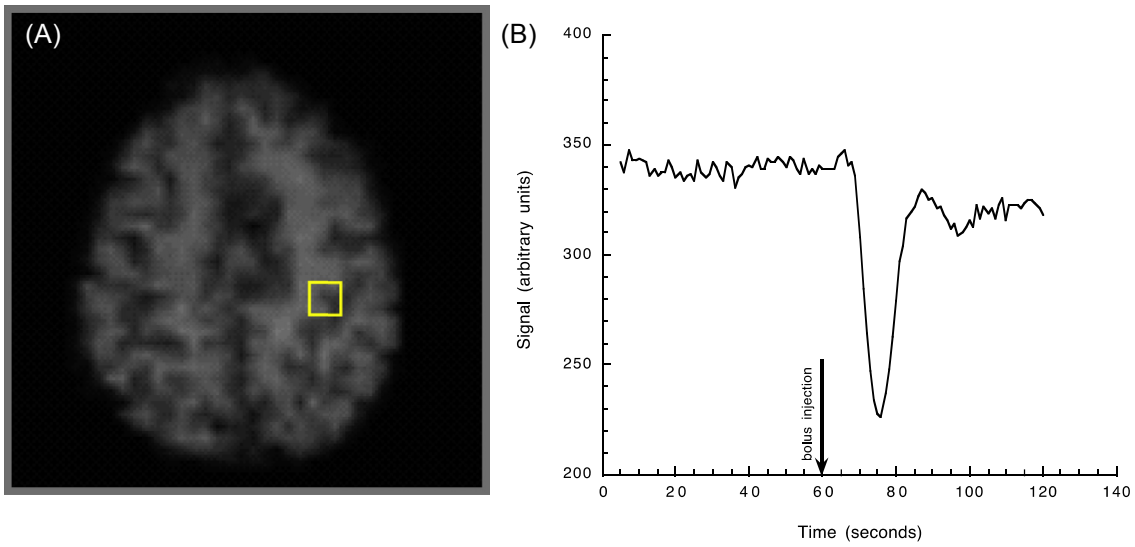


FIGURE 2 DSC data. (A) An echoplanar image collected during the bolus administration of a Gd contrast agent. (B) A signal time course from a voxel within the echoplanar image in (A). Note the transient decrease in the signal intensity as the bolus of contrast agent passes through the brain tissue. This decrease is due to the susceptibility effect of the contrast agent.

In addition to measuring CBV, CBF can also be determined from the same dynamic data. The quantification of CBF from DSC imaging data requires the measurement of the AIF and the deconvolution of the tissue concentration time curve. While there are many ways to perform the deconvolution, the model-independent singular value decomposition approach has emerged as the standard approach.[54]

DSC Imaging Methodology

A typical rCBV image protocol lasts only about 1–3 min, with images collected approximately every 1 s throughout this time period (see Figure 2). Baseline images are first acquired, followed by the bolus administration of contrast agent, during which the collection of images continues both during and after contrast agent administration. To create the rCBV maps the signal versus time data are converted into T2* (or T2) relaxation rate (ΔR2* or ΔR2) versus time data, which is proportional to tissue contrast agent concentration. These data can then be integrated (i.e., added up over time) to give rCBV for each image voxel (see Figure 3). This description provides only the most basic implementation of a DSC rCBV protocol and the data analysis. Although seemingly straightforward, there are several issues regarding implementation and analysis that must be considered to appropriately use these methods. Several of these issues are briefly discussed here.

Choice of DSC Imaging Sequence

To acquire DSC image data, fast imaging techniques are required. In most cases, echoplanar imaging (EPI) methods are used with some more recent studies using spiral-based imaging methods.[32,55] There also exists a choice in the type of EPI or spiral-based sequence used. Options include gradient-echo (GRE) techniques, spin-echo (SE) techniques, or image sequences that acquire both GRE and SE data,[56,57] or multiple-echo GRE data.[32,36,55,58] The GRE and SE methods differ in their sensitivity to vessel diameter. While GRE techniques are equally sensitive to all vessel diameters, SE methods have a maximal sensitivity to microvessels.[59] When using an image sequence with which both GRE and SE data are simultaneously collected, maps of total and microvascular blood volume, as well as a GRE/SE ratio related to the mVD, are computed. Results from one of the first studies using a simultaneous GRE/SE method in patients are given in Figure 4. This approach is similar to previous studies performed in a rat tumor model.[60,61]

With the more recent implementation of multiple-echo GRE (spiral based[32,62,63]) or multiple-echo GRE plus SE data (e.g.,[33,35,36]), the R2* value can be computed directly (as opposed to ΔR2*) such that any confounding T1 effects are implicitly eliminated. These sequences have the added advantage of being capable of simultaneously collecting DCE data if the first echo time is sufficiently short. Additional important advantages of the multiple-echo GRE data is that a precontrast T1 measurement is no longer needed for the DCE calculations and the data can be obtained using just a single dose of Gd contrast agent, such that a preload dose is no longer needed[63]. (See more on the rationale for using a contrast agent preload below.)

The image sequences used in rCBV mapping are T2 or T2* weighted to enable them to be sensitive to the susceptibility effect described above. To maximize this sensitivity, attention must be paid to the choice of imaging

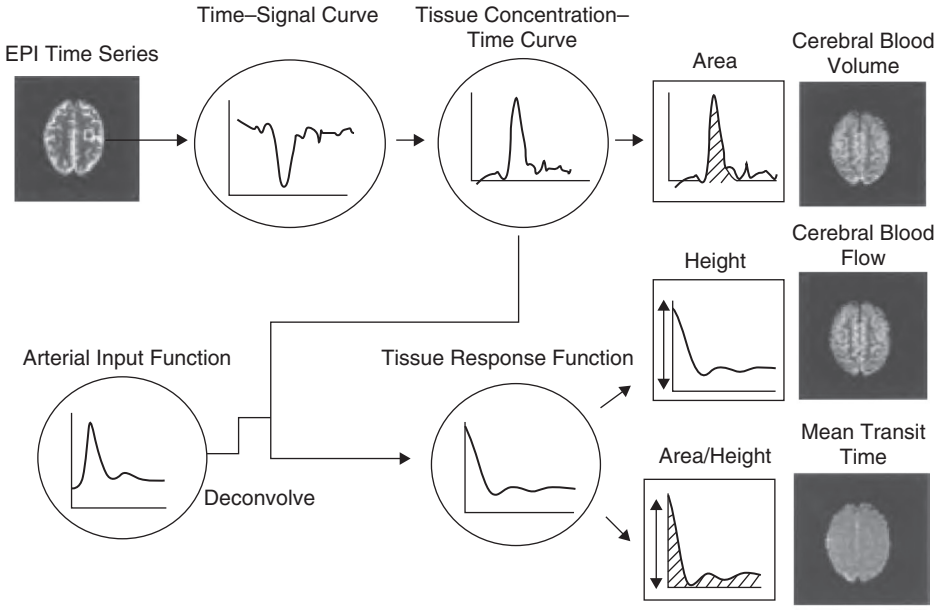


FIGURE 3 Diagram explaining calculation of rCBV, CBF, and MTT using the DSC imaging technique. Signal–time course data for each voxel are converted to T2* relaxation rate changes (ΔR2*), which are assumed proportional to the tissue contrast agent concentration. Maps of rCBV are obtained by determining area below the trace concentration–time curve. Maps of rCBF are obtained by determining the height of the tissue response function. To obtain the tissue response function, the AIF must be deconvolved from the measured tissue concentration–time curve. EPI, echoplanar imaging. *Adapted by permission from AJR 2005; 185:763–767.*

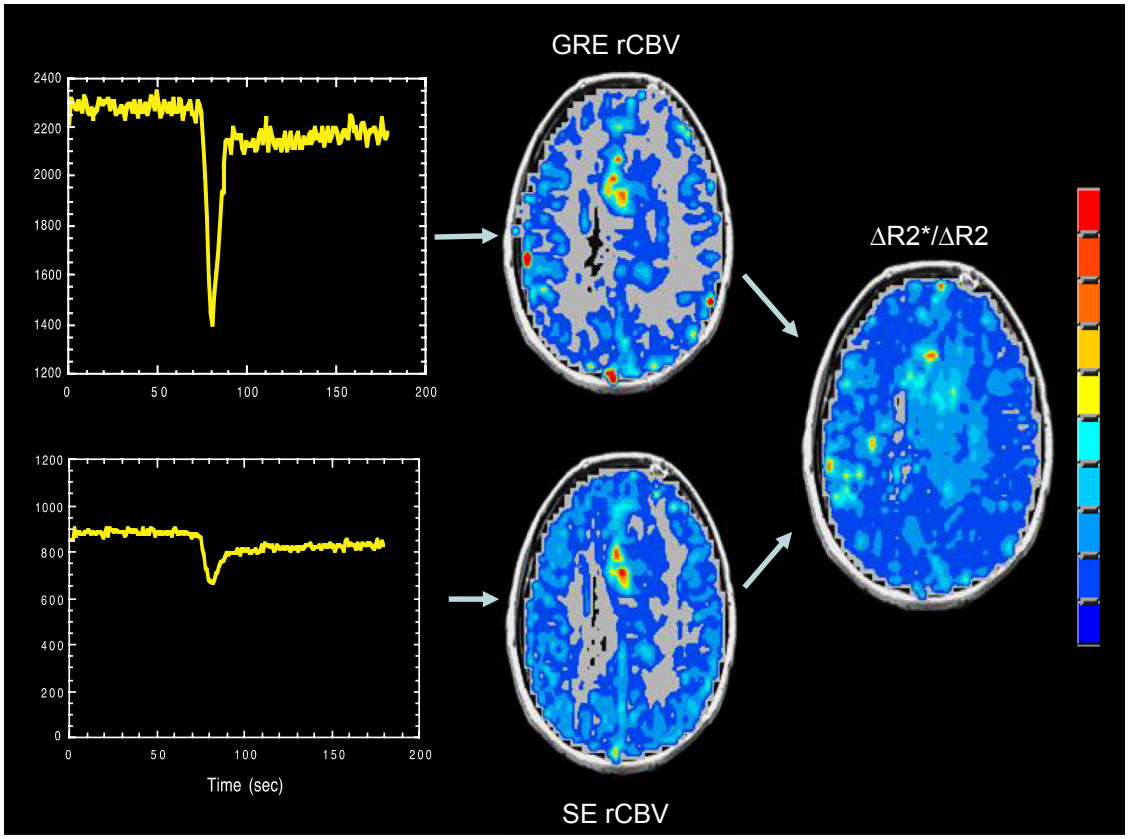


FIGURE 4 Example of data and image information that can be collected when simultaneously collecting GRE and SE DSC data. Example of GRE and SE time courses are shown at left. The resulting GRE and SE rCBV maps from a patient with a grade III astrocytoma are displayed in the center. The GRE rCBV provides information about total blood volume, while the SE rCBV map gives information about the microvascular blood volume. The GRE-to-SE relaxation rate ratio map, shown at right, provides a measure of the mVD.

parameters. Detailed analyses of the SNR of rCBV maps, and its dependence on the choice of experimental parameters and processing strategies, have been undertaken.[64,65] To maximize the SNR of rCBV maps it was recommended that the input bolus duration be as short as possible, that a sufficient number of baseline images be collected, and that the imaging parameters (TE, TR, α) be optimized for the dose of contrast agent. Specifically, as previously shown with simulations, a minimum of 30 baseline points is recommended to give a sufficient CNR. An optimal TE would be equal to the postcontrast tissue T2. However, not knowing this a priori, and since the contrast remains largely intravascular in brain, the TE is set equal to the precontrast T2, which is typically about 20–30 ms for T2* and 110 ms for T2. To get a good measure of an AIF, if CBF is to be determined, a TR close to 1 s is recommended. And finally, for best CNR, a flip angle equal to the Ernst angle is best. This is typically around 72° at 1.5 T and 80° at 3.0 T.

Postprocessing of DSC Imaging Data

In the work of Boxerman et al., [64] it was also suggested that the straightforward integration of the signal time course, rather than a γ-variate fit of the time course, is the most reliable and practical method of determining rCBV, at least in normal brain. In another study four different postprocessing methods were compared for the determination of rCBV and CBF using Monte Carlo simulations and in patients with cerebral ischemia.[66] The rCBV was determined by two different methods that numerically integrate the tracer concentration–time curves, with one approach integrating over the whole time series and the other limiting the integration to the first pass. In addition, two other methods were applied that take recirculation into account. One method used a γ-variate fit, while the other method determined CBV by deconvolving the tissue–time curve with the AIF and then integrating the resulting residue function. The study showed clear differences in precision and accuracy among these methods for the determination of relative as well as absolute CBV. For rCBV measurements simple numerical integration over the whole image range had clear advantages in terms of high SNR and modest computational requirements. Although γ-variate fitting and deconvolution both demonstrated accurate rCBV measurements, these numerical manipulations introduced additional noise in the maps and increased computational complexity. For the determination of absolute CBV, the two methods that minimize recirculation effects were shown to be most accurate. Of the two approaches, the deconvolution approach gave maps with higher SNR compared to γ-variate fitting. And because the deconvolution approach is necessary for the determination of CBF, this choice seems the most logical when absolute values are desired.

Contrast Agent Leakage Effects

Additional issues arise when using DSC imaging methods to determine rCBV in brain tumors in particular. Specifically, determination of brain tumor rCBV from the contrast-enhanced MRI signal can be complicated by a leaky BBB, as is often the case with tumors. Under these conditions, contrast agent leaks out of the vasculature into the brain or tumor tissue, thereby diminishing the susceptibility effect (i.e., producing a smaller signal decrease) of the contrast agent passage through the vasculature. This feature may lead to an underestimation or overestimation of rCBV depending on contrast dose and image sequence settings. Various levels of consideration have been given to this issue. Some investigators performed rCBV imaging without leakage correction,[67–70] but did mention it as a possible confounding factor. Other authors have included data in their studies only if leakage was not demonstrated.[70] Some investigators use low-flip-angle GRE[71–73] or dual-TE[74] methods to minimize the T1 effects that occur with agent extravasation. Yet another approach is to manage this effect by both minimizing its impact during data collection and applying a correction during postprocessing.[56,57,75,76] One approach is to first administer a preload of contrast agent to diminish any T1 changes that might subsequently occur during the bolus administration. Then, after collecting the dynamic data, leakage is detected and fit on a voxel-wise basis.[77–79] With this approach it was demonstrated that GRE rCBV significantly correlated with tumor grade while the uncorrected maps did not.[56,57,78] This approach was validated in an animal study in which leakage-corrected rCBV was compared to rCBV determined with long-lived intravascular contrast agents.[80] Another study demonstrated that the optimal preload dose and timing to distinguish tumor from treatment effect was a 0.05–0.1 mmol Gd/kg dose with 5–6-min incubation time before collecting the DSC data.[75] Contrast agent leakage can also confound the determination of CBF. Though the effect is less profound compared to CBV, it does contribute inaccuracies.[81] Consequently, a postprocessing correction algorithm was also developed for purposes of measuring CBF in brain tumors.[82] This approach was also shown to be insensitive to variations in tissue MTTs as further confirmed in patients with brain tumors.[76]

As just described, most attention has been paid to minimizing the T1 effects resulting from agent extravasation. Although the T1 minimization sequences and postprocessing algorithms correct for T1 enhancement effects, they may not correct for possible T2- and T2*-weighted signal changes that result from loss of compartmentalization or increased sensitivity to dipolar T2 effects.[83] These effects can be significant and result in *overestimations* of blood volume.

In an effort to better understand and compare the various DSC methods, and their ability to compensate for both

T1 and T2/T2* leakage effects, a comparison study was performed in which the most commonly published acquisition and postprocessing methods were compared in 22 patients with high-grade gliomas.[32] In this study it was possible to directly compare two acquisition techniques in each patient. Then six different postprocessing methods were applied. The question addressed was which approach best distinguished high-grade tumor from reference brain. Results demonstrated two best approaches (Figure 5). The first approach used a preload followed by postprocessing correction for leakage, as described above. The second best approach used a dual-echo spiral-based acquisition, which as previously mentioned has the added advantage of providing both DCE and DSC information. Several subsequent publications using dual-echo methods are proving them to be a comprehensive solution to perfusion imaging in brain tumors.[36,63]

Distinction of Glioma Tumor Grade

One of the characteristic features of high-grade tumors relative to low-grade tumors is greater capillary density. Because rCBV is generally considered to reflect capillary density, it is reasonable to suppose that high-grade tumors have higher rCBV than low-grade tumors. Therefore, by using this DSC MRI method, several laboratories have demonstrated the feasibility of determining rCBV in patients with brain tumors.[56,64,65,67–69,71,84–89] Many additional studies suggest that MRI-derived rCBV may better differentiate histologic tumor types than conventional MRI and provide information to predict glial tumor grade.[56,68,69,71,85,90] Example postcontrast and rCBV image maps of low- and high-grade gliomas are given in Figure 6.

In most studies, the greatest rCBV values measured in a high-grade brain neoplasm are generally found to be much higher than in normal white matter and approximately the same as, or higher than, rCBV values in gray matter.[91] In these studies, investigators have typically measured the region of highest rCBV within a tumor, taking into account the fact that tumors are characteristically heterogeneous with regard to vascular supply and, thus, rCBV. Many studies have been performed to attempt to distinguish high-grade gliomas from other types of primary brain tumors (e.g., low-grade gliomas, CNS lymphoma, and meningiomas) and metastases. The rCBV values in various series are often expressed as a ratio of the highest rCBV in the tumor compared to a representative rCBV value in a normal brain region (typically normal-appearing white matter in either the same hemisphere or the contralateral hemisphere). The resultant ratio is referred to using various terms, of which the most common is the rCBV ratio or normalized rCBV.

A study using the combined GRE/SE sequence,[57] described above, emphasizes the importance of the choice of the tumor ROI on the study results. When extracting mean data from ROIs of the entire tumor, the GRE rCBV and ratio information showed statistically significant differences between low-grade and high-grade tumors, while the SE rCBV information did not.[56,57] However, when extracting the rCBV information from blood volume "hot spots" or areas with the highest microvessel blood volume, a significant correlation was also found between SE rCBV and glioma grade.[57] This

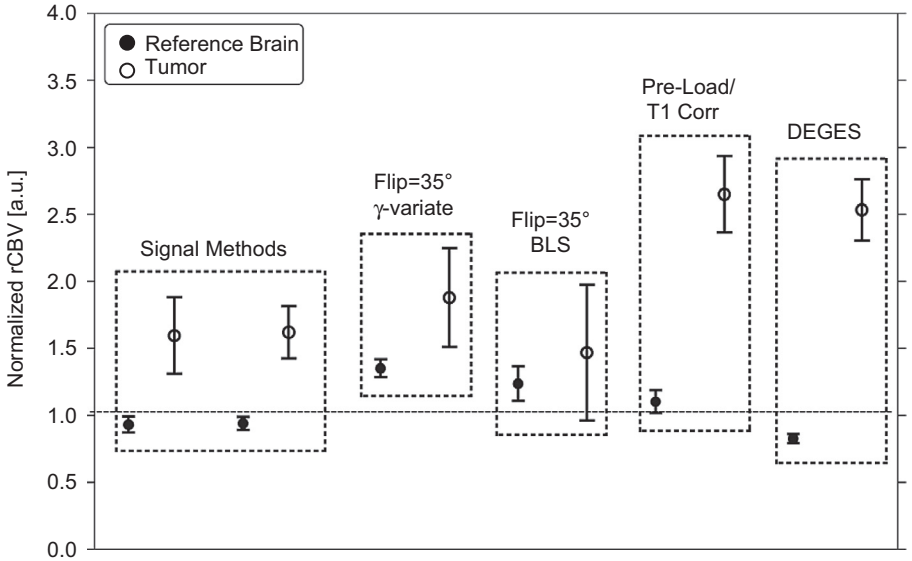


FIGURE 5 Summary of results previously reported[32] for which several different acquisition and postprocessing approaches were used to create rCBV maps in patients with high-grade glioma. The methods that best distinguished tumor from reference brain were determined to be approaches in which a preload dose of contrast agent was given followed by application of a postprocessing correction algorithm (Pre-Load/T1 Corr) and a dual-echo GRE spiral-based method (DEGES). Other approaches shown are those based on analysis of the signal (Signal Methods), with low flip angle and γ-variate fit of the data (Flip = 35° γ-variate), and with postbolus baseline subtraction (Flip = 35° BLS).

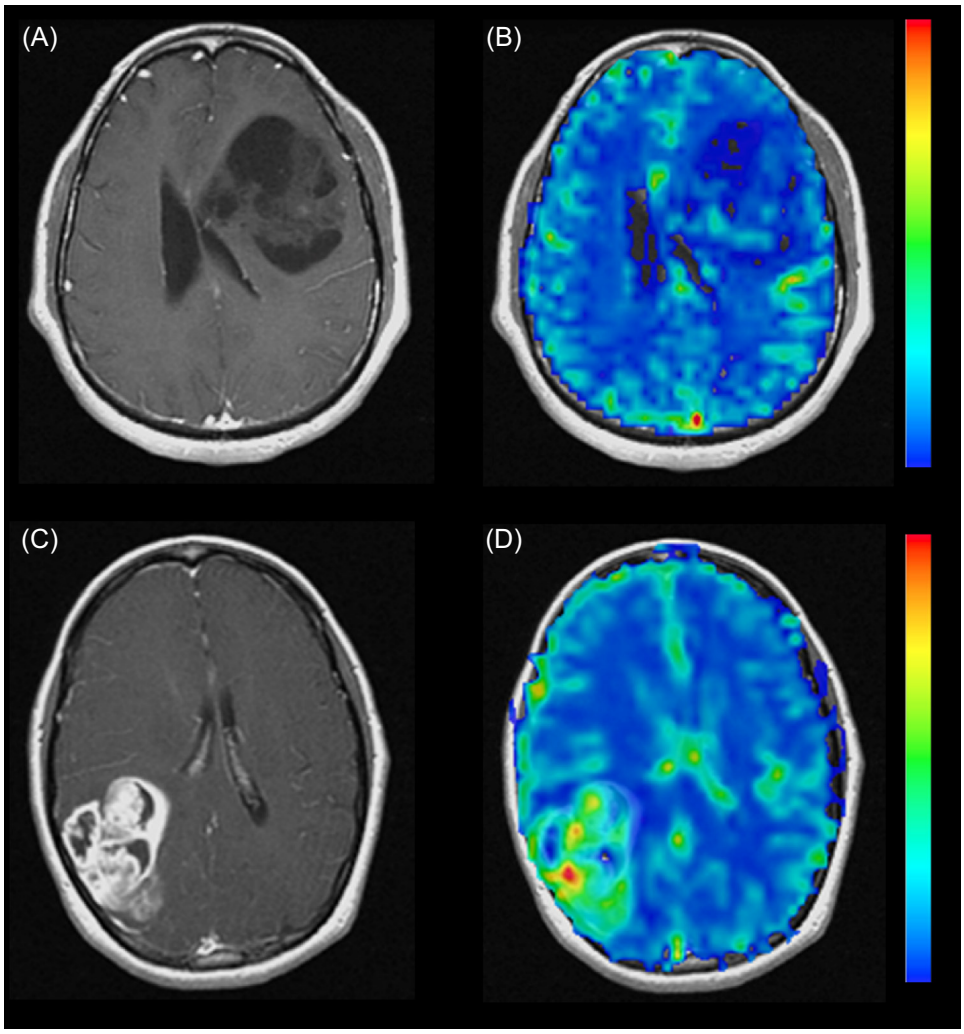


FIGURE 6 (A, C) T1-weighted contrast-enhanced images and (B, D) GRE rCBV maps from a 46-year-old male diagnosed with a low-grade astrocytoma (A, B) and a 45-year-old female diagnosed with a glioblastoma multiforme (C, D).

finding is consistent with the histopathologist's approach of assessing tumor angiogenesis, which is performed by evaluating areas of highest microvessel density.

Distinction of High-Grade Gliomas from Other Neoplasms

DSC-based studies have been generally successful in distinguishing high-grade glial neoplasms from other cerebral neoplasms. A number of studies have indeed verified the hypothesis that the mean values of regions of highest rCBV in high-grade gliomas are substantially higher than the mean values of regions of highest rCBV in low-grade gliomas.[92,93] One exception that has been noted is that of low-grade oligodendrogliomas. In one series that used a threshold rCBV ratio of 1.5 to distinguish high-grade tumors from low-grade tumors, the investigators found that this threshold had 100% sensitivity for detecting high-grade gliomas but that two of four low-grade oligodendrogliomas had rCBV ratios above this threshold.[93] In the same study, two of nine low-grade astrocytomas had rCBV ratios that exceeded the threshold ratio.

Distinction of high-grade glioma from CNS lymphoma is another difficulty that neuroradiologists face with some frequency based on the similar imaging features of the two types of tumors on conventional MRI studies. In one study, lymphoma lesions could be distinguished from high-grade glial neoplasms on the basis of lower mean rCBV values.[94] The authors also found that primary CNS lymphoma lesions typically had a time-signal intensity curve characterized by an increase in signal intensity above baseline following the initial decrease in signal intensity. Such an increase has been shown to be associated with marked leakage of contrast material across a very leaky BBB; if not taken into account when analyzing DSC images, such an increase in signal intensity can produce lower-than-expected rCBV measurements.[95]

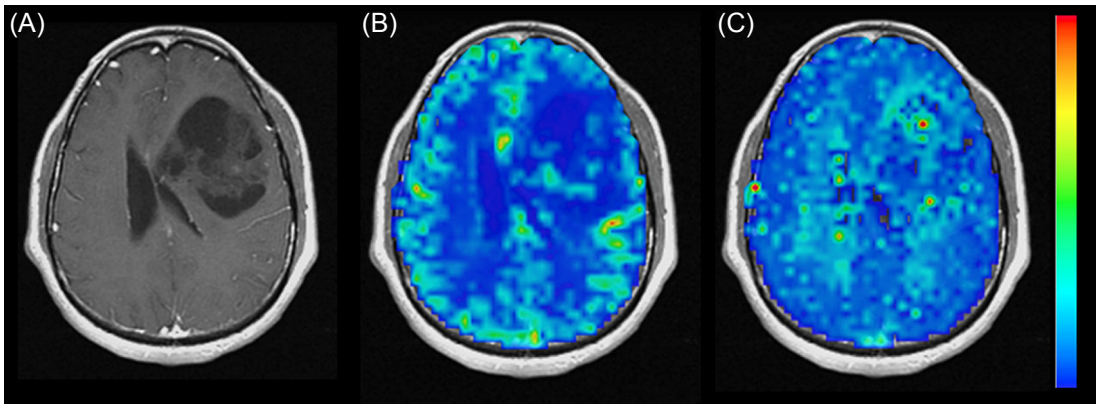


FIGURE 7 (A) T1-weighted contrast-enhanced images and (B) GRE rCBF and (C) GRE MTT maps from a 46-year-old male diagnosed with a low-grade astrocytoma. These are from the same patient shown in Figure 3.

In another such example, dural metastases from non-CNS sources were found to have significantly lower rCBV values than lesions with which they could be confused on radiological grounds, i.e., meningiomas.[96]

Potential Role of CBF to Characterize Brain Tumors

Measurement of CBF provides information not derived from CBV measures. For example, it has been shown that areas of high vessel density may not necessarily correspond to well-perfused (oxygenated) areas.[97] Blood flow within solid tumors is spatially and temporally heterogeneous.[97–100] The importance of tumor heterogeneity as a factor influencing the response to treatment has been well described.[15,97,101] Blood flow is necessary for the hematogenous delivery of anticancer agents. Decreased perfusion can result in tissue hypoxia, which diminishes the tumor's sensitivity to radiation treatment.[102] Therefore, measurement of CBF should aid in monitoring the progress of therapies.[103] This may be of particular importance for antivascular agents that have been shown to induce acute and massive tumor hemostasis.[104,105] Consequently, measurement of CBF provides functional information about the tumor vasculature, which is complementary to the morphologic measurement provided by CBV images. Example CBF images, also derived from DSC data, are given in Figure 7. These images were determined using the singular-value decomposition method after correcting the data for contrast agent leakage effects.[82]

Assessment of Tumor Vascular Architecture

As mentioned above, the use of combined GRE/SE DSC techniques has also shown that a measure of a voxel's mVD can also be determined. In particular, owing to the different sensitivities of GE and SE to vessel diameter, theory has shown that the ratio of GE and SE relaxation rates ($\Delta R2^*/\Delta R2$) is proportional to the mVD.[59] A strong correlation between this ratio and an independent measure of vessel diameter has been demonstrated in animal tumor models.[60,61] It was demonstrated for the first time in patients that the ratio was significantly correlated with tumor grade.[56,57]

Assessment of tumor vessel architecture, with measurements of such parameters as mVD, may be important to our understanding of treatment effects. Several studies have demonstrated changes in vascular architecture with tumor growth,[106] in response to treatment, and under various conditions such as hypoxia. It has been suggested that administration of individual antiangiogenic agents may block specific angiogenic pathways and thus result in different patterns of tumor vessel formation.[107] In one study using DSC methods, rats treated with the corticosteroid dexamethasone showed that the mVD and overall architecture were much more like that in normal brain.[108] This result may be explained by the fact that dexamethasone inhibits VEGF expression[109,110] and vessels become dilated when both VEGF and angiopoietin-2 are present.[106]

MR Perfusion Imaging Assessment of Peritumoral Regions

Definition of tumor margins on cross-sectional imaging studies is one of the more difficult tasks the neuroradiologist encounters in assessing imaging studies of patients with contrast-enhancing brain tumors. The problem would be relatively simple if one could assume that the margins of a contrast-enhancing lesion coexisted with the margins of the tumor. However, numerous reasons exist for believing this assumption is generally invalid. First, histological analysis of high-grade brain neoplasms frequently shows gross or microscopic evidence of tumor extension beyond the regions that contrast enhance on imaging studies. Second, many tumors do not contrast enhance (or weakly enhance) on imaging studies. Therefore, use of

enhancing regions to demarcate tumor extent is fruitless. For these reasons, neuroradiologists have turned to imaging techniques other than solely conventional contrast-enhanced CT or MRI to attempt to define actual tumor extent. The major techniques for this application are advanced MRI techniques (e.g., MR spectroscopy, diffusion imaging, and perfusion imaging) and nuclear medicine techniques (e.g., positron emission tomography). This review focuses solely on the role of MR perfusion imaging to define tumor margins.

In one study, investigators using DSC methods to study tumor margins found that rCBV values in the peritumoral regions of high-grade gliomas were significantly higher than in metastases.[111] However, in the same study, rCBV in metastases was substantially higher than in gliomas, which seems at variance with the finding of higher rCBV in peritumoral regions of metastases. Another study also found significantly higher rCBV values in the peritumoral regions of high-grade gliomas than in metastases; in that study, rCBV values in the two types of tumors being studied were very similar.[112]

MR Perfusion Imaging for Assessment of Tumor Therapy

A number of well-designed studies to monitor response to tumor therapy have been performed in animal models. In more recent years many more studies have used MR perfusion imaging to assess tumor response in patients. Animal studies will be discussed first.

In one study using a murine breast tumor model and DCE technique, investigators used a heavily T1-weighted three dimensional spoiled-gradient-refocused acquisition in a steady-state pulse sequence and a macromolecular contrast medium to assess response following treatment with anti-VEGF antibody.[113,114] The study found both decreased tumor growth rates and decreased microvascular permeability following treatment. In another study that also used DCE technique and rats harboring a tumor raised from human glioblastoma multiforme cell lines, investigators showed a significant decrease in microvascular permeability after therapy with a monoclonal antibody raised against VEGF.[115]

With regard to therapeutic trials in humans, in one of the first trials of an antiangiogenesis therapy for human brain tumors, early decreases in rCBV (measured on DSC MRI) and degree of contrast enhancement (measured on DCE imaging) were seen.[116] In another study, investigators sought to determine whether the rCBV measured in tumors prior to therapy would allow prediction of treatment outcome.[117] The pretreatment rCBV did not allow such prediction but instead the change in rCBV after the first 6 weeks of therapy did allow prediction of treatment outcome at 6 months.[117] Change in rCBV was substantially more sensitive in prediction of outcome than change in tumor size over the same period. These early results are largely consistent with those from single-center[118,119] and multicenter studies[120] in which patients with recurrent glioblastoma were treated with bevacizumab. In these studies either pretreatment rCBV or changes in rCBV were shown to be predictive of overall survival.

Distinction of Tumor Recurrence from Radiation Necrosis

Another problem that neuroradiologists encounter on a fairly regular basis is distinction of tumor recurrence from radiation necrosis. The problem lies in the fact that both processes can produce marked interruption of the BBB (and subsequent contrast enhancement after intravenous infusion of contrast material) and mass effect. Thus, the distinction of radiation necrosis from tumor recurrence using conventional contrast-enhanced MRI and CT imaging is often difficult. Alternative imaging techniques, such as fluorodeoxyglucose positron-emission tomography and MR spectroscopy, are increasingly used in an attempt to distinguish radiation necrosis from residual tumor.[121] MR perfusion imaging has also been brought to bear on distinguishing these two entities. The theoretical basis for the use of perfusion MRI lies in the fact that recurrent high-grade tumor is marked by angiogenesis (which would typically be associated with high rCBV) and tumor necrosis is generally associated with lack of rCBV elevation.[122] In one study, investigators used dynamic MRI to use rate of contrast enhancement to distinguish high-grade tumor recurrence from radiation necrosis.[123] In that study, signal enhancement–time curves were analyzed by fitting to a sigmoidal-exponential function and the resultant maximal enhancement rates were calculated as the first derivative of the fitted curve. The mean maximal enhancement rate in tumor recurrence was significantly higher than in radiation necrosis; cases of mixed tumor recurrence and radiation necrosis had values that were intermediate between solely tumor recurrence and solely radiation necrosis. Similarly, another study used DSC imaging in an attempt to distinguish recurrent tumor from radiation necrosis in 20 cases.[89] Recurrent tumor was consistently found to have a high rCBV, ratio whereas radiation necrosis was seen to have low rCBV relative to contralateral normal brain tissue. Yet another report has shown that it is possible to depict a difference by DSC technique between low-grade astrocytomas following radiation treatment and normal brain.[124] Finally, even more recently it was shown that rCBV could be used to distinguish tumor from post-treatment radiation effects,[125] and the rCBV threshold can be used to create maps of fractional tumor burden.[126]

ARTERIAL SPIN-LABELING TECHNIQUES

MR perfusion imaging using ASL has begun to show promise as a technique for hemodynamic assessment of brain tumors. ASL is a completely noninvasive MRI technique because it does not require infusion of exogenous tracer material. Instead, a subject's own blood is used as an intrinsic tracer. Arterial blood outside the imaging plane is labeled using an inversion pulse and, upon entering the imaging section, spins within blood exchange with tissue water within capillaries.[127] By subtracting an image of the target tissue obtained prior to blood labeling from an image obtained after magnetized spins have entered the target slice, a hemodynamic image is obtained. Preliminary studies using animals harboring tumors have shown promising results for measuring various hemodynamic parameters within tumors.[128] Work in humans with brain tumors has shown the ability to distinguish high-grade gliomas from low-grade gliomas as well as very good correlation of the ratio of tumor blood flow to CBF as determined by the ASL and DSC techniques.[127] More recently, the use of the more advanced pseudo-continuous ASL techniques demonstrates a very good correlation with the DSC-determined blood flow.[129] Example ASL images obtained form a healthy volunteer are given in Figure 8. An important advantage for ASL is that exogenous contrast agent is not used. A disadvantage for brain tumors is that tortuous vasculature with lengthy transit times may serve to underestimate flow in areas of tumor, thus falsely underestimating the aggressive nature of some tumors. However, given the important advantages of ASL these issues must be more fully explored.

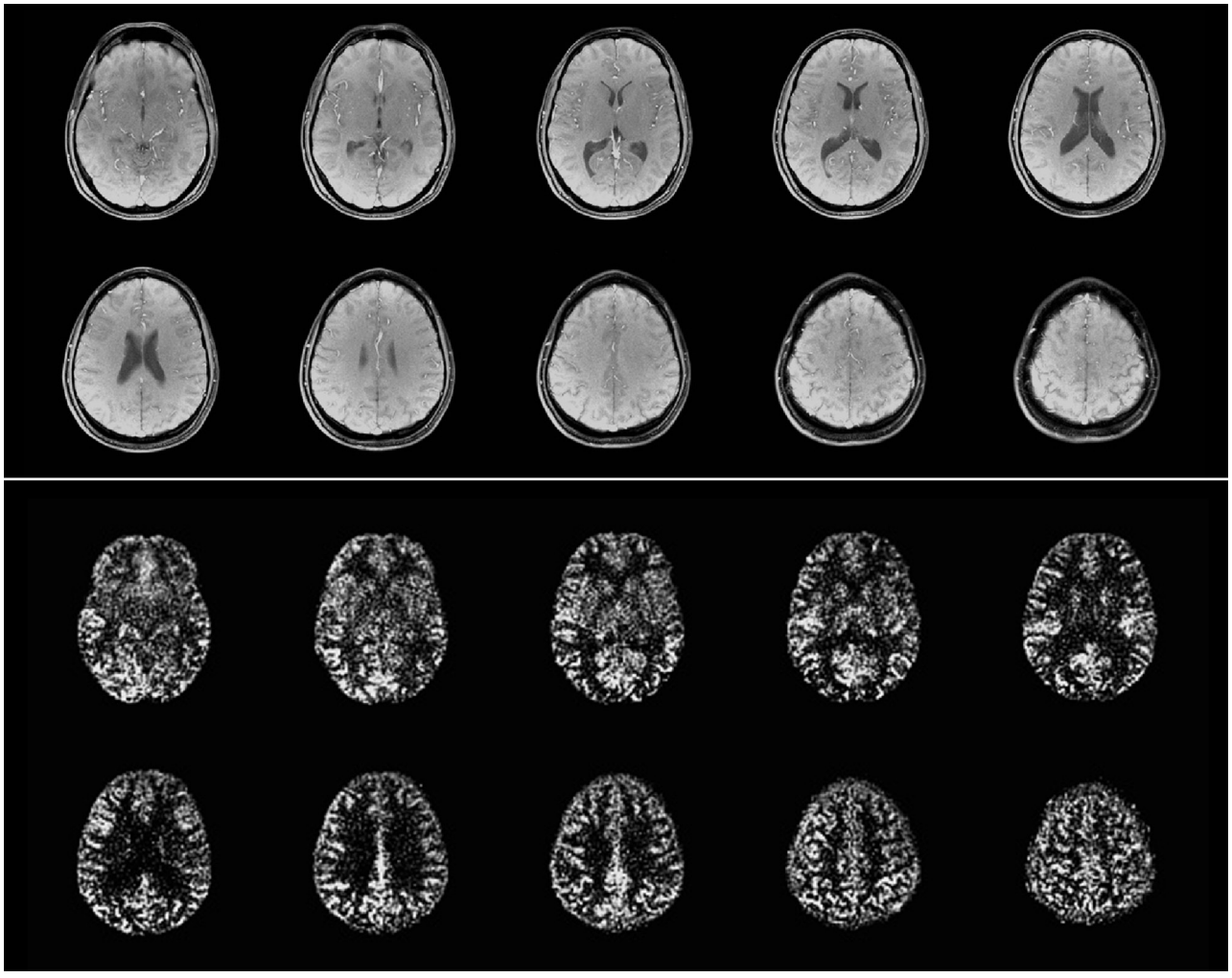


FIGURE 8 T1-weighted anatomic (upper images) and ASL images (lower images) obtained from a healthy volunteer on a 3-T MRI system. The ASL images were obtained using a background-suppressed PICORE/QUIPSSII tagging scheme implemented with a multishot, SE spiral-out sequence, TI2 = 1600 ms, TI1 = 700 ms, tag thickness = 20 cm, tag gap = 1 cm, TE = 11 ms, TR = 3000 ms. *Images are courtesy of Eric Paulson, Medical College of Wisconsin.*

CT PERFUSION IMAGING

In recent years, CT perfusion imaging has gained acceptance as a valuable imaging technique for assessment of some CNS diseases, such as cerebral ischemia. However, because MRI remains the preferred technique for assessment of brain tumors, reports of CT perfusion studies of rCBV for the evaluation of brain tumors are much fewer in number than reports of MRI for the same purpose. However, CT perfusion imaging for assessment of brain tumors has been well validated in animal studies.[130] In humans, CT perfusion imaging has been reported to be of value in the assessment of head and neck tumors (possibly reflecting the fact that CT imaging remains the preferred technique for evaluation of neck tumors at many institutions). For instance, using a technique that assesses not only the initial phase of contrast enhancement but also the time–signal intensity curve over the first few minutes after infusion of contrast material, investigators have examined regional blood flow, capillary permeability, and relative compartmental volumes in human neck tumors.[131] Those investigators found higher regional blood flow in neck neoplasms compared to normal muscle, but attributed that higher blood flow to a higher regional blood volume rather than to higher flow per unit plasma volume. Published examples of CT perfusion imaging for assessment of brain tumors remain confined at this point to small series or case reports. In a report of five cases of brain tumors assessed using CT perfusion imaging, high-grade gliomas were found to produce heterogeneous rCBV maps with regions of high rCBV, whereas low-grade gliomas had only low rCBV.[132] These findings are similar to those reported using MRI. In one series of patients with various diagnoses studied by CT perfusion, the investigators reported markedly elevated rCBV and rCBF within a contrast-enhancing tumor in a patient with a malignant brain neoplasm.[133] Another case report reported CT perfusion imaging findings in a patient with a high-grade glioma who could not undergo MRI because of the presence of a cardiac pacemaker.[134] CT perfusion imaging showed moderately elevated rCBV and markedly elevated rCBF and mean permeability surface flow within the tumor compared to normal tissue. Finally, CT perfusion findings have been reported for two patients with brain metastases developing from a non-CNS origin, of which one also underwent MR perfusion imaging using the DCE technique.[135] In both patients, the tumors were seen to contrast enhance on conventional CT imaging and both had markedly increased permeability–surface area measurements on CT perfusion. One tumor was seen to have normal rCBF and only mildly elevated rCBV while the other tumor had markedly increased rCBF and rCBV both. In the latter patient, regions of highest permeability slightly differed on CT perfusion imaging compared to regions of highest permeability on MRI. However, the regions of high rCBV on CT perfusion imaging conformed relatively well to regions of tumor having high rCBV on MR perfusion imaging.

References

1. Kaiser WA, Zeitler E. MR imaging of the breast: fast imaging sequences with and without Gd-DTPA. *Radiology*. 1989;17:681–686.
2. Stack JP, et al. Breast disease: tissue characterization with Gd-DTPA enhancement profiles. *Radiology*. 1990;174:491–494.
3. Kelcz F, et al. Reducing the false positive gadolinium-enhanced breast MRI results through parameters analysis of the enhancement profile. In: *12th Annual Meeting of the Society of Magnetic Resonance in Medicine*. 1993. [New York].
4. Noseworthy MD, Morton G, Wright GA. A comparison of normal and cancerous prostate using dynamic T1 and T2* weighted MRI. In: *7th Annual Meeting of the international Society of Magnetic Resonance in Medicine*. 1999. [Philadelphia].
5. Hawihorst H, et al. Uterine cervical carcinoma: comparison of standard and pharmacokinetic analysis of time-intensity curves for assessment of tumor angiogenesis and patient survival. *Cancer Res*. 1998;58:3598–3602.
6. Buckley DL, et al. Microvessel density in invasive breast cancer assessed by dynamic Gd-DTPA enhanced MRI. *J Magn Reson Imaging*. 1997;7:461–464.
7. Tofts PS, Kermode AG. Measurement of the blood–brain barrier permeability and leakage space using dynamic MR imaging: 1. Fundamental concepts. *Magn Reson Med*. 1991;17:357–367.
8. Tofts PS, et al. Estimating kinetic parameters from dynamic contrast-enhanced T1-weighted MRI of a diffusable tracer: standardized quantities and symbols. *J Magn Reson Imaging*. 1999;10:223–232.
9. St Lawrence KS, Lee TY. An adiabatic approximation to the tissue homogeneity model for water exchange in the brain: I. Theoretical derivation. *J Cereb Blood Flow Metab*. 1998;18:1365–1377.
10. Johnson JA, Wilson TA. A model for capillary exchange. *Am J Physiol*. 1966;210:1299–1303.
11. Ludemann L, Hamm B, Zimmer C. Pharmacokinetic analysis of glioma compartments with dynamic Gd-DTPA-enhanced magnetic resonance imaging. *Magn Reson Imaging*. 2000;18:1201–1214.
12. Harrer JU, et al. Comparative study of methods for determining vascular permeability and blood volume in human gliomas. *J Magn Reson Imaging*. 2004;20(5):748–757.
13. Ludemann L, et al. Quantitative measurement of leakage volume and permeability in gliomas, meningiomas and brain metastases with dynamic contrast-enhanced MRI. *Magn Reson Imaging*. 2000;23:833–841.
14. Henderson E, et al. Simultaneous MRI measurement of blood flow, blood volume, and capillary permeability in mammary tumors using two different contrast agents. *J Magn Reson Imaging*. 2000;12:991–1003.
15. Vajkoczy P, Menger MD. Vascular microenvironment in gliomas. *J Neuro-Oncol*. 2000;50(1–2):99–108.
16. van Dijke CF, et al. Mammary carcinoma model: correlation of macromolecular contrast-enhanced MR imaging characterizations of tumor microvasculature and histologic capillary density. *Radiology*. 1996;198(3):813–818.
17. Daldrup H, et al. Correlation of dynamic contrast-enhanced MR imaging with histologic tumor grade: comparison of macromolecular and small-molecular contrast media. *Am J Roentgenol*. 1998;171(4):941–949.
18. Larsson C, et al. T1 in high-grade glioma and the influence of different measurement strategies on parameter estimations in DCE-MRI. *J Magn Reson Imaging*. 2015;42(1):97–104.

19. Patlak CS, Blasberg RG, Fenstermacher JD. Graphical evaluation of blood-to-brain transfer constants from multiple-time uptake data. *J Cerebr Blood Flow Metab*. 1983;3:1–7.
20. Kenney J, et al. Measurement of blood–brain barrier permeability in a tumor model using magnetic resonance imaging with gadolinium-DTPA. *Magn Reson Med*. 1992;27:68–75.
21. Ewing JR, et al. Patlak plots of Gd-DTPA MRI data yield blood–brain transfer constants concordant with those of 14C-sucrose in areas of blood–brain opening. *Magn Reson Med*. 2003;50(2): 283–292.
22. Choyke PL, Dwyer AJ, Knopp MV. Functional tumor imaging with dynamic contrast enhanced magnetic resonance imaging. *JMRI*. 2003;17:509–520.
23. Sung K, et al. Simultaneous T(1) and B(1) (+) mapping using reference region variable flip angle imaging. *Magn Reson Med*. 2013;70(4):954–961.
24. van Schie JJ, et al. Feasibility of a fast method for B1-inhomogeneity correction for FSPGR sequences. *Magn Reson Imaging*. 2015; 33(3):312–318.
25. Yarnykh VL. Optimal radiofrequency and gradient spoiling for improved accuracy of T1 and B1 measurements using fast steady-state techniques. *Magn Reson Med*. 2010;63(6):1610–1626.
26. Evelhoch J, et al. Expanding the use of magnetic resonance in the assessment of tumor response to therapy: workshop report. *Cancer Res*. 2005;65(16):7041–7044.
27. Henderson E, Rutt BK, Lee TY. Temporal sampling requirements for the tracer kinetics modeling of breast disease. *Magn Reson Imaging*. 1998;16:1057–1073.
28. Rijpkema M, et al. Method for quantitative mapping of dynamic MRI contrast agent uptake in human tumors. *J Magn Reson Imaging*. 2001;14(4):457–463.
29. Brix G, et al. Tracer kinetic modelling of tumour angiogenesis based on dynamic contrast-enhanced CT and MRI measurements. *Eur J Nucl Med Mol Imaging*. 2010;37(suppl 1):S30–S51.
30. Aerts HJ, Jaspers K, Backes WH. The precision of pharmacokinetic parameters in dynamic contrast-enhanced magnetic resonance imaging: the effect of sampling frequency and duration. *Phys Med Biol*. 2011;56(17):5665–5678.
31. Paulson ES, Prah DE, Schmainda KM. Compensation of confounding T1 and T2 dipolar and residual susceptibility effects in DSC-MRI using dual-echo SPIRAL. In: *Proceedings of the International Society for Magnetic Resonance in Medicine*. 2007.
32. Paulson ES, Schmainda KM. Comparison of dynamic susceptibility-weighted contrast-enhanced MR methods: recommendations for measuring relative cerebral blood volume in brain tumors. *Radiology*. 2008;249(2):601–613.
33. Quarles CC, et al. Comparison of dual-echo DSC-MRI- and DCE-MRI-derived contrast agent kinetic parameters. *Magn Reson Imaging*. 2012;30(7):944–953.
34. Schmiedeskamp H, et al. Combined spin- and gradient-echo perfusion-weighted imaging. *Magn Reson Med*. 2012;68(1):30–40.
35. Schmiedeskamp H, et al. Simultaneous perfusion and permeability measurements using combined spin- and gradient-echo MRI. *J Cereb Blood Flow Metab*. 2013;33(5):732–743.
36. Skinner JT, et al. Evaluation of a multiple spin- and gradient-echo (SAGE) EPI acquisition with SENSE acceleration: applications for perfusion imaging in and outside the brain. *Magn Reson Imaging*. 2014;32(10):1171–1180.
37. Blaimer M, et al. Multiband phase-constrained parallel MRI. *Magn Reson Med*. 2013;69(4):974–980.
38. Degani H, et al. Mapping of patholophysiologic features of breast tumors by MRI at high spatial resolution. *Nat Med*. 1997;3: 780–782.
39. Mayr NA, et al. MR microcirculation assessment in cervical cancer: correlations with histomorphological tumor markers and clinical outcome. *J Magn Reson Imaging*. 1999;10:267–276.
40. Padhani AR. Dynamic contrast-enhanced MRI in clinical oncology: current status and future directions. *J Magn Reson Imaging*. 2002;16:407–422.
41. Gossmann A, et al. Dynamic contrast-enhanced magnetic resonance imaging as a surrogate marker of tumor response to anti-angiogenic therapy in a xenograft model of glioblastoma multiforme. *J Magn Reson Imaging*. 2002;15:223–240.
42. Knopp MV, et al. Pathophysiologic basis of contrast enhancement in breast tumors. *J Magn Reson Imaging*. 1999;10:260–266.
43. Hulka CA, et al. Dynamic echo-planar imaging of the breast: experience in diagnosing breast carcinoma and correlation with tumor angiogenesis. *Radiology*. 1997;205(3):837–842.
44. Jung BC, et al. Comparison of glioblastomas and brain metastases using dynamic contrast-enhanced perfusion MRI. *J Neuroimaging*. 2015.
45. Bauer AH, et al. Differentiation of solitary brain metastasis from glioblastoma multiforme: a predictive multiparametric approach using combined MR diffusion and perfusion. *Neuroradiology*. 2015;57(7):697–703.
46. Lund R, et al. Using rCBV to distinguish radiation necrosis from tumor recurrence in malignant gliomas. In: *47th Annual Meeting of American Society for therapeutic Radiology and oncology*. 2005. [Denver, CO].
47. Li X, et al. Glioma grading by microvascular permeability parameters derived from dynamic contrast-enhanced MRI and intratumoral susceptibility signal on susceptibility weighted imaging. *Cancer Imaging*. 2015;15:4.
48. Choi HS, et al. Glioma grading capability: comparisons among parameters from dynamic contrast-enhanced MRI and ADC value on DWI. *Korean J Radiol*. 2013;14(3):487–492.
49. Ahn SS, et al. Prediction of methylguanine methyltransferase promoter methylation in glioblastoma using dynamic contrast-enhanced magnetic resonance and diffusion tensor imaging. *J Neurosurg*. 2014;121(2):367–373.
50. Shin KE, et al. DCE and DSC MR perfusion imaging in the differentiation of recurrent tumour from treatment-related changes in patients with glioma. *Clin Radiol*. 2014;69(6):e264–e272.
51. Kim HS, et al. Which combination of MR imaging modalities is best for predicting recurrent glioblastoma? Study of diagnostic accuracy and reproducibility. *Radiology*. 2014;273(3):831–843.
52. Huang W, et al. Variations of dynamic contrast-enhanced magnetic resonance imaging in evaluation of breast cancer therapy response: a multicenter data analysis challenge. *Transl Oncol*. 2014;7(1):153–166.
53. Rosen BR, et al. Perfusion imaging with NMR contrast agents. *Magn Reson Med*. 1990;14:249–265.
54. Ostergaard L, et al. High resolution measurement of cerebral blood flow using intravascular tracer bolus passages. Part I: Mathematical approach and statistical analysis. *Magn Reson Med*. 1996;36:715–725.
55. Paulson ES, Prah DE, Schmainda KM. Correction of confounding leakage and residual susceptibility effects in dynamic susceptibility contrast MR imaging using dual-echo SPIRAL. In: *Proceedings American Society of Neuroradiology*. 2007. [Chicago].
56. Donahue KM, et al. Utility of simultaneously acquired gradient-echo and spin-echo cerebral blood volume and morphology maps in brain tumor patients. *Magn Reson Med*. 2000;43:845–853.
57. Schmainda KM, et al. Characterization of a first-pass gradient-echo spin-echo method to predict brain tumor grade and angiogenesis. *Am J Neuroradiol*. 2004;25:1524–1532.
58. Vonken EP, et al. Simultaneous quantitative cerebral perfusion and Gd-DTPA extravasation measurement with dual-echo dynamic susceptibility contrast MRI. *Magn Reson Med*. 2000;43(6):820–827.
59. Boxerman J, et al. The intravascular contribution to fMRI signal change: Monte Carlo modeling and diffusion-weighted studies in vivo. *Magn Reson Med*. 1995;34:4–10.

60. Dennie J, et al. NMR imaging of changes in vascular morphology due to tumor angiogenesis. *Magn Reson Med*. 1998;40:793–799.
61. Tropres I, et al. Vessel size imaging. *Magn Reson Med*. 2001;45: 397–408.
62. Paulson ES, Prah DE, Schmainda KM. Correction of contrast agent extravasation effects in DSC-MRI using Dual-Echo spiral provides better reference for evaluating PASL CBF estimates in brain tumors. In: *Proceedings International Society of Magnetic Resonance in Medicine, 15th Annual Meeting*. 2007. [Berlin].
63. Schmainda KM, et al. Simultaneous measurement of DSC- and DCE-MRI parameters using dual-echo spiral with a single dose of gadolinium in comparison to single-echo GRE-EPI methods in brain tumors. In: *Proceedings of the International Society of Magnetic Resonance in Medicine*. 2015. [Toronto, Ontario, Canada].
64. Boxerman JL, Rosen BR, Weisskoff RM. Signal-to-Noise analysis of cerebral blood volume maps from dynamic NMR imaging studies. *J Magn Reson Imaging*. 1997;7(3):528–537.
65. Hou L, et al. Optimization of fast acquisition methods for whole-brain relative cerebral blood volume (rCBV) mapping with susceptibility contrast agents. *J Magn Reson Imaging*. 1999;9:233–239.
66. Perkio J, et al. Evaluation of four postprocessing methods for determination of cerebral blood volume and mean transit time by dynamic susceptibility contrast imaging. *Magn Reson Med*. 2002;47:973–981.
67. Aronen HJ, et al. Ultrafast imaging of brain tumors. *Top Magn Reson Imaging*. 1993;5:14–24.
68. Aronen HJ, et al. Cerebral blood volume maps of gliomas: comparison with tumor grade and histologic findings. *Radiology*. 1994;191:41–51.
69. Aronen HJ, et al. High microvascular blood volume is associated with high glucose uptake and tumor angiogenesis in human gliomas. *Clin Cancer Res*. 2000;6(6):2189–2200.
70. Fuss M, et al. Tumor angiogenesis of low-grade astrocytomas measured by dynamic susceptibility contrast-enhanced MRI (DSC-MRI) is predictive of local tumor control after radiation therapy. *Int J Radiat Oncol Biol Phys*. 2001;51(2):478–482.
71. Maeda M, et al. Tumor vascularity in the brain: evaluation with dynamic susceptibility-contrast MR imaging. *Radiology*. 1993;189:233–238.
72. Cha S. Perfusion imaging of brain tumors. *Top Magn Reson Imaging*. 2004;15(5):279–289.
73. Knopp EA, et al. Glial neoplasms: dynamic contrast-enhanced T2*-weighted MR imaging. *Radiology*. 1999;211(3):791–798.
74. Heiland S, et al. Simultaneous assessment of cerebral hemodynamics and contrast agent uptake in lesions with disrupted blood–brain barrier. *Magn Reson Imaging*. 1999;17(1):21–27.
75. Hu LS, et al. Optimized preload leakage-correction methods to improve the diagnostic accuracy of dynamic susceptibility-weighted contrast-enhanced perfusion MR imaging in posttreatment gliomas. *AJNR Am J Neuroradiol*. 2010;31(1):40–48.
76. Bjornerud A, et al. T1- and T2*-dominant extravasation correction in DSC-MRI: part I–theoretical considerations and implications for assessment of tumor hemodynamic properties. *J Cereb Blood Flow Metab*. 2011;31(10):2041–2053.
77. Weisskoff RM, et al. Simultaneous blood volume and permeability mapping using a single Gd-based contrast injection. In: *Society of Magnetic Resonance in Medicine, 2nd Annual Meeting*. 1994. [San Francisco].
78. Boxerman J, Schmainda KM, Weisskoff RM. Relative cerebral blood volume maps corrected for contrast agent extravasation significantly correlate with glioma tumor grade whereas uncorrected maps do not. *Am J Neuroradiol*. 2006;27:859–867.
79. Boxerman JL, Schmainda KM, Weisskoff RM. Relative cerebral blood volume maps corrected for contrast agent extravasation significantly correlate with glioma tumor grade, whereas uncorrected maps do not. *AJNR Am J Neuroradiol*. 2006;27(4):859–867.
80. Boxerman JL, et al. The role of preload and leakage correction in gadolinium-based cerebral blood volume estimation determined by comparison with MION as a criterion standard. *AJNR Am J Neuroradiol*. 2012;33(6):1081–1087.
81. Quarles CC, Ward BD, Schmainda KM. Improving the reliability of obtaining tumor hemodynamic parameters in the presence of contrast agent extravasation. *Magn Reson Med*. 2005;53(6):1307–1316.
82. Quarles CC, Ward BD, Schmainda KM. Improving the reliability of obtaining tumor hemodynamic parameters in the presence of contrast agent extravasation. *Magn Reson Med*. 2005;53:1307–1316.
83. Quarles CC, et al. Dexamethasone normalizes brain tumor hemodynamics as indicated by dynamic susceptibility contrast MRI perfusion parameters. *Technol Cancer Res Treat*. 2005;4(3): 245–249.
84. Guckel F, et al. Assessment of cerebral blood volume with dynamic susceptibility contrast enhanced gradient-echo imaging. *J Comput Assisted Tomogr*. 1994;18(3):344–351.
85. Bruening R, et al. Echo-planar MR determination of relative cerebral blood volume in human brain tumors: T1 versus T2 weighting. *Am J Neuroradiol*. 1996;17:831–840.
86. Siegal T, et al. Utility of relative cerebral blood volume mapping derived from perfusion magnetic resonance imaging in the routine follow up of brain tumors. *J Neurosurg*. 1997;86:22–27.
87. Hacklander T, Reichenbach JR, Modder U. Comparison of cerebral blood volume measurements using the T1 and T2* methods in Normal human brains and brain tumors. *J Comput Assisted Tomogr*. 1997;21(6):857–866.
88. Zhu XP, et al. Quantification of endothelial permeability, leakage space, and blood volume in brain tumors using combined T1 and T2* contrast-enhanced dynamic MR imaging. *J Magn Reson Imaging*. 2000;11:575–585.
89. Sugahara T, et al. Posttherapeutic intraaxial brain tumor: the value of perfusion-sensitive contrast-enhanced MR imaging for differentiating tumor recurrence from nonneoplastic contrast-enhancing tissue. *Am J Neuroradiol*. 2000;21:901–909.
90. Sugahara T, et al. Perfusion-sensitive MR imaging of gliomas: comparison between gradient-echo and spin-echo echo-planar imaging techniques. *Am J Neuroradiol*. 2001;22(7):1306–1315.
91. Aronen HJ, et al. Echo-planar MR cerebral blood volume mapping of gliomas. Clinical utility. *Acta Radiol*. 1995;36(5):520–528.
92. Bulakbasi N, et al. Assessment of diagnostic accuracy of perfusion MR imaging in primary and metastatic solitary malignant brain tumors. *Am J Neuroradiol*. 2005;26:2187–2199.
93. Lev MH, et al. Glial tumor grading and outcome prediction using dynamic spin-echo MR susceptibility mapping compared with conventional contrast-enhanced MR: confounding effect of elevated rCBV of oligodendrogliomas. *Am J Neuroradiol*. 2004;25:214–221.
94. Hartmann M, et al. Distinguishing of primary cerebral lymphoma from high-grade glioma with perfusion-weighted magnetic resonance imaging. *Neurosci Lett*. 2003;338(2):119–122.
95. Wong JC, Provenzale JM, Petrella JR. Perfusion MR imaging of brain neoplasms. *Am J Neuroradiol*. 2000;174:1147–1157.
96. Kremer S, et al. Contribution of dynamic contrast MR imaging to the differentiation between dural metastasis and meningioma. *Neuroradiology*. 2004;46(8):642–648.
97. Gillies RJ, et al. Causes and effects of heterogeneous perfusion in tumors. *Neoplasia*. 1999;1(3):197–207.
98. Jain RK. Determinants of tumor blood flow: a review. *Cancer Res*. 1988;48:2641–2658.
99. Hamberg LM, et al. Spatial heterogeneity in tumor perfusion measured with functional computed tomography at 0.05 μl resolution. *Cancer Res*. 1994;54:6032–6036.
100. Eskey CJ, et al. 2H-Nuclear magnetic resonance imaging of tumor blood flow: spatial and temporal heterogeneity in a tissue-isolated mammary adenocarcinoma. *Cancer Res*. 1992;52:6010–6019.

101. Jain RK. Physiological resistance to the treatment of solid tumors. In: Teicher BA, ed. *Drug Resistance in Oncology*. New York: Marcel Dekker, Inc.; 1993:87–105.
102. Durand RE, LePard NE. Modulation of tumor hypoxia by conventional chemotherapeutic agents. *Int J Radiat Oncol*. 1994;29(3):481–486.
103. Gee MS, et al. Doppler ultrasound imaging detects changes in tumor perfusion during antivascular therapy associated with vascular anatomic alterations. *Cancer Res*. 2001;61:2974–2982.
104. Tozer GM, et al. Combretastatin A-4 phosphate as a tumor vascular-targeting agent: early effects in tumors and normal tissues. *Cancer Res*. 1999;59:1626–1634.
105. Dark GG, et al. Combretastatin A-4, an agent that displays potent and selective toxicity toward tumor vasculature. *Cancer Res*. 1997;57:1829–1834.
106. Holash J, et al. Vessel cooption, regression, and growth in tumors mediated by angiopoietins and VEGF. *Science*. 1999;284:1994–1998.
107. Bernsen HJ, et al. Suramin treatment of human glioma xenografts; effects on tumor vasculature and oxygenation status. *J Neuro-Oncol*. 1999;44:129–136.
108. Badruddoja MA, et al. Antiangiogenic effects of dexamethasone in 9L gliosarcoma assessed by MRI cerebral blood volume maps. *Neuro Oncol*. 2003;5(4):235–243.
109. Heiss JD, et al. Mechanism of dexamethasone suppression of brain tumor-associated vascular permeability in rats. *J Clin Invest*. 1996;98:1400–1408.
110. Machein MR, et al. Differential downregulation of vascular endothelial growth factor by dexamethasone in normoxic and hypoxic rat glioma cells. *Neuropathol Appl Neurobiol*. 1999;25:104–112.
111. Chiang IC, Kuo YT, Lu CY. Distinction between high-grade gliomas and solitary metastases using peritumoral 3T magnetic resonance spectroscopy, diffusion, and perfusion imaging. *Neuroradiology*. 2004;46:619–627.
112. Law M, et al. High-grade gliomas and solitary metastases: differentiation by using perfusion and proton spectroscopic MR imaging. *Radiology*. 2002;222:715–721.
113. Pham CD, et al. Magnetic resonance imaging detects suppression of tumor vascular permeability after administration of antibody to vascular endothelial growth factor. *Cancer Invest*. 1998;16(4):225–230.
114. Brasch R, et al. Assessing tumor angiogenesis using macromolecular MR imaging contrast agents. *J Magn Reson Imaging*. 1997;7(1):68–74.
115. Gossmann A, et al. Dynamic contrast-enhanced magnetic resonance imaging as a surrogate marker of tumor response to anti-angiogenic therapy in xenograft model of glioblastoma multiforme. *J Magn Reson Imaging*. 2002;15:233–240.
116. Provenzale JM, Glavez MM, Leeds NE. MR imaging evaluation of a novel anti-angiogenesis agent, PTK787. In: *Radiological Society of North America*. 2002.
117. Essig M, et al. Assessment of brain metastases with dynamic susceptibility-weighted contrast-enhanced MR imaging: initial results. *Radiology*. 2003;228:193–199.
118. Schmainda KM, et al. Dynamic-susceptibility contrast agent MRI measures of relative cerebral blood volume predict response to bevacizumab in recurrent high-grade glioma. *Neuro Oncol*. 2014;16(6):880–888.
119. Kickingereder P, et al. Relative cerebral blood volume is a potential predictive imaging biomarker of bevacizumab efficacy in recurrent glioblastoma. *Neuro Oncol*. 2015;17(8):1139–1147.
120. Schmainda KM, et al. Dynamic susceptibility contrast MRI measures of relative cerebral blood volume as a prognostic marker for overall survival in recurrent glioblastoma: results from the ACRIN 6677/RTOG 0625 multicenter trial. *Neuro Oncol*. 2015.
121. Rock JP, et al. Associations among magnetic resonance spectroscopy, apparent diffusion coefficients, and image-guided histopathology with special attention to radiation necrosis. *Neurosurgery*. 2004;54(5):1111–1117.
122. Cha S, et al. Dynamic, contrast-enhanced perfusion MRI in mouse gliomas: correlation with histopathology. *Magn Reson Med*. 2003;49:848–855.
123. Hazle JD, et al. Dynamic imaging of intracranial lesions using fast spin-echo imaging: differentiation of brain tumors and treatment effects. *J Magn Reson Imaging*. 1997;7:1084–1093.
124. Wenz F, et al. Effect of radiation on blood volume in low-grade astrocytomas and normal brain tissue: quantification with dynamic susceptibility contrast MR imaging. *Am J Roentgenol*. 1996;166(1):187–193.
125. Hu L, et al. Relative cerebral blood volume values to differentiate high-grade glioma recurrence from posttreatment radiation effect: direct correlation between image-guided tissue histopathology and localized dynamic susceptibility-weighted contrast perfusion MR imaging measurements. *Am J Neuroradiol*. 2009;30(3):552–558.
126. Hu LS, et al. Reevaluating the imaging definition of tumor progression: perfusion MRI quantifies recurrent glioblastoma tumor fraction, pseudoprogression, and radiation necrosis to predict survival. *Neuro Oncol*. 2012;14(7):919–930.
127. Warmuth C, Gunther M, Zimmer C. Quantification of blood flow in brain tumors: comparison of arterial spin labeling and dynamic susceptibility-weighted contrast-enhanced MR imaging. *Radiology*. 2003;228:523–532.
128. Silva AC, Kim SG, Garwood M. Imaging blood flow in brain tumors using arterial spin labeling. *Magn Reson Med*. 2000;44:169–173.
129. Jarnum H, et al. Perfusion MRI of brain tumours: a comparative study of pseudo-continuous arterial spin labelling and dynamic susceptibility contrast imaging. *Neuroradiology*. 2010;52(4):307–317.
130. Cenic A, et al. A CT method to measure hemodynamics in brain tumors: validation and application to cerebral blood flow maps. *Am J Neuroradiol*. 2000;21:462–470.
131. Brix G, et al. Regional blood flow, capillary permeability, and compartmental volumes: measurement with dynamic CT-initial experience. *Radiology*. 1999;210:269–276.
132. Leggett D, Miles KA, Kelly BB. Blood–brain barrier and blood volume imaging of cerebral glioma using functional CT: a pictorial review. *Eur J Radiol*. 1999;30:185–190.
133. Nabavi DG, et al. CT assessment of cerebral perfusion: experimental validation and initial clinical experience. *Radiology*. 1999;213:141–149.
134. Eastwood JD, Provenzale JM. Cerebral blood flow, blood volume, and vascular permeability of cerebral glioma assessed with dynamic CT perfusion imaging. *Neuroradiology*. 2003;45:373–376.
135. Roberts HC, et al. Dynamic, contrast-enhanced CT of human brain tumors: quantitative assessment of blood volume blood flow, and microvascular permeability: report of two cases. *Am J Neuroradiol*. 2002;23:828–832.

CHAPTER

32

Positron Emission Tomography (PET) and Single-Photon Emission Computed Tomography (SPECT) Physics

Marie Foley Kijewski

Department of Radiology, Brigham and Women's Hospital, Harvard Medical School, Boston, MA, USA

INTRODUCTION

The purpose of emission tomography is to estimate the distribution of a radiotracer from external measurements of the pattern of photons emerging from the brain. Some of these photons are detected, and certain information about them recorded, by the scanner. These external measurements are termed "projections," and each measurement in a projection represents, ideally, the sum of radioactivity concentration along a line through the brain. From these measured projection data sets and knowledge of certain aspects of the single-photon emission computed tomography (SPECT) or positron emission tomography (PET) instrument, estimated images of the distribution of radioactivity are mathematically reconstructed. All modern SPECT and PET scanners image the three-dimensional (3D) distribution of radioactivity, either as a stack of two-dimensional (2D) transaxial images or directly as a 3D volume.

Image reconstruction techniques fall into two categories: analytic and iterative. Reconstruction by analytic methods is rapid and straightforward, as it involves solution of the inverse reconstruction problem (i.e., determining the original distribution from knowledge of its projections) by an algorithm. The underlying mathematics were published in 1917 by Radon.[1] Iterative reconstruction consists of a repeated updating of an initial image based on comparison of calculated projections of the current image estimate to the measured projections. Many iterative approaches have been developed; they differ in the criterion to be minimized and the algorithm for updating the image estimates, as well as in the statistical and physical models they incorporate. This approach has the potential to be more accurate, because it can incorporate more information about the physics of the imaging process, and to have better noise properties, as it uses a more realistic statistical model. Iterative reconstruction algorithms were initially used only in research applications because of the long reconstruction times. These times have been reduced significantly because of improvements in computer processing speed and advances in efficiency of the reconstruction algorithms, and iterative algorithms are now in clinical use.

Brain SPECT or PET images are interpreted by visual inspection by a physician or analyzed for measurements of physical quantities, such as activity concentration, size of tumor, or parameters of dynamic acquisitions.

SPECT IMAGING

Introduction to SPECT Physics

SPECT imaging is based on detection of gamma-radiation from radioisotopes that emit one photon of a particular energy per nuclear decay, characterized by a particular half-life. (Some radioisotopes used in SPECT emit significant numbers of photons at each of several energies.) For optimal imaging, photon energy should be in the hundred-kiloelectron volt (keV) range; the energy must be high enough that significant numbers of photons escape the body, even from deep structures, but not so high that they have little probability of being stopped by the detector (see Anger Camera Section). The energy (140 keV) of the photon emitted by the most commonly used SPECT radioisotope, ^{99m}Tc, is ideal. The injected

Handbook of Neuro-Oncology Neuroimaging, Second Edition
http://dx.doi.org/10.1016/B978-0-12-800945-1.00032-X

© 2016 Elsevier Ltd. All rights reserved.

tracer amounts are limited by dosimetry considerations because, in contrast to X-ray imaging, the radioactivity remains in the patient for an extended period of time, in declining concentrations as it decays and is excreted. Therefore, the emission rate is low, and imaging normally takes a long time (20–30 min for SPECT vs a few seconds for X-ray computed tomography (CT)). Furthermore, the statistical quality of emission CT images is poor, because they are formed with relatively few photons.

SPECT Instrumentation

Anger Camera

The most commonly used SPECT instrument is the Anger camera[2] (see Figure 1). A photon that traverses a collimator hole strikes a scintillating crystal, most commonly made of sodium iodide (NaI). This material provides good detection efficiency and relatively good energy resolution (9% full-width at half-maximum at 140 keV) at reasonable cost. Each photon is converted in the crystal to many lower-energy photons in the visible-light range. These, in turn, are detected by an array, usually hexagonal, of photomultiplier tubes, which convert the light photons to electrical current. Each scintillation in the crystal generates a signal in several photomultiplier tubes; those closest to the interaction will receive the greatest amount of light. Positioning electronics yield an estimate of the location of the interaction based on the relative signal from each tube. The energy of each detected photon is also estimated by a pulse-height analyzer.

Collimator

A collimator is a device used to restrict the photon acceptance angle to provide positional information for detected photons. A SPECT collimator is a thick sheet of metal of high atomic number, usually lead or tungsten, pierced by an array of holes. In theory, only photons that traverse these holes without striking the septa between them can be detected. In practice, some photons penetrate the septa and are detected, degrading the resolution and contrast of the reconstructed image. This is more likely for isotopes that emit higher-energy photons, such as ^{111}In, frequently used for tumor imaging,[3] with primary gamma-ray emissions at 171 and 245 keV. In parallel-hole collimators (see Figure 2), all holes are parallel to one another and perpendicular to the detector face. The fundamental design parameter for such a collimator is the hole size; smaller holes provide better information on the location of the emission and, consequently, better spatial resolution, but accept fewer photons, thereby increasing noise. Sensitivity is a crucial consideration for SPECT imaging, as the fraction of photons striking a collimator that traverse it without being absorbed is on the order of 1/1000. In an effort to increase sensitivity, a number of focusing collimator designs have been proposed[4–11]; fan-beam collimators focus only in the transaxial (within-plane) direction, whereas cone-beam collimators focus in both transaxial and axial directions. Several groups have designed hybrid collimation systems consisting of cone-beam or multi-pinhole collimators, for increased sensitivity, paired with fan- or parallel-beam collimators, for data sufficiency.[12–14] Focusing collimators lead to improved spatial resolution, as well as improved sensitivity, owing to magnification (see Figure 2).

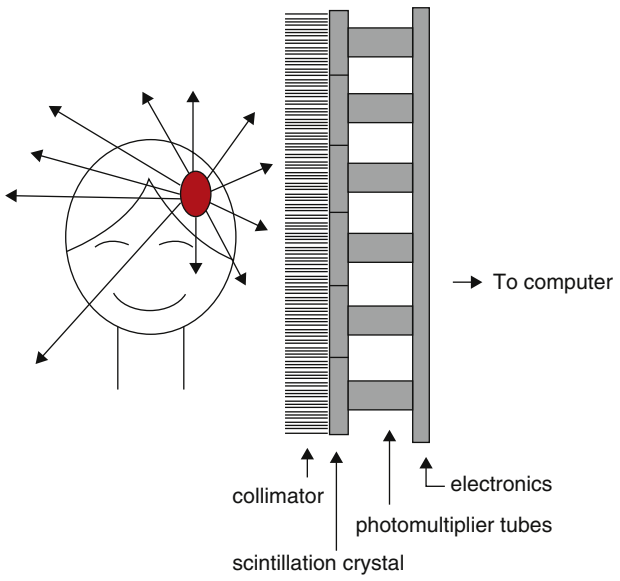


FIGURE 1 Diagram of an Anger camera. *Courtesy of Dr. Mi-Ae Park.*

SPECT Image Reconstruction and Correction

The major physical effects that cause the image measurements to deviate from their assumed line projections are limited spatial resolution, photon attenuation, and photon scatter. Spatial resolution is determined by characteristics of the collimator and of the crystal. Because each collimator hole accepts photons originating within an extended volume rather than along a line, the pattern of photons striking the detector is a blurred version of the true projection through the radioactivity distribution. This blurring increases with distance from the collimator,

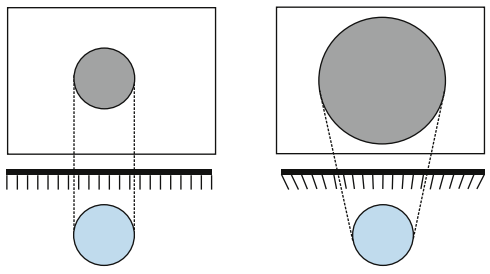


FIGURE 2 Diagrams of parallel-hole (left) and cone-beam (right) collimators. *Courtesy of Dr. Mi-Ae Park.*

leading to variable spatial resolution within the reconstructed image. Further blurring takes place within the crystal. Because the intrinsic resolution of the crystal and the geometry of the collimators are well characterized, it is, in theory, possible to mathematically remove the blurring from the projections. This can be accomplished prior to analytical reconstruction by inverse filtering or within an iterative reconstruction algorithm by incorporating the resolution characteristics into the system model. In practice, because the measured projections are noisy versions of the true projections, resolution recovery is accompanied by amplification of image noise no matter how it is implemented. Another approach to correcting effects of limited spatial resolution, which does not amplify noise, is to incorporate a priori anatomical information or homogeneity constraints based on other imaging modalities.[15] Some emitted photons do not escape the brain, but undergo interactions with the tissue (see Figure 3). The likelihood of an emitted photon escaping the brain depends on the location of the emission and the density and atomic number of the anatomical structures along the photon path. The probability of an emitted photon being lost to attenuation is greatest for photons originating near the center of the brain, because these photons must traverse the greatest amount of tissue (averaged over all projection angles) to escape the brain and be detected. The effects of attenuation on reconstructed images are a negative bias in reconstructed activity concentration and an increase in image noise; both of these are greatest at the center of the brain. Several exact analytical correction methods[16-19] have been proposed; however, the most widely used remains the approximate technique of Chang.[20] These methods do not take into account the heterogeneous density of brain structures, most importantly, the higher density of the skull. Attenuation correction can also be incorporated into an iterative reconstruction algorithm. SPECT/CT systems provide patient-specific attenuation maps, as well as registered anatomical images.[21] It should be noted that although correction methods compensate for the negative bias due to attenuation, thereby improving the accuracy of the reconstructed voxel values, they do not affect the increase in image noise.[22]

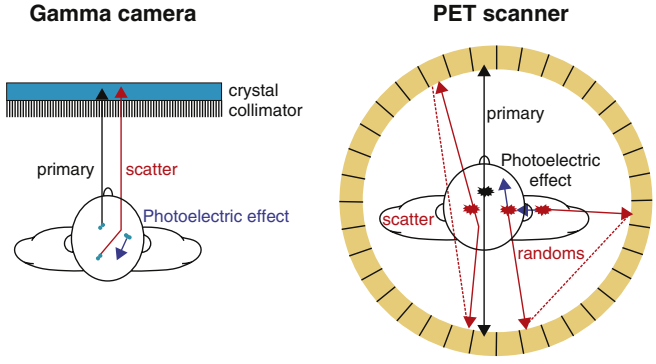


FIGURE 3 Illustration of types of events in SPECT (left) and PET (right) scanners. *Courtesy of Dr. Georges El Fakhri.*

Although patient-specific attenuation maps are crucial for accurate attenuation correction in whole-body imaging, they are less important for brain SPECT because of the smaller attenuating volume and more homogeneous density. The value of nonuniform attenuation correction in the brain depends on the imaging task; for example, Rajeevan et al.[23] reported that nonuniform attenuation correction yielded more accurate estimates of absolute activity concentration within brain regions of interest (ROI) than did uniform attenuation correction, whereas the accuracy of ROI-to-background ratio estimates was not improved.

Attenuated photons are either fully absorbed by patient tissue in a photoelectric event or partially absorbed, with the residual energy carried off as a lower-energy photon in a different direction (Compton scatter) (see Figure 3). Those scattered photons that retain enough energy to be accepted within the energy window may be detected; because the emission event is assumed to have occurred along the path of the scattered photon, rather than along the path of the original photon, scattered photons contribute to the reconstructed image at the wrong location. The effects of detection of scattered photons on the reconstructed image are reduced contrast and a positive bias in reconstructed voxel values. The acceptance of scattered photons is controlled by the energy window settings; narrow energy windows reduce the amount of scatter in the data set. Because the energy resolution of the detectors is not perfect, however, narrow energy windows also lead to rejection of some primary photons. There are two basic approaches to scatter compensation. The first approach estimates the amount of scatter at each point in the projection data set, so that it can be subtracted from the projections, and the second incorporates scatter modeling into the reconstruction algorithm. The first approach, subtracting an estimate of the scatter from the projections, leads to a more accurate image but increases noise, because fewer photons contribute to the image. A number of methods based on this approach, and differing in the method used to estimate the contribution of scatter, have been proposed; the most commonly used are the dual-energy-window method of Jaszczak[24] and the triple-energy-window method of Ogawa.[25] Several multiple-energy-window methods have also been proposed[26-29]; this more complex approach can, for brain imaging, lead to performance in estimation tasks approaching that of perfect scatter rejection.[26] Not all SPECT instruments, however, have the capability to collect photons in multiple-energy windows. The second approach, incorporating scatter modeling into the reconstruction algorithm, essentially uses the scattered photons by restoring them to their correct location, rather

than removing them. This approach should, in theory, lead to more accurate images without increasing noise as much as the scatter-rejection techniques. The major disadvantage of this approach is that accurate modeling of scatter is computationally demanding. A review of scatter correction techniques is given by Hutton et al.[30]

PET IMAGING

Introduction to PET Physics

PET radioisotopes have unstable nuclei in which a proton decays to a neutron, emitting a positron, the antiparticle of the electron, with the same rest mass (511 keV) but opposite charge, and a neutrino, a chargeless and (almost) massless particle, which does not interact with matter (see Figure 4). The positron travels some distance, depending on its initial kinetic energy, through tissue before interacting with an electron; this annihilation yields two 511-keV photons traveling in (nearly) opposite directions. The positron range in tissue, on the order of a few millimeters, places a fundamental limit on the spatial resolution of PET imaging. Although the annihilation photon energy is much higher than optimal for imaging purposes, the potential for coincidence imaging more than compensates for this shortcoming. When two photons are detected in opposed detectors within the coincidence timing window, a "true" coincidence event is recorded, and the annihilation is assumed to have occurred somewhere along the line of response (LOR) connecting the two detectors (see Figure 3). This electronic collimation has advantages over the physical collimation, which is necessary for SPECT. The absence of the physical collimator, which absorbs a large fraction of the incident photons, is the major reason for the higher (by one or two orders of magnitude) sensitivity of PET compared to SPECT.

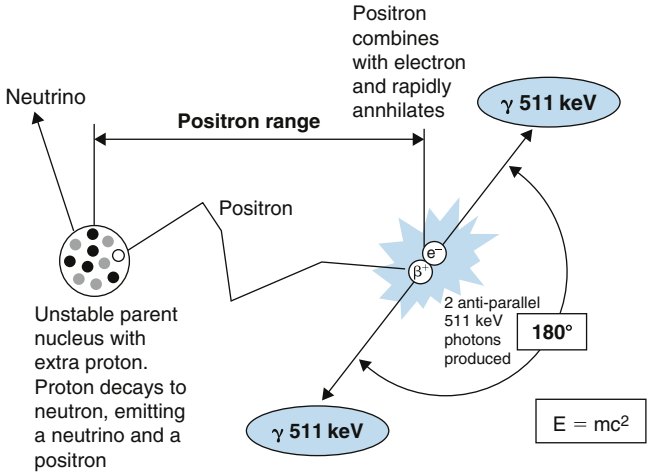


FIGURE 4 Illustration of positron emission and decay. *Courtesy of Dr. Georges El Fakhri.*

Some annihilation events do not generate a coincidence event, because only one of the photons strikes a detector; the "singles" count rate is the total of all detected counts. There are also some erroneous coincidences, termed "randoms," which occur when single photons from each of two annihilations are detected in coincidence (see Figure 3). Although in whole-body PET imaging the randoms rate sometimes exceeds the true coincidence rate, in brain imaging the randoms rate seldom exceeds 25% of the true rate. The randoms rate can be minimized by using fast scintillators and fast detector electronics.

Annihilation photons may undergo Compton scatter, just as single photons may, and strike a detector in coincidence with the other photon in the pair (see Figure 3). If the energy of the scattered photon falls within the detector energy window, then a spurious true coincidence will be recorded. This yields inaccurate positioning, analogous to inaccurate positioning due to detection of scattered radiation in SPECT. Furthermore, some positron emitters generate additional gamma-rays, which can also result in false coincidences.

PET Instrumentation

Detector Materials

The choice of radiation detectors for PET instruments requires trade-offs among several detector characteristics, including physical density, atomic number, scintillation speed, and light output. The stopping power is determined by physical density and effective atomic number; high stopping power is desirable, as it leads to increased sensitivity. Atomic number also determines the ratio of photoelectric events to Compton scattering events; because photoelectric events are preferred for imaging, high atomic number is desirable. Faster crystals make possible narrower coincidence timing windows and, therefore, fewer random coincidences.

The original PET instruments used thallium-doped NaI, but modern PET scanners use other crystals with higher stopping power, such as bismuth germinate, cerium-doped lutetium oxyorthosilicate (LSO), and gadolinium oxyorthosilicate (GSO). LSO and GSO are faster than the other materials, and GSO has the best energy resolution, making possible better scatter rejection.

Detector Configurations

Most modern PET scanners use multiple rings of detectors, with each detector in coincidence with a number of detectors on the opposite side of the ring (and, in some cases, with detectors in other rings; see below). A variant of the ring configuration is a polygonal array, in which each detector is in coincidence with detectors on the opposing face. Less expensive options include

partial rings, which require rotation of the detector array for acquisition of a complete set of data, and single-crystal detectors, similar to those in SPECT systems, but with the capability for coincidence imaging.[31] One such system, the PENNPET, consists of a hexagonal array of large-area detectors; it has been designed for brain imaging and is in use at a number of centers.

The spatial resolution of a typical PET scanner is determined by the size of the individual crystals. Block detectors were recently introduced to avoid the cost of more, smaller crystals and their associated individual photomultiplier tubes and electronics.[32] A block detector consists of a large crystal that is divided into an array of subelements by partial cuts, normal to the face, that are filled with reflective material. Modern systems using rings of block detectors can have up to 20,000 detector elements. This design improves spatial resolution, but at the cost of some loss of sensitivity owing to the reduction in active crystal surface. Another innovation, used in several commercial systems, is the pixelated detector matrix, which consists of a set of small crystals coupled to a single light guide, viewed by an array of photomultiplier tubes.

The original PET scanners used septa between slices to define image planes, preventing cross-slice coincidences (2D PET). This configuration leads to the most accurate imaging, because it minimizes random coincidences and detection of scattered photons; it also, however, reduces sensitivity. In some systems, coincidences between adjacent slices are also acquired. In 3D PET, septa are not used; coincidences are accepted from the entire field of view, leading to greatly increased sensitivity compared to 2D. There is significant axial variation in sensitivity, with the highest sensitivity at the center and lowest sensitivity at the most extreme axial positions. The disadvantages of the 3D geometry, increased scatter and randoms, are less significant for brain than for whole-body PET.

Advances in PET detectors and electronics have spurred the development of instruments with time-of-flight capability. Time-of-flight information, based on differences in arrival time of the two annihilation photons, makes it possible to localize an event to a segment of the LOR. Several commercial PET/CT systems are available with timing resolution in the 500–600 ps range.[33,34] Although the benefits of time-of-flight information are greater for body than for brain imaging, significant improvements in image quality have been reported for brain PET imaging incorporating time-of-flight information.[35]

PET Image Reconstruction and Correction

Before PET data can be reconstructed, it must be corrected for several physical effects. Corrections for dead time, a count-rate-dependent phenomenon by which the detector is paralyzed and stops recording counts, and for varying sensitivity among detectors are relatively straightforward for brain imaging. A certain number of detected coincidences are random, that is, single photons from each of two different annihilations are detected in coincidence (see Figure 3). The most commonly used approach to correct for randoms is to subtract from the coincidence data for each LOR an estimate of the number of random coincidences, obtained by using a delayed timing window.[36]

Attenuation correction of PET data is simpler than correction of PET data, because, in contrast to SPECT, the probability of detection is uniform everywhere along a LOR. The correction factor depends only on the total thickness and density of tissue along the LOR. All that is necessary, then, for attenuation correction in PET is an estimate of the total attenuation along the LOR. Patient-specific measurements can be obtained by a transmission scan, using either an external radioisotope source or an X-ray tube mounted on the PET scanner or an integrated PET/CT system.

Detection of scattered photons emerging from the patient that retain enough energy to be accepted by the detection system causes the coincidence event to be assigned to the wrong LOR; as in SPECT, this leads to reduced contrast and a positive bias in reconstructed voxel activity concentration values. The first line of defense against scattered radiation is discrimination on the basis of energy; this is not very effective in PET, because of the relatively poor energy resolution of PET detector materials. The simplest approach to scatter correction is to estimate the amount of scatter at each point in the measured projection data and mathematically remove it from the projection data set. The estimates of scatter can be based on the measurements outside the projection of the body contour (presumably consisting only of scatter)[37] or on data acquisition in two,[38] three,[39] or many[40] energy windows. A more accurate but much more complex approach is to use Monte Carlo simulations to determine scatter estimates.[41-43] Finally, scatter modeling can be incorporated into an iterative reconstruction algorithm.[44-46] A review of scatter correction for brain PET imaging is given by Zaidi.[47]

References

1. Radon J. Über die bestimmung von funktionen durch ihre integralwerte längs gewisser mannigfaltigkeiten. *Berichte Sächsische Akademie der Wissenschaften, Leipzig*. 1917;69:262–277.
2. Anger HO. Scintillation camera. *Rev Sci Instrum*. 1958;29:27–33.
3. Bakker WH, Albert R, Bruns C, et al. [In-111-DTPA-D-Phe1]-octreotide, a potential radiopharmaceutical for imaging of somatostatin receptor-positive tumors – synthesis, radiolabeling and in vitro validation. *Life Sci*. 1991;49:1583–1591.
4. Lalush DS. Dual-planar circular-orbit cone-beam SPECT. *J Nucl Med*. 1998;39:22P.

5. Kamphuis C, Beekman FJ. The use of offset cone-beam collimators in a dual head system for combined emission transmission brain SPECT: a feasibility study. *IEEE Trans Nucl Sci*. 1998;45:1250–1254.
6. Li JY, Jaszczak RJ, VanMullekom A, et al. Half-cone beam collimation for triple-camera SPECT systems. *J Nucl Med*. 1996;37:498–502.
7. Gullberg GT, Zeng GL, Datz FL, et al. Review of convergent beam tomography in single photon emission computed tomography. *Phys Med Biol*. 1992;37:507–534.
8. Jaszczak RJ, Greer KL, Coleman RE. SPECT using a specially designed cone beam collimator. *J Nucl Med*. 1988;29:1398–1405.
9. Jaszczak RJ, Floyd CE, Manglos SH, Greer KL, Coleman RE. Cone beam collimation for single photon emission computed tomography – analysis, simulation, and image reconstruction using filtered backprojection. *Med Phys*. 1986;13:484–489.
10. Hawman EG, Hsieh J. An astigmatic collimator for high-sensitivity SPECT of the brain. *J Nucl Med*. 1986;27:930.
11. Jaszczak RJ, Chang LT, Murphy PH. Single photon emission computed tomography using multi-slice fan beam collimators. *IEEE Trans Nucl Sci*. 1979;26:610–618.
12. King MA, Zubal IG, Mukherjee JM, et al. Design of a combined fan and multi-pinhole collimator combination for clinical I-123 DaTscan imaging on dual-headed SPECT systems. In: Yu B, ed. *2012 IEEE Nuclear Science Symposium and Medical Imaging Conference Record*. 2012:3170–3173.
13. Park MA, Moore SC, Kijewski MF. Brain SPECT with short focal-length cone-beam collimation. *Med Phys*. 2005;32:2236–2244.
14. Ter-Antonyan R, Jaszczak RJ, Greer KL, et al. Combination of converging collimators for high-sensitivity brain SPECT. *J Nucl Med*. 2009;50:1548–1556.
15. Erlandsson K, Buvat I, Pretorius PH, Thomas BA, Hutton BF. A review of partial volume correction techniques for emission tomography and their applications in neurology, cardiology and oncology. *Phys Med Biol*. 2012;57:R119–R159.
16. Bellini S, Piacentini M, Cafforio C, Rocca F. Compensation of tissue absorption in emission tomography. *IEEE Trans Acoust Speech Signal Process*. 1979;27:213–218.
17. Gullberg GT, Budinger TF. The use of filtering methods to compensate for constant attenuation in single photon emission computed tomography. *IEEE Trans Biomed Eng*. 1981;28:142–157.
18. Metz C.E., Pan X.C. A unified analysis of exact methods of inverting the 2-D exponential radon transform, with implications for noise control in SPECT. *IEEE Trans Med Imaging*. 1995;14:643–658.
19. Tretiak O, Metz C. The exponential Radon transform. *SIAM J Appl Math*. 1980;39:341–354.
20. Chang LT. Method for attenuation correction in radionuclide computed tomography. *IEEE Trans Nucl Sci*. 1978;25:638–643.
21. Tang HR, Da Silva AJ, Matthay KK, et al. Neuroblastoma imaging using a combined CT scanner-scintillation camera and I-131-MIBG. *J Nucl Med*. 2001;42:237–247.
22. Kijewski MF, Muller SP, Moore SC. Nonuniform collimator sensitivity: improved precision for quantitative SPECT. *J Nucl Med*. 1997;38:151–156.
23. Rajeevan N, Zubal IG, Ramsby SQ, et al. Significance of nonuniform attenuation correction in quantitative brain SPECT imaging. *J Nucl Med*. 1998;39:1719–1726.
24. Jaszczak RJ, Chang LT, Stein NA, Moore FE. Whole-body single-photon emission computed tomography using dual, large-field-of-view scintillation cameras. *Phys Med Biol*. 1979;24:1123–1143.
25. Ogawa K, Harata Y, Ichihara T, Kubo A, Hashimoto S. A practical method for position-dependent Compton scatter correction in single photon emission CT. *IEEE Trans Med Imaging*. 1991;10:408–412.
26. Moore SC, Kijewski MF, Muller SP, Rybicki F, Zimmerman RE. Evaluation of scatter compensation methods by their effects on parameter estimation from SPECT projections. *Med Phys*. 2001;28:278–287.
27. Haynor DR, Kaplan MS, Miyaoka RS, Lewellen TK. Multiwindow scatter correction techniques in single-photon imaging. *Med Phys*. 1995;22:2015–2024.
28. Gagnon D, Todd-Pokropek A, Arsenault A, Dupras G. Introduction to holospectral imaging in nuclear medicine for scatter subtraction. *IEEE Trans Med Imaging*. 1989;8:245–250.
29. Koral KF, Wang XQ, Rogers WL, Clinthorne NH, Wang XH. SPECT Compton scattering correction by analysis of energy spectra. *J Nucl Med*. 1988;29:195–202.
30. Hutton BF, Buvat I, Beekman FJ. Review and current status of SPECT scatter correction. *Phys Med Biol*. 2011;56:R85–R112.
31. Karp JS, Muehllehner G, Mankoff DA, et al. Continuous-slice Penn-PET – a positron tomograph with volume imaging capability. *J Nucl Med*. 1990;31:617–627.
32. Casey ME, Nutt R. A multicrystal 2-dimensional BGO detector system for positron emission tomography. *IEEE Trans Nucl Sci*. 1986;33:460–463.
33. Jakoby BW, Bercier Y, Conti M, et al. Physical and clinical performance of the mCT time-of-flight PET/CT scanner. *Phys Med Biol*. 2011;56:2375–2389.
34. Surti S, Kuhn A, Werner ME, et al. Performance of Philips Gemini TF PET/CT scanner with special consideration for its time-of-flight imaging capabilities. *J Nucl Med*. 2007;48:471–480.
35. Nagaki A, Onoguchi M, Matsutomo N. Clinical validation of high-resolution image reconstruction algorithms in brain F-18-FDG-PET: effect of incorporating Gaussian filter, point spread function, and time-of-flight. *Nucl Med Comm*. 2014;35:1224–1232.
36. Hoffman EJ, Huang SC, Phelps ME, Kuhl DE. Quantitation in positron emission computed tomography. 4. Effect of accidental coincidences. *J Comput Assist Tomogr*. 1981;5:391–400.
37. Bailey DL, Meikle SR. A convolution-subtraction scatter correction method for 3D PET. *Phys Med Biol*. 1994;39:411–424.
38. Grootoonk S, Spinks TJ, Sashin D, Spyrou NM, Jones T. Correction for scatter in 3D brain PET using a dual energy window method. *Phys Med Biol*. 1996;41:2757–2774.
39. Shao LX, Freifelder R, Karp JS. Triple energy window scatter correction technique in PET. *IEEE Trans Med Imaging*. 1994;13:641–648.
40. Bentourkia M, Msaki P, Cadorette J, Lecomte R. Energy-dependence of scatter components in multispectral PET imaging. *IEEE Trans Med Imaging*. 1995;14:138–145.
41. Levin CS, Dahlbom M, Hoffman EJ. A Monte-Carlo correction for the effect of Compton scattering in 3D PET brain imaging. *IEEE Trans Nucl Sci*. 1995;42:1181–1185.
42. Zaidi H. Relevance of accurate Monte Carlo modeling in nuclear medical imaging. *Med Phy*. 1999;26:574–608.
43. Kim KS, Son YD, Cho ZH, Ra JB, Ye JC. Ultra-Fast Hybrid CPU-GPU Multiple Scatter Simulation for 3-D PET. *IEEE J Biomed Health Inform*. 2014;18:148–156.
44. Floyd CE, Jaszczak RJ, Greer KL, Coleman RE. Inverse Monte-Carlo as a unified reconstruction algorithm for ECT. *J Nucl Med*. 1986;27:1577–1585.
45. Beekman FJ, Kamphuis C, Frey EC. Scatter compensation methods in 3D iterative SPECT reconstruction: a simulation study. *Phys Med Biol*. 1997;42:1619–1632.
46. Hutton BF, Baccarne V. Efficient scatter modelling for incorporation in maximum likelihood reconstruction. *Eur J Nucl Med*. 1998;25:1658–1665.
47. Zaidi H. Comparative evaluation of scatter correction techniques in 3D positron emission tomography. *Eur J Nucl Med*. 2000;27:1813–1826.

CHAPTER

33

Positron Emission Tomography (PET) and Single Photon Emission Computed Tomography (SPECT) Imaging

Randy Yeh[1], *Vesselin Z. Miloushev*[2], *Masanori Ichise*[3]

[1]Nuclear Medicine and Molecular Imaging, Department of Radiology, Columbia University Medical Center, New York, NY, USA; [2]Neuroradiology, Department of Radiology, Columbia University Medical Center, New York, NY, USA; [3]Molecular Neuroimaging Program, Molecular Imaging Center, National Institute of Radiological Sciences, Chiba, Japan

OVERVIEW

Incidence and Prevalence

Brain tumors are generally divided into primary brain tumors and metastatic brain tumors. Furthermore, categories are importantly distinguished by tumors that are native or untreated and those that are recurrent following treatment. The overall annual incidence of primary brain tumors worldwide is 3.7 per 100,000 for males and 2.6 per 100,000 in females,[1] with an estimated 23,380 new cases and 14,320 deaths in the United States for 2014.[2] The diagnostic power of radiopharmaceuticals is primarily evidenced in characterizing primary brain tumors, and hence this overview will focus on applications to primary brain tumors, both native and recurrent. The most common form of adult primary brain tumor are gliomas, which account for more than 90% of primary brain tumors in patients over the age of 20 years and 60% of all primary brain tumors.[3] Gliomas are classified into increasing grades of malignancy based on histopathology. The World Health Organization (WHO) grading system, which is based on cellularity, is the most commonly used classification system.[4]

Brain Tumor Classification

Primary brain tumors are graded based on the WHO brain tumor classification system, which accounts for the cell type of origin, histological features, and genetic mutations. The cellularity of gliomas is characterized into four classes (WHO grades I–IV), according to the degree of malignancy, ranging from the lowest, grade I, to the least well-differentiated, grade IV (i.e., glioblastoma).[5] The survival rate diminishes significantly as tumor grade progresses from grade I to IV, with a 5-year survival of 3.3% for grade IV glioblastoma compared with over 70% for lower grade tumors such as grade I pilocytic astrocytoma or grade II oligodendrogliomas.[1]

NEUROIMAGING

Computed Tomography (CT) and Magnetic Resonance Imaging (MRI)

Brain magnetic resonance imaging (MRI) is currently the preferred imaging modality in diagnosing and monitoring the treatment of brain tumors. MRI has superior soft tissue contrast to CT, however artifacts related to susceptibility, field inhomogeneity, signal to noise limitations, and patient motion may limit its applicability. In these cases, CT and the nuclear medicine methods that incorporate it (single photon emission computed tomography (SPECT) and positron emission tomography/computed tomography (PET/CT)) may be useful alternatives. Furthermore, CT can be useful as an alternative if there is a contraindication to MRI, such as in cases of nonMRI compatible implanted devices or patient intolerance due to claustrophobia. MRI is an excellent imaging modality to identify

Handbook of Neuro-Oncology Neuroimaging, Second Edition
http://dx.doi.org/10.1016/B978-0-12-800945-1.00033-1

© 2016 Elsevier Ltd. All rights reserved.

lesions, but sometimes lacks the specificity to distinguish tumor progression from posttreatment effects, where complementary nuclear medicine tracers show efficacy.

The basic sequences that comprise a brain MRI examination include T1-weighted and T2-weighted imaging, fluid-attenuated T2-weighted imaging, diffusion-weighted imaging, susceptibility-weighted imaging, and postcontrast imaging. There are many variations on these basic sequences and a multitude of so-called "advanced" or "functional" methods; these include perfusion imaging, MRI spectroscopy, diffusion tensor imaging, and functional MRI to name a few, which are discussed in greater detail elsewhere in this volume. Hybrid modalities such as PET/MRI as well as novel molecular tracers in combination hyperpolarization of small molecules show promise in revolutionizing the field of brain tumor imaging. This rapid pace of method development in MRI combined with development of complementary radiopharmaceuticals will hopefully address the greatest current challenge: assessing the degree of tumor response following treatment and expanding the understanding of tumor biology on a molecular level.

SPECT Imaging

SPECT imaging is a versatile, widely available technique to localize the emission of a variety of tracer compounds. The radiopharmaceuticals employed with SPECT can be categorized into a number of broad categories as follows: regional cerebral blood flow compounds ([^{99m}Tc]HMPAO and [^{99m}Tc]ECD); cationic compounds (thallium-201(^{201}Tl), technetium-99m methoxyisobutylisonitrile ([^{99m}Tc]MIBI), technetium-99m tetrofosmin ([^{99m}Tc]tetrofosmin)); labeled amino acids ([^{123}I]iodo-α-methyltyrosine ([^{123}I]IMT)); labeled antibodies; labeled somatostatin analogs ([^{111}In] octreotide); and apoptosis compounds ([^{123}I]anexcin).

The disadvantage of SPECT is its slightly inferior spatial resolution to that of PET. However, this limitation may be offset by some of the major advantages of SPECT that are related to the more cost-effective availability of SPECT tracers compared with PET tracers. Yet, for functional imaging with either SPECT or PET to be a viable clinical or research tool for imaging of brain tumors, it must provide information that cannot be obtained by other anatomic imaging modalities, primarily MRI.[6] The pertinent information and thus proposed added benefit expected to be obtained from SPECT imaging of brain tumors relates to whether: (1) tracer uptake correlates with tumor histological grade and hence tracer uptake may be used as a diagnostic or prognostic indicator; and (2) tracer uptake can be used to indicate postoperative tumor recurrence or it can distinguish between tumor recurrence and radiation necrosis.

Perfusion Agents: [^{99m}Tc]HMPAO and [^{99m}Tc]ECD

The two most popular brain SPECT compounds for assessment of relative cerebral blood flow (rCBF) are [^{99m}Tc]HMPAO and [^{99m}Tc]ECD. Both of these compounds are lipophilic and readily cross the intact blood–brain barrier (BBB), where they are converted to hydrophilic compounds that are not able to easily cross back across the BBB. In general, rCBF compounds are not routinely used in the assessment of brain tumors, although historically, these compounds were used in combination with ^{201}Tl for differentiation of malignant brain lesions from benign tumors[7] as well as differentiating tumor recurrence from postradiation changes.[8]

The uptake of ^{201}Tl requires the breakdown of the BBB, which is an important consideration in imaging low-grade gliomas where there may not be breakdown of the BBB. In contrast, rCBF compounds do not require such breakdown and accumulate in lower grade tumors. Despite this potential added value, the use of nuclear medicine compounds for perfusion imaging has largely been supplanted by MRI and CT perfusion techniques.

Labeled Cations: Thallium-201(^{201}Tl) and Technetium-99m methoxyisobutylisonitrile ([^{99m}Tc]MIBI)

Thallium-201

Thallium-201 is a chemical analog of potassium, and its tumor uptake appears to be related to multiple factors including alterations in the BBB, Na^+/K^+ ATPase pump activity, and blood flow.[9,10] Although low energy X-rays (68–80 KeV) from ^{201}Tl decays are not optimal for imaging, the long physical half-life of 73 h is a convenient feature of ^{201}Tl. Typically, ^{201}Tl SPECT brain imaging is performed 15 min after bolus intravenous injection of 2–5 mCi of ^{201}Tl and additional delayed SPECT imaging may be performed a few hours after.

Many authors have investigated ^{201}Tl SPECT for determining tumor grade.[11–18] Uptake of ^{201}Tl generally correlates with histological tumor grade, however there is considerable overlap between tumor types. In part, this may be due to tumor heterogeneity, BBB breakdown, and partial volume effects, as well as the fact that some low-grade tumors such as pilocytic astrocytoma intrinsically show high ^{201}Tl uptake.[11,12,15]

Thalium-201 may be useful for the detection of recurrence in gliomas (Figure 1). Historically, there is considerable heterogeneity in studies that have reported on the ability of ^{201}Tl to differentiate recurrence of gliomas from posttreatment changes; metaanalytic confidence interval estimates for sensitivity were 43–100% and for specificity were 25–100%.[19] However, studies have shown specificities and sensitivities approaching 95% when combined with MRI for the detection of recurrent glioma.[20] This has prompted some authors to

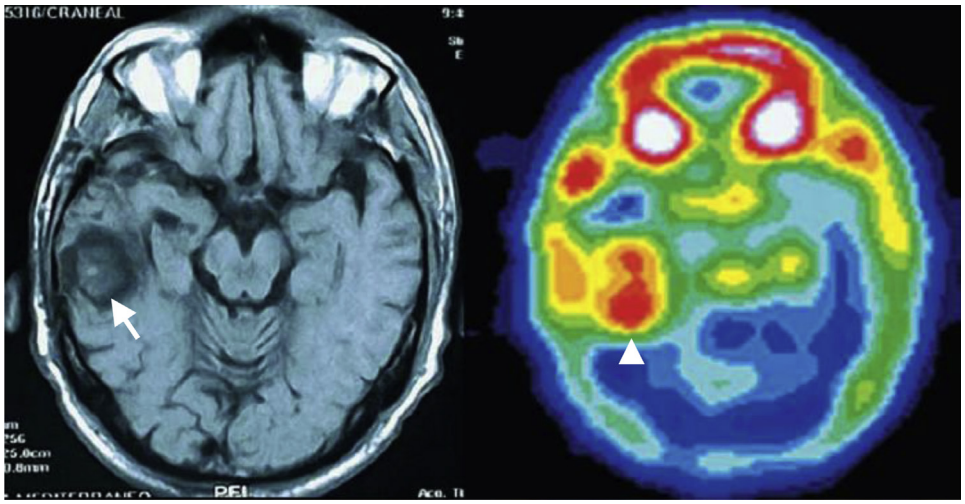


FIGURE 1 ^{201}Tl SPECT images of tumor recurrence versus radiation necrosis. Inconclusive MRI scan (left) for tumor recurrence in the right temporal lobe (arrow), alongside a ^{201}Tl SPECT image (right) of local radiotracer uptake at the margins of the primary lesion (arrowhead). *Modified and reproduced with permission from Gomez-Rio et al. ^{201}Tl SPECT in low-grade gliomas: diagnostic accuracy in differential diagnosis between tumour recurrence and radionecrosis.* Eur J Nucl Med Mol Imaging. *31:1237–1243. Copyright © 2004 Springer-Vertag Gmbh, Heidelberg Germany. All rights reserved.*

recommend ^{201}Tl as the optimal imaging technique for differentiating glioma recurrence from posttreatment effects.[21]

Technetium-99m MIBI

[^{99m}Tc]MIBI is a cationic compound that accumulates in cytoplasm and mitochondria as a result of passive diffusion across the potential of the polarized cellular/organelle membrane. Like ^{201}Tl, [^{99m}Tc]MIBI is normally excluded from the brain by the BBB and therefore, tumor uptake appears to be mainly related to BBB breakdown. The normal MIBI distribution is in the choroid plexus, scalp, and pituitary gland, but not in normal brain parenchyma. Normal uptake in the choroids can be confounding and limit evaluation of deep periventricular tumors.[6] Despite this limitation, a meta-analysis of [^{99m}Tc]MIBI SPECT in the assessment of glioma recurrence following radiation therapy demonstrated a pooled sensitivity of 90% and specificity of 92%.[22,23] Although [^{99m}Tc]MIBI has better imaging characteristics than ^{201}Tl (140 KeV and higher allowable injection dose of up to 30 mCi), studies designed to evaluate the usefulness of [^{99m}Tc]MIBI for diagnosis, prognosis, and detection of tumor recurrence have not yet convincingly shown its superiority to ^{201}Tl,[24–28] although some studies suggest that [^{99m}Tc]MIBI has increased specificity over ^{201}Tl.[29]

[^{99m}Tc]MIBI has also been studied as a both a prognostic biomarker for patient survival and predictive biomarker of chemotherapy treatment response. Beauchesne et al.[29] showed via a quantitative analysis of [^{99m}Tc]MIBI uptake that MIBI SPECT findings correlated with survival time in patients following chemoradiotherapy, and therefore may be helpful in establishing prognosis. In assessing chemotherapy response, [^{99m}Tc]MIBI SPECT has been shown to be an early indicator of treatment failure, demonstrating tumor progression on average four months prior to changes detected on MR.[30] Interestingly, [^{99m}Tc]MIBI is eliminated from cells by P-glycoprotein, which also acts as an energy-driven efflux pump for several antineoplastic agents. However, multiple drug resistance (MDR)-1 gene expression as demonstrated by [^{99m}Tc]MIBI does not appear to correlate with chemoresistance in gliomas.[27,29,30]

Labeled Amino Acids: [^{123}I]Iodo-α-Methyltyrosine

^{123}I possesses favorable SPECT imaging characteristics (γ rays of 159 keV and a physical half-life of 13 h) with well-known and well–characterized synthetic procedures to incorporate it into biologically relevant molecules such as the amino acid analog, methytyrosine. [^{123}I]iodo-α-methyltyrosine ([^{123}I]IMT) is an SPECT tracer developed as a less expensive alternative to the PET compound, methyl-[^{11}C]-L-methionine ([^{11}C]MET), which requires an on-site cyclotron for production. However, this benefit is offset by the limited commercial availability of ^{123}I.

[^{123}I]IMT is a radiolabeled amino acid (tyrosine) analog, which is taken up in the brain by carrier mediated, stereoselective active transport systems across both the BBB and cellular membranes. While [^{123}I]IMT is not incorporated into cellular proteins, the cellular uptake of [^{123}I]IMT in glioma cells is a biomarker of cellular proliferation.[6,31]

As a marker of cellular proliferation, [^{123}I]IMT has been shown to be useful in brain tumor detection, diagnosis of post-therapeutic tumor recurrence, and differentiating brain tumors from nonneoplastic lesions.[23,32–35]

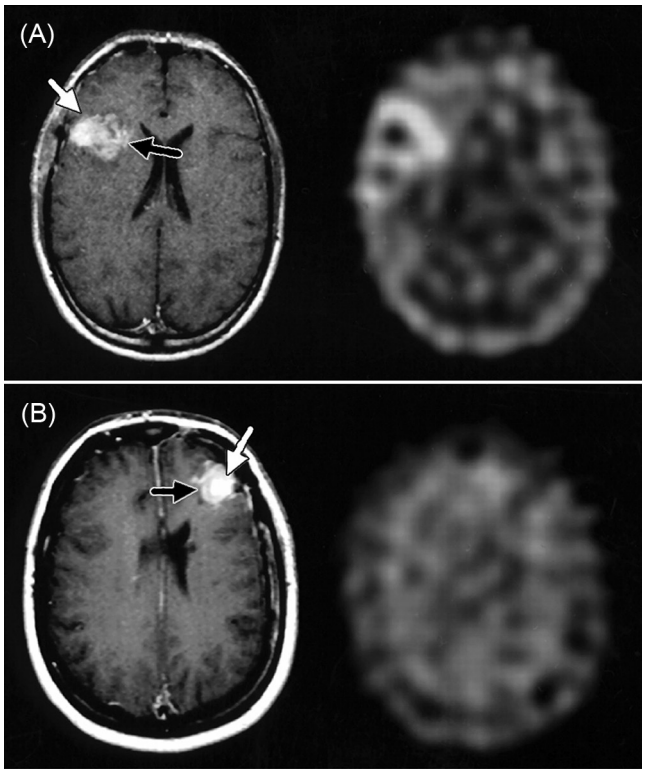


FIGURE 2 In patients with anaplastic astrocytoma, examples of [^{123}I]IMT SPECT studies with (A) and without (B) focal IMT uptake at resection site. (A) On left, MR image (T1-weighted after administration of gadolinium-DTPA) shows resection cavity (white arrow) and rim of contrast enhancement (black arrow). Resection cavity contains blood and is, therefore, hyperintense in T1-weighted image. On right, [^{123}I]IMT SPECT image shows intense uptake of [^{123}I]IMT at resection margin. This patient died six months after SPECT study. (B) On left, MR image shows resection cavity (white arrow) and surrounding contrast enhancement (black arrow). However, on right, [^{123}I]IMT SPECT image shows no clear focal IMT uptake. This patient was still alive after 38 months of follow-up. *Reproduced with permission from Weber et al. Correlation between postoperative 3-[^{123}I]iodo-L-α-methyltyrosine uptake and survival in patients with gliomas.* J Nucl Med. *42:1144–1150. Copyright © 2001, Society of Nuclear Medicine. All rights reserved.*

Weber et al.,[36] for example, demonstrated that focal [^{123}I]IMT uptake correlates with residual tumor following resection and is associated with decreased survival (Figure 2). However, [^{123}I]IMT does not appear to be able to distinguish between differing tumor histological grades.[33]

Comparisons between IMT SPECT and fluorodeoxyglucose (FDG)-PET have suggested that [^{123}I]IMT is superior to FDG in tumor detection and delineating tumor extent as well as identifying low-grade recurrences, while only FDG was able to accurately grade recurrences.[34,36] Thus, [^{123}I]IMT SPECT may be a viable alternative to the more expensive [^{11}C]MET PET, which requires an on-site cyclotron facility to produce the short-lived ^{11}C.

PET Imaging

Brain tumor imaging with [^{18}F]FDG was the first oncological application of PET.[37] The role of PET in the evaluation of brain tumors is continuingly evolving and expanding as new radiopharmaceuticals become available. Unfortunately, at the present time, the only compound approved by the Food and Drug Administration is [^{18}F]FDG. However, promising research with novel PET radiotracers using radiolabeled amino acids (i.e., [^{18}F]FET and [^{11}C]MET) and radiolabeled nucleosides (i.e., [^{18}F]FLT) may eventually change the landscape of molecular imaging in brain tumors.

[^{18}F]FDG-PET

[^{18}F]FDG is a glucose analogue that is actively transported across the intact BBB and phosphorylated by hexokinase to form flourodeoxyglucose-6-phosphate, trapping the compound in the cell. FDG uptake is generally high in high-grade tumors due to increased glucose metabolism, with a positive correlation between increased glycolysis and malignancy (the Warburg hypothesis).[38] Currently, FDG-PET imaging is an adjunct technique in cases where MRI, and to a lesser extent CT, is unable to establish a diagnosis or answer the clinical question that needs to be addressed. The areas where FDG-PET has been shown to be of value include tumor detection, defining tumor extent and degree of malignancy, posttreatment assessment of tumor response, and identification of tumor recurrence versus radiation necrosis.[39]

Tumor Detection

Since the first introduction of FDG-PET imaging, it has been recognized that the technique is very sensitive for detecting high-grade gliomas (Figure 3) and less accurate for the identification of lower grade lesions.[40,41] Additionally, certain extraaxial tumors such as pituitary tumors may show FDG avidity (Figure 4). However, FDG-PET is somewhat hampered by the high physiological uptake in normal brain parenchyma, as glucose is the obligatory energy substrate for the brain, limiting the sensitivity for tumor detection.[38] This limitation is most pronounced in low-grade tumors, which demonstrate only modestly increased FDG uptake, similar to that of normal white matter and decreased compared to normal gray matter.[37,38] Additionally, FDG imaging can be confounded by uptake in areas of inflammation or infection. To overcome these limitations, the use of serial delayed scanning has been reported to enhance visualization of some tumors since FDG washout from the tumor is delayed relative to normal surrounding brain parenchyma.[41] In addition, it is helpful to delay follow-up scanning postchemotherapy for one to two weeks and

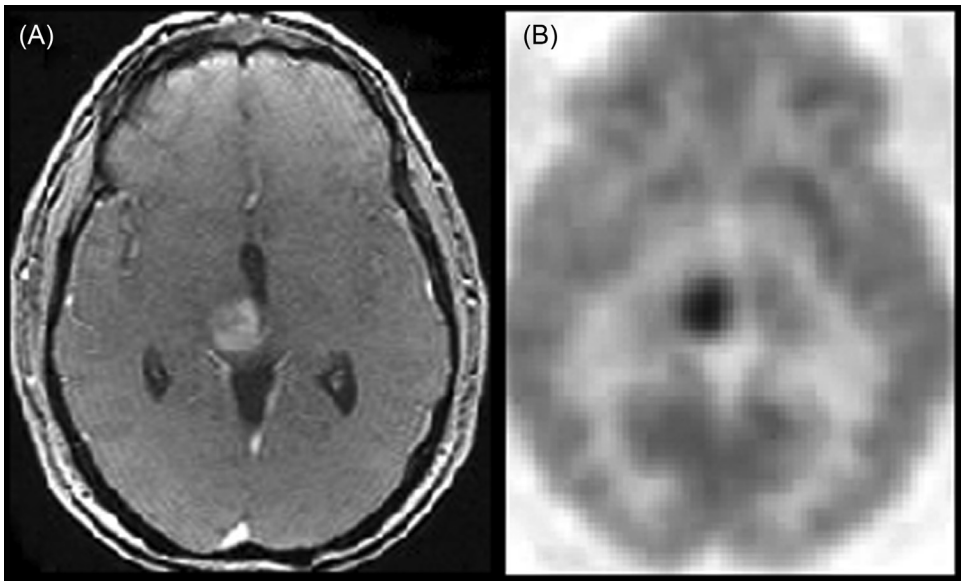


FIGURE 3 Right parathalamic astrocytoma in a 44-year-old man complaining of headaches. (A) Postcontrast T1 axial MR reveals a focal enhancing lesion medial to the right thalamus. (B) Axial FDG-PET at the same level reveals a corresponding hypermetabolic lesion confirming a malignant tumor (grade III astrocytoma).



FIGURE 4 Unsuspected pituitary tumor in an elderly male referred for a PET/CT study to assess progressive cognitive dysfunction. (A) Axial FDG-PET reveals a focal, hypermetabolic, midline lesion at the level of the temporal lobes. (B) Axial noncontrast CT reveals a soft tissue mass with bone erosion of the surrounding sella turcica. (C) Fused FDG-PET/CT images confirming a pituitary tumor.

postradiation therapy for six to eight weeks, in order to reduce uptake from accompanying inflammation following treatment.[42]

Tumor Grading and Degree of Malignancy

Early PET studies showed that the degree of glial cell malignancy, based on histopathology, directly correlated with the degree of tumor glycolytic activity observed on FDG-PET imaging.[40] In fact, some investigators have suggested that the level of FDG uptake is a better measure of the malignancy potential and aggressiveness of individual brain tumors than actual histopathology.[43] Additionally, several studies have demonstrated the prognostic value of FDG uptake in brain tumors in both high- and low-grade tumors.[44–46] In patients with histologically proven high-grade brain gliomas (WHO grade III and IV), patients with tumors exhibiting markedly elevated glucose metabolism will have a shorter survival time than those with lower glucose metabolism.[46] Similar findings have been demonstrated in patients with low-grade gliomas.[44] FDG imaging can be also useful in detecting lesions that have transformed from low-grade histopathological tumors into higher-grade tumors with a resultant greater degree of malignancy and aggressiveness, and associated decreased survival.[39,44,45] Such a determination is very important, as

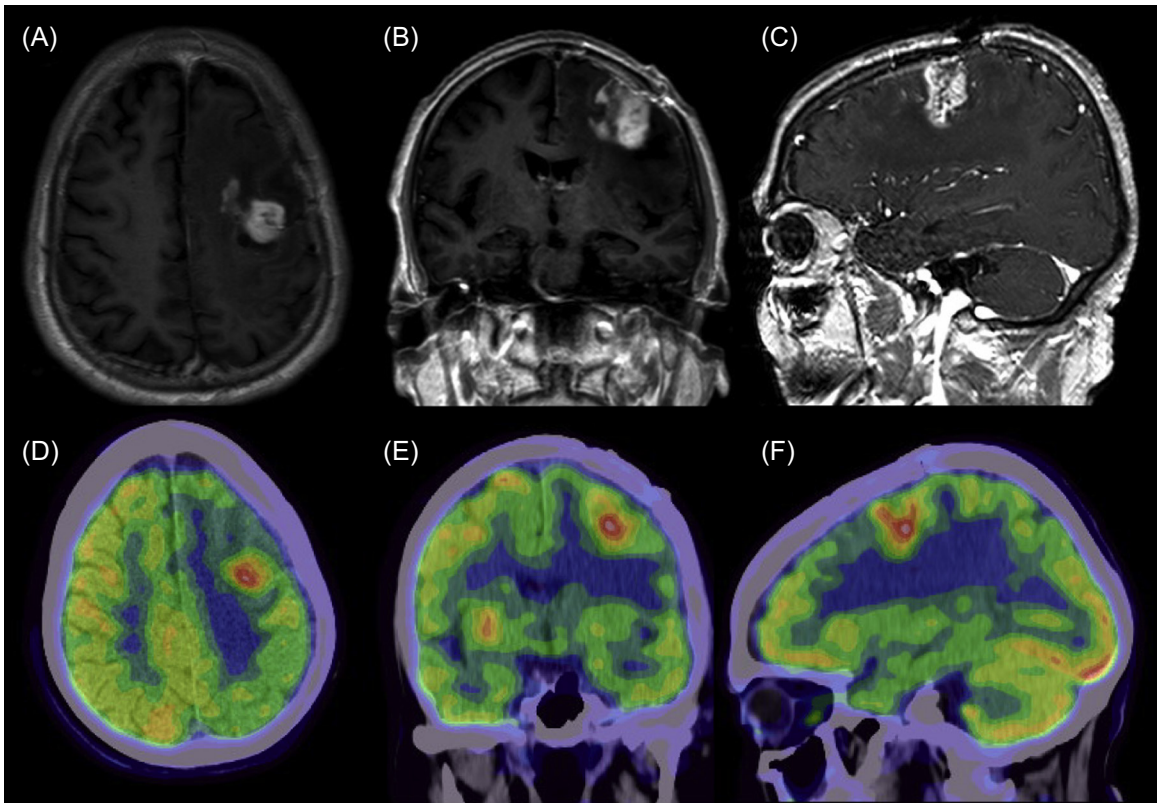


FIGURE 5 Recurrent grade IV glioblastoma in a 66-year-old woman post treatment (surgery followed by concurrent chemoradiotherapy). (A) Axial, (B) coronal, and (C) sagittal T1 postcontrast MR reveal irregular and nodular enhancement within the left frontoparietal resection cavity. (D) Axial, (E) coronal, and (F) sagittal-fused FDG-PET/CT reveal a hypermetabolic focus corresponding with area of nodular enhancement on MR representing recurrent disease.

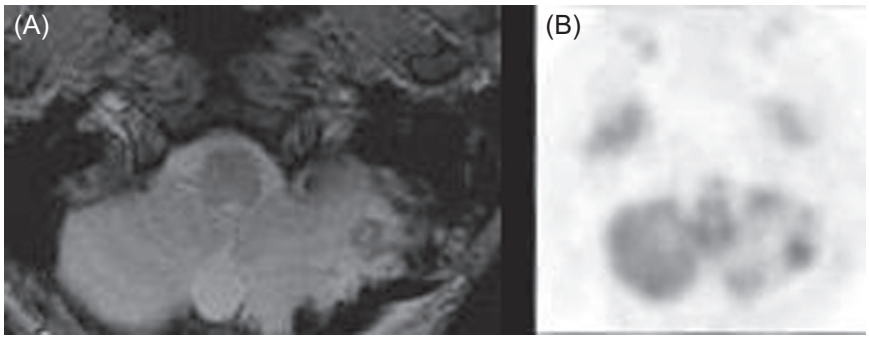


FIGURE 6 Recurrent cerebellar tumor in a 52-year-old man who is post treatment (surgery and radiation) for an astrocytoma grade III involving the left cerebellum hemisphere. (A) Axial MR, at the level of the cerebellum, reveals postsurgical changes and a nonenhancing focus involving the lateral aspect of the left cerebellum. (B) Axial FDG-PET, at the comparable level, reveals diffuse hypometabolism of the left cerebellar hemisphere secondary to prior radiation treatment to this region and a hypermetabolic focus corresponding to the lesion seen on MR that is consistent with recurrent tumor.

the subsequent treatment management would likely be changed significantly.

Follow-up Assessment and Monitoring Treatment

The ability of FDG to assess tumor glucose metabolism is a very important aspect of brain tumor evaluation, particularly in the follow-up assessment of patients after treatment.

While there are a number of areas where PET imaging has proven to be useful in the follow-up assessment and detection of tumor recurrence following therapy (Figures 5–7), there are also a number of significant drawbacks to the use of FDG-PET in follow-up assessment.

The major issue issues to be answered following treatment can generally be addressed using MRI.

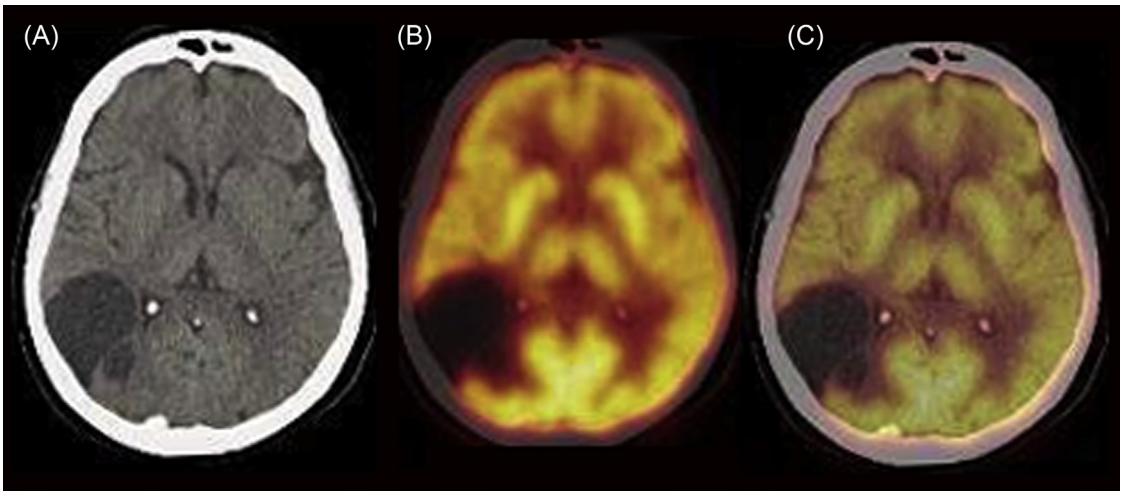


FIGURE 7 PET/CT Postoperative assessment of a grade III/IV right parietal temporal astrocytoma. (A) Axial noncontrast CT, (B) FDG-PET, and (C) fused FDG-PET/CT reveals postoperative changes with no uptake in the resection cavity to suggest tumor recurrence.

This technique is usually adequate for assessing the response to treatment by monitoring the reduction in tumor size, edema, and gadolinium contrast enhancement, and remains the imaging gold standard for response assessment in clinical trials.[47] However, MRI has significant limitations, as both postcontrast enhancement and increased T2/fluid-attenuated inversion recovery signal are nonspecific and may not always accurately assess treatment response. This problem is more pronounced in the setting of chemoradiation and/or corticosteroid administration, which can alter the amount of postcontrast enhancement.[47] MRI lacks the specificity to differentiate radiation necrosis from viable residual or recurrent tumor, and as a corollary, it cannot specifically determine the histological grade of tumor recurrence.[3] In such cases, FDG-PET imaging specifically in combination with advanced MRI techniques such as functional imaging, may be warranted.

FDG-PET has a sensitivity and specificity of 80–90% and 50–90%, respectively, for distinguishing radiation necrosis from recurrent tumor and is particularly useful in cases where MRI is unable to make the distinction.[48] Caution should be employed in the follow-up of brain tumors after radiation therapy, as there is a significant degree of inflammatory response that can confound the uptake within the tumor, potentially leading to an equivocal or false positive interpretation for recurrent tumor. Conversely, recent radiation therapy, low-grade tumors, and small tumor volume are potential causes of false negatives.[48] As a result, the general recommendation is that an FDG-PET scan should not be performed until a minimum of six to eight weeks following completion of radiation therapy. In addition, since FDG is avidly taken up in the highly metabolic cortical gray matter, lower metabolically active residual or recurrent lesions may be easily masked by surrounding normal brain activity.

Other Applications

Other potential applications and future areas of investigation of FDG-PET include prediction of treatment response and PET guidance for biopsy planning and radiation therapy. An investigation showed that early changes in glucose metabolic rate on FDG-PET predicted response to patients receiving temozolomide, a standard chemotheraupeutic agent for gliomas; however, it was not effective in predicting response to combination temozolamide plus radiation therapy.[38,49] In biopsy planning, FDG-PET has demonstrated superiority compared with CT or MRI alone in high-grade gliomas, although its added value remains limited.[38,50] This is particularly important given the heterogeneous histology within a given tumor and the need for accurate tumor grading.

Novel PET Tracers: [^{11}C]MET, [^{18}F]FET, and [^{18}F]FLT

[^{11}C] methionine

Amino acid and nucleoside analogs have the advantage of low native uptake in normal brain and are thus able to better delineate tumors than FDG. [^{11}C]methylmethionine ([^{11}C]MET) is one of several amino acid analogs that have been developed as PET tumor imaging agents.[51] [^{11}C]MET uptake in tumors generally reflects the protein synthesis rate, because [^{11}C]MET is transported via amino acid transporters across the cell membrane and is incorporated into proteins. However, [^{11}C]MET also seems to be incorporated into phospholipids through the S-adenylmethionine pathway.[52] Disadvantages of [^{11}C]MET are its uptake in acutely ischemic and inflammatory brain tissue,[53] its short half-life of 20 min, and the need for an on-site cyclotron facility; although the [^{18}F] versions of [^{11}C]MET may overcome the latter disadvantages. Yet,

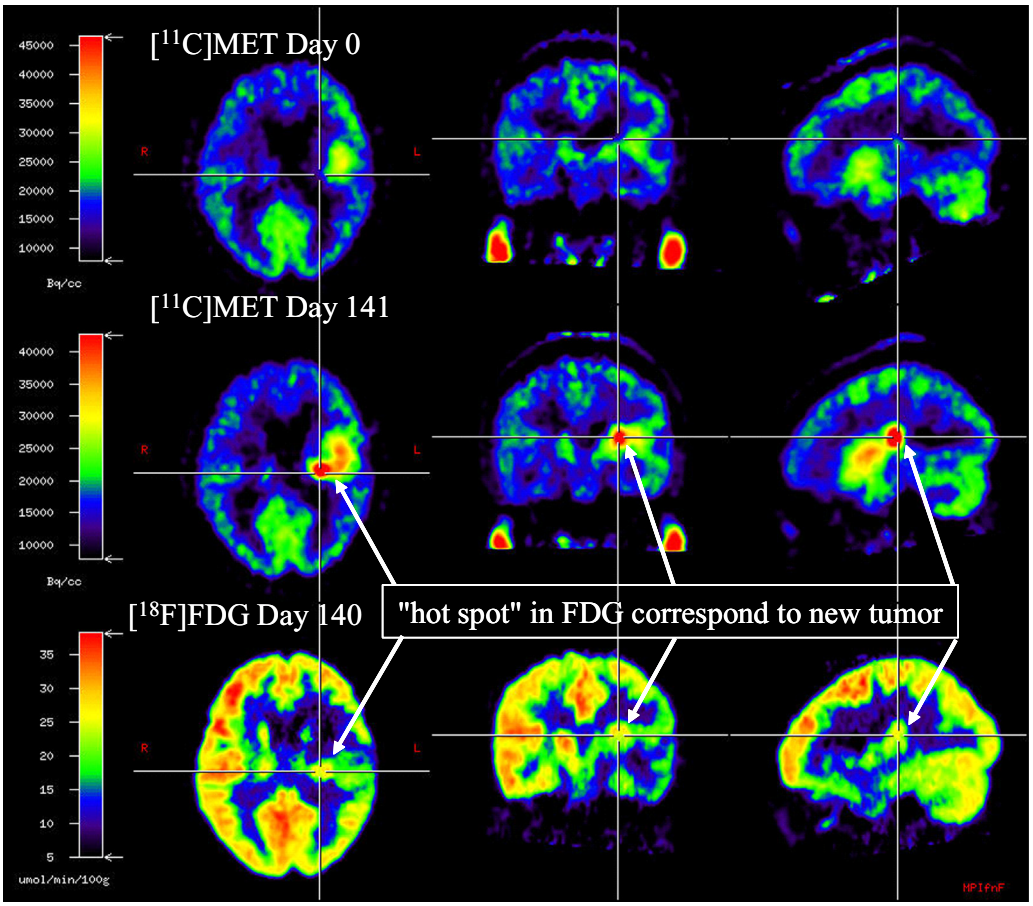


FIGURE 8 Growth of glioblastoma. [11C]methyl-methionine ([11C]MET) PET brain images of a patient with glioblastoma at day 0 (top row) and day 141 (middle row) and [18F]FDG images of the brain of same patient at day 140. Due to lower background brain activity, the delineation of tumor extent and visualization of new tumor growth is much better for ([11C]MET) than for [18F]FDG. *Reproduced with permission from Karl Herholtz, MD, University of Cologne, Germany. All rights reserved.*

[11C]MET performs better than [18F]FDG in defining the extent of tumor involvement and detecting tumor recurrence (Figure 8) including low-grade gliomas. Amino acid tracers, such as [11C]MET, thus appear to play a complementary role to [18F]FDG.[54–59,35] [11C]MET may be useful for monitoring chemotherapy in gliomas (Figure 9).[60,61]

[18F] Fluoroethyl-L-Tyrosine

[18F]fluoroethyl-L-tyrosine (FET) is another amino acid analog that has shown efficacy in determining glioma grade and differentiating recurrence from radiation necrosis.[62–65] The selective uptake of [18F]FET may be due to specific amino acid transporters. While the tracer has shown high sensitivity for detecting gliomas, its specificity is reduced due to passive flux through regions of BBB breakdown.[66] However, one of the most promising features of [18F]FET is the ability to detect nonenhancing, biologically active tumor components.[67] This feature may be useful for determining initial resection margins, as well as adding to the MRI assessment of the degree of tumor infiltration in the peripheral region of signal abnormality surrounding an enhancing component.

3′-deoxy-3′-[18F]fluorothymidine

The thymidine nucleoside analog 3′-deoxy-3′-[18F] fluorothymidine ([18F]FLT) is based on the gold standard for determination of cell proliferation in cell culture, radiolabeled thymidine.[68] [18F]FLT uptake reflects the activity of thymidine kinase-1, an enzyme expressed during the DNA synthesis phase of the cell cycle.[69] There is a linear correlation of quantitative [18F]FLT uptake in recurrent gliomas with the immunohistochemistry marker of cell proliferation, Ki-67, with a stronger correlation than that seen with [18F]FDG.[70–72] For the evaluation of gliomas, relative [18F]FLT uptake within gliomas is greater than relative [18F]FDG uptake (Figure 10), but lower than [11C]MET.[68,73,74] Hence, [18F]FLT PET may be an alternative tool to [18F]FDG or [11C]MET PET in evaluating brain tumors, particularly chemotherapeutic tumor response.

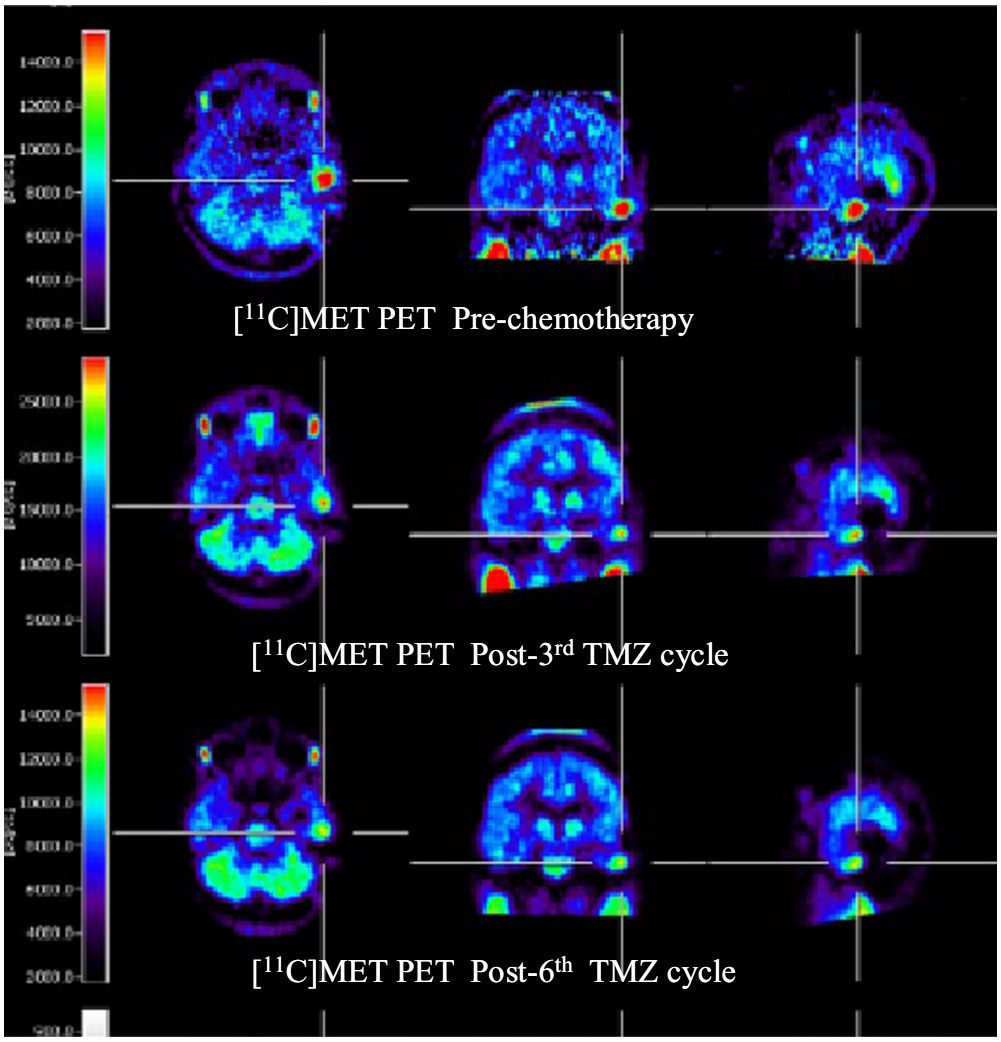


FIGURE 9 [11C]methyl-methionine ([11C]MET) PET in monitoring chemotherapy. Patient with oligoastrocytoma (WHO grade III) was treated with six cycles of temozolomide (TMZ). Reduced [11C]MET uptake in the left temporal lobe tumor as a metabolic response to TMZ chemotherapy is evident after third TMZ cycle (middle and bottom rows). *Modified and Reproduced with permission from Galldiks et al. Use of (11)C-methionine PET to monitor the effects of temozolomide chemotherapy in malignant gliomas.* Eur J Nucl Med Mol Imaging. *February 1:1–9 [Epub ahead of print]. Copyright © 2006 Springer-Vertag Gmbh, Heidelberg Germany. All rights reserved.*

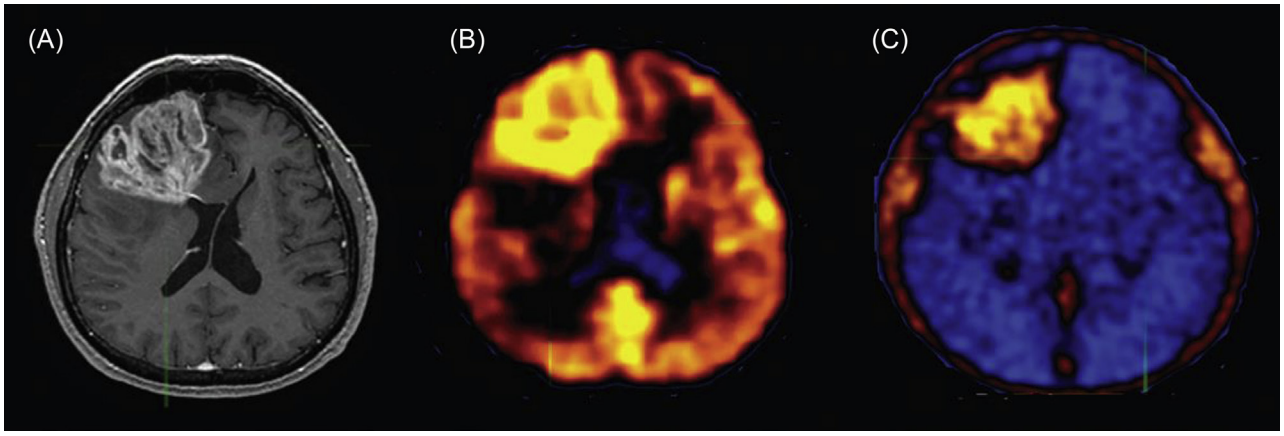


FIGURE 10 Newly diagnosed glioblastoma. (A) MRI (contrast enhanced T1-weighted image) shows large area of contrast enhancement in right frontal lobe. Both [18F]FDG-PET (B) and [18F]FLT PET (C) show increased uptake in same area. *Reproduced with permission from Chen et al. Imaging proliferation in brain tumors with 18F-FLT PET: comparison with 18F-FDG.* J Nucl Med. *46: 945–952. Copyright © 2005, Society of Nuclear Medicine. All rights reserved.*

CONCLUSIONS

SPECT and PET imaging of brain tumors provides information that is complementary to MRI. These functional brain tumor imaging techniques are evolving with the continuing development of new radiopharmaceuticals that ultimately aim to be biomarkers for determining tumor histological grade, detection of postoperative tumor recurrence, distinguishing between tumor recurrence and radiation necrosis, and assessing response to therapy.

References

1. Bondy ML, Scheurer ME, Malmer B, et al. Brain tumor epidemiology C. Brain tumor epidemiology: consensus from the Brain Tumor Epidemiology Consortium. *Cancer*. October 1, 2008;113 (7 Suppl):1953–1968.
2. American Cancer Society. *Cancer Facts and figures 2014*. Atlanta, Ga: American Cancer Society; 2014.
3. Del Sole A, Falini A, Ravasi L, et al. Anatomical and biochemical investigation of primary brain tumours. *Eur J Nucl Med*. December 2001;28(12):1851–1872.
4. Louis DN, Ohgaki H, Wiestler OD, et al. The 2007 WHO classification of tumours of the central nervous system. *Acta Neuropathol*. August 2007;114(2):97–109.
5. Altieri R, Agnoletti A, Quattrucci F, et al. Molecular biology of gliomas: present and future challenges. *Transl Med UniSa*. September 2014;10:29–37.
6. Benard F, Romsa J, Hustinx R. Imaging gliomas with positron emission tomography and single-photon emission computed tomography. *Semin Nucl Med*. April 2003;33(2):148–162.
7. Schwartz RB, Holman BL, Polak JF, et al. Dual-isotope single-photon emission computerized tomography scanning in patients with glioblastoma multiforme: association with patient survival and histopathological characteristics of tumor after high-dose radiotherapy. *J Neurosurg*. July 1998;89(1):60–68.
8. Schwartz RB, Carvalho PA, Alexander 3rd E, Loeffler JS, Folkerth R, Holman BL. Radiation necrosis vs high-grade recurrent glioma: differentiation by using dual-isotope SPECT with ^{201}TI and ^{99m}Tc-HMPAO. *AJNR Am J Neuroradiol*. November–December 1991;12(6):1187–1192.
9. Ancri D, Basset JY, Lonchampt MF, Etavard C. Diagnosis of cerebral lesions by thallium 201. *Radiology*. August 1978;128(2): 417–422.
10. Kaplan WD, Takvorian T, Morris JH, Rumbaugh CL, Connolly BT, Atkins HL. Thallium-201 brain tumor imaging: a comparative study with pathologic correlation. *J Nucl Med*. January 1987;28(1):47–52.
11. Kim KT, Black KL, Marciano D, et al. Thallium-201 SPECT imaging of brain tumors: methods and results. *J Nucl Med*. June 1990;31(6):965–969.
12. Oriuchi N, Tamura M, Shibazaki T, et al. Clinical evaluation of thallium-201 SPECT in supratentorial gliomas: relationship to histologic grade, prognosis and proliferative activities. *J Nucl Med*. December 1993;34(12):2085–2089.
13. Dierckx RA, Martin JJ, Dobbeleir A, Crols R, Neetens I, De Deyn PP. Sensitivity and specificity of thallium-201 single-photon emission tomography in the functional detection and differential diagnosis of brain tumours. *Eur J Nucl Med*. July 1994;21(7):621–633.
14. Ishibashi M, Taguchi A, Sugita Y, et al. Thallium-201 in brain tumors: relationship between tumor cell activity in astrocytic tumor and proliferating cell nuclear antigen. *J Nucl Med*. December 1995;36(12):2201–2206.
15. Ricci M, Pantano P, Pierallini A, et al. Relationship between thallium-201 uptake by supratentorial glioblastomas and their morphological characteristics on magnetic resonance imaging. *Eur J Nucl Med*. May 1996;23(5):524–529.
16. Staffen W, Hondl N, Trinka E, Iglseder B, Unterrainer J, Ladurner G. Clinical relevance of ^{201}Tl-chloride SPET in the differential diagnosis of brain tumours. *Nucl Med Commun*. April 1998;19(4): 335–340.
17. Sun D, Liu Q, Liu W, Hu W. Clinical application of ^{201}Tl SPECT imaging of brain tumors. *J Nucl Med*. January 2000;41(1):5–10.
18. Gomez-Rio M, Martinez Del Valle Torres D, Rodriguez-Fernandez A, et al. (201)Tl-SPECT in low-grade gliomas: diagnostic accuracy in differential diagnosis between tumour recurrence and radionecrosis. *Eur J Nucl Med Mol Imaging*. September 2004;31(9): 1237–1243.
19. Vos MJ, Tony BN, Hoekstra OS, Postma TJ, Heimans JJ, Hooft L. Systematic review of the diagnostic accuracy of ^{201}Tl single photon emission computed tomography in the detection of recurrent glioma. *Nucl Med Commun*. June 2007;28(6):431–439.
20. Gomez-Rio M, Rodriguez-Fernandez A, Ramos-Font C, Lopez-Ramirez E, Llamas-Elvira JM. Diagnostic accuracy of 201Thallium-SPECT and ^{18}F-FDG-PET in the clinical assessment of glioma recurrence. *Eur J Nucl Med Mol Imaging*. May 2008;35(5):966–975.
21. Shah AH, Snelling B, Bregy A, Patel PR, Tememe D. Discriminating radiation necrosis from tumor progression in gliomas: a systematic review what is the best imaging modality? *J Neuro-Oncol*. 2013;112(2):141–152.
22. Cheng X, Li Y, Xu Z, Li D, Wang J. A meta-analysis of ^{99m}Tc-MIBI SPECT for detection of recurrent glioma after radiation therapy. *J Clin Neurosci*. March 2011;18(3):307–312.
23. Biersack HJ, Coenen HH, Stocklin G, et al. Imaging of brain tumors with L-3-[^{123}I]iodo-alpha-methyl tyrosine and SPECT. *J Nucl Med*. January 1989;30(1):110–112.
24. O'Tuama LA, Treves ST, Larar JN, et al. Thallium-201 versus technetium-99m-MIBI SPECT in evaluation of childhood brain tumors: a within-subject comparison. *J Nucl Med*. July 1993;34(7):1045–1051.
25. Bagni B, Pinna L, Tamarozzi R, et al. SPET imaging of intracranial tumours with ^{99}Tcm-sestamibi. *Nucl Med Commun*. April 1995;16(4):258–264.
26. Soler C, Beauchesne P, Maatougui K, et al. Technetium-99m sestamibi brain single-photon emission tomography for detection of recurrent gliomas after radiation therapy. *Eur J Nucl Med*. December 1998;25(12):1649–1657.
27. Yokogami K, Kawano H, Moriyama T, et al. Application of SPET using technetium-99m sestamibi in brain tumours and comparison with expression of the MDR-1 gene: is it possible to predict the response to chemotherapy in patients with gliomas by means of ^{99m}Tc-sestamibi SPET? *Eur J Nucl Med*. April 1998;25(4): 401–409.
28. Nishiyama Y, Yamamoto Y, Fukunaga K, Satoh K, Kunishio K, Ohkawa M. Comparison of ^{99}Tcm-MIBI with ^{201}Tl chloride SPET in patients with malignant brain tumours. *Nucl Med Commun*. June 2001;22(6):631–639.
29. Beauchesne P, Pedeux R, Boniol M, Soler C. ^{99m}Tc-sestamibi brain SPECT after chemoradiotherapy is prognostic of survival in patients with high-grade glioma. *J Nucl Med*. March 2004;45(3):409–413.
30. Bleichner-Perez S, Le Jeune F, Dubois F, Steinling M. ^{99m}Tc-MIBI brain SPECT as an indicator of the chemotherapy response of recurrent, primary brain tumors. *Nucl Med Commun*. December 2007;28(12):888–894.

31. Langen KJ, Muhlensiepen H, Holschbach M, Hautzel H, Jansen P, Coenen HH. Transport mechanisms of 3-[^{123}I]iodo-alpha-methyl-L-tyrosine in a human glioma cell line: comparison with [3H]methyl]-L-methionine. *J Nucl Med*. July 2000;41(7): 1250–1255.
32. Kuwert T, Woesler B, Morgenroth C, et al. Diagnosis of recurrent glioma with SPECT and iodine-123-alpha-methyl tyrosine. *J Nucl Med*. January 1998;39(1):23–27.
33. Schmidt D, Gottwald U, Langen KJ, et al. 3-[^{123}I]Iodo-alpha-methyl-L-tyrosine uptake in cerebral gliomas: relationship to histological grading and prognosis. *Eur J Nucl Med*. July 2001;28(7):855–861.
34. Bader JB, Samnick S, Moringlane JR, et al. Evaluation of l-3-[^{123}I] iodo-alpha-methyltyrosine SPET and [18F]fluorodeoxyglucose PET in the detection and grading of recurrences in patients pretreated for gliomas at follow-up: a comparative study with stereotactic biopsy. *Eur J Nucl Med*. February 1999;26(2):144–151.
35. Sasaki M, Kuwabara Y, Yoshida T, et al. A comparative study of thallium-201 SPET, carbon-11 methionine PET and fluorine-18 fluorodeoxyglucose PET for the differentiation of astrocytic tumours. *Eur J Nucl Med*. September 1998;25(9):1261–1269.
36. Weber WA, Dick S, Reidl G, et al. Correlation between postoperative 3-[(^{123})I]iodo-L-alpha-methyltyrosine uptake and survival in patients with gliomas. *J Nucl Med*. August 2001;42(8):1144–1150.
37. Chen W. Clinical applications of PET in brain tumors. *J Nucl Med*. September 2007;48(9):1468–1481.
38. la Fougere C, Suchorska B, Bartenstein P, Kreth FW, Tonn JC. Molecular imaging of gliomas with PET: opportunities and limitations. *Neuro Oncol*. August 2011;13(8):806–819.
39. Vanheertum R, Greenstein E, Tikofsky R. 2-deoxy-fluorglucose-positron emission tomography imaging of the brain: current clinical applications with emphasis on the dementias. *Semin Nucl Med*. 2004;34(4):300–312.
40. Di Chiro G, Patronas N, DeLapaz RL et al.
41. Spence AM, Muzi M, Mankoff DA, et al. ^{18}F-FDG PET of gliomas at delayed intervals: improved distinction between tumor and normal gray matter. *J Nucl Med*. October 2004;45(10):1653–1659.
42. Pirotte B, Goldman S, Massager N, et al. Comparison of ^{18}F-FDG and ^{11}C-methionine for PET-guided stereotactic brain biopsy of gliomas. *J Nucl Med*. August 2004;45(8):1293–1298.
43. Alavi JB, Alavi A, Chawluk J, et al. Positron emission tomography in patients with glioma. A predictor of prognosis. *Cancer*. September 15, 1988;62(6):1074–1078.
44. De Witte O, Levivier M, Violon P, et al. Prognostic value positron emission tomography with [^{18}F]fluoro-2-deoxy-D-glucose in the low-grade glioma. *Neurosurgery*. September 1996;39(3):470–476; discussion 476–477.
45. Padma MV, Said S, Jacobs M, et al. Prediction of pathology and survival by FDG PET in gliomas. *J Neuro-Oncol*. September 2003;64(3):227–237.
46. Patronas NJ, Di Chiro G, Kufta C, et al. Prediction of survival in glioma patients by means of positron emission tomography. *J Neurosurg*. June 1985;62(6):816–822.
47. Wen PY, Macdonald DR, Reardon DA, et al. Updated response assessment criteria for high-grade gliomas: response assessment in neuro-oncology working group. *J Clin Oncol*. April 10, 2010;28(11): 1963–1972.
48. Langleben DD, Segall GM. PET in differentiation of recurrent brain tumor from radiation injury. *J Nucl Med*. November 2000;41(11):1861–1867.
49. Charnley N, West CM, Barnett CM, et al. Early change in glucose metabolic rate measured using FDG-PET in patients with high-grade glioma predicts response to temozolomide but not temozolomide plus radiotherapy. *Int J Radiat Oncol Biol Phys*. October 1, 2006;66(2):331–338.
50. Pirotte BJ, Lubansu A, Massager N, Wikler D, Goldman S, Levivier M. Results of positron emission tomography guidance and reassessment of the utility of and indications for stereotactic biopsy in children with infiltrative brainstem tumors. *J Neurosurg*. November 2007;107(5 Suppl):392–399.
51. Kubota K, Yamada K, Fukada H, et al. Tumor detection with carbon-11-labelled amino acids. *Eur J Nucl Med*. 1984;9(3):136–140.
52. Ishiwata K, Kubota K, Murakami M, Kubota R, Senda M. A comparative study on protein incorporation of L-[methyl-3H]methionine, L-[1-^{14}C]leucine and L-2-[^{18}F]fluorotyrosine in tumor bearing mice. *Nucl Med Biol*. November 1993;20(8):895–899.
53. Jacobs A. Amino acid uptake in ischemically compromised brain tissue. *Stroke*. October 1995;26(10):1859–1866.
54. Herholz K, Holzer T, Bauer B, et al. 11C-methionine PET for differential diagnosis of low-grade gliomas. *Neurology*. May 1998;50(5): 1316–1322.
55. Kaschten B, Stevenaert A, Sadzot B, et al. Preoperative evaluation of 54 gliomas by PET with fluorine-18-fluorodeoxyglucose and/or carbon-11-methionine. *J Nucl Med*. May 1998;39(5):778–785.
56. Chung JK, Kim YK, Kim SK, et al. Usefulness of 11C-methionine PET in the evaluation of brain lesions that are hypo- or isometabolic on ^{18}F-FDG PET. *Eur J Nucl Med Mol Imaging*. February 2002;29(2): 176–182.
57. Jager PL, Vaalburg W, Pruim J, de Vries EG, Langen KJ, Piers DA. Radiolabeled amino acids: basic aspects and clinical applications in oncology. *J Nucl Med*. March 2001;42(3):432–445.
58. Ogawa T, Inugami A, Hatazawa J, et al. Clinical positron emission tomography for brain tumors: comparison of fludeoxyglucose F 18 and L-methyl-^{11}C-methionine. *AJNR Am J Neuroradiol*. February 1996;17(2):345–353.
59. Pauleit D, Floeth F, Tellmann L, et al. Comparison of O-(2-^{18}F-fluoroethyl)-L-tyrosine PET and 3-^{123}I-iodo-alpha-methyl-L-tyrosine SPECT in brain tumors. *J Nucl Med*. March 2004;45(3): 374–381.
60. Herholz K, Kracht LW, Heiss WD. Monitoring the effect of chemotherapy in a mixed glioma by C-11-methionine PET. *J Neuroimaging*. July 2003;13(3):269–271.
61. Galldiks N, Kracht LW, Burghaus L, et al. Use of ^{11}C-methionine PET to monitor the effects of temozolomide chemotherapy in malignant gliomas. *Eur J Nucl Med Mol Imaging*. May 2006;33(5): 516–524.
62. Floeth FW, Pauleit D, Sabel M, et al. ^{18}F-FET PET differentiation of ring-enhancing brain lesions. *J Nucl Med*. May 2006;47(5): 776–782.
63. Popperl G, Gotz C, Rachinger W, Gildehaus FJ, Tonn JC, Tatsch K. Value of O-(2-[^{18}F]fluoroethyl)- L-tyrosine PET for the diagnosis of recurrent glioma. *Eur J Nucl Med Mol Imaging*. November 2004;31(11):1464–1470.
64. Dunet V, Maeder P, Nicod-Lalonde M, Lhermitte B, Pollo C, Bloch J, et al. Combination of MRI and dynamic FET PET for initial glioma grading. *Nuklearmedizin*. August 6, 2014;53(4):155–161.
65. Dunet V, Rossier C, Buck A, Stupp R, Prior JO. Performance of ^{18}F-fluoro-ethyl-tyrosine (^{18}F-FET) PET for the differential diagnosis of primary brain tumor: a systematic review and Metaanalysis. *J Nucl Med*. February 2012;53(2):207–214.
66. Hutterer M, Nowosielski M, Putzer D, et al. [^{18}F]-fluoro-ethyl-L-tyrosine PET: a valuable diagnostic tool in neuro-oncology, but not all that glitters is glioma. *Neuro Oncol*. March 2013;15(3):341–351.
67. Nowosielski M, DiFranco MD, Putzer D, et al. An intra-individual comparison of MRI, [^{18}F]-FET and [^{18}F]-FLT PET in patients with high-grade gliomas. *PLoS One*. 2014;9(4):e95830.
68. Shields AF, Grierson JR, Dohmen BM, et al. Imaging proliferation in vivo with [F-18]FLT and positron emission tomography. *Nat Med*. November 1998;4(11):1334–1336.

69. Rasey JS, Grierson JR, Wiens LW, Kolb PD, Schwartz JL. Validation of FLT uptake as a measure of thymidine kinase-1 activity in A549 carcinoma cells. *J Nucl Med*. September 2002;43(9):1210–1217.
70. Yamamoto Y, Ono Y, Aga F, Kawai N, Kudomi N, Nishiyama Y. Correlation of ^{18}F-FLT uptake with tumor grade and Ki-67 immunohistochemistry in patients with newly diagnosed and recurrent gliomas. *J Nucl Med*. December 2012;53(12):1911–1915.
71. Chalkidou A, Landau DB, Odell EW, Cornelius VR, O'Doherty MJ, Marsden PK. Correlation between Ki-67 immunohistochemistry and ^{18}F-fluorothymidine uptake in patients with cancer: a systematic review and meta-analysis. *Eur J Cancer*. December 2012;48(18):3499–3513.
72. Chen W, Cloughesy T, Kamdar N, et al. Imaging proliferation in brain tumors with ^{18}F-FLT PET: comparison with ^{18}F-FDG. *J Nucl Med*. June 2005;46(6):945–952.
73. Jacobs AH, Thomas A, Kracht LW, et al. 18F-fluoro-L-thymidine and 11C-methylmethionine as markers of increased transport and proliferation in brain tumors. *J Nucl Med*. December 2005;46(12):1948–1958.
74. Choi SJ, Kim JS, Kim JH, et al. [^{18}F]3′-deoxy-3′-fluorothymidine PET for the diagnosis and grading of brain tumors. *Eur J Nucl Med Mol Imaging*. June 2005;32(6):653–659.

CHAPTER

34

Advanced Methionine Positron-Emission Tomography Imaging for Brain Tumor Diagnosis, Surgical Planning, and Treatment

Arash Kardan, Martin Satter

Departments of Nuclear Medicine, /PET, Kettering Memorial Hospital, Kettering, OH, USA

Tumors of the central nervous system are a heterogeneous group with an incidence rate of 20.5 per 100,000 people each year, the most common being meningiomas (35.5%) and gliomas (30%).[1] While 97% of meningiomas are benign, 54% of gliomas are highly malignant glioblastomas. For the diagnosis and classification of these aggressive central nervous system tumors, internationally accepted guidelines have been formulated.[2] Grading is based primarily on histologic criteria, such as cell density, nuclear and cellular atypia, number of mitoses, and vascular endothelial proliferation. The World Health Organization (WHO) classifies the gliomas into four grades, with grades I and II being low grade, grade III being anaplastic, and grade IV, glioblastoma multiforme, being the highest grade with the worst prognosis.[3]

Survival rates are 35.7% at 1 year and 4–7% at 5 years for glioblastoma of WHO grade IV. Survival rates for astrocytomas and oligodendrogliomas of WHO grade III are 60–80% at 1 year and 26–46% at 5 years, while WHO grade II astrocytomas and oligodendrogliomas have survival rates of 94% at 1 year and 67% at 5 years.[4] Clearly, the projected survival for a patient is based upon histologic grading, which in turn is based on the associated tissue biopsy; however, tissue biopsies may not prove to be representative of the actual pathology, given the frequent heterogeneity of gliomas and nonspecific guidance that comes from traditional anatomic imaging such as magnetic resonance imaging (MRI) and computed tomography (CT).[5]

Neuroimaging allows for the noninvasive evaluation of glioma and is one of the key factors for guiding individualized therapy and patient management, since accurate diagnosis and demarcation of viable tumor tissue are required for treatment planning as well as assessment of any treatment response. Conventional imaging modalities like MRI and CT reveal morphological information but are of comparatively limited value for the assessment of more specific and reproducible information about the biology and metabolic activity of a tumor.

Positron-emission tomography (PET) imaging allows highly sensitive measurements (in the picomolar range) of biochemically active molecules labeled with short-lived positron-emitting radionuclides (radiotracers). Positrons emitted from the nucleus of PET radiopharmaceuticals subsequently annihilate on contact with electrons after traveling a short distance within the tissue (mean range, 0.2 up to 1.5 mm, depending on the mean energy of the positron). Each annihilation results in a pair of 511-keV photons traveling in opposite directions that can be counted by detector units, which commonly are arranged in ring structures surrounding the subject. When two opposing detectors simultaneously register a pair of photons (time window, 500–1000 ps), the annihilation event is counted and assigned to a line of response joining the two relevant detectors.

Accordingly, a PET scan consists of the acquisition of a large number of lines of response, which are used to reconstruct three-dimensional images by means of standard tomographic techniques that also include scatter correction, randoms correction, and the effects of attenuation to obtain an accurate image of the radioactive distribution. The physics of coincidence detection enable high spatial resolution and high sensitivity, which are necessary to perform dynamic data acquisition. The spatial resolution of state-of-the-art clinical PET scanners as of this writing is about 5–6 mm.[6]

http://dx.doi.org/10.1016/B978-0-12-800945-1.00034-3

© 2016 Elsevier Ltd. All rights reserved.

Molecular imaging with PET is increasingly implemented in neuro-oncology, since it provides additional metabolic information about the tumor, both for patient management and for evaluation of newly developed therapeutics. Various molecular processes have been designated as key to tracking tumor biology, leading to the development of PET radiopharmaceuticals designed to monitor glucose consumption, expression of amino acid transporters, proliferation rate, membrane biosynthesis, and hypoxia. Useful PET radiopharmaceuticals should have unaltered biological properties compared with the unlabeled molecule, should not be easily dissociable from the radionuclide, and should ideally come with low nonspecific uptake in the background or blood in order to obtain higher contrast PET images. Typically, several hundred million cells in relatively close proximity must accumulate the radiotracer to visualize them against the background.[7]

The glucose analogue 2-[^{18}F]fluoro-2-deoxy-D-glucose ([^{18}F]FDG) is the most frequently used radiotracer to measure the local metabolic rate of glucose that represents a common pathway of neurochemical activity in the brain.[8,9] Imaging of brain tumors with [^{18}F]FDG was the first oncologic application of PET.[10–12] [^{18}F]FDG is actively transported across the blood–brain barrier (BBB), where it is phosphorylated and subsequently trapped intracellularly.

[^{18}F]FDG uptake is generally high in high-grade tumors. The increased uptake was suggested to be related to changes in transport rate via modulation of glucose transporter proteins.[13] [^{18}F]FDG PET was proposed to be useful for imaging of gliomas because of increased glucose metabolism in high-grade gliomas as well as a positive correlation between the glycolysis rate and malignancy. The amount of [^{18}F]FDG accumulation in a primary brain tumor correlates with the histologic tumor grade, cell density, and survival.[9,14–17] High uptake of [^{18}F]FDG in a previously known low-grade tumor establishes the diagnosis of anaplastic transformation[18,19] (see Figures 1 and 2).

Some studies have demonstrated the diagnostic limitations of [^{18}F]FDG PET in the evaluation of brain tumors.[20,21] Glucose is the primary substrate of energy supply to the brain, providing approximately 95% of the required ATP, and is also tightly connected to neuronal activity. High physiologic brain glucose metabolism will then correlate with high uptake of [^{18}F]FDG in the brain. The diagnostic accuracy of [^{18}F]FDG is hampered by the high physiologic glucose metabolism in different brain areas, such as the cerebral cortex, the basal ganglia, and the thalamus, significantly limiting the sensitivity for detection as well as the specificity for delineation of glioma-involved tissue from adjacent normal brain.

Because of the high rate of physiologic glucose metabolism in normal brain tissue, the detectability of tumors with only modest increases in glucose metabolism, such as low-grade tumors and in some cases recurrent high-grade tumors, can be difficult. The clear demarcation of glioma is most notably impeded in low-grade gliomas, which undergo only modest radiotracer uptake, similar to that of white matter, and decreased uptake compared with gray matter.[21,22] [^{18}F]FDG uptake in low-grade tumors is usually similar to that in normal white matter, and uptake in high-grade tumors can be less than or similar to that in normal gray matter, thus decreasing the sensitivity of lesion detection.[23]

The coupling of [^{18}F]FDG uptake and glucose metabolism in tumors can be radically different from that in normal tissue. It was demonstrated that [^{18}F]FDG uptake in tumors could be increased, whereas glucose metabolism could not.[24] Furthermore, [^{18}F]FDG uptake can vary greatly; high-grade tumors may have uptake that is only similar to or slightly above that in white matter, especially after treatment.[12] Low contrast to background can also be found in some high-grade gliomas, where [^{18}F]FDG uptake was found to be similar to or less than in the cerebral cortex.[25] Finally, [^{18}F]FDG is known to accumulate in macrophages and inflammatory tissue, potentially making the distinction between glioma and an acute or chronic inflammatory process challenging.

Amino acid and analogue amino acid PET tracers constitute an additional class of tumor-imaging agents.[26,27] They are particularly useful for imaging brain tumors because of the high uptake in tumor tissue and low uptake in normal brain tissue and, thus, higher tumor-to-normal contrast ratio. Amino acids are transported into the cell via several carrier-mediated processes.[27] Amino acid imaging is based on the observation that amino acid transport is generally increased in malignant transformation.[34,35] In animal models, the upregulation of amino acid transporters in the supporting vasculature of brain tumor tissue has been demonstrated as responsible for the increased facilitation of amino acid transport into the tumor cell.[36]

Factors involved in this active transport have been reviewed and include flux of the amino acid to the tissue, the intrinsic activity of the amino acid transporter, and the rate of intracellular amino acid metabolism.[29] Amino acid transport is generally accepted to be the rate-limiting step, even for the few amino acid tracers that are incorporated into the proteins. The relationship between proliferative activity and amino acid transport was investigated in three glioma cell lines.[37] The authors utilized unmetabolized amino acid to demonstrate that increased amino acid transport in tumor cells involves all phases of the cell cycle and that upregulation of amino acid transport (L and A systems) occurs in the absence of increased vascular permeability. Thus, amino acid transport is increased in tumor cells regardless of the phase of the cell cycle, and this upregulation of transport does not depend on breakdown of the BBB. An earlier study showed that amino acid transport into brain tumors does not depend on, but may be enhanced by, a breakdown in the BBB.[38]

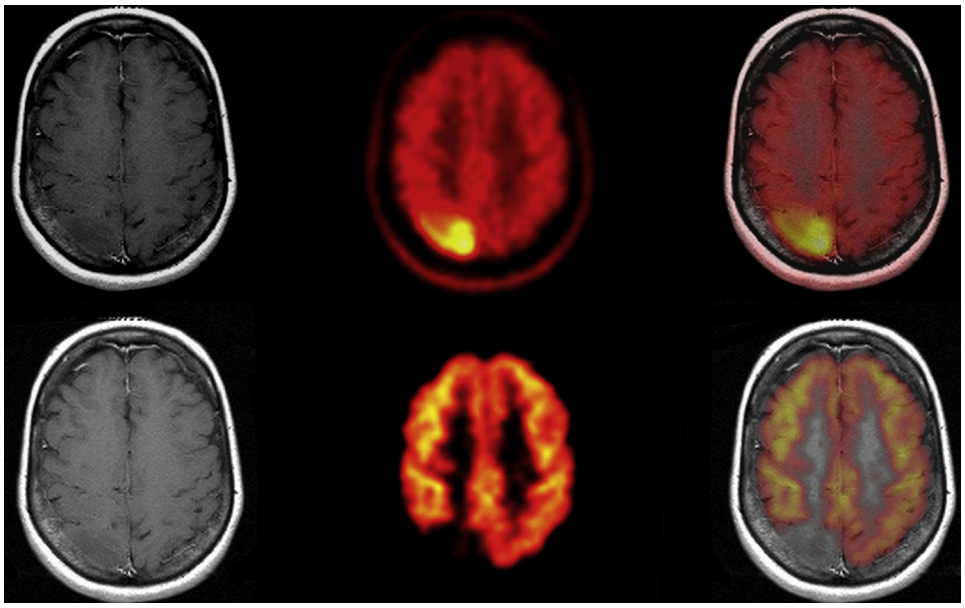


FIGURE 1 Row 1, MR, [^{11}C]methionine PET, coregistered [^{11}C]methionine PET to MR; row 2, MR, [^{18}F]FDG PET, coregistered [^{18}F]FDG PET to MR; 64-year-old female at the time of initial diagnosis. PET scans demonstrated elevated [^{11}C]methionine uptake (row 1) with decreased [^{18}F]FDG uptake (row 2) suggestive of low-grade histology. Contemporaneous intravenous contrast-enhanced T1-weighted MR demonstrates no definite corresponding anatomic abnormality. [^{11}C]Methionine PET image guidance was used for stereotactic single-pass biopsy target with [^{11}C]methionine PET total tumor volume used in resection margin planning. Final pathology was consistent with oligoastrocytoma, WHO grade III (with 1p19q codeletion). *Courtesy of the Charles F. Kettering Memorial Hospital Department of Nuclear Medicine/PET.*

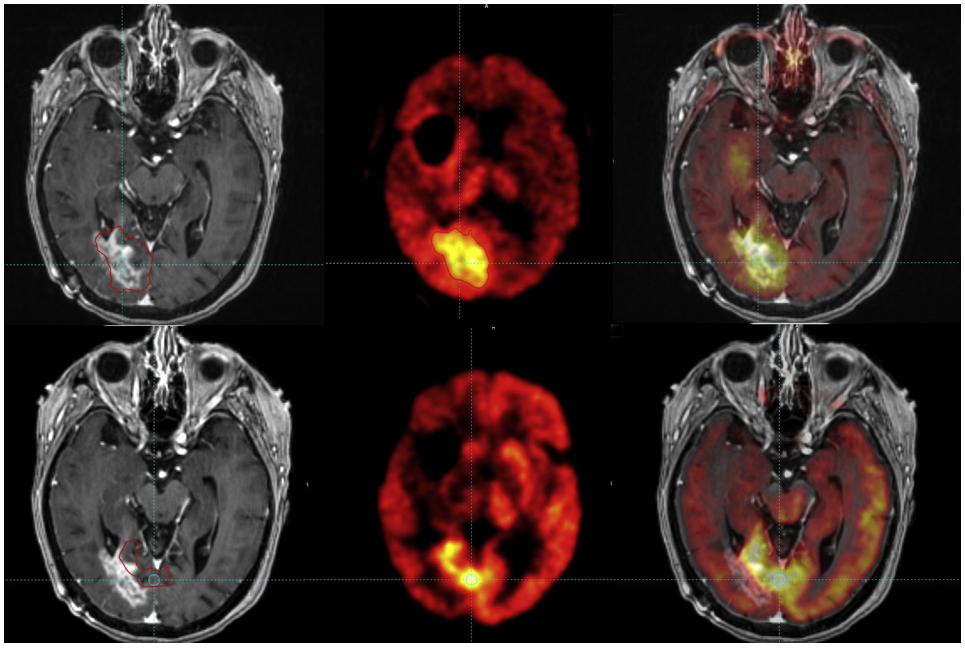


FIGURE 2 Row 1, MR, [^{11}C]methionine PET; coregistered [^{11}C]methionine PET to MR; row 2, MR, [^{18}F]FDG PET, coregistered [^{18}F]FDG PET to MR; 71-year-old female (64 years old at the time of initial diagnosis; same patient as in Figure 1). Follow-up [^{11}C]methionine PET scan performed 7 years after initial diagnosis demonstrates new increased uptake (row 1) with associated matching focal [^{18}F]FDG uptake (row 2) localized to the superior resection cavity margin and corresponding to new anatomic abnormality on intravenous contrast-enhanced T1 MR image. The matching methionine/FDG uptake is suggestive of high-grade transformation within residual/recurrent disease. [^{11}C]Methionine PET better delineates the tumor margins and total volume and was used for stereotactic PET image-guided single-pass biopsy. Final pathology was consistent with high-grade glioblastoma, WHO grade IV. *Courtesy of the Charles F. Kettering Memorial Hospital Department of Nuclear Medicine/PET.*

The best-studied amino acid tracer is [^{11}C]methionine.[27,28] Because of the short half-life of ^{11}C (20 min), an onsite cyclotron is a prerequisite for [^{11}C]methionine use in brain tumor imaging and has limited its implementation into clinical practice. The longer half-life of ^{18}F (110 min) allows for offsite production of an ^{18}F-labeled amino acid PET radiotracer and transport to a clinical site. For this reason, several ^{18}F-labeled aromatic amino acid analogues have been developed for tumor imaging.[29] The 3,4-dihydroxy-6-[^{18}F]fluoro-L-phenylalanine ([^{18}F]FDOPA) metabolite 3-*O*-methyl-6-[^{18}F]fluoro-L-DOPA has also been investigated for brain tumor imaging with PET.[32] The diagnostic accuracy of [^{18}F]FDOPA has been reported to be superior to that of [^{18}F]FDG in evaluating recurrent low-grade and high-grade gliomas.[33] Tumor uptake of *O*-(2-[^{18}F]fluoroethyl)-L-tyrosine and [^{18}F]FDOPA has been reported to be similar to that of [^{11}C]methionine.[30,31]

The uptake of [^{11}C]methionine is mainly determined by a specific carrier-mediated mechanism and correlates with the proliferative activity and microvessel density of the tumor cells.[39–42] The [^{11}C]methionine uptake in gliomas is influenced by its specific activity in plasma, the transfer across the BBB, the intracellular metabolism, and the incorporation of [^{11}C]methionine in proteins.[43,44] Although disruption of the BBB is not a prerequisite for increased [^{11}C]methionine uptake, a damaged BBB may enhance leakage of the tracer to the extracellular space and contribute to the increased uptake in malignant gliomas.[45]

In short, uptake of [^{11}C]methionine is significant in low-grade astrocytoma but typically not as high as observed in glioblastoma. However, [^{11}C]methionine uptake is often higher in meningioma (lack of BBB) than in glioblastoma. In contrast, [^{18}F]FDG uptake is higher in glioblastoma than in meningioma. Therefore, transport across the BBB is not the rate-limiting step for [^{18}F]FDG, whereas transport across the BBB does appear to be the rate-limiting step for amino acid tracers such as [^{11}C]methionine. The superiority of [^{11}C]methionine PET over [^{18}F]FDG PET for evaluating glioma is based on the low background uptake of [^{11}C]methionine in normal brain tissue, providing good contrast with tumor uptake. In accordance, [^{11}C]methionine is better than [^{18}F]FDG in delineating gliomas[46] (see Figure 3).

[^{11}C]Methionine uptake has been demonstrated to correlate with tumor grade.[43,47] However, high interindividual variability in [^{11}C]methionine uptake does not allow for accurate noninvasive initial grading.[48] On the other hand, [^{11}C]methionine has been demonstrated to be effective in identifying malignant progression in patients already diagnosed with glioma with a sensitivity of 90% and specificity of 92.3% for the detection of malignant transformation.[49] Detailed immunohistochemical analysis demonstrated a significant correlation between changes in [^{11}C]methionine uptake and the expression of vascular endothelial growth factor in these patients.[49]

Several studies have suggested better outcome for patients for whom amino acid PET images coregistered to MRI are utilized for treatment planning (image-guided surgery and/or radiation therapy) and follow-up versus patients for whom MRI alone is used.[50–54] Tumor margins of low-grade gliomas are often better delineated by [^{11}C]methionine than assessed on T1-weighted contrast-enhanced MRI.[55–57]

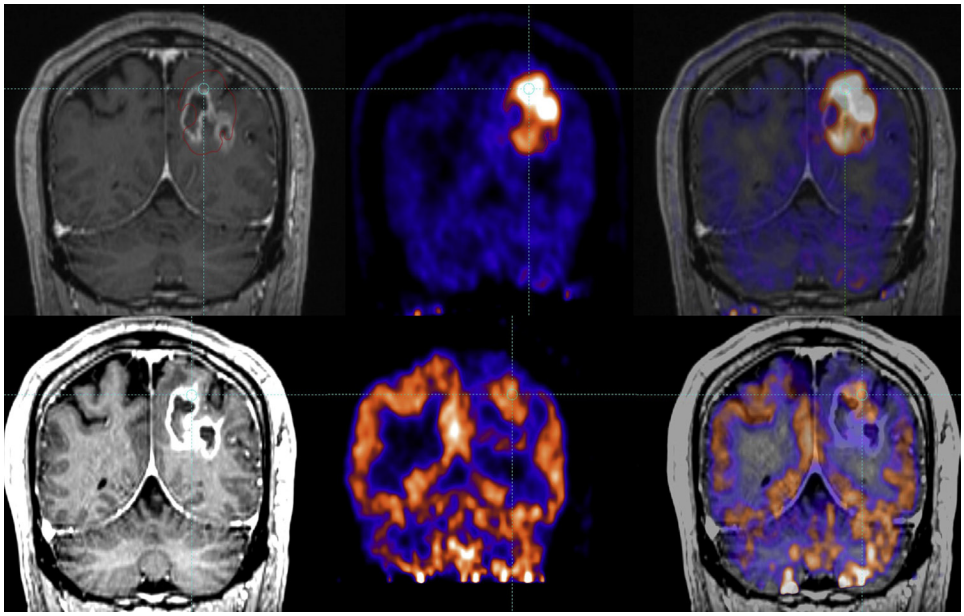


FIGURE 3 MR, [^{11}C]methionine PET, coregistered [^{11}C]methionine PET to MR; MR, [^{18}F]FDG PET, coregistered [^{18}F]FDG PET/MR, 67-year-old male at the time of initial diagnosis. [^{11}C]Methionine PET scan demonstrates heterogeneous uptake with the most focal and intense tracer accumulation demarcating viable tumor components versus necrotic or cystic changes. [^{11}C]Methionine PET image guidance was used for stereotactic single-pass biopsy target. Final pathology was consistent with high-grade glioblastoma, WHO grade IV. *Courtesy of the Charles F. Kettering Memorial Hospital Department of Nuclear Medicine/PET.*

A direct local comparison of signal changes on presurgical MRI and [^{11}C]methionine with stereotactic biopsies showed that [^{11}C]methionine detected solid tumor components as well as infiltration areas with high sensitivity and specificity, providing histological proof for the superior role of [^{11}C]methionine in delineating the tumor extent of gliomas.[58] Interestingly, the infiltrative part of low-grade gliomas included in this study showed higher [^{11}C]methionine uptake compared with the corresponding solid tumor component, suggesting that areas of tumor invasion/infiltration may have a higher demand for amino acids such as methionine[58] (see Figure 4).

Perfusion studies using dynamic contrast perfusion MRI in combination with PET have established a positive correlation between [^{11}C]methionine uptake and tumor vascularity in gliomas.[59,60] The regional cerebral blood volume (CBV) of the tumors correlated strongly with [^{11}C]methionine uptake and was significantly higher in high-grade than in low-grade gliomas.[59] Stereotactic coregistration of CBV and [^{11}C]methionine showed that both imaging parameters were associated with histopathological features of endothelial proliferation and mitotic activity but not with necrosis.[60]

Low-grade oligodendrogliomas show a generally higher [^{11}C]methionine uptake than astrocytomas of similar malignancy grade despite their more indolent clinical behavior. Higher [^{11}C]methionine uptake in oligodendrogliomas is probably related to a higher cell density and larger cell turnover in oligodendrogliomas compared to astrocytic tumors.[61] Oligodendrogliomas are also known to have a higher microvessel density, consistent with increased CBV values found in oligodendrogliomas.[59] These data demonstrate that high microvessel density in gliomas does not necessarily relate to endothelial cell proliferation (see Figure 5).

In application to daily clinical practice, molecular PET imaging techniques may be used in diagnostic evaluation of suspected gliomas when conventional diagnostics fail to give reliable information or are considered too insensitive.[62] In such scenarios, [^{11}C]methionine may change clinical decisions for patients with brain tumor.[63] [^{11}C]Methionine can assist in differential diagnosis of tumor from nontumor lesions. In a consecutive series of 196 patients with suspected brain tumors, differentiation between gliomas and nontumor lesions by [^{11}C]methionine was correct in 79%, using a baseline threshold of 1.47 for [^{11}C]methionine uptake. Diagnosis was verified by histological examination in 170 patients or by clinical follow-up and additional investigations (cerebrospinal fluid examination or follow-up MRI) in the remainder.[28]

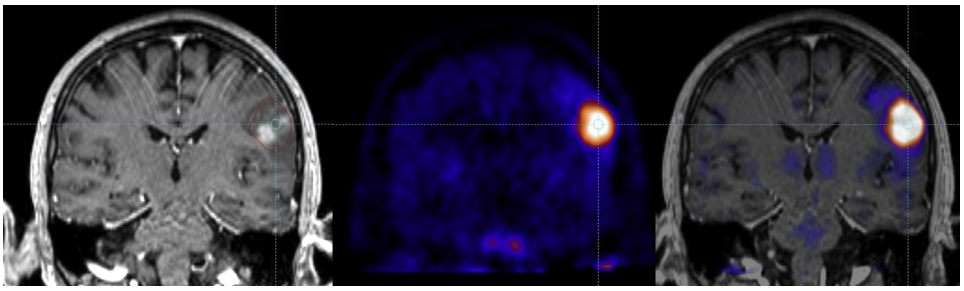


FIGURE 4 MR, [^{11}C]methionine PET, coregistered [^{11}C]methionine PET to MR; 59-year-old male with a remote history of carcinoid tumor of the abdomen. [^{11}C]Methionine PET scan demonstrates intense uptake with an estimation of the full extent of tumor volume greater than that seen on intravenous contrast-enhanced T1-weighted MR. The contrast-enhanced MR tumor volume was measured as 2.3 cm^3 versus [^{11}C]methionine tumor volume measured as 9.6 cm^3. [^{11}C]Methionine PET image guidance was used for stereotactic single-pass biopsy target. Final pathology was consistent with glioblastoma multiforme, WHO grade IV. *Courtesy of the Charles F. Kettering Memorial Hospital Department of Nuclear Medicine/PET.*

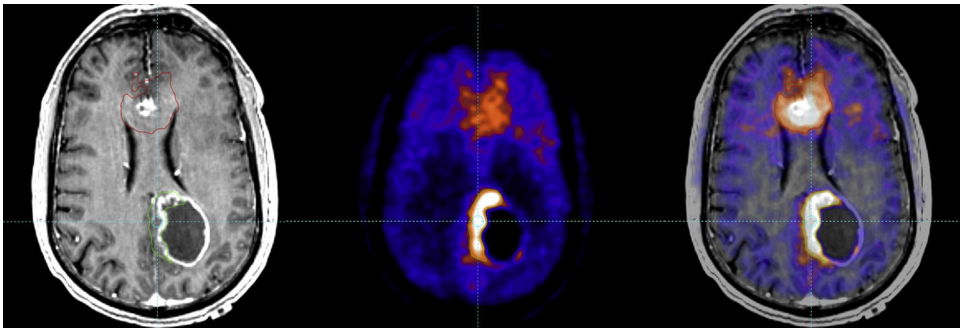


FIGURE 5 MR, [^{11}C]methionine PET, coregistered [^{11}C]methionine PET to MR, 76-year-old male at the time of initial diagnosis. [^{11}C]Methionine demonstrated multifocal abnormalities and distinguished between viable tumor components versus necrotic or cystic changes. [^{11}C]Methionine PET image guidance was utilized for stereotactic single-pass biopsy, targeting the highest potential grade viable tumor component (crosshairs). Final pathology was consistent with glioblastoma multiforme, WHO grade IV. *Courtesy of the Charles F. Kettering Memorial Hospital Department of Nuclear Medicine/PET.*

In a series of 39 children and young adults (between 2 and 21 years of age) with suspected brain neoplasms, the diagnostic accuracy of [^{11}C]methionine with regard to differentiating tumors from nontumor brain lesions showed a sensitivity of 83% and a specificity of 92%.[64]

The combination of [^{18}F]FDG and [^{11}C]methionine for guidance of stereotactic biopsy was studied in 32 patients with unresectable gliomas.[80] The dual-tracer approach was proposed for these patients because they presented with a tumor considered unresectable and located in the cortical or subcortical gray matter, and therefore likely to be of lower sensitivity on [^{18}F]FDG. PET images were coregistered with MRI and were analyzed to determine which tracer offered the best information for target (resection) definition. All 32 patients had histologically documented glioma: 10 glioblastomas, 12 anaplastic astrocytomas, and 10 low-grade gliomas. [^{18}F]FDG uptake was equal to or less than uptake in the surrounding gray matter in 18 patients, including 3 with glioblastoma, 6 with anaplastic astrocytoma, and 9 with low-grade glioma. [^{18}F]FDG was used for target selection when its uptake was found to be higher in tumor than in gray matter (14 patients).

[^{11}C]Methionine was used for target selection when [^{18}F]FDG uptake was less than or equal to uptake in gray matter (18 patients). Sixty-one of the 70 stereotactic trajectories were based on PET-defined targets and showed abnormal [^{11}C]methionine uptake. All 61 [^{11}C]methionine-positive trajectories yielded a diagnosis of tumor. The remaining nine trajectories were [^{11}C]methionine negative and nondiagnostic. The authors concluded from the study that because [^{11}C]methionine provides a more sensitive signal, it is the tracer of choice for single-tracer PET-guided neurosurgical procedures on gliomas[65] (see Figure 6).

There is a relationship between angiogenesis and amino acid uptake.[41,49] Often, functional imaging with [^{11}C]methionine reveals a larger volume of tumor than that demonstrated on contrast-enhanced MRI, indicating additional regions of tumor infiltration.[66] In a series of 30 patients with suspected primary or recurrent brain tumor on MRI, patients were investigated with [^{11}C]methionine, which was utilized to plot stereotactic biopsy utilizing intraoperative neuronavigation. [^{11}C]Methionine demonstrated a sensitivity of 87% and a specificity of 89% for detection of solid tumor and demonstrated significantly higher uptake in areas of infiltration[58] (see Figure 7).

In another series, 442 children (birth through 15 years of age) were referred for evaluation of a newly diagnosed brain lesion. Of these, 85 were studied with PET utilizing

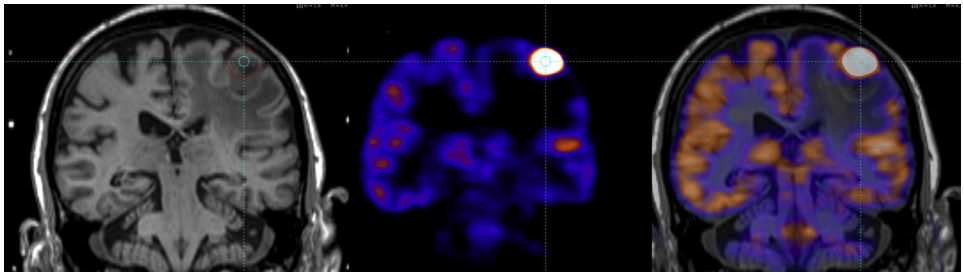


FIGURE 6 MR, [^{11}C]methionine PET, coregistered [^{11}C]methionine PET to MR; 52-year-old male at the time of initial diagnosis. [^{11}C]Methionine PET scan demonstrated intense, well-circumscribed accumulation. Contemporaneous intravenous contrast-enhanced T1-weighted MR demonstrated no associated corresponding anatomic abnormality. There was a substantial discrepancy between [^{11}C]methionine PET and MRI tumor volume estimation on T2-weighted fluid-attenuated inversion recovery sequence images (not shown). The smaller [^{11}C]methionine PET total tumor volume estimation qualified the patient for Gamma Knife radiosurgery as a treatment option. [^{11}C]Methionine PET tumor volume was used in Gamma Knife radiosurgery planning. Final pathology was consistent with metastatic melanoma. *Courtesy of the Charles F. Kettering Memorial Hospital Department of Nuclear Medicine/PET.*

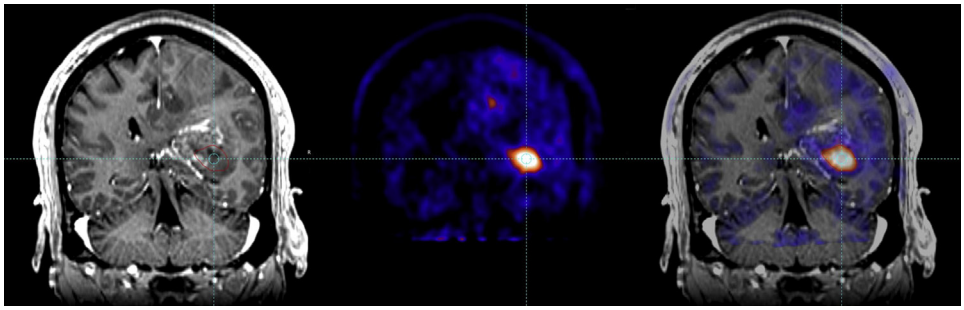


FIGURE 7 MR, [^{11}C]methionine PET, coregistered [^{11}C]methionine PET to MR; 52-year-old male at the time of initial diagnosis. [^{11}C]Methionine PET scan demonstrates intense, focal tracer accumulation in a region heterogeneous in appearance on contemporaneous intravenous contrast-enhanced T1-weighted MR images. [^{11}C]Methionine PET image guidance was used for stereotactic single-pass biopsy target with [^{11}C]methionine PET total tumor volume used in resection margin planning. Final pathology was consistent with an oligodendroglioma, WHO grade II (with 1p19q codeletion). *Courtesy of the Charles F. Kettering Memorial Hospital Department of Nuclear Medicine/PET.*

FDG PET and/or [11C]methionine in cases in which MR images were unable to assist in selecting accurate biopsy targets (35 patients) or to delineate tumors for maximal resection (50 patients). In surgical cases, PET and MR images were combined in image fusion planning for stereotactic biopsies or navigation-based resections. The preoperative planning images were compared postoperatively with MRI and PET findings and histological data for evaluating the clinical impact on the diagnostic yield and tumor resection. The PET data influenced surgical decisions or procedures in all cases.

The use of PET imaging helped to better differentiate indolent from active components in complex lesions (in 12 patients), improved target selection and diagnostic yield of stereotactic biopsies without increasing the sampling (see Figure 8), provided additional prognostic information, reduced the amount of tissue needed for biopsy sampling in brain-stem lesions (in 20 cases), better delineated lesions that were poorly delineated on MRI and that infiltrated functional cortex (in 50 cases), significantly increased the amount of tumor tissue removed in cases in which total resection influenced survival (in 20 cases), guided resection in hypermetabolic areas (in 15 cases), improved early postoperative detection of residual tumor (in 20 cases), avoided unnecessary reoperation (in 5 cases), and supported the decision to undertake early second-look resection (in 8 cases) (see Figure 9).[67]

In another study, PET-guided volumetric resection in high-grade gliomas was evaluated in a series of 66 consecutive patients who underwent preoperative PET imaging with [18F]FDG and [11C]methionine, which was then coregistered with MR images for image-guided surgery. In all cases (35 anaplastic gliomas—20 astrocytomas, 10 oligoastrocytomas, 5 oligodendrogliomas—and 31 glioblastomas), the level and distribution of PET

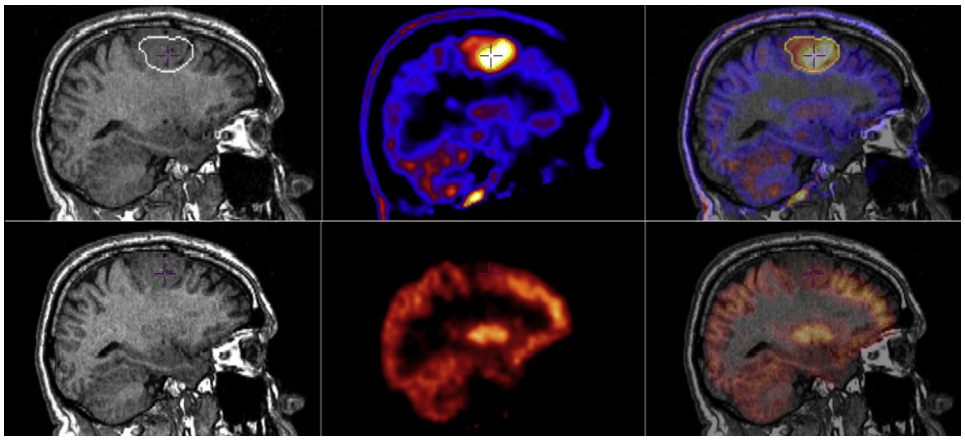


FIGURE 8 Row 1, MR, [11C]methionine PET, coregistered [11C]methionine PET to MR; row 2, MR, [18F]FDG PET, coregistered [18F]FDG PET to MR; 58-year-old male at the time of initial diagnosis. PET scans demonstrated elevated [11C]methionine (row 1) uptake with decreased [18F]FDG (row 2) uptake, suggestive of low-grade histology. [11C]Methionine PET image guidance was used for stereotactic single-pass biopsy target with [11C]methionine PET total tumor volume used in resection margin planning. Final pathology was consistent with astrocytoma, WHO grade II. *Courtesy of the Charles F. Kettering Memorial Hospital Department of Nuclear Medicine/PET.*

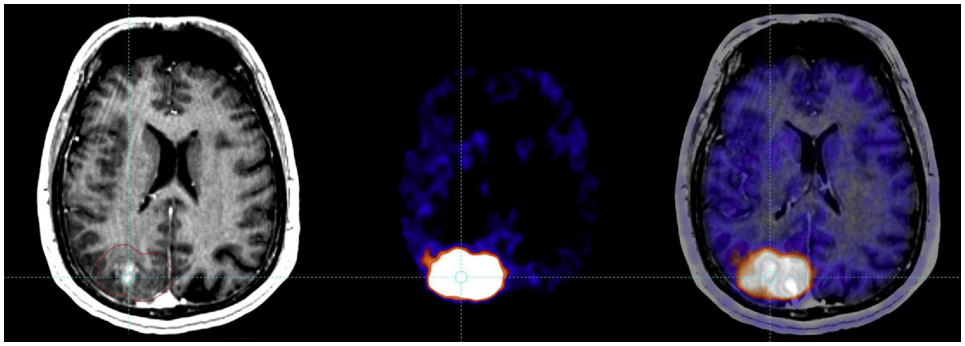


FIGURE 9 MR, [11C]methionine PET, coregistered [11C]methionine PET to MR; 66-year-old male at the time of initial diagnosis. [11C]Methionine PET scan demonstrated intense uptake with an estimation of full extent of tumor volume greater than that seen on intravenous contrast-enhanced T1-weighted MR. Contrast-enhanced MR tumor volume was estimated at 6.8 cm^3 versus [11C]methionine tumor volume estimation of 33.7 cm^3. [11C]Methionine PET image guidance was used for stereotactic single-pass biopsy target with [11C]methionine PET total tumor volume used in resection margin planning. Final pathology was consistent with glioblastoma multiforme, WHO grade IV. *Courtesy of the Charles F. Kettering Memorial Hospital Department of Nuclear Medicine/PET.*

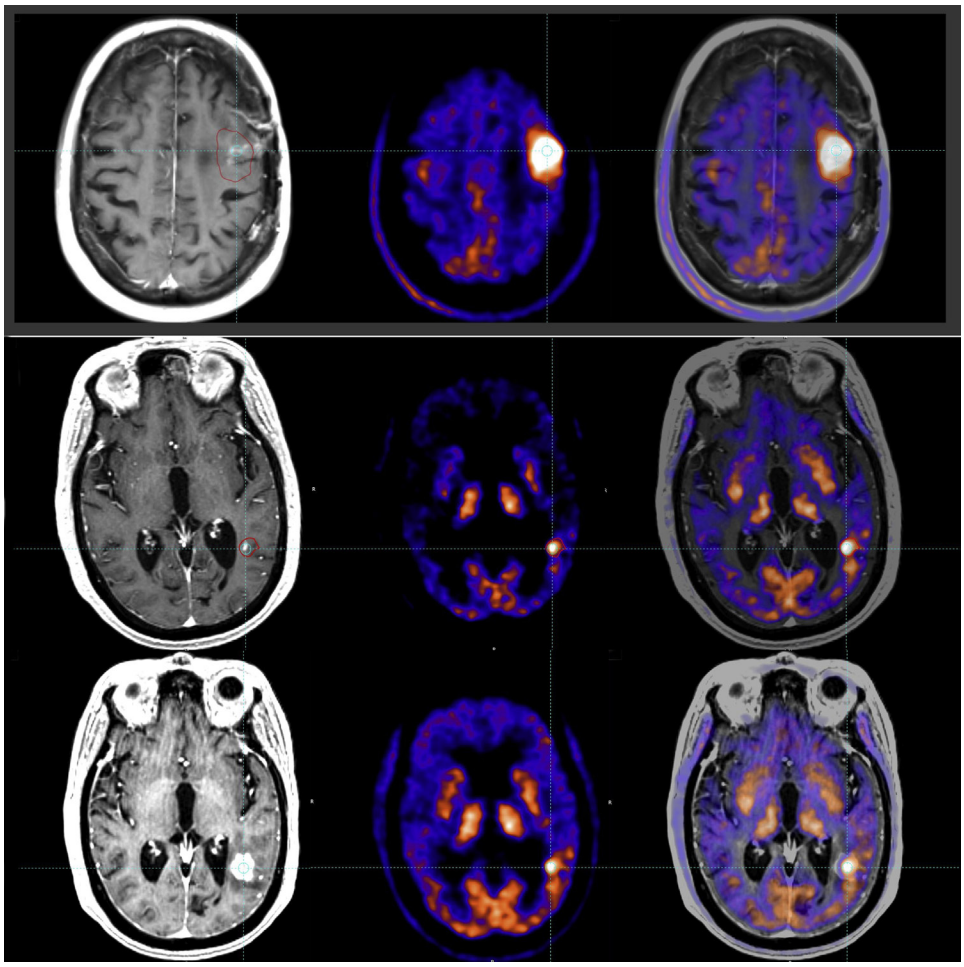


FIGURE 10A Row 1, MR, [^{11}C]methionine PET, coregistered MR to PET; row 2, MR, [^{11}C]methionine PET, coregistered MR to PET; row 3, MR, [^{11}C]methionine PET, coregistered MR to PET; 64-year-old female at the time of initial diagnosis; glioblastoma, WHO grade IV. Follow-up [^{11}C] methionine PET scan (row one) performed 4 years after initial surgery demonstrated intense tracer uptake consistent with residual/recurrent tumor volume adjacent to the original site of resection in the left frontotemporal lobe. [^{11}C]Methionine PET scan repeated 3 months later (row 2) demonstrated focal abnormal tracer accumulation in the posterior periventricular left lateral ventricle corresponding to a new focal abnormality on contemporaneously performed contrast-enhanced T1-weighted MR. Intravenous contrast-enhanced MR repeated an additional 3 months later demonstrated interval progression of an anatomic abnormality on intravenous contrast-enhanced T1-weighted MR in the posterior periventricular left lateral ventricle corresponding to the site of focal abnormal tracer accumulation on the prior [^{11}C]methionine PET. [^{11}C]Methionine PET images were utilized in surgical planning including PET-guided stereotactic first-pass biopsy followed by a PET image-guided Neuroblate laser thermoablation procedure. Final pathology was consistent with high-grade glioblastoma, WHO grade IV. *Courtesy of the Charles F. Kettering Memorial Hospital Department of Nuclear Medicine/PET.*

tracer uptake were analyzed to define a PET contour projected on MRI scans to define a final target contour for volumetric resection. Maximal tumor resection was accomplished in each case, with the intention to remove the entire abnormal metabolic area, as defined on PET, comprised in the surgical planning. Early postoperative MRI and PET assessed tumor resection. Survival analysis was performed separately in anaplastic gliomas and glioblastoma multiforme according to the presence or absence of residual tracer uptake on postoperative PET and according to the presence or absence of residual contrast enhancement on postoperative MRI.

In all procedures, PET contributed to defining a final target contour different from that obtained with MRI alone. Postoperatively, 46 of 66 patients had no residual PET tracer uptake (total PET resection), 23 of 66 had no residual MRI contrast enhancement. No additional neurological morbidity due to the technique was reported. A total PET tracer uptake resection was associated with a significantly longer survival in anaplastic gliomas ($P = 0.0071$) and in glioblastoma multiforme ($P = 0.0001$). A total MRI contrast-enhancement resection was not correlated with a significantly better survival, neither in anaplastic gliomas ($P = 0.6089$) nor in glioblastoma multiforme ($P = 0.6806$) (see Figures 10 (A), (B) and 11).[68]

In the posttreatment follow-up and management of patients with brain tumor, the differentiation between recurrent tumor (as a sign of treatment failure) and

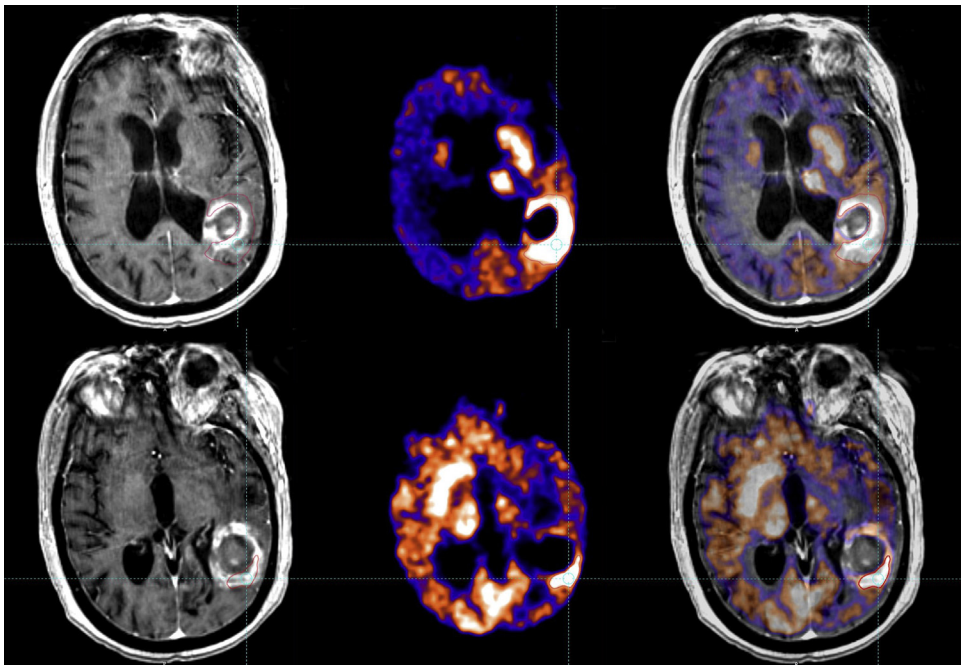


FIGURE 10B Row 1, MR, [^{11}C]methionine PET, coregistered MR to PET; row 2, MR, [^{18}F]FDG PET, coregistered MR to PET. *Courtesy of the Charles F. Kettering Memorial Hospital Department of Nuclear Medicine/PET.*

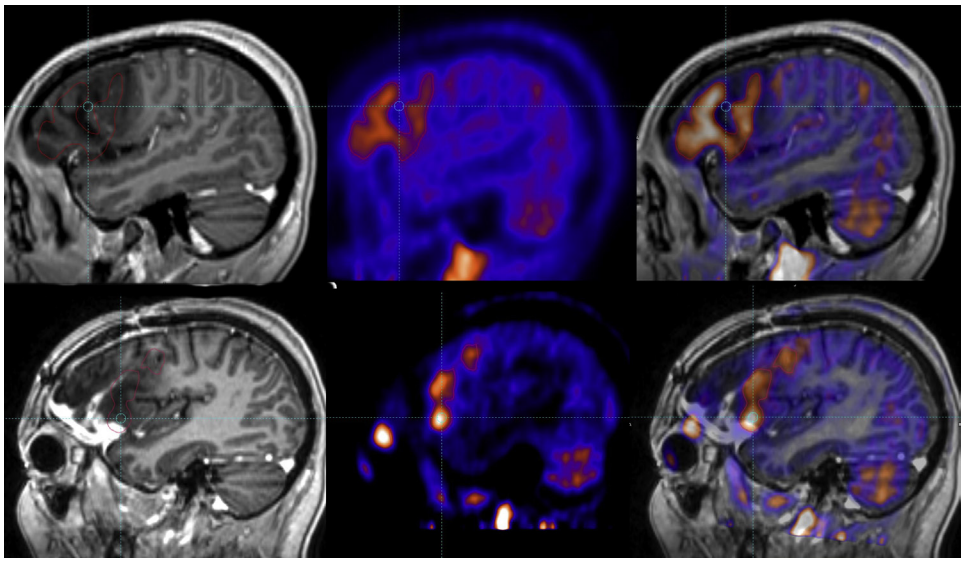


FIGURE 11 Row 1, MR, [^{11}C]methionine PET, coregistered [^{11}C]methionine PET to MR; row 2, MR, [^{11}C]methionine PET, coregistered [^{11}C]methionine PET to MR; 29-year-old female at time of initial diagnosis. [^{11}C]Methionine PET scan was done at the time of initial diagnosis (row 1). [^{11}C]Methionine PET total tumor volume estimation was used in image-guided surgery for stereotactic single-pass biopsy target and resection margin planning. Final pathology was consistent with oligodendroglioma, WHO grade II. [^{11}C]Methionine PET scan was repeated months after resection (row 2), demonstrating focal residual/recurrent tumor at the periphery of the resection margins. [^{11}C]Methionine PET scan information led to additional surgery. *Courtesy of the Charles F. Kettering Memorial Hospital Department of Nuclear Medicine/PET.*

necrosis (as an indicator of success) is essential. For that application, [^{11}C]methionine PET coregistered to MRI has a reported high sensitivity and specificity (~75%) (see Figure 12).[69–72]

As PET imaging with [^{11}C]methionine has been demonstrated to be useful in the delineation of tumor volume, the technique has been successfully used for planning of target volume prior to radiotherapy.[73] PET (or SPECT)/MRI fusion with [^{11}C]methionine and ^{123}I-labeled α-methyltyrosine was studied in 44 patients with recurrent glioblastoma after surgery and postoperative conventional radiotherapy. Fused imaging was used to delineate the volume in planning for fractional stereotactic radiotherapy. This volume was compared with the

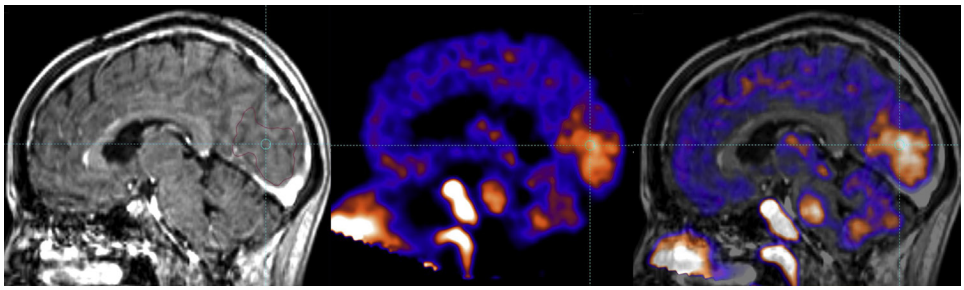


FIGURE 12 MR, [^{11}C]methionine PET, coregistered [^{11}C]methionine PET to MR; 36-year-old female at the time of initial diagnosis. [^{11}C]Methionine PET scan demonstrated intense uptake with an estimation of full extent of tumor volume greater than that seen on contemporaneously acquired intravenous contrast-enhanced T1-weighted MR, which does not show an associated anatomic abnormality in the same region. Contrast-enhanced MR tumor volume is indiscernible versus [^{11}C]methionine tumor volume measured as 18.4 cm^3. Final pathology was consistent with astrocytoma, WHO grade III. *Courtesy of the Charles F. Kettering Memorial Hospital Department of Nuclear Medicine/PET.*

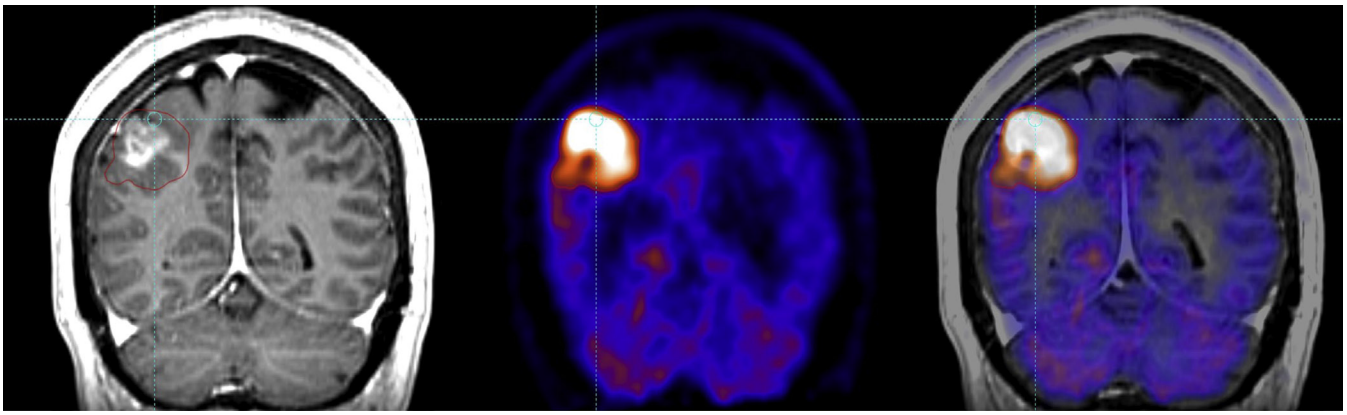


FIGURE 13A MR, [^{11}C]methionine PET, coregistered [^{11}C]methionine PET to MR; 66-year-old female. [^{11}C]Methionine PET scan demonstrated intense uptake with an estimation of full extent of tumor volume greater than that seen on intravenous contrast-enhanced T1-weighted MR. Contrast-enhanced MR tumor volume was measured as 9.6 cm^3 versus [^{11}C]methionine PET tumor volume measured as 18.5 cm^3. [^{11}C]Methionine PET image guidance was used for stereotactic single-pass biopsy target with [^{11}C]methionine PET total tumor volume used in resection margin planning. Final pathology was consistent with glioblastoma multiforme, WHO grade IV. *Courtesy of the Charles F. Kettering Memorial Hospital Department of Nuclear Medicine/PET.*

volume determined using CT or MRI alone. A significant survival advantage was found: a 9-month median survival in patients whose treatment volume was based on fused PET/MRI, versus a 5-month median survival in patients whose treatment planning was based on CT or MRI alone[74] (see Figures 13 (A) and (B)).

There is considerable uncertainty with regard to the indication for and the chances of success of chemotherapy in patients with gliomas.[75] Because chemotherapy may have substantial side effects that interfere with the quality of life, a method to assess its efficacy early during treatment is needed. Monitoring of metabolic changes in tumors may provide an objective measure of response to treatment with temozolomide (TMZ). In the event of tumor resistance to TMZ, one could switch to a second-line chemotherapeutic regimen with potentially different agents before bone marrow reserves are compromised. With conventional anatomic imaging with CT and MRI, the extent of contrast enhancement in malignant gliomas has been used as an indicator of therapeutic response, and definitions have been proposed for partial response, minor response, stable disease, or progressive disease.[76]

Contrast enhancement, however, is dependent upon BBB damage and necrosis, which may be induced by therapy or occur spontaneously during tumor progression, making contrast enhancement an unreliable distinguishing feature in differentiating posttherapy changes from tumor residual, recurrence, or progression after therapy.[77] Therefore, imaging of the effectiveness of anticancer therapy by assessing the extent of MRI contrast enhancement is limited by the lack of distinction between tumor extent and contrast-enhancing necrosis. In addition, contrast uptake may be substantially reduced by dexamethasone, which is often necessary to reduce edema in progressing tumors and thus confounds contrast enhancement as an indicator of therapeutic efficiency.[78,79]

Since morphological imaging often does not adequately reflect underlying tumor biology and its metabolic activity, there is a considerable incentive to develop alternative measures of therapeutic response in humans. [^{18}F]FDG has been successfully used to

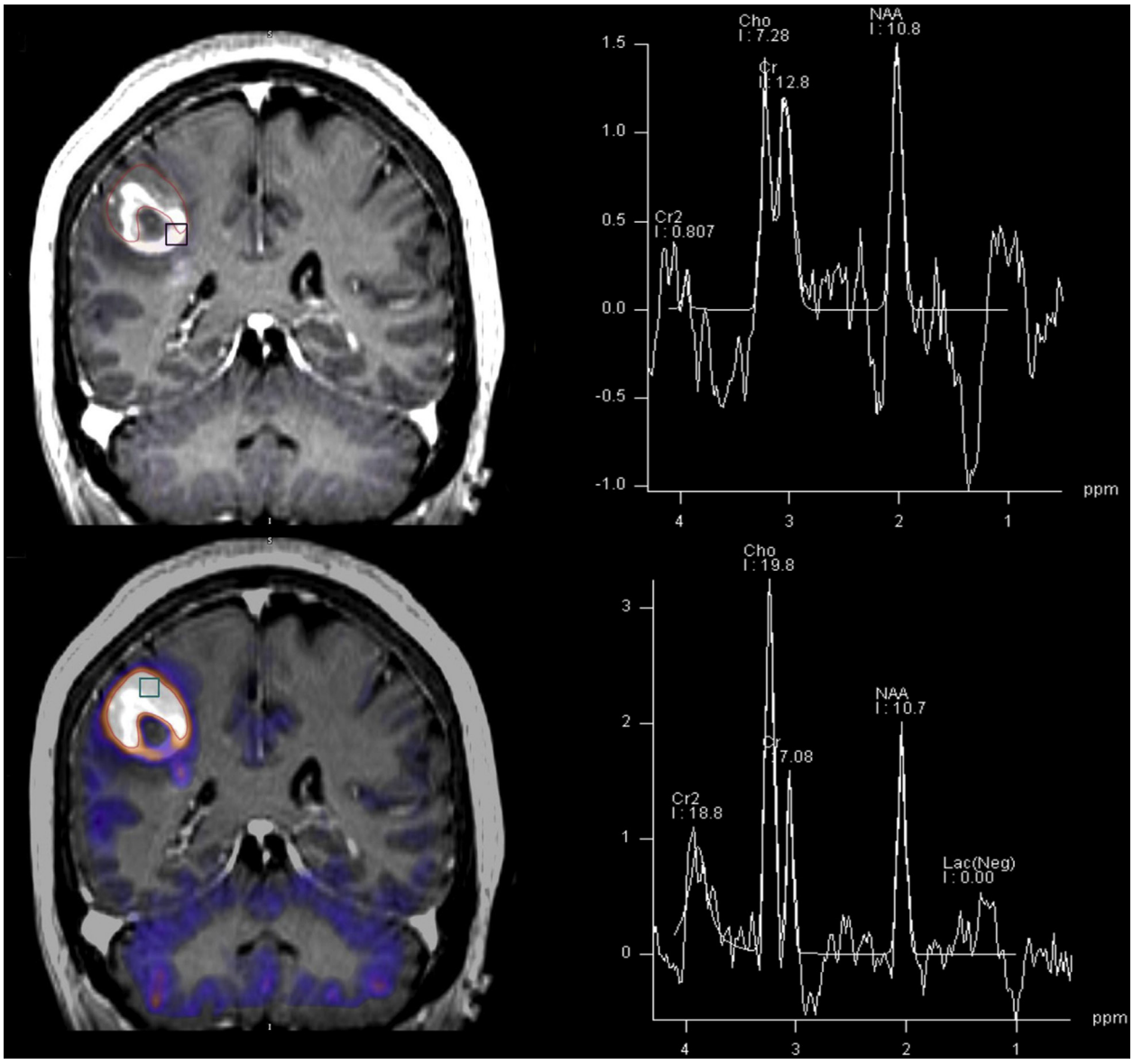


FIGURE 13B Intravenous contrast-enhanced T1-weighted MR, MR-guided MR spectroscopy, coregistered [^{11}C]methionine PET to MR, [^{11}C]methionine PET-guided MR spectroscopy, MR-guided MR spectroscopy demonstrating nonelevated choline levels relative to *N*-acetylaspartate levels suggestive of nonmalignant etiology. [^{11}C]Methionine PET-guided MR spectroscopy demonstrating elevated choline to *N*-acetylaspartate ratio concordant with malignant etiology (biopsy-proven). [^{11}C]Methionine PET scan demonstrates heterogeneous uptake with the most focal and intense tracer accumulation demarcating viable tumor components versus necrotic or cystic changes. Final pathology was consistent with glioblastoma multiforme, WHO grade IV. *Courtesy of the Charles F. Kettering Memorial Hospital Department of Nuclear Medicine/PET.*

monitor TMZ chemotherapy in gliomas.[80] However, FDG uptake is known to be nonspecific, with high FDG accumulation observed not only in viable cancer cells but also in inflammatory cells and granulation tissue.[81] A further clinically relevant issue is the limited contrast between normal brain tissue and some lower grade tumors, which increases the potential for false-negative FDG PET studies.[46] Therefore, other metabolic tracers, such as positron-emitter-labeled amino acids, have been proposed as new indicators of tumor activity.[46]

Several studies have demonstrated metabolic functional imaging with [^{11}C]methionine and amino acid PET imaging to be able to detect response to chemotherapy early in the course of treatment, suggesting that deactivation of amino acid transport is an early sign of response to chemotherapy.[89–91]

In a case report, the effect of chemotherapy with procarbazine, CCNU, and vincristine in an anaplastic oligoastrocytoma was successfully monitored by serial [^{11}C]methionine PET scans, highlighting the potential of this technique to monitor chemotherapy.[82] It provides a more accurate assessment of tumor extent than does contrast enhancement on CT and MRI.[28,58,83,84] Accumulation is largely due to carrier-mediated transport, which

is not altered by dexamethasone and permits distinction between tumors and contrast-enhancing necrosis.[28,85,86] [11C]Methionine is transported by the LAT1 amino acid transporter, which is highly expressed in cultured cells and malignant tumors.[27,87] Once transported into cells, [11C]methionine undergoes complex metabolism and is incorporated into proteins, suggesting that uptake may reflect the metabolic needs of brain tumors.[88] Several studies have demonstrated metabolic functional imaging with [11C]methionine and amino acid PET imaging to be able to detect response to chemotherapy early in the course of treatment, suggesting that deactivation of amino acid transport is an early sign of response to chemotherapy.[89–91]

In summary, an accurate, more comprehensive assessment of brain tumor extent and biology is frequently more feasible with metabolic [11C]methionine amino acid PET imaging compared to morphologic contrast-enhanced, high-resolution MR or CT scans. The disparity in tumor volume measured via [11C]methionine scans versus MR or CT scans is greatest in the assessment of low-grade gliomas. In addition, as the current WHO classification scheme gives way to more specific genomic profiling, the ability to predict low-grade gliomas that are on the verge of high-grade transformation will become an additional important clinical qualifier directing treatment strategy. This will add even more value to PET biochemical imaging, with novel PET radiopharmaceutical development resulting in the ability to image, and therefore characterize, more complex tumor biology.

Thus, functional and metabolic imaging with PET will continue to expand and further assist neuro-oncologists in gaining deeper insight into tumor biology through "true molecular imaging." When fully integrated as an applied science within a comprehensive multidisciplinary clinical program, PET imaging information combined with morphologic imaging information can be utilized to optimize the full course of patient care, from improving initial diagnosis through guidance toward more specific, personalized treatment plans.

References

1. Dolecek TA, Propp JM, Stroup NE, Kruchko C. CPTRUS statistical report: primary brain and central nervous tumors diagnosed in the United States in 2005-2009. *Neuro-oncol*. 2012;14(suppl 5):v1–v49.
2. Kleihues P, Cavenee WK. *Tumors of the Nervous System*. Lyon, France: International Agency for Research on Cancer; 1997.
3. Louis DN, Ohgaki H, Wiestler OD, et al. The 2007 WHO classification of tumours of the central nervous system. *Acta Neuropathol*. 2007;114:97–109.
4. Yang P, Wang Y, Peng X, et al. Management and survival rates in patients with glioma in China (2004-2010): a retrospective study from a single institution. *J Neurooncol*. 2013;113:259–266.
5. Paulus W, Peiffer J. Intratumoral histologic heterogeneity of gliomas: a quantitative study. *Cancer*. 1989;64:442–447.
6. Fougere C, Suchorska B, Bartenstein P, et al. Molecular imaging of gliomas with PET: opportunities and limitations. *Neuro-Oncology*. 2011;13(8):806–819.
7. Gambhir SS. Molecular imaging of cancer with positron emission tomography. *Nat Rev Cancer*. 2002;2:683–693.
8. Di Chiro G. Positron emission tomography using [18F] fluorodeoxyglucose in brain tumors. A powerful diagnostic and prognostic tool. *Invest Radiol*. 1987;22:360–371.
9. Di Chiro G, DeLaPaz RL, Brooks RA, et al. Glucose utilization of cerebral gliomas measured by [18F] fluordeoxyglucose and positron emission tomography. *Neurology*. 1982;32:1323–1329.
10. Patronas NJ, Di Chiro G, Brooks RA, et al. [18F] fluorodeoxyglucose and positron emission tomography in the evaluation of radiation necrosis of the brain. *Radiology*. 1982;144:885–889.
11. Di Chiro G, Oldfield E, Wright DC, et al. Cerebral necrosis after radiotherapy and/or intrarterial chemotherapy for brain tumors: PET and neuropathologic studies. *AJR*. 1988;150:189–197.
12. Wong TZ, van der Westhuizen GJ, Coleman RE. Positron emission tomography imaging of brain tumors. *Neuroimaging Clin N Am*. 2002;12:615–626.
13. Nagamatsu S, Sawa H, Wakizaka A, et al. Expression of facilitative glucose transporter isoforms in human brain tumors. *J Neurochem*. 1993;61:2048–2053.
14. Alavi JB, Alavi A, Chawluk J, et al. Positron emission tomography in patients with glioma. A predictor of prognosis. *Cancer*. 1988;62:1074–1078.
15. Herholz K, Peitrzyk U, Voges J, et al. Correlation of glucose consumption and tumor cell density in astrocytomas: a stereotactic PET study. *J Neurosurg*. 1993;79:853–858.
16. Patronas NJ, Di Chiro G, Kufta, et al. Prediction of survival in glioma patients by means of positron emission tomography. *J Neurosurg*. 1985;62:816–822.
17. Barker II FG, Chang SM, Valk PE, et al. 18-fluorodeoxyglucose uptake and survival of patients with suspected recurrent malignant glioma. *Cancer*. 1997;79:115–126.
18. Padoma MV, Said S, Jacobs M, et al. Prediction of pathology and survival by FDG PET in gliomas. *J Neurooncology*. 2003;64:227–237.
19. De Witte O, Levivier M, Violon P, et al. Prognostic value of positron emission tomography imaging with [18F]fluoro-2-D-glucose in the low-grade glioma. *J Neurosurg*. 1996;39:470–477.
20. Olivero WC, Dulebohn SC, Lister JR. The use of PET in evaluating patients with primary brain tumors: is it useful? *J Neurol Neurosurg Psychiatry*. 1995;58:250–252.
21. Ricci PE, Karis JP, Heiserman JE, et al. Differentiating recurrent tumor from radiation necrosis: time for re-evaluation of positron emission tomography? *Am J Neuroradiol*. 1998;19:407–413.
22. Weber W, Bartenstein P, Gross MW, et al. Fluorine-18-FDG PET and iodine-123-IMT SPECT in the evaluation of brain tumors. *J Nucl Med*. 1997;38:802–808.
23. Chen W. Clinical applications of PET in brain tumors. *J Nucl Med*. 2007;48:1468–1481.
24. Krohn KA, Mankaoff DA, Muzi M, et al. True tracers: comparing FDG with glucose and FLT with Thymidine. *Nucl Med Biol*. 2005;32:663–671.
25. Schifter T, Hoffman JM, Hanson MW, et al. Serial FDG-PET studies n the prediction of survival in patients with primary brain tumors. *J Comput Assist Tomogr*. 1993;17:509–561.
26. Ishiwata K, Kutota K, Murakami M, et al. Re-evaluation of amino acid PET studies: can the protein synthesis rates in brain and tumor tissues be measured in vivo? *J Nucl Med*. 1993;34:1936–1943.
27. Jager PL, Vaalburg W, Pruim J, et al. Radiolabeled amino acids: basic aspects and clinical applications in oncology. *J Nucl Med*. 2001;42:432–445.
28. Herholz K, Holzer T, Bauer B, et al. 11C-Methionine PET for differential diagnosis of low-grade gliomas. *Neurology*. 1998;50:1316–1322.
29. Laverman P, Boerman OC, Corstens FH, et al. Fluorinated amino acids for tumour imaging with postitron emission tomography. *Eur J Nucl Med Mol Imaging*. 2002;29:681–690.

30. Weber WA, Waster JH, Grosu AL, et al. *O*-(2-[18F]fluoroethyl)-L-tyrosine and L-[methyl-11C]methionine uptake in brain tumors: initial results of a comparative study. *Eur J Nucl Med*. 2000;27:542–549.
31. Becherer A, Karanikas G, Szabo M, et al. Brain tumour imaging with PET: a comparison between [18F]flluorodopa and [11C]methionine. *Eur J Nucl Med Mol Imaging*. 2003;30:1561–1567.
32. Beuthien-Baumann B, Bredow J, Burchert W, et al. 3-*O*-Methyl-6-[18F]fluoro-L-DOPA and its evaluation in brain tumour imaging. *Eur J Nucl Med Mol Imaging*. 2003;30:1004–1008.
33. Chen W, Silverman DHS, Delaloye S, et al. 18F-FDOPA PET imaging of brain tumors: comparison study with 18F-FDG PET and evaluation of diagnostic accuracy. *J Nucl Med*. 2006;47:904–911.
34. Isselbacher KJ. Sugar and amino acid transport by cells in culture: differences between normal and malignant cells. *N Engl J Med*. 1972;286:929–933.
35. Busch H, Davis JR, Honig GR, et al. The uptakes of a variety of amino acids into nuclear proteins of tumors and other tissues. *Cancer Res*. 1959;19:1030–1039.
36. Miyagawa T, Oku T, Uehara H, et al. "Facilitated" amino acid transport is upregulated in brain tumors. *J Cereb Blood Flow Metab*. 1998;18:500–509.
37. Sasajima T, Miyagawa T, Oku T, et al. Proliferation-dependent changes in amino acid transport and glucose metabolism in glioma cell lines. *Eur J Nucl Med Mol Imaging*. 2004;31:1244–1256.
38. Roelcke U, Radu EW, von Ammon K, et al. Alteration of blood–brain barrier in human brain tumors: comparison of [18F]fluorodeoxyglucose, [11C]methionine and rubidium-82 using PET. *J Neurol Sci*. 1995;132:20–27.
39. Bergstrom M, Lundqvist H, Ericson K, et al. Comparison of the accumulation kinetics of L-(methyl-C)-methionine and D-(methyl-C)-methionine in brain tumors studied with positron emission tomography. *Acta Radiol*. 1987;28:225–229.
40. Sato N, Suzuki M, Kuwata N, et al. Evaluation of the malignancy of glioma using C-methionine positron emission tomography and proliferating cell nuclear antigen staining. *Neurosurg Rev*. 1999;22:210–214.
41. Kracht M, Friese M, Herholz K, et al. Methyl-[C]-L-methionine uptake as measured by positron emission tomography correlates to microvessel density in patients with glioma. *Eur J Nucl Med Mol Imaging*. 2003;30:868–873.
42. Okita Y, Kinoshita M, Goto T, et al. C-methionine uptake correlates with tumor cell density rather than with microvessel density in glioma: a stereotactic image-histology comparison. *Neuro Imag*. 2010;49:2977–2982.
43. Derlon JM, Bourdet C, Bustany P, et al. [11C]L-Methionine uptake in gliomas. *Neurosurg*. 1989;25:720–728.
44. Goldman S, Levivier M, Pirotte B, et al. Regional methionine and glucose uptake in high-grade gliomas: a comparative study on PET-guided stereotactic biopsy. *J Nucl Med*. 1997;38:1459–1462.
45. Sasaki M, Kuwabara Y, Yoshida T, et al. A comparative study of thallium-201 SPECT, carbon-11 methionine PET and fluorine-18 fluorodeoxyglucose PET for the differentiation of astrocytic tumours. *Eur J Nucl Med*. 1998;25:1261–1269.
46. Kaschten B, Stevenaert A, Sadzot B, et al. Preoperative evaluation of 54 gliomas by PET with fluorine-18-fluorodeoxyglucose and/or carbon-11-methionine. *J Nucl Med*. 1998;39:778–785.
47. Ogawa T, Shishido F, Kanno I, et al. Cerebral glioma: evaluation-with methionine PET. *Radiol*. 1993;186:45–53.
48. Ceyssens S, Van Laere K, de Groot T, et al. [11C]methionine PET, histopathology, and survival in primary brain tumors and recurrence. *Am J Neuroradiol*. 2006;27:1432–1437.
49. Ulrich RT, Kracht L, Brunn A, et al. Methyl-L-11C-Methionine PET as a diagnostic marker for malignant progression in patients with glioma. *J Nucl Med*. 2009;50:1962–1968.
50. Tanaka Y, Nariai T, Momose T, et al. Glioma surgery using a a multimodal navigation system with integrated metabolic images. *J Neurosurg*. 2009;110:163–172.
51. Grosu AL, Weber WA, Riedel E, et al. L-(methyl-11C) methionine positron emission tomography for target delineation in resected high-grade gliomas before radiotherapy. *Int J Radiat Oncol Biol Phys*. 2005;63:64–74.
52. Weber DC, Zilli T, Buchegger F, et al. [18F]fluoroethyltyrosin-positron emission tomography-guided radiotherapy for high-grade glioma. *Radiat Oncol*. 2008;3:44.
53. Vees H, Senthamizhchelvan S, Mirabell R, et al. Assessment of various strategies for 18F-FET PET-guided delineation of target volumes in high-grade glioma patients. *Eur J Nucl Med Mol Imaging*. 2009;36:182–193.
54. Nariai T, Tanaka Y, Wakimoto H, et al. Usefulness of L-[methyl-11C]methionine-positron emission tomography as a biological monitoring tool in the treatment of glioma. *J Neurosurg*. 2005;103: 498–507.
55. Pallud J, Varlet P, Devaux B, et al. Diffuse low-grade oligodendrogliomas extend bewond MRI-defined abnormalities. *Neurol*. 2010;74:1724–1731.
56. Pallud J, Capelle L, Taillandier L, et al. Prognostic significance of imaging contrast enhancement for WHO grade II gliomas. *Neuro Oncol*. 2009;11:176–182.
57. Dhermain FG, Hau P, Lanfermann H, et al. Advanced MRI and PET imaging for assessment of treatment response in patients with gliomas. *Lancet Neurol*. 2010;9:906–920.
58. Kracht LW, Miletic H, Busch S, et al. Delineation of brain tumor extent with [11C]L-methionine positron emission tomography: ocal comparison with stereotactic histopathology. *Clin Canc Res*. 2004;10:7163–7170.
59. Sadeghi N, Salmon I, Tang BN, et al. Correlation between dynamic susceptibility contrast perfusion MRI and methionine metabolism in brain gliomas: preliminary results. *J Mag Res Imaging*. 2006;24: 989–994.
60. Sadeghi N, Salmon I, Decaestecker C, et al. Stereotactic comparison among cerebral blood volume, methionine uptake, and histopathology in brain glioma. *Am J Neuroradiol*. 2007;28:455–461.
61. Derlon JM, Petit-Taboue MC, Chapon F, et al. The in vivo metabolic pattern of low-grade brain gliomas: a positron emission tomographic study using F-fluorodeoxyglucose and C-L-methylmethionine. *Neurosurgery*. 1997:276–288.
62. Minn H. PET and SPECT in low-grade glioma. *Eur J Radiol*. 2005;56:171–178.
63. Yamane T, Sakamoto S, Senda M. Clinical Impact of C-methionine PET on expected management of patients with brain neoplasm. *Eur J Nucl Med Mol Imag*. 2010;37:685–690.
64. Galldiks N, Kracht LW, Berthold F, et al. [C]-L-Methionine positron emission tomography in the management of children and young adults with brain tumors. *J Neuro-Onc*. 2010;96:231–239.
65. Pirotte B, Goldman S, Massager N, et al. Combined use of 18F-fluorodeoxyglucose and 11C-methionine in 45 positron emission tomography-guided stereotactic brain biopsies. *J Nucl Med*. 2004;45:1293–1298.
66. Ericson K, Lilja A, Bergstrom M, et al. Positron emission tomography with ([11C])methyl-L-methionine, [11C]D-glucose, and [68Ga]EDTA in supratentorial tumors. *J Comput Assist Tomogr*. 1985;9:683–689.
67. Pirotte B, Lubansu A, Massager N, et al. Clinical impact of integrating positron emission tomography during surgery in 85 children with brain tumors. *J Neurosurg Pediatr*. 2010;5:486–499.
68. Pirotte B, Levivier M, Goldman S, et al. Positron emission tomography-guided volumetric resection of supra tentorial high-grade gliomas: a survival analysis in 66 consecutive patients. *Neurosurgery*. 2009;64:471–481.
69. Thiel A, Pietrzyk U, Sturm V, et al. Enhanced accuracy in differential diagnosis of radiation necrosis by positron emission tomography-magnetic resonance imaging coregistration: technical case report. *Neurosurgery*. 2000;46:232–234.

70. Tsuyuguchi N, Takami T, Sunada I, et al. Methionine positron emission tomography for differentiation of recurrent brain tumor and radiation necrosis after stereotactic radiosurgery: In malignant glioma. *Ann Nucl Med*. 2004;18:291–296.
71. Terakawa Y, Tsuyuguchi N, Iwai Y, et al. Diagnostic accuracy of 11C-methionine PET for differentiation of recurrent brain tumors from radiation necrosis after radiotherapy. *J Nucl Med*. 2008;49:694–699.
72. Van Laere K, Ceyssens S, Van Calenbergh F, et al. Direct comparison of 18F-FDG and 11C-methionine PET in suspected recurrence of gllioma: sensitivity, inter-observer variability and prognostic value. *Eur J Nucl Med Mol Imaging*. 2005;32:39–51.
73. Nuutinen J, Sonninen P, Lehikoinen P, et al. Radiotherapy treatment planning and long-term follow up with [11C]methionine PET in patients with low-grade astrocytoma. *Inter J Rad Onc Biol Phys*. 2000;48:43–52.
74. Grosu AL, Weber WA, Franz M, et al. Reirradiation of recurrent high-grade gliomas using amino acid PET (SPECT)/CT/MRI image fusion to determine gross tumor volume for stereotactic fractional radiotherapy. *Int J Radiat Oncol Biol Phys*. 2005;63:511–519.
75. Burton EC, Prados MD. Malignant gliomas. *Curr Treat Options Oncol*. 2000;1:459–468.
76. Grant R, Liang BC, Slattery J, et al. Chemotherapy response criteria in malignant glioma. *Neurology*. 1997;48:1336–1340.
77. Levivier M, Becerra A, De Witte O, et al. Radiation necrosis or recurrence. *J Neurosurg*. 1996;84:148–149.
78. Cairncross JG, Macdonald DR, Pexman JH, et al. Steroid induced CT changes in patients with recurrent malignant glioma. *Neurology*. 1988;38:724–726.
79. Ostergaard L, Hochberg FH, Rabinov JD, et al. Early changes measured by magnetic resonance imaging in cerebral blood flow, blood volume, and blood–brain barrier permeability following dexamethasone treatment in patients with brain tumors. *J Neurosurg*. 1999;90:300–305.
80. Brock CS, Young H, O'Reily SM, et al. Early evaluation of tumour metabolic response using [18F]fluorodeoxyglucose and positron emission tomography: a pilot study following the phase II chemotherapy schedule for temozolomide I recurrent high-grade gliomas. *Br J Cancer*. 2000;82:608–615.
81. Kubota R, Yamada S, Kubota K, et al. Intratumoral distribution of fluorine-11-fluorodeoxyglucose in vivo: high accumulation in macrophages and granulation tissues studied by microautoradiography. *J Nucl Med*. 1992;33:1972–1980.
82. Herholz K, Kracht LW, Heiss WD. Monitoring the effect of chemotherapy in a mixed glioma by C-11-methionine PET. *J Neuroimaging*. 2003;13:269–271.
83. Tovi M, Lilja A, Bergstrom M, et al. Delineation of gliomas with magnetic resonance imaging using Gd-DTPA in comparison with computed tomography and positron emission tomography. *Acta Radiol*. 1990;31:417–429.
84. Pauleit D, Floeth F, Hamacher K, et al. O-(2-[18F]fluoroethyl)-L-tyrosine PET combined with MRI improves the diagnostic assessment of cerebral gliomas. *Brain*. 2005;128:678–683.
85. Reinhardt MJ, Kubota K, Yamada S, et al. Assessment of cancer recurrence I residual tumors after fractionated radiotherapy: a comparison of fluorodeoxyglucose, L-methionine and thymidine. *J Nucl Med*. 1997;38:280–287.
86. Sonoda Y, Kumabe T, Takahashi T, et al. Clinical usefulness of 11C-MET PET and 201Tl SPECT for differentiation of recurrent glioma from radiation necrosis. *Neurol Med Chir*. 1998;38:342–348.
87. Kim do K, Kanai Y, Choi HW, et al. Characterization of the system L amino acid transporter in T24 human bladder carcinoma cells. *Biochim Biophys Acta*. 2002;1565:112–121.
88. Bustany P, Chatel M, Derlon JM, et al. Brain tumor protein synthesis and histological grades: a study by positron emission tomography (PET) with C11-L-Methionine. *J Neurooncol*. 1986;3:397.
89. Galldiks N, Kracht LW, Burghaus L, et al. Use of 11C-methionine PET to monitor the effects of temozolomide chemotherapy in malignant gliomas. *Eur J Nucl Med Mol Imaging*. 2006;33:516–524.
90. Wyss M, Hofer S, Bruehlmeier M, et al. Early metabolic response in temozolomide treated low-grade glioma patients. *J Neurooncol*. 2009;95:87–93.
91. Galldiks N, Kracht LW, Burghaus L, et al. Patient-tailored, imaging-guided, long-term temozolomide chemotherapy in patients with glioblastoma. *Mol Imaging*. 2010;9:40–46.

CHAPTER

35

Ultra-High-Field Magnetic Resonance Imaging of Brain Tumors

Gregory A. Christoforidis

Department of Radiology, University of Chicago, Chicago, IL, USA

INTRODUCTION

The Food and Drug Administration has indicated that human imaging up to 8.0T is considered a "nonsignificant risk" for adults. Currently, imaging above 8.0T is available only on research protocols approved by an institutional review board and the informed consent of the subjects. Ultra-high-field (UHF) magnetic resonance imaging (MRI) generally refers to imaging at field strengths of 7T or more. This chapter reviews the current experience with the imaging of brain tumors at UHF strengths and potential clinical applications currently in transitional research.

Imaging of brain tumors attempts to define a tumor's anatomic location, its extent, and the intrinsic characteristics predictive tumor of behavior, as well as neurologic function that may be affected. MRI at higher field strengths has the potential to improve all of these goals. Compared to lower field strengths, the higher signal-to-noise ratio (SNR) obtained at higher field strengths allows for greater spatial resolution (leading to a more detailed assessment of the relationship of the tumor to adjacent structures such as gray matter, subarachnoid space, and blood vessels), more detailed MR spectroscopy (with ability to resolve more metabolites), and the ability to lead to higher resolution multinuclear imaging (phosphorus, sodium, etc.) and chemical exchange saturation transfer (CEST) imaging. Although higher field strength has resulted in greater spatial resolution, the visualized extent of brain tumors imaged at 8 and 1.5T has not differed. Finally, because greater susceptibility effects occur at higher field strengths, elements present within the tumor bed with greater magnetic susceptibility are expected to contrast against the tumor background. Such components may include foci of hemorrhage, iron-containing structures or components labeled with susceptibility-based contrast agents, and vessels containing deoxyhemoglobin. Technical and clinical challenges exist, which need to be overcome to realize the full potential of brain tumor imaging at UHF strengths.

SPATIAL RESOLUTION

Higher SNR is the major advantage with UHFMRI. SNR is computed as the ratio of the signal derived from tissue and the noise in an air-filled region outside the head, whereas contrast-to-noise ratio (CNR) is the signal difference between two adjacent structures divided by the noise as shown in Figure 1. For some regions, up to a 15-fold SNR improvement is achieved with 8T compared with 1.5T. Note in Figure 2 that with similar pulse sequences differences in SNR are clearly visualized. However, practical limitations, most notably RF inhomogeneity, susceptibility artifacts, tissue relaxation times, and suboptimal pulse sequences, still hamper UHFMRI. The RF coils used for UHF (>7T) are often transverse electromagnetic resonators.[1–3] At this field strength, these volume coils are unfortunately quite inhomogeneous in terms of the B1 fields, not only for the volume, but also for various locations on the same image. These coils tend to demonstrate the best image quality (highest SNR) within the central portion of the brain, although conventional single-transmit coils may result in a factor of 2 signal variation across an 8T acquired image of the brain owing to RF inhomogeneity (see below). However, RF inhomogeneities can be in part overcome by using multitransmit (parallel transmit) and multireceive (parallel receive) RF coils.

http://dx.doi.org/10.1016/B978-0-12-800945-1.00035-5

© 2016 Elsevier Ltd. All rights reserved.

Although increased spatial resolution is possible at lower field strengths with surface coil imaging and smaller field of view, the signal is limited by radio frequency penetration. The higher SNR possible at higher field strengths allows for deeper radio frequency penetration. Imaging at lower field strengths using surface coils and small field of view has resulted in improved signal-to-noise ratio derived from the surface of the brain.[4] Such techniques have been applied toward the detection of cortical dysplasia in the setting of childhood epilepsy[5] and smaller voxel size for MR spectroscopy along the surface of the brain, but not the deeper structures. UHFMRI allows for greater signal to noise through both superficial and deeper structures of the brain. This has allowed for imaging with larger matrix size.

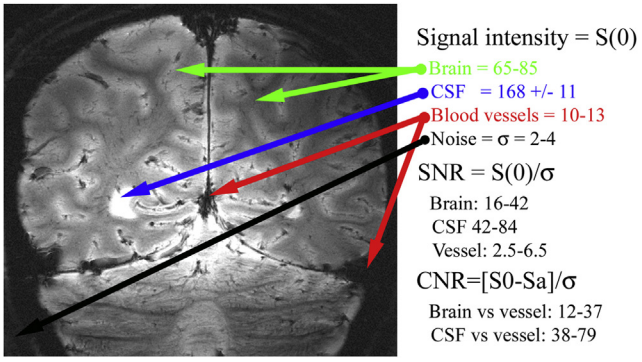


FIGURE 1 Calculation of signal-to-noise ratio (SNR) and contrast to-noise ratio (CNR) in a normal subject imaged at 8T. CSF, cerebrospinal fluid.

Comparison of 1.5 and 8.0T images derived from patients with brain tumors has not been shown to demonstrate any greater tumor extent based on signal changes associated with tumor infiltration. However, the relationships of involved tumor to adjacent anatomic structures are more clearly depicted with higher resolution imaging. In addition, areas of questionable infiltration at lower field strengths are more clearly depicted with higher field strength imaging. Higher-resolution images allow for a more detailed characterization of tumoral architecture and relationship to adjacent anatomic structures (Figure 3). Septations within the tumor bed stand out more readily when present. Using a 9.4T MRI unit Fatterpekar et al. were able to demonstrate lamination of the cerebral cortex within

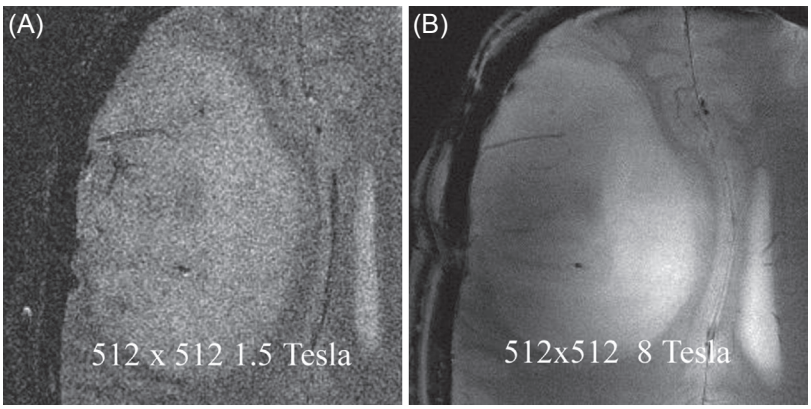


FIGURE 2 Improved signal-to-noise ratio at 8T vs 1.5T. The four- to fivefold signal-to-noise advantage of 8T is clearly demonstrated when comparing gradient-echo MR images using similar parameters acquired at 1.5T (A) and 8T (B) in a subject with anaplastic astrocytoma.

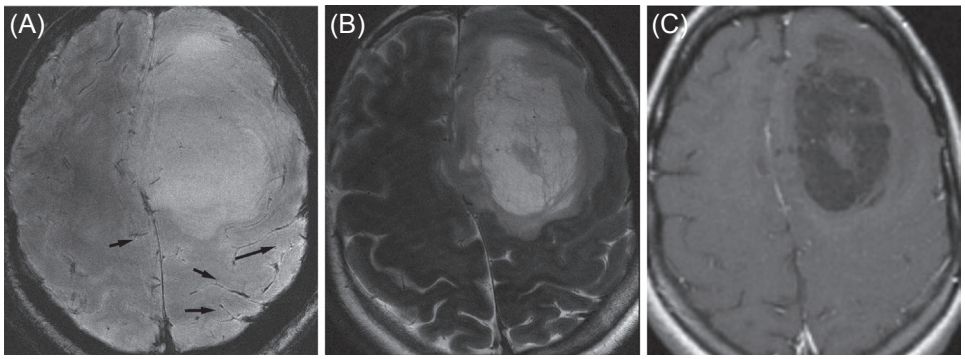


FIGURE 3 8T MRI in a patient with low-grade oligodendroglioma. 8T gradient echo (GE) (A), RARE (B), and 1.5T T1W gadolinium (C) images of a WHO grade II oligodendroglioma. Note the ability to resolve fine septations within the tumor on the RARE image. Even though cortical penetrating veins are visualized within the tumor bed (arrows), no foci of irregular vessels suggestive of neovascularity were resolved within the tumor bed of 8T GE imaging.

fixed specimens, albeit using acquisition times that lasted 14 h.[6] Although such image acquisitions are unrealistic in a clinical setting, the imaging is useful in the understanding of expected signal intensity profiles from the human cortex. High-resolution image acquisitions acquired in vivo have been obtained at matrix sizes as large as 2048 × 2048.[7] In our experience, in vivo imaging of the cortex of the human brain often displays a laminar appearance on gradient-echo UHFMRI using a 1024 × 1024 matrix size in which the middle layers have slightly lower signal intensity relative to the cortex. This can be explained by the higher concentration of normal microvascular structures in the middle layers of the cortex. It is expected that higher resolution imaging will lead to the observation of findings that otherwise could not be resolved and allow the depiction of smaller normal anatomic structures. Thus imaging at UHF strengths has the potential for image interpretation with greater sophistication than possible at lower field strengths.

MAGNETIC SUSCEPTIBILITY

Magnetic susceptibility is the magnetic response of a substance to a magnetic field and can result in local magnetic field inhomogeneities and signal loss. These effects are proportional to field strength and the differences in susceptibility of two regions. Magnetic susceptibility increases with field strength. It can result from macroscopic effects such as the interface between substances (e.g., around air cavities or at the interface between bone and soft tissues) or it can result from microscopic effects such as paramagnetic materials (e.g., unpaired electrons in blood products) or ferromagnetic materials (e.g., iron). The effects can vary depending on the size, shape, and direction of the object relative to the external field. Magnetic susceptibility can result in the ability to visualize microscopic structures with susceptibility effects. Because gradient-echo images do not have a refocusing pulse, they are especially sensitive to effects from magnetic susceptibility. This results in increased visibility of microhemorrhage; deposition of paramagnetic and superparamagnetic substances such as gadolinium, deoxyhemoglobin or iron within the tissues; or blood vessels.

The most unique results with brain tumor imaging thus far have been found using high-resolution (<200 μm) proton density/T2*-weighted gradient-echo axial images. On these images hundreds of small linear low-signal regions correspond to the microvasculature of the brain (Figures 4–6). As mentioned earlier, the

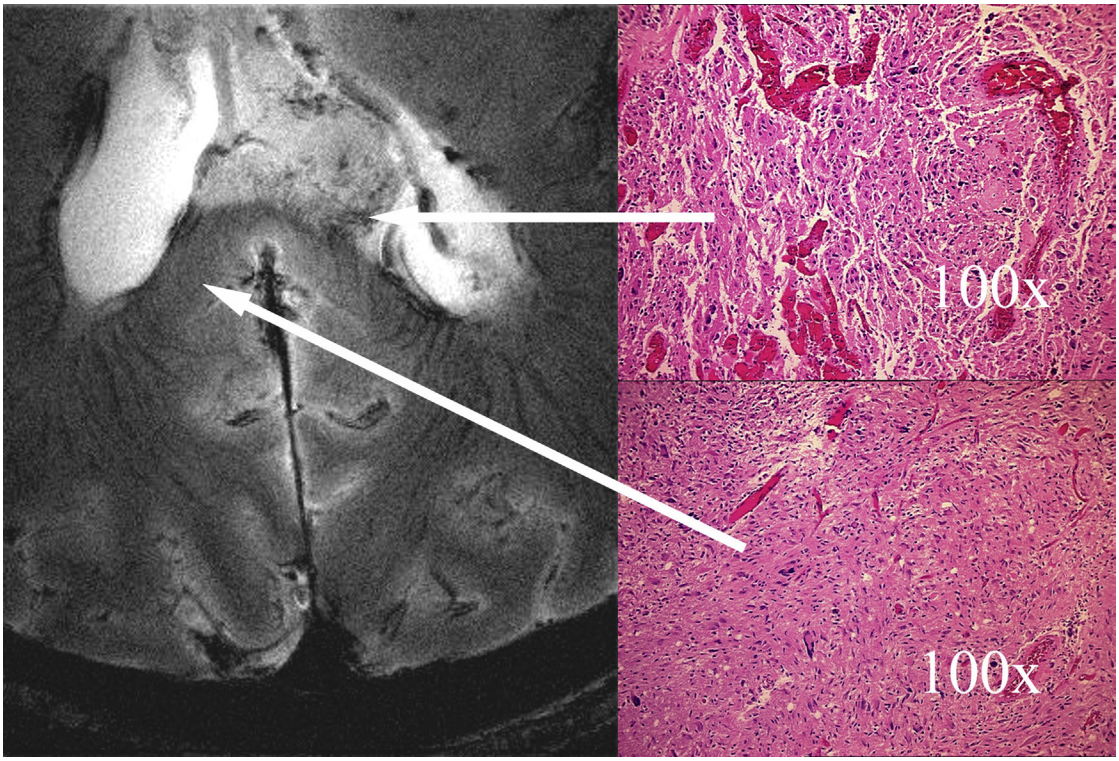


FIGURE 4 Histopathologic correlation to high-resolution 8T gradient echo (GE) MRI. Glioblastoma was imaged within an intact fresh cadaver using 8T GE MRI using a 1024 × 1024 matrix giving an in-plane resolution of 196 μm. Directed specimens were obtained at autopsy. Areas of serpiginous signal voids seen on 8T MRI (in this case probably related to deoxy- or methemoglobin in vessels) correspond to areas of enlarged microvessels and increased microvascular density on hematoxylin and eosin stain. Areas of the tumor with smaller microvessels and low microvascular density had few signal voids on 8T MRI.

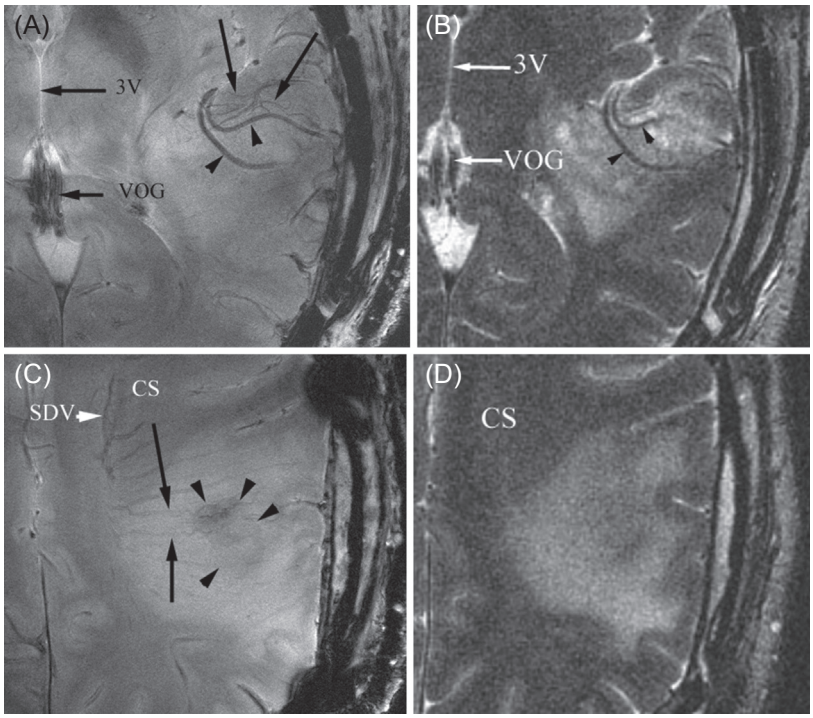


FIGURE 5 Microvascularity within a glioblastoma 8T gradient echo MRI with a 1024 × 1024 matrix and in-plane resolution of 196 μm (A and C) is compared to fast spine echo T2 images with a 512 × 512 matrix (B and D) in a patient with glioblastoma. Images were cropped to demonstrate microvascular structures. Arrowheads (A and B) demonstrate arterial structures within the sylvian fissure (identified in both exams). The smaller venous structures draining the tumor (arrows) are observed only on the 8T images (arrowheads). Signal loss adjacent to a focus of distorted microvasculature (C, arrowheads) is thought to represent microvasculature beyond the resolution of this scan (VOG, vein of Galen; 3V, third ventricle; CS, centrum semiovale).

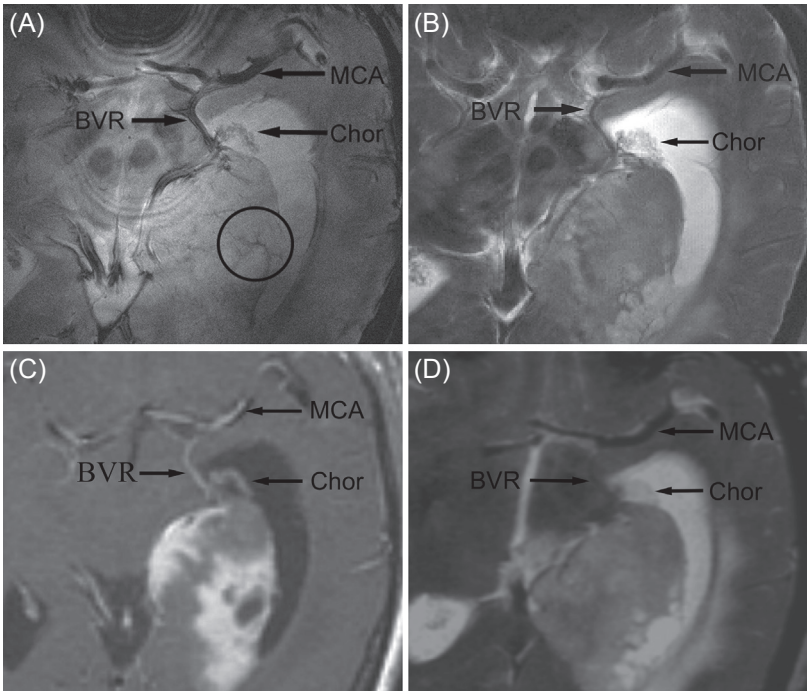


FIGURE 6 Microvascularity within a high-grade pleomorphic xanthoastrocytoma. 8T gradient echo (GE) (A), 8T RARE (B), 1.5T T1 with gadolinium (C), and 1.5T fast spine echo T2 (D) of a high-grade pleomorphic xanthoastrocytoma. Note the identification of foci of microvascularity within the tumor bed (circle). Venous structures, such as the basal vein of Rosenthal (BVR), appear substantially larger relative to arterial structures, such as the middle cerebral artery (MCA), of equivalent size on the GE images relative to the 8T RARE and the 1.5T images owing to susceptibility. Finally, the 8T images display detail within anatomic structures such as the choroid plexus (Chor) better than the 1.5T images.

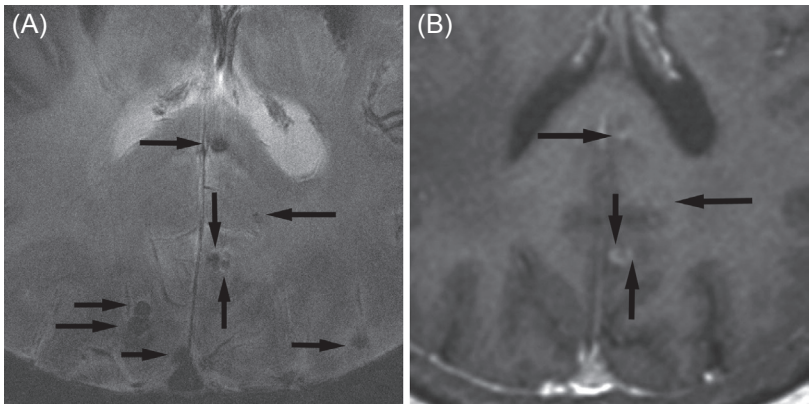


FIGURE 7 Identification of metastases on high-resolution 8T gradient echo (GE) imaging. Comparison of high-resolution 8T GE MRI (A) to postgadolinium 1.5T 3D FSPGR (B) images in a patient with metastases along the occipital lobes and splenium of the corpus callosum. Note the difference in the conspicuity of the metastatic foci (arrows) between the two studies. Some of the metastases identified on the 1.5T SPGR image are not seen on the 8T image. This is probably related to a combination of the higher signal-to-noise ratio attained at 8T imaging and susceptibility effects resulting from the metastatic foci.

images demonstrate a susceptibility-based signal void for cerebral vasculature with visualization of the cortical penetrating vessels, transcallosal veins, and transmedullary veins. The expected diameter of some of these vessels is less than 100 μm. This susceptibility-based image contrast is attributed to the presence of deoxyhemoglobin, primarily within the venous structures, and results in a blood oxygen level-dependent (BOLD) contrast. T2* in venous blood is very short—the vessels are seen as low-signal regions. Because of their sensitivity to subtle local field variations, gradient-echo imaging is most suitable for this purpose. Similar BOLD contrast images have been acquired at lower magnetic field strength[3,9,10] (Figure 7).

Tumor growth is believed to depend on angiogenesis. Folkman proposed that without angiogenesis tumor growth is limited to several millimeters of thickness.[11] Furthermore, tumor cells are believed to induce angiogenesis by secreting a number of growth factors (angiogenesis factors), which stimulate endothelial cells.[11–14] Glioblastoma has been shown to be one of the most vascularized tumors in humans.[15] One therapeutic strategy for patients with brain tumors involves the development of agents that modulate angiogenesis.[11,14,15] Validation of techniques that monitor angiogenesis is key to the development of such strategies. It therefore follows that the imaging identification of angiogenic vessels may serve as a marker for response to antiangiogenesis treatment. Histopathologic methods grading angiogenesis have been based on the number of vessels, degree of glomeruloid vascular structure formation, and endothelial cytology.[15] More recently microvascular density counting using panendothelial staining techniques (e.g., factor VIII, CD34) has been used to quantify angiogenesis and has been found to act as an independent prognosticator.[16–18] It should therefore follow that an imaging assessment of vascular density within a tumor bed may act as an indicator of tumoral angiogenesis.

High-field MRI at 8T using 1024 × 1024 matrix size has been able to visualize vasculature to approximately 100 μm in size.[8] This type of high-resolution imaging has been able to directly identify vascular features within a tumor bed.[19] The MRI findings of distorted vasculature include enlargement of transmedullary veins, increased tortuosity, and increased apparent vessel density[19,20] giving a "tumoral pseudoblush" appearance.[21] Previous studies have demonstrated that apparent vessel density in a nude mouse glioma model as identified by 4.7T gradient-echo MR images significantly correlates with the histopathologically identified density of blood-containing vessels.[22] High-resolution MRI of apparent vascular density has been successfully used as an assay for angiogenesis in this same animal model.[23,24] Using gradient-echo 8T imaging, it has been possible to identify microvascularity within brain tumors in humans (see Figures 5 and 6). The tumor bed can be analyzed for foci with vascular distortion. These foci of microvascularity can then be assessed for microvessel size and concentration compared with that found in gray matter and white matter. Semiquantitative determination of the number of foci with areas of abnormal vasculature, as well as the size and density of the abnormal microvascular structures relative to gray matter and white matter, has been noted to correlate with tumoral grade.[25] In addition, foci of vascular distortion within the tumor bed on gradient-echo 8T MRI correspond to areas of increased cerebral blood volume on dynamic contrast-enhanced 1.5T MRI.[26] Finally, in our experience, directed brain tumor biopsies derived from foci corresponding to microvascular distortion on gradient-echo 8T MRI have corresponded to areas of increased microvascularity and neovascularity on histopathology.[21] However,

differentiation of increased microvascular visibility due to radiation microvessel hyalinosis from tumoral microvascularity may not be possible.[21] Preliminary results indicate that longitudinal imaging of malignant gliomas during the course of antiangiogenic treatment allows for the assessment of changes in tumor vascularization over time.[27] Further improvement in spatial resolution would be possible with larger matrix size; however, the acquisition times may be prohibitively long for routine in vivo work.

Conventional MRI displays images in terms of signal amplitude (magnitude images). Phase imaging (also known as susceptibility-weighted imaging (SWI)) displays images in terms of phase shifts. As such they highlight anatomic structures with susceptibility effects including iron-containing structures, venous vasculature, and cortex and filter out susceptibility effects due to field inhomogeneities. RF inhomogeneity is reflected as a variation in signal-to-noise ratio.[28] As a result flow voids from arteries (Figure 10, arrows) are suppressed and venous structures (Figure 10, arrowheads) are enhanced. Phase imaging therefore has the potential to allow the differentiation of arteries from veins or calcium from hemosiderin.

More recently the use of ultrasmall particle iron oxide (USPIO) contrast agents has been shown to increase the visibility of these microvascular structures in a rodent model. The total volume of increased microvascularity within the tumor bed identified on 8T MRI following the intravenous administration of USPIO (see Figure 8) is substantial. It is interesting that foci exist within the tumor bed, some of which show microvascularity prior to USPIO injection and others do not. Since visualization of microvasculature prior to USPIO injection depends on the BOLD effect, these differences may relate to differences in deoxyhemoglobin concentration between

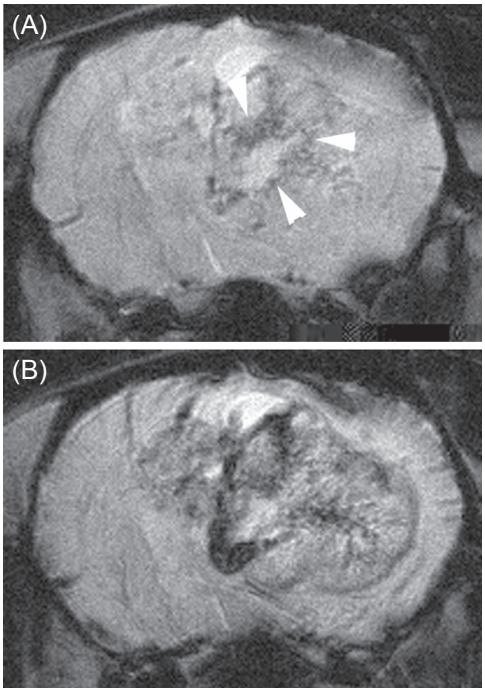


FIGURE 8 Ultrasmall superparamagnetic iron oxide (USPIO) enhancement of microvascularity in the F98 glioma. Fischer rats bearing the F98 glioma were initially imaged while ventilated on 100% O_2 (A) and following intravenous administration of 2mg Fe/kg USPIO intravascular contrast agent (B). These rats were imaged at 8T using high-resolution gradient echo (GE) imaging. In-plane resolution here is 78 μm. Compare microvascularity identified on the precontrast image with microvascularity identified on the postcontrast image. Note the increase in conspicuity in hypointense serpiginous vessels within the tumor bed. Vessel conspicuity centrally within the tumor bed prior to contrast injection in these rats, which were ventilated with 100% oxygen, may be related to hypoxia (arrowheads). Their visibility on GE T2 images results from deoxyhemoglobin within those vessels. This method can increase the conspicuity of microvascularity within tumors and potentially identify regions of hypoxia within the tumor bed.

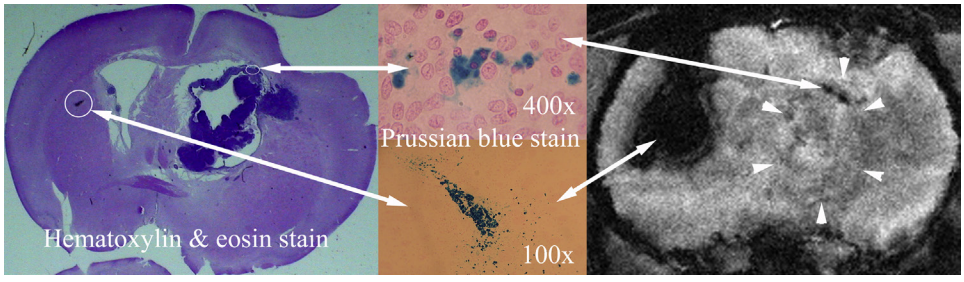


FIGURE 9 Detection of microglia migration in an F98 rat glioma model. Two hundred microliters of ultrasmall superparamagnetic iron oxide (USPIO) intravascular contrast agent (0.1 mmol/ml) was injected into the right hemisphere of a Fischer rat brain to allow endocytosis by microglia. Two weeks later, 10^5 F98 glioma cells were injected into the contralateral caudate nucleus. Serial 8T gradient echo (GE) high-resolution MR scans with in-plane resolution of 78 μm were performed to monitor the microglial migration. Ten days after implantation of F98 glioma cells, the rat was sacrificed. The 8T GE images from immediately prior to sacrifice display profound signal loss at the USPIO injection site. Note the size of this signal loss relative to the iron particles on histopathology. A few microglial cells were identified in the tumor region containing the USPIO particles on histology. It is impressive that 8T GE MRI is sensitive enough to visualize only a few USPIO-labeled cells.

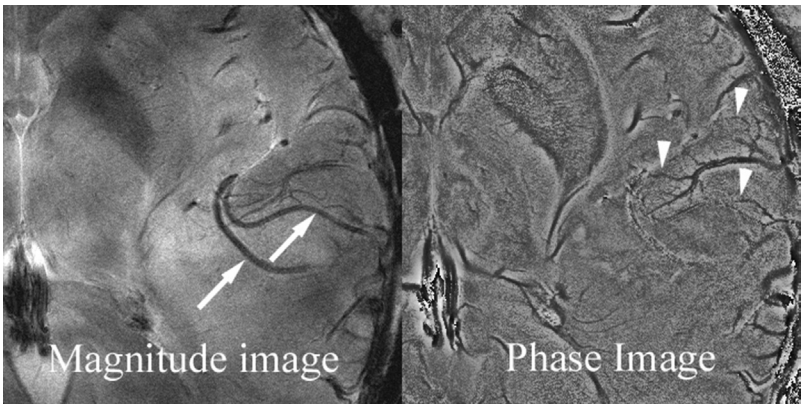


FIGURE 10 Conventional MRI displays images in terms of signal amplitude (magnitude images). Phase images (a.k.a. susceptibility weighted imaging) are displayed in terms of phase shifts. As such they highlight anatomic structures with susceptibility effects including iron-containing structures and paramagnetic effects from deoxyhemoglobin within venous vasculature and cortex and filter out susceptibility effects due to field inhomogeneities. RF inhomogeneity is reflected as a variation in signal-to-noise. As a result flow voids from arteries (arrows) are suppressed and venous structures containing paramagnetic deoxyhemoglobin (arrowheads) are enhanced. This can serve as a method to distinguish arterial from venous structures.

regions within the tumor bed. As such it would lend support to the hypothesis that this type of imaging may be useful in identifying foci of hypoxia within the tumor bed.

IMAGING TUMOR OXYGENATION

Tumor hypoxia is known to protect against radiation treatment. Fractionated doses of radiation delivered during periods of higher oxygenation result in more effective tumoral suppression. The identification of tumor tissues that are hypoxic by nature can result in improved treatment planning.[29–34] The identification of deoxyhemoglobin is thought to indirectly assess tumoral oxygenation via noninvasive means. Deoxyhemoglobin can be assessed via direct measurements of T2* relaxation or BOLD signal behavior. Studies using electron paramagnetic resonance oximetry have been able to demonstrate that BOLD imaging can be used to assess and quantify tumoral oxygenation within tumor models.[31] Similarly, near-infrared spectroscopy measurements of deoxyhemoglobin have been shown to correlate well with tissue deoxyhemoglobin concentration.[35]

It has been shown that tumor perfusion and vessel reactivity can vary between tumor types.[36,37] A decrease in vessel reactivity can result in inefficient oxygen delivery. On the other hand, this difference may result from vessel tortuosity, which in turn may limit erythrocyte access in certain parts of the tumor bed, resulting in lower deoxyhemoglobin concentration and thereby less BOLD effect with lesser visualization of these vascular structures. Exogenous contrast agents would, however, have the opportunity to visualize the total perfused vascular volume.[37] Because tumoral oxygenation is critical in influencing tumor response to radiation and some chemotherapeutic agents, imaging of hypoxic regions could provide an in vivo marker for potential treatment response.[38] Images derived from Fischer rodents bearing the F98 glioma have been compared to immunohistochemical stains using a nitroimidazole agent. These indicate that the BOLD effect identified within abnormal microvasculature of brain tumors may be able to indirectly identify hypoxic regions associated with microvascularity.[29,30]

CELLULAR MAGNETIC RESONANCE IMAGING

Currently approved MRI contrast agents are water-soluble gadolinium-based conjugates, which depend on breakdown of the blood–brain barrier and cause enhancement either by increased vascularization of the tumor bed or by accumulation in the interstitial tissues. As such they are not necessarily an accurate representation of tumor extent.

Iron oxide agents can become incorporated by cells and tag them. This leads to the ability to image them using susceptibility-based sequences on MRI. Via the process of endocytosis, cell types that have been incubated and successfully labeled with ferumoxides have included mesenchymal stem cells, astrocytes, oligodendrocyte progenitor cells, mononuclear cells, and

microglia cells.[39,40] These labeled cells have then been directly implanted into the brain and followed over time. In the setting of central nervous system pathology, microglia cells appear to most efficiently take up iron oxides. Alternatively, USPIO particles directly injected into the brain have been shown to be taken up predominantly by microglia cells via phagocytosis. Microglia cells can then be seen to migrate toward glial tumors and can be used to outline the tumor on MRI. Higher resolution and higher susceptibility effects are expected to favor the use UHFMRI over lower field strengths in detecting cells labeled with USPIO. An example is provided in Figure 9.

In tumor models, macrophages and microglia cells have been shown to surround and infiltrate the tumor in amounts ranging from 20% to 40% of the tumor cell mass.[39,41–43] It is not clear whether these cells act as immune defense or to promote glioma invasion and proliferation.[44–46] Glioma cells have the ability to secrete cytokines and attract microglia cells.[39,47] Thus microglia cells labeled with iron oxide can be used to localize gliomas. Even solitary invading tumor cells have been detected with USPIO-labeled microglia cells.[39] Potential pitfalls in imaging the trafficking of mononuclear cells and stem cells within the central nervous system with contrast agents include potential inability to readily distinguish from other pathologies as well as similar signal loss from tumor components with susceptibility effects such as hemorrhage.

MAGNETIC RESONANCE SPECTROSCOPY

MR spectroscopy (MRS) has the potential to provide insight into the metabolite makeup within brain tissue and neoplasms. Higher field strengths are expected to afford proton MRS of cerebral metabolites with increased sensitivity and spectral dispersion. In addition to increased SNR at higher field strengths, the chemical shift differences between metabolite resonance frequencies proportionally increase the separation of metabolite MRS spectra thus allowing for increased differentiation of more peaks.[48] The B1 field inhomogeneities, greater susceptibility effects, and RF power deposition at UHF strengths represent technical challenges that need to be overcome to fully realize the benefits of UHF MRS. In some investigations, the sensitivity threshold for detecting concentration changes was 0.2 μmol/g for most of the quantified metabolites.[49] Furthermore, changes in the concentration of metabolites have been observed during physiologic stimulation of the visual cortex.[50] In addition to proton MRS, ^{31}P MRS has the potential to image phospholipid metabolites and potentially differentiate various tumor types;[51–53] however, their application to brain neoplasms has yet to be assessed at UHFs.

MULTINUCLEAR IMAGING AND CHEMICAL EXCHANGE SATURATION TRANSFER IMAGING

The greater SNR afforded by UHFMRI relative to lower field strengths has the potential to image and quantify pathophysiologic changes, which may prove useful when assessing cellular proliferation as well as tumoral intracellular and extracellular environments. Such an assessment may lend itself to the characterization of the metabolic behavior of individual tumors, which may in turn be predictive of future tumoral behavior and treatment response.[54–56] UHFs enhance our ability to image the brain using nuclei other than water hydrogen protons, including sodium, phosphorus, and chlorine.[54] Compared to proton imaging, imaging of other nuclei leads to lower spatial resolution mainly due to significantly lower tissue concentrations relative to water, but also due to shorter relaxation times and lower sensitivities resulting from lower gyromagnetic ratios relative to hydrogen. Tissue sodium concentration (TSC) maps of the human brain at 9.4T have been shown to achieve a spatial resolution of 3 mm^3. Preliminary results indicate that TSC maps may be able to assess early tumoral response to treatment.[57]

CEST MRI represents a method in which low concentrations of molecules with chemically exchangeable protons (e.g., amine, amide, hydroxyl) are selectively saturated with an RF pulse to detect them with greater sensitivity indirectly via the water signal. CEST MRI thus enables the detection of endogenous metabolites depending on their proton concentration, saturation time, and exchange rate, as well as potential water pool shine-through effects. CEST MRI has the potential to provide metabolic imaging, which includes, among others, pH, amide, enzyme, and nitrous oxide maps. Preliminary results indicate that CEST MRI may assist in glioma grading and differentiation of tumor recurrence from radiation necrosis.[58,59] Analogous to MRS, as field strength increases so does the separation of the radio frequency resonance, allowing for more precise selective saturation of exchangeable protons with resonances near that of water. Furthermore, the longer T1 decays at higher fields allow for greater saturation and ultimately increased signal return.[60]

The capabilities of UHF MRI as they apply to brain tumor imaging have yet to be fully explored. It is expected that with time the higher SNRs derived from higher field strengths will result in improved spatial resolution not only of microvascularity but also functional imaging, dynamic contrast enhancement, spectroscopic imaging, and MRI derived from protons other than water.

Acknowledgment

NCI 1R21CA/NS92846-01A1.

References

1. Haacke EM, Tkach JA, Parrish TB, Reducing T. Dephasing in gradient field-echo imaging. *Radiology*. 1989;170:457–462.
2. Ibrahim TS, Abduljalil AM, Lee R, Baertlein BA, Robitaille PML. Analysis of B1 field profiles and SAR values for multi-strut transverse electromagnetic RF coils in high field MRI application. *Phys Med Biol*. 2001;46:2545–2555.
3. Ibrahim TS, Lee R, Abduljalil AM, Baertlein BA, Robitaille PML. Effect of RF coil excitation on field inhomogeneity at ultra high fields: a field optimized TEM resonator. *Magn Reson Imaging*. 2001;19:1339–1347.
4. Wald LL, Crvajal L, Moyer SE, et al. Phased array detectors and an automated intensity correction algorithm for high resolution MR imaging of the human brain. *Magn Reson Med*. 1995;34:433–439.
5. Grant PE, Barkovich AJ, Wald LL, Dillon WP, Laxe KD, Vigneron DB. High-resolution surface coil MR of cortical lesions in medically refractory epilepsy: a prospective study. *Am J Neuradiol*. 1997;18:291–301.
6. Fatterpekar GM, Naidich TP, Delman BN, et al. Cytoarchitecture of the human cerebral cortex: MR microscopy of excised specimens at 9.4 Tesla. *Am J Neuroradiol*. 2002;23:1313–1321.
7. Robitaille PM, Abduljalil AM, Kangarlu A. Ultra high resolution imaging of the human head at 8 Tesla: 2K × 2K for Y2K. *J Comput Assist Tomogr*. 2000;24:2–8.
8. Christoforidis GA, Bourekas EC, Baujan M, et al. High resolution MRI of the deep brain vascular anatomy at 8 Tesla: susceptibility-based enhancement of the venous structures. *J Comput Assist Tomogr*. 1999;23:857–866.
9. Reichenbach JR, Essig M, Haacke EM, Lee BC, Przetak C, Kaiser WA, et al. High-resolution venography of the brain using magnetic resonance imaging. *Magnetic Reson Mater Phys Biol Med (MAGMA)*. August 1998;6(1):62–69.
10. Reichenbach JR, Barth M, Haacke EM, Klarhofer M, Kaiser WA, Moser E. High-resolution MR venography at 3.0 Tesla. *J Comput Assist Tomogr*. 2000 Nov-Dec;24(6):949–957.
11. Folkman J. Angiogenesis in cancer, vascular, rheumatoid and other dissease. *Nat Med*. 1995;1:27–31.
12. Plate KH, Risau W. Angiogenesis in malignant gliomas. *Glia*. 1995;15:339–347.
13. Weller RO, Foy M, Cox S. The development and ultrastructure of the microvasculature in malignant gliomas. *Neuropathol Appl Neurobiol*. 1977;3:307–322.
14. Haddad SF, Moore SA, Schlefer RL, Goeken JA. Vascular smooth muscle hyperplasia underlies the formation of glomeruloid vascular structures in glioblastoma multiforme. *J Neuopath Exp Neurol*. 1992;51:488–492.
15. Brem S, Cotran R, Folkman J. Tumor angiogenesis: a quantitative method for histologic grading. *J Nat Cancer Inst*. 1972;48:347–356.
16. Weidner N. Tumoral vascularity as a prognostic factor in cancer patients: the evidence continues to grow. *J Pathol*. 1998;184:119–122.
17. Fox SB. Tumour angiogenesis and prognosis. *Histopathology*. 1997;30:294–301.
18. Eberhard A, Kahlert S, Goede V, Hemmerlein B, Plate KH, Augustin HG. Heterogeneity of angiogenesis and blood vessel maturation in human tumores: implications for antiangiogenic tumor therapies. *Cancer Res*. 2000;60:1388–1393.
19. Christoforidis GA, Grecula JC, Newton HB, et al. Visualization of microvascularity within glioblastoma multiforme utilizing 8 Tesla high-resolution magnetic resonance imaging. *Am J Neuroradiol*. 2002;23:1553–1556.
20. Christoforidis GA, Kangarlu A, Abduljalil AM, et al. Susceptibility based imaging of glioblastoma microvascularity at 8 T: correlation of MR imaging and postmortem pathology. *AJNR Am J Neuroradiol*. 2004;25(5):756–760.
21. Christoforidis GA, Yang M, Abduljalil A, et al. "Tumoral pseudoblush" identified within gliomas at high-spatial-resolution ultrahigh-field-strength gradient-echo MR imaging corresponds to microvascularity at stereotactic biopsy. *Radiology*. 2012;264:210–217.
22. Abramovich R, Frenkiel D, Neeman M. Analysis of subcutaneous angiogenesis by gradient echo magneticc resonance imaging. *Mag Reson Med*. 1998;39:813–824.
23. Abramovich R, Marikovsky M, Meir G, Neeman M. Stimulation of tumour angiogenesis by proximal wound: spatial and temporal analysis by MRI. *Br J Cancer*. 1998;77:440–447.
24. Abramovich R, Meir G, Neeman M. Neovascularization induced growth of implanted C6 glioma multicellular spheroids: magnetic resonance microimaging. *Cancer Res*. 1995;55:1956–1962.
25. Christoforidis GA, Varakis K, Newton HB, et al. Comparison of brain tumor microvcascularity identified on gradient echo 8 T MRI with perfusion MRI at 1.5 T. In: *International Society for Magnetic Resonance in Medicine Tenth Scientific Meeting and Exhibition Program*. 2002:317.
26. Christoforidis GA, Yang M, Abduljalil A, et al. Correlation of microvascularity identified within human gliomas between 8T gradient echo MRI. In: *Joint Annal Meeting International Society for Magnetic Resonance in Medicine – European Society for Magnetic Resonance in Medicine and Biology*. 2007:551.
27. Grabner G, Nöbauer I, Elandt K, et al. Longitudinal brain imaging of five malignant glioma patients treated with bevacizumab using susceptibility-weighted magnetic resonance imaging at 7 T. *Magn Reson Imaging*. 2012;30:139–147.
28. Abduljalil AM, Schmalbrock P, Novak V, Chakeres DW. Enhanced gray and white matter contrast of phase susceptibility-weighted images in ultra-high field magnetic resonance imaging. *J Magn Reson Imaging*. September 2003;18(3):284–290.
29. Novak V, Christoforidis G. Clinical promise: clinical imaging at ultra high field. In: Robitaille PM, Berliner L, eds. *Ultrahigh Field Magnetic Resonance Imaging (Biological Magnetic Resonance 26)*. Springer; 2006:411–432.
30. Christoforidis GA, Yang M, Kontzialis MS, et al. High resolution ultra high field magnetic resonance imaging of glioma microvascularity and hypoxia using ultra-small particles of iron oxide. *Invest Radiol*. July 2009;44(7):375–383.
31. Dunn JF, O'Hara JA, Zaim-Wadhiri Y, et al. Changes in oxygenation of intracranial tumors with carbogen: a bold MRI and EPR oximetry study. *J Magn Reson Imag*. 2002;16:511–521.
32. Veninga T, Langendijk HA, Slotman BJ, et al. Reirradiation of primary brain tumors: survival, clinical response and prognosic factors. *Radiother Oncol*. 2001;59:127–137.
33. Hockel M, Schlenger K, Aral B. Association between tumor hypoxia and malignant progression in advanced cancer of the uterine cervix. *Cancer Res*. 1996;56:4509–4515.
34. Overgaard J, Horsman MR. Modification of hypoxia-induced radioresistance in tumors by the use of oxygen and sensitizers. *Semin Radiat Oncol*. 1996;6:10–21.
35. Punwani S, Ordidge RJ, Cooper CE, Amess P, Clemence M. MRI measurements of cerebral deoxyhemoglobin concentration- correlation with near infrared spectroscopy (NIRS). *NMR Biomed*. 1998;11:281–289.
36. Neeman M, Dafni H, Bukhari O, Braun RD, Dewirst MW. In vivo BOLD contrast MRI mapping of subcutaneous vascular function and maturation: validation by intravital microscopy. *Magn Reson Med*. 2001;45:887–898.
37. Robinson SP, Rijken PFJW, Howe FA, et al. Tumor vascular architecture and function evaluated by non-invasive susceptibility MRI methods and immunohistochemistry. *J Magn Res Imag*. 2003;17:445–454.

38. Yetkin FZ, Mendelsohn D. Hypoxia imaging in brain tumors. *Neuroimag Clin N Am*. 2002;12:537–552.
39. Fleige G, Nolte C, Synowitz F, et al. Magnetic labeling of activated Microglia in experimental gliomas. *Neoplasia*. 2001;3:489–499.
40. Moore A, Marecos E, Bogdanove Jr A, Weissleder R. Tumoral distribution of long-circulating dextran coated iron oxide nanoparticles in a rodent model. *Radiology*. 2000;214:568–574.
41. Roggendorf W, Strupp S, Paulus W. Distribution and characterization of microglia/macrophages in human brain tumors. *Acta Neuropathol Berl*. 1996;92:288–293.
42. Morimura T, Neuchrist C, Kitz K, et al. Monocyte subpopulations in human gliomas: expression of Fc and complement receptors and correlation with tumor proliferation. *Acta Neuropathol Berl*. 1990;80:287–294.
43. Wood GW, Morantz RA. Immunohistologic evaluation of the lymphoreticular infiltrate of human central nervous sytem tumors. *J Natl Cancer Inst*. 1979;62:485–491.
44. Huettner C, Czub S, Kerkau S, Roggendorf W, Tonn JC. Interleukin 10 is expressed in human glikomas in vivo and increases glioma cell proliferation and motility in vitro. *Anticancer Res*. 1997;17: 3217–3224.
45. Taniguchi Y, Ono K, Yoshida S, Tanaka R. Antigen-presenting capability of glial cells under glioma-harboring conditions and the effect of glioma derived factors on antigen presentation. *J Neuroimmunol*. 2000;111:177–185.
46. Wagner S, Czub S, Greif M, et al. Microglial/macrophage expression of interleukin 10 in human glioblastomas. *Int J Cancer*. 1999;82:12–16.
47. Badie B, Schartner J, Klaver J, Vorpahl J. In vitro modulation of microglia motility by glioma cells is mediated by hepatocyte growth factor/scatter factor. *Neurosurgery*. 1999;44:1077–1082.
48. Juchem C, Muller-Bierl B, Schick F, Logothetis NK, Pfeuffer J. Combined passive and active shimming for in vivo MR spectroscopy at high magnetic fields. *J Magn Reson*. December 2006;183(2):278–289. [Epub September 29, 2006].
49. Mangia S, Tkac I, Gruetter R, et al. Sensitivity of single-voxel H-1-MRS in investigating the metabolism of the activated human visual cortex at 7T. *Magn Reson Imaging*. 2006;24(4):343–348.
50. Mangia S, Tkac I, Gruetter R, et al. Sustained neuronal activation raises oxidative metabolism to a new steady-state level: evidence from (1)H NMR spectroscopy in the human visual cortex. *J Cereb Blood Flow Metab*. 2007;27:1055–1063.
51. Maudsley AA, Hilal SK, Perman WH, Simon HE. Spatially resolved high-resolution spectroscopy by 4-Dimensional NMR. *J Magnetic Reson*. 1983;51(1):147–152.
52. Sammet S, Koch RM, Murdoch JB, Schmalbrock P, Duraj J, Knopp MV. In: *Chemical Shift Imaging of the Human brain at 7T. Radiological Society of North America (RSNA) 92nd Annual Meeting, Chicago, USA*. 2006. [abstract].
53. Koch RM, Sammet S, Schmalbrock P, Duraj J, Thompson M, Knopp MV. In: *Diffusion Tensor imaging and Fiber Tracking of the Optic Nerve at 7T. Society of Molecular Imaging (SMI), 5th Annual Meeting, Hawaii, USA*. 2006. [abstract].
54. Balchandani P, Naidich T. Ultra-high field MR neuroimaging. *Am J Neurradiol*. 2014. [Epub ahead of print].
55. Bartha R, Megyesi JF, Watling CJ. Low-grade glioma: correlation of short echo time 1H-MR spectroscopy with 23Na MR imaging. *Am J Neurradiol*. 2006;29:464–470.
56. Ouwerkerk R, Bleich KB, Gillen JS, Pomper MG, Bottomley PA. Tissue sodium concentration in human brain tumors as measured with 23Na MR imaging. *Radiology*. 2003;227(2):529–537.
57. Thulborn KR, Atkinson IC, Vilano JL. Quantitative sodium MR imaging and sodium bioscales for the management of brain tumors. *Neuroimag Clin N Am*. 2009;19:615–624.
58. Kogan F, Hariharan H, Reddy R. Chemical exchange saturation transfer (CEST) imaging: description of technique and potential clinical applications. *Curr Radiol Rep*. 2013;1:102–114.
59. Zaiss M, Windschuh J, Paech D, et al. Relaxation-compensated CEST-MRI of the human brain at 7T: unbiased insight into NOE and amide signal changes in human glioblastoma. *Neuroimage*. February 26, 2015;112:180–188.
60. Polders DL, Hoogduin JM. Chemical exchange saturation transfer MR imaging: potential clinical applications. *Pet Clin*. 2013;8: 245–257.

CHAPTER

36

Neuroimaging of Brain Tumors in Animal Models of Central Nervous System Cancer

Yanping Sun[1], *Herbert B. Newton*[2]

[1]Brigham and Women's Hospital, Harvard Medical School, Boston, MA, USA; [2]Division of Neuro-Oncology, Departments of Neurology and Neurosurgery, Dardinger Neuro-Oncology Center, Wexner Medical Center at The Ohio State University and James Cancer Hospital and Solove Research Institute, Columbus, OH, USA

INTRODUCTION

For several decades, animal models of human cancers of the central nervous system (CNS) have played essential roles as tools for the development of novel anticancer therapies. Orthotopically implanting xenografts of human tumors into immunodeficient rodents has been a valuable preclinical research methodology for more than 30 years,[1–5] and advances in genetically engineered mouse (GEM) models and other animal models (e.g., canine, zebrafish) hold promise as a new class of models that may more closely mimic the human pathology.[6–9] Increasingly, neuroimaging is being used in combination with these animal models to gather preclinical data that are unavailable with endpoint histological analysis alone and that are readily translated to the observations in clinical settings, where similar diagnostic imaging protocols are used.

Owing to interanimal variability, histological evaluations of the effects of therapeutic interventions on GEMs or xenograft models of brain cancer typically require large numbers of animals to attain statistical significance for survival curves and other measurements of disease parameters, such as tumor mass or proliferation. Noninvasive imaging methods can be used to monitor disease progression in vivo within the same animal and, in contrast to the clinic, where patients typically undergo neuroimaging evaluation after presenting with symptoms that result from advanced disease, longitudinal experiments in GEMs or xenograft animals can provide detailed information regarding disease progression as well as the effects of treatment. Imaging modalities such as magnetic resonance imaging (MRI), micro-positron emission tomography (microPET), single-photon emission computed tomography (SPECT), and optical imaging give the research investigator a powerful set of tools with which to investigate the biological mechanisms of disease and the effects of novel treatments.

MAGNETIC RESONANCE IMAGING OF SMALL ANIMAL MODELS OF CENTRAL NERVOUS SYSTEM CANCER

MRI of small animals is a versatile tool for investigating tumor extent and physiology, allowing the investigator to probe a wide variety of anatomical and physiological parameters noninvasively and in a single experimental setting. Dedicated MRI systems for animal research typically operate at much higher magnetic field strengths, ranging from 4.7 to 11.7 T as opposed to the 1.5–3.0 T range of most clinical scanners.[10] The higher field strength of these systems allows investigators to obtain images at higher spatial resolution than is possible using most clinical systems and enables a variety of measurements that can provide insights into tumor physiology and vasculature.[11] Dedicated animal scanners have a smaller bore (inner diameter of the superconducting magnet), making higher magnetic field strengths easier to achieve; nonetheless, the large-bore, lower-field-strength systems used clinically can also be used for the investigation of small animals.[10]

Distinguishing Malignant Tissue from Normal Brain Parenchyma

Strategies that are used in clinical MRI for investigating cancer are also applicable to imaging experiments

Handbook of Neuro-Oncology Neuroimaging, Second Edition
http://dx.doi.org/10.1016/B978-0-12-800945-1.00036-7

© 2016 Elsevier Ltd. All rights reserved.

using animal models.[12] Spin–spin or transverse relaxation (T2) and spin–lattice or longitudinal relaxation (T1) rates are intrinsic tissue parameters whose differences produce the exceptional soft-tissue contrast that is visible in MR images.[11,13] Factors affecting T1 and T2 include water mobility, membrane integrity, apoptosis, and other physiological features at the cellular and subcellular levels. Prolonged T1 and T2 values are common features of malignant brain tumors and a change in T1 and T2 can be indicative of a response to treatment.[14] T1 and T2 relaxation times of human U87 brain tumors have been reported in a mouse model of glioblastoma multiforme (GBM),[15] and more detailed measurements of T2-related relaxation have revealed biexponential signal decay characteristics that may reflect intra- and extracellular water volumes.[16,17] Figure 1(A) illustrates the contrast produced by a T2-weighted image to distinguish malignant tumor tissue from the surrounding brain parenchyma in a xenograft model of GBM in a mouse bearing a large tumor. Viable tumor tissue near the border of the proliferating tumor appears hyperintense, while necrotic tissue in the tumor core appears darker than tissue in the surrounding tumor and brain. While T1 and T2 contrast are valuable parameters to differentiate tumor tissue from normal brain neuropil, they often provide suboptimal contrast for segmentation and volume reconstruction owing to the heterogeneity of contrast throughout the tumor and the frequent presence of poorly defined transitional zones between core tumor tissue and the normal brain.

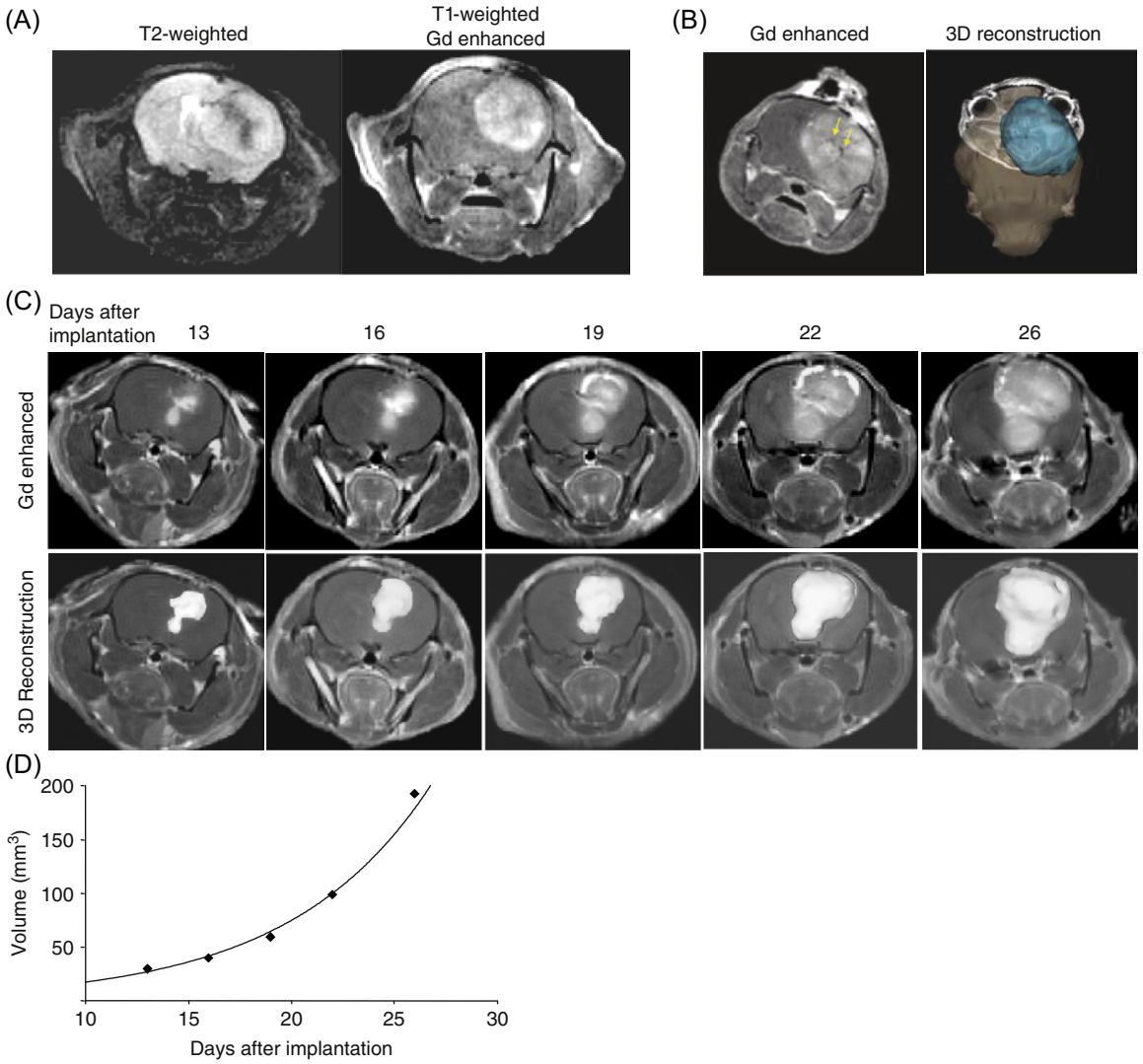


FIGURE 1 **Identification of malignant tumor tissue in animal models of GBM by MRI.** (A): MR images that distinguish tumor tissue from surrounding brain parenchyma by using T2 contrast (T2 weighted) and T1 contrast following the administration of an exogenous contrast agent, gadolinium–DTPA (Gd enhanced). (B): 3D reconstruction of tumor, produced by segmentation of Gd-enhanced images. (C): Time course, Gd-enhanced images, and corresponding 3D reconstructions of tumors from a single animal in a longitudinal investigation. (D): Quantitative measurements of tumor volume as a function of time from the subject in (C). *(A, C, D): Courtesy of Dr. Y. Sun, Small Animal Imaging, Brigham and Women's Hospital, Harvard Medical School. (B): Reroduced with permission from Schmidt NO, et al (2004). Antiangiogenic therapy by local intracerebral microinfusion improves treatment efficiency and survival in an orthotopic human glioblastoma model. Clinical Cancer Research 10:1255–1262.*

To provide enhanced differentiation of tumor tissue from normal brain tissue, contrast agents such as gadolinium–diethylenetriaminepentaacetic acid (Gd-DTPA)[18,19] that perturb the local magnetic field to create contrast detectable by MRI can be introduced into the blood of the animal. Ordinarily, these contrast agents are restricted to the vascular compartment in the brain, but in the vicinity of tumor tissue, the compromised blood–brain barrier (BBB) causes leakage of the contrast agent into the surrounding tissue, where it remains for a period of time after the agent has been cleared from the blood.[20] This residual contrast agent causes local changes in T1 and T2 relaxation that can be accentuated by MRI sequences. Figure 1(A) illustrates the comparison of a Gd-DTPA contrast agent-enhanced image of an orthotopic GBM xenograft tumor to a T2-weighted image acquired in the absence of the contrast agent. The clearly delineated regions of compromised BBB integrity (presumed to reflect the presence of tumor tissue) provide the investigator with a clear picture of tumor extent that can be used for reliable segmentation and volume assessment (see Figure 1(B)).

Following tumor growth within the same animal over time using quantitative volume measurements (see Figures 1(B–D)) provides valuable information describing disease progression that can be used to assess the impact of treatments. High-resolution multislice MRI that differentiates tumor tissue from the surrounding neuropil of the brain enables the investigator to construct three-dimensional models of the tumor (see Figure 1(B)). These models enable a more accurate calculation of tumor volume than estimation using geometric primitives (i.e., spheres or ellipsoids), as is often done following histological measurements of maximum tumor length, depth, and height.[21] This improved accuracy can be especially relevant during advanced stages of disease, when tumor infiltration into surrounding areas of the brain is often asymmetrical.

In addition to producing T1- and T2-weighted images with tissue contrast that is a complex function of both of these parameters, it is possible to explicitly quantify T1 and T2 as well as other measures such as proton density (ϱ_0) at each pixel in the image. When combined with anatomical images of the same slices the T1 and T2 of various anatomical aspects of the tumor are easily evaluated. Figure 2(A) illustrates the changes in calculated T1 and calculated T2 between normal brain tissue and GBM tissue, providing quantitative information that can be more easily compared with results from other experiments.

Measuring Vascular Parameters by Magnetic Resonance Imaging

Cerebral blood volume (CBV), cerebral blood flow (CBF), and macrovascular architecture can also be assessed by MRI to provide information about tumor physiology and the effects of treatment. Tumor-related angiogenesis often causes a disorganized proliferation of vessels that deleteriously affects blood flow within the tumor with respect to healthy tissue[22] and alters the volume of blood in the vascular compartment within the tumor in a manner that can be specific to tumor type.[23] The perfusion and altered CBV of the local tissue can be detected by MRI with the use of blood pool contrast agents in dynamic contrast-enhanced (DCE) imaging protocols[24] or through the use of water in arterial blood as an endogenous tracer in a variety of techniques referred to as arterial spin labeling (ASL).[25] Additionally, macrovascular changes in the cerebral vasculature can result from the angiogenic processes of advanced tumors and can be directly visualized using MR angiography (MRA).

Blood pool contrast agents such as Gd-DTPA alter the magnetic susceptibility of the blood and induce magnetic field gradients within and around blood vessels, causing a detectable drop in the MR signal that can be large (30–50%) in T2*-weighted images and that is dependent on the volume of blood in the voxel from which the signal is detected.[26] In DCE experiments, rapid image acquisitions record this transient drop in signal as a bolus of injected contrast agent arrives at the tissue of interest. The dynamics and extent of signal change in response to the intravenously administered contrast agent permit a calculation of local CBV or CBF. In animal studies, it has been reported that MRI-derived CBV in 9L rat brain tumors correlated with histological measures of microvessel density[27]—observations that complement clinical work in glioma patients in which relative CBV maps permit the differentiation of glioma vascularization types and show a good correlation with the histological grading of the tumors.[28]

The ASL technique offers particular advantages over contrast-enhanced imaging by eliminating the need for exogenous contrast agents.[29–32] In ASL imaging methods, spatially selective radiofrequency pulses are used to perturb the nuclear spins of the water in arterial blood that is in, or flowing to, the brain. After a period of time has elapsed to allow these perturbed spins to flow into or wash out from the imaged tissue, exchange of perturbed spins with unperturbed spins produces a measurable change in signal intensity reflective of perfusion. When the appropriate pulse sequences are used, this signal change can be converted into a quantitative value for blood flow, as shown in Figure 2(A) (CBF).[33] Figure 2(B) illustrates the labeled and unlabeled images acquired in a typical ASL experiment and the subtraction process yielding a perfusion-weighted image that reveals a deficit of perfusion (hypointense area) within the tumor.

Blood flowing in macrovessels within the brain can be visualized by MRA using a variety of pulse sequences that are sensitive to signal from blood that flows into the field of view during the acquisition (i.e., time-of-flight

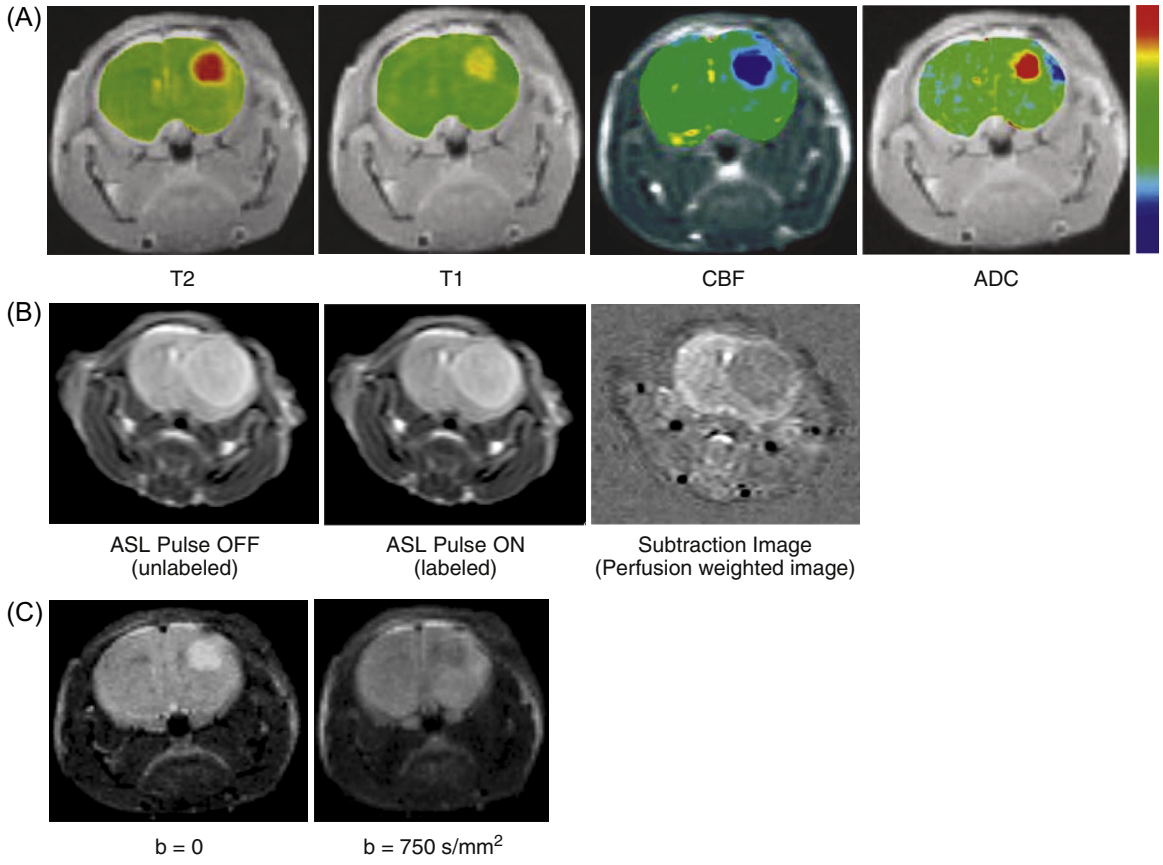


FIGURE 2 **Quantitative measurements of tumor physiology and perfusion by MRI.** (A): False-color images illustrating quantitative values of T2, T1, CBF, and apparent diffusion coefficient (ADC) obtained in vivo from a mouse bearing a GBM tumor. The color bar to the right indicates the color legend for values between the maximum (red) and the minimum (blue) values of the reported parameters with ranges of T2, 0–72 ms; T1, 500–3000 ms; ADC, 0–1.0 mm^2/s; CBF, 0–400 mL/100 g/min. (B): Images illustrating the arterial spin labeling (ASL) acquisitions that reveal perfusion-related contrast, apparent as a hypointense region (reflecting reduced perfusion) within the tissue of the tumor. (C): Signal attenuation in the tumor region was observed on high-diffusion-weighted image ($b = 750\,s/mm^2$) due to the higher ADC value of tumor tissue relative to normal brain tissue. A: T2, T1, and ADC *(C): Reproduced with permission from Sun Y et al (2004). Quantification of water diffusion and relaxation times of human U87 tumors in a mouse model. NMR Biomed 17(6):399–404. (A): CBF: Reproduced with permission from Sun Y et al (2004). Perfusion MRI of U87 brain tumors in a mouse model. Magn Reson Med 51(5):893–899. (B): Courtesy of Dr. Y. Sun, Small Animal Imaging, Brigham and Women's Hospital, Harvard Medical School.*

MRA protocols) or by using exogenous contrast agents. This measurement can be valuable to assess vascular changes that result from pathogenic angiogenesis. Figure 3 illustrates pathological changes in the vasculature in the vicinity of a spontaneously occurring choroid plexus tumor in GEMs[34] and illustrates the high level of detail that can be obtained with MRA to investigate the architecture of cerebral vessels in small animals.

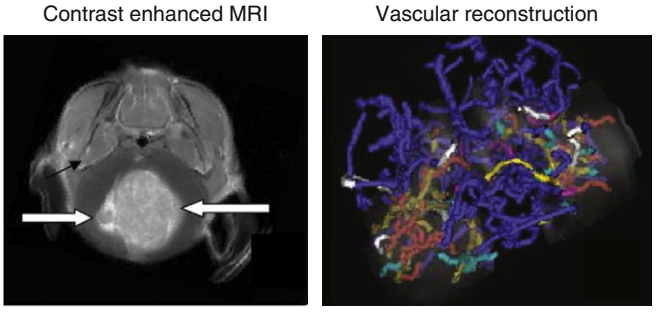


FIGURE 3 **MRA investigation of a spontaneously occurring choroid plexus tumor in a GEM. (Left)** Gadolinium-enhanced T1 image showed the location of the large tumor. (Right) Three-dimensional visualization of the magnified segmented tumor (gray) drawn at partial opacity and with vessels color-coded relative to the tumor surface. Blue, outside; red, inside; gold, traverse; cyan, entering or exiting; white, traversing vessels with fewer than five vessel points within the tumor. There is marked neoangiogenesis producing an increase in vessel number both within and surrounding the tumor. *Reproduced with permission from Brubaker LM et al (2005). Magnetic resonance angiography visualization of abnormal tumor vasculature in genetically engineered mice. Cancer Res 65(18):8218–8223.*

Probing Cellular Structure and Organization by Diffusion Magnetic Resonance Imaging

As water molecules diffuse through space and through the magnetic field gradients that are applied during an MRI scan, the protons within acquire shifts in phase that erode the detected MR signal. Imaging protocols specifically designed to exploit this phenomenon are able to detect the ability of water in the extracellular spaces of the brain to diffuse microscopic distances

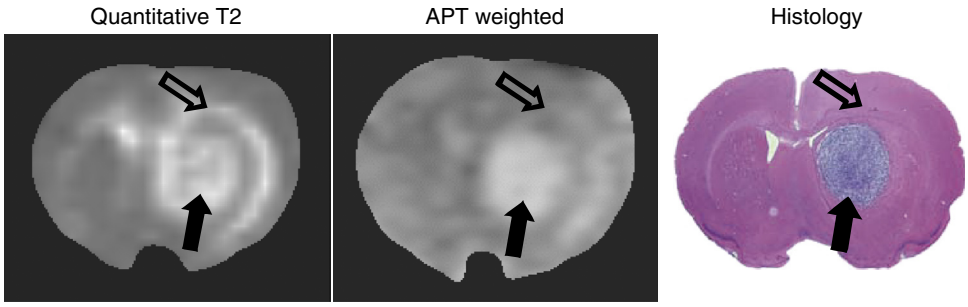


FIGURE 4 Quantitative T2- and APT-weighted images of a 9L brain tumor with corresponding histology. Comparison of T2 map, APT-weighted image, and corresponding histology for a rat 9L brain tumor. The hyperintense peritumoral tissue (open arrow) in the T2 map is normal in the APT-weighted image. *Courtesy of Drs. J. Zhou and P. van Zijl, Johns Hopkins University Medical School.*

in one or several directions.[35–37] Diffusion-weighted images (DWIs) are sensitive to this molecular movement of water and can be used to probe the structure of biologic tissues at a microscopic level. Differences in cellular organization and differences in the integrity of cellular membranes within tumors affect the movement of water molecules and can distinguish tumor tissue from normal brain in DWIs.[38]

The diffusion characteristics of extracellular water can be quantified by MRI in experiments that directly assess the apparent diffusion coefficient (ADC) by acquiring images with varying amounts of diffusion weighting, referred to as the *b*-factor. At high diffusion weighting (high *b*-value), tissues with lower ADC appear hyperintense relative to regions of higher ADC. Figure 2(C) illustrates a T2-weighted image without diffusion weighting ($b=0$); the tumor appears hyperintense relative to normal brain tissue owing to the longer T2 value of this tissue. The adjacent panel shows a more heavily diffusion-weighted image ($b=750\,s/mm^2$), in which signal within the tumor is attenuated owing to the higher ADC value in this region. Quantitative maps of ADC can be calculated on a pixel-by-pixel basis as shown in Figure 2(A) (ADC). Tumor tissue (red) is readily differentiated from normal brain tissue by the significantly higher ADC value compared to normal brain (green). Analyses of changes in ADC from the tumor core, through the tumor edge, to the surrounding tissue have been reported previously.[15]

Quantitative diffusion measurements have been shown to be sensitive to tissue cellular size, extracellular volume, and membrane permeability.[39] DWI has been used in the clinical management of primary brain tumors[40,41] and has been used to distinguish tumor types and viability[42] in animal models. Changes in ADC have been used as a biomarker for changes in the cellular structure of tumor tissue during tumor progression and to distinguish tissue compartments in early, intermediate, and advanced stages of disease.[38] Consistently high diffusion in necrotic tissue, relative to solid tumor, provides a rationale for the use of diffusion imaging to monitor cellular changes following anticancer therapies,[14] making ADC quantification a potentially valuable means of assessing treatment response in animal experiments.

Assessment of Tissue Protein/Peptide Fragments Using Amide Proton Transfer

A novel MRI method has been developed in which contrast is generated based on the tissue content of mobile protein and peptide fragments. These fragments contain amide protons in each of the peptide bonds that are in direct exchange with water protons. It has been shown that this interaction can be used to detect the presence of these fragments using the approach of chemical exchange saturation transfer (CEST) MRI.[43,44] When exchangeable protons are selectively saturated by radio-frequency irradiation, the saturation is transferred to the water protons through proton exchange. The solvent (water) pool is considerably larger than the solute pool and proton exchange quickly returns nonsaturated protons to the peptide and protein fragments. When an amide proton saturating pulse is applied for a period of several seconds, an enhanced saturation of water occurs at a concentration that is much higher than that of the solute, and this enhanced saturation can be detected by MRI. This CEST principle was first demonstrated on small solutes[45] and later on proteins in solution.[46,47] Using this technique, a study of 9L gliomas in rat brain revealed that tumor protein contrast can be valuable for distinguishing tumor tissue from normal brain.[48] Figure 4 illustrates that amide proton transfer (APT)-weighted imaging can be used to delineate malignant tumor tissue in certain cases in which T2-weighted contrast is ambiguous. In the 9L tumor illustrated in the figure, both edema and malignant tumor tissue appear as hyperintense areas in the T2-weighted image, but only the tumor tissue appears hyperintense on the APT-weighted image, as confirmed by histological analysis. It was demonstrated that this contrast can also be detected in brain tumor patients.[49] The relatively uniform intensity of the tumor in the APT-weighted images may further benefit investigators by reducing the confusion of tumors that

present with highly heterogeneous contrast using traditional imaging modalities, such as T2 contrast.

Probing Tumor Metabolism by Magnetic Resonance Spectroscopy

Nuclear MR (NMR) spectroscopy has been used by physicists and chemists to study molecular structure and mobility since the 1950s. Spatially selective NMR spectroscopy, or MRS, can complement other MRI methods to obtain detailed biochemical information from a specific anatomical location within the living animal that can be used as a prognostic or diagnostic marker in studies of cancer. Several NMR-active isotopes are available for MRS study: ^{31}P and ^{1}H are the most common nuclei used in vivo; ^{1}H is an effective nucleus for investigating metabolite concentrations, while ^{31}P can be used in bioenergetics and in the investigation of local lipid content. ^{23}Na can be applied in investigations of cellular energetics, and ^{13}C and ^{19}F have been used to investigate several other aspects of metabolism. These are just a few applications of this active field of research, and the reader is directed to several reviews that discuss the use of MRS in detail.[50–53]

Among investigations of cancer, numerous studies have demonstrated that MRS can characterize the chemical fingerprint for various tumor types as well as discriminating tumor from nonneoplastic lesions and from the effects of radiation.[54–57] In general, decreased *N*-acetylaspartate (NAA) and creatine (Cr) concentrations and increased choline (Cho) concentrations correlate with tumor grade. Increases in lipid and lactate concentrations are also observed in some gliomas. Reduction of NAA is probably due to neuronal death or damage, while the decrease in Cr may arise from changes in cell energetics. Increased Cho (and in some cases lipid) is believed to reflect changes in increased membrane synthesis. Lactate is a by-product of anaerobic metabolism and is believed to accumulate when tumor growth outpaces neovascularization. More recently it has been demonstrated that MRS is useful in predicting response to therapy and in assessing response to therapy.[58–60] It has also been shown that changes in the Cho resonance can predict response to therapy weeks to months before changes are observed by anatomical imaging. ^{1}H MRS has been used to study the correlation between the ^{1}H MRS lipid signal, necrosis, and lipid droplets during C6 rat glioma development.[61] ^{31}P MRS spectra were used to evaluate the effects of lonidamine in the 9L tumor model,[62] and ^{13}C and ^{31}P MRS was used to investigate the regulation of phosphocholine and phosphoethanolamine levels in rat glioma.[63]

Figure 5 illustrates ^{1}H MRS spectra obtained from an intracranial 9L tumor in rat, which demonstrated a decrease in Cho/Cr ratio and increase in the lipid/lactate resonance peak (1.3 ppm) intensity for treated 9L tumor compared with untreated tumor spectra.[64] The sensitivity of serial MRS measurement has revealed that MRS can deliver important data for the evaluation of tumor responses to treatment. The integration of spectroscopic studies and imaging techniques into preclinical animal model investigations provides a valuable avenue in drug discovery.

IN VIVO BIOLUMINESCENCE IMAGING

Bioluminescence imaging (BLI) is an experimental technique that uses light-emitting proteins (luciferases) found naturally in insects, bacteria, and plants as optical reporters ideal for cell labeling in vivo. Luciferases are proteins with enzymatic activity that, in the presence

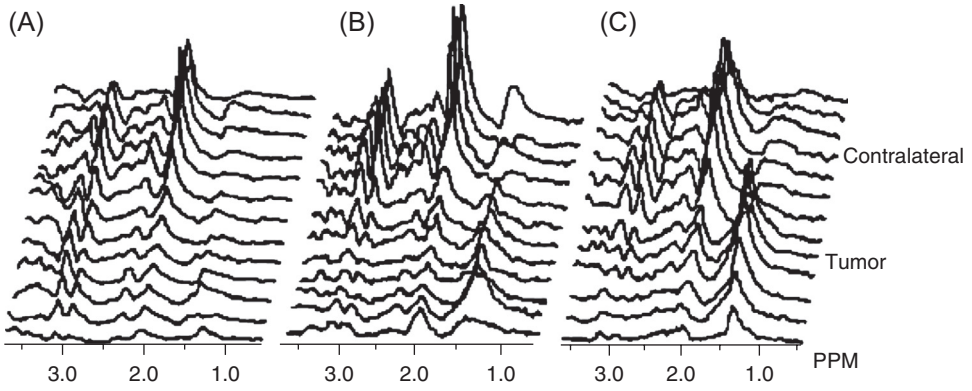


FIGURE 5 Spatially localized ^{1}H MR spectra obtained from a rat brain harboring (A) an untreated intracranial 9L and a treated glioma on the (B) sixth and (C) ninth day following initiation of daily treatments with tezacitabine (FMdC) (15 mg/kg, ip). Each series of spectra was obtained from 25-μL voxels along a column through the rat brain. In the contralateral side, resonances were observed corresponding to NAA, Cr, and Cho at 2.0, 3.0, and 3.2 ppm, respectively. Untreated 9L tumors showed absence of NAA, increased Cho, and decreased Cr compared with the contralateral brain spectra. FMdC-treated tumors showed a progressive increase in the lipid + lactate resonance intensity (1.3 ppm) and decreased Cho intensity on days 6 and 9 of treatment. *Reproduced with permission from Ross BD et al (2003). Evaluation of (E)-2-deoxy-2′-(fluoromethylene) cytidine on the 9L rat brain tumor model using MRI. NMR Biomed 16(2):67–76.*

of ATP, oxygen, and the appropriate substrate (typically luciferin), catalyze the oxidation of the substrate in a reaction that results in the emission of a photon. The photons emitted have broad spectral distributions with peaks between 538 and 582 nm for various firefly luciferases, but considerable emission occurs at longer wavelengths (>600 nm) and this radiation propagates more easily through tissue for detection by sensitive external cameras. Photons readily traverse several millimeters of tissue and thin bones, such as the mouse cranium, and can be detected noninvasively by cooled, charge-coupled device cameras housed inside compartments sealed against external light.[65–67]

In orthographic xenograft models using transplanted cells that have been genetically engineered to express luciferase, tumor proliferation can be monitored using straightforward techniques and a modest detection system.[68–70] Tumor cells harboring a gene that encodes luciferase under the control of a constitutively activated promoter accumulate luciferase in the cytoplasm. Because luciferase-coding DNA is propagated as tumor cells divide, this optical label endures in future generations of cells and can be used to monitor tumor growth within the same animal over time. To assay the quantity of cells containing luciferase, luciferin is administered systemically to anesthetized animals before a period of photo-acquisition. Luciferin is a small molecule that readily crosses the BBB and cellular membranes and can be easily administered systemically at doses on the order of 150 mg/kg.[68,71,72] Luminescence reaches its peak level within 10–20 min, and the image acquisition times are relatively short (from several seconds to a few minutes).[73,74] Several studies have documented a high degree of correlation between bioluminescence and MRI volumetric measurements.[68,70,78] Rapid image acquisition and ease of the imaging procedure allow multiple mice to be imaged simultaneously, making this a very high throughput technique; it is not unreasonable for one system to process more than 200 mice per day.

The dependence of the light-emitting reaction on the presence of luciferase from sustained expression of the luciferase gene, ATP, oxygen, and the presence of unmetabolized substrate makes BLI subject to cellular viability. This sensitivity has been examined in conjunction with diffusion MRI to suggest that BLI signal loss may be a surrogate marker of cell death, for example, in response to a chemotherapeutic being investigated.[75] Other factors, such as translocation to deeper tissue with increased absorption or loss of luciferase expression in tumor cell progeny, may also affect the detected signal in longitudinal studies. It is also probable that volume measurement as a function of photon emission is less sensitive to tumor morphology than volume measurements using 3D reconstruction techniques, which may be sensitive to partial volume effects in MRI. However, factors such as substrate concentration, reaction rates, rate of substrate clearance, and internal absorption and scattering of photons complicate precise quantitative analyses. The scattering of emitted light presents an additional challenge for the spatial resolution of luciferase-harboring cells, but work to develop reliable bioluminescence tomography is promising.[76,77]

Figure 6 illustrates the application of BLI to track intracranial tumor growth in a xenograft mouse model of GBM. Bioluminescence increases exponentially over time (see Figure 6(B)), consistent with the expected change in tumor volume.[70,74,78] Quantitative volume measurements determined by MRI are highly correlated with BLI measurements (see Figure 6(C)) and have been shown to exhibit a log–linear correlation for up to 4 weeks following implantation.[70,78]

MOLECULAR IMAGING OF SMALL ANIMALS

Micro-Positron Emission Tomography

PET is a medical imaging technique that is used clinically to assess local tissue metabolism and the local concentration of molecules of interest, such as cell surface receptors, often at picomolar concentrations.[79] MicroPET technology was developed as a scaled-down version of clinical PET systems to bring these imaging capabilities to preclinical research using animals.[80] Technologically, microPET systems have delivered a solution to the problems of increased demand for sensitivity and spatial resolution as a result of the small size of the animals being investigated, with resolution that surpasses 2 mm in each direction (<8 mm^3). In both clinical and animal imaging, radioactive isotopes of oxygen (^{15}O), nitrogen (^{13}N), carbon (^{11}C), and fluorine (^{18}F) are added to molecules that either participate in a metabolic pathway of interest or bind selectively with a molecular target of interest and are administered to the patient or animal and allowed to accumulate in the target tissue prior to scanning.

Image formation is made possible through the acquisition of many detected events that occur as these radioactive isotopes decay. The isotopes used in imaging experiments decay with varying half-lives and in all cases the decay results in the production of a positron that quickly annihilates with a nearby electron resulting in the emission of two γ-rays. The γ-rays travel away from the locus of annihilation on opposed and nearly collinear trajectories. The near-collinearity of these trajectories permits the calculation of a line of response (LOR) when arrayed sensors in the scanner register simultaneous γ-ray detections. By collecting multiple LORs over a period of minutes, a 3D reconstruction of the emission volume can be produced using traditional tomographic methods.[80,81]

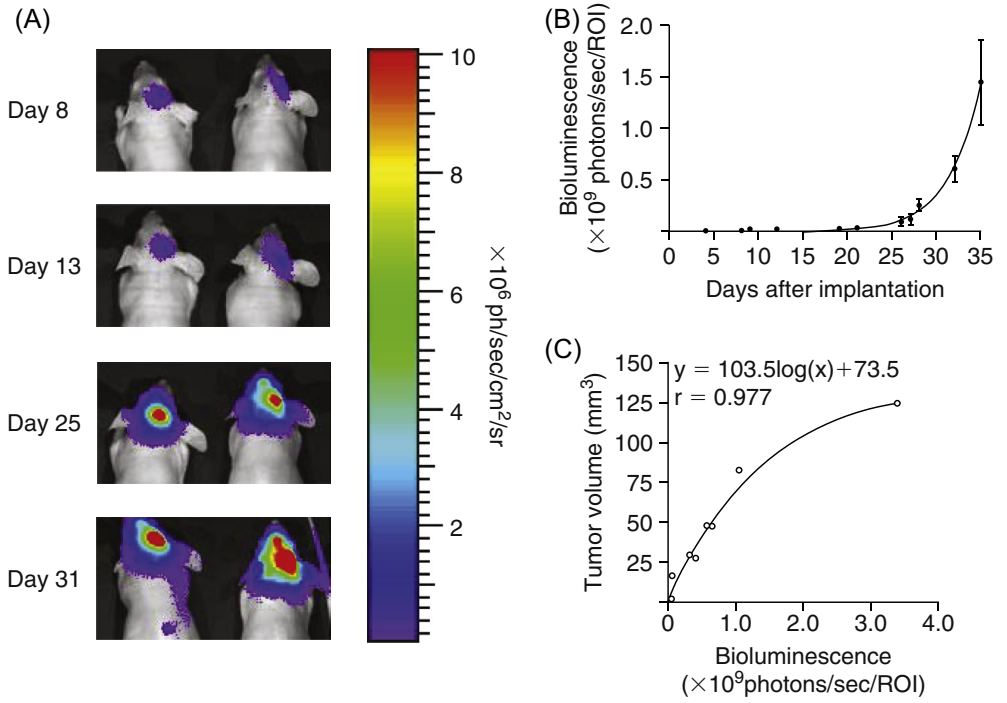


FIGURE 6 **BLI of GBM xenografts reveals increases in luminescence that are correlated with tumor growth and quantitative volume measurements determined by MRI.** Luciferase-expressing U87 cells were stereotactically implanted into the right hemisphere of NCr nude mice. (A) Dim-light photographs of two representative animals overlaid with a false-color representation of photonic flux (photons/s/cm^2/sr) at the indicated times after intracranial tumor cell implantation. (B) The bioluminescence through standardized regions of interest (photons/s/ROI) was found to increase exponentially and (C) was highly correlated with tumor volume measurements determined by MR imaging. *Reproduced with permission from Rubin JB et al (2003). A small-molecule antagonist of CXCR4 inhibits intracranial growth of primary brain tumors. Proc Natl Acad Sci USA 100(23):13513–13518. Copyright (2003) National Academy of Sciences, USA.*

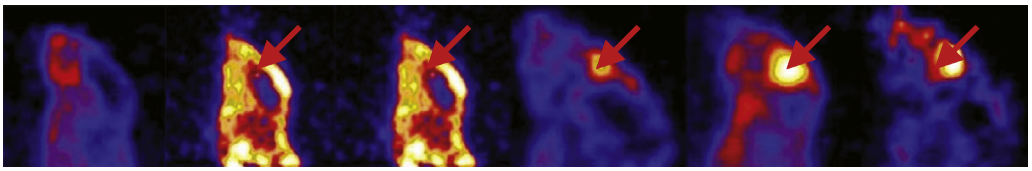


FIGURE 7 **MicroPET images of GBM tumor growth within a single rat using ^{18}F integrated into an RGD peptide.** Serial microPET scans of the same mouse before (day 0) and after inoculation of U87 human glioblastoma cells to the forebrain. Sagittal images were obtained as 10-min static scans at 30 min post-administration of 200 mCi of ^{18}F FB-RGD and reconstructed using a filtered back-projection algorithm. *Reproduced with permission from Chen X et al (2006). Longitudinal microPET imaging of brain tumor growth with F-18-labeled RGD peptide. Mol Imaging Biol 8(1):9–15.*

In oncological investigations, tissue metabolism is often measured by PET with the administration of radiolabeled fluorodeoxyglucose (FDG), which accumulates in cells as a function of cellular demand for glucose. FDG-PET is commonly employed as a diagnostic tool in clinical oncology, owing to the higher-than-normal metabolism of most malignant neoplasms, including many tumors of the brain.[82–84] However, the ability of PET and microPET to reveal the presence and distribution of specific cell surface receptors has shifted much of the focus of current animal research toward the investigation of molecules that may play pathogenic roles in the cancers of the brain. Integrins represent one example of molecular targets being investigated by microPET, on the basis that tumor expression of integrins has been shown to play an essential role in tumor angiogenesis, and antagonists of integrin receptors are currently being evaluated as potential therapies for tumorigenic cancers.[85]

Figure 7 illustrates the results of a longitudinal microPET study following tumor growth within the same animal in an orthotopic U87 xenograft model of GBM. ^{18}F was incorporated into an arginine-glycine-aspartic acid (RGD) peptide, a potent α_v-integrin antagonist, and administered to localize brain regions containing high concentrations of α_v-integrin receptors, areas colocalized

with tumor tissue and vascular endothelium resulting from pathological angiogenesis. The technique used by Chen et al. is applicable to microPET investigations of other cell surface targets with the availability of appropriate radiolabeled ligands.[86]

Micro-Single-Photon Emission Computed Tomography

SPECT operates on principles similar to those of PET, with the important distinction that the radionuclides used in SPECT experiments exhibit longer half-lives and emit γ-photons of varying energies that are generally lower than those emitted by isotopes used in PET experiments. For small-animal imaging, the energy of the photons is in the range of 25–511 keV.[87] The formation of SPECT images requires the use of a collimator that determines the direction of the photon as it travels between the source and the detector. In clinical SPECT systems, the collimator has parallel holes that are oriented to image a large field of view appropriate for a human subject. This resolution is not good enough for imaging small animals, however, so most SPECT experiments investigating animals typically require the higher spatial resolution afforded by pinhole collimators. Several dedicated small-animal pinhole SPECT systems have been developed in recent years,[88–92] and it has been reported that volumetric resolution on the order of 0.1 μl can be achieved,[91] making this modality well suited to studies of molecular binding or uptake with submillimeter resolution in the living animal. Although the detection efficiency of microSPECT systems is much lower than that of microPET, dynamic studies are still often possible because of the longer half-life of SPECT tracers.

High-resolution SPECT provides a valuable tool in the development and evaluation of radiopharmaceutical agents and in molecular research. In combination with small-animal MRI, multipinhole microSPECT with submillimeter resolution has been used to follow the development of disease in mouse models over time,[93,94] and the use of multiple energy windows to perform dual-isotope imaging has also been reported.[93] Figure 8 illustrates concomitant SPECT and MRI of a U87 GBM xenograft in a mouse model and reflects the ability of SPECT to distinguish malignant tumor tissue by means of a vitronectin-binding radioligand (99mTc-NC100692, 1 mCi).[95] The development of highly sensitive SPECT systems with exceptional spatial resolution has created a broad range of new applications of molecular imaging in animal research.

Animal models will continue to play an indispensable role in the investigation of CNS cancer and in the search for novel therapies. In studies using these models, noninvasive neuroimaging techniques afford the investigator important capabilities that include and exceed the capabilities of clinical diagnostic imaging. Common among all noninvasive imaging modalities is the benefit of performing measurements in vivo, typically in longitudinal evaluations within the same animal that can provide a more sensitive assay of therapeutic response. A variety of measurements of disease status and drug action can be obtained, whether using MRI and MRS, optical imaging technologies, molecular techniques such as PET and SPECT, or other technologies that are being continually improved for application to the investigation of brain tumors in small animals, such as microCT,[96–99] contrast enhanced ultrasonography,[100] and photoacoustic tomography.[101] Each imaging technique has specific limitations, and the combination of multiple techniques has become an increasingly popular strategy to leverage the strengths of different modalities within a single experiment, as in Figure 8. The combination of molecular imaging techniques with high-resolution anatomical or physiological imaging can be used to determine the pharmacodynamic and pharmacokinetic actions of drugs and to determine whether novel therapeutics modulate their intended targets in vivo. These capabilities, and the increasing frequency of the use of small-animal imaging, bode well for the translation of in vitro biology to in vivo animal models and ultimately to observations expected in the clinic.

RECENT ADVANCES

Numerous investigators continue to explore "cutting-edge" imaging techniques in animal models of brain tumors, in an effort to improve the ability of clinicians to prognosticate, diagnose, and provide treatment for their patients.[102–107] For example, in the report from Wang and Zhou, they used quantitative diffusion tensor imaging (DTI) to study a rat glioma model (F98, GBM xenografts, 9L gliosarcoma).[102] Quantitative DTI proved very useful in assessing the tumor microstructure and tumor cell invasion into the adjacent gray and white matter. Aryal et al. used DCE MRI to study U251 xenografts in athymic rats and assess for plasma volume, forward transfer constant, interstitial volume fraction (ve), and distribution volume (VD).[103] They found that ve and/or VD was significantly correlated with tumor cellularity ($p < 0.001$ for both). The authors concluded that this technique has utility in assessing tumor cellularity and pathophysiology in a noninvasive fashion. In the study by Cho and colleagues, they investigated the use of MRI with 5-aminolevulinic acid (5-ALA) in BALB/c nude mice implanted with U87 glioma cells.[104] They noted that the administration of 5-ALA increased the intracellular iron concentration in glioma cells by promoting the synthesis

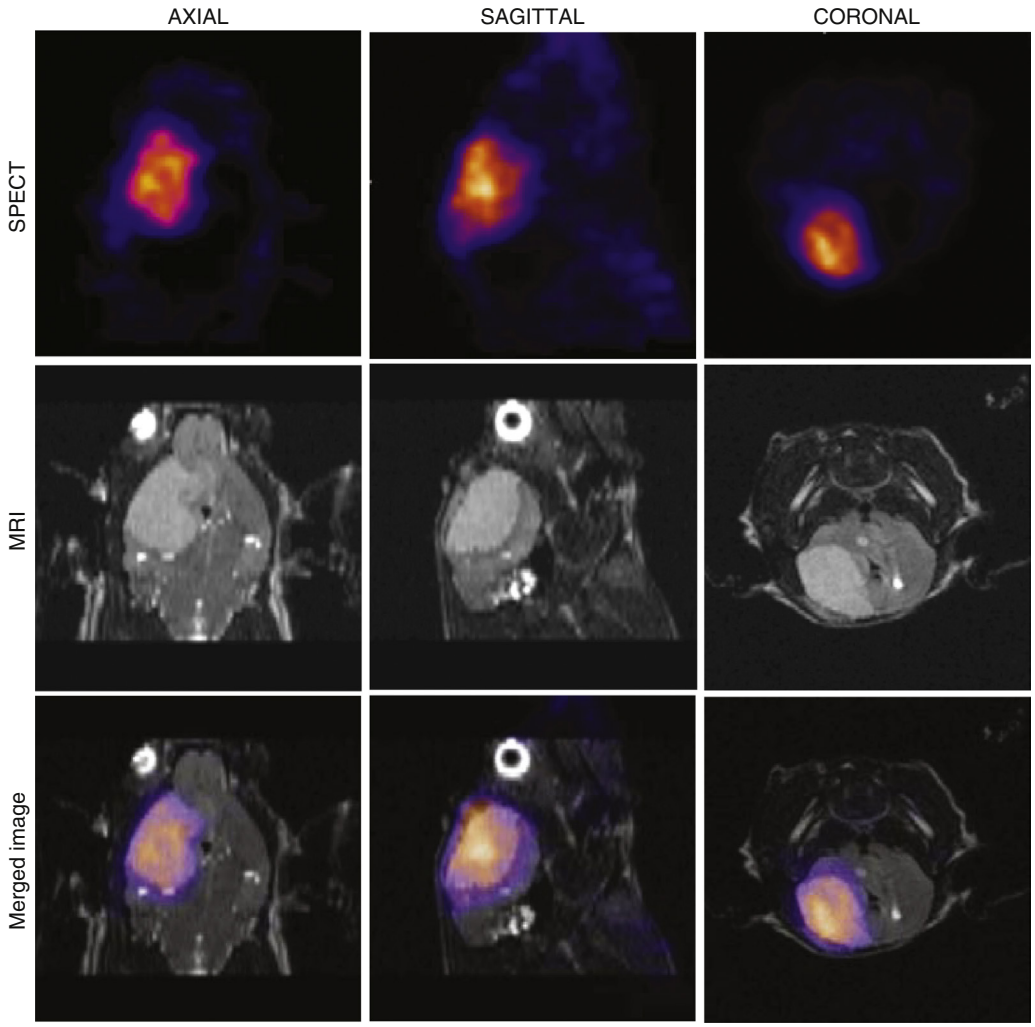


FIGURE 8 **MicroSPECT images of GBM tumor in mice using a vitronectin-binding radioligand (99mTc-NC100692).** Multimodality SPECT and MR images reveal a large tumor in axial, coronal, and sagittal planes in a mouse bearing a U87 cell xenograft. The coregistered data confirm that both modalities reveal tumor tissue in the same loci. *Courtesy of J. W. Barnes and Dr. M. W. Kieran, Department of Pediatric Oncology, Dana-Farber Cancer Institute, Harvard Medical School.*

of heme, which is the metabolite of 5-ALA. Since intracellular iron is readily detected by MRI, 5-ALA may aid in the identification of high-grade foci in glial tumors. Perez-Torres and co-workers used a Gamma Knife-irradiated mouse glioma model to study the ability of MRI to differentiate between glioma tumor tissue and radiation necrosis—which is a common clinical problem in patients.[105] They used DWI and ADC, as well as magnetization transfer contrast and the magnetization transfer ratio (MTR) in irradiated and nonirradiated animals. ADC was proven to be a better technique than MTR for differentiating glioma from radiation injury. However, MTR was more sensitive to both tumor and radiation injury than ADC and may have a role in detecting lesions that do not enhance strongly on T1-GAD images. Using a mouse glioma model, Blasiak et al. studied the use of susceptibility-weighted imaging (SWI) to improve the ability to image the rim of a growing glial tumor—which would be very helpful in the surgical assessment of and planning for brain tumor patients.[106] They used SWI in combination with superparamagnetic iron oxide nanoparticles, in comparison to standard contrast-enhanced imaging, to assess the tumor core, tumor rim, and growing edge of the tumor. The data suggested that SWI, in combination with the targeted superparamagnetic nanoparticles, was more sensitive and efficient at imaging and defining the growing edge–normal brain interface. A report by Schepkin discussed the use of sodium MRI in the imaging of gliomas in animal models.[107] At ultrahigh field strengths, such as 9.4 and 21.1 T, sodium MRI showed an improved ability to monitor tumor response to chemotherapy in comparison to diffusion MRI. Conversely, sodium MRI was also better able to predict early resistance to therapy.

References

1. Simeonova I, Huillard E. In vivo models of brain tumors: roles of genetically engineered mouse models in understanding tumor biology and use in preclinical studies. *Cell Mol Life Sci*. 2014;71:4007–4026.
2. Pierce AM, Keating AK. Creating anatomically accurate and reproducible intracranial xenografts of human brain tumors. *J Vis Exp*. September 24, 2014;91:52017. http://dx.doi.org/10.3791/52017.
3. Janbazian L, Karamchandani J, Das S. Mouse models of glioblastoma: lessons learned and questions to be answered. *J Neurooncol*. May 2014;118(1):1–8.
4. Kegelman TP, Hu B, Emdad L, et al. In vivo modeling of malignant glioma: the road to effective therapy. *Adv Cancer Res*. 2014;121:261–330.
5. Hicks J, Platt S, Kent M, Haley A. Canine brain tumours: a model for the human disease? *Vet Comp Oncol*. May 18, 2015. http://dx.doi.org/10.1111/vco.12152. [Epub ahead of print].
6. Eden CJ, Ju B, Murugesan M, et al. Orthotopic models of pediatric brain tumors in zebrafish. *Oncogene*. 2015;34:1736–1742.
7. Lu X, et al. Selective inactivation of p53 facilitates mouse epithelial tumor progression without chromosomal instability. *Mol Cell Biol*. 2001;21(17):6017–6030.
8. Hallahan AR, et al. The SmoA1 mouse model reveals that notch signaling is critical for the growth and survival of sonic hedgehog-induced medulloblastomas. *Cancer Res*. 2004;64(21):7794–7800.
9. Lin W, et al. Interferon-gamma induced medulloblastoma in the developing cerebellum. *J Neurosci*. 2004;24(45):10074–10083.
10. Pirko I, et al. Magnetic resonance imaging, microscopy, and spectroscopy of the central nervous system in experimental animals. *NeuroRx*. 2005;2(2):250–264.
11. Westbrook C. *Handbook of MRI Technique*. 2nd ed. Oxford, UK: Blackwell Publishing; 1999.
12. Sorensen AG. Magnetic resonance as a cancer imaging biomarker. *J Clin Oncol*. 2006;24(20):3274–3281.
13. Cameron IL, Ord VA, Fullerton GD. Characterization of proton NMR relaxation times in normal and pathological tissues by correlation with other tissue parameters. *Magn Reson Imaging*. 1984;2(2):97–106.
14. Chenevert TL, McKeever PE, Ross BD. Monitoring early response of experimental brain tumors to therapy using diffusion magnetic resonance imaging. *Clin Cancer Res*. 1997;3(9):1457–1466.
15. Sun Y, et al. Quantification of water diffusion and relaxation times of human U87 tumors in a mouse model. *NMR Biomed*. 2004;17(6):399–404.
16. Schad LR, et al. Multiexponential proton spin-spin relaxation in MR imaging of human brain tumors. *J Comput Assist Tomogr*. 1989;13(4):577–587.
17. Macri MA, et al. Spin-lattice relaxation in murine tumors after in vivo treatment with interferon alpha/beta or tumor necrosis factor alpha. *Magn Reson Med*. 1992;23(1):12–20.
18. Villringer A, et al. Dynamic imaging with lanthanide chelates in normal brain: contrast due to magnetic susceptibility effects. *Magn Reson Med*. 1988;6(2):164–174.
19. Rosen BR, Belliveau JW, Chien D. Perfusion imaging by nuclear magnetic resonance. *Magn Reson Q*. 1989;5(4):263–281.
20. Runge VM, et al. Visualization of blood–brain barrier disruption on MR images of cats with acute cerebral infarction: value of administering a high dose of contrast material. *AJR Am J Roentgenol*. 1994;162(2):431–435.
21. Schmidt KF, et al. Volume reconstruction techniques improve the correlation between histological and in vivo tumor volume measurements in mouse models of human gliomas. *J Neurooncol*. 2004;68(3):207–215.
22. Lim M, Cheshier S, Steinberg GK. New vessel formation in the central nervous system during tumor growth, vascular malformations, and Moyamoya. *Curr Neurovasc Res*. 2006;3(3):237–245.
23. Cha S, et al. Differentiation of low-grade oligodendrogliomas from low-grade astrocytomas by using quantitative blood-volume measurements derived from dynamic susceptibility contrast-enhanced MR imaging. *AJNR Am J Neuroradiol*. 2005;26(2):266–273.
24. Hylton N. Dynamic contrast-enhanced magnetic resonance imaging as an imaging biomarker. *J Clin Oncol*. 2006;24(20):3293–3298.
25. Barbier EL, Lamalle L, Decorps M. Methodology of brain perfusion imaging. *J Magn Reson Imaging*. 2001;13(4):496–520.
26. Buxton RB. *Introduction to Functional Magnetic Resonance Imaging: Principles and Techniques*. New York: Cambridge University Press; 2002. 523.
27. Pathak AP, et al. MR-derived cerebral blood volume maps: issues regarding histological validation and assessment of tumor angiogenesis. *Magn Reson Med*. 2001;46(4):735–747.
28. Ludemann L, Hamm B, Zimmer C. Pharmacokinetic analysis of glioma compartments with dynamic Gd-DTPA-enhanced magnetic resonance imaging. *Magn Reson Imaging*. 2000;18(10):1201–1214.
29. Williams DS, et al. Magnetic resonance imaging of perfusion using spin inversion of arterial water. *Proc Natl Acad Sci USA*. 1992;89(1):212–216.
30. Calamante F, et al. Measuring cerebral blood flow using magnetic resonance imaging techniques. *J Cereb Blood Flow Metab*. 1999;19(7):701–735.
31. Detre JA, et al. Noninvasive MRI evaluation of cerebral blood flow in cerebrovascular disease. *Neurology*. 1998;50(3):633–641.
32. Silva AC, Kim SG, Garwood M. Imaging blood flow in brain tumors using arterial spin labeling. *Magn Reson Med*. 2000;44(2):169–173.
33. Sun Y, et al. Perfusion MRI of U87 brain tumors in a mouse model. *Magn Reson Med*. 2004;51(5):893–899.
34. Brubaker LM, et al. Magnetic resonance angiography visualization of abnormal tumor vasculature in genetically engineered mice. *Cancer Res*. 2005;65(18):8218–8223.
35. Westbrook C, Kaut C. *MRI in Practice*. 2nd ed. Oxford, UK: Blackwell Science, Inc; 1998. 326.
36. Bammer R. Basic principles of diffusion-weighted imaging. *Eur J Radiol*. 2003;45(3):169–184.
37. Mitchell D. *MRI Principles*. New York, NY: W.B. Saunders Company; 1999.
38. Herneth AM, Guccione S, Bednarski M. Apparent diffusion coefficient: a quantitative parameter for in vivo tumor characterization. *Eur J Radiol*. 2003;45(3):208–213.
39. Latour LL, et al. Time-dependent diffusion of water in a biological model system. *Proc Natl Acad Sci USA*. 1994;91(4):1229–1233.
40. Krabbe K, et al. MR diffusion imaging of human intracranial tumours. *Neuroradiology*. 1997;39(7):483–489.
41. Chenevert TL, et al. Diffusion magnetic resonance imaging: an early surrogate marker of therapeutic efficacy in brain tumors. *J Natl Cancer Inst*. 2000;92(24):2029–2036.
42. Eis M, Els T, Hoehn-Berlage M. High resolution quantitative relaxation and diffusion MRI of three different experimental brain tumors in rat. *Magn Reson Med*. 1995;34(6):835–844.
43. Zhou J, et al. Using the amide proton signals of intracellular proteins and peptides to detect pH effects in MRI. *Nat Med*. 2003;9(8):1085–1090.
44. van Zijl PC, et al. Mechanism of magnetization transfer during on-resonance water saturation. A new approach to detect mobile proteins, peptides, and lipids. *Magn Reson Med*. 2003;49(3):440–449.
45. Ward KM, Aletras AH, Balaban RS. A new class of contrast agents for MRI based on proton chemical exchange dependent saturation transfer (CEST). *J Magn Reson*. 2000;143(1):79–87.

46. Goffeney N, et al. Sensitive NMR detection of cationic-polymer-based gene delivery systems using saturation transfer via proton exchange. *J Am Chem Soc*. 2001;123(35):8628–8629.
47. McMahon MT, et al. Quantifying exchange rates in chemical exchange saturation transfer agents using the saturation time and saturation power dependencies of the magnetization transfer effect on the magnetic resonance imaging signal (QUEST and QUESP): Ph calibration for poly-L-lysine and a starburst dendrimer. *Magn Reson Med*. 2006;55(4):836–847.
48. Zhou J, et al. Amide proton transfer (APT) contrast for imaging of brain tumors. *Magn Reson Med*. 2003;50(6):1120–1126.
49. Jones CK, et al. Amide proton transfer imaging of human brain tumors at 3T. *Magn Reson Med*. 2006;56(3):585–592.
50. Gillies RJ, Morse DL. In vivo magnetic resonance spectroscopy in cancer. *Annu Rev Biomed Eng*. 2005;7:287–326.
51. Nelson SJ. Multivoxel magnetic resonance spectroscopy of brain tumors. *Mol Cancer Ther*. 2003;2(5):497–507.
52. Bachelard H. Landmarks in the application of 13C-magnetic resonance spectroscopy to studies of neuronal/glial relationships. *Dev Neurosci*. 1998;20(4–5):277–288.
53. Howe FA, et al. Proton spectroscopy in vivo. *Magn Reson Q*. 1993;9(1):31–59.
54. Preul MC, et al. Using pattern analysis of in vivo proton MRSI data to improve the diagnosis and surgical management of patients with brain tumors. *NMR Biomed*. 1998;11(4–5):192–200.
55. Castillo M, Kwock L. Proton MR spectroscopy of common brain tumors. *Neuroimaging Clin N Am*. 1998;8(4):733–752.
56. Wald LL, et al. Serial proton magnetic resonance spectroscopy imaging of glioblastoma multiforme after brachytherapy. *J Neurosurg*. 1997;87(4):525–534.
57. Olsen KI, et al. Advanced magnetic resonance imaging techniques to evaluate CNS glioma. *Expert Rev Neurother*. 2005;5(6 suppl):S3–S11.
58. Lazareff JA, Gupta RK, Alger J. Variation of post-treatment H-MRSI choline intensity in pediatric gliomas. *J Neurooncol*. 1999;41(3):291–298.
59. Graves EE, et al. Serial proton MR spectroscopic imaging of recurrent malignant gliomas after gamma knife radiosurgery. *AJNR Am J Neuroradiol*. 2001;22(4):613–624.
60. Tzika AA, et al. Proton magnetic spectroscopic imaging of the child's brain: the response of tumors to treatment. *Neuroradiology*. 2001;43(2):169–177.
61. Zoula S, et al. Correlation between the occurrence of 1H-MRS lipid signal, necrosis and lipid droplets during C6 rat glioma development. *NMR Biomed*. 2003;16(4):199–212.
62. Ben-Yoseph O, et al. Mechanism of action of lonidamine in the 9L brain tumor model involves inhibition of lactate efflux and intracellular acidification. *J Neurooncol*. 1998;36(2):149–157.
63. Gillies RJ, Barry JA, Ross BD. In vitro and in vivo 13C and 31P NMR analyses of phosphocholine metabolism in rat glioma cells. *Magn Reson Med*. 1994;32(3):310–318.
64. Ross BD, et al. Evaluation of (E)-2′-deoxy-2′-(fluoromethylene) cytidine on the 9L rat brain tumor model using MRI. *NMR Biomed*. 2003;16(2):67–76.
65. Viviani VR. The origin, diversity, and structure function relationships of insect luciferases. *Cell Mol Life Sci*. 2002;59(11):1833–1850.
66. Shah K, Weissleder R. Molecular optical imaging: applications leading to the development of present day therapeutics. *NeuroRx*. 2005;2(2):215–225.
67. Choy G, Choyke P, Libutti SK. Current advances in molecular imaging: noninvasive in vivo bioluminescent and fluorescent optical imaging in cancer research. *Mol Imaging*. 2003;2(4):303–312.
68. Rehemtulla A, et al. Rapid and quantitative assessment of cancer treatment response using in vivo bioluminescence imaging. *Neoplasia*. 2000;2(6):491–495.
69. Vorechovsky I, et al. Somatic mutations in the human homologue of Drosophila patched in primitive neuroectodermal tumours. *Oncogene*. 1997;15(3):361–366.
70. Rubin JB, et al. A small-molecule antagonist of CXCR4 inhibits intracranial growth of primary brain tumors. *Proc Natl Acad Sci USA*. 2003;100(23):13513–13518.
71. Contag CH, et al. Visualizing gene expression in living mammals using a bioluminescent reporter. *Photochem Photobiol*. 1997;66(4):523–531.
72. Honigman A, et al. Imaging transgene expression in live animals. *Mol Ther*. 2001;4(3):239–249.
73. Edinger M, et al. Noninvasive assessment of tumor cell proliferation in animal models. *Neoplasia*. 1999;1(4):303–310.
74. Kung AL. Harnessing the power of fireflies and mice for assessing cancer mechanisms. *Drug Discov Today*. 2005;2:153–158.
75. Rehemtulla A, et al. Molecular imaging of gene expression and efficacy following adenoviral-mediated brain tumor gene therapy. *Mol Imaging*. 2002;1(1):43–55.
76. Chaudhari AJ, et al. Hyperspectral and multispectral bioluminescence optical tomography for small animal imaging. *Phys Med Biol*. 2005;50(23):5421–5441.
77. Wang G, et al. In vivo mouse studies with bioluminescence tomography. *Opt Express*. 2006;14(17):7801–7809.
78. Szentirmai O, et al. Noninvasive bioluminescence imaging of luciferase expressing intracranial U87 xenografts: correlation with magnetic resonance imaging determined tumor volume and longitudinal use in assessing tumor growth and antiangiogenic treatment effect. *Neurosurgery*. 2006;58(2):365–372. discussion 365–72.
79. Bergstrom M, Grahnen A, Langstrom B. Positron emission tomography microdosing: a new concept with application in tracer and early clinical drug development. *Eur J Clin Pharmacol*. 2003;59(5–6):357–366.
80. Chatziioannou AF. Molecular imaging of small animals with dedicated PET tomographs. *Eur J Nucl Med Mol Imaging*. 2002;29(1):98–114.
81. Turkington TG, Coleman RE. Clinical oncologic positron emission tomography: an introduction. *Semin Roentgenol*. 2002;37(2):102–109.
82. Weber WA, Avril N, Schwaiger M. Relevance of positron emission tomography (PET) in oncology. *Strahlenther Onkol*. 1999;175(8):356–373.
83. Di Chiro G. Positron emission tomography using [18F] fluorodeoxyglucose in brain tumors. A powerful diagnostic and prognostic tool. *Invest Radiol*. 1987;22(5):360–371.
84. Del Sole A, et al. Anatomical and biochemical investigation of primary brain tumours. *Eur J Nucl Med*. 2001;28(12):1851–1872.
85. Tucker GC. Integrins: molecular targets in cancer therapy. *Curr Oncol Rep*. 2006;8(2):96–103.
86. Chen X, et al. Longitudinal microPET imaging of brain tumor growth with F-18-labeled RGD peptide. *Mol Imaging Biol*. 2006;8(1):9–15.
87. King MA, et al. Introduction to the physics of molecular imaging with radioactive tracers in small animals. *J Cell Biochem Suppl*. 2002;39:221–230.
88. Jaszczak RJ, et al. Pinhole collimation for ultra-high-resolution, small-field-of-view SPECT. *Phys Med Biol*. 1994;39(3):425–437.
89. Ishizu K, et al. Ultra-high resolution SPECT system using four pinhole collimators for small animal studies. *J Nucl Med*. 1995;36(12):2282–2287.
90. Weber DA, Ivanovic M. Ultra-high-resolution imaging of small animals: implications for preclinical and research studies. *J Nucl Cardiol*. 1999;6(3):332–344.
91. Beekman FJ, et al. U-SPECT-I: a novel system for submillimeter-resolution tomography with radiolabeled molecules in mice. *J Nucl Med*. 2005;46(7):1194–1200.

92. Moore S, et al. A triple-detector, multiple-pinhole system for SPECT imaging of rodents. *J Nucl Med*. 2004;45(5):97.
93. Mahmood A, et al. Following disease progression in small animals with μ-SPECT. *Technetium, Rhenium and Other Metals in Chemistry and Nuclear Medicine*. vol. 7. Padova: SGEditoriali; 2006. 465–470.
94. Hua J, et al. Noninvasive imaging of angiogenesis with a 99mTc-labeled peptide targeted at alphavbeta3 integrin after murine hindlimb ischemia. *Circulation*. 2005;111(24):3255–3260.
95. Barnes JW, et al. EMD121974 targeting of αvβ3 integrin inhibits orthotopic Glioblastoma multiforme. *Am Assoc Cancer Res*. 2006. Washington, DC.
96. Ritman EL. Molecular imaging in small animals–roles for micro-CT. *J Cell Biochem Suppl*. 2002;39:116–124.
97. Psarros TG, Mickey B, Giller C. Detection of experimentally induced brain tumors in rats using high resolution computed tomography. *Neurol Res*. 2005;27(1):57–59.
98. Seemann MD, Beck R, Ziegler S. Vivo tumor imaging in mice using a state-of-the-art clinical PET/CT in comparison with a small animal PET and a small animal CT. *Technol Cancer Res Treat*. 2006;5(5):537–542.
99. Winkelmann CT, et al. Microimaging characterization of a B16-F10 melanoma metastasis mouse model. *Mol Imaging*. 2006;5(2):105–114.
100. Ellegala DB, et al. Imaging tumor angiogenesis with contrast ultrasound and microbubbles targeted to alpha(v)beta3. *Circulation*. 2003;108(3):336–341.
101. Ku G, et al. Imaging of tumor angiogenesis in rat brains in vivo by photoacoustic tomography. *Appl Opt*. 2005;44(5):770–775.
102. Wang S, Zhou J. Diffusion tensor magnetic resonance imaging of rat glioma models: a correlation study of MR imaging and histology. *J Comput Assist Tomogr*. 2012;36:739–744.
103. Ayral MP, Nagaraja TN, Keenan KA, et al. Dynamic contrast enhanced MRI parameters and tumor cellularity in a rat model of cerebral glioma at 7 T. *Magn Reson Med*. 2014;71:2206–2214.
104. Cho HR, Kim DH, Kim D, et al. Malignant glioma: MR maging by using 5-aminolevulinic acid in an animal model. *Radiol*. 2014;272:720–730.
105. Perez-Torres CJ, Engelbach JA, Cates J, et al. Toward distinguishing recurrent tumor from radiation necrosis: DWI and MTC in a Gamma knife-irradiated mouse glioma model. *Int J Radiat Oncol Biol Phys*. 2014;90:446–453.
106. Blasiak K, Landry J, Tyson R, et al. Molecular susceptibility weighted imaging of the glioma rim in a mouse model. *J Neurosci Methods*. 2014;226:132–138.
107. Schepkin VD. Sodium MRI of glioma in animal models at ultra-high magentic fields. *NMR Biomed*. July 15, 2015. http://dx.doi.org/10.1002/nbm.347. [Epub ahead of print].

CHAPTER

37

RANO Criteria: Application to Response Assessment in Clinical Trials

Mithun G. Sattur[1], *Michael A. Vogelbaum*[1,2]

[1]Rose Ella Burkhardt Brain Tumor and NeuroOncology Center, Cleveland Clinic, Cleveland, OH, USA;
[2]Department of Surgery (Neurosurgery), Cleveland Clinic Lerner College of Medicine of Case Western Reserve University, Cleveland, OH, USA

INTRODUCTION

Infiltrative glioma, and in particular glioblastoma (GBM), continues to challenge neuro-oncologists owing to the lack of definitive therapy and the frustrating outcomes of patients. The median survival of patients with newly diagnosed GBM ranges from 12 to 14 months under the current standard of care of biopsy or maximally safe surgical resection followed by concurrent radiotherapy and temozolomide (TMZ) along with adjuvant TMZ.[1] Upon the diagnosis of recurrence, the prognosis is more dismal and the median survival of these patients is between 24 and 40 weeks, with a 6-month progression-free survival of only about 15%.[2,3]

A modest breakthrough for recurrent GBM was achieved in 2009 with the accelerated approval of bevacizumab for this indication. Bevacizumab is a monoclonal antibody against vascular endothelial growth factor (VEGF), and it acts as an antiangiogenic agent. Since its approval, bevacizumab, at times in combination with another chemotherapeutic drug, has become the standard of care for recurrent GBM in the United States.[4]

The fundamental near-term metric of the results of GBM therapy is based upon imaging of the tumor and the changes that occur as a result of therapeutic intervention, typically with use of magnetic resonance imaging (MRI). Hence, the assessment of therapeutic response or failure to respond to treatment is inseparably linked to radiographic response, especially with use of contrast-enhanced images.[5] This barometer of response assessment has been the basis for the role that bevacizumab has come to play in the management of recurrent GBM.[6] The dramatic radiographic response often observed in terms of reduction and/or disappearance of contrast enhancement following initial treatment with bevacizumab led to the conclusion that there is a very high radiographic objective response rate (ORR) and progression-free survival (PFS) with this drug. Yet the overall survival rates continued to remain poor and the patterns of recurrence were suspected to be diffuse and infiltrative (these issues are addressed in further detail below). This discordance between imaging-based response and ultimate patient outcome led many investigators to conclude that the traditional criteria for tumor response assessment were inadequate and insufficient.

To review in brief, imaging criteria for brain tumor progression have evolved from the initial Levin criteria, which emphasized the use of contrast-enhanced computed tomography (CT) to assess the degree of contrast enhancement, edema, and mass effect.[7] A pivotal change occurred with the publication of the Macdonald criteria in 1990, which combined corticosteroid usage and clinical status along with contrast-enhanced tumor measurements in two dimensions on CT or MRI to classify responses into four categories, namely complete response, partial response, stable disease, and progressive disease.[8] The Macdonald criteria were quickly and widely adopted, enabling these objective criteria to be used effectively to make meaningful comparisons across clinical trials. These criteria have been extensively used for RANO in therapy trials.[9] Of note, it is important to remember that the original paper described the criteria specifically with respect to enhancing tumors because enhancement is a key property of high-grade gliomas.[8] There is also a one-dimensional (1D) measurement technique promulgated by the RECIST working group, which initially was proposed for radiographic assessment of solid organ tumors and has

Handbook of Neuro-Oncology Neuroimaging, Second Edition
http://dx.doi.org/10.1016/B978-0-12-800945-1.00037-9

© 2016 Elsevier Ltd. All rights reserved.

been applied to high-grade gliomas, but is not as widely received in the neuro-oncology community.[9,10]

To address these shortcomings a multinational working group was formed to address endpoint assessment in neuro-oncology. This group proposed a set of criteria, which are now termed the Response Assessment in Neuro-Oncology (RANO) criteria.[11]

RANO CRITERIA FOR GLIOMAS

The RANO criteria proposed several key refinements in assessment technique, the salient features of which follow. It is important to note that the RANO criteria assume the use of MRI:

1. Calculation of contrast-enhancing disease as measurable and nonmeasurable disease with particular care in recognizing that cystic areas representing surgical resection cavities or tumor cysts or necrosis are considered nonmeasurable unless the walls consist of nodular components measuring ≥10 mm.
2. Recognition of pseudoprogression (PsP) as an important cause of contrast enhancement early during therapy with the use of concomitant chemoradiation and the possibility of equating this increased enhancement with tumor progression. The RANO criteria introduced a time frame of 12 weeks[12] within which progression is defined only if it occurs outside the high-dose region or 80% isodose line (or if pathological confirmation occurs). The accurate distinction of PsP from true progression is of paramount importance—if true progression is mistakenly diagnosed as PsP, then ineffective therapy will be continued, and if the other way around, falsely high response rates will be documented with any change in therapy instituted.
3. To avoid the confounding influence of surgery on contrast enhancement[13,14] the baseline postoperative scan has to be performed within 24–48 h after surgery and no later than 72 h.[15,16]
4. T2/fluid attenuation inversion recovery (FLAIR) imaging signals are an integral component of the criteria and have to be assessed for significant change during the course of therapy. This vital inclusion versus the Macdonald criteria became necessary owing to the increasing use of antiangiogenics, which changed the relevance of contrast changes in the tumor and added a possible change in the recurrence patterns (specifically bevacizumab, as detailed further in this chapter).
5. Steroid therapy continues to be assessed as a surrogate indicator of disease burden and its effect on neurological function.
6. Clinical evaluation is recommended at the clinician's discretion and, like the Macdonald criteria, the specific details of the "bedside" neurological assessment are not specifically described. Decline in Karnofsky performance status (KPS) or Eastern Cooperative Oncology Group (ECOG) scores or World Health Organization performance scores is taken into account to consider neurologic deterioration.

Given that patients who progress on bevacizumab have a reported overall survival of only about 2.2–4.1 months,[17] indicating the lack of effective salvage therapies, most clinical trials will continue to use this agent along with other novel drugs and combinations. This fact heightens the sense of urgency of standardizing an effective and reliable response assessment system, and the RANO criteria are a step in that direction.

Although the RANO criteria represent a significant advancement in response assessment the authors have maintained from the outset that it is a work in evolution.[11] They anticipated the use of newer physiologic imaging techniques to play a greater role, especially in patients receiving antiangiogenics who develop a predominant nonenhancing pattern to their recurrent disease, in recognition upfront that even these criteria would be inadequate in certain cases. In the following sections, the individual components of the RANO criteria will be critically analyzed in detail. It is to be noted that although the driving concept behind the collaborative effort was to standardize imaging criteria for response assessment, the RANO working group is continually making attempts to establish guidelines for clear endpoints in clinical trials for malignant gliomas[18,19] in addition to diseases such as brain metastases[20,21] and low-grade gliomas.[22] Table 1 lists the salient publications by RANO regarding the above. These aspects are also addressed later in the chapter.

TABLE 1 Publications on Response Assessment by the RANO Group

- Wen PY, Macdonald DR, Reardon DA, et al. Updated response assessment criteria for high-grade gliomas: Response Assessment in Neuro-Oncology working group. *J Clin Oncol*. 2010;28(11):1963–1972.
- Galanis E, Wu W, Cloughesy T, et al. Phase 2 trial design in neuro-oncology revisited: a report from the RANO group. *Lancet Oncol*. 2012;13(5):e196–204.
- Lin NU, Lee EQ, Aoyama H, et al. Challenges relating to solid tumour brain metastases in clinical trials, part 1: patient population, response, and progression. A report from the RANO group. *Lancet Oncol*. 2013;14(10):e396–406.
- Lin NU, Wefel JS, Lee EQ, et al. Challenges relating to solid tumour brain metastases in clinical trials, part 2: neurocognitive, neurological, and quality-of-life outcomes. A report from the RANO group. *Lancet Oncol*. 2013;14(10):e407–416.
- van den Bent MJ, Wefel JS, Schiff D, et al. Response Assessment in Neuro-Oncology (a report of the RANO group): assessment of outcome in trials of diffuse low-grade gliomas. *Lancet Oncol*. 2011;12(6):583–593.
- Vogelbaum MA, Jost S, Aghi MK, et al. Application of novel response/progression measures for surgically delivered therapies for gliomas: Response Assessment in Neuro-Oncology (RANO) working group. *Neurosurgery*. 2012;70(1):234–243.

KEY ASPECTS OF IMAGING AND CLINICAL CRITERIA USED FOR RANO EVALUATION

T1 Contrast-Enhancing Disease

The assessment of T1 contrast-enhancing disease includes an evaluation of measurable and nonmeasurable disease. Measurable disease is defined as bidimensionally contrast-enhancing lesions with clearly defined margins by CT or MRI scan, with two perpendicular diameters of at least 10 mm, visible on two or more axial slices that are, preferably, at most, 5 mm apart with 0-mm skip. Measuring tumor around a cyst or surgical cavity is acknowledged as difficult and is considered measurable only with nodular components measuring ≥10 mm. Of note, the empty space of the cyst or cavity is not included in the measurement. Nonmeasurable disease is defined as either unidimensionally measurable lesions, masses with margins not clearly defined, or lesions with maximal perpendicular diameters less than 10 mm. A unique difficulty arises with patients who have undergone complete resection of all enhancing tumor. Such patients can be enrolled only in studies measuring PFS or overall survival (OS) and not response rates as endpoints, since there is no "response" that can be quantified.[11] That said, they can be followed for recurrence, and thus progression, although even this is not without problems.[23,24] Surgical therapies such as convection-enhanced delivery of gene- or immune-therapy agents, chemotherapy wafers, and radiosurgery add another confounding aspect due to treatment-related changes in enhancement patterns on posttreatment scans.[25,26] The important caveat of contrast enhancement as a surrogate marker of tumor activity is the phenomenon of PsP. It is defined by increased contrast enhancement and occurs in 20–30% of patients following standard radiation therapy with concomitant TMZ.[12,27] It is noted to be more common in tumors with methylated methyl guanine methyl transferase (MGMT) status.[28] The timing of the highest risk for PsP after chemoradiation may range between 3[29] and 6 months.[30] Hence, despite the RANO stated time frame of 12 weeks, there is the possibility that PsP does occur outside of this time window.[31]

One important aspect of disease measurement that remains in the RANO guidelines is that measurement is to be performed with the use of a 2D method similar to the earlier MacDonald criteria.[8,11,32] Several studies have compared the simultaneous use of RANO and RECIST (1D) criteria to monitor tumor response and have found strong concordance among these methods.[32–34] The ubiquity of the use of MacDonald criteria in clinical studies[24] has made the 2D method entrenched in response assessment in trials conducted over recent years. Intuitively, however, volumetric 3D measurements of tumors should be more accurate representations of actual tumor diameters and therefore should be able to detect smaller changes along the course of treatment. This difference in precision should be more obvious with recurrent GBM because of their complex geometrical shapes, presence of cysts and/or cavities with necrosis, and multifocal disease. Volumetric assessment also can help quantify nonmeasurable enhancing disease.[35] Volumetric tumor assessment has been shown to correlate with patient survival in trials based on bevacizumab therapy with intraclass correlation coefficients as high as 0.97.[4,36,37] There is also correlation between the ratio of abnormal FLAIR signal and the enhancing tissue volume, termed the relative nonenhancing tumor ratio, with PFS and OS in recurrent GBM patients treated with bevacizumab.[38] The adoption of the volumetric technique has even been shown to overcome erroneous 2D measurements that might occur with changes in head position during MR image acquisition between serial scans.[39]

Three-dimensional volumetric analysis still requires manual identification of regions of interest and as of this writing is too labor intensive for a busy clinical practice.[35,39] However, progressive improvements in software capabilities are occurring and consequently volumetric measurements may eventually be the "standard" for documenting the physical dimensions of brain tumors and the changes that occur with treatment.

T2/FLAIR Imaging

As alluded to earlier, a significant paradigm change to response assessment has occurred with the increasing use of antiangiogenic agents such as bevacizumab. Bevacizumab continues to be part of numerous clinical trials in recurrent GBM,[40] and it and other antiangiogenic agents target tumor vascularization via multiple steps that converge on the VEGF pathway, which is known to play a key role in GBM.[41] Independent of their antitumor effects, antiangiogenic agents can produce a profound change in imaging characteristics consequent to a dramatic, early reduction in contrast enhancement, an effect that has been termed pseudoresponse[42,43] Bevacizumab normalizes tumor vasculature, decreases vessel permeability, and thereby reduces contrast enhancement.[44] This is not necessarily an antitumor effect, and it may be responsible for the discrepancy in clinical trials between the exceptional objective radiographic response rates of 29–42% with bevacizumab[7,45] and the poor impact of this drug on OS.[7,46,47]

Measurements of enhancement alone are probably not an adequate indicator of the extent of GBM disease volume at baseline, and this discrepancy becomes even more problematic in the setting of VEGF inhibition as the relationship of enhancing tumor volume to total volume of disease becomes even more distorted.[7] Therefore the durability of a response and whether it is sustained on serial imaging have become new factors to consider in

assessing response to treatment, and a period of 4 weeks is accepted as the minimum duration that the response persists.[11] In addition, and possibly by logical extension, it has been noted that treatment with anti-VEGF therapy reduces the incidence of PsP; therefore, any increase in enhancement in the setting of these agents should probably be interpreted as true progression.[48]

Another issue of immediate relevance is the pattern of recurrence and progression of GBM in patients who have been treated with these agents.[49,50] There have been repeated observations that there is an increased incidence of infiltrative nonenhancing tumor growth occurring after antiangiogenic treatment that is evident on T2/FLAIR imaging.[46,51–53] Nearly 5–10% of patients treated with bevacizumab have been found to have evidence of progression only on T2/FLAIR images without increased contrast-enhancing disease.[54] The significance of such a recurrence pattern as to whether it portends a worse OS is uncertain.[32,54–58] Boxerman et al. in their prospective study mention that survival is not different between isolated FLAIR progressors and nonprogressors and may paradoxically end up diminishing the specificity of imaging progression for predicting outcome.[37] Regardless, one of the most significant improvements in the RANO criteria was to include T2/FLAIR imaging as part of the response assessment.

Progression with respect to T2/FLAIR disease is defined as "significant increase in the non-enhancing lesion not caused by co-morbid events such as radiation therapy, demyelination, ischemic injury, infection, seizures, post-operative changes, or other treatment effect."[11] Some features that are more suggestive of cellular infiltration by tumor are mass effect, infiltration of the cortical ribbon, location outside the radiation field, intermediate signal intensity between gray matter and vasogenic edema, inhomogeneous signal changes, and lack of finger-like "tentacles" of edema.[53] Yet it is practically quite difficult to distinguish true infiltration by tumor from the other potential causes enumerated above, which cause virtually identical T2/FLAIR changes. The challenges to the unequivocal recognition of this assessment criterion were acknowledged by the RANO investigators, beginning with issues as basic as what constitutes "significant" changes. In the context of clinical trials for recurrent disease the confusion becomes more apparent with such patients who are heavily pretreated, often with multiple surgeries, chemotherapy, and focused radiation therapy regimens including radiosurgery.

Naturally there have been attempts to recognize T2/FLAIR progression with more certainty and also its quantification to enable serial follow-up comparisons.[59–61] The principle behind these techniques is that the T2 relaxation times differ between normal brain, infiltrative tumor areas, and areas of edema.[62,63] MRI scans obtained before the start of therapy and during therapy are analyzed to generate quantitative maps of T2 relaxation times in different regions of interest, which are manually identified. Voxel-wise subtraction between the T2 maps from posttreatment and pretreatment time periods is performed to quantify the extent of T2 change with treatment and these data may be displayed in the form of color-coded maps. These studies have been able to demonstrate the effect of bevacizumab in reducing edema and the infiltrative tumor-type pattern on progression.[59,61] However, it is apparent that absolute values of these relaxation times are not sufficient to discriminate between tissue types, and more importantly, consistent correlation of change on the differential maps and survival has not come forth yet.

Corticosteroid Use

The use of glucocorticoids to reduce cerebral edema and improve neurologic function in malignant glioma patients is very commonplace both at first diagnosis and at recurrence.[1,45] Since steroid dependence has a host of side effects that may add to substantial morbidity, reduction in dose is considered an improvement in clinical status.

Assessment of Patient Well-Being and Neurological Functioning

In the context of patient care management the fundamental bedrock of assessment remains diligent bedside clinical examination, whether in clinical trials or routine care.[64] Accordingly the RANO criteria have recognized that clinical status should be documented as an important component of response assessment, but does not specify one particular standard. Assessments may take the form of physician-rated outcomes (KPS, Medical Research Council scale for muscle strength, Common Terminology Criteria for Adverse Events), patient-reported outcomes (European Organization for Research and Treatment of Cancer brain tumor module (EORTC-BN), MD Anderson Symptom Inventory (MDASI)), and objective tests in the form of neurocognitive test battery (Hopkins Verbal Learning Test–Revised, Trail Making Test A and B, and multilingual aphasia examination and oral word association test).[21] In general formal neurocognitive testing provides a reliable assessment of neurologic integrity.[65] Subjective patient-reported assessments, though appealing, have not been found to correlate well with objective neurocognitive status.[66] Many practical concerns complicate the use of any of the three types of measures. Some of these include the heterogeneity of neurologic manifestations, frequency of test administration, short progression durations with diseases such as recurrent GBM, floor and ceiling effects in certain tests, the

phenomenon of response shift, nonuniformity between trials and historical controls, and patient compliance, especially when they are taken off protocol treatment.[21] It is proposed that protocols, especially in clinical trials, include baseline cognitive assessments, a prespecified assessment schedule through the study, and tests to evaluate multiple functional domains; ensure compliance of patients and investigators; and use stratification based on performance status. It is also important to perform these evaluations at the same time as the imaging.

With the foregoing background we shall now discuss how the fundamental aspects of RANO criteria apply to response assessment in the context of clinical trials.

APPLICATION OF RANO CRITERIA TO HIGH-GRADE GLIOMAS

Response assessment has a broad connotation and implies a barometer of gauging the effectiveness of therapy, not necessarily restricted to imaging, though this is inextricably linked. Rigorous research in molecular-targeted therapies for malignant gliomas has identified several candidate therapies with potential clinical benefit. These drugs are typically studied in phase 2 trials for clinical efficacy before transitioning to phase 3 trials. However, choosing appropriate primary (and auxiliary) endpoints to study in order to demonstrate benefit is not a straightforward matter.[18] The current trial landscape, with multiple possible novel/conventional agents alone or in combination in a limited patient population, financial constraints, lack of reliable historical controls, and inconsistent proof of meaningful activity of otherwise promising drugs in phase 3 randomized trials, makes this an issue of some urgency. With regard to endpoints, the following three measures have been used as traditional parameters of therapeutic efficacy.

ORR is the endpoint most directly tied to radiographic parameters. In addition to being a relatively early endpoint, it is probably the most direct measure of therapeutic effect.[18,67] ORR is not affected by disease natural history and there is already a significant historical database of ORR with cytotoxic drugs and bevacizumab. It is by far the most expeditious endpoint criterion for early phase 2 trials of novel therapies. However, the most obvious problem with imaging response assessment has been discussed in detail above. In addition, many agents, including targeted therapies, have the effect of producing stable disease on imaging rather than tumor regression. Blinded centralized radiologic review may solve some of the methodological issues, especially bias, but may not be feasible or cost-effective for phase 2 trials.

OS as an endpoint is considered the gold standard in oncology,[67] as it lends itself to easy and precise measurement. Because a disease such as GBM is progressive without periods of prolonged quiescence and has short survival times in general, improvements in OS can be considered to mirror the therapeutic efficacy of an agent. However, OS as a primary endpoint is prone to being affected by salvage therapies. Also, the experimental arm of the phase 2 trial of the investigational agent may differ from historical controls with regard to eligibility criteria, salvage therapy use, start times, and the level of general medical care and this will have an impact on comparisons of OS.[18] Choosing an OS rate by defining OS at a defined time point may expedite translation into phase 3 studies. For such an objective, however, PFS may be preferable.

PFS has many advantages such as shorter time to event, potentially bigger effect sizes than OS, and not being affected by salvage therapies.[18,67] The relation between PFS and OS may not be deemed as one of default surrogacy, but there are good data to suggest that PFS correlates well with OS,[68–70] more so with PFS at fixed time points (such as PFS-6). Ultimately, since PFS is predicated upon defining progression on imaging, the very factors making imaging assessment difficult make this a "vulnerable" parameter.

APPLICATION OF RANO CRITERIA TO LOW-GRADE GLIOMAS

Low-grade gliomas (LGG), comprising oligodendroglioma, astrocytoma, and mixed oligoastrocytoma, are predominantly nonenhancing tumors and are defined by their T2/FLAIR signal abnormality. Imaging response using traditional criteria is inadequate since these were designed for high-grade enhancing tumors.[22] T2/FLAIR imaging measurements also have poor sensitivity to detecting either response or progression given the slow growth rate[71] and indolent nature of "true" LGG and low-risk LGG. Also, radiological progression may occur without any clinical symptoms. Linear measurements tend to have poor reproducibility owing to the irregular shape and anisotropic growth pattern, and its relation to cross-sectional area or absolute volume depends on initial tumor size, which becomes important when comparing data across studies. Another important fact is that despite significant clinical benefit with regard to seizure and/or disease control, ORR may be very low or even absent.[72] Hence an additional response category termed "minor response" is applied to LGG studies and is defined by RANO as 25–50% reduction in the T2/FLAIR signal from baseline.[22] Also progression needs to be distinguished into two types: enhancement-related progression, suggestive of malignant transformation, and increase of a still nonenhancing tumor. Regarding endpoints for LGG trials, there are several nuances. The use of OS tends to be complicated

because of two reasons: the long survival times in LGG patients, which necessitate long-term follow-up, which is expensive and can be unreliable because of attrition, and the effect of salvage treatments, which have a high chance of being administered owing to prolonged survival.[71] In addition, large sample sizes are needed because of small therapeutic effects that are attributable to interventions.[22] PFS appears to be an attractive endpoint in reliably assessing the therapeutic efficacy of a trial agent and is not subject to the effects of subsequent therapies. Unfortunately, the same issues that plague assessment of radiological progression apply to PFS. Even with considering clinical status as required by RANO criteria, there exists the problem of encountering increase in tumor size on imaging yet without clinical symptoms. Alternatively the toxic side effects of therapy, such as those associated with radiation therapy, may lead to clinical decline despite stability on imaging. This dilemma appears as a recurring theme in endpoint assessment in neuro-oncology and further compels the use of tools to detect neurological and clinical deterioration that affect a patient's general well-being.[73] Accordingly, trials for LGG should include neurocognitive tests that cover multiple domains and can be administered in short duration. Patient-reported symptom burden would need to include a module such as MDASI-BT, and quality of life measures should be captured with brain tumor-specific scales like EORTC-BN20 or FACT-Br. An additional important factor that should be accounted for in LGG patients is seizure activity,[74] and this can be captured with a scale such that 50% or greater decrease in seizure frequency is indicative of response.[22]

DEVELOPMENT OF RANO CRITERIA FOR BRAIN METASTASES

Brain metastases present a unique conundrum when considering response assessment owing to all the foregoing issues, plus the additional problems of different methods used in different trials of addressing extracranial disease and the inclusion of different tumor types.[20] The last is increasingly important because of recognition of molecular markers within a given tumor type (lung cancer, for instance) that respond differently to local and systemic therapy. Additionally the question of whether imaging response by itself can serve as a surrogate endpoint for clinical benefit has evidence both for[75,76] and against.[77] The robustness of defining imaging response depends on whether the trial is phase 2 or 3 and whether the focus is on local (intracranial) or systemic therapy. A particularly vexing problem is the high incidence of radionecrosis after stereotactic radiosurgery (SRS).[78,79] By extension this problem of identifying an objective central nervous system (CNS) imaging response affects PFS as an endpoint in phase 2 and 3 trials. PFS in turn should be clearly identified separately for intracranial and extracranial disease depending on whether the trial focuses on local CNS therapy (surgery, SRS, or whole-brain radiation) or systemic therapy, but in general overall PFS is generally more appropriate. The choice of OS as an endpoint is subject to being affected more by extra-CNS disease. Collection and archiving of imaging data linked to outcome data in trials are paramount to allow future comparisons of measurement techniques, response criteria, and their associations with outcome.[20] Of course it is indispensable to include scales of neurological function and well-being as endpoints, mostly in phase 3 trials, but also in some instances in nonrandomized phase 2 trials.

FUTURE DIRECTIONS FOR RANO

Role of Biomarkers

Tumor tissue biomarkers in predicting response to therapy have been explored intensely and it is well established that loss of 1p and 19q and MGMT methylation status are useful in this regard.[80] IDH1 status also is similarly beneficial.[72] Genomic biomarkers have been explored in attempts to improve prognostication in GBM patients.[81] A 2014 publication[67] by the Targeted Therapies Working Group has made an in-depth recommendation of the latest applicability of tumor biomarkers, appropriate use of endpoints, and trial design. Accordingly they suggest that patient subgroups should be identified beforehand based on biomarker status and then enrolled in trials to serve as a means toward prognostic enrichment. Since these biomarkers are tumor tissue-based analyses, they may not have practical use in serial monitoring of disease activity. More attractive would be biomarkers assessable through peripheral blood/plasma DNA analysis. This is currently in the experimental stage.[82]

Advanced Imaging Techniques as Biomarkers

Continual attempts are being made to assess the utility of advanced imaging markers to enable response assessment in a reliable manner with consistent correlation with endpoints. If found to have significant correlation, these parameters themselves may possibly serve as endpoints for rapid screening of therapeutic efficacy in early phase 2 studies of novel molecular agents. Unfortunately none of the modalities discussed below have turned out to be robust enough for such use. That said, the issue of distinguishing true tumor progression

versus PsP in malignant gliomas (following chemoradiation) and brain metastases (following radiosurgery) is reasonably aided by these.

PERFUSION MAGNETIC RESONANCE IMAGING

Dynamic contrast-enhanced and dynamic susceptibility-weighted contrast-enhanced MRI can assess perfusion both in regions of contrast-enhancing tumor and in the nonenhancing T2/FLAIR areas. Studies have documented the ability to distinguish between true progression and radiation effect.[83] With regard to therapy response it is attractive to utilize perfusion studies in patients on treatment with antiangiogenic agents in view of their profound effects on tumor vasculature, and there is evidence of correlation with OS.[84,85] Yet the problem remains that there is significant overlap in the relative capillary blood volume (rCBV) values of tumor tissue, edematous regions, radiation-affected tissue, and normal brain, and changes also variably depend on differential changes in edema, proliferative tumor, or cellularity.[60] Even on serial imaging there is a possibility of not recognizing responders or nonresponders if they demonstrate only subtle/intermediate rCBV changes between scans.[86] Most of the data remain class III and thus limit validity and widespread applicability.[87]

DIFFUSION MAGNETIC RESONANCE IMAGING

Diffusion-weighted MRI (DW-MRI) characterizes tissue in terms of apparent diffusion coefficient (ADC) values, which are primarily determined by cell density and can reflect the degree of cellularity and edema in different tumor and peritumoral regions.[88] DW-MRI has been shown to differentiate PsP from true tumor progression, with lower ADC values (restricted diffusion–high cellularity) within true tumor areas.[89] The addition of DW-MRI to the postsurgery scanning protocol has been suggested in order to document periresection ischemia/edema at baseline.[20] Studies have correlated changes in ADC over treatment with survival in both newly diagnosed and recurrent GBMs.[90] Volumetric segmentation of the tumor can be done with both the T1-enhancing region and the T2/FLAIR abnormality, and ADC values of these voxels can be analyzed and compared between pre- and posttreatment scans.[91] The whole problem remains the significant overlap in absolute values of these parameters between tumor tissue, edema, necrotic tissue, radiation-affected areas, and indeed normal white matter. Values of mean ADC also overlap between patients to a significant extent and most data of diffusion MRI in brain tumor trials again remain class III with attendant issues of validity.

MAGNETIC RESONANCE SPECTROSCOPY

Studies investigating tumor and peritumoral metabolite ratios using proton MR spectroscopy (^{1}H MRSI) have shown changes with bevacizumab therapy in GBM on serial scans that correlate with outcome.[92] ^{1}H MRSI has been applied to distinguish true recurrence from PsP.[93] There are several technical problems, such as long acquisition times, low spatial resolution, inadequate separation of metabolite peaks, inadequate tools for image processing for clinical use, and discordant voxel placement on serial MRI exams that interfere with standardization.

Combining the above techniques into a multiparametric MRI protocol seems attractive[94] and there has been demonstration of a correlation of increase in tumor infiltrative areas with PFS.[60] Certain issues will still continue to interfere with validation: the choice of contralateral "normal" brain parenchyma as the region of reference for most of the above MRI techniques, which is still not standardized; the possibility of underestimating small active tumor foci; and difficulty with large-scale generalization to routine clinical practice owing to the time-intensive nature of postprocessing and data display. These should improve with rapid software evolution.

POSITRON EMISSION TOMOGRAPHIC IMAGING

Positron emission tomographic (PET) imaging, utilizing various isotopes including [^{18}F]fluorodeoxyglucose (^{18}FDG), fluorothymidine (^{18}FLT), and fluoroethyl-L-tyrosine, has been explored in the context of identifying biomarkers for response to antiangiogenic therapies. Owing to baseline high metabolic uptake of glucose by the brain ^{18}FDG PET may have less sensitivity. ^{18}FLT PET uptake changes in tumor have been shown to be predictive of both PFS and OS, with ^{18}FLT PET being capable of identifying treatment responders earlier than MRI.[95] Similar investigations with FDOPA have found sensitive correlation between uptake changes along with bevacizumab therapy and survival.[96] Of course, as with the advanced MR techniques, generalized applicability across all centers is limited owing to issues of cost, availability, and expertise.

SUMMARY

Rigorous and effective criteria to assess the response of gliomas and brain metastases to therapy are of paramount importance in neuro-oncology, with applicability to both daily clinical practice and evaluation of an increasing number of therapeutic agents in a constrained research environment. The RANO working group is continually making efforts toward refining conventional MRI-based criteria while exploring novel imaging techniques. In addition RANO efforts are directed toward optimizing scales that assess neurological function and general well-being, which are assuming increasing importance because of the limitations of traditional assessment parameters. Such assessments are crucial with agents that tend to promote stable disease on radiology and to ascertain that clinical activity does not come at the price of toxicity and neurologic dysfunction. The RANO working group does not intend for its criteria to be permanent; future RANO updates will incorporate new developments in clinical care and assessment of outcome toward the goal of maintaining uniform and standardized methods for performing assessments of patients with brain tumors.

References

1. Stupp R, Mason WP, van den Bent MJ, et al. Radiotherapy plus concomitant and adjuvant temozolomide for glioblastoma. *N Engl J Med*. 2005;352:987–996.
2. Norden AD, Drappatz J, Muzikansky A, et al. An exploratory survival analysis of anti-angiogenic therapy for recurrent malignant glioma. *J Neurooncol*. 2009;92:149–155.
3. Gilbert M. Recurrent glioblastoma: a fresh look at current therapies and emerging novel approaches. *Seminars Oncol*. 2011;38: S21–S33.
4. Ellingson BM, Kim HJ, Woodworth DC, et al. Recurrent glioblastoma treated with bevacizumab: contrast-enhanced T1-weighted subtraction maps improve tumor delineation and aid prediction of survival in a multicenter clinical trial. *Radiology*. 2014;271(1): 200–210.
5. Leu K, Pope WB, Cloughesy TF, Lai A, et al. Imaging biomarkers for antiangiogenic therapy in malignant gliomas. *CNS Oncol*. 2013;2(1):33–47.
6. Desjardins A, Friedman HS. Bevacizumab therapy for glioblastoma: a passionate discussion. *CNS Oncol*. 2014;3(1):1–3.
7. Kreisl TN, Kim L, Moore K, et al. Phase II trial of single-agent bevacizumab followed by bevacizumab plus irinotecan at tumor progression in recurrent glioblastoma. *J Clin Oncol*. 2009;27(5):740–745.
8. Macdonald DR, Cascino TL, Schold Jr SC, Cairncross JG. Response criteria for phase II studies of supratentorial malignant gliomas. *J Clin Oncol*. 1990;8(7):1277–1280.
9. Therasse P, Arbuck SG, Eisenhauer EA, et al. New guidelines to evaluate the response to treatment in solid tumors. European Organization for Research and Treatment of Cancer, National Cancer Institute of the United States, National Cancer Institute of Canada. *J Natl Cancer Inst*. 2000;92(3):205–216.
10. Eisenhauer EA, Therasse P, Bogaerts J, et al. New response evaluation criteria in solid tumours: revised RECIST guideline (version 1.1). *Eur J Cancer*. 2009;45(2):228–247.
11. Wen PY, Macdonald DR, Reardon DA, et al. Updated response assessment criteria for high-grade gliomas: Response Assessment in Neuro-Oncology working group. *J Clin Oncol*. 2010;28(11):1963–1972.
12. Brandsma D, Stalpers L, Taal W, Sminia P, van den Bent MJ. Clinical features, mechanisms, and management of pseudoprogression in malignant gliomas. *Lancet Oncol*. 2008;9(5):453–461.
13. Cairncross JG, Pexman JH, Rathbone MP, DelMaestro RF. Postoperative contrast enhancement in patients with brain tumor. *Ann Neurol*. 1985;17(6):570–572.
14. Cairncross JG, Pexman JH, Rathbone MP. Post-surgical contrast enhancement mimicking residual brain tumor. *Can J Neurol Sci*. 1985;12(1):75.
15. Henegar MM, Moran CJ, Silbergeld DL. Early postoperative magnetic resonance imaging following nonneoplastic cortical resection. *J Neurosurg*. 1996;84(2):174–179.
16. Ulmer S, Braga TA, Barker 2nd FG, Lev MH, Gonzalez RG, Henson JW. Clinical and radiographic features of peritumoral infarction following resection of glioblastoma. *Neurology*. 2006;67(9): 1668–1670.
17. Reardon DA, Peters KB, Vredenburgh JJ, et al. Phase 2 study of carboplatin, irinotecan, and bevacizumab for recurrent glioblastoma after progression on bevacizumab therapy. *Cancer*. 2011;117: 5351–5535.
18. Reardon DA, Galanis E, DeGroot JF, et al. Clinical trial end points for high-grade glioma: the evolving landscape. *Neuro Oncol*. 2011;13(3):353–361.
19. Galanis E, Wu W, Cloughesy T, Lamborn K, et al. Phase 2 trial design in neuro-oncology revisited: a report from the RANO group. *Lancet Oncol*. 2012;13(5):e196–204.
20. Lin NU, Lee EQ, Aoyama H, et al. Challenges relating to solid tumour brain metastases in clinical trials, part 1: patient population, response, and progression. A report from the RANO group. *Lancet Oncol*. 2013;14(10):e396–406.
21. Lin NU, Wefel JS, Lee EQ, et al. Challenges relating to solid tumour brain metastases in clinical trials, part 2: neurocognitive, neurological, and quality-of-life outcomes. A report from the RANO group. *Lancet Oncol*. 2013;14(10):e407–416.
22. van den Bent MJ, Wefel JS, Schiff D, et al. Response Assessment in Neuro-Oncology (a report of the RANO group): assessment of outcome in trials of diffuse low-grade gliomas. *Lancet Oncol*. 2011;12(6):583–593.
23. van den Bent MJ, Vogelbaum MA, Wen PY, Macdonald DR, Chang SM. End point assessment in gliomas: novel treatments limit usefulness of classical Macdonald's Criteria. *J Clin Oncol*. 2009;27(18):2905–2908.
24. Chinot OL, Macdonald DR, Abrey LE, Zahlmann G, Kerloëguen Y, Cloughesy TF. Response assessment criteria for glioblastoma: practical adaptation and implementation in clinical trials of antiangiogenic therapy. *Curr Neurol Neurosci Rep*. 2013;13(5):347.
25. Vogelbaum MA, Jost S, Aghi MK, et al. Application of novel response/progression measures for surgically delivered therapies for gliomas: Response Assessment in Neuro-Oncology (RANO) working group. *Neurosurgery*. 2012;70(1):234–243.
26. Westphal M, Ylä-Herttuala S, Martin J, et al. ASPECT Study Group. Adenovirus-mediated gene therapy with sitimagene ceradenovec followed by intravenous ganciclovir for patients with operable high-grade glioma (ASPECT): a randomised, open-label, phase 3 trial. *Lancet Oncol*. 2013;14(9):823–833.
27. Linhares P, Carvalho B, Figueiredo R, Reis RM, Vaz R. Early pseudoprogression following chemoradiotherapy in glioblastoma patients: the value of RANO evaluation. *J Oncol*. 2013;2013:690585.
28. Brandes AA, Franceschi E, Tosoni A, et al. MGMT promoter methylation status can predict the incidence and outcome of pseudoprogression after concomitant radiochemotherapy in newly diagnosed glioblastoma patients. *J Clin Oncol*. 2008;26(13): 2192–2197.

29. Brandes AA, Tosoni A, Spagnolli F, et al. Disease progression or pseudoprogression after concomitant radiochemotherapy treatment: pitfalls in neurooncology. *Neuro Oncol*. 2008;10(3):361–367.
30. Chaskis C, Neyns B, Michotte A, De Ridder M, Everaert H. Pseudoprogression after radiotherapy with concurrent temozolomide for high-grade gliomas : clinical observations and working recommendations. *Surg Neurol*. 2009;72(4):423–428.
31. Nasseri M, Gahramanov S, Netto JP, et al. Evaluation of pseudoprogression in patients with glioblastoma multiforme using dynamic magnetic resonance imaging with ferumoxytol calls RANO criteria into question. *Neuro Oncol*. 2014;16(8):1146–1154.
32. Gállego Pérez-Larraya J, Lahutte M, Petrirena G, et al. Response assessment in recurrent glioblastoma treated with irinotecan-bevacizumab: comparative analysis of the Macdonald, RECIST, RANO, and RECIST + F criteria. *Neuro Oncol*. 2012;14(5):667–673.
33. Galanis E, Buckner JC, Maurer MJ, et al. Validation of neuroradiologic response assessment in gliomas: measurement by RECIST, two-dimensional, computer-assisted tumor area, and computer-assisted tumor volume methods. *Neuro Oncol*. 2006;8(2):156–165.
34. Shah GD, Kesari S, Xu R, Batchelor TT, et al. Comparison of linear and volumetric criteria in assessing tumor response in adult high-grade gliomas. *Neuro Oncol*. 2006;8(1):38–46.
35. Kanaly CW, Mehta AI, Ding D, et al. A novel, reproducible, and objective method for volumetric magnetic resonance imaging assessment of enhancing glioblastoma. *J Neurosurg*. 2014;121(3):536–542.
36. Huang RY, Rahman R, Hamdan A, et al. Recurrent glioblastoma: volumetric assessment and stratification of patient survival with early posttreatment magnetic resonance imaging in patients treated with bevacizumab. *Cancer*. 2013;119(19):3479–3488.
37. Boxerman JL, Zhang Z, Safriel Y, et al. Early post-bevacizumab progression on contrast-enhanced MRI as a prognostic marker for overall survival in recurrent glioblastoma: results from the ACRIN 6677/RTOG 0625 Central Reader Study. *Neuro Oncol*. 2013;15(7):945–954.
38. Ellingson BM, Cloughesy TF, Lai A, Nghiemphu PL, Mischel PS, Pope WB. Quantitative volumetric analysis of conventional MRI response in recurrent glioblastoma treated with bevacizumab. *Neuro Oncol*. 2011;13(4):401–409.
39. Reuter M, Gerstner ER, Rapalino O, Batchelor TT, Rosen B, Fischl BJ. Impact of MRI head placement on glioma response assessment. *Neuro Oncol*. 2014;118(1):123–129.
40. de Groot JF, Mandel JJ. Update on anti-angiogenic treatment for malignant gliomas. *Curr Oncol Rep*. 2014;16(4):380.
41. Sorensen AG, Jain RK, Batchelor TT, Chi AS. Angiogenesis as a therapeutic target in malignant gliomas. *Oncologist*. 2009;14(6):621–636.
42. Brandsma D, van den Bent MJ. Pseudoprogression and pseudoresponse in the treatment of gliomas. *Curr Opin Neurol*. 2009;22(6):633–638.
43. Clarke JL, Chang S. Pseudoprogression and pseudoresponse: challenges in brain tumor imaging. *Curr Neurol Neurosci Rep*. 2009;9(3):241–246.
44. Batchelor TT, Sorensen AG, di Tomaso E, et al. AZD2171, a pan-VEGF receptor tyrosine kinase inhibitor, normalizes tumor vasculature and alleviates edema in glioblastoma patients. *Cancer Cell*. 2007;11(1):83–95.
45. Friedman HS, Prados MD, Wen PY, et al. Bevacizumab alone and in combination with irinotecan in recurrent glioblastoma. *J Clin Oncol*. 2009;27(28):4733–4740.
46. Norden AD, Young GS, Setayesh K, et al. Bevacizumab for recurrent malignant gliomas: efficacy, toxicity, and patterns of recurrence. *Neurology*. 2008;70(10):779–787.
47. Zuniga RM, Torcuator R, Jain R, et al. Efficacy, safety and patterns of response and recurrence in patients with recurrent high-grade gliomas treated with bevacizumab plus irinotecan. *J Neurooncol*. 2009;91(3):329–336.
48. Pinho MC, Polaskova P, Kalpathy-Cramer J, et al. Low incidence of pseudoprogression by imaging in newly diagnosed glioblastoma patients treated with cediranib in combination with chemoradiation. *Oncologist*. 2014;19(1):75–81.
49. Chamberlain MC. Radiographic patterns of relapse in glioblastoma. *J Neurooncol*. 2011;101(2):319–323.
50. Wick W, Wick A, Weiler M, Weller M. Patterns of progression in malignant glioma following anti-VEGF therapy: perceptions and evidence. *Curr Neurol Neurosci Rep*. 2011;11:305–312.
51. de Groot JF, Fuller G, Kumar AJ, et al. Tumor invasion after treatment of glioblastoma with bevacizumab: radiographic and pathologic correlation in humans and mice. *Neuro Oncol*. 2010;12(3):233–242.
52. Gerstner ER, Chen PJ, Wen PY, Jain RK, Batchelor TT, Sorensen G. Infiltrative patterns of glioblastoma spread detected via diffusion MRI after treatment with cediranib. *Neuro Oncol*. 2010;12(5):466–472.
53. Pope WB, Young JR, Ellingson BM. Advances in MRI assessment of gliomas and response to anti-VEGF therapy. *Curr Neurol Neurosci Rep*. 2011;11(3):336–344.
54. Taal W, Oosterkamp HM, Walenkamp AM, et al. Single-agent bevacizumab or lomustine versus a combination of bevacizumab plus lomustine in patients with recurrent glioblastoma (BELOB trial): a randomised controlled phase 2 trial. *Lancet Oncol*. 2014;15(9):943–953.
55. Ananthnarayan S, Bahng J, Roring J, et al. Time course of imaging changes of GBM during extended bevacizumab treatment. *J Neurooncol*. 2008;88(3):339–347.
56. Quant EC, Norden AD, Drappatz J, et al. Role of a second chemotherapy in recurrent malignant glioma patients who progress on bevacizumab. *Neuro Oncol*. 2009;11(5):550–555.
57. Wick A, Dörner N, Schäfer N, et al. Bevacizumab does not increase the risk of remote relapse in malignant gliomas. *Ann Neurol*. 2011;69(3):586–592.
58. Pope WB, Sayre J, Perlina A, Villablanca JP, Mischel PS, Cloughesy TF. MR imaging correlates of survival in patients with high-grade gliomas. *AJNR Am J Neuroradiol*. 2005;26:2466–2474.
59. Hattingen E, Jurcoane A, Daneshvar K, et al. Quantitative T2 mapping of recurrent glioblastoma under bevacizumab improves monitoring for non-enhancing tumor progression and predicts overall survival. *Neuro Oncol*. 2013;15(10):1395–1404.
60. Artzi M, Bokstein F, Blumenthal DT, et al. Differentiation between vasogenic-edema versus tumor-infiltrative area in patients with glioblastoma during bevacizumab therapy: a longitudinal MRI study. *Eur J Radiol*. 2014;83(7):1250–1256.
61. Ellingson BM, Cloughesy TF, Lai A, et al. Quantification of edema reduction using differential quantitative T2 (DQT2) relaxometry mapping in recurrent glioblastoma treated with bevacizumab. *J Neurooncol*. 2012;106(1):111–119.
62. Oh J, Cha S, Aiken AH, et al. Quantitative apparent diffusion coefficients and T2 relaxation times in characterizing contrast enhancing brain tumors and regions of peritumoral edema. *J Magn Reson Imaging*. 2005;21(6):701–708.
63. Hoehn-Berlage M, Tolxdorff T, Bockhorst K, Okada Y, Ernestus RI. In vivo NMR T2 relaxation of experimental brain tumors in the cat: a multiparameter tissue characterization. *Magn Reson Imaging*. 1992;10(6):935–947.
64. Pasieka JL. Dare to be Oslerian: embracing the value of clinical medicine in today's surgical practice. *Surgery*. 2010;148(6):1047–1056.
65. Meyers CA, Brown PD. Role and relevance of neurocognitive assessment in clinical trials of patients with CNS tumors. *J Clin Oncol*. 2006;24(8):1305–1309.
66. Armstrong TS, Gilbert MR. Net clinical benefit: functional endpoints in brain tumor clinical trials. *Curr Oncol Rep*. 2007;9(1):60–65.

67. Alexander BM, Galanis E, Yung WK, et al. Brain malignancy steering committee clinical trials planning workshop: report from the Targeted Therapies working group. *Neuro Oncol*. August 26, 2014. [PII:nou154. Epub ahead of print].
68. Ballman KV, Buckner JC, Brown PD, et al. The relationship between six-month progression-free survival and 12-month overall survival end points for phase II trials in patients with glioblastoma multiforme. *Neuro Oncol*. 2007;9(1):29–38.
69. Lamborn KR, Yung WK, Chang SM, et al. For North American brain tumor consortium. Progression-free survival: an important end point in evaluating therapy for recurrent high-grade gliomas. *Neuro Oncol*. 2008;10(2):162–170.
70. Han K, Ren M, Wick W, et al. Progression-free survival as a surrogate endpoint for overall survival in glioblastoma: a literature-based meta-analysis from 91 trials. *Neuro Oncol*. 2014;16(5):696–706.
71. van den Bent MJ, Afra D, de Witte O, et al. Long-term efficacy of early versus delayed radiotherapy for low-grade astrocytoma and oligodendroglioma in adults: the EORTC 22845 randomised trial. *Lancet*. 2005;366(9490):985–990.
72. Sofietti R, Baumert BG, Bello L, et al. Guidelines on management of low-grade gliomas: report of an EFNS-EANO task force. *Eur J Neurol*. 2010;17(9):1124–1133.
73. Gotay CC, Kawamoto CT, Bottomley A, Efficace F. The prognostic significance of patient-reported outcomes in cancer clinical trials. *J Clin Oncol*. 2008;26(8):1355–1363.
74. Chang EF, Potts MB, Keles GE, et al. Seizure characteristics and control following resection in 332 patients with low-grade gliomas. *J Neurosurg*. 2008;108(2):227–235.
75. Lin NU, Dieras V, Paul D, et al. Multicenter phase II study of lapatinib in patients with brain metastases from HER2-positive breast cancer. *Clin Cancer Res*. 2009;15(4):1452–1459.
76. Li J, Bentzen SM, Renschler M, Mehta MP. Regression after whole-brain radiation therapy for brain metastases correlates with survival and improved neurocognitive function. *J Clin Oncol*. 2007;25(10):1260–1266.
77. Chang EL, Wefel JS, Hess KR, et al. Neurocognition in patients with brain metastases treated with radiosurgery or radiosurgery plus whole-brain irradiation: a randomised controlled trial. *Lancet Oncol*. 2009;10(11):1037–1044.
78. Hoefnagels FW, Lagerwaard FJ, Sanchez E, et al. Radiological progression of cerebral metastases after radiosurgery: assessment of perfusion MRI for differentiating between necrosis and recurrence. *J Neurol*. 2009;256(6):878–887.
79. Mitsuya K, Nakasu Y, Horiguchi S, et al. Perfusion weighted magnetic resonance imaging to distinguish the recurrence of metastatic brain tumors from radiation necrosis after stereotactic radiosurgery. *J Neurooncol*. 2010;99(1):81–88.
80. Ahmed R, Oborski MJ, Hwang M, Lieberman FS, Mountz JM. Malignant gliomas: current perspectives in diagnosis, treatment, and early response assessment using advanced quantitative imaging methods. *Cancer Manag Res*. 2014;24(6):149–170.
81. Nicolasjilwan M, Hu Y, Yan C, et al. TCGA Glioma Phenotype Research Group. Addition of MR imaging features and genetic biomarkers strengthens glioblastoma survival prediction in TCGA patients. *J Neuroradiol*. 2014. [2 PII:S0150-9861(14) 00187–4].
82. Tanaka S, Louis DN, Curry WT, Batchelor TT, Dietrich J. Diagnostic and therapeutic avenues for glioblastoma: no longer a dead end? *Nat Rev Clin Oncol*. 2013;10(1):14–26.
83. Hu LS, Eschbacher JM, Heiserman JE, et al. Reevaluating the imaging definition of tumor progression: perfusion MRI quantifies recurrent glioblastoma tumor fraction, pseudoprogression, and radiation necrosis to predict survival. *Neuro Oncol*. 2012;14(7):919–930.
84. Sorensen AG, Batchelor TT, Zhang WT, et al. A "vascular normalization index" as potential mechanistic biomarker to predict survival after a single dose of cediranib in recurrent glioblastoma patients. *Cancer Res*. 2009;69(13):5296–5300.
85. Hu LS, Eschbacher JM, Dueck AC, et al. Correlations between perfusion MR imaging cerebral blood volume, microvessel quantification, and clinical outcome using stereotactic analysis in recurrent high-grade glioma. *AJNR Am J Neuroradiol*. 2012;33(1):69–76.
86. Essock-Burns E, Lupo JM, Cha S, et al. Assessment of perfusion MRI-derived parameters in evaluating and predicting response to antiangiogenic therapy in patients with newly diagnosed glioblastoma. *Neuro Oncol*. 2011;13(1):119–131.
87. Ryken TC, Aygun N, Morris J, et al. The role of imaging in the management of progressive glioblastoma: a systematic review and evidence-based clinical practice guideline. *J Neurooncol*. 2014;118(3):435–460.
88. Provenzale JM, McGraw P, Mhatre P, Guo AC, Delong D. Peritumoral brain regions in gliomas and meningiomas: investigation with isotropic diffusion-weighted MR imaging and diffusion-tensor MR Imaging. *Radiology*. 2004;232:451–460.
89. Chu HH, Choi SH, Ryoo I, et al. Differentiation of true progression from pseudoprogression in glioblastoma treated with radiation therapy and concomitant temozolomide: comparison study of standard and high-b-value diffusion-weighted imaging. *Radiology*. 2013;269(3):831–840.
90. Pope WB, Qiao XJ, Kim HJ, et al. Apparent diffusion coefficient histogram analysis stratifies progression-free and overall survival in patients with recurrent GBM treated with bevacizumab: a multicenter study. *J Neurooncol*. 2012;108:491–498.
91. Ellingson BM, Malkin MG, Rand SD, et al. Volumetric analysis of functional diffusion maps is a predictive imaging biomarker for cytotoxic and anti-angiogenic treatments in malignant gliomas. *J Neurooncol*. 2011;102:95–103.
92. Ratai EM, Zhang Z, Snyder BS, et al. Magnetic resonance spectroscopy as an early indicator of response to anti-angiogenic therapy in patients with recurrent glioblastoma: RTOG 0625/ACRIN 6677. *Neuro Oncol*. 2013;15(7):936–944.
93. Costanzo A Di, Scarabino T, Trojsi F, et al. Recurrent glioblastoma multiforme versus radiation injury: a multiparametric 3-T MR approach. *Radiol Med*. 2014;119(8):616–624.
94. Liberman G, Louzoun Y, Aizenstein O, et al. Automatic multimodal MR tissue classification for the assessment of response to bevacizumab in patients with glioblastoma. *Eur J Radiol*. 2013;82(2):e87–94.
95. Schwarzenberg J, Czernin J, Cloughesy TF, et al. 3′-deoxy-3′-18F-fluorothymidine PET and MRI for early survival predictions in patients with recurrent malignant glioma treated with bevacizumab. *J Nucl Med*. 2012;53(1):29–36.
96. Harris RJ, Cloughesy TF, Pope WB, et al. 18F-FDOPA and 18F-FLT positron emission tomography parametric response maps predict response in recurrent malignant gliomas treated with bevacizumab. *Neuro Oncol*. 2012;14(8):1079–1089.

CHAPTER

38

Malignant Astrocytomas

A. Drevelegas[1], *D. Chourmouzi*[1], *N. Papanicolaou*[2], *K. Drevelegas*[1,2]

[1]Department of Radiology, Interbalkan Medical Center, Thessaloniki, Greece; [2]Karolinska Institute, Solna, Sweden

Gliomas are the most common primary brain tumors in adults and account for 40–50% of all intracranial tumors. They may manifest at any age, but preferentially affect adults. Their peak incidence is in the 5th and 6th decade of life. They are slightly more common in men than in women (1.5/1 ratio) and significantly more common in white than in black individuals. Gliomas can affect any part of the central nervous system (CNS), but they usually occur more supratentorially in adults and infratentorially in children.[1]

The clinical symptoms of the tumor depend on the anatomical location of the neoplasm in the brain. Headache, seizures, hemiparesis, personality changes, visual loss, gait disturbances, and signs of increased intracranial pressure are among the most common clinical manifestations.[2]

More than half of all glial tumors are astrocytic tumors. The pathologic classification and grading of astrocytomas are controversial, but on the other hand they are also critical for assessment of prognosis and treatment. A simple grading system for gliomas relies upon recognition of four parameters: nuclear atypia, mitoses, endothelial proliferation, and necrosis. The presence of two or more of the above-described features in a glioma places the tumor in the high-grade category.[3] High-grade or malignant gliomas are tumors with both expansive and infiltrative growth. They show some degree of anaplasia, without any cleavage plane, and in microscopic examination tumor cells are known to extend beyond the tumor margins. Anaplastic astrocytoma (AA; WHO grade III) and glioblastoma multiforme (GBM; WHO grade IV), the most common primary malignant brain tumors, are classified as high-grade gliomas or malignant astrocytomas. This histologic behavior is a consequence of multiple genetic changes that accumulate during stepwise progression.[4] Since 2005, tremendous progress has been made in our understanding of the critical events that accompany astroglial transformation and malignant progression[5] (see Table 1). Gliosarcoma, a rare tumor (WHO grade IV) composed of both neoplastic glial and mesenchymal cells, is also reviewed here with the high-grade neoplasms.

I. Anaplastic astrocytoma (WHO grade III) is an infiltrating lesion with biology and average age of diagnosis intermediate between simple low-grade astrocytomas and GBM. Although some AAs arise as new primaries, 65–75% result from dedifferentiation of low-grade gliomas (LGGs).[6] The course of progression of LGGs to AA varies considerably, with time intervals ranging from less than 1 year to more than 10 years, the mean interval being 4–5 years. The designation of a tumor as AA reflects a distinct histological classification of malignant glioma characterized by an abundance of pleomorphic astrocytes with evidence of mitosis.[7] On the other hand, they lack the necrosis and significant vascular proliferation that characterize GBM.

Anaplastic astrocytomas appear in a slightly higher age group than low-grade astrocytomas. They can occur at any age, but most commonly in the 4th–6th decade of life. The cerebral hemispheres are the most common location of these tumors. Seizures and focal neurologic deficits represent the most common clinical symptoms.

Although AA are malignant tumors, they have a better prognosis and a higher likelihood of response to treatment than GBM. The median survival rate for the patients with these tumors is 2–3 years.

On CT scans AA present as ill-defined inhomogeneous lesions. Calcification is rarely encountered and only in cases of preexisting LGGs with malignant transformation. Peritumoral edema may be present as a hypodense area. After the administration of contrast

http://dx.doi.org/10.1016/B978-0-12-800945-1.00038-0
© 2016 Elsevier Ltd. All rights reserved.

TABLE 1 Genetic Abnormalities in Astrocytic Tumors

Tumor Type	Chromosome Deviation	Gene Alteration	Growth Factor Amplification/Overexpression
Astrocytoma	+7q, −22q	*−p53*	PDGFR-α
Anaplastic astrocytoma	1, +7q, −9p, −10, −13q, +19, +20, −22q	*−p53* *−p16* *−Rb*	
Primary glioblastoma	1, −4q, −6q, +7q, 8q, −9p, −10, −13q, −17p, 19, +20, −22q	*+MDM2* *−PTEN* *−p16* *−Rb*	EGFR
Secondary glioblastoma	−4q, −9p, −10, −13q, −17p	*−p53* *−p16* *−Rb* *−DCC*	PDGFR-α

+, chromosomic gain or gene amplification/overexpression.
-, chromosomic loss or gene inactivation.
PDGFR-α; platelet-derived growth factor receptor α.
EGFR, epidermal growth-derived factor receptor.
From the book Imaging of brain tumors with pathological correlations, *A. Drevelegas (Ed.), with kind permission of Springer Science and Business Media.*

material, the tumors either do not enhance or show focal, nodular, or heterogeneous enhancement[8,9] (see Figure 1(a) and (b)). On MRI the appearance of AA may be quite variable. On T1-weighted images they appear heterogeneously iso- to hypointense. T2-weighted images reflect better the heterogeneous composition of the AA, with areas of high signal intensity representing the tumor itself and the peritumoral vasogenic edema. Tumor cells can be identified either in the most distant aspect of peritumoral edema or occasionally in areas depicted as normal on T2-weighted images outside the margins of peritumoral edema. On T1-weighted images after the administration of contrast medium they show heterogeneous or patchy enhancement[10] (see Figure 1(c)–(e)).

In terms of imaging characteristics, AAs may be difficult to differentiate from GBMs. However, the margins of AA are less defined and exhibit a moderate amount of mass effect, vasogenic edema, and heterogeneity. They show a minimal amount of hemorrhage, as opposed to findings in GBM. Necrosis, the imaging hallmark of GBM, is absent. AAs may also mimic the appearance of low-grade astrocytomas and can present as a well-demarcated, homogeneous nonenhancing mass.[11,12] A nonenhancing supratentorial neoplasm does not always equate with low-grade malignancy. In one study, 40% of nonenhancing lesions proved to be anaplastic astrocytomas[13] (see Figure 2). MRI is the modality of choice for tumor surveillance and potential malignant transformation over time (see Figure 3).

II. Glioblastoma multiforme (WHO grade IV) is the most common brain tumor, accounting for more than half of all gliomas and 15–20% of all intracranial tumors. About 50–60% of all astrocytic tumors are classified as GBM. Although they represent only 1–2% of all malignancies, the incidence of GBMs is in the range of two or three new cases per 100,000 population per year.[14]

GBMs may occur at any age but most commonly affect adults, with a peak incidence between 45 and 70 years. In childhood, GBMs are relatively uncommon compared to adults and account for 7–9% of all pediatric intracranial tumors.

GBMs occur most commonly in the subcortical white matter of the temporal, parietal, frontal, and occipital lobes. In a series of 987 GBMs from University Hospital Zurich, the most frequently affected sites were the temporal (31%), parietal (24%), frontal (23%), and occipital (16%) lobes.[15] The basal ganglia may also be involved. Brain-stem GBMs are infrequent and occur most commonly in children, as a result of transformation of preexisting low-grade glioma, and the cerebellum and spinal cord are rare sites for this neoplasm.

The most common clinical symptoms in GBMs include seizures, headaches, personality changes, focal neurologic deficits, speech impairment, cranial nerve involvement, and increased intracranial pressure. Glioblastoma represents an aggressive tumor with an ominous prognosis.

Glioblastomas can arise "de novo" (primary glioblastomas) or after progression of an AA (secondary glioblastoma). Primary GBMs account for the vast majority of cases (60%) in adults older than 50 years. After a short clinical history, usually less than 3 months, they manifest de novo (i.e., without clinical or histopathological evidence of a preexisting, less malignant precursor lesion). Secondary GBMs (40%) typically develop in younger patients (<45 years) through

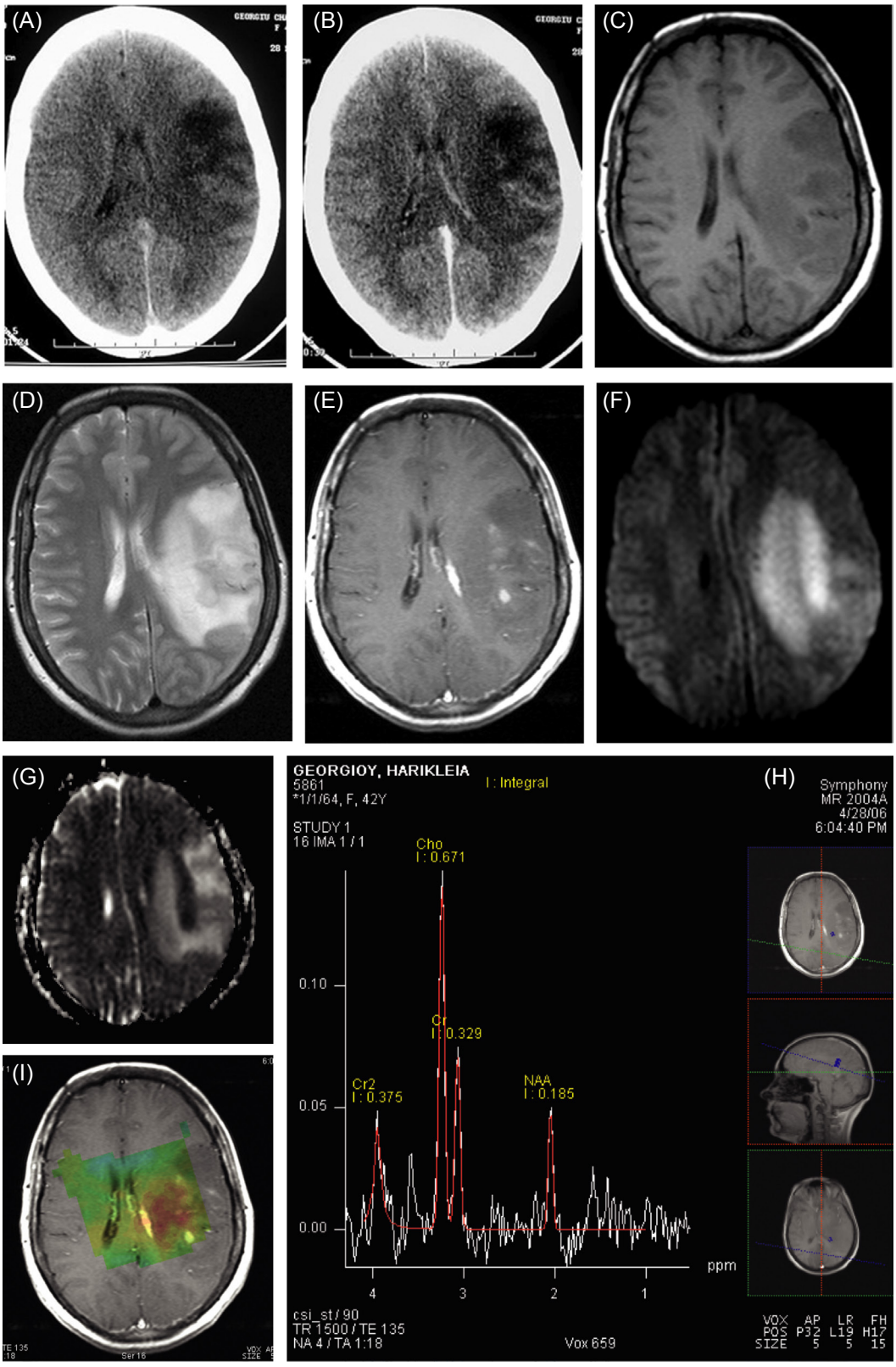


FIGURE 1 Anaplastic astrocytoma. (A) NCCT shows a heterogeneous, hypodense left parietal lobe mass. (B) After the administration of contrast medium the mass remains predominantly hypodense and only a small area of enhancement is present (arrow). (C) Axial T1-weighted image (T1WI) shows a slightly hypointense lesion with thickened left parietal cortex. (D) On axial T2-weighted image the lesion is heterogeneously hyperintense with peritumoral edema. (E) On axial postcontrast T1WI the hypointense lesion shows patchy enhancement, which exhibits high signal intensity on diffusion-weighted image (F) and low signal intensity on ADC map (G) owing to restricted diffusion. (H) Long TE (135 ms) spectrum demonstrates elevated choline and reduced NAA at the area of tumor plus edema. (I) Choline (Cho)/creatine (Cr) spectral map shows abnormal Cho/Cr with red color.

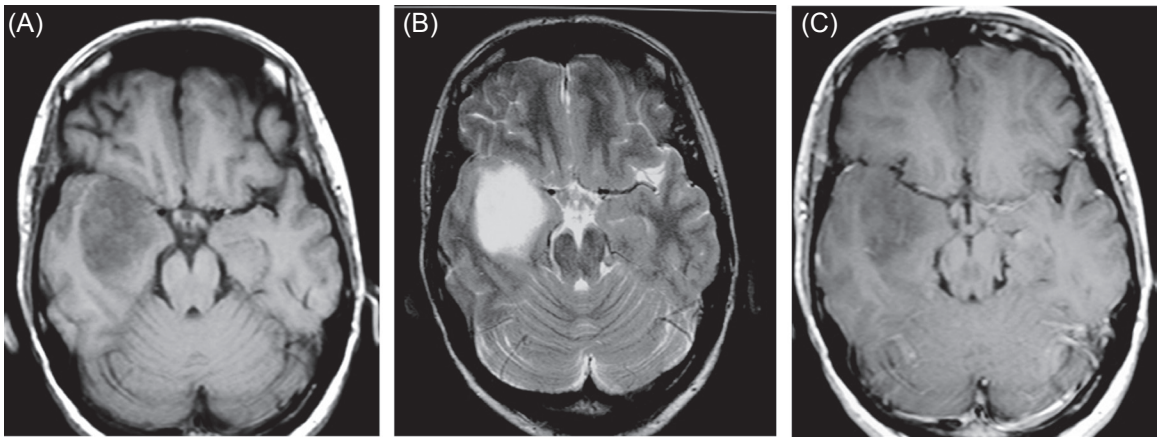


FIGURE 2 Anaplastic astrocytoma of the left temporal lobe. (A) Axial T1-weighted image shows a space occupying hypointense mass. (B) On T2-weighted image the mass shows homogeneous high signal intensity. (C) On postcontrast T1-weighted image the mass is unenhanced.

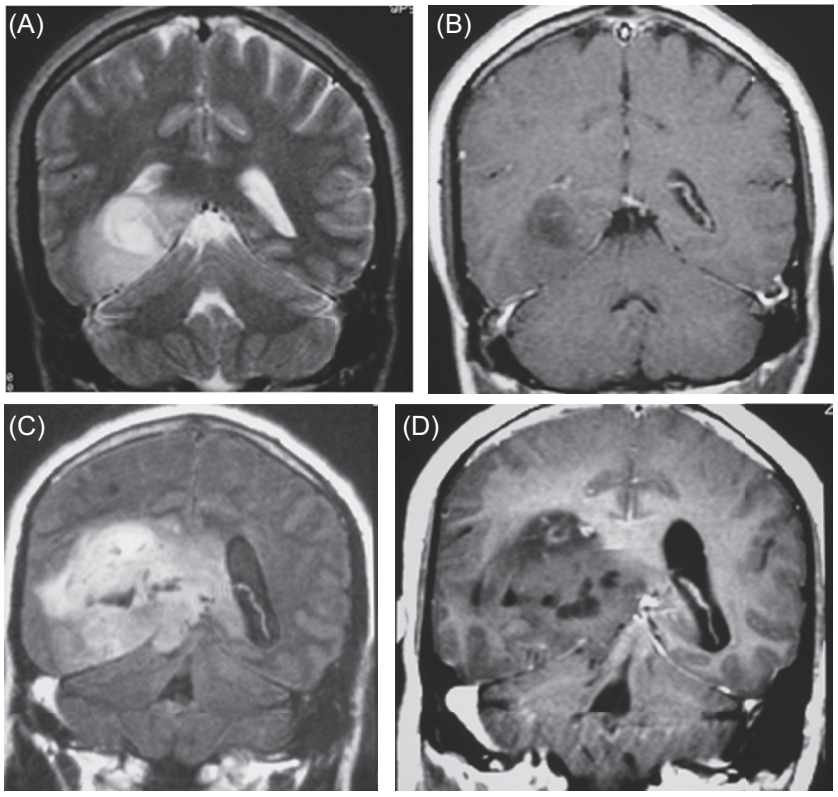


FIGURE 3 Evolution of low-grade glioma to anaplastic astrocytoma. (A) Coronal T2 and (B) postcontrast T1-weighted images in a 35-year-old man with temporal lobe seizures show a heterogeneous nonenhanced mass. Biopsy revealed an infiltrating low-grade astrocytoma. Three years later (C) coronal FLAIR and (D) postcontrast T1-weighted images show significant enlargement of the mass. Stereotactic biopsy showed anaplastic astrocytoma.

malignant progression from a low-grade astrocytoma (WHO grade II) or AA (WHO grade III).

Despite the progress in surgery, radiation therapy, and chemotherapy, the mean survival time for patients with GBM ranges between 12 and 15 months. Only exceptional patients survive beyond 2 years.[16]

On nonenhanced CT GBMs appear as central low-density lesions that reflect necrosis, located usually in the centrum semiovale. Necrosis is the imaging hallmark of GBMs.[17,18] Calcification is rare in GBMs and when present is thought to be related to a preexisting low-grade astrocytoma. They are heterogeneous owing to the reflecting sites

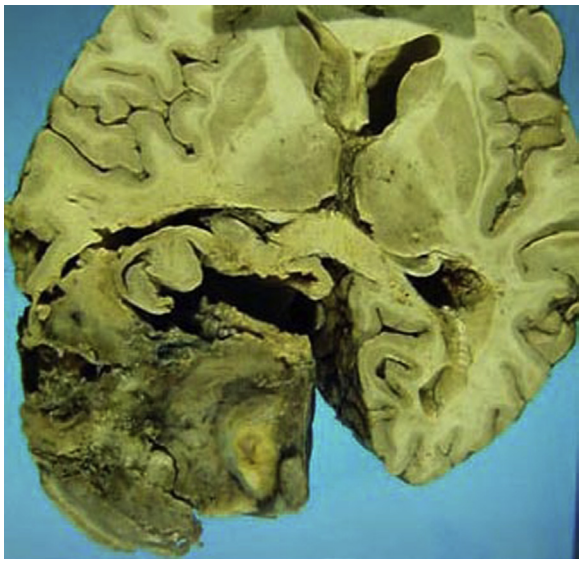


FIGURE 4 Glioblastoma multiforme. Gross specimen shows a large heterogeneous tumor occupying the right occipital lobe with necrotic and hemorrhagic areas.

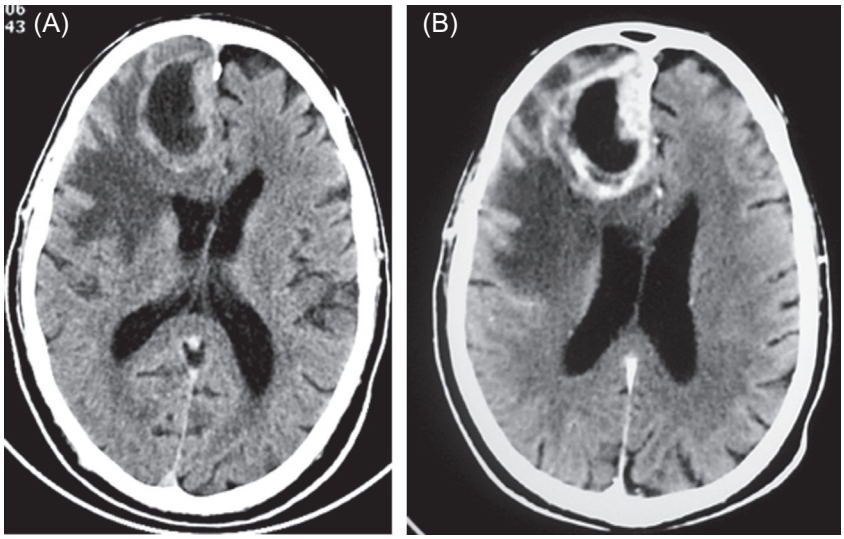


FIGURE 5 Axial (A) noncontrast and (B) postcontrast CTs in a patient with glioblastoma multiforme show a thick and nodular ring-like enhancing mass with central necrosis. Note also the mass effect and the surrounding white matter edema.

of necrosis, hemorrhage, and increased cellularity (see Figure 4). Hemorrhage was reported in approximately 19% of patients with GBM and in approximately 12% of patients with low-grade lesions.[19] In addition to necrosis and hemorrhage, another characteristic radiologic feature is the presence of edema, which surrounds the tumor, extends along the adjacent white matter tracts, and usually produces significant mass effect. After the administration of contrast material they usually show marked heterogeneous ring-like enhancement with thick, shaggy, irregular, and nodular walls (see Figures 5 and 6).

On T1-weighted images, GBMs appear as heterogeneous masses with central necrosis, thick irregular margins, and peritumoral edema (see Figures 7(a) and 8(a)). After the administration of contrast medium they show inhomogeneous or irregular ring-like enhancement (see Figures 7(b) and 8(b)). The thick and irregular enhanced rim surrounds a hypointense central area consistent with necrosis within the tumor. The peripheral nonenhancing low attenuation zone represents vasogenic edema. The enhanced ring-like structure does not represent the outer tumor border, because infiltrating glioma cells can be identified easily within, and occasionally beyond, a 2-cm margin.

On T2-weighted images GBM appears as a heterogeneous mass with high signal intensity. The heterogeneous appearance may be due to central necrosis,

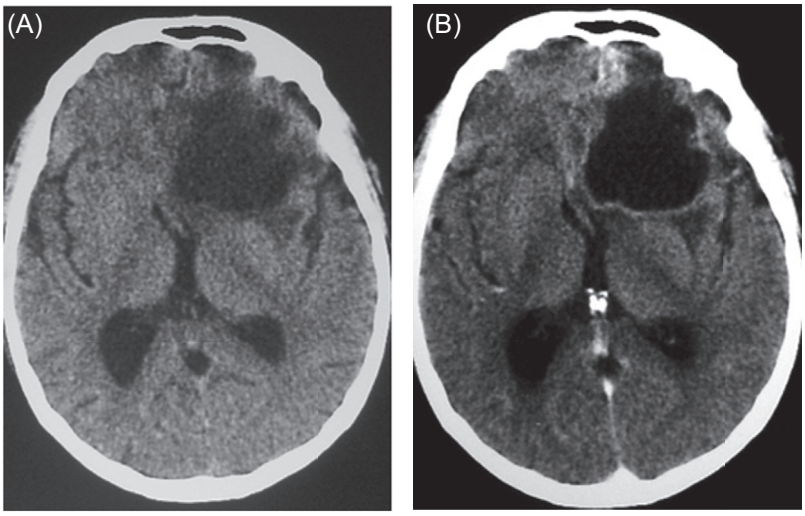


FIGURE 6 Glioblastoma multiforme. (A) Noncontrast CT shows a hypodense mass in the left frontal lobe. (B) Postcontrast CT shows a centrally necrotic mass with thin ring-like enhancement. Note also the surrounding mass effect and the midline shift.

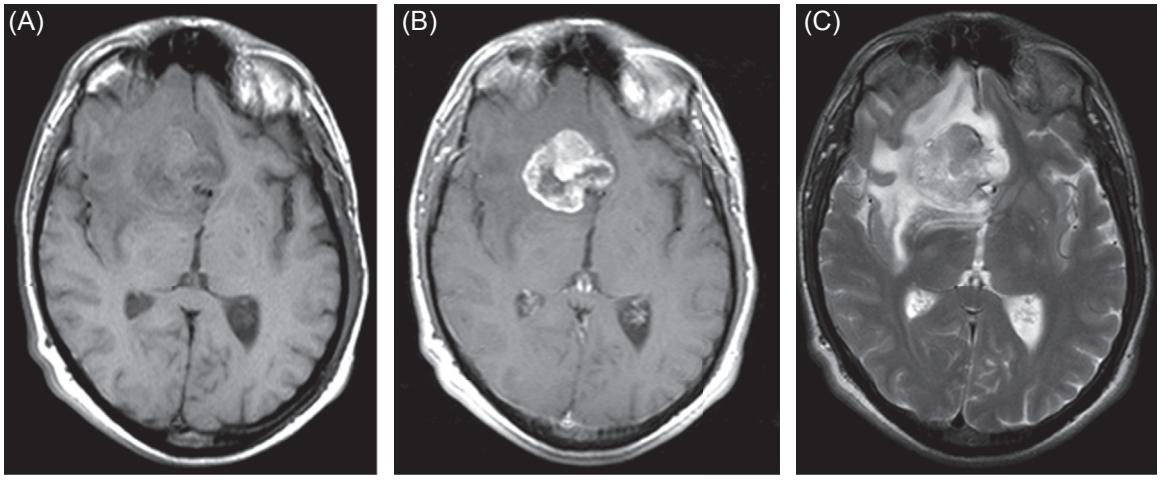


FIGURE 7 Glioblastoma multiforme. (A) Noncontrast T1-weighted image shows a heterogeneous mass in the right frontal lobe. (B) After the administration of contrast medium thick and irregular ring-like enhancement is seen with central necrosis. (C) Axial T2-weighted image shows a heterogeneous mass with peritumoral vasogenic edema extending along the adjacent white matter.

hemorrhage, and tumor vascularity. Prominent peritumoral vasogenic edema is always present and is better appreciated in T2- compared with T1-weighted images. The vasogenic edema is produced by abnormal neoplastic vessels, which lack the normal blood–brain barrier, resulting in transudation of fluids and proteins into the extracellular space. Although MR imaging is the most sensitive method for depicting abnormal amounts of tissue water, discrimination of tumor tissue from edema in terms of signal characteristics has proved unreliable. The white matter edema produced by GBMs is very extensive and actually represents tumor plus edema[20–23] (see Figures 7(c) and 8(c)).

GBMs may disseminate along various pathways but most commonly along the white matter tracts to involve the contralateral hemisphere. Spread across the corpus callosum, internal capsule, optic radiations, and anterior and posterior commissure is typical. Symmetric extension through the corpus callosum gives rise to the so-called "butterfly" appearance (see Figure 9). Subependymal spread of GBM can occur and is correlated with a poor prognosis. Spread along the neuraxis via the cerebrospinal fluid is also well documented and, incidentally, has been found to have a 6–20% incidence in autopsy series. Extracranial metastases of GBMs are very rare and occur most commonly in patients after surgery. However, surgery is not a prerequisite for extracranial metastatic spread of primary CNS malignant disease; extraneural metastases have been described in patients who had not undergone previous surgery. The incidence of symptomatic metastases is certainly lower than the incidence seen at postmortem and is due to the short survival of the affected patients.[24–28]

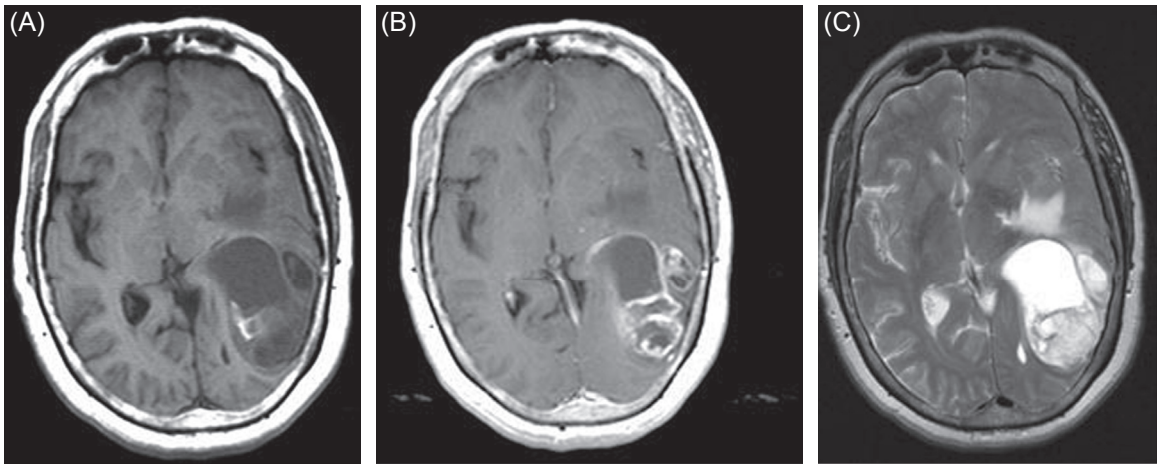


FIGURE 8 Glioblastoma multiforme. (A) Noncontrast T1WI shows a large cystic left parieto-occipital tumor with intratumoral hemorrhage (arrow). (B) Postcontrast T1WI shows irregular ring-like enhancement. (C) On T2-weighted image the cavitary necrosis shows high signal intensity and the solid component of the tumor appears heterogeneous.

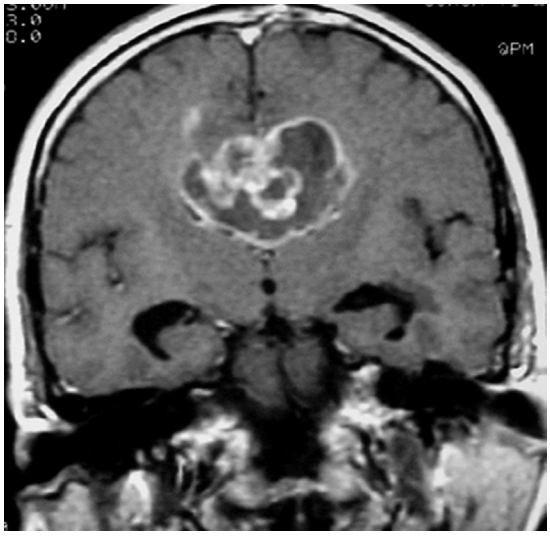


FIGURE 9 Coronal postcontrast T1-weighted MR image shows an enhancing mass extending through the corpus callosum to both frontal and parietal lobes (butterfly GBM).

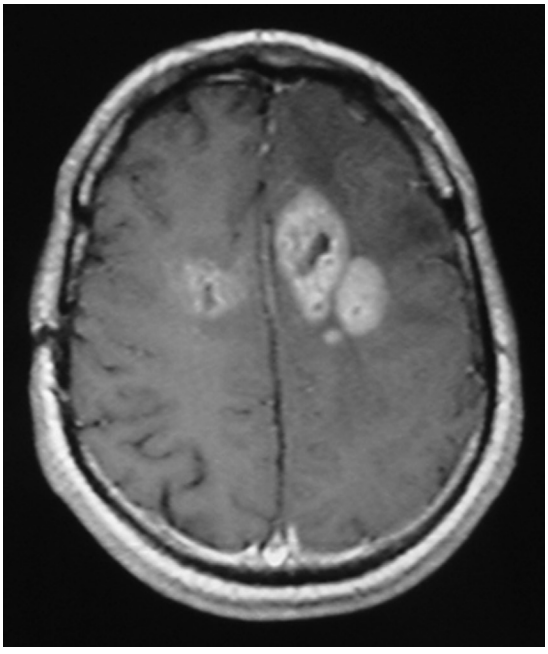


FIGURE 10 Axial postcontrast T1-weighted image demonstrates multiple, nodular enhanced lesions in both hemispheres. Biopsy proved multifocal GBM.

The vast majority of GBMs are solitary lesions. Multifocal or multicentric tumors occur rarely, in only 0.5–1% of cases.[29] Multicentric tumors are described as widespread lesions in different lobes or hemispheres, without the evidence of possible intracranial spread or microscopic connection. On the other hand, those with either gross or microscopic continuity are defined as multifocal (see Figure 10). The most frequent dissemination route in this group is the meningeal–subarachnoid space, followed by the subependymal, intraventricular route and direct brain penetration through white matter tracts.[30–32]

Studies of human neoplasms have demonstrated that increased malignancy is associated with increased neovascularity. Microvascular proliferation (i.e., angiogenesis) is one of the most important criteria for determining the malignancy of gliomas. Tumor capillaries provide not only nutrients to growing tumor cells, but also a route for spread and infiltration far beyond the site of the parent tumor.[33] Angiogenesis is an important parameter in assessing the grading of gliomas.

Although MRI is the modality of choice in the evaluation of brain tumors, conventional T1 and T2 sequences, as well as postcontrast MRI, have been unable to discriminate neoplastic cells from peritumoral edema or to determine tumor margins accurately. On the other hand, radiologic grading of tumors with conventional MR imaging is not always accurate, with sensitivity in identifying high-grade gliomas (HGGs) ranging from 55.1% to 83.3%.[34–37]

The development of techniques capable of accurately depicting tumor margins and grades in vivo is important for determination of the most appropriate treatment for gliomas. The implementation of echo-planar imaging allowed the development of advanced imaging techniques such as diffusion-weighted imaging (DWI) and dynamic contrast-enhanced perfusion, providing physiologic information that complements the anatomic information available with conventional MR imaging. Today advanced MR imaging is a key modality not only for lesion diagnosis, but also for evaluating the extension, type, and grade of the tumor. Additionally, it provides some new insights for neuroradiology practice, such as targeting stereotactic biopsies to tumor areas of likely higher grades, distinguishing radiation necrosis from tumor infiltration, and assessing tumor response to therapy.[38,39]

DWI uses a pair of strong magnetic gradient pulses to dephase and subsequently rephase protons. Protons with higher diffusion rates show a loss of phase coherence and a low MR signal, whereas protons with slow or restricted diffusion will largely rephase and appear as a high MR signal. The information provided reflects the viability and structure of tissue on a cellular level. Quantitative information on restricted diffusion of water molecules can be obtained by calculating the apparent diffusion coefficient (ADC). DWI has proved clinically useful in the evaluation of cerebral ischemia, infection, and tumors.[40–42]

The role of DWI in patients with brain tumors has been investigated. ADCs could provide useful information in the diagnosis of patients with brain tumors, such as tumor malignancy and peritumoral infiltration. Tumor cellularity and tumor grade have been correlated with ADC values. Brain neoplasms with higher cellularity or higher grades show a significant reduction in the value of the ADC and a marked increase in the signal of diffusion-weighted images. The low ADC values in tumor probably reflect a decreased volume of extracellular space due to increased tumor cellularity, high nuclear/cytoplasmic ratio, and increased intracellular viscosity, with subsequent restriction of water motion. Lower ADCs indicate mostly malignant glioma and higher ADCs low-grade gliomas[43–45] (see Figure 1(f) and (g)). In a study by Higano et al. the minimum ADC varies significantly between WHO grade III ($(1.026+0.21)\times10^{-3}\,mm^2/s$) and WHO grade IV gliomas ($(0.83+0.14)\times10^{-3}\,mm^2/s$) at a value of $1000\,s/mm^2$.[46]

A study performed at our institution on 70 consecutive patients with a diagnosis of primary intracranial glioma immediately before undergoing surgical resection revealed an inverse correlation between minimum ADC values and degree of malignancy. The mean minimum ADC for LGGs was $(1.4920\pm0.2774)\times10^{-3}\,mm^2/s$, for HGGs grade III $(1.1106\pm0.4627)\times10^{-3}\,mm^2/s$, and for high-grade gliomas grade IV $(0.8931\pm0.1611)\times10^{-3}\,mm^2/s$.[47] Other investigators have failed to find a significant difference between the ADC values of HGGs and low-grade tumors.

There is an effort to define glioma margins using diffusion tensor imaging. MR diffusion tensor imaging allows the identification and characterization of white matter tracts according to the direction and degree of their anisotropic water diffusion. Quantifying the degree of anisotropy in terms of metrics such as the fractional anisotropy offers insight into white matter development and degradation. There are fractional anisotropy changes in the white matter of glioblastomas that might indicate cellular infiltration beyond the area of the tumor enhancement. Within the tumor center, white matter fibers are displaced by cellular infiltration, and fractional anisotropy is reduced, whereas in the periphery and in a narrow rim of white matter surrounding the tumor, this parameter could be preserved or even increased by fiber compression due to the space-occupying effect of the tumor[48–50] (see Figure 11(a)–(c)).

Several studies suggest that contrast enhancement alone is not sufficient to predict tumor grade, because 20% of LGGs demonstrate contrast enhancement, whereas one-third of high-grade tumors do not.[36] Although contrast enhancement indicates disruption of the blood–brain barrier, it is not particularly effective at revealing the underlying regional vascularity. Precise determination of the regional vascularity is important, given that the degree of vascular proliferation is an important parameter for the histopathologic grading of gliomas.

The introduction into clinical practice of echo-planar MR imaging allowed the estimation of parameters that reflect tissue vascularization. Perfusion-weighted imaging provides useful information about the microcirculation in brain tissue. This technique requires the dynamic (bolus) intravenous administration of an MR contrast agent. As the paramagnetic contrast agent passes through the intravascular compartment, it causes local field inhomogeneities that result in magnetic susceptibility effects with a decrease in signal on multiple repeated T2* images that can be measured. This signal drop depends on both the vascular concentration of contrast agent and the concentration of small vessels per voxel of tissue.[51,52] Changes in signal intensity may be used to calculate an image of the relative cerebral blood volume (rCBV).

In brain tumors, cerebral blood volume (CBV) maps are particularly sensitive for depicting the microvasculature of a tumor and therefore its aggressiveness and proliferative potential. Several studies have found statistically significant correlations between tumor rCBV

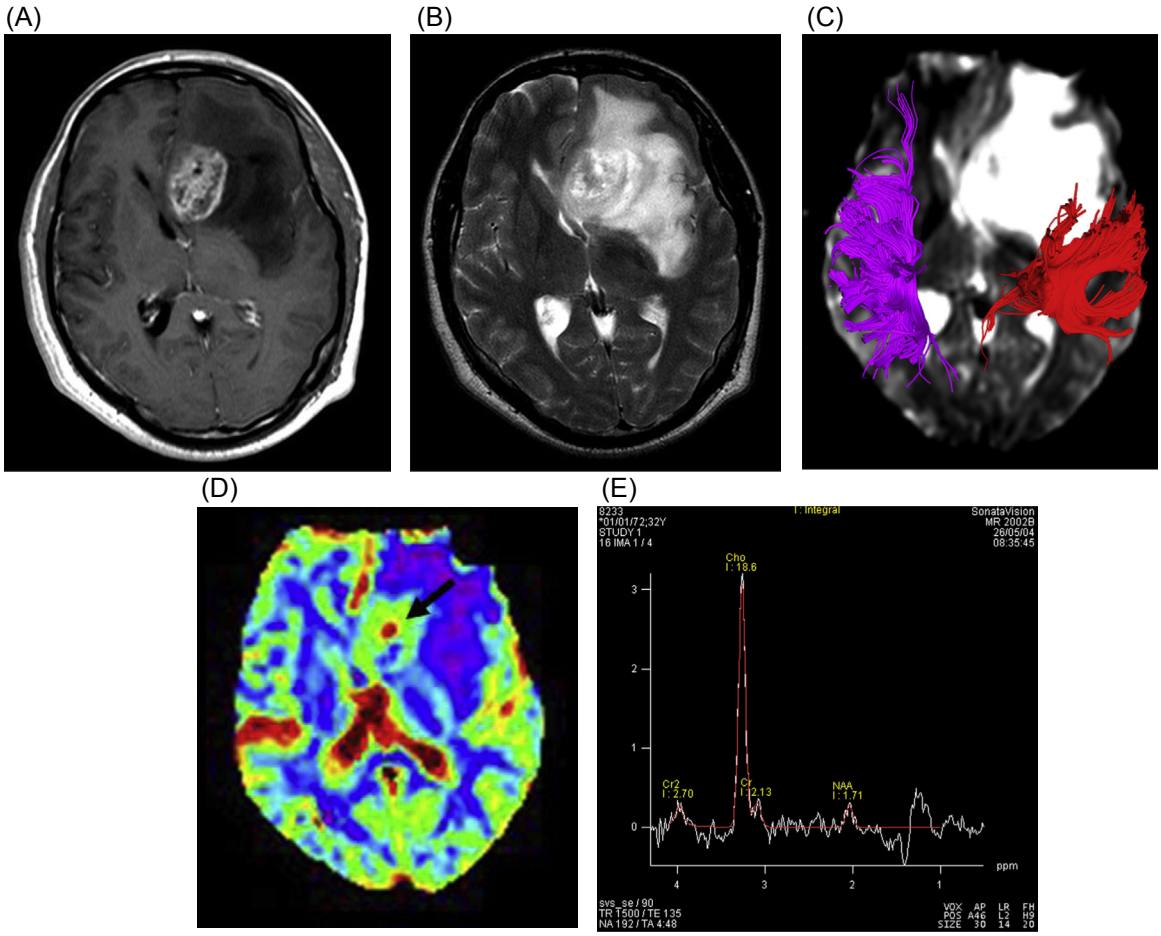


FIGURE 11 Glioblastoma multiforme. (A) Axial post-gadolinium T1-weighted image shows inhomogeneous contrast enhancement of the tumor, located in the left basal ganglia area. (B) On T2 weighting the tumor appears inhomogeneous, surrounded by extensive edema. (C) Diffusion tensor-based tractography reveals extensive infiltration and displacement of internal capsule fibers near the tumor. (D) Perfusion map demonstrates increased CBV at the center of the tumor (arrow). (E) Significantly elevated choline peak (Cho/Cr = 8.51) is shown on a long TE spectrum (TE = 135 ms) obtained from the enhancing part of the tumor.

and glioma grade. HGGs demonstrate higher rCBV values than low-grade tumors, and the low-grade tumors with contrast enhancement present with low rCBV (see Figures 11(d) and 12).[53–56] Several studies have shown that LGGs have maximal rCBV values of between 1.11 and 2.14, and HGGs have maximal rCBV values that range between 3.54 and 7.32.[57] In clinical practice, 95–100% sensitivity has been reported for differentiating HGGs from LGGs using thresholds of 1.75 and 1.5 for rCBV, respectively. In our study LGGs showed maximum rCBV of 0.7575 ± 0.2944, gliomas grade III 3.3425 ± 1.7020, and gliomas grade IV 6.3894 ± 3.0974. A sensitivity of 100%, specificity of 98%, and diagnostic accuracy of 98% were found for differentiating HGGs from LGGs using a threshold for maximum rCBV between 1.625 and 1.735.[47]

On the basis of differences between HGGs and LGGs in terms of vascular heterogeneity, Emblem et al.[58] proposed an alternative method to differentiate HGGs from LGGs using normalized blood volume histogram analysis of the entire tumor volume. Whole-lesion histogram analysis represents a more comprehensive method of quantification and information extraction compared to traditional two-dimensional region of interest (ROI) generation on a single slice (see Figure 13). Apparently, histogram analysis does not suffer from personal bias introduced by the person drawing the ROI; however, it requires the availability of a robust and accurate segmentation algorithm. In addition, the final outcome of a two-dimensional ROI-based measurement method is a single number that suffers from averaging effects, especially when heterogeneous lesions are studied.

CBV measurements can also be used to reduce the sampling error in the histopathologic diagnosis of gliomas, improving the selection of targets for stereotactic biopsy. High-CBV areas represent the best stereotactic biopsy site for accurate grading of astrocytomas.[55,59]

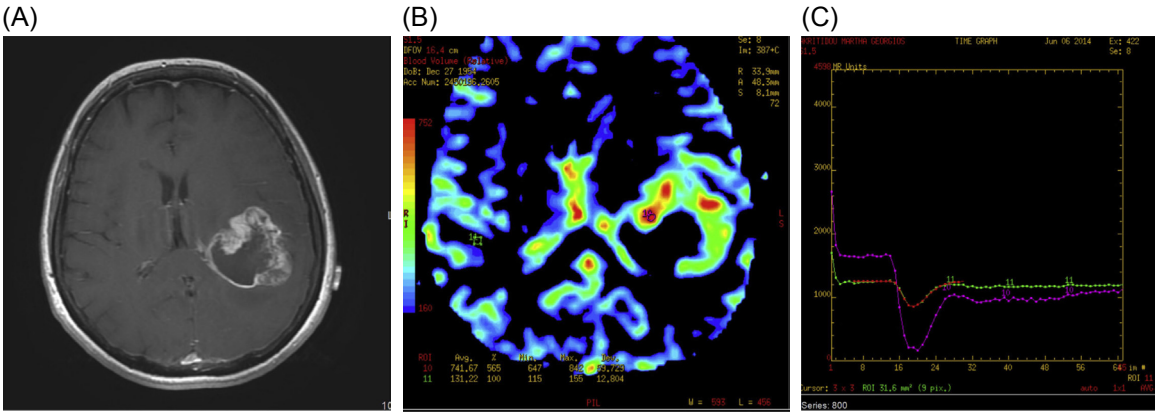


FIGURE 12 (A) Glioblastoma presents with rim enhancement pattern on post-gadolinium T1-weighted axial image, whereas (B) on perfusion color map it demonstrates increased rCBV. (C) Time-intensity curve shows significant signal drop in the area of the tumor as opposed to normal contralateral white matter, indicative of high-grade tumor.

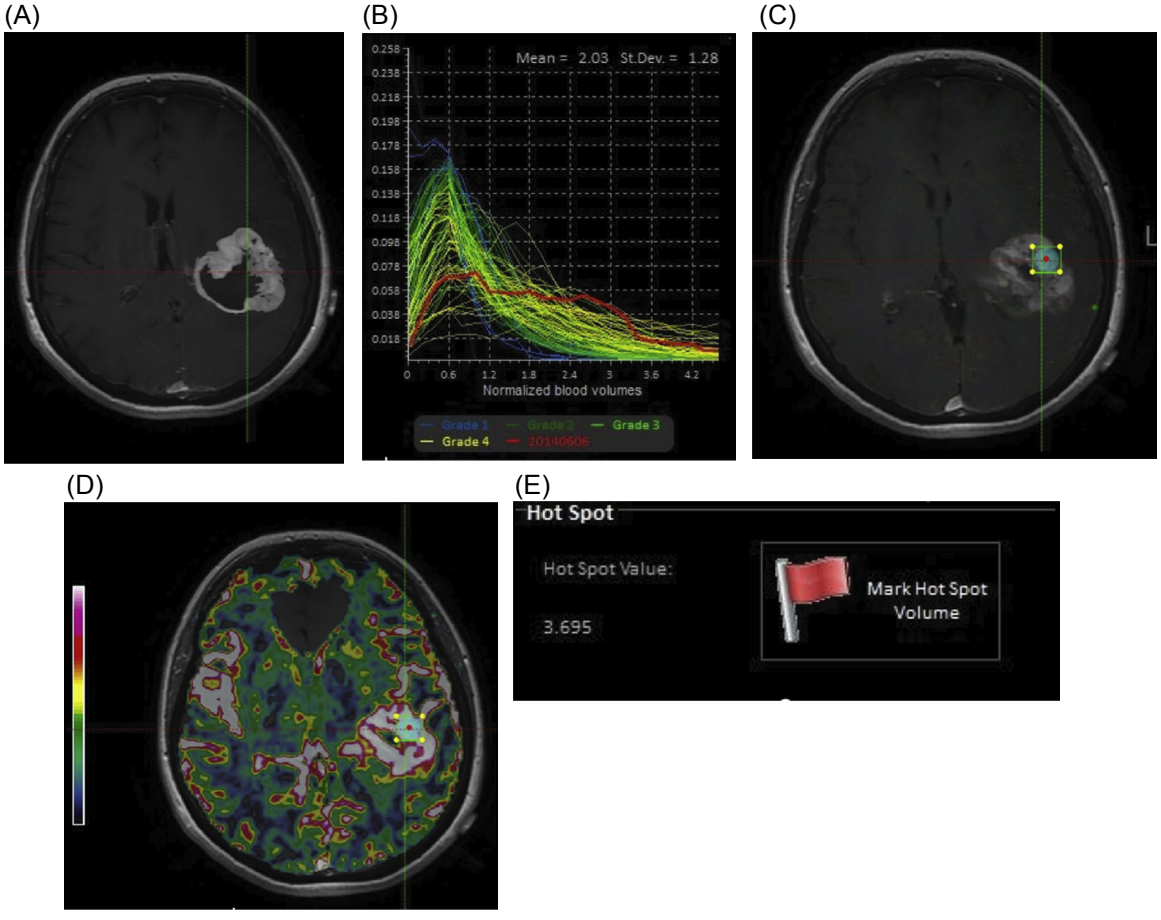


FIGURE 13 Histogram analysis on a patient with glioblastoma multiforme. (A) Post-gadolinium T1-weighed axial image showing peripheral enhancement of the tumor. (B) Normalized histogram (red line) of normalized blood volume obtained from the enhancing parts of the tumor. The histogram is broad and short in amplitude owing to the heterogeneity in vascularity that is a common feature of high-grade tumors. In the background, histograms of known gliomas are shown for which blue corresponds to grade I, dark green to grade II, light green to grade III, and yellow to grade IV. (C) Region of interest is shown on a post-gadolinium T1-weighted axial image and (D) normalized blood volume map, from which (E) the hot-spot ratio was calculated.

MR spectroscopy (MRS) is a noninvasive technique that allows in vivo measurements of certain tissue metabolites. By suppressing the water signal, the relative concentrations of non-water, proton-containing metabolites from discrete tissue regions can be quantified. There is certainly compelling evidence that MRS provides important supplementary information to conventional MR imaging. In normal brain, the principal metabolite signals that can be measured by MRS are choline (Cho), creatine (Cr), *N*-acetylaspartate (NAA), and lactate (Lac).[60,61] Each metabolite resonates at a specific frequency (ppm), and each one reflects specific cellular and biochemical processes.

Cho is a cell membrane marker. The increase in Cho in simple terms is attributed to cell membrane turnover and proliferation. An elevation in Cho may be due to either cell membrane synthesis or destruction or both. Cho is most prominent in regions with high neoplastic cellular density and is progressively lower in moderate and low-grade tumors. Some highly malignant tumors and some GBMs may show low Cho because of extensive necrosis.[62–64]

Cr is a marker of "energy metabolism" and is reduced in tumors because of the increased metabolic activity of tumors consuming energy. NAA is a marker of neuronal density and viability, and it is generally felt to be neuron specific. The decrease in NAA represents the replacement of normal-functioning neurons and axons by any disease that adversely affects neuronal integrity.[61,62]

Lac is a product of anaerobic glycolysis and is present only in minute amounts in normal brain. It appears when tumors outgrow their blood supply and start utilizing anaerobic glycolysis. Lac levels increase significantly in necrotic and cystic tumors.

Lipids are products of brain destruction and are found in necrotic portions of tumors. Myoinositol is a glial cell marker and osmolyte hormone receptor mechanism.

The basic metabolite changes common to brain tumors include elevation in Cho, Lac, and lipids, with a decrease in NAA and Cr (see Figures 1(h), 1(i), and 11(e)). As a general rule, as malignancy increases, NAA and Cr decrease, and Cho, Lac, and lipids increase. Myoinositol can also be used to differentiate LGGs and HGGs. LGGs express higher levels of myoinositol compared with HGGs. This may be due to the lack of activation of phosphatidylinositol metabolism resulting in the accumulation of myoinositol in LGGs.[65–67]

There is extensive literature demonstrating the metabolite ratios of Cho/Cr, NAA/Cr, NAA/Cho, and Cho/NAA and the presence of lipids and Lac to be useful in grading tumors and predicting tumor malignancy.

Several investigations have noted a significant difference in Cho/Cr, Cho/NAA, and NAA/Cr ratios for differentiating between LGGs and HGGs.

Law et al. demonstrated that a threshold value of 1.56 for Cho/Cr provides sensitivity, specificity, and positive and negative predictive values of 75.8, 47.5, 81.2, and 39.6%, respectively, for the determination of HGG versus a LGG. In the same study, a threshold value of 1.6 for Cho/NAA provided 74.2, 62.5, 85.6, and 44.6% for the sensitivity, specificity, and positive and negative predictive values, respectively, for determination of a HGG.[57]

In our study the Cho/Cr ratio was 1.5230 ± 0.4578 and Cho/NAA 1.4520 ± 0.8845 for LGGs, Cho/Cr 2.2157 ± 0.5498 and Cho/NAA 2.0345 ± 0.9206 for grade III gliomas, and Cho/Cr 2.8222 ± 0.8002 and Cho/NAA 3.0650 ± 1.7313 for grade IV gliomas.

A Cho/Cr ratio threshold between 1.685 and 1.885 for the determination of HGG versus LGG provided sensitivity, specificity, and diagnostic accuracy of 70, 98, and 94%, respectively.[47]

The differential diagnosis of GBM includes abscess, metastasis, lymphoma, and tumefactive multiple sclerosis (MS). Brain abscess remains a diagnostic challenge because the presenting clinical manifestations and neuroradiological appearances are often nonspecific. Imaging findings helpful in the differential diagnosis include a thin wall with ring-like enhancement that is often thinner along the medial margin, daughter rings, and hypointense rim on T2-weighted images[68,69] (see Figure 14(a) and (b)). Most studies have reported increased ADC values in the necrotic component of tumors as opposed to abscesses. Noguchi et al.[70] found that the necrotic components of tumors had ADC values in the range of $(2.2–3.2) \times 10^{-3}\,mm^2/s$, in contrast to abscesses that had ADC values of less than $0.7 \times 10^{-3}\,mm^2/s$. In another study, the calculated ADC values of the enhancing component of GBM were in the range of 0.78×10^{-3} to 1.79×10^{-3} (mean, 1.14×10^{-3})[71] (see Figure 14(c) and (d)). However, there are reported cases of tumors demonstrating marked hyperintensity on DW–MRI with extremely low ADC values in the necrotic center, similar to what has been reported for abscesses. Restricted diffusion within these lesions could be due to a variety of causes, including intratumoral hemorrhage, cytotoxic edema in the early phases of cell death, thick sterile liquefaction, or pyogenic superinfection.[72–75]

MRS can also noninvasively contribute to the establishment of the differential diagnosis between tumors and abscesses. The spectrum of the abscess cavity shows elevation of lactate, acetate, succinate, and alanine and some amino acids, and this spectrum appears significantly different from that of necrotic or cystic brain tumor.[76]

Intracranial metastases and primary malignant gliomas are two common brain tumors encountered in adults.

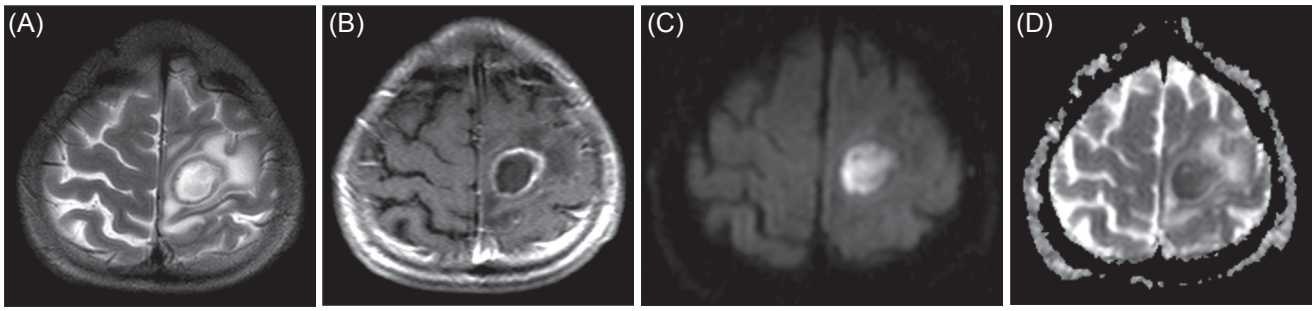


FIGURE 14 Diffusion study in a patient with brain abscess. (A) Axial T2-weighted image shows a well-defined lesion with hypointense rim and perilesional edema. (B) Post-gadolinium T1-weighted image demonstrates ring-like enhancement. (C) Diffusion-weighted image ($b = 1000\,mm^2/s$) shows high signal intensity within the lesion, whereas (D) the same area in the corresponding ADC map presents with low signal intensity due to restricted diffusion.

The management of these two tumors is totally different and can potentially affect the clinical outcome. When the clinical findings are nonspecific, conventional MR imaging characteristics may be similar and unable to differentiate between the two entities.

DWI techniques can be helpful in distinguishing solitary intra-axial metastatic lesions from HGGs. Studies showed that both contrast-enhancing portions and peritumoral edema of metastasis have higher ADC than HGGs. However, the distinction between metastases and HGGs is often difficult to make based on ADC values, as some HGGs also exhibit high ADC values.[45,77–79]

Perfusion MR imaging and spectroscopy may also be used to differentiate high-grade primary gliomas from solitary metastases. Law et al.[80] found a significant difference between the mean rCBV value within the peritumoral region in HGGs, which was 1.31 ± 0.97, suggesting increased peritumoral perfusion due to tumor infiltration, and the mean rCBV surrounding metastatic tumors, which was 0.39 ± 0.19, consistent with compression of capillaries by vasogenic edema (see Figure 15(a)–(c)). No difference has been demonstrated between the intratumoral rCBV values of HGGs and metastases. In the same study they found elevated Cho/Cr (2.28 ± 1.24) in the peritumoral regions of HGGs, in keeping with tumoral infiltration. No increase in the Cho/Cr (0.76 ± 0.23) was found in the peritumoral region of metastases, which again suggests vasogenic edema (see Figure 15(d)–(g)). In the same study there was also no significant difference in the peritumoral NAA/Cr between the two groups because there was no neuronal replacement or destruction in the peritumoral region of either pathologic condition.

The differential diagnosis of primary CNS lymphoma (PCNSL) from malignant astrocytoma can be based on the periventricular and deep gray matter location of lymphoma and on hypo- or isointensity of PCNSL on T2-weighted images, whereas HGG shows high signal intensity. On postcontrast T1-weighted images PCNSL shows intense homogeneous enhancement (see Figure 16(a) and (b)). However, less commonly, PCNSL may be hyperintense on T2-weighted images and may show ring-like enhancement especially in immunocompromised patients. In these cases it can be difficult to distinguish PCNSL from HGG on the basis of conventional MR imaging features.

DWI techniques showed that the mean ADC value in lymphomas is lower than that of HGGs, reflecting the increased cellularity of lymphomas[81,82] (see Figure 16(c) and (d)). Neovascularization is absent in PCNSLs, in contrast to HGGs; therefore perfusion-weighted images can also be used to distinguish the two entities. The lower rCBV values of PCNSLs may be helpful in differentiating from other brain tumors such as HGGs[83] (see Figure 16(e)).

The MR spectrum of PCNSL is characterized by increased Cho, Lac, and lipids and is associated with decreases in NAA, Cr, and myoinositol levels. This metabolite pattern can also be found in malignant astrocytomas. However, if the analysis of the solid portion of the tumor shows a significant increase in lipids, it is probably lymphoma.[84]

The conventional MRI features of tumefactive MS may mimic those of HGGs. Both lesions may show variable contrast enhancement, perilesional edema, mass effect, and central necrosis. The pathologic difference between tumefactive MS and HGGs is the absence of angiogenesis in MS, which demonstrates low rCBV values, as opposed to gliomas, which are characterized by neovascularization and angiogenesis resulting in a significant elevation of rCBV.[85]

In spectroscopy there is some overlap between tumefactive MS and HGGs. There is Cho elevation in MS from astrogliosis, demyelination, and inflammation; Lac is found from anaerobic glycolysis and a decrease in NAA from neuronal and axonal damage. However, the NAA/Cr ratio is higher in both the enhancing and the central regions in MS. Hence, the

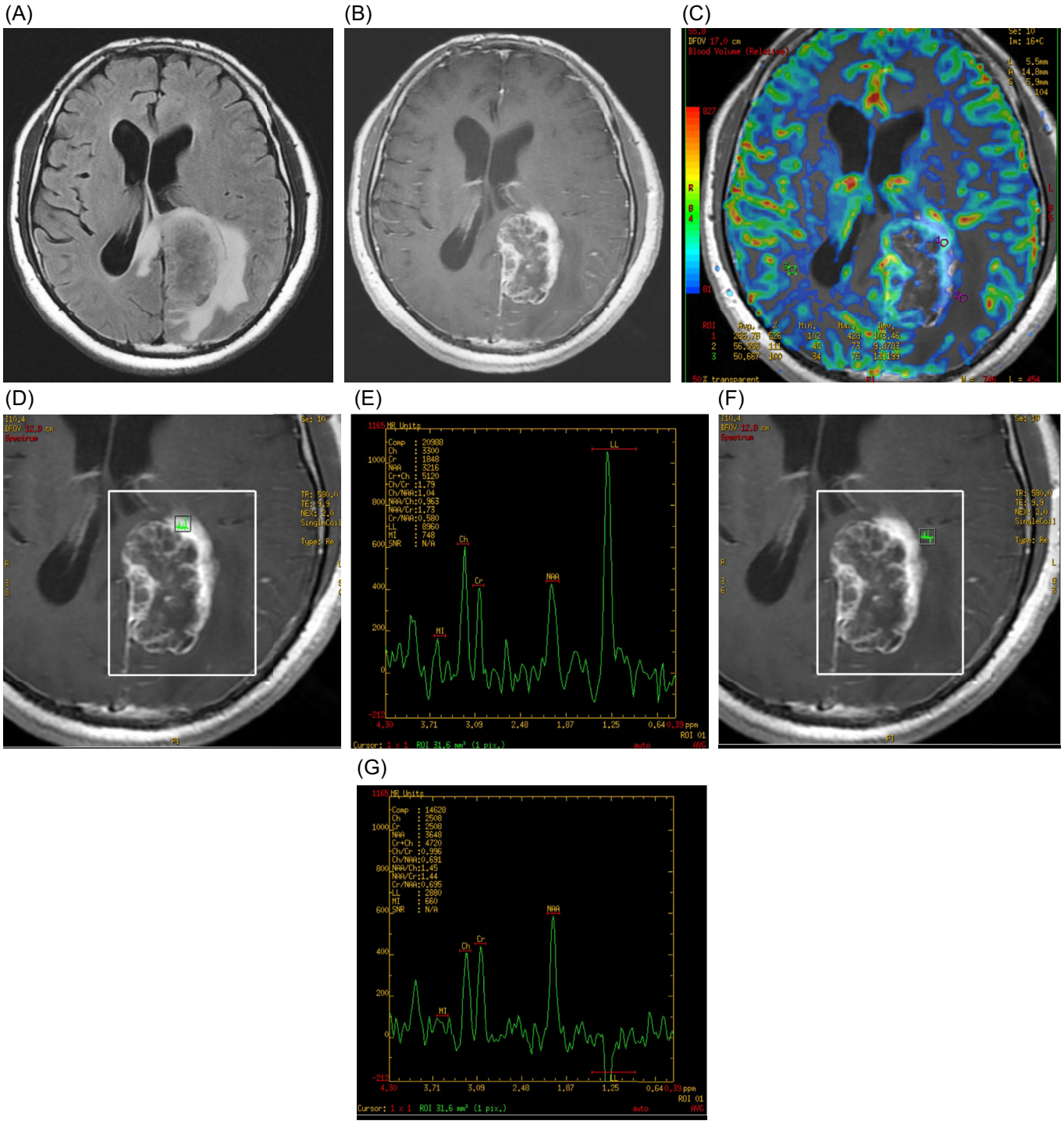


FIGURE 15 Brain metastasis. (A) Axial FLAIR and (B) post-gadolinium T1-weighted images show an enhancing lesion surrounded by edema. (C) On perfusion color map the tumor demonstrates high rCBV values, whereas the area of perilesional edema demonstrates low rCBV values due to capillary compression by vasogenic edema. (D, E) Long TE (135 ms) spectrum obtained from the enhancing lesion shows elevation of Cho, decrease in NAA, and lipid/lactate (LL) peak, whereas in (F, G) peritumoral edema Cho is within the normal range.

combination of reduced perfusion and moderate NAA reduction can help differentiate tumefactive MS from HGGs.[86,87]

Posttherapeutic MR examinations are used routinely to differentiate therapy-induced necrosis from residual or recurrent tumor. On conventional MRI, abnormal contrast enhancement on postcontrast T1-weighted images and the pattern of hyperintensity on T2-weighted images are used to discriminate these entities. Features that are inspected for assessment of

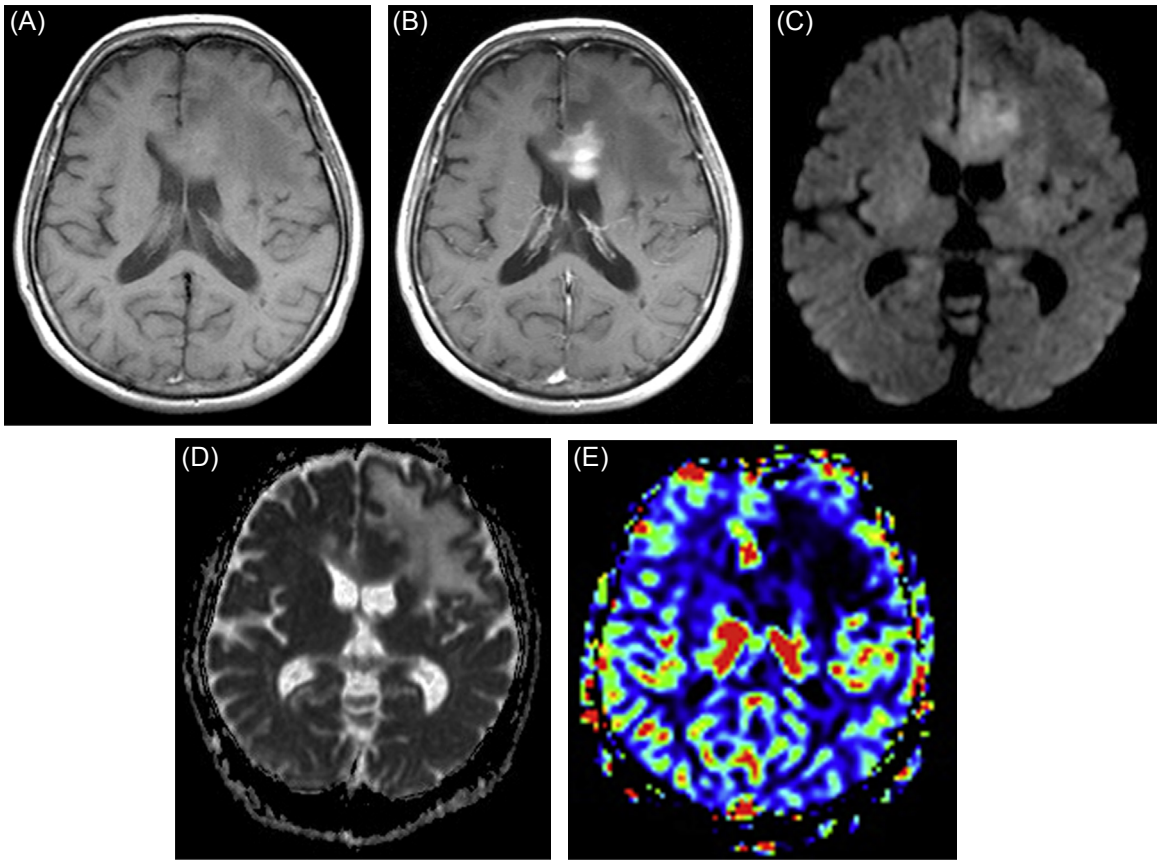


FIGURE 16 Primary cerebral lymphoma. (A) Noncontrast T1-weighted image shows an isointense mass involving the genu of the corpus callosum. (B) After the administration of contrast medium the mass shows intense enhancement. (C) On diffusion-weighted image ($b = 1000\,mm^2/s$) the tumor shows high signal intensity, whereas (D) on the ADC map it exhibits low signal intensity due to restricted diffusion (arrowhead). (E) On perfusion color map the tumor and the adjacent edema demonstrate low CBV values.

tumor progression are regions of abnormal contrast enhancement on postcontrast T1-weighted images and the volume of hyperintensity on T2-weighted images. Other certain conventional MR imaging findings suggesting predominant glioma progression are corpus callosum involvement, conjunction with multiple enhancing lesions without crossing of the midline, and subependymal spread.[88] Although such morphological changes are indicative of the existence of the disease, it is often difficult to determine whether an enhanced lesion represents tumor recurrence, especially when the enhancement is initially observed.

Perfusion MR imaging may be helpful for differentiating recurrent tumors from posttherapeutic necrosis. Elevated rCBV values most likely represent recurrent tumor, whereas decreased rCBV values are more likely to represent radionecrosis due to vascular injury (see Figure 17(a) and (b)). Studies found that if the rCBV ratio of an enhancing lesion is more than 2.6 or less than 0.6, tumor recurrence or radiation necrosis, respectively, should be strongly suspected.[89]

MRS has a significant clinical impact on posttreatment evaluation of intracranial neoplasms and it is useful for identifying recurrent tumor earlier than conventional MRI and differentiating residual or recurrent tumor from posttreatment abnormality.

Evidence of radiation necrosis is typically observed within 3–6 months after therapy and is characterized by decreases in Cho, Cr, and NAA and increased lipid and Lac levels. On the other hand, elevated Cho levels and greater Cho/NAA ratio suggest tumor recurrence (see Figure 17(c) and (d)).

Increases in lipid and Lac levels are less specific than elevated Cho levels because they may result from both tissue necrosis and radiation-induced necrosis.

Follow-up of these lesions is crucial for accurate diagnosis.[90]

III. Gliosarcoma (WHO grade IV) is a rare tumor composed of glial and sarcomatous components. The glial component usually demonstrates the typical features of GBM. Although oligodendroglial cells are occasionally recognized, in most cases the glial cells are

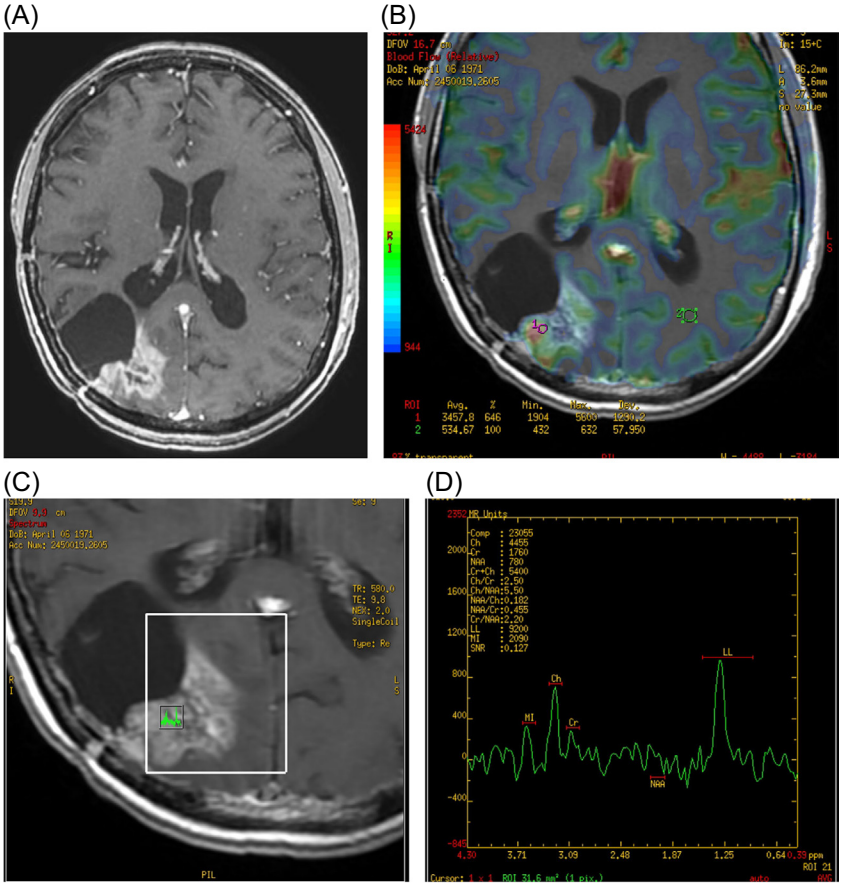


FIGURE 17 Glioblastoma multiforme recurrence. (A) Postoperative axial post-gadolinium T1-weighted image shows a porencephalic cyst with inhomogeneous peripheral enhancement. (B) On perfusion MRI the enhancing component demonstrates increased CBV indicating tumor recurrence. (C, D) MR spectroscopy shows markedly increased Cho, decreased NAA levels, and lipid/lactate peak.

astrocytic, with a tissue pattern of a GBM. As expected, heterogeneity is a feature of the glial component. Additional variation is recognized in the mesenchymal component. Malignant fibrous histiocytoma is the most frequent sarcomatous component. Fibrosarcoma, with smooth and striated muscle sarcoma, as well as bone or cartilaginous sarcoma, may also be found.[91–93] Gliosarcomas are peripherally located and involve the temporal, parietal, and occipital lobes.[94–96] Posterior fossa gliosarcomas have also been reported. Radiation-induced gliosarcoma may appear at the site of a treated intracranial neoplasm.[97] Most patients with gliosarcomas are in their 5th–7th decade. Extracranial metastasis of the sarcomatous component is common, occurring in 15–30% of all gliosarcomas.[98]

On plain CT most tumors appear as slightly hyperdense lesions because of their high vascularity and cellularity. After contrast administration gliosarcomas show marked enhancement and may mimic a meningioma, when the tumor is located near the skull or falx. Gliosarcomas, however, are less homogeneously hyperdense than meningiomas, do not have a large base in contact with the skull, and are virtually always associated with peritumoral edema. In other cases, the CT appearance is that of an intracerebral mass with irregular and peripheral enhancement and large necrotic areas, similar to malignant astrocytomas or glioblastomas.[99,100]

On MR they have an inhomogeneous or cystic appearance, with surrounding vasogenic edema. They are intra-axial but abutting a dural surface with intense heterogeneous tumor enhancement. On T2-weighted images they have intermediate signal intensity with peripheral high signal intensity, due to the surrounding edema (see Figure 18). Hemorrhage and necrosis are common.[101,102]

Gliosarcoma should be included in the differential diagnosis of any tumor that appears to be intra-axial but abuts a dural surface and shows imaging characteristics similar to gray matter on T2-weighted images. Gliosarcomas are considered to have an aggressive course, with a prognosis similar to that of GBM.[92,102]

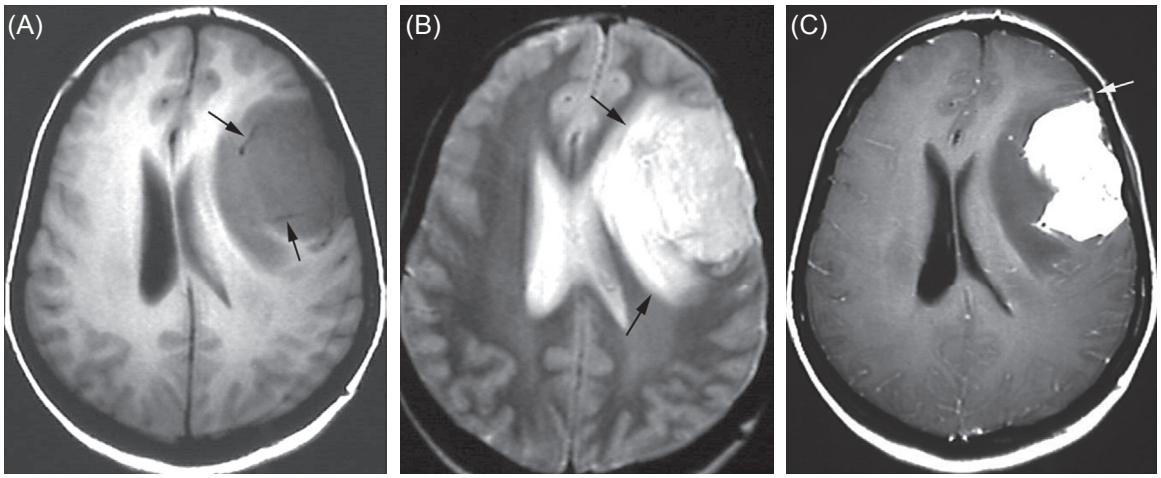


FIGURE 18 Gliosarcoma. (A) Axial T1WI shows a hypointense lesion with intratumoral vessels (arrows). (B) On axial T2WI the mass as well as the adjacent edema (arrows) shows high signal intensity. (C) On axial postcontrast T1WI the tumor shows intense homogeneous enhancement. Note the close relation of the mass with the dura, which is enhanced in a way that mimics meningioma (arrow). *From the book* Imaging of brain tumors with pathological correlations, *A. Drevelegas (Ed.), with kind permission of Springer Science and Business Media.*

References

1. Davis FG, McCarthy B, Jukich P. The descriptive epidemiology of brain tumors. *Neuroimaging Clin N Am*. 1999;9:581–594.
2. Karkavelas G, Taskos N. Epidemiology, histological classification and clinical course of brain tumors. In: Drevelegas A, ed. *Imaging of Brain Tumors with Histological Correlations*. Berlin Heidelberg New York: Springer-Verlag; 2002:1–10.
3. Daumas-Duport C, Scheihauer B, O'Fallon J, Kelly P. Grading of astrocytomas. A simple and reproducible method. *Cancer*. 1988;62:2152–2165.
4. Louis DN, Cavenee WK. Molecular biology of central nervous system neoplasms. In: De Vita VT, Hellman S, Rosenberg SA, eds. *Cancer: Principles and Practice of Oncology*. Philadelphia: Lippincott Raven Publishers; 1997:2013–2022.
5. Goussia AC, Polyzoidis K, Kyritsis AP. Molecular abnormalities in gliomas. In: Drevelegas A, ed. *Imaging of Brain Tumors with Histological Correlations*. Berlin Heidelberg New York: Springer-Verlag; 2002:27–35.
6. Parisi JE, Scheithauer BW. Glial tumors. In: Nelson JS, Parisi JE, Scheithauer BW, eds. *Principles and practice of neuropathology*. St Louis: Mosby; 1993:123–183.
7. See SJ, Gilbert MR. Anaplastic astrocytoma: diagnosis, prognosis, and management. *Semin Oncol*. 2001;31:618–634.
8. Philippon JH, Clemenceau SH, Fauchon FH, Foncin JF. Supratentorial low-grade astrocytomas in adults. *Neurosurgery*. 1993;32:554–559.
9. Castillo M, Scatliff JH, Bouldin TW, Suzuki K. Radiologic–pathologic correlation: intracranial astrocytoma. *AJNR*. 1992;13:1609–1616.
10. Watanabe M, Tanaka R, Takeda N. Magnetic resonance imaging and histopathology of cerebral gliomas. *Neuroradiology*. 1992;35:463–469.
11. Barker 2nd FG, Chang SM, Huhn SL, et al. Age and the risk of anaplasia in magnetic resonance-nonenhancing subratentorial cerebral tumors. *Cancer*. 1997;80:936–941.
12. Kondziolka D, Lunsford LD, Martinez AJ. Unreliability of contemporary neurodiagnostic imaging in evaluation of suspected adult supratentorial (low-grade) astrocytoma. *J Neurosurg*. 1993;79:533–536.
13. Ginsberg LE, Fuller GN, Hashmi M, Leeds NE, Schomer DF. The significance of lack of MR contrast enhancement of supratentorial brain tumors in adults: histopathological evaluation of a series. *Surg Neurol*. 1998;49:436–440.
14. Boring CC, Squires TS, Tong T. Cancer statistics. *CA Cancer J Clin*. 1993;43:7–26.
15. Kleihues P, Burger PC, Collins VP, Newcomb EW, Ohgaki H, Cavenee WK. Glioblastoma. In: Kleihues P, Cavenee WK, eds. *Pathology and Genetics of Tumours of the Nervous System*. 2nd ed. Lyon, France: IARC Press; 2000:29–39. 1993.
16. Becker LE. Central neuronal tumors in childhood: relationship to dysplasia. *J Neuro-Oncol*. 1995;24:13.
17. Burger PC, Heinz ER, Shibata T, Kleihues P. Topographic anatomy and CT correlations in the untreated glioblastomas multiforme. *J Neurosurg*. 1988;68:698–704.
18. Lilja A, Bergstrom K, Spannare B, Olsson Y. Reliability of CT in assessing histopathological features of malignant supratentorial gliomas. *J Comput Assist Tomogr*. 1981;5:625–636.
19. Kondziolka D, Bernstein M, Resch L, et al. Significance of hemorrhage into brain tumors: clinicopathological study. *J Neurosurg*. 1987;67:852–857.
20. Earnest F, Kelly PJ, Scheithauer BW, et al. Cerebral astrocytomas: histopathologic correlation of MR and CT contrast enhancement with stereotactic biopsy. *Radiology*. 1988;166:823–827.
21. Atlas SW. Adult supratentorial tumors. *Sem Roentgenol*. 1990; 25:130–154.
22. Tovi M, Lilja A, Erickson A. MR imaging in cerebral gliomas: tissue component analysis in correlation with histopathology of whole-brain specimens. *Acta Radiol*. 1994;35:495–505.
23. Drevelegas A, Karkavelas G. High-grade gliomas. In: Drevelegas A, ed. *Imaging of Brain Tumors with Histological Correlations*. Berlin Heidelberg New York: Springer-Verlag; 2002:109–135.
24. Boleslaw H, Liwinics L, Rubinstein J. The pathways of extraneural spread in metastasizing gliomas. *Hum Pathol*. 1979;10:453–467.
25. Dolman CL. Lymph node metastases as a first manifestation of glioblastoma multiforme. *J Neurosurg*. 1974;41:607–609.
26. Vestosick FT, Selker RG. Brain stem and spinal metastases of supratentorial glioblastomas multiforme: a clinical series. *Neurosurgery*. 1990;27:516–522.
27. Taha M, Ahmad A, Wharton S, Jellinek D. Extra-cranial metastasis of glioblastoma multiforme presenting as acute parotitis. *Br J Neurosurg*. 2005;193:48–51.
28. Rees JH, Smirniotopoulos JG, Jones RV, Wong K. Glioblastoma multiforme: radiologic–pathologic correlation. *Radiographics*. 1996; 16:1413–1438.
29. Barnard RO, Geddes JF. The incidence of multifocal gliomas: a histologic study of large hemisphere sections. *Cancer*. 1987;60: 1519–1531.

30. Prather JL, Long JM, van Heertum R, Hardman J. Multicentric and isolated multifocal glioblastomas multiforme simulating metastatic disease. *Br J Radiol*. 1975;48:10–15.
31. Lafitte F, Morel-Precetti S, Martin-Duverneuil N, et al. Multiple glioblastomas: CT and MR features. *Eur Radiol*. 2001;11:131–136.
32. Jawahar A, Weilbaecher C, Shorter C, Stout N, Nanda A. Multicentric glioblastoma multiforme determined by positron emission tomography: a case report. *Clin Neurol Neurosurg*. 2003;106:38–40.
33. Scherer HJ. The role of vascular proliferation in the growth of brain tumors. *Brain*. 1940;63:1–35.
34. Dean BL, Drayer BP, Bird CR, et al. Gliomas: classification with MR imaging. *Radiology*. 1990;174:411–415.
35. Moller-Hartmann W, Herminghaus S, Krings T, et al. Clinical application of proton magnetic resonance spectroscopy in the diagnosis of intracranial mass lesions. *Neuroradiology*. 2002;44: 371–381.
36. Knopp EA, Cha S, Johnson G, et al. Glial neoplasms: dynamic contrast-enhanced T2*-weighted MR imaging. *Radiology*. 1999;211: 791–798.
37. Law M, Yang S, Wang H, et al. Glioma grading: sensitivity, specificity, and predictive values of perfusion MR imaging and proton MR spectroscopic imaging compared with conventional MR imaging. *AJNR*. 2003;24:1989–1998.
38. Chang YW, Yoon HK, Shin HJ, Roh HG, Cho JM. MR imaging of glioblastoma in children: usefulness of diffusion/perfusion-weighted MRI and MR spectroscopy. *Pediatr Radiol*. 2003;33:836–842.
39. Moffat BA, Chenevert TL, Lawrence TS, et al. Functional diffusion map: a noninvasive MRI biomarker for early stratification of clinical brain tumor response. *Proc Natl Acad Sci*. 2005;102:5524–5529.
40. Drevelegas A. Imaging modalities in brain tumors. In: Drevelegas A, ed. *Imaging of Brain Tumors with Pathologic Correlations*. Berlin Heidelberg New York: Springer-Verlag; 2002:11–25.
41. Mullins ME, Schaefer PW, Sorensen AG, et al. CT and conventional and diffusion-weighted MR imaging in acute stroke: study in 691 patients at presentation to the emergency department. *Radiology*. 2002;224:353–360.
42. Schaefer PW, Ozsunar Y, He J, et al. Assessing tissue viability with MR diffusion and perfusion imaging. *Am J Neuroradiol*. 2003;24:436–443.
43. Lam WW, Poon WS, Metreweli C. Diffusion MR imaging in glioma: does it have any role in the preoperation determination of grading of glioma? *Clin Radiol*. 2002;57:219–225.
44. Kono K, Inoue Y, Nakayama K, et al. The role of diffusion-weighted imaging in patients with brain tumors. *Am J Neuroradiol*. 2001;22:1081–1088.
45. Krabbe K, Gideon P, Wagn P, et al. MR diffusion imaging of human intracranial tumors. *Neuroradiology*. 1997;39:483–489.
46. Higano S, Yun X, Kumabe T, et al. Malignant astrocytic tumors: clinical importance of apparent diffusion coefficient in prediction of grade and prognosis. *Radiology*. December 2006;241(3):839–846.
47. Danai Chourmouzi Theses: New MR techniques in diagnosis and grading of brain tumors. National Archive of PhD Theses http://hdl.handle.net/10442/hedi/34579.
48. Tropine A, Vucurevic G, Delani P, et al. Contribution of diffusion tensor imaging to delineation of gliomas and glioblastomas. *J Magn Reson Imaging*. 2004;20:905–912.
49. Roberts TP, Liu F, Kassner A, Mori S, Guha A. Fiber density index correlates with reduced fractional anisotropy in white matter of patients with glioblastoma. *Am J Neuroradiol*. 2005;26:2183–2186.
50. Lu S, Ahn D, Johnson G, Cha S. Peritumoral diffusion tensor imaging of high-grade gliomas and metastatic brain tumors. *Am J Neuroradiol*. 2003;24:937–941.
51. Baird AE, Benfield A, Schlaug G, et al. Enlargement of human cerebral ischemic lesions volumes measured by diffusion-weighted magnetic resonance imaging. *Ann Neurol*. 1997;41:581–589.
52. Wilms G, Sunaert S, Flamen P. Recent developments in brain tumour diagnosis. In: Demaerel P, Baert AL, Demaerel P, eds. *Recent Advances in Diagnostic Neuroradiology*. Berlin Heidelberg New York: Springer; 2001:119–135.
53. Cha S, Knopp EA, Johnson G, et al. Intracranial mass lesions: dynamic contrast enhanced susceptibility-weighted echo-planar perfusion MR imaging. *Radiology*. 2002;223:11–29.
54. Maia Jr AC, Malheiros SM, da Rocha AJ, et al. MR cerebral blood volume maps correlated with vascular endothelial growth factor expression and tumor grade in nonenhancing gliomas. *Am J Neuroradiol*. 2005;26:777–783.
55. Yang D, Korogi Y, Sugahara T, et al. Cerebral gliomas: prospective comparison of multivoxel 2D chemical-shift imaging proton MR spectroscopy, echoplanar perfusion and diffusion-weighted MRI. *Neuroradiology*. 2002;44:656–666.
56. Rollin N, Guyotat J, Streichenberger N, et al. Clinical relevance of diffusion and perfusion magnetic resonance imaging in assessing intra-axial brain tumors. *Neuroradiology*. 2006;48:150–159.
57. Law M, Yang S, Wang H, et al. Glioma grading: sensitivity, specificity and predictive value of perfusion MRI and proton spectroscopic imaging compared with conventional MR imaging. *Am J Neuroradiol*. 2003;24:1989–1998.
58. Emblem KE, Nedregaard B, Nome T, et al. Glioma grading by using histogram analysis of blood volume heterogeneity from MR-derived cerebral blood volume maps. *Radiology*. 2008;247: 808–817.
59. Lev MH, Rosen BR. Clinical applications of intracranial perfusion MR imaging. *Neuroimaging Clin N Am*. 1999;9:309–331.
60. Law M. Perfusion and MRS for brain tumor diagnosis. In: Edelman RR, ed. *Clinical Magnetic Resonance Imaging*. Saunders; 2005:1215–1247.
61. Pomper MG, Port JD. New techniques in MR imaging of brain tumors. *Magn Reson Imaging Clin N Am*. 2000;8:691–713.
62. Castillo M, Kwock L. Proton MR spectroscopy of common brain tumors. *Neuroimaging Clin N Am*. 1998;8:733–752.
63. Brandao LA. Introduction and technique. In: Bandao LA, ed. *MR Spectroscopy of the Brain*. Philadelphia: Lippincott Williams & Wilkins; 2004:1–15.
64. Gupta RK, Cloughesy TF, Sinha U, et al. Relationships between choline magnetic resonance spectroscopy, apparent diffusion coefficient and quantitative histopathology in human glioma. *J Neurooncol*. 2000;50:215–226.
65. Tedeschi G, Lundbom N, Raman R, et al. Increased choline signal coinciding with malignant degeneration of cerebral gliomas: a serial proton magnetic resonance spectroscopy imaging study. *J Neurosurg*. 1997;87:516–524.
66. Urenjak J, Williams SR, Gadian DG, Noble M. Specific expression of *N*-acetylaspartate in neurons, oligodendrocyte- type-2 astrocyte progenitors, and immature oligodendrocytes in vitro. *J Neurochem*. 1992;59:55–61.
67. Negendank WG, Sauter R, Brown TR, et al. Proton magnetic resonance spectroscopy in patients with glial tumors: a multicenter study. *J Neurosurg*. 1996;84:449–458.
68. Haimes AB, Zimmerman RD, Morgello S, et al. MR imaging of brain abscesses. *Am J Roentgenol*. 1989;152:1073–1085.
69. Kim YJ, Chang KH, Song IC, et al. Brain abscess and necrotic or cystic brain tumor: discrimination with signal intensity on diffusion-weighted MR imaging. *Am J Roentgenol*. 1998;171:1487–1490.
70. Noguchi K, Watanabe N, Nagayoshi T, et al. Role of diffusion-weighted echo-planar MRI in distinguishing between brain brain abscess and tumor: a preliminary report. *Neuroradiology*. 1999;41:171–174.
71. Stadnik TW, Chaskis C, Michotte A, et al. Diffusion-weighted MR imaging of intracerebral masses: comparison with conventional MR imaging and histologic findings. *Am J Neuroradiol*. 2001;22:969–976.

72. Batra A, Tripathi RP. Atypical diffusion-weighted magnetic resonance findings in glioblastoma multiforme. *Australas Radiol*. 2004;48:388–391.
73. Tung GA, Evangelista P, Rogg JM, Duncan 3rd JA. Diffusion-weighted MR imaging of rim-enhancing brain masses: is markedly decreased water diffusion specific for brain abscess? *Am J Roentgenol*. 2001;177:709–712.
74. Hakyemez B, Erdogan C, Yildirim N, Parlak M. Glioblastoma multiforme with atypical diffusion-weighted MR findings. *Br J Radiol*. 2005;78:989–992.
75. Holtas S, Geijer B, Stromblad LG, Maly-Sundgren P, Burtscher IM. A ring-enhancing metastasis with central high signal on diffusion-weighted imaging and low apparent diffusion coefficients. *Neuroradiology*. 2000;42:824–827.
76. Lai PH, Li KT, Hsu SS, et al. Pyogenic brain abscess: findings from in vivo 1.5-T and 11.7-T in vitro proton MR spectroscopy. *Am J Neuroradiol*. 2005;26:279–288.
77. Stadnik TW, Demaerel P, Luypaert RR, et al. Imaging tutorial: differential diagnosis of bright lesions on diffusion-weighted MR images. *Radiographics*. 2003;23:e7.
78. Chiang IC, Kuo YT, Lu CY, et al. Distinction between high-grade gliomas and solitary metastases using peritumoral 3-T magnetic resonance spectroscopy, diffusion, and perfusion imagings. *Neuroradiology*. 2004;46:619–627.
79. Lu S, Ahn D, Johnson G, et al. Diffusion-tensor MR imaging of intracranial neoplasia and associated peritumoral edema: introduction of the tumor infiltration index. *Radiology*. 2004;232:221–228.
80. Law M, Cha S, Knopp EA, et al. High-grade gliomas and solitary metastases: differentiation by using perfusion and proton spectroscopic MR imaging. *Radiology*. 2002;222:715–721.
81. Guo AC, Cummings TJ, Dash RC, Provenzale JM. Lymphomas and high-grade astrocytomas: comparison of water diffusibility and histologic characteristics. *Radiology*. 2002;224:177–183.
82. Hiwatashi A. Brain neoplasms. In: Moritani T, Ekholm S, Westesson P-L, eds. *Diffusion – Weighted MR Imaging of the Brain*. Berlin Heidelberg New York: Springer; 2003:161–179.
83. Hartmann M, Heiland S, Harting I, et al. Distinguishing of primary cerebral lymphoma from high-grade glioma with perfusion-weighted magnetic resonance imaging. *Neurosci Lett*. 2003;338:119–122.
84. Harting I, Hartmann M, Jost G, et al. Differentiating primary central nervous system lymphoma from glioma in humans using localised proton magnetic resonance spectroscopy. *Neurosci Lett*. 2003;342:163–166.
85. Cha S, Pierce S, Knopp EA, et al. Dynamic contrast-enhanced T2*-weighted MR imaging of tumefactive demyelinating lesions. *Am J Neuroradiol*. 2001;22:1109–1116.
86. Arnold DL, Matthews PM, Francis GS, O'Connor J, Antel JP. Proton magnetic resonance spectroscopic imaging for metabolic characterization of demyelinating plaques. *Ann Neurol*. 1992;31:235–241.
87. Davie CA, Hawkins CP, Barker GJ, et al. Serial proton magnetic resonance spectroscopy in acute multiple sclerosis lesions. *Brain*. 1994;117:49–58.
88. Mullins ME, Bares GD, Schaefer PW, et al. Radiation necrosis versus glioma recurrence: conventional MR imaging clues to diagnosis. *Am J Neuroradiol*. 2005;26:1967–1972.
89. Sugahara T, Korogi Y, Tomiguchi S, et al. Posttherapeutic intraaxial brain tumor: the value of perfusion sensitive contrast-enhanced MR imaging for differentiating tumor recurrence from nonneoplastic contrast-enhancing tissue. *Am J Neuroradiol*. 2000;21:901–919.
90. Law M, Hamburger M, Johnson G, et al. Differentiating surgical from non-surgical lesions using perfusion MR imaging and proton MR spectroscopic imaging. *Technol Cancer Res Treat*. 2004;3:557–565.
91. Banerjee AK, Sharma BS, Kak VK, Ghatak NR. Gliosarcoma with cartilage formation. *Cancer*. 1989;63:518–523.
92. Morantz RA, Feigin I, Ransohoff 3rd J. Clinical and pathological study of 24 cases of gliosarcoma. *Neurosurgery*. 1976;45:398–408.
93. Coons SW, Ashby LS. Pathology of intracranial neoplasms. *Neuroimaging Clin N Am*. 1999;9:615–649.
94. Beute BJ, Fobben ES, Hubschmann O, Zablow A, Eanelli T, Solitare GB. Cerebellar gliosarcoma: report of a probable radiation-induced neoplasm. *Am J Neuroradiol*. 1991;12:554–556.
95. Kim DS, Kang SK, Chi JG. Gliosarcoma: a case with unusual epithelial feature. *J Korean Med Sci*. 1999;14:345–350.
96. Meis JM, Martz KL, Nelson JS. Mixed glioblastoma multiforme and sarcoma. A clinicopathologic study of 26 radiation therapy oncology group cases. *Cancer*. 1991;67:2342–2349.
97. Lach M, Wallace CJ, Krcek J, Curry B. Radiation-associated gliosarcoma. *Can Assoc Radiol J*. 1996;47:209–212.
98. Cerame MA, Guthikonda M, Kohli CM. Extraneural metastases in gliosarcoma: a case report and review of the literature. *Neurosurgery*. 1985;17:413–418.
99. Maiuri F, Stella L, Benvenuti D, Giamundo A, Pettinato G. Cerebral gliosarcomas: correlation of computed tomographic findings, surgical aspect, pathological features, and prognosis. *Neurosurgery*. 1990;26:261–267.
100. Sakurai T, Abe J, Hayashi T, Sekino H, Tadokoro M. A case of gliosarcoma associated with large cyst. *No Shinkei Geka*. 1993;21:637–640.
101. Dwyer KW, Naul LG, Hise JH. Gliosarcoma: MR features. *J Comput Assist Tomogr*. 1996;20:719–723.
102. Galanis E, Buckner JC, Dinapoli RP, et al. Clinical outcome of gliosarcoma compared with glioblastoma multiforme: North Central Cancer Treatment Group results. *J Neurosurg*. 1998;89:425–430.

CHAPTER

39

Low-Grade Astrocytomas

John M. Collins, Gregory A. Christoforidis

Department of Radiology, University of Chicago, Chicago, IL, USA

INTRODUCTION

Astrocytic neoplasms include a group of central nervous system tumors derived from astrocytic cells, which vary in degree of malignancy, location, and extent of infiltration. A variety of tumor types comprise this set of lesions, and these are to some degree distinguished from one another by their tendency to affect different central nervous system locations, age groups, or genders.[1,2] Astrocytomas can be divided into infiltrative types (75%) and noninfiltrative types (25%). Noninfiltrative astrocytomas include pilocytic astrocytoma, pilomyxoid astrocytoma (PMA), pleomorphic xanthoastrocytoma, subependymal giant cell astrocytoma, and desmoplastic cerebral astrocytoma of infancy.[3–6] Infiltrative astrocytomas include the low-grade well-differentiated diffuse astrocytoma,[7] as well as more aggressive, higher grade varieties, which are described in other chapters.

The identification of an astrocytic lesion, as opposed to an oligodendroglioma or neuronal tumor, relies on the identification of cellular morphology reminiscent of astrocytes. The differentiation of a nonneoplastic gliosis from a low-grade astrocytoma from a higher grade astrocytoma depends on the presence or frequency of other histopathologic features. These include cellularity, degree of nuclear atypia, frequency of mitotic activity, necrosis, and vascular endothelial proliferation.[1,8] As a general rule of thumb, increased cellularity or nuclear atypia, as well as the identification of mitotically active cells, signals an increase in grade. Among astrocytomas, and with one exception, which will be discussed in a following section, necrosis and microvascular endothelial proliferation are indicators of the highest grade, most malignant astrocytoma, the glioblastoma multiforme (GBM; WHO grade IV). At the other end of the spectrum, however, the distinction between an indolent well-differentiated grade II astrocytoma and benign reactive gliosis can sometimes be difficult. Both conditions may present as a mild relative increase in the number and size of astrocytes. A diagnosis of neoplasia is made when the cellularity is particularly high, and when the cells are fairly uniform in size and morphology. Reactive astrocytes, in contrast, are usually to be found at varying stages of reactivity, and the cells will reflect this with variability of cellular size, nuclear size, and nuclear morphology. Where histologic categorization fails to provide a definitive diagnosis, assessment of the lesion's genetic makeup may provide a fallback option because it is now well established that certain mutations are more likely to be found in specific tumor types. Investigation into the genetic makeup of tumors is perhaps the most promising and exciting development in neuro-oncologic research in recent years. It is well recognized that certain mutations or chromosomal rearrangements confer a better or worse prognosis, independent of the histologic type and WHO grade of the tumor and differing treatment responses.[9] These considerations currently influence treatment decisions, at least in a limited fashion, and are likely to play a more central role in the future.

After reviewing imaging methods that can potentially distinguish low- from high-grade astrocytomas, this chapter reviews the imaging characteristics of individual types of low-grade astrocytomas. The chapter ends with a brief discussion of gliomatosis cerebri, which is a widespread and diffuse infiltration of tumor cells that straddles the categories of low- and high-grade tumor.

PHYSIOLOGIC IMAGING

Many imaging modalities have been utilized in an attempt to noninvasively differentiate high- and low-grade gliomas. Proton magnetic resonance spectroscopy (MRS), positron emission tomography (PET) imaging, cerebral blood volume mapping, and single-photon emission computed tomography (SPECT) are all modalities that have been employed toward this end. Tools such as these to help predict the biological behavior of a lesion

http://dx.doi.org/10.1016/B978-0-12-800945-1.00039-2
© 2016 Elsevier Ltd. All rights reserved.

are greatly needed, as it has been known for some time that conventional imaging features such as morphology, signal characteristics, and degree of enhancement are not always reliable indicators of a tumor's aggressiveness.[10]

MRS can be used to quantify various metabolites within a sample of tumor tissue. The most relevant metabolites include *N*-acetylaspartate (NAA), a neuronal marker; choline (Cho), a cell membrane component; lactate, a marker for anaerobic metabolism and necrosis; creatine, a marker for energy metabolism; and myoinositol, a metabolite that is primarily found in astrocytes and has been shown to be more abundant in low-grade gliomas relative to higher grade gliomas.[11] MRS of brain tumors has been studied for over 2 decades now.[12] In general, primary brain tumors demonstrate reduced levels of NAA and increased levels of choline relative to normal brain tissue. Elevated choline levels are thought to represent areas of increased tumor cellularity and proliferative activity, for which building blocks for membrane construction (choline) are in high demand,[13–17] whereas decreased NAA is thought to represent decreased neuronal density and viability.[13,16] Elevated levels of lactate have been identified in higher grade tumors, perhaps representing the anaerobic metabolism and necrosis that characterize an aggressive tumor whose metabolic needs outstrip vascular supply.[18,19] The presence of lactate should be interpreted with caution, though, as this metabolite can also be found in lower grade and benign tumors as well as nonneoplastic abnormalities.[15,20,21]

Contrast reagents have been used for decades to characterize brain tumors. Lesions that enhance are more easily detected visually, and in cases in which lesions are small and induce no edema in the surrounding brain, they may be detected only by virtue of their enhancement. Furthermore, the pattern of enhancement, and even the lack of enhancement, can help to narrow the differential diagnosis. Enhancement of tumors has been shown to depend on the degree of disruption of the blood–brain barrier, as well as tumoral microvascularity. The extent and pattern of enhancement can vary depending on the choice and dosage of contrast agent used, pulse sequence selected to visualize the enhancement, time from contrast bolus injection to imaging, field strength, and medication history, including exposure to corticosteroid or antiangiogenic chemotherapies.[22–30] As field strength increases both T1 and T1 shortening increase. As a result, the degree of contrast enhancement increases as well. Tumor-to-brain contrast after gadolinium administration at 3-T imaging compared to 1.5 T has been shown to be significantly higher.[24] Contrast-to-noise ratio at 3 T has been shown to be 2.8 times higher than at 1.5 T using the same contrast dosing and 1.3 times higher when using half the contrast dose. Extent of contrast enhancement increases with contrast dose.[25] The time course of MR imaging following contrast administration affects signal intensity. Peak signal intensity occurs at 25–35 min; however, there is no diagnostically significant change after 5 min. It is generally accepted that contrast-enhanced MR imaging of brain tumors should not begin until 2–5 min after contrast administration.[22] Comparison of gadolinium dimeglumine versus gadopentate dimeglumine contrast reagents in a multisite study has shown that gadopentate was superior in both qualitative and quantitative assessments of brain-to-tumor contrast.[23] In general, contrast-enhancing lesions are more likely to be higher grade, though this concept should be used with great caution. Lack of enhancement carries a two out of three chance for low-grade tumor, but some reports indicate that up to 40% of low-grade tumors may show some enhancement, and some of the lowest grade, prognostically most favorable lesions (e.g., pilocytic astrocytoma) almost always enhance.[31,32] As a result, alternate imaging methods predictive of tumor grade have been studied.

Dynamic MR imaging studies attempt to characterize tumor vascular dynamics by imaging differences in the signal intensity of a tumor as contrast reagents course through the vascular bed using T1-weighted, T2-weighted, or T2*-weighted techniques. Contrast leakage across a vascular bed is influenced by vascular permeability, contrast binding within the vascular bed, hematocrit, and contrast reagent concentration within the blood. Choice of postprocessing methods can influence signal-to-noise ratio and overall precision and accuracy obtained with dynamic contrast imaging.[33] Ultimately, data derived from these imaging sequences are used to study the cerebral blood volume, blood flow, blood–brain barrier permeability, and water-exchange kinetics of the neoplastic tissue relative to normal brain tissue. Among these parameters, relative cerebral blood volume (rCBV) mapping has received the most attention in characterizing tumor grade. rCBV is used as a surrogate marker for microvascularity. Higher rCBV implies a greater degree of microvascularity, which in turn implies a more aggressive, higher grade tumor. rCBV mapping uses perfusion magnetic resonance imaging (MRI) techniques to construct a map of the relative blood volume per unit of tissue within the brain. Animal studies have indicated that rCBV corresponds to the vascular concentration of contrast agent.[34,35] Areas of low rCBV within a tumor, compared to normal white matter or gray matter, have been suggested to correlate with lower tumor grade, whereas areas of higher rCBV correlate with higher grade. On the basis of this type of data, surgical biopsy may be directed toward more aggressive areas of the tumor, which results in a more accurate diagnosis and more reliable prognostic information. It is important to note that rCBV is independent of the degree of lesion enhancement, such that tumors that show minimal or no enhancement may still have elevated rCBV.

For example, rCBV has been shown to correlate with vascular endothelial growth factor (VEGF) expression and histologic grade in nonenhancing gliomas.[36] rCBV measurements have been shown to assist in identifying "low-grade" gliomas that are either high-grade gliomas misdiagnosed as a result of sampling error or low-grade gliomas undergoing transformation to a higher grade.[37] Vascular permeability, another parameter that can be derived from dynamic imaging, has been suggested to relate to the presence of VEGF and angiogenesis.[38] Indeed, dynamic contrast enhancement methods using T1 and T2* techniques have been used to assess vascular permeability within a tumor bed and have been shown to correlate with tumor grade as well.[39] It is noteworthy that although the use of corticosteroid is known to alter the degree of lesion enhancement and peritumoral edema, potentially confounding the diagnosis or follow-up of brain tumors, perfusion parameters within the lesion (including rCBV) do not seem to be significantly affected.[40]

Diffusion weighted imaging (DWI) techniques have allowed insight into characterizing tumor composition and behavior. Isotropic conventional DWI characterizes the diffusion of water in three directions. Conventional DWI provides information about the diffusion of water within a given region of tissue and can be used to predict the internal tissue composition. The DWI appearance of a tumor, or more accurately, the calculated apparent diffusion coefficient (ADC) maps, have been suggested to be influenced by tumor cellularity and total nuclear area and thus have the potential to assist in the characterization and grading of brain tumors.[41] For example, high-grade gliomas have been reported to be associated with decreased diffusivity values. Although in theory the DWI or ADC characteristics of a lesion may assist in the differentiation of high-grade, low-grade, and nonglio-matous tumors, this has not always been shown to be consistently reliable.[41] Some authors suggest that ADC maps can help determine the extent of tumor invasion, though again, this remains controversial. Some preliminary evidence indicates that ADC mapping may help in the assessment of brain tumor response to therapy and in the differentiation of radiation necrosis from tumor recurrence.[41] Diffusion tensor imaging (DTI), a more intense type of diffusion imaging that requires the characterization of water diffusion in at least six directions (and typically many more for high-quality imaging), is able to display and quantify the relationship between intra-axial tumors and adjacent white matter fiber tracts. When postprocessed appropriately, DTI can be used to generate tractography images that allow for the localization of major white matter tracts relative to the tumor. In this way, preoperative identification of the anatomic relationship between the neoplastic tissue and the critical white matter pathways may assist the surgeon when planning the extent to which a brain tumor can be removed while preserving functionality. Furthermore, DTI and tractography may be able to predict the infiltrative pattern of spread characteristic of diffuse astrocytoma and higher grade astrocytomas, thereby distinguishing them from circumscribed gliomas and metastases that tend not to infiltrate. It has been hypothesized that identification of these patterns may be able to differentiate tumor types.[42] Fractional anisotropy (FA), another parameter that can be calculated from a DTI data set, quantifies the degree to which water molecules are confined to diffusion in one specific direction. The theory behind FA is that in much of the brain, the diffusion of water is relatively restricted to a single direction or trajectory by the presence of thick bundles of highly ordered, highly directional axons. Water is permitted to diffuse along these structures, but not across them, and the more strictly directional the diffusion, the higher the FA value. When FA values are seen to decrease, this may reflect a disordering of the underlying axonal tracts, perhaps owing to the presence of an infiltrative neoplasm. When FA is reduced to very low levels, frank destruction of the underlying normal brain may be suspected. Because FA values normally differ depending on location, they are compared to similar regions of interest in the normal-appearing brain or in the contralateral hemisphere. Unlike ADC values, FA values have been shown to differ in peritumoral signal abnormality associated with infiltrating tumors such as gliomas compared to noninfiltrating tumors such as meningiomas.[43] Although FA values have been found to be low within the tumor beds of both high- and low-grade gliomas, interrogation of the central portion of the tumor compared with the peripheral portion of the tumor appears to differ slightly in low- but not high-grade gliomas.[44] This suggests greater disorganization within the peripheral portion of the tumor bed of high-grade gliomas compared to low-grade gliomas. It is critical to point out that measurements obtained via DWI methods could potentially be influenced by therapeutic effects such as radiation, chemotherapy, and steroid use.

PET imaging has also been used to separate high- from low-grade tumors by distinguishing hypometabolic from hypermetabolic tumors. Metabolic activity within brain tumors has been studied extensively using PET with a large number of markers. Applications include measurement of blood flow, blood volume, oxygen use, glucose use, glucose transport, amino acid uptake, protein synthesis, blood–brain barrier integrity, cerebral pH, membrane metabolism, and nucleic acid synthesis.[45] Tumor grade has been studied by measuring either glucose uptake using [^{18}F]fluorodeoxyglucose (FDG) or amino acid uptake by using [^{11}C]methylmethionine. Low-grade gliomas demonstrate normal or lower glucose or amino acid uptake relative to normal brain tissue.[12,16,45]

PET imaging of astrocytomas with FDG has been shown to be predictive of tumor progression and able to differentiate tumor recurrence from radiation necrosis. Newer innovative techniques focus on the visualization of specific biological molecules, such as PET imaging of VEGF receptor expression, a marker of angiogenesis.[46]

SPECT imaging of brain tumors has been studied predominantly with thallium-201 (^{201}Tl) and technetium-99m hexamethylpropyleneamine oxime (^{99m}Tc-HMPAO). Because thallium behaves biologically like potassium, imaging of ^{201}Tl can act as a marker for the function of the sodium potassium pump. Thallium thus acts as a measure of metabolic activity. The ratio of ^{201}Tl uptake in the tumor in question relative to normal brain has been used to predict which tumors are low grade and to distinguish viable tumor from radiation necrosis.[47,48] ^{99m}Tc-HMPAO can act as a measure of tissue perfusion, as the degree of tracer uptake in brain parenchyma (or tumor) is directly proportional to blood flow. Much like perfusion MRI, tumor recurrence shows an increase in uptake of ^{99m}Tc-HMPAO and can help increase the accuracy of ^{201}Tl SPECT differentiation of recurrent tumor from radiation necrosis.

DIFFUSE ASTROCYTOMA

Diffuse astrocytoma (see Figures 1–5) is a well-differentiated but diffusely infiltrative tumor classified as a WHO grade II lesion. It comprises 10–15% of all astrocytic tumors and about 9% of all brain gliomas.[2,7] Diffuse astrocytoma is characterized by a high degree of astrocytic cellular differentiation. The component cells are usually easily recognized as astrocytic in morphology, and as discussed above, it can sometimes be difficult to distinguish these low-grade neoplastic astrocytes from nonneoplastic reactive astrocytes. The neoplastic cells are found in an environment of neuroglial fibrils and are often accompanied by degenerative microscopic cysts. Mean age at presentation is 34 years, with a slight male predilection, with a peak incidence between ages 30 and 40. Approximately, 10% occur under the age of 20 and 30% over the age of 45. The most frequently encountered subtype is the fibrillary astrocytoma composed of cells that have irregularly shaped nuclei and little if any visible cytoplasm. Other subtypes include the gemistocytic astrocytoma, which by definition must be composed of at least 20% of cells displaying the gemistocytic morphology of plump eosinophilic cells with eccentric nuclei. Gemistocytic astrocytoma is more prone to degeneration into higher grade tumors, though despite this, it is still considered a WHO grade II lesion. The protoplasmic astrocytoma is a rare variant with low cellular density and frequent areas of mucoid degeneration and microcyst formation. Common to all three of these subtypes is the complete or near-complete absence of mitotic activity. Necrosis and microvascular proliferation are also, by definition, absent.

On macroscopic examination these tumors have a firm rubbery consistency, which expands the involved brain. They sometimes contain calcifications. Macroscopic and microscopic cysts can occur with these tumors and, if extensive, may give them a gelatinous appearance.[7] They infiltrate adjacent and distant brain. Any grade II astrocytoma may progress to a more malignant phenotype over time. Progression to higher grade (see Figure 4) can result from a variety of pathways, including the overexpression of proteins involved with cellular proliferation, the inactivation of genes responsible for apoptosis, and the deregulation of the normal cell cycle.[49] Markers for proliferative activity such as the MIB-1 index and molecular markers such as p53 overexpression have been useful in predicting which low-grade diffuse astrocytomas will transform into higher grades.[7,9,49] Gemistocytic astrocytomas, given their higher rate of dedifferentiation, carry a less favorable prognosis than either the fibrillary or the protoplasmic version.[50]

Diffuse astrocytomas most frequently arise from the supratentorial brain and the brain stem. The supratentorial location is the most frequent site in all age groups, with a special predilection for the frontal and temporal lobes.[6] The brain stem is the second most frequent site of involvement and is more often seen in children. Cerebellar location is rare. Brain-stem lesions are often associated with a poorer prognosis, irrespective of histologic subtype or genetic markers, in part because of the limited chance for a complete resection in this location. Tectal plate lesions often produce symptoms earlier owing to obstruction of the aqueduct of Sylvius, resulting in hydrocephalus. In this location, low-grade astrocytomas can be distinguished from other lesions such as hamartomas based on size. Most lesions under 4 cc volume tend to be hamartomas, whereas most lesions over 10 cc volume tend to be neoplastic.[51]

On imaging, these tumors classically appear homogeneous on all modalities. They can, in fact, be difficult to detect by computed tomography (CT) as they tend to be close in density to the background brain and usually do not enhance (see Figure 4). MRI therefore is more sensitive than CT in detecting these tumors.[12,52–54] It has been well documented that neoplastic cells can potentially extend far beyond the imaging margins of the tumor as delineated by contrast enhancement or FLAIR hyperintensity.[55–57] Indeed, there is a threshold cellular density that must be achieved before the lesion can be detected on MRI.[58] They display low signal on T1-weighted imaging (T1WI) and higher signal on T2WI with little or no enhancement following gadolinium administration. However, because contrast enhancement is well known to occur in grade II diffuse astrocytoma (up to 40% in

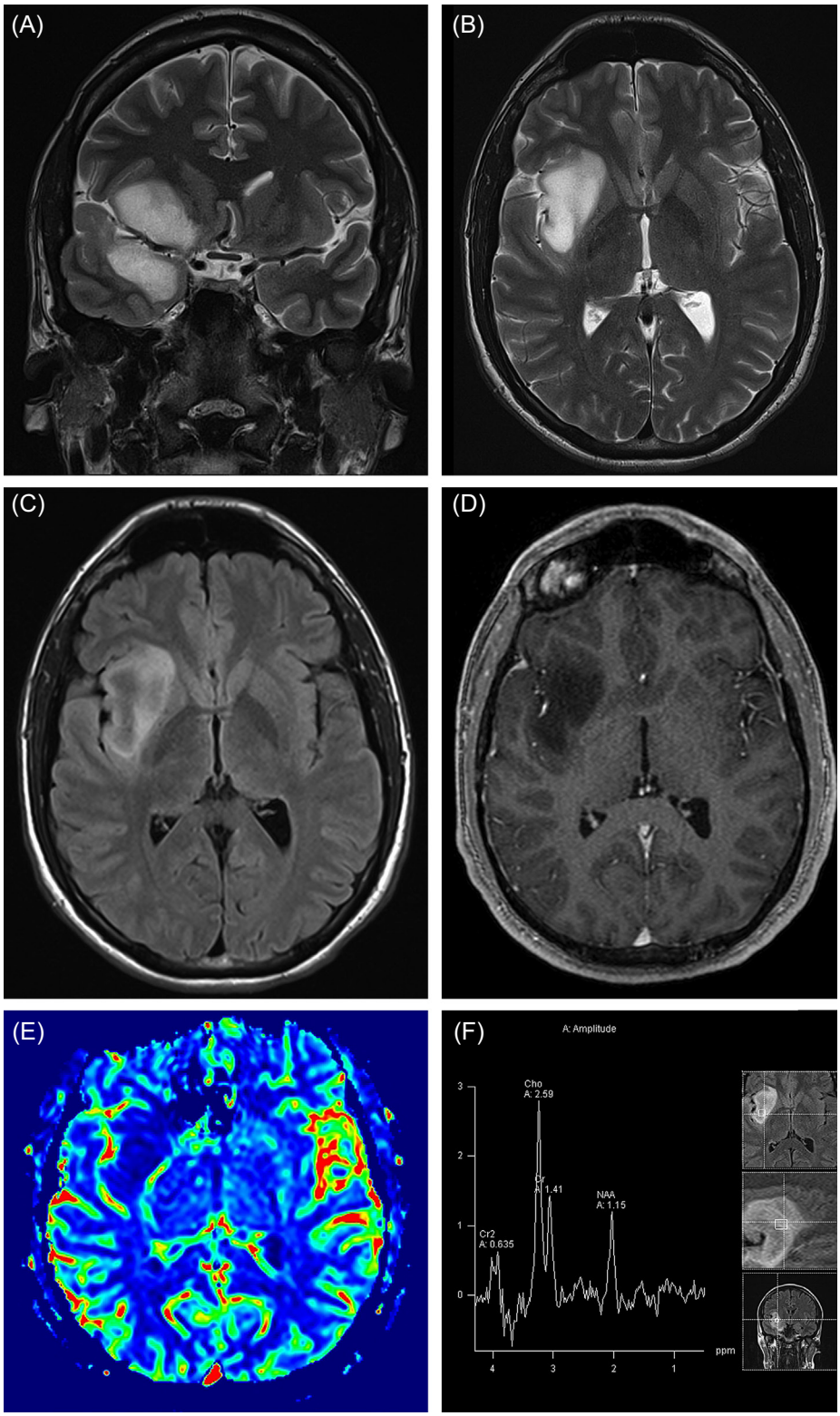


FIGURE 1 **Grade II fibrillary astrocytoma.** (A) Coronal T2, (B) axial T2, and (C) axial FLAIR MR images demonstrating a T2 hyperintense mass, which straddles the Sylvian fissure to involve the inferior frontal and temporal lobes. Heterogeneity on the FLAIR sequence may reflect variability in tumor cellularity and microcystic content. (D) Axial T1 postcontrast image shows no enhancement. (E) rCBV imaging shows the tumor to possess a relatively lower vascularity than normal white matter. (F) MR spectroscopy demonstrates reversal of the Cho and NAA peaks characteristic of tumor. The Cho peak is not quite as high, nor the NAA peak quite as low, as one would expect for a very high-grade tumor such as a grade IV GBM.

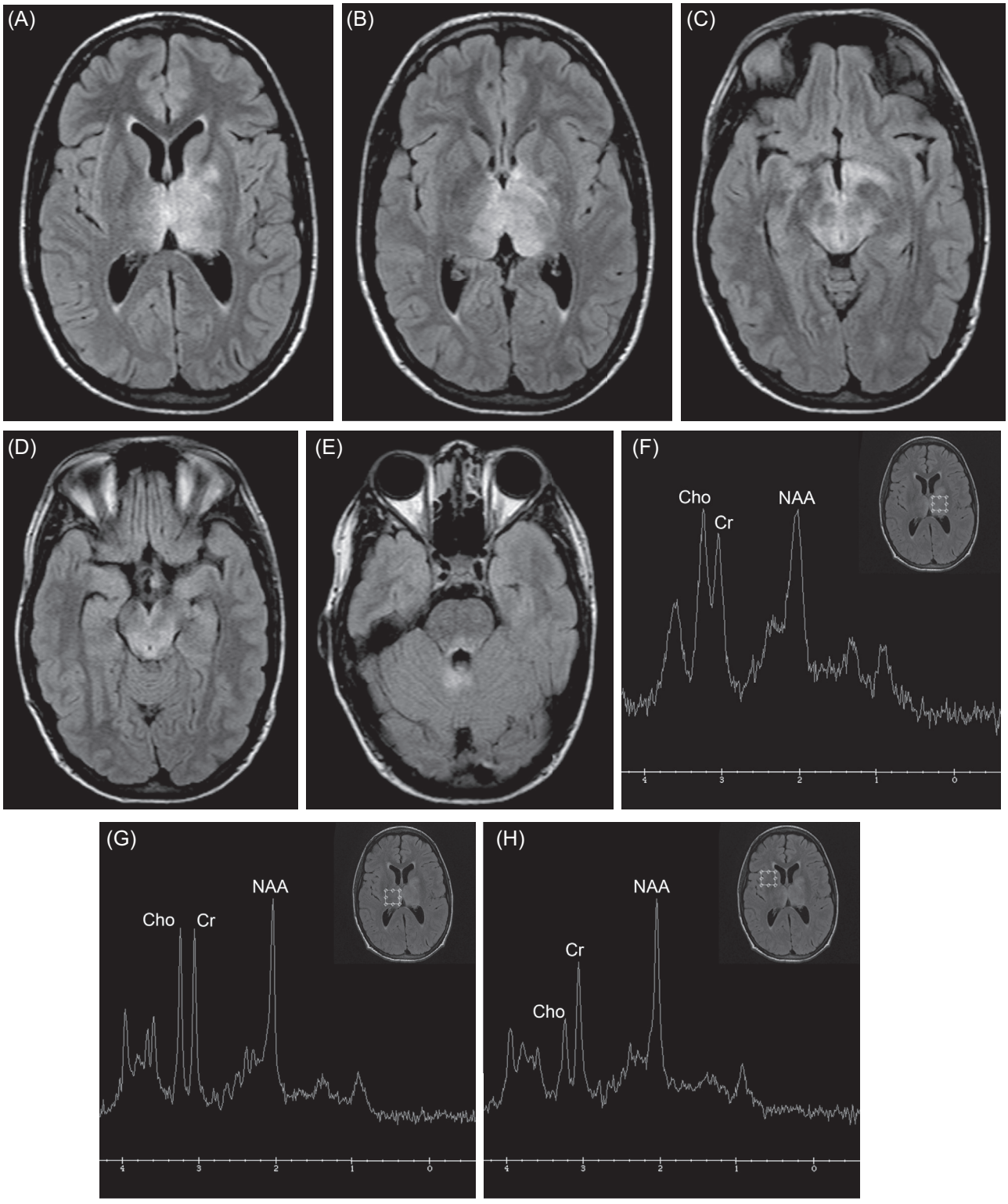


FIGURE 2 **Grade II astrocytoma with a widely infiltrative appearance on imaging.** (A–E) Axial FLAIR images demonstrating another grade II astrocytoma, this time showing a frankly infiltrative appearance on imaging. Tumor is visible in the bilateral thalami, hypothalamus, left basal ganglia, brain stem, and cerebellar vermis. MR spectroscopy obtained in areas where FLAIR would suggest higher tumor cellularity (F, left thalamus), lower tumor cellularity (G, right thalamus), and no tumor (H, right basal ganglia). Note the progressively decreasing Cho peak and increasing NAA peak as one moves from areas of high to low to no tumor cellularity.

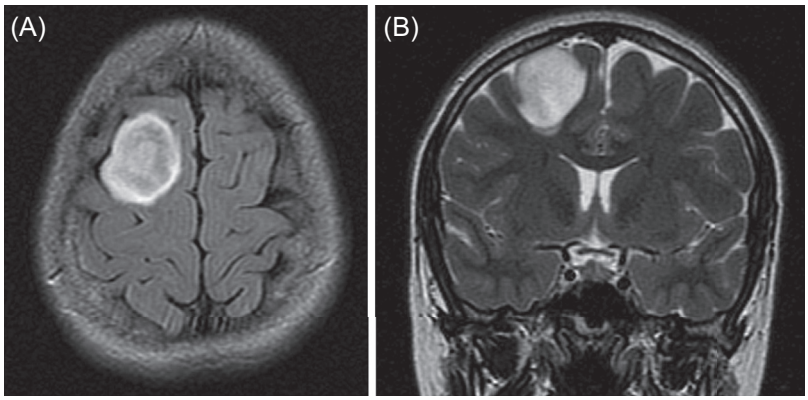


FIGURE 3 **Grade II astrocytic tumor with a very circumscribed appearance on imaging.** (A) Axial FLAIR and (B) coronal T2 MR images showing a grade II tumor in the right superior frontal gyrus. In contrast to the lesion in Figure 2, this tumor seems to show very well-circumscribed margins, which might suggest a noninfiltrative histology. Nevertheless, this was a diffuse astrocytoma at pathology. MRI cannot be relied upon to accurately assess the presence or absence of infiltration.

some studies), it is not thought to be a reliable marker for histopathologic grade, nor does it carry any significance for prognosis, as nonenhancing and enhancing lesions behave similarly.[32,55,59,60] CT reveals tumoral calcifications in 20% of cases.[60,61] Well-differentiated diffuse astrocytomas may spread to gray matter and may have cystic foci on imaging, but typically lack peritumoral edema and exert little or no mass effect.[52,55] When the tumor infiltrates the cortex it may be confused with infarction or cortical-based tumors such as oligodendroglioma or ganglioglioma. The margins of a diffuse astrocytoma may appear quite circumscribed and easy to define on imaging (as in Figure 3), or they may fade gradually or infiltrate irregularly in such a way as to defy accurate measurement (as in Figure 2). Regardless of the imaging appearance, it should always be remembered that a grade II diffuse astrocytoma is inherently infiltrative and that tumor cells will almost always extend beyond the margins of visible signal abnormality on MRI.

Imaging has been shown to have the potential to predict progression of WHO grade II astrocytomas to higher grades and the likelihood of poor outcome. Larger tumor volumes and involvement of more than one lobe as depicted on T2-weighted MRI have been shown to be associated with worse outcomes and transformation to higher grades.[62] Whereas the presence of enhancement on initial diagnosis of a grade II astrocytoma does not affect prognosis, the development of new enhancement on serial imaging follow-up may indicate transformation to a higher grade (as in Figure 4). Of course, in the appropriate context, a radiation-induced effect may also account for changes in enhancement. Several studies have shown the utility of rCBV maps in identifying higher grade tumors and tumors more likely to progress and in predicting patient survival.[37,63–65] Higher rCBV is thought to be associated with microvascularity and therefore angiogenesis. Inconsistencies between histopathology and dynamic susceptibility contrast-enhanced MRI may be attributable to misdiagnosis or sampling error on biopsy. In a 25-patient study, fibrillary WHO grade II astrocytomas with higher rCBV were shown to be associated with earlier recurrence following fractionated stereotactic radiotherapy relative to those with lower rCBV (see Figure 5).[66]

NONINFILTRATIVE ASTROCYTOMAS

These tumors are relatively well circumscribed compared to diffuse astrocytomas. In general, they carry a good prognosis, because they grow indolently and their circumscribed nature makes complete resection feasible in some cases. Several subtypes have been identified and are described below.

Pilocytic Astrocytoma

Pilocytic astrocytomas (see Figures 6–12) usually present in the first 2 decades of life. They often arise from the hypothalamus, optic nerve, optic chiasm, brain stem, and cerebellum or, less commonly, the cerebral hemispheres. They are included among the few tumors that characteristically arise from the corpus callosum (see Figure 9). These tumors are classified by the WHO as grade I lesions.[6] Classically, they are composed of alternating areas of compact and spongy tissue. The name "pilocytic" (directly translated as "hair cell") is derived from the long hair-like projections originating from the neoplastic astrocytes. The compact tissue contains a higher density of bipolar neoplastic astrocytes along with their hair-like processes, as well as Rosenthal fibers. The spongiform tissue contains, on a background matrix of microcysts, a looser mixture of multipolar cells, which contain in their cytoplasm eosinophilic granular bodies.

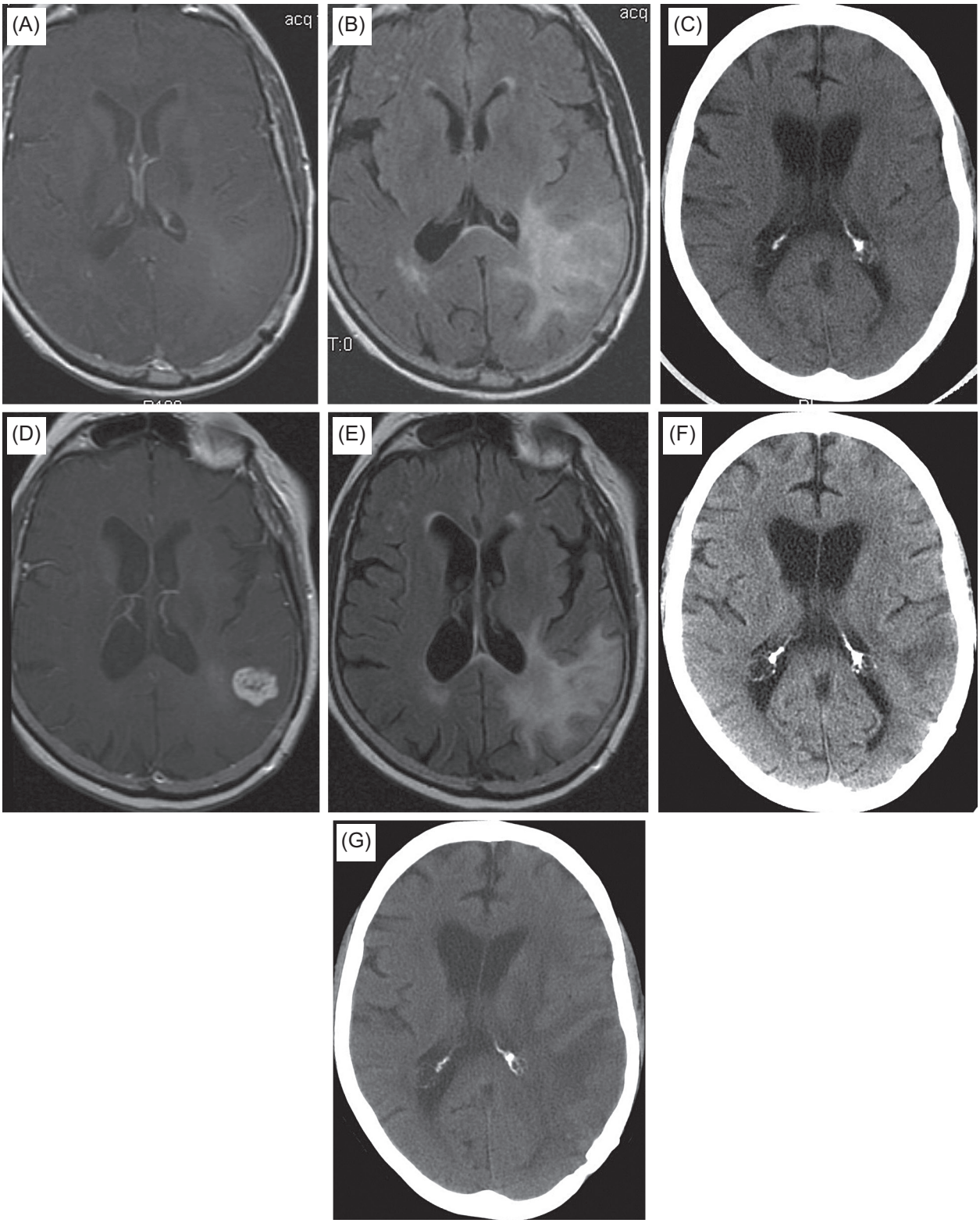


FIGURE 4 **Anaplastic transformation of low-grade astrocytoma.** Sixty-one-year-old female patient presenting with aphasia and discovered to have a WHO grade II astrocytoma involving the left temporal and parietal lobes. (A) The lesion did not enhance on postcontrast images but (B) demonstrated extensive signal abnormality on FLAIR. (C) The tumor was much less conspicuous on a contrast-enhanced CT scan of the head. She underwent conformal radiation and chemotherapy. One year later the imaging characteristics of the tumor changed. (D) The tumor enhanced, but (E) the extent of the signal abnormality on FLAIR did not change significantly. (F) There was some hypodensity noted on CT within the tumor bed. (G) Three months later the tumor showed significant progression on CT and the patient expired shortly thereafter.

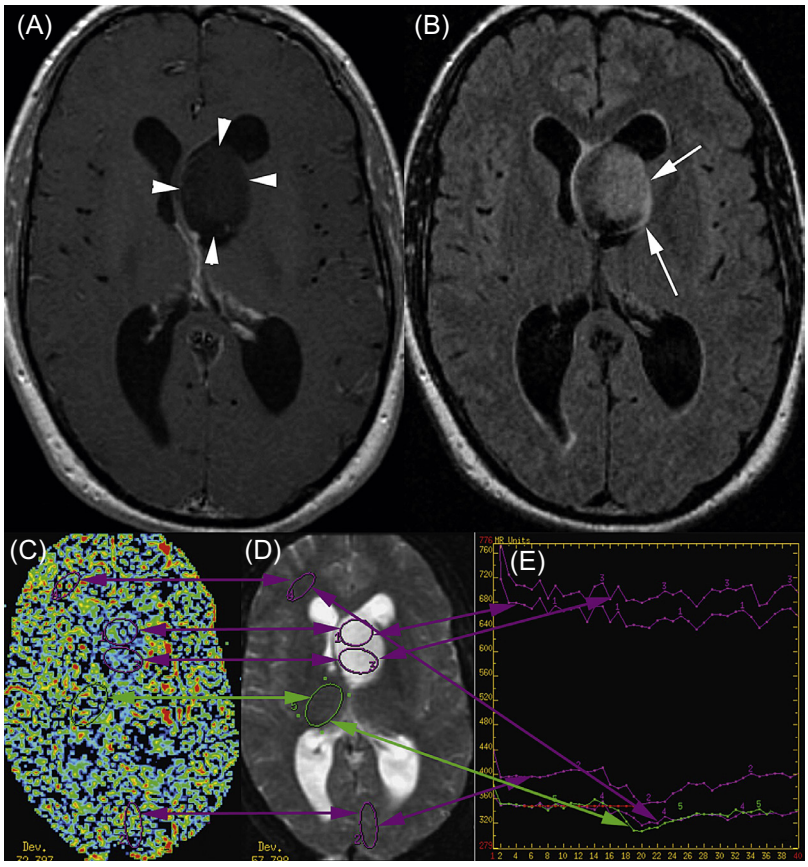


FIGURE 5 **Exophytic low-grade astrocytoma near the foramen of Monro.** (A) Thirty-five-year-old male presenting with headaches and nausea was found to have a mass on MRI (arrowheads) associated with ventriculomegaly. (B) The lesion did not enhance on postcontrast images and appeared to arise from the region of the foramen of Monro. Its lack of enhancement and heterogeneity suggested against most tumors that typically occur in this location, such as subependymal giant cell astrocytoma and central neurocytoma. Subependymomas, although they do not enhance and can have a similar appearance, are unusual in this age group. (C) T2 echo-planar perfusion studies with cerebral blood volume maps and (D) regions of interest depicted on (E) time–activity curves indicate low microvascularity suggestive of low-grade neoplasm. Biopsy revealed WHO grade II diffuse astrocytoma on MRI.

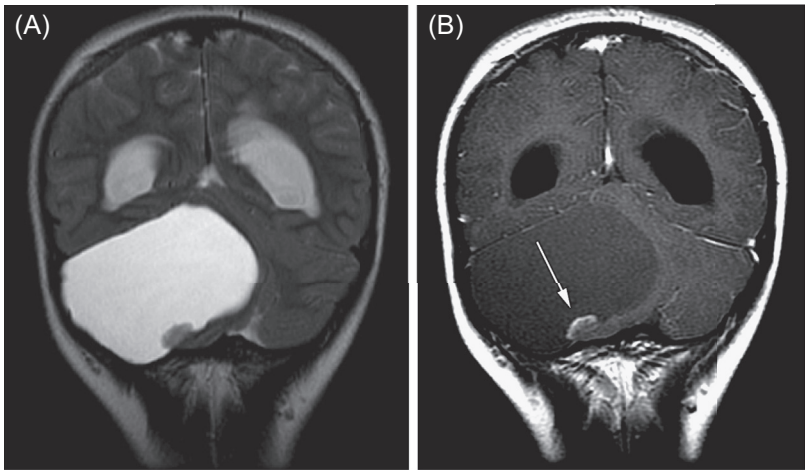


FIGURE 6 **Large predominantly cystic pilocytic astrocytoma of the cerebellum.** (A) Coronal T2 and (B) coronal T1 postcontrast MR images showing a large and predominantly cystic tumor in the right cerebellum with a small enhancing mural nodule (arrow).

Pilocytic astrocytomas are slow growing and have been found to spontaneously stabilize or regress. They are characterized by the presence of numerous vessels that assume a glomeruloid or wickerwork pattern on histology and which account for their typically prominent enhancement. This vascular pattern has been referred to by some sources as microvascular proliferation, though unlike the microvascular proliferation seen in grade IV astrocytomas (GBM), the endothelial cells usually remain single layered and nonproliferative. Rosenthal fibers are highly eosinophilic corkscrew-like filaments found within the astrocytic processes. They are characteristic of pilocytic astrocytoma, but they need not be present to make the diagnosis, and they are also found in a variety of other tumors as well as nonneoplastic reactive astrocytes. The presence of eosinophilic granular bodies is

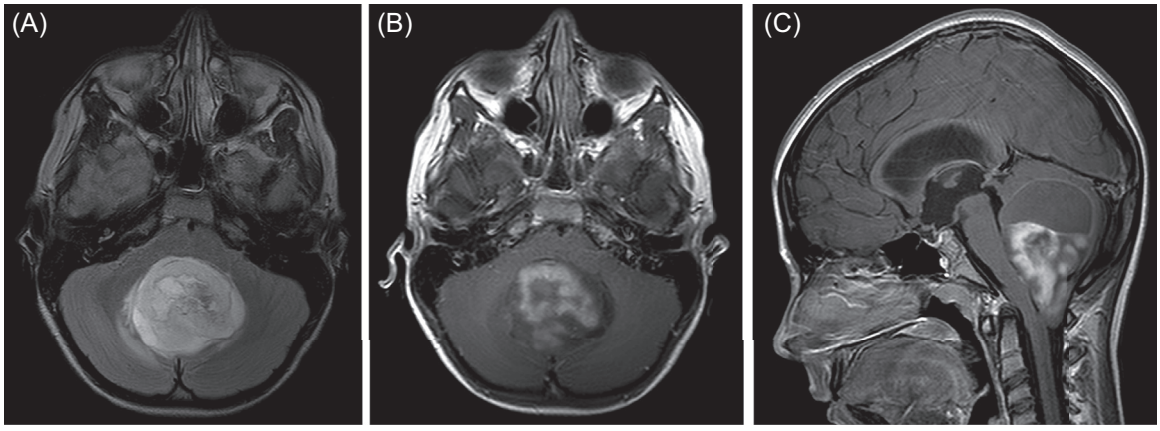


FIGURE 7 **Cerebellar cystic and solid pilocytic astrocytoma.** (A) Axial FLAIR, (B) axial T1 postcontrast, and (C) sagittal T1 postcontrast MR images showing a pilocytic astrocytoma that contains a more substantial solid component. The proportion of solid and cystic material can vary considerably in pilocytic astrocytoma.

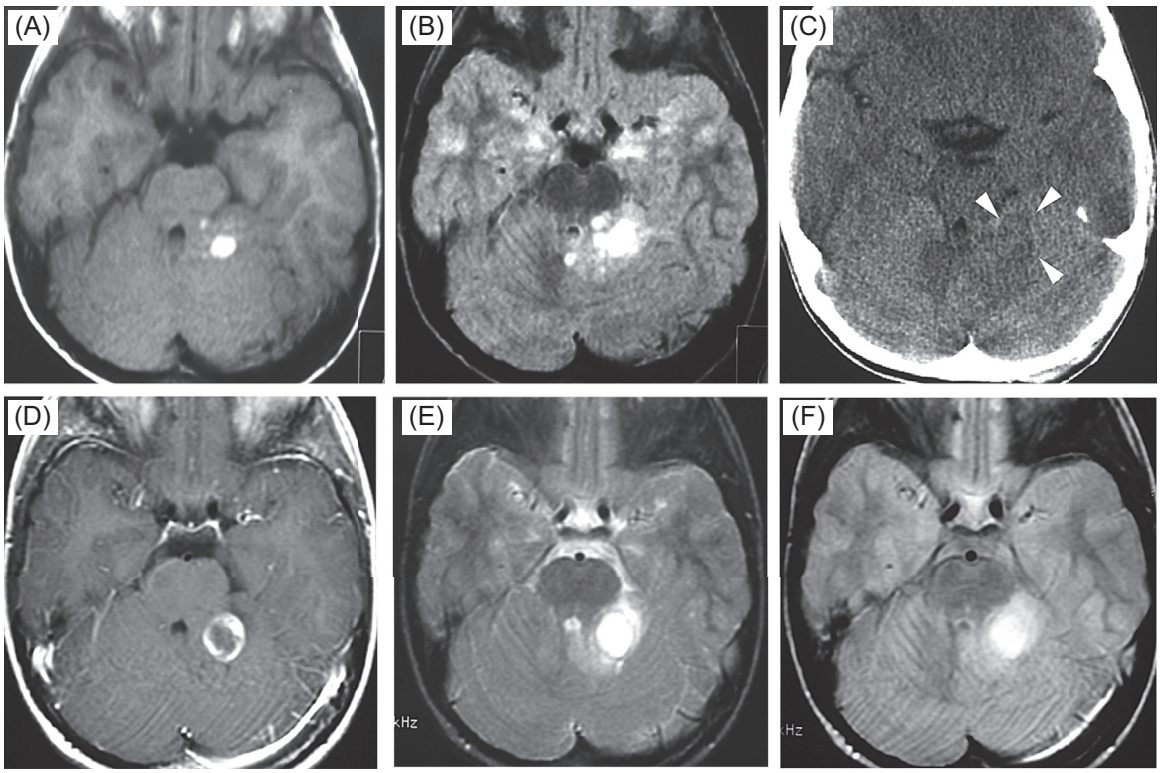


FIGURE 8 **Pilocytic astrocytoma with cystic generation.** (A) Nine-year-old boy presenting with headache due to a left cerebellar neoplasm. (B) FLAIR images show extension of signal abnormality beyond the enhancing borders of the tumor. (C) The tumor is less conspicuous on CT (arrowheads). (D) One year later, the tumor developed a cystic component with ring enhancement, which follows cerebrospinal fluid intensity (E) on T2 but (F) not on proton density imaging.

considered a marker for low-grade neoplasms and this feature can be found in ganglion cell tumors and pleomorphic xanthoastrocytoma, as well as pilocytic astrocytoma. Again, they are helpful but not required to make the diagnosis. Pilocytic astrocytoma exhibits a paucity of consistent genetic abnormalities predictive of outcome.[49] It is, however, interesting that these tumors may display abnormalities on chromosome 17 in the same region as the neurofibromatosis type I (NFI) gene, and patients with NFI have a higher incidence of pilocytic astrocytomas.[67] Pilocytic astrocytomas may spread locally, and very uncommonly they have been found to spread via cerebrospinal fluid (CSF) dissemination.[6,60,68,69] It is not unusual for pilocytic astrocytoma to encroach upon the subarachnoid space and to invade the leptomeninges in microscopic fashion. When this occurs, it does not imply

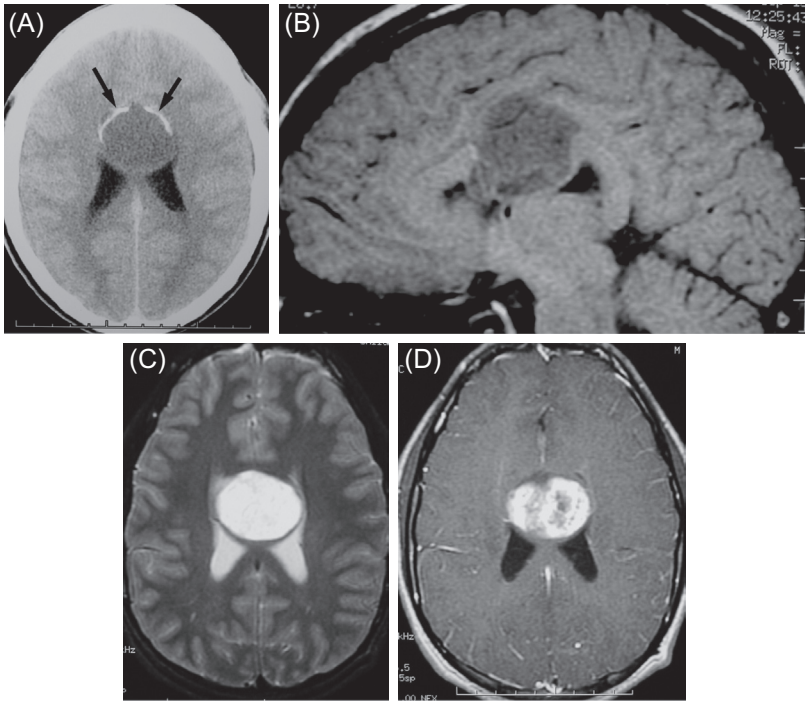


FIGURE 9 **Pilocytic astrocytoma of the corpus callosum.** (A) Axial CT, (B) sagittal T1, (C) axial T2, and (D) axial postgadolinium T1 MR images of a pilocytic astrocytoma centered in the corpus callosum. Note the calcification, which occasionally accompanies this tumor type (arrows). Pilocytic astrocytomas differ from other tumors involving the corpus callosum because they are usually well circumscribed and not typically associated with vasogenic edema.

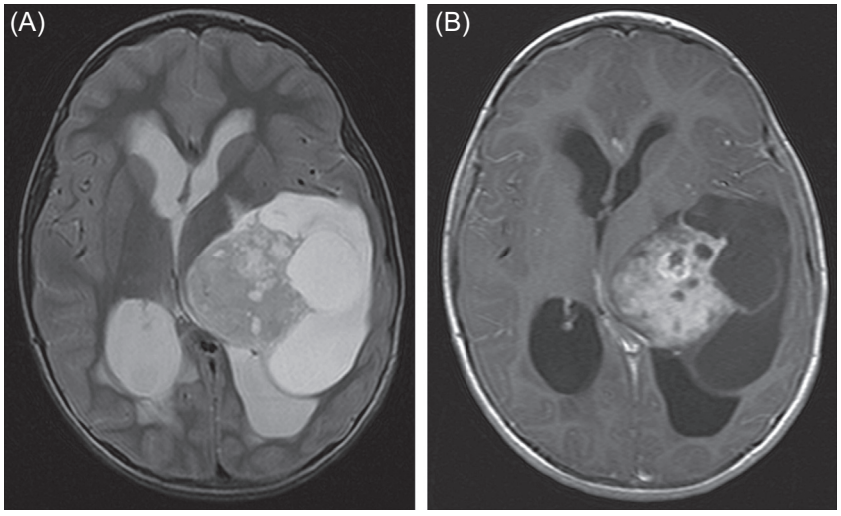


FIGURE 10 **Giant supratentorial pilocytic astrocytoma.** (A) Axial T2 and (B) T1 postcontrast MR images showing a very large cystic and solid tumor arising in the left cerebral hemisphere. Notice that despite the tumor's size and associated mass effect, there is minimal edema in the surrounding parenchyma.

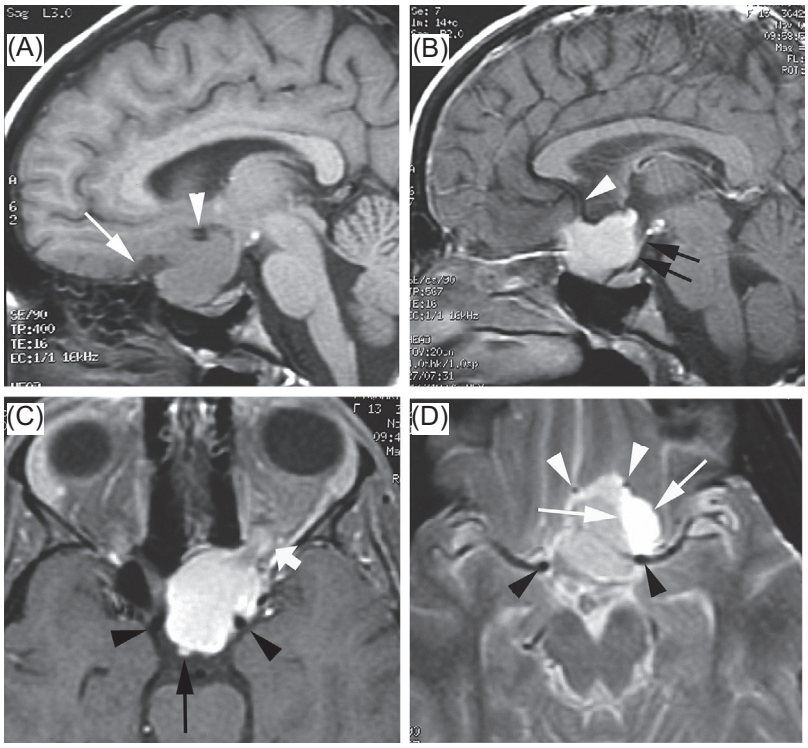


FIGURE 11 **Pilocytic astrocytoma involving the hypothalamus and optic nerves.** (A) T1 parasagittal, (B) postgadolinium T1 midline sagittal, (C) postgadolinium T1 axial, and (D) T2 axial images through the suprasellar region demonstrate a pilocytic astrocytoma with a cystic component (white arrows in (A) and (D)). The lesion is isointense to gray matter on T1- and slightly hyperintense to gray matter on T2-weighted images. Note the tumor's relationship to the anterior cerebral arteries (white arrowheads), the distal internal carotid arteries (black arrowheads), and the infundibular stalk of the pituitary. Also note growth of the tumor along the optic nerve (wide white arrow).

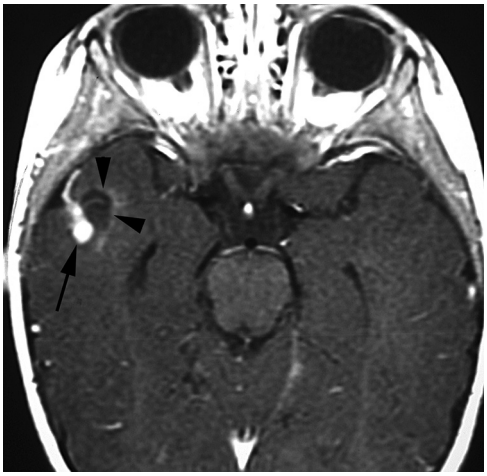


FIGURE 12 **Pilocytic astrocytoma involving the temporal lobe.** Pilocytic astrocytomas can arise from the supratentorial brain as depicted on this T1 postgadolinium MR image. This cyst (arrowheads) and enhancing mural nodule (arrow) appearance in this location can also be seen with ganglioglioma and pleomorphic xanthoastrocytoma.

impending dissemination. Malignant transformation has been reported with pilocytic astrocytoma, but it is an exceptionally rare event. In general, these lesions are considered to have little if any risk of degeneration, and patient survival is excellent, with 10-year survival up to 96% for patients diagnosed at younger ages. The acquisition of histopathologic features suggestive of malignant transformation, such as multiple mitoses per high-power field or palisading necrosis, has been reported to occur; however, the outcome is not always grim in such cases.[6] Indeed, proliferative indices such as MIB-1 labeling ranging up to 4%, and TP53 genetic mutations, which may portend poorer prognosis in other histologies, do not have the same implication for pilocytic astrocytomas.

On cross-sectional imaging they are identified as well-circumscribed tumors. Classically they present as a cystic lesion with an enhancing mural nodule (see Figures 6–8). In actual practice, the proportions of cystic to solid tissue are highly variable and range from nearly entirely cystic to entirely solid. Cystic components are identified in approximately 68% of cases, and if not present on initial diagnosis, cysts may develop over time as the lesion is followed (see Figure 8). In general, the chiasmatic location is associated with a lesser incidence of cyst formation (see Figure 11). On CT, the solid component of the tumor typically appears hypodense (43%) or isodense (51%) and is much less commonly hyperdense (6%). Calcifications have been reported in approximately 11% of CT cases (see Figure 9). On MRI they present as well-circumscribed tumors (96%) with benign morphologic features and rarely cause vasogenic edema (5%). On MRI they display

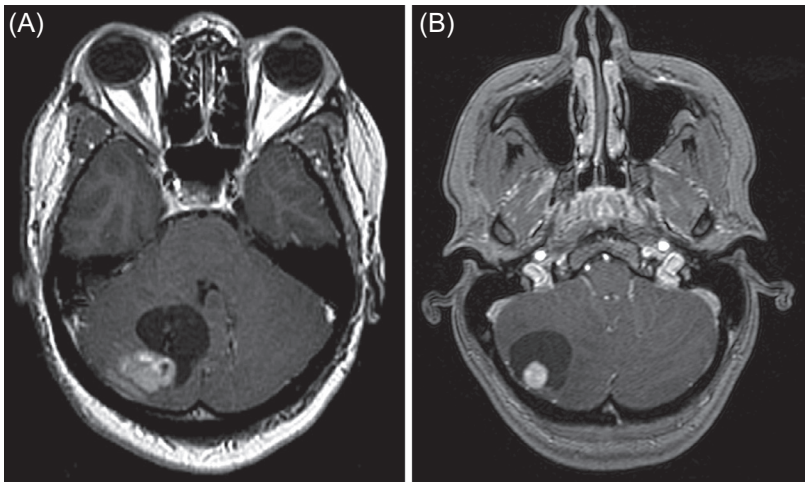


FIGURE 13 **Differential diagnosis for a cyst with mural nodule in the cerebellum.** (A and B) Axial postcontrast images of two different patients both show a cystic lesion with an enhancing mural nodule. On pathology, the tumor in (A) was a pilocytic astrocytoma, and the tumor in (B) was a hemangioblastoma. These lesions can be indistinguishable on imaging as in this case. Patient age will be a far more useful discriminator in such a situation. In a pediatric patient, pilocytic astrocytoma is far more common than hemangioblastoma (assuming the patient does not have von Hippel Lindau syndrome). The opposite would be true for an adult.

contrast enhancement in 94% of cases, which is thought to be related to the vascular nature of these tumors. Again, the higher density of vessels seen in these tumors does not imply an aggressive phenotype as it would for other histologies and grades. On T1-weighted imaging, they tend to be of lower signal intensity relative to gray matter. On T2-weighted imaging, they are of higher signal relative to gray matter. The T2 signal intensity of the solid component is similar to that of CSF in 50% of cases and may even be mistaken for cystic tissue (see Figure 9) until the postcontrast images are inspected. This feature differs from medulloblastomas, for example, which are T2 isointense to gray matter, thus offering a way to distinguish these two very different lesions, which often occur in the same geographic regions and in the same patient demographic.[70] Varying imaging presentations may include solid tumor as well as multicystic tumor. In most locations they have a round or oval shape; however, in the chiasmatic location they have been found to have a multilobulated shape. MR spectroscopy can reveal an elevated lactate peak in these tumors, again not a sign of aggressive behavior or malignant potential.[20] In general, they are distinguished from other cystic tumors on the basis of location and patient age (see Figure 13).[6,12,71,72] When atypical imaging features are seen, such as invasion of adjacent structures or rapid growth, there may be corresponding atypical histologic features as well (see Figure 14).

Pilomyxoid Astrocytoma

PMA (see Figures 15 and 16) is a low-grade astrocytoma, which, up to the late 1990s, was classified as a pilocytic astrocytoma.[6] In fact, this lesion may represent up to 10% of tumors previously classified as pilocytic.[73] Histologically, PMAs have a monomorphic bipolar cellular pattern on a highly mucoid matrix. The tumor characteristically lacks both Rosenthal fibers and eosinophilic granular bodies.[6] It tends to occur in early childhood, but has been identified in adults.[74] These tumors are most often found in the hypothalamic/chiasmatic region and are more likely to be solid enhancing tumors with homogeneously high signal on T2-weighted images. Furthermore, this signal may feather into the adjacent white matter, which can help distinguish PMA from pilocytic astrocytoma. CSF dissemination is also more likely than in pilocytic astrocytoma. Proton MRS of PMA has shown a decreased concentration of choline, creatine, and NAA. This pattern differs from pilocytic astrocytoma, which tends to display elevated choline and decreased creatine and NAA.[75] Given that PMA is rare and relatively newly described, data regarding its biological behavior and prognosis are scant. There is little doubt, however, that this tumor behaves more aggressively than pilocytic astrocytoma. CSF dissemination is not uncommon, and multiple recurrences following resection have been reported. The degree to which these difficulties influence survival is not quite as clear, however. Whereas an early study suggested reduced survival for patients with pilomyxoid versus pilocytic astrocytoma,[76] a more recent study found no significant survival difference.[73] The WHO classifies this lesion as grade II.

Pleomorphic Xanthoastrocytoma

Pleomorphic xanthoastrocytoma (PXA) (see Figures 17 and 18) is a tumor with a varied histologic appearance. It is generally classified as WHO grade II neoplasm, but a grade of III may occasionally be assigned

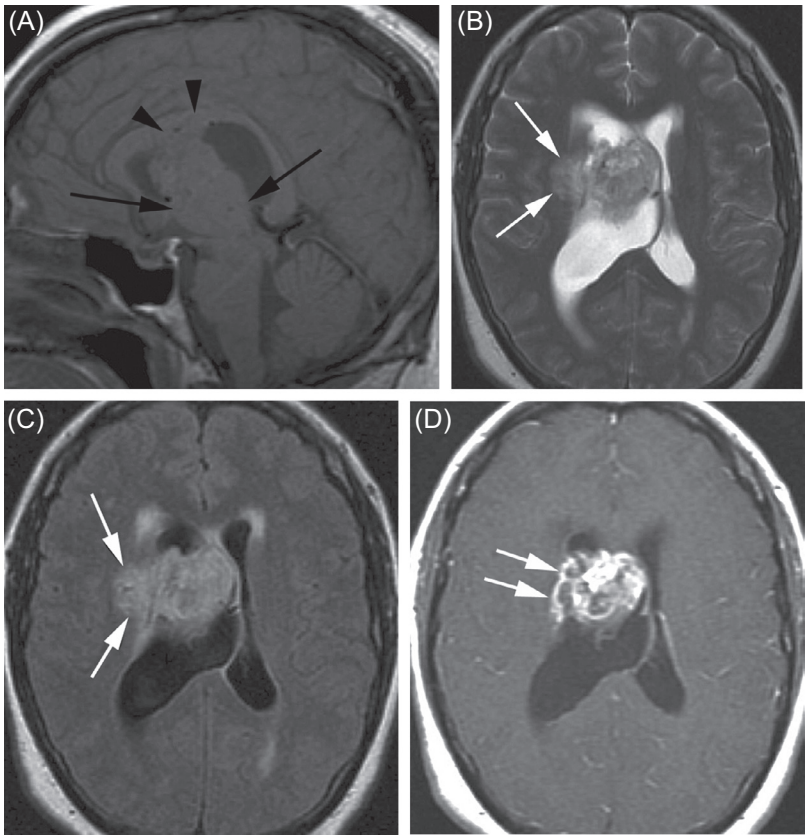


FIGURE 14 **Atypical pilocytic astrocytoma.** (A) Sagittal T1, (B) axial T2, (C) axial FLAIR, and (D) axial postgadolinium T1 images of a pilocytic astrocytoma that displayed aggressive features on histopathology including an increase in proliferative activity. The neoplasm spans between the corpus callosum (black arrowheads) and the thalamus (black arrows). There is apparent invasion of adjacent centrum semiovale (white arrows) suggestive of a more aggressive neoplasm.

when aggressive histopathologic features are present. Characteristics distinguishing PXA include spindly cells as well as mononucleated or multinucleated giant cells with intracellular accumulation of lipid droplets often surrounded by a thick reticulin-laden basement membrane.[4] Gross evaluation indicates that they involve the leptomeninges as well as the underlying brain. Their peripheral location suggests that they arise from subpial astrocytes.[77] These tumors have been rarely shown to transform into, or coexist with, ganglioglioma.[4,78,79] If only a small amount of tumor is provided to the pathologist for analysis, PXA may be confused with glioblastoma, and even with an adequate sample, distinction from ganglioglioma can be problematic. In these cases, the MRI and CT appearance of the tumor may assist pathologic interpretation.[80]

Like pilocytic astrocytomas, PXAs occur more frequently in the first 2 decades of life. Unlike pilocytic astrocytomas, they occur more commonly in the cerebral hemispheres, with a predilection for the temporal lobes. On imaging, PXAs classically have a cyst and mural nodule appearance and may be difficult to distinguish from gangliogliomas (see Figure 17). Imaging features of low grade, such as lack of peritumoral edema and calvarial scalloping, frequently accompany these tumors. On CT these tumors have a cystic appearance in half the cases and rarely contain calcifications. Angiography reveals that these tumors are hypervascular and receive supply from the meningeal arteries.[81] MRI reveals that relative to gray matter, the solid component is of similar signal intensity on T1-weighted images and increased signal on T2-weighted sequences.[81,82] Because of their peripheral location, they can be confused with meningioma on imaging.[12,81] Other differential considerations when identifying a tumor with characteristics of PXA include pilocytic astrocytoma, ganglioglioma, and oligodendroglioma.

Subependymal Giant-Cell Astrocytoma

Subependymal giant-cell astrocytoma (SGA) (see Figures 19 and 20) is a low-grade primary brain tumor assigned a WHO grade I classification. As the name implies, these tumors are composed of large ganglioid astrocytes, which are located along the wall of the lateral ventricle. They invariably occur in the setting of tuberous sclerosis and affect the region near the foramen of

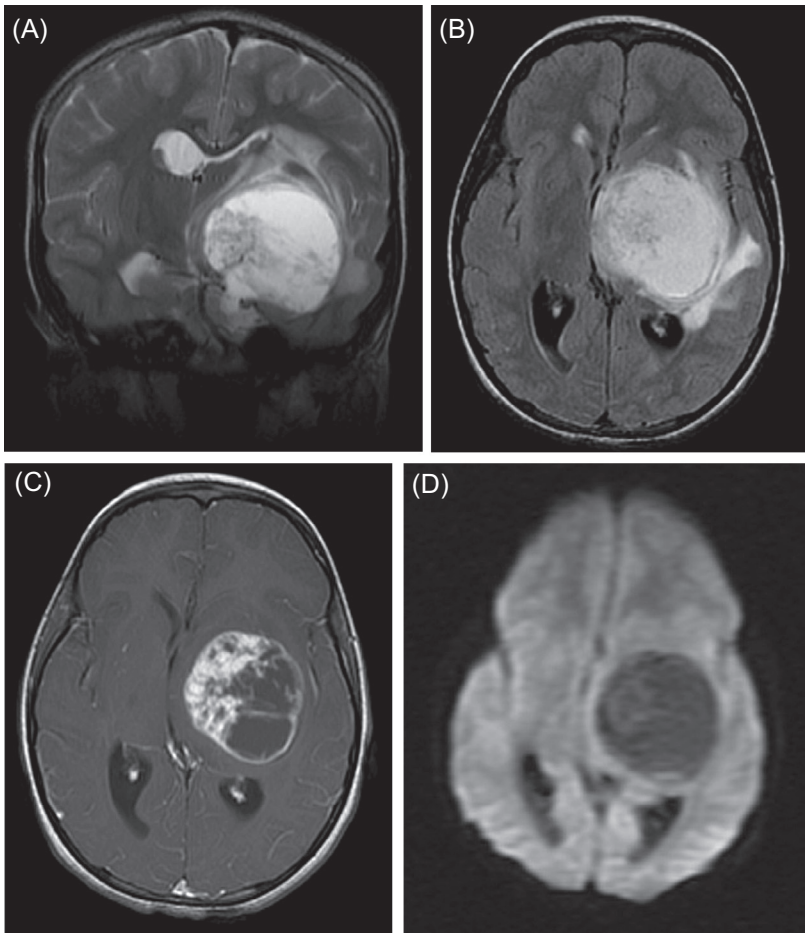


FIGURE 15 **Pilomyxoid astrocytoma.** (A) Coronal and (B) axial T2 MR images show a large, very T2 hyperintense mass involving the left thalamus, hypothalamus, and basal ganglia. Note the greater degree of T2 hyperintense signal in the surrounding parenchyma compared to a pilocytic astrocytoma. (C) Axial T1 postcontrast image shows partial enhancement of the lesion. (D) On DWI, the lesion demonstrates an increase in diffusion (lower signal) relative to normal brain, which may reflect the myxoid or mucoid matrix of this tumor.

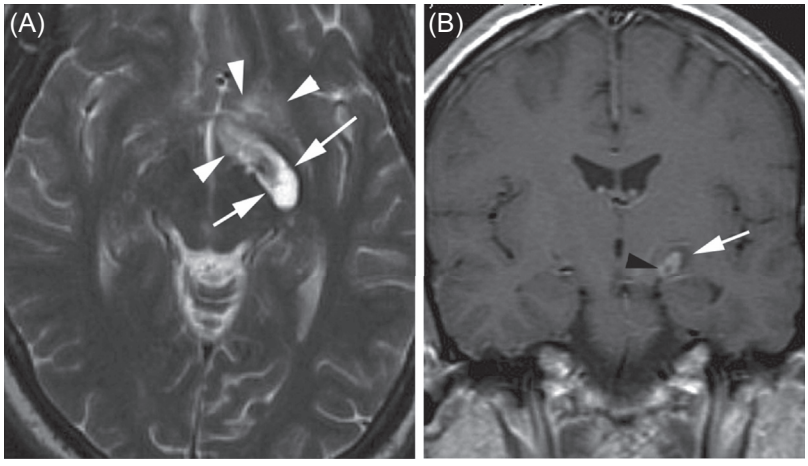


FIGURE 16 **Pilomyxoid astrocytoma.** (A) T2 axial and (B) postgadolinium coronal T1 images through the brain of a 36-year-old male with a hypothalamic cystic lesion. Note the cystic component (arrows) and the infiltration into adjacent brain (arrowheads).

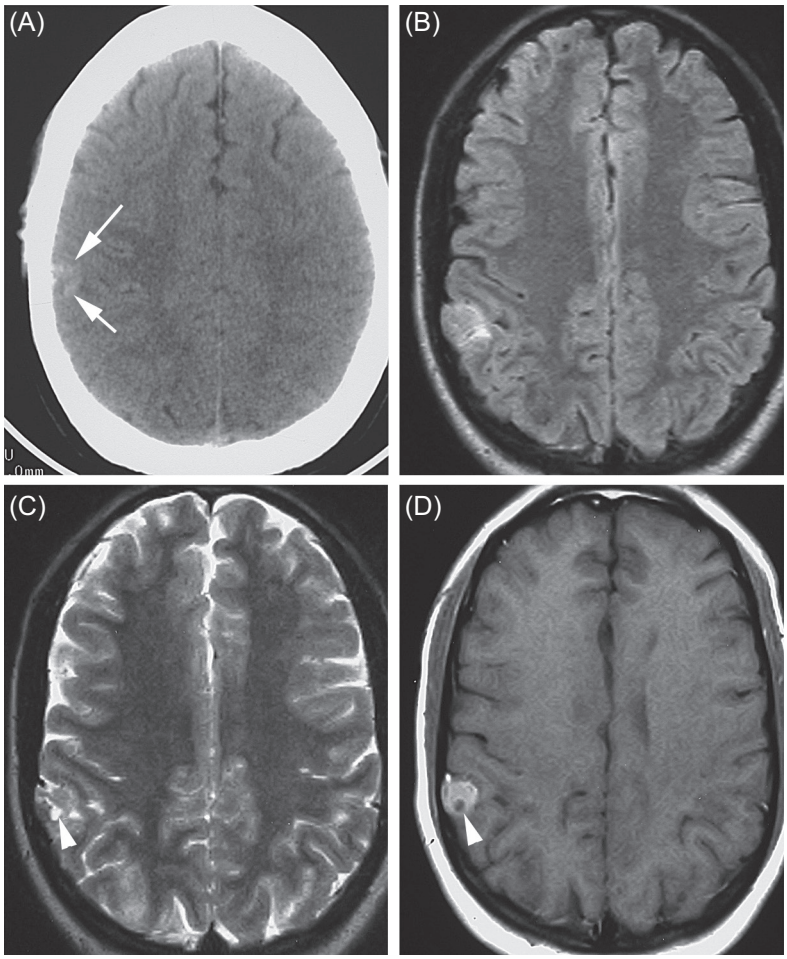


FIGURE 17 **Pleomorphic xanthoastrocytoma.** A 25-year-old male presenting with seizure. (A) Axial CT, (B) axial FLAIR, (C) axial T2, and (D) axial postgadolinium T1 MR images of a low-grade pleomorphic xanthoastrocytoma located in the right parietal lobe cortex. Note the hyperdense appearance on CT (arrow). Distinguishing features for this tumor type include a well-circumscribed appearance, cyst formation (arrowheads), cortical location, and contrast enhancement. It would be difficult to distinguish this tumor from other cortically based tumors such as metastasis or ganglioglioma. Because of frequent association with a dural tail they may appear similar to cystic meningiomas.

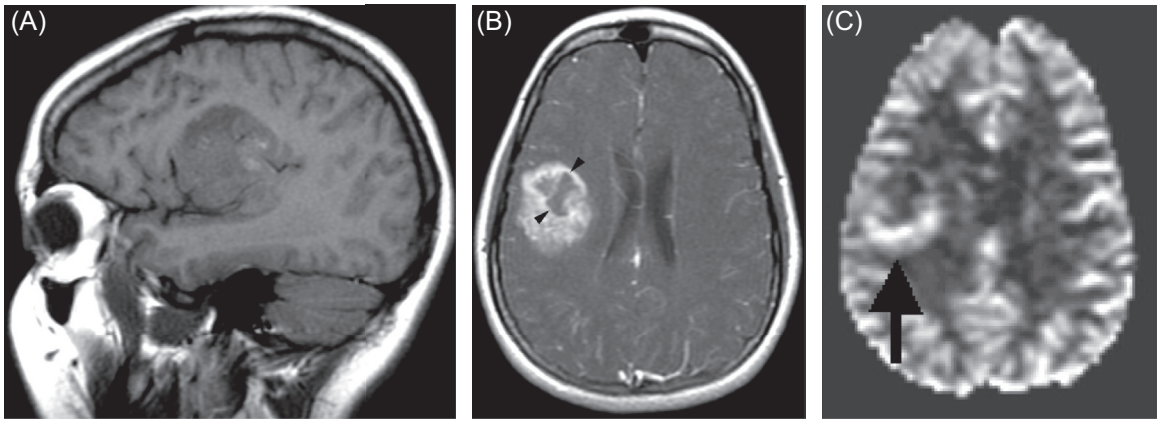


FIGURE 18 **Pleomorphic xanthoastrocytoma.** (A) Sagittal T1, (B) axial postgadolinium T1, and (C) axial relative cerebral blood volume MRI map of a WHO grade III pleomorphic xanthoastrocytoma centered in the inferior right frontal gyrus. Note the cortical location as well as the presence of a cystic-appearing component (arrowheads) and an enhancing component as well as isointense signal relative to gray matter on T1, all features of PXA. Because the tumor is well circumscribed and not associated with vasogenic edema, it is not readily distinguished from a grade II PXA on conventional MRI. Although higher cerebral blood volume in a portion of the tumor (arrow) is suggestive of higher grade in astrocytomas, in PXA this finding may just be an indication of increased vascularity unrelated to grade.

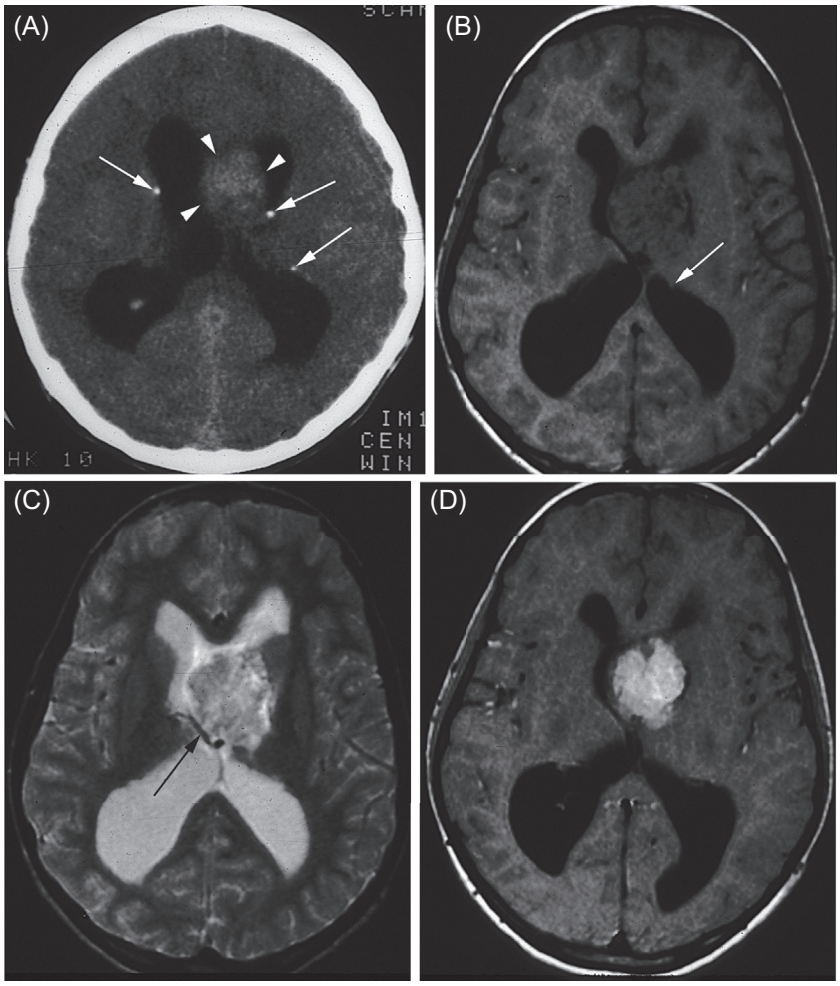


FIGURE 19 **Subependymal giant-cell astrocytoma.** (A) Axial CT, (B) axial T1, (C) axial T2, and (D) axial postgadolinium T1 MR images of a subependymal giant-cell astrocytoma (SGA) located at the left foramen of Monro (arrowheads) in a patient with tuberous sclerosis. Note that subependymal nodules (white arrows) are more conspicuous on the CT examination than on the MRI. Note the relationship of the tumor to the internal cerebral vein (black arrow), which may affect surgical planning. The tumor is hyperdense on CT and heterogeneous on T2 and T1 MRI, and it enhances following contrast. These features, although typical of SGA, are also features found in most lateral ventricular tumors. The diagnosis is made on the basis of stigmata of tuberous sclerosis such as the presence of subependymal nodules and cortical tubers.

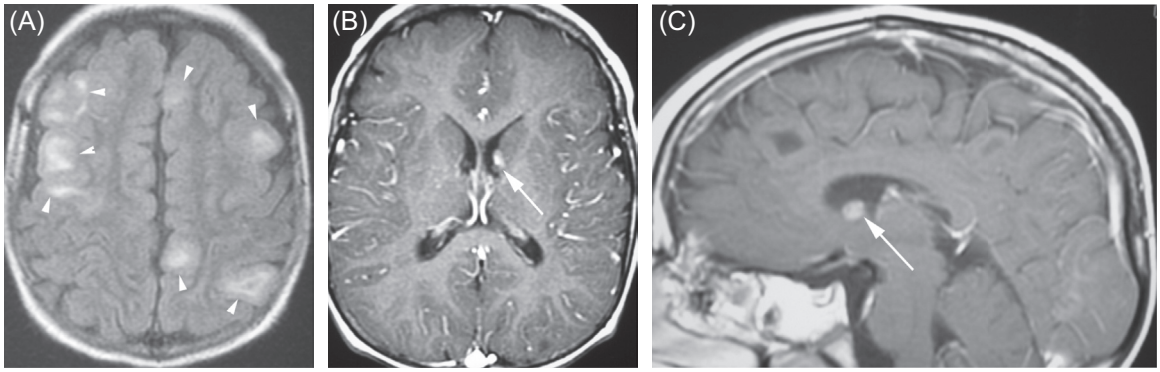


FIGURE 20 **Cortical tubers with subependymal giant-cell astrocytoma.** (A) Axial FLAIR, (B) axial T1 postgadolinium, and (C) sagittal T1 postgadolinium MR images of a cognitively impaired patient with seizures and adenoma sebaceum. Among pulse sequences, FLAIR MRI displays cortical tubers (arrowheads) most effectively. A 5-mm enhancing lesion near the foramen of Monro (arrows) most likely represents a subependymal giant-cell astrocytoma. Because of their propensity to enlarge, aggressive follow-up MRI or surgical removal is often suggested.

Monro, potentially obstructing the flow of CSF and causing hydrocephalus. The presence of more aggressive histopathologic features such as increased mitoses, nuclear pleomorphism, necrosis, and endothelial proliferation have not been associated with shorter survival times as they would in other tumors.[5,12,78,81]

SGAs occur in 6–16% of patients with tuberous sclerosis. In addition to identifying this tumor in its typical location near the foramen of Monro, the identification of stigmata related to tuberous sclerosis in the same patient confirms the diagnosis of SGA (see Figure 20).[83–88] SGA is one of the few brain tumors that may be identified at birth and should therefore be included in the differential diagnosis of neonatal brain tumors when appropriate. On ultrasound, the mass tends to be isoechoic with hyperechoic foci representing calcification or hemorrhage. Intrinsic CT features include the presence of calcifications and a hyperdense appearance relative to cortex (see Figure 19). Tumoral calcifications are thought to relate to small areas of prior hemorrhage. Contrast enhancement is common with these tumors on both CT and MRI. Associated stigmata of tuberous sclerosis include the presence of cortical tubers and subependymal nodules. In general, cortical tubers are more readily apparent on MRI (see Figure 20), whereas calcified subependymal nodules are more readily identified on CT (see Figure 19).[83,84,87] The extent of brain involvement with cortical tubers has been shown to correlate with the severity of disease in these patients.[83,86,87] Patients with tuberous sclerosis probably benefit from annual surveillance for these tumors during childhood. Patients with biopsy-proven asymptomatic SGA who do not undergo resection should be imaged annually. If the tumor grows or changes its enhancement pattern, this may serve as an indication to increase the frequency of imaging surveillance or to surgically remove the tumor.[89] It should be emphasized that larger tumors near the foramen of Monro and symptomatic presentation are associated with higher morbidity. It has been suggested that any lesion near the foramen of Monro greater than 5 mm in size with incomplete calcification should be removed as soon as there is clear evidence of growth on serial scans.[90] Early resection of these tumors results in improved overall outcome. Differential considerations on imaging include other intraventricular tumors such as central neurocytoma, metastasis, oligodendroglioma, pilocytic astrocytoma, and meningioma. SGA can be distinguished from these tumors on imaging by the identification of features of tuberous sclerosis as described above.[85]

GLIOMATOSIS CEREBRI

Gliomatosis cerebri (see Figure 21) is a condition in which a large portion of the brain becomes diffusely infiltrated by neoplastic glial cells.[91] Whereas all diffuse astrocytomas are infiltrative, gliomatosis differs from most of these in that, in the classic version, there is no recognizable focality on imaging or pathology. By definition, neoplastic cells spread through at least three lobes of the brain, and indeed, the disease may extend to involve every lobe as well as the brain stem and spinal cord. The cell of origin is usually astrocytic, though other cell types may dominate the picture, including oligodendroglia and mixed varieties.[91,92] The WHO classifies this disease as a grade III neoplasm because, in terms of biological behavior and prognosis, gliomatosis is on equal footing with other grade III brain tumors. Individual biopsy specimens, however, may not meet the criteria for a grade III astrocytic designation, and of course, with such a large extent of disease, nonrepresentative sampling is an issue. Gliomatosis may be subclassified into primary and secondary types, the former arising as an independent entity in its own right, and the latter arising in the context of a preexisting focal glial neoplasm.[91] Another classification scheme involves the designation of type 1, or classic gliomatosis, for disease in which neoplastic cells are spread evenly over multiple lobes without focality, and type 2, in which the even neoplastic spread exists with superimposed lumpy, more focal masses.

Gliomatosis cerebri was an autopsy diagnosis prior to the advent of MRI. This reflects the impossibility of establishing the diagnosis on the basis of one or a few limited biopsies. Furthermore, it was not even always clear that patients were suffering from a neoplastic disease, as focal or localizing symptoms were often absent. Nowadays, imaging plays a critical role in the diagnosis and the essential features have been well defined.[93–96] Gliomatosis may be visible to some degree on CT as diffuse hypoattenuation through a large region of white matter. The finding is likely to be subtle, though, and in some cases, it may not be detectable. MRI demonstrates the abnormality far more sensitively and the extent of disease as predicted on MRI matches well with that found at autopsy.[91,93,96] Diffuse T2 hyperintensity will be seen extending through a large region of white matter, with correlating T1 hypointensity, involving at least three lobes. Normal structures are expanded and deformed but not destroyed. The pattern of signal abnormality may be smooth and uniform (type 1, or classic), or there may be superimposed more focal tumor nodules (type 2). Small areas of scattered enhancement may be seen, but the bulk of the process typically does not enhance. On DWI, signal may be normal or increased.

Although data on survival are somewhat varied, all indicate that gliomatosis cerebri carries a poor prognosis.[97–100] Survival of up to 40 months has been reported, though it would seem that an estimate of between 12 and 24 months is probably more realistic. Chemotherapy and radiation may help to prolong life in gliomatosis. Beyond biopsy to establish the diagnosis, however, there is no role for surgery in the management of this widespread diffuse disease.

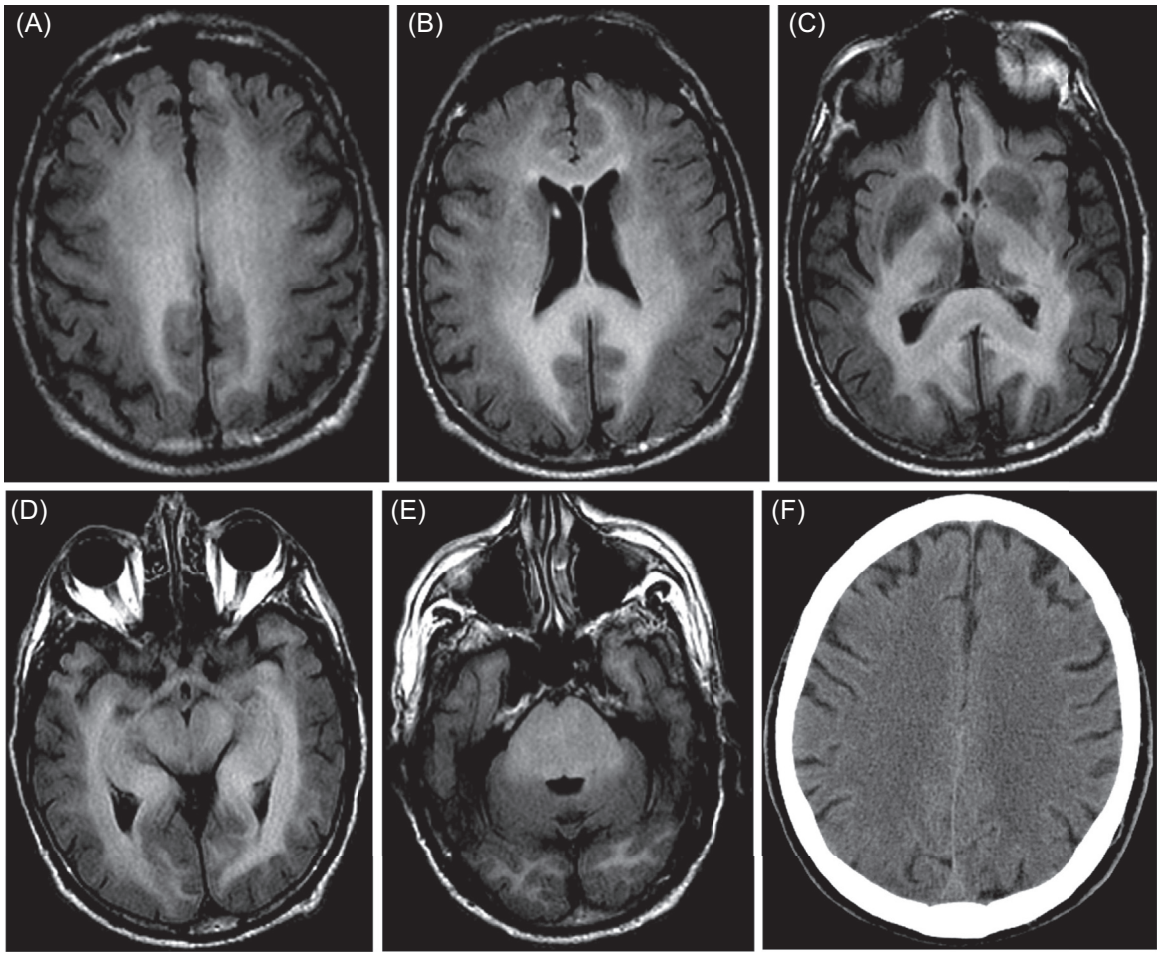


FIGURE 21 **Gliomatosis cerebri**. (A–E) Axial FLAIR images demonstrate diffuse and symmetric thickening and hyperintensity throughout the entire cerebral white matter compatible with classic (type I) gliomatosis cerebri. (F) Although the abnormality is striking and easily detected on MRI, it can be very subtle and potentially overlooked on CT, as in this case, in which only a very subtle white matter hypodensity suggests the underlying disease.

References

1. Astrocytic tumors. In: Louis DN, Ohgaki H, Wiestler OD, Cavenee WK, eds. *The 2007 WHO Classification of Tumours of the Central Nervous System*. 4th ed. Lyon, France: International Agency for Research on Cancer; 2007:13–52.
2. Ostrom QT, Gittleman H, Farah P, et al. CBTRUS statistical report: primary brain and central nervous system tumors diagnosed in the United States in 2006–2010. *Neuro Oncol*. 2013;15(suppl 2):ii1–ii56.
3. Brat DJ, VandenBerg SR, Figarella-Branger D, Taratuto AL. Desmoplastic infantile astrocytoma and ganglioglioma. In: Louis DN, Ohgaki H, Wiestler OD, Cavenee WK, eds. *The 2007 WHO Classification of Tumours of the Central Nervous System*. 4th ed. Lyon, France: International Agency for Research on Cancer; 2007:96–98.
4. Giannini C, Paulus W, Louis DN, Liberski PP. Pleomorphic xanthoastrocytoma. In: Louis DN, Ohgaki H, Wiestler OD, Cavenee WK, eds. *The 2007 WHO Classification of Tumours of the Central Nervous System*. 4th ed. Lyon, France: International Agency for Research on Cancer; 2007:22–24.
5. Lopes MBS, Wiestler OD, Stemmer-Rachamimov AO, Sharma MC. Tuberous sclerosis complex and subependymal giant cell astrocytoma. In: Louis DN, Ohgaki H, Wiestler OD, Cavenee WK, eds. *The 2007 WHO Classification of Tumours of the Central Nervous System*. 4th ed. Lyon, France: International Agency for Research on Cancer; 2007:218–221.
6. Scheithauer BW, Hawkins C, Tihan T, VandenBerg SR, Burger PC. Pilocytic astrocytoma. In: Louis DN, Ohgaki H, Wiestler OD, Cavenee WK, eds. *The 2007 WHO Classification of Tumours of the Central Nervous System*. 4th ed. Lyon, France: International Agency for Research on Cancer; 2007:14–21.
7. Von Deimling A, Burger PC, Nakazato Y, Ohgakia H, Kleihues P. Diffuse astrocytoma. In: Louis DN, Ohgaki H, Wiestler OD, Cavenee WK, eds. *The 2007 WHO Classification of Tumours of the Central Nervous System*. 4th ed. Lyon, France: International Agency for Research on Cancer; 2007:25–29.
8. Rivera-Zengotita M, Yachnis AT. Gliosis versus glioma?: don't grade until you know. *Adv Anat Pathol*. 2012;19(4):239–249.
9. Bourne TD, Schiff D. Update on molecular findings, management and outcome in low-grade gliomas. *Nat Rev Neurol*. 2010;6(12):695–701.
10. Chamberlain MC, Murovic JA, Levin VA. Absence of contrast enhancement on CT brain scans of patients with supratentorial malignant gliomas. *Neurology*. 1988;38(9):1371–1374.
11. Castillo M, Smith JK, Kwock L. Correlation of myo-inositol levels and grading of cerebral astrocytomas. *AJNR Am J Neuroradiol*. 2000;21(9):1645–1649.
12. Sanders WP, Christoforidis GA. Imaging of low grade primary brain tumors. In: Rock JP, ed. *The Practical Management of Low-Grade Primary Brain Tumors*. Philadelphia: Lippincott Williams & Wilkins; 1999:5–32.

13. Castillo M, Kwock L. Proton MR spectroscopy of common brain tumors. *Neuroimaging Clin N Am*. 1998;8(4):733–752.
14. Gupta RK, Sinha U, Cloughesy TF, Alger JR. Inverse correlation between choline magnetic resonance spectroscopy signal intensity and the apparent diffusion coefficient in human glioma. *Magn Reson Med*. 1999;41(1):2–7.
15. Ott D, Hennig J, Ernst T. Human brain tumors: assessment with in vivo proton MR spectroscopy. *Radiology*. 1993;186(3):745–752.
16. Pomper MG, Port JD. New techniques in MR imaging of brain tumors. *Magn Reson Imaging Clin N Am*. 2000;8(4):691–713.
17. Shimizu H, Kumabe T, Shirane R, Yoshimoto T. Correlation between choline level measured by proton MR spectroscopy and Ki-67 labeling index in gliomas. *AJNR Am J Neuroradiol*. 2000;21(4):659–665.
18. Fulham MJ, Bizzi A, Dietz MJ, et al. Mapping of brain tumor metabolites with proton MR spectroscopic imaging: clinical relevance. *Radiology*. 1992;185(3):675–686.
19. Gotsis ED, Fountas K, Kapsalaki E, Toulas P, Peristeris G, Papadakis N. In vivo proton MR spectroscopy: the diagnostic possibilities of lipid resonances in brain tumors. *Anticancer Res*. 1996;16(3B):1565–1567.
20. Hwang JH, Egnaczyk GF, Ballard E, Dunn RS, Holland SK, Ball WS. Proton MR spectroscopic characteristics of pediatric pilocytic astrocytomas. *AJNR Am J Neuroradiol*. 1998;19(3):535–540.
21. Chernov MF, Kasuya H, Nakaya K, et al. (1)H-MRS of intracranial meningiomas: what it can add to known clinical and MRI predictors of the histopathological and biological characteristics of the tumor? *Clin Neurol Neurosurg*. 2011;113(3):202–212.
22. Abdullah ND, Mathews VP. Contrast issues in brain tumor imaging. *Neuroimaging Clin N Am*. 1999;9(4):733–749.
23. Knopp MV, Runge VM, Essig M, et al. Primary and secondary brain tumors at MR imaging: bicentric intraindividual crossover comparison of gadobenate dimeglumine and gadopentetate dimeglumine. *Radiology*. 2004;230(1):55–64.
24. Trattnig S, Ba-Ssalamah A, Noebauer-Huhmann IM, et al. MR contrast agent at high-field MRI (3 Tesla). *Top Magn Reson Imaging*. 2003;14(5):365–375.
25. Yuh WT, Fisher DJ, Engelken JD, et al. MR evaluation of CNS tumors: dose comparison study with gadopentetate dimeglumine and gadoteridol. *Radiology*. 1991;180(2):485–491.
26. Thompson EM, Dosa E, Kraemer DF, Neuwelt EA. Correlation of MRI sequences to assess progressive glioblastoma multiforme treated with bevacizumab. *J Neurooncol*. 2011;103(2):353–360.
27. Siauve N, Clement O. Utility of MRI contrast agents for diagnosis and treatment follow-up in cancer. *Bulletin du Cancer*. 2007;94(2):139–146.
28. Pichler J, Pachinger C, Pelz M, Kleiser R. MRI assessment of relapsed glioblastoma during treatment with bevacizumab: volumetric measurement of enhanced and FLAIR lesions for evaluation of response and progression–a pilot study. *Eur J Radiol*. 2013;82(5):e240–245.
29. Mathews MS, Linskey ME, Hasso AN, Fruehauf JP. The effect of bevacizumab (Avastin) on neuroimaging of brain metastases. *Surg Neurol*. 2008;70(6):649–652; discussion 653.
30. Ambady P, Bettegowda C, Holdhoff M. Emerging methods for disease monitoring in malignant gliomas. *CNS Oncol*. 2013; 2(6):511–522.
31. Barker FG, Chang SM, Huhn SL, et al. Age and the risk of anaplasia in magnetic resonance-nonenhancing supratentorial cerebral tumors. *Cancer*. 1997;80(5):936–941.
32. Scott JN, Brasher PM, Sevick RJ, Rewcastle NB, Forsyth PA. How often are nonenhancing supratentorial gliomas malignant? A population study. *Neurology*. 2002;59(6):947–949.
33. Kotys MS, Akbudak E, Markham J, Conturo TE. Precision, signal-to-noise ratio, and dose optimization of magnitude and phase arterial input functions in dynamic susceptibility contrast MRI. *J Magn Reson Imaging*. 2007;25(3):598–611.
34. Aronen HJ, Gazit IE, Louis DN, et al. Cerebral blood volume maps of gliomas: comparison with tumor grade and histologic findings. *Radiology*. 1994;191(1):41–51.
35. Lev MH, Rosen BR. Clinical applications of intracranial perfusion MR imaging. *Neuroimaging Clin N Am*. 1999;9(2):309–331.
36. Maia AC, Malheiros SM, da Rocha AJ, et al. MR cerebral blood volume maps correlated with vascular endothelial growth factor expression and tumor grade in nonenhancing gliomas. *AJNR Am J Neuroradiol*. 2005;26(4):777–783.
37. Law M, Oh S, Johnson G, et al. Perfusion magnetic resonance imaging predicts patient outcome as an adjunct to histopathology: a second reference standard in the surgical and nonsurgical treatment of low-grade gliomas. *Neurosurgery*. 2006;58(6):1099–1107; discussion 1099–1107.
38. Dvorak HF, Brown LF, Detmar M, Dvorak AM. Vascular permeability factor/vascular endothelial growth factor, microvascular hyperpermeability, and angiogenesis. *Am J Pathol*. 1995;146(5):1029–1039.
39. Provenzale JM, Wang GR, Brenner T, Petrella JR, Sorensen AG. Comparison of permeability in high-grade and low-grade brain tumors using dynamic susceptibility contrast MR imaging. *AJR Am J Roentgenol*. 2002;178(3):711–716.
40. Bastin ME, Carpenter TK, Armitage PA, Sinha S, Wardlaw JM, Whittle IR. Effects of dexamethasone on cerebral perfusion and water diffusion in patients with high-grade glioma. *AJNR Am J Neuroradiol*. 2006;27(2):402–408.
41. Moritani T. *Diffusion-weighted mr imaging of the brain*. 2nd ed. New York: Springer; 2009.
42. Talos IF, Zou KH, Kikinis R, Jolesz FA. Volumetric assessment of tumor infiltration of adjacent white matter based on anatomic MRI and diffusion tensor tractography. *Acad Radiol*. 2007;14(4):431–436.
43. Provenzale JM, McGraw P, Mhatre P, Guo AC, Delong D. Peritumoral brain regions in gliomas and meningiomas: investigation with isotropic diffusion-weighted MR imaging and diffusion-tensor MR imaging. *Radiology*. 2004;232(2):451–460.
44. Goebell E, Paustenbach S, Vaeterlein O, et al. Low-grade and anaplastic gliomas: differences in architecture evaluated with diffusion-tensor MR imaging. *Radiology*. 2006;239(1):217–222.
45. Kracht LW, Jacobs AH, Heiss WD. Metabolic imaging. In: Bernstein MM, Berger MS, eds. *Neuro-oncology: the Essentials*. 2nd ed. New York: Thieme; 2008.
46. Cai W, Chen K, Mohamedali KA, et al. PET of vascular endothelial growth factor receptor expression. *J Nucl Med*. 2006; 47(12):2048–2056.
47. Hustinx R, Alavi A. SPECT and PET imaging of brain tumors. *Neuroimaging Clin N Am*. 1999;9(4):751–766.
48. Schwartz RB, Carvalho PA, Alexander E, Loeffler JS, Folkerth R, Holman BL. Radiation necrosis vs high-grade recurrent glioma: differentiation by using dual-isotope SPECT with 201TI and ^{99m}Tc-HMPAO. *AJNR Am J Neuroradiol*. 1991;12(6):1187–1192.
49. Pollack IF, Hamilton RL, Finkelstein SD, Lieberman F. Molecular abnormalities and correlations with tumor response and outcome in glioma patients. *Neuroimaging Clin N Am*. 2002;12(4):627–639.
50. Babu R, Bagley JH, Park JG, Friedman AH, Adamson C. Low-grade astrocytomas: the prognostic value of fibrillary, gemistocytic, and protoplasmic tumor histology. *J Neurosurg*. 2013;119(2):434–441.
51. Ternier J, Wray A, Puget S, Bodaert N, Zerah M, Sainte-Rose C. Tectal plate lesions in children. *J Neurosurg*. 2006;104(6 suppl): 369–376.
52. Holland BA, Brant-Zawadzki M, Norman D, Newton TH. Magnetic resonance imaging of primary intracranial tumors: a review. *Int J Radiat Oncol Biol Phys*. 1985;11(2):315–321.
53. McGinnis BD, Brady TJ, New PF, et al. Nuclear magnetic resonance (NMR) imaging of tumors in the posterior fossa. *J Comp Assist Tomogr*. 1983;7(4):575–584.

54. Grafin von Einsiedel H, Loffler W. Nuclear magnetic resonance imaging of brain tumors unrevealed by CT. *Eur J Radiol*. 1982;2(3):226–234.
55. Earnest F, Kelly PJ, Scheithauer BW, et al. Cerebral astrocytomas: histopathologic correlation of MR and CT contrast enhancement with stereotactic biopsy. *Radiology*. 1988;166(3):823–827.
56. Greene GM, Hitchon PW, Schelper RL, Yuh W, Dyste GN. Diagnostic yield in CT-guided stereotactic biopsy of gliomas. *J Neurosurg*. 1989;71(4):494–497.
57. Kelly PJ, Daumas-Duport C, Kispert DB, Kall BA, Scheithauer BW, Illig JJ. Imaging-based stereotaxic serial biopsies in untreated intracranial glial neoplasms. *J Neurosurg*. 1987;66(6):865–874.
58. Swanson KR, Alvord EC, Murray JD. A quantitative model for differential motility of gliomas in grey and white matter. *Cell Prolif*. 2000;33(5):317–329.
59. Pallud J, Capelle L, Taillandier L, et al. Prognostic significance of imaging contrast enhancement for WHO grade II gliomas. *Neuro Oncology*. 2009;11(2):176–182.
60. Jayaraman MV, Boxerman JL. Adult brain tumors. In: Atlas SW, ed. *Magnetic Resonance Imaging of the Brain and spine*. Vol. 1. Philadelphia, PA: Lippincott Williams and Wilkins; 2009:445–590.
61. Holland BA, Kucharczyk W, Brant-Zawadzki M, Norman D, Haas DK, Harper PS. MR imaging of calcified intracranial lesions. *Radiology*. 1985;157(2):353–356.
62. Mariani L, Siegenthaler P, Guzman R, et al. The impact of tumour volume and surgery on the outcome of adults with supratentorial WHO grade II astrocytomas and oligoastrocytomas. *Acta Neurochir (Wien)*. 2004;146(5):441–448.
63. Spampinato MV, Schiarelli C, Cianfoni A, et al. Correlation between cerebral blood volume measurements by perfusion-weighted magnetic resonance imaging and two-year progression-free survival in gliomas. *Neuroradiol J*. 2013;26(4):385–395.
64. Law M, Oh S, Babb JS, et al. Low-grade gliomas: dynamic susceptibility-weighted contrast-enhanced perfusion MR imaging–prediction of patient clinical response. *Radiology*. 2006;238(2): 658–667.
65. Bisdas S, Kirkpatrick M, Giglio P, Welsh C, Spampinato MV, Rumboldt Z. Cerebral blood volume measurements by perfusion-weighted MR imaging in gliomas: ready for prime time in predicting short-term outcome and recurrent disease? *AJNR Am J Neuroradiol*. 2009;30(4):681–688.
66. Fuss M, Wenz F, Essig M, et al. Tumor angiogenesis of low-grade astrocytomas measured by dynamic susceptibility contrast-enhanced MRI (DSC-MRI) is predictive of local tumor control after radiation therapy. *Int J Radiat Oncol Biol Phys*. 2001;51(2): 478–482.
67. Raffel C. Molecular biology of pediatric gliomas. *J Neurooncol*. 1996;28(2–3):121–128.
68. Guitierrez JA. Classification and pathobiology of low-grade glial and glioneuronal neoplasms. In: Rock JP, ed. *The practical management of low-grade primary brain tumors*. Philadelphia: Lippincott Williams & Wilkins; 1999:33–67.
69. Bian SX, McAleer MF, Vats TS, Mahajan A, Grosshans DR. Pilocytic astrocytoma with leptomeningeal dissemination. *Childs Nerv Syst*. 2013;29(3):441–450.
70. Arai K, Sato N, Aoki J, et al. MR signal of the solid portion of pilocytic astrocytoma on T2-weighted images: is it useful for differentiation from medulloblastoma? *Neuroradiology*. 2006;48(4):233–237.
71. Coakley KJ, Huston J, Scheithauer BW, Forbes G, Kelly PJ. Pilocytic astrocytomas: well-demarcated magnetic resonance appearance despite frequent infiltration histologically. *Mayo Clin Proc*. 1995;70(8):747–751.
72. Lee YY, Van Tassel P, Bruner JM, Moser RP, Share JC. Juvenile pilocytic astrocytomas: CT and MR characteristics. *AJR Am J Roentgenol*. 1989;152(6):1263–1270.
73. Bhargava D, Sinha P, Chumas P, et al. Occurrence and distribution of pilomyxoid astrocytoma. *Br J Neurosurg*. 2013;27(4):413–418.
74. Komotar RJ, Mocco J, Zacharia BE, et al. Astrocytoma with pilomyxoid features presenting in an adult. *Neuropathology*. 2006; 26(1):89–93.
75. Cirak B, Horská A, Barker PB, Burger PC, Carson BS, Avellino AM. Proton magnetic resonance spectroscopic imaging in pediatric pilomyxoid astrocytoma. *Childs Nerv Syst*. 2005;21(5):404–409.
76. Tihan T, Fisher PG, Kepner JL, et al. Pediatric astrocytomas with monomorphous pilomyxoid features and a less favorable outcome. *J Neuropathol Exp Neurol*. 1999;58(10):1061–1068.
77. Weldon-Linne CM, Victor TA, Groothuis DR, Vick NA. Pleomorphic xanthoastrocytoma. Ultrastructural and immunohistochemical study of a case with a rapidly fatal outcome following surgery. *Cancer*. 1983;52(11):2055–2063.
78. Zülch KJ. *Brain Tumors Their Biology and Pathology*. Third Completely Revised ed. Berlin, Heidelberg: Springer; 1986. Berlin Heidelberg.
79. Daumas-Duport C, Scheithauer B, O'Fallon J, Kelly P. Grading of astrocytomas. A simple and reproducible method. *Cancer*. 1988;62(10):2152–2165.
80. Rippe DJ, Boyko OB, Radi M, Worth R, Fuller GN. MRI of temporal lobe pleomorphic xanthoastrocytoma. *J Comp Assist Tomogr*. 1992;16(6):856–859.
81. Yoshino MT, Lucio R. Pleomorphic xanthoastrocytoma. *AJNR Am J Neuroradiol*. 1992;13(5):1330–1332.
82. Petropoulou K, Whiteman ML, Altman NR, Bruce J, Morrison G. CT and MRI of pleomorphic xanthoastrocytoma: unusual biologic behavior. *J Comp Assist Tomogr*. 1995;19(6):860–865.
83. Altman NR, Purser RK, Post MJ. Tuberous sclerosis: characteristics at CT and MR imaging. *Radiology*. 1988;167(2):527–532.
84. Hahn JS, Bejar R, Gladson CL. Neonatal subependymal giant cell astrocytoma associated with tuberous sclerosis: MRI, CT, and ultrasound correlation. *Neurology*. 1991;41(1):124–128.
85. Jelinek J, Smirniotopoulos JG, Parisi JE, Kanzer M. Lateral ventricular neoplasms of the brain: differential diagnosis based on clinical, CT, and MR findings. *AJNR Am J Neuroradiol*. 1990;11(3):567–574.
86. Jeong MG, Chung TS, Coe CJ, Jeon TJ, Kim DI, Joo AY. Application of magnetization transfer imaging for intracranial lesions of tuberous sclerosis. *J Comp Assist Tomogr*. 1997;21(1):8–14.
87. Nabbout R, Santos M, Rolland Y, Delalande O, Dulac O, Chiron C. Early diagnosis of subependymal giant cell astrocytoma in children with tuberous sclerosis. *J Neurol Neurosurg Psychiatry*. 1999;66(3):370–375.
88. Turgut M, Akalan N, Ozgen T, Ruacan S, Erbengi A. Subependymal giant cell astrocytoma associated with tuberous sclerosis: diagnostic and surgical characteristics of five cases with unusual features. *Clin Neurol Neurosurg*. 1996;98(3):217–221.
89. Clarke MJ, Foy AB, Wetjen N, Raffel C. Imaging characteristics and growth of subependymal giant cell astrocytomas. *Neurosurg Focus*. 2006;20(1):E5.
90. de Ribaupierre S, Dorfmuller G, Bulteau C, et al. Subependymal giant-cell astrocytomas in pediatric tuberous sclerosis disease: when should we operate? *Neurosurgery*. 2007;60(1):83–89; discussion 89–90.
91. Fuller GN, Kros JM. Gliomatosis cerebri. In: Louis DN, Ohgaki H, Wiestler OD, Cavenee WK, eds. *The 2007 WHO Classification of Tumours of the Central Nervous System*. 4th ed. Lyon, France: International Agency for Research on Cancer; 2007:50–52.
92. Di Ieva A, Gaetani P, Giannini M, et al. Oligodendroglial gliomatosis cerebri. Case report. *J Neurosurg Sci*. 2006;50(4):123–125.
93. del Carpio-O'Donovan R, Korah I, Salazar A, Melancon D. Gliomatosis cerebri. *Radiology*. 1996;198(3):831–835.
94. Desclée P, Rommel D, Hernalsteen D, Godfraind C, de Coene B, Cosnard G. Gliomatosis cerebri, imaging findings of 12 cases. *J Neuroradiol*. 2010;37(3):148–158.

95. Park S, Suh YL, Nam DH, Kim ST. Gliomatosis cerebri: clinicopathologic study of 33 cases and comparison of mass forming and diffuse types. *Clin Neuropathol*. 2009;28(2):73–82.
96. Shin YM, Chang KH, Han MH, et al. Gliomatosis cerebri: comparison of MR and CT features. *AJR Am J Roentgenol*. 1993;161(4):859–862.
97. Taillibert S, Chodkiewicz C, Laigle-Donadey F, Napolitano M, Cartalat-Carel S, Sanson M. Gliomatosis cerebri: a review of 296 cases from the ANOCEF database and the literature. *J Neurooncol*. 2006;76(2):201–205.
98. Sun LM, Lui CC, Huang SC, Lu K, Wang CJ. Diagnosis and results of treatment with radiation therapy in gliomatosis cerebri patient: case report. *Chang Gung Med J*. 2001;24(3):196–201.
99. Perkins GH, Schomer DF, Fuller GN, Allen PK, Maor MH. Gliomatosis cerebri: improved outcome with radiotherapy. *Int J Radiat Oncol Biol Phys*. 2003;56(4):1137–1146.
100. Kim DG, Yang HJ, Park IA, et al. Gliomatosis cerebri: clinical features, treatment, and prognosis. *Acta Neurochir (Wien)*. 1998;140(8):755–762.

CHAPTER

40

Imaging of Oligodendrogliomas

William Ankenbrandt[1], *Nina Paleologos*[2]

[1]Department of Radiology, North Shore University Health System, The University of Chicago Pritzker School of Medicine, Chicago, IL, USA; [2]Rush Medical College, Rush University, Chicago, IL, USA

INTRODUCTION

The role of clinical imaging of brain tumors is to provide sufficient data for diagnosis and appropriate care of the patient. After initial tumor detection, additional imaging techniques may help in narrowing the differential diagnosis, biopsy or resection planning, judging prognosis, radiation therapy (RT) planning, and disease assessment over time. We review standard computed tomography (CT) and magnetic resonance imaging (MRI) of the brain useful in the evaluation of oligodendrogliomas and review what is known about the characteristics of oligodendrogliomas on positron-emission tomography (PET) and physiologic MR methods of imaging, such as MR spectroscopy (MRS) and two types of perfusion imaging—dynamic susceptibility-weighted contrast-enhanced (DSC) and dynamic contrast-enhanced (DCE) MRI.

CHARACTERISTICS OF OLIGODENDROGLIOMAS ON ROUTINE COMPUTED TOMOGRAPHY AND MAGNETIC RESONANCE IMAGES

In most cases, standard neuroimaging with either CT or MRI allows primary brain tumors to be distinguished from other intra-axial lesions, such as cerebritis, abscess, infarct, and vascular malformation. Specific cellular histopathology may be suspected owing to imaging characteristics; however, it is not specifically distinguishable by neuroimaging. Astrocytomas and oligodendrogliomas, in particular, cannot be differentiated from one another based on imaging alone. However, there are some characteristics on routine imaging that may favor oligodendroglioma over astrocytoma. These include predominance of cortical involvement, presence of calcification on CT, heterogeneous attenuation/signal including in some cases presence of intratumoral cysts, and presence of subtle, patchy, or "lacy" enhancement.[1] See Figures 1–3 for variable appearances of grade II oligodendrogliomas and Figures 4 and 5 for two different-appearing images showing what proved to be grade III (anaplastic) oligodendrogliomas. MRI is better than CT at demonstrating enhancement in malignant brain tumors.[2] Contrast enhancement and endothelial hyperplasia have been shown to negatively correlate with survival in "classical" oligodendrogliomas.[3]

On CT, low-grade oligodendrogliomas typically appear as nonenhancing low-density masses. High-grade or anaplastic tumors may enhance to a variable degree. Calcification is found microscopically in 90% of oligodendrogliomas.[4] Calcifications may also be seen on CT and, when detectable, are often coarse (see Figures 1(B) and 4(A)). Calcification is not specific to oligodendroglioma, but is quite common. The reported prevalence of calcification detected on CT varies widely but is at least 20%.[5,6]

MRI is superior to CT in delineating these tumors, which appear as a regional area of increased signal on T2-weighted and fluid-attenuated inversion recovery (FLAIR) images. They frequently involve the cortex, which probably explains the high incidence of seizures in these patients. They may be large at the time of presentation. Oligodendrogliomas are frequently heterogeneous on T1-weighted images, and cysts and areas of hemorrhage may be present. Low-grade tumors characteristically do not show enhancement. High-grade or anaplastic tumors commonly, but not always, have areas of blood–brain barrier breakdown manifesting as contrast enhancement.[2] Assessment of tumor grade by stereotactic biopsy or from tissue obtained at subtotal resection is prone to sampling error because oligodendrogliomas, especially large ones, contain regions of

Handbook of Neuro-Oncology Neuroimaging, Second Edition
http://dx.doi.org/10.1016/B978-0-12-800945-1.00040-9

© 2016 Elsevier Ltd. All rights reserved.

variable histology. A small area of enhancement in part of a large predominantly nonenhancing tumor probably represents higher grade pathology in that area. Histology obtained from nonenhancing areas of the same partially enhancing tumor may be of lower grade, thus resulting in "sampling error" or undergrading of the tumor histologically. The absence of contrast enhancement does not rule out high-grade histology. White and colleagues, in a study of conventional MRI features of oligodendroglioma, found that the presence of contrast enhancement had a sensitivity of only 63% and a specificity of 50% in differentiating anaplastic from low-grade tumors.[7]

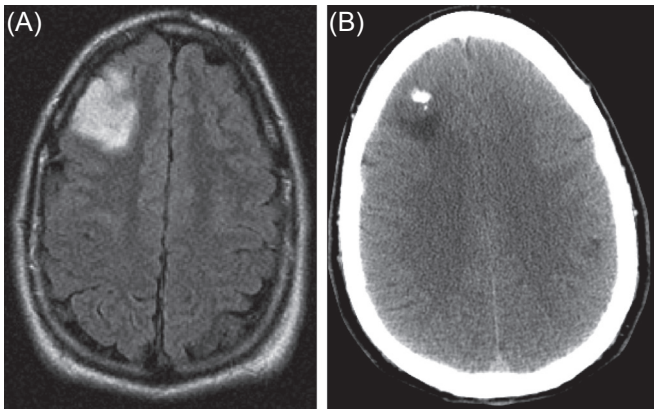


FIGURE 1 (A and B) WHO grade II oligodendroglioma. The lesion is a small frontal cortically based tumor with high signal on FLAIR (A). Note coarse calcification within the lesion on CT (B). The lesion did not enhance with gadolinium.

DIFFUSION-WEIGHTED IMAGING

Typically part of a routine MR examination of the brain, diffusion-weighted imaging (DWI) is classically thought of as a stroke-imaging tool, but is helpful in tumor imaging as well. The physical assumption behind the technique is that water in tissue is constantly in motion, flowing from intracellular to extracellular space and from one volume box of imaging data (voxel) to another. Energy, in the form of rapid magnetic-field gradient changes, is applied to hydrogen atoms of water, which precess or "spin." Hydrogen atoms in water molecules free to move within a gradient field will have random phase. They will lose phase coherence, and the

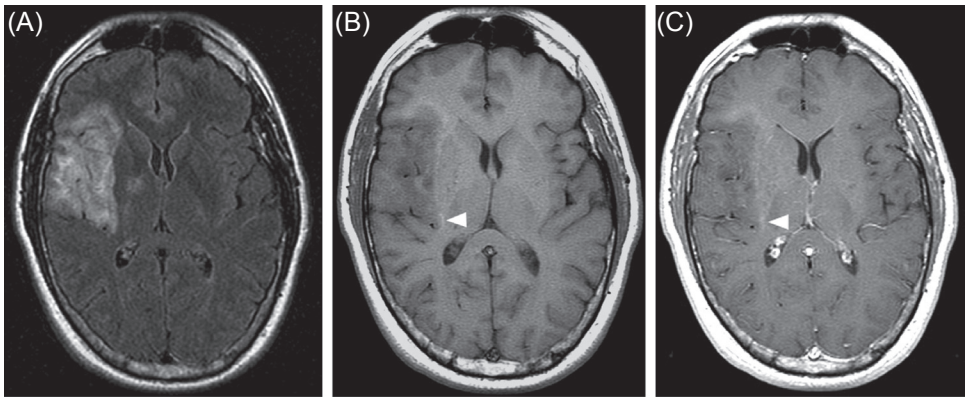


FIGURE 2 (A–C) WHO grade II oligodendroglioma. This right insular/subinsular tumor has little heterogeneity, the sort of mass that could be misinterpreted as an infarct. Some infarcts in this location are misinterpreted as tumor. Note cortical predominance of the lesion. There are areas of subtle T1 shortening at the margin of the tumor, but careful comparison between pre- and post-gadolinium T1-weighted images shows no enhancement separable from baseline increased T1 signal (B and C, arrowheads).

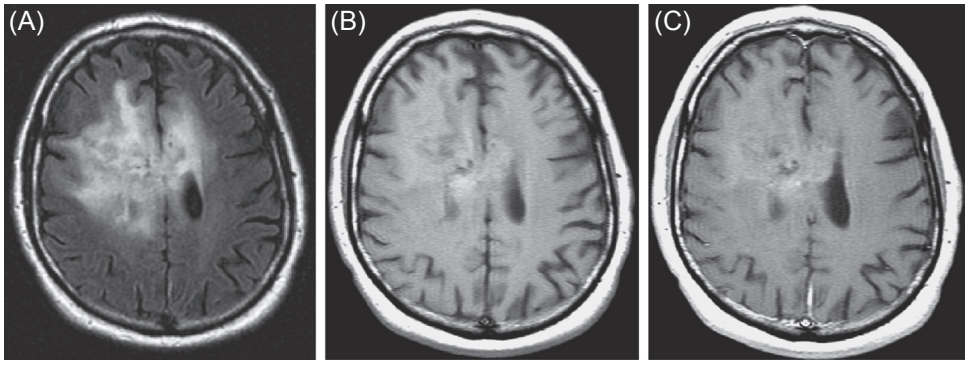


FIGURE 3 (A–C) WHO grade II oligodendroglioma. This lesion is markedly heterogeneous and presented at very large size. At presentation it had already crossed the body of the corpus callosum. There is no demonstrable enhancement separable from baseline T1 shortening (B and C).

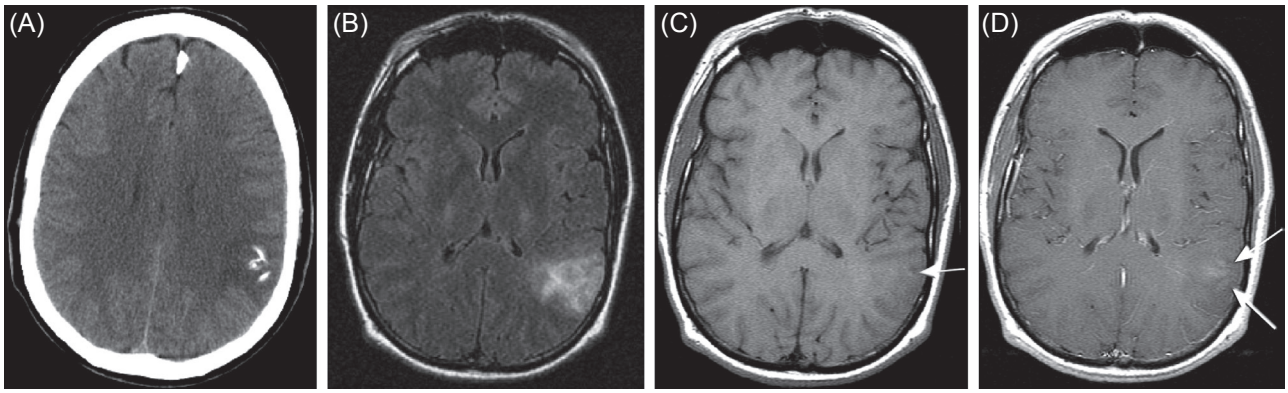


FIGURE 4 (A–D) Anaplastic (WHO grade III) oligodendroglioma. CT shows coarse calcification within the lesion (A). Note the lack of heterogeneity and minimal enhancement. By carefully comparing pre- and post-gadolinium images it can be established that there is faint enhancement (C and D, arrows). Interestingly, both this tumor and the much more "aggressive"-appearing tumor in Figure 5 were found to have chromosome 1p and 19q deletions, predicting favorable response to therapy.

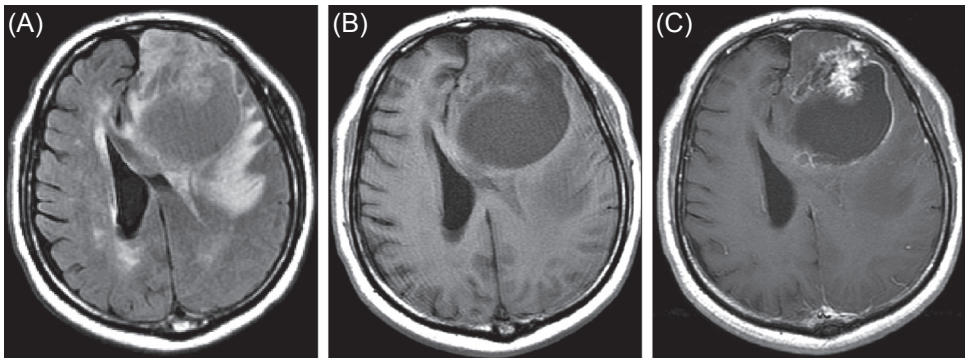


FIGURE 5 (A–C) Anaplastic (WHO grade III) oligodendroglioma. Partially cystic, partially solid, heterogeneous mass with prominent gadolinium enhancement (C). There is marked edema (A) and mass effect, with subfalcine herniation. Chromosome 1p and 19q deletions were confirmed, just as in the more "benign"-appearing anaplastic oligodendroglioma in Figure 4.

resultant image will lose signal intensity. Water trapped, or whose free diffusion is "restricted," will have hydrogen atoms spinning in greater phase coherence with one another, with resultant greater signal intensity.[8,9]

Restricted diffusion, with a low apparent diffusion coefficient (ADC), in the postoperative setting adjacent to a resection cavity may indicate postoperative infarct, and this is very helpful to recognize, since the infarcted brain will enhance with gadolinium in the subacute phase, beginning about a week after the operation and sometimes persisting for a month or more, which may complicate interpretation of follow-up scans since it could be confused with recurrent, enhancing tumor (see Figure 6).

Low ADC within a tumor has been correlated with increased tumor cellularity and higher grade neoplasia.[10] Other processes, such as abscess following biopsy, or intratumoral infarction, can also have restricted diffusion. Restricted diffusion related to infarction typically reverses within about 5 days, so short-interval follow-up MRI may be helpful. Persistently low ADC in part of a tumor probably indicates higher cellularity within that part. Low ADC has been found to correlate with elevated choline (Cho) on MRS of gliomas.[11]

MAGNETIC RESONANCE SPECTROSCOPY

Malignancy is characterized by accelerated cell division (high "mitotic index"), which is detectable on proton (^{1}H) MRS (hereinafter "MRS") as elevated Cho. Cho elevation occurs when there is rapid cell membrane synthesis. The N–CH_3 group of Cho, the first major peak from the left on MRS, has a resonance at 3.2 ppm. This is positioned immediately to the left of creatine (Cr), which has a peak at 3.0 ppm. *N*-Acetylaspartate (NAA) is the third major peak from the left, with a resonance at 2.0 ppm. These three peaks represent the most common metabolites evaluated, with Cr typically used as the putative reference, since it changes little with most disease processes. NAA, a marker of intact neurons, will be depressed in many disease processes, including in some oligodendrogliomas and other primary brain tumors.

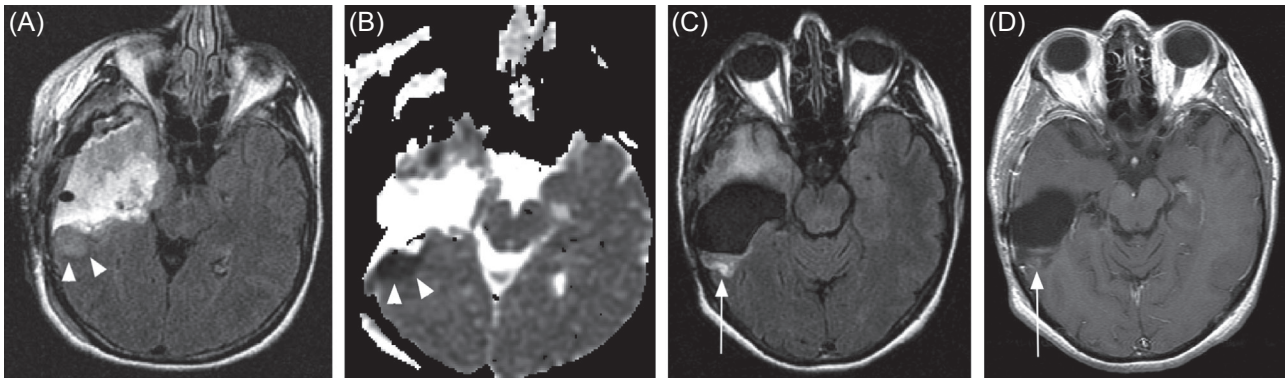


FIGURE 6 (A–D) Postoperative day 1 status after resection of right temporal oligodendroglioma. There is very subtle increased signal posterior to the right temporal surgical resection cavity on FLAIR images, with corresponding low signal on ADC maps indicating restricted diffusion and acute ischemia (A and B, arrowheads). Follow-up MRI shows a more distinct, focal area of increased signal on FLAIR (C, arrow), with focal enhancement (D, arrow). Because DWI was performed on the immediate postoperative scan, it can be confidently predicted that the enhancement that subsequently developed in the location where there was restricted diffusion represents blood–brain barrier breakdown secondary to infarction and *not* recurrent tumor.

Long TE multivoxel MRS may be used to evaluate the three principal metabolites (Cho, Cr, NAA) in each box of a grid placed over a larger part of the tumor and usually including also a portion of presumably normal brain. Long TE single-voxel MRS in abnormal brain is compared to an area or areas of brain with normal-appearing signal intensity. 3-T MRS may be preferable because of higher signal-to-noise ratio (SNR); however, 1.5-T scanners are more readily available for clinical scanning. The SNR is acceptable on a 1.5-T magnet, especially if a phased array head coil is used.[12]

MRS as an initial diagnostic tool for oligodendrogliomas can be misleading if considered in isolation from other imaging findings, since low-grade gliomas may have only modest depression of NAA and little or no demonstrable elevation of Cho (see Figure 7). The finding of faint or lacy enhancement in a heterogeneous, cortically based primary tumor with less than 2/1 elevation of the Cho/Cr ratio may favor an oligodendroglioma. A Cho/Cr ratio of greater than 2/1 is suggestive of high-grade neoplasm, as is a Cho/NAA ratio greater than 0.8.[13]

One MRS finding that may help distinguish oligodendroglioma from astrocytoma preoperatively is myoinositol (MI), an astroglial marker that is particularly elevated in low-grade astrocytomas.[14] A caveat is that glycine (resonance 3.4–3.7 ppm) overlaps the MI peak, has been found in high-grade primary tumors, and has been demonstrated to be elevated on MRS in a rare case of oligodendroglial gliomatosis cerebri.[15] Glycine elevation has been also reported in astrocytoma.[16] The glutamine plus glutamate peak may be higher in oligodendrogliomas than in astrocytomas, and one of the resonances is immediately adjacent to MI, further muddying the waters. Elevation of MI is also found in multiple sclerosis plaques, human immunodeficiency virus infection, and metachromatic leukodystrophy, and it is normally much higher in infants than in adults.[17] Absence of MI elevation in a suspected low-grade glioma may favor oligodendroglioma. MI and other "minor metabolites" are best detected using a low TE. This could be done as an additional sequence after the standard high TE sequence, if time permits.

An elevated lipid–lactate combined peak suggests higher grade oligodendroglioma, but the combined peak is also elevated in infections.[18]

MRS is perhaps most helpful in following oligodendrogliomas and other primary gliomas that have been treated. After surgery, with or without RT, there is often a margin of increased T2 signal intensity (T2 prolongation) adjacent to the resection cavity. If routine follow-up MRI shows growth of the area of abnormal signal, MRS can be used to attempt to distinguish incidental postoperative gliosis or signal changes related to RT from those changes related to tumor progression. Sometimes, however, MRS is nondiagnostic owing to the proximity of the cavity and magnetic field heterogeneity caused by blood degradation products and other contents of the cavity.

MAGNETIC RESONANCE PERFUSION AND PERMEABILITY IMAGING

Dynamic Susceptibility-Weighted Contrast-Enhanced Perfusion Imaging

High-grade oligodendrogliomas, as well as many low-grade oligodendrogliomas, have elevated relative cerebral blood volume (rCBV) compared to normal white matter (see Figure 8). The conclusion that high-grade tumors can be distinguished from low-grade tumors based on elevated rCBV may not be true for oligodendrogliomas, but nonetheless DSC imaging may be helpful

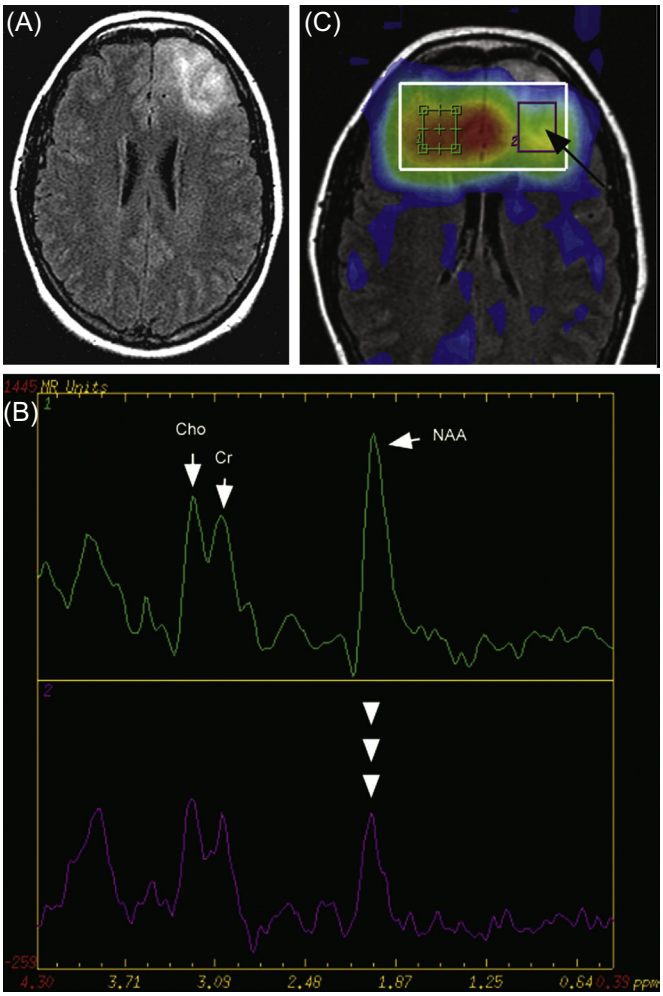


FIGURE 7 (A–C) Grade II mixed glioma (oligoastrocytoma). Many low-grade tumors will not show significant elevation of Cho on ^{1}H MRS. This left frontal infiltrating tumor shows moderate depression of NAA as the only abnormality of the three major peaks (B, arrowheads). (C) A spectroscopic image map showing distribution of NAA within the sampled area. Note decrease in NAA levels (in this image, higher concentrations are red, lower are blue or green; the arrow points to a predominantly blue and green region in the left frontal lobe) approximately corresponding to the area of increased signal on FLAIR (A).

to distinguish tumor from other etiologies and to distinguish recurrent tumor from radiation necrosis.[19] Herpes encephalitis and toxoplasmosis tend to have low rCBV; most infarcts have low rCBV; bacterial abscesses are variable; and tumefactive demyelination has slightly lower rCBV than high-grade tumor, with presence of vessels running through the lesion on the echoplanar (EP) source images possibly favoring demyelination over tumor.[20]

rCBV is approximated as the area under the time–intensity curve in a perfusion study performed with the DSC technique. Each curve represents the signal loss due to the T2* effect of concentrated gadolinium as the contrast material passes through each image slice, and each voxel, over time. Normally the curve has a steep downslope and relatively steep upslope as well. In tumors that have elevated rCBV, the peak is deeper, with a larger area under the curve representing higher rCBV. The area under the curve can be depicted for each voxel as a particular color in a scale typically progressing through a rainbow spectrum from blue to red. With a color map of rCBV for the entire slice being evaluated, it is straightforward for non-color-blind individuals to determine whether the rCBV for the area of signal abnormality in question is greater than that of adjacent presumably normal white matter.

Unfortunately, for color-blind individuals, the color scale most commonly employed includes a red–green scale. The color range provided to the interpreting radiologist is operator-dependent. Also, many standard PACS are black and white. To get around these problems, using the gray-scale diagnostic (not screen-saved) image, a region of interest (ROI) is placed over the area in question and another over presumably normal brain tissue in an analogous "mirror" location in the contralateral hemisphere and/or over presumably normal white matter.

In one study, the role of rCBV was examined in the characterization of low-grade versus high-grade oligodendroglial tumors and found no statistical difference in rCBV between the low- and the high-grade tumors.[21] Sample size in this study was small and only three anaplastic tumors were analyzed with large ROIs (measuring 20–40 mm^2), which are known to negatively affect sensitivity in the detection of focal areas of increased vascularization in anaplastic neoplasms. In another study, using smaller ROIs, rCBV was significantly different between low-grade (1.61 ± 1.20) and high-grade tumors (5.45 ± 1.96), with an optimal rCBV ratio cutoff value in identification of anaplastic tumors of 2.14.[22] The authors found that the sensitivity of rCBV in grading oligodendroglial tumors was 100%, indicating that all high-grade tumors were correctly classified, but that the specificity of rCBV measurement was 86% with a cutoff value of 2.14, indicating that a few low-grade oligodendroglial tumors may be incorrectly classified as high grade. They suggest that rCBV ratios can be used more confidently to exclude the presence of anaplasia within oligodendroglial tumors than vice versa. Whether low-grade oligodendrogliomas with high rCBV behave more aggressively than those with lower rCBV or whether those tumors are being undergraded owing to sampling error needs further investigation. In a study by Jenkins and colleagues, rCBV did not distinguish histology subtype or grade but did show that 1p19q-deleted oligodendrogliomas are more likely to have elevated rCBV.[23]

When comparing dynamic T2* signal dropout curves, the baseline of the curve will be higher in areas with increased T2 signal than in areas that have normal T2 signal. In other words, the entire curve will be shifted above the level of the comparison region, so they will

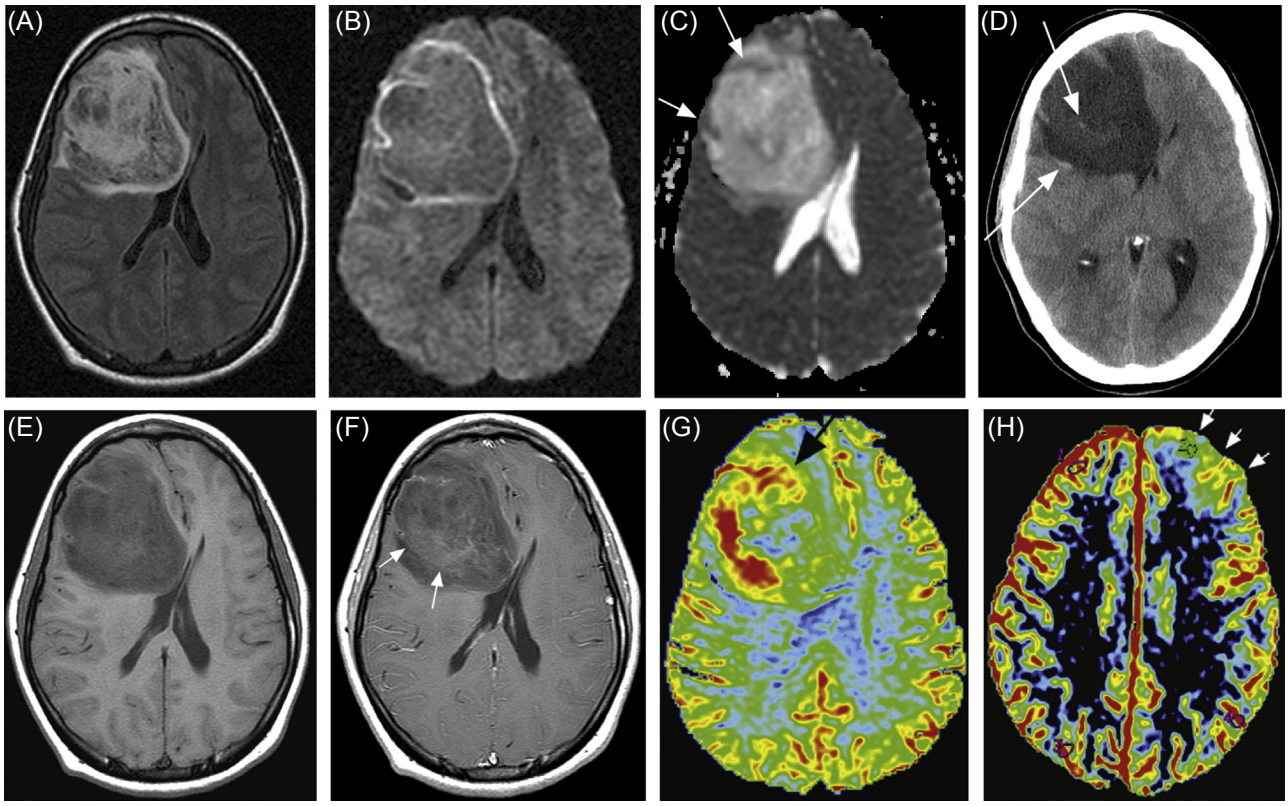


FIGURE 8 (A–E) Grade II mixed glioma (oligoastrocytoma). (A) FLAIR. (B and C) DWI, $B = 1000$, and ADC map. Areas of predominantly T2 shine-through are present at the periphery of the tumor (B). The ADC map helps determine which areas have restricted diffusion (C, arrows). (D) CT shows faint calcifications (arrows). (E and F) Pre- and post-gadolinium T1-weighted images suggest faint, patchy enhancement (F, arrows). (G) Negative enhancement integral image (approximating rCBV) shows areas of markedly increased rCBV in this low-grade tumor. Note that not all of the areas of increased blood volume correspond to areas of gadolinium enhancement (black arrow). (H) One caveat: some low-grade oligodendrogliomas and mixed gliomas have low rCBV. This is a different grade II mixed glioma and is the same tumor as in Figure 7. There is predominantly low rCBV in the region of tumor infiltration (arrows).

not be automatically superimposable. Although most oligodendrogliomas will not be confused with metastases, high-grade lesions with ring enhancement could have an appearance similar to that of solitary metastasis. Evaluation of the perfusion curve may help distinguish metastasis from primary tumor. Primary tumor is more likely to have a curve that rapidly returns to near baseline, whereas metastasis is more likely to return to less than 50% of baseline. Also, it has been shown that rCBV in the peritumoral region of primary enhancing brain tumors is higher within this region of so-called "infiltrative edema" compared to the analogous peritumor region, representing vasogenic edema surrounding a solitary metastasis.[24,25] DSC perfusion MR has also been shown to be helpful in distinguishing high-grade brain neoplasm from brain abscess.[26]

Magnetic Resonance Permeability Imaging—Dynamic Contrast-Enhanced Imaging

For trials of new therapies for oligodendroglioma, it may be helpful to attempt to quantify the degree of vascular permeability in a tumor, since it has been proposed that tumors with greater vascular permeability may have improved response to chemotherapy due to more efficient drug delivery. Permeability as measured by dynamic MR perfusion techniques may correlate with tumor grade.[27,28] DCE perfusion imaging has been proposed as a quantitative method of measuring vascular permeability by assessing a time–intensity curve after administration of contrast.[29] Unlike DSC, which relies on a first-pass T2* effect, DCE is a dynamic T1-weighted imaging method that measures the extent of contrast enhancement over time. Thus far it has been employed predominantly as a research tool. It has been shown that mapping permeability can be accomplished concurrently with DSC imaging using a single gadolinium bolus.[30]

FUNCTIONAL MAGNETIC RESONANCE IMAGING AND FRACTIONAL ANISOTROPY

Functional Magnetic Resonance Imaging

Blood oxygen level-dependent functional MRI (fMRI) of the brain is helpful in the preoperative evaluation of

tumors, especially those that are thought to encroach on measurably "eloquent" anatomic areas, such as those functional regions responsible for motor activity and for generation and comprehension of language. The technique relies on detection of very small differences in blood flow due to upregulation of flow in metabolically active functional areas. Paradoxically, there will be a measurable *increase* in blood oxygen in metabolically active areas because the upregulation of flow due to regional vasodilatation overcomes the increased oxygen extraction related to metabolic activity. Total oxygen extraction is greater in the functionally active area, but the oxygen extraction fraction is decreased. This is measurable on EP T2*-weighted imaging because deoxyhemoglobin has a strong paramagnetic effect that reduces signal by increasing spin-phase incoherence. Areas that have a higher ratio of oxyhemoglobin to deoxyhemoglobin will therefore have slightly (2–7%) higher signal intensity on T2*-weighted images.[31,32]

Because differences in signal are very small, interpretation requires postprocessing of source image maps that are created during a task (e.g., finger tapping) and at rest. Essentially the block of slices obtained during the task is compared to the block of slices at rest, and areas that have statistically significantly higher signal during the task are considered to be functionally active areas. In clinical fMRI it is helpful to have a reference of activation in grouped normal volunteers so that the patient's fMRI can be compared to the expected pattern of activation with each language and motor task.

Oligodendrogliomas are often cortically based and may infiltrate functionally active, eloquent brain areas. fMRI is most helpful for preoperative planning when complete resection is contemplated for tumors that are thought, based either on clinical data (e.g., aphasia or hemiparesis) or on routine imaging findings (e.g., tumor encroaching on or infiltrating precentral gyrus, frontal operculum, or superior or middle temporal gyrus), to involve highly eloquent brain regions.

Functional data sets are acquired with 5-mm-thick EP sections. Since the EP images have poor tissue contrast relative to standard diagnostic imaging sequences, the processed data showing color maps of areas of activation are superimposed not on the original EP images, but on a separately acquired set of images. A software is used to merge the image locations of the original functional dataset with diagnostic-quality brain images, typically FLAIR and SPGR images.

Diffusion Tensor Imaging—Fractional Anisotropy

Diffusion tensor imaging (DTI) is sometimes employed preoperatively to attempt to establish the location of important fiber tracts, such as the corticospinal tract, and to determine whether there is displacement, infiltration, or destruction of such tracts. The diffusion-weighted images displayed as part of routine MRI are "isotropic"—that is, the differences in directional water diffusivity (greater ease of diffusion along axonal tracts, for example) are essentially nullified by averaging of directional anisotropy. DTI makes use of multidirectional diffusion gradients to maximize detection of anisotropy. The goal of DTI is to discover for each voxel which way water diffuses most readily, and this has been shown, in an experimental cat model, to be along the orientation of major white matter fiber tracts.[33] A simple map of directional anisotropy (most commonly calculated as "fractional anisotropy") can approximate white matter tract configurations by displaying diffusivity along three principal axes in three colors.[34,35] Tractography can also be performed by creating an ROI in a seed location and examining tracts that emanate from that area. An ROI can be placed around a functional area of brain to see if tumor encroaches on associated tracts, or it could be placed over part of the corticospinal tract to determine whether tumor encroaches on the tract or infiltrates subcortical fibers leading to the corticospinal tract. Tractography is highly operator-dependent and time-consuming, so three-direction color maps are most commonly used in clinical practice.

POSITRON-EMISSION TOMOGRAPHY

PET gives metabolic information on tumor in vivo and is discussed in detail with regard to its usage in differentiating recurrent brain tumor from radiation injury, and in guiding stereotactic biopsy and radiation target volumes, elsewhere in this book. Oligodendrogliomas show a higher uptake on [^{11}C]methionine PET than astrocytomas, and anaplastic oligodendrogliomas have an increased uptake compared to low-grade tumors.[36,37] In one study of 27 low-grade tumors, which had undergone diagnostic surgery, but no other treatment, low uptake of [^{11}C]methionine was found to be a predictor of long time to tumor progression in oligodendrogliomas, but not in astrocytomas or oligoastrocytomas.[38] The activity volume index, a metabolic index generated from an automated semiquantification of PET with methionine, has been shown to decrease in patients with low-grade oligodendrogliomas responding to procarbazine, CCNU, and vincristine chemotherapy.[39]

IMAGING DIFFERENTIATION OF TUMOR PROGRESSION FROM PSEUDO-PROGRESSION

Usually within 3 months, and at times even up to 6 months, following the completion of RT, especially in conjunction with temozolomide, there may be

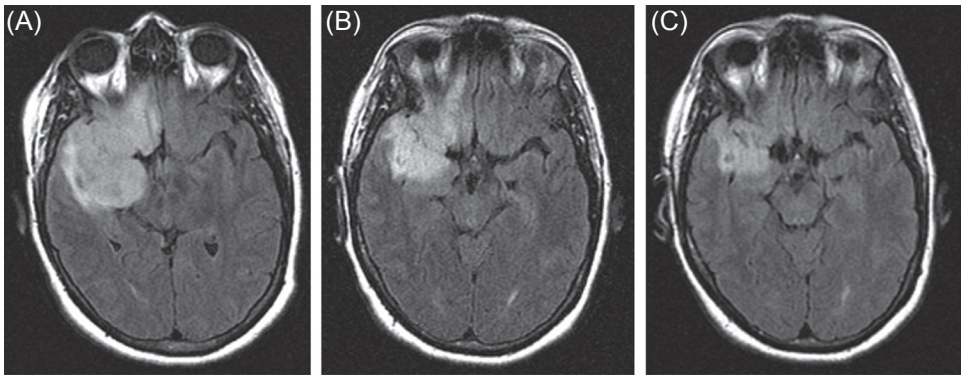


FIGURE 9 (A–C) (A) Grade II oligodendroglioma, baseline after biopsy. (B) Grade II oligodendroglioma following 10 months of antineoplastic therapy with temodar. (C) Grade II oligodendroglioma following 20 months of temodar.

enlargement of treated pathologically enhancing areas, new areas of enhancement in previously nonenhancing tumor, and associated progression of surrounding increased T2 signal. If on follow-up, without change in treatment regimen, this enhancement and adjacent increased T2 signal are shown to improve relative to the pretreatment baseline, the previous scan that was obtained within the 6-month post-RT window is deemed to have represented "pseudo-progression." A high association between methylguanine-methyltransferase promoter methylation and pseudo-progression has been appreciated and, especially in those patients whose tumors are methylated, pseudo-progression may correlate with therapeutic response.[40,41]

Pseudo-progression is very difficult to prospectively diagnose. These early post-RT changes usually should be assessed as indeterminate, with the understanding that they may represent genuine tumor progression or pseudo-progression. DSC perfusion MRI may be employed in an attempt to identify true tumor progression, based on elevated rCBV, but because of limited sensitivity and specificity in areas of partially resected and treated tumor, many times the most prudent solution is to obtain a short-interval follow-up MRI(s) to observe how these changes evolve.

OTHER TREATMENT-RELATED IMAGING CHANGES

Other treatments such as dexamethasone have long been known to alter imaging appearance. Antiangiogenic agents such as bevacizumab, an anti-vascular endothelial growth factor monoclonal antibody, may produce a distinct and rapid decrease in contrast enhancement. This quick decrease in enhancement suggests a change in vascular permeability with vascular "normalization" of the blood–brain barrier.[41] This decrease in contrast enhancement may or may not indicate reduction in underlying high-grade tumor volume, but still may result in improved clinical function with a reduction in steroid dependence. Interpretation of imaging in the era of these sorts of therapies is an ongoing area of investigation.

CONCLUSION

Physiologic imaging techniques developed since 1995 can add helpful information to aid in diagnosis, treatment planning, and follow-up evaluation of oligodendrogliomas and mixed gliomas. While MRI is no substitute for histology, diagnostic confidence can be increased by selective application of these newer imaging techniques. The goal of imaging is to relatively noninvasively assess oligodendrogliomas, with the hope of monitoring effective therapy (see Figure 9), but also to identify potential tumor recurrence in a reliable and timely fashion.

References

1. Daumas-Duport C, Varlet P, Tucker ML, et al. Oligodendrogliomas. Part 1: patterns of growth, histological diagnosis, clinical and imaging correlations: a study of 153 cases. *J Neuro Oncol*. 1997;34:37–59.
2. Graif M, Bydder GM, Steiner RE, et al. Contrast-enhanced MR imaging of malignant brain tumors. *Am J Neuroradiol*. 1985;6:855–862.
3. Daumas-Duport C, Tucker ML, Kolles H, et al. Oligodendrogliomas. Part II: a new grading system based on morphological and imaging criteria. *J Neuro Oncol*. 1997;34:61–78.
4. Burger PC, Scheithauer BW, Vogel FS. *Surgical Pathology of the Nervous System and Its Coverings*. New York, NY: Churchill Livingstone; 2002.
5. Lee YY, Van Tassel P. Intracranial oligodendrogliomas: imaging findings in 35 treated cases. *Am J Roentgenol*. 1989;152:361–369.
6. Vonofakos D, Marcu H, Hacker H. Oligodendrogliomas: CT patterns with emphasis on features indicating malignancy. *J Comput Assist Tomogr*. 1979;3:783–788.
7. White ML, Zhang Y, Kirby P, et al. Can tumor contrast enhancement be used as a criterion for differentiating tumor grades of oligodendrogliomas? *Am J Neuroradiol*. 2005;26:784–790.
8. Mosely ME, Kucharczyk J, Mintorovitch J, et al. Diffusion-weighted MR imaging of acute stroke: correlation with T2-weighted and magnetic susceptibility-enhanced MR imaging in cats. *Am J Neuroradiol*. 1990;11:423–429.

9. Atlas SW. *Magnetic Resonance Imaging of the Brain and Spine*. Lippincott-Raven Publishers; 1998. [Chapter 2] – The Basis of MR Contrast from Flow and Diffusion.
10. Sugahara T, Korogi Y, Kochi M, et al. Usefulness of diffusion-weighted MRI with echo-planar technique in the evaluation of cellularity in gliomas. *J Magn Reson Imaging*. 1999;9:53–60.
11. Gupta RK, Sinha U, Cloughesy TF, Alger JR. Inverse correlation between choline magnetic resonance spectroscopy signal intensity and the apparent diffusion coefficient in human glioma. *Magn Reson Med*. 1999;41:2–7.
12. Inglese M, Spindler M, Babb JS, et al. Field, coil, and echo-time influence on sensitivity and reproducibility of brain proton MR spectroscopy. *Am J Neuroradiol*. 2006;27:684–688.
13. Stadlbauer A, Gruber S, Nimsky C, et al. Preoperative grading of gliomas by using metabolite quantification with high-spatial-resolution proton MR spectroscopic imaging. *Radiology*. 2006; 238:958–969.
14. Castillo M, Smith JK, Kwock L. Correlation of myo-inositol levels and grading of cerebral astrocytomas. *Am J Neuroradiol*. 2000;21:1645–1649.
15. Gutowski NJ, Gómez-Ansón B, Torpey N, et al. Oligodendroglial gliomatosis cerebri: ^{1}H-MRS suggests elevated glycine/inositol levels. *Neuroradiology*. 1999;41:650–653.
16. Londono A, Castillo M, Armao D, et al. Unusual MR spectroscopic imaging pattern in an astrocytoma: lack of elevated choline and high myo-inositol and glycine levels. *Am J Neuroradiol*. 2003;24:942–945.
17. Ross BD, Colletti P, Lin A. Magnetic resonance spectroscopy of the brain: neurospectroscopy. In: Edelman RR, Hellelink JR, Zlatkin MB, Crues JV, eds. *Clinical Magnetic Resonance Imaging*. 3rd ed. New York: Saunders/Elsevier; 2006:1850–1851.
18. Rijpkema M, Schuuring J, van der Meulin Y, et al. Characterization of oligodendrogliomas using short echo time ^{1}H MR spectroscopic imaging. *NMR Biomed*. 2003;16:12–18.
19. Law M, Yang S, Wang H, et al. Glioma grading: sensitivity, specificity, and predictive values of perfusion MR imaging and proton MR spectroscopic imaging compared to conventional MR imaging. *Am J Neuroradiol*. 2003;24:1989–1998.
20. Cha S, Knopp EA, Johnson G, et al. Intracranial mass lesions: dynamic contrast-enhanced susceptibility-weighted echo-planar perfusion MR imaging. *Radiology*. 2002;223:11–29.
21. Xu M, See SJ, Ng WH, et al. Comparison of magnetic resonance spectroscopy and perfusion-weighted imaging in presurgical grading of oligodendroglial tumors. *Neurosurgery*. 2005;56:919–926.
22. Spampinato MV, Smith JK, Kwock L, et al. Cerebral blood volume measurements and proton MR spectroscopy in grading of oligodendroglial tumors. *Am J Roentgenol*. 2007;188:204–212.
23. Jenkinson MD, Smith TS, Joyce KA, et al. Cerebral blood volume, genotype and chemo sensitivity in oligodendroglial tumors. *Neuroradiology*. October 2006;48(10):703–713.
24. Law M, Cha S, Knopp EA, et al. High-grade gliomas and solitary metastases: differentiation by using perfusion and proton spectroscopic MR imaging. *Radiology*. 2002;222:715–721.
25. Cha S. Update on brain tumor imaging: from anatomy to physiology. *Am J Neuroradiol*. 2006;27:475–487.
26. Holmes TM, Petrella JR, Provenzale JM. Distinction between cerebral abscesses and high-grade neoplasms by dynamic susceptibility contrast perfusion MRI. *Am J Radiol*. 2004;183:1247–1252.
27. Provenzale JM, Wang GR, Brenner T, et al. Comparison of permeability in high-grade and low-grade brain tumors using dynamic susceptibility contrast MR imaging. *Am J Radiol*. 2002;178:711–716.
28. Roberts HC, Roberts TP, Brasch RC, et al. Quantitative measurement of microvascular permeability in human brain tumors achieved using dynamic contrast-enhanced MR imaging: correlation with histologic grade. *Am J Neuroradiol*. 2000;21:891–899.
29. Tofts PS, Kermode AG. Measurement of the blood–brain barrier permeability and leakage space using dynamic MR imaging. Fundamental concepts. *Magn Reson Med*. 1991;17:357–367.
30. Donahue KM, Krouwer HG, Rand SD, et al. Utility of simultaneously acquired gradient-echo and spin-echo cerebral blood volume and morphology maps in brain tumor patients. *Magn Reson Med*. 2000;43:845–853.
31. Brown GG, Jernigan TL, Cato M. Functional magnetic resonance imaging in neuropsychiatric disorders. In: Edelman RR, Hellelink JR, Zlatkin MB, Crues JV, eds. *Clinical Magnetic Resonance Imaging*. 3rd ed. New York: Saunders/Elsevier; 2006:1807.
32. Ogawa S, Lee TM, Kay AR, Tank DW. Brain magnetic resonance imaging with contrast dependent on blood oxygenation. *Proc Natl Acad Sci USA*. 1990;87:9868–9872.
33. Moseley ME, Cohen Y, Kucharczyk J, et al. Diffusion-weighted MR imaging of anisotropic water diffusion in cat central nervous system. *Radiology*. 1990;176:439–446.
34. Witwer BP, Moftakhar R, Hasan KM, et al. Diffusion-tensor imaging of white matter tracts in patients with cerebral neoplasm. *J Neurosurg*. 2002;97:568–575.
35. Jellison BJ, Field AS, Medow J, et al. Diffusion tensor imaging of cerebral white matter: a pictorial review of physics, fiber tract anatomy, and tumor imaging patterns. *Am J Neuroradiol*. 2004;25:356–369.
36. Van den Bent MJ, Kros JM. Oligodendrogliomas and mixed gliomas. In: Schiff D, O'Neill BP, eds. *Principles of Neuro-Oncology*;15. New York: McGraw-Hill; 2005:311–332.
37. Derlon JM, Chapon F, Noel MH, et al. Non-invasive grading of oligodendrogliomas: correlation between in vivo metabolic pattern and histopathology. *Eur J Nucl Med*. 2000;27:778–787.
38. Ribum D, Smits A. Baseline ^{11}C-methionine PET reflects the natural course of grade 2 oligodendrogliomas. *Neurol Res*. 2005;27:516–521.
39. Tang BN, Sadeghi N, Branle F, et al. Semi-quantification of methionine uptake and flair signal for the evaluation of chemotherapy in low-grade oligodendroglioma. *J Neurooncol*. 2005;71:161–168.
40. Fatterpekar GM, Galheigo D, Narayana A, Johnson G, Knopp E. Treatment-related change versus tumor recurrence in high grade gliomas: a diagnostic conundrum- use of dynamic susceptibility contrast-enhanced (DSC) perfusion MRI. *AJR*. 2012;198:19–26.
41. da Cruz Jr H, Rodriguez I, Domingues RC, et al. Pseudoprogression and pseudoresponse: imaging challenges in the assessment of posttreatment glioma. *Am J Neuroradiol*. 2011;32:1978–1985.

CHAPTER

41

Primary Central Nervous System Lymphoma

Herbert B. Newton[1], *H. Wayne Slone*[2], *Eric C. Bourekas*[1,2]

[1]Division of Neuro-Oncology, Departments of Neurology and Neurosurgery, Dardinger Neuro-Oncology Center, Wexner Medical Center at The Ohio State University and James Cancer Hospital and Solove Research Institute, Columbus, OH, USA; [2]Dardinger Neuro-Oncology Center, Departments of Radiology, Wexner Medical Center at The Ohio State University and James Cancer Hospital and Solove Research Institute, Columbus, OH, USA

INTRODUCTION

Primary central nervous system lymphoma (PCNSL) is defined as the presentation of extranodal lymphoma confined to the central nervous system (CNS).[1–3] While the vast majority of CNS lymphomas (80–90%) are primary lesions, they are relatively uncommon, accounting for only about 1–2% of all lymphomas. The incidence of PCNSL has increased since the mid-1980s in both the immunocompromised and immunocompetent populations. Previously accounting for only about 1% of all CNS neoplasms, they currently represent 3–6% of all primary brain tumors.[2,3]

The prevalence of PCNSL continues to be significantly higher in immunocompromised than immunocompetent patients. A dramatic increase in the incidence of PCNSL in the immunocompromised population occurred in the early 1980s, coinciding with the first reported cases of acquired immunodeficiency syndrome (AIDS). Patients with AIDS continue to account for the largest group of immunocompromised patients with CNS lymphoma, and PCNSL in an human immunodeficiency virus (HIV)-seropositive patient is an AIDS-defining condition. Other immunocompromised states associated with CNS lymphoma include organ transplantation, Wiskott-Aldrich Syndrome, congenital immune deficiency syndromes, and prolonged immunosuppressive therapy.[1–3] Additionally, there have been reports of CNS lymphoma related to autoimmune diseases such as Sjogren's Syndrome and systemic lupus erythematosus. Clinical data suggest that up to 6% of AIDS patients will develop PCNSL.[2,3] In transplant patients, the risk is about 1–5% (1–2% for renal transplant patients, and 2–7% for cardiac, lung, and liver transplant patients).[4–6] Patients with congenital immune deficiency syndromes carry a risk of 4%. A growing body of evidence has linked Epstein–Barr virus with the pathogenesis of CNS lymphoma in AIDS patients.[7]

Although CNS lymphomas are responsive to chemotherapy and radiation, prognosis remains poor, with high rates of recurrence.[1–3] Chemotherapy can be delivered systemically or intrathecally. Some patients have been treated with intraarterial delivery of chemotherapeutic agents following disruption of the blood–brain barrier.[8–10] Although surgical intervention is often necessary for diagnostic purposes, surgical resection provides no therapeutic benefit, and is generally reserved for cases in which the tumor might cause brain herniation.[1–3] However, some authors are now challenging these traditional views, and feel that surgical intervention may be appropriate in selected cases.[11]

Lymphomas can be divided into the Hodgkin's and nonHodgkin's types.[7] NonHodgkin's lymphoma can be further subdivided by cell type and grade, and these classifications have long been a source of controversy. The vast majority of PCNSLs are high-grade tumors of the nonHodgkin's B cell type.[1–3,7] Primary T cell lymphoma of the CNS is rare, and CNS involvement by Hodgkin's lymphoma is even more rare.[12–14] The imaging features of CNS lymphoma are variable, and attempts at correlating imaging features with histologic subtypes have yielded inconsistent results.[15–19] Therefore, the diagnosis of PCNSL hinges upon stereotactic biopsy and histologic assessment. Nevertheless, neuroimaging can suggest the diagnosis, leading to timely initiation of appropriate therapy. In this chapter, we will discuss the characteristic imaging features of this aggressive neoplasm.

© 2016 Elsevier Ltd. All rights reserved.

GENERAL IMAGING FEATURES

Anatomical Distribution

An overwhelming majority of PCNSL lesions occur in the brain, but they can also occur in the spinal cord, meninges, globe, and cerebrospinal fluid (CSF).[15–19] Of those primary CNS lesions occurring in the brain, supratentorial lesions occur much more commonly than those in the posterior fossa, accounting for 80–90% of all lesions.[15–17] One-half to two-thirds of lesions have been reported to occur in the cerebral hemispheres, with the white matter of the frontal lobes being the most common location, followed by the temporal, parietal, and occipital lobes. The central deep gray matter of the basal ganglia, thalamus, and hypothalamus, often reported as a classic location for CNS lymphoma, accounts for about one-third of lesions. Approximately 10% of lesions occur in the posterior fossa, and only 1% is found in the spinal cord.[1–3,15–19]

A characteristic feature of PCNSL is its tendency to contact ependymal or meningeal surfaces, with leptomeningeal involvement seen in about 12% of cases.[1–3,15–19] Corpus callosum involvement is also relatively common, reported in some series to be nearly as common as involvement of the deep gray matter. Frontal lobe lesions that cross the genu of the corpus callosum create the classic "butterfly" pattern. Dural involvement is uncommon, and often mimics meningioma in its presentation. In untreated CNS lymphoma, calcification, hemorrhage, and cysts are only rarely seen.[15–17,20] Another characteristic finding of CNS lymphoma is the relatively little mass effect and edema relative to lesion size.[15–17]

Computed Tomography and Magnetic Resonance Imaging

On computed tomography (CT), CNS lymphoma usually presents as an iso- or hyperdense mass relative to brain parenchyma on unenhanced scans, and almost all lesions demonstrate contrast enhancement[1–3,15,17,21–24] (see Figure 1). However, a negative CT examination does not exclude the diagnosis, with false negative rates of up to 38% having been reported on initial diagnostic scans (although these rates are currently likely to be lower given advances in CT technology).[25] Magnetic resonance imaging (MRI) is more sensitive, and is currently the imaging modality of choice in the evaluation of CNS lymphoma.[1–3,15–19] On MRI, the lesions usually present as well-demarcated masses that are isointense to hypointense relative to gray matter on T1-weighted sequences. The T2-weighted imaging characteristics can be more variable. Initial reports described these lesions to be predominantly hyperintense to gray matter on T2-weighted sequences. Studies indicate that more than half the lesions are hypointense to isointense relative to gray matter.[15–17,21] The hypointensity on T2-weighted imaging, as well as the hyperattenuation on CT, is attributable to the dense cellularity of the tumor and high nucleus-to-cytoplasm ratio.[1–3,7] Higher T2 signal intensity within CNS lymphoma lesions has been correlated with higher degrees of necrosis.[15–17] Using fluid attenuated inversion recovery (FLAIR) sequences, which are T2-weighted, the imaging characteristics are similar to traditional T2 sequences. A variable pattern can be seen on diffusion-weighted imaging (DWI). While most tumors demonstrate elevated water diffusibility, the dense cellularity of CNS lymphoma often results in restricted diffusion (high signal) on DWI.[26] As with CT, most lesions enhance with contrast administration (see Figures 2–4); treatment with steroids may result in decreased enhancement or nonenhancement.[15–17] Imaging findings of PCNSL in children are variable, but often similar to those seen in adults.[27]

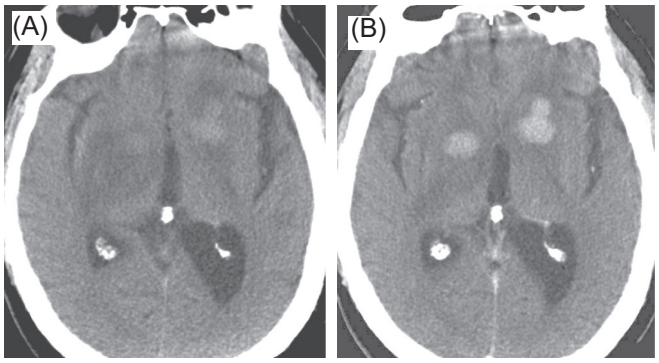


FIGURE 1 Sixty-one-year-old male who presented with gait disturbance and slurred speech. Biopsy yielded B cell PCNSL. (A) Noncontrast CT demonstrates bilateral hyperdense lesions involving the deep gray and white matter. Surrounding low density is consistent with edema. (B) The lesions demonstrate homogeneous enhancement with the administration of contrast.

Angiography

The angiographic appearance of CNS lymphoma is highly variable. A common finding is that of an avascular mass with little vessel displacement or involvement.[28] Jack et al., described a homogeneous vascular stain that appeared in the late arterial or early venous phase in 12 of 29 patients with PCNSL who underwent cerebral angiography.[29] Vascular encasement may rarely be seen.[15–19] Lesions involving the meninges may demonstrate a dural supply, and are also a rare finding.[30] Angiography plays little role in the diagnosis of CNS lymphoma. There has been an increasing role for endovascular techniques in the treatment of CNS lymphoma, with the use of blood–brain barrier disruption to deliver intraarterial chemotherapy.[9,10] Osmotic disruption of the blood–brain barrier is achieved by the infusion of

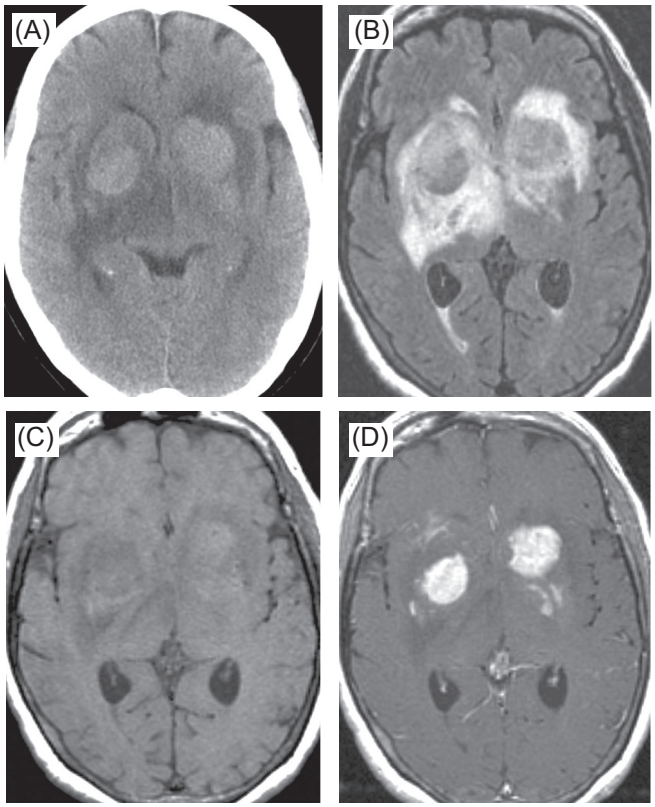


FIGURE 2 Seventy-three-year-old female with progressive motor weakness and biopsy-proven PCNSL of the B cell type. (A) Hyperdense masses are seen involving the basal ganglia bilaterally on noncontrast CT, with surrounding edema. (B) On MRI, FLAIR sequence shows the masses to be isointense to gray matter, with surrounding high-T2 signal related to edema. On pregadolinium (C) and postgadolinium (D) sequences, the lesions demonstrate fairly homogeneous contrast enhancement.

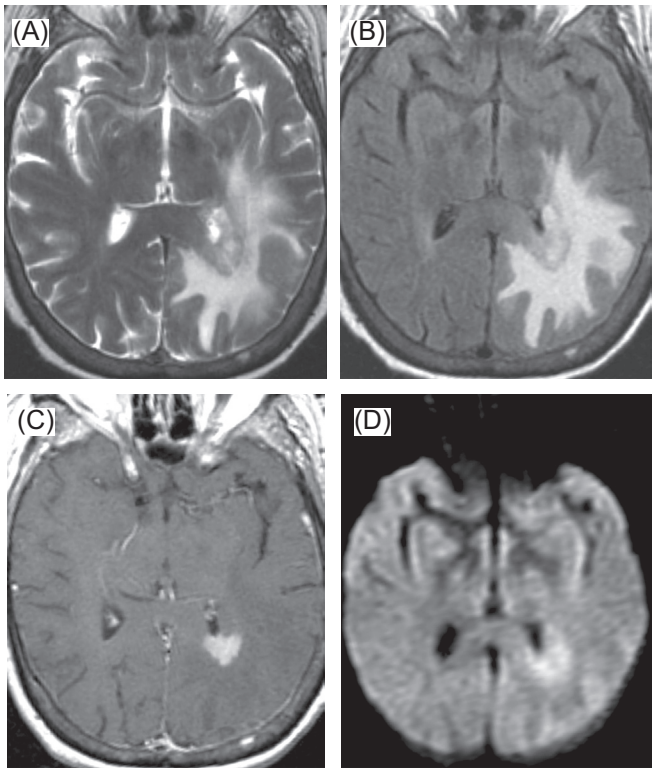


FIGURE 3 In this 62-year-old female with PCNSL, a periventricular lesion in the deep white matter of the left cerebral hemisphere is isointense to gray matter on the T2 (A) and FLAIR (B) sequences, with surrounding hyperintensity related to edema. The lesion demonstrates homogeneous enhancement on the postgadolinium T1 sequence (C), and restricted diffusion (high signal) on DWI (D).

intraarterial mannitol into the desired cerebrovascular distribution, followed by the intraarterial administration of the chemotherapeutic agent (see Figure 5).[8]

Other Imaging Modalities

Cross-sectional imaging studies (CT and MRI) are the most commonly utilized imaging modalities in the diagnosis and management of CNS lymphoma.[15–19] However, several studies have reported on the utility of thallium-201 single photon emission computed tomography (SPECT) and F-18 fluorodeoxyglucose (FDG) positron emission tomography (PET) in CNS lymphoma.[31–35] Generally, CNS lymphoma lesions demonstrate hypermetabolic activity on PET imaging, and increased radiopharmaceutical uptake with SPECT imaging. While most brain neoplasms will demonstrate similar findings, PET and SPECT may help differentiate neoplastic from benign processes, where the activity will be relatively less intense. These imaging modalities may be particularly useful in differentiating CNS lymphoma from infectious or inflammatory lesions in AIDS patients (Imaging Patterns in Immunocompetent vs Immunocompromised Patients Section), and in monitoring response to therapy.

Imaging Patterns in Immunocompetent versus Immunocompromised Patients

In immunocompetent patients, PCNSL most commonly presents as a solitary supratentorial lesion in the cerebral hemispheres.[15–19] The vast majority of lesions in immunocompetent patients demonstrate homogeneous contrast enhancement.[15–19,24] Lesions in the immunocompromised host are more likely to be multiple, with a more variable enhancement pattern.[1–3,36] Central necrosis is also more common in immunocompromised patients. This often results in a ring pattern on imaging: the central area of necrosis results in T2 hyperintensity, with a densely cellular, T2 hypointense rim, surrounded by T2 hyperintensity peripherally related to edema.[1–3] The pattern is reversed on T1-weighted imaging, with a T1 hyperintense ring surrounded by T1 hypointense edema. There is usually intense ring enhancement with contrast, which may be smooth or irregular[15–17,25] (see Figure 6). Periventricular enhancement, although relatively uncommon, is very specific for CNS lymphoma in AIDS patients.[37]

Neurological complications are common in patients infected with HIV. These patients often present with neurological symptoms and multifocal brain lesions on CT or MRI, many of which demonstrate ring enhancement. The most likely etiology in this scenario is cerebral toxoplasmosis, but the differential diagnosis includes PCNSL as well as other (less common) infectious processes including neurosyphilis and progressive multifocal leukoencephalopathy. Definitive diagnosis requires brain biopsy, which is associated with the morbidity and

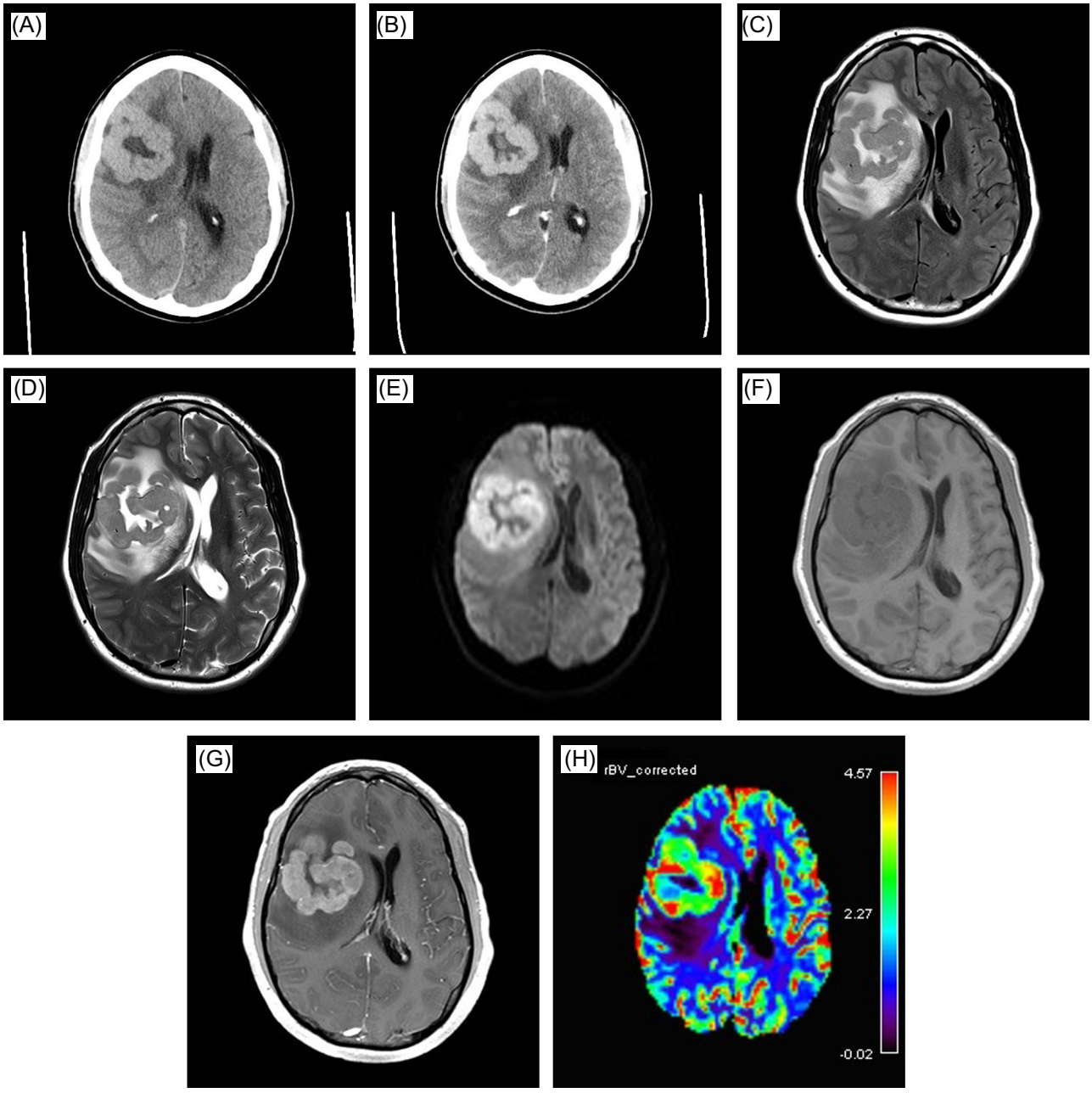


FIGURE 4 This is a 49-year-old male who presented with persistent dull aching headache after a motor vehicle accident a week ago. He did hit his head against the dashboard and sustained a small laceration on the scalp. When the headache persisted he decided to go to see a doctor and had a screening cranial CT scan. (A) The CT without contrast demonstrates a hyperdense appearance of the solid portion of the tumor, which is characteristic of PCNSL, due to high cellularity. Low density vasogenic edema surrounds the mass, resulting in mass effect and midline shift. (B) The postcontrast CT demonstrates enhancement of the solid portion of the mass. On the subsequent MRI scan, the axial FLAIR (C) and T2-weighted (D) images demonstrate the hypointense solid peripheral portion of the tumor relative to the hyperintense surrounding edema. Fluid signal is noted centrally in both images. The diffusion-weighted image (E) shows hyperintense restricted diffusion in the solid portion of the tumor. T2-weighted hypointensity and restricted diffusion are characteristic of PCNSL due to high cellularity. The T1-weighted axial images before (F) and after (G) contrast reveal enhancement of the solid part of the tumor. There is a high degree of perfusion noted within the tumor on the perfusion-weighted imaging (H).

mortality of an invasive procedure. Standard practice has been to place the patient empirically on antitoxoplasmosis therapy for a two-week period. If the lesions respond, the diagnosis is confirmed. If the lesions fail to respond or worsen, an alternative diagnosis such as PCNSL is entertained, and the patient may go on to brain biopsy if indicated (see Figure 7). The obvious downfall to this approach is that if the presumptive diagnosis of toxoplasmosis is incorrect, the underlying disease process may progress and the patient's chances for prolonged survival may be decreased. In this scenario, thallium-201 SPECT or F-18 FDG PET, particularly when combined with toxoplasma serology, may be helpful in arriving at the correct diagnosis in a more timely fashion.[31–35]

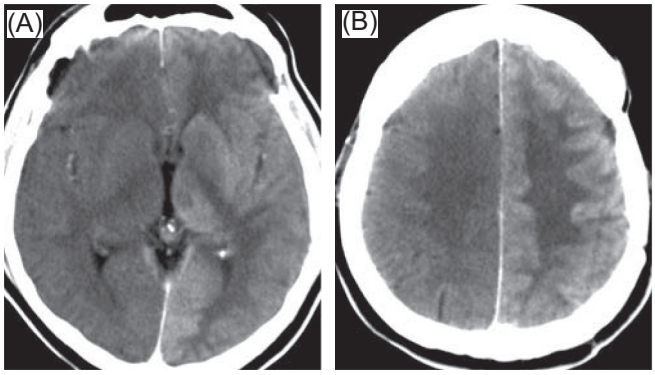


FIGURE 5 In this 46-year-old male with PCNSL, osmotic disruption of the blood–brain barrier (BBB) was achieved with the intraarterial infusion of mannitol into the left internal carotid artery (ICA), immediately followed by infusion of the chemotherapeutic regimen. Contrast enhanced CT was then performed to evaluate the degree of BBB disruption. The study shows asymmetrically increased enhancement of the left cerebral hemisphere in the distribution of the left ICA (A,B), consistent with adequate BBB disruption.

Differential Diagnosis of Primary CNS Lymphoma

Differential considerations in the diagnosis of PCNSL based on imaging findings include gliomas (usually higher grade lesions like glioblastoma multiforme) (see Figure 6), metastases (from extracranial sources or from other brain primaries), abscess and other types of infection, and granulomatous processes such as sarcoidosis (see Figure 8) and tuberculosis.[1–3] Active demyelinating disease can mimic PCNSL, and primitive neuroectodermal tumor should be considered in the pediatric population.[38] T2 hypointensity, when present, can help differentiate

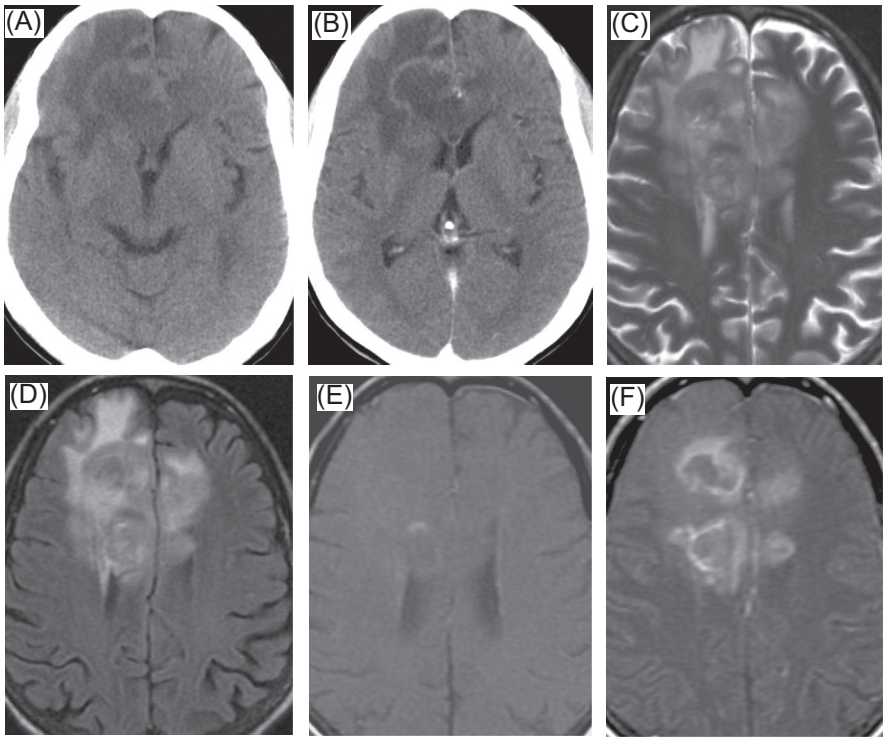


FIGURE 6 Forty-four-year-old female with history of HIV who presented with high fevers and headache. Differential diagnosis included toxoplasmosis and PCNSL. She was started empirically on antitoxoplasma therapy, but did not respond. An alternative diagnosis of PCNSL was then made, and the patient improved with steroids. CT without (A) and with (B) contrast demonstrates a lesion in the right frontal lobe, extending into the corpus callosum, with a ring pattern of enhancement and surrounding edema. On MRI, T2 (C) and FLAIR (D) sequences show lesions involving the frontal lobes bilaterally, extending into the corpus callosum. Increased signal within these lesions is likely related to necrosis, with the surrounding high signal secondary to edema. The areas of the lesion that are isointense to normal brain parenchyma indicate the densely cellular areas. These are also the areas that enhance with gadolinium, seen on the pre- (E) and postcontrast (F) sequences, resulting in the ring enhancement pattern.

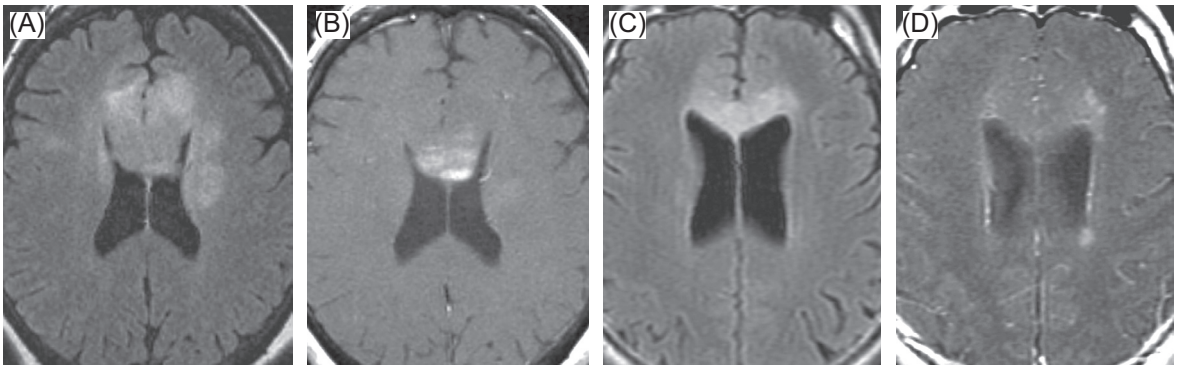


FIGURE 7 Two patients with similar imaging findings. The first is a 68-year-old female with new onset seizure. On MRI, FLAIR sequence (A) shows abnormal high signal in the corpus callosum and periventricular regions. The postcontrast T1 sequence (B) shows enhancement in the corpus callosum. The second patient is a 51-year-old male with progressive neurologic deterioration. Again, there is abnormal signal in the periventricular region on FLAIR (C), and subtle enhancement in the corpus callosum and periventricular region on postcontrast T1 (D). The first patient had a high-grade astrocytoma, while the second patient had PCNSL.

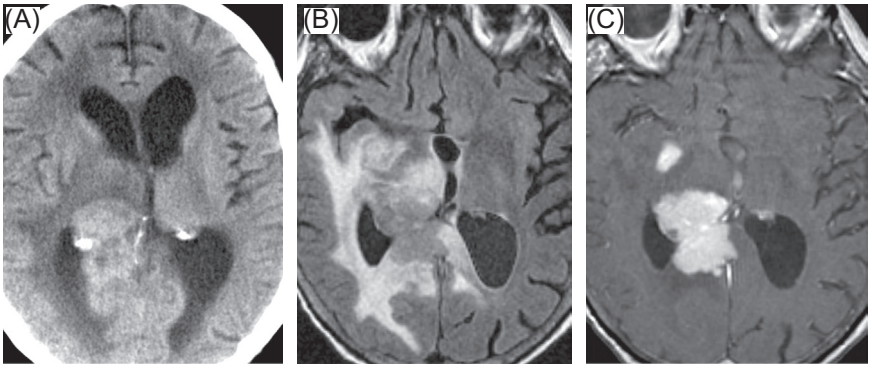


FIGURE 8 Seventy-four-year-old male with changes in mental status and difficulty with ambulation. Noncontrast CT showed a hyperdense mass involving the deep gray matter on the right, extending into the splenium of the corpus callosum, with surrounding edema (A). MRI showed an isointense lesion in the same distribution with surrounding high signal edema on the FLAIR sequence (B). On the postcontrast T1 sequence (C), the lesion demonstrated homogeneous enhancement, with an enhancing satellite lesion more anteriorly. The patient had a known history of sarcoidosis, and the initial explanation for the neurological symptoms and imaging findings was neurosarcoidosis. He went on to biopsy, and the diagnosis was B cell PCNSL.

CNS lymphoma from other brain neoplasms and demyelinating disease, which are both more likely to be hyperintense on T2-weighted sequences. Distinguishing brain abscess from CNS lymphoma can be more difficult, as both can demonstrate ring-like enhancement and increased signal on DWI. Brain abscesses are typically associated with a moderate to large amount of surrounding vasogenic edema, while PCNSL typically generates only mild edema relative to lesion size, and this feature can sometimes be useful in making the diagnosis. The differentiation of PCNSL from toxoplasmosis can be virtually impossible in the immunocompromised population based on conventional imaging techniques. As discussed in the previous section, both can demonstrate ring enhancement patterns and multicentricity, and alternative imaging modalities may help make the diagnosis more rapidly (Imaging Patterns in Immunocompetent vs Immunocompromised Patients Section). Secondary CNS lymphoma usually involves the leptomeninges, and patients typically present with cranial nerve palsies (see Figure 9).

UNCOMMON MANIFESTATIONS OF PRIMARY CNS LYMPHOMA

Primary Leptomeningeal Lymphoma

Primary leptomeningeal lymphoma is a rare presentation of PCNSL, characterized by lymphomatous involvement of the leptomeninges in the absence of parenchymal CNS or systemic involvement. It accounts for fewer than 8% of all PCNSLs.[39] The most common clinical symptoms are those of raised intracranial pressure.[40] Meningismus, cranial neuropathies, or spinal radiculopathies have also been described.[39–41] CSF analysis has been inconsistent in showing the presence of malignant cells. Histologic analyses have revealed both B and T cell primary lymphoma of the leptomeninges.[42,43]

Neuroimaging can often be unremarkable, or show nonspecific findings such as hydrocephalus. Less common findings include meningeal calcification, and meningeal or cranial nerve enhancement.[43] Proton density

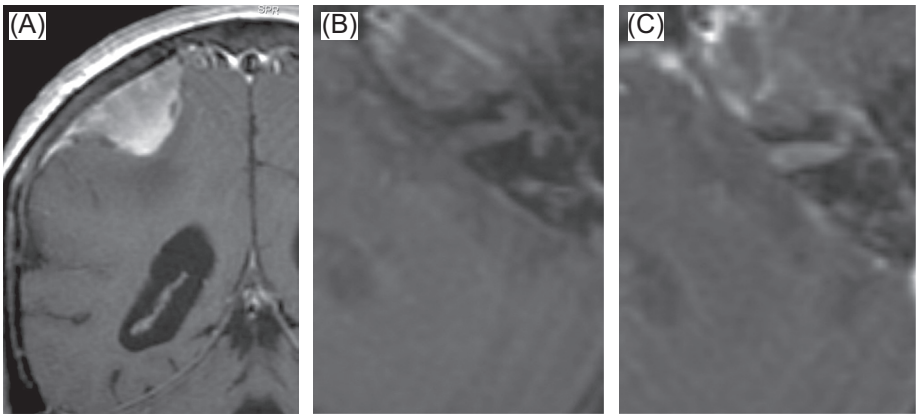


FIGURE 9 Seventy-one-year-old female with systemic follicular lymphoma who presented with ataxia, slurred speech, and diplopia. Coronal postgadolinium T1-weighted sequence shows an enhancing dural-based mass overlying the right parietal convexity (A). Precontrast (B) and postcontrast (C) axial images through the region of the internal auditory canal (IAC) on the left demonstrates abnormal and asymmetric enhancement in the left IAC. The diagnosis was secondary leptomeningeal lymphoma.

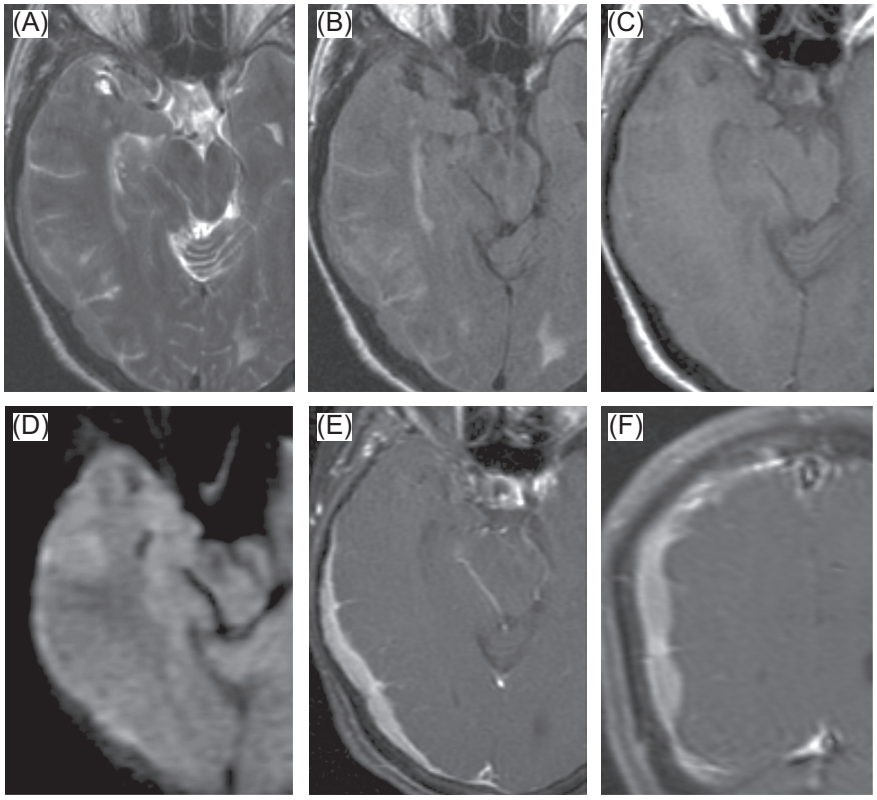


FIGURE 10 Sixty-four-year-old female with recurrent falls, headache, and vertigo. Biopsy confirmed primary leptomeningeal lymphoma. On MRI, axial T2 (A), FLAIR (B), and precontrast T1 (C) sequences demonstrate a dural-based lesion that is nearly isointense to brain parenchyma on all pulse sequences. There is also signal abnormality involving the subarachnoid space along the right cerebral convexity on the FLAIR sequence. On DWI (D), the lesion demonstrates slightly increased signal (restricted diffusion). Axial (E) and coronal (F) postgadolinium sequences show homogeneous enhancement of the lesion.

or (fluid-attenuated inversion recovery) FLAIR MRI sequences may demonstrate high signal intensity in the subarachnoid space, although this is a nonspecific finding and can also be seen with other processes such as subarachnoid hemorrhage and meningeal inflammation of any cause. A very rare presentation of primary leptomeningeal lymphoma is that of a cerebellopontine angle mass.[44] Only a few cases have been reported, and a lesion in this location may show effacement of the basal cisterns and enlargement of the ventricles on imaging. Due to its nonspecific clinical and imaging findings, the diagnosis of primary leptomeningeal lymphoma can be difficult, and requires a high index of suspicion (see Figure 10). Primary parenchymal CNS lymphoma with

meningeal extension and systemic lymphoma with meningeal spread are both more common entities (see Figure 9), and must be excluded.

Intravascular Lymphomatosis

Intravascular lymphomatosis is a rare type of B cell nonHodgkin's lymphoma characterized by the aggressive intravascular proliferation of lymphoid cells. The process is systemic and any organ can be involved, with or without clinical manifestation. The skin and CNS are the most frequent sites of involvement, with a neurological presentation in over 80% of cases having been reported.[45] Isolated CNS involvement is frequent, and is difficult to distinguish from other cerebral microangiopathies.[46] Presenting symptoms include mental status changes, dementia, and focal or nonlocalizing neurologic deficits as a result of ischemia caused by vessel occlusion.[46–48] The disease affects predominantly small blood vessels, more specifically arterioles, capillaries, and postcapillary venules.[46] A few reports have described involvement of the cortical veins and dural sinuses, although this is rare.[49]

Diagnosis can be elusive, as hematologic abnormalities are commonly absent, and CSF analysis is nonspecific. Prognosis remains poor, with a mortality rate over 80%. The success of therapy hinges on an early diagnosis prior to irreversible ischemic damage. Diagnosis is based upon biopsy of suspected sites of involvement. However, as the lesions are small and often located deep within the brain parenchyma, they are prone to sampling error; it is not uncommon for biopsy results to be nondiagnostic or fail to show the presence of intravascular tumor cells. Additionally, lesions found in sensitive areas of the brain may preclude biopsy. For these reasons, it is estimated that in up to 80% of cases, diagnosis is not made until histologic evaluation at autopsy.[46]

Imaging findings are variable, but intravascular lymphoma most commonly presents as multiple lesions scattered throughout the cerebral hemispheres, with the brainstem and cerebellum less frequently involved.[46,47] Of the hemispheric lesions, the subcortical white matter is more commonly affected than the cortex and subcortical nuclei. These lesions typically demonstrate hyperintensity on T2-weighted MR sequences, which appears to correlate with edema and gliosis on biopsy.[47] This can be a nonspecific finding, often difficult to distinguish from age-related white matter changes. Another common presentation of intravascular lymphomatosis is that of multifocal areas of ischemia and infarction, not surprising given the underlying pathology of small vessel occlusion.[50] Lesions in various stages of evolution can be seen at one time. In the acute phase, ischemic lesions demonstrate high signal intensity on DWI. Hyperintensity can also initially be seen on FLAIR sequences (see Figure 11). As these lesions evolve, they follow the expected signal characteristics of an ischemic small vessel stroke; the DWI hyperintensity will resolve, with persistence of abnormal FLAIR signal.[46] The chronic stage of these lesions is characterized by tissue loss and T2 hyperintensity, likely representing gliosis as a result of chronic ischemia and tissue damage. Subsequently, the T2 hyperintense lesions described earlier in this paragraph may be along the spectrum of ischemic changes related to vessel occlusion. Enhancement patterns are also variable, with less than one-third of lesions demonstrating enhancement with gadolinium on initial imaging. When enhancement is present, it can manifest as parenchymal mass-like enhancement or meningeal enhancement.[46,47] Spinal cord involvement is fairly common, but the sensitivity of MRI in detecting these lesions is low; fewer than 40% of patients with autopsy-proven cord lesions had an abnormal MRI. When present, the most common signal abnormality was T2 hyperintensity. DWI and FLAIR signal abnormalities can be partially reversible, and may correlate with response to chemotherapy.[46]

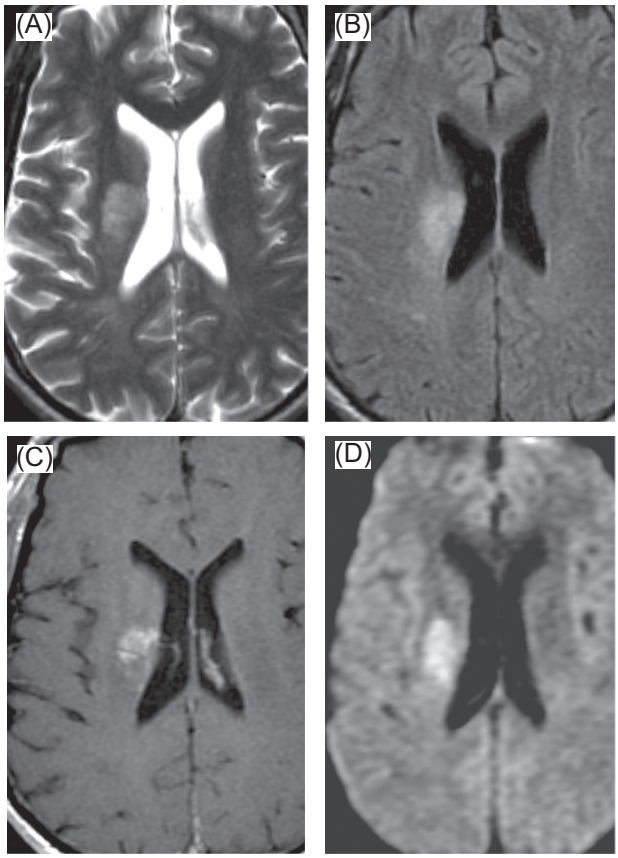


FIGURE 11 Forty-eight-year-old male with diffuse large B cell lymphoma, who presented with an acute basal ganglia infarct. Biopsy showed intravascular lymphomatosis. Axial T2 (A) and FLAIR (B) MRI sequences demonstrate abnormal high signal in the basal ganglia on the right. The postcontrast axial T1 sequence shows the lesion to enhance (C). On DWI (D), the lesion demonstrates restricted diffusion, consistent with history of recent infarct.

Lymphomatosis Cerebri

In contrast to the usual presentation of PCNSL as solitary or multiple mass lesions within the CNS, lymphomatosis cerebri is an extremely rare form of CNS lymphoma that manifests as a diffuse, infiltrative process without formation of a distinct mass. The entity was first described in 1999,[51] and only about five cases have been reported in the literature since that time. In all of the reported cases, the clinical presentation was that of a rapidly progressive dementia. MRI demonstrated a diffuse white matter process with relative sparing of gray matter, and a diffusely infiltrating B cell lymphoma was confirmed in those cases that went to autopsy.[52] Contrast enhancement may be absent, suggesting that the blood–brain barrier remains intact.[53] Because the clinical and imaging features are similar to those of other diffuse white matter disorders, such as demyelinating disease, leukodystrophy, small vessel ischemic disease, viral disease, Binswanger's disease, or infiltrating glioma (gliomatosis cerebri), biopsy is necessary for accurate diagnosis.

Primary Lymphoma of the Spinal Cord

Accounting for about 1% of all PCNSLs, primary intramedullary spinal lymphoma is extremely rare, with only a handful of reported cases.[1–3,7] Patients commonly present with focal neurologic deficits, including pain, paresthesias, and paresis. MRI typically reveals an intramedullary lesion with T2 hyperintensity and intense enhancement with the administration of gadolinium.[54–56] Surrounding edema may be present as well. Lymphomas of both B and T cell origin have been described in this location. The imaging findings are nonspecific, and differential considerations include malignant glioma, metastatic disease, and inflammatory processes such as multiple sclerosis and acute transverse myelitis. CSF analysis can often be nonspecific, and histopathological evaluation may be necessary for diagnosis.

Primary CNS Hodgkin's Lymphoma

CNS involvement in Hodgkin's lymphoma is uncommon, and is seen in fewer than 1% of patients with the disease.[1–3,7,57] When present, CNS involvement is usually secondary to disseminated disease elsewhere in the body, and occurs at the time of relapse in most patients. Hodgkin's lymphoma as a primary intracranial lesion is exceedingly rare, with only a few case reports in the literature.[57–59] Clinical symptoms at presentation are variable, ranging from memory loss and hemiparesis to cranial nerve palsies. Although meningeal involvement is common, neuroimaging may also reveal a parenchymal lesion without dural attachment. In cases where the meninges are involved, lesions may be indistinguishable from meningioma in clinical presentation and imaging features.[60]

Primary Intraocular Lymphoma

Intraocular lymphoma is a subset of PCNSL that may occur as a solitary lesion, or in association with lymphoma elsewhere in the CNS. Primary lymphoma of the globe often progresses to the CNS parenchyma and meninges. Patients often present with symptoms of chronic vitreitis, including complaints of blurred vision and floaters.[1–3,7,61] Diagnosis is contingent upon histologic analysis, and is often delayed until a prolonged course of treatment for idiopathic vitreitis has failed.[61,62] Vitrectomy specimen or vitreous aspirate reveals diffuse large B cell lymphoma in most cases (although T cell lymphomas have also been reported). Neuroimaging plays little role in the diagnosis, but is routinely performed to assess for concurrent CNS disease.

Low-Grade PCNSL

Low-grade lymphoma of the CNS is relatively rare, although its true incidence is currently unknown.[7] One series of 40 patients with low-grade PCNSL described differences in clinical, pathological, and radiological features compared to the more common high-grade subtype.[63] In this series, seizures were the most common symptom at presentation, while mental status changes were rare. The reverse is true in high-grade PCNSL, where mental status changes are common at presentation and seizures are less frequent. Due to the indolent course of the low-grade subtype, mean time to diagnosis from symptom onset is often longer relative to the high-grade subtype (approximately 15 months in this series compared with approximately three months for high-grade PCNSL). Prognosis is typically better for the low-grade subtype. Both B cell and T cell histologic types were identified. While B cell cases were much more common, the incidence of T cell cases in this series (20%) was much higher than that reported for PCNSL of the high-grade subtype. On imaging, lesions of the low-grade subtype were more likely to demonstrate hyperintensity on T2-weighted MRI sequences and moderate or heterogeneous contrast enhancement, and less likely to be periventricular in location compared with the high-grade subtype.

Mucosa-Associated Lymphoid Tissue Lymphoma of the CNS

Mucosa-associated lymphoid tissue (MALT) lymphomas are characterized as low-grade B cell lymphomas that occur in extranodal tissue.[7] They were initially described in the GI tract, but have since been reported to develop in

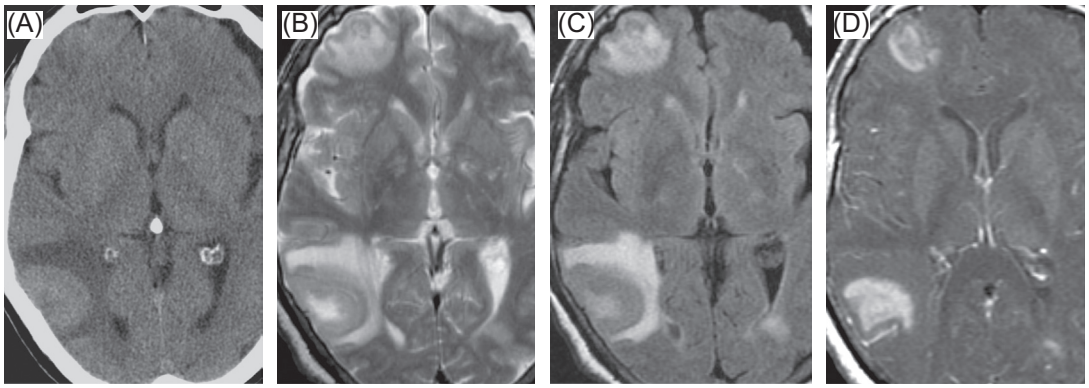


FIGURE 12 Seventy-nine-year-old male with seizures and biopsy-proven PCNSL of the T cell subtype. Noncontrast CT (A) shows a subcortical hyperdense mass in the right parieto–occipital region with surrounding edema. On MRI, T2 (B) and FLAIR (C) sequences show additional lesions in the right frontal lobe and left periventricular region. All three lesions enhance with gadolinium on the postcontrast sequence (D).

a variety of extranodal tissues. More recently, there have been reports of MALT lymphomas arising from the meninges. Now classified as extranodal marginal zone B cell lymphoma of MALT-type, these lesions are often present in the CNS as well-defined, dural-based masses that mimic meningiomas both in clinical presentation and imaging features.[64–66] There have also been a few reports of MALT lymphoma presenting as a cerebellopontine angle mass.[67] Due to its localized nature and slow growth, surgical resection with or without adjuvant therapies is often curative.

Primary T cell CNS Lymphoma

PCNSL of the T cell type (TPCNSL) is rare, with the majority of cases having been reported in the immunocompetent population.[7] There have been a few reports of AIDS-related TPCNSL, and in these patients an association with the human T cell lymphotropic virus type I has been found.[68] In the largest published series of TPCNSL (45 patients), the presentation and outcome were similar to the B cell subtype.[69] Imaging may reveal solitary or multiple lesions, which demonstrate variable enhancement patterns. The following imaging characteristics were described on MRI in a series of seven patients: tendency to be subcortical in location, relatively high incidence of hemorrhage, ring pattern of enhancement, and cystic areas consistent with necrosis[70] (see Figure 12). Primary spinal and leptomeningeal lymphomas of the T cell subtype have also been reported.[71]

References

1. Deckert M, Engert A, Bruck W, et al. Modern concepts in the biology, diagnosis, differential diagnosis, and treatment of primary central nervous system lymphoma. *Leukemia*. 2011;25:1797–1807.
2. Gerstner ER, Batchelor TT. Primary central nervous system lymphoma. *Arch Neurol*. 2010;67:291–297.
3. Schulz CJ, Bovi J. Current management of primary central nervous system lymphoma. *Int J Rad Oncol Biol Phys*. 2010;76:666–678.
4. Boubenider S, Hiesse C, Goupy C, et al. Incidence and consequences of post-transplantation lymphoproliferative disorders. *J Nephrol*. 1997;10:136–145.
5. Penn I. Incidence and treatment of neoplasia after transplantation. *J Heart Lung Transpl*. 1993;12:S328–S336.
6. Penn I. Posttransplantation de novo tumors in liver allograft recipients. *Liver Transpl Surg*. 1996;2:52–59.
7. Giannini C, Dogan A, Salomao DR. CNS lymphoma: a practical diagnostic approach. *J Neuropathol Exp Neurol*. 2014;73:478–494.
8. Doolittle ND, Petrillo A, Bell S, et al. Blood–brain barrier disruption for the treatment of malignant brain tumors: the National Program. *J Neurosci Nurs*. 1998;30:81–90.
9. Fortin D, Desjardins A, Benko A, et al. Enhanced chemotherapy delivery by intraarterial infusion and blood–brain barrier disruption in malignant brain tumors: the Sherbrooke experience. *Cancer*. 2005;103:2606–2615.
10. Siegal T, Zylber-Katz E. Strategies for increasing drug delivery to the brain: focus on brain lymphoma. *Clin Pharmacokinet*. 2002;41:171–186.
11. Weller M, Martus P, Roth P, et al. Surgery for primary CNS lymphoma? Challenging a paradigm. *Neuro-Oncol*. 2012;14:1481–1484.
12. Gijtenbeek JM, Rosenblum MK, DeAngelis LM. Primary central nervous system T-cell lymphoma. *Neurology*. 2001;57:716–718.
13. Lee DK, Chung CK, Kim HJ, et al. Multifocal primary CNS T cell lymphoma of the spinal cord. *Clin Neuropathol*. 2002;21:149–155.
14. Hirmiz K, Foyle A, Wilke D, et al. Intracranial presentation of systemic Hodgkin's disease. *Leuk Lymphoma*. 2004;45:1667–1671.
15. Haldorsen IS, Espeland A, Larsson EM. Central nervous system lymphoma: characteristic findings on traditional and advanced imaging. *ANJR Am J Neuroradiol*. 2011;32:984–992.
16. Yap KK, Sutherland T, Liew E, et al. Magnetic resonance features of primary central nervous system lymphoma in the immunocompetent patient: a pictorial essay. *J Med Imag Rad Oncol*. 2012;56:179–186.
17. Partovi S, Karimi S, Lyo JK, et al. Multimodality imaging of primary CNS lymphoma in immunocompetent patients. *Br J Radiol*. 2014;87:20130684.
18. Lolli V, Tampieri D, Melancon D, Delpilar Cortes M. Imaging in primary central nervous system lymphoma. *Neuroradiol J*. 2010;23:680–689.
19. Schulte-Altedorneburg G, Heuser L, Pels H. MRI patterns in recurrence of primary CNS lymphoma in immunocompetent patients. *Eur J Radiol*. 2012;81:2380–2385.
20. Jenkins CN, Colquhoun IR. Characterization of primary intracranial lymphoma by computed tomography: an analysis of 36 cases and a review of the literature with particular reference to calcification haemorrhage and cyst formation. *Clin Radiol*. 1998;53:428–434.

21. Slone HW, Blake JJ, Shah R, et al. CT and MRI findings of intracranial lymphoma. *AJR Am J Roentgenol*. 2005;184:1679–1685.
22. Gliemroth J, Kehler U, Gaebel C, et al. Neuroradiological findings in primary cerebral lymphomas of non-AIDS patients. *Clin Neurol Neurosurg*. 2003;105:78–86.
23. Suwanwela N, Tantanatrakool B, Suwanwela NC. Intracranial lymphoma: CT and MR findings. *J Med Assoc Thai*. 2001;84(suppl 1): S228–S243.
24. Herrlinger U, Schabet M, Bitzer M, et al. Primary central nervous system lymphoma: from clinical presentation to diagnosis. *J Neuro-Oncol*. 1999;43:219–226.
25. Remick SC, Diamond C, Migliozzi JA, et al. Primary central nervous system lymphoma in patients with and without the acquired immune deficiency syndrome. *Medicine*. 1990;69:345–360.
26. Cotton F, Ongolo-Zogo P, Louis-Tisserand G, et al. Diffusion and perfusion MR imaging in cerebral lymphomas. *J Neuroradiol*. 2006;33:220–228. [French].
27. Porto L, Kieslich M, Schwabe D, et al. Central nervous system lymphoma in children. *Pediatr Hematol Oncol*. 2005;22:235–246.
28. Tallroth K, Katevuo K, Holsti L, Andersson U. Angiography and computed tomography in the diagnosis of primary lymphoma of the brain. *Clin Radiol*. 1981;32:383–388.
29. Jack CR, Reese DF, Scheithauer BW. Radiographic findings in 32 cases of primary CNS lymphoma. *AJR Am J Roentgenol*. 1986;146:271–276.
30. Spillane JA, Kendall BE, Moseley IF. Cerebral lymphoma: clinical radiological correlation. *J Neurol Neurosurg Psychiatry*. 1982;45:199–208.
31. Heald AE, Hoffman JM, Bartlett JA, Waskin HE. Differentiation of central nervous system lesions in AIDS patients using positron emission tomography (PET). *Int J STD AIDS*. 1996;7:337–346.
32. Lorberboym M, Estok L, Machac J, et al. Rapid differential diagnosis of cerebral toxoplasmosis and primary central nervous system lymphoma by thallium-201 SPECT. *J Nucl Med*. 1996;37:1150–1154.
33. Pierce MA, Johnson MD, Maciunas RJ, et al. Evaluating contrast-enhancing brain lesions in patients with AIDS by using positron emission tomography. *Ann Intern Med*. 1995;123:594–598.
34. Pomper MG, Constantinides CD, Barker PB, et al. Quantitative MR spectroscopic imaging of brain lesions in patients with AIDS: correlation with [11C-methyl]thymidine PET and thallium-201 SPECT. *Acad Radiol*. 2002;9:398–409.
35. Skiest DJ, Erdman W, Chang WE, et al. SPECT thallium-201 combined with Toxoplasma serology for the presumptive diagnosis of focal central nervous system mass lesions in patients with AIDS. *J Infect*. 2000;40:274–281.
36. Thurnher MM, Rieger A, Kleibl-Popov C, et al. Primary central nervous system lymphoma in AIDS: a wider spectrum of CT and MRI findings. *Neuroradiology*. 2001;43:29–35.
37. Dina TS. Primary central nervous system lymphoma versus toxoplasmosis in AIDS. *Radiology*. 1991;179:823–828.
38. DeAngelis LM. Primary central nervous system lymphoma imitates multiple sclerosis. *J Neuro-Oncol*. 1990;9:177–181.
39. Lachance DH, O'Neill BP, Macdonald DR, et al. Primary leptomeningeal lymphoma: report of 9 cases, diagnosis with immunocytochemical analysis, and review of the literature. *Neurology*. 1991;41:95–100.
40. Kim HJ, Ha CK, Jeon BS. Primary leptomeningeal lymphoma with long-term survival: a case report. *J Neuro-Oncol*. 2000;48:47–49.
41. Shenkier TN. Unusual variants of primary central nervous system lymphoma. *Hematol Oncol Clin North Am*. 2005;19:651–664, vi.
42. Grove A, Vyberg M. Primary leptomeningeal T-cell lymphoma: a case and a review of primary T-cell lymphoma of the central nervous system. *Clin Neuropathol*. 1993;12:7–12.
43. King A, Wilson H, Penney C, Michael W. An unusual case of primary leptomeningeal marginal zone B-cell lymphoma. *Clin Neuropathol*. 1998;17:326–329.
44. Berciano J, Jimenez C, Figols J, et al. Primary leptomeningeal lymphoma presenting as cerebellopontine angle lesion. *Neuroradiology*. 1994;36:369–371.
45. Treves TA, Gadoth N, Blumen S, Korczyn AD. Intravascular malignant lymphomatosis: a cause of subacute dementia. *Dementia*. 1995;6:286–293.
46. Baehring JM, Henchcliffe C, Ledezma CJ, et al. Intravascular lymphoma: magnetic resonance imaging correlates of disease dynamics within the central nervous system. *J Neurol Neurosurg Psychiatry*. 2005;76:540–544.
47. Williams RL, Meltzer CC, Smirniotopoulos JG, et al. Cerebral MR imaging in intravascular lymphomatosis. *AJNR Am J Neuroradiol*. 1998;19:427–431.
48. Albrecht R, Krebs B, Reusche E, et al. Signs of rapidly progressive dementia in a case of intravascular lymphomatosis. *Eur Arch Psychiatry Clin Neurosci*. 2005;255:232–235.
49. Kenez J, Barsi P, Majtenyi K, et al. Can intravascular lymphomatosis mimic sinus thrombosis? A case report with 8 months' follow-up and fatal outcome. *Neuroradiology*. 2000;42:436–440.
50. Kinoshita T, Sugihara S, Matusue E, et al. Intravascular malignant lymphomatosis: diffusion-weighted magnetic resonance imaging characteristics. *Acta Radiol*. 2005;46:246–249.
51. Bakshi R, Mazziotta JC, Mischel PS, et al. Lymphomatosis cerebri presenting as a rapidly progressive dementia: clinical, neuroimaging and pathologic findings. *Dement Geriatr Cogn Disord*. 1999;10:152–157.
52. Rollins KE, Kleinschmidt-DeMasters BK, Corboy JR, et al. Lymphomatosis cerebri as a cause of white matter dementia. *Hum Pathol*. 2005;36:282–290.
53. Lai R, Rosenblum MK, DeAngelis LM. Primary CNS lymphoma: a whole-brain disease? *Neurology*. 2002;59:1557–1562.
54. Herrlinger U, Weller M, Küker W. Primary CNS lymphoma in the spinal cord: clinical manifestations may precede MRI detectability. *Neuroradiology*. 2002;44:239–244.
55. Schild SE, Wharen RE, Menke DM, et al. Primary lymphoma of the spinal cord. *Mayo Clin Proc*. 1995;70:256–260.
56. Bekar A, Cordan T, Evrensel T, Tolunay S. A case of primary spinal intramedullary lymphoma. *Surg Neurol*. 2001;55:261–264.
57. Deckert-Schlüter M, Marek J, Šetlík M, et al. Primary manifestation of Hodgkin's disease in the central nervous system. *Virchows Arch*. 1998;432:477–481.
58. Ashby MA, Barber PC, Holmes AE, et al. Primary intracranial Hodgkin's disease. A case report and discussion. *Am J Surg Pathol*. 1988;12:294–299.
59. Clark WC, Callihan T, Schwartzberg L, Fontanesi J. Primary intracranial Hodgkin's lymphoma without dural attachment. Case report. *J Neurosurg*. 1992;76:692–695.
60. Johnson MD, Kinney MC, Scheithauer BW, et al. Primary intracerebral Hodgkin's disease mimicking meningioma: case report. *Neurosurgery*. 2000;47:454–456.
61. Hormigo A, Abrey L, Heinemann MH, DeAngelis LM. Ocular presentation of primary central nervous system lymphoma: diagnosis and treatment. *Br J Haematol*. 2004;126:202–208.
62. Levy-Clarke GA, Chan CC, Nussenblatt RB. Diagnosis and management of primary intraocular lymphoma. *Hematol Oncol Clin North Am*. 2005;19:739–749.
63. Jahnke K, Korfel A, O'Neill BP, et al. International study on low-grade primary central nervous system lymphoma. *Ann Neurol*. 2006;59:755–762.
64. Pavlou G, Pal D, Bucur S, et al. Intracranial non-Hodgkin's MALT lymphoma mimicking a large convexity meningioma. *Acta Neurochir (Wien)*. 2006;148:791–793.
65. Rottnek M, Strauchen J, Moore F, Morgello S. Primary dural mucosa-associated lymphoid tissue-type lymphoma: case report and review of the literature. *J Neuro-Oncol*. 2004;68:19–23.
66. Tu PH, Giannini C, Judkins AR, et al. Clinicopathologic and genetic profile of intracranial marginal zone lymphoma: a primary low-grade CNS lymphoma that mimics meningioma. *J Clin Oncol*. 2005;23:5718–5727.

67. Itoh T, Shimizu M, Kitami K, et al. Primary extranodal marginal zone B-cell lymphoma of the mucosa-associated lymphoid tissue type in the CNS. *Neuropathology*. 2001;21:174–180.
68. Calderon EJ, Japon MA, Chinchon I, et al. Primary lymphoma of the central nervous system and HTLV-I infection. *Haematologia (Budap)*. 2002;31:365–367.
69. Shenkier TN, Blay JY, O'Neill BP, et al. Primary CNS lymphoma of T-cell origin: a descriptive analysis from the international primary CNS lymphoma collaborative group. *J Clin Oncol*. 2005;23:2233–2239.
70. Kim EY, Kim SS. Magnetic resonance findings of primary central nervous system T-cell lymphoma in immunocompetent patients. *Acta Radiol*. 2005;46:187–192.
71. Lee DK, Chung CK, Kim HJ, et al. Multifocal primary CNS T cell lymphoma of the spinal cord. *Clin Neuropathol*. 2002;21:149–155.

CHAPTER

42

Pituitary and Sellar Region Lesions

Eric C. Bourekas[1,2], *Lilja Bjork Solnes*[3], *H. Wayne Slone*[1]

[1]Dardinger Neuro-Oncology Center, Departments of Radiology, Wexner Medical Center at The Ohio State University and James Cancer Hospital and Solove Research Institute, Columbus, OH, USA; [2]Division of Neuro-Oncology, Departments of Neurology and Neurosurgery, Dardinger Neuro-Oncology Center, Wexner Medical Center at The Ohio State University and James Cancer Hospital and Solove Research Institute, Columbus, OH, USA; [3]Division of Nuclear Medicine, Johns Hopkins, Baltimore, MD, USA

INTRODUCTION

Sellar and juxtasellar lesions are common, with up to 27% of people having incidental pituitary tumors at autopsy.[1] Clinically, tumors in this region frequently present with endocrine abnormalities or symptoms related to mass effect on subjacent structures. Mass lesions in this region are not uncommon, accounting for 15–20% of all intracranial neoplasms. The most common lesions in adults are pituitary adenomas and meningiomas, while the most common lesions in children are craniopharyngiomas and hypothalamic/chiasmatic gliomas. In a review of 131 cases, Johnsen et al. found that 54.2% of all lesions in this region were adenomas, 10.7% meningiomas, 9.6% craniopharyngiomas, and 4.6% chiasmatic or hypothalamic gliomas.[2] The radiologic evaluation of suspected sellar and suprasellar lesions should include contrast-enhanced multiplanar magnetic resonance imaging (MRI) with dedicated small field-of-view images through the region of interest. The exact protocol varies by institution and various protocols will be discussed later. In those patients in whom MRI is contraindicated, a contrast-enhanced computed tomography (CT) scan may be done, although the soft-tissue resolution is poor and significant artifact renders this examination suboptimal. Often the imaging characteristics of a lesion along with clinical history including the patient's age will be helpful in formulating a differential diagnosis and aid in the clinical decision-making tree.

ANATOMY

The sella turcica is a bony depression in the sphenoid bone. The sella is bordered laterally by the cavernous sinuses, superiorly by the diaphragma sellae (dural fold), anteroinferiorly by the sphenoid sinus, and posteriorly by the pontine cistern. The pituitary gland normally sits within the sella. The gland itself is composed of an anterior lobe, intermediate (vestigial) lobe, and posterior lobe. The anterior lobe, adenohypophysis, forms about 75–80% of the gland and is a center for hormone synthesis, including thyroid-stimulating hormone, adrenocorticotropic hormone (ACTH), and prolactin. The posterior lobe, neurohypophysis, is connected to the hypothalamus by the pituitary stalk and receives hormones from the hypothalamus via the pituitary stalk (i.e., antidiuretic hormone). The two can be differentiated on imaging because the posterior lobe characteristically demonstrates increased T1 signal on unenhanced images, while the anterior lobe is isointense to gray matter on T1-weighted images. However, in the first 6 weeks of life the anterior pituitary is bright as well on T1-weighted images in 82%.[3] The size and configuration of the pituitary gland are thought to vary by age and sex. In adults, the gland is slightly larger in females compared to males. The height of a normal gland can be up to 9 mm.[4] The gland tends to enlarge during puberty and pregnancy. Therefore, caution must be exercised in suggesting pituitary gland pathology in young adolescent patients and women of childbearing age.

IMAGING

Although CT is used at some institutions for the evaluation of the sellar and juxtasellar regions, evaluation of this region is hampered by beam hardening artifacts related to the dense bone and by metallic artifacts from

© 2016 Elsevier Ltd. All rights reserved.

dental fillings. Soft-tissue resolution is poor compared with MRI. However, CT is excellent for the evaluation of adjacent bony structures and the presence or absence of calcifications, both of which can be important in the differential diagnosis. CT should be used only as the primary mode of evaluation in patients in which there is a contraindication to MRI. In these patients, 1-mm axial and coronal sections are obtained postcontrast, with precontrast images in one plane being useful.

MRI, because of its multiplanar capability and superior soft-tissue resolution, is the examination of choice for evaluation of sellar and juxtasellar lesions. Involvement of the subjacent structures such as the optic chiasm, cavernous sinus, sphenoid sinus, orbit, temporal lobes, and carotid arteries can be better evaluated with MRI. A small field of view of 16–20 cm, with thin sections of 3 mm or less, and high resolution, with a matrix of 256 × 256, are essential. T1- and T2-weighted images are generally obtained, with T1-weighted images after contrast administration. Sagittal and coronal imaging is most useful for imaging the pituitary and cavernous sinus region. At our institution we obtain a high-resolution three-dimensional sequence in the coronal plane with contrast for optimal evaluation of the pituitary. Because the pituitary lacks a blood–brain barrier, it enhances intensely, early, and more so than tumors, so that tumors generally appear as areas of nonenhancement. Dynamic T1-weighted fast spin echo imaging after a bolus of contrast can detect lesions not seen on standard imaging in 10–14% of cases.[5,6] However, in 12.5–17% of cases, lesions are better seen with standard postcontrast images and in 8–9% of cases lesions are seen with standard imaging and not with dynamic imaging.[6] For these reasons, standard imaging is used in most cases, with dynamic imaging performed in problem cases.

Incidental lesions are frequently identified on MRI in the sellar region owing to increased soft-tissue resolution. Autopsy studies reveal incidental pituitary pathology in up to 27% of cases, most being incidental microadenomas or pars intermedia cysts.[1] Focal 2- to 3-mm lesions on imaging will prove to be incidental as often as they are endocrinologically significant.[1] In patients with incidental lesions, with normal laboratory values and no clinical symptoms, stability over a 2-year period on follow-up imaging suggests a benign etiology and no further studies are necessary.[7]

Venous sampling of the inferior petrosal or cavernous sinus is an invasive study that can be valuable in the diagnosis of a suspected adenoma, and in particular Cushing's disease, in cases in which imaging has failed to identify a lesion. Catheters are placed from each of the femoral veins into the internal jugular veins and then advanced into each of the inferior petrosal sinuses.[8] Blood samples are obtained from each side both before and after stimulation with corticotropin-releasing hormone and analyzed. This technique can reliably distinguish pituitary Cushing's disease due to a microadenoma from ectopic ACTH syndrome in patients with negative imaging and can frequently lateralize the lesion.[9,10] Although inferior petrosal sinus sampling is usually performed, it has been shown that bilateral, simultaneous cavernous sinus sampling, using corticotropin-releasing hormone, is as accurate as inferior petrosal sinus sampling in detecting Cushing's disease and perhaps more accurate in lateralizing the abnormality within the pituitary gland.[11] However, this procedure is not without risk. Miller et al. reported that 0.2–0.5% of patients undergoing the procedure suffered a major neurologic complication thought to be related to venous hypertension.[12]

The discussion that follows is based on whether a lesion is solid, mixed solid and cystic, or cystic, although this is a somewhat oversimplified approach. Clearly lesions that tend to be solid, such as adenomas, can be cystic or mixed, and lesions that tend to be mixed solid and cystic, such as craniopharyngiomas, can be purely solid or purely cystic.

SOLID LESIONS

Pituitary Adenoma

Adenomas arise from the adenohypophyseal cells and are the most common tumors of the sella turcica in adults. Although many different classification schemes exist, pituitary adenomas are most commonly classified according to size and function (functioning versus nonfunctioning adenomas).[13–15] Lesions smaller than 1 cm are classified as *microadenomas* and those larger than 1 cm are classified as *macroadenomas*. Microadenomas tend to be functioning lesions, whereas macroadenomas are usually nonfunctioning lesions.

Johnsen et al. reported that 54% of sellar and juxtasellar lesions in their series were pituitary adenomas.[2] Pituitary adenomas are usually seen in adults and are uncommon in children, representing less than 3% of all pediatric intracranial tumors.[16] However, pituitary adenomas occurring in the pediatric population are thought to be more aggressive lesions and warrant more aggressive therapy than their adult counterparts.[17] The clinical presentation may be related to the size of the lesion, presence or absence of hormone secretion, or degree of local invasion.

Approximately 60–70% of adenomas present with symptoms related to hormone secretion, while the remainder present with symptoms related to mass effect.[18] Microadenomas most commonly present with a clinical picture reflecting the hormone excess. The most common functioning adenomas are prolactinomas. Other functioning adenomas include ACTH-secreting tumors, thyroid-stimulating hormone-secreting tumors, and growth hormone-secreting tumors. Nonsecreting

adenomas go unrecognized until they produce symptoms such as visual compromise, due to compression of the optic chiasm, nerve, or tract, or cranial nerve pathology due to local invasion of the cavernous sinus.

Although adenomas are overwhelmingly benign, they have been known to metastasize, with seeding of the cerebrospinal fluid (CSF),[19] and are associated with an increased morbidity and mortality due to an increased incidence of cardiovascular disease and cerebrovascular disease.[20,21] Patients with nonfunctioning adenomas and acromegaly have also been shown to have a significantly higher incidence of malignancy than the general population.[22]

The imaging appearance of pituitary adenomas is nonspecific, and no inference to histology can be made from the sellar patterns. On MRI, microadenomas appear as areas of nonenhancement (Figure 1). This reflects the difference in enhancement pattern of normal pituitary tissue compared with enhancement patterns of adenomas. The gland is not generally enlarged, although the contour of the gland may be changed, with the upper margin becoming convex, the floor of the sella demonstrating a downsloping, or with deviation of the infundibulum. It has been reported that more than 90% of microadenomas can be detected by contrast-enhanced MRI.[1]

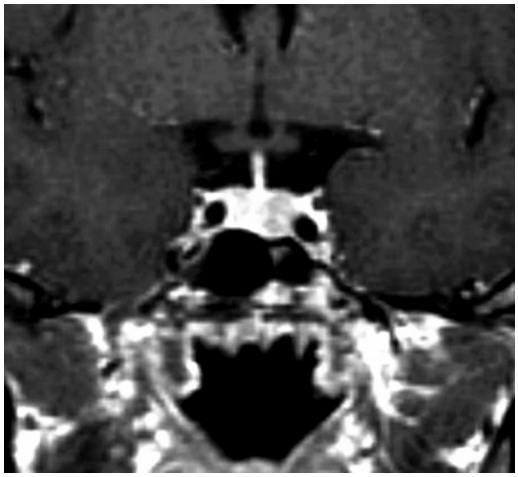


FIGURE 1 Microadenoma. Conventional coronal T1-weighted image with contrast through the pituitary. The patient is a 21-year-old female with headaches. She was not found to have significant endocrine abnormalities. The image demonstrates a small hypointense (nonenhancing relative to the pituitary) lesion of the left pituitary consistent with a microadenoma.

The MRI appearance of macroadenomas can be variable although typically they follow gray matter signal on all sequences (Figure 2). Cystic changes can be seen in up to 18% of cases (Figure 7).[23] Enhancement is also variable although generally intense and somewhat heterogeneous (Figures 3 and 4). A typical figure-of-eight configuration can be seen owing to compression of the tumor at the diaphragma sella (Figure 5). Calcifications can be seen, although they are not commonly associated with adenomas.[24] Adenomas may also hemorrhage, especially in the setting of treatment with bromocriptine (Figure 6). Although more commonly seen in the setting of craniopharyngiomas, edema can be seen along the optic tracts in the setting of any pituitary lesion compressing the optic tracts (Figure 8).[25] Saeki et al. proposed that this edema-like pattern is seen because of dilated Virchow–Robinson spaces, due to drainage obstruction related to the presence of a pituitary lesion.[25]

Invasion of adjacent structures is seen in up to 35% of cases and is not indicative of malignancy (Figures 8–10).[26] Approximately 10% of pituitary adenomas involve the cavernous sinus (Figures 3, 6, and 10).[27] Knowledge of involvement of the cavernous sinus is important in surgical planning because of increased morbidity/mortality related to the surgery, regardless of histologic grade of the tumor. It has been reported that encasement of the carotid artery is the most specific sign of cavernous sinus invasion.[28] Cottier et al. suggest that if the tumor encases the internal carotid artery by 25%

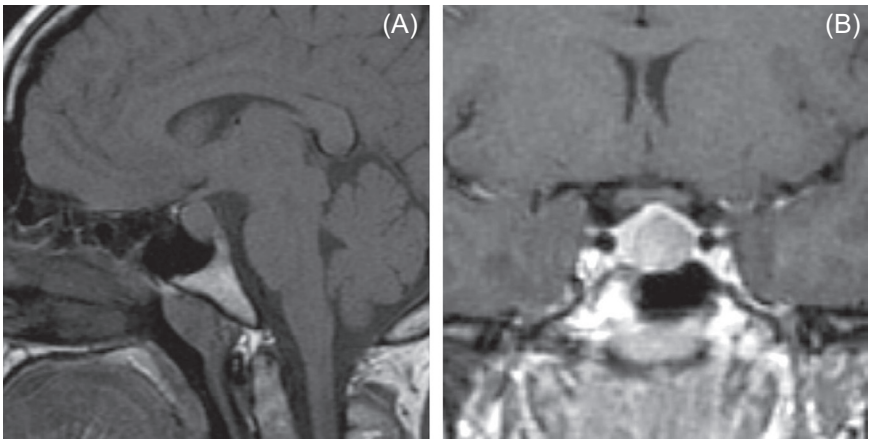


FIGURE 2 Macroadenoma. (A) Sagittal T1-weighted image precontrast. (B) Coronal T1-weighted image postcontrast. Images demonstrate a mass lesion of the sella and suprasellar region. The unenhanced lesion has signal similar to gray matter on T1-weighted images and demonstrates mild-to-moderate contrast enhancement.

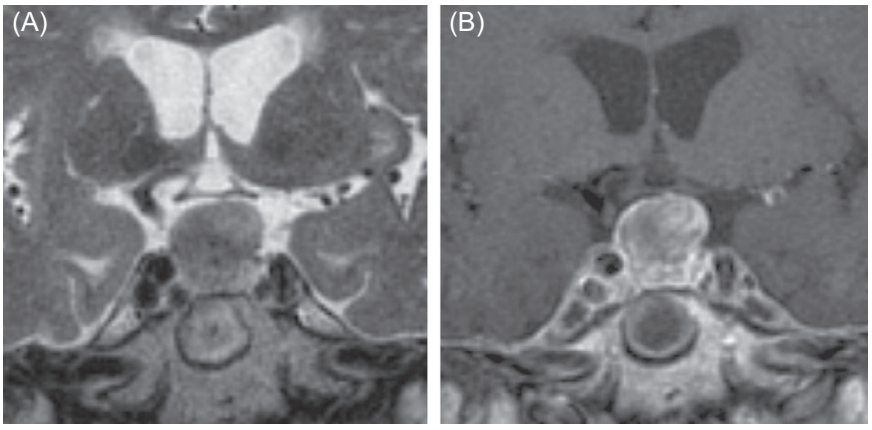


FIGURE 3 Macroadenoma. (A) Coronal T2-weighted image. (B) Coronal T1-weighted image postcontrast. Images reveal a predominantly peripherally enhancing macroadenoma in a 78-year-old male, invading the right cavernous sinus and compressing the optic.

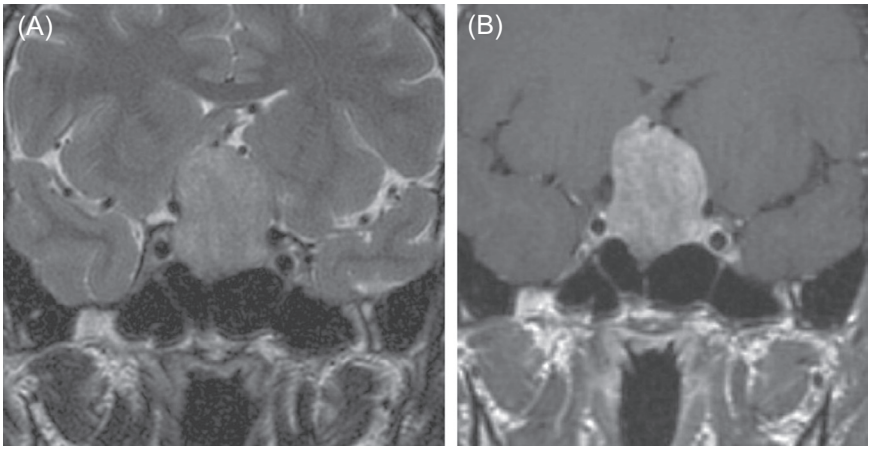


FIGURE 4 Macroadenoma. (A) Coronal T2-weighted image. (B) Coronal T1-weighted image postcontrast. Sellar and suprasellar pituitary adenoma, which displaces adjacent vasculature and optic chiasm. The patient's initial complaint was of visual disturbances.

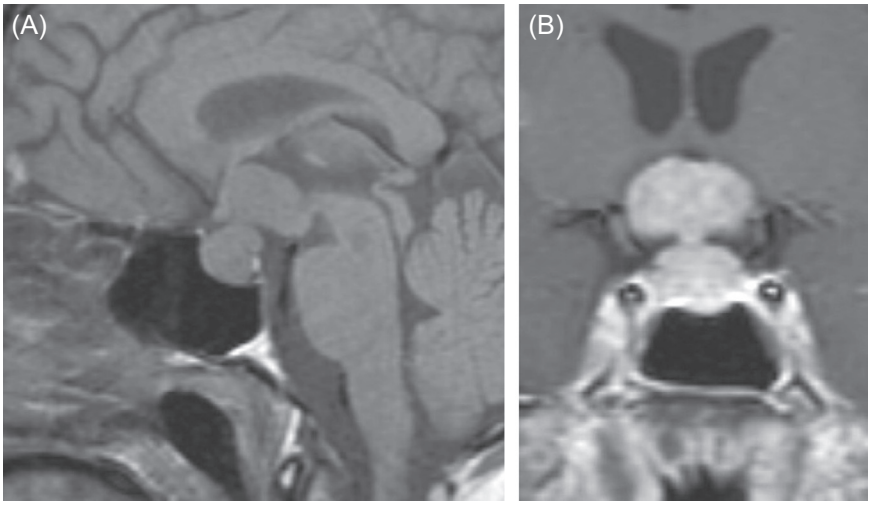


FIGURE 5 Macroadenoma. (A) Sagittal T1-weighted image precontrast. (B) Coronal T1-weighted image postcontrast. The patient is a 46-year-old male with lung cancer metastatic to the brain. However, given the stability of this lesion and its configuration "classic figure-of-eight," it was thought that the pituitary lesion represented an incidental macroadenoma. The waist of the lesion is caused by the diaphragma sella through which the lesion has passed.

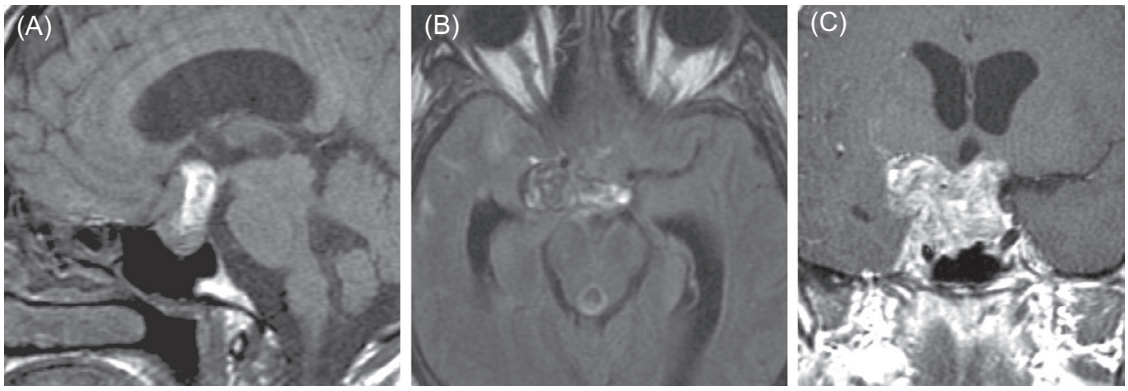


FIGURE 6 Invasive macroadenoma with possible calcifications versus hemorrhage. (A) Sagittal T1-weighted image. (B) Axial fluid-attenuated inversion recovery (FLAIR) image. (C) Post-contrast-enhanced coronal T1-weighted image. This is an invasive macroadenoma, involving the cavernous sinus, which demonstrates areas of increased signal on T1-weighted images before the administration of contrast as well as areas of decreased signal on FLAIR and T2-weighted images. These foci may represent calcifications or hemorrhage.

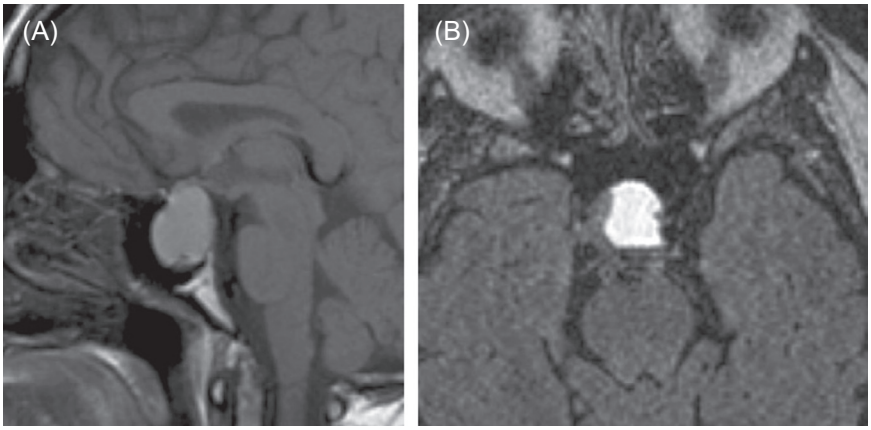


FIGURE 7 Cystic macroadenoma. (A) Sagittal T1-weighted image shows a hyperintense lesion involving the sella and suprasellar region. (B) Axial FLAIR image shows a bright focus within the lesion thought to represent cystic change.

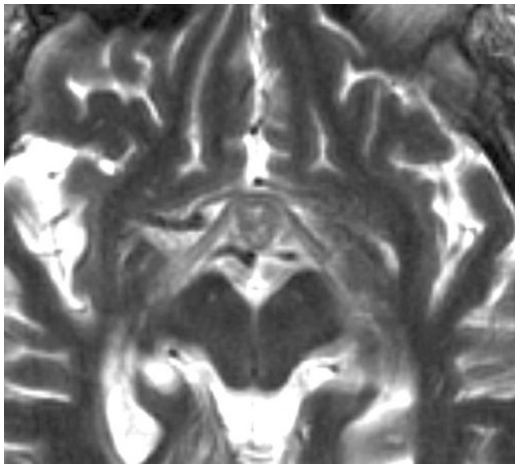


FIGURE 8 Macroadenoma with edematous changes involving the optic tracts bilaterally. Axial T2-weighted image shows abnormal high signal in the optic tracts bilaterally compatible with edema related to a pituitary adenoma occupying the suprasellar region.

or less, or the margin drawn between the medial aspect of the supra- and intracavernous internal carotid artery was not invaded by tumor, the negative predictive value was 100%.[29] Asymmetric tentorial enhancement has also been described as a useful sign for suggesting invasion or severe compression by a sellar tumor on the cavernous sinus.[30]

Prolactinomas and growth-hormone-secreting tumors can be treated medically.[31] Bromocriptine is commonly used in prolactinomas, with MRI used to evaluate the patient's response to therapy.[32] A decrease in tumor size can be seen as early as 1 week after the start of therapy. Additionally, MRI can detect posttherapy hemorrhage into macroadenomas and mass effect or inferior herniation of the chiasm as a result of a decrease in the tumor size.[33] Bromocriptine has been associated with an increased incidence of intratumoral hemorrhage, also known as pituitary apoplexy.[34] The clinical syndrome is characterized by sudden headache, vomiting, visual

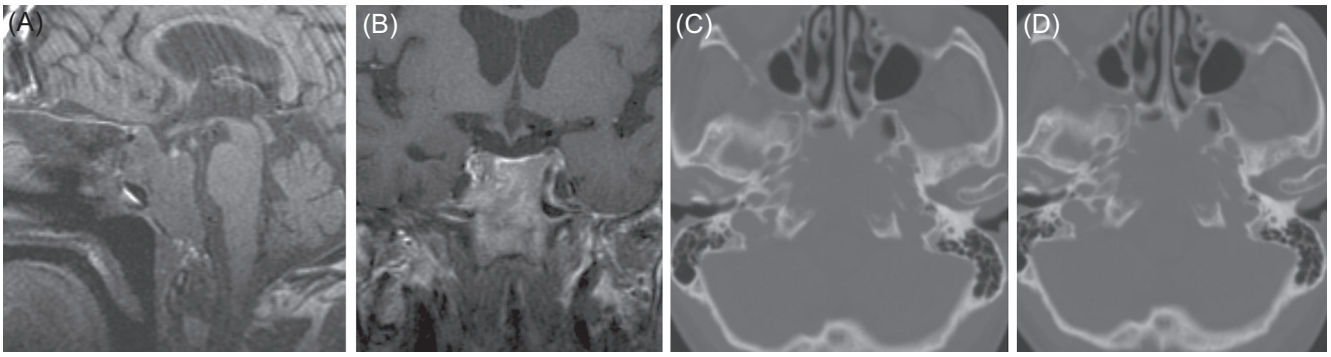


FIGURE 9 Invasive macroadenoma. (A) Sagittal T1-weighted image without contrast. (B) Coronal T1-weighted post-contrast-enhanced image. Images demonstrate a mass in the pituitary region, which appears to invade the clivus. (C and D) Axial CT images at the level of the clivus (bone windows) show destruction of much of the clivus related to an invasive adenoma. This is an 80-year-old male who had a CT scan of the head following a syncopal episode.

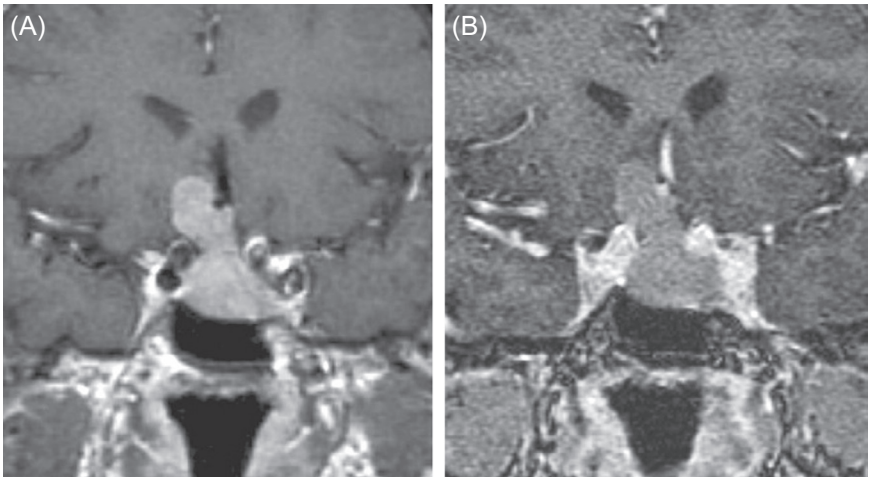


FIGURE 10 Invasive macroadenoma. (A) Coronal T1-weighted postcontrast. (B) Thin-section T1-weighted postcontrast. Images show a macroadenoma extending into the inferior right frontal lobe. The lesion invades the left cavernous sinus. Patient presented because of visual disturbances in the left eye.

impairment, and meningismus, caused by rapid enlargement of an adenoma owing to hemorrhagic infarction.[35] Subarachnoid hemorrhage and vasospasm have been reported.[36] Octreotide is commonly used in patients with acromegaly due to excess secretion of growth hormone.[37] Transsphenoidal surgery is the preferred approach to the resection of pituitary adenomas because it is associated with lower morbidity and mortality than the transcranial approach, which is generally the preferred approach for large tumors.[38]

Meningioma

Meningiomas are the second most common primary brain tumors of the sellar and juxtasellar region, representing 11% of tumors in this region and second only to pituitary adenomas.[2,23] Ten percent of all meningiomas occur in the parasellar region. Meningiomas can arise from the diaphragma sella (Figure 11), tuberculum sella, medial sphenoid ridge, optic nerve sheaths, clinoids (Figure 12), cavernous sinus (Figure 13), or clivus, as well as the planum sphenoidale (Figure 14). Rarely, meningiomas can be intrasellar, probably arising from the diaphragma or tuberculum sella and growing downward. Clinically, patients usually present with visual disturbances because of involvement of the cavernous sinus and without endocrine dysfunction.

On CT, calcification is common, as is hyperostosis. Contrast enhancement is typically intense. MRI is the examination of choice for meningiomas because of its multiplanar capability. On MRI, meningiomas are typically isointense to gray matter on T1 and isointense or mildly to moderately hyperintense on T2-weighted images and demonstrate homogeneous and relatively intense contrast enhancement (Figure 14), in contrast to macroadenomas in which enhancement is not as intense and somewhat heterogeneous.[39] A dural tail is helpful although not diagnostic, being present in up to 57% of

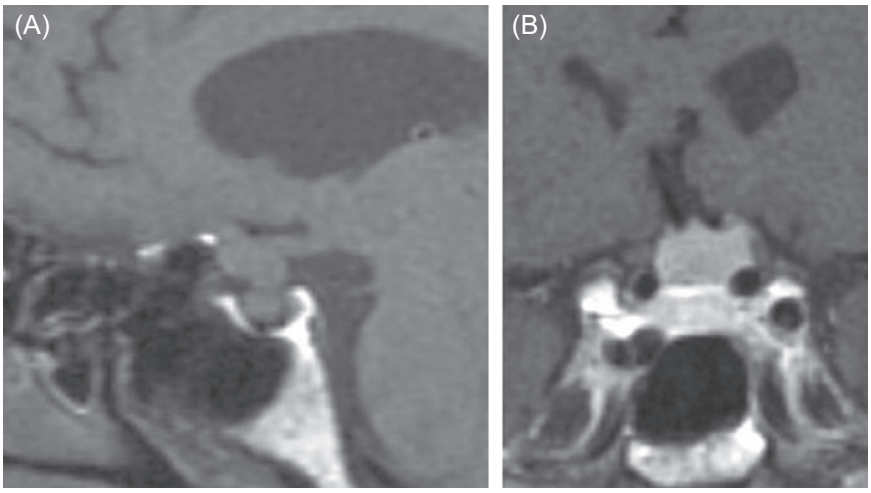


FIGURE 11 Meningioma of the diaphragma sella. (A) Precontrast T1-weighted sagittal mage. (B) Coronal post-contrast-enhanced image shows a uniformly enhancing lesion arising from the diaphragmatic sella. The normally enhancing pituitary can be seen as a separate structure inferior to the lesion.

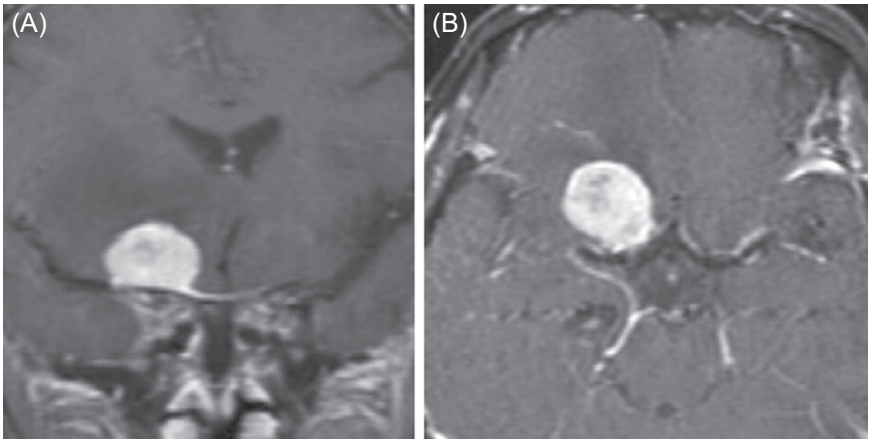


FIGURE 12 Clinoid meningioma. (A) Coronal T1-weighted post-contrast-enhanced image. (B) Axial T1-weighted post-contrast-enhanced image. Images show a homogeneously enhancing lesion, which abuts the left anterior clinoid process. The coronal image also shows a classic dural tail (enhancement of the subjacent dura) extending across the planum sphenoidale, suggesting the diagnosis of meningioma.

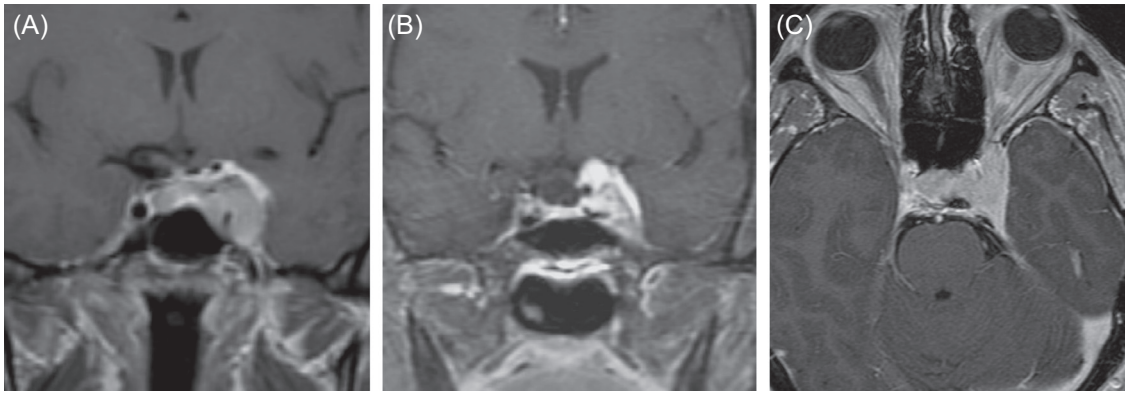


FIGURE 13 Meningioma of the cavernous sinus. (A and B) Coronal post-contrast-enhanced T1-weighted image. (C) Axial T1-weighted post-contrast-enhanced image. The patient had transient vision loss. Images show a relatively homogeneously enhancing mass involving the left cavernous sinus, encasing and narrowing the internal carotid artery, which is characteristic of meningiomas. Patient was a 51-year-old female with a history of left-sided visual disturbances.

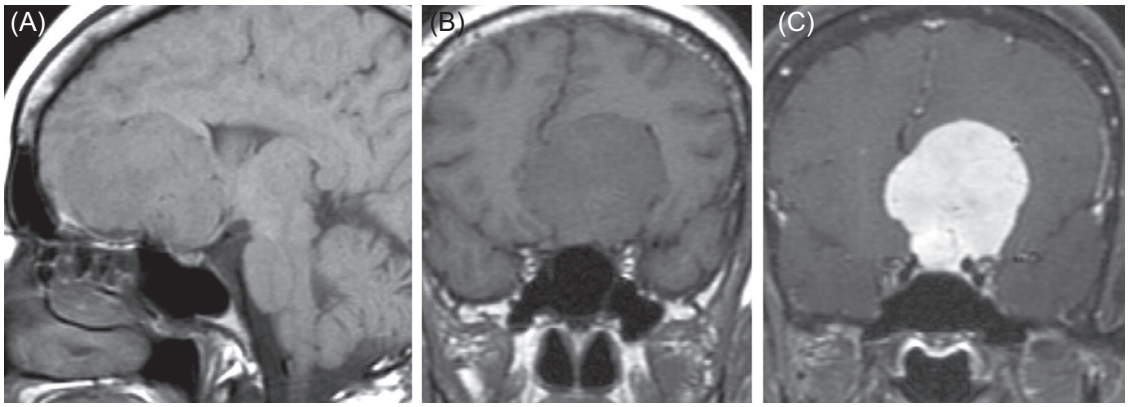


FIGURE 14 Meningioma of the planum sphenoidale. (A) Sagittal T1-weighted image demonstrates a mass lesion arising from the region of the planum sphenoidale along the midline, which is essentially isointense to gray matter. (B) Coronal T1-weighted image without contrast shows an isointense lesion in the anterior cranial fossa. (C) Coronal T1-weighted image postcontrast shows intense and uniform enhancement. The imaging findings are classic for a meningioma of the planum sphenoidale.

cases (Figure 12(A)).[2] The epicenter of the lesion is usually not in the sella, with the sella almost always being normal and the pituitary gland easily identified. This is the major distinguishing factor from macroadenomas.[39] Another distinguishing factor is the fact that meningiomas typically encase and constrict the carotids (Figure 13), whereas macroadenomas may encase but typically do not constrict vessels. Invasion of the carotid artery is frequently seen, even when there is no evidence of narrowing of the artery.[40] Making the diagnosis preoperatively is important since meningiomas are treated via craniotomy rather than by a transsphenoidal approach. Surgical resection is considered to be the treatment of choice for meningiomas, whenever this can be accomplished with acceptable morbidity; however, radiosurgery can also be an effective management strategy for many patients with meningiomas.[41]

Chiasmatic and Hypothalamic Gliomas

Gliomas of the hypothalamus and optic pathways represent 5% of pediatric intracranial tumors.[42] The vast majority represent slow-growing pilocytic astrocytomas, although malignant gliomas and in particular glioblastoma multiforme may occur, especially in adults.[43] The most common locations for pilocytic astrocytomas are the cerebellum, optic nerve and chiasm, and hypothalamic region.[44] Pilocytic astrocytomas occur most commonly in the first 2 decades of life—75% of cases.[45] The mean age of presentation is 5 years.[46] An association with neurofibromatosis 1 (NF-1) has been reported with up to 15–21% of NF-1 patients developing pilocytic astrocytomas, usually involving the optic nerve or chiasm.[47,48]

It is difficult to discern the site of origin of chiasmatic/hypothalamic gliomas by imaging in most cases, since both the optic chiasm and the hypothalamus are involved regardless of the site of origin.[49] For this reason, both are discussed as one entity. Chiasmatic gliomas may occasionally demonstrate extension along the optic tracts or optic nerves, thus indicating their site of origin. Patients usually present with visual symptoms, headaches, and endocrine abnormalities. Endocrine abnormalities occur in 42%, with growth hormone deficiency being the most common.[46,50]

MRI is the examination of choice. The lesions tend to be solid with microcyst formation. They are usually iso- or hypointense on T1-weighted images and hyperintense on T2-weighted images and demonstrate variable enhancement with contrast. These lesions do not typically hemorrhage or calcify. The sella and its contents are usually normal.[46,50]

Generally the treatment of choice for pilocytic astrocytomas is resection, except for lesions involving the optic pathway and hypothalamic region, for which the treatment of choice is chemotherapy and radiation.[44] Chemotherapy may be used to postpone radiation treatment until after the age of 5, which may reduce neurological morbidity.[42] Chiasmatic/hypothalamic gliomas are more aggressive in the very young and in adults.[42,51,52] In NF-I the course is more indolent.[42] Survival is 93% at 5 years and 74% at 10 years, with chiasmatic lesions having a 19-year 44% survival.[53] The prognosis of chiasmatic gliomas is worse than with optic nerve gliomas.[53]

Germinoma

The sellar and suprasellar region is the second most common location of central nervous system (CNS) germ cell tumors; the most common location is the pineal gland. The most commonly occurring CNS germ cell tumor is a germinoma. Other germ cell tumors such as teratomas, embryonal carcinomas, choriocarcinomas, and mixed tumors are much less common intracranially, particularly in the sellar and suprasellar region.

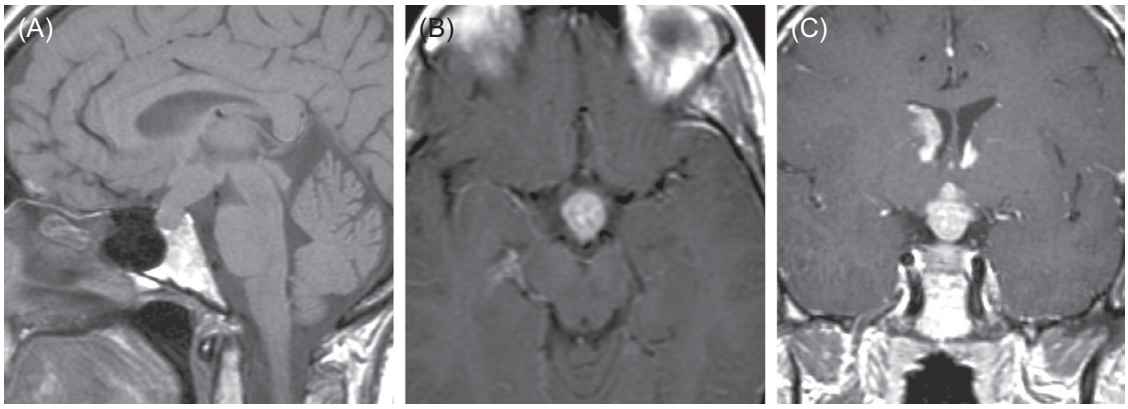


FIGURE 15 Germinoma. (A) T1-weighted sagittal. (B) Axial T1-weighted postcontrast. (C) Coronal T1-weighted postcontrast. Images show a lobulated mass, which appears to enhance uniformly in the sellar/suprasellar region. Patient was a 28-year-old female complaining of abnormal menses. Abnormal enhancement is also seen in the region of the lateral ventricles bilaterally compatible with tumor involvement.

However, these lesions are not as common as other CNS tumors, representing approximately 0.5–3% of all CNS tumors.[54] These lesions occur in children and young adults. Synchronous pineal and suprasellar lesions occur in 6–12% of germinomas and are considered diagnostic.[55] Primary suprasellar germinomas have no sex predilection, in contrast to pineal germinomas, which show a male predominance.[50] The clinical presentation often includes hypopituitarism, diabetes insipidus, and visual disturbances.

On MRI, the mass appears as a well-marginated, round or lobulated, homogeneous tumor with prolonged T1 and T2 relaxation times, which strongly enhances after gadolinium administration (Figure 15). The presence of these imaging findings in a young patient, along with a clinical history of diabetes insipidus, is a strong clue to the diagnosis of germinoma.[56] Also, germinomas may secrete β-human chorionic gonadotropin or α-fetoprotein, which can be detected in the CSF or blood and can aid in the preoperative diagnosis. Germinoma cells frequently spread through the CSF. Therefore, imaging the entire neural axis may be helpful.

Biopsy is necessary prior to treatment, except in the case of synchronous suprasellar and pineal lesions. The lesions are extremely radiosensitive, with over 90% of patients being effectively treated with radiation therapy alone. Germinomas, however, are also very chemosensitive, with reports suggesting that the dose and volume of radiation required can be lessened with the addition of adjuvant chemotherapy.[57] At our institution intra-arterial chemotherapy after disruption of the blood–brain barrier has been used with good results. Radical resection offers no benefit over biopsy with subsequent radiation and/or chemotherapy, making the preoperative diagnosis very important in decision-making.[58] Prognosis is good, with 10- and 20-year survival rates of 92.7% and 80.6%, respectively.[59]

Metastasis

Metastases to the pituitary gland represent 1–4% of pituitary tumors, with 50% being of breast origin and 20% from the lung.[60] Metastases to the sellar, suprasellar, or parasellar region may arise in the sphenoid bone or sinus, cavernous sinus, pituitary gland, hypothalamus, or surrounding soft tissues. It may be difficult to distinguish a metastasis from a primary pituitary abnormality on the basis of imaging alone; however, the presence of bony destruction or the history of a known primary tumor may be helpful. The incidence of pituitary metastases ranges from 0.14 to 28.1% of all brain metastases, the incidence being higher in autopsy series.[61] Sellar metastases appear to favor the posterior lobe of the pituitary and the pituitary stalk, which may be related to the difference in blood supply compared with the anterior lobe.[62] The posterior lobe of the pituitary derives its blood supply primarily from arterial blood flow, whereas the anterior lobe receives most of its blood supply from portal vessels. These patients frequently present with diabetes insipidus, which occurs in 33–70% of patients with symptomatic pituitary metastases, in contrast to only 1–2% of patients with pituitary adenomas (Figures 16 and 17). Primary carcinomas of the pituitary gland are rare.[63] Metastases to the gland are more common.

Schwannoma

Schwannomas, which are tumors derived from the myelin sheath of peripheral nerves, can be found involving the cranial nerves within the cavernous sinus and parasellar regions. In general, pituitary function is not affected; however, often the cranial nerves III, IV, V, and VI are affected within the cavernous sinuses or in the suprasellar and prepontine cisterns. Schwannomas most commonly arise from the trigeminal nerve but may involve other cranial nerves as well.[64] Remodeling of the

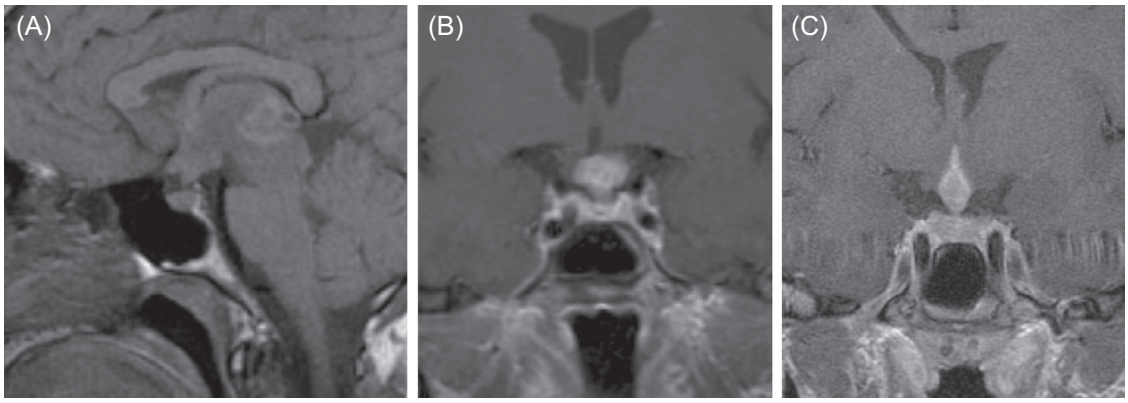


FIGURE 16 Metastatic anaplastic oligodendroglioma involving the pituitary stalk. (A) T1-weighted sagittal image. (B and C) Post-contrast-enhanced coronal T1-weighted images show an irregular suprasellar lesion involving the infundibulum. The patient is a 19-year-old male with a history of anaplastic oligodendroglioma in the right frontal lobe. Multiple lesions seen on brain MRI were thought to represent multifocal metastases due to CSF seeding.

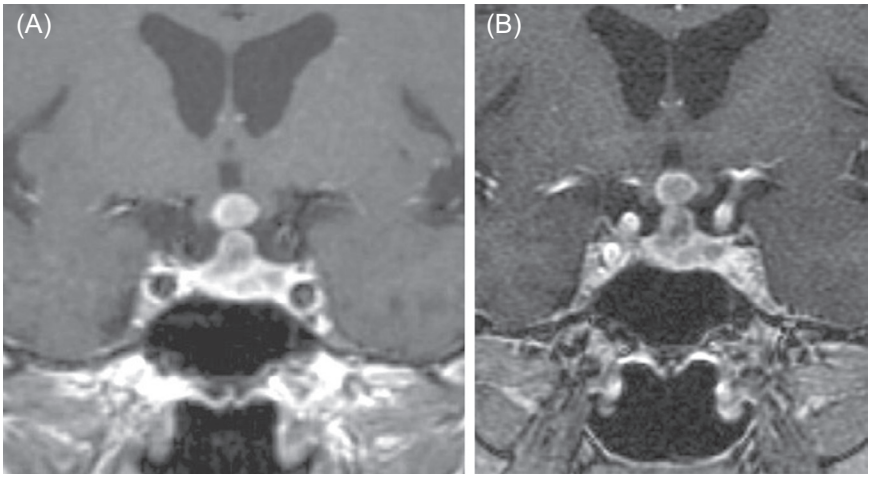


FIGURE 17 Infundibular metastases. (A) Coronal T1-weighted image through the sellar region and (B) coronal SPGR post-contrast-enhanced image through the infundibulum demonstrate a small enhancing lesion of the infundibulum in a patient with renal cell carcinoma representing metastatic disease.

skull base foramina where individual nerves exit may occur. When multiple lesions are seen, neurofibromatosis should be considered. On CT, schwannomas usually are hyperdense lesions with homogeneous enhancement, and they may be hard to differentiate from meningiomas. On MRI, they may be isointense or hyperintense to gray matter on T1-weighted images, with dense and homogeneous enhancement.[64]

Hypothalamic Hamartoma

A hamartoma of the tuber cinereum usually presents as precocious puberty in a young child.[65] It is important to differentiate this lesion from a hypothalamic glioma, because the prognosis for hamartoma is much more favorable. Imaging is best with thin-section coronal and sagittal MRI. The findings are usually characteristic: The mass arises from the undersurface of the hypothalamus and is exophytic. The nodular mass (<1 cm) hangs into the suprasellar cistern adjacent to the mammillary bodies. On T1-weighted images, the signal is isointense with normal brain and on T2-weighted images there is mild hyperintensity or isointensity. The distinguishing feature is that these lesions do not usually enhance with contrast administration.

Pituitary Hyperplasia

The pituitary gland commonly enlarges during puberty and pregnancy. The gland may also increase in size in the setting of endocrine disequilibrium. For example, in the setting of primary hypothyroidism, the pituitary gland will grow in size. This hyperplasia is thought to be related to lack of negative feedback on the hypothalamus by circulating thyroid hormone.[66] On imaging, the pituitary gland will appear enlarged, but will not show any

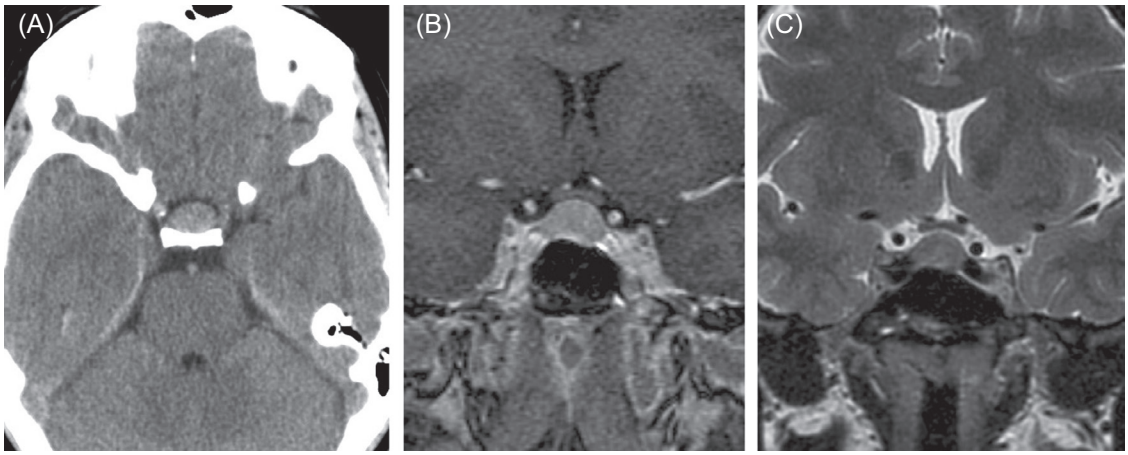


FIGURE 18 Pituitary hyperplasia. (A) Axial CT scan through the region of the pituitary shows a homogeneously enhancing mass. (B) Coronal post-contrast-enhanced SPGR image demonstrates a prominent pituitary gland, which enhances homogeneously. (C) Coronal T2-weighted image shows a prominent pituitary with uniform signal. Patient was a young female who had undergone a total thyroidectomy followed by ^{131}I therapy for thyroid cancer.

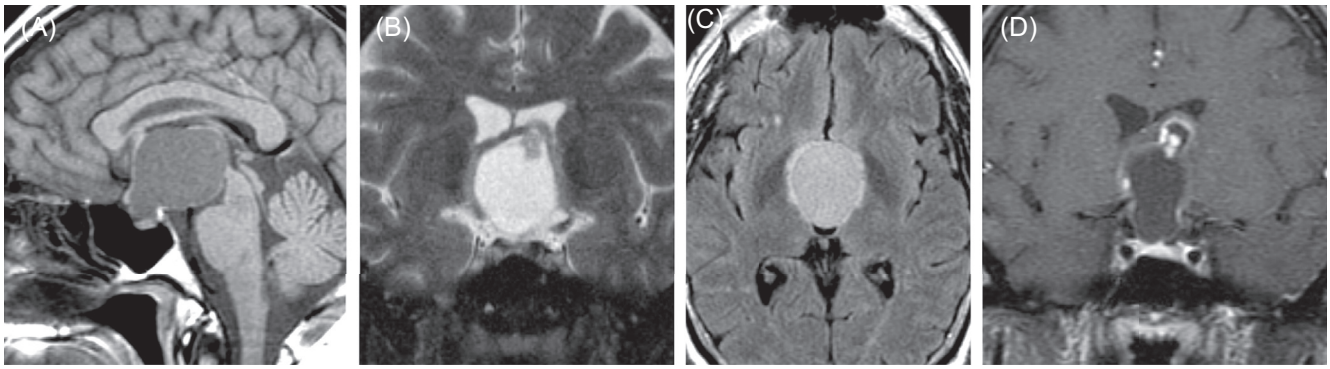


FIGURE 19 Craniopharyngioma—cystic. (A) Sagittal T1-weighted image. (B) Axial T2-weighted image. (C) Axial FLAIR. (D) Coronal T1-weighted post-contrast-enhanced image. The images demonstrate a predominantly cystic mass lesion in the suprasellar region. Post-contrast-enhanced images as well as the T2-weighted images show an enhancing solid nodular density associated with this cystic mass, suggesting the diagnosis of craniopharyngioma.

nonenhancing lesions or nonuniformity on post-contrast-enhanced images (Figure 18). Following therapy for hypothyroidism, the gland will decrease in size.[67]

MIXED SOLID AND CYSTIC LESIONS

Craniopharyngioma

Craniopharyngiomas are the most common intracranial tumor of nonglial origin in children, comprising up to 10% of pediatric brain tumors.[31,68,69] They are formed from ectodermal remnants of Rathke's pouch and are composed of a squamous epithelium. Craniopharyngiomas can occur anywhere from the floor of the third ventricle (hypothalamus) to the pharyngeal tonsils, with 67% being found in the suprasellar region. These tumors have a bimodal incidence, with peaks in the first and fifth decades. Although they are histologically benign, they are behaviorally aggressive, invading adjacent structures and thus making resection difficult. Recurrence is local, although meningeal seeding has been described.[70]

Two distinct subtypes are recognized: the adamantinous, which tend to occur in children, and the squamous–papillary variants, which tend to occur in adults.[71] Craniopharyngiomas are thought to be part of a continuum of ectodermally derived cystic epithelial lesions, which includes arachnoid cysts, Rathke's cleft cysts, epidermoids, and dermoids, with craniopharyngiomas being at the more aggressive end of the spectrum.[72] They typically present because of mass effect on the chiasm and hydrocephalus, with visual disturbances, headaches, and pituitary and hypothalamic dysfunction. Endocrine deficiency is seen in 80%, with growth hormone deficiency noted in 75%.[73]

Craniopharyngiomas can be predominantly cystic (Figure 19), mixed cystic/solid (Figure 20), or entirely

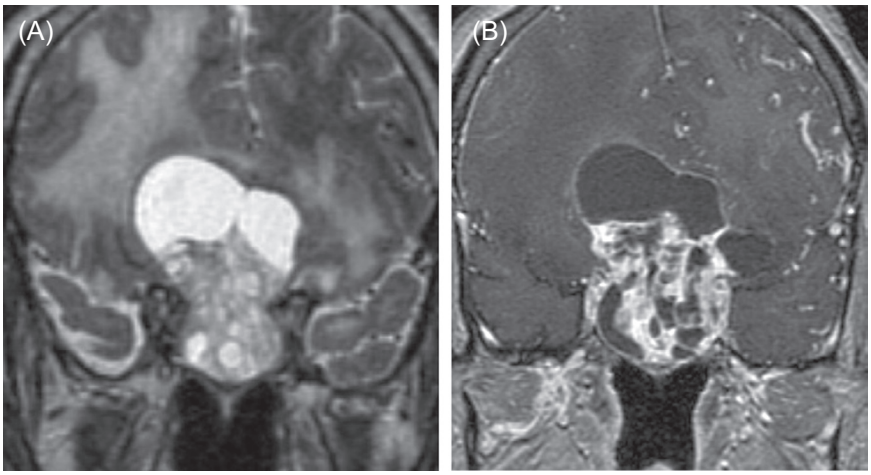


FIGURE 20 Mixed solid and cystic craniopharyngioma. (A) Coronal T2-weighted image. (B) Coronal T1-weighted post-contrast-enhanced image. The images show a mixed solid/cystic lesion centered in the suprasellar cistern with marked enhancement of the solid component on post-contrast-enhanced images. The mass compresses and may invade the third ventricle, resulting in hydrocephalus.



FIGURE 21 Solid craniopharyngioma. Coronal T1-weighted post-contrast-enhanced image shows a solid lesion in the suprasellar region, which is a nonspecific finding. This lesion was resected and found to represent a solid craniopharyngioma.

solid (Figure 21), although the mixed solid and cystic appearance is rather characteristic. Hemorrhage is not an uncommon finding, particularly within cystic portions of the tumors. Craniopharyngiomas may grow to compress the optic chiasm superiorly, to displace the normal pituitary gland and stalk, to invade the cavernous sinuses, and even to encase or occlude the carotid arteries. CT is the examination of choice for evaluation of calcification, which is seen in 87% of cases (Figure 23).[74] On MRI, high signal intensity on T1- and T2-weighted images is seen in cysts with high cholesterol content or with subacute hemorrhage. Craniopharyngiomas can also be of low signal intensity on T1-weighted images if the cyst contains a large amount of keratin.[75] Fluid levels can be seen in cystic regions. Adamantinous craniopharyngiomas tend to be primarily cystic or mixed cystic–solid lesions that tend to occur in children, whereas squamous–papillary subtypes tend to be predominately solid or mixed solid–cystic and occur in adults.[71] Distinguishing between the two has a prognostic significance since adamantinous tumors tend to recur. MRI can be helpful in distinguishing between the two, with encasement of vessels, a lobulated shape, and the presence of hyperintense cysts favoring adamantinous tumors, and a round shape, presence of hypointense cysts, and a predominately solid appearance being seen with squamous–papillary tumors.[71] Calcification, encasement of vessels, and recurrence favor adamantinous craniopharyngiomas.[71] Enhancement tends to be heterogeneous, with the solid portions of the lesion enhancing after the administration of contrast (Figure 20). Preoperative differentiation from arachnoid cysts, Rathke's cleft cysts, epidermoids, and dermoids can be difficult. Calcification and solid components are features more commonly seen with craniopharyngiomas.[74] In adults, calcified aneurysms must be part of the differential of calcified lesions in the sellar, parasellar, and suprasellar regions.

Treatment is primarily surgical, with the efficacy of radiotherapy being well documented. Gamma Knife radiosurgery may also play a role, although there are no specific guidelines.[76] Recurrence-free survival after total resection is 86.9% at 5 years, but falls to 48.8% with subtotal resection.[77]

Epidermoid and Dermoid

Epidermoids and dermoids are uncommon, slow-growing masses that account for 1% of all intracranial

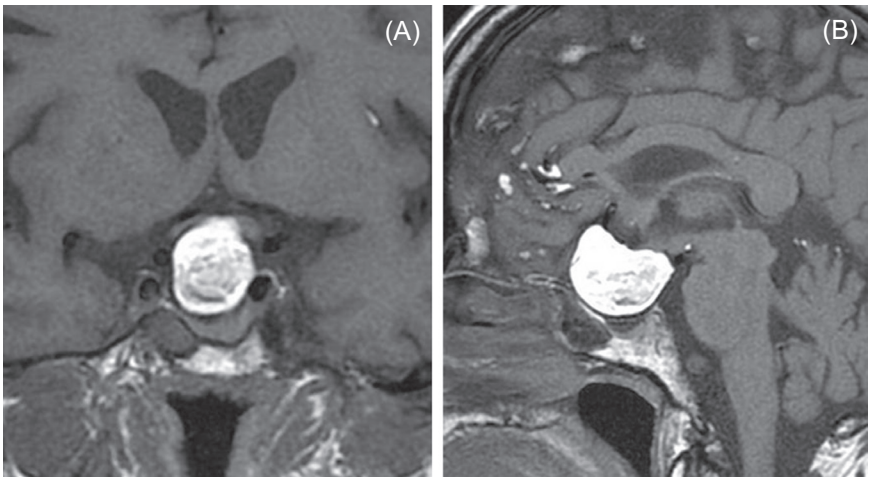


FIGURE 22 Ruptured dermoid. (A) Coronal T1-weighted and (B) sagittal T1-weighted images demonstrate a large hyperintense mass lesion of an enlarged sella and suprasellar extension compressing the optic chiasm, consistent with a dermoid. (B) Note the droplets of increased signal in the CSF spaces indicating that the dermoid has ruptured, thus explaining the patient's headaches.

neoplasms.[78] These lesions are similar in their development, histology, behavior, and imaging and for this reason are discussed together. Both lesions are generally considered developmental/congenital masses rather than neoplastic, arising from ectodermal heterotopias. Both cysts are lined with stratified squamous epithelium, with dermoids adding mesodermal elements such as hair, sebaceous glands, and sweat glands.

Epidermoids are slightly more common than dermoids intracranially. They typically spread along the basal surfaces, with the cerebellopontine angles being the most common location, followed by the parasellar region.[79–81] They are extra-axial lesions with only 1.5% being intracerebral.[82] They are overwhelmingly benign, although they can be malignant in rare cases. Average age of presentation is 37.3 years, with a male-to-female ratio of 3:2.[78] The symptomatic onset is generally slow, lasting 2 years or more, although for suprasellar lesions it is much shorter.[82] Presenting symptoms may include headaches, visual problems, cranial nerve symptoms, and seizures, which typically indicate rupture. Rupture can produce aseptic meningitis, which can be lethal, although not necessarily so.

Epidermoids on CT appear as hypodense masses, with irregular borders and rare contrast enhancement. Dense lesions have been reported and calcification is occasionally seen.[81,83] On MRI, they typically are of low signal on T1- and of increased signal on T2-weighted images, following that of CSF on all pulsing sequences.[78] Classically, they can be differentiated from arachnoid cysts on diffusion-weighted images, on which these lesions show restricted diffusion and are bright, whereas arachnoid cysts are not bright.

Dermoids are midline lesions, occurring in the parasellar, frontobasal region, or posterior fossa.[84] Average age of presentation is 36.2 years with a male-to-female ratio of 3:1.[78] The complications of dermoids are similar to those of epidermoids. They can present with headaches, seizures, meningeal signs, and TIAs.[84,85] Most of these symptoms are indicative of rupture, which produces a chemical or aseptic meningitis and which can be lethal in some cases.[84,86] The CT appearance of dermoids is similar to that of epidermoids. Their MRI appearance depends on the amount of fat present, although generally they are of increased signal on both T1- and T2-weighted images.[78] CT or MRI can both make the diagnosis of rupture although MRI is the preferred preoperative study (Figure 22).[85]

Treatment is surgery, with 86% being in good or excellent condition postoperatively. The 20-year survival of epidermoids is 92.8%, with good survival even with recurrence.[78] Epidermoids have a classic mother-of-pearl appearance at surgery.

Rathke's Cleft Cyst

Rathke's cleft cysts are epithelial cysts that arise from Rathke's pouch remnants. Small Rathke's cleft cysts are commonly found at autopsy in 12–33% of normal pituitary glands, with cysts noted by imaging being much less common.[87] They are usually found in the pars intermedia between the anterior and the posterior lobes of the pituitary.[88] Histologically, they have a single row of cuboidal or columnar epithelial lining in contrast to craniopharyngiomas, which have a squamous epithelial lining.

Rathke's cleft cysts are usually intrasellar cysts (Figure 23), but may be intrasellar and suprasellar, rarely purely suprasellar, and have been described even in the sphenoid sinus.[89] They may be asymptomatic, although they frequently present with endocrine abnormalities, headaches, and visual field defects, especially when there is suprasellar extension.[74] Nishioka et al. found that the presence of anterior pituitary dysfunction or headaches

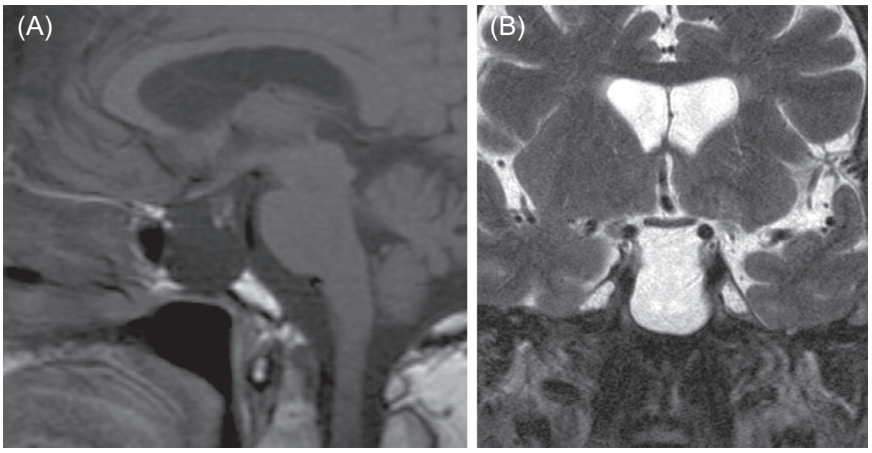


FIGURE 23 Rathke's cleft cyst. (A) Sagittal T1-weighted image without contrast demonstrates a cystic intrasellar lesion. (B) Coronal T2-weighted image shows that this cystic structure follows the CSF signal. The sella is expanded. This lesion was thought to represent a Rathke's cleft cyst. Similar findings could be seen in the setting of empty sella or arachnoid cyst.

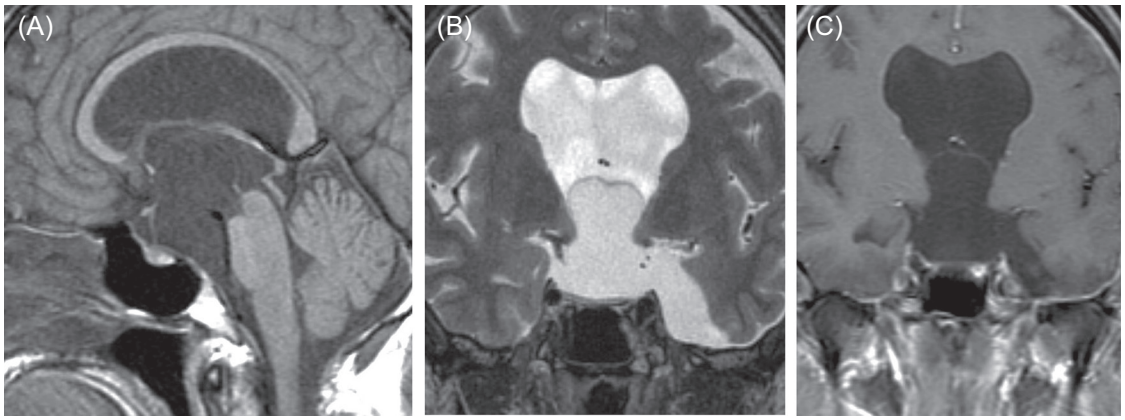


FIGURE 24 Arachnoid cyst. (A) Sagittal T1-weighted image. (B) Coronal T2-weighted image. (C) Coronal T1-weighted post-contrast-enhanced image. Images show a nonenhancing lesion centered in the sellar/suprasellar region, which follows CSF signal on all sequences and was thought to represent an arachnoid cyst. Patient was scanned following a traumatic event. The arachnoid cyst was an incidental finding.

was not related to cyst size but was more likely to be present in patients whose cyst demonstrated a high/isointense T1-weighted signal, as opposed to those demonstrating low signal intensity.[90] The mean age of presentation is 38 years, with a female predominance of 2:1.[31,91] Teramoto et al. found that 87% of incidental lesions found in the medial aspect of the pituitary gland were Rathke's cleft cysts, whereas 74% of incidental lesions centered in the lateral gland represented adenomas.[92]

On CT, the sella may be normal or slightly expanded. The cysts can usually be seen as an area of low attenuation that is similar to CSF. Calcification is seen in approximately 13% of cases—usually peripherally, in contrast to craniopharyngiomas, in which calcification is seen in 87% of cases.[74] Peripheral rim enhancement may be seen.[23] On MRI, the cysts are usually isointense with CSF on all pulse sequences (Figure 23). Occasionally, they may have a more unusual signal due to varying cyst fluid composition. Cyst wall biopsy and aspiration, usually transsphenoidal, is considered to be curative with a low recurrence rate of 5%.[72,91]

Arachnoid Cyst

These nonneoplastic cysts are a rare cause of cystic lesions in the sellar region. As noted previously, it has been suggested that they are a part of a continuum of epithelial cysts at the more benign end of the spectrum behaviorally. They are thought to be developmental lesions arising from an imperforate membrane of Liliequist, which develops into a diverticulum and subsequently a cyst when it loses its communication with the subarachnoid space.[93] They tend to present at an older age, usually the fifth decade, with headaches, visual field defects, and impotence.[74] On MRI, these sellar and/or suprasellar cysts follow CSF signal on all pulsing sequences (Figure 24), as do epidermoids, but with no restricted diffusion, which helps distinguish them from

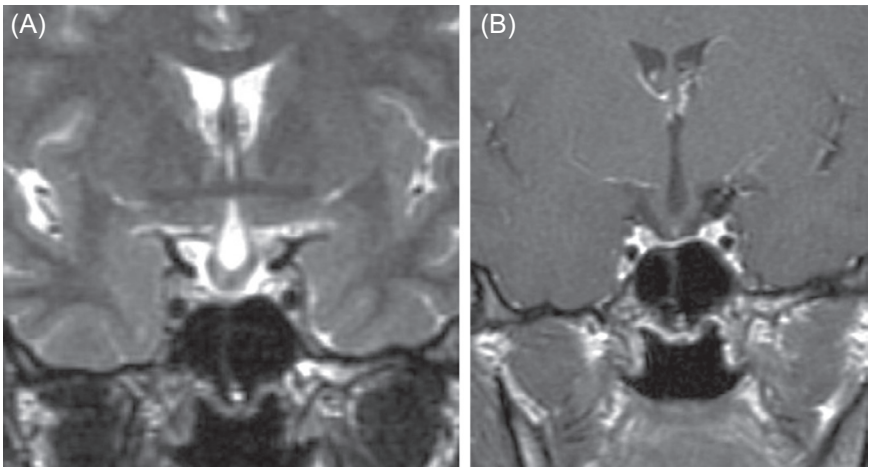


FIGURE 25 Empty sella. (A) Coronal T2-weighted image. (B) Coronal T1-weighted postcontrast. Images show an empty sella with downward herniation of the optic chiasm. Patient was a young female with panhypopituitarism.

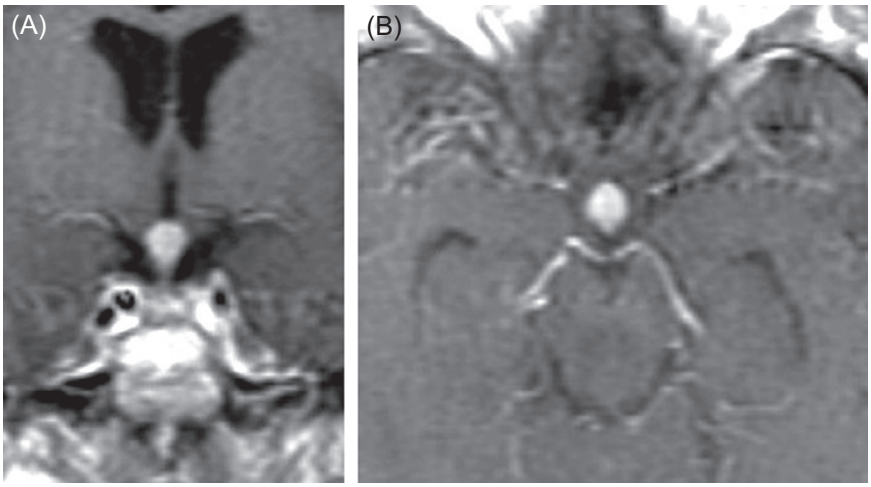


FIGURE 26 Lymphoma. (A) Coronal and (B) axial T1-weighted images following the administration of contrast demonstrate an enhancing lesion involving the pituitary stalk in a patient with a history of systemic lymphoma. Findings resolved following chemotherapy for lymphoma.

epidermoids. They are well defined, with no calcification and no enhancement.[50,74]

Empty Sella

The term "empty sella" refers to a condition in which the sella is filled with CSF with significant flattening of the pituitary gland with possible enlargement of the sella turcica (Figure 25). The etiology for this finding is thought to be a defect in the diaphragma sella, which exposes the sella and its contents to CSF pulsations that over time enlarge the sella and flatten the gland. It is generally considered an incidental finding, with most patients with this finding demonstrating no clinical symptoms. However, some patients may have endocrine deficiencies, headaches, or visual disturbances. A strong statistical correlation between an empty sella and idiopathic intracranial hypertension or pseudo-tumor has been established.[94]

PITUITARY STALK LESIONS

The thickness of the normal pituitary stalk is approximately 2 mm. The normal stalk enhances markedly on CT and MRI with contrast. The most common clinical problem associated with disease of the pituitary stalk is diabetes insipidus. When this is present, there usually is absence of the normal hyperintensity of the posterior pituitary noted on T1-weighted MRI. Diabetes insipidus may also occur as a result of transection of the pituitary stalk.

The differential diagnosis of a thickened stalk includes sarcoidosis, tuberculosis, histiocytosis X, germinoma, lymphoma (see Figure 26), leukemia, metastasis

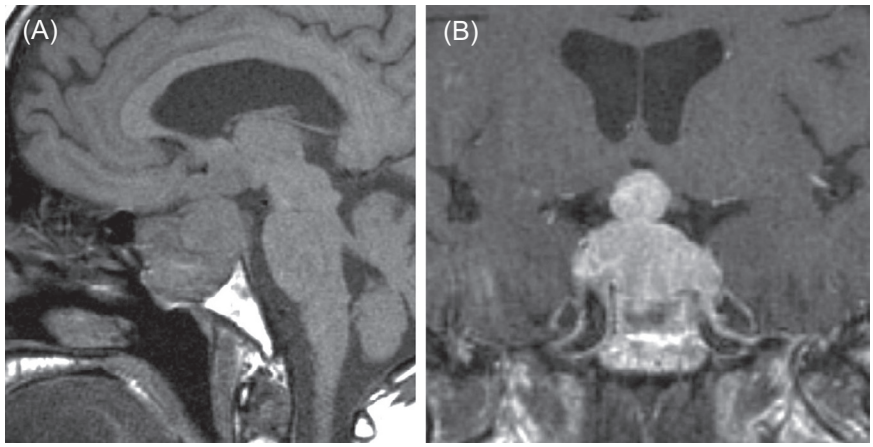


FIGURE 27 Neurosarcoidosis. (A) Sagittal T1-weighted image. (B) Coronal T1-weighted image after contrast administration. Images show a lobulated mass involving the sellar and suprasellar region, which enhances on postcontrast images. The patient was a 62-year-old male complaining of visual disturbances with known sarcoidosis. His symptoms improved following a steroid regimen.

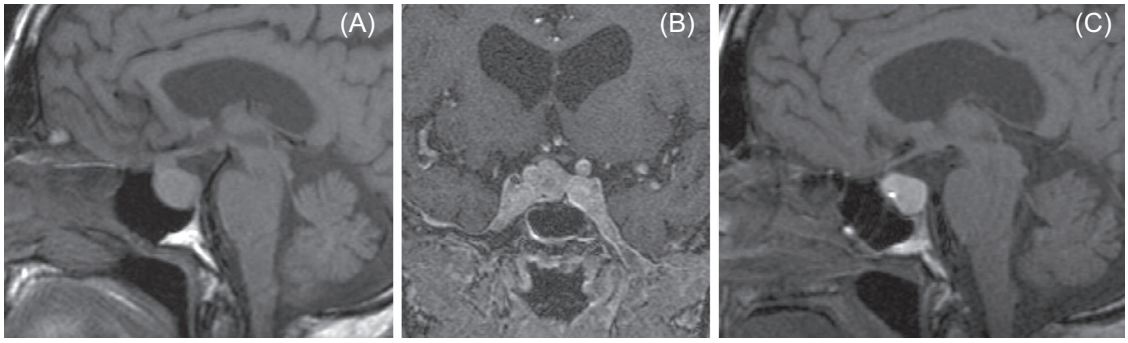


FIGURE 28 Lymphocytic hypophysitis. (A) T1-weighted sagittal image showing a pituitary mass. (B) Coronal thin-section T1-weighted image following the administration of contrast shows enhancement of this lesion. The patient was a 74-year-old male who presented with headaches. (C) Follow-up T1-weighted sagittal image showing increased T1 signal within the lesion thought to represent hemorrhage.

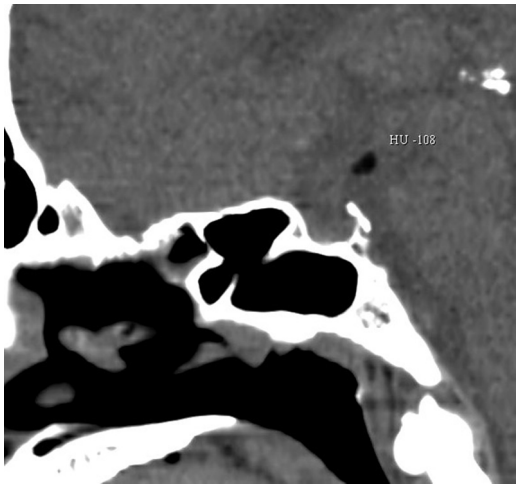


FIGURE 29 Suprasellar lipoma. Midline sagittal CT image without contrast reveals a low-density lesion, measuring −108 HU, of the suprasellar cistern representing an incidental lipoma. This was an incidental finding in a patient complaining of headache.

(Figures 17 and 18), and ectopic posterior pituitary. A thickened stalk can also be due to an extension of a glioma from the hypothalamus.

Clinical findings may help in sorting out the etiology for pituitary stalk thickening. For example, in patients with neurosarcoidosis or tuberculous infiltration of the stalk, the chest radiograph is generally abnormal and may be helpful in the differentiation from histiocytosis X. Clinically, patients with histiocytosis X may have skin lesions, otitis media, or bone lesions, in addition to interstitial lung disease.[95]

Neurosarcoidosis causing clinical symptoms is an uncommon manifestation of sarcoidosis. It has been reported that symptomatic neurosarcoidosis occurs in up to 5% of patients.[96] The most common clinical symptoms include cranial nerve dysfunction, aseptic meningitis related to leptomeningeal spread, hydrocephalus, and dysfunction of the hypothalamic–pituitary axis such as diabetes insipidus.[96,97] Neurosarcoidosis commonly affects the leptomeninges with findings of basilar

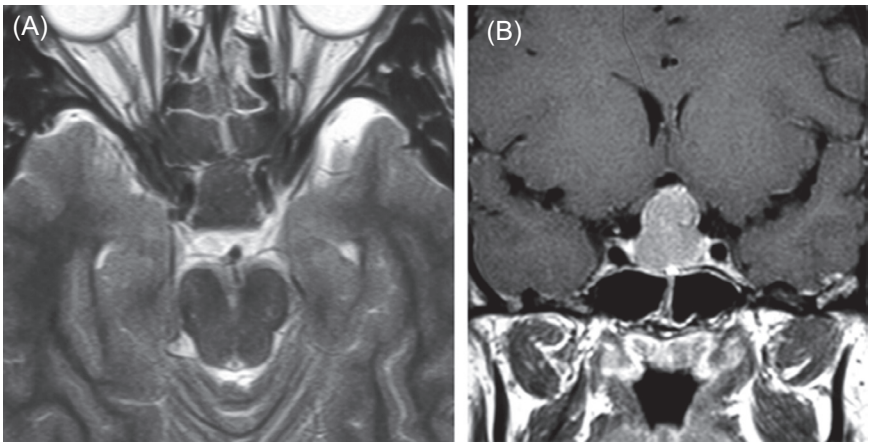


FIGURE 30 Choristoma. (A) Axial T2-weighted image and (B) axial T1-weighted post-contrast-enhanced image show a well-circumscribed sellar/juxtasellar mass that enhances uniformly. Its appearance is suggestive of an adenoma. Histology after resection revealed a choristoma.

leptomeningitis affecting the pituitary gland region and subjacent structures.[97] Mass lesions as a result of sarcoid are less common (Figure 27).

MISCELLANEOUS LESIONS

Lymphocytic hypophysitis is a rare entity affecting the pituitary gland and stalk. It is thought to represent an inflammatory disorder, although the exact cause is unknown.[98] Clinically, patients may complain of headache, visual disturbances, symptoms related to diabetes insipidus, or abnormal menses. The pituitary hormone levels may be depressed. On imaging, the lesion may present as a mass involving the adenohypophysis and mimic pituitary adenomas (Figure 7) and/or present as a mass primarily involving the infundibulum and the neurohypophysis. Lymphocytic hypophysitis may regress following steroid therapy.

Recently, ipilimumab-associated autoimmune hypophysitis has been described in patients with metastatic melanoma treated with ipilimumab. Ipilimumab-induced hypophysitis is more frequent among older and male patients. Fatigue and headache are the most frequent initial clinical manifestations, and enlargement of the pituitary gland at MRI is present in the majority of patients. Those who receive more than three cycles of ipilimumab have more fatigue and arthritis. Adrenal insufficiency is more prevalent in men and can be fatal. Glucocorticoid therapy and hormone replacement are required in most patients and pituitary function recovery is uncommon. The MRI appearance is the same as with lymphocytic hypophysitis (Figure 28).[100]

Other entities should be considered in the differential diagnosis of lesions centered in the sellar and juxtasellar regions. These include aneurysms, lymphoma, leukemia, teratoma, chordoma, chondrosarcoma, melanoma, nasopharyngeal carcinoma, mucoceles, lipoma (Figure 29), hemangioma,[99] pituitary astrocytomas,[100] xanthogranuloma, and choristoma[101] (Figure 30).

References

1. Elster AD. Modern imaging of the pituitary. *Radiology*. 1993;187:1–14.
2. Johnsen DE, Woodruff WW, Allen IS, et al. MR imaging of the sellar and junxtasellar regions. *Radiographics*. 1991;11:727–758.
3. Dietrich RB, Lis LE, Greensite FS, Pitt D. Normal MR appearance of the pituitary gland in the first 2 years of life. *AJNR Am J Neuroradiol*. 1995;16:1413–1419.
4. Wolpert SM, Molitch ME, Goldman JA, Wood JB. Size, shape and appearance of the normal female pituitary gland. *AJR*. 1984;143:377–381.
5. Miki Y, Matsuo M, Nishizawa S, et al. Pituitary adenomas and normal pituitary tissue: enhancement patterns on gadopentetate-enhanced MR imaging. *Radiology*. 1990;177:36.
6. Bartynski WS, Lin L. Dynamic and conventional spin-echo MR of pituitary microlesions. *Am J Neuroradiol*. 1997;18(5):965–972.
7. Naidich MJ, Russell EJ. Current approaches to imaging of the sellar region and pituitary. *Endocrinol Metab Clin North Am*. 1999;28(1):45–79.
8. Miller DL, Doppman JL, Nieman LK, et al. Petrosal sinus sampling: discordant lateralization of ACTH-secreting pituitary microadenomas before and after stimulation with corticotropin-releasing hormone. *Radiology*. 1990;176:429.
9. Graham KE, Samuel MH, Nesbit GM, et al. Cavernous sinus sampling is highly accurate in distinguishing cushing's disease from the ectopic adrenocorticotropin syndrome and in predicting intrapituitary tumor location. *J Clin Endocrinol Metab*. 1999;84(5):1602–1610.
10. Mamelak AN, Dowd CF, Tyrrell JB, McDonald JF, Wilson CB. Venous angiography is needed to interpret inferior petrosal sinus and cavernous sinus sampling data for lateralizing adrenocorticotropin-secreting adenomas. *J Clin Endocrinol Metab*. 1996;81(2):475–481.
11. Oliverio PJ, Monsein LH, Wand GS, Debrun GM. Bilateral simultaneous cavernous sinus sampling using corticotropin-releasing hormone in the evaluation of cushing disease. *AJNR Am J Neuroradiol*. 1996;17:1669–1674.

12. Miller DL, Doppman JL, Peterman SB, Nieman LK, Oldfield EH, Chang R. Neurologic complication of petrosal sinus sampling. *Radiology*. 1992;185:143–147.
13. Asa SL. The pathology of pituitary tumors. *Clin North Am*. 1999;28(1):13–43.
14. Kovacs K, Scheithauer B, Horvath E, Lloyd R. The world health organization classification of adenohypophysial neoplasms. *Cancer*. 1996;78(3):502–510.
15. Mindermann T. Letter to the editor: classification of pituitary adenomas. *Acta Neurochir*. 1997;139:267–270.
16. Poussaint TY, Barnes PD, Anthony DC, Spack N, Scott RM, Tarbell NJ. Hemorrhagic pituitary adenomas of adolescence. *AJNR Am J Neuroradiol*. 1996;17(10):1907–1912.
17. Fisher B, Gasper LE, Stitt LW, Noone BE. Pituitary adenomas in adolescents: a biologically more aggressive disease? *Radiology*. 1994;192:869–872.
18. Evanson EJ. Imaging of the pituitary gland. *Imaging*. 2002; 14:93–102.
19. De Boucaud L, Dousset V, Caillaud P, Viaud B, Guerin J, Caille JM. Metastases from a pituitary adenoma: MRI. *Neuroradiology*. 1999;41(10):785–787.
20. Brada M, Burchell L, Ashley S, Traish D. The incidence of cerebrovascular accidents in patients with pituitary adenoma. *Int J Radiat Oncol Biol Phys*. 1999;45(3):693–698.
21. Nilsson B, Gustavsson-kadaka E, Bengtsson B, Jonsson B. Pituitary adenomas in Sweden between 1958 and 1991: incidence, survival and mortality. *J Clin Endocrinol Metab*. 2000;85(4):1420–1425.
22. Popovic V, Damjanovic S, Micic D, et al. Increased incidence of neoplasia in patients with pituitary adenomas. *Clin Endocrinol*. 1998;49:441–445.
23. Simonetta AB. Imaging of suprasellar and parasellar tumors. *Neuroimaging Clin North Am*. 1999;9(4):717–732.
24. Majos C, Coll S, Aguilera C, Acebes JJ, Pons LC. Imaging of giant pituitary adenomas. *Neuroradiology*. 1998;40:651–655.
25. Saeki N, Uchino Y, Murai H, et al. MR imaging study of edema-like change along the optic tract in patients with pituitary region tumors. *Am J Neuroradiol*. 2003;24:336–342.
26. Levy RA, Quint DJ. Giant pituitary adenoma with unusual orbital and skull base extension. *AJR Am J Roentgenol*. 1998;170(1):194–196.
27. Ahmadi J, North CM, Segall HD, Zee CS, Weiss MH. Cavernous invasion by pituitary adenomas. *AJR*. 1986;146:257–262.
28. Scotti G, Yu C, Dillon WP, et al. MR imaging of cavernous sinus involvement by pituitary adenomas. *AJR*. 1988;151:799–806.
29. Cottier JP, Destrieux C, Vinikoff-Sonier C, Jan M, Herbreteau D. MRI diagnosis of cavernous sinus invasion by pituitary adenomas. *Ann Endocrinol*. 2000;61(3):269–274.
30. Nakasu Y, Nakasu S, Ito R, Mitsuya K, Fujimoto O. Tentorial enhancement on MR image is a sign of cavernous sinus involvement in patients with sellar tumors. *Am J Neuroradiol*. 2001;22:1528–1533.
31. Freda PU, Post KD. Differential diagnosis of sellar masses. *Endocrinol Metab Clin North Am*. 1999;28(1):81–117.
32. Pinzone JJ, Katznelson L, Danila DC, Pauler DK, Miller CS, Klibanski A. Primary medical therapy of micro- and macroprolactinomas in men. *J Clin Endocrinol Metab*. 2000;85(9):3053–3057.
33. Lundin P, Bergstrom K, Nyman R, et al. Macroprolactinomas: serial MR imaging in long-term bromocriptine therapy. *AJNR Am J Neuroradiol*. 1992;13:1287.
34. Yousem DM, Arrington JA, Zinreich JS, Kumar AJ, Bryan RN. Pituitary adenomas: possible role of bromocriptine in intratumoral hemorrhage. *Radiology*. 1989;170(1):239–243.
35. Randeva H, Schoebel J, Byrne J, Esiri M, Adams CBT, Wass JAH. Classical pituitary apoplexy: clinical features, management and outcome. *Clin Endocrinol*. 1999;51:181–188.
36. Sanno N, Ishii Y, Sugiyama M, et al. Subarachnoid hemorrhage and vasospasm due to pituitary apoplexy after pituitary function tests. *Acta Neurochir*. 1999;141:1009–1010.
37. Melmed S. Acromegaly. *Metabolism*. 1996;45(8):51–52.
38. Giovanelli M, Losa M, Mortini P. Surgical therapy of pituitary adenomas. *Metabolism*. 1996;45(8):115–116.
39. Cappabianca P, Cirillo S, Alfieri A, et al. Pituitary macroadenoma and diaphragma sellae meningioma: differential diagnosis on MRI. *Neuroradiology*. 1999;41:22–26.
40. Sen C, Hague K. Meningiomas involving the cavernous sinus: histological factors affecting the degree of resection. *J Neurosurg*. 1997;87:535–543.
41. Stafford SL, Pollock BE, Foote RL, et al. Meningioma radiosurgery: tumor control, outcomes, and complications among 190 consecutive patients. *Neurosurgery*. 2001;49(5):1029–1038.
42. Janss AJ, Grundy R, Cnaan A, et al. Optic pathway and hypothalamic/chiasmatic gliomas in children younger than age 5 years with a 6-year follow-up. *Cancer*. 1995;75(4):1051–1059.
43. Barbaro NM, Rosenblum ML, Maitland CG, Hoyt WF, Davis RL. Malignant optic glioma presenting radiologically as a "cystic" suprasellar mass: case report and review of the literature. *Neurosurgery*. 1982;11(6):787–789.
44. Koeller KK, Rushing EJ. Pilocytic astrocytoma: radiology-pathologic correlation. *Radiographics*. 2004;24:1693–1708.
45. Wallner KE, Gonzales MF, Edwards MSB, Wara WM, Sheline GE. Treatment of juvenile pilocytic astrocytomas. *J Neurosurg*. 1988;69:171–176.
46. Collet-Solberg PF, Sernyak H, Satin-Smith M, et al. Endocrine outcome in long-term survivors of low-grade hypothalamic/chiasmatic glioma. *Clin Endocrinol*. 1997;47(1):79–85.
47. Deliganis AV, Geyer JR, Berger MS. Prognostic significance of type 1 neurofibromatosis (von Recklinghausen disease) in childhood optic glioma. *Neurosurgery*. 1996;38:1114–1119.
48. Lewis RA, Gerson LP, Axelson KA, Riccardi VM, Whitford RP. von Recklinghausen neurofibromatosis. II. Incidence of optic nerve gliomata. *Opthalmology*. 1984;91:929–935.
49. Albert A, Lee BC, Saint-Louis L, Deck MD. MRI of optic chiasm and optic pathways. *AJNR Am J Neuroradiol*. 1986;7(2):255–258.
50. Freda PU, Wardlaw SL. Clinical review 110: diagnosis and treatment of pituitary tumors. *J Clin Endocrinol Metab*. 1999; 84(11):3859–3866.
51. Alshail E, Rutka JT, Becker LE, Hoffman HJ. Optic chiasmatic-hypothalamic glioma. *Brain Pathol*. 1997;7(2):799–806.
52. Nishio S, Takeshita I, Fujiwara S, Fukui M. Optico-hypothalamic glioma: an analysis of 16 cases. *Childs Nerv Syst*. 1993;9(6):334–338.
53. Rodriguez LA, Edwards MS, Levin VA. Management of hypothalamic gliomas in children: an analysis of 33 cases. *Neurosurgery*. 1990;26(2):242–246.
54. Fischbein NJ, Dillon W, Barkovich AJ. *Teaching Atlas of Brain Imaging*. New York: Thieme; 2000:62–64.
55. Sugiyama K, Uozumi T, Kiya K, et al. Intracranial germ cell tumor with synchronous lesions in the pineal and suprasellar regions: six cases and review of the literature. *Surg Neurol*. 1992;38: 114–120.
56. Kollias SS, Barkovich AJ, Edwards MS. Magnetic resonance analysis of suprasellar tumors of childhood. *Pediatr Neurosurg*. 1991;17(6):284–303.
57. Packer RJ, Cohen BH, Consy K. Intracranial germ cell tumors. *Oncologist*. 2000;5(4):312–320.
58. Sawamura Y, de Tribolet N, Ishii N, Abe H. Management of primary intracranial germinomas: diagnostic surgery or radical resection. *J Neurosurg*. 1997;87(2):262–266.
59. Matsutani M, Sano K, Takakura K, et al. Primary intracranial germ cell tumors: a clinical analysis of 153 histologically verified cases. *J Neurosurg*. 1997;86(3):446–455.
60. McCutcheon IE, Kitagawa RH, Sherman SI, Bruner JM. Adenocarcinoma of the salivary gland metastatic to the pituitary gland: case report. *Neurosurgery*. 2001;48(5):1161–1166.
61. Chiang MF, Brock M, Patt S. Pituitary metastases. *Neurochirurgia*. 1990;33:127–131.

62. Buonaguidi R, Ferdeghini M, Faggionato F, Tusini G. Intrasellar metastases mimicking a pituitary adenoma. *Surg Neurol*. 1983;20:373–378.
63. Pernicone PJ, Scheithauer BW, Sebo TJ. Pituitary carcinoma. *Cancer*. 1997;79:804–812.
64. Eisenberg MD, Al-Mefty O, DeMonte F, Burson GT. Benign nonmeningeal tumors of the cavernous sinus. *Neurosurgery*. 1999;44(5):949–954.
65. Hahn FJ, Leinbrock LG, Huseman CA, Makos MM. The MR appearance of hypothalamic hamartoma. *Neuroradiology*. 1988; 30:67.
66. Shimoto T, Hiroto H, Kanji K, et al. Rapid progression of pituitary hyperplasia in humans with primary hypothyroidism: demonstration with MR imaging. *Radiology*. 1999;213:383–388.
67. Hutchins WW, Crues JV, Miya P, Pojunas KW. MR demonstration of pituitary hyperplasia and regression after therapy for hypothyroidism. *AJNR Am J Neuroradiol*. 1990;11:410.
68. Young SC, Zimmerman REA, Nowell MA, et al. Giant cystic craniopharyngiomas. *Neuroradiology*. 1987;29:468.
69. Khafaga Y, Jenkin D, Kanaan I, Hassounah M, Shabanah MA, Gray A. Craniopharyngioma in children. *Int J Radiat Oncol Biol Phys*. 1998;42(3):601–606.
70. Gupta k, Kuhn MJ, Shevlin DW, Wacaser LE. Metastatic craniopharyngioma. *Am J Neuroradiol*. 1999;20:1059–1060.
71. Sartoretti-Schefer S, Wichmann W, Aguzzi A, Valavanis A. MR differentiation of adamantinous and squamous-papillary craniopharyngiomas. *Am J Neuroradiol*. 1997;18(1):77–87.
72. Harrison MJ, Morgello S, Post KD. Epithelial cystic lesions of the sellar and parasellar region: a continuum of ectodermal derivatives? *J Neurosurg*. 1994;80:1018–1025.
73. Lafferty AR, Chrousos GP. Pituitary tumors in children and adolescents. *J Clin Endocrinol Metab*. 1999;84(12):4317–4323.
74. Shin JL, Asa SL, Woodhouse LJ, Smyth HS, Ezzat S. Cystic lesions of the pituitary: clinicopathological features distinguishing craniopharyngioma, Rathke's cleft cyst, and arachnoid cyst. *J Clin Endocrinol Metab*. 1999;84(11):3972–3982.
75. Pusey E, Kortman KE, Flannigan BD, et al. MR of craniopharyngiomas: tumor delineation and characterization. *AJNR Am J Neuroradiol*. 1987;8:443.
76. Laws ER, Vance ML. Radiosurgery for pituitary tumors and craniopharyngiomas. *Neurosurg Clin N Am*. 1999;10(2):327–336.
77. Fahlbusch R, Honegger J, Paulus W, Huk W, Buchfelder M. Surgical treatment of craniopharyngiomas: experience with 168 patients. *J Neurosurg*. 1999;90:237–250.
78. Yaşargil MG, Abernathey CD, Sarioglu AÇ. Microsurgical treatment of intracranial dermoid and epidermoid tumors. *Neurosugery*. 1989;23(4):561–567.
79. Mori K, Handa H, Moritake K, Takeuchi J, Nakano Y. Suprasellar epidermoid. *Neurochirurgia*. 1982;25(4):138–142.
80. Yamakawa K, Shitara N, Genka S, Manaka S, Takakura K. Clinical course and surgical prognosis of 33 cases of intracranial epidermoid tumors. *Neurosurgery*. 1989;24(4):568–573.
81. Horowitz BL, Chari MV, James R, Bryan RN. MR of intracranial epidermoid tumors: correlation of in vivo imaging with in vitro 13C spectroscopy. *Am J Neuroradiol*. 1990;11(2):299–302.
82. Netsky MG. Epidermoid tumors. Review of the literature. *Surg Neurol*. 1988;29(6):477–483.
83. Braun IF, Naidich TP, Leeds NE, Koslow M, Zimmerman HM, Chase NE. Dense intracranial epidermoid tumors. Computed tomographic observations. *Radiology*. 1977;122(3):717–719.
84. Wilms G, Casselman J, Demaerel P, Plets C, De Haene I, Baert AL. CT and MRI of ruptured intracranial dermoids. *Neuroradiology*. 1991;33(2):149–151.
85. Smith AS, Benson JE, Blaser SI, Mizushima A, Tarr RW, Bellon EM. Diagnosis of ruptured intracranial dermoid cyst: value MR over CT. *AJNR Am J Neuroradiol*. 1991;12(1):175–180.
86. Cohen JE, Abdallah JA, Garrote M. Massive rupture of suprasellar dermoid cyst into ventricles. Case illustration. *J Neurosurg*. 1997;87(6):963.
87. El-Mahdy W, Powall M. Transsphenoidal management of 28 symptomatic Rathke's cleft cysts, with special references to visual and hormonal recovery. *Neurosurgery*. 1998;42:6–7.
88. Takanashi J, Tada H, Barkovich AJ, Saeki N, Kohno Y. Pituitary cysts in childhood evaluated by MR imaging. *Am J Neuroradiol*. September 2005;26:2144–2147.
89. Megdiche-Bazarbacha H, Hammouda KB, Aicha AB, et al. Intrasphenoidal rathke cleft cyst. *AJNR Am J Neuroradiol*. 2006; 27:1098–1100.
90. Nishioka H, Haraoka J, Izawa H, Ikeda Y. Magentic resonance imaging, clinical manifestations, and management of Rathke's cleft cyst. *Clin Endocrinol*. 2006;64(2):184–188.
91. Voelker JL, Campbell RL, Muller J. Clinical, radiographic and pathologic features of symptomatic Rathke's cleft cysts. *J Neurosurg*. 1991;74(4):535–544.
92. Teramoto A, Hirakawa K, Sanno N, Osamura Y. Incidental pituitary lesions in 1000 unselected autopsy specimens. *Radiology*. 1994;193:161–164.
93. Fox JL, Al-Mefty O. Suprasellar arachnoid cysts: an extension of the membrane of Liliequist. *Neurosurgery*. 1980;7:615–618.
94. Foley KM, Posner JB. Does pseudotumor cerebri cause the empty sella syndrome and benign intracranial hypertension? *Neurology*. 1975;25:565–569.
95. Tien RD, Newton TH, McDermott MW, et al. Thickened pituitary stalk on MR images in patients with diabetes insipidus and Langerhans cell histiocytosis. *AJNR Am J Neuroradiol*. 1990;11:707.
96. Smith JK, Matheus MG, Castillo M. Imaging manifestations of neurosarcoidosis. *AJR*. 2004;182:289–295.
97. Hollander MD, Friedman DP. Neuroradiology case of the day. *Radiographics*. 1998;18:1608–1611.
98. Ahmadi J, Meyers GS, Segall HD, Sharma OP, Hinton DR. Lymphocytic adenohypophysitis: contrast-enhanced MR imaging in five cases. *Radiology*. 1995;195:30–34.
99. Bourekas EC, Tzalonikou M, Christoforidis GA. Cavernous hemangioma of the optic chiasm. *AJR*. 2000;175(3):888–891.
100. Araujo PB, Coelho MC, Arruda M, Gadelha MR, Neto LV. Ipilimumab-induced hypophysitis: review of the literature. *J Endocrinol Invest*. May 10, 2015;38(11):1159–1166. [Epub ahead of print].
101. Nishizawa S, Yokoyama T, Hinokuma K, et al. Pituitary astrocytoma: magnetic resonance and hormonal characteristics. *J Neurosurg*. 1997;87:131.

CHAPTER

43

Neoplasms of the Cranial Nerves

Nicholas C. Ferraro, Michael E. Ivan, Ricardo J. Komotar

Department of Neurosurgery, University of Miami–Miller School of Medicine, Miami, FL, USA

Neoplasms of the cranial nerves are rare and often benign lesions. These lesions often present with pain, numbness, or weakness in a cranial nerve distribution. Unless malignant, these lesions are slow growing. Below we describe many of the various types and locations of cranial nerve tumors. Their epidemiology, pathology, presenting signs and symptoms, imaging characteristics, and management will also be discussed.

NERVE SHEATH NEOPLASMS

Schwannomas

Introduction

Schwannomas are benign neoplasms of the peripheral nerve sheath. They arise along the peripheral nerves just distal to the oligodendroglial–Schwann junction. Schwannomas are typically encapsulated and composed of well-differentiated Schwann cells, whose normal function is to insulate the peripheral nerves with myelin. They occur both intracranially and intraspinally, with schwannomas comprising 10–15% of all intracranial tumors and 78% of lesions found within the cerebellopontine angle (CPA).[1–3]

Pathology

Grossly schwannomas are globoid, encapsulated masses that are tan in color and can be associated or not with cysts and hemorrhage. Microscopically the neoplastic Schwann cells form two distinctive cellular patterns. Areas of compact, elongated cells with occasional nuclear palisading are referred to as Antoni A and areas of less cellular, loosely textured cells with indistinct processes and variable lipidization are referred to as Antoni B[4] (Figure 1). The Antoni A growth pattern consists of closely apposed tumor cells forming nuclear palisades (Verocay bodies) (Figure 2). The tumor cells constitutively express the S-100 protein. Other immunohistochemical markers, Leu-7 and calretinin, are often expressed as well and the tumor cells may focally express glial fibrillary acidic protein. They are usually negative for myelin basic protein and epithelial membrane antigen.[4]

Imaging

The characteristic appearance of a schwannoma on computed tomography (CT) is iso- or hypodense compared to the normal brain parenchyma (Figure 3). Schwannomas can also demonstrate cystic components or calcification, with the latter only rarely occurring[5] (Figure 4). Although not the preferred imaging modality to evaluate schwannomas, CT is the best option when evaluating the bony anatomy of the skull base in relation to the tumor. The bony anatomy of the skull base and its relation to the tumor are important for several reasons. First, it can provide the practitioner with a tentative diagnosis. Schwannomas have the tendency to widen the foramina through which they pass, whereas meningiomas do not (Figure 5). This can be especially useful in smaller tumors that do not demonstrate significant enhancement.[6–8] Second, it aids the surgeon in the operative plan. For instance, with acoustic schwannomas an evaluation of the air cells, degree of pneumatization of the temporal bone, and relationship of the semicircular canals, vestibule, jugular bulb, and internal auditory meatus is a critical step in the surgical planning. However, artifact from the petrous bone is a major limiting factor to the use of CT in the imaging of posterior fossa lesions.[8]

Since the advent of magnetic resonance imaging (MRI), it has become the imaging modality of choice for schwannomas. Most schwannomas are visible on noncontrasted T1-weighted images but not on T2-weighted images, on which the tumor may be isointense with

Handbook of Neuro-Oncology Neuroimaging, Second Edition
http://dx.doi.org/10.1016/B978-0-12-800945-1.00043-4

© 2016 Elsevier Ltd. All rights reserved.

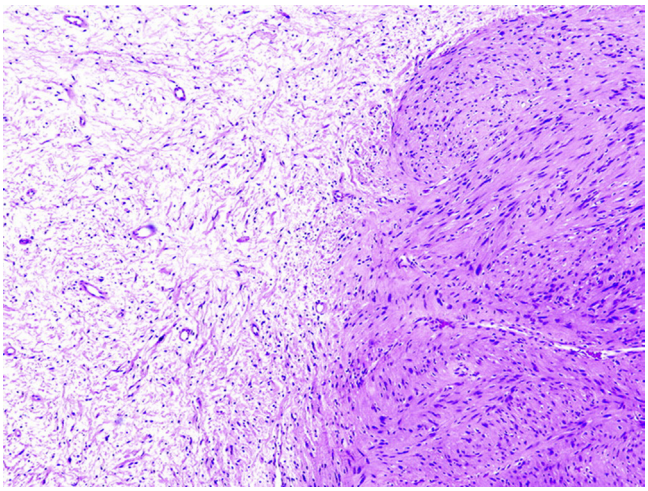


FIGURE 1 Schwannoma. Note the Antoni A area on the left (dense) and Antoni B area on the right (loose).

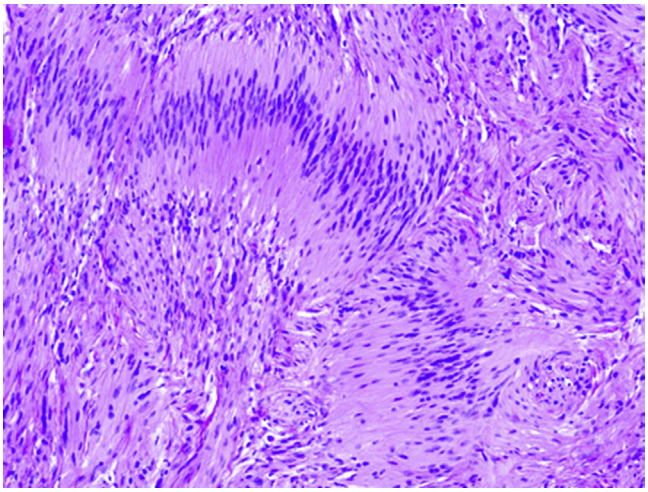


FIGURE 2 Schwannoma. Note the Verocay body.

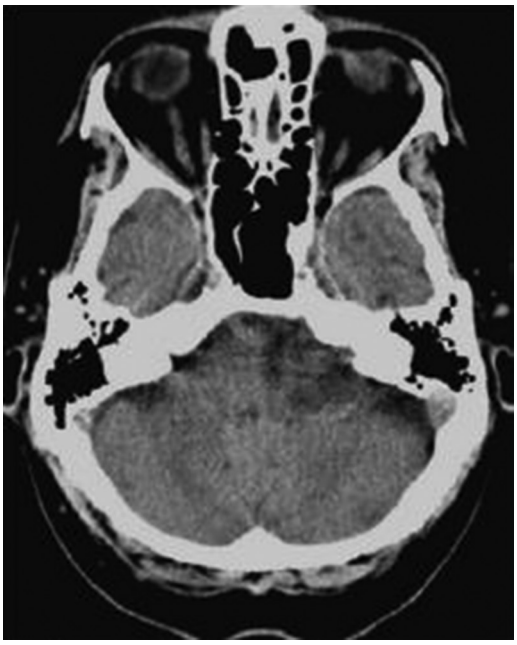


FIGURE 3 CT without contrast demonstrating left-sided acoustic neuroma.

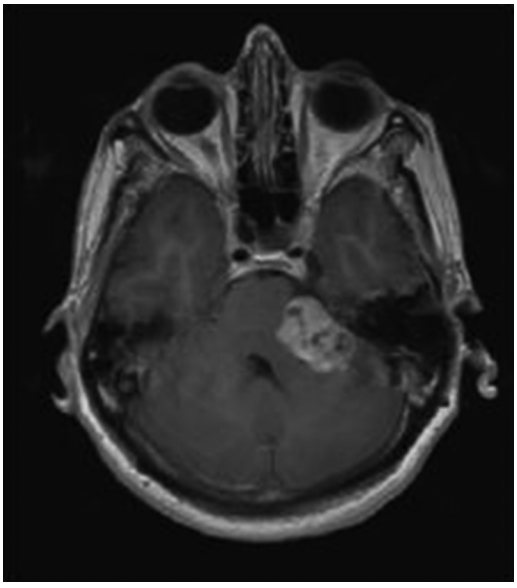


FIGURE 4 MRI with gadolinium demonstrating left-sided acoustic neuroma. Note the presence of microcysts within the tumor.

cerebrospinal fluid (CSF). They demonstrate avid uptake of gadolinium after administration and the use of contrast allows for the detection of lesions as small as 2–3 mm. Two new MRI sequences, T2 fast spin echo and three-dimensional Fourier transformation–constructive interference in steady-state sequence (CISS), allow for high-resolution imaging of the labyrinthine and CSF interface with bone and soft tissue (Figure 6). This enables the surgeon or neuroradiologist to delineate tumor, vessels, and nerves without the use of contrast.[9]

Cranial Nerve VIII—Acoustic Neuroma (Vestibular Schwannoma)

Cranial nerve VIII (CN VIII) is the most common location for intracranial schwannomas, accounting for 6–8% of all intracranial tumors.[10] Ironically, the term acoustic neuroma is a misnomer because schwannomas rarely involve the cochlear division. Instead they have a predilection to arise from the vestibular portion of CN VIII. It was previously believed that all vestibular schwannomas preferentially occurred on the superior vestibular division; however, newer data suggest this is not true.[5] Clemis et al. concluded that 50–60% of tumors arose from the superior vestibular nerve, 40–50% from the inferior vestibular nerve, and <10% from the cochlear nerve.[11] There is a female predilection ratio of 1.5–2 per liter and

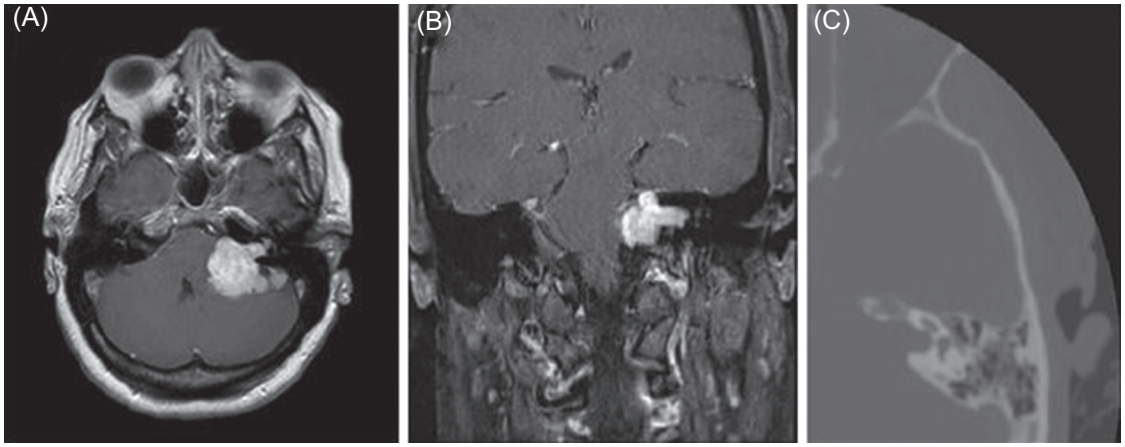


FIGURE 5 (A and B) Axial and coronal T1-weighted MRI with gadolinium. Note the extension of the tumor into the internal acoustic canal. (C) CT bone window. Note the widening of the foramina.

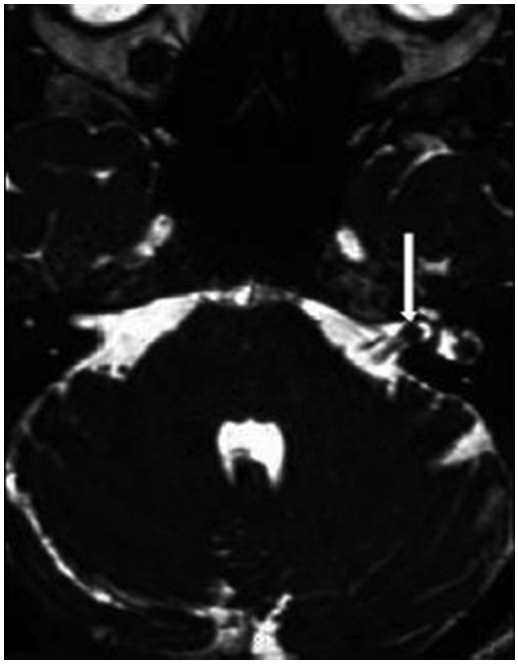


FIGURE 6 MRI CISS demonstrating an intracanalicular vestibular schwannoma.

they occur predominantly in the third to sixth decades of life.[5,8,12] Approximately 90% of schwannomas are solitary and arise de novo, whereas 4% are associated with neurofibromatosis type 2 (NF-2) and 5% are multiple without an association with NF-2.[12]

The most common symptoms of acoustic neuroma are unilateral sensorineural hearing loss, unsteadiness, tinnitus, mastoid pain or otalgia, headache, facial numbness, and diplopia.[13] Unilateral or asymmetric sensorineural hearing loss is almost always the initial symptom and has been present usually for a median of 1–3 years at the time of diagnosis.[14] The type of hearing loss, sensorineural or conductive, can be indicative of the location of the schwannoma. In sensorineural hearing loss, the schwannoma is typically located within the cisternal or intracanalicular segment. In conductive hearing loss, the schwannoma will usually be found in the tympanic or mastoid segment.[15–17] Thomsen et al. found that in patients with lesions >4 cm, 58% will exhibit cerebellar dysfunction, and 53% will have corneal or facial hypoesthesia.[18]

Plain tomography of the internal acoustic meatus will demonstrate enlargement of the porus acousticus in approximately 80–90% of cases.[19] A difference greater than 1–2 mm between the two sides is significant, especially when associated with differences in canal shape, evidence of bone erosion, or shortening of the posterior wall.[20] Acoustic neuromas have the same imaging characteristics as schwannomas on CT. However, schwannomas of the CPA have specific imaging findings on CT and MRI, which aid in the differentiation between other tumors common to the CPA, specifically meningiomas. Unlike acoustic neuromas, meningiomas are hyperdense on CT prior to administration of contrast and they rarely enlarge the porus acousticus. However, erosion of the posterior portion of the petrous pyramid or areas of hyperostosis can be seen in meningiomas and is rare in acoustic neuromas.[20] Meningiomas also have the tendency to contain calcifications. Moller et al. found a rate of 25% of calcification in their series.[21] The presence of a dural tail, often better visualized on a T1-weighted contrast-enhanced MRI, is also associated with a meningioma (Figure 7). Finally, acoustic schwannomas are associated with a more globular appearance and cystic changes and are often centered at the porus acousticus.[22]

Over time the management of vestibular schwannomas has evolved along with improving microsurgical techniques and radiation-based therapies; however, the current management is complex and dependent on

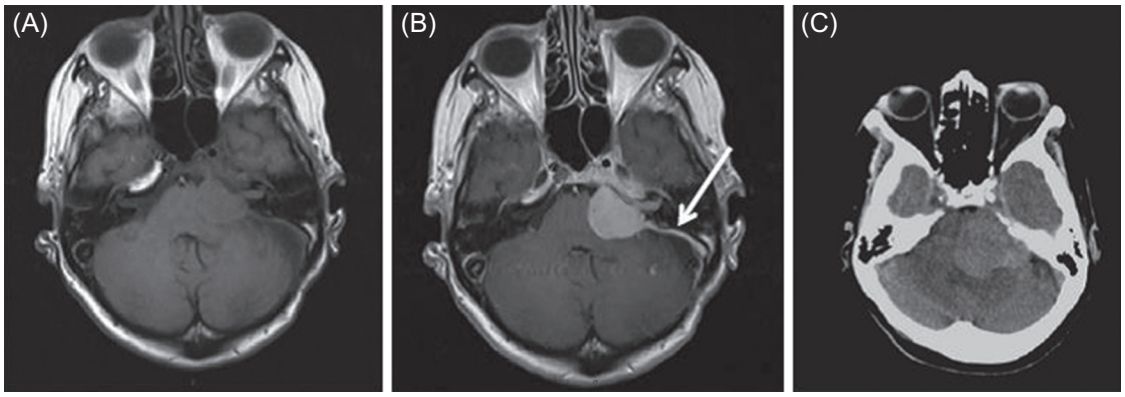


FIGURE 7 Left-sided CPA meningioma. (A) T1-weighted MRI precontrast. (B) T1-weighted MRI postcontrast. Note the presence of the dural tail (arrow). (C) CT without contrast. Note the tumor is hyperdense to the brain parenchyma.

multiple variables: hearing status, tumor size, tumor location, presence of bilateral tumors, and age. In today's practice, management of vestibular schwannomas involves conservative management, surgical resection (complete resection, subtotal resection for decompression of facial nerve), and radiosurgery.

One of the most important aspects of surgical management of vestibular schwannomas is the timing of surgery. It is estimated that vestibular schwannomas grow at an average rate of between 0.02 and 1 cm/year.[23] In general, it is recommended to observe smaller tumors and wait for evidence of their growth on serial imaging. However, watchful waiting is not the most appropriate course of action when the patients are younger, since their tumors have a tendency to be more aggressive, or for lesions larger than 2.0 cm, as any further growth would cause an unacceptable surgical risk.[24] If left untreated all vestibular schwannomas will result in hearing loss.

The primary goal in vestibular neuroma surgery and other treatment modalities is to preserve hearing. Interestingly, in patients with NF-2 their tumors were found to be more likely to demonstrate infiltration of the cochlear nerve and inner ear. This fact makes functional hearing preservation in this patient population more difficult than in patients who present with sporadic tumors.[25]

The dilemma facing any neurosurgeon when contemplating a surgery on a patient with a vestibular schwannoma is the role of tumor size. Operating early when the tumor is smaller has been shown to improve outcomes in regard to functional hearing and facial preservation. More importantly, operating early is the best hope of preserving long-term hearing.[24] However, any operation, no matter how small the tumor is, has an inherent risk of hearing loss. Yet, waiting until the tumor shows some growth on serial imaging or the patient begins to demonstrate signs of hearing loss will increase the risk of postoperative deafness. Studies have shown that the risk of postoperative deafness increases with increasing tumor size.[8] With large, symptomatic tumors treatment should not be delayed for fear of postoperative hearing loss. In these cases subtotal tumor removal, which involves decompressing the internal auditory canal, or radiosurgery (<3 cm) is the most appropriate course of action. In addition to possible damage to the cochlear nerve and inner ear caused by surgery, damage to the facial nerve is one of the more common complications of vestibular schwannoma surgery.[26]

In patients with unilateral or bilateral small tumors, radiosurgery, and even fractionated radiosurgery, has demonstrated tumor control rates comparable to those of surgical resection with improved hearing preservation and decreased facial palsy rates.[24] With time, further studies may demonstrate the efficacy of fractionated radiosurgery on all types of acoustic neuromas.

Nonvestibular Schwannomas

Cranial Nerve V—Trigeminal Schwannomas (Neuromas)

Following the vestibular nerve, the trigeminal nerve (CN V) is the second most common cranial nerve to be involved with schwannomas. However, trigeminal schwannomas comprise only 0.8–8% of all intracranial schwannomas.[27,28] Trigeminal schwannomas have a peak incidence in the fourth and fifth decades of life and they have a slight predilection for woman. Trigeminal schwannomas typically arise from the gasserian ganglion, but they have been known to arise proximally from the trigeminal root and distally in the postganglionic divisions. The ophthalmic branch (V_1) is the most commonly involved compared to the maxillary (V_2) or mandibular (V_3) branch.[29] In 1955, Jefferson proposed a classification system of trigeminal schwannomas based on of their location. Type A refers to tumors contained predominantly in the middle fossa. Type B refers to



FIGURE 8 T1-weighted MRI postcontrast of trigeminal neuroma. Note the cystic nature of the schwannoma and its extension into Meckel's cave.

tumors in the posterior fossa, and the type C tumor is a dumbbell tumor with elements in both the posterior and the middle fossa and is contiguous through the porus trigeminus.[29]

A sensory disturbance of the ipsilateral face is the most common presenting complaint of patients with trigeminal schwannomas (neurinomas). Other symptoms include focal seizures, hemiparesis, hearing disturbances, gait disturbances, elevated intracranial pressure, otalgia, involvement of the cranial nerves of the extraocular muscles, and occasionally posterior fossa signs.[27,30,31] Sensory disturbances are most common with tumors located within the middle fossa. These tumors can extend into the cavernous sinus or into the orbital apex causing exophthalmos. Tumors located within the posterior fossa typically present with hearing loss, tinnitus, or gait disturbance.[30]

Large tumors that originate at the root of the trigeminal ganglion often produce a syndrome known as CPA syndrome. Patients will present with hearing loss, facial weakness, ataxia, and spasticity. The first two are secondary to the stretching of CNs VII and VIII by the tumor. The last two are results of compression of the brain stem and cerebellum.[29,32]

On plain films trigeminal schwannomas will demonstrate the truncation of the petrous apex with smooth margins. Other common findings on plain radiographs include enlargement of the skull base foramina, erosion of the dorsum and lateral aspect of the clinoid processes or sella, as well as enlargement of the superior orbital fissure.[33,34] MRI also offers the added benefit of differentiating between a schwannoma and a meningioma (Figure 8). Using the dynamic spin-echo (TR/TE 200/15 ms) MRI, practitioners are able to better appreciate the more varied dynamic patterns of meningiomas compared to schwannomas.[35]

Cranial Nerve VII—Facial Nerve Schwannomas

The facial nerve is the third most common location for intracranial schwannomas. It accounts for 1.9% of all intracranial schwannomas.[36] Facial nerve schwannomas typically present in the fourth and fifth decades of life and have a definitive predilection for the female population.[37] Furthermore, several series have shown a 15–21% association rate of neurofibromatosis in patients with facial nerve schwannomas.[35–37]

Schwann cells begin to cover the facial nerve approximately 2 mm after it exits the brain stem. It is from this point and distal that schwannomas will occur. Several series have shown that the most common location for schwannomas of the facial nerve is the geniculate ganglion.[15,36,38] Facial schwannomas also have the capacity to be multicentric, occurring simultaneously in the various branches and segments of the nerve.[8]

Common presenting symptoms include hearing loss, tinnitus, vertigo, facial pain, facial paralysis, hemifacial spasm, and otalgia. It is hearing loss that is the most common initial presenting symptom, occurring in 41–91% of cases. Although not an early symptom, facial weakness will occur in 46–90% of patients.[16,36]

Enlarged segments of the facial nerve canal filled with a homogeneously enhancing mass are diagnostic of a facial nerve schwannoma[8] (Figure 9). Owing to the close proximity to the vestibular nerve, facial nerve schwannomas are often confused with vestibular schwannomas, especially when located in the cisternal or canalicular segment of the facial nerve. O'Donoghue found a misdiagnosis rate of 36% in these tumors.[36]

Cranial Nerves IX, X, XI—Jugular Foramen Schwannomas

After glomus tumors, schwannomas are the second most common tumors of the jugular foramen. Approximately 90% of jugular foramen schwannomas arise from the glossopharyngeal or vagus nerve.[39,40] Samii et al. classified jugular foramen schwannomas into four groups based on their location. Type A tumors are those located primarily within the CPA with minimal enlargement of the jugular foramen. Type B tumors are primarily located within the jugular foramen with some intracranial extension. Type C tumors are primarily extracranial with extension into the jugular foramen. Type D tumors are dumbbell-shaped tumors with both intra- and extracranial components. Similar to most schwannomas, these tumors usually present in the third to fifth decades of life, with a slight female predilection.[41]

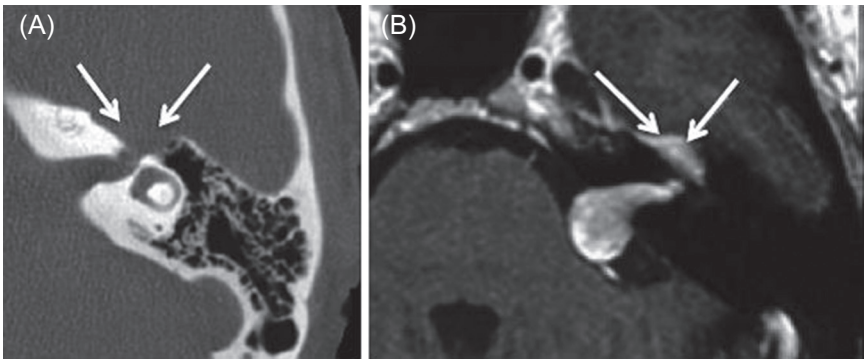


FIGURE 9 (A) CT bone window of facial nerve schwannoma. Note the widening of the facial nerve canal. (B) T1-weighted MRI postcontrast. Note the tumor's extension into the facial nerve canal. *Ref. 108.*

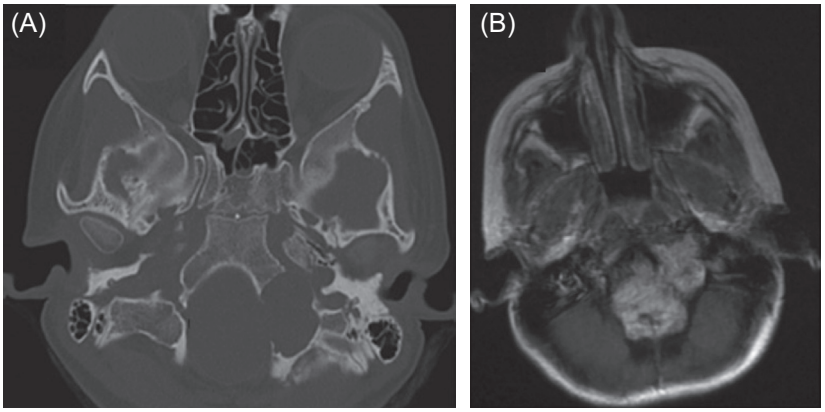


FIGURE 10 (A) CT bone window of a jugular foramen schwannoma. Note the widening of the jugular foramen along with the scalloping of the margins. (B) T1-weighted MRI of the same tumor. Note the extension of the tumor through the jugular foramen. *Ref. 109.*

CT scan will demonstrate the architecture of the jugular foramen and adjacent skull base. With jugular foramen schwannomas the jugular foramen is enlarged with smooth/scalloped borders as opposed to glomus tumors, which demonstrate irregular borders with bone destruction.[42] MRI allows for a more detailed evaluation of the vascular supply of the tumor and the relationship to the major vessels, architecture of the sigmoid sinus, and the jugular bulb (Figure 10). MRI allows for improved visualization of the vascularity of the tumor, helping to differentiate it from glomus tumors, which often demonstrate multiple signal voids.[42]

Cranial Nerve XII—Hypoglossal Nerve Schwannomas

Since the original report of a hypoglossal nerve schwannoma by de Martel in 1933, there have been 70 reported cases in the literature.[8,43] The hypoglossal nerve is a purely motor nerve and is therefore a rare location for schwannomas (Figure 11). Two series with a total of 35 patients with a hypoglossal nerve schwannoma showed a 14% rate of being afflicted with neurofibromatosis.[44,45] Interestingly, hypoglossal schwannomas have an even higher predilection for the female population. In one series of 30 patients, females comprised 83% of all patients with schwannomas of CN XII.[44,45]

Most patients do not initially present with complaints associated with their tongue. Complaints of symptoms associated with raised intracranial pressure, brain-stem and cerebellum compression, or lower cranial nerve dysfunction are what most patients with hypoglossal nerve schwannomas present with. In fact, Odake found a 67% rate of dysfunction of the cranial nerves in the jugular foramen in patients with hypoglossal schwannomas.[46]

The thickness of the occipital condyle will often limit the expansion of the hypoglossal canal by schwannomas. Cerebral angiography will help in the differential diagnosis as well. Unlike jugular foramen schwannomas or glomus tumors, hypoglossal schwannomas will not infiltrate or obstruct the jugular bulb.[5,8]

Cranial Nerves III, IV, VI—Extraocular Nerve Schwannomas

Like schwannomas that arise from the hypoglossal nerve, schwannomas from the extraocular nerves are extremely rare due to them being purely motor nerves. Just like other schwannomas of the cranial nerves,

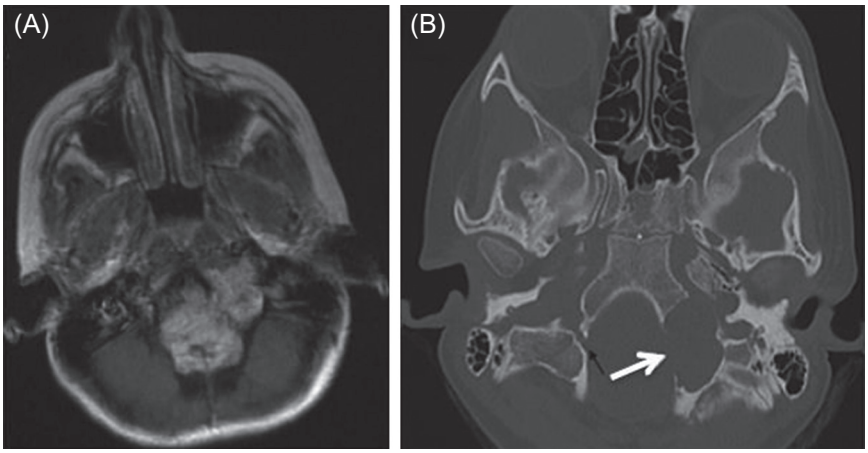


FIGURE 11 (A) T1-weighted MRI postcontrast demonstrating a left-sided hypoglossal schwannoma. (B) CT bone window of the same patient showing the expansion of the hypoglossal canal (arrow). *Ref. 110.*

extraocular nerve schwannomas have a peak incidence in the fourth and fifth decades of life and have a slight female predilection.[47]

In 1937, Tarlov was able to demonstrate the transition zone between the central and the peripheral nerve (oligodendroglial–Schwann junction) in the extraocular nerves. Both the oculomotor and the trochlear nerves acquire the first Schwann cell at approximately 0.6 mm after leaving the brain stem. The abducens nerve receives its first Schwann cell slightly before the other two at 0.5 mm from the brain stem.[48] Owing to the close proximity of the oligodendroglial–Schwann junction to the brain stem, extraocular nerve schwannomas that have a very proximal origin (cisternal) can often be confused with intrinsic tumors of the brain stem.[49]

In 1992, Celli et al. devised a classification scheme of the extraocular nerve schwannomas based on their location. In fact, this system is highly analogous to the one used by Jefferson in 1955 to describe trigeminal neuromas.[29,47] Celli created three different groups: cisternal, cavernous, and cisternocavernous (dumbbell-shaped). Which tumors fall into which categories is fairly self-explanatory. The cisternal schwannomas are predominantly located within the subarachnoid space around the brain stem. The cavernous group will be primarily located within the cavernous sinus and the cisternocavernous group will have significant portions of the tumor located within both locations. As with most tumors, the symptoms will depend on the location of the lesion.[47]

Most oculomotor nerve schwannomas have an equal distribution between the cisternal and the cavernous. Cisternal tumors have the tendency to grow rostrally into the interpeduncular and suprasellar cisterns causing compression of the brain stem, third ventricle, and hypothalamus. Tumors of the cavernous variety result in compression of the nerves within the cavernous sinus.[8,47] This results in a cavernous sinus syndrome whose symptoms include chemosis, proptosis, ophthalmoplegia, Horner syndrome, and sensory loss within the V_1 distribution. Occasionally, the tumor will also compress the optic nerve resulting in an orbital apex syndrome (ophthalmoplegia and visual loss).[8] Celli et al. found that approximately 70% of patients with an oculomotor schwannoma will present with an isolated CN III palsy. If the tumor progresses to a larger size, it can cause unilateral exophthalmos along with neuralgia and sensory disturbances along the distribution of V_1.[47]

Interestingly, schwannomas of the trochlear nerve rarely present with trochlear nerve palsies. Celli et al. found that less than 44% of patients with trochlear nerve schwannomas presented with a palsy of that cranial nerve. Furthermore, Celli found that up to one-third of these patients present with a palsy of the oculomotor nerve.[47] Schwannomas of the trochlear nerve are usually the cisternal variety. Their growth patterns usually demonstrate growth upward into the tentorial incisura or medially into the prepontine or interpeduncular cisterns.[8] When these tumors grow to a large size within the ambient cistern they will compress the superior cerebellar and cerebral peduncles. This results in an ipsilateral limb ataxia and a contralateral spastic hemiparesis. This syndrome was first described by Bendheim and Berg in 1981 and called "ataxic hemiparesis."[50]

Unlike schwannomas of the oculomotor and trochlear nerves, those of the abducens nerve are primarily the cisternocavernous variety. The most common signs and symptoms are those of parent nerve dysfunction and raised intracranial pressure (ICP). If the tumor grows to a large enough size, patients may also demonstrate palsies of the other cranial nerves within the cavernous sinus or hemiparesis.[8]

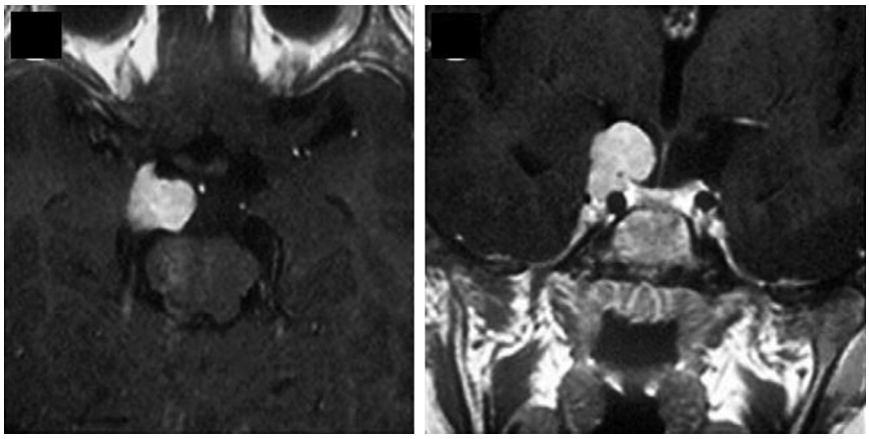


FIGURE 12 T1-weighted MRI of a schwannoma of the oculomotor nerve. *Ref. 111.*

Imaging characteristics of schwannomas of the extraocular nerves will demonstrate bone changes on radiographs and CT similar to those of schwannomas of the other cranial nerves. There is evidence of scalloping of the petrous apex, clinoids, and sella in cisternocavernous tumors. Widening of the superior orbital fissure or erosion of the floor of the middle fossa can be seen in patients with cavernous schwannomas (Figure 12).

Cranial Nerve I—Olfactory Nerve Schwannomas

Of all the cranial nerves, the olfactory nerve is the least likely to be affected by a schwannoma. To date, only 35 cases of olfactory nerve schwannomas have been reported in the world literature. Therefore, little is known about them. The tumors are believed to arise from the fila olfactoria where the oligodendroglial–Schwann junction occurs approximately 0.5 mm past the olfactory bulb.[48] The majority of the reported cases have occurred in young males. Most patients present with anosmia, visual changes, seizures, and other symptoms of elevated ICP.

CT is the most useful imaging modality in the differential as it will reveal scalloping or hyperostosis of the floor of the anterior fossa, with the former being specific for schwannoma and the latter for meningioma.

Management of Nonvestibular Schwannomas

For most nonvestibular schwannomas surgical resection remains the primary method of treatment. Complete resection results in a cure. However, owing to the proximity of most nonvestibular schwannomas to other critical structures, a complete resection is not often possible. This is especially true for schwannomas located within the cavernous sinus or the jugular foramen and those involving the hypoglossal nerve.

In trigeminal schwannomas, surgical resection remains the primary method of treatment in symptomatic patients. The most common postoperative complications include cranial nerve palsies (abducens, oculomotor), CSF leak, and hydrocephalus. In a series of 47 patients with trigeminal schwannomas, the main complaint was facial hypesthesia, with a permanent abducens palsy occurring in only three patients. There were no cases of patient mortality. Within this same series a total resection rate of 91.5% was achieved.[26]

Most of these common surgical risks can be avoided with radiosurgery. The evidence for the use of stereotactic radiosurgery (SRS) is promising and this treatment has been increasing. In a series of 16 patients (average tumor volume 5.3 cc), Huang et al. demonstrated a 100% tumor control rate with regression in nine patients and no growth in seven. No patients demonstrated new cranial nerve deficitis.[51] Furthermore, in a series of 13 patients with trigeminal neuromas who underwent SRS therapy, nine showed evidence of regression, four had no change, and none showed evidence of progression.[52]

Like trigeminal neurinomas, current management of facial nerve schwannomas includes surgical resection or SRS. As seen in surgery for vestibular schwannomas, the main risks of surgical resection include facial paralysis, hearing loss, CSF leak, meningitis, and hydrocephalus. In a series of 12 patients, Symon et al. was able to achieve complete resection in all 12 patients. There was no report of mortality, and facial nerve function was partially restored in all patients with the use of nerve grafting procedures.[8,15]

With a lower side-effect profile, radiosurgery has been increasingly used in the treatment of facial nerve schwannomas. A series of six patients showed good outcomes at 46 months with preserved facial function and hearing.[53] More studies are needed to further evaluate the role of SRS in facial nerve schwannomas. However, the outcomes of SRS use in the other varieties of nonvestibular schwannomas provide indirect evidence of its potential efficacy for tumor control and decreased side effects.

Like schwannomas of Meckel's cave or those confined within the cavernous sinus, surgical resection

of jugular foramen schwannomas caries significant risk of morbidity. This must be balanced with the fact that complete surgical resection is the only option that offers a cure. The main risk associated with surgical resection of a jugular foramen schwannoma is damage to the cranial nerves, which traverse this cranial foramen, resulting in difficulty with swallowing and speaking. In fact, postoperative dysphagia and hoarseness are common.[41,54,55]

Although not the primary method of therapy, radiosurgery of jugular foramen schwannomas has demonstrated good outcomes with few side effects. One series of 17 patients with a jugular foramen schwannoma who underwent Gamma Knife radiosurgery had a mean follow-up of 64 months. MRI showed reduced tumor size in 13 cases and no size change in four cases. The tumor growth control rate was 100%, with one patient demonstrating transient hoarseness.[56] In the review by Hamm et al., a total of five patients with jugular foramen schwannomas underwent SRS. Two of the patients demonstrated tumor regression on follow-up MRI, two showed no change, and one showed progression.[52] Further evidence of the benefit of SRS in jugular foramen schwannomas was demonstrated by Zhang et al. His group studied a total of 27 patients diagnosed with a jugular foramen schwannoma and treated with SRS. They found a tumor control rate of 96%. Two patients were lost to follow-up, 11 tumors decreased (44%), 13 remained unchanged, and one progressed. Symptoms improved in 64% of patients and there were no new cranial nerve deficits.[57]

Owing to their rarity, the management of hypoglossal schwannomas is dictated by the surgeon's preference. With the significant morbidity associated with surgical resection, radiosurgery for these lesions has become a good option in the treatment paradigm. Few cases report the use of radiosurgery for these lesions. However, one patient with a hypoglossal schwannoma in the series by Elsharkawy et al. was treated with radiosurgery. Postoperatively, the patient demonstrated lower cranial nerve palsies and tremors of his extremities, which progressed to a loss of ambulation and speech. In his final follow-up MRI, his tumor had demonstrated an increase in size compared to his pre-radiosurgery imaging.[58]

Schwannomas of the oculomotor, trochlear, and abducens nerve are extremely rare and, therefore, reports of surgical experience and results of SRS are sparse within the literature and limited to small series or case reports. Despite this, most schwannomas of the cisternal or cisternocavernous variety are candidates for surgical resection. Complete surgical resection is curative, but parent nerve sacrifice is almost always required, resulting in permanent dysfunction of that nerve.[8,47]

SRS has advantages over surgical resection in schwannomas of CNs III, IV, and VI. First, the procedure is less invasive and the risk of injury to adjacent cranial nerves is less. Second, sacrifice of the parent nerve is not necessary. Kim et al. published a series of eight patients with schwannomas from the cranial nerves controlling the extraocular muscles (two oculomotor, five trochlear, one abducens) who underwent SRS. Postoperative MRI demonstrated tumor regression in all eight patients with a mean progression-free survival of 21 months with no reported complications during the period of follow-up. Four of the five patients with a trochlear nerve schwannoma had improvement of the preoperative complaint of diplopia. There was no noted improvement in the patients with the oculomotor schwannoma.[59] The main limitation of SRS is when tumors are located next to eloquent or radiosensitive structures, like the optic apparatus. When large tumors occur in these regions, a subtotal resection to debulk the tumor is performed prior to SRS to decrease the radiation dose to the susceptible region.[8]

GLIAL NEOPLASMS

Optic Pathway Gliomas

Introduction

Optic pathway tumors account for 2–5% of all pediatric brain tumors. The most common type of tumor of the optic nerve/pathway is a low-grade glioma, with pilocytic astrocytomas being the most common subtype, followed by fibrillary astrocytomas. However, high-grade gliomas (including glioblastoma multiforme) have been known to occur in this region, particularly in the adult population.[60,61] Roughly 11–30% of children affected with NF-1 are diagnosed with optic pathway tumors. In patients with NF-1 and an optic pathway glioma (OPG), their tumors have the tendency to be benign, multifocal, bilateral, and located within the optic nerves.[62–64] Most OPGs associated with NF-1 present in early childhood with the peak incidence occurring between 4 and 6 years of age.[65] OPGs located within the chiasm are not usually associated with NF-1 and have a more aggressive course. Several series have found that roughly 25% of OPGs are confined to the optic disc and nerve with 40–75% involving the chiasm.[66–68]

Pathology

Grossly, pilocytic astrocytomas are well-circumscribed lesions with a heterogeneous consistency that contains both firm and mucoid areas. Pilocytic astrocytomas can also contain focal areas of calcification as well as a mural nodule with an associated cyst. Microscopically, pilocytic astrocytomas have a biphasic pattern

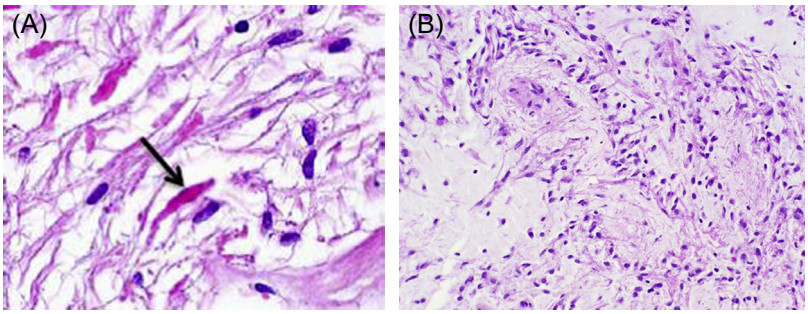


FIGURE 13 (A) Pilocytic astrocytoma. Note the presence of Rosenthal fibers (arrow). (B) Pilomyxoid astrocytoma. Note the absence of Rosenthal fibers.

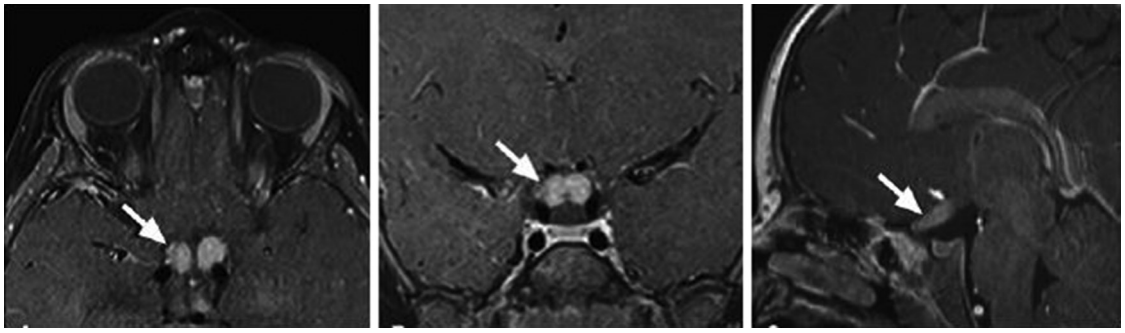


FIGURE 14 T1-weighted MRI postcontrast of an optic nerve/chiasm glioma. Note the suprasellar location and expansion of the nerve and chiasm. *Ref. 112*.

with Rosenthal fibers and eosinophilic granular bodies (Figure 13(A)). Nuclear pleomorphism and hyperchromasia are usually present but are not clinically or prognostically significant findings.[4]

Another variant of low-grade gliomas (LGGs) within the OPG group is pilomyxoid astrocytomas (PMAs). These groups of tumors, although still considered LGGs, have a more aggressive course than their cousins, pilocytic astrocytomas. Microscopically, PMAs will demonstrate piloid cells in a loose fibrillary and myxoid background. Unlike pilocytic astrocytomas, they lack Rosenthal fibers and eosinophilic granular bodies are rare[69] (Figure 13(B)). A unique aspect of these tumors is that their spread is dependent on their association with NF-1. If the tumor is associated with NF-1, it will demonstrate a perineural spread of the tumor. On the other hand, if there is no association with NF-1 the tumor will spread intraneurally.[64]

The presenting signs and symptoms in children affected with OPG are dependent on the location of the tumor. Patients with intraorbital lesions will present with proptosis and painless unilateral vision loss. In their series of patients with OPG and NF-1, Listerneck et al. found that patients with chiasmatic lesions often presented with endocrinopathy (diencephalic syndrome), decreased visual acuity, and symptoms of raised ICP (hydrocephalus). Interestingly, the group also found that patients who were diagnosed with an OPG of the optic nerve purely based on screening had no evidence of decreased visual acuity or progression.[8] Furthermore, all six patients with decreased visual acuity without proptosis had chiasmatic lesions.[65]

Imaging

MRI is the imaging modality of choice for OPGs. Most lesions have a tendency to be solid with the presence of the occasional microcyst. They are usually iso- or hypointense on T1-weighted images and hyperintense on T2-weighted images and demonstrate heterogeneous enhancement with contrast administration[5,70,71] (Figure 14). Several other MRI sequences can be of use in evaluating the tumor margins/extent of spread. Fat suppression will aid in discerning the intraorbital margins of the tumor and fluid-attenuated inversion recovery (FLAIR) or T2-weighted imaging is useful in identifying tracking along postchiasmal fiber pathways.[8]

Management

Currently, management of OPG includes observation, surgery, radiotherapy, or chemotherapy. The determination of the treatment modality is dependent on multiple factors. Age, tumor location, and symptomatology (visual loss, endocrine disturbance, hydrocephalus, or mass effect) are the most important. In 2003, Astrup advocated for the following management algorithm for

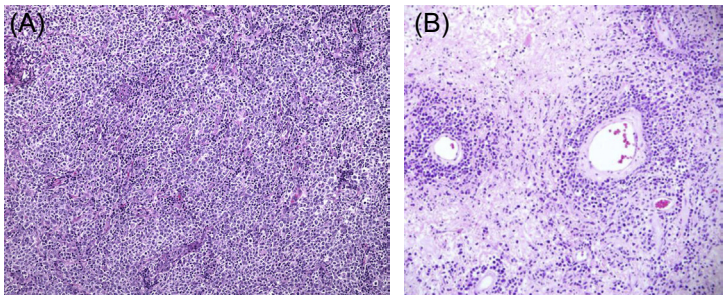


FIGURE 15 Primary CNS lymphoma (diffuse B-cell). (A) Note the abundant cytoplasm, prominent nucleoli, and dense nuclear chromatin. (B) PCNSL has the tendency to invade the perivascular spaces, called "angiotropism."

OPGs: observation for newly diagnosed OPG, resection for progressive intraorbital tumors, radiotherapy for progressive chiasmatic tumors in older children, and chemotherapy (carboplatin and vincristine) in children younger than 5 years.[72]

PRIMARY CENTRAL NERVOUS SYSTEM LYMPHOMA

Introduction

Primary central nervous system lymphoma (PCNSL) is a variant of non-Hodgkin lymphoma and accounts for roughly 3% of all the primary CNS tumors diagnosed in the United States each year. Immunodeficiency, either congenital or acquired, is the only known risk factor for PCNSL. Approximately 2–13% of individuals diagnosed with acquired immunodeficiency syndrome (AIDS) will be diagnosed with PCNSL.[12,24] The median age of diagnosis as well as sex distribution of PCNSL is dependent on the etiology of the disease. In immunocompetent patients, the median age of diagnosis is 64 years in the series by Murray et al., with a male predilection of 1.5:1. On the other hand, immunocompromised patients had a much earlier median age of diagnosis and a much stronger male predilection. Immunocompromised patients, specifically those with AIDS, had a median age of onset of 39 years and a male predilection of 17:1.[73–76]

In immunocompetent PCNSL patients, lesions are solitary in 65% of cases and are most frequently located, in descending order, in the cerebral hemisphere, thalamus or basal ganglia, corpus callosum, periventricular region, and cerebellum. Reports of extra-axial PCNSL are rare and tumors limited to the cranial nerves are even rarer. Of the reported cases in the literature, the oculomotor nerve is the most commonly affected, followed by optic nerve.[77,78] There are several reports of PCNSL involvement of the trochlear nerve in the cavernous sinus as well as the trigeminal nerve at the region of Meckel's cave.[79–81] Interestingly, there is one report of a patient presenting with PCNSL of the bilateral internal acoustic meatus who presented with bilateral palsies of CN VII and CN VIII.[82] Direct invasion of the leptomeninges by PCNSL from a parenchymal lesion is the most common cause of cranial nerve palsies in PCNSL.[83,84]

An even rarer form of PCNSL is one that is confined solely to the leptomeninges, called primary leptomeningeal lymphoma (PLML). Lachance et al. reported an estimated incidence of 7% of PLML in PCNSL.[85] In a series of 48 patients, Taylor et al., in the International Primary CNS Lymphoma Collaborative Group report, found 33 (68%) patients who presented with cranial neuropathy. CNs VI and VIII were the most affected at 31% and 17%, respectively.[83]

Pathology

Diffuse large B-cell lymphoma accounts for 90% of all PCNSLs, with the other 10% comprising low-grade lymphomas, Burkitt lymphomas, or T-cell lymphomas.[86] Macroscopically PCNSL appears as a bulky and irregular mass that is brown or cream in color and may contain focal areas of necrosis or hemorrhage.[8,24]

PCNSL has a unique feature, which is not demonstrated in its systemic counterparts, that can only be appreciated microscopically. PCNSL is unique in its angiotropism. The neoplastic lymphocytes will invade along the perivascular spaces with perivascular cuffing and vessel wall infiltration.[24] The periphery of the tumor is typically composed of a T-lymphocyte infiltrate. Diffuse large-cell lymphoma is characterized by large lymphoid cells containing abundant cytoplasm, prominent nucleoli, and dense nuclear chromatin (Figure 15). These features are what give the "starry-sky" appearance to PCNSL.[4]

Imaging

CT and MRI are the most common imaging modalities for PCNSL. Currently, gadolinium-enhanced MRI is the imaging modality of choice. On CT PCNSL appears iso- or hyperdense relative to brain parenchyma on unenhanced scans, and lesions typically demonstrate contrast enhancement.

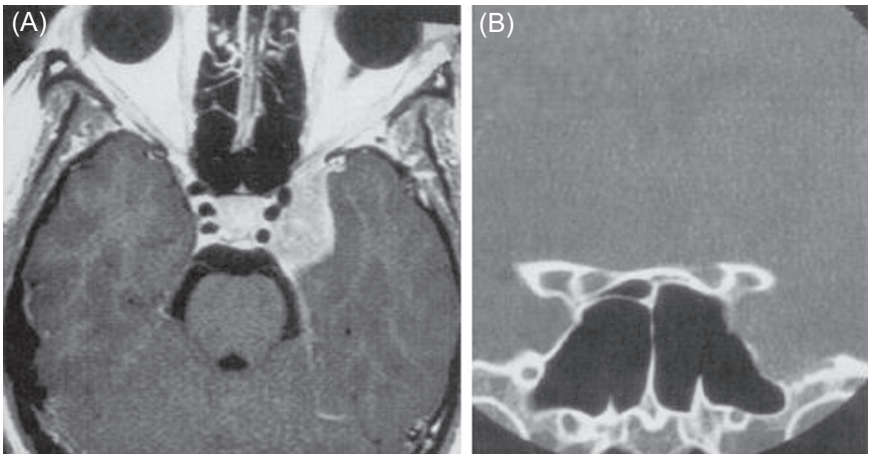


FIGURE 16 (A) T1-weighted MRI postcontrast demonstrating a tumor (PCNSL) invading Meckel's cave. (B) CT bone window demonstrating sclerotic changes of the petrous apex and lateral wall of the sphenoid sinus. *Ref. 81*.

On MRI, the lesions are typically well demarcated and isointense to hypointense relative to gray matter on T1-weighted sequences. The lesions, however, have a variable appearance on T2-weighted imaging. Some lesions are predominantly hyperintense to gray matter on T2-weighted sequences, with more than half of lesions being hypointense to isointense relative to gray matter[87–89] (Figure 16). FLAIR sequences demonstrate findings similar to those seen on T2-weighted sequences, and diffusion-weighted imaging will often demonstrate restricted diffusion.[90] Newer imaging modalities have been utilized to help in the differential between PCNSL and other entities that have similar radiographic appearances. Thallium-201 single-photon-emission CT (SPECT) and [^{18}F]fluorodeoxyglucose (FDG) positron-emission tomography (PET) are two of the most commonly used. Generally, CNS lymphoma lesions demonstrate hypermetabolic activity on PET imaging and increased uptake with SPECT imaging.[91–105]

In cases of PLML the imaging has the potential to demonstrate nonspecific findings like hydrocephalus. Other imaging findings, although not as commonly seen, are meningeal calcification and meningeal or cranial nerve enhancement.[96]

Imaging of cranial nerve involvement by PCNSL demonstrates findings similar to those seen in parenchymal CNS lymphoma. The nerves will demonstrate enlargement of the affected region and the lesions are typically isointense on T1-weighted and T2-weighted imaging, with homogeneous enhancement after gadolinium administration. In their series of five patients with non-Hodgkin lymphoma involving the cranial base, Han et al. tried to establish imaging criteria based on MRI. In their patients they found that the signal intensity in T1- and T2-weighted images was similar to that of the brain parenchyma and lesions were homogeneously enhanced with gadolinium. There was infiltration along the dural surface that resembled the dural tail of a meningioma but without hyperostotic reaction and internal carotid artery narrowing, thus differentiating the lesion from a meningioma.[97]

Management

PCNSL is typically a nonsurgical disease. Most cases of PCNSL can be diagnosed based on the imaging findings on CT, MRI, SPECT, and/or FDG PET. If imaging is not diagnostic in the immunocompetent patient, CSF should be obtained, as malignant cells in the CSF are found approximately 20% of the time in this patient population.[98,99] A positive CSF sample will negate the need for a biopsy. Of note, lymphomas are very sensitive to steroid therapy, with cell death and tumor regression occurring as early as 24 h after initiation of therapy. Therefore, if the diagnosis is uncertain steroids should be held until it is determined if a biopsy is necessary. Unlike the immunocompetent patient, biopsy of a suspected PCNSL lesion in a patient with AIDS carries a much higher surgical risk.[100] However, needle biopsy for tissue diagnosis is the appropriate course of management when CSF is negative for lymphoma, imaging is nontypical for toxoplasmosis, toxoplasmosis titers are negative, there is evidence of progression of the lesion after antitoxoplasmosis therapy, there is rapid neurological deterioration, or there are discordant CSF Epstein–Barr virus and thallium-201 SPECT scans.[101,102]

Once the diagnosis of PCNSL is made, the management is no longer surgical. Steroids, as previously mentioned, play a major role in the therapy and even diagnosis of PCNSL. Up to 40% of patients will see a regression of their PCNSL following administration of steroids.[102] Even 15% of patients will have a complete response after administration.[103] However, PCNSL is a systemic disease and recurrence will eventually happen

at the same or a distant site.[26] Radiation therapy was used in the past with good results, but has since been abandoned because of the severe neurotoxicity of the therapy.[26] SRS has even been used for small, focal lesions but series have shown that it is not successful at distant control or the prevention of recurrence.[104,105]

As of this writing, the standard of care for PCNSL is methotrexate-based chemotherapy. Studies have shown improved survival when high-dose methotrexate or high-dose cytarabine is used.[106] Furthermore, both methotrexate and cytarabine have excellent blood–brain barrier penetration.[26] Although there are significant side effect profiles for these two drugs (bone marrow suppression, neutropenia, mucositis), neither has demonstrated increased neurotoxicity regardless of route of administration (intravenous or intrathecal).[106] Using these two compounds, physicians have seen an increase in the median survival times ranging from 33 to 60 months.[107,108]

References

1. Chandler CL, Ramsden RT. Acoustic schwannoma. *Br J Hosp Med*. 1993;49:335–343.
2. D'Alessandro G, Giovnni M, Iannizzi L, et al. Epidemiology of primary intracranial tumors in the Valle d'Aosta during the 6-yr period. *Neuroepidemiology*. 1986–1991;14:139–146.
3. Barker DJP, Weller RO, Garfield JS. Epidemiology of primary tumors of the brain and spinal cord: a regional survey in Southern England. *J Neurol Neurosurg Psychiatry*. 1976;39:290–296.
4. Chimelli LM, Lowe JS, Harding B, et al. *Neuropathology, a Reference Text of CNS Pathology*. Elsevier Health Sciences; 2013.
5. Newton HB. *Handbook of Neuro-Oncology Neuroimaging*. Academic Press; 2007.
6. Curton D. CT of acoustic neuroma and other tumors of the ear. *Radiol Clin North Am*. 1984;22(1):77–105.
7. Graham MD. The jugular bulb. Its anatomic and clinical considerations in contemporary otology. *Arch Otolaryngol*. 1975;101(9): 560–564.
8. Kaye AH, Laws ER. *Brain Tumors: An Encyclopedic Approach*. Edinburgh: Saunders/Elsevier; 2012. [Print].
9. Casselman JW, Kuhweide R, Ampe W, Meeus L, Steyaert L. Pathology of the membranous labyrinth: comparison of T1- and T2-weighted and gadolinium-enhanced spin-echo and 3DFT-CISS imaging. *AJNR Am J Neuroradiol*. 1993;14(1):59–69.
10. Cushing H. *Tumors of the Nervus Acousticus and the Syndrome of the Cerebellopontine Angle*. Philadelphia, PA: WB Saunders; 1931.
11. Clemis JD, Ballad WJ, Baggot PJ, Lyon ST. Relative frequency of inferior vestibular schwannoma. *Arch Otolaryngol Head Neck Surg*. 1986;112(2):190–194.
12. Louis DN. *WHO Classification of Tumours of the Central Nervous System*. Lyon: International Agency for Research on Cancer; 2007. [Print].
13. Hardy DG, Macfarlane R, Baguley D, Moffat DA. Surgery for acoustic neurinoma. An analysis of 100 translabyrinthine operations. *J Neurosurg*. 1989;71(6):799–804.
14. Johnson EW. Auditory test results in 500 cases of acoustic neuroma. *Arch Otolaryngol*. 1977;103(3):152–158.
15. Symon L, Cheesman AD, Kawauchi M, Bordi L. Neuromas of the facial nerve: a report of 12 cases. *Br J Neurosurg*. 1993;7(1):13–22.
16. King TT, Morrison AW. Primary facial nerve tumors within the skull. *J Neurosurg*. 1990;72(1):1–8.
17. Yamaki T, Morimoto S, Ohtaki M, et al. Intracranial facial nerve neurinoma: surgical strategy of tumor removal and functional reconstruction. *Surg Neurol*. 1998;49(5):538–546.
18. Thomsen J, Tos M. Acoustic neuroma: clinical aspects, audiovestibular assessment, diagnostic delay, and growth rate. *Am J Otol*. 1990;11(1):12–19.
19. Pulec JL, House WF. Transtemporal bone microsurgical removal of acoustic neuromas. Facial nerve involvement and testing in acoustic neuromas. *Arch Otolaryngol*. 1964;80:685–692.
20. Valvassori GE. Radiologic evaluation of eighth nerve tumors. *Am J Otolaryngol*. 1984;5(4):270–280.
21. Möller A, Hatam A, Olivecrona H. The differential diagnosis of pontine angle meningioma and acoustic neuroma with computed tomography. *Neuroradiology*. 1978;17(1):21–23.
22. Wu EH, Tang YS, Zhang YT, Bai RJ. CT in diagnosis of acoustic neuromas. *AJNR Am J Neuroradiol*. 1986;7(4):645–650.
23. Pulec JL, House WF, Britton BH. A system of management of acoustic neuroma based on 364 cases. *Trans Am Acad Ophthalmol Otolaryngol*. 1971;75(1):48–55.
24. Winn HR. *Youmans Neurological Surgery, 4-Volume Set* Expert Consult—Online and Print. W.B. Saunders Company; 2011.
25. Linthicum FH, Brackmann DE. Bilateral acoustic tumors. A diagnostic and surgical challenge. *Arch Otolaryngol*. 1980;106(12): 729–733.
26. Quinones-Hinojosa A. *Schmidek and Sweet–Operative Neurosurgical Techniques, Indications, Methods and Results*. Saunders; 2012.
27. Mccormick PC, Bello JA, Post KD. Trigeminal schwannoma. Surgical series of 14 cases with review of the literature. *J Neurosurg*. 1988;69(6):850–860.
28. Pollack IF, Sekhar LN, Jannetta PJ, Janecka IP. Neurilemomas of the trigeminal nerve. *J Neurosurg*. 1989;70(5):737–745.
29. Jefferson G. The trigeminal neurinomas with some remarks on malignant invasion of the gasserian ganglion. *Clin Neurosurg*. 1953;1:11–54.
30. Nager GT. Neurinomas of the trigeminal nerve. *Am J Otolaryngol*. 1984;5(5):301–333.
31. Yasui T, Hakuba A, Kim SH, Nishimura S. Trigeminal neurinomas: operative approach in eight cases. *J Neurosurg*. 1989;71(4):506–511.
32. Mello LR, Tänzer A. Some aspects of trigeminal neurinomas. *Neuroradiology*. 1972;4(4):215–221.
33. Holman CB, Olive I, Svien HJ. Roentgenologic features of neurofibromas involving the gasserian ganglion. *Am J Roentgenol Radium Ther Nucl Med*. 1961;86:148–153.
34. Palacios E, Macgee EE. The radiographic diagnosis of trigeminal neurinomas. *J Neurosurg*. 1972;36(2):153–156.
35. Ikushima I, Korogi Y, Kuratsu J, et al. Dynamic MRI of meningiomas and schwannomas: is differential diagnosis possible? *Neuroradiology*. 1997;39(9):633–638.
36. O'donoghue GM, Brackmann DE, House JW, Jackler RK. Neuromas of the facial nerve. *Am J Otol*. 1989;10(1):49–54.
37. Isamat F, Bartumeus F, Miranda AM, Prat J, Pons LC. Neurinomas of the facial nerve. Report of three cases. *J Neurosurg*. 1975;43(5):608–613.
38. Horn KL, Crumley RL, Schindler RA. Facial neurilemmomas. *Laryngoscope*. 1981;91(8):1326–1331.
39. Graham MD, Larouere MJ, Kartush JM. Jugular foramen schwannomas: diagnosis and suggestions for surgical management. *Skull Base Surg*. 1991;1(1):34–38.
40. Song MH, Lee HY, Jeon JS, Lee JD, Lee HK, Lee WS. Jugular foramen schwannoma: analysis on its origin and location. *Otol Neurotol*. 2008;29(3):387–391.
41. Samii M, Babu RP, Tatagiba M, Sepehrnia A. Surgical treatment of jugular foramen schwannomas. *J Neurosurg*. 1995;82(6): 924–932.
42. Badie B. *Neurosurgical Operative Atlas, Neuro-oncology*. Thieme; 2007.

43. Ho CL, Deruytter MJ. Navigated dorsolateral suboccipital transcondylar (NADOSTA) approach for treatment of hypoglossal schwannoma. Case report and review of the literature. *Clin Neurol Neurosurg*. 2005;107(3):236–242.
44. Fujiwara S, Hachisuga S, Numaguchi Y. Intracranial hypoglossal neurinoma: report of a case. *Neuroradiology*. 1980;20(2):87–90.
45. Morelli RJ. Intracranial neurilemmoma of the hypoglossal nerve. Review and case report. *Neurology*. 1966;16(7):709–713.
46. Odake G. Intracranial hypoglossal neurinoma with extracranial extension: review and case report. *Neurosurgery*. 1989;24(4): 583–587.
47. Celli P, Ferrante L, Acqui M, Mastronardi L, Fortuna A, Palma L. Neurinoma of the third, fourth, and sixth cranial nerves: a survey and report of a new fourth nerve case. *Surg Neurol*. 1992;38(3): 216–224.
48. Tarlov I. Structure of the nerve root. II: differentiation of sensory from motor roots; observations on identification of function in roots of mixed cranial nerves. *Arch Neurol Psychiatry*. 1937;37:1338–1355.
49. Garen PD, Harper CG, Teo C, Johnston IH. Cystic schwannoma of the trochlear nerve mimicking a brain-stem tumor. Case report. *J Neurosurg*. 1987;67(6):928–930.
50. Bendheim PE, Berg BO. Ataxic hemiparesis from a midbrain mass. *Ann Neurol*. 1981;9(4):405–407.
51. Huang CF, Kondziolka D, Flickinger JC, Lunsford LD. Stereotactic radiosurgery for trigeminal schwannomas. *Neurosurgery*. 1999;45(1):11–16.
52. Hamm KD, Gross MW, Fahrig A, et al. Stereotactic radiotherapy for the treatment of nonacoustic schwannomas. *Neurosurgery*. 2008;62(5 suppl):A29–A36.
53. Madhok R, Kondziolka D, Flickinger JC, Lunsford LD. Gamma knife radiosurgery for facial schwannomas. *Neurosurgery*. 2009;64(6):1102–1105.
54. Hakuba A, Hashi K, Fujitani K, Ikuno H, Nakamura T, Inoue Y. Jugular foramen neurinomas. *Surg Neurol*. 1979;11(2):83–94.
55. Kadri PA, Al-mefty O. Surgical treatment of dumbbell-shaped jugular foramen schwannomas. *Neurosurg Focus*. 2004;17(2):E9.
56. Peker S, Sengöz M, Kılıç T, Pamir MN. Gamma knife radiosurgery for jugular foramen schwannomas. *Neurosurg Rev*. 2012;35(4):549–553.
57. Zhang N, Pan L, Dai JZ, Wang BJ, Wang EM, Cai PW. Gamma knife radiosurgery for jugular foramen schwannomas. *J Neurosurg*. 2002;97(5 suppl):456–458.
58. Elsharkawy M, Xu Z, Schlesinger D, Sheehan JP. Gamma knife surgery for nonvestibular schwannomas: radiological and clinical outcomes. *J Neurosurg*. 2012;116(1):66–72.
59. Kim IY, Kondziolka D, Niranjan A, Flickinger JC, Lunsford LD. Gamma knife surgery for schwannomas originating from cranial nerves III, IV, and VI. *J Neurosurg*. 2008;109(suppl):149–153.
60. Janss AJ, Grundy R, Cnaan A, et al. Optic pathway and hypothalamic/chiasmatic gliomas in children younger than age 5 years with a 6-year follow-up. *Cancer*. 1995;75(4):1051–1059.
61. Barbaro NM, Rosenblum ML, Maitland CG, Hoyt WF, Davis RL. Malignant optic glioma presenting radiologically as a "cystic" suprasellar mass: case report and review of the literature. *Neurosurgery*. 1982;11(6):787–789.
62. Binning MJ, Liu JK, Kestle JR, Brockmeyer DL, Walker ML. Optic pathway gliomas: a review. *Neurosurg Focus*. 2007;23(5):E2.
63. Czyzyk E, Józwiak S, Roszkowski M, Schwartz RA. Optic pathway gliomas in children with and without neurofibromatosis 1. *J Child Neurol*. 2003;18:471–478.
64. Dutton JJ. Gliomas of the anterior visual pathway. *Surv Ophthalmol*. 1994;38:427–452.
65. Listernick R, Charrow J, Greenwald M, Mets M. Natural history of optic pathway tumors in children with neurofibromatosis type 1: a longitudinal study. *J Pediatr*. 1994;125(1):63–66.
66. Grill J, Couanet D, Cappelli C, et al. Radiation-induced cerebral vasculopathy in children with neurofibromatosis and optic pathway glioma. *Ann Neurol*. 1999;45(3):393–396.
67. Jenkin D, Angyalfi S, Becker L, et al. Optic glioma in children: surveillance, resection, or irradiation? *Int J Radiat Oncol Biol Phys*. 1993;25(2):215–225.
68. Khafaga Y, Hassounah M, Kandil A, et al. Optic gliomas: a retrospective analysis of 50 cases. *Int J Radiat Oncol Biol Phys*. 2003;56(3):807–812.
69. Komotar RJ, Burger PC, Carson BS, et al. Pilocytic and pilomyxoid hypothalamic/chiasmatic astrocytomas. *Neurosurgery*. 2004;54(1):72–79.
70. Collet-solberg PF, Sernyak H, Satin-smith M, et al. Endocrine outcome in long-term survivors of low-grade hypothalamic/chiasmatic glioma. *Clin Endocrinol (Oxf)*. 1997;47(1):79–85.
71. Horger M, Vogel MN, Beschorner R, et al. T2 and DWI in pilocytic and pilomyxoid astrocytoma with pathologic correlation. *Can J Neurol Sci*. 2012;39(4):491–498.
72. Astrup J. Natural history and clinical management of optic pathway glioma. *Br J Neurosurg*. 2003;17(4):327–335.
73. Beral V, Peterman T, Berkelman R, Jaffe H. AIDS-associated non-Hodgkin lymphoma. *Lancet*. 1991;337(8745):805–809.
74. So YT, Beckstead JH, Davis RL. Primary central nervous system lymphoma in acquired immune deficiency syndrome: a clinical and pathological study. *Ann Neurol*. 1986;20(5):566–572.
75. Snider WD, Simpson DM, Aronyk KE, Nielsen SL. Primary lymphoma of the nervous system associated with acquired immunedeficiency syndrome. *N Engl J Med*. 1983;308(1):45.
76. Küker W, Nägele T, Korfel A, et al. Primary central nervous system lymphomas (PCNSL): MRI features at presentation in 100 patients. *J Neurooncol*. 2005;72(2):169–177.
77. Sato H, Hashimoto T, Yoneda S, Hirabayashi K, Oguchi K, Higuchi K. Lymphoma as a cause of isolated oculomotor nerve palsy. *J Clin Neurosci*. 2011;18(9):1256–1258.
78. Tsutsumi K, Horiuchi T, Aoyama T, Hongo K. Isolated primary malignant lymphoma arising from the optic chiasm. *J Clin Neurosci*. 2013;20(12):1783–1786.
79. Barreira junior AK, Moura FC, Monteiro ML. Bilateral cavernous sinus non-Hodgkin's lymphoma as the presenting sign of acquired immunodeficiency syndrome: case report. *Arq Bras Oftalmol*. 2011;74(2):130–131.
80. Jaiswal AK, Tripathi M, Chandra PS, Sharma MC, Mahapatra AK. An unusual case of primary lymphoma of the skull base extending from cerebellopontine angle to cavernous sinus and orbit. A case report. *J Neurosurg Sci*. 2000;44(3):145–148.
81. Abdel aziz KM, Van loveren HR. Primary lymphoma of Meckel's cave mimicking trigeminal schwannoma: case report. *Neurosurgery*. 1999;44(4):859–862.
82. Lenarz M, Durisin M, Becker H, Lenarz T, Nejadkazem M. Primary central nervous system lymphoma presenting as bilateral tumors of the internal auditory canal. *Skull Base*. 2007;17(6):409–412.
83. Taylor JW, Flanagan EP, O'neill BP, et al. Primary leptomeningeal lymphoma: International primary CNS lymphoma collaborative group report. *Neurology*. 2013;81(19):1690–1696.
84. Gastaldi M, Ferrario A, Basilico C, et al. Primary leptomeningeal CNS lymphoma presenting as bilateral facial nerve palsy. *J Neurol Sci*. 2014;344(1–2):234–235.
85. Lachance DH, O'neill BP, Macdonald DR, et al. Primary leptomeningeal lymphoma: report of 9 cases, diagnosis with immunocytochemical analysis, and review of the literature. *Neurology*. 1991;41(1):95–100.
86. Miller DC, Hochberg FH, Harris NL, Gruber ML, Louis DN, Cohen H. Pathology with clinical correlations of primary central nervous system non-Hodgkin's lymphoma. The Massachusetts General Hospital experience 1958–1989. *Cancer*. 1994;74(4):1383–1397.

87. Koeller KK, Smirniotopoulos JG, Jones RV. Primary central nervous system lymphoma: radiologic-pathologic correlation. *Radiographics*. 1997;17(6):1497–1526.
88. Coulon A, Lafitte F, Hoang-xuan K, et al. Radiographic findings in 37 cases of primary CNS lymphoma in immunocompetent patients. *Eur Radiol*. 2002;12(2):329–340.
89. Slone HW, Blake JJ, Shah R, Guttikonda S, Bourekas EC. CT and MRI findings of intracranial lymphoma. *AJR Am J Roentgenol*. 2005;184(5):1679–1685.
90. Cotton F, Ongolo-zogo P, Louis-tisserand G, et al. Diffusion and perfusion MR imaging in cerebral lymphomas. *J Neuroradiol*. 2006;33(4):220–228.
91. Heald AE, Hoffman JM, Bartlett JA, Waskin HA. Differentiation of central nervous system lesions in AIDS patients using positron emission tomography (PET). *Int J STD AIDS*. 1996;7(5):337–346.
92. Lorberboym M, Estok L, Machac J, et al. Rapid differential diagnosis of cerebral toxoplasmosis and primary central nervous system lymphoma by thallium-201 SPECT. *J Nucl Med*. 1996;37(7):1150–1154.
93. Skiest DJ, Erdman W, Chang WE, Oz OK, Ware A, Fleckenstein J. SPECT thallium-201 combined with toxoplasma serology for the presumptive diagnosis of focal central nervous system mass lesions in patients with AIDS. *J Infect*. 2000;40(3):274–281.
94. Pomper MG, Constantinides CD, Barker PB, et al. Quantitative MR spectroscopic imaging of brain lesions in patients with AIDS: correlation with [11C-methyl]thymidine PET and thallium-201 SPECT. *Acad Radiol*. 2002;9(4):398–409.
95. Pierce MA, Johnson MD, Maciunas RJ, et al. Evaluating contrast-enhancing brain lesions in patients with AIDS by using positron emission tomography. *Ann Intern Med*. 1995;123(8):594–598.
96. King A, Wilson H, Penney C, Michael W. An unusual case of primary leptomeningeal marginal zone B-cell lymphoma. *Clin Neuropathol*. 1998;17(6):326–329.
97. Herrlinger U, Schabet M, Bitzer M, Petersen D, Krauseneck P. Primary central nervous system lymphoma: from clinical presentation to diagnosis. *J Neurooncol*. 1999;43(3):219–226.
98. Behin A, Hoang-xuan K, Carpentier AF, Delattre JY. Primary brain tumours in adults. *Lancet*. 2003;361(9354):323–331.
99. Skolasky RL, Dal pan GJ, Olivi A, Lenz FA, Abrams RA, Mcarthur JC. HIV-associated primary CNS lymorbidity and utility of brain biopsy. *J Neurol Sci*. 1999;163(1):32–38.
100. Kasamon YL, Ambinder RF. AIDS-related primary central nervous system lymphoma. *Hematol Oncol Clin North Am*. 2005;19(4):665–687. vi-vii.
101. Sparano JA. Clinical aspects and management of AIDS-related lymphoma. *Eur J Cancer*. 2001;37(10):1296–1305.
102. Weller M. Glucocorticoid treatment of primary CNS lymphoma. *J Neurooncol*. 1999;43(3):237–239.
103. Dong Y, Pan L, Wang B, et al. Stereotactic radiosurgery in the treatment of primary central nervous system lymphoma. *Chin Med J*. 2003;116(8):1166–1170.
104. Kenai H, Yamashita M, Nakamura T, Asano T, Momii Y, Nagatomi H. Gamma knife surgery for primary central nervous system lymphoma: usefulness as palliative local tumor control. *J Neurosurg*. 2006;105(suppl):133–138.
105. Blay JY, Conroy T, Chevreau C, et al. High-dose methotrexate for the treatment of primary cerebral lymphomas: analysis of survival and late neurologic toxicity in a retrospective series. *J Clin Oncol*. 1998;16(3):864–871.
106. Omuro AM, Deangelis LM, Yahalom J, Abrey LE. Chemoradiotherapy for primary CNS lymphoma: an intent-to-treat analysis with complete follow-up. *Neurology*. 2005;64(1):69–74.
107. Sughrue ME, Yang I, Aranda D, et al. The natural history of untreated sporadic vestibular schwannomas: a comprehensive review of hearing outcomes. *J Neurosurg*. 2010;112(1):163–167.
108. Wiggins RH, Harnsberger HR, Salzman KL, Shelton C, Kertesz TR, Glastonbury CM. The many faces of facial nerve schwannoma. *AJNR Am J Neuroradiol*. 2006;27(3):694–699.
109. Eldevik OP, Gabrielsen TO, Jacobsen EA. Imaging findings in schwannomas of the jugular foramen. *AJNR Am J Neuroradiol*. 2000;21(6):1139–1144.
110. Santarius T, Dakoji S, Afshari FT, et al. Isolated hypoglossal schwannoma in a 9-year-old child. *J Neurosurg Pediatr*. 2012;10(2):130–133.
111. Yang SS, Li ZJ, Liu X, Li Y, Li SF, Zhang HD. Pediatric isolated oculomotor nerve schwannoma: a new case report and literature review. *Pediatr Neurol*. 2013;48(4):321–324.
112. Avery RA, Fisher MJ, Liu GT. Optic path way gliomas. *J Neuroophthalmol*. 2011;31(3):269–278.

CHAPTER

44

Meningeal Tumors

John M. Collins, Gregory A. Christoforidis
Department of Radiology, University of Chicago, Chicago, IL, USA

INTRODUCTION

The most common neoplasms to arise from the meninges have meningothelial cell origin. Collectively referred to as meningiomas, this category includes many different subtypes, which differ in histologic features and behavioral characteristics. These include low-grade meningiomas, as well as the more aggressive atypical and anaplastic meningiomas. Although much rarer, a full complement of mesenchymal nonmeningothelial tumors (lipoma, leiomyoma, solitary fibrous tumor, sarcoma, etc.) can also arise in the meninges. Among the mesenchymal nonmeningothelial tumors arising from the meninges, hemangiopericytoma is the most commonly encountered of the group. Rarer still are the melanocytic tumors, the primary meningeal lymphomas, and some varieties of histiocytosis. All these meningeal tumors are distinguished from other intracranial tumors by their extra-axial location and in many cases their rich vascular supply. Their extra-axial location often makes them amenable to surgical resection and cure. Imaging and image interpretation for these lesions therefore aim to establish their extra-axial location; identify any invasion of adjacent structures, such as the calvarium, the brain, or the dural venous sinuses; confirm their vascular nature; and identify associations that might hint at a congenital or inherited underlying process such as neurofibromatosis. After reviewing a basic approach to imaging of these tumors, this chapter goes on to take a closer look at individual meningeal tumor types.

IMAGING OF EXTRA-AXIAL TUMORS

Features common to extra-axial meningeal tumors that can help distinguish them from intra-axial tumors may include broad dural attachment, displacement of the cortex away from the calvarium, an accordion-like folding of brain parenchyma adjacent to the lesion, and oftentimes a thin cerebrospinal fluid space interposed between the lesion and the adjacent brain (Figures 1 and 2). Because of their tendency to be vascular, these tumors often have high cerebral blood volumes when applying perfusion magnetic resonance imaging (MRI) techniques, and they characteristically lack an *N*-acetylaspartate (NAA) peak on MRI spectroscopy (Figures 3 and 4). Preoperative planning for meningeal tumor surgery and embolization includes a thorough imaging evaluation. This can help identify the location and extent of the tumor, the vascularity of the tumor, any potential invasion of large vessels such as the internal carotid artery (ICA), or draining veins such as the dural venous sinuses. The location of the tumor should give the neurointerventionalist insight into the vascular supply of the tumor.[1–6] Imaging features such as the pattern of enhancement or presence of calcifications may help in assessing tumoral vascularity and tumor type (Figures 5–15). Imaging may help assess whether sacrifice of the ICA may be necessary or whether the tumor has occluded the dural sinuses. If there is suspicion of invasion of adjacent dural venous sinuses, angiographic methods that evaluate these structures, such as CT angiography (CTA), MR venography, or conventional angiography, can assist the surgeon in planning a resection.

MENINGIOMAS

Meningiomas were first described in 1614 by Felix Paster.[6–8] Meningiomas are tumors that are thought to arise from the arachnoid cap cells found in the arachnoid granulations.[7,9] Meningioma represents the most common benign intracranial tumor and is in fact the most common overall primary intracranial tumor. According to the 2013 statistical report from the U.S. Central Brain Tumor Registry, meningioma accounts for almost 36% of

Handbook of Neuro-Oncology Neuroimaging, Second Edition
http://dx.doi.org/10.1016/B978-0-12-800945-1.00044-6

© 2016 Elsevier Ltd. All rights reserved.

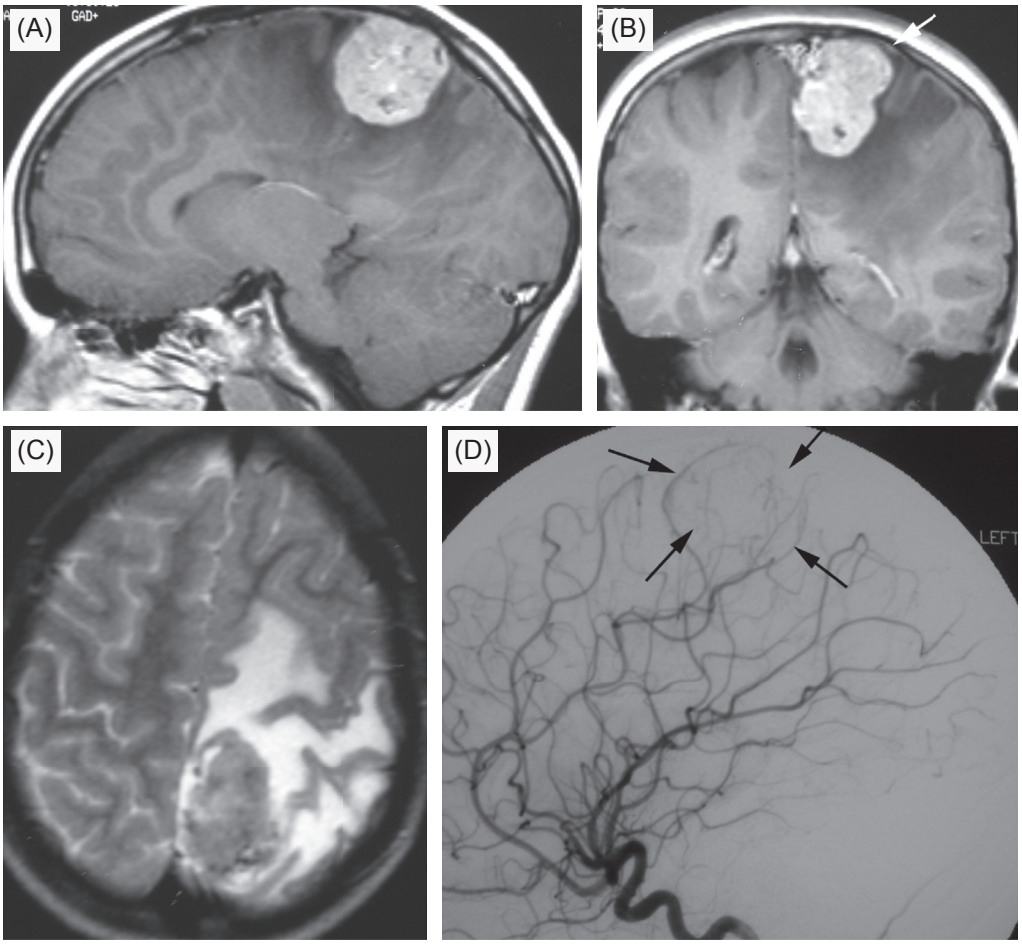


FIGURE 1 **Intra-axial glioma mimicking a meningioma.** (A) Sagittal and (B) coronal post-gadolinium T1 and (C) axial T2 images of a heterogeneously enhancing mass closely applied to the dura. On coronal imaging there appears to be cortex partially surrounding the mass (arrow). There is no cleft of cerebrospinal fluid separating the tumor from adjacent brain to confirm extra-axial location. (D) Lateral view of left internal carotid angiogram demonstrates microvascularity within the tumor bed (arrows) but no tumor blush. This helps confirm intra-axial location.

all intracranial tumors.[10] The reported annual incidence in the United States is approximately 7 per 100,000 population, and autopsy studies suggest an overall prevalence of 1.4%. Many meningiomas undoubtedly go undetected during life and so the real numbers are likely to be higher. Peak incidence is in the sixth and seventh decades of life and there is a 2:1 female predilection. Meningiomas can occur in multiples (Figure 5), which may signal an inherited predisposition, and they can develop along with other tumor types, as is often seen in neurofibromatosis type II (Figure 8).[11] Increasing age and female sex are well established as markers of higher risk for the development of a meningioma. Radiation exposure, at both high and low levels, also conveys increased risk.[12,13] Data regarding the influence of environmental factors, reproductive status, and hormone exposure have been somewhat conflicting. However, reports exist that suggest an increased risk with higher body mass index, higher parity, exposure to hormone replacement therapy (but not oral contraceptive use), and a history of uterine leiomyoma.[14–16] Interestingly, meningiomas have also been associated with a history of head trauma.[17]

Meningiomas have historically been divided into many subtypes based on their histologic features. The World Health Organization (WHO) classification systems lists 15 distinct subtypes, of which meningothelial, fibrous, and transitional are the most common.[7–9,11] Many of these subtypes are identical in their indolent, nonaggressive behavior. Furthermore, most are indistinguishable on imaging, and thus the distinctions are largely academic. Some meningiomas, however, manifest a more aggressive behavior, showing relatively faster growth rates and a greater tendency to invade brain parenchyma, to recur after surgery, and even to metastasize to distant sites. The WHO classification therefore superimposes a three-tiered grading scheme, which is meant to identify those lesions that may behave more mischievously. Grade I meningiomas are considered benign. They tend not to invade the adjacent brain or calvarium, grow slowly, induce little parenchymal edema

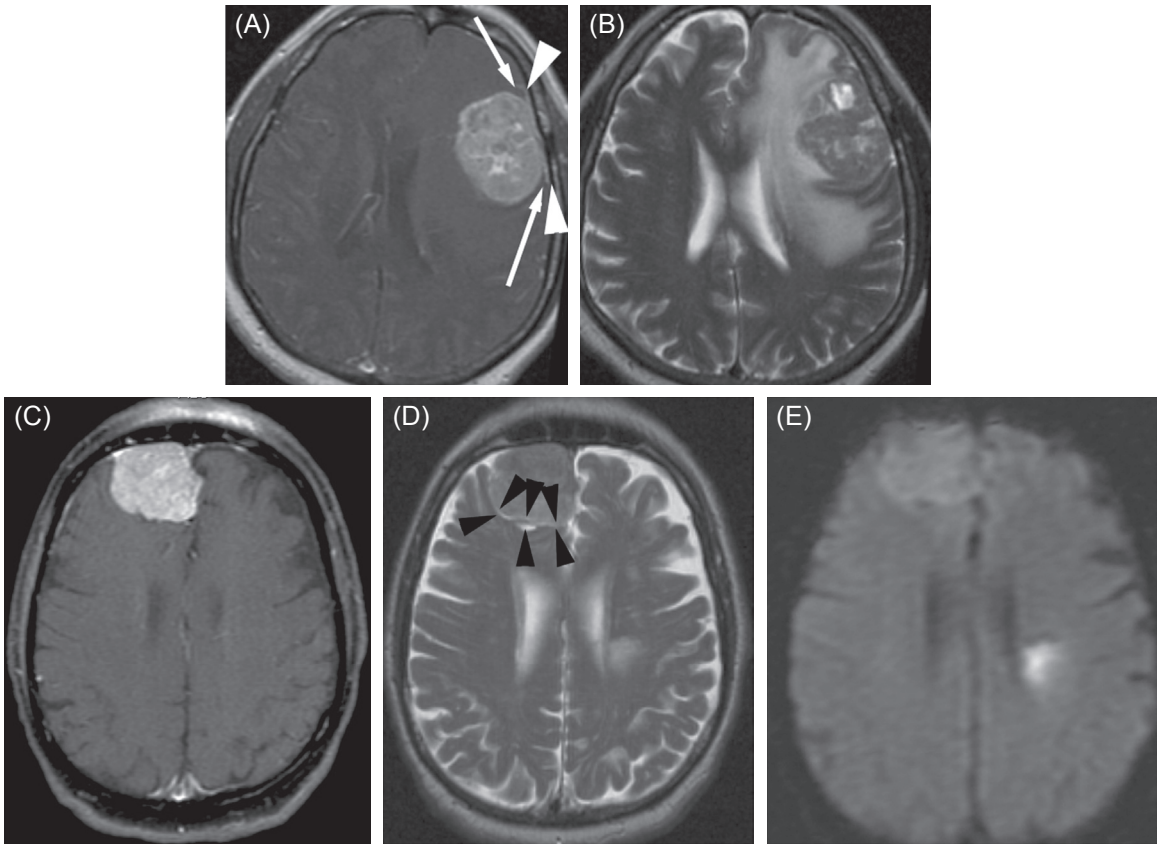


FIGURE 2 **Intra-axial metastasis compared to an extra-axial meningioma.** (A) Axial T2 and (B) axial post-gadolinium T1 images of a peripherally located mass with dural tail sign (white arrowheads) raise the question of extra-axial tumor with extensive vasogenic edema. Normal tissue begins to surround the tumor (white arrows) and no cerebrospinal fluid cleft is identified adjacent to the tumor. Meningioma, however, is still a differential consideration. Compare this to (C) T2 and (D) post-gadolinium T1 images from a different patient with a homogeneously enhancing extra-axial meningioma. Note the cerebrospinal fluid cleft surrounding the mass (black arrowheads). (E) Diffusion MRI of the meningioma demonstrates no significant diffusion restriction (high signal focus in the left hemisphere is a subacute infarction).

until they become large, and typically do not recur after a complete resection. Grade II meningiomas are termed atypical, and although the statistics vary, these tumors may comprise up to 20% of all meningiomas that come to clinical attention (Figures 9 and 10). Grade III meningiomas are termed anaplastic (Figure 11), and these may account for 1.0–2.8% of all meningiomas.[11] WHO grade II and III meningiomas occur more frequently in children and males. The distinction between grades is made based on the observed level of cellularity, atypia, and mitoses at histologic assessment. The application of a grade is independent of the overall meningioma subtype, and it is the grade rather than the subtype that best predicts prognosis. As one would expect, prognosis decreases with increasing grade. Some reports indicate a less than 2-year median survival for the most aggressive varieties. Anaplastic meningiomas, for example, recur after surgery 50–94% of the time and have even been known to metastasize to the lung, pleura, bone, and liver.[11,18]

Surgical removal of meningiomas continues to be the most effective method of treating these tumors, at least for the lower grades. For higher grade lesions, surgery and radiotherapy form the mainstay of treatment. When these modalities fail, however, there are few additional tools available to the neuro-oncologist, as these lesions tend to be resistant to most chemotherapy regimens.[19,20] By way of providing for an easier and more complete tumor resection, preoperative embolization has become an accepted and valuable procedure serving to devascularize highly vascular meningiomas without disturbing the blood supply to the adjacent normal structures. Embolization of a meningioma softens the tumor, reduces intraoperative blood loss and surgical time, and assists in more complete tumor removal. Advances in microcatheter technology and embolic agents and advances in the understanding of the functional anatomy of the head and neck have further contributed to the refinement and extent of endovascular techniques (Figures 16 and 17).[1,6,21]

Imaging Evaluation

Meningiomas are typically intracranial in origin but can also be found within the orbit and spinal canal.[11] Rare occurrences have been reported in almost every organ.

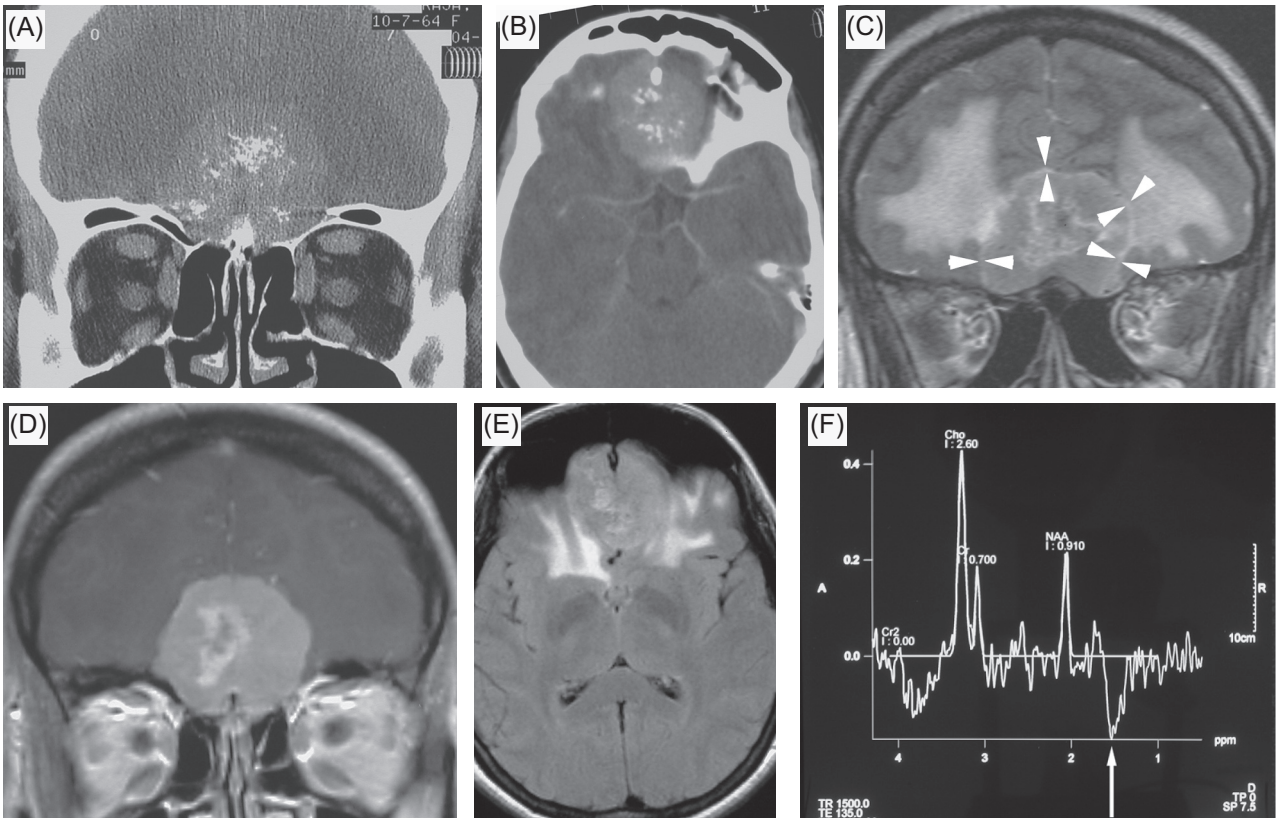


FIGURE 3 **Olfactory groove meningioma with MR spectroscopy.** Patient presenting with anosmia. (A) Noncontrast coronal and (B) contrast-enhanced axial CT scans demonstrate a peripherally located mass similar in density to gray matter with a broad base to the dura associated with calcifications within the tumor bed. Further investigation was performed with (C) T2 coronal, (D) post-gadolinium coronal, (E) axial FLAIR, and (F) MR spectroscopy. Extra-axial location is confirmed by a narrow cerebrospinal fluid cleft (arrowheads) on T2 imaging (C). The mass is associated with vasogenic edema and is heterogeneous in signal characteristics and contrast enhancement. Heterogeneity can be in part attributed to calcification. (F) MR spectroscopy reveals low NAA, high choline, and inverse lipid/lactate (arrow) peaks.

Intracranially, meningiomas occur most frequently along the cerebral convexities, especially along the falx cerebri. Intracranial origins, in order of decreasing frequency of occurrence, include the parafalcine location, the falx, the sphenoid ridges, and the posterior fossa (including petroclival location and foramen magnum). In addition, they are found at the tuberculum sellae, olfactory grooves, tentorium, optic nerves, and petrous ridges.[22] Purely intraventricular meningiomas also occur, most often developing in the atria of the lateral ventricles and with a slight preference for the left side. Symptoms and signs of meningioma vary according to size and location. Patients present with headache alone up to 36% of the time (as in Figures 4 and 5),[23,24] whereas other symptoms may be due to compression of adjacent structures such as cranial nerves (Figures 3, 7, and 12) or obstruction of the ventricles (Figures 13, 16, and 18).

Computed tomography (CT) imaging of meningioma demonstrates an isodense or slightly hyperdense tumor with a 15–20% incidence of tumoral calcifications (Figure 3). Calcifications are more common in fibroblastic or transitional subtypes, with dense calcifications occurring in psammomatous subtypes. On nonenhanced CT scans, they are sharply circumscribed and tend to be hyperdense or isodense relative to brain. Meningiomas that are isodense may be difficult to identify on noncontrast CT (Figure 5). Meningiomas, however, typically enhance uniformly following contrast administration, allowing for easier identification. They can also elicit changes in the adjacent bony structures, usually in the form of hyperostosis, in up to 20% of cases (Figures 8 and 16). Hyperostosis associated with meningioma has not been shown to correlate with either tumor size or grade, and although it may be tempting to ascribe it to nonneoplastic reactive bony changes, in some cases the hyperostotic bone has been shown to contain tumor cells.[23,25] It is therefore difficult or impossible to determine if the appearance of sclerosis in adjacent bone is the result of a slow, benign, and reactive osseous proliferation or from a slow tumor invasion into the bone itself. This is, of course, a very significant distinction to make, as the presence of true bony invasion may completely alter the surgical approach. Conventional imaging is currently limited in this regard, but there may be added benefit to taking a

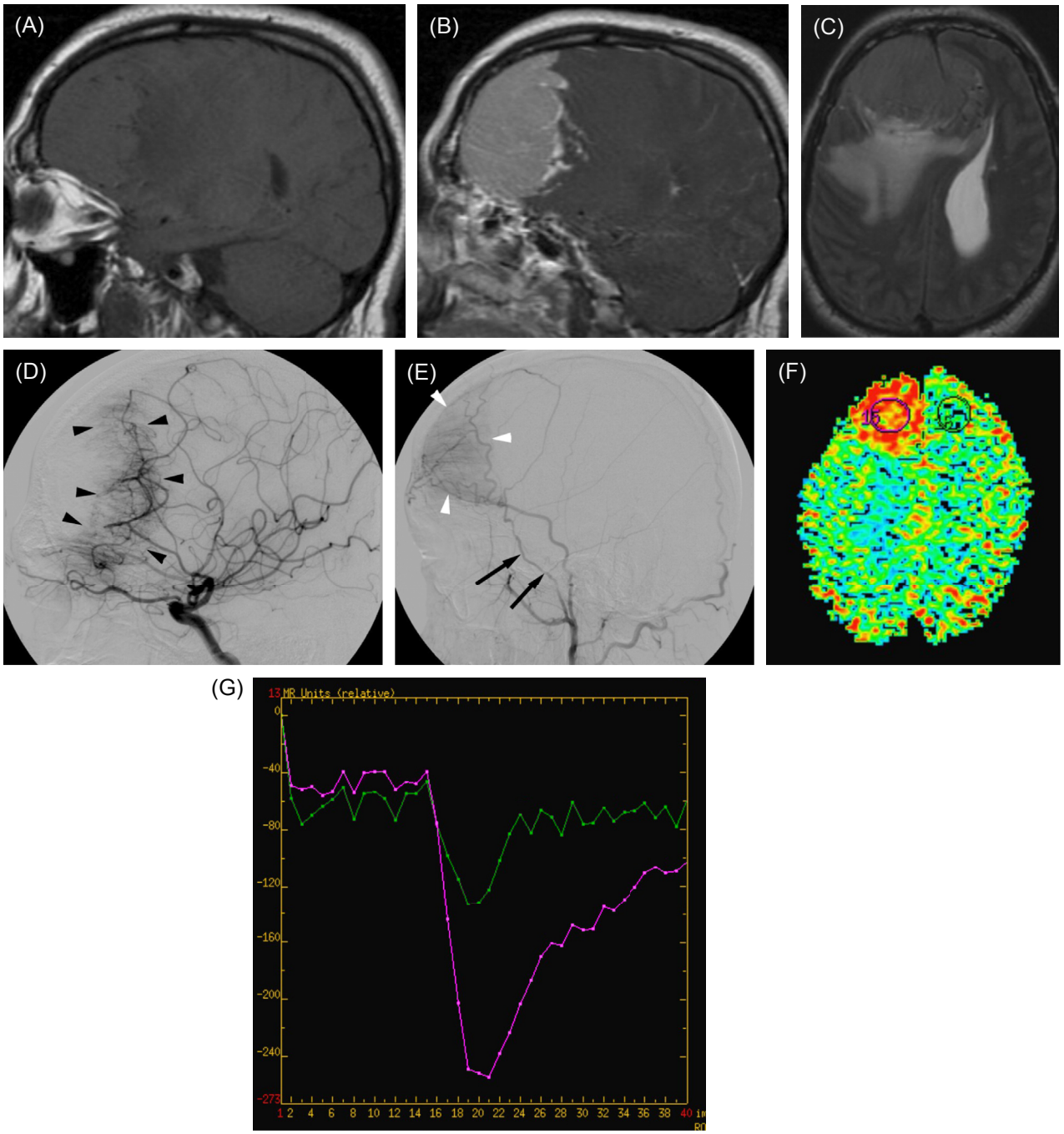


FIGURE 4 **Perfusion MRI of a large meningioma.** This patient presented with headaches with no other symptoms. He was found to have a sizable meningioma. (A) T1 sagittal, (B) T1 post-gadolinium sagittal, (C) T2 axial, (D) lateral internal carotid artery injection, (E) lateral external carotid artery injection, (F) axial perfusion cerebral blood volume map, and (G) time–intensity curves are shown here. Note the pial supply to the meningioma (black arrowheads) on the internal carotid artery injection (D), as well as the middle meningeal artery (arrow) supply on the external carotid artery injection. Note that on perfusion imaging the meningioma demonstrates a hyperperfusing mass with delayed contrast washout on time–intensity curves (purple curve) relative to normal brain tissue (green curve).

multimodal approach, including PET, in the preoperative assessment of select patients.[26] More aggressive tumors sometimes demonstrate frank lytic or destructive changes (Figure 11). However, a lytic appearance has also been associated with intraosseous meningioma, which can still be of low grade[27] (Figure 17). Additional CT findings of meningioma include abnormal enlargement of the paranasal sinuses.[28] Areas of hypodensity within the tumor can reflect the presence of cysts or trapped cerebrospinal fluid (CSF).[23] Hypodensity may also stem from fatty transformation, as with the rare lipomatous meningiomas.[29,30] Some meningiomas lack the typical solid pattern of

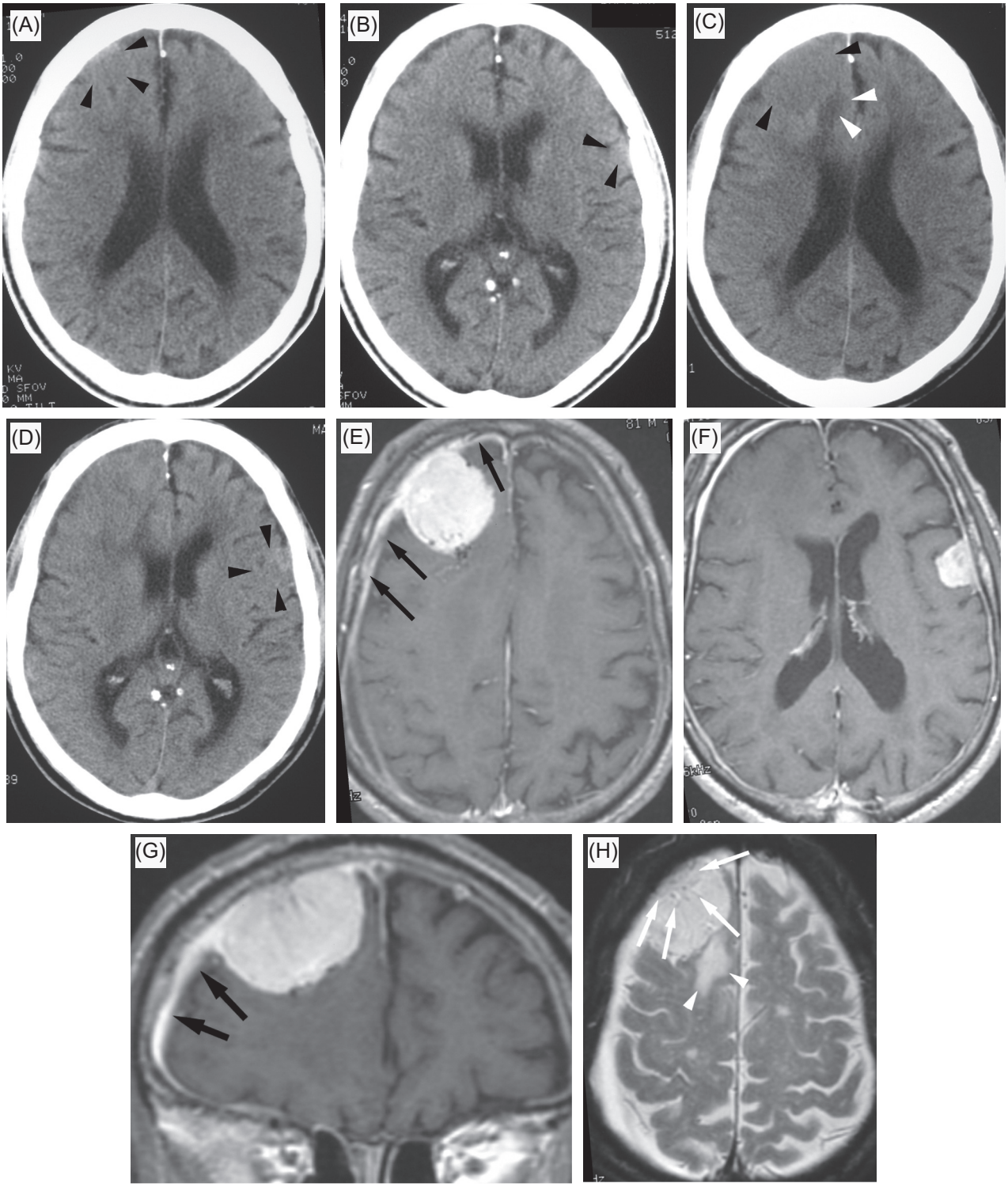


FIGURE 5 **Subtle meningioma on noncontrast CT.** A patient who presented with headache underwent a head CT. (A, B) Two meningiomas are not readily identified on noncontrast CT images of the brain (arrowheads) owing to small size and isodensity relative to adjacent brain. (C) Follow-up CT of the head after a second presentation 4 years later displays a small amount of vasogenic edema (white arrowheads) adjacent to one of the two neoplasms (C, D). (E, F) Post-gadolinium axial and (G) coronal and (H) T2-weighted MRI of the brain suggest that this patient has multiple meningiomas. Note the dural reaction adjacent to the tumor (black arrows) and the flow voids within the tumor (white arrows).

enhancement, showing instead a heterogeneous or ring-like pattern, which can mimic other tumor types, even high-grade glioma. Hemorrhage and necrosis within the tumor bed also result in a heterogeneous appearance on both noncontrast and contrast-enhanced CT.[31,32]

Edema within the white matter adjacent to a meningioma occurs in up to 75% of cases[33] and can usually be seen on CT, but is best displayed on MRI (Figures 3–5, 9, 11, 13, 16, 18). The source of this edema is controversial but thought to arise either from repeated mechanical injury to the adjacent brain or in response to factors secreted by the tumor.[23] It is not possible to predict histologic subtype, venous occlusion, or tumoral vascularity based on the finding of edema on imaging[23,34–36] (Figures 9 and 10). Some studies have suggested that there may be an association between edema, brain invasion, and recurrence.[37] Secretory meningiomas have been shown to produce a greater amount of edema.[38]

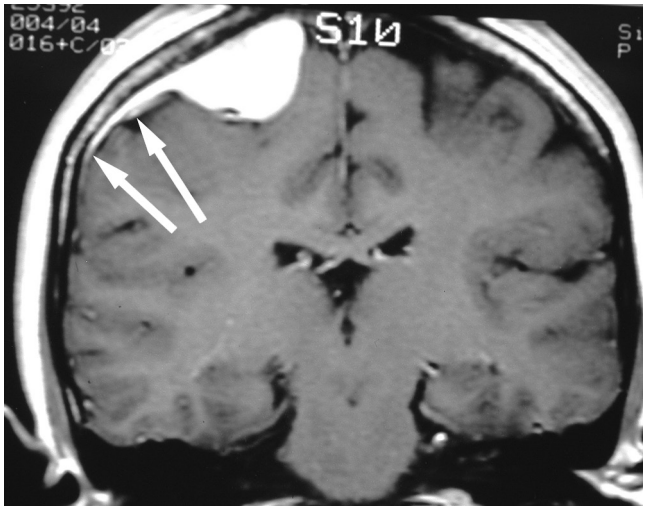


FIGURE 6 **Low-grade meningioma with dural tail.** Post-gadolinium coronal T1 MRI demonstrating a dural tail (arrow) and no evidence for vasogenic edema.

Magnetic Resonance Imaging

Whereas a meningioma may first be encountered on CT, complete imaging assessment requires contrast-enhanced MRI. The MR signal intensity of meningiomas varies on T1, T2/FLAIR, and proton density (PD) sequences. On T1-weighted images, they tend to be rather similar in signal intensity to the brain parenchyma. Meningiomas are usually relatively hyperintense to brain on T2/FLAIR and even more so on PD, though there is a wide range. They are usually not light-bulb bright on T2 images, however, and this feature can help distinguish them from other extra-axial lesions (inflammatory, metastatic, etc.), which tend to be brighter. There is, nevertheless, a wide range, and some meningiomas can appear quite bright on T2 (Figure 5), whereas others appear quite T2 dark, especially in contrast to any T2-bright edema that the lesion may be inducing in the surrounding parenchyma (Figure 16). On postcontrast T1 imaging, solid uniform enhancement is the expected finding, though of course any areas of cystic degeneration will bring some heterogeneity to the picture.

Postcontrast MRI is superior to contrast-enhanced CT in detection of the so-called dural tail in which the edges of an enhancing dural-based tumor taper away to blend with

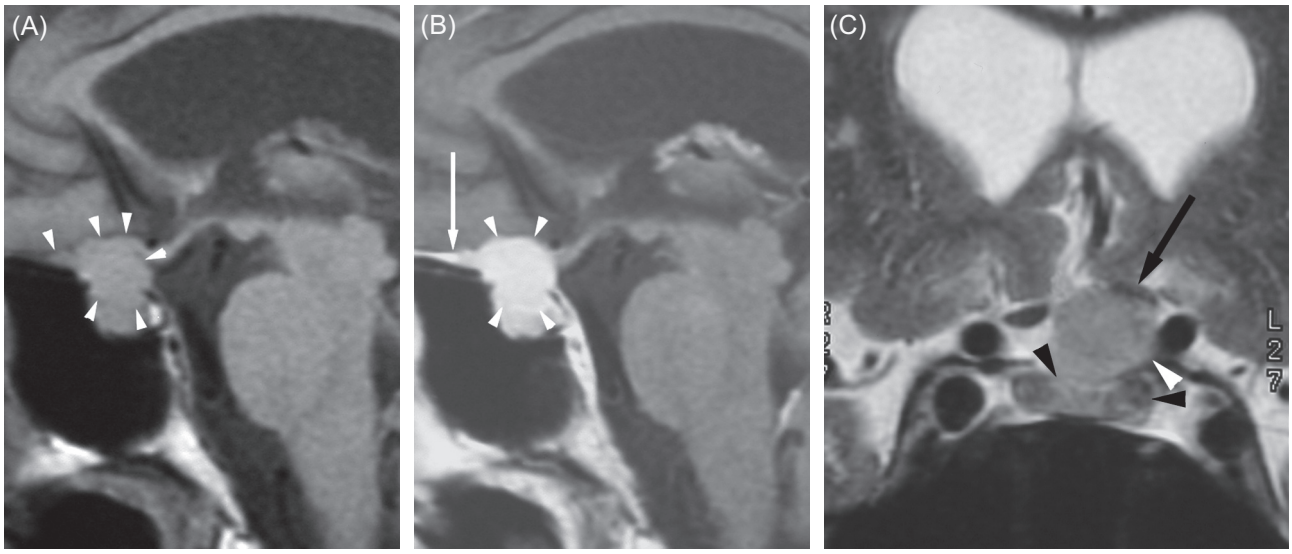


FIGURE 7 **Meningioma of the diaphragma sellae.** (A) Sagittal T1, (B) post-gadolinium sagittal T1, and (C) coronal T2 demonstrate a neoplasm along the sellae. The most common tumor in this location is pituitary adenoma; however, certain features may suggest a different diagnosis. The dural attachment and dural tail suggest the diagnosis of meningioma. A dural tail is less commonly seen with pituitary adenoma. Note a clear separation between the meningioma (white arrowheads) and the pituitary gland (black arrowheads) especially on the T2 images. Note the displacement of the optic nerve (black arrow), which can account for the patient's symptoms of loss of visual acuity.

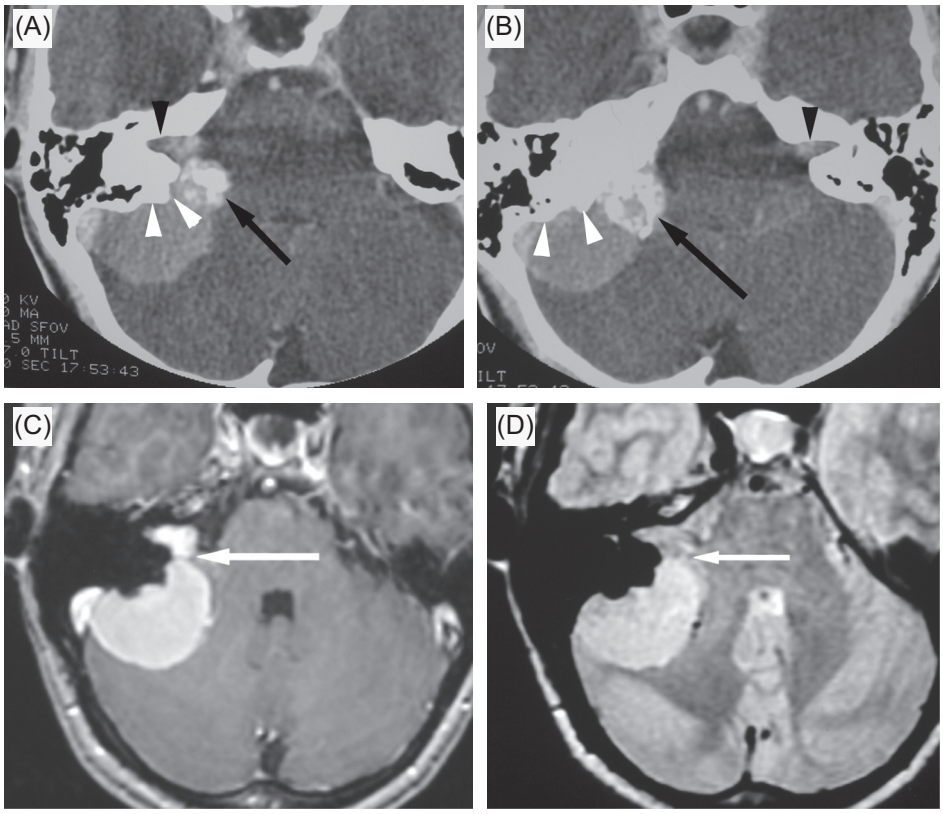


FIGURE 8 **Meningioma in neurofibromatosis type II.** (A, B) Axial enhanced CT demonstrates a right cerebellopontine angle (CPA) cistern extra-axial mass associated with calcifications (black arrows) and hyperostosis (white arrowheads), which are features suggestive of meningioma. Enlargement of the internal auditory canals associated with enhancing lesions (black arrowheads) suggests vestibular schwannomas, which are the most common CPA cistern lesions. (C) Post-gadolinium MRI identifies bilateral vestibular schwannomas and a cleft separating the CPA cistern lesion from the internal auditory canal lesion. (D) Furthermore, the internal auditory canal lesion and the CPA cistern lesion differ in intensity of enhancement and proton density signal. This suggests the diagnosis of neurofibromatosis II with bilateral vestibular schwannomas and a right CPA cistern meningioma.

the underlying dura (Figures 7 and 8). This imaging feature is often cited as a way to distinguish meningioma from other lesions, for example, cerebellopontine (CP) angle meningioma from a CP angle schwannoma (Figure 8). This finding can be useful in some cases, but it is not adequately specific to meningioma to rely upon it when the information might result in a change in therapy. The dural tail has been shown to occur with lymphoma, peripheral gliomas, and schwannomas.[39] The exact nature of the dural tail itself remains a topic of some debate and investigation. The specific question of whether the dural tail represents reactive hypervascularity or true tumor infiltration is very critical in planning a strategy for treatment. Complete surgical resection of the entire tumor, including any areas of bony or dural invasion, offers the best chance for cure and is therefore the goal of the surgeon whenever possible. However, inclusion of the dural tail can add centimeters to a resection margin, and inclusion within a radiation field can substantially increase dose to the patient. Desire to avoid these added risks has prompted several studies correlating histology to radiology, and there is some disagreement among them. One early report suggested that the dural tail most likely represents a nonneoplastic reactive phenomenon.[39] More recent studies suggest quite the opposite, that in a large number of cases, the dural tail is indeed infiltrated by histochemically verified tumor cells and that this invasion may even extend into normal-appearing dura.[40,41] Therefore, a cautious approach currently involves resection of the entire tumor including any dural tail and a margin of normal dura. Where complete resection is not an option, the same extent of tissue is included in the radiation field.

In addition to the anatomic location of the tumor, other factors that have an impact on the likelihood and difficulty of a complete resection include invasion of adjacent bone, invasion of brain parenchyma (suggesting a higher grade lesion), and the consistency of the tumor. In addition to the CT findings discussed above, MRI may help identify bone invasion by revealing frank tumor-like enhancement within the marrow space. A number of conventional MRI parameters have been associated with higher grade and/or brain parenchymal invasion, including tumor capsule enhancement, heterogeneous enhancement, and particularly indistinctness of the tumor–brain interface.[42,43] Finally, tumor consistency at surgery is related to the difficulty and likelihood of achieving a complete resection, with firmer, more fibrous lesions being more difficult.

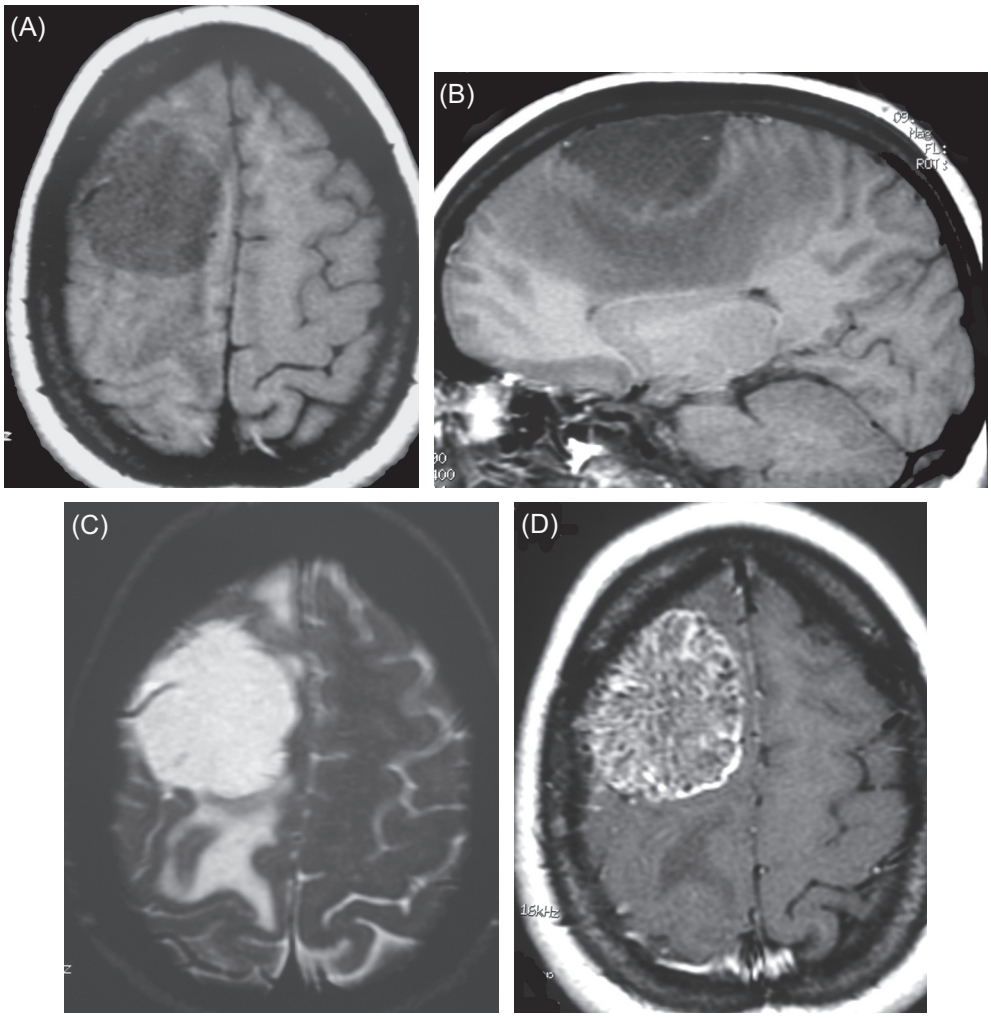


FIGURE 9 **Atypical meningioma.** (A) Axial T1, (B) sagittal T1, (C) axial T2, and (D) post-gadolinium T1 MR images demonstrate an extra-axial mass adjacent to the right frontal lobe associated with vasogenic edema and mass effect. Histopathology revealed atypical meningioma.

Of the parameters tested, T2 signal seems to be the most reliable. Tumors that are T2 hypointense relative to brain are more likely to be firm or fibrous, whereas T2 hyperintense lesions are more likely to be soft.[44]

Advanced MRI techniques are often not necessary to make the diagnosis of a meningioma because conventional imaging features are usually adequate for diagnosis. There may, however, be some additional information to gain by performing these studies, and their utility is still being assessed in specific contexts. Proton magnetic resonance spectroscopy (MRS) of meningioma will classically show a choline-only spectrum, with elevated choline-to-creatine ratio and little or no NAA, reflecting the nonneural origin of the lesion.[45,46] A detectable alanine peak is sometimes mentioned as relatively specific for meningioma, but this finding is not consistently seen. Although a lack of NAA and other metabolites is the norm, a variety of patterns can be seen in newly diagnosed untreated meningiomas, possibly representing the presence of fatty elements or necrotic regions. Whereas some patterns on MRS may help to discriminate typical WHO grade I tumors from the more aggressive varieties, it is not yet clear if MRS adds much to the conventional MR findings (discussed above), which propose to do the same.[47–49] Meningiomas are vascular lesions and as such demonstrate "hypervascularity" on perfusion imaging. Perhaps more useful than any of the calculated perfusion maps may be the simple time–intensity curve obtained from a region of interest placed within the meningioma. This will typically show a more rapid and larger change in signal intensity during the first pass of contrast relative to normal brain. Furthermore, the signal within a meningioma is slower to recover after bolus passage and will not fully recover to a level equivalent to brain parenchyma (Figure 4). This is believed to reflect the increased size, number, or tortuosity of vessels in tumor compared to normal brain. Also contributing may be the ease of passage of contrast molecules through meningioma vessels, which are typically derived from external carotid artery branches and which therefore possess no blood–brain barrier.

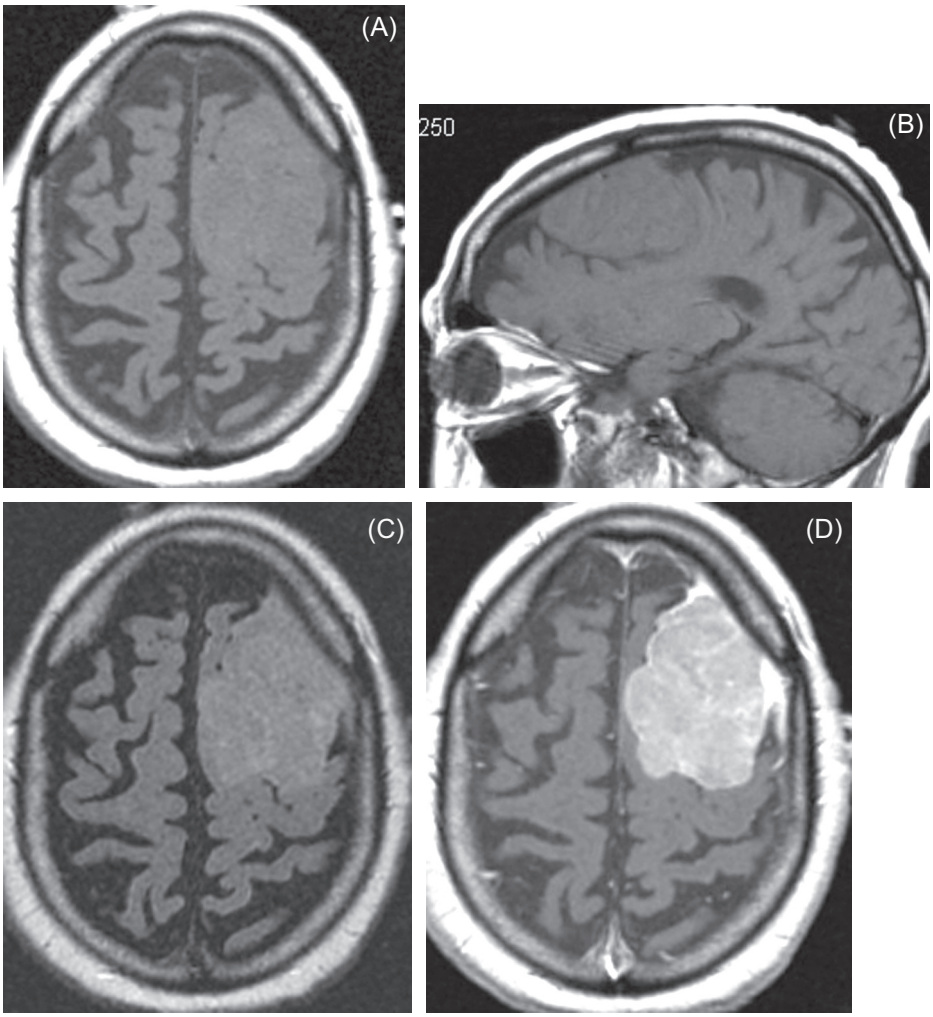


FIGURE 10 **Atypical meningioma.** (A) Axial T1, (B) sagittal T1, (C) axial FLAIR, and (D) post-gadolinium T1 MR images demonstrate a lobulated extra-axial mass adjacent to the left frontal lobe without associated vasogenic edema whose histopathology revealed atypical meningioma.

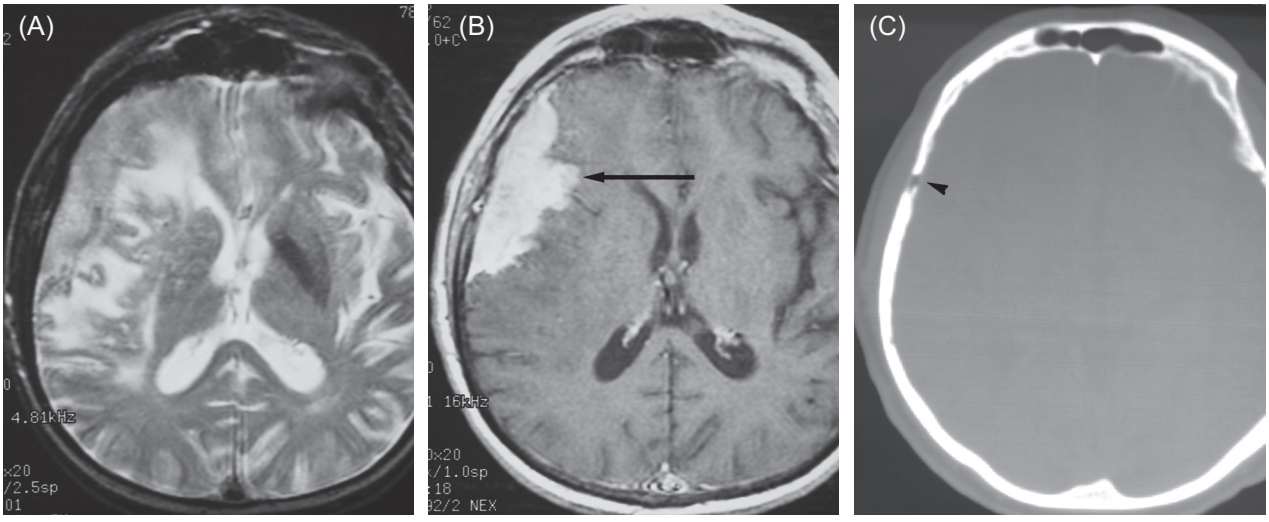


FIGURE 11 **Malignant meningioma.** (A) Axial T2 and (B) axial post-gadolinium T1 MRI demonstrate a mass with a broad base toward the dura with irregular margins suggesting tumor invasion into the brain (arrow) and adjacent vasogenic edema. (C) An axial bone window CT demonstrates bone lysis (arrowhead). On histopathology this was found to be a malignant meningioma.

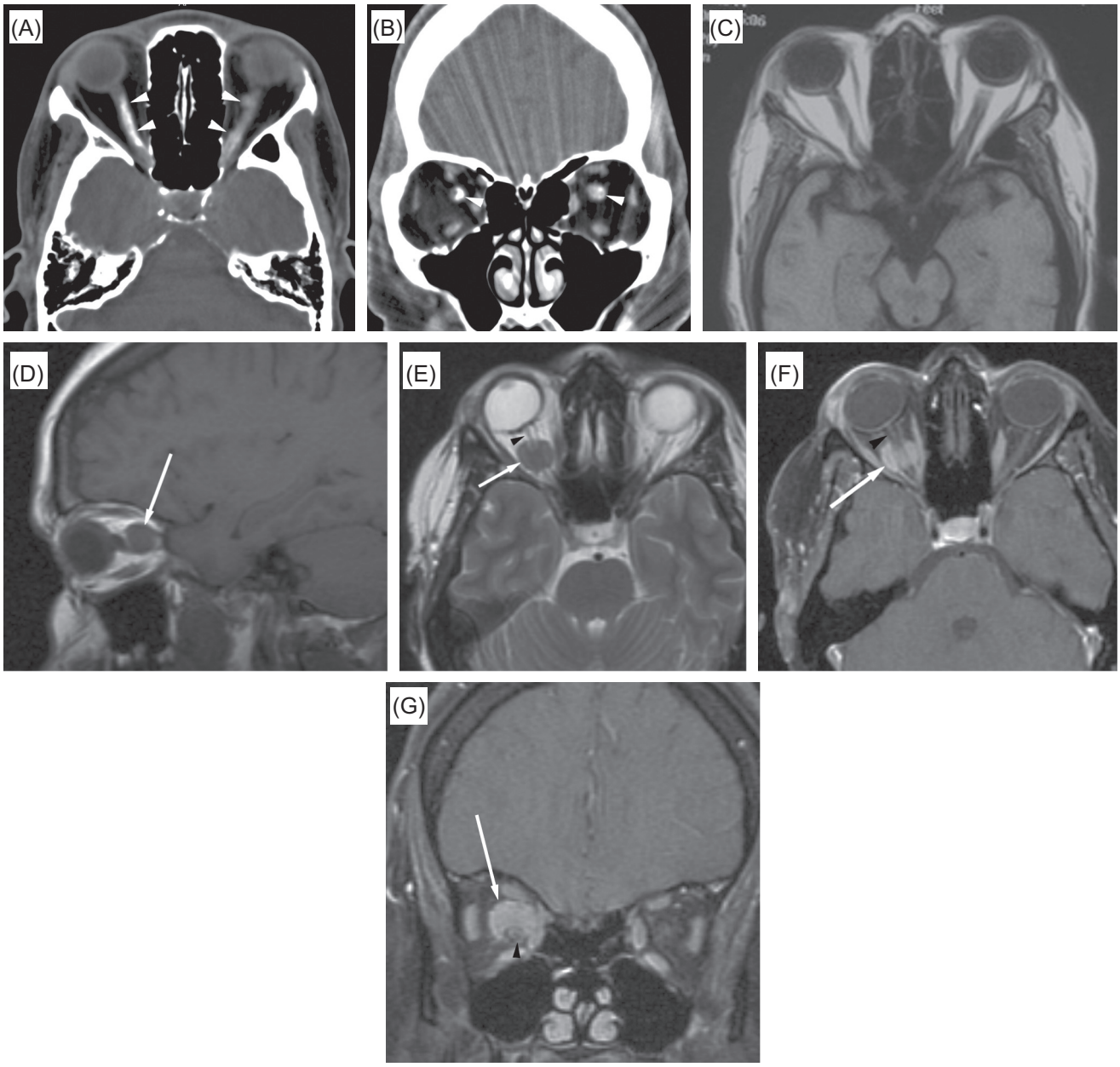


FIGURE 12 **Optic nerve meningiomas.** (A) Axial and (B) coronal CT scans of a patient with "tram-track calcifications" along the optic nerves (white arrowheads), which (C) are faintly visible on T1 MRI as dark outlining. Tram-track calcifications favor the diagnosis of meningioma. (D) Sagittal T1, (E) axial T2, and post-gadolinium fat-suppressed (F) axial and (G) coronal T1 images of the orbits in a different patient demonstrate a more mass-like meningioma (arrows) arising from the nerve sheath and surrounding the optic nerve (black arrowhead).

On occasion, though, some meningiomas may receive a larger proportion of blood from the ICA distribution, for example, in lesions that parasitize the pial vasculature. As the ICA vasculature does indeed contain a blood–brain barrier, which would limit extravascular efflux of contrast, it has been suggested that this variant supply may be predicted by a perfusion time–intensity curve, which is closer in depth and degree of recovery to that of normal parenchyma.[50] Perfusion MRI may also be useful in separating typical from atypical meningiomas. Of the parameters tested, volume transfer constant, a measure of capillary permeability, may be best able to make this distinction.[51]

Angiographic Evaluation

Angiographic assessment of meningiomas is useful for preoperative planning and embolization. Angiographic evaluation of these tumors depends on their location and the vascular territory that they occupy as depicted on multiplanar contrast-enhanced MRI. Information derived from angiography should include[4] the dural

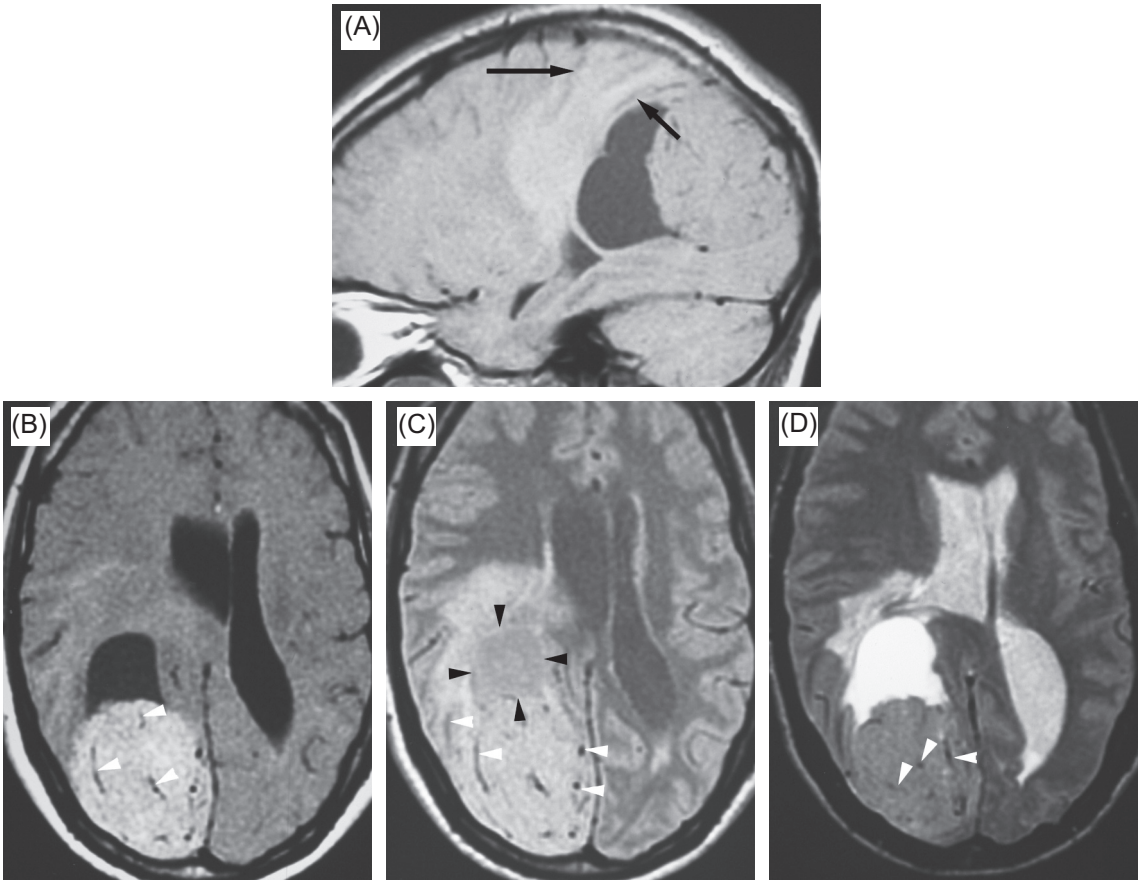


FIGURE 13 **Cystic meningioma.** (A) Sagittal T1, (B) axial post-gadolinium T1, (C) axial proton density, and (D) axial T2 MR images of a cystic meningioma. Note that the cystic component does not follow cerebrospinal fluid on the proton density image (black arrowheads). Note the vascular flow voids within the tumor bed (white arrowheads). Note the accordion-like effect of this extra-axial mass on the adjacent cortical layers (black arrows).

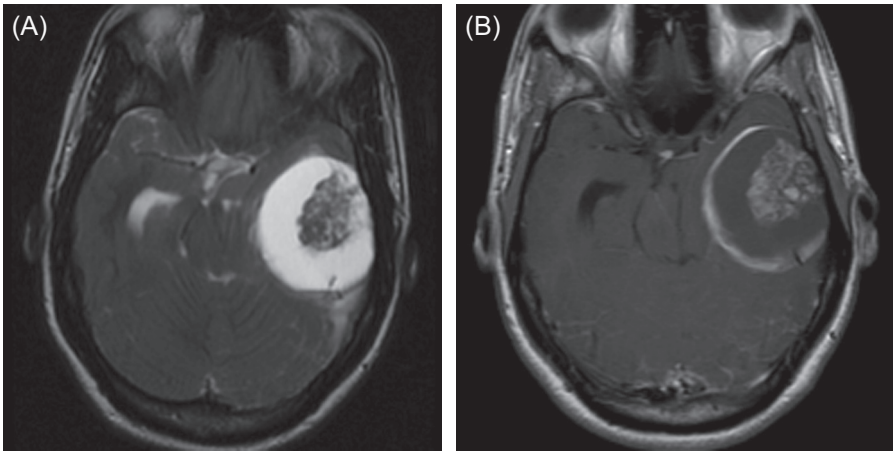


FIGURE 14 **Cystic meningioma.** (A) Axial T2 and (B) T1 postcontrast MR images demonstrate an unusual nodule within a cyst presentation. It is doubtful that meningioma would top the differential list for this lesion, and in fact, one might reasonably entertain an infectious etiology before meningioma. Nevertheless, this lesion was diagnosed as an atypical (WHO grade II) meningioma.

arteries supplying the tumor; the pial arteries supplying the tumor; the relationship of dural/pial arterial supply to the tumor; the detection of arterioarterial anastomoses; the detection of abnormal origin of dural supplying arteries; the displacement of pial arteries; the transosseous supply of the tumor; the compression and/or encasement of the internal carotid, vertebral, or basilar arteries with skull base meningiomas; the collateral circulation to the brain; the intensity of tumor staining and flow characteristics of the tumor; the venous drainage of the tumor; the cortical venous changes; and the status and patency of adjacent major dural venous sinuses (Figures 4, 16, 17).

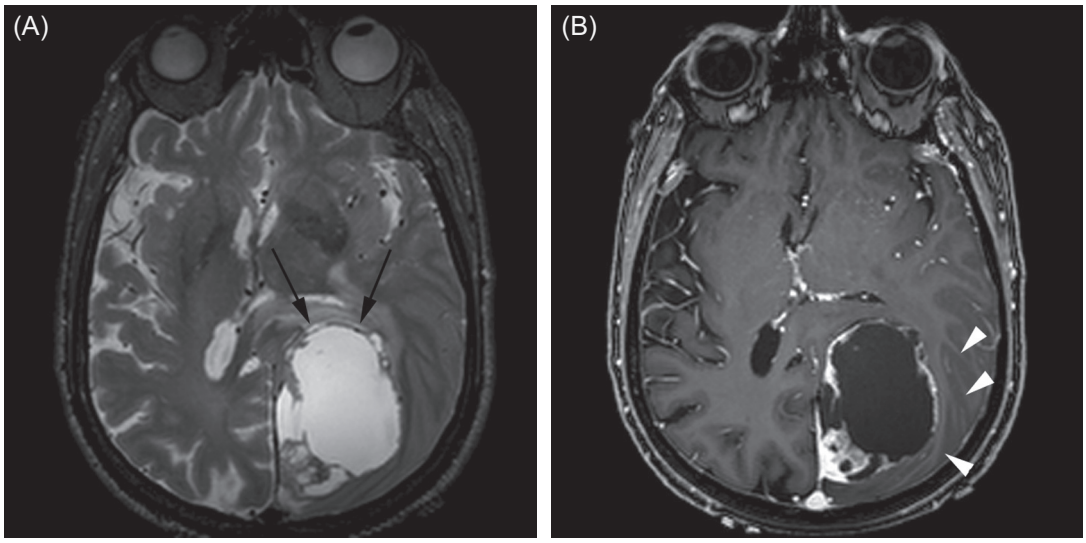


FIGURE 15 **Cystic meningioma.** (A) Axial T2 and (B) T1 postcontrast MR images demonstrate a nearly entirely cystic lesion with a thin-ragged margin of enhancing tissue. Although on first glance, this lesion was felt to be intra-axial and probably a glioma, the accordion-like folding of the adjacent gyri (white arrowheads) and a thin rim of CSF signal along the margin of the tumor (black arrows) ultimately favored an extra-axial location. This lesion came back from pathology as an atypical meningioma.

Characteristic angiographic findings for meningiomas include dilation of meningeal feeding arteries, radiating intratumoral dural arteries, and a fairly homogeneous tumoral blush of varying intensity that persists into the late venous phase.[22,52] Degree of vascularity can vary depending on histologic subtype. Angioblastic and transitional types tend to be more vascular than fibroblastic varieties. Psammomatous subtypes are sometimes avascular.[11] The blood supply to a meningioma is typically derived from meningeal vasculature (Figures 4 and 16); however, additional supply or exclusive supply can be derived from transosseous vessels (Figure 17), pial vessels (Figure 4), and even choroidal vessels with intraventricular meningiomas (Figure 18).[1]

At the current state of development of endovascular techniques, safe and efficient embolization of pial supply to a meningioma is rarely possible.[53] As a result, embolization of meningiomas is most effective when an exclusive meningeal supply is present. In the case of meningioma with a dominant pial supply, embolization is indicated if the dural supply to the tumor is difficult to access at surgery. This is often the case with basal meningiomas and posterior fossa meningiomas.

In general, meningiomas of the convexity, parasagittal area, and falx cerebri receive dural supply from the branches of the ipsilateral middle meningeal artery. Those located closer to the midline may also receive supply from the contralateral middle meningeal artery. When meningiomas involving the convexities extend through the calvaria into the subgaleal space, they may receive transosseous supply from scalp arteries. Depending on their location, these meningiomas may receive supply from the superficial temporal, posterior auricular, or occipital arteries.[1,4]

Meningiomas involving the anterior portion of the falx may also receive supply from the artery of the falx cerebri, which arises from the anterior ethmoidal artery of the ophthalmic artery. Furthermore, meningiomas involving the free margin of the tentorium and the wall of the inferior sagittal sinus often receive supply from the dural branches of the pericallosal and callosomarginal arteries. These arteries are usually not accessible to superselective embolization because of their size and distal origin.[1,4] Because the territories involved are more dangerous, special care should be taken when embolization via the ophthalmic artery or cerebral vasculature is considered. In a similar manner, meningiomas arising from the olfactory groove and those arising from the planum sphenoidale may receive dural supply from the anterior and posterior ethmoidal arterial branches of the ophthalmic artery.

Meningiomas involving the cavernous sinus and parasellar region typically receive arterial supply from branches of the cavernous ICA such as the inferolateral trunk (Figure 16), the meningohypophyseal trunk, the accessory meningeal artery, the cavernous branch of the middle meningeal artery, and the recurrent meningeal branches of the ophthalmic artery (Figures 16 and 17).[1,2,4] Special considerations for embolization via arterial feeders in this region have been described earlier in this chapter. In addition, in cases in which there is encasement of the ICA or suspicion of invasion of the ICA as depicted on MRI or angiography, permanent balloon occlusion of the ICA preoperatively may be an option.

When meningiomas are located in the middle cranial fossa or on the greater wing of the sphenoid, they typically receive supply from the sphenoidal branch of the middle meningeal artery. Meningiomas arising from the tentorial leaf can be divided into three types on the

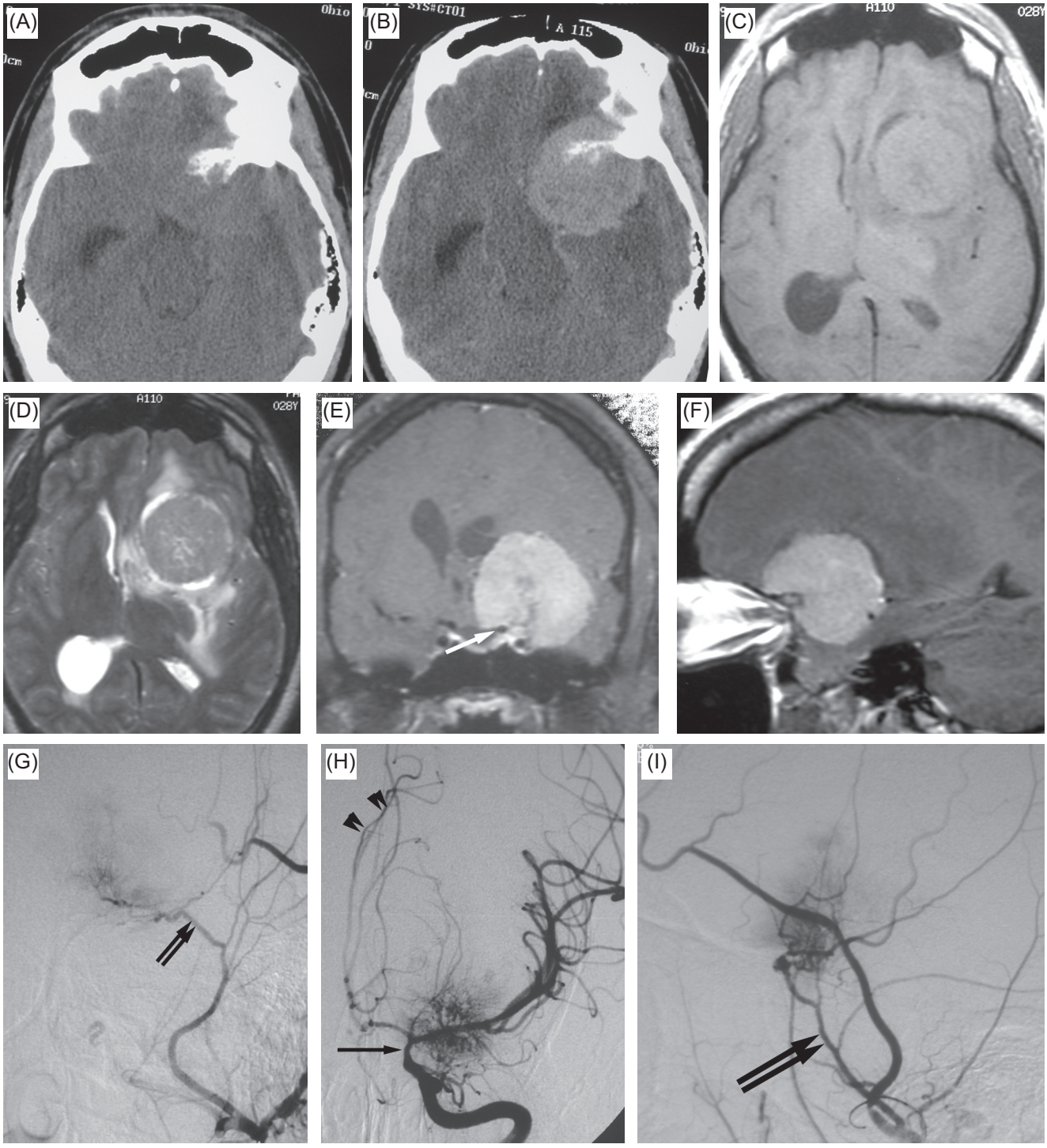


FIGURE 16 **Paracavernous meningioma with angiography and embolization.** Unlike pituitary adenomas, meningiomas often narrow the intracranial carotid artery. Axial CT scans (A) without and (B) with contrast demonstrate an enhancing mass isodense to gray matter associated with adjacent hyperostosis of the sphenoid bone. Axial (C) T1, (D) T2, and post-gadolinium T1 (E) coronal and (F) sagittal MR images demonstrate homogeneous enhancement of this mass, which surrounds the internal carotid artery (white arrow). Anteroposterior and lateral projections of (G and I) external carotid artery and (H and J) internal carotid artery arteriograms demonstrate the vascularity of the meningioma predominantly supplied via the internal carotid artery branches. Unlike pituitary adenomas, meningiomas tend to narrow the internal carotid artery, as in this case (black arrow). There is also displacement of the anterior cerebral artery (double arrowheads) due to this subfrontal mass. Embolization was performed via the inferior frontal branch of the middle meningeal artery (double arrows) and via the inferolateral trunk (L, white arrowhead) of the internal carotid artery using balloon assistance (K, white arrow). (M) At the end of the embolization the only supply left was via the recurrent meningeal artery from the ophthalmic artery. Embolization assists the surgeon in removing meningiomas more completely and with less blood loss.

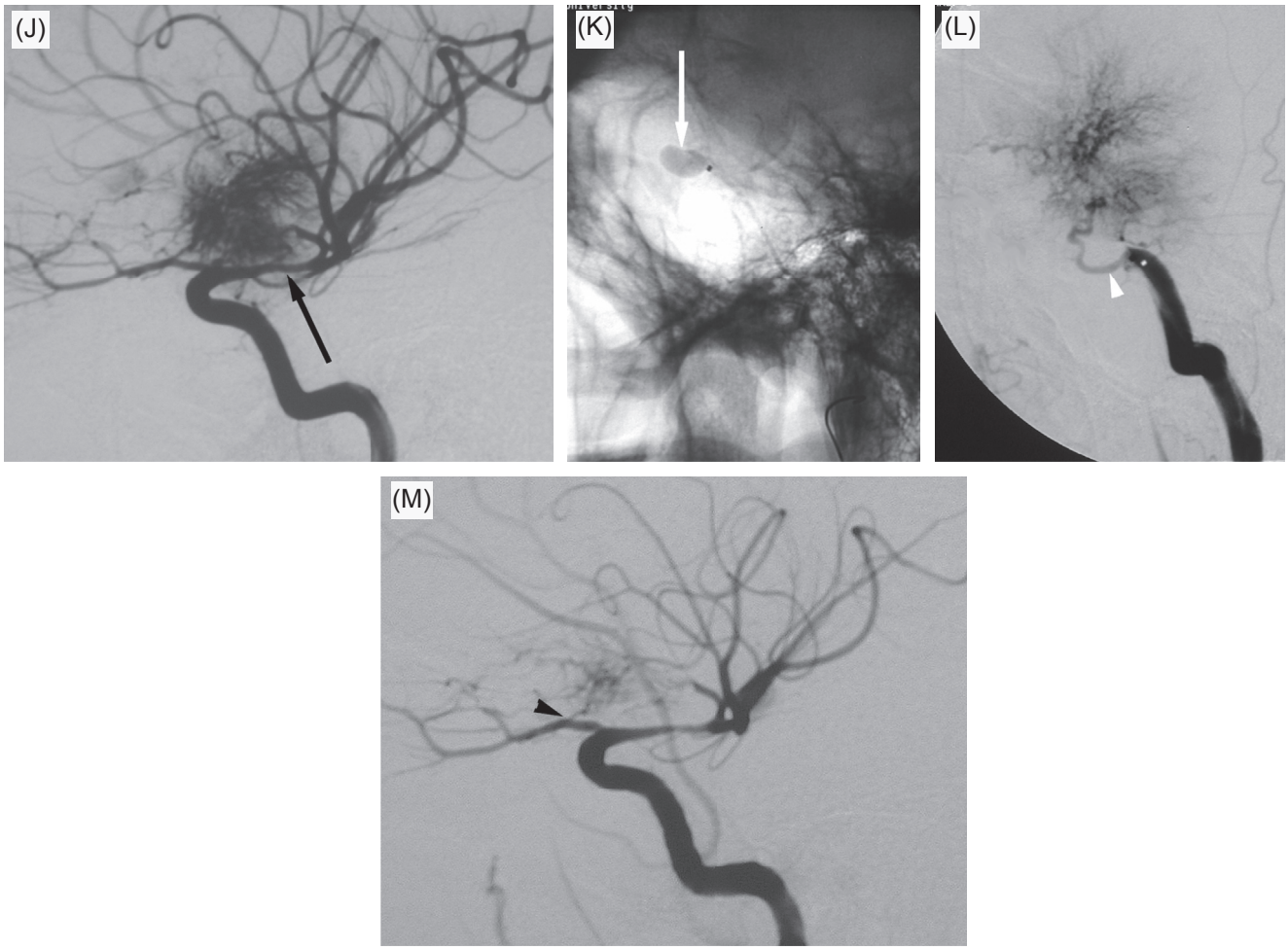


FIGURE 16 **Cont'd.**

basis of location: those arising from the medial tentorial leaf, those arising from the anterolateral tentorial leaf, and those arising from the posterior tentorial leaf. Meningiomas arising from the medial tentorial leaf have a tendency to recruit supply from the marginal tentorial artery, which usually arises from the posterior bend of the cavernous carotid artery. However, it has also been found to arise from the horizontal portion of the cavernous carotid, the ophthalmic artery, the lacrimal artery, and the accessory meningeal artery.[4] Meningiomas arising from the anterolateral portion of the tentorial leaf typically receive arterial supply from the lateral clival branch of the posterior bend of the cavernous carotid artery and the basal tentorial branch of the petrosquamosal branch of the middle meningeal artery. Arterial supply to meningiomas arising from the posterior portion of the tentorium can be divided into supratentorial and infratentorial supply. The supratentorial supply usually includes middle meningeal supply via petrosquamosal branches and parieto-occipital tentorial branches. Infratentorial supply includes branches of the mastoid artery, branches of the posterior meningeal artery, and the posterior falx artery. Origins of the posterior meningeal artery and the posterior falx artery are variable and may arise from the vertebral artery, the posterior inferior cerebellar artery, or the occipital artery. In addition, the posterior meningeal artery has been found to arise from the neuromeningeal trunk of the ascending pharyngeal artery.[1]

Petroclival meningiomas and meningiomas along the posterior surface of the petrous bone and of the cerebellopontine angle are supplied by clival branches of the ICA anteriorly, branches of the petrosal branch of the middle meningeal artery superiorly, the ascending branch of the mastoid artery posteriorly, and the jugular and hypoglossal branches of the ascending pharyngeal artery inferiorly and centrally. The anterior inferior cerebellar artery (AICA) often provides additional supply via the subarcuate artery.[1] Meningiomas adjacent to the cerebellar convexity typically receive supply from the posterior meningeal artery and the artery of the falx cerebelli. In addition, posterior fossa meningiomas frequently receive supplementary pial supply via the superior cerebellar artery (SCA), the AICA, and/or the posterior inferior cerebellar artery (PICA)[1,54].

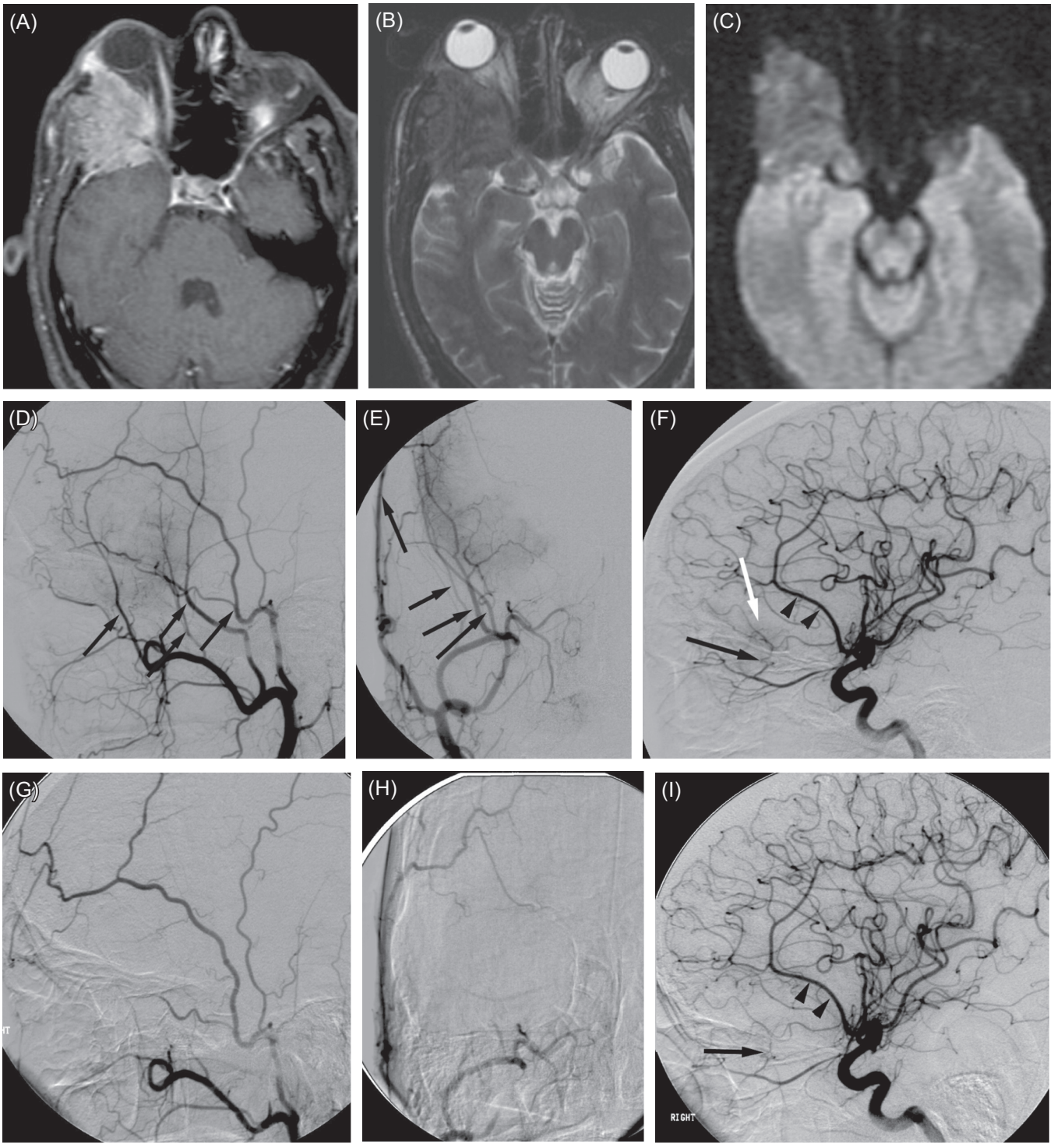


FIGURE 17 **Intraosseous meningioma before and after embolization.** (A) Axial post-gadolinium T1, (B) axial T2, and (C) axial diffusion MR images before embolization of an intraosseous meningioma involving the right sphenoid bone, orbit, and middle cranial fossa. The signal on diffusion imaging suggests lower grade. Pre- and postembolization (D and G) lateral and (E and H) anteroposterior external carotid artery (ECA) and (F and I) lateral internal carotid artery (ICA) arteriograms demonstrate arterial supply (black arrows, D and E) via ECA branches, including superficial temporal, deep temporal, accessory meningeal, and middle meningeal, as well as ICA supply via the recurrent meningeal artery from the ophthalmic artery (black arrow, F). Postembolization there is minimal tumor blush on the ICA injection (white arrow, F) which was not embolized. Note the mass effect on the anterior cerebral artery (black arrowheads, F and I). (J) Postembolization there is substantially reduced contrast enhancement. High (K) T2 and (L) diffusion signal within the tumor represent the effect of embolization.

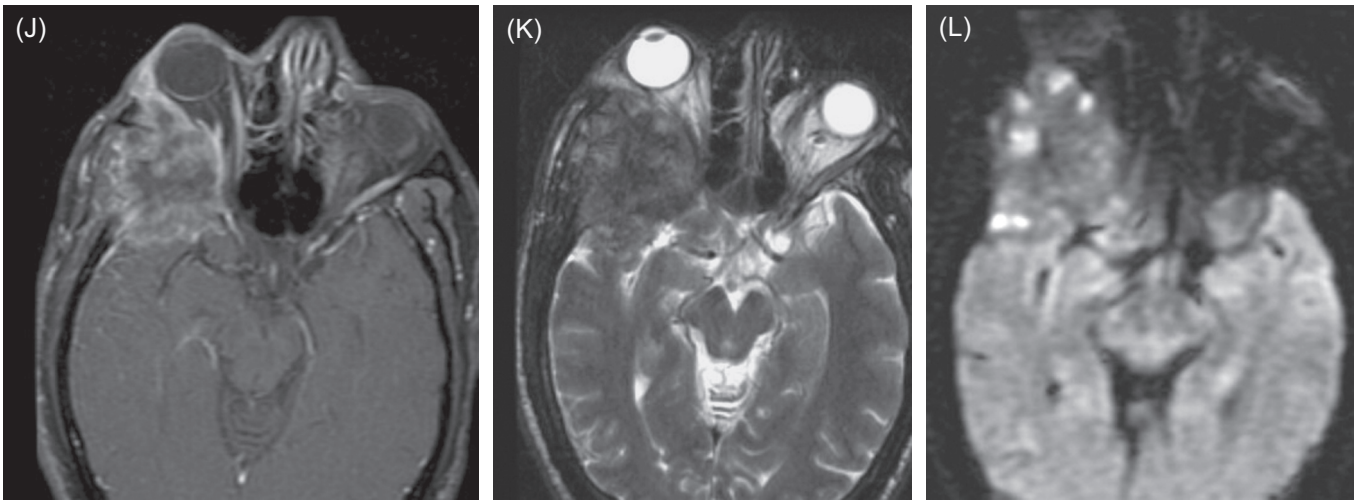


FIGURE 17 Cont'd.

Imaging Meningiomas Postembolization

Maps of relative regional cerebral blood volume have been shown to provide hemodynamic information regarding tumor perfusion and as such can monitor the treatment effect of embolization in meningiomas.[55] Comparing T1 post-gadolinium imaging to dynamic MR using a contrast bolus indicates that following embolization some areas of embolized tumor may enhance in a delayed fashion owing to slow collateral flow (Figure 17). Tumor necrosis has also been demonstrated on the basis of MRS. The spectroscopic data indicate high concentrations of lactate at 24 h after embolization, followed by broad aliphatic signal several days later.[56–61] Lipid signal appears to be associated with softer tumor at surgery. Persistence of a lactate signal is felt to indicate incomplete tumor embolization. Spectroscopic experiments have suggested that the process of tumoral necrosis is complete 4 days following embolization. Based on this information surgery should be planned following completion of the process of necrosis.[58,60] Sequential MRIs following embolization have shown that areas that did not enhance in the immediate postembolization period variably did so over the next few days, especially along the periphery of the tumor bed. Histopathologically, this area of "reenhancement" corresponded to vital tissue.[56] On the basis of MR findings it has been suggested that MRI and MRS following embolization may serve a purpose to identify revascularization and establish the presence of fatty degeneration of the meningioma.[56]

MESENCHYMAL, NONMENINGOTHELIAL TUMORS

As the name implies, mesenchymal tumors originate from nonmeningothelial cells that happen to be resident in the meninges. The most common of these tumors is the hemangiopericytoma (Figures 19–22). They also include tumors arising from adipose tissue, solitary fibrous tumors, fibrohistiocytic tumors, muscle tumors, osteocartilagenous tumors, neoplasms arising from elements of the vessel wall, and meningeal sarcomas. Their imaging varies depending on the cell of origin. For example, fibrous tumors tend to be very dense, and on MRI display low T1 and T2 signal owing to a lack of water. Lipomas are hypodense on CT and display high signal on T1-weighted imaging, which suppresses with pulse sequence in which a fat saturation pulse is applied. Chemical shift artifact can also be seen with fatty or lipomatous lesions on T2 images (Figure 23). Ultimately, these mesenchymal nonmeningothelial tumors are rare, with hemangiopericytomas representing 0.4–1%, lipomas up to 0.4%, and sarcomas less than 0.1% of all intracranial tumors.[11,62] With the exception of rhabdomyosarcomas, which occur predominantly in children, there is no documented predilection for age or sex and no documented preferential location.

Hemangiopericytoma

Intracranial hemangiopericytomas are rare tumors of mesenchymal origin arising from vascular pericytes within the meninges that are indistinguishable on histopathologic analysis from hemangiopericytomas arising from elsewhere in the body. Although hemangiopericytomas were initially described elsewhere in the body, intracranial hemangiopericytomas were first described in 1954 by Begg and Garret after they identified one case of dural-based hemangiopericytoma and reviewed six cases of dural-based tumors previously labeled as angioblastic subtypes of meningioma.[63-65] They constitute approximately 0.4–1% of all central nervous system (CNS) neoplasms and tend to occur in younger age groups relative to meningiomas, with a mean presenting

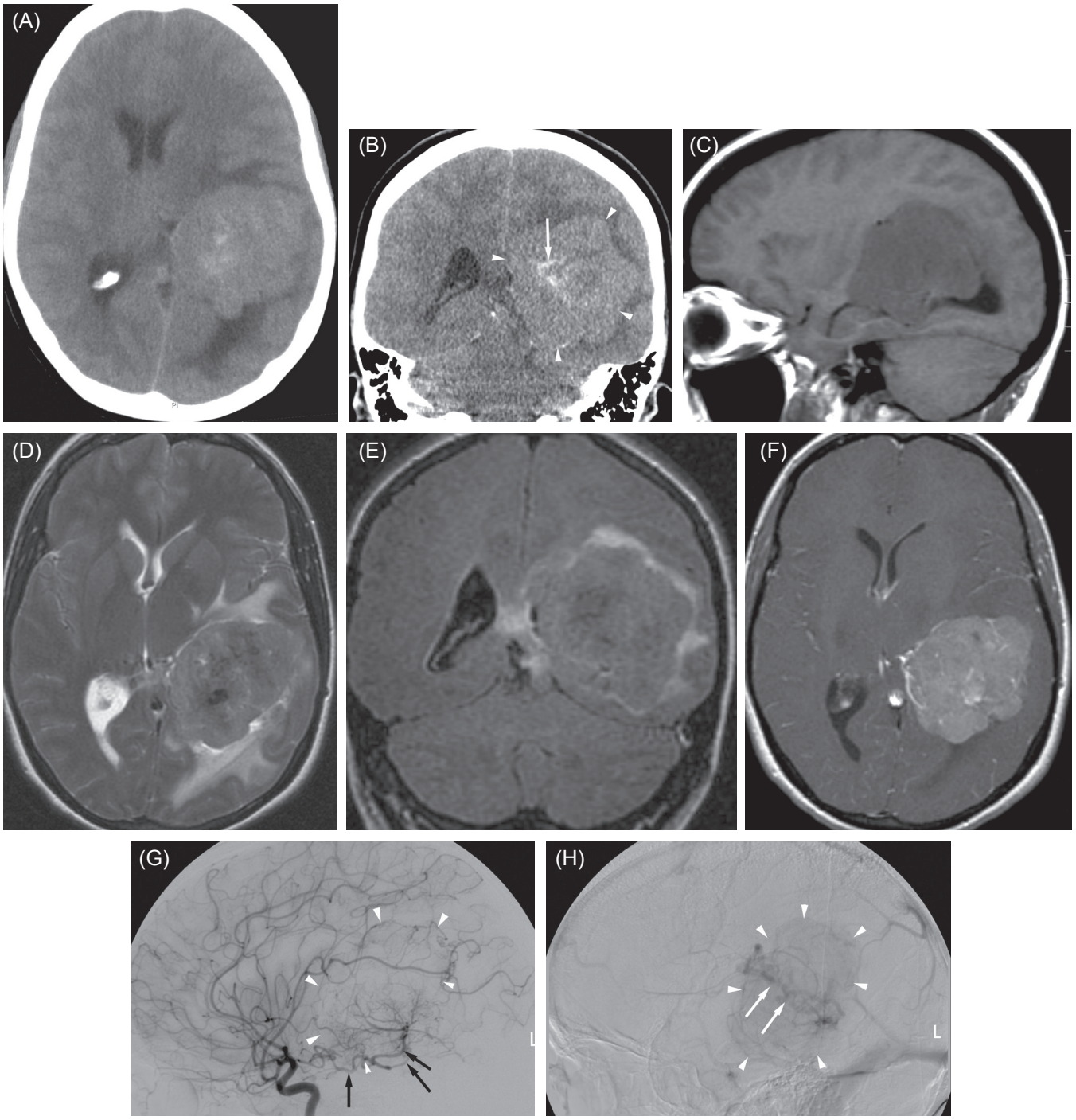


FIGURE 18 **Intraventricular meningioma.** (A) Axial and (B) coronal CT scans demonstrate an intraventricular mass (white arrowheads) associated with calcifications (white arrow). (C) Sagittal T1, (D) axial T2, (E) coronal FLAIR, and (F) post-gadolinium T1 images confirm an intraventricular mass. (G) Lateral left internal carotid angiogram demonstrates anterior choroidal artery supply (black arrows) on arterial phase and (H) sustained vascular blush with enlarged draining veins (white arrows) on late venous phase.

age of 37–44 and a male/female ratio of 1:4. Males tend to present at a younger age than females.[66] Hemangiopericytomas are highly vascular neoplasms with a propensity to invade adjacent structures, recur following surgical resection, and metastasize. Aggressive management with complete resection, radiation therapy, and frequent and prolonged follow-up is advocated.[67]

Their extra-axial location and similar imaging features may lead to their confusion with more aggressive meningiomas. In contrast to meningiomas, hemangiopericytomas (Figures 19–22) tend to be larger (greater than 4 cm), lobular, extra-axial, and heterogeneously hyperdense tumors that enhance on CT with no evidence of calcification.[63,65,67] They may have a broad-based attachment to

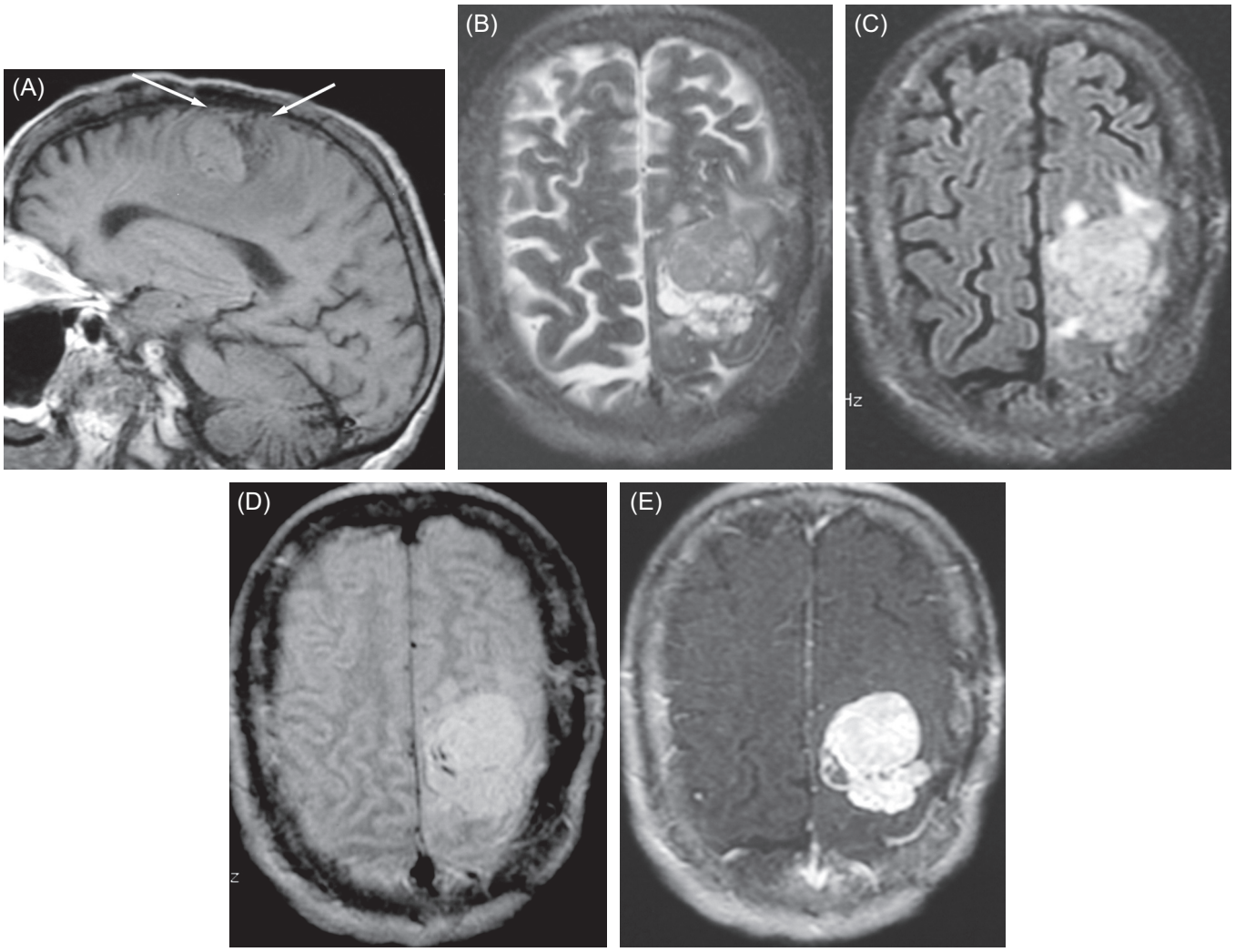


FIGURE 19 **Recurrent hemangiopericytoma.** (A) Sagittal T1, (B) axial T2, (C) axial FLAIR, (D) axial proton density, and (E) post-gadolinium T1 MR images of an extra-axial mass heterogeneous in signal characteristics on T1 and T2 but similar to gray matter. This mass has a narrow dural attachment (arrows) and associated vasogenic edema.

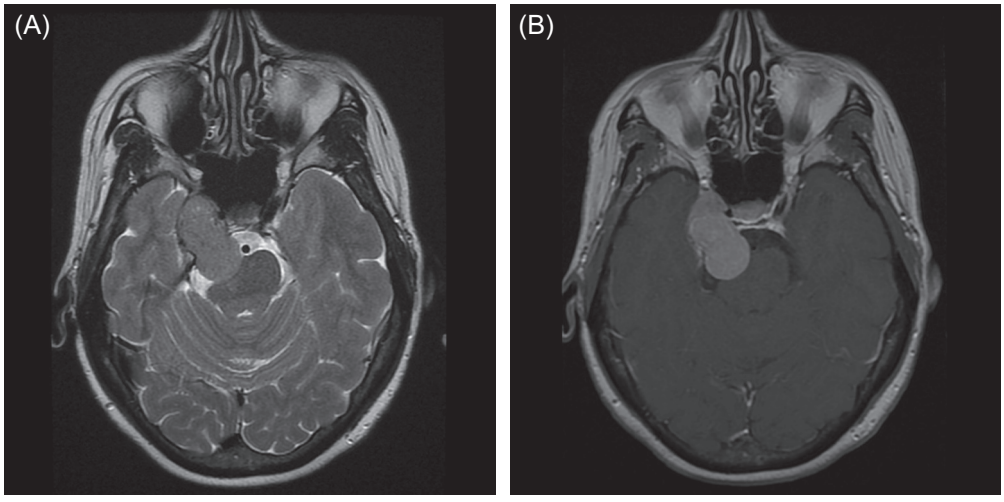


FIGURE 20 **Hemangiopericytoma.** (A) Axial T2 and (B) T1 postcontrast MR images demonstrate a lobular tumor, which seems to be centered on the right cavernous sinus with extension into the prepontine cistern. The differential for this lesion would also include a nerve sheath tumor, though the relatively low T2 signal should favor a primary dural lesion such as meningioma or, as it turned out to be, hemangiopericytoma.

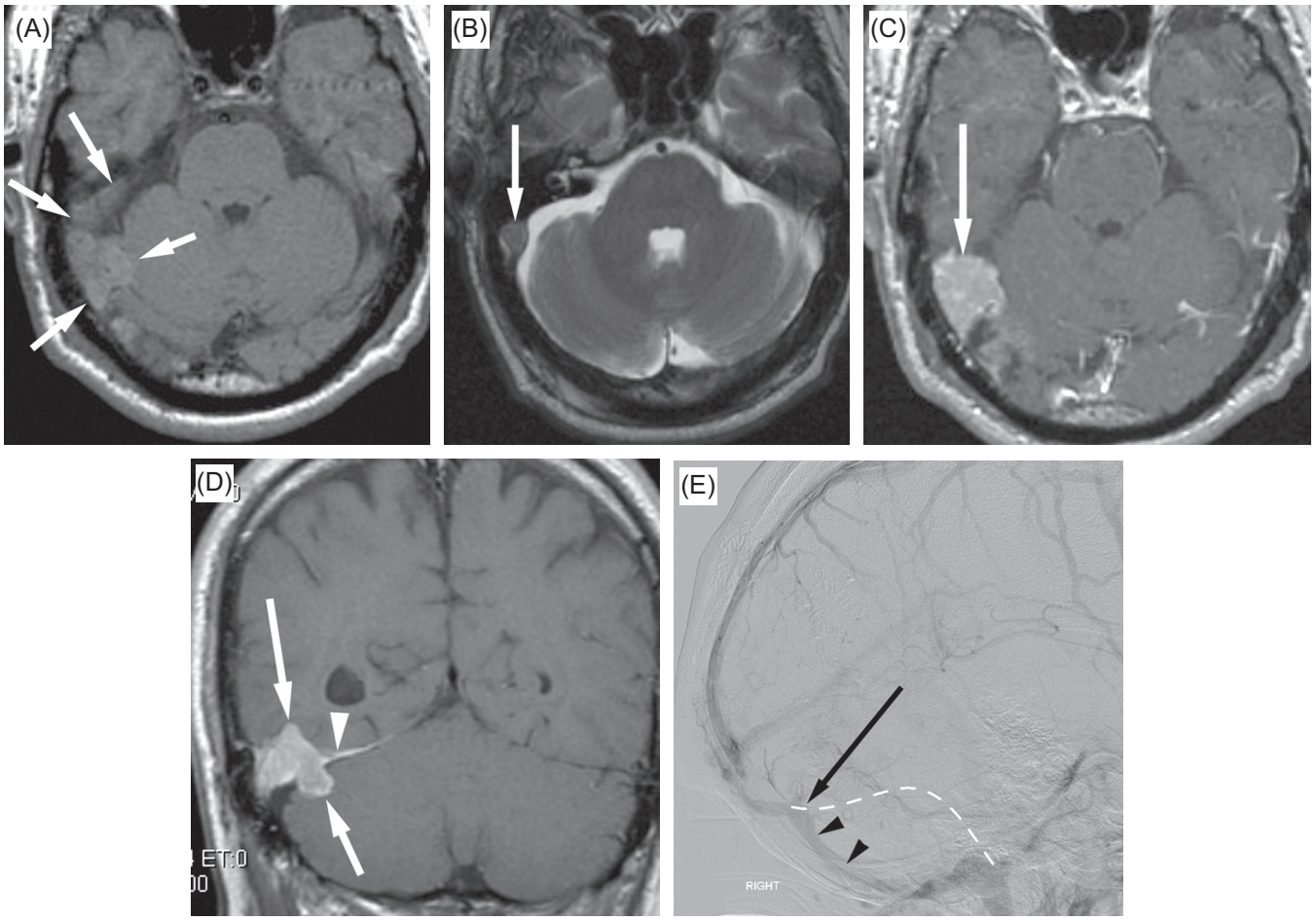


FIGURE 21 **Recurrent hemangiopericytoma with dural sinus invasion.** (A) Axial T1, (B) axial T2, (C) post-gadolinium axial, and (D) coronal T1 MR images of a recurrent hemangiopericytoma invading the transverse and sigmoid sinuses (white arrows) with possible spread along the tentorium (white arrowhead). (E) Venous phase of a lateral right internal carotid arteriogram demonstrates occlusion of the right transverse sinus (black arrow) with collateral venous drainage (black arrowheads). The normal course of the sigmoid sinus is indicated by the dashed white line.

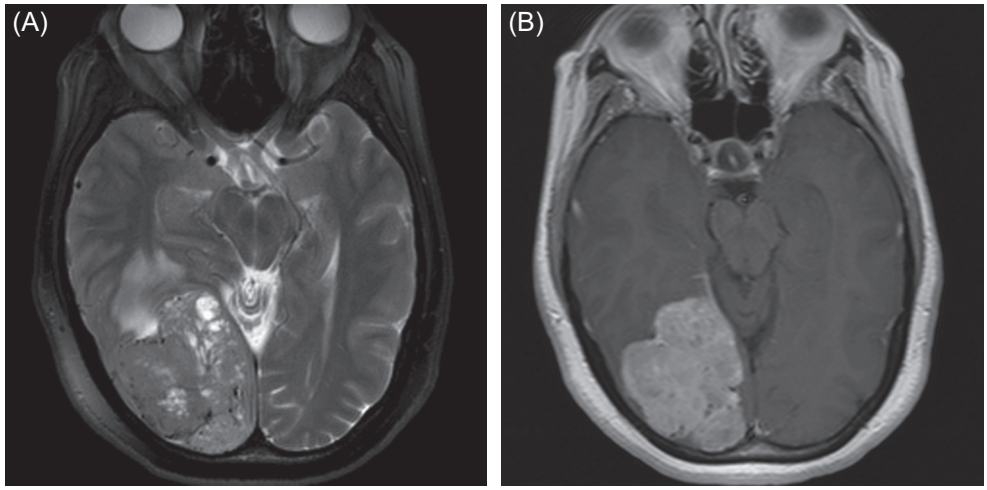


FIGURE 22 **Anaplastic hemangiopericytoma.** (A) Axial T2 and (B) T1 postcontrast MR images show an enhancing, T2-heterogeneous mass along the right occipital lobe, read by pathology as an anaplastic hemangiopericytoma. There is nothing on imaging to distinguish this lesion from a higher grade meningioma.

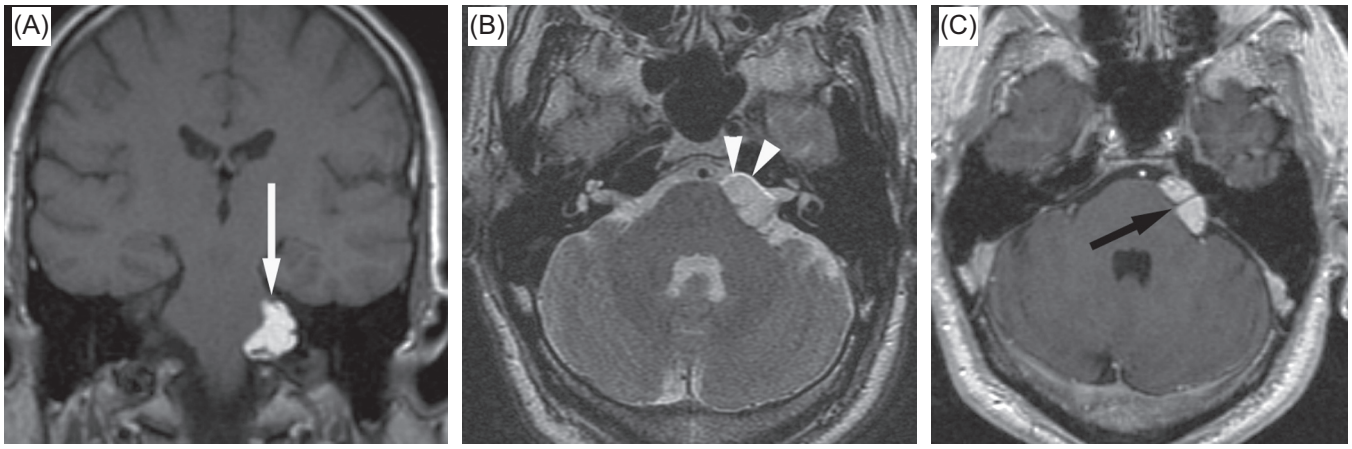


FIGURE 23 **Cerebellopontine angle cistern lipoma.** (A) Coronal T1, (B) axial T2, and (C) post-gadolinium axial SPGR T1 MR images of a right cerebellopontine angle cistern lipoma (white arrow). Chemical shift artifact (white arrowheads) suggests lipid content within the tumor. The seventh and eighth cranial nerves are noted to course through the tumor (black arrow).

the dura, similar to meningioma, but often they show a narrow dural attachment and tend to be taller than wide. On CT, in contradistinction to meningioma, they are more frequently associated with lysis rather than hyperostosis of adjacent bone. There is some evidence to suggest that bone lysis is more frequently associated with anaplastic hemangiopericytoma, whereas lack of bone lysis on CT is more frequently associated with well-differentiated forms. Hyperostosis has not been reported with hemangiopericytomas. Contrast enhancement tends to be heterogeneous but can also be homogeneous.

On MRI, hemangiopericytomas are usually either homogeneously or heterogeneously isointense to gray matter on T1-weighted imaging, but can be hypointense or hyperintense. They are usually homogeneously or heterogeneously isointense relative to gray matter on T2-weighted imaging.[65,67] As a rule they tend to have prominent serpentine vascular signal voids. A significant amount of adjacent brain edema is almost always seen with these tumors.[65] As on CT contrast-enhanced MRI usually displays heterogeneous enhancement, and there may be an associated dural tail.

Angiographic findings include supply similar to meningiomas with numerous corkscrew vessels. Early venous drainage, which is atypical for meningioma, is the norm for hemangiopericytoma. MRS demonstrates increased choline and myoinositol peaks and mildly increased lipid peaks.[67]

Melanocytic Lesions

Melanocytic lesions are rare (0.06–0.1% of brain tumors) neoplasms arising from leptomeningeal melanocytes. These can be either diffuse or circumscribed and include malignant melanoma, melanocytoma, and neurocutaneous melanosis.[68] Melanocytoma is the most common of these and has an annual incidence of 1 per 10 million population.

Melanocytomas are considered benign lesions with a tendency to invade and recur locally. Melanocytomas are suspected to arise from melanocytes, which are cells of neural crest origin to be found scattered along the surface of the brain. Case reports in the literature indicate that they tend to be isodense or hyperdense relative to gray matter on CT with homogeneous enhancement and display high signal on T1- and low signal on T2-weighted imaging. Hemorrhage within the tumor may influence the imaging appearance. To a large degree, the signal characteristics depend on the melanin concentration within the tumor. The paramagnetic effect of melanin results in both T1 and T2 shortening.[69–72] Differential considerations for melanocytoma include pigmented meningioma, melanotic schwannoma, and melanoma. Progression of melanocytoma to malignant melanoma has been described.[73]

Diffuse melanocytosis represents leptomeningeal proliferation of melanocytic cells. On imaging, this entity presents with diffuse leptomeningeal thickening with high signal on T1-weighted MRI.[70] Diffuse melanocytosis carries a poor prognosis.[62] Malignant melanomas display more aggressive features such as pleomorphism, high mitotic rates, necrosis, hemorrhage, invasion of the brain, radioresistance, and also a poor prognosis. Meningeal melanomatosis refers to malignant melanoma with diffuse meningeal spread.[62]

Other Rare Lesions

Additional entities reported to affect the meninges include lymphoma and benign histiocytic tumors.[74] Both of these entities are more commonly found in other organ systems and, as primary meningeal lesions, are exceedingly rare. For example, primary dural lymphoma, as distinct

from primary CNS lymphoma and metastatic systemic lymphoma, represents less than 1% of all lymphomas. It is typically of the mucosal-associated lymphoid tissue (MALT) subtype and carries a significantly better prognosis than primary CNS or other systemic lymphomas.[75] On imaging, primary dural lymphoma is difficult to distinguish from meningioma, presenting as a somewhat hyperdense dural mass on CT, with iso- to hypointensity on T2 images and solid or heterogeneous enhancement (Figure 24). The histiocytic tumors comprise a varied group of disorders that all have in common the abnormal proliferation of cells of histiocytic lineage.[76] All of these so-called histiocytoses affect other organ systems more commonly than the meninges. For example, Langerhans cell histiocytosis can often be seen in the hypothalamic–pituitary axis and the skull, Rosai-Dorfman disease is typically found in the lymph nodes, and Erdheim-Chester disease most commonly presents in the skin and long bones. When these conditions affect the meninges, the imaging presentation is generally very similar to meningioma (Figure 25).

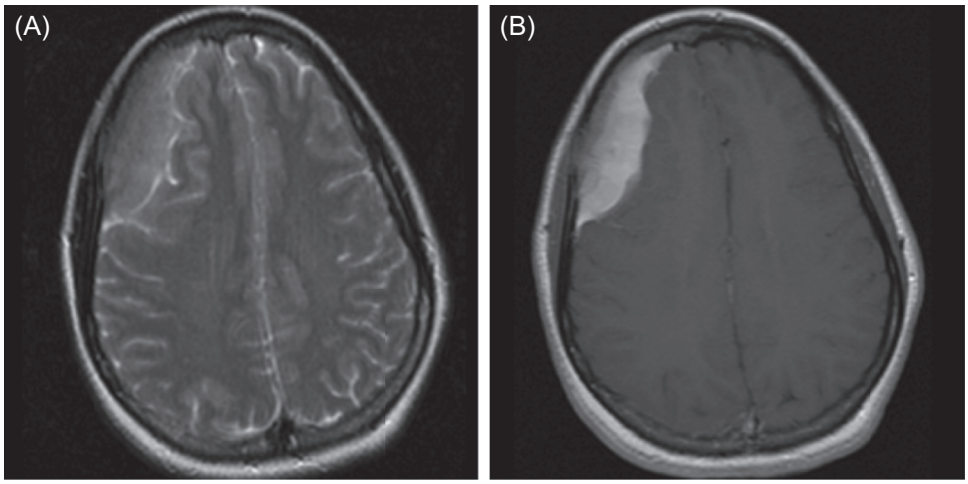


FIGURE 24 **Primary dural lymphoma.** (A) Axial T2 and (B) postcontrast T1 MR images demonstrate a homogeneously enhancing, T2 isointense dural-based mass along the right frontal lobe. Meningioma topped the differential list. On close inspection, though, one can appreciate a loss of definition of the inner table of the calvarium, which would suggest the possibility of a somewhat more aggressive lesion. On biopsy, this was diagnosed as MALT lymphoma and felt to be primary to the dura as no other systemic disease was found.

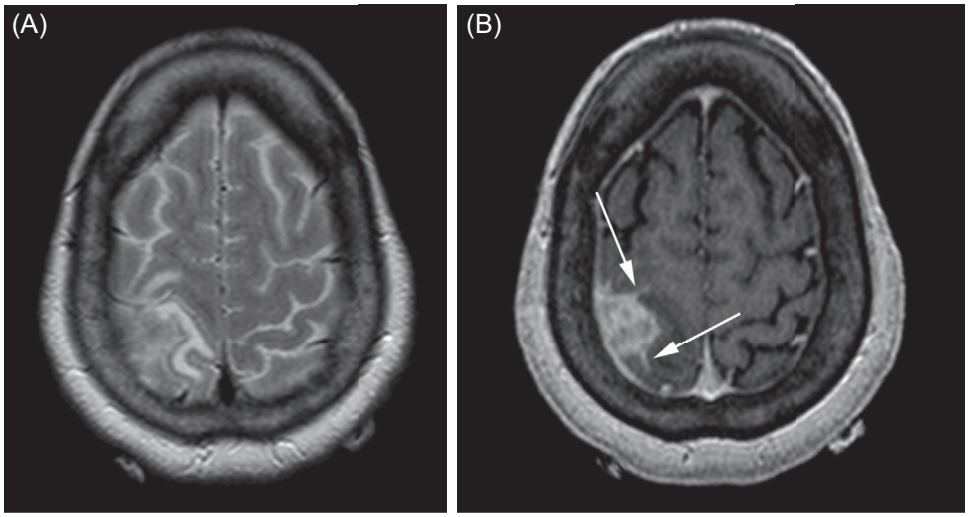


FIGURE 25 **Rosai-Dorfman disease.** (B) Axial T2 MR image showing an iso- to hyperintense mass situated just posterior to the right central sulcus. (B) On the T1 postcontrast image this lesion is enhancing and demonstrates broad contact with the dura, which is itself thickened and enhancing. Note that along the margins of the lesion, there are thin wisps of enhancement, which extend into the adjacent sulci (white arrows). Although this pattern of enhancement is not specific, it would be unusual in a typical meningioma, and so the differential was broadened to include higher grade dural tumors, lymphoma, and even nonneoplastic inflammatory processes. Pathology returned the diagnosis of Rosai-Dorfman disease.

References

1. Christoforidis G, Valavanis A. Embolization of meningiomas. *Neurointerventionist*. 2003;4:43–53.
2. Lasjaunias PL, Berenstein A. Surgical neuroangiography. In: *Functional Anatomy of Craniofacial Arteries*. Vol. 1. Berlin: Springer; 1987.
3. Valavanis A. Interventional neuroradiology for head and neck surgery. In: Cummings CW, ed. *Otolaryngology–Head and Neck Surgery: Update* 2. St. Louis: Mosby–Year Book; 1990:206–223.
4. Valavanis A. Embolization of intracranial and skull base tumors. In: Valavanis A, Alvarez H, eds. *Interventional Neuroradiology*. Berlin; New York: Springer-Verlag; 1993:63–91.
5. Valavanis A. Interventional radiology in the neck. In: Panje WR, Atiyah RA, eds. Head and Neck Surgery/3, Neck/ed. by Panje WR, with contributions by: Atiyah RA-2, completely rev. ed. Stuttgart: Thieme; 1998:487–493.
6. Valavanis A, Christoforidis GC. Tumors of the head and neck. In: Byrne JV, ed. *Interventional Neuroradiology: Theory and Practice*. Oxford; New York: Oxford University Press; 2002:213–234.
7. Black PM. Meningiomas. *Neurosurgery*. April 1993;32(4):643–657.
8. Bondy M, Ligon BL. Epidemiology and etiology of intracranial meningiomas: a review. *J Neuro-Oncol*. September 1996;29(3):197–205.
9. Langford LA. Pathology of meningiomas. *J Neuro-Oncol*. September 1996;29(3):217–221.
10. Ostrom QT, Gittleman H, Farah P, et al. CBTRUS statistical report: primary brain and central nervous system tumors diagnosed in the United States in 2006–2010. *Neuro Oncol*. November 2013;15 (Suppl 2):ii1–ii56.
11. Paulus W, Scheithauer BW, Perry A. Mesenchymal, non-meningothelial tumours. In: Louis DN, Ohgaki H, Wiestler OD, Cavenee WK, eds. *The 2007 WHO Classification of Tumours of the Central Nervous System*. 4th ed Lyon, France: International Agency for Research on Cancer; 2007:173–177.
12. Sadetzki S, Mandelzweig L. Exposure to ionizing radiation and glioma risk. In: Mehta MP, ed. *Principles and Practice of Neuro-Oncology: a Multidisciplinary Approach*. New York: Demos Medical; 2011:26–30.
13. Sadetzki S, Flint-Richter P, Ben-Tal T, Nass D. Radiation-induced meningioma: a descriptive study of 253 cases. *J Neurosurg*. November 2002;97(5):1078–1082.
14. Johnson DR, Olson JE, Vierkant RA, et al. Risk factors for meningioma in postmenopausal women: results from the Iowa Women's Health Study. *Neuro Oncol*. September 2011;13(9):1011–1019.
15. Qi ZY, Shao C, Huang YL, Hui GZ, Zhou YX, Wang Z. Reproductive and exogenous hormone factors in relation to risk of meningioma in women: a meta-analysis. *PloS One*. 2013;8(12):e83261.
16. Yen YS, Sun LM, Lin CL, Chang SN, Sung FC, Kao CH. Higher risk for meningioma in women with uterine myoma: a nationwide population-based retrospective cohort study. *J Neurosurg*. March 2014;120(3):655–661.
17. Phillips LE, Koepsell TD, van Belle G, Kukull WA, Gehrels JA, Longstreth Jr WT. History of head trauma and risk of intracranial meningioma: population-based case-control study. *Neurology*. June 25, 2002;58(12):1849–1852.
18. Surov A, Gottschling S, Bolz J, et al. Distant metastases in meningioma: an underestimated problem. *J Neuro-Oncol*. May 2013;112(3):323–327.
19. Kaley T, Barani I, Chamberlain M, et al. Historical benchmarks for medical therapy trials in surgery- and radiation-refractory meningioma: a RANO review. *Neuro Oncol*. June 2014;16(6):829–840.
20. Fathi AR, Roelcke U. Meningioma. *Curr Neurol Neurosci Rep*. April 2013;13(4):337.
21. Engelhard HH. Progress in the diagnosis and treatment of patients with meningiomas. Part I: diagnostic imaging, preoperative embolization. *Surg Neurol*. February 2001;55(2):89–101.
22. Hasso AN, Bell SA, Tadmor R. Intracranial vascular tumors. *Neuroimaging Clin N Am*. November 1994;4(4):849–870.
23. Buetow MP, Buetow PC, Smirniotopoulos JG. Typical, atypical, and misleading features in meningioma. *Radiographics*. November 1991;11(6):1087–1106.
24. Drevelegas A, Karkavelas G, Hourmouzi D, Boulogianni G, Petridis A, Dimitriadis A. Meningeal tumors. In: Drevelegas A, ed. *Imaging of Brain Tumors with Histological Correlations*. Berlin; New York: Springer; 2002:177–214.
25. Pieper DR, Al-Mefty O, Hanada Y, Buechner D. Hyperostosis associated with meningioma of the cranial base: secondary changes or tumor invasion. *Neurosurgery*. April 1999;44(4):742–746; discussion 746–747.
26. Tateishi U, Tateishi K, Hino-Shishikura A, Torii I, Inoue T, Kawahara N. Multimodal approach to detect osseous involvement in meningioma: additional value of F-Fluoride PET/CT for conventional imaging. *Radiology*. July 25, 2014:132118.
27. Tokgoz N, Oner YA, Kaymaz M, Ucar M, Yilmaz G, Tali TE. Primary intraosseous meningioma: CT and MRI appearance. *AJNR Am J Neuroradiol*. September 2005;26(8):2053–2056.
28. Miller NR, Golnik KC, Zeidman SM, North RB. Pneumosinus dilatans: a sign of intracranial meningioma. *Surg Neurol*. November 1996;46(5):471–474.
29. Bolat F, Kayaselcuk F, Aydin MV, Erdogan B, Ulusan S, Zorludemir S. Lipidized or lipomatous meningioma, which is more appropriate? A case report. *Neurol Res*. October 2003;25(7):764–766.
30. Kubota Y, Ueda T, Kagawa Y, Sakai N, Hara A. Microcystic meningioma without enhancement on neuroimaging–case report. *Neurologia Medico-Chirurgica*. May 1997;37(5):407–410.
31. Roosen N, Deckert M, Lumenta CB, Stork W, Gahlen D. Endotheliomatous meningioma with coalescing microcysts, presenting as an hypodense lesion with ring enhancement on computed tomography. *Neurochirurgia*. September 1989;32(5):160–163.
32. Yashi M, Sasaki M, Ono T. Ring-enhanced malignant meningioma mimicking a brain metastasis from a renal cell carcinoma. *Urol Int*. 2003;70(1):80–82.
33. Bradac GB, Ferszt R, Bender A, Schorner W. Peritumoral edema in meningiomas. A radiological and histological study. *Neuroradiology*. 1986;28(4):304–312.
34. Domingo Z, Rowe G, Blamire AM, Cadoux-Hudson TA. Role of ischaemia in the genesis of oedema surrounding meningiomas assessed using magnetic resonance imaging and spectroscopy. *Br J Neurosurg*. October 1998;12(5):414–418.
35. Kizana E, Lee R, Young N, Dorsch NW, Soo YS. A review of the radiological features of intracranial meningiomas. *Australas Radiol*. November 1996;40(4):454–462.
36. Pistolesi S, Fontanini G, Camacci T, et al. Meningioma-associated brain oedema: the role of angiogenic factors and pial blood supply. *J Neuro-Oncol*. November 2002;60(2):159–164.
37. Mantle RE, Lach B, Delgado MR, Baeesa S, Belanger G. Predicting the probability of meningioma recurrence based on the quantity of peritumoral brain edema on computerized tomography scanning. *J Neurosurg*. September 1999;91(3):375–383.
38. Probst-Cousin S, Villagran-Lillo R, Lahl R, Bergmann M, Schmid KW, Gullotta F. Secretory meningioma: clinical, histologic, and immunohistochemical findings in 31 cases. *Cancer*. May 15, 1997; 79(10):2003–2015.
39. Nagele T, Petersen D, Klose U, Grodd W, Opitz H, Voigt K. The "dural tail" adjacent to meningiomas studied by dynamic contrast-enhanced MRI: a comparison with histopathology. *Neuroradiology*. May 1994;36(4):303–307.
40. Wen M, Jung S, Moon KS, et al. Immunohistochemical profile of the dural tail in intracranial meningiomas. *Acta Neurochir (Wien)*. December 2014;156(12):2263–2273.
41. Slot KM, Verbaan D, Uitdehaag BM, et al. Can excision of meningiomas be limited to resection of tumor and radiologically abnormal dura? Neuronavigation-guided biopsies of dural tail and seemingly normal dura, with a review of literature. *World Neurosurg*. December 2014;82(6):e832–e836.

42. Kawahara Y, Nakada M, Hayashi Y, et al. Prediction of high-grade meningioma by preoperative MRI assessment. *J Neuro-Oncol*. May 2012;108(1):147–152.
43. Lin BJ, Chou KN, Kao HW, et al. Correlation between magnetic resonance imaging grading and pathological grading in meningioma. *J Neurosurg*. August 22, 2014:1–8.
44. Hoover JM, Morris JM, Meyer FB. Use of preoperative magnetic resonance imaging T1 and T2 sequences to determine intraoperative meningioma consistency. *Surg Neurol Int*. 2011;2:142.
45. Qi ZG, Li YX, Wang Y, et al. Lipid signal in evaluation of intracranial meningiomas. *Chin Med J*. December 5, 2008;121(23):2415–2419.
46. Buhl R, Nabavi A, Wolff S, et al. MR spectroscopy in patients with intracranial meningiomas. *Neurol Res*. January 2007;29(1):43–46.
47. Yue Q, Isobe T, Shibata Y, Kawamura H, Anno I, Matsumura A. Usefulness of quantitative proton MR spectroscopy in the differentiation of benign and malignant meningioma. *Sheng wu yi xue gong cheng xue za zhi = J Biomed Eng = Shengwu yixue gongchengxue zazhi*. December 2011;28(6):1103–1109.
48. Majos C, Alonso J, Aguilera C, et al. Utility of proton MR spectroscopy in the diagnosis of radiologically atypical intracranial meningiomas. *Neuroradiology*. March 2003;45(3):129–136.
49. Chernov MF, Kasuya H, Nakaya K, et al. (1)H-MRS of intracranial meningiomas: what it can add to known clinical and MRI predictors of the histopathological and biological characteristics of the tumor? *Clin Neurol Neurosur*. April 2011;113(3):202–212.
50. Saloner D, Uzelac A, Hetts S, Martin A, Dillon W. Modern meningioma imaging techniques. *J Neuro-Oncol*. September 2010;99(3):333–340.
51. Yang S, Law M, Zagzag D, et al. Dynamic contrast-enhanced perfusion MR imaging measurements of endothelial permeability: differentiation between atypical and typical meningiomas. *AJNR Am J Neuroradiol*. September 2003;24(8):1554–1559.
52. Lasjaunias P, Berenstein A. Surgical neuroangiography. *Endovascular Treatment of Craniofacial Lesions*. Vol. 2. Berlin, Heidelberg: Springer; 1987. SpringerLink: http://dx.doi.org/10.1007/978-3-642-71188-6.
53. Kaji T, Hama Y, Iwasaki Y, Kyoto Y, Kusano S. Preoperative embolization of meningiomas with pial supply: successful treatment of two cases. *Surg Neurol*. September 1999;52(3):270–273.
54. Masters LT, Nelson PK. Pre-operative angiography and embolisation of petroclival meningiomas. *Interv Neuroradiol: J Peritherapeutic Neuroradiol Surg Proced Relat Neurosci*. September 30, 1998;4(3):209–221.
55. Bruening R, Wu RH, Yousry TA, et al. Regional relative blood volume MR maps of meningiomas before and after partial embolization. *J Comp Assist Tomogr*. January–February 1998;22(1):104–110.
56. Bendszus M, Warmuth-Metz M, Klein R, et al. Sequential MRI and MR spectroscopy in embolized meningiomas: correlation with surgical and histopathological findings. *Neuroradiology*. January 2002;44(1):77–82.
57. Houkin K, Kamada K, Sawamura Y, Iwasaki Y, Abe H, Kashiwaba T. Proton magnetic resonance spectroscopy (1H-MRS) for the evaluation of treatment of brain tumours. *Neuroradiology*. February 1995;37(2):99–103.
58. Jungling FD, Wakhloo AK, Hennig J. In vivo proton spectroscopy of meningioma after preoperative embolization. *Magn Reson Med: Off J Soc Magn Reson Med/Soc Magn Reson Med*. August 1993;30(2):155–160.
59. Kallmes DF, Evans AJ, Kaptain GJ, et al. Hemorrhagic complications in embolization of a meningioma: case report and review of the literature. *Neuroradiology*. December 1997;39(12):877–880.
60. Tymianski M, Willinsky RA, Tator CH, Mikulis D, TerBrugge KG, Markson L. Embolization with temporary balloon occlusion of the internal carotid artery and in vivo proton spectroscopy improves radical removal of petrous-tentorial meningioma. *Neurosurgery*. November 1994;35(5):974–977; discussion 977.
61. Wakhloo AK, Juengling FD, Van Velthoven V, Schumacher M, Hennig J, Schwechheimer K. Extended preoperative polyvinyl alcohol microembolization of intracranial meningiomas: assessment of two embolization techniques. *AJNR Am J Neuroradiol*. May–Jun 1993;14(3):571–582.
62. Jellinger K, Paulus W. Mesenchymal, non-meningothelial tumors of the central nervous system. *Brain Pathol*. January 1991;1(2):79–87.
63. Alen JF, Lobato RD, Gomez PA, et al. Intracranial hemangiopericytoma: study of 12 cases. *Acta Neurochir (Wien)*. 2001;143(6):575–586.
64. Begg CF, Garret R. Hemangiopericytoma occurring in the meninges: case report. *Cancer*. May 1954;7(3):602–606.
65. Chiechi MV, Smirniotopoulos JG, Mena H. Intracranial hemangiopericytomas: MR and CT features. *AJNR Am J Neuroradiol*. August 1996;17(7):1365–1371.
66. Giannini C, Rushing EJ, Hainfellner JA. Haemangiopericytoma. In: Louis DN, Ohgaki H, Wiestler OD, Cavenee WK, eds. *The 2007 WHO Classification of Tumours of the Central Nervous System*. 4th ed Lyon, France: International Agency for Research on Cancer; 2007:178–180.
67. Fountas KN, Kapsalaki E, Kassam M, et al. Management of intracranial meningeal hemangiopericytomas: outcome and experience. *Neurosurg Rev*. April 2006;29(2):145–153.
68. Perry A, Brat DJ. Melanocytic lesions. In: Louis DN, Ohgaki H, Wiestler OD, Cavenee WK, eds. *The 2007 WHO Classification of Tumours of the Central Nervous System*. 4th ed Lyon, France: International Agency for Research on Cancer; 2007:181–183.
69. Kiecker F, Hofmann MA, Audring H, et al. Large primary meningeal melanoma in an adult patient with neurocutaneous melanosis. *Clin Neurol Neurosur*. June 2007;109(5):448–451.
70. Offiah CJ, Laitt RD. Case report: intracranial meningeal melanocytoma: a cause of high signal on T1- and low signal on T2-weighted MRI. *Clin Radiol*. March 2006;61(3):294–298.
71. Chow M, Clarke DB, Maloney WJ, Sangalang V. Meningeal melanocytoma of the planum sphenoidale. Case report and review of the literature. *J Neurosurg*. May 2001;94(5):841–845.
72. Hamasaki O, Nakahara T, Sakamoto S, Kutsuna M, Sakoda K. Intracranial meningeal melanocytoma. *Neurologia Medico-Chirurgica*. November 2002;42(11):504–509.
73. Roser F, Nakamura M, Brandis A, Hans V, Vorkapic P, Samii M. Transition from meningeal melanocytoma to primary cerebral melanoma. Case report. *J Neurosurg*. September 2004;101(3):528–531.
74. Smith AB, Horkanyne-Szakaly I, Schroeder JW, Rushing EJ. From the radiologic pathology archives: mass lesions of the dura: beyond meningioma-radiologic-pathologic correlation. *Radiographics*. March–April 2014;34(2):295–312.
75. Deckert M, Paulus W. Malignant lymphomas. In: Louis DN, Ohgaki H, Wiestler OD, Cavenee WK, eds. *The 2007 WHO Classification of Tumours of the Central Nervous System*. 4th ed Lyon, France: International Agency for Research on Cancer; 2007:188–192.
76. Paulus W, Perry A. Histiocytic tumors. In: Louis DN, Ohgaki H, Wiestler OD, Cavenee WK, eds. *The 2007 WHO Classification of Tumours of the Central Nervous System*. 4th ed Lyon, France: International Agency for Research on Cancer; 2007:193–196.

CHAPTER

45

Intracranial Schwannomas

D. Bradley Welling

Department of Otology and Laryngology, Harvard Medical School, Massachusetts Eye and Ear and Massachusetts General Hospital, Boston, MA, USA

INTRODUCTION

Intracranial schwannomas are often solitary encapsulated tumors that grow along the sensory distribution of cranial and spinal nerve or nerve roots. The most common of these is the vestibular schwannoma (VS), which was first described at autopsy in 1777 and later in a patient in 1833 by Sir Charles Bell.[1] Acoustic neuroma (also termed neurinoma, neurilemmoma, neurofibroma, and neuroma) is a misnomer as it arises from the vestibular division of cranial nerve (CN) VIII and originates from Schwann cells and does not contain nerve tissue. A better and more accurate term is VS. Schwannomas comprise approximately 5–10% of all intracranial tumors and are predominantly located in the cerebellar pontine angle (CPA).[2,3] The clinical incidence is between 0.92 and 1.9 per 100,000 and they often present between the ages of 40 and 60 years.[3,4] Temporal bone histopathology shows an incidence of VSs of 2.4–3.5%, but incidental VSs are identified in only 0.2% of the population on magnetic resonance imaging (MRI) in asymptomatic patients.[4,5] Among these, 80–90% arise from the vestibular branch or ganglion of CN VIII, predominantly from the inferior vestibular nerve.[6–8] There is a female-to-male predilection ratio of approximately 1.5–2:1.[4]

About 90–95% of VSs are solitary and 5–10% bilateral as seen in neurofibromatosis 2 (NF2) patients. Conversely 95% of NF2 patients develop bilateral VSs.[5] While almost all isolated VS patients have somatic involvement, about 6% are mosaic for the NF2 gene mutation.[6] In these instances the age of the individual at presentation is the most important determinant of risk of NF2, with patients less than 30 years of age at high risk for the disease and those greater than 55 years of age with negligible risk. NF2-associated schwannomas are more likely to present in children or young adults.

After the vestibular portion of the eighth CN (Figures 1–4), the next most common location of intracranial schwannomas is the fifth CN, representing approximately 0.2% of intracranial tumors[7] (see Figure 5). These arise either from the nerve root at the CPA or Meckel's cave for intradural locations or extradurally from the Gasserian ganglion. They tend to be more varied in appearance and are more often associated with cystic components (see Figure 6). There are also sporadic reports of trochlear, abducens, facial, vagal, glossopharyngeal, and hypoglossal schwannomas in the literature[8–11] (see Figures 7–10). Facial schwannomas tend to arise at the geniculate ganglion. They may present initially with sensorineural hearing loss rather than facial nerve palsy, as the acoustic nerve is more thinly myelinated. Intraparenchymal schwannomas are exceedingly rare, with a slight male predilection of 1.6:1. They are seen in younger age groups (<30 years of age) and have been reported in periventricular, brain-stem, and sellar locations.[12–15]

Schwann cells originate from neural crest cells that migrate with the growing neurites during nerve development. All myelinated fibers are ensheathed by Schwann cells, except at the nodes of Ranvier, to facilitate rapid transmission of electric impulses via saltatory conduction. Unlike neurofibromas, which contain all elements of nerve including Schwann cells, nerve fibers, and fibroblasts causing splaying of the axon, schwannomas do not contain any neural tissue.[15]

PATHOLOGY

Histologically, VSs are composed of a variable continuum of two patterns. The Antoni type A (see Figure 11) component is more compact, consisting of interwoven

Handbook of Neuro-Oncology Neuroimaging, Second Edition
http://dx.doi.org/10.1016/B978-0-12-800945-1.00045-8

© 2016 Elsevier Ltd. All rights reserved.

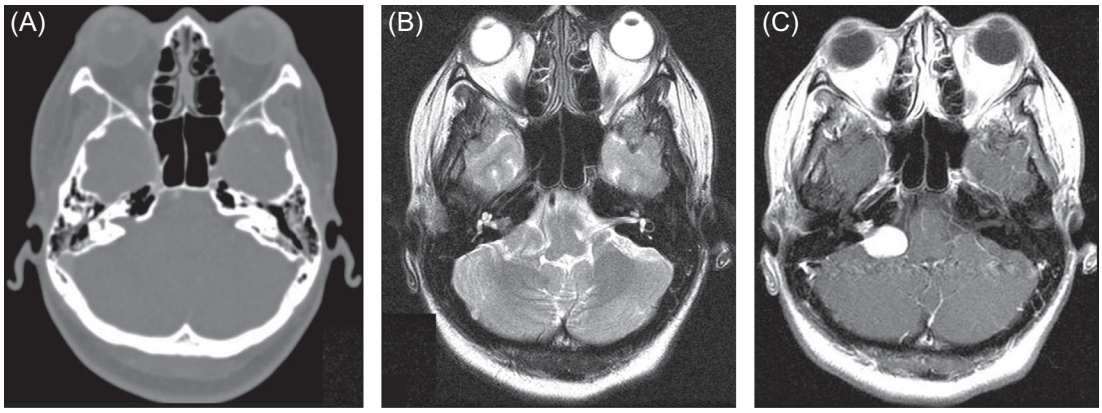


FIGURE 1 Right vestibular schwannoma demonstrating (A) an enlarged internal auditory canal on axial CT; (B) slight brain-stem compression of the pons onT2 axial; and (C) T1 post-gadolinium enhancement of the tumor.

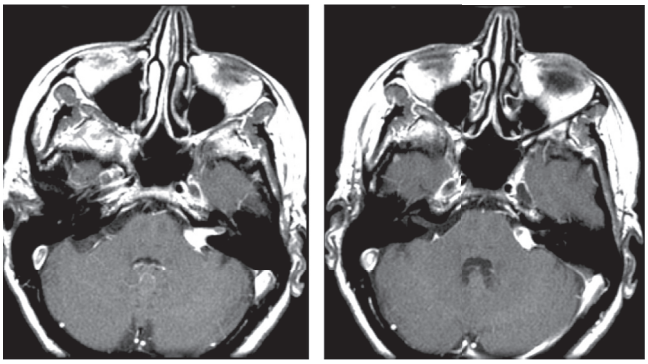


FIGURE 2 Left-vestibular schwannoma with both intra- and extra-canalicular components on axial T1 post-gadolinium images.

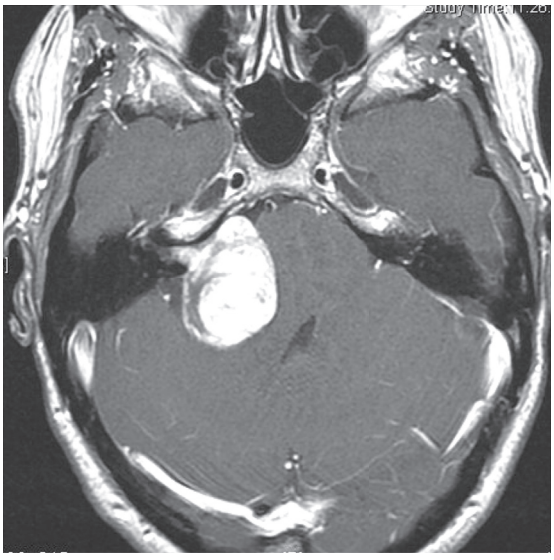


FIGURE 3 Large nonhomogeneously enhancing right vestibular schwannoma on axial T1 post contrast image. Note shift of the brain stem from tumor compression.



FIGURE 4 FIESTA image demonstrates high-resolution visualization of bilateral seventh and eighth nerve complex (arrows).

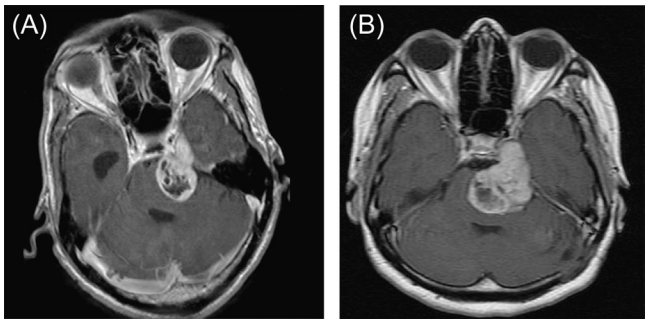


FIGURE 5 Postcontrast fat suppression left fifth nerve schwannomas extending into Meckel's cave. (A) *Case courtesy of Dr. Desai, P.K., Radiopaedia.org, rID: 10864.* (B) *Courtesy of Dr. Gupta, K., Radiopaedia.org, rID: 14454.*

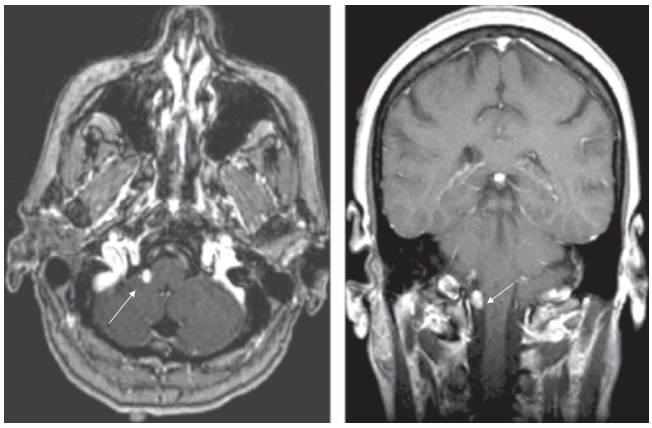


FIGURE 6 Axial (left) and coronal (right) post-gadolinium T1 images of a small right third-nerve schwannoma.

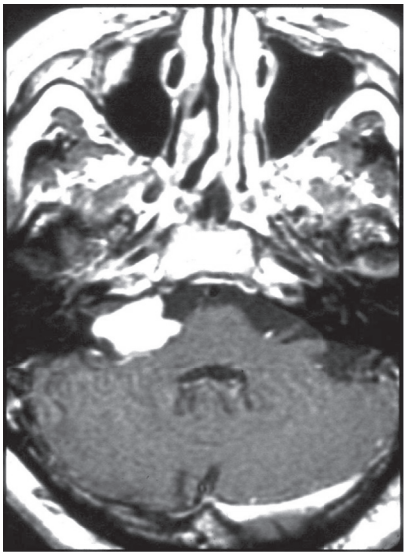


FIGURE 7 Homogeneously enhancing right hypoglossal schwannoma on axial T1 post-gadolinium images.

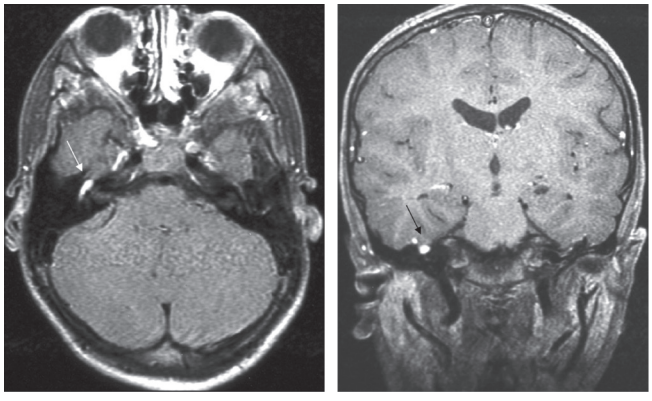


FIGURE 8 Axial T1 (left) post-gadolinium and coronal (right) of a right facial nerve schwannoma involving the geniculate ganglion (arrows).

bundles of fusiform cells, collagen whorls, and reticulin fibers. They may arrange in a palisading pattern around a nuclear-free zone, named a Verocay body. The more loosely packed Antoni type B (see Figure 11) is made up of spindle and polygonal cells randomly scattered within a loose matrix often with microcystic or mucinous areas that may coalesce to form larger cysts. Occasionally other variants are seen, consisting of fibroblastic changes with dense collagen bands, calcification, fatty or xanthomatous changes, and intratumoral vascular thrombosis (hyaline thickening of vascular wall), or sometimes even hemorrhage. Ancient change in schwannoma describes a histologic variant with biphasic features that result from degenerative changes from a long-standing tumor.[16] The spindle-shaped cells stain positively for S-100 protein and vimentin.

Malignant schwannomas (1%) are very rare and are more commonly seen in NF2 patients. These tumors are characterized by focal areas of extremely high cellularity, pleomorphism, and mitosis in an otherwise typically benign tumor. They can either arise from preexisting tumors (latency 10–20 years) or can arise de novo, often seen in a younger age group (15–39 years). The rare intraparenchymal schwannomas are thought to originate from perivascular Schwann cells of innervated arteries, dural CN sites, or ectopic cell rests.[16]

Clinically VSs often present with tinnitus followed by gradual and progressive asymmetric hearing loss. Even in NF2 patients with bilateral tumors, the hearing loss is usually asymmetric initially, but profound bilateral deafness may eventually ensue. About 10% of VS present with sudden hearing loss, although of all patients with sudden hearing loss, only 1% have associated VSs. The mechanism was previously thought to be secondary to acute vascular compromise of the cochlea or cochlear nerve.[4,14] Recently, protein deposition in the cochlea, especially the scala media, has been found to correlate with hearing loss. This association may explain why tumor size does not necessarily correlate to hearing loss. The nature of the protein deposition seen on MRI in the cochlea in the fluid-attenuated inversion recovery sequence is still under study[17] (see Figure 12). Disequilibrium is a symptom in about half of the VS patients when carefully questioned, but true vertigo is rare and disequilibrium is the presenting symptom in only about 10% of patients. Interestingly, involvement of CN V by compression from a VS causes hypoesthesia or dysesthesia prior to facial nerve paresis, as the sensory nerves are more sensitive to the tumor presence than is the motor component of the seventh CN. Diplopia suggests cavernous sinus extension, and vertigo and lower CN palsies signify lower or skull base involvement.[2]

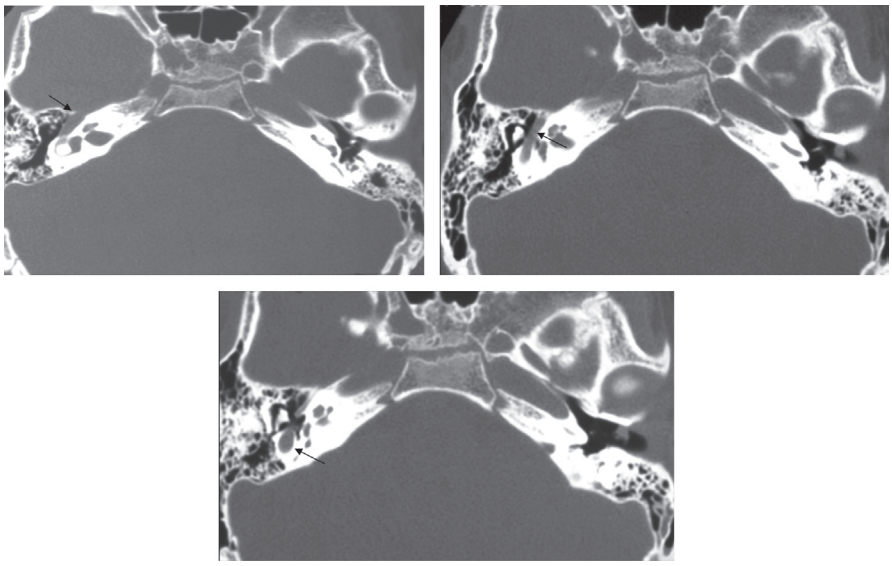


FIGURE 9 Same patient as in Figure 8 demonstrating (clockwise top left) bony enlargement of the course of the right facial nerve secondary to schwannoma (arrows).

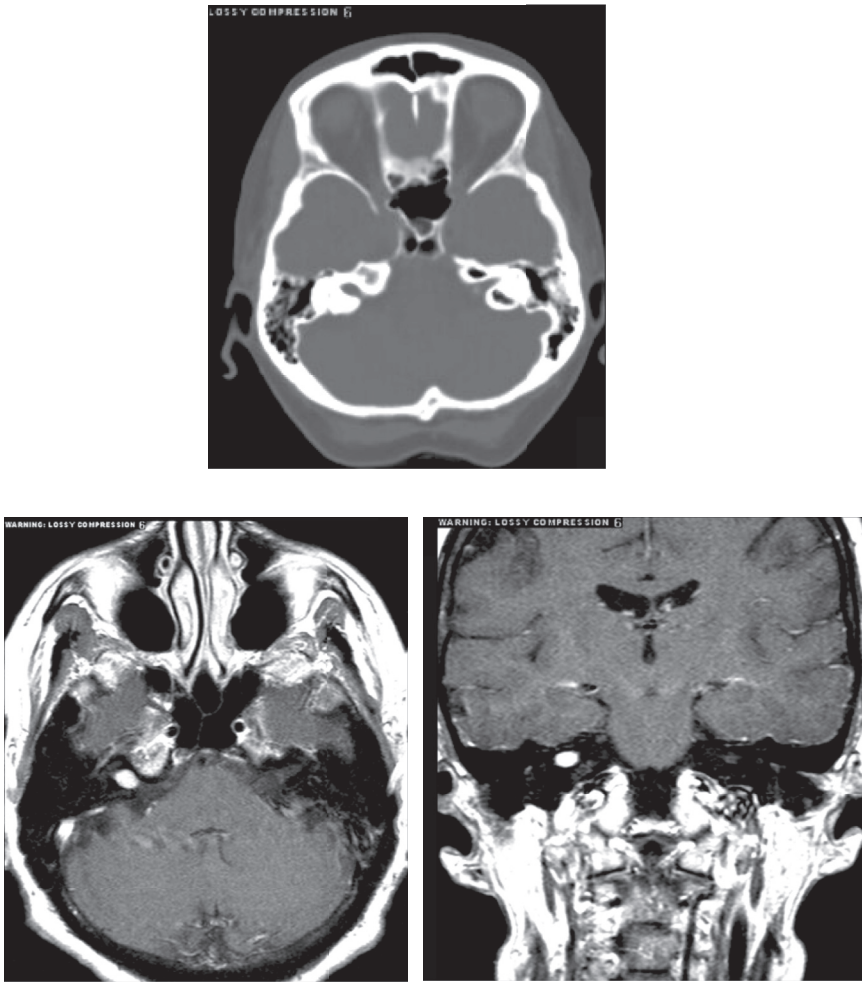


FIGURE 10 Patient with right facial nerve schwannoma demonstrating (top) bony enlargement of the internal auditory canal and enhancement post-gadolinium (bottom-left) on T1 axial and coronal (bottom-right) along the course of the right facial nerve.

IMAGING

The development of MRI with contrast has markedly facilitated the diagnosis of eighth nerve schwannomas, especially the small intracanalicular tumors. Prior to MRI, widening of the internal auditory canal (IAC) could sometimes be detected on computed tomography (CT) but could not reliably detect tumors less than 1 cm.[18] These tumors on MRI enhance intensely with gadolinium complexes. Contrast enhancement tends to have a rapid initial decrease (15 min after injection) followed by a slower decline.[19] Maximum enhancement can be reasonably anticipated within the half-hour after injection. Contrast gives an overall sensitivity of almost 100%.[20,21] On CT, schwannomas are isodense or have low signal density relative to brain and sometimes contain a cystic component or calcification. Rarely a lipid-rich and larger Antoni A-component tumor can impart a lower attenuation on CT.[22]

In earlier studies about 70% of the time there was widening of the IAC best seen with bone windows on thin-section CT images (see Figure 1). The majority of eighth nerve schwannomas have both intra- and extracanalicular components. Some authors have suggested that the reason for this location is that the transitional zone between the oligodendrocytes and the Schwann cells (the so-called Obersteiner-Redlich zone) lies in close proximity to the vestibular ganglion at the opening of the porus acusticus. Schwannomas could then grow bidirectionally from this junction (see Figure 1(C)).[23,24] Origin at or near Scarpa's ganglia is more common, however, than origin at the transitional junction.[25] The next most common pattern is purely intracanalicular (see Figure 12), followed rarely by a predominantly extracanalicular lesion.

On T1 MR images they tend to be iso- or hypointense to brain while heterogeneously hyperintense on T2 sequence. It is thought that mucopolysaccharide contributes to lower T1 signal while collagen imparts a low T2 signal.[18,19] In fact, there has been description of a "target" sign on T2 sequence whereby centrally a low signal is seen secondary to fibrocollagen surrounded by peripheral high signal from myxomatous matrix. It was thought that this so-called "target" sign is not seen in malignant schwannomas.[26] Long-standing schwannomas are also more likely to have cystic degenerative changes and hemorrhage.

Schwannomas tend to be slow growing, most at a rate of about 0.02 cm/year, some at 0.2 cm/year, and rarely at 1 cm/year.[21] Most present as medium-sized lesions of about 2 cm with 2–4 cm defined as large lesions and >4 cm as giant schwannomas (see Figure 3). Pregnancy may accelerate the growth of schwannomas with worsening of symptoms.[27]

Segmented volumetric analysis of tumor size has been established and found to be more accurate for measurement of growth in both sporadic unilateral VSs and NF2-associated VSs than linear measurements. Complex three-dimensional tumors make linear assessments less accurate. In a study of sporadic VS, the estimated average growth rate was 50 mm^3/

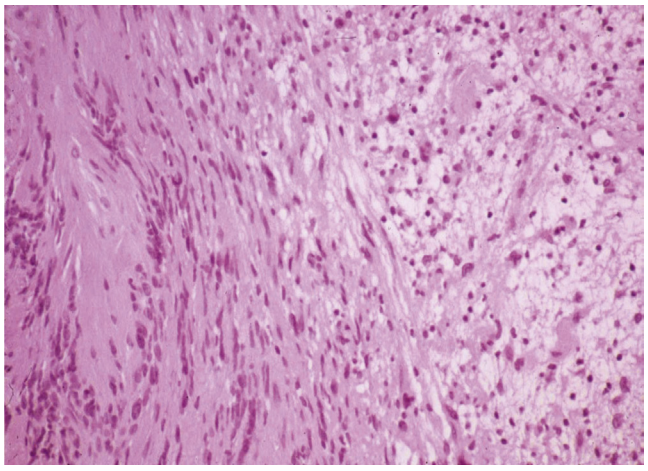


FIGURE 11 Hematoxylin and eosin stained vestibular schwannoma demonstrating palisading schwannoma cells on the left (Antoni A pattern) and loosely packed irregular schwannoma cells on the right (Antoni B pattern).

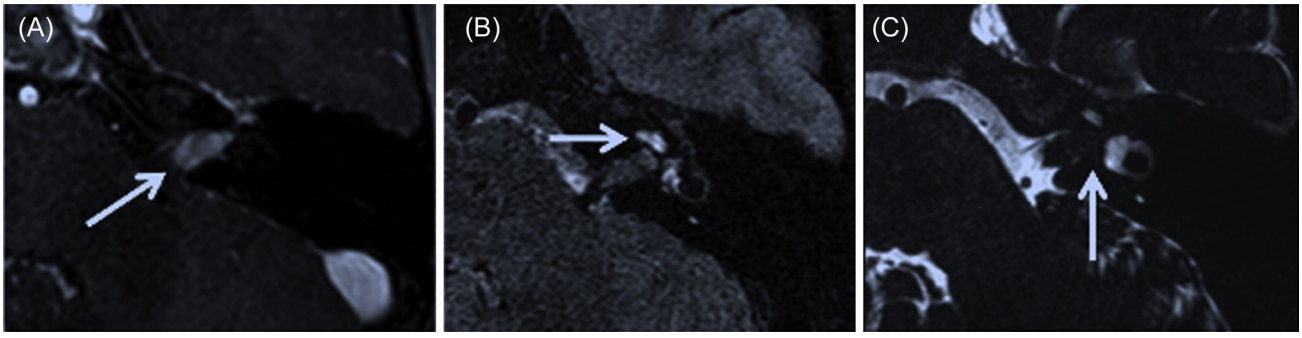


FIGURE 12 MRI of the left internal auditory canal (IAC) tumor in (A) T1 post-gadolinium showing tumor (arrow); (B) fluid-attenuated inversion recovery sequence showing elevated signal indicating protein in the basal turn of the left cochlea (arrow); (C) VISTA reveals cochlear aperture obstruction without fluid in distal IAC (arrow). *Courtesy Holliday et al. Ref. 17.*

year.[28] Growth was detected in 75% more tumors volumetrically than by linear measurement estimates. A similar finding was reported by Harris et al. in NF2-associated VSs with growth detected in 29% more tumors by volumetric analysis than by linear measurements.[29]

A standard MR protocol as recommended by the Consensus Conference in 2012 includes the following:

Series No.	MRI Series Name	Type of Pulse Sequence	Slice Thickness (mm)
1	Localizer	Gradient echo	5
2	Calibration scan	Gradient echo	6
3	Sagittal T1	Spin echo	5
4	Axial DIFF	Spin echo	5
5	Axial FLAIR T2	Inversion recovery	5
6	Axial T2	Fast spin echo	5
7	Ax T1 IAC precontrast	Spin echo	3
8	Ax 3D FIESTA high resolution	FIESTA	0.8
9	Ax T1 IAC FS postcontrast	Spin echo	3
10	Cor T1 IAC FS postcontrast	Spin echo	3
11	Ax post-FS T1 SPGR	SPGR	2.5
12	Ax post-whole brain	Spin echo	5

Ax, axial orientation; Cor, coronal orientation; T1, T1 weighted; T2, T2 weighted; DIFF, diffusion-weighted sequence; FLAIR, fluid attenuated inversion recovery sequence; IAC, internal auditory canal; FIESTA, fast imaging employing steady-state acquisition; IAC FS, internal auditory canal with fat saturation; SPGR, spoiled gradient recalled.
Modified from Ref. 31.

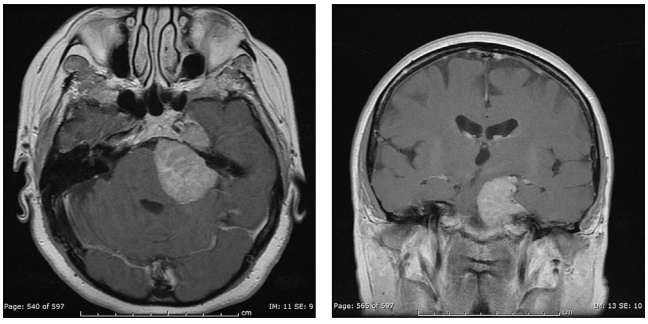


FIGURE 13 T1 post-gadolinium cerebellopontine angle and Meckel's cave meningioma on axial and coronal sections. *Case courtesy of Dr. Frank Gaillard, Radiopaedia.org, rID: 9128.*

Main differentials for schwannoma are from meningioma (see Figure 14), metastasis (see Figure 15), and other extra-axial processes such as epidermoid (see Figure 16) and nonacoustic schwannoma.

As most schwannomas occur at the CPA one often needs to differentiate this from a meningioma. There are a few observations that can help in such instances. Schwannomas tend to be isodense and calcify less commonly on CT. They are globular and centered at the porus acusticus with acute margins, while meningiomas often arise along the petrous bone and are more sessile in shape with obtuse margins. Schwannomas are also more heterogeneous in appearance with cystic changes and tend to widen the IAC. Meningiomas, on the other hand, are more commonly associated with a dural tail (see Figures 14 and 17) and may calcify.

After radiotherapy, greater than 80% (most centrally) show loss of enhancement (see Figure 18), 5% have an increase, and about 11% are without changes. There is, however, no correlation between the volume of tumor to enhancement.[31] Adjacent brain, such as the pons, may also show mild enhancement after radiation.[32,33]

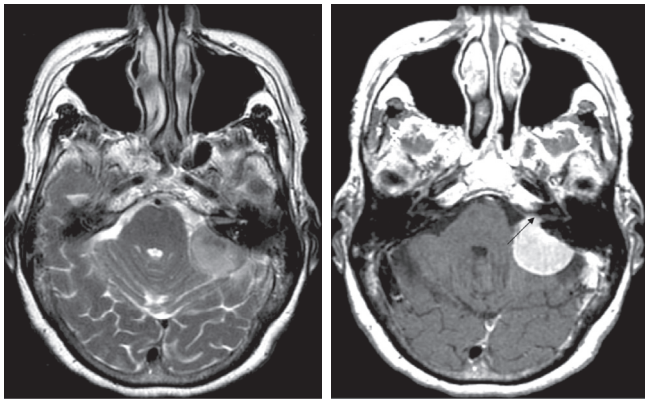


FIGURE 14 Meningioma along posterior fossa plate with small intrusion into the internal auditory canal (arrow). T2 axial (left) and T1 post-gadolinium (right) MRI.

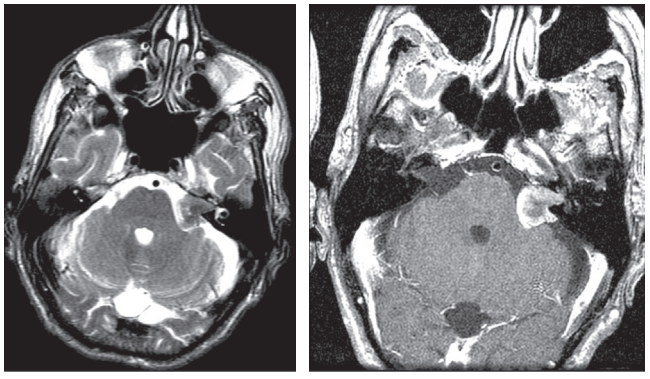


FIGURE 15 A rare mesothelioma metastasis to left internal auditory canal. T2 and T1 (left and right) postcontrast axial images.

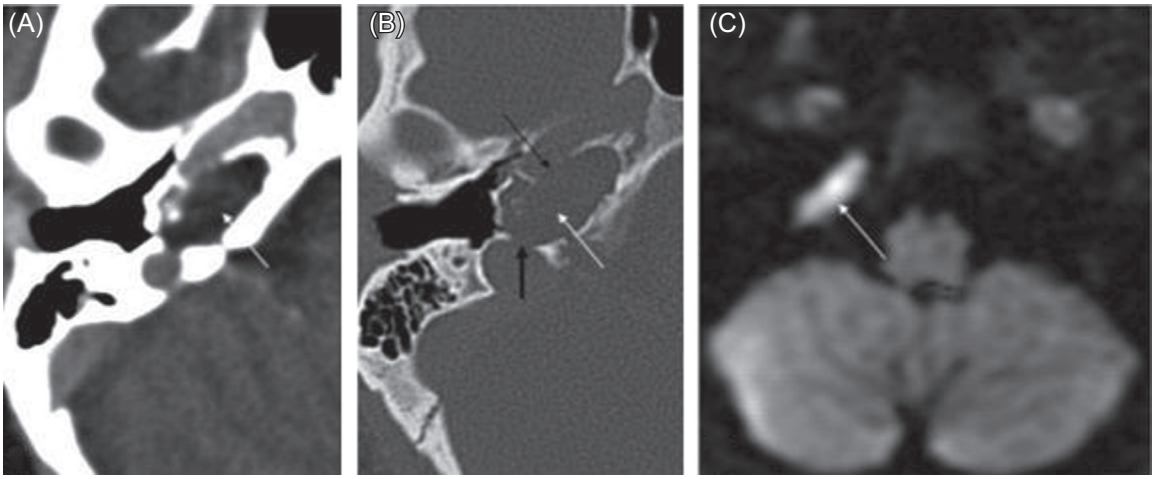


FIGURE 16 Cholesteatoma of the petrous apex. Contrast-enhanced high-resolution CT with a soft-tissue window (A) and a bone window (B) show an oval well-delineated, nonenhancing lesion (white arrows) with erosion of the posterior wall of the pyramidal segment of the internal carotid artery (thin black arrow) and the anterior wall of the jugular bulb (thick black arrow). (C) Diffusion-weighted image demonstrates diffusion restriction in the lesion (white arrow), supporting the diagnosis of a cholesteatoma. *Used with permission from Hsu, L. Intracranial Schwannomas. From Newton HB Jolesz, FA eds.* Handbook of Neuro-Oncology Neuroimaging. *Elsevier; 2007:408–418.*

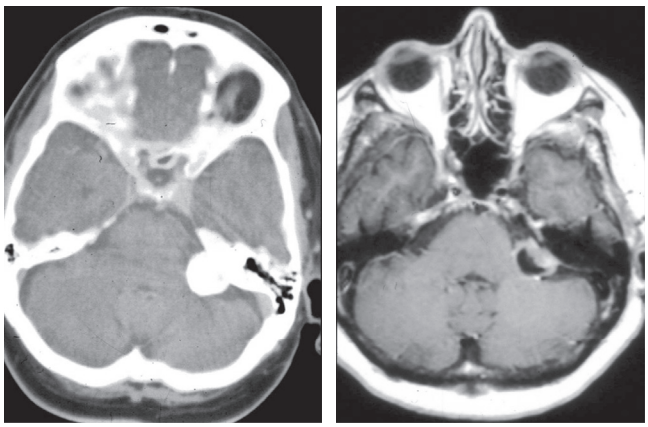


FIGURE 17 Axial noncontrast CT (left) and post-gadolinium T1 images (right) show a calcified left CPA meningioma.

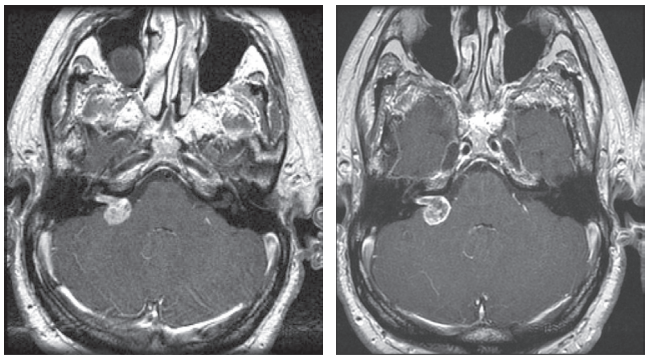


FIGURE 18 Axial post-gadolinium T1 images show heterogeneous enhancing right vestibular schwannoma before (left) and decreased enhancement and necrosis after radiation (right).

NEUROFIBROMATOSIS 2

NF2 is an autosomal dominant highly penetrant cancer-predisposing syndrome that does not have any sex or racial predilection.[34] The disorders in half of affected patients are due to new gene mutations, while the other 50% are inherited.[35,36] They often present with multiple CN schwannomas and bilateral VS by the age of 30 (Figures 19–21). By definition, bilateral VSs constitute a diagnosis of NF2. About 18% of patients manifest tumors before 15 years of age and often develop spinal tumors and skin lesions. Past classifications have included the Wishart type, which has an early onset (~ 20s), multiple tumors including bilateral VSs, and a severe clinical and rapid course. A second or Gardner type has a later presentation, bilateral VSs, and a more benign course, with fewer tumors. The third or segmental NF2, which constitutes about 25% of cases, has somatic mosaicism with mutation occurring during embryogenesis rather than germ-line DNA resulting in altered genetic material in only a portion of the patient's cells.[30] There really is a continuum between the severe and the mild phenotypes. Familial genetic mutations, which are inherited, do not necessarily mean the phenotype will be the same in all family members, as one mutation is acquired.

It is thought that the disorder arises from the alteration or loss of genetic material and occasional translocation of the NF2 gene locus[37] on chromosome 22q12.2, which codes for a protein named "merlin" (moezin–ezrin–radixin-like protein). It has high homology to a family of cytoskeletal-associated proteins and possesses tumor suppression activity.[38,39] This gene consists of 110 kilobases with 16 constitutive exons and an alternatively

spliced exon.[38,39] There are at least 150 different mutations described, of which most are point mutations.[40] Missense mutations are thought to give a milder form of the disease, while nonsense, frameshifting,[41,42] and truncating mutations[42] are associated with more severe phenotypes. The deletion or mutation results in increased risk of development of schwannomas, meningiomas, ependymomas, gliomas, and juvenile posterior subcapsular lenticular opacity.[43–45] Variability in expression results in differing size, location, and number of tumors. A milder phenotypic form of the disease is often seen in individuals with somatic mosaicism with unilateral VS and other ipsilateral tumors.[44] Genetic testing of these patients may give misleading information because their lymphocytes can be normal, thus necessitating direct tumor tissue analysis for proper diagnosis.[47] Reports indicate 25–30% of NF2 patients without a family history are mosaic for the mutation.[47–49] The prevalence of NF2 is approximately 1 in 210,000 with an incidence of 1 in 30,000–40,000 (Figure 22).[50]

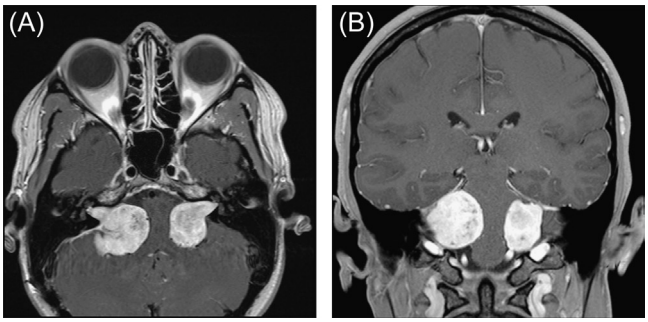


FIGURE 19 MRI T1 post-gadolinium image of an NF2 patient with large bilateral vestibular schwannomas. (A) Axial and (B) coronal. Note: Brain-stem compression, but no hydrocephalus. *Case courtesy of Dr. Frank Gaillard, Radiopedia.org, rID:9128.*

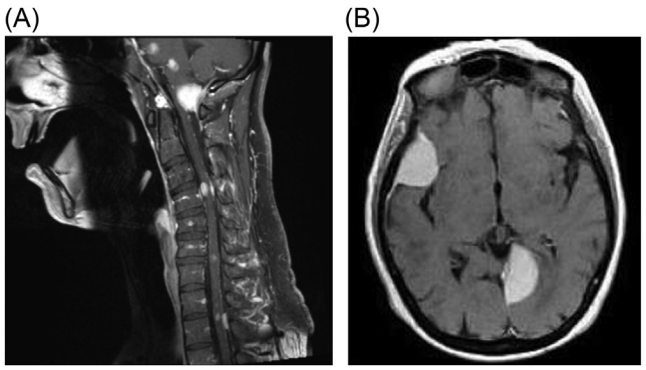


FIGURE 20 MRI T1 post-gadolinium of an NF2 patient on (A) sagittal view demonstrating intra-axial tumors within the spinal cord consistent with ependymomas (arrows) and extra-axial meningiomas or schwannomas and (B) large intracranial meningiomas with enhanced dura tails (arrows).

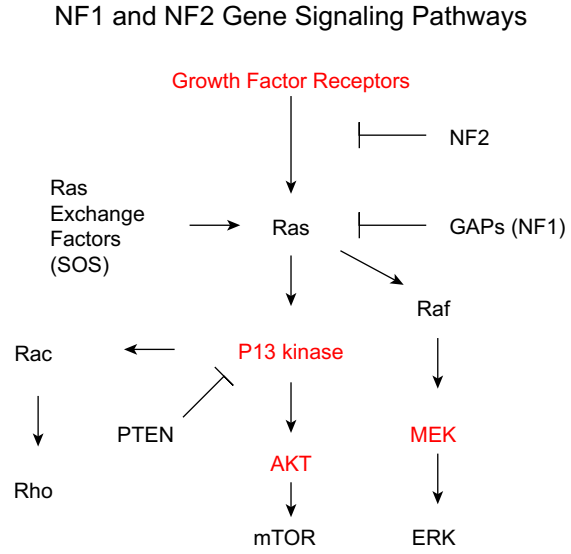


FIGURE 22 The NF2 gene elaborates a protein (merlin or schwannomin) which is shown as a suppressor of tumor growth with similar activity to the Ras suppression of NF1. Intervention at multiple points along the tumor pathways is being targeted with clinical trials.

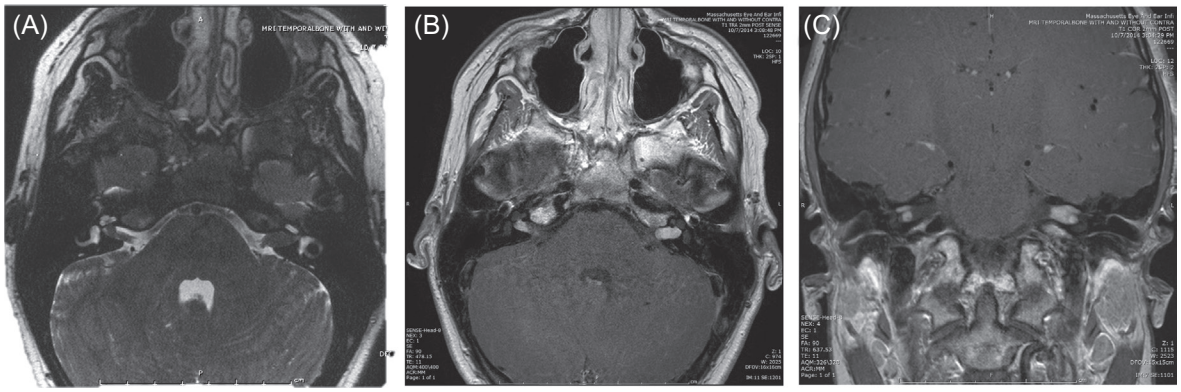


FIGURE 21 MR images from a 12-year-old NF2 patient with (A) T2 images demonstrating some spinal fluid in the IAC and tumor adjacent to the modiolus of the cochlea (arrow), also shown in (B) a T1 post-gadolinium image. Both also demonstrate left VS filling the IAC. In (C), a coronal T1-weighted image with contrast shows both superior and inferior vestibular nerve tumors on the right and a probable tumor of separate origin in the left IAC also.

Over the years there have been various modifications of the National Institutes of Health consensus criteria for the diagnosis of NF2 listed, as of this writing, as[30]:

- Bilateral VSs
- First-degree relative with NF2 AND
  - Unilateral VS OR
  - Any two of meningioma, schwannoma, glioma, neurofibroma, cataract
- Unilateral VS AND any two of meningioma, schwannoma, glioma, neurofibroma, posterior subcapsular lenticular opacities
- Multiple meningiomas AND
  - Unilateral VS OR
  - Any two of schwannoma, glioma, neurofibroma, cataract

In addition to diagnostic purposes, genetic testing is also employed in the early detection of patients (primarily children of classically affected parents) for earlier intervention options.

Unlike sporadic schwannomas, the tumors associated with NF2 tend to be multinodular,[51] may have foci in the cochlear and facial nerves, and are bilateral and occur at a younger age (20s and 30s). Fifty percent of patients have concomitant meningiomas. Patients often present with tinnitus and hearing loss, balance problems, and seizures.[52] Facial paralysis is delayed unless a facial nerve tumor is present. Malignant transformation is rare and can be iatrogenic from prior radiation. There have been reports of malignant transformation of about 0.5% in radiated schwannomas, with 41% of these occurring in NF2 patients, which represent only 5% of VSs.[53] The authors estimate a 10-fold increase in malignant change in non-NF2-associated schwannomas following radiation (15.6/100,000 in non-NF2 compared to 1–2/100,000 cases). Other symptoms are mass effect from meningiomas, nonacoustic schwannomas, skin tumors, and presenile cataracts, the last two most often being the initial presentation in children.

Spinal tumors are also found in two-thirds of patients and are debilitating and difficult to manage.[51] Although the tumors are rarely malignant they are situated in proximity to vital structures that result in high morbidity and mortality. Usual time of survival from initial diagnosis is about 15 years, with average age of death at 36 years.[50] The age at presentation, presence of meningioma, and whether treatment was conducted at a specialty center are all predictors of mortality risk. Mononeuropathy in childhood and polyneuropathy in adults not directly associated with tumors are increasingly being recognized.[51]

There has been a concerted effort to identify targetable pathways in the formation of NF2-associated tumors and to seek new treatment compounds and combinations that might successfully reverse tumor progression in schwannoma and meningioma. Some of the representative pathways are shown.

MANAGEMENT AND TREATMENT

The average growth rate for VS is approximately 1 mm^3 per year. The tumor size and location, age, NF2 status, and degree of hearing loss are important factors in the management of these patients. There is no correlation between initial tumor size and growth rate. In the sporadic population most can be followed with MRI every 6–12 months under the so-called expectant management.[46]

For microsurgery there are primarily three basic surgical approaches, each with their unique advantages and risks. In 1960, Dr. William House reintroduced the translabyrinthine approach for patients with poor preoperative hearing. It is generally used when the speech discrimination score (SDS) is poorer than 70%. In NF2 patients this surgical approach may be used in conjunction with an auditory brain-stem implant.[46,47] The primary advantage is that the facial nerve can be identified as it attaches to the anterior face of the tumor, giving a more direct dissection plane between the tumor and the facial nerve.[54] Also, less cerebellar retraction is necessary than with the suboccipital approach.

The retrosigmoid or suboccipital approach is potentially a hearing preservation approach. Some surgeons prefer this approach whether or not hearing is salvageable, largely dependent upon their experience. Older studies reported a high residual tumor rate (18%) for tumors that extended laterally into the IAC; however, removal of the posterior wall of the IAC and endoscopic visualization of the lateral IAC have reduced this markedly.

The third approach is via the middle cranial fossa and is best for small intracanalicular (<1.0 cm) tumors with good preoperative hearing. The potential risks of this technique include seizures due to retraction of the temporal lobe. In our hands, there is no increased rate of postoperative cerebrospinal fluid (CSF) leak nor increased incidence of facial nerve damage with this approach.

In NF2 patients a multidisciplinary approach to diagnosis, evaluation, and treatment at an experienced center is the key for the optimal management of their disease. Surgical resection remains a cornerstone for treatment of VS, with the best results obtained for smaller tumors (<1.5 cm), which are medially positioned in the IAC leaving a fundal cap of CSF laterally in the canal next to the cochlea. Debulking or subtotal resection of a larger tumor is reserved for patients with worsening symptoms or brain-stem compression[49]; however, residual hearing

may be lost even with tumor decompression because of vascular supply to the cochlea. Brain-stem compression is a concern with large bilateral tumors, and tumors may need to be resected despite residual useful hearing to prevent hydrocephalus and death. For small bilateral tumors (<1.5 cm) and good preoperative hearing (speech discrimination score >75%), the smaller tumor is resected while attempting to preserve hearing. If successful, the second VS is also removed. If hearing is not preserved in the first ear, watchful waiting is recommended for the second tumor. As long as hearing is viable, the larger lesion may be observed unless there is brain-stem compression, which would lead to hydrocephalus. If the tumor size is equal bilaterally the side with worse hearing will undergo initial resection (Figure 23).

Postoperative complications include CSF leak (8%), infection (1%), and postoperative headache, particularly with the suboccipital approach with removal of the posterior lip of the porus acusticus. The overall rate of hearing preservation is variable dependent on tumor size and location. Facial nerve function is graded from I to VI (good to poor) at 6–12 months after surgery. It may be splayed during surgery, especially for >1.5-cm lesions that are cystic and thus more adherent. Overall rate is 82% with good follow-up (grade I/II) breaking down as 92% in Retrosigmoid (RSA), 89% in middle cranial fossa (MCF), and 73% for Translabynnthine (TLA).[46,47]

CSF leak is often seen during the first 2–3 or 10–14 days after surgery. It can occur at various locations including the incision site, tympanic membrane, eustachian tube, and nasopharynx. The overall rate is 8%, with a breakdown of 6% for MCF, 9% TLA, and 11% RSA.[50,51] Postoperative infections are often aseptic and thought to be due to irritation from bone dust or hemorrhage. They occur in about 2% of MCF and 3% in both RSA and TLA. Steroid treatment in this population has been helpful.[50–52,55] Finally, headache may persist up to 3 months after surgery with an overall rate of 10%, seen most in RSA (21%) and less in MCF and TLA.[51,53,56,57]

In general, tumors that measure greater than 1.5 cm in the axial plane at the CPA have higher risk for facial nerve injury from surgery than from radiation therapy. Solid tumors also fare better than cystic ones. Outpatient stereotactic radiation treatment (single dose or fractionated)—primarily Gamma Knife—is also an alternative to surgery with better long-term control in non-NF2 patients, 95% versus 60%.[58] In the late 1980s and early 1990s about 79% had normal facial nerve function after 5 years from radiation, with 51% without hearing loss. With lower doses of about 13 Gy, there has been a further decrease in posttreatment dysfunction approaching 1.1% in facial and 2.6% in trigeminal nerves, with 71% hearing preservation and an overall 80–97% control rate. On imaging tumors may initially enlarge during the first 6 months to a year after radiation owing to edema. Very infrequently a large tumor undergoes initial surgical debulking followed by radiation.[47] Tinnitus seems more likely to improve following resection (52%) than when stereotactic radiation is given (16%). Tinnitus is aggravated by radiation treatment in 74% of patients as opposed to 11% of patients who report increased tinnitus following translabyrinthine excision of tumor.[56]

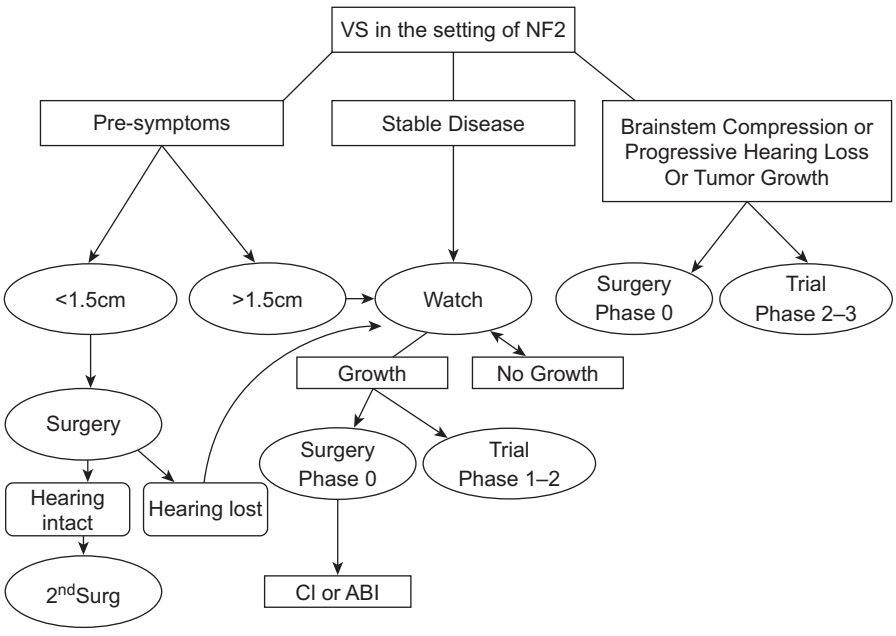


FIGURE 23 A treatment paradigm for patients with NF2 can be useful to examine various considerations. Individual treatment is necessary; however, because of the multifocal, highly complex nature of the disease process.

The risks and benefits of radiation therapy should also be carefully weighed to prevent untoward malignant transformation of existing tumors, especially in individuals with an inactive copy of a tumor suppression gene. There are sporadic reports of malignant triton tumors and squamous cell carcinoma transformation secondary to radiation.[59,60] The upper limit for tumor size for radiation therapy is about 3 cm maximum in the axial plane given that postradiation swelling may cause further brain-stem compression and hydrocephalus.

The prognosis of NF2 patients is certainly guarded, as they face potential progressive neurologic decline. The rate of decline is variable, however. Progressive cranial-base tumor growth can lead to lower CN dysfunction and may lead to chronic aspiration, gastrostomy tube dependence, or recurrent pneumonia and is often the root cause of death. Patients diagnosed from 1970 to 1990 were found to have a 15-year life expectancy from the time of diagnosis (see Figure 19), but improved diagnosis and early intervention have improved current life expectancies.

Some patients with NF2 may benefit from cochlear implants when hearing has been lost from compression, radiation, or surgery if the cochlear nerves are still intact. Preimplantation electrical stimulation of the cochlea via an electrode placed directly on the promontory of the cochlea may be useful to detect if the patient still has potential for electrical stimulation of hearing prior to implantation.[61]

Imaging provides information on size, site, presence or absence, and preoperative planning and postoperative follow-up of tumors. In addition it also serves as a noninvasive way to monitor tumor growth as well as recurrent or residual lesions over time with or without prior treatment.

Regarding chemotherapy, although no FDA-approved NF2 chemotherapeutic agents exist, patients with severe disease have been treated with chemotherapeutic agents. Inhibitors directed at the ErbB receptor family, AKT/PI3 kinase signaling pathway, and vascular endothelial growth factor have shown evidence of inhibition of NF2 VS growth (see Figures 16–18). In particular bevacizumab has shown initial improved hearing and tumor reduction in early trials in about half of the patients treated. Further preclinical work is indicated to identify effective medical treatments.

Genetic testing should be offered for first-degree relatives of NF2 patients and genetic counseling should be offered to NF2 patients. Support groups such as the Acoustic Neuromas Association (www.anausa.org) and the Children's Tumor Foundation (www.ctf.org) provide many educational and social resources for patients and families affected by NF2.

Schwannomatosis is a disease genetically and clinically distinct from NF2 and characterized by multiple schwannomas, which tend to be nonintradermal and nonvestibular but include intracranial, spinal root, and peripheral nerves. Schwannomatosis may be associated with meningiomas as well, but only in about 5%, far less than the 50% association with NF2. Familial cases of schwannomatosis demonstrate autosomal dominant inheritance with variable expression and penetrance. Germ-line mutations in the SMARCB1 (SWI/SNF chromatin remodeling complex) gene are responsible for approximately 20% of schwannomatosis, with 50% in familial cases. The LZTR1 (leucine-zipper-like transcription regulator) gene was found mutated in 80% of patients who do not have a SMARCB1 mutation.[55–57]

In summary, sporadic and NF2 VSs are typically benign tumors with morbidity and mortality mostly attributed to lesion size and location. Thin-section MRI, especially with contrast, remains the imaging modality of choice for the diagnosis of these tumors as well as for pre- and postoperative planning and follow-up. Microsurgery, stereotactic radiation, and observation are the current treatment options, with chemotherapeutic compounds under current investigation.

References

1. Bell C. *The Nervous System of the Human Body*. Washington, DC: Green; 1833.
2. Chandler CL, Ramsden RT. Acoustic schwannoma. *Br J Hosp Med*. 1993;49:335–343.
3. D'Alessandro G, Giovnni M, Iannizzi L, et al. Epidemiology of primary intracranial tumors in the Valle d'Aosta during the 6-yr period. 1986–1991. *Neuroepidemiology*. 1995;14:139–146.
4. Henschen F. Concerning the history and pathogenesis for cerebellopontine angle tumors. *Arch Psychiatry*. 1915;56:21.
5. Vernooij MW, Ikran MA, Tanghe HL, et al. Incidental findings on brain MRI in the general population. *NEJM*. 2007;357:1821–1828.
6. Barker DJP, Weller RO, Garfield JS. Epidemiology of primary tumors of the brain and spinal cord: a regional survey in southern England. *J Neurol Neurosurg Psychiatry*. 1976;39:290–296.
7. Jacob A, Robinson Jr LL, Bortman JS, et al. Nerve of origin, tumor size, hearing preservation, and facial nerve outcomes in 359 vestibular schwannoma resections at a tertiary care academic center. *Laryngoscope*. 2007;117:2087–2092.
8. Khrais T, Romano G, Sanna M. Nerve origin of vestibular schwannoma: a prospective study. *J Larynogl Otol*. 2008;1122:128–131.
9. Consensus Development panel. National Institute of Health Consensus Development Conference Statement on Acoustic Neuroma December 11–13, 1991. *Arch Neurol*. 1994;51:201–207.
10. Lin D, Hegarty JL, Fischbein NJ, et al. The prevalence of "incidental" acoustic neuroma. *Arch Otolaryngol Head Neck Surg*. 2005; 131:241–244.
11. Mohyuddin A, Neary WJ, Wallace A, et al. Molecular genetic analysis of the NF2 gene in young patients with unilateral vestibular schwannomas. *J Med Genet*. 2002;39:315–322.
12. Shisano G, Olivecrona H. Neurinomas of the Gasserian ganglion and trigeminal root. *J Neurosurg*. 1960;17:306–322.
13. Celli P, Ferrante L, Acqui M, et al. Neurinoma of the third, fourth and sixth cranial nerves and report of a new fourth nerve case. *Surg Neurol*. 1992;38:216–224.
14. Morey RA, Halliday GC. Neurinomas of facial nerve. Report of a case. *J Neurosurg*. 1965;23:539–541.

15. Lanotte M, Giordana MT, Forni C, et al. Schwannoma of the cavernous sinus. *J Neurosurg Sci*. 1992;36:233–238.
16. Lantos PL, Louis DN, Rosenblum MK, Kleihues P. Chapter 11 Tumors of the Nervous System in Greenfields Neuropathology. 7th ed. In: Graham DI, Lantos PL eds. vol. 2:897–909.
17. Holliday MA, Kim HJ, Zalewski CK, et al. Audiovestibular characteristics of small cochleovestibular schwannomas in neurofibromatosis type 2. *Otolaryngol Head Neck Surg*. 2014;151:117–124.
18. Welling DB, Glasscock ME, Woods CI, et al. Acoustic Neuroma: a cost-effective approach. *Otolaryngol Head Neck Surg*. 1990;103: 364–370.
19. Hatam A, Bergstrom M, Moller A, et al. Early contrast enhancement of acoustic neuroma. *Neuroradiology*. 1978;17:31–33.
20. Curtin HD. Rule out eighth nerve tumor: contrast enhanced T1-weighted or high resolution T2-weighted MR? *AJNR*. 1997;18: 1834–1838.
21. Schmalbrock P, Chakeres DW, Monroe JW, et al. Assessment of internal auditory canal tumors: a comparison of contrast-enhanced T1-weighted and steady- state T2-weighted gradient-echo MR imaging. *AJNR*. 1999;20:1207–1213.
22. Wu E, Tang Y, Zhang Y, et al. CT in diagnosis of acoustic neuromas. *AJNR*. 1986;7:745–750.
23. Schuknecht H. *Pathology of the Ear*. Cambridge, Mass: Harvard University Press; 1974.
24. Bebin J. Pathophysiology of Acoustic Tumors. *Diagnosis*. vol. I. Baltimore: University Park Press; 1979.
25. Xenellis JE, Linthicum FH. On the myth of the Glial/Schwann junction (Obersteiner-Redlich zone): origin of vestibular Nerve Schwannomas. 2003;24:1.
26. Press GA, Hesselink JR. MR imaging of cerebellopontine angle and internal auditory canal lesions at 1.5 T. *AJNR*. 1988;9:241–251.
27. Kasantikul V, Brown WJ. Estrogen receptors in acoustic neurilemmomas. *Surg Neurol*. 1981;15:105–109.
28. Walz PC, Bush ML, Robinett Z, et al. Three-dimensional segmented volumetric analysis of sporadic vestibular schwannomas: comparison of segmented and linear measurements. *Otolaryngol Head Neck Surg*. 2012;147:737–743.
29. Harris GJ, Plotkin SR, MacCollin M, et al. Three-dimensional volumetrics for traking vestibular schwannoma growth in nuruofibromatosis type II. *Neurosurgery*. 2008;62:1314–1319.
30. Blakeley JO, Evans DG, Adler J, et al. Consensus recommendations for current treatments and accelerating clinical trials for patients with neurofibromatosis type 2. *Am J Med Genet A*. 2012;158A:24–41.
31. Nakamura H, Jokura H, Takahashi K, et al. Serial follow-up MR imaging after gamma knife radiosurgery for vestibular schwannoma. *AJNR*. 2000;21:1540–1546.
32. Noren G, Arndt J, Hindmarsh T. Stereotacticradiosurgery in cases of acoustic neurinoma: further experiences. *Neurosurgery*. 1983;13:12–22.
33. Thomsen J, Tos M, Borgesen SE. Gamma knife: hydrocephalus as a complication of stereotactic radiosurgical treatment of an acoustic neuroma. *Am J Otol*. 1990;11:330–333.
34. Martuza RL, Eldridge R, Wertelecki W, et al. Neurofibromatosis 2: clinical and DNA linkage studies of a large kindred. *N Engl J Med*. 1988;318:684–688.
35. MacCollin M, Ramesh V, Jacoby LB, et al. Mutational analysis of patients with neurofibromatosis 2. *Am J Hum Genet*. 1994;55:314–320.
36. Parry DM, MacCollin MM, Kaiser-Kupfer MI, et al. Germ-line mutations in the neurofibromatosis 2 gene: correlations with disease severity and retinal abnormalities. *Am J Hum Genet*. 1996;59: 529–539.
37. Tsilchorozidou T, Menko F, Lalloo F, et al. Constitutional rearrangements of chromosome 22 as a cause of neurofibromatosis. *J Med Genet*. 2004;41:529–534.
38. Trofatter JA, MacCollin MM, Rutter JL, et al. A novel moesin-, ezrin, radixin-like gene is a candidate for the neurofibromatosis 2 tumor suppressor. *Cell*. 1993;72:791–800.
39. Rouleau GA, Merel P, Lutchman M, et al. Alteration in a new gene encoding a putative membrane-organizing protein causes neurofibromatosis type 2. *Nature*. 1993;363:515–521.
40. Legoix P, Sarkissian HD, Cazes L, et al. Molecular characterization of germline NF2 gene rearrangements. *Genomics*. 2000;65:62–66.
41. Evans DG, Trueman L, Wallace A, et al. Genotype/phenotype correlations in type 2 neurofibromatosis (NF2): evidence for more severe disease associated with truncating mutations. *J Med Genet*. 1998;35:450–455.
42. Welling DB. Clinical manifestiations of mutations in the neurofibromatosis type 2 gene in vestibular schwannomas (acoustic neuromas). *Laryngoscope*. 1998;108:178–189.
43. Baser ME, Friedman JM, Aeschliman D, et al. Predictors of the risk of mortality in neurofibromatosis 2. *Am J Hum Genet*. 2002;71:715–723.
44. Evans DG, Huson SM, Donnai D, et al. A clinical study of type 2 neurofibromatosis. *Q J Med*. 1992;84:603–618.
45. Mautner VF, Tatagiba M, Guthoff R, et al. Neurofibromatosis 2 in the pediatric age group. *Neurosurgery*. 1993;33:92–96.
46. Barbi G, Rossier E, Vossbeck S, et al. Constitutional de novo interstitial deletion of 8 Mb on chromosome 22q12.1–12.3 encompassing the neurofibromatosis type 2 (NF2) locus in a dysmorphic girl with severe malformations. *J Med Genet*. 2002;39:E6.
47. MacCollin M, Jacoby L, Jones D, et al. Somatic mosaicism of the neurofibromatosis 2 tumor suppressor gene. *Neurology*. 1997;48A:429.
48. Moyhuddin A, Baser ME, Watson C, et al. Somatic mosaicism in neurofibromatosis 2: prevalence and risk of disease transmission to offspring. *J Med Genet*. 2003;40:459–463.
49. Kluwe L, Mautner V, Heinrich B, et al. Molecular study of frequency of mosaicism in neurofibromatosis 2 patients with bilateral vestibular schwannomas. *J Med Genet*. 2003;40:109–114.
50. Evans DG, Huson SM, Donnai D, et al. A genetic study of type 2 neurofibromatosis in the United Kingdom. I. Prevalence, mutation rate, fitness, and confirmation of maternal transmission effect on severity. *J Med Genet*. 1992;29:841–846.
51. Sperfeld AD, Hein C, Schroder JM, et al. Occurrence and characterization of peripheral nerve involvement in neurofibromatosis type 2. *Brain*. 2002;125:996–1004.
52. Parry DM, Eldridge R, Kaiser-Kupfer MI, et al. Neurofibromatosis 2 (NF2): clinical characteristics of 63 affected individuals and clinical evidence for heterogeneity. *Am J Med Genet*. 1994;52:450–461.
53. Serefis C, Torren M, Paraskevopoulou C, et al. Malignant transformation in vestibular schwannoma: report of a single case, literature search, and debate. *J Neurosurg*. 2014;121:160–166.
54. Jaaskelainen J, Paetau A, Pyykko I, et al. Interface between the facial nerve and large acoustic neurinomas. Immunohistochemical study of the cleavage plane in NF2 and non-NF2 cases. *J Neurosurg*. 1994;80:541–547.
55. MacCollin M, Woodfin W, Kronn D, et al. Schwannmatosis: a clinical and pathologic study. *Neurology*. 1996;46:1072–1079.
56. Park SH, Oh HS, Jeon JH, et al. Change in tinnitus after treatment of vestibular schwannoma: microsurgery vs. Gamma knife radiosurgery. *Yonsei Med J*. 2014;55:19–24.
57. MacCollin M, Willet C, Heinrich B, et al. Familial schwannomatosis: exclusion of the NF2 locus as the germline event. *Neurology*. 2003;60:1968–1974.
58. Smith MJ, Isidor B, Beetz C, et al. Mutations in LZTR1 add to the complex heterogeneity of schwannomatosis. *Neurology*. 2015; 84:141–147.
59. Harsha WJ, Backous DP. Counseling patients on surgical options for treating acoustic neuroma. *Otolaryngologic Clin NA August*. 2005; vol. 38:643–652.
60. Wackym PA. Stereotactic radiosurgery, microsurgery and expectant management of acoustic neuroma. Basis for informed consent. In: *Otolaryng Clinics of NA August*. 2005;vol. 38:653–670.
61. Neff BA, Wiet RM, Lasak JM, et al. Cochlear implantation in the neurofibromatosis type 2 patient: long-term follow up. *Laryngoscope*. 2007;117:1069–1072.

CHAPTER

46

Diencephalic and Other Deep Brain Tumors

A. Drevelegas[1], D. Chourmouzi[1], E. Xinou[2], K. Drevelegas[1,3]

[1]Department of Radiology, Interbalkan Medical Center, Thessaloniki, Greece; [2]Department of Radiology, Theagenio Cancer Hospital, Thessaloniki, Greece; [3]Karolinska Institute, Solna, Sweden

The diencephalon is one of the most highly developed structures of the human central nervous system and consists of two major components: the thalamus, a key structure for transmitting information to the cerebral hemispheres, and the hypothalamus, which integrates the functions of the autonomic nervous system and endocrine hormone release from the pituitary gland.[1] Tumors that affect the thalamus and the basal ganglia can develop as primary tumors or secondarily from neighboring tumors that invade the deep portions of the cerebrum.[2] Therefore, we will classify deep brain tumors either as primary neoplasms or as neighboring tumors that invade the diencephalic or the deep telencephalic structures.

PRIMARY DIENCEPHALIC TUMORS

Basal Ganglia–Thalami

Thalamic tumors are generally considered together with basal ganglionic tumors, although the thalami are part of the diencephalon. Basal ganglia and thalamic tumors account for 10% of supratentorial tumors in children, and nearly two-thirds of these neoplasms involve the thalami.[3] Thalamic tumors account for approximately 1–1.5% of all brain tumors;[4–7] they are slightly more common in children than in adults and involve significant diagnostic, prognostic, and therapeutic problems.[8,9]

Their deep location makes them difficult to treat, mainly because surgery is rarely feasible.[10–15] Radiation therapy with or without adjuvant chemotherapy[16] is still considered to be the basic treatment. They are predominantly low-grade astrocytomas,[11] but oligodendrogliomas, ganglion cell tumors, germinal neoplasms, primitive neuroectodermal tumors, lymphomas, and metastases can also arise from the basal ganglia and thalamic region.[2]

Gliomas

Gliomas can be divided into two broad categories: well-circumscribed gliomas like pilocytic astrocytomas and infiltrating or diffuse gliomas, including fibrillary astrocytomas, oligodendrogliomas, and gliomatosis cerebri. In the first category, the extent of excision is a powerful prognostic factor, whereas the prognosis in the latter is related more closely to the histologic grade.[17] According to Wald, the number of astrocytic tumors was 147 (77%) among 191 cases of thalamic tumors assessed by histological examination.[3]

Pilocytic Astrocytoma

Pilocytic astrocytomas (PAs) represent the prototype of benign circumscribed astrocytomas, usually without a tendency to infiltrate and progress toward anaplasia.[5] Macroscopically, PAs can be seen as homogeneous solid, heterogeneous–multicystic, or predominantly cystic tumors, occasionally with calcifications developing in the solid portions. Hemorrhages are very unusual.[18,19] PAs are tumors with a characteristic, heterogeneous "biphasic" histological appearance, consisting of spongy areas alternating with other more cellular regions. In the thalami, PAs are much less frequent than in the cerebellum, optic-chiasmatic region, and cerebral hemispheres.[5]

Computed tomography (CT)/magnetic resonance imaging (MRI) features are characterized by a well-circumscribed appearance, with sharp margins and variable size, mass effect, and degree of perilesional edema. The typical cerebellar presentation of a cystic tumor with a mural nodule (Figure 1) or a thick solid rim is rarely encountered in the thalami, where solid tumors predominate, with or without small cystic areas.[5]

CT may demonstrate a well-circumscribed mass that is homogeneous in cases of solid or predominantly solid tumors and heterogeneous in multicystic

Handbook of Neuro-Oncology Neuroimaging, Second Edition
http://dx.doi.org/10.1016/B978-0-12-800945-1.00046-X

© 2016 Elsevier Ltd. All rights reserved.

neoplasms. Cystic areas should be barely hypodense and similar to cerebrospinal fluid (CSF). Solid portions may be iso- to hypodense in comparison to brain parenchyma.[20] Sometimes hyperdense foci of calcification can be detected.[2]

On MRI, cysts may be iso- or hyperintense to CSF in all pulse sequences. Nevertheless, the degree of hyperintensity of the cysts depends on the biochemical characteristics of the cystic fluid. Solid areas are usually isointense or discretely hypointense relative to normal brain on T1-weighted images (T1WI). On intermediate and T2WI, solid areas are usually hyperintense and do not show restriction on diffusion-weighted imaging (DWI) (Figure 2).[21,22]

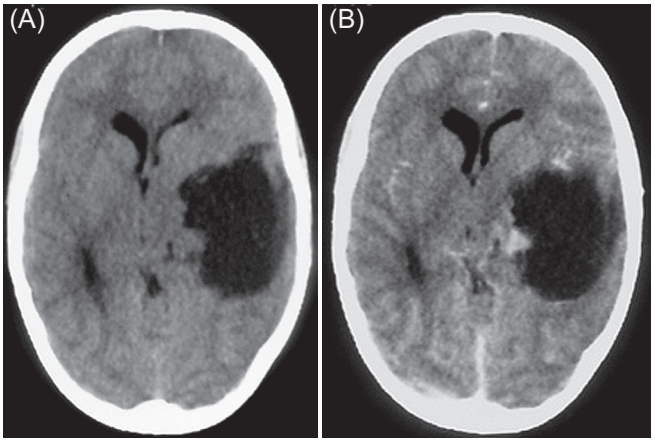


FIGURE 1 PA. (A) Axial noncontrast CT scan shows an isodense left-thalamic mural nodule with a hypodense cyst extending to the adjacent structures. (B) On axial postcontrast CT scan the mural nodule shows intense and homogeneous enhancement. The wall of the cyst remains unenhanced.

Usually, the solid portion of the tumor enhances after contrast administration (Figure 3).[23,24] If MRI depicts calcifications, they normally induce a decrease in signal in all sequences. Rarely, they are depicted as areas of hyperintensity on T1WI. Surrounding edema should be minimal or undetectable.[25] The inhomogeneity of PA may lead to the suspicion of malignant astrocytoma, but the well-defined margins, bright contrast enhancement, low signal on DWI, and lack of necrosis usually lead to a correct preoperative diagnosis.[5]

Diffuse or Infiltrating Astrocytoma

Diffuse astrocytomas are less common in children than in adults. They can be classified as low-grade diffuse astrocytomas (LGDA), anaplastic astrocytomas (AA), and glioblastoma multiforme (GBM).[20,24]

LGDAs usually enlarge but do not destroy brain structures.[25] Cyst and hemorrhage are uncommon, and calcification may be seen in up to 20% of cases.[24,26] CT may demonstrate a homogeneous, poorly circumscribed hypodense lesion with occasional contrast

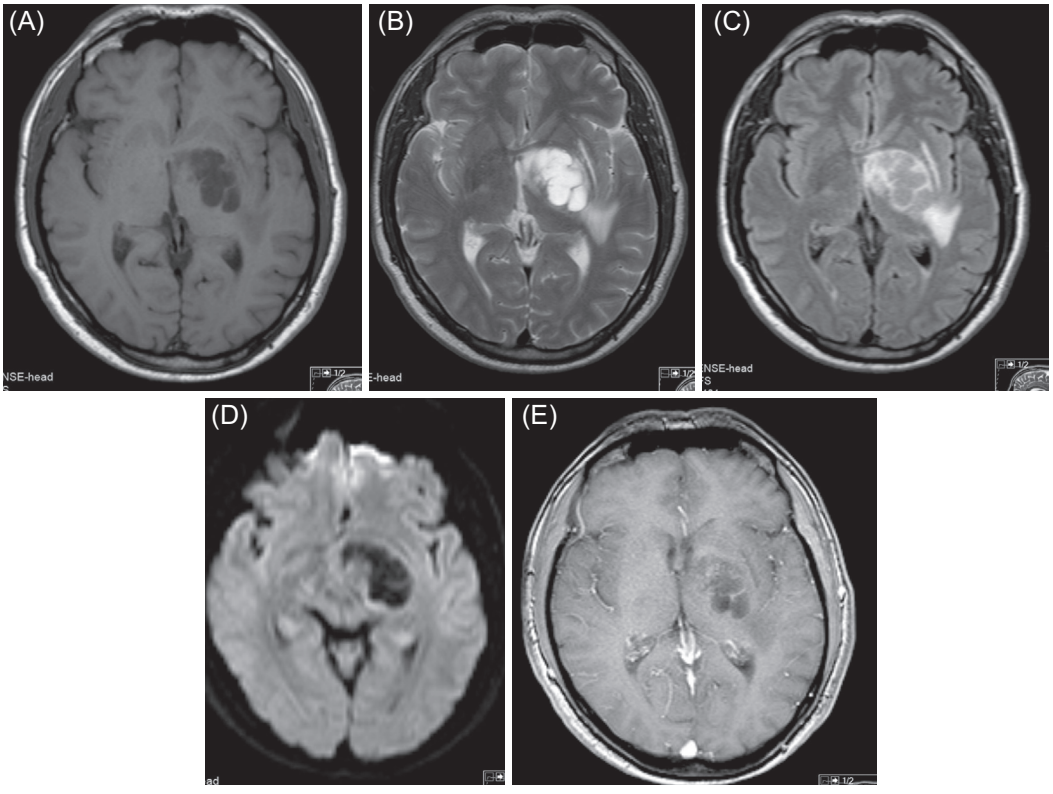


FIGURE 2 PA. The tumor involves deep structures such as thalamus, internal capsule, and lentiform nucleus. It is multicystic with low signal intensity on T1WI (A), high on T2-weighted (B), and FLAIR (C) images. NoS evidence of restricted diffusion seen on DWI (D). On axial postcontrast T1WI (E) foci of mild enhancement are seen.

enhancement.[20,24] Sometimes the tumor is relatively isodense and mass effect may be the only detectable imaging sign.

LGDAs are usually hypointense on T1WI, hyperintense on intermediate and T2WI, and demonstrate no or variable enhancement.[20,22,24] Surrounding vasogenic edema is an uncommon radiological finding (Figure 4).[20,22,24] On fluid-attenuated inversion recovery (FLAIR) and IR images, ill-defined hyperintense regions are noted in the subthalamic areas, the cerebral peduncles, or the internal capsule, revealing marginal infiltration, as perilesional edema is usually lacking or extremely limited.[5]

AAs are biologically more aggressive neoplasms with imaging findings similar to those of LGDA, except for the more frequent contrast enhancement and vasogenic edema.[24]

On the other hand, the typical features of AA are the inhomogeneity of MR signal on T1WI and T2WI, due to variable cellularity and vascularity, the presence of heterogeneous contrast enhancement, and extensive edema. Thus, inhomogeneity, irregular contrast enhancement, and extensive edema should be considered as characteristics of anaplasia, but also the extensive infiltrative growth is to be maintained as an indicator of malignancy and of dismal prognosis (Figure 5).[5]

GBM is far more common in adults than in children, as is progression from astrocytoma to GBM. Thalamic GBM appears as a fairly localized mass lesion with extensive vasogenic edema.[5] Necrosis and microvascular proliferation are histological characteristics that induce typical imaging manifestations.[24,26]

CT and MRI appearance of thalamic GBM is markedly inhomogeneous, usually with central necrosis, possible cavitation and fluid/fluid levels, and frequent hemorrhage at all stages of evolution (Figure 6(A) and (B)). On T1WI GBM appears with low or mixed signal intensity, while on T2WI, the recognition of central necrosis is more distinct, showing heterogeneous intensity and degraded blood products, while peripheral areas exhibit relatively low signal intensity (high cellularity). Flow voids related to vascular proliferation may also be observed.[24] Despite its circumscribed appearance, thalamic GBM may have small finger-like marginal extensions that represent their tendency to infiltrate adjacent tissues or spread more

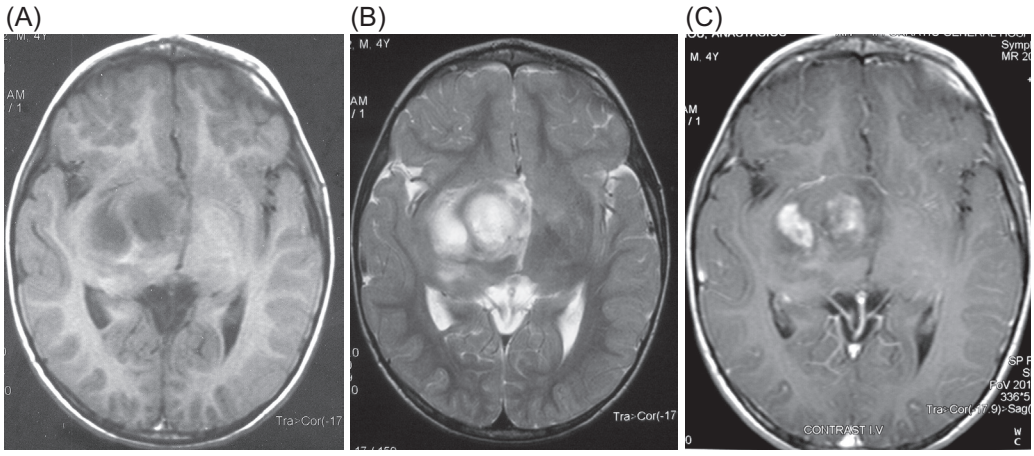


FIGURE 3 Right thalamic PA. The tumor appears hypointense on T1WI (A) and hyperintense on T2WI (B) and shows marked enhancement after contrast injection (C).

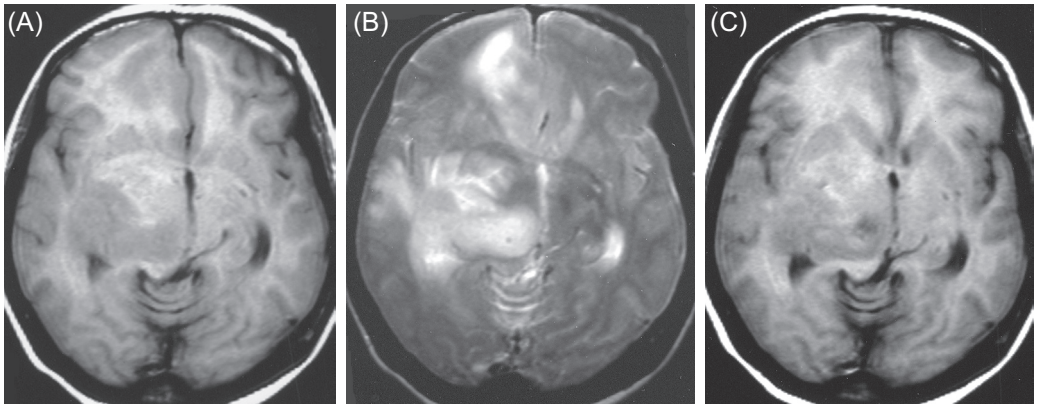


FIGURE 4 Right thalamic glioma. The tumor appears hypointense on non-contrast T1-weighted image (A) and hyperintense on T2-weighted image (B) with infiltration of the adjacent structures (internal capsule, parietal and frontal lobe). Post-gadolinium T1-weighted image (C) shows subtle contrast enhancement.

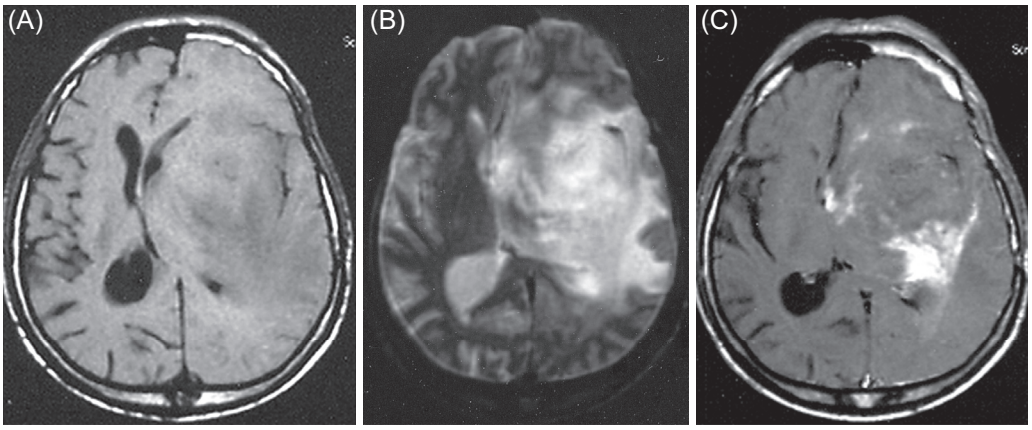


FIGURE 5 AA. (A) Axial T1WI shows a low signal mass in the left thalamus extending to adjacent structures and displacing the midline structures. (B) On axial T2WI the mass shows high signal intensity extending to the ipsilateral parietal lobe. (C) After contrast administration the mass shows inhomogeneous enhancement.

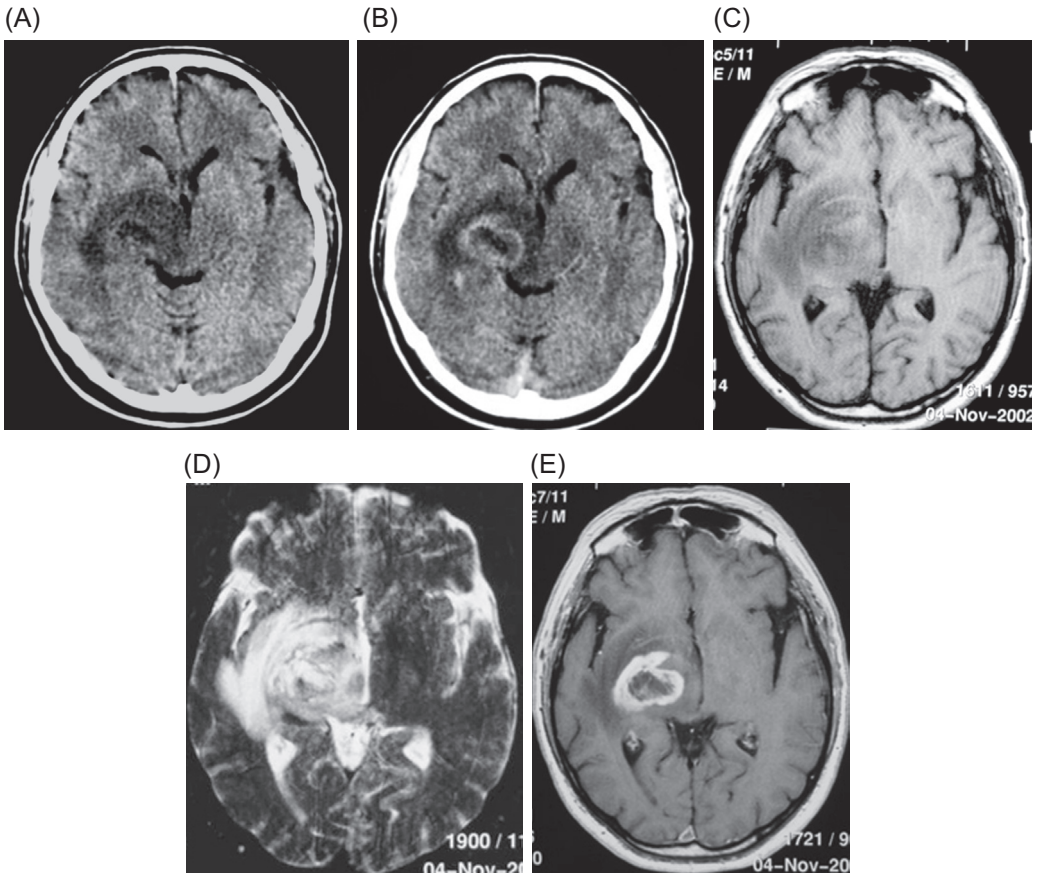


FIGURE 6 GBM. (A) Noncontrast CT scan shows a hypodense left thalamic mass, which shows ring-like enhancement after the contrast medium administration (B). On noncontrast T1WI (C) the mass appears inhomogeneously hypointense and on T2WI (D) inhomogeneously hyperintense surrounded by high signal intensity edema. (E) Axial postcontrast T1WI shows a rim-enhancing mass.

diffusely, producing intraventricular and craniospinal leptomeningeal CSF seeding.[5,27]

Little or no vasogenic edema is typical with all grades of thalamic astrocytoma. This may be due to a paucity of white matter pathways in this area.[28]

On postcontrast T1WI strong and inhomogeneous enhancement is seen (Figure 6).

Advanced imaging techniques such as diffusion, perfusion, and spectroscopy have improved the characterization of the physiology and metabolism of the tumors noninvasively, leading to improved diagnosis and better detection of recurrence, as well as improving image-guided biopsy and assessing tumor response in therapy (Figure 7).[29–32]

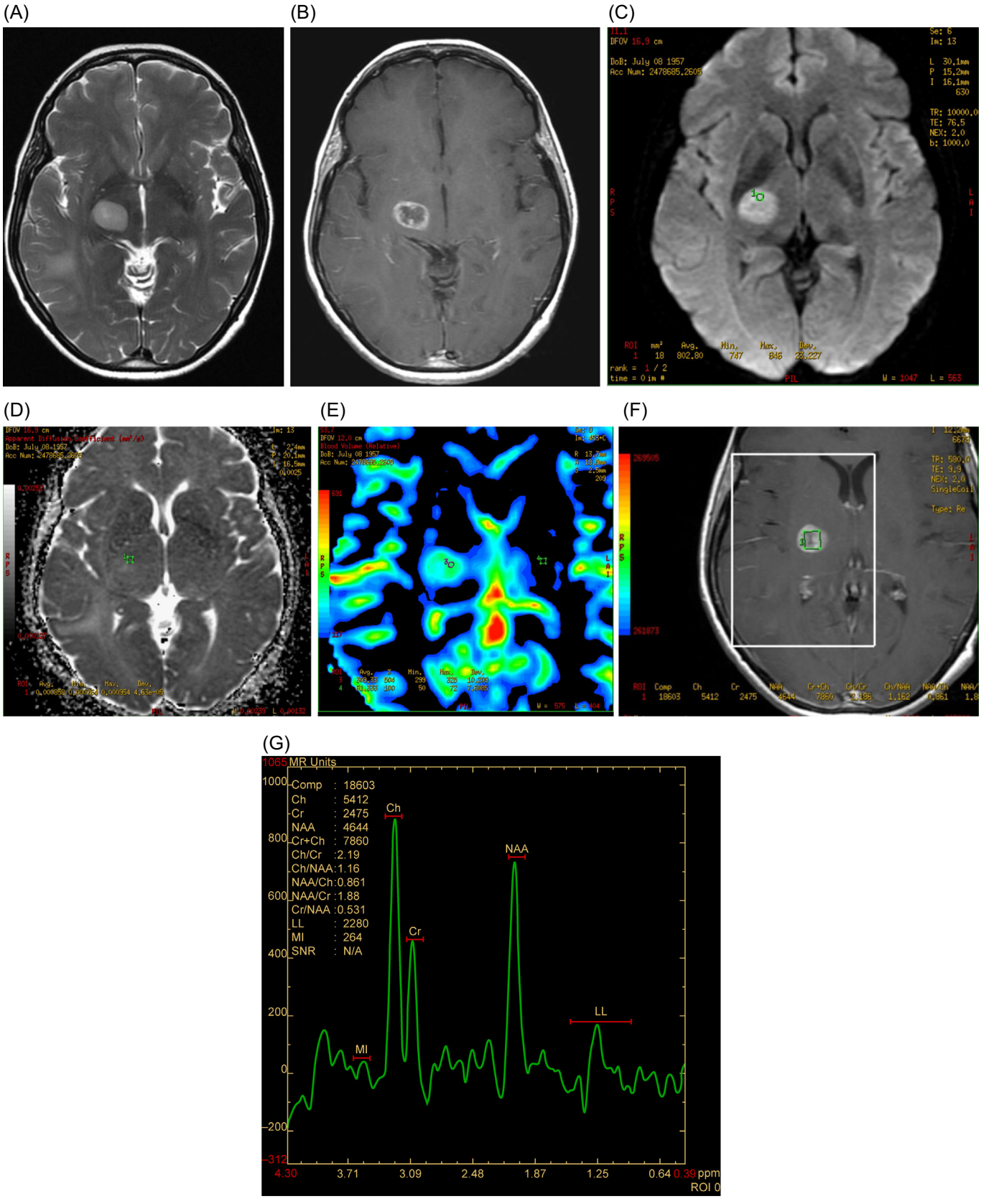


FIGURE 7 Right thalamic GBM. Axial T2WI (A) shows a right-thalamic high-signal mass. On postcontrast T1WI (B) shows thick ring-like enhancement. On DWI (C), the mass shows high signal with low apparent diffusion coefficient (D). Perfusion color map (E) shows marked increased relative capillary blood volume. MRS (F and G) shows increase in choline levels and lipid/lactate peak due to intratumoral necrosis.

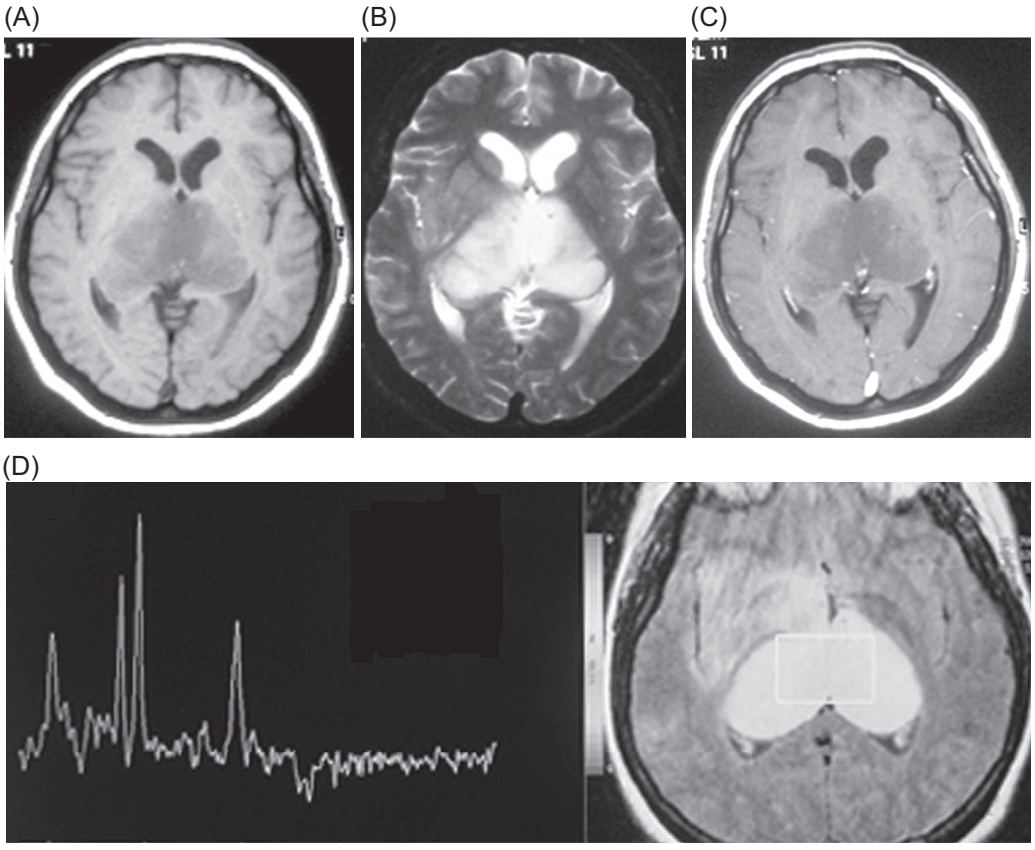


FIGURE 8 BTG. Axial T1WI (A) and T2WI (B) show enlargement of both thalami with low signal intensity on T1, high signal intensity on T2, and infiltration of the right basal ganglia and adjacent parietal cortex. (C) On postcontrast MRI the tumor remains unenhanced. (D) MRS demonstrates higher peak of creatine than choline and reduced NAA. Biopsy proved a fibrillary astrocytoma.

Bilateral Thalamic Glioma

Among the primary thalamic gliomas, a type known as bilateral thalamic glioma (BTG) has been identified, in which a large tumor appears symmetrically in both thalami and is accompanied by behavioral impairments varying from personality changes to dementia. BTG is rare among the thalamic tumors and has a very poor prognosis despite therapy.[6,33–35]

These tumors are generally low grade at presentation and produce remarkably symmetric areas of radiographic abnormality, in some cases with extension that is equally symmetric, into the adjacent basal ganglia and midbrain.[9,36,37] They are usually undetectable on CT, whereas on FLAIR and T2WI they appear as diffuse, homogeneous high-intensity areas (Figure 8(A–C)).[38–40]

The differential diagnosis of BTG includes brainstem encephalitis, acute necrotizing encephalopathy, mitochondrial encephalomyopathy, and deep cerebral venous thrombosis.[9] The acute onset of signs and symptoms favors infarction or inflammatory process over thalamic neoplasm.[41]

BTG may originate in the subependymal glia and hence have primary relation to the medial areas of the thalamus.[42] The tumor can spread across the midline via the interthalamic adhesion and the roof or floor of the third ventricle.[6,42]

Metabolic analysis of BTGs by MR spectroscopy (MRS) shows a higher peak of creatine (Cr) than choline, in contrast to the increased peak of choline (Cho) usually observed in low-grade gliomas. The MR *N*-acetylaspartate (NAA) signal is decreased in the BTGs, as is usually observed in low-grade gliomas (Figure 8(D)).[36]

Oligodendrogliomas and Mixed Gliomas

The pathological features of oligodendrogliomas (ODGs) and mixed gliomas (MGs) provide the basis for imaging findings: they are circumscribed, heterogeneous lesions that frequently contain calcification, cysts, and hemorrhage or blood degradation products; calcification is the most typical finding of ODG. Thus, a thalamic ODG or MG resembles a malignant astrocytoma, but appears more circumscribed and more frequently calcified, and without necrosis. The signal intensity is heterogeneous on both T1WI and T2WI, because calcification and proteinaceous cystic content can also induce hyperintensity counterparts in T1WI (Figure 9). The extent of edema and rapid increase in size support the hypothesis of the tumor being anaplastic.[5]

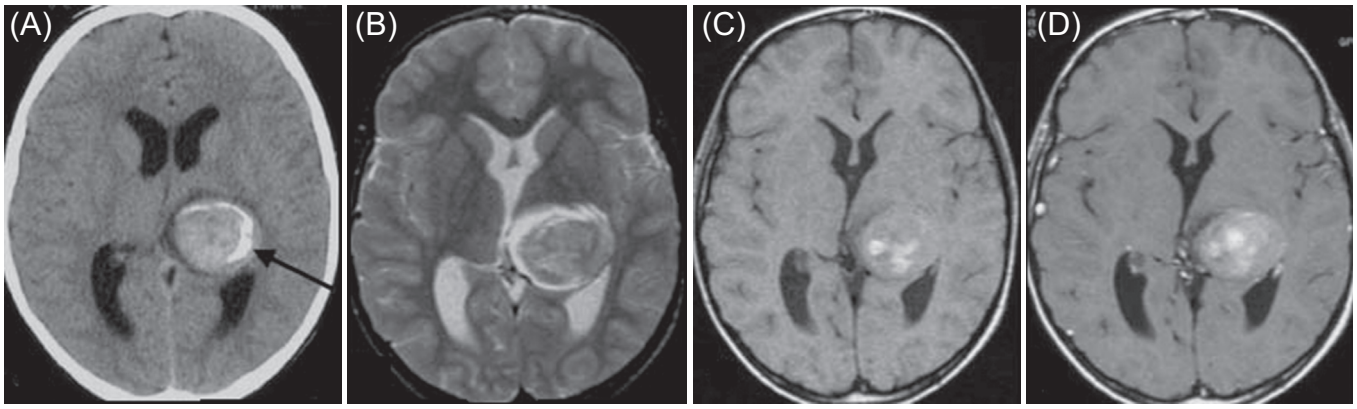


FIGURE 9 ODG of the left thalamus in a 7-year-old female. (A) Axial CT scan demonstrates a rounded, well-circumscribed, and slightly isodense mass with peripheral calcification (arrow) located in the left thalamus. The lesion appears inhomogeneously hypointense on T2WI (B), with little central hyperintense hemorrhagic foci on T1WI (C) and mild enhancement after contrast injection (D). *Reprinted from the Ref. 5, with kind permission of Springer Science and Business Media.*

Ganglion Cell Tumors

Gangliogliomas and gangliocytomas (GG–GC) are more common in children than in adults.[43] The thalamic location is exceedingly rare and a definite preoperative neuroradiological diagnosis is virtually impossible because their imaging features are similar to their astrocytic counterparts (pilocytic, fibrillary, anaplastic) and because in the deep location they lack the calvarial scalloping that supports correct recognition in the typically superficial temporal location.[5] They are usually well-circumscribed, benign, and nonprogressive tumors that are frequently cystic and calcify.[5,19] In the rarely encountered thalamic GG–GC, the cystic appearance predominates, with sharp margins and focal areas of contrast enhancement.[5,44] Calcification results in areas of T1 hyperintensity, and signal intensity is highly variable on T2WI (Figure 10).[5]

MRS analysis indicates that GG–GC has higher NAA/Cho and Cr/Cho ratios relative to other tumors.[45] These ratios can be related to both higher levels of NAA and a discrete drop in Cho reflecting the little aggressiveness of these tumors. As ganglion cell tumors are frequently cystic, they may show a peak of lactic acid, like many other cystic processes.[45,46] Because of their deep location and benign clinical behavior, long-term imaging follow-up is often carried out, and no progression has been confirmed.[5]

Germ-Cell Tumors

Germ-cell tumors (GCTs) usually grow up from the pineal gland or in the suprasellar area, but up to 15% occur in the thalamus and the basal ganglia, and are usually unilateral.[47] Most thalamic GCTs actually originate outside the thalami and infiltrate the thalami from the posterior or anterior walls of the third ventricle.[5] The most common presenting symptom is hemiparesis, caused by tumor invasion of the internal capsule, followed by cognitive deterioration.[48]

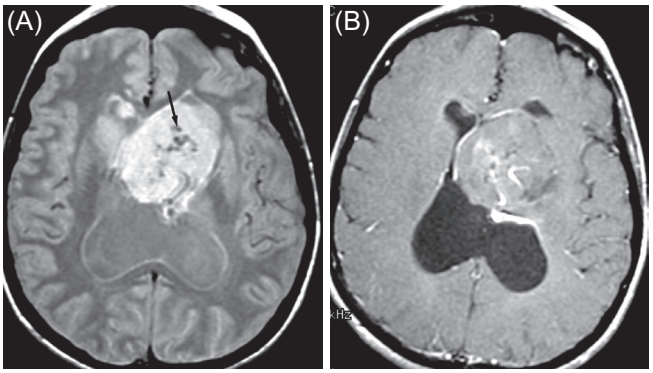


FIGURE 10 Gangliocytoma in the left basal ganglia. (A) Axial proton density image shows a mass with high signal intensity and central calcifications (arrow). (B) Post-gadolinium T1WI shows internal focal and linear enhancement.

Germinoma is the most common GCT, usually appears in the second or early third decade of life, and shows a striking male predominance.[21,43,47,49,50] A high prevalence of intracranial germinoma in the Far East is well documented, but the reason is unknown.[50,51] Histologically, germinomas range from benign processes to highly malignant neoplasms with a tendency to metastasize throughout the CSF spaces.[52]

The prognosis of germinoma is significantly better than with the other GCTs, with the 5-year survival rate approaching 80%.[52–54] Because of the good response to chemotherapy and radiotherapy, early detection and treatment are very important.[55] However, diagnosis of germinoma in the basal ganglia and thalamus is usually delayed because of minimal or nonspecific clinical findings in the relatively early stage.[56]

In the early stage of basal ganglionic germinomas, CT may not show any abnormality, despite neurological symptoms. An irregularly defined, slightly hyperdense area without mass effect is the early CT sign of

germinoma in the basal ganglia[57–60] (Figure 11). On the other hand, demonstration of an ill-defined hyperintense area on both T2WI and T1WI without contrast enhancement and especially atrophy of the ipsilateral basal ganglia are early diagnostic MRI features.[61–63]

In advanced stages, germinomas show a typical infiltrative pattern and CT density/MR signal intensity that make them difficult to differentiate from neuroepithelial tumors.[5] In fact, the rich cellularity of germinomas is represented by moderate hyperintensity on unenhanced CT and quite intense contrast enhancement (Figure 12(A)).[5,64] The infiltrating tumor appears heterogeneous on T1WI and T2WI, with cystic areas and hemorrhage, especially in large lesions, and shows heterogeneous intense enhancement and moderate perilesional edema (Figure 12(B–D)).[5,56] Intratumoral calcification is frequent and presents as nodular or spotty hyperdensity on CT and on T1WI. Unlike typical germinomas in pineal or suprasellar regions, thalamic and basal ganglionic germinomas show a higher tendency to cystic formation, hemorrhage, calcification, and progressive infiltration into the internal capsule, which may in turn cause cerebral hemiatrophy.[58] Cystic changes and hemorrhage seem to be attributed to the more rapid enlargement of the germinomas in the basal ganglia and thalamus compared to those in the pineal body and suprasellar region.[56]

Choriocarcinoma, yolk-sac tumor, embryonic cell carcinoma, and endodermal sinus tumors are highly malignant subtypes of GCT.[43] These high-grade tumors are heterogeneous on CT and MRI, and except for the occurrence of hemorrhage in choriocarcinoma, there is no imaging peculiarity that could help in distinguishing them from other tumors.[21,43,47] For this purpose, laboratory examinations of tumor markers are useful: choriocarcinoma releases human chorionic gonadotropin, yolk sac tumor α-fetoprotein, and embryonic cell carcinoma both human chorionic gonadotropin and α-fetoprotein.[57]

When GCT is suspected, contrast material is very useful in detecting CSF spread in the brain and spine, a relatively common and early finding.[20–22,43] The differential diagnosis should include glioma, primary central nervous system (CNS) lymphoma, and primitive neuroectodermal tumors.[5]

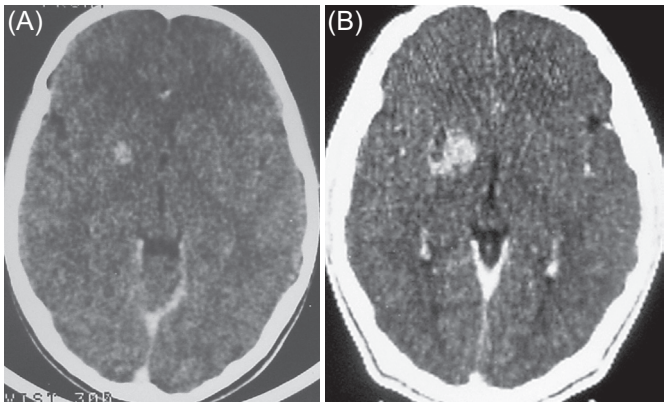


FIGURE 11 Basal ganglia germinoma. Postcontrast CT scan (A) shows a small strongly enhanced lesion. On postcontrast CT scan (B) 1 year later, the lesion shows increase in size and cystic degeneration. Histologic examination after stereotactic biopsy revealed a germinoma.

Primitive Neuroectodermal Tumors

Primitive neuroectodermal tumors (PNETs) account for 15–25% of pediatric brain tumors, typically appearing during the first 10 years of life, but only rarely arise in the thalamus.[20,26,43,65] The vast majority are medulloblastomas, developing characteristically in the posterior fossa. Those PNETs arising inside the supratentorial compartment are rare neoplasms, comprising 15% of all CNS PNETs.[43,66] Pineoblastoma, which is the most frequent neoplasm of this group of supratentorial PNETs, grows up from the pineal gland, and we will not consider it as a primary basal ganglia–thalamic tumor.[2,66] Generally, PNETs growing up from the supratentorial brain usually arise from the deep cerebral white matter.[19,43]

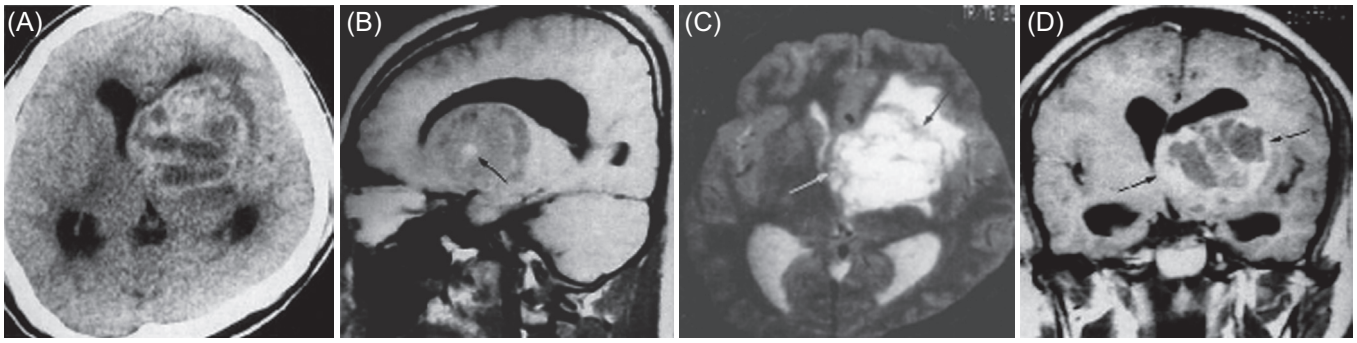


FIGURE 12 Basal ganglia germinoma in a 17-year-old male with history of vomiting and seizures for 2 months. (A) Noncontrast CT scan shows a multicystic mass with hyperdense solid areas located in the left basal ganglia. (B) Left parasagittal T1WI shows a slightly hypointense mass with central focal hemorrhage (arrow). (C) Axial T2WI shows a hyperintense multiseptated mass with moderate peritumoral edema (arrows). (D) Postcontrast T1WI shows intense enhancement of the solid portion of the mass (arrows). *Reprinted from the Ref. 56, with permission from the American Journal of Roentgenology.*

While PNETs are dense cellular well-circumscribed neoplasms, they are microscopically invasive, with extension of tumor cells beyond a reactive desmoplastic glial pseudocapsule.[2,52] Supratentorial PNETs are remarkable for their inhomogeneity.[2] CT and MRI show a well-defined heterogeneous expansive lesion, with cystic and necrotic areas and calcifications in most of the cases.[20–22,24,43] The solid portions of the tumor are often hyperdense on CT and relatively hypointense on T2WI, because of their high cellularity and nuclear-to-cytoplasmic ratio.[21] Despite their large size, PNETs typically induce only minimal surrounding edema, which may be the best clue to correct preoperative diagnosis.[19,20,67] Enhancement is usually diffuse and heterogeneous (Figure 13).[28] Contrast material administration is also useful in demonstrating the presence of leptomeningeal tumor implants, which are common in PNETs.[20,21,23,43]

MRS may be used to define the malignant behavior of PNETs. As in astrocytomas, the rise of the Cho peak is an indicator of their aggressiveness.[46] The NAA/Cho and Cr/Cho ratios are lower in PNETs than in astrocytomas and ependymomas, which is related to the more significant drop in Cho levels in PNETs.[2,31]

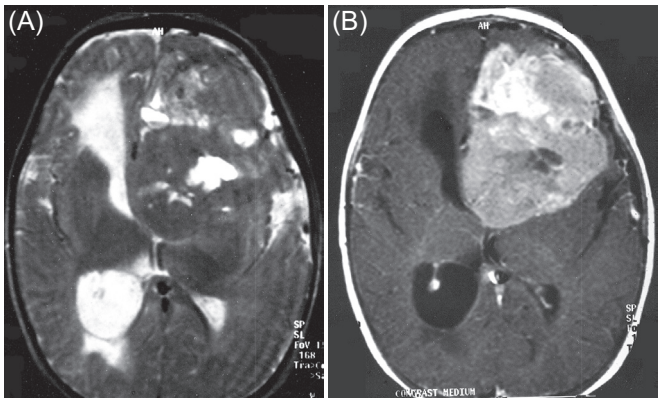


FIGURE 13 PNET in a 1-year-old male. (A) Axial T2WI demonstrates a slightly hypointense lesion with focal hyperintensities located in the left basal ganglia. (B) Post-gadolinium T1WI shows diffuse intense inhomogeneous enhancement of the mass extending to the adjacent frontal lobe.

Atypical Rhabdoid–Teratoid Tumors

Atypical rhabdoid–teratoid tumors (ARTTs) are very rare neoplasms that are included within the group of embryonal tumors, together with the PNETs. The microscopic distinctive feature of ARTTs is the presence of rhabdoid cells.[2,5] These highly malignant tumors affect almost exclusively infants and children younger than 3 years, and in this age group they develop characteristically in the posterior fossa.[2,5] In older patients, the incidence of supratentorial ARTT is strikingly higher.[68] They can rarely arise from the basal ganglia and thalamus, but those that appear in the cerebral hemispheres or the pineal gland can also invade through to the deep brain.[69] Imaging cannot distinguish ARTT from classic PNET.[2] Consequently, these malignant tumors appear at diagnosis as a large heterogeneous mass that contains necrosis, areas of high cellularity (hypointense on T2WI), and hemorrhage. They also demonstrate extensive surrounding edema and mass effect and intense heterogeneous enhancement (Figure 14). The prognosis is poor and CSF seeding is common.[5]

Lymphomas

Primary cerebral lymphomas (PCLs) are infrequent nonglial intracranial neoplasms that constitute 1–6% of malignant CNS tumors and are predominantly of B-cell origin.[2,70,71] Their incidence has increased since acquired immunodeficiency syndrome (AIDS) was first recognized.[72,73] PCLs can occur anywhere in the brain but the most common locations are the periventricular white matter and the corpus callosum.[74,75] Up to 17% of PCLs arise in the basal ganglia, thalamus, and hypothalamus.[76,77] It has also been reported that up to 75% of lymphomatous masses are seen to be in contact with

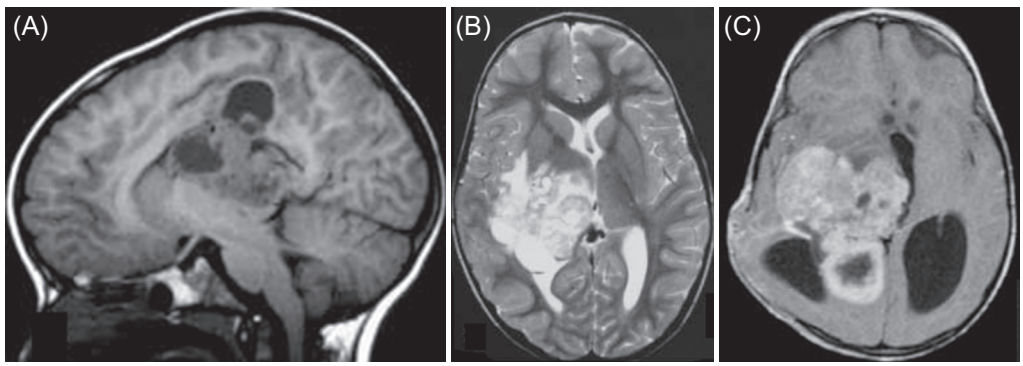


FIGURE 14 ARTT in a 2-year-old female. (A) Sagittal T1WI, (B) axial T2WI, and (C) axial T1WI after contrast injection demonstrate a huge inhomogeneous deep located mass, which has its epicenter in the right thalamus. The lesion shows multiple macro- and microcystic components, as well as necrosis. The signal of the solid component appears mildly hypointense on T1WI and mildly hyperintense on T2WI (suggesting high cellularity), with intense contrast enhancement. *Reprinted from the Ref. 5, with kind permission of Springer Science and Business Media.*

ependymal, meninges, or both.[21] PCL has a distinct tendency for perivascular extension, whereas leptomeningeal or ependymal involvement occurs in about 12% of the cases.[78]

A 5-year survival rate of more than 30% can be achieved, when combining chemotherapy and radiotherapy treatment.[79] Nevertheless, because of the rapid course of PCL, a delay in whole-brain irradiation and chemotherapy markedly decreases the effectiveness of the treatment and survival. Therefore, early diagnosis is critical.[80]

In most cases, PCLs in the basal ganglia and thalamus show distinctive neuroimaging features that allow differentiation from the more common glial tumors.[5] PCL classically appears as a predominantly hyperdense mass on CT, relatively hypointense on T2WI, and hyperintense on DWI, representing restricted diffusion, features that are attributed to dense cellularity, and high nuclear-to-cytoplasmic ratio of neoplastic cells[24,77,81] (Figure 15). Surrounding edema is mild and much less extensive than is seen with primary glial tumors or metastases.[82] Calcifications and hemorrhage are uncommon before treatment.[24,83] In both postcontrast CT and MRI, PCL usually shows strong homogeneous enhancement in immunocompetent patients and ring enhancement in AIDS patients, due to central necrosis (Figure 16).[21,25,73,77] The detection of enhancement along perivascular spaces on MRI is also characteristic of PCL, allowing differential diagnosis from other malignant processes.[21]

MRS of PCL shows almost complete loss of NAA, decrease in Cr, and massive increase in Cho, lactate, and lipids, whereas the myoinositol peak appears normal or slightly decreased.[31,76]

The differential diagnosis of PCL in immunocompetent patients includes glioma, metastasis, PNET, multiple sclerosis, and meningioma.[84,85] A hyperdense lesion on CT and a periventricular T2 hypointense mass with mild surrounding edema and ependymal seeding on MRI favor the diagnosis of PCL.[73] In immunocompromised patients, PCL should be differentiated from toxoplasmosis abscesses.[74,86]

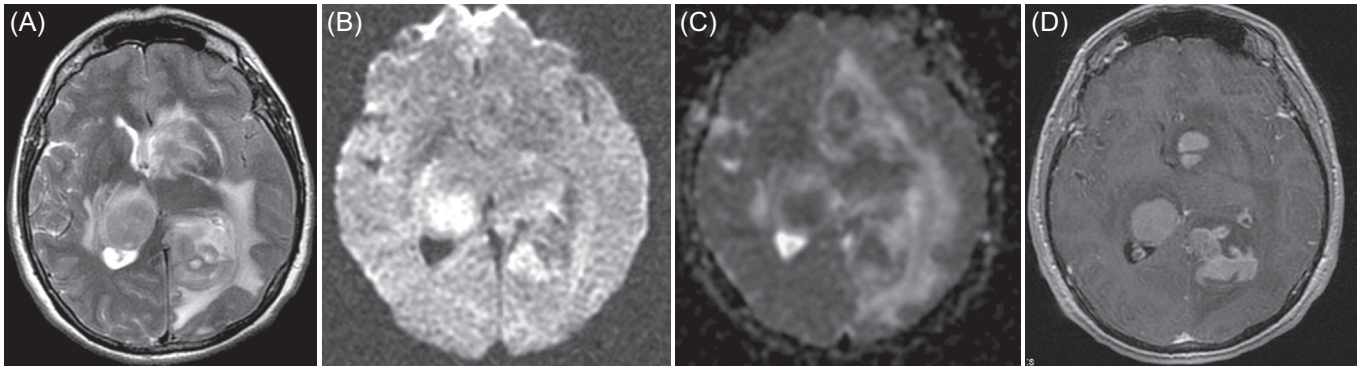


FIGURE 15 Pathologically proven multifocal B-cell lymphoma in a 60-year-old woman. On axial T2WI (A), multiple relatively hypointense lesions are seen involving the right thalamus, left basal ganglia, and occipital lobe. On DWI (B), the lesions show high signal intensity and low on apparent diffusion coefficient map (C). On postcontrast T1WI (D) strong and homogeneous enhancement is seen.

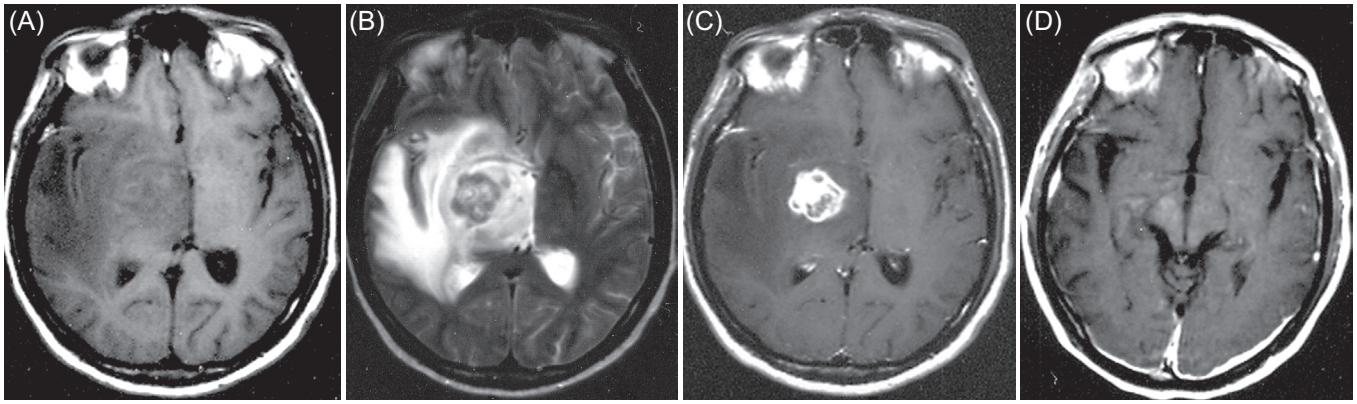


FIGURE 16 Thalamic lymphoma in a patient with AIDS. (A) Axial T1WI shows an extensive low signal area located in the right parietal and thalamic region. (B) On axial T2WI a low-signal right-thalamic lesion with high-signal central foci is seen surrounded by high-signal-intensity peritumoral edema. (C) Post-gadolinium axial T1WI shows intense and inhomogeneous enhancement with central necrosis. (D) A few months after therapy the tumor is almost completely resolved, but simultaneous meningeal enhancement is seen.

Metastases

Metastatic CNS tumors now account for up to 50% of all brain tumors and affect primarily the brain parenchyma.[87] It has been estimated that 80–85% of brain metastases are located supratentorially. The frontal and parietal lobes of the cerebral hemispheres are most commonly affected, with the corticomedullary junction being the earliest site of involvement.[88] Basal ganglia and thalamus are rare locations and are involved only in 3% of the cases.[87]

Metastases may result from hematogenous spread of distant tumors or from CSF seeding of CNS tumors.[2] In adults, hematogenous metastases mostly come from tumors of lung, breast, gastrointestinal tract, genitourinary tract, and skin (melanoma), whereas in children, they mostly come from sarcomas, Wilms tumor, and hepatoblastoma.[2,21] PNETs, astrocytomas, ependymomas, germinomas, pineoblastomas, and choroid plexus carcinomas in children and glioblastomas and lymphomas in adults often show CSF spread when the diagnosis is made.

Most intracerebral metastases are multiple, regardless of the site of origin. However, there is a high incidence of solitary metastasis, estimated to range from 30% to 50%, which is especially common in melanoma, lung, and breast carcinoma.[21] The imaging findings of hematogenous metastases are nonspecific. They are usually surrounded by prominent edema, which follows white matter boundaries and does not usually cross the corpus callosum. Contrast enhancement can be solid and nodular, as well as ring-like (Figure 17).

The differential diagnosis includes abscess, demyelinating disease, thromboembolic stroke, and multifocal malignant glioma.[87]

Hypothalamus–Optic Chiasm

In midsagittal sections, the human hypothalamus is bound anteriorly by the lamina terminalis, posteriorly by a plane drawn between the posterior commissure and the caudal limit of the mammillary body, and superiorly by the hypothalamic sulcus. Ventrally, the hypothalamus encompasses the floor of the third ventricle, the inferior surface of which presents to the subarachnoid space below and is termed the tuber cinereum (gray swelling). The lateral boundaries include the internal capsule, cerebral peduncle, and subthalamus on each side.[89]

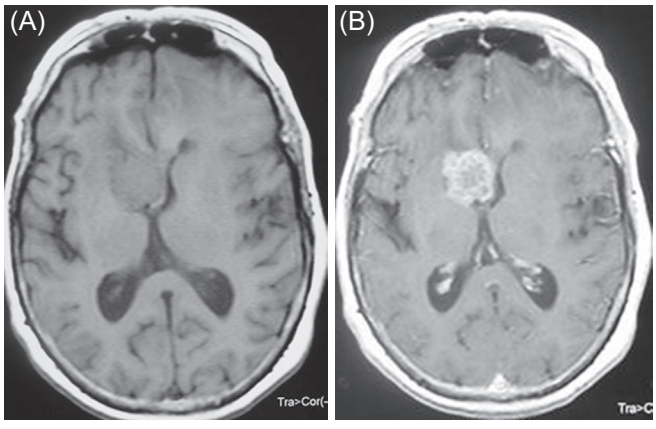


FIGURE 17 Basal ganglia metastasis. Pre- (A) and postcontrast (B) axial T1WI shows an isointense lesion involving the right caudate nucleus, which enhances markedly and heterogeneously.

Hypothalamic and Chiasmatic Gliomas

Gliomas of the hypothalamus and optic pathways represent 5% of pediatric intracranial tumors and 25–30% of pediatric suprasellar tumors with 60% involving the optic chiasm and hypothalamus.[90–92] These tumors occur mostly in children, especially in those under 10 years of age. There is an equal male-to-female distribution.[93] A definite association of hypothalamic/chiasmatic gliomas with neurofibromatosis type I is noted in 33% of patients.[90,91] The vast majority are slow-growing PAs, although malignant histology and in particular GBM may occur, especially in adults over 50 years of age.[94,95]

The distinction between hypothalamic and chiasmatic gliomas often depends on the predominant position of the tumor. Chiasmatic gliomas may occasionally demonstrate extension along the optic tracts or optic nerves, whereas hypothalamic tumors grow into the third ventricle, often leading to hydrocephalus.[52,96] In many cases, especially in larger gliomas, it is difficult to determine the exact site of origin as the hypothalamus and chiasm are inseparable. For this reason, they are discussed as a single entity based on their similar histology, clinical presentation, and management.[93]

Patients with hypothalamic/chiasmatic gliomas usually present with visual symptoms, headaches, and endocrine abnormalities, due to hypothalamic dysfunction.[91,96] A rare but characteristic presentation of these tumors is the diencephalic syndrome, which is characterized by profound emaciation with normal caloric intake, absence of cutaneous adipose tissue, locomotor hyperreactivity, euphoria, and alertness.[97] Typically, gliomas associated with this syndrome are larger, occur at a younger age, and are often more aggressive than other gliomas arising in this region.[98]

Hypothalamic and chiasmatic gliomas are predominantly solid tumors, with cystic changes occurring in larger hypothalamic tumors.[91] They are usually isointense or hypointense relative to gray matter on T1WI and moderately to markedly hyperintense on T2WI. After contrast administration, chiasmatic tumors usually show intense, heterogeneous enhancement, whereas pre- and postchiasmatic tumors show lesser degrees of enhancement (Figure 18).[52,91,98,99] Hyperintense signal may be seen extending into the optic radiations and lateral geniculate bodies on T2WI, due either to tumor infiltration or to tumor-related edema (Figure 19).[52]

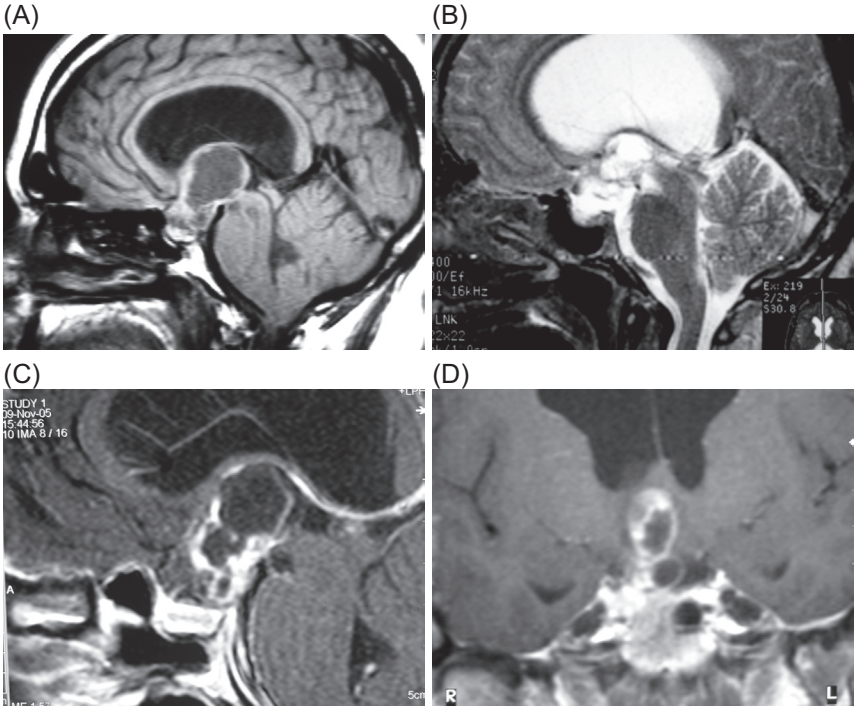


FIGURE 18 Chiasmatic/hypothalamic PA. (A) Sagittal T1WI shows a cystic tumor involving the hypothalamus and optic chiasm. (B) On T2WI the tumor appears heterogeneously hyperintense. Postcontrast sagittal (C) and coronal (D) images show intense heterogeneous enhancement. Note the enlargement of the lateral ventricles due to the invagination of the tumor within the third ventricle.

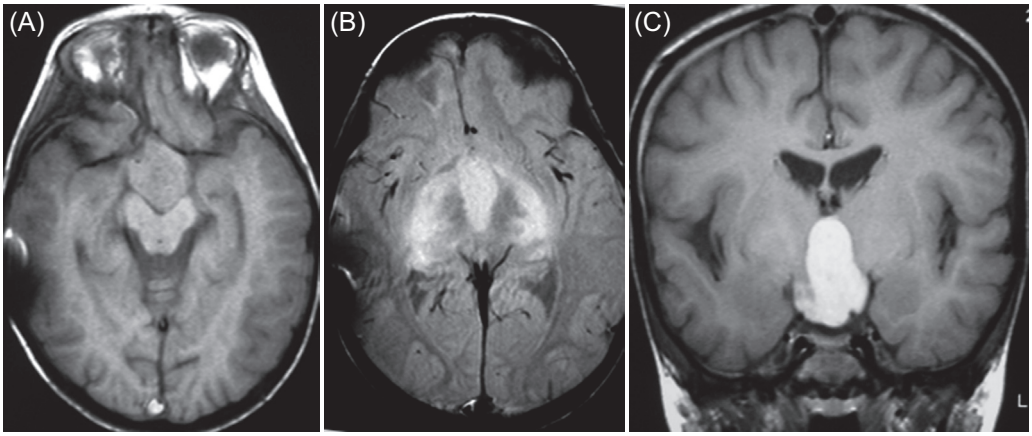


FIGURE 19 Chiasmatic/hypothalamic PA. (A) T1WI shows an isointense suprasellar mass. (B) On proton-density image the mass is hyperintense and the optic radiations and the lateral geniculate bodies also show high signal intensity. (C) Coronal postcontrast T1WI shows intense and homogeneous enhancement of the mass.

Only subtotal tumor resection is possible because of the involvement of visual pathways and the pituitary–hypothalamic axis.[100] While the rates of recurrence and progression of untreated lesions are similar regardless of location, mortality from those involving both the chiasm and the hypothalamus is much higher. However, 20–50% of untreated lesions will not progress.[95]

Hamartoma

Hypothalamic hamartomas are rare congenital non-neoplastic heterotopias with prevalence estimated as high as 1 in 50,000 to 100,000.[101] They typically present in young males but are not uncommon in females.[52] Although they do not invade surrounding tissues, they do have the potential for slow growth and may be quite large.[93] The hypothalamic hamartoma syndrome traditionally comprises the clinical triad of central precocious puberty, epilepsy (gelastic seizures), and developmental retardation.[102]

Hypothalamic hamartomas have been classified radiologically on the basis of the breadth of attachment to the tuber cinereum (sessile versus pedunculated) or the presence of more than minimal distortion of the outline of the third ventricle (intrahypothalamic versus parahypothalamic) or using a combination of size,

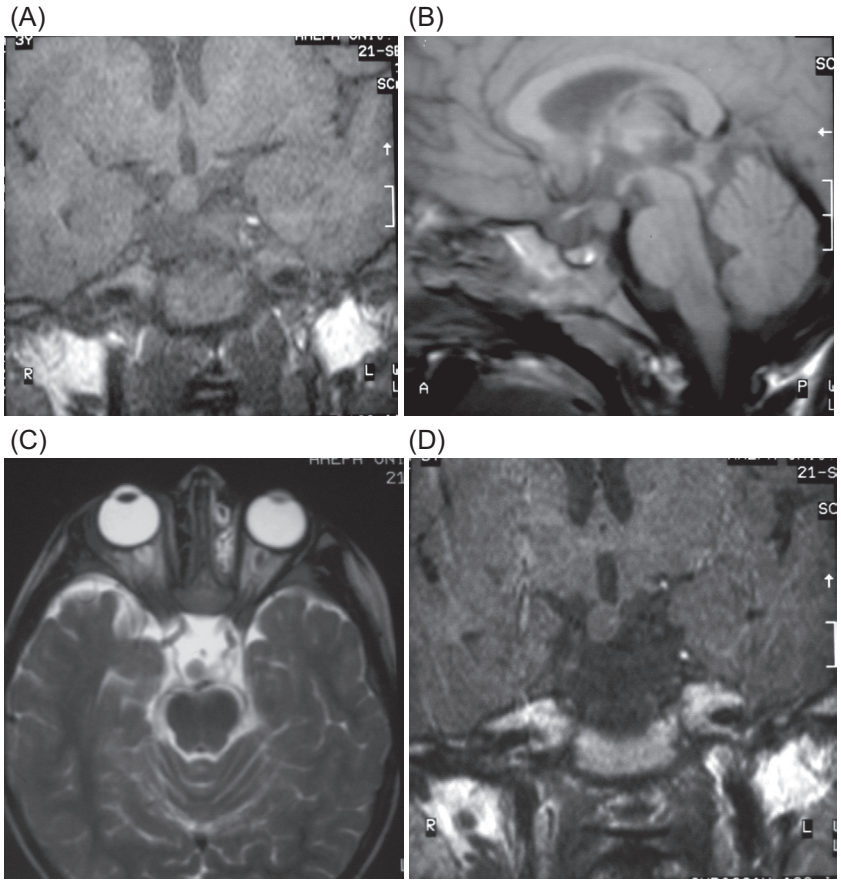


FIGURE 20 Tuber cinereum hamartoma. Coronal (A) and sagittal (B) T1WI shows an isointense mass located between the infundibulum and the mammillary bodies. On axial T2WI (C) the mass remains isointense and does not enhance after contrast injection on T1WI (D).

breadth of attachment, distortion of the hypothalamus, and location of attachment (types Ia, Ib, IIa, and IIb).[103–105] These classifications have attempted to correlate the clinical features observed with the physical properties of the hamartomas.[104,106] Hypothalamic hamartomas associated with epilepsy usually have sessile attachment to the hypothalamus and displace normal hypothalamic structures, whereas those associated with precocious puberty are usually pedunculated.[102–105,107–109]

Most patients with hypothalamic hamartoma have a sporadic form of the disease, without family history or risk of recurrence and without associated congenital anomalies. However, roughly 5% of the population with the intrahypothalamic subtype of hypothalamic hamartoma have Pallister–Hall syndrome, which can include anomalies such as postradial polydactyly, bifid epiglottis, and imperforate anus.[102,110]

On MRI, hypothalamic hamartomas are uniformly isointense to gray matter on T1WI and slightly hyperintense or isointense on T2WI with no enhancement after gadolinium administration, thereby demonstrating the integrity of the blood–brain barrier (Figure 20).[103,109,111–118] Cyst formation and calcifications have been rarely reported.[94,109,119] Arachnoid cysts occurring in association with hypothalamic hamartomas have been also rarely reported, suggesting either a common antecedent or a causal relationship.[109,120–122]

MRS has shown lower NAA and higher myoinositol concentration than normal thalamic gray matter or frontal lobe white and gray matter.[109,123] These findings suggest reduced neuronal density and relative gliosis compared with normal gray matter.[109]

Differential diagnosis includes craniopharyngioma, hypothalamic and chiasmatic glioma, GCT, and metastasis.

Chordoid Glioma

Chordoid glioma is a new clinicopathological entity that occurs in the region of the hypothalamus–anterior third ventricle.[124] This tumor was named chordoid glioma because of its distinctive histologic appearance, reminiscent of chordoma, and its avid staining with glial fibrillary acidic protein.[125] Although the incidence of chordoid glioma cannot yet be evaluated because of its recent description, it seems to be an uncommon tumor. The clinical presentation is related to the local mass effect of the tumor and includes headaches, obstructive hydrocephalus, homonymous hemianopsia, and hypothalamic dysfunction.[124] Distinctive imaging characteristics are its consistent location, ovoid shape with the greater

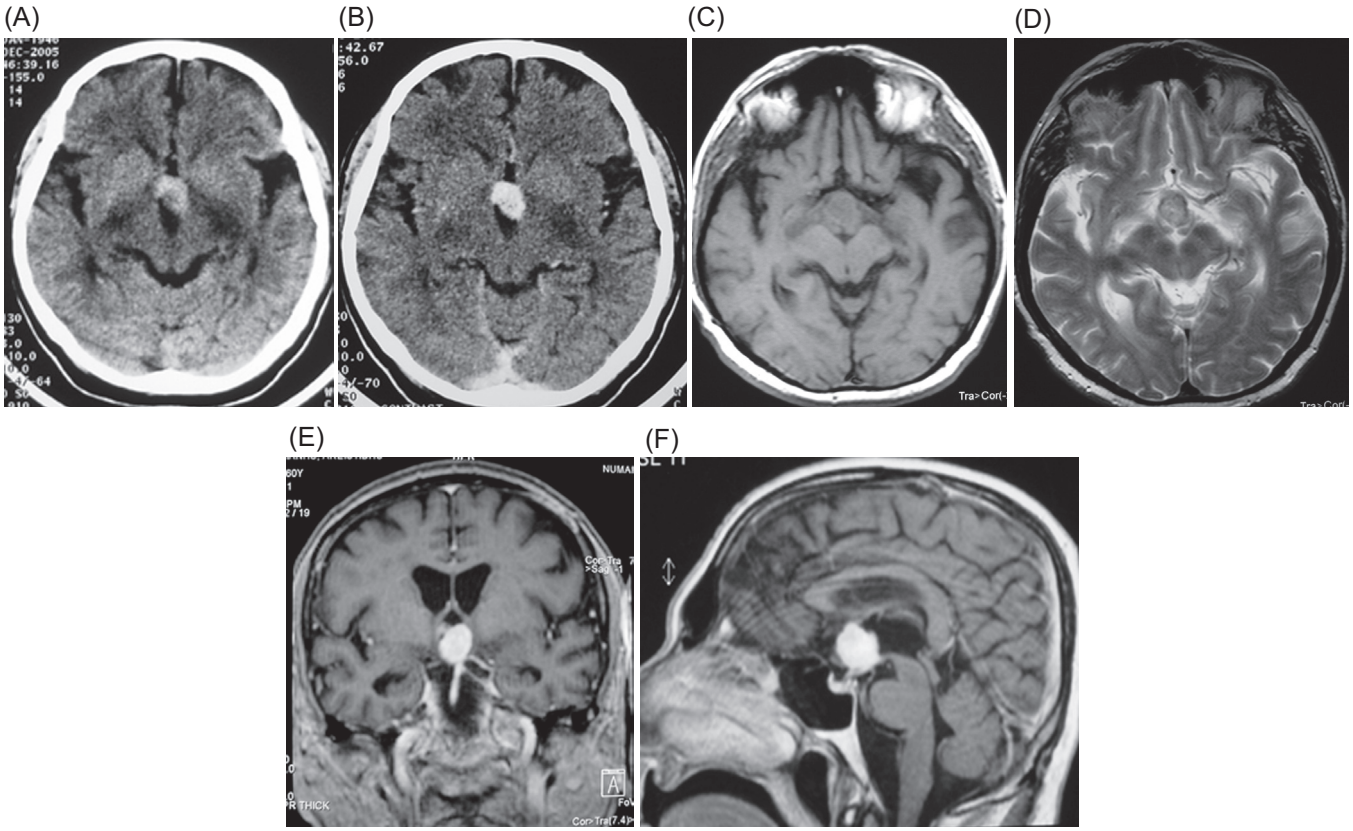


FIGURE 21 Chordoid glioma in the hypothalamic–third-ventricle region in a 59-year-old male. Noncontrast CT scan (A) demonstrates a hyperdense suprasellar lesion, which on postcontrast CT scan (B) shows intense and homogeneous enhancement. On axial T1WI (C) and T2WI (D) the lesion in the hypothalamic area is relatively isointense. Contrast-enhanced coronal (E) and sagittal (F) T1WI shows dense and homogeneous enhancement. Note the ovoid shape of the lesion with the greater dimension in the superoinferior orientation and the posterior displacement of the infundibulum.

dimension in the superoinferior orientation, hyperdensity on CT scans, relative isointensity on T2WI, and uniform intense contrast enhancement. Sagittal MR images clearly depict the infundibulum to be displaced posteriorly, whereas Rathke cleft cysts and tuber cinereum hamartomas generally displace the infundibulum anteriorly (Figure 21).[125,126] The differential diagnosis also includes lymphomas, meningiomas, and hypothalamic/chiasmatic gliomas. The current treatment of choice for chordoid glioma is surgical resection.[124]

Lymphoma

Primary CNS lymphomas are infrequent tumors that may arise from various parts of the brain, with deep hemispheric periventricular white matter being the most common. Lymphomatous involvement of the hypothalamic–third-ventricular area is extremely rare and appears usually in patients with AIDS.[80,127,128] The usual clinical manifestations are hypopituitarism and psychiatric and memory disturbances.[127,128] As a diffuse, intrinsic tumor that tends to infiltrate or replace the brain tissue rather than displace or compress it, a hypothalamic–third-ventricular lymphoma should more accurately be considered a hypothalamic lymphoma that has secondarily invaded the third-ventricle cavity.[129,130] Unfortunately, in many cases neither CT nor MRI can provide an exact delimitation between the tumor and the third ventricle margins and this may lead to topographical misdiagnosis.[131] On CT and MRI, hypothalamic lymphomas appear as homogeneous isointense masses, which show marked homogeneous enhancement after contrast administration (Figure 22).[128]

Miscellaneous Masses

Other entities that should be considered in the differential diagnosis of a hypothalamic lesion are neurosarcoidosis, lipoma, and osteolipoma.[132–135]

TUMORS THAT SECONDARILY INVADE THE DEEP BRAIN

Tumors that arise from the cerebral hemispheres, the cerebral ventricles, and the pineal gland can invade the diencephalon, but they are not actually deep brain tumors.

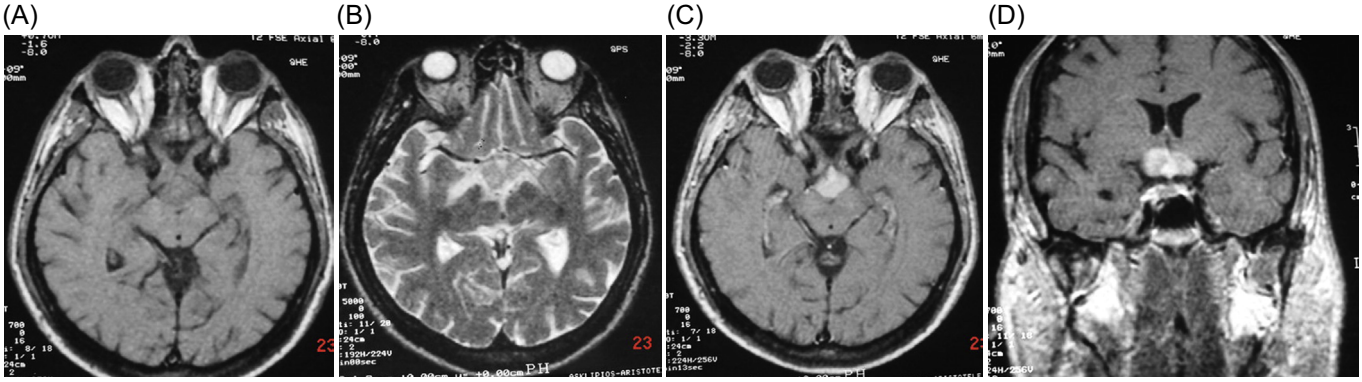


FIGURE 22 Hypothalamic non-Hodgkin lymphoma. (A) Axial T1WI shows a hypointense lesion in the suprasellar region. (B) On axial T2WI the lesion appears slightly hyperintense. Axial (C) and coronal (D) T1WI after contrast injection show intense and homogeneous enhancement of the lesion. Biopsy proved a hypothalamic non-Hodgkin B-cell lymphoma.

Peripheral Brain Tumors

The same tumors that arise from the deep brain can be diagnosed peripherally in the cerebral hemispheres. Low- and high-grade astrocytomas, PNETs, and supratentorial ependymomas can invade the deep brain after developing from the white matter of the cerebral hemispheres.

Ventricular Tumors

Choroid plexus tumors, subependymal giant cell tumors, ependymomas, subependymomas, and central neurocytomas are ventricular tumors that can occasionally spread to the deep brain.

Pineal Gland Tumors

Pineal gland tumors include GCTs, pineocytomas, and pineoblastomas, which are discussed in detail in a different chapter.

References

1. Martin JH. Development of CNS. In: Martin JH, ed. *Neuroanatomy: Text and Atlas*. Elsevier; 1989:32–53.
2. Garcia-Santos JM, Torres del Rio S, Sanchez A, Martinez-Lage JF. Basal ganglia and thalamic tumours: an imaging approximation. *Childs Nerv Syst*. 2002;18:412–425.
3. Wald SL, Fogelson H, McLaurin RL. Cystic thalamic gliomas. *Childs Brain*. 1982;9:381–393.
4. Cheek WR, Taveras JM. Thalamic tumors. *J Neurosurg*. 1966;24:505–513.
5. Colosimo C, di Lella GM, Tartaglione T, Riccardi R. Neuroimaging of thalamic tumors in children. *Childs Nerv Syst*. 2002;18:426–439.
6. McKissock W, Paine KW. Primary tumours of the thalamus. *Brain*. 1958;81:41–63.
7. Tovi D, Schisano G, Liljeqvist B. Primary tumors of the region of the thalamus. *J Neurosurg*. 1961;18:730–740.
8. Allen JC. Initial management of children with hypothalamic and thalamic tumors and the modifying role of neurofibromatosis-1. *Pediatr Neurosurg*. 2000;32:154–162.
9. Yoshida M, Fushiki S, Takeuchi Y, Takanashi M, Imamura T, Shikata T, et al. Diffuse bilateral thalamic astrocytomas as examined serially by MRI. *Childs Nerv Syst*. 1998;14:384–388.
10. Arseni C. Tumors of the basal ganglia; their surgical treatment. *AMA Arch Neurol Psychiatry*. 1958;80:18–24.
11. Bernstein M, Hoffman HJ, Halliday WC, Hendrick EB, Humphreys RP. Thalamic tumors in children. Long-term follow-up and treatment guidelines. *J Neurosurg*. 1984;61:649–656.
12. Drake JM, Joy M, Goldenberg A, Kreindler D. Computer- and robot-assisted resection of thalamic astrocytomas in children. *Neurosurgery*. 1991;29:27–33.
13. Lyons MK, Kelly PJ. Computer-assisted stereotactic biopsy and volumetric resection of thalamic pilocytic astrocytomas. Report of 23 cases. *Stereotact Funct Neurosurg*. 1992;59:100–104.
14. Matsumoto K, Higashi H, Tomita S, Furuta T, Ohmoto T. Resection of deep-seated gliomas using neuroimaging for stereotactic placement of guidance catheters. *Neurol Med Chir (Tokyo)*. 1995;35:148–155.
15. Steiger HJ, Gotz C, Schmid-Elsaesser R, Stummer W. Thalamic astrocytomas: surgical anatomy and results of a pilot series using maximum microsurgical removal. *Acta Neurochir (Wien)*. 2000;142:1327–1336. Discussion 1336–1337.
16. Packer RJ, Ater J, Allen J, Phillips P, Geyer R, Nicholson HS, et al. Carboplatin and vincristine chemotherapy for children with newly diagnosed progressive low-grade gliomas. *J Neurosurg*. 1997;86:747–754.
17. Burger PC, Cohen KJ, Rosenblum MK, Tihan T. Pathology of diencephalic astrocytomas. *Pediatr Neurosurg*. 2000;32:214–219.
18. Becker LE. Pathology of pediatric brain tumors. *Neuroimaging Clin N Am*. 1999;9:671–690.
19. Naidich TP, Zimmerman RA. Primary brain tumors in children. *Semin Roentgenol*. 1984;19:100–114.
20. Luh GY, Bird CR. Imaging of brain tumors in the pediatric population. *Neuroimaging Clin N Am*. 1999;9:691–716.
21. Atlas SW, Lavi E. Intra-axial brain tumors. In: Atlas SW, ed. *Magnetic Resonance Imaging of the Brain and Spine*. 2nd ed. Philadelphia, Pennsylvania: Lippincott Williams & Wilkins; 1996:315–422.
22. Edwards-Brown MK. Supratentorial brain tumors. *Neuroimaging Clin N Am*. 1994;4:437–455.
23. Castillo M. Contrast enhancement in primary tumors of the brain and spinal cord. *Neuroimaging Clin N Am*. 1994;4:63–80.
24. Koeller KK. *Central nervous system neoplasms: intraaxial* RSNA Categorical Course in Diagnostic Radiology: Neuroradiology; 2000: 105–121.
25. Gore JC, Kennan RP. Contrast agents and relaxation effects. In: Atlas SW, ed. *Magnetic Resonance Imaging of the Brain and Spine*. 2nd ed. Philadelphia, Pennsylvania: Lippincott Williams & Wilkins; 1996:89–107.

26. Bleyer WA. Epidemiologic impact of children with brain tumors. *Childs Nerv Syst*. 1999;15:758–763.
27. Kumar R, Jain R, Tandon V. Thalamic glioblastoma with cerebrospinal fluid dissemination in the peritoneal cavity. *Pediatr Neurosurg*. 1999;31:242–245.
28. Lefton DR, Pinto RS, Silvera VM, DeLara FA, Schwartz JB, Haller JO. Radiologic features of pediatric thalamic and hypothalamic tumors. *Crit Rev Diagn Imaging*. 2000;41:237–278.
29. Price SJ. The role of advanced MR imaging in understanding brain tumour pathology. *Br J Neurosurg*. December 2007;21(6):562–575.
30. Kao HW, Chiang SW, Chung HW, Tsai FY, Chen CY. Advanced MR imaging of gliomas: an update. *Biomed Res Int*. 2013;2013:970586.
31. Gupta A, Young RJ, Karimi S, Sood S, Zhang Z, Mo Q, et al. Isolated diffusion restriction precedes the development of enhancing tumor in a subset of patients with glioblastoma. *AJNR Am J Neuroradiol*. August 2011;32(7):1301–1306.
32. Hu LS, Eschbacher JM, Dueck AC, Heiserman JE, Liu S, Karis JP, et al. Correlations between perfusion MR imaging cerebral blood volume, microvessel quantification, and clinical outcome using stereotactic analysis in recurrent high-grade glioma. *AJNR Am J Neuroradiol*. January 2012;33(1):69–76.
33. Hirano H, Yokoyama S, Nakayama M, Nagata S, Kuratsu J. Bilateral thalamic glioma: case report. *Neuroradiology*. 2000;42:732–734.
34. Partlow GD, del Carpio-O'Donovan R, Melanson D, Peters TM. Bilateral thalamic glioma: review of eight cases with personality change and mental deterioration. *AJNR Am J Neuroradiol*. 1992;13:1225–1230.
35. Uchino M, Kitajima S, Miyazaki C, Shibata I, Miura M. Bilateral thalamic glioma – case report. *Neurol Med Chir (Tokyo)*. 2002;42: 443–446.
36. Esteve F, Grand S, Rubin C, Hoffmann D, Pasquier B, Graveron-Demilly D, et al. MR spectroscopy of bilateral thalamic gliomas. *AJNR Am J Neuroradiol*. 1999;20:876–881.
37. Reardon DA, Gajjar A, Sanford RA, Heideman RL, Walter AW, Thompson SJ, et al. Bithalamic involvement predicts poor outcome among children with thalamic glial tumors. *Pediatr Neurosurg*. 1998;29:29–35.
38. Carter DJ, Wiedmeyer DA, Antuono PG, Ho KC. Correlation of computed tomography and postmortem findings of a diffuse astrocytoma: a case report. *Comput Med Imaging Graph*. 1989;13:491–494.
39. Rogers LR, Weinstein MA, Estes ML, Cairncross JG, Strachan T. Diffuse bilateral cerebral astrocytomas with atypical neuroimaging studies. *J Neurosurg*. 1994;81:817–821.
40. Yanaka K, Kamezaki T, Kobayashi E, Matsueda K, Yoshii Y, Nose T. MR imaging of diffuse glioma. *AJNR Am J Neuroradiol*. 1992;13:349–351.
41. Levy RA, Quint DJ. Bilateral thalamic venous infarctions mimicking tumor. *AJR Am J Roentgenol*. 1994;163:226–227.
42. Smyth GE, Stern K. Tumors of the thalamus, a clinicopathological study. *Brain*. 1938;61:339–374.
43. Barkovich AJ. Brain tumors in childhood. In: Barkovich AJ, ed. *Paediatric Neuroimaging*. New York: Raven; 1990:149–204.
44. Fujimura M, Kayama T, Kumabe T, Yoshimoto T. Ganglioglioma in the basal ganglia totally resected by a trans-distal Sylvian approach. *Tohoku J Exp Med*. 1995;175:211–218.
45. Wang Z, Sutton LN, Cnaan A, Haselgrove JC, Rorke LB, Zhao H, et al. Proton MR spectroscopy of pediatric cerebellar tumors. *AJNR Am J Neuroradiol*. 1995;16:1821–1833.
46. Taylor JS, Ogg RJ, Langston JW. Proton MR spectroscopy of pediatric brain tumors. *Neuroimaging Clin N Am*. 1998;8:753–779.
47. Sumida M, Uozumi T, Kiya K, Mukada K, Arita K, Kurisu K, et al. MRI of intracranial germ cell tumours. *Neuroradiology*. 1995;37:32–37.
48. Tamaki N, Lin T, Shirataki K, Hosoda K, Kurata H, Matsumoto S, et al. Germ cell tumors of the thalamus and the basal ganglia. *Childs Nerv Syst*. 1990;6:3–7.
49. Huh SJ, Kim IH, Ha SW, Park CI. Radiotherapy of germinomas involving the basal ganglia and thalamus. *Radiother Oncol*. 1992;25:213–215.
50. Kobayashi T, Kageyama N, Kida Y, Yoshida J, Shibuya N, Okamura K. Unilateral germinomas involving the basal ganglia and thalamus. *J Neurosurg*. 1981;55:55–62.
51. Shih CJ. Intracranial tumors in Taiwan. A cooperative survey of 1200 cases with special reference to intracranial tumors in children. *Taiwan Yi Xue Hui Za Zhi*. 1977;76:515–527.
52. Jones BV, Patterson RJ. Supratentorial tumors. In: Ball Jr WS, ed. *Pediatric Neuroradiology*. Philadelphia: Lippincott-Raven; 1997:369–442.
53. Allen JC. Controversies in the management of intracranial germ cell tumors. *Neurol Clin*. 1991;9:441–452.
54. Jennings MT, Gelman R, Hochberg F. Intracranial germ-cell tumors: natural history and pathogenesis. *J Neurosurg*. 1985;63:155–167.
55. Kim DI, Yoon PH, Ryu YH, Jeon P, Hwang GJ. MRI of germinomas arising from the basal ganglia and thalamus. *Neuroradiology*. 1998;40:507–511.
56. Moon WK, Chang KH, Kim IO, Han MH, Choi CG, Suh DC, et al. Germinomas of the basal ganglia and thalamus: MR findings and a comparison between MR and CT. *AJR Am J Roentgenol*. 1994;162:1413–1417.
57. Komatsu Y, Narushima K, Kobayashi E, Ebihara R, Enomoto T, Nose T, et al. CT and MR of germinoma in the basal ganglia. *AJNR Am J Neuroradiol*. 1989;10:S9–S11.
58. Higano S, Takahashi S, Ishii K, Matsumoto K, Ikeda H, Sakamoto K. Germinoma originating in the basal ganglia and thalamus: MR and CT evaluation. *AJNR Am J Neuroradiol*. 1994;15:1435–1441.
59. Mutoh K, Okuno T, Ito M, Fujii T, Mikawa H, Moritake K, et al. Ipsilateral atrophy in children with hemispheric cerebral tumors: CT findings. *J Comput Assist Tomogr*. 1988;12:740–743.
60. Soejima T, Takeshita I, Yamamoto H, Tsukamoto Y, Fukui M, Matsuoka S. Computed tomography of germinomas in basal ganglia and thalamus. *Neuroradiology*. 1987;29:366–370.
61 Okamoto K, Ito J, Ishikawa K, Morii K, Yamada M, Takahashi N, et al. Atrophy of the basal ganglia as the initial diagnostic sign of germinoma in the basal ganglia. *Neuroradiology*. 2002;44: 389–394.
62. Takano T, Matsui E, Yamano T, Shimada M, Nakasu Y, Handa J. Sequential MRI findings in a patient with a germ cell tumor in the basal ganglia. *Brain Dev*. 1993;15:283–287.
63. Takeda N, Fujita K, Katayama S, Uchihashi Y, Okamura Y, Nigami H, et al. Germinoma of the basal ganglia. An 8-year asymptomatic history after detection of abnormality on CT. *Pediatr Neurosurg*. 2004;40:306–311.
64. Wong LW, Jayakumar CR. Germinoma of the basal ganglia and thalamus–CT and MRI findings. *Singapore Med J*. 1997;38: 444–446.
65. Rorke LB, Trojanowski JQ, Lee VM, Zimmerman RA, Sutton LN, Biegel JA, et al. Primitive neuroectodermal tumors of the central nervous system. *Brain Pathol*. 1997;7:765–784.
66 Becker LE, Halliday WC. Central nervous system tumors of childhood. *Perspect Pediatr Pathol*. 1987;10:86–134.
67. Figeroa RE, el Gammal T, Brooks BS, Holgate R, Miller W. MR findings on primitive neuroectodermal tumors. *J Comput Assist Tomogr*. 1989;13:773–778.
68. Rorke LB, Packer RJ, Biegel JA. Central nervous system atypical teratoid/rhabdoid tumors of infancy and childhood: definition of an entity. *J Neurosurg*. 1996;85:56–65.
69. Martinez-Lage JF, Nieto A, Sola J, Domingo R, Costa TR, Poza M. Primary malignant rhabdoid tumor of the cerebellum. *Childs Nerv Syst*. 1997;13:418–421.
70. Jellinger KA, Paulus W. Primary central nervous system lymphomas–an update. *J Cancer Res Clin Oncol*. 1992;119:7–27.

71. Ling SM, Roach 3rd M, Larson DA, Wara WM. Radiotherapy of primary central nervous system lymphoma in patients with and without human immunodeficiency virus. Ten years of treatment experience at the University of California San Francisco. *Cancer*. 1994;73:2570–2582.
72. Belman AL. Pediatric neuro-AIDS. *Update Neuroimaging Clin N Am*. 1997;7:593–613.
73. Ruiz A, Post MJ, Bundschu C, Ganz WI, Georgiou M. Primary central nervous system lymphoma in patients with AIDS. *Neuroimaging Clin N Am*. 1997;7:281–296.
74. Drevelegas A. Lymphomas and hematopoietic neoplasms. In: Drevelegas A, ed. *Imaging of Brain Tumors with Histological Correlation*. Berlin Heidelberg: Springer-Verlag; 2002:215–225.
75. Lee YY, Bruner JM, Van Tassel P, Libshitz HI. Primary central nervous system lymphoma: CT and pathologic correlation. *AJR Am J Roentgenol*. 1986;147:747–752.
76. Kuker W, Nagele T, Korfel A, Heckl S, Thiel E, Bamberg M, et al. Primary central nervous system lymphomas (PCNSL): MRI features at presentation in 100 patients. *J Neurooncol*. 2005;72:169–177.
77. Zimmerman RA. Central nervous system lymphoma. *Radiol Clin North Am*. 1990;28:697–721.
78. Rosenthal MA, Green MD. Cerebral lymphoma. In: Kaye AH, Laws Jr ER, eds. *Brain Tumors*. Edinburgh: Churchill-Livingstone; 1995:861–869.
79. Gliemroth J, Kehler U, Gaebel C, Arnold H, Missler U. Neuroradiological findings in primary cerebral lymphomas of non-AIDS patients. *Clin Neurol Neurosurg*. 2003;105:78–86.
80. Erdag N, Bhorade RM, Alberico RA, Yousuf N, Patel MR. Primary lymphoma of the central nervous system: typical and atypical CT and MR imaging appearances. *AJR Am J Roentgenol*. 2001;176:1319–1326.
81. Buhring U, Herrlinger U, Krings T, Thiex R, Weller M, Kuker W. MRI features of primary central nervous system lymphomas at presentation. *Neurology*. 2001;57:393–396.
82. Vandermarcq P, Drapeau C, Ferrie JC. Imaging aspects of primary cerebral lymphoma. *Neurochirurgie*. 1997;43:363–368.
83. Ricci PE. Imaging of adult brain tumors. *Neuroimaging Clin N Am*. 1999;9:651–669.
84. Kelly WM, Brant-Zawadzki M. Acquired immunodeficiency syndrome: neuroradiologic findings. *Radiology*. 1983;149:485–491.
85. Tubman DE, Frick MP, Hanto DW. Lymphoma after organ transplantation: radiologic manifestations in the central nervous system, thorax, and abdomen. *Radiology*. 1983;149:625–631.
86. Cordoliani YS, Derosier C, Pharaboz C, Jeanbourquin D, Schill H, Cosnard G. Primary brain lymphoma in AIDS. 17 cases studied by MRI before stereotaxic biopsies. *J Radiol*. 1992;73:367–376.
87. Osborn AG. Neoplasms and tumorlike lesions. In: Osborn AG, et al., ed. *Diagnostic Imaging: Brain*. Salt Lake City, Utah: Amirsys; 2004:140–143.
88. Patronas NJ. Brain metastasis. In: Drevelegas A, ed. *Imaging of Brain Tumors with Histological Correlation*. Berlin Heidelberg: Springer-Verlag; 2002:253–276.
89. Nauta WH, Haymaker W. Hypothalamic nuclei and fiber connections. In: Haymaker W, Anderson E, Nauta WJH, eds. *The Hypothalamus*. Springfield: Thomas; 1969:136–209.
90. Janss AJ, Grundy R, Cnaan A, Savino PJ, Packer RJ, Zackai EH, et al. Optic pathway and hypothalamic/chiasmatic gliomas in children younger than age 5 years with a 6-year follow-up. *Cancer*. 1995;75:1051–1059.
91. Collet-Solberg PF, Sernyak H, Satin-Smith M, Katz LL, Sutton L, Molloy P, et al. Endocrine outcome in long-term survivors of low-grade hypothalamic/chiasmatic glioma. *Clin Endocrinol*. 1997;47:79–85.
92. Rodriguez LA, Edwards MS, Levin VA. Management of hypothalamic gliomas in children: an analysis of 33 cases. *Neurosurgery*. 1990;26:242–246.
93. Kucharczyk W, Montanera WJ, Becker LE. The sella turcica and parasellar region. In: Atlas SW, ed. *Magnetic Resonance Imaging of the Brain and Spine*. 2nd ed. Philadelphia, Pennsylvania: Lippincott Williams & Wilkins; 1996:871–930.
94. Rauschning W. Brain tumors and tumorlike masses: classification and differential diagnosis. In: Osborn AG, ed. *Diagnostic Neuroradiology*. St Louis: Mosby; 1994:401–528.
95. Alvord Jr EC, Lofton S. Gliomas of the optic nerve or chiasm. Outcome by patients' age, tumor site, and treatment. *J Neurosurg*. 1988;68:85–98.
96. Bourekas EC, Miller JW, Christoforidis GA. Masses of the sellar and juxtasellar region. In: Drevelegas A, ed. *Imaging of Brain Tumors with Histological Correlation*. Berlin Heidelberg: Springer-Verlag; 2002:227–252.
97. Russell A. A diencephalic syndrome of emaciation in infancy and childhood. *Arch Dis Child*. 1951;26:274.
98. Poussaint TY, Barnes PD, Nichols K, Anthony DC, Cohen L, Tarbell NJ, et al. Diencephalic syndrome: clinical features and imaging findings. *AJNR Am J Neuroradiol*. 1997;18:1499–1505.
99. Osborn AG. Sella and pituitary. In: Osborn AG, et al., ed. *Diagnostic Imaging: Brain*. Salt Lake City, Utah: Amirsys; 2004:12–15.
100. Namba S, Nishimoto A, Yagyu Y. Diencephalic syndrome of emaciation (Russell's syndrome). Long-term survival. *Surg Neurol*. 1985;23:581–588.
101. Weissenberger AA, Dell ML, Liow K, Theodore W, Frattali CM, Hernandez D, et al. Aggression and psychiatric comorbidity in children with hypothalamic hamartomas and their unaffected siblings. *J Am Acad Child Adolesc Psychiatry*. 2001;40:696–703.
102. Kerrigan JF, Ng YT, Chung S, Rekate HL. The hypothalamic hamartoma: a model of subcortical epileptogenesis and encephalopathy. *Semin Pediatr Neurol*. 2005;12:119–131.
103. Boyko OB, Curnes JT, Oakes WJ, Burger PC. Hamartomas of the tuber cinereum: CT, MR, and pathologic findings. *AJNR Am J Neuroradiol*. 1991;12:309–314.
104. Arita K, Ikawa F, Kurisu K, Sumida M, Harada K, Uozumi T, et al. The relationship between magnetic resonance imaging findings and clinical manifestations of hypothalamic hamartoma. *J Neurosurg*. 1999;91:212–220.
105. Valdueza JM, Cristante L, Dammann O, Bentele K, Vortmeyer A, Saeger W, et al. Hypothalamic hamartomas: with special reference to gelastic epilepsy and surgery. *Neurosurgery*. 1994;34:949–958.
106. Freeman JL. The anatomy and embryology of the hypothalamus in relation to hypothalamic hamartomas. *Epileptic Disord*. 2003;5:177–186.
107. Debeneix C, Bourgeois M, Trivin C, Sainte-Rose C, Brauner R. Hypothalamic hamartoma: comparison of clinical presentation and magnetic resonance images. *Horm Res*. 2001;56:12–18.
108. Jung H, Neumaier Probst E, Hauffa BP, Partsch CJ, Dammann O. Association of morphological characteristics with precocious puberty and/or gelastic seizures in hypothalamic hamartoma. *J Clin Endocrinol Metab*. 2003;88:4590–4595.
109. Freeman JL, Coleman LT, Wellard RM, Kean MJ, Rosenfeld JV, Jackson GD, et al. MR imaging and spectroscopic study of epileptogenic hypothalamic hamartomas: analysis of 72 cases. *AJNR Am J Neuroradiol*. 2004;25:450–462.
110. Hall JG, Pallister PD, Clarren SK, Beckwith JB, Wiglesworth FW, Fraser FC, et al. Congenital hypothalamic hamartoblastoma, hypopituitarism, imperforate anus and postaxial polydactyly – a new syndrome? Part I: clinical, causal, and pathogenetic considerations. *Am J Med Genet*. 1980;7:47–74.
111. Barral V, Brunelle F, Brauner R, Rappaport R, Lallemand D. MRI of hypothalamic hamartomas in children. *Pediatr Radiol*. 1988;18:449–452.
112. Burton EM, Ball Jr WS, Crone K, Dolan LM. Hamartoma of the tuber cinereum: a comparison of MR and CT findings in four cases. *AJNR Am J Neuroradiol*. 1989;10:497–501.

113. Chong BW, Newton TH. Hypothalamic and pituitary pathology. *Radiol Clin North Am*. 1993;31:1147–1153.
114. Hahn FJ, Leibrock LG, Huseman CA, Makos MM. The MR appearance of hypothalamic hamartoma. *Neuroradiology*. 1988;30:65–68.
115. Lona Soto A, Takahashi M, Yamashita Y, Sakamoto Y, Shinzato J, Yoshizumi K. MRI findings of hypothalamic hamartoma: report of five cases and review of the literature. *Comput Med Imaging Graph*. 1991;15:415–421.
116. Marliani AF, Tampieri D, Melancon D, Ethier R, Berkovic SF, Andermann F. Magnetic resonance imaging of hypothalamic hamartomas causing gelastic epilepsy. *Can Assoc Radiol J*. 1991;42:335–339.
117. Striano S, Striano P, Sarappa C, Boccella P. The clinical spectrum and natural history of gelastic epilepsy-hypothalamic hamartoma syndrome. *Seizure*. 2005;14:232–239.
118. Turjman F, Xavier JL, Froment JC, Tran-Minh VA, David L, Lapras C. Late MR follow-up of hypothalamic hamartomas. *Childs Nerv Syst*. 1996;12:63–68.
119. Prasad S, Shah J, Patkar D, Gala B, Patankar T. Giant hypothalamic hamartoma with cystic change: report of two cases and review of the literature. *Neuroradiology*. 2000;42:648–650.
120. Booth TN, Timmons C, Shapiro K, Rollins NK. Pre- and postnatal MR imaging of hypothalamic hamartomas associated with arachnoid cysts. *AJNR Am J Neuroradiol*. 2004;25:1283–1285.
121. Kuzniecky R, Guthrie B, Mountz J, Bebin M, Faught E, Gilliam F, et al. Intrinsic epileptogenesis of hypothalamic hamartomas in gelastic epilepsy. *Ann Neurol*. 1997;42:60–67.
122. Nishio S, Morioka T, Hamada Y, Kuromaru R, Fukui M. Hypothalamic hamartoma associated with an arachnoid cyst. *J Clin Neurosci*. 2001;8:46–48.
123. Martin DD, Seeger U, Ranke MB, Grodd W. MR imaging and spectroscopy of a tuber cinereum hamartoma in a patient with growth hormone deficiency and hypogonadotropic hypogonadism. *AJNR*. 2003;24:1177–1180.
124. Pomper MG, Passe TJ, Burger PC, Scheithauer BW, Brat DJ. Chordoid glioma: a neoplasm unique to the hypothalamus and anterior third ventricle. *AJNR Am J Neuroradiol*. 2001;22:464–469.
125. Brat DJ, Scheithauer BW, Staugaitis SM, Cortez SC, Brecher K, Burger PC. Third ventricular chordoid glioma: a distinct clinicopathologic entity. *J Neuropathol Exp Neurol*. 1998;57:283–290.
126. Simonetta AB. Imaging of suprasellar and parasellar tumors. *Neuroimaging Clin N Am*. 1999;9:717–732.
127 Lee MT, Lee TI, Won JG, Chau WK, Yang HJ, Li JC, et al. Primary hypothalamic lymphoma with panhypopituitarism presenting as stiff-man syndrome. *Am J Med Sci*. 2004;328:124–128.
128. Pascual JM, Gonzalez-Llanos F, Roda JM. Primary hypothalamic-third ventricle lymphoma. Case report and review of the literature. *Neurocir Astur*. 2002;13:305–310.
129. Lanzieri CF, Sabato U, Sacher M. Third ventricular lymphoma: CT findings. *J Comput Assist Tomogr*. 1984;8:645–647.
130. Namasivayam J, Teasdale E. The prognostic importance of CT features in primary intracranial lymphoma. *Br J Radiol*. 1992;65:761–765.
131. Shelton 3rd CH, Phillips CD, Laws ER, Larner JM. Third ventricular lesion masquerading as suprasellar disease. *Surg Neurol*. 1999;51:177–180.
132. Kurt G, Dogulu F, Kaymaz M, Emmez H, Onk A, Baykaner MK. Hypothalamic lipoma adjacent to mamillary bodies. *Childs Nerv Syst*. 2002;18:732–734.
133. Bognar L, Balint K, Bardoczy Z. Symptomatic osteolipoma of the tuber cinereum. Case report. *J Neurosurg*. 2002;96:361–363.
134. Mackenzie IR, Girvin JP, Lee D. Symptomatic osteolipoma of the tuber cinereum. *Clin Neuropathol*. 1996;15:60–62.
135. Wittig H, Kasper U, Warich-Kirches M, Dietzmann K, Roessner A. Hypothalamic osteolipoma: a case report. *Gen Diagn Pathol*. 1997;142:361–364.

CHAPTER

47

Neuroimaging of Glioneuronal Tumors

Jeffrey J. Raizer, Priya Kumthekar

Department of Neurology, Northwestern University, Feinberg School of Medicine, Chicago, IL, USA

INTRODUCTION

Neuronal and mixed neuronal–glial tumors are a rare but important group of primary brain tumors. With the exception of gangliioglioma and dysplastic gangliocytoma of the cerebellum, the remaining tumors have been described since 1985.[1–7] These tumors are usually benign and often curable with surgical resection. For this reason, histologic diagnosis is important to avoid unnecessary treatment with radiation therapy (RT) or chemotherapy (CTX). In cases in which there has been incomplete resection or malignant degeneration occurs, RT or CTX may have a role, but the "true" benefits, if any, often remain unknown. This chapter reviews the available literature using CTX to treat glioneuronal tumors. Reasons to use CTX include recurrent tumors after radiation, in place of RT to avoid the long-term sequelae in young patients, and for patients who refuse RT. Definitive recommendations cannot be made as most reports are limited to case reports or small numbers of patients, and the type of CTX is often different for an individual tumor type. We hope that this review will provide a framework to assist physicians in deciding on optimal treatment from diagnosis and beyond with the understanding that much remains unknown and new drugs are rapidly becoming available.

CENTRAL NEUROCYTOMA

Clinical

Central neurocytoma was first described in 1982 and further characterized in 1993.[4,8] The intraventricular location of the central neurocytoma makes it unique among the neuronal tumors. The imaging hallmark of this tumor is its association with the septum pellucidum. However, in the past this tumor was often misclassified as an intraventricular oligodendroglioma. They make up 0.25–0.5% of intracranial tumors.[8] The majority of these tumors (75%) present between 20 and 40 years of age without a gender predilection.[1,2] They usually present in the second and third decades of life with symptoms of increased intracranial pressure, due to their intraventricular location within the lateral and third ventricles.[8,9] Patients complain of headache and visual changes and on exam there may be papilledema and ataxia.[2,3] The clinical course is short, typically less than 6 months, prior to presentation. Rare cases of sudden death due to acute ventricular obstruction have been reported.[1] Reports of extraventricular neurocytomas have been described with symptoms associated with the location of the tumor.[10,11]

Pathology

Central neurocytomas are thought to arise from germinal matrix cells in the septum pellucidum or the periventricular region. This accounts for the typical intraventricular location. The cells of the germinal matrix are progenitor cells that can differentiate into both neuronal and glial tissue. Consequently, central neurocytomas may have both neuronal and glial cell types present although those tumors that have a glial component are more frequently extraventricular in location.[1,4,5]

Central neurocytomas consist of small uniform cells with round or oval nuclei. There is scant surrounding cytoplasm, creating a perinuclear halo or "fried egg" appearance, which occurs owing to a fixation artifact.[1,2,6–8] Mitotic figures are infrequent, as are vascular proliferation and necrosis. Focal calcifications may be present. Immunostains help differentiate this tumor from an oligodendroglioma. Central neurocytomas stain positive for markers of neuronal differentiation, including synaptophysin (a normal protein of presynaptic

Handbook of Neuro-Oncology Neuroimaging, Second Edition
http://dx.doi.org/10.1016/B978-0-12-800945-1.00047-1

© 2016 Elsevier Ltd. All rights reserved.

vesicles) and neuron-specific enolase (NSE) as well as hexaribonucleotide-binding protein-3 (NeuN), and typically negative for epithelial markers such as epithelial membrane antigen and vimentin.[9] Central neurocytomas may also stain positive for glial fibrillary acidic protein (GFAP); however, when present this is thought to reflect reactive astrocytes trapped at the tumor margin rather than reactivity of glial-origin tumor cells.[9] Neuronal characteristics such as microtubules, neurosecretory granules, clear vesicles, and synapses are seen with electron microscopy. These ultrastructural traits define the central neurocytoma.[1,2,6–8] Although a central neurocytoma is felt to be a relatively benign tumor characterized by indolent growth, the behavior of this tumor is uncertain. The several cases of poor outcome secondary to its aggressive behavior, recurrence, and cerebrospinal fluid (CSF) dissemination led to the reclassification of this tumor in 1999 to a World Health Organization (WHO) grade II to reflect its uncertain malignant potential.[4] The best indicator of the behavior of this tumor is the labeling index (LI), which is typically low in central neurocytoma. A higher LI of the tumor portends a worse prognosis. One study[10] found that if the LI is less than 2% there is only 22% relapse, whereas the rate of relapse is nearly three times greater (63%) if the index is greater than 2%. Atypical neurocytomas have an LI > 5%, focal necrosis, vascular proliferation, and increased mitotic activity.[10] Their intraventricular location lends neurocytomas to disseminate within the neuroaxis and even intraperitoneally via ventriculoperitoneal (VP) shunt.[12–15]

Imaging

A central neurocytoma is typically a supratentorial tumor arising from the septum pellucidum or ventricle wall. Koeller et al.[1] reports that 50% are located in the lateral ventricle near the foramen of Monroe, 15% are in both the lateral and the third ventricle, and 3% are isolated to the third ventricle. There is a report of a central neurocytoma in the fourth ventricle.[5] Bilateral involvement of the ventricles is present in 13% of cases. These tumors are occasionally reported in an extraventricular location such as the cerebrum, cerebellum, and spinal cord. There may be CSF dissemination.[1,5,11]

Computerized tomography for central neurocytomas typically shows a well-circumscribed intraventricular isodense to hyperdense tumor often with cystic changes.[4,8] The tumor may abut and bow the septum pellucidum. Clumped, amorphous, globular calcifications are seen in 50% of these tumors. Following administration of contrast there is mild to moderate enhancement. Associated findings of hydrocephalus and monoventricular dilatation may be present.[1,3,7]

Magnetic resonance imaging (MRI) appearance (Figures 1 and 2) is high signal on T1 and T2 with variable contrast enhancement.[4,8] The solid portions of the tumor are isointense to gray matter on T1-weighted images. The T2 characteristics are variable with areas that are isointense to mildly hyperintense. Areas of high T2 signal with corresponding low T1 signal correlate to cystic regions. Areas of very low T1 and T2 signal or flow voids may represent calcifications, hemorrhagic regions, or vessels. There is variable enhancement.[1,3,7] Peritumoral edema is infrequent and if present may be an indicator of invasion through the ventricular wall into the brain parenchyma or of a highly aggressive tumor.[12,13]

The differential diagnoses to be considered for these intraventricular tumors include intraventricular oligodendrogliomas, intraventricular astrocytomas, intraventricular meningiomas, subependymomas, ependymomas, choroid plexus papillomas, colloid cysts, intraventricular teratomas, and dermoid tumors, as they may possess similar imaging characteristics. In the

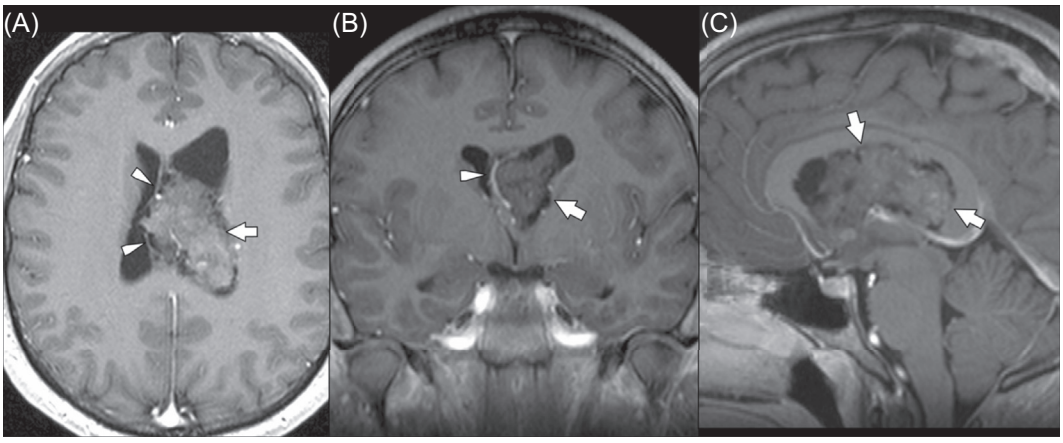


FIGURE 1 Central neurocytoma. Axial (A), coronal (B), and sagittal (C) postcontrast T1 images show the tumor (arrows) filling and expanding the left lateral ventricle. Note the close association with the septum pellucidum (arrowheads) on the axial and coronal views. The mass is predominately isointense on T1-weighted imaging with only minimal enhancement.

absence of distinguishing imaging features, advanced imaging techniques may help make the diagnosis.

Magnetic resonance spectroscopy (MRS) is a one such advanced imaging method whereby metabolites of a targeted tissue are measured. Based on the various ratios of the metabolites detected conclusions may be made regarding the nature of the tissue present. *N*-Acetylaspartate (NAA) is produced by normally functioning mature neurons and serves as a neuronal marker. Under conditions of neuronal cell loss the amount of NAA decreases. Choline and its derivatives (phosphocholine, phosphatidylcholine, and glycerophosphocholine) participate in cell membrane synthesis and breakdown. Elevation of choline corresponds to increased cell proliferation and cell turnover. Higher choline levels suggest a more aggressive tumor type.[8,14]

Given these markers, the results from several cases of MRS performed on known central neurocytomas are contrary to what would be predicted. The amount of the neuronal marker NAA is decreased relative to normal values. However, it is felt that although the neuronal cells in central neurocytomas are highly differentiated, they are still too immature to produce NAA. MRS of central neurocytomas also shows increased choline that classically reflects aggressive tumor types. In most tumors there is a linear correlation between the increased choline and the MIB-1 LI; in central neurocytomas this is not the case.[14] Several MRS studies[8,14,15] also demonstrate the presence of a glycine peak. Glycine is not present in normal brain tissue or in most brain tumors. This metabolite, so far, appears unique to the central neurocytomas, although the absence of glycine does not exclude the diagnosis.[8,15–17] MRS of extraventricular central neurocytomas are equivalent to the intraventricular version.[16]

Other imaging techniques have also been employed to predict the biologic behavior and potential prognosis of central neurocytomas especially in light of the fact that the histologic appearance often belies the nature of the tumor.[18] Positron emission tomography (PET) is an imaging technique that measures various

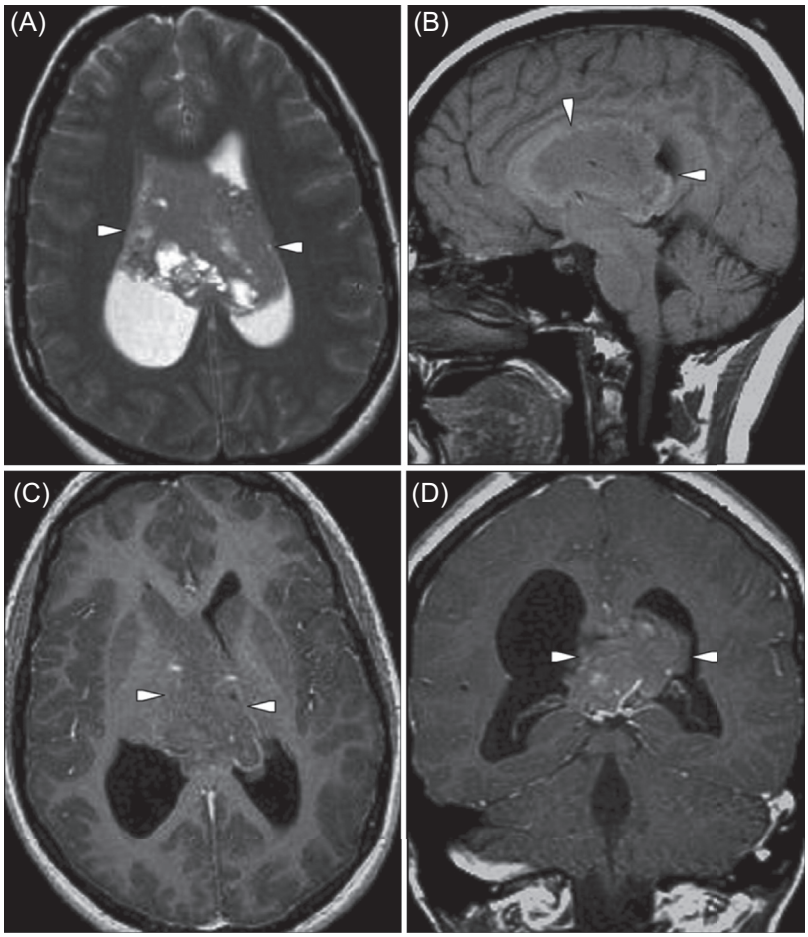


FIGURE 2 Central neurocytoma. Axial T2-weighted images (A) of a different patient show a large tumor involving both lateral ventricles (arrowheads). It is isointense to gray matter with some irregular areas of high T2 signal correlating to cystic regions. There are a few very small foci of very low signal present, which may represent calcifications, hemorrhage, or vessels. (B) A noncontrast sagittal T1 image shows the isointense mass (arrowheads) filling the lateral ventricles. Axial and coronal (C, D) postcontrast images demonstrate the lesion to have only minimal enhancement. *Courtesy of Dr Eric Bartlett.*

metabolic indices. PET uses various labeled tracers to assess hemodynamic and metabolic information about various tumors. In tumors the cerebral circulation, as measured by regional cerebral blood flow and volume, varies depending on the tumor's histology. In central neurocytomas these perfusion parameters are elevated. Oxygen metabolism is always reduced in tumors owing to the anaerobic metabolism. However, the reduction of the cerebral metabolic rate of oxygen in central neurocytomas is less so than that in other brain tumors. This may help distinguish this tumor from more malignant ones. [^{18}F]Fluorodeoxyglucose (FDG) can be used to measure the metabolic rate of glucose within the tumor. Increased metabolic rate of glucose is a characteristic of malignant brain tumors.[4,17,19] In a study performed by Mineura et al.[12] most of the central neurocytomas they investigated had low metabolic rates of glucose. However, one of the central neurocytomas sampled had a relatively increased glucose metabolism. This particular tumor showed rapid regrowth 4 months after partial resection. Ohtani et al.[19] present a case report in which a central neurocytoma had an extremely high uptake of FDG, even greater than the normal brain cortex. Upon resection this tumor was noted to have atypical histological features and an elevated MIB-1 LI of 7%. Consequently, the cerebral metabolic rate of glucose may be useful not only as a predictor of the proliferation potential of the tumor at the time of diagnosis, but potentially as a tool to assess residual tumor during treatment.

Thallium-201 single-photon emission computed tomography (^{201}Tl SPECT) is a technique that reflects changes in blood–brain barrier permeability and regional blood flow typically making elevation of ^{201}Tl retention a reflection of malignancy in brain tumors. However, studies have shown increased uptake of ^{201}Tl in central neurocytomas that does not correspond to the MIB-1 LI.[14] The underlying reason for this discrepancy is unknown. On angiography, some central neurocytomas show moderate vascularity, but most are relatively nonvascular, demonstrating displacement of the normal vascular structures and associated with vascular blush in the venous phase.

Treatment

The primary treatment of these tumors is surgical irrespective of location.[9–11,17,18] Gross total resection (GTR) has resulted in 5-year local control rates of 90–100% and 5-year survival rates of 90–100% and 10 year survival rate of 83% in one report.[16] For subtotal resection (STR) without any adjuvant therapy, these rates were 46–70% and 77–86%, respectively.[20] RT to the primary tumor has been advocated only for lesions that are subtotally resected to increase local control and survival.[17,19] However, the exact role of radiation is unclear as some patients with an STR do not recur and have survivals similar to those with GTR. Stereotactic radiosurgery has been used in some cases of STR tumors with good local control.[20–22] The use of CTX in these tumors is limited and does not appear to play a role in treatment with the limited data published.[14,17,18,23–25]

GANGLIOGLIOMA AND GANGLIOCYTOMA

Gangliogliomas were first named by Perkins in 1926.[1] Gangliogliomas account for 1.3% of all brain tumors and are composed of neuronal and glial elements, while gangliocytomas (WHO grade I) are composed predominantly of neoplastic neurons.[26] They are most commonly located in the temporal lobe and frequently present with seizures. They usually present before the age of 30 with a male/female ratio of 1–2/1,[27] and account for 1–11% in children and less than 1% in adults. The location of ganglioglioma is most commonly in the cerebral hemispheres with involvement of the temporal lobes, followed by the frontal lobes, occipital lobes, and parietal lobes. Much less common is the posterior fossa, where involvement of the cerebellum and brain stem is reported. Size may be variable and ranges from 1 to 10.5 cm, and an increase in tumor diameter and volume is seen in patients <10 years of age compared to those who are older.[26,27]

Pathology

Gangliocytomas are composed of irregular groups of large multipolar neurons often with dysplastic features; nonneoplastic glial elements and reticulin fibers make up the stroma.[26] Gangliogliomas have a neoplastic glial component, usually astrocytes.[26] By immunohistochemistry, these tumors stain for synaptophysin, GFAP, and less so for chromogranin. LIs are less than 3%, but increased growth fraction and p53 may be associated with tumor recurrence. Despite these tumors being benign, reports of malignant degeneration, drop metastases, and dissemination via a VP shunt have been published.[28–34] Malignant change is usually in the glial elements, leading to features similar to a glioblastoma. Features of anaplasia appear to be a negative prognostic factor.[35–38] Mutations of the proto-oncogene BRAF (V600E) have also been found in approximately 20% of gangliogliomas.[39] BRAF V600E mutational status is found by VE1 immunohistochemistry and direct DNA sequencing and has treatment implications that will be discussed later with treatment of these tumors.

Imaging

Imaging on computed tomography (CT) scan with contrast shows a solid mass or cyst with a mural nodule both well circumscribed.[40,41]They are usually isodense or hypodense but can be hyperdense; most enhance after the administration of contrast, which can be homogeneous or heterogeneous or have a ring pattern.[40,41] Calcifications are common.[40,41] These tumors can be solid or cystic, the latter is often hypodense, while solid ones can be any density. Solid tumors are more likely to homogeneously enhance, while cystic ones inhomogeneously enhance. CT scan may be normal in some cases, and intratumoral hemorrhage is a rare event.[40,41]

MRI appearance (Figures 3 and 4) is hypointense, isointense, hyperintense, or mixed relative to brain on T1 in decreasing order and almost always hyperintense on T2.[41] They are often well circumscribed. Enhancement is more common than not, but is variable and may be solid, rim, or nodular.[41] Peritumoral edema may be seen.[40,41] Cystic components may be hypointense on T1 but hypertense on T2. MR perfusion of these tumors has a relative cerebral blood volume greater than other low-grade gliomas; a nonsignificant trend correlates with enhancement but not with increased grade.[41] On MRS, compared to the contralateral normal hemisphere, there is reduced choline (Cho)/creatine (Cr) and NAA/Cr ratio and an increased Cho/NAA ratio; the NAA/Cr ratio is relatively higher than gliomas, probably from the neuronal component of the tumor.[41]

On advanced imaging, including angiography and PET, the appearance has not been widely characterized. In one study looking at angiography with gangliogliomas, most lesions were found to be avascular;[40,42] however, one patient was shown to have a vascular blush. On PET imaging with FDG these tumors were shown to be hypometabolic compared to normal brain in almost all cases, others were normometabolic, and corresponded to a low-grade histology; but one case of a grade I/II ganglioglioma was hypermetabolic.[41] The dimensions on PET and SPECT imaging both correlated well with size on MRI. SPECT imaging also correlated with tumor grade and with uptake being increased if the tumor was high grade but not if low grade.[40]

Gangliogliomas may also occur in the spinal cord. They have a difference in length compared to spinal cord astrocytomas or ependymomas, an average length of eight vertebral bodies compared to four.[43] Most occur in the cervical spine but can involve the whole cord and are eccentrically located.[43] Tumoral cysts appear to be more common than in astrocytomas or ependymomas; bony erosion is also more common than in astrocytomas.[43] On T1 they most often have a mixed signal intensity and less often are hypointense; the mixed density differs from astrocytomas or ependymomas. On T2, they are slightly more likely to have a homogeneous signal than heterogeneous.[43] Edema is not a common finding.[43] The enhancement pattern varies but most often is patchy with enhancement reaching the surface of the cord.[43]

Treatment

The mainstay of treatment for ganglioglioma is surgery. Many large retrospective case series have highlighted the important role of surgery in these tumors[40,41,44] for potential cure. Long-term survival rates with surgery alone are excellent.[27,44] Several series have found no increased survival with adjuvant RT,[35,36,40,45,46] but for anaplastic lesions this may be of some benefit especially when not completely resected.[37,42] Some reports show concern that radiation may predispose to malignant degeneration; therefore, it is typically considered at recurrence or for higher grade transformations.[30,32]

CTX is not routinely utilized in the treatment of ganglioglioma and no randomized clinical trials exist to

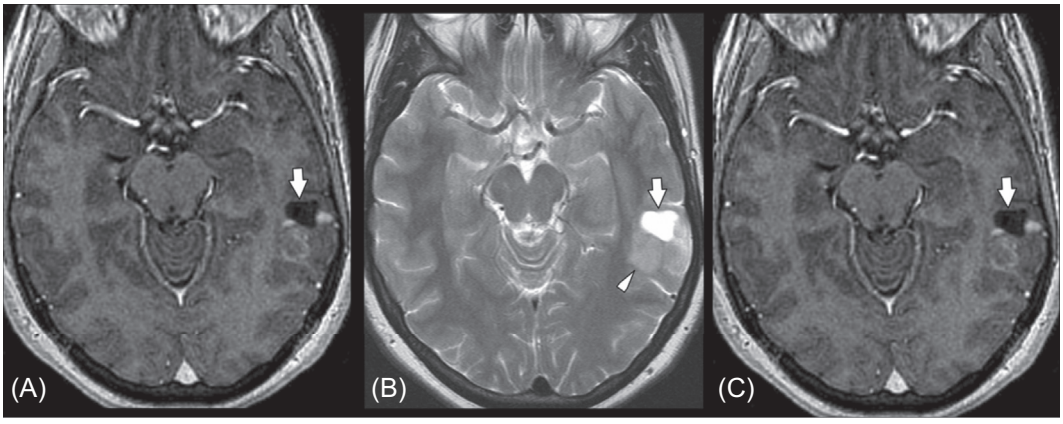


FIGURE 3 Ganglioglioma. (A) An axial T1-weighted image shows an irregularly shaped hypointense lesion within the left temporal lobe. (B) On the T2-weighted sequence, the lesion is high signal (arrow) with surrounding less intense edema (arrowhead). (C) There is peripheral nodular enhancement on the postcontrast axial T1-weighted image.

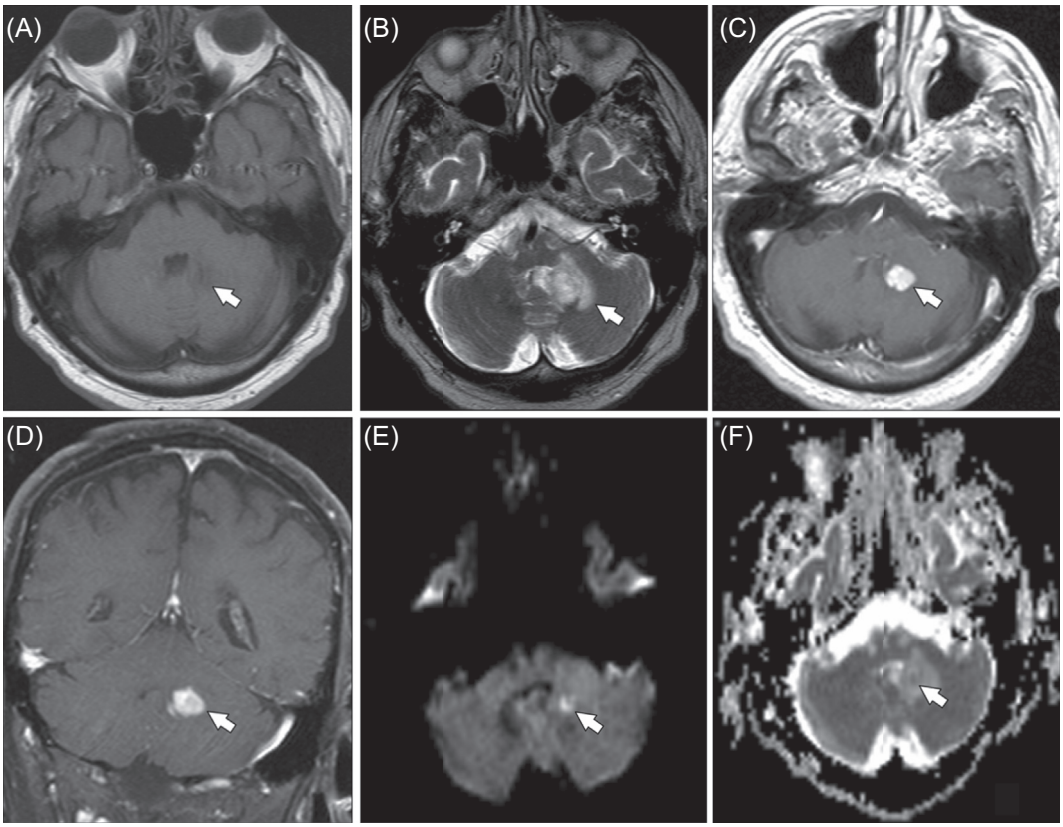


FIGURE 4 Ganglioglioma. (A) An axial T1-weighted image faintly shows an area of diminished signal (arrow) in the medial aspect of the left cerebellum. (B) The T2-weighted image shows a larger area of abnormal hyperintensity (arrow) corresponding to the lesion and the surrounding edema. (C) Postcontrast axial and (D) coronal show avid enhancement of the lesion (arrow). (E) The B1000 diffusion-weighted sequence demonstrates high signal with faint corresponding low ADC signal (F) within a portion of the tumor (arrows) consistent with an area of restricted diffusion.

evaluate its efficacy. There are, however, a handful of published reports of patients being treated with various CTX regimens for gangliogliomas, some of which were anaplastic or malignant.[30,34,47,48] In most case reports, patients who have been treated with CTX (often not noted as to type) have also been treated with RT, so the true benefit is difficult to assess; in several series there was no benefit, patients did poorly, or there was no specific mention of outcome.[36–38,44,46,47,49] In a series of 34 patients with gangliogliomas, one patient was treated with nitrosourea and one with Accutane after STR and irradiation, with stable disease at 4 and 39 months, respectively.[40] Sasaki et al.[48] treated one patient with a recurrent ganglioglioma that became progressively more anaplastic with each recurrence with local methotrexate without any tumor activity. Kaba et al.[50] treated a patient with a ganglioglioma that underwent malignant transformation with *cis*-retinoic acid with almost complete resolution of the lesion. Hassell et al.[51] treated one patient with recurrent spinal cord ganglioglioma with carboplatin (560 mg/m^2/month) for 11 cycles; the patient had a radiographic and clinical stabilization for 17 months. Another report describes a patient with leptomeningeal dissemination who had no response to postradiation ACNU.[33] As a whole, limited data exist for prolonged disease control of ganglioglioma with traditional CTX.

Emerging targeted therapies appear to provide a potential benefit to patients with ganglioglioma. As previously stated, activating mutations of the proto-oncogene BRAF have been found in multiple tissue studies with gangliogliomas.[52,53] As a result, Vemurafenib, a BRAF inhibitor, has been used to treat ganglioglioma with some noted efficacy. One such report described a brain-stem ganglioglioma treated successfully with vemurafenib and vincristine with noted radiographic and clinical disease response.[49] Given the combination therapy, the specific response to vemurafenib was unclear. Another publication reported on three patients treated with vemurafenib monotherapy, with two of the three showing a sustained clinical and radiographic response to vemurafenib.[54]

DESMOPLASTIC INFANTILE GANGLIOGLIOMA AND DESMOPLASTIC INFANTILE ASTROCYTOMA

Desmoplastic infantile astrocytoma (DIA), first described by Taratuto in 1982,[7] and desmoplastic infantile ganglioglioma (DIG), described by VandenBerg in 1987,[5]

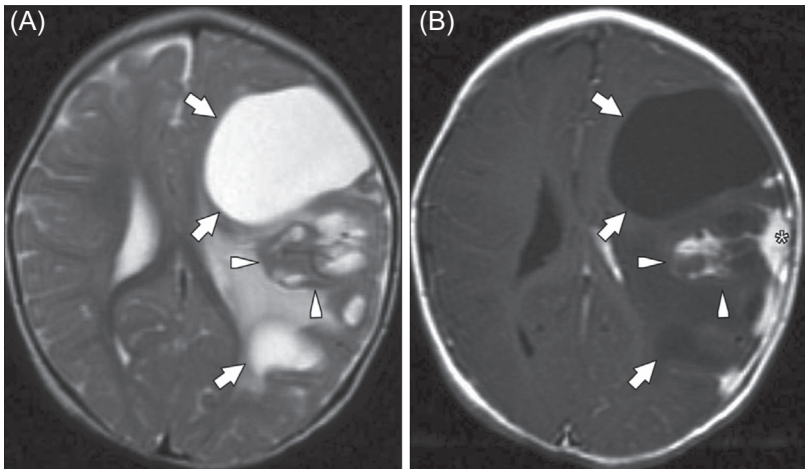


FIGURE 5 DIG. (A) An axial T2-weighted image demonstrates a tumor involving predominately the left frontal lobe extending into the parietal lobe. There is a large, high-signal cystic component, as well as some additional smaller cysts (arrows). The solid components (arrowheads) are isointense to brain parenchyma. There is surrounding high T2 edema and mass effect on the left lateral ventricle. (B) A postcontrast axial T1-weighted image demonstrates the low signal cystic components (arrows). There is enhancement of the solid component (arrowheads) that is avid at the site of attachment to the dura (asterisk). *Courtesy of Dr Francine Kim.*

are rare WHO grade I tumors. They are characterized by a mix of neuronal and glial elements surrounded by a desmoplastic reaction.[5,7] Almost all cases occur in children of <2 years with a male/female ratio of 1.7/1.[7,55] For both histologies, children commonly present with increase in head circumference, bulging fontanelles, and downward ocular deviation ("sunset sign"); other symptoms include seizures, paresis, and increased muscle tone and reflexes.[7,55]

Pathology

Histologically, both tumors are composed of neoplastic astrocytes and a prominent reticulin-rich, desmoplastic stroma (DIA), in some cases with a variable extent of neuronal differentiation (DIG); they are often adherent to the dura and involve multiple lobes. Immunohistochemical stains are positive for GFAP, vimentin, and synaptophysin and the LI is low.[7] Similar to other neuronal tumors such as ganglioglioma, the BRAF V600E mutation has also been found in both DIA and DIG tumors and may have similar treatment implications with the use of BRAF inhibitors.[52,56]

Imaging

Neuroimaging on MRI and CT is similar for both of these entities (Figure 5). On CT, these tumors are large hypodense cystic masses with a solid isodense or slightly hyperdense superficial portion that shows contrast enhancement. MRI on T1 shows a hypointense cystic mass with an isointense peripheral solid component that enhances; on T2 the cyst is hyperintense and the solid portion is heterogeneous.[7,55,57]

Treatment

Although the tumors appear histologically malignant, their course is usually benign,[58–60] although reports of central nervous system dissemination and malignant transformation do exist.[61–63] The primary mode of treatment is surgical with the aim of GTR.[55,58–60,64] In fact, some reports have demonstrated stable follow-up and even spontaneous regression after partial resection.[64,65]

There are only a few patients who have received CTX for DIG/DIA. Duffner et al.[66] reported on four patients with DIG treated with vincristine (0.065 mg/kg; maximum 1.5 mg on days 1–8), cyclophosphamide (65 mg/kg on day 1) for two 28-day cycles, and then cisplatin (4 mg/kg on day 1) and etoposide (6.5 mg/kg on days 3 and 4) for one 28-day cycle; this sequence was repeated for up to 2 years and RT was not used. Case 1 was a 5-month-old boy disease free more than 36 months after diagnosis after 24 months of treatment. Case 2 was an 8-month-old boy treated for 12 months whose tumor remained stable 42 months after diagnosis. Case 3 was a 4-month-old boy treated for 24 months; he had a complete response and was well 5 years after diagnosis. Case 4 was a 7-month-old boy treated for 18 months who had a partial response and was well 4 years after diagnosis. VandenBerg et al.[5] reported on 11 patients, three of whom had surgery, RT, and then CTX. Of these three, one was treated with vincristine and dactinomycin, while the CTX used in the other two was not specified. Ultimately, two of the three patients died. De Munnynck et al.[67] report a case of a 2-year-old girl with a malignant DIG based on histology, radiographic appearance, and clinical aggressiveness. MRI 1 month after surgery revealed tumor progression and she was initially started on a combination of vincristine (0.15 mg/m^2) and carboplatin (550 mg/m^2) for one cycle with a decrease in the tumor. Three cycles of carboplatin (200 mg/m^2 for 24 h on days 1–4) and etoposide (100 mg/m^2 for 24 h on days 1–4) were then

given, followed by one cycle of high-dose carboplatinum (500 mg/m^2 for 24 h on days 1–4) and etoposide (200 mg/m^2 for 24 h on days 1–4) with autologous stem cell rescue. She had a further reduction in tumor volume. She remained stable on maintenance vincristine (1.5 mg/m^2) and cisplatin (80 mg/m^2) for 4 weeks × 3 cycles but then progressed 11 months after surgery. She was subsequently placed on tamoxifen (120 mg/m^2) without response and died soon after. One patient with a partially resected DI tumor was treated with RT and CTX (type not noted) but died nonetheless.[57]

DYSEMBRYOPLASTIC NEUROEPITHELIAL TUMOR

Dysembryoplastic neuroepithelial tumors (DNETs) are low-grade, cortically based tumors that were described as a distinct entity by Daumas-Duport et al. in 1988.[3] DNETs are located primarily in the temporal lobes and are associated with drug-resistant epilepsy. They occur most frequently in the second and third decades, with a male predominance.

Pathology

DNETs are nodular-appearing lesions with glioneuronal elements that histologically have both glial and neuronal elements of differentiation. As such, they show GFAP positivity with their glial elements and "floating neurons" that are synaptophysin positive with their neuronal elements. The LI is low and cortical dysplasia may be seen. These are usually benign tumors; however, there are reports of malignant transformation.[68,69] Analogous to the other neuronal tumors discussed, BRAF V600E mutations have also been observed in DNETs.[70]

Imaging

On CT scan DNETs are most commonly well-demarcated hypodense lesions (although rarely isodense or hypodense) with a pseudocystic appearance and may contain calcifications (Figure 6).[71–73] These calcifications are seen in about 20% of DNET cases, and most DNETs are heterogeneous in density without mass effect or edema.[73]

On T1 MRI DNETs are hypointense and on T2 hyperintense and well demarcated (Figure 6).[74] About one-third enhance on CT or MRI and often have ring-like features or a faint margin of enhancement.[3,75] Most lesions are cystic, even multicystic in nature, and have a shorter T1 than CSF and appear hypointense, isointense, or hyperintense on proton density imaging.[73,74] This signal pattern is due to the abundant myxoid interstitial matrix and accounts for the differences with CSF. The solid portion is isointense and approximately half have contrast enhancement and may appear multinodular.[73,76] The margins on MRI may not be as well defined as on CT. Calvarial changes can be seen, especially for lesions extending to the cortical margin.[71,76] For lesions in the mesial temporal or insular region this is unlikely to occur.

On T2 MRI sequences, DNETs are hyperintense with well-demarcated margins.[74,76] Despite cystic appearance on MRI, cysts are infrequently seen histologically and edema and mass effect are also not typically seen.[73,74,76] Rare cases have shown hemorrhage,[73,74,76] and with high-resolution imaging, septations can be seen on MRI within the lesion. Fernandez et al.[76] also described a "spatial" distribution of DNETs as triangular mostly or as rectangular or round. On MRI these lesions can change over time with the development of contrast enhancement, without necessarily indicating a change in grade.

In advanced imaging with FDG and [^{11}C]methionine PET these lesions are typically inactive, especially if in the mesial temporal lobe, or with mild uptake; uptake has no bearing on contrast enhancement, and increased activity suggests another diagnosis. For patients evaluated by FDG PET, all were hypometabolic, and normal [^{11}C]Met uptake has been shown to make the diagnosis of ganglioglioma more likely.[77] SPECT with Tc99m-HMPAO can have normal perfusion or hypoperfusion.[74] MRS in one patient showed a reduced NAA and the Cho/Cr and Cho/NAA ratios are lower than for other gliomas, although most studies have shown normal spectroscopy for DNET patients.[74]

Treatment

Surgical resection is the main treatment, with excellent long-term outcomes even for subtotally resected tumors.[3,71,72,75] There are no randomized trials evaluating CTX or radiation for these tumors as of this writing and generally these modalities are reserved for nonresectable or recurrent tumors. There does not appear to be a role for external-beam RT for these tumors, although there has been one report on the potential efficacy of stereotactic radiosurgery for DNETs in which a patient with intractable epilepsy remained seizure free after almost 2 years following treatment of a nonresectable DNET with stereotactic radiosurgery.[78] There are no reports of CTX in the treatment of DNET, except in cases for which the diagnosis was incorrect, but there does not appear to be any indication for its use.

These lesions are most commonly found in the temporal lobes—they can be medial or lateral but also frontal, parietal, and occipital[73,74,76]; size is from 1 to 5 cm.[74] Reports of DNETs occurring in the pons, thalamus, basal ganglia, cerebellum, and third ventricle and septum pellucidum all exist. Varying degrees of hydrocephalus were present, with the tumors ranging from 1 to 3 cm. They were nonenhancing in all but one case in which

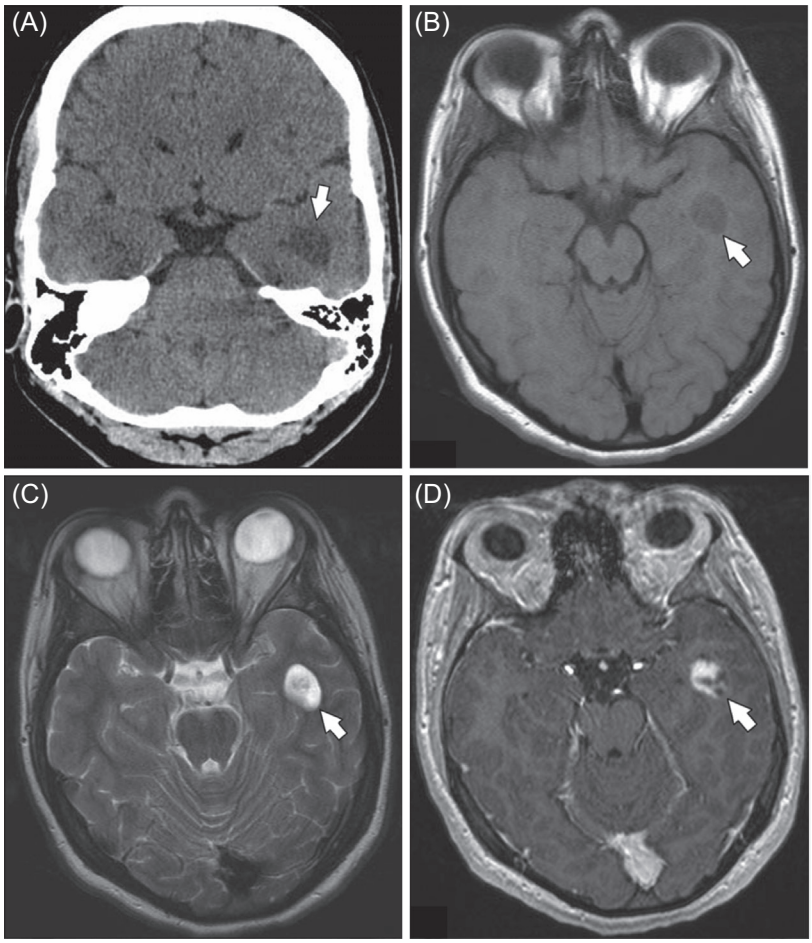


FIGURE 6 DNET. (A) Axial CT shows a small rounded area of low attenuation in the left temporal lobe. (B) Axial T1- and (C) T2-weighted images show the same rounded lesion with low T1 and high T2 signal. There is no surrounding edema. (D) A postcontrast axial T1 image shows heterogeneous enhancement.

there was minimal peripheral enhancement. They were hypointense on T1 and hyperintense on T2 or proton density; varying edema was noted.

DYSPLASTIC GANGLIOCYTOMA OF THE CEREBELLUM

Dysplastic gangliocytoma of the cerebellum (WHO grade I), also known as Lhermitte–Duclos disease, is a rare hamartomatous or nonneoplastic tumor of the cerebellar cortex that most commonly presents with increased intracranial pressure and hydrocephalus, headache, cerebellar symptoms, and cranial nerve palsies.[79,80] It usually presents in the third or fourth decade with no gender predominance.[79,80] This condition has been noted to occur in association with Cowden disease, a phakomatosis that is associated with multiple hamartomas and other systemic neoplasms.[79,80] Cowden disease occurs owing to a mutation in the phosphatase and tensin homolog (PTEN) gene and is also known as PTEN hamartoma syndrome. In addition to dysplastic gangliocytoma of the cerebellum, it is also associated with[81] breast carcinoma, follicular carcinoma of the thyroid, and endometrial carcinoma.

Pathology

On histopathology, the lesion is characterized by large neuronal cells that expand the granular and molecular layers.[79,80] There have been no reports of malignant transformation of this tumor and its clinical course is benign.

Imaging

MRI shows a hypointense lesion on T1 with little or no enhancement and is hyperintense on T2 (Figure 7).[79,80]

Treatment

The optimal treatment is surgical excision and decompression to relieve symptoms of increased intracranial pressure.[79,80] There are no reports of CTX or RT for this

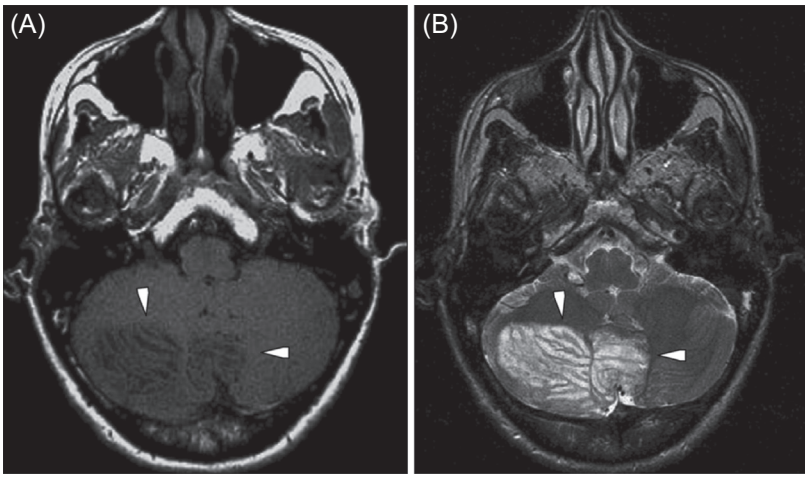


FIGURE 7 Lhermitte–Duclos. (A) Axial T1 and (B) T2 images show the classic striated cerebellum of Lhermitte–Duclos. This lesion involves both a portion of the right cerebellum and the vermis. There are stripes of low T1 signal with corresponding high T2 signal representing the abnormal granular layer and the diminished white matter. These stripes alternate with isointense regions that are made up of the expanded outer molecular layer and the adjacent leptomeningeal surfaces. *Courtesy of Dr Eric Bartlett.*

lesion and there does not appear to be any indication to use these, even when incompletely resected.

CEREBELLAR LIPONEUROCYTOMA

First recognized by Bechtel in 1978,[6] this is a well-differentiated neurocytic tumor (WHO grade I or II) that occurs in the fifth and six decades, with a slight male predominance.[73,82] It typically occurs in the cerebellar lobes or vermis and presents with symptoms consistent with its location in the posterior fossa—dizziness, headache, vomiting, and gait disturbance, similar to dysplastic gangliogliocytoma of the cerebellum.

Pathology

Many of these tumors are reported to occur with the lateral ventricle, and according to the 2007 WHO classification, these are WHO grade II tumors.[83] They contain round neoplastic cells with a consistent neuronal and focal lipomatous differentiation and a low rate of proliferation. There is focal GFAP expression and also NSE and synaptophysin staining; LI is low.[82]

Imaging

CT scan imaging shows a well-circumscribed mass in the posterior fossa often with associated hydrocephalus. The tumor is isodense to hypodense to brain with moderate patchy contrast enhancement.[73] It may have a cystic component.[73] One case report of a presumed liponeurocytoma had evidence of hemorrhage on CT scan without contrast.[73] On T1 MRI, the mass is isodense to hypodense, with areas of hyperintensity correlating to the fat density seen on CT scans; these tumors may have a cystic component.[73,84] There is irregular enhancement postcontrast. On T2 and proton density, the tumor is heterogeneous and has variable hyperintensity compared to normal cortex. [73] The cyst rim is not contrast enhancing and is isointense to CSF on T2 and proton density. Edema is minimal when present.[73,84] Hemorrhage may be seen on MRI that is subacute to chronic but may be lipid.[84] The lipomatous component may be hyperintense to a variable degree on T1 MRI and enhancement is minimal.[82,85]

Tumor Management

Surgical resection is the primary approach to treatment of this tumor and GTR may allow for a cure. It is possible, though, for patients to have recurrence of their tumor,[73] and one report of this tumor acting more aggressively exists; this tumor recurred despite RT; the patient underwent a second resection and was treated with CTX per a medulloblastoma protocol, but outcome or response was not noted.[86] The treatment is surgical, but for STR lesions, radiation may prevent relapse, but the limited number of cases makes any definite recommendations difficult.[84] There are no reports of CTX for these tumors so it role is unknown.

References

1. Perkins OC. Ganglioglioma. *Arch Pathol Lab Med*. 1926;2:11–17.
2. Lhermitte J, Duclos P. Sur un ganglioneurome diffus du coertex du cervelet. *Bull Assoc Fran Etude Cancer*. 1920;9:99–107.
3. Daumas-Duport C, Scheithauer BW, Chodkiewicz JP, Laws Jr ER, Vedrenne C. Dysembryoplastic neuroepithelial tumor: a surgically curable tumor of young patients with intractable partial seizures. Report of thirty-nine cases. *Neurosurgery*. 1988;23: 545–556.

4. Hassoun J, Gambarelli D, Grisoli F, et al. Central neurocytoma. An electron-microscopic study of two cases. *Acta Neuropathol Berl*. 1982;56:151–156.
5. VandenBerg SR, May EE, Rubinstein LJ, et al. Desmoplastic supratentorial neuroepithelial tumors of infancy with divergent differentiation potential ("desmoplastic infantile gangliogliomas"). Report on 11 cases of a distinctive embryonal tumor with favorable prognosis. *J Neurosurg*. 1987;66:58–71.
6. Bechtel JT, Patton JM, Takei Y. Mixed mesenchymal and neuroectodermal tumor of the cerebellum. *Acta Neuropathol Berl*. 1978;41:261–263.
7. Taratuto AL, Monges J, Lylyk P, et al. Meningocerebral astrocytoma attached to the dura with "desmoplastic" reaction. *Proc IX Int Congr Neuropathol Viena*. 1982:5–10.
8. Hassoun J, Soylemezoglu F, Gambarelli D, et al. Central neurocytoma: a synopsis of clinical and histological features. *Brain Pathol*. 1993;3:297–306.
9. Schmidt MH, Gottfried ON, von Koch CS, Chang SM, McDermott MW. Central neurocytoma: a review. *J Neuro Oncol*. 2004;66:377–384.
10. Brat DJ, Scheithauer BW, Eberhart CG, Burger PC. Extraventricular neurocytomas: pathologic features and clinical outcome. *Am J Surg Pathol*. 2001;25:1252–1260.
11. Giangaspero F, Cenacchi G, Losi L, et al. Extraventricular neoplasms with neurocytoma features. A clinicopathological study of 11 cases. *Am J Surg Pathol*. 1997;21:206–212.
12. Soylemezoglu F, Scheithauer BW, Esteve J, Kleihues P. Atypical central neurocytoma. *J Neuropathol Exp Neurol*. 1997;56: 551–556.
13. Rades D, Fehlauer F, Schild SE. Treatment of atypical neurocytomas. *Cancer*. 2004;100:814–817.
14. Eng DY, DeMonte F, Ginsberg L, Fuller GN, Jaeckle K. Craniospinal dissemination of central neurocytoma. Report of two cases. *J Neurosurg*. 1997;86:547–552.
15. Elek G, Slowik F, Eross L, et al. Central neurocytoma with malignant course. Neuronal and glial differentiation and craniospinal dissemination. *Pathol Oncol Res*. 1999;5:155–159.
16. Lubrano V, Francois P, Londou A, Vasiljevic A, Roche PH. French society of neurosurgery. Outcomes after surgery for central neurocytoma: results of a French multicentre retrospective study. *Acta Neurochir*. July 2013;155(7):1261–1269.
17. Schild SE, Scheithauer BW, Haddock MG, et al. Central neurocytomas. *Cancer*. 1997;79:790–795.
18. Sgouros S, Carey M, Aluwihare N, Barber P, Jackowski A. Central neurocytoma: a correlative clinicopathologic and radiologic analysis. *Surg Neurol*. 1998;49:197–204.
19. Rades D, Fehlauer F. Treatment options for central neurocytoma. *Neurology*. 2002;59:1268–1270.
20. Kim JW, Kim DG, Chung HT, et al. Radiosurgery for central neurocytoma: long term outcome and failure pattern. *J Neurooncol*. December 2013;115(3):505–511.
21. Anderson RC, Elder JB, Parsa AT, Issacson SR, Sisti MB. Radiosurgery for the treatment of recurrent central neurocytomas. *Neurosurgery*. 2001;48:1231–1237.
22. Tyler-Kabara E, Kondziolka D, Flickinger JC, Lunsford LD. Stereotactic radiosurgery for residual neurocytoma. Report of four cases. *J Neurosurg*. 2001;95:879–882.
23. Dodds D, Nonis J, Mehta M, Rampling R. Central neurocytoma: a clinical study of response to chemotherapy. *J Neuro Oncol*. 1997;34:279–283.
24. Brandes AA, Gardiman M, et al. Chemotherapy in patients with recurrent and progressive central neurocytoma. *Cancer*. 2000;88:169–174.
25. von Koch CS, Schmidt MH, Uyehara-Lock JH, Berger MS, Chang SM. The role of PCV chemotherapy in the treatment of central neurocytoma: illustration of a case and review of the literature. *Surg Neurol*. 2003;60:560–565.
26. Nelson JS, Bruner JM, Wiestler OD, VandenBerg SR. Ganglioglioma and gangliocytoma. In: Kleihues P, Cavenee WK, eds. *Pathology and Genetics: Tumours of the Nervous System*. 2000:96–98.
27. Zentner J, Wolf HK, Ostertun B, et al. Gangliogliomas: clinical, radiological, and histopathological findings in 51 patients. *J Neurol Neurosurg Psychiatry*. 1994;57:1497–1502.
28. Hukin J, Siffert J, Velasquez L, Zagzag D, Allen J. Leptomeningeal dissemination in children with progressive low-grade neuroepithelial tumors. *Neuro Oncol*. 2002;4:253–260.
29. Araki M, Fan J, Haraoka S, et al. Extracranial metastasis of anaplastic ganglioglioma through a ventriculoperitoneal shunt: a case report. *Pathol Int*. 1999;49:258–263.
30. Jay V, Squire J, Becker LE, Humphreys R. Malignant transformation in a ganglioglioma with anaplastic neuronal and astrocytic components. Report of a case with flow cytometric and cytogenetic analysis. *Cancer*. 1994;73:2862–2868.
31. Jay V, Squire J, Blaser S, Hoffman HJ, Hwang P. Intracranial and spinal metastases from a ganglioglioma with unusual cytogenetic abnormalities in a patient with complex partial seizures. *Childs Nerv Syst*. 1997;13:550–555.
32. Rumana CS, Valadka AB. Radiation therapy and malignant degeneration of benign supratentorial gangliogliomas. *Neurosurgery*. 1998;42:1038–1043.
33. Nakajima M, Kidooka M, Nakasu S. Anaplastic ganglioglioma with dissemination to the spinal cord: a case report. *Surg Neurol*. 1998;49:445–448.
34. Kurian NI, Nair S, Radhakrishnan VV. Anaplastic ganglioglioma: case report and review of the literature. *Br J Neurosurg*. 1998;12:277–280.
35. Rumana CS, Valadka AB, Contant CF. Prognostic factors in supratentorial ganglioglioma. *Acta Neurochir Wien*. 1999;141:63–68.
36. Lang FF, Epstein FJ, Ransohoff J, et al. Central nervous system gangliogliomas. Part 2: clinical outcome. *J Neurosurg*. 1993;79:867–873.
37. Krouwer HG, Davis RL, McDermott MW, Hoshino T, Prados MD. Gangliogliomas: a clinicopathological study of 25 cases and review of the literature. *J Neurooncol*. 1993;17:139–154.
38. Hirose T, Scheithauer BW, Lopes MB, et al. Ganglioglioma: an ultrastructural and immunohistochemical study. *Cancer*. 1997;79: 989–1003.
39. Koelsche C, Wöhrer A, Jeibmann A, et al. Mutant BRAF V600E protein in ganglioglioma is predominantly expressed by neuronal tumor cells. *Acta Neuropathol*. June 2013;125(6):891–900.
40. Selch MT, Goy BW, Lee SP, et al. Gangliogliomas: experience with 34 patients and review of the literature. *Am J Clin Oncol*. 1998;21:557–564.
41. Im SH, Chung CK, Cho BK, et al. Intracranial ganglioglioma: preoperative characteristics and oncologic outcome after surgery. *J Neurooncol*. 2002;59:173–183.
42. Haddad SF, Moore SA, Menezes AH, VanGilder JC. Ganglioglioma: 13 years of experience. *Neurosurgery*. 1992;31:171–178.
43. Patel U, Pinto RS, Muller DC, et al. MR of spinal cord ganglioglioma. *AJNR Am J Neuroradiol*. May 1998;19(5):879–887.
44. Luyken C, Blumcke I, Fimmers R, et al. Supratentorial gangliogliomas: histopathologic grading and tumor recurrence in 184 patients with a median follow-up of 8 years. *Cancer*. 2004;101:146–155.
45. Celli P, Scarpinati M, Nardacci B, Cervoni L, Cantore GP. Gangliogliomas of the cerebral hemispheres. Report of 14 cases with long-term follow-up and review of the literature. *Acta Neurochir Wien*. 1993;125:52–57.
46. Silver JM, Rawlings III CE, Rossitch Jr E, Zeidman SM, Friedman AH. Ganglioglioma: a clinical study with long-term follow-up. *Surg Neurol*. 1991;35:261–266.
47. Johnson Jr JH, Hariharan S, Berman J, et al. Clinical outcome of pediatric gangliogliomas: ninety-nine cases over 20 years. *Pediatr Neurosurg*. 1997;27:203–207.

48. Sasaki A, Hirato J, Nakazato Y, Tamura M, Kadowaki H. Recurrent anaplastic ganglioglioma: pathological characterization of tumor cells. Case report. *J Neurosurg*. 1996;84:1055–1059.
49. Rush S, Foreman N, Liu A. Brainstem ganglioglioma successfully treated with vemurafenib. *J Clin Oncol*. April 1, 2013;31(10): e159–e160.
50. Kaba SE, Langford LA, Yung WK, Kyritsis AP. Resolution of recurrent malignant ganglioglioma after treatment with cis-retinoic acid. *J Neurooncol*. 1996;30:55–60.
51. Hassall TE, Mitchell AE, Ashley DM. Carboplatin chemotherapy for progressive intramedullary spinal cord low-grade gliomas in children: three case studies and a review of the literature. *Neuro Oncol*. 2001;3:251–257.
52. Dougherty MJ, Santi M, Brose MS, et al. Activating mutations in BRAF characterize a spectrum of pediatric low-grade gliomas. *Neuro Oncol*. July 2010;12(7):621–630. http://dx.doi.org/10.1093/neuonc/noq007. Epub February 14, 2010.
53. Schindler G, Capper D, Meyer J, et al. Analysis of BRAF V600E mutation in 1,320 nervous system tumors reveals high mutation frequencies in pleomorphic xanthoastrocytoma, ganglioglioma and extra-cerebellar pilocytic astrocytoma. *Acta Neuropathol*. March 2011;121(3):397–405.
54. Bautista F, Paci A, Minard-Colin V, et al. Vemurafenib in pediatric patients with BRAFV600E mutated high-grade gliomas. *Pediatr Blood Cancer*. June 2014;61(6):1101–1103.
55. Tamburrini G, Colosimo Jr C, Giangaspero F, Riccardi R, Di RC. Desmoplastic infantile ganglioglioma. *Childs Nerv Syst*. 2003;19:292–297.
56. Koelsche C, Sahm F, Paulus W, et al. BRAF V600E expression and distribution in desmoplastic infantile astrocytoma/ganglioglioma. *Neuropathol Appl Neurobiol*. April 2014;40(3):337–344.
57. Trehan G, Bruge H, Vinchon M, et al. MR imaging in the diagnosis of desmoplastic infantile tumor: retrospective study of six cases. *AJNR Am J Neuroradiol*. 2004;25:1028–1033.
58. Sugiyama K, Arita K, Shima T, et al. Good clinical course in infants with desmoplastic cerebral neuroepithelial tumor treated by surgery alone. *J Neurooncol*. 2002;59:63–69.
59. VandenBerg SR. Desmoplastic infantile ganglioglioma and desmoplastic cerebral astrocytoma of infancy. *Brain Pathol*. 1993;3:275–281.
60. Sperner J, Gottschalk J, Neumann K, et al. Clinical, radiological and histological findings in desmoplastic infantile ganglioglioma. *Childs Nerv Syst*. 1994;10:458–462.
61. Setty SN, Miller DC, Camras L, Charbel F, Schmidt ML. Desmoplastic infantile astrocytoma with metastases at presentation. *Mod Pathol*. 1997;10:945–951.
62. Phi JH, Koh EJ, Kim SK, Park SH, Cho BK, Wang KC. Desmoplastic infantile astrocytoma: recurrence with malignant transformation into glioblastoma: a case report. *Childs Nerv Syst*. December 2011;27(12):2177–2181.
63. Prakash V, Batanian JR, Guzman MA, Duncavage EJ, Geller TJ. Malignant transformation of a desmoplastic infantile ganglioglioma in an infant carrier of a nonsynonymous TP53 mutation. *Pediatr Neurol*. July 2014;51(1):138–143.
64. Mallucci C, Lellouch-Tubiana A, Salazar C, et al. The management of desmoplastic neuroepithelial tumours in childhood. *Childs Nerv Syst*. 2000;16:8–14.
65. Takeshima H, Kawahara Y, Hirano H, et al. Postoperative regression of desmoplastic infantile gangliogliomas: report of two cases. *Neurosurgery*. 2003;53:979–983.
66. Duffner PK, Burger PC, Cohen ME, et al. Desmoplastic infantile gangliogliomas: an approach to therapy. *Neurosurgery*. 1994;34: 583–589.
67. De MK, Van GS, Van CF, et al. Desmoplastic infantile ganglioglioma: a potentially malignant tumor? *Am J Surg Pathol*. 2002;26: 1515–1522.
68. Moazzam AA, Wagle N, Shiroishi MS. Malignant transformation of DNETs: a case report and literature review. *Neuroreport*. August 20, 2014;25(12):894–899.
69. Ray WZ, Blackburn SL, Casavilca-Zambrano S, et al. Clinicopathologic features of recurrent dysembryoplastic neuroepithelial tumor and rare malignant transformation: a report of 5 cases and review of the literature. *J Neurooncol*. September 2009;94(2):283–292.
70. Lee D, Cho YH, Kang SY, Yoon N, Sung CO, Suh YL. BRAF V600E mutations are frequent in dysembryoplastic neuroepithelial tumors and subependymal giant cell astrocytomas. *J Surg Oncol*. October 24, 2014.
71. Daumas-Duport C, Varlet P, Bacha S, et al. Dysembryoplastic neuroepithelial tumors: nonspecific histological forms—a study of 40 cases. *J Neurooncol*. 1999;41:267–280.
72. Raymond AA, Halpin SF, Alsanjari N, et al. Dysembryoplastic neuroepithelial tumor. Features in 16 patients. *Brain*. 1994;117(Pt 3): 461–475.
73. Ostertun B, Wolf HK, Campos MG, et al. Dysembryoplastic neuroepithelial tumors: MR and CT evaluation. *AJNR Am J Neuroradiol*. March 1996;17(3):419–430.
74. Lee DY, Chung CK, Hwang YS, et al. Dysembryoplastic neuroepithelial tumor: radiological findings (including PET, SPECT, and MRS) and surgical strategy. *J Neurooncol*. April 2000;47(2):167–174.
75. Daumas-Duport C, Pietsch T, Lantos PL. Dysembryoplastic neuroepithelial tumour. *Pathol Genet Tumours Nerv Syst*. 2000:103–106.
76. Fernandez C, Girard N, Paz Paredes A, Bouvier-Labit C, Lena G, Figarella-Branger D. The usefulness of MR imaging in the diagnosis of dysembryoplastic neuroepithelial tumor in children: a study of 14 cases. *AJNR Am J Neuroradiol*. May 2003;24(5):829–834.
77. Rheims S, Rubi S, Bouvard S, et al. Accuracy of distinguishing between dysembryoplastic neuroepithelial tumors and other epileptogenic brain neoplasms with [^{11}C]methionine PET. *Neuro Oncol*. October 2014;16(10):1417–1426.
78. Kwon KH, Lee JI, Hong SC, Seo DW, Hong SB. Gamma knife radiosurgery for epilepsy related to dysembryoplastic neuroepithelial tumor. *Stereotact Funct Neurosurg*. 2006;84(5–6):243–247.
79. Nowak DA, Trost HA. Lhermitte-Duclos disease (dysplastic cerebellar gangliocytoma): a malformation, hamartoma or neoplasm? *Acta Neurol Scand*. 2002;105:137–145.
80. Wiestler OD, Padberg GW, Steck PA. Cowden disease and dysplastic gangliocytoma of the cerebellum/Lhermitte-Duclos disease. In: Kleihues P, Cavenee WK, eds. *Pathology and Genetics: Tumours of the Nervous System*. 2000:235–237.
81. Pilarski R, Burt R, Kohlman W, Pho L, Shannon KM, Swisher E. Cowden syndrome and the PTEN hamartoma tumor syndrome: systematic review and revised diagnostic criteria. *J Natl Cancer Inst*. November 6, 2013;105(21):1607–1616.
82. Kleihues P, Chimelli L, Giangaspero F. Cerebellar liponeurocytoma. *Pathol Genet Tumours Nerv Syst*. 2000:110–111.
83. Louis DN, Ohgaki H, Wiestler OD, et al. The 2007 WHO classification of tumours of the central nervous system. *Acta Neuropathol*. August 2007;114(2):97–109.
84. Jackson TR, Regine WF, Wilson D, Davis DG. Cerebellar liponeurocytoma. Case report and review of the literature. *J Neurosurg*. 2001;95:700–703.
85. Cacciola F, Conti R, Taddei GL, Buccoliero AM, Di LN. Cerebellar liponeurocytoma. Case report with considerations on prognosis and management. *Acta Neurochir Wien*. 2002;144:829–833.
86. Jenkinson MD, Bosma JJ, Du PD, et al. Cerebellar liponeurocytoma with an unusually aggressive clinical course: case report. *Neurosurgery*. 2003;53:1425–1427.

CHAPTER

48

Pineal Region Tumors

Edward Yang[1], *Susan N. Chi*[2], *Victoria Michelle Silvera*[1]

[1]Department of Radiology, Boston Children's Hospital, Boston, MA, USA; [2]Dana-Farber/Boston Children's Cancer and Blood Disorder Center, Dana-Farber Cancer Institute and Boston Children's Hospital, Boston, MA, USA

INTRODUCTION

Masses intrinsic to the pineal gland are uncommon and caused by a small number of tumor types, most of which are similar in imaging appearance. As a result, it is difficult to provide a specific diagnosis based on the imaging characteristics alone. Nonetheless, it is possible to narrow potential diagnostic considerations to a limited number of pathologic entities based on a careful analysis of the imaging. This analysis begins with the exclusion of pathology extrinsic to the pineal gland (e.g., tectal, thalamic, and dural lesions). Following careful consideration of clinical features (e.g., age, sex, and tumor markers) and imaging characteristics, an ordered and manageable differential can be suggested. To review this systematic approach to pineal region masses, the anatomy and function of the pineal gland will be considered followed by a review of the epidemiology of pineal lesions, a discussion of imaging features of pineal region tumors, and last, an overview of treatment and prognosis of these lesions.

ANATOMY, FUNCTION, AND NORMAL IMAGING

The pineal gland is a midline, ovoid structure located at the anterior aspect of the quadrigeminal plate cistern, between the two superior colliculi of the tectum (Figure 1(A) and (B)). The gland arises from the posterior wall of the third ventricle, to which it is attached by the pineal stalk.[1] The pineal stalk is composed of a superior lamina, which merges with the habenular commissure (attached to the thalami), and an inferior lamina, which is attached to the posterior commissure bridging the upper midbrain. The two laminae are separated by the suprapineal recess of the third ventricle. The cistern of the velum interpositum is located between the two layers of the tela choroidea, lies superior to the pineal gland and inferior to the splenium, and contains the internal cerebral veins. Owing to these anatomic relationships, intrinsic lesions of the pineal gland have a predictable pattern of regional mass effect: they encroach on the posterior aspect of the third ventricle, elevate the internal cerebral veins, deform the tectum of the midbrain, and occasionally cause aqueductal compression.

The pineal gland is predominantly made up of pineocytes, which are specialized neuronal cells with features of photoreceptors. A small portion (5%) of the pineal gland consists of astrocytes.[2] This cellular composition explains the signal intensity of the gland on magnetic resonance imaging (MRI), which is similar in appearance to gray matter. Following injection of contrast, the gland enhances avidly owing to a fenestrated capillary bed.[3] While it may appear bright on diffusion-weighted imaging (DWI) trace maps like other gray matter structures (Figure 1(C)), the normal pineal gland will have apparent diffusion coefficient (ADC) values similar to the remainder of the brain parenchyma. This feature may help distinguish it from some pathologic conditions.[4] According to cross-sectional studies of gland size, the pineal gland is relatively small in infancy, with a mean volume reported to be 27 mm;[3] enlarges by the age of 2 to approximately 56–100 mm^3; and stabilizes in size thereafter.[5,6] The gland plays a role in regulating circadian rhythms and responses to seasonal changes, body temperature, and levels of circulating hormones such as melatonin.[7,8]

EPIDEMIOLOGY AND PATHOLOGY

Pineal region tumors can be divided into four categories: germ-cell tumors, pineal parenchymal tumors, tumors of supporting tissues of the pineal gland (e.g.,

Handbook of Neuro-Oncology Neuroimaging, Second Edition
http://dx.doi.org/10.1016/B978-0-12-800945-1.00048-3

© 2016 Elsevier Ltd. All rights reserved.

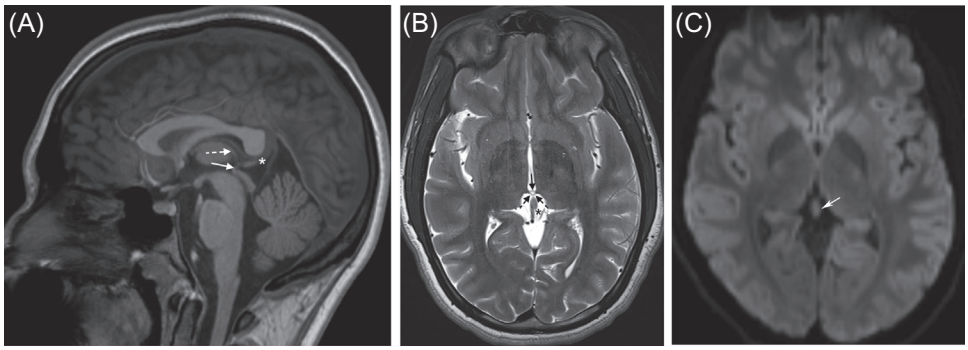


FIGURE 1 Normal pineal gland on MRI. (A) Sagittal T1-weighted magnetization prepared rapid aquisition gradient echo (MPRAGE) image demonstrates the normal pineal gland (anterior to the asterisk) suspended from the inferior and superior lamina (solid and dashed white lines, respectively). (B) Axial T2-weighted image through the pineal gland (anterior to the asterisk) depicts the continuation of the inferior and superior lamina into the posterior and habenular commissures (solid and dashed black lines, respectively). (C) Trace DWI map through the pineal gland shows the normal hyperintensity of the gland (arrow), similar to gray matter.

astrocytoma), and tumors arising from nearby structures (e.g., thalamic astrocytomas and choroid plexus tumors).[2] The last category represents lesions extrinsic to the pineal gland, while the first three categories represent lesions intrinsic to the pineal gland.

As a group, tumors of the pineal region are relatively uncommon, accounting for only 0.4–1% of brain tumors across all ages and 3–8% of brain tumors in children.[9–13] The incidence of pineal tumors is higher in East Asia, where pineal tumors account for 2.2–8% of brain tumors and 10–12.5% of all pediatric brain tumors.[14,15]

The most common tumors in the pineal region are germ-cell tumors, which account for 40–80% of all pineal neoplasms depending on the case series examined.[9,16–19] Germinomas represent the most common germ-cell tumor type, representing 40–80% of pineal region germ-cell tumors and two-thirds of all intracranial germinomas. The remainder of germ-cell tumors are nongerminomatous germ-cell tumors (NGGCTs), such as embryonal carcinoma, endodermal sinus tumor (a.k.a. yolk sac tumor), choriocarcinoma, teratoma, and mixed germ-cell tumors. Germ-cell tumors are strongly male-predominant in the pineal region (particularly germinomas), but show no gender predilection for other locations.[20,21] The peak age for germ-cell tumors is the second decade.[22]

Pineal parenchymal tumors account for 11–40% of all pineal region tumors.[19] These tumors can be divided into pineocytomas, pineoblastomas, and, as of the 2007 World Health Organization (WHO) Classification of Central Nervous System Tumors,[23] papillary tumors of the pineal region (PTPRs) and pineal parenchymal tumors of intermediate differentiation (PPTIDs). Pineocytomas are classified as WHO grade I tumors, PTPRs and PPTIDs as WHO grade II or III tumors (the criteria for which have not yet been fully established), and pineoblastomas as WHO grade IV tumors. PPTIDs fall midway in the spectrum between pineocytomas and pineoblastomas, but PTPRs represent unique tumors thought to derive from ependymal remnants of a structure within the pineal gland known as the subcommissural organ.[24] While the age of presentation for pineal parenchymal tumors is broad, there is a correlation between higher tumor grade and younger age: pineoblastomas are most commonly a disease of children and pineocytomas a disease of middle to late age.[25] Some larger case series suggest a female predominance for pineal parenchymal tumors, but this trend is not readily apparent in review of smaller studies.[25,26] One important group at risk for pineoblastoma is patients with germ-line mutations in the retinoblastoma gene *Rb.* In the era during which radiotherapy rather than chemotherapy was favored in the treatment of retinoblastoma, pineoblastoma was found in up to 8% of patients. Using modern-day chemotherapeutic regimens, pineoblastoma is observed in 1% of patients with this mutation.[27]

Masses arising from supporting cells within the pineal gland or surrounding structures include astrocytomas, ependymomas, choroid plexus papillomas and carcinomas, lymphomas, gangliogliomas, dermoid and epidermoid cysts, meningiomas, and metastases. The incidence and origin of these lesions are difficult to establish based on review of the literature as historical case series used varying pathologic criteria for study inclusion and did not always clarify whether "pineal region" tumors were primarily centered within or outside the pineal gland.[28,29] In our experience, tumors arising from structures external to the pineal gland can be distinguished from intrinsic pineal tumors with careful image analysis, and intrinsic pineal astrocytomas are rare. This contrasts with historical series that suggest that up to 20% of pineal region tumors are astrocytomas.[16,17,30–32]

CLINICAL

Patients with pineal region tumors most commonly present with symptoms related to compression of the cerebral aqueduct and obstructive hydrocephalus.[17,33,34] These symptoms include headaches, nausea and

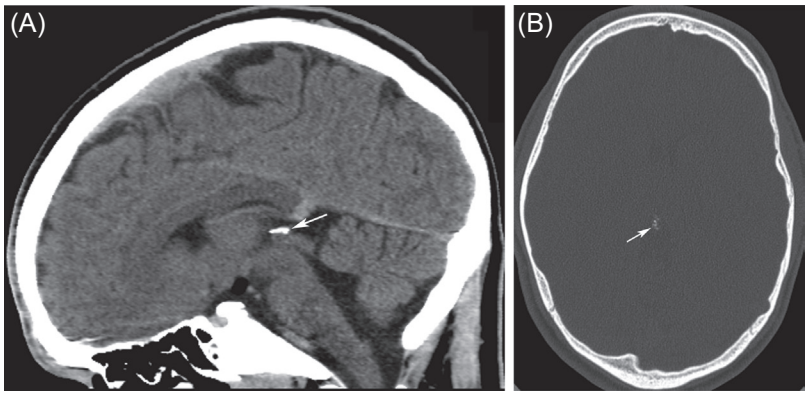


FIGURE 2 Normal pineal calcification on CT. Sagittal soft tissue kernel (A) and axial bone kernel (B) reconstructions. The calcification is compact (arrow, A), coarse in appearance (arrow, B), and without associated soft tissue mass.

vomiting, drowsiness, blurred and double vision, sixth cranial nerve palsy, and papilledema. With compression or invasion of the midbrain, ophthalmological signs may be observed, including impairment of upward gaze, dilated pupils unreactive to light but responsive to accommodation, and convergence retractory nystagmus (rhythmic convergence of the eyes and retraction of the eyes into the orbits, usually elicited by attempting to look upward). This constellation of signs is also known as Parinaud syndrome. Diabetes insipidus may occur if the floor of the third ventricle or the hypothalamus is involved by direct tumoral extension or by disseminated tumor. Less common symptoms include hemiparesis, third-nerve palsy, ataxia, precocious puberty, hypogonadism, seizures, hemorrhage (apoplexy), enuresis, weight loss, and even movement disorders—these unusual symptoms can occur even without apparent tumor dissemination and may result in a delay in diagnosis.[35–37] Despite the multitude of biological systems in which the pineal gland participates, destruction of the gland by tumor, treatment, or resection generally does not produce a measurable effect on intrinsic pineal functions such as the sleep–wake cycle.[38–41]

IMAGING

Pineal Calcification

The pineal gland undergoes progressive calcification with age. Historic cohorts suggest that pineal calcification is rare in children less than 6 years of age and that fewer than 11% of children between the ages of 11 and 14 show pineal calcification. With modern-day multidetector computed tomography (CT) scanners with multiplanar reconstruction capabilities, detection of pineal calcification earlier in life is probably normal, but these earlier normal limits still need to be defined. By the age of 20 years, pineal calcification is present in 40% of the normal population.[42] Normal pineal calcification is described as compact, sand-like or granular in appearance, and less than 1 cm in size (Figure 2). By contrast, pineal calcification that is dispersed or engulfed by solid tumor is frequently seen in germ-cell and pineal parenchymal tumors (see below).[28,30,43,44]

Pineal Cysts

Typical-appearing benign pineal cysts are unilocular or multilocular, have smooth (i.e., nonnodular) walls measuring less than 2 mm thick, and show peripheral enhancement (Figures 3 and 4).[45] Pineal cysts typically have proteinaceous fluid signal characteristics (i.e., signal brighter than cerebrospinal fluid (CSF) on fluid-attenuated inversion recovery (FLAIR) and/or T1-weighted images) and contain internal septations in up to a quarter of cases in one pediatric series.[46,47] Invasion of adjacent structures is absent, and there is minimal or no mass effect on adjacent structures (e.g., the tectum may be flattened but the aqueduct remains unobstructed).[48] The enhancement pattern of pineal cysts is peripheral and curvilinear without nodular or solid-appearing enhancing components, though some gradation may be present, particularly favoring the posterior portion of the cyst.[49] Enhancement of a pineal cyst due to seepage of gadolinium into the cyst fluid can be observed on delayed postcontrast imaging[50] and should not be mistaken for tumoral enhancement. A pineal cyst can be distinguished from a cyst of the velum interpositum by the location of the internal cerebral veins (Figure 5). A pineal cyst will displace the internal cerebral veins away from the gland, whereas a cyst of the velum interpositum will incorporate the internal cerebral veins along its lateral walls.

Early literature raised concern over pineal cysts because of reports of symptomatic patients with cysts as small as 8 mm in size.[34] These concerns were increased after the realization that almost all pineal parenchymal and germ-cell tumors can present with cysts as an imaging feature.[51–55] Additionally, several case

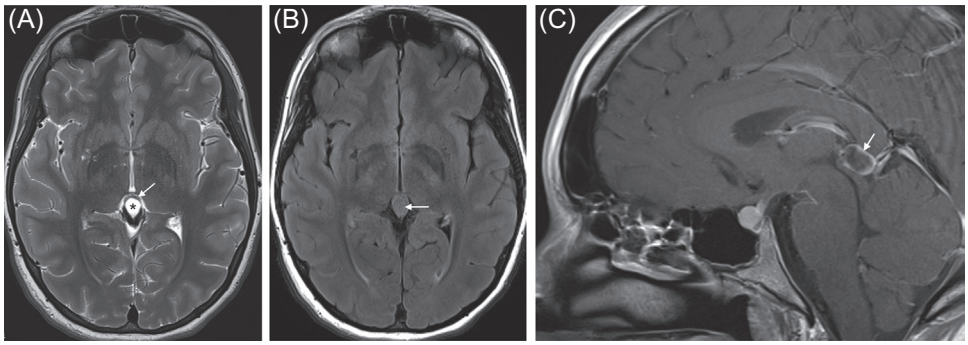


FIGURE 3 Typical benign pineal cyst first detected as part of a seizure evaluation and unchanged in size and appearance over a period of 5 years. (A) Axial T2-weighted MR image demonstrates a unilocular pineal cyst (asterisk) with a smooth cyst wall and a normal volume of solid pineal tissue along the anterior margin of the cyst (arrow). (B) Axial FLAIR MR image demonstrates proteinaceous fluid signal within the cyst (arrow), which is typical. (C) Sagittal T1-weighted postcontrast MR image illustrates smooth curvilinear enhancement of the cyst margin (arrow).

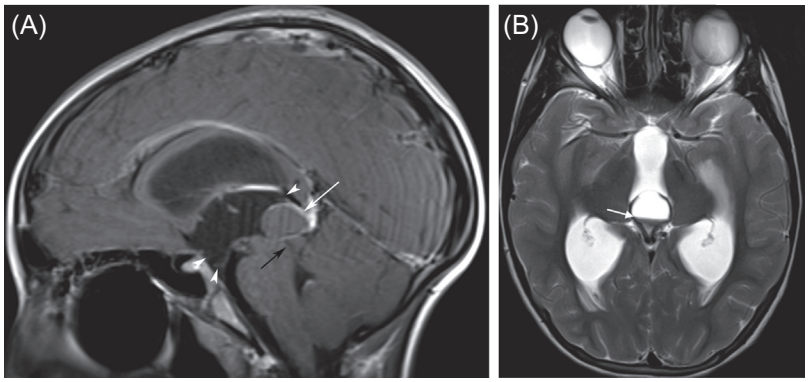


FIGURE 4 Hemorrhagic pineal cyst with obstructive hydrocephalus in a 12-year-old female evaluated for escalating headaches. (A) Sagittal T1-weighted postcontrast MR image reveals a large pineal mass with smooth peripheral enhancement (white arrow). There is obstruction of the cerebral aqueduct (black arrow) and distension of the recesses of the third ventricle (arrowheads) consistent with obstructive hydrocephalus. (B) Axial T2-weighted MR image through the pineal gland demonstrates a unilocular cyst and contains a hematocrit level (arrow) consistent with recent hemorrhage. The patient underwent an endoscopic third ventriculostomy and biopsy of the pineal cyst, which was negative for tumor.

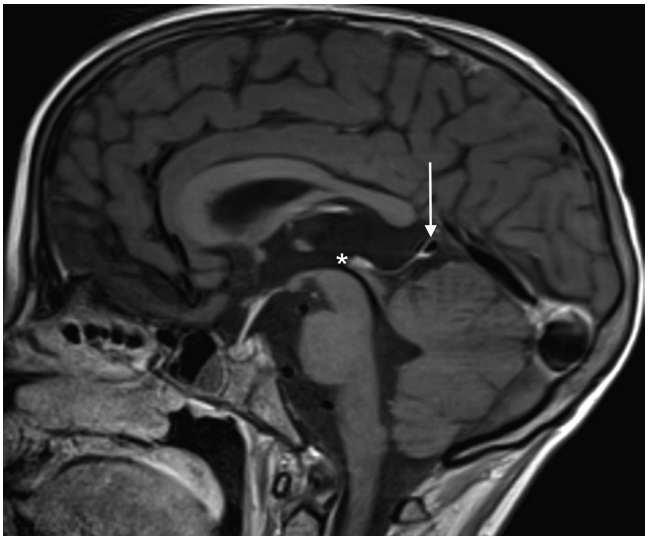


FIGURE 5 Cistern of the velum interpositum cyst. Sagittal T1-weighted sampling perfection with application optimized contrasts using different flip angle evolution (SPACE) postcontrast MR image depicts a cyst within the cistern of the velum interpositum. The pineal gland (posterior to asterisk) is located along the anterior margin of the cyst. The internal cerebral vein (arrow) is displaced away from the splenium.

reports and case series emphasized the difficulty in distinguishing pineal cysts from pineal tumors even with high-quality imaging.[56–59]

However, a more nuanced view has developed with time. To begin with, it has been demonstrated that up to 40% of normal patients will have cystic change within the pineal gland[3,6,60,61] and up to 1–2% of patients will have pineal cysts greater than 5 mm in size.[46,62] These numbers comport well with autopsy series.[63] Pineal cysts become increasingly common during childhood before peaking in frequency in early adulthood. There is a slight increased prevalence of pineal cysts in females compared to males.[46,62] Large studies with imaging follow-up demonstrate that changes in pineal cyst size are rare, that pineal cysts more often decrease in size than increase, and that pineal cysts are not commonly associated with symptoms.[46,48,49] Finally, it has been noted that there is almost always some radiographic hint of neoplasm within cystic pineal tumors (e.g., the cyst will contain nodular soft tissue or have an abnormally thick cyst wall).[34,52] Therefore, many experts suggest that imaging surveillance is necessary

only for pineal cysts with atypical features such as soft tissue nodularity, abnormal wall thickening, or large size (e.g., greater than 15 mm) or for those associated with neurologic symptoms referable to the pineal region, with the remainder of cysts being followed clinically.[45,48,52,64]

Pineal Region Germ-Cell Tumors

The most common tumors of the pineal region are germ-cell tumors, and germinomas are the most common germ-cell tumor in this region. These tumors are believed to derive from fetal germinal cells, similar to gonadal germ cells, that migrated to the fetal central nervous system early in development and persisted.[2,65] Germ-cell tumors are classified by cell type and may be benign or malignant.

Germinoma

Germinomas are histologically identical to testicular seminomas and ovarian dysgerminomas. They are characterized by large multipotential germ cells.[21] Approximately two-thirds of germinomas are centered in the pineal region and one-third are located in the suprasellar cistern, with small numbers seen elsewhere within the brain, such as within the basal ganglia and periventricular white matter.[20,66] Although most germinomas are not associated with hormonal secretion, a small subset of germinomas containing syncytiotrophoblastic cells secrete β-human chorionic gonadotropin (β-HCG).[67]

Germinomas are generally small to moderate in size (1–3 cm).[51] On CT, germinomas are well circumscribed, smoothly bordered, hyperdense and enhance homogeneously,[30,68] features typical of a compact hypercellular neoplasm. At least a third of cases demonstrate coarse focal calcification engulfed by tumor (Figure 6).[43,68,69] On MRI (Figures 7 and 8), germinomas tend to be homogeneous in appearance and intermediate in signal on T2-weighted images (isointense to gray matter). Tumoral cysts are present in 44–58% of cases.[54,70] ADC measures, if cystic foci within the tumor are excluded from the analysis, may show restricted diffusion in solid portions of tumor.[71] Standardized uptake values on positron emission tomography imaging do not help distinguish germinomas from pineal parenchymal tumors.[51,69]

The vector of tumor growth is usually in the ventral direction, with tumor encroachment or extension into the posterior aspect of the third ventricle. Tumoral invasion into the adjacent thalami or midbrain is occasionally encountered.[33,37] Leptomeningeal dissemination of tumor into the intracranial or spinal CSF compartment can be seen at presentation, with rates of dissemination in the range of 9–36%.[37,66,72]



FIGURE 6 Noncontrast CT of a germinoma in a 7-year-old child presenting with headaches and diabetes insipidus. The hyperdense germinoma (white arrow) engulfs the pineal calcification (black arrow) rather than dispersing it, as is seen in pineal parenchymal tumors. The patient had concurrent disease in the suprasellar cistern explaining the diabetes insipidus.

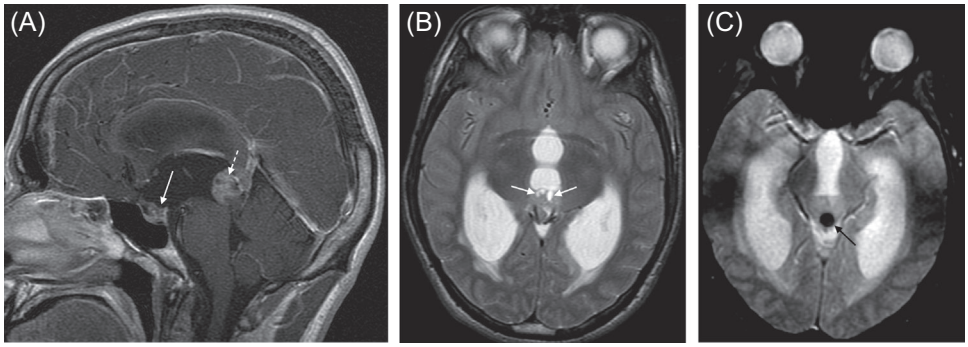


FIGURE 7 Synchronous pineal and suprasellar germinoma in an 18-year-old male with diabetes insipidus. (A) Sagittal T1-weighted postcontrast MR image demonstrates a solidly enhancing pineal mass (dashed arrow) with irregular, enhancing soft tissue within the suprasellar region (arrow). (B) Axial T2-weighted MR image confirms that the areas of differential enhancement within the anterior portion of the pineal mass represent small cysts (arrows). (C) Axial T2* gradient-echo MR image just caudal to image B depicts calcification (arrow) engulfed by the tumor.

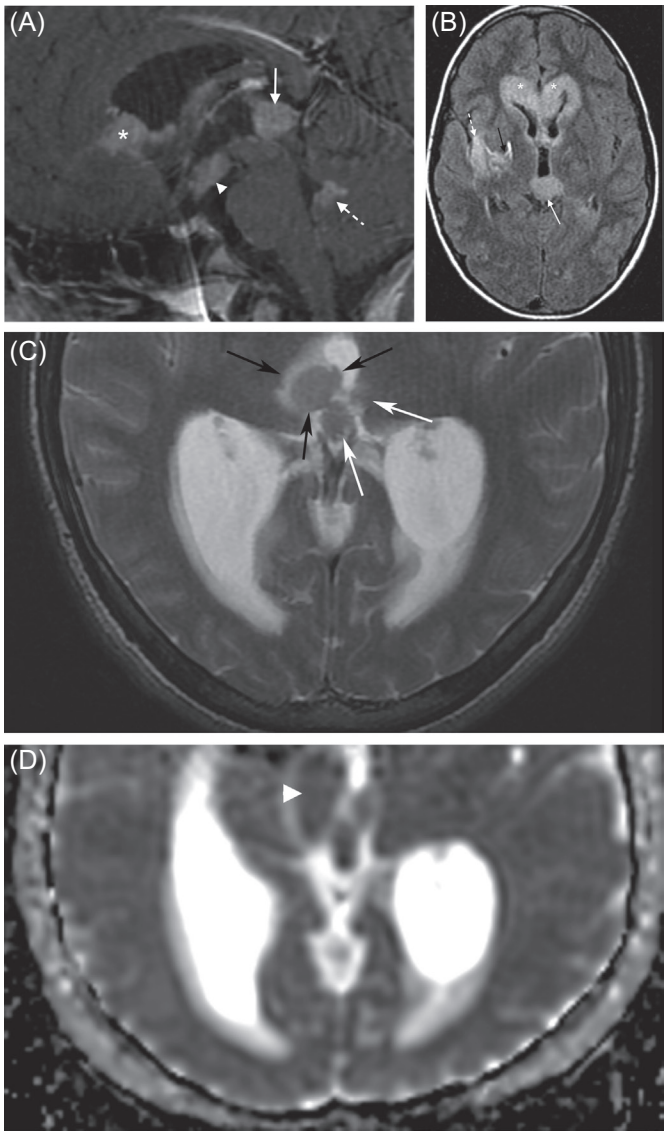


FIGURE 8 Variant manifestations of germinomas in two different patients. (A) Sagittal T1-weighted postcontrast MR image demonstrates synchronous disease in the suprasellar (arrowhead) and pineal region (solid arrow) as well as intraventricular dissemination involving the frontal horns (asterisk) and fourth ventricle (dashed arrow). (B) Axial FLAIR image shows pineal region tumor (solid white arrow) and periventricular tumor in the frontal lobe white matter (asterisk), right insula (dashed arrow), and right basal ganglia (black arrow). (C, D) An axial T2-weighted MR image in a different patient (C) and ADC map from DWI (D) illustrate a pineal region germinoma (white arrows) with local invasion into the right thalamus (black arrows) and restricted diffusion (white arrowhead).

Nongerminomatous Germ-Cell Tumors

NGGCTs include embryonal carcinomas, endodermal sinus (yolk sac) tumors, choriocarcinomas, teratomas, and mixed germ-cell tumors. Pineal teratomas contain three defined germ-cell layers with varying levels of differentiation (e.g., immature, mature, or mature with malignant degeneration). The other NGGCTs represent malignant degeneration of germ-cell derivatives (e.g., placental cells in choriocarcinomas).[73]

Many of the NGGCTs will express tumor markers, which can be detected in serum and CSF. Tumor markers include β-HCG, α-fetoprotein (AFP), and placental alkaline phosphatase.[20,74] Elevated β-HCG levels are seen in choriocarcinoma containing pineal tumors and germinomas with syncytiotrophoblastic giant cells. Yolk sac tumor-containing lesions show elevated AFP.

NGGCTs are typically larger than germinomas. As a group, NGGCTs are more heterogeneous in signal intensity and enhancement than germinomas and almost always contain tumoral cysts (Figures 9–11). Occasionally proteinaceous fluid or hemorrhage is observed within an NGGCT (choriocarcinomas in particular are reported to be more commonly associated with intratumoral hemorrhage, a finding that has been described in several cases but is not felt to be a proven trend).[20,54,68,70,75] Excluding areas of proteinaceous or hemorrhagic fluid signal, NGGCTs are similar in signal intensity on MRI to other high-grade pineal tumors, namely iso- or hypointense on T1-weighted images and intermediate on T2-weighted images (i.e., similar in signal to gray matter).[54] NGGCTs contain calcification in up to 50% of tumors, but the pattern of calcification is generally more multifocal and smaller than the single coarse calcification typically seen in germinomas.[20,43,68] Teratomas are unique for the occasional presence of macroscopic fat.[28,30] Apart from mature teratomas, the borders of NGGCTs tend to be irregular and the tumor often invades adjacent structures, which is suggested by edema along the tumor margins.[54,68]

Pineal Parenchymal Tumors

Pineocytomas, PPTIDs, and pineoblastomas can be conceptualized as pineocyte neoplasms with varying degrees of malignancy/dedifferentiation while maintaining hints of their pineocyte lineage such as continued photoreceptor expression.[19,25,76,77] At the most differentiated end of the spectrum are pineocytomas, which show expression of neuronal markers, absence of atypia, and infrequent mitoses (MIB-1 antibody proliferation indices reported to be less than 2%). For PPTIDs, atypia is present with variable loss of neuronal markers, and mitoses are more frequent (0–10 per 10 high-power fields; MIB 8–12%). At the least differentiated end of the spectrum are pineoblastomas, which are characterized by marked hypercellularity, poorly defined microscopic margins, and a high mitotic rate (MIB 24–27%). Pineoblastomas are the largest tumors (mean size of 4.2 cm) in the spectrum, occur in the youngest patients (mean age of 13 years), and show the highest propensity to disseminate and recur (historically up to 73%). Pineocytomas represent the smallest tumors (2.6 cm in size on average) in the oldest patients (mean age of 47 years), with the lowest tendency to disseminate

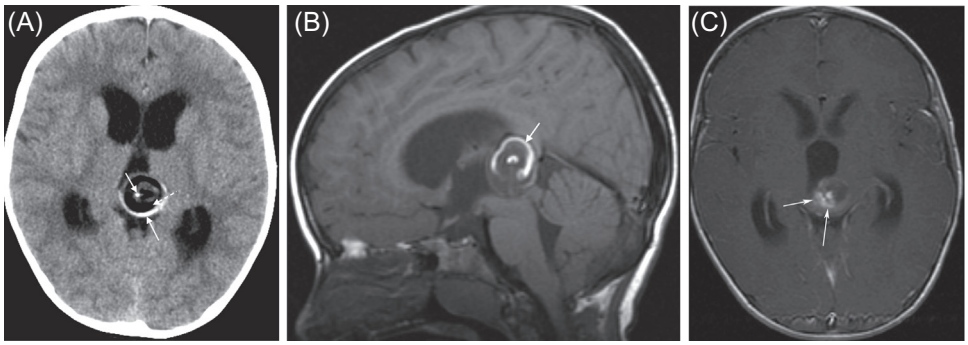


FIGURE 9 Mature teratoma. (A) Axial noncontrast CT shows a heterogeneous mass with tumoral calcification (solid arrows) and fatty components (dashed arrow). (B) Sagittal T1-weighted MR image without contrast demonstrates the fatty component (arrow) in an arc-like configuration. The calcified component is less well appreciated. (C) Axial T1-weighted postcontrast MR image demonstrates mild tumoral enhancement (arrows).

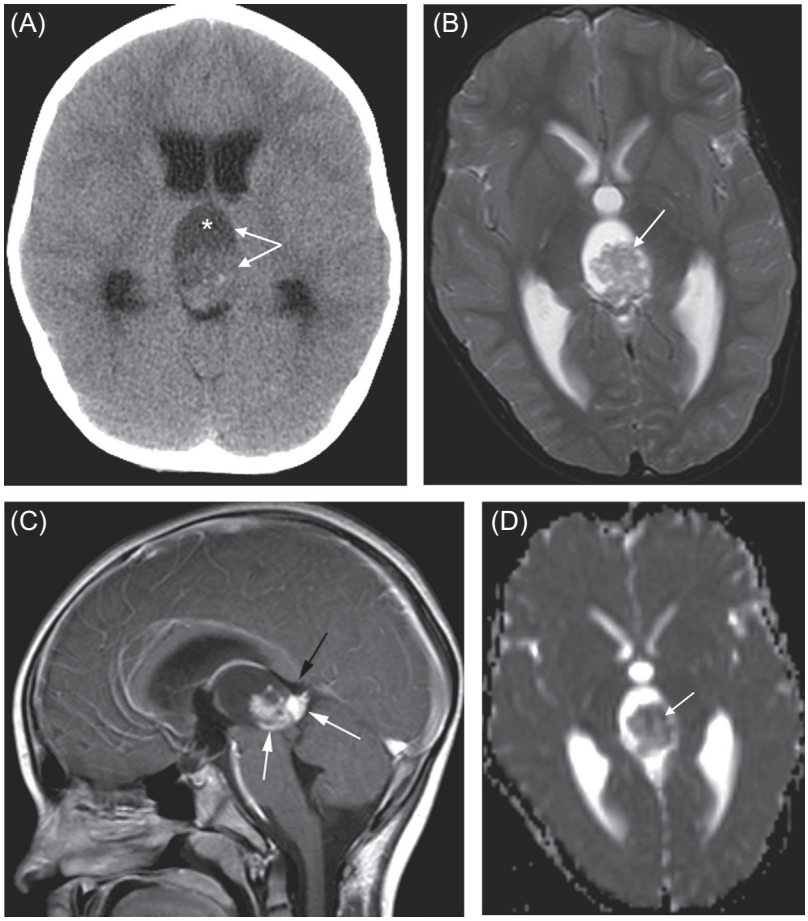


FIGURE 10 Immature teratoma in a 5-year-old boy presenting with headache, nausea, and vomiting. (A) Axial CT without contrast demonstrates a large pineal region tumor (arrows) with the cystic component (asterisk) filling the third ventricle. There is associated hydrocephalus. (B) Axial T2-weighted MR image shows that the solid portion of the tumor (arrow) is isointense to gray matter. (C) Sagittal T1-weighted postcontrast MR image shows the avid enhancement of the solid portion of tumor (white arrow). Note the superior displacement of the internal cerebral veins (black arrow) and distension of the third ventricle secondary to hydrocephalus. (D) ADC map from diffusion-weighted MRI demonstrates that the solid component of the tumor (arrow) has diffusivity coefficients similar to or higher than background brain parenchyma.

or recur (no tumor dissemination was reported in the Fauchon series of 76 patients). The PPTIDs are intermediate in size and age of presentation. The frequencies of tumor dissemination (for grade III tumors) and tumor recurrence (for both grade II and grade III tumors) are slightly less than for pineoblastomas. Papillary tumors of the pineal gland do not clearly fit into this schema as they are believed to arise from the subcommissural organ and have immunohistochemistry characteristics suggesting ependymal differentiation.[78]

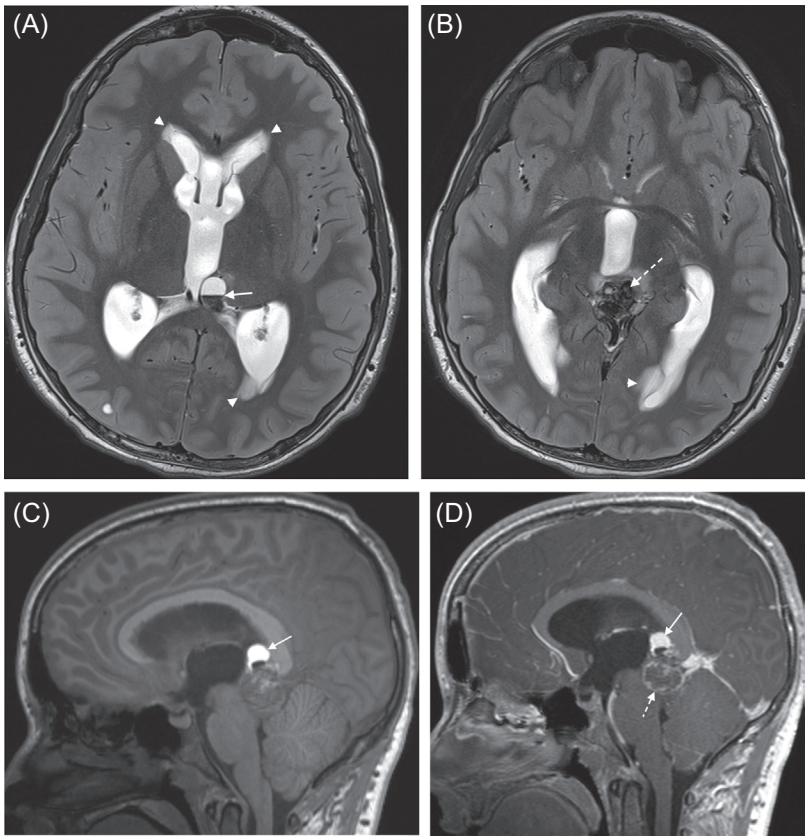


FIGURE 11 Malignant mixed germ-cell tumor with yolk sac tumor and choriocarcinoma components (AFP and β-HCG both elevated) in a 12-year-old male with headaches and Parinaud syndrome. (A, B) Axial T2-weighted MR images demonstrate a pineal mass with a hematocrit level (arrow) in a superiorly located cyst (A) and blood products (dashed arrow) within the solid component of the lesion (B) consistent with a hemorrhagic pineal mass. There is obstructive hydrocephalus with transependymal edema (arrowheads). (C, D) Sagittal T1-weighted MR images before (C) and after (D) contrast confirm the presence of intrinsic T1 hyperintensity (arrow) in the mass consistent with blood products; there is irregular enhancement (dashed arrow, D) of the solid portions of the lesion.

While the relative incidence of the different pineal parenchymal tumors is difficult to determine owing to the rarity of these tumors and the evolving pathologic classification, historical series suggest that pineoblastomas account for 40–80% of pineal parenchymal tumors, pineocytomas for 20–40%, and the remainder of tumors are papillary or intermediate differentiation tumors.[26,69,79]

In general, pineal parenchymal tumors are iso-to hypointense on T1-weighted images and become progressively darker on T2-weighted images with increasing tumoral cellularity, with the caveat that a finely calcified or mineralized tumor will appear dark on T2-weighted images and simulate a hypercellular tumor.

Pineoblastomas

Pineoblastomas are embryonal tumors that resemble primitive neuroectodermal tumors (PNETs). However, both shared and unique transcriptional/genetic alterations distinguish pineoblastoma from supratentorial PNETs and medulloblastomas.[80,81] So while supratentorial PNETs and pineoblastomas are often studied together, the validity of this grouping is being reconsidered as more genomic information becomes available.

On CT, pineoblastomas are usually hyperdense and have variable calcification (Figures 12 and 13).[30,43,44,69,82] When calcification is present, it often has a dispersed pattern as is seen in other pineal parenchymal tumors, although instances of central calcification are also observed.[44] MRI features suggestive of malignancy include heterogeneous signal characteristics and findings of local tumoral invasion (i.e., extension into the thalamus or midbrain).[44,82] On DWI, a spectrum of ADC values is reported, but a propensity for low diffusivity (Figures 12(C) and 13(B)), in keeping with a highly cellular tumor, is expected, especially when minimum ADC values are analyzed.[4,51,69] Generally, there is a tendency for these tumors to be isointense to gray matter on T2-weighted imaging.[44,51,82] CSF tumor dissemination at presentation can be seen and is reported in the range of 14–32%.[83]

Pineocytomas

On CT, pineocytomas contain calcification in over 50% of cases and the calcifications are usually

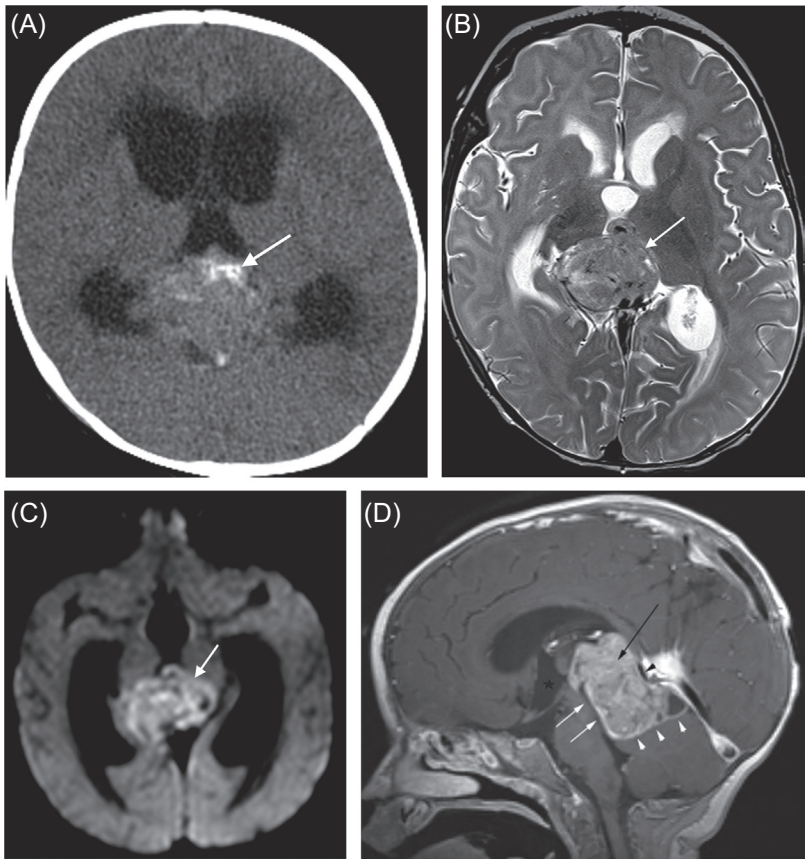


FIGURE 12 Pineoblastoma in a 6-month-old boy presenting with lethargy. (A) Noncontrast CT of the head demonstrates a large solid pineal region mass with dispersed, fine calcifications (arrow) typical of a pineal parenchymal tumor. There is obstructive hydrocephalus. (B) Axial T2-weighted MR image demonstrates that the signal of the solid component of the mass (arrow) is isointense to gray matter. (C) Diffusion-weighted MRI reveals marked restricted diffusion (arrow) consistent with a hypercellular mass. (D) Sagittal T1-weighted SPACE postcontrast MRI demonstrates avid enhancement (black arrow) of the mass. Note the significant mass effect: there is effacement of the cerebral aqueduct (white arrows), downward displacement of the cerebellum (white arrowheads), and upward displacement of the internal cerebral vein (black arrowhead). There is also dilation of the third ventricle (asterisk) from the obstructive hydrocephalus.

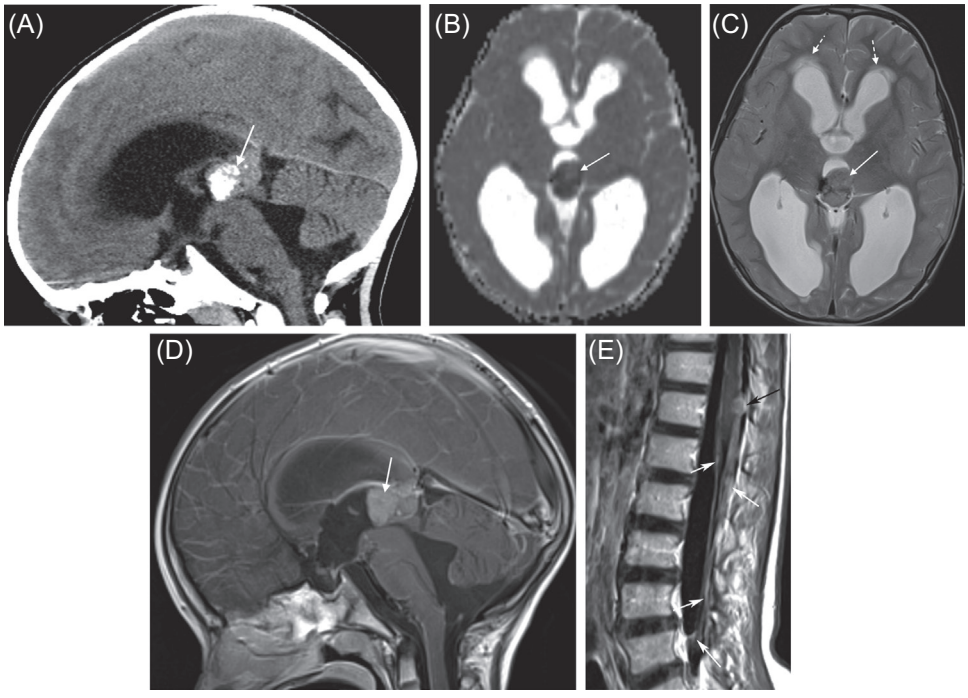


FIGURE 13 Pineoblastoma with tumor dissemination in a 5-year-old boy with headaches and back pain. (A) Sagittal reformatted CT image of the head without contrast demonstrates stippled calcification (arrow) of the pineal region mass. (B) The ADC map from diffusion-weighted MR imaging shows restricted diffusion of the lesion (arrow) consistent with a highly cellular neoplasm. (C) The axial T2-weighted MRI demonstrates mild hypointensity of the mass (solid arrow) relative to normal gray matter signal. There is transependymal edema (dashed arrows) of CSF from the obstructive hydrocephalus. (D) Sagittal T1 postcontrast image confirms avid enhancement of tumor (arrow). (E) Sagittal T1-weighted post-contrast MRI of the lumbar spine reveals irregular thickening of the cauda equina (white arrows) and a more focal nodular tumor implant along the dorsal conus medullaris (black arrow), indicative of CSF dissemination of the pineal tumor.

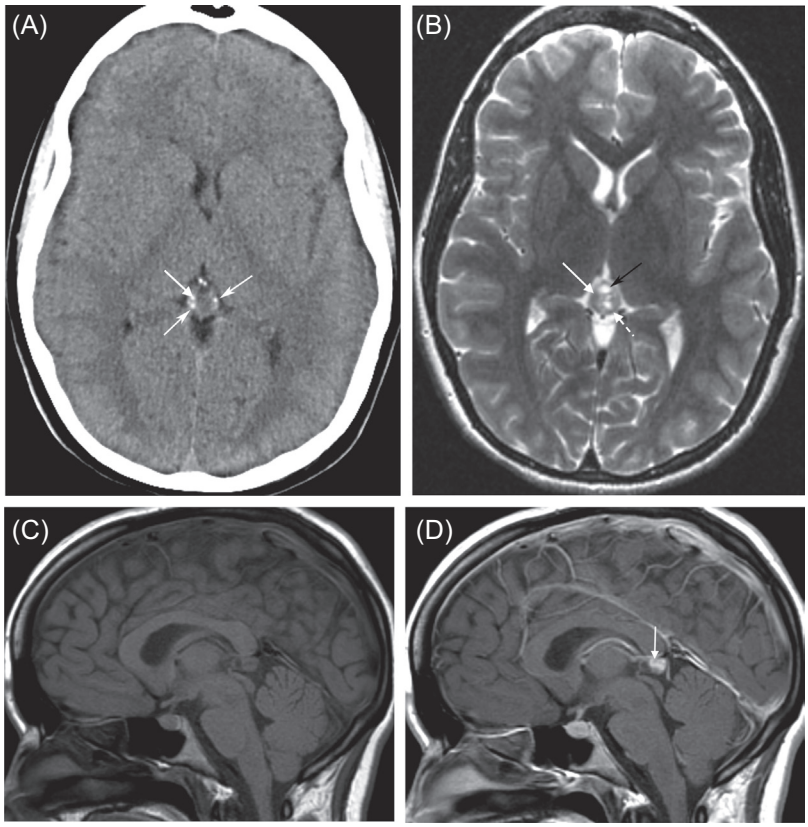


FIGURE 14 Pineocytoma incidentally detected in an 18-year-old female with head trauma. (A) CT of the head without contrast demonstrates dispersed fine calcification (arrows) at the margins of a heterogeneous-appearing pineal gland. (B) Axial T2-weighted MRI shows that the heterogeneous pineal gland corresponds to a cystic (black arrow) and solid mass (solid, white arrow) with mural thickening (dashed white arrow) between the cystic components. (C, D) Sagittal T1-weighted MRI precontrast (C) and postcontrast (D) confirms solid enhancement (arrow) of the lesion. Although the patient was asymptomatic from the lesion, it enlarged over several months, prompting resection.

peripherally dispersed.[30,43,44,69,82,84] Pineocytomas are completely solid in 76% of cases and are typically medium-sized masses with a mean size of approximately 2.0 cm.[52] The typical MRI characteristics are those of a homogeneously enhancing solid mass, with a minority of cases having areas of cystic change and a few reported cases having pronounced cystic changes (Figure 14).[30,44,52,56,69,82] The ADC values of pineocytomas overlap with other pineal tumors, but the minimum ADC values have been suggested to lie in the range of normal background parenchyma, unlike PPTIDs and pineoblastomas.[4,69] Dissemination of pineocytomas is extremely uncommon, except for one pediatric case series in which CSF dissemination was reported in three of six patients.[25,85]

Pineal Parenchymal Tumors of Intermediate Differentiation

Approximately 100 cases of PPTID have been reported in the literature and in these cases the imaging features appear to be similar to those of other pineal parenchymal tumors. The mean size of PPTID falls midway between pineocytomas and pineoblastomas, in the range of 3.1–3.4 cm.[25] On CT, calcifications are inconsistently observed, but when present, they tend to be dispersed peripherally, similar in appearance to pineocytomas.[51,53,69] The CT attenuation of PPTID overlaps with other pineal parenchymal tumors, measuring approximately 40–50 Hounsfield units.[69] MRI signal characteristics are variable and tumors may be iso- to hypointense on T1-weighted images and are of variable signal intensity on T2-weighted images (Figure 15). Enhancement may be homogeneous or heterogeneous, cysts are seen in up to 72% of cases, and margins may be well demarcated or infiltrative.[53,86] Minimum ADC values are midway between the restricted diffusion of pineoblastomas and the normal diffusivity of pineocytomas.[4] Tumor dissemination at presentation is seen in up to one-third of cases (for grade III but not for grade II PPTID, according to the Jouvet criteria), which is less common than what is seen in patients with pineoblastomas but more common than dissemination rates for pineocytomas. Tumor recurrences are approximately 26% (primarily local) for grade II PPTID and 56% (more frequently spinal) for grade III PPTID.[25,77]

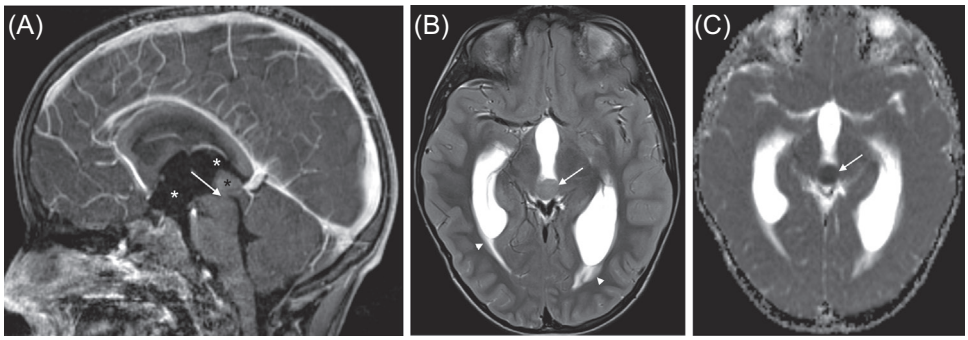


FIGURE 15 PPTID in an 8-year-old boy. (A) Sagittal T1-weighted postcontrast MR image depicts obstruction of the aqueduct (arrow) and distension of the third ventricle (white asterisks) by an enhancing pineal mass (black asterisk). (B) Axial T2-weighted image demonstrates that the pineal mass (arrow) is similar in signal intensity to gray matter. There is transependymal edema (arrowheads) from the hydrocephalus. (C) ADC map from diffusion-weighted MRI indicates marked restricted diffusion of the tumor (arrow) consistent with a hypercellular tumor. The resected tumor had aggressive features but did not fulfill criteria for a pineoblastoma. It was treated as a grade III PPTID.

Papillary Tumors of the Pineal Region

PTPRs are believed to arise from a distinct population of cells within the pineal gland known as the subcommissural organ and have ependymal markers, which suggests a different pathogenesis compared to other pineal parenchymal tumors. The number of reported PTPRs is on the order of 100 total cases, which probably overstates their frequency based on studies of pineal parenchymal tumors of all types. As a result, making representative statements on the imaging appearance of these tumors is limited. Reported cases have generally been cystic and solid in appearance, heterogeneously enhancing, and moderate to large in size (size range 2.0–5.0 cm).[78,87] Solid portions of tumor are generally hypodense on CT and on MRI are iso- to hypointense on T1-weighted images and iso- to hyperintense on T2-weighted images relative to brain cortex (Figure 16). Occasionally, intrinsic T1 shortening (bright signal) has been observed, which is an unusual finding among pineal tumors that do not contain macroscopic fat (i.e., teratomas), hemorrhage, or calcification as an alternative explanation.[88] DWI is not consistently reported in published case series, but where available, ADC values appear to fall in the range of background parenchyma.[51,89] In the largest case series of PTPRs, CSF dissemination was seen in only one of 44 cases at presentation, but 16% eventually developed CSF dissemination and 57% local tumor recurrence.[87]

Other Lesions

Other tumors may occur in the pineal region, such as astrocytomas (Figures 17 and 18), choroid plexus papillomas and carcinomas, meningiomas, ependymomas, atypical teratoid rhabdoid tumors, and metastases.[2,17,33,73,90–92] Nonneoplastic masses in the pineal region include congenital lesions such as arachnoid cysts (Figure 19), lipomas (Figure 20), and dermoid and epidermoid cysts; vascular anomalies such as cavernous malformations, arteriovenous malformations, and vein of Galen malformations (Figure 21); and atrial diverticula from hydrocephalus. Dermoid cysts are circumscribed, nonenhancing masses that may contain fat and typically have restricted diffusion. Lipomas are fatty lesions that may contain calcification, show chemical shift artifact, or undergo signal suppression with MRI fat saturation techniques and do not enhance. Epidermoid cysts are nonenhancing, lobulated lesions that are characterized by striking restricted diffusion. Meningiomas usually have an attachment to the free edge of the tentorium with an enhancing dural tail, are hypointense on T2-weighted images, and show intense enhancement. In our experience, glial neoplasms intrinsic to the pineal gland are unusual, as opposed to tumors that arise from nearby structures and encroach upon the pineal gland such as tectal and thalamic tumors. These extrinsic tumors should be suspected when the pineal gland is intact and displaced. Occasionally a rare or atypically located tumor is found in the pineal region (Figure 22).

MAKING A DIAGNOSIS

As emphasized in this chapter, the imaging appearances of pineal neoplasms overlap considerably. Nonetheless, careful image analysis can lead to a limited differential and guide an efficient patient workup.

As a first step, differentiation must be made between intrinsic and extrinsic pineal region masses. For example, a lesion that is centered within the tectum or thalamus and extends into the pineal region is suggestive of an astrocytoma rather than a primary pineal lesion. There is also a limited differential diagnosis for extra-axial masses in the pineal region: a homogeneous-appearing nonenhancing mass with signal characteristics that mirror CSF is an arachnoid cyst; a homogeneous appearing nonenhancing fatty lesion is a lipoma; a nonenhancing

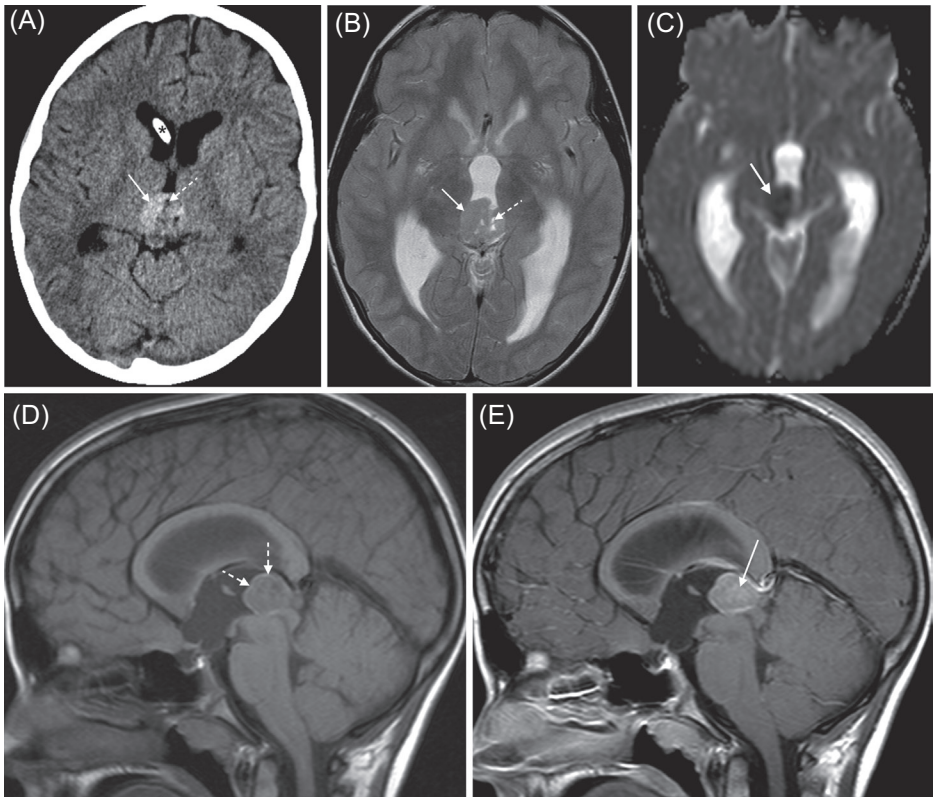


FIGURE 16 PTPR in an 11-year-old boy with headaches, nausea, and vomiting. (A) Noncontrast head CT shows a hyperdense mass in the pineal region (solid arrow) with microcysts (dashed arrow). A ventriculostomy catheter (asterisk) has been placed for hydrocephalus. (B) Axial T2-weighted MRI shows microcysts (dashed arrow) within the lesion. The solid component of the tumor shows signal isointense to gray matter (solid arrow). (C) The ADC map from diffusion-weighted MRI shows diffusion restriction (arrow). Based on the data from (A–C), a hypercellular tumor such as pineoblastoma might be suspected. (D, E). However, sagittal T1-weighted MRI before (D) and after (E) contrast shows some intrinsic hyperintensity (dashed arrows) not attributable to calcification or hemorrhage. There is mildly heterogeneous enhancement (arrow) of the lesion.

lesion with reduced diffusivity is usually an epidermoid; and an enhancing lesion with a dural tail is typically a meningioma.

Once a lesion is determined to be intrinsic to the pineal gland, careful analysis of the cystic component and calcifications is required. In particular, cystic changes should be scrutinized for unusual features such as mural soft tissue nodularity and unusually thick (>2 mm) walls that suggest neoplasm as opposed to a benign pineal cyst. The calcification pattern is also important: normal pineal calcification is typically compact and often solitary, whereas dispersed calcification is encountered in many pineal tumors. The presence of mass effect and symptoms referable to the pineal region or evidence of increased intracranial pressure (such as headache, vomiting, and upward gaze paralysis) also suggest a clinically significant mass.

Detection of specific imaging findings may narrow the diagnostic possibilities. For instance, a pineal mass that shows bright signal on T1-weighted images that cannot be explained by hemorrhage, calcium, or fat is suggestive of a PTPR, whereas a tumor containing fatty foci probably represents a teratoma. Signs of lesion aggressiveness are also helpful: malignant NGGCTs, pineoblastomas, and high-grade PPTIDs are generally larger, more heterogeneous in signal and enhancement, darker on T2-weighted imaging, hyperdense on CT, diffusion restricting, and frequently accompanied by CSF dissemination. Similar-appearing tumors that are more homogeneous in signal and enhancement and contain fewer cysts are more suggestive of germinomas. Integration of imaging with clinical data also assists with diagnosis, as pineoblastomas and germ-cell tumors are more commonly encountered in children, and tumor markers such as β-HCG and AFP suggest a malignant NGGCT.

In the appropriate clinical setting and with supportive radiographic findings, the oncologic diagnosis of an NGGCT can be made based on tumor markers alone (detected within serum and CSF). Other pineal region tumor histologies are best determined by tissue sampling. Procuring tumor tissue is also important for molecular analysis of the tumor. Therefore the radiologist's observations and impressions help determine the best approach to making a diagnosis and help guide treatment (e.g., stereotactic biopsy vs open biopsy, surgical debulking vs maximal resection of tumor).

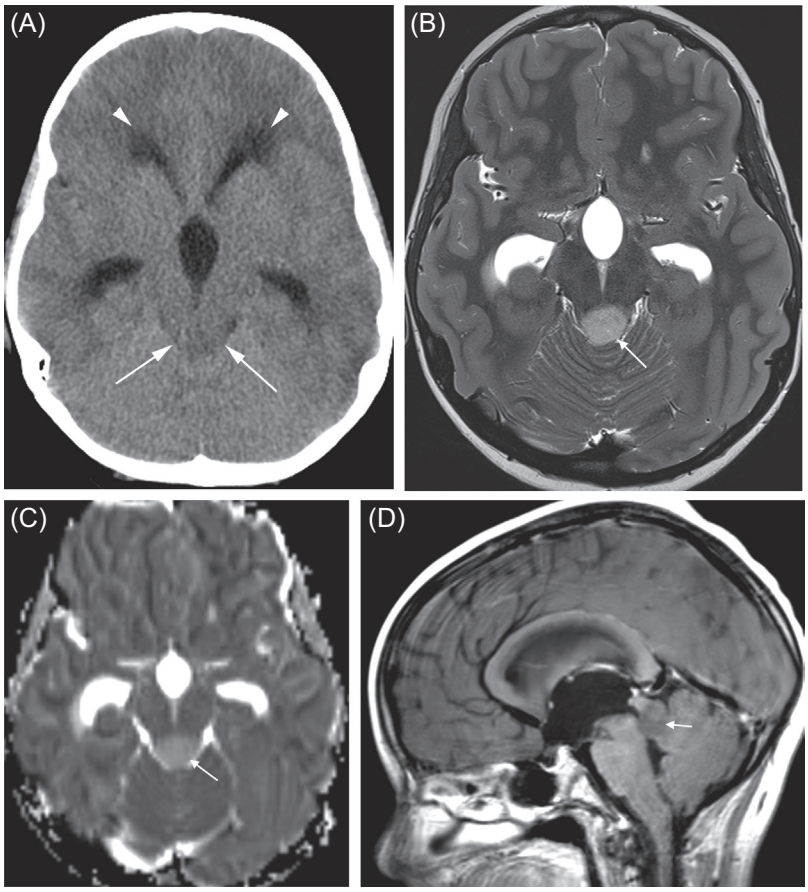


FIGURE 17 Tectal glioma in an 8-year-old with headaches. (A) Noncontrast CT of the head demonstrates hydrocephalus with transependymal edema (arrowheads). There is fullness of the tectum (arrow). (B) Axial T2-weighted MRI confirms the presence of a mass (arrow), hyperintense in signal. (C) ADC map from diffusion-weighted MRI shows the lesion has facilitated diffusion (arrow). (D) Sagittal T1-weighted SPACE postcontrast MRI shows that the mass (arrow) is nonenhancing. The imaging findings are typical of a low-grade tectal glioma and the patient underwent CSF diversion without biopsy.

TREATMENT AND PROGNOSIS

Germinomas are highly radiosensitive, and the majority of germinomas are curable by craniospinal irradiation (CSI) alone with historical survival rates approaching 90% at 10 years.[93] However, these excellent survival statistics were achieved at the cost of long-term complications, which include neurocognitive impairment, radiation vasculopathy, and treatment-induced secondary tumors. Therefore, treatment strategies that minimize radiation dose and/or volume and utilize adjuvant chemotherapy continue to evolve.[66,74]

Malignant NGGCTs secrete either β-HCG or AFP or both and are generally diagnosed based on these tumor markers. First-line therapy for NGGCTs is chemotherapy followed by CSI. If induction chemotherapy does not result in a complete response, surgery prior to CSI is considered. The purpose of surgery is twofold: to establish the nature of the residual soft tissue within the tumor bed and to resect this soft tissue if it represents tumor. Soft tissue residua may be composed of granulation tissue, viable tumor, or differentiated teratoma (remaining after treatment of the malignant elements of the NGGCT). The last scenario is a well-recognized entity called the "growing teratoma" syndrome. With the exception of mature pineal region teratomas, which are benign tumors curable by surgical resection without adjuvant therapy (as shown by the upward of 80% 10-year survival rates[93]), most NGGCTs have a more guarded prognosis than germinomas do. Taken as a group, 5-year survival rates of NGCCTs range between 40% and 70%[94] although, depending on the malignant composition of the tumor (particularly tumors that contain choriocarcinoma, yolk sac tumor, and embryonal carcinoma), 3-year survival rates as low as 9% can be seen.[20] Malignant teratomas have 3-year survival rates in the range of 28–50% and immature teratomas have 10-year survival rates in the range of 45–86%.[20,93]

Pineal parenchymal tumors are generally treated with maximal surgical resection. In cases of pineoblastoma, adjuvant irradiation and high-dose chemotherapy

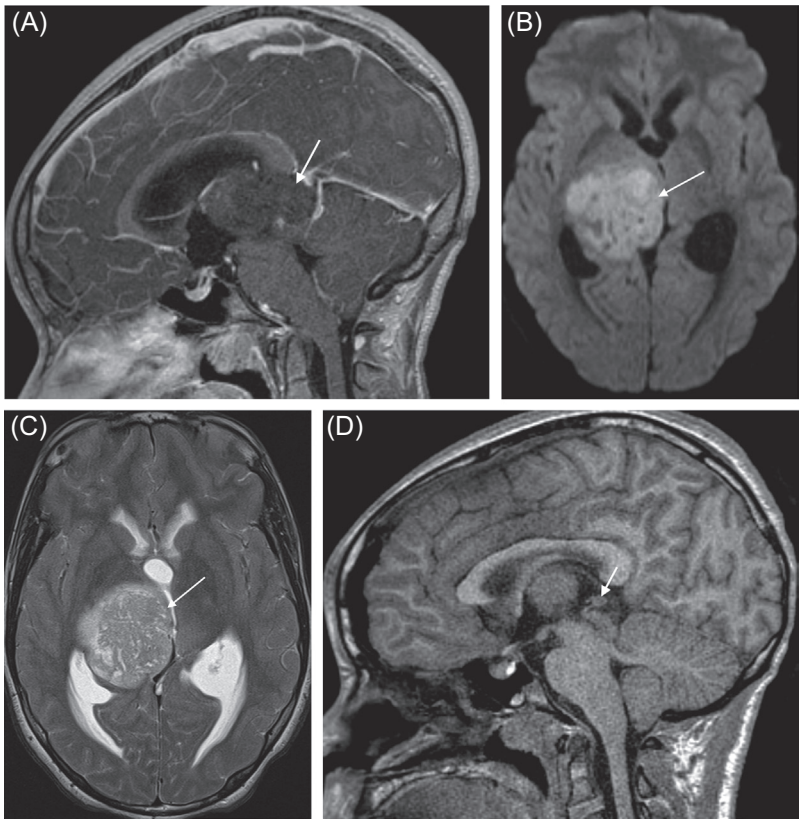


FIGURE 18 Glioblastoma multiforme simulating a pineal parenchymal tumor in a 13-year-old boy evaluated for left-sided esotropia. (A) Sagittal T1-weighted spoiled gradient-echo MR postcontrast image demonstrates a large, nonenhancing mass (arrow) obscuring the native pineal gland. (B) Trace map from diffusion-weighted MRI indicates restricted diffusion (arrow) of the tumor consistent with hypercellularity. (C) Axial T2-weighted MRI shows that the lesion is isointense to gray matter (arrow), but is centered in the right thalamus and extending into the pineal region. The findings are consistent with a highly cellular thalamic tumor such as a glioblastoma multiforme. (D) Sagittal T1 MPRAGE image after partial right thalamic tumor resection demonstrates a normal appearance of the pineal gland (arrow), which is no longer obscured by the thalamic lesion.

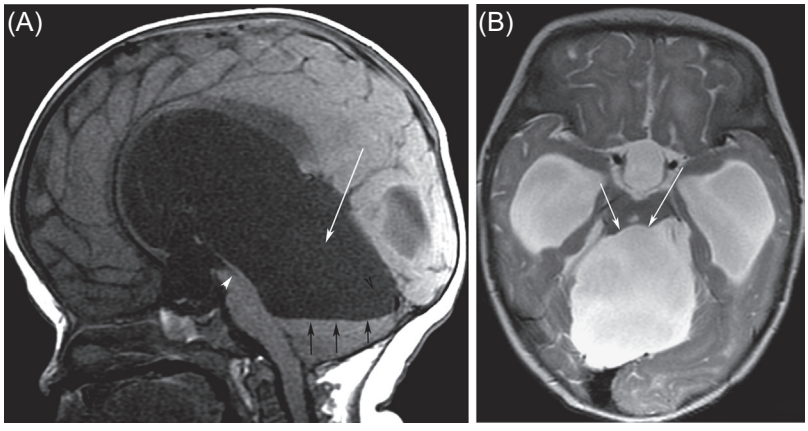


FIGURE 19 Arachnoid cyst. (A) Sagittal T1-weighted MR image shows a very large cyst (white arrow) with compression of the aqueduct (arrowhead) and cerebellum (black arrows). (B) Axial T2-weighted MRI shows the marked mass effect on the tectum (arrows) and obstructive hydrocephalus.

regimens are necessary. Historically, the overall survival rate of pineablastomas has been as low as 10% at 5 years.[25] Newer treatment protocols report 5-year survival rates in the range of 23–73%, with a general trend toward improved survival relative to other supratentorial PNETs. Factors that correlate with a worse outcome include age less than 5 years at presentation, tumor larger than 5 cm, subtotal resection, and tumor dissemination at presentation.[83,95] Pineocytomas are generally treated with maximal surgical



FIGURE 20 Pineal lipoma. Noncontrast CT scan demonstrates a pineal region lipoma (solid arrow). The calcified pineal gland (dashed arrow) lies anterior to the fatty mass.

resection and have good outcomes with 5-year survival rates as high as 91%.[25] The optimal treatment choice for PPTID is less well established and successful treatment is reported using postoperative irradiation, chemotherapy, or both.[25,26,86,96] The role of stereotactic radiosurgery for local control following local tumor progression is controversial in these patients.[97,98] When patients with PPTID are subdivided using the Jouvet methodology, grade II PPTIDs have 74% survival rates and the grade III PPTIDs 39% at 5 years.[25,99] PTPRs have a good prognosis with 5-year survival rates of 80% following maximal surgical resection and adjuvant therapy (usually irradiation, sometimes irradiation and chemotherapy, and rarely chemotherapy alone) in the largest reported case series of 44 patients, despite a high incidence of tumor recurrence.[87]

Benign pineal region masses such as mature teratomas, meningiomas, dermoid and epidermoid cysts, and choroid plexus papillomas are curable by surgery alone.

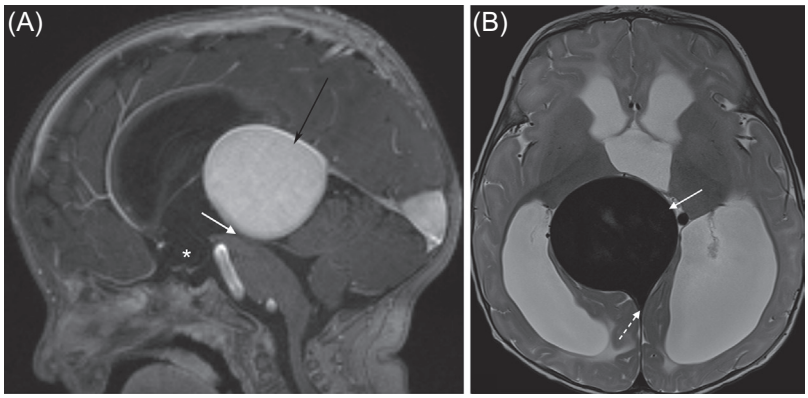


FIGURE 21 Vein of Galen malformation in a 6-month-old with macrocephaly. (A) Sagittal T1-weighted MPRAGE postcontrast MRI demonstrates a large enhancing structure (black arrow) in the pineal region. There is compression of the aqueduct (white arrow) and ballooning of the third ventricle (asterisk) consistent with obstructive hydrocephalus. (B) Axial T2-weighted MR imaging shows that the enhancing structure corresponds to a large flow void (arrow) emptying into the straight sinus (dashed arrow), consistent with a vein of Galen malformation.

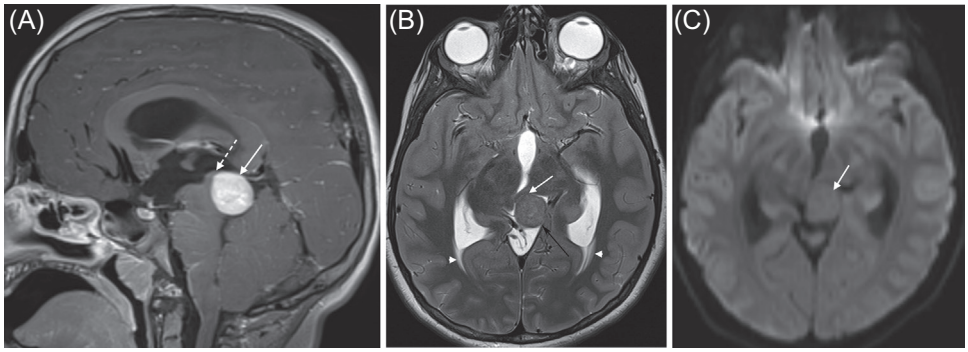


FIGURE 22 Solitary fibrous tumor discovered as part of a headache workup in an 11-year-old female. (A) Postcontrast sagittal T1-weighted SPACE MRI demonstrates an enhancing mass (arrow) abutting to the posterior aspect of the pineal gland (dashed arrow). (B) On the axial T2-weighted MR image, the mass (black arrow) is hypointense to gray matter and compresses the tectum (white arrow), causing hydrocephalus with transependymal edema (arrowheads). (C) Trace map from diffusion imaging shows intermediate diffusion characteristics (arrow).

Astrocytoma treatments are based on the tumor grade and location, analogous to treatments for tumors of similar histology elsewhere in the brain. For example, pediatric tectal gliomas typically undergo CSF diversion and observation, and thalamic astrocytomas are treated based on tumor histology.[100,101]

SUMMARY

There are a small number of tumor histologies that are intrinsic to the pineal gland, and the prognosis for these tumors varies dramatically depending on the tumor type. Unfortunately, there are relatively few imaging features that can guide the radiologist in making a specific diagnosis. A systematic analysis is required for masses in the pineal region. First, the mass must be accurately identified as intrinsic or extrinsic (i.e., extra-axial space, thalamus, or tectum) to the pineal gland. If the pineal gland demonstrates cystic change, further scrutiny to search for atypical features is necessary to determine the likelihood of tumor versus pineal cyst. Any solid tissue should be assessed for features that suggest a specific histology (e.g., T1 shortening and diffusion restriction) or malignancy (e.g., large size, poor margination, invasion of adjacent structures, and CSF dissemination). Clinical information and tumor markers can prove decisive in diagnosing a germ-cell tumor. While this approach rarely yields a specific diagnosis, careful assessment of imaging can facilitate an orderly workup of a pineal mass, help guide the surgeon in biopsy and surgical planning, and aid the clinician in monitoring the patient during treatment and follow-up.

References

1. *Anatomy: Pineal Region*. Amirsys Inc.; 2005–2013 Accessed 04.09.13.
2. Smith AB, Rushing EJ, Smirniotopoulos JG. From the archives of the AFIP: lesions of the pineal region: radiologic-pathologic correlation. *Radiographics*. November 2010;30(7):2001–2020.
3. Inoue Y, Saiwai S, Miyamoto T, Katsuyama J. Enhanced high-resolution sagittal MRI of normal pineal glands. *J Comput Assist Tomogr*. March–April 1994;18(2):182–186.
4. Zhu L, Ren G, Li K, et al. Pineal parenchymal tumours: minimum apparent diffusion coefficient in prediction of tumour grading. *J Int Med Res*. 2011;39(4):1456–1463.
5. Sumida M, Barkovich AJ, Newton TH. Development of the pineal gland: measurement with MR. *AJNR Am J Neuroradiol*. February 1996;17(2):233–236.
6. Sun B, Wang D, Tang Y, et al. The pineal volume: a three-dimensional volumetric study in healthy young adults using 3.0 T MR data. *Int J Dev Neurosci*. November 2009;27(7):655–660.
7. Apuzzo M, Gruen P. Pineal physiology. In: Wilkins R, Rengachary S, eds. *Neurosurgery*. New York: Mcgraw-Hill; 1996:977–994.
8. Macchi MM, Bruce JN. Human pineal physiology and functional significance of melatonin. *Front Neuroendocrinol*. September–December 2004;25(3–4):177–195.
9. Hoffman HJ, Yoshida M, Becker LE, Hendrick EB, Humphreys RP. Pineal region tumors in childhood. Experience at the Hospital for Sick Children. 1983. *Pediatr Neurosurg*. 1994;21(1):91–103. discussion 104.
10. Russell DS, Rubinstein LJ. *Pathology of Tumors of the Nervous System*. 4th ed. Baltimore: Wiliams & Wilkins; 1977. 284–295.
11. Surawicz TS, McCarthy BJ, Kupelian V, Jukich PJ, Bruner JM, Davis FG. Descriptive epidemiology of primary brain and CNS tumors: results from the Central Brain Tumor Registry of the United States, 1990–1994. *Neuro Oncol*. January 1999;1(1):14–25.
12. Kaatsch P, Rickert CH, Kuhl J, Schuz J, Michaelis J. Population-based epidemiologic data on brain tumors in German children. *Cancer*. December 15, 2001;92(12):3155–3164.
13. Dolecek TA, Propp JM, Stroup NE, Kruchko C. CBTRUS statistical report: primary brain and central nervous system tumors diagnosed in the United States in 2005–2009. *Neuro Oncol*. November 2012;14(suppl 5):v1–49.
14. Koide O, Watanabe Y, Sato K. Pathological survey of intracranial germinoma and pinealoma in Japan. *Cancer*. April 15, 1980;45(8):2119–2130.
15. Oi S. Recent advances and racial differences in therapeutic strategy to the pineal region tumor. *Childs Nerv Syst*. January–February 1998;14(1–2):33–35.
16. DeGirolami U, Schmidek H. Clinicopathological study of 53 tumors of the pineal region. *J Neurosurg*. October 1973;39(4):455–462.
17. Edwards MS, Hudgins RJ, Wilson CB, Levin VA, Wara WM. Pineal region tumors in children. *J Neurosurg*. May 1988;68(5):689–697.
18. Oi S, Matsuzawa K, Choi JU, Kim DS, Kang JK, Cho BK. Identical characteristics of the patient populations with pineal region tumors in Japan and in Korea and therapeutic modalities. *Childs Nerv Syst*. January–February 1998;14(1–2):36–40.
19. Hirato J, Nakazato Y. Pathology of pineal region tumors. *J Neurooncol*. September 2001;54(3):239–249.
20. Matsutani M, Sano K, Takakura K, et al. Primary intracranial germ cell tumors: a clinical analysis of 153 histologically verified cases. *J Neurosurg*. March 1997;86(3):446–455.
21. Bjornsson J, Scheithauer BW, Okazaki H, Leech RW. Intracranial germ cell tumors: pathobiological and immunohistochemical aspects of 70 cases. *J Neuropathol Exp Neurol*. January 1985;44(1):32–46.
22. Korogi Y, Takahashi M, Ushio Y. MRI of pineal region tumors. *J Neurooncol*. September 2001;54(3):251–261.
23. Louis DN, Ohgaki H, Wiestler OD, et al. The 2007 WHO classification of tumours of the central nervous system. *Acta neuropathol*. August 2007;114(2):97–109.
24. Jouvet A, Fauchon F, Liberski P, et al. Papillary tumor of the pineal region. *Am J Surg Pathol*. April 2003;27(4):505–512.
25. Fauchon F, Jouvet A, Paquis P, et al. Parenchymal pineal tumors: a clinicopathological study of 76 cases. *Int J Radiat Oncol Biol Phys*. March 1, 2000;46(4):959–968.
26. Villa S, Miller RC, Krengli M, et al. Primary pineal tumors: outcome and prognostic factors–a study from the Rare Cancer Network (RCN). *Clin Transl Oncol*. November 2012;14(11):827–834.
27. Abramson DH, Dunkel IJ, Marr BP, Francis J, Gobin YP. Incidence of pineal gland cyst and pineoblastoma in children with retinoblastoma during the chemoreduction era. *Am J Ophthalmol*. December 2013;156(6):1319–1320.
28. Zimmerman RA, Bilaniuk LT, Wood JH, Bruce DA, Schut L. Computed tomography of pineal, parapineal, and histologically related tumors. *Radiology*. December 1980;137(3):669–677.
29. Regis J, Bouillot P, Rouby-Volot F, Figarella-Branger D, Dufour H, Peragut JC. Pineal region tumors and the role of stereotactic biopsy: review of the mortality, morbidity, and diagnostic rates in 370 cases. *Neurosurgery*. November 1996;39(5):907–912. discussion 912–904.

30. Ganti SR, Hilal SK, Stein BM, Silver AJ, Mawad M, Sane P. CT of pineal region tumors. *AJR Am J Roentgenol*. March 1986;146(3):451–458.
31. Cho BK, Wang KC, Nam DH, et al. Pineal tumors: experience with 48 cases over 10 years. *Childs Nerv Syst*. January–February 1998;14(1–2):53–58.
32. Tong T, Zhenwei Y, Xiaoyuan F. MRI and 1H-MRS on diagnosis of pineal region tumors. *Clin Imaging*. November–December 2012;36(6):702–709.
33. Tien RD, Barkovich AJ, Edwards MS. MR imaging of pineal tumors. *AJR Am J Roentgenol*. July 1990;155(1):143–151.
34. Fleege MA, Miller GM, Fletcher GP, Fain JS, Scheithauer BW. Benign glial cysts of the pineal gland: unusual imaging characteristics with histologic correlation. *AJNR Am J Neuroradiol*. January 1994;15(1):161–166.
35. Dolendo MC, Lin TP, Tat OH, Chong QT, Timothy LK. Parkinsonism as an unusual presenting symptom of pineal gland teratoma. *Pediatr Neurol*. April 2003;28(4):310–312.
36. Higashi K, Katayama S, Orita T. Pineal apoplexy. *J Neurol Neurosurg Psychiatry*. November 1979;42(11):1050–1053.
37. Crawford JR, Santi MR, Vezina G, et al. CNS germ cell tumor (CNSGCT) of childhood: presentation and delayed diagnosis. *Neurology*. May 15, 2007;68(20):1668–1673.
38. Etzioni A, Luboshitzky R, Tiosano D, Ben-Harush M, Goldsher D, Lavie P. Melatonin replacement corrects sleep disturbances in a child with pineal tumor. *Neurology*. January 1996;46(1):261–263.
39. Jan JE, Tai J, Hahn G, Rothstein RR. Melatonin replacement therapy in a child with a pineal tumor. *J Child Neurol*. February 2001;16(2):139–140.
40. Ellis DL, Kanter J, Walsh JW, Drury SS. Posterior fossa syndrome after surgical removal of a pineal gland tumor. *Pediatr Neurol*. December 2011;45(6):417–419.
41. Mittal VA, Karlsgodt K, Zinberg J, Cannon TD, Bearden CE. Identification and treatment of a pineal region tumor in an adolescent with prodromal psychotic symptoms. *Am J Psychiatry*. September 2010;167(9):1033–1037.
42. Zimmerman RA, Bilaniuk LT. Age-related incidence of pineal calcification detected by computed tomography. *Radiology*. March 1982;142(3):659–662.
43. Chang T, Teng MM, Guo WY, Sheng WC. CT of pineal tumors and intracranial germ-cell tumors. *AJR Am J Roentgenol*. December 1989;153(6):1269–1274.
44. Nakamura M, Saeki N, Iwadate Y, Sunami K, Osato K, Yamaura A. Neuroradiological characteristics of pineocytoma and pineoblastoma. *Neuroradiology*. July 2000;42(7):509–514.
45. Choy W, Kim W, Spasic M, Voth B, Yew A, Yang I. Pineal cyst: a review of clinical and radiological features. *Neurosurg Clin N Am*. July 2011;22(3):341–351. vii.
46. Al-Holou WN, Terman SW, Kilburg C, et al. Prevalence and natural history of pineal cysts in adults. *J Neurosurg*. December 2011;115(6):1106–1114.
47. Whitehead MT, Oh CC, Choudhri AF. Incidental pineal cysts in children who undergo 3-T MRI. *Pediatr Radiol*. July 14, 2013.
48. Barboriak DP, Lee L, Provenzale JM. Serial MR imaging of pineal cysts: implications for natural history and follow-up. *AJR Am J Roentgenol*. March 2001;176(3):737–743.
49. Al-Holou WN, Maher CO, Muraszko KM, Garton HJ. The natural history of pineal cysts in children and young adults. *J Neurosurg Pediatr*. February 2010;5(2):162–166.
50. Mamourian AC, Yarnell T. Enhancement of pineal cysts on MR images. *AJNR Am J Neuroradiol*. July–August 1991;12(4):773–774.
51. Dumrongpisutikul N, Intrapiromkul J, Yousem DM. Distinguishing between germinomas and pineal cell tumors on MR imaging. *AJNR Am J Neuroradiol*. March 2012;33(3):550–555.
52. Fakhran S, Escott EJ. Pineocytoma mimicking a pineal cyst on imaging: true diagnostic dilemma or a case of incomplete imaging? *AJNR Am J Neuroradiol*. January 2008;29(1):159–163.
53. Komakula S, Warmuth-Metz M, Hildenbrand P, et al. Pineal parenchymal tumor of intermediate differentiation: imaging spectrum of an unusual tumor in 11 cases. *Neuroradiology*. August 2011;53(8):577–584.
54. Liang L, Korogi Y, Sugahara T, et al. MRI of intracranial germ-cell tumours. *Neuroradiology*. May 2002;44(5):382–388.
55. Sato TS, Kirby PA, Buatti JM, Moritani T. Papillary tumor of the pineal region: report of a rapidly progressive tumor with possible multicentric origin. *Pediatr Radiol*. February 2009;39(2):188–190.
56. Engel U, Gottschalk S, Niehaus L, et al. Cystic lesions of the pineal region–MRI and pathology. *Neuroradiology*. June 2000;42(6):399–402.
57. Mandera M, Marcol W, Bierzynska-Macyszyn G, Kluczewska E. Pineal cysts in childhood. *Childs Nerv Syst*. November 2003;19(10–11):750–755.
58. Hayashida Y, Hirai T, Korogi Y, et al. Pineal cystic germinoma with syncytiotrophoblastic giant cells mimicking MR imaging findings of a pineal cyst. *AJNR Am J Neuroradiol*. October 2004;25(9):1538–1540.
59. Steven DA, McGinn GJ, McClarty BM. A choroid plexus papilloma arising from an incidental pineal cyst. *AJNR Am J Neuroradiol*. May 1996;17(5):939–942.
60. Mamourian AC, Towfighi J. Pineal cysts: MR imaging. *AJNR Am J Neuroradiol*. November–December 1986;7(6):1081–1086.
61. Pu Y, Mahankali S, Hou J, et al. High prevalence of pineal cysts in healthy adults demonstrated by high-resolution, noncontrast brain MR imaging. *AJNR Am J Neuroradiol*. October 2007;28(9):1706–1709.
62. Al-Holou WN, Garton HJ, Muraszko KM, Ibrahim M, Maher CO. Prevalence of pineal cysts in children and young adults. Clinical article. *J Neurosurg Pediatr*. September 2009;4(3):230–236.
63. Cooper ER. The human pineal gland and pineal cysts. *J Anat*. October 1932;67(Pt 1):28–46.
64. Osborn AG, Preece MT. Intracranial cysts: radiologic-pathologic correlation and imaging approach. *Radiology*. June 2006;239(3):650–664.
65. Jennings MT, Gelman R, Hochberg F. Intracranial germ-cell tumors: natural history and pathogenesis. *J Neurosurg*. August 1985;63(2):155–167.
66. Schoenfeld A, Haas-Kogan DA, Molinaro A, et al. Pure germinomas of the central nervous system: treatment strategies and outcomes. *J Neurooncol*. September 5, 2014.
67. Lim do H, Yoo KH, Lee NH, et al. Intensive chemotherapy followed by reduced-dose radiotherapy for biopsy-proven CNS germinoma with elevated beta-human chorionic gonadotropin. *J Neurooncol*. April 2014;117(2):279–285.
68. Fujimaki T, Matsutani M, Funada N, et al. CT and MRI features of intracranial germ cell tumors. *J Neurooncol*. 1994;19(3):217–226.
69. Kakigi T, Okada T, Kanagaki M, et al. Quantitative imaging values of CT, MR, and FDG-PET to differentiate pineal parenchymal tumors and germinomas: are they useful? *Neuroradiology*. April 2014;56(4):297–303.
70. Sumida M, Uozumi T, Kiya K, et al. MRI of intracranial germ cell tumours. *Neuroradiology*. January 1995;37(1):32–37.
71. Douglas-Akinwande AC, Ying J, Momin Z, Mourad A, Hattab EM. Diffusion-weighted imaging characteristics of primary central nervous system germinoma with histopathologic correlation: a retrospective study. *Acad Radiol*. November 2009;16(11):1356–1365.
72. Maity A, Shu HK, Janss A, et al. Craniospinal radiation in the treatment of biopsy-proven intracranial germinomas: twenty-five years' experience in a single center. *Int J Radiat Oncol Biol Phys*. March 15, 2004;58(4):1165–1170.

73. Smirniotopoulos JG, Rushing EJ, Mena H. Pineal region masses: differential diagnosis. *Radiographics*. May 1992;12(3):577–596.
74. Thakkar JP, Chew L, Villano JL. Primary CNS germ cell tumors: current epidemiology and update on treatment. *Med Oncol*. June 2013;30(2):496.
75. Zee CS, Segall H, Apuzzo M, et al. MR imaging of pineal region neoplasms. *J Comput Assisted Tomogr*. January–February 1991;15(1):56–63.
76. Han SJ, Clark AJ, Ivan ME, Parsa AT, Perry A. Pathology of pineal parenchymal tumors. *Neurosurg Clin N Am*. July 2011;22(3): 335–340. vii.
77. Jouvet A, Saint-Pierre G, Fauchon F, et al. Pineal parenchymal tumors: a correlation of histological features with prognosis in 66 cases. *Brain pathol*. January 2000;10(1):49–60.
78. Poulgrain K, Gurgo R, Winter C, Ong B, Lau Q. Papillary tumour of the pineal region. *J Clin Neurosci*. August 2011;18(8):1007–1017.
79. Schild SE, Scheithauer BW, Schomberg PJ, et al. Pineal parenchymal tumors. Clinical, pathologic, and therapeutic aspects. *Cancer*. August 1, 1993;72(3):870–880.
80. Adamski J, Ramaswamy V, Huang A, Bouffet E. Advances in managing medulloblastoma and intracranial primitive neuroectodermal tumors. *F1000Prime Rep*. 2014;6:56.
81. Miller S, Rogers HA, Lyon P, et al. Genome-wide molecular characterization of central nervous system primitive neuroectodermal tumor and pineoblastoma. *Neuro Oncol*. August 2011;13(8):866–879.
82. Chiechi MV, Smirniotopoulos JG, Mena H. Pineal parenchymal tumors: CT and MR features. *J Comput Assisted Tomogr*. July–August 1995;19(4):509–517.
83. Tate M, Sughrue ME, Rutkowski MJ, et al. The long-term postsurgical prognosis of patients with pineoblastoma. *Cancer*. January 1, 2012;118(1):173–179.
84. Nakagawa H, Iwasaki S, Kichikawa K, et al. MR imaging of pineocytoma: report of two cases. *AJNR Am J Neuroradiol*. January–February 1990;11(1):195–198.
85. D'Andrea AD, Packer RJ, Rorke LB, et al. Pineocytomas of childhood. A reappraisal of natural history and response to therapy. *Cancer*. April 1, 1987;59(7):1353–1357.
86. Ito T, Kanno H, Sato K, et al. Clinicopathologic study of pineal parenchymal tumors of intermediate differentiation. *World Neurosurg*. May–June 2014;81(5–6):783–789.
87. Fauchon F, Hasselblatt M, Jouvet A, et al. Role of surgery, radiotherapy and chemotherapy in papillary tumors of the pineal region: a multicenter study. *J Neurooncol*. April 2013;112(2):223–231.
88. Chang AH, Fuller GN, Debnam JM, et al. MR imaging of papillary tumor of the pineal region. *AJNR Am J Neuroradiol*. January 2008;29(1):187–189.
89. Cerase A, Vallone IM, Di Pietro G, Oliveri G, Miracco C, Venturi C. Neuroradiological follow-up of the growth of papillary tumor of the pineal region: a case report. *J Neurooncol*. December 2009;95(3):433–435.
90. Fang AS, Meyers SP. Magnetic resonance imaging of pineal region tumours. *Insights Imaging*. June 2013;4(3):369–382.
91. Magrini S, Feletti A, Marton E, Longatti P. Gliomas of the pineal region. *J Neurooncol*. July 3, 2013.
92. Meyers SP, Khademian ZP, Biegel JA, Chuang SH, Korones DN, Zimmerman RA. Primary intracranial atypical teratoid/rhabdoid tumors of infancy and childhood: MRI features and patient outcomes. *AJNR Am J Neuroradiol*. May 2006;27(5):962–971.
93. Kyritsis AP. Management of primary intracranial germ cell tumors. *J Neurooncol*. January 2010;96(2):143–149.
94. Robertson PL, DaRosso RC, Allen JC. Improved prognosis of intracranial non-germinoma germ cell tumors with multimodality therapy. *J Neurooncol*. March 1997;32(1):71–80.
95. Pizer BL, Weston CL, Robinson KJ, et al. Analysis of patients with supratentorial primitive neuro-ectodermal tumours entered into the SIOP/UKCCSG PNET 3 study. *Eur J Cancer*. May 2006;42(8): 1120–1128.
96. Yi JW, Kim HJ, Choi YJ, et al. Successful treatment by chemotherapy of pineal parenchymal tumor with intermediate differentiation: a case report. *Cancer Res Treat*. September 2013;45(3):244–249.
97. Clark AJ, Sughrue ME, Ivan ME, et al. Factors influencing overall survival rates for patients with pineocytoma. *J Neurooncol*. November 2010;100(2):255–260.
98. Wilson DA, Awad AW, Brachman D, et al. Long-term radiosurgical control of subtotally resected adult pineocytomas. *J Neurosurg*. August 2012;117(2):212–217.
99. Lutterbach J, Fauchon F, Schild SE, et al. Malignant pineal parenchymal tumors in adult patients: patterns of care and prognostic factors. *Neurosurgery*. July 2002;51(1):44–55. discussion 55–46.
100. Pollack IF, Pang D, Albright AL. The long-term outcome in children with late-onset aqueductal stenosis resulting from benign intrinsic tectal tumors. *J Neurosurg*. April 1994;80(4):681–688.
101. Albright AL. Feasibility and advisability of resections of thalamic tumors in pediatric patients. *J Neurosurg*. May 2004;100(5 suppl Pediatrics):468–472.

CHAPTER

49

Chordomas and Other Skull Base Tumors

Eric C. Bourekas[1,2], *Herbert B. Newton*[2], *H.Wayne Slone*[1]

[1]Dardinger Neuro-Oncology Center, Departments of Radiology, Wexner Medical Center at The Ohio State University and James Cancer Hospital and Solove Research Institute, Columbus, OH, USA; [2]Division of Neuro-Oncology, Departments of Neurology and Neurosurgery, Dardinger Neuro-Oncology Center, Wexner Medical Center at The Ohio State University and James Cancer Hospital and Solove Research Institute, Columbus, OH, USA

CHORDOMA

Chordomas are rare, locally aggressive, low-grade to intermediate-grade malignant tumors that arise from embryonic notochord remnants or ectopic notochordal tissue, usually within bone.[1] They represent 4% of all primary bone tumors but only 0.2–1% of primary intracranial tumors.[1,2] Since first being described in 1894 by Ribbert, little more than 1000 cases have been reported.[2] They usually occur along the midline, anywhere from the spheno–occipital synchondrosis of the clivus to the sacro–coccygeal region (see Figures 1–4). Cranial chordomas represent approximately one-third of all chordomas, with 15–33% being spinal chordomas and 29–49% being sacral chordomas.[1–3] Cranial chordomas typically occur at the spheno–occipital synchondrosis of the clivus and less commonly at the basisphenoid and basioccipital synchondroses, but may occur anywhere along the midline, having been described in the nose,[4] nasal septum,[5] oropharynx,[6] ethmoid sinus,[7] sphenoid sinus, maxilla, retropharyngeal extraosseous,[8] retroclival extradural,[9] intradural,[10] sella turcica (see Figure 4),[11–13] suboccipital region,[14] and nasopharynx.[15] Cranial chordomas can occur off midline in 14% of cases, and have been described in the cavernous sinus (see Figure 5), jugular foramen (see Figure 6)[16–18] cerebellopontine angle,[19] intradural cerebellar,[20] and temporal bone at the petrous apex.[21]

The overall incidence of chordomas is 0.08 per 100,000. They are more common in whites than blacks (4:1)[1,2] and more common in males than females, as much as 2:1 in one series.[3] Median age of diagnosis is 58.5 years, although in blacks the median age of diagnosis is much younger, at 27 years. The median age for cranial tumors is 49 years, which is much younger than the median age of presentation for sacral tumors, 69 years. The younger age of cranial presentation may in part relate to the earlier manifestation of symptoms. Females also have a greater likelihood of cranial presentation, as do blacks. Cranial chordomas are more common in females and typically occur at a younger age.[1,2]

Pathology

Grossly, chordomas are soft, gelatinous, semitranslucent blue-gray, multilobulated tumors. Histologically, although there are no absolute or specific histologic features, there are four criteria used for the diagnosis of chordoma that are fairly constant: (1) a lobular arrangement of cells; (2) a tendency for the cells to grow in cords, irregular bands, or pseudoacinar forms; (3) production of abundant intercellular mucinous matrix; and most characteristically (4) the presence of large physaliphorous and vacuolated cells.[1,15] There are two different histologic types of chordomas: typical or classic chordomas and chondroid chordomas. Typical chordomas are primarily made up of cords of physaliphorous cells. The chondroid variant of chordomas, first described by Heffelfinger et al., in 1973, has a striking histologic resemblance to chondrosarcomas and chondromas, with the stroma resembling hyaline cartilage with neoplastic cells in lacunae.[1,3] The chondroid variant represents approximately 14% of all chordomas, although almost all chondroid chordomas occur in the cranial region and represent a third of all chordomas in the spheno–occipital region. They are more common in females, present at a younger age, and are believed to be associated with a better prognosis.[3] Typical chordomas

Handbook of Neuro-Oncology Neuroimaging, Second Edition
http://dx.doi.org/10.1016/B978-0-12-800945-1.00049-5

© 2016 Elsevier Ltd. All rights reserved.

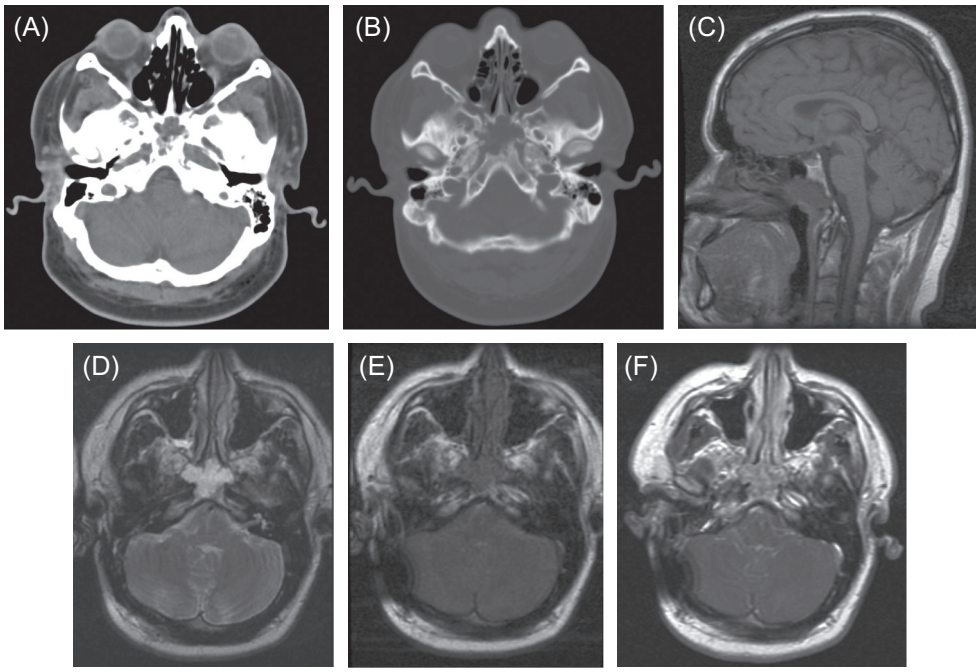


FIGURE 1 **Typical chordoma.** Thirty-year-old male with a history of a cochlear implant presented with right facial pain, headache, and fever. Immunostains were positive for cytokeratin AE1/AE3 and S-100 protein. (A) CT of the head without contrast and (B) CT of the head with bone windowing demonstrate a lytic lesion of the clivus. (C) MRI sagittal T1-weighted image without contrast demonstrates the mass of the clivus, isointense to muscle and projecting into the nasopharynx. (D) MRI axial T2-weighted image without contrast shows that the mass is lobulated and of increased signal. The signal is relatively uniform which occurs in only 21%. (E) MRI axial T1-weighted image without contrast. The lesion is of low signal and (F) MRI axial T1-weighted image with contrast demonstrates relatively homogeneous enhancement.

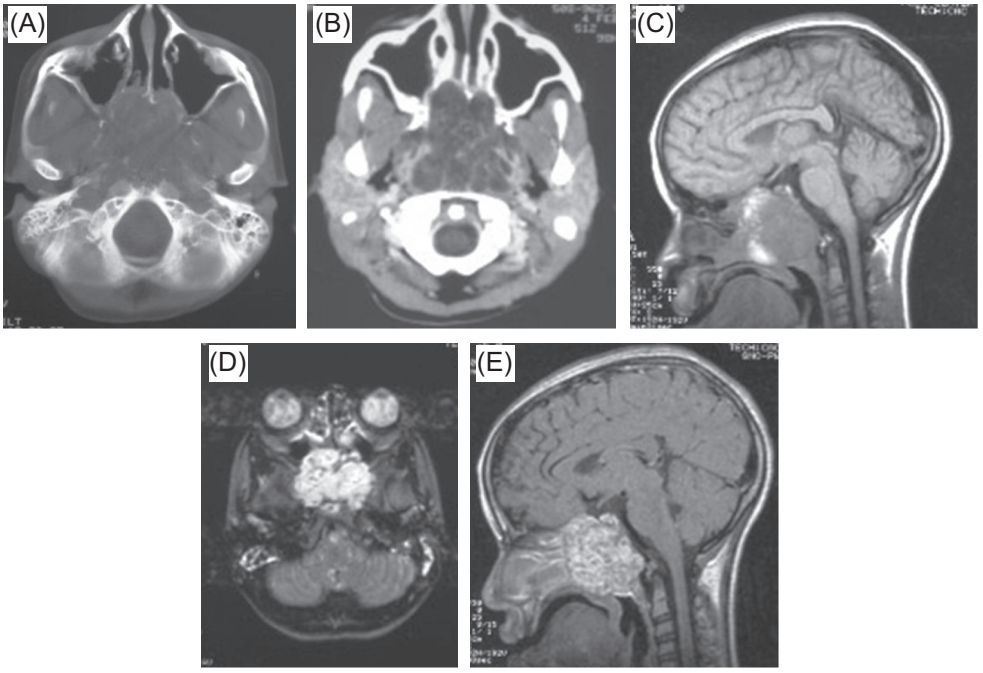


FIGURE 2 **Typical chordoma.** (A) CT of the head with bone window demonstrates a large, destructive, multilobulated mass of the clivus and nasopharynx. (B) CT of the head with contrast: after contrast the mass shows enhancing septations. (C) MRI sagittal T1-weighted image without contrast shows that the mass has destroyed the clivus posteriorly but maintains a CSF interface between it and the brainstem. (D) MRI axial T2-weighted image without contrast: on this image the mass is hyperintense with septations of low signal separating lobulated areas of increased signal, rather classic for a chordoma. (E) MRI sagittal T1-weighted image with contrast; the mass enhances rather intensely as most chordomas do with a lobulated, honeycomb appearance which is characteristic for chordomas.

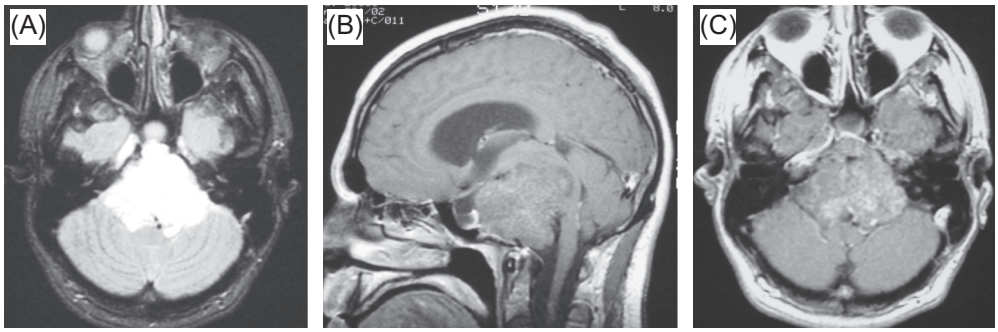


FIGURE 3 **Typical chordoma.** (A) MRI axial T2-weighted image reveals a very large, lobulated mass of the clivus that is hyperintense. (B) MRI sagittal and (C) Axial T1-weighted images with contrast demonstrate only mild enhancement of the large clival lesion with severe compression and posterior displacement of the brainstem. *Courtesy of Steven P. Meyers M.D., University of Rochester, Rochester, New York.*

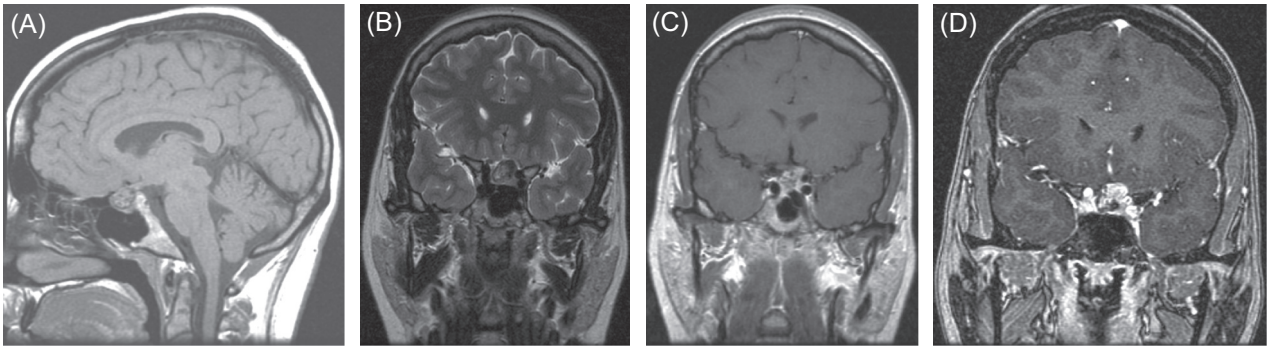


FIGURE 4 **Chondroid chordoma of the sella.** Twenty-two-year-old female with irregular menses. The imaging was initially interpreted as an adenoma (A) MRI sagittal T1-weighted image demonstrates a heterogeneous mass of the sella with foci of increased signal which may represent hemorrhage or calcification. (B) MRI coronal T2-weighted image: the sellar and slightly suprasellar mass is heterogeneous but primarily isointense to cortex. (C) MRI coronal T1-weighted image with contrast and (D) coronal T1-weighted three-dimensional spoiled gradient recalled acquisition in steady state (SPGR) image postcontrast demonstrate heterogeneous but intense enhancement of the sellar lesion which extends to the suprasellar region anterior to the optic chiasm and involves the intracranial segment of the left optic nerve.

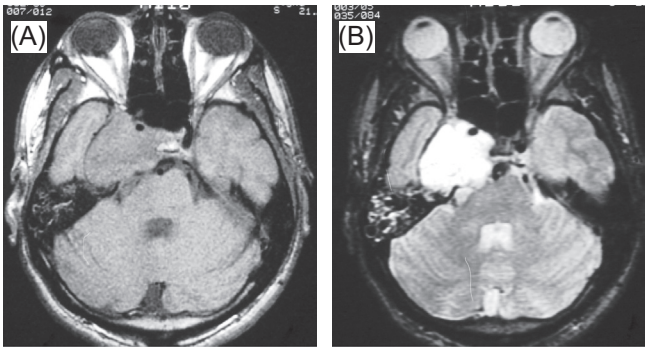


FIGURE 5 **Chondroid chordoma.** (A) MRI axial T1-weighted image without contrast demonstrates the large mass in the region of the cavernous sinus, isointense to brain with partial encasement of the carotid artery. (B) MRI axial T2-weighted image shows the hyperintense lesion. *Courtesy of Steven P. Meyers M.D., University of Rochester, Rochester, New York.*

are almost always positive for epithelial markers such as cytokeratin (CK) and epithelial membrane antigen (EMA) and positive for S-100 protein in 44–76.5 % of cases.[22,23] Chondroid chordoma stain positive for S-100 protein in 85–100% of cases but in only one-third of cases for CK and EMA.[22,23] Chordomas also stain strongly with vimentin.

Clinical Presentation

Symptoms generally depend on the location of the tumor. Diplopia is the most common symptom, being noted in 64% of cases in one series.[1,24–29] Diplopia is due to cranial nerve palsies of which cranial nerve VI is the most commonly involved.[1,25,28,30] Headaches are the second most common symptom in cranial skull base chordomas and are noted in 32%.[1,24–29] They are usually occipital or retroorbital. Tinnitus and hearing loss may also be symptoms[31] as can neck pain with clival chordomas.[1,32] Other symptoms may include facial pain and dysesthesia, decreased vision, gait disturbance, and vertigo.[1,24]

Imaging

Magnetic resonance (MR) and computed tomography (CT) are both useful modalities used in the evaluation of chordomas and generally both are obtained. Both modalities are equivalent in the detection of the tumor but MR is better in evaluating the extent of the tumor and delineating its relationship to the vasculature which is critical

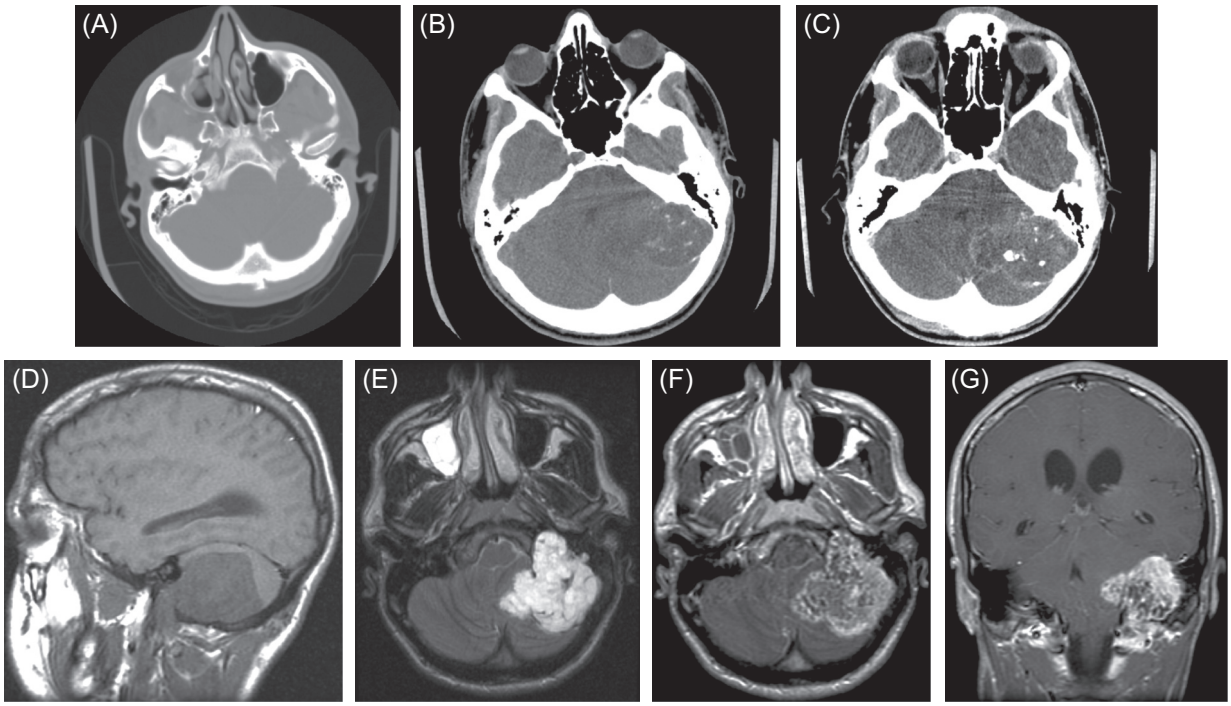


FIGURE 6 **Jugular fossa chondroid chordoma.** Twenty-two-year-old white male who presented to the emergency department complaining of a 3–4 day history of emesis, vertigo, headache, and right eye central vision loss. (A) Axial temporal bone CT demonstrates erosion of the bony margins of the jugular foramen on the left. (B) Unenhanced axial CT image demonstrates a large, slightly hypodense, left posterior fossa mass, with scattered calcifications, that results in compression of the fourth ventricle and displacement of the fourth ventricle to the right. (C) CT after contrast, there is mild heterogeneous and primarily peripheral enhancement. (D) MRI sagittal unenhanced T1-weighted image shows the large, hypointense posterior fossa mass extending through the jugular foramen. (E) MRI axial fast spin-echo T2-weighted image shows the large, multilobulated, (F) postcontrast axial T1-weighted image, and (G) sagittal postcontrast T1-weighted image demonstrate the heterogeneous, honeycomb enhancement of the lesion, typical of chordomas.

in surgical planning.[1,33] CT is better in demonstrating bone destruction and the presence of calcifications.

On CT, chordomas are typically homogeneous and isodense to muscle, expansile, destructive, and lytic lesions of the skull base.[1] CT is excellent in assessing the degree of osteolysis.[34] Thin section CT is most useful in defining the anatomy of bone destruction at the skull base and the extent of calcifications. Foci of calcification may also be seen in fewer than 50% of cases and are difficult to distinguish from sequestered bone fragments.[1,34] In typical chordomas, calcifications within the lesion are more likely to represent sequestered bone fragments, while in chondroid chordomas these are more likely to be tumoral dystrophic calcifications. After contrast, the tumors demonstrate heterogeneous enhancement (see Figures 1(A), 1(B), 2(A), 2(B), 6(A), 6(B), and 6(C)).[1]

MR imaging (MRI), because of its superior soft tissue contrast and multiplanar capability, is the exam of choice in delineating the anatomic extension of chordomas and defining involvement of adjacent and critical structures.[1] Chordomas involve the cavernous sinus in 60% of cases, the petrous apex in 48%, intradural 48%, upper clivus 48%, sphenoid sinus 44%, middle clivus 32%, lower clivus 24%, and occipital condyle in 24%, with less common involvement of the nasopharynx, infratemporal fossa, jugular foramen, and C2–3 to name a few.[1,24] Sagittal images are ideal in defining the posterior margin of the tumor, its relationship to the brainstem and nasopharynx and intradural extension. Coronal images are most useful in showing involvement of the cavernous sinus, which is most common, and of the optic chiasm.[33,35,36] Chordomas are generally isointense to hypointense on T1-weighted images (T1WI) with 75% being isointense.[1,33,37] The T1WI images are especially useful in defining tumor–cerebrospinal fluid interfaces.[22] Foci of increased signal on T1WI may be seen reflecting hemorrhage and mucinous collections.[37] On T2-weighted images (T2WI) they are typically of increased signal that is heterogeneous in 79%,[37] with 70% demonstrating septations of low signal, separating lobulated areas of increased signal (see Figures 2(D) and 6(E)).[33,37,38] Chondroid chordomas tend to be brighter on T1WI and less intense than typical chordomas on T2WI, secondary to lower water content in the cartilage-like tissue.[33] Almost all chordomas enhance after intravenous contrast administration, with 81% enhancing heterogeneously (see Figures 1–6).[37] A lobulated, honeycomb appearance after gadolinium contrast is rather characteristic (see Figure 2(E)).[39]

Overall, CT and MRI are complementary exams in the imaging of chordomas, and both are usually needed for treatment planning.[1] The imaging appearance of chordoma, however, is not pathognomonic. Imaging studies cannot reliably distinguish chordoma from chondrosarcoma or other skull base lesions. Histological studies are necessary for confirmation of the specific diagnosis.[1,38]

Chordomas have been detected on positron emission tomography (PET) using [^{18}F]fluorodeoxyglucose (FDG) and [^{11}C]methionine (MET).[40,41] In 12 of 15 (80%) patients imaged prior to treatment with carbon ion radiotherapy, the chordomas were clearly visible on the baseline MET PET study with a mean tumor to nontumor ratio of 3.3 ± 1.7. The methionine uptake decreased significantly to 2.3 ± 1.4 after carbon ion radiotherapy. A significant reduction in tumor MET uptake of 24% was observed after carbon ion radiotherapy. Ninety-three percent of patients showed no local recurrence after carbon ion radiotherapy with a median follow-up time of 20 months. This indicates that MET PET could potentially provide important tumor metabolic information for the therapeutic monitoring of chordomas after treatment.[41] Further work remains prior to PET being routinely used.

Treatment

Surgery is the mainstay of treatment of chordomas. Radical resection is the key factor in longer survival and improved quality of life with longer survival associated with more extensive tumor removal.[1,29,42–46] The location of the tumor, its invasive nature, its proximity to and involvement of critical neural (cranial nerves, optic chiasm, brain stem) and vascular (carotid, vertebral, basilar arteries) structures frequently prevents complete resection with radical removal achieved in only 44% in one series.[1,24] Radical surgical removal and high-dose radiation therapy, particularly proton beams are effective in tumor control. High-dose radiation therapy, especially fractionated proton beam or combined proton–photon beam therapy, has been shown to provide good tumor control and acceptable rates of complication.[1,47–49] Radiation is more effective when given after surgery rather than after tumor recurrence, and its effectiveness has been related to the volume of residual tumor.[1,44] Gamma Knife has been used as adjunctive therapy but limited experience does not permit meaningful conclusions.[50,51] The same is true of brachytherapy with implantation of ^{125}I seeds.[52,53] Chemotherapy generally plays no role in the initial treatment of chordomas. The role of chemotherapy is in patients with metastatic disease and locally advanced recurrent disease where systemic palliative therapy that includes thalidomide retards disease progression.[1,54] Imatinib mesylate and other targeted molecular therapies have been found to have antitumor activity in selected patients with chordomas.[1,55]

Local relapse is the predominant type of treatment failure seen in up to 95% of treatment failures, with surgical pathway recurrence and metastatic disease also possible.[56] Metastatic disease has been reported in 7–14% of cases, with metastases to bone and lungs being most common and lymph node, brain, and abdominal visceral involvement reported.[1,56–58] In the largest series of chordomas by McMaster et al., the median survival for all races, genders, and locations was 6.29 years. Median survival was longer for females (7.25 years) than for males (5.93 years) but this was not statistically significant.[2] Other studies however have suggested that female gender, as well as tumor necrosis of greater than 10% in biopsy specimens, and tumor volume of greater than 70 ml, are independent predictors of shortened survival after radiation therapy.[59] In the McMaster series, median survival was higher for cranial chordomas (6.94 years) compared with spinal (5.88 years) and sacral (6.48 years), with median survival for females higher than males (7.70 vs 6.42 years).[1,2] The overall 5-, 10- and 20-year survival rates were 67.7%, 39.9%, and 13.1%, respectively.[1,2] Following local relapse 5-year survival has been reported as 5%.[56]

CHONDROSARCOMA

Chondrosarcomas of the skull base are uncommon neoplasms that can resemble chordomas, and indeed are frequently misdiagnosed as such. In the largest review of 200 skull base chondrosarcomas by Rosenberg et al., around 37% of lesions diagnosed as chordomas at other institutions had their diagnosis changed to chondrosarcoma.[60] They are malignant tumors that produce cartilage matrix. Primary chondrosarcomas arise de novo, whereas secondary chondrosarcomas arise from preexisting lesions such as Paget's, enchondromas, osteochondromas, etc. Overall, they are the third most common primary malignant bone tumor after multiple myeloma and ostreosarcoma, and represent 20–27% of all primary malignant bone tumors.[61] Craniofacial chondrosarcomas represent 2% of all chondrosarcomas and have a predilection for skull base.[61] Only 6% of skull base tumors are chondrosarcomas with chordomas being more common skull base tumors.[61] Unlike chordomas, which tend to be midline lesions, the majority of chondrosarcomas occur off midline with 6% of the tumors arising in the sphenoethmoid complex, 28% originating in the clivus (see Figure 7), and 66% occurring in the temporo–occipital junction (see Figure 8).[60,62] The mean age of presentation is 39 years, which is younger than for chordomas. They are slightly more common in females, with a female to male ratio of 1.3/1.[60]

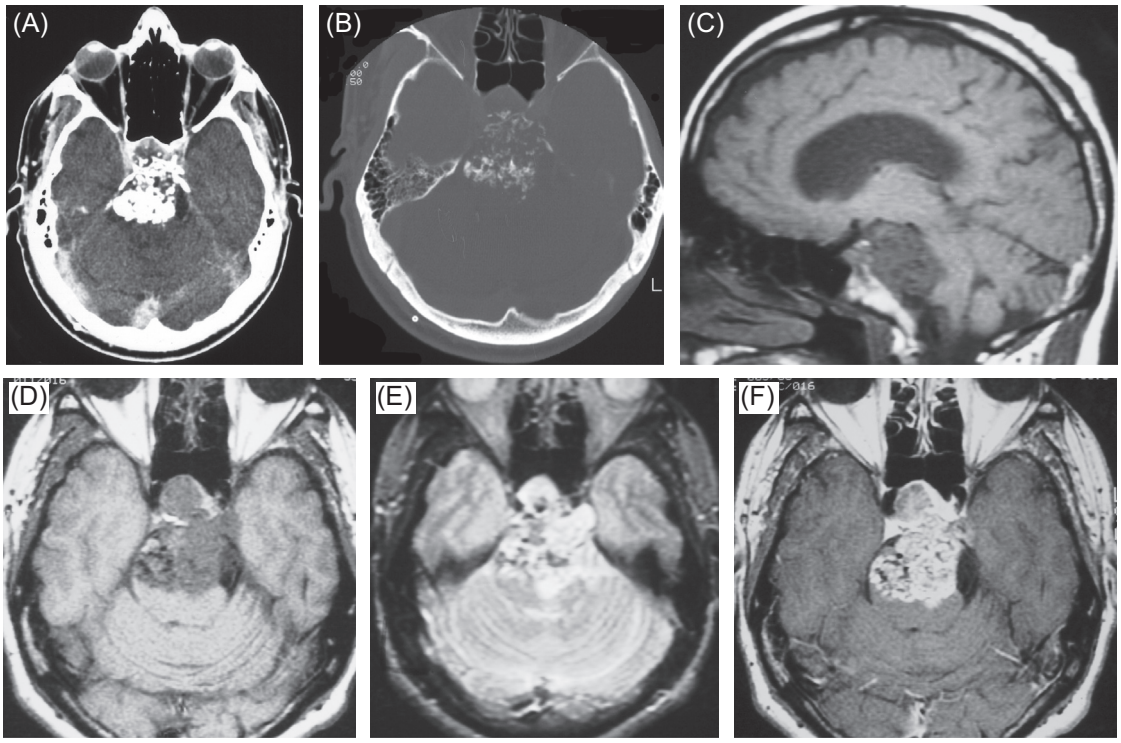


FIGURE 7 **Conventional grade I chondrosarcoma.** (A) Axial CT of the head with contrast with soft tissue window and (B) bone window demonstrates a heavily calcified mass of the clivus with arcuate and ring-shaped mineralization classic for a chondrosarcoma. (C) Sagittal T1-weighted and (D) axial T1-weighted images both without contrast demonstrate a large hypodense and slightly heterogeneous mass of the clivus causing compression of the brainstem. (E) Axial T2-weighted image demonstrates the mass to be hyperintense but heterogeneous with areas of low signal caused by matrix mineralization, fibrocartilaginous elements, or both. (F) Axial T1-weighted image postcontrast demonstrates intense but heterogeneous enhancement. *Courtesy of Robert Tarr M.D. Case Western Reserve University, Cleveland, Ohio.*

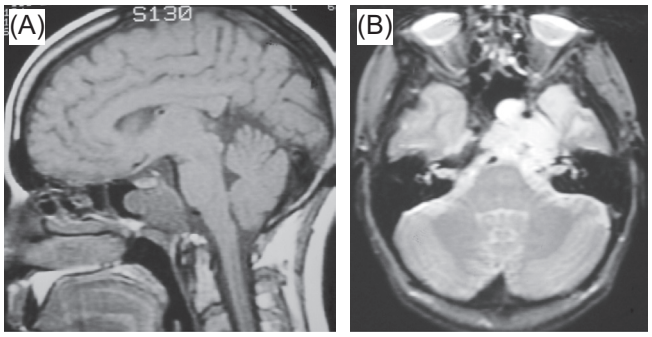


FIGURE 8 **Conventional grade I chondrosarcoma.** (A) MRI sagittal T1-weighted image demonstrates a lobulated hypointense mass of the clivus, extending into the sphenoid sinus. (B) Axial T2-weighted image shows the mass is heterogeneous, hyperintense, and encasing the left carotid artery. *Courtesy of Steven P. Meyers M.D., University of Rochester, Rochester, New York.*

Pathology

Histologically, the majority of skull base chondrosarcomas (63%) are mixed hyaline and myxoid tumors, with 29.5% being pure myxoid and 7.5% classified as hyaline chondrosarcomas.[60] The myxoid cartilage is the component that causes diagnostic confusion with chordoma. Myxoid chondrosarcomas can be distinguished from chordoma on morphologic grounds because the neoplastic chondrocytes are relatively small, contain diminished amounts of cytoplasm, and do not grow in cohesive groups, nests, or sheets. Most tumors (50.5%) are grade I, 28.5% mixed grades I and II, 21% pure grade II, with grade III being uncommon (in fact 0% in Rosenberg's study).[60] Chondrosarcomas are subclassified into conventional or classic (hyaline/myxoid), dedifferentiated, clear cell, and mesenchymal subtypes. The conventional type of chondrosarcoma is the most common cartilage tumor to develop in the skull base and the least aggressive.[60,63] Typically low-grade chondrosarcomas may undergo dedifferentiation and become highly malignant tumors with a poor prognosis.[64] They almost always (98.9%) stain for S-100 protein and do not stain for keratin. Faint staining for EMA can be seen in a minority of cases.[60]

Clinical Presentation

The presenting symptoms of chondrosarcomas are similar to those of chordomas previously described and include hearing loss, pulsatile tinnitus, vertigo, headache, diplopia due to cranial nerve palsies of cranial nerves III, IV, and VI, facial pain and paresthesias due to cranial nerve V palsy, and facial spasm or facial paresis due to cranial nerve VII involvement to name a few.[65]

Imaging

Imaging is unfortunately nonspecific and generally unable to distinguish between chordomas and chondrosarcomas.[66] On CT, chondrosarcomas frequently contain matrix calcifications or sequestered bony fragments (see Figure 7(A) and 7(B)). Matrix mineralization is seen in 44–80% of cases.[62,67] Matrix calcification may demonstrate the typical chondroid pattern of ring, arc, or snowflake-like foci. Peripheral eggshell-like calcification has also been described. Extensive chondroid calcification tends to occur in lower grade classic chondrosarcomas.[63,68] On unenhanced CT the masses may be of increased or decreased density relative to brain parenchyma and may mildly or moderately enhance.[66] On MRI chondrosarcomas are of low to intermediate signal on T1 (see Figures 7(C), 7(D), and 8(A)) and high signal on T2 with heterogeneous signal noted in 59% caused by matrix mineralization, fibrocartilaginous elements, or both (see Figures 7(E) and 8(B)). The margins tend to be multilobulated and well defined. Contrast enhancement is noted in 100% and is heterogeneous in 73% (see Figure 7(F)).[62]

Treatment

The goal of surgery is complete resection[69]; however, gross total removal is only achieved in a small percentage due to tumor location and frequent involvement of adjacent critical structures such as the cavernous sinus, carotid and basilar arteries, optic chiasm, etc.[60] Surgery combined with proton beam irradiation can yield excellent results with 5- and 10-year progression free survival rates of 70% and 45%, respectively, compared with 5- and 10-year survival rates of chordoma which have been reported to be approximately 51% and 35%, respectively, despite similar aggressive management. Rosenberg et al. reported using high-dose postoperative fractionated precision radiation therapy, combining conformal megavoltage and charged particle irradiation using the 160 MeV proton beam, with a median dose of 72.1 Cobalt–Gray equivalent, given in 38 fractions.[60]

OTHER SKULL BASE TUMORS

Malignant tumors outnumber benign ones at the skull base and metastases are more common than primary tumors.[60] Of the primary tumors, an overwhelming majority are chordomas and chondrosarcomas.[1,60] Besides chordoma and chondrosarcoma, there are many other tumors that have been reported to involve the skull base and that should be considered. These include meningioma, metastasis, invasive adenoma, craniopharyngioma, glomus tumors, plasmacytoma, lymphoma, giant cell tumor, nasopharyngeal carcinoma, eosinophilic granuloma, rhabdomyosarcoma, adenoid cystic carcinoma, benign fibrous histiocytoma, chondroblastoma, ameloblastoma, chondroma, osteogenic sarcoma, and enchondroma.[70]

References

1. Newton HB. Chordoma. In: Raghavan D, Brecher M, Johnson DH, et al., eds. *Textbook of Uncommon Cancer*. 4th ed. Vol. 54. Chichester: Wiley; 2012:721–732.
2. McMaster ML, Goldstein AM, Bromley CM, Ishibe N, Parry DM. Chordoma: incidence and survival patterns in the United States, 1973–1995. *Cancer Causes Control*. 2001;12:1–11.
3. Heffelfinger MJ, Dahlin DC, MacCarty CS, Beabout JW. Chordomas and cartilaginous tumors at the skull base. *Cancer*. 1973;32:410–420.
4. Mou Z, Liu Z. Primary chordoma of the nose. *Chin Med J*. 2003;116:154–156.
5. Scartozzi R, Couch M, Sciubba J. Chondroid chordoma of the nasal septum. *Arch Otolaryngol Head Neck Surg*. 2003;129:244–246.
6. Gladstone HB, Bailet JW, Rowland JP. Chordoma of the oropharynx: an unusual presentation and review of the literature. *Otolaryngol Head Neck Surg*. 1998;118:104–107.
7. Loughran S, Badia L, Lund V. Primary chordoma of the ethmoid sinus. *J Laryngol Otol*. 2000;114:627–629.
8. Wang YP, Lee KS, Chen YJ, Huang JK. Extraosseous chordoma of the retropharyngeal space. *Otolaryngol Head Neck Surg*. 2004;130:383–385.
9. Warakaulle DR, Anslow P. A unique presentation of retroclival chordoma. *J Postgrad Med*. 2002;48:285–287.
10. Mapstone TB, Kaufman B, Ratcheson RA. Intradural chordoma without bone involvement: nuclear magnetic resonance (NMR) appearance. Case report. *J Neurosurg*. 1983;59:535–537.
11. Kakuno Y, Yamada T, Hirano H, Mori H, Narabayashi I. Chordoma in the sella turcica. *Neurol Med Chir (Tokyo)*. 2002;42:305–308.
12. Haridas A, Ansari S, Afshar F. Chordoma presenting as pseudoprolactinoma. *Br J Neurosurg*. 2003;17:260–262.
13. Thodou E, Kontogeorgos G, Scheithauer BW, et al. Intrasellar chordomas mimicking pituitary adenoma. *J Neurosurg*. 2000;92:976–982.
14. Carpentier A, Blanquet A, George B. Suboccipital and cervical chordomas: radical resection with vertebral artery control. *Neurosurg Focus*. 2001;10:E4.
15. Batsakis JG, Kittleson AC. Chordomas. Otorhinolaryngologic presentation and diagnosis. *Arch Otolaryngol*. 1963;78:168–175.
16. Ramina R, Maniglia JJ, Fernandes YB, et al. Jugular foramen tumors: diagnosis and treatment. *Neurosurg Focus*. 2004;17:E5.
17. Iwasaki S, Ito K, Takai Y, Morita A, Murofushi T. Chondroid chordoma at the jugular foramen causing retrolabyrinthine lesions in both the cochlear and vestibular branches of the eighth cranial nerve. *Ann Otol Rhinol Laryngol*. 2004;113:82–86.
18. Itoh T, Harada M, Ichikawa T, Shimoyamada K, Katayama N, Tsukune Y. A case of jugular foramen chordoma with extension to the neck: CT and MR findings. *Radiat Med*. 2000;18:63–65.
19. Okamoto K, Furusawa T, Ishikawa K, Sasai K, Tokiguchi S. Focal T2 hyperintensity in the dorsal brain stem in patients with vestibular schwannoma. *AJNR Am J Neuroradiol*. 2006;27:1307–1311.
20. Dow GR, Robson DK, Jaspan T, Punt JA. Intradural cerebellar chordoma in a child: a case report and review of the literature. *Childs Nerv Syst*. 2003;19:188–191.
21. Khmel'nitskaia NM, Zavarzin BA. Chordoma of the temporal bone. *Vestn Otorinolaringol*. 2000:58–59.
22. Mitchell A, Scheithauer BW, Unni KK, Forsyth PJ, Wold LE, McGivney DJ. Chordoma and chondroid neoplasms of the sphenooccput. An immunohistochemical study of 41 cases with prognostic and nosologic implications. *Cancer*. 1993;72:2943–2949.

23. Meis JM, Giraldo AA. Chordoma. An immunohistochemical study of 20 cases. *Arch Pathol Lab Med*. 1988;112:553–556.
24. Al Mefty O, Borba LA. Skull base chordomas: a management challenge. *J Neurosurg*. 1997;86:182–189.
25. Forsyth PA, Cascino TL, Shaw EG, et al. Intracranial chordomas: a clinicopathological and prognostic study of 51 cases. *J Neurosurg*. 1993;78:741–747.
26. Raffel C, Wright DC, Gutin PH, Wilson CB. Cranial chordomas: clinical presentation and results of operative and radiation therapy in twenty-six patients. *Neurosurgery*. 1985;17:703–710.
27. Rich TA, Schiller A, Suit HD, Mankin HJ. Clinical and pathologic review of 48 cases of chordoma. *Cancer*. 1985;56:182–187.
28. Volpe R, Mazabraud A. A clinicopathologic review of 25 cases of chordoma (a pleomorphic and metastasizing neoplasm). *Am J Surg Pathol*. 1983;7:161–170.
29. Watkins L, Khudados ES, Kaleoglu M, Revesz T, Sacares P, Crockard HA. Skull base chordomas: a review of 38 patients, 1958-88. *Br J Neurosurg*. 1993;7:241–248.
30. Chetiyawardana AD. Chordoma: results of treatment. *Clin Radiol*. 1984;35:159–161.
31. Zhang H, Zhang D, Sun Y, et al. The study of 11 cases of chordoma in the skull base or neck. *Lin Chuang Er Bi Yan Hou Ke Za Zhi*. 2006;20:251–253.
32. Alvarado R, Gomez J, Morale SG, Davis CP. Neck pain: common complaint, uncommon diagnosis–symptomatic clival chordoma. *South Med J*. 2004;97:83–86.
33. Sze G, Uichanco III LS, Brant-Zawadzki MN, et al. Chordomas: MR imaging. *Radiology*. 1988;166:187–191.
34. Meyer JE, Oot RF, Lindfors KK. CT appearance of clival chordomas. *J Comput Assist Tomogr*. 1986;10:34–38.
35. Oot RF, Melville GE, New PF, et al. The role of MR and CT in evaluating clival chordomas and chondrosarcomas. *AJR Am J Roentgenol*. 1988;151:567–575.
36. Erdem E, Angtuaco EC, Van Hemert R, Park JS, Al Mefty O. Comprehensive review of intracranial chordoma. *Radiographics*. 2003;23:995–1009.
37. Meyers SP, Hirsch Jr WL, Curtin HD, Barnes L, Sekhar LN, Sen C. Chordomas of the skull base: MR features. *AJNR Am J Neuroradiol*. 1992;13:1627–1636.
38. Doucet V, Peretti-Viton P, Figarella-Branger D, Manera L, Salamon G. MRI of intracranial chordomas. Extent of tumour and contrast enhancement: criteria for differential diagnosis. *Neuroradiology*. 1997;39:571–576.
39. Drummond DS, Wenzel DM, Kudryk W. Spheno-occipital chondroid chordoma. *J Otolaryngol*. 1997;26:197–200.
40. Lin CY, Kao CH, Liang JA, Hsieh TC, Yen KY, Sun SS. Chordoma detected on F-18 FDG PET. *Clin Nucl Med*. 2006;31:506–507.
41. Zhang H, Yoshikawa K, Tamura K, et al. Carbon-11-methionine positron emission tomography imaging of chordoma. *Skeletal Radiol*. 2004;33:524–530.
42. Hug EB, Loredo LN, Slater JD, et al. Proton radiation therapy for chordomas and chondrosarcomas of the skull base. *J Neurosurg*. 1999;91:432–439.
43. Arnold H, Herrmann HD. Skull base chordoma with cavernous sinus involvement. Partial or radical tumour-removal? *Acta Neurochir (Wien)*. 1986;83:31–37.
44. Berson AM, Castro JR, Petti P, et al. Charged particle irradiation of chordoma and chondrosarcoma of the base of skull and cervical spine: the Lawrence Berkeley Laboratory experience. *Int J Radiat Oncol Biol Phys*. 1988;15:559–565.
45. Gay E, Sekhar LN, Rubinstein E, et al. Chordomas and chondrosarcomas of the cranial base: results and follow-up of 60 patients. *Neurosurgery*. 1995;36:887–896.
46. Sen CN, Sekhar LN, Schramm VL, Janecka IP. Chordoma and chondrosarcoma of the cranial base: an 8-year experience. *Neurosurgery*. 1989;25:931–940.
47. Austin JP, Urie MM, Cardenosa G, Munzenrider JE. Probable causes of recurrence in patients with chordoma and chondrosarcoma of the base of skull and cervical spine. *Int J Radiat Oncol Biol Phys*. 1993;25:439–444.
48. Hug EB, Fitzek MM, Liebsch NJ, Munzenrider JE. Locally challenging osteo- and chondrogenic tumors of the axial skeleton: results of combined proton and photon radiation therapy using three-dimensional treatment planning. *Int J Radiat Oncol Biol Phys*. 1995;31:467–476.
49. Austin-Seymour M, Munzenrider J, Goitein M, et al. Fractionated proton radiation therapy of chordoma and low-grade chondrosarcoma of the base of the skull. *J Neurosurg*. 1989;70:13–17.
50. Lanzino G, Dumont AS, Lopes MB, Laws Jr ER. Skull base chordomas: overview of disease, management options, and outcome. *Neurosurg Focus*. 2001;10:E12.
51. Muthukumar N, Kondziolka D, Lunsford LD, Flickinger JC. Stereotactic radiosurgery for chordoma and chondrosarcoma: further experiences. *Int J Radiat Oncol Biol Phys*. 1998;41:387–392.
52. Gutin PH, Leibel SA, Hosobuchi Y, et al. Brachytherapy of recurrent tumors of the skull base and spine with iodine-125 sources. *Neurosurgery*. 1987;20:938–945.
53. Kumar PP, Good RR, Skultety FM, Leibrock LG. Local control of recurrent clival and sacral chordoma after interstitial irradiation with iodine-125: new techniques for treatment of recurrent or unresectable chordomas. *Neurosurgery*. 1988;22:479–483.
54. Schonegger K, Gelpi E, Prayer D, et al. Recurrent and metastatic clivus chordoma: systemic palliative therapy retards disease progression. *Anticancer Drugs*. 2005;16:1139–1143.
55. Casali PG, Messina A, Stacchiotti S, et al. Imatinib mesylate in chordoma. *Cancer*. 2004;101:2086–2097.
56. Fagundes MA, Hug EB, Liebsch NJ, Daly W, Efird J, Munzenrider JE. Radiation therapy for chordomas of the base of skull and cervical spine: patterns of failure and outcome after relapse. *Int J Radiat Oncol Biol Phys*. 1995;33:579–584.
57. Singh W, Kaur A. Nasopharyngeal chordoma presenting with metastases. Case report and review of literature. *J Laryngol Otol*. 1987;101:1198–1202.
58. Yuh WT, Flickinger FW, Barloon TJ, Montgomery WJ. MR imaging of unusual chordomas. *J Comput Assist Tomogr*. 1988;12:30–35.
59. O'Connell JX, Renard LG, Liebsch NJ, Efird JT, Munzenrider JE, Rosenberg AE. Base of skull chordoma. A correlative study of histologic and clinical features of 62 cases. *Cancer*. 1994;74:2261–2267.
60. Rosenberg AE, Nielsen GP, Keel SB, et al. Chondrosarcoma of the base of the skull: a clinicopathologic study of 200 cases with emphasis on its distinction from chordoma. *Am J Surg Pathol*. 1999;23:1370–1378.
61. Murphey MD, Walker EA, Wilson AJ, Kransdorf MJ, Temple HT, Gannon FH. From the archives of the AFIP: imaging of primary chondrosarcoma: radiologic-pathologic correlation. *Radiographics*. 2003;23:1245–1278.
62. Meyers SP, Hirsch Jr WL, Curtin HD, Barnes L, Sekhar LN, Sen C. Chondrosarcomas of the skull base: MR imaging features. *Radiology*. 1992;184:103–108.
63. Cure JK, Bhatia M, Richardson MS, Conway WF. General case of the day. Myxoid chondrosarcoma of the cavernous sinus. *Radiographics*. 1995;15(5):1231–1234.
64. Littrell LA, Wenger DE, Wold LE, et al. Radiographic, CT, and MR imaging features of dedifferentiated chondrosarcomas: a retrospective review of 174 de novo cases. *Radiographics*. 2004;24(5):1397–1409.

65. Neff B, Sataloff RT, Storey L, Hawkshaw M, Spiegel JR. Chondrosarcoma of the skull base. *Laryngoscope*. 2002;112(1):134–139.
66. Pamir MN, Ozduman K. Analysis of radiological features relative to histopathology in 42 skull-base chordomas and chondrosarcomas. *Eur J Radiol*. 2006;58(3):461–470.
67. Grossman RI, Davis KR. Cranial computed tomographic appearance of chondrosarcoma of the base of the skull. *Radiology*. 1981;141(2):403–408.
68. Lee YY, Van Tassel P. Craniofacial chondrosarcomas: imaging findings in 15 untreated cases. *AJNR Am J Neuroradiol*. 1989;10:165–170.
69. Stapleton SR, Wilkins PR, Archer DJ, Uttley D. Chondrosarcoma of the skull base: a series of eight cases. *Neurosurgery*. 1993;32(3):348–355.
70. Laine FJ, Nadel L, Braun IF. CT and MR imaging of the central skull base. Part 2. Pathologic spectrum. *Radiographics*. 1990;10:797–821.

CHAPTER

50

Pediatric Brain Tumors

Sanjay P. Prabhu, Tina Young Poussaint

Department of Radiology, Division of Neuroradiology, Boston Children's Hospital, Harvard Medical School, Boston, MA, USA

INTRODUCTION

The most common type of solid tumor among children is the pediatric brain tumor, which is the second most frequent childhood malignancy after leukemia[1] and the leading cause of death from solid tumors in this population. About 7% of the brain tumors reported to the Central Brain Tumor Registry of the United States between 2006 and 2010 occurred in persons younger than 20.[2] Among children ages 0–19, the incidence rate for all primary brain and central nervous system (CNS) tumors was roughly 5.3 per 100,000[2] with approximately 4350 new cases of childhood primary malignant and nonmalignant CNS tumors expected to be diagnosed each year in the United States.[2] The prevalence rate of all pediatric (ages 0–19) primary brain and CNS tumors was estimated at 35.4 per 100,000 with more than 28,000 children estimated to be living with this diagnosis in the United States in 2004.[3]

Our ability to reach an accurate preoperative diagnosis of the pediatric brain tumor hinges largely on magnetic resonance imaging (MRI), which is the ideal modality for defining tumor extent, developing an effective treatment plan, and implementing image-guided therapies involving surgery, radiotherapy, and chemotherapy. Indeed, because of MRI's unique multiplanar capability, its ability to provide detailed structural and anatomical information, and its ability to produce images of superior resolution,[4] MRI is unrivaled as a superior diagnostic tool. It is also the central modality for tumor follow-up including tumor response, progression, and treatment effects. Craniospinal MR with gadolinium is the modality of choice for detection of tumor dissemination in the cerebrospinal fluid (CSF) pathways.[5] Computed tomography (CT) is used for the assessment of calcification and cortical bony involvement, especially in lesions such as craniopharyngioma and orbital, sinonasal, petrous temporal, skull base, and cranial calvarial lesions. Other imaging procedures that aid in localization and in guiding surgical and radiation therapy include stereotactic MR and CT, the open magnet, and intraoperative sonography. Image fusion with reconstructions is used for stereotaxis, radiosurgery, stereotactic radiotherapy, and image-guided surgery.

Functional assessment of the brain can be performed using modalities such as single photon emission computed tomography (SPECT) and positron emission tomography (PET). Depending on the type of tracer used, PET and SPECT are also used to assess metabolic activity in brain tumors and are useful in distinguishing tumor from radiation necrosis or scar.[6]

Advanced MR techniques such as MR perfusion imaging, MR diffusion imaging, and MR spectroscopy (MRS) help further characterize the hemodynamics, cellularity, and metabolism of any suspected neoplasms. Functional MRI (fMRI) using blood oxygen level-dependent imaging is used to map the eloquent areas to assess risk of a surgical procedure, select patients for invasive intraoperative mapping, and guide the surgical resection of the tumor (Figure 1).[7–9] In addition, fMRI may help improve the understanding of mechanisms of cognitive deficits and avenues for intervention for children with brain tumors.[10]

The ability of these advanced MR techniques, separately and in combination, to elucidate the physiologic characteristics of pediatric tumors is proving essential in reaching accurate and timely diagnoses, developing effective postsurgical treatment plans, and implementing regular and responsive follow-up. MR perfusion imaging, MR diffusion imaging, and MRS are described briefly below; they are covered in depth by other contributors to this book.

MR perfusion imaging is used to evaluate cerebral perfusion dynamics by analysis of the hemodynamic

http://dx.doi.org/10.1016/B978-0-12-800945-1.00050-1
© 2016 Elsevier Ltd. All rights reserved.

parameters of relative cerebral blood volume, relative cerebral blood flow, and mean transit time. The techniques used to perform perfusion imaging include T2*-weighted dynamic susceptibility contrast (DSC), arterial spin labeling techniques, and permeability-based T1-weighted dynamic contrast-enhanced perfusion techniques.[11] MR perfusion can be used for preoperative tumor grading, evaluating tumor margins, and selecting stereotactic biopsy sites by identifying the perfusion in a portion of tumor and differentiating radiation necrosis versus tumor recurrence.[12,13] A major limitation to the use of DSC MR perfusion in pediatric brain tumors is the need for large-bore intravenous catheter placement to enable rapid delivery of gadolinium-based contrast

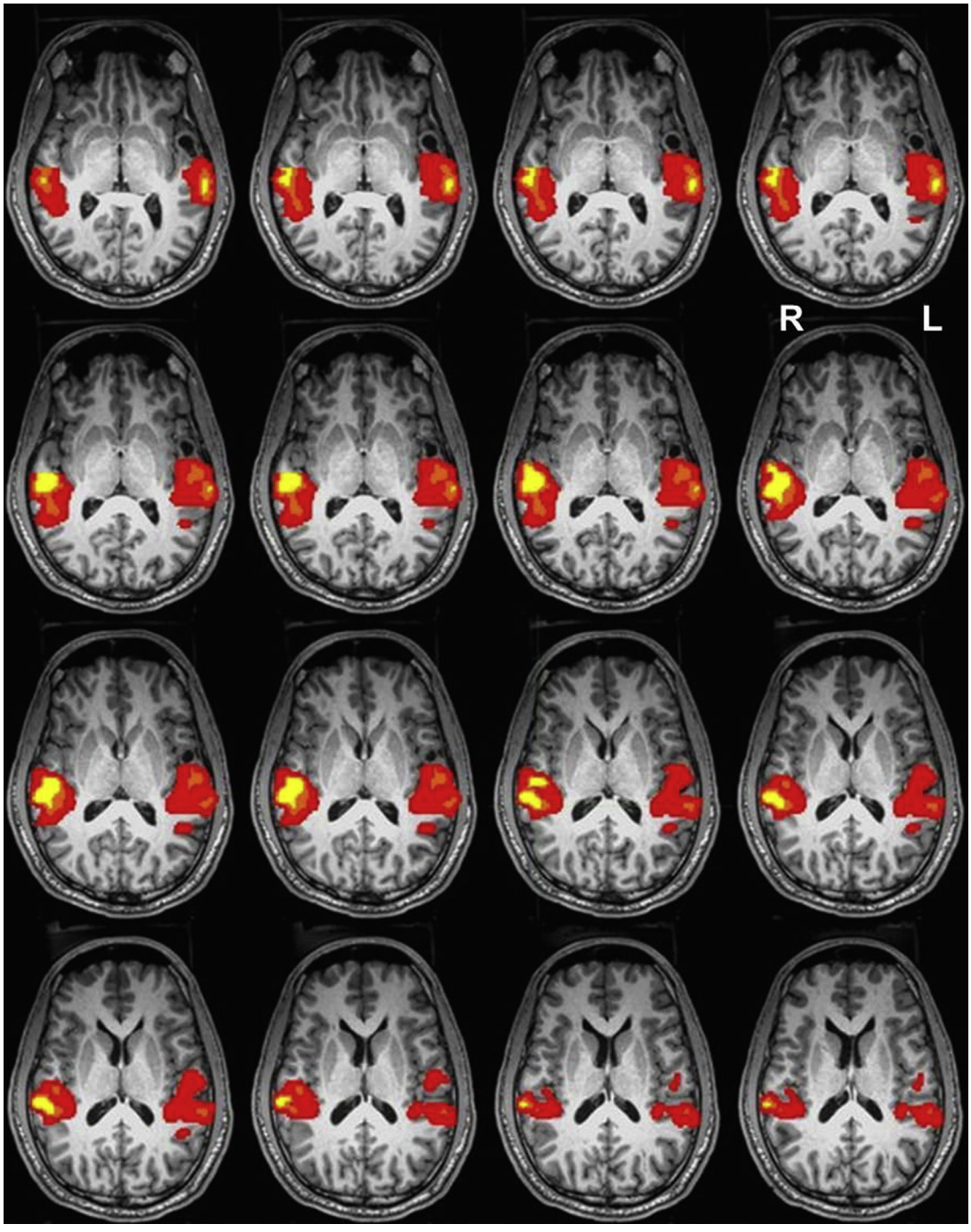


FIGURE 1 fMRI activation of passive narrative language processing in a 17-year-old male patient with a left temporal lobe tumor shows bilateral activation of the primary auditory cortex in the middle superior temporal gyri and right-lateralized language activation in the posterior half of the superior temporal gyrus with some support from the left hemisphere.

medium to generate an optimal first-pass curve. This can be challenging in young children, particularly when they are sick or on steroids. Other problems with the DSC technique include the image distortion caused by intratumoral hemorrhage and the underestimation of regional cerebral blood volume (CBV) owing to leakage through tumor capillaries.

Permeability-based perfusion techniques rely on the increased leakage of contrast medium through tumor vessel walls. Advantages of permeability-based perfusion techniques over DSC techniques in children include more manageable injection rates (1–2 ml/s), superior anatomic resolution, and absence of T2* susceptibility artifacts observed on the echo-planar DSC imaging.

Arterial spin labeling perfusion has had increasing clinical availability in children, with the advantage of using blood as an endogenous tracer. It therefore does not require contrast administration and is repeatable. In pediatric brain tumors it can be used to distinguish high-grade from low-grade tumors.[14]

MR diffusion-weighted imaging (DWI) using predominately echoplanar techniques has also been useful in characterizing tissue and tumor cellularity, in gauging tumor response to treatment,[15] in grading tumors, and in distinguishing tissue types.[16–19] Diffusion tensor imaging (DTI) is a derivative of DWI performed by acquiring diffusion data in six or more directions, which enables determination of the direction and magnitude of water diffusion. Connecting the direction of diffusion in neighboring voxels using various sets of mathematical algorithms enables the creation of a three-dimensional map of white matter tracts affected by the tumor, a technique called tractography. These white matter tractography maps provide information about fiber bundle direction and tract integrity, which can be used for presurgical planning (Figure 2). Coregistration of tractography data with functional MR data can help predict deficits following surgery resulting from white matter damage.[20] Moreover, FA using DTI is helpful in assessing treatment-induced white matter changes in children.[21,22] More refined diffusion techniques like diffusion spectrum imaging can resolve crossing white matter tracts to the scale of a single voxel,[23] but their role in the evaluation of pediatric brain tumors has not been validated.

Proton nuclear MRS, a noninvasive in vivo technique that provides additional metabolic diagnostic indices beyond anatomic information, has been extensively used to evaluate brain tumors. Specifically, it enables the radiologist to identify tumor tissue, to grade tumors, to differentiate tumor types, to distinguish active tumor from radiation necrosis or scar tissue, to guide stereotactic biopsy sites, and to determine early response to treatment.[11]

Another advance in MRI of brain tumors is the increasing availability of intraoperative scanners.[24] These scanners enable preoperative guidance for stereotactic biopsy and for planning tumor resection and provide a review of the resection site for residual tumor prior to closure of the craniotomy.[25] Intraoperative DTI can help confirm preservation of fiber tracts and minimize postoperative deficits.

More recently, MR-guided laser-induced thermal therapy is emerging as an alternative to conventional surgery to reduce morbidity following tumor resection (Figure 3).

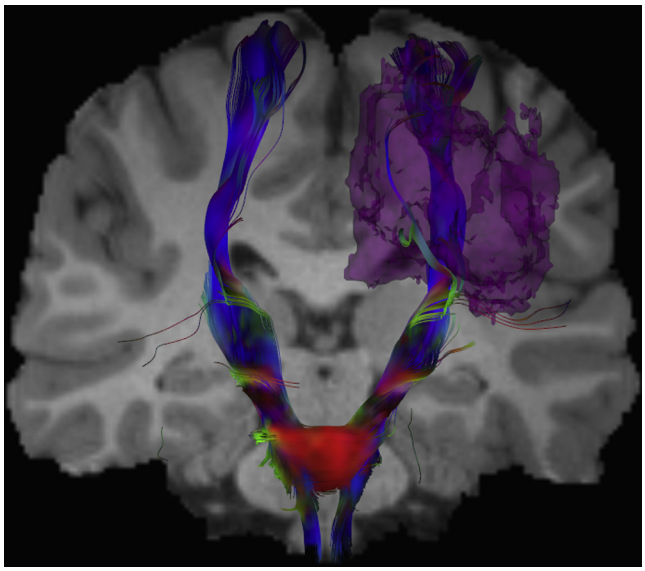


FIGURE 2 Diffusion tractography in a 5-year-old male with a large frontal lobe tumor shows the right-sided corticospinal tracts passing through the lesion.

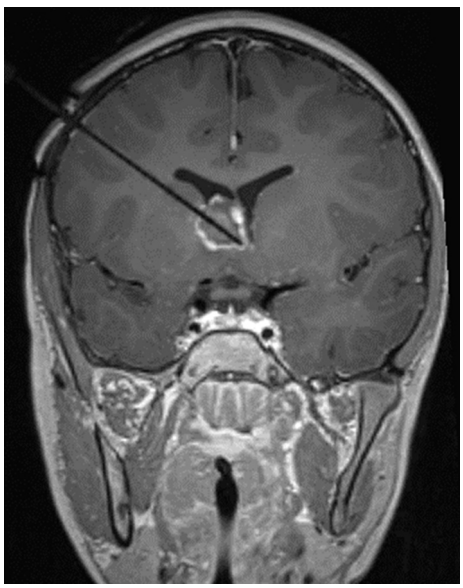


FIGURE 3 Coronal contrast-enhanced magnetization-prepared rapid gradient echo (MPRAGE) image shows a laser ablation probe extending into a hypothalamic hamartoma with the needle tip within the lesion in the hypothalamus. Enhancement around the tip indicates the areas that have been ablated by the procedure.

SPECIFIC PEDIATRIC BRAIN TUMORS

Tumors such as meningiomas, Schwann-cell tumors, metastases from outside the brain, and pituitary tumors rarely present in children,[26] but are commonly found in adults. In children, the vast majority of brain tumors are primary CNS lesions.[27] Pediatric brain tumors are typically classified pathologically or by location; classification by location helps limit the differential diagnosis. *In this chapter, tumors of the cerebral hemispheres, posterior fossa tumors, sellar and suprasellar tumors, and parameningeal tumors will be classified by location*. Pineal region tumors will be covered elsewhere in this book.

Tumors of the Cerebral Hemispheres

Astrocytomas

Astrocytomas are the most common childhood tumors of the CNS, accounting for approximately one-third of all pediatric supratentorial tumors.[2] The grading of astrocytomas has been defined by the World Health Organization (WHO) or St. Anne-Mayo system and is predictive of patient survival.[28,29] In pediatrics, the modified WHO classification of CNS tumors has become the standard classification system. Astrocytomas can be classified as low grade (WHO grades I and II) or high grade (WHO grades III and IV). Low-grade gliomas (LGGs) may consist of relatively pure tumors such as a juvenile pilocytic (grade I) or fibrillary (grade II) astrocytoma or mixed populations of both glial and neuronal lineages, such as ganglioglioma or glioneurocytoma. Another approach to pediatric gliomas is based on location rather than grade and recognizes the unique aspects of the environment in which tumors of a particular histology grow and their effect on the treatment response and prognosis.

Pilocytic astrocytomas are typically well demarcated, with the T2 signal abnormality matching the amount of gadolinium enhancement, occasionally presenting with an associated cyst. Higher grades of malignancy are usually heterogeneous in signal intensity with ill-defined margins, edema, hemorrhage, necrosis, mass effect, and irregular enhancement (Figure 4(A–C)).

Perfusion studies in adults and children have measured the relative CBV (rCBV) in the assessment of glioma grade and have demonstrated that low-grade astrocytomas have a significantly lower average rCBV than high-grade astrocytomas, such as anaplastic astrocytomas or glioblastoma multiforme.[30–36] One of the pitfalls of perfusion imaging in children is that pilocytic astrocytomas can have a high blood volume that mimics high-grade tumors on perfusion imaging alone.[37]

Diffusion imaging studies in astrocytomas have demonstrated a significant negative correlation between apparent diffusion coefficient (ADC) values and WHO astrocytic tumor grades for tumor grades II through IV.[38] Moreover, ADC values have been found to inversely correlate with tumor cellularity (Figure 4(D)).[16]

MRS is uniquely able to measure the higher choline (Cho) to creatine (Cr) ratio that is characteristic of HGGs; MRS has thus shown great utility in distinguishing HGGs from LGGs[39] and has enhanced overall diagnostic accuracy. Along these same lines, Tzika et al. have examined normalized Cho and lipids as the physiologic characteristic that distinguishes high-grade from low-grade tumors in children.[40]

Supratentorial Primitive Neuroectodermal Tumors

Supratentorial primitive neuroectodermal tumors (PNETs) are found in younger children with a mean age of 5 years.[41] These tumors are often large and sharply demarcated and may be solid and homogeneous or

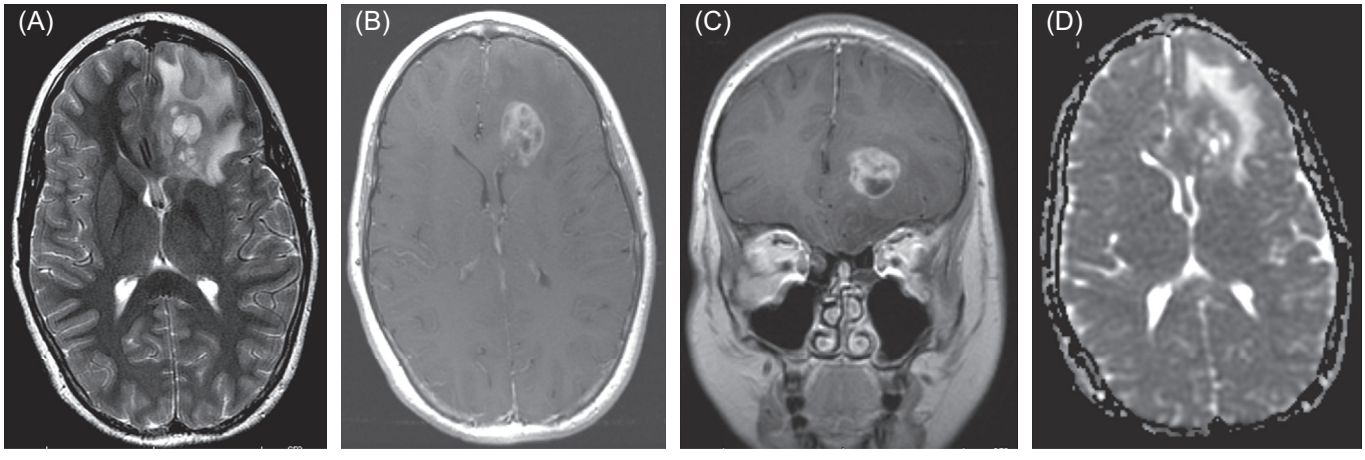


FIGURE 4 Supratentorial glioblastoma multiforme in 15-year-old boy with seizures. (A) Axial T2 MR image demonstrates heterogeneous mass within left frontal lobe with extensive surrounding edema. (B and C) Axial and coronal T1 image with gadolinium demonstrates heterogeneous enhancing tumor. (D) Axial diffusion ADC map demonstrates restricted diffusion (arrow) in the solid component of the mass.

heterogeneous with cyst, calcification, or hemorrhage[42] on CT and MRI. Frequently, calcification is seen on CT. Following contrast, there is heterogeneous enhancement. These tumors can occur in either the cerebral hemispheres or the lateral ventricles (Figure 5(A–F)). The differential diagnosis of supratentorial tumors similar to PNET includes other large heterogeneous tumors such as atypical teratoid/rhabdoid tumors and ependymoma.

Supratentorial Ependymoma

Supratentorial ependymomas represent 40% of all ependymomas. These tumors typically occur in children younger than 5 years. On CT, these tumors are heterogeneous with calcification and cyst formation. On MRI, these tumors are heterogeneous, containing cysts, calcification, and occasional hemorrhage;[43] they usually demonstrate irregular, heterogeneous enhancement with gadolinium.

Subependymal Giant Cell Tumor

Tuberous sclerosis (TS), an autosomal dominant multisystem disease linked to chromosomes 9 and 16, is caused by a mutation of the TSC1 and TSC2 genes that encode for hamartin and tuberin proteins, respectively.[44,45] Neuroimaging findings include subependymal and cortical tubers, white matter lesions, and subependymal giant cell astrocytomas.[46,47] Subependymal giant cell tumors are of mixed glioneuronal lineage associated with subependymal nodules that have symptoms such as hydrocephalus, interval growth, or papilledema. These tumors are seen in approximately 10% of patients with TS.[46] They arise from the lateral ventricle near the foramen of Monro and present with obstructive hydrocephalus between the ages of 10 and 30.[48] These tumors are often calcified on CT; on MR, they are hypointense or isointense on T1-weighted images and are isointense to hyperintense on T2-weighted sequences. Following contrast,

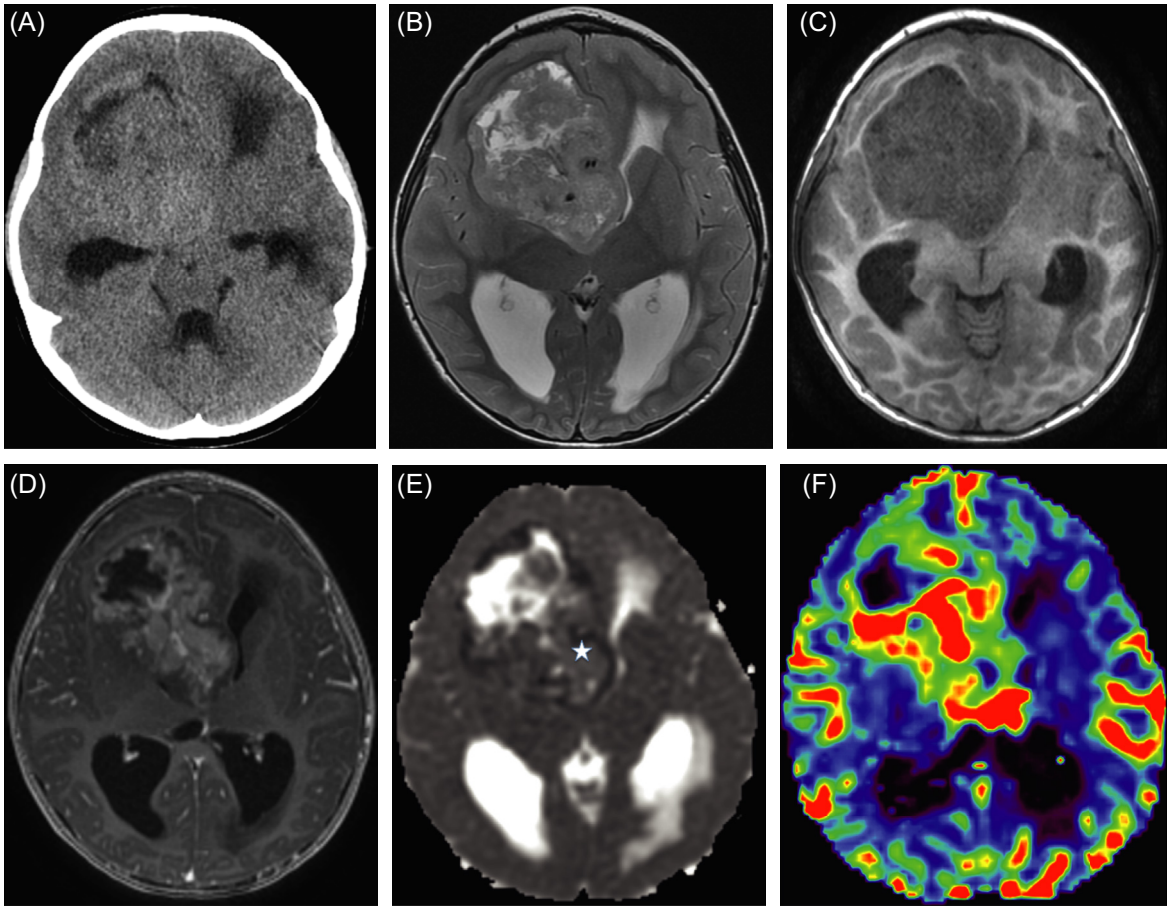


FIGURE 5 Supratentorial PNET in a 4-year-old girl with headache, nausea, and vomiting. (A) CT image demonstrates large right frontal heterogeneous dense mass. (B) Axial T2 MRI demonstrates heterogeneous T2 signal within the mass. (C) Axial T1 MRI before gadolinium shows intermediate signal intensity. (D) Axial T1 MRI after gadolinium demonstrates areas of avid enhancement of the solid components and nonenhancing foci anteriorly consistent with areas of necrosis. (E) Axial diffusion MRI shows restricted diffusion (asterisk) in the solid components of the mass. (F) Axial perfusion-weighted image show relative increased blood volume within the solid components of the tumor on the rCBV maps.

these tumors uniformly enhance and are often associated with subependymal nodules and cortical tubers (Figure 6).

Neuronal and Mixed Neuronal–Glial Tumors

These tumors are characterized by neuronal and glial differentiation. Tumors in this category include gangliocytoma, ganglioglioma, dysembryoplastic neuroepithelial tumor (DNT), central neurocytoma, paraganglioma, and cerebellar liponeurocytoma.[41]

Dysembryoplastic Neuroepithelial Tumor

DNT is a benign tumor associated with intractable, partial complex seizures occurring in children and young adults. These tumors are located either cortically or supratentorially and are often associated with cortical dysplasias occurring most commonly in the temporal and frontal lobes.[49] On CT, the tumor is typically hypodense with minimal or absent enhancement. On MR, the lesion is well circumscribed; it is hypointense on T1-weighted images and hyperintense on T2-weighted images without surrounding edema and with minimal enhancement (Figure 7). There may be remodeling of the calvarium.

Choroid Plexus Tumors

The most common types of choroid plexus tumors in childhood are choroid plexus papilloma and choroid plexus carcinoma. Choroid plexus tumors represent 2–4% of brain tumors in children.[41]

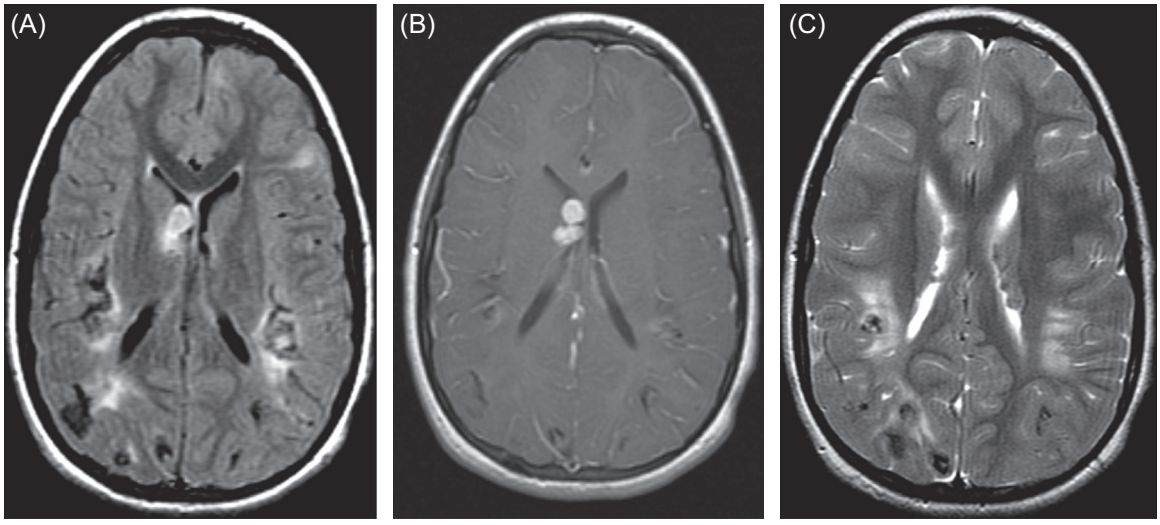


FIGURE 6 TS and subependymal giant cell astrocytoma. (A) Axial fluid-attenuated inversion recovery MRI demonstrates multiple calcified cortical tubers and hyperintense mass at the right foramen of Monro. (B) Axial T1 MRI with gadolinium demonstrates enhancing subependymal giant cell astrocytoma at the right foramen of Monro. (C) Axial T2 MRI shows hypointense calcified cortical tubers and bilateral subependymal nodules.

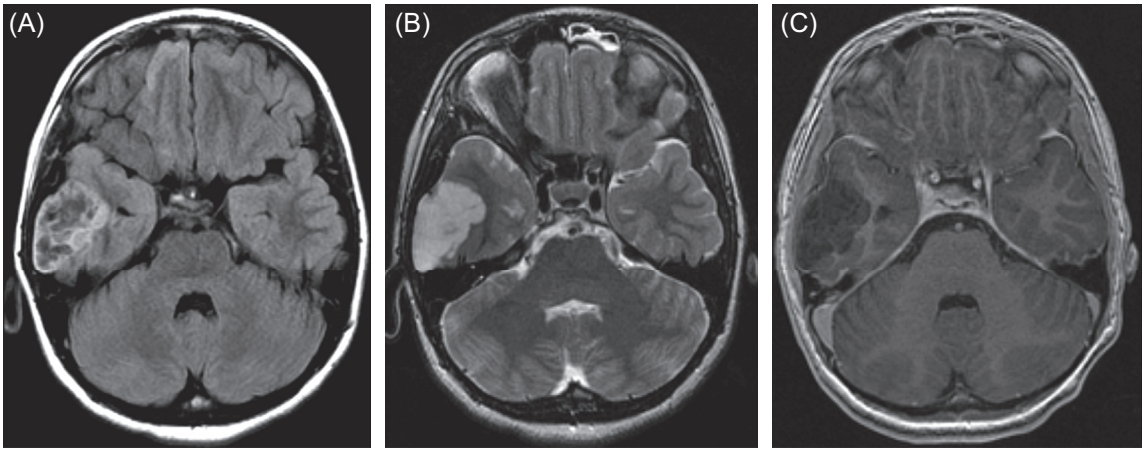


FIGURE 7 DNT tumor in an 11-year-old boy with seizures. (A and B) Axial fluid-attenuated inversion recovery and T2 MRI demonstrate sharply circumscribed, nonenhancing, multiseptated hyperintense mass extending to the cortex of the right temporal lobe. (C) Axial T1 image with gadolinium shows the tumor does not enhance.

Choroid Plexus Papilloma

Choroid plexus papillomas are intraventricular tumors that are well circumscribed. In children, these tumors arise in the lateral ventricle, often the trigone, whereas in adults, they are found in the fourth ventricle. Choroid plexus papillomas are lobulated in appearance and are associated with hydrocephalus often containing punctate regions of calcification, hemorrhage, and vascular flow voids. The hydrocephalus may arise from CSF overproduction and/or obstruction. Imaging features on CT include a lobulated intraventricular mass with calcification and homogeneously intense enhancement. MR features include T1 isointense to hypointense signal with T2 hypointensity and intense contrast enhancement (Figure 8). On MRS, these tumors exhibit a significantly higher level of myoinositol, low Cr, and decreased Cho compared to choroid plexus carcinomas.[50,51]

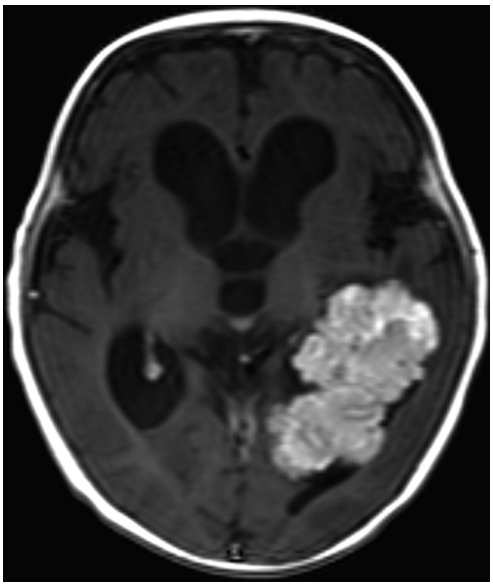


FIGURE 8 Choroid plexus papilloma in a 7-month-old boy presenting with irritability, nausea, and vomiting. Axial MRI with gadolinium shows large intraventricular lobulated mass in left lateral ventricle with intense enhancement. There is moderate enlargement of the lateral and third ventricles.

Choroid Plexus Carcinoma

Choroid plexus carcinomas represent 20–40% of choroid plexus tumors. They are heterogeneous on MR, extend beyond the margin of the ventricle, and are associated with edema and mass effect (Figure 9). Both choroid plexus papilloma and carcinoma can seed the CSF pathways.

On MRS, choroid plexus carcinomas have elevated Cho levels compared to choroid plexus carcinomas[50] and lower Cr and Cr/total Cho ratios than other pediatric brain tumors.[51]

Posterior Fossa Tumors

The common posterior fossa tumors of childhood include medulloblastoma, cerebellar astrocytoma, brainstem glioma, and ependymoma. Less frequent posterior fossa tumors include atypical teratoid/rhabdoid tumors, hemangioblastoma, dermoid–epidermoid tumors, acoustic schwannomas, meningioma, teratoma, and skull-base tumors. Skull-base tumors such as carcinoma, metastasis, sarcoma, histiocytosis, chordoma, and paraganglioma[52] may invade the posterior fossa. Presenting symptoms include head tilt, cranial nerve palsies, ataxia, headache, nausea, and vomiting.

Medulloblastoma

Medulloblastoma is a PNET arising from the fetal granular layer of the cerebellum or the posterior medullary velum. Genomic characteristics of medulloblastoma have demonstrated that medulloblastoma can be divided into four molecular groups: wingless, sonic hedgehog, group 3,

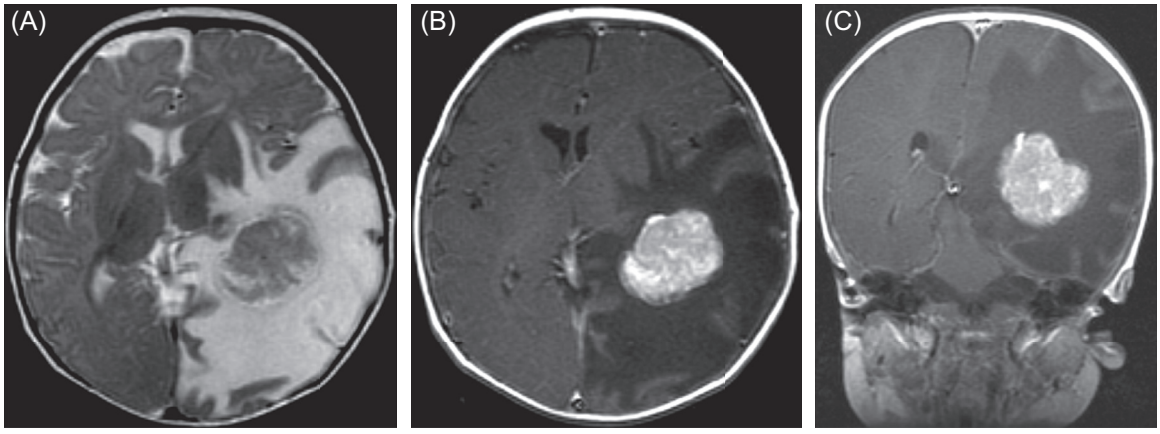


FIGURE 9 Choroid plexus carcinoma in a 5-month-old girl presenting with nausea, vomiting, lethargy, and apnea. (A) Axial T2 MRI demonstrates hypointense mass centered in the trigone of the left lateral ventricle with extensive surrounding edema in the adjacent white matter. (B and C) Axial and coronal T1 MRI with gadolinium demonstrates enhancing mass in the left trigone of the lateral ventricle.

and group 4.[53] It is the most common tumor of the posterior fossa in childhood, representing 15–20% of brain tumors in children and 30–40% of posterior fossa neoplasms.[52] Medulloblastomas usually arise in the midline within the vermis with growth into the fourth ventricle.[54–59] This differs from adults and older children, in whom the tumor is found laterally in the cerebellar hemispheres.[55,60] On CT, the tumor is typically characterized as hyperdense; and on MR, the tumor is viewed on T1-weighted images as hypointense (Figure 10(A)) and on T2-weighted images as hypointense to gray matter (Figure 10(B)).[56] On diffusion MRI, these tumors demonstrate restricted diffusion due to high cellularity within the tumor (Figure 10(C)).[61] Homogeneous enhancement is usually seen following gadolinium administration (Figure 11(A) and 11(B)). To identify leptomeningeal enhancement and seeding, the entire craniospinal axis must be screened (Figure 11(C) and (D)). In addition, MRS of untreated pediatric has demonstrated a significantly elevated taurine concentration compared to other tumors.[51,62,63] Cr/Cho and *N*-acetylaspartate (NAA)/Cho ratios have been used to differentiate between normal cerebellar tissue and posterior fossa tumors such as PNET, ependymoma, and juvenile pilocytic astrocytoma.[64] A 2014 study suggested that tumor location and enhancement pattern were predictive of molecular subgroups of pediatric medulloblastoma and may potentially serve as a surrogate for genomic testing.[65] In this study, sonic hedgehog tumors were seen to occur in the cerebellar hemispheres, wingless tumors were more likely to be localized to the cerebellar peduncle or cerebellopontine angle cistern, and groups 3 and 4 tumors predominated within the midline fourth ventricle. In addition, midline group 4 tumors were characterized most often as lesions with minimal or no enhancement.

Cerebellar Astrocytomas

Cerebellar astrocytoma, one of the most common posterior fossa tumors (second only to medulloblastoma), is often

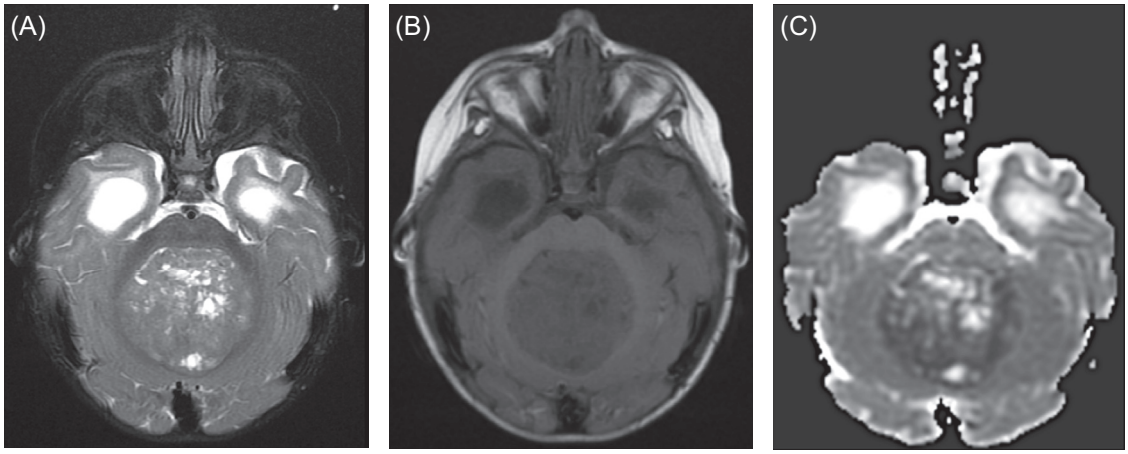


FIGURE 10 Medulloblastoma. (A) Axial T2 fat sat MRI shows hypointense mass in fourth ventricle. (B) Axial diffusion MRI of a medulloblastoma shows restricted diffusion in mass. (C) Sagittal T1 MRI with gadolinium shows enhancing fourth ventricular mass.

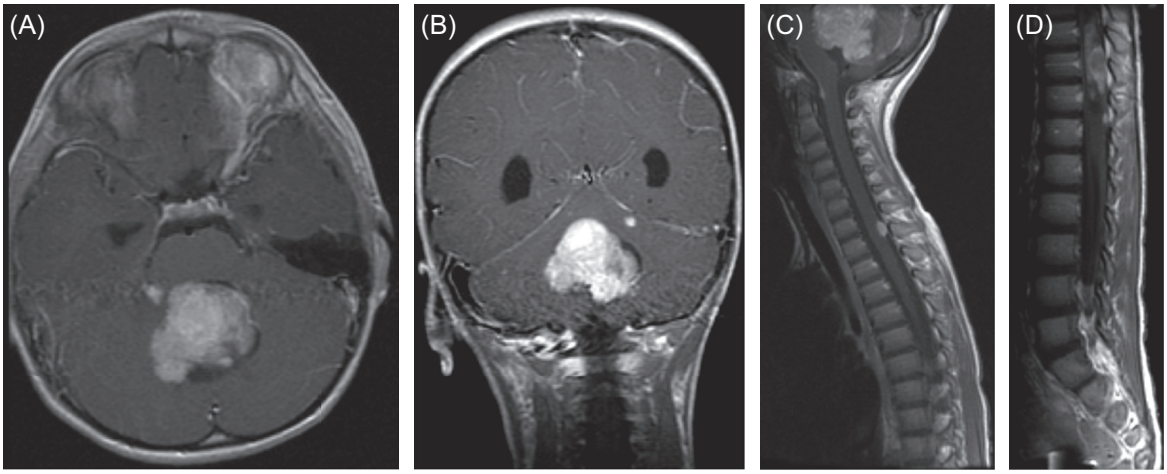


FIGURE 11 Medulloblastoma with spinal leptomeningeal seeding. (A and B) Axial and coronal T1 MRI with gadolinium shows enhancing posterior fossa mass. (C and D) Sagittal T1 MRI with gadolinium show spinal leptomeningeal seeding.

diagnosed as a juvenile pilocytic astrocytoma with excellent survival after gross total surgical resection.[66–68] Cerebellar astrocytomas can occur in the midline or in the cerebellar hemispheres. These tumors are often associated with hydrocephalus owing to compression of the aqueduct or fourth ventricle. The classic appearance is a cerebellar mass consisting of a large cyst with a solid tumor nodule. However, the imaging spectrum of appearances may include cystic, solid, or a mix of cystic and solid presentations. Macrocysts or microcysts can form and the tumor can be grossly cystic or solid. On CT and MR, a cyst with enhancement of the solid nodular component is typically found (Figure 12).

The solid, enhancing component of cerebellar pilocytic astrocytomas has greater ADC values than other pediatric cerebellar tumors such as ependymoma, rhabdoid tumor, and medulloblastoma.[61]

MRS of these tumors has demonstrated high lactate concentrations and consistently high Cho content and Cho/NAA and Cho/Cr ratios despite the benign clinical course of this tumor type.[69]

Brain-Stem Tumors

Brain-stem tumors represent 10–20% of all CNS tumors in childhood. These tumors can be categorized as diffuse and focal.

Pontine Tumors

Patients with diffuse pontine gliomas commonly present with multiple cranial nerve palsies, long tract signs, and ataxia.[70,71] Typically, these tumors can cause the pons to expand by more than 50% and can infiltrate into the medulla or midbrain. Diagnosis is based on the characteristic changes on MRI of diffuse, T2-weighted, hyperintense expansion of the brain stem without biopsy. Despite multiple treatment approaches, the prognosis is poor, with long-term survival <10%.[72] From a pathological standpoint, these tumors represent high-grade lesions. On CT, these tumors are of low density or isodense. On MR, they are typically isointense to hypointense on T1-weighted images and are hyperintense on T2 images. Enhancement is usually absent or minimal (Figure 13).

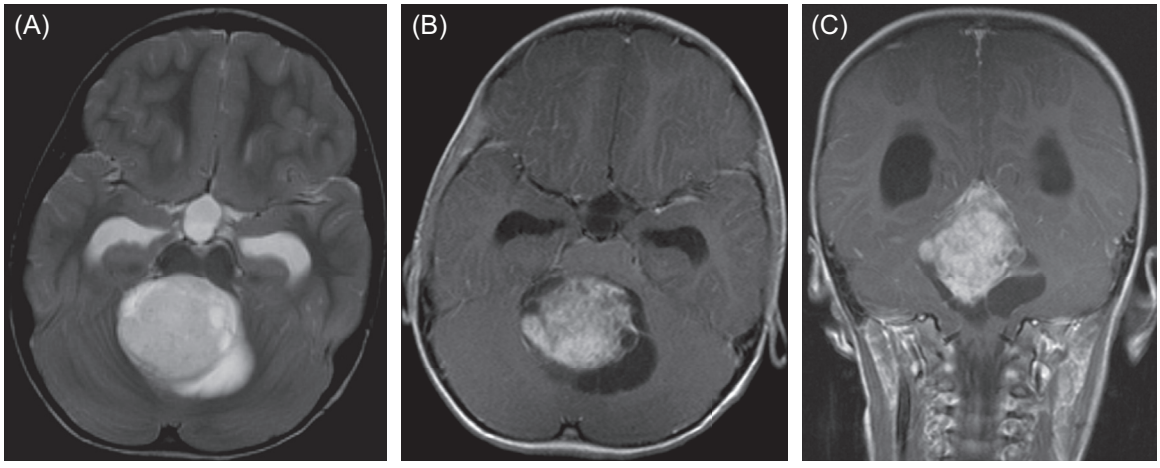


FIGURE 12 Posterior fossa juvenile pilocytic astrocytoma. (A) Axial T2 MRI of hyperintense mass in posterior fossa with hydrocephalus. (B and C) Axial and coronal T1 MRI show enhancing tumor nodule with cysts within the tumor.

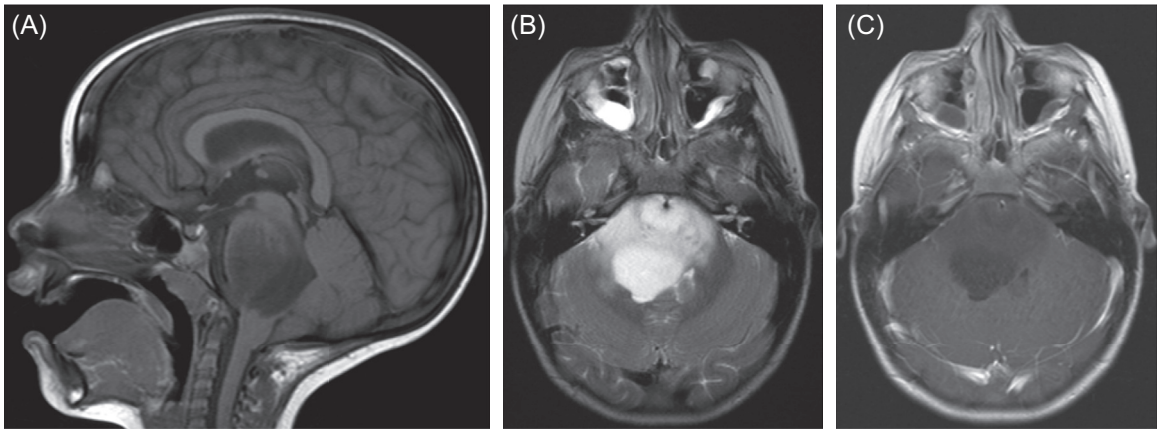


FIGURE 13 Diffuse pontine glioma. (A) Sagittal T1 MRI shows expansile hypointense mass in the pons with mass effect on the fourth ventricle. (B) Axial T2 MRI shows encasement of the basilar artery and large hyperintense pontine mass with mass effect on the fourth ventricle. (C) Axial T1 MRI with gadolinium shows no enhancement within the mass.

Calcification and hemorrhage within the tumor are rare. A study by Poussaint et al. found that patients with diffuse intrinsic brain-stem glioma, presence of larger tumors at presentation, and greater decreases in tumor volume and diffusion values had longer survival intervals.[73] Conversely, enhancement at baseline and over time was significantly associated with shorter survival. Tumor enhancement was associated with shorter survival, lower tumor diffusion values (increased cellularity), and a smaller drop in diffusion values after radiotherapy (RT).

Using multivoxel MRS, Laprie et al. followed eight patients with diffuse pontine glioma after radiotherapy.[74] Spectroscopy in these tumors was evaluated before RT, at response, and at recurrence. Cho/NAA and Cho/Cr values within the imaging abnormalities were significantly higher than the mean values in normal-appearing regions. Cho/NAA values decreased in studies performed from diagnosis to the time of response to RT followed by an increase at the time of relapse.

A 2011 prospective study of 38 patients suggested Cho/NAA ratio and variance in Cho/NAA values among different voxels within a tumor were each predictive of shorter survival in patients with diffuse brain-stem gliomas.[75] In another study, two pediatric patients with diffuse pontine tumors improved clinically following RT; however, MRS showed an overall increase in Cho/Cr and Cho/NAA ratios indicating tumor progression.[76] Unfortunately, the disease progressed in both patients. These studies demonstrate the potential utility of MRS in determining tumor response or lack of response to therapy. The presence of a relatively high concentration of a metabolite at 2.6 ppm that was tentatively labeled as citrate has been observed in diffuse intrinsic brain-stem gliomas at presentation, which declined significantly with time in progressing brain-stem glioma (Figure 14).[77]

MR DTI of brain-stem gliomas has been reported by Helton et al.[78] This technique can provide visualization and quantification of tumor involvement in the brain stem by measuring the degree to which the tumor has invaded white matter tracts. They found that: (1) the corticospinal tracts and transverse pontine fibers were more affected than the medial lemnisci; and (2) fractional anisotropy (FA) and the ADC were significantly ($p < 0.05$) altered in the tracts of all patients with pontine tumors compared to control groups. Another study by Prabhu et al. comprising three patients with diffuse brain-stem gliomas (BSGs) demonstrated serial changes in ADC and FA values and tractography data in pediatric BSG including initial tumor infiltration, which improved transiently on treatment and was followed subsequently by loss of tract anisotropy during tumor progression.[79]

In a study of 40 newly diagnosed diffuse intrinsic BSG patients using fluorodeoxyglucose (FDG) PET, Zukotynski et al. found that when FDG uptake involved at least half of the tumor, there was poorer survival than in children with uptake less than 50% of the tumor. Decreased survival was associated with intense FDG PET tracer uptake. When there was higher FDG uptake in diffuse intrinsic BSG associated with enhancement, there was restricted diffusion within the tumor consistent with increased cellularity.[80]

Focal pontine gliomas are uncommon, representing 5–10% of BSGs.[72] They may have an exophytic component.[81] These tumors also demonstrate marked enhancement and have a better prognosis than diffuse pontine gliomas.[82]

Medullary Tumors

Cervicomedullary astrocytomas are a unique group of brain-stem tumors with a good prognosis compared to the diffuse pontine group of BSGs.[83,84] On CT, these tumors are isodense; on MR, these tumors are isointense on T1-weighted images and are hyperintense on T2-weighted images. They are typically well circumscribed, often demonstrate enhancement, and are described pathologically as pilocytic astrocytomas (Figure 15).[85] These tumors probably originate in the upper cervical cord and grow upward toward the obex into the medulla and are dorsally exophytic.[86]

Diffuse medullary tumors are poorly defined lesions centered in the medulla that can extend into the pons or upper cervical cord and have a poorer prognosis than the dorsally exophytic type of tumor.

Midbrain Tumors

Tumors of the midbrain include focal and diffuse midbrain tumors and tectal tumors. The focal midbrain tumor has a better prognosis than the diffuse. Tectal tumors are a unique subset of tumors of the brain stem. These tumors are often low-grade pilocytic astrocytomas, present with obstructive hydrocephalus, and usually do not require treatment beyond CSF diversion such as third ventriculostomy. Before the advent of MR, patients with this tumor were frequently misdiagnosed as having aqueductal stenosis on CT. On MR, the lesions are usually isointense on T1-weighted images and hyperintense on T2-weighted images without enhancement (Figure 16). Tumors larger than 2.5 cm in diameter with enhancement are significant radiologic predictors of those patients who will need further treatment beyond CSF diversion.[87] In a study of 40 children with tectal tumors, the only factor predictive of tumor enlargement was lesion volume at presentation ($p = 0.002$). Lesions with volume less than 4 cm^3 were likely to follow a benign course. All large lesions defined as a volume greater than 10 cm^3 at presentation eventually required treatment.[88]

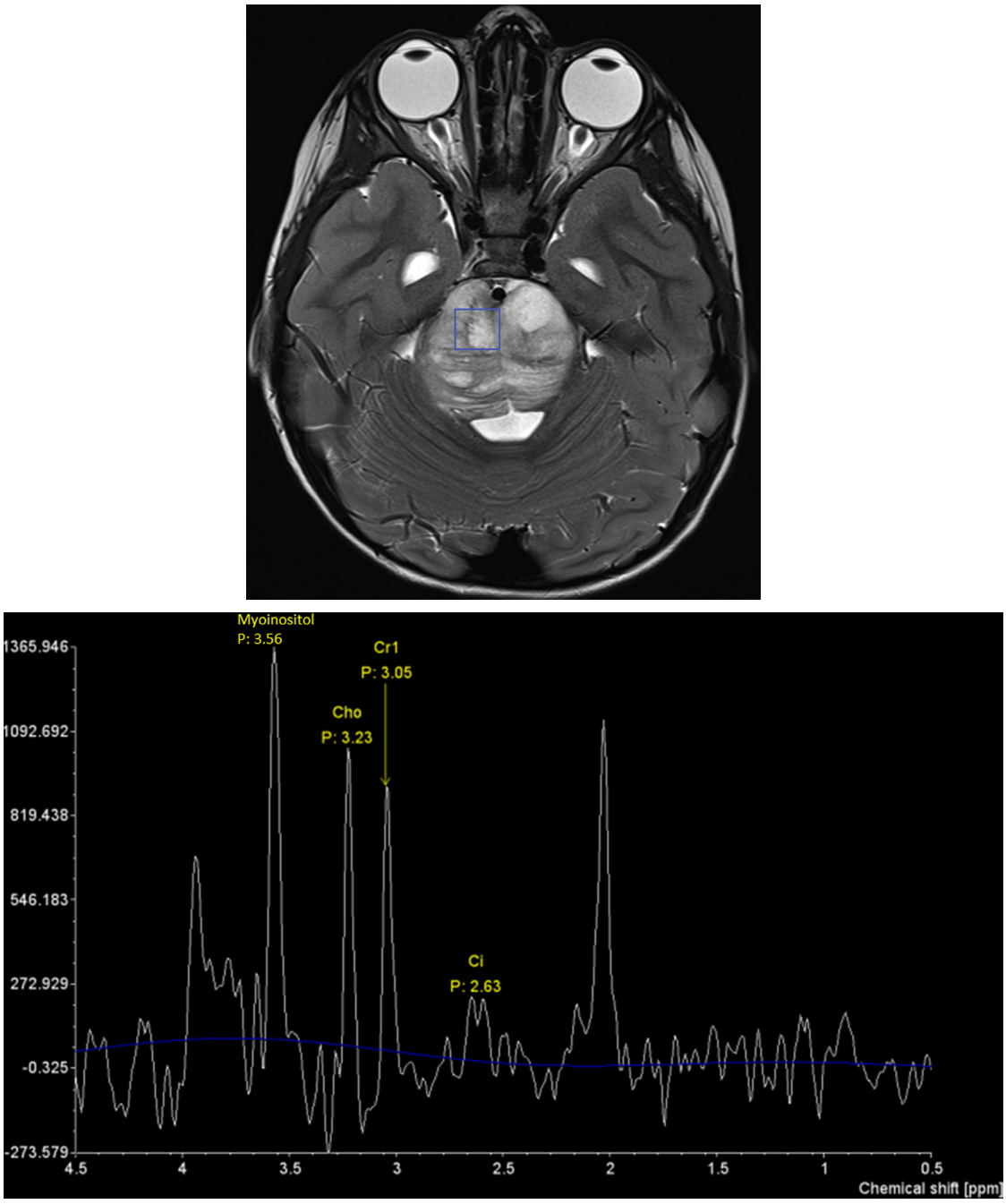


FIGURE 14 Short TE (30 ms) multivoxel spectroscopy shows presence of a prominent peak at 2.6 ppm corresponding to citrate in a brain-stem glioma within a processed voxel located over the center of a large lesion centered in the brain stem with signal characteristics of a diffuse intrinsic brain-stem glioma in a 7-year-old female.

Ependymomas

Ependymomas constitute 6–12% of all intracranial tumors in children and 8–15% of posterior fossa tumors in children.[41] They are the fourth most common posterior fossa tumor in children following medulloblastoma, cerebellar astrocytoma, and BSG. Ependymomas arise from ependymal cells lining the ventricles; they grow out of the fourth ventricle via the foramina of Luschka and Magendie into the cisterna magna, basilar cisterns, and cerebellopontine angles and through the foramen magnum into the upper cervical canal around the spinal cord. On CT, the tumor reveals mixed density with punctate calcification in 50% of cases with variable enhancement. These tumors are heterogeneous on MR, reflecting a combination of solid component, cyst, calcification, necrosis, edema, or hemorrhage.[89] On T1-weighted

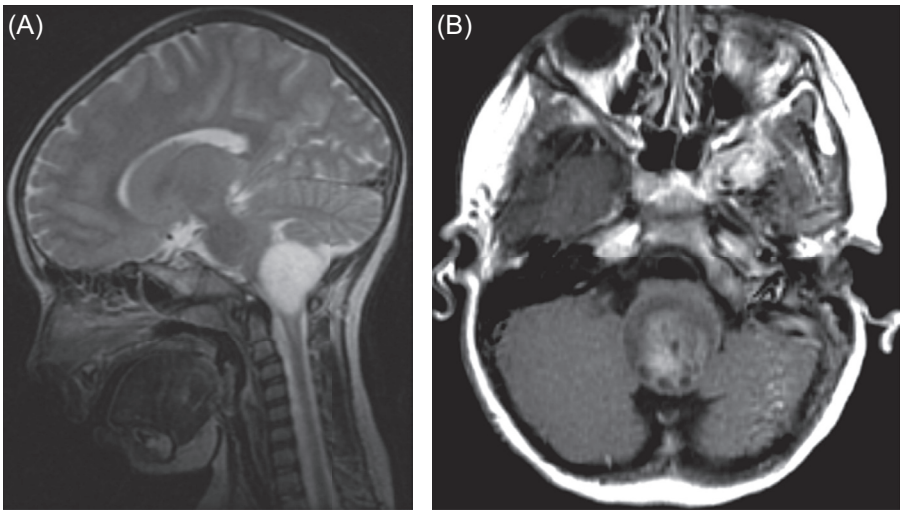


FIGURE 15 Cervicomedullary astrocytoma. (A) Sagittal T2 MRI demonstrates hyperintense cervicomedullary mass. (B) Axial T1 MRI with gadolinium shows mild enhancement and tiny cysts posteriorly.

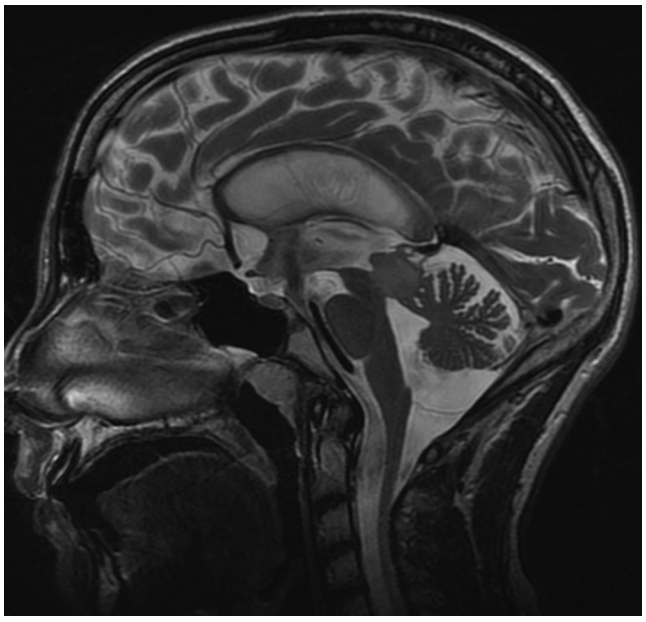


FIGURE 16 Tectal glioma. Sagittal T2 image shows expansile tectal mass (arrow) obstructing the aqueduct of Sylvius.

images, ependymomas are usually hypointense; and on T2-weighted images, the mass is often isointense to gray matter with foci of dark T2 signal, related to calcification or blood, and foci of bright T2 signal, related to cyst or necrosis within the tumor. Following contrast administration, there is heterogeneous enhancement in the tumor (Figure 17).

Atypical Teratoid/Rhabdoid Tumors

Of all atypical teratoid/rhabdoid tumors, the majority (94%) are intra-axial, occurring in the infratentorial component in 47% of cases.[90] The imaging features are identical to those of medulloblastoma; however, the prognosis is worse, with a median survival rate with disseminated leptomeningeal tumor of 16 months (Figure 18).[91] These tumors occur at a younger age, are predominately seen in females, and have a propensity to seed.[91] These tumors are distinguished by mutation or deletion of both copies of the hSNF5/INI1 gene, which maps to chromosome band 22q11.2 and is observed in approximately 70% of primary tumors.[92]

Sellar and Suprasellar Tumors

Sellar and suprasellar tumors in children include craniopharyngioma, chiasmatic/hypothalamic glioma, hypothalamic hamartoma, pituitary adenoma, germ-cell tumors, Langerhans cell histiocytosis, Rathke's cleft cysts, arachnoid cysts, and dermoid/epidermoid cysts. The most common sellar and suprasellar tumors are craniopharyngioma and chiasmatic/hypothalamic glioma.

Craniopharyngioma

Craniopharyngioma is a benign (WHO grade I) neoplasm arising in the suprasellar or intrasellar region. These tumors arise from remnants of Rathke's pouch (i.e., the craniopharyngeal duct) and are composed of characteristic squamous epithelium.[93] They represent 1–5% of all intracranial tumors and constitute 50% of the suprasellar tumors seen in childhood.[94] They have a bimodal distribution, occurring in childhood and adolescence and older adults in their 50s. In children, the clinical presentation includes headache, visual field defects, diplopia, and short stature, with occasional hydrocephalus and papilledema present. Classically, these are cystic tumors filled with cholesterol-rich fluid grossly resembling motor oil. The tumors are usually intrasellar, suprasellar, or both.

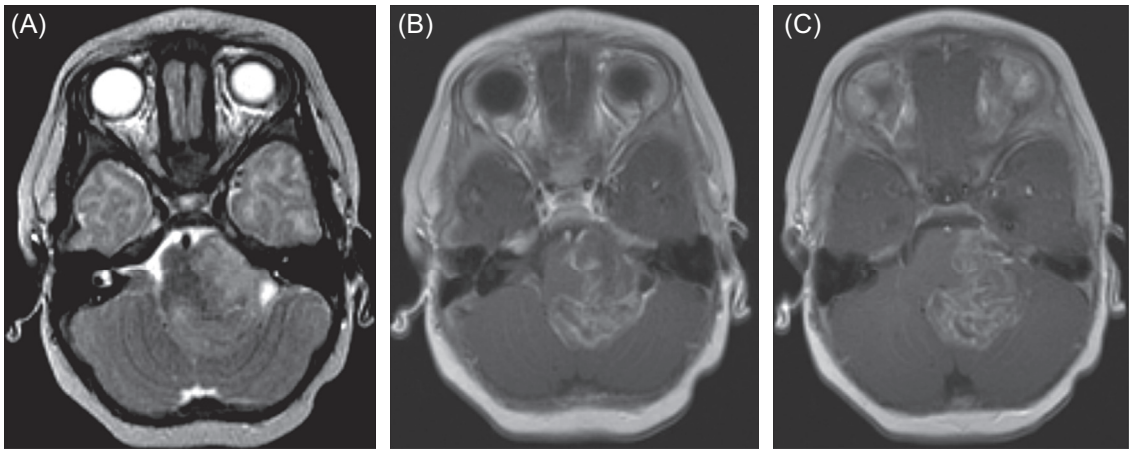


FIGURE 17 Posterior fossa ependymoma. (A) Axial T2 MRI demonstrates mass within fourth ventricle extending through the left foramen of Luschka. (B and C) Axial T1 MRI with gadolinium demonstrates heterogeneously enhancing fourth-ventricular tumor extending through the left foramen of Luschka.

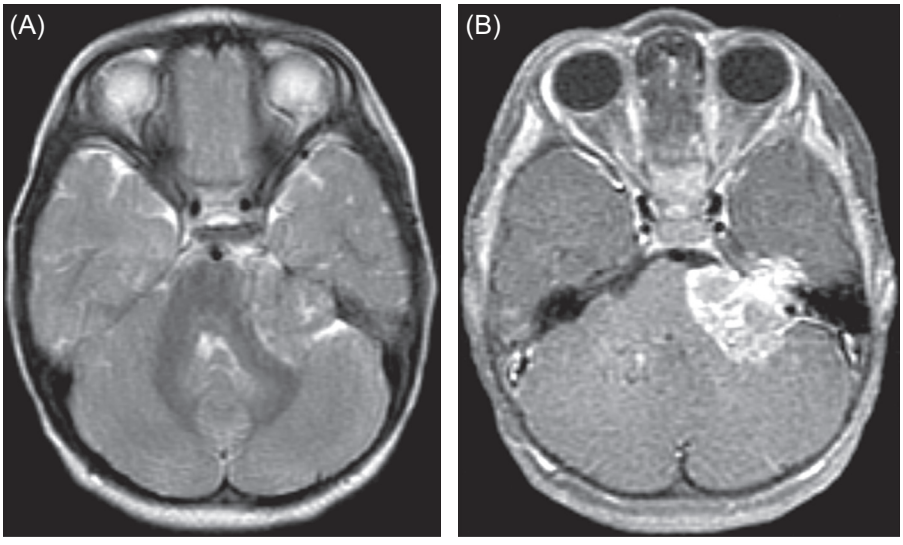


FIGURE 18 Posterior fossa rhabdoid tumor in 20-month-old infant with left facial nerve paralysis. (A) Axial T2 MRI shows hypointense mass in left cerebellopontine angle cistern. (B) Axial T1 MRI with gadolinium shows enhancing left cerebellopontine angle mass.

Craniopharyngiomas can compress, envelop, or infiltrate adjacent structures and produce a reactive gliosis, although they are histologically benign. Hetelekidis et al. have demonstrated that if the tumor is greater than 5 cm, there is a greater likelihood of recurrence.[95] In many cases, surgical extirpation is difficult, and with a high rate of recurrence, adjuvant RT is often necessary. On CT, 90% of craniopharyngiomas are cystic and calcified.[96,97] On MRI, these tumors have variable signal characteristics depending on the contents of the cyst and the presence of calcium. On CT, the solid component of the tumor may be isodense or hypodense and on MRI, T1 isointense to hypointense with T2 isointensity to hyperintensity. The calcified component is of increased attenuation on CT and often T2 hypointense on MRI. The cystic component may be of high or low T1 intensity and T2 hyperintense. Following gadolinium administration, peripheral enhancement of the cyst as well as heterogeneous enhancement of the solid component generally occurs (Figure 19).

Chiasmatic/Hypothalamic Gliomas

These tumors constitute 5% of pediatric intracranial tumors.[98] Chiasmatic/hypothalamic tumors are often low-grade astrocytomas and pilocytic. Between 20% and 50% of patients with chiasmatic/hypothalamic tumors have neurofibromatosis type 1 (NF1). NF1 is the most common of the phakomatoses, inherited as an autosomal dominant disorder localized on chromosome 17 with variable penetrance. Optic gliomas are the most common tumor of the CNS in NF1.[99] These gliomas

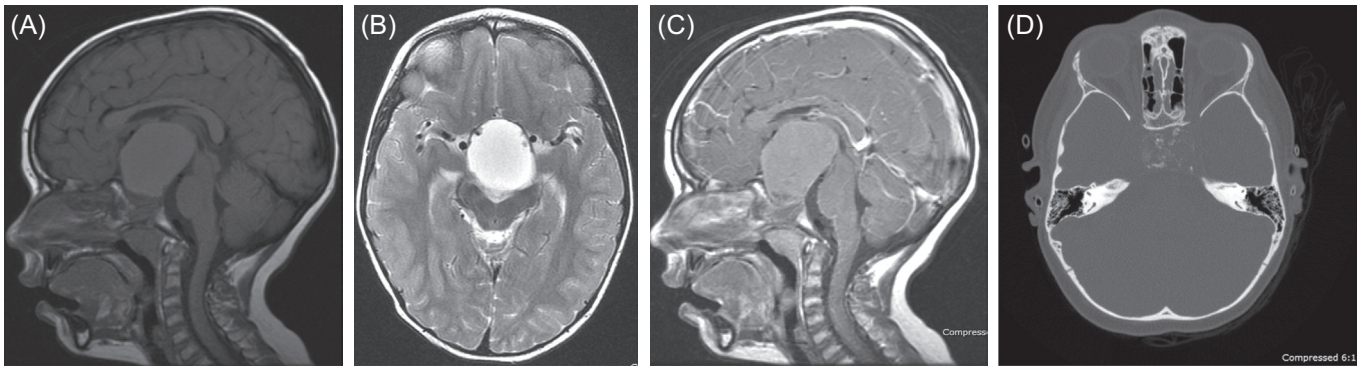


FIGURE 19 Craniopharyngioma. (A) Sagittal T1 MRI shows large sellar and suprasellar mass with bright T2 signal superiorly and small amount of hypointense signal inferiorly in the sella. (B) Axial T2 MRI shows predominantly hyperintense mass in the suprasellar region. (C) Sagittal T1 MRI with gadolinium shows mild enhancement of the inferior solid component in the sella and peripheral enhancement of the superior cystic component. (D) Axial CT image shows stippled calcification within the mass.

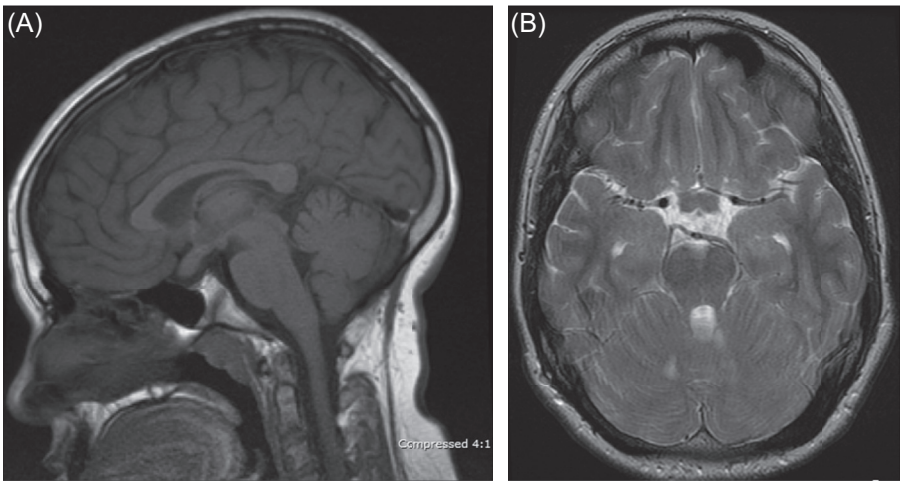


FIGURE 20 Optic chiasm glioma in 14-year-old male with NF1. (A) Sagittal T1 MRI shows a thickened optic chiasm (arrow). (B) Axial T2 MRI shows thickened optic chiasm and NF spots in cerebellum.

may involve any portion of the optic pathway, including one or both optic nerves, the chiasm (Figure 20), the tracts, the lateral geniculate bodies, or the optic radiations. Other intracranial lesions that may be seen in NF1 include vacuolization in the myelin (i.e., NF spots), plexiform neurofibromas, and other astrocytomas (Figure 21).[100] The clinical presentation of optic glioma is most often characterized by decreased visual acuity, though other symptoms including visual field defects, optic atrophy, hydrocephalus, or hypothalamic dysfunction and papilledema may be seen.[101] These lesions are usually T1-hypointense and T2-hyperintense with typically homogeneous gadolinium enhancement and, in large tumors, heterogeneous enhancement. MRI with fat suppression leads to optimal visualization of the optic pathways.[102] Spontaneous regression of optic gliomas in patients with and without NF1 has been reported.[103]

Diencephalic syndrome is also commonly associated with hypothalamic/chiasmatic astrocytomas and may be the underlying cause of failure to thrive in infancy in a rare number of cases. Clinical characteristics include severe emaciation in the setting of normal linear growth. The tumors associated with this unusual syndrome are often larger in size, occur at a younger age, and are more aggressive than those associated with other presentations (Figure 22). Despite low-grade histologic findings, these tumors may seed throughout the CSF pathways. This syndrome serves as a model for studying growth hormone resistance and metabolic regulation of adiposity.[104]

Hypothalamic Hamartoma

Hypothalamic hamartomas are masses of mature ganglionic tissue, located between the pituitary stalk and the mammillary bodies, involving the region of the tuber cinereum. They do not demonstrate invasion or growth.[105] Often the patients are male, presenting with symptoms including precocious puberty, gelastic seizures, hyperactivity, and developmental delay. On CT, there is a suprasellar mass, isodense with gray matter, noncalcified, and rarely cystic. On MRI, a well-demarcated mass is present

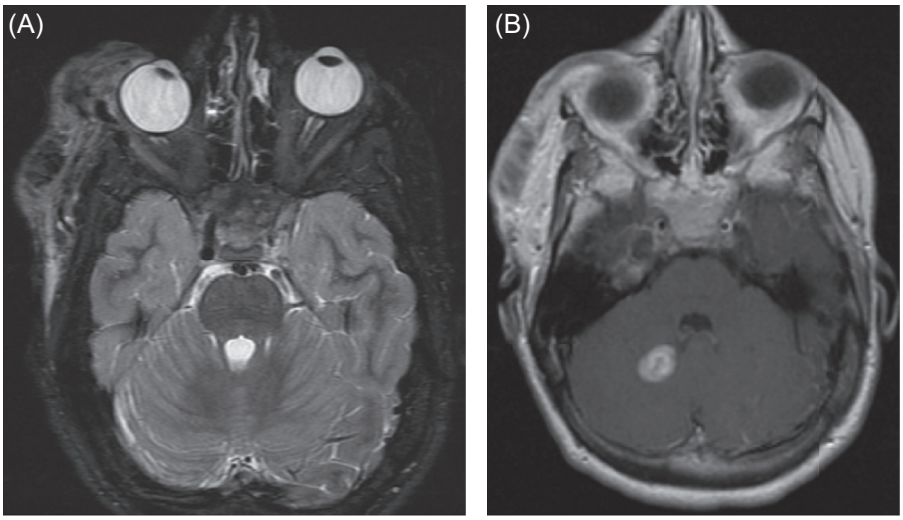


FIGURE 21 18-year-old girl with NF1, right facial plexiform neurofibroma, and left cerebellar astrocytoma. (A) Axial fast spin-echo inversion recovery (FSEIR) MRI demonstrates right facial plexiform neurofibroma (arrow). (B) Axial T1 MRI with gadolinium shows right cerebellar pilocytic astrocytoma.

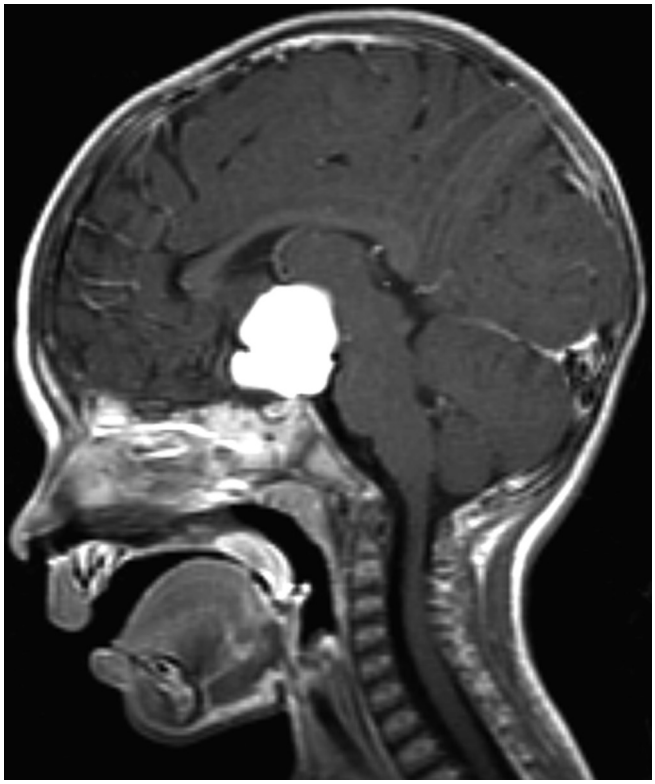


FIGURE 22 Diencephalic syndrome in a 13-month-old girl with failure to thrive. Sagittal T1 MRI with gadolinium shows enhancing suprasellar mass.

within or adjacent to the tuber cinereum or mammillary bodies. The hamartomas are T1-isointense and T2-isointense to slightly hyperintense to gray matter without enhancement (Figure 23). In a study using short-echo-time point-resolved spectroscopy sequences, Amstutz et al. sampled hypothalamic hamartomas.[106] Sequences were used to compare Cho, NAA, and myoinositol (mI) resonances by using a Cr reference. Spectral ratios and T2 signal-intensity ratios of the hamartomas were then compared with histopathologic findings. In 14 hypothalamic hamartomas, a spectrum of increased mI/Cr ratios was seen. Those tumors with markedly elevated mI/Cr demonstrated an increased glial component compared with the remaining tumors. Increased glial component was also found to have a positive correlation with hyperintensity of lesions on T2-weighted images.[106]

Other studies have identified a subgroup of patients with hypothalamic hamartoma and associated congenital anomalies including hypoplasia of the olfactory bulbs, absence of the pituitary gland, cardiac and renal anomalies, imperforate anus, craniofacial anomalies, syndactyly, and short metacarpal—clinical features characterizing the autosomal dominant Pallister–Hall syndrome.[107,108]

Germ-Cell Tumors

CNS germ-cell tumors in childhood occur commonly in the suprasellar region and pineal region and may be germinomas or nongerminomatous germ-cell tumors. These patients may clinically present with central diabetes insipidus (DI), wasting, precocious puberty, or growth failure. On imaging, a mass may be seen involving the suprasellar region or there may be thickening of the infundibulum (Figure 24). On CT, these lesions are well defined and slightly hyperdense. On MRI, they are T1-hypointense, T2-hypointense, and markedly enhancing. CSF seeding is not uncommon. On occasion, there may be an associated pineal region germinoma, which may be metastatic or synchronous.

Suprasellar germinomas often present with central DI. On MRI, the normally seen posterior pituitary bright spot is absent.[109] The mechanism of central DI is thought to be the interruption of transport of the vasopressin

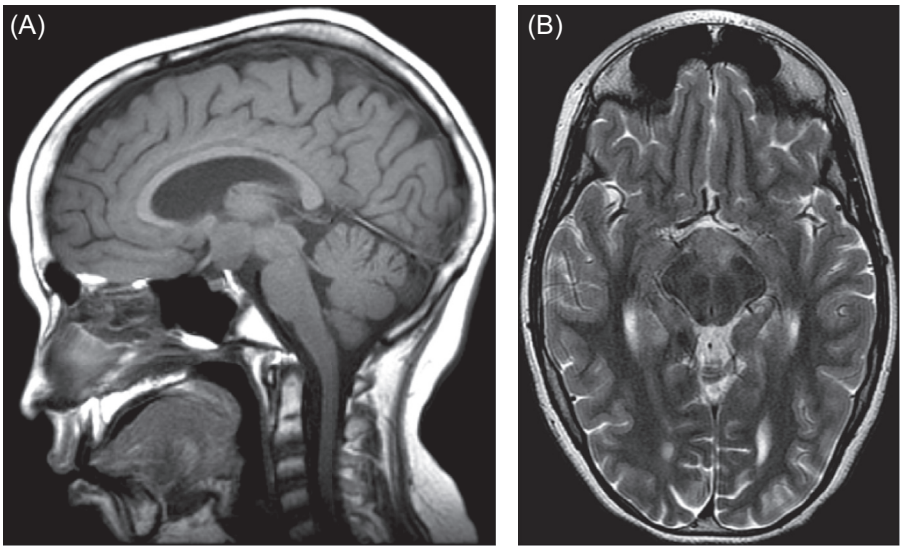


FIGURE 23 Hypothalamic hamartoma. (A) Sagittal T1 MRI shows hypointense hypothalamic mass (arrow). (B) Axial T2 MRI shows isointense hypothalamic mass (arrow).

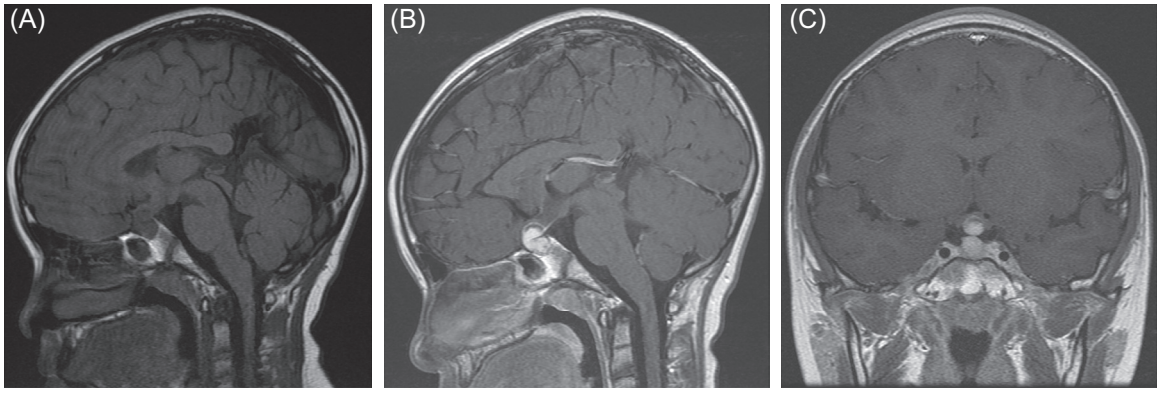


FIGURE 24 Nongerminomatous germ-cell tumor of suprasellar region in a 10-year-old girl with central diabetes insipidus. (A) Sagittal T1 MRI shows loss of posterior pituitary bright spot (arrow). (B and C) Sagittal and coronal T1 image shows thickened enhancing infundibulum and sellar mass.

neurosecretory granules along the hypothalamic–neurohypophyseal pathway. Central DI and the absence of the posterior bright spot may precede other clinical and imaging features of hypothalamic tumor by months or years. Therefore, follow-up MRI with gadolinium is recommended in all of these patients.[110] Other causes of pituitary stalk thickening include Langerhans histiocytosis, lymphocytic hypophysitis, and rare entities such as sarcoidosis and lymphoma.

Teratomas occur more often in the pineal region than in the suprasellar region. They are classified as mature or immature depending on whether the tissue components resemble mature adult tissues or immature embryonic tissues. On CT and MRI, the mass often contains fat, bone, or cartilage with heterogeneous density and intensity characteristics. These patients may present with precocious puberty.

Pituitary Adenomas

Pituitary adenomas are uncommon in childhood and represent less than 3% of all intracranial tumors.[111] The clinical presentation depends on tumor size, hormonal activity, and extrasellar extent. Pituitary adenomas are divided into hormonally active and inactive types, with the majority being hormonally active and most commonly prolactin-secreting. These lesions tend to occur in adolescence; they are often microadenomas (<1 cm) and are most often prolactinomas (Figure 25). Macroadenomas are greater than 1 cm in diameter and are often prolactinomas in patients presenting with neuroendocrine symptoms, visual field deficits, and headache. The majority of macroadenomas in adolescence are hemorrhagic and often occur in males.[112]

On MRI, pituitary adenomas are T1-hypointense in the majority of cases. Less frequently, adenomas are T1-isointense or hyperintense.[113] On T2 images, adenomas are often hyperintense or isointense, and macroadenomas are usually hyperintense.[113] Macroadenomas may invade the cavernous sinuses, may extend superiorly into the suprasellar cistern, and can compress the optic chiasm. Immediately following gadolinium administration, the lesion will be hypointense compared to the normal gland.

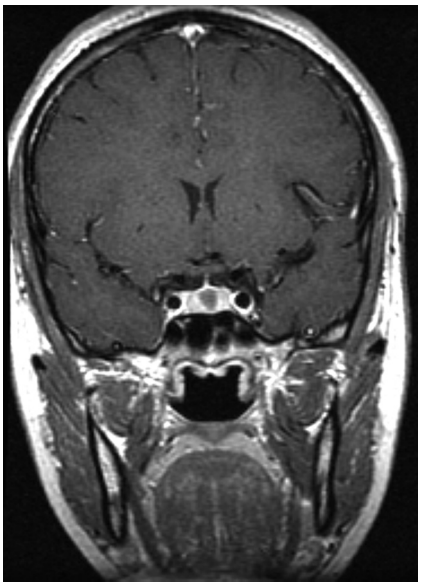


FIGURE 25 Prolactinoma. Coronal T1 MRI with gadolinium shows a nonenhancing pituitary microadenoma (arrow).

Langerhans Cell Histiocytosis

Systemic Langerhans cell histiocytosis may include involvement of the pituitary stalk and hypothalamus. These patients may present with DI; MRI shows loss of the normal posterior pituitary bright spot.[114] MRI may also demonstrate a solitary mass in the region of the median eminence of the pituitary stalk or thickening of the infundibulum. On CT, the mass is isodense, and on MRI, the lesion is T1 isointense and T2 hyperintense. Following gadolinium administration, there is marked enhancement.

Parameningeal and Metastatic Tumors

Parameningeal tumors are extradural but contiguous with the CNS. They may arise from or involve the scalp, cranial vault, cranial base, orbits, sinuses or pharynx, petrous temporal structures, or soft tissues of the face or neck. The parameningeal neoplastic processes encountered in childhood include those of osseous, chondroid, or myeloid (reticuloendothelial) origin; other mesenchymal origin tumors; and those arising from notochordal elements including neuroblastoma, rhabdomyosarcoma, histiocytosis, plexiform neurofibroma, and angiofibroma (Figure 26).[115]

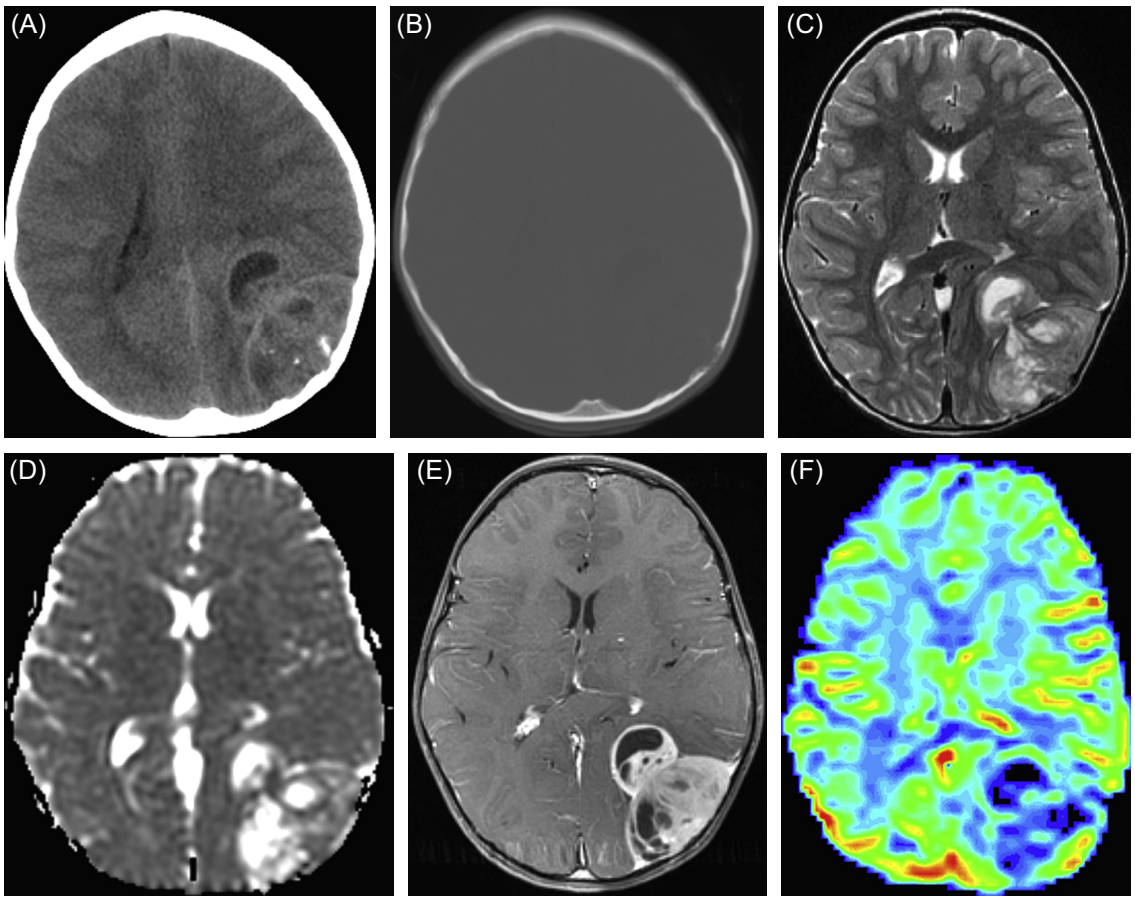


FIGURE 26 Supratentorial extra-axial Ewing sarcoma. (A) Axial CT image demonstrates heterogeneously dense mass lesion in the left parietal lobe with scattered calcification. (B) Axial CT bone window image demonstrates lytic destruction of the left parietal bone. (C) Axial T2 MRI demonstrates large heterogeneous extra-axial tumor compressing the left occipital lobe with mass effect on the left parietal lobe. (D) Axial MR diffusion ADC map demonstrates restricted diffusion within the mass. (E) Axial T1 MRI with gadolinium demonstrates nodular heterogeneous enhancement of the mass. (F) Axial T2* MR perfusion image demonstrates increased perfusion in central areas of the mass.

Metastatic disease to the brain is rare and, when present, is commonly leptomeningeal disease from a primary brain tumor. However, when brain metastases in childhood occur, they generally arise from sarcomas such as Ewing sarcoma and rhabdomyosarcoma.[116]

CONCLUSION

MRI has emerged as the imaging gold standard for pediatric brain tumors. It is constantly evolving and it now provides incredibly detailed structural, anatomic, metabolic, and functional data without the potentially harmful effects of ionizing radiation. The precise pretherapy, intraoperative, and postoperative images produced by MRI allow the physician to accurately detect, diagnose, treat, and follow a wide range of malignancies affecting the CNS.

More recently, MRI has proven an indispensable tool in implementing extremely sophisticated, technologically advanced surgeries that are executed under computer-assisted image guidance. Because of MRI's ability to achieve precise localization and targeting, brain tumor excision is now accomplished with exceptional accuracy and without causing damage to surrounding healthy tissue, which is of particular benefit to the developing pediatric brain.

Advanced MRI techniques like MR perfusion imaging, MRS, diffusion imaging, and DTI are constantly furthering the quality and types of data that are generated. These techniques, when combined with other modalities such as CT, SPECT, and PET, are resulting in (1) more accurate and timely diagnoses; (2) interventions tailored to the individual needs of the patient; and (3) improved assessment of response to treatment.

Thus equipped with extremely detailed disease profiles, the entire medical team—from the diagnosing neuroradiologist to the treating neurosurgeon and neuro-oncologist—is able to implement the most responsive and effective therapeutic interventions from the moment the tumor is detected to complete eradication or remission. In the near future, computer-assisted robotics should also play an important role in maximizing the utility of MRI and other imaging modalities. Of immediate benefit is the practice of combining modalities to generate the most comprehensive "picture" of the tumor, including accurate staging, which, in turn, leads to successful surgical and postoperative outcomes. In adopting the most effective treatment approach to pediatric brain tumors, the physician increasingly chooses MRI as the imaging foundation upon which suspected malignancies are diagnosed and established malignancies are evaluated and destroyed.

In summary, this chapter aimed to convey (1) the advantages of MRI in treating pediatric brain tumors (especially when used in tandem with other modalities); and (2) the MRI features that are unique to specific lesions affecting the CNS. It is hoped that further advances in neuroimaging, when coupled with advances in molecular typing of tumors, will allow more tailored and individualized treatment of tumor types in the future.

References

1. Gurney J, Smith M, Bunin G. CNS and miscellaneous intracranial and intraspinal neoplasms. In: Ries L, Smith M, Gurney J, eds. *Cancer Incidence and Survival among Children and Adolescents: United States SEER Program 1975–1995 NIH Publication No 99-4649*. Bethesda, MD: National Cancer Institute SEER Program; 1999:51–63.
2. Ostrom QT, Gittleman H, Farah P, et al. CBTRUS statistical report: primary brain and central nervous system tumors diagnosed in the United States in 2006–2010. *Neuro Oncol*. 2013;15(Suppl 2): ii1–56.
3. Porter KR, McCarthy BJ, Freels S, Kim Y, Davis FG. Prevalence estimates for primary brain tumors in the United States by age, gender, behavior, and histology. *Neuro Oncol*. 2010;12:520–527.
4. Poussaint TY. Magnetic resonance imaging of pediatric brain tumors: state of the art. *Top Magn Reson Imaging*. 2001;12:411–433.
5. Dunbar SF, Barnes PD, Tarbell NJ. Radiologic determination of the caudal border of the spinal field in cranial spinal irradiation. *Int J Radiat Oncol Biol Phys*. 1993;26:669–673.
6. Hustinx R, Alavi A. SPECT and PET imaging of brain tumors. *Neuroimaging Clin N Am*. 1999;9:751–766.
7. Voss J, Meier TB, Freidel R, et al. The role of secondary motor and language cortices in morbidity and mortality: a retrospective functional MRI study of surgical planning for patients with intracranial tumors. *Neurosurg Focus*. 2013;34:E7.
8. Sunaert S. Presurgical planning for tumor resectioning. *J Magn Reson Imaging*. 2006;23:887–905.
9. Wengenroth M, Blatow M, Guenther J, Akbar M, Tronnier VM, Stippich C. Diagnostic benefits of presurgical fMRI in patients with brain tumours in the primary sensorimotor cortex. *Eur Radiol*. 2011;21:1517–1525.
10. Robinson KE, Pearson MM, Cannistraci CJ, et al. Neuroimaging of executive function in survivors of pediatric brain tumors and healthy controls. *Neuropsychology*. 2014;28:791–800.
11. Poussaint TY, Rodriguez D. Advanced neuroimaging of pediatric brain tumors: MR diffusion, MR perfusion, and MR spectroscopy. *Neuroimaging Clin N Am*. 2006;16:169–192.
12. Cha S, Knopp EA, Johnson G, Wetzel SG, Litt AW, Zagzag D. Intracranial mass lesions: dynamic contrast-enhanced susceptibility-weighted echo-planar perfusion MR imaging. *Radiology*. 2002;223:11–29.
13. Lefranc M, Monet P, Desenclos C, et al. Perfusion MRI as a neurosurgical tool for improved targeting in stereotactic tumor biopsies. *Stereotact Funct Neurosurg*. 2012;90:240–247.
14. Yeom KW, Mitchell LA, Lober RM, et al. Arterial spin-labeled perfusion of pediatric brain tumors. *AJNR Am J Neuroradiol*. 2014;35:395–401.
15. Provenzale JM, Mukundan S, Barboriak DP. Diffusion-weighted and perfusion MR imaging for brain tumor characterization and assessment of treatment response. *Radiology*. 2006;239:632–649.
16. Gauvain KM, McKinstry RC, Mukherjee P, et al. Evaluating pediatric brain tumor cellularity with diffusion-tensor imaging. *AJR Am J Roentgenol*. 2001;177:449–454.
17. Kono K, Inoue Y, Nakayama K, et al. The role of diffusion-weighted imaging in patients with brain tumors. *AJNR Am J Neuroradiol*. 2001;22:1081–1088.

18. Mardor Y, Roth Y, Lidar Z, et al. Monitoring response to convection-enhanced taxol delivery in brain tumor patients using diffusion-weighted magnetic resonance imaging. *Cancer Res*. 2001;61:4971–4973.
19. Ross BD, Chenevert TL, Rehemtulla A. Magnetic resonance imaging in cancer research. *Eur J Cancer*. 2002;38:2147–2156.
20. Witwer BP, Moftakhar R, Hasan KM, et al. Diffusion-tensor imaging of white matter tracts in patients with cerebral neoplasm. *J Neurosurg*. 2002;97:568–575.
21. Khong PL, Kwong DL, Chan GC, Sham JS, Chan FL, Ooi GC. Diffusion-tensor imaging for the detection and quantification of treatment-induced white matter injury in children with medulloblastoma: a pilot study. *AJNR Am J Neuroradiol*. 2003;24:734–740.
22. Khong PL, Leung LH, Chan GC, et al. White matter anisotropy in childhood medulloblastoma survivors: association with neurotoxicity risk factors. *Radiology*. 2005;236:647–652.
23. Wedeen VJ, Wang RP, Schmahmann JD, et al. Diffusion spectrum magnetic resonance imaging (DSI) tractography of crossing fibers. *Neuroimage*. 2008;41:1267–1277.
24. Samdani A, Jallo GI. Intraoperative MRI: technology, systems, and application to pediatric brain tumors. *Surg Technol Int*. 2007;16:236–243.
25. Jolesz FA, Talos IF, Schwartz RB, et al. Intraoperative magnetic resonance imaging and magnetic resonance imaging-guided therapy for brain tumors. *Neuroimaging Clin N Am*. 2002;12:665–683.
26. Pollack IF. Brain tumors in children. *N Engl J Med*. 1994;331:1500–1507.
27. Packer R, Pollack I. *Pediatric Brain Tumors, Brain Tumor Progress Review Group*. Bethesda, MD: National Cancer Institute; 2000.
28. Puget S, Boddaert N, Veillard AS, et al. Neuropathological and neuroradiological spectrum of pediatric malignant gliomas: correlation with outcome. *Neurosurgery*. 2011;69:215–224.
29. Daumas-Duport C, Beuvon F, Varlet P, Fallet-Bianco C. Gliomas: WHO and Sainte-Anne hospital classifications. *Ann Pathol*. 2000;20:413–428.
30. Aronen HJ, Gazit IE, Louis DN, et al. Cerebral blood volume maps of gliomas: comparison with tumor grade and histologic findings. *Radiology*. 1994;191:41–51.
31. Fayed N, Modrego PJ. The contribution of magnetic resonance spectroscopy and echoplanar perfusion-weighted MRI in the initial assessment of brain tumours. *J Neurooncol*. 2005;72:261–265.
32. Jackson A, Kassner A, Annesley-Williams D, Reid H, Zhu XP, Li KL. Abnormalities in the recirculation phase of contrast agent bolus passage in cerebral gliomas: comparison with relative blood volume and tumor grade. *AJNR Am J Neuroradiol*. 2002;23:7–14.
33. Knopp EA, Cha S, Johnson G, et al. Glial neoplasms: dynamic contrast-enhanced T_2*-weighted MR imaging. *Radiology*. 1999;211:791–798.
34. Law M, Yang S, Wang H, et al. Glioma grading: sensitivity, specificity, and predictive values of perfusion MR imaging and proton MR spectroscopic imaging compared with conventional MR imaging. *AJNR Am J Neuroradiol*. 2003;24:1989–1998.
35. Sugahara T, Korogi Y, Kochi M, et al. Correlation of MR imaging-determined cerebral blood volume maps with histologic and angiographic determination of vascularity of gliomas. *AJR Am J Roentgenol*. 1998;171:1479–1486.
36. Sugahara T, Korogi Y, Kochi M, Ushio Y, Takahashi M. Perfusion-sensitive MR imaging of gliomas: comparison between gradient-echo and spin-echo echo-planar imaging techniques. *AJNR Am J Neuroradiol*. 2001;22:1306–1315.
37. Ball Jr WS, Holland SK. Perfusion imaging in the pediatric patient. *Magn Reson Imaging Clin N Am*. 2001;9:207–230.
38. Yamasaki F, Kurisu K, Satoh K, et al. Apparent diffusion coefficient of human brain tumors at MR imaging. *Radiology*. 2005;235:985–991.
39. Magalhaes A, Godfrey W, Shen Y, Hu J, Smith W. Proton magnetic resonance spectroscopy of brain tumors correlated with pathology. *Acad Radiol*. 2005;12:51–57.
40. Tzika AA, Astrakas LG, Zarifi MK, et al. Multiparametric MR assessment of pediatric brain tumors. *Neuroradiology*. 2003;45:1–10.
41. Kleihues P, Cavenee WK, eds. *World Health Organization Classification of Tumours: Pathology and Genetics of Tumours of the Nervous System*. Lyon, France: IARC Press; 2000.
42. Figeroa RE, el Gammal T, Brooks BS, Holgate R, Miller W. MR findings on primitive neuroectodermal tumors. *J Comput Assist Tomogr*. 1989;13:773–778.
43. Furie DM, Provenzale JM. Supratentorial ependymomas and subependymomas: CT and MR appearance. *J Comput Assist Tomogr*. 1995;19:518–526.
44. Haines JL, Short MP, Kwiatkowski DJ, et al. Localization of one gene for tuberous sclerosis within 9q32–9q34, and further evidence for heterogeneity. *Am J Hum Genet*. 1991;49:764–772.
45. Kandt RS, Haines JL, Smith M, et al. Linkage of an important gene locus for tuberous sclerosis to a chromosome 16 marker for polycystic kidney disease. *Nat Genet*. 1992;2:37–41.
46. Goh S, Butler W, Thiele EA. Subependymal giant cell tumors in tuberous sclerosis complex. *Neurology*. 2004;63:1457–1461.
47. Mizuguchi M, Takashima S. Neuropathology of tuberous sclerosis. *Brain Dev*. 2001;23:508–515.
48. Houser OW, Gomez MR. CT and MR imaging of intracranial tuberous sclerosis. *J Dermatol*. 1992;19:904–908.
49. Koeller KK, Dillon WP. Dysembryoplastic neuroepithelial tumors: MR appearance. *AJNR Am J Neuroradiol*. 1992;13:1319–1325.
50. Krieger MD, Panigrahy A, McComb JG, et al. Differentiation of choroid plexus tumors by advanced magnetic resonance spectroscopy. *Neurosurg Focus*. 2005;18:E4.
51. Panigrahy A, Krieger MD, Gonzalez-Gomez I, et al. Quantitative short echo time 1H-MR spectroscopy of untreated pediatric brain tumors: preoperative diagnosis and characterization. *AJNR Am J Neuroradiol*. 2006;27:560–572.
52. Barkovich A. *Pediatric Neuroimaging*. 4th ed. Philadelphia: Lippincott Williams & Wilkins; 2005.
53. Taylor MD, Northcott PA, Korshunov A, et al. Molecular subgroups of medulloblastoma: the current consensus. *Acta Neuropathol*. 2012;123:465–472.
54. Bourgouin PM, Tampieri D, Grahovac SZ, Leger C, Del Carpio R, Melancon D. CT and MR imaging findings in adults with cerebellar medulloblastoma: comparison with findings in children. *AJR Am J Roentgenol*. 1992;159:609–612.
55. Koci TM, Chiang F, Mehringer CM, et al. Adult cerebellar medulloblastoma: imaging features with emphasis on MR findings. [see comments]. *AJNR Am J Neuroradiol*. 1993;14:929–939.
56. Meyers SP, Kemp SS, Tarr RW. MR imaging features of medulloblastomas. *AJR Am J Roentgenol*. 1992;158:859–865.
57. Rollins N, Mendelsohn D, Mulne A, et al. Recurrent medulloblastoma: frequency of tumor enhancement on Gd-DTPA MR imaging. *AJNR Am J Neuroradiol*. 1990;11:583–587.
58. Zerbini C, Gelber RD, Weinberg D, et al. Prognostic factors in medulloblastoma, including DNA ploidy. *J Clin Oncol*. 1993;11:616–622.
59. Kuhl J. Modern treatment strategies in medulloblastoma. *Childs Nerv Syst*. 1998;14:2–5.
60. Maleci A, Cervoni L, Delfini R. Medulloblastoma in children and in adults: a comparative study. *Acta Neurochir (Wien)*. 1992;119:62–67.
61. Rumboldt Z, Camacho DL, Lake D, Welsh CT, Castillo M. Apparent diffusion coefficients for differentiation of cerebellar tumors in children. *AJNR Am J Neuroradiol*. 2006;27:1362–1369.
62. Kovanlikaya A, Panigrahy A, Krieger MD, et al. Untreated pediatric primitive neuroectodermal tumor in vivo: quantitation of taurine with MR spectroscopy. *Radiology*. 2005;236:1020–1025.

63. Tong Z, Yamaki T, Harada K, Houkin K. In vivo quantification of the metabolites in normal brain and brain tumors by proton MR spectroscopy using water as an internal standard. *Magn Reson Imaging*. 2004;22:1017–1024.
64. Wang Z, Sutton LN, Cnaan A, et al. Proton MR spectroscopy of pediatric cerebellar tumors. *AJNR Am J Neuroradiol*. 1995;16:1821–1833.
65. Perreault S, Ramaswamy V, Achrol AS, et al. MRI surrogates for molecular subgroups of medulloblastoma. *AJNR Am J Neuroradiol*. 2014;35:1263–1269.
66. Gjerris F, Klinken L. Long-term prognosis in children with benign cerebellar astrocytoma. *J Neurosurg*. 1978;49:179–184.
67. Pencalet P, Maixner W, Sainte-Rose C, et al. Benign cerebellar astrocytomas in children. *J Neurosurg*. 1999;90:265–273.
68. Campbell JW, Pollack IF. Cerebellar astrocytomas in children. *J Neuro-oncol*. 1996;28:223–231.
69. Hwang JH, Egnaczyk GF, Ballard E, Dunn RS, Holland SK, Ball Jr WS. Proton MR spectroscopic characteristics of pediatric pilocytic astrocytomas. *AJNR Am J Neuroradiol*. 1998;19:535–540.
70. Epstein F, Wisoff JH. Intrinsic brainstem tumors in childhood: surgical indications. *J Neurooncol*. 1988;6:309–317.
71. Littman P, Jarret P, Bilaniuk L, et al. Pediatric brainstem gliomas. *Cancer*. 1980;45:2787–2792.
72. Freeman CR, Farmer JP. Pediatric brain stem gliomas: a review. *Int J Radiat Oncol Biol Phys*. 1998;40:265–271.
73. Poussaint TY, Kocak M, Vajapeyam S, et al. MRI as a central component of clinical trials analysis in brainstem glioma: a report from the Pediatric Brain Tumor Consortium (PBTC). *Neuro Oncol*. 2011;13:417–427.
74. Laprie A, Pirzkall A, Haas-Kogan DA, et al. Longitudinal multivoxel MR spectroscopy study of pediatric diffuse brainstem gliomas treated with radiotherapy. *Int J Radiat Oncol Biol Phys*. 2005;62:20–31.
75. Steffen-Smith EA, Shih JH, Hipp SJ, Bent R, Warren KE. Proton magnetic resonance spectroscopy predicts survival in children with diffuse intrinsic pontine glioma. *J Neurooncol*. 2011;105:365–373.
76. Thakur SB, Karimi S, Dunkel IJ, Koutcher JA, Huang W. Longitudinal MR spectroscopic imaging of pediatric diffuse pontine tumors to assess tumor aggression and progression. *AJNR Am J Neuroradiol*. 2006;27:806–809.
77. Seymour ZA, Panigrahy A, Finlay JL, Nelson Jr MD, Bluml S. Citrate in pediatric CNS tumors? *AJNR Am J Neuroradiol*. 2008;29:1006–1011.
78. Helton KJ, Phillips NS, Khan RB, et al. Diffusion tensor imaging of tract involvement in children with pontine tumors. *AJNR Am J Neuroradiol*. 2006;27:786–793.
79. Prabhu SP, Ng S, Vajapeyam S, et al. DTI assessment of the brainstem white matter tracts in pediatric BSG before and after therapy: a report from the Pediatric Brain Tumor Consortium. *Childs Nerv Syst*. 2011;27:11–18.
80. Zukotynski KA, Fahey FH, Kocak M, et al. Evaluation of 18F-FDG PET and MRI associations in pediatric diffuse intrinsic brain stem glioma: a report from the Pediatric Brain Tumor Consortium. *J Nucl Med*. 2011;52:188–195.
81. Hoffman HJ. Dorsally exophytic brain stem tumors and midbrain tumors. *Pediatr Neurosurg*. 1996;24:256–262.
82. Farmer JP, Montes JL, Freeman CR, Meagher-Villemure K, Bond MC, O'Gorman AM. Brainstem gliomas. A 10-year institutional review. *Pediatr Neurosurg*. 2001;34:206–214.
83. Robertson PL, Allen JC, Abbott IR, Miller DC, Fidel J, Epstein FJ. Cervicomedullary tumors in children: a distinct subset of brainstem gliomas. *Neurology*. 1994;44:1798–1803.
84. Epstein F, Wisoff J. Intra-axial tumors of the cervicomedullary junction. *J Neurosurg*. 1987;67:483–487.
85. Poussaint TY, Yousuf N, Barnes PD, et al. Cervicomedullary astrocytomas of childhood: clinical and imaging follow-up. *Pediatr Radiol*. 1999;29:662–668.
86. Epstein F, Farmer J. Brain-stem glioma growth patterns. *J Neurosurg*. 1993;78:408–412.
87. Poussaint TY, Kowal JR, Barnes PD, et al. Tectal tumors of childhood: clinical and imaging follow-up. *AJNR Am J Neuroradiol*. 1998;19:977–983.
88. Ternier J, Wray A, Puget S, Bodaert N, Zerah M, Sainte-Rose C. Tectal plate lesions in children. *J Neurosurg*. 2006;104:369–376.
89. Chen CJ, Tseng YC, Hsu HL, Jung SM. Imaging predictors of intracranial ependymomas. *J Comput Assist Tomogr*. 2004;28:407–413.
90. Meyers SP, Khademian ZP, Biegel JA, Chuang SH, Korones DN, Zimmerman RA. Primary intracranial atypical teratoid/rhabdoid tumors of infancy and childhood: MRI features and patient outcomes. *AJNR Am J Neuroradiol*. 2006;27:962–971.
91. Rorke LB, Packer RJ, Biegel JA. Central nervous system atypical teratoid/rhabdoid tumors of infancy and childhood: definition of an entity. *J Neurosurg*. 1996;85:56–65.
92. Biegel JA. Molecular genetics of atypical teratoid/rhabdoid tumor. *Neurosurg Focus*. 2006;20:E11.
93. Petito CK, DeGirolami U, Earle KM. Craniopharyngiomas: a clinical and pathological review. *Cancer*. 1976;37:1944–1952.
94. Bunin GR, Surawicz TS, Witman PA, Preston-Martin S, Davis F, Bruner JM. The descriptive epidemiology of craniopharyngioma. [see comments]. *J Neurosurg*. 1998;89:547–551.
95. Hetelekidis S, Barnes PD, Tao ML, et al. 20-year experience in childhood craniopharyngioma. [see comments]. *Int J Radiat Oncol Biol Phys*. 1993;27:189–195.
96. Pusey E, Kortman KE, Flannigan BD, Tsuruda J, Bradley WG. MR of craniopharyngiomas: tumor delineation and characterization. *AJR Am J Roentgenol*. 1987;149:383–388.
97. Kollias S, Barkovich A, Edwards M. Magnetic resonance analysis of suprasellar tumors of childhood. *Pediatr Neurosurg*. 1991–1992;17:284–303.
98. Janss AJ, Grundy R, Cnaan A, et al. Optic pathway and hypothalamic/chiasmatic gliomas in children younger than age 5 years with a 6-year follow-up. *Cancer*. 1995;75:1051–1059.
99. Aoki S, Barkovich AJ, Nishimura K, et al. Neurofibromatosis types 1 and 2: cranial MR findings. *Radiology*. 1989;172:527–534.
100. Rodriguez D, Young Poussaint T. Neuroimaging findings in neurofibromatosis type 1 and 2. *Neuroimaging Clin N Am*. 2004;14:149–170.
101. Barnes PD, Robson CD, Robertson RL, Poussaint TY. Pediatric orbital and visual pathway lesions. *Neuroimaging Clin N Am*. 1996;6:179–198.
102. Simon J, Szumowski J, Totterman S, et al. Fat suppression MR imaging of the orbit. *AJNR Am J Neuroradiol*. 1988;9:961–968.
103. Parsa CF, Hoyt CS, Lesser RL, et al. Spontaneous regression of optic gliomas: thirteen cases documented by serial neuroimaging. *Archives Ophthalmol*. 2001;119:516–529.
104. Fleischman A, Brue C, Poussaint TY, et al. Diencephalic syndrome: a cause of failure to thrive and a model of partial growth hormone resistance. *Pediatrics*. 2005;115:e742–748.
105. Poussaint TY, Gudas T, Barnes PD. Imaging of neuroendocrine disorders of childhood. *Neuroimaging Clin N Am*. 1999;9:157–175.
106. Amstutz DR, Coons SW, Kerrigan JF, Rekate HL, Heiserman JE. Hypothalamic hamartomas: correlation of MR imaging and spectroscopic findings with tumor glial content. *AJNR Am J Neuroradiol*. 2006;27:794–798.
107. Clarren SK, Alvord Jr EC, Hall JG. Congenital hypothalamic hamartoblastoma, hypopituitarism, imperforate anus, and postaxial polydactyly–a new syndrome? Part II: neuropathological considerations. *Am J Med Genet*. 1980;7:75–83.

108. Hall JG, Pallister PD, Clarren SK, et al. Congenital hypothalamic hamartoblastoma, hypopituitarism, imperforate anus and postaxial polydactyly–a new syndrome? Part I: clinical, causal, and pathogenetic considerations. *Am J Med Genet*. 1980;7:47–74.
109. Tien R, Kucharczyk J, Kucharczyk W. MR imaging of the brain in patients with diabetes insipidus. *AJNR Am J Neuroradiol*. 1991;12:533–542.
110. Appignani B, Landy H, Barnes P. MR in idiopathic central diabetes insipidus of childhood. *AJNR Am J Neuroradiol*. 1993;14:1407–1410.
111. Haddad S, VanGilder J, Menezes A. Pediatric pituitary tumors. *Neurosurgery*. 1991;29:509–514.
112. Poussaint TY, Barnes PD, Anthony DA, Spack N, Scott RM, Tarbell NJ. Hemorrhagic pituitary adenomas of adolescence. *AJNR Am J Neuroradiol*. 1996;17:1907–1912.
113. Kucharczyk W, Davis D, Kelly W, et al. Pituitary adenoma: high resolution MRI at 1.5 T. *Radiology*. 1986;161:761–765.
114. Maghnie M, Arico M, Villa A, Genovese E, Beluffi G, Severi F. MR of the hypothalamic-pituitary axis in Langerhans cell histiocytosis. *AJNR Am J Neuroradiol*. 1992;13:1365–1371.
115. Barnes PD, Robertson RL, Young poussaint T. Structural imaging of CNS tumors. In: Black PM, Loeffler JS, eds. *Cancer of the Nervous System*. Cambridge: Blackwell Science; 1997:54–97.
116. Bouffet E, Doumi N, Thiesse P, et al. Brain metastases in children with solid tumors. *Cancer*. 1997;79:403–410.

CHAPTER

51

Papillary Glioneuronal Tumors

Herbert B. Newton[1], *H. Wayne Slone*[2], *Eric C. Bourekas*[1,2]

[1]Division of Neuro-Oncology, Departments of Neurology and Neurosurgery, Dardinger Neuro-Oncology Center, Wexner Medical Center at The Ohio State University and James Cancer Hospital and Solove Research Institute, Columbus, OH, USA; [2]Dardinger Neuro-Oncology Center, Departments of Radiology, Wexner Medical Center at The Ohio State University and James Cancer Hospital and Solove Research Institute, Columbus, OH, USA

INTRODUCTION

Papillary glioneuronal tumors (PGNTs) are rare lesions of the central nervous system, first described in 1998 by Komori and colleagues in a series of nine patients.[1] The 2007 World Health Organization (WHO) classification recognizes PGNT as a member of the group of neuronal and mixed neuronal–glial tumors, and as a variant of gangliolioma.[2–4] Since the initial report by Komori, there have been more than 70 cases of PGNT reported in the literature.[5–34] PGNTs usually occur in children and young adults, although there have been infrequent reported cases in patients over the age of 50 years.[5] Patients with PGNT have ranged in age from 4 to 83 years, with a median age at diagnosis of 23 years (see Table 1). Approximately 35% of cases develop in children less than 18 years of age, with roughly 60% occurring by 26 years. There is a nonsignificant predilection for PGNT to occur more often in females than males (53.5% vs 46.5%).[5] Symptoms are noted prior to diagnosis in 90% of patients, with the most common presenting complaints being headache (61%) and seizures (33%). Other reported presenting symptoms include nausea and vomiting (23%), visual disturbances (19%), difficulty with comprehension (15%), vertigo or ataxia (9%), hemiparesis (9%), memory loss (6%), change in mood (6%), and abnormality of gait and coordination (5%). An additional 6% of patients are symptom free at diagnosis, with their tumor being discovered incidentally by a computed tomography (CT) or magnetic resonance imaging (MRI) scan. The duration of symptoms ranges from 1 day (seizure) to 16 years (drug resistant epilepsy cured after gross tumor resection).[5,23] There does not appear to be any association with congenital abnormalities or heritable syndromes.

Pathology. On pathological examination, PGNT is a mixed tumor consisting of gliovascular pseudopapillary structures composed of hyalinized blood vessels upon which layers of astrocytes are anchored.[1–4] The interpapillary space contains a variable number of cells with neuronal nuclear features, ranging from small immature neurocytes to large mature ganglion cells (see Figure 1). PGNT has been well-characterized immunohistochemically. The perivascular astrocytes stain positive for glial fibrillary acidic protein and S-100 protein, but are negative for synaptophysin, class III β-tubulin, and neuron-specific enolase. The interpapillary neuronal cells stain positive for synaptophysin, class III β-tubulin, and neuron-specific enolase. Mitoses are rare or absent in typical cases of PGNT, and necrosis is usually absent.[1–4] MIB-1 proliferation indices from the case reports in the literature ranged from 0.5 to 50%, with a median of 1.8%.[5–34] This low proliferation index and the absence of mitoses and necrosis suggest that PGNT is usually a low-grade tumor.[1–4] However, cases with higher proliferation indices, ranging from 5 to 50%, have also been reported in more aggressive cases.[6–9,30,32–34] In a meta-analysis of PGNT cases, the Ki-67 labeling index was found on Cox proportional hazards regression analysis to be a significant variable ($p = 0.003$).[5] For example, a 1% increase in Ki-67 positive tumor cells extended the risk of progression by 10%. In addition, tumors with anaplastic features, such as focal necrosis and vascular proliferation, have also been reported (see Figure 2).

Molecular studies of PGNT suggest a different profile than the more common high-grade gliomas.[2–4] For

© 2016 Elsevier Ltd. All rights reserved.

TABLE 1 Summary of PGNT Characteristics From the Literature ($N = 71$)

Age (Years)	4–83 (Median:23)
Sex (%)	
Male	46.5
Female	53.5
Presenting Symptoms (%)	
Headache	61
Seizures	33
Nausea/vomiting	23
Visual disturbance	19
Comprehension difficulty	15
Papilledema/optic atrophy	13
Vertigo/ataxia	9
Hemiparesis	9
Memory loss	6
Mood disturbance	6
None	6
Abnormality of gait and coordination	5

References 1,5–34.

example, the tumors do not usually express p53, amplification of the epidermal growth factor receptor (EGFR), or the EGFR vIII mutant variant, which are common in high-grade astrocytomas in adults. Codeletion of 1p and 19q is also not present in PGNT, even though it is common in many oligodendrogliomas and mixed oligoastrocytomas. Loss of the PTEN tumor suppressor gene is noted in some cases. Methylation of the O^6-methylguanine-DNA methyltransferase promoter has also been documented in several tumors. Mutations of IDH1 and IDH2 have not been reported thus far, even though these are commonly found in adults with gliomas that have a good prognosis.

Treatment. PGNT is classified as a low-grade tumor—therefore, whenever possible, the definitive approach should be gross total resection (GTR) of the mass. In approximately 80% of published cases, GTR has been the initial treatment option, with another 20% undergoing a partial resection or, rarely, biopsy.[5] In patients with a GTR or extensive partial resection, no further treatment is necessary. For cases with a more aggressive or anaplastic version of PGNT, further treatment with radiotherapy (RT) and/or chemotherapy may be necessary. In approximately 11.3% of published cases, RT alone or in combination with temozolomide (TEM) has been used in the postoperative setting.[5–8,30,33] Chemo-RT, as used more commonly for high-grade gliomas (e.g., glioblastoma multiforme), has been shown to be very effective for several patients with aggressive PGNTs.[7,30,33,35] One patient who had significant tumor recurrence after an initial response to chemo-RT and adjuvant TEM, responded to intraarterial chemotherapy with carboplatin for over a year, until end-stage progression with extraneural metastases.[33]

Progression-free survival and overall survival for PGNT is generally very good, considering its low-grade histology and biology in the majority of patients.[2–4] In a meta-analysis by Schlamann and colleagues, the 1.5-year progression-free survival rate for all published cases of PGNT was 86%.[5] For the entire cohort of PGNT, the 1.5-year overall survival rate was 98%.

GENERAL IMAGING FEATURES

In a review of the entire series of published cases of PGNT, 97.2% of tumors (69/71) were located in the supratentorial region, mainly in the major lobes.[5] Another case presented in the posterior fossa; there were no tumors with a spinal cord origin. Unusual locations at presentation included the pineal gland and intraventricular, within the lateral ventricle.[30,32] The intraventricular tumor was disseminated at presentation, with spread into the third and fourth ventricles. The pineal case was also aggressive, with malignant features. The posterior fossa tumor was located within the fourth ventricle, and was hemorrhagic at presentation.[29] PGNT occurs more often in the left hemisphere, and may be seen in any lobe of the brain, but appears to have a predilection for the frontal (36%) and temporal (33%) lobes. The parietal lobes (13%) and occipital lobes (6%) are much less frequently involved.[36] Tumor size can range from 1.0 to 9.0 cm, with a median size of 4.0 cm. In roughly 59% of the cases, the tumor was larger than 3.5 cm in diameter.[5] The majority of PGNTs contain a cystic component (91.8%), with or without a mural nodule, although there have been reports of PGNTs with only a solid component (8.2%). The most common radiologic presentation is a tumor with a cystic region and a solid component, noted in 41.0% of reported cases.[5] Tumors with a cystic region and a classic mural nodule are also fairly common, reported in another 37.7% of cases. Purely cystic tumors have also been reported in 13.1% of cases. Enhancement of PGNTs is very common, reported in 95.2% of cases.[5] The specific type of enhancement is variable, and can include a ring configuration, homogeneous, or heterogeneous. The presence of calcifications has been reported in several cases. Peritumoral edema and

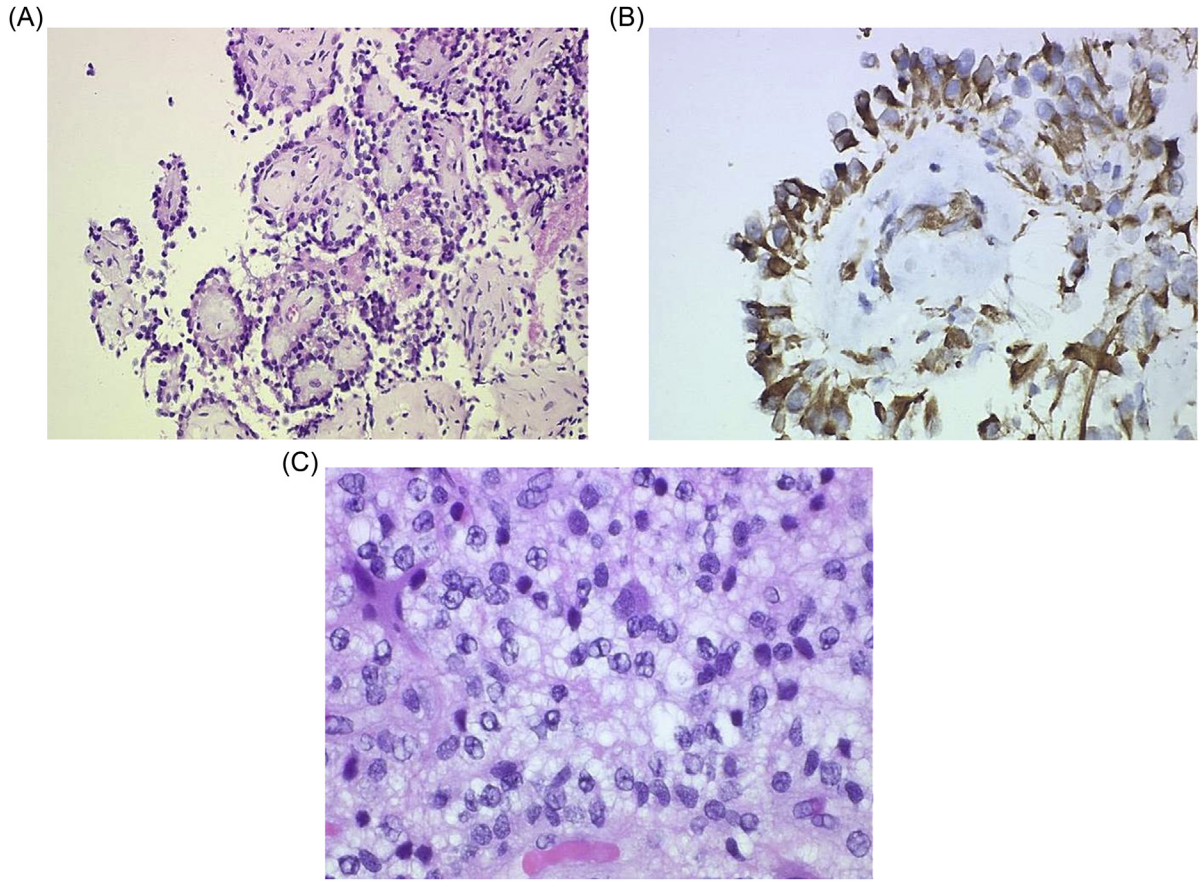


FIGURE 1 Pathology from a typical case of PGNT. (A) Papillary processes lined by mildly pleomorphic glial elements (H & E stain). (B) Higher power view demonstrating the mildly pleomorphic glial elements that are positively stained by GFAP. (C) Section of tumor demonstrating the neuronal components of the mass, with vesicular nuclei and prominent nucleoli (H & E stain). There is a large ganglion cell with copious cytoplasm in the center of the field.

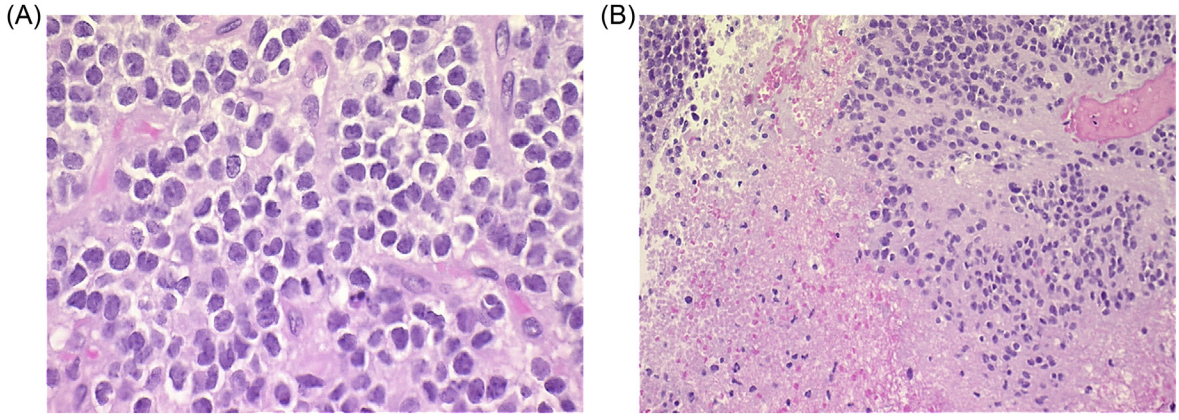


FIGURE 2 Pathological specimens from a patient with an anaplastic PGNT. (A) High-power micrograph demonstrating pleomorphic tumor cells, with mitotic figures in the lower central portion of the field (H & E stain). Some of the cells also have nuclei with prominent nucleoli that appear neuronal. (B) A focus of necrosis, in the lower right portion of the field (H & E stain).

mass effect have also been reported in a few cases of more aggressive tumors.[6,7] Intratumoral hemorrhage is an uncommon imaging feature of PGNT, noted in fewer than 10% of all cases.[36]

Features of PGNT on CT. Reports of PGNT that include radiological assessment by CT are very uncommon.[36] In general, the tumor will appear as a low-to-medium density cystic mass arising from one

of the major lobes, often near the lateral ventricle. The tumor tends to be well circumscribed, with minimal surrounding edema, and may show a variable amount of calcification. The solid component of the tumor is most often isodense when there is calcification present, and hypodense without any concomitant calcification. Calcification is always accompanied by a cystic component within the tumor. When the tumors are isodense with calcification, the Hounsfield units ranged from 35 to 37. Tumors without calcification that appeared hypodense had Hounsfield units of around 30. After administration of contrast, the tumor will usually demonstrate a variable amount of homogeneous or heterogeneous enhancement. The enhancement can be within a solid component of the tumor, or within a mural nodule.

Features of PGNT on MRI. The radiological features of PGNT on MRI have been well described by many authors.[5–37] On noncontrast T1 images, the tumor appears as a hypointense mass in 93.2% of the cases (see Figure 3).[5,36] In the other 6.8% of cases, the mass is hyperintense; no isointense tumors have been described thus far. On T2 and fluid-attenuated inversion recovery (FLAIR) images, PGNTs appear as hyperintense lesions in 100% of cases (see Figure 3).[5] The cystic component of the tumor is imaged very clearly, and is present in over 90% of all cases. The solid component can be a mural nodule or a solid mass associated with a cyst. In approximately 7% of cases, the tumor only has a solid component. For the majority of cases, the solid component will be well circumscribed, with minimal if any evidence for infiltration into the surrounding brain parenchyma. On T1 images with infusion of contrast, there is enhancement noted in approximately 95% of cases (see Figure 3).[5] The enhancement can be within the solid component of the mass, or within a mural nodule, and is typically very robust. The pattern of enhancement is variable, and can be homogeneous, heterogeneous, or in a ring configuration. In diffusion-weighted images (DWI), tumors were a heterogeneous mix of hypointensity and isointensity in approximately 57% of cases.[36] In the other 43%, the tumors were homogeneously isointense on the DWI.

UNCOMMON MANIFESTATIONS OF PGNT

The majority of PGNTs arise within the major lobes of the supratentorial region, often deep in the white matter close to the ventricles, but a few have been described in atypical locations, including the pineal gland and inside the ventricles (lateral and fourth ventricles).[5,29,30,32] As noted above, most PGNTs will have a cystic component, but purely solid tumors have been described in fewer than 10% of cases. Similarly, the vast majority of PGNTs demonstrate robust enhancement. However, minimal enhancement or a complete lack of enhancement can be noted in fewer than 5% of cases. The presence of intratumoral hemorrhage is also very uncommon, only being described in a single case of a PGNT arising in the fourth ventricle.[29]

Most PGNTs are low grade in terms of their histology, biological behavior, and imaging features. However, there have been reported cases in which the tumor has more anaplastic histology and behaves in a more aggressive fashion, including features on CT and MRI.[5–7,30,32,33] Several tumors have been described with peritumoral edema and mass effect, with compression of regional neural structures and the ventricles (see Figure 4). The presence of edema and mass effect is very uncommon, and suggests a more aggressive variety of PGNT. Another atypical case involved a tumor of the lateral ventricles that had intraventricular dissemination at presentation, with enhancing nodular disease in the third and fourth ventricles.[30] On pathological examination, the tumor did not have the typical papillary morphology, and had a high Ki-67 labeling index. Another anaplastic PGNT has also been reported that had multiple recurrences locally in the brain, and eventually had extraneural metastases to the lungs and pleura (see Figure 5).[7,33]

DIFFERENTIAL DIAGNOSIS ON MRI

In most patients with PGNT, there is a typical presentation of increasing headaches—with or without seizures—in a child or young adult, with a mass on MRI in the deep frontal or temporal lobes, that has cystic and solid components, and other features consistent with a low-grade glioma.[5,36] However, even in these "classic" cases, there are still other tumor types that cannot be excluded by imaging criteria. The tumor most likely to be confused with PGNT is ganglioglioma, which also has a predilection for the temporal lobes. However, most gangliogliomas develop in the temporal lobe cortex, while most PGNTs prefer the deeper temporal white matter closer to the lateral ventricle. In addition, PGNTs are more often cystic than typical low-grade gangliogliomas, and have a higher rate of enhancement. The calcification rate for PGNTs is also much higher than that of gangliogliomas (75% vs 28%).[36] Another tumor that can appear similar to PGNT is pleomorphic xanthoastrocytoma (PXA), which can also present as a supratentorial mass with a mural nodule.[5,36] However, PXA is typically located near the cortex and leptomeningeal region, and not deeper towards the ventricles. In addition, calcification

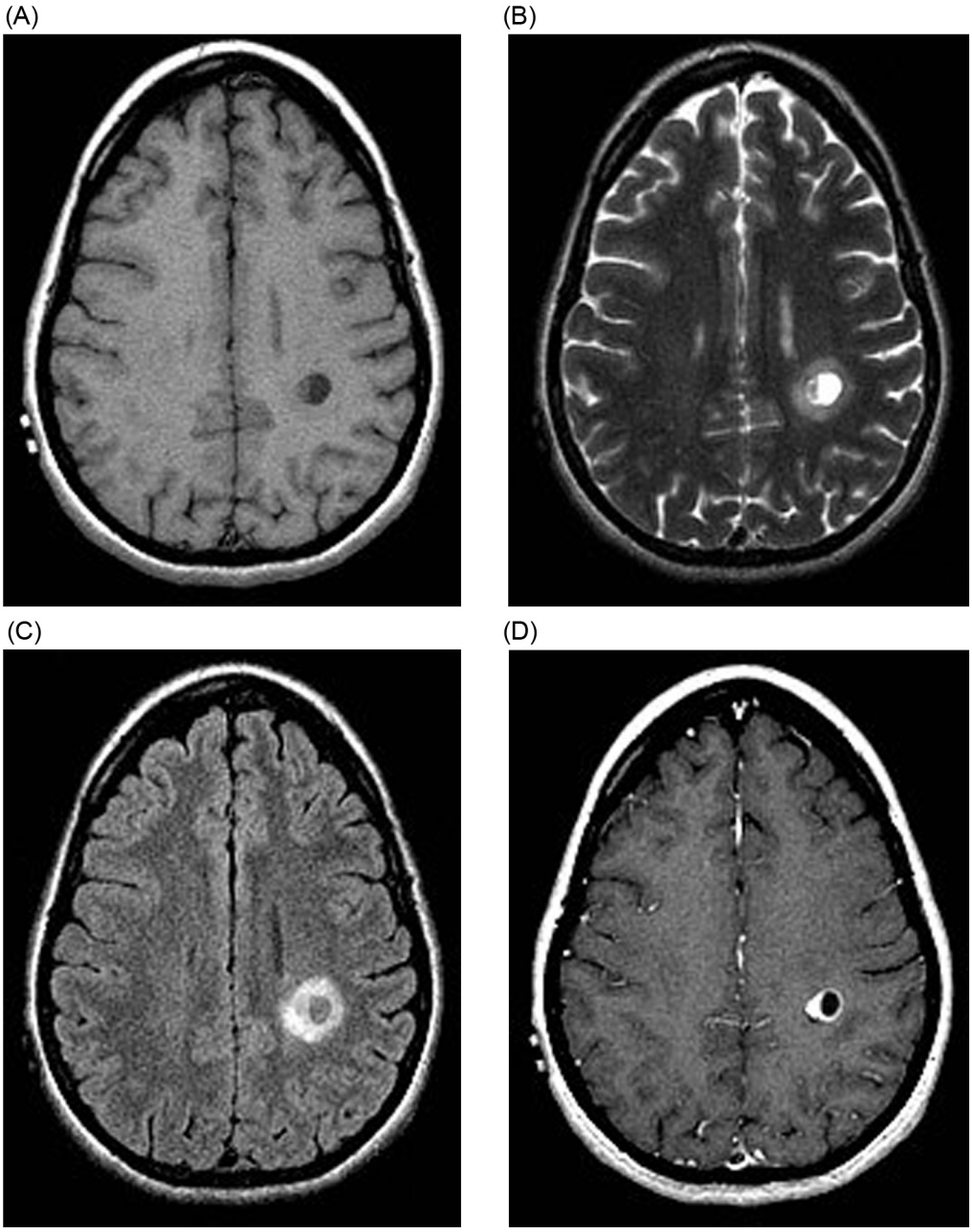


FIGURE 3 The patient is a 26-year-old female who presented with headaches and seizures. (A) Axial T1-weighted image shows a 1.3 cm well-defined, noninfiltrative, hypointense mass lesion of the left parietal lobe with a cystic component. (B) Axial T2-weighted image shows the cystic component to be of increased signal with an isointense to white matter solid component medially and a small amount of surrounding edema. (C) Axial FLAIR images demonstrate the cystic component to be isointense to white matter with the solid component medially of increased signal with a small amount of surrounding edema. (D) Axial T1-weighted image after contrast demonstrates a well-defined, peripherally enhancing lesion with a solidly enhancing solid component medially and a larger cystic component laterally. Seven years after gross total resection, there is no evidence of tumor recurrence.

in PXA is very rare. Pilocytic astrocytomas can appear similar on MRI to PGNT, and have a very comparable clinical demographic.[5] They are often enhancing and cystic, with fairly circumscribed tumoral edges. Supratentorial extraventricular ependymomas might occasionally appear similar to PGNT.[36] However, the ependymomas are not often as cystic, and have a much higher rate of intratumoral hemorrhage (57%). Other tumors to be included on the differential diagnosis of PGNT include cystic high-grade gliomas (astrocytomas, oligodendrogliomas) and dysembryoplastic neuroepithelial tumor.[5,36]

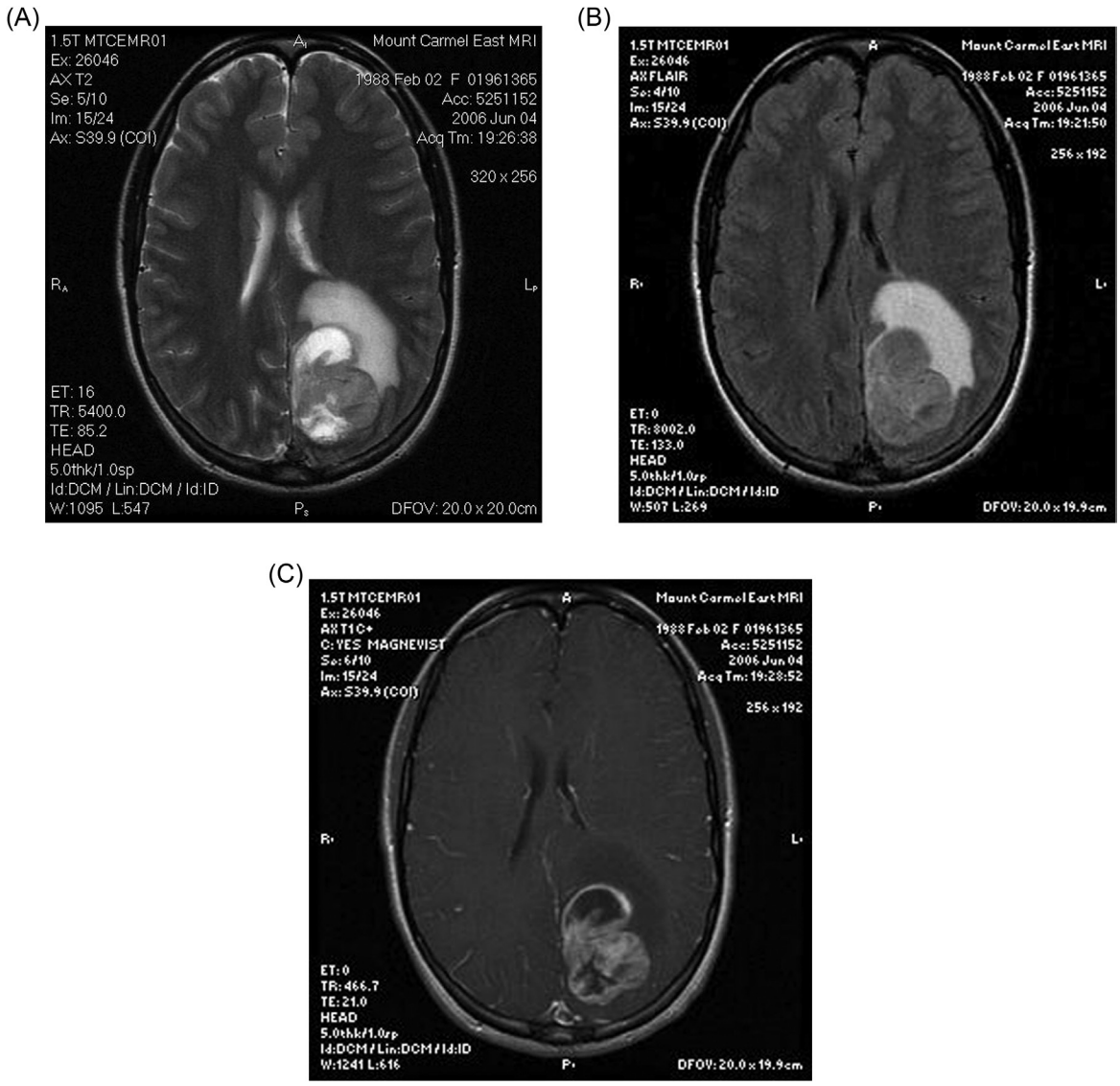


FIGURE 4 Patient with an aggressive, anaplastic PGNT, who presented with seizure activity, headaches, and a mild right-sided visual field defect. (A and B) Non-contrast T2 and FLAIR images—note the large, noncystic mass in the left occipital–parietal region, with a high-signal abnormality consistent with edema, and mass effect displacing the body of the lateral ventricle. (C) T1 contrast enhanced image—note the heterogeneously enhancing mass and region of low-signal abnormality.

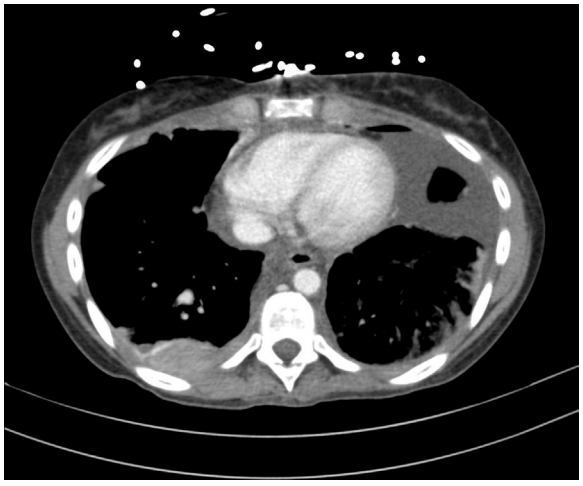


FIGURE 5 CT chest of patient reported in references 7,33, demonstrating a posterior pleural-based mass in the right lung. On biopsy, the pathology was consistent with anaplastic PGNT, with features similar to the patient's primary brain tumor.

Acknowledgments

The authors would like to thank Shawna Huckell and Nicole Ghaffari for research assistance. Dr. Newton was supported in part by National Cancer Institute grant, CA 16058 and the Dardinger Neuro-Oncology Center Endowment Fund.

References

1. Komori T, Scheithauer BW, Anthony DC, et al. Papillary glioneuronal tumor: a new variant of mixed neuronal-glial neoplasm. *Am J Surg Pathol*. 1998;22:1171–1183.
2. Louis DN, Ohgaki H, Wiestler OD, et al. The 2007 WHO classification of tumours of the central nervous system. *Acta Neuropathol*. 2007;114:97–109.
3. Myung JK, Byeon SJ, Kim B, et al. Papillary glioneuronal tumors: a review of clinicopathologic and molecular genetic studies. *Am J Surg Pathol*. 2011;35:1794–1805.
4. Edgar MA, Rosenblum MK. Mixed glioneuronal tumors. Recently described entities. *Arch Pathol Lab Med*. 2007;131:228–233.
5. Schlamann A, von Bueren AO, Hagel C, et al. An individual patient data meta-analysis on characteristics and outcome of patients with papillary glioneuronal tumor, rosette glioneuronal tumor with neuropil-like islands and rosette forming glioneuronal tumor of the fourth ventricle. *PLoS One*. July 3, 2014;9(7):e101211.
6. Vaquero J, Coca S. Atypical papillary glioneuronal tumor. *J Neuro-Oncol*. 2007;83:319–323.
7. Newton HB, Dalton J, Ray-Chaudhury A, et al. Aggressive papillary glioneuronal tumor: case report and literature review. *Clin Neuropathol*. 2008;27:317–324.
8. Atri S, Sharma MC, Sarkar C, et al. Papillary glioneuronal tumor: a report of a rare case and review of the literature. *Childs Nerv Syst*. 2007;23:349–353.
9. Ishizawa T, Komori T, Shibahara J, et al. Papillary glioneuronal tumor with minigemistocytic components and increased proliferative activity. *Hum Pathol*. 2006;37:627–630.
10. Bouvier-Labit C, Daniel L, Dufour H, et al. Papillary glioneuronal tumour: clinicopathological and biochemical study of one case with 7-year follow up. *Acta Neuropathol*. 2000;99:321–326.
11. Prayson RA. Papillary glioneuronal tumor. *Arch Pathol Lab Med*. 2000;124:1820–1823.
12. Broholm H, Madsen FF, Wagner AA, et al. Papillary glioneuronal tumor – a new tumor entity. *Clin Neuropathol*. 2002;21:1–4.
13. Barnes NP, Pollock JR, Harding B, et al. Papillary glioneuronal tumour in a 4-year-old. *Pediatr Neurosurg*. 2002;36:266–270.
14. Tsukayama C, Arakawa Y. A papillary glioneuronal tumor arising in an elderly woman: a case report. *Brain Tumor Pathol*. 2002;19:35–39.
15. Lamszus K, Makrigeorgi-Butera M, Laas R, et al. 24-year-old female with a 6-month history of seizures. *Brain Pathol*. 2003;13:115–117.
16. Kordek R, Hennig R, Jacobsen E, et al. Papillary glioneuronal tumor – a new variant of benign mixed brain neoplasm. *Pol J Pathol*. 2003;54:75–78.
17. Ebato M, Tsunoda A, Maruki C, et al. Papillary glioneuronal tumor with highly degenerative pseudopapillary structure accompanied by specific abortive glial cells: a case report. *No Shinkei Geka*. 2003;31:1185–1190.
18. Borges G, Bonilha L, Menezes AS, et al. Long term follow-up in a patient with papillary glioneuronal tumor. *Arq Neuropsiquiatr*. 2004;62:869–872.
19. Stosic-Opincal T, Peric V, Gavrilovic S, et al. Papillary glioneuronal tumor. *Am J Roentgenol*. 2005;185:265–267.
20. Vajtai I, Kappeler A, Lukes A, et al. Papillary glioneuronal tumor. *Pathol Res Pract*. 2006;202:107–112.
21. Celli P, Caroli E, Giangaspero F, et al. Papillary glioneuronal tumor: case report and literature review. *J Neuro-Oncol*. 2006;80:185–189.
22. Epelbaum S, Kujas M, Van Effenterre R, et al. Two cases of papillary glioneuronal tumours. *Br J Neurosurg*. 2006;20:90–93.
23. Chen L, Piao Y, Xu Q, et al. Papillary glioneuronal tumor: a clinicopathological and immunohistochemical study of two cases. *Neuropathology*. 2006;26:243–248.
24. Buccoliero AM, Giordano F, Mussa F, et al. Papillary glioneuronal tumor radiologically mimicking a cavernous hemangioma with hemorrhagic onset. *Neuropathology*. 2006;26:206–211.
25. Kuo Y, Edgar MA, Luther N, et al. Novel low-grade glioneuronal neoplasm presenting in an octogenarian: case report and review of the literature. *Clin Neurol Neurosurg*. 2006;108:426–432.
26. Dim DC, Lingamfelter DC, Taboada EM, et al. Papillary glioneuronal tumor: a case report and review of the literature. *Hum Pathol*. 2006;37:914–918.
27. Konya D, Peker S, Ozgen S, et al. Superficial siderosis due to papillary glioneuronal tumor. *J Clin Neurosci*. 2006;13:950–952.
28. Radotra BD, Kumar Y, Bhatia A, et al. Papillary glioneuronal tumor: a new entity awaiting inclusion in WHO classification. *Diagn Pathol*. 2007;8:2–6.
29. Ulivieri S, Oliveri G, Cerease A, Miracco C. Papillary glioneuronal tumor of the fourth ventricle: case report and review of the literature. *G Chir*. 2010;31:368–370.
30. Yano H, Nakayama N, Hirose Y, et al. Intraventricular glioneuronal tumor with disseminated lesions at diagnosis – a case report. *Diag Pathol*. 2011;6:119. http://dx.doi.org/10.1186/1746-1595-6-119.
31. Agarwal S, Sharma MC, Singh G, et al. Papillary glioneuronal tumor – a rare entity: report of four cases and brief review of literature. *Childs Nerv Syst*. 2012;28:1897–1904.
32. Kaloostian PE, Chen H, Tran HP. Malignant papillary glioneuronal tumor of the pineal gland: case presentation and literature review of a distinct entity. *Am J Case Rep*. 2013;14:164–168.
33. Bourekas EC, Bell SD, Ladwig NR, et al. Anaplastic papillary glioneuronal tumor with extraneural metastases. *J Neuropathol Exp Neurol*. 2014;73:474–476.
34. Momota H, Fujii M, Tatematsu A, et al. Papillary glioneuronal tumor with a high proliferative component and minigemistocytes in a child. *Neuropathology*. 2014;34:484–490. http://dx.doi.org/10.1111/neup.12123.
35. Newton HB. Chemotherapy of high-grade astrocytomas. In: Newton HB, ed. *Handbook of Brain Tumor Chemotherapy*. vol. 24. London: Elsevier Medical Publishers/Academic Press; 2006:347–363.
36. Tan W, Huang W, Xiong J, et al. Neuroradiological features of papillary glioneuronal tumor: a study of 8 cases. *J Comput Assist Tomogr*. 2014;38:634–638.
37. Xiao H, Ma L, Lou X, Gui Q. Papillary glioneuronal tumor: radiological evidence of a newly established tumor entity. *J Neuroimaging*. 2011;21:297–302.

CHAPTER

52

Intracranial Metastases

Arastoo Vossough[1], *John W. Henson*[2]

[1]Children's Hospital of Philadelphia, Philadelphia, PA, USA and Hospital of the University of Pennsylvania, Philadelphia, PA, USA; [2]Piedmont Brain Tumor Center, Atlanta, GA, USA

INTRODUCTION

Brain metastases are the most common intracranial tumors in adults. Approximately 97,800 to 170,000 new cases are diagnosed in the United States each year.[1,2] There is an equal male-to-female ratio. Melanoma is the tumor most likely to produce brain metastases. Metastases from lung, breast, unknown primary, melanoma, and colon cancer are the most commonly encountered tumors. The majority of intracranial metastases are parenchymal, with a smaller number in the subarachnoid space, and rarely to other structures such as choroid plexus or the pituitary gland. Presumably reflecting blood flow, approximately 80% of brain metastases are located supratentorially, 15% in the cerebellum, and 5% in the brain stem.[3,4] However, abdominal and pelvic cancers of gastrointestinal, prostate, and uterine primaries disproportionately metastasize to the posterior fossa.[3] Although metastases are often located at gray–white matter junctions, any site may occur. It is thought that tumor emboli lodge in arterioles, where changes in vessel caliber allow metastatic emboli to adhere to the vessel wall.

Brain metastases are usually rounded in shape and almost always enhance (see Figure 1(A)), except when they are hemorrhagic and thus already demonstrate T1-weighted hyperintensity on pregadolinium images. Multiple metastatic lesions are seen in 60–75% of all cases as determined by gadolinium-enhanced magnetic resonance imaging (MRI).[2,5] Melanoma and small-cell lung carcinoma metastases are most likely to be multiple. Metastases typically have surrounding vasogenic edema, although this rule is routinely broken in smaller lesions. Extent of edema is not a differentiating feature among the causes of enhancing masses. Hemorrhage is common with melanoma and lung. Dystrophic calcification is rare except with some indolent metastatic cancers or years following radiation therapy. Atrial myxoma can produce embolic brain metastases and distal cerebral aneurysms.[6] Systemic malignancies can metastasize into meningiomas.

Despite the above typical characteristics, in a prospective study of 48 adult patients who were initially thought to have a single brain metastasis by MRI, 11% were found on biopsy to have a different diagnosis.[7] Modern neuroimaging techniques have the potential of increasing the sensitivity and specificity of cerebral metastasis detection.

COMPUTED TOMOGRAPHY

On noncontrast-enhanced head computed tomography (CT) scans, metastases are typically hypodense to isodense, well circumscribed, and rounded (see Figure 1). Some may have necrotic low attenuation centers; cystic changes may occur. Low-attenuation vasogenic edema usually surrounds the lesion, particularly lesions over about 10 mm in size. Metastases are occasionally hyperdense, which may indicate the presence of hemorrhage, especially in hemorrhage-prone tumors such as melanoma, choriocarcinoma, renal cell carcinoma, thyroid carcinoma, neuroblastoma, and lung cancers. Mild hyperdensity is seen in tumors with high cellularity and high nuclear-to-cytoplasmic ratios, such as lymphoma and small-cell lung cancer. Metastases are rarely hyperdense secondary to calcification, though indolent or previously irradiated metastases can calcify. Punctate calcification may produce only mild elevation of Hounsfield units and can be very difficult to distinguish from petechial hemorrhage.

Almost all metastases enhance with iodinated contrast secondary to breakdown of the blood–brain barrier and angiogenesis (see Figure 1(B)). Enhancement can be homogeneous or a ring configuration. Enhancement is a time-dependent phenomenon, with near-maximal enhancement being present by approximately 5–10 min

Handbook of Neuro-Oncology Neuroimaging, Second Edition
http://dx.doi.org/10.1016/B978-0-12-800945-1.00052-5

© 2016 Elsevier Ltd. All rights reserved.

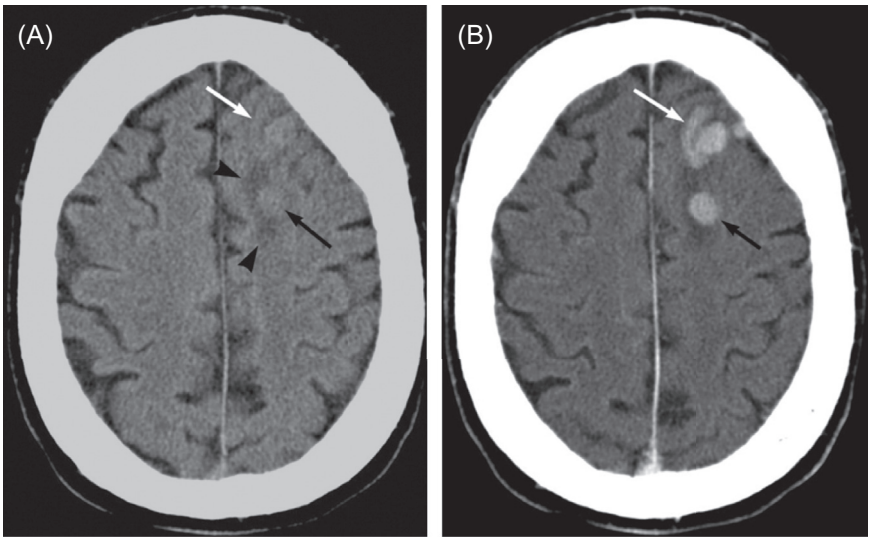


FIGURE 1 Computed tomography (CT) in a 51-year-old patient with brain metastases from breast cancer. (A) Noncontrast CT scan showing hypodense edema (*arrowheads*) surrounding an isodense round brain metastatic focus in the subcortical left frontal white matter (*black arrow*). A second isodense focus within the cortex is barely detectable given the similar attenuation compared to the cortical gray matter (*white arrow*). (B) CT after the administration of iodinated contrast greatly increases the conspicuity of the metastatic foci, and now the cortical lesion (*white arrow*) is clearly visualized. Minimal edema is present. The extent of edema surrounding an enhancing brain mass does not aid in the differential diagnosis of the lesion.

after contrast administration. High-dose contrast with delayed imaging at 1 h may detect additional lesions in a significant number of patients.[8] Immediate imaging after injection of contrast, such as with CT angiography (CTA), is not suitable for metastasis detection. When a brain-tumor-induced seizure is in the differential diagnosis of a transient neurological event, CTA should include a routine postcontrast image set obtained a few minutes after administration of the contrast bolus.

The sensitivity of CT may be reduced with posterior fossa lesions and isodense hemorrhagic metastases. Coronal reformatting of helically acquired images can occasionally aid in the identification of small lesions near the vertex, along the tentorium, and in the posterior fossa.[9] Hemorrhage loses its hyperdensity over 14–28 days, and hemorrhage in profoundly anemic patients and in patients who are highly anticoagulated can be isodense.

Although not as sensitive as MRI, CT remains very useful for the detection of parenchymal metastases.

MAGNETIC RESONANCE IMAGING

Conventional Magnetic Resonance Imaging

On MRI, most metastases are slightly hypointense to isointense with respect to gray matter on T1-weighted images, with surrounding hypointense vasogenic edema (see Figure 2). Marked central hypointensity is characteristic of necrotic or cystic tumors. On T2-weighted images, most metastases are isointense to hyperintense compared to gray matter with surrounding edema that is markedly hyperintense and extends into white matter in a pattern reminiscent of "fingers" (see Figure 2). Marked central hyperintensity is seen in necrotic, hemorrhagic tumors or with highly proteinaceous cystic or necrotic areas. Hemorrhagic metastases demonstrate variable signal intensities depending on the stage of hemorrhage. Adenocarcinomas demonstrate T2 hypointensity for unknown reasons and without correlation to the presence of mucin, blood products, iron, or calcium.[10] Cellular metastases with high nuclear-to-cytoplasmic ratios, such as lymphomas, and calcified metastases may also demonstrate T2 hypointensity. Peripheral gray matter lesions and lesions without significant edema can be missed on unenhanced MRI. Unenhanced MRI can also fail to demonstrate small nodules hidden by edema from other more dominant lesions. Lesions missed on CT and unenhanced MRI are almost always less than 10 mm in size.

Almost all metastases enhance following intravenous contrast injection on both CT and MRI secondary to blood–brain barrier breakdown and tumor angiogenesis (see Figure 2(D)). Davis et al. have shown that gadolinium-enhanced MRI is superior to double-dose delayed CT for lesion detection, anatomic localization, and differentiation of solitary versus multiple metastases.[8] Metastases may enhance in a solid or ring-like configuration; the wall of the ring is usually thick and irregular. There may be a stage at which metastases grow avascularly; therefore, they do not enhance on routine MRI, but are large enough to be detected on T2-weighted MR sequences.[8]

Contrast enhancement may be strikingly decreased by steroid therapy. In addition, contrast enhancement may be altered by radiation or chemotherapy. The presence of

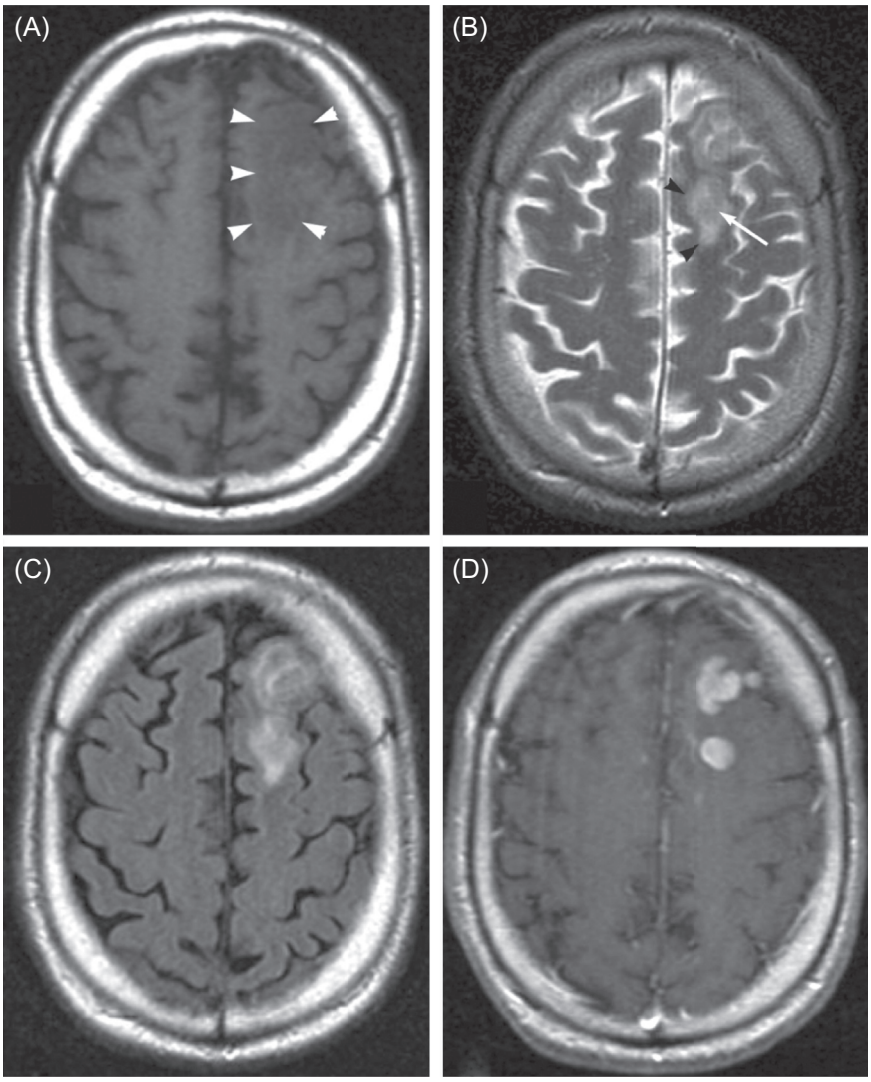


FIGURE 2 Conventional MRI sequences in the same patient as shown in Figure 1. (A) Axial T1-weighted image without contrast shows a slightly hypointense area in the left frontal lobe (*arrowheads*). (B) Axial fast spin-echo T2-weighted image showing hyperintense vasogenic edema (*black arrowheads*) surrounding a slightly less bright metastatic lesion in the left frontal lobe white matter (*white arrow*). The metastatic lesion itself is relatively hypointense to the edematous surrounding white matter, presumably due to dense cell packing within the tumor. (C) Axial T2 fluid-attenuated inversion recovery image showing mild extent of hyperintense vasogenic edema. (D) Axial T1-weighted image after the intravenous administration of gadolinium contrast shows avid, solid enhancement of the metastatic foci.

intrinsic T1-weighted hyperintensity from hemorrhage can obscure enhancement. Gadolinium enhancement may be visible on T2 fluid-attenuated inversion recovery (FLAIR) images. Miliary metastases are characterized by diffuse spread of small tumor nodules in the brain. Lesions of varying sizes may sometimes indicate the occurrence of multiple embolic events over time.

MRI is frequently employed in the differential diagnosis of newly detected brain masses. Malignant gliomas and metastases frequently have similar enhancement patterns, and it is often not possible to differentiate between the two on conventional MRI. However, metastatic lesions are much more likely to be multiple, and metastatic lesions are typically rounded, whereas gliomas show a more "geographic" pattern of enhancement, extending into adjacent gyri or other structures through infiltration. The extent of edema is not a reliable differentiating characteristic. Areas of glioma infiltration into brain adjacent to the enhancing mass show less T2 hyperintensity than does vasogenic edema and often lack the so-called "finger" appearance.

Differentiating hemorrhagic metastases from nonneoplastic hemorrhagic lesions is frequently difficult. The findings that suggest tumor include the presence of enhancement in nonhemorrhagic areas of the lesion, an incomplete ring of T2-weighted hypointensity representing hemosiderin, delayed evolution of hemorrhage-related signal change over several weeks, worsening enhancement or enlargement over this time, and persistence of vasogenic edema for several weeks.

Tumefactive demyelinating lesions are usually seen in young patients and the lesions show an incomplete ring of enhancement.

Carcinomatous encephalitis or miliary metastasis is a rare form of metastatic disease to the brain, usually from primary lung carcinoma.

Techniques to Increase Lesion Conspicuity

There are several strategies to further improve the detection of metastases by MRI:

1. Double- and triple-dose contrast: Increased lesion detection may be achieved by increasing the contrast dose beyond the standard 0.1 mmol/kg of body weight. There is a relatively linear relationship between lesion contrast ratio and intravenous contrast dose over the range of 0.05–0.3 mmol/kg.[11] In a larger series specifically evaluating brain metastasis, it was shown that triple-dose gadolinium MRI increases mean lesion contrast, increases qualitative conspicuity of lesions, detects additional small lesions, and, in a subset of patients, would have changed the choice of therapy.[12] Increased contrast-to-noise ratio and visual assessment ratings were also shown to be superior in a randomized trial.[13] Lesions greater than 10 mm will be seen at all dose levels. The utility of higher dose gadolinium mainly lies in the ability to reveal smaller lesions, especially less than 5 mm.[12,14]
2. Delayed imaging: Several studies of standard-dose gadolinium-enhanced MRI also looked at delayed imaging and showed improvement in the detection of small lesions with delayed imaging. Although delayed imaging improves the detection of small metastases, high-dose (0.3 mmol/kg) imaging is more effective at increasing lesion detection.[12] One study of the effective time window for scanning concluded that the postcontrast scan should be started with a 2–5-min delay after injection of contrast medium, and there was no major advantage in waiting longer.[15]
3. Slice thickness: Studies have shown the detection of additional tiny metastatic lesions when 1-mm-thick T1-weighted images, compared to routine 5-mm skip 1 mm images, are used for radiosurgery planning. This is most likely secondary to reduced volume averaging with thin-slice studies.[16]
4. Magnetization transfer (MT): MT increases the contrast of enhancing and nonenhancing lesions by suppressing background signal and is achieved by selectively saturating the signal from the immobile water protons. MT can be used to improve lesion contrast of gadolinium-enhanced brain lesions on T1-weighted spin-echo images. In one study, MT resulted in a 108% improvement in the contrast-to-noise ratio compared with conventional T1-weighted gadolinium-enhanced images.[17] Some studies have suggested that use of standard gadolinium dose with MT is equivalent to triple-dose gadolinium-enhanced MRI with conventional spin-echo techniques.[17,18] While the use of triple dose with MT further increases contrast, it does not result in detection of additional tumors.[18]
5. Newer contrast agents: MRI contrast agents with higher T1 relaxivity have been shown to improve the sensitivity of brain metastasis detection. Gadobenate dimeglumine significantly increased the sensitivity compared to gadopentetate dimeglumine, gadodiamide, and gadoterate meglumine at similar doses.[19] Gadobenate dimeglumine has also been shown to have similar sensitivity at reduced doses compared to standard-dose gadodiamide.[20]
6. Higher field MRI: Higher field MR magnets above 1.5 T now have widespread clinical availability. It has been shown that 3.0-T imaging both increases the subjective assessment of brain metastases and produces significantly higher signal-to-noise and contrast-to-noise ratios compared to 1.5 T.[21] Gadolinium administration produces higher contrast between tumor and normal brain on 3.0-T than on 1.5-T imaging,[22] resulting in better detection of brain metastases and leptomeningeal involvement.[21] The relatively improved detection rate using higher contrast doses is maintained at high field. Use of MT in high-field imaging may not be feasible owing to energy absorption limits or undesired effects of deep gray nuclei signal, but a fat-saturated spin-echo T1-weighted image at high field may produce a similar effect for increasing lesion detection.
7. Gradient-echo T2* sequences and melanoma imaging: Despite its relative rarity as a systemic neoplasm, melanoma is the third most common primary to produce brain metastasis. Approximately one-half of melanoma metastases are hyperintense on T1-weighted images prior to the administration of gadolinium, while other cerebral metastases rarely demonstrate T1 hyperintensity. Melanin itself may lead to T1 shortening and melanoma metastases have a propensity for hemorrhage, with methemoglobin also producing T1 shortening. Additionally, melanin and blood products may also produce susceptibility effects on T2* images due to the presence of metal ions including iron, copper, manganese, and zinc (see Figure 3). T2*-weighted signal loss and T1 shortening are both five times more common in melanoma metastases than in lung cancer metastases.[23] Three-quarters of melanoma metastases had either susceptibility effect or intrinsic T1 hyperintensity and 7% of melanoma lesions were detected principally on

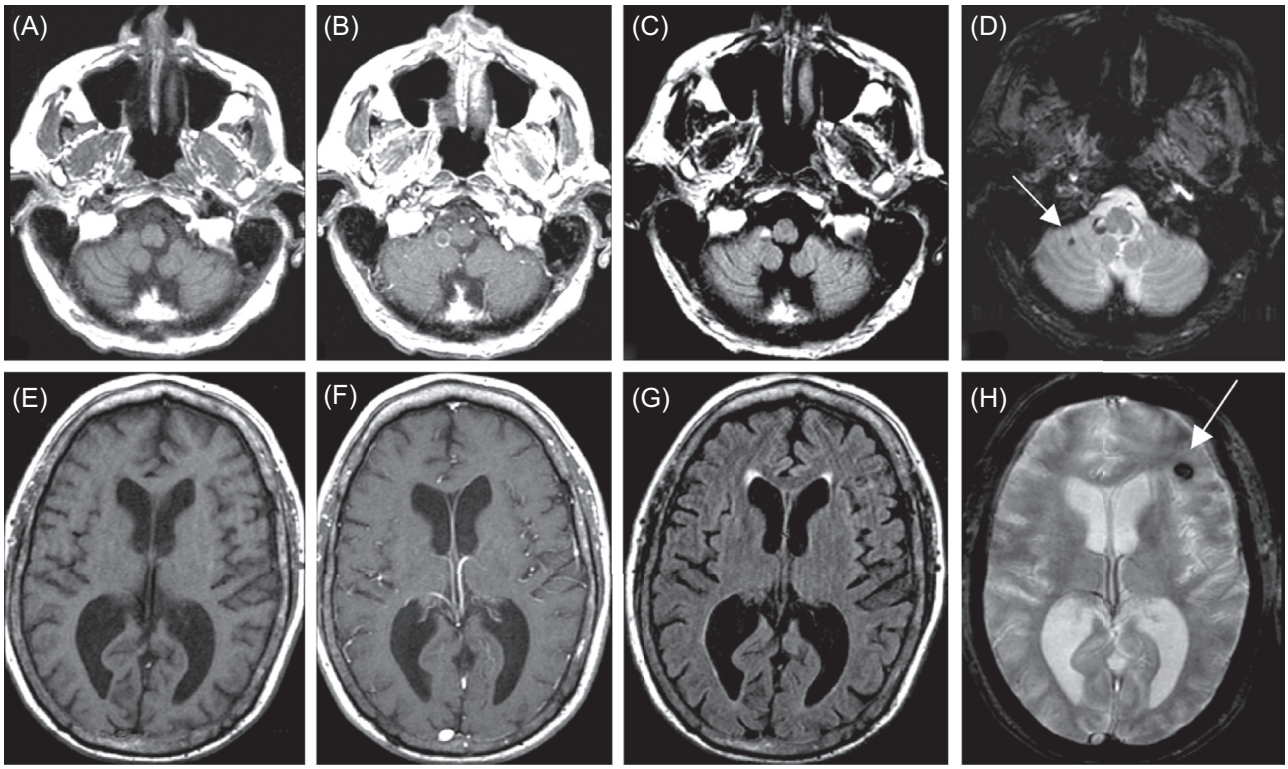


FIGURE 3 Melanoma brain metastases detected on T2* imaging sequences. T1-weighted sequences before (A, E) and after (B, F) administration of gadolinium, T2 FLAIR sequences (C, G), and T2*-weighted sequences (D, H) are shown. T1 isointense, nonenhancing lesions are seen in the right cerebellar hemisphere lesion (top row) and left frontal lobe (bottom row). An additional small lesion is seen on T2* image in the right cerebellar hemisphere. A subtle abnormality can be seen in the left frontal lobe on the FLAIR image (G), but the lesion is markedly more conspicuous on the T2*-weighted image (H).

T2*-weighted sequences.[23] These findings highlight the value of the T2*-weighted sequence in patients with known melanoma who are undergoing central nervous system (CNS) staging.

Diffusion-Weighted Imaging

Technical aspects of diffusion-weighted imaging (DWI) are discussed in Chapters 27 and 28. Metastatic tumors with dense cell packing or high nuclear-to-cytoplasmic ratio, such as lymphoma, small-cell lung cancer, medulloblastoma, and other primitive neuroectodermal tumors, can show restricted diffusion on DWI (see Figure 4). Diffusion imaging aids in the differentiation of cystic neoplasms and abscesses and can play a role in delineating cystic from solid components in metastases.[24]

There is no significant difference in the fractional anisotropy (FA) values of either the enhancing or the nonenhancing peritumoral portions of high-grade gliomas and solitary brain metastases.[25,26] However, when peritumoral FA values were expressed as a differential from values "expected" in bland edema, there was a significant difference between metastases and gliomas. Expected FA values were predicted from a linear regression of FA onto apparent diffusion coefficient for a series of bland edema cases; the difference between expected and observed FA was named the "tumor infiltration index."[27] Also the peritumoral mean diffusivity of metastatic lesions measured significantly greater than that of gliomas.[26,27] Displacement of subcortical white matter fibers by subjective visual assessment of diffusion tensor tractography images (as opposed to tract disruption or invasion) is also more commonly seen in metastases compared to high-grade gliomas.[25,28]

Diffusion anisotropy is highly sensitive to microstructural changes that do not appear on conventional imaging. Unfortunately, this high sensitivity is accompanied by relatively low pathologic specificity, such that useful diffusion tensor imaging-based tissue characterization may ultimately require the use of more sophisticated approaches. For example, the major eigenvalue of the diffusion tensor (reflecting diffusivity in the longitudinal direction) was found to be significantly lower in the peritumoral white matter surrounding high-grade gliomas than in metastases, even when the anisotropy showed no difference.[29]

Perfusion-Weighted Imaging

Technical aspects of perfusion-weighted imaging (PWI) are discussed in Chapter 31. The importance of

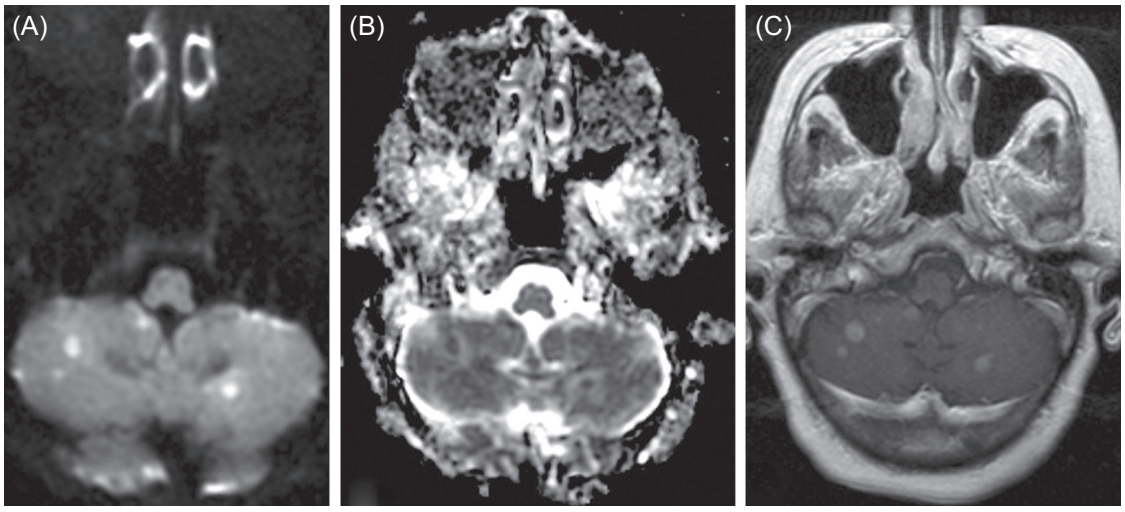


FIGURE 4 DWI in metastatic small-cell lung cancer to the brain. (A) DWI shows multiple foci of increased signal in the cerebellum bilaterally, initially raising the question of embolic infarcts. (B) Apparent diffusion coefficient (ADC) maps confirm low ADC and restricted diffusion in these lesions, along with surrounding hyperintensity and vasogenic edema. (C) Postcontrast T1-weighted image demonstrates solid and punctate enhancement in these lesions. By comparison, infarcts show enhancement after 1–2 weeks, but rarely show ring enhancement.

tumor angiogenesis in the regulation of tumor growth and development of metastatic disease has been demonstrated. Metastatic tumors to the brain induce neovascularization as they grow and expand. These neovessels resemble those of the primary systemic tumor with fenestrated membranes and open endothelial junctions, in contrast to normal brain capillaries with an intact blood–brain barrier with its tight junctions and continuous basement membrane.[30]

PWI could not reliably differentiate metastatic tumors from high-grade gliomas when relative cerebral blood volume (rCBV) was measured in the enhancing portion of the tumors, since both are highly vascular tumors and demonstrate increased rCBV (see Figure 5). However, rCBV was significantly higher within the peritumoral region of primary gliomas compared to metastatic lesions. The reason is thought to lie in the different histopathologic milieu of the peritumoral region. In primary gliomas, the peritumoral region represents a variable combination of vasogenic edema and tumor cell infiltration, whereas in metastatic lesions, the peritumoral region represents pure vasogenic edema due to leaky capillaries.[31,32] More recent work has suggested that the shape of the enhancement curve can distinguish between glioblastoma and hypovascular metastasis.[33] Permeability analysis has not been helpful in distinguishing these two entities.

Differentiation of metastases from low-grade gliomas is usually not a diagnostic dilemma, owing to the general lack of contrast enhancement and minimal peritumoral edema in diffuse low-grade gliomas. Low-grade gliomas often have low rCBV compared to metastases and high-grade gliomas.[32]

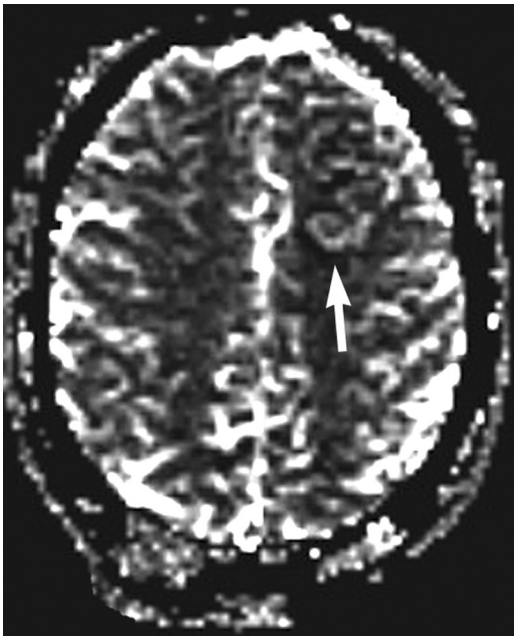


FIGURE 5 PWI in a patient with breast cancer brain metastasis. This is an rCBV-weighted image of the perfusion study, demonstrating increased rCBV in the round metastatic focus in the left frontal white matter (*arrow*).

Magnetic Resonance Spectroscopy

Technical aspects of magnetic resonance spectroscopy (MRS) are discussed in Chapter 30. *N*-acetylaspartate is low or absent in most metastases, consistent with the lack of neuroglial elements.[34–36] Metastatic lesions show an elevated choline/creatine ratio, as do gliomas.[36–38] Metastatic lesions were initially thought to

be distinguishable from high-grade gliomas by the presence of lipid and lactate peaks, lack of creatine, and increased lipid/creatine ratio.[39,40] However, in areas of central necrosis in high-grade gliomas, there is often the presence of lactate and lipid, as well as a lack of creatine, therefore decreasing the specificity of the above findings.[41] Nevertheless, the finding of high choline in the *peritumoral* region of a lesion is more likely to represent a glioma rather than a metastasis, since, as noted earlier, the peritumoral region of metastases is typically pure vasogenic edema, whereas in gliomas, it represents a combination of tumor cell infiltration and vasogenic edema.[41] Increased choline/creatine ratio can sometimes distinguish areas of tumor recurrence from radiation necrosis.

NUCLEAR MEDICINE TECHNIQUES

Single-photon-emission CT (SPECT) is a method in which γ photons emitted from a patient injected with a radiotracer are detected with a rotating gamma camera. Thallium-201 is a potassium analog tracer that localizes in tumors. SPECT imaging with thallium-201 has been used chiefly in the evaluation of primary tumors, but also shows accumulation in metastatic tumors.[42,43] One group has shown that delayed thallium imaging may have some utility in differentiation of high-grade glioma and metastases.[43] One group reported a sensitivity of 70% for both thallium-201 and technetium-99m MIBI SPECT in the detection of cerebral metastases. SPECT thallium scanning is not useful for following tumors that do not demonstrate thallium uptake and cannot reliably be used for screening.

Positron-emission tomography (PET) has been used extensively in the evaluation and follow-up of primary brain tumors, especially for distinguishing between necrosis from radiation and chemotherapy and recurrent tumor; residual tumor usually demonstrates increased fluorodeoxyglucose (FDG) uptake, and necrosis from radiation or chemotherapy usually demonstrates decreased FDG uptake. In one study, FDG PET detected only 50–68% of metastases from non-CNS neoplasms[44] and in another study, only 61% of metastatic lesions in the brain were identified by PET.[45] Coregistration of PET with MRI improved the sensitivity for detecting metastatic recurrence from 65% to 86%.[46] Unsuspected brain metastases were detected in only 0.7% undergoing PET scanning for evaluation of extracranial neoplasms.[47] In another large study, unsuspected cerebral or skull metastases were detected in only 0.4% of patients and the authors concluded that FDG PET screening for cerebral lesions in patients with non-CNS malignancy has little clinical impact.[48] One reason for the low sensitivity of PET may be the fact that metastases are often located close to the high-FDG-uptake gray matter at the gray–white junction and hence are more difficult to identify.

There is variability in FDG accumulation in metastases of different pathologies as well as among lesions of similar pathology. When a metastasis demonstrates increased FDG uptake similar to a high-grade primary tumor, FDG PET could be useful in following the response to treatment and in distinguishing recurrent tumor from necrosis secondary to radiation or chemotherapy. FDG PET should not be used as a screening method or for following lesions that are isometabolic or hypometabolic. New tracers are continuously being developed for PET imaging, which may further increase the utility of this modality in the evaluation of brain metastases.

MENINGEAL METASTASES

Approximately 8% of patients with systemic cancer have evidence of meningeal metastasis at autopsy.[8] The most common clinical presentations are headache, mental status change, cranial and spinal nerve dysfunction, gait disturbance, and leg and lower back pain. CSF cytology is specific, but remains negative in 5–10% of patients.[8] The most common primary tumors to spread to the meninges are breast carcinoma, lung carcinoma, melanoma, lymphoma, and leukemia. Most frequently, metastatic disease spreads to the meninges hematogenously via small meningeal vessels. Superficial parenchymal lesions and skull metastases may, however, directly invade the meninges.

Leptomeningeal metastases are more common than pachymeningeal metastases. Pachymeningeal metastases are frequently associated with calvarial metastases, but isolated dural metastases can be seen in breast cancer, lymphoma, leukemia, prostate cancer, and neuroblastoma. Metastases involving the dura may result in subdural effusions and can also lead to venous sinus thrombosis, either by direct invasion or by compression.

Noncontrast-enhanced CT is quite insensitive in detecting meningeal carcinomatosis. Contrast-enhanced CT is more sensitive than nonenhanced T1- and T2-weighted MR images, but inferior to contrast MRI. MRI with gadolinium is most commonly used to detect pachymeningeal and leptomeningeal metastases, but T2 FLAIR imaging can show hyperintensity in the subarachnoid spaces and can assist in detection of diffuse leptomeningeal disease (see Figure 6). Diffuse meningeal enhancement is the most common MR finding. Other findings include focal meningeal enhancement, nodular meningeal enhancement, and hydrocephalus. Meningeal metastases invade the

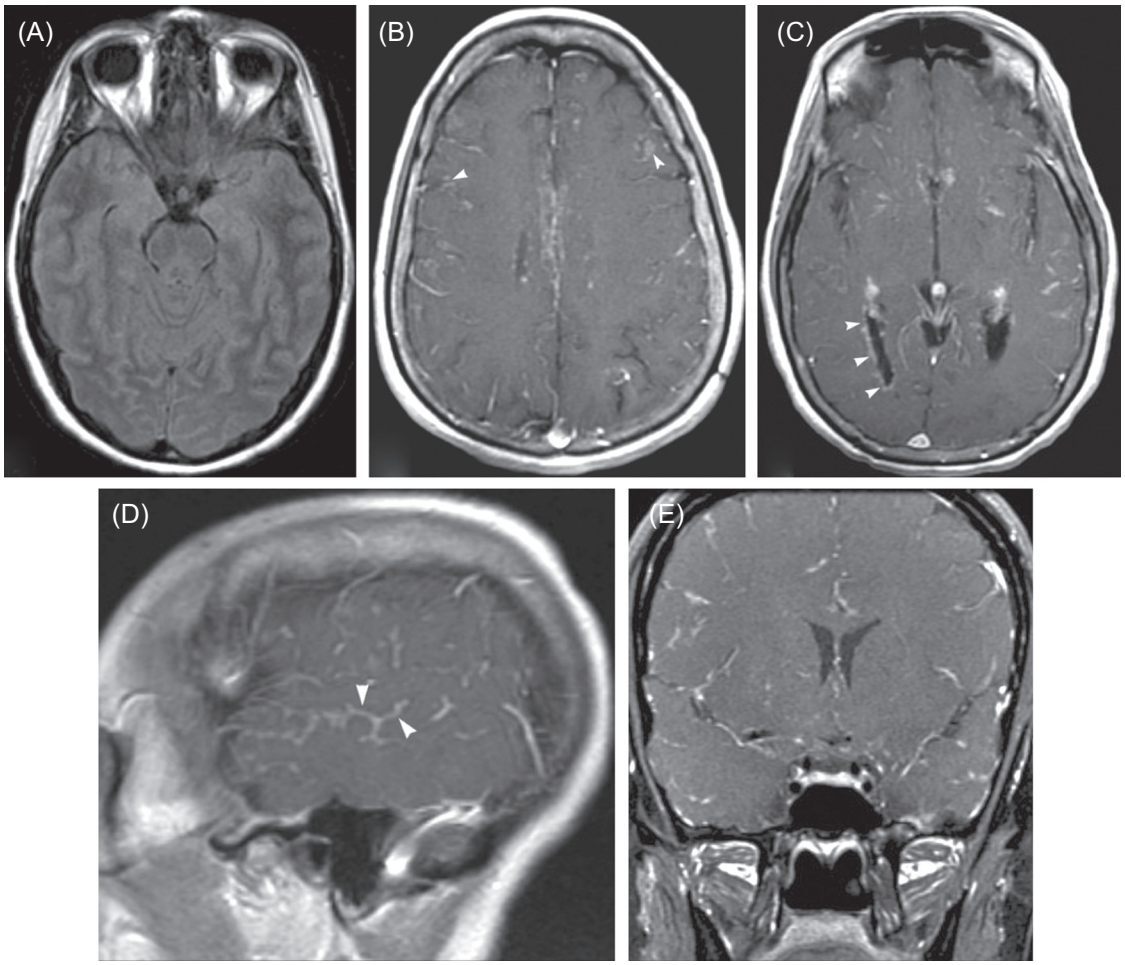


FIGURE 6 MRI of leptomeningeal metastases and potential mimickers. (A) Axial T2 FLAIR image demonstrating abnormal diffuse sulcal hyperintensity in a 58-year-old patient with nonsmall-cell lung carcinoma. (B) Axial postcontrast T1-weighted MRI in the same patient, showing abnormal enhancement of the sulci and leptomeninges, some of which have a nodular appearance (*arrowheads*). (C) Axial postcontrast T1-weighted MRI in the same patient, showing abnormal enhancement of the ependymal surface of the lateral ventricles (*arrowheads*). (D) Sagittal postcontrast T1-weighted MRI with better demonstration of sulcal leptomeningeal enhancement (*arrowheads*). (E) Abnormal diffuse sulcal enhancement on coronal postcontrast T1-weighted MRI in a 32-year-old patient with neurosarcoidosis. Inflammatory and infectious processes of the meninges may at times be indistinguishable from meningeal metastases.

underlying parenchyma via Virchow–Robin spaces and may produce parenchymal T2 hyperintensity, mass effect, and contrast enhancement.

Although MRI with gadolinium is sensitive for detecting meningeal disease, it is not specific. Diffuse linear or focal linear can be seen in both neoplastic and inflammatory lesions (see Figure 6(E)). Postoperatively, most patients have brain, pial, and dural enhancement. In patients with mass lesions causing obstructive hydrocephalus, meningeal enhancement may be secondary to vascular stasis rather than to carcinomatosis. In addition, dural enhancement adjacent to a parenchymal tumor does not always indicate invasion. Discontinuous enhancing dura adjacent to a mass correlates with dural invasion, but uniformly enhancing dura near a parenchymal tumor is more often not due to dural invasion.

IMAGING APPROACH IN BRAIN METASTASES

New developments in neuroimaging are increasing the sensitivity for the detection of brain metastases. Given these advances, one question raised is whether the additional information has clinical usefulness, especially in terms of patient outcome and in relation to new therapeutic choices. Given a choice of multiple treatment options, the second question that must be answered is which imaging modality is appropriate for which group of patients. A reasonable approach would base screening on neurologic symptoms, primary tumor staging, and cell type. Neuroimaging screening for brain metastases is generally indicated in patients with any stage of disease or cell type who present with focal or nonfocal neurologic symptoms or unexplained systemic symptoms.

Screening of asymptomatic patients is controversial and dependent on the primary tumor. A large number of patients with metastatic malignant melanoma harbor brain metastases.

Another issue is the imaging evaluation of patients presenting with a brain mass in the absence of known malignancy. Patients present to their physician or to the emergency ward with neurological symptoms and a brain mass is discovered on neuroimaging. When brain metastasis and malignant glioma are the major clinical considerations, the search for a systemic tumor can be seen as an approach to selecting a biopsy site. In the absence of a history of systemic cancer, a series of radiological studies usually follows, which may include CT imaging of the chest, abdomen, and pelvis; radionuclide bone scan; and whole-body FDG PET imaging. Mavrakis et al. performed a retrospective analysis the presenting features and diagnostic workup of patients with neurologic symptoms as the presenting manifestation of cancer.[49] Clinical features were not useful in predicting primary versus metastatic tumor. Brain MRI and chest CT together identified the ultimate site of diagnostic biopsy in 97% of patients who present with a newly detected brain mass. The clinical and imaging features of these patients can be used to optimize the diagnostic workup of patients with newly detected brain masses.

CONCLUSION

High-resolution MRI with intravenous gadolinium has greatly enhanced the ability to detect and characterize metastases as well as to reasonably differentiate them from other intracranial processes. Combination of conventional MRI with more advanced techniques of DWI, PWI, MRS, and PET can be useful in the evaluation and management of patients with intracranial metastases. Nevertheless, additional research is needed to further determine which imaging modality is most appropriate for specific patient populations and to determine whether or how the newer imaging techniques are useful in terms of patient outcome.

References

1. Johnson JD, Young B. Demographics of brain metastasis. *Neurosurg Clin N Am*. July 1996;7(3):337–344.
2. Hutter A, Schwetye KE, Bierhals AJ, McKinstry RC. Brain neoplasms: epidemiology, diagnosis, and prospects for cost-effective imaging. *Neuroimaging Clin N Am*. May 2003;13(2):237–250, x–xi.
3. Posner JB. Management of brain metastases. *Rev Neurol (Paris)*. 1992;148(6–7):477–487.
4. Delattre JY, Krol G, Thaler HT, Posner JB. Distribution of brain metastases. *Arch Neurol*. July 1988;45(7):741–744.
5. Sze G, Milano E, Johnson C, Heier L. Detection of brain metastases: comparison of contrast-enhanced MR with unenhanced MR and enhanced CT. *AJNR Am J Neuroradiol*. July–August 1990;11(4):785–791.
6. Radoi MP, Stefanescu F, Arsene D. Brain metastases and multiple cerebral aneurysms from cardiac myxoma: case report and review of the literature. *Br J Neurosurg*. December 2012;26(6):893–895.
7. Patchell RA, Tibbs PA, Walsh JW, et al. A randomized trial of surgery in the treatment of single metastases to the brain. *N Engl J Med*. February 22, 1990;322(8):494–500.
8. Schaefer PW, Budzik Jr RF, Gonzalez RG. Imaging of cerebral metastases. *Neurosurg Clin N Am*. July 1996;7(3):393–423.
9. Wei SC, Ulmer S, Lev MH, Pomerantz SR, Gonzalez RG, Henson JW. Value of coronal reformations in the CT evaluation of acute head trauma. *AJNR Am J Neuroradiol*. February 2010;31(2):334–339.
10. Carrier DA, Mawad ME, Kirkpatrick JB, Schmid MF. Metastatic adenocarcinoma to the brain: MR with pathologic correlation. *AJNR Am J Neuroradiol*. January 1994;15(1):155–159.
11. Yuh WT, Fisher DJ, Mayr-Yuh NA, et al. Review of the use of high-dose gadoteridol in the magnetic resonance evaluation of central nervous system tumors. *Invest Radiol*. August 1992;27(suppl 1):S39–S44.
12. Yuh WT, Tali ET, Nguyen HD, Simonson TM, Mayr NA, Fisher DJ. The effect of contrast dose, imaging time, and lesion size in the MR detection of intracerebral metastasis. *AJNR Am J Neuroradiol*. February 1995;16(2):373–380.
13. Haustein J, Laniado M, Niendorf HP, et al. Triple-dose versus standard-dose gadopentetate dimeglumine: a randomized study in 199 patients. *Radiology*. March 1993;186(3):855–860.
14. Akeson P, Larsson EM, Kristoffersen DT, Jonsson E, Holtas S. Brain metastases–comparison of gadodiamide injection-enhanced MR imaging at standard and high dose, contrast-enhanced CT and non-contrast-enhanced MR imaging. *Acta Radiol*. May 1995;36(3):300–306.
15. Akeson P, Nordstrom CH, Holtas S. Time-dependency in brain lesion enhancement with gadodiamide injection. *Acta Radiol*. January 1997;38(1):19–24.
16. Engh JA, Flickinger JC, Niranjan A, Amin DV, Kondziolka DS, Lunsford LD. Optimizing intracranial metastasis detection for stereotactic radiosurgery. *Stereotact Funct Neurosurg*. 2007;85(4):162–168.
17. Finelli DA, Hurst GC, Gullapali RP, Bellon EM. Improved contrast of enhancing brain lesions on postgadolinium, T1-weighted spin-echo images with use of magnetization transfer. *Radiology*. February 1994;190(2):553–559.
18. Knauth M, Forsting M, Hartmann M, Heiland S, Balzer T, Sartor K. MR enhancement of brain lesions: increased contrast dose compared with magnetization transfer. *AJNR Am J Neuroradiol*. November–December 1996;17(10):1853–1859.
19. Colosimo C, Ruscalleda J, Korves M, et al. Detection of intracranial metastases: a multicenter, intrapatient comparison of gadobenate dimeglumine-enhanced MRI with routinely used contrast agents at equal dosage. *Invest Radiol*. February 2001;36(2):72–81.
20. Runge VM, Parker JR, Donovan M. Double-blind, efficacy evaluation of gadobenate dimeglumine, a gadolinium chelate with enhanced relaxivity, in malignant lesions of the brain. *Invest Radiol*. May 2002;37(5):269–280.
21. Ba-Ssalamah A, Nobauer-Huhmann IM, Pinker K, et al. Effect of contrast dose and field strength in the magnetic resonance detection of brain metastases. *Invest Radiol*. July 2003;38(7):415–422.
22. Nobauer-Huhmann IM, Ba-Ssalamah A, Mlynarik V, et al. Magnetic resonance imaging contrast enhancement of brain tumors at 3 tesla versus 1.5 tesla. *Invest Radiol*. March 2002;37(3):114–119.
23. Gaviani P, Mullins ME, Braga TA, et al. Improved detection of metastatic melanoma by T2*-weighted imaging. *AJNR Am J Neuroradiol*. March 2006;27(3):605–608.
24. Bukte Y, Paksoy Y, Genc E, Uca AU. Role of diffusion-weighted MR in differential diagnosis of intracranial cystic lesions. *Clin Radiol*. March 2005;60(3):375–383.

25. Tsuchiya K, Fujikawa A, Nakajima M, Honya K. Differentiation between solitary brain metastasis and high-grade glioma by diffusion tensor imaging. *Br J Radiol*. June 2005;78(930):533–537.
26. Lu S, Ahn D, Johnson G, Cha S. Peritumoral diffusion tensor imaging of high-grade gliomas and metastatic brain tumors. *AJNR Am J Neuroradiol*. May 2003;24(5):937–941.
27. Lu S, Ahn D, Johnson G, Law M, Zagzag D, Grossman RI. Diffusion-tensor MR imaging of intracranial neoplasia and associated peritumoral edema: introduction of the tumor infiltration index. *Radiology*. July 2004;232(1):221–228.
28. De La Cruz L, Magalhães F, Domingues R, Domingues R, Rosen BR, Sorensen AG. Assessment of brain tumor with diffusion tensor imaging and tractography. In: *Paper Presented at RSNA Annual Meeting*; 2005. [Chicago].
29. Wiegell MR, Henson JW, Tuch DS. Diffusion tensor imaging shows potential to differentiate infiltrating from non-infiltrating tumors. In: *Paper Presented at: Proceedings of the (ISMRM) Eleventh Scientific Meeting*; 2003. [Toronto].
30. Groothuis DR. The blood–brain and blood-tumor barriers: a review of strategies for increasing drug delivery. *Neuro Oncol*. January 2000;2(1):45–59.
31. Bertossi M, Virgintino D, Maiorano E, Occhiogrosso M, Roncali L. Ultrastructural and morphometric investigation of human brain capillaries in normal and peritumoral tissues. *Ultrastruct Pathol*. January–February 1997;21(1):41–49.
32. Cha S. Perfusion MR imaging of brain tumors. *Top Magn Reson Imaging*. October 2004;15(5):279–289.
33. Jung BC, Arevalo-Perez J, Lyo JK, et al. Comparison of glioblastomas and brain metastases using dynamic contrast-enhanced perfusion MRI. *J Neuroimaging*. August 3, 2015. http://dx.doi.org/10.1111/jon.12281.
34. Kwock L, Smith JK, Castillo M, et al. Clinical applications of proton MR spectroscopy in oncology. *Technol Cancer Res Treat*. February 2002;1(1):17–28.
35. Poptani H, Gupta RK, Roy R, Pandey R, Jain VK, Chhabra DK. Characterization of intracranial mass lesions with in vivo proton MR spectroscopy. *AJNR Am J Neuroradiol*. September 1995;16(8):1593–1603.
36. Bruhn H, Frahm J, Gyngell ML, et al. Noninvasive differentiation of tumors with use of localized H-1 MR spectroscopy in vivo: initial experience in patients with cerebral tumors. *Radiology*. August 1989;172(2):541–548.
37. Castillo M, Kwock L, Mukherji SK. Clinical applications of proton MR spectroscopy. *AJNR Am J Neuroradiol*. January 1996;17(1):1–15.
38. Sijens PE, Knopp MV, Brunetti A, et al. 1H MR spectroscopy in patients with metastatic brain tumors: a multicenter study. *Magn Reson Med*. June 1995;33(6):818–826.
39. Ishimaru H, Morikawa M, Iwanaga S, Kaminogo M, Ochi M, Hayashi K. Differentiation between high-grade glioma and metastatic brain tumor using single-voxel proton MR spectroscopy. *Eur Radiol*. 2001;11(9):1784–1791.
40. Bulakbasi N, Kocaoglu M, Ors F, Tayfun C, Ucoz T. Combination of single-voxel proton MR spectroscopy and apparent diffusion coefficient calculation in the evaluation of common brain tumors. *AJNR Am J Neuroradiol*. February 2003;24(2):225–233.
41. Law M. MR spectroscopy of brain tumors. *Top Magn Reson Imaging*. October 2004;15(5):291–313.
42. Dierckx RA, Martin JJ, Dobbeleir A, Crols R, Neetens I, De Deyn PP. Sensitivity and specificity of thallium-201 single-photon emission tomography in the functional detection and differential diagnosis of brain tumours. *Eur J Nucl Med*. July 1994;21(7):621–633.
43. Kojima Y, Kuwana N, Noji M, Tosa J. Differentiation of malignant glioma and metastatic brain tumor by thallium-201 single photon emission computed tomography. *Neurol Med Chir (Tokyo)*. September 1994;34(9):588–592.
44. Griffeth LK, Rich KM, Dehdashti F, et al. Brain metastases from non-central nervous system tumors: evaluation with PET. *Radiology*. January 1993;186(1):37–44.
45. Rohren EM, Provenzale JM, Barboriak DP, Coleman RE. Screening for cerebral metastases with FDG PET in patients undergoing whole-body staging of non-central nervous system malignancy. *Radiology*. January 2003;226(1):181–187.
46. Chao ST, Suh JH, Raja S, Lee SY, Barnett G. The sensitivity and specificity of FDG PET in distinguishing recurrent brain tumor from radionecrosis in patients treated with stereotactic radiosurgery. *Int J Cancer*. June 20, 2001;96(3):191–197.
47. Larcos G, Maisey MN. FDG-PET screening for cerebral metastases in patients with suspected malignancy. *Nucl Med Commun*. March 1996;17(3):197–198.
48. Ludwig V, Komori T, Kolb D, Martin WH, Sandler MP, Delbeke D. Cerebral lesions incidentally detected on 2-deoxy-2-[18F]fluoro-D-glucose positron emission tomography images of patients evaluated for body malignancies. *Mol Imaging Biol*. October 2002;4(5):359–362.
49. Mavrakis AN, Halpern EF, Barker 2nd FG, Gonzalez RG, Henson JW. Diagnostic evaluation of patients with a brain mass as the presenting manifestation of cancer. *Neurology*. September 27, 2005;65(6):908–911.

CHAPTER

53

Nonneoplastic Mass Lesions of the Central Nervous System

S.B. Omay[1], *K.K. Atsina*[1], *J.M. Baehring*[1,2]

[1]Department of Neurosurgery, Yale School of Medicine, New Haven, CT, USA; [2]Departments of Neurology and Medicine, Yale School of Medicine, New Haven, CT, USA

Nonneoplastic mass lesions of the central nervous system (CNS) mimic tumors clinically and radiographically; their etiology is diverse. Although nonneoplastic mass lesions may also require surgical resection, recognition of such lesions and an accurate diagnosis utilizing only imaging modalities may, at times, spare the patient from invasive procedures. Failing to differentiate between the two may delay treatment in malignant tumors or result in unnecessary treatment in nonneoplastic lesions.[1] When surgery is required, utilization of imaging modalities to accurately predict a diagnosis may help the neurosurgeon plan the intervention accordingly. This chapter provides an overview of nonneoplastic mass lesions and their characteristics on neuroimaging studies.

DEVELOPMENTAL ABNORMALITIES

Pineal cysts

These lesions are benign cysts composed of an inner layer of gliotic tissue with pineal parenchymal tissue and connective tissue as the outer layer.[2] Their incidence (>5 mm) was found to be 2.6% in adults in retrospective magnetic resonance imaging (MRI) studies,[3] while other studies reported their prevalence as 25–40% of cases in autopsy series and in 23% of patients in imaging studies of normal volunteers.[4] Pineal cysts are usually asymptomatic lesions found incidentally. The majority of these lesions remain stable[7] and can be followed by repeat imaging, but rapid enlargement may require histological diagnosis and surgical resolution of the mass effect.

On MRI, pineal cysts are round or oval, thin walled, and well circumscribed (Figure 1A). They typically demonstrate signal intensity similar to that of cerebrospinal fluid (CSF) on T1- and T2-weighted images. On fluid-attenuated inversion recovery (FLAIR) images, the signal may not be completely suppressed owing to proteinaceous contents. On gadolinium-enhanced images, enhancement of the cyst wall occurs in most pineal cysts but is typically incomplete; this finding has been attributed to fragmentation of the pineal parenchyma as the cyst enlarges. On the other hand, at delayed imaging, uniform enhancement of the cyst has been reported.[5] The mechanism behind this finding is not understood, but it may be related to passive diffusion of the contrast agent through the cyst wall or to active secretion of contrast agent by the cyst wall.[4] Fine internal septa and internal cysts may be seen at high-resolution imaging. The differential diagnosis includes cystic tumors such as astrocytoma, pineocytoma, and pineoblastoma.[6]

Arachnoid cysts

Arachnoid cysts are collections of CSF localized with the arachnoid membranes. They are extra-axial by definition. They are more prevalent in males and mostly present in the pediatric population.[8] Arachnoid cysts can present in many different locations. Most commonly, they are found within the middle cranial fossa with an incidence of 42% followed by retrocerebellar and convexity locations.[8] Depending on location, arachnoid cysts may present with headaches, seizures, and rarely hemorrhage in the cyst. In patients with symptomatic arachnoid cysts, treatment may lead to lasting relief of focal neurological deficits; treatment modalities involve endoscopic or open fenestration and shunt placement.[8,9]

Arachnoid cysts present as extra-axial masses, they are well circumscribed and cause calvarial remodeling.

© 2016 Elsevier Ltd. All rights reserved.

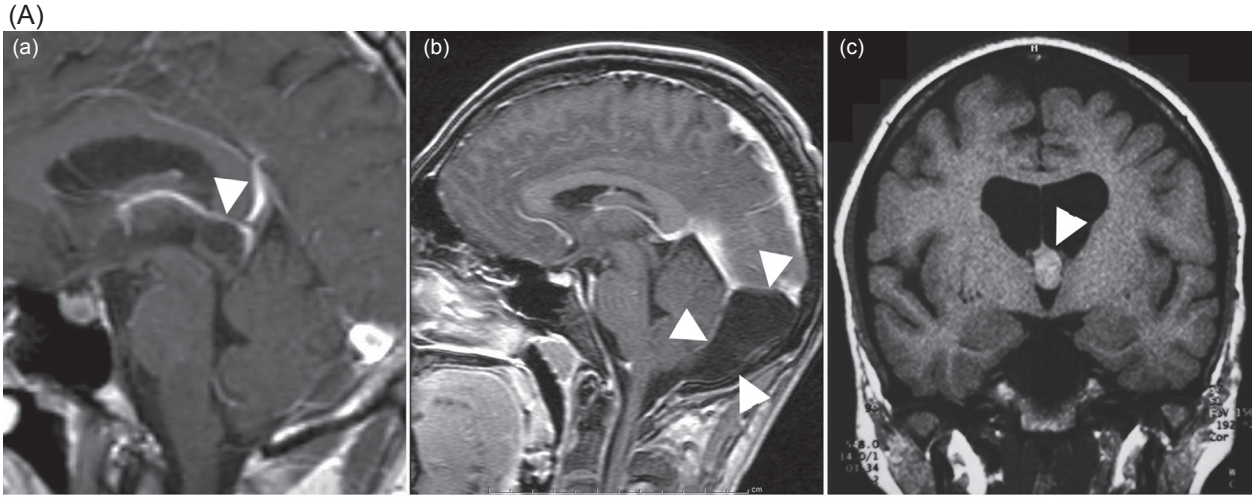


FIGURE 1A Developmental mass lesions. (a) Pineal cyst (arrowhead). There is flattening of the quadrigeminal plate. The cyst wall is regular and does not enhance (T1W with gadolinium). (b) Arachnoid cyst (arrowheads). There is mass effect on the cerebellum (T1W with gadolinium). (c) Colloid cyst (arrowhead). Cyst content is slightly hyperintense compared to normal white matter (T1W).

They follow CSF density and intensity in computed tomography (CT) and MRI, respectively. They do not enhance with contrast. Diffusion-weighted imaging fails to reveal restriction of water diffusion, which helps differentiate arachnoid cysts from epidermoid tumors.[10]

Epidermoid Cysts

Epidermoid cysts are developmental lesions believed to arise from midline ectodermal cells that are displaced during embryogenesis, or from multipotent embryonic cells or displaced otic capsule cells (for those arising in the cerebellopontine angle (CPA)). They tend to occur off midline and are most commonly found in the CPA as well as the petrous apex and in the parasellar area.[11–13] Clinical presentation is dependent on location: CPA lesions present with symptoms of hearing loss, tinnitus, and sometimes trigeminal neuralgia; parasellar lesions cause headache and visual symptoms. Although technically difficult owing to adhesions to neighboring neurovascular structures, total excision is the recommended treatment for these lesions. They are likely to recur in subtotally resected cases.[11] Pathologically they are composed of keratinized squamous epithelium. Although rare, secondary development of squamous carcinoma has been reported.[14]

On imaging studies, epidermoids tend to be hypodense on CT and may show calcification. They follow CSF intensity on MRI with T1-weighted (T1W) hypointensity and T2W hyperintensity, but FLAIR signal suppression is incomplete. Perilesional edema is uncommon. Typically there is no enhancement. Lesional margins may be irregular. Characteristically they show restricted diffusion of water.[15,16]

Dermoid Cysts

Dermoid cysts are also developmental lesions containing dermal elements like hair, hair follicles, or sweat glands. They are rarer compared to epidermoid cysts, constituting about 0.05% of all brain masses.[17] They tend to occur in younger patients with an average age of 15 years.[18] In contrast to epidermoid cysts, which contain keratin and epithelial cell debris, dermoid cysts contain elements of the dermis including hair, hair follicles, dental enamel, sweat glands, and sebaceous and apocrine glands.[16] Dermoids tend to be closer to the midline, with the vermian and parasellar regions as the most common sites of presentation. Treatment of these lesions is surgical. Incomplete resection leads to recurrence many years later as these lesions tend to grow indolently.

On CT imaging, dermoids appear as a well-defined hypodense mass (Figure 1B). Calcifications are common. On MRI, they are hyperintense on T1W imaging and heterogeneous on T2W sequences.[10]

Neuroenteric Cysts

Neuroenteric or neuroepithelial cysts are developmental malformations. Most commonly encountered locations are the spinal column, pontomedullary junction, CPA, craniocerebral junction, and parasellar area.[19] They are mostly localized ventrally and extra-axial within the spinal column. Spinal neuroenteric cysts are associated with vertebral anomalies such as hemivertebrae, fused vertebrae, or diastematomyelia and more complex syndromes such as Klippel–Feil syndrome. The cyst wall usually is composed of cuboidal, columnar, or ciliated epithelium, with or without goblet cells or microvilli resembling gastrointestinal epithelium. Symptoms

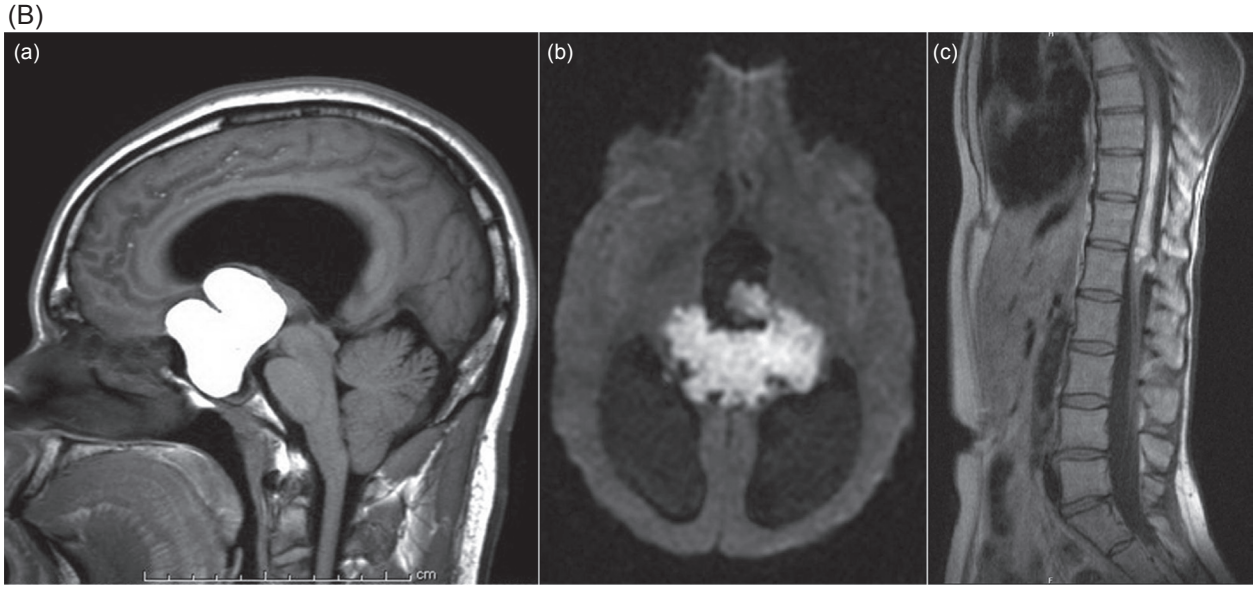


FIGURE 1B Developmental mass lesions. (a) Dermoid cyst. A large hyperintense lesion expands the pituitary fossa and extends into the base of frontal lobe and hypothalamus (T1W). (b) Epidermoid cyst. A large mass with a cauliflower-like appearance compresses the tectum of the midbrain. There is restriction of water diffusion (DWI). (c) Lipoma of the thoracic spinal cord. A large hyperintense mass lesion is seen within the center of the cord. It appears to be tethered to the posterior dura at its caudal end (T1W).

are related to location and most commonly related to mass effect.[20] Surgery is usually reserved for symptomatic lesions. The goal is for complete cyst wall resection, except in situations of adherence to critical structures. For complex, unresectable cysts, shunting into the subarachnoid space may be considered.

MRI signal intensity varies with the cyst contents but most commonly is similar to CSF with T1 hypointensity and T2 hyperintensity. T2 signal may be hyperintense relative to CSF. These lesions do not enhance with contrast.[10,21]

Intracranial Lipoma

Intracranial lipomas are rare (<0.1%) malformations secondary to faulty differentiation of the primitive meninges.[22] They are mostly found in the midline, especially over the corpus callosum in the pericallosal cistern but also in the quadrigeminal and interpeduncular cisterns.[23] There is an association with agenesis of the corpus callosum, spinal dysraphism, and other developmental abnormalities of the CNS.[24] These lesions are usually incidental findings on imaging studies and very rarely require a surgical intervention. However, they may cause hydrocephalus due to obstruction requiring shunting. Seizures have been reported to be associated with sylvian cistern lipomas.[24]

On CT, lipomas are well-defined hypodense lesions with occasional peripheral calcification, They usually have a CT density of between −50 Hounsfield units (HU) and −100 HU.[23] On MRI, they appear as homogeneous, hyperintense masses on T1W images (hypointense on fat-suppressed sequences) and hyperintense on T2W images. They do not enhance.[23]

Epithelial Cysts of the Central Nervous System

These lesions are characterized by a glial wall with an epithelial lining similar to ependyma or choroid plexus.[25] They are thought to arise from neuroectodermal progenitor cells. Other terms have been used to describe lesions, like ependymal cyst, choroid cyst, choroidal–epithelial cyst, and glioependymal cyst.[26] Unless they are very large and cause mass effect, they are asymptomatic and usually found incidentally. On CT, neuroepithelial cysts appear as smooth, round to ovoid, nonenhancing lesions with a central low density resembling CSF. They may display internal septations; they rarely calcify. Intraparenchymal cysts appear well circumscribed with well-defined cyst margins. Because the cyst wall is typically thin, intraventricular cysts and cysts located within the cisterns may be difficult to distinguish from the surrounding CSF. On MRI, the cyst fluid largely resembles CSF on both T1W and T2W images.[25] However, the cyst fluid may appear slightly hyperintense to CSF on T1W images. These lesions do not enhance.[25,27]

Colloid Cysts

Colloid cysts account for 0.5–1% of all brain masses. They are commonly third ventricular lesions located anteriorly within the ventricle. Patients present with

headaches, which are secondary to persistent or intermittent obstruction of the foramen of Monro.[28] Obstruction resulting in acute hydrocephalus has been described as a cause of sudden death.[29] The cell of origin is still a subject of debate but studies suggest an endodermal origin.[28,30] Treatment options include observation for small and asymptomatic lesions or surgical management with microsurgical or neuroendoscopic resection.[28]

Anterior third ventricular location is key in imaging diagnosis of these lesions. CT and MRI signal characteristics are dependent on the composition of the cyst content. T1W signal correlates with cholesterol concentration (two-thirds of them being hyperintense on nonenhanced T1W images), whereas T2W signal is variable. They show no enhancement, not even in the cyst wall.[31]

Rathke Cleft Cysts

Rathke cleft cysts (RCCs) originate from embryonic remnants of Rathke's pouch and are benign cystic lesions with variable size.[32] Content is usually a thick, mucoid material consisting of cholesterol and protein.[33] RCCs typically present within the sella in the pars intermedia of the pituitary gland or, rarely, suprasellar.[34,35] Small cysts are asymptomatic, incidentally found on imaging. Larger lesions present with signs of mass effect such as headache, pituitary malfunction, or visual field deficits.[35] Small, asymptomatic RCCs do not require surgical intervention. When symptomatic, the goal of surgery is cyst drainage and safe removal of as much of the capsule as possible. Cyst fenestration and drainage via an endonasal/sublabial transsphenoidal approach are the most commonly used methods to achieve this goal.[35,36]

On imaging, RCCs are well-circumscribed lesions. The pituitary gland is usually around or under the cyst, creating the sign of "the egg in a cup."[37] On CT, they usually appear as low or isodense homogeneous lesions or with slight hyperdensity relative to the brain parenchyma sometimes with ring-like enhancement.[36] On MRI, they appear as well-demarcated cystic lesions with homogeneous signal intensity. Signal intensity varies with the composition of the cyst content. T2 hypointense signal intensity is highly suggestive of RCC, as it distinguishes it from chordomas, chondroid tumors, abscesses, mucoceles, and lipomas, all characterized by hyperintense T2 signal.[38]

Cholesteatoma

These are rare middle-ear and mastoid process lesions characterized by destructive, expansile growth. Pathologically, they consist of keratinized squamous epithelium. Patients typically come to medical attention in their 20 s. Most patients present with ear discharge and conductive hearing loss. Less common manifestations are ipsilateral Bell palsy, tinnitus, imbalance, and headaches. Cholesteatomas may be congenital or acquired. The standard management is surgical resection. CT scans through the temporal bones demonstrate a hypodense expansile lesion without enhancement (Figure 1C).[39] MRI reveals hyperintense T1W and hypointense T2W signal without postcontrast enhancement. Restricted water diffusion on diffusion-weighted imaging (DWI) helps in distinguishing a cholesteatoma from other middle ear masses.[40]

Hamartomas

CNS hamartomas are slow-growing lesions occurring in the tuber cinereum and inferior hypothalamus. They may be entirely asymptomatic or present with epilepsy (gelastic seizures), developmental delay, and central precocious puberty. They are isointense to normal cortex on T1WI and may be slightly hyperintense on T2WI. Ictal single-photon emission computed tomography (SPECT) studies have revealed increased perfusion. These lesions do not enhance. Symptomatic lesions may be resected.[41,42]

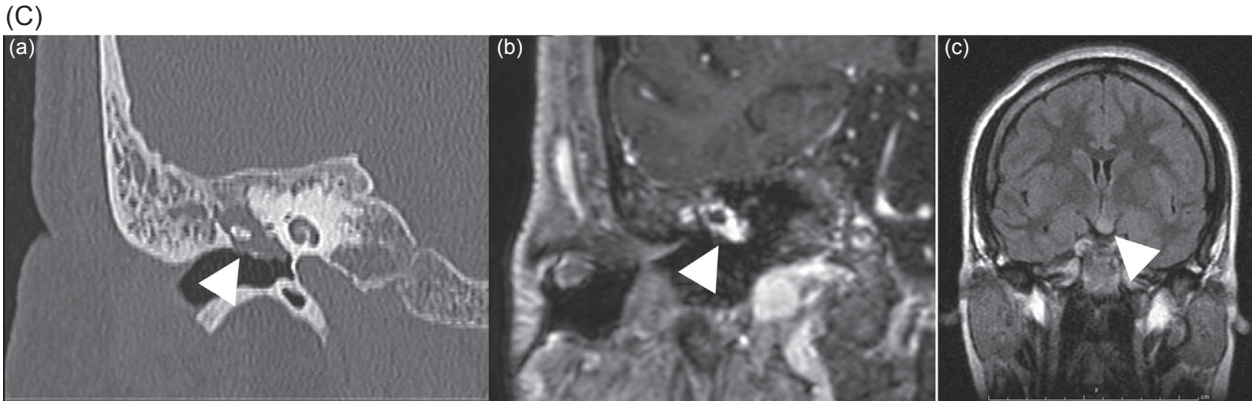


FIGURE 1C Developmental mass lesions. (a, b) Cholesteatoma (arrowhead). A small mass lesion is noted in the right epitympanum. ((a) High-resolution CT of the right temporal bone, coronal view. (b) T1W with gadolinium). (c) Hamartoma (arrowhead). A hyperintense mass lesion is noted in the left hypothalamus (FLAIR).

INFLAMMATORY DISORDERS

Autoimmune Encephalitis

These pathologies arise from altered immune response targeting intracellular or cell surface antigens. Limbic encephalitis and rhombencephalitis are often paraneoplastic conditions that typically present in a subacute timeline. The clinical picture may involve confusion, agitation, hallucinations, seizures, and sleep disturbance. Antibodies to onconeural intracellular antigens such as Hu, Ma, and Ri are associated with certain malignancies such as small-cell lung cancer, testicular germ-cell tumors, thymoma, and Hodgkin lymphoma.[43–45] Immune-mediated encephalitis with autoantibodies targeting neuronal cell surface antigens are much more common than those mediated by intracellular antigens, have a better overall prognosis, and are less commonly paraneoplastic.[44,45] Treatment includes steroids and immunomodulatory therapy.[44,45]

T2W and FLAIR sequences reveal hyperintense signal in the medial temporal lobes and hippocampi. This is often subtle and may be entirely absent. When prominent and asymmetric, it may mimic infiltrative or non-infiltrative glioma (pleomorphic xanthoastrocytoma, ganglioglioma).

Primary Central Nervous System Vasculitis

Often a multifocal disease affecting small- to medium-sized cerebral blood vessels, primary CNS vasculitis can occasionally present as a mass lesion. Corticosteroids should be used with caution before a definitive diagnosis is established, as they may alter the histopathologic features profoundly. A biopsy is often required.

On brain MRI, lesions are hyperintense on T2W images and hypointense on T1W images. There may be patchy contrast enhancement, signs of acute or subacute ischemia, or hemorrhage.[46]

Sarcoidosis

Sarcoidosis is a chronic, multisystem granulomatous inflammatory disease of unclear etiology. A biopsy is required for diagnosis but can often be acquired from extraneural sites. Corticosteroids remain the mainstay of therapy. Sarcoidosis gives rise to a basal meningitis resulting in cranial neuropathies. However, when small parenchymal granulomas coalesce into a single mass it may mimic a neoplastic lesion.[47] Large sarcoid granulomas are hypodense on CT. Depending on lesion location they may give rise to obstructive or communicating hydrocephalus. On MRI, lesions on T1W are iso- to hypointense and display variable T2W signal patterns. They enhance after gadolinium administration, as do the thickened basal meninges.[48,49] Dural involvement may be diffuse or focal and mass-like, and the latter may resemble a meningioma or nerve sheath tumor.[6]

Inflammatory Pseudotumor

Inflammatory pseudotumor (IPT) comprises a heterogeneous group of lesions sharing common histological features (Figure 2). These include fibroblastic and myofibroblastic proliferation with inflammatory infiltrates comprising acute and chronic inflammatory cells, including plasma cells. Infections, malignancies, radiotherapy, and surgery have been reported to precede this pathology.[50] IPT has aggressive clinical features and is typically characterized by locally destructive or infiltrative features that mimic malignant neoplasms.[76] The usual treatment for brain IPT is surgical resection combined with corticosteroids or radiation therapy. Recurrence is common within 2 years of primary surgery.[51] Complete resection is advocated whenever possible.[76] CT scans demonstrate lesion enhancement as well as associated bony destruction. On MRI, lesions are T2W hyperintense and enhance homogeneously.[52]

Rosai–Dorfman Disease

Rosai–Dorfman disease (RDD), also referred to as sinus histiocytosis with massive lymphadenopathy, is an uncommon benign lymphoproliferative disorder with an estimated incidence of approximately 100 cases per year in the United States.[53,54] It involves the CNS infrequently, usually as dural-based masses. Intraparenchymal involvement is less common.[54] In localized presentations, surgical resection is the therapy of choice; however, resection is not always possible and other therapeutic modalities may be required for disease management.[54]

On CT, RDD lesions present as homogeneous hyperdense masses. Perilesional edema and mass effect on adjacent structures are common. MRI reveals single or multiple well-defined lesions that are isointense on T1W and enhance avidly after gadolinium administration. On T2W RDD lesions appear as heterogeneous masses hypo- or isointense to the contiguous dura.[54,55] They have to be distinguished from meningiomas.

Idiopathic Pachymeningitis

Idiopathic hypertrophic pachymeningitis is a rare chronic inflammatory process that gives rise to thickening of the dura mater. Mass-like presentations have been described (tumefactive pachymeningitis).[56] Histopathologically, there is fibrosis with inflammatory cell infiltration. Patients typically present with cranial neuropathies and headaches, but depending on location and

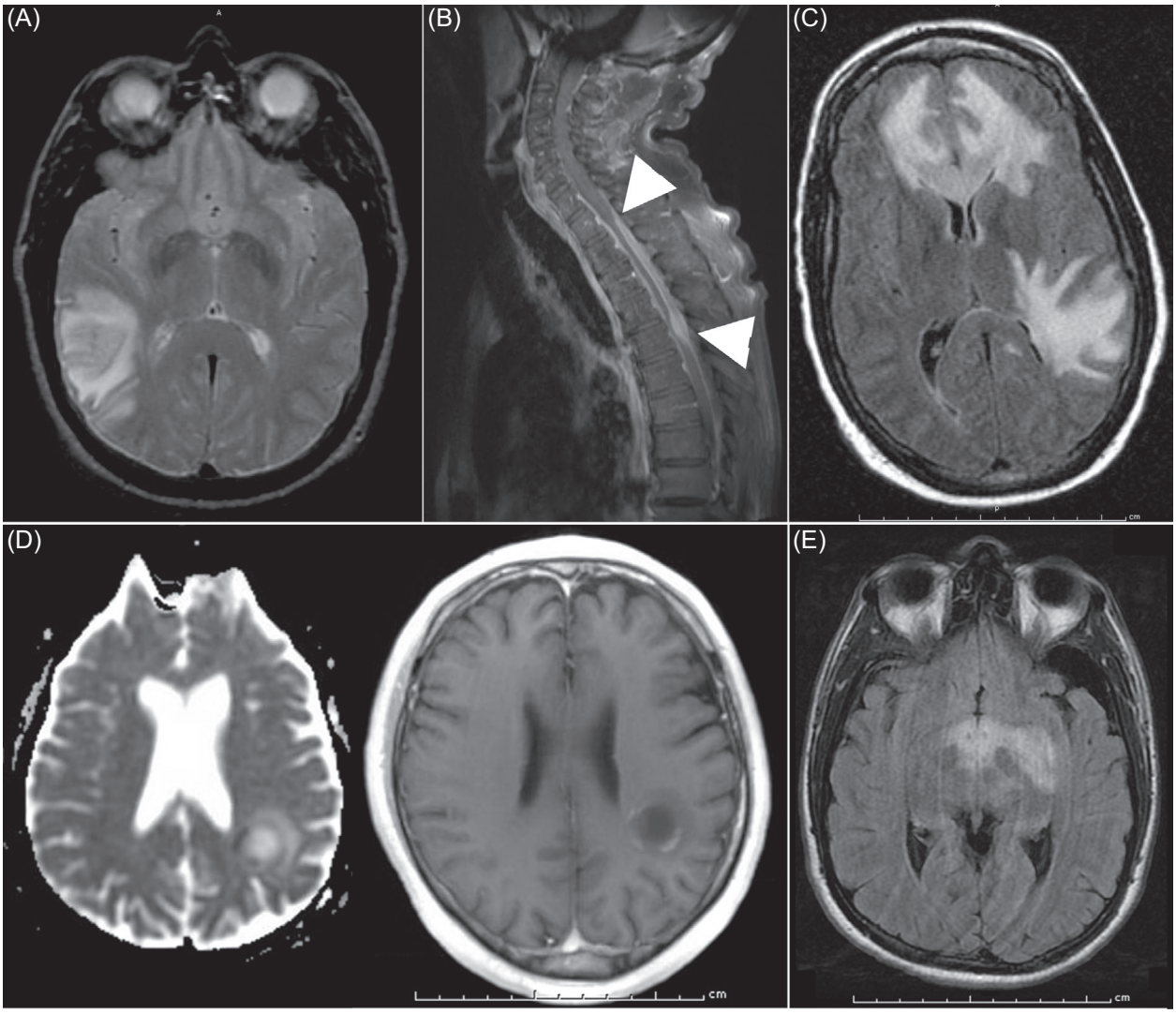


FIGURE 2 Inflammatory mass lesions. (A) Primary CNS angiitis on the background of congophilic angiopathy. A hyperintense lesion, mostly vasogenic edema, is seen in the right temporoparietal area (T2W). (B) IPT. There is a homogeneously enhancing mass lesion in the thoracic epidural space compressing the cord circumferentially (T1W with gadolinium). (C) Acute demyelinating encephalitis. Two inflammatory lesions surrounded by extensive vasogenic edema are seen in the genu of the corpus callosum and the subependymal white matter in the left centrum semiovale (FLAIR). (D) Single acute demyelinating lesion in the left frontoparietal white matter. There is restriction of water diffusion at the margin. The C-shaped enhancement pattern helps distinguish it from abscesses and rim-enhancing neoplasms (apparent diffusion coefficient map (left), T1W with gadolinium (right)). (E) Paraneoplastic encephalitis. A hyperintense lesion is seen in the left basal ganglia, mesial temporal lobe, and anterior commissure mimicking an infiltrative neoplasm (FLAIR).

extent, a variety of symptoms and signs are possible. Immunosuppression and immunomodulation have been shown to be effective therapies in most patients. On MRI, diffuse, prominent pachymeningeal thickening and enhancement are noted, resembling meningioma en plaque.[57] The thickened dura is T1W hypointense and displays mixed signal intensity on T2W.[58]

Tolosa–Hunt Syndrome

Tolosa–Hunt syndrome is a steroid-responsive granulomatous disease of the cavernous sinus and orbital apex. Clinical presentation is painful ophthalmoplegia.[59] Thickening of the cavernous sinus on the afflicted side may be visible on CT. The inflamed dura is iso- to hyperintense on T1W and hyperintense on T2W. Contrast enhancement is common during active disease[60] and resolves with steroid therapy.[61] As lesions are deep seated and small, patients are often treated empirically, mandating close surveillance imaging.[61]

Infundibulitis and Hypophysitis

Infundibulitis and hypophysitis are rare clinical entities, which may present alone or in a combined fashion. They are marked by lymphocytic infiltration on

histological analysis. Patients may present with diabetes insipidus or other neurohypophyseal endocrinopathies, often in the postpartum period or in the third trimester of pregnancy.[62] On MRI the characteristic T2W hyperintense signal of the neurohypophysis is absent. The affected areas are isointense on T1W, hypointense on T2W, and enhance with gadolinium. Pituitary stalk or gland may be thickened, resembling an adenoma.[63] Response to steroids or other immunomodulatory agents is highly suggestive of primary autoimmune or lymphocytic etiology.[64]

Demyelinating Encephalitis

Demyelinating disorders may present as cerebral mass lesions. Tumefactive demyelination occurs in the setting of multiple sclerosis and acute disseminated encephalomyelitis. Histopathologically lesions are characterized by demyelination and relative preservation of axon cylinders. Tumefactive lesions of MS are typically periventricular and multiple and follow the course of intramedullary veins. There is little perilesional vasogenic edema or mass effect.[65] The lesions are hypointense on T1W and hyperintense on T2W. Enhancement pattern is heterogeneous and creates an incomplete faint ring, an appearance distinguishing demyelination from tumor or abscess.[1,66,67] Perfusion-weighted MRI reveals decreased cerebral blood volume in demyelinating tumefactive lesions compared to neoplasms.[68] On diffusion-weighted MRI, demyelinating lesions are largely characterized by increased diffusivity in the center of the lesion. Only in the acute stage there may be restricted diffusion in the margin of the lesion.[8]

INFECTIONS

Bacterial Infections and Brain Abscess

Brain abscesses are focal, encapsulated infectious lesions within the brain parenchyma. They result from hematogenous or contiguous spread of an infection, penetrating trauma, or barrier breakdown from a neurosurgical procedure. Abscesses from hematogenous spread of bacteria tend to form in the distribution of the middle cerebral artery at the gray–white matter junction.[69] Contiguous spread occurs in patients with infections of the paranasal sinuses, middle ear, or mastoid process.[70] The most common causative organisms are *Streptococcus viridans* and *Staphylococcus aureus*.[71] Patients with right to left shunts (arteriovenous fistulas, cardiac defects) are at higher risk. In the immunocompromised host, *Nocardia* or *Listeria* species are encountered.[72] A detailed exposure history and consideration of endemic pathogens are crucial to establish a definitive diagnosis. Patients present with headaches, nausea, fever, and an altered sensorium. Small abscesses may be eradicated by antibiotherapy alone but most lesions require surgical drainage. Substantial mass effect, periventricular location, signs of increased intracranial pressure, and presence of a foreign body mandate surgical intervention.[73]

MRI is more sensitive than CT, especially at the early cerebritis stage (Figure 3A). The center of a mature brain abscess is hypointense on T1W and hyperintense on T2W. The surrounding capsule is T2 hypointense and displays peripheral enhancement after contrast administration. Perilesional edema is often profound, a distinguishing feature from tumors.[74] Bacterial abscesses in the immunocompetent host are characterized by profound restriction of water diffusion, a feature otherwise seen only in mucoid metastases or epidermoid cysts.[71] Occasionally, multiple abscesses may mimic metastatic brain tumors.[1] CNS listeriosis affects the brain stem and can mimic an infiltrative glioma. Abscess formation is common.[75,76]

Tuberculosis can give rise to pachymeningitis, leptomeningitis, and cerebral parenchymal granuloma formation. The last, characterized by central caseous necrosis surrounded by granulomatous inflammation, has to be distinguished from malignant gliomas or metastases. The margin of these lesions enhances avidly. Signal on diffusion-weighted MRI is variable.[76] Cerebral syphilitic gumma is a rare manifestation of tertiary syphilis, which is caused by *Treponema pallidum*. Histopathologically, gummas are granulomatous inflammatory lesions with distinct microvascular changes such as intimal thickening and perivascular inflammation. On MRI, these lesions enhance and are surrounded by vasogenic edema.[78]

Fungal Infections

Fungal brain abscesses resemble bacterial ones. Given their typical occurrence in immunocompromised hosts, appearance on DWI and degree of perilesional vasogenic edema are variable. Examples are cryptococcoma and aspergilloma (Figure 3B). Owing to its tendency to invade blood vessels, aspergillosis may give rise to ischemic strokes.

Parasitic Infections

Neurocysticercosis

This infection is caused by *Taenia solium*, whose intermediate host is the pig. Parasitic cysts form at the gray–white matter junction and in the central nuclei. In their final stage, cyst contents are T1W hypointense and T2W hyperintense. Water diffusivity is not restricted. Peripheral enhancement and perilesional vasogenic edema are common.[76]

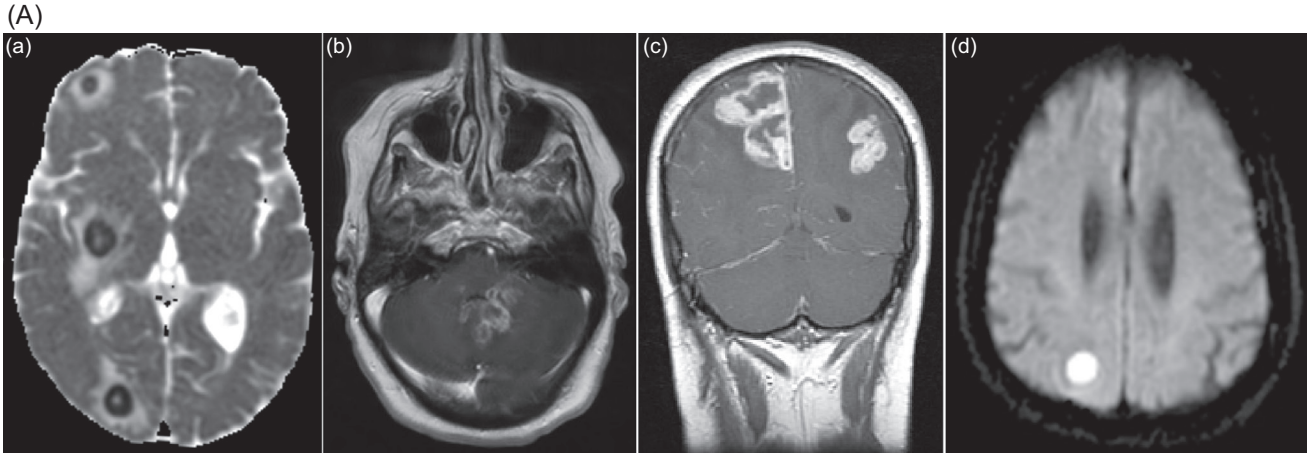


FIGURE 3A Infections. (a) Multiple bacterial abscesses are seen scattered throughout the right internal carotid artery territory, the result of embolization from an infected pseudoaneurysm within the cavernous portion of the vessel (apparent diffusion coefficient map). (b) *Listeria* rhombencephalitis. Heterogeneous contrast enhancement is noted in brain stem and midline cerebellar structures (T1W with gadolinium). (c) Tuberculosis. Multiple heterogeneously enhancing mass lesions involving dura and cerebral parenchyma are seen in both hemispheres (T1W with gadolinium). (d) Nocardiosis. An abscess is seen in the right parietal region (DWI).

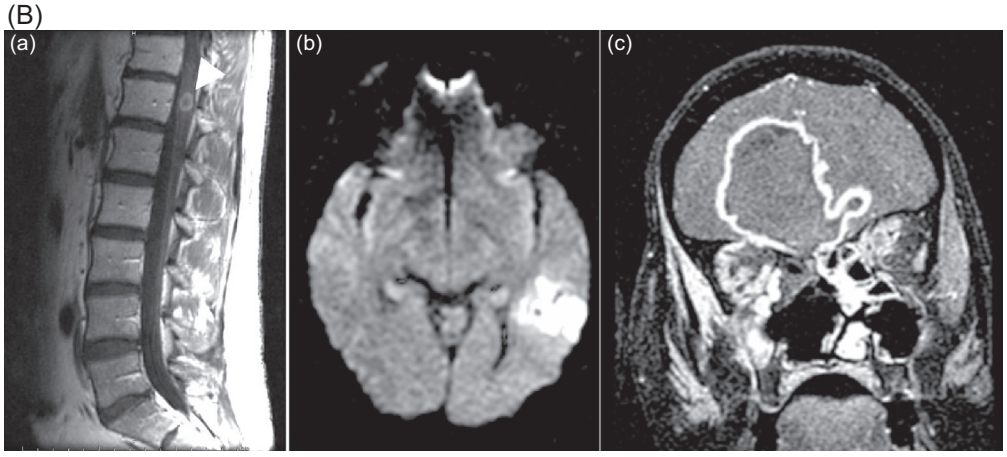


FIGURE 3B (a) Cryptococcoma of the conus medullaris (arrowhead; T1W with gadolinium). (b) Aspergilloma (diffusion-weighted MRI). (c) Mucor abscess in the right frontal lobe (T1W with gadolinium).

Toxoplasmosis

This infection is caused by *Toxoplasma gondii,* whose definitive host is the cat (Figure 3C). Toxoplasmic lesions have a necrotic center surrounded by inflammatory cells. They occur as single or multiple lesions of variable size and are located at the gray–white matter junction. T1W and T2W images reveal isointense lesions with an irregular and thick rim of enhancement and perilesional vasogenic edema.[76]

Viral Infections

Herpes Encephalitis

Herpes simplex encephalitis is the main cause of sporadic viral encephalitis. Like most other pathogenic viruses, it affects gray matter. Owing to its predilection for the mesial temporal lobe and its asymmetric distribution it can resemble infiltrative glioma. Patients present with altered sensorium and seizures.[77] The infection often starts in the anterior part of the temporal lobe and then extends posteriorly. The lesion is T1W hypointense in the acute stage. In the chronic lesion, laminar necrosis is seen as a fine line of T1W hyperintense signal within the cortex. On T2W, areas of inflammation and vasogenic edema are hyperintense. Enhancement is subtle and often peripheral. Gradient-echo sequences may reveal intralesional microhemorrhages. The early lesion is characterized by restricted water diffusion within the cortex reflecting cytotoxic edema. As the disease progresses and neuronal cell membranes are compromised, the apparent diffusion coefficient increases.[76]

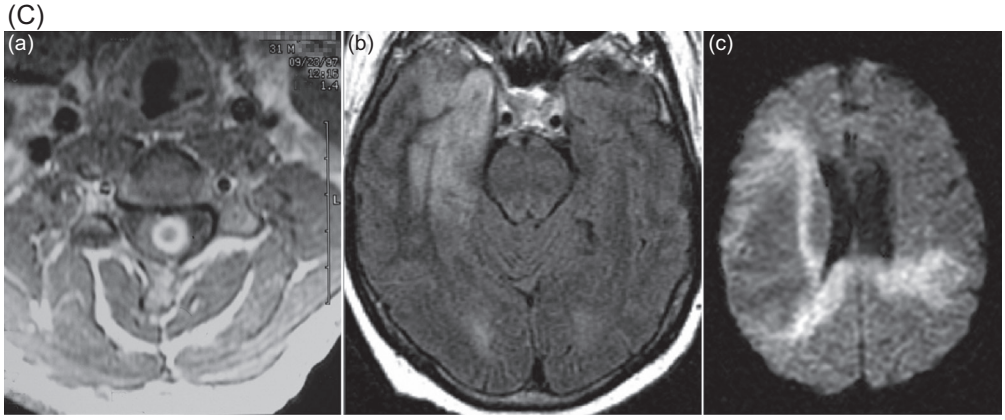


FIGURE 3C (a) Toxoplasmosis abscess in the cervical spinal cord (T1W with gadolinium). (b) Herpes simplex encephalitis. Hyperintense signal is noted, affecting predominantly gray matter of the right temporal lobe (FLAIR). (c) Progressive multifocal leukoencephalopathy. The large lesion affecting both hemispheres displays restriction of water diffusion at its growing edge and increased diffusivity in the center (DWI).

Progressive Multifocal Leukoencephalopathy

Progressive multifocal leukoencephalopathy lesions predominantly affect the parieto-occipital white matter. The center of the lesion is T1W hypointense and T2W hyperintense. As cell membrane destruction is complete in this part of the lesion, water diffusivity is increased. Cytotoxic edema and preserved oligodendroglial membranes characterize the margin of the lesion histopathologically. This is reflected by restricted water diffusion.

CEREBROVASCULAR LESIONS

Ischemic Infarctions

Ischemic strokes, especially at the subacute stage, may occasionally be mistaken for a neoplasm. Wedge-shaped configuration with the broad base on the cortex, involvement of gray and white matter of a single vascular territory (venous or arterial), laminar necrosis, and pseudonormalization on apparent diffusion coefficient support the diagnosis of a stroke. Conversely, early stages of malignant gliomas (markedly increased cellularity without central necrosis) may resemble an ischemic stroke (Figure 4).[1]

Intracranial Hemorrhage

Intracranial hemorrhage (ICH) may have a mass-like appearance. It results from uncontrolled hypertension, trauma, or vascular lesions such as hemorrhagic stroke, arteriovenous malformation, aneurysm, or dural sinus thrombosis. An important feature of intracranial hemorrhage imaging is the evolution over time secondary to degradation of blood products. Treatment is defined by the causative pathology, but if the hemorrhage is large enough to cause mass effect or hydrocephalus, surgical intervention may be required. Head CT is widely used as the initial imaging modality to diagnose acute ICH. Hyperdense in the acute stage, ICH becomes isodense in the subacute stage with possible ring enhancement and hypodense in the chronic stage. On MRI, hyperacute blood is iso- to hypointense on T2W images. In the subacute stage, signal becomes T1W and T2W hyperintense. As macrophages invade the hematoma from the periphery toward the center, T2 signal turns hypointense and T1W signal isointense. Susceptibility weighted imaging (SWI) signal is hyperintense in the acute stage and hypointense in the chronic stage.[79] Cavernomas are characterized by heterogeneous central T2W signal and a hypointense rim.[80] They are not visible by conventional angiography. Arteriovenous malformation (AVM) has prominent flow voids on T1W and T2W images. SWI sequences may reveal a hypointense rim secondary to previous hemorrhage.[81] Differential diagnosis is difficult at the acute stage of acute hemorrhage, such that repeat imaging is often necessary within 6 weeks to identify underlying pathology. Aneurysm are easily diagnosed with CT, MR, and conventional angiography. However, on MRI aneurysms may occasionally resemble a neoplasm, especially when their lumen is partially thrombosed.[82]

OTHER ENTITIES

Extramedullary Hematopoiesis

Mostly related to thalassemia and myelofibrosis, extramedullary hematopoiesis is rare in the cranial vault and the spinal canal and is usually an incidental finding, but on rare occasions it can cause mass effect and present with neurologic dysfunction. CT reveals heterogeneous density in the extra-axial space (Figure 5). MRI demonstrates extra-axial masses that are isointense on T1W and hypointense on T2W images with postcontrast enhancement.[83,84]

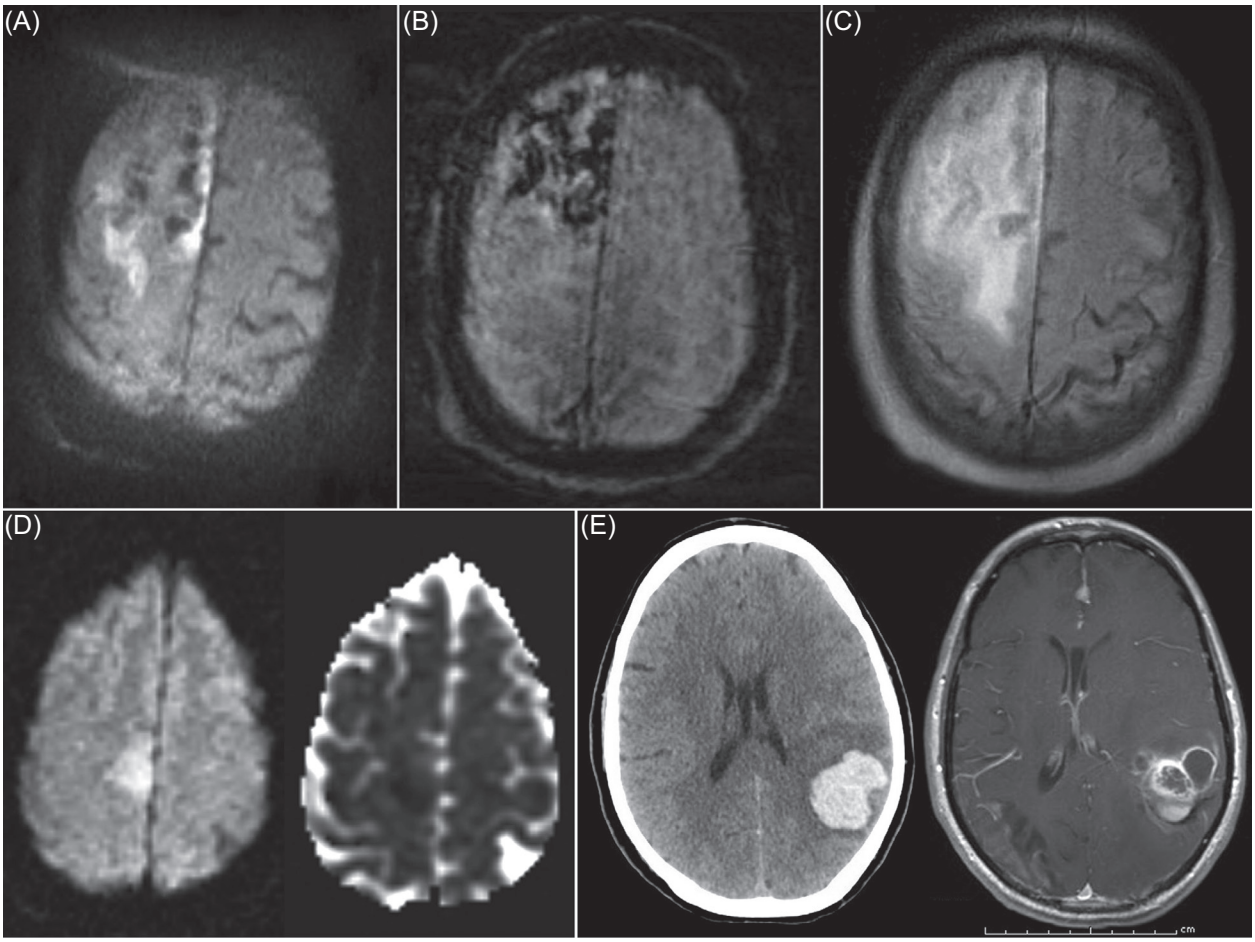


FIGURE 4 Cerebrovascular lesions mimicking tumors and vice versa. (A–C) Subacute ischemic infarction in the right anterior cerebral artery territory. There is susceptibility artifact in a cortical pattern indicative of hemorrhagic transformation ((A) DWI; (B) susceptibility-weighted MRI; (C) FLAIR). (D) A small area of restricted water diffusion indicative of increased cellularity is noticed in the right frontal parasagittal region. Biopsy revealed glioblastoma multiforme. (E) A left frontal hematoma is seen in the left frontal lobe. Repeat imaging 2 months later shows a heterogeneously enhancing mass lesion within the resolving hematoma. Biopsy revealed malignant glioma.

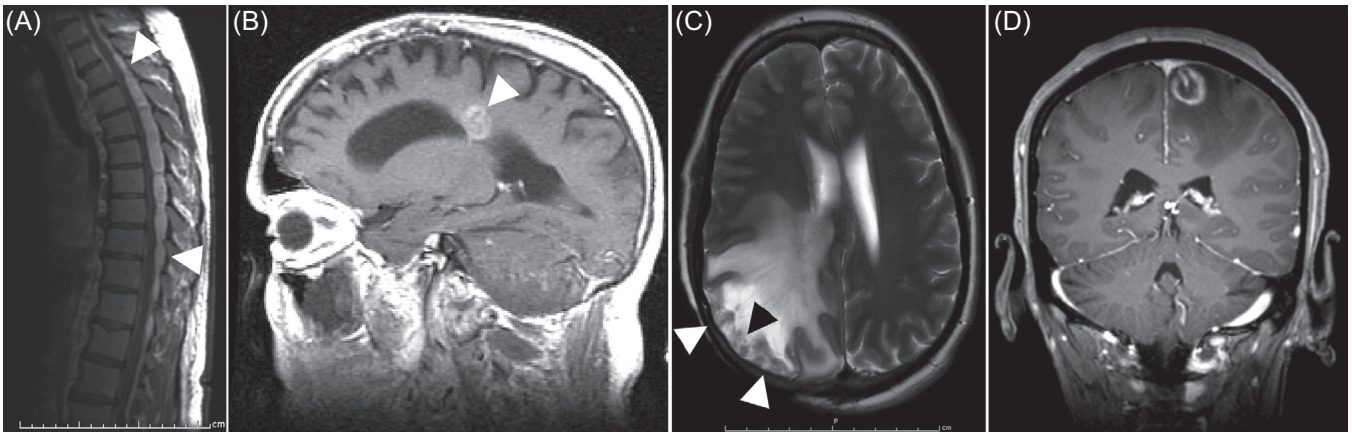


FIGURE 5 Other entities. (A) Extramedullary hematopoiesis. A hyperintense mass lesion compresses the thoracic spinal cord posteriorly (arrowheads; T1W). (B) Amyloidoma. A subependymal heterogeneously enhancing mass lesion is seen adjacent to the body of the left lateral ventricle. Biopsy revealed amorphous material identified as β-amyloid by immunohistochemistry (T1W with gadolinium). (C) Radiation necrosis. A superficial inflammatory mass is seen in the right parietal lesion (arrowheads). There is extensive vasogenic edema in the underlying white matter. The patient had received radiosurgery to a scalp melanoma (T2W). (D) Polymorphic posttransplant lymphoproliferative disorder. A heterogeneously enhancing mass lesion is seen in the left frontal parasagittal region (T1W with gadolinium).

Amyloidoma

Like in amyloid angiopathy and senile plaques, amyloidoma is also formed by the deposition of amyloid protein and presents as single or multiple intracranial masses. Surgical intervention may be required for diagnosis but only rarely for mass effect. Imaging characteristics including enhancement patterns vary.[85]

Radiation Necrosis

Radiation necrosis (RN), also referred to as pesudoprogression, poses a considerable diagnostic challenge as it is difficult to differentiate from tumor recurrence. Clinically, both pathologies present with signs and symptoms of focal mass effect. Therapy involves corticosteroids, bevacizumab, or surgical intervention. Radiologically, a "soap bubble" appearance on post-gadolinium sequences has been described as characteristic for RN. Perfusion-weighted MRI may reveal increased cerebral blood volume in tumors and decreased cerebral blood volume in RN. [^{18}F]Fluorodeoxyglucose PET, SPECT, and MR spectroscopy provide additional information but none of these studies has sufficient sensitivity or specificity.[86]

Polymorphic Posttransplant Lymphoproliferative Disorder

Occurring in organ transplant recipients on chronic immunosuppression, these lesions represent unchecked B-cell polyclonal or oligoclonal hyperplasia and may involve the CNS. Clinical symptoms are variable and depend on the location of the lesions. First-line therapy is reduction of immunosuppression. They may present as multiple hemispheric masses with variable MRI features and enhancement patterns, depending on their cellularity. Left untreated, degeneration into lymphoma occurs. This is reflected by MRI findings (restriction of water diffusion, homogeneous or rim enhancement.[87]

References

1. Huisman TA. Tumor-like lesions of the brain. *Cancer Imaging*. 2009;9. Spec No. A: S10–S13.
2. Hirato J, Nakazato Y. Pathology of pineal region tumors. *J Neurooncol*. 2001;54:239–249.
3. Sener RN. The pineal gland: a comparative MR imaging study in children and adults with respect to normal anatomical variations and pineal cysts. *Pediatr Radiol*. 1995;25:245–248.
4. Pu Y, Mahankali S, Hou J, et al. High prevalence of pineal cysts in healthy adults demonstrated by high-resolution, noncontrast brain MR imaging. *AJNR Am J Neuroradiol*. 2007;28:1706–1709.
5. Mamourian AC, Yarnell T. Enhancement of pineal cysts on MR images. *AJNR Am J Neuroradiol*. 1991;12:773–774.
6. Smith AB, Horkanyne-Szakaly I, Schroeder JW, Rushing EJ. From the radiologic pathology archives: mass lesions of the dura: beyond meningioma-radiologic-pathologic correlation. *Radiographics*. 2014; 34:295–312.
7. Barboriak DP, Lee L, Provenzale JM. Serial MR imaging of pineal cysts: implications for natural history and follow-up. *AJR Am J Roentgenol*. 2001;176:737–743.
8. Al-Holou WN, Terman S, Kilburg C, Garton HJ, Muraszko KM, Maher CO. Prevalence and natural history of arachnoid cysts in adults. *J Neurosurg*. 2013;118:222–231.
9. Boutarbouch M, El Ouahabi A, Rifi L, Arkha Y, Derraz S, El Khamlichi A. Management of intracranial arachnoid cysts: institutional experience with initial 32 cases and review of the literature. *Clin Neurol Neurosurg*. 2008;110:1–7.
10. Osborn AG, Preece MT. Intracranial cysts: radiologic-pathologic correlation and imaging approach. *Radiology*. 2006;239:650–664.
11. Altschuler EM, Jungreis CA, Sekhar LN, Jannetta PJ, Sheptak PE. Operative treatment of intracranial epidermoid cysts and cholesterol granulomas: report of 21 cases. *Neurosurgery*. 1990;26:606–613; discussion 14.
12. Yamakawa K, Shitara N, Genka S, Manaka S, Takakura K. Clinical course and surgical prognosis of 33 cases of intracranial epidermoid tumors. *Neurosurgery*. 1989;24:568–573.
13. Kaylie DM, Warren FM, Haynes DS, Jackson CG. Neurotologic management of intracranial epidermoid tumors. *Laryngoscope*. 2005;115:1082–1086.
14. Vellutini EA, de Oliveira MF, Ribeiro AP, Rotta JM. Malignant transformation of intracranial epidermoid cyst. *Br J Neurosurg*. 2014;28:507–509.
15. Ikushima I, Korogi Y, Hirai T, et al. MR of epidermoids with a variety of pulse sequences. *AJNR Am J Neuroradiol*. 1997;18:1359–1363.
16. Smirniotopoulos JG, Chiechi MV. Teratomas, dermoids, and epidermoids of the head and neck. *Radiographics*. 1995;15:1437–1455.
17. Orakcioglu B, Halatsch ME, Fortunati M, Unterberg A, Yonekawa Y. Intracranial dermoid cysts: variations of radiological and clinical features. *Acta Neurochir Wien*. 2008;150:1227–1234; discussion 34.
18. Gormley WB, Tomecek FJ, Qureshi N, Malik GM. Craniocerebral epidermoid and dermoid tumours: a review of 32 cases. *Acta Neurochir Wien*. 1994;128:115–121.
19. Cai C, Shen C, Yang W, Zhang Q, Hu X. Intraspinal neurenteric cysts in children. *Can J Neurol Sci*. 2008;35:609–615.
20. Kim CY, Wang KC, Choe G, et al. Neurenteric cyst: its various presentations. *Childs Nerv Syst*. 1999;15:333–341.
21. Khosla A, Wippold FJ. CT myelography and MR imaging of extramedullary cysts of the spinal canal in adult and pediatric patients. *AJR Am J Roentgenol*. 2002;178:201–207.
22. Truwit CL, Barkovich AJ. Pathogenesis of intracranial lipoma: an MR study in 42 patients. *AJR Am J Roentgenol*. 1990;155:855–864. discussion 65.
23. Jabot G, Stoquart-Elsankari S, Saliou G, Toussaint P, Deramond H, Lehmann P. Intracranial lipomas: clinical appearances on neuroimaging and clinical significance. *J Neurol*. 2009;256:851–855.
24. Yildiz H, Hakyemez B, Koroglu M, Yesildag A, Baykal B. Intracranial lipomas: importance of localization. *Neuroradiology*. 2006;48:1–7.
25. Neuroepithelial cyts, porencephaly and perivascular spaces. In: Thomas P, Naidich MC, Cha S, Smirniotopoulos JG, eds. *Imaging of the Brain*. Elsevier; 2013.
26. Ghatak NR, Hirano A, Kasoff SS, Zimmerman HM. Fine structure of an intracerebral epithelial cyst. *J Neurosurg*. 1974;41:75–82.
27. Guermazi A, Miaux Y, Majoulet JF, Lafitte F, Chiras J. Imaging findings of central nervous system neuroepithelial cysts. *Eur Radiol*. 1998;8:618–623.
28. Pollock BE, Huston J. Natural history of asymptomatic colloid cysts of the third ventricle. *J Neurosurg*. 1999;91:364–369.
29. Mathiesen T, Grane P, Lindgren L, Lindquist C. Third ventricle colloid cysts: a consecutive 12-year series. *J Neurosurg*. 1997;86: 5–12.
30. Ho KL, Garcia JH. Colloid cysts of the third ventricle: ultrastructural features are compatible with endodermal derivation. *Acta Neuropathol*. 1992;83:605–612.

31. Bender B, Honegger JB, Beschorner R, Ernemann U, Horger M. MR imaging findings in colloid cysts of the sellar region: comparison with colloid cysts of the third ventricle and Rathke's cleft cysts. *Acad Radiol*. 2013;20:1457–1465.
32. Isono M, Kamida T, Kobayashi H, Shimomura T, Matsuyama J. Clinical features of symptomatic Rathke's cleft cyst. *Clin Neurol Neurosurg*. 2001;103:96–100.
33. Karavitaki N, Wass JA. Non-adenomatous pituitary tumours. *Best Pract Res Clin Endocrinol Metab*. 2009;23:651–665.
34. Wen L, Hu LB, Feng XY, et al. Rathke's cleft cyst: clinicopathological and MRI findings in 22 patients. *Clin Radiol*. 2010;65:47–55.
35. Trifanescu R, Ansorge O, Wass JA, Grossman AB, Karavitaki N. Rathke's cleft cysts. *Clin Endocrinol Oxf*. 2012;76:151–160.
36. Kim JE, Kim JH, Kim OL, et al. Surgical treatment of symptomatic Rathke cleft cysts: clinical features and results with special attention to recurrence. *J Neurosurg*. 2004;100:33–40.
37. Brassier G, Morandi X, Tayiar E, et al. Rathke's cleft cysts: surgical-MRI correlation in 16 symptomatic cases. *J Neuroradiol*. 1999;26: 162–171.
38. Bonneville F, Cattin F, Marsot-Dupuch K, Dormont D, Bonneville JF, Chiras J. T1 signal hyperintensity in the sellar region: spectrum of findings. *Radiographics*. 2006;26:93–113.
39. El-Bitar MA, Choi SS, Emamian SA, Vezina LG. Congenital middle ear cholesteatoma: need for early recognition–role of computed tomography scan. *Int J Pediatr Otorhinolaryngol*. 2003;67:231–235.
40. Dubrulle F, Souillard R, Chechin D, Vaneecloo FM, Desaulty A, Vincent C. Diffusion-weighted MR imaging sequence in the detection of postoperative recurrent cholesteatoma. *Radiology*. 2006;238:604–610.
41. Burton EM, Ball WS, Crone K, Dolan LM. Hamartoma of the tuber cinereum: a comparison of MR and CT findings in four cases. *AJNR Am J Neuroradiol*. 1989;10:497–501.
42. Maixner W. Hypothalamic hamartomas–clinical, neuropathological and surgical aspects. *Childs Nerv Syst*. 2006;22:867–873.
43. Graus F, Saiz A, Dalmau J. Antibodies and neuronal autoimmune disorders of the CNS. *J Neurol*. 2010;257:509–517.
44. Lancaster E, Martinez-Hernandez E, Dalmau J. Encephalitis and antibodies to synaptic and neuronal cell surface proteins. *Neurology*. 2011;77:179–189.
45. Vincent A, Buckley C, Schott JM, et al. Potassium channel antibody-associated encephalopathy: a potentially immunotherapy-responsive form of limbic encephalitis. *Brain*. 2004;127:701–712.
46. Birnbaum J, Hellmann DB. Primary angiitis of the central nervous system. *Arch Neurol*. 2009;66:704–709.
47. Gascón-Bayarri J, Mañá J, Martínez-Yélamos S, Murillo O, Reñé R, Rubio F. Neurosarcoidosis: report of 30 cases and a literature survey. *Eur J Intern Med*. 2011;22. e125–e32.
48. Shah R, Roberson GH, Curé JK. Correlation of MR imaging findings and clinical manifestations in neurosarcoidosis. *AJNR Am J Neuroradiol*. 2009;30:953–961.
49. Smith JK, Matheus MG, Castillo M. Imaging manifestations of neurosarcoidosis. *AJR Am J Roentgenol*. 2004;182:289–295.
50. Tsutsumi Y, Kanamori H, Kawamura T, et al. Inflammatory pseudotumor of the brain following hematopoietic stem cell transplantation. *Bone Marrow Transpl*. 2005;35:1123–1124.
51. Häusler M, Schaade L, Ramaekers VT, Doenges M, Heimann G, Sellhaus B. Inflammatory pseudotumors of the central nervous system: report of 3 cases and a literature review. *Hum Pathol*. 2003;34:253–262.
52. Segawa Y, Yasumatsu R, Shiratsuchi H, et al. Inflammatory pseudotumor in head and neck. *Auris Nasus Larynx*. 2014;41:321–324.
53. Warrier R, Chauhan A, Jewan Y, Bansal S, Craver R. Rosai-Dorfman disease with central nervous system involvement. *Clin Adv Hematol Oncol*. 2012;10:196–198.
54. Sandoval-Sus JD, Sandoval-Leon AC, Chapman JR, et al. Rosai-Dorfman disease of the central nervous system: report of 6 cases and review of the literature. *Med Baltim*. 2014;93:165–175.
55. Adeleye AO, Amir G, Fraifeld S, Shoshan Y, Umansky F, Spektor S. Diagnosis and management of Rosai-Dorfman disease involving the central nervous system. *Neurol Res*. 2010;32:572–578.
56. Kazem IA, Robinette NL, Roosen N, Schaldenbrand MF, Kim JK. Best cases from the AFIP: idiopathic tumefactive hypertrophic pachymeningitis. *Radiographics*. 2005;25:1075–1080.
57. Kupersmith MJ, Martin V, Heller G, Shah A, Mitnick HJ. Idiopathic hypertrophic pachymeningitis. *Neurology*. 2004;62:686–694.
58. Friedman DP, Flanders AE. Enhanced MR imaging of hypertrophic pachymeningitis. *AJR Am J Roentgenol*. 1997;169:1425–1428.
59. La Mantia L, Curone M, Rapoport AM, Bussone G, Society IH. Tolosa-Hunt syndrome: critical literature review based on IHS 2004 criteria. *Cephalalgia*. 2006;26:772–781.
60. Lee JH, Lee HK, Park JK, Choi CG, Suh DC. Cavernous sinus syndrome: clinical features and differential diagnosis with MR imaging. *AJR Am J Roentgenol*. 2003;181:583–590.
61. Jain R, Sawhney S, Koul RL, Chand P. Tolosa-Hunt syndrome: MRI appearances. *J Med Imaging Radiat Oncol*. 2008;52:447–451.
62. Quencer RM. Lymphocytic adenohypophysitis: autoimmune disorder of the pituitary gland. *AJNR Am J Neuroradiol*. 1980;1:343–345.
63. Pisaneschi M, Kapoor G. Imaging the sella and parasellar region. *Neuroimaging Clin N Am*. 2005;15:203–219.
64. Abe T. Lymphocytic infundibulo-neurohypophysitis and infundibulo-panhypophysitis regarded as lymphocytic hypophysitis variant. *Brain Tumor Pathol*. 2008;25:59–66.
65. Given CA, Stevens BS, Lee C. The MRI appearance of tumefactive demyelinating lesions. *AJR Am J Roentgenol*. 2004;182:195–199.
66. McAdam LC, Blaser SI, Banwell BL. Pediatric tumefactive demyelination: case series and review of the literature. *Pediatr Neurol*. 2002;26:18–25.
67. Smirniotopoulos JG, Murphy FM, Rushing EJ, Rees JH, Schroeder JW. Patterns of contrast enhancement in the brain and meninges. *Radiographics*. 2007;27:525–551.
68. Cha S, Pierce S, Knopp EA, et al. Dynamic contrast-enhanced T2*-weighted MR imaging of tumefactive demyelinating lesions. *AJNR Am J Neuroradiol*. 2001;22:1109–1116.
69. Bakshi R, Wright PD, Kinkel PR, et al. Cranial magnetic resonance imaging findings in bacterial endocarditis: the neuroimaging spectrum of septic brain embolization demonstrated in twelve patients. *J Neuroimaging*. 1999;9:78–84.
70. Yen PT, Chan ST, Huang TS. Brain abscess: with special reference to otolaryngologic sources of infection. *Otolaryngol Head Neck Surg*. 1995;113:15–22.
71. Brouwer MC, Coutinho JM, van de Beek D. Clinical characteristics and outcome of brain abscess: systematic review and meta-analysis. *Neurology*. 2014;82:806–813.
72. Cunha BA. Central nervous system infections in the compromised host: a diagnostic approach. *Infect Dis Clin North Am*. 2001;15:567–590.
73. Ratnaike TE, Das S, Gregson BA, Mendelow AD. A review of brain abscess surgical treatment–78 years: aspiration versus excision. *World Neurosurg*. 2011;76:431–436.
74. Chang SC, Lai PH, Chen WL, et al. Diffusion-weighted MRI features of brain abscess and cystic or necrotic brain tumors: comparison with conventional MRI. *Clin Imaging*. 2002;26:227–236.
75. Hatipoglu HG, Gurbuz MO, Sakman B, Yuksel E. Diffusion-weighted magnetic resonance imaging in rhombencephalitis due to Listeria monocytogenes. *Acta Radiol*. 2007;48:464–467.
76. Sarrazin JL, Bonneville F, Martin-Blondel G. Brain infections. *Diagn Interv Imaging*. 2012;93:473–490.
77. Levitz RE. Herpes simplex encephalitis: a review. *Heart Lung*. 1998;27:209–212.
78. Li JC, Mahta A, Kim RY, Saria M, Kesari S. Cerebral syphilitic gumma: a case report and review of the literature. *Neurol Sci*. 2012;33:1179–1181.
79. Linfante I, Llinas RH, Caplan LR, Warach S. MRI features of intracerebral hemorrhage within 2 hours from symptom onset. *Stroke*. 1999;30:2263–2267.

80. Pinker K, Stavrou I, Knosp E, Trattnig S. Are cerebral cavernomas truly nonenhancing lesions and thereby distinguishable from arteriovenous malformations? MRI findings and histopathological correlation. *Magn Reson Imaging*. 2006;24:631–637.
81. Geibprasert S, Pongpech S, Jiarakongmun P, Shroff MM, Armstrong DC, Krings T. Radiologic assessment of brain arteriovenous malformations: what clinicians need to know. *Radiographics*. 2010;30:483–501.
82. Hacein-Bey L, Provenzale JM. Current imaging assessment and treatment of intracranial aneurysms. *AJR Am J Roentgenol*. 2011;196:32–44.
83. Haidar S, Ortiz-Neira C, Shroff M, Gilday D, Blaser S. Intracranial involvement in extramedullary hematopoiesis: case report and review of the literature. *Pediatr Radiol*. 2005;35:630–634.
84. Lee CM, Salzman KL, Blumenthal DT, Gaffney DK. Intracranial extramedullary hematopoiesis: brief review of response to radiation therapy. *Am J Hematol*. 2005;78:151–152.
85. Gandhi D, Wee R, Goyal M. CT and MR imaging of intracerebral amyloidoma: case report and review of the literature. *AJNR Am J Neuroradiol*. 2003;24:519–522.
86. Chao ST, Ahluwalia MS, Barnett GH, et al. Challenges with the diagnosis and treatment of cerebral radiation necrosis. *Int J Radiat Oncol Biol Phys*. 2013;87:449–457.
87. Castellano-Sanchez AA, Li S, Qian J, Lagoo A, Weir E, Brat DJ. Primary central nervous system posttransplant lymphoproliferative disorders. *Am J Clin Pathol*. 2004;121:246–253.

CHAPTER

54

Neuroimaging Issues in Assessing Response to Brain Tumor Therapy

Brendan J. McCullough[2,3,4], *John W. Henson*[1]

[1]Piedmont Brain Tumor Center, Atlanta, GA, USA; [2]Radia Inc., Lynwood, WA, USA; [3]Swedish Neuroscience Institute, Seattle, WA, USA; [4]Department of Health Services, University of Washington, Seattle, WA, USA

IMAGING APPEARANCE OF GLIOMAS OF THE ADULT CEREBRAL HEMISPHERES

Primary brain tumors of the adult cerebral hemisphere are primarily composed of diffusely infiltrating astrocytomas. These tumors are remarkable for the degree to which their magnetic resonance imaging (MRI) characteristics reflect their histopathologic features (Figure 1). In general, diffusely infiltrating fibrillary astrocytomas are hypointense on T1-weighted images (T1WIs) and hyperintense on T2-weighted (T2WI) or fluid-attenuated inversion recovery (FLAIR) images. Mildly restricted diffusion is said to reflect increased cellularity. Susceptibility artifact may be seen with old hemorrhage or less often with mineralization. Enhancement is present when the blood–brain barrier (BBB) is not effective at containing gadolinium contrast material within the vasculature.

Low-grade diffuse astrocytomas (LGAs; World Health Organization (WHO) grade II) are generally homogeneous in appearance with mild expansion of the affected parenchyma, reflecting mildly increased cellularity. Gray and white matter are involved with tumor, and thus the junction becomes indistinct. Although these tumors often appear well circumscribed, neoplastic cells generally infiltrate the adjacent normal-appearing brain. There is no enhancement with gadolinium-based contrast agents, indicative of an intact BBB. Relative cerebral blood volume (rCBV) is normal or mildly elevated, reflecting the absence of significant angiogenesis.

Anaplastic astrocytomas (AAs; WHO grade III) typically demonstrate greater mass effect than LGAs because of their relatively increased cellular proliferation. Margins are more blurred and the tumor may appear grossly infiltrative. Contrast enhancement is common, but 30–50% will not enhance.[1] The risk of high-grade histopathology in a nonenhancing astrocytoma rises with age, such that by 45 years of age, the likelihood of finding high-grade tumor is 50%.[2] Enhancement reflects an absent or ineffective BBB and is also associated with microvascular angiogenesis. When enhancement is present, it is typically focal or patchy and rarely ringlike. Angiogenesis also results in increased rCBV. Enhancement and elevated rCBV are both associated with increased risk of early recurrence and shortened survival.[1,3] Relative CBV may vary throughout the tumor; as such, rCBV maps have been used to predict regions of tumor with the highest grade to guide stereotactic biopsy.[4] Vasogenic edema may or may not be present.

Glioblastoma multiforme (GBM; WHO grade IV) generally demonstrates a thick, peripheral ring of enhancing tumor with a central necrotic core. Intratumoral hemorrhage and calcification are common and further contribute to a heterogeneous appearance. Tumor cells have a higher nuclear-to-cytoplasm ratio than LGAs, resulting in lower T2 signal and mildly restricted diffusion on diffusion-weighted imaging (DWI). The enhancing component of the tumor typically has significantly elevated rCBV, indicative of angiogenesis. There is surrounding, poorly circumscribed hyperintensity on T2WI/FLAIR due to infiltrative tumor and vasogenic edema. Angiogenesis is often present within this infiltrative component, resulting in moderately elevated rCBV, reflecting the mixture of tumor and normal cells.

Oligodendrogliomas are nonastrocytic glial neoplasms that follow GBM and AA in prevalence. These tumors are commonly peripherally based, resulting in infiltration and expansion of the cortex. Unlike astrocytomas, low-grade oligodendrogliomas demonstrate coarse

http://dx.doi.org/10.1016/B978-0-12-800945-1.00054-9
© 2016 Elsevier Ltd. All rights reserved.

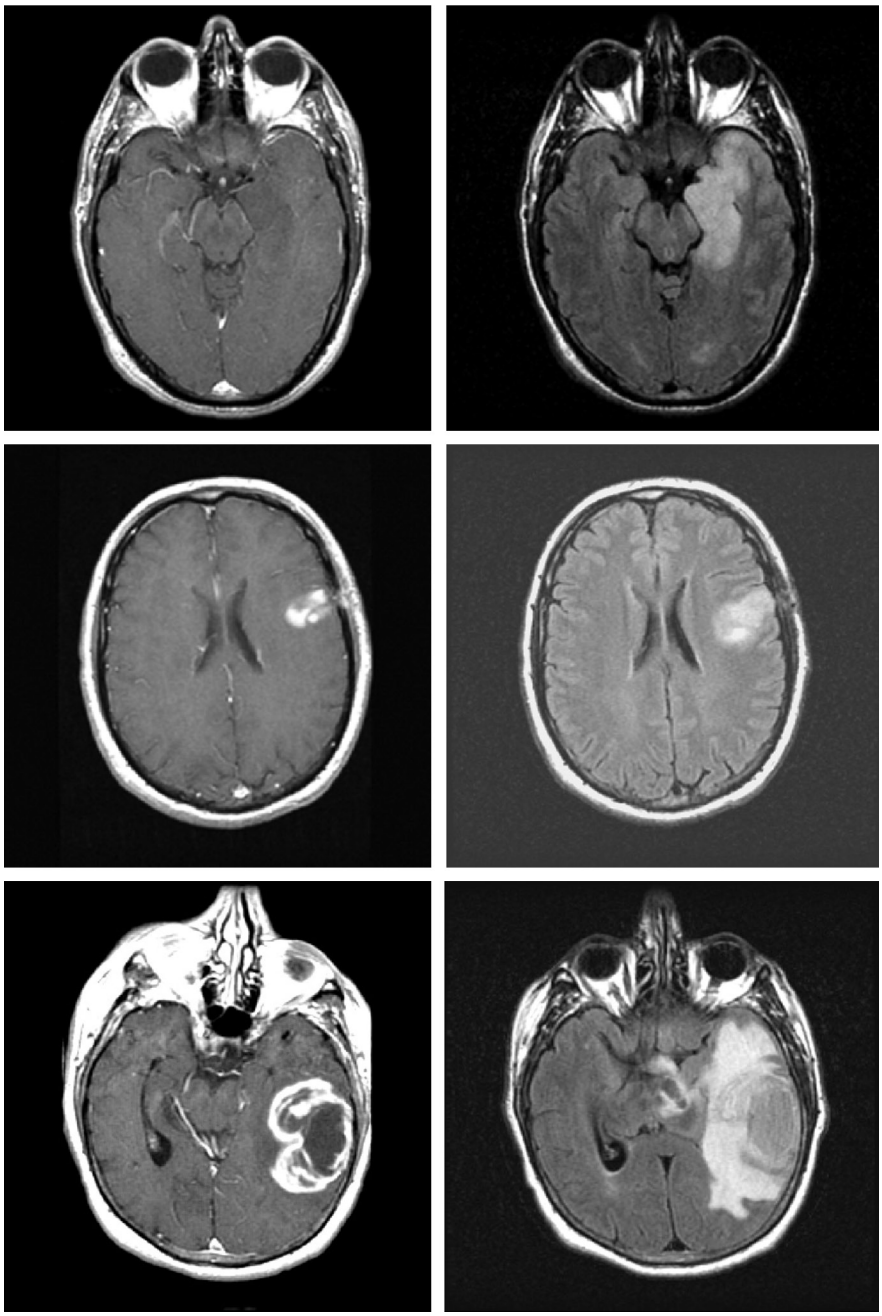


FIGURE 1 Imaging findings of astrocytomas reflect the histopathological features of these tumors. Comparison of the imaging findings in low-grade astrocytoma (top row), anaplastic astrocytoma (middle row), and glioblastoma multiforme (bottom row). The left column shows axial gadolinium-enhanced T1WIs and the right column shows FLAIR images. See the text for discussion of the correlation between imaging features of these tumor grades and histological findings.

calcification (70–90%), enhancement (50%), cystic degeneration (20%), and occasionally hemorrhage, all contributing to a heterogeneous appearance. These tumors may also be quite vascular, resulting in significantly elevated rCBV despite low-grade histological and more benign clinical features. Therefore, enhancement does not carry the same negative implication for oligodendrogliomas as for diffuse astrocytoma. This difference is even more extreme with the benign and strongly enhancing pilocytic astrocytoma, and thus enhancement must be interpreted through the lens of histopathology. For the purposes of measuring tumors during clinical trials, therefore, it is easy to see that enhancement is a complicated feature.

Oligoastrocytomas comprise a mixed population of tumor cells resembling an oligodendroglioma and

fibrillary astrocytoma. The mixed histopathological appearance is reflected in mixed imaging features leading to a nonspecific appearance. Anaplastic variants of oligodendrogliomas and oligoastrocytomas also cannot be reliably distinguished from low-grade lesions by imaging. However, surrounding vasogenic edema, intratumoral hemorrhage, and cystic degeneration tend to be greater with higher-grade lesions.

EVOLUTION OF DIFFUSE GLIOMAS IN ADULTS

Diffusely infiltrating gliomas have a well-known tendency to become more histologically anaplastic and clinically aggressive over time, evolving toward glioblastoma.[5–7] This evolution is called anaplastic progression and results from a stepwise accumulation of genetic alterations within tumor cells. Although the true incidence of anaplastic progression is difficult to determine, approximately 50% of LGAs undergo radiographic changes consistent with anaplastic progression, while the remainder show gradual growth presumably as low-grade lesions.[7] In one study of 19 consecutive patients undergoing reoperation for low-grade glioma, histopathological analysis showed evidence of progression in 58% of tumors.[8] New enhancement was present on the preoperative MRI in 10 of 11 (91%) of those with progression and in one of eight (13%) without progression. Additionally, anaplastic progression of an LGA to a high-grade lesion is also more rapid in older patients.[9]

Glioblastoma arising from an LGA is termed "secondary glioblastoma." Although histologically and radiographically indistinguishable from de novo, or primary, glioblastoma, there are important genetic and clinical differences between the two, suggesting they arise from distinct pathways. From a genetic perspective, epidermal growth factor receptor overexpression is commonly identified in primary glioblastoma (40–60%) and is associated with a more aggressive tumor phenotype.[10,11] Isocitrate dehydrogenase mutations, conversely, are more commonly seen in lower-grade gliomas and secondary glioblastomas compared to primary glioblastomas (70–80% vs 5–10%, respectively).[12] These mutations are associated with a more favorable prognosis. Clinically, primary glioblastomas typically arise in older adults (peaking in the seventh to eighth decades). Secondary glioblastomas tend to occur in younger patients (peaking one to two decades earlier), reflecting the younger age of diagnosis of the precursor lower-grade glioma. Survival is also longer in younger patients with glioblastoma, probably reflecting a slower course with secondary glioblastoma.

IMAGING DIFFUSE GLIOMAS FOLLOWING DIAGNOSIS AND TREATMENT

Low-Grade Gliomas

Despite classical literature to the contrary, low-grade gliomas are not stable. Growth occurs as gradual enlargement of nonenhancing, T2/FLAIR hyperintensity on MRI. For example, serial imaging of 27 untreated WHO grade II tumors demonstrated that tumor diameter increased an average of 4 mm per year.[13] Furthermore, tumor infiltration generally extends beyond the signal abnormality evident on MRI. As such, the "watch and wait" paradigm has largely been abandoned in favor of early, maximal safe resection.

Following surgery, the role of imaging is first to determine the extent of resection (EOR). EOR has repeatedly been shown to be associated with improved overall survival.[10] This is true for gross total resection compared to debulking surgery, but even in patients with subtotal resection the amount of residual tumor is inversely correlated with overall survival.[14] Since this risk is potentially modifiable, reoperation should be considered if substantial residual disease could be safely removed. Furthermore, extended or "supratotal" resection has been suggested to improve outcomes over standard, gross total resection.[15] Presumably this addresses tumor cells that extend beyond the margins evident on imaging.

Although controversial, adjuvant treatments such as chemotherapy and radiotherapy are generally not employed with low-grade gliomas following resection unless there are risk factors for early progression or malignant transformation. Risk factors include increased age, subtotal or partial resection, and rapid early progression following surgery. Radiotherapy has also been shown to be beneficial for treating intractable seizures that may limit quality of life.

After surgical resection, the rationale behind serial imaging surveillance is the early detection of tumor progression. As mentioned above, progression of low-grade gliomas during the premalignant phase is slow, necessitating long-term comparison. Figure 2 illustrates this pattern of growth in a patient with a left frontal low-grade oligoastrocytoma who reported increasing severity of the seizures affecting language function. Compared to the recent prior study, there was no change evident to explain the patient's clinical deterioration. However, comparison to an earlier, baseline study revealed a clear, gradual increase in tumor size. This observation provided a reasonable radiographic basis for understanding the clinical progression, and the patient was begun on oral chemotherapy with subsequent improvement in her symptoms. Thus, it is of utmost importance to compare each new MRI study

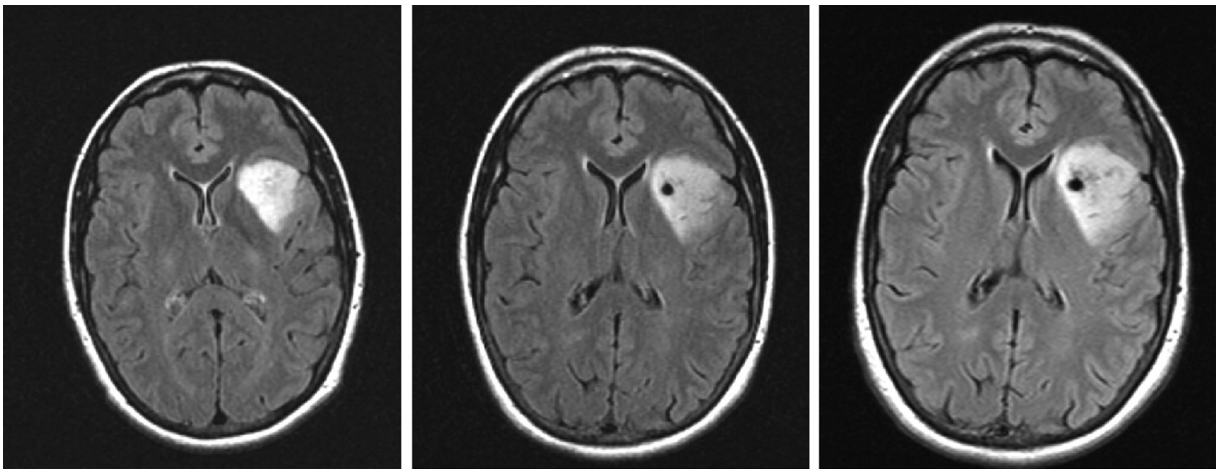


FIGURE 2 Gradual growth of an untreated low-grade oligoastrocytoma over a 4-year interval (left image in 1999 at diagnosis, middle image in 2002, and right image in 2003). Comparison of axial FLAIR images reveals slow enlargement of the tumor. The patient's seizures began to worsen in 2003. Mandonnet and coworkers (2003) showed that untreated low-grade oligodendrogliomas enlarge about 4 mm in cross-sectional diameter each year.

with prior studies over as long a period as possible to detect the presence of gradual interval growth that could escape detection if comparison is limited to the most recent prior examination.

Patients with low-grade gliomas may receive treatment when their tumors show growth or when there are symptoms, such as poorly controlled seizures, that might benefit from therapy. Treatment may consist of involved field irradiation or chemotherapy without irradiation. In these patients "response" of the tumor may consist of shrinkage of the lesion or stabilization of size, with or without decrease in target symptoms (e.g., decrease in seizure frequency). Clinical experience indicates that stabilization is the most common form of response. When shrinkage does occur in LGAs or low-grade oligodendrogliomas it is usually minor in degree (i.e., insufficient to qualify for a partial response as defined below) and is often apparent only after 1 year or more following initiation of therapy.

In the case of anaplastic progression within low-grade gliomas, a new focus of rapidly growing, contrast-enhancing tumor appears within an existing, nonenhancing mass. These patients are treated aggressively with irradiation and chemotherapy at the time progression is recognized. The imaging considerations regarding assessment of treatment responses in these patients are the same as those described below for high-grade gliomas.

High-Grade Gliomas

Patients who are diagnosed with high-grade gliomas (WHO grade III and IV) are usually treated with maximal resection followed by a combination of involved field irradiation and chemotherapy. Immediate postoperative imaging is performed to identify residual enhancing disease as a prognostic marker or potentially as an indication for reoperation.

Imaging may also identify new areas of restricted diffusion presumably due to ischemic injury (infarct) during surgery. This infarcted tissue will enhance on subsequent exams, usually evolving to nonenhancing encephalomalacia within 3 months, although prolonged enhancement has been described for up to 6 months in this context.[16]

On surveillance imaging, stability in the size of the tumor is the most common outcome with treatment, especially with astrocytomas. As such, radiographic outcomes are generally measured as "progression-free survival" (further discussed below). Shrinkage is common only with anaplastic oligodendrogliomas with the 1p/19q codeletion, in which case it is often seen within 3 months of initiation of therapy (Figure 3). Shrinkage may occur in the size of nodular enhancing disease and in the area of hyperintense T2-weighted signal. Tumor cysts often do not change in size even when the surrounding tumor is shrinking. The size of the enhancing component is often seen to decrease with the introduction of antiangiogenic therapies (e.g., bevacizumab), but this may represent changes in contrast permeability rather than true response (further discussed below).

As practitioners of neuro-oncology are acutely aware, the vast majority of high-grade gliomas demonstrate progressive enlargement within months of diagnosis. Progression most often is declared when there is enlargement of one or more enhancing nodules within the tumor or appearance of a new nodular area of enhancement either locally at the tumor margin or distantly elsewhere in the brain. In the early months following chemoradiation, pseudoprogression should also be considered (further discussed below). Increase in the extent

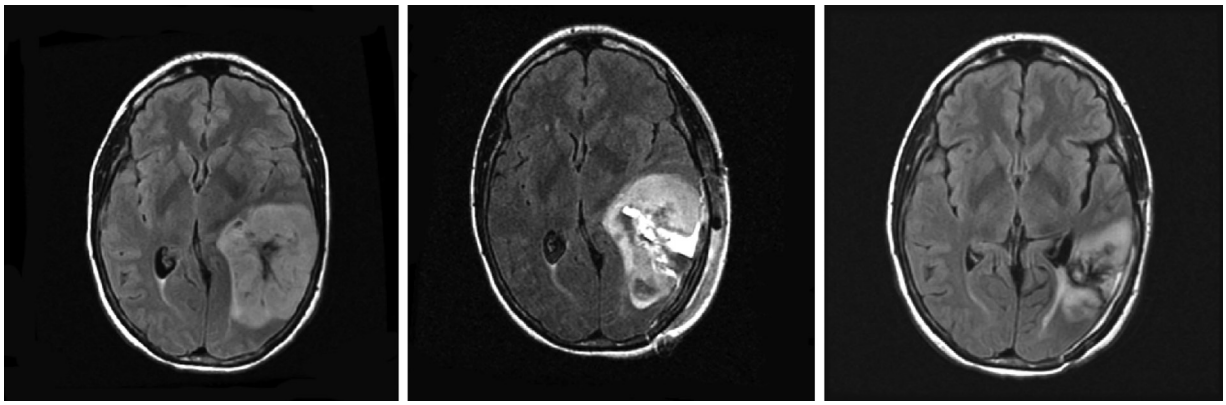


FIGURE 3 Marked shrinkage of brain tumors is commonly seen only with 1p– anaplastic oligodendrogliomas and primary central nervous system lymphomas. In this example, a 1p– anaplastic oligodendroglioma involuted following three cycles of oral chemotherapy without irradiation. The left image is preoperative, the middle image was taken following a subtotal resection, and the right image was taken following three monthly cycles of oral chemotherapy with temozolomide.

of hyperintensity on T2/FLAIR sequences is nonspecific and could represent treatment effects or progression of infiltrative disease. In patients receiving antiangiogenic therapy, progression may not be evident on contrast-enhanced scans and may be detectable only on T2/FLAIR or diffusion-weighted sequences. Increases in the size of a tumor cyst and the appearance of hemorrhage when there is stability of the remainder of the lesion do not qualify as tumor progression.

RELATED ISSUES

Pseudoprogression

In the era of radiotherapy with concurrent temozolomide (i.e., Stupp protocol) as the standard of care for high-grade glioma treatment,[17] enhancement concerning for early progressive disease is observed in approximately 50% of patients most commonly within 90 days, but up to 6 months, following the end of radiation. Of those, the enhancement will regress or stabilize in approximately 40% without a change in treatment, a finding that is not consistent with progressive disease.[18] On histopathological analysis, the enhancing tissue shows inflammation and necrosis without active tumor.[19] This phenomenon has been termed pseudoprogression and is believed to be the imaging manifestation of increased permeability of the BBB from radiotherapy and potentiated by chemotherapy. The enhancement may be accompanied by increased vasogenic edema and clinical deterioration. Pseudoprogression has been shown to be associated with methylated methylguanine methyltransferase (MGMT) promoter[20] and increased overall survival.[21]

Pseudoprogression is indistinguishable from early progressive disease on conventional MRI. Advanced imaging techniques, most notably measurements of rCBV,[22] have demonstrated statistically significant differences, but values overlap between groups limiting sensitivity and specificity. Permeability is being studied as a distinguishing feature. Lesions outside the high-dose radiation field are not considered for pseudoprogression. For the time being, however, serial imaging and biopsy are the key diagnostic studies. Unfortunately, pseudoprogression may worsen on one or more serial 4-week interval scans before showing improvement. This can make the diagnosis of pseudoprogression difficult. Exclusion of patients from clinical trials with early worsening could lead to a bias for either improved (pseudoprogression) or worsened (early true progression) survival.

Angiogenesis Inhibitors

Angiogenesis inhibitors, most notably bevacizumab (Avastin; Genentech, South San Francisco, CA, USA), are a relatively new class of drugs intended to disrupt tumor neovascularity. Bevacizumab is a monoclonal antibody targeting vascular endothelial growth factor A.

On imaging, bevacizumab results in marked reduction in the volume and intensity of tumor enhancement as early as 1–2 days after treatment initiation (Figure 4). This is believed to be due to decreased permeability (normalization) of the BBB rather than true antitumoral effects. As such, this effect has been termed pseudoresponse. Decreased vasogenic edema and mass effect, along with marked clinical improvement, are also commonly seen.

A pattern of gliomatosis cerebri can be seen in patients receiving bevacizumab. This may be accompanied by gradual deterioration of cognitive function and gait. There is some evidence that bevacizumab may increase the risk of aggressive infiltration.[23]

In phase III clinical trials of bevacizumab administered at the time of diagnosis, median progression-free

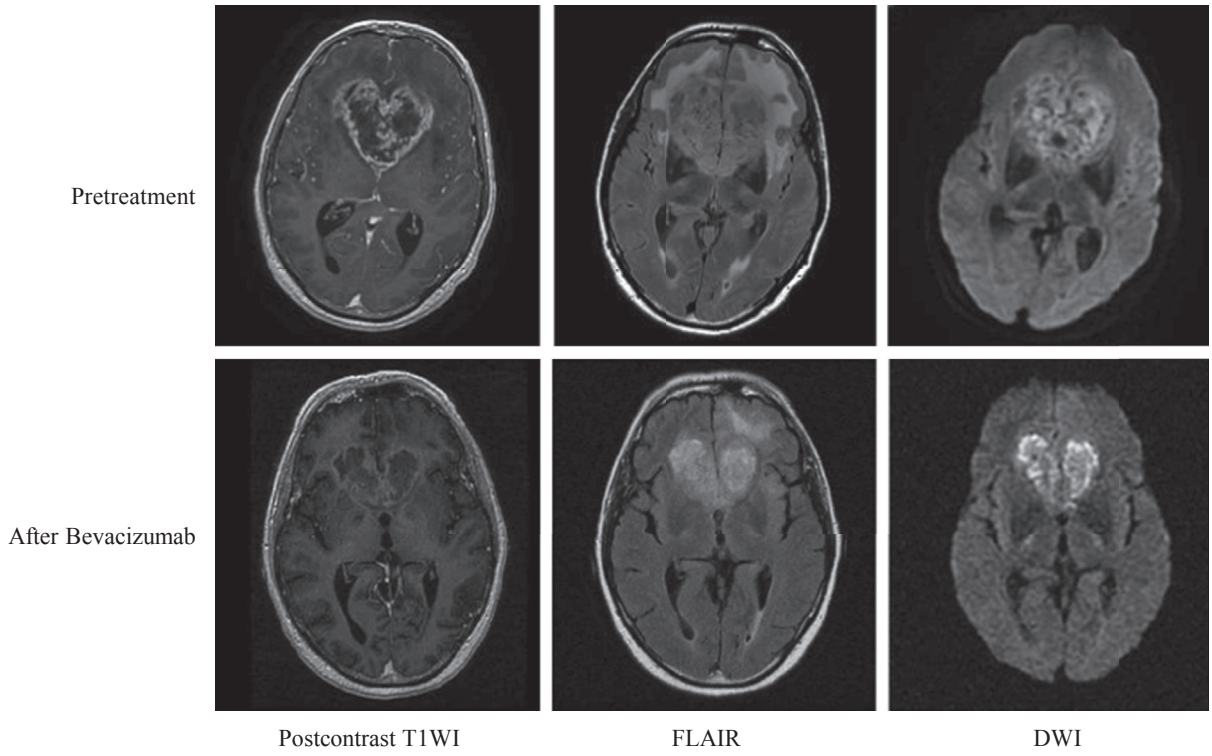


FIGURE 4 Bevacizumab commonly results in marked radiographic response in tumors. In this example, pretreatment MRI shows an avidly enhancing, "butterfly" glioblastoma with marked surrounding infiltrative edema on FLAIR sequence (top row). Following institution of bevacizumab therapy, enhancement is nearly absent, tumor size is decreased, and surrounding infiltrative edema is greatly reduced (bottom row). Tumor often becomes more prominent on DWI, which may be the most useful sequence for monitoring tumor stability on subsequent scans.

survival (PFS) was approximately 10 months.[24,25] However, there is variability in the appearance of progression on imaging. Progression may be evident as the return and enlargement of enhancing tumor or it may be evident only as expanding, nonenhancing tumor on FLAIR or diffusion-weighted images.[26] Additionally, there is evidence suggesting the pattern of response is predictive of overall survival.[27] Bevacizumab did not improve overall survival, compared to radiation and temozolomide alone.

USE OF IMAGING IN CLINICAL TRIALS

Enormous effort has been put into clinical trials of new agents for malignant gliomas. A new drug or treatment is evaluated using the standard three-phase design.[28] Phase I studies are intended to evaluate the safety of a new drug or treatment and to determine the maximal tolerated dose. Phase II studies continue to evaluate safety but they are also designed to examine the efficacy of the new treatment in a limited number of patients. Phase III studies are intended to establish the efficacy of the new therapy in the context of current therapies using a large sample of patients.

Survival is considered the gold standard of efficacy in the evaluation of new cancer therapies. Phase III clinical trials, therefore, employ this measure as their primary endpoint and do not rely heavily on imaging. Phase II studies, however, utilize imaging as a surrogate measure of survival to more quickly evaluate new therapies in order to recommend promising ones for definitive, phase III trials. Additionally, phase II studies are usually performed in patients with progressive tumors. Any survival measurement would be complicated by the administration of prior therapy or any subsequent salvage therapy.

Imaging, however, is an indirect measure of the cellular response to therapy. Contrast enhancement reflects disruption of the BBB, making it an indirect marker of malignancy. Signal abnormality on T2/FLAIR sequences may be due to the different water contents of tumor cells themselves compared to normal parenchyma (greater or less), or it may be the manifestation of acute and chronic changes elicited by the tumor, treatments, or a combination of the two. Standardization of imaging evaluation has therefore evolved over time, following the lead of general oncology but adapting to the unique features of the central nervous system.

QUANTIFICATION OF TUMOR RESPONSE BY IMAGING

Macdonald Criteria

The modern system of imaging evaluation of tumors in phase II neuro-oncology clinical trials was established by the publication of the so-called Macdonald criteria in 1990.[29] The goal of this publication was to establish uniform measurement and response criteria for malignant gliomas in clinical trials.

Similar to existing criteria in general oncology at the time, the Macdonald criteria (Table 1) primarily evaluate response by the change in size of the enhancing tumor. The measurement is defined as the product of the largest perpendicular diameters of enhancement on serial, cross-sectional imaging. However, Macdonald criteria also consider concurrent corticosteroid use and changes in neurological status. Corticosteroids may decrease the size of the tumor on imaging and can improve clinical signs and symptoms irrespective of the therapy being evaluated. Neurological symptoms may not improve with successful therapy (i.e., "fixed deficits"), but unequivocal neurological deterioration could be indicative of treatment failure regardless of imaging changes.

The Macdonald criteria divide response to therapy into four categories (Table 2): Complete response (CR) is the disappearance of all enhancing tumor on scans at least 1 month apart in a neurologically stable or improved patient not on corticosteroids. Partial response (PR) requires ≥50% reduction in the size of the tumor in a neurologically stable or improved patient. The patient can be on corticosteroids, but the dose must not be increasing. Progressive disease (PD) is ≥25% increase in the size of the enhancing tumor or new enhancing tumor. Neurological deterioration with stable or increasing steroid requirements also counts as PD. Stable disease (SD) is defined as not meeting the above conditions.

TABLE 1 Comparison of Measurement Techniques between Response Criteria

	Macdonald	RECIST	RANO
Enhancement	Product of bidirectional measurements	Unidirectional diameter	Product of bidirectional measurements
Minimum size	Not specified	10 mm	10 mm
Multiple lesions	Not specified	Sum of diameters	Sum of products
FLAIR	Not considered	Not considered	Considered, but qualitative assessment
Corticosteroids	Considered	Not considered	Considered
Neurological status	Considered	Not considered	Considered
Other			No enrollment within 12 weeks of chemoradiation

TABLE 2 Comparison of Response Assessment between Criteria

	Macdonald	RECIST	RANO
Complete response	• Complete disappearance of enhancing lesion. • No new lesions. • No corticosteroids. • Clinically stable or improved.	• Complete disappearance of enhancing lesions. • No new lesions.	• Complete disappearance of enhancing lesions. • No new lesions. • Stable or improved nonenhancing FLAIR lesion. • No corticosteroids. • Clinically stable or improved.
Partial response	• ≥50% decrease in size of enhancing lesion. • No new lesions. • Stable or reduced corticosteroids. • Clinically stable or improved.	• ≥30% decrease in size of enhancing lesions. • No new lesions.	• ≥50% decrease in size of enhancing lesions. • No new lesions. • Stable or improved nonenhancing FLAIR lesion. • Stable or reduced corticosteroids. • Clinically stable or improved.
Stable disease	Not meeting other criteria.	Not meeting other criteria.	Not meeting other criteria.
Progressive disease	• ≥25% increase in size of enhancing lesion. • New lesions. • Clinical deterioration.	• ≥20% increase in size of enhancing lesions. • New lesions.	• ≥25% increase in size of enhancing lesions. • New lesions. • Significantly increased nonenhancing FLAIR lesion. • Clinical deterioration.

There are important limitations to the Macdonald criteria. Lesions are often irregularly shaped or surround a resection cavity, making reproducible measurements of disease challenging and hence limiting interobserver agreement. Strict rules for measurement of enhancing lesions were not given (e.g., diameters that include cystic, necrotic, or hemorrhagic areas). A minimum lesion size was not defined. Nonenhancing tumor is not considered, and therefore low-grade gliomas that typically do not show contrast enhancement cannot be assessed. Multifocal disease is not considered. Enhancement may be a less reliable indicator of disease in the context of antiangiogenic agents, most notably bevacizumab. Finally, there is no provision for pseudoprogression and pseudoresponse.

RESPONSE EVALUATION CRITERIA IN SOLID TUMORS

Since the publication of the Macdonald criteria, general oncology has largely adopted the Response Evaluation Criteria in Solid Tumors (RECIST) and subsequent revision (RECIST 1.1) as the standard response criteria for clinical trials.[30,31] RECIST differs from the Macdonald criteria in the following ways (Table 1): Lesion measurements are one-dimensional (maximum diameter of enhancement); target lesions must have a minimum diameter (10 mm by CT or MRI); multiple target lesions are considered (up to five), and the sum of their maximum diameters is followed as a measure of overall disease burden; nontarget, "immeasurable" disease is considered on a qualitative basis; and evaluation is limited to imaging data—clinical status and medications, such as corticosteroid use, are not considered. RECIST categorizes responses as CR, PR, PD, and SD in a manner similar to the Macdonald criteria with minor differences (Table 2). RECIST has been shown to have good concordance with bidirectional measurements and Macdonald criteria in high-grade glioma trials,[32–34] but it has not achieved widespread use in glioma trials.

RESPONSE ASSESSMENT IN NEURO-ONCOLOGY

More recently, the Response Assessment in Neuro-Oncology (RANO) working group published criteria (Table 1) intended to draw on preexisting criteria but to address their shortcomings.[35] As with the Macdonald criteria, lesions are scored as the product of bidirectional, perpendicular diameters of the enhancing component of the tumor. Corticosteroid use and neurological status are considered in the same way. Drawing from RECIST, lesions must have diameters of at least 10 mm to be considered measurable. When there are multiple lesions, the products of bidirectional diameters are summed together as a measure of overall disease burden. Lesion measurements must not include the resection cavity or cystic components. RANO criteria add additional requirements. Nonenhancing, T2/FLAIR hyperintense progression is also considered, but the writers left out specific criteria as to what constitutes nonenhancing progression, acknowledging that progressive disease, radiation effects, and decreased steroid dose, as well as other factors, can all have a similar appearance. To avoid confusing pseudoprogression with true early progression, they advocate excluding patients from trials for progressive disease until at least 12 weeks after radiation therapy (unless the progression is clearly outside of the radiation field or progression is proven by histopathology).

RESPONSE AS A SURROGATE FOR SURVIVAL

Progression-Free Survival

CR and PR are seen only in approximately 10% of patients with newly diagnosed malignant gliomas[34] and probably even less in patients with progressive disease. As a result, phase II clinical trials typically measure the duration of SD as PFS. The percentage of patients with PFS at a defined time of 6 or 12 months (PFS6 and PFS12, respectively) is then compared to historical controls or less often to a control group within the study.

There are advantages and disadvantages to using PFS in phase II trials. PFS (particularly PFS6) allows a decision to be made about the potential efficacy of a new treatment in a relatively time-efficient manner. Using a defined 6- or 12-month interval limits time-dependent assessment variation seen with "time-to-progression" outcome measures and provides a standardized measure for comparing results with historical data, mitigating the need for a concurrent, control treatment group. However, PFS primarily measures SD, a weaker biological effect than tumor shrinkage. Furthermore, using historical controls adds additional, potentially unmeasured differences between the treatment and the control groups that limit the validity of the comparison. PFS can be used with difficulty in studies of angiogenesis inhibitors.

Radiographic Response as a Surrogate for Overall Survival

The use of radiographic response in clinical trials assumes that it is a valid surrogate measure for overall survival. Past phase II and III trials provide a window through which to evaluate this assumption.

Overall, PFS has proven to be a strong predictor of overall survival. PFS6, the most commonly used measure, was shown to be significantly associated with overall survival in patients with primary glioblastoma

($n = 1348$), recurrent WHO grade III glioma ($n = 159$), and recurrent glioblastoma ($n = 345$ and 437 in different studies) using pooled data from multiple clinical trials.[36,37] PFS as a time-dependent marker for overall survival had a hazard ratio of 16.2 (95% confidence interval: 13.2–19.8) in newly diagnosed glioblastoma, indicating a strong relationship between progression on imaging and shorter survival. Ballman et al. also performed a simulation study to determine how often study decisions based on PFS6 results would predict decisions made by overall survival at 12 months and found agreement in 88% of cases. Additionally, clinical trials in anaplastic oligodendroglioma and AA have shown that radiographic response correlates with overall survival.[38,39]

Radiographic response is imperfect as a surrogate for survival in glioma trials, however. First, although pooled data present a convincing picture of agreement between PFS and overall survival, individual trials may be outliers. The best-described example is that of bevacizumab. Two separate phase II clinical trials in patients with recurrent glioblastoma demonstrated significantly improved rates of PFS6.[40,41] Subsequent phase III randomized controlled trials in patients with newly diagnosed glioblastoma again showed significantly improved PFS with bevacizumab compared to placebo, but overall survival was not improved.[24,25] The most likely explanation for the discrepancy with prior studies is the marked difficulty of measuring progression in patients on bevacizumab.

Second, radiographic response (CR and PR) has been shown to be a poor predictor of survival. Lamborn et al. separated patients with recurrent WHO grade III and IV glioma based on radiographic response according to the Macdonald criteria.[37] There was no significant association between radiographic response (CR or PR) and survival in this sample. However, the number of patients with radiographic response was low for both grade III (14 patients; 9%) and grade IV (30 patients; 7%) tumors, limiting statistical power to detect a difference. Grant et al. also failed to demonstrate an association between radiographic response and survival in 136 patients with malignant glioma.[42] However, in both of these examples, PFS was predictive of survival.

TECHNICAL ASPECTS OF MEASURING RESPONSE AND PROGRESSION

Although the problems discussed above represent limitations for clinical trials of new brain tumor therapies, neuroimaging is still the best available tool for evaluating response in the phase II setting. Currently, MRI is the mainstay of diagnostic neuroimaging. CT is a valuable tool for triaging patients with acute clinical changes, but MRI is far more sensitive for evaluation of underlying pathology.

Technical Considerations

The sequences performed as part of the MRI protocol must be carefully chosen to best evaluate the pathology of interest while minimizing the time required. Long exams are more likely to suffer from motion artifact as patients tire of being in the scanner and holding still. The technical parameters of the sequences, slice and skip thicknesses, contrast type and dose, and even the order in which sequences are acquired can all alter the appearance of lesions, necessitating standardization for all participants in a trial and across sites.

Measurements of pathological lesions are most commonly based on axial postcontrast images. Traditionally, 5 mm, skip 0 mm spin echo-based T1WIs have been used (leading to minimal lesion diameters of 10 mm, or twice the slice thickness, in RANO and RECIST criteria). However, three-dimensional (3D) gradient recalled echo-based T1-weighted sequences with isotropic voxel acquisitions of approximately 1 mm^3 have become commonly available. These offer superior spatial resolution, minimizing the effects of volume averaging over the slice thickness, although at the cost of slightly reduced contrast resolution. These sequences are optimal for clinical trials.

Postcontrast sequences should be performed at a specified interval following contrast administration for each exam and at least 5 min after injection. Since enhancement is dependent on contrast leakage across the disrupted BBB, gradual accumulation of contrast material and increased enhancement may be seen on successive acquisitions. Other sequences not affected by gadolinium contrast (e.g., T2WI) can be performed immediately following contrast administration to optimize scanner utilization. Intervening sequences also help to maintain consistency of the postcontrast interval.

Computer-Aided Volumetric Analysis

Current gradient-echo-based MRI sequences allow high-resolution, 3D acquisitions. This technology lends itself to semiautomated volumetric measurements in which the user selects lesions on axial postcontrast T1WI and the computer automatically calculates a 3D volume (Figure 5). There are several advantages to this technique. First, it is more sensitive for the detection of early progression, especially with smaller lesions.[43,44] Second, intra- and interobserver reliability is excellent. Third, it is ideal for complex lesions with cystic or necrotic components or lesions along resection cavity margins because the volume measurement can be limited to the enhancing portions.

There are drawbacks with automated volumetric analysis. The radiologist must check the perimeter determined by the software for accuracy, adding a degree of subjectivity, potential error, and time. T1-hyperintense blood products and enhancing infarct are difficult to exclude from the automated analysis and may add further error.

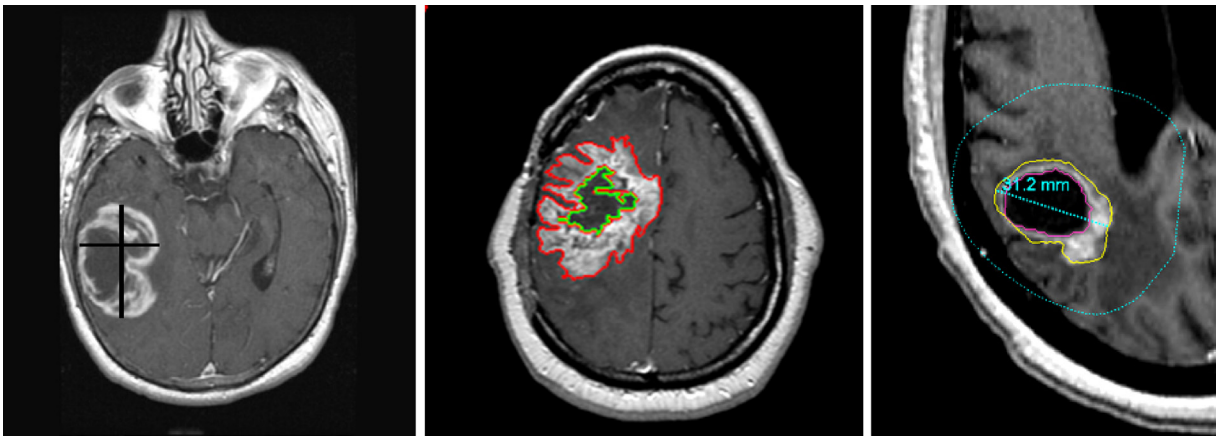


FIGURE 5 Illustration of the common, orthogonal diameters approach to brain tumor measurement (left image). The difficulties with this approach are described in detail in the text. Computer-aided volumetric approach for measurement of an irregularly shaped glioblastoma containing a significant region of nonenhancing, necrotic tumor (center image). The program calculates enhancing volume, central nonenhancing volume, and total lesion volume. Another case of glioblastoma (right image) comparing RECIST and volumetric measurements.

Comparison of Diameter and Volumetric Approaches

Multiple studies have compared diameter and volumetric-based approaches to the detection of response in clinical trials.[33,43–45] These studies have shown that three perpendicular diameters to estimate volume had the lowest degree of concordance with 1D (single linear measurement as in RECIST), 2D (two orthogonal measurements as in the Macdonald and RANO criteria), and volumetric approaches. The volumetric approach had the lowest intra- and interobserver variability. It also had the highest rates of response rate, probably reflecting the higher sensitivity to small changes in size.[33] For example, PR would have been declared in 8% of 284 scans using the 1D measurement, compared to 17% using the volumetric approach.

Timing of Imaging

Baseline imaging for clinical trials is required, ideally within 14 days prior to initiation of treatment. Preoperative and postoperative scans, if prior to the trial, should be available to help identify preexisting disease. Postoperative scans should be done within 72 h of surgery, after which time enhancing granulation tissue will be present along the margins of the resection cavity that is indistinguishable from enhancing tumor.

Follow-up studies are performed according to treatment protocol, but most commonly after every second cycle or every 2 months. The same imaging technique and protocol must be used at every time point. Small differences in technique can result in significant variability in tumor measurements. For example, in one study minor changes in head position in the same patient resulted in up to 22% difference in the product of manual bidirectional measurements (the difference in computer-assisted volumetric measurement using the same dataset was less than 5%).[46] The type of MRI scanner (i.e., 1.5-T vs 3.0-T) should be maintained if possible.

Additionally, confirmation of response at 4 weeks is generally required in clinical trials to avoid overestimating the response rate. If confirmation is not available, response is not considered adequately assessed and should not be included in the clinical trial.

Image Interpretation and Measurements

The Macdonald criteria, RECIST, and most recently RANO have attempted to provide a framework for identifying and measuring disease over time in clinical trials (Table 1). In general, these techniques follow the size of contrast-enhancing disease on axial images using perpendicular diameters (or unidirectional diameter in the case of RECIST). However, several issues often arise on image interpretation and measurement in neuro-oncology.

First, high-grade gliomas (glioblastoma in particular) are heterogeneous in appearance on imaging, with irregular, peripheral enhancement and central cystic or necrotic regions. Avoiding the cystic or necrotic regions with caliper measurements is effectively impossible in many cases. However, this limitation is often mitigated by the fact that most clinical trials follow disease after the primary, heterogeneous tumor has been resected. Recurrent disease generally begins as smaller, homogeneous enhancement along the resection cavity margins. Although this enhancement lends itself to standardized definitions of a measurable lesion (provided it meets the size minimum for measurable disease), it is often crescent-shaped along the margin of the resection cavity, again making measurements with bi- or unidirectional diameters challenging. Computer-assisted volumetric assessment can more accurately measure the enhancing component in these cases (described above), but this technique has not achieved widespread use in clinical trials.

Second, enhancement may not be a reliable indicator of disease in the context of angiogenesis inhibitors (e.g., bevacizumab), as discussed above.

Third, to minimize the potential for interobserver variation, clinical trials will often utilize a system of central review. Generally, specific sequences of anonymized data are transferred to a central imaging center to be reviewed in a blinded manner. Central review is usually employed to confirm response status, with the primary clinical interpretation being the responsibility of the patient's neuro-oncologist.

Imaging Pitfalls

Several additional problems arise in clinical trial imaging and are worth noting. First, contrast enhancement can be difficult to distinguish from intrinsic T1-weighted hyperintensity of blood products. This issue is especially difficult on the immediate postoperative MRI scan (i.e., the study performed within 72h of surgery) since extensive signal changes from blood products are routinely present. A detailed, side-by-side comparison of the pre- and postcontrast enhanced images is required. Occasionally the intrinsically T1-weighted hyperintense postoperative blood products along the surgical margin can obscure the presence of residual enhancing disease, and these foci become apparent only on further follow-up studies when the blood product-related signal has resolved.

Second, areas of restricted diffusion occur in two-thirds of patients following surgery for malignant gliomas (Figure 6). These foci evolve into encephalomalacia, consistent with the presence of infarction. Follow-up studies reveal enhancement in about one-half of these infarcts, a finding that could easily be misinterpreted as persistent or progressive tumor if the presence of the perioperative infarct is not realized. Thus, it is important

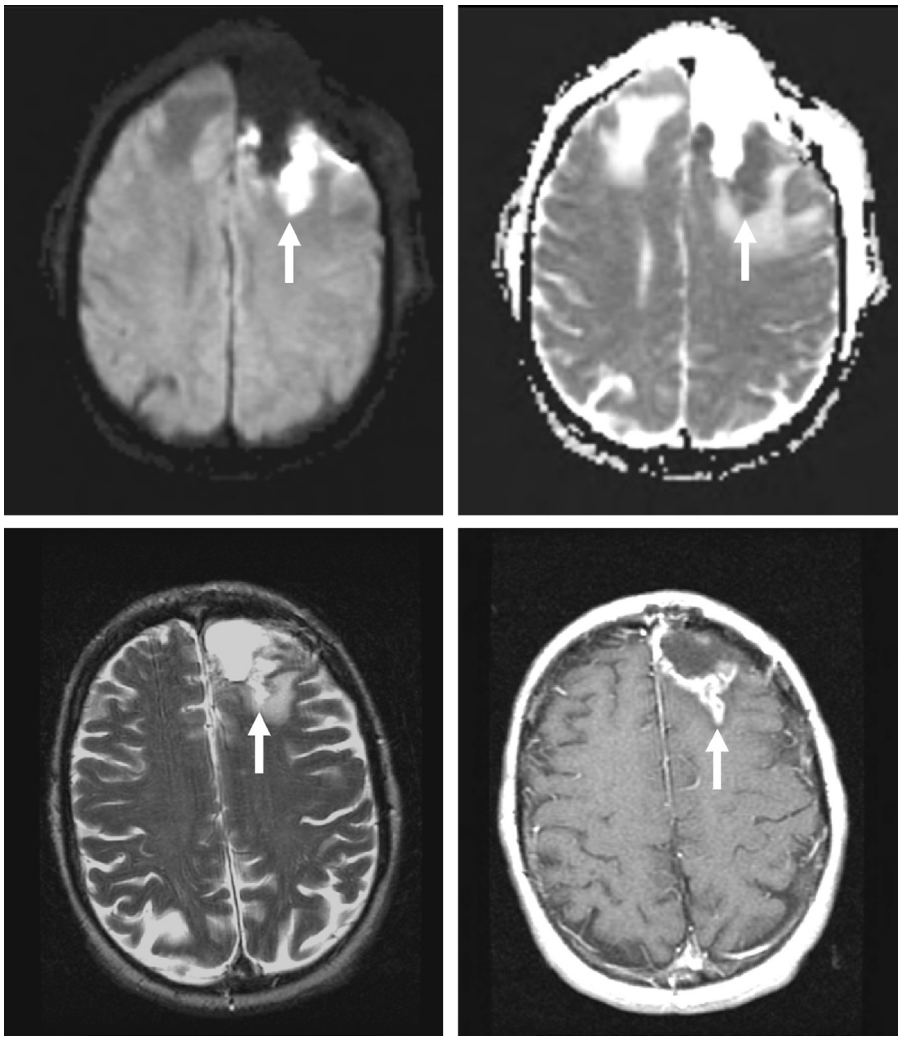


FIGURE 6 Two-thirds of patients undergoing surgery for malignant gliomas have infarcts in their tumors on the immediate postoperative MRI scan. These infarcts often demonstrate nodular gadolinium enhancement on subsequent studies, a finding that could be easily confused with tumor. Immediate postoperative DWI (upper left) and apparent diffusion coefficient (upper right) show restricted diffusion (arrows), followed by a 3-month postoperative T2WI (lower left) and gadolinium-enhanced T1WI showing enhancement within the infarct (lower right).

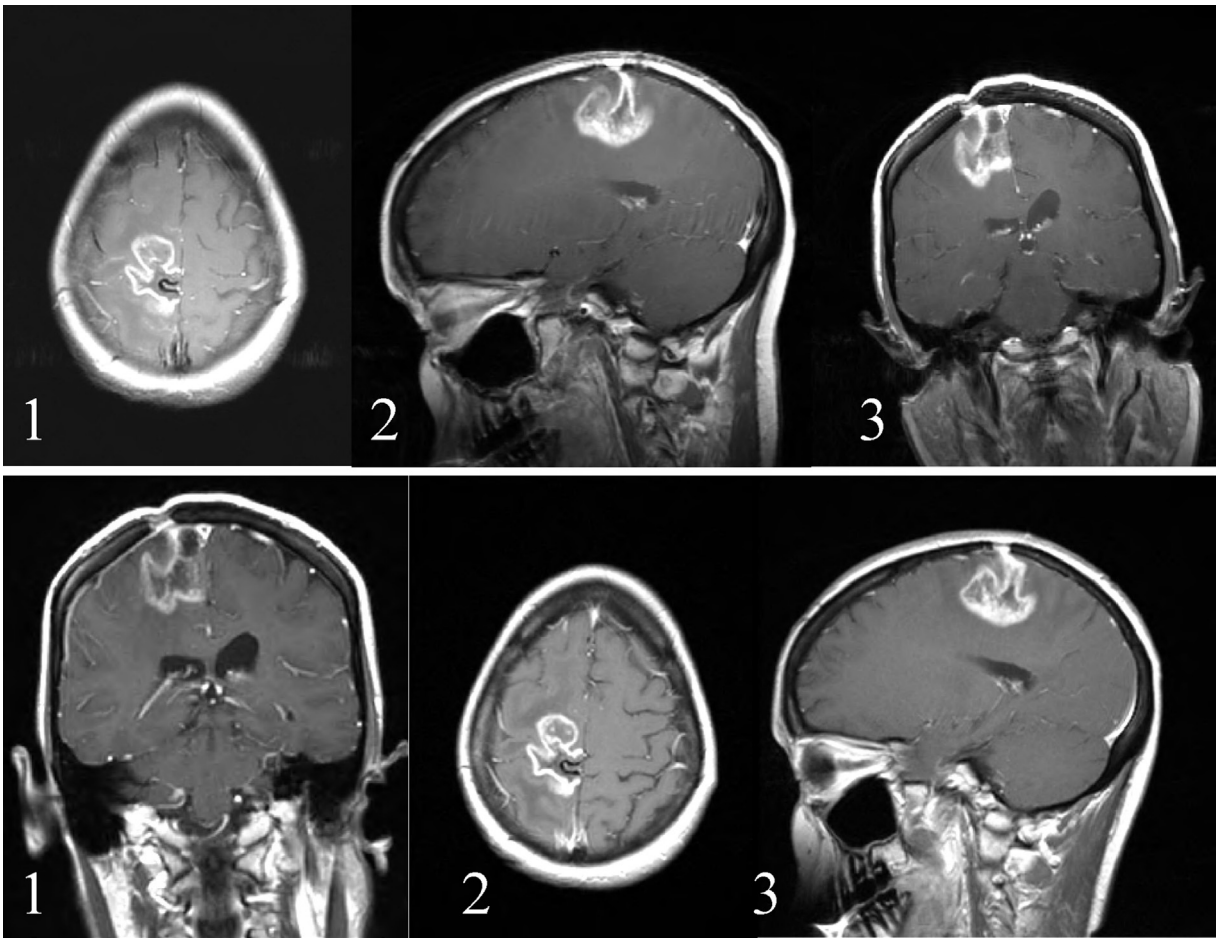


FIGURE 7 Contrast enhancement within brain tumors is a dynamic process. A standardized imaging protocol is important for the purposes of direct comparison. In this case the usual acquisition order of the triplanar images was reversed in the lower row, producing marked differences between the coronal images. The numbers refer to order in which the images were acquired.

to review the immediate postoperative diffusion-weighted image when evaluating an area of focal nodular enhancement for serial measurement.

Third, gadolinium enhancement is a time-dependent phenomenon, and this fact can result in significant changes in apparent lesion size between the initial and the final enhanced sequences (Figure 7). Since each sequence takes approximately 3–5 min to acquire, significant time can elapse prior to the second or third sequence. The images should always be obtained in the same sequence at about the same time interval to avoid misinterpretation of response or progression. Evaluation of the degree of enhancement within the deep cerebral veins (e.g., internal cerebral veins) and within the nasal mucosa can help to confirm the presence of an adequate dose of gadolinium.

SUMMARY

MRI is an indispensable tool in the day-to-day clinical management of patients with brain tumors as well as the assessment of new therapeutic agents in neuro-oncology clinical trials. In this chapter, we have reviewed the role of imaging in diagnosis, treatment, and surveillance of brain tumors. We also reviewed the conceptual and technical challenges of using imaging as a surrogate measure of pathology in clinical trials.

References

1. Chaichana KL, Kosztowski T, Niranjan A, et al. Prognostic significance of contrast-enhancing anaplastic astrocytomas in adults. *J Neurosurg*. 2010;113(2):286–292. http://dx.doi.org/10.3171/2010.2.JNS091010.
2. Barker FG, Chang SM, Huhn SL, et al. Age and the risk of anaplasia in magnetic resonance-nonenhancing supratentorial cerebral tumors. *Cancer*. 1997;80(5):936–941.
3. Law M, Young RJ, Babb JS, et al. Gliomas: predicting time to progression or survival with cerebral blood volume measurements at dynamic susceptibility-weighted contrast-enhanced perfusion MR imaging. *Radiology*. 2008;247(2):490–498. http://dx.doi.org/10.1148/radiol.2472070898.
4. Maia ACM, Malheiros SMF, da Rocha AJ, et al. Stereotactic biopsy guidance in adults with supratentorial nonenhancing gliomas: role of perfusion-weighted magnetic resonance imaging. *J Neurosurg*. 2004;101(6):970–976. http://dx.doi.org/10.3171/jns.2004.101.6.0970.

5. Kleihues P, Soylemezoglu F, Schäuble B, Scheithauer BW, Burger PC. Histopathology, classification, and grading of gliomas. *Glia*. 1995;15(3):211–221. http://dx.doi.org/10.1002/glia.440150303.
6. Recht LD, Lew R, Smith TW. Suspected low-grade glioma: is deferring treatment safe? *Ann Neurol*. 1992;31(4):431–436. http://dx.doi.org/10.1002/ana.410310413.
7. Recht LD, Bernstein M. Low-grade gliomas. *Neurol Clin*. 1995;13(4):847–859.
8. Martino J, Taillandier L, Moritz-Gasser S, Gatignol P, Duffau H. Re-operation is a safe and effective therapeutic strategy in recurrent WHO grade II gliomas within eloquent areas. *Acta Neurochir (Wien)*. 2009;151(5):427–436. http://dx.doi.org/10.1007/s00701-009-0232-6. [Discussion 436].
9. Shafqat S, Hedley-Whyte ET, Henson JW. Age-dependent rate of anaplastic transformation in low-grade astrocytoma. *Neurology*. 1999;52(4):867–869.
10. Bernstein M, Berger MS, eds. *Neuro-Oncology: the Essentials*. 3rd ed. New York: Thieme; 2014.
11. Ostrom QT, Bauchet L, Davis FG, et al. The epidemiology of glioma in adults: a "state of the science" review. *Neuro Oncol*. 2014;16(7):896–913. http://dx.doi.org/10.1093/neuonc/nou087.
12. Parsons DW, Jones S, Zhang X, et al. An integrated genomic analysis of human glioblastoma multiforme. *Science*. 2008;321(5897):1807–1812. http://dx.doi.org/10.1126/science.1164382.
13. Mandonnet E, Delattre J-Y, Tanguy M-L, et al. Continuous growth of mean tumor diameter in a subset of grade II gliomas. *Ann Neurol*. 2003;53(4):524–528. http://dx.doi.org/10.1002/ana.10528.
14. Ius T, Isola M, Budai R, et al. Low-grade glioma surgery in eloquent areas: volumetric analysis of extent of resection and its impact on overall survival. A single-institution experience in 190 patients: clinical article. *J Neurosurg*. 2012;117(6):1039–1052. http://dx.doi.org/10.3171/2012.8.JNS12393.
15. Yordanova YN, Moritz-Gasser S, Duffau H. Awake surgery for WHO grade II gliomas within "noneloquent" areas in the left dominant hemisphere: toward a "supratotal" resection. Clinical article. *J Neurosurg*. 2011;115(2):232–239. http://dx.doi.org/10.3171/2011.3.JNS101333.
16. Smith JS, Cha S, Mayo MC, et al. Serial diffusion-weighted magnetic resonance imaging in cases of glioma: distinguishing tumor recurrence from postresection injury. *J Neurosurg*. 2005;103(3):428–438. http://dx.doi.org/10.3171/jns.2005.103.3.0428.
17. Stupp R, Mason WP, van den Bent MJ, et al. Radiotherapy plus concomitant and adjuvant temozolomide for glioblastoma. *N Engl J Med*. 2005;352(10):987–996. http://dx.doi.org/10.1056/NEJMoa043330.
18. Kruser TJ, Mehta MP, Robins HI. Pseudoprogression after glioma therapy: a comprehensive review. *Expert Rev Neurother*. 2013;13(4):389–403. http://dx.doi.org/10.1586/ern.13.7.
19. Chamberlain MC, Glantz MJ, Chalmers L, Van Horn A, Sloan AE. Early necrosis following concurrent Temodar and radiotherapy in patients with glioblastoma. *J Neurooncol*. 2007;82(1):81–83. http://dx.doi.org/10.1007/s11060-006-9241-y.
20. Brandes AA, Franceschi E, Tosoni A, et al. MGMT promoter methylation status can predict the incidence and outcome of pseudoprogression after concomitant radiochemotherapy in newly diagnosed glioblastoma patients. *J Clin Oncol*. 2008;26(13):2192–2197. http://dx.doi.org/10.1200/JCO.2007.14.8163.
21. Gahramanov S, Muldoon LL, Varallyay CG, et al. Pseudoprogression of glioblastoma after chemo- and radiation therapy: diagnosis by using dynamic susceptibility-weighted contrast-enhanced perfusion MR imaging with ferumoxytol versus gadoteridol and correlation with survival. *Radiology*. 2013;266(3):842–852. http://dx.doi.org/10.1148/radiol.12111472.
22. Kong D-S, Kim ST, Kim E-H, et al. Diagnostic dilemma of pseudoprogression in the treatment of newly diagnosed glioblastomas: the role of assessing relative cerebral blood flow volume and oxygen-6-methylguanine-DNA methyltransferase promoter methylation status. *AJNR Am J Neuroradiol*. 2011;32(2):382–387. http://dx.doi.org/10.3174/ajnr.A2286.
23. Norden AD, Young GS, Setayesh K, et al. Bevacizumab for recurrent malignant gliomas: efficacy, toxicity, and patterns of recurrence. *Neurology*. 2008;70(10):779–787. http://dx.doi.org/10.1212/01.wnl.0000304121.57857.38.
24. Chinot OL, Wick W, Mason W, et al. Bevacizumab plus radiotherapy-temozolomide for newly diagnosed glioblastoma. *N Engl J Med*. 2014;370(8):709–722. http://dx.doi.org/10.1056/NEJMoa1308345.
25. Gilbert MR, Dignam JJ, Armstrong TS, et al. A randomized trial of bevacizumab for newly diagnosed glioblastoma. *N Engl J Med*. 2014;370(8):699–708. http://dx.doi.org/10.1056/NEJMoa1308573.
26. Schaub C, Greschus S, Seifert M, et al. FLAIR-only progression in bevacizumab-treated relapsing glioblastoma does not predict short survival. *Oncology*. 2013;85(3):191–195. http://dx.doi.org/10.1159/000354692.
27. Nowosielski M, Wiestler B, Goebel G, et al. Progression types after antiangiogenic therapy are related to outcome in recurrent glioblastoma. *Neurology*. 2014;82(19):1684–1692. http://dx.doi.org/10.1212/WNL.0000000000000402.
28. Batchelor T, Stanley K, Andersen J. Clinical trials in neuro-oncology. *Curr Opin Neurol*. 2001;14(6):689–694.
29. Macdonald DR, Cascino TL, Schold SC, Cairncross JG. Response criteria for phase II studies of supratentorial malignant glioma. *J Clin Oncol*. 1990;8(7):1277–1280.
30. Therasse P, Arbuck SG, Eisenhauer EA, et al. New guidelines to evaluate the response to treatment in solid tumors. European Organization for Research and Treatment of Cancer, National Cancer Institute of the United States, National Cancer Institute of Canada. *J Natl Cancer Inst*. 2000;92(3):205–216.
31. Eisenhauer EA, Therasse P, Bogaerts J, et al. New response evaluation criteria in solid tumours: revised RECIST guideline (version 1.1). *Eur J Cancer*. 2009;45(2):228–247. http://dx.doi.org/10.1016/j.ejca.2008.10.026.
32. Gállego Pérez-Larraya J, Lahutte M, Petrirena G, et al. Response assessment in recurrent glioblastoma treated with irinotecan-bevacizumab: comparative analysis of the Macdonald, RECIST, RANO, and RECIST + F criteria. *Neuro Oncol*. 2012;14(5):667–673. http://dx.doi.org/10.1093/neuonc/nos070.
33. Shah GD, Kesari S, Xu R, et al. Comparison of linear and volumetric criteria in assessing tumor response in adult high-grade gliomas. *Neuro Oncol*. 2006;8(1):38–46. http://dx.doi.org/10.1215/S1522851705000529.
34. Galanis E, Buckner JC, Maurer MJ, et al. Validation of neuroradiologic response assessment in gliomas: measurement by RECIST, two-dimensional, computer-assisted tumor area, and computer-assisted tumor volume methods. *Neuro Oncol*. 2006;8(2):156–165. http://dx.doi.org/10.1215/15228517-2005-005.
35. Wen PY, Macdonald DR, Reardon DA, et al. Updated response assessment criteria for high-grade gliomas: response assessment in neuro-oncology working group. *J Clin Oncol*. 2010;28(11):1963–1972. http://dx.doi.org/10.1200/JCO.2009.26.3541.
36. Ballman KV, Buckner JC, Brown PD, et al. The relationship between six-month progression-free survival and 12-month overall survival end points for phase II trials in patients with glioblastoma multiforme. *Neuro Oncol*. 2007;9(1):29–38. http://dx.doi.org/10.1215/15228517-2006-025.
37. Lamborn KR, Yung WKA, Chang SM, et al. Progression-free survival: an important end point in evaluating therapy for recurrent high-grade gliomas. *Neuro Oncol*. 2008;10(2):162–170. http://dx.doi.org/10.1215/15228517-2007-062.
38. Cairncross JG, Ueki K, Zlatescu MC, et al. Specific genetic predictors of chemotherapeutic response and survival in patients with anaplastic oligodendrogliomas. *J Natl Cancer Inst*. 1998;90(19):1473–1479.

39. Prados MD, Seiferheld W, Sandler HM, et al. Phase III randomized study of radiotherapy plus procarbazine, lomustine, and vincristine with or without BUdR for treatment of anaplastic astrocytoma: final report of RTOG 9404. *Int J Radiat Oncol Biol Phys*. 2004;58(4):1147–1152. http://dx.doi.org/10.1016/j.ijrobp.2003.08.024.
40. Kreisl TN, Kim L, Moore K, et al. Phase II trial of single-agent bevacizumab followed by bevacizumab plus irinotecan at tumor progression in recurrent glioblastoma. *J Clin Oncol*. 2009;27(5):740–745. http://dx.doi.org/10.1200/JCO.2008.16.3055.
41. Friedman HS, Prados MD, Wen PY, et al. Bevacizumab alone and in combination with irinotecan in recurrent glioblastoma. *J Clin Oncol*. 2009;27(28):4733–4740. http://dx.doi.org/10.1200/JCO.2008.19.8721.
42. Grant R, Liang BC, Slattery J, Greenberg HS, Junck L. Chemotherapy response criteria in malignant glioma. *Neurology*. 1997;48(5):1336–1340. http://dx.doi.org/10.1212/WNL.48.5.1336.
43. Sorensen AG, Patel S, Harmath C, et al. Comparison of diameter and perimeter methods for tumor volume calculation. *J Clin Oncol*. 2001;19(2):551–557.
44. Warren KE, Patronas N, Aikin AA, Albert PS, Balis FM. Comparison of one-, two-, and three-dimensional measurements of childhood brain tumors. *J Natl Cancer Inst*. 2001;93(18):1401–1405.
45. Poussaint TY, Jaramillo D, Chang Y, Korf B. Interobserver reproducibility of volumetric MR imaging measurements of plexiform neurofibromas. *AJR Am J Roentgenol*. 2003;180(2):419–423. http://dx.doi.org/10.2214/ajr.180.2.1800419.
46. Reuter M, Gerstner ER, Rapalino O, Batchelor TT, Rosen B, Fischl B. Impact of MRI head placement on glioma response assessment. *J Neurooncol*. 2014;118(1):123–129. http://dx.doi.org/10.1007/s11060-014-1403-8.

CHAPTER

55

Pseudoprogression in Neuro-Oncology: Overview, Pathophysiology, and Interpretation

Nancy Ann Oberheim Bush[1,3], *Soonmee Cha*[2,3], *Susan M. Chang*[3], *Jennifer L. Clarke*[1,3]

[1]Department of Neurology, University of California, San Francisco, CA, USA; [2]Department of Radiology and Biomedical Imaging, University of California, San Francisco, CA, USA; [3]Department of Neurological Surgery, University of California, San Francisco, CA, USA

OVERVIEW OF PSEUDOPROGRESSION

Glioblastoma (GBM) is the most common malignant primary brain tumor, with an incidence of 3.19 cases per 100,000 person years.[1] With the current standard of medical treatment, consisting of maximal safe resection followed by external beam radiation and concomitant temozolomide (TMZ), and then maintenance chemotherapy, median overall survival (OS) for patients with newly diagnosed GBM is 12–18 months.[2,3] Treatment efficacy is measured by OS, radiographic response, and progression-free survival (PFS), or duration of tumor control.[4,5] Radiographic response rate has become an important endpoint when evaluating the efficacy of treatment regimens.[4] Typically, increased enhancement (>25%) on a T1-weighted magnetic resonance imaging (MRI) scan using gadolinium-based contrast 1–6 months after chemoradiation therapy (CRT) can represent either true tumor progression or, if transient or not serially progressive, a phenomenon now known as pseudoprogression.

Pseudoprogression is defined as a radiographic increase in enhancement and/or edema on MRI without tumor progression. This transient increase in enhancement and/or edema stabilizes or resolves without further changes in management (Figure 1). This phenomenon can be distinguished from classic radiation necrosis, which occurs 3 months to greater than 1 year after CRT and does not have immediate resolution. The incidence of pseudoprogression in GBM patients undergoing standard therapy is between 14% and 50%.[6–14] Currently, it is primarily diagnosed on follow-up imaging; however, there is a drive for improved diagnostic methods on initial evaluation. Pseudoprogression can be completely asymptomatic or, in one-third of patients, can be accompanied by symptoms related to increased intracranial pressure, including headache, nausea, focal neurologic deficits, alterations of consciousness, and seizure.[15] It must also be distinguished from peri-ictal pseudoprogression, which is a transient MRI abnormality in the setting of the development of a seizure.[16] Typically focal cortical or leptomeningeal enhancing lesions in the setting of seizure are seen, which then normalize after 1–3 months. This preferentially occurs among long-term survivors, and management is focused on treatment with antiepileptic medications.[16]

Recognizing pseudoprogression is important for a number of reasons. Primarily, discontinuing therapy, typically adjuvant TMZ, owing to pseudoprogression may be denying effective therapy for patients with responsive disease, and currently there are limited therapeutic options. Second-line agents are typically less effective; therefore it is important to continue first-line therapies when appropriate. If a patient has true progression, it is important to recognize this early and begin either clinical trials or second-line therapies. Furthermore, enrollment of patients with pseudoprogression inappropriately into clinical trials for treatment failure may bias treatment results by overestimating the investigational treatment's efficacy, especially if radiographic response is a means of evaluating efficacy. Conversely, it is important to discontinue ineffective treatments so as to minimize disease resistance and exposure to unnecessary treatments and toxicity. Therefore, accurate

http://dx.doi.org/10.1016/B978-0-12-800945-1.00055-0
© 2016 Elsevier Ltd. All rights reserved.

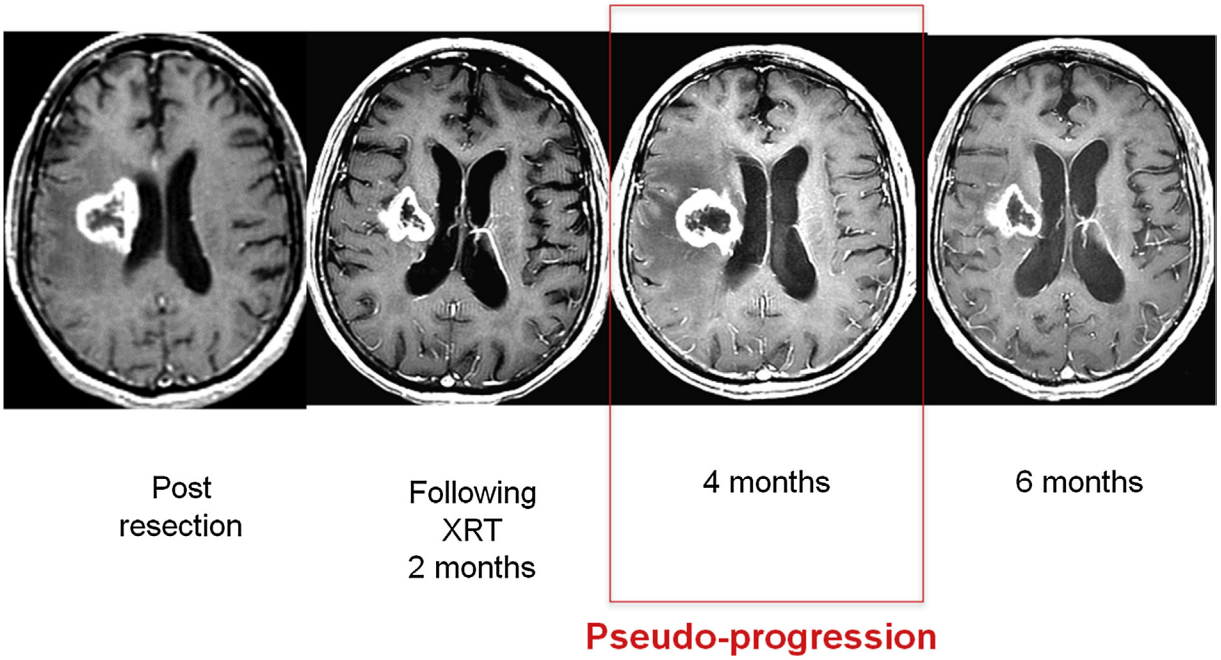


FIGURE 1 MRI series of an 80-year-old woman with a GBM treated with radiation therapy (RT) and concurrent TMZ who stopped therapy in the setting of worsening enhancement at 4 months and had spontaneous improvement, demonstrating the phenomenon of pseudoprogression.

differentiation between pseudoprogression and true disease progression is imperative.

HISTORY

Although pseudoprogression has become a prominent factor in the management of glioma patients only since about 2005, it was probably first observed more than 25 years before that. In 1979, Hoffman et al., published a series of 51 glioma patients evaluated by contrast-enhanced brain computerized tomography (CT) and radionuclide scans for response to radiotherapy using the Levin criteria.[17,18] They reported that 28% of the patients showed radiographic improvement or stabilization without a change in therapy. This suggests that transient changes that mimic tumor progression were apparent and not infrequent on early postradiation radiologic evaluations. This was followed by the first published case series of serial CT imaging in three patients with GBM after surgery and radiation that demonstrated regression of enhancement originally seen after treatment mimicking tumor progression.[19] In 1988 Cascino et al. described four patients with postradiotherapy changes seen on CT scan that improved or stabilized on repeat imaging without further treatment.[20] In 1990, the MacDonald criteria were published characterizing response criteria for phase II studies of patients with high-grade gliomas.[21] Within this seminal paper, the appearance of transient postradiotherapy progression was noted; and it was suggested that no new therapies should be initiated for recurrent high-grade gliomas until 1–2 months post-radiation treatment.[21]

The incidence of pseudoprogression, as well as factors influencing the phenomenon, has become better understood since 2005. In 2004, de Wit et al. conducted a study to determine the frequency of transient MRI lesions following radiotherapy in a cohort of patients treated within two different prospective phase III trials with radiotherapy alone.[8] They concluded that one-third of patients with evidence of disease progression on MRI on their first imaging evaluation after radiotherapy had improved or stabilized lesions on follow-up scans without further intervention. They further concluded that patients that had evidence of progressive lesions within 3 months of initial therapy should not be included in phase II trials on recurrent glioma.[8] In 2007, it was first suggested that TMZ-based CRT may influence the incidence of pseudoprogression. Chamberlain et al. published a case series of 51 newly diagnosed GBM patients treated with the now widely accepted TMZ–CRT (EORTC/NCIC).[2,6] They noted that 51% of the patients failed clinically and radiographically within 6 months of completion of CRT and were considered to have progressive GBM. Of these patients, 15 underwent reoperation, in seven of which (47%) histopathology was interpreted as necrosis without evidence of tumor. Therefore, the authors concluded that early radiation necrosis can mimic tumor progression and can influence further management decisions. Furthermore, the phenomenon of pseudoprogression was not confined to the first post-CRT MRI, but rather was seen in approximately one-third of patients during

continuation of TMZ therapy. Finally, this study also suggested the importance in TMZ therapy of clinically significant radiosensitization.

The incidence of pseudoprogression was further characterized by Taal et al., in 2008, in a cohort of 85 patients with malignant glioma (68 with GBM and 17 with anaplastic glioma) treated with TMZ-based CRT.[10] Of the 85 patients included in the study, 42% had evidence of disease progression as evidenced by greater than 25% increase in the product of the orthogonal maximum tumor diameters on the first post-radiation therapy (RT) scan 4 weeks after completion of therapy. Of these, 50% were subsequently diagnosed as having pseudoprogression as defined as improvement or stabilization of clinical and radiographic findings on a stable or decreased dose of steroids and continuation of planned therapy; this constituted 25% of the total patient population. The authors also reported that only one-third of patients with pseudoprogression were clinically symptomatic. Finally, they reported that survival in patients with pseudoprogression was comparable to that in those without and better than in patients with true progression. More recent studies based on Canadian populations with GBM using the EORTC/NCIC TMZ-based regimen have found an incidence of pseudoprogression of 32–50%[13,14]

The link of pseudoprogression to methylguanine methyltransferase (MGMT) gene promoter methylation was described in 2008.[22] Brandes et al. studied 208 patients with newly diagnosed GBM treated with TMZ–CRT followed by 12 cycles of postradiotherapy TMZ. One hundred three patients underwent MGMT methylation status, and 35% were found to have MGMT promoter methylation. At the first post-CRT MRI, 49% of all patients were found to have apparent disease progression. TMZ was continued in all patients, and on follow-up imaging, 64% of the patients with changes on their initial MRI were subsequently diagnosed with pseudoprogression because of improvement or stabilization of their initial imaging findings, leading to a conclusion that pseudoprogression occurs in 30% of patients on first MRI after CRT. Interestingly, of the patients diagnosed with pseudoprogression, 66% had a methylated MGMT promoter. Conversely, patients with unmethylated tumors had higher rates of disease progression (3/1). It was also first postulated in this study that patients that develop pseudoprogression may have improved survival perhaps due to an improved treatment response.

Based on the Brandes study in 2008, MGMT status predicted pseudoprogression in 91.3% of methylated cases and tumor recurrence in 59% of unmethylated cases, suggesting a strong link between MGMT promoter status and pseudoprogression.[22] This was reiterated in a study in 2011 by Kong et al., who showed that there was a significantly higher incidence of pseudoprogression in patients with MGMT methylation, 37.5% compared to 24.2% ($p = 0.019$).[23]

PATHOPHYSIOLOGY

Histology

The histologic characteristics of pseudoprogression remain incompletely understood and characterized. This is partly due to the complexity of brain tissue changes seen as a result of both radiation and chemotherapy toxicity. Active tumor recurrence is usually characterized by microvascular proliferation in conjunction with highly cellular tumor tissue. This is in contrast to histologic analysis of enhancing tissue consistent with pseudoprogression, which is usually paucicellular (Figure 2).[24] There is usually a low density of pleomorphic tumor cells with a low mitotic index. Furthermore, there is evidence of coagulation necrosis, which is seen as brightly eosinophilic. Hyalinization of vessel walls is common, as well as fibrinoid necrosis. Telangiectatic vessels can also be seen, but are less specific. Both fibrillary and gemistocytic astrocytes can be seen, usually at low density. Widely scattered pleomorphic astrocytes are most consistent with irradiated tumor and are commonly present in tissue consistent with pseudoprogression.[24]

Other biomarkers, including Ki67 and p53 overexpression, may also be useful in distinguishing pseudoprogression; however, the current evidence remains unclear. In 2011, a Korean group studied p53 overexpression as a potential biomarker for predicting pseudoprogression. They found that 87.5% of patients with pseudoprogression had p53 overexpression compared to 30% with true disease progression ($p = 0.03$).[25] However, another group found that p53 expression had no predictive value for pseudoprogression; rather, Ki67 was a valuable marker.[26] In this study, the Ki67 index, which is a marker of the level of cellular proliferation, was significantly higher compared to patients with true progression, with a median of 20% compared to 10%, respectively ($p = 0.0016$). This study also demonstrated that all patients with Ki67 indices greater than 20% were diagnosed with pseudoprogression, suggesting that this could be a very useful biomarker to differentiate the two entities. Although this seems counterintuitive, the authors postulate that this could be due to the fact that RT–TMZ induces cell death during the replication phase of the cell cycle, and therefore the increased Ki67 index could represent initial effects of treatment. This study also did not specifically investigate the cell types associated with the high levels of proliferation. Potentially, this could also represent high levels of inflammatory cells within patients with pseudoprogression. Further studies investigating the utility of both p53 and Ki67

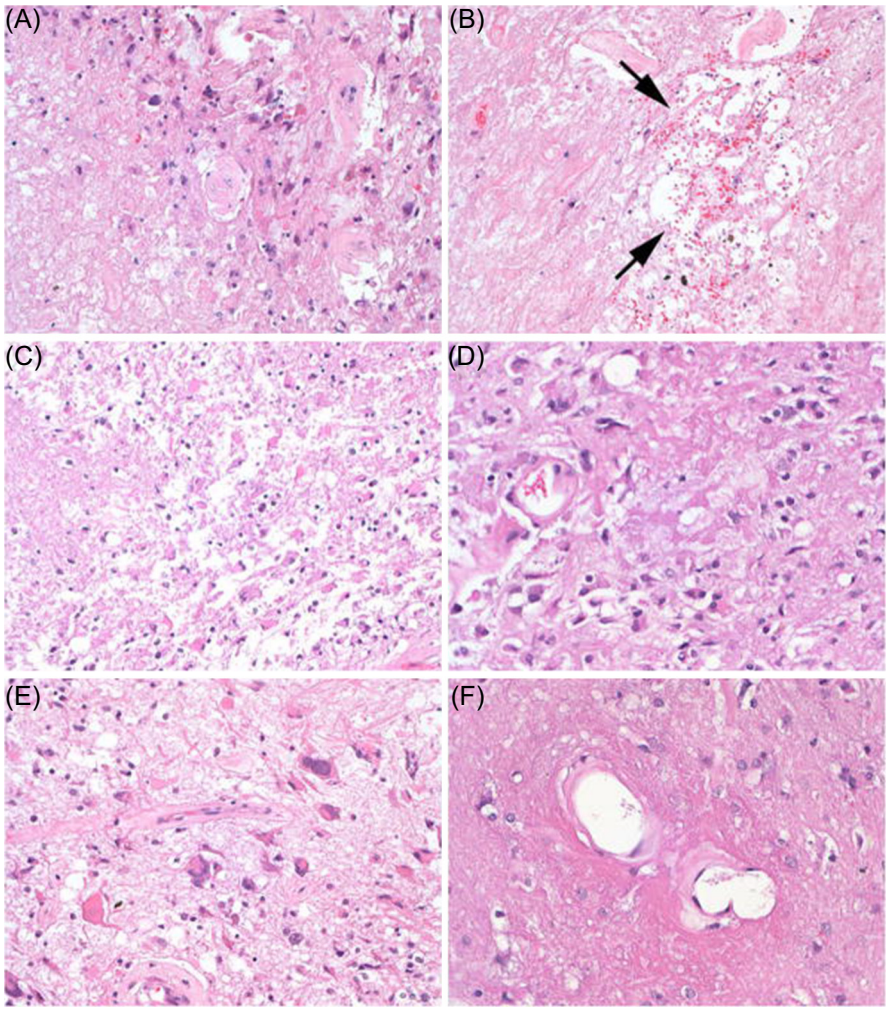


FIGURE 2 Histological features of treatment effect—pseudoprogression. (A) Necrosis, left, hyalinized vessels, and pleomorphic tumor cells in low density are considered evidence of treatment effect, not expressions of recurrent or residual active high-grade tumor. (B) Areas of brightly eosinophilic coagulation necrosis are common effects of treatment. Telangiectatic vessels (arrows) are additional, but less specific, features. (C) Necrosis in this treated lesion is associated with fibrillary and gemistocytic astrocytes in low density. It can be difficult in cases such as this to determine whether these cells are reactive or neoplastic. Even if the latter, we did consider them evidence of tumor recurrence. (D) Well-differentiated neoplastic astrocytes in low numbers were not interpreted as evidence of recurrent active, high-grade glioma. Coagulation necrosis in a paucicellular lesion such as this is typical of treatment effect. (E) Widely scattered pleomorphic astrocytes consistent with irradiated tumor cells were not taken as evidence of active high-grade astrocytoma. (F) Fibrinoid necrosis of vessels is a common feature of treatment effect. *With permission, from Ref. 24.*

should be performed to further clarify the utility of these biomarkers.

Theories of Pathophysiology

In line with the incomplete characterization of the histology of pseudoprogression, the pathophysiology also remains poorly understood. It is theorized that there are two components to pseudoprogression: vascular injury and treatment-related cellular effects. It is postulated that the primary phenomenon leading to the transient nature of the effect is vascular endothelial damage leading to increased permeability of the blood–brain barrier (BBB). CRT has been shown to lead to disruption of the BBB associated with increased vasogenic edema and contrast enhancement on MRI.[27] This is coupled with the antitumor effects of CRT, leading to an inflammatory tissue environment. Evidence of inflammation is commonly seen histologically on re-resected tissue. The combination of these effects perhaps leads to the radiographic finding of pseudoprogression, which resolves in time. The idea that MGMT promoter methylation leads to higher rates of pseudoprogression presumably relates to an enhanced treatment response, increased BBB disruption, and inflammation, resulting in radiographic pseudoprogression.

It is also debated whether pseudoprogression is on a continuum with radiation necrosis, differentiated only

by time, or is its own entity. Certainly many of the histologic features of pseudoprogression are similar to those of radiation necrosis, and some studies suggest that pseudoprogression can progress to radiation necrosis in some cases.[10,15] Others, however, would suggest that pseudoprogression is a result of radiation injury to the tumor itself, while radiation necrosis is defined as injury to normal brain parenchyma. Furthermore, radiation necrosis is a histological diagnosis. This is in contrast to the transient phenomenon of pseudoprogression.

INTERPRETATION

Methods of Differentiation between Progression and Pseudoprogression

Pseudoprogression in itself is a radiographic occurrence, defined as a transient increase in enhancement and/or edema on MRI without tumor progression. It remains a retrospective diagnosis and at this time no single imaging technique is adequate to completely differentiate pseudoprogression from true tumor progression. Furthermore, there is a paucity of large studies comparing imaging modalities to better distinguish disease progression versus pseudoprogression, as more effort has been placed on distinguishing progression versus radiation necrosis.

The criteria for assessment of GBM and the presence of pseudoprogression has evolved over time. Prior to 1990, patient response to therapy was assessed using the Levin criteria as well as the World Health Organization (WHO) oncology response criteria.[18,28] With the Levin criteria, CT scan and radionuclide scintiscan were used as qualitative measurements, accounting for multiple factors including edema and mass effect, to predict deterioration.[18] The WHO response criteria used contrast-enhanced CT scans to measure tumor area. The usefulness of both of these criteria was limited in that they were quite subjective and contrast enhancement is now known to be affected by multiple factors, not just tumor progression.

The Macdonald criteria published in 1990 were established to further define disease progression after initial radiotherapy by standardizing definitions of radiographic response. These criteria use two-dimensional measurements of enhancing tumor by multiplying the largest cross-sectional diameter of enhancing tumor on the same axial image on CT or MRI.[21] Additionally, corticosteroid dosing and clinical assessment were used as a surrogate for tumor progression at 3 months postradiotherapy.[21] They classified patient responses into four categories—complete response, partial response, stable disease, and progressive disease. However, there were several obstacles with the use of the Macdonald criteria, including the difficulty in measuring irregularly shaped tumors, difficulty in measuring lesions in the walls of cystic or surgical cavities, lack of guidance of the assessment of multifocal tumors, lack of measurement of nonenhancing aspects of the tumor, as well as interobserver variability.[29] Subsequently, it was shown that this method is only 66.7–93.5% sensitive and 50–63.9% specific in differentiating tumor recurrence from radiation necrosis or pseudoprogression.[30]

The Response Evaluation Criteria in Solid Tumors (RECIST) guidelines for solid tumors (including gliomas) have also been previously used for determination of tumor progression. These guidelines were introduced in 2000 and updated in 2009.[31,32] They use a unidimensional measurement based on the longest diameter of a lesion in the axial plane. The individual diameters are summed when multiple lesions are present. However, these guidelines do not take treatments or clinical status into account.[31,32] Despite this, comparison studies have shown good concordance between the RECIST guidelines and the Macdonald criteria in measuring response and progression with irinotecan and bevacizumab combination therapy in relapsed GBM.[33]

After the Macdonald criteria were published, it became increasingly understood that these criteria needed to be altered to account for the variability in contrast-enhancing lesions and noncontrasting tumor, as well as the timing of the radiographic scans with respect to treatment. With the development of new imaging techniques, primarily T2-weighted or fluid-attenuated inversion recovery (FLAIR) MRI, the importance of noncontrast-enhancing tumor that is FLAIR positive became understood. This pattern on imaging, corresponding to infiltrative disease or diffuse tumor growth, was not taken into account with previous response criteria, including both Macdonald and RECIST. This is further complicated by the use of vascular endothelial growth factor inhibitors, antiangiogenic agents that can dramatically reduce contrast enhancement and edema. However, resistance to such agents can include infiltrative tumor growth, possibly along preexisting vasculature, which can be non-contrast-enhancing. These complexities were not taken into account in the previously used criteria.[34–37] Finally, the phenomenon of pseudoprogression was becoming more widely appreciated; therefore the timing of scans in relation to treatments is now understood to be an important factor in the accurate determination of tumor progression compared to pseudoprogression.

AVAglio Protocol

In 2009, the multicenter phase III AVAglio trial (BO21990, NCT00943826) was initiated. This randomized, placebo-controlled trial was designed to investigate the efficacy of radiotherapy and TMZ with or without bevacizumab in patients with newly diagnosed GBM.

To improve on the accuracy and reproducibility of the radiologic response assessment, all aspects were standardized, including image acquisition, timing of assessments, and a centralized review.[38] Furthermore, it adapted the Macdonald criteria to encompass assessment of nonenhancing tumor by use of a T2/FLAIR imaging component as well as qualitative assessments. In the AVAglio protocol, a distinction between index and nonindex lesions was created. Index lesions were defined as all measureable lesions that were contrast-enhancing with clear borders >10 mm identified at baseline. Nonindex lesions were defined as contrast-enhancing lesions that were too small or irregular in shape to be considered index lesions as well as nonenhancing lesions consistent with tumor and were assessed both quantitatively and qualitatively to further define disease progression. Additionally, the AVAglio protocol standardized the assessment of possible pseudoprogression in its study. At the first assessment after radiotherapy (4 weeks posttreatment), if the investigator noted a greater than 25% increase in index lesions or progression of existing nonindex lesions relative to the baseline assessment, then the recommended assessment was pseudoprogression and repeat evaluation should be confirmed 2 months later. If this follow-up scan showed stable disease or partial response the diagnosis of pseudoprogression was confirmed. If, however, the images showed further tumor progression, then progressive disease was diagnosed; the date of the first scan following radiotherapy was considered the date of progression.

RANO Criteria

The Response Assessment in Neuro-oncology (RANO) working group then published updated criteria in 2010 to address and standardize the response of high-grade gliomas to therapy in response to new imaging techniques and impacts of new therapeutic agents as well as the AVAglio trial (Tables 1 and 2).[39] Similar to the Macdonald criteria, the RANO criteria use the product of the maximal cross-sectional enhancing diameters to establish the size of contrast-enhancing lesions. Measurable disease is defined as bidimensionally contrast-enhancing lesions with clearly defined margins using either MRI or CT scan of at least 10 mm, visible on two or more axial slices. These criteria address tumor surrounding cysts or surgical cavities, stating that unless they have a nodular component measuring greater than or equal to 10 mm in diameter, they should be considered nonmeasurable. Nonmeasurable disease is defined as masses with unclear margins, unidimensionally measurable lesions, or lesions smaller than 10 mm. If there are multiple contrast-enhancing lesions, the sum of the products of the perpendicular diameters of at least the two largest lesions and at most five lesions should be measured. Owing to the acceptance of the high rates of pseudoprogression within the first 12 weeks after radiotherapy, the RANO criteria used this time frame to define disease progression. Prior to 12 weeks after the completion of CRT, progression was defined only if there were new areas of enhancement outside of the high-dose radiation field or with evidence of viable tumor on histopathologic sampling (Table 2). After 12 weeks following the completion of CRT, disease progression was defined as new contrast-enhancing lesions outside the field of radiation on stable or increasing doses of corticosteroids, an increase by greater than or equal to 25% in the sum of the products of perpendicular diameters on stable or increasing doses of corticosteroids, clinical deterioration not attributable to concurrent medication or comorbid conditions, and, if the patient is on antiangiogenic therapy, significant increase in T2/FLAIR nonenhancing lesion on stable or increasing doses of corticosteroids and not felt to be a result of comorbid events (Table 2).

Limitations of Current Systems

It is interesting to note that pseudoprogression is treated somewhat differently between the RANO and the

TABLE 1 Summary of the Proposed RANO Response Criteria[39]

Criterion	CR	PR	SD	PD
T1 gadolinium-enhancing disease	None	≥50% ↓	<50% ↓ but <25% ↑	≥25% ↑[a]
T2/FLAIR	Stable or ↓	Stable or ↓	Stable or ↓	↑[a]
New lesion	None	None	None	Present[a]
Corticosteroids	None	Stable or ↓	Stable or ↓	NA[b]
Clinical status	Stable or ↑	Stable or ↑	Stable or ↑	↓[a]
Requirement for response	All	All	All	Any[a]

Abbreviations: RANO, Response Assessment in Neuro-oncology; CR, complete response; PR, partial response; SD, stable disease; PD, progressive disease; FLAIR, fluid-attenuated inversion recovery; NA, not applicable.

[a]*Progression occurs when this criterion is present.*

[b]*Increase in corticosteroids alone will not be taken into account in determining progression in the absence of persistent clinical deterioration.*

AVAglio criteria. The RANO criteria define that progression can be defined only within 12 weeks of completion of radiotherapy with the development of new enhancement outside of the radiation field or histopathologic confirmation.[39] AVAglio uses a more specific definition of pseudoprogression, suggesting that all patients with an initial observed increased in enhancement undergo a follow-up scan at 12 weeks to document a change in this enhancement pattern, so that pseudoprogression can be diagnosed. However, since this first MRI following treatment initiation is used as the new baseline scan for patients with confirmed pseudoprogression, there is no restaging and these patients are excluded from response analyses, which is not an issue with the RANO criteria. Additionally, a limitation of both criteria includes the ability to assess nonenhancing lesions more objectively and the development or persistence of pseudoprogression past 12 weeks. This was highlighted in a 2014 study by Nasseri et al.[40] In this study, 56 patients with GBM who had conventional MRI findings concerning for progression of disease following CRT were enrolled, and dynamic susceptibility-weighted contrast-enhanced p-MRI-Fe was used to distinguish true progression from pseudoprogression using relative cerebral blood volume (rCBV) values. Twenty-seven patients were found to have pseudoprogression and in eight of these 27 patients (30%), pseudoprogression occurred later than 3 months following CRT. This mirrored the previously reported results in the classic paper by Chamberlain et al. that suggested that pseudoprogression can be seen up to 6 months following treatment.[6] This questions the strictly defined time period of 12 weeks used in both the RANO and the AVAglio criteria.

NOVEL IMAGING TECHNIQUES

As the radiographic changes on conventional MRI are indistinguishable between true early disease progression and pseudoprogression, yet have dramatic implications, novel imaging and clinical techniques are being developed to further differentiate these alternatives (Table 3). Some radiographic patterns seen on conventional MRI (axial T1, T2, and post-gadolinium T1-weighted) are suggestive of progressive disease, such as involvement of the corpus callosum with either subependymal spread or multiple enhancing lesions; however, they are not prevalent enough to confirm progression versus postradiation changes.[41] A 2011 study evaluated conventional MRIs of 321 patients with GBM undergoing CRT, 93 of which had evidence of pseudoprogression.[12] This study evaluated 11 MRI signs that may be potentially helpful in distinguishing progression versus pseudoprogression. Of the 11, only one, subependymal enhancement, was predictive for early progression with 38.1% sensitivity and 93.3% specificity, but had a 41.8% negative predictive value. This study highlighted how difficult it is to distinguish these entities with conventional MRI alone. New advanced imaging techniques such as diffusion-weighted MRI (DWI/ADC), MR perfusion imaging, diffusion-tensor imaging, arterial spin, MR spectroscopy, and positron emission tomography (PET)-based strategies are now being evaluated for their potential utility. However, some of the limitations of these new strategies include the lack of prospective assessment and validation in independent cohorts of large enough sizes, as well as a lack of tissue-based confirmatory studies.

TABLE 2 RANO Definitions of Progressive Disease[39]

First Progression	Definition
Progressive disease <12 weeks after completion of CRT	Progression can be defined using diagnostic imaging only if there is new enhancement outside of the radiation field (beyond the high-dose region or 80% isodose line) or if there is unequivocal evidence of viable tumor on histopathologic sampling (e.g., solid tumor areas (i.e., >70% tumor cell nuclei in areas), high or progressive increase in MIB-1 proliferation index compared with prior biopsy, or evidence for histologic progression or increased anaplasia in tumor). Note: Given the difficulty of differentiating true progression from pseudoprogression, clinical decline alone, in the absence of radiographic or histologic confirmation of progression, will not be sufficient for definition of progressive disease in the first 12 weeks after completion of concurrent CRT.
Progressive disease ≥12 weeks after CRT completion	1. New contrast-enhancing lesion outside of radiation field on decreasing, stable, or increasing doses of corticosteroids. 2. Increase by ≥25% in the sum of the products of perpendicular diameters between the first postradiotherapy scan, or a subsequent scan with smaller tumor size, and the scan at 12 weeks or later on stable or increasing doses of corticosteroids. 3. Clinical deterioration not attributable to concurrent medication or comorbid conditions is sufficient to declare progression on current treatment but not for entry onto a clinical trial for recurrence. 4. For patients receiving antiangiogenic therapy, significant increase in T2/FLAIR nonenhancing lesion may also be considered progressive disease. The increased T2/FLAIR must have occurred with the patient on stable or increasing doses of corticosteroids compared with baseline scan or best response after initiation of therapy and not be a result of comorbid events (e.g., effects of radiation therapy (RT), demyelination, ischemic injury, infection, seizures, postoperative changes, or other treatment effects).

TABLE 3 Overview of Imaging Techniques Used to Distinguish Progression from Pseudoprogression[89]

Imaging Method	Patterns Associated with ePD	Strengths	Limitations	References
Conventional MRI	Involvement of callosum with either subependymal spread or multiple enhancing lesions	Available	Unable to distinguish ePD and PsP	3,4
Diffusion-weighted MRI	Lower mean ADC and ADC ratios	Characterizes cellular density	Dependent on sampling method, confounded by vascularity and necrosis	5–7
MR perfusion (DSC)	Increased rCBV in areas of enhancement	rCBV correlates with histologic diagnosis and survival	Vascular leak, cutoff values vary	8–20
Delayed-contrast extravasation MRI	Fast clearance of contrast is associated with active tumor	Fast clearance areas histologically correlate with active tumor	Only pilot studies thus far	21
MR spectroscopic imaging	Higher Cho/Cr and Cho/NAA ratios	Captures metabolic activity	Difficult to interpret heterogeneous tissue	22–29
Arterial spin imaging	Correlation with grade III labeling (blood vessels)	Independent predictor of tumor progression	Only modestly improves diagnostic accuracy over DSC	30
PET	Variable	FDG PET widely available, C-Met with less background	FDG PET with poor sensitivity and specificity, new tracers with more promising results, but most not widely available	31–44

Abbreviations: MRI, magnetic resonance imaging; MR, magnetic resonance; ePD, early progressive disease; PsP, pseudoprogression; ADC, apparent diffusion coefficient; DSC, dynamic susceptibility-weighted contrast-enhanced perfusion MR imaging; rCBV, relative cerebral blood volume; Cho, choline; Cr, creatinine; NAA, N-acetylaspartate; PET, positron emission tomography; FDG, ^{18}F-labeled fluorodeoxyglucose; C-Met, [^{11}C]methionine.

Diffusion Weighted Magnetic Resonance Imaging

DWI measures water diffusion within tissue, a putative measurement of edema. The apparent diffusion coefficient (ADC) quantifies the impedance or mobility of water molecules and may be used to help differentiate between edema, necrosis, and tumor tissue as a marker of cellular density. The first group to use DWI to distinguish recurrent tumor from treatment-related effects was Hein et al. in 2004.[42] This retrospective review of conventional and DWI MR images of 18 patients 4 weeks after completion of radiation found that ADC ratios (ADC of enhancing lesion to ADC of contralateral normal white matter) and ADC values were significantly lower in recurrent tumors compared to radiation injury, confirmed by either histology or clinical course and subsequent imaging. Similar results have been found in other retrospective studies as well as in a prospective study of 17 patients (20 lesions) evaluated with DWI and ADC imaging.[43,44] In the prospective study, five regions of interest within each area of contrast enhancement were evaluated; the maximal ADC values were significantly smaller in the patients with recurrence versus those with radiation injury, suggesting that DWI may be a useful tool in differentiating tumor recurrence versus pseudoprogression.

DWI has been used to specifically evaluate true progression versus pseudoprogression in a study by Lee et al.[45] This retrospective study found higher incidences of restricted diffusion in patients with true progression than in those with pseudoprogression 12 weeks after completion of concomitant CRT with TMZ. The true progression patients had higher incidences of homogeneous or multifocal high signal intensity on DWI (7 of 10 patients, 70%), whereas rim high or no high-intensity signal (10 of 12 patients, 83%) was seen in patients with pseudoprogression with a sensitivity of 80%, a specificity of 83%, and an accuracy of 81.2%.

The use of contrast-enhanced susceptibility-weighted imaging (CE-SWI) also has been shown to be valuable in differentiating tumor recurrence. CE-SWI has been shown to have improved visualization of the heterogeneity of tissue, including tissue necrosis, microvascularity, and defects within the BBB.[46] In a study by Al Sayyari et al. ADC profiles from CE-SWI were compared to conventional MRI from 17 patients with high-grade primary brain tumors with new enhancing lesions.[47] Again, patients with a diagnosis of tumor recurrence had significantly reduced ADC measurements within the enhancement volume.

A 2014 study used both ADC values and rCBV to differentiate tumor progression from pseudoprogression.[48] Thirty-five patients with GBM with new or increased size of enhancing lesions after concomitant CRT and surgical resection were evaluated with combined histograms using both ADC values and relative cerebral blood flow (rCBF). The multiparametric approach (rCBF × ADC) had a sensitivity of 82% and a specificity of 100% and

was the best predictor of true tumor progression and survival compared to uniparametric approaches.

Although the use of DWI/ADC imaging alone or in combination with other imaging techniques holds promise, larger and more prospective studies will need to be completed to verify its utility in distinguishing true progression from pseudoprogression.

Perfusion Imaging

Dynamic susceptibility-weighted contrast-enhanced perfusion MR imaging (DSC) is a T2-weighted MRI that can estimate tissue microvascular density by measuring rCBV. This is in contrast to dynamic contrast-enhanced (DCE) MRI, which is a T1-based image that measures vascular permeability. These two techniques provide information on absolute blood flow, blood volume, and relative blood volume, which can then be a biomarker for tumor progression over time, as GBMs are highly vascular tumors associated with increased blood volume and blood flow. This technique was first used in 2009 to differentiate tumor progression from radiation effects and pseudoprogression. Hu et al. published a prospective study of 13 patients with high-grade gliomas with contrast-enhancing lesions on follow-up scans.[49] Three-tesla gradient-echo DSC as well as contrast-enhanced T1-weighted images were performed preoperatively. Intraoperatively, stereotactic locations of multiple biopsies were captured and coregistered to the imaging sets, which allowed for calculation of localized rCBV. The rCBV values were then correlated to the histopathology from the biopsies to determine areas of tumor progression versus radiation effects. Forty specimens from 13 patients were collected. Of the tissue that was deemed tumor, the rCBV ranged from 0.55 to 4.64, while tissue with radiation effects had a range of rCBV from 0.21 to 0.71. The authors selected a threshold value of 0.71, which enabled an optimized differentiation of recurrent tumor from radiation effects with a sensitivity of 91.7% and a specificity of 100%. Multiple subsequent studies also confirmed similar results that radiation effects have lower rCBV compared to tumor tissue.[50–56]

In 2011, Kong et al. published a prospective study of 90 patients with high-grade glioma treated with adjuvant chemoradiation.[23] Fifty-nine of these patients developed new or enlarging lesions following their therapy. They performed DSC perfusion MR imaging to determine rCBV and also established MGMT promoter methylation status for all the patients. They found that there was a significant difference in the mean rCBV between pseudoprogression and real tumor progression ($p = 0.003$), with a rCBV ratio of >1.47, having an 81.5% sensitivity and 77.8% specificity. They also noted that the unmethylated MGMT promoter group had a significant difference in mean rCBV between real and pseudoprogression, but the methylated MGMT promoter group did not. Several other groups published studies demonstrating significantly lower median rCBV in patients with pseudoprogression compared to true progression, but the sensitivities and specificities varied. One found that, depending on the threshold selected, one could achieve 100% sensitivity and 75% specificity (threshold <1.8) or 100% specificity and 69% sensitivity (threshold <2.4).[57] Furthermore, although many studies achieve significantly different rCBVs between tumor tissue and pseudoprogression, the thresholds selected vary greatly and range from 0.7 to 2.4.[49,57] Therefore, the optimal threshold has yet to be determined and validated for widespread clinical use.

One complicating factor in the use of DSC perfusion imaging is the issue of vascular leak; CRT is known to disrupt the BBB, which could allow for the leak of gadolinium-based contrast agents into the interstitial fluid, which could result in the underestimation of rCBV values.[58] To circumvent this issue, one group has focused on using alternative contrast agents that are unable to cross the disrupted BBB with MR perfusion studies. Gahramanov et al. investigated the use of ferumoxytol for measurement of rCBV compared to the classic gadolinium-based contrast agents such as gadoteridol.[55] In this study of 19 patients who had evidence of recurrent high-grade gliomas on conventional MRI, contrast agent leakage maps and rCBV were derived from perfusion imaging with gadoteridol and ferumoxytol. A threshold of rCBV >1.75 indicated tumor and <1.75 indicated pseudoprogression. Patients with an rCBV of <1.75 using ferumoxytol were associated with a significantly greater median survival of 591 days, compared to rCBV of >1.75 with a median survival of 163 days ($p < 0.001$). Notably, the subsequent determination of disease progression versus pseudoprogression was not formally reported in this study, but it does suggest that MRI with the use of ferumoxytol is probably able to differentiate between tumor progression and pseudoprogression and does not require contrast agent leakage correction as do the gadolinium-based agents.

The widespread use of antiangiogenic agents has added complexity to the interpretation of pseudoprogression in high-grade gliomas, as these agents have been shown to strikingly decrease contrast enhancement on MRI studies. In a study by Artzi et al., 14 patients with GBM undergoing bevacizumab treatment were longitudinally evaluated with multiple MR scans including conventional, diffusion, dynamic susceptibility contrast, DCE imaging, and MR spectroscopy (MRS).[59] This study focused on nonenhancing FLAIR-positive lesions, attempting to differentiate between infiltrative tumor and vasogenic edema. They found that areas of infiltrative tumor were characterized by increased perfusion compared to areas of vasogenic edema, which had reduced perfusion and increased FLAIR values, suggesting that the characterization of non-contrast-enhancing

lesions that are FLAIR positive by MR perfusion may also differentiate the presence of infiltrative tumor in the setting of treatments with antiangiogenic treatments such as bevacizumab.

Finally, DSC MRI may also have predictive value when obtained during chemoradiation. Tsien et al. used DSC MRI to calculate rCBV and rCBF as well as a parametric response map (PRM), which is a voxel-by-voxel analysis, prior to treatment as well as after 3 weeks of CRT in 27 patients in a prospective trial.[60] Thirteen patients had stable disease or partial response, and 14 patients had apparent progression, six of which were deemed to have pseudoprogression by clinical course or surgical resection. Based on the voxel-by-voxel PRM analysis, significantly reduced blood volume at the third week was found in patients with progressive disease compared to pseudoprogression or patients with stable disease ($p < 0.01$). However, change in average percentage of neither rCBV nor rCBF was significantly different from progression and pseudoprogression at these time points. Therefore, CBV from DSC MRI may be an early biomarker for response and differentiating between progression and pseudoprogression during treatment with CRT in patients with higher grade gliomas.

Delayed Contrast Extravasation Magnetic Resonance Imaging

Delayed-contrast extravasation MRI is a novel technique that calculates delayed enhancement subtraction maps, which depict the spatial distribution of contrast accumulation and clearance within tissue, blood vessels, and CSF. This technique can be used to detect subtle disruptions in the BBB. Zach et al. adapted this technique for use in patients with primary brain tumors to differentiate between true and pseudoprogression.[61] In their study of 13 patients with GBM undergoing standard chemoradiation, patients were scanned by delayed-contrast extravasation MRI and followed for up to 19 months posttherapy. They found that there were two patterns of enhancement maps: one that showed slowed contrast clearance from the tissue compared to contrast accumulation and a fast population in which clearance was faster than accumulation. Histological correlation found that the fast population consisted of morphologically active tumor, compared to the slow population, which consisted of nontumor tissue. They found that true progression was associated with a significant increase in the fast component of the enhancing lesion, where pseudoprogression had an increase in the slow component with no significant change in the fast. This suggests that this technique may serve as an early predictor of progression versus pseudoprogression for patients undergoing standard therapies for GBM; however, further larger studies must be completed before its validity is confirmed.

Magnetic Resonance Spectroscopy

MRS is a technique that is used to detect various metabolites within tissues, the most common of which in brain are choline (Cho), *N*-acetylaspartate (NAA), creatinine (Cr), lipid, and lactate. Typically tumors have elevated levels of Cho because of increased cell membrane phospholipids and decreased NAA compared to normal white matter. In contrast, necrotic tissue is characterized by elevated lipid and lactate levels. This technique has been applied in several studies to help differentiate early tumor progression from pseudoprogression and other radiation effects. The original studies used single-voxel MRS, in which the concentration of a metabolite is assessed at a single voxel. These studies demonstrated that pure tumor or pure necrosis could be easily distinguished by this method; however, because of the heterogeneity of contrast-enhancing lesions in postradiation patients, the interpretation was complicated and was rarely definitive in mixed tissues.[62–64]

The technique was then adapted to multislice two-dimensional (2D) multivoxel methods for coverage of a larger region and the ability to investigate multiple regions within heterogeneous tissue. Weybright et al. used 2D chemical shift imaging MRS to evaluate areas of new contrast enhancement in 29 patients with previously treated brain tumors.[65] They found that the Cho/Cr and Cho/NAA ratios were significantly higher and the NAA/Cr ratio significantly lower in areas of tumor compared to radiation injury ($p < 0.0001$). However, they also noted that areas of radiation injury had significantly higher Cho/Cr and Cho/NAA ratios compared to normal white matter. Additionally, when a cutoff value was applied retrospectively 96% of patients (27/28) were correctly classified as either recurrence or radiation injury. This technique was further adapted to 3D MRS enabling evaluation of even larger volumes of interest. Zeng et al. used this technique in 28 patients with new contrast-enhancing lesions after treatment for high-grade glioma.[66] They found that the Cho/NAA and Cho/Cr ratios were significantly higher in recurrent tumor compared to areas of radiation injury ($p < 0.01$), and the NAA/Cr ratios were lower in recurrent tumor than in radiation injury ($p = 0.02$), with a sensitivity of 94%, specificity of 100%, and diagnostic accuracy of 96.2%.

MRS has also been combined with other imaging modalities such as DWI, DSC, and perfusion imaging.[67–69] In one study of 55 patients with new contrast-enhancing lesions after surgery and radiation with high-grade gliomas, MRS was combined with DWI.[68] This study demonstrated significantly elevated Cho/NAA and Cho/Cr ratios in recurrent tumor compared to areas of radiation necrosis ($p < 0.01$), as well as significantly higher ADC values and ratios in areas of radiation injury compared to recurrent tumor ($p < 0.01$), similar to

the previous studies. The combination, however, of MRS (Cho/NAA and Cho/Cr) plus ADC ratios classified 96.4% of patients accurately between tumor recurrence and radiation injury, compared to 85.5% using MRS alone. These results were mirrored in a smaller study of 15 patients that demonstrated that the combination of DWI, DSC, and MRS modalities significantly improved diagnostic accuracy from 84–87% to 93.3% ($p < 0.05$) of tumor recurrence versus radiation injury.[69] These studies suggest that the combination of multiple modalities with MRS may improve its efficacy for differentiating tumor progression from pseudoprogression.

Arterial Spin Imaging

Arterial spin imaging or labeling (ASL) is a technique in which arterial blood water is magnetically labeled and then imaged to measure tissue perfusion. It has been used in conjunction with DSC MRI to distinguish early progression from pseudoprogression in GBM patients. In a retrospective study of 117 patients with newly diagnosed GBM who underwent surgical resection and CRT, patients who underwent both ASL and DSC perfusion MRI were classified as having either tumor recurrence (34 patients) or pseudoprogression (28 patients) based on subsequent clinical course, radiologic findings, or histopathologic diagnosis.[70] ASL imaging was classified into three grades—grade I was equal to white matter, grade II was equal to gray matter, and grade III was equal to blood vessels—and was correlated with DSC perfusion MRI via histogram parameters. Pseudoprogression was observed in 53.6% of patients with grade I and 46.4% of patients with grade II ASL imaging and in 0% of patients with grade III. Conversely, tumor recurrence was seen in 20.6% of patients with grade I, 32.3% of patients with grade II, and 47.1% of patients with grade III ASL imaging, and ASL grade was found to be an independent predictor of tumor progression (odds ratio, 4.73; $p = 0.0017$). Furthermore, ASL improved the diagnostic accuracy of DSC perfusion MRI with 12.9% more accurate results than DSC perfusion MRI alone. However, larger and prospective studies need to be completed for this technique to be validated clinically.

Positron Emission Tomographic Imaging

Because conventional imaging with MRI has failed to completely differentiate early tumor progression from pseudoprogression, PET imaging has also been used in this setting. PET imaging with ^{18}F-labeled fluorodeoxyglucose (FDG) is used in many oncologic settings, but its utility in the brain is limited by the high glucose metabolism in brain tissue, creating high background activity. Furthermore, studies have shown that radiation necrosis and areas of inflammation can also have increased glucose metabolism, complicating interpretation of tumor recurrence.[71] Early studies using FDG PET to evaluate for recurrent tumor versus radiation necrosis had high rates of both false-positive and false-negative findings with unacceptably low sensitivities and specificities (86% and 22%, when using white matter for comparison).[72] A repeat study reported a sensitivity and specificity of FDG PET–CT to be 70% and 97%, respectively, consistent with the poor sensitivity previously published.[73]

Because FDG PET has shown limited utility in the determination of early progression compared to pseudoprogression, investigations into novel tracers with decreased background within brain tissue have occurred including [^{13}N]NH_3 PET, 3′-deoxy-3′-[^{18}F]fluorothymidine (^{18}F-FLT) PET, [^{11}C]methionine (^{11}C-Met) PET, *O*-(2-[^{18}F] fluoroethyl)-L-tyrosine (FET) PET, and 3,4-dihydroxy-6-[^{18}F]fluoro-L-phenylalanine (^{18}F-FDOPA) PET. In a study of only seven patients, [^{13}N]NH_3 PET was efficacious in the differentiation of recurrence from radiation necrosis 6 months after completion of radiotherapy; the scans were concordant 100% with the final diagnosis.[74] However, this tracer has not been studied at earlier time points more consistent with pseudoprogression. ^{18}F-FLT PET is another tracer that holds promise, as it has been used for detection of high-grade gliomas and prognostications during treatments.[75,76] A 2012 small study combined the technique of FLT PET with sodium (^{23}Na) MRI to use complementary approaches to assess tumor function over time to attempt to assess for tumor response.[77] This combined technique, however, has not yet been applied to the challenge of differentiation between early progression and pseudoprogression.

^{11}C-Met has also been investigated in several studies. In the first study published using this tracer in glioma patients, 11 patients were evaluated after receiving stereotactic radiosurgery after primary treatments.[78] In this study, the ^{11}C-Met PET had a sensitivity, specificity, and accuracy in detecting tumor recurrence of 100%, 60%, and 82%, respectively. In a study of 26 glioma patients treated with radiotherapy after primary treatment, however, the sensitivity and specificity of ^{11}C-Met PET for differentiation of recurrence compared to radiation effects was only 75% and 75%.[79] In a larger more recent study, FDG PET and ^{11}C-Met PET were directly compared in 37 patients with concern for primary brain tumor recurrence. Tripathi et al. found that ^{11}C-Met PET was superior to FDG PET in that the sensitivity and specificity of FDG PET was 81.2% and 88.9%, respectively, compared to a sensitivity and specificity of ^{11}C-Met PET of 94.7% and 88.89%, respectively, and had less intraobserver variability.[80] Despite these promising results, other studies suggest that DWI MRI is more effective at differentiating radiation effects from tumor progression than ^{11}C-Met PET when directly compared.[54] Therefore, further

studies with this tracer need to be performed before its clinical utility is established.

Additionally, FET PET has also been investigated in multiple studies for its utility in distinguishing recurrence. In a study by Rachinger et al., 45 patients with a diagnosis of tumor recurrence after various therapies were investigated with FET PET.[81] They found that FET PET had a sensitivity and specificity of 100% and 92.9%, respectively, which was significantly better compared to MRI, with sensitivity and specificity of 93.5% and 50%, respectively. A follow-up prospective study was then completed with FET PET. In this study, 31 patients with glioma underwent FET PET imaging after suspicion of recurrence based on MRI.[82] In 26 patients, FET PET imaging indicating tumor was concurrent with biopsy results, with discordant results in five patients, leading to a positive predictive value of 84%.

^{18}F-FDOPA is an ^{18}F-labeled dopamine precursor that has also been used for PET imaging, with the advantage that it is believed to require active transport for tissue uptake and does not rely on BBB breakdown. In a preliminary study of 51 patients being evaluated for brain tumor recurrence, ^{18}F-FDOPA PET had a sensitivity of 97% and a specificity of 86% for tumor recurrence.[83] Follow-up studies also suggest that this technique may have utility in earlier detection of recurrence than MRI and may improve detection of nonenhancing tumors as well.[84] However, further larger and prospective studies will need to be completed to validate its utility in this clinical context.

BIOLOGIC DIFFERENTIATION

In addition to imaging methods, there have been several avenues of research into biologic and immunologic methods of predicting recurrence compared to pseudoprogression. The prognostic value of MGMT promoter methylation as well as its relation to pseudoprogression has been well established as described above. One recent study investigated the usefulness of a semiquantitative approach of determining MGMT promoter methylation status in determining the occurrence of pseudoprogression. By using methylation-specific multiplex ligation probe amplification to evaluate MGMT promoter methylation status, in conjunction with the standard methylation-specific polymerase chain reaction, a diagnostic accuracy of 93% was achieved for the identification of pseudoprogression.[85] Isocitrate dehydrogenase (IDH1) mutation status has also been investigated for its utility in determining pseudoprogression versus true progression. In a retrospective study of 32 patients with high-grade gliomas who had undergone surgery and CRT, IDH1 mutation analysis from the tumor blocks was performed on the patients with evidence of early progression on MRI within 6 months of completion of therapy.[86] This study reported that the sensitivity and specificity of the IDH1 mutation for detecting pseudoprogression was 66.7% and 100%, respectively, suggesting that the IDH1 mutation may be a useful biomarker in the prediction of pseudoprogression; however, this mutation is known to have a low prevalence in primary high-grade glioma, which may limit its utility.

Additionally, a study has investigated the prognostic value of $CD4^+$ and $CD8^+$ tumor-infiltrating lymphocytes (TILs) in glioma. Han et al. investigated 284 gliomas by immunohistochemical staining of tissue microarray for $CD4^+$, $FoxP3^+$, and $CD8^+$ TILs.[87] They found that high $CD4^+$ and low $CD8^+$ TIL levels were an independent predictor of poor PFS and poor OS.[87] Furthermore, higher rates of pseudoprogression were found in patients with high $CD4^+$ TILs and high $CD8^+$ TILs ($p = 0.007$). This suggests that there may be an immune-related component to the phenomenon of pseudoprogression. A drawback of this method, however, is that is requires tumor tissue for its use in differentiating true progression versus pseudoprogression.

Less invasive approaches have also been investigated with the use of telomerase promoter-based assays to detect tumor cells within the peripheral blood. A 2014 pilot prospective study evaluated detection of tumor cells in the peripheral blood of patients with high-grade glioma using an adenoviral detection system to successfully detect circulating tumor cells based on telomerase activity in patients with brain tumors.[88] Their limited data suggest that the detection of these circulating tumor cells may be predictive of clinical course with higher cell numbers in patients with evidence of progression compared to patients with pseudoprogression. It is appealing to have a peripheral blood-based method helping to determine tumor recurrence; however, a formal large-scale trial of this method must be performed to establish its clinical utility.

CONCLUSIONS

The differentiation of true early progression from pseudoprogression remains a fundamental issue in the field of neuro-oncology. The correct diagnosis can dramatically influence a patient's treatment course. Furthermore, it is a critical issue in the design and implementation of clinical trials, as the inability to distinguish pseudoprogression from true progression can markedly cloud results, leading to inappropriate conclusions. At this time, there is little known about the underlying pathology of pseudoprogression, but it is theorized to be a combination of vascular injury and treatment-related cellular effects. Unfortunately, conventional anatomic MRI is insufficient to adequately distinguish true early

progression from pseudoprogression, and in real time the diagnosis can only be retrospective. Despite multiple investigations into alternate forms of MRI, arterial spin, PET, and MRS imaging, a definitive imaging modality to distinguish these entities has yet to be determined. Alternative approaches through biomarkers have also been explored and hold promise for the future. The continued study of the phenomenon of pseudoprogression is imperative for the future of GBM research.

References

1. Dolecek TA, Propp JM, Stroup NE, Kruchko C. CBTRUS statistical report: primary brain and central nervous system tumors diagnosed in the United States in 2005–2009. *Neuro Oncol*. 2012;14 (suppl 5):v1–49.
2. Stupp R, Mason WP, van den Bent MJ, Weller M, Fisher B, Taphoorn MJ, et al. Radiotherapy plus concomitant and adjuvant temozolomide for glioblastoma. *N Engl J Med*. 2005;352:987–996.
3. Wen PY, Kesari S. Malignant gliomas in adults. *N Engl J Med*. 2008;359:492–507.
4. Quant EC, Wen PY. Response assessment in neuro-oncology. *Curr Oncol Rep*. 2011;13:50–56.
5. Reardon DA, Galanis E, DeGroot JF, Cloughesy TF, Wefel JS, Lamborn KR, et al. Clinical trial end points for high-grade glioma: the evolving landscape. *Neuro Oncol*. 2011;13:353–361.
6. Chamberlain MC, Glantz MJ, Chalmers L, Van Horn A, Sloan AE. Early necrosis following concurrent Temodar and radiotherapy in patients with glioblastoma. *J Neurooncol*. 2007;82:81–83.
7. Gunjur A, Lau E, Taouk Y, Ryan G. Early post-treatment pseudoprogression amongst glioblastoma multiforme patients treated with radiotherapy and temozolomide: a retrospective analysis. *J Med Imaging Radiat Oncol*. 2011;55:603–610.
8. de Wit MC, de Bruin HG, Eijkenboom W, Sillevis Smitt PA, van den Bent MJ. Immediate post-radiotherapy changes in malignant glioma can mimic tumor progression. *Neurology*. 2004;63:535–537.
9. Brandes AA, Tosoni A, Spagnolli F, Frezza G, Leonardi M, Calbucci F, et al. Disease progression or pseudoprogression after concomitant radiochemotherapy treatment: pitfalls in neurooncology. *Neuro Oncol*. 2008;10:361–367.
10. Taal W, Brandsma D, de Bruin HG, Bromberg JE, Swaak-Kragten AT, Smitt PA, et al. Incidence of early pseudo-progression in a cohort of malignant glioma patients treated with chemoirradiation with temozolomide. *Cancer*. 2008;113:405–410.
11. Chaskis C, Neyns B, Michotte A, De Ridder M, Everaert H. Pseudoprogression after radiotherapy with concurrent temozolomide for high-grade glioma: clinical observations and working recommendations. *Surg Neurol*. 2009;72:423–428.
12. Young RJ, Gupta A, Shah AD, Graber JJ, Zhang Z, Shi W, et al. Potential utility of conventional MRI signs in diagnosing pseudoprogression in glioblastoma. *Neurology*. 2011;76:1918–1924.
13. Roldan GB, Scott JN, McIntyre JB, Dharmawardene M, de Robles PA, Magliocco AM, et al. Population-based study of pseudoprogression after chemoradiotherapy in GBM. *Can J Neurol Sci*. 2009;36:617–622.
14. Sanghera P, Perry J, Sahgal A, Symons S, Aviv R, Morrison M, et al. Pseudoprogression following chemoradiotherapy for glioblastoma multiforme. *Can J Neurol Sci*. 2010;37:36–42.
15. Brandsma D, van den Bent MJ. Pseudoprogression and pseudoresponse in the treatment of gliomas. *Curr Opin Neurol*. 2009;22:633–638.
16. Rheims S, Ricard D, van den Bent M, Taillandier L, Bourg V, Desestret V, et al. Peri-ictal pseudoprogression in patients with brain tumor. *Neuro Oncol*. 2011;13:775–782.
17. Hoffman WF, Levin VA, Wilson CB. Evaluation of malignant glioma patients during the postirradiation period. *J Neurosurg*. 1979;50:624–628.
18. Levin VA, Crafts DC, Norman DM, Hoffer PB, Spire JP, Wilson CB. Criteria for evaluating patients undergoing chemotherapy for malignant brain tumors. *J Neurosurg*. 1977;47:329–335.
19. Graeb DA, Steinbok P, Robertson WD. Transient early computed tomographic changes mimicking tumor progression after brain tumor irradiation. *Radiology*. 1982;144:813–817.
20. Cascino TL, Kimmel DW, Dinapoli RP, et al. Report of four cases with a resolving syndrome which otherwise simulates recurrent brain tumor. *Neurology*. 1988;38:306.
21. Macdonald DR, Cascino TL, Schold Jr SC, Cairncross JG. Response criteria for phase II studies of supratentorial malignant glioma. *J Clin Oncol*. 1990;8:1277–1280.
22. Brandes AA, Franceschi E, Tosoni A, Blatt V, Pession A, Tallini G, et al. MGMT promoter methylation status can predict the incidence and outcome of pseudoprogression after concomitant radiochemotherapy in newly diagnosed glioblastoma patients. *J Clin Oncol*. 2008;26:2192–2197.
23. Kong DS, Kim ST, Kim EH, Lim DH, Kim WS, Suh YL, et al. Diagnostic dilemma of pseudoprogression in the treatment of newly diagnosed glioblastomas: the role of assessing relative cerebral blood flow volume and oxygen-6-methylguanine-DNA methyltransferase promoter methylation status. *AJNR Am J Neuroradiol*. 2011;32:382–387.
24. Woodworth GF, Garzon-Muvdi T, Ye X, Blakeley JO, Weingart JD, Burger PC. Histopathological correlates with survival in reoperated glioblastomas. *J Neurooncol*. July 2013;113(3):485–493.
25. Kang HC, Kim CY, Han JH, Choe GY, Kim JH, Kim IA. Pseudoprogression in patients with malignant gliomas treated with concurrent temozolomide and radiotherapy: potential role of p53. *J Neurooncol*. 2011;102:157–162.
26. Pouleau HB, Sadeghi N, Baleriaux D, Melot C, De Witte O, Lefranc F. High levels of cellular proliferation predict pseudoprogression in glioblastoma patients. *Int J Oncol*. 2012;40:923–928.
27. Cao Y, Tsien CI, Shen Z, Tatro DS, Ten Haken R, Kessler ML, et al. Use of magnetic resonance imaging to assess blood–brain/blood-glioma barrier opening during conformal radiotherapy. *J Clin Oncol*. 2005;23:4127–4136.
28. Miller AB, Hoogstraten B, Staquet M, Winkler A. Reporting results of cancer treatment. *Cancer*. 1981;47:207–214.
29. van den Bent MJ, Vogelbaum MA, Wen PY, Macdonald DR, Chang SM. End point assessment in gliomas: novel treatments limit usefulness of classical Macdonald's criteria. *J Clin Oncol*. 2009;27: 2905–2908.
30. Caroline I, Rosenthal MA. Imaging modalities in high-grade gliomas: pseudoprogression, recurrence, or necrosis? *J Clin Neurosci*. 2012;19:633–637.
31. Eisenhauer EA, Therasse P, Bogaerts J, Schwartz LH, Sargent D, Ford R, et al. New response evaluation criteria in solid tumours: revised RECIST guideline (version 1.1). *Eur J Cancer*. 2009;45:228–247.
32. Therasse P, Arbuck SG, Eisenhauer EA, Wanders J, Kaplan RS, Rubinstein L, et al. New guidelines to evaluate the response to treatment in solid tumors. European Organization for Research and Treatment of Cancer, National Cancer Institute of the United States, National Cancer Institute of Canada. *J Natl Cancer Inst*. 2000;92:205–216.
33. Gallego Perez-Larraya J, Lahutte M, Petrirena G, Reyes-Botero G, Gonzalez-Aguilar A, Houillier C, et al. Response assessment in recurrent glioblastoma treated with irinotecan-bevacizumab: comparative analysis of the Macdonald, RECIST, RANO, and RECIST + F criteria. *Neuro Oncol*. 2012;14:667–673.
34. Norden AD, Young GS, Setayesh K, Muzikansky A, Klufas R, Ross GL, et al. Bevacizumab for recurrent malignant gliomas: efficacy, toxicity, and patterns of recurrence. *Neurology*. 2008;70:779–787.

35. de Groot JF, Fuller G, Kumar AJ, Piao Y, Eterovic K, Ji Y, et al. Tumor invasion after treatment of glioblastoma with bevacizumab: radiographic and pathologic correlation in humans and mice. *Neuro Oncol*. 2010;12:233–242.
36. Gerstner ER, Chen PJ, Wen PY, Jain RK, Batchelor TT, Sorensen G. Infiltrative patterns of glioblastoma spread detected via diffusion MRI after treatment with cediranib. *Neuro Oncol*. 2010;12:466–472.
37. Rubenstein JL, Kim J, Ozawa T, Zhang M, Westphal M, Deen DF, et al. Anti-VEGF antibody treatment of glioblastoma prolongs survival but results in increased vascular cooption. *Neoplasia*. 2000;2:306–314.
38. Chinot OL, de La Motte Rouge T, Moore N, Zeaiter A, Das A, Phillips H, et al. AVAglio: phase 3 trial of bevacizumab plus temozolomide and radiotherapy in newly diagnosed glioblastoma multiforme. *Adv Ther*. 2011;28:334–340.
39. Wen PY, Macdonald DR, Reardon DA, Cloughesy TF, Sorensen AG, Galanis E, et al. Updated response assessment criteria for high-grade gliomas: response assessment in neuro-oncology working group. *J Clin Oncol*. 2010;28:1963–1972.
40. Nasseri M, Gahramanov S, Netto JP, Fu R, Muldoon LL, Varallyay C, et al. Evaluation of pseudoprogression in patients with glioblastoma multiforme using dynamic magnetic resonance imaging with ferumoxytol calls RANO criteria into question. *Neuro Oncol*. 2014;16:1146–1154.
41. Mullins ME, Barest GD, Schaefer PW, Hochberg FH, Gonzalez RG, Lev MH. Radiation necrosis versus glioma recurrence: conventional MR imaging clues to diagnosis. *AJNR Am J Neuroradiol*. 2005;26:1967–1972.
42. Hein PA, Eskey CJ, Dunn JF, Hug EB. Diffusion-weighted imaging in the follow-up of treated high-grade gliomas: tumor recurrence versus radiation injury. *AJNR Am J Neuroradiol*. 2004;25:201–209.
43. Asao C, Korogi Y, Kitajima M, Hirai T, Baba Y, Makino K, et al. Diffusion-weighted imaging of radiation-induced brain injury for differentiation from tumor recurrence. *AJNR Am J Neuroradiol*. 2005;26:1455–1460.
44. Sundgren PC, Fan X, Weybright P, Welsh RC, Carlos RC, Petrou M, et al. Differentiation of recurrent brain tumor versus radiation injury using diffusion tensor imaging in patients with new contrast-enhancing lesions. *Magn Reson Imaging*. 2006;24:1131–1142.
45. Lee WJ, Choi SH, Park CK, Yi KS, Kim TM, Lee SH, et al. Diffusion-weighted MR imaging for the differentiation of true progression from pseudoprogression following concomitant radiotherapy with temozolomide in patients with newly diagnosed high-grade gliomas. *Acad Radiol*. 2012;19:1353–1361.
46. Pinker K, Noebauer-Huhmann IM, Stavrou I, Hoeftberger R, Szomolanyi P, Weber M, et al. High-field, high-resolution, susceptibility-weighted magnetic resonance imaging: improved image quality by addition of contrast agent and higher field strength in patients with brain tumors. *Neuroradiology*. 2008;50:9–16.
47. Al Sayyari A, Buckley R, McHenery C, Pannek K, Coulthard A, Rose S. Distinguishing recurrent primary brain tumor from radiation injury: a preliminary study using a susceptibility-weighted MR imaging-guided apparent diffusion coefficient analysis strategy. *AJNR Am J Neuroradiol*. 2010;31:1049–1054.
48. Cha J, Kim ST, Kim HJ, Kim BJ, Kim YK, Lee JY, et al. Differentiation of tumor progression from pseudoprogression in patients with posttreatment glioblastoma using multiparametric histogram analysis. *AJNR Am J Neuroradiol*. 2014;35:1309–1317.
49. Hu LS, Baxter LC, Smith KA, Feuerstein BG, Karis JP, Eschbacher JM, et al. Relative cerebral blood volume values to differentiate high-grade glioma recurrence from posttreatment radiation effect: direct correlation between image-guided tissue histopathology and localized dynamic susceptibility-weighted contrast-enhanced perfusion MR imaging measurements. *AJNR Am J Neuroradiol*. 2009;30:552–558.
50. Gahramanov S, Raslan AM, Muldoon LL, Hamilton BE, Rooney WD, Varallyay CG, et al. Potential for differentiation of pseudoprogression from true tumor progression with dynamic susceptibility-weighted contrast-enhanced magnetic resonance imaging using ferumoxytol vs. gadoteridol: a pilot study. *Int J Radiat Oncol Biol Phys*. 2011;79:514–523.
51. Hu X, Wong KK, Young GS, Guo L, Wong ST. Support vector machine multiparametric MRI identification of pseudoprogression from tumor recurrence in patients with resected glioblastoma. *J Magn Reson Imaging*. 2011;33:296–305.
52. Narang J, Jain R, Arbab AS, Mikkelsen T, Scarpace L, Rosenblum ML, et al. Differentiating treatment-induced necrosis from recurrent/progressive brain tumor using nonmodel-based semiquantitative indices derived from dynamic contrast-enhanced T1-weighted MR perfusion. *Neuro Oncol*. 2011;13:1037–1046.
53. Fatterpekar GM, Galheigo D, Narayana A, Johnson G, Knopp E. Treatment-related change versus tumor recurrence in high-grade gliomas: a diagnostic conundrum–use of dynamic susceptibility contrast-enhanced (DSC) perfusion MRI. *AJR Am J Roentgenol*. 2012;198:19–26.
54. Kim YH, Oh SW, Lim YJ, Park CK, Lee SH, Kang KW, et al. Differentiating radiation necrosis from tumor recurrence in high-grade gliomas: assessing the efficacy of 18F-FDG PET, 11C-methionine PET and perfusion MRI. *Clin Neurol Neurosurg*. 2010;112:758–765.
55. Gahramanov S, Muldoon LL, Varallyay CG, Li X, Kraemer DF, Fu R, et al. Pseudoprogression of glioblastoma after chemo- and radiation therapy: diagnosis by using dynamic susceptibility-weighted contrast-enhanced perfusion MR imaging with ferumoxytol versus gadoteridol and correlation with survival. *Radiology*. 2013;266:842–852.
56. Young RJ, Gupta A, Shah AD, Graber JJ, Chan TA, Zhang Z, et al. MRI perfusion in determining pseudoprogression in patients with glioblastoma. *Clin Imaging*. 2013;37:41–49.
57. Graber JJ, Young RJ, Gupta A, Shah D, Chan TA, Zhang Z, et al. Magnetic resonance (MR) perfusion imaging to differentiate early progression from pseudoprogression following chemoradiotherapy for glioblastoma (GBM). *J Clin Oncol*. 2011;2009:29.
58. Gahramanov S, Muldoon LL, Li X, Neuwelt EA. Improved perfusion MR imaging assessment of intracerebral tumor blood volume and antiangiogenic therapy efficacy in a rat model with ferumoxytol. *Radiology*. 2011;261:796–804.
59. Artzi M, Bokstein F, Blumenthal DT, Aizenstein O, Liberman G, Corn BW, et al. Differentiation between vasogenic-edema versus tumor-infiltrative area in patients with glioblastoma during bevacizumab therapy: a longitudinal MRI study. *Eur J Radiol*. 2014;83:1250–1256.
60. Tsien C, Galban CJ, Chenevert TL, Johnson TD, Hamstra DA, Sundgren PC, et al. Parametric response map as an imaging biomarker to distinguish progression from pseudoprogression in high-grade glioma. *J Clin Oncol*. 2010;28:2293–2299.
61. Zach L, Guez D, Last D, Daniels D, Grober Y, Nissim O, et al. Delayed contrast extravasation MRI for depicting tumor and non-tumoral tissues in primary and metastatic brain tumors. *PLoS One*. 2012;7:e52008.
62. Schlemmer HP, Bachert P, Herfarth KK, Zuna I, Debus J, van Kaick G. Proton MR spectroscopic evaluation of suspicious brain lesions after stereotactic radiotherapy. *AJNR Am J Neuroradiol*. 2001;22:1316–1324.
63. Rock JP, Hearshen D, Scarpace L, Croteau D, Gutierrez J, Fisher JL, et al. Correlations between magnetic resonance spectroscopy and image-guided histopathology, with special attention to radiation necrosis. *Neurosurgery*. 2002;51:912–919. discussion 919–920.
64. Rock JP, Scarpace L, Hearshen D, Gutierrez J, Fisher JL, Rosenblum M, et al. Associations among magnetic resonance spectroscopy, apparent diffusion coefficients, and image-guided histopathology with special attention to radiation necrosis. *Neurosurgery*. 2004;54:1111–1117. discussion 1117–1119.

65. Weybright P, Sundgren PC, Maly P, Hassan DG, Nan B, Rohrer S, et al. Differentiation between brain tumor recurrence and radiation injury using MR spectroscopy. *AJR Am J Roentgenol*. 2005;185: 1471–1476.
66. Zeng QS, Li CF, Zhang K, Liu H, Kang XS, Zhen JH. Multivoxel 3D proton MR spectroscopy in the distinction of recurrent glioma from radiation injury. *J Neurooncol*. 2007;84:63–69.
67. Bobek-Billewicz B, Stasik-Pres G, Majchrzak H, Zarudzki L. Differentiation between brain tumor recurrence and radiation injury using perfusion, diffusion-weighted imaging and MR spectroscopy. *Folia Neuropathol*. 2010;48:81–92.
68. Zeng QS, Li CF, Liu H, Zhen JH, Feng DC. Distinction between recurrent glioma and radiation injury using magnetic resonance spectroscopy in combination with diffusion-weighted imaging. *Int J Radiat Oncol Biol Phys*. 2007;68:151–158.
69. Matsusue E, Fink JR, Rockhill JK, Ogawa T, Maravilla KR. Distinction between glioma progression and post-radiation change by combined physiologic MR imaging. *Neuroradiology*. 2010;52: 297–306.
70. Choi YJ, Kim HS, Jahng GH, Kim SJ, Suh DC. Pseudoprogression in patients with glioblastoma: added value of arterial spin labeling to dynamic susceptibility contrast perfusion MR imaging. *Acta Radiol*. 2013;54:448–454.
71. Chen W. Clinical applications of PET in brain tumors. *J Nucl Med*. 2007;48:1468–1481.
72. Ricci PE, Karis JP, Heiserman JE, Fram EK, Bice AN, Drayer BP. Differentiating recurrent tumor from radiation necrosis: time for re-evaluation of positron emission tomography? *AJNR Am J Neuroradiol*. 1998;19:407–413.
73. Santra A, Kumar R, Sharma P, Bal C, Kumar A, Julka PK, et al. F-18 FDG PET-CT in patients with recurrent glioma: comparison with contrast enhanced MRI. *Eur J Radiol*. 2012;81:508–513.
74. Xiangsong Z, Weian C. Differentiation of recurrent astrocytoma from radiation necrosis: a pilot study with ^{13}N-NH_3 PET. *J Neurooncol*. 2007;82:305–311.
75. Chen W, Cloughesy T, Kamdar N, Satyamurthy N, Bergsneider M, Liau L, et al. Imaging proliferation in brain tumors with ^{18}F-FLT PET: comparison with ^{18}F-FDG. *J Nucl Med*. 2005;46:945–952.
76. Wardak M, Schiepers C, Dahlbom M, Cloughesy T, Chen W, Satyamurthy N, et al. Discriminant analysis of (1)(8)F-fluorothymidine kinetic parameters to predict survival in patients with recurrent high-grade glioma. *Clin Cancer Res*. 2011;17:6553–6562.
77. Laymon CM, Oborski MJ, Lee VK, Davis DK, Wiener EC, Lieberman FS, et al. Combined imaging biomarkers for therapy evaluation in glioblastoma multiforme: correlating sodium MRI and F-18 FLT PET on a voxel-wise basis. *Magn Reson Imaging*. 2012;30: 1268–1278.
78. Tsuyuguchi N, Takami T, Sunada I, Iwai Y, Yamanaka K, Tanaka K, et al. Methionine positron emission tomography for differentiation of recurrent brain tumor and radiation necrosis after stereotactic radiosurgery–in malignant glioma. *Ann Nucl Med*. 2004;18:291–296.
79. Terakawa Y, Tsuyuguchi N, Iwai Y, Yamanaka K, Higashiyama S, Takami T, et al. Diagnostic accuracy of 11C-methionine PET for differentiation of recurrent brain tumors from radiation necrosis after radiotherapy. *J Nucl Med*. 2008;49:694–699.
80. Tripathi M, Sharma R, Varshney R, Jaimini A, Jain J, Souza MM, et al. Comparison of F-18 FDG and C-11 methionine PET/CT for the evaluation of recurrent primary brain tumors. *Clin Nucl Med*. 2012;37:158–163.
81. Rachinger W, Goetz C, Popperl G, Gildehaus FJ, Kreth FW, Holtmannspotter M, et al. Positron emission tomography with O-(2-[18F]fluoroethyl)-l-tyrosine versus magnetic resonance imaging in the diagnosis of recurrent gliomas. *Neurosurgery*. 2005;57:505–511. discussion 505–511.
82. Mehrkens JH, Popperl G, Rachinger W, Herms J, Seelos K, Tatsch K, et al. The positive predictive value of O-(2-[18F]fluoroethyl)-L-tyrosine (FET) PET in the diagnosis of a glioma recurrence after multimodal treatment. *J Neurooncol*. 2008;88:27–35.
83. Chen W, Silverman DH, Delaloye S, Czernin J, Kamdar N, Pope W, et al. 18F-FDOPA PET imaging of brain tumors: comparison study with 18F-FDG PET and evaluation of diagnostic accuracy. *J Nucl Med*. 2006;47:904–911.
84. Ledezma CJ, Chen W, Sai V, Freitas B, Cloughesy T, Czernin J, et al. 18F-FDOPA PET/MRI fusion in patients with primary/recurrent gliomas: initial experience. *Eur J Radiol*. 2009;71:242–248.
85. Park CK, Kim J, Yim SY, Lee AR, Han JH, Kim CY, et al. Usefulness of MS-MLPA for detection of MGMT promoter methylation in the evaluation of pseudoprogression in glioblastoma patients. *Neuro Oncol*. 2011;13:195–202.
86. Motegi H, Kamoshima Y, Terasaka S, Kobayashi H, Yamaguchi S, Tanino M, et al. IDH1 mutation as a potential novel biomarker for distinguishing pseudoprogression from true progression in patients with glioblastoma treated with temozolomide and radiotherapy. *Brain Tumor Pathol*. 2013;30:67–72.
87. Han S, Zhang C, Li Q, Dong J, Liu Y, Huang Y, et al. Tumour-infiltrating CD4(+) and CD8(+) lymphocytes as predictors of clinical outcome in glioma. *Br J Cancer*. 2014;110:2560–2568.
88. Macarthur KM, Kao GD, Chandrasekaran S, Alonso-Basanta M, Chapman C, Lustig RA, et al. Detection of brain tumor cells in the peripheral blood by a telomerase promoter-based assay. *Cancer Res*. 2014;74:2152–2159.
89. Kruser TJ, Mehta MP, Robins HI. Pseudoprogression after glioma therapy: a comprehensive review. *Expert Rev Neurother*. 2013;13:389–403.

CHAPTER

56

Pitfalls in the Neuroimaging of Brain Tumors

Erik B. Nine[1], *Haricharan Reddy*[2], *Eric C. Bourekas*[3,4], *H. Wayne Slone*[3]

[1]Department of Radiology, North Shore Medical Center, Salem, MA, USA; [2]Diversified Radiology, Denver, CO, USA; [3]Dardinger Neuro-Oncology Center, Departments of Radiology, Wexner Medical Center at The Ohio State University and James Cancer Hospital and Solove Research Institute, Columbus, OH, USA; [4]Division of Neuro-Oncology, Departments of Neurology and Neurosurgery, Dardinger Neuro-Oncology Center, Wexner Medical Center at The Ohio State University and James Cancer Hospital and Solove Research Institute, Columbus, OH, USA

INTRODUCTION

Each year, more than 200,000 people are newly diagnosed with a primary or metastatic brain tumor. Accurate diagnosis and grading of brain tumors are critical to determining prognosis and therapy. Imaging plays a critical role in these processes. Certain imaging characteristics, such as the pattern of enhancement and alteration of signal on magnetic resonance imaging (MRI), or density alterations on computed tomography, suggest a brain tumor. However, imaging of brain tumors is frequently not so straightforward. Many entities can mimic a brain tumor. These mimics of tumors include inflammatory, infectious, demyelinating, and cerebrovascular diseases, among others. Once the diagnosis has been made and treatment initiated, it is important to determine response to therapy and differentiate tumor recurrence from treatment-related complications. In this chapter, we discuss pitfalls in the neurological imaging of brain tumors categorized by location: extra-axial, the meninges, and intra-axial. We focus on the mimics of brain tumors in each location.

IMAGING FEATURES

Extra-axial and Meningeal Tumors

Meningioma and lymphoma are common extra-axial brain tumors. A common mimic of these lesions is sarcoidosis, which may be difficult to distinguish from a brain tumor.[1] Low signal intensity on diffusion-weighted imaging (DWI) helps distinguish sarcoidosis from lymphoma or meningioma, which is often mildly hyperintense on DWI.

Infectious granulomas such as tuberculosis may mimic meningiomas. Pulmonary involvement as well as clinical parameters can help differentiate these entities. Other infectious etiologies, which can present with ring-enhancing lesions simulating brain tumor, include aspergillosis and toxoplasmosis. These patients are often immunocompromised. Paranasal sinus disease is usually the origin of intracranial aspergillus.

Intracranial foreign body granulomas can simulate meningiomas. Gel foam, shunt tubing, suture, cotton, or acrylate monomer can cause similar MRI characteristics. Low signal on T1-weighted images, heterogeneous high signal on T2-weighted images, and contrast enhancement are the typical MRI features.[1] Close correlation with history regarding type of surgery and length of time from surgery can assist in the diagnosis.

Whenever meningioma is a diagnostic consideration, other neoplastic processes that should be considered include lymphoma, dural-based metastasis, and plasmacytoma. Of note, the dural tail sign, which is often associated with a meningioma, is a pitfall, as it can be seen with any lesion involving the dura.[2]

Meningeal enhancement is seen in leptomeningeal metastases or even primary tumors such as lymphoma. It is important to differentiate leptomeningeal from pachymeningeal or dural enhancement. Other causes of leptomeningeal enhancement include infectious meningitis (bacterial, tuberculosis, fungal, syphilis, and viral), granulomatous

http://dx.doi.org/10.1016/B978-0-12-800945-1.00056-2

© 2016 Elsevier Ltd. All rights reserved.

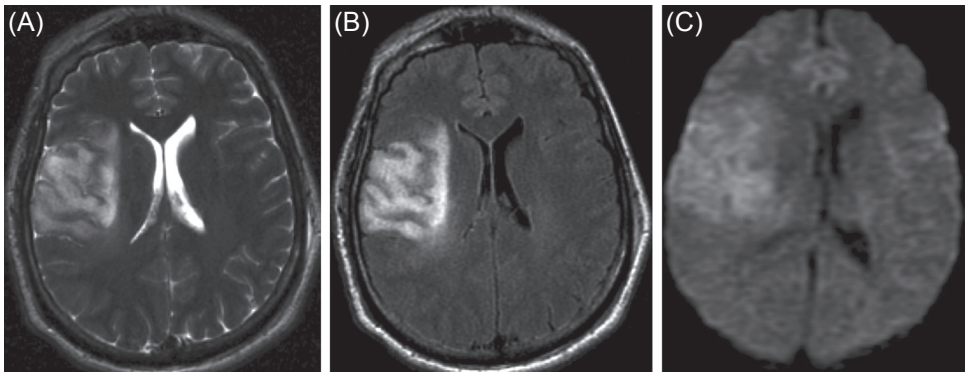


FIGURE 1 A 49-year-old male with seizure activity and loss of consciousness. (A) T2-weighted MR image shows infiltrative area of increased signal involving both gray and white matter in the right MCA distribution mimicking infarct. (B) FLAIR sequence reveals mild gyral thickening and surrounding edema and mild mass effect. (C) Of note, there is mild restricted diffusion on the DWI sequences, not to the degree expected with infarction. Findings suggest infiltrative tumor. Subsequent biopsy yielded oligodendroglioma.

meningitis (sarcoidosis), subacute subarachnoid hemorrhage, subacute cerebral infarction, and Sturge–Weber syndrome. Differential considerations for dural or pachymeningeal enhancement include infection (skull-base osteomyelitis), intracranial hypotension, iatrogenic etiologies (after craniotomy or shunt insertion or after lumbar puncture), venous thrombosis, and granulomatous meningitis (sarcoidosis). Correlation with the history usually narrows the differential diagnosis. Idiopathic intracranial hypotension shows diffuse pachymeningeal enhancement as well as other findings, including the "sagging" brain.

In addition to enhancement, hyperintensity of the cerebrospinal fluid (CSF) on fluid-attenuated inversion recovery (FLAIR) imaging is often noted with leptomeningeal metastases. Other processes such as subarachnoid hemorrhage and infection can result in similar hyperintensity. Bright CSF on FLAIR imaging is not always indicative of subarachnoid disease. If the patient has been administered 100% O_2, the CSF may be bright. Bright CSF can also be a result of diffusion of gadolinium contrast into the CSF in the setting of renal insufficiency.

Intra-axial Lesions

Cerebral infarction is one of the most common mimics of a brain tumor. It is usually straightforward to differentiate brain tumor from infarct, especially if the clinical history is known and the characteristic imaging findings are seen in a vascular distribution. When there is an atypical clinical course or unreliable history, differentiating cerebral infarction from brain tumor may be difficult (see Figure 1).

An acute ischemic stroke may present with an ill-defined cerebral lesion with mass effect, with or without parenchymal enhancement. These findings may be similar to a glioma. DWI is crucial in this setting and usually will demonstrate a greater degree of hyperintensity (i.e., restricted diffusion) in the setting of an infarct, compared to neoplasm. However, this may not be conclusive and short-term follow-up is necessary in these patients.

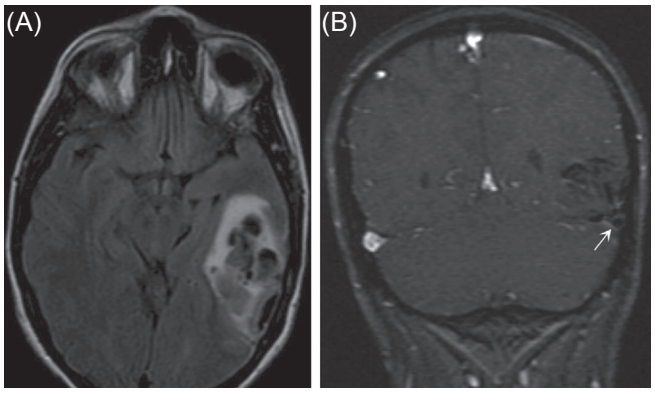


FIGURE 2 A 36-year-old HIV-positive female with a 3-day history of global headache. (A) On MRI, FLAIR sequence shows a heterogeneous signal mass involving white and gray matter, with surrounding edema, which could suggest neoplasm; however, this is nonspecific. (B) Coronal MR venogram shows left transverse dural venous sinus thrombosis (arrow), which indicates that the parenchymal lesion is actually a hemorrhagic venous infarct.

Subacute infarction is even more likely to mimic a brain tumor. Subacute infarction often demonstrates contrast enhancement. Moreover, DWI may be falsely negative, as pseudonormalization of the apparent diffusion coefficient can mask the infarction on imaging. Variable contrast enhancement can also mimic a neoplasm. However, the vascular distribution, gyral enhancement, and minimal to no mass effect are more characteristic of subacute infarction.

Venous infarction may simulate brain tumor, as it does not occur in a vascular territory, has more extensive white matter lesions, can show hemorrhagic change, can have irregular contrast enhancement, and can appear similar to peritumoral edema. If a lesion is not in a typical vascular distribution or there are multifocal high-signal changes on T2-weighted imaging, further inspection for evidence of venous infarction should be made via MR venography (see Figure 2).

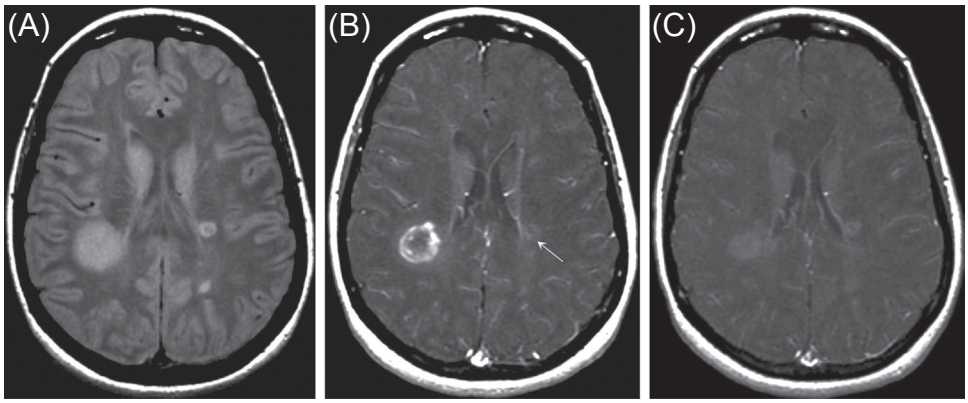


FIGURE 3 (A) A 48-year-old female with weakness and suspected MS. There are several periventricular lesions in the deep white matter of both cerebral hemispheres present on the initial FLAIR sequences. (B) One of the lesions shows thick rim enhancement in the posterior right frontal lobe following gadolinium administration, raising the possibility of neoplasm. (C) However, the lack enhancement of several other periventricular lesions (arrow), as well as partial interval decrease in size and enhancement on the 7-month follow-up examination, suggests demyelination.

Hematoma may be indistinguishable from brain tumor. History and follow-up imaging can help make this differentiation.

A large aneurysm with surrounding edema may mimic a brain tumor. If the aneurysm is partially or completely thrombosed, it may exhibit ring enhancement or peripheral calcifications as imaging features. Laminated calcification morphology may be characteristic.

Tumefactive multiple sclerosis (MS) can mimic brain tumors such as gliomas (see Figure 3). The lack of mass effect and edema may help in the differential diagnosis. Also, incomplete rim enhancement and mildly restricted diffusion are typical of MS lesions.

Intracranial parenchymal sarcoidosis can also mimic a brain tumor. The findings of neurosarcoidosis are nonspecific. Parenchymal lesions may be either solitary or multiple and can be infratentorial or supratentorial. They usually exhibit moderate edema. It is difficult to distinguish sarcoid from brain tumors such as glioma, metastases, or lymphoma. Associated findings may include involvement of the basal leptomeninges and cranial nerves.

Neurosyphilis is becoming more common, owing to the spread of acquired immunodeficiency syndrome worldwide. Focal meningovascular neurosyphilis (cerebral gumma) can present as a solitary or multiple ring-enhancing subcortical masses.

Differentiating cerebral abscesses from necrotic tumor is difficult on conventional MRI. DWI helps in distinguishing these entities. Increased signal in DWI and decreased apparent diffusion coefficient (ADC) values suggest brain abscesses (see Figure 4). The converse is true for brain tumors. In addition, the ring enhancement of an abscess is typically smooth and thinner adjacent to the ventricular system. The capsule of an abscess often shows low T2 and high T1 signal. In contrast, an irregular and thickened rim of enhancement is typical of brain tumors.

In the human immunodeficiency virus (HIV) patient, differentiating toxoplasmosis from lymphoma may be difficult, as both may demonstrate ring enhancement. Further differentiation may be made utilizing positron-emission tomography (PET) imaging, thallium-201 SPECT imaging, and MR spectroscopy.

RECURRENCE VERSUS TREATMENT-RELATED COMPLICATIONS

The diagnosis of radiation necrosis on imaging remains challenging, in part because the pattern of abnormal enhancement closely mimics that of recurrent brain tumor (see Figure 5). Tumor recurrence is suggested by new, nodular enhancement. In contrast, treatment-related complications such as postradiation therapy changes, necrosis, and abscess formation usually will not demonstrate new nodular enhancement.

MRI manifestations of radiation necrosis are cystic or finger-like foci of abnormally increased signal intensity within white matter on T2-weighted images. Rim or possibly nodular enhancement may be present,[2–4] as there is often diffuse damage to the blood–brain barrier. The degree of enhancement can vary with time. The enhancement pattern may be heterogeneous and lesions may appear discontinuous with surrounding areas of nonenhancing necrosis. Vasogenic edema and regional mass effect may be minimal or extensive. These findings are often nonspecific and may not permit differentiation from tumor recurrence.

Assessment of ADC ratios in the enhancing regions of a brain tumor during the follow-up evaluation after therapy may be useful in differentiating radiation effects from tumor recurrence or progression.[5]

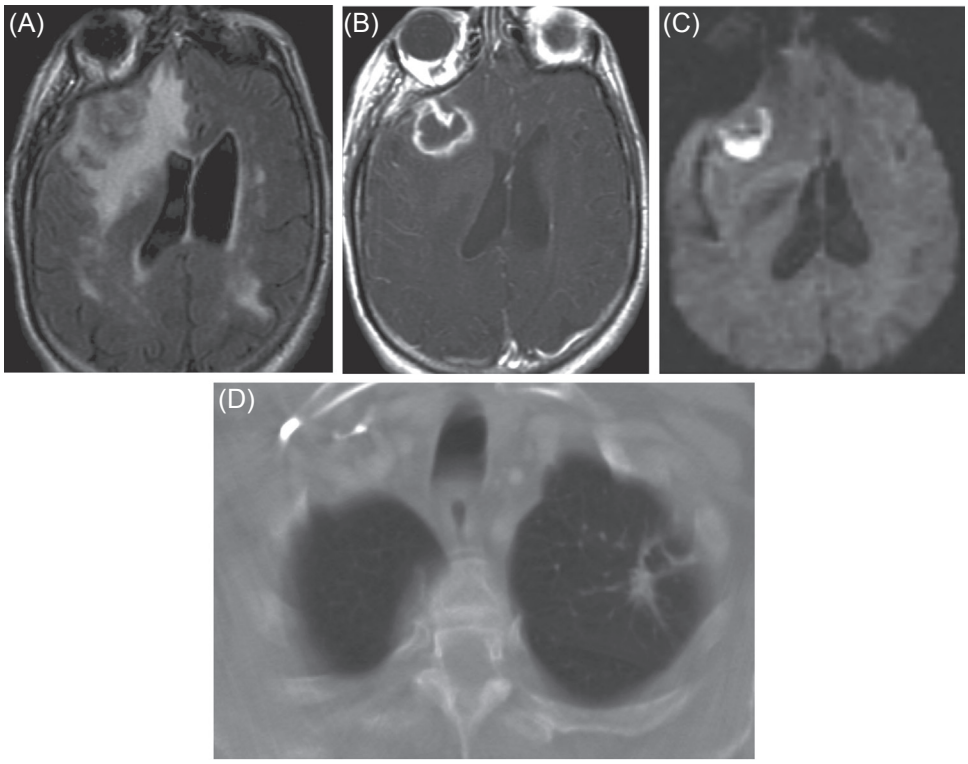


FIGURE 4 A 69-year-old male with 3-day history of weakness and dizziness. A contrast-enhanced MRI was performed, which demonstrated a heterogeneous mass in the right frontal lobe with surrounding increased FLAIR signal consistent with vasogenic edema. (A) Administration of intravenous gadolinium confirms circumferential rim enhancement suggesting primary or metastatic brain malignancy. (B) DWI confirms marked increased signal. (C) suggesting parenchymal abscess. Further workup later revealed a cavitary left upper lobe lung lesion. (D) Biopsy revealed *Nocardia* infection.

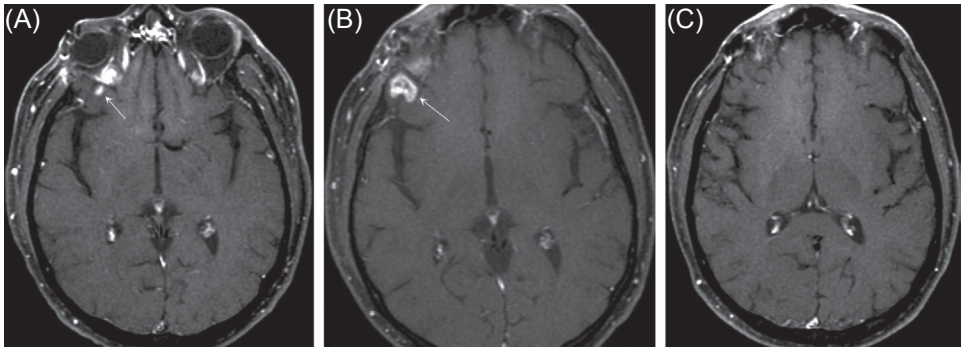


FIGURE 5 A 51-year-old male with history of right lacrimal adenocystic carcinoma following intraoperative high-dose-rate brachytherapy and external beam radiation therapy now presents with persistent headache. Initial T1-weighted gadolinium-enhanced MRI reveals a rim-enhancing lesion in the frontal lobe adjacent to the orbital apex, which enlarged over a 7-month period (arrow). (A, B) Differential diagnosis of a recurrent rim-enhancing lesion included tumor extension versus radiation necrosis. Initial PET evaluation of the brain was normal. Two-year delayed follow-up T1-weighted contrast-enhanced images reveal resolution of the rim-enhancing signal abnormality. (C) confirming radiation necrosis.

Additionally, numerous metabolic imaging techniques have been evaluated to help distinguish recurrent neoplasm from radiation-related posttreatment changes. Previous studies have demonstrated diminished levels of choline-containing compounds in brain parenchyma affected by chronic radiation necrosis compared with tumor, which typically shows an elevated choline-to-creatine ratio.[6] PET utilizing [^{18}F] fluorodeoxyglucose will also assist in differentiating neoplasm from radiation necrosis by determining relative glucose metabolism.[7,8] Despite advances in metabolic imaging, differentiating recurrent neoplasm from radiation necrosis remains difficult. More recently, MRI with diffusion and more importantly perfusion imaging has been used to differentiate recurrent tumor from radiation necrosis and pseudoprogression.[9]

References

1. Central Brain Tumor Registry of the United States. *Statistical Report: Primary Brain Tumors in the United States, 1992–1997*. Chicago: Central Brain Tumor Registry of the United States (Pub.); 2000.
2. Bourekas EC, Wildenhain P, Lewin JS, et al. The dural tail revisited. *AJNR Am J Neuroradiol*. 1995;16:1514–1516.
3. Lee AW, Cheung LO, Ng SH, et al. Magnetic resonance imaging in the clinical diagnosis of late temporal lobe necrosis following radiotherapy for nasopharyngeal carcinoma. *Clin Radiol*. 1990;12:256–270.
4. Chan YL, Leung SF, King AD, Choi PH, Metreweli C. Late radiation injury to the temporal lobes: morphologic evaluation at MR imaging. *Radiology*. 1999;213:800–807.
5. Kumar AJ, Leeds NE, Fuller GN, et al. Malignant gliomas: MR imaging spectrum of radiation therapy- and chemotherapy-induced necrosis of the brain after treatment. *Radiology*. 2000;217:377–384.
6. Hein PA, Eskey CJ, Dunn JF, Hug EB. Diffusion-weighted imaging in the follow-up of treated high-grade gliomas: tumor recurrence versus radiation injury. *AJNR Am J Neuroradiol*. 2004;25:201–209.
7. Fulham MJ, Bizzi A, Dietz MJ, et al. Mapping of brain tumor metabolites with proton MR spectroscopic imaging: clinical relevance. *Radiology*. 1992;185:675–686.
8. Chao ST, Suh JH, Raja S, Lee SY, Barnett G. The sensitivity and specificity of FDG PET in distinguishing recurrent brain tumor from radionecrosis in patients treated with stereotactic radiosurgery. *Int J Cancer*. 2001;96:191–197.
9. Prager AJ, Martinez N, Beal K, Omuro A, Zhang Z, Young RJ. Diffusion and perfusion MRI to differentiate treatment-related changes including pseudoprogression from recurrent tumors in high-grade gliomas with histopathologic evidence. *AJNR Am J Neuroradiol*. 2015;36:877–885.

CHAPTER

57

Neuroradiology of Leptomeningeal Metastases

Emilie Le Rhun[1,2], *Sophie Taillibert*[3], *Marc C. Chamberlain*[4]

[1]Breast Unit, Department of Medical Oncology, Oscar Lambret Center, Lille Cedex, France; [2]Department of Neuro-oncology, Neurosurgery, Roger Salengro Hospital, University Hospital, Lille Cedex, France; [3]Department of Neurology Mazarin and Department of Radiation Oncology, Pitié-Salpétrière Hospital, University Pierre et Marie Curie, Paris VI, Paris, France; [4]Department of Neurology and Neurological Sciences, Fred Hutchinson Cancer Research Center, University of Washington, Seattle, Washington, USA

INTRODUCTION

Leptomeningeal metastasis (LM) is the third most common central nervous system (CNS) metastatic complication of systemic cancer and additionally is seen in patients with primary brain cancers. Because the entire neuraxis is contained by a cerebrospinal fluid (CSF) compartment, which circulates, all regions of the CNS may be involved by LM, which may result in multifocal neurological signs and symptoms. LM occurs in approximately 5% of patients with systemic cancer at autopsy, of whom 10–15% present initially with cancer that is with LM.[1,2] Premorbid diagnosis of LM is much less frequent (1–3%), reflecting in part the failure to consider the diagnosis of LM and the difficulty in making the diagnosis antemortem.[1,3,4]

Diagnosis is problematic, as the disease is often not considered because of the pleomorphic manifestations of LM and occurrence in patients with extraneural sites of metastases. Useful tests to establish diagnosis and guide treatment of LM include CSF cytology, magnetic resonance imaging (MRI) of the brain and spine, and radioisotope CSF flow studies (FS). LM is most commonly diagnosed when malignant cells are found by cytology (in instances of solid tumors) or flow cytometry (in hematological cancers) examination of the CSF. However, multiple examinations of the CSF may be required to make the diagnosis by CSF cytology.[1,3,4] In addition, CSF cytology is negative in 40–50% of patients in whom the diagnosis is confirmed at the time of autopsy.[5] This suggests a high incidence of LM that is cytology negative, thereby requiring corroborative tests to assist in diagnosing LM.

Assessing the extent of CNS disease radiographically in patients with LM is of clinical value, as documenting large-volume subarachnoid disease or CSF flow obstruction is of prognostic significance and may alter treatment. This chapter summarizes the imaging modalities used to evaluate patients with LM, including cranial and spine MRI as well as radioisotope CSF FS (Table 1).

CNS IMAGING MODALITIES IN LM

Several different imaging techniques of the CNS are available and often are clinically useful in patients with LM. Both cranial computed tomography (CT) and MRI following intravenous contrast administration (CE-CT/Gd-MRI) may demonstrate abnormalities consistent with LM and may be used to make the diagnosis of LM regardless of CSF cytology or flow cytometry.[5,6] CT myelography (CT-M) and radioisotope CSF FS may demonstrate radiographic findings consistent with LM as well. ^{18}F-Fluorodeoxyglucose positron emission tomography–CT has a limited resolution for the detection of LM and consequently is rarely useful in either the diagnosis or the management of patients with LM.[7]

Cranial CE-CT is abnormal in approximately 26–56% of patients with LM.[5,6,8–12] However, LM may be mistaken for parenchymal brain disease in nearly a quarter of patients with LM, based upon a single study.[12]

© 2016 Elsevier Ltd. All rights reserved.

TABLE 1 Leptomeningeal Metastases Disease Staging

Leptomeningeal Metastases: Method of Evaluation
CSF analysis for pathologic confirmation
Contrast-enhanced computed tomography (CT) brain scans
Contrast-enhanced brain and spine MRI
CSF FS by either lumbar or ventricular administration of radioisotope
CT myelography (for patients unable to undergo MRI)

Adapted from Ref. 2.

TABLE 2 Comparison of Cranial CT and MRI in Leptomeningeal Metastases

Leptomeningeal Metastases: Comparative MR and CT Brain Imaging		
	Imaging Techniques	
Findings	**MRI**	**CT**
Abnormal enhancement	71%	29%
Nodules	43%	36%
• Subarachnoid	36%	29%
• Parenchymal	43%	29%
Hydrocephalus	7%	7%

Adapted from Ref. 18.

Several reports have compared cranial CE-CT and MRI in the diagnosis of LM. In two studies, MRI performed without contrast enhancement was compared to CE-CT.[13,14] Of a total of 30 patients reported, MR without gadolinium was abnormal in 35% compared with 53% evaluated with CE-CT. Regions of abnormal sulcal, cisternal, ependymal, and tentorial enhancement seen with CE-CT had normal signal intensity on noncontrast MRI. CE-CT was, therefore, superior to noncontrast MRI in the evaluation of patients with LM.

Other studies have compared cranial CE-CT and Gd-MRI. Mathews compared CE-CT with Gd-MRI in a canine model of experimental bacterial meningitis.[15] Unenhanced MRI was not useful in identifying meningitis in that study. However, T1-weighted (T1W) Gd-MRI was superior to CE-CT in detecting abnormal leptomeningeal enhancement and complications of meningitis including cerebritis and ventriculitis. Similar findings were also demonstrated by Frank et al. in a rabbit model of LM.[16] Sze et al. studied normal and abnormal meningeal enhancement in three groups of patients and found that Gd-MRI was more sensitive than CE-CT in the detection of meningeal abnormalities, especially in patients with LM.[17] In a cohort of 14 consecutive patients with LM, Chamberlain et al. demonstrated that Gd-MRI has a higher specificity and sensitivity than CE-CT in the evaluation of LM

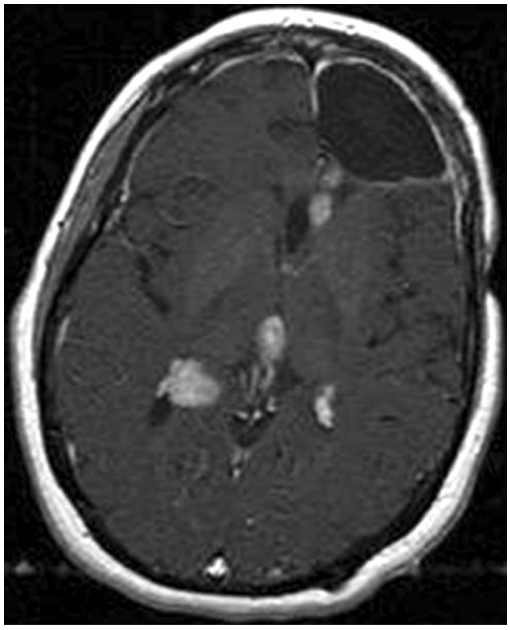


FIGURE 1 T1W axial MRI with gadolinium. Intraventricular nodules in the left ventricular atrium and third and left lateral ventricles (breast cancer).

(Table 2).[18] Additionally, any abnormalities detected by CE-CT were also detected by Gd-MRI. In the majority of patients with LM, Gd-MRI is particularly useful in demonstrating bulky (large-volume) disease, a pattern of disease most responsive to radiotherapy or systemic chemotherapy. Despite the superiority of Gd-MRI to CE-CT in the evaluation of LM, both modalities had a high incidence of false-negative studies (30% by Gd-MRI, 58% by CE-CT) in the above-mentioned study of 14 patients with CSF-positive LM. Normal findings by either examination do not exclude a diagnosis of LM. Data from Chamberlain and others indicate that Gd-MRI is the preferred imaging modality for diagnosing LM and suggest that CE-CT may be unnecessary (see Figures 1–10, 14, 17, 19, 20).[18]

Myelographic features characteristic of LM include parallel longitudinal striations due to thickened nerved roots in the cauda equina, nerve root sleeve filling defects, widening of the spinal cord, varying degrees of CSF flow block, subarachnoid nodules, and scalping of the subarachnoid membranes.[4,9,19–22] A number of studies have evaluated patients with LM by spine imaging, employing either CT-M or spine MRI (S-MRI).[3,4,19–27] However, relatively few studies have compared both CT-M and S-MRI in patients with LM.[9,21] Sze et al. compared spinal Gd-MRI with CT-M in 12 patients with LM.[24] They concluded that spinal Gd-MRI was competitive with, and sometimes superior to, CT-M in demonstrating intradural extramedullary spinal diseases in LM. In another study by Chamberlain, in 61 patients with LM, CT-M and S-MRI were compared. Very few



FIGURE 2 T1W axial MRI with gadolinium. Bilateral frontal lateral convexities, subarachnoid tumor (breast cancer).

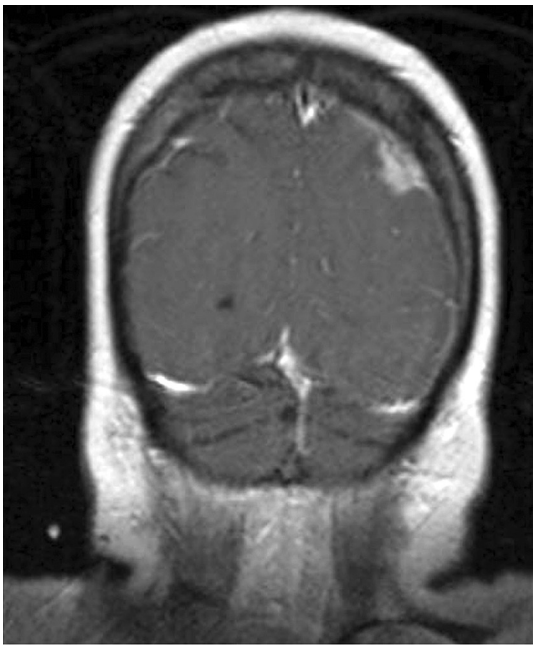


FIGURE 4 T1W coronal MRI with gadolinium. Focal subarachnoid tumor, left lateral parietal convexity (breast cancer).

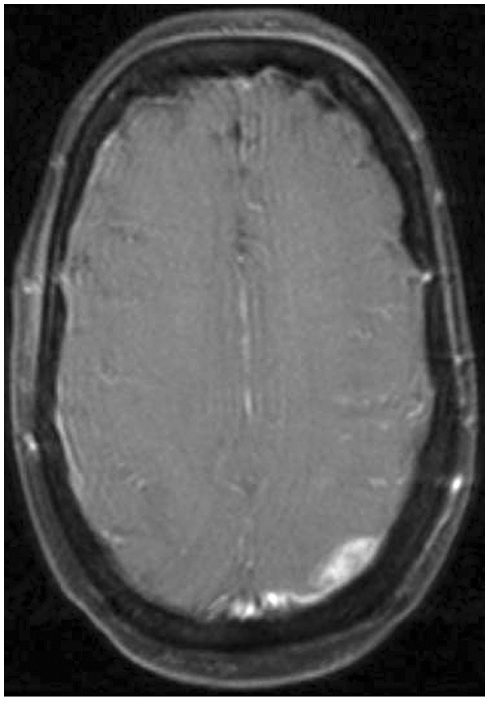


FIGURE 3 T1W axial MRI with gadolinium. Focal subarachnoid tumor, left lateral parietal convexity (breast cancer).

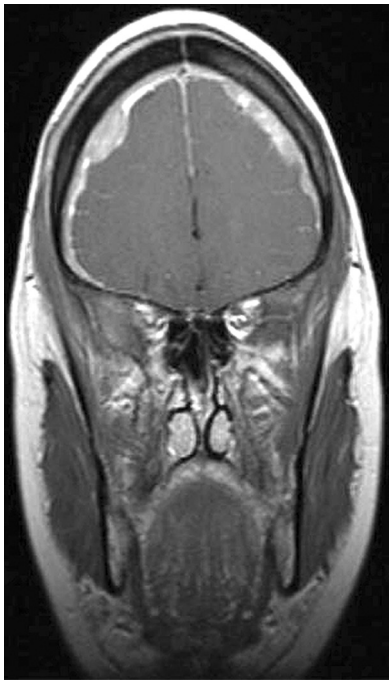


FIGURE 5 T1W coronal MRI with gadolinium. Bilateral frontal lateral convexities, subarachnoid tumor (breast cancer).

discordant results (<10%) were observed when comparing CT-M and S-MRI, and in general CT-M and S-MRI were complementary in evaluating patients with LM.[28] The differences were usually quantitative and not qualitative, notwithstanding that S-MRI better demonstrated coexisting epidural spinal cord compression and intradural intramedullary spinal cord metastases, two CNS complications of metastatic systemic cancer requiring emergent



FIGURE 6 T1W coronal MRI with gadolinium. Bilateral frontal lateral convexities, subarachnoid tumor (breast cancer).



FIGURE 8 T1W sagittal MRI with gadolinium. Enhancement of falx (melanoma).



FIGURE 7 T1W sagittal MRI with gadolinium. Subarachnoid tumor over superior convexity frontal lobe (breast cancer).

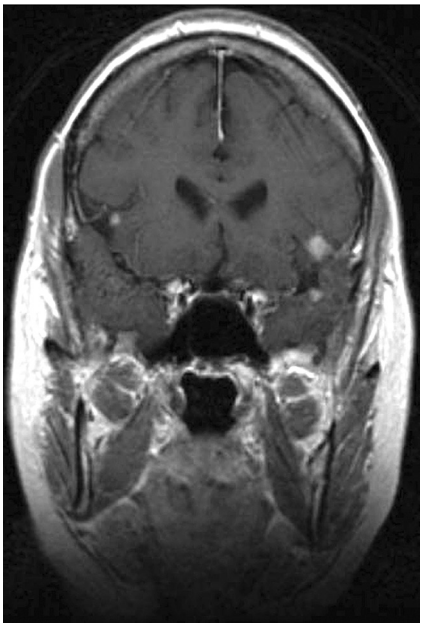


FIGURE 9 T1W coronal MRI with gadolinium. Subarachnoid nodules in right and left sylvian cisterns (melanoma).

radiotherapy. Therefore, S-MRI would appear to be the preferable spine imaging modality for patients with LM (see Figures 11–13, 15, 16, 18).

CSF flow interruption is not uncommon in LM. Compartmentalization of the CSF as documented by radioisotope CSF FS pathologically appears to be a consequence of tumor resulting in adhesions of the subarachnoid space. These subarachnoid adhesions are below the radiographic sensitivity of either CT or MRI in the overwhelming majority of patients with LM. By contrast, ^{111}In–diethylenetriamine pentaacetic acid (DTPA) or ^{99}Tc macroaggregated albumin CSF FS is sensitive in demonstrating compartmentalization of CSF pathways compared to enhanced S-MRI,



FIGURE 10 T1W coronal MRI with gadolinium. Subarachnoid tumor with lateral and inferior subarachnoid space of left temporal lobe (melanoma).



FIGURE 12 T1W sagittal MRI with gadolinium. Multiple subarachnoid nodules, both ventral and dorsal (dorsal > ventral) to the thoracic spinal cord (non-small-cell lung cancer).



FIGURE 11 T1W sagittal MRI with gadolinium. Multiple subarachnoid nodules, both ventral and dorsal to the cervical and upper thoracic spinal cord (non-small-cell lung cancer).



FIGURE 13 T1W sagittal MRI with gadolinium. Multiple subarachnoid nodules involving the lumbar sac and cauda equina (non-small-cell lung cancer).

CT-M, or enhanced cranial MRI/CT imaging.[23,28,29] The reasons for this increased sensitivity may reflect the dynamic nature of radioisotope CSF FS, whereby radionuclide is passively carried by CSF bulk flow in a physiologic antegrade manner. However, FS are informative only with respect to compartmentalization of CSF and provide no information regarding the volume of leptomeningeal disease, an aspect of LM best addressed by CT-M or cranial or spinal Gd-MRI[2,23,28–30] (Table 3).

A study by Chamberlain compared three methods of spine imaging in a series of 61 patients with LM[28] (Table 4). The study utilized sequential FS, CT-M, and S-MRI in each patient and demonstrated findings similar



FIGURE 14 T1W coronal MRI with gadolinium. Thick subarachnoid tumor overlying the left frontal lateral convexity (prostate cancer).



FIGURE 15 T1W sagittal MRI with gadolinium. Multiple subarachnoid nodules, both ventral and dorsal to the cervical spinal cord (ependymoma).

to those previously described for cranial CE-CT and Gd-MRI.[2–4,9,19–27] Although infrequently present in patients with LM, both CT-M and S-MRI were superior to FS in detecting epidural spinal cord metastases. Additionally CT-M and S-MRI were superior to FS in demonstrating leptomeningeal enhancement and spinal subarachnoid nodules. In this study, both S-MRI and FS provided the best radiographic assessment, wherein S-MRI was superior for detecting both large- and small-volume disease and FS best demonstrated interruption of CSF flow.[28] In vivo CSF flow is evaluable at select institutions by novel flow-dependent MRI techniques, and in

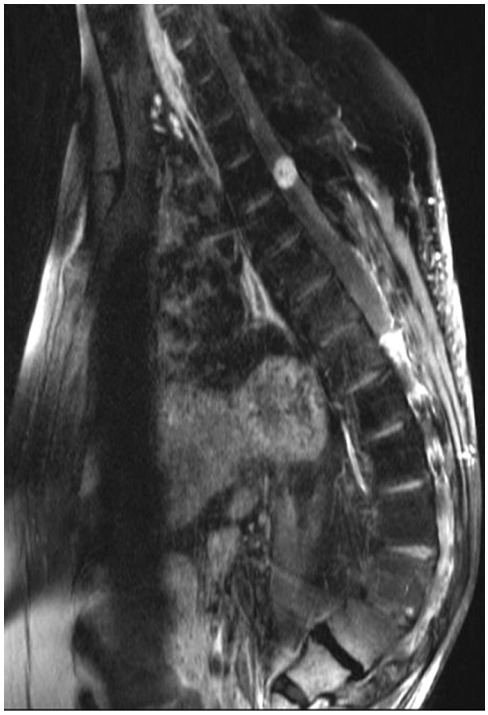


FIGURE 16 T1W sagittal MRI with gadolinium. A large subarachnoid nodule ventral to the thoracic spinal cord immediately above a tumor affecting the lumbar space (ependymoma).

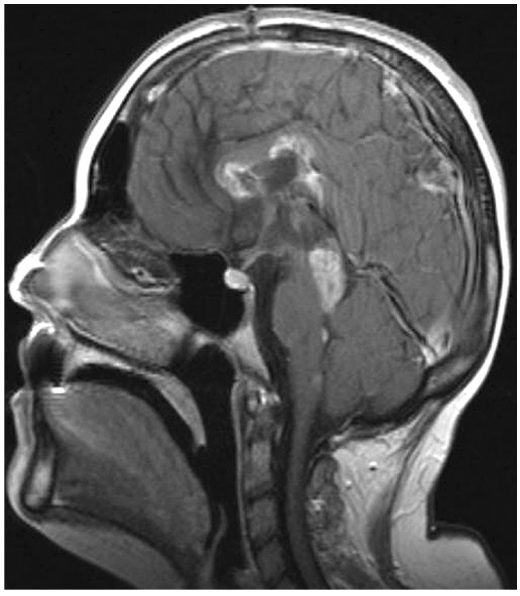


FIGURE 17 T1W sagittal MRI with gadolinium. A corpus callosum-based tumor with dissemination to the collicular cistern and floor of the fourth ventricle (glioblastoma).

the future, detection and quantification of CSF flow by MRI may obviate the need for radionuclide CSF FS.[31,32]

In conclusion, LM is a pathologic diagnosis that is determined by the demonstration of neoplastic cells in the CSF. However, in instances of a nondiagnostic CSF examination, i.e., negative CSF cytology or flow



FIGURE 18 T1W sagittal MRI with gadolinium. Subarachnoid tumor nodules ventral and dorsal to the cervical spinal cord (ependymoma).

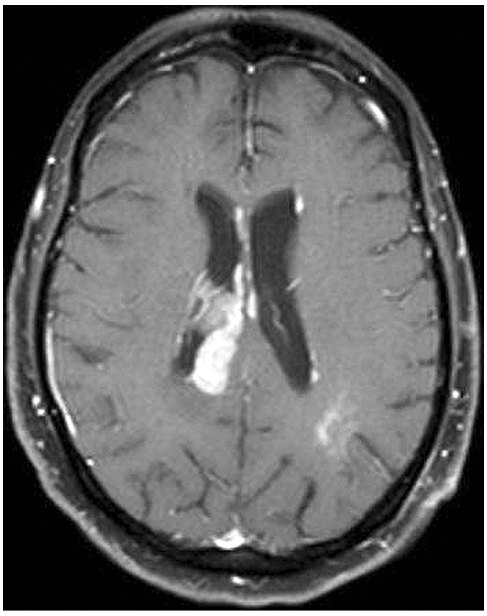


FIGURE 20 T1W axial MRI with gadolinium. Intraventricular tumor dissemination with ependymal implants in the right and left lateral ventricles (primary CNS lymphoma).

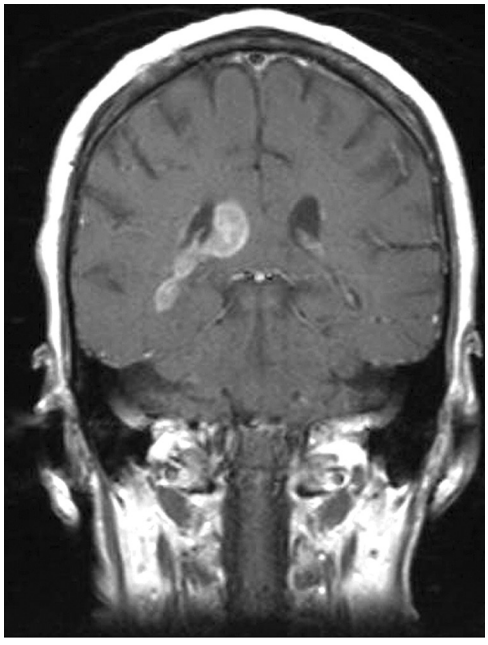


FIGURE 19 T1W coronal MRI with gadolinium. Intraventricular tumor extending from the right lateral ventricle, subependymal (primary CNS lymphoma).

cytometry, brain and spine Gd-MRI may be diagnostic of LM (see Figures 1–14). In patients suspected of or with definitive LM, parenchymal or subarachnoid disease (best detected by cerebral and S-MRI) or CSF compartmentalization (best detected by FS) occurs sufficiently often to warrant combined study with both cerebral and S-MRI and FS.

TABLE 3 Comparison of Spine Imaging in Leptomeningeal Metastases

LM: Comparative Spine Imaging			
Patient Population ($n = 63$)	**Image Modality**		
	Spine MR	**CT-M**	**CSF FS**
57% Normal			
43% Abnormal	34%	33%	33%

Adapted from Ref. 28.

BRAIN AND SPINE MRI

Because LM involves the entire neuraxis, imaging of the entire neuraxis is required to adequately assess the extent of CNS disease. MRI following intravenous contrast administration (Gd-MRI) is the technique of choice, as mentioned above.[7,18] The sensitivity of MRI for LM depends in part on the type of primary cancer.[33] One study found that MRI was capable of detecting 100% of cases of LM from solid tumors.[34] However, in most studies, Gd-MRI has a reported sensitivity varying from 70% to 87%.[35–38] The specificity of Gd-MRI is estimated at 75–94% in solid cancers.[34–36] In one study, Gd-MRI showed a 30% incidence of false-negative results and consequently negative CNS imaging does not exclude the diagnosis of LM in a patient with typical signs and symptoms.[18]

Contrast-enhanced T1W and fluid-attenuated inversion recovery (FLAIR) MRI sequences appear to be

TABLE 4 Abnormalities of Spine Imaging as a Function of Clinical Presentation

	Clinical Presentation				
	Normal Neurological Examination	**Cerebral Dysfunction**	**Cranial Nerve Palsies**	**Spinal Cord Dysfunction**	**Multilevel Dysfunction**
No. of patients (% total)	14 (23%)	3 (5%)	21 (34%)	30 (49%)	6 (10%)
Imaging modality	(No. of patients with abnormal study)				
CT-M	0	1	7	16	5
S-MRI	1	3	5	15	4
FS	1	2	6	18	6

CT-M = Computed tomographic myelography.
S-MRI = Contrast-enhanced spine magnetic resonance imaging.
FS = ^{111}In–DTPA CSF flow study.
Adapted from Ref. 28.

most sensitive in detecting LM.[39–43] In centers employing contrast-enhanced FLAIR MRI meningeal abnormalities consistent with LM may be demonstrated by early-enhanced FLAIR images.[43,44] However, contrast-enhanced T1W Gd-MRI is superior to unenhanced FLAIR or contrast-enhanced fast FLAIR images for the detection of LM, particularly for abnormalities involving the basal cisterns and cranial nerves.[37,41] The sensitivity of unenhanced FLAIR, contrasted-enhanced fast FLAIR, and contrast-enhanced T1W Gd-MR images for detecting LM was 12%, 41%, and 59%, respectively, in a single study. The specificity of unenhanced FLAIR, contrasted-enhanced fast FLAIR, and contrast-enhanced T1W Gd-MR images for detecting LM was 93%, 88%, and 93%, respectively.[41] Importantly the increase in signal intensity seen on FLAIR MRI in LM has been described in numerous other conditions, including subarachnoid hemorrhage, infectious meningitis, stroke, subdural hematoma, dural venous thrombosis, status epilepticus, patients receiving supplemental oxygen, and previous (24–48 h) administration of gadolinium chelate.[45]

The coronal and axial plane is the most useful in making the MRI diagnosis of LM, as enhancement is less conspicuous with sagittal scans.[17,18] Delayed T1W images may improve the detection of leptomeningeal enhancement in LM.[46] Gadolinium should be injected 10 min before data acquisition and the slice thickness should be 5 mm or less. The gadolinium enhancement pattern seen in LM is dependent on several technical factors including the strength of the MRI magnet, type of pulse sequence, and volume of contrast administered.[42] During follow-up of patients with LM and while on treatment, repeat MRI should be performed ideally on the same device.

At the time of diagnosis of LM, brain MRI should include axial T1W, axial FLAIR, axial diffusion, axial T2*, post-gadolinium three-dimensional (3D) and post-gadolinium 3D FLAIR sequences. S-MRI should include a post-gadolinium sagittal T1 sequence. Spine sagittal T1W sequences without contrast and sagittal fat-suppression T2-weighted (T2W) sequences, combined with axial T1W images with contrast of regions of interest, may also be useful at LM diagnosis. During follow-up of patients with LM, brain MRI should include post-gadolinium 3D and post-gadolinium 3D FLAIR sequences and S-MRI should include a post-gadolinium sagittal T1 sequence.[39]

Several radiographic abnormalities are consistent with LM and may be used to render a radiographic diagnosis of LM regardless of CSF cytology or flow cytometry.[6,33,47] Typical MRI abnormalities include (1) sulcal–cisternal enhancement or obliteration, (2) ependymal–subependymal enhancement, (3) cerebellar folia enhancement, (4) irregular tentorial enhancement, (5) cranial nerve enhancement and/or enlargement, (6) subarachnoid enhancing nodules, (7) intraventricular enhancing nodules, and (8) spinal nerve root enhancement or intradural–extramedullary enhancing nodules, especially in the cauda equina. Pial enhancement of the spinal cord has been termed by Kramer as "sugar coating."[21] The most frequent brain MRI findings are subarachnoid nodules (35–50%) and pial enhancement (15–50%). Similarly, the most frequent S-MRI findings are subarachnoid nodules (8–10%), focal pial enhancement (6–10%), and nerve root enhancement (4–13%).[39,47,48]

In a retrospective case series, Chamberlain analyzed the MRI data of 165 patients with solid tumor LM, among whom 125 patients had positive CSF cytology and 40 had negative CSF cytology. The study included as well 50 patients with lymphoma-related LM and 25 patients with leukemia-related LM.[48] Abnormalities found by brain MRI and consistent with LM were more frequent in cytology-negative solid tumor patients versus cytology-positive solid tumor patients (80 vs 40%, $p = 0.03$). Normal brain was more common in hematologic cancers versus solid tumors (80–84% vs 60%, $p = 0.05$). These data

TABLE 5 Contrast-Enhanced MRI of the Brain and Spine in Leptomeningeal Metastasis

Region	Solid Tumor		Lymphoma	Leukemia
	Cytology Negative ($n=40$); % (n)	Cytology Positive ($n=125$); % (n)	Flow Cytometry Positive ($n=50$); % (n)	Flow Cytometry Positive ($n=25$); % (n)
BRAIN				
Total	75 (30)	40 (50)	15 (8)	1 (4)
Hydrocephalus	10 (4)	5 (6)	3 (3)	4 (1)
Nodules	50 (20)	35 (44)	15 (8)	8 (2)
• Subarachnoidal	25 (10)	10 (12)	3 (2)	0
◦ Ventricular	10 (4)	5 (6)	3 (2)	0
• Parenchymal	50 (20)	32 (40)	12 (6)	8 (2)
Pial enhancement	50 (20)	15 (19)	6 (3)	8 (2)
• Focal	40 (16)	10 (12)	3 (2)	8 (2)
• Diffuse	10 (4)	5 (6)	3 (2)	0
Ependymal enhancement	10 (4)	5 (6)	6 (3)	4 (1)
Sulci enhancement	10 (4)	5 (6)	3 (2)	8 (2)
Folia enhancement	10 (4)	10 (12)	3 (2)	4 (1)
Cranial enhancement	10 (4)	5 (6)	3 (2)	4 (1)
SPINE				
Total	35 (14)	15 (19)	20 (10)	12 (3)
Nodules	25 (10)	10 (13)	6 (3)	4 (1)
• Subarachnoid	20 (8)	8 (10)	6 (3)	4 (1)
• Parenchymal	5 (2)	2 (3)	0	0
Pial enhancement	20 (8)	10 (13)	15 (8)	8 (2)
• Focal	15 (6)	8 (10)	12 (6)	4 (1)
• Diffuse	5 (2)	2 (3)	3 (2)	4 (1)
Nerve root enhancement	10 (4)	10 (13)	12 (6)	8 (2)
NORMAL				
Total	0	60 (75)	80 (40)	84 (21)

Patients with multiple metastases were counted in every subcategory.
Adapted from Ref. 48.

are shown in Table 5. S-MRI was abnormal in 12–35% of the cases, depending on the LM category. Nodular disease constituted the most common MRI abnormality followed by pial enhancement. The incidence of both nodular and pial enhancement was twice as frequent in the intracranial compared with the intraspinal compartment ($p=0.02$). No difference was observed in brain or S-MRI abnormalities when comparing symptomatic versus asymptomatic patients with LM ($p=0.18$).[48]

In conclusion, the most frequent MRI findings are subarachnoid and parenchymal enhancing nodules (10–35%) and diffuse or focal pial enhancement (10–20%).[12,39] The most common locations affected by LM include enhancement of the basilar cisterns, cerebellar folia, cranial nerves, and lumbar intradural nerve roots, particularly those in the cauda equina.[40,49] Radiographic spine involvement by MRI is present in 15–25% of the patients with LM. Indirect signs such as communicating hydrocephalus may also be observed in 5–10% of patients with solid tumors and 3–4% of hematologic malignancies.[6,8–11,48,50] Coexistent parenchymal metastases may be associated in 38–52% of breast cancer patients with LM, in 56–82% of lung cancer patients with LM, and in 54–83% of melanoma patients with LM.[51–62]

In a retrospective study, MRI results of pretreatment brain and spine imaging were correlated with survival

in 240 patients with LM.[48] In this study, contrast-enhancing nodules were characterized as subarachnoid, ventricular, or parenchymal. Patients were subdivided into small- (<10 mm) or large- (>10 mm) volume disease based on the diameter of the enhancing nodules seen by Gd-MRI. Pial enhancement was defined as focal, diffuse, or none. Other abnormalities characterized and tabulated were ependymal, sulci, folia, cranial nerve, or spinal root enhancement as either present or absent. All patients were treated with intra-CSF chemotherapy (predominantly liposomal cytarabine) and site-specific radiotherapy (to sites of symptomatic disease, sites of large-volume disease, and sites of CSF flow obstruction). Overall, radiotherapy was administered to 45% of patients. Systemic chemotherapy was used in the majority (90%) of patients with hematologic cancers and in approximately 27% of solid tumor-related LM patients. In this study, solid tumor-related LM had a higher incidence of patients with abnormal MRI findings as well as patients with large-volume LM disease compared to hematological cancer-related LM. Median overall survival was similar in solid tumor-related LM patients with positive or negative CSF cytology. However, survival in patients with solid tumor-related LM with large-volume disease was significantly less than in patients with either normal MRI findings or small-volume disease ($p = 0.03$).[48]

Large nodules, defined as >10 mm in size, are easily and reproducibly measured by MRI. Other common radiologic findings seen by MRI in LM, for example, leptomeningeal, cranial nerve, or spinal nerve root enhancement, do not easily lend themselves to quantification.[48] Consequently, for the majority of patients with LM and radiographic findings consistent with LM, the radiographic findings of LM are nonmeasurable. Furthermore the reproducibility of measuring subarachnoid nodules is subject to inter-MRI variability due to slice thickness, patient positioning, and contrast conspicuity.[48]

Differential Diagnosis

Any irritation of the leptomeninges can result in enhancement on MRI, and consequently the differential diagnosis is extensive. Therefore findings by neuroradiology must be interpreted in the clinical context. Leptomeningeal enhancement has been described following a lumbar puncture probably due to either introduction of blood into the subarachnoid space or induction of low-pressure postlumbar puncture syndrome.[17] Focal dural enhancement and thickening are commonly seen after craniotomy.[17,63–65] On thin 3D T2W sequences, subarachnoid trabeculae, such as the membrane of Liliequist, can be detected and potentially confused with subarachnoid nodules often seen in LM.[40] In patients with a high degree of skin pigmentation, deposition of leptomeningeal melanin characterized by T2W hypointensity especially along the medulla oblongata may be seen.[40,66]

Pachymeningitis is characterized by diffusely enhancing meninges with corresponding thickening of both the arachnoid and the dura. This finding may be seen with any chronic inflammatory process affecting the leptomeninges, including CNS vasculitis (as in Wegener's granulomatosis),[67] Moyamoya disease,[68] sarcoidosis, inflammatory autoimmune diseases such as rheumatoid arthritis,[69,70] and infectious diseases (tuberculous pachymeningitis).[71,72] Aplastic anemia[73] and the intracranial hypotension syndrome, either spontaneous or following a lumbar puncture or ventricular shunt, may result in leptomeningeal enhancement due to enlargement of leptomeningeal vessels.[40,65,73] Metastatic infiltration of the skull may result in diffuse dural thickening preferentially affecting the cerebral convexities and skull base with relative sparing of the falx and tentorium.[40]

Focal thickening and enhancement of the dura may occur adjacent to a metastatic skull lesion. The differential diagnosis of focal thickening of the meninges may also include meningioma or other dural-based lesions such as dural metastasis. A wide variety of other disorders can be considered in an appropriate clinical context, including meningeal sarcoidosis, primary CNS lymphoma without parenchymal disease, hemangiopericytoma, plasmacytoma, plasma cell granuloma, inflammatory pseudotumors (as occasionally seen in patients with systemic disorders such as rheumatoid arthritis, Behçet disease, and Castelman disease), solitary fibrous tumor, amyloid, leptomeningeal melanocytic tumors such as melanocytomas and neurocutaneous melanosis, tuberculoma, primary meningeal sarcoma, gliosarcoma, leiomyosarcoma, and Rosai–Dorfman disease.[66,74–80] Local intracranial infections such as sinusitis or mastoiditis may also result in focal meningeal enhancement.[80]Dural fistula, cerebral ischemia, sinus thrombosis, Sturge–Weber disease, subdural hematoma, and carotid stent insertions have also been described in association with a focal enhancement and thickening of the meninges.[17,40,81,82] Focal or diffuse subarachnoid enhancement may be observed in any infectious meningitis, as for example, meningococcal meningitis, pneumococcal and tuberculous meningitis or cryptococcosis,[83,84] viral encephalitis and meningoencephalitis, and leptomeningeal neurosarcoidosis.[85–89] The presence of symmetric and bilateral enhancement of all spinal nerve roots and cranial nerves without associated focal tumor suggests a diagnosis of infectious or inflammatory meningoradiculitis such a neuroborreliosis or Guillain–Barré syndrome. [40]

RADIOISOTOPE CSF FLOW STUDIES

Normal CSF flow is a consequence of both transmitted choroidal arterial pulsations and bulk flow resulting from continuous CSF production. Radionuclide CSF FS, or so-called radionuclide ventriculography, provides a safe physiological assessment of the functional anatomy of the various CSF compartments and constitutes the technique of choice to evaluate CSF flow dynamics as mentioned above.[2,23,90,91] CSF FS permits detection of CSF flow abnormalities, which are often not apparent by conventional neuroradiographic imaging,[28,29,92,93] and is more sensitive in demonstrating compartmentalization of CSF pathways than are S-MRI, CT-M, and cranial MRI or CT imaging (see Figures 21–23).[23,28,29] Approximately 50% of patients with LM will manifest CSF flow abnormalities.[28,29,92,93]

CSF flow can be evaluated using either 10 to 20 MBq (270–540 μCi) of ^{111}In–DTPA or 74 MBq (200 μCi) of ^{99}Tc macroaggregated albumin radioisotopes.[28,91] The pattern of CSF circulation and time to appearance of regionally administered chemotherapy are similar whether the radioisotope is given by an intraventricular or intralumbar administration. Imaging acquisition is performed after 15 min, 6 h, 24 h, and 48 h and should include the lumbar, thoracic, and cervical subarachnoid spaces using a posterior coronal imaging technique, whereas the brain is studied with coronal (anterior) and sagittal images.

Failure of radionuclide to appear in a given CSF compartment is operationally defined as CSF flow block.[18] Failure of radioisotope movement can be defined as complete or partial obstruction of CSF flow. In most centers, partial CSF flow obstruction is not considered as constituting a CSF flow block. The site of CSF flow interruption may be identified as either in the brain (ventricular, skull base, or convexity) or in the spine (cervical, thoracic, or lumbar). CSF flow abnormalities in LM are most commonly observed at the base of the brain, in the spinal subarachnoid space (especially at the level of the cauda equina), and over the cerebral convexities.[28,91,93,95]

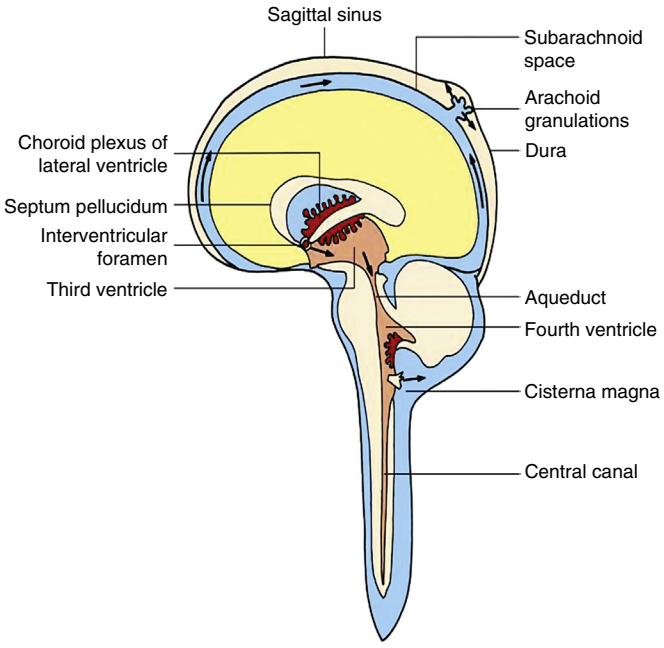


FIGURE 21 Cartoon of normal CSF flow.

Table 6 demonstrates the normal times of appearance of ^{111}In–DTPA in various CSF compartments following intraventricular injection of radionuclide in 30 adult patients with LM.[23] For a similar study, performed in children, the normal time to appearance of radioisotope in various CSF compartments following ventricular injection is seen in Table 7.[29] In a separate study, 20 consecutive adult patients with LM were evaluated by intralumbar-administered ^{111}In–DTPA (see Table 8). Results from patients in this study with normal CSF FS can be seen in Table 4.[28]

Abnormal CSF circulation has been demonstrated in 10–70% of patients with LM.[28,48,96,101] CSF FS were more commonly abnormal in LM from solid tumors than in LM from hematologic malignancies (25–28% vs 10–20%, $p = 0.04$). The spine was slightly more common than the brain as the site of obstruction ($p = 0.05$).[48] The results are detailed in Table 9.

Compartmentalization of CSF as documented by FS is an important consideration in patients with LM considered for intra-CSF chemotherapy, as homogeneous distribution of administered chemotherapy within the CSF is critical for effective treatment.[2,23] Four clinical studies have suggested that radioisotope CSF FS have prognostic significance in patients with LM and independently predict survival in patients with LM who are considered candidates for intra-CSF therapy.[48,91,94,96] Treatment of CSF flow blocks by involved-field radiotherapy and reestablishment of normal CSF flow documented by posttreatment radioisotope CSF FS ensure both homogeneous distribution of chemotherapy administered via CSF and treatment of the entire neuraxis in patients with LM. Reestablishment of CSF flow with involved-field radiotherapy followed by intra-CSF chemotherapy led to longer survival, lower rates of treatment-related morbidity, and a lower rate of death from progressive LM, compared with the group that had persistent CSF blocks.[48,91,94] CSF flow obstruction documented by radioisotope FS is another criterion by which to assess patients for applicability of intra-CSF chemotherapy, independent of the patient's performance status, neurologic disability, and extent and activity of systemic disease.

Radioisotope CSF FS documenting CSF flow predicts for distribution of intra-CSF chemotherapy. In patients with LM not considered candidates for intra-CSF therapy,

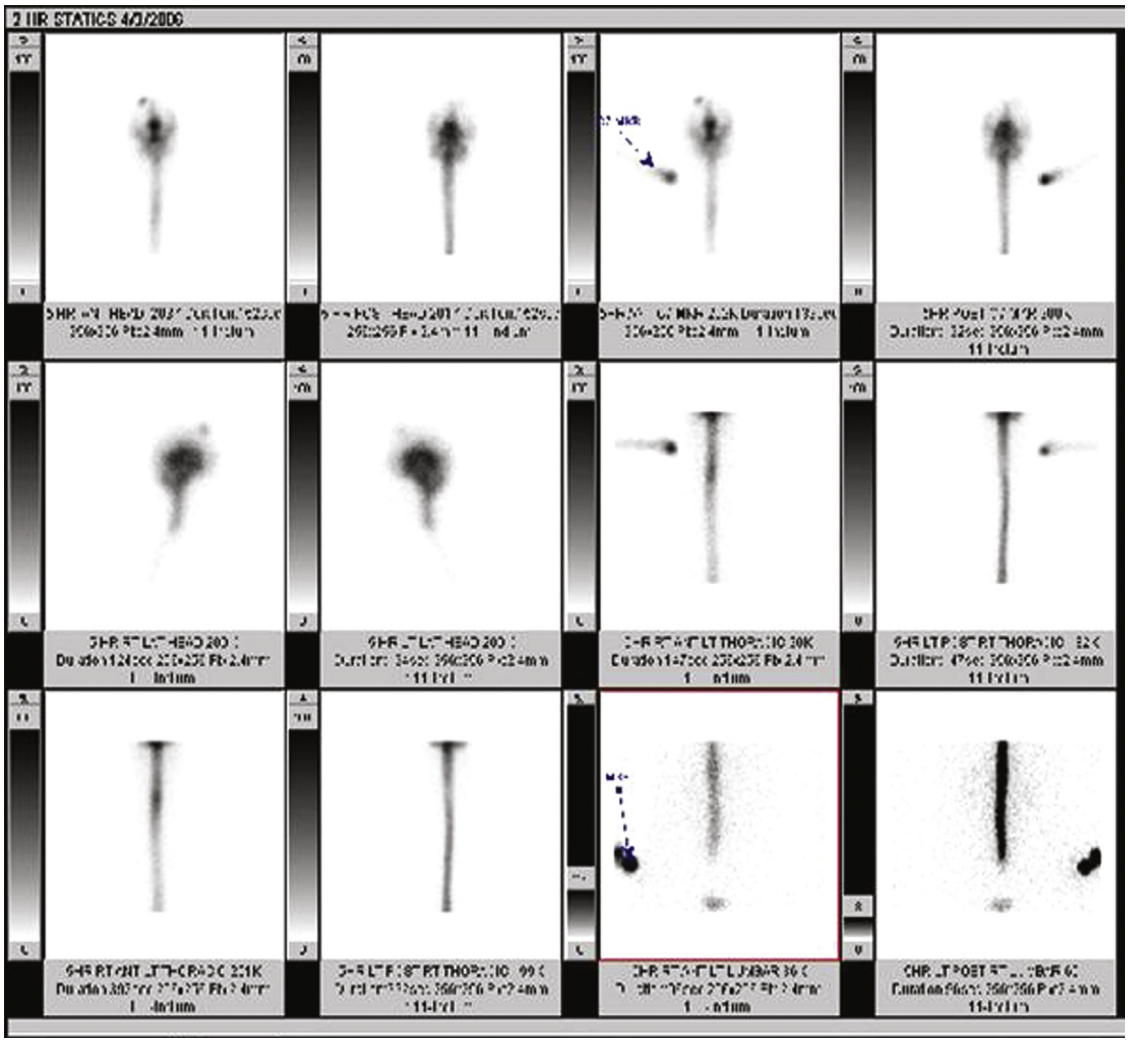


FIGURE 22 ^{111}In-DTPA CSF FS. Radioisotope was injected into an Ommaya device implanted in the right lateral ventricle, showing normal CSF flow.

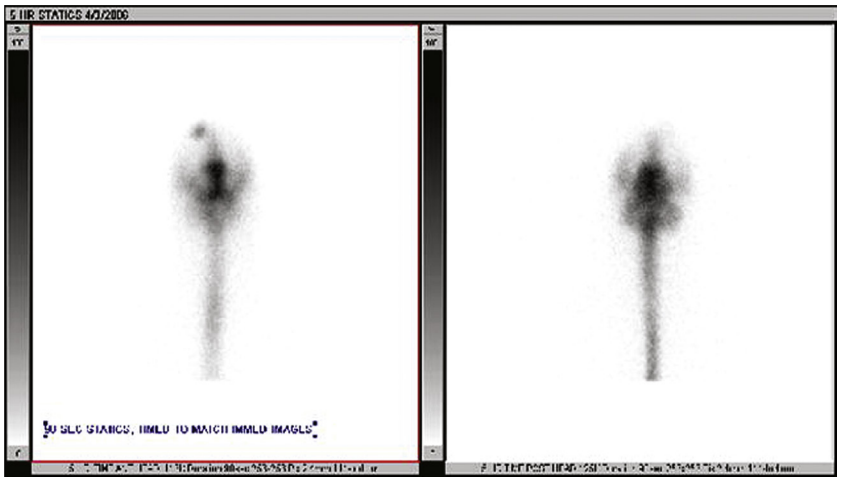


FIGURE 23 ^{111}In-DTPA CSF FS. Twenty-four-hour delayed study showing CSF obstruction over lateral cerebral convexities.

TABLE 6 Adult Leptomeningeal Metastasis: Normal Compartmental Appearance of ^{111}In–DTPA Following Intraventricular Administration

			CSF Compartment: Time to Appearance (min)				
				Spinal Subarachnoid			
	mCi ^{111}In–DTPA	Ventricular System	Cisterna Magna/Basal Cisterns	Cervical Cord	Thoracic Cord	Lumbar Cord	Sylvian Cistern
Median	700	1	5	15	20	30	50
Range	500–900	0–5	5–15	5–20	10–20	25–50	35–90

Adapted from Ref. 93.

TABLE 7 Pediatric Leptomeningeal Metastasis: Normal Compartmental Appearance of ^{111}In–DTPA CSF Flow Studies Following Intraventricular Administration

	CSF Compartment: Time to Appearance (min)					
			Spinal Subarachnoid			
	Ventricular System	Cisterna Magna/Basal Cisterns	Cervical Cord	Thoracic Cord	Lumbar Cord	Sylvian Cistern
Median	1	5	8	15	35	80
Range	0–3	3–5	5–10	10–30	20–45	60–90

Adapted from Ref. 93.

TABLE 8 Normal Compartmental Appearance of ^{111}In–DTPA Following Intralumbar Administration to Adult Patients with Leptomeningeal Metastasis

		CSF Compartment: Time to Appearance (min)						
		Spinal Subarachnoid						
	mCi ^{111}In–DTPA	Lumbar Cord	Thoracic Cord	Cervical Cord	Cisterna Magna/Basal Cisterns	Sylvian Cistern	Ventricular System	Cerebral Convexities
Median	500	1	22.5	32.5	37.5	65	1440	1440
Range	450–600	0–1	20–25	30–35	35–40	60–70	1440	1440

Adapted from Ref. 93.

TABLE 9 Radioisotope Cerebrospinal Fluid Flow Study in Leptomeningeal Metastasis

	Solid Tumor	Lymphoma		Leukemia
Site of Obstruction	Cytology Negative ($n = 40$); % (n)	Cytology Positive ($n = 125$); % (n)	Flow Cytometry Positive ($n = 50$); % (n)	Flow Cytometry Positive ($n = 25$); % (n)
BRAIN				
Total	10 (4)	9 (11)	4 (2)	8 (2)
Ventricular	2.5 (1)	2 (2)	0	0
Skull base	2.5 (1)	2 (2)	0	0
Convexity	5 (2)	5 (7)	4 (2)	8 (2)
SPINE				
Total	15 (6)	19 (24)	6 (3)	12 (3)
Cervical	2.5 (1)	4 (6)	0	4 (1)
Thoracic	2.5 (1)	4 (6)	2 (1)	0
Lumbar	10 (4)	10 (12)	4 (2)	8 (2)
NORMAL				
Total	75 (30)	72 (90)	90 (45)	80 (20)

Adapted from Ref. 48.

for example, a patient with leukemic meningitis being treated with craniospinal irradiation, CSF FS would not be required as part of the CNS staging. Notwithstanding this observation, no study has yet to document differences in CSF drug levels above and below the sites of CSF flow interruption as demonstrated by radioisotope CSF FS. A not infrequent mechanism of LM relapse appears to involve CSF compartmentalization, thereby interrupting intra-CSF drug distribution.[94] Recurrent LM with CSF compartmentalization is therapeutically difficult to treat, notwithstanding the administration of intra-CSF chemotherapy, and often involves a change in intra-CSF drug therapy and the use of site-specific CNS radiotherapy. In general, CSF compartmentalization demonstrated by radionuclide CSF FS often proves recalcitrant to medical therapy.[23,28,29] Patients failing radiotherapy to a site of CSF block as demonstrated by FS essentially never demonstrate reestablishment of normal CSF flow when treated with intra-CSF chemotherapy only.[23,28,29,94] Similar to prior reports, following CSF block-directed radiotherapy, only 50% of brain and 35% of spine subarachnoid blocks respond with restoration of normal CSF flow.[102] In patients with CSF flow obstruction refractory to site of obstruction therapy, including involved-field radiotherapy and intra-CSF chemotherapy, limited survival, rapid leptomeningeal disease progression, and death due to progressive CSF disease are predicted. The rationale for radioisotope CSF FS is straightforward; intra-CSF chemotherapy, to be effective, assumes homogeneous distribution of chemotherapy within the CSF compartments, thereby ensuring exposure of tumor cells to chemotherapy regardless of their location in the CSF or leptomeninges. Therefore, patients studied by CSF FS before administration of intra-CSF chemotherapy who demonstrate obstruction of CSF flow would appear to be poor candidates for regional chemotherapy unless normal communication of the CSF can be reestablished.

CONCLUSIONS

MRI with gadolinium enhancement is the technique of choice to evaluate patients with suspected LM.[18] Because LM involves the entire neuraxis, imaging of the entire CNS is required in patients considered for further treatment. T1W sequences, with and without contrast, combined with fat-suppression T2W and FLAIR sequences, constitute the standard MRI examination.[39,97] Gd-MRI has been shown to have a higher sensitivity than CE-CT in several series of LM,[18,24] and is similar to CT-M for the evaluation of the spine, but significantly better tolerated by patients.[28,35] Any irritation of the leptomeninges may result in their enhancement on MRI. Some changes, such as cranial nerve enhancement on cranial imaging and intradural extramedullary enhancing nodules on S-MRI (most frequently seen in the cauda equina), can be considered diagnostic of LM in patients with cancer. Lumbar puncture itself can rarely cause a meningeal reaction leading to dural–arachnoidal enhancement, such that imaging should be obtained preferably prior to the procedure.[91,98] Nonetheless Gd-MRI has a 30% incidence of false-negative results, so that a normal study does not exclude the diagnosis of LM. On the other hand, in cases with a typical clinical presentation, abnormal Gd-MRI alone is adequate to establish the diagnosis of LM.[2,6,36,98,99]

Radionuclide studies using either ^{111}In–DTPA or ^{99}Tc macroaggregated albumin constitute the technique of choice to evaluate CSF flow dynamics.[100,101] Abnormal CSF circulation has been demonstrated in 10–70% of patients with LM with blocks commonly occurring at the skull base, at the spinal canal, and over the cerebral convexities.[28,96,101] Patients with interruption of CSF flow demonstrated by radionuclide ventriculography have been shown in four clinical series to have decreased survival compared to those with normal CSF flow.[89,94,101,102] Involved-field radiotherapy to the site of CSF flow obstruction restores flow in 35% of patients with spinal disease and 50% of patients with intracranial disease.[102] Reestablishment of CSF flow with involved-field radiotherapy followed by intra-CSF chemotherapy leads to longer survival, lower rates of treatment-related morbidity, and lower rate of death from progressive LM compared to the group that had persistent CSF blocks.[28,101] These findings may reflect that CSF flow abnormalities prevent homogeneous distribution of intra-CSF chemotherapy, resulting in (1) protected sites where tumor can progress and (2) accumulation of drug at other sites leading to neurotoxicity and systemic toxicity. Based on this, many experts recommend that intra-CSF chemotherapy be preceded by a radionuclide FS and, if a block is found, that radiotherapy be administered in an attempt to reestablish normal flow.[91,102]

References

1. Theodore WH, Gendelman S. Meningeal carcinomatosis. *Arch Neurol*. 1981;38:696–699.
2. Chamberlain MC. Leptomeningeal metastasis: review of current concepts. *Curr Opin Oncol*. 1992;4(3):533–539.
3. Olson ME, Dhernik NL, Posner JB. Infiltration of the leptomeninges by systemic cancer: a clinical and pathologic study. *Arch Neurol*. 1974;30:122–137.
4. Wasserstrom WR, Glass JP, Postner JB. Diagnosis and treatment of leptomeningeal metastases from solid tumors: experience with 90 patients. *Cancer*. 1985;49:759–772.
5. Glass JP, Melamed M, Chernik NL, Posner JB. Malignant cells in cerebrospinal fluid (CSF): the meaning of a positive CSF cytology. *Neurology*. 1979;28:1369–1375.
6. Lee Y, Glass JP, Geoffrey A, Wallace S. Cranial-computed tomographic abnormalities in leptomeningeal metastasis. *AJR Am J Radiol*. 1984;143:1035–1039.
7. Lombardi G, Zustovich F, Farina P, et al. Neoplastic meningitis from solid tumors: new diagnostic and therapeutic approaches. *Oncologist*. 2011;16(8):1175–1188.

8. Jaeckle KA, Krol G, Posner JB. Evolution of computed tomographic abnormalities in leptomeningeal metastasis. *Ann Neurol*. 1985;17:85–89.
9. Krol G, Sze G, Malkin M, Walker R. MR of cranial and spinal meningeal carcinomatosis: comparison with CT and myelography. *AJNR Am J Neuroradiol*. 1988;9:709–714.
10. Enzmann DR, Krikorin CY, Hayward R. Computed tomography in leptomeningeal spread in tumor. *J Comput Assist Tomogr*. 1978;2:445–448.
11. Ascherl GF, Hilal SK, Brisman R. Computed tomography of disseminated meningeal and ependymal malignant neoplasms. *Neurology*. 1981;31:567–574.
12. Collie DA, Brush JP, Lammie GA, et al. Imaging features of leptomeningeal metastases. *Clin Radiol*. 1999;54(11):765–771.
13. Davis PC, Freedman NC, Fry SM. Leptomeningeal metastasis: MR imaging. *Radiology*. 1987;163:449–454.
14. Barloon TJ, Uyuh WT, Yang CJ. Spinal subarachnoid tumor seeding from intracranial metastasis: MR findings. *J Comput Assist Tomogr*. 1987;11:242–244.
15. Mathews VP, Kuharik MA, Edwards MK, D'Amour PG, Azzarelli B, Dreesen RG. Gd-DTPA-enhanced MR imaging of experimental bacterial meningitis: evaluation and comparison with CT. *AJNR Am J Neuroradiol*. 1988;9:1045–1050.
16. Frank JA, Girton M, Dwyer AJ, Wright DC, Cohen PJ, Doppman JL. Meningeal carcinomatosis in the VX2 rabbit tumor model: detection with Gd-DTPA-enhanced MR imaging. *Radiology*. 1988;167:825–829.
17. Sze G, Soletsky S, Bronen R, Krol G. MR imaging of the cranial meninges with emphasis on contrast enhancement and meningeal carcinomatosis. *AJNR Am J Neuroradiol*. 1989;10(5): 965–975.
18. Chamberlain MC, Sandy AD, Press GA. Leptomeningeal metastasis: a comparison of gadolinium-enhanced MR and contrast-enhanced CT of the brain. *Neurology*. 1990;40:435–438.
19. Little JR, Dale AJD, Okazaki H. Meningeal carcinomatosis: clinical manifestations. *Arch Neurol*. 1974;30:138–143.
20. Pedersen AG, Paulson OB, Gyldensted C. Metrizamide myelography in patients with small cell carcinoma of the lung suspected of meningeal carcinomatosis. *J Neurooncol*. 1985;3:85–89.
21. Kramer ED, Rafto S, Packer RJ, Zimmerman RA. Comparison of myelography with CT follow-up versus gadolinium MRI for subarachnoid metastatic disease in children. *Neurology*. 1991;41:46–50.
22. Kim KS, Ho SU, Weinberg PE, Lee C. Spinal leptomeningeal infiltration by systemic cancer: myelographic features. *AJR Am J Radiol*. 1982;139:361–365.
23. Chamberlain MC, Corey-Bloom J. Leptomeningeal metastases: ^{111}Indium-DTPA CSF flow studies. *Neurology*. 1991; 41:1765–1769.
24. Sze G, Abramson A, Krol G, et al. Gadolinium-DTPA in the evaluation of intradural extramedullary spinal disease. *AJNR Am J Neuroradiol*. 1988;9:153–163.
25. Wiener MD, Boyko OB, Friedman HS, Hockenberger B, Oakes WJ. False-positive spinal MR findings for subarachnoid spread of primary CNS tumor in postoperative pediatric patients. *AJNR Am J Neuroradiol*. 1990;11:1100–1103.
26. Rippe DF, Boyko OB, Friedman HS, et al. Gd-DTPA-enhanced MR imaging of leptomeningeal spread of primary CNS tumor in children. *AJNR Am J Neuroradiol*. 1990;11:329–332.
27. Lim V, Sobel DF, Zyroff J. Spinal cord pial metastases: MR imaging with gadopentetate dimeglumine. *AJNR Am J Neuroradiol*. 1990;11:975–982.
28. Chamberlain MC. Comparative spine imaging in leptomeningeal metastases. *J Neurooncol*. 1995;23:233–238.
29. Chamberlain MC. Pediatric leptomeningeal metastasis: ^{111}Indium-DTPA CSF flow studies. *J Child Neurol*. 1994;9:150–154.
30. Chamberlain MC. New approaches to and current treatments of leptomeningeal metastases. *Curr Opin Neurol*. 1994;7:492–500.
31. Feinberg DA. Modern concepts of brain motion and cerebrospinal fluid flow. *Radiology*. 1992;185:630–632.
32. Schellinger D, LeBihan D, Sunder SR, et al. MR of slow CSF flow in the spine. *AJNR Am J Neuroradiol*. 1992;13:1393–1403.
33. Chamberlain MC, Glantz M, Groves MD, Wilson WH. Diagnostic tools for neoplastic meningitis: detecting disease, identifying patient risk, and determining benefit of treatment. *Semin Oncol*. 2009;36(4 suppl 2):s35–S45.
34. Zeiser R, Burger JA, Bley TA, Windfuhr-Blum M, Schulte-Mönting J, Behringer DM. Clinical follow-up indicates differential accuracy of magnetic resonance imaging and immunocytology of the cerebral spinal fluid for the diagnosis of neoplastic meningitis - a single centre experience. *Br J Haematol*. 2004;124(6):762–768.
35. Freilich RJ, Krol G, DeAngelis LM. Neuroimaging and cerebrospinal fluid cytology in the diagnosis of leptomeningeal metastasis. *Ann Neurol*. 1995;38(1):51–57.
36. Straathof CS, de Bruin HG, Dippel DW, Vecht CJ. The diagnostic accuracy of magnetic resonance imaging and cerebrospinal fluid cytology in leptomeningeal metastasis. *J Neurol*. 1999;246(9):810–814.
37. Singh SK, Agris JM, Leeds NE, Ginsberg LE. Intracranial leptomeningeal metastases: comparison of depiction at FLAIR and contrast-enhanced MR imaging. *Radiology*. 2000;217(1):50–53.
38. Chamberlain MC. Leptomeningeal metastasis. *Curr Opin Oncol*. 2010;22:627–635.
39. Le Rhun E, Taillibert S, Chamberlain MC. Carcinomatous meningitis: leptomeningeal metastases in solid tumors. *Surg Neurol Int*. 2013;4(suppl 4):s265–S688.
40. Dietemann JL, Correia Bernardo R, Bogorin A, et al. Normal and abnormal meningeal enhancement: MRI features. [Article in French] *J Radiol*. 2005;86(11):1659–1683.
41. Singh SK, Leeds NE, Ginsberg LE. MR imaging of leptomeningeal metastases: comparison of three sequences. *AJNR Am J Neuroradiol*. 2002;23(5):817–821.
42. Mahendru G, Chong V. Meninges in cancer imaging. *Cancer Imaging*. 2009;9:S14–S21. Spec No A.
43. Hirota T, Ishihara K, Akazawa K, Kubota T, Yamada K, Nishimura T. Case report: delayed post-contrast fluid-attenuated inversion recovery image for depicting meningeal carcinomatosis. *Br J Radiol*. 2004;77(918):528–531.
44. Mathews VP, Caldemeyer KS, Lowe MJ, Greenspan SL, Weber DM, Ulmer JL. Brain: gadolinium-enhanced fast fluid-attenuated inversion-recovery MR imaging. *Radiology*. 1999;211:257–263.
45. Morris JM, Miller GM. Increased signal in the subarachnoid space on fluid-attenuated inversion recovery imaging associated with the clearance dynamics of gadolinium chelate: a potential diagnostic pitfall. *AJNR Am J Neuroradiol*. 2007;28(10):1964–1967.
46. Pui M, Langston J, Arai Y. Gd-DTPA enhancement of CSF in meningeal carcinomatosis. *J Comput Assist Tomogr*. 1993;17:940–944.
47. Taillibert S, Laigle-Donadey F, Chodkiewicz C, Sanson M, Hoang-Xuan K, Delattre JY. Leptomeningeal metastases from solid malignancy: a review. *J Neurooncol*. 2005;75(1):85–99.
48. Chamberlain MC. Comprehensive neuraxis imaging in leptomeningeal metastasis : a retrospective case series. *CNS Oncol*. 2013;2(2):121–128.
49. Fink KR, Fink JR. Imaging of brain metastases. *Surg Neurol Int*. 2013;4(suppl 4):S209–S219.
50. Watanabe M, Tanaka R, Takeda N. Correlation of MRI and clinical features in meningeal carcinomatosis. *Neuroradiology*. 1993;35:512–515.
51. Regierer AC, Stroux A, Kühnhardt D, et al. Contrast-enhancing meningeal lesions are associated with longer survival in breast Cancer-related leptomeningeal metastasis. *Breast Care (Basel)*. 2008;3(2):118–123.
52. Gauthier H, Guilhaume MN, Bidard FC, et al. Survival of breast cancer patients with meningeal carcinomatosis. *Ann Oncol*. 2010;21(11):2183–2187.

53. Rudnicka H, Niwinska A, Murawska M. Breast cancer leptomeningeal metastasis—the role of multimodality treatment. *J Neurooncol*. 2007;84:57–62.
54. Niwińska A, Rudnicka H, Murawska M. Breast cancer leptomeningeal metastasis: propensity of breast cancer subtypes for leptomeninges and the analysis of factors influencing survival. *Med Oncol*. 2013;30(1):408.
55. Meattini I, Livi L, Saieva C, et al. Prognostic factors and clinical features in patients with leptominengeal metastases from breast cancer: a single center experience. *J Chemother*. 2012;24(5):279–284.
56. Lara-Medina F, Crismatt A, Villarreal-Garza C, et al. Clinical features and prognostic factors in patients with carcinomatous meningitis secondary to breast cancer. *Breast J*. 2012;18(3):233–241.
57. Le Rhun E, Taillibert S, Zairi F, et al. A retrospective case series of 103 consecutive patients with leptomeningeal metastasis and breast cancer. *J Neurooncol*. 2013;113(1):83–92.
58. Park JH, Kim YJ, Lee JO, et al. Clinical outcomes of leptomeningeal metastasis in patients with non-small cell lung cancer in the modern chemotherapy era. *Lung Cancer*. 2012;76(3):387–392.
59. Umemura S, Tsubouchi K, Yoshioka H, et al. Clinical outcome in patients with leptomeningeal metastasis from non-small cell lung cancer: Okayama Lung Cancer Study Group. *Lung Cancer*. 2012;77(1):134–139.
60. Morris PG, Reiner AS, Szenberg OR, et al. Leptomeningeal metastasis from non-small cell lung cancer: survival and the impact of whole brain radiotherapy. *J Thorac Oncol*. 2012;7(2):382–385.
61. Harstad L, Hess KR, Groves MD. Prognostic factors and outcomes in patients with leptomeningeal melanomatosis. *Neuro Oncol*. 2008;10(6):1008–1010.
62. Raizer JJ, Hwu WJ, Panageas KS, et al. Brain and leptomeningeal metastases from cutaneous melanoma: survival outcomes based on clinical features. *Neuro Oncol*. 2008;10:199–207.
63. Burke JW, Podrasky AE, Bradley Jr WG. Meninges: benign postoperative enhancement on MR images. *Radiology*. 1990;174:99–102.
64. Leach JL, Jones BV, Tomsick TA, Stewart CA, Balko MG. Normal appearance of arachnoid granulations on contrast-enhanced CT and MR of the brain: differentiation from dural sinus disease. *AJNR Am J Neuroradiol*. 1997;18:594–595.
65. Smirniotopoulos JG, Murphy FM, Rushing EJ, Rees JH, Schroeder JW. Patterns of contrast enhancement in the brain and meninges. *Radiographics*. 2007;27(2):525–551.
66. Gebarski SS, Blaivas MA. Imaging of normal leptomeningeal melanin. *AJNR Am J Neuroradiol*. 1996;17:55–60.
67. Spranger M, Schwab S, Meinck HM, et al. Meningeal involvement in Wegener's granulomatis confirmed and monitored by positive circulating antineutrophil cytoplasm in cerebrospinal fluid. *Neurology*. 1997;48:263–265.
68. Heijmen L, van Dijk EJ, Goraj B, van Laarhoven HW. Moyamoya disease misdiagnosed as leptomeningeal metastases. *J Clin Oncol*. 2012;30(36):e382–385.
69. Agildere AM, Tutar NU, Yucel E, Coskun M, Benli S, Aydin P. Parencyhmeningitis and optic neuritis in rheumatoid arthritis: MR findings. *Br J Radiol*. 1999;72:404–407.
70. Cellerini M, Gabbrielli S, Maddali Bongi S, Cammelli D. MRI of cerebral rheumatoid parenchymeningitis: report of two cases with follow-up. *Neuroradiology*. 2001;43:147–150.
71. Demaerel P, Wilms G, Marchal G. MRI findings in tuberculous meningo-encephalitis. *RÖFO Fortschr Röntgenstr*. 1990;152: 384–387.
72. Goyal M, Scharma A, Mishra NK, Gaikwad SB, Sharma MC. Imaging appearance of parechymeningeal tuberculosis. *AJR Am J Roentgenol*. 1997;169:1421–1424.
73. Asano T, Hayashida M, Ogawa K, Adachi K, Teramoto A, Yamamoto M. Hypertrophic cranial pachymeningitis in a patient with aplastic anemia. *Ann Hematol*. 1998;77(6):279–282.
74. Nayak L, Abrey LE, Iwamoto FM. Intracranial dural metastases. *Cancer*. 2009;115(9):1947–1953.
75. Buttner A, Pfluger T, Weis S. Primary meningeal sarcomas in two children. *J Neurooncol*. 2001;52:181–188.
76. River Y, Schwartz A, Gomori JM, Schoffer D, Siegal T. Clinical significance of diffuse dural enhancement detected by magnetic resonance imaging. *J Neurosurg*. 1996;85:777–783.
77. Sandhu FA, Schellinger D, Martuza RL. A vascular sarcoid mass mimicking a convexity meningioma. *Neuroradiology*. 2000; 42:195–198.
78. Guma A, Aguilera C, Acebes J, Arruga J, Pons L. Meningeal involvement in Behcet's disease: MRI. *Neuroradiology*. 1998;40:512–515.
79. Demaerel P, Robberecht W, Casteels I, et al. Focal leptomeningeal MR enhancement along the chiasm as a presenting sign of multiple sclerosis. *J Comput Assist Tomogr*. 1995;19:297–298.
80. Horowitz S, Thomas C, Gruener G, Nand S, Shea JF. MR of leptomeningeal spinal and posterior fossa amyloid. *AJNR Am J Neuroradiol*. 1998;19:900–902.
81. Nemzek W, Postma G, Poirier V, Hecht S. MR features of pachymeningitis presenting with sixth-nerve palsy secondary to sphenoid sinusitis. *AJNR Am J Neuroradiol*. 1995;16:960–963.
82. Wilkinson Stroke, 2003 Wilkinson ID, Griffiths PD, Hoggard N, Cleveland TJ, Gaines PA, Venables GS. Unilateral leptomeingeal enhancement after carotid stent insertion detected by magnetic resonance imaging. *Stroke*. 2000;31:2274–2275.
83. Tayfun C, Ucoz T, Tasar M, et al. Diagnostic value of MRI in tuberculous meningitis. *Eur Radiol*. 1996;6:380–386.
84. Arnder L, Castillo M, Heinz ER, Scatliff JG, Enterline D. Unusual pattern of enhancement in cryptococcal meningitis: in vivo findings with postmortem correlation. *J Comput Assist Tomogr*. 1996;20:1023–1026.
85. Fukui MB, Meltzer CC, Kanal E, Smirnioptopoulos JG. MR imaging of the meninges. Part II. Neoplastic disease. *Radiology*. 1996;201:605–612.
86. Bode MK, Tikkakoski T, Tuisku S, Kronqvist E, Tuominen H. Isolated neurosarcoidosis MR findings and pathologic correlation. *Acta Radiol*. 2001;42:563–567.
87. Pickhut D, Heywang-Kobrunner SH. Neurosarcoidosis: evaluation with MRI. *J Neuroradiol*. 2000;27:185–188.
88. Wilson JD, Castillo M, Van Tassel P. MRI features of intracranial sarcoidosis mimicking meningiomas. *Clin Imaging*. 1994;18:184–188.
89. Christoforidis GA, Spickler EM, Recio MV, Mehta BM. MR of CNS sarcoidosis: correlation of imaging features to clinical symptoms and response to treatment. *AJNR Am J Neuroradiol*. 1999;20:655–669.
90. Chamberlain M. Leptomeningeal metastases: a review of evaluation and treatment. *J Neurooncol*. 1998;37:271–284.
91. Glantz M, Hall WA, Cole BF, et al. Diagnosis, management, and survival of patients with leptomeningeal cancer based on cerebrospinal fluid-flow studies. *Cancer*. 1995;75:2919–2931.
92. Haaxma-Reiche H, Piers DA, Beekhuis H. Normal cerebrospinal fluid dynamics: a study with intraventricular injection of ^{111}In-DTPA in leukemia and lymphoma without meningeal involvement. *Arch Neurol*. 1989;46:997–999.
93. Grossman SA, Trump CL, Chen DCP, Thompson G, Camargo E. Cerebrospinal fluid flow abnormalities in patients with neoplastic meningitis. *Am J Med*. 1982;73:641–647.
94. Chamberlain MC, Kormanik P. Prognostic significance of ^{111}Indium-DTPA CSF flow studies. *Neurol*. 1996;46(6):1674–1677.

95. Chamberlain MC. Neoplastic meningitis. *Oncologist*. 2008;13: 967–977.
96. Mason WP, Yeh SD, DeAngelis LM. ^{111}Indium-diethylenetriamine pentaacetic acid cerebrospinal fluid flow studies predict distribution of intrathecally administered chemotherapy and outcome in patients with leptomeningeal metastases. *Neurology*. 1998;50(2):438–444.
97. Schuknecht B, Huber P, Buller B, et al. Spinal leptomeningeal neoplastic disease. Evaluation by MR, myelography and CT myelography. *Eur Neurol*. 1992;32(1):11–16.
98. Mittl Jr RL, Yousem DM. Frequency of unexplained meningeal enhancement in the brain after lumbar puncture. *AJNR Am J Neuroradiol*. 1994;15(4):633–638.
99. Lyons MK, Meyer FB. Cerebrospinal fluid physiology and the management of increased intracranial pressure. *Mayo Clin Proc*. 1990;75:684–707.
100. Schumacher M, Orszagh M. Imaging techniques in neoplastic meningiosis. *J Neurooncol*. 1998;38(2–3):111–120.
101. Trump DL, Grossman SA, Thompson G, Murray K. CSF infections complicating the management of neoplastic meningitis. Clinical features and results of therapy. *Arch Intern Med*. 1982;142(3):583–586.
102. Chamberlain MC, Kormanik P, Jaeckle KA, Glantz M. ^{111}Indium-diethylenetriamine pentaacetic acid CSF flow studies predict distribution of intrathecally administered chemotherapy and outcome in patients with leptomeningeal metastases. *Neurology*. 1999;52:216–217.

CHAPTER

58

Imaging of Epidural Spinal Cord Compression

Tanvir Rizvi[1], *Max Wintermark*[2], *David Schiff*[3]

[1]Radiology and Medical Imaging, University of Virginia Health System, Charlottesville, VA, USA; [2]Neuroradiology Division, Department of Radiology, Stanford University, Stanford, CA, USA; [3]Neuro-Oncology Center, University of Virginia Health System, Charlottesville, VA, USA

CLINICAL BACKGROUND

Metastatic epidural spinal cord compression occurs when cancer metastasizes to the spine or epidural space and secondarily causes compression of the spinal cord.[1] It has been estimated that 5% of patients with systemic cancer at autopsy have pathologic evidence of tumor invading the epidural space.[2] A 2011 study in the United States found a 3.4% annual incidence of epidural spinal cord compression (ESCC) requiring hospitalization in patients dying from cancer.[3] Although nearly all malignancies may potentially involve the spine and/or epidural space, in a 2011 study, lung cancer (25%), prostate cancer (16%), and multiple myeloma (11%) were the most common causes, with 15% patients with multiple myeloma and 14% with lymphoma experiencing ESCC requiring hospitalization.[3]

Multiple epidural metastases have been reported in approximately 9–49% of patients with ESCC,[4–7] and the site of epidural metastatic disease varies from 68% in the thoracic spine to 16% in the lumbosacral spine and 15% in the cervical spine.[8] Approximately 20% of patients with spinal metastatic disease will have at least two sites of epidural involvement at some time during the disease.[9] Though multiplicity has been associated with specific tumor type,[6] this has not been confirmed by other investigators.[10] The incidence of ESCC is expected to increase owing to improved survival of cancer patients. Additionally, in those patients who survive long enough, recurrent spinal epidural metastasis is not uncommon. In a study of 103 patients, van der Sande et al. showed that recurrent spinal epidural metastasis occurred in 19% of the patients with prior spinal epidural metastases and slightly more often in the patients with breast cancer (21%) than in the patients with other primary tumors (17%). About one-half of the patients surviving 2 years and nearly all patients surviving 3 years or longer developed recurrent spinal epidural metastases.[11] Because of this potential for multiple epidural metastases and their association with ESCC, many authorities advocate diagnostic imaging of the entire spine.[5,10]

Metastatic ESCC is a medical emergency that needs rapid diagnosis and treatment to prevent permanent paralysis.[12] Clinically, metastatic ESCC is nearly always preceded by back or neck pain, which on average has been present for 2 months when metastatic ESCC is diagnosed.[13] In fact, back pain is the presenting symptom in 80–96% of patients.[14] Weakness (76%), bowel and bladder dysfunction (57%), and sensory loss (35–51%) may also be seen at the time of diagnosis.[14]

The functional outcome of ESCC is influenced by many variables, with the pretreatment neurologic status being the most important determinant of functional prognosis.[15,16] Bowel and bladder dysfunction is an unfavorable prognostic sign[14] and the extent of subarachnoid block is related to the degree of motor and sphincter dysfunction.[16,17] Furthermore, the degree of thecal sac/cord compression correlates positively with the degree of neurologic impairment[18] and is directly related to functional outcome.[19] The presence of vertebral body collapse is also an ominous finding.[20] The duration of sensory and motor changes has been considered an important prognostic factor.[21] However, other studies have shown that the duration of the worst degree of neurologic dysfunction may be a more important prognostic factor than the entire duration of weakness.[17] The radiosensitivity of the primary tumor is also an important prognostic factor for the clinical response.[14,16,22,23] Breast, prostate, small-cell lung cancer, lymphoma, and multiple myeloma are most radiosensitive, while renal cell and melanoma are extremely radioresistant.[22,23] Studies have found that 74% of paraparetic patients with radiosensitive tumors became ambulatory after radiation therapy; however, only 34% of those harboring less radiosensitive tumors were able to regain ambulation.[14,24]

Handbook of Neuro-Oncology Neuroimaging, Second Edition
http://dx.doi.org/10.1016/B978-0-12-800945-1.00058-6

© 2016 Elsevier Ltd. All rights reserved.

PATHOPHYSIOLOGY

Broadly, spinal tumors can be organized according to their location outside or within the dura of the spinal canal as extradural or intradural and outside or within the arachnoid as extramedullary or intramedullary. A single tumor can reside in more than one compartment. The epidural space is the most common site of metastases producing injury to the spinal cord. Epidural compression represents 97% of spinal cord metastatic lesions.[25]

Various anatomic patterns of spread have been proposed for spinal epidural metastases.[17,22,23,26] Arterial spread to bone marrow with resultant vertebral body collapse and formation of anterior epidural mass is the most commonly proposed mechanism.[27] Kim et al. in a prospective study of 59 patients found hematogenous spread to the spine in 51 (86%) cases.[17] The vertebral body is involved more commonly than the posterior elements presumably because of its larger volume and highly vascular marrow, which promotes proliferation of tumor cells.[26] In a study utilizing computed tomography (CT) of the vertebral column, pedicle destruction was identified only in the presence of vertebral body involvement.[27] The initial location of metastasis is within the posterior vertebral body where the basivertebral arterial plexus is present.[28] Subsequently, the basivertebral veins or other penetrating vessels provide entry into the valveless epidural venous sinuses,[29] which can lead to circumferential soft tissue compression of the spinal cord in 22% of cases.[26] Such hematogenous dissemination from vertebral bone metastases to the dura is a frequent pathway in patients with breast carcinoma.[30] Alternatively, there may be direct infiltration of the dura from vertebral lesions.[26]

Spinal epidural metastases can also spread via the intervertebral foramina from a paravertebral source.[17,22,26] Kim et al. found direct extension from a paravertebral mass through bone or intervertebral foramina in 8 of 59 cases (14%).[17] This transforaminal pattern of spread comprises a significantly smaller proportion, approximately 10% of spinal epidural metastases cases,[26] and is frequently associated with lung cancer and lymphoma.[17,31] Epidural extension of lymphoma from a vertebral body is also common.[32]

The pathophysiology of neurologic symptoms may be due to a vascular phenomenon. It is hypothesized that the soft tissue material may impinge upon the epidural venous plexus resulting in venous hypertension and vasogenic edema.[22,33] Venous hypertension may be complicated by hematomyelia at the site of vascular compression.[29] Epidural tumor itself[22,26] or vertebral body collapse with extradural mass[23] may also have a direct mass effect on the spinal cord leading to neurologic deterioration.

EPIDURAL ANATOMY

Understanding the anatomy of the epidural space (Figure 1) is important, as it is frequently involved in neoplastic diseases. The epidural space surrounds the dural sac. It is bounded anteriorly by the posterior longitudinal

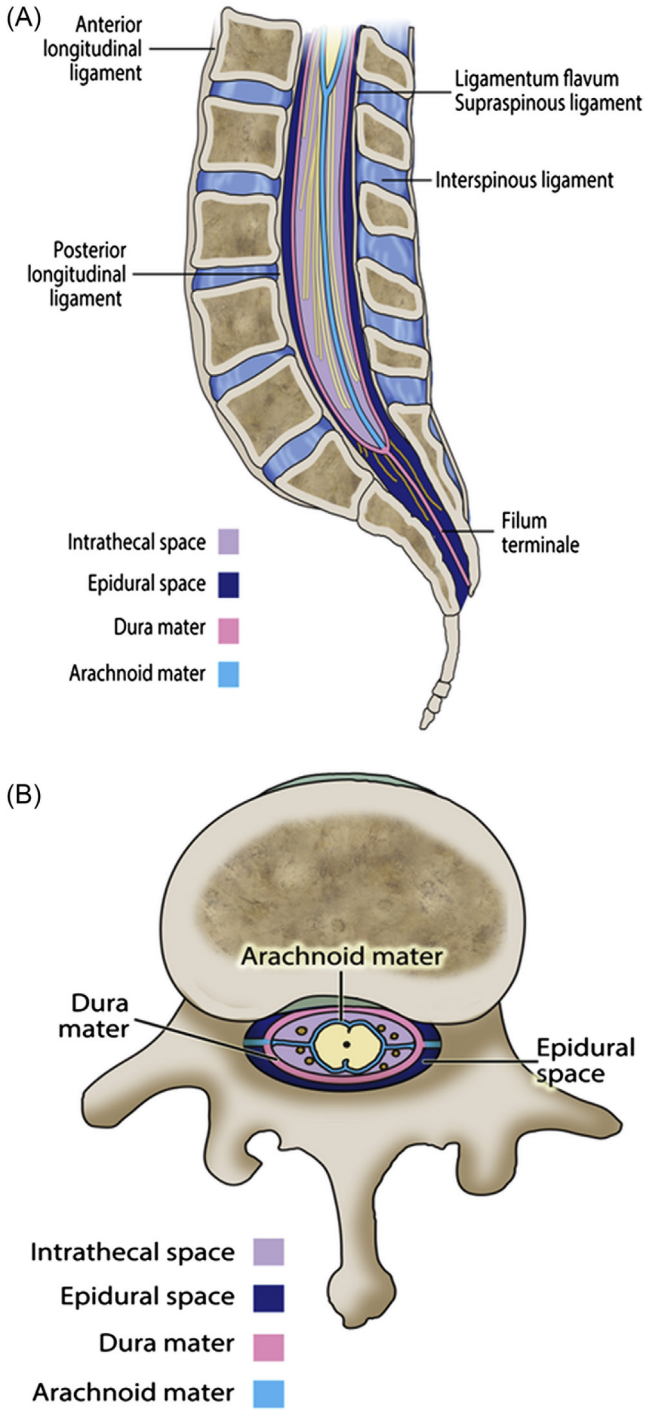


FIGURE 1 Illustration of the individual spaces of the lumbar spinal canal including intrathecal and epidural space in the sagittal (A) and axial (B) planes along with an illustration of the leptomeningeal and dural layers. *Illustrations by Philip Cohen, University of Virginia Health System.*

ligament, posteriorly by the ligamentum flavum and the periosteum of laminae, and laterally by the pedicles of the spinal column and the intervertebral foramina containing their neural elements. The epidural space communicates freely with the paravertebral space through the intervertebral foramina. Superiorly the space is anatomically closed at the foramen magnum where the spinal dura attaches to the endosteal dura of the cranium. Inferiorly the epidural space ends at the sacral hiatus, which is closed by the sacral hiatus.[34,35] As the size of the dural sac relative to the epidural space decreases at the L4–L5 level, the posterior longitudinal ligament falls away from the anterior dura and fat fills the anterior epidural space.[35]

The epidural space contains loose areolar connective tissue, fat, lymphatics, arteries, an extensive plexus of veins, and the spinal nerve roots as they exit the dural sac. The epidural venous plexus is a valveless system that communicates with the basivertebral vein; the intracranial sigmoid, occipital, and basilar venous sinuses; and the azygous system.[34,35] In the thoracolumbar region (T10–L2 level), the basivertebral vein originates from this venous plexus and extends into the vertebral bodies.

In the cervicothoracic region, there is minimal epidural fat and the dura contacts the lamina. The posterior epidural space is continuous with a thin layer of epidural fat between the lamina and the dura (Figure 2). In comparison, in the lumbar region, the anteroposterior dimension of the posterior epidural space is greater, averaging 5.0–6.0 mm in adult males (Figure 3).[34] Areas of epidural fat under the ligamentum flavum of the lumbar spine extend under the laminae, but are separated by areas where the posterior dura contacts, but does not adhere to, the periosteum of the lamina. Contact with the pedicles also divides the posterior epidural space from the lateral epidural space.[36]

The anterior dura adheres tightly to the posterior longitudinal ligament, which stretches across the intervertebral disks to form the anterior epidural space between the posterior longitudinal ligament and the periosteum of the vertebral body.[34] The dura and posterior longitudinal ligaments blend with the annular ligament, dividing the anterior epidural space into vertical compartments at each vertebral level. In areas immediately next to the intervertebral disks, dense connective tissue extensions extend superiorly and inferiorly, dividing the anterior epidural space into lateral halves. In the lumbar region, a membranous extension of the posterior longitudinal ligament joins with the neural elements laterally and isolates the anterior epidural space from the posterior and lateral epidural space.[36] In the case of lumbar vertebral metastasis associated with anterior epidural carcinomatous infiltration, Hutzelmann



FIGURE 2 Sagittal T1-weighted image of the thoracic spine shows relatively less epidural fat compared to that in the lumbar spine in Figure 3.

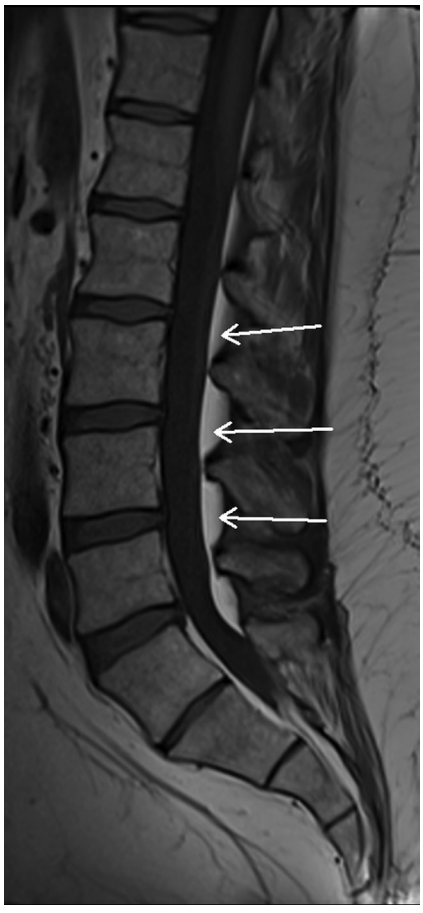


FIGURE 3 Sagittal T1-weighted image of the lumbar spine shows relatively abundant epidural fat in comparison to the thoracic spine in Figure 2.

et al. observed that infiltrations tend to respect the midline. This phenomenon was observed to be uni- or bilateral in 88.3% of all cases with intraspinal anterior epidural carcinomatous infiltration, especially in that part of the vertebral body where the basal vertebral venous plexus was located.[37] This phenomenon is probably due to the anatomy of the vertebral body and especially its stabilization by the posterior longitudinal ligament. This imaging feature may be helpful in delineating vertebral body metastases with epidural infiltration from intraspinal processes, which proceed with the destruction of the vertebral body.

IMAGING

The diagnosis of ESCC requires demonstration of extrinsic compression of the thecal sac by the tumor. Magnetic resonance imaging (MRI) is considered the most specific and sensitive modality for evaluating spinal neoplastic lesions.[29] Other alternative modalities can be used when MRI is contraindicated (like pacemaker, aneurysm clip, and certain cochlear implants). Therefore it is useful to understand the appearance of spinal tumors with other modalities.

Radiography

Plain radiographs are often used as the first imaging modality, as they are relatively inexpensive and easily available. However, they suffer from a high false-negative rate of 10–17%.[2] At least 50% of bone must be destroyed before it is radiographically detectable.[23,27] Pedicular erosion predicts epidural disease in only 31% cases (Figure 4).[27] Radiographs cannot evaluate paraspinal tumor invasion through the neural foramina or soft tissue impingement of the thecal sac.[23] It may be difficult to assess the clinically relevant lesion with radiography alone if there are multiple lesions.[22] Despite these limitations, bone destruction is often seen with ESCC. The series by Kim et al. demonstrated that 86% of patients had vertebral body destruction at the level of ESCC.[17] Radiographic abnormalities with symptoms have an even greater predictive value. Rodichok et al. found that 91% of patients with back pain, myelopathy/radiculopathy, and evidence of bone destruction on radiographs had ESCC.[38,39] However, in cases of lymphoma, plain radiographs are not as useful, as bony destruction is seen only in 30–42% of patients.[31] Preservation of the disk space suggests infectious disease over metastases.[27]

Myelography and Computed Tomographic Myelography

Before the widespread availability and usage of MRI, myelography was the gold standard for the evaluation of ESCC, with the added advantage of obtaining a cerebrospinal fluid (CSF) sample at the time of the procedure. In myelography, intrathecal contrast opacifies the intradural/subarachnoid space and demonstrates epidural metastases as extradural defects. Typically, conventional myelography and postmyelographic CT are equally sensitive to MRI for epidural metastases that cause cord compression. However, Carmody et al. found MRI to be more sensitive than conventional myelography when cord compression had not yet developed, enabling detection of spinal metastases that are subtly encroaching upon the subarachnoid space owing to improved cross-sectional resolution.[40] The addition of cross-sectional anatomy of CT to myelography increases detection of bony and paravertebral metastases. CT myelography may be helpful in cases in which magnetic susceptibility artifact from orthopedic hardware on MRI obscures the spinal canal.[41]

Myelography is relatively safe and accurate for the evaluation of ESCC. It is a less attractive diagnostic procedure because of its many disadvantages, including exposure to diagnostic radiation and being an invasive procedure requiring introduction of intrathecal contrast. Both the puncture and the contrast agent can produce side effects and rarely significant adverse effects. The side effects of water-soluble contrast media are well known. Certain medications are contraindicated with myelographic contrast as they

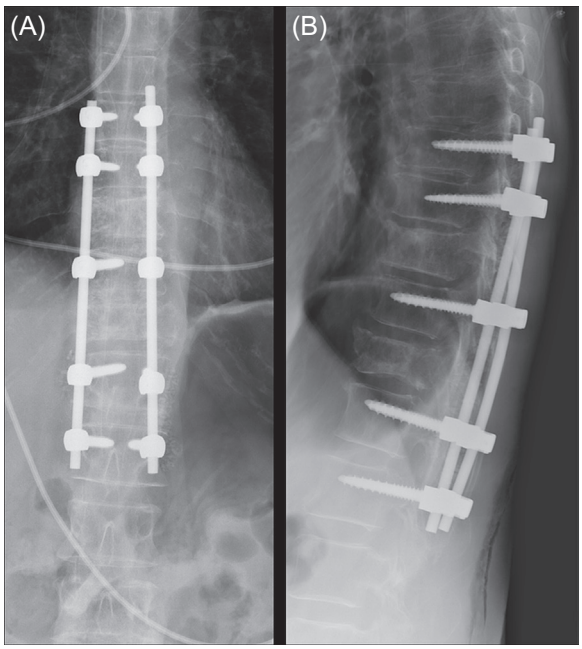


FIGURE 4 Anteroposterior (A) and lateral (B) radiographs of thoracolumbar spine show pathological compression fractures of T10 and T12 vertebrae from breast primary. On AP view, right pedicle destruction is seen at T10 and both pedicle destructions at T12 vertebral level. Posterior instrumented fusion from T8 to L2 level is also seen.

lower the seizure threshold and have to be withheld for a period of time. There is also a risk of further neurologic deterioration after lumbar puncture,[42] nerve root avulsion,[43] and puncture-site hematomas that can occasionally lead to death.[44,45] When there are two areas of myelographic block, the study may not be able to demonstrate the extent of either lesion or detect an intervening lesion in the unopacified segment. Although CT myelography will allow assessment of the spinal canal in cases with apparent block, in some cases, a second puncture with contrast injection rostral to the block may be required to delineate the superior extent of the epidural disease.[10] Because of these limitations, myelography should be reserved for those patients who cannot undergo a technically adequate MRI, including those patients with MRI-incompatible hardware, including pacemakers, or with metallic foreign bodies close to vital structures.

Computed Tomography

Unenhanced CT is relatively insensitive for identification of extradural metastatic involvement. Bone destruction is often seen with ESCC. O'Rourke et al. found the presence of cortical disruption around the neural canal to be highly associated with epidural compression,[46] and CT in particular provides better delineation of cortical bone than MRI. Multidetector spiral CT with re-formations may be used as a screening tool, but the soft tissue contrast is poor compared to MRI (Figure 5). CT-guided or CT fluoroscopically guided biopsy of paraspinal and epidural masses may be useful to obtain histological diagnosis (Figure 6).[8]

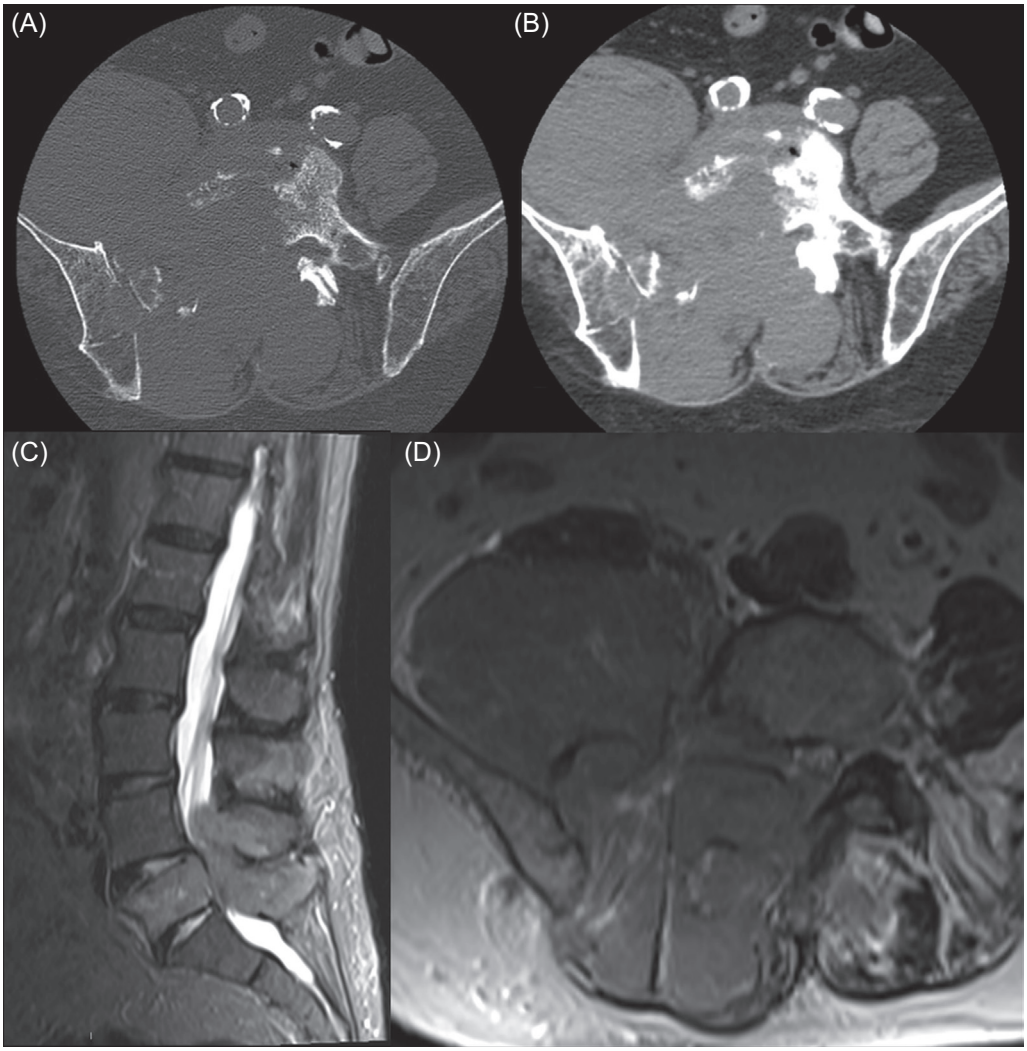


FIGURE 5 A 79-year-old male with lumbosacral soft tissue mass involving L4 and L5 right posterior elements and L5 vertebral body with epidural component compromising the spinal canal. CT bone and soft tissue window (A and B) demonstrates bone destruction and soft tissue component. MR sagittal and axial T2-weighted sequences (C and D) show the lesion with better contrast between the spinal canal filled with CSF, which appears bright, and the soft tissue, appearing iso- to mildly hyperintense.



FIGURE 6 Axial image of CT-guided biopsy on the same patient as in Figure 5 in prone position shows a needle placed in the right paravertebral soft tissue mass at the L4 level. Biopsy result was plasmablastic lymphoma.

Nuclear Medicine

Bone scan and [^{18}F]fluorodeoxyglucose positron emission tomography (^{18}F-FDG PET) are often used in the assessment of metastatic disease but are of limited utility in the evaluation of spinal epidural disease. Radionuclide bone scanning is a relatively sensitive tool for diagnosing vertebral body metastases; however, it has a high frequency of false-positive results, with a specificity of only 53%.[27] It is limited in its ability to define the anatomic extent of destruction, which requires further imaging for better delineation. It is not helpful in the detection of spinal cord compression. Some studies have found that MRI is more sensitive than single-photon emission CT bone scintigraphy for the detection of metastatic disease,[40,41,47] but may not be as sensitive for the detection of small metastases in the posterior elements.[48] Metser et al. studied the role of ^{18}F-FDG PET/CT in the assessment of secondary malignant involvement of the spinal column. Of 242 lesions, ^{18}F-FDG PET alone detected significantly more malignant lesions than did CT alone (96% vs 68%, respectively); however, this modality detected epidural extension of tumor, neural foramen involvement, or a combination of both in only 33% of cases.[49] Fusion of metabolic PET data with cross-sectional CT anatomy can help localize metastatic disease to the epidural space (Figure 7).

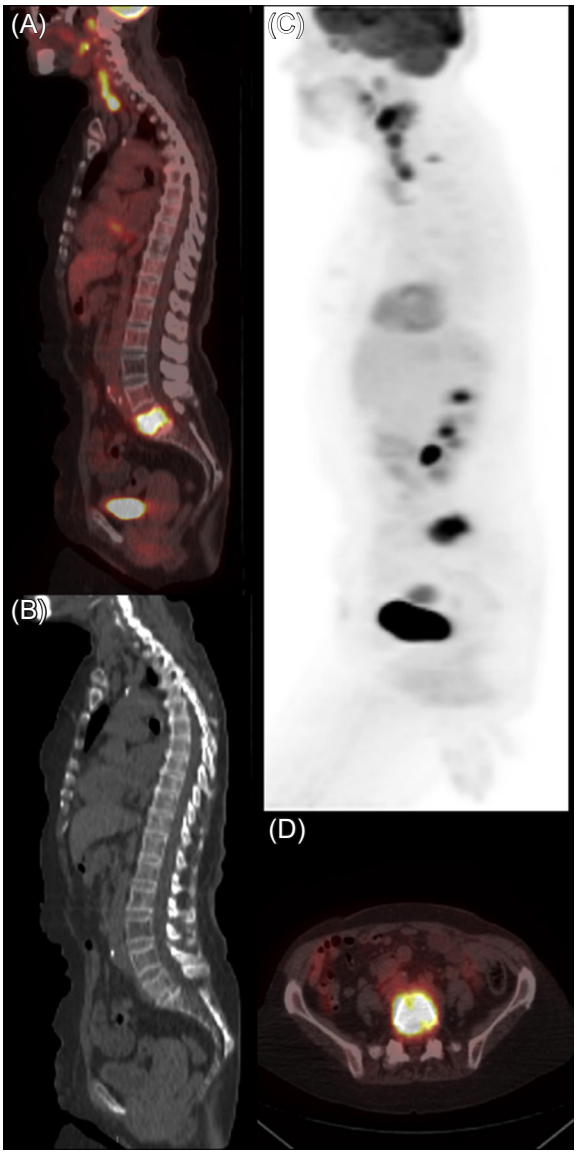


FIGURE 7 PET/CT of a 67-year-old male with Hodgkin lymphoma. Sagittal fused PET/CT (A), sagittal CT (B), maximum intensity projection (C), and fused PET/CT axial (D) images show a hypermetabolic lesion with pathological fracture of the L5 vertebra associated with epidural compromise of the spinal canal. Hypermetabolic neck lymph nodes are also seen.

Magnetic Resonance Imaging

MRI has become the modern gold standard for the evaluation of spinal epidural metastasis.[13,40,50–53] In addition to demonstrating the presence and extent of bone involvement, MRI delineates the presence and location of paravertebral and epidural extension, degree of neural compromise, and thecal sac impingement. It is noninvasive, has increased sensitivity relative to CT or myelography, and does not use ionizing radiation, which is particularly advantageous in the lumbar area where gonadal exposure may occur. Additional advantages of MRI include the ability to evaluate the spinal cord, nerve roots, and disks, while their location and morphology are less completely evaluated on myelography. The multiplanar capabilities, as well as the superior soft tissue discrimination and contrast resolution of MRI, enable a highly accurate evaluation of the nature and extent

of epidural lesions.[53] MRI can detect widely separated lesions, which may not be identified by CT myelography if they cause minimal subarachnoid compression or if they are located between two areas of myelographic block. In symptomatic epidural metastases, identifying multiple areas of metastatic disease is critical, particularly when deciding between surgery and radiotherapy or in the delineation of radiation ports. For asymptomatic epidural metastases, Schiff et al. showed that it may be safe to omit MRI of the cervical spine when there is radiographically verified thoracic or lumbar ESCC.[10] However, since the likelihood of an asymptomatic or unsuspected second site of epidural disease is higher in the thoracic and lumbosacral spine, thorough imaging of these regions is advisable.[10]

The fundamentals of MR physics are detailed in other sections of this text. Briefly, an MR image is determined by the spatial allocation of individual MR signals that represent the corresponding anatomical structure. The magnetic field is spatially varied such that the nuclear spins demonstrate different precessional frequencies at different positions. The frequency and phase of each nuclear spin are acquired in the presence of radio-frequency pulsations and magnetic gradients and stored in a matrix of voxels (k-space). The MR image is a mathematical reconstruction (Fourier transformation) of these data.

Imaging of the cervical and thoracic spine requires higher spatial resolution in comparison to the lumbar spine. Also, motion artifact related to swallowing and respiration and pulsation from the thoracoabdominal vessels is more problematic in the cervical and thoracic spine, respectively. In conventional MRI, the phase-encoding steps are performed in sequential order by switching a magnetic field gradient and this determines the measurement time. With techniques such as parallel imaging, the raw data are simultaneously acquired at an accelerated pace via two or more receiver coils with varied spatial sensitivity.[54,55] Parallel imaging exploits the difference in sensitivities between individual coil elements in a receive array to reduce the number of gradient encoding steps required for imaging. The shortened measurement time is of particular benefit in examinations with breath-hold technique. Although there may be lower signal-to-noise ratio compared to "complete" measurement results, higher resolution may be achieved with similar measurement times through phase oversampling and averaging. Phased-array surface coils, which cover a large volume with several smaller coils, are used in spine parallel imaging and can be used to achieve an optimized signal-to-noise ratio (SNR) over a large field of view.[56] Phased-array coils have an increased number of elements to enable faster dynamic scans with the consequent reduction of motion artifacts.

Sagittal and axial T1-weighted (short TR (time to recovery)/short TE (echo time)) and T2-weighted (long TR/long TE) are the typical sequences used in the evaluation of spinal metastatic disease. Fast spin-echo (FSE) imaging, also known as turbo spin-echo, has replaced conventional spin-echo (SE) imaging of the spine owing to improved time efficiency and image quality.[57] FSE sequences collect small segments of k-space after each radiofrequency (RF) pulse for excitation.[57] This enables decreased overall imaging time, thereby lessening the potential for patient motion and enabling additional signal averages, which improve signal.

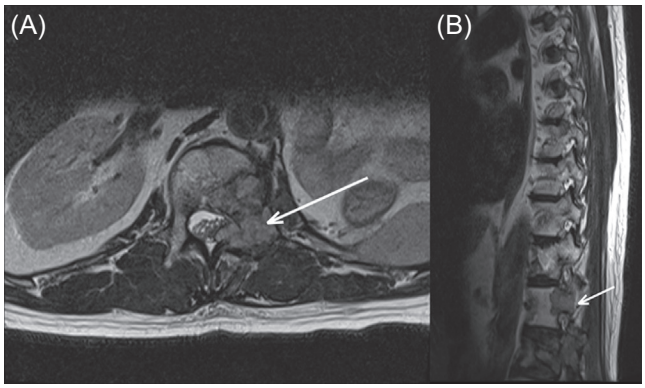


FIGURE 8 (A) Axial and (B) sagittal T2-weighted images in a 56-year-old male with renal cell carcinoma (note left nephrectomy on axial image) demonstrates soft tissue mass in the left epidural space with mass effect on the thecal sac on the axial image and involvement of T11, T12, and L1 vertebrae on the sagittal image. The relatively hypointense appearance compared to hyperintense CSF on T2-weighted image (arrows) demonstrates compromise of the thecal sac and nerve roots to better effect.

The FSE strategy is particularly helpful in T2-weighted imaging to take advantage of the long TR intervals to accommodate a relatively long echo train. These heavily T2-weighted studies produce marked contrast between the CSF, the conus medullaris, and the extradural tissues. However, the fat remains relatively bright despite its short T2 on FSE sequences and may decrease detection of tumor.[58] The degree of compromise of the thecal sac, spinal cord, and nerve roots can be easily assessed on heavily T2-weighted images on which the CSF is particularly bright (Figure 8).[59] However, CSF flow can create problems including signal loss, spurious signal, and blurred interfaces, particularly on those sequences that produce myelographic contrast and for those that suppress CSF signal intensity (Figure 9).[57] In the lumbar spine, CSF pulsation is dramatically dampened.[57] While lymphoid malignancies are often isointense with marrow on T2-weighted images, most metastatic carcinomas and sarcomas give higher signal intensity than fat, suggesting that MRI findings may be used to distinguish between these pathologies.[60] Sze et al. found that long TR sequences without contrast material also showed equally good delineation.[61] Additionally, the presence of apparently bright disks on T2-weighted images may be



FIGURE 9 Sagittal T2-weighted image demonstrates CSF pulsation artifacts within the posterior aspect of the thecal sac in the thoracic spine (arrows) in a 15-year-old male being evaluated for pineal germinoma metastatic deposits.

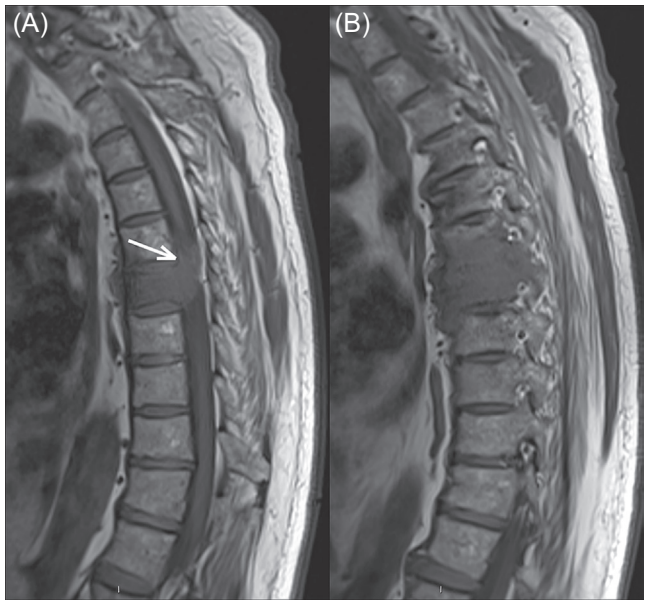


FIGURE 10 Sagittal T1-weighted image in midline (A) demonstrates abnormal hypointense marrow signal involving the T7 vertebral body with an anterior and posterior epidural component (arrow). A right paramidline sagittal T1-weighted image (B) demonstrates involvement of the T6 vertebra as well. CT-guided biopsy proved poorly differentiated metastatic lung adenocarcinoma.

a subtle sign of diffuse replacement of normal fatty bone marrow in the vertebrae.[62]

T1-weighted FSE imaging is helpful to identify marrow replacement processes, such as metastases. Normal vertebrae in young adults are composed primarily of hematopoietic bone marrow containing significant amounts of fat (from 25% to 50%).[63] With aging, the marrow is converted to even larger amounts of fat and correspondingly, the mean percentage volume of hematopoietic marrow decreases progressively, with the result that in the eighth decade of life it is about half of that present in the first decade (29.2% vs 57.9%).[64,65] This is useful in detection of pathology, as an abnormal hypointense focus is sharply contrasted to the normal hyperintense fatty marrow in the adult spine. Tumors tend to be hypointense on noncontrast T1-weighted images, reflecting replacement of fatty bone marrow, increased water content, and hypercellularity (Figure 10).[66] In acute compression fractures, the distinction between nonneoplastic involvement and tumor replacement of marrow is difficult because both may display low T1 signal. The former is due to marrow edema (Figure 11) and the latter due to the tumor itself (Figure 12). Postgadolinium imaging may not be helpful because lesions may be obscured as they enhance to the isointensity of the adjacent marrow on the T1-weighted sequences (Figure 12).[50] Also, acute compression fractures can enhance (Figure 11).

Epidural space lesions, however, may be difficult to detect on unenhanced T1-weighted sequences, and further evaluation with contrast-enhanced images or long TR images may be necessary.[50] Sze et al. demonstrated the utility of gadolinium in characterizing possible epidural tumor by delineating the extent of tumor and outlining regions of spinal cord compression.[50,60] This is helpful in the cervical and thoracic spines where there is a relative lack of prominent ligaments and epidural fat, which typically increase the conspicuity of lesions projecting from the spine. The timing of postcontrast imaging can be used to differentiate tumor from a herniated intervertebral disk, demonstrating delayed enhancement (Figure 13).[67] Early contrast images may help in localizing tumor for biopsy. Enhanced MRI may be used for posttreatment assessment of epidural tumor. After radiation therapy, decreased vascularity can explain relatively diminished enhancement on MRI. It is prudent to compare serial images with the baseline, as untreated epidural neoplasms can vary in the degree of enhancement.[50] Gadolinium-enhanced MRI is also helpful in evaluating mimics like intradural/intramedullary lesions and subarachnoid seeding (Figure 14).

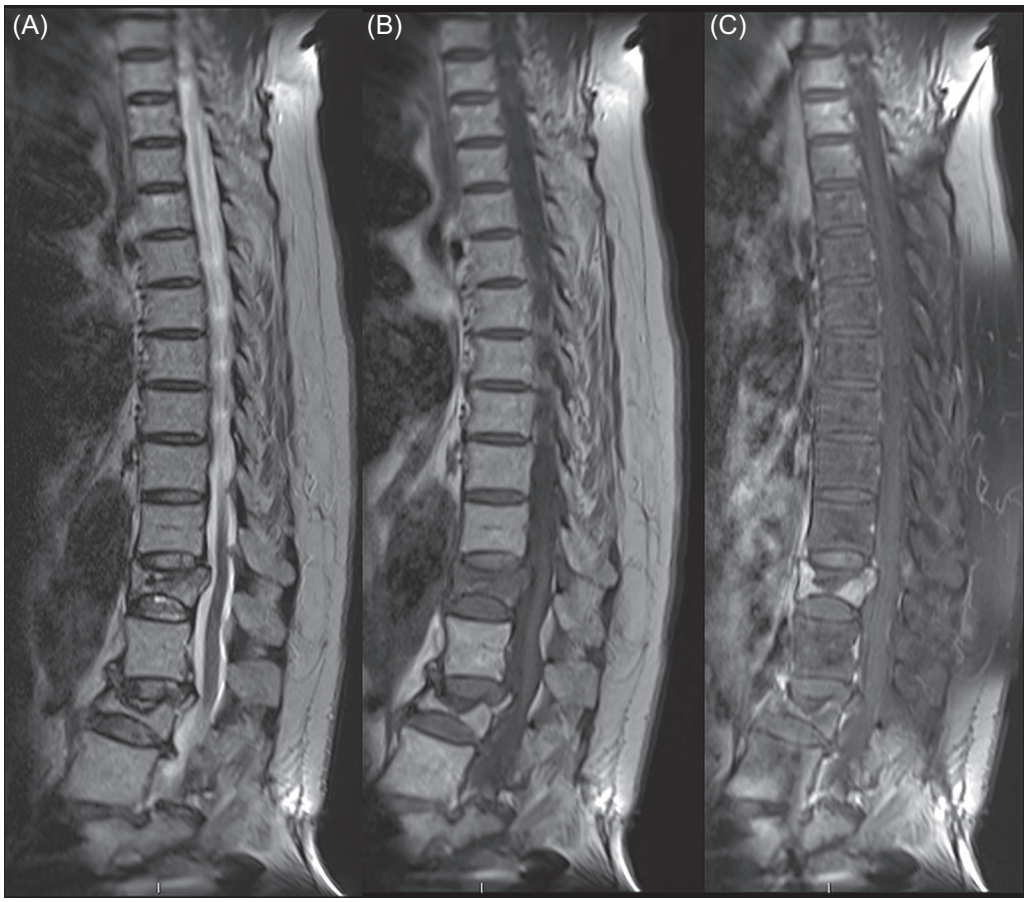


FIGURE 11 Sagittal T2 (A), sagittal T1 (B), and sagittal T1 postcontrast fat-saturated sequence (C) demonstrate acute compression fracture of the T11 vertebra with retropulsion into the central canal and enhancement related to edema in a 74-year-old female. An old compression fracture of the L1 vertebra is also noted.



FIGURE 12 Sagittal STIR (A), sagittal T1 (B), and sagittal postcontrast T1 fat-saturated (C) sequences demonstrate metastatic compression fracture of the T11 vertebra with retropulsion resulting in moderate canal compromise in a 61-year-old male. The primary was a poorly differentiated lung adenocarcinoma. Note the relative hypointensity on T1-weighted sequence and diffuse enhancement on postcontrast sequence compared with normal marrow hyperintensity on T1-weighted sequence.



FIGURE 13 Sagittal T2 (A) and postcontrast sagittal T1 fat-saturated (B) images demonstrate a peripherally enhancing lesion in the ventral epidural space representing herniated disk material extending posteriorly from the L5–S1 intervertebral disk space level.

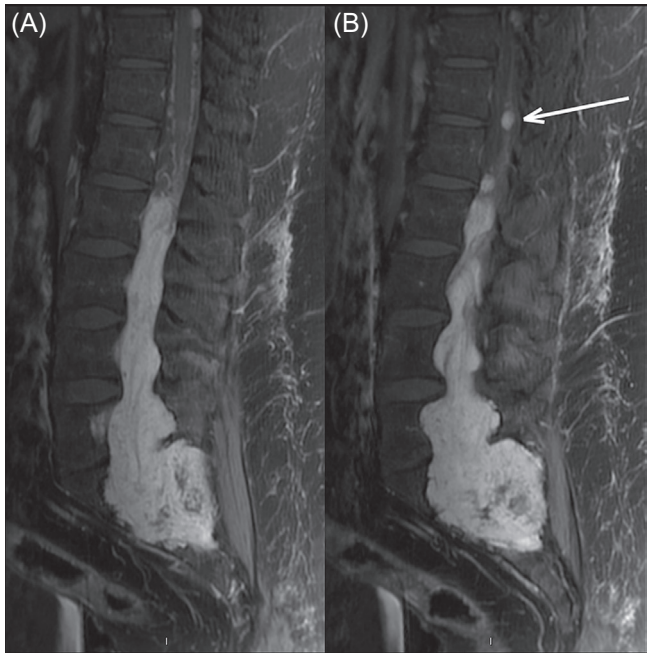


FIGURE 14 Sagittal T1 postcontrast fat-saturated images in the midline (A) and parasagittal planes (B) demonstrate large enhancing lobulated mass in the lumbosacral spinal canal representing myxopapillary ependymoma. Nodular enhancing foci along the posterior aspect of the conus medullaris (arrow) represent areas of subarachnoid seeding.

Sze et al. have reported the efficacy of gadolinium in detecting even small lesions in the intradural extramedullary space.[61]

Gradient-echo (GRE) imaging is more often used in the cervical and thoracic spine to produce myelogram-like images.[68,69] In GRE imaging, the RF pulse is applied with a partial flip angle (<90°) and the gradients are then inverted to refocus the excited spins without the application of a 180° pulse. Although the absent 180° pulse enables faster imaging, it makes the images more susceptible to local field inhomogeneities (Figure 15(A)). The relatively long TEs and large voxel size in routine two-dimensional GRE studies result in considerable susceptibility artifact at the bone–soft issue interface, which exaggerates the true degree of bony canal and neural foraminal stenosis.[57] However, by producing a myelographic effect with bright CSF, GRE images can depict regions of impingement (Figure 15(B)).

Diffusion-weighted imaging (DWI) is an established method for studying cerebral disease processes, but previous use of DWI in the spine was limited for technical reasons.[57] Baur et al. were able to use DWI with a steady-state free procession sequence to distinguish benign vertebral compression fractures from pathologic compression fractures.[70] In contrast, Castillo et al. showed that DWI of the spine had no advantage in the detection and characterization of vertebral metastases compared with noncontrast T1-weighted imaging, although it was considered superior to T2-weighted imaging.[71] DWI is challenging to perform in the spine because of the small cross-sectional area of the spinal canal and interfaces distorting the signal. The only practical use remains that of differentiating metastatic tumor infiltration from benign fracture edema.[72]

Fat-saturation techniques can be used to suppress the signal from normal adipose tissue to reduce chemical shift artifact or improve visualization of uptake of contrast material. A frequency-selective saturation RF pulse with the same resonance frequency as that of lipids is applied to each slice-selection RF pulse and a homogeneity spoiling gradient pulse is applied immediately after the saturation pulse to diphase the lipid signal. Thus, the signal excited by the subsequent slice-selection pulse contains no contribution from lipid. This method is lipid-specific, is reliable for tissue characterization, and allows good demarcation of small anatomic details.[73] Because subtle low-intensity lesions can be obscured by the high signal intensity of marrow fat on routine T1-weighted SE imaging, suppression of marrow fat can be helpful in detecting metastatic lesions in the spine. This is particularly important in the elderly population because of the heterogeneous fatty vertebral marrow.[74] Low-intensity lesions enhance after the administration of gadolinium and can be obscured; therefore, fat suppression of postcontrast images can be useful to differentiate normally enhancing marrow from a pathologic lesion (Figure 16).

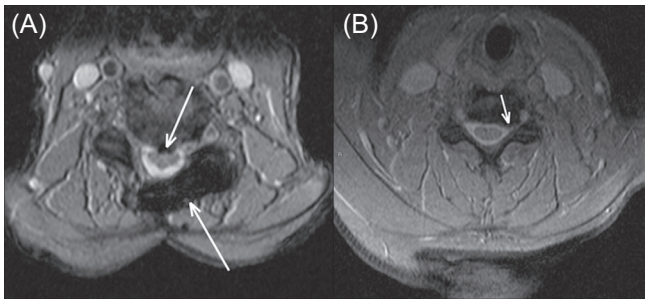


FIGURE 15 (A) Axial GRE image demonstrates overestimation of spinal canal narrowing due to magnetic susceptibility artifact caused by posterior osteophytes (arrow) and artifacts generated from a left lamelloplasty (arrow). (B) Axial GRE image shows an effaced ventral thecal sac and severe left neural foraminal stenosis (arrow) due to a disk–osteophyte complex better seen against relatively bright CSF.



FIGURE 16 Postcontrast sagittal T1-weighted image with fat saturation shows multiple enhancing bone lesions involving the vertebral bodies of T12, L2–L5, and S1 and spinous processes of T12, L1, and L5. Note an epidural-enhancing component at the T12 level (arrow) causing a mass effect over the thecal sac. The metastatic lesions enhance, while normal marrow is suppressed.

The disadvantages of this technique are its susceptibility to static field inhomogeneities; misregistration artifact, particularly due to foreign bodies like metal or air collections; and unreliability with low-field-strength magnets.

Another method for suppression of fat signal is inversion-recovery imaging, which is based on differences in the T1 of tissues. In a short T1 (tau) inversion-recovery (STIR) sequence, a 180° pulse is applied and the longitudinal magnetization of adipose tissue recovers faster than that of water (shorter T1). Subsequently, a 90° pulse is applied at the null point of the adipose tissue, which produces no signal, whereas water will still produce a signal. This technique is less sensitive to magnetic field inhomogeneities and has a high sensitivity for the detection of neoplasms and infectious processes because of its ability to show the combined effects of prolonged T1 and T2 relaxation times of these pathologic tissues in a background of hypointense fat-suppressed marrow (Figure 17).[57,75,76] However, this imaging sequence has a low SNR and is limited because of the motion artifacts caused by CSF pulsation. The drawback of STIR and inversion recovery FSE sequences (IRFSE) is their failure to show epidural metastatic disease because CSF and epidural tumor both have high signal intensity, making CSF indistinguishable from metastatic disease.[74] Mehta et al. demonstrated that T1-weighted, FSE, and fat-saturated FSE sequences were superior to STIR and IRFSE in the detection of epidural metastatic disease.[74]

Fluid-attenuated inversion recovery (FLAIR) is an inversion-recovery sequence in which the inversion time is chosen to null the CSF signal and the TR and TE are chosen to provide heavy T2-weighting. This is useful in the spine because pulsation artifact from CSF flow, which is troublesome on SE and FSE T2-weighted sequences, is negated with FLAIR. T1 FLAIR provides thinner slices and higher spatial resolution in less time than the conventional two-dimensional SE imaging for routine spine studies. It also provides greater CSF suppression and improved cord-to-CSF contrast by using the inherent magnetization transfer effect to suppress CSF in postcontrast studies.[77] This sequence also allows increased conspicuity of lesions of the spinal cord and bone marrow and reduces hardware-related artifacts compared with conventional T1-weighted sequences. It may be considered as the preferred lumbar spine imaging sequence compared to T1-weighted FSE, as it has demonstrated superior CSF nulling, better conspicuousness of normal anatomic structures and degenerative and metastatic lesions, and improved image contrast.[78]

CSF flow imaging based on the phase-contrast technique provides information about the phase (or direction) of flow and the velocity (or magnitude) of CSF flow such that no signal is detected from stationary tissue. Prominent epidural venous plexus can be differentiated from solid tumor, metastatic disease, inflammatory disease, or herniated disk with MR CSF flow images.[79] When there is prominence of the epidural plexus due to spondylosis, the extent of the plexus can be seen on



FIGURE 17 Sagittal STIR sequence shows hyperintense signal in the T5 vertebra (arrow) resulting from marrow edema with hypointense fat-suppressed marrow in the rest of the vertebral bodies. Also note the posterior epidural tissue in the thoracic spinal canal from the T1 to T10 level (arrows) with a mass effect on the spinal cord at the T4–T5 level. This was proven to be osteomyelitis and epidural abscess.

flow images. However, epidural involvement by tumor or scar component will not show flow.[80]

Alteration of the spinal cord structural integrity due to various diseases such as metastases, abscess, or spondylosis is a major cause of motor dysfunction and can be assessed by using diffusion tensor imaging (DTI) methods. In a study of 15 symptomatic and 11 normal volunteers, Facon et al. evaluated the diagnostic accuracy of apparent diffusion coefficient (ADC), fractional anisotropy (FA), and fiber tracking in both acute and slowly progressive spinal cord compressions.[81] They found that FA has the highest sensitivity and specificity in the detection of acute spinal cord abnormalities. In another study by Yoo et al. involving 15 patients with cervical myelopathy and five healthy volunteers, the cervical myelopathy subgroup showed significantly reduced FA and increased ADC compared to the healthy subgroup.[82] They concluded that the use of DTI to quantify the extent of myelopathological changes in compressive myelopathy could be more reliable than any other existing diagnostic tools and might provide invaluable information about selecting the optimal treatment for compressive myelopathy and predicting surgical outcomes and prognosis.

With higher magnetic strength, there are advantages of higher SNR, which would be double at 3.0 T in comparison to 1.5 T, enabling improved contrast or spatial resolution.[83,84] There is also the potential advantage of decreased scan times without reduction in image quality, which is helpful in reducing patient motion artifacts. The improved SNR may reveal subtle structural and pathologic details involving the cervical and lumbar spinal elements, such as nerve roots, neural foramina, and intracanalicular lesions.[85] Increased magnetic strength brings with it issues of increased energy deposition (specific absorption rate); increased effects of magnetic susceptibility differences of tissues, particularly at tissue–bone and tissue–air interfaces; increased chemical shift artifact, which degrades standard SE images; and alterations in the T1 and T2 relaxation times.[85] Improvements in sequences, data sampling, and postprocessing software have benefited the attainable spatial and temporal resolution to the point at which the fine depiction of anatomical structure and pathological processes is now routine.[86]

While MRI has revolutionized the detection of spinal epidural metastases, it has inherent disadvantages. Some patients who have contraindications to MRI, such as pacemakers or cochlear implants, will require other modalities for primary evaluation. Although not a contraindication to spine MR, metallic hardware in the area of scanning may, in some cases, limit the delineation of anatomic detail. Sedation and adequate analgesia can facilitate obtaining an MRI in those patients with pain and/or claustrophobia. Nevertheless, patient motion cannot always be controlled by sedation or analgesia and continues to be the most vexing problem during sequences requiring long acquisition times. Marrow heterogeneity due to osteopenia, myeloinfiltrative processes, and anemia can complicate interpretation of MRI. Hematopoietic marrow of younger patients is also difficult to assess in the setting of a neoplastic process involving the extradural spine. As mild to moderate degenerative changes evolve, the marrow may demonstrate T1 hypointensity and T2 hyperintensity and may enhance to some extent after administration of Gd-DTPA, which may confound the imaging diagnosis. Mild hyperemia and marrow edema associated with fractures can also enhance.[50]

MRI is increasingly used for guiding, monitoring, and controlling percutaneous procedures and surgery. The rapid development of interventional techniques in radiology has led to integration of imaging with computers, new therapy devices, and operating room-like conditions. This has projected as faster and more accurate imaging and hence more demanding procedures have been applied to the repertoire of the interventional radiologist. By combining features of various other imaging modalities and adding some more into them,

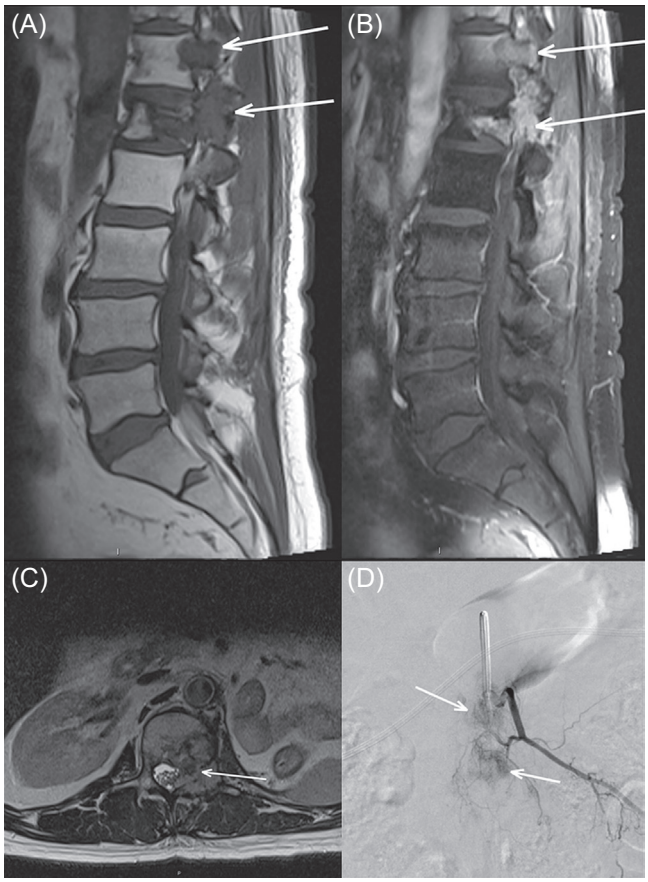


FIGURE 18 Sagittal T1 precontrast (A) and T1 postcontrast T1 fat-saturated (B) images of metastatic renal cell carcinoma show hypointense enhancing lesions involving the T12 and L1 vertebral bodies and left pedicle and laminae (arrows). Axial T2-weighted (C) image at the L1 vertebral level shows an epidural component with thecal sac displacement to the right (arrow). Note the left nephrectomy. Selective digital subtraction catheter angiogram (D) shows vascular tumor blush at the T12 and L1 levels on the left side (arrows), which was successfully embolized with polyvinyl alcohol particles prior to surgical decompression and stabilization.

interventional MRI has the potential to extend interventional radiology techniques, minimally invasive therapies, and surgery. The term "interventional MRI" covers all those procedures that are performed under MRI guidance.[87] Preoperative endovascular embolization of highly vascular metastases such as those from melanoma, renal cell carcinoma, and thyroid carcinoma can be performed to minimize intraoperative blood loss (Figure 18). Angiographic embolization within 48 h of the operative procedure may preclude the recruitment of adjacent nonembolized vessels.[88]

IMAGING DIFFERENTIAL DIAGNOSIS

The radiological differential diagnosis of an epidural mass includes metastases, lymphoma, hemorrhage, radiation-induced tumor, and inflammatory/infectious process. History is critical in establishing the neuro-oncologic clinical setting to aid in obtaining the appropriate imaging study and in accurate interpretation of the diagnostic images. In addition to evaluating the imaging characteristics of the epidural mass, assessment of any additional abnormalities helps in further narrowing the differential diagnosis.

The pathophysiology and examples of metastases to the epidural space have been discussed earlier in the chapter. It is important to emphasize lymphoma, as it can commonly extend into the epidural space directly from a vertebral body, which is usually the cause of cord compression with lymphoma.[32] The soft tissue component demonstrates iso- to hypointensity relative to muscle on the T1-weighted image (T1WI) and variable iso- to hyperintensity on the T2WI and enhances uniformly and intensely. It is often multisegmental and can infiltrate through the neural foramina, which is typical of lymphoma. Isolated hematogenous involvement of only the epidural space occurs rarely in metastatic lesions and more frequently in lymphoma.[31] Lymphoma has a predilection for the thoracic spine and has a tendency to spread over several vertebral levels.[89] There may be thickened enhancing nerve roots with or without focal nodules. Intramedullary tumors may be present, may show variable patchy and/or confluent enhancement, and may be infiltrative or discrete (Figure 19). Other hematologic malignancies, such as multiple myeloma, have also been associated with spinal epidural disease.[90] In multiple myeloma, the vertebral body marrow may demonstrate an inhomogeneous pattern with foci of T1 hypointensity in a background of diffusely low signal.[91] Spinal cord compression due to amyloid deposits has been reported in multiple myeloma.[92,93]

Infection and malignancy can be differentiated by various features. These were described in a study involving the lower spine.[94] Infectious processes usually involve more than one vertebra. While intervertebral disk involvement is seen more often with infection and very rarely with malignant disease, neural arch involvement is seen more often with malignant disease. In cases of direct spread of infection into the epidural space from diskitis/osteomyelitis, the abscesses are often located in the anterior aspect of the spinal canal. Epidural abscesses are often multisegmental and fusiform, centered on and contiguous with the diseased disk and adjacent vertebral bodies. Spinal epidural abscesses can also result from hematogenous spread of bacteria usually from a cutaneous or mucosal source. They can be circumferential, and the posterior epidural space is involved in 80% of the cases from a hematogenous source.[95] Radiography may demonstrate end-plate erosion and vertebral body weight loss. Myelographic findings of extradural mass impeding upon the thecal sac are nonspecific. CT shows an enhancing epidural mass narrowing the canal along with the osseous changes. The lesion is iso- to hypointense on T1WI and hyperintense on T2WI and STIR MRI

sequences. There may be homogeneous or heterogeneous phlegmon, peripherally enhancing necrotic lesion, and prominent enhancing anterior epidural veins or basivertebral plexus above or below the abscess (Figure 20). Signal alterations in the cord may be due to direct infection, cord compression, and/or cord ischemia.

The differential diagnosis of an epidural mass in a patient with treated cancer includes radiation-induced secondary tumor and inflammatory/infectious process.

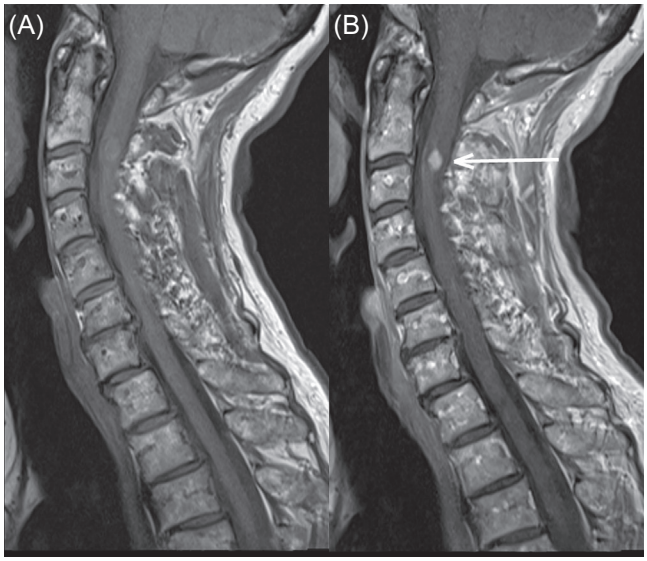


FIGURE 19 Pre- (A) and postcontrast (B) sagittal T1WIs of cervical spine demonstrate an expansile isointense intramedullary lesion with areas of discrete enhancement (arrow) representing an ependymoma.

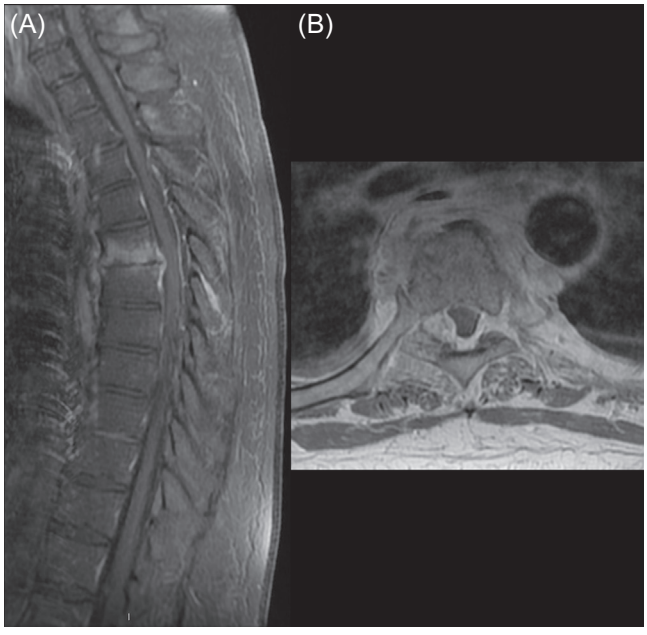


FIGURE 20 Sagittal postcontrast T1WI with fat saturation (A) and axial postcontrast T1WI (B) demonstrate acute diskitis and osteomyelitis at the T5–T6 level with right epidural abscess displacing the thecal sac and spinal cord to the left and causing moderate canal stenosis.

However, osteoradionecrosis has been reported to present as a metastatic epidural spinal lesion within a previously irradiated port[96] and is a serious complication in the treatment of head and neck malignancies. The lesion demonstrates hypointensity on T1WI and variable hyperintensity on T2WI sequence. CT finding of sclerosis and then progression over time are more specific for osteoradionecrosis (Figure 21). In a 2014 study, Alhilalai et al. found a significant overlap of standard uptake values on PET in patients with osteoradionecrosis and tumor recurrence. CT findings provided more reliable diagnostic tools, with a solid or cystic mass strongly associated with tumor recurrence and bony sclerosis seen only with osteoradionecrosis.[97]

Inflammatory processes including granulomatous disease can also involve the epidural space.[98–100] Granulomatous infections caused by tuberculosis (TB), brucellosis, fungi, and parasites, including hydatid disease

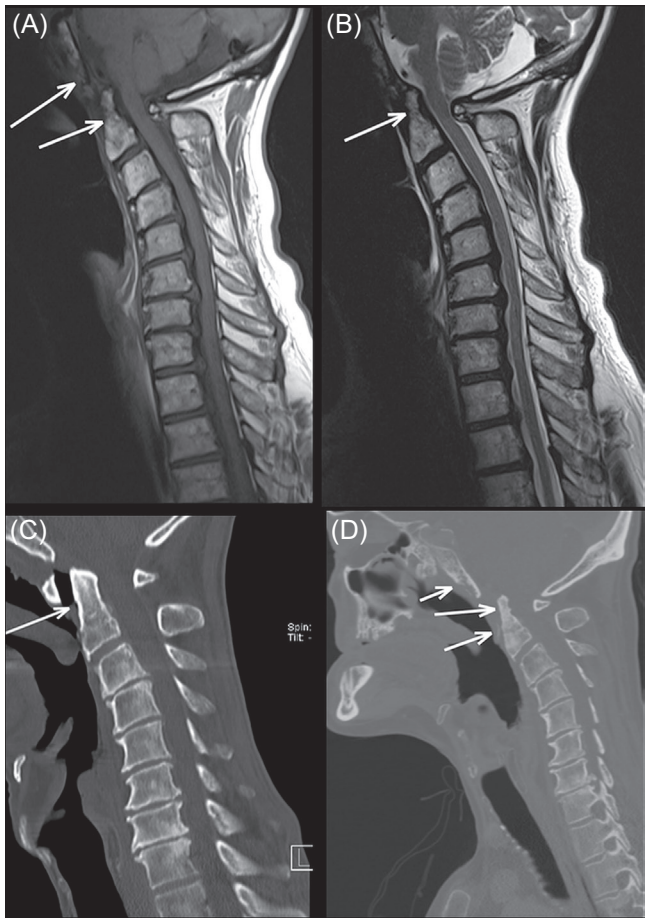


FIGURE 21 Sagittal T1- (A) and T2- (B) weighted sequences demonstrate erosion and marrow replacement process in the clivus and odontoid process (arrows) in a patient with squamous cell oropharyngeal carcinoma postchemoradiation. Note radiation-related fatty replacement of marrow as a relatively hyperintense signal in the rest of the vertebrae. The erosive marrow changes are better seen on CT sagittal reconstructions with progression over 1 year 4 months (C and D). Note the anterior arch of dens is resorbed and there is increased erosion on image (D, arrows) resulting in spinal instability at the atlantodental joint.

(*Echinococcus*), have some imaging findings different from those seen with nonspecific bacterial infection.[95] For example, TB spreads via the anterior longitudinal ligament with relatively limited disk involvement in comparison to degree of vertebral body and paraspinal infection and with frequent thoracic segment involvement.[95] In a study by Colmenero et al., epidural and paravertebral masses were present in 68.3% and 78% of cases of TB osteomyelitis, respectively.[98] This was significantly greater than in cases of pyogenic and *Brucella* osteomyelitis.[95] *Brucella* infection also commonly involves the lumbar spine and the epidural space.[95] SAPHO syndrome, in which the acronym SAPHO stands for synovitis, acne, palmoplantar pustulosis, hyperostosis, and osteitis, is an interesting entity.[101] MRI demonstrates enhancement of vertebral end plates indicating spondylodiscitis. CT shows sclerosis, hyperostosis, and erosion of the vertebral end plates (Figure 22). The pathogenesis of this syndrome remains unknown, although some authors have described an association with psoriatic arthritis, inflammatory chronic intestinal diseases, and *Propionibacterium* acnes.[102]

Rarely, inflammatory arthropathy (e.g., tophaceous gout, renal osteoarthropathy, calcium pyrophosphate dihydrate crystal deposition) can have a soft tissue component in addition to the osseous disease. Gout of the axial skeleton is unusual, presenting with a range of symptoms from neck or back pain to various neurologic syndromes, including radiculopathy, myelopathy, and cauda equina syndrome.[103] Radiographs may be normal or may show nonspecific degenerative changes. CT is useful to demonstrate focal facet joint erosion, which is a more characteristic imaging feature of gout than with osteoarthritis.[104] Tophaceous lesions produce abnormal T1 and T2 signal intensities and enhance with gadolinium. Epidural tophus can extend beneath the posterior longitudinal ligament over two vertebral levels, as well as involving the intervening intervertebral disks and portions of the adjacent end plates.[105] Similar MRI findings have been reported in cases of cord compression secondary to gout of the cervical spine.[106] Calcium pyrophosphate dihydrate deposition in the transverse ligament of the atlas has been reported to cause cervical myelopathy.[107] It can be seen as a nonenhanced isointense extradural mass on a T1WI and a heterogeneous signal mass on a T2WI. CT can show calcifications in the retrodental region with erosion of the dens and compression of the cervicomedullary junction (Figure 23). There is instability at the atlantodental joint.

Epidural/subdural hematoma should be considered in the differential diagnosis when a long segmental epidural mass displays high signal on both T1WI and T2WI.[90] There is usually no significant postgadolinium enhancement; however, there are case reports of patchy enhancement of hyperacute/acute epidural hematoma.[108] In the absence of trauma, as in

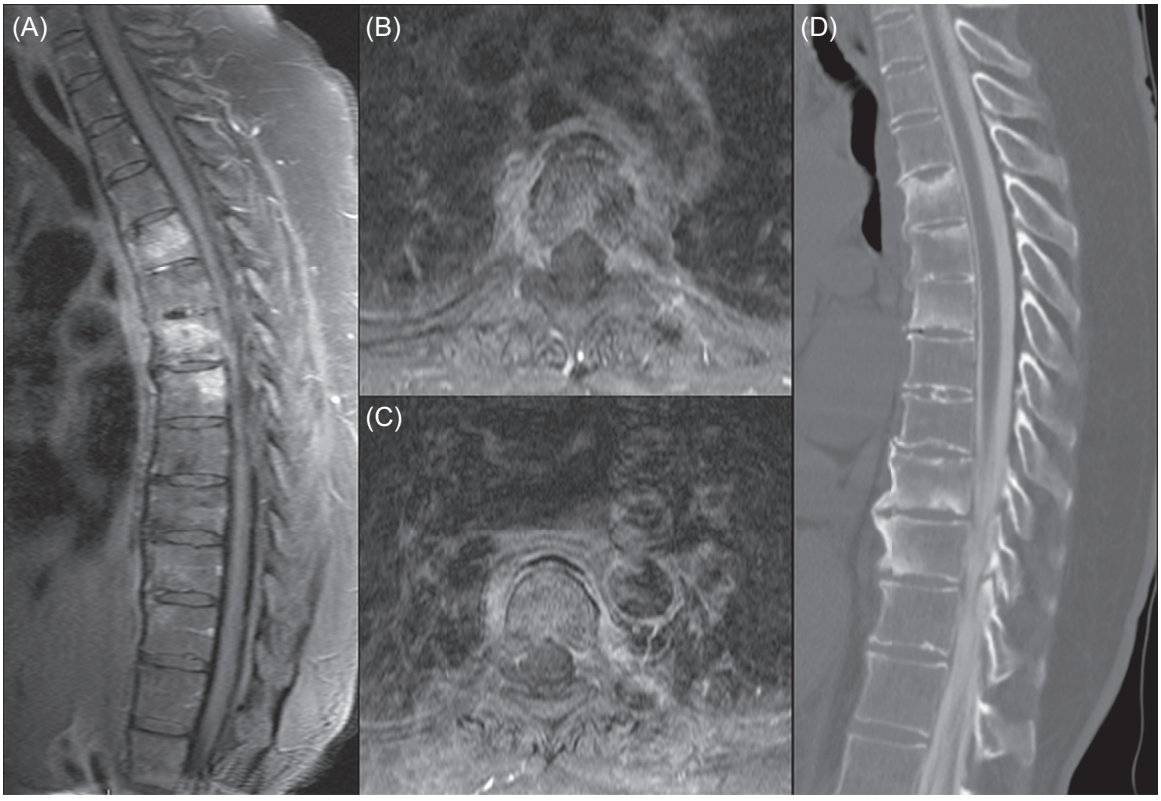


FIGURE 22 Postcontrast sagittal T1 fat-saturated (A) and axial T1 fat-saturated (B and C) images demonstrate enhancement in multiple thoracic vertebrae with enhancing pre- and paravertebral soft tissue. Thoracic CT myelogram bone window (D) shows end-plate irregularity, sclerosis, and anterior beaking osteophytes consistent with SAPHO syndrome.

spontaneous epidural hemorrhage, the vertebrae are intact.[109] Depending on the age of the blood products, the hemorrhage may be hypo-, iso-, or hyperintense. It can be eccentric, multilocular, or multisegmental (Figure 24). Uncommonly, an epidural CSF collection can be seen after trauma or after surgery. It demonstrates CSF signal intensities on all sequences (Figure 25) as opposed to a soft tissue epidural mass.

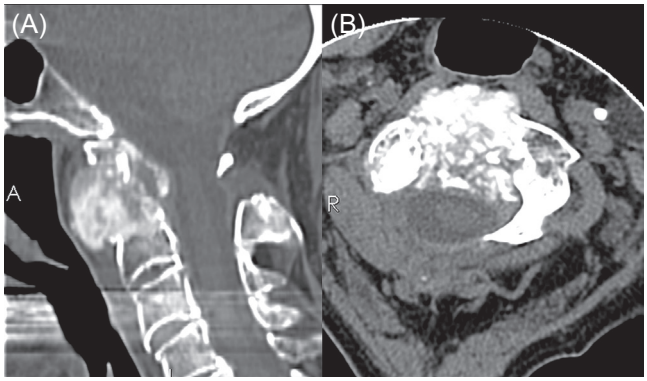


FIGURE 23 Sagittal (A) and axial (B) reconstructed CT slices at the craniovertebral junction show a soft tissue mass posterior to the dens with calcifications and erosion of the dens resulting in a mild mass effect over the cervicomedullary junction in a case of calcium pyrophosphate dihydrate deposition or pseudogout. This results in instability at the atlantodental joint.

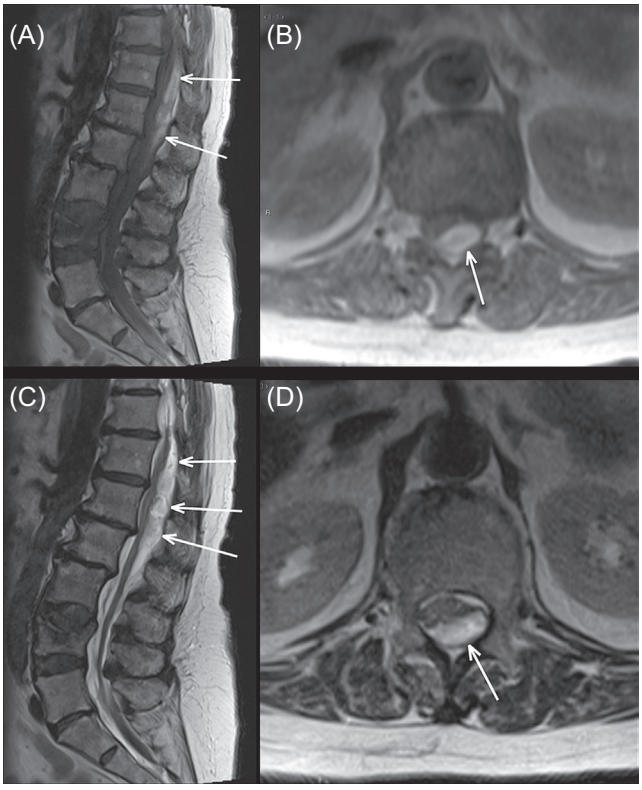


FIGURE 24 Sagittal (A) and axial (B) T1WIs of lower thoracic and lumbar spine demonstrate a T1-hyperintense epidural collection representing epidural hematoma on the left dorsal aspect from the T10–L2 vertebral levels displacing the thecal sac anteriorly and to the right in a 73-year-old female who sustained a ground-level fall. Sagittal (C) and axial (D) T2WIs show heterogeneous hyperintense signal in a dorsal epidural hematoma. Also note a burst compression fracture of the L4 vertebral body that has low signal on T1- and high signal on T2-weighted sequence representing marrow edema.

When a focal epidural mass at the level of the intervertebral disk space is identified, a disk extrusion should be considered. An intervertebral disk extrusion has a narrow contiguous segment with the parent disk while a sequestered disk has no continuity with the parent disk. On T1WI the disk material is isointense to the parent disk and iso- to hyperintense on T2WI depending on the degree of hydration (Figure 26(A–D)). The disk demonstrates peripheral enhancement (Figure 26(B)), but can demonstrate diffuse enhancement if imaged longer than 30 min after contrast injection. These are most commonly seen at the L4–L5 or L5–S1 level.

Sometimes extensive soft tissue material that is hyperintense on T1WI and low density on CT insinuates in the epidural space. This may represent epidural lipomatosis, which is an aberrant excess of epidural fat, often related to exogenous or endogenous steroids. The majority of cases are idiopathic and the thoracic and lumbar spinal canal is equally involved. There can be mass effect on the thecal sac and nerve roots. Borre et al. quantified normal and pathological amounts of epidural fat in a large study, grading it from I through III, and found that all grade III patients exhibited radiculopathy.[110] The lesion is homogeneously hyperintense on T1WI, is hypointense on T2WI, and does not enhance. Fat-saturation

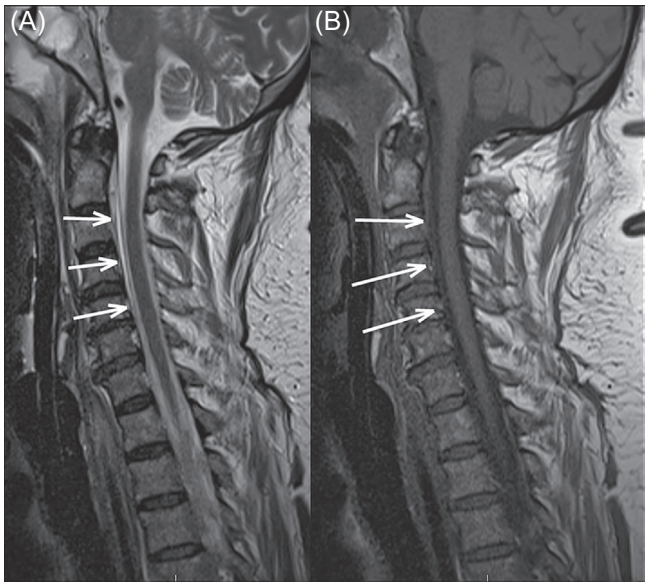


FIGURE 25 (A) Sagittal unenhanced T2WIs show an anterior epidural fluid collection slightly more hyperintense than CSF (arrows) from C2 through the C4–C5 level and that does not cause any mass effect on spinal cord. (B) Sagittal unenhanced T1-weighted sequence shows the collection to be isointense to CSF. This represents a thin epidural hygroma in a 62-year-old after a motor vehicle accident.

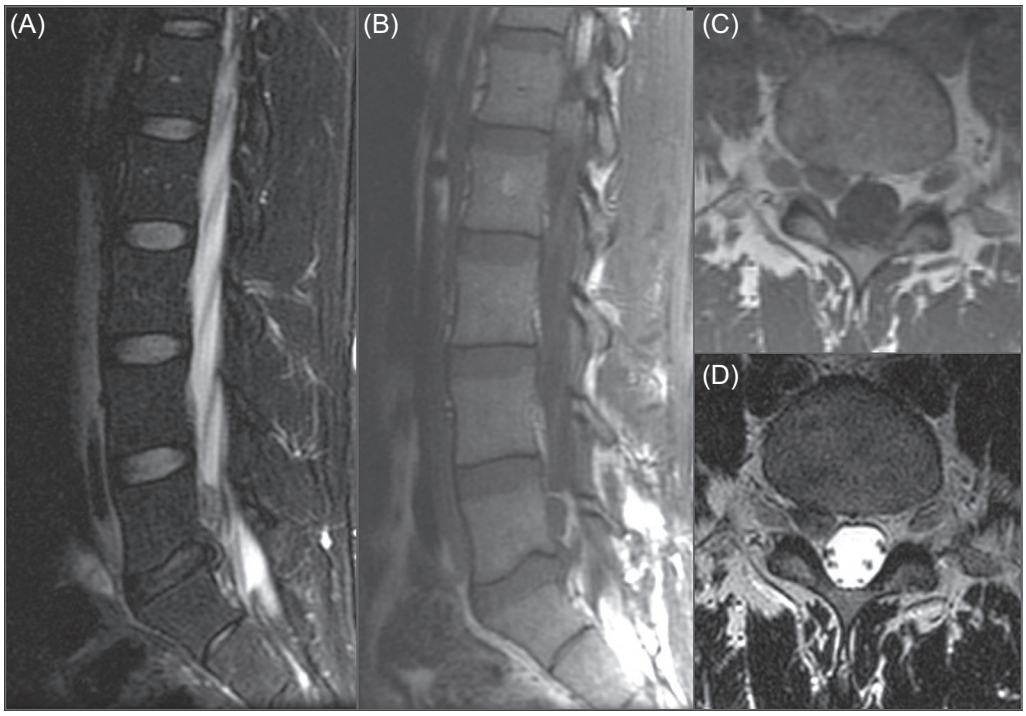


FIGURE 26 Sagittal GRE (A) image shows disk degeneration at the L5–S1 level. A heterogeneously hyperintense lesion is seen in the ventral epidural space posterior to the L5 vertebral body representing a sequestered disk. It does not demonstrate any connection with the parent disk and has a signal different from the parent disk. It represents superior migration of a sequestered disk. Sagittal postcontrast T1 (B) image shows isointense signal with peripheral enhancement. Axial T1 (C) image shows the sequestered disk to have isointense signal and be located in the right ventral epidural space with mild mass effect on the thecal sac. Axial T2 (D) image shows the sequestered disk material to have hypointense signal.

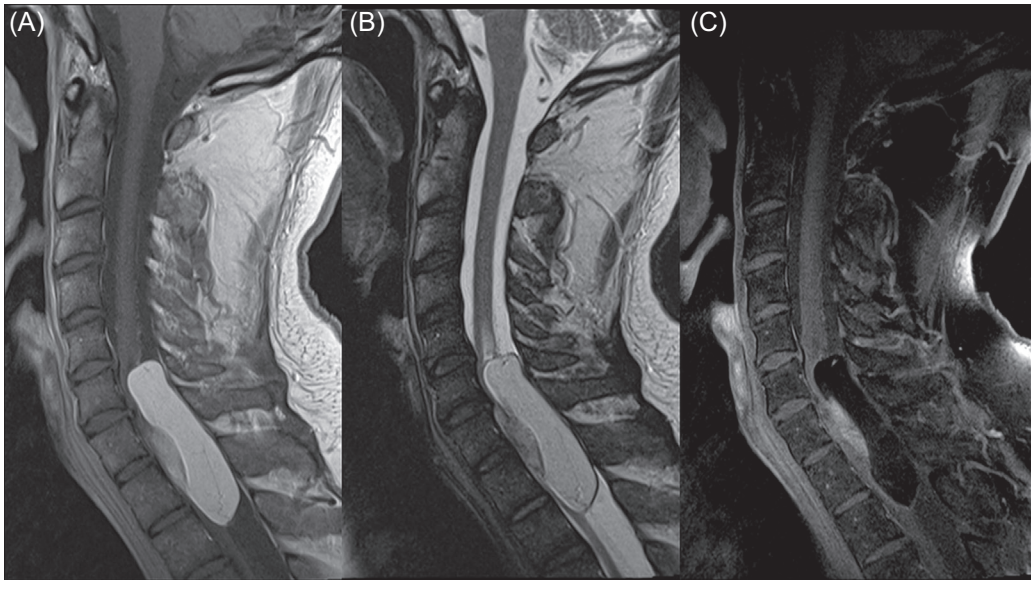


FIGURE 27 Sagittal T1 (A), T2 (B), and postcontrast fat-saturated (C) sequences show an intradural, extramedullary hyperintense lesion on T1W and T2W sequences from the C6 to the T2 level with nulling of fat on fat-saturated sequence. The anterior enhancing component represents dysplastic compression spinal cord parenchyma. This was surgically excised and returned a lipoma.

techniques such as STIR can be used to confirm adipose tissue. Intradural lipomas are rare but have similar signal characteristics and suppression on fat-saturated sequences (Figure 27).

The rare entity of ossification of the posterior longitudinal ligament (OPLL) can have a confounding T2-hypointense appearance if first encountered on MRI. OPLL is ventrally located in the cervical spine and CT is

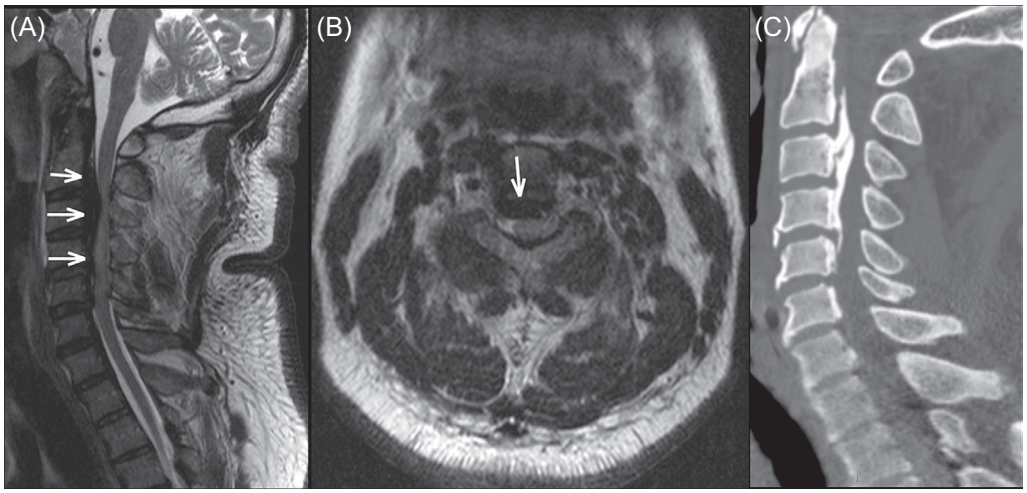


FIGURE 28 Sagittal T2WI (A) shows a hypointense lesion along the posterior aspect of the C2 through C5 vertebral bodies with mass effect and compression of cervical spinal cord. Axial T2WI (B) shows effacement of ventral CSF space and mass effect over the cervical spinal cord. Reconstructed CT image in the sagittal plane (C) shows the hyperdense flowing area in the spinal canal along the posterior aspect of the C2–C5 vertebral bodies representing OPLL. The patient underwent a posterior decompression to relieve cord compression.

best at demonstrating the bone. There is no enhancement of this ossified ligament (Figure 28).

Extramedullary hematopoiesis (EH) has also been described to be a cause of ESCC.[111,112] EH is a compensatory mechanism of coping with several hematological disorders, but is always of long duration. It is hypothesized that such hematopoietic tissue in the spinal cord vicinity arises from embryonal rests in the extradural areolar tissue of mesodermal origin.[113] These patients are expected to have good recovery despite long-standing neurological deficits.[113] On MRI, it can manifest as paravertebral and epidural masses, which are isointense on T1- and T2-weighted sequences and demonstrate intermediate enhancement. On CT, they can be seen as paravertebral soft tissue masses (Figure 29). An important finding to recognize is the diffuse low to intermediate T1 signal of the vertebral body marrow as a result of displacement of fatty marrow by hematopoietic elements. Technetium colloid scanning can also be used to demonstrate ectopic marrow formation.[114]

Primary tumors of the dura, such as fibromas, fibromatosis, and sarcomas, are rare,[30] but given their extradural location, they may cause spinal cord compression. Meningiomas can rarely be intraosseous, extradural (7%), or paraspinous in location. Extradural meningiomas are thought to arise from arachnoid rests.[115] An extradural meningioma may easily be mistaken for a spinal metastasis even at surgery; therefore it requires intraoperative histology.[116] Most often these lesions are isointense to the cord on T1WI and T2WI, but some may be hyperintense on T2WI. Hypointensity within the lesion is probably due to calcification. Very vascular meningiomas can have prominent flow voids. Bony changes are more frequent when a meningioma

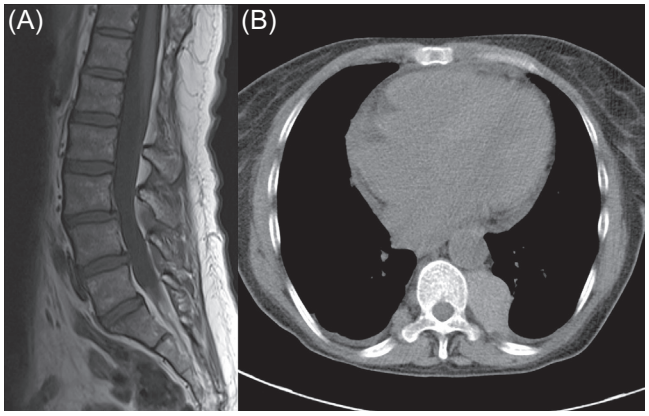


FIGURE 29 Sagittal T1WI (A) demonstrates diffuse vertebral bone marrow heterogeneous hypointensity, which can be seen in patients with myeloinfiltrative and marrow recruitment processes like anemia. (B) Contrast-enhanced axial CT image shows enhancing paravertebral masses, larger on the left side, representing EH.

is extradural, including widened intervertebral foramen, pedicle erosion, or, rarely, invasion of the vertebral body.[115]

Schwannomas are an additional extradural neoplasm to consider, as about 7% of schwannomas are purely extradural.[117] Schwannomas are well-marginated lesions, which can be very hyperintense on T2WI owing to intratumoral cystic formation or necrosis. Areas of T2 hypointensity may be due to dense cellularity, hemorrhage, or collagen deposition (Figure 30(A) and (B)).[118] Intense enhancement may be uniform, heterogeneous, or peripheral (Figure 30(C)). CT can demonstrate adjacent bone erosion and/or remodeling, such as enlarged neural foramina, expansion of the central canal, or posterior body of the vertebrae.

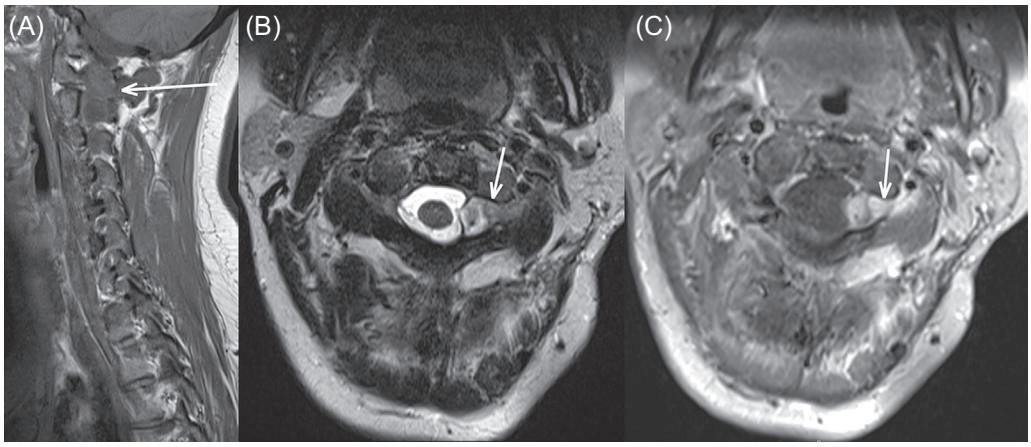


FIGURE 30 Sagittal unenhanced T1WI (A) demonstrates an isointense lobulated extradural mass lesion extending through the left C1–C2 neural foramen. Axial T2WI (B) demonstrates hyperintense signal within this lesion and enhancement on postcontrast axial T1W sequence representing schwannoma in a 37-year-old female with neurofibromatosis type 2. Lumbar schwannoma, thoracic meningioma, and ependymoma were also present in the same patient.

References

1. Cole JS, Patchell RA. Metastatic epidural spinal cord compression. *Lancet Neurol*. May 2008;7(5):459–466.
2. Bach F, Larsen BH, Rohde K, Børgesen SE, Gjerris F, Bøge-Rasmussen T, et al. Metastatic spinal cord compression. Occurrence, symptoms, clinical presentations and prognosis in 398 patients with spinal cord compression. *Acta Neurochir (Wien)*. 1990;107(1–2):37–43.
3. Mak KS, Lee LK, Mak RH, Wang S, Pile-Spellman J, Abrahm JL, et al. Incidence and treatment patterns in hospitalizations for malignant spinal cord compression in the United States, 1998–2006. *Int J Radiat Oncol Biol Phys*. July 1, 2011;80(3):824–831.
4. Boogerd W, van der Sande JJ, Kröger R. Early diagnosis and treatment of spinal epidural metastasis in breast cancer: a prospective study. *J Neurol Neurosurg Psychiatry*. December 1992;55(12):1188–1193.
5. van der Sande JJ, Kröger R, Boogerd W. Multiple spinal epidural metastases; an unexpectedly frequent finding. *J Neurol Neurosurg Psychiatry*. November 1990;53(11):1001–1003.
6. Helweg-Larsen S, Hansen SW, Sørensen PS. Second occurrence of symptomatic metastatic spinal cord compression and findings of multiple spinal epidural metastases. *Int J Radiat Oncol Biol Phys*. October 15, 1995;33(3):595–598.
7. Heldmann U, Myschetzky PS, Thomsen HS. Frequency of unexpected multifocal metastasis in patients with acute spinal cord compression. Evaluation by low-field MR imaging in cancer patients. *Acta Radiol*. May 1997;38(3):372–375.
8. Kornblum MB, Wesolowski DP, Fischgrund JS, Herkowitz HN. Computed tomography-guided biopsy of the spine. A review of 103 patients. *Spine (Phila Pa 1976)*. January 1, 1998;23(1):81–85.
9. Black P. Spinal metastasis: current status and recommended guidelines for management. *Neurosurgery*. December 1979;5(6):726–746.
10. Schiff D, O'Neill BP, Wang CH, O'Fallon JR. Neuroimaging and treatment implications of patients with multiple epidural spinal metastases. *Cancer*. October 15, 1998;83(8):1593–1601.
11. van der Sande JJ, Boogerd W, Kröger R, Kappelle AC. Recurrent spinal epidural metastases: a prospective study with a complete follow up. *J Neurol Neurosurg Psychiatry*. May 1999;66(5):623–627.
12. Ribas ES, Schiff D. Spinal cord compression. *Curr Treat Options Neurol*. August 2012;14(4):391–401.
13. Portenoy RK, Lipton RB, Foley KM. Back pain in the cancer patient: an algorithm for evaluation and management. *Neurology*. January 1987;37(1):134–138.
14. Gilbert RW, Kim JH, Posner JB. Epidural spinal cord compression from metastatic tumor: diagnosis and treatment. *Ann Neurol*. January 1978;3(1):40–51.
15. Zevallos M, Chan PY, Munoz L, Wagner J, Kagan AR. Epidural spinal cord compression from metastatic tumor. *Int J Radiat Oncol Biol Phys*. June 1987;13(6):875–878.
16. Helweg-Larsen S, Sørensen PS, Kreiner S. Prognostic factors in metastatic spinal cord compression: a prospective study using multivariate analysis of variables influencing survival and gait function in 153 patients. *Int J Radiat Oncol Biol Phys*. March 15, 2000;46(5):1163–1169.
17. Kim RY, Spencer SA, Meredith RF, Weppelmann B, Lee JY, Smith JW, et al. Extradural spinal cord compression: analysis of factors determining functional prognosis–prospective study. *Radiology*. July 1990;176(1):279–282.
18. Helweg-Larsen S, Johnsen A, Boesen J, Sørensen PS. Radiologic features compared to clinical findings in a prospective study of 153 patients with metastatic spinal cord compression treated by radiotherapy. *Acta Neurochir (Wien)*. 1997;139(2):105–111.
19. Barcena A, Lobato RD, Rivas JJ, Cordobes F, de Castro S, Cabrera A, et al. Spinal metastatic disease: analysis of factors determining functional prognosis and the choice of treatment. *Neurosurgery*. December 1984;15(6):820–827.
20. Harrington KD. The use of methylmethacrylate for vertebral-body replacement and anterior stabilization of pathological fracture-dislocations of the spine due to metastatic malignant disease. *J Bone Joint Surg Am*. January 1981;63(1):36–46.
21. Khan FR, Glicksman AS, Chu FC, Nickson JJ. Treatment by radiotherapy of spinal cord compression due to extradural metastases. *Radiology*. September 1967;89(3):495–500.
22. Schiff D. Spinal cord compression. *Neurol Clin*. February 2003;21(1):67–86, viii.
23. Gabriel K, Schiff D. Metastatic spinal cord compression by solid tumors. *Semin Neurol*. December 2004;24(4):375–383.
24. Findlay GF. Adverse effects of the management of malignant spinal cord compression. *J Neurol Neurosurg Psychiatry*. August 1984;47(8):761–768.
25. Spinazzé S, Caraceni A, Schrijvers D. Epidural spinal cord compression. *Crit Rev Oncol Hematol*. December 2005;56(3):397–406.

26. Mut M, Schiff D, Shaffrey ME. Metastasis to nervous system: spinal epidural and intramedullary metastases. *J Neurooncol*. October 2005;75(1):43–56.
27. Grant R, Papadopoulos SM, Sandler HM, Greenberg HS. Metastatic epidural spinal cord compression: current concepts and treatment. *J Neurooncol*. 1994;19(1):79–92.
28. Algra PR, Heimans JJ, Valk J, Nauta JJ, Lachniet M, Van Kooten B. Do metastases in vertebrae begin in the body or the pedicles? Imaging study in 45 patients. *AJR Am J Roentgenol*. June 1992;158(6):1275–1279.
29. Arguello F, Baggs RB, Duerst RE, Johnstone L, McQueen K, Frantz CN. Pathogenesis of vertebral metastasis and epidural spinal cord compression. *Cancer*. January 1, 1990;65(1):98–106.
30. Fukui MB, Meltzer CC, Kanal E, Smirniotopoulos JG. MR imaging of the meninges. Part II. Neoplastic disease. *Radiology*. December 1996;201(3):605–612.
31. Haddad P, Thaell JF, Kiely JM, Harrison EG, Miller RH. Lymphoma of the spinal extradural space. *Cancer*. October 1976;38(4):1862–1866.
32. Li MH, Holtås S, Larsson EM. MR imaging of spinal lymphoma. *Acta Radiol*. July 1992;33(4):338–342.
33. Ushio Y, Posner R, Posner JB, Shapiro WR. Experimental spinal cord compression by epidural neoplasm. *Neurology*. May 1977;27(5):422–429.
34. Westbrook JL, Renowden SA, Carrie LE. Study of the anatomy of the extradural region using magnetic resonance imaging. *Br J Anaesth*. October 1993;71(4):495–498.
35. Blomberg RG, Olsson SS. The lumbar epidural space in patients examined with epiduroscopy. *Anesth Analg*. February 1989;68(2):157–160.
36. Blomberg R. The dorsomedian connective tissue band in the lumbar epidural space of humans: an anatomical study using epiduroscopy in autopsy cases. *Anesth Analg*. July 1986;65(7):747–752.
37. Hutzelmann A, Palmié S, Freund M. Abstract: Vertebral body metastases: characteristic MRI findings in epidural infiltration. *Aktuelle Radiol*. July 1997;7(4):169–172.
38. Rodichok LD, Harper GR, Ruckdeschel JC, Price A, Roberson G, Barron KD, et al. Early diagnosis of spinal epidural metastases. *Am J Med*. June 1981;70(6):1181–1188.
39. Rodichok LD, Ruckdeschel JC, Harper GR, Cooper G, Prevosti L, Fernando L, et al. Early detection and treatment of spinal epidural metastases: the role of myelography. *Ann Neurol*. December 1986;20(6):696–702.
40. Carmody RF, Yang PJ, Seeley GW, Seeger JF, Unger EC, Johnson JE. Spinal cord compression due to metastatic disease: diagnosis with MR imaging versus myelography. *Radiology*. October 1989;173(1):225–229.
41. Beltran J, Noto AM, Chakeres DW, Christoforidis AJ. Tumors of the osseous spine: staging with MR imaging versus CT. *Radiology*. February 1987;162(2):565–569.
42. Hollis PH, Malis LI, Zappulla RA. Neurological deterioration after lumbar puncture below complete spinal subarachnoid block. *J Neurosurg*. February 1986;64(2):253–256.
43. Kennedy TF, Steinfeld JR. Nerve rootlet avulsion as a complication of myelography with the Cualtico needle. *Radiology*. May 1976;119(2):389.
44. Abla AA, Rothfus WE, Maroon JC, Deeb ZL. Delayed spinal subarachnoid hematoma: a rare complication of C1–C2 cervical myelography. *AJNR Am J Neuroradiol*. May–June 1986;7(3):526–528.
45. Rogers LA. Acute subdural hematoma and death following lateral cervical spinal puncture. Case report. *J Neurosurg*. February 1983;58(2):284–286.
46. O'Rourke T, George CB, Redmond 3rd J, Davidson H, Cornett P, Fill WL, et al. Spinal computed tomography and computed tomographic metrizamide myelography in the early diagnosis of metastatic disease. *J Clin Oncol*. April 1986;4(4):576–583.
47. Algra PR, Bloem JL, Tissing H, Falke TH, Arndt JW, Verboom LJ. Detection of vertebral metastases: comparison between MR imaging and bone scintigraphy. *Radiographics*. March 1991;11(2):219–232.
48. Kosuda S, Kaji T, Yokoyama H, Yokokawa T, Katayama M, Iriye T, et al. Does bone SPECT actually have lower sensitivity for detecting vertebral metastasis than MRI? *J Nucl Med*. June 1996;37(6):975–978.
49. Metser U, Lerman H, Blank A, Lievshitz G, Bokstein F, Even-Sapir E. Malignant involvement of the spine: assessment by 18F-FDG PET/CT. *J Nucl Med*. February 2004;45(2):279–284.
50. Sze G, Krol G, Zimmerman RD, Deck MD. Malignant extradural spinal tumors: MR imaging with Gd-DTPA. *Radiology*. April 1988;167(1):217–223.
51. Kienstra GE, Terwee CB, Dekker FW, Canta LR, Borstlap AC, Tijssen CC, et al. Prediction of spinal epidural metastases. *Arch Neurol*. May 2000;57(5):690–695.
52. Jennelle RL, Vijayakumar V, Vijayakumar S. A systematic and evidence-based approach to the management of vertebral metastasis. *ISRN Surg*. 2011;2011:719715. http://dx.doi.org/10.5402/2011/719715. Epub 2011 Aug 2.
53. Masaryk TJ. Neoplastic disease of the spine. *Radiol Clin North Am*. July 1991;29(4):829–845.
54. Sodickson DK, McKenzie CA, Ohliger MA, Yeh EN, Price MD. Recent advances in image reconstruction, coil sensitivity calibration, and coil array design for SMASH and generalized parallel MRI. *MAGMA*. January 2002;13(3):158–163.
55. Pruessmann KP. Encoding and reconstruction in parallel MRI. *NMR Biomed*. May 2006;19(3):288–299.
56. Roemer PB, Edelstein WA, Hayes CE, Souza SP, Mueller OM. The NMR phased array. *Magn Reson Med*. November 1990;16(2):192–225.
57. Ruggieri PM. Pulse sequences in lumbar spine imaging. *Magn Reson Imaging Clin N Am*. August 1999;7(3):425–437, vii.
58. Henkelman RM, Hardy PA, Bishop JE, Poon CS, Plewes DB. Why fat is bright in RARE and fast spin-echo imaging. *J Magn Reson Imaging*. September–October 1992;2(5):533–540.
59. Sevick RJ, Wallace CJ. MR imaging of neoplasms of the lumbar spine. *Magn Reson Imaging Clin N Am*. August 1999;7(3):539–553, ix.
60. Negendank WG, al-Katib AM, Karanes C, Smith MR. Lymphomas: MR imaging contrast characteristics with clinical-pathologic correlations. *Radiology*. October 1990;177(1):209–216.
61. Sze G, Abramson A, Krol G, Liu D, Amster J, Zimmerman RD, et al. Gadolinium-DTPA in the evaluation of intradural extramedullary spinal disease. *AJR Am J Roentgenol*. April 1988;150(4):911–921.
62. Castillo M, Malko JA, Hoffman Jr JC. The bright intervertebral disk: an indirect sign of abnormal spinal bone marrow on T1-weighted MR images. *AJNR Am J Neuroradiol*. January–February 1990;11(1):23–26.
63. Ricci C, Cova M, Kang YS, Yang A, Rahmouni A, Scott Jr WW, et al. Normal age-related patterns of cellular and fatty bone marrow distribution in the axial skeleton: MR imaging study. *Radiology*. October 1990;177(1):83–88.
64. Dunnill MS, Anderson JA, Whitehead R. Quantitative histological studies on age changes in bone. *J Pathol Bacteriol*. October 1967;94(2):275–291.
65. Dooms GC, Fisher MR, Hricak H, Richardson M, Crooks LE, Genant HK. Bone marrow imaging: magnetic resonance studies related to age and sex. *Radiology*. May 1985;155(2):429–432.
66. Daffner RH, Lupetin AR, Dash N, Deeb ZL, Sefczek RJ, Schapiro RL. MRI in the detection of malignant infiltration of bone marrow. *AJR Am J Roentgenol*. February 1986;146(2):353–358.
67. Ross JS, Delamarter R, Hueftle MG, Masaryk TJ, Aikawa M, Carter J, et al. Gadolinium-DTPA-enhanced MR imaging of the postoperative lumbar spine: time course and mechanism of enhancement. *AJR Am J Roentgenol*. April 1989;152(4):825–834.

68. Enzmann DR, Rubin JB. Cervical spine: MR imaging with a partial flip angle, gradient-refocused pulse sequence. Part I. General considerations and disk disease. *Radiology*. February 1988;166(2):467–472.
69. Enzmann DR, Rubin JB. Cervical spine: MR imaging with a partial flip angle, gradient-refocused pulse sequence. Part II. Spinal cord disease. *Radiology*. February 1988;166(2):473–478.
70. Baur A, Stäbler A, Brüning R, Bartl R, Krödel A, Reiser M, et al. Diffusion-weighted MR imaging of bone marrow: differentiation of benign versus pathologic compression fractures. *Radiology*. May 1998;207(2):349–356.
71. Castillo M, Arbelaez A, Smith JK, Fisher LL. Diffusion-weighted MR imaging offers no advantage over routine noncontrast MR imaging in the detection of vertebral metastases. *AJNR Am J Neuroradiol*. May 2000;21(5):948–953.
72. Oztekin O, Ozan E, Hilal Adibelli Z, Unal G, Abali Y. SSH-EPI diffusion-weighted MR imaging of the spine with low b values: is it useful in differentiating malignant metastatic tumor infiltration from benign fracture edema? *Skelet Radiol*. July 2009;38(7):651–658.
73. Delfaut EM, Beltran J, Johnson G, Rousseau J, Marchandise X, Cotten A. Fat suppression in MR imaging: techniques and pitfalls. *Radiographics*. March-April 1999;19(2):373–382. Review. Erratum in: Radiographics July–August 1999;19(4):1092.
74. Mehta RC, Marks MP, Hinks RS, Glover GH, Enzmann DR. MR evaluation of vertebral metastases: T1-weighted, short-inversion-time inversion recovery, fast spin-echo, and inversion-recovery fast spin-echo sequences. *AJNR Am J Neuroradiol*. February 1995;16(2):281–288.
75. Fleckenstein JL, Archer BT, Barker BA, Vaughan JT, Parkey RW, Peshock RM. Fast short-tau inversion-recovery MR imaging. *Radiology*. May 1991;179(2):499–504.
76. Rahmouni A, Divine M, Mathieu D, Golli M, Dao TH, Jazaerli N, et al. Detection of multiple myeloma involving the spine: efficacy of fat-suppression and contrast-enhanced MR imaging. *AJR Am J Roentgenol*. May 1993;160(5):1049–1052.
77. Melhem ER, Israel DA, Eustace S, Jara H. MR of the spine with a fast T1-weighted fluid-attenuated inversion recovery sequence. *AJNR Am J Neuroradiol*. March 1997;18(3):447–454.
78. Lavdas E, Vlychou M, Arikidis N, Kapsalaki E, Roka V, Fezoulidis IV. Comparison of T1-weighted fast spin-echo and T1-weighted fluid-attenuated inversion recovery images of the lumbar spine at 3.0 Tesla. *Acta Radiol*. April 2010;51(3):290–295.
79. Levy LM. MR imaging of cerebrospinal fluid flow and spinal cord motion in neurologic disorders of the spine. *Magn Reson Imaging Clin N Am*. August 1999;7(3):573–587.
80. Levy LM, Di Chiro G. MR phase imaging and cerebrospinal fluid flow in the head and spine. *Neuroradiology*. 1990;32(5):399–406.
81. Facon D, Ozanne A, Fillard P, Lepeintre JF, Tournoux-Facon C, Ducreux D. MR diffusion tensor imaging and fiber tracking in spinal cord compression. *AJNR Am J Neuroradiol*. June–July 2005;26(6):1587–1594.
82. Yoo WK, Kim TH, Hai DM, Sundaram S, Yang YM, Park MS, et al. Correlation of magnetic resonance diffusion tensor imaging and clinical findings of cervical myelopathy. *Spine J*. August 2013;13(8):867–876.
83. Edelstein WA, Glover GH, Hardy CJ, Redington RW. The intrinsic signal-to-noise ratio in NMR imaging. *Magn Reson Med*. August 1986;3(4):604–618.
84. Shapiro MD. MR imaging of the spine at 3T. *Magn Reson Imaging Clin N Am*. February 2006;14(1):97–108.
85. Phalke VV, Gujar S, Quint DJ. Comparison of 3.0 T versus 1.5 T MR: imaging of the spine. *Neuroimaging Clin N Am*. May 2006;16(2):241–248, ix.
86. Fries P, Runge VM, Kirchin MA, Watkins DM, Buecker A, Schneider G. Magnetic resonance imaging of the spine at 3 Tesla. *Semin Musculoskelet Radiol*. September 2008;12(3):238–252.
87. Blanco RT, Ojala R, Kariniemi J, Perälä J, Niinimäki J, Tervonen O. Interventional and intraoperative MRI at low field scanner–a review. *Eur J Radiol*. November 2005;56(2):130–142.
88. Broaddus WC, Grady MS, Delashaw Jr JB, Ferguson RD, Jane JA. Preoperative superselective arteriolar embolization: a new approach to enhance resectability of spinal tumors. *Neurosurgery*. November 1990;27(5):755–759.
89. Lyons MK, O'Neill BP, Marsh WR, Kurtin PJ. Primary spinal epidural non-Hodgkin's lymphoma: report of eight patients and review of the literature. *Neurosurgery*. May 1992;30(5):675–680.
90. Li MH, Holtås S, Larsson EM. MRI of extradural spinal tumours at 0.3 T. *Neuroradiology*. 1993;35(5):370–374.
91. Laurat E, Cazalets C, Sébillot M, Bernard M, Caulet-Maugendre S, Grosbois B. Localized epidural and bone amyloidosis, rare cause of paraplegia in multiple myeloma. *Amyloid*. March 2003;10(1):47–50.
92. Okacha N, Chrif E, Brahim E, Ali A, Abderrahman E, Gazzaz M, et al. Extraosseous epidural multiple myeloma presenting with thoracic spine compression. *Joint Bone Spine*. January 2008;75(1):70–72.
93. Belber CJ, Graham DL. Multiple myeloma-associated solitary epidural amyloidoma of C2–C3 without bony connection or myelopathy: case report and review of the literature. *Surg Neurol*. December 2004;62(6):506–509. Discussion 509.
94. Hovi I, Lamminen A, Salonen O, Raininko R. MR imaging of the lower spine. Differentiation between infectious and malignant disease. *Acta Radiol*. November 1994;35(6):532–540.
95. Calderone RR, Larsen JM. Overview and classification of spinal infections. *Orthop Clin North Am*. January 1996;27(1):1–8.
96. Mut M, Schiff D, Miller B, Shaffrey M, Larner J, Shaffrey C. Osteoradionecrosis mimicking metastatic epidural spinal cord compression. *Neurology*. January 25, 2005;64(2):396–397.
97. Alhilali L, Reynolds AR, Fakhran S. Osteoradionecrosis after radiation therapy for head and neck cancer: differentiation from recurrent disease with CT and PET/CT imaging. *AJNR Am J Neuroradiol*. July 2014;35(7):1405–1411.
98. Stäbler A, Reiser MF. Imaging of spinal infection. *Radiol Clin North Am*. January 2001;39(1):115–135.
99. Adachi M, Hayashi A, Ohkoshi N, Nagata H, Mizusawa H, Shoji S, et al. Hypertrophic cranial pachymeningitis with spinal epidural granulomatous lesion. *Intern Med*. August 1995;34(8):806–810.
100. Balériaux DL, Neugroschl C. Spinal and spinal cord infection. *Eur Radiol*. March 2004;14(suppl 3):E72–E83.
101. Canella C, Costa F, d'Oliveira I, Albuquerque E, Marchiori E. SAPHO syndrome. *Joint Bone Spine*. January 2014;81(1):90.
102. Assmann G, Simon P. The SAPHO syndrome–are microbes involved? *Best Pract Res Clin Rheumatol*. June 2011;25(3):423–434.
103. Barrett K, Miller ML, Wilson JT. Tophaceous gout of the spine mimicking epidural infection: case report and review of the literature. *Neurosurgery*. May 2001;48(5):1170–1172. Discussion 1172–1173.
104. Fenton P, Young S, Prutis K. Gout of the spine. Two case reports and a review of the literature. *J Bone Joint Surg Am*. May 1995;77(5):767–771.
105. Yen PS, Lin JF, Chen SY, Lin SZ. Tophaceous gout of the lumbar spine mimicking infectious spondylodiscitis and epidural abscess: MR imaging findings. *J Clin Neurosci*. January 2005; 12(1):44–46.
106. Duprez TP, Malghem J, Vande Berg BC, Noel HM, Munting EA, Maldague BE. Gout in the cervical spine: MR pattern mimicking diskovertebral infection. *AJNR Am J Neuroradiol*. January 1996;17(1):151–153.
107. Doita M, Shimomura T, Maeno K, Nishida K, Fujioka H, Kurosaka M. Calcium pyrophosphate dihydrate deposition in the

transverse ligament of the atlas: an unusual cause of cervical myelopathy. *Skeletal Radiol*. July 2007;36(7):699–702.
108. Chang FC, Lirng JF, Chen SS, Luo CB, Guo WY, Teng MM, et al. Contrast enhancement patterns of acute spinal epidural hematomas: a report of two cases. *AJNR Am J Neuroradiol*. March 2003;24(3): 366–369.
109. Boukobza M, Guichard JP, Boissonet M, George B, Reizine D, Gelbert F, et al. Spinal epidural haematoma: report of 11 cases and review of the literature. *Neuroradiology*. August 1994;36(6): 456–459.
110. Borré DG, Borré GE, Aude F, Palmieri GN. Lumbosacral epidural lipomatosis: MRI grading. *Eur Radiol*. July 2003;13(7):1709–1721.
111. Chourmouzi D, Pistevou-Gompaki K, Plataniotis G, Skaragas G, Papadopoulos L, Drevelegas A. MRI findings of extramedullary haemopoiesis. *Eur Radiol*. 2001;11(9):1803–1806.
112. Ghieda U, Elshimy M, El Beltagi AH. Progressive spinal cord compression due to epidural extramedullary hematopoiesis in thalassemia intermedia. A case report and literature review. *Neuroradiol J*. February 2013;26(1):111–117.
113. Abbassioun K, Amir-Jamshidi A. Curable paraplegia due to extradural hematopoietic tissue in thalassemia. *Neurosurgery*. December 1982;11(6):804–807.
114. Singh S, Gunatunga I, Bartley L, Facey P, Rees J, Fielding P. Paraspinal extramedullary hematopoiesis diagnosed using Tc-99m sulfur colloid. *Clin Nucl Med*. November 2008;33(11):794–796.
115. Sato N, Sze G. Extradural spinal meningioma: MRI. *Neuroradiology*. June 1997;39(6):450–452.
116. Zevgaridis D, Thomé C. Purely epidural spinal meningioma mimicking metastatic tumor: case report and review of the literature. *Spine (Phila Pa 1976)*. September 15, 2002;27(18):E403–E405.
117. Conti P, Pansini G, Mouchaty H, Capuano C, Conti R. Spinal neurinomas: retrospective analysis and long-term outcome of 179 consecutively operated cases and review of the literature. *Surg Neurol*. January 2004;61(1):34–43. Discussion 44.
118. Friedman DP, Tartaglino LM, Flanders AE. Intradural schwannomas of the spine: MR findings with emphasis on contrast-enhancement characteristics. *AJR Am J Roentgenol*. June 1992;158(6):1347–1350.

CHAPTER

59

Neuroimaging for Surgical Treatment Planning of Neoplastic Disease of the Spine

Carlos R. Goulart[1], *Tobias A. Mattei*[2], *Michael A. Weicker*[1], *Ehud Mendel*[1]

[1]Department of Neurological Surgery, The Ohio State University – Wexner Medical Center, The James Cancer Hospital, Columbus, OH, USA; [2]Department of Neurosurgery, Brain & Spine Center – InvisionHealth, Buffalo, NY, USA

INTRODUCTION

Low-back pain (LBP) is one of the most common causes of disability in the world and its negative economical impact is massive.[1,2] Unfortunately, a specific diagnosis for back pain does not occur in up to 85% of patients.[3] Moreover, as much as 70% of the population will experience at least one episode of LBP during their lives.[4] Owing to the difficulty in pinpointing a clear diagnosis in the majority of cases, the pain is considered to be benign in origin.[5]

Nonetheless, serious spine pathologies might also present for the first time as an episode of LBP. These pathologies include spinal malignancy, fractures, or infection. The prevalence of these conditions is between 1% and 5% of all patients presenting with LBP.[3,4,6] Although most guidelines recommend against routine imaging studies for patients with LBP, there are specific red-flag symptoms that should prompt a more detailed exam, including an imaging investigation.[7] The use of red flags in a primary care setting is suitable when applied in combination with judicious clinical judgment of the pain characteristics.[7,8]

Levack et al.[9] reported a series of 319 patients with a median delay of 2 months in the diagnosis of cord compression after the initial complaint of pain to a primary care physician. This delay in the diagnosis is commonly seen in patients with vertebral metastasis, in which the most common initial complaint is new-onset back or neck pain. Such delay might increase the complexity of the available therapeutic surgical options as well as decreasing the benefits the patient might receive from it.[10]

Most patients will have pain before neurological deficits arise and the neurological function status usually correlates with their prognosis.[11] Therefore, for an early diagnosis to be done it is crucial to know when there should be a high index of suspicion for vertebral neoplasia in patients with back pain.

Warning signs will include symptoms such as nocturnal pain, neurological dysfunction, and gait disturbance. Also, symptoms that might indicate systemic disease, like weight loss or organ dysfunction, are important clues. When there is increased suspicion for vertebral lesions an anamnesis should include questioning for any known history of neoplasia or associated habits and comorbidities that increase the likelihood for cancer, such as recent positive cancer screening, family history, smoking history, environmental and occupational exposures, human immunodeficiency virus, inflammatory diseases, and carcinoma in situ. The immediate workup will derive from the symptoms and anamnesis and might include blood cell counts, electrolytes, prostate-specific antigen, and serum and urine protein electrophoresis if there is suspicion for multiple myeloma.[8]

A very important point to be highlighted is that in patients with known primary cancer there should be no assumption of routine or nonspecific back pain (Figure 1). The physician must have a very low threshold to order an imaging study in these cases because of the risk of missing a metastatic lesion to the spine that might cause serious consequences for the patient, such as fractures and spinal cord compression with neurological deficits that could be permanent if not addressed in time.

The spine is the most common site of bone metastasis, which is the third most frequent site of distant metastatic disease after lung and liver.[12,13] Autopsy studies show that between 30% and 90% of patients who die of cancer will have spinal metastasis.[13–15] Of those patients who

http://dx.doi.org/10.1016/B978-0-12-800945-1.00059-8

© 2016 Elsevier Ltd. All rights reserved.



FIGURE 1 Myxoid liposarcoma. This is a 49-year-old male patient with previous diagnosis of metastatic myxoid liposarcoma, who had already undergone a sacral laminectomy for removal of a large intracanalicular tumor and now presented with midthoracic pain and myelopathy. The MRI of the thoracic spine revealed a lesion with signal intensity compatible with liposarcoma invading the posterior portion of the T9 vertebral body (arrow) and extending to the epidural space ((A): sagittal T2 MRI; (B): axial T2 MRI). The patient was submitted to a T6–T12 posterior pedicle screw fixation followed by an anterolateral transthoracic T9 vertebrectomy with en bloc resection of the lesion and reconstruction of the anterior vertebral column with an expandable cage. (C): Intraoperative fluoroscopy during the anterolateral transthoracic procedure. (D): Postoperative CT scan demonstrating the final 360° instrumentation.

develop spinal metastasis up to 50% will need some treatment for the diverse complications deriving from it, such as pain, instability, and spinal cord compression.[13,16–19] Additionally, symptomatic metastatic spinal disease will become more prevalent as the long-term survival improves for many common cancers owing to more effective treatment plans.

The peak of incidence in spinal metastases occurs between 40 and 65 years of age because of the increased risk of cancer in this population.[13] The most frequent primary cancers sending metastases to the spine are breast cancer, lung, and prostate tumors. These types of cancer are not only prevalent but also avid for bones.[20,21] In a study by Brihaye et al. the authors found that 16.5% of symptomatic spine metastases came from breast cancer, 15.6% from lung cancer, and 9.2% from prostate cancer.[22]

The majority of spine metastases occur in the extradural compartment (osseous spine), more commonly in the vertebral bodies followed by the paravertebral

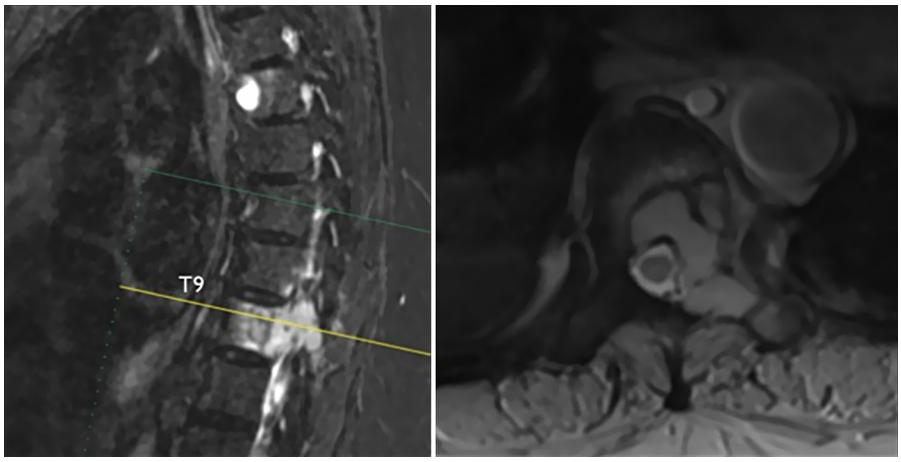


FIGURE 2 Thoracic spine metastatic lesion in a 71-year-old female with a metastasis from a neuroendocrine carcinoma presenting with 2 weeks of refractory axial neck pain and no radiculopathy.

areas and epidural region. The other two possibly affected compartments are the intradural and intramedullary, which are less frequent and usually secondary to cerebrospinal fluid (CSF) seeding.[13,23,24]

The thoracic spine is the most frequent portion to be affected by metastases (70%), followed by the lumbar spine (20%), cervical spine, and sacrum.[25] Since pain due to nonneoplastic processes is less common in the thoracic spine than in the cervical or lumbar spine, pain in this region should raise the suspicion of cancer and prompt further workup[10,13] (Figure 2).

METASTATIC SPINAL TUMORS

Metastatic tumors will present with a variable pattern of symptoms but usually including pain with or without motor or autonomic dysfunction and sensory dysfunction. Symptoms are dependent on the degree of bone destruction, compression causing myelopathy or nerve root impingement, and the extent of the primary disease (Figure 3).

Fast-growing tumors have a steep progression of symptoms. Lytic tumors more commonly lead to a bone destruction that will cause pathological fractures or deformities (Figure 4). A palpable mass, although not common, might be present in the paraspinal or rectal region in the case of sacral masses[10,26] (Figure 5).

PRIMARY BONE TUMORS

Primary tumors of the vertebral column correspond to only a small portion (10%) of all tumors of the spine.[27] Their presentation is similar to the metastatic tumors, with pain being the most common initial complaint. Since the physical examination is not very helpful in this setting imaging studies are essential. X-rays might offer some clue to the initial diagnosis and reveal the location of the tumor. Nonetheless computed tomography (CT) and magnetic resonance imaging (MRI) followed by fine-needle aspiration biopsy are essential for further understanding of the condition and surgical planning.[28,29] The imaging findings are discussed later in the chapter.

The most frequent benign primary spinal bone tumors include aneurysmal bone cyst, chondroma and enchondroma, eosinophilic granuloma, fibrous dysplasia, hemangioma, osteoid osteoma, and osteoblastoma. The management strategies for these tumors, as well as the metastatic ones, include different treatment modalities such as chemotherapy, embolization, or radiation depending on type and location of the lesion. Nonetheless, in contrast with spinal metastasis the goal with primary tumors can be total eradication through surgical resection.[28,29] The basic imaging characteristics that may assist in the differentiation among different primary bone tumors are summarized in Tables 1 and 2.

For primary spine tumors, especially for the malignant subtypes, en bloc resection with free margins has been demonstrated to be the best alternative to increase long-term survival and recurrence-free survival.[30,31]

In their series on spinal chordomas, Boriani et al. demonstrated that in patients treated with intralesional resection recurrence happened in less than 2 years in all of them. On the other hand, 12 of the 18 patients treated with en bloc resections were continuously disease free at an average of 8 years (Figure 6). Moreover, the six patients who did have a recurrence were previously treated with other techniques or had positive margins after resection.[32]

If an MRI suggests a primary malignant bone tumor of the spine (Tables 1 and 2), the next step in management should be a core needle biopsy to confirm the diagnosis.

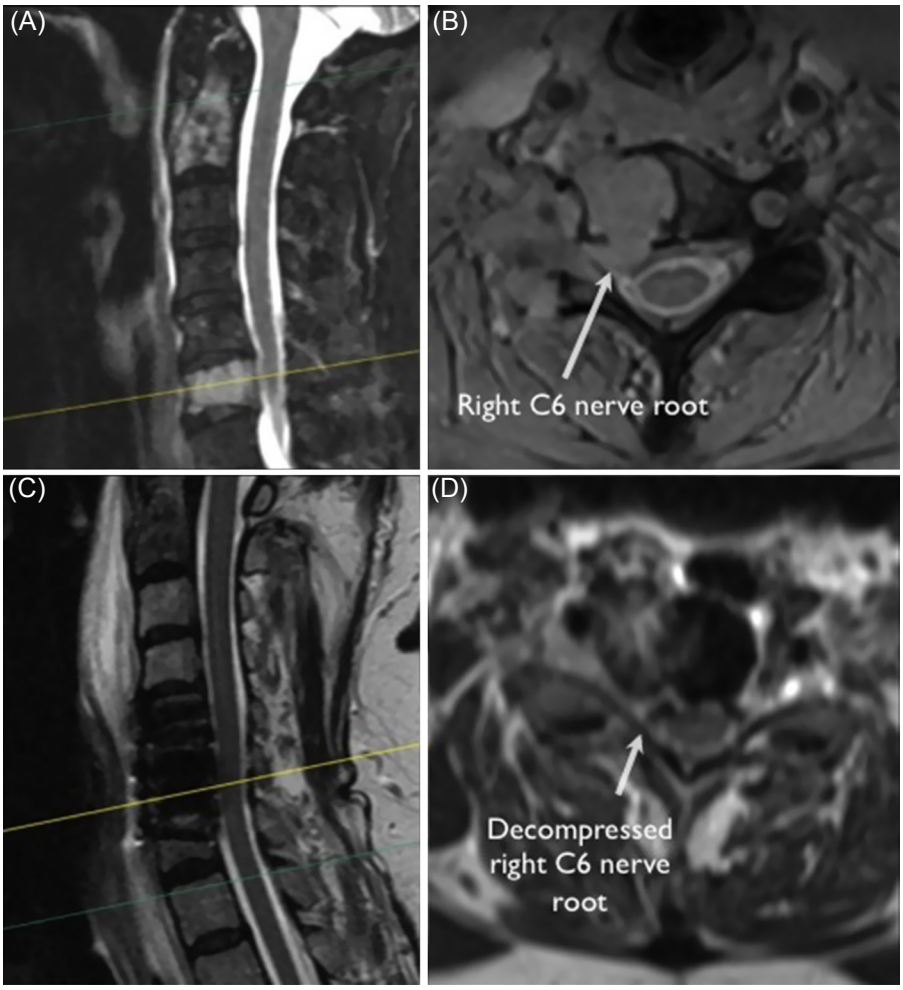


FIGURE 3 Metastatic lesion in a 71-year-old female with neuroendocrine carcinoma. (A) and (B): Metastatic lesion compressing the C6 nerve root. (C) and (D): Decompressed C6 nerve root after surgery with C6 corpectomy + C5–C7 plating.

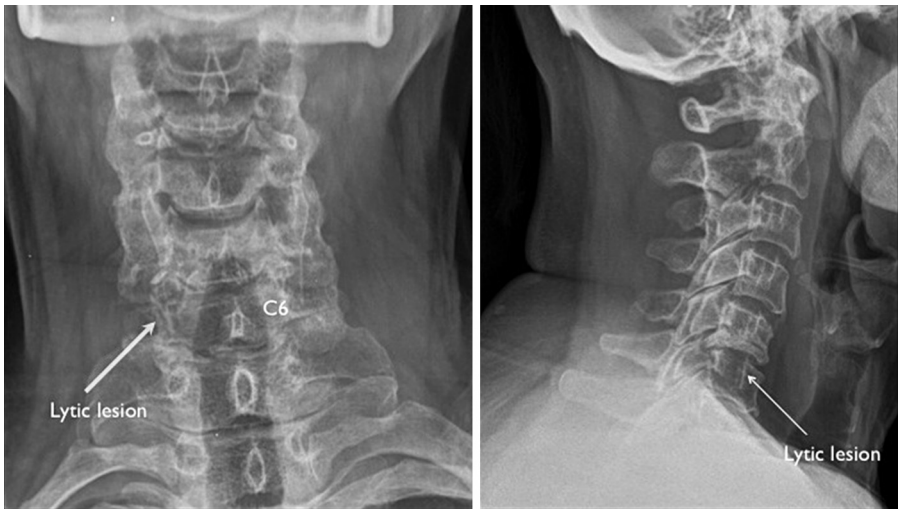


FIGURE 4 Lytic metastatic lesion in the C6 vertebra.



FIGURE 5 A 32-year-old female patient that noticed a growing mass in the middle of her thoracic region. Postcontrast T1 MRI sequences ((A): sagittal; (B): axial) demonstrating the large paraspinal lesion extending from the T10 to the L1 level. The core needle biopsy was compatible with a neuroectodermal tumor/Askin tumor (a type of Ewing sarcoma of the chest wall). The patient was subjected to chemotherapy with complete disappearance of the lesion after nine cycles. Postcontrast MRI (T1 sequence) after chemotherapy ((C): sagittal; (D): axial)—the arrows indicate the site of the previous location of the lesion.

TABLE 1 Imaging Characteristics of Benign Primary Bone Tumors

Tumor Type	CT Scan Findings	MRI Findings
Chondroma	Calcifications, osteolytic	T1 hypointense to intermediate signal; T2 hyperintense signal
Eosinophilic granuloma	Osteolytic destruction of vertebral bodies with possible collapse	T1 isointense; T2 hyperintense with soft tissue swelling
Fibrous dysplasia	Osteolytic and expansive; "ground glass" appearance with sclerotic margins	T1 and T2 with variable intensity
Hemangioma	Polka dots of bone on CT	T1 isointense; T2 hyperintense; +gadolinium enhancement
Aneurysmal bone cyst	"Soap bubble" appearance; osteolytic	Heterogeneous on T1 and T2; +gadolinium enhancement
Osteoid osteoma	Nidus with sclerotic border and low attenuation	T1 nidus with intermediary signal intensity; T2 hypointense; +gadolinium enhancement in the nidus

An incisional biopsy should not be done for the same reason, as the intralesional resection is discouraged, as this will increase the local recurrence to nearly 100% (Figure 7). The staging of these tumors is to be made according to the Weinstein–Boriani–Biagini system and the Enneking grade.[33]

Patients who undergo such surgeries should be aware of their complexity and extent. En bloc resection is one of the most challenging surgical procedures in the spine and when it occurs in areas close to important structures—such as the cervical spine—they might become even harder to perform. The patient has to understand that to

TABLE 2 Imaging Characteristics of Malignant Primary Bone Tumors

Tumor Type	CT Findings	MRI Findings
Chordoma (Figure 15)	Expansive, osteolytic, sclerotic	T1 hypointense; T2 hyperintense; irregular gadolinium enhancement
Chondrosarcoma (Figure 6)	Expansive and osteolytic; cortical expansion and erosion	T2 hyperintense; +gadolinium enhancement with "rings and arcs" pattern
Ewing sarcoma (Figure 5)	Osteolytic	T1 isointense; T2 iso- to hyperintense; +gadolinium enhancement
Multiple myeloma	Lytic, osteoporotic	T1 hypointense; T2 hyperintense; +gadolinium enhancement
Giant cell tumor	Osteolytic, sometimes cystic appearance	T1 hypointense; T2 hypointense; possible hemorrhage; +gadolinium enhancement
Osteosarcoma (Figure 14)	Lytic and destructive with matrix mineralization	T1 hypointense; T2 hyperintense

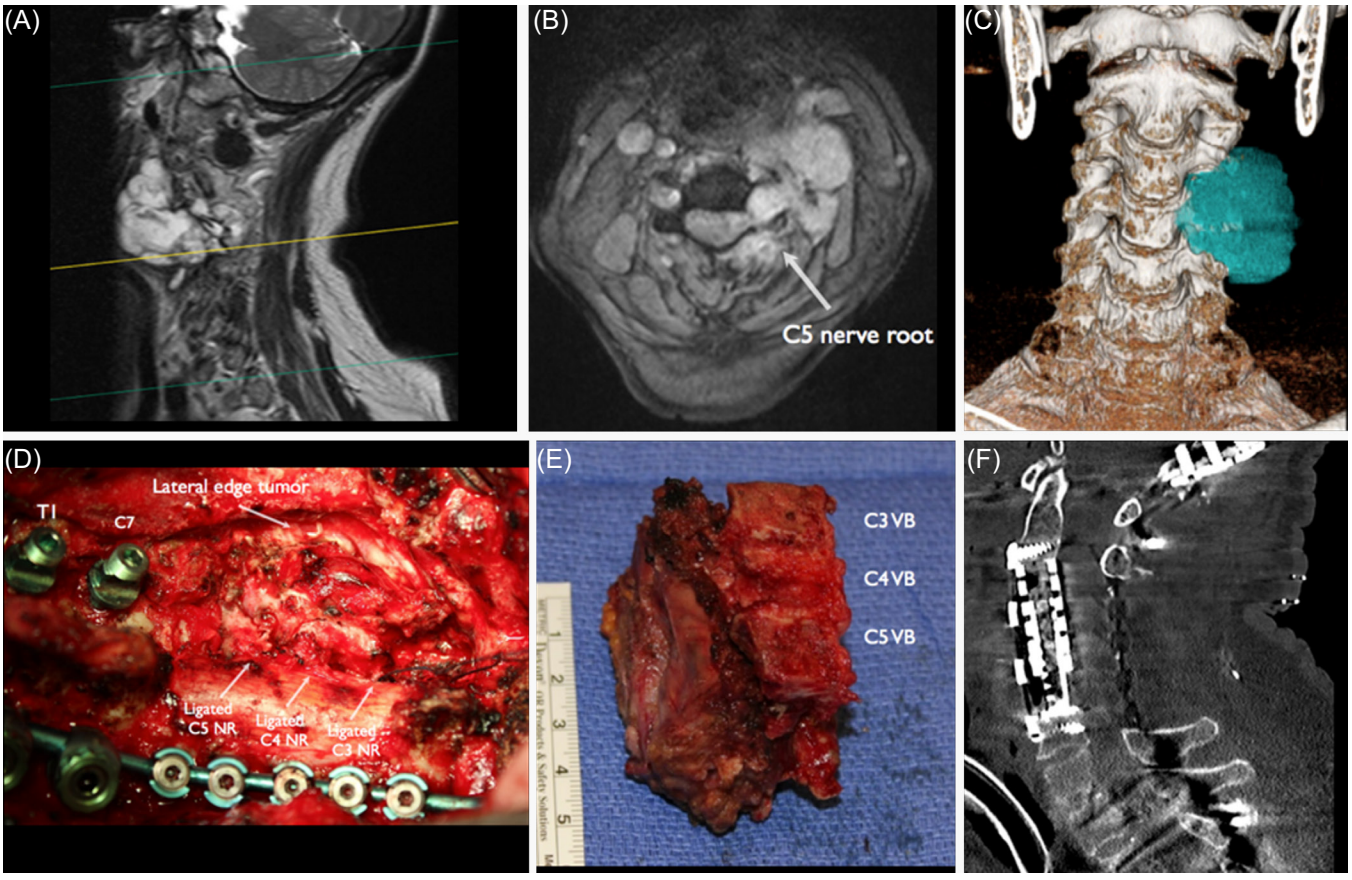


FIGURE 6 Sagittal (A) and axial (B) MRI of the cervical spine (T2 sequences) demonstrating a tumoral lesion involving the C3, C4, and C5 vertebral bodies, extending anterolaterally to the left side with involvement of the left vertebral artery and infiltration of the left C3, C4, and C5 nerve roots (C). The CT-guided core needle biopsy revealed the diagnosis of a chondrosarcoma. The patient was submitted to en bloc resection of the lesion in four surgical stages, consisting in a midline posterior approach to the cervicothoracic spine for a occipito-T3 instrumentation; endovascular ligation of the left vertebral artery; a second posterior surgical approach for surgical ligation of the left vertebral artery as well as the C3, C4, and C5 nerve roots that were involved by tumor (D); and a final anterior approach, during which the tumor was delivered en bloc after C3, C4, and C5 partial corpectomies on the left (E). The postoperative CT scan ((F): three-dimensional reconstruction) demonstrated the final construct involving a robust 360° fixation with reconstruction of the anterior and middle column with cage and a long posterior (occipito-T3) instrumentation.

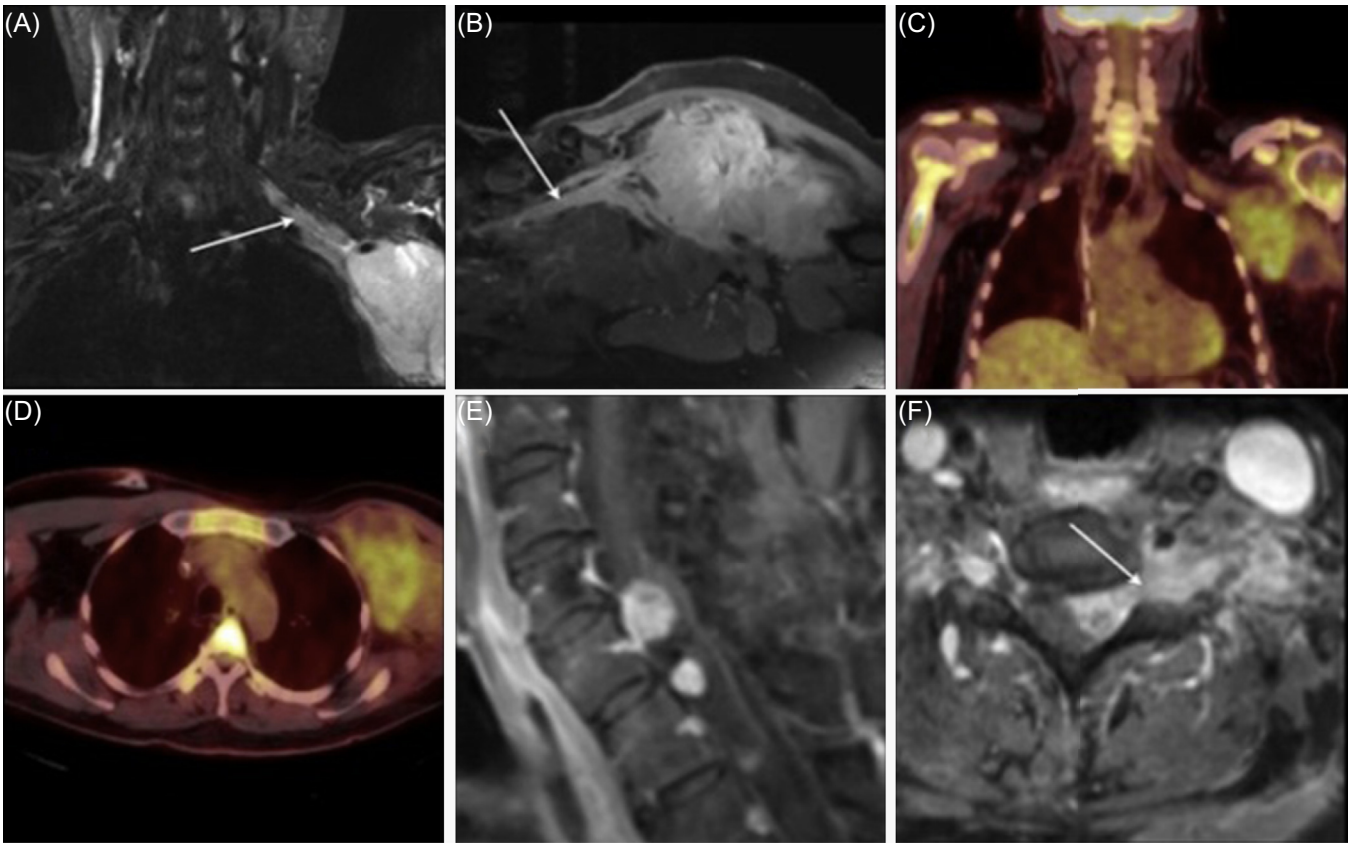


FIGURE 7 Images of a 53-year-old male presenting with left arm radiculopathy. The MRI of the brachial plexus revealed a large lesion in the left shoulder region, which extended proximally through the brachial plexus. Postcontrast T1 MRI ((A): sagittal; (B): axial). The PET CT scan demonstrated a hypermetabolic lesion ((C): coronal; (D): axial). The core needle biopsy provided the diagnosis of a high-grade spindle-cell sarcoma suggestive of monophasic synovial sarcoma. The patient was submitted to left upper extremity amputation and surgical resection of the lesion (which was performed in a non-en-bloc fashion) by another surgical team. Three years later, despite adjuvant chemotherapy, the patient presented with recurrence of the lesion proximally, at the emergence of the cervical nerve roots. Late follow-up MRI (3 years after the initial surgery), T1 postcontrast, is shown ((E): sagittal; (F): axial).

achieve long-term survival permanent neurological deficits deriving from the surgery could ensue. This is especially true when dealing with tumors next to functional nerve roots and vertebral arteries[33,34] (Figure 8).

EXTRAMEDULLARY INTRADURAL SPINAL TUMORS

Up to 85% of extramedullary intradural spinal tumors (EISTs) are meningiomas, nerve sheath tumors (neurofibromas and schwannomas), and ependymomas. The remaining types comprise lipomas, paragangliomas, spinal nerve myxomas, leptomeningeal metastases, lymphomas, sarcomas, and vascular tumors.[35–37]

Meningiomas

Meningiomas present more commonly in women ages 50–70 years but can occur in any group age. They usually arise from the dura mater closer to a spinal nerve root sleeve and more frequently in the thoracic spine (80%)[35] (Figure 9).

In imaging studies spinal meningiomas are isointense or hypointense on T1-weighted images and slightly hyperintense or hypointense on T2-weighted MRI. In contrast exams they enhance intensely and habitually present a "dural tail" sign.[35,38–41] Often their attachment to the dura will be broad based, and duroplasty after tumor resection will be necessary to avoid CSF leak. Calcification occurs in 85% of meningiomas. They are usually single lesions; if multiple meningiomas are present one should suspect neurofibromatosis type II.[35]

Nerve Sheath Tumors

Spinal nerve sheath tumors (SNSTs) are the most frequent EISTs and include schwannomas (neuromas, neurinoma, neurilemmomas) and neurofibromas. Schwannomas might result in cystic degeneration and hemorrhage. Typically SNSTs are found on the dorsal

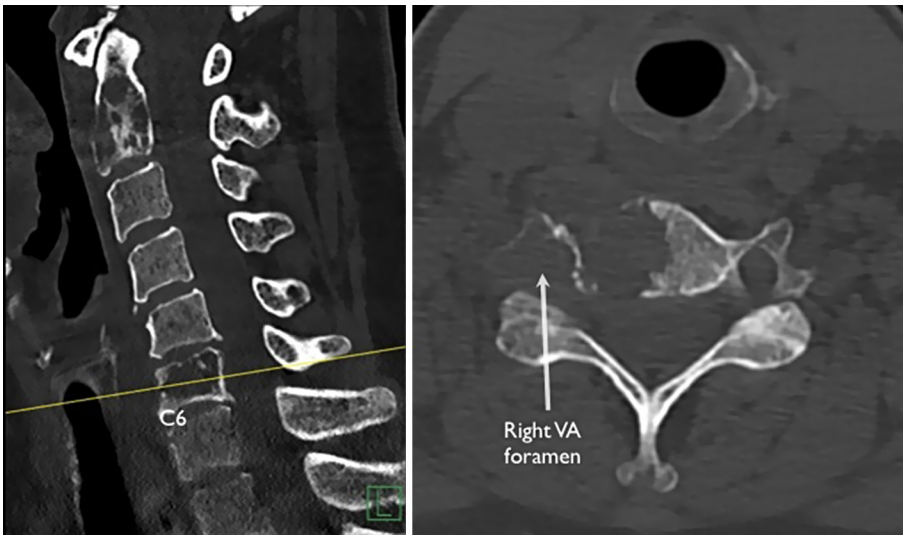


FIGURE 8 Metastatic lesion encasing the right vertebral artery.

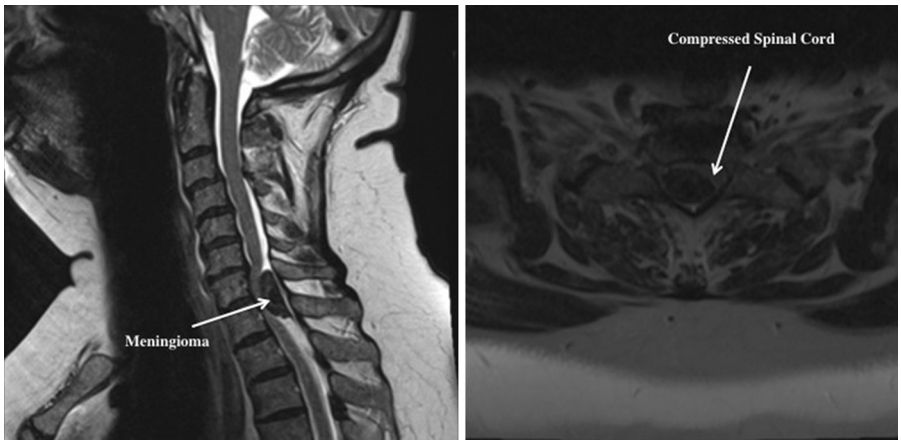


FIGURE 9 T1-weighted MRI of an intradural meningioma compressing the cervical spinal cord.

sensory roots and by mechanical displacement of the nerve roots could cause radicular pain. If bilateral vestibular schwannomas are present, association with neurofibromatosis II should be investigated.[42]

The most commonly affected areas of the spine are cervical and lumbar. Their peak incidence is the fourth decade of life and 90% of them are benign. SNSTs are isointense on T1-weighted MRIs and have hyperintense signal on T2-weighted images. Unfortunately enhancement with contrast does not follow a strict pattern. Nonetheless a dumbbell shape on the MRI is helpful and when present there is an 80% positive predictive value for the tumor to be SNST.[38,42,43]

INTRAMEDULLARY TUMORS

Intramedullary spinal tumors represent only 5–10% of all spinal tumors in adults but happen more frequently in children, accounting for 35% of the spinal tumors in this population. These tumors are usually glial in origin (90%) and the most common types are the ependymomas (60%) and astrocytomas (30%). The remaining 10% are composed of the hemangioblastomas (2–8%) and intramedullary metastases (2%).[35,44]

Ependymomas

Fifty percent of all ependymomas will occur in the spine; half are intramedullary and half are located in the filum terminale. They happen most commonly between the third and the fifth decades, but can be present at any age. These tumors are well-circumscribed and seldom infiltrate the dura. Their recurrence rate is very low if a thorough resection is achieved. On T1-weighted images they are hypo- or isointense and are hyperintense on T2-weighted MRIs. Enhancement with contrast is variable.[35,38]

Cellular ependymomas arise from the ependymal lining of the central canal, which gives their typical

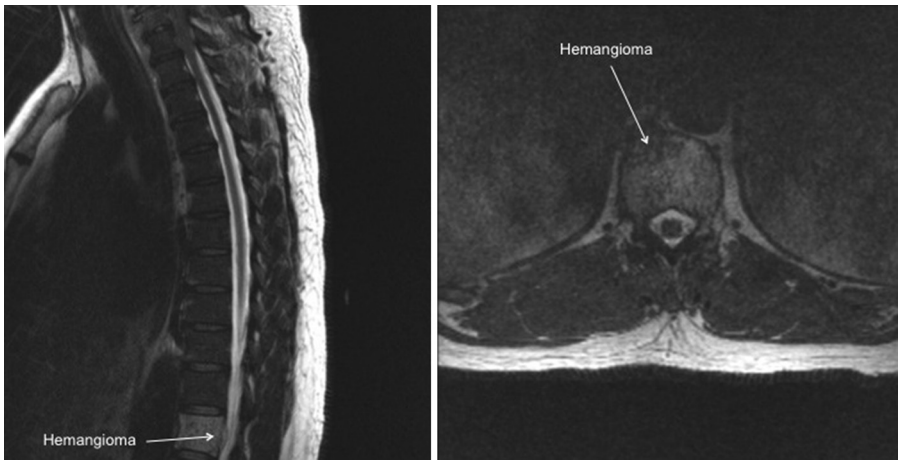


FIGURE 10 T2-weighted MRI of a hemangioma in the thoracic spine.

concentric appearance. They happen more frequently in the cervical or upper thoracic region. On imaging they will be hyperintense on T2-weighted images. On T1-weighted MRI they are hypo- or isointense compared to the spinal cord signal. Their enhancement in contrasted exams is variable. Specifically in the cervical region they can present with a syrinx. If the tumor is large enough spinal cord edema might occur. Additionally, polar cyst formations and hemorrhage are sometimes associated.[44–46]

Astrocytomas

Astrocytomas characteristically present as focal fusiform expansions in the spinal cord, commonly in the cervical and thoracic regions. Their margins are usually irregular. They might have an associated cystic component or edema and syrinx.[47] Astrocytomas will most frequently be hypo- or isointense on T1-weighted images.[35] On T2-weighted images they will be hyperintense. Owing to their heterogeneous enhancement they may be difficult to distinguish from other types of intramedullary tumors.[47]

Hemangioblastomas

Up to 75% of the hemangioblastomas will present as localized spinal cord masses. Homogeneous contrast enhancement happens with smaller masses that are more frequently associated with syrinx and spinal cord edema. Heterogeneous enhancement happens with larger hemangioblastomas due to hemorrhage, mural noduli, and flow void consequent to enlarged feeding or draining vessels.[35] Additionally the smaller hemangiomas are isointense on T1-weighted images and hyperintense on T2-weighted images. Instead the larger tumors will have iso- or hypointense signal on T1-weighted images and will be heterogeneous on T2-weighted images[48] (Figure 10).

Although the postoperative prognosis in patients with intramedullary tumors depends on preoperative neurological status, tumor histology, and amount of residual disease after surgery, the majority of intramedullary tumors are eligible for resection with potential for cure without adjuvant therapy.[35] This is especially true for ependymoma, pilocytic astrocytoma, and hemangioblastoma. The surgical planning in these cases depends on the use of anatomic and functional imaging studies such as high-field MRI.

Tractography, also known as diffusion tensor-fiber tracking (DT-FT) and diffusion tensor imaging (DTI), is an imaging method used to evaluate the direction and integrity of white matter tracts. Only since 2005 has this technique established itself in the management of spinal cord pathologies.[49–53]

Although their role in spine surgery has not been completely defined yet, one of the main uses for DTI and DT-FT would be to differentiate invasion from compression in intramedullary tumors. For instance, astrocytomas usually present an infiltrative nature, while ependymomas tend to displace white matter tracts rather than destroy them.[54–56] This would influence the surgical planning and the resectability of these tumors, aiding in the characterization of margins for intramedullary spinal cord neoplasms.[55]

SURGICAL INTERVENTION FOR SPINAL TUMORS

As the vast majority of spinal column tumors are metastatic in origin, and these patients usually have advanced stage of cancer, the goal of surgery is not oncological cure. As aforementioned, the goal of oncological cure or control is reserved for patients with primary bone tumors that undergo en bloc resection or patients with a single metastatic lesion in whom the primary disease is well controlled. The potential benefits of surgery, especially in

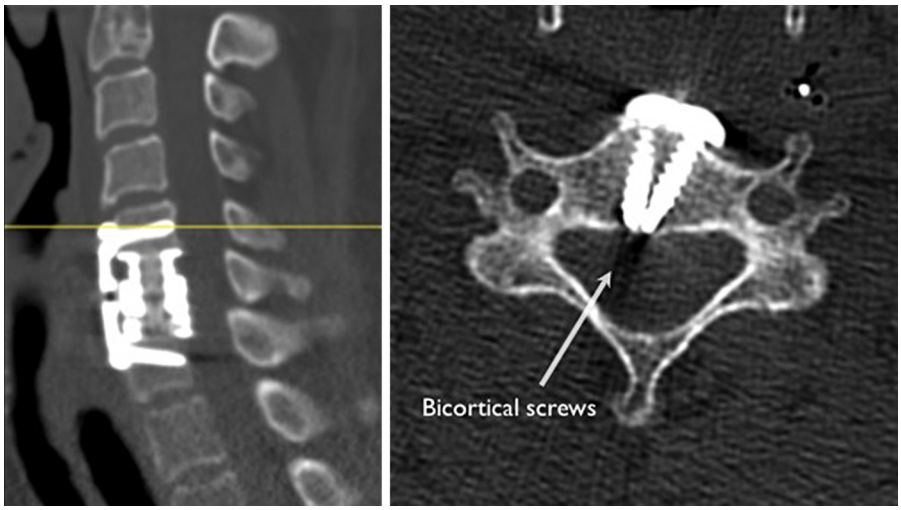


FIGURE 11 Metastatic tumor removal and spine stabilization in the cervical spine.

the case of metastatic disease, should be balanced against the risks of such a major surgical procedure. The recovery time for spine tumor surgery is usually long—lasting between 1 and 2 months. This will delay treatment of the systemic disease with chemotherapy and radiation therapy in order to avoid possible wound complications.[57] Additionally, the general health conditions of these patients, such as coagulation, nutritional status, and expected survival time, are essential in the planning of these surgeries.

In this context the goals and the surgical approach should be established in harmony with the appropriate indications, which include neurological symptoms, oncological control (conditional to the type of tumor), biomechanical problems, and refractory pain (Figure 11).

Neurological symptoms are caused by spinal cord or nerve root compression. Rapid neurological deterioration or even rapidly growing tumors (as defined by serial MRI surveillance) in the epidural space that will cause spinal cord compression in a short period of time are indications for surgery. This allows the patient to keep his or her ambulatory status for a longer period, improving the quality of life and avoiding complications consequent to being bedridden such as infections, pneumonia, and deep vein thrombosis. Several studies demonstrated that in these cases and in combination with radiotherapy there is an increase in the 1-year survival of these patients with better functional status.[57,58]

Biomechanical instability is not well defined in the literature, but gross movement on dynamic X-rays should raise concerns. Kostuik and colleagues concluded that the spine was stable if no more than two of six segments were destroyed and it was unstable if three or more segments were destroyed.[59] Additionally they noted that the spine was unstable if the angular deformity caused by vertebral collapse was more than 20° and in these cases it should be stabilized surgically.[59]

Refractory or limiting pain is another indication for spine surgery. All types of spine tumors can cause pain. The pain can arise from periosteal expansion or pathologic collapse. Radicular pain will ensue when the tumor affects the foramina and it can be addressed with nerve root ligation during surgery. Nocturnal and weight-bearing pain are symptoms of bony destruction by the tumor. This bony destruction can lead to pathologic fractures that cause a mechanical type of pain that can be solved with surgical treatment.

En Bloc Resection of Single Metastasis to the Spine

The management of solitary metastases to the spine is often controversial. A prognostic scoring system to direct the surgical planning was developed by Tomita et al. In their study they concluded that en bloc resection should be reserved for those patients with solitary or isolated bone metastasis of either slow or moderate growth based on the primary tumor origin behavior.[60] In a study by Cloyd et al. the mean disease-free survival in patients with single metastatic disease of the spine was 12 months in those with positive margins and 24 months when the margins were negative.[34]

NEUROIMAGING PREOPERATIVE PLANNING

Magnetic Resonance Imaging Features in Spinal Metastasis

MRI is crucial in the evaluation, biopsy guiding, and surgical planning of spinal metastatic diseases. The MRI provides information concerning the bone marrow and

demonstration of the affected bony levels and adds valuable evidence of any spinal cord or neural compression. For the demonstration of bone marrow abnormalities, helpful in the differentiation of malignant and benign changes, the combination of T1-weighted spin-echo and STIR MRI sequences are particularly useful.[61,62]

T1-weighted imaging is valuable in detecting spinal metastasis. This derives from the differences between water and fat signals. The fatty yellow marrow will demonstrate higher signal intensity; thus any lesion with lower signal will easily appear as a hypointense lesion. Moreover, the red marrow, which contains a more balanced amount of water and fat, is hypointense compared to fat alone and hyperintense compared to the muscles. Therefore any replacement of the bone marrow will be demonstrated as a hypointensity compared to normal marrow.[61,63]

A study by Carroll et al. verified that when using 1.5-T MRI a hypointensity in the marrow offers an accuracy of 94% in identifying metastasis, compared to the muscle signal, and 98% compared to the intervertebral disc signal.[64] Nonetheless, it is important to note that in another study using a 3-T MRI the accuracy of the comparison was actually better using the muscle signal (89%) than the disc signal (78%).[62]

Owing to their higher water content, metastatic lesions will be brighter than bone marrow on T2-weighted images. The lesions can present with a bright rim of high signal around them, forming a halo, which provides a 75% sensitivity and 99.5% specificity for metastatic lesions. Unfortunately, this finding is not common.[65] On the other hand, a point of high signal intensity in the center of the bone lesion is a very specific (99.5% specificity) indicator of normal red marrow with a 95% sensitivity.[65]

The use of contrasted MRI provides valuable feedback to identify the exact compartment where the tumors is and the degree of spinal cord compression. This might guide the surgical indication and extent of the procedure to be offered, such as a simpler surgery, like a decompressive laminectomy, versus a more complex and aggressive approach, such as a circumferential resection and vertebrectomy with reconstruction divided in two surgical procedures, one through the back and one through the front.[66,67]

To evaluate the enhancing metastatic lesions in the T1-weighted sequence it is important to revert to techniques to suppress normal fatty marrow to avoid possible misleading isointensity of the lesion with the normal marrow.[68] By suppressing the fatty marrow signal background a T1 postcontrast with fat saturation will allow a more accurate view of the lesion. The combination of T1-weighted and either fat-saturation T2-weighted or STIR images is a very good option to evaluate the extent of bone marrow compromise. On fat-suppressed, T1-weighted images, metastases will have mixed-to-high signal intensity, while nonneoplastic lesions have low signal intensity.[69,70] Nonetheless the physician should be aware that fat-saturation techniques might be impaired by artifact from spinal hardware.

Leptomeningeal Metastasis

Leptomeningeal metastasis (LM) is one of the most severe complications in cancer patients and is a major cutoff for surgery. It occurs in approximately 4–15% of all patients with solid tumors. Breast cancer, lung cancer, and melanoma are some of the most common types of tumors to progress with LM.[71] Systemic treatment might delay the manifestation of LM but, unfortunately, once it occurs the prognosis is very poor and the median survival is around 8 weeks (range, 4–11 weeks).[72,73] These patients will not benefit from surgical procedures at this point. Waki et al., in a series of 85 patients with LM from solid tumors, concluded that palliative treatment is the most plausible option for these patients because of their short survival.[74] Some previous studies have shown that intrathecal chemotherapy for LM in breast cancer patients did not yield either a neurological response or a survival benefit.[75,76]

MRI with gadolinium enhancement is the examination of choice to evaluate patients with suspected LM. Any patient with possible LM that is being considered for surgery should have an entire neuraxis MRI before treatment decisions are made. Nonetheless, a normal MRI with gadolinium study does not exclude the diagnosis of LM and if LM is still suspected the gold standard workup is CSF cytology.[77–80]

Diffusion-Weighted Imaging

The utility of diffusion-weighted imaging (DWI) on differentiating benign from metastatic spinal lesions is controversial in the literature. This technique estimates the tissue-specific molecular diffusion of protons. Highly cellular tissues such as neoplastic ones will present a diminished apparent diffusion coefficient due to the exaggerated amount of cellular membranes restricting the diffusion. Castillo et al. considered in a series that DWI of the spine had no advantage compared to noncontrast T1-weighted MRI in detecting and defining the vertebral metastases, but the same study considered DWI to be superior to T2-weighted imaging.[81,82]

COMPUTED TOMOGRAPHY

CT scan is an excellent exam for bone evaluation. It can diagnose a bony metastatic lesion up to 6 months before regular X-rays.[83] The resolution is much higher than in plain X-rays, offering accuracy in analyzing trabecular bone. When contrast is administered soft tissue masses will be demonstrated in one-third of the cases. Sensitivity and specificity of CT scan are high for evaluating

vertebral collapse, vertebral body, foraminal and pedicle involvement, cortical destruction, paravertebral masses, and extension to the epidural space. Cortical destruction is an important clue to determining tumor origin but it may be difficult to identify when osteoporosis or degenerative changes are associated.[84–86]

CT is a great tool to use in surgical planning. With the evaluation of the bone quality and pedicles involvement one may decide between a transpedicular or posterolateral approach for a vertebroplasty or to guide the decision about the pedicle screws placement.[87]

Some findings are highly suggestive of malignancy. The collapse of a vertebral body due to porotic bone might present with a burst-like appearance, which is a sign of cortical fracture. Lesions located in the cervical vertebrae, single vertebra lesions, and backward angulation also suggest malignant origin.[86]

Differentiation of Lytic versus Blastic Spinal Disease

CT is very important in differentiating between lytic and blastic lesions. Lytic lesions almost invariably will present in the posterior cortex causing destruction of the cortex and the pedicle. These lesions will exhibit diffuse enhancement in contrast exams.[86]

Tumors that typically present with lytic metastases include breast, lung, kidney, thyroid, oropharyngeal, melanoma, adrenal, and uterus. Mixed lytic and sclerotic lesion may occur in breast and lung cancer. But this mixed pattern is more commonly seen with ovarian, testicular, and cervical carcinomas.[86]

Sclerotic lesions are more rare than lytic lesions. They are highly dense with a heterogeneous appearance; the boundaries are commonly blurred with the presence of spongiform bone and periosteal reaction. As a consequence usually the vertebrae affected with blastic lesions are more stable compared with lytic lesions. On the other hand they are harder to drill during surgery, increasing the difficulty in performing vertebrectomies. The places with sclerosis may be nodular or mottled in the imaging examination. It is not possible to visualize normal bone trabeculae in these cases. Cortical involvement is very uncommon as well as the presence of a paravertebral mass. On contrast exams these lesions have a variable pattern depending on the amount of sclerosis.[84,86]

DIFFERENTIAL DIAGNOSIS OF SPINAL TUMORS

On imaging exams spinal metastasis and bone tumors can be confused with other benign pathologies such as aneurysmal bone cysts, hemangiomas, eosinophilic granulomas, and infections. Some features that might aid in the differential diagnosis of osteomyelitis are the frequent involvement of the disc space and vertebral body in infectious pathologies. They present with hypointense signal on the T1-weighted MRI and hyperintensity on the T2-weighted MRI.[88]

In contrast, in tumor cases the discs will not be involved and appear with normal signal intensities on T1- and T2-weighted MRI. Also, loss of destruction of the vertebral body end plate is seen in infection more frequently than with tumor. Infections usually spread to contiguous vertebral bodies and this is another feature that differentiates it from tumor presentation. Moreover, tumors will not affect the fat soft tissue around the area where they are present, but infection will commonly affect the fat visualization owing to diffuse edema.[88] It is highly important not only to differentiate infectious lesions from tumors but also to avoid surgery in infected patients until complete resolution of the infection, as there is a high rate of contamination of the spinal hardware in patients with concomitant infection, even in sites distant from the spine, owing to hematogenous seeding.[89]

DYNAMIC X-RAYS

One of the most important points in the surgical planning is the evaluation of spine instability as aforementioned in this chapter. Functional radiograph is an important tool in this setting. Intervertebral kinematics based on functional flexion–extension radiography will provide the necessary information on the spine stability to guide surgical management.[90–92] Specifically, forward displacement of the vertebrae greater than 3.5 mm and an angle between adjacent end plates greater than 11° are considered signs of instability.[93]

POSITRON EMISSION TOMOGRAPHY SCAN

Bone scintigraphy, using 99mTc-methylene diphosphonate, is the most frequently used imaging procedure for the assessment of bone metastases. It is easily accessible, offers high sensitivity, and allows the evaluation of the whole skeleton. Nonetheless, many patients with metastasis will not show the classical patterns in this exam.[94,95] Bone scintigraphy has several limitations since it cannot detect associated soft-tissue changes. Many benign abnormalities that could affect the bone might lead to inaccurate results and consequently its specificity is low.[95]

In this context, positron emission tomography (PET)/CT using [^{18}F]fluorodeoxyglucose (^{18}F-FDG), which is already an established tool in the staging of most types of cancer, proves to have a role in spine oncology. In contrast with bone scan, which is capable of evaluating only the mineral turnover, ^{18}F-FDG PET/CT provides a

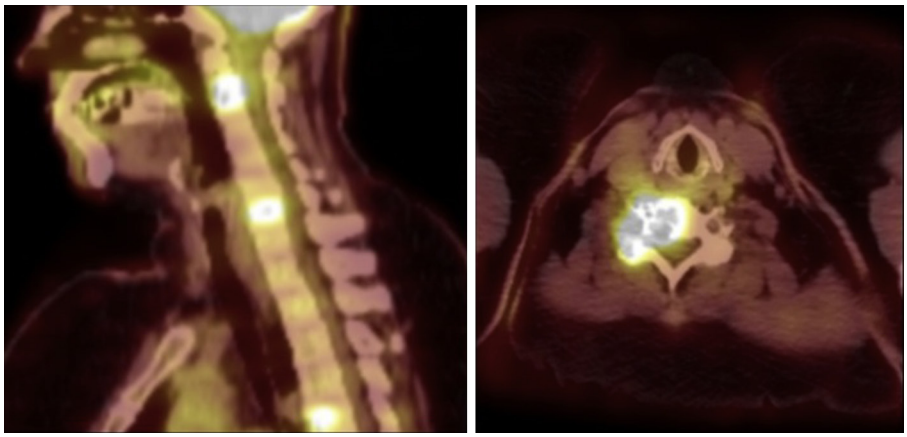


FIGURE 12 PET/CT showing several points of ^{18}F-FDG uptake due to metastatic foci with bone marrow infiltration.

deeper evaluation of bone pathology based on the glucose metabolism that is altered in cancer pathology. This characteristic allows for the differentiation between benign and malignant lesions.[95] Additionally, it will provide a good idea of bone marrow infiltration, and this is one of the most crucial aspects in tumor screening and staging that will enable earlier and precise therapy and decrease morbidity due to pain or complications[96–98] (Figure 12).

Nonetheless, it is important to highlight that MRI is superior to ^{18}F-FDG PET in detecting bone marrow infiltration and metastases, especially in patients with solid tumors and lymphoma. Therefore PET/CT, although useful to add information, should not replace the MRI. In a study by Ghanem et al. MRI provides greater sensitivity (78%), specificity (88%), and diagnostic accuracy (82%) than PET/CT in the detection of bone marrow infiltration and metastasis. Moreover, MRI provides information regarding associated conditions, such as pathological fractures, presence of epidural disease, and intramedullary and intraspinal metastases. These will all affect the surgical planning and therapeutic options for these patients. In suspected cases when cancer patients present with bone pain, neurological symptoms, and a negative PET/CT, an MRI of the spine must be performed to exclude bone marrow metastasis or infiltration.[99]

Additionally, false-positive PET/CT results might be caused by fractures. In suspected cases cross-sectional CT or MRI can differentiate the ^{18}F-FDG uptake caused by fractures and the ^{18}F-FDG accumulation due to tumor infiltration.[100]

SINGLE-PHOTON EMISSION COMPUTED TOMOGRAPHY/COMPUTED TOMOGRAPHY

Compared with planar scintigraphy, single-photon emission CT (SPECT) improves the sensitivity in bone scanning. Nonetheless, SPECT still has low specificity and it cannot offer precise anatomical information, which impairs the ability to distinguish between benign and malignant lesions in the spine.[101,102] But when combined with a CT, SPECT has improved diagnostic utility with better accuracy for the bone pathology in question.[103] Fused SPECT/CT images have better spatial and density resolution, providing a well-defined view of the affected anatomical sites. The osteolytic or osteoblastic changes that might indicate the occurrence of metastatic spine disease can also be satisfactorily evaluated using SPECT/spiral CT.

ANGIOGRAPHY

In the performance of spine surgery, tumor hypervascularity leads to major intraoperative blood loss and consequently increased morbidity.[104–106] The metastatic tumors most commonly associated with high intraoperative blood loss are renal cell carcinoma, thyroid carcinoma, multiple myeloma, and hepatocellular carcinoma.[107–109] When uncontrolled hemorrhage occurs intraoperatively, surgery might be interrupted, impairing tumor resection ability. Complications deriving from excessive bleeding, such as paraplegia due to epidural hematoma, are reported in the literature.[107]

In this scenario preoperative arterial embolization of hypervascular spinal tumors arises as an important tool to reduce blood loss.[110–114] One should be aware that the relation between the preoperative MRI enhancement and hypervascularity in the angiography is not reliable. Many studies have demonstrated that in patients who are not embolized prior to surgery the intraoperative blood loss estimations range from 4350 to 8750 mL.[102,104,107,114] In contrast, in the patients who have their tumors embolized preoperatively the surgical blood loss decreases to a range from 300 to 4300 mL.[102]

Several large series emphasize the importance of preoperative embolization, especially in known hypervascular tumors. Nonetheless, it should be highlighted that in many patients in whom angiography showed complete

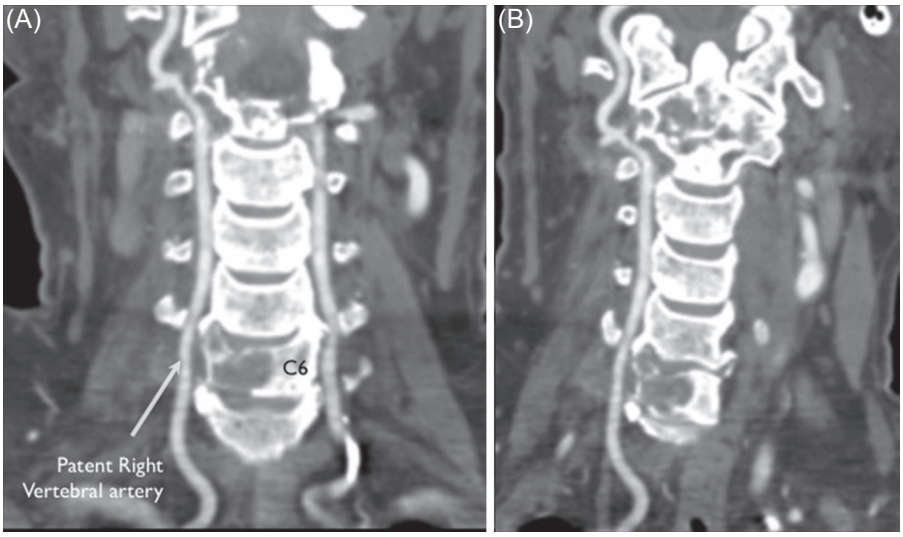


FIGURE 13 (A): Angiography pre-en-bloc resection demonstrating vertebral artery patent in the contralateral side. (B): Angiography postembolization of the left vertebral artery.

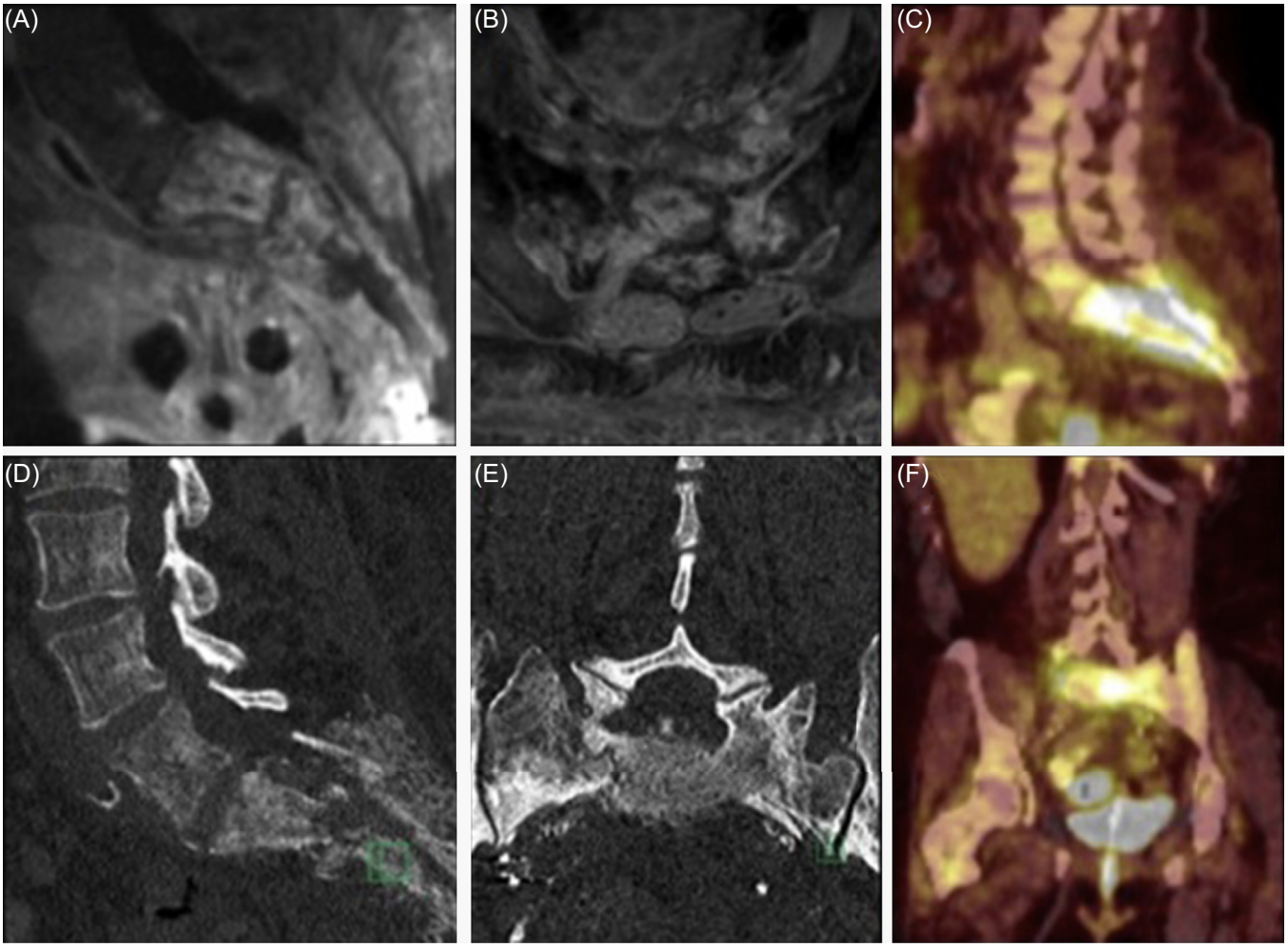


FIGURE 14 Images of a 59-year-old female patient presenting with a radiation-induced osteosarcoma after radiotherapy for a cervix carcinoma. The patient was submitted to a surgical procedure for en bloc resection of the lesion but the procedure was aborted because of the extensive fibrosis and adherence of the iliac vessels to the retroperitoneum. Preoperative postcontrast T1 MRI ((A): sagittal; (B): axial) demonstrating the contrast-enhancing lesion affecting the whole sacrum. CT scan demonstrating the intense remodeling of the sacrum with new areas of abnormal osteogenesis, a pattern that is typical of osteosarcomas ((D): sagittal; (E): coronal). PET CT scan demonstrating the hypermetabolic lesion in the sacrum and posterior sacral elements. Note that the lesion affects the whole sacrum extending laterally up to the sacroiliac joints ((C): sagittal; (F): coronal).

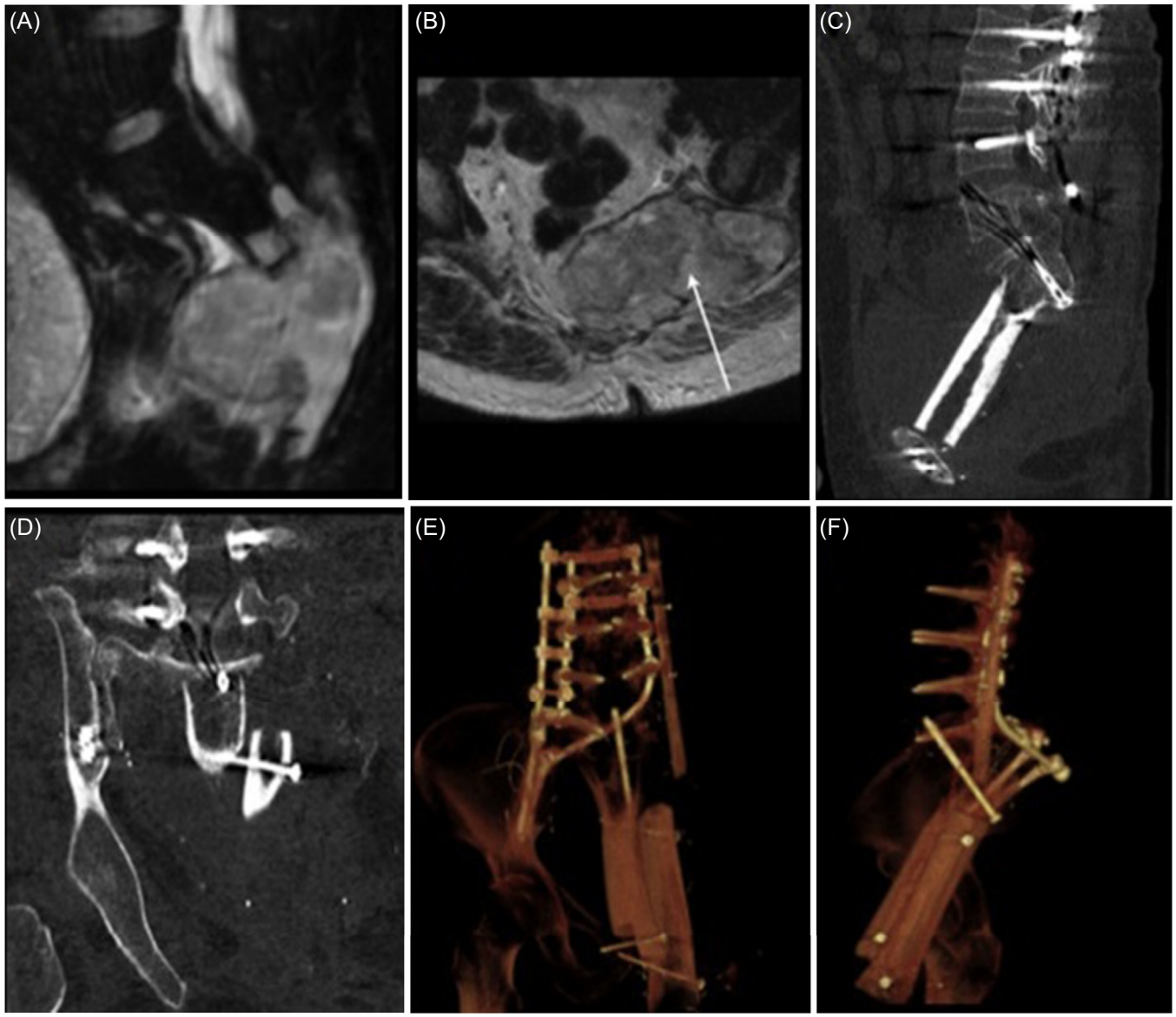


FIGURE 15 Images of a 50-year-old male patient presenting with left buttock and leg pain. The MRI of the lumbosacral spine revealed a large lesion affecting the lower sacrum and extending anteriorly into the presacral area ((A): sagittal T2 MRI; (B): axial T2 MRI). After a core needle biopsy revealing the diagnosis of a chordoma, the patient was submitted to an en bloc resection of the lesion with left external hemipelvectomy, amputation of the left lower limb, and lumbopelvic reconstruction using femoral and fibular vascularized bone grafts that were removed from the sacrificed limb. Postoperative CT scan demonstrating the final construct ((C): sagittal; (D): coronal; (E): anteroposterior three-dimensional reconstruction; and (F): lateral three-dimensional reconstruction).

embolization, significant blood loss still occurred during surgery.[102,106] The reason is that intraoperative blood loss in cancer patients is a multifactorial process that will vary between patient, type of tumor, technique used for the embolization, and surgical technique.[109]

When the surgeon is performing an en bloc resection in the cervical spine, angiography is essential in the surgical planning. Owing to technical difficulties, when the tumor has a close relation with the foramina, in dealing with the significant venous plexus that surrounds the vertebral arteries and also in cases in which the tumor engulfs one of the vertebral arteries, the endovascular occlusion of the affected artery is recommended. Moreover, angiography will provide adequate information about the posterior circulation through a balloon occlusion test to confirm the feasibility of sacrificing one of the vertebral arteries[33] (Figure 13).

CONCLUSIONS

In patients with new-onset LBP, the majority of cases will arise from benign conditions. Nonetheless, spinal cancer might present for the first time as an episode of

new-onset back or neck pain. Imaging studies are essential in evaluating these patients. They are valuable tools to provide diagnosis deriving from imaging characteristics or imaging-guided biopsy. CT scan and MRI are essential in the surgical planning to address the extent of disease, the compartment affected, and the degree of bone destruction. Contrasted MRIs are crucial to evaluate intradural tumors and spinal cord compression. MRI tractography might be used to guide the resection of intramedullary lesions. Angiography is essential in evaluating the vertebral arteries in cases of en bloc resection of primary bone tumors. Angiography should be used to evaluate the vascularity of determined types of tumor and it might be followed by embolization to decrease intraoperative bleeding. The combination of imaging studies affects decision-making in vertebroplasty, screw placement, and type of approach and aggressiveness of the procedure. A multidisciplinary team should assess patients with spinal cancer.

References

1. Atlas SJ, Deyo RA. Evaluating and managing acute low back pain in the primary care setting. *J Gen Intern Med*. February 2001;16(2):120–131.
2. Deyo RA, Weinstein JN. Low back pain. *N Engl J Med*. February 1, 2001;344(5):363–370.
3. Deyo RA, Rainville J, Kent DL. What can the history and physical examination tell us about low back pain? *JAMA*. August 12, 1992;268(6):760–765.
4. Koes BW, van Tulder MW, Thomas S. Diagnosis and treatment of low back pain. *BMJ*. June 17, 2006;332(7555):1430–1434.
5. Koes BW, van Tulder M, Lin CW, Macedo LG, McAuley J, Maher C. An updated overview of clinical guidelines for the management of non-specific low back pain in primary care. *Eur Spine J*. December 2010;19(12):2075–2094.
6. Henschke N, Maher CG, Refshauge KM, et al. Prevalence of and screening for serious spinal pathology in patients presenting to primary care settings with acute low back pain. *Arthritis Rheum*. October 2009;60(10):3072–3080.
7. Downie A, Williams CM, Henschke N, et al. Red flags to screen for malignancy and fracture in patients with low back pain: systematic review. *BMJ*. 2013;347:f7095.
8. Henschke N, Maher CG, Ostelo RW, de Vet HC, Macaskill P, Irwig L. Red flags to screen for malignancy in patients with low-back pain. *Cochrane Database Syst Rev*. 2013;2:CD008686.
9. Levack P, Graham J, Collie D, et al. Don't wait for a sensory level–listen to the symptoms: a prospective audit of the delays in diagnosis of malignant cord compression. *Clin Oncol*. December 2002;14(6):472–480.
10. Sciubba DM, Gokaslan ZL. Diagnosis and management of metastatic spine disease. *Surg Oncol*. November 2006;15(3):141–151.
11. Arguello F, Baggs RB, Duerst RE, Johnstone L, McQueen K, Frantz CN. Pathogenesis of vertebral metastasis and epidural spinal cord compression. *Cancer*. January 1, 1990;65(1):98–106.
12. Aaron AD. The management of cancer metastatic to bone. *JAMA*. October 19, 1994;272(15):1206–1209.
13. Sciubba DM, Petteys RJ, Dekutoski MB, et al. Diagnosis and management of metastatic spine disease. A review. *J Neurosurg Spine*. July 2010;13(1):94–108.
14. Sundaresan N, Kroll G, DiGiacinto G. Metastatic tumors of the spine. In: Sundaresan N, Schmidek HH, Schiller AL, Rosenthal D, eds. *Tumors of the Spine: Diagnosis and Clinical Management*. Philadelphia: WB Sanders; 1990:279–304.
15. Wong DA, Fornasier VL, MacNab I. Spinal metastases: the obvious, the occult, and the impostors. *Spine*. January 1990;15(1):1–4.
16. Bell GR. Surgical treatment of spinal tumors. *Clin Orthop Relat Res*. February 1997;(335):54–63.
17. Bilsky MH, Lis E, Raizer J, Lee H, Boland P. The diagnosis and treatment of metastatic spinal tumor. *Oncologist*. 1999;4(6):459–469.
18. Walsh GL, Gokaslan ZL, McCutcheon IE, et al. Anterior approaches to the thoracic spine in patients with cancer: indications and results. *Ann Thorac Surg*. December 1997;64(6):1611–1618.
19. York JE, Wildrick DM, Gokaslan ZL. Metastatic tumors. In: Benzel EC, Stillerman CB, eds. *The Thoracic Spine*. St. Louis: Quality Medical Publishing; 1999:392–411.
20. Constans JP, de Divitiis E, Donzelli R, Spaziante R, Meder JF, Haye C. Spinal metastases with neurological manifestations. Review of 600 cases. *J Neurosurg*. July 1983;59(1):111–118.
21. Helweg-Larsen S, Sorensen PS. Symptoms and signs in metastatic spinal cord compression: a study of progression from first symptom until diagnosis in 153 patients. *Eur J Cancer*. 1994;30A(3):396–398.
22. Brihaye J, Ectors P, Lemort M, Van Houtte P. The management of spinal epidural metastases. *Adv Tech Stand Neurosurg*. 1988;16:121–176.
23. Khanna AJ, Shindle MK, Wasserman BA, et al. Use of magnetic resonance imaging in differentiating compartmental location of spinal tumors. *Am J Orthop*. October 2005;34(10):472–476.
24. Osborn AG. Cysts, tumors, and tumorlike lesions of the spine and spinal cord. In: Osborn AG, ed. *Diagnostic Neuroradiology*. St. Louis, Missouri: Mosby; 1994:876–918.
25. Ross JS, Brant-Zawadzki M, Moore KR, Crim J, Chen MZ, Katzman GL. Neoplasms, cysts, and other masses. In: Ross JS, ed. *Diagnostic Imaging: Spine*. vol. 4. Manitoba, Canada: AMIRSYS; 2005:1–126.
26. Weinstein JN, McLain RF. Primary tumors of the spine. *Spine*. November 1987;12(9):843–851.
27. Hsu W, Kosztowski TA, Zaidi HA, Dorsi M, Gokaslan ZL, Wolinsky JP. Multidisciplinary management of primary tumors of the vertebral column. *Curr Treat Options Oncol*. April 2009;10(1–2):107–125.
28. Ropper AE, Cahill KS, Hanna JW, McCarthy EF, Gokaslan ZL, Chi JH. Primary vertebral tumors: a review of epidemiologic, histological, and imaging findings, Part I: benign tumors. *Neurosurgery*. December 2011;69(6):1171–1180.
29. Ropper AE, Cahill KS, Hanna JW, McCarthy EF, Gokaslan ZL, Chi JH. Primary vertebral tumors: a review of epidemiologic, histological and imaging findings, part II: locally aggressive and malignant tumors. *Neurosurgery*. January 2012;70(1):211–219. discussion 219.
30. Yamazaki T, McLoughlin GS, Patel S, Rhines LD, Fourney DR. Feasibility and safety of en bloc resection for primary spine tumors: a systematic review by the Spine Oncology Study Group. *Spine*. October 15, 2009;34(22 suppl):S31–S38.
31. Yang X, Wu Z, Xiao J, et al. Chondrosarcomas of the cervical and cervicothoracic spine: surgical management and long-term clinical outcome. *J Spinal Disord Tech*. February 2012;25(1):1–9.
32. Boriani S, Bandiera S, Biagini R, et al. Chordoma of the mobile spine: fifty years of experience. *Spine*. February 15, 2006;31(4):493–503.
33. Mattei TA, Mendel E. En bloc resection of primary malignant bone tumors of the cervical spine. *Acta Neurochir*. May 1, 2014.
34. Cloyd JM, Acosta Jr FL, Polley MY, Ames CP. En bloc resection for primary and metastatic tumors of the spine: a systematic review of the literature. *Neurosurgery*. August 2010;67(2):435–444. discussion 444–445.

35. Abul-Kasim K, Thurnher MM, McKeever P, Sundgren PC. Intradural spinal tumors: current classification and MRI features. *Neuroradiology*. April 2008;50(4):301–314.
36. Beall DP, Googe DJ, Emery RL, et al. Extramedullary intradural spinal tumors: a pictorial review. *Curr Probl Diagn Radiol*. September–October 2007;36(5):185–198.
37. Chamberlain MC, Tredway TL. Adult primary intradural spinal cord tumors: a review. *Curr Neurol Neurosci Rep*. June 2011;11(3):320–328.
38. Arnautovic K, Arnautovic A. Extramedullary intradural spinal tumors: a review of modern diagnostic and treatment options and a report of a series. *Bosn J Basic Med Sci*. October 2009;9(suppl 1): 40–45.
39. Bloomer CW, Ackerman A, Bhatia RG. Imaging for spine tumors and new applications. *Top Magn Reson Imaging*. April 2006;17(2):69–87.
40. Traul DE, Shaffrey ME, Schiff D. Part I: spinal-cord neoplasms-intradural neoplasms. *Lancet Oncol*. January 2007;8(1):35–45.
41. Zimmerman RA, Bilaniuk LT. Imaging of tumors of the spinal canal and cord. *Radiol Clin N Am*. September 1988;26(5): 965–1007.
42. Jeon JH, Hwang HS, Jeong JH, Park SH, Moon JG, Kim CH. Spinal schwannoma; analysis of 40 cases. *J Korean Neurosurg Soc*. March 2008;43(3):135–138.
43. Ozawa H, Kokubun S, Aizawa T, Hoshikawa T, Kawahara C. Spinal dumbbell tumors: an analysis of a series of 118 cases. *J Neurosurg Spine*. December 2007;7(6):587–593.
44. Duong LM, McCarthy BJ, McLendon RE, et al. Descriptive epidemiology of malignant and nonmalignant primary spinal cord, spinal meninges, and cauda equina tumors, United States, 2004–2007. *Cancer*. September 1, 2012;118(17):4220–4227.
45. Choi JY, Chang KH, Yu IK, et al. Intracranial and spinal ependymomas: review of MR images in 61 patients. *Korean J Radiol*. October–December 2002;3(4):219–228.
46. Sun B, Wang C, Wang J, Liu A. MRI features of intramedullary spinal cord ependymomas. *J Neuroimaging*. October 2003;13(4):346–351.
47. Westphal M. Intramedullary tumors. In: Tonn JC, Westphal M, Rutka JT, Grossman SA, eds. *Neuro-Oncology of CNS Tumors*. Heidelberg: Springer; 2005:499–504.
48. Baker KB, Moran CJ, Wippold 2nd FJ, et al. MR imaging of spinal hemangioblastoma. *AJR Am J Roentgenol*. February 2000;174(2):377–382.
49. Choudhri AF, Whitehead MT, Klimo Jr P, Montgomery BK, Boop FA. Diffusion tensor imaging to guide surgical planning in intramedullary spinal cord tumors in children. *Neuroradiology*. February 2014;56(2):169–174.
50. Lee JW, Kim JH, Park JB, et al. Diffusion tensor imaging and fiber tractography in cervical compressive myelopathy: preliminary results. *Skelet Radiol*. December 2011;40(12):1543–1551.
51. Mohamed FB, Hunter LN, Barakat N, et al. Diffusion tensor imaging of the pediatric spinal cord at 1.5T: preliminary results. *AJNR Am J Neuroradiol*. February 2011;32(2):339–345.
52. Mulcahey MJ, Samdani A, Gaughan J, et al. Diffusion tensor imaging in pediatric spinal cord injury: preliminary examination of reliability and clinical correlation. *Spine*. June 1, 2012;37(13):E797–E803.
53. Phillips NS, Sanford RA, Helton KJ, et al. Diffusion tensor imaging of intraaxial tumors at the cervicomedullary and pontomedullary junctions. Report of two cases. *J Neurosurg*. December 2005;103(6 suppl):557–562.
54. Ducreux D, Lepeintre JF, Fillard P, Loureiro C, Tadie M, Lasjaunias P. MR diffusion tensor imaging and fiber tracking in 5 spinal cord astrocytomas. *AJNR Am J Neuroradiol*. January 2006;27(1):214–216.
55. Setzer M, Murtagh RD, Murtagh FR, et al. Diffusion tensor imaging tractography in patients with intramedullary tumors: comparison with intraoperative findings and value for prediction of tumor resectability. *J Neurosurg Spine*. September 2010;13(3): 371–380.
56. Thurnher MM, Law M. Diffusion-weighted imaging, diffusion-tensor imaging, and fiber tractography of the spinal cord. *Magn Reson Imaging Clin N Am*. May 2009;17(2):225–244.
57. Laufer I, Iorgulescu JB, Chapman T, et al. Local disease control for spinal metastases following "separation surgery" and adjuvant hypofractionated or high-dose single-fraction stereotactic radiosurgery: outcome analysis in 186 patients. *J Neurosurg Spine*. March 2013;18(3):207–214.
58. Lee CH, Kwon JW, Lee J, et al. Direct decompressive surgery followed by radiotherapy versus radiotherapy alone for metastatic epidural spinal cord compression: a meta-analysis. *Spine*. April 20, 2014;39(9):E587–E592.
59. Kostuik JP, Weinstein JN. Differential diagnosis and surgical treatment of metastatic spine tumors. In: Frymoyer JW, Ducker TB, Hadler NM, Kostuik JP, Weinstein JN, Whitecloud III TS, eds. *The Adult Spine*. New York: Raven Press; 1991:861–888.
60. Tomita K, Kawahara N, Kobayashi T, Yoshida A, Murakami H, Akamaru T. Surgical strategy for spinal metastases. *Spine*. February 1, 2001;26(3):298–306.
61. Baur A, Stabler A, Bruning R, et al. Diffusion-weighted MR imaging of bone marrow: differentiation of benign versus pathologic compression fractures. *Radiology*. May 1998;207(2):349–356.
62. Zhao J, Krug R, Xu D, Lu Y, Link TM. MRI of the spine: image quality and normal-neoplastic bone marrow contrast at 3 T versus 1.5 T. *AJR Am J Roentgenol*. April 2009;192(4):873–880.
63. Daffner RH, Lupetin AR, Dash N, Deeb ZL, Sefczek RJ, Schapiro RL. MRI in the detection of malignant infiltration of bone marrow. *AJR Am J Roentgenol*. February 1986;146(2):353–358.
64. Carroll KW, Feller JF, Tirman PF. Useful internal standards for distinguishing infiltrative marrow pathology from hematopoietic marrow at MRI. *J Magn Reson Imaging*. March–April 1997;7(2):394–398.
65. Schweitzer ME, Levine C, Mitchell DG, Gannon FH, Gomella LG. Bull's-eyes and halos: useful MR discriminators of osseous metastases. *Radiology*. July 1993;188(1):249–252.
66. Carmody RF, Yang PJ, Seeley GW, Seeger JF, Unger EC, Johnson JE. Spinal cord compression due to metastatic disease: diagnosis with MR imaging versus myelography. *Radiology*. October 1989;173(1):225–229.
67. Hansen-Algenstaedt N, Knight R, Beyerlein J, Gessler R, Wiesner L, Schaefer C. Minimal-invasive stabilization and circumferential spinal cord decompression in metastatic epidural spinal cord compression (MESCC). *Eur spine J*. September 2013;22(9):2142–2144.
68. Schmidt GP, Schoenberg SO, Reiser MF, Baur-Melnyk A. Whole-body MR imaging of bone marrow. *Eur J Radiol*. July 2005;55(1):33–40.
69. Mirowitz SA, Apicella P, Reinus WR, Hammerman AM. MR imaging of bone marrow lesions: relative conspicuousness on T1-weighted, fat-suppressed T2-weighted, and STIR images. *AJR Am J Roentgenol*. January 1994;162(1):215–221.
70. Uchida N, Sugimura K, Kajitani A, Yoshizako T, Ishida T. MR imaging of vertebral metastases: evaluation of fat saturation imaging. *Eur J Radiol*. September 1993;17(2):91–94.
71. Chamberlain MC. Leptomeningeal metastases: a review of evaluation and treatment. *J Neurooncol*. May 1998;37(3):271–284.
72. Grossman SA, Krabak MJ. Leptomeningeal carcinomatosis. *Cancer Treat Rev*. April 1999;25(2):103–119.
73. Le Rhun E, Taillibert S, Chamberlain MC. Carcinomatous meningitis: leptomeningeal metastases in solid tumors. *Surg Neurol Int*. 2013;4(suppl 4):S265–S288.

74. Waki F, Ando M, Takashima A, et al. Prognostic factors and clinical outcomes in patients with leptomeningeal metastasis from solid tumors. *J Neurooncol*. June 2009;93(2):205–212.
75. Boogerd W, van den Bent MJ, Koehler PJ, et al. The relevance of intraventricular chemotherapy for leptomeningeal metastasis in breast cancer: a randomised study. *Eur J Cancer*. December 2004;40(18):2726–2733.
76. Orlando L, Curigliano G, Colleoni M, et al. Intrathecal chemotherapy in carcinomatous meningitis from breast cancer. *Anticancer Res*. September-October 2002;22(5):3057–3059.
77. Chamberlain MC, Sandy AD, Press GA. Leptomeningeal metastasis: a comparison of gadolinium-enhanced MR and contrast-enhanced CT of the brain. *Neurology*. March 1990;40(3 Pt 1): 435–438.
78. Freilich RJ, Krol G, DeAngelis LM. Neuroimaging and cerebrospinal fluid cytology in the diagnosis of leptomeningeal metastasis. *Ann Neurol*. July 1995;38(1):51–57.
79. Schumacher M, Orszagh M. Imaging techniques in neoplastic meningiosis. *J Neurooncol*. June–July 1998;38(2–3):111–120.
80. Sze G, Soletsky S, Bronen R, Krol G. MR imaging of the cranial meninges with emphasis on contrast enhancement and meningeal carcinomatosis. *AJR Am J Roentgenol*. November 1989;153(5):1039–1049.
81. Byun WM, Shin SO, Chang Y, Lee SJ, Finsterbusch J, Frahm J. Diffusion-weighted MR imaging of metastatic disease of the spine: assessment of response to therapy. *AJNR Am J Neuroradiol*. June-July 2002;23(6):906–912.
82. Castillo M, Arbelaez A, Smith JK, Fisher LL. Diffusion-weighted MR imaging offers no advantage over routine noncontrast MR imaging in the detection of vertebral metastases. *AJNR Am J Neuroradiol*. May 2000;21(5):948–953.
83. Salvo N, Christakis M, Rubenstein J, et al. The role of plain radiographs in management of bone metastases. *J Palliat Med*. February 2009;12(2):195–198.
84. Guillevin R, Vallee JN, Lafitte F, Menuel C, Duverneuil NM, Chiras J. Spine metastasis imaging: review of the literature. *J Neuroradiol*. December 2007;34(5):311–321.
85. Kamholtz R, Sze G. Current imaging in spinal metastatic disease. *Semin Oncol*. April 1991;18(2):158–169.
86. Shah LM, Salzman KL. Imaging of spinal metastatic disease. *Int J Surg Oncol*. 2011;2011:769753.
87. Chiras J, Depriester C, Weill A, Sola-Martinez MT, Deramond H. [Percutaneous vertebral surgery. Technics and indications]. *J Neuroradiol*. June 1997;24(1):45–59.
88. An HS, Vaccaro AR, Dolinskas CA, Cotler JM, Balderston RA, Bauerle WB. Differentiation between spinal tumors and infections with magnetic resonance imaging. *Spine*. August 1991; 16(8 suppl):S334–S338.
89. Kasliwal MK, Tan LA, Traynelis VC. Infection with spinal instrumentation: review of pathogenesis, diagnosis, prevention, and management. *Surg Neurol Int*. 2013;4(suppl 5):S392–S403.
90. Dimnet J, Pasquet A, Krag MH, Panjabi MM. Cervical spine motion in the sagittal plane: kinematic and geometric parameters. *J Biomech*. 1982;15(12):959–969.
91. Panjabi MM, Lydon C, Vasavada A, Grob D, Crisco 3rd JJ, Dvorak J. On the understanding of clinical instability. *Spine*. December 1, 1994;19(23):2642–2650.
92. White 3rd AA, Johnson RM, Panjabi MM, Southwick WO. Biomechanical analysis of clinical stability in the cervical spine. *Clin Orthop Relat Res*. 1975;109:85–96.
93. Bifulco P, Cesarelli M, Romano M, Fratini A, Sansone M. Measurement of intervertebral cervical motion by means of dynamic x-ray image processing and data interpolation. *Int J Biomed Imaging*. 2013;2013:152920.
94. Resnick D. Skeletal metastasis. In: Resnick D, ed. *Bone and Joint Imaging*. Philadelphia: Pennsylvania Saunders Company; 1996:1076–1091.
95. Uchida K, Nakajima H, Miyazaki T, et al. (18)F-FDG PET/CT for diagnosis of osteosclerotic and osteolytic vertebral metastatic lesions: comparison with bone scintigraphy. *Asian Spine J*. June 2013;7(2):96–103.
96. Altehoefer C, Ghanem N, Hogerle S, Moser E, Langer M. Comparative detectability of bone metastases and impact on therapy of magnetic resonance imaging and bone scintigraphy in patients with breast cancer. *Eur J Radiol*. October 2001;40(1):16–23.
97. Bares R. Skeletal scintigraphy in breast cancer management. *Q J Nucl Med*. March 1998;42(1):43–48.
98. Baur A, Stabler A, Nagel D, et al. Magnetic resonance imaging as a supplement for the clinical staging system of Durie and Salmon? *Cancer*. September 15, 2002;95(6):1334–1345.
99. Ghanem NA, Pache G, Lohrmann C, et al. MRI and (18)FDG-PET in the assessment of bone marrow infiltration of the spine in cancer patients. *Eur Spine J*. November 2007;16(11):1907–1912.
100. Fayad LM, Cohade C, Wahl RL, Fishman EK. Sacral fractures: a potential pitfall of FDG positron emission tomography. *AJR Am J Roentgenol*. November 2003;181(5):1239–1243.
101. Bellah RD, Summerville DA, Treves ST, Micheli LJ. Low-back pain in adolescent athletes: detection of stress injury to the pars interarticularis with SPECT. *Radiology*. August 1991;180(2):509–512.
102. Kobayashi K, Okuyama C, Kubota T, Nakai T, Ushijima Y, Nishimura T. Do short-time SPECT images of bone scintigraphy improve the diagnostic value in the evaluation of solitary lesions in the thoracic spine in patients with extraskeletal malignancies? *Ann Nucl Med*. October 2005;19(7):557–566.
103. Zhang Y, Shi H, Cheng D, et al. Added value of SPECT/spiral CT versus SPECT in diagnosing solitary spinal lesions in patients with extraskeletal malignancies. *Nucl Med Commun*. May 2013;34(5):451–458.
104. Berkefeld J, Scale D, Kirchner J, Heinrich T, Kollath J. Hypervascular spinal tumors: influence of the embolization technique on perioperative hemorrhage. *AJNR Am J Neuroradiol*. May 1999;20(5):757–763.
105. Breslau J, Eskridge JM. Preoperative embolization of spinal tumors. *J Vasc Interv Radiol*. November–December 1995;6(6):871–875.
106. Manke C, Bretschneider T, Lenhart M, et al. Spinal metastases from renal cell carcinoma: effect of preoperative particle embolization on intraoperative blood loss. *AJNR Am J Neuroradiol*. May 2001;22(5):997–1003.
107. Olerud C, Jonsson Jr H, Lofberg AM, Lorelius LE, Sjostrom L. Embolization of spinal metastases reduces peroperative blood loss. 21 patients operated on for renal cell carcinoma. *Acta Orthop Scand*. February 1993;64(1):9–12.
108. Shi HB, Suh DC, Lee HK, et al. Preoperative transarterial embolization of spinal tumor: embolization techniques and results. *AJNR Am J Neuroradiol*. November–December 1999;20(10):2009–2015.
109. Thiex R, Harris MB, Sides C, Bono CM, Frerichs KU. The role of preoperative transarterial embolization in spinal tumors. A large single-center experience. *Spine J*. February 2013;13(2):141–149.
110. Benati A, Da Pian R, Mazza C, et al. Preoperative embolisation of a vertebral haemangioma compressing the spinal cord. *Neuroradiology*. 1974;7(3):181–183.
111. Kobayashi K, Ozkan E, Tam A, Ensor J, Wallace MJ, Gupta S. Preoperative embolization of spinal tumors: variables affecting intraoperative blood loss after embolization. *Acta Radiol*. October 1, 2012;53(8):935–942.
112. Prabhu VC, Bilsky MH, Jambhekar K, et al. Results of preoperative embolization for metastatic spinal neoplasms. *J Neurosurg*. March 2003;98(2 suppl):156–164.
113. Wilson MA, Cooke DL, Ghodke B, Mirza SK. Retrospective analysis of preoperative embolization of spinal tumors. *AJNR Am J Neuroradiol*. April 2010;31(4):656–660.
114. Wirbel RJ, Roth R, Schulte M, Kramann B, Mutschler W. Preoperative embolization in spinal and pelvic metastases. *J Orthop Sci*. May 2005;10(3):253–257.

CHAPTER

60

Imaging of Plexopathy in Oncologic Patients

Andrew D. Schweitzer[1], *George Krol*[2]

[1]Department of Radiology, Division of Neuroradiology, Weill Cornell Medicine New York, NY, USA; [2]Division of Neuroradiology, Memorial Sloan Kettering Cancer Center, New York, NY, USA

INTRODUCTION

The general term "plexopathy" is often used to describe symptomatology related to plexus involvement caused by a variety of conditions, including tumor infiltration and inflammatory, traumatic, postsurgical, and postradiation changes. In oncologic patients, such involvement may be due to tumor arising from the nerve fibers (e.g., neurofibroma), direct spread of primary neoplasm from the adjacent organs (breast, lung), compression/infiltration by regional metastases (metastatic nodes), or iatrogenic factors, particularly treatment by surgical intervention or radiation. Patients may present with pain, paresthesias, focal weakness, autonomic symptoms, sensory deficits, and muscle atrophy.[1–3] Physical examination fares rather poorly in assessment of the process. Conventional radiologic methods have been utilized all along in an attempt to localize and further characterize the causes of plexopathy, although with rather dismal results. A "quantum step" in progress was made with the introduction of computed tomography (CT) and magnetic resonance imaging (MRI). Technical improvements have made it possible to visualize individual nerves directly.[4–7] A reliable method of visualization of diseased nerve/plexus seems more difficult to find. As new techniques are introduced, improving resolution and depicting more detail and the chemical composition of tissue, there arises a need for more thorough knowledge of imaging utility in the normal and diseased states.

NORMAL ANATOMY OF PLEXUSES

Plexus is defined as a network of connections of nerve roots, giving rise to further interconnecting or terminal branches. As ventral (motor) and dorsal (sensory) roots leave the spinal cord, they soon unite within the spinal canal to form a spinal nerve. After exiting the neural foramina, they form a network of interconnections (plexus), from ventral roots, trunks, and cords to individual nerves. Although there are many such stations in the body, the three main plexuses are cervical, brachial, and lumbosacral. Plexopathy may result when any of the above segments of the plexus becomes involved. Since it may not be possible to visualize directly the abnormality within the nerve, one may have to rely on altered adjacent tissue to make a diagnosis. Thus, the knowledge of normal configuration, adjacent tissue characteristics, and spatial relationships of plexus components in reference to bony landmarks, vascular structures, and muscles is very important in the detection of abnormality and interpretation of plexus disease.

Cervical and Brachial Plexus

The cervical plexus lies on the ventral surface of the medial scalene and levator scapulae muscles. It is formed by ventral rami of the cervical nerves C1 through C4. Each ramus at the C2, C3, and C4 levels divides into two branches, superior and inferior. These in turn unite in the following way: superior branch of C2 with C1, inferior branch of C2 with superior branch of C3, inferior branch of C3 with superior branch of C4, and inferior branch of C4 joins C5, to become part of the brachial plexus. Terminal cutaneous, muscular, and communicating branches supply skin and muscles in the occipital area, upper neck, supraclavicular, upper pectoral region, and diaphragm.

The brachial plexus is formed by the ventral rami of spinal nerves exiting through the neural foramina of the cervical spine at the C5–T1 levels (dorsal rami innervate posterior paravertebral muscles). Inconsistent contributions may arise from the C4 and T2 segments. As the spinal nerves leave the foramina between the vertebral

Handbook of Neuro-Oncology Neuroimaging, Second Edition
http://dx.doi.org/10.1016/B978-0-12-800945-1.00060-4

© 2016 Elsevier Ltd. All rights reserved.

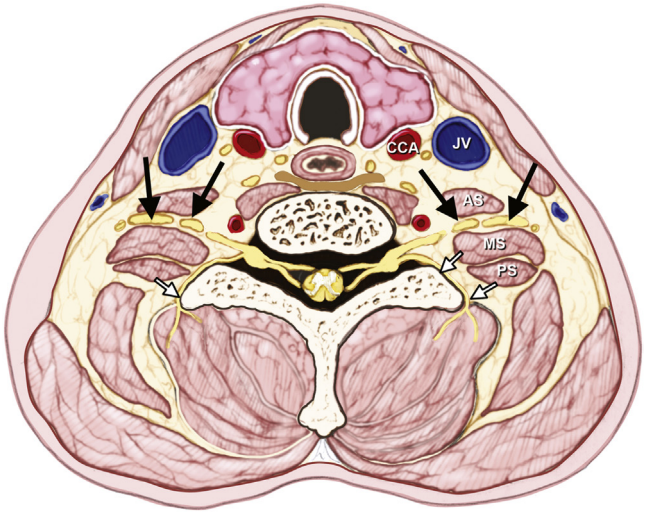


FIGURE 1 Diagram of an anatomical section through the lower cervical spine in the axial plane. Ventral rami of spinal nerves exiting through the neural foramina unite between anterior and middle scalene muscles to form the brachial plexus (arrows). Posterior rami innervate the posterior paraspinal musculature (open arrows). AS, MS, PS, anterior, middle, and posterior scalene muscles; CCA, common carotid artery; JV, jugular vein.

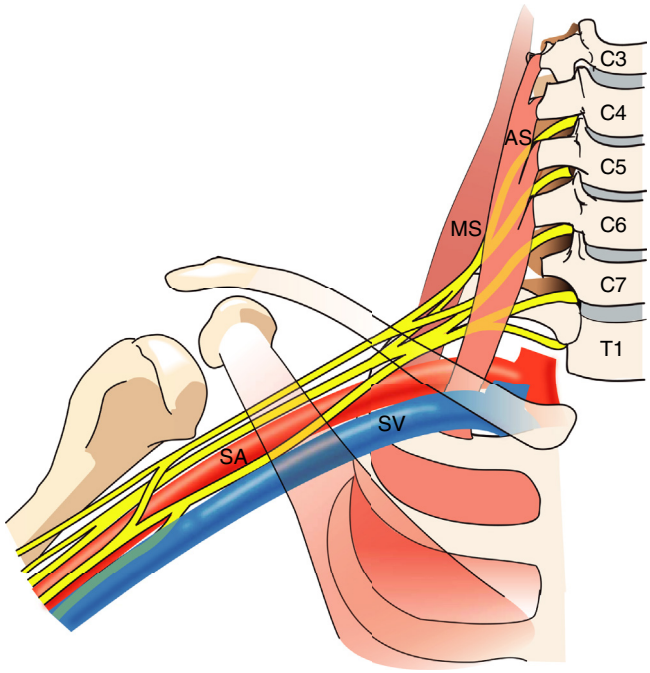


FIGURE 2 Brachial plexus proceeds laterally toward the axillary fossa through the scalene triangle (bordered by anterior and middle scalene muscles anteroposteriorly and first rib inferiorly), where it is located posterior to the subclavian artery. Subclavian vein travels anteriorly to the anterior scalene muscle. SA, subclavian artery; SV, subclavian vein.

artery anteriorly and the facet joint posteriorly, they soon create the first station of connections between anterior and middle scalene muscles: C5 and C6 nerves unite to form the superior trunk, C7 becomes the middle trunk, and C8 and T1 form the inferior trunk. The subclavian artery proceeds with the brachial plexus components within the triangle, anteriorly to the trunks, and the subclavian vein courses in front of the anterior scalene muscle. The trunks divide just lateral to the lateral margin of the scalene muscles into three anterior and three posterior divisions. Pectoralis major and serratus anterior muscles constitute anterior and posterior boundaries, respectively. Anterior divisions of the superior and middle trunks join to form the lateral cord; anterior division of the inferior trunk becomes the medial cord and posterior divisions of all three trunks unite to form the posterior cord. The medial cord, which receives fibers from the inferior C8–T1 trunk, gives off the ulnar nerve. The lateral cord, containing contributions from the superior and middle trunks (C5–C7), becomes the largest nerve of the upper extremity, the median nerve. The posterior cord contains fibers from all three trunks (C5–T1); its main pathway is the radial nerve. Other terminal branches include suprascapular, musculocutaneous, axillary, thoracodorsal, medial cutaneous, and long thoracic nerves (Figures 1–3).[8,9]

Lumbosacral Plexus

The lumbosacral plexus is formed by ventral rami of the lumbar and sacral nerves, T12 through S4. The lumbar part is formed by roots from T12 to L4 and the sacral component by L4–S4 roots. These divide into anterior and posterior divisions, which give rise to anterior and posterior branches, respectively. Anterior branches of the lumbar plexus include (in the craniocaudal direction) iliohypogastric, ilioinguinal, genitofemoral, and obturator nerves; the same of the sacral plexus are the tibial component of the sciatic nerve, posterior femoral cutaneous, and pudendal nerves. Posterior branches of the lumbar plexus include lateral femoral cutaneous and femoral nerves and those of the sacral plexus are the peroneal component of the sciatic nerve and the superior and inferior gluteal and piriformis nerves. The roots of the lumbar plexus lie on the ventral surface of the posterior abdominal wall, proceeding in diagonal fashion anterolaterally, between fibers of the psoas and iliacus muscles. The largest femoral nerve continues behind the inguinal ligament, supplying anterior and medial aspects of the thigh. The sacral plexus proceeds laterally along the posterior wall of the pelvis, where it lies between iliac vessels anterolaterally and piriform muscle posteromedially (Figure 4). Terminal branches innervate the pelvic organs, and the sciatic nerve, the largest nerve of the body, proceeds through the greater sciatic notch to supply regions of the posterior thigh and below the knee.[8]

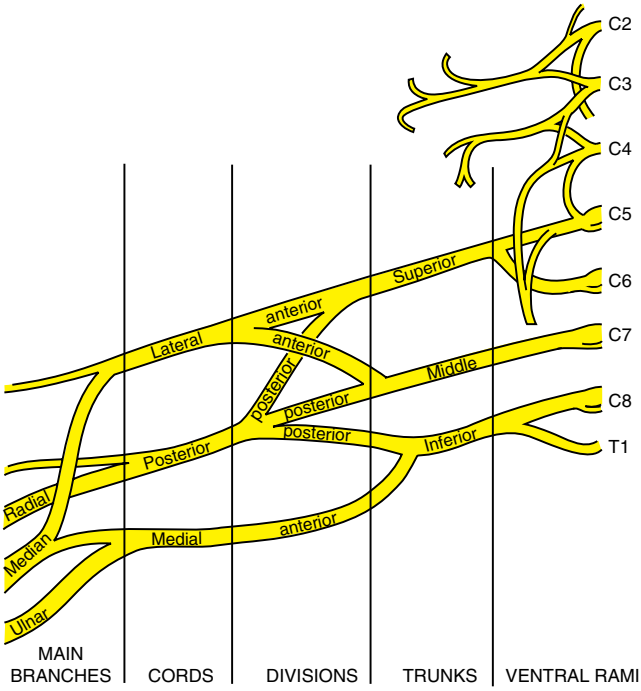


FIGURE 3 Schematic representation of the cervical and brachial plexus network. Cervical plexus (C1–C4): ventral rami C2, C3, and C4 divide, giving off a superior and inferior branch at each level. Superior branch of C2 and C1 ramus unite to form the ansa cervicalis. Adjacent inferior and superior branches of C2, C3, and C4 merge and give off lesser occipital, greater auricular, transverse cervical, supraclavicular, and phrenic nerves (unmarked). Brachial plexus (C5–T1): superior, middle, and inferior trunks are formed by ventral rami of C5/C6, C7, and C8/T1, respectively. Each trunk divides into anterior and posterior divisions. Anterior divisions of the superior and middle trunks form the lateral cord; anterior division of the inferior trunk becomes the medial cord and posterior divisions of all three trunks unite to form the posterior cord. Major nerves of the arm: median, ulnar, and radial receive contributions predominantly from lateral, medial, and posterior cords, respectively.

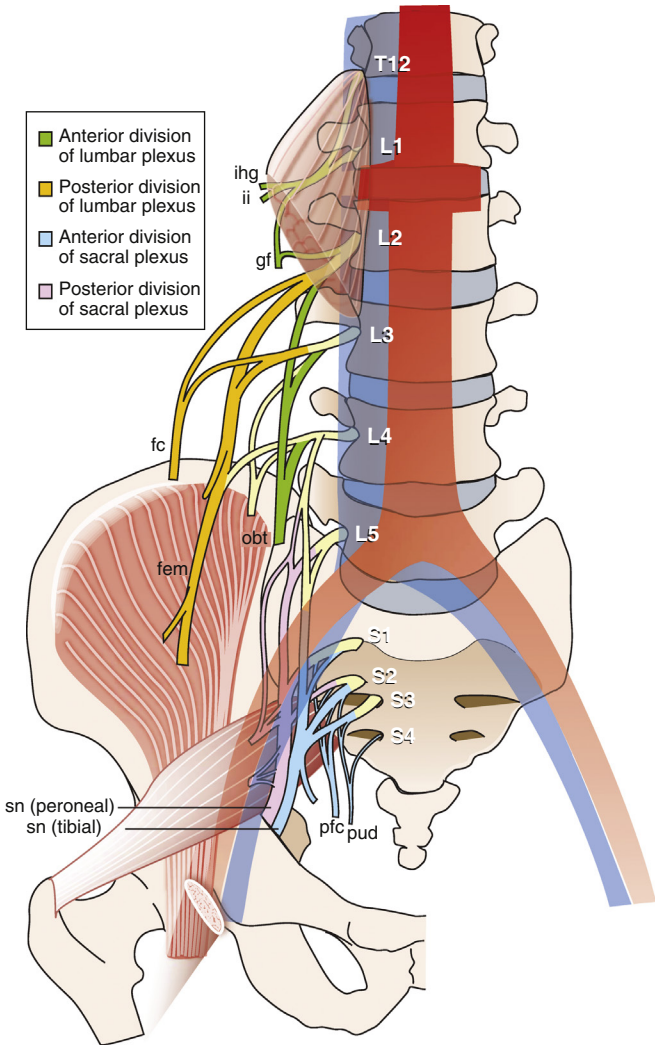


FIGURE 4 Simplified coronal diagram of the lumbosacral plexus, depicted on a background of psoas, iliacus, and piriformis muscles. Anatomy of the lumbosacral plexus is much less intricate and more variable than that of the brachial plexus. Anterior and posterior divisions unite and divide to form terminal branches (the trunks and cords are not distinguished). Anterior divisions of the lumbar plexus unite to form iliohypogastric (ihg), ilioinguinal (ii), genitofemoral (gf), and obturator (obt) branches, whereas posterior divisions give rise to femoral cutaneous (fc) and femoral (fem) nerves. Of the sacral plexus, anterior divisions divide to give rise to the tibial component of the sciatic nerve (sn), posterior femoral cutaneous (pfc), and pudendal nerves (pud), while posterior divisions give off the peroneal component of the sciatic nerve (sn), part of the femoral cutaneous, gluteal, and piriformis nerves.

RADIOGRAPHIC METHODS OF IMAGING

Evaluation of a plexus with conventional radiography is difficult and yields little information.[10] However, it may be used in preliminary evaluation of plexopathy, mainly to exclude a major abnormality, such as bone destruction, fracture, lung infiltration, or ligamentous calcifications. The development of CT heralded major progress in imaging and its utility in detection of plexus disease was realized by early investigators.[11–16] Further anatomical detail and tissue characteristics have been provided by MRI. Special sequences have been developed for selective imaging of nerve tissue (neurography). Sonography and positron emission tomography (PET) scanning also have been reported to provide valuable contributions.[17–19] Development of the picture archiving system has revolutionized the way studies are viewed and interpreted by radiologists. Perhaps the best example is the cine mode option, which creates a three-dimensional perception, allowing for better understanding of the extent and configuration of lesions and their relation to adjacent normal structures, particularly vessels. However, despite valuable contributions from the above imaging methods, the assessment of the plexus regions frequently presents a challenging problem for clinicians as well as radiologists.

Technique—Computed Tomography

Because of its small size, the cervical plexus is rarely evaluated radiographically as a separate entity. Rather, it is included as a part of the head, cervical spine, or neck examinations. The cervical plexus extends from C1 down to C4; thus scanning from the skull base down to C5, utilizing a small field of view (FOV) (25 cm), is sufficient. The anatomical brachial plexus extends approximately from C5 down to the T2 vertebral level. Adequate coverage of the plexus is provided by scanning the region from C4 to T3. We extend the lower range with a larger FOV down to T6, to include more peripheral components. Contiguous 4- to 5-mm spaced axial sections should be obtained. Coned-down views of the area in question may be added to the study. The elements of normal plexus are small and are depicted as nodular or linear areas of soft tissue density. They are difficult to identify and may not be outlined at all,[20] particularly on inferior quality examination. Contrast injection is recommended,[12] not only for identification of normal vascular structures and differentiation from lymph nodes, but also for more complete information on the enhancement pattern of the lesion. For this purpose, an intravenous injection in dynamic mode is preferred, using an initial bolus of 50 mL, followed by contiguous infusion at the rate of 1 mL/s to a total of 100 mL of nonionic contrast (Omnipaque 300 or equivalent). The infusion should be administered on the site opposite to the suspected pathology, since high concentrations of intravenous contrast may produce streaking artifacts, obscuring detail.[20]

Adequate coverage of the lumbosacral plexus includes axial sections from T12 down to the tip of the coccyx, to visualize the greater sciatic notches (GSN). Axial images with 4- to 5-mm slice thickness and FOV large enough to include both sacroiliac joints are usually sufficient. Oral contrast given 2 h in advance may be beneficial in assessment of lumbosacral plexus pathology, mainly to delineate the distal urinary tract and colon, respectively.

Technique—Magnetic Resonance

The main advantages of MRI over CT are the ability to perform multiplanar scanning without needing to change the patient's position and superior resolution and tissue characterization.[21–23] Adequate anatomical coverage of the plexus must be ensured. Thus, for the brachial plexus, axial sections from level C3 down to T6, coronal sections including both glenohumeral joints, and sagittal sections to cover both axillary fossas should be obtained. For the lumbosacral plexus, the coverage in the axial plane needs to extend from T12 to the coccyx. Sections of 5-mm thickness/0.25 gap are obtained in the axial, sagittal, and coronal planes. We prefer scanning in direct axial, sagittal, and coronal planes,[24] although oblique scanning planes have been advocated for the brachial[25] and sacral plexus,[26] to optimize visualization of plexus components and the sciatic nerve. High-resolution MRI is recommended in at least two orthogonal planes.[27] T1, fast spin-echo (FSE) T2, and short tau inversion recovery (STIR; which results in fat suppression) should be obtained. The use of phased-array coils is recommended for greater resolution of detail.[28,29] More recent MRI protocols have included a number of three-dimensional (3D) sequences as options for plexus characterization.[7,30–32] The advantage of 3D acquisition is that it can be reformatted into any plane, as required by the patient's anatomy or the presence of pathology. Another sequence applied to plexus imaging is diffusion-weighted imaging (DWI); benefits include suppression of most background tissues (i.e., fat, muscles, and vascular structures), while drawbacks include visualization of background tissues with high DWI signal (i.e., lymph nodes, bone marrow, and veins with slow flow).[31,33,34] Postcontrast T1-weighted images (with or without fat suppression) should be obtained after intravenous administration of a gadolinium-based contrast agent.

The feasibility of diffusion tensor MRI and fiber tractography of the sacral plexus has been demonstrated at 1.5 and 3 T[35–37] as a means to assess the architecture of neural fiber bundles, as well as microstructural properties such as fractional anisotropy.

According to American College of Radiology (ACR) appropriateness criteria, MRI without and with contrast has an appropriateness score of 8 (1 being least appropriate and 9 being most appropriate) for the evaluation of brachial, lumbar, or sacral plexopathy of sudden or chronic onset, that is post-traumatic, or that is related to neoplasm (before or after radiation therapy).[38]

Visualization of Normal Plexus Components on Computed Tomography and Magnetic Resonance

Conventional (noncontrast) CT offers rather poor definition of intraspinal anatomy. Nerve roots exiting through foramina are more consistently seen, particularly in lumbar spine and sacrum, because of larger size and more abundant epidural fat (Figure 5). They are depicted as punctate or linear structures of muscle density, contrasting against the adjacent darker fat within the foramen or vicinity (Figure 6). Trunks and cords of the brachial plexus are usually blended with muscle fibers and major vessels more distally. With abundant fat tissue, individual nerve components may be visible as discrete, linear areas of soft tissue density, proceeding posteriorly along the subclavian artery (Figure 7). Those of the lumbar plexus enter the paraspinal musculature (psoas) and are difficult to identify with certainty. Femoral and obturator nerves may be visible, contrasted against the intrapelvic/intra-abdominal fat. The largest

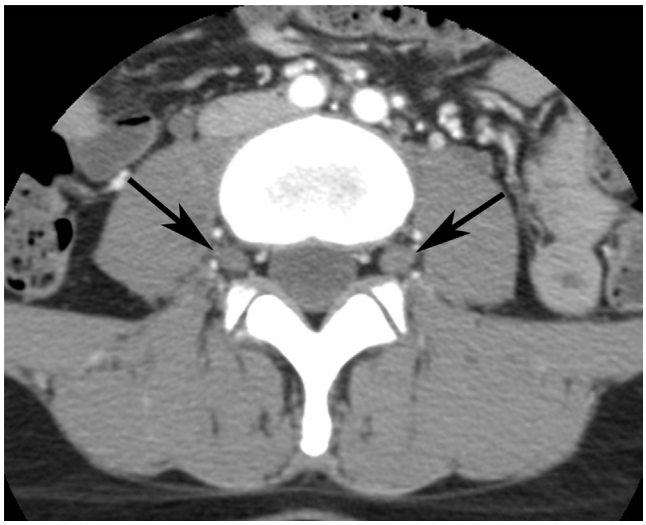


FIGURE 5 Axial CT section through the inferior plate of L3. Nerve roots are clearly seen bilaterally (arrows), contrasting against the low background density of fat tissue.



FIGURE 7 Axial CT image, depicting spatial arrangement of the neurovascular bundle (arrows from front): subclavian vein, artery, and fibers of brachial plexus.



FIGURE 6 Sagittal reconstruction a CT image through the plane of the foramina. Nerve root (arrow) surrounded by epidural fat. Note lytic bone lesion below, not compromising the lumen of the foramen.

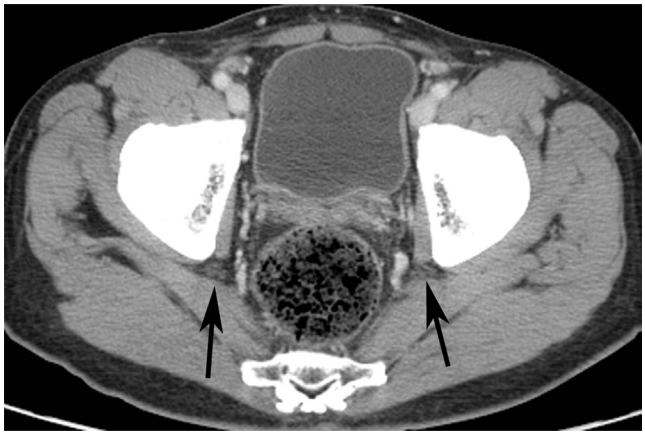


FIGURE 8 Axial CT section through the GSN. Sciatic nerves (arrows) are visualized in the lateral aspect of the GSN, posterior to the ischial spine.

sciatic nerve (Figure 8) is more consistently identified in the lateral aspect of GSN, posterior to the ischial spine.[12–15]

MR depicts the plexus components with much greater accuracy[21–47] and can be further improved when phased-array coils are used.[29,39] Conventional T1-weighted sequences are routinely utilized to assess nerve morphology. Fat-suppressed heavily T2-weighted sequences are used to evaluate nerve signal characteristics. Although individual nerves down to 2 mm in diameter can be seen,[29] much of the success depends upon relaxation properties of adjacent tissues. Thus, even a

smaller branch surrounded by fat or fluid (i.e., cerebrospinal fluid (CSF)) can be seen clearly, while a larger neural trunk encompassed by infiltrative process will blend with the abnormal tissue and may not be recognized at all. T2-weighted sequences (fast spin echo (FSE)) provide the best detail of normal nerve when a contrast interphase of fluid (CSF) or abnormal tissue (e.g., edema) is present. Thus, spinal nerves within the canal are demonstrated in good detail on T1 and T2 sequences, because they contrast against fat (epidural) and fluid (CSF), respectively.

Special sequences have been designed to create a "myelographic effect," termed "MR myelography," depicting the spinal cord and nerve roots within the thecal sac throughout the spine.[41] Fat-suppression sequences (STIR being most commonly used) nullify fat signals, thus rendering background fatty tissue darker and nerves more clearly visible.[42,43] The option can be applied to both T1- and T2-weighted sequences and is most valuable in conjunction with contrast enhancement.

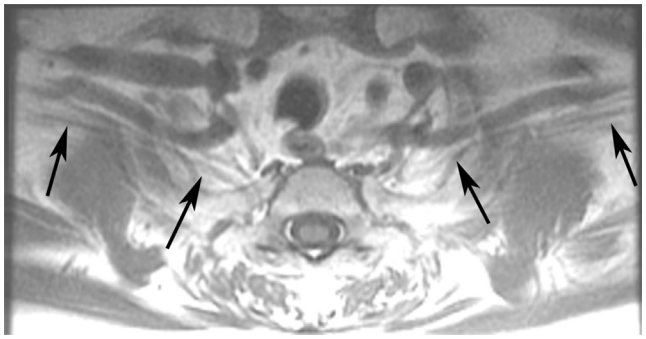


FIGURE 9 MRI of the brachial plexus. Long segments of plexus fibers (arrows) are demonstrated on an axial T1-weighted image. Subclavian arteries and veins are visualized anteriorly.

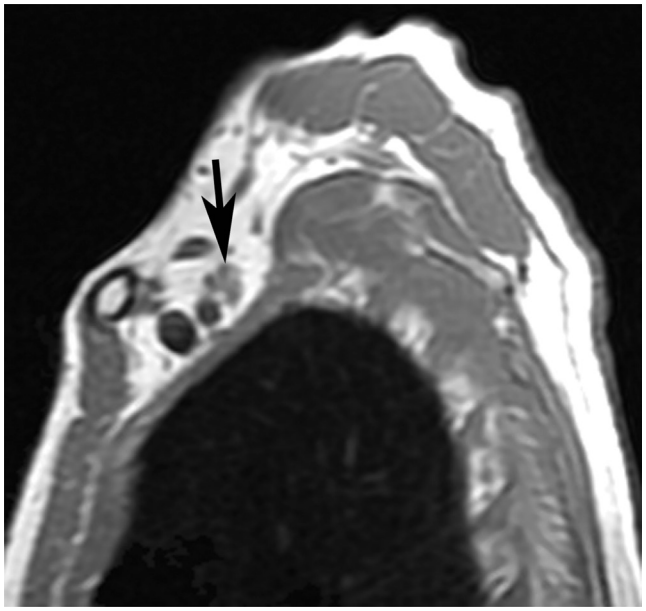


FIGURE 10 Sagittal T1-weighted image through the axillary fossa on the same patient as Figure 9 in Chapter 53. Brachial plexus components (arrow) depicted as nodular, somewhat irregular soft tissue densities, posterior to the artery and vein (rounded, lower intensity structures anteriorly).

The normal neural components of the plexus can be identified with variable success on a good-quality MR scan. Nerve roots within the foramina and immediate vicinity are routinely seen. As they descend with the muscle fibers, trunks and cords of the brachial plexus can be identified on axial images, proceeding between the anterior and the middle scalene group laterally, to exit through the scalene triangle. Extended segments of the plexus may be demonstrated on one well-placed axial and/or coronal T1-weighted anatomical image (Figure 9). Sagittal sections through and lateral to the scalene triangle outline the individual divisions as punctate areas of soft tissue intensity within the fatty background, with the subclavian artery and vein anteriorly (Figure 10). Similarly, the lumbar and sacral roots within the subarachnoid space and neural foramina are seen in great detail, while the interconnecting network within the psoas complex is more difficult to identify. On axial sections, the femoral nerve may be visualized as a single trunk proceeding anterolaterally along the ventral aspect of the posterior abdominal wall. The greater sciatic nerve within the notch is more consistently seen, either as a single, oval-shaped structure or as a cluster of several smaller individual nerves (Figure 11).[7,22,23]

Abnormal Nerve

When involved by a disease, nerve tissue may exhibit swelling, focal or diffuse infiltration, edema, cyst formation, or necrosis. In the early stage, when there is no enlargement of peripheral nerve(s), these changes may not be appreciated on imaging modalities but become more apparent as the process progresses. On CT, abnormal nerve or plexus may appear locally or diffusely enlarged or become indistinguishable from adjacent structures because of infiltrative process or fibrosis. In the brachial plexus, this may be manifested as general thickening of the neurovascular bundle (Figure 12). Greater tissue discrimination allows MR to assess the character and extent of disease more precisely. T1-weighted images may show segmental or diffuse enlargement, and increased T2 intensity may be seen within the nerve in the case of involvement by infiltrative process or edema. The extent of the abnormal T2 signal may be demonstrated to better advantage on STIR sequences (Figure 13). Contiguity (or disruption) of the nerve, increased diameter, change of course or contour (compression), altered intrinsic intensity or enhancement within an involved or a compressed segment of the nerve may be observed. Neurography, utilizing a combination of T1, T2, and STIR sequences, and phased-array surface coils depict these findings

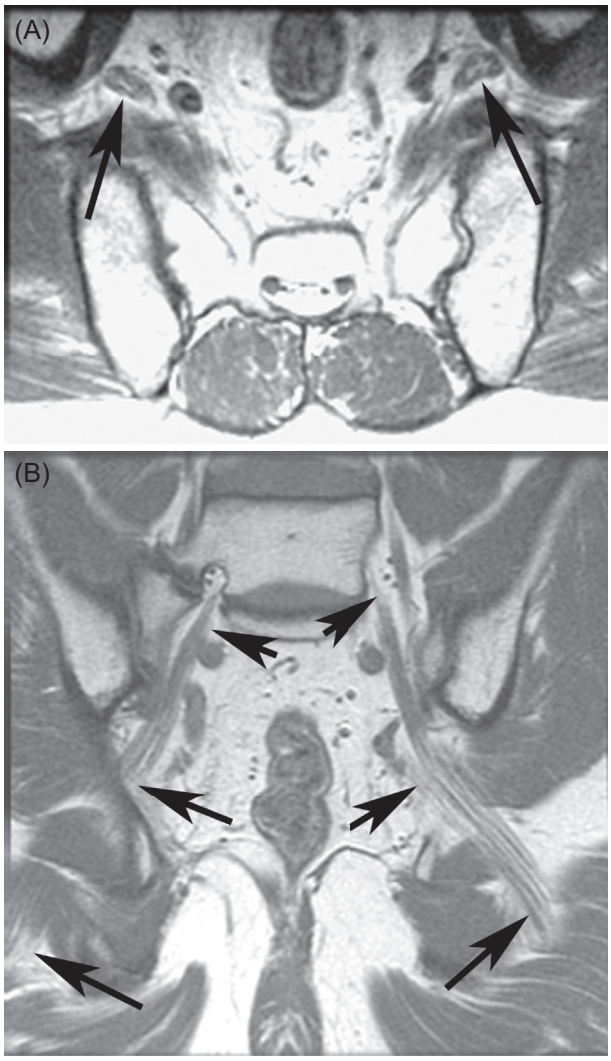


FIGURE 11 Sciatic nerves (arrows) depicted on axial (A) and coronal (B) T1-weighted MR images through the pelvic region, as a conglomerate of individual fibers.

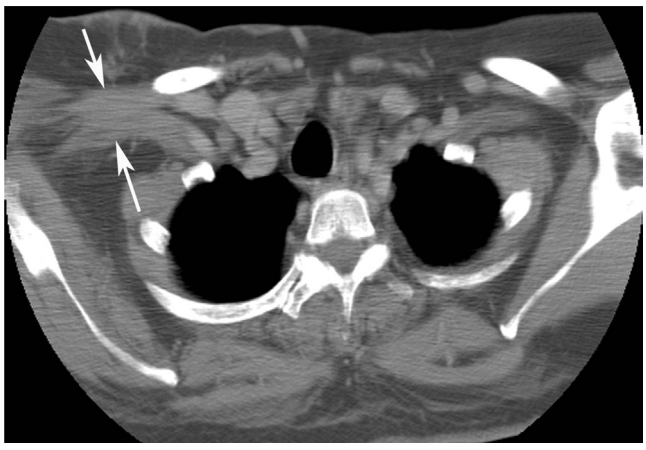


FIGURE 12 Recurrent breast cancer. Axial CT image demonstrates general thickening of the neurovascular bundle (arrows).

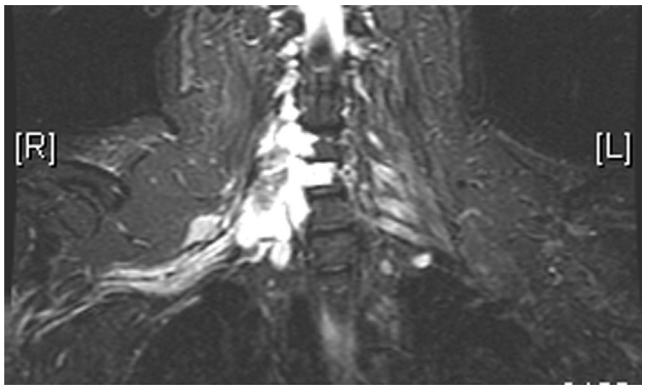


FIGURE 13 Coronal STIR MR noncontrast sequence enhances visualization of the tumor tissue (bright areas on the right side).

with greater accuracy.[5,44–46] In a study of 15 patients with neuropathic leg pain and negative conventional MR conducted by Moore et al., it proved definitely superior, revealing casual abnormality accounting for clinical findings in all cases.[47]

An interesting phenomenon of increased T2 intensity within normal nerves, mimicking abnormal tissue, was initially reported by Chappell et al.[48] They observed signal hyperintensity within the peripheral nerve as the orientation of the longitudinal axis of the nerve approached 55° to the main magnetic field Bo. As the brachial plexus is usually scanned close to this "magic angle," T2 hyperintensity within the nerve or plexus should thus be interpreted with caution, to avoid a false-positive reading. Administration of contrast is essential in the proper evaluation of the extent of disease. Generally, enhancement of an intraspinal or peripheral nerve after administration of a conventional dose of gadolinium-based contrast is considered pathological.

As fractional anisotropy is lost in nerve injury and regained in nerve repair, diffusion tensor MRI and fiber tractography have the potential to assess nerve injury and regeneration.[37]

Imaging Method of Choice

As radiographs yield very limited information on plexus involvement, early reports praised the ability of CT to demonstrate anatomical detail of normal and diseased plexus.[13,14] As early as 1988, Benzel et al. considered CT a method of choice in the evaluation of location and extent of nerve sheath tumors of sciatic nerve and sacral plexus, important in determination of the resectability of these lesions.[11] Hirakata et al. found CT to be helpful in the assessment of patients with Pancoast tumors.[16] They reported obliteration of the fat plane between scalene muscles on CT to be an indication of brachial plexus involvement. The addition of sagittal, coronal, and oblique reformatted images improved visualization

of the brachial plexus and helped to diagnose tumor recurrence.[49] Soon after the introduction of MR and as early as 1987, Castagno and Shuman anticipated that the new modality may have substantial clinical utility in evaluating patients with suspected brachial plexus tumor.[50] The advantages of MR over CT in the assessment of plexus were reported in comparative studies by several investigators.[51–53] In the evaluation of 64 patients with brachial plexopathy of diverse cause by Bilbey et al., the sensitivity of MR was 63%, specificity 100%, and accuracy 77%.[54] In a subgroup of patients with trauma and neoplasm these were even higher (81%, 100%, and 88%, respectively). Better anatomical definition provided by MR was considered to improve patient care in the study by Collins et al.[55] More recently, in the study of patients with plexopathy following the treatment of breast cancer, Qayyum et al. reported high reliability of MR, with specificity of 95%, positive predictive value of 96%, and negative predictive value of 95%.[56] MR without and with contrast enhancement is also the method of choice in evaluating a patient with plexopathy at our institution.

PRIMARY PLEXUS NEOPLASMS

Primary tumors of peripheral nerve (plexus) are rare, constituting approximately 1% of all cancers. According to the World Health Organization classification proposed in 2000, four groups are distinguished:

1. schwannomas,
2. neurofibromas,
3. perineuriomas,
4. malignant peripheral nerve sheath tumors (MPNSTs).

Neurofibromas and schwannomas are most prevalent. On MR, these tumors usually present as well-defined, rounded or oval masses, oriented along the longitudinal axis of the nerve (Figure 14). Larger size or plexiform appearance favors neurofibroma, particularly in patients with neurofibromatosis (Figure 15). Both are iso- or slightly hyperintense on T1- and hyperintense on T2-weighted sequences, showing homogeneous or inhomogeneous enhancement. Marked T2 hyperintensity may be seen in some patients.[57–61] Capsule can be identified in approximately 70% of schwannomas and 30% of neurofibromas.[58] A "target sign" consisting of a central low-intensity area within the lesion on T2-weighted sequence was found to be much more frequent in neurofibromas.[62,63] On CT, low density (in reference to the muscle) was a common feature of plexus tumors and contrast enhancement varied from moderate to marked, as reported by Vestraete.[64] Perineuriomas, rare benign tumors of the peripheral nerve sheath perineurium, can be intra- or extraneural in location and typically present as a painless, slowly progressive mononeuropathy. Local recurrence of a perineurioma after resection is very rare, even when there are positive margins.[65] MPNSTs are rare, arising either as a spontaneous mutation or within preexisting neurofibroma, usually as a transformation to spindle-cell sarcoma.[66] It may be difficult to distinguish these tumors from their benign counterparts. Larger size, internal heterogeneity, poor definition of the peripheral border, invasion of fat planes, and adjacent edema favor the malignant variant.[67–70] Extremely rarely other malignancies can arise from the nerve proper.[71] There are no pathognomonic radiographic features that could be totally attributed to a particular group; thus thorough knowledge of clinical information, such as age, gender, duration of symptoms, history of von Recklinghausen disease, etc., is very helpful while interpreting the imaging studies.

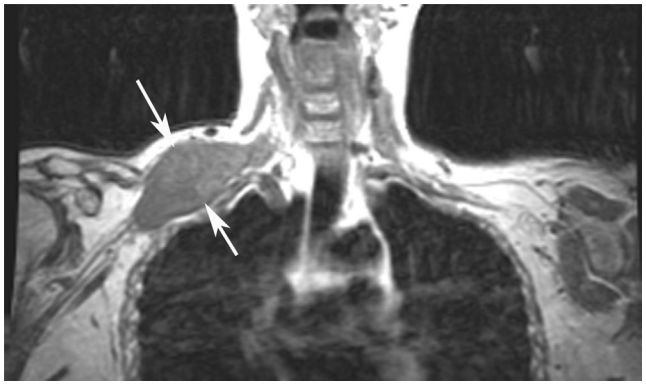


FIGURE 14 Brachial plexus schwannoma, depicted on coronal T1-weighted MR image. Fusiform mass is oriented along the longitudinal axis of the plexus.



FIGURE 15 Patient with neurofibroma. Large mass is demonstrated in axillary fossa (T). There is also marked thickening of all components of the plexus bilaterally (arrows).

EXTRINSIC PLEXUS TUMORS

Plexus may be compressed or infiltrated by an extrinsic neoplasm arising from adjacent structures, with breast, neck, lung, and lymph node malignancies being the most common offenders for brachial region and pelvic tumors for lumbosacral plexus (Figures 16 and 17). Clinically, pain is a prominent feature of residual or recurrent tumor.[1] Although the local extent of the lesion may be depicted adequately by CT, infiltration of the plexus is difficult to diagnose, except for advanced disease with gross infiltration of the plexus region (Figure 18). In a study of 14 patients with Pancoast tumor, obliteration of the fat planes between the scalene muscles on CT was found to be suggestive of plexus involvement.[16] The potential of MR in evaluation of the extent of thoracic malignancies and brachial plexus involvement was realized as early as 1989.[72] In the study of chest wall tumors by Fortier, MR clearly delineated the margins and revealed evidence of muscle, vascular, or bone invasion.[73] T1 and T2 signal characteristics were nonspecific (apart from lipomas), not allowing for confident distinction of benign from malignant process. Qayyum et al. considered MR to be a reliable and accurate tool in the evaluation of brachial plexopathy due to tumor, reporting sensitivity and positive predictive value of 96% and specificity and negative predictive value of 95%.[56] Tagliafico et al. reported overall diagnostic accuracy of 93.3% for MR in the diagnosis of mass lesion.[74] Currently, MR without and with contrast remains a method of choice for the assessment of local tumor extent and plexus involvement. PET scanning is considered useful in the evaluation of patients with plexopathy, mainly by excluding recurrent tumor, especially when the primary tumor is known to be fluorodeoxyglucose avid.[18,19,75]



FIGURE 16 MPNST, coronal T1-weighted MR image (the same patient as in Figure 13 in Chapter 53). The tumor (arrows) is poorly defined and infiltrates adjacent cervical vertebrae.



FIGURE 17 Axial CT section through the thoracic inlet of a patient with lymphoma. Neurovascular elements (arrows) are buried in massive lymphadenopathy.

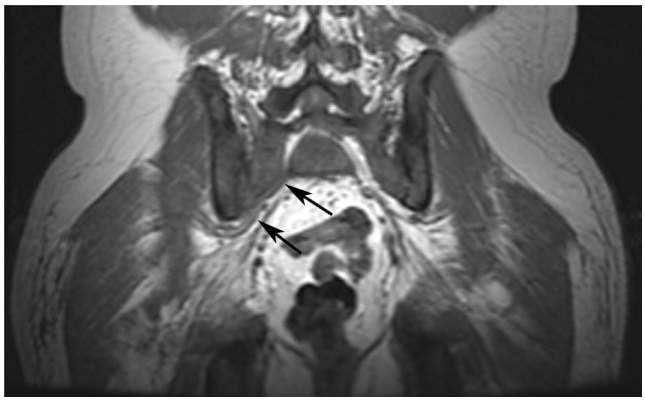


FIGURE 18 Coronal T1 MR image through the pelvis of a patient with extensive bone metastases from prostate cancer and right hip and extremity pain. The fat plane separating nerve fibers of the plexus from abnormal bone is obliterated on the right, compared to the left (arrows).

RADIATION INJURY

Plexopathy is a recognized complication of radiation therapy, occurring most commonly in the brachial plexus[1] following regional treatment of breast, lung, or neck cancer. The clinical presentation of radiation-induced fibrosis (RIF) is that of a protracted course with low-grade pain often coexisting with cutaneous radiation changes, as opposed to recurrent tumor, which progresses more rapidly, with pain being a dominant symptom. In the brachial plexus, RIF is more common than tumor to result in upper trunk involvement owing to its longer course through the radiation field and less tissue shielding it from radiation.[76] Three forms are recognized: acute ischemic, transient, and delayed (radiation fibrosis), the third being most common.[77–79] RIF occurs

usually within the first few years after completion of treatment, although latent periods as long as 22 years have been reported.[80,81] It is dose-dependent and more likely to occur above 6000 cGy and with larger fraction sizes. Younger patients and those receiving cytotoxic therapy are more vulnerable.[1,82] Changes are confined to the radiation port with a clearly demarcated margin from nonirradiated tissue. The main role of imaging is to distinguish this chronic iatrogenic process from a recurrent tumor, which generally carries an unfavorable prognosis. CT may demonstrate poor definition of neurovascular bundle and increased density of regional fat, without recognizable soft tissue mass,[83] and MR may reveal thickening and indistinct outline of plexus components, again without identifiable focal mass (Figures 19 and 20). There is no uniform agreement



FIGURE 19 Coronal CT reconstruction image of a patient with extensive infiltration of neurovascular structures and scalene muscle complex due to metastatic cholangiocarcinoma. Note normal neurovascular bundle on the right side (arrows).

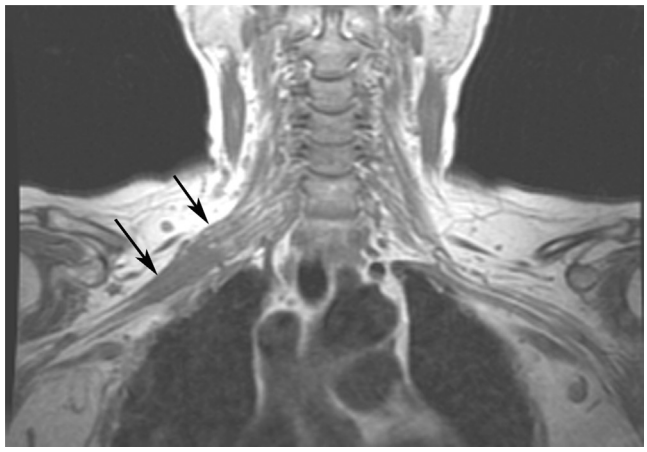


FIGURE 20 Patient with breast cancer and suspected postradiation right brachial plexopathy. MR reveals matting and thickening of the right neurovascular bundle (arrows) without recognizable soft tissue mass, consistent with clinical diagnosis of RIF.

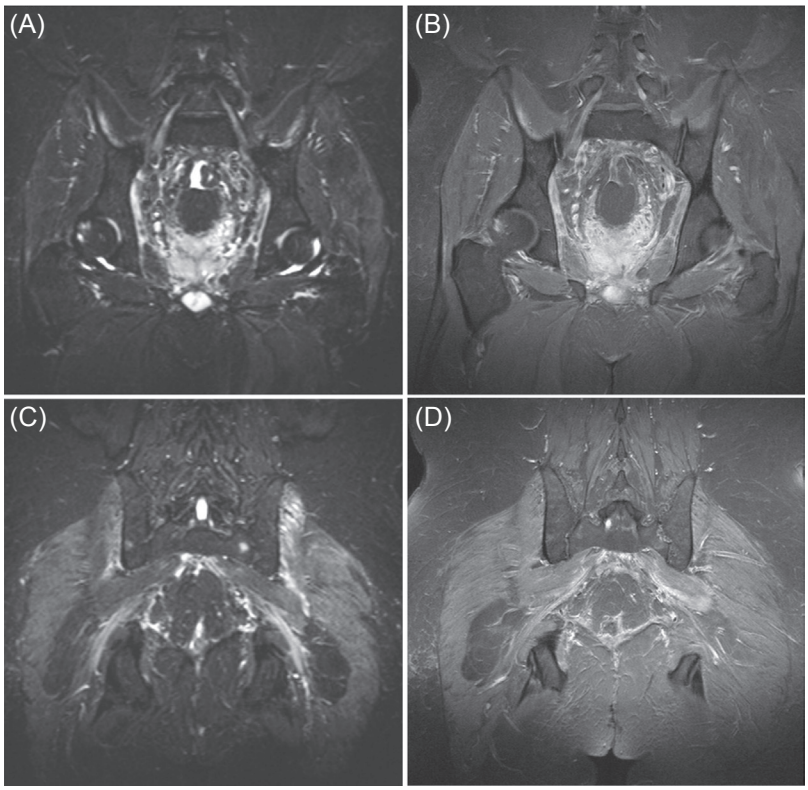


FIGURE 21 Bilateral lumbosacral radiation plexopathy in a 52-year-old man with rectal cancer status post-radiation therapy and bilateral leg pain. Coronal fat-suppressed T2 (A and C) and fat-suppressed postcontrast T1 (B and D) images of the lumbosacral plexus show T2 hyperintensity and enhancement of the bilateral L5 nerve roots (A and B) and sciatic nerves (C and D) without associated mass, consistent with radiation plexopathy. *Images courtesy of J. Levi Chazen, MD, Weill Cornell Medical Center, New York-Presbyterian Hospital, New York, NY.*

as to signal intensity patterns and contrast enhancement of RIF. While some investigators reported low intensity of both T1- and T2-weighted sequences,[84] others described variable signal changes.[85–87] Parascalene and interscalene T2 hyperintensity was reported by Bowen et al.[88] and the degree of T2 hyperintensity was found to correspond with severity of fibrosis by Hoeller et al.[87] Positive contrast enhancement was reported by most investigators, even in very delayed cases.[85] Figure 21 shows acute bilateral lumbosacral radiation plexopathy. The main utility of MRI in distinguishing between recurrent tumor and radiation injury may not be to definitively confirm the presence of radiation injury, but the ability to exclude tumor recurrence with high certainty given its high negative predictive value (over 90%).[56,74,87] To minimize the risk of radiation injury to the brachial plexus during intensity-modulated radiotherapy (e.g., for head and neck cancer), CT has shown utility in contouring the brachial plexus prior to irradiation.[89]

SUMMARY

Clinical assessment of plexus involvement by primary neoplasm, metastases, or conditions related to treatment is limited, and imaging studies (CT, MR) are routinely requested to characterize further the nature and extent of the process. With its many advantages over CT, MRI, with and without contrast, is considered the imaging modality of choice in evaluation of plexus disease at the time of writing. Utilizing high-resolution devices, we are now able to visualize individual nerves (MR neurography). In cases in which there is clinical uncertainty between recurrent tumor and radiation injury, MR has been shown to have a high negative predictive value in excluding tumor recurrence. While higher field strength (3 T) MR may offer superior resolution and improved options for functional imaging, magnetic field inhomogeneity and artifacts related to susceptibility are amplified. As for the "state of the art" approach at present, it includes thorough clinical examination, followed by high-resolution phase-array MR, with and without contrast. Dynamic CT should be reserved for patients unable to have MR and instances in which additional information on bone detail or vascular anatomy is also needed. PET scanning plays a role complementary to MR in the assessment of neoplastic involvement.

References

1. Kori SH, et al. Brachial plexus lesions in patients with cancer: 100 cases. *Neurology*. 1981;31(1):45–50.
2. Aguilera Navarro JM, et al. Neoplastic lumbosacral plexopathy and 'hot foot'. *Neurologia*. 1993;8(8):271–273.
3. Jaeckle KA. Neurological manifestations of neoplastic and radiation-induced plexopathies. *Semin Neurol*. 2004;24(4):385–393.
4. Filler AG, et al. Magnetic resonance neurography. *Lancet*. 1993; 341(8846):659–661.
5. Filler AG, et al. Application of magnetic resonance neurography in the evaluation of patients with peripheral nerve pathology. *J Neurosurg*. 1996;85(2):299–309.
6. Aagaard BD, et al. MR neurography. MR imaging of peripheral nerves. *Magn Reson Imaging Clin N Am*. 1998;6(1):179–194.
7. Freund W, et al. MR neurography with multiplanar reconstruction of 3D MRI datasets: an anatomical study and clinical applications. *Neuroradiology*. 2007;49:335–341.
8. Clemente DC. The peripheral nervous system. In: *Gray's Anatomy*. 30th American ed. Philadelphia: Lea & Febiger; 1985:1149–1282.
9. Castillo M. Imaging the anatomy of the brachial plexus: review and self-assessment module. *Am J Roentgenol*. 2005;185(6 suppl): S196–S204.
10. Posniak HV, et al. MR imaging of the brachial plexus. *Am J Roentgenol*. 1993;161(2):373–379.
11. Benzel EC, et al. Nerve sheath tumors of the sciatic nerve and sacral plexus. *J Surg Oncol*. 1988;39(1):8–16.
12. Cooke J, et al. The anatomy and pathology of the brachial plexus as demonstrated by computed tomography. *Clin Radiol*. 1988;39(6):595–601.
13. Dietemann JL, et al. Anatomy and computed tomography of the normal lumbosacral plexus. *Neuroradiology*. 1987;29(1):58–68.
14. Gebarski KS, et al. The lumbosacral plexus: anatomic-radiologic-pathologic correlation using CT. *Radiographics*. 1986;6(3):401–425.
15. Gebarski KS, et al. Brachial plexus: anatomic, radiologic, and pathologic correlation using computed tomography. *J Comput Assist Tomogr*. 1982;6(6):1058–1063.
16. Hirakata K, et al. Computed tomography of Pancoast tumor. *Rinsho Hoshasen*. 1989;34(1):79–84.
17. Graif M, et al. Sonographic evaluation of brachial plexus pathology. *Eur Radiol*. 2004;14(2):193–200.
18. Hathaway PB, et al. Value of combined FDG PET and MR imaging in the evaluation of suspected recurrent local-regional breast cancer: preliminary experience. *Radiology*. 1999;210(3):807–814.
19. Ahmad A, et al. Use of positron emission tomography in evaluation of brachial plexopathy in breast cancer patients. *Br J Cancer*. 1999;79(3–4):478–482.
20. Krol G, Strong E. Computed tomography of head and neck malignancies. *Clin Plast Surg*. 1986;13(3):475–491.
21. Carriero A, et al. Magnetic resonance imaging of the brachial plexus. *Anat Radiol Med (Torino)*. 1991;81(1–2):73–77.
22. Gierada DS, Erickson SJ. MR imaging of the sacral plexus: abnormal findings. *Am J Roentgenol*. 1993;160(5):1067–1071.
23. Gierada DS, et al. MR imaging of the sacral plexus: normal findings. *Am J Roentgenol*. 1993;160(5):1059–1065.
24. Blake LC, et al. Sacral plexus: optimal imaging planes for MR assessment. *Radiology*. 1996;199(3):767–772.
25. Panasci DJ, et al. Advanced imaging techniques of the brachial plexus. *Hand Clin*. 1995;11(4):545–553.
26. Almanza MY, et al. Dual oblique MR method for imaging the sciatic nerve. *J Comput Assist Tomogr*. 1999;23(1):138–140.
27. Stoll G, et al. Magnetic resonance imaging of the peripheral nervous system. *J Neurol*. 2009;256(7):1043–1051.
28. Kichari JR, et al. MR imaging of the brachial plexus: current imaging sequences, normal findings, and findings in a spectrum of focal lesions with MR-pathologic correlation. *Curr Probl Diagn Radiol*. 2003;32(2):88–101.
29. Maravilla KR, Bowen BC. Imaging of the peripheral nervous system: evaluation of peripheral neuropathy and plexopathy. *Am J Neuroradiol*. 1998;19(6):1011–1023.
30. Viallon M, et al. High-resolution and functional magnetic resonance imaging of the brachial plexus using an isotropic 3D T2 STIR (Short Term Inversion Recovery) SPACE sequence and diffusion tensor imaging. *Eur Radiol*. 2008;18(5):1018–1023.

31. Mallouhi A, et al. 3 T MR tomography of the brachial plexus: structural and microstructural evaluation. *Eur J Radiol*. 2012;81(9): 2231–2245.
32. Tagliafico A, et al. Brachial plexus assessment with three-dimensional isotropic resolution fast spin echo MRI: comparison with conventional MRI at 3.0 T. *Br J Radiol*. 2012;85(1014):e110–e116.
33. Takahara T, et al. Subtraction of unidirectionally encoded images for suppression of heavily isotropic objects (SUSHI) for selective visualization of peripheral nerves. *Neuroradiology*. 2011;53(2): 109–116.
34. Tanaka H, et al. Secondary neurolymphomatosis detected by whole-body diffusion-weighted magnetic resonance imaging: a case report. *J Clin Exp Hematop*. 2013;53(3):221–226.
35. Vargas MI, et al. Diffusion tensor imaging (DTI) and tractography of the brachial plexus: feasibility and initial experience in neoplastic conditions. *Neuroradiology*. 2010;52(3):237–245.
36. Tagliafico A, et al. Brachial plexus MR imaging: accuracy and reproducibility of DTI-derived measurements and fibre tractography at 3.0-T. *Eur Radiol*. 2011;21(8):1764–1771.
37. Van der Jagt PKN, et al. Architectural configuration and microstructural properties of the sacral plexus: a diffusion tensor MRI and fiber tractography study. *Neuroimage*. 2012;62(3):1792–1799.
38. Bowen BC, Seidenwurm DJ for the Expert Panel on Neurologic imaging. Plexopathy. *AJNR Am J Neuroradiol*. 2008;29(2):400–402.
39. Blair DN, et al. Normal brachial plexus: MR imaging. *Radiology*. 1987;165(3):763–767.
40. Bowen BC, et al. The brachial plexus: normal anatomy, pathology, and MR imaging. *Neuroimaging Clin N Am*. 2004;14(1):59–85. vii–viii.
41. Gasparotti R, et al. Three-dimensional MR myelography of traumatic injuries of the brachial plexus. *Am J Neuroradiol*. 1997;18(9):1733–1742.
42. Tien RD, et al. Improved detection and delineation of head and neck lesions with fat suppression spin-echo MR imaging. *Am J Neuroradiol*. 1991;12(1):19–24.
43. Howe FA, et al. Magnetic resonance neurography. *Magn Reson Med*. 1992;28(2):328–338.
44. Dailey AT, et al. Magnetic resonance neurography for cervical radiculopathy: a preliminary report. *Neurosurgery*. 1996;38(3):488–492. discussion 492.
45. Erdem CZ, et al. High resolution MR neurography in patients with cervical radiculopathy. *Tani Girisim Radyol*. 2004;10(1):14–19.
46. Lewis AM, et al. Magnetic resonance neurography in extraspinal sciatica. *Arch Neurol*. 2006;63(10):1469–1472.
47. Moore KR, et al. The value of MR neurography for evaluating extraspinal neuropathic leg pain: a pictorial essay. *Am J Neuroradiol*. 2001;22(4):786–794.
48. Chappell KE, et al. Magic angle effects in MR neurography. *Am J Neuroradiol*. 2004;25(3):431–440.
49. Fishman EK, et al. Multiplanar CT evaluation of brachial plexopathy in breast cancer. *J Comput Assist Tomogr*. 1991;15(5):790–795.
50. Castagno AA, Shuman WP. MR imaging in clinically suspected brachial plexus tumor. *Am J Roentgenol*. 1987;149(6):1219–1222.
51. Rapoport S, et al. Brachial plexus: correlation of MR imaging with CT and pathologic findings. *Radiology*. 1988;167(1):161–165.
52. Thyagarajan D, et al. Magnetic resonance imaging in brachial plexopathy of cancer. *Neurology*. 1995;45(3 Pt 1):421–427.
53. Taylor BV, et al. Magnetic resonance imaging in cancer-related lumbosacral plexopathy. *Mayo Clin Proc*. 1997;72(9):823–829.
54. Bilbey JH, et al. MR imaging of disorders of the brachial plexus. *J Magn Reson Imaging*. 1994;4(1):13–18.
55. Collins JD, et al. Compromising abnormalities of the brachial plexus as displayed by magnetic resonance imaging. *Clin Anat*. 1995;8(1):1–16.
56. Qayyum A, et al. Symptomatic brachial plexopathy following treatment for breast cancer: utility of MR imaging with surface-coil techniques. *Radiology*. 2000;214(3):837–842.
57. Baba Y, et al. MR imaging appearances of schwannoma: correlation with pathological findings. *Nippon Igaku Hoshasen Gakkai Zasshi*. 1997;57(8):499–504.
58. Cerofolini E, et al. MR of benign peripheral nerve sheath tumors. *J Comput Assist Tomogr*. 1991;15(4):593–597.
59. Soderlund V, et al. MR imaging of benign peripheral nerve sheath tumors. *Acta Radiol*. 1994;35(3):282–286.
60. Saifuddin A. Imaging tumours of the brachial plexus. *Skelet Radiol*. 2003;32(7):375–387.
61. Hayasaka K, et al. MR findings in primary retroperitoneal schwannoma. *Acta Radiol*. 1999;40(1):78–82.
62. Bhargava R, et al. MR imaging differentiation of benign and malignant peripheral nerve sheath tumors: use of the target sign. *Pediatr Radiol*. 1997;27(2):124–129.
63. Burk Jr DL, et al. Spinal and paraspinal neurofibromatosis: surface coil MR imaging at 1.5 T1. *Radiology*. 1987;162(3):797–801.
64. Verstraete KL, et al. Nerve sheath tumors: evaluation with CT and MR imaging. *J Belge Radiol*. 1992;75(4):311–320.
65. Hornick JL, Fletcher CD. Soft tissue perineurioma: clinicopathologic analysis of 81 cases including those with atypical histologic features. *Am J Surg Pathol*. 2005;29(7):845–858.
66. Antonescu C, Woodruff J. Primary tumors of cranial, spinal and peripheral nerves. In: McLendon RE, Rosenblum KM, Bigner DD, eds. *Russell and Rubinstein's Pathology of Tumors of the Nervous System*. 7th ed. London: Hodder Arnold; 2006:787–835.
67. Levine E, et al. Malignant nerve-sheath neoplasms in neurofibromatosis: distinction from benign tumors by using imaging techniques. *Am J Roentgenol*. 1987;149(5):1059–1064.
68. Fuchs B, et al. Malignant peripheral nerve sheath tumors: an update. *J Surg Orthop Adv*. 2005;14(4):168–174.
69. Geniets C, et al. Imaging features of peripheral neurogenic tumors. *JBR-BTR*. 2006;89(4):216–219.
70. Amoretti N, et al. Peripheral neurogenic tumors: is the use of different types of imaging diagnostically useful? *Clin Imaging*. 2006;30(3):201–205.
71. Descamps MJ, et al. Primary sciatic nerve lymphoma: a case report and review of the literature. *J Neurol Neurosurg Psychiatr*. 2006;77(9): 1087–1089.
72. Templeton PA, Zerhouni EA. MR imaging in the management of thoracic malignancies. *Radiol Clin North Am*. 1989;27(6):1099–1111.
73. Fortier M, Mayo JR, Swensen SJ, Munk PL, Vellet DA, Muller NL. MR imaging of chest wall lesions. *Radiographics*. 1994;14(3):597–606.
74. Tagliafico, et al. Diagnostic accuracy of MRI in adults with suspect brachial plexus lesions: a multicentre retrospective study with surgical findings and clinical follow-up as reference standard. *Eur J Radiol*. 2013;81(10):2666–2672.
75. Rosen, et al. FDG PET, PET/CT, and breast cancer imaging. *Radiographics*. 2007;27(suppl 1):S215–S229.
76. Gosk, et al. Radiation-induced brachial plexus neuropathy – aetiopathogenesis, risk factors, differential diagnosis, symptoms and treatment. *Folia Neuropathol*. 2007;45(1):26–30.
77. Gerard JM, Franck N, Moussa Z, Hildebrand J. Acute ischemic brachial plexus neuropathy following radiation therapy. *Neurology*. 1989;39(3):450–451.
78. Salner AL, et al. Reversible brachial plexopathy following primary radiation therapy for breast cancer. *Cancer Treat Rep*. 1981;65(9–10): 797–802.
79. Maruyama Y, Mylrea MM, Logothetis J. Neuropathy following irradiation. An unusual late complication of radiotherapy. *Am J Roentgenol Ther Nucl Med*. 1967;101(1):216–219.
80. Fathers E, et al. Radiation-induced brachial plexopathy in women treated for carcinoma of the breast. *Clin Rehabil*. 2002;16(2):160–165.
81. Nich C, et al. An uncommon form of delayed radio-induced brachial plexopathy. *Chir Main*. 2005;24(1):48–51.
82. Olsen NK, Pfeiffer P, Johannsen L, Schroder H, Rose C. Radiation induced brachial plexopathy: neurological follow-up in 161 recurrence free breast cancer patients. *Int J Radiat Biol Phys*. 1993;26(1):43–49.

83. Cascino TL, et al. CT of the brachial plexus in patients with cancer. *Neurology*. 1983;33(12):1553–1557.
84. Wittenberg KH, Adkins MC. MR imaging of nontraumatic brachial plexopathies: frequency and spectrum of findings. *Radiographics*. 2000;20(4):1023–1032.
85. Wouter van Es H, et al. Radiation-induced brachial plexopathy: MR imaging. *Skelet Radiol*. 1997;26(5):284–288.
86. Dao TH, et al. Tumor recurrence versus fibrosis in the irradiated breast: differentiation with dynamic gadolinium-enhanced MR imaging. *Radiology*. 1993;187(3):751–755.
87. Hoeller U, et al. Radiation-induced plexopathy and fibrosis. Is magnetic resonance imaging the adequate diagnostic tool? *Strahlenther Onkol*. 2004;180(10):650–654.
88. Bowen BC, et al. Radiation-induced brachial plexopathy: MR and clinical findings. *Am J Neuroradiol*. 1996;17(10):1932–1936.
89. Hall, et al. Development and validation of a standardized method for contouring the brachial plexus: preliminary dosimetric analysis among patients treated with IMRT for head-and-neck cancer. *Int J Radiat Oncol Biol Phys*. 2008;72(5):1362–1367.

CHAPTER

61

Imaging of Peripheral Neurogenic Tumors

Randall Lawrence Baldassarre[1], *Ken Alexander Nakanote*[2], *Tudor Hesketh Hughes*[1]

[1]Department of Radiology, UCSD Medical Center, San Diego, CA, USA; [2]School of Medicine, University of California, San Diego, CA, USA

INTRODUCTION

Normal peripheral nerves develop from axons migrating from the neural tube and elements from the neural crest. They are supported by connective tissue stroma and Schwann cells.[1] Myelinated fibers have one axon encased by one Schwann cell. Unmyelinated fibers have many axons encased by one Schwann cell. Each individual axon is surrounded by an endoneurium. Groups of axons are bundled together and encased by the perineurium. Multiple groups of axons running together produce a peripheral nerve and this is encased by the epineurium. This produces a fasicular appearance of peripheral nerves on imaging with magnetic resonance imaging (MRI) or ultrasound.[2–4] Nerve signal conduction is energy dependent and hence there is a profuse blood supply in the immediately adjacent soft tissues.

The presentation and clinical or imaging findings of neurogenic tumors will depend on the nerve involved. Most often these will be painless masses. Sometimes they will become tender to palpation and shooting pains in the nerve distribution will develop. When produced clinically this is Tinel's sign. If nerve transmission is affected then secondary effects on muscles supplied by the nerve may become apparent with weakness and wasting.

The location of the mass may be a useful indicator as to the type of lesion. If a plantar digital nerve is involved a Morton neuroma may be suspected; if a mass is seen beneath the fingernail a glomus tumor is a consideration; and if the median nerve is enlarged a neural fibrolipoma may be the cause. Peripheral nerve sheath tumors (PNSTs) tend to involve large nerve trunks, and nerve sheath ganglia are often seen about the knee.

All forms of medical imaging may assist in the correct diagnosis of PNSTs. These may range from the less sensitive and less specific, but also inexpensive, radiographs through ultrasound, gallium or methylene diphosphonate (MDP) nuclear medicine, and computed tomography (CT), to the more expensive, more accurate contrast-enhanced MRI and positron emission tomography (PET)/CT. Often, however, no one imaging technique is used in isolation, since different techniques are often complementary. It is also very important to always consider radiation dosage in the selection of technique, particularly when multiple follow-up studies are contemplated.

With imaging the shape of the lesion can lead to a diagnosis of nerve sheath tumor. The "string sign" refers to vertical soft tissue extending from both ends of the mass and represents the entering and exiting nerve. The "split-fat sign" refers to the displaced fat surrounding the neurovascular bundle and tumor. With MRI a target pattern that is the reverse of that normally seen in tumors may be apparent. This has low signal centrally and high signal peripherally on fluid-sensitive imaging. Following intravenous gadolinium, the opposite signal pattern may occur, which is also the reverse of most tumors, and this combination is virtually diagnostic of a nerve sheath tumor. Enhancement is more often nonspecific. Should imaging show central calcification, necrosis, or hemorrhage in a tumor otherwise resembling a PNST, then ancient schwannoma should be considered. Another form of MRI, tractography, is gaining momentum for nerve imaging, but yielding less consistent results in the periphery than within the brain.

Although biopsy of the mass can be diagnostic, this is often painful with smaller lesions.

http://dx.doi.org/10.1016/B978-0-12-800945-1.00061-6
© 2016 Elsevier Ltd. All rights reserved.

BENIGN PERIPHERAL NERVE SHEATH TUMORS

Benign PNSTs are divided into neurilemoma (schwannoma) and neurofibroma. They are similar lesions clinically and on imaging, but differ histologically and in their frequency of association with neurofibromatosis 1 (NF1). Both contain elements related to the Schwann cell. Neurilemoma is composed entirely of Schwann cells, but neurofibromas contain all elements of peripheral nerves, including fibroblasts, Schwann cells, and neurites.

Neurilemoma

Neurilemoma is also known as benign schwannoma and neurinoma. These tend to occur in the 20- to 30-year age group with an equal sex distribution. They represent approximately 5% of all benign soft tissue tumors.[5,6] Common sites are the flexor surfaces of the upper and lower extremities, particularly the ulnar and peroneal nerves. Classically the tumor lies eccentric to the native nerve, with the normal nerve components (fascicles) maintained. Histologically they are composed of two types of tissue: Antoni A and B tissue types. Antoni A tissue is central in location and of high cellularity with bundles or fascicles of spindle cells. If the Antoni A tissue predominates, then the tumor is referred to as a cellular schwannoma. It is this part of the tumor that enhances strongly. Antoni B tissue is peripheral and relatively hypocellular, contains myxoid tissue, and is of high water content, accounting for the high signal on T2-weighted (T2W) images. These tissue types are often intermixed and with varying amounts of the two tissues. They are immunohistochemical S100 protein positive.[5–7]

Neurilemoma is usually solitary and shows slow growth. At presentation it is usually an asymptomatic mass less than 5 cm in diameter.[6,7] Fusiform on small nerves, and eccentric on larger nerves, they grow within the epineurium. Because of the nerve to which they are attached, they are mobile side to side, but fixed longitudinally in the line of the nerve. When they are multiple, approximately 5% of patients will be found to have NF1.[6]

Large neurilemomas may degenerate, and when they do so they are refereed to as ancient schwannomas. In this case they may show cystic change, areas of calcification, hemorrhage, or fibrosis.[6,7]

Treatment can be complete surgical resection if they can be separated from the underlying nerve or are superficial and the nerve can be spared.[8] If not, partial resection may suffice and recurrence is rare. Malignant transformation is rare.

Neurofibroma

Like neurilemoma, these also occur in the 20- to 30-year age group with equal sex distribution.[9] They also represent approximately 5% of benign soft tissue tumors.[5] Although similar in many ways to neurilemoma when imaged, they are histologically different, with no Antoni cellular histology, but rather have abundant central collagen.[5–7] They are immunohistochemical S100 protein positive, but less so than neurilemoma.[5] Degeneration is less common than with neurilemoma. There are three classic types: localized (90%), diffuse (typically subcutaneous in the neck), and plexiform (pathognomonic of NF1). The localized form is not associated with NF1 in 90% of cases and in which case are referred to as solitary. When solitary, malignant change is rare. They are usually superficial and at presentation are less than 5 cm in diameter and painless.[5,8] They are fusiform on the native nerve and surgically inseparable. On a large nerve they remain within the epineurium and are encapsulated. On a small nerve, they extend beyond the epineurium, but are still well defined.[5,8]

The diffuse form is usually seen in children and young adults involving the head and neck. Ninety percent of these are not associated with NF1. They are poorly defined subcutaneous, plaque-like infiltrates.

The plexiform type of PNST is essentially pathognomonic for NF1. It has been described as having a "bag of worms" appearance. These tend to follow the course of a nerve and to be a diffuse, multinodular, coalescent sheet-like mass consisting of diffuse soft tissue or nerve enlargement. They may involve the skin, subcutaneous tissue, or deeper nerves and cause distortion of bone growth. In addition they may cause disfigurement and/or functional disability and cause massive enlargement of extremities (elephantiasis neuromatosa).[10]

IMAGING OF BENIGN PERIPHERAL NERVE SHEATH TUMORS

Five good review articles on the imaging of PNSTs are listed in the reference section.[11–14] Radiographically, they usually have either a normal X-ray or a nonspecific soft tissue mass, rarely with surrounding fat outlining the mass (Figure 1). Bony erosion may be seen in longstanding cases, and this has a sclerotic margin compatible with the slow growth of the tumor (Figure 2). Calcification is uncommon and when present may suggest an ancient schwannoma with degeneration (Figure 3). If the tumor is associated with NF1 then some of the associated osseous abnormalities of this condition may be seen, such as pseudoarthrosis or elephantiasis neuromatosa with bony overgrowth.

Angiography may show displaced vessels or corkscrew vessels at either end of the tumor.[15,16] Scintigraphy with MDP will show only mild increased uptake at all phases unless the tumor is calcified. Gallium 67 (^{67}Ga) shows increased uptake in malignant PNSTs, but not those that are benign.[17,18]

With sonography (ultrasound), both neurofibroma and neurilemoma are usually solid noncompressible, well-defined hypoechoic soft tissue masses (Figure 4) that have faint distal acoustic enhancement. Occasionally they may have a coarse echotexture, or have focal hyperechoic areas thought to be due to collagen-rich regions within the tumor. Ultrasound can also have a target-like appearance with a ring of increased echoes within the tumor and when present is virtually pathognomonic of a neurogenic tumor. As with other imaging, fusiform shape and string sign suggest a neurogenic tumor (Figure 5).[2,3,19,20] Ultrasound can also dynamically assess for side-to-side movement with absence of longitudinal movement suggestive of PNST. It had been hoped that ultrasound with its very high superficial resolution would be able to distinguish neurofibroma and neurilemoma on the basis of fusiform versus eccentric enlargement, but studies suggest that sonography may not satisfactorily distinguish between neurilemoma and neurofibroma, as the characteristic eccentric pattern associated with the former is often not observed, and instead a centrally positioned tumor may be visualized with both PNSTs.[21,22]

Because of the lipid in Schwann cells and relatively high water content, benign PNSTs are low attenuation on unenhanced CT, on the order of 5–25 Houndsfield units. Should this become increased or heterogeneous, then transformation to a malignant PNST should be considered. As with plain films, calcification is uncommon and when present may suggest an ancient schwannoma with degeneration (Figure 3(A)). CT may also show central necrosis, again suggesting an ancient schwannoma. CT may also show a target-like appearance with increased density centrally due to increased collagen.[23–25]

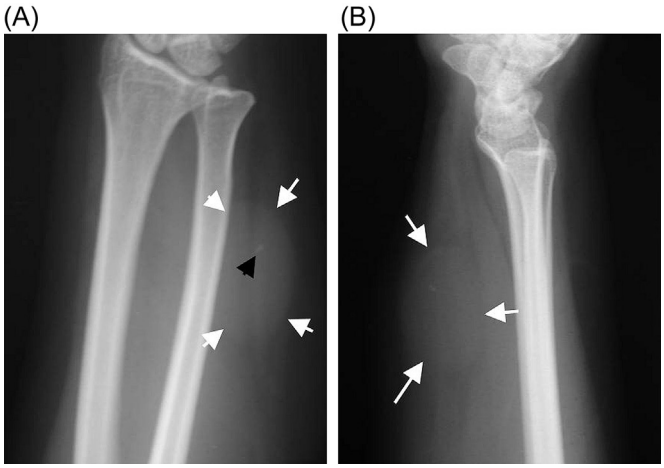


FIGURE 1 A 40-year-old female with neuroma of the right forearm. The posteroanterior (A) and lateral (B) radiographs of the forearm show a well-defined fusiform mass (outlined by white arrows). Note the "split fat" around the mass and the apparent entering and exiting nerve on the lateral view. A small fleck of calcification could indicate early degeneration (black arrowhead).

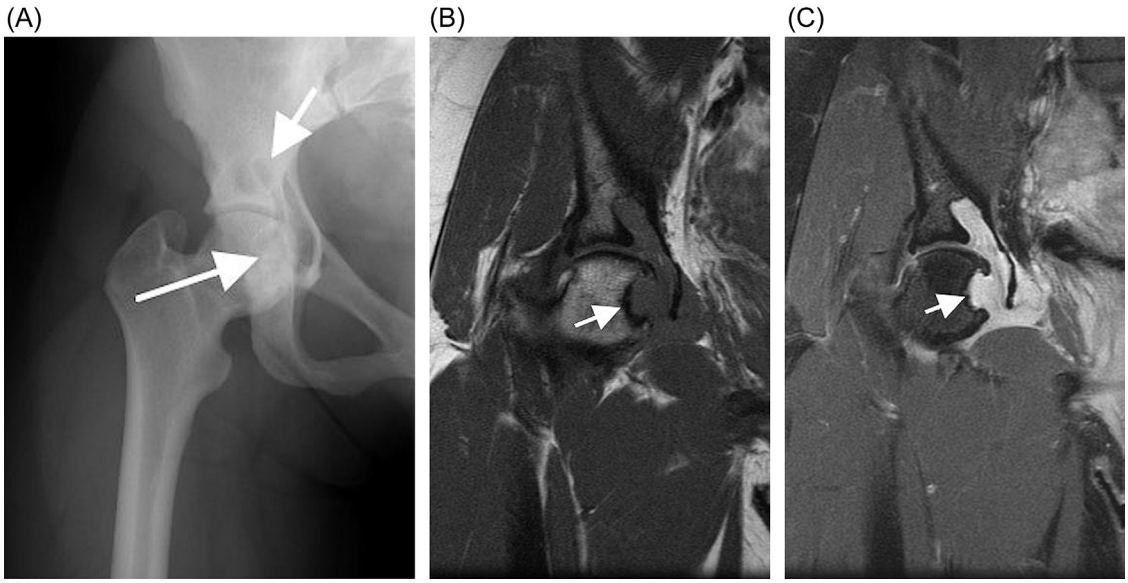


FIGURE 2 A 35-year-old female with NF1. The frontal radiograph (A) of the right hip shows well-defined erosions with thin sclerotic margins involving the femoral head and superomedial acetabulum (white arrows). The coronal T1 (B) and coronal T1 fat-saturation post-intravenous gadolinium (C) images demonstrate the intra-articular neurofibroma, which strongly enhances and is causing the mechanical bony erosion (white arrows).

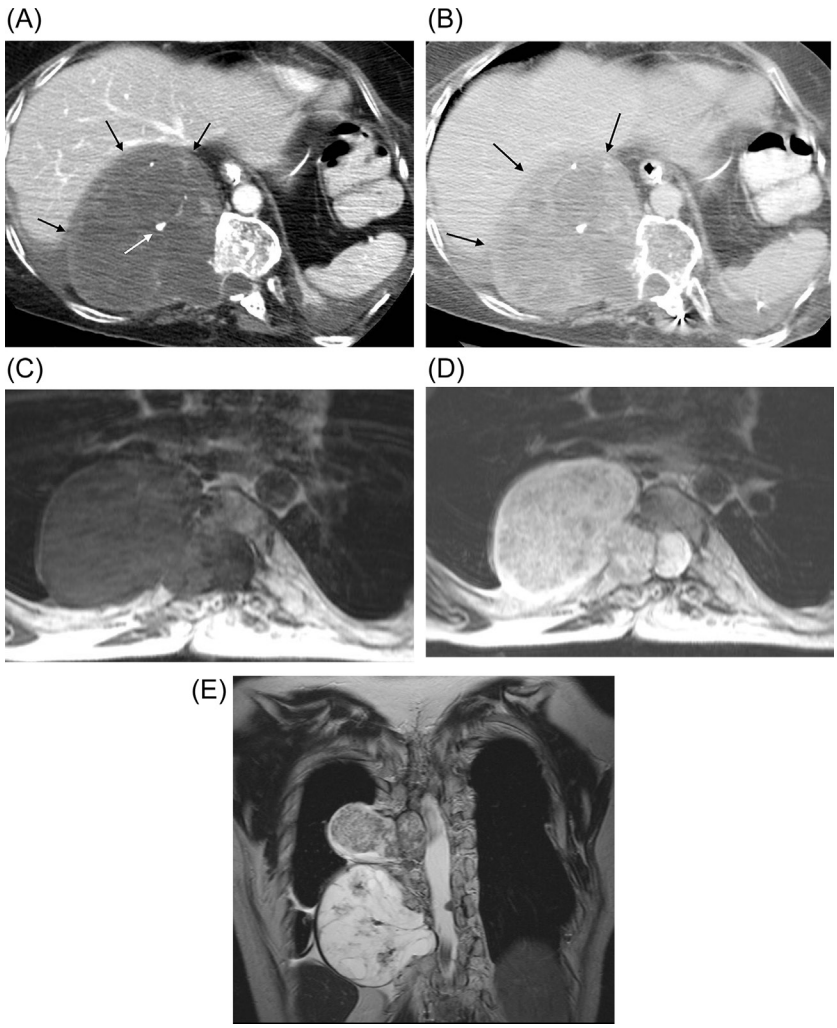


FIGURE 3 A large right paravertebral ancient schwannoma is seen in this 37-year-old female with NF1. (A) The arterial phase and (B) the equilibrium phase of an abdominal CT scan. The tumor is outlined (black arrows). Note the areas of calcification (white arrow) and the early arterial (septal) enhancement with later heterogeneous enhancement. Note also the vertebral erosion. (C) Axial T1 image shows the homogeneous intermediate signal and (D) axial T2 image the heterogeneous pattern often seen in neurogenic tumors owing to their fasicular pattern. The coronal T2 image (E) shows additional other tumors arising from the spine.

MRI is considered to be the superior imaging modality for demonstrating the classic findings of PNSTs.[26] These include fusiform shape, visualization of the entering and exiting nerve, target signs, split-fat sign, fascicular sign, and associated muscle atrophy. However, it is not usually possible to separate neurofibroma from neurilemoma by imaging. The MR signal is T1 isointense to muscle and T2 with variable increased signal.[27,28]

The fusiform shape of the tumor and the visualization of the entering and exiting nerve giving a tail to the tumor are considered the most important features that distinguish neurogenic tumors from nonneurogenic tumors when using MRI (Figure 6).[27] Normally the margins of the tumor are distinct, and if they become indistinct then malignant PNST or diffuse/plexiform NF should be considered. The "target sign" refers to increased peripheral signal with fluid-sensitive imaging from high water content and myxoid tissue.[29] The low signal center is due to the Antoni A tissue high cellularity, with bundles or fascicles of spindle cells in the case of neurilemoma (Figure 7), and central fibrosis with high collagen content in the case of neurofibroma (Figure 8). This is the reverse of most other tumors, which, owing to central necrosis, have increased fluid signal centrally. The "fascicular sign" refers to the pattern of the signal within the tumor being similar to a normal peripheral nerve,[8] with multiple ring-like structures, which are most conspicuous on T2W imaging (Figures 7 and 9). The "split-fat sign"[24] refers to the way the fat of normal neuronal fascial planes wraps around the mass, producing a thin high-signal rim

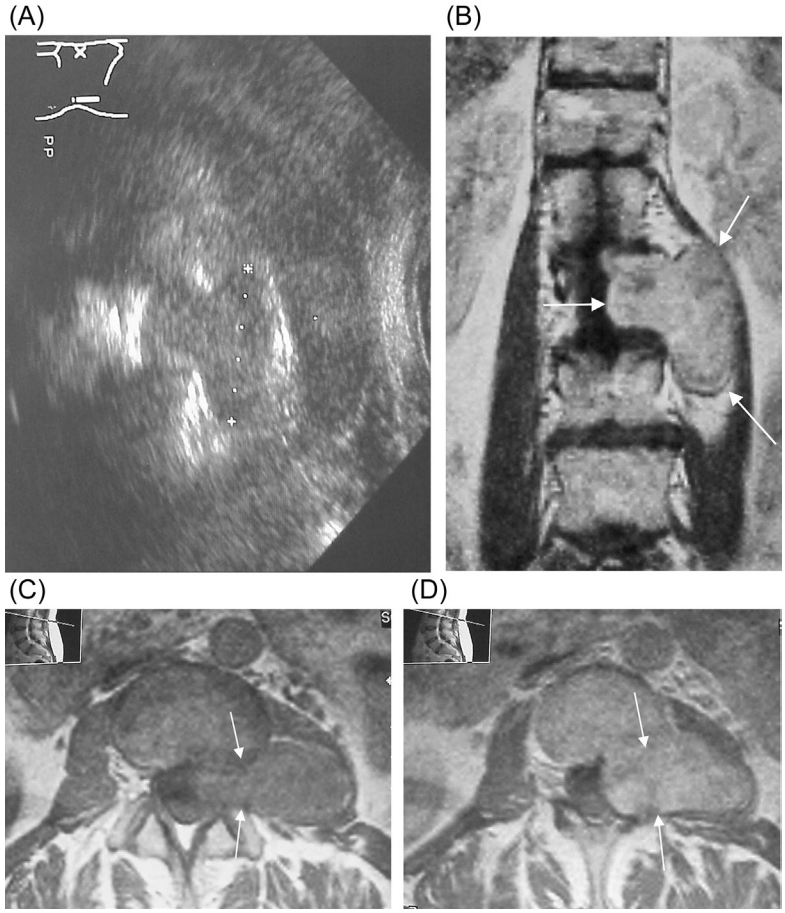


FIGURE 4 A 55-year-old female having ultrasound for deep vein thrombosis evaluation who was found to have a neurilemoma emerging from the left L2–3 neural foramen. Ultrasound scan of the left flank (A), coronal plane, rotated 90° to match the coronal T1W MRI of the lumbar spine (B). The tumor is shown by calipers on the ultrasound and by three white arrows on the MRI. Additional axial T1W (C) and axial T1 post-intravenous gadolinium (D) images show the enlargement of the foramen by the tumor and the mild enhancement (white arrows).

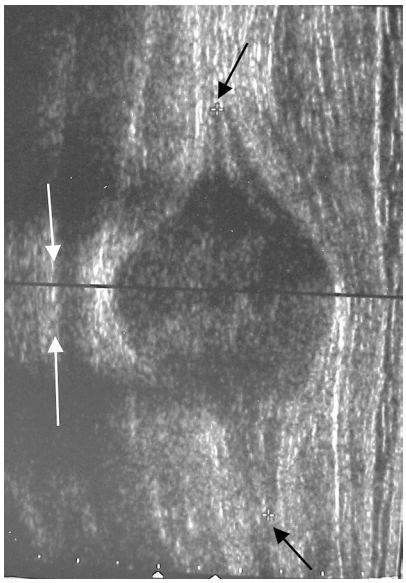


FIGURE 5 Common peroneal nerve neurofibroma. Longitudinal ultrasound rotated 90° shows a well-defined, fusiform, hypoechoic solid mass with posterior acoustic enhancement (white arrows). Note that the entering and exiting nerve (black arrows) lies centrally, suggesting neurofibroma rather than neurilemoma.



FIGURE 6 Common peroneal nerve neuroma (white arrows) just above the knee in a 54-year-old female. Coronal T1W (A) and coronal protein density with fat saturation (B) clearly show the fusiform shape and the entering and exiting nerve. In addition the protein density images show a mild target sign with peripheral high signal.

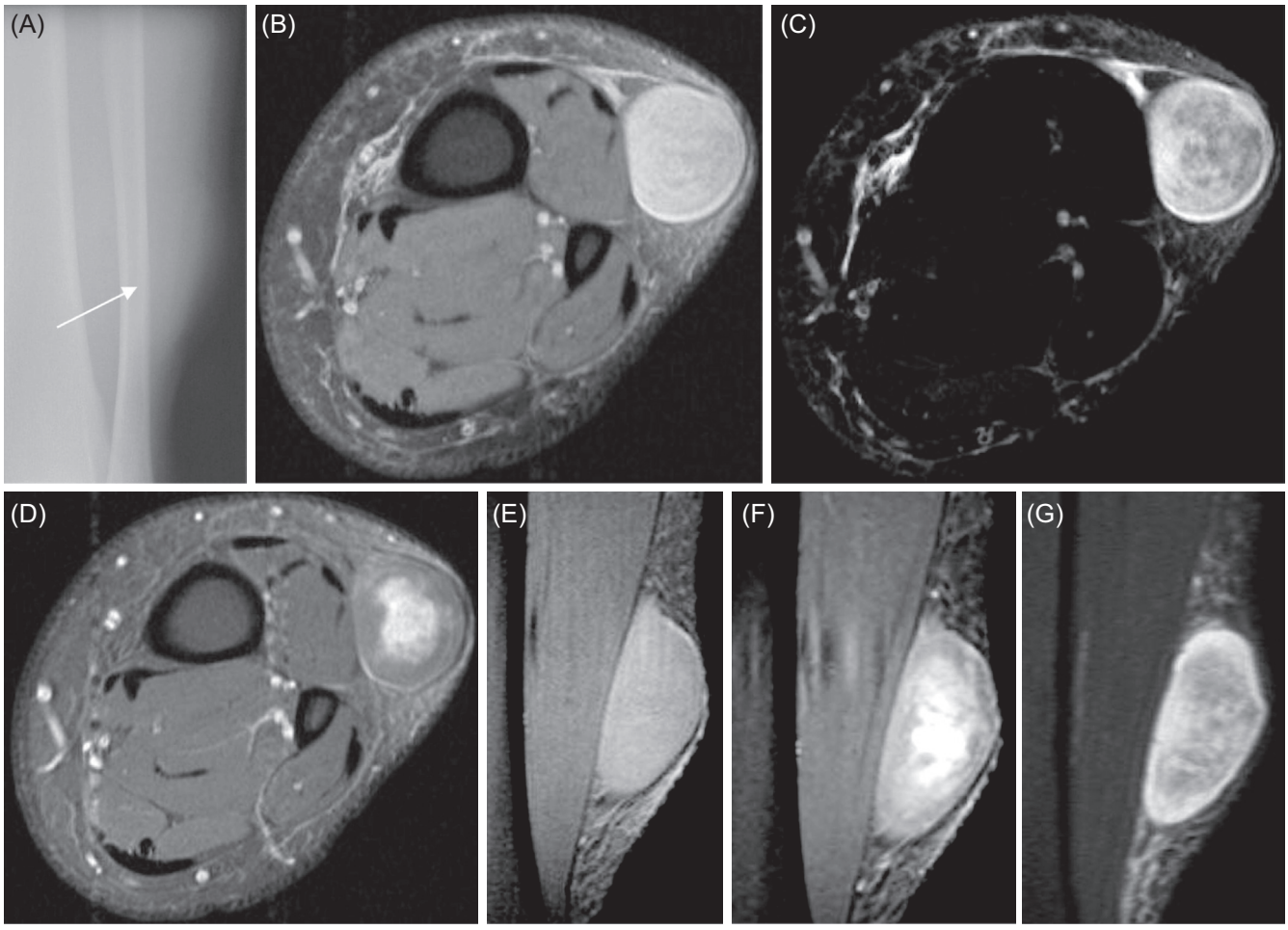


FIGURE 7 Subcutaneous neurilemoma of the anterolateral aspect of the distal left calf in a 23-year-old man. The frontal radiograph (A) shows a focal soft tissue fullness of the lateral calf (white arrow). The three axial MR images, protein density with fat saturation (B), T2W with fat saturation (C), and T1W fat saturation post-intravenous gadolinium (D), and the three coronal images, T1W with fat saturation pre-gadolinium (E) and post-gadolinium (F) and protein density with fat saturation (G), show some of the characteristic image findings. The fasicular pattern is seen best on (B), the peripheral high signal on fluid-sensitive images producing the target sign on (C) and (G), and central enhancement on (D–F) combined.

with triangles at either end on T1W imaging (Figure 10). This is, however, nonspecific and seen with other tumors that are intermuscular rather than intramuscular. Following intravenous gadolinium (Gd), a useful diagnostic feature is enhancement that follows a reverse target sign of that seen with T2W (center/cellular area enhances more than periphery) (Figures 7 and 8). This is again the reverse of most nonneurogenic tumors, which enhance at the growing periphery rather than the necrotic center, and as such is almost pathognomonic of benign PNSTs. However, this is not the norm, and enhancement is variable for both benign and malignant tumors. Malignant PNSTs usually have more enhancement.[8]

Plexiform neurofibromas appear as large lobulated masses following the course of peripheral nerves (Figure 11), particularly the sciatic nerve (Figure 12). They are usually high signal on T2W (occasionally low owing to high collagen content) and low signal on T1W images with variable enhancement.

NEUROFIBROMATOSIS 1

This is one of the most common genetic diseases, which, in addition to the findings of multiple PNSTs, also shows many other relatively distinctive features due to accompanying mesodermal dysplasia. It is one of the neurocutaneous syndromes or phakomatoses, along with tuberous sclerosis, Von Hippel–Lindau, ataxia telangiectasia, and Sturge–Weber–Dimitri syndromes. NF1 was the first phakomatosis to be recognized, described by von Recklinghausen,[30] and has become known as von Recklinghausen disease of bone. There are eight variants numbered NF I–VIII, but 90% of these are NF1 and 9% NF2. NF1 has an incidence of 1 in 3000 and when

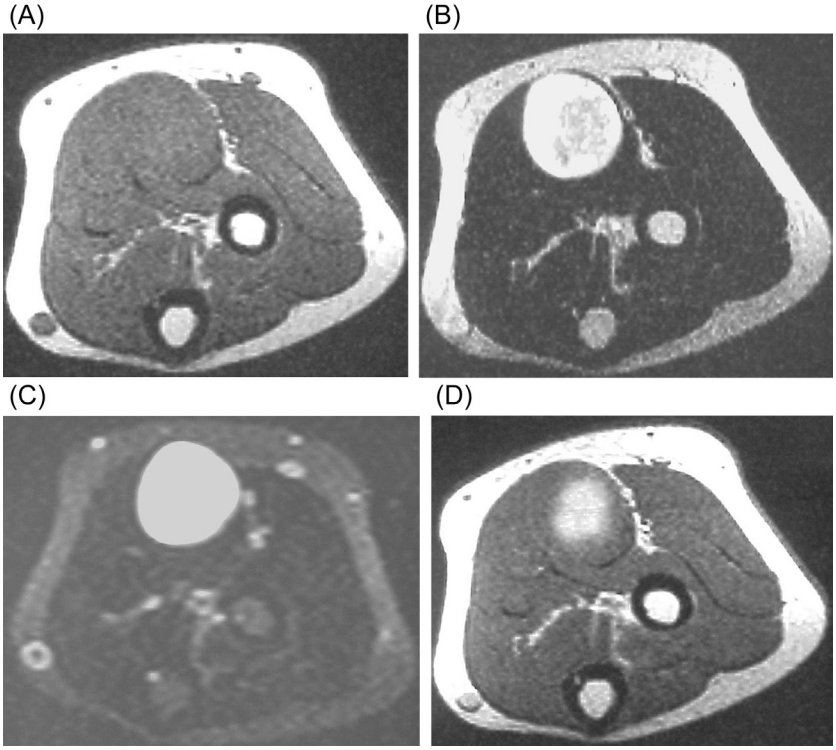


FIGURE 8 Neurofibroma of the anterior compartment of the middle forearm. Axial images, T1W (A), T2W (B), STIR (C), and T1 fat saturation post-intravenous gadolinium (D), show the pathognomonic signal characteristics of a PNST. Isointense to muscle on T1W, high peripheral signal on T2W, very bright with STIR, and central enhancement following gadolinium.

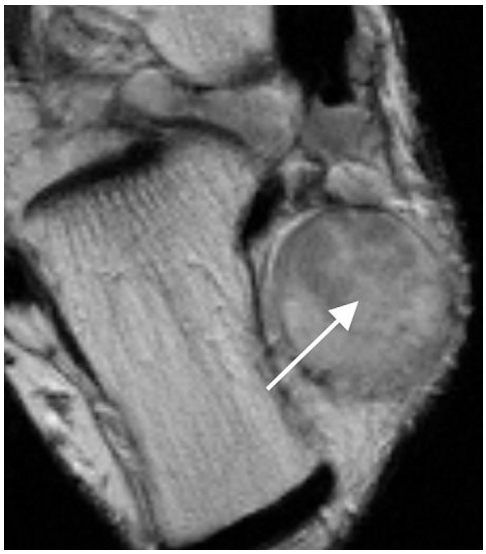


FIGURE 9 A 26-year-old man with NF1 and a large neurilemoma of the tibial nerve extending into its medial and lateral plantar nerve branches, which shows a partial fasicular pattern on this axial T2W image (white arrow).

hereditary is autosomal dominant, owing to a defect at the pericentric location of chromosome 17, but 50% are spontaneous mutations.[31,32] Increased paternal age increases the number of cases of new mutations. The gene at the above location codes for the production of the protein neurofibromen, which appears to be a tumor suppressor. The PNSTs of NF1 may be localized, diffuse, or plexiform. NF1 presents with the classic triad of cutaneous lesions, skeletal deformity, and mental retardation. The diagnostic criteria for NF1 are shown in Table 1. In addition there may be manifestations of the accompanying mesodermal dysplasia, which can present as a range of musculoskeletal deformities of which scoliosis is the most common. These are shown in Table 2.

All three types of neurofibroma mentioned above (localized, diffuse, and plexiform) can be associated with NF1.[33] However, most of the localized and diffuse variants are not associated with NF1, but the presence of a plexiform neurofibroma is virtually pathognomonic of NF1. Neurofibromas in patients with NF1 tend to involve the skin and subcutaneous tissues, but also the peripheral nerve trunks. Neurofibromas in patients with NF1 tend to be multiple and more often involve deep large nerves than do solitary neurofibromas.

NEURAL FIBROLIPOMA

This has also been referred to as fibrolipomatous hamartoma, perineural lipoma, or intraneural lipoma, but neural fibrolipoma is the preferred name. As the name suggests, the pathology is that of fatty (fibrofatty)

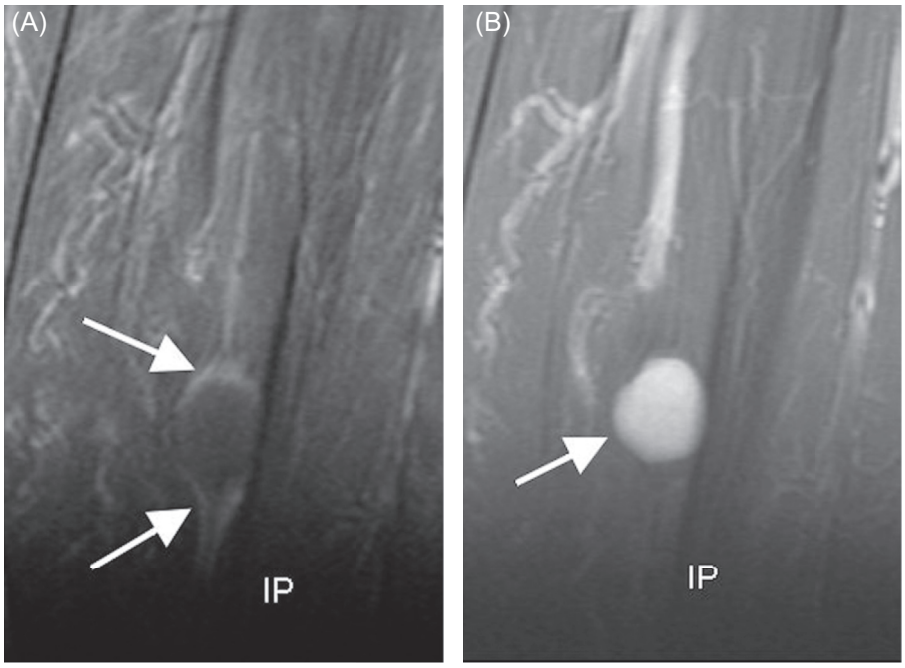


FIGURE 10 Neurilemoma within the flexor hallucis longus muscle of the calf in a 46-year-old female. Coronal T1W (A) and T1 fat saturation post-intravenous gadolinium (B) show the split-fat sign with triangles of fat at either end of the tumor, high signal on T1W (white arrow) and suppressing on the fat-saturation image. Note the central enhancement (white arrow).

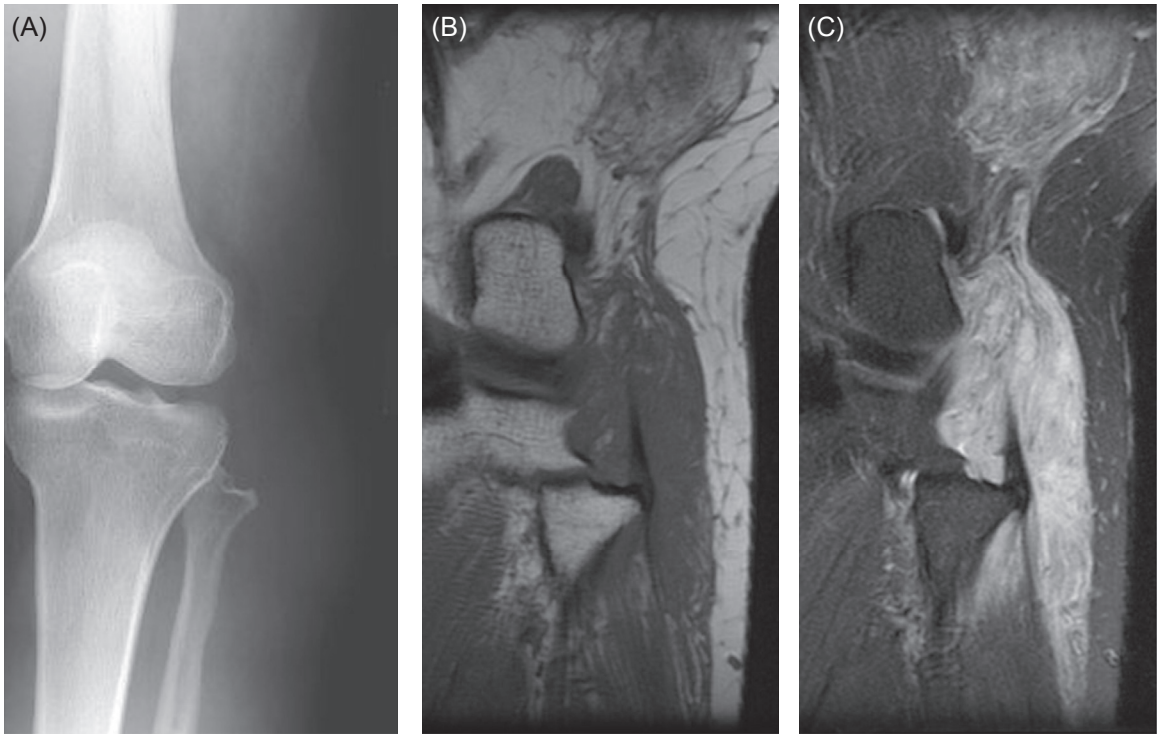


FIGURE 11 A 35-year-old female with NF1 demonstrates a classic plexiform neurofibroma along the course of the common peroneal nerve. The frontal radiograph (A) shows an ill-defined soft tissue mass laterally and erosion of the proximal fibula. The coronal MRIs, T1W (B) and T1 fat saturation post-intravenous Gd (C), show a large heterogeneous serpentine mass resembling a "bag of worms," with strong enhancement and additional bony erosion of the adjacent tibia.

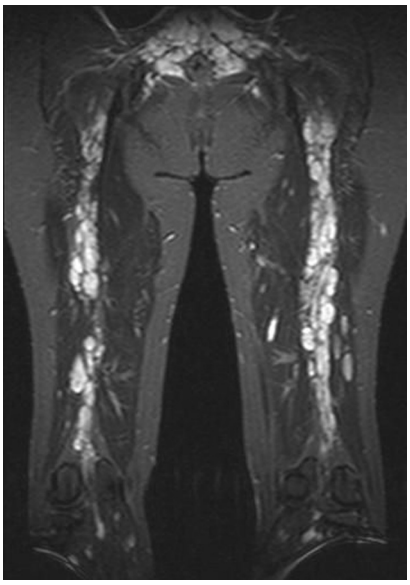


FIGURE 12 A 29-year-old female with NF1. The coronal T2W fat saturation image shows extensive plexiform neurofibromas following the course of the sciatic nerve bilaterally.

TABLE 1 Diagnostic Criteria for NF1

Diagnostic criteria for NF1 are two or more of the following:

- Six or more café-au-lait macules
  - >5 mm prepubertal
  - >15 mm postpubertal
- Two or more neurofibromas or one plexiform neurofibroma
- Axillary or inguinal freckling
- Optic glioma
- Two or more Lisch nodules (hamartoma of the iris)
- Distinctive bone lesion
  - Sphenoid dysplasia
  - Pseudoarthrosis
- First degree relative with NF1

TABLE 2 Manifestations of the Mesodermal Dysplasia of Neurofibromatosis Type 1

- Scoliosis (short or long segment)
- Kyphosis (often predominates)
- Facial or orbital dysplasia
- Lambdoid suture defects (left sided)
- Pseudoarthrosis (tibia + congenital)
- Periosteal abnormalities (reaction or cyst)
- Multiple nonossifying fibroma or fibroxanthomas
- Rib deformity (ribbon ribs)
- Posterior vertebral scalloping (dural ectasia)
- Elephantiasis neuromatosa
- Mesodermal dysplasia pseudofracture

infiltration of the nerve and this usually presents in a child or young adult, with equal sex distribution, as a slowly enlarging soft mass. Approximately 90% involve the upper extremity and 85% the median nerve. Hence the mass is often felt in the palmar region or may present as carpal tunnel syndrome.[34–36]

In 30–70% of cases the neural fibrolipoma is associated with macrodystrophia lipomatosa (Figure 13). When involving the distal nerves this presents as bony and soft tissue overgrowth in the associated sclerotomes (mesenchymal-derived tissues supplied by specific nerve root) of the affected nerve as macrodactyly and hence is often in the second + third digits of the hand (Figure 14). This diffuse increase in fibroadipose and osseous overgrowth ceases at puberty, but can lead to secondary osteoarthrosis (Figure 15).[37]

Radiographs of the affected area may show a soft tissue mass due to the neural fibrolipoma and/or the macrodystrophia lipomatosa or the bony overgrowth and secondary osteoarthrosis. Ultrasound shows a cable-like appearance of the enlarged nerve, with alternating hyper- and hypoechoic strands. MRI is nearly always diagnostic and shows the enlarged nerve with low signal fascicles and surrounding fat.

TRAUMATIC NEUROMA

Traumatic neuroma is not a neoplasia, but rather an overgrowth of normal nerve components trying to regenerate the injured nerve, particularly the axons,[8,38,39] and as such is a hamartoma. This represents a normal pattern of healing and is often asymptomatic. These can be divided into two major groups. The first is the spindle type, which is due to chronic friction to the nerve at a point of irritation or microtrauma due to stretching or compressing of the nerve by localized scar tissue. These are internal focal fusiform swellings (Figure 16). The second type is the lateral or terminal type, which is secondary to partial or total transection of a nerve and produces a bulbous swelling at the site of injury, if partial, or on the proximal nerve stump if there has been complete transection.[40–44]

They present 1–12 months postinjury with pain and shooting sensations in the nerve distribution if bumped or palpated (Tinel's sign). Pain that is associated with a neuroma does not always have a precise topography and is often difficult to distinguish from phantom limb pain. They are most common in the lower extremity after limb amputation or surgery and are occasionally seen in the brachial plexus and radial nerve.[41] Histologically they are tangled masses of axons and other peripheral nerve components, sometimes with partial formation of a fasicular pattern. They have no malignant potential.

Ultrasound (US) imaging shows a nonspecific hypoechoic mass, unless the history is noted and the

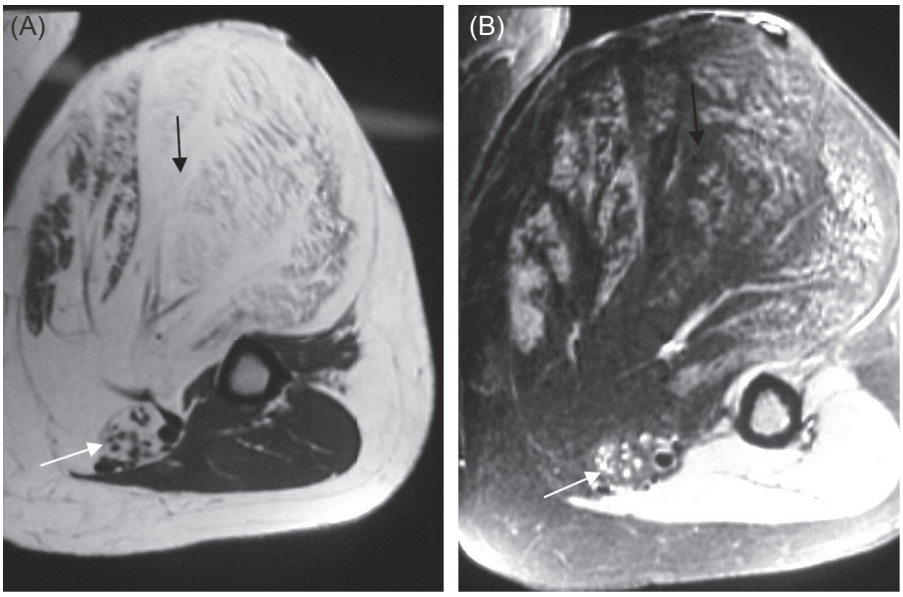


FIGURE 13 A 47-year-old man with a long history of left arm overgrowth that spares the fourth and fifth digits. Axial T1W (A) and protein density with fat-saturation (B) images of the upper arm demonstrate fatty infiltration of the median nerve (white arrows) and fatty overgrowth with muscle atrophy of the anterior compartment of the arm (black arrows) in this patient with median nerve neural fibrolipoma and accompanying macrodystrophia lipomatosa of the biceps and brachialis muscles. Although the median nerve does not supply the anterior compartment of the arm musculature, it has the same nerve root distribution as the musculocutaneous nerve of the arm, which does supply these muscles. *Courtesy of Dexter Witte, MD, Baptist Memorial Hospital, Memphis, TN.*

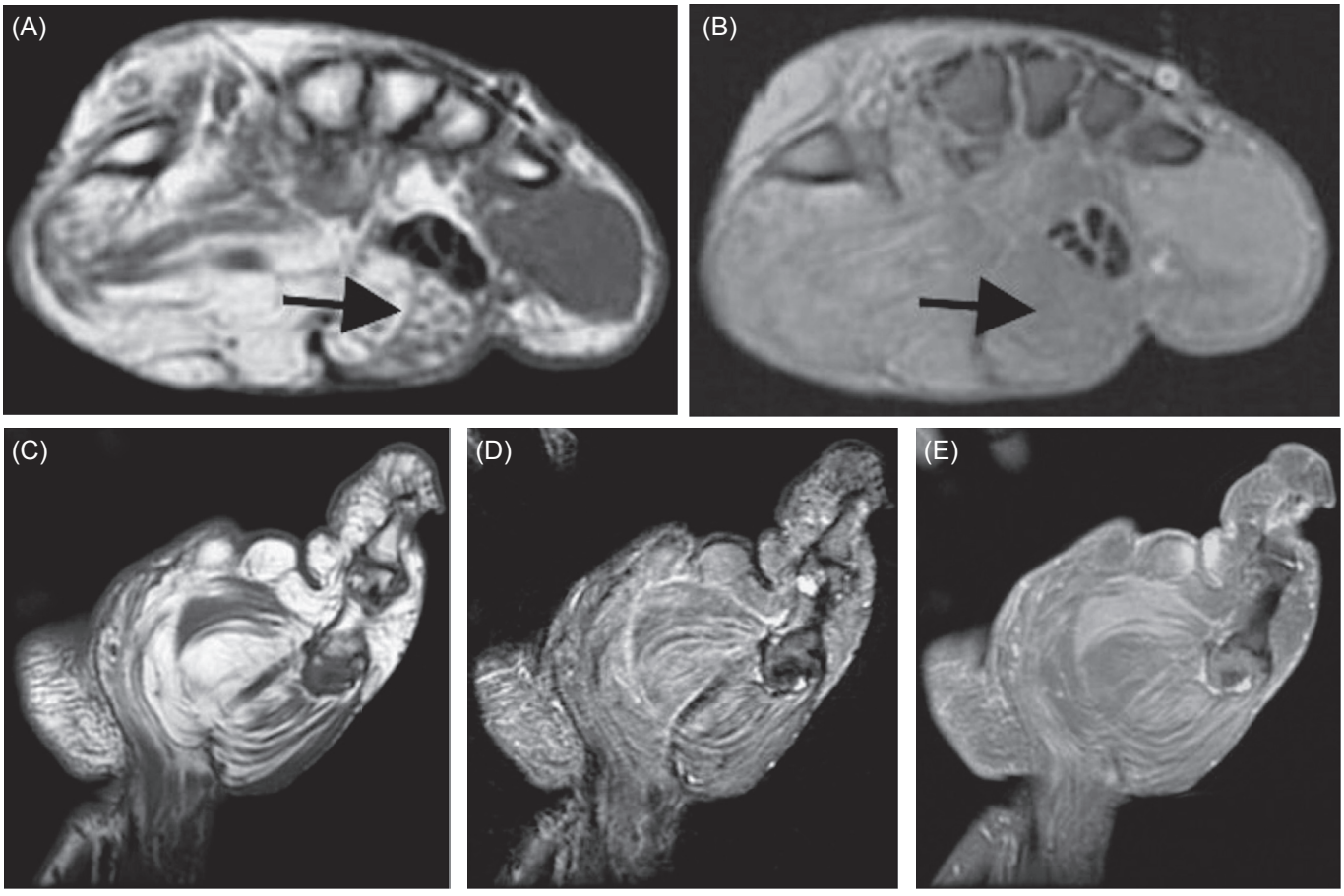


FIGURE 14 A 39-year-old man with neural fibrolipoma of the median nerve and accompanying macrodystrophia lipomatosa of the distal median nerve distribution. Axial T1W (A), axial T1W with fat saturation post-intravenous Gd (B), coronal T1W (C), coronal T2 with fat saturation (D), and coronal T1W with fat saturation post-intravenous Gd (E). This is the classic location and appearance of these conditions. Note the fatty infiltration of the median nerve, which loses signal with fat saturation and does not enhance (black arrows), and fatty overgrowth of the thumb, seen best on the coronal images.

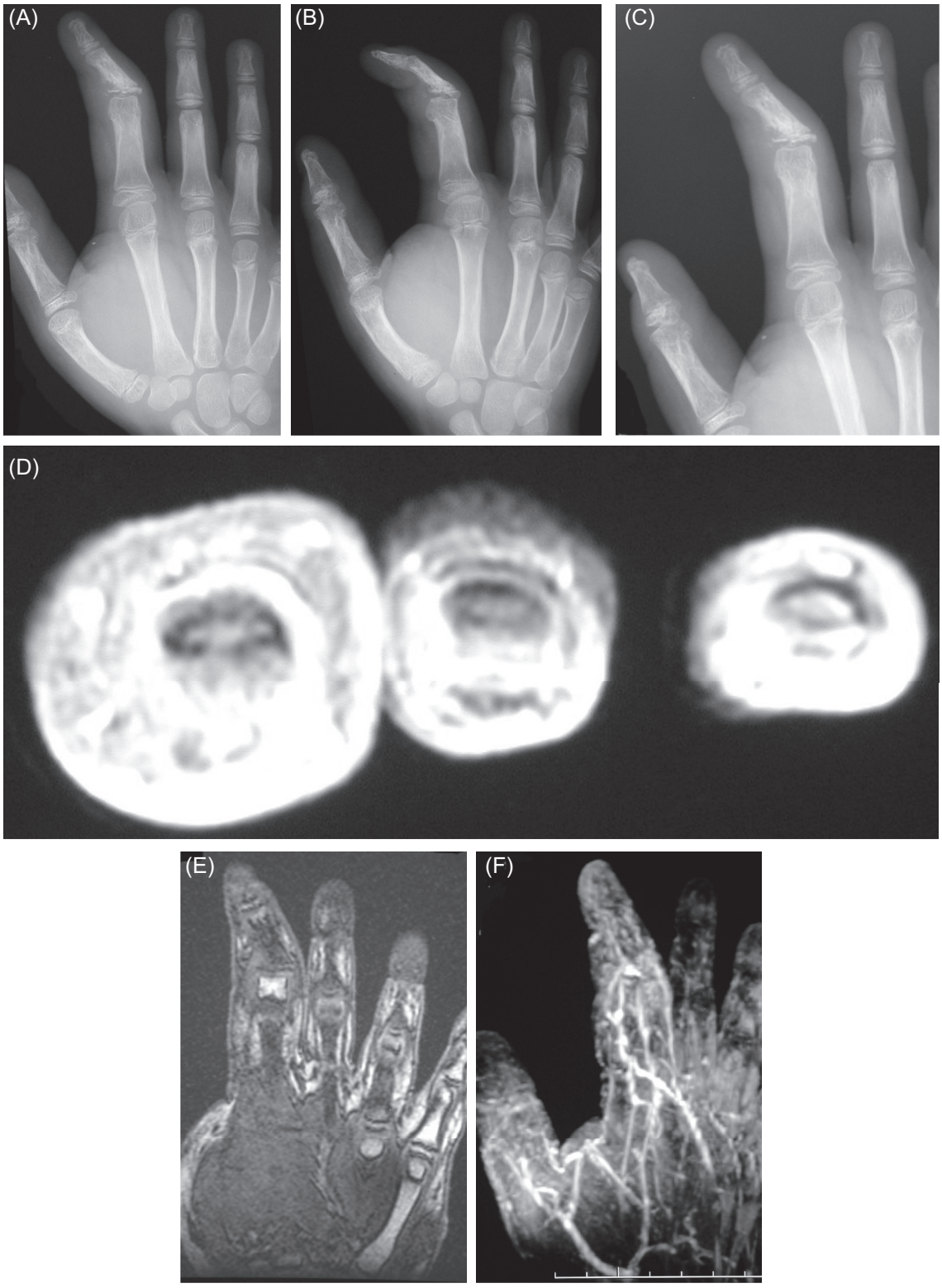


FIGURE 15 A 14-year-old boy with a median nerve neural fibrolipoma and accompanying macrodystrophia lipomatosa involving the index finger. Posteroanterior (A), oblique (B), and close-up oblique (C) radiographs of the right hand show the bony and soft tissue overgrowth of the index finger and secondary osteoarthrosis of the proximal interphalangeal joint. The axial (D) and coronal (E) T1W images show the significant soft tissue and bony overgrowth and the coronal T1W with fat saturation post-intravenous Gd magnetic resonance angiogram (F) shows the accompanying increase in blood flow to that ray.

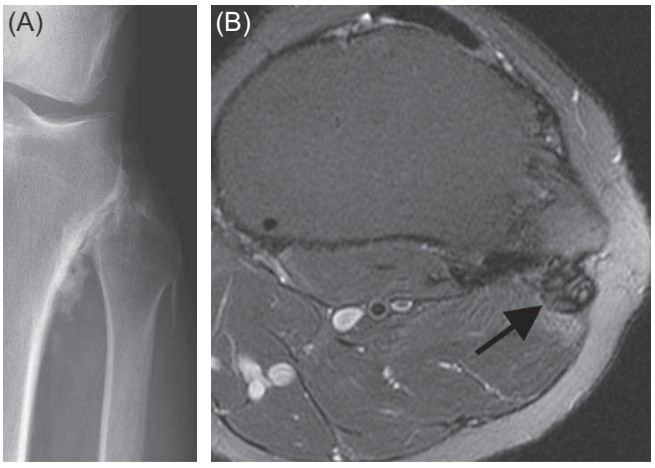


FIGURE 16 Spindle-type traumatic neuroma of the common peroneal nerve. AP radiograph of the lateral aspect of the left knee shows posttraumatic dystrophic ossification in the region of the expected course of the common peroneal nerve (A). Axial proton density image (B) at the level of the proximal fibula shows fusiform enlargement of the common peroneal nerve with maintenance of the fasicular pattern (black arrow) secondary to the chronic irritation of the nerve by the posttraumatic changes to the adjacent tissues.

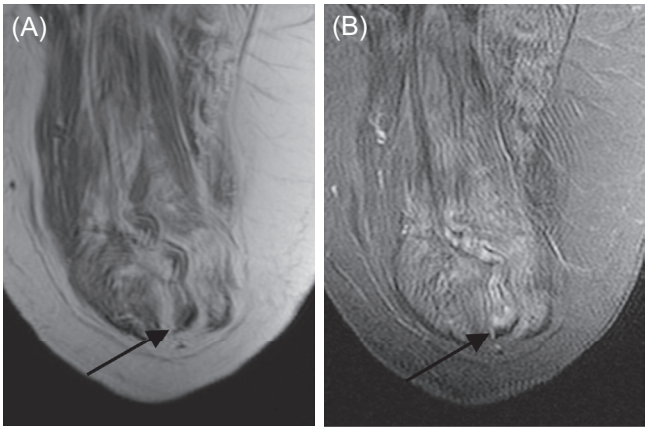


FIGURE 17 Terminal-type traumatic neuroma of the sciatic nerve stump in a 60-year-old female who is 4 years postamputation and has had 1 month of pain. Coronal T1W (A) and coronal T2W with fat saturation (B) images of the left thigh show the tortuous sciatic nerve surrounded by fat ending in a bulbous tip with increased fluid signal (black arrows).

native nerve is observed. With CT scanning the attenuation is that of muscle and hence nonspecific.[42] With MRI there is intermediate signal on T1W images and intermediate to high signal on T2W imaging, occasionally with a heterogeneous ring (fascicular) pattern (Figure 16). When surrounded by fat, as is often the case owing to accompanying muscle atrophy (Figure 17), the lesions are well defined. Often if a larger nerve is involved the association of the tumor with the severed nerve can be made (Figure 17), but with smaller nerves this will be difficult. There is variable enhancement following intravenous Gd (Figure 18).[43–45]

NERVE SHEATH GANGLION

A ganglion is a myxoid collection of inspissated fluid surrounded by a fibrous capsule of compressed tissue. These are often multiloculated. They are thought to arise secondarily to a very minor injury to fibrous connective tissue, which then produces a loculated fluid collection.

Nerve sheath ganglia are usually seen in the nerves about the knee (peroneal, tibial). It is debated as to whether they originate within the nerve or arise in the proximal tibiofibular joint and extend to involve the nerve. They may present as a mass if the ganglion is of a large size, but commonly present with foot drop (peroneal nerve) even when of a small size. This is because of the proximity to the osseoligamentous peroneal tunnel between the two heads of the peroneus longus, which arise from the proximal fibula, forming a tunnel through which the nerve passes. Here the nerve becomes compressed by the ganglion.[46,47]

Imaging of nerve sheath ganglia will reveal a well-defined cystic mass. Hence on US there will be an anechoic structure, possibly with some septation, with increased through transmission.[48] With CT the density will be slightly above water owing to inspissation and proteinaceous material.[49] With MRI the mass will have low signal on T1, occasionally with slight increase over that of water because of the proteinaceous material; have high signal (light bulb lesion) with T2W imaging; and show a thin rim of enhancement following intravenous Gd due to the compressed tissue at the periphery.[50] The other major finding with MRI will be the secondary effects upon the muscles supplied by that nerve (Figure 19). For the fibular tunnel this will be both the peroneal and the anterior compartments of the leg. Initially there is seen to be muscle edema with mild enhancement and subsequently over many months of compression fatty atrophy with loss of the edema and enhancement.

MORTON NEUROMA

Morton neuroma is actually a perineural fibrosis induced by friction on the plantar nerve at the level of the metatarsal heads.[5] It is far more common in women (up to 18/1), which has led to the speculation that it is induced by the wearing of high heals.[51,52] These cause dorsiflexion at the metatarsophalangeal joints and stretch the plantar nerve at its point of bifurcation into the digital nerves, as it passes over the intermetatarsal ligament. Other provocative factors include arthritis, ganglion cysts, running, ballet, or an enlarged intermetatarsal bursa[53] as may be seen in rheumatoid arthritis.[54]

Another theory is that it is induced by ischemia.[55] There is often an associated inflammatory response with fluid seen in the adjacent intermetatarsal bursa and surrounding soft tissue hyperemia. Morton neuromas are most commonly seen at the third interspace between the third and fourth metatarsal heads. This is thought to be the most common

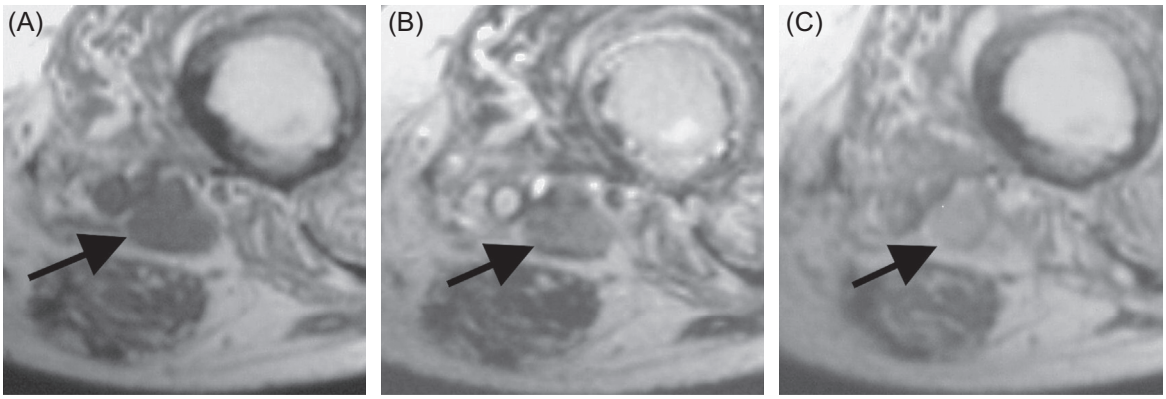


FIGURE 18 Terminal-type traumatic neuroma of the sciatic nerve stump in a 71-year-old man whose status is post-above-knee amputation of the left leg. Axial T1W (A), axial T2W (B), and axial T1W post-intravenous Gd (C) images show a well-defined mass (black arrows) of low signal on T1W, intermediate signal on T2W, and moderate enhancement post-Gd.

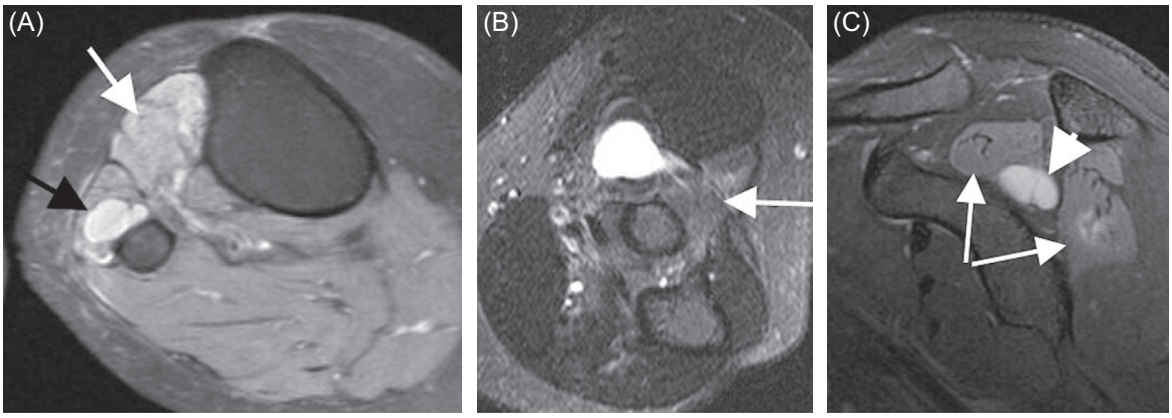


FIGURE 19 Three different patients with ganglia at osseoligamentous tunnels causing nerve-entrapment syndromes. Common peroneal nerve ganglion (A): axial T2W with fat saturation shows the ganglion (black arrow) and the accompanying muscle edema in the peroneal and anterior compartments of the leg (white arrow). Posterior interosseous nerve of the forearm entrapment by a ganglion arising in the annular periradial recess and compressing the nerve beneath the arcade of Frohse at the proximal supinator muscle (B): axial T2W with fat saturation. The edema is seen in the posterior compartment of the forearm and in the supinator muscle (white arrow). Suprascapular nerve ganglion compressing the nerve in the suprascapular notch in a 26-year-old man (C) (white arrowhead), sagittal proton density with fat saturation and causing edema of both the supra- and the infraspinatus muscles (white arrows).

site because the medial and lateral plantar nerves combine in this interspace to produce a slightly larger interdigital nerve, or because there is more tethering of the nerve owing to the two nerves combining. The second interspace is the next most common: Hauser neuroma. They are uncommon at the first interspace, where they go by the name of Heuter neuroma, and rare in the fourth interspace.[56]

Histologically there is thickening of the epineural fascicles, perineural fibrosis with high collagen content (Renaut bodies), and loss of the myelinated fibers.

Clinically there may be localized pain or pain radiating to the toes.[57] This is brought on by exercise or by palpation. A unilateral distribution predominates. The actual neuroma is not usually palpable, but an accompanying inflamed bursa may be. The size of the lesion relates to symptoms, with many smaller lesions seen at imaging being found to be asymptomatic.

Radiographs are invariably normal, but sometimes increased intermetatarsal distance can suggest a large neuroma (Figure 20). They are principally used to exclude other pathology. US shows a round or ovoid hypoechoic mass with internal echoes in the intermetatarsal space. US being a dynamic interactive investigation, the mass can easily be correlated with the patient's symptoms by pressure on the probe and seen to move between the metatarsals when finger pressure is applied dorsally. This is the US equivalent of Mulder's click or sign produced by side-to-side squeezing of the forefoot. Any accompanying bursitis is seen as an anechoic adjacent lesion. Color or power Doppler is a useful adjunct to assess the associated inflammation of the bursitis.[58,59] Imaging with sonography has yielded a sensitivity of 85%, with false negatives attributable to small size of the neuroma and sonographer technique.[60]

MR signal characteristics (Figure 20) are of low signal on T1W images, best seen on coronal T1 non-fat-saturated imaging. With T2W imaging the signal is variable, but generally remains relatively low or equal to fat. Hence conspicuity on T2W images is less good. Because of this

the tumor is better seen with fat saturation (but still not as good as on T1 imaging), and this also brings out any accompanying intermetatarsal bursitis, which will be high signal intensity with T2W imaging. Enhancement with intravenous Gd will often demonstrate peripheral enhancement and will increase sensitivity over T2W imaging.[61] It is also helpful in separating fibrosis (enhances solidly) from bursa (enhances peripherally). Intermetatarsal bursitis often coexists with, or causes, a Morton neuroma. The presence of small asymptomatic neuromas can be normal when 3 mm or less in the first to third intermetatarsal spaces. Zanetti and colleagues[62] have shown that MRI is 90% accurate, positive predictive value 100%, and negative predictive value 60% and introduced the following diagnostic criteria: (1) centered in neurovascular bundle at the intermetatarsal space on the plantar side of the intermetatarsal ligament, (2) well demarcated, and (3) signal intensity equal to muscle on T1W. Erickson and coworkers[63] showed intermetatarsal bursal fluid in 67% of patients with neuroma. With prone imaging the neuroma is plantar to "virtual" plantar cortical line. With supine and weight-bearing imaging the neuroma migrates dorsally. The shape and transverse measurement change. Neuromas are most conspicuous on prone images. This is important since neuromas larger than 5 mm have a much better surgical outcome.[64,65]

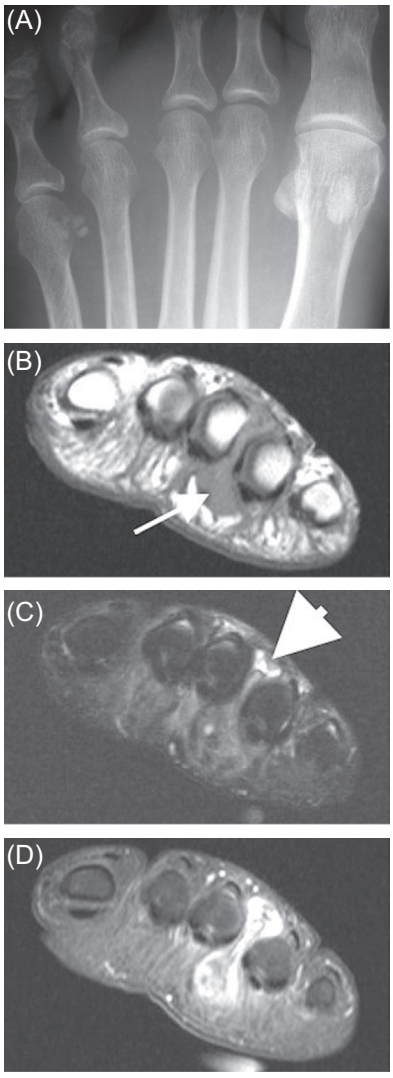


FIGURE 20 A 51-year-old female with a third-interspace Morton neuroma. AP radiograph of the left foot (A), coronal T1W (B), coronal T2W with fat saturation (C), and coronal T1W with fat saturation post-intravenous Gd (D). The radiograph suggests widening of the third interspace. The MR images show a well-defined mass of low T1 signal (white arrow), which stays of relatively low signal on T2W images apart from accompanying bursal fluid seen dorsally (white arrowhead). Following Gd, there is intense enhancement of the neuroma and periphery of the bursa.

GLOMUS TUMOR

This nearly always benign, usually solitary tumor most often presents in adults, with equal sex distribution, unless in the most common location beneath the nail (subungual glomus tumor), when it is more common in women. Seventy-five percent occur in the hand, with the second most common site being the sole of the foot. It arises from the neuromyoarterial glomus. Histologically there are three types: vascular, myxoid, and solid, ranging from more vascular to more glomus cells. Symptoms are out of proportion to the small size of the lesion, which is usually less than 1 cm in size, and include localized tenderness, intense intermittent pain, and cold sensitivity, at times mistaken for Raynaud disease.[66] Although the symptoms of a glomus tumor can be nonspecific, the combination of imaging study findings described below helps paint a consistent picture of when glomus should be considered.[67]

Imaging with plain films (Figure 21) and CT may show well-defined bony erosion with a thin sclerotic margin of the adjacent bone if the lesion is subungual.

For lesions about 2.0 mm in size, US studies show well-circumscribed tumor with clear margins.[67] The tumors mostly appear homogeneous and hypoechoic. Another morphological trait seen by US are phalangeal bone erosions. Bone erosions are a break in the hyperechoic outline of the bony cortex. This bone deformity is found in about half of the glomus tumor cases and can actually be the only finding present in glomus tumors.[67] Bone erosions, or scalloping, often occur at the distal phalanx. Plain radiographs may be used to detect erosions, but US has a higher sensitivity.[68] When they are present, however, the tumor tends to be larger on average (>2 mm). Compared to radiographs and MRI, US is a superior method at detecting erosions. A 10- to 18-MHz transducer is recommended and has been shown to resolve erosions as small as 1.0 mm.[67,69] Functional US studies for glomus tumor evaluation includes color Doppler to examine relative blood flow velocities. A vast majority of glomus tumors appear hypervascular either within or adjacent

to the lesion. This property is observed independent of the presence of bony erosions.[67] The sensitivity of gray-scale US detection of glomus tumor tends to be quite high (86%) and this value increases further when bony erosions are included in the diagnostic criteria (93%).[67]

MRI of glomus tumor requires high-resolution MRI. Standard MRI is not sufficient to make a diagnosis especially for occult tumor cases.[70] MRI shows a lesion of low signal on T1W and high signal on T2W with strong enhancement (Figure 22).[71,72]

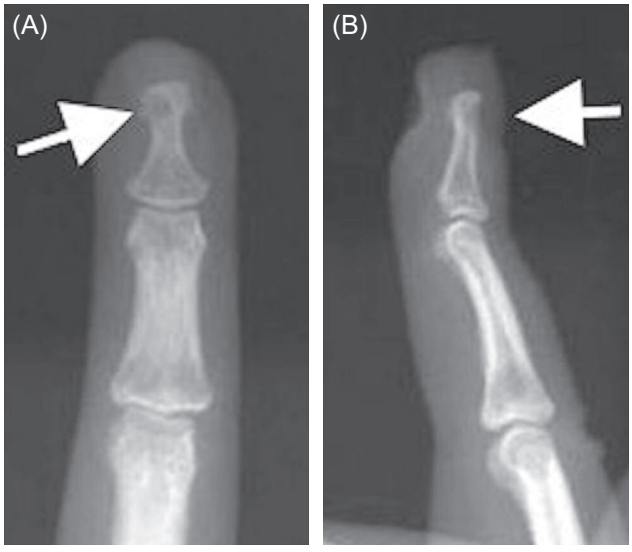


FIGURE 21 Subungual glomus tumor of the finger. AP (A) and lateral (B) radiographs of the ring finger show a subungual lucency (arrows) due to bony erosion by the tumor.

MALIGNANT PERIPHERAL NERVE SHEATH TUMORS

Malignant PNST is now the accepted name for tumors that previously may have been called neurosarcoma or malignant schwannoma.[73] These account for 5–10% of all soft tissue sarcomas.[73,74] They tend to occur in the 20- to 50-year age range. There is a nearly even sex distribution overall, but when the tumor occurs in a patient with NF1, there is a strong male predominance of up to 80%.[8,73] They are associated with NF1 in 25–70% of cases, and when they are, they occur a decade earlier than otherwise. The potential for degeneration of a benign PNST in a patient with NF1 to a malignant PNST is approximately 5%. Malignant PNSTs may also be secondary to radiotherapy, in which case there is usually a 10- to 20-year lag period from radiotherapy to presentation. This accounts for 11% of malignant PNSTs.[73,75]

Malignant PNSTs commonly involve large nerves such as the sciatic nerve and sacral and brachial plexi.[76] They present with a painful, rapidly enlarging mass, usually larger than 5 cm, often with neurologic symptoms and weakness. The tumor spreads along the nerve and hence may still have a fusiform shape.

Imaging is useful in helping to differentiate benign from malignant PNSTs. Benign PNSTs on MRI will show a well-circumscribed homogeneous low T1 signal and variable high T2 signal and may show a target sign of a central zone of low signal with surrounding increased signal on T2W images.[77] Malignant PNSTs

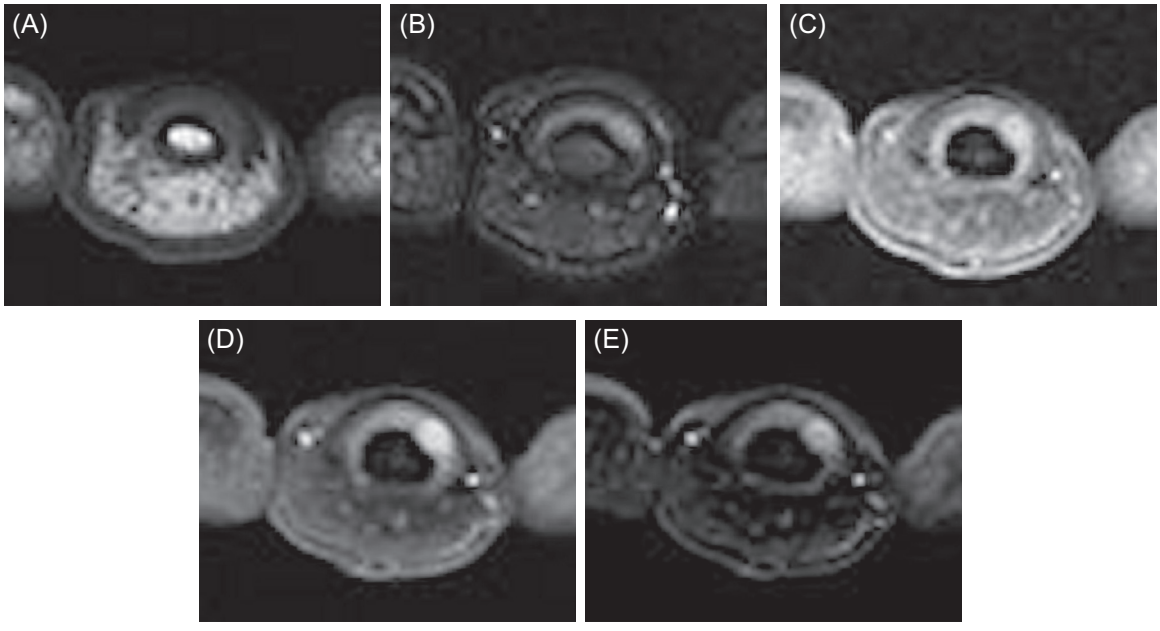


FIGURE 22 Subungual glomus tumor of the finger in a 37-year-old female. Axial MRI images: T1W (A), T2 with fat saturation (B), T1 with fat saturation pre-Gd (C), T1 with fat saturation post-Gd (D), and subtraction of (C) from (D) and (E). The technique shows the added advantage of subtraction in enhancing contrast.

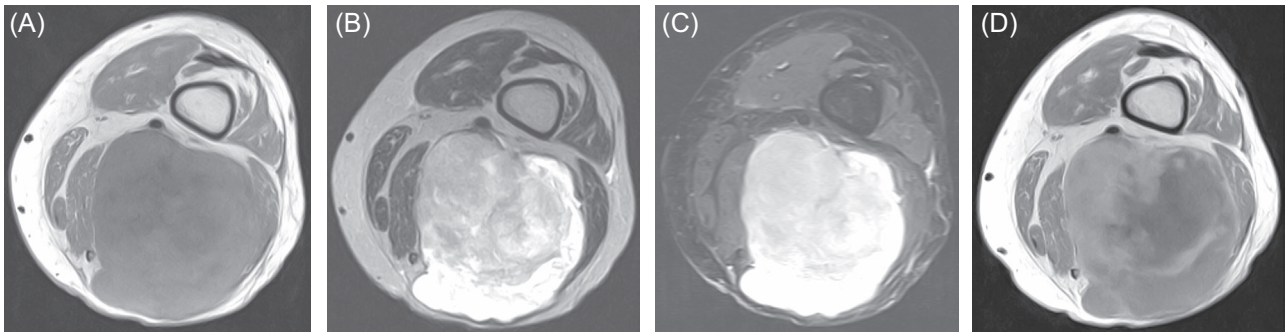


FIGURE 23 MPNST of the sciatic nerve just above the knee occurring in a 47-year-old man with known history of NF1. The mass has been present for 10 months and is painful and enlarging. Axial T1W (A), axial T2W (B), axial STIR (C), and axial T1W post-intravenous Gd (D). Note the large size of the lesion, its location along the line of the sciatic nerve, its heterogeneous signal, and its heterogeneous enhancement. *Courtesy of Robert Downey Boutin, MD, Medical Director, MedTel International, Davis, CA.*

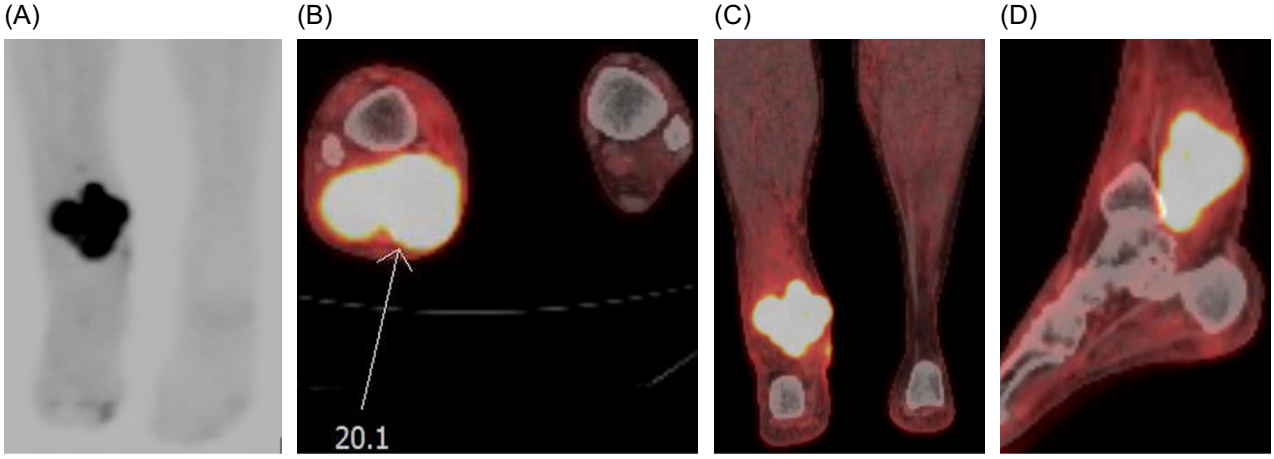


FIGURE 24 A 36-year-old man with NF1 with the development of an MPNST of the right lower leg. PET/CT images; coronal maximum intensity projection (A); axial, coronal, and sagittal fused images (B–D) showing the intense uptake in the tumor with an SUV_{max} of 20.1.

(Figure 23) show a heterogeneous mass[78] with areas of hyperintensity due to hemorrhage and necrosis and with infiltrative margins. Calcification is seen in 10–15% of tumors. The target sign on T2W imaging and post-Gd is less often seen. In a 2010 study, the following criteria resulted in a sensitivity of 60% and specificity of 90% when at least two criteria were present[79]: increased largest dimension of mass, presence of peripheral enhanced pattern, presence of perilesional edema-like zone, or intratumoral cystic lesion. The characteristic MRI features suggestive of malignant PNSTs are still observed with some benign PNSTs such that complete excision is often required for definitive diagnosis.[80]

Nuclear imaging of malignant PNST (MPNST) was traditionally with ^{67}Ga. When a ^{67}Ga citrate nuclear medicine study of PNST is positive, it is usually sarcomatous.[17,18] More recently PET and PET combined with CT (PET/CT) have proven useful diagnostic tools. Rather than looking solely at morphology, PET examines relative metabolic activity of tissues to distinguish MPNSTs from benign neoplastic processes. PET detects relative metabolic activity by measuring volumetric distribution as the standardized uptake value (SUV) of the radiotracer fluorodeoxyglucose (FDG) or carbon-11 methionine (^{11}C). Since 1995, ^{18}FDG-PET and PET/CT have emerged as useful tools in discriminating between benign PNSTs and transformation to MPNSTs, particularly in patients with NF1. These imaging modalities may reduce the number of surgical resections and are useful in biopsy planning.[81]

The sensitivity for detection of malignant lesions with PET ranged from 89% to 100% with a specificity between 72% and 100%.[82] Although there is no consensus on thresholds, maximum SUVs (SUV_{max}) <2.5 are generally benign and may be followed with clinical examination and repeat imaging.[82,83] SUV_{max} of 3.5 or greater is a reasonable threshold for further evaluation with biopsy, though false positives are likely to be seen at lower values. Indeed, there is a well-described overlap of SUV_{max} in the literature for benign and malignant lesions. Tumors with SUV_{max} greater than 7.0 are unlikely to be benign.[83] This was also shown to be useful in patients with underlying NF1[84] (Figure 24).

Absolute measures of SUV can possess considerable variability and less diagnostic utility as stand-alone values. PET SUV data are instead used to compute a semiquantitative SUV ratio between the tumor and the liver (T/L). Normalizing SUV data in this manner can increase

the sensitivity and specificity of MPNST diagnosis by PET. Conversely, sensitivity and specificity diminish if an MPNST has a particularly low or high SUV or the patient's liver has a high SUV. Sensitivity and specificity for suspicious lesions are optimized when the SUV T/L ratio is ≥1.5. Suspicious lesions are candidates for biopsy with possible surgical intervention.[85] Patients whose SUV T/L ratio is <1.5 are considered to have nonsuspicious lesions that should only be monitored. In a 2009 study, 3.5 was determined to be a meaningful cutoff point for T/L.[86] Additionally PET alone has been shown to be about as effective in diagnosing MPNSTs as coregistered PET/CT, although PET/CT is more useful for planning biopsy approaches.[81]

The time of FDG injection in PET imaging in these studies has ranged from 60 min to 4 h, with the latter posited to yield better sensitivity.[86,87] The potential utility of 90-min and 4-h imaging was investigated[88] and results show uptake is high in MPNSTs on both early and delayed imaging, with a time-dependent increase, and tends to stay lower for benign PNST.

FDG-PET may also allow for prediction of malignant transformation of benign PNSTs.[89–91] Increase in PNST volume, for instance, correlated with SUV >2.0 compared with lower values.[90] Among NF1 patients with suspicious lesions that were clinically concerning for MPNSTs, there was increased FDG uptake (SUV_{max} 2.7–19.5 g/ml) compared with nonsuspicious lesions (SUV_{max} 0.5–2.2 g/ml) despite benign findings on biopsy.[91] Further longitudinal studies are required to determine the natural course of such lesions.

Another radiotracer used in PET analysis of PNSTs is [^{11}C]methionine. This radiolabeled L-amino acid shows enhanced uptake particularly in tumors, in which cell proliferation is enhanced. Malignant tumors show significantly increased expression of transporters for this amino acid.[81] There are several situations in which [^{11}C]methionine might be favored over FDG as a radiotracer. If tumor and liver SUV values are similar (T/L equals approximately 1), the sensitivity and specificity of FDG-PET measurements diminish for diagnosis of MPNSTs. The ^{11}C tracer can be used as an alternative when FDG-PET results are equivocal because no liver-baseline is needed for a ^{11}C measurement. One major downside to ^{11}C imaging is its short 20-min half-life, compared to 110 min for FDG. Thus ^{11}C tracer requires constant cyclotron radionucleotide production.[81]

The rarity of MPNSTs limits the number of patients that have been assessed in these studies. Future work in this area is likely to better delineate parameters such as SUV thresholds for diagnosis and further workup, grading of MPNSTs, and prognosis.

These are usually high-grade sarcomas. As with other sarcoma metastases, metastases from MPNSTs go principally to the lung and bone. Local nodes are seen in only 9% of patients. Surgical excision and adjuvant chemotherapy and/or radiotherapy are the treatment of choice, but still 40–50% recur and 40–60% metastasize. The 5-year survival is approximately 44% and disease-specific mortality is greater than 40%, but is worse in the older patient with larger and more central lesions. Having underlying NF1 does not affect prognosis.[75,92,93]

METASTASES TO NERVES

Hematogenous metastases to nerves are rare and when seen involve the larger nerve trunks, such as the sciatic nerve (Figure 25). Direct invasion of peripheral nerves tends to occur to the brachial plexus, particularly with apical lung tumors (Pancoast tumors), and to the lumbosacral plexus with colorectal and gynecological

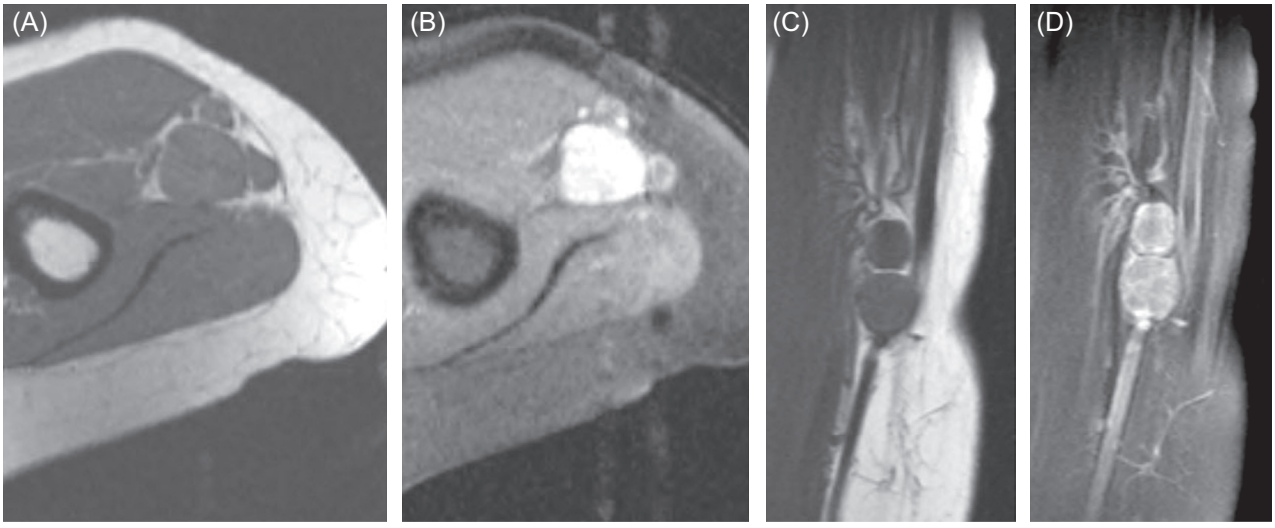


FIGURE 25 Metastatic melanoma to the median nerve of the arm in a 74-year-old female. Axial T1W (A), axial STIR (B), coronal T1W (C), and coronal T1W with fat saturation post-intravenous Gd (D). Note the location of the lesion in relation to the exiting nerve trunk, the high signal of the lesion on STIR images, and heterogeneous peripheral enhancement.

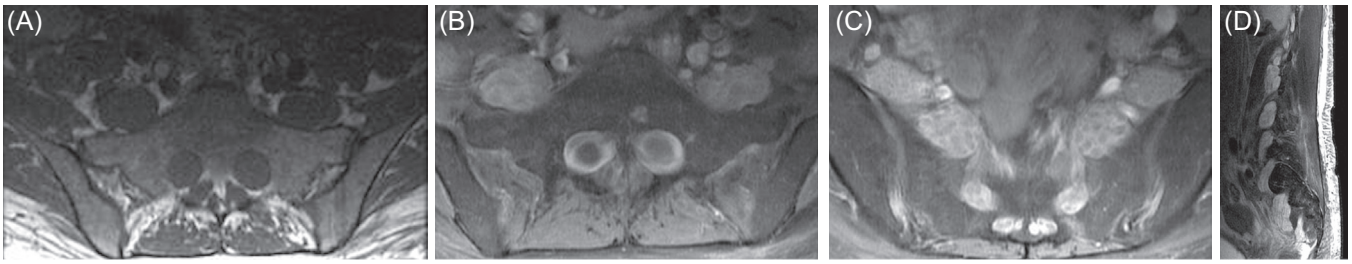


FIGURE 26 A 33-year-old female with refractory acute myeloid leukemia. The axial T1W image (A), axial T1W images with fat saturation following intravenous Gd (B) and (C), and sagittal T2W image with fat saturation (D) show presumed leukemic infiltration of nerve roots about the sacral plexus.

malignancy.[94–96] Diffuse infiltration of nerves may also occur with myelogenous leukemia (Figure 26).

SECONDARY SIGNS

In addition to the direct visualization of a neurogenic tumor, there may also be times when the secondary effects of nerve compression will be visualized by changes in the muscles supplied by that nerve.[97] This most often occurs when the tumor causes nerve entrapment at a fibro-osseous tunnel. These tunnels are most commonly adjacent to joints, when a nerve passes between a fixed structure such as the bone and a movable object such as the attachment of a tendon or ligament. Examples of such sites in the upper extremity include the suprascapular nerve in the suprascapular notch or spinoglenoid notch, the posterior interosseous nerve as it passes deep to the arcade of Frohse at the proximal aspect of the supinator muscle, the anterior interosseous nerve as it passes between the aponeurotic two heads of the flexor digitorum superficialis, and the median nerve in the carpal tunnel.

Within the lower extremity such sites include the common peroneal nerve in the fibular tunnel between the two heads of the peroneus longus and the tibial nerve or its branches, the medial and lateral plantar nerves, within the tibial tunnel on the medial aspect of the ankle. Examples of the patterns of muscle edema and atrophy are shown (Figures 19 and 27).

Muscle edema occurs 2–4 weeks after an acute injury and more gradually with nerve compression. This is because of water shift from intracellular to extracellular compartments, probably due to the loss of the energy-dependent pump. If the muscle is reinnervated at an early stage, eventually it will return to normal. Once fatty atrophy develops after several months some muscle damage will be irreversible.

SUMMARY

The combination of location, shape, and signal characteristics can usually lead to a diagnosis of a nerve sheath tumor or, less specifically, neurogenic tumor. The separation of neurilemoma from neurofibroma is problematic. High-resolution US may now be able to separate these in some cases, when the nerve can be seen in relation to the tumor. The larger and more heterogeneous a lesion is, in the presence of pain, suggests malignant nerve sheath tumor.

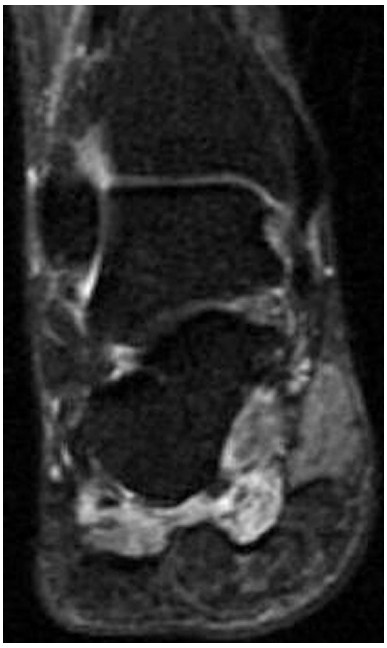


FIGURE 27 Coronal proton density with fat-saturation image of the hind foot. Note the high signal in all of the muscles of the plantar aspect compatible with either tibial nerve or combined medial and lateral plantar nerve compression, probably in the tibial tunnel.

References

1. Damjanov I, Linder J. Anderson's pathology. In: Kissane JM, ed. *Peripheral Nervous System*. 10th ed. St Louis, MO: Mosby; 1996: 2799–2803.
2. Fornage BD. Peripheral nerves of the extremities: imaging with US. *Radiology*. 1988;167:179–182.
3. Graif M, Seton A, Nerubai J, Horoszowski H. Sciatic nerve: sonographic evaluation and anatomic-pathologic considerations. *Radiology*. 1991;181:405–408.
4. Ikeda K, Haughton VM, Ho KC, Nowicki BH. Correlative MR-anatomic study of the median nerve. *AJR*. 1996;167:1233–1236.
5. Kransdorf MJ. Benign soft-tissue tumors in a large referral population: distribution of specific diagnoses by age, sex, and location. *AJR*. 1995;164:395–402.

6. Harkin JC, Reed RJ. Tumors of peripheral nervous system. In: *Atlas of Tumor Pathology, 2nd Ser, Fasc 3*. Washington, DC: Armed Forces Institute of Pathology; 1969:29–120.
7. Stout AP. The peripheral manifestations of the specific nerve sheath tumor (neurilemmoma). *Am J Cancer*. 1935;24:751–796.
8. Kransdorf M, Murphey MD. Neurogenic tumors. In: *Imaging of Soft Tissue Tumors*. Philadelphia: Saunders; 1997:235–273.
9. Resnick D. Tumors and tumor like lesions of soft tissues. In: Resnick D, ed. *Diagnosis of Bone and Joint Disorders*. 4th ed. Philadelphia: Saunders; 2002:4219–4222.
10. Harris WC, Alpert WJ, Marcinko DE. Elephantiasis neuromatosa in von Recklinghausen's disease. *J Am Podiatr Assoc*. 1982;72:70–72.
11. Lin J, Martel W. Cross sectional imaging of peripheral nerve sheath tumors. Characteristic signs on CT, MR imaging, and sonography. *AJR*. 2001;176:75–82.
12. Murphey M, Sean Smith W, Smitteh SE, Kransdorf MJ, Temple HT. Imaging of musculoskeletal neurogenic tumors: radiologic-pathologic correlation. *Radiographics*. 1999;19:1253–1280.
13. Pilvaki M, Chourmouzi D, Kiziridou A, Skordalaki A, Zarampoukas T, Drevelengas A. Imaging of peripheral nerve sheath tumors with pathologic correlation. Pictorial review. *Eur J Radiol*. 2004;52: 229–239.
14. Kamran SC, Shinagare AB, Howard SA, Hornick JL, Ramaiya NH. A–Z of malignant peripheral nerve sheath tumors. *Cancer Imaging*. October 26, 2012;12:475–483.
15. Berlin O, Stener B, Lindahl S, Irstam L, Lodding P. Vascularization of peripheral neurilemomas: angiographic, computed tomographic, and histologic studies. *Skeletal Radiol*. 1986;15:275–283.
16. Stener B, Angervall L, Nilsson L, Wickbom I. Angiographic and histologic studies of the vascularization of peripheral nerve tumors. *Clin Orthop Relat Res*. 1969;666:113–124.
17. Levine E, Huntrakoon M, Wetzel LH. Malignant nerve sheath neoplasms in neurofibromatosis: distinction from benign tumors by using imaging techniques. *AJR*. 1987;149:1059–1064.
18. Hammond JA, Driedger AA. Detection of malignant change in neurofibromatosis (von Recklinghausen's) by gallium-67 scanning. *Can Med Assoc J*. 1987;119:252–253.
19. Beggs I. Pictorial review: imaging of peripheral nerve tumours. *Clin Radiol*. 1997;52:8.
20. Beggs I. Sonographic appearance of nerve tumors. *J Clin Ultrasound*. 1999;27:363–368.
21. Tsai W, Chiou H, Chou Y, Wang H, Chiou S, Chang C. Differentiation between schwannomas and neurofibromas in the extremities and superficial body: the role of high-resolution and color Doppler ultrasonography. *J Ultrasound Med*. 2008;27(2):168–169, 161–166.
22. Reynolds DL, Jacobson JA, Inampudi P, Jamadar DA, Ebrahim FS, Hayes CW. Sonographic characteristics of peripheral nerve sheath tumors. *AJR Am J Roentgenol*. 2004;182(3):741–744.
23. Kumar AJ, Kuhajda FP, Martinez CR, Fishman EK, Jezic DV, Siegelman SS. Computed tomography of extracranial nerve sheath tumors with pathologic correlation. *J Comput Assist Tomogr*. 1983;7:857–865.
24. Cohen LM, Schwartz AM, Rockoff SD. Benign schwannomas: pathologic basis for CT inhomogeneities. *AJR*. 1983;147:141–143.
25. Thiebot J, Laissy JP, Delangre T, Biga N, Liotard A. Benign solitary neurinomas of the sciatic and popliteal nerves: CT study. *Neuroradiology*. 1991;33:186–188.
26. Chee DW, Peh WC, Shek TW. Pictorial essay: imaging of peripheral nerve sheath tumours. *Can Assoc Radiol J*. August 2011;62(3):176–182.
27. Cerofolini E, Landi A, DeSantis G, Mairorana A, Canossi G, Romagnoli R. MR of benign peripheral nerve sheath tumors. *J Comput Assist Tomogr*. 1991;15:593–597.
28. Soderlund V, Goranson H, Bauer HC. MR imaging of benign peripheral nerve sheath tumors. *Acta Radiol*. 1994;35:282–286.
29. Suh JS, Abenoza P, Galloway HR, Everson LI, Griffiths HJ. Peripheral (extracranial) nerve tumors: correlation of MR imaging and histologic findings. *Radiology*. 1992;183:341–346.
30. von Recklinghausen F. *Ueber die multiplen fibrome der haut und ihre beziehung zu den multiplen neuromen*. Berlin, Germany: August Hirchwald; 1882.
31. National Institutes of Health. Consensus development. *Neurofibromatosis Arch Neurol*. 1988;45:575–578.
32. National Institutes of Health Conference. Neurofibromatosis 1 (Recklinghausen disease) and neurofibromatosis 2 (bilateral acoustic neurofibromatosis): an update. *Ann Intern Med*. 1990;113:39–52.
33. Hillier JC, Moskovic E. The soft tissue manifestations of neurofibromatosis type 1. *Clin Radiol*. 2005;60:960–967.
34. Silverman TA, Enzinger FM. Fibrolipomatous hamartoma of nerve: a clinicopathologic analysis of 26 cases. *Am J Surg Pathol*. 1985;9:7–14.
35. Cavallaro MC, Taylor JAM, Gorman JD, Haghighi P, Resnick D. Imaging findings in a patient with fibrolipomatous hamartoma of the median nerve. *AJR*. 1993;161:837–838.
36. Evans HA, Donnelly LF, Johnson ND, Blebea JS, Stern PJ. Fibrolipoma of the median nerve: MRI. *Clin Radiol*. 1997;52:304–307.
37. Ban M, Kamiya H, Sato M, Kitajima Y. Lipofibro-matous hamartoma of the median nerve associated with macrodactyly and port-wine stain. *Pediatr Dermatol*. 1998;15:378–380.
38. Enzinger FM, Weiss SW. Benign tumors of peripheral nerves. In: *Soft Tissue Tumors*. 3rd ed. St Louis, MO: Mosby; 1995:821–888.
39. Spencer PS. The traumatic neuroma and proximal stump. *Bull Hosp Joint Dis*. 1974;35:85–102.
40. Huber GC, Lewis D. Amputation neuromas: their development and prevention. *Arch Surg*. 1920;1:85–113.
41. Gupta RK, Mehta VS, Banerji AK, Jain RK. MR evaluation of brachial plexus injuries. *Neuroradiology*. 1989;31:377–381.
42. Singson RD, Feldman F, Slipman CW, Gonzalez E, Rosenberg ZS, Kiernan H. Postamputation neuromas and other symptomatic stump abnormalities: detection with CT. *Radiology*. 1987;162:743–745.
43. Boutin RD, Pathria MN, Resnick D. Disorders in the stumps of amputee patients: MR imaging. *AJR*. 1998;171:497–501.
44. Singson RD, Feldman F, Staron R, Fechtner D, Gonzalez E, Stein J. MRI of postamputation neuromas. *Skeletal Radiol*. 1990; 19:259–262.
45. Henrot P, Stines J, Walter F, Martinet N, Paysant J, Blum A. Imaging of the painful lower limb stump. *Radiographics*. 2000;20:S219–S235.
46. Yamazaki H, Saitoh S, Seki H, Murakami N, Misawa T, Takaoka K. Peroneal nerve palsy caused by intraneural ganglion. *Skeletal Radiol*. 1999;28:52–56.
47. Nucci F, Artico M, Santoro A, et al. Intraneural synovial cyst of the peroneal nerve: report of two cases and review of the literature. *Neurosurgery*. 1990;26:339–344.
48. Leijten FS, Arts W-F, Puylaert JBCM. Ultrasound diagnosis of an intraneural ganglion cyst of the peroneal nerve. *J Neurosurg*. 1992;76:538–540.
49. Gambari PI, Giuliani G, Poppi M, Pozzati E. Ganglionic cysts of the peroneal nerve at the knee: CT and surgical correlation. *J Comput Assist Tomogr*. 1990;14:801–803.
50. Leon J, Marano G. MRI of peroneal nerve entrapment due to a ganglion cyst. *Magn Reson Imaging*. 1987;5:307–309.
51. Alexander IJ, Johnson KA, Parr JW. Morton's neuroma: a review of recent concepts. *Orthopedics*. 1987;10:103–106.
52. Mann RA, Reynolds JC. Interdigital neuroma: a critical analysis. *Foot Ankle*. 1983;3:238–243.
53. Theumann NH, Pfirrmann CWA, Chung CB, et al. Intermetatarsal spaces: analysis with MR bursography, anatomic correlation, and histopathology in cadavers. *Radiology*. 2001;221(2):478–484.
54. Zanetti M, Weishaupt D. MR imaging of the forefoot: Morton neuroma and differential diagnoses. *Semin Musculoskelet Radiol*. 2005;9(3):175–186.
55. Zanetti M, Strehle JK, Zollinger H, Hodler J. Morton neuroma and fluid in the intermetatarsal bursae on MR images of 70 asymptomatic volunteers. *Radiology*. 1997;203:516–520.

56. Larson E, Barrett S, Battiston B, Maloney C, Dellon A. Accurate nomenclature for forefoot nerve entrapment. *J Am Podiatr Med Assoc*. 2005;95:298–306.
57. Wu KK. Morton neuroma and metatarsalgia. *Curr Opin Rheumatol*. 2000;12(2):131–142.
58. Redd RA, Peters VJ, Emery SF, Branch HM, Rifkin MD. Morton neuroma: sonographic evaluation. *Radiology*. 1989;171:415–417.
59. Kaminsky S, Griffin L, Milsap J, Page D. Is ultrasonography a reliable way to confirm the diagnosis of Morton's neuroma. *Orthopedics*. 1997;20:37–39.
60. Quinn TJ, Jacobson JA, Craig JG, van Holsbeeck MT. Sonography of Morton's neuromas. *AJR Am J Roentgenol*. 2000;174(6):1723–1728.
61. Terk MR, Kwong PK, Suthar M, Horvath BC, Colletti PM. Morton neuroma: evaluation with MR imaging performed with contrast enhancement and fat suppression. *Radiology*. 1993;189(1):239–241.
62. Zanetti M, Ledermann T, Zollinger H, Hodler J. Efficacy of MR imaging in patients suspected of having Morton's neuroma. *AJR*. 1997;168:529–532.
63. Erickson SJ, Canale PB, Carrera GF, et al. Interdigital (Morton) neuroma: high-resolution MR imaging with solenoid coil. *Radiology*. 1991;181:833–836.
64. Weishaupt D, Treiber K, Kundert H-P, et al. Morton neuroma: MR imaging in prone, supine, and upright eight-bearing body positions. *Radiology*. 2003;226(3):849–856.
65. Zanetti M, Strehle JK, Kundert HP, Zollinger H, Hodler J. Morton neuroma: effect of MR imaging findings on diagnostic thinking and therapeutic decisions. *Radiology*. 1999;213(2):583–588.
66. Abdelrahman MH, Hammoudeh M. Glomus tumor presenting as raynaud's phenomenon. *Case Rep Med*. 2012;2012:380540.
67. Chiang YP, Hsu CY, Lien WC, Chang YJ. Ultrasonographic appearance of subungual glomus tumors. *J Clin Ultrasound*. 2014;42(6):336–340.
68. Debnath SC, Roy SK, Kaqiry RR. Subungual glomus tumor- clinical presentation and treatment. *Bangladesh J Plastic Surg*. 2012;3(2): 45–48.
69. Grechenig W, Clement HG, Fellinger M, et al. Scope and limitations of ultrasonography in the documentation of fractures—an experimental study. *Arch Orthop Trauma Surg*. 1998;117:368.
70. King ESJ. Glomus tumor. *Aust N Z J Surg*. 1954;23:280.
71. Drape JL, Idy-Peretti I, Goettmann S, et al. Subungual glomus tumors: evaluation with MR imaging. *Radiology*. 1995;195(2):507–515.
72. Theumann NH, Goettmann S, Le Viet D, et al. Recurrent glomus tumors of fingertips: MR imaging evaluation. *Radiology*. 2002;223:143–151.
73. Enzinger FM, Weiss SW. Malignant tumors of the peripheral nerves. In: *Soft Tissue Tumors*. 3rd ed. St Louis, MO: Mosby; 1995:889–928.
74. Kransdorf MJ. Malignant soft-tissue tumors in large referral population: distribution of diagnoses by age, sex, location. *AJR*. 1995;164:129–134.
75. Wanebo JE, Malik JM, VandenBerg SR, Wanebo HJ, Driesen N, Presing JA. Malignant peripheral nerve sheath tumors: a clinicopathologic study of 28 cases. *Cancer*. February 1993;71:1247–1253.
76. Ducatman DB, Scheithauer BW, Piepgras DG, Reiman HM, Ilstrup DM. Malignant peripheral nerve sheath tumors: a clinicopathologic study of 120 cases. *Cancer*. 1986;57:2006–2021.
77. Bhargava R, Parham DM, Lasater OE, Chari RS, Chen G, Fletcher BD. MR imaging differentiation of benign and malignant peripheral nerve sheath tumors: use of the target sign. *Pediatr Radiol*. 1997;27:124–129.
78. Mann FA, Murphy WA, Totty WG, Manaster BJ. Magnetic resonance imaging of peripheral nerve sheath tumors: assessment by numerical visual fuzzy cluster analysis. *Invest Radiol*. 1990;25:1238–1245.
79. Wasa J, Nishida Y, Tsukushi S, et al. MRI features in the differentiation of malignant peripheral nerve sheath tumors and neurofibromas. *AJR Am J Roentgenol*. 2010;194(6):1568–1574.
80. Crim JR, Seeger LL, Yao L, Chandnani V, Eckardt JJ. Diagnosis of soft-tissue masses with MR imaging: can benign masses be differentiated from malignant ones? *Radiology*. 1992;185:581–586.
81. Bredella MA1, Torriani M, Hornicek F, et al. Value of PET in the assessment of patients with neurofibromatosis type 1. *Am J Roentgenol*. 2007;189(4):928–935.
82. Treglia G, Taralli S, Bertagna F, et al. Usefulness of whole-body fluorine-18-fluorodeoxyglucose positron emission tomography in patients with neurofibromatosis type 1: a systematic review. *Radiol Res Pract*. 2012;2012:431029.
83. Karabatsou K, Kiehl TR, Wilson DM, et al. Potential role of 18fluorodeoxyglucose-positron emission tomography/computed tomography in differentiating benign neurofibroma from malignant peripheral nerve sheath tumor associated with neurofibromatosis 1. *Neurosurgery*. 2009;65:A160–A170.
84. Otsuka H, Graham MM, Kubo A, Nishitani H. FDG-PET/CT findings of sarcomatous transformation in neurofibromatosis: a case report. *Ann Nucl Med*. February 2005;19(1):55–58.
85. Combemale P, Valeyrie-Allanore L, Giammarile F, et al. Utility of 18F-FDG PET with a semi-quantitative index in the detection of sarcomatous transformation in patients with neurofibromatosis type 1. *PLoS One*. 2014;9(2):e85954. http://dx.doi.org/10.1371/journal.pone.0085954.
86. Ferner RE, Golding JF, Smith M, et al. [18F]2-fluoro-2-deoxy-D-glucose positron emission tomography (FDG PET) as a diagnostic tool for neurofibromatosis 1 (NF1) associated malignant peripheral nerve sheath tumours (MPNSTs): a long-term clinical study. *Ann Oncol*. 2008;19:390–394.
87. Cardona S, Schwarzbach M, Hinz U, et al. Evaluation of F18-deoxuglucose positron emission tomography (FDG-PET) to assess the nature of neurogenic tumors. *Eur J Surg Oncol*. 2003;29:536–541.
88. Warbey VS, Ferner RE, Dunn JT, Calonje E, O'Doherty MJ. FDG PET CT in diagnosis of MPNST in NF1. *Eur J Nucl Med Mol Imaging*. 2009;36.
89. Brenner W, Friedrich RE, Gawad KA, et al. Prognostic relevance of FDG PET in patients with neurofibromatosis type-1 and malignant peripheral nerve sheath tumors. *Eur J Nucl Med Mol Imaging*. 2006;33:428–432.
90. Fisher MJ, Basu S, Dombi E, et al. The role of [18F]-fluorodeoxyglucose positron emission tomography in predicting plexiform neurofibroma progression. *J Neurooncol*. 2008;87(2):165–171.
91. Meany H, Dombi E, Reynolds J, et al. 18-fluorodeoxyglucose-positron emission tomography (FDG-PET) evaluation of nodular lesions in patients with neurofibromatosis type 1 and plexiform neurofibromas (PN) or malignant peripheral nerve sheath tumors (MPNST). *Pediatr Blood Cancer*. 2013;60:59–64.
92. Anghileri M, Miceli R, Fiore M, et al. Malignant peripheral nerve sheath tumors: prognostic factors and survival in a series of patients treated at a single institution. *Cancer*. 2006;107:1065–1074.
93. Wong WW, Hirose T, Scheithauer BW, et al. Malignant peripheral nerve sheath tumour: analysis of treatment outcome. *Int J Radiat Oncol Biol Phys*. 1998;42:351–360.
94. Nagao E, Nishie A, Yoshimitsu K, et al. Gluteal muscular and sciatic nerve metastases in advanced urinary bladder carcinoma: case report. *Abdom Imaging*. 2004;29(5):619–622.
95. Jaeckle KA. Nerve plexus metastases. *Neurol Clin*. 1991;9(4): 857–866.
96. Hirota N, Fujimoto T, Takahashi M, Fukushima Y. Isolated trigeminal nerve metastases from breast cancer: an unusual cause of trigeminal mononeuropathy. *Surg Neurol*. 1998;49(5):558–561.
97. Allieu Y, Mackinnon S, eds. *Nerve Compression Syndromes of the Upper Limb*. Martin Dunitz; 2002.

CHAPTER

62

Neuroimaging of Cerebrovascular Complications in Cancer Patients

Prashant Nagpal[1], *Shehanaz Ellika*[2], *Rajan Jain*[3]

[1]Department of Radiology, University of Iowa Hospitals and Clinics, Iowa City, IA, USA; [2]Department of Radiology, Henry Ford Hospital, Detroit, MI, USA; [3]Department of Radiology, New York University School of Medicine, New York, NY, USA

INTRODUCTION

Cerebrovascular disease should be considered at the top of differentials in any cancer patient who presents with neurological symptoms. In cancer patients, cerebrovascular disease is the second most common cause of pathologically proven central nervous system (CNS) disease after metastases, with a large autopsy series reporting the presence of cerebrovascular disease in 14.6% of cancer patients.[1] It is symptomatic in the majority of the patients. The literature is divided among the most common cause of stroke in cancer patients, with a few studies showing atherosclerosis as the most common cause,[1] whereas other studies show embolic phenomenon as the most common cause.[2] These reports suggest that the etiopathogenesis of cerebrovascular disease is different in cancer patients than in the general population. Apart from the host factors, the etiology can be categorized as a direct effect of tumor, paraneoplastic syndromes, treatment complications, or a combination of these factors. Aggressive treatment approaches with multimodality management such as radiation therapy, chemotherapy, or combination therapies can cause additional stress, leading to unusual or accelerated cerebral vasculature disorders. As in the general population with neurological symptoms, imaging plays a very important role in diagnosis and treatment planning in the subset of the population with cancer. Sometimes the neurological symptoms may be the presenting feature of a cancer and in this population, imaging can guide diagnosis of the cancer.

The imaging workup in cancer patients with CNS symptoms typically starts with cerebral computed tomography (CT), which is less sensitive for diagnosis of stroke but is very useful in differentiating hemorrhagic stroke from ischemic stroke. Magnetic resonance imaging (MRI) is usually used after CT imaging, as it is more sensitive and specific for the diagnosis of various etiologies of stroke. CT/MRI angiography and venography can accurately depict the CNS vascular system and may guide interventions rather than diagnose pathologies in most cases. Perfusion imaging using MR or CT perfusion techniques can help in assessment of cerebral blood flow that further aids in evaluation of the cause and extent of cerebrovascular compromise. Imaging features of the cerebrovascular complications associated with tumors, mostly with CNS malignancies, either directly related to the tumor or related to the effects of the therapy, are reviewed in this chapter, with an emphasis on various advanced imaging techniques.

TUMOR-RELATED CEREBROVASCULAR COMPLICATIONS

Coagulopathy

Cancer is itself considered a hypercoagulable state that may predispose to stroke. Hypercoagulability is often related to activation of the coagulation cascade by cancer cells.[3] Stroke may also be related to disseminated intravascular coagulation (DIC), which can cause hemorrhagic stroke, or nonbacterial thrombotic endocarditis (NBTE), which typically causes embolic stroke. Thrombotic episodes may precede the diagnosis of malignancy by months or years and can present as migratory superficial thrombophlebitis (Trousseau syndrome), idiopathic venous

Handbook of Neuro-Oncology Neuroimaging, Second Edition
http://dx.doi.org/10.1016/B978-0-12-800945-1.00062-8

© 2016 Elsevier Ltd. All rights reserved.

thrombosis, NBTE (i.e., marantic endocarditis), DIC, or thrombotic microangiopathy (e.g., hemolytic–uremic syndrome) or with arterial thrombosis.[4] NBTE is a manifestation of the hypercoagulable state in cancer patients and is characterized by the formation of sterile platelet–fibrin vegetations on cardiac valves. The possibility of NBTE should be considered in all cancer patients who develop an acute stroke syndrome or in cancer patients presenting with cerebral embolism of unknown etiology.[5] The diagnosis of NBTE typically requires transesophageal echocardiography. Few studies have highlighted the use of D-dimer for diagnosis of hypercoagulability in cancer patients, but its utility is limited given the elevation of D-dimer in 30.5–90% of patients with cancer in various studies.[6–8] NBTE is most commonly associated with adenocarcinomas of the lung, ovary, biliary system, pancreas, and stomach. On neuroimaging, multiple and often hemorrhagic infarcts are seen in multiple vascular territories caused by embolization of cardiac platelet–fibrin vegetations or by thrombotic occlusion of medium- and small-sized vessels. Cerebral angiography can detect vascular occlusions typically involving middle cerebral artery branches.[9] Diffusion-weighted imaging can show multiple small (<10 mm), medium (10–30 mm), or large (>30 mm) areas of restricted diffusion in multiple territories in NBTE as opposed to infective endocarditis, which can have a single lesion, territorial infarction, or disseminated punctate lesions.[10]

Venous Thrombosis

Cerebral venous thrombosis (CVT) as a complication of cancer can occur as a result of primary hypercoagulability or direct tumor invasion by primary cancer/metastases or as a "paraneoplastic phenomenon," or it could be related to treatment agents like L-asparaginase.[11,12] CVT is seen more commonly with hematologic malignancies. The usual clinical presentation is with isolated headache, intracranial hypertension syndrome, seizures, a focal lobar syndrome, and encephalopathy.[13]

Initial imaging is typically done with a noncontrast CT (NCCT) scan that can show dense triangle sign due to occlusion of the superior sagittal sinus by a hyperdense clot or hyperdensity along the transverse sinus or, rarely, a cord sign due to visualization of a thrombosed cortical vein. NCCT can also demonstrate indirect signs of CVT that include hemorrhagic infarcts not conforming to an arterial vascular territory, nonspecific brain swelling, cortical sulcal effacement, or loss of gray–white matter differentiation.[14] Multifocal hemorrhagic infarcts are almost as frequent as nonhemorrhagic infarcts in CVT.[15,16] Contrast-enhanced CT can show the empty delta sign (Figure 1(A)), due to filling defects from a nonenhancing clot in the lumen and enhancement of small collateral veins in the walls of the sinus. Prominent

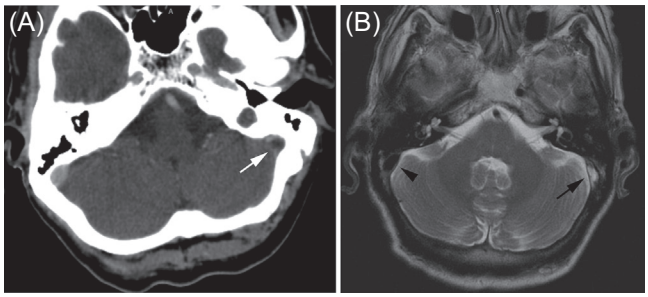


FIGURE 1 (A) Contrast-enhanced CT scan in a patient with small-cell lung carcinoma showing "empty delta sign" involving the left sigmoid sinus, a filling defect seen due to thrombosis (arrow). (B) Axial T2-weighted MR image showing loss of flow void in the left sigmoid sinus suggestive of thrombosis (arrow). Normal flow void is seen in the right sigmoid sinus (arrowhead).

tentorial enhancement may be seen due to venous collaterals and congestion. However, in up to 30% of cases, initial CT scan can be nondiagnostic particularly in patients with isolated intracranial hypertension.[16]

MRI is very sensitive in diagnosing CVT. Absence of blood flow in the thrombosed sinus results in loss of normal flow void seen on fast spin-echo images (Figure 1(B)). Various signal abnormalities in the involved dural sinus can be seen on MRI depending on the time interval between onset of thrombosis and imaging. MRI also helps to better delineate the associated parenchymal changes such as edema or hemorrhagic or nonhemorrhagic infarcts that occur secondary to venous drainage obstruction. Diffusion-weighted imaging (DWI) and apparent diffusion coefficient (ADC) pattern seen in venous infarcts are variable and heterogeneous, markedly different from that seen in pure arterial infarcts suggestive of vasogenic edema mixed with cytotoxic edema. This difference probably corresponds in part to the much better recovery observed in nonhemorrhagic venous infarcts with normal or increased ADC. It has been shown that within the venous infarct, even the areas with reduced ADC initially can be reversible.[17] MR venography (MRV) is currently the best noninvasive method for assessment of the cerebral venous system. In MRV, flow within the vein rises to bright signal intensity, and absence of flow is characterized by reduced signal intensity. MRV can be done using two-dimensional (2D) and 3D phase-contrast and time-of-flight (TOF) as well as 3D contrast-enhanced thin-section gradient-echo techniques. The TOF imaging can be limited by saturation effects at in-plane flow and by inclusion of substances with a short T1 relaxation time, like methemoglobin. On the other hand 3D phase-contrast MR angiography has a drawback of longer acquisition times, making it more susceptible to motion artifacts. Moreover, it requires an idea of flow velocity to prevent aliasing.[18] Compared with 2D TOF, 3D contrast-enhanced thin-section gradient-echo techniques are more sensitive to dural sinus thrombosis

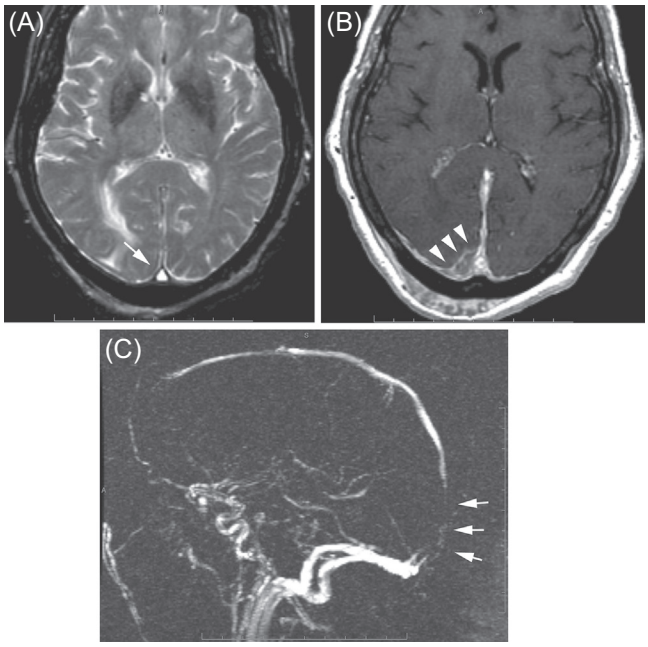


FIGURE 2 A 59-year-old female with metastatic breast carcinoma. (A) T2-weighted image showing loss of normal flow void and hyperintense signal in the superior sagittal sinus (arrow). (B) Postcontrast T1-weighted axial image showing enhancing dural metastases encasing and occluding the superior sagittal sinus (arrowheads). (C) Phase-contrast MR venogram showing nonvisualization of the posterior part of the superior sagittal sinus (arrows).

and are less affected by saturation artifacts.[19] With the advent of multislice CT scanners, CT venogram can be obtained very quickly with a high yield for diagnoses of venous sinus thrombosis. CT venography has been shown to be superior to MRV in visualizing dural sinuses or smaller cerebral veins with low flow and is at least equivalent in the diagnosis of dural sinus thrombosis.[18,20] CT venogram can be easier to interpret and have fewer artifacts than MRV and may be especially helpful in the very acute or late stages of CVT, when MRI can be misleading. Catheter angiography, which has been used extensively in the past to diagnose venous sinus thrombosis, has a limited role now, with the advent of various noninvasive techniques. The most reliable sign of CVT is the partial or complete lack of opacification of veins or dural sinuses on angiography. Some indirect angiographic signs include dilated collateral veins with a corkscrew appearance and delayed venous emptying.

CVT due to direct tumor invasion shows associated enhancing parenchymal, dural, or calvarial metastases encasing, compressing, or infiltrating the dural venous sinuses on CT or MRI (Figure 2). Differentiation of tumor thrombus from bland thrombus based on imaging findings can be difficult. Enhancement of thrombus filling an occluded venous sinus could not only be seen with tumor (Figure 3) but can also occur in subacute bland thrombus with neovascularization.

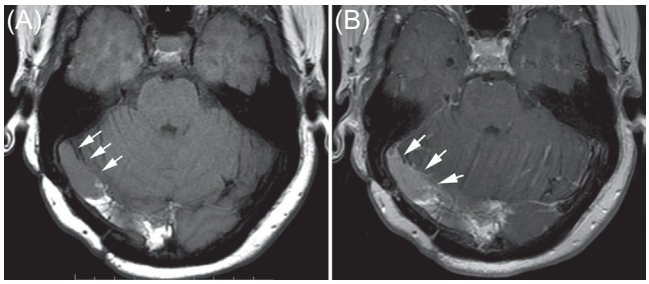


FIGURE 3 Axial (A) pre- and (B) postcontrast T1-weighted MR images in a patient presenting with venous sinus thrombosis showing an enhancing filling defect within the distal part of the right transverse sinus, which revealed tumor thrombus from an undifferentiated metastatic carcinoma on histopathology.

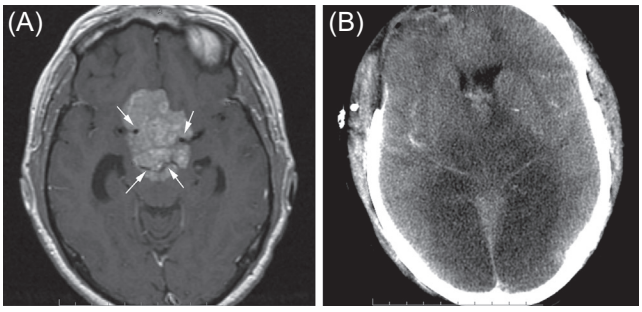


FIGURE 4 (A) Postcontrast T1-weighted axial MR image in a patient with a large suprasellar meningioma showing encasement of bilateral internal carotid artery terminus, basilar tip, and bilateral posterior cerebral arteries by the meningioma (arrows). (B) Postoperative CT scan showing bilateral posterior cerebral artery territory infarcts due to vascular compression and edema.

Direct Tumor-Related Compromise of Arterial Vasculature

Direct tumor-related stroke is an uncommon complication of intracranial neoplasms that is mostly due to encasement, compression, displacement, or invasion of intracranial vessels by tumors. Tumors that have been associated with direct arterial compromise include craniopharyngiomas, suprasellar germinomas, hypothalamic tumors, pituitary adenomas (usually with apoplexy), meningiomas, and astrocytomas.[21–23] Meningiomas arising from skull base and cavernous sinus regions can encase and narrow vessels forming the circle of Willis and compromise the cerebral blood blow. MRI with MRA can demonstrate the narrowing or occlusion of the major intracranial vessels by meningioma (Figure 4). Although uncommon, various reports in the literature have highlighted the direct effects of high-grade gliomas leading to ischemic stroke (Figure 5). It is well known that high-grade gliomas infiltrate the adjacent structures and have been shown to cause dissection of the middle cerebral artery,[24] arterial narrowing,[25] and vessel luminal obliteration.[26–28]

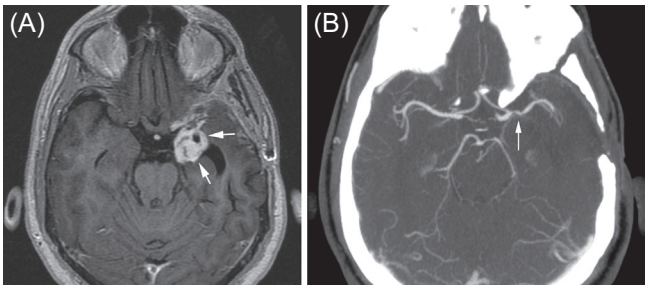


FIGURE 5 (A) Postcontrast T1-weighted axial images in a patient with recurrent anaplastic astrocytoma showing an enhancing lesion in the left temporal lobe, abutting the left middle cerebral artery (MCA) 3 years after external beam and stereotactic radiosurgery (60 Gy). (B) CT angiogram showing focal narrowing of the M1 segment of the left MCA.

Leptomeningeal Metastases

Tumor-related stroke could also occur owing to vascular involvement by leptomeningeal spread of cancer. Leptomeningeal metastases or carcinomatous meningitis results from metastatic spread to the cerebral vessels in the Virchow–Robin spaces. These can cause stroke either by vascular occlusion/spasm or by causing vasculopathic changes in the cerebral vessels.[29,30] Ischemic stroke has been described as a rare cause of focal cerebral symptoms in patients with carcinomatous meningitis.[31] Imaging is very helpful in diagnosis of leptomeningeal metastases. CT is usually the first-line modality but has limited utility in diagnosis of metastases. MRI is the best investigation for diagnosis of leptomeningeal metastases and has been shown to be more sensitive (reported sensitivity of 100%) than cerebrospinal fluid (CSF) analysis for diagnosis.[32] Nodular pial enhancement is one of the characteristic features of leptomeningeal metastases on gadolinium-enhanced MRI. Other features of leptomeningeal metastases that can be seen on MRI include hydrocephalus (often noncommunicating), multifocal cranial and spinal neural enhancement, and diffuse arachnoid enhancement.[32] Digital subtraction angiography is rarely used for diagnosis but can show segmental narrowing and wall irregularities in multiple proximal and distal vessels in the setting of leptomeningeal metastases from carcinoma.[31,33]

Tumor Emboli and Neoplastic Aneurysms

Infarction due to tumor emboli presenting with cerebral ischemia can be seen in patients with primary or metastatic neoplasm due to embolization of tumor fragments into the arterial circulation. This typically occurs mostly with lung cancer during surgical resection. Cardiac myxomas and choriocarcinomas are the two tumors most commonly associated with neoplastic aneurysms.[34–36] Cardiac myxomas are most common in the left atrium and hence are associated with systemic embolization in approximately 30–45% of cases, cerebral circulation being involved in one-half of these instances.[37–39] The source of embolus could be the tumor itself or thrombus on the surface of the tumor. Since the middle cerebral artery (MCA) contributes to the majority of blood supply to the brain, the MCA territory is most frequently affected (Figure 6).[40] Hematogenous spread of the tumor cells with tumor emboli can progress to development of parenchymal brain metastases (Figure 7) and

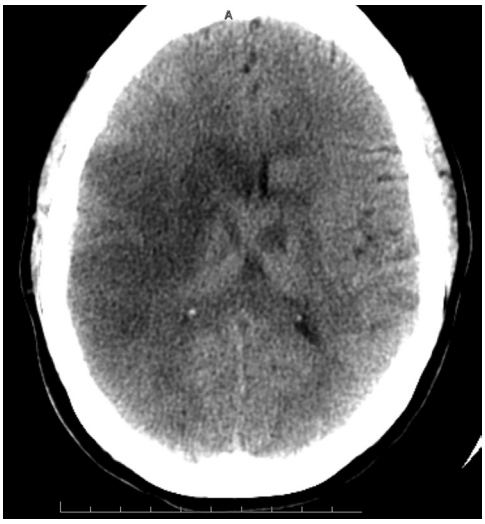


FIGURE 6 Noncontrast CT scan in a 34-year-old female with left atrial myxoma showing large acute infarct involving the right MCA territory along with multiple small infarcts in the left basal ganglia.

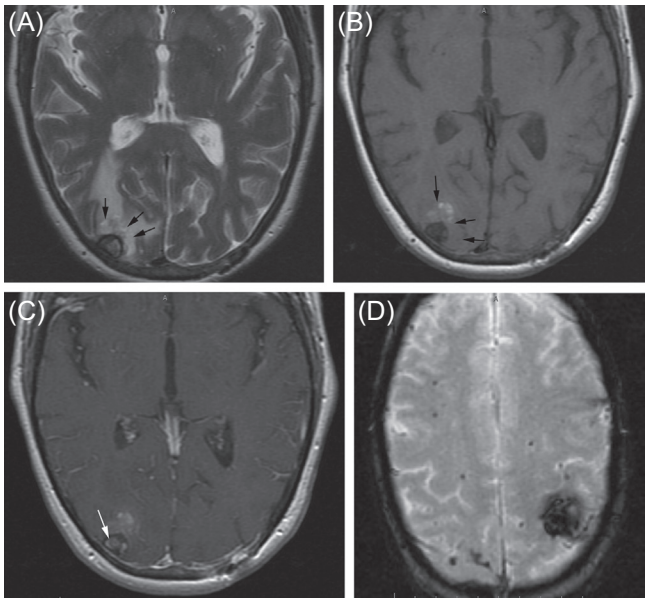


FIGURE 7 Axial (A) T2 and (B) pre- and (C) postcontrast T1-weighted MR images in a patient with atrial myxoma showing hemorrhagic lesion (arrows) with central enhancement (white arrow) in the right occipital lobe. (D) Axial gradient-echo image at the supratentorial level shows multiple blooming artifacts due to multiple other small hemorrhagic metastases, mostly at the corticomedullary junction, suggesting hematogenous spread and shower of tumor emboli.

intracerebral hemorrhage and rarely can also lead to formation of neoplastic aneurysms.[41] Neoplastic aneurysms are usually caused by tumor cells that lodge in smaller, distal, peripheral arteries, attach to the vessel wall, and invade the internal elastic lamina causing weakening of the endothelium and hence causing pseudoaneurysm formation similar to mycotic aneurysms.[42,43] These aneurysms have classically been diagnosed by catheter angiography and usually appear as irregular, fusiform, distal vessel aneurysms.

Tumor-Related Hemorrhagic Stroke

Tumor-related hemorrhage is the most common cause of hemorrhage in patients with solid tumors and occurs more commonly in metastases than in primary brain neoplasms. Lung, melanoma, and breast are the common metastatic solid tumors associated with hemorrhage, whereas leukemia is the most common hematological malignancy associated with tumor hemorrhage.[44] Primary neoplasms like pituitary adenomas, gliomas, meningiomas, schwannomas, oligodendrogliomas, and primitive neuroectodermal tumors have also been associated with intratumoral hemorrhage.[45] The mechanism of hemorrhage is probably due to rapid tumor growth with tumor necrosis, rupture of newly formed blood vessels, and invasion of adjacent cerebral blood vessels by tumors.[46] Hemorrhage usually produces acute symptoms that may be the presenting symptoms or be superimposed on the chronic course of the disease. The patients typically present with focal neurological deficit, headache, seizures, or sometimes with encephalopathy-like symptoms. Imaging of hemorrhage within a tumor (especially in a primary brain tumor or single metastasis) can present a diagnostic dilemma since hemorrhage obscures the mass lesion on imaging. On imaging, characteristics such as atypical location, multiple hemorrhagic sites, disproportionate vasogenic edema, and early enhancement may suggest a neoplastic hemorrhage. Various studies have shown promise using dual-energy CT for differentiation of tumor bleed and pure bleed.[47,48] True noncontrast images and postcontrast-enhanced images with two tube energies help to further obtain virtual noncontrast, color-coded iodine overlay and fusion images of iodine overlay. These help to identify tumor enhancement that gets masked by hemorrhage on conventional CT.[49]

On MRI, hemorrhagic tumors can also show heterogeneous signal characteristics due to blood products in different stages of evolution mixed with tumor (Figure 8). Delayed pattern of evolution of the hematoma can be seen in hemorrhagic neoplasms.[45,50] Neoplastic hemorrhage can also be differentiated from nonneoplastic hemorrhage by the absence of a well-defined complete hemosiderin rim around the hemorrhage.[51,52] This is due

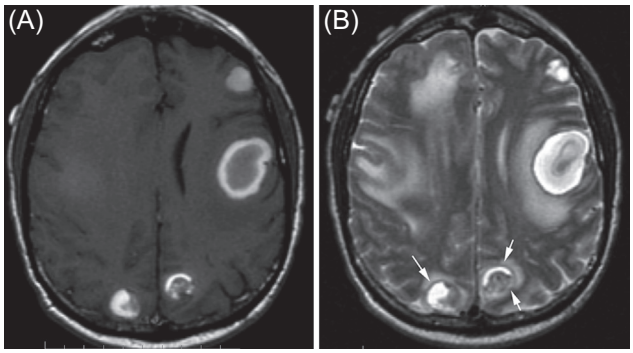


FIGURE 8 (A) Axial precontrast T1-weighted MR image showing multiple lesions showing hyperintense signal suggestive of subacute methemoglobin in a patient with metastatic amelanotic melanoma. (B) Axial T2-weighted image showing heterogeneous hyperintense lesions with incomplete peripheral hemosiderin rim and surrounding edema.

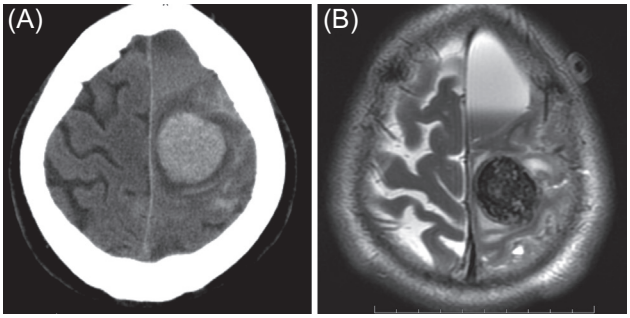


FIGURE 9 Axial (A) noncontrast CT and (B) T2-weighted MR images showing intratumoral and subarachnoid hemorrhage in a patient with a meningioma.

to the persistent and marked disruption of the blood–brain barrier that occurs with intracranial tumors and allows more efficient removal of the hemosiderin-laden macrophages.[51]

Hemorrhage may be purely intratumoral or may extend into the adjacent brain parenchyma depending upon the location of tumor and mechanism of hemorrhage. Similarly, hemorrhage can extend into the extra-axial spaces and tumors can be associated with subarachnoid, intraventricular, subdural, or epidural hemorrhage (Figure 9). Superficial tumors can rarely present with multiple episodes of subarachnoid hemorrhage and resultant superficial siderosis (SS). SS is caused by deposition of blood products in the leptomeninges, subpial tissue of the brain and spinal cord, and cranial nerves as a result of hemorrhage in the subarachnoid space. Bergmann glia of the cerebellum have a tendency toward accelerated ferritin synthesis and hence the cerebellum is preferentially involved in SS.[53] Various intracranial tumors such as ependymomas, oligodendrogliomas, astrocytomas, and vascular spinal tumors can be a source of repeated hemorrhages causing SS (Figure 10).[54] On MRI, in addition to the mass lesion, there is characteristic marginal T2 hypointensity around the brain stem, cerebellum, spinal cord, and cranial nerves.

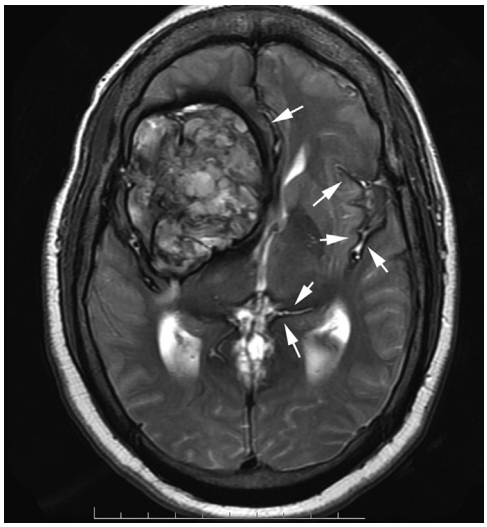


FIGURE 10 Axial T2-weighted image in a patient with oligodendroglioma showing a large heterogeneous intensity hemorrhagic tumor with hypointense signal along the pial surface of the brain parenchyma suggesting SS (arrows).

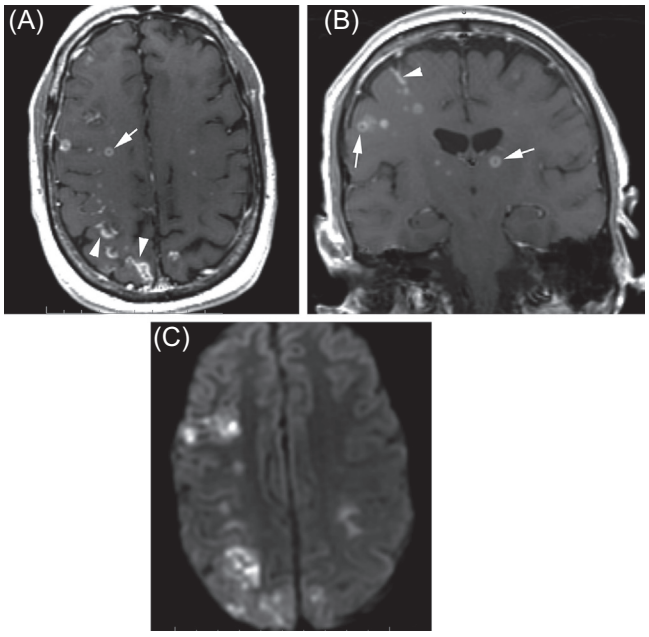


FIGURE 11 Postcontrast T1-weighted (A) axial and (B) coronal images in a patient with mycosis fungoides and CNS aspergillosis showing multiple, small, ring-enhancing abscesses (arrows) predominantly involving the corticomedullary junction and the basal ganglia. Multiple areas of gyral enhancement are also noted, suggesting cerebritis (arrowheads). (C) DWI shows corresponding areas of restricted diffusion (low ADC—not shown here) suggesting hematogenous spread and septic infarcts.

INFECTION-RELATED CEREBROVASCULAR COMPLICATIONS

Infection in cancer patients occurs owing to immunosuppression that is either related to antineoplastic therapy or induced by tumor. In severely immunocompromised hosts, angioinvasive pathogens like *Aspergillus* gain access to the systemic circulation and disseminate to end organs such as brain causing infarction or hemorrhage as the early radiologic presentation.[55] Owing to narrowing and acute angle branching of vessels, pyogenic abscesses and metastatic lesions have a predilection for the corticomedullary junction in the brain.[56] However, *Aspergillus* lesions are more commonly seen in the basal ganglia and thalami owing to involvement of perforating artery territories. MRI can show multiple disseminated small septic infarcts, which will involve the basal ganglia, thalami, and corpus callosum in addition to cortical and corticomedullary junction infarcts.[55,57–59] As these lesions are infarcts, DWI may also be useful for detecting early lesions and can be beneficial in differentiating these from progressive multifocal leukoencephalopathy and tumoral lesions. Associated cortical/gyral enhancement may suggest cerebritis. Further progression to multiple ring-enhancing abscesses, usually measuring less than 3 mm, can be seen commonly in the basal ganglia and at the corticomedullary junction, which may also show restricted diffusion in the necrotic component on DWI (Figure 11).[58] Although rare, *Candida* infections can present with encephalopathy and progressive cerebral signs. *Candida* brain abscesses are often associated with candidemia and endocarditis.[60]

Mycotic aneurysms are a rare complication of bacterial or fungal infections in immunosuppressed cancer patients. Most cerebral mycotic aneurysms developing in the course of bacterial endocarditis are multiple and are located along the distal branches, particularly of the MCA, and rarely in the posterior circulation.[61,62] These can rupture causing parenchymal or subarachnoid hemorrhage, but can also be found associated with cerebritis and abscesses. Among the fungal pathogens, *Aspergillus* is the most common causative agent of infective aneurysms.[63] Pathologically, there is septic embolization of the vasa vasorum or lumen of the artery with resultant focal arteritis, necrosis, and aneurysm formation.[64]

On imaging, it is difficult to distinguish infective and noninfective (berry) aneurysm, but infective aneurysms tend to be peripherally located and are fusiform in appearance (Figure 12).[65,66] But in approximately 33% of cases mycotic aneurysms are centrally located and differentiation based on location may be difficult.[67] Other features that may point toward diagnosis of mycotic aneurysm on imaging include arterial stenosis or occlusion close to the aneurysm, rapid change in morphology of the aneurysm, or presence of other infected aneurysms.[66] Both CT and MR angiography are excellent modalities for diagnosis of cerebral aneurysm with reported sensitivity and specificity of 92.8–94% and 90.2–100%, respectively, for 64-row multidetector CT compared to digital subtraction angiography (DSA).[68,69] Three-tesla MRI has shown to be comparable to multidetector computed tomography (MDCT)

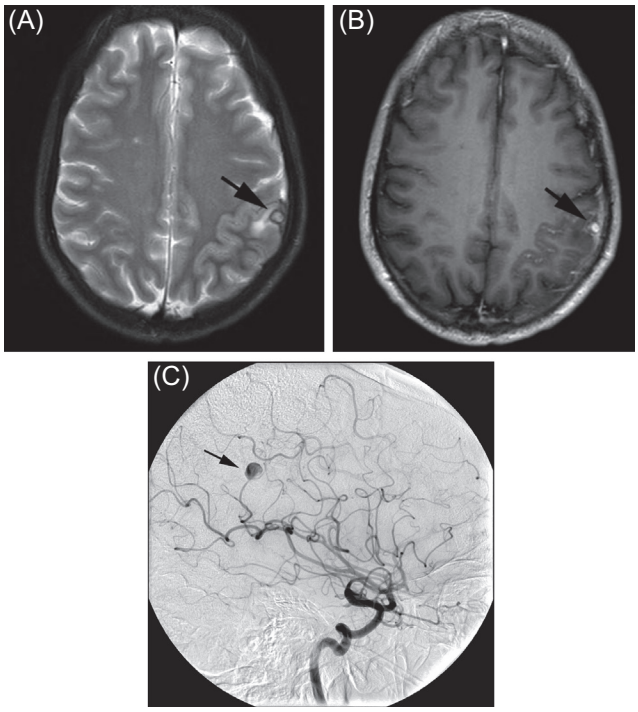


FIGURE 12 Axial (A) T2- and (B) postcontrast T1-weighted MR images in a patient with a distal mycotic aneurysm showing a small round peripheral lesion with peripheral hypointense rim and surrounding edema, showing central enhancement (arrow). (C) Oblique projection of a left internal carotid angiogram showing a distal left MCA aneurysm filling with contrast (arrow). *Courtesy of Dr Dheeraj Gandhi.*

for diagnosis of these aneurysms,[70] but DSA scores over both CT and MRI for diagnosis of small (<3 mm) aneurysms because of its high inherent spatial resolution.[71] Management of mycotic aneurysms is still a topic of debate but most studies have shown that both endovascular and neurosurgical techniques are equally safe and effective.[72]

THERAPY-RELATED CEREBROVASCULAR COMPLICATIONS

Radiation-Induced Cerebrovascular Complications

The radiation-induced vascular insult is an important cause of morbidity and mortality in cancer patients who receive head and neck radiation. The hypothesis of radiation-induced vascular disease is an acceleration of the atherosclerotic process probably due to endothelial cell damage, fibrosis of the intima–media layer, and development of atheromatous plaques, which is increased by occlusive changes in the vasa vasorum leading to ischemia of the arterial wall.[73,74] Radiation therapy administered for head and neck cancers or lymphoma is best known to cause carotid artery stenosis. Carotid duplex ultrasound detected 70% stenosis of the internal carotid artery in 11.7% patients irradiated for head and neck cancers in one series.[74]



FIGURE 13 Lateral projection of a left common carotid artery digital subtraction angiogram in a patient with previously irradiated undifferentiated carcinoma of the neck showing marked irregularity of the distal common carotid artery, external carotid, and internal carotid artery with contrast extravasation (arrowheads) suggestive of carotid blowout. Poor contrast opacification of the internal carotid artery is suggestive of occlusion (arrow).

Radiation-induced carotid artery lesions seem to have a disproportionately long segment involvement within the irradiated field, and not confined to the bifurcation,[75] and thus can be differentiated from the atherosclerotic stenosis. In addition, they are often associated with occlusion of other cervical arteries within the radiation portal.[76] In patients with nasopharyngeal cancer, radiation therapy has been linked to development of temporal lobe necrosis. Pathologically, in addition to direct radiation-induced injury, there is higher intima-media thickness and occurrence of plaque formation in carotid arteries of patients with temporal lobe necrosis.[77,78]

Carotid blowout syndrome is a rare but devastating complication of radiation therapy in the neck. Risk factors include radical tumor resection, flap necrosis, wound infection, and recurrent or persistent tumor in addition to radiation therapy. Carotid blowout can be classified as threatened, impending, or acute.[79,80] Threatened carotid blowout is when the vessel is exposed but there is no hemorrhage; impending blowout is when there is pseudoaneurysm formation that may be associated with intermittent hemorrhage. The third stage is acute carotid blowout with exsanguinating hemorrhage (Figure 13). Traditionally, emergency surgical ligation of the common carotid artery or the proximal internal carotid artery without provocative testing was the mainstay of treatment[79] but since the technique was associated with high chances of cerebral ischemia, various endovascular techniques like permanent

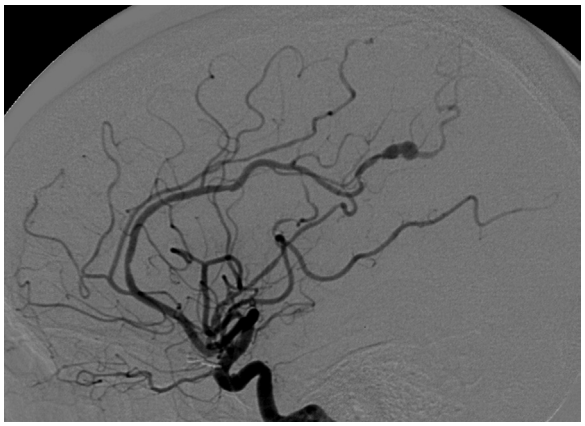


FIGURE 14 Lateral oblique projection of internal carotid angiogram in a patient who underwent radiation therapy 5 years previously showing irregularity and focal dilatation of one of the distal MCA branches due to radiation-induced vasculopathy.

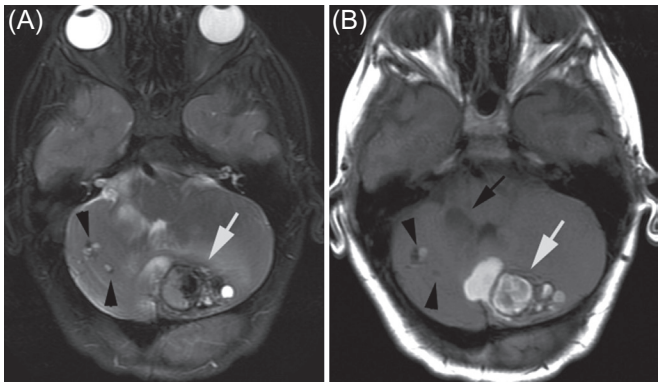


FIGURE 15 (A) Axial T2- and (B) T1-weighted MR images obtained 3 years after involved field radiation therapy at age 3 years for a posterior fossa ependymoma showing a large hemorrhagic, mixed-signal-intensity lobulated lesion (white arrow) in the left cerebellar hemisphere and vermis. Two more small cavernomas (black arrowheads) are seen in the right cerebellum. Postoperative changes (black arrow) are noted in the right cerebellum. *From Ref. 91, Figure 2(A) and (B).*

balloon occlusion or overlapping covered stents have been successfully used.[80–82] The various endovascular techniques are shown to have lesser mortality and morbidity compared to surgical ligation of the carotid artery.

Radiation-induced vasculopathy of larger intracranial vessels is a rare complication of radiation therapy and its incidence has a considerable correlation with radiation dose and age at the time of radiation therapy.[83] This occurs mostly in a delayed fashion following treatment to the tumors around the circle of Willis and can be accelerated in neurocutaneous syndromes.[84] Catheter angiography usually shows irregularity, narrowing, focal dilatation, or even occlusion of the affected vessels (Figure 14). Cerebral infarcts can be seen in the distribution of the affected vessels. When large or medium-sized vessels are affected, a Moyamoya-like pattern due to collateral formation can be seen on angiography. A Moyamoya-like pattern with development of small immature collateral vessels can also be produced by some tumors that cause slow occlusion of the major intracranial vessels.[85]

Mineralizing microangiopathy is another pathological entity, usually attributed to the combined toxicity of cranial irradiation and chemotherapy (usually intrathecal methotrexate), but can rarely be seen with radiotherapy alone.[86] It is characterized by the presence of mineralized deposits in the small vessels. Radiation therapy produces hyalinization and fibrinoid necrosis of small arteries and arterioles with endothelial proliferation and calcium deposition.[87–89] Dystrophic calcifications in the basal ganglia, subcortical white matter, and vascular border zones of the cerebral cortex are the usual imaging manifestations of this entity.[90]

Brain irradiation is also known to cause vascular malformations that can present with intracranial hemorrhage or can be asymptomatic and found on follow-up imaging.[91] Capillary telangiectasias usually occur 3–9 months after radiation, whereas cavernous malformations can have a latency period ranging from 1 to 26 years.[92–95] Appearance of a new hemorrhagic lesion in a patient previously treated with radiation, especially if treated in childhood, should always raise the possibility of a cavernoma in addition to neoplastic recurrence or metastases.[91] The diagnosis of radiation-induced cavernoma is made by typical popcorn-like appearance of cavernoma nidus with little or no surrounding edema on MRI (Figure 15, from Ref. 91, Figure 2(A) and (B)). Sometimes MRI characteristics can be blurred by the presence of acute hemorrhage and follow-up imaging can be useful in such cases.

Chemotherapy-Related Cerebrovascular Complications

Chemotherapy is an integral part of multimodal treatment for a wide variety of malignancies. The risk of cerebrovascular events increases in patients receiving adjuvant chemotherapy for a variety of hematological and solid malignancies.[96–98] L-Asparaginase, cisplatin, 5-fluorouracil, and methotrexate are well-recognized chemotherapeutic agents associated with stroke.[98] The underlying pathophysiology of these events remains obscure; however, both acute and long-term vascular toxicity may be associated with these agents.[99] The imaging findings in chemotherapy-associated ischemic stroke are similar to the appearance of ischemic stroke elsewhere.

Methotrexate (MTX) therapy is known to induce small-vessel vasculopathy that clinically mimics stroke and has a characteristic appearance on imaging.[100,101] Areas of restricted diffusion and hyperintensity on T2-weighted imaging are usually located in the periventricular white matter, particularly in the centrum semiovale,[102,103] and can be seen in 15–75% of patients during MTX chemotherapy.[104]

Despite restricted diffusion on MRI, patients often recover spontaneously from MTX-induced neurotoxicity.[90] DWI shows high signal on DW images and low ADC, suggesting cytotoxic edema; however, DWI findings are reversible, suggesting a transient metabolic derangement over an angiopathic or demyelinating process.[105]

Another commonly used chemotherapeutic agent associated with various neurovascular complications is L-asparaginase. It is commonly used in combination therapy for treatment of both adult and pediatric acute lymphoblastic leukemia. L-Asparaginase causes alterations in the level of antithrombin III and fibrinogen and is known to cause both hemorrhage and thromboembolic events,[106] with studies suggesting a fibrinogen level of <50 mg/dL as a risk factor for thrombotic events.[107] A study of 238 patients treated with L-asparaginase showed cerebral hemorrhages in 2.1% and cerebral thrombosis and thromboembolism in 4.2% of patients.[108] L-asparaginase-associated sinus thrombosis occurs usually during the remission/induction period, but has also been observed during the later course of polychemotherapy.[109] Patients usually present with severe headaches, and MR or CT venography can be used for the radiological confirmation of the sinus thrombosis.

Posterior reversible encephalopathy syndrome (PRES) is another neuroradiological entity associated with the use of chemotherapeutic agents that consists usually of a reversible encephalopathy, with predominant involvement of the posterior white matter. It usually occurs in association with acute hypertensive crisis and eclampsia, but has also been seen following treatment with immunosuppressive or chemotherapy agents.[110–112] On conventional catheter angiography, focal and diffuse areas of narrowing alternating with focal vasodilation often producing a string-of-beads appearance can be identified.[113] On perfusion MRI, there is a decrease in relative cerebral blood volume, confirming cerebral hypoperfusion and vasogenic edema from vasculopathy as the trigger for this entity rather than hyperperfusion from sudden elevations in systemic blood pressure exceeding the autoregulatory capability of the brain vasculature, as initially described by Hinchey et al.[111,112,114] The selective involvement of structures perfused by the posterior circulation and the rapid reversibility of symptoms indicate loss of autoregulation of the vertebrobasilar system, probably due to its relatively sparse sympathetic innervation. Classically, MR findings are typically those of vasogenic edema, with T2 and fluid-attenuated inversion recovery (FLAIR) hyperintensities predominantly involving the posterior parieto-occipital regions of the brain bilaterally. FLAIR images can show the lesions of PRES better owing to suppression of the adjacent CSF signal. These lesions usually show higher ADC on DWI and ADC maps that is suggestive of vasogenic edema, unlike cytotoxic edema in ischemic strokes that will have lower ADC.[111,114] Sometimes, when the condition is severe, there may be disruption of the blood–brain barrier, thereby leading to hemorrhage, enhancement on gadolinium-enhanced images, and cytotoxic edema with low ADC on DWI. These imaging features when present are associated with adverse clinical outcome.[114,115] Prompt reversal of triggering factor can lead to complete clinical recovery, with reversal of MRI lesions, but there may be persistent neurological sequelae, and if untreated, permanent neurologic deficit, or even death, may occur as a result of the ensuing cerebral infarctions or hemorrhages.[116]

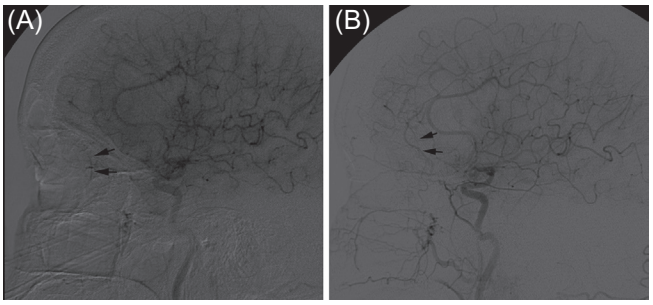


FIGURE 16 A 49-year-old patient with left frontal meningioma, who underwent preoperative endovascular embolization of the middle meningeal artery branches with polyvinyl alcohol (PVA) particles, complained of complete vision loss in the left eye following embolization. (A) Pre- and (B) postembolization lateral projection internal carotid arteriograms showing disappearance of choroidal blush due to occlusion of the retinal artery because of inadvertent embolization of PVA particles through arterial anastomoses.

Endovascular Therapy-Related Cerebrovascular Complications

Preoperative embolization of brain tumors such as meningioma is used to induce hemostasis and necrosis of the tumor for easier surgical manipulation and surgical removal of the tumor with less intraoperative blood loss.[117,118] Histologically, there is extensive tumor infarction after embolization that can also induce spontaneous intratumoral or subarachnoid hemorrhage due to rupture of fragile tumor vessels in a large, necrotic meningioma.[117,119] Usually dural branches of the external carotid artery branches supplying the tumor are amenable to embolization, but it is also possible to safely embolize dural branches of the internal carotid or vertebral arteries supplying the tumor.[120] Apart from the desired effects of preoperative embolization there may be inadvertent embolization of particulate embolic agent to the vessels supplying the normal brain. Ischemic stroke or blindness can occur because of very small extracranial–intracranial arterial anastomoses that open up because of altered flow hemodynamics during embolization (Figure 16). With the use of microcatheters that allow superselective angiography and precise delivery of embolizing agents, there is a reduction in the incidence of these complications.[120,121]

MISCELLANEOUS TUMOR-RELATED CEREBROVASCULAR CONDITIONS

Primary Angiitis of Central Nervous System

Primary angiitis of the CNS (PACNS) is a noninfectious granulomatous angiitis that has no clear etiological association, but some reports have shown its association with Hodgkin lymphoma.[23,122,123] It typically involves small- and medium-sized arteries of the brain and spinal cord and to a lesser degree may also involve small veins and venules. Associated infarction, hemorrhage, and demyelination and axonal degeneration can be seen in the adjacent brain parenchyma. The pathogenesis of this condition is unclear; however, a hypersensitivity reaction as well as autoimmune response has been suggested.[124,125] Symptomatology is variable and includes headache, focal or global neurological dysfunction, confusion, intellectual deterioration, memory loss, or malaise. T2-weighted MRI shows hyperintense foci representing ischemia, infarction, or inflammatory changes involving both the cortex and the white matter.[124,126,127] Postcontrast images show enhancing linear lesions predominantly involving brain stem and white matter that represent inflammation of the perforating arteries and perivascular tissues (Figure 17). Other less common presentations include hemorrhage[124,127] or focal lesion that may simulate a neoplasm.[128] Patients with Hodgkin disease who initially present with neurological symptoms due to PACNS have been shown to have a better outcome than those who present initially with the Hodgkin disease and later go on to develop PACNS.[23]

Intravascular Lymphomatosis

Intravascular lymphomatosis (IVL) is a rare intravascular subtype of extranodal large-cell lymphoma characterized by selective presence of neoplastic lymphomatous cells within the lumen of CNS blood vessels with no/minimal extravascular infiltration. Based on clinical presentation, it has been divided into two types: a conventional European type and an Asian variant. In the European variant, patients present with CNS or cutaneous disease, whereas in the Asian variant patients present with hepatosplenomegaly and pancytopenia.[129,130] When there is CNS involvement, malignant cells may cause multifocal vascular occlusion resulting in diffuse thrombosis. The entity shows poor response to therapy and is characterized by an extremely aggressive clinical course.[131] The affected blood vessels show reactive endothelial cells adjacent to lymphoma cells, and complete occlusion of vessel lumen can be seen.[132] Isolated CNS involvement with IVL may pose a diagnostic challenge since it may be difficult to distinguish these from other vasculitides such as primary angiitis of the CNS. MRI usually shows multifocal hyperintense lesions in the deep white matter on T2-weighted images that correlate with edema and gliosis seen on biopsy.[133–136] Small vessels (arterioles, capillaries, postcapillary venules) are more commonly involved than large vessels. Owing to the ischemic nature of the lesions in IVL the imaging findings are more pronounced on DWI in the acute phase.

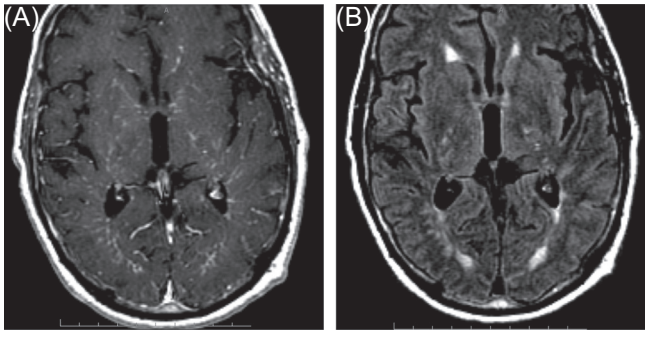


FIGURE 17 (A) Axial postcontrast T1-weighted image in a patient with Hodgkin lymphoma and associated PACNS showing extensive linear enhancement through the white matter suggestive of vasculitis. (B) Axial FLAIR image showing a few corresponding white matter lesions.

SUMMARY

Cerebrovascular complications associated with malignancies occur owing to a myriad of tumor, host, and treatment factors and can significantly contribute to morbidity and mortality in cancer patients. Any patient with a known cancer presenting with new neurological deficit should be evaluated to rule out cerebrovascular compromise in addition to tumor progression, recurrence, or metastases. In addition, a thromboembolic or hemorrhagic stroke as the initial presentation can also lead to diagnosis of an occult malignancy in a small but significant subset of cancer patients. Neuroimaging studies, particularly evaluating the cerebral vasculature, can help define the cause of stroke and thus help manage these patients. With development of perfusion imaging, the imaging has gone beyond morphological diagnosis and now can help predict the pathology. With further technical advancements like dual-energy CT and higher-strength MR scanners, the role of imaging in these patients continues to grow.

References

1. Graus F, Rogers LR, Posner JB. Cerebrovascular complications in patients with cancer. *Medicine (Baltimore)*. 1985;64(1):16–35.
2. Cestari DM, Weine DM, Panageas KS, Segal AZ, DeAngelis LM. Stroke in patients with cancer: incidence and etiology. *Neurology*. 2004;62(11):2025–2030.
3. Lee AY. Cancer and thromboembolic disease: pathogenic mechanisms. *Cancer Treat Rev*. 2002;28(3):137–140.

4. Levine M. Treatment of thrombotic disorders in cancer patients. *Haemostasis*. 1997;27(suppl 1):38–43.
5. Rogers LR, Cho ES, Kempin S, Posner JB. Cerebral infarction from non-bacterial thrombotic endocarditis. Clinical and pathological study including the effects of anticoagulation. *Am J Med*. 1987;83(4):746–756.
6. ten Wolde M, Kraaijenhagen RA, Prins MH, Büller HR. The clinical usefulness of D-dimer testing in cancer patients with suspected deep venous thrombosis. *Arch Intern Med*. 2002;162(16):1880–1884.
7. Dirix LY, Salgado R, Weytjens R, et al. Plasma fibrin D-dimer levels correlate with tumour volume, progression rate and survival in patients with metastatic breast cancer. *Br J Cancer*. 2002;86(3):389–395.
8. Gouin-Thibault I, Samama MM. Laboratory diagnosis of the thrombophilic state in cancer patients. *Semin Thromb Hemost*. 1999;25(2):167–172.
9. Rogers LR. Cerebrovascular complications in cancer patients. *Neurol Clin*. 2003;21(1):167–192.
10. Singhal AB, Topcuoglu MA, Buonanno FS. Acute ischemic stroke patterns in infective and nonbacterial thrombotic endocarditis: a diffusion-weighted magnetic resonance imaging study. *Stroke*. 2002;33(5):1267–1273.
11. Lee AY, Levine MN. Venous thromboembolism and cancer: risks and outcomes. *Circulation*. 2003;107(23 suppl 1):I17–I21.
12. Priest JR, Ramsay NK, Steinherz PG, et al. A syndrome of thrombosis and hemorrhage complicating L-asparaginase therapy for childhood acute lymphoblastic leukemia. *J Pediatr*. 1982;100(6):984–989.
13. Ferro JM, Canhao P. Cerebral venous sinus thrombosis: update on diagnosis and management. *Curr Cardiol Rep*. 2014;16(9):523.
14. Chiewvit P, Piyapittayanan S, Poungvarin N. Cerebral venous thrombosis: diagnosis dilemma. *Neurol Int*. 2011;3(3):e13.
15. Raizer JJ, DeAngelis LM. Cerebral sinus thrombosis diagnosed by MRI and MR venography in cancer patients. *Neurology*. 2000;54(6):1222–1226.
16. Crassard I, Bousser MG. Cerebral venous thrombosis. *J Neuroophthalmol*. 2004;24(2):156–163.
17. Ducreux D, Oppenheim C, Vandamme X, et al. Diffusion-weighted imaging patterns of brain damage associated with cerebral venous thrombosis. *AJNR Am J Neuroradiol*. 2001;22(2):261–268.
18. Khandelwal N, Agarwal A, Kochhar R, et al. Comparison of CT venography with MR venography in cerebral sinovenous thrombosis. *AJR Am J Roentgenol*. 2006;187(6):1637–1643.
19. Liang L, Korogi Y, Sugahara T, et al. Normal structures in the intracranial dural sinuses: delineation with 3D contrast-enhanced magnetization prepared rapid acquisition gradient-echo imaging sequence. *AJNR Am J Neuroradiol*. 2002;23(10):1739–1746.
20. Ozsvath RR, Casey SO, Lustrin ES, Alberico RA, Hassankhani A, Patel M. Cerebral venography: comparison of CT and MR projection venography. *AJR Am J Roentgenol*. 1997;169(6):1699–1707.
21. Lath R, Rajshekhar V. Massive cerebral infarction as a feature of pituitary apoplexy. *Neurol India*. 2001;49(2):191–193.
22. Mori K, Takeuchi J, Ishikawa M, Handa H, Toyama M, Yamaki T. Occlusive arteriopathy and brain tumor. *J Neurosurg*. 1978;49(1):22–35.
23. Rosen CL, DePalma L, Morita A. Primary angiitis of the central nervous system as a first presentation in Hodgkin's disease: a case report and review of the literature. *Neurosurgery*. 2000;46(6):1504–1508. Discussion 1508–1510.
24. Aoki N, Sakai T, Oikawa A, Takizawa T, Koike M. Dissection of the middle cerebral artery caused by invasion of malignant glioma presenting as acute onset of hemiplegia. *Acta Neurochir (Wien)*. 1999;141(9):1005–1008.
25. Zuchner S, Kawohl W, Sellhaus B, Mull M, Mayfrank L, Kosinski CM. A case of gliosarcoma appearing as ischaemic stroke. *J Neurol Neurosurg Psychiatry*. 2003;74(3):364–366.
26. Pina S, Carneiro Â, Rodrigues T, et al. Acute ischemic stroke secondary to glioblastoma. A case report. *Neuroradiol J*. 2014;27(1):85–90.
27. Obeid M, Ulane C, Rosenfeld S. Pearls & Oy-sters: large vessel ischemic stroke secondary to glioblastoma multiforme. *Neurology*. 2010;74(13):e50–51.
28. Chen H, Cebula H, Schott R, Dietemann JL, Froelich S. Glioblastoma multiforme presenting with ischemic stroke: case report and review of the literature. *J Neuroradiol*. 2011;38(5):304–307.
29. Lokan J, Galea L, Arumugaswamy A, Grigg A. Cerebral Hodgkin lymphoma causing leptomeningeal foam cell vasculopathy with cerebral infarction. *Leuk Lymphoma*. 2013;54(6):1321–1323.
30. Moonis M, Smith TW. Meningeal gliomatosis presenting as multiple cerebral infarcts: a case report. *Neurology*. 1996;46(6):1760–1762.
31. Klein P, Haley EC, Wooten GF, VandenBerg SR. Focal cerebral infarctions associated with perivascular tumor infiltrates in carcinomatous leptomeningeal metastases. *Arch Neurol*. 1989;46(10):1149–1152.
32. Collie DA, Brush JP, Lammie GA, et al. Imaging features of leptomeningeal metastases. *Clin Radiol*. 1999;54(11):765–771.
33. Wall JG, Weiss RB, Norton L, et al. Arterial thrombosis associated with adjuvant chemotherapy for breast carcinoma: a cancer and leukemia group B study. *Am J Med*. 1989;87(5):501–504.
34. Zairi F, De Saint Denis T, Thines L, Bourgeois P, Lejeune JP. Ruptured cerebral oncotic aneurysm from choriocarcinoma: report of two cases and review of the literature. *Acta Neurochir (Wien)*. 2011;153(2):353–357.
35. Wang J, Wang R, Zhao J. Ruptured cerebral aneurysm from choriocarcinoma. *J Clin Neurosci*. 2013;20(9):1324–1326.
36. Kalafut M, Vinuela F, Saver JL, Martin N, Vespa P, Verity MA. Multiple cerebral pseudoaneurysms and hemorrhages: the expanding spectrum of metastatic cerebral choriocarcinoma. *J Neuroimaging*. 1998;8(1):44–47.
37. Branch Jr CL, Laster DW, Kelly Jr DL. Left atrial myxoma with cerebral emboli. *Neurosurgery*. 1985;16(5):675–680.
38. Price DL, Harris JL, New PF, Cantu RC. Cardiac myxoma. A clinicopathologic and angiographic study. *Arch Neurol*. 1970;23(6):558–567.
39. Reynen K. Cardiac myxomas. *N Engl J Med*. 1995;333(24):1610–1617.
40. Hofmann E, Becker T, Romberg-Hahnloser R, Reichmann H, Warmuth-Metz M, Nadjmi M. Cranial MRI and CT in patients with left atrial myxoma. *Neuroradiology*. 1992;34(1):57–61.
41. Jean WC, Walski-Easton SM, Nussbaum ES. Multiple intracranial aneurysms as delayed complications of an atrial myxoma: case report. *Neurosurgery*. 2001;49(1):200–202. Discussion 202–203.
42. Murata J, Sawamura Y, Takahashi A, Abe H, Saitoh H. Intracerebral hemorrhage caused by a neoplastic aneurysm from small-cell lung carcinoma: case report. *Neurosurgery*. 1993;32(1):124–126.
43. Nomura R, Yoshida D, Kim K, Kobayashi S, Teramoto A. Intracerebral hemorrhage caused by a neoplastic aneurysm from pleomorphic lung carcinoma. *Neurol Med Chir (Tokyo)*. 2009;49(1):33–36.
44. Velander AJ, DeAngelis LM, Navi BB. Intracranial hemorrhage in patients with cancer. *Curr Atheroscler Rep*. 2012;14(4):373–381.
45. Rudoltz MS, Regine WF, Langston JW, Sanford RA, Kovnar EH, Kun LE. Multiple causes of cerebrovascular events in children with tumors of the parasellar region. *J Neurooncol*. 1998;37(3):251–261.
46. Kondziolka D, Bernstein M, Resch L, et al. Significance of hemorrhage into brain tumors: clinicopathological study. *J Neurosurg*. 1987;67(6):852–857.
47. Kim SJ, Lim HK, Lee HY, et al. Dual-energy CT in the evaluation of intracerebral hemorrhage of unknown origin: differentiation between tumor bleeding and pure hemorrhage. *AJNR Am J Neuroradiol*. 2012;33(5):865–872.
48. Phan CM, Yoo AJ, Hirsch JA, Nogueira RG, Gupta R. Differentiation of hemorrhage from iodinated contrast in different intracranial compartments using dual-energy head CT. *AJNR Am J Neuroradiol*. 2012;33(6):1088–1094.

49. De Cecco CN, Darnell A, Rengo M, et al. Dual-energy CT: oncologic applications. *AJR Am J Roentgenol*. 2012;199(5 suppl):S98–S105.
50. Atlas SW, Grossman RI, Gomori JM, et al. Hemorrhagic intracranial malignant neoplasms: spin-echo MR imaging. *Radiology*. 1987;164(1):71–77.
51. Grossman RI, Gomori JM, Goldberg HI, et al. MR imaging of hemorrhagic conditions of the head and neck. *Radiographics*. 1988;8(3):441–454.
52. Gomori JM, Grossman RI, Goldberg HI, Hackney DB, Zimmerman RA, Bilaniuk LT. Occult cerebral vascular malformations: high-field MR imaging. *Radiology*. 1986;158(3):707–713.
53. Kumar N. Neuroimaging in superficial siderosis: an in-depth look. *AJNR Am J Neuroradiol*. 2010;31(1):5–14.
54. Fearnley JM, Stevens JM, Rudge P. Superficial siderosis of the central nervous system. *Brain*. 1995;118(Pt 4):1051–1066.
55. DeLone DR, Goldstein RA, Petermann G, et al. Disseminated aspergillosis involving the brain: distribution and imaging characteristics. *AJNR Am J Neuroradiol*. 1999;20(9):1597–1604.
56. Delattre JY, Krol G, Thaler HT, Posner JB. Distribution of brain metastases. *Arch Neurol*. 1988;45(7):741–744.
57. Miaux Y, Ribaud P, Williams M, et al. MR of cerebral aspergillosis in patients who have had bone marrow transplantation. *AJNR Am J Neuroradiol*. 1995;16(3):555–562.
58. Keyik B, Edguer T, Hekimoglu B. Conventional and diffusion-weighted MR imaging of cerebral aspergillosis. *Diagn Interv Radiol*. 2005;11(4):199–201.
59. Guermazi A, Gluckman E, Tabti B, Miaux Y. Invasive central nervous system aspergillosis in bone marrow transplantation recipients: an overview. *Eur Radiol*. 2003;13(2):377–388.
60. Hagensee ME, Bauwens JE, Kjos B, Bowden RA. Brain abscess following marrow transplantation: experience at the Fred Hutchinson Cancer Research Center, 1984–1992. *Clin Infect Dis*. 1994;19(3):402–408.
61. Meena AK, Sitajayalakshmi S, Prasad VS, Murthy JM. Mycotic aneurysm on posterior cerebral artery: resolution with medical therapy. *Neurol India*. 2000;48(3):276–278.
62. Frazee JG, Cahan LD, Winter J. Bacterial intracranial aneurysms. *J Neurosurg*. 1980;53(5):633–641.
63. Clare CE, Barrow DL. Infectious intracranial aneurysms. *Neurosurg Clin N Am*. 1992;3(3):551–566.
64. Molinari GF, Smith L, Goldstein MN, Satran R. Pathogenesis of cerebral mycotic aneurysms. *Neurology*. 1973;23(4):325–332.
65. Chun JY, Smith W, Halbach VV, Higashida RT, Wilson CB, Lawton MT. Current multimodality management of infectious intracranial aneurysms. *Neurosurgery*. 2001;48(6):1203–1213. Discussion 1213–1214.
66. Chapot R, Houdart E, Saint-Maurice JP, et al. Endovascular treatment of cerebral mycotic aneurysms. *Radiology*. 2002;222(2):389–396.
67. Lee WK, Mossop PJ, Little AF, et al. Infected (mycotic) aneurysms: spectrum of imaging appearances and management. *Radiographics*. 2008;28(7):1853–1868.
68. Pozzi-Mucelli F, Bruni S, Doddi M, Calgaro A, Braini M, Cova M. Detection of intracranial aneurysms with 64 channel multidetector row computed tomography: comparison with digital subtraction angiography. *Eur J Radiol*. 2007;64(1):15–26.
69. Lubicz B, Levivier M, François O, et al. Sixty-four-row multisection CT angiography for detection and evaluation of ruptured intracranial aneurysms: interobserver and intertechnique reproducibility. *AJNR Am J Neuroradiol*. 2007;28(10):1949–1955.
70. Nael K, Villablanca JP, Mossaz L, et al. 3-T contrast-enhanced MR angiography in evaluation of suspected intracranial aneurysm: comparison with MDCT angiography. *AJR Am J Roentgenol*. 2008;190(2):389–395.
71. Papke K, Kuhl CK, Fruth M, et al. Intracranial aneurysms: role of multidetector CT angiography in diagnosis and endovascular therapy planning. *Radiology*. 2007;244(2):532–540.
72. Allen LM, Fowler AM, Walker C, et al. Retrospective review of cerebral mycotic aneurysms in 26 patients: focus on treatment in strongly immunocompromised patients with a brief literature review. *AJNR Am J Neuroradiol*. 2013;34(4):823–827.
73. Murros KE, Toole JF. The effect of radiation on carotid arteries. A review article. *Arch Neurol*. 1989;46(4):449–455.
74. Cheng SW, Wu LL, Ting AC, Lau H, Lam LK, Wei WI. Irradiation-induced extracranial carotid stenosis in patients with head and neck malignancies. *Am J Surg*. 1999;178(4):323–328.
75. Loftus CM, Biller J, Hart MN, Cornell SH, Hiratzka LF. Management of radiation-induced accelerated carotid atherosclerosis. *Arch Neurol*. 1987;44(7):711–714.
76. Melliere D, Becquemin JP, Berrahal D, Desgranges P, Cavillon A. Management of radiation-induced occlusive arterial disease: a reassessment. *J Cardiovasc Surg (Torino)*. 1997;38(3):261–269.
77. Chen J, Dassarath M, Yin Z, Liu H, Yang K, Wu G. Radiation induced temporal lobe necrosis in patients with nasopharyngeal carcinoma: a review of new avenues in its management. *Radiat Oncol*. 2011;6:128.
78. Ye J, Rong X, Xiang Y, Xing Y, Tang Y. A study of radiation-induced cerebral vascular injury in nasopharyngeal carcinoma patients with radiation-induced temporal lobe necrosis. *PLoS One*. 2012;7(8):e42890.
79. Chaloupka JC, Putman CM, Citardi MJ, Ross DA, Sasaki CT. Endovascular therapy for the carotid blowout syndrome in head and neck surgical patients: diagnostic and managerial considerations. *AJNR Am J Neuroradiol*. 1996;17(5):843–852.
80. Haas RA, Ahn SH. Interventional management of head and neck emergencies: carotid blowout. *Semin Interv Radiol*. 2013;30(3):245–248.
81. Farivar BS, Lee DH, Khalil A, Abrol S, Flores L. Carotid blowout syndrome: endovascular management of acute hemorrhage with tapering overlapped covered stents. *Ann Vasc Surg*. 2014;28.
82. Dequanter D, Shahla M, Paulus P, Aubert C, Lothaire P. Transarterial endovascular treatment in the management of life-threatening carotid blowout syndrome in head and neck cancer patients: review of the literature. *J Mal Vasc*. 2013;38(6):341–344.
83. Brant-Zawadzki M, Anderson M, DeArmond SJ, Conley FK, Jahnke RW. Radiation-induced large intracranial vessel occlusive vasculopathy. *AJR Am J Roentgenol*. 1980;134(1):51–55.
84. Omura M, Aida N, Sekido K, Kakehi M, Matsubara S. Large intracranial vessel occlusive vasculopathy after radiation therapy in children: clinical features and usefulness of magnetic resonance imaging. *Int J Radiat Oncol Biol Phys*. 1997;38(2):241–249.
85. Rajakulasingam K, Cerullo LJ, Raimondi AJ. Childhood moyamoya syndrome. Postradiation pathogenesis. *Childs Brain*. 1979;5(5):467–475.
86. Rabin BM, Meyer JR, Berlin JW, Marymount MH, Palka PS, Russell EJ. Radiation-induced changes in the central nervous system and head and neck. *Radiographics*. 1996;16(5):1055–1072.
87. Chen CY, Zimmerman RA, Faro S, Bilaniuk LT, Chou TY, Molloy PT. Childhood leukemia: central nervous system abnormalities during and after treatment. *AJNR Am J Neuroradiol*. 1996;17(2):295–310.
88. Parker BR. Leukemia and lymphoma in childhood. *Radiol Clin North Am*. 1997;35(6):1495–1516.
89. Shanley DJ. Mineralizing microangiopathy: CT and MRI. *Neuroradiology*. 1995;37(4):331–333.
90. Keime-Guibert F, Napolitano M, Delattre JY. Neurological complications of radiotherapy and chemotherapy. *J Neurol*. 1998;245(11):695–708.

91. Jain R, Robertson PL, Gandhi D, Gujar SK, Muraszko KM, Gebarski S. Radiation-induced cavernomas of the brain. *AJNR Am J Neuroradiol*. 2005;26(5):1158–1162.
92. Hassler O, Movin A. Microangiographic studies on changes in the cerebral vessels after irradiation. 1. Lesions in the rabbit produced by 60Co gamma-rays, 195kV and 34MV roentgen rays. *Acta Radiol Ther Phys Biol*. 1966;4(4):279–288.
93. Heckl S, Aschoff A, Kunze S. Radiation-induced cavernous hemangiomas of the brain: a late effect predominantly in children. *Cancer*. 2002;94(12):3285–3291.
94. Reinhold HS, Hopewell JW. Late changes in the architecture of blood vessels of the rat brain after irradiation. *Br J Radiol*. 1980;53(631):693–696.
95. Chourmouzi D, Papadopoulou E, Kontopoulos A, Drevelegas A. Radiation-induced intracranial meningioma and multiple cavernomas. *BMJ Case Rep*. 2013;2013.
96. Czaykowski PM, Moore MJ, Tannock IF. High risk of vascular events in patients with urothelial transitional cell carcinoma treated with cisplatin based chemotherapy. *J Urol*. 1998;160(6 Pt 1):2021–2024.
97. El Amrani M, Heinzlef O, Debroucker T, Roullet E, Bousser MG, Amarenco P. Brain infarction following 5-fluorouracil and cisplatin therapy. *Neurology*. 1998;51(3):899–901.
98. Saynak M, Cosar-Alas R, Yurut-Caloglu V, Caloglu M, Kocak Z, Uzal C. Chemotherapy and cerebrovascular disease. *J BUON*. 2008;13(1):31–36.
99. Gerl A. Vascular toxicity associated with chemotherapy for testicular cancer. *Anticancer Drugs*. 1994;5(6):607–614.
100. Gosavi TD, Ahmad MT, Lee LH, Lim SH. Methotrexate induced leucoencephalopathy: a stroke mimic. *Ann Indian Acad Neurol*. 2013;16(3):418–421.
101. Rollins N, Winick N, Bash R, Booth T. Acute methotrexate neurotoxicity: findings on diffusion-weighted imaging and correlation with clinical outcome. *AJNR Am J Neuroradiol*. 2004;25(10):1688–1695.
102. Asato R, Akiyama Y, Ito M, et al. Nuclear magnetic resonance abnormalities of the cerebral white matter in children with acute lymphoblastic leukemia and malignant lymphoma during and after central nervous system prophylactic treatment with intrathecal methotrexate. *Cancer*. 1992;70(7):1997–2004.
103. Matsumoto K, Takahashi S, Sato A, et al. Leukoencephalopathy in childhood hematopoietic neoplasm caused by moderate-dose methotrexate and prophylactic cranial radiotherapy–an MR analysis. *Int J Radiat Oncol Biol Phys*. 1995;32(4):913–918.
104. Mahoney Jr DH, Shuster JJ, Nitschke R, et al. Acute neurotoxicity in children with B-precursor acute lymphoid leukemia: an association with intermediate-dose intravenous methotrexate and intrathecal triple therapy–a pediatric oncology group study. *J Clin Oncol*. 1998;16(5):1712–1722.
105. Haykin ME, Gorman M, van Hoff J, Fulbright RK, Baehring JM. Diffusion-weighted MRI correlates of subacute methotrexate-related neurotoxicity. *J Neurooncol*. 2006;76(2):153–157.
106. Hunault-Berger M, Chevallier P, Delain M, et al. Changes in antithrombin and fibrinogen levels during induction chemotherapy with L-asparaginase in adult patients with acute lymphoblastic leukemia or lymphoblastic lymphoma. Use of supportive coagulation therapy and clinical outcome: the CAPELAL study. *Haematologica*. 2008;93(10):1488–1494.
107. Beinart G, Damon L. Thrombosis associated with L-asparaginase therapy and low fibrinogen levels in adult acute lymphoblastic leukemia. *Am J Hematol*. 2004;77(4):331–335.
108. Fleischhack G, Solymosi L, Reiter A, Bender-Gotze C, Eberl W, Bode U. Imaging methods in diagnosis of cerebrovascular complications with L-asparaginase therapy. *Klin Padiatr*. 1994;206(4):334–341.
109. Corso A, Castagnola C, Bernasconi C. Thrombotic events are not exclusive to the remission induction period in patients with acute lymphoblastic leukemia: a report of two cases of cerebral sinus thrombosis. *Ann Hematol*. 1997;75(3):117–119.
110. Ay H, Buonanno FS, Schaefer PW, et al. Posterior leukoencephalopathy without severe hypertension: utility of diffusion-weighted MRI. *Neurology*. 1998;51(5):1369–1376.
111. Bartynski WS. Posterior reversible encephalopathy syndrome, part 1: fundamental imaging and clinical features. *AJNR Am J Neuroradiol*. 2008;29(6):1036–1042.
112. Hinchey J, Chaves C, Appignani B, et al. A reversible posterior leukoencephalopathy syndrome. *N Engl J Med*. 1996;334(8):494–500.
113. Bartynski WS, Boardman JF. Catheter angiography, MR angiography, and MR perfusion in posterior reversible encephalopathy syndrome. *AJNR Am J Neuroradiol*. 2008;29(3):447–455.
114. Hugonnet E, Da Ines D, Boby H, et al. Posterior reversible encephalopathy syndrome (PRES): features on CT and MR imaging. *Diagn Interv Imaging*. 2013;94(1):45–52.
115. Covarrubias DJ, Luetmer PH, Campeau NG. Posterior reversible encephalopathy syndrome: prognostic utility of quantitative diffusion-weighted MR images. *AJNR Am J Neuroradiol*. 2002;23(6):1038–1048.
116. Keyserling HF, Provenzale JM. Atypical imaging findings in a near-fatal case of posterior reversible encephalopathy syndrome in a child. *AJR Am J Roentgenol*. 2007;188(1):219–221.
117. Gruber A, Killer M, Mazal P, Bavinzski G, Richling B. Preoperative embolization of intracranial meningiomas: a 17-years single center experience. *Minim Invasive Neurosurg*. 2000;43(1):18–29.
118. Hieshima GB, Everhart FR, Mehringer CM, et al. Preoperative embolization of meningiomas. *Surg Neurol*. 1980;14(2):119–127.
119. Bendszus M, Monoranu CM, Schutz A, Nolte I, Vince GH, Solymosi L. Neurologic complications after particle embolization of intracranial meningiomas. *AJNR Am J Neuroradiol*. 2005;26(6):1413–1419.
120. Borg A, Ekanayake J, Mair R, et al. Preoperative particle and glue embolization of meningiomas: indications, results, and lessons learned from 117 consecutive patients. *Neurosurgery*. 2013;73 (2 suppl operative):244–251. Discussion 252.
121. Raper DM, Starke RM, Henderson F, et al. Preoperative embolization of intracranial meningiomas: efficacy, technical considerations, and complications. *AJNR Am J Neuroradiol*. 2014;35(9):1798–1804.
122. Grimm S, Chamberlain M. Hodgkin's lymphoma: a review of neurologic complications. *Adv Hematol*. 2011;2011. 624578.
123. Yuen RW, Johnson PC. Primary angiitis of the central nervous system associated with Hodgkin's disease. *Arch Pathol Lab Med*. 1996;120(6):573–576.
124. Greenan TJ, Grossman RI, Goldberg HI. Cerebral vasculitis: MR imaging and angiographic correlation. *Radiology*. 1992;182(1):65–72.
125. Kolodny EH, Rebeiz JJ, Caviness Jr VS, Richardson Jr EP. Granulomatous angiitis of the central nervous system. *Arch Neurol*. 1968;19(5):510–524.
126. Campi A, Benndorf G, Filippi M, Reganati P, Martinelli V, Terreni MR. Primary angiitis of the central nervous system: serial MRI of brain and spinal cord. *Neuroradiology*. 2001;43(8):599–607.
127. Pomper MG, Miller TJ, Stone JH, Tidmore WC, Hellmann DB. CNS vasculitis in autoimmune disease: MR imaging findings and correlation with angiography. *AJNR Am J Neuroradiol*. 1999;20(1):75–85.
128. Calabrese LH, Duna GF. Evaluation and treatment of central nervous system vasculitis. *Curr Opin Rheumatol*. 1995;7(1):37–44.

129. Armitage JO. My treatment approach to patients with diffuse large B-cell lymphoma. *Mayo Clin Proc*. 2012;87(2):161–171.
130. Mizutani T. Neurological disturbances caused by intravascular lymphomatosis. *Brain Nerve*. 2011;63(5):443–449.
131. Glass J, Hochberg FH, Miller DC. Intravascular lymphomatosis. A systemic disease with neurologic manifestations. *Cancer*. 1993;71(10):3156–3164.
132. Chapin JE, Davis LE, Kornfeld M, Mandler RN. Neurologic manifestations of intravascular lymphomatosis. *Acta Neurol Scand*. 1995;91(6):494–499.
133. al-Chalabi A, Sivakumaran M, Holton J, West KP, Wood JK, Abbott RJ. A case of intravascular malignant lymphomatosis (angiotropic lymphoma) with raised perinuclear antineutrophil cytoplasmic antibody titres–a hitherto unreported association. *Clin Lab Haematol*. 1994;16(4):363–369.
134. Hashimoto H, Naritomi H, Kazui S, et al. Presymptomatic brain lesions on MRI in a patient with intravascular malignant lymphomatosis. *J Neuroimaging*. 1998;8(2):110–113.
135. Wick MR, Mills SE. Intravascular lymphomatosis: clinicopathologic features and differential diagnosis. *Semin Diagn Pathol*. 1991;8(2):91–101.
136. Liow K, Asmar P, Liow M, et al. Intravascular lymphomatosis: contribution of cerebral MRI findings to diagnosis. *J Neuroimaging*. 2000;10(2):116–118.

CHAPTER

63

Neuroimaging in Paraneoplastic Syndromes

Justin T. Jordan[1], *Steven Vernino*[2]

[1]Massachusetts General Hospital, Department of Neurology, Division of Neuro-Oncology, Boston, MA, USA;
[2]Department of Neurology & Neurotherapeutics, University of Texas Southwestern Medical Center, Dallas, TX, USA

Imaging studies are an important component in the evaluation of paraneoplastic neurological syndromes. Characteristic magnetic resonance imaging (MRI) abnormalities are found in several (but not all) of these syndromes. Generally, imaging findings are best seen on fluid-attenuated inversion recovery (FLAIR) and T2 sequences and demonstrate little or no contrast enhancement. The lack of contrast enhancement helps to distinguish paraneoplastic disorders from malignant disease. Similarly, normal diffusion-weighted imaging and angiography may help distinguish from ischemic vascular disease. Conversely, there are many central nervous system (CNS) paraneoplastic disorders that have no associated MRI abnormalities. In these cases, imaging of the neuraxis is still necessary to evaluate for alternative (and more common) neurological diagnoses such as inflammatory or demyelinating disease, mass lesions, or vascular abnormalities. Finally, most paraneoplastic disorders of the peripheral or autonomic nervous systems also have no associated imaging abnormalities.

When evaluating possible paraneoplastic neurological syndromes, nonneurological diagnostic imaging is also critical to detect systemic malignancies. Most patients with neurological paraneoplastic syndromes present with neurological symptoms prior to their diagnosis of cancer.[1–4] In patients with known cancer, the onset of neurological symptoms may herald the recurrence of tumor. Tumors in these patients tend to be small and localized. Serological studies and assessment of cancer risk factors can help identify possible sites of malignancy, though often imaging studies are necessary to find these lesions prior to diagnostic biopsy. Utilization of multiple imaging modalities can improve the early detection of small malignancies.[3,5]

PARANEOPLASTIC CEREBELLAR DEGENERATION

Despite the dramatic and disabling symptoms of this disorder, imaging of the cerebellum is usually unremarkable early in the disease course of paraneoplastic cerebellar degeneration (PCD) (see Figure 1(A)). The cerebellum and associated brainstem nuclei typically appear normal on cranial MRI.[6] Abnormal MRI signal or contrast enhancement is distinctly unusual, but may be seen in rare cases with rapid progression.[7] In a few isolated reports of fulminant cerebellar degeneration, FLAIR abnormalities in the cerebellar parenchyma may represent vasogenic edema. Signal abnormalities in the brainstem or mesial temporal lobes may be seen when PCD coexists with other paraneoplastic disorders (such as brainstem or limbic encephalitis). Even when conventional imaging is normal, positron emission tomographic (PET) imaging may show hypermetabolism in the cerebellar cortex.[8]

Months after the development of symptoms, cranial MRI and computed tomography (CT) may begin to show diffuse cerebellar atrophy corresponding to permanent neuronal loss. The cerebellum becomes diffusely atrophic, although the loss of tissue is most notable in midline structures (see Figure 1).

PARANEOPLASTIC LIMBIC ENCEPHALITIS

In cases of paraneoplastic limbic encephalitis (PLE) that are not associated with N-methyl-D-aspartate receptor (NMDAR) antibodies (addressed separately), cranial MRI is often abnormal. The usual pattern is unilateral

© 2016 Elsevier Ltd. All rights reserved.

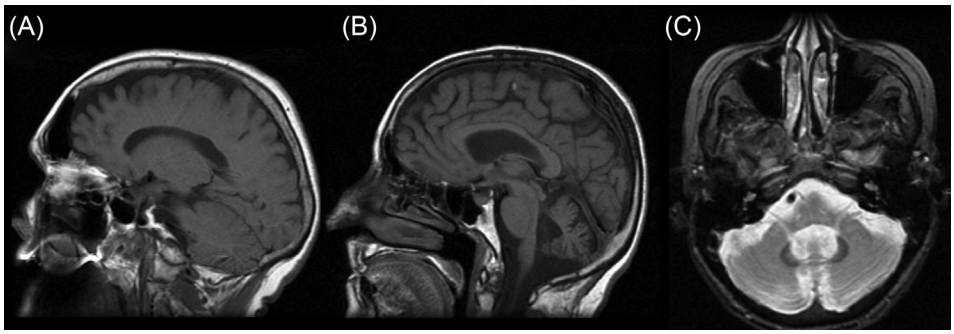


FIGURE 1 Paraneoplastic cerebellar degeneration. (A) Off-midline sagittal T1 spin echo image demonstrates the relative lack of atrophy often seen early in the course of PCD. Despite severe neurological disability, initial brain imaging studies are usually normal. (B) Sagittal T1 spin-echo MRI shows prominent cerebellar atrophy. This is the most common finding in more advanced cases. (C) Axial T2-weighted image through the cerebellum demonstrates atrophy without signal abnormality.

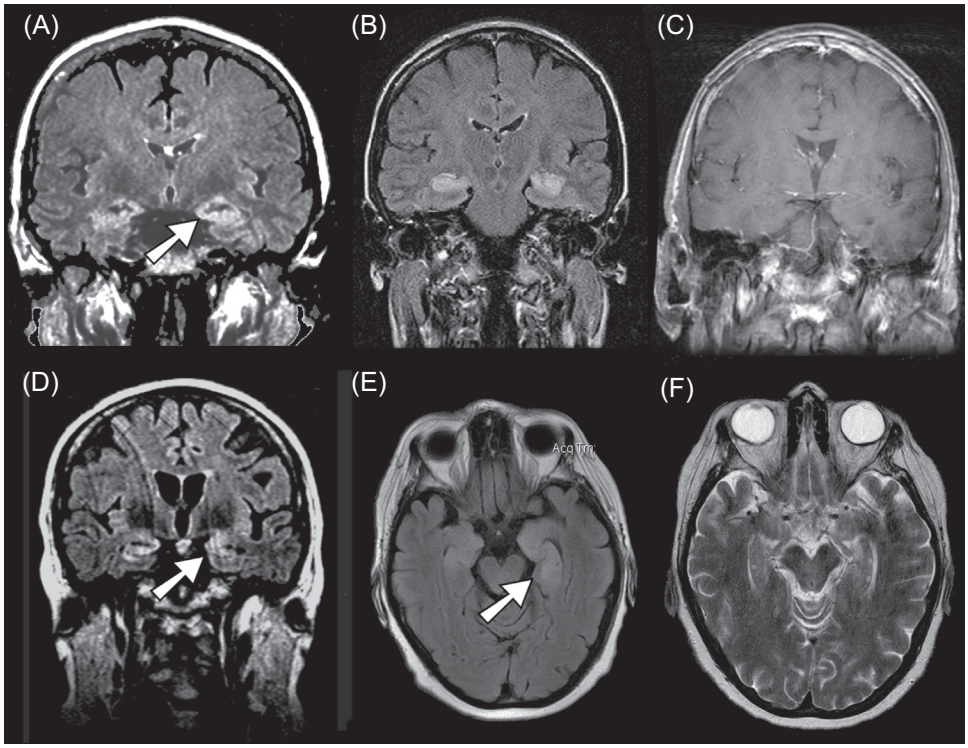


FIGURE 2 Paraneoplastic limbic encephalitis. (A) Coronal FLAIR image through the mesial temporal lobes shows increased signal involving the hippocampus (arrow) and amygdala. These signal abnormalities are often present bilaterally but may be asymmetric. Early in the disease course, there is minimal cortical or mesial temporal atrophy. These changes can be similar to those seen in herpes encephalitis. (B) Nearly identical findings can be seen in nonparaneoplastic autoimmune limbic encephalitis. Coronal FLAIR image from a patient with limbic encephalitis and voltage-gated potassium channel antibodies. (C) The mesial temporal abnormalities in PLE generally show no enhancement on gadolinium-enhanced images. (D–F) MR images from a patient with PLE show that the imaging abnormalities are best appreciated on coronal FLAIR images (D, arrow). They can also be seen on axial FLAIR images (E, arrow) although the mesial temporal area is also prone to artifact on the axial FLAIR sequence. PLE abnormalities are usually not conspicuous on the axial T2 scan (F).

or bilateral (asymmetric) T2/FLAIR hyperintensity in the mesial temporal lobes, involving the amygdala and hippocampal formations (see Figure 2).[9] In addition to the mesial temporal areas, other limbic structures may also become involved, especially the insular cortex (see Figure 3). Several reports have shown that limbic areas may appear hypermetabolic on cranial PET imaging (see Figure 3),[10,11] sometimes even in the setting of normal MRI.[12] One retrospective analysis of MRI and PET imaging in 18 limbic encephalitis patients suggested that antibodies directed at intracellular markers (Hu, Ri, GAD) are more likely to show mesiotemporal PET abnormality than those directed at cell surface markers (VGKC, NMDAR).[13] Because of the location and subtlety of these MRI abnormalities, if present at all, they may be missed on standard axial MRI series. Coronal T2/FLAIR

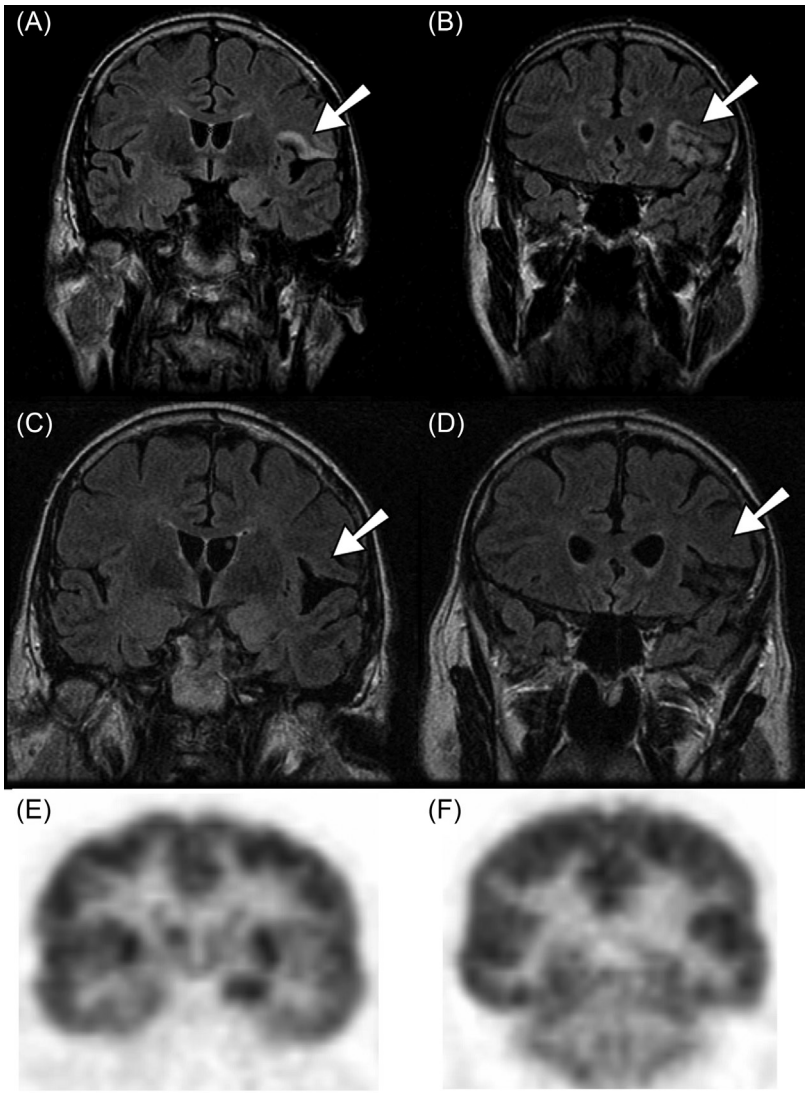


FIGURE 3 Paraneoplastic limbic encephalitis. (A) A 3-T coronal FLAIR image through the mesial temporal lobes shows increased signal in the left mesial temporal lobe and in the left frontal operculum (arrow). (B) Adjacent coronal FLAIR image anterior to (A) showing the extension of the abnormal signal to involve the anterior left frontal operculum and anterior insular cortex (arrow). (C and D) Coronal FLAIR images demonstrating improvement in the opercular and insular signal (arrows) after immunosuppression treatment. Signal abnormality in the left amygdala persists. (E and F) PET imaging with [^{18}F]FDG demonstrates hypermetabolism in the areas of abnormal T2 signal seen in panels (A and B). The PET abnormalities are presumed to represent active inflammation.

sequences with thin sections through the mesial temporal lobes may optimize the detection of these abnormalities (see Figure 2). A newly described MRI technique of quantitative FLAIR analysis may also increase the sensitivity and reduce the subjectivity of such imaging.[14] Gadolinium enhancement is minimal, if present at all, and tends to be more common in PLE associated with particular antibodies such as anti-Ma2.[15] The imaging appearance and typical regions of involvement of PLE have significant overlap with other, often more aggressive, pathologies. Differentiation from herpes encephalitis is an important primary consideration. Herpes encephalitis tends to cause insular and diffuse temporal lobe changes, with a greater degree of enhancement and greater local mass effect than PLE, although the signal changes and areas of involvement have significant overlap (see Figure 4).[16] As such, prompt cerebrospinal fluid analysis and empiric antiviral treatment are still important when herpes infection is a consideration. Additional considerations of mesial temporal sclerosis, gliomatosis cerebri, acute disseminated encephalomyelitis, and non-PLE can have imaging abnormalities identical to those of PLE.[17–19]

In a study of PLE at the Mayo Clinic, cranial MRI was abnormal in 89% of the cases.[20] Nearly all cases showed increased T2 and FLAIR signal in the mesial temporal lobe. Bilateral temporal lobe abnormalities were present in 69%, while abnormal contrast enhancement was seen in only 21%. In those cases,

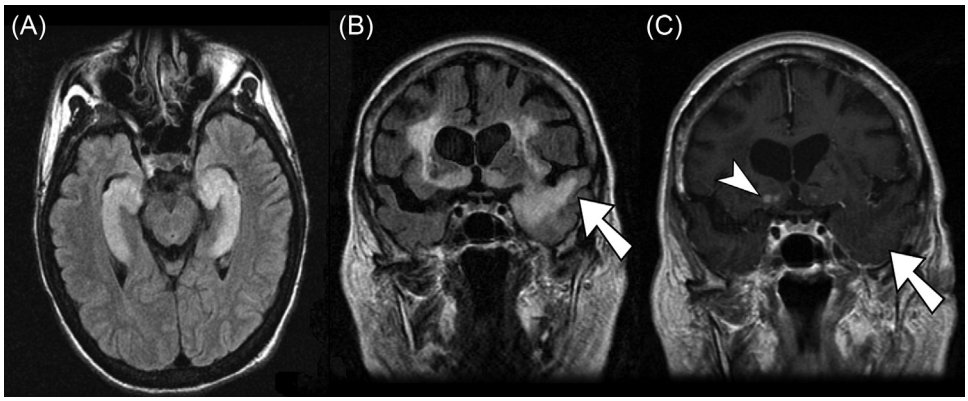


FIGURE 4 Limbic encephalitis. (A) Axial FLAIR image showing extensive signal abnormality, which is highly restricted to the mesial temporal lobe in a patient with PLE associated with Hodgkin lymphoma. Gadolinium-enhanced T1 images were unremarkable in this case. (B) Coronal FLAIR image in a case of herpes simplex encephalitis shows signal abnormalities extending throughout the left temporal lobe, insular cortex, and bilateral medial thalamus. The findings in herpes encephalitis involve the limbic areas of the brain but are typically more extensive. (C) Gadolinium-enhanced T1 coronal image shows areas of contrast enhancement in the thalamus (arrowhead). The left temporal lobe shows low signal and increased volume consistent with vasogenic edema. This degree of contrast enhancement and swelling would be very unusual for PLE.

the enhancing tissue comprised only a small volume of the total signal abnormality. Extratemporal cortical signal abnormalities were observed in 37%, ranging from diffuse hemispheric cortical and subcortical signal abnormalities in bilateral hemispheres to involvement of insular cortex.

Over time, the mesial temporal lobe T2 hyperintensity may improve, replaced by focal temporal lobe or generalized, cerebral cortical atrophy. In untreated cases, mesial temporal atrophy can be profound (see Figure 5).

NMDAR ENCEPHALITIS

For cases of NMDAR encephalitis, brain MRI is normal in approximately 50%. In the other half of patients, nonspecific T2/FLAIR hyperintensity may be seen in the hippocampus, insula, basal ganglia, brainstem, or cerebellum, which occasionally may be contrast enhancing and transient.[1,21] MR spectroscopy has not shown any added diagnostic benefit in these cases. Data regarding the use of brain fluorodeoxyglucose (FDG) PET imaging in cases of NMDAR encephalitis have been mixed, with some cases reporting cortical hypometabolism[22,23] and others reporting focal hypermetabolism, which may be reversible with treatment.[24,25]

The majority of NMDAR encephalitis cases are in women, and there is a high likelihood of ovarian teratoma in these patients. Screening for these pelvic tumors may be done with ultrasound as an initial step, either transvaginal or transabdominal.[3] If no tumor is found, recommendations vary on whether to use CT or MRI of the pelvis next, which have approximately equal sensitivity.[3,26] If still no tumor is found, annual MRI of the pelvis is recommended thereafter, in case of an undiscovered tumor with interval growth.[26] FDG PET has not been formally studied in screening for ovarian teratomas, but most teratomas associated with NMDAR encephalitis are mature cystic teratomas and therefore do not take up FDG. As such, FDG PET is not recommended for ovarian teratoma screening.[3]

PARANEOPLASTIC BRAINSTEM ENCEPHALITIS

Various patterns of imaging abnormalities have been reported with paraneoplastic brainstem encephalitis. Often the MRI is normal[27,28]; however, varying patterns of abnormal T2/FLAIR signal in the brainstem have been reported (see Figure 6).[15,29,30] Enhancement in this cohort of patients is uncommon. Imaging in patients with isolated opsoclonus/myoclonus, however, is generally normal.

PARANEOPLASTIC CHOREA

Identifiable MRI abnormalities have been occasionally reported in paraneoplastic chorea and include nonenhancing increased T2/FLAIR signal in the basal ganglia (see Figure 7)[31] or striatum,[32] or isolated T1 hyperintensity in the basal ganglia.[33] Occasionally, these abnormalities may be seen in conjunction with typical changes in PLE. The increased T2 and FLAIR signals may resolve in concert with clinical improvement. The MRI abnormalities in paraneoplastic chorea are reminiscent of those seen in sporadic Creutzfeldt–Jacob disease (CJD) and acute disseminated encephalomyelitis, and there may be some overlap in the

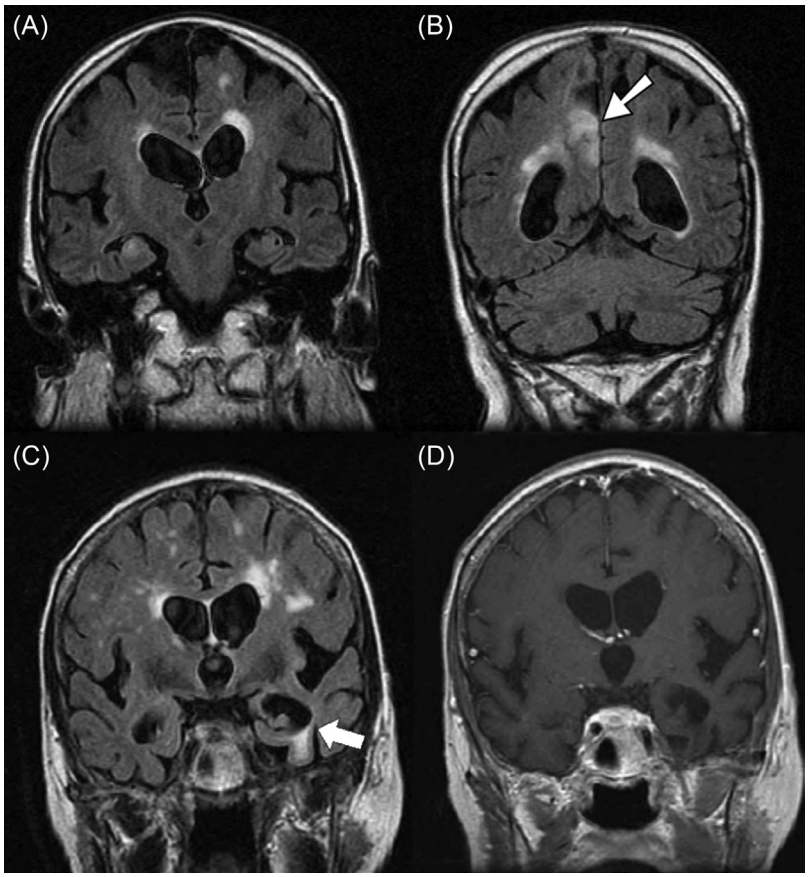


FIGURE 5 Paraneoplastic limbic encephalitis. Later in the course of PLE, prominent mesial temporal atrophy typically develops. (A) Coronal FLAIR image demonstrates moderate bilateral temporal atrophy and abnormal increased right mesial temporal lobe signal. (B) Coronal FLAIR image more posteriorly demonstrates abnormal increased signal in the posterior right cingulate gyrus (arrow). (C) Coronal FLAIR MRI from a patient with untreated PLE (2 years after onset of symptoms) shows severe asymmetric temporal atrophy with relative preservation of frontoparietal cortex. An area of signal abnormality persists in the inferior temporal cortex. (D) T1-weighted coronal image after gadolinium shows no enhancement of these abnormalities.

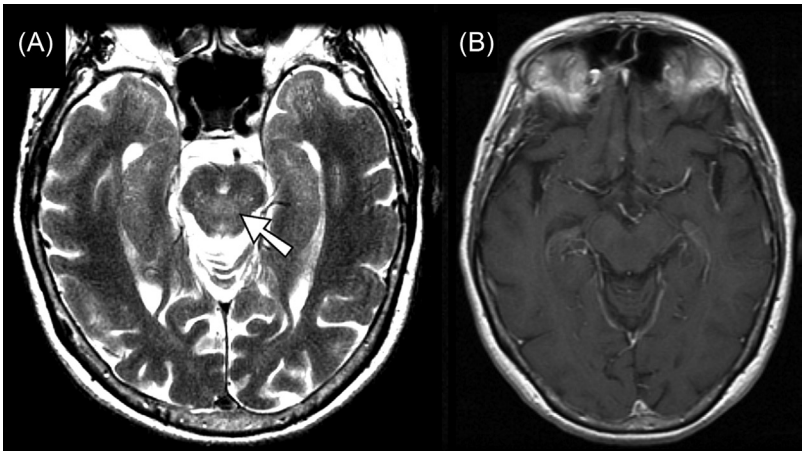


FIGURE 6 Paraneoplastic brainstem encephalitis. (A) Thin-section axial fast spin echo T2 sequence through the midbrain shows abnormal increased T2 signal in the tegmentum and tectum (arrow). Many cases of brainstem encephalitis have no obvious imaging abnormalities. (B) Axial postgadolinium T1 image at the same level demonstrates no corresponding enhancement. The lack of enhancement helps differentiate this entity from other infectious and inflammatory disorders.

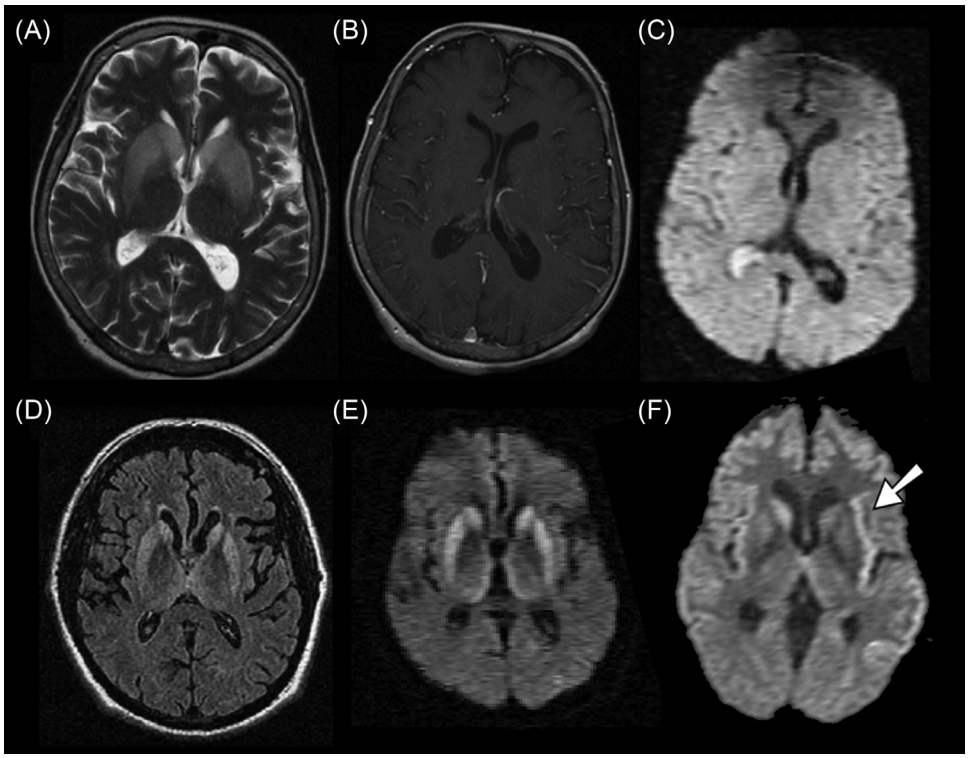


FIGURE 7 Paraneoplastic chorea. (A) Axial spin echo T2 image shows increased signal in the caudate and anterior putamen consistent with "striatal encephalitis." Similar findings are present on FLAIR images. (B) Axial postgadolinium T1 image at the same level shows no enhancement. (C) Diffusion-weighted images show normal signal in the basal ganglia. The lack of restricted diffusion is characteristic of paraneoplastic chorea and effectively eliminates CJD and ischemia as alternative diagnoses. (D) In CJD, axial FLAIR image demonstrates similar abnormal T2 signal in the basal ganglia. (E) However, on diffusion-weighted imaging, these abnormalities are associated with restricted diffusion. (F) In a different patient with CJD, a diffusion-weighted image shows abnormality both in the right caudate and along the cortical ribbon of the left insula. Paraneoplastic disorders may show abnormalities of the striatum (chorea) or insular cortex (PLE) but diffusion abnormalities are not seen.

clinical presentation of these disorders. However, diffusion imaging in paraneoplastic chorea is normal, which differentiates it from CJD radiographically (see Figure 7).

PARANEOPLASTIC MYELOPATHY

In cases of paraneoplastic myelopathy, gadolinium-enhancing, T2/FLAIR hyperintensities in long tracts have been reported, which are often symmetrical and longitudinally extensive (more than three vertebral segments).[34,35] As such, imaging may overlap with alternative causes of inflammatory myelitis, such as multiple sclerosis or neuromyelitis optica, and so additional imaging of the entire neuraxis may be useful to evaluate for additional diagnostic lesions for these diseases. Further, whereas MRI abnormalities may be difficult to discern between local tumor and inflammation, including paraneoplastic myelitis, FDG PET is a useful addition in this evaluation, as neoplastic lesions are much more avid than nonneoplastic lesions.[34,36]

IMAGING OF OCCULT MALIGNANCY IN PATIENTS WITH PARANEOPLASTIC DISORDERS

One of the greatest challenges in evaluating patients with a suspected paraneoplastic disorder (PND) is obtaining a cancer diagnosis. The majority of new diagnoses of PND occur in patients without a history of cancer.[1–4] In most circumstances, conventional body imaging studies (CT, ultrasonography, etc.) will reveal the malignancy and identify a site for diagnostic biopsy. However, tumors in patients with PND may be missed on initial imaging studies since they are often small with limited, if any, metastases. Yet, patients with well-recognized paraneoplastic syndromes and onconeural antibodies are very likely (85–90% in most series) to harbor a malignancy, and early tumor diagnosis and treatment are important to improve outcome. Several studies have shown that [^{18}F]FDG whole-body PET improves tumor detection when conventional imaging studies are normal (see Figure 8).[37,38] When limited to patients with PND

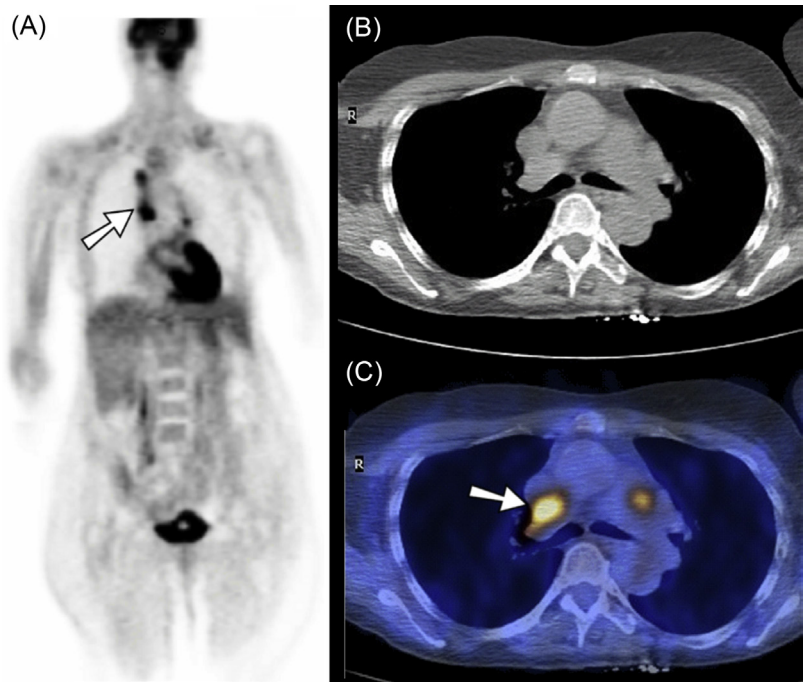


FIGURE 8 PET imaging for cancer diagnosis. (A) Coronal whole-body [^{18}F]FDG PET image shows abnormal hypermetabolism in right paratracheal and right hilar regions suggesting a lung primary. This patient had PLE and antibodies against both Hu and CRMP-5. (B) Noncontrast axial CT scan of the chest in this patient was interpreted as showing no abnormalities. (C) Coregistration of the PET images with the CT allows identification of hypermetabolic mediastinal lymph nodes. Biopsy of the most prominent lesion (arrow) confirmed a diagnosis of small-cell lung carcinoma.

associated with well-defined antibodies, the sensitivity of PET was reported to be 80–90%.[39,40] Given its relative sensitivity, yet increased cost, PET has a definite role in evaluating patients with definite PND when conventional oncological screening studies are negative.

SUMMARY

Neuroimaging has a definite role in the diagnostic evaluation of PND of the CNS. Whereas some well-defined paraneoplastic neurologic disorders may have characteristic imaging abnormalities, neurological imaging is important in all such disorders to exclude additional or alternative diagnoses. In patients with suspected PND (based on serology and clinical presentation), imaging of the body including FDG PET imaging is important for early detection of small malignancies.

References

1. Dalmau J, Gleichman AJ, Hughes EG, et al. Anti-NMDA-receptor encephalitis: case series and analysis of the effects of antibodies. *Lancet Neurol*. December 2008;7(12):1091–1098.
2. Graus F, Keime-Guibert F, Rene R, et al. Anti-Hu-associated paraneoplastic encephalomyelitis: analysis of 200 patients. *Brain*. June 2001;124(Pt 6):1138–1148.
3. Titulaer MJ, Soffietti R, Dalmau J, et al. Screening for tumours in paraneoplastic syndromes: report of an EFNS task force. *Eur J Neurol*. January 2011;18(1):19-e3.
4. Titulaer MJ, Wirtz PW, Willems LN, van Kralingen KW, Smitt PA, Verschuuren JJ. Screening for small-cell lung cancer: a follow-up study of patients with Lambert–Eaton myasthenic syndrome. *J Clin Oncol*. September 10, 2008;26(26):4276–4281.
5. Berner U, Menzel C, Rinne D, et al. Paraneoplastic syndromes: detection of malignant tumors using [(18)F]FDG-PET. *Q J Nucl Med*. June 2003;47(2):85–89.
6. Scheid R, Voltz R, Briest S, Kluge R, von Cramon DY. Clinical insights into paraneoplastic cerebellar degeneration. *J Neurol Neurosurg Psychiatry*. April 2006;77(4):529–530.
7. de Andres C, Esquivel A, de Villoria JG, Graus F, Sanchez-Ramon S. Unusual magnetic resonance imaging and cerebrospinal fluid findings in paraneoplastic cerebellar degeneration: a sequential study. *J Neurol Neurosurg Psychiatry*. April 2006;77(4):562–563.
8. Choi KD, Kim JS, Park SH, Kim YK, Kim SE, Smitt PS. Cerebellar hypermetabolism in paraneoplastic cerebellar degeneration. *J Neurol Neurosurg Psychiatry*. April 2006;77(4):525–528.
9. Tuzun E, Dalmau J. Limbic encephalitis and variants: classification, diagnosis and treatment. *Neurologist*. September 2007;13(5):261–271.
10. Fakhoury T, Abou-Khalil B, Kessler RM. Limbic encephalitis and hyperactive foci on PET scan. *Seizure*. October 1999;8(7):427–431.
11. Kassubek J, Juengling FD, Nitzsche EU, Lucking CH. Limbic encephalitis investigated by ^{18}FDG-PET and 3D MRI. *J Neuroimaging*. January 2001;11(1):55–59.
12. Ances BM, Vitaliani R, Taylor RA, et al. Treatment-responsive limbic encephalitis identified by neuropil antibodies: MRI and PET correlates. *Brain*. August 2005;128(Pt 8):1764–1777.
13. Baumgartner A, Rauer S, Mader I, Meyer PT. Cerebral FDG-PET and MRI findings in autoimmune limbic encephalitis: correlation with autoantibody types. *J Neurol*. November 2013;260(11):2744–2753.
14. Wagner J, Schoene-Bake JC, Malter MP, et al. Quantitative FLAIR analysis indicates predominant affection of the amygdala in antibody-associated limbic encephalitis. *Epilepsia*. September 2013;54(9):1679–1687.

15. Dalmau J, Graus F, Villarejo A, et al. Clinical analysis of anti-Ma2-associated encephalitis. *Brain*. August 2004;127(Pt 8):1831–1844.
16. Oyanguren B, Sanchez V, Gonzalez FJ, et al. Limbic encephalitis: a clinical-radiological comparison between herpetic and autoimmune etiologies. *Eur J Neurol*. August 14, 2013;20(12):1566–1570.
17. Thieben MJ, Lennon VA, Boeve BF, Aksamit AJ, Keegan M, Vernino S. Potentially reversible autoimmune limbic encephalitis with neuronal potassium channel antibody. *Neurology*. April 13, 2004;62(7):1177–1182.
18. Sakai K, Yoshita M, Samuraki M, Yamada M. Acute disseminated encephalomyelitis with medial temporal lesions mimicking acute limbic encephalitis. *Clin Neurol Neurosurg*. January 2011;113(1):72–74.
19. Nagata R, Ikeda K, Nakamura Y, et al. A case of gliomatosis cerebri mimicking limbic encephalitis: malignant transformation to glioblastoma. *Intern Med*. 2010;49(13):1307–1310.
20. Lawn ND, Westmoreland BF, Kiely MJ, Lennon VA, Vernino S. Clinical, magnetic resonance imaging, and electroencephalographic findings in paraneoplastic limbic encephalitis. *Mayo Clin Proc*. November 2003;78(11):1363–1368.
21. Dalmau J, Lancaster E, Martinez-Hernandez E, Rosenfeld MR, Balice-Gordon R. Clinical experience and laboratory investigations in patients with anti-NMDAR encephalitis. *Lancet Neurol*. January 2011;10(1):63–74.
22. Morooka M, Kubota K, Minamimoto R, et al. ^{18}F-FDG and 11C-methionine PET/CT findings in a case with anti-NMDA (NR2B) receptor encephalitis. *Clin Nucl Med*. April 2012;37(4):400–402.
23. Pillai SC, Gill D, Webster R, Howman-Giles R, Dale RC. Cortical hypometabolism demonstrated by PET in relapsing NMDA receptor encephalitis. *Pediatr Neurol*. September 2010;43(3):217–220.
24. Maeder-Ingvar M, Prior JO, Irani SR, Rey V, Vincent A, Rossetti AO. FDG-PET hyperactivity in basal ganglia correlating with clinical course in anti-NDMA-R antibodies encephalitis. *J Neurol Neurosurg Psychiatry*. February 2011;82(2):235–236.
25. Maqbool M, Oleske DA, Huq AH, Salman BA, Khodabakhsh K, Chugani HT. Novel FDG-PET findings in anti-NMDA receptor encephalitis: a case based report. *J Child Neurol*. October 2011;26(10):1325–1328.
26. Florance NR, Davis RL, Lam C, et al. Anti-N-methyl-D-aspartate receptor (NMDAR) encephalitis in children and adolescents. *Ann Neurol*. July 2009;66(1):11–18.
27. Moragas M, Martinez-Yelamos S, Majos C, Fernandez-Viladrich P, Rubio F, Arbizu T. Rhombencephalitis: a series of 97 patients. *Medicine*. July 2011;90(4):256–261.
28. Saiz A, Bruna J, Stourac P, et al. Anti-Hu-associated brainstem encephalitis. *J Neurol Neurosurg Psychiatry*. April 2009;80(4):404–407.
29. Barnett M, Prosser J, Sutton I, et al. Paraneoplastic brain stem encephalitis in a woman with anti-Ma2 antibody. *J Neurol Neurosurg Psychiatry*. February 2001;70(2):222–225.
30. Taraszewska A, Piekarska A, Kwiatkowski M, Wierzba-Bobrowicz T, Czorniuk-Sliwa A. A case of the subacute brainstem encephalitis. *Folia Neuropathol*. 1998;36(4):217–220.
31. Vernino S, Tuite P, Adler CH, et al. Paraneoplastic chorea associated with CRMP-5 neuronal antibody and lung carcinoma. *Ann Neurol*. May 2002;51(5):625–630.
32. Vigliani MC, Honnorat J, Antoine JC, et al. Chorea and related movement disorders of paraneoplastic origin: the PNS EuroNetwork experience. *J Neurol*. November 2011;258(11):2058–2068.
33. Vick A, Kraemer RR, Morris JL, et al. A 60-year-old woman with chorea and weight loss. *J Gen Intern Med*. June 2012;27(6):747–751.
34. Flanagan EP, McKeon A, Lennon VA, et al. Paraneoplastic isolated myelopathy: clinical course and neuroimaging clues. *Neurology*. June 14, 2011;76(24):2089–2095.
35. Flanagan EP, Keegan BM. Paraneoplastic myelopathy. *Neurol Clin*. February 2013;31(1):307–318.
36. Flanagan EP, Hunt CH, Lowe V, et al. [(18)F]-fluorodeoxyglucose-positron emission tomography in patients with active myelopathy. *Mayo Clin Proc*. November 2013;88(11):1204–1212.
37. Rees JH, Hain SF, Johnson MR, et al. The role of [^{18}F]fluoro-2-deoxyglucose-PET scanning in the diagnosis of paraneoplastic neurological disorders. *Brain*. November 2001;124(Pt 11):2223–2231.
38. Hadjivassiliou M, Alder SJ, Van Beek EJ, et al. PET scan in clinically suspected paraneoplastic neurological syndromes: a 6-year prospective study in a regional neuroscience unit. *Acta Neurol Scand*. March 2009;119(3):186–193.
39. Linke R, Schroeder M, Helmberger T, Voltz R. Antibody-positive paraneoplastic neurologic syndromes: value of CT and PET for tumor diagnosis. *Neurology*. July 27, 2004;63(2):282–286.
40. Younes-Mhenni S, Janier MF, Cinotti L, et al. FDG-PET improves tumour detection in patients with paraneoplastic neurological syndromes. *Brain*. October 2004;127(Pt 10):2331–2338.

Index

'*Note*: Page numbers followed by "f" indicate figures and "t" indicate tables.'

A
Abscess
  brain. *See* Brain abscess
  epidural, 735–736
N-Acetylaspartate(NAA), 170, 199, 238, 252, 440
  bilateral thalamic glioma, 560
  central neurocytoma, 575
  DNETs, 580
  ganglioglioma, 561, 577
  glioblastoma multiforme, 431
  meningioma, 519
  metastatic brain tumors, 648–649
  oligodendrogliomas, 463
  pontine tumors, 622
  primary cerebral lymphomas, 564
  primitive neuroectodermal tumors, 563
Acetylcholine receptors (AChR), 108
Acoustic neuroma, 263–264, 504–506
  computed tomography, 505
  magnetic resonance imaging, 505
Acoustic schwannomas, 5, 503, 505. *See also* Schwannomas
Acquired immunodeficiency syndrome (AIDS)
  and PCNSL, 471, 474–475, 513–514
  primary cerebral lymphomas, 563–564, 564f
  and TPCNSL, 480
Acromegaly, 264–265, 487–488
Active demyelinating disease
  and PCNSL, 475–476
Active optical trackers, 211
Activity volume index, oligodendroglioma, 467
Acute disseminated encephalomyelitis, 814–816
Acute ischemic stroke, 91
Acute promyelocytic leukemia (APML), 85
Acute stroke, neuroimaging of, 89
Adamantinous craniopharyngiomas, 493–494
Adenocarcinoma, 63, 87f
Adenohypophysis, 483
Adenoid cystic carcinoma, skull base, 609
Adenoma
  pediatric pituitary, 628
  pituitary. *See* Pituitary adenomas
Adrenocorticotropic hormone-secreting adenomas, 265
Advanced imaging techniques, 252–253
Advanced magnetic resonance imaging, 220
  for brain tumors, 167–182
  diffusion-weighted imaging (DWI), 167–168
    differential diagnosis, grading, monitoring of progression, and response, 167–168
  diffusion tensor imaging, 168
  microvascular imaging, 172–177
    perfusion-weighted imaging, 173–176
    T1-weighted permeability imaging, 176–177
  MR spectroscopy (MRS), 169–172
    in assessment of treatment response, 171–172
    in differential diagnosis, grading, surgical planning, and follow-up, 170–171
Alanine, magnetic resonance spectroscopy, 170
Albumin–Gd–diethylenetriaminepentaacetic acid (DTPA), 337
Algebraic reconstruction algorithm, 146–147
Alkylating agents, 134
  busulfan, 134
  ifosfamide, 134
Allergic/nonallergic reactions, 153
Allergy, 6
α-fetoprotein, 65, 491
α-interferon, 71t
Ameloblastoma, skull base, 609
American Society for Radiation Oncology (ASTRO), 28
Amide proton transfer (APT)
  tissue protein/peptide fragments assessment using, 399–400
  -weighted imaging, 399–400
AMIGO (advanced multimodality image-guided operating room), 211–212
Amino acid, 372
  labeled, 361–362
5-Aminolevulinic acid (5-ALA), 403–404
Amyloidoma, 663
Anaplasia, 12–13
Anaplastic astrocytoma (AA), 9–10, 45–46, 46f, 421–422, 423f, 667, 668f
  magnetic resonance imaging, 557, 558f
  thalamus, 556–557
Anaplastic ependymomas, 45
Anaplastic meningioma, 14f
Anaplastic oligodendroglioma, 11–12, 235, 307f, 381–382, 492f, 670
Anaplastic progression, 669–670
Anastrozole, 71
Aneurysm, 152, 661, 699
Aneurysmal bone cyst
  computed tomography, 749t
  magnetic resonance imaging, 749t
Anger camera, 354, 354f
Angiitis, primary
  of central nervous system, 806
Angiogenesis, 17, 72, 195, 346, 389–390, 427, 667
Angiogenesis inhibitors, 671–672
Angiography
  benign peripheral nerve sheath tumors, 779
  gangliocytoma, 577
  ganglioglioma, 577
  hemangiopericytoma, 539
  meningiomas, 520f, 529–533, 532f–536f
  PCNSL, 472–473, 475f
  spinal tumors, 757–759, 758f
Angiopoietins, 55
Angiotropism, 513, 513f
Animal models, of CNS cancer, 395–400
  magnetic resonance imaging (MRI)
    amide proton transfer, 399–400
    diffusion imaging, 398–399
    magnetic resonance spectroscopy, 400
    malignant tissue versus normal brain parenchyma, 395–397
    vascular parameters, 397–398
Annexin II, 79
Annihilation photons, 356
Annual Medical Image Computing and Computer Assisted Intervention DTI challenge, 218
Anterior primary ramus (APR), 111
Anthracycline antibiotics, 136
Antiangiogenesis therapy, 293–295, 338, 346
Antibiotherapy, brain abscess, 659
Anticoagulation, 101–102
"Anti-CV2" antibodies, 107
Antimetabolites, 132–134
  5-fluorouracil (5-FU), 134
  cytosine arabinoside, 134
  methotrexate, 132–134
Anti-NMDAR encephalitis, 106
Antitoxoplasmosis therapy, 474–475
Antoni A, in schwannoma, 503, 504f
Antoni B, in schwannoma, 41–42, 503, 504f
Antoni type A
  vestibular schwannoma, 543–545, 547f
Antoni type B
  vestibular schwannoma, 543–545, 547f

Apparent diffusion coefficient (ADC), 167–168, 262, 274–275, 279, 281–286, 292, 399, 441, 585, 688–689, 699–700
  germinomas, pineal tumor, 589
  glioblastoma multiforme, 428, 431
  oligodendrogliomas, 463
  pediatric astrocytomas, 616, 616f
  pineoblastomas, 592
  pineocytomas, 592–594
  pontine tumors, 622
  PPTIDs, 594, 595f
  and primary intracranial gliomas, 428
  in spinal cord compression, 734
  values, 415
Apparent diffusion constant maps, 301
Arachnoid cyst, 496–497, 654
  magnetic resonance imaging, 496–497, 496f, 598f
Arginine-glycine-aspartic acid (RGD) peptide, 402–403
Arterial compromise, tumor-related, 799
Arterial input function (AIF), 336–337
Arterial spin imaging
  pseudoprogression, 691
Arterial spin labeling (ASL), 335, 347, 397
  pediatric brain tumors, 615
Arterial vasculature
  cerebrovascular complications, 799, 799f–800f
Aseptic meningitis, 132
L-Asparaginase, 80–81, 86, 99, 136
Aspergillosis, 697
Astrocytic lesion, 439
Astrocytic tumors, 10t
Astrocytoma, 9–10, 10f, 35, 597f, 753
  cerebellar, 620–621
  cervicomedullary, 624f
  diffuse, 442–445, 443f–447f, 556–558
    computed tomography, 442–445, 446f
    magnetic resonance imaging, 442–445
  diffusely infiltrating, 667, 668f
  fibrillary, 442, 443f, 445
  gemistocytic, 442
  genetic abnormalities in, 422t
  gliomatosis cerebri, 456, 457f
  grade 2, 329f
  infiltrating. *See* Astrocytoma, diffuse
  infiltrative, 439
  localized, 11
  low-grade, 439–460
    lesion enhancement, 440
  malignant, 419–438
  noninfiltrative, 439, 445–456
  pediatric, 616
  pilocytic, 445–451, 447f–452f
  pilomyxoid, 445, 451
  pleomorphic xanthoastrocytoma, 451–452, 454f
  protoplasmic, 442
  of spinal cord, 45–46, 46f, 48–49
  subependymal giant-cell astrocytoma, 452–456, 455f
  thalamus, 555–556
  treatment, 599–600
Ataxic hemiparesis, 509
Atherosclerosis, 130, 797
Atomic number, 356
Atrial myxoma, 643, 650f
Attenuated photons, 355–356
Attenuation correction, 354–355, 357
Atypical rhabdoid-teratoid tumors (ARTTs)
  magnetic resonance imaging, 563, 563f
  thalamus, 563
Autoantibodies, neuronal paraneoplastic, 105t
Autoimmune encephalitis (AE), 106, 657
Autoimmunity, 103
AVAglio protocol
  limitations, 686–687
  pseudoprogression, 685–686

B
B cell markers, 14–15
Back pain, epidural spinal cord compression, 60, 723
Bacterial infections
  and brain abscess, 659
Basal ganglia
  germinoma, 561–562
    computed tomography, 561–562, 562f
    magnetic resonance imaging, 562, 562f
  metastases, 565, 565f
  tumors, 555–565
Basic pulse sequence, 158–159
BAX expression, 7, 23–24
Benign fibrous histiocytoma, skull base, 609
Benign peripheral nerve sheath tumors, 778
  angiography, 779
  computed tomography, 779, 780f
  imaging, 778–782
  magnetic resonance imaging, 780–782, 781f–785f
  neurilemoma, 778
  neurofibroma, 778
β-human chorionic gonadotropin (β-HCG), 65, 491
  nongerminomatous germ-cell tumors, 590
  pineal tumor germinomas, 589
Bevacizumab (BEV), 17–19, 30, 50, 72, 81, 136, 409, 671–672, 672f
  oligodendrogliomas, 468
  for radionecrosis, 128
  vestibular schwannoma, 553
Biexponential model, 305–308
Bilateral thalamic glioma (BTG), 560
  computed tomography, 560
  magnetic resonance imaging, 560, 560f
  magnetic resonance spectroscopy, 560, 560f
Bioluminescence imaging (BLI), 400–401, 402f
Biomarker, 273–274, 292–293
  advanced imaging techniques as, 414–415
  role of, 414
Biopsy
  magnetic resonance spectroscopy, 328
  meningeal, 65
  sarcoidosis, 657
  solid lesions, 491, 613–615
  stereotactic, 15, 376, 429, 461–462
  sural nerve, 134–135
  surgical, 118
Bismuth germinate, 356
Bisphosphonates, 61
Blood–brain barrier (BBB), 28, 174, 176, 336, 338, 342, 360, 372, 397
Blood flowing in macrovessels within the brain, 397–398
Blood oxygen level-dependent (BOLD) imaging, 198, 219, 289–290, 387–389, 391
Boltzman distribution function, 194
Bone
  primary tumors, 747–751, 750f–752f
  scintigraphy, 756
Brachial plexopathies, 114, 131–132
  evaluation, 117
Brachial plexus (BP), 111–112, 112f, 763–764, 764f–765f
  differential diagnosis, 116
Brachytherapy, 15–16
  chordomas, 607
BRAF (V600E), 576, 580
Brain, electric field distribution within, 249–251
  computational model, 249–250
  experimental evidence, 249
  future modeling developments, 251
  modeling results, 250–251
Brain, radiation-induced neurologic complications to, 125
Brain abscess, 659
  and glioblastoma multiforme, 431
  and PCNSL, 475–476
Brain hemorrhage, 79
Brain metastases, 6, 432, 433f
  development of RANO criteria for, 414
Brain stem, diffuse astrocytomas in, 442
BRAIN trial, 18
Brain tumor resection under intraoperative MRI guidance, 207–211
  instrument tracking and neuronavigation, 210–211
  intraoperative detection of complications, 210
  intraoperative dynamic contrast imaging, 210
  multimodality imaging, 207–208
  rationale, 207
  rigid and nonrigid image registration for surgical guidance, 208
Brain tumor surgery, general considerations in, 217
Brain tumors, 3
  advanced magnetic resonance imaging of, 167–182
  classification, 359
  CNS infarction as a result of treatment of, 94–96
  CNS infarction caused by, 94
  diffusion magnetic resonance imaging in, 273–300
    assessment of extra-axial tumors, 279–280
    clinical use, 279
    intra-axial cystic masses, characterization of, 281

intraoperative diffusion imaging, 290–291
physical basis, 274–279
posttreatment evaluation, 291–295
potential future applications, 295–296
preoperative planning and peritumoral margins, 285–290
stratifying tumor histology, 284–285
tumor grading, 281–284
incidence and prevalence, 359
magnetic resonance spectroscopy, 440
MRI of, 194
special considerations for fMRI measurements using, 321–322
Brain tumors, diffusion imaging of, 301–316
characterization of brain tumors
with a single diffusion coefficient derived from conventional diffusion-weighted images, 302–304, 303f–304f
with multiple diffusion parameters derived from highly diffusion-weighted images, 305–309
magnetic resonance diffusion imaging, 301–302
nerve fiber tract integrity, assessment of, 309–312
Brain-stem encephalitis, 106
paraneoplastic, 814
Brain-stem gliomas (BSGs), 622
Brain-stem tumors, pediatric, 621–622
Branched-chain amino acids, magnetic resonance spectroscopy, 170
Breast cancer, 115
neoplastic meningitis (NM), 63, 66, 71–73
plexopathies, 131–132
triple negative status of, 63
Breast carcinoma, 113
Breast-feeding, X-ray contrast agent safety, 153
Broca's area, 320–322
Bromocriptine, pituitary adenoma, 485, 487–488
Busulfan, 134
b-value, 165

C

[^{11}C]methionine, 238–239, 365–366, 373f–380f, 374–376, 379–380, 382, 467, 580, 607
[^{11}C]methyl-methionine ([^{11}C]MET) PET, 367f, 441–442
Calcium pyrophosphate dihydrate deposition
spinal epidural disease differential diagnosis, 737–738, 738f
Candida brain abscesses, 81–82
Capecitabine, 71
Capillary telangiectasias, 804
Carboplatin, ganglioglioma, 577–578
Carcinoembryogenic antigen (CEA), 65
Carcinomatous encephalitis, 646
Carcinomatous meningitis, 63
Carmustine, 49–50
Carotid artery, 130, 485–490
Carotid blowout syndrome, 803–804
Carotid endarterectomy, 129
Catheter angiography, 94
for CNS infarction, 94
Cations, labeled, 360–361
technetium-99m MIBI, 361
thallium-201, 360–361
Cauda equina syndrome, 69, 118
Cavernous angiomas, 130
Cavernous sinus syndrome, 509
CBV–CBF/MTT mismatch, 92
CD19, 14–15
CD20, 14–15, 136
CD45, 14–15
CD79a, 14–15
Cellsave Preservative tubes, 65
CellSearch technology, 65
Cellular magnetic resonance imaging, 391–392
Cellular telephones, 5
Central necrosis, in immunocompromised patients, 473
Central nervous system
leptomeningeal metastases. *See* Leptomeningeal metastases (LM)
primary angiitis. *See* Primary central nervous system lymphoma (PCNSL)
vascular disease, 79
Central nervous system infarction, 89–98
caused by brain tumors, 94
imaging evaluation of, 89–94
catheter angiography, 94
computed tomography, 89–92
magnetic resonance, 92–94
in neurooncology, 94–96
as a result of treatment of brain tumors, 94–96
spinal cord infarction, 96
Central nervous system cancer/tumors, 10t, 42t, 231–232, 371, 395–401
in vivo bioluminescence imaging, 400–401
magnetic resonance imaging, 395–400
amide proton transfer, 399–400
diffusion MRI, 398–399
magnetic resonance spectroscopy, 400
malignant tissue versus normal brain parenchyma, 395–397
vascular parameters, measuring, 397–398
molecular imaging of small animals, 401–403
micro-positron emission tomography, 401–403
micro-single-photon emission computed tomography, 403
recent advances, 403–404
Central neurocytoma, 573–576
computed tomography, 574
magnetic resonance imaging, 574, 574f–575f
magnetic resonance spectroscopy, 575
pathology, 573–574
treatment, 576
Central volume formula, 91
Cerebellar astrocytoma, 620–621
pediatric, 627f
Cerebellar degeneration, paraneoplastic, 811
Cerebellar hemangioblastomas, 284, 619–620
Cerebellar liponeurocytoma, 582
computed tomography, 582
magnetic resonance imaging, 582
pathology, 582
treatment, 582
Cerebellar syndrome, 134
Cerebellopontine angle (CPA) meningioma, 525–526, 526f
Cerebellopontine angle (CPA) syndrome, 507
Cerebral abscesses, 699, 700f
Cerebral blood flow (CBF), 91, 219, 335, 340, 341f, 397
potential role of, 345
Cerebral blood volume (CBV), 91, 335, 339, 342, 397
glioblastoma multiforme, 428–429, 430f
high grade gliomas, 428–429
Cerebral embolism, 80, 797–798
Cerebral hemispheres, pediatric tumors of, 616–619
Cerebral infarction, 80, 99, 698
Cerebral ischemia in cancer patients, 80
Cerebral metastases, 262–263
Cerebral perfusion, 91
Cerebral septic emboli, 81–82
Cerebral syphilitic gumma, 659
Cerebral venous thrombosis (CVT), 80, 99
clinical features, 99–100
diagnosis, 100–101
etiology, 99
treatment, 101–102
Cerebrospinal fluid (CSF), 63, 158, 218, 279
CSF cytology, 64–65, 67, 73
CSF flow
fast spin-echo (FSE) imaging, 729–730, 733–734
imaging pitfalls, 698
radioisotope studies, 715–718, 715f–716f, 717t
measurement, 117
PCNSL, 514
neoplastic meningitis, 64–65
pathways, 12–13
Cerebrovascular complications
computed tomography, 797–803, 798f–801f, 805
infection-related, 802–803, 802f–803f
magnetic resonance imaging, 797–806, 799f–806f
therapy-related, 803–805
chemotherapy, 804–805
endovascular therapy, 805, 805f
radiation, 803–804, 803f–804f
tumor-related, 797
arterial vasculature, 799, 799f–800f
coagulopathy, 797–798
intravascular lymphomatosis, 806
leptomeningeal metastases, 800
primary angiitis of central nervous system, 806, 806f
tumor emboli and neoplastic aneurysms, 800–801, 800f
tumor-related hemorrhagic stroke, 801, 801f–802f
venous thrombosis, 798–799, 798f–799f

Cerebrovascular lesions, 661
Cerium-doped lutetium oxyorthosilicate (LSO), 356
Cervical meningiomas, 42
Cervical myelopathy
  spinal epidural disease differential diagnosis, 737–738, 738f
Cervical plexopathies, 115–116
Cervical plexus, 111, 112f, 763–764, 764f–765f
Cervicomedullary astrocytomas, 622, 624f
Cetuximab, 136
Chamberlain, 50–51
Chemical exchange saturation transfer (CEST) imaging, 385, 392, 399–400
Chemical shift fat saturation, 164
Chemical shift imaging, 327. *See also* Magnetic resonance imaging (MRI)
Chemoradiation therapy (CRT), glioblastoma (GBM), 681–684, 686
Chemotherapy
  central neurocytoma, 576
  cerebellar liponeurocytoma, 582
  cerebrovascular complications due to, 804–805
  chordomas, 607
  desmoplastic infantile astrocytoma, 579–580
  desmoplastic infantile ganglioglioma, 579–580
  DNETs, 580
  epidural spinal cord compression (ESCC), 61
  ganglioglioma, 577–578
  germinomas, 491, 597
  gliomas, 669
  gliomatosis cerebri, 456
  glioneuronal tumors, 573
  of intramedullary spinal cord metastases (ISCM), 57–58
  intravascular lymphomatosis, 478
  of metastatic brain tumors (MBTs), 28–30
  neoplastic meningitis, 70
  nongerminomatous germ-cell tumors, 597
  optic pathway gliomas, 512–513
  papillary glioneuronal tumors, 636
  papillary tumors of the pineal region, 597–599
  PCNSL, 471, 515
  pilocytic astrocytomas, 490
  pineoblastoma, 586, 597–599
  of primary brain tumors (PBTs), 16–19
  primary cerebral lymphomas, 564
  of primary SCT, 49–51
  thalamic tumors, 555
  vascular disorders, 81
  vestibular schwannoma, 553
Chemotherapy-induced cognitive impairment, 132–136
  alkylating agents, 134
    busulfan, 134
    ifosfamide, 134
  anthracycline antibiotics, 136
  antimetabolites, 132–134
    5-fluorouracil (5-FU), 134
    cytosine arabinoside, 134
    methotrexate, 132–134
  L-asparaginase, 136
  monoclonal antibodies, 136
    bevacizumab, 136
    cetuximab, 136
    ipilumimab, 136
    rituximab, 136
    trastuzumab, 136
  platinum-based agents, 134–135
    cisplatin, 134–135
    oxaliplatin, 135
  taxanes, 135
  vincristine, 135–136
Chemotherapy-related cerebrovascular complications
  computed tomography, 805
  magnetic resonance imaging, 804–805
Chiasmatic gliomas, 490
Chiasmatic tumors, pediatric, 625–626
Cho/NAA ratio (CNR), 171
Cholesteatoma, 656
Choline (Cho), 170–171, 327, 440
  bilateral thalamic glioma, 560
  central neurocytoma, 575
  DNETs, 580
  ganglioglioma, 561, 577
  glioblastoma multiforme, 431
  high-grade gliomas, 432
  magnetic resonance spectroscopy, 170
  metastatic brain tumors, 648–649
  oligodendrogliomas, 463
  pontine tumors, 622
  primary cerebral lymphomas, 564
  primitive neuroectodermal tumors, 563
Chondroblastoma, skull base, 609
Chondroid chordomas, 43–44
Chondroma
  computed tomography, 749t, 759f
  magnetic resonance imaging, 749t, 759f
  skull base, 609
Chondrosarcomas, 37, 607–609
  clinical presentation, 608
  computed tomography, 608f, 609, 750f, 750t
  hyaline, 608
  magnetic resonance imaging, 608f, 609, 750t
  myxoid, 608
  pathology, 608
  treatment, 609
Chordoid glioma, 567–568
  computed tomography, 567–568, 568f
  magnetic resonance imaging, 567–568, 568f
Chordomas, 603–607
  clinical presentation, 605
  computed tomography, 604f–606f, 605–607
  magnetic resonance imaging, 604f–606f, 605–607
  pathology, 603–605
  positron emission tomography, 607
  of spine, 43–44, 44f
  treatment, 607
Chorea, 107
  paraneoplastic, 814–816
Choriocarcinoma, 562, 590
Choristoma, 499, 499f
Choroid plexus carcinomas
  pediatric, 619, 619f
Choroid plexus papillomas
  pediatric, 619, 619f
Choroid plexus tumors, 618–619
Chronic kidney disease (CKD), 185–186
Cine-CT scanner, 145
Cisplatin, 28–29, 81, 134–135
  cytarabine, 49–50
  desmoplastic infantile ganglioglioma, 579–580
Clinical target volume (CTV), 231–232
Clinical trial
  bevacizumab (BEV), 30
  in oncology, 73
  use of imaging in, 672
Clinical utility of MRA, 93–94
Coagulopathy
  cerebrovascular complications, 797–798
  intracranial hemorrhage, 85
  vascular disorders, 79
Cognitive dysfunction, 128
Cognitive impairment, chemotherapy-induced, 132–136
Collimator, 354
Colloid cysts, 655–656
Compartmental volumes, 335
Complete response (CR), 49–50
Computed tomographic myelography, epidural spinal cord compression, 726–727
Computed tomography (CT), 28, 89–92, 143–150, 195, 231, 260–261, 359–360, 371
  acoustic neuroma, 505
  aneurysmal bone cyst, 749t
  arachnoid cysts, 653–654
  astrocytoma
    anaplastic, 421–422
  basal ganglia germinoma, 561–562, 562f
  benign peripheral nerve sheath tumors, 779, 780f
  bilateral thalamic glioma, 560
  central neurocytoma, 574
  cerebellar astrocytoma, 620–621
  cerebellar liponeurocytoma, 582
  chemotherapy-related cerebrovascular complications, 805
  cholesteatoma, 656, 656f
  chondroma, 749t–750t, 759f
  chondrosarcomas, 608f, 609, 750f, 750t
  chordoid glioma, 567–568, 568f
  chordomas, 604f–606f, 605–607
  choroid plexus papillomas, 619
  colloid cysts, 656
  complications, 127
  contrast agents, 151–156
    current applications of, 152
  craniopharyngioma, 493–494, 625, 626f
  CT perfusion (CTP), disadvantages of, 92
    for acute stroke, 91–92
    advantages of, 92
    quantitative, 92
  CT perfusion imaging, 348
  CT–MR image integration, 261
  dermoids, 495, 654

desmoplastic infantile astrocytoma, 579
desmoplastic infantile ganglioglioma, 579
diffuse astrocytomas, 442–445, 446f
direct tumor-related compromise of arterial vasculature, 799, 799f–800f
DNETs, 580, 581f
eosinophilic granuloma, 749t
ependymomas, 623–624
epidermoids, 495, 654
epidural spinal cord compression, 727, 727f–728f
epithelial cysts, 655
Ewing sarcoma, 749f, 750t
extramedullary hematopoiesis, 661
facial nerve schwannomas, 508f
fibrous dysplasia, 749t
gangliocytoma, 577
gangliogliomas, 561–562, 577
germ-cell tumors, 627–628
germinomas, pineal tumor, 589, 589f
giant cell tumor, 750t
glioblastoma, 682, 685–687
glioblastoma multiforme, 424–425, 425f–426f, 557–558, 558f
gliomatosis cerebri, 456
gliosarcoma, 435
glomus tumor, 790
hemangioma, 749t
hemangiopericytoma, 536–539
historical development, 145–146, 151
  dual source CT, 146
  helical CT, 146
  multiple detector array CT, 146
  rotate/rotate geometry, 145
  rotate/stationary geometry, 145
  stationary/stationary geometry, 145
  translate/rotate geometry, 145
hypoglossal nerve schwannomas, 509f
hypothalamic hamartomas, 626–627
hypothalamic lymphoma, 568
image reconstruction, 146–149
infection-related cerebrovascular complications, 802–803
inflammatory pseudotumor, 657
intracranial hemorrhage, 86, 661
intracranial lipomas, 655
jugular foramen schwannomas, 508, 508f
Langerhans cell histiocytosis, 629
leptomeningeal metastases, 705–711, 706t, 800
low-grade diffuse astrocytomas, 556–557
medullary tumors, 622
medulloblastoma, 619–620
melanocytomas, 539
meningioma, 488–490, 505, 522–525, 522f, 524f, 526f, 528f, 536f
metastatic brain tumors, 643–644, 644f, 649–650
midbrain tumors, 622
multiple myeloma, 750t
nerve sheath ganglion, 788
neuroimaging response assessment, 675
NMDAR encephalitis, 814
noncontrast computed tomography (NCCT), 89–91
nongerminomatous germ-cell tumors, 591f
occult malignancy, 816–817, 817f
olfactory nerve schwannomas, 510
oligodendrogliomas, 461–462, 462f–463f
osteoid osteoma, 749t
osteosarcoma, 750t, 758f
Pancoast tumors, 769–770
papillary glioneuronal tumors, 637–638, 640f
papillary tumors of the pineal region, 595, 596f
paraneoplastic cerebellar degeneration, 811
PCNSL, 472, 472f–474f, 513, 514f
pediatric brain tumors, 613
pediatric dysembryoplastic neuroepithelial tumor, 618
physics of, 143–156
pilocytic astrocytomas, 450–451, 555–556, 556f
pineal calcification, 587, 587f
pineal lipomas, 599f
pineoblastomas, 592, 593f
pineocytomas, 592–594, 594f
pituitary hyperplasia, 493f
pituitary stalk lesions, 497
pleomorphic xanthoastrocytoma, 452
plexopathy, 765–766, 771f
  visualization of normal plexus components, 766–768
pontine tumors, 621–622
PPTIDs, 594
primary cerebral lymphomas, 564
primitive neuroectodermal tumors, 563
Rathke cleft cysts, 496, 656
Rosai-Dorfman disease, 657
sarcoidosis, 657
schwannomas, 491–492, 503, 504f–505f
sellar/juxtasellar lesions, 483–484
side effects and toxicity, 152–154
spinal tumors, 755–756
subependymal giant cell astrocytomas, 456, 617–618
suprasellar lipoma, 498f
supratentorial ependymomas, 617
supratentorial primitive neuroectodermal tumors, 616–617, 617f
tectal gliomas, 597f
Tolosa-Hunt syndrome, 658
traumatic neuroma, 785–788
tumor emboli and neoplastic aneurysms, 800–801, 800f
tumor-related hemorrhagic stroke, 801, 801f
venous thrombosis, 798–799, 798f
vestibular schwannoma, 544f, 547, 549f
X-ray contrast agents, general principle of, 151–152
Computed tomography angiography (CTA)
  for acute stroke, 91
  CTA source images (CTA-SI), 91
  metastatic brain tumors, 643–644
Computer-aided volumetric analysis, 675–676, 676f
Comsol Multiphysics, 244
Conductive hearing loss, and acoustic neuroma, 505
Congenital immune deficiency syndromes, and PCNSL, 471
Consensus DCE model, 336
Contrast agents, magnetic resonance imaging, 646
Contrast enhanced MRA (CE MRA), for CNS infarction, 93
Contrast materials (CMs), 151, 153
Contrast media
  advanced techniques using, 186–188
  in neuroimaging, 183–184
Contrast-enhanced computed tomography, 100–101, 409–410
Contrast-enhanced magnetic resonance imaging (MRI), 327
Contrast-enhanced susceptibility-weighted imaging (CE-SWI)
  pseudoprogression, 688
Contrast-induced AKI, 154
Contrast-to-noise ratio (CNR), 195, 338, 385
Conventional diffusion-weighted images, single diffusion coefficient derived from, 302–304, 303f–304f
Cortical mapping, 220–221, 224
Cortical stimulation testing, 221–222
Corticospinal tract, 90f, 93, 286–288, 290, 467
Corticosteroids, 73, 412, 440–441
  of epidural spinal cord compression (ESCC), 60–61
  inflammatory pseudotumor, 657
  sarcoidosis, 657
Cowden disease, 581
Cranial exposure to therapeutic ionizing radiation, 4
Cranial nerve I (CN I), schwannoma, 510
Cranial nerve III (CN III), schwannoma, 508–510
Cranial nerve IV (CN IV), schwannoma, 508–510
Cranial nerve V (CN V), schwannoma, 506–507
Cranial nerve VI (CN VI), schwannoma, 508–510
Cranial nerve VII (CN VII), schwannoma, 507
Cranial nerve VIII (CN VIII), schwannomas, 504–506
Cranial nerve IX (CN IX), schwannoma, 507–508
Cranial nerve X (CN X), schwannoma, 507–508
Cranial nerve XI (CN XI), schwannoma, 507–508
Cranial nerve XII (CN XII), schwannoma, 508
Cranial nerve tumors
  glial neoplasms, 511–513
  nerve sheath neoplasms, 503–511
  primary central nervous system lymphoma, 513–515
Cranial nerves, target proximity to, 258
Cranial neuropathies, 132

Craniopharyngioma, 493–494
computed tomography, 493–494
magnetic resonance imaging, 493–494, 493f–494f
pediatric, 624–625
skull base, 609
Craniotomy, meningioma, 488–490
Cranium, electric field distribution within, 249–251
computational model, 249–250
experimental evidence, 249
future modeling developments, 251
modeling results, 250–251
Creatine (Cr), 440
bilateral thalamic glioma, 560
DNETs, 580
gangliogliomas, 561, 577
glioblastoma multiforme, 431
high-grade gliomas, 432
magnetic resonance spectroscopy, 170
metastatic brain tumors, 648–649
pontine tumors, 622
primary cerebral lymphomas, 564
primitive neuroectodermal tumors, 563
Creutzfeldt–Jacob disease (CJD), 814–816
Cushing disease, venous sampling, 484
Cw*01 variant, 5
CyberKnife, 27, 49
CyberKnife radiosurgery, 57, 259–260, 260f
Cyclooxygenase-2 (COX-2), 7, 23–24
Cyclophosphamide (CTX), 28, 49–50
desmoplastic infantile ganglioglioma, 579–580
Cystic memningioma, 530f–531f
Cytarabine, 70, 71t
PCNSL, 515
Cytokeratin (CK), chordomas, 603–605
Cytosine arabinoside, 134

D

Dabrafenib, 72
Dactinomycin, desmoplastic infantile ganglioglioma, 579–580
Deep brain, invasion by cerebral hemisphere tumors, 568–569
Degree of anisotropy, 168
Delayed contrast extravasation magnetic resonance imaging, pseudoprogression, 690
Delayed radiation myelopathy (DRM), 131
Delta brush, 106
Dementia, 128
Demyelinating encephalitis, 659
2-Deoxy-2-(^{18}F)fluoro-D-glucose (FDG), 253
3′-Deoxy-3′-[^{18}F]fluorothymidine, 366
Deoxyhemoglobin, 210, 391
DepoCyt, 70, 71t
Dermoid cysts, pineal region, 595
Dermoids, 37, 494–495, 654, 655f
computed tomography, 495
magnetic resonance imaging, 495
Desmoplastic infantile astrocytoma (DIA), 578–580
computed tomography, 579
magnetic resonance imaging, 579
pathology, 579
treatment, 579–580
Desmoplastic infantile ganglioglioma (DIG), 578–580
computed tomography, 579
magnetic resonance imaging, 579, 579f
pathology, 579
treatment, 579–580
Detector configurations, positron emission tomography (PET) imaging, 356–357
Detector materials, positron emission tomography (PET) imaging, 356
Dexamethasone, 57, 381–382
oligodendrogliomas, 468
Diabetes insipidus, pituitary stalk, 497
Dielectric resonance, 200
Diencephalic syndrome, 565, 626, 627f
Diencephalic tumors, 555–568
basal ganglia-thalamus, 555–565
hypothalamus-optic chiasm, 565–568
Diencephalon, 555
Diffuse astrocytic tumors, 9–10
Diffuse astrocytomas, 556–558
Diffuse gliomas
in adults, evolution, 669
high-grade gliomas, 670–671, 671f
low-grade gliomas, 669–670, 670f
Diffuse melanocytosis, 539
Diffuse tensor tractography, 441
Diffusion anisotropy, 309–312
Diffusion imaging
in brain tumors, 302
intraoperative, 290–291
Diffusion kurtosis MR imaging (DKI), 274, 278–279, 281–283
-based fiber tractography, 295
-based tractography, 295
Diffusion magnetic resonance imaging
assessment of extra-axial tumors, 279–280
in brain tumors, 273–300
clinical use, 279
intra-axial cystic masses, characterization of, 281
intraoperative diffusion imaging, 290–291
medulloblastoma, 619–620
pediatric brain tumors, 613
physical basis, 274–279
diffusion kurtosis MR imaging, 278–279
diffusion tensor MR imaging, 275–276
diffusion-weighted MR imaging, 274–275
posttreatment evaluation, 291–295
potential future applications, 295–296
limitations, 295–296
preoperative planning and peritumoral margins, 285–290
stratifying tumor histology, 284–285
tumor grading, 281–284
Diffusion spectrum imaging (DSI), 274, 295
Diffusion tensor imaging (DTI), 118, 165, 168, 193, 218–219, 403–404, 441
glioblastoma multiforme, 428, 429f
hemangioblastomas, 753
oligodendrogliomas, 467
pediatric brain tumors, 615
pontine tumors, 622
for preoperative assessment, surgical guidance, and follow-up of brain tumors, 168
spine metastases, 734
Diffusion tensor MR imaging (DT-MRI), 208, 273–276, 279, 283, 289–291, 295
Diffusion tensor tractography, 312
Diffusion tensor-based clustered images (DTcls), 168
Diffusion tensor-fiber tracking (DT-FT)
hemangioblastomas, 753
Diffusion tractography, pediatric brain tumors, 615, 615f
Diffusion values, 302–303, 305t
Diffusion-tensor imaging (DTI), 309–310, 312
Diffusion-weighted imaging (DWI), 165, 167–168, 196–197, 273–274, 279, 281, 284–286, 292–295, 302–309, 398–399, 441
cerebral abscesses, 699
cholesteatoma, 656
demyelinating encephalitis, 659
in differential diagnosis, 697–698
differential diagnosis, grading, monitoring of progression, and response, 167–168
diffusion tensor imaging, 168
glioblastoma multiforme, 428, 432, 559f
intravascular lymphomatosis, 478, 478f
ischemic infarctions, 662f
metastatic brain tumors, 647, 648f
oligodendrogliomas, 462–463, 464f
papillary glioneuronal tumors, 638
papillary tumors of the pineal region, 595, 596f
pediatric brain tumors, 615
pilocytic astrocytomas, 556, 556f
pineoblastomas, 592, 593f
primary cerebral lymphomas, 564, 564f
primary CNS lymphoma, 432, 472, 473f
pseudoprogression, 688–689
spine, 732, 755
tectal gliomas, 597f
vestibular schwannoma, 549f
Diffusion-weighted MRI (DW-MRI), 274–275, 415
3,4-Dihydroxy-6-[^{18}F]fluoro-L-phenylalanine ([^{18}F] FDOPA)
Diplopia, 64, 605
Direct cortical stimulation (DCS), 317, 319, 323–324
Direct tumor-related compromise of arterial vasculature
computed tomography, 799, 799f–800f
magnetic resonance imaging, 799, 799f–800f
Disseminated encephalomyelitis, 811–813
Disseminated intravascular coagulation (DIC), 79, 85
Dixon techniques, 164
Docetaxel, 135
Dose delivery, 233
Dose volume histograms (DVHs), 231–232
Dose-dependent side effects, 153
Dose-independent and unpredictable side effects, 153
Dose–volume histogram (DVH), 235
Doxetaxel, 28–29

Doxorubicin, 81
Dual source CT, 146
Dural venous sinuses, 93, 519
Dural-based metastasis, 697
Dynamic contrast agent MRI perfusion techniques, 335–336
Dynamic contrast enhanced (DCE) imaging, 186–187, 252, 335–339, 397, 689–690
  basic principles, 336–337
  to characterize gliomas and predict treatment response, 338, 339f
  to characterize non-CNS tumors, 338
  imaging methodology, 337–338
  toward standardization of DCE acquisition and postprocessing methods, 339
Dynamic spin-echo magnetic resonance imaging
  trigeminal schwannomas, 507, 507f
Dynamic susceptibility contrast (DSC) imaging, 335, 339–346
  assessment of tumor vascular architecture, 345
  basic principles, 339–340
  cerebral blood flow (CBF), potential role of, 345
  distinction of tumor recurrence from radiation necrosis, 346
  glioma tumor grade, distinction of, 343–344
  high-grade gliomas versus other neoplasms, 344–345
  methodology, 340–343
    choice of DSC imaging sequence, 340–342
    contrast agent leakage effects, 342–343
    postprocessing of DSC imaging data, 342
  MR perfusion imaging assessment of peritumoral regions, 345–346
  MR perfusion imaging for assessment of tumor therapy, 346
Dynamic susceptibility contrast-weighted imaging using T2- or T2*-weighted imaging (DSC-MRI), 186–187
Dynamic susceptibility-weighted contrast-enhanced (DSC) perfusion imaging, 689–690
  oligodendrogliomas, 464–466, 466f
Dynamic X-rays, spinal tumors, 756
Dysembryoplastic neuroepithelial tumors (DNETs), 580–581, 618
  computed tomography, 580, 581f
  magnetic resonance imaging, 580, 581f
  pathology, 580
  positron emission tomography, 580
  single-photon emission computed tomography, 580
  treatment, 580–581
Dysplastic cerebellar gangliocytoma, 581–582
  magnetic resonance imaging, 581, 582f
  pathology, 581
  treatment, 581–582

E

Early disease progression (EP), 236–237
Early–delayed radiation myelopathy, 131
  delayed radiation myelopathy (DRM), 131
  late–delayed myelopathy, 131
  radiogenic lower motor neuron disease, 131
  vascular changes, 131
Echo time (TE), 158–159
Echoes, 164
Echoplanar imaging (EPI) methods, 195, 340, 428
Edema, 302
  pituitary adenoma, 485, 487f
EF-14, 247–249
Electric field
  distribution within cranium and brain, 249–251
    computational model, 249–250
    experimental evidence, 249
    future modeling developments, 251
    modeling results, 250–251
  physics of, 243–244
Electrical cortical stimulation (ECS), 221–222
Electrocorticography (ECG), 221–222
Electrodiagnostic (EDX) testing, 118
Electromagnetic digitizers, 211
Elekta Gamma Knife system, 233
Elephantiasis neuromatosa, 778
Emboli
  septic, 81–82
  tomor, 80, 85, 643, 800–801
Embolization, meningioma, 521, 531, 532f–535f
Embryonal tumors, 3, 12–13, 13t
Embryonic cell carcinoma, 562
Empty sella, 497, 497f
En bloc resection of single metastasis to spine, 754
Encephalitis
  acute demyelinating, 658f
  autoimmune, 657
  demyelinating, 659
  herpes simplex encephalitis, 660
  paraneoplastic, 658f
Encephalopathy, acute, 125
Enchondroma, skull base, 609
Endocrine disorders, 130–131
Endodermal sinus tumors, 562
Endovascular techniques, 94
  meningioma, 521
Endovascular therapy
  cerebrovascular complications due to, 805, 805f
  -related cerebrovascular complications magnetic resonance imaging, 805, 805f
Eosinophilic granuloma
  computed tomography, 749t
  magnetic resonance imaging, 749t
  skull base, 609
Ependymomas, 35, 45, 752–753
  intradural, 37
  myxopapillary, 37
  pediatric, 623–624
  spinal, 37
  supratentorial, pediatric, 617
Epidemiology
  of intramedullary spinal cord metastases (ISCM), 38
  of metastatic brain tumors (MBTs), 6–7
  of primary brain tumors (PBTs), 3–6
  of primary SCT, 35–37
Epidermal growth factor (EGF), 55
Epidermal growth factor receptor (EGFR), 5, 7, 23–24, 66
Epidermoid, 654, 655f
Epidermoid cysts, pineal region, 595
Epidermoid tumors, 37
Epidermoids, 37, 494–495
  computed tomography, 495
  magnetic resonance imaging, 495
Epidural hematoma, 737, 757
Epidural hemorrhage, 85, 87
Epidural lipomatosis, 738–739, 739f
Epidural space, 59
Epidural spinal cord compression (ESCC)
  in adult neoplasms, 59–62
    clinical features, 60
    corticosteroids, 60–61
    diagnosis, 60
    etiology, 59–60
    prognosis, 61
    treatment, 61
  clinical background, 723
  epidural anatomy, 724, 724f
  imaging, 726–735
    computed tomographic myelography, 726–727
    computed tomography, 727, 727f–728f
    differential diagnosis, 735–740, 736f–741f
    magnetic resonance imaging, 728–735, 729f–735f
    myelography, 726–727
    nuclear medicine, 728
    radiography, 726, 726f
  incidence, 723
  metastatic, 723
  multiple epidural metastases, 723
  pathophysiology, 724–726
  prognostic factor, 723
Epidural venous plexus, 725, 733–734
Epidural/subdural hematoma, spinal epidural disease differential diagnosis, 737, 738f
Epilepsy, 222, 566–567
Epithelial cysts, 655
Epithelial membrane antigen (EMA), chordomas, 603–605
Epstein-Barr virus, 471
Equilibrium magnetization, 157, 160
ERCC1, 5
ERCC2, 5
Erdheim-Chester disease, 539–540
Erlotinib, 71–72
Etoposide, 28, 50–51, 71t
  desmoplastic infantile ganglioglioma, 579–580
Ewing sarcoma, 629f
  computed tomography, 749f, 750t
  magnetic resonance imaging, 749f, 750t

Expanded pulse sequence diagram, 163–164
Extended Tofts Model, 337
Extent of resection (EOR), 669
Extra-axial tumor
  assessment of, 279–280
  imaging features, 697–698
  meningeal tumors, 519
Extracellular matrix (ECM), 23–24
Extracellular volume fraction, 167
Extramedullary hematopoiesis (EH), 661
  spinal epidural disease differential diagnosis, 740, 740f
Extramedullary intradural spinal tumors, 751–752
  meningiomas, 751, 752f
  nerve sheath tumors, 751–752
Extramedullary spinal cord tumors, 35, 48
Extranodal B-cell non-Hodgkin lymphoma, 80
Extraocular nerve schwannomas, 508–510
  classification, 509
  magnetic resonance imaging, 510–511, 510f
  management of, 511
Extremely low frequency magnetic fields (ELFs), 5

F

2-[18F]fluoro-2-deoxy-D-glucose ([18F]FDG), 372, 376, 380–381
[18F]fluorodeoxyglucose (FDG) PET, 362–365, 415, 441–442
  central neurocytoma, 575–576
  chordomas, 607
  DNETs, 580
  follow-up assessment and monitoring treatment, 364–365
  PCNSL, 473–475, 514
  tumor detection, 362–363
  tumor grading and degree of malignancy, 363–364
[18F]fluoroethyl-L-tyrosine (FET), 366
Facial nerve schwannomas, 507
  computed tomography, 508f
  magnetic resonance imaging, 508f
  management of, 510
Fast spin-echo (FSE) imaging, 195, 729–730
Fat signal suppression
  fat-saturation technique, 732–733
  inversion-recovery imaging, 733
Fiber tracking, in spinal cord compression, 734
Fibrillary astrocytoma, 442, 443f, 445
Fibroblast growth factors, 55
Fibromas, spinal epidural disease differential diagnosis, 740
Fibromatosis, spinal epidural disease differential diagnosis, 740
Fibrosarcoma, 434–435
Fibrous dysplasia
  computed tomography, 749t
  magnetic resonance imaging, 749t
FIESTA, vestibular schwannoma, 544f
Filtered back-projection, 146–147, 148f
Fluid attenuated inversion recovery (FLAIR), 128, 160, 231, 733
  autoimmune encephalitis, 657
  bilateral thalamic glioma, 560
  for CNS infarction, 92–93
  craniopharyngioma, 493f
  hamartomas, 656f
  hemangiopericytoma, 537f
  images, 184
  imaging signals, 410–411
  intravascular lymphomatosis, 478, 478f
  ischemic infarctions, 662f
  low-grade diffuse astrocytomas, 557
  meningioma, 522f, 525, 536f
  metastatic brain tumors, 644–645, 649–650, 650f
  oligodendrogliomas, 461–462, 462f, 464f, 466f
  optic pathway gliomas, 512
  papillary glioneuronal tumors, 638, 639f
  PCNSL, 472, 473f–474f
  pineal cysts, 588f, 653
  primary leptomeningeal lymphoma, 476–478, 477f
  tissue, 327
  vestibular schwannoma, 547f
Flow-related enhancement, 93
Fludeoxyglucose positron emission tomography (FDG-PET), 126
Fluorodeoxyglucose (FDG) PET, 362–365, 402
  metastatic brain tumors, 649
  pontine tumors, 622
Fluoroethyl-L-tyrosine, 415
Fluorothymidine (18FLT), 415
5-Fluorouracil (5-FU), 81, 134
Focused ultrasound (FUS), 213
Folinic acid, 70
Foreign body granulomas, 697
Fourier slice theorem, 147
Fourier transformation, 147, 148f, 162
Fractional anisotropy (FA), 168, 276, 286, 289, 441
  FA index, 309
  metastatic brain tumors, 647
  oligodendrogliomas, 467
  pontine tumors, 622
  in spinal cord compression, 734
Fractionated stereotactic radiotherapy, 233
Frequency encoding, 162
Functional brain mapping techniques, 225–226
Functional diffusion imaging, 292
Functional imaging, 261–262
Functional magnetic resonance imaging (fMRI), 207–208, 219–220, 222, 224, 290, 317–326
  blood oxygen level–dependent (BOLD fMRI)
  effects of brain tumors and prior surgery on the fMRI signal, 322
  general considerations, 317–318
  interpretation pitfalls, 322–324
  language fMRI, 320
    lateralization, 320
    localization, 320–321
  oligodendrogliomas, 466–467
  pediatric brain tumors, 613, 614f
  sensory/motor, 318–319
  special considerations for fMRI measurements using brain tumor patients, 321–322
  surgical outcomes and future developments, 324–325
Fungal infections, 659
Fungal sepsis, 81–82
Fusiform Schwann cells, 42–43

G

Gadobenate dimeglumine, 184t, 646
Gadobutrol, 184t
Gadodiamide, 184t
Gadofosveset, 184t
Gadolinium, 93, 183, 329
Gadolinium chelates, 184–185
Gadolinium contrast agents, 188–189
Gadolinium dimeglumine, 440
Gadolinium oxyorthosilicate (GSO), 356
Gadolinium-based contrast agents (GBCAs), 183–186, 189
Gadolinium-based molecules, 198
Gadolinium–diethylenetriaminepentaacetic acid (Gd-DTPA), 397
Gadolinium-enhanced MRI
  metastatic brain tumors, 644
Gadomer-17, 337
Gadopentate dimeglumine, 440
Gadopentetate dimeglumine, 184t
Gadoteric acid, 184t
Gadoteridol, 184t
Gadoversetamide, 184t
Gadoxetic acid, 184t
Gamma Knife, 27, 607
  radiation therapy, vestibular schwannoma, 552
  radiosurgery, 259, 259f
    craniopharyngioma, 494
    jugular foramen schwannomas, 511
    planning, 233
Gangliocytoma (GC), 576–578
  angiography, 577
  computed tomography, 577
  magnetic resonance imaging, 577
  pathology, 576
  positron emission tomography, 577
  single-photon emission computed tomography, 577
  thalamus, 561
  treatment, 577–578
Ganglioglioma (GG), 576–578, 638–639
  angiography, 577
  computed tomography, 561–562, 577
  magnetic resonance imaging, 561, 561f, 577, 577f–578f
  magnetic resonance spectroscopy, 561
  pathology, 576
  positron emission tomography, 577
  single-photon emission computed tomography, 577
  thalamus, 561
  treatment, 577–578

Ganglion cell tumors, 561
Gefitinib, 71–72
Gemistocytic astrocytoma, 442
Genetically engineered mouse (GEM) models, 395
Germ-cell tumors (GCTs)
  pediatric, 627–628
  pineal gland, 586, 589–590
  thalamus, 561–562
Germinoma, 490–491, 491f, 561
  basal ganglia, 561–562
  pineal tumor, 586, 589
    computed tomography, 589, 589f
    magnetic resonance imaging, 589, 589f–590f
  treatment, 597
Giant cell astrocytomas, subependymal, 617–618, 618f
Giant cell tumor
  computed tomography, 750t
  magnetic resonance imaging, 750t
  skull base, 609
  supratentorial, pediatric, 617–618
Glial fibrillary acidic protein (GFAP), 10–11, 573–574
Glial hypothesis, 127–128
Glial neoplasms, 511–513
Glioblastoma, 10, 389, 409, 411–412, 669, 676, 681–683
  arterial spin imaging, 691
  computed tomography, 682, 685–687
  delayed contrast extravasation magnetic resonance imaging, 690
  diffusion weighted magnetic resonance imaging, 688–689
  efficacy of alternating electric fields therapy for, 246–249
  growth of, 366f–367f
  magnetic resonance imaging, 681, 682f, 685–687
  magnetic resonance spectroscopy, 690–691
  perfusion imaging, 689–690
  positron emission tomographic imaging, 691–692
  secondary, 669
Glioblastoma multiforme (GBM), 3, 9–11, 11f, 45–46, 46f, 171–172, 395–396, 421–429, 425f, 431–434, 511, 667, 668f
  computed tomography, 557–558, 558f
  differential diagnosis of, 431
  diffusion tensor imaging, 428, 429f
  diffusion-weighted imaging, 428, 559f
  magnetic resonance imaging, 557–558, 558f–559f, 598f, 616f
  magnetic resonance spectroscopy, 559f
  metastases, 426, 432
  multifocal/multicentric tumors, 427
  perfusion-weighted imaging, 428
  primary, 422–424
  recurrence, 434, 435f
  secondary, 422–424
  supratentorial, 616f
  thalamus, 556–557
  TTFields for, 243
Gliomas, 3–6, 9, 130, 265–266, 273, 278–279, 281–283, 288, 330, 421, 667–669
  basal ganglia, 555
  cellularity of, 359, 392
  chiasmatic, 490
  chordoid, 567–568
  grade I, 265–266
  grade II, 266
  grade III, 235, 266
  grade IV, 235, 266
  grading system for, 421
  high-grade gliomas, 273, 288–289, 670–671, 671f, 676
    application of RANO criteria to, 413
  hypothalamic, 490, 565–566
  low-grade gliomas, 669–670, 670f
    application of RANO criteria to, 413–414
  mixed, 560
  optic chiasm, 565–566
  and PCNSL, 475–476
  pontine, 621f
    magnetic resonance imaging, 621f
  and predict treatment response
    dynamic contrast enhanced (DCE) imaging to characterize, 338
  versus radiation necrosis, 188
  RANO criteria for, 410
  tectal, 595f, 624f
    computed tomography, 597f
    diffusion-weighted imaging, 597f
    magnetic resonance imaging, 597f
    treatment, 599–600
  thalamic, 555, 557f, 560
  tumor grade, distinction of, 343–344
Gliomatosis cerebri, 456, 457f
  classification, 456
  computed tomography, 456
  magnetic resonance imaging, 456
Glioneuronal tumors, 573–584
  central neurocytoma, 573–576
  cerebellar liponeurocytoma, 582
  desmoplastic infantile astrocytoma, 578–580
  desmoplastic infantile ganglioglioma, 578–580
  dysembryoplastic neuroepithelial tumors, 580–581
  dysplastic gangliocytoma of the cerebellum, 581–582
  gangliogliomaand gangliocytoma, 576–578
Gliosarcoma, 10, 421, 434–435
  computed tomography, 435
  magnetic resonance imaging, 435, 436f
  posterior fossa, 434–435
  radiation-induced, 434–435
Glomeruloid structures, 24–25
Glomus tumor, 790–791
  computed tomography, 790
  magnetic resonance imaging, 790–791, 791f
  skull base, 609
Glycine, central neurocytoma, 575
Gradient echo (GRE), 164, 196–197, 646–647
  acquisitions, 183–184
  of brain tumor, 196f
  imaging, spine, 732
  sequences, 210
  techniques, 340, 342
Grading and differential diagnosis, 327–328
Granulomatous infections, spinal epidural disease differential diagnosis, 736–737, 737f
Gray matter, 302, 308–309
Gross total resection (GTR)
  central neurocytoma, 576
  papillary glioneuronal tumors, 636
Gross tumor volume (GTV), 231–232
Growing teratoma syndrome, 597
Growth hormone-secreting adenomas, 264–265
Gummas, 659

H

Hamartomas, 442, 656
  hypothalamic, 492, 566–567, 626–627, 628f
  magnetic resonance imaging, 567, 567f
Hazard ratio (HR), 17
Helical CT, 146
Hemangioblastomas, 37, 44, 44f, 753
Hemangioma
  computed tomography, 749t
  magnetic resonance imaging, 749t
Hemangiopericytoma, 519, 535–539
  angiography, 539
  computed tomography, 536–539
  FLAIR, 537f
  magnetic resonance imaging, 537f–539f, 539
Hematologic malignancies, spinal epidural disease differential diagnosis, 735
Hematoma, 699
Hemodynamic response function (HRF), 198
Hemolytic uremic syndrome, 86
Hemorrhage, 43, 85
Hemorrhagic metastases, magnetic resonance imaging, 644–646
Hemosiderin pigment, 44
Hereditary syndrome, 4
Herpes simplex encephalitis, 660
High bandwidth (BW) pulses, 201
High magnetic field, 195–196
High-angular-resolution diffusion imaging (HARDI), 274
High-field (HF) magnetic resonance imaging, 193–202, 646
  brain tumors, 194
  high-resolution imaging, 196–197
  magnetic susceptibility, 197–198
  MRI
    comparison with other techniques, 195
    physics, 193–194
  pathology
    direct measure of, 195
    indirect measure of, 194–195
  pros and cons, 195–196
  radio frequency
    issues, 200–201
    penetration, 199–200
  static magnetic field, 198–199

High-grade gliomas (HGGs), 273. *See also* Astrocytoma; malignant; Gliomas
  versus other neoplasms, 344–345
  practical application of radiotherapy in, 233–235
  vascular heterogeneity, 429
Highly diffusion-weighted images, multiple diffusion parameters derived from characterization of brain tumors with, 305–309
High-resolution imaging, 196–197
High-resolution magic angle spinning (HR-MAS), 332
Hippocampal dysfunction, 128
Hippocampal neurogenesis, 129
Hippocampal sparing, 129
Histiocytoma, malignant fibrous, 434–435
Histiocytosis X, pituitary stalk lesions, 498
Histogram analysis, glioblastoma multiforme, 429, 430f
Hodgkin lymphoma, 81–82, 471, 479
Horner syndrome, 115–116
Hounsfield units (HU), 148
Human immunodeficiency virus, 699
Human leukocyte antigens (HLAs), 5
Hydrogen (^{1}H), 193–194
2-Hydroxyglutarate (2-HG), 172
Hydroxyurea, 49–50
Hyperleukocytosis, 85
Hyperplasia, pituitary, 492–493
Hyperthyroidism, iodine-induced, 154
Hypodensity, 89
Hypoglossal nerve schwannomas, 508
  computed tomography, 509f
  magnetic resonance imaging, 509f, 511
  management of, 511
Hypophysitis, 658–659
Hypothalamic gliomas, 490, 565–566
  magnetic resonance imaging, 565, 566f
Hypothalamic hamartomas, 492, 626–627, 628f
Hypothalamic tumors, 565–568
  pediatric, 625–626
Hypoxia, tumor, 391

I

Idiopathic pachymeningitis, 657–658
Ifosfamide, 134
Image contrast mechanisms, 158–160
  basic pulse sequence, 158–159
  echo time (TE), 158–159
  imaging parameters repetition time, 158–159
  inversion recovery, 160
  proton density, 159–160
  proton density images, 160
  T1-weighted images, 160
  T2-weighted images, 160
Image reconstruction, 353
  computed tomography (CT), 146–149
Image-guided surgery, 374, 377–378
Imaging criteria for brain tumor progression, 409–410
Imaging parameters repetition time, 158–159
Imaging pitfalls
  imaging features, 697–699
    extra-axial and meningeal tumors, 697–698
    intra-axial lesions, 698–699
  recurrence versus treatment-related complications, 699–700
Imaging tumor oxygenation, 391
Imatinib mesylate, chordomas, 607
Immunocompetent patients, PCNSL in, 473–475, 513–514
Immunocompromised patients, PCNSL in, 473–475, 513
Immunosuppression in cancer patients, 81–82
In vivo bioluminescence imaging, 400–401
Increased intracranial pressure (ICP), 125
^{111}Indium-diethylenetriamine pentaacetic acid, 66
Infection, spinal epidural disease differential diagnosis, 735–736, 736f
Infection-related cerebrovascular complications, 802–803, 802f–803f
  computed tomography, 802–803
  magnetic resonance imaging, 802–803, 802f–803f
Infectious granulomas, 697
Infiltrative edema, 465–466
Infiltrative glioma, 409
Inflammation, spinal epidural disease differential diagnosis, 736–737, 737f
Inflammatory arthropathy, spinal epidural disease differential diagnosis, 737–738
Inflammatory pseudotumor (IPT), 657
Inflammatory disorders, 657–659
Infundibulitis, 658–659
Interleukins, 55
Internal carotid artery (ICA), 222
  radiation to, 257
Intervertebral disk extrusion, spinal epidural disease differential diagnosis, 738, 739f
Intra-axial cystic masses, characterization of, 281
Intra-axial lesions, imaging features, 698–699, 698f
Intracranial foreign body granulomas, 697
Intracranial hemorrhage (ICH), 80, 85–88, 661
  clinical presentation, 86
  diagnosis, 86–87
  etiology, 85–86
    coagulopathy, 85
    treatment effects, 86
    tumor-related hemorrhages, 85
  management, 87
Intracranial lipomas, 655
Intracranial meningiomas, 36
Intracranial parenchymal sarcoidosis, 699
Intracranial schwannomas. *See* Vestibular schwannoma (VS)
Intracranial tumor, 80–81, 231
  treatment effects, 81
Intracranial veno-occlusive disease, 99–102
  clinical features, 99–100
  diagnosis, 100–101
  etiology, 99
    metastatic cerebral venous thrombosis, 99
    nonmetastatic cerebral venous thrombosis, 99
  treatment, 101–102
IntraCSF therapy, neoplastic meningitis, 70
Intradural ependymomas, 37
Intradural lipomas, spinal epidural disease differential diagnosis, 738–739, 739f
Intradural tumors, 35
Intramedullary ependymomas, 45, 45f
Intramedullary spinal cord metastases (ISCM), 55–58
  chemotherapy of, 57–58
  epidemiology of, 38
  pathology of, 55–56
  percentage of, by primary tumor site, 38t
  radiation therapy of, 57
  surgical therapy of, 56–57
Intramedullary tumors, 35, 752–753
  astrocytomas, 753
  ependymomas, 752–753
  hemangioblastomas, 753
  spinal epidural disease differential diagnosis, 735, 736f
Intraocular lymphoma, primary, 479
Intraoperative diffusion imaging, 290–291
Intraoperative dynamic contrast imaging, 210
Intraoperative image-guided surgery, 224–225
Intraoperative imaging modalities, 217
Intraoperative MR imaging (iMRI), 205, 224–225, 290
  and brain tumor resection, 207–211
    instrument tracking and neuronavigation, 210–211
    intraoperative detection of complications, 210
    intraoperative dynamic contrast imaging, 210
    multimodality imaging, 207–208
    rationale, 207
    rigid and nonrigid image registration for surgical guidance, 208
  patient positioning, 206–207
  safety, 206
Intraparenchymal tumors, 44
Intravascular lymphomatosis, 80, 95f, 478, 478f
  cerebrovascular complications, 806
  magnetic resonance imaging, 806
Intravoxel incoherent motion (IVIM) analysis, 167–168
Introductory magnetic resonance imaging physics, 157–166
  chemical shift fat saturation, 164
  diffusion-weighted imaging (DWI), 165
  external magnetic field, protons, and equilibrium magnetization, 157
  fluid attenuated inversion recovery (FLAIR), 160
  image contrast mechanisms, 158–160
    basic pulse sequence, 158–159
    echo time (TE), 158–159

imaging parameters repetition time, 158–159
inversion recovery, 160
proton density, 159–160
proton density images, 160
T1-Weighted, and T2-weighted images, 160
T1-weighted images, 160
T2-weighted images, 160
Larmor precession and MRI signal, 157
making an image, 161–164
echoes, 164
expanded pulse sequence diagram, 163–164
frequency encoding, 162
gradient echoes, 164
k-space, 162
magnetic field gradients, spatial frequencies, and k-space, 162
phase encoding, 162–163
slice selection, 163
spatial localization by magnetic field gradients, 161–162
spin echoes, 164
two-dimensional versus three-dimensional imaging techniques, 164
motion compensation, 165
parallel imaging, 165–166
radiofrequency energy and resonance, 157–158
relaxation, 158
T1 and T2, 158
T2*, 158
short tau inversion recovery (STIR), 161
susceptibility-weighted imaging (SWI), 165
Invasive adenoma, skull base, 609
Invasive imaging, 231
Inversion recovery, 160
Inversion recovery FSE sequences (IRFSE), 733
Inversion-recovery imaging, fat signal suppression, 733
Iodine-induced hyperthyroidism, 154
Ipilimumab-associated autoimmune hypophysitis, 499
Ipilumimab, 136
Irinotecan, 17–18
Iron oxide-based contrast agents, 198
Ischemic cerebrovascular events disorders vascular disorders, 80
Ischemic infarctions, 661
Ischemic penumbra, 91
Isocitrate dehydrogenase (IDH) mutation, 172, 328, 692
Isocitrate dehydrogenase mutations, in gliomas, 669
Iterative reconstruction, 353

J

Jugular foramen schwannomas, 507–508
computed tomography, 508, 508f
magnetic resonance imaging, 508, 508f, 511
management of, 510–511
Juxtasellar lesions. *See* Sellar region tumors

K

Karnofsky Performance Status (KPS) score, 6–7
Ki67
labeling index, 9–10, 14–15, 635, 638
pseudoprogression, 683–684
k-space, 162
Kurtosis model, 305–308

L

Labeling index (LI), 573–574, 580
Lacrimal adenocystic carcinoma, magnetic resonance imaging, 700f
Lactate (Lac), 327–328, 440
glioblastoma multiforme, 431
magnetic resonance spectroscopy, 170
oligodendrogliomas, 464
Lambert–Eaton syndrome (LES), 108
Langerhans cell histiocytosis, 539–540
pediatric, 629
Language fMRI, 320
lateralization, 320
localization, 320–321
Language localization, 321
Language networks, 222
Large vessel atherosclerosis, 130
Larmor precession and MRI signal, 157
Laser-induced thermal therapy, pediatric brain tumors, 615, 615f
Late–delayed myelopathy, 131
Leptomeningeal carcinomatosis, 184f
Leptomeningeal lymphoma, primary, 477f, 479
Leptomeningeal metastases (LM), 649, 697–698, 705
in adults, 717t
brain MRI, 711–714
cerebrovascular complications, 800
in children, 717t
CNS imaging modalities, 705–711, 706f–711f
computed tomography, 800
cranial CT and MRI, comparison, 706t
CSF cytology, 705
differential diagnosis, 714
disease staging, 706t
magnetic resonance imaging, 755, 800
radioisotope CSF flow studies, 715–718, 715f–716f, 717t
spine imaging
abnormalities, 712t
comparison, 711t
MRI, 711–714
Leptomeninges, 66
Letrozole, 71
Leukemia, 80
Leukoencephalopathy, 128
Lhermitte-Duclos disease, 581–582
Li-Fraumeni syndrome, 4
Light-emitting diodes (LEDs), 211
Limbic encephalitis, 104–106
paraneoplastic, 811–814
Limitations and future directions, 225–226
Line of response (LOR), 401
Linear accelerator (LINAC) radiosurgery, 232–233, 259, 259f
Line-scan diffusion imaging (LSDI) technique, 301–302
Lipids
glioblastoma multiforme, 431
magnetic resonance spectroscopy, 170
oligodendrogliomas, 464
Lipomas, 37, 535
intracranial, 655
pineal region, 595
computed tomography, 599f
Low-back pain (LBP), 745
Lower motor neuron syndrome, 131
Low-grade astrocytomas, 439–460
Low-grade diffuse astrocytomas (LGDA), 667, 668f
computed tomography, 556–557
magnetic resonance imaging, 557, 557f
thalamus, 556–557
Low-grade gliomas (LGGs), 172, 413–414, 511–512
and anaplastic astrocytoma, 421, 424f
cerebral blood volume, 428–429
contrast enhancement, 428
metabolites, 431
pediatric, 616
vascular heterogeneity, 429
Low-grade neoplasms, 286–288
Low-grade PCNSL, 479
Luciferase-coding DNA, 401
Luciferases, 400–401
Luciferin, 401
Lumbar plexopathies, 114–115
Lumbosacral (LS) plexus, 112, 764, 765f
differential diagnosis, 116
evaluation, 118
Lumbosacral tumors, 43–44
Lutetium oxyorthosilicate (LSO), 356
Lymphocytic hypophysitis, 499
magnetic resonance imaging, 498f
Lymphoma, 85
hypothalamus, 568
computed tomography, 568
magnetic resonance imaging, 568, 569f
imaging features, 697
pituitary stalk thickening, 497f
skull base, 609
spinal epidural disease differential diagnosis, 735
of the spine, 37
thalamus, 563–564
Lymphomatosis cerebri, 479
Lytic versus blastic spinal disease, differentiation, 756

M

MacDonald criteria, 409–410, 673–674, 676
glioblastoma, 682, 685–686
limitations, 674
measurement technique, 673t
response assessment, 673t
Macroadenomas, pituitary, 484
Macrovascular architecture, 397

Magnetic field
external, 157
gradients, 161–162
inhomogeneities, 387, 733, 773
radiofrequency, 157
strength, 395
Magnetic resonance angiography (MRA), 188–189, 397–398, 398f
clinical utility of, 93–94
for CNS infarction, 93–94
contrast enhanced MRA, 93
phase contrast, 93
time-of-flight, 93
Magnetic resonance contrast agents, 183–192
advanced techniques using contrast media, 186–188
contrast media in neuroimaging, 183–184
future applications, 189
magnetic resonance angiography, 188–189
safety, 184–186
adverse reactions, 184–185
nephrogenic systemic fibrosis, 185–186
Magnetic resonance diffusion imaging, 301–302
Magnetic resonance image-guided neurosurgery, 203–216
brain tumor resection under intraoperative MRI guidance, 207–211
instrument tracking and neuronavigation, 210–211
intraoperative detection of complications, 210
intraoperative dynamic contrast imaging, 210
multimodality imaging, 207–208
rationale, 207
rigid and nonrigid image registration for surgical guidance, 208
coregistration of ultrasound with preoperative MRI and iMRI, 211–214
MRI-guided thermal ablations and focused ultrasound surgery, 212–214
image-guided therapy systems, 205–207
choice of MRI scanner and procedural flow, 206
patient positioning, 206–207
safety, 206
Magnetic resonance imaging (MRI), 28, 205, 231, 261, 273, 281, 359–360, 371, 409, 440–441
acoustic neuroma, 505
amyloidoma, 662f
anaplastic astrocytomas, 557, 558f
aneurysmal bone cyst, 749t
arachnoid cyst, 496–497, 496f, 598f, 653–654, 654f
aspergilloma, 660f
astrocytoma, 753
anaplastic, 421–422, 424f
atypical pediatric rhabdoid tumors, 624, 625f
atypical rhabdoid-teratoid tumors, 563, 563f
autoimmune encephalitis, 657
basal ganglia germinoma, 562, 562f
benign peripheral nerve sheath tumors, 780–782, 781f–785f
bilateral thalamic glioma, 560, 560f
of brain, 711–714
brain abscess, 659, 660f
of brain tumors, 194
central neurocytoma, 574, 574f–575f
cerebellar astrocytoma, 620–621, 621f
cerebellar liponeurocytoma, 582
cerebral abscesses, 699
chemotherapy-related cerebrovascular complications, 804–805
chiasmatic gliomas, 490
chiasmatic/hypothalamic tumors, 626f–627f
cholesteatoma, 656
chondroma, 749t
chondrosarcoma, 608f, 609, 750f, 750t
chordoid glioma, 567–568, 568f
chordomas, 604f–606f, 605–607
choristoma, 499f
choroid plexus carcinomas, 619, 619f
choroid plexus papillomas, 619, 619f
for CNS infarction, 92–94
catheter angiography, 94
clinical utility of MRA, 93–94
contrast enhanced MRA (CE MRA), 93
diffusion-weighted imaging (DWI), 92–93
MR angiography (MRA), 93–94
phase contrast (PC) MRA, 93
time-of-flight (TOF) MRA, 93
colloid cysts, 656
comparison with other techniques, 195
craniopharyngioma, 493–494, 493f–494f, 625, 626f
cryptococcoma, 660f
demyelinating encephalitis, 659
dermoid, 495, 654, 655f
desmoplastic infantile astrocytoma, 579
desmoplastic infantile ganglioglioma, 579, 579f
diencephalic syndrome, 627f
diffuse astrocytomas, 442–445
direct tumor-related compromise of arterial vasculature, 799, 799f–800f
DNETs, 580, 581f
dysplastic cerebellar gangliocytoma, 581, 582f
empty sella, 497f
endovascular therapy-related cerebrovascular complications, 805, 805f
eosinophilic granuloma, 749t
ependymomas, 623–624, 625f, 752–753
epidermoids, 495, 654, 655f
epidural spinal cord compression (ESCC), 60, 725f, 728–735
epithelial cysts, 655
Ewing sarcoma, 629f, 749f, 750t
extramedullary hematopoiesis, 661, 662f
extraocular nerve schwannomas, 510–511, 510f
facial nerve schwannomas, 508f
fibrous dysplasia, 749t
with gadolinium enhancement (MR-Gd), 66
gangliocytoma, 577
ganglioglioma, 561, 561f, 577, 577f–578f
germ-cell tumors, 627–628, 628f
germinoma, 491, 491f
pineal tumor, 589, 589f–590f
giant cell tumor, 750t
glioblastoma, 681, 682f, 685–687
glioblastoma multiforme, 425–426, 426f–427f, 429f, 434, 557–558, 558f–559f, 598f, 616f
gliomatosis cerebri, 456
gliosarcoma, 435, 436f
glomus tumor, 790–791, 791f
-guided tissue ablation, 213
hamartomas, 567, 567f
hemangioblastomas, 753, 753f
hemangioma, 749t
hemangiopericytoma, 537f–539f, 539
herpes simplex encephalitis, 660
hypoglossal nerve schwannomas, 509f, 511
hypothalamic and optic chaisma gliomas, 565, 566f
hypothalamic hamartoma, 492, 626–627, 628f
hypothalamic lymphoma, 568, 569f
to identify CVT, 100–101
idiopathic pachymeningitis, 657–658
infection-related cerebrovascular complications, 802–803, 802f–803f
inflammatory pseudotumor, 657, 658f
infundibulitis/hypophysitis, 658–659
intracranial hemorrhage, 86, 661
intracranial lipomas, 655
intravascular lymphomatosis, 478, 478f, 806
ischemic infarctions, 662f
jugular foramen schwannomas, 508, 508f, 511
lacrimal adenocystic carcinoma, 700f
Langerhans cell histiocytosis, 629
Larmor precession and, 157
leptomeningeal metastases, 705–711, 706f–711f, 706t, 755, 800
low-grade diffuse astrocytomas, 557, 557f
lumbar spine, epidural fat, 725, 725f
lymphocytic hypophysitis, 498f, 499
lymphoma, 497f
malignant peripheral nerve sheath tumors, 791–792, 792f
medullary tumors, 622, 624f
medulloblastoma, 619–620, 620f
melanocytomas, 539
melanoma, 646–647, 647f
meningioma, 488–490, 489f–490f, 505, 506f, 519, 520f–523f, 525–535, 525f–528f, 530f–536f, 751, 752f
metastases to nerves, 565f, 793–794, 793f–794f
metastatic brain tumors, 644–646, 645f, 649–650, 650f
midbrain tumors, 622
Morton neuroma, 789–790, 790f
multiple myeloma, 750t
neoplastic meningitis (NM), 65
for neoplastic plexopathies, 117
nerve sheath ganglion, 788, 789f
neural fibrolipoma, 785, 786f–787f

neurocysticercosis, 659, 660f
neuroenteric cysts, 655
neuroimaging response assessment, 667, 669–671, 675
neurosarcoidosis, 498f
NMDAR encephalitis, 814
nongerminomatous germ-cell tumors, 590, 591f–592f
oligodendrogliomas, 461–462, 462f, 464, 560, 561f
optic chiasm glioma, 625–626, 626f
optic pathway gliomas, 512, 512f
osteoid osteoma, 749t
osteosarcoma, 750t, 758f
papillary glioneuronal tumors, 638–639, 639f–640f
papillary tumors of the pineal region, 595, 596f
paraneoplastic brain stem encephalitis, 814, 815f
paraneoplastic cerebellar degeneration, 811, 812f
paraneoplastic chorea, 814–816, 816f
paraneoplastic limbic encephalitis, 811–814, 812f–815f
paraneoplastic myelopathy, 816
PCNSL, 472, 473f–474f, 513–514, 514f
pediatric brain tumors, 613
pediatric dysembryoplastic neuroepithelial tumor, 618, 618f
physics, 193–194
pilocytic astrocytomas, 450–451, 556, 556f–557f, 566f
pilomyxoid astrocytoma, 452, 453f
pineal cysts, 588f, 653, 654f
pineal gland, 586f
pineal parenchymal tumors, 592
pineal region tumors, 596
pineoblastomas, 592, 593f
pineocytomas, 592–594, 594f
pitfalls, 697
pituitary metastases, 491, 492f
pituitary adenomas, 485–488, 485f–488f, 628, 629f
pituitary hyperplasia, 493f
pituitary stalk lesions, 497
pleomorphic xanthoastrocytoma, 452
plexopathy, 765–766, 770f–771f
  visualization of normal plexus components, 766–768
polymorphic posttransplant lymphoproliferative disorder, 662f
pontine tumors, 621–622, 621f
PPTIDs, 594, 595f
primary angiitis of central nervous system, 806, 806f
primary central nervous system vasculitis, 657
primary cerebral lymphomas, 564, 564f
primary dural lymphoma, 540f
primary intramedullary spinal lymphoma, 479
primary leptomeningeal lymphoma, 476–478
primary T cell CNS lymphoma, 480, 480f
primitive neuroectodermal tumors, 563, 563f
progressive multifocal leukoencephalopathy, 661
prolactinoma, 628, 629f
quantitative measurements of tumor physiology and perfusion by, 398f
radiation-induced cerebrovascular complications, 804, 804f
radiation necrosis, 662f, 699, 700f
Rathke's cleft cysts, 495–496, 496f, 656
Rosai-Dorfman disease, 540f, 657
sarcoidosis, 657
schwannomas, 491–492, 503–504, 504f–505f
sellar/juxtasellar lesions, 484
of small animal models of central nervous system cancer, 395–400
  malignant tissue versus normal brain parenchyma, 395–397
  probing cellular structure and organization by diffusion MRI, 398–399
  probing tumor metabolism by magnetic resonance spectroscopy, 400
  tissue protein/peptide fragments assessment using amide proton transfer, 399–400
  vascular parameters measurement by MRI, 397–398
spinal metastasis, 747–749, 749f–750f, 749t–750t, 751–755, 752f–753f, 758f
spinal nerve sheath tumors, 752
spine imaging, 711–714
subependymal giant cell astrocytomas, 456, 617–618, 618f
supratentorial ependymomas, 617
supratentorial primitive neuroectodermal tumors, 616–617, 617f
1.5-T MRI, 195–196
3.0-T intraoperative MRI, 290–291
tectal gliomas, 597f, 624f
thoracic spine, epidural fat, 725, 725f
Tolosa-Hunt syndrome, 658
toxoplasmosis, 660, 661f
traumatic neuroma, 785–788, 788f–789f
trigeminal schwannomas, 507, 507f
tumor emboli and neoplastic aneurysms, 800–801, 800f
tumor progression, 126
tumor-related hemorrhagic stroke, 801, 801f–802f
vein of Galen malformations, 599f
venous thrombosis, 798–799, 799f
vestibular schwannoma, 544f–550f, 547, 548t
Magnetic resonance myelography, 118
Magnetic resonance perfusion imaging, 415, 440–441
  assessment of tumor therapy, 346
  meningioma, 523f
  pediatric brain tumors, 613–615
  peritumoral regions, 345–346
Magnetic resonance permeability imaging, oligodendrogliomas, 466
Magnetic resonance spectroscopy (MRS), 169–172, 238, 252, 273–274, 327–334, 392, 415, 440
  3-T, 464
  in assessment of treatment response, 171–172
  bilateral thalamic glioma, 560, 560f
  central neurocytoma, 575
  cerebellar astrocytoma, 621, 621f
  choroid plexus carcinomas, 619
  choroid plexus papillomas, 619
  clinical applications, 327–332
  contrast-enhanced, 327
  differential diagnosis, 330–332
    grading, surgical planning, and follow-up, 170–171
    low-grade tumors, malignant transformation of, 330
    radiation necrosis and recurrent tumor, differentiation of, 330–332
    recurrent disease, 330
  differentiating toxoplasmosis from lymphoma, 699
  future directions, 332
  gangliogliomas, 561
  glioblastoma multiforme, 431–432, 434, 559f
  grading and differential diagnosis, 327–328
  hamartomas, 567
  medulloblastoma, 619–620
  meningioma, 522f, 527–529
  metastatic brain tumors, 648–649
  neoplastic versus nonneoplastic, 327
  oligodendrogliomas, 463–464, 465f
  pediatric astrocytomas, 616
  pediatric brain tumors, 613, 615
  pilocytic astrocytoma, 450–451
  pilomyxoid astrocytoma, 452
  pontine tumors, 622, 623f
  primary cerebral lymphomas, 564
  primitive neuroectodermal tumors, 563
  probing tumor metabolism by, 400
  prognosis and survival, 328
  pseudoprogression, 690–691
  therapy guidance, 328–330
    radiation planning, 329–330
    surgical planning, 328
  treatment efficacy/response, assessment of, 330
    chemotherapy, 330
    radiation, 330
    serial monitoring, 330
Magnetic resonance venography (MRV), 93, 101f
Magnetic susceptibility, 197–198, 387–391
Magnetization transfer (MT), magnetic resonance imaging, 646
Magnetization transfer ratio (MTR), 403–404
Magnetization-prepared rapid gradient echo (MPRAGE), pediatric brain tumors, 615f
Magnetoencephalography (MEG), 220–221, 317
Malignant astrocytomas, 419–438
Malignant cells, 80

Malignant peripheral nerve sheath tumors (MPNSTs), 770, 791–793
magnetic resonance imaging, 791–792, 792f
Malignant psoas syndrome, 115
Malignant tissue versus normal brain parenchyma, 395–397
Malignant tumor tissue identification in animal models of GBM by MRI, 396f
Maximum intensity projections (MIP), 91
Maxwell's equations, 249
Mean transit time (MTT), 91, 335, 341f, 342
Mean vessel diameter (mVD), 335
Medial cord lesions, 114
Medullary tumors, pediatric, 622, 624f
Medulloblastoma, pediatric, 3, 12–13, 13f, 450–451, 562
Megestrol, 71
Melanocytic lesions, 539
Melanocytomas, 539
computed tomography, 539
magnetic resonance imaging, 539
Melanoma, 63, 66, 643
magnetic resonance imaging, 646–647, 647f
Mementine, 129
Meningeal metastatic brain tumors, 649–650
Meningeal tumors, 519–542
extra-axial tumors, 519
imaging evaluation, 521–525
imaging features, 697–698
mesenchymal, nonmeningothelial tumors, 535–540
hemangiopericytoma, 535–539
melanocytic lesions, 539
other rare lesions, 539–540
postembolization, 534f–535f, 535
Meninges, tumors of, 13t–14t
Meningiomas, 13–15, 14f, 42, 42f, 130, 263, 495–496, 519–535
angiography, 520f, 529–533, 532f–536f
cerebellopontine angle, 525–526, 526f
classification, 520–521
computed tomography, 488–490, 505, 522–525, 522f, 524f, 526f, 528f
FLAIR, 522f, 525, 536f
imaging features, 697
magnetic resonance imaging, 488–490, 489f–490f, 505, 506f, 519, 520f–523f, 525–535, 525f–528f, 530f–536f
magnetic resonance spectroscopy, 522f, 527–529
pineal region, 595
skull base, 609
spinal epidural disease differential diagnosis, 740
spine, 36
Meningothelial meningiomas, 13–14
Merlin, 549–550
Metabolic imaging, 327
Metastases
infundibular, 492f
and oligodendrogliomas, 465–466
pituitary, 491, 492f
skull base, 609
thalamus, 565
magnetic resonance imaging, 565f
Metastases to nerves, 793–794
magnetic resonance imaging, 793–794, 793f–794f
Metastatic brain tumors (MBTs), 23–34, 643–652
chemotherapy of, 28–30
computed tomography, 643–644, 644f, 649–650
computed tomography angiography, 643–644
diffusion-weighted imaging, 647, 648f
epidemiology of, 6–7
fractional anisotropy, 647
gadolinium-enhanced MRI, 644
imaging approach, 650–651
magnetic resonance imaging, 644–646, 645f, 649–650, 650f
techniques to increase lesion conspicuity, 646–647
magnetic resonance spectroscopy, 648–649
meningeal, 649–650
nuclear medicine techniques, 649
pathology of, 23–25
perfusion-weighted imaging, 647–648, 648f
positron-emission tomography, 649
primary sites of, 24t
radiation therapy of, 26–28
single-photon-emission computerized tomography, 649
surgical therapy of, 25–26
Metastatic cerebral venous thrombosis, 99
Metastatic lesions, 59
Metastatic spinal tumors, 747
Metastatic tumors, pediatric, 629–630
Metformin-induced lactic acidosis, 154
Methionine positron-emission tomography imaging, 371–382
Methotrexate, 70, 71t, 132–134
Methotrexate-based chemotherapy PCNSL, 515
3-*O*-Methyl-6-[^{18}F]fluoro-L-DOPA, 374
5-(3-Methyl-1-triazeno)imidazole-4-carboxamide, 16
Methylated methylguanine methyltransferase (MGMT), 411, 671
Methylguanine methyltransferase (MGMT), 17
and pseudoprogression, 683, 692
Methyl-[^{11}C]-L-methionine ([^{11}C]MET), 361
Methytyrosine, 361
MIB-1 index, 442
Microadenomas, pituitary, 484–485
MicroPET images, 402f
MicroSPECT images, 403, 404f
Microvascular hyalinization, 43
Microvascular imaging
in brain tumors, 172–177
perfusion-weighted imaging, 173–176
T1-weighted permeability imaging, 176–177
Microvascularity, 388f
Microvascular proliferation, and gliomas, 427
Midbrain tumors, pediatric, 622
Middle cerebral artery (MCA) territory infarct, 89, 90f
Miliary metastasis, 646
Minimum ADC (ADCmin), 168
Mixed gliomas (MGs), thalamus, 560
Molecular imaging of small animals, 401–403
micro-positron emission tomography, 401–403
micro-single-photon emission computed tomography, 403
Molecular imaging with PET, 372
Molecular neuropathology, 12
Molecular therapeutics, 19–20, 30, 51
Molecular/"targeted" treatment
of primary brain tumors (PBTs), 19–20
of primary SCT, 51
Monitoring radiation, 295
Monoclonal antibodies, cetuximab, 136
bevacizumab, 136
ipilumimab, 136
rituximab, 136
trastuzumab, 136
Monte Carlo simulations, 342, 357
Morton neuroma, 788–790
magnetic resonance imaging, 789–790, 790f
Motion compensation, 165
Motor mapping, 222
Motor-evoked potentials (MEPs), 221
Mucormycosis species, 81–82
Mucosa-associated lymphoid tissue (MALT) lymphomas, 479–480
Multichannel coils, 201
Multiexponential model, 305–308
Multileaf collimators, 232–233
Multimodal imaging techniques, 89
Multimodality imaging, 207–208
for guiding brain tumor resection, 207–208
Multinuclear imaging and chemical exchange saturation transfer imaging, 392
Multiple detector array CT, 146
Multiple drug resistance (MDR)-1 gene expression, 361
Multiple myeloma
computed tomography, 750t
magnetic resonance imaging, 750t
spinal epidural disease differential diagnosis, 735
Multiple sclerosis (MS), 699, 699f
tumefactive
and glioblastoma multiforme, 432–433
Multiple-refocusing techniques, 195
Multiple-time-graphic method, 337
Multislice CT, 146
Murine double minute-2 (MDM2), 5
Myasthenia gravis (MG), 108
Myelography
epidural spinal cord compression, 726–727
Myelopathy, 60–61
paraneoplastic, 816
Myelosuppression, 70
Myoinositol (MI), 431, 440
magnetic resonance spectroscopy, 170
oligodendrogliomas, 464
Myxoid liposarcoma, 745, 746f
Myxopapillary ependymomas, 37, 43, 43f

N

Nasopharyngeal carcinoma, skull base, 609
Navigated transcranial magnetic stimulation (nTMS), 221
Near-infrared spectroscopy, 317
Necrosis, 10–11, 45–46
Necrotic tumor, differentiating cerebral abscesses from, 699
Neoplastic aneurysms
  cerebrovascular complications, 800–801, 800f
  computed tomography, 800–801, 800f
  magnetic resonance imaging, 800–801, 800f
Neoplastic disease of spine, 745–749, 749f–750f, 749t–750t, 751–753, 752f–753f, 758f, 759–760
  angiography, 757–759, 758f
  computed tomography, 747, 749f–750f, 749t–750t, 755–756, 758f–759f
  differential diagnosis, 756
  diffusion-weighted imaging (DWI), 755
  dynamic X-rays, 756
  extramedullary intradural spinal tumors, 751–752
    meningiomas, 751, 752f
    nerve sheath tumors, 751–752
  intramedullary tumors, 752–753
    astrocytomas, 753
    ependymomas, 752–753
    hemangioblastomas, 753
  lytic versus blastic spinal disease, differentiation, 756
  metastatic spinal tumors, 747
  positron emission tomography scan, 756–757, 757f
  preoperative planning, 754–755
    leptomeningeal metastasis, 755
    magnetic resonance imaging features in spinal metastasis, 754–755
  primary bone tumors, 747–751, 750f–752f
  single-photon emission computed tomography/computed tomography, 757
  surgical intervention for spinal tumors, 753–754, 754f
    en bloc resection of single metastasis to spine, 754
  X-rays, 747
Neoplastic meningitis (NM), 63–78
  clinical features, 64
  diagnosis, 64–66
    CSF analysis, 64–65
    neuroradiographic studies, 66
  epidemiology, 63
  evaluation and response to treatment, 67
  experimental agents, 72–73
    intraCSF experimental agents, 72–73
    supportive care, 73
  intraCSF therapy, 70
  pathogenesis, 63–64
  prognosis, 66–67
  regional chemotherapy for, 71t
  staging, 66
  systemic therapy, 70–72
  treatment, 67–70
    algorithm of, 68f–69f
    chemotherapy, 70
    radiotherapy, 69–70
    surgery, 67–69
Neoplastic plexopathies, 111–124
  associated neoplastic disorders, 115–116
    Pancoast syndrome, 115–116
  classification, 111
  clinical features, 114–115
  differential diagnosis, 116
    postradiation plexopathy, 116
  epidemiology and risk factors, 113
  evaluation, 117–118
  management, 118–120
  pathogenesis and pathophysiology, 113–114
  plexus anatomy, 111–112
    brachial plexus (BP), 111–112
    cervical plexus, 111
    lumbosacral plexus (LS), 112
  prognosis and future perspectives, 120
Neoplastic versus nonneoplastic lesions, 327
Nephrogenic systemic fibrosis (NSF), 185–186
Nerve fiber tract integrity, assessment of, 309–312
Nerve sheath ganglion, 788
  computed tomography, 788
  magnetic resonance imaging, 788, 789f
Neural fibrolipoma, 783–785
  magnetic resonance imaging, 785, 786f–787f
Neural sheath tumors (NSTs), 111, 113–114
  benign peripheral, 778
  evaluation, 117–118
  malignant peripheral, 791–793
  management, 118–119
  nonvestibular schwannomas, 506–511
  prognosis, 120
  schwannomas, 503–511
Neurilemoma, 778
Neurocysticercosis, 659
Neuroendocrine dysfunction, 130–131
Neuroenteric cysts, 654–655
Neuroepithelial cysts, 654–655
Neuroepithelial origin, tumors of, 9
Neuroepithelial tissue, tumors of, 10t
Neurofibromas, 35–36, 42–43, 43f, 47, 778
  magnetic resonance imaging, 770, 770f
  multiple, 47
  plexiform, pediatric, 627f
Neurofibromatosis 1 (NF1), 4, 113, 782–783
  chiasmatic/hypothalamic tumors, 625–626
  and optic pathway gliomas, 511–512
  and pilocytic astrocytoma, 445–450, 490
Neurofibromatosis 2 (NF2), 4
  vestibular schwannoma, 504–506, 543, 545, 549–551, 550f, 552f, 553
Neurogenic sarcomas, 111
Neurohypophysis, 483
Neuroimaging issues, in response assessment
  angiogenesis inhibitors, 671–672
  complete response, 673, 673t
  computed tomography, 675
  diffuse gliomas
    in adults, evolution of, 669
    high-grade gliomas, 670–671, 671f, 676
    low-grade gliomas, 669–670, 670f
  gliomas of adult cerebral hemispheres, 667–669, 668f
  imaging in clinical trials, 672
  magnetic resonance imaging, 667, 669–671, 675
  partial response, 673, 673t
  progressive disease, 673, 673t
  pseudoprogression, 671
  Response Assessment in Neuro-Oncology (RANO), 674
  Response Evaluation Criteria in Solid Tumors (RECIST), 674
  response quantification, 673–674
    Macdonald criteria, 673–674, 673t
  stable disease, 673, 673t
  surrogate for survival, response as, 674–675
    overall survival, radiographic response as, 674–675
    progression-free survival, 674
  technical aspects, 675–678
    computer-aided volumetric analysis, 675–676, 676f
    diameter and volumetric approaches, comparison, 676
    image interpretation and measurements, 676–677
    imaging pitfalls, 677–678, 677f–678f
    technical considerations, 675
    timing of imaging, 676
Neurological stimulation (NS), 198
Neurolymphomatosis, 113–114
Neuromas, 506–507
Neuronal paraneoplastic autoantibodies, 105t
Neuronal-glial tumors, neuronal and mixed, 618
Neuronavigation, 210–211, 376
Neuron-specific enolase (NSE), 573–574
Neuroradiology, 231
Neurosarcoidosis, pituitary stalk thickening, 498–499, 498f
Neurosurgical treatment planning, 217–230
  brain tumor surgery, general considerations in, 217
  functional applications, 222–224
    language localization, 222–224
    motor mapping, 222
  intraoperative image-guided surgery, 224–225
  for language activation with superimposed tract reconstruction of the arcuate fasciculus, 223f
  limitations and future directions, 225–226
  for motor tasks with superimposed DTI-derived corticospinal tracts, 223f
  preoperative imaging strategies, 217–222
    diffusion tensor imaging, 218–219
    electrocorticography and electrical cortical stimulation, 221–222
    functional magnetic resonance imaging, 219–220
    magnetoencephalography, 220–221
    transcranial magnetic stimulation, 221
    Wada testing, 222

Neurosyphilis, 699
Neurovascular coupling (NVC), 317
Neurovascular uncoupling (NVU), 322
Nevoid basal cell carcinoma syndrome, 4
NMDAR encephalitis, magnetic resonance imaging, 814
  computed tomography, 814
  positron emission tomography, 814
Nonbacterial thrombotic endocarditis (NBTE), 80
Non-CNS tumors, dynamic contrast enhanced (DCE) imaging to characterize, 338
Noncontrast computed tomography (NCCT), for acute stroke, 89–91
Nonfunctioning adenomas, 265
Nongerminomatous germ-cell tumors (NGGCTs)
  pineal tumor, 586, 590
    computed tomography, 592f
    magnetic resonance imaging, 590, 591f–592f
  treatment, 597
Non-Hodgkin lymphoma, 471
  hypothalamic, 569f
  intravascular lymphomatosis, 478, 478f
Nonmeasurable disease, 411
Nonmetastatic cerebral venous thrombosis, 99
Nonneoplastic mass lesions, 653–666
  cerebrovascular lesions, 661
  developmental abnormalities, 653–656
  infections, 659–661
  inflammatory disorders, 657–659
Nonopioid analgesics, for neoplastic plexopathies, 119
Nonparaneoplastic encephalitis, 106
Non-small-cell lung cancer (NSCLC), 6–7, 23–24
Nonvestibular schwannomas, 506–511
  management of, 510–511
Normal-appearing white matter (NAWM), 173–174
Normalized blood volume histogram analysis, glioblastoma multiforme, 429
Normalized CBV (nCBV), 173
NovoTTF-100A device, 246–249, 246f
Nuclear medicine
  epidural spinal cord compression, 728
  metastatic brain tumors, 649
Nuclear MR (NMR) spectroscopy, 400
Nutritional deficiency, 79

O

O^6-methylguanine-DNA-methyltransferase (MGMT), 5
  of glioblastoma, 126
Objective response rate (ORR), 409, 413
Occult malignancy
  computed tomography, 816–817, 817f
  positron emission tomography, 816–817, 817f
Occult malignancy imaging, 816–817
Octreotide, 487–488
Olfactory nerve schwannomas, 510
  computed tomography, 510
Oligoastrocytomas, 11–12, 668–669
Oligodendrogliomas (ODGs), 11–12, 12f, 461–470, 667–668
  computed tomography, 461–462, 462f–463f
  diffusion tensor imaging, 467
  diffusion-weighted imaging, 462–463, 464f
  DSC perfusion imaging, 464–466, 466f
  fractional anisotropy, 467
  functional magnetic resonance imaging, 466–467
  magnetic resonance imaging, 461–462, 462f, 464, 560, 561f
  magnetic resonance permeability imaging, 466
  magnetic resonance spectroscopy, 463–464, 465f
  metastases, 492f
  positron-emission tomography, 467
  pseudo-progression, 467–468
  thalamus, 560
  treatment-related imaging changes, 468
Ommaya reservoir, 67
Opioid monotherapy, for neoplastic plexopathies, 119
Opsoclonus–myoclonus syndrome (OMS), 107
Optic chaisma gliomas, 565–566
  magnetic resonance imaging, 565, 566f
  pediatric, 626f
Optic chiasma tumors, 565–568
Optic nerve meningiomas, 529f
Optic pathway gliomas (OPGs), 511–513
  magnetic resonance imaging, 512, 512f
  management, 512–513
  pathology, 511–512
Organ transplantation, and PCNSL, 471
Orthographic xenograft models, 401
Ossification of the posterior longitudinal ligament (OPLL), spinal epidural disease differential diagnosis, 739–740, 740f
Osteogenic sarcoma, skull base, 609
Osteoid osteoma
  computed tomography, 749t
  magnetic resonance imaging, 749t
Osteoradionecrosis, 736
Osteosarcoma
  computed tomography, 750t, 758f
  magnetic resonance imaging, 750t, 758f
Outpatient stereotactic radiation, vestibular schwannoma, 552
Overall survival (OS), 411, 413
Oxaliplatin, 135
Oxygenation, imaging tumor, 391

P

p53, 5, 442
  pseudoprogression, 683–684
Pachymeningeal metastases, 649
Paclitaxel, 135
Pallister-Hall syndrome, 567, 627
Pancoast syndrome, 115–116
  computed tomography, 769–771
  prognosis, 120
  treatment of, 119–120
Papillary glioneuronal tumors (PGNTs), 635–642
  anaplastic, 637f
  characteristics, 636t
  computed tomography, 637–638, 640f
  diffusion-weighted imaging, 638
  features, 636–638
  magnetic resonance imaging, 638, 639f–640f
  differential diagnosis, 638–639
  pathology, 635–636, 637f
  treatment, 636
  uncommon manifestations, 638
Papillary tumors of the pineal region (PTPRs), 586, 595
  computed tomography, 595, 596f
  diffusion-weighted imaging, 595, 596f
  magnetic resonance imaging, 595, 596f
  treatment, 597–599
Paragangliomas, 37
Parallel imaging, 165–166, 201
  spine, 729
Parameningeal tumors, pediatric, 629–630
Paranasal sinus disease, 697
Paraneoplastic brain stem encephalitis, 106
  magnetic resonance imaging, 814, 815f
Paraneoplastic cerebellar degeneration (PCD), 104
  computed tomography, 811
  magnetic resonance imaging, 811, 812f
  positron emission tomography, 811
Paraneoplastic chorea, 107
  magnetic resonance imaging, 814–816, 816f
Paraneoplastic limbic encephalitis (PLE), 105
  magnetic resonance imaging, 811–814, 812f–815f
  positron emission tomography, 811–813, 813f
Paraneoplastic myelopathy
  magnetic resonance imaging, 816
  positron emission tomography, 816
Paraneoplastic neurological disorders (PNDs), 103–104, 106t
Paraneoplastic neurological syndromes, 104t, 811
Paraneoplastic syndromes, 103–110, 811
  brain-stem encephalitis, 106
  computed tomography, 811, 814, 816–817, 817f
  evaluation and treatment, 108–109
  laboratory findings, 108
  Lambert–Eaton syndrome (LES), 108
  limbic encephalitis, 104–106
  magnetic resonance imaging, 811–816, 812f–816f
  myasthenia gravis (MG), 108
  NMDAR encephalitis, 814
  occult malignancy imaging, 816–817
  opsoclonus–myoclonus, 107
  paraneoplastic brain stem encephalitis, 814
  paraneoplastic cerebellar degeneration (PCD), 104, 811, 812f
  paraneoplastic chorea, 107, 814–816

paraneoplastic limbic encephalitis, 811–814, 812f
paraneoplastic myelopathy, 816
peripheral nervous system disorders, 107
positron emission tomography, 811–814, 813f, 816–817, 817f
Parasitic infections, 659–660
Parenchymal lesions, 479, 699
Parenchymal tumors, pineal, 586
Parinaud syndrome, 586–587
Partial responses (PR), 49–50
Pathology
of intramedullary spinal cord metastases (ISCM), 55–56
of metastatic brain tumors (MBTs), 23–25
of selected primary brain tumors, 9–15
of selected primary spinal cord tumors, 41–46
Patient Registry Dataset (PRiDe), 247
Patlak plot, 337
Pediatric brain tumors, 613–634
cerebral hemispheres, 616–619
choroid plexus carcinomas, 619, 619f
choroid plexus papillomas, 619, 619f
computed tomography, 613
diffusion MRI, 613
diffusion tensor imaging, 615
diffusion tractography, 615, 615f
diffusion-weighted imaging, 615
dysembryoplastic neuroepithelial tumor, 618
functional MRI, 613, 614f
laser-induced thermal therapy, 615, 615f
magnetic resonance imaging, 613
magnetic resonance spectroscopy, 613, 615
medullary tumors, 622
midbrain tumors, 622
MPRAGE, 615f
parameningeal and metastatic tumors, 629–630
perfusion MRI, 613–615
permeability-based perfusion techniques, 615
pontine tumors, 621–622
positron emission tomography, 613
posterior fossa tumors, 619–624
proton nuclear MRS, 615
sellar and suprasellar tumors, 624–629
single photon emission computed tomography, 613
PENNPET, 356–357
Perfusion, definition of, 335
Perfusion imaging, 91
arterial spin-labeling techniques, 347
CT perfusion imaging, 348
dynamic contrast agent MRI perfusion techniques, 335–336
dynamic contrast enhanced (DCE) imaging, 336–339, 466
acquisition and postprocessing methods, 339
basic principles, 336–337
to characterize gliomas and predict treatment response, 338, 339f
to characterize non-CNS tumors, 338
imaging methodology, 337–338
dynamic susceptibility contrast (DSC) imaging, 339–346
basic principles, 339–340
cerebral blood flow (CBF), potential role of, 345
glioma tumor grade, distinction of, 343–344
high-grade gliomas versus other neoplasms, 344–345
methodology, 340–343
MR perfusion imaging assessment of peritumoral regions, 345–346
MR perfusion imaging for assessment of tumor therapy, 346
tumor recurrence versus radiation necrosis, 346
tumor vascular architecture, assessment of, 345
magnetic resonance, 94, 613–615
pseudoprogression, 689–690
Perfusion-weighted imaging (PWI), 173, 659
glioblastoma multiforme, 428, 432, 434
in diagnosis, grading, operative planning, and follow-up of brain tumors, 173–176
metastatic brain tumors, 647–648, 648f
Perineuriomas, 770
Peripheral brain tumors, 569
Peripheral nervous system, 111, 132, 777
disorders, 107
primary tumors, 770
Peripheral neurogenic tumors, 777
angiography, 779
benign peripheral nerve sheath tumors, 778
imaging, 778–782, 779f–785f
neurilemoma, 778
neurofibroma, 778
computed tomography, 779, 780f, 785–788, 790
glomus tumor, 790–791, 791f
magnetic resonance imaging, 780–782, 781f–785f, 785–792
malignant peripheral nerve sheath tumors, 791–793, 792f
metastases to nerves, 793–794, 793f–794f
Morton neuroma, 788–790, 790f
nerve sheath ganglion, 788, 789f
neural fibrolipoma, 783–785, 786f–787f
neurofibromatosis 1, 782–783
diagnostic criteria, 785t
mesodermal dysplasia manifestation, 785t
secondary signs, 789f, 794, 794f
sonography, 779
traumatic neuroma, 785–788, 788f–789f
Peritumoral edema, 236, 302–303, 421–422, 636–637
Peritumoral regions, MR perfusion imaging assessment of, 345–346
Perivascular pseudorosettes, 45
Permeability imaging, T1-weighted, 176–177
Permeability MRI, 188
Permeability-based perfusion techniques, 615
Phase contrast (PC) MRA, 93
Phase encoding, 162–163
Phosphatase and tensin homolog (PTEN) gene, 581
Photon and proton radiosurgery, 258
Photons
annihilation, 356
attenuated, 355–356
scattered, 355–356
Physaliphorous, 43–44
Physiology-based MRI methods, 273–274
Pilocytic astrocytoma (PA), 11, 15, 445–451, 447f–452f, 490, 511–512, 512f, 638–639
computed tomography, 450–451, 555–556, 556f
diffusion-weighted imaging, 556, 556f
magnetic resonance imaging, 450–451, 556, 556f–557f, 566f
magnetic resonance spectroscopy, 450–451
pediatric, 616
posterior fossa juvenile, 621f
spinal, 45f
thalamus, 555–556
Pilomyxoid astrocytomas (PMAs), 445, 451, 512
Pineal cysts, 587–589, 653
magnetic resonance imaging, 588f, 653, 654f
Pineal gland, 585
calcification, 587
magnetic resonance imaging, 586f
Pineal gland tumors, 569
Pineal parenchymal tumors, 590–595
of intermediate differentiation (PPTIDs), 586, 590–591, 594
computed tomography, 594
magnetic resonance imaging, 594, 595f
treatment, 597–599
magnetic resonance imaging, 592
treatment, 597–599
Pineal region tumors, 585–602
anatomy and function, 585
clinical features, 586–587
diagnosis, 595–596
epidemiology, 585–586
germ cell tumors, 589–590
magnetic resonance imaging, 596
papillary tumors of the pineal region, 595
pathology, 585–586
pineal parenchymal tumors, 590
solitary fibrous tumor, 599f
treatment and prognosis, 597–600
Pineoblastomas, 562, 586, 590–592
computed tomography, 592, 593f
diffusion-weighted imaging, 592, 593f
magnetic resonance imaging, 592, 593f
treatment, 597–599
Pineocytomas, 590–594
computed tomography, 592–594, 594f
magnetic resonance imaging, 592–594, 594f
treatment, 597–599

Pitch, 146
Pituitary adenomas, 264–265, 484–488
  adrenocorticotropic hormone (ACTH), 265
  growth hormone-secreting adenomas, 264–265
  magnetic resonance imaging, 485–488, 485f–488f
  nonfunctioning, 484–485
  pediatric, 628
  prolactinomas, 264
Pituitary apoplexy, 487–488
Pituitary hyperplasia, 492–493
Pituitary stalk lesions, 497–499
Planned target volume (PTV), 231–232
Plasmacytoma, 697
  skull base, 609
Platelet-derived growth factor (PDGF), 55
Platinum-based agents, 134–135
  cisplatin, 134–135
  oxaliplatin, 135
Pleomorphic tumor cells, 683
Pleomorphic xanthoastrocytoma (PXA), 11, 451–452, 454f, 638–639
  computed tomography, 452
  magnetic resonance imaging, 452
Plexopathy in oncologic patients, 131–132, 763
  abnormal nerve, 768–769
  computed tomography, 765–766, 769f, 771f–772f
    visualization of normal plexus components, 766–768, 767f
  extrinsic plexus tumors, 771
  imaging method of choice, 769–770
  magnetic resonance imaging, 765–766, 769f–772f
    visualization of normal plexus components, 766–768, 768f–769f
  positron emission tomography, 765, 771
  primary plexus neoplasms, 770
  radiation injury, 771–773, 772f
  sonography, 765
Plexuses
  anatomy, 111–112
    brachial plexus (BP), 111–112
    cervical plexus, 111
    lumbosacral (LS) plexus, 112
  extrinsic plexus tumors, 771, 771f
  normal anatomy, 763–764, 764f–765f
    cervical and brachial plexus, 763–764
    lumbosacral plexus, 764
  primary plexus neoplasms, 770, 770f
Point-resolved spin echo (PRESS), 169–170
Polymerase chain reaction, 65
Polymorphic posttransplant lymphoproliferative disorder, 663
Pontine tumors, pediatric, 621–622
Positron emission and decay, 356f
Positron emission tomography (PET), 195, 317, 356–357, 362–366, 371, 401–403, 415, 441–442, 792–793, 792f
  central neurocytoma, 575–576
  chordomas, 607
  differentiating toxoplasmosis from lymphoma, 699
  DNETs, 580
  epidural spinal cord compression, 728, 728f
  [18F]FDG-PET, 362–365
    follow-up assessment and monitoring treatment, 364–365
    tumor detection, 362–363
    tumor grading and degree of malignancy, 363–364
  gangliocytoma, 577
  ganglioglioma, 577
  metastatic brain tumors, 649
  NMDAR encephalitis, 814
  novel PET tracers, 365–366
    [11C] methionine, 365–366
    3′-deoxy-3′-[18F]fluorothymidine, 366
    [18F]fluoroethyl-L-tyrosine (FET), 366
  occult malignancy, 816–817, 817f
  oligodendrogliomas, 467
  paraneoplastic cerebellar degeneration, 811
  paraneoplastic limbic encephalitis, 811–813, 813f
  paraneoplastic myelopathy, 816
  PCNSL, 473–475, 514
  pediatric brain tumors, 613
  PET image reconstruction and correction, 357
  PET instrumentation, 356–357
    detector configurations, 356–357
    detector materials, 356
  PET physics, 356
  plexopathy, 116, 765, 771
  pontine tumors, 622
  pseudoprogression, 691–692
  spinal tumors, 756–757, 757f
Posterior fossa tumors, pediatric, 619–624
Postradiation plexopathy, 116, 120
Prednisone, 49–50
Preoperative planning and peritumoral margins, 285–290
Primary angiitis of central nervous system (PACNS)
  cerebrovascular complications, 806, 806f
  magnetic resonance imaging, 806, 806f
Primary bone tumors, 747–751
Primary brain tumors (PBTs), 9–22, 359
  chemotherapy of, 16–19
  epidemiology of, 3–6
  molecular/“targeted” treatment, 19–20
  pathology of, 9–15
  radiation therapy of, 15–16
  surgical therapy of, 15
Primary central nervous system lymphoma (PCNSL), 14–15, 471–482, 513–515, 568
  anatomical distribution, 472–476
  angiography, 472–473, 475f
  angiotropism, 513, 513f
  chemotherapy, 471
  computed tomography, 472, 472f–474f, 513, 514f
  CSF measurement, 514
  cytarabine, 515
  differential diagnosis of, 476f, 479
  diffusion-weighted imaging, 472, 473f
  and glioblastoma multiforme, 432
  Hodgkin’s lymphoma, 479
  immunocompetent versus immunocompromised patients, 473–475
  intraocular lymphoma, 479
  intravascular lymphomatosis, 478, 478f
  low-grade, 479
  lymphomatosis cerebri, 479
  magnetic resonance imaging, 472, 473f–474f, 564f, 567
  management, 514–515
  methotrexate-based chemotherapy, 515
  mucosa-associated lymphoid tissue lymphomas, 479–480
  pathology, 513
  positron emission tomography, 473–475, 514
  prevalence of, 471
  primary intramedullary spinal lymphoma, 479
  primary leptomeningeal lymphoma, 477f, 479
  radiation therapy, 514–515
  single photon emission computed tomography, 473–475
  single-photon-emission CT, 514
  surgery, 471
  T cell CNS lymphoma, 480, 480f
  and toxoplasmosis, 474–476, 475f
  uncommon manifestations, 476–480
Primary central nervous system vasculitis, 657
Primary cerebral lymphomas (PCLs)
  computed tomography, 564
  diffusion-weighted imaging, 564, 564f
  magnetic resonance imaging, 564, 564f
  magnetic resonance spectroscopy, 564
  thalamus, 563–564
Primary dural lymphoma, 539–540
  magnetic resonance imaging, 540f
Primary glioblastomas, 422–424
Primary intramedullary spinal lymphoma, 479
Primary leptomeningeal lymphoma (PLML), 513–514
Primary spinal cord tumors (SCTs), 41–54
  in adults, 36t
  anatomic distribution of, 36t
  chemotherapy of, 49–51
  in children, 36t
  epidemiology of, 35–37
  molecular/“targeted” treatment, 51
  pathology of, 41–46
  radiation therapy of, 48–49
  surgical therapy of, 46–48
Primary T cell lymphoma, 471
Primitive neuroectodermal tumors (PNETs), 12–13, 592
  computed tomography, 563
  magnetic resonance imaging, 563, 563f
  magnetic resonance spectroscopy, 563
  supratentorial, pediatric, 617f, 622
  thalamus, 562–563
  treatment, 597–599
Procarbazine, 16, 49–50
Progression-free survival (PFS), 15, 409, 413–414, 674–675

Progressive disease (PD), 251–252, 673
RANO definitions of, 687t
Progressive multifocal leukoencephalopathy, 661
Prolactinomas, 264, 484–485, 487–488
pediatric, 628, 629f
PROPELLER technique, 165
Prophylactic cranial irradiation (PCI), 27
Proton beam radiosurgery, 260
Proton density, 159–160
images, 160
Proton gantry system, 261f
Proton magnetic resonance spectroscopy (^{1}H MRS), 327–328, 331
Proton nuclear magnetic resonance spectroscopy, pediatric brain tumors, 615
Protoplasmic astrocytoma, 442
Psammomatous lesions, 42
Pseudoprogression (PsP), 126, 188, 236–239, 247, 410–411, 415, 671
biologic differentiation, 692
defined, 681
history, 682–683
and methylguanine methyltransferase (MGMT), 683, 692
novel imaging techniques, 687–693
arterial spin imaging, 691
delayed contrast extravasation magnetic resonance imaging, 690
diffusion weighted magnetic resonance imaging, 688–689
magnetic resonance spectroscopy, 690–691
perfusion imaging, 689–690
positron emission tomographic imaging, 691–692
oligodendrogliomas, 467–468
overview, 681–682
pathophysiology, 683–685
histology, 683–684, 684f
theories, 684–685
and progression, differentiation between, 685–686, 692–693
AVAglio protocol, 685–687
Response Assessment in Neuro-Oncology, 686–687
Pseudoresponse, 188, 411, 671
PTEN hamartoma syndrome, 581
Pure sensory neuropathy, 107

Q

Quality assurance (QA) of imaging and dose delivery, 233

R

Radiation-associated tumor formation, 266
Radiation-induced cerebrovascular complications, 81
magnetic resonance imaging, 804, 804f
Radiation-induced fibrosis (RIF), 771–773
computed tomography, 772f
magnetic resonance imaging, 772f
Radiation-induced secondary tumor, spinal epidural disease differential diagnosis, 736, 736f
Radiation-induced vascular malformations, 130
Radiation necrosis (RN), 236–239, 663
on imaging, 697
tumor recurrence versus, 346
Radiation planning, magnetic resonance spectroscopy, 329–330
Radiation therapy (RT), 48–49, 61, 96, 116
cerebrovascular complications due to, 803–804, 803f–804f
chondrosarcomas, 609
chordomas, 607
delineating pseudo-progression, true disease progression, and radiation necrosis, 236–239
and delivery, 231–233
desmoplastic infantile ganglioglioma, 579–580
DNETs, 580
future directions, 239
germinoma, 491
glioneuronal tumors, 573
of intramedullary spinal cord metastases (ISCM), 57
of metastatic brain tumors (MBTs), 26–28
neuroimaging, 231
PCNSL, 514–515
practical application of radiotherapy in high-grade glioma, 233–235
of primary brain tumors (PBTs), 15–16
of primary SCT, 48–49
quality assurance of imaging and dose delivery, 233
stereotactic radiosurgery (SRS), 233
thalamic tumors, 555
treatment toxicity, 236
use of neuroimaging for, 231–242
vestibular schwannoma, 552–553
Radiation Therapy Oncology Group (RTOG), 16, 26–27, 233
Radiofrequency (RF), 93, 335
energy and resonance, 157–158
issues, 200–201
penetration, 199–200
Radiogenic lower motor neuron disease, 131
Radiographic response as, surrogate for overall survival, 674–675
Radioisotope CSF flow studies, 715–718, 717t
Radionecrosis, 127–128
treatment of, 128
Radionuclide scintiscan, glioblastoma, 685
Radiosurgery
acoustic neuroma, 506
central neurocytoma, 576
clinical applications of, 262–266
acoustic neuromas, 263–264
cerebral metastases, 262–263
gliomas, 265–266
meningiomas, 263
nonfunctioning adenomas, 265
pituitary adenomas, 264–265
radiation-associated tumor formation, 266
delivery of, 258–260
CyberKnife platform, 259–260
Gamma Knife system, 259
LINAC, 259
photon and proton radiosurgery, 258
proton beam radiosurgery, 260
epidural spinal cord compression (ESCC), 61
extraocular nerve schwannomas, 511
facial nerve schwannomas, 510
foundations of, 257–258
target location, 257
target proximity to cranial nerves, 258
target size, 257
hypoglossal nerve schwannomas, 511
jugular foramen schwannomas, 510–511
meningioma, 488–490
PPTIDs, 597–599
trigeminal schwannomas, 510
Radiotherapy (RT), 17, 19, 57
complications of, 125–130, 126t
acute (0–14 days), 125
early delayed (4 weeks to months), 125–127
late delayed (months to years), 127–130
gliomas, 669
-induced tumors, 129–130
inflammatory pseudotumor, 657
meningioma, 521
neoplastic meningitis, 69–70
optic pathway gliomas, 512–513
papillary glioneuronal tumors, 636
pineoblastoma, 586
pontine tumors, 621–622
primary cerebral lymphomas, 564
and radiosurgery, 258f
vascular disorders, 81
Rapid acquisition by relaxation enhancement (RARE), 197–198
Rathke cleft cysts (RCCs), 495–496, 656
computed tomography, 496
magnetic resonance imaging, 495–496, 496f
Recurrence versus treatment-related complications, 699–700
Regions of interest (ROIs), 169–170, 338
Relative capillary blood volume (rCBV), 173–176, 175f, 186–187
maps, 339, 341f, 342–343
pediatric astrocytomas, 616
values, 415
Relative cerebral blood flow (rCBF), 360, 688–690
Relative cerebral blood volume (rCBV), 238, 440–441, 686–687, 689–690
diffuse astrocytomas, 445
glioblastoma multiforme, 428, 430f, 432, 434
metastatic brain tumors, 648
oligodendrogliomas, 464–465, 466f
Relaxation, 158
T1 and T2, 158
T2*, 158
Relaxivity, 183–184
Resonance, radiofrequency energy and, 157–158
Response assessment, 409, 410t, 411–415

Response Assessment in Neuro-Oncology (RANO), 251–252, 674, 676
application of
to high-grade gliomas, 413
to low-grade gliomas, 413–414
development of, for brain metastases, 414
diffusion-weighted MRI (DW-MRI), 415
future directions for, 414–415
advanced imaging techniques as biomarkers, 414–415
role of biomarkers, 414
glioblastoma, 686
for gliomas, 410
key aspects of imaging and clinical criteria used for, 411–413
assessment of patient well-being and neurological functioning, 412–413
corticosteroid use, 412
T1 contrast-enhancing disease, 411
T2/FLAIR imaging, 411–412
limitations, 686–687
magnetic resonance spectroscopy, 415
measurement technique, 673t
perfusion magnetic resonance imaging, 415
positron emission tomographic (PET) imaging, 415
progressive disease, definitions, 687t
pseudoprogression, 686
response assessment, 673t
working group, 67
Response Evaluation Criteria in Solid Tumors (RECIST), 67, 674, 676
glioblastoma, 685
measurement technique, 673t
response assessment, 673t
Resting-state fMRI (RS-fMRI), 324–325
Retrosigmoid approach, vestibular schwannoma, 551
"Reverse omega" sign, 318
Rhabdoid tumors, atypical, pediatric, 624
Rhabdomyosarcoma, skull base, 609
Rhombencephalitis, subacute, 126–127
Rickham style reservoir, 67
Rituximab, 71t, 81, 136
Rosai-Dorfman disease (RDD), 539–540, 657
magnetic resonance imaging, 540f
Rosenthal fibers, 44–46, 445–450

S

S4 APR, 112
Sacral plexus, 112
SAPHO syndrome, spinal epidural disease differential diagnosis, 736–737, 737f
Sarcoidosis, 657
and PCNSL, 475–476, 476f
Sarcoma, 80–81
spinal epidural disease differential diagnosis, 740
Scattered photons, 355–356
Schwannomas, 15, 36, 41–42, 42f, 47, 113, 491–492, 503–511
acoustic, 5
computed tomography, 503, 504f–505f
cranial nerve VIII, 504–506
magnetic resonance imaging, 503–504, 504f–505f, 770, 770f
nonvestibular, 506–511
pathology, 503
spinal epidural disease differential diagnosis, 740, 741f
trigeminal, 506–507
vestibular, 504–506
Schwannomatosis, 553
Secondary glioblastomas, 422–424, 669
Sellar region tumors, 483–502
anatomy, 483
incidental lesions, 484
mixed solid/cystic lesions, 493–497
pituitary stalk lesions, 497–499
solid lesions, 484–493
Sellar tumors, 624–629
Sella turcica, 483, 497
Sensitivity encoding (SENSE), 201
Sensorineural hearing loss, and acoustic neuroma, 505
Sensory ganglionopathy, 107
Sensory/motor fMRI, 318–319
Sensory neuronopathy, 107
Septic emboli, 81–82
Serial monitoring using MRSI, 330
Short tau inversion recovery (STIR), 161, 733
Signal-to-noise ratio (SNR), 194–196, 198–199, 295, 336–337, 385, 386f
Simultaneous acquisition of spatial harmonics (SMASH), 201
Single photon emission computed tomography (SPECT), 353–356, 360–362, 361f, 442
central neurocytoma, 576
gangliocytoma, 577
ganglioglioma, 577
hamartomas, 656
image reconstruction and correction, 354–356
instrumentation, 354
Anger camera, 354, 354f
collimator, 354
labeled amino acids, 361–362
labeled cations, 360–361
technetium-99m MIBI, 361
thallium-201, 360–361
metastatic brain tumors, 649
PCNSL, 473–475, 514
pediatric brain tumors, 613
perfusion agents, 360
physics, 353–354
spinal tumors, 757
Single-shot echoplanar imaging, 173
brain tumor, 301
Sinograms, 146
Sinus histiocytosis with massive lymphadenopathy. *See* Rosai-Dorfman disease (RDD)
Skin hemangiomas, 4
Skull base tumors, 609
Slice selection, 163
Small-cell lung carcinoma, 27, 38, 63, 103–104, 107
Small vessel disease, 130
SMART syndrome, 81
Sodium iodide (NaI), 354
Solitary neurofibromas, 113
Somnolence syndrome, 126
Sonography
benign peripheral nerve sheath tumors, 779
plexopathy, 765
Spatial localization by magnetic field gradients, 161–162
Spatial resolution, 354–355, 385–387
Specific absorption rate (SAR), 199–200
Spinal anaplastic astrocytomas, 45–46, 46f
Spinal astrocytoma, 37, 45–46, 46f, 48–49
Spinal chordoma, 43–44, 44f
Spinal cord, 131
acute, 131
compression, 60
early–delayed radiation myelopathy, 131
delayed radiation myelopathy (DRM), 131
late–delayed myelopathy, 131
radiogenic lower motor neuron disease, 131
vascular changes, 131
infarction, 96
oligodendrogliomas, 37
primary lymphoma of, 479
Spinal cord tumors (SCT), 55
epidemiology, 35–40
intramedullary spinal cord metastases (ISCM), 38
primary SCT, 35–37
Spinal ependymomas, 37
Spinal epidural metastases, 723
Spinal glioblastoma multiforme (GBM), 45–46, 46f
Spinal hemangioblastomas, 44, 44f
Spinal meningiomas, 36, 42, 42f
Spinal nerve sheath tumors (SNSTs), 751–752
Spinal neurofibroma, 42–43, 43f, 47
Spinal radiosurgery, epidural spinal cord compression (ESCC), 61
Spinal schwannoma, 41–42, 42f, 47
Spinal stabilization surgery, 47–48
Spinal tumors
angiography, 757–759, 758f
computed tomography, 755–756
differential diagnosis, 756
diffusion-weighted imaging (DWI), 755
dynamic X-rays, 756
extramedullary intradural, 751–752
meningiomas, 751, 752f
nerve sheath tumors, 751–752
lytic versus blastic spinal disease, differentiation, 756
magnetic resonance imaging, 754–755
metastatic, 747
positron emission tomography scan, 756–757, 757f
single-photon emission computed tomography/computed tomography, 757
surgical intervention, 753–754, 754f
en bloc resection of single metastasis to spine, 754

Spinal-axis radiation therapy, 15–16
Spine
  en bloc resection of single metastasis to, 754
  magnetic resonance imaging, 711–714
  meningiomas of, 521–522
  metastatic tumors, 745–747, 748f–749f
  neoplasms, 37
Spin-echo (SE) techniques, 164, 183–184, 274–275, 340
Spine imaging
  abnormalities, 712t
  comparison, 711t
  magnetic resonance imaging, 711–714
Spin–lattice/longitudinal relaxation rates, 395–396
Spin–spin/transverse relaxation, 395–396
Spiral computed tomography, 146
Spoiled gradient-echo (SPGR) image, 208, 210, 337
Sporadic neurofibromas, 113
Staphylococcus aureus, 659
Staphylococcus epidermidis, 70
STAR (stereotactic alignment radiosurgery) system, 260, 260f
Static magnetic field, 198–199
Stereotactic radiosurgery (SRS), 15–16, 27, 233, 257–272, 414
  central neurocytoma, 576
  clinical applications of radiosurgery, 262–266
    acoustic neuromas, 263–264
    cerebral metastases, 262–263
    gliomas, 265–266
    meningiomas, 263
    nonfunctioning adenomas, 265
    pituitary adenomas, 264–265
    radiation-associated tumor formation, 266
  delivery of radiosurgery, 258–260
    CyberKnife platform, 259–260
    Gamma Knife system, 259
    LINAC, 259
    photon and proton radiosurgery, 258
    proton beam radiosurgery, 260
  DNETs, 580
  extraocular nerve schwannomas, 511
  facial nerve schwannomas, 510
  foundations of radiosurgery, 257–258
    target location, 257
    target proximity to cranial nerves, 258
    target size, 257
  jugular foramen schwannomas, 511
  neuroimaging and radiosurgery, 260–262
    computerized tomography, 260–261
    CT–MR image integration, 261
    functional imaging, 261–262
    magnetic resonance imaging (MRI), 261
  PPTIDs, 597–599
  trigeminal schwannomas, 510
Stopping power, 356
Streptococcus viridans, 659
Stretched exponential model, 305–308
Stroke, ischemic, 661
Subdural hematomas, treatment of, 87
Subdural hemorrhages, 81, 87
Subependymal giant-cell astrocytoma (SGA), 452–456, 455f
  computed tomography, 456
  magnetic resonance imaging, 456
  ultrasound, 456
Suboccipital approach, vestibular schwannoma, 551
Subtotal resection (STR), central neurocytoma, 576
Supplementary motor area (SMA), 318
Supraclavicular plexus, 111–112
Suprasellar lipoma, 498f
Suprasellar tumors, 624–629
Supratentorial brain, diffuse astrocytomas in, 442
Surgery
  central neurocytoma, 576
  cerebellar liponeurocytoma, 582
  chondrosarcomas, 609
  chordomas, 607
  DNETs, 580
  extraocular nerve schwannomas, 511
  facial nerve schwannomas, 510
  ganglioglioma, 577
  hypoglossal nerve schwannomas, 511
  jugular foramen schwannomas, 510–511
  Rosai-Dorfman disease, 657
  spinal tumors, 753–754, 754f
    en bloc resection of single metastasis to spine, 754
    preoperative planning, 754–755
  trigeminal schwannomas, 510
  vestibular schwannomas, 506, 551–552
Surgical planning, magnetic resonance spectroscopy, 328
Surgical therapy
  of intramedullary spinal cord metastases (ISCM), 56–57
  of metastatic brain tumors (MBTs), 25–26
  of primary brain tumors (PBTs), 15
  of primary SCT, 46–48
Surrogate for survival, response as, 674–675
  overall survival, radiographic response as, 674–675
  progression-free survival, 674
Survivin, 118–119
Susceptibility weighted imaging (SWI), 165, 184, 390, 403–404
  intracranial hemorrhage, 661
  ischemic infarctions, 662f
Synaptophysin, 573–574
Syringomyelia, 37
Systemic therapy, neoplastic meningitis, 70–72
Systemic tumor cells, 23

T

T cell CNS lymphoma, primary (TPCNSL), 480, 480f
T1 contrast-enhanced and T2/FLAIR sequences, 236
T1 contrast-enhancing disease, 411
T1 weighted images, 160, 231
  anaplastic astrocytoma, 421–422, 424f
  craniopharyngioma, 493–494
  diffuse astrocytomas, 442–445
  glioblastoma multiforme, 425, 426f–427f, 429f, 433–434
  PCNSL, 472
  pilocytic astrocytoma, 450–451
  primary CNS lymphoma, 432, 434f
  sellar/juxtasellar lesions, 484
T1-SPECT technique, 127
T1-weighted permeability imaging, 176
  in diagnosis, grading, and follow-up of brain tumors, 176–177
T2/FLAIR imaging, 411–412
T2 shine-through effect, 274–275
T2-weighted images, 160, 167
  anaplastic astrocytoma, 421–422
  craniopharyngioma, 493–494
  diffuse astrocytomas, 442–445
  glioblastoma multiforme, 425–426, 433–434
  gliosarcoma, 435, 436f
  MRI, 231
  oligodendrogliomas, 466–467
  PCNSL, 472
  pilocytic astrocytoma, 450–451
  pilomyxoid astrocytoma, 452, 453f
  primary CNS lymphoma, 432
  sellar/juxtasellar lesions, 484
Taenia solium, 659
Tamoxifen, 50–51, 71, 81
  for NST management, 118–119
Taxanes, 135
^{99}Tc macroaggregated albumin, 66
Tc99m SPECT, DNETs, 580
Technetium-99m hexamethylpropyl-eneamine oxime (^{99m}Tc-HMPAO), 442
Technetium-99m MIBI, 361
Telangiectasia, 130
Temozolomide, 16–19, 28–29, 50, 237–238, 247–249, 380, 409, 681–683
  papillary glioneuronal tumors, 636
TEM resonator, 200–201
Teratoid tumors, atypical, pediatric, 624
Teratomas, 37
  pediatric, 628
  pineal region, 590, 591f
  treatment, 597
Thalamic tumors, 555–565
Thalidomide, 28–29
Thallium-201 (^{201}Tl), 360–361, 442
Thallium-201 single photon emission computed tomography (201Tl SPECT)
  central neurocytoma, 576
  PCNSL, 473–475, 514
Therapeutic ionizing radiation, cranial exposure to, 4
Therapy monitoring, 295
Therapy-related cerebrovascular complications, 803–805
  chemotherapy, 804–805
  endovascular therapy, 805, 805f
  radiation, 803–804, 803f–804f
ThioTEPA, 70, 71t
Thoracic spine metastatic lesion, 747f
3D tractography, 208
3D-Slicer software package, 211
Thrombocytopenia, 79, 85
Thrombosis, 43
  in metastatic CVT, 102

Time-of-flight (TOF) MRA, 93, 188–189
Tinea capitis, 4
Tissue heterogeneity, 250–251
Tissue plasminogen activator, 65
Tissue protein/peptide fragments assessment using amide proton transfer, 399–400
Tissue sodium concentration (TSC) maps, 392
Tolosa-Hunt syndrome, 658
Tophaceous lesions, spinal epidural disease differential diagnosis, 737–738
Topotecan, 28, 71t, 72
Toxicity of brain radiation, 236
Toxoplasmosis, 660, 697
  and PCNSL, 474–476, 475f–476f
Transcranial magnetic spectroscopy, 317
Transcranial magnetic stimulation (TMS), 221
Transfer constant (K^{trans}), 335–336
Transforming growth factors (TGFα and TGFβ), 55
Transient cognitive impairment, 126
Translabyrinthine approach, vestibular schwannoma, 551
Transmit SENSE/receive SENSE, 201
Transsphenoidal surgery, pituitary adenoma, 487–488
Transverse electromagnetic design, 200–201
Trastuzumab, 136
  Phase I, 71t
Traumatic neuroma, 785–788
  computed tomography, 785–788
  magnetic resonance imaging, 785–788, 788f–789f
Treponema pallidum, 659
Tricarboxylic acid (TCA) cycle, 327–328
Trigeminal schwannomas, 506–507
  classification, 506–507
  magnetic resonance imaging, 507, 507f
  management of, 510
  symptoms of, 507
True disease progression, 236–239
Tuber cinereum hamartoma, 567f
Tuberculosis (TB), 659, 697
  spinal epidural disease differential diagnosis, 736–737
Tuberous sclerosis, 4
  and subependymal giant-cell astrocytoma, 456
  pediatric, 617–618
Tumefactive multiple sclerosis (MS), 699, 699f
Tumor emboli, 80, 85, 643, 800–801
  cerebrovascular complications, 800–801, 800f
  computed tomography, 800–801, 800f
  magnetic resonance imaging, 800–801, 800f
Tumor grading, 281–284
Tumor histology, stratifying, 284–285
Tumor hypoxia, 391
Tumorigenesis, 5
Tumor infiltration, 64
Tumor infiltration index, 647
Tumor metabolism, probing by magnetic resonance spectroscopy, 400
Tumor recurrence versus radiation necrosis, 346
Tumor treating fields (TTFields), 243–256
  basic principles, 243–246
  cell biology effects of, 244–246
  clinical application of, 246–249
    efficacy of alternating electric fields therapy for glioblastoma, 246–249
  electric field distribution within cranium and brain, 249–251
    computational model, 249–250
    experimental evidence, 249
    future modeling developments, 251
    modeling results, 250–251
  imaging in patients treated with TTFields therapy, 251–253
    advanced imaging techniques, 252–253
    early experience, 253
    pseudoprogression and other treatment-related changes, 247
    response criteria, 251–252
  mechanisms of action of, 244
  NovoTTF-100A device, 246–247, 246f
  physics of electric fields, 243–244
  preclinical findings and pilot trials, 244–246
Tumor vascular architecture, assessment of, 345
Tumor-related cerebrovascular complications, 797
  arterial vasculature, 799, 799f–800f
  coagulopathy, 797–798
  intravascular lymphomatosis, 806
  leptomeningeal metastases, 800
  primary angiitis of central nervous system, 806, 806f
  tumor emboli and neoplastic aneurysms, 800–801, 800f
  tumor-related hemorrhagic stroke, 801, 801f–802f
  venous thrombosis, 798–799, 798f–799f
Tumor-related hemorrhages, 85
Tumor-related hemorrhagic stroke
  cerebrovascular complications, 801, 801f–802f
  computed tomography, 801, 801f
  magnetic resonance imaging, 801, 801f–802f
Turbo spin-echo imaging, 729
Turcot syndrome, 4
Two-dimensional versus three-dimensional imaging techniques, 164
Type A reactions, 153
Type B reactions, 153
Tyrosine kinase inhibitors (TKIs), 71–72

U

Ultrahigh field (UHF) animal magnets, 198
Ultrahigh field (UHF) MRI, 385–392
  cellular magnetic resonance imaging, 391–392
  imaging tumor oxygenation, 391
  magnetic resonance spectroscopy (MRS), 392
  magnetic susceptibility, 387–391
  multinuclear imaging and chemical exchange saturation transfer imaging, 392
  spatial resolution, 385–387
Ultrasmall superparamagnetic iron oxide (USPIO), 189, 198, 390–392, 390f
Urokinase-type plasminogen activator, 65

V

Variable flip-angle (VFA) imaging, 337
Varicella zoster reactivation, 81–82
Vascular disorders, 79–84
  coagulopathy, 79
  infection, 81–82
  intracranial tumor, 80–81
    treatment effects, 81
  ischemic cerebrovascular events disorders, 80
Vascular endothelial growth factor (VEGF), 17, 50, 55, 65, 72, 85, 338, 409
  and rCBV, 440–441
Vascular hypothesis, 127–128
Vascular malformations, 130
  intracranial hemorrhage, 661
Vascular parameters measurement by MRI, 397–398
Vascular permeability, 440–441
  oligodendrogliomas, 466
Vascular proliferation, 10–11, 45–46
Vasculopathy, 130–131
  large vessel atherosclerosis, 130
  neuroendocrine dysfunction, 130–131
  small vessel disease, 130
  vascular malformations, 130
Vein of Galen malformations, 595
  magnetic resonance imaging, 599f
Vemurafenib, 72
  ganglioglioma, 577–578
Venous infarction, 698
Venous sinus thrombosis, 81
Venous thrombosis
  cerebrovascular complications, 798–799, 798f–799f
  computed tomography, 798–799, 798f
  magnetic resonance imaging, 798–799, 799f
Ventricular tumors, 569
Verocay body, 41–42
  in schwannoma, 503, 504f
  vestibular schwannoma, 543–545, 547f
Vessel hyperdensity, 91
Vestibular schwannoma (VS), 504–506, 543
  computed tomography, 544f, 547, 549f
  diffusion-weighted imaging, 549f
  FIESTA, 544f
  FLAIR, 547f
  magnetic resonance imaging, 544f–550f, 547, 548t
  neurofibromatosis 2, 543, 545, 549–551, 550f, 552f, 553
  pathology, 543–545
  treatment, 551–553
Vincristine, 49–50, 135–136
  desmoplastic infantile ganglioglioma, 579–580
  ganglioglioma, 577–578

Viral infections, 660–661
Virchow–Robin space, 55, 80
VISTA, vestibular schwannoma, 547f
Von Hippel-Lindau Syndrome (VHLS), 37, 47–48

W
WADA test, 320
Wada testing, 222
Wernicke's area, 320–321, 323–324
White matter (WM), 168, 302, 308–310
White matter—cerebrospinal fluid (WM–CSF) interface, 250
Whole brain external beam irradiation, 26–27
Whole-brain radiation therapy (WBRT), 69, 262–263
Windowing and leveling, 148–149

X
X-ray contrast agents, development of, 151
general principle of, 151–152
X-ray detectors, 145

Y
Yolk-sac tumor, 562